AD-A280 382

IEEE ®

The American Physical Society

Proceedings
of the
1993
Particle Accelerator
Conference

DTIC
S ELECTE
JUN 1 3 1994
F

Volume 1 of 5
Pages 1–747

94-17989

DTIC QUALITY INSPECTED 1

94 6 10 096

1993 IEEE Particle Accelerator Conference

IEEE

The
American
Physical
Society

1993 Particle Accelerator Conference, Washington, D.C., 17–20 May

Conference Chairman
Christoph Leemann, *CEBAF*
Annie Soltys, Executive Assistant
Telephone: (804) 249-7575
E-mail: soltys@cebaf.gov
Fax: (804) 249-5024

Organizing Committee
M. Allen, *SLAC*
W. Barletta, *LLNL*
K. Berkner, *LBL*
D. Berley, *NFS*
J. Bisognano, *CEBAF*
R. Briggs, *SSCL*
Y. Cho, *ANL*
L. Costrell, *NBS*
M. Craddock, *U. of BC*
W. K. Dawson, *TRIUMF*
H. Edwards, *FNAL*
S. Holmes, *FNAL*
S. Krinsky, *BNL*
H. Lustig, *APS*
C. Roberson, *ONR*
S. Schriber, *LANL*
D. Sutter, *DOE*
S. Tazzari, *U. of Rome II & INFN*
M. Tigner, *Cornell*
W. T. Weng, *BNL*

Program Committee
J. Bisognano, Chair, *CEBAF*
Telephone: (804) 249-7521
E-mail: bisognano@cebaf.gov
H. Edwards, Deputy Chair, *FNAL*

Program Treasurer
Julie Leverenz
Telephone: (804) 249-7642
E-mail: leverenz@cebaf.gov

Conference Editor
Steven T. Corneliussen, *CEBAF*
Telephone: (804) 249-7582
E-mail: corneliussen@cebaf.gov

Editorial Assistant
Linda Carlton
Telephone: (804) 249-7690
E-mail: carlton@cebaf.gov
Fax: (804) 249-5024

18-May-94

Box 2 of 2

DEFENSE TECHNICAL INFORMATION CENTER
BUILDING 5, CAMERON STATION
ALEXANDRIA, VA 22304-6145
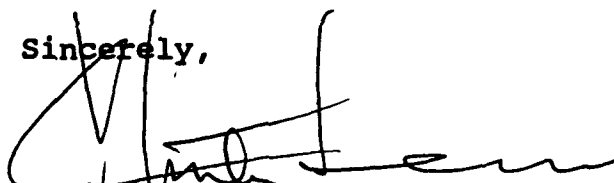
REF.: GRANT NO. N00014-93-1-0623

Dear Sir or Madam:

Enclosed please find two (2) copies of the
Proceedings of the 1993 Particle Accelerator
Conference (PAC93). The above-referenced $15,000
grant from the Office of Naval Research helped
fund the cost of publishing the Proceedings,
enabling us to keep the registration fee to a
minimum.

On behalf of the conference organizers and the
more than 1300 participants, thank you for
supporting PAC93.

Sincerely,

Christoph W. Leemann
Conference Chairman

cc: D. Galicki, IEEE

Conference Organizers and Staff

Conference Chair	Christoph W. Leemann, CEBAF
Program Chair	Joseph J. Bisognano, CEBAF
Deputy Program Chair	Helen Edwards, FNAL
Local Arrangements Chair	Isidoro E. Campisi, CEBAF
Program Coordinator	Avril Quarrie, CEBAF

Organizing Committee

C. Leemann, CEBAF

M. Allen, SLAC	R. Briggs, SSCL	H. Edwards, FNAL	S. Schriber, LANL
W. Barletta, LLNL	Y. Cho, ANL	S. Holmes, FNAL	D. Sutter, DOE
K. Berkner, LBL	L. Costrell, NIST	S. Krinsky, BNL	S. Tazzari, INFN
D. Berley, NSF	M. Craddock, TRIUMF	H. Lustig, APS	M. Tigner, Cornell
J. Bisognano, CEBAF	W. K. Dawson, TRIUMF	C. Roberson, ONR	W. Weng, BNL

Program Committee

J. Bisognano, CEBAF	H. Edwards, FNAL		
T. 'Antaya, MSU	J. Hinkson, LBL	J. Madey, Duke	R. Sheffield, LANL
W. Barletta, LLNL	F. R. Huson, TAC	P. Mantsch, FNAL	G. Shenoy, ANL
I. Ben-Zvi, BNL	G. Jackson, FNAL	J. Marriner, FNAL	K. Shepard, ANL
J. Brennan, BNL	R. Jayakumar, SSCL	J. McGill, SSCL	S. Simrock, CEBAF
S. Chattopadhyay, LBL	C. Joshi, UCLA	J. Nation, Cornell	C. Sinclair, CEBAF
R. Cooper, LANL	T. Katsouleas, USC	D. Neuffer, CEBAF	P. Sprangle, NRL
M. Cornacchia, SSRL	Y. Kimura, KEK	D. Olsen, ORNL	J. Strait, FNAL
M. de Jong, AECL	L. Klaisner, SLAC	H. Padamsee, Cornell	R. Sundelin, CEBAF
P. Debenham, DOE	H. Klein, Goethe Univ.	R. Pollock, Indiana	D. Sutter, DOE
G. Dutto, TRIUMF	M. Knott, ANL	D. Proch, DESY	M. Syphers, SSCL
L. Evans, CERN	S. Krinsky, BNL	D. W. Reid, LANL	J. Watson, SSCL
T. Fessenden, LBL	S. Kurokawa, KEK	M. Reiser, Maryland	G. Westenskow, LLNL
R. Gerig, SSCL	R. Kustom, ANL	J. Rosenzweig, UCLA	K. Whitham, Titan Beta
R. Hamm, AccSys	K. Leung, LBL	R. Ruth, SLAC	F. Willeke, DESY
R. Hardekopf, LANL	G. Loew, SLAC	J. Seeman, SLAC	E. Willen, BNL
M. Harrison, BNL	P. Lucas, FNAL	R. Shafer, LANL	R. Witkover, BNL

Conference Staff

Meeting Planner	PJ Meals
Conference Treasurer	Julia B. Leverenz
Companions' Suite Coordinator	Sarah Ingels
CEBAF Tour Coordinator	Tammy L. Hudson
Conference Administrator	Yvonne B. Casalino
Executive Assistant	Annie Soltys
Industrial Exhibits	Trade Associates, Inc. (Rockville, Md.)

Proceedings and Publications

Conference Editor	Steven T. Corneliussen
Proceedings Compiler	Linda Carlton
Photography	Twin Lens Photo (Silver Spring, Md.)

The 1993 Particle Accelerator Conference

The fifteenth biennial Particle Accelerator Conference met May 17–20, 1993, in Washington, D.C., at the Omni Shoreham Hotel. Previously, the first, second, third, sixth, ninth, and twelfth of the series were also held at the Shoreham, and once again this site proved especially well suited for the interdisciplinary exchanges that are at the heart of the gathering. Since its inception in 1965, the conference had been organized under the auspices of the Institute of Electrical and Electronics Engineers. With the 1993 conference, the American Physical Society Division of Physics of Beams has joined with the IEEE Nuclear and Plasma Sciences Society in co-sponsorship. A memorandum of understanding has been signed to continue this relationship for future years. The support of these two major professional organizations gives the Particle Accelerator Conference a unique breadth of perspective and full recognition in both the engineering and physics communities. Conference attendance, although somewhat lower than that of the 1991 San Francisco meeting, exceeded 1300, including about 300 from outside North America. This year's 1291 papers set a record.

The Opening Plenary Session began with C. H. Llewellyn Smith's incisive talk on the "Frontiers of High Energy Particle and Nuclear Physics," which highlighted successes and limitations of the standard model as well as the puzzle of the baryon number of the universe and the experimental challenges of the Higgs, CP violation, and quark-gluon plasmas. Then B. Wiik described the very fruitful first year of HERA operations, notable for excellent beam-beam tune shift stability and physics data of remarkable clarity. After the intermission, Paul Horn of IBM startled the audience with his frank comments on the frailty of a national competitiveness argument for justifying the construction of large accelerators. Although listeners were far from convinced, Horn's comments generated healthy discussion throughout the meeting. On a more positive note, the closing talk of J. Kirz on "Soft X-Ray Microscopy with Synchrotron Radiation" clearly demonstrated with fascinating photomicroscopy of biological systems the value of accelerator technology for applications outside physics research.

The program followed a new set of topical categories that stressed the commonalities of the underlying accelerator technology and the evolution of accelerator science in recent years. In general, talks and poster papers were arranged by accelerator types rather than energy. A half-session dedicated to accelerator control systems was very well attended. During the Photon Source parallel session, the spectacular speed in commissioning and reaching beam performance milestones at the Advanced Light Source at Berkeley, the European Synchrotron Radiation Facility at Grenoble, and the SRRC in Taiwan was reported. The Advanced Accelerator Concepts presentations included John Blewett's R. R. Wilson Prize account of his involvement in many innovative accelerator developments during his career and C. Clayton's report on successful high-gradient acceleration with plasma beat waves. S. Schultz discussed the possibilities of photonic band-gap structures for particle acceleration. In the Magnet session, K. Halbach explored novel uses of permanent magnets, and R. Scanlan discussed advanced superconductors that exhibit very high critical current. Radioactive beam production and applications were overviewed by J. D'Auria and G. Alton. During the Multiparticle Beam Dynamics Session, R. Ryne explored the profound impact that massively parallel processors will have on 3-D simulation within the next few years. These are among the very many fine papers which can be found in this proceedings.

During the banquet awards ceremony, the IEEE PAC Technology Awards went to T. Collins for his invention of the long straight section and his lattice designs for Fermilab, and to L. Anderson and Y. Mori for their invention of the optically pumped negative hydrogen ion source. The APS R. R. Wilson Prize was presented to J. Blewett for his contributions to synchrotron radiation physics, alternate gradient focusing in linacs, and other developments in machine design and construction. J. Palkovic received the APS dissertation award, and R. Sheffield, J. Fraser, and M. Ross accepted awards from the U.S. Particle Accelerator School for achievements in accelerator physics and technology. New fellows of the APS and IEEE were also announced. The political satire group Capitol Steps entertained at the banquet and had the courage to present their "science nerd" routine to an audience of physicists and engineers.

The first part of the Closing Plenary Session comprised progress reports on large-scale initiatives: the Japanese B-factory and linear collider programs, the Large Hadron Collider at CERN, and the U.S. Supercollider. The final two talks explored more fundamental aspects of accelerator technology and its limits. R. Jameson discussed the mechanisms for halo formation in the high-current hadron linacs that are required for applications such as nuclear waste transmutation. For these machines, low residual beam loss is critical to prevent machine activation. M. Tigner closed the conference by delineating the fundamental limits on usable beam energy and luminosity for high energy physics that are implied by falling cross sections and rational electrical power budgets. The path to a PeV collider appears difficult.

The accelerator community experienced the loss of three of its most productive and creative talents during this past year, and their colleagues took the opportunity of the conference to honor them. The Single-Particle Beam Dynamics session was dedicated to the memory of L. Jackson Laslett, who laid the foundation of much of our understanding of nonlinear and collective phenomena in accelerators. The Multiparticle Beam Dynamics session was dedicated to the renowned beam dynamicist I. M. Kapchinskiy, and his last paper was presented by his co-worker N. V. Lazarev. During the awards ceremony, H. Winick accepted G. Fischer's APS Fellowship certificate and commented on his many contributions, including his most recent work on understanding the effects of tidal forces on LEP.

C. W. Leemann
Conference Chair

J. J. Bisognano
Program Chair

Five-Volume Contents

Each volume begins with this five-volume table of contents and ends with the five-volume author index. The chairmen's foreword and a list of conference organizers and staff appear as front matter in Volume 1. A list of conference participants precedes the author index in Volume 5.

Volume 1

Five-Volume Contents

Proceedings of the 1993 Particle Accelerator Conference

Proceedings of the 1993 Particle Accelerator Conference

High-Current Accelerators   *Chair: T. Fessenden*

Poster presentations:

Volume 2

RF Structures   Chair: D. Reid

Poster presentations:

Power Technology and Miscellaneous Subsystems   *Chair: D. Reid*

Poster presentations:

Photon Sources   *Chair: J. Galayda*

Proceedings of the 1993 Particle Accelerator Conference

Volume 3

Hadron RF Linacs, Cyclotrons, Radioactive Beams   *Chair: R. Pollock*

Poster presentations:

Accelerator Control Systems   *Chair: D. Gurd*

Poster presentations:

Proceedings of the 1993 Particle Accelerator Conference

Lepton Circular Colliders, Synchrotrons, and Microtrons   *Chair: A. Sessler*

Poster presentations:

Instrumentation and Beam Feedback   Chair: R. Shafer

Poster presentations:

*Each volume begins with this five-volume table of contents
and ends with the five-volume author index. The chairmen's
foreword and a list of conference organizers and staff
appear as front matter in Volume 1. A list of conference
participants precedes the author index in Volume 5.*

Each volume begins with this five-volume table of contents and ends with the five-volume author index. The chairmen's foreword and a list of conference organizers and staff appear as front matter in Volume 1. A list of conference participants precedes the author index in Volume 5.

Volume 4

Advanced Accelerator Concepts   Chair: C. Joshi

Magnets, Cryogenics, and Alignment   *Chair: J. Strait*

Proceedings of the 1993 Particle Accelerator Conference

Each volume begins with this five-volume table of contents and ends with the five-volume author index. The chairmen's foreword and a list of conference organizers and staff appear as front matter in Volume 1. A list of conference participants precedes the author index in Volume 5.

Particle Sources, Beam Formation, and Matching   *Chair: J. Fraser*

Proceedings of the 1993 Particle Accelerator Conference

Volume 5

Multiparticle Beam Dynamics   *Chair: M. Reiser*

Poster presentations:

Proceedings of the 1993 Particle Accelerator Conference

Proceedings of the 1993 Particle Accelerator Conference

Hadron and e-p Colliders and Hadron Synchrotrons   *Chair: D. Edwards*

Poster presentations:

Vacuum Technology   *Chair: D. Edwards*

Poster presentations:

HERA Operations and Physics

B. H. Wiik
University of Hamburg and
Deutsches Elektronen-Synchrotron DESY
Notkestrasse 85 - 22603 Hamburg, Germany

Abstract

HERA is designed to collide 820 GeV protons with 30 GeV electrons in 4 interaction regions spaced equidistant around its 6.3 km circumference. The initial commissioning of the HERA collider was successfully completed in the summer of 1992 with the start up of the experimental programme. In the talk I'll first focus on the performance of the accelerator and on the operational experience. At present two general pupose detectors H1 and ZEUS have been installed in two of the four interaction regions of HERA. I'll briefly review the layout and the performance of these detectors and then report on the first physics results. At the end I'll comment on a possible fixed target programme at HERA using targets installed in the circulating electron and proton beams.

I. INTRODUCTION

Last year the electron-proton collider HERA [1] and its large multipurpose detectors H1 [2] and ZEUS [3] made the transition from a virtual to a real source of data on electron-proton interactions in a new, greatly expanded kinematic region.

The HERA project is a truly international effort. It was built within the framework of a collaboration where institutions in 10 countries contributed either components built at home or delegated skilled manpower to work on the project at DESY. Also the large detectors H1 and ZEUS have been built and are exploited by international collaborations. Only some 25% of the 750 physicists presently involved in the programme are from German institutions while the remainder comes from 69 institutions in 15 countries.

Data taking by H1 and ZEUS started at the end of May 1992 and continued to November 8, with a 7 weeks shutdown in August and September. The remaining time until early December was used for machine studies.

During this period a total, integrated luminosity of 58 nb^{-1} was delivered to each of the experiments and data corresponding to some 30 nb^{-1} were recorded.

Both experiments functioned from the outset and they have already analyzed and published a series of papers on deep inelastic scattering at low x [4,5], on photo production [6,7] and on the search for new particles [8,9].

The winter shutdown 92/93 has been used to upgrade the control system and to prepare HERA for multibunch operation. Improvements to the detectors and to the data acquisition system have also been made.

II. HERA

2.1 Overview

HERA is made of two independent accelerators designed to store respectively 820 GeV protons and 30 GeV electrons and to collide the two counterrotating beams head on in four interaction regions spaced equidistant around its 6.5 km long circumference.

The layout of the accelerator complex is shown in Fig. 1.
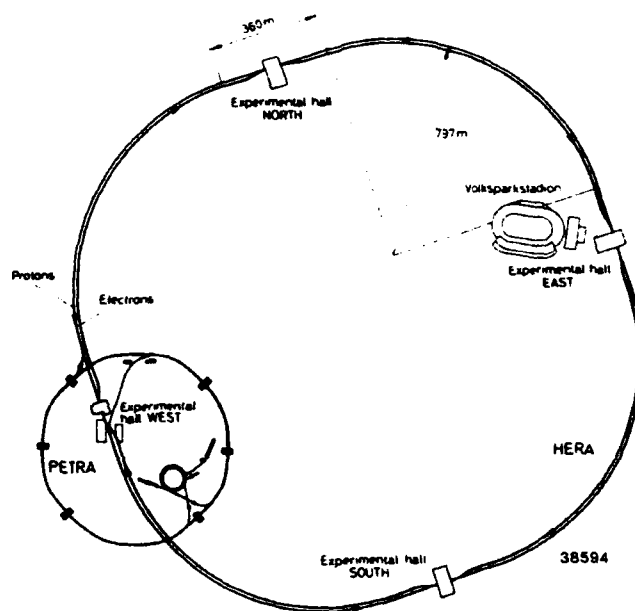
Fig. 1.
The layout of the HERA accelerator complex.

The general purpose detectors H1 and ZEUS are installed in straight section North, respectively South. In straight section East the HERMES experiment, designed to scatter longitudinally polarized electrons on polarized H, D and He^3 targets installed in the internal electron beam, will be installed. An experiment, designed to measure the CP violation in the b b̄ system, using an internal wire target in the halo of the proton beam, is being considered. If approved, this experiment will be installed in straight section West.

2.2 The HERA Electron Ring

The injection into the electron ring works well with an efficiency of roughly 80%.

The design energy of 30 GeV was reached using the normal and the superconducting RF system [10] in parallel. However, to have sufficient safety margin in the case an RF station is lost, the HERA operating energy was chosen to be 26.7 GeV.

The superconducting RF system is made of 16 four cell superconducting 500 MHz cavities assembled pairwise into 8 cryostats. The S.C. RF system has now been in operation for some 10000hrs. It has been very reliable and it provides nearly a third of the total circumferential voltage of 160 MV.

During the 1992 run the maximum current which could be stored with lifetimes on the order of a few hours was limited to roughly 3 mA at 26.7 GeV. This limit may have been due to dust particles trapped in the strong field of the circulating electron beam. Using the proton loss monitors, the beam loss was traced back to two vacuum chambers hit by synchrotron radiation from a reverse bend magnet. Replacing these vacuum chambers seems to have solved the problems. A total of 27 mA have now been stored in 100 bunches compared to the design value of 60 mA in 210 bunches.

A 5 MHz bandwidth multibunch feedback system needed to control coupled bunch instabilities, has been installed and successfully commissioned.

The observed transverse beam polarization [11] is shown in Fig. 2 as a function of synchrotron tune and beam energy. The buildup time of 25.8 min is consistent with the measured masimum beam polarization of 58 ± 5%. A high polarization can be achieved routinely.
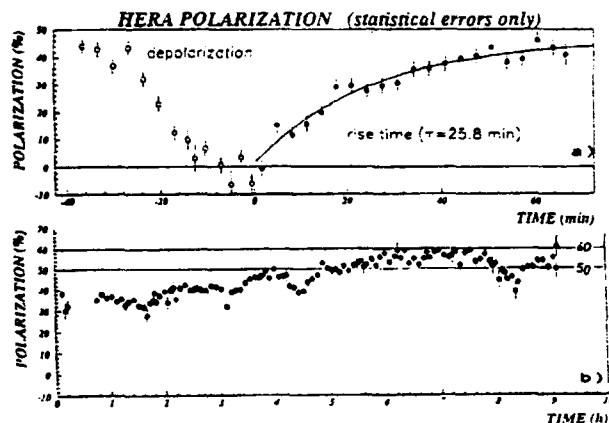
Fig. 2.
a) The transverse electron beam polarization as a function of time. The build up of transverse polarization is easily seen.
b) Beam polarization during a long storage.

2.3 The HERA Proton Ring

The operation of the HERA proton ring has been greatly eased by the reliability and the stability of the accelerator. In particular the refrigerator and the superconducting magnet system have been extremely reliable.

A total of 2156 superconducting magnets and correction coils are installed in the HERA proton ring. None of the magnets in the ring had to be removed during 2½ years of operation. Only a few beam induced and no spurious quenches have been observed.

The field quality of the superconducting magnets is seriously affected by persistent magnetization currents. However, the strength of persistent current multipoles vary little from magnet to magnet and are well reproducible and can hence be compensated by correction coils wound directly on the dipole and quadrupole beam pipes.

In order to determine the required strength of the correction elements at injection and during acceleration, the dipole and sextupole fields are measured continously in two superconducting reference magnets, powered in series with the ring magnets.

The proton beam lifetime at injection is on the order of 10hrs after a careful cycling of the magnets and after correction of persistent current multipoles using the scheme outlined above.

The geometric acceptance is larger than 2π mm mrad and the dynamic acceptance is of order 1π mm mrad. The design value of the unnormalized 2σ transverse emittance is 0.5 π mm mrad at injection. Including magnet cycling the proton filling time is roughly 1 hour.

The proton injection efficiency is of order 95%.

Only small beam losses occur during the acceleration cycle from 40 GeV by 820 GeV. The single bunch current is limited to $4 \cdot 10^{10}$ protons/bunch compared to the design value of 10^{11} protons/bunch. So far at most 160 proton bunches with low currents have been stored. With 90 bunches a total of 17 mA have been stored compared to the design value of 160 mA in 210 bunches.

The measured proton lifetime at 820 GeV for 10 bunches each with 25% of its design intensity is several weeks. The measured normalized 2σ emittance is on the order of 25 π mm mrad in agreement with the design value.

2.4 Colliding Beams

The luminosity is measured using the bremsstrahlungs reaction e+p=e+γ+p with the electron and the photon detected in coincidence. A maximum luminosity of $2.5 \cdot 10^{29}$ cm^{-2}s^{-1} with 9 bunches in each beam has been observed corresponding to 25% of the design luminosity per bunch crossing. The observed proton tune shifts are close to their design values of 0.001, wheras the electron tune shifts are a factor of two below design.

During the 1992 run the number of electron bunches was limited to 10 by the maximum electron current which could be stored in the ring. This limit has now been raised to 27 mA corresponding to 100 bunches at design current. A total of 160 proton bunches has been stored in HERA. The number of protons per bunch has so far been limited by the proton injectors and by losses during beam transfers to 25% of the design value.

In the 1993 run we thus expect to be able to raise the number of colliding bunches to 100 in each ring with the same bunch currents as in 1992. This would yield a peak luminosity of order $2 \cdot 10^{30} \text{cm}^{-2}\text{s}^{-1}$.

The proton beam lifetime is strongly dependent on the transverse dimensions of the electron beam and is maximized when the cross sections of the two beams match at the interaction point and the beams are well centered. The values of the β-functions at the interaction point has been adjusted to match the transverse size of the two beams. Under these conditions the proton beam lifetime is of order 50 hours compared to a typical 4 hour lifetime of the electron beam. Thus in general protons are filled once every 24 hours wheras electrons are dumped and reinjected every 4 to 5 hours.

The stored currents, luminosity and the specific luminosity as measured using the H1 luminosity detector is plotted in Fig. 3.
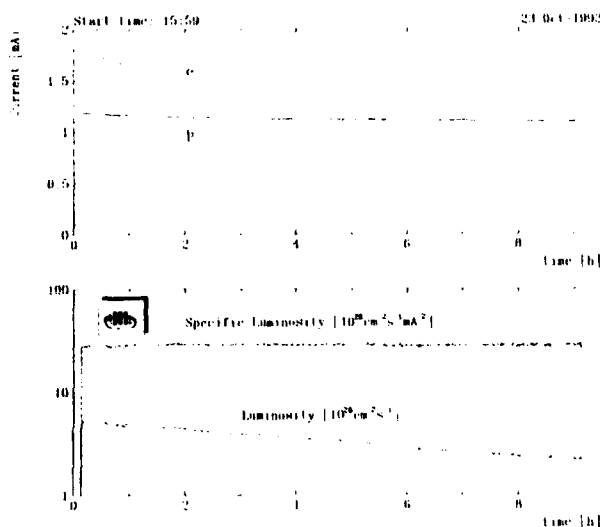
Fig. 3.
The stored currents, the luminosity and the specific luminosity as measured by the H1 detector as a function of storage time.

The specific luminosity, defined as $L / I_p \cdot I_e$ is a measure of beam overlap and transverse beam dimensions. Wheras the luminosity drops by a factor of 2 during the 9 hours storage time the specific luminosity remains nearly constant. This demonstrates the stability of the two rings and that the proton beam emittance remains constant over the fill. It also demonstrates that the proton beam emittance is not strongly influenced by noise in the electron beam - i. e. there is negligible cross talk between the two beams.

III. THE PHYSICS

3.1 Introduction

In a deep inelastic electron-proton collision the incoming electron interacts directly with one of the quarks in the proton

by means of a spacelike current, charged or neutral. This results in a very simple final state topology. The struck quark will materialize as one or several jets of hadrons whose momentum components transverse to the beam axis are balanced by the transverse momentum of the final state electron (or neutrino). The remainder of the proton will appear as a sharply collimated jet of hadrons travelling along the initial proton direction.

This event topology is indeed observed at HERA as shown for a neutral current event e+p→e+X in Fig. 4.
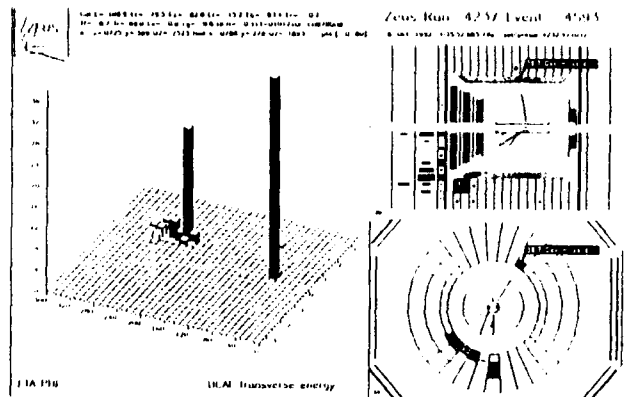
Fig. 4.
Deep inelastic neutral current event observed by the ZEUS detector at HERA.

A deep inelastic process is described in terms of

$$-Q^2 = (k - k')^2 \quad \text{and} \quad \nu = {pQ}/{m\rho}$$

where the fourmomenta of the incident lepton, the final state lepton and the incident proton are denoted by k, k' and p. Often the scaled variables $x=Q^2/2m\nu$ and $y=\nu/\nu_{max}$ are used. With HERA, present maximum values of $Q^2 = 600$ GeV^2 and $\nu = 400$ GeV which are available in fixed target experiments can be extended by nearly two orders of magnitude to Q^2 and ν values of order 30000 GeV^2 and 40000 GeV.

A complete up-to-date discussion on HERA physics can be found in reference 12.

3.2 Physics Results

3.2.1 Deep inelastic neutral current events

The kinematic region in 1/x and Q^2 available to HERA and to a 600 GeV muon beam incident on a proton at rest is plotted in Fig. 5.

3
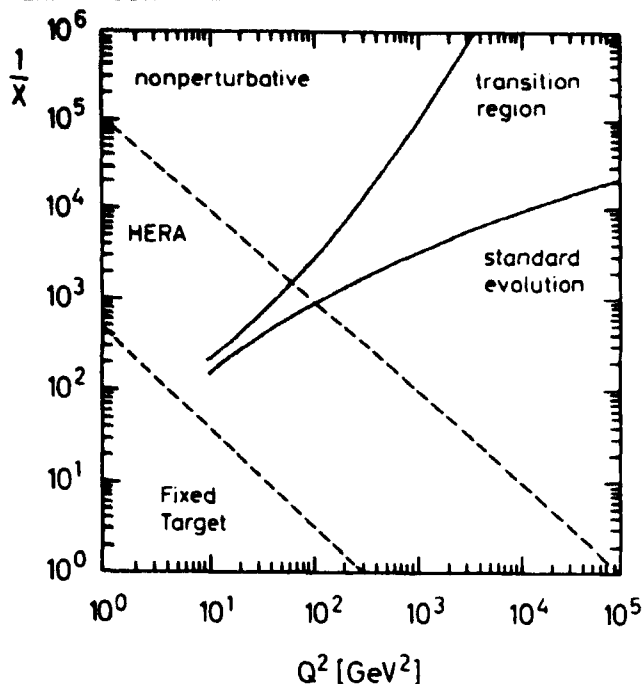
Fig. 5.
The kinematic region in 1/x and Q^2 available at HERA and with a 600 GeV muon beam incident on protons at rest. The perturbative and non-perturbative domains are separated by a transition region.

The kinematic region can be divided into three main areas: a QCD perturbative region located in the lower right hand corner at moderate x and large Q^2, a non-perturbative region in the left hand upper corner and a transition region in between.

At low x-values the structure functions are dominated by the gluon distribution function $xG(x,Q^2)$. Extrapolating $xG(x,Q^2)$, as determined in the perturbative region, towards small x for constant Q^2 leads to a steeply increasing function that violates unitarity. Since the gluon density increases with 1/x, the gluon-gluon interaction can no longer be neglected although the gluon-gluon coupling $\alpha_s(Q^2)$ is still small. In this transition region one may be able to use the parton language and the behaviour of the structure functions may be described by adding a recombination term to the perturbative evolution equations.

A further extrapolation in 1/x yields a very dense partonic system. Although the coupling constant is still small the effective interactions are strong due to the high parton densities. In this region the perturbative approach breaks down and the parton picture may not be applicable.

At HERA the structure functions can be explored down to x-values of 10^{-4}, a factor of 100 below the region available in fixed target experiments. Both experiments reports data on e+p→e+X. The details of the experiments and the data reduction can be found elsewhere [4,5]. The formfactor $F_2(x,Q^2)$ measured by the H1 collaboration is plotted in Fig. 6 versus x for Q^2 = 15 GeV^2 and Q^2 = 30 GeV^2. Note the rise in the formfactors towards lower values of x, reflecting the increase in gluon density.
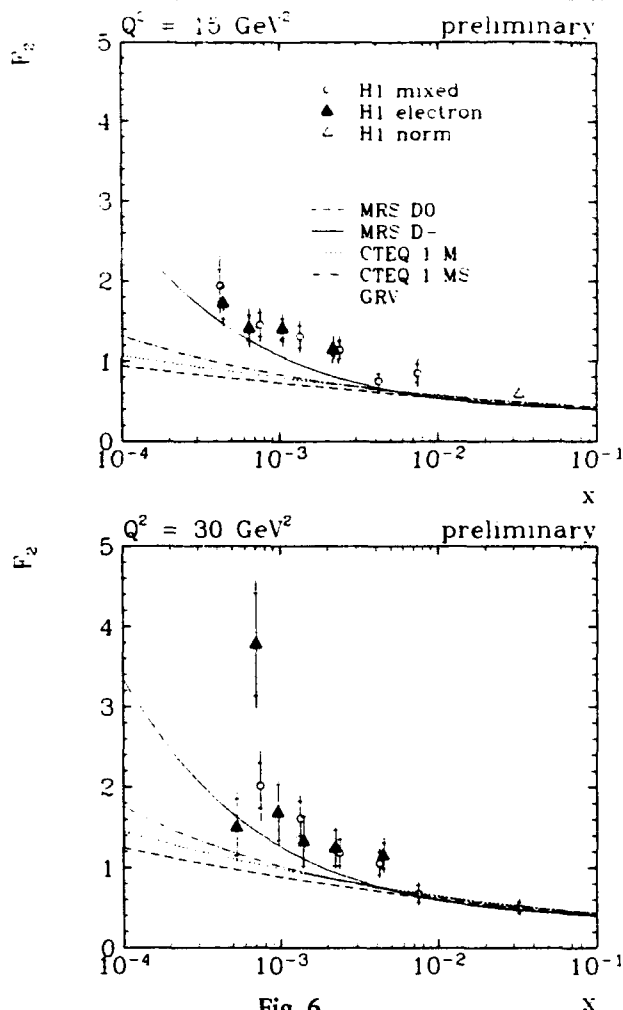
Fig. 6.

The formfactor $F_2(x,Q^2)$ plotted versus x for Q^2 = 15 GeV^2 and Q^2 = 30 GeV^2. The data are from the H1 collaboration.

3.2.2 Photoproduction

The photon is a particle with unique properties. On the one hand it is a fundamental gauge boson with well defined couplings to basic fermions and gauge bosons, on the other hand, part of the time the photon behaves like a strongly interacting vector boson. For larger values of $p_\perp$, the photon interacts indeed dominantly via its hadronic constituents, quarks and gluons, yielding resolved photon events. The total photon-photon section has previously been studied for center of mass energies up to 18 GeV. Both experiments reports [6,7] data on the total photoproduction cross section:
H1 quotes at a c. m. of 200 GeV:

$$\sigma_T(\gamma p) = (150 \pm 15(stat.) \pm 19(syst.))\mu b$$

ZEUS reports at a c. m. of 210 GeV:

$$\sigma_T(\gamma p) = (154 \pm 16(stat.) \pm 32(syst.))\mu b.$$

The data are in good agreement with predictions based on Regge models and show an increase with energy similar to that observed in the p-p total cross section.

The hadronic character of the photon can also be observed directly in the final state. A pointlike interaction between the

4

quark and the photon will in general yield two jets of hadrons from quark fragmentation. If the photon interacts via one of its hadronic constituents then we will observe, in addition to the two hadron jets at large angles also a jet along the incident electron direction resulting from the fragmentation of the remains of the photon. Lego plots, showing the two classes of events, are depicted in Fig. 7.
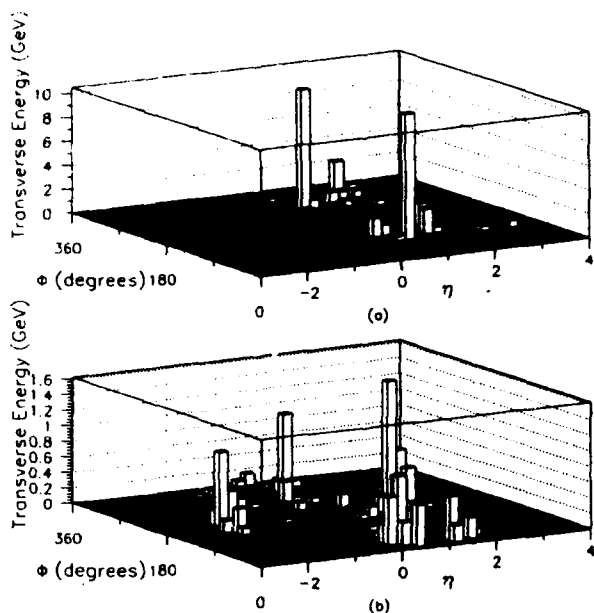
Fig. 7.

Deposited energy in photoproduction events as a function of

q and $\eta = -\ln\tan\frac{\theta}{2}$ measured by the ZEUS collaboration.

The occurance of resolved photon events have been confirmed by a detailed analysis [6,7].

3.2.3 Search for new particles

HERA is ideally suited to search for leptoquarks, exotic particles with mixed electron baryon quantum numbers. Leptoquarks occur naturally in composite models in which leptons and quarks are made of common building blocks and in various technicolour models. Particles with mixed baryon-lepton quantum numbers also occur in certain classes of supersymmetric models. The favoured leptoquark decay mode is into an electron and a quark jet.

Leptoquark production will thus lead to a neutral-current type final state and will show up in the x-distribution of neutral-current events as a bump at

x=(Mass of Leptoquark)^2/(Center of Mass energy)^2.

Both groups quote mass limits [8,9] as a function of the electron-quark coupling constant. Assuming this coupling strength to be of order $e = \sqrt{4\pi\alpha}$, the experiments find that

the mass of an (eu)-bound state must be above roughly 170 GeV depending somewhat on the helicity structure of the eu coupling.

3.3 Fixed target experiments

HERA offers the intriquing possibility of carrying out high luminosity, high duty cycle experiments by using internal targets in both the electron and the proton beam.

The aproved HERMES experiment plans to use the longitudinally polarized electron beam incident on a polarized H, D or He^3 gas jet target to investigate the nucleon spin structure. Given the good duty cycle the experiments can measure the scattered electron in coincidence with the hadronic final state.

The ARGUS collaboration are investigating the possibility of doing fixed target b-physics at HERA by positioning a thin wire target in the halo of the proton beam. Indeed, early studies using an internal target at HERA have given promising results. Although the primary goal is to

measure the CP-violating parameters in $B^0 \rightarrow \psi_\psi K_s^0$ channel

a series of other experiments on B physics can also be carried out.

IV. REFERENCES

[1] For a recent review including references see
F. Willeke, Proceedings of the XII International
Accelerator Conference, Hamburg, July (1992).

[2] For a recent review including references see
F. Brusse, Proceedings of the International Conference
on High Energy Physics, Dallas, July (1992).

[3] For a recent review including references see
D. Coldwell, Proceedings of the International
Conference on High Energy Physics, Dallas, July (1992).

[4] H1 Collaboration, T. Ahmed et al.,
Phys. Lett. B299 (1993), 385.

[5] ZEUS Collaboration, M. Derrick et al.,
Phys. Lett. B303 (1993), 183,
Phys. Lett. B306 (1993), 158.

[6] ZEUS Collaboration, M. Derrick et al.,
Phys. Lett. B293 (1992), 465,
Phys. Lett. B297 (1992), 404.

[7] H1 Collaboration, T. Ahmed et al.,
Phys. Lett. B297 (1992), 205,
Phys. Lett. B299 (1992), 374.

[8] ZEUS Collaboration, M. Derrick et al.,
Phys. Lett. B306 (1993), 173.

[9] H1 Collaboration, T. Ahmed et al.,
DESY 93-029.

[10] A. Matheisen et al., Proc. IEEE Part. Acc. Conf.,
San Francisco (1991) 2429, 1.

[11] D. P. Barber et al., Nucl. Inst. and Methods.,
A329 (1993), 79.

[12] Physics at HERA,
Proc. of the Workshop, Hamburg, October (1991).

Nonlinear Beam Dynamics Experiments at the IUCF Cooler Ring

S.Y. Lee

Department of Physics, Indiana University, Bloomington, IN 47405

Abstract

Results of nonlinear beam dynamics experiments at the IUCF Cooler Ring in past two years are discussed. Our experiments include studies on (1) betatron motion at 1-D resonance island, (2) linear coupling correction, (3) Hamiltonians determined experimentally from 2-D difference and sum resonances, (4) longitudinal phase space tracking, (5) beam response to rf phase modulation, (6) beam response to rf voltage modulation, (7) synchro-betatron coupling induced by dipole field modulation and (8) attractors of a weak dissipative Hamiltonian system.

1 INTRODUCTION

There have been many nonlinear beam dynamics experiments in the past. [1-5] The beam-beam interaction Experiments at Novosibirsk VEPP-4 measured particle loss and lifetime at various nonlinear resonance conditions and similar experiments at the SPS observed large background in detector area when a high order resonance is encountered. [1] More recently, due to advances in electronics, large amounts of data can be recorded for post analysis, where the Poincaré maps becomes a powerful tool in the study of nonlinear dynamics. [3-5] Nonlinear perturbations in the accelerator include sextupoles, octupoles, and higher order multipoles. These anharmonic terms usually do not significantly perturb the particle motion in phase space except when the betatron tunes are near to a resonance condition with $m\nu_s + n\nu_x = \ell$ (m, n, ℓ integers), where the Poincaré map deviates from a simple ellipse.

This paper reports highlights of recent nonlinear beam dynamics experiments performed at the IUCF Cooler Ring, which is one of recently completed storage rings with electron cooling. [6] Fig. 1 shows the IUCF Cooler Ring geometry. The lattice properties are $C = 86.8$ m, with $\nu_s = 3.8$, $\nu_x = 4.8$ and $\hat{D}_s = 4.0$ m. The beam rigidity varies from 1 Tm to 3.6 Tm with proton kinetic energy ranges from 45 to 500 MeV. At 45 MeV, the revolution period is $T_0 = 969$ ns. The 95% emittance is electron cooled to $\epsilon \sim 0.3\pi$ mm-mrad with $\sigma_s \approx 0.7$ mm. The available dynamical aperture is about 20π mm-mrad. There are two rf systems capable of operating at harmonic numbers from $h = 1$ to 13. Our experiment started in December 1990, when the cooler experiment CE22 was approved by the Program Advisory Committee. The first test of experimental hardware was in May 1991. We completed 50 shifts of beam time in March 30, 1993 and are requesting 50 shifts for a new series of beam dynamics experiments. Currently, our hardware/software can digitise 6D phase space up to 256K turns. In past two years, we have studied $3\nu_s, 4\nu_s, \nu_s - \nu_x, \nu_s - 2\nu_x, \nu_s + 2\nu_x$ transverse reso-
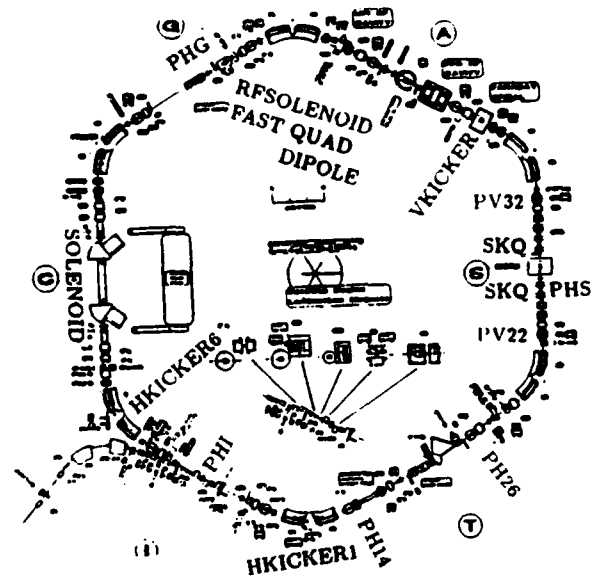
Figure 1: The schematic drawing of the IUCF Cooler Ring. The BPMs used are marked as PH or PV.

nances and studied longitudinal synchrotron Poincaré map with rf phase modulation, rf voltage modulation and the synchro-betatron coupling. From these experimental data, we were able to derive nonlinear Hamiltonian at nonlinear resonance conditions. [5-6] In section 2, the experimental procedure and some results will be reported. Section 3 will discuss future plan and conclusions.

2 NONLINEAR BEAM EXPERIMENTS

Our experimental procedure started with a single bunch being kicked transversely with various transverse angular deflections, θ_K, by a pulsed deflecting magnet within one revolution or kicked longitudinally by rf phase shifter or rf phase modulation or rf voltage modulation. The subsequent beam-centroid displacement was measured by two BPMs (four BPMs for both x and z degrees of freedom) for betatron motion. The synchrotron motion was tracked by 1 BPM located at a high dispersion region with $D_s = 4.0$ m for the momentum deviation and 1 WGM or a sum signal with a phase detector relative to the rf wave to obtain the synchrotron phase. The turn-by-turn beam positions were digitised and recorded in transient recorders up to 256K memory in 8 channels for the 6D phase space. The number of turns for the particle tracking can be increased by digitising once in every P turns (the rate divider), where P varies from 1 to 99. Important issues in these experiments are (1) the stability of beam closed orbit and be-
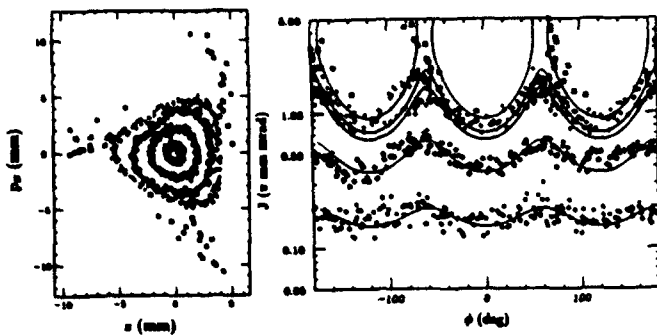
Figure 2: Poincaré maps at third order resonance.
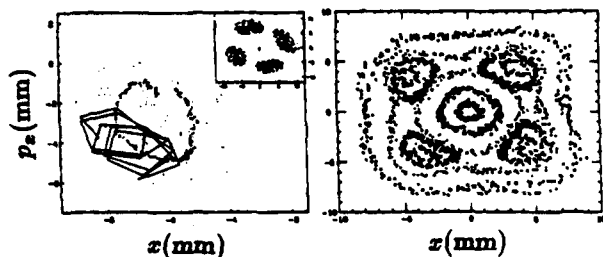
Figure 3: The Poincaré map at the fourth order resonance (left) is shown in the inset. The effect of the linear coupling motion is shown as a winding motion around an island fixed point. The Poincaré map after linear coupling correction is shown on the right.

tatron tunes, (2) the resolution of beam position monitor, (3) linearity and dynamical range of the amplifier, (4) digitization bandwidth for the time resolution and (5) careful preparation of the beam condition. Depending on physics issues, the available memory can be also important. For most of electron storage rings, the damping time is of the order of milliseconds and the betatron amplitude decoheres in hundred revolutions, the amount of memory buffer is not important. For the study of diffusion process in the hadron storage ring, large memory becomes necessary.

Besides hardware issues, beam properties in storage rings are also very important in nonlinear beam dynamics experiments. To better simulate single particle motion, nonlinear beam dynamics studies prefer a small emittance beam. The BPM measures the centroid of the charge distribution. With a smaller beam size, dynamics of resonance islands can be explored. The oscillation frequencies inside the island can be measured. The effect of betatron decoherence is smaller for smaller beam size also. When the bunch of particles is kicked to a large betatron amplitude, particles with different betatron tunes decohere in the betatron phase space. Although each particle may remain in a large betatron amplitude of a hollow beam, the centroid of the bunch becomes zero due to decoherence, which limits the number of measurable turns. Another important issue is the linear coupling, which may not destroy the island but it will mess up the interpretation of

nonlinear experiments. Besides, linear coupling is also an important topic in nonlinear beam dynamics experiments, where careful measurement of $\nu_x + \nu_z = n$ resonance remains to be seen.

The conditions for most of our experiments were $h = 1$, $\eta \approx -0.86$, $\phi_0 = 0$. We chose an rf voltage of 41 V to obtain a synchrotron frequency of about 262 Hz in order to avoid harmonics of the 60 Hz ripple. Sometimes, we chose $f_{syn} = 540$ Hz in order to improve the resolution of the $\frac{\Delta p}{p}$ measurement.

2.1 Transverse Beam Dynamics Experiments

The Hamiltonian for particles encountering a single resonance, $m\nu_x + n\nu_z = \ell$, $m \geq 0$, is given by

$$H = H_0(J_x, J_z) + g J_x^{\frac{|m|}{2}} J_z^{\frac{|n|}{2}} \cos(m\phi_x + n\phi_z - \ell\theta + \chi) \quad (1)$$

where g is determined by nonlinear elements in the accelerator. The unperturbed Hamiltonian H_0, is given by $H_0(J_1, J_2) = \nu_{x0}J_x + \nu_{z0}J_z + \frac{1}{2}\alpha_{xx}J_x^2 + \alpha_{xz}J_xJ_z + \frac{1}{2}\alpha_{zz}J_z^2 + \cdots$. The Hamiltonian in the single resonance approximation is integrable. Particle trajectories follow invariant tori of the Hamiltonian flow.

A special class of the above Hamiltonian is a 1D parametric resonance, i.e. $m\nu_x = \ell$ or $n\nu_z = \ell$. Most previous experiments [2-4] was set up to study these resonances, where stable regions of phase space around stable fixed points (SFP) are called islands. The beam was kicked onto a resonance island to study properties of the Hamiltonian flow. With a small emittance beam, details of island motion could be studied. Fig. 2 shows the Poincaré maps at the third order resonance condition. The Hamiltonian for third order resonance is given by, $H = \delta J_x + \frac{1}{2}\alpha_{xx}J_x^2 + \frac{(2J_x)^{3/2}}{48\pi}F\cos(3(\phi_x + \chi))$, where ϕ_x is the betatron phase, $\delta = \nu_x - \frac{\ell}{3}$, with ℓ integer, and $Fe^{i3\chi} = \int \beta_x^{3/2}\frac{B''}{B\rho}e^{i3\phi_x}ds$ with B'' as the 2nd derivative of the magnetic field. The relative magnitude of F and $\alpha_{xx}J_x^{1/2}$ determine the characteristics of the 3rd order resonance islands. For a third order slow extraction process, a small detuning parameter and good linear coupling correction are important in achieving high efficiency.

The fourth order 1D resonance data (inset) is shown on the left side of Fig. 3. Because of the linear coupling, the Poincaré map winds around fixed points of a resonance island. The linear coupling at the IUCF Cooler may arise from the solenoidal field at the electron cooling section. Averaging the winding motion of linear coupling reveals an ellipse around an island's fixed point. [4] Eliminating the linear coupling with skew quadrupoles, the right side of Fig. 3 shows the fourth order resonance Poincaré maps [4], which give greater precision in predicting the nonlinear Hamiltonian of the synchrotron.

On the 2D $\nu_x - 2\nu_z = -6$ resonance, Fig. 4 shows the characteristic x, z nonlinear coupling resonance data vs revolution number. The corresponding FFT spectrum exhibits typical nonlinear coupling sidebands. Tranforming the 2D
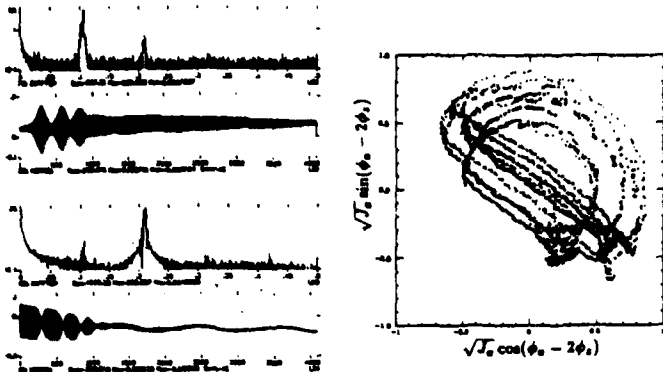
Figure 4: The measured x and z position vs turn number are shown for the experiment at $\nu_x - 2\nu_z = -6$ resonance condition. The Poincaré map in the resonance frame is shown on the right.

Figure 5: The response of sinusoidal modulation to the rf phase for $\frac{\Delta p}{p}$ and ϕ vs revolutions are shown on the left frame. The measured peak amplitude and the modulation period is shown as a function of the modulation frequency.

data in the resonance frame, i.e. $(\sqrt{J_x}\cos\phi_1, \sqrt{J_x}\sin\phi_1)$ with $\phi_1 = \phi_x - 2\phi_z$, the Poincaré maps in resonant frame becomes invariant tori. These data, shown in Fig. 4, was used to derive the 2D Hamitonian experimentally. [4] Although the aperture may be reduced because of the energy exchange between horizontal and vertical planes, the difference resonances are intrinsically stable. On the other hand, particle motion is unstable at a sum resonance, where the beam intensity becomes too low to make any meaningful measurement. A ferrite Panofsky quadrupole [7] was constructed to change the betatron tunes in 1 μs so that a beam bunch with reasonable intensity is tracked at the sum resonance condition. Parts of our successful initial results at $\nu_x + 2\nu_z$ resonance are reported in these proceedings. [4]

2.2 Longitudinal Dynamics Experiments

Longitudinal beam dynamics experiments are also important. The phase space coordinates, (ϕ, δ), with the normalized off momentum $\delta = \frac{h\eta}{\nu_s}\frac{\Delta p}{p}$, obey the mapping equations,

$$\phi_{n+1} = \phi_n + 2\pi\nu_s\delta_n + \Delta\varphi(\theta), \qquad (2)$$

$$\delta_{n+1} = \delta_n - 2\pi\nu_s(1 + A(\theta))\sin\phi_{n+1} - \frac{4\pi\alpha}{\omega_0}\delta_n, \qquad (3)$$

where the orbital angle θ is used as the time variable, $\Delta\varphi(\theta)$ is the rf phase error, $A(\theta)$ is the rf voltage error, and α is the phase space damping coefficient due to electron cooling at the IUCF Cooler Ring. The damping time for 45 MeV protons was measured to be about 0.4 sec or $\alpha = 2.5\,\text{s}^{-1}$ at an electron current of 0.75 A. Thus $\alpha \ll \omega_s$. The rf phase and voltage errors can arise from the noise of power supply or external modulation in the rf system, or from synchro-betatron coupling. The SB coupling is important to electron storage rings, where the fractional parts of the synchrotron and betatron tunes are of the same order of magnitude. For the SSC, where the synchrotron frequency varies from 7 Hz at injection energy to 4 Hz

at 20 TeV, SB coupling may arise from ground vibration. At RHIC, the synchrotron frequency ramps through 60 Hz around 17 GeV/c for heavy ion beams, SB coupling may result from power supply ripple.

To understand the dynamics of synchrotron motion in the presence of phase or voltage errors, we examine first the Hamiltonian. Neglecting the damping term ($\alpha = 0$), the synchrotron equation of motion, can be derived from the Hamiltonian, $H = \frac{1}{2}\nu_s\delta^2 + \nu_s(1 + A(\theta))[1 - \cos\phi] + \delta\Delta\varphi(\theta)$. Let us transform the phase space coordinates, (ϕ, δ), into $(\tilde{\phi}, \tilde{\delta})$ by $F_2(\phi, \tilde{\delta}) = (\phi - \Delta\varphi(\theta))\tilde{\delta}$. The new Hamiltonian becomes, $H = \frac{1}{2}\nu_s\tilde{\delta}^2 + \nu_s(1 + A(\theta))[1 - \cos(\tilde{\phi} + \Delta\varphi(\theta))]$, where the potential energy term is now independent of the momentum variable. The phase coordinate $\tilde{\phi}$ is relative to the revolution frequency.

Consider now the case that both the phase and the voltage errors are small and sinusoidal, i.e. $\Delta\varphi = \nu_1 a\cos\nu_1\theta$ and $A = \varepsilon\sin\nu_2\theta$ with $a, \varepsilon \ll 1$. The Hamiltonian system can be expanded in terms of the action-angle of the unperturbed Hamiltonian, i.e. $J = \frac{1}{2\pi}\oint\tilde{\delta}d\tilde{\phi}$. For our experiments with a small action, $J \leq 2$, the action-angle canonical transformation can be carried out approximately by the generating function, $F_1(\phi, \psi) = -\frac{\tilde{\phi}^2}{2}\tan\psi$ with $\tilde{\phi} = \sqrt{2J}\cos\psi$, $\tilde{\delta} = -\sqrt{2J}\sin\psi$. The new Hamiltonian can be approximated by,

$$H \approx \nu_s J - \frac{\nu_s}{16}J^2 + \Delta H_0 + \sum_{k=1}\Delta H_{2k}^{(\pm)} + \sum_{k=0}\Delta H_{2k+1}^{(\pm)}. \qquad (4)$$

The corresponding perturbed synchrotron tune is given by $\tilde{\nu}_s \approx \nu_s(1 - \frac{J}{8})$, which is a good approximation to the exact synchrotron tune up to about $J \approx 2.5$. The nonlinear resonance terms arising from the unperturbed Hamiltonian, $\Delta H_0 = \nu_s[-\frac{J}{2}\cos 2\psi - 2\sum_{k=1}^{\infty}(-)^k J_{2k}(\sqrt{2J})\cos 2k\psi]$, are not important because $\nu_s \leq 10^{-3}$ is a small number so that the resonance condition occurs at $2k\nu_s = $ integer with a large k, where the resonance strength, proportional to J_{2k}, is very small. Here J_{2k} are Bessel functions of the first kind.

The Hamiltonian due to the external modulation induces parametric resonances at harmonics of the synchrotron frequency, i.e.

$$\Delta H_n^{(\pm)} = \begin{cases} (-)^k a \nu_s J_{2k+1}(\sqrt{2J}) \sin(\nu_1\theta \pm (2k+1)\psi) \\ (-)^{k+1} \epsilon \nu_s J_{2k}(\sqrt{2J}) \sin(\nu_2\theta \pm 2k\psi). \end{cases}$$

(5)

The resonances due to external modulation are sometimes called parametric resonances. The resonances due to the voltage modulation are located at even multiples of the synchrotron harmonics and the resonances due to the phase modulation are located at odd synchrotron harmonics. When the modulation frequency, ν_1 or ν_2, equals to the multiples of the synchrotron frequency, the coherent kick due to resonance condition dominates the beam dynamics. Making the canonical transformation to the resonance precessing frame with the generating function, $F_2(\psi, \tilde{J}) = (\psi - \frac{\nu_m}{n}\theta - \frac{\pi}{2n})\tilde{J}$, the time averaged Hamiltonian becomes,

$$\langle H \rangle = (\nu_s - \frac{\nu_m}{n})\tilde{J} - \frac{\nu_s}{16}\tilde{J}^2 - \nu_s f J_n(\sqrt{2\tilde{J}})\cos(n\tilde{\psi}), \quad (6)$$

where J_n is the Bessel function, f, aside from a possible $\pm$ sign, stands either for a or ϵ and ν_m stands either ν_1 or ν_2. The particle trajectory will be located on the tori of the time independent Hamiltonian flow. The longitudinal Hamiltonian is therefore almost identical to that of the transverse resonant Hamiltonian of Eq. (1). Hereafter, we drop the tilde notation for simplicity. Since the Hamitonian in Eq. (6) is time independent, it is a constant of motion. The particle trajectories, obeying the Hamilton-Jacobi equation,

$$\dot{J} = -\frac{1}{2^n n!}\nu_s c(2J)^{n/2}\sin n\psi, \quad (7)$$

$$\dot{\psi} = (\nu_s - \frac{\nu_m}{n}) - \frac{\nu_s}{8}J - \frac{\nu_s f J_n'(\sqrt{2J})}{\sqrt{2J}}\cos n\psi, \quad (8)$$

are tori with constant Hamitonian values. The fixed points, which determine charachteristics of tori, are given by $\dot{J} = 0$, $\dot{\psi} = 0$. There are in general n stable (SFP) and n unstable (UFP) fixed points. (There is a possible extra fixed point at $J = 0$ arising from the unperturbed Hamiltonian). The Hamiltonian flow corresponds to a torus about an SFP.

For illustration, we consider the lowest order parametric resonance at $\nu_m \approx \nu_s$ due to the rf phase modulation. Using $g = \sqrt{2J}\cos\psi$ with $\psi = 0$ or π as the rf phase coordinate of the fixed point, the equation for g becomes,

$$\frac{\nu_s}{16}g^3 - (\nu_s - \nu_m)g + \frac{\nu_s a}{2} = 0, \quad (9)$$

which has three possible solutions at modulation frequencies below the critical frequency ν_c called the bifurcation frequency given by $\nu_c = \nu_s[1 - \frac{3}{16}(4a)^{2/3}]$. When the modulation frequency is below ν_c, there are two SFPs and one UFP. Beyond the bifurcation frequency, only the outer SFP exists.
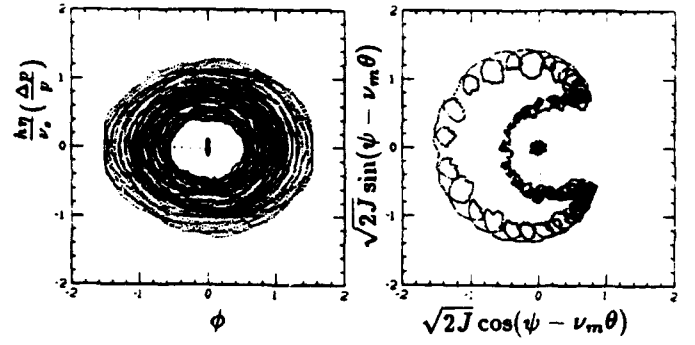
Figure 6: The response of the bunch at 42° initial phase kick to the sinusoidal modulation at a modulation amplitude of 1.3°. The Poincaré map of (δ, ϕ) is shown on the left frame and the Poincaré map in the resonance frame on the right

At the IUCF Cooler Ring, we measured Poincaré maps of the beam with phase or voltage modulations. [5] When the bunch is kicked with an rf phase shift, the synchrotron tune, measured as a function of the synchrotron amplitude, was found in excellent agreement with theory. When the rf phase is modulated sinusoidally, the response of the bunch motion located initially at the origin shows characteristics of parametric resonant system (Fig. 5). The modulation period shown in Fig. 5 characterizes the tune of the motion about an SFP. The modulation amplitude characterizes the intercept of the torus with the phase axis. The peak response and the peak modulation period occur at the same modulation frequency, which reflects the condition that the separatrix of these two resonant islands pass through the origin of the rf bucket, which is the initial condition of the beam. Figure 6 demonstrates that the reduction of the Poincaré map in the resonance frame revealing indeed the simplicity of the Hamiltonian flow of Eq. (6) from experimental data.

The rf phase modulation may also arise from synchro-betatron coupling. For proton storage rings, the synchrotron tune is small, therefore synchro-betatron coupling is usually not important. However dipole field modulation at a non-zero dispersion function location can change the circumference by $\Delta C = D_x \theta(t)$. The corresponding rf phase difference becomes, $\Delta \phi = 2\pi h \frac{\Delta C}{C}$. In our experiment, the maximum rf phase shift per turn was $\hat{\Delta\phi} = 0.78 \times 10^{-5}\hat{B}_m$ [Gauss] radians. Because the synchrotron frequency is much smaller than the revolution frequency in proton storage rings, the phase errors of each turn accumulate. The modulation phase amplitude is enhanced by the factor $\frac{\omega_0}{2\pi\omega_s}$. In this run, the injected beam was cooled and simultaneously modulated by a small dipole. A window frame ferrite dipole magnet was used to produce the transvese dipole modulation. [7] The horizontal dispersion function was $D_x \approx 4.0$ m at the modulation dipole location. The result is shown in Fig. 7, where the inset shows
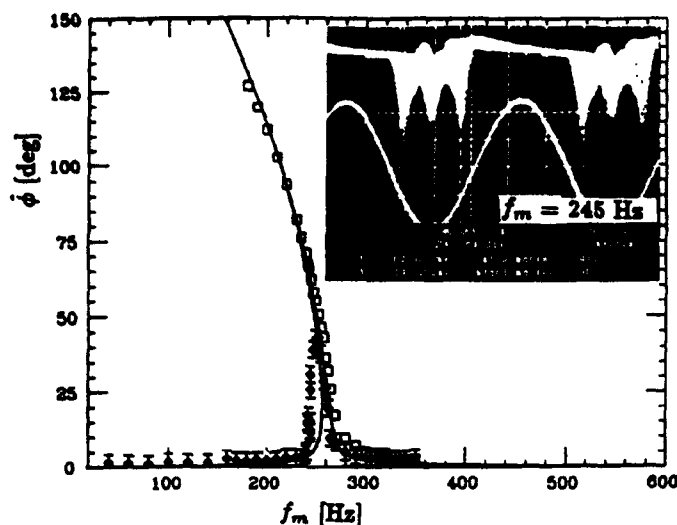
Figure 7: The inlet shows the trace of signal from a wall gap monitor triggered by the rf frequency. The measured phase amplitude of the outer beamlet is shown to compare with the fixed points of the Hamiltonian.

the trace of the bunch shape accumulated on an oscilloscope. It appears that the beam split into two beamlets. The phase amplitudes of the outer and the inner beamlets measured from the oscilloscope and digitized phase detector are also plotted in Fig. 7, where lines are solutions of Eq. (9). Because of the phase space damping due to electron cooling, particles in the phase space are trapped into the islands of the resonant Hamiltonian. These beamlets are observed to rotate about the center of the bucket at the modulation frquency. Results from similar measurements for the voltage modulation at $\nu_m \approx 2\nu_s$ indicate that the beam split into three beamlets. The measured phase amplitude of the outer beamlet agrees well with the fixed point of the Hamiltonian (6). Data analysis of these experiments will be reported shortly. [5]

3   CONCLUSION

Recent advances in fast digitizing electronics and also the availability of small emittance storage rings offer us the possibility of long term tracking of betatron and synchrotron motion. Combined with recent advances in numerical nonlinear beam dynamics methods of using Taylor map, Lie algebraic and canonical perturbation techniques, nonlinear beam dynamics experiments are timely and important in supporting, verifying and guiding theories. Our experiments indicates that indeed a particle motion in synchrotron obeys Hamiltonian flow. In particular, the longitudinal phase space experiments reveals the simplicity of invariant tori. They are simple and predictable. Our results can therefore be used to set the tolerance for high energy accelerators on errors associated with rf voltage and phase modulations, such as ground motion, the power supply ripple etc.

The limitations of nonlinear beam dynamics experiments rest on 1) finite beam size, 2) decoherence of betatron motion, 3) uncontroled tune modulation. These limitations reflect however a realistic storage ring environment. Theoretical calculations are usually limited by its difficulties in predicting the realistic environment. Our next phase of experiments will begin with rf phase/voltage modulation to create longitudinal island structure and study the particle motion when a second harmonic modulation at the island tune is applied. However, transverse beam dynamics remains to be our major focus. With a successful sum resonance experiment [4] by using the Panofsky quadrupole for the tune jump, we will study 2-D resonances. We will not forget the survival plot either. All these experiments require careful planning and beam conditioning. These difficult experiments have just begun to take place.

4   REFERENCES

[1] A.B. Temnykh, p.5, Proc. of the 3rd Adv. ICFA beam dynamics workshop, ed. I. Koop and G. Tumaikin, Novosibirsk (1989); L. Evans, et.al., Proc. of EPAC Rome, p.619, (1988); L. Evans, J. Gareyte, A. Hilaire, and F. Schmidt, Proc. of IEEE PAC, Chicago, p. 1376 (1989); L. Evans, et.al., ibid. 1403(1989); L. Evans, CERN SPS/83-38;

[2] M. Cornacchia and L. Evans, Part. Accel. 19, 125(1986); P.L. Morton, et. al., IEEE Tran. Nucl. Sci. NS-32, 2291 (1985). D.A. Edwards, R.P. Johnson, and F. Willeke, Part. Accel. 19, 145 (1986). A. Chao, et al., Phys. Rev. Lett. 61, 2752 (1988); N. Merminga, et al., Proc. EPAC, p.791 (1988). T. Satogata, et al., Phys. Rev. Lett., 68, 1838 (1992); P. Krejcik, Proc. ICFA Beam Dynamics Workshop II (Lugano), CERN 88-04, p.145 (1988).

[3] J. Bridge, et al., Part. Acc. 28, 1 (1990). E. Crosbie, et al., IEEE PAC, p.1624 (1991); J. Liu, et al., Ph.D. Thesis, Univ. of Wisconsin, (1993) unpublished.

[4] S.Y. Lee, et al., Phys. Rev. Lett. 67, 2767 (1991); D.D Caussyn, et al., Phys. Rev. A46, 7942 (1992); M. Ellison, et al., these proceedings, Y. Wang, et al., these proceedings.

[5] M. Ellison, et al., Phys. Rev. Lett. 70, 591 (1993); D.D. Caussyn et al., these proceedings; M. Syphers, et al., "Experimental Study of Synchrotron Coupling and Strange Attractors", submitted to the Phys. Rev. Lett., March (1993); these proceedings. Y. Wang, et al., "On Synchro-Betatron Coupling induced by Dipole Modulations", to be published; H. Huang, et al., "Experimental determination of the Hamiltonian for synchrotron motion with the rf phase modulation", to be published; D. Li, et al., "Experimental measurement of resonance islands induced by the rf voltage modulation", to be published.

[6] R.E. Pollock, Proc. of IEEE Part. Acc. Conf., p.17 (1989).

[7] J. Budnick, T. Hall, D. Li, S.Y. Lee, these proceedings.

The Preservation of Low Emittance Flat Beams*

T. O. RAUBENHEIMER

Stanford Linear Accelerator Center, Stanford University, Stanford, CA 94309

Abstract

Many future linear collider designs require beams with very small transverse emittances and large emittance ratios $\epsilon_x \gg \epsilon_y$. In this paper, we will discuss issues associated with the preservation of these small emittances during the acceleration of the beams. The primary sources of transverse emittance dilution in a high energy linear accelerator are the transverse wakefields, the dispersive errors, RF deflections, and betatron coupling. We will discuss the estimation of these effects and the calculation of tolerances that will limit the emittance dilution with a high degree of confidence. Since the six-dimensional emittance is conserved and only the projected emittances are increased, these dilutions can be corrected if the beam has not filamented (phase mixed). We discuss methods of correcting the dilutions and easing the tolerances with beam-based alignment and steering techniques, and non-local trajectory bumps. Finally, we discuss another important source of luminosity degradation, namely, pulse-to-pulse jitter.

Introduction

In this paper, we will discuss emittance preservation in the linear accelerators of future linear colliders. Currently, many groups around the world are designing the "next generation" of e^-/e^+ linear collider which would have center-of-mass energies ranging from $\frac{1}{2}$ to 2 TeV [1]. Although some designs are more extreme than others, they all specify beams with low emittances and a large aspect ratio ϵ_x/ϵ_y, i.e. flat beams. Parameters for the various designs are listed in Table 1 and a discussion of the differences can be found in Ref. 2.

There are three principal reasons for using low emittance flat beams: first, the small emittances allow for small spot sizes at the IP which is needed to achieve the required luminosity. Second, flat beams take advantage of the natural asymmetry of the damping ring based sources and of the final focus; quadrupole focusing is asymmetric and a flat beam final focus is easier to design than a round beam final focus. Third, for a given cross sectional area and charge, flat beams generate less beamstrahlung than round beams; the beamstrahlung increases the energy spread and causes detector backgrounds. In fact, a simple scaling suggests that very large aspect ratios are needed at the higher energies of 1 to 2 TeV to keep reasonable detector backgrounds [3].

Although low emittance flat beams are desirable from the standpoint of the luminosity and the IP physics, there is the obvious disadvantage that the low emittance beams need to be generated and then the emittances must be preserved during the subsequent acceleration and manipulation. In this paper, we will discuss issues pertinent to emittance preservation during the acceleration; these issues, as well as issues relevant in the damping rings, are described in more detail in Ref. 4.

Sources of Dilution

In a high energy linear accelerator, the principal sources of emittance dilution or luminosity reduction are conservative dilutions and pulse-to-pulse jitter. A conservative emittance dilution arises when the transverse or longitudinal degrees of freedom become coupled. In this case, the six-dimensional emittance is conserved but the projected emittances, which are the values relevant at the IP, are increased. It can easily be shown that coupling of two planes always increases the smaller of the two projected emittances from the uncoupled value.

Thus, the primary sources of dilution in the linacs of a future linear collider are:

- Dispersive errors: $\delta \rightarrow (y, y')$
- Transverse wakefields: $z \rightarrow (y, y')$
- RF deflections: $z \rightarrow (y, y')$
- Betatron coupling: $(x, x') \rightarrow (y, y')$
- Multi-bunch effects: $z \rightarrow (y, y')$
- Pulse-to-pulse jitter: $t \rightarrow (y, y')$

Because the emittance dilutions are conservative, they can be corrected, i.e., the emittance can be uncoupled, provided that the dilution has not filamented (phase mixed). The filamentation occurs because the beam has a spread in betatron oscillation frequency due to an energy spread in the beam, space charge forces, ions trapped in long bunch trains, etc.

Bare Machine Tolerances

It is straightforward to calculate alignment tolerances assuming only simple 1-to-1 trajectory correction, i.e., the trajectory is corrected to zero the beam position monitors (BPMs) located at the focusing quadrupoles; we refer to these tolerances as "bare machine tolerances." Approximate tolerances to limit the principal single bunch dilutions to 25% of the design emittance with a 95% confidence are listed in Table 2. Brief descriptions of the formula used in these calculations can be found in Refs. 5 and 6 and more detailed derivations can be found in Ref. 4.

The first tolerance is on the amplitude of a betatron oscillation injected into the linac which will filament and increase the projected emittance; this tolerance is simply related to the injected beam size specifies the minimum BPM precision (reading-to-reading measurement jitter) since the trajectory needs to be resolved at this level. The second tolerance is that on random misalignments of the quadrupoles and BPMs. With standard trajectory correction, the trajectory is deflected to follow these random misalignments. This leads to anomalous dispersion and wakefield errors since the beam is off-axis in the cavities. The third tolerance is on the random misalignments of the cavities which leads to wakefield dilutions and the last tolerance is on the rotational alignment of the quadrupoles which leads to betatron coupling.

In all designs, these bare machine tolerances are very tight and thus we must consider methods of correcting the emittance dilutions. There are essentially two approaches: non-local correction where the beam emittance is mini-

Table 1. Parameters of future linear collider designs for 500 GeV c.o.m.

	CLIC	VLEPP	JLC	NLC	DLC	TESLA
$\gamma\epsilon_x$ [mm-mrad]	1.8	20	5.5	5	10	20
$\gamma\epsilon_y$ [mm-mrad]	0.2	0.08	0.08	0.05	1	1
Part./bunch [10^{10}]	0.6	20	1.3	0.7	2.2	2.5
Bunches/pulse	4	1	20	90	172	1600
Rep. rate [Hz]	1700	300	150	180	50	12

Table 2. Bare machine tolerances for 25% ϵ dilution

Source	CLIC	VLEPP	JLC	NLC	DLC	TESLA
Injected betatron osc. with BNS damping	3.5 μm	1.5 μm	0.7 μm	0.7 μm	7 μm	15 μm
BPM and quad. misalignments	0.5 μm	0.2 μm	5 μm	4 μm	20 μm	50 μm
Accel. section misalignments	0.4 μm	0.4 μm	1.4 μm	5 μm	15 μm	300 μm
Quadrupole rotations	1 mrad	0.2 mrad	0.3 mrad	0.3 mrad	1 mrad	1 mrad
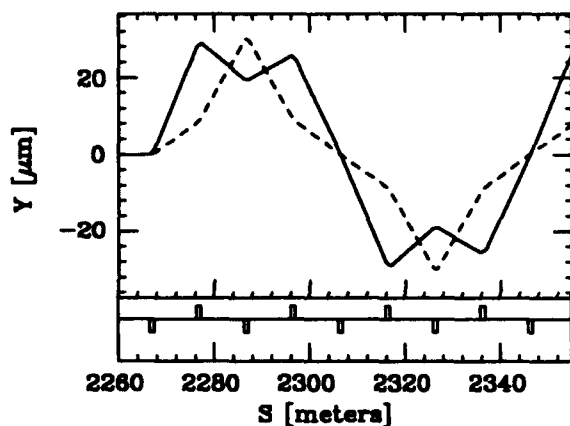
Fig. 1 A non-dispersive bump (solid) compared with a betatron oscillation (dashes); from Ref. 4.

Table 3. Non-dispersive bumps in the NLC with 70 μm RF structure misalignments

Uncorrected dilution	11.7$\pm$2 ϵ_{y0}
Initial conditions (y_0, y_0')	9.8$\pm$1 ϵ_{y0}
2 Non-disp. bumps (near front)	2.6$\pm$.2ϵ_{y0}
4 Non-disp. bumps	1.4$\pm$.1ϵ_{y0}
6 Non-disp. bumps	1.1$\pm$.02 ϵ_{y0}

mized at diagnostic stations and local correction where one effectively attempts to re-align the linac.

using skew quadrupoles to cancel the betatron coupling. Because the dilutions cannot be corrected after they filament, the spacing between diagnostic stations must be small compared to the filamentation length; in the NLC design, the linacs need to be divided into four sections.

In the SLC, simple betatron oscillations are used to reduce the effects of the wakefield dilutions [7], but, in most future linear collider designs, both dispersive and wakefield errors are important. Thus, one needs to have orthogonal correction for the two effects. This is possible using non-dispersive bumps to correct the wakefield tails and non-wakefield bumps for the dispersive errors; a non-dispersive bump is illustrated in Fig. 1.

Table 3 lists the average of twenty simulations of the NLC where non-dispersive bumps were used to correct for 70 μm rms random accelerator section misalignments. The average uncorrected dilution is over 1000%. As additional pairs of non-dispersive bumps are added, pairs of bumps separated by 90° in betatron phase are needed for orthogonal control, the emittance dilution is corrected to 10% on average. Thus, the bare machine tolerance of 5 μm on the accelerator section alignment could be eased to a more reasonable 70 μm with this non-local correction.

The difficulties with this approach are: (1) the beam emittance and tails need to be measured accurately to correct the dilution, (2) multiple stations are needed to prevent filamentation of the dilutions, and (3) the technique is sensitive to changes in the linac energy profile and quadrupole settings since it depends upon the phase advance between the dilutions and the corrections.

Non-local ϵ Correction

To perform non-local emittance correction, the linac is interspersed with diagnostic stations where the beam emittance is measured. Then, the emittance couplings are removed using trajectory bumps to compensate the dispersive errors, transverse wakefields, and RF deflections, using kickers or special structures to re-align bunch trains, and

Local ϵ Correction

Local emittance correction involves correcting the emittance dilutions at their source, typically using information from the BPMs and not from emittance measurements. There are a few techniques that have been proposed. To align the quadrupoles one can: (1) vary independent power quadrupole power supplies as suggested in
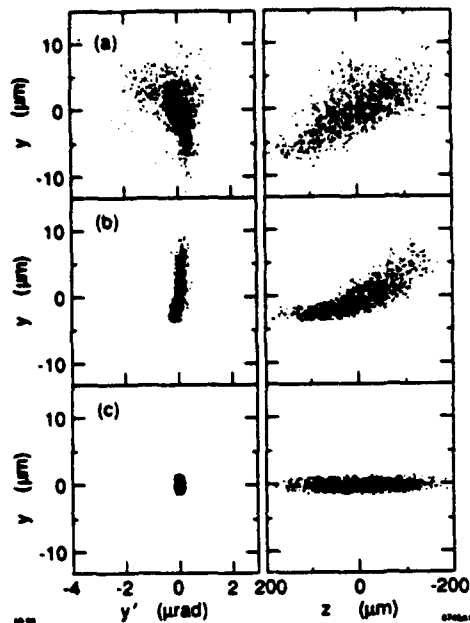
Fig. 2 The beam distribution after (a) 1-to-1,
(b) DF, and (c) WF correction at the end of the
250 GeV NLC linac. The left-hand plots are the
y-y' phase space while the right-hand plots are
the beam in y-z space; from Ref. 10.
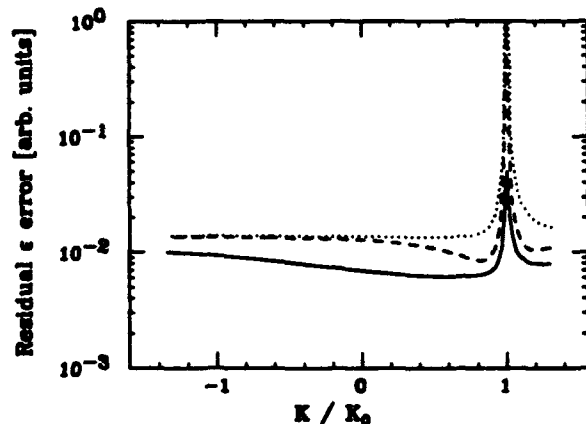
Fig. 3 Effectiveness of DF type correction ver-
sus the energy deviation or quadrupole scaling
(K/K_0) used. The curves correspond to cases
where the rms alignment of the BPMs rela-
tive to the quadrupoles is $2\sigma_{prec}$ (solid), $10\sigma_{prec}$
(dashes), and $100\sigma_{prec}$ (dots).

the VLEPP design, (2) use the beam-based alignment like
that used in the SLC [8], or (3) use specialized trajectory
correction techniques such as the Dispersion-Free (DF) or
Wake-Free (WF) techniques [9,10]. To align the acceler-
ating structures, BPMs could be build into the structures
with a very high accuracy as suggested in the CLIC de-
sign, or, the dipole wakefield, induced by the beam, might
be measured directly and then minimized.

In all cases, the best alignment that can be attained
is limited by the BPM precision (the reading-to-reading
jitter of the BPM measurement) and is roughly *indepen-*

dent of the magnitude of the misalignments. To limit the
emittance dilution to 6% using these techniques, the BPM
precision in the VLEPP and CLIC designs must be roughly
$\sigma_{prec} \sim 100$ nm, while the JLC and NLC designs require a
precision of $\sigma_{prec} \sim 1\,\mu$m and the DLC and TESLA designs
need $\sigma_{prec} \sim 10\,\mu$m.

The SLC beam-based alignment technique has been
demonstrated experimentally [8] and there has been ex-
tensive simulation of the other approaches. Simulations
results using the VLEPP approach can be found in Ref. 1
while simulations using the DF and WF correction tech-
niques are described in Refs. 9–12. Results from one simu-
lation in the NLC are plotted in Fig. 2 where the quadru-
poles and BPMs were randomly misaligned with a $70\,\mu$m
rms and the BPM precision was assumed to be $2\,\mu$m. Using
just the standard 1-to-1 trajectory correction, the emit-
tance is increased by a factor of 2400%. Using the DF
technique, the dilution is reduced to roughly 1000%, but
wakefield tails, due to the non-zero trajectory in the struc-
tures, are still apparent. Then, using the WF technique,
the emittance dilution is reduced to less than 10%.

Finally, the various correction approaches can be stud-
ied using analytic techniques [13]. The effectiveness of the
DF technique is illustrated in Fig. 3. Here, the residual
emittance dilution is plotted versus the magnitude of the
quadrupole scaling (K/K_0); the BPMs were assumed to
be aligned to the quadrupole magnets with rms errors
of $2\sigma_{prec}$ (solid), $10\sigma_{prec}$ (dashes), and $100\sigma_{prec}$ (dots).
The large peak at a quadrupole scaling of $K/K_0 = 1.0$ is
roughly equivalent to the 1-to-1 steering technique, while
the values near 0.8 corresponds to the DF technique and
the values near -1.0 approximate the SLC beam-based
alignment approach. Notice that, using the DF or beam-
based alignment techniques, the residual is roughly *inde-
pendent* of the initial alignment and instead only depends
upon the BPM precision.

The primary difficulty with these approaches is that
the beam emittance is not actually measured, instead, the
alignment information is inferred from the BPM measure-
ments. Thus, one would not want to use these techniques
alone without also having non-local diagnostic stations to
correct for residual dilutions.

Pulse-to-Pulse Jitter

Another source of luminosity degradation is pulse-to-
pulse jitter. The jitter can arise from motion of the quad-
rupole magnets, dipole power supply fluctuations, pulsed
kickers, or noise from the klystrons in concert with the
RF deflections. The induced oscillation will then either
filament, increasing the projected emittance, or shift the
beam centroid so the beams do not fully overlap at colli-
sion; this later effect is partially ameliorated by the beam-
beam pinch.

Usually, the most severe effect is due to the motion
of the quadrupole magnets. This motion arises from mo-
tion of the ground and the support structures in addition
to turbulence in the cooling flows and vibrations trans-
mitted through the RF feeds. Extensive measurements of
the ground motion relevant to linear colliders have been
made around the world. Some examples can be found in
Refs. 14–17.

Assuming that the motion is uncorrelated from magnet to magnet, tolerances on the linac quadrupoles are typically a few nanometers in the small emittance designs and tens of nanometers to a 100 nanometers in the DLC and TESLA designs. At low frequencies, $f \sim 0.15$ Hz, the amplitude of the ground motion tends to be very large, the order of microns, while at higher frequencies, $f \gtrsim 1$ Hz, the motion is at the level of a few nanometers. Fortunately, the motion is highly correlated at low frequencies where the amplitude of the motion is large. When the quadrupole motion is correlated, the beam response is small at frequencies below the first resonance where the wavelength of the motion is equal to the betatron wavelength. An example of the beam response y_{beam}/y_{quad} to correlated motion in the NLC design is plotted in Fig. 4 versus the frequency multiplied by the cosine of the angle of incidence; the first resonance occurs at 2.5 Hz, assuming a wave parallel to the linac.

Of course, the higher frequency motion, which is dominated by cultural (man made) noise, is not correlated over long distances. In an attempt to model recent measurements [18] we have calculated the response with a frequency dependent random phase such that the correlation length is given by $l_c \approx 100/(f + 0.03)$. The average of 16 seeds is plotted in Fig. 5. Notice that the response to the low frequency motion is significantly larger than that calculated for purely correlated motion.

To reduce the effect of the ground motion, one can use feedbacks, based on either the beam position or the actual motion of the quadrupoles. In addition, one needs to have well designed support structures with resonances where the feedback systems can reduce the response or where the ground motion is not significant. Typically, active feedbacks are needed on the IP quadrupoles, where the tolerances are much tighter. But, installing such a system on each of the hundreds of quadrupoles in the linacs becomes expensive and complex. Thus, it is desirable to use a few beam-based feedback systems to stabilize the trajectory. Unfortunately, the frequency response of the beam-based system depends upon the linear collider repetition rate. Simple analysis of the broadband feedbacks suggest that they can begin damping at frequencies below $f_{rep}/6$. More realistic feedback designs have much lower crossover frequencies. For example, the SLC fast feedbacks begin damping at frequencies below $f_{rep}/30$ [19].

Results from the SLC

Three elements crucial for a future linear collider have been demonstrated at the SLC; these, as well as other recent SLC results, are described in Refs. 20–22. First, beam-based alignment techniques [8] have been used to reduce the rms alignment of the quadrupoles to roughly 60 μm; this is four times the BPM precision of 15 μm. Second, fast feedback systems are used to stabilize the beam trajectory and energy [19]; currently, there are over 28 fast feedbacks operating in the SLC. Third, trajectory bumps have been used to decrease the emittance dilutions in the linac.

The SLC has been running with "flat" beams since March 1993 [21,22]. In normal operation, bunches of over 3×10^{10} particles are accelerated from 1.2 GeV to 47 GeV.
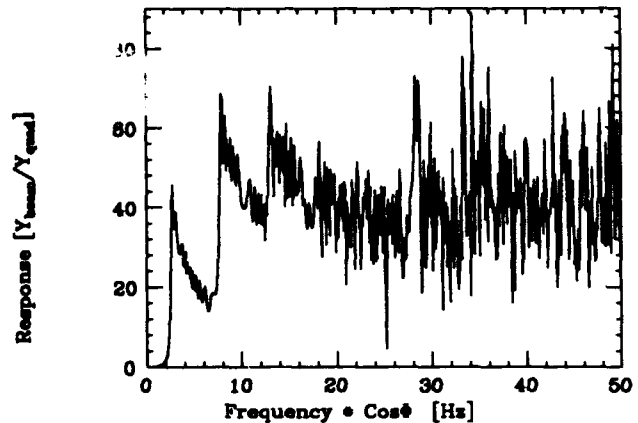
Fig. 4   Beam response to correlated motion of the linac quadrupoles in the 1 TeV c.o.m. NLC design.
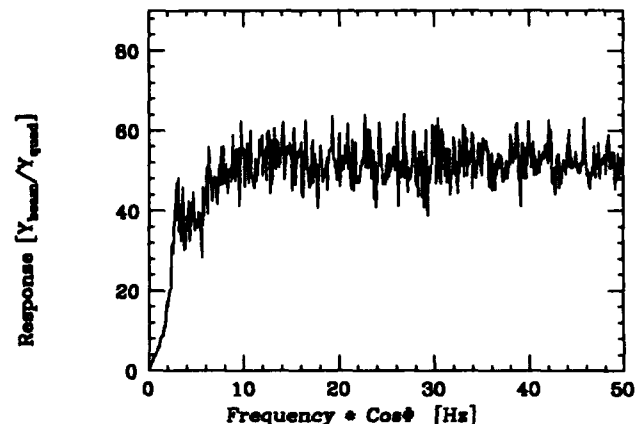
Fig. 5   Beam response to motion having a correlation length given by $l_c = 100/(f + 0.03)$ in the 1 TeV c.o.m. NLC design.

At the beginning of the linac, the rms beam emittances are roughly $\gamma\epsilon_x = 30$ mm-mrad and $\gamma\epsilon_y = 3$ mm-mrad. Without trajectory bumps to correct the emittance dilution, the emittances measured at the end of the linac are roughly $\gamma\epsilon_x = 60 \sim 80$ mm-mrad and $\gamma\epsilon_y = 20 \sim 50$ mm-mrad. With trajectory bumps, the emittances are reduced to roughly $\gamma\epsilon_x = 40 \sim 50$ mm-mrad and $\gamma\epsilon_y = 5 \sim 10$ mm-mrad; at lower currents, vertical emittances of $\gamma\epsilon_y = 2$ mm-mrad have been attained. The electron beam trajectory, with the emittance bumps, is shown in Fig. 6. The reduction in the emittance achieved with the bumps is equivalent to reducing the alignment errors by roughly a factor of three.

Figure 7 is a history of the emittances measured at the end of the linac during a week in April 1993. The fast fluctuations are thought to be due to changes in the linac energy profile which changes the phase relation between the emittance correction bumps and the sources of the dilution; this is one problem with non-local correction techniques and a feedback system is planned to compensate the phase errors.

Summary

We have discussed the principal sources of emittance dilution in future linear colliders and have listed some
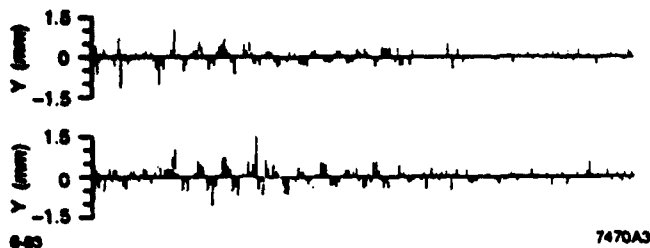
Fig. 6 e^- x and y trajectories in the SLC with emittances of roughly $\gamma\epsilon_x \approx 40\,\text{mm-mrad}$ and $\gamma\epsilon_y \approx 6\,\text{mm-mrad}$. Notice the large betatron oscillations used to control the emittance dilutions.
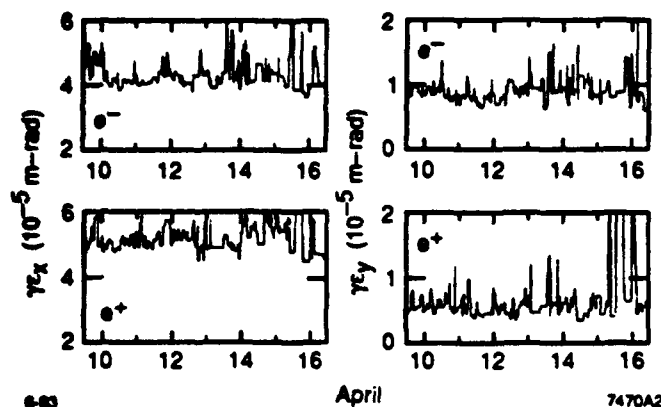
Fig. 7 e^- and e^+ emittances at the end of the SLC linac recorded over roughly one week in time.

"bare machine" alignment tolerances. In all designs, these alignment tolerances are extremely tight. Thus, detailed correction, tuning, and recovery procedures must be an integral part of a future linear collider design. In a linear collider the bare machine tolerances cannot be considered alone — emittance correction is needed just as orbit correction is needed in a storage ring. The emittance correction can be performed with a combination of local and non-local techniques. The local techniques are limited by the BPM precision while the non-local techniques are limited by the beam size measurement and by filamentation (phase mixing). Finally, jitter is another important source of luminosity reduction and feedback systems are essential.

A number of experiments have been performed or are being planned to fully verify the feasibility of preserving the necessary emittances. Foremost, of course, is the SLC which has demonstrated very impressive results. In addition, there is the FFTB project at SLAC, the ATF project at KEK, the ASSET project at SLAC, and multi-bunch and RF studies are planned for all of the linear collider designs.

References

[1] There are many future linear collider that are being designed around the world. Current parameters can be found in: *Proc. of the ECFA Workshop on e^+e^- Linear Colliders: LC92*, Garmisch-Partenkirchen, Germany (1992).

[2] B. Siemann, "Overview of Linear Collider Designs," *Presented at the 1993 IEEE Part. Acc. Conf.*, Washington D.C. (1993).

[3] J. Irwin, private communication.

[4] T. O. Raubenheimer, "Generation and Acceleration of Low Emittance Flat Beams for Future Linear Colliders," Ph.D. Thesis, Stanford University, SLAC-387 (1991).

[5] H. Henke, "Transport and Acceleration of Low Emittance Electron Beams," *Proc. of the 1988 Linear Acc. Conf.*, Williamsburg, VA (1988).

[6] R. Ruth, "Emittance Control in Linear Colliders," *Proc. of the 1991 IEEE Part. Acc. Conf.*, San Francisco, CA (1991).

[7] J. T. Seeman, F.-J. Decker, I. Hsu, "The Introduction of Trajectory Oscillations to Reduce Emittance Growth in the SLC Linac," *Proc. of the XVth Conf. on High Energy Acc.*, Hamburg, Germany (1992).

[8] C. Adolphsen, et. al., "Beam Based Alignment Technique for the SLC Linac," *Proc. of the 1989 IEEE Part. Acc. Conf.*, Chicago, IL. (1989).

[9] T. O. Raubenheimer and R. D. Ruth, "A Dispersion-Free Trajectory Correction Technique for Linear Colliders," *Nucl. Instr. Meth.*, A302:191 (1991).

[10] T. O. Raubenheimer, "A New Technique of Correcting Emittance Dilutions in Linear Colliders," *Nucl. Instr. Meth.*, A306:61 (1991).

[11] G. Guignard, "Treatment of Nonlinearities in Achromatic Trajectory Correction for Future Linacs," *Proc. of the 1992 European Part. Acc. Conf.*, Berlin, Germany (1992).

[12] A. Monsier, data presented at: *TESLA Collaboration Meeting*, Fermilab, IL, March 10–12, 1993.

[13] C. Adolphsen and T. O. Raubenheimer, "Method to Evaluate Steering and Alignment Algorithms for Controlling Emittance Growth," *Presented at the 1993 IEEE Part. Acc. Conf.*, Washington D.C. (1993).

[14] G. E. Fischer, "Ground Motion: An Introduction for Accelerator Builders," it Proc. of the 1992 CERN Acc. School on Magnetic Measurement and Alignment, Montreux, Switzerland (1992).

[15] J. Rossbach, "Fast Ground Motion at HERA," DESY 89–023 (1989).

[16] B. Baklakov, et.al., "Investigation of Seismic Vibrations and Relative Displacements of Linear Collider VLEPP Elements," *Proc. of the 1991 IEEE Part. Acc. Conf.* San Francisco, CA (1991).

[17] Y. Ogawa, et. al., "Vibrational Issues Regarding Linac Beam Characteristics," *Proc. of the 1992 Linear Acc. Conf.*, Ottawa, Canada (1992).

[18] V. Balakin and V. Shiltsev, data presented at: *Workshop on Emittance Preservation in Linear Colliders*, KEK Laboratory, Tsukuba, Japan, April 19–23, 1993.

[19] F. Rouse, et. al., "A Database Driven Fast Feedback System for the SLC," *Nucl. Inst. Meth.*, A316:343 (1992).

[20] M. Ross, "Recent SLC Developments," *Presented at the 1993 IEEE Part. Acc. Conf.*, Washington D.C. (1993).

[21] C. Adolphsen, T. Barklow, F.-J. Decker, P. Emma, P. Krejcik T. Limberg, M. Minty, N. Phinney, P. Raimondi, T. Raubenheimer, M. Ross, J. Seeman, R Siemann, W. Spence, N. Walker, M. Woodley, "Flat Beams in the SLC," *Presented at the 1993 IEEE Part. Acc. Conf.*, Washington D.C. (1993).

[22] C. Adolphsen, F.-J. Decker, J. Seeman, "Flat Beam Studies in the SLC Linac," *Presented at the 1993 IEEE Part. Acc. Conf.*, Washington D.C. (1993).

Long-Term Stability Studies for CERN-LHC

W. Scandale
CERN, CH-1211 Geneva 23, Switzerland

Abstract

In the modern hadron colliders, like LHC, SSC and RHIC, the stability of the single-particle motion is basically determined by the field-shape imperfections of the superconducting dipoles and quadrupoles, especially during the injection flat bottom, when the effect of the persistent currents is maximum and the transverse size of the beam is large. The non-linear fields are at the origin of two effects: the betatron tunes change with the amplitude and the momentum of the circulating particles, and, for certain combinations of the horizontal, vertical, and synchrotron tunes, non-linear resonances are excited. These phenomena have a destabilizing influence on the particle motion, over a time-scale extending up to several million turns. Some precautions can make the motion of the particles less sensitive to the non-linear components of the guiding fields. Correcting multipoles can be foreseen in the regular cells, to reduce the non-linear tune-shift caused by the systematic components of the field errors. The variations of the orbit functions can be limited along the insertions. The closed orbit and the linear coupling can be corrected sufficiently well. Finally the ripple of the power supplies can be reduced as much as possible. Most of these concepts have been embedded in the design of the LHC and their beneficial effects on the dynamic aperture have been extensively evaluated by computer simulations.

1. INTRODUCTION

The motion of charged particles in circular accelerators is basically governed by the magnetic field of the guiding dipoles and the focusing quadrupoles. Intentional and non intentional non-linear fields are in general also present, the side-effect of which is to induce losses at large amplitude. Sextupoles are used to reduce the chromaticity and octupoles make the tune dependent on the amplitude, which is sometime exploited to improve the current-dependent behavior. In hadron accelerators, the destabilizing action of chromaticity sextupoles is self-compensated to a large extent due to the regularity of the lattice. However, usually, a strongly focused lattice is necessary to reduce the sensitivity to field errors, and this in turn produces two adverse effects: the strength of chromaticity sextupoles has to be increased, therefore the beam stability is reduced, and the space available for dipoles along the ring is shortened with a consequent decrease of the maximum beam energy. Unintentional multipoles due to unavoidable imperfections of the guiding and focusing fields introduce additional non-linearities, which represent the greatest hazard. However, compromises are to be found between making magnetic fields as uniform as possible and keeping the magnet cost low. This is a difficult achievement especially for superconducting magnets, whose quality depends on the mechanical tolerances of the coil geometry, rather than on the shape of the poles. Both in the Tevatron and in the Hera magnets, typical deviations from uniformity have been limited to about one part in ten thousand at 2.5 centimetres from the magnet axis. Similar values, properly extrapolated with the inner coil diameter and the superconducting filament size, are expected to be reached in the magnets of the SSC, the LHC, and RHIC.

The single-particle approach provides a sufficiently simple, reliable and coherent model of the real accelerator to investigate performances related to non-linear dynamics. The key issue is to estimate the stability of the motion over the operational cycle of the accelerator. In a linear machine with irrational tunes the motion is stable and regular all around the closed reference orbit near the magnetic axis. The non-linear fields add a tune dependence with the amplitude, which shifts tunes to rational values, provoking resonant phenomena accompanied in the phase space by islands of finite area surrounded by thin chaotic layers. The islands and the chaotic layers exist through the entire phase space. However, at small amplitude, trajectories follow invariant surfaces, the KAM tori[1], and remain stable for indefinite time. As amplitude increases, the islands become larger until they overlap. Beyond that point, the chaotic layers become interconnected and the particle motion is no longer bounded. This is the domain in which the non-linear forces are able to provoke particle losses, that sometimes may occur after millions of turns. The border between regular and chaotic motion is called dynamic aperture. This is analytically well defined for $1\frac{1}{2}$ dimensional ($1\frac{1}{2}$-D) systems only[2]. With more degrees of freedom, particles in stochastic layers, even close to the origin, may escape through the entire phase space, due to the so called Arnold diffusion. However, for all practical purposes, the border between mostly regular and mostly chaotic trajectories can be used as the dynamic aperture.

Both analytical and numerical tools are used to estimate the dynamic aperture as a function of various machine parameters. Improvements of the linear lattice and correction schemes are studied to reduce the influence of the non-linear forces, and to specify upper limits for the magnet imperfections. The final confirmation is in general performed with numerical simulations in which the particle position is tracked element by element around the machine for large numbers of turns.

Simpler dynamical systems, such as the Hénon map[3], are advantageously used to investigate mechanisms of long-term losses.

Machine experiments with existing accelerators, in which non-linear perturbations are deliberately introduced, allow comparisons with predictions of numerical simulations.

In the following sections three subjects are reviewed, with special emphasis for the case of the LHC: the tools by which predictions on beam stability are formulated, the particular applications on accelerator design, and finally the outcome of the experiments performed in the CERN-SPS and in the FNAL-TEVATRON.

2. TOOLS FOR DYNAMIC APERTURE ESTIMATES

2.1. Tracking Simulations

Simulations with thin-lens approximation and symplectic integrators are considered as the master tool for quantitative estimates of particle behavior in the LHC with non-linear elements. They provide exact solutions of the equation of motion for a dynamical system approximating the accelerator. A sequence of linear transfer matrices interleaved with localized polynomial non-linearities is to be computed. Reliable results are easily obtained, since computer rounding errors can be kept under control[4]. However a vast computing power is required to get reliable estimates of the dynamic aperture as a function of various lattice and beam parameters. A fully realistic description of the accelerator structure is difficult if not impossible. Simplifications are also imposed by limitations in computing power. Thin-lens description of guiding and focusing fields is used, and do not imply relevant changes to orbit functions. Ignoring fringing fields, and representing non-linearities with equivalent thin-lenses is also considered acceptable.

Two computer codes are routinely used to describe LHC lattice models and compute particle trajectories of given initial conditions: MAD[5], developed at CERN, and SIXTRACK[6], developed at DESY. Both of them have scalar versions to be processed in the modern farms of workstations as well as vectorized versions to make use of modern parallel processors.

2.2. Maps

In linear lattices, particle coordinates can be propagated along the accelerator azimuth by Twiss transfer matrices.

The use of maps can be extended to non-linear dynamics with some precautions. This extension, originally motivated by the need to speed-up long-term tracking simulations in hadron colliders, in fact provides a powerful tool to handle dynamical quantities, like the tune dependence with the amplitude and the momentum, the distortion functions and the smear, the high-order non-linear invariants, and finally the Fourier harmonic coefficients of the resonance driving terms. Non-linear matrices can be constructed very efficiently with Differential Algebra techniques using Taylor expansion to some high order of algebraic operators[7]. One-turn Taylor maps resulting from the composition of all the linear and non-linear elements in the accelerator, are inherently not symplectic because of the high order truncation, therefore inappropriate to preserve volume in phase space. A way to restore symplecticity, whose physical meaning, however, is not fully understood, is to replace the truncated map with a Normal Form[8], that is an integrable map, represented by a rotation of an angle depending on the amplitude of the orbit. In practice this is performed by a local change of coordinates in the phase space, which brings intricate orbits into circles. However, the normalized map has an optimized order of accuracy. Above it, the approximation is improved at lower amplitude and worsened at higher amplitude. The domain of convergency is limited by resonances of low order that are allowed by the truncated Taylor map. There are ways to handle the first limiting resonance, with Resonant Normal Forms, which are not yet made of practical use.

In the LHC, the mapping approach based on Taylor expansion and Normal Form is used to evaluate the dependence of tune-shift on the amplitude and the momentum due to systematic field-shape imperfections[9]. By this it is possible to identify the multipoles that are more dangerous for the stability of the motion, taking into account the quite strong high order cross terms, and to define and optimize the most suited scheme of multipolar correctors.

High order Taylor maps are also used to estimate the dynamic aperture in a faster way than with the usual element by element tracking[10]: however, in the LHC, this approach is non-controversial only for simulations up to few 10^4 turns. By increasing the order of the map the violation of area preserving transport can be made arbitrarily small, but the map size grows exponentially and the computing speed decreases accordingly. An interesting result is that one can correlate the accuracy of the truncated Taylor map tracking to the size of the high order terms in the map. Alternatively, one can restore the symplecticity of the Taylor map by a linear scaling transformation to the particle coordinates at each turn. The transformation is staged in three different scale transformations, two in the transverse and one in the longitudinal directions respectively, characterized by three different scaling factors chosen in a suitable manner to ensure that the Liouville's theorem is obeyed, at least in average. In fact, there is an infinite set of possibilities for the choice of the three scaling factors. The additional criterion to determine the final choice is based on the following arguments. It is assumed that Taylor maps up to order 11th are sufficient for an accurate description of the beam dynamics in the LHC, at least in the region of the phase-space where the motion is regular or only weakly chaotic. The beam trajectories are computed both with element-by-element tracking and with Taylor maps with initial values of the scaling factors. The difference of amplitudes in the phase-space of the two results are estimated in few iterations by slightly varying the scaling factors. From that one can optimize the scaling factors in such a way that the amplitude differences between the direct tracking and the iteration of the Taylor map is constant as a function of the number of turns. The comparison between direct tracking and iteration of truncated maps with and without dynamic re-scaling has been made for a large number of turns: the agreement is two orders of magnitude better with re-scaling that without.

2.3. Early indicators of chaos

Early indicators of chaotic motion have been used to speed

up the estimate of the dynamic aperture in the LHC. The exponential divergence of two initially very close trajectories is a criterion for chaos, a linear growth indicating regular motion. The exponential coefficient, called Lyapunov exponent[11], can be used to localize stochastic layers in the phase space and eventually to identify the stability border below which its value is zero. The routine way to evaluate the Lyapunov coefficient is to track simultaneously two particles with a slightly different initial amplitude, and to compute periodically and plot their mutual distance[12]. An equivalent method is based on the analytical evaluation of the Jacobian in the phase space domain of interest[13]. A third possibility is to compute the slow change of an action invariant[14]. The predictability of all three methods is enhanced when the non-linear deformation of the phase space is removed by Lie algebraic or Normal Forms type change of coordinates. It is currently admitted that through early indicators of chaos a conservative estimate of the dynamic aperture can be obtained with about ten times less computing power than for standard tracking.

2.4 Figure of merit and data processing

The linear aperture, based on smear and tuneshift with the amplitude, and the short-term dynamic aperture were widely used in the past[15] to estimate non-linear effects, since threshold values for detuning and amplitude distortion were considered sufficient to ensure long-term stability. However, the validity of this extrapolation has not been confirmed by deeper studies. Therefore, intensive tracking and sophisticated data processing are preferred nowadays to estimate the dynamic aperture, after a preliminary selection of rather few significant cases, on the basis of short-term simulations. Results are presented in graphical form: survival plots depict the maximum number of stable turns as a function of starting amplitude[16]. These plots and early indicators of chaos provide a practical estimate of the stable region. Dense survival plots are ragged and show a large spread in the survival time close to the chaotic border, rapidly decreasing at larger amplitudes. Such an irregular shape reflects the local origin of the particle instability: at moderate amplitude in presence of weaker perturbations, the escape time is largely influenced by microscopic changes of initial coordinates; at large amplitude, instead there are only fast losses. Under the influence of non-linearities, particles migrate across different nests of resonances, which can be at least phenomenologically correlated to average lifetime. The loss mechanism is in general sudden: the particle may stay confined even for millions of turns and then diverge in a few thousand turns.

3. APPLICATIONS IN ACCELERATOR DESIGN

The LHC must operate with negligible loss for long periods, up to 10^8 turns, in spite of the unavoidable field shape imperfections. An upper limit to unintentional multipoles and practical compensation strategies have to be devised for a safe operation. This implies a thorough understanding of the influence of the non-linearities on the long-term behavior of particle trajectories. Analytical methods available are not yet fully exploited. Numerical simulations are too heavy and time consuming for an exhaustive overview of all the possible situations. Nevertheless, remarkable progress has been made through heuristic approaches proposed in the recent past, based on the investigation of simplified non-linear models of the LHC lattice and on the use of empiric criteria for beam stability.

Too crude simplifications of the lattice structure itself have dramatic effects on non-linear performances. Cell lattice models with only regular cells and no interaction regions show a regular azimuthal pattern of the orbit functions and in particular of the betatronic phase advance leading to unrealistic enhancement of the particle stability. They are in general used for numerical studies of simple dynamical systems as the Hénon map. A more realistic way to drop the insertions is to replace them with equivalent rotation matrices. Part of the chromatic aberration and some unintentional field errors are disregarded in this way. However, relevant informations can be gained with less computing power and complexity, especially during the injection plateau, where the stability of motion is mainly determined by non-linear perturbations in the arcs. This approach was used to determine the optimum value for the length and the phase advance of the LHC cell[17], fixed to about 100 m and 90 degrees, respectively. More advanced studies are based on models with realistic descriptions of the insertions.

The field-shape imperfections are equivalent to multipoles up to large order, which can be expressed as the sum of two parts, one systematic and the other random. The general agreement is to stop at order 11th in the multipolar expansion and to neglect correlations between random multipoles of different orders. Systematic errors are larger at injection due to persistent currents. Large low-order (3rd and 5th) values provoke a sizeable detuning with the amplitude and the momentum, which can be corrected either locally[18], as in the LHC lattice version 2, or using a clever cancellation of the detuning terms by means of Sympson rules[19], as in the LHC lattice version 1. In the latter case, multipolar correctors are to be located near the main quadrupoles as well as at about the middle of each half cell[9]. Octupolar imperfections have, in the LHC, a particular behavior related to the symmetry of the magnetic field in two-in-one magnets: the integrated value along the azimuth is expected to be zero, therefore the detuning with the amplitude is expected to be self-compensated without specific correctors. Large high-order (7th and 9th) systematic multipoles destabilize off-momentum particles and have to be minimized by design: tolerable values for the LHC have been found to be of the order of $2 \cdot 10^{-6}$ and $5 \cdot 10^{-7}$ units at 1 cm radius, respectively.

Random imperfections, which vary from magnet to magnet due to manufacturing tolerances, are the main source of non-linear resonances and distortion functions. Statistical distributions can be easily predicted, but are insufficient for a complete knowledge of the non-linear optics, since resonance strengths depend on the specific sequence of the random errors around the ring rather than on statistical properties. Therefore,

criteria for magnet design are to be studied on several non-linear lattices, with different sequences of random multipoles. In fact, there are many parameters that limit the stability of the particle motion in the LHC, therefore the first task is to identify the most important ones, in order to reduce to a reasonable amount the enormous need of computing time required for an exhaustive set of simulations. Parameters routinely considered in the accelerator models are residual closed orbit, linear coupling due to imperfections, synchrotron motion, and main power supplies ripple. Chromaticity and non-linear detuning are corrected with suited set of correctors. Special cases with some residual uncompensated chromaticity are considered as well. Short-term dynamic aperture is first evaluated by tracking particles of different starting amplitudes for 10^3 turns. This is fast and well suited for a first exploration of the space parameters, and is also sufficient to reveal the most important features of the non-linear phase space. Ten different seeds are used to fix the test samples of the random errors. Appropriate subsets of them are considered to disentangle the effects of the dipole imperfections from those of the quadrupole imperfections in a machine with a perfect closed orbit and no linear coupling. By choosing three representative seeds in each distribution, i.e. one with the smallest, one with the largest, and one with an average value of the aperture, one can easily check the combined effect of the dipole and the quadrupole errors and identify a limited number of representative sets of non-linear lattice models to be investigated with long-term tracking simulations. With this strategy[20], beam stability has been found to be strongly influenced by linear lattice parameters like tune, residual linear coupling, and peak-ß values in the insertion quadrupoles as well as by a residual chromaticity of a few units. Instead, residual closed orbit associated to magnet misalignment and tune ripple of a few 10^{-4} units showed a weak interference with beam stability.

Particles above the stable region are expected to diffuse towards the vacuum pipe at a speed strongly increasing with the transverse amplitude. A set of collimators[21] is used to absorb them before they hit the magnets and provoke an unwanted deposition of energy in the superconducting coils. The transverse position of the primary collimator defines the mechanical aperture of the accelerator. It is basically fixed taking into account the mechanical tolerances of the cold bore and of the thermal screen of the main magnets, the expected peak-values of the closed-orbit, of the dispersion, and of the ß-function modulation, and, of course, the optimum value of the separation between the primary and the secondary collimators. For a safe operation, careful matching of physical aperture and stability border is to be performed[20]. With a small mechanical aperture, trajectories with small amplitude oscillations only are allowed, which are weakly perturbed even in presence of large field-shape imperfections, whilst, with larger mechanical apertures, and larger amplitude oscillations, the non-linear perturbation becomes larger and the size of the magnetic errors start to play a leading role for the dynamic aperture. On the other hand, we believe that particles with amplitudes up to the chaotic boundary are stable, although the

non-linear perturbations induce a finite smear of their trajectories, whilst particles with larger amplitudes may become unstable after a sufficiently large number of turns. Ideally, the chaotic limit should be equal to the dynamic aperture evaluated in presence of collimators, in which case only the unstable particles will be intercepted by the collimators. In this respect the mechanical size and the field quality of the LHC at injection have been found to be well matched to a value of 6 σ, i.e. of 7.2 mm, which is considered a wise choice for the needed dynamic and physical aperture.

Strategies of magnet sorting have been invented, by which the magnets are installed in such a sequence in the machines as to minimize the combined non-linear effects. For practical and theoretical reasons, the sorting scheme should be as local as possible and must refer to a limited kind of multipoles. Different solutions have been proposed[22]. By introducing a quasi-periodicity of multipoles every two betatronic wavelengths, the harmonic content of non-linearities can be shifted away from harmful frequencies. Alternatively, small groups of magnets, typically ten, are ordered in such a way to minimize a broad band of non-linear driving terms computed to 2nd perturbative order, contributing to resonances up to order 12th. The first method is used in the LHC and the SSC, the last method is used for HERA and is still under investigation for the LHC.

Diffusion with steady state increase of the amplitude has never been detected in numerical simulations, even in presence of external tune modulation, contrary to what is usually observed with beam-beam interaction. Due to resonance crossing and non-linear coupling, migration of particles in the tune diagram and mixing of horizontal and vertical oscillations are well visible in long-term tracking results. However large increases in amplitude and particle losses are sudden and unpredictable, even if they occur after a large number of turns.

4. EXPERIMENTS

In the last decade, experiments have been devised to study the effect of high-order resonances under controlled conditions. The hope is that by comparing theoretical or numerical results with experimental ones, it may be possible to define suitable criteria for beam stability and evaluate their predictive power. This is an ambitious goal, since real machines are much more complicated than models used in tracking codes or analytical evaluations. There are many phenomena, like collective instabilities, synchro-betatron resonances, linear imperfections affecting the orbit functions, the linear coupling, the closed orbit, non-linear imperfections due to fringing fields and saturations, which may take a long time to be quantified in order to disentangle single-particle effects from measurements. However, analysis of operating situations provides a wealth of informations which can be exploited to bridge the gap between models and reality. These experiments have been performed in the CERN-SPS and the FNAL-TEVATRON which are already well understood, so that clear conditions could be defined, spurious effect eliminated and phenomena under study carefully isolated, with reasonably small effort. Having repeated similar

measurements in different accelerators is invaluable to help in distinguishing results of general interest from those which are just a property of the machine used. Common motivations of the two experiments are related to the refinement of aperture and field quality criteria for future large hadron accelerators, like LHC or SSC. A common procedure consists in exciting already existing sextupoles in order to introduce in a controlled fashion non-linearities in an otherwise linear lattice. To probe large amplitudes, a pencil beam with small emittance and momentum spread is used, to which a large enough coherent deflection is applied. In a few hundred turns, a 'hollow' distribution of charges is created around the central orbit due to nonlinear filamentation, whose behavior is observed with several instruments: current transformers record lifetime, Schottky noise detectors give tune and tune-spread, flying wires provide transverse profile, and orthogonal pairs of position monitors are able to produce a phase space portrait.

In the experiment E778 at FNAL[23], sextupoles were exciting strongly the third integer resonance together with the higher-order ones. Smear, injection efficiency and short-term dynamic aperture were measured and compared with tracking. The agreement is good, however long-term losses could not be quantitatively reproduced. The existence of stable nonlinear resonance islands was demonstrated experimentally by observing coherent persistent signals of particles captured into them. Tune modulation effects were explored and compared with those of 1-D forced pendulum.

In the experiments at the SPS[24], the sextupolar excitation chosen such as to minimize the third integer resonance. Detuning compensation was experimentally tested by using existing octupoles. A 30% increase of dynamic aperture resulted from a factor ten reduction of tune-spread. This provides experimental guidance in devising correction schemes for large hadron accelerators. However most of the emphasis was put on the study of slow diffusion induced by power supply ripple, and controlled modulation of a special quadrupole. The diffusion coefficient was measured as a function of the amplitude, the modulation frequency and depth, and the tune. It was obtained by scraping the beam tail with horizontal and vertical collimators, retracting them suddenly by a few mm, and observing the beam lifetime to estimate the time taken by the particles to fill the gap created by the retraction. Diffusion immediately sets in when tune modulation is turned on, and there is evidence that a ripple which leads to tune modulation of 10^{-3} cannot be tolerated in a machine with strong non-linearities. A tune modulation at two frequencies is more destructive than a modulation at a single frequency for the same overall depth. The agreement with numerical simulations is of the order of 20%, however the strong dependence of diffusion on modulation depth and the dependence on frequency are not yet understood.

Recent experiments at FNAL[25] have also addressed the problem of ripple induced diffusion. Intensity and transverse profile were recorded and used to deduce a phenomenological dependence of the diffusion coefficient on amplitude. The proposed model assumes a threshold amplitude, below which there is no diffusion, and above which the diffusion speed

increases as a polynomial of the amplitude. A steady reduction of beam size was pointed out which was never observed at the SPS. This is likely to be typical of the regime of large losses explored at FNAL.

The phenomenological model of FNAL for diffusion has been found to be in contradiction with some results of the CERN experiment as well as with the sudden manifestation of fast amplitude growth in tracking[26]. More general models of diffusion based on Markov process with jumps, using master equations on status transition probability are under investigation.

5. TRENDS

Studies of theoretical aspects of the LHC related to non-linearities are being pursued, to develop new tools for stability estimate, and to understand diffusion in 1-D and 2-D Hénon map models. However, the main tools to evaluate beam stability in the design lattice will continue to be tracking simulations and maps associated to Differential Algebra methods, whose potentiality seems to be far from being fully exploited. Experiments are likely to be vigorously pursued, to compare predictions with real world in a controlled fashion, and to clarify features of slow diffusion in presence of external modulation and non-linear fields.

6. REFERENCES

[1]   V.I. Arnold, "Mathematical Methods of Classical Mechanics", Springer-Verlag, 1978.
[2]   B.V. Chirikov, Physics Report 52 N. 5, p. 263 (1979).
[3]   M. Q. Hénon, Quarterly of Appl. Math. 27, 291 (1969).
[4]   E. Lohrmann, P. Wilhelm, Particle Acc. 19, p. 99 (1986).
[5]   H. Grote, C. Iselin, CERN/SL/90-13 (AP) Rev.2 (1991).
[6]   F. Schmidt, CERN/SL/AP 91-52 (1991).
[7]   M. Berz, Particle Acc. 24, 109 (1989).
[8]   A.Bazzani, et al., Il Nuovo Cimento, Vol. 102 B, N. 1 (1988).
      E. Forrest, J. Irwin, M. Berz, Particle Acc. 24, p. 91 (1989).
[9]   W. Scandale, et al., Particle Acc. 35, p. 53 (1991).
[10] R. Kleiss, F. Schmidt, F. Zimmermann, Particle Acc. Vol.41, N.2 (1993).
[11] A. M. Lyapunov, "Stability of Motion", Ac. Press (1966).
[12] F.Schmidt, F. Willeke, F. Zimmermann, Particle Acc. 35, p. 249 (1991).
[13] F. Zimmermann, Dipl. Thesis, DESY-HER.
[14] J.Irwin, Y. Yan, IEEE PAC 89, p. 1340 (1989).
[15] A. Chao et al., CERN 88-04, p. 152 (1988).
[16] F. Galluccio, F. Schmidt, EPAC 90, p.640 (1990).
[17] M. Bassetti et al., IEEE PAC 87, p. 1284 (1987).
[18] M. Giovannozzi, F.Schmidt, "General Normal Forms procedure to correct Tune-Shift and Non-Linear Chromaticity for Large Accelerators like the LHC", these proceedings.
[19] D. Neuffer, CERN 88-04, p. 179 (1988).
[20] Z. Guo, T. Risselada, W. Scandale, EPAC 92, p.637 (1992).
[21] Design Study of the LHC, CERN 91-03, p. 115 (1991).
[22] R. Gluckstern, S. Ohnuma, IEEE PAC 85, p. 2315 (1985).
      F. Willeke, DESY-HERA 87-12 (1987).
      W. Scandale, L. Wang, CERN SPS 89-41 (AMS) (1989).
[23] L. Merminga et al., IEEE PAC 89, p. 1429 (1989).
[24] D. Brandt et al., EPAC 90, p.1438 (1990),
      X. Altuna et al., CERN SL/91-41 (AP) (1991).
[25] T. Chen et al, Phys.Rev.Lett., Vol 68 N.1, p.33 (1992).
[26] A. Gerasimov, FERMILAB-Pub-92/185 (1992).

Emittance Growth in a
Low Energy Proton Beam

John A. Palkovic
Superconducting Supercollider Laboratory *
2550 Beckleymeade Avenue
Dallas, TX 75237

Abstract

We have measured emittances in a low energy proton beam at energies between 19 and 45 KeV and currents between 9 and 39 mA. The rms emittance of the space charge dominated proton beam, as measured by a moving-slit emittance probe, grew by an average amount of 60% in a propagation distance of 2.5 cm. An Abel inversion procedure was applied to the measured transverse charge distribution of the proton beam in order to calculate the electrostatic field energy, which is the driving quantity for emittance growth. We have found that all of the emittance growth is due to a halo containing $\simeq$ 10% of the beam particles.

I. INTRODUCTION

This paper is a report on an experimental investigation of space-charge driven emittance growth in a low-energy proton beam. The emittance[1] growth of a space charge dominated beam is given by a differential equation which relates the change of the emittance with z, the axial length coordinate, to changes in the field energy: [1]

$$\frac{d\epsilon^2}{dz} = -\frac{KX^2}{2}\frac{d}{dz}\left(\frac{U}{W_0}\right),\qquad(1)$$

where $U = W - W_u$ and W is given by

$$W = \pi\varepsilon_0\int_0^\infty rE_r^2 dr.\qquad(2)$$

Physically, W_u is the electrostatic field energy per unit length of a uniform beam with the same current and energy as the real beam. It is calculated from

$$W_u = W_0\left(1 + 4\ln(b/X)\right),\ b \geq X,\qquad(3)$$

where b is the radius of the (assumed present) beam pipe and $X = 2\sqrt{\overline{x^2}}$ is twice the width of the beam. $W_0 = (eN)^2/16\pi\varepsilon_0$ is the field energy within the uniform beam,

---

[1]The rms emittance of a beam is given by the formula

$$\epsilon_x = \frac{4}{p_z}\sqrt{\langle x^2\rangle\langle p_x^2\rangle - \langle xp_x\rangle^2}$$

where p_z is the average momentum of the particles in the direction of motion of the beam; x and p_x are a transverse displacement and momentum, respectively. With an azimuthally symmetric beam, $\epsilon_x = \epsilon_y = \epsilon$.
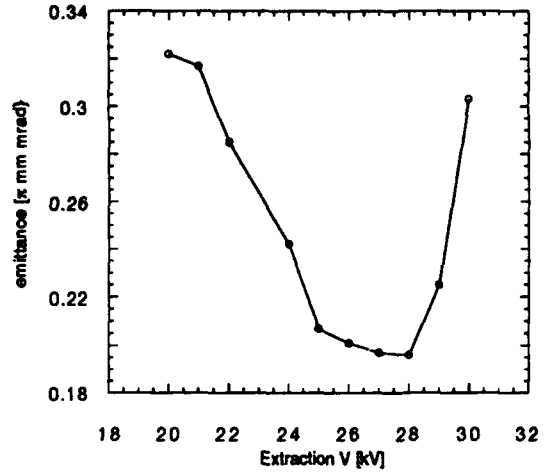
Figure 1. Emittance vs. extraction voltage.

with the logarithmic term giving the contribution from the field outside of the beam.

The proton beam was generated by a duoplasmatron which is capable of producing proton currents in excess of 100 mA. However, the peak current in the experiment was limited by the acceptance of the emittance probe to 30 mA or less. The primary diagnostic used in the experiment was the moving slit emittance probe. In addition, a toroidal current transformer and a Faraday cup were used for current measurement.

A set of measurements was done solely on the "young" beam immediately out of the ion source. The emittance seen out of the source depends on many factors — filament current, arc voltage, gas pressure, etc. A reproducible method of generating a beam with a given emittance was needed. It was found that for any setting of the ion source parameters used to produce extracted beam, there was a minimum value of emittance that was obtained as the extraction voltage was varied. This is shown in Fig. 1. The procedure to acquire data that was used for the emittance measurements was to change the ion source arc voltage and the accelerating voltage to produce a desired energy and current, then the extraction voltage was varied until a minimum emittance was found. This ensured that the beam was matched into the accelerating column.

By varying the extraction voltage, the shape of the "plasma emissive meniscus" from which the beam is extracted in the expansion cup of the duoplasmatron is changed. [2] This directly affects the angular distribution of

---

21

the emitted beam, as ions tend to leave along trajectories normal to the meniscus. Since the shape of the distribution function $f(x, x')$ is changed, the emittance changes.

II. ABEL INVERSION

As was mentioned above, the emittance growth of a space charge dominated beam is driven by the electrostatic field energy of the beam. Thus we are interested in calculating the electrostatic field energy from the measured distribution function of the beam. A necessary part of this process is the Abel inversion of the density profile. It is easy to extract the distribution $f(x)$ from the measured data. Since the beam is azimuthally symmetric, what is needed is $f(r)$. It is straightforward to calculate the electric field from $f(r)$ by solving Poisson's equation.

A moving-slit emittance probe measures the projection of the six-dimensional beam phase-space onto the transverse "trace-space" $x - x'$. [2] The intensity $I(x)$ of the integrated signal measured at a particular value of x, is given by

$$I(x) = \int_{-\infty}^{+\infty} f(r)dy. \tag{4}$$

Using the fact that x, y, and r are related by the Pythagorean theorem, dy can be expressed in terms of dr to yield

$$I(x) = 2 \int_{x}^{+\infty} \frac{rf(r)dr}{\sqrt{r^2 - x^2}}. \tag{5}$$

We say that $I(x)$ is the Abel transform of $f(r)$. This is an integral equation which must now be solved for $f(r)$, the quantity of physical interest. The solution can be written as [3]

$$f(r) = -\frac{1}{\pi} \int_{r}^{\infty} \frac{\left(\frac{dI}{dx}\right) dx}{\sqrt{x^2 - r^2}}. \tag{6}$$

The literature on the numerical evaluation of Eq. (6) is large. This form of the solution is not suitable for application to experimental data, for several reasons. There is a singularity in the integrand, and the evaluation of the derivative dI/dx tends to introduce large errors, since the intensity $I(x)$ is discretely sampled. Therefore, we would like to express the inverse transform in a different form. Also, real data has a noise component, which can be amplified by the inversion process, particularly for points near the origin. [4] It is desirable to remove the noise with a digital filter while processing the data.

It can be shown that the Fourier, Hankel, and Abel transforms form a set known as the FHA cycle; i.e., applying the Abel transform and then the Fourier transform to a function, we obtain the Hankel transform.[3] The Fourier and Hankel transform can be computed with fast Fourier transform (FFT) algorithms, thus decreasing the computation time required. [5]

We write the Fourier transform of Eq. (4) as

$$\mathcal{F}\{I(x)\} = \int_{-\infty}^{+\infty} \int_{-\infty}^{+\infty} f(r)exp(-i2\pi xq)dxdy \tag{7}$$

Using a standard identity from the theory of Bessel functions, Eq. (7) can be recast as

$$\mathcal{F}\{I(x)\} = 2\pi \int_{0}^{+\infty} rf(r)J_0(2\pi rq)dr \tag{8}$$

The right hand side of Eq. (8) is the Hankel transform of $f(r)$. The inverse Hankel transform is identical to the forward Hankel transform, hence Eq. (7) and (8) lead to

$$f(r) = 2\pi \int_{0}^{+\infty} qJ_0(2\pi rq) \int_{-\infty}^{+\infty} I(x)exp(-i2\pi xq)dxdq \tag{9}$$

Eq. (9) is the form which was used for the inversion of the experimental data. This result has several advantages over Eq. (6). There is no singularity in the integrand. The data can be filtered in the transform domain to smooth it. [6] Considering the baseband nature of the data, a low pass filter is appropriate. A filter with a bandwidth of 0.2 times the Nyquist frequency was used. This smoothing is an important part of the Abel inversion process. Without smoothing the output would contain noise which is the Abel transform of the input noise. The use of FFT routines increases the speed with which the calculations can be done on a computer, and the absence of the derivative in Eq. (9) removes a source of (numerical) uncertainty in the analysis.

Given the radial distribution function $f(r)$, we wish to calculate the field energy per unit length of the beam W, since that is the driving quantity for emittance growth. The radial electric field is easily calculated from Gauss' law; with the electric field determined, the field energy per unit length can be calculated from Eq. (2).

III. DATA INTERPRETATION

The result of an Abel inversion for a measured beam distribution is shown in Fig.(2). The high frequency noise evident in $I(x)$ is completely gone after Abel inversion to obtain $f(r)$. It has to be remembered that the uncertainty in $f(r)$ is largest near the origin of r when comparing the results of two inversions. [4] Since it is the product r and $f(r)$ which is integrated to obtain $E_r(r)$, the input noise does introduce uncertainty into W. This was born out in the experiments, which showed that W varied by $\pm 5\%$ over a set of 20 runs taken with identical ion source parameter settings.

The two most important quantities observed were the beam emittance and the electrostatic field energy of the beam distribution. We recall that it is the electrostatic field energy that drives the emittance growth. A total of 370 emittance was studied.

One observation that was made concerns the shape of the function $f(r)$. Emittance was measured at three different positions along the beam axis. We shall call them z_1, z_2, and z_3. At position z_1, we observed that the beam had a hollow shape. This is illustrated by the distribution in Fig. 3, which shows the result of the Abel inversion procedure for a single emittance run. This shape can be changed
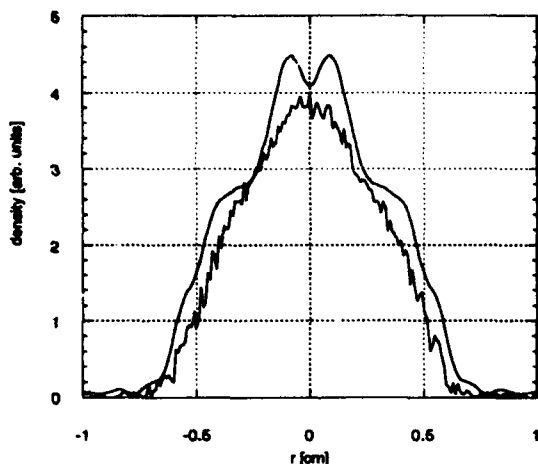
Figure 2. Input x density and inverted density $f(r)$ for 45 keV proton beam. The upper curve is the radial density, which is plotted with negative abscissa values for comparison.
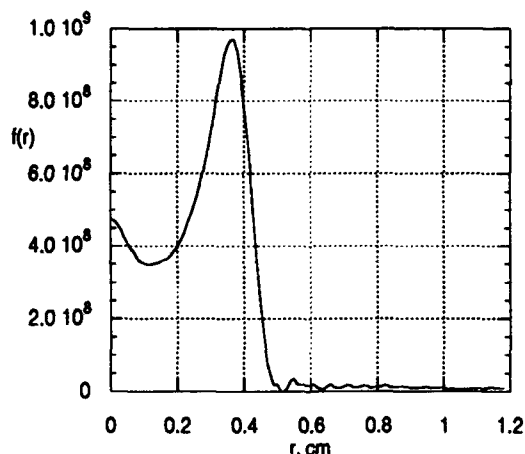
Figure 3. "Hollow" beam distribution from the z_1 position. The ordinate is in cm^{-3}.

somewhat by varying the ion source parameters. However, we found that the hollow shape was predominant at the z_1 position with the extraction optics tuned for minimum emittance as stated above.

When the emittance probe was moved out 5.9 cm to z_2, it was found that the beam was no longer hollow. It had assumed more of a flattened shape, with a "peak" in the middle, as in Fig. 4. As before, the figure corresponds to a single emittance run. Moving another 2.5 cm to position z_3, the beam has assumed an even more pronounced peaked shape in its distribution. This is shown in Fig. 5, which shows a typical beam. The interpretation is that the particles on the edge of the beam at position z_1 have moved into the region near the beam axis due to an inward component of radial velocity. Of course, the space charge of the beam also contributes to development of this shape,
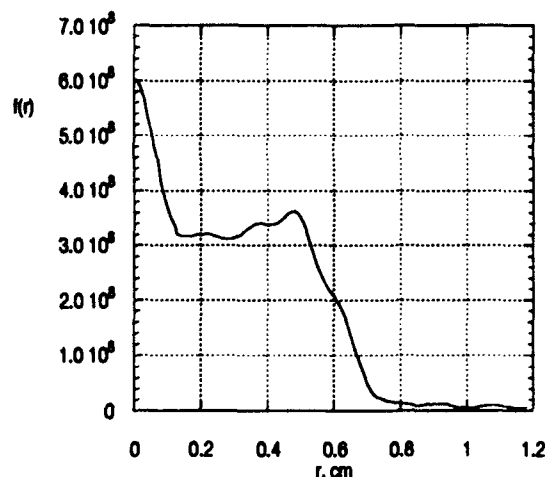
Figure 4. Sample beam distribution at the z_2 position.

although it is not easy to untangle the two contributions.

An important statement of the theory of space charge dominated beams is the equation of energy conservation given by

$$T + W = const. \tag{10}$$

where W is the field energy/unit length of the beam, defined above, and T is given by

$$T = p_z \left\langle x'^2 \right\rangle \left(\frac{I}{q}\right), \tag{11}$$

where $x' = p_x/p_z$. Eq. 11 is derived from a similar result in the literature. [7] Physically, T is the transverse kinetic energy per unit length of the beam. The two quantities T and W were tabulated for each emittance run. We find that the average value of $T + W$, as measured at the three longitudinal positions, is constant within the statistical spread in the data. The results, tabulated from all the data, are shown in Table III..

A correlation was found between the quantity U of Eq. (1) and the rms width of the beam. This is plotted in Fig. (6). This particular correlation was unexpected when first seen. This is perhaps the most striking relationship found in the data. We know of no satisfactory quantitative explanation for it. Qualitatively, the relationship seen is that the smaller beams have more nonlinear field energy. This quantity is strongly dependent on the shape of the distribution function. It is considered to be a property of the duoplasmatron. Although not shown on the graph, the points with the largest U values come mostly from the emittance measurements at position z_1, immediately outside the exit of the ion source.

Perhaps the most dramatic prediction of emittance growth theory is the large "explosive" growth of emittance that a beam experiences when injected into a uniform focusing channel. This growth is predicted to occur in a distance $\lambda_p/4 = m\omega_p/p_z$, where ω_p is the plasma frequency of the beam. [8] Several comments are appropriate before
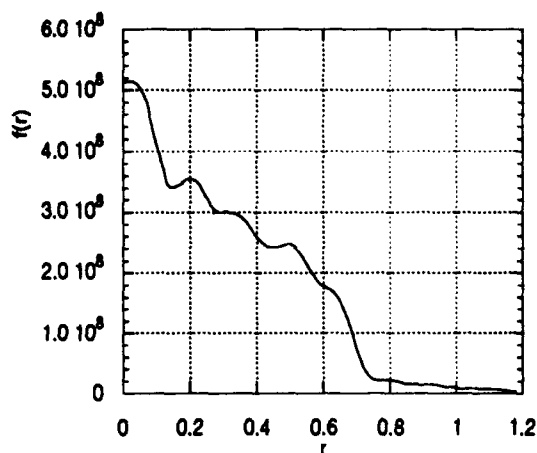
Figure 5. Sample beam distribution at the z_3 position.

Figure 6. Nonlinear field energy U (dimensionless) vs. rms beam size in cm.

Table 1
Field energy vs. position. T and W are measured in Joules/m.

$T + W$	z,cm
$(2.9 \pm 1.6) \times 10^{-6}$	0.0
$(5.1 \pm 3.2) \times 10^{-6}$	5.9
$(6.5 \pm 3.5) \times 10^{-6}$	8.4

we reach any conclusion on the nature of any such growth in the data presented here.

Rms fitting procedures suffer from a sensitivity to outliers; that is, a small subset of data points that are far from the mean can contribute a large amount to the rms value. In our case, these outliers came from electrical noise on the wires in the backplane of the emittance measuring apparatus. The effect of the noise on the rms emittance calculated from the measured beam data was to make the calculated rms emittance much larger than the true rms emittance of the beam. The outliers introduced by noise could increase the rms emittance by a factor of 2-4. Measurements taken with no beam incident on the probe indicated random noise voltages were present at the $V \leq 0.015$ Volt level. In order to eliminate this spurious contribution to the emittance, a cut was taken at the 0.015 volt level. It was seen that approximately 10% of the wire readings in a typical emittance run contribute to the calculation, the other 90% being noise since little or no beam was incident on these wires.

As was done with the field energy data, it is possible to tabulate the average rms emittances for the three positions at which emittance data was taken. This is shown in Table 1. There is no significant growth in the rms emittance as the beam propagates from z_1 to z_2, a distance of 5.9 cm. As the beam moves from z_2 to z_3, however, the average measured emittance has grown by a factor of 1.6. This certainly qualifies as a large, fast growth.

Figure 7. RMS emittance vs. fraction of beam removed.

The typical value of $\lambda_p/4$ for the beams measured was 13.3 cm. Simulations published in the literature often neglect the emittance of the initial beam, and also assume that the beam is subjected to an external force field. In addition, the initial distributions are idealized abstractions which do not completely simulate the charge distribution of a real beam. It is not clear how to relate this observation of emittance growth in a drifting beam to published emittance growth curves. It is plausible that the sharp growth seen is strongly dependent on the initial distribution.

We have found that almost all of the emittance growth is due to particles in the "halo" of the beam, i.e. particles which are positioned near the edge of the distribution in phase space. Fig. (7) is an illustration of this effect. This figure was produced by taking two sets of emittance runs and then increasing the level of the cut from the minimum level (0.015 volts) upward until there was no emittance growth evident at all. Then the fraction of beam removed is calculated. This is proportional to the volume of the

Table 1. RMS Emittance vs. position for low-energy proton beam

ϵ, $\pi mm - mrad$	z, cm
$0.98 \pm .31$	0.0
$1.02 \pm .32$	5.9
$1.60 \pm .15$	8.4

distribution that is removed, i.e. the change in the integral

$$V = \int \int f(x, x') dx dx'. \qquad (12)$$

We see that all of the emittance growth is due to the approximately 10% of the beam particles which are in the halo of the beam. In the core of the beam, the curve is flat. In the upper curve, which represents data from position z_3, a larger percentage of the beam has moved into the halo. This contributes significantly to the rms emittance.

IV. CONCLUSION

In conclusion, there has been much excellent theoretical work published in the field of low energy beam transport. We have performed some new measurements to test the most important aspect of the theory of emittance growth in a space charge dominated beam. The results obtained are not inconsistent with the theory. This is not surprising, since it is well founded in classical physics. We have found some new correlations which were not predicted by the theory.

It is a well known fact that emittance grows for almost any beam as it propagates through most any kind of transport line or accelerating structure. The dynamics of this process for a cold space charge dominated beam were predicted to show an explosive growth, and that has been observed. Another important prediction is the constancy of the field energy sum for a drifting beam, $T + W$. This is also verified, although not with high precision. We have found that the emittance growth observed is due entirely to particles in the halo of the beam. If a cut is taken in an emittance run data set which removes 10% of the beam particles, the emittance growth vanishes.

V. ACKNOWLEDGEMENT

VI. REFERENCES

[1] T.P. Wangler., K.R. Crandall, R.S. Mills, and M. Reiser, IEEE Trans. Nucl. Sci. **32**, 2196 (1985).

[2] C. Lejeuene. volume 13 C of *Advances in Electronics and Electron Physics*, pg. 207. Academic Press, 1980.

[3] R.N. Bracewell. *The Fourier Transform and Its Applications*. McGraw-Hill, New York, 1977.

[4] L.M. Smith. *IEEE Transactions on Information Theory*, **34**, 158, 1988.

[5] L.M. Smith. *Journal Quantum Spectroscopy and Radiation Transfer*, **39**, 367, 1988.

[6] J.F. Kaiser and W.A. Reed. *Review of Scientific Instruments*, **48**, 1447, 1977.

[7] I. Hoffman and J. Struckmeier. *Particle Accelerators*, **21**, 69, 1987.

[8] O.A. Anderson. *Particle Accelerators*, **21**,197, 1987.

Proton extraction from the CERN-SPS by a bent crystal

The RD22 Collaboration [1]
Presented by S. Weisz, CERN
CH 1211 - Geneva 23

Abstract

An experiment is being performed at the CERN-SPS to study the feasibility of extracting protons from the halo of a 120 GeV stored beam by means of planar channeling in a 8.5 mrad bent silicon monocrystal. Two different techniques have been used to bring the protons into the crystal. In one case a kicker magnet was repeatedly energized to displace particles up to 100 microns inside the crystal front face. In the other case a continuous flux of impinging particles was obtained by powering electrostatic plates with a white noise excitation. In both cases we observed an extracted beam of channeled particles. The detection was performed with several large size scintillators, a fluorescent screen, a scintillation hodoscope, and a pair of microstrip gas chambers. Extraction efficiencies of the order of 10% were measured.

I. INTRODUCTION

Planar channeling can occur when a proton beam is sent onto a monocrystal with an incident angle relative to the main crystalline planes smaller than a given critical angle [2]. The impinging particles are confined between the atomic planes and can eventually be deflected if the crystal is mechanically bent [3]. The main features of planar channeling are now well established from the theoretical point of view [4]:

- The critical angle Ψ_p varies with the beam momentum P as $1/\sqrt{P}$. The surface acceptance, which is the probability that incident particles within the critical angle get initially channeled, does not depend

- Multiple scattering on electrons can kick channeled particles out of the guiding potential. The dechanneling length is proportional to P in a straight crystal.

- The curvature of the bent crystal introduces additional losses due to centrifugal forces acting on particles when entering the curved region. The reduction of the deflection efficiency is function of the ratio P/R, where R is the bending radius.

Bending efficiencies of about 50%, with a deflection of 2.4 mrad, have been measured with 450 GeV protons channeled in a silicon crystal [5]. These results were obtained on a highly parallel external beam with an angular divergence of $\pm 3 \mu$rad, less than the critical angle for planar channeling at this energy $\Psi_p(450 \text{ GeV}) = \pm 7 \mu$rad. Extraction of 70 GeV protons from an internal circulating beam was reported with a much lower efficiency of about 1.5×10^{-4} [6].

It has been proposed to use the technique of crystal channeling to extract protons from the beam halo of both future multi-TeV colliders SSC [7] and LHC [8], allowing fixed target experiments to run in a parasitic mode. The main expected difficulty comes from a reduction of the channeling efficiency when the protons hit the crystal with small impact parameters and remain close to the surface where defaults of the crystalline structure can occur. One is also concerned about the alignment of the crystal relative to the circulating beam. The aim of the RD22 experiment [9] is to investigate these effects in the environment of a real accelerator. The experimental equipment was installed in the CERN-SPS and became operational by mid 1992.

II. EXPERIMENTAL LAYOUT

The experimental set-up, located in Straight Section 5 of the CERN-SPS, is shown schematically in Figure 1. The vacuum tank contains two silicon monocrystals, each 3 cm long, 1 cm high and 1.5 mm thick. Their upper and lower edges are clamped onto cylindrical formers to bend the crystal {110} lattice planes by 8.5 mrad. Each crystal is mounted on a goniometer which can move horizontally into the beam and which can provide angular adjustment with a resolution of up to 4 μrad. Four beam scrapers, three in the horizontal plane and one in the vertical plane, are used for a precise positioning of the beam. Protons are extracted in the horizontal plane, towards the centre of the ring. The deflected beam stays in the vacuum pipe for about 15 meters and exits through a 0.2 mm thick stainless steel window.

The three scintillators S1,S2 and S3 form a telescope to detect and count the extracted protons. The light outputs of scintillators S4 and S5 are attenuated to operate at high fluxes. S4 is in the extracted beam line while S5 is placed on the opposite side to monitor background. TV1 is a scintillating (Cesium Iodide) screen read by a CCD TV camera providing an immediate image of the extracted beam [10]. Hh and Hv are two hodoscope planes 32×32 mm^2, 1 mm pitch, to measure horizontal and vertical profiles. C1 and C2 are pairs of Micro Strip Gas Chambers (MSGC) [11], 25×25 mm^2, with horizontal and vertical strips (200 μm pitch), spaced by 1 meter. Their spatial resolution is better than 100 μm. They are used to measure the direction and profiles of the extracted beam. Counter S3, the hodoscope and the MSGCs are mounted on a movable table to follow the position of the extracted beam and account for the parallax between the two crystals.
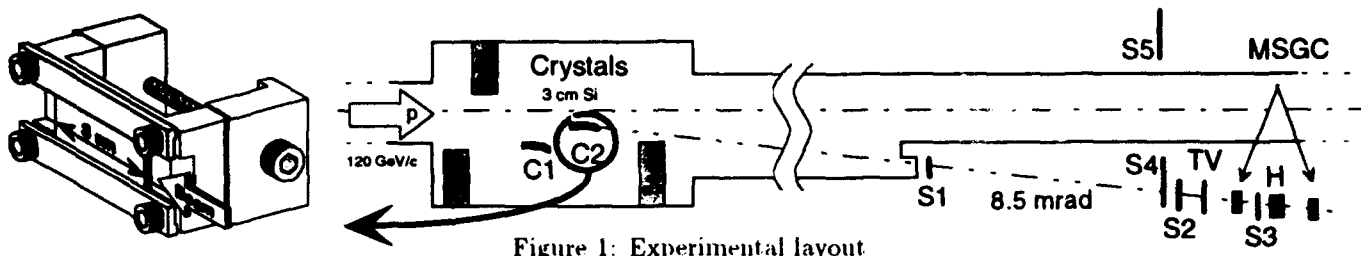
Figure 1: Experimental layout

III. KICK MODE

First evidence of extraction by crystal channeling with a circulating 120 Gev/c beam was obtained using the so called "kick mode". A fast kicker magnet was energized during one SPS revolution (23 μs) to displace horizontally the circulating beam about 100 μm at the crystal position. The inner edge of the crystal was 10 mm from the nominal closed orbit, about 3 σ of the beam size after emittance blow up, so that only a very small fraction ($\sim 10^{-4}$) of the stored protons could hit the crystal at each kick. The horizontal β function was 90 m at the crystal location, leading to an horizontal angular spread of 1.1 μrad for the proton trajectories when they first enter the crystal. This is much less than the critical channeling angle $\Psi_p(120$ GeV$)$ = $\pm 14\mu$rad. The time between two consecutive kicks was long enough for the beam filamentation to refill the originally available phase space.
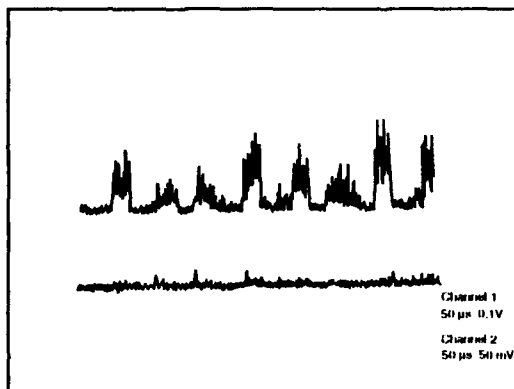
Figure 2: Extraction signal in "kick mode"

A clear signal synchronised with the kicker magnet excitation was observed in the S4 counter after angular adjustment of the crystal (upper trace of Figure 2). The toothed pattern results from the betatron motion of the proton beam which is successively displaced towards the crystal or away from it. The lower trace of Figure 2 shows the S5 counter which essentially recorded particles produced by nuclear interaction in the crystal. The amplitude of both traces were about equal when the crystal was not aligned and no channeling occurred.

IV. CONTINUOUS EXTRACTION

The continuous extraction was achieved by exciting an electrostatic deflector with amplitude tunable white noise. Each circulating proton received a small random horizontal

kick when passing between the electrodes of the deflector, and the global effect was a continuous blow-up of the horizontal emittance of the beam. Under these conditions, the crystal received protons in a steady-state regime with impact parameters in the micron range. The hodoscope counting rate as a function of the crystal tilt angle is shown on Figure 3.
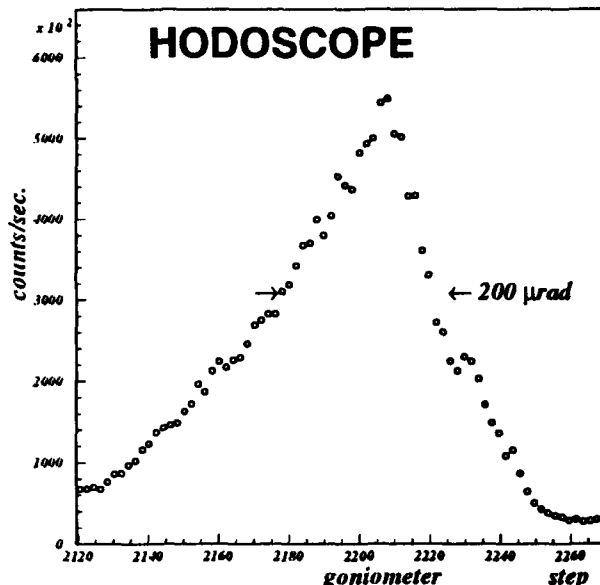
Figure 3: Hodoscope response versus crystal tilt

The distribution has a σ of $\sim 90\mu$rad, much larger than the channeling acceptance expected from the critical angle Ψ_p. The peak position corresponds to the same goniometer setting as the one that gave the maximum signal of channeled protons in the kick mode.

Our present understanding of the large angular response curve is the following: The clamping of the crystal on its bender introduces stresses and the crystal curvature is not perfectly uniform. An X-ray survey of the crystal surface, prior to its installation on the CERN-SPS, indicated that the orientation of the crystalline planes varies at the entrance and exit edges as one departs from the middle plane. By displacing the beam vertically along the crystal entrance face, we observed a shift of the peak position of the angular response curve as shown on Figure 4.

The extracted beam was observed on the TV screen and recorded by the hodoscope and the MSGCs. The horizontal profile obtained with the hodoscope is displayed on Figure 5. The width of the distribution corresponds to a beam divergence of $\sigma \sim 40\mu$rad at the crystal exit, again larger than the critical angle Ψ_p that one would expect.
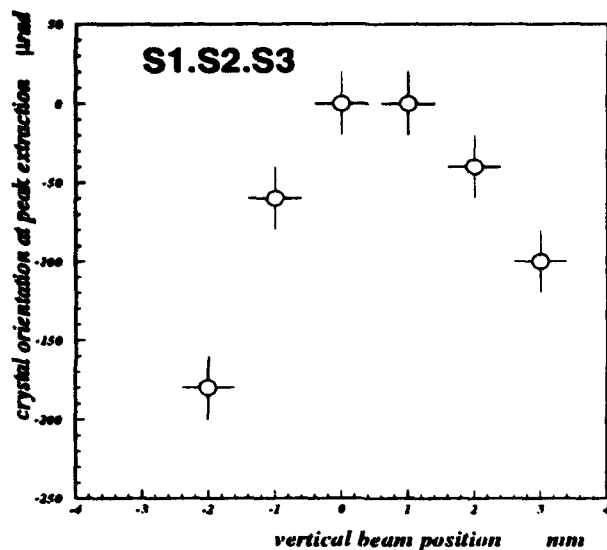
Figure 4: Peak position versus beam height
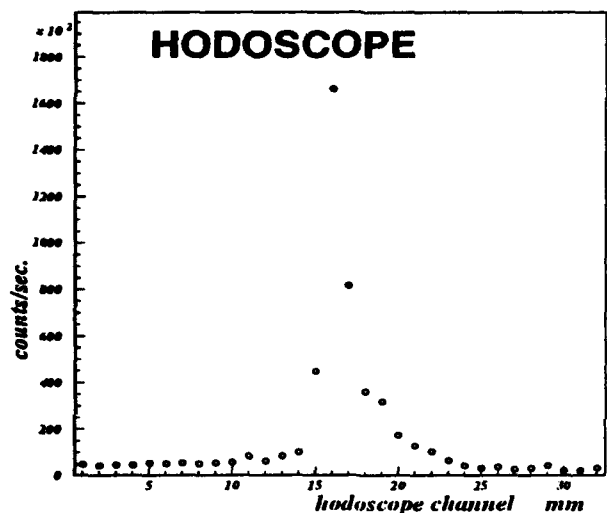
Figure 5: Horizontal profile of extracted beam

The extraction efficiency is defined as the ratio of extracted protons to the number of protons initially hitting the crystal. The number of extracted protons was deduced from the counting rates in S1,S2 and S3 while the fraction of the beam hitting the crystal was constantly monitored through the beam lifetime measurement.

Sample	Crystal 1	Crystal 2
Protons on Crystal (Hz)	$6.7 \ 10^6$	$10. \ 10^6$
$S1 \cdot S2 \cdot S3$ rate (Hz)	$.61 \ 10^6$	$.74 \ 10^6$
Background rate (Hz)	$.27 \ 10^5$	$.39 \ 10^5$
Efficiency	$12 \pm 3 \ \%$	$10 \pm 3 \ \%$

Table 1: Extraction Efficiencies

The S1·S2·S3 acceptance is limited by S3 and defined a $1.9 \ 10^{-6}$ Steradian solid angle containing the extracted beam. The background was estimated in the surrounding $6.9 \ 10^{-6}$ Steradian still covered by the S1·S2 coincidence. With conservative counter efficiencies of $90\pm10\%$, one gets the extraction efficiencies of Table 1.

V. CONCLUSIONS AND PROSPECTS

Stable continuous proton extraction from the periphery of a 120 GeV/c beam circulating in the CERN-SPS was achieved by means of particle channeling in a bent silicon monocrystal. The intensity of the extracted beam could be controlled by the strength of the excitation used to blow up the horizontal emittance. We tested successively 2 crystals and extraction efficiencies of $\sim$ 10% were measured with both samples.

Large widths were observed for both the channeling acceptance and the deflected beam. Mechanical distortions of the crystals could explain the effects and we will investigate the problem using different bending devices during the course of 1993.

We wish to thank the Beam Transfer, the Beam Instrumentation and the Operation groups of the CERN SL Division for their help.

VI. REFERENCES

[1] The RD22 Collaboration: H. Akbari[2], R. Bellazzini[5], A. Brez[5], M.P. Bussa[7], L. Busso[7], A. Calcaterra[3], G. Carboni[5], F. Costantini[5], R. De Sangro[3], K. Elsener[2], G. Ferioli[2], F. Ferroni[6], G. Fidecaro[2], M. Gyr[2], W. Herr[2], A. Hilaire[2], J. Klem[2], L. Lanceri[8], M.M. Massai[5], S.P. Moller[1], S. Morganti[6], O. Palamara[4], R. Santacesaria[6], W. Scandale[2], R. Schmidt[2], F. Tosello[7], E. Uggerhoj[1], B. Vetterman[2], E. Weisse[2], S. Weisz[2],
[1]ISA, University of Aarhus, Aarhus, Denmark
[2]CERN, Geneva, Switzerland
[3]Laboratori Nazionali di Frascati, Frascati, Italy
[4]Università di Lecce and INFN, Lecce, Italy
[5]Università di Pisa and INFN, Pisa, Italy
[6]Università 'La Sapienza' and INFN, Roma, Italy
[7]Università di Torino and INFN, Torino, Italy
[8]Università di Trieste and INFN, Trieste, Italy

[2] J. Lindhard, Kgl. Danske Vid. Selsk. Mat. Fys. Medd. 34 no. 14 (1964).

[3] J.A. Ellison, Nucl. Phys. B206 (1982), 205.

[4] See e.g. Relativistic Channeling, NATO ASI Vol. 165, eds. R.A. Carrigan jr. and J.A. Ellison (Plenum Press, 1986).

[5] K. Elsener et al., "High efficiency beam deflection by planar channeling in bent silicon crystals", this conference.

[6] A.A. Asseev et al., EPAC Proceedings (1992), 1493.

[7] The SFT collaboration,"An expression of Interest in a Super Fixed Target Beauty Facility (SFT) at the Superconducting Super Collider", Fermi-Lab (1990).

[8] W. Scandale,"Experimental Insertion for the LHC" in: Large Hadron Collider Workshop (1990), CERN 90-10, ECFA 90-133, Vol III p 760.
The LHB Collaboration, 'Measurement of CP violation in B-decays using an extracted beam', Proceeding of the Meeting on LHC Physics and Detectors (1992).

[9] B.N. Jensen et al.,"Proposal to test the beam extraction by crystal channeling at the SPS: a first step towards a LHC extracted beam", CERN/DRDC 91-25, DRDC/P29.

[10] J. Bosser et al., PAC Proceedings (1987), 732.

[11] F. Angelini et al., NP 23A (1991), 254.

Longitudinal Tracking with Phase and Amplitude Modulated RF *

D.D. Caussyn[a], M. Ball[a], B. Brabson[a], J. Budnick[a], A. W. Chao[b], J. Collins[a],
V. Derenchuk[a], S. Dutt[b], G. East[a], M. Ellison[a], T. Ellison[a], D. Friesel[a], B. Hamilton[a],
H. Huang[a], W.P. Jones[a], S.Y. Lee[a], D. Li[a], M.G. Minty[c], S. Nagaitsev[a], K.Y. Ng[e],
X. Pei[a], T. Sloan[a], M. Syphers[b], Y. Wang[a], Y.T. Yan[b], P.L. Zhang[b]

Abstract

Synchrotron motion was induced by phase shifting the rf of the Indiana University Cyclotron Facility (IUCF) cooler-synchrotron. The resulting coherent-bunch motion was tracked in longitudinal phase space for as many as 700 000 turns, or for over 350 synchrotron oscillations. Results of recent experimental studies of longitudinal motion in which the rf phase and amplitude were harmonically modulated are also presented. Comparisons of experimental data with numerical simulations, assuming independent particle motion, are made. Observed multiparticle effects are also discussed.

I. Introduction

The IUCF cooler storage ring and synchrotron accelerator was the first of many similar accelerator storage rings designed specifically to employ electron cooling to produce and use high quality medium energy ion beams for nuclear research [1]. This machine has also been a near ideal laboratory for conducting accelerator physics experiments. For a beam of 45 MeV protons the equilibrium 95% emittance or phase space area is about 0.3π mm mrad with a relative momentum spread full width at half maximum, FWHM, of about 0.0001. The motion of a beam bunch with this small an emittance can closely simulate single particle motion. Several experiments studying transverse motion near betatron resonances[2] have demonstrated this advantage. In the last year, we have applied many of the same techniques for studying transverse motion on a turn-by-turn basis to a study of longitudinal motion, some of which has been reported previously [3].

Since its discovery in 1945 by McMillan and Veksler[4] synchrotron motion has come to be relatively well understood. For a system with time-independent system parameters, the difference equations describing the longitudinal motion are

$$\delta_{n+1} = \delta_n + \frac{eV}{\beta^2 E}(\sin\phi_n - \sin\phi_0) - 2\alpha\delta_n \quad (1)$$

$$\phi_{n+1} = \phi_n + 2\pi h\eta\delta_{n+1}, \quad (2)$$

where δ is the fractional momentum deviation of a particle from that of a synchronous particle, and ϕ is the phase of the particle relative to the rf, with the subscripts on these variables indicating the turn number. In addition, η is the phase slip factor, ϕ_0 is the phase of a synchronous particle, which for a stored beam is 0 deg, h is the harmonic number, α is the damping coefficient, V is the rf voltage, e is the particle's charge, E is the particle's total energy, and β is the usual relativistic factor.

Assuming that the system is not dissipative, these difference equations can be approximated by the differential equations of motion which can be found from the Hamiltonian H given by

$$H = \frac{1}{2}h\omega_0\eta\delta^2 + \frac{eV\omega_0}{2\pi\beta^2 E}[(\cos\phi - \cos\phi_0 + (\phi - \phi_0)\sin\phi_0)]$$

where ω_0 is the particle revolution frequency. While the difference equations provide a more exact description of the motion, Hamiltonian mechanics can be useful for gaining insight on the motion. Even when the beam is electron cooled, the damping is small enough that the approximations in using Hamiltonian mechanics still result in a reasonable description of the motion.

We have experimentally tracked the beam in ten-turn intervals, and made comparisons of the observed motion with the theory. The response of the beam due to modulating the phase and the voltage of the rf, was also easily measured using the same techniques.

II. Procedure and Results

The experiment began with a beam bunch stored in the IUCF cooler ring having about 3×10^8 protons with kinetic energy of about 45 MeV. The IUCF cooler ring has a circumference of 86.82 m, η was about -0.86, and we were using an rf system with a frequency of 1.03148 MHz with a harmonic number h of one. The beam bunch was about 60 ns (or 5.4 m) FWHM. The beam was injected into the cooler ring in a 10 s cycle, with injection and electron cooling being completed within the first 5 s.

Since measurements of longitudinal motion were being made, the phase lock feedback loop for the rf, which is normally on, was switched off. Phase shifting and phase modulation of the beam relative to the rf was achieved by phase shifting or modulating the rf control signal. The rf cavity had a Q value of about 40 at a frequency of 1 MHz, with a resulting half-power bandwidth of 25 kHz so the response to a step phase shift occurs in about 40 turns, which is relatively short compared to the shortest synchrotron period used of about 1920 turns.

The phase of the beam was determined from the relative phase between the signal from a pickup coil in the rf cavity,
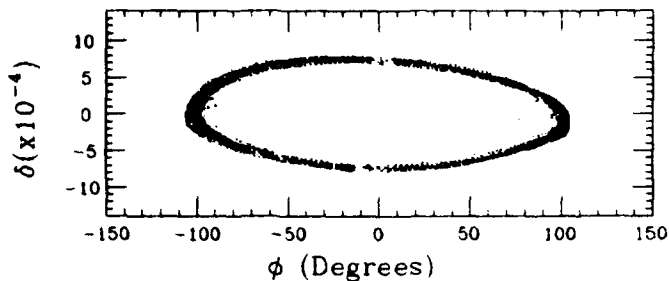
Figure 1: A longitudinal phase space plot after inducing a synchrotron oscillation by making a sudden shift in the rf phase. The asymmetry observed here is due to a defect in the phase detector used.

Figure 2: A plot of the measured beam response to phase modulation for two different phase modulation amplitudes. The solid lines are the results from a numerical simulation using Eqs. 1 and 2.

Figure 3: A plot showing the ϕ signal on a digital oscilloscope. The upper trace is with the electron-cooling "on", and the lower trace is with the cooling "off".

and the sum signal from a beam position monitor (BPM) after it had been passed through a 1.4 MHz low pass filter. The work being reported here was conducted over a period of time in which three different types of phase detectors [5] were used. The first two phase detectors had either an inadequate range of operation, or an uneven response over its full range. Our final phase detector had a range of 720 deg and replaced the first two.

The momentum deviation of the beam was found from the deviation of the beam from the closed orbit Δx_{co} measured by a BPM in a region of high dispersion D_s. The fractional momentum deviation δ, could then be found from $\delta = \Delta x_{co}/D_s$ where D_s was measured to be 3.9 m. The position signal was passed through a 3 kHz low pass filter to remove the effects of any coherent betatron oscillations.

Both the δ and phase signals were digitized using our data aquisition system which has been described elsewhere[2]. As many as 16384 points were digitized in time intervals which were integer multiples of the beam revolution period. A typical measurement of the longitudinal phase space variables after inducing a synchrotron oscillation is shown in Fig. 1 as a Poincaré plot, where every tenth turn is plotted. Similar data was taken for induced synchrotron oscillations having initial phase amplitudes in the range from 10 to 150 deg measured in fifty-turn intervals. The synchrotron tune ν_s, which is the ratio of the synchrotron frequency to the revolution frequency, was determined for each case from a fast-Fourier transform (FFT), or from a measurement of the synchrotron period and was found to shift with amplitude as expected from theory[3]. This data was also used to estimate the damping time for the synchrotron oscillation due to the electron cooling. The $1/e$ damping time was found to be about 400 ms, which corresponds to a value of α in Eq.(1) of about 2.5×10^{-6}.

The longitudinal response of the beam to forced phase oscillations was also studied. In this case an additional term $\Delta\phi_{rf}$ must be included in Eq. (2) where $\Delta\phi_{rf} = a(\sin\omega_m t_{n+1} - \sin\omega_m t_n)$ with a the phase modulation amplitude, ω_m the angular frequency of the rf phase modulation, and t_n and t_{n+1} the beam arrival times at the rf
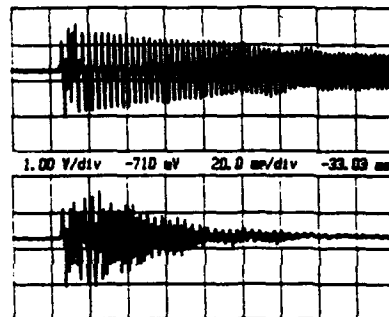
cavity, which are approximately multiples of the revolution period for a synchronous particle. Experimentally this was accomplished by modulating the phase of the rf with various a and ω_m. The transient response was then measured.

The amplitude response A_m was found by measuring the peak phase amplitude and normalizing it by dividing by a. The frequency response was characterized by measuring the beat period T_m of the phase signal. In Fig. 2, the measured responses as a function of phase modulation frequency are plotted for two different phase modulation amplitudes. The synchrotron frequency was about 536 Hz in this case. The sudden transition from the lower stable solution to the upper stable solution near a frequency called the bifurcation frequency is evident in this figure[3, 6]. This is a characteristic shared by many other parametric resonant systems[7].

An interesting aspect of these measurements was the relative insignificance of decoherence when the electron cooling was optimized. In Fig. 3, the phase amplitude as a function of time is shown for two cases where the applied phase shift was about 150 deg. In the first case the electron energy was optimized to maximize cooling. In the
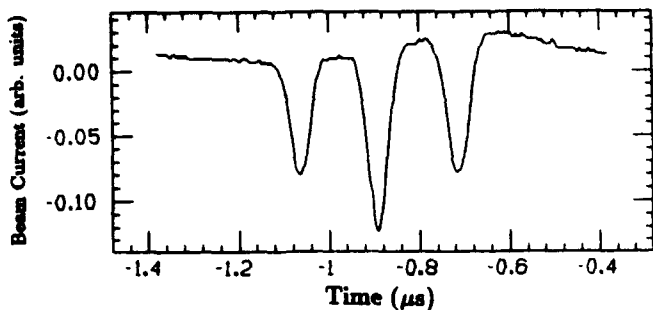
Figure 4: Equilibrium bunch shape for 5% voltage modulation where ν_m is 4.75×10^{-4}.

Figure 5: Beam response for 5% voltage modulation.

second case, the electron energy was shifted 20 ms prior to the start of the measurement so that electron cooling would be negligible (the electron velocity was shifted by about 0.5%). Note that the damping of the coherent signal due to decoherence in the absence of electron cooling is relatively rapid.

The response of the beam to rf voltage modulation was also investigated. At this time, we chose to study the equilibrium or steady-state response of the beam after the transient had time to damp out. Experimentally, this was accomplished by modulating the reference voltage in the automatic level control (ALC) circuit for the rf voltage by some fractional amount ϵ. The motion in this case is described by the difference equations after multiplying V in Eq.(1) by $1 - \epsilon \sin \omega_m t$. The revolution frequency in this case was 1.03168 MHz and the small amplitude synchrotron tune ν_{s_0} (without voltage modulation) was 2.55×10^{-4}.

We found that when the beam was allowed to reach equilibrium, it frequently split into multiple bunches in a process that could take several seconds to occur. It was also observed that the degree to which this occurred depended on the beam current. In Fig. 4, the BPM sum signal trace from a fast digital oscilloscope is shown for a modulation tune of 4.75×10^{-4} with the rf voltage modulated by 5%. By making an appropriate canonical transformation to a rotating reference frame, Hamiltonian methods reveal that the particles accumulated at the locations of stable fixed points (SFP) in this rotating reference frame[8].

Since the various phase detectors we employed were not intended for use with multiple bunches, we used an oscilloscope to measure the peak phase amplitude for the response. The measured responses, as maximum phase, are plotted in Fig. 5. The large responses were obtained by starting the voltage modulation at injection where the beam occupies a larger amount of phase space. The gap in the measured response for ν_m from 4.91×10^{-4} to 5.02×10^{-4} occurred due to the small separation of the SFP's compared to the full width of the particle distribution of about 40 deg. For ν_m above about 5.02×10^{-4}, the response could again be determined since the SFP at the origin becomes an unstable fixed point (UFP), producing a greater separation between the remaining SFP's. The
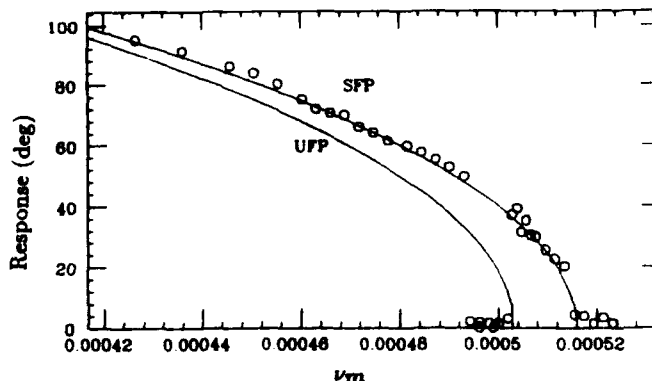
solid lines in Fig. 5 correspond to the maximum phases of the observed SFP's and of a nearby UFP[8].

III. Conclusions

We have found that the experimental techniques used for turn-by-turn tracking in studying transverse motion are equally effective for studying single-particle longitudinal motion, at least in the case of transient motion. The steady-state motion was somewhat more difficult to study. In this case, the beam bunch may separate into two or more bunches within an rf bucket. Phase space tracking of individual bunches then becomes difficult. Multiparticle aspects of the motion we have observed are interesting in their own right. The rate at which the bunch splitting occurs, the dependence of the amount of beam accumulating at each SFP on the beam current, and the relationship between decoherence and electron cooling may be of practical interest in schemes in which these effects are to be used for slow particle extraction, or in trying to understand bunch diffusion.

References

[1] R.E. Pollock, *Proc. 1989 IEEE P.A.C., Acc. Eng. and Tech.*, Chicago, IL, p. 17; D.L. Friesel, T.J. Ellison, and P. Schwandt, *Nucl. Inst. Meth.* B40/41 927 (1989); Timothy JP Ellison, Dennis L. Friesel, and Robert J. Brown, ibid, pp. 633–635; T. Ellison, "Electron Cooling", Indiana University, Bloomington, Indiana, Ph.D. Dissertation, 1990 (unpublished).

[2] S.Y. Lee, et al., Phys. Rev. Lett. 67, 3768 (1991); D.D. Caussyn, et al., Phys. Rev. A 46, 7942 (1992).

[3] M. Ellison, et al., Phys. Rev. Lett., Phys. Rev. Lett. 70 591, (1993).

[4] E.M. McMillan, Phys. Rev., 68, 143 (1945); V.I. Veksler, Compt. Rend. Acad. Sci. U.S.S.R., 43, 329 (1944); ibid. 44, 365 (1944).

[5] Roland E. Best, *Phase Locked Loops, Theory, Design, and Applications* (McGraw-Hill, 1984) pp. 7-9.

[6] H. Huang, et al., to be published.

[7] D.D'Humieres, M.R. Beasley, B.A. Huberman, and Libchaber, Phys. Rev. A 26, 3483 (1982).

[8] D. Li, et al., to be published.

31

Measurement of Spin Motions in a Storage Ring Outside the Stable Polarization Direction[*]

N. Akchurin[(1)], L. Badano[(2)], A. Bravar[(1,3)], M. Conte[(2)], J. Hall[(4)], H. Kreiser[(9)],
J. McPherson[(1)], F. Olchowski[(1)], Y. Onel[(1)], A. Penso[(3)], A. Pisent[(5)],
M. Pusterla[(6)], T. Rinckel[(7)], R. Rossmanith[(8)]

[(1)] Department of Physics, University of Iowa, Iowa City, IA 52242, USA

[(2)] Dipartimento di Fisica dell'Universita di Genova, INFN Sezione di Genova,
Via Dodecaneso 33, I-16146 Genova, Italy

[(3)] INFN Sezione di Trieste, Via Valerio 2, I-34127 Trieste, Italy

[(4)] University of New Mexico, Albuquerque, New Mexico, USA

[(5)] INFN LNL, Via Roma 4, 35020 Legnaro (PD), Italy

[(6)] Dipartimento di Fisica dell'Universita di Padova, INFN Sezione die Padova
Via Marzolo 8, I-35131 Padova, Italy

[(7)] IUCF, 2401 Milo B. Sampson Lane, Bloomington, Indiana 47408, USA

[(8)] CEBAF, 12000 Jefferson Ave., Newport News, Virginia 23606, USA

[(9)] I. Inst. fuer Experimentalphysik, Luruper Chaussee 149, D-2000 Hamburg 52, Germany

Abstract

Polarized, stored beams are becoming a more and more important tool in nuclear and high energy physics. In order to measure the beam polarization in a storage ring the polarization vector of the stored beam has to aim, revolution for revolution, over a period of seconds to minutes, into the same, so-called "stable", direction. In this paper measurements at the Indiana University Cooler Ring (IUCF) are described in which for the first time in a storage ring oscillations of the polarization vector around this stable direction have been measured [1]. The existence and the dynamics of such oscillations are, for instance, important for a new proposed technique for polarising stored hadron beams [2].

I. INTRODUCTION

The behaviour of polarized beams was studied both in electron-positron storage rings [3,4] and proton storage rings [5].

The theoretical description of the polarization in these storage rings is mainly based on a formalism introduced by Derbenev and Kondratenko [6] and later by Chao [7]. The basic concept is the following: all the trajectories in a storage ring can be calculated relative to the closed orbit, a (fictive) trajectory, which repeats itself from one revolution to another. The behaviour of the polarization can be calculated in a similar way. A polarization vector is found along this closed orbit which also repeats itself from one revolution to another. This vector is called n-axis.

The thinking in terms of an ever-recurring polarization direction is highly supported by the polarimetry used in storage rings. In order to measure polarisation with sufficient accuracy, the measurements have to be performed over several seconds or minutes [8].

In this paper the first measurements on the stability of time-varying spin components are reported. The practical importance of an oscillating polarisation is described somewhere else [2,9]. The measurements were performed at the Cooler Ring of the Indiana University Cyclotron Facility (IUCF) in Bloomington, Indiana. Recently a Siberian Snake was installed in this ring for demonstration purposes [5]. The snake consists of a solenoid which rotates the polarisation by 180 degrees around the momentum axis and skew quadrupoles. The skew quadrupoles are located on each side of the solenoid. The authors of this paper used this Snake, the existing polarised source and the existing polarimeter [10] to measure time-dependent spin motions.

II. THE STABLE SPIN DIRECTION

Particle and spin motion are related to each other. When the particle is deflected by an angle α around a certain axis its spin is rotated around this axis by an angle ψ:

$$\frac{g-2}{2}\gamma\alpha = G\gamma\alpha = \psi \qquad (1)$$

where g is the proton g factor and γ the Lorentz factor. The numerical value of G is 1.7928. Equation (1) is a direct consequence of the well known BMT-equation on the behaviour of the spin $\vec{S}$ in a magnetic field [11]:

$$\frac{d\vec{S}}{dt} = \frac{e}{\gamma m}\vec{S} \times [(1+G\gamma)\vec{B}_\perp + (1+G)\vec{B}_\parallel] \qquad (2)$$

For the experiment an energy was chosen in which the spin performs two revolutions during one revolution of the beam: $G\gamma = 2$. For a machine consisting only of bending magnets the energy corresponding to $G\gamma = 2$ is 108.4 MeV. A more careful analysis [5,12] showed that the solenoid of the cooler also contributes to the spin tune and the correct energy for $G\gamma = 2$ is 106.2 MeV. The solenoid of the Siberian Snake rotates the spin around the momentum axis by an angle of 180 degrees. The required field strength for a 180 degree rotation can be derived from equation (2).

The n-axis of a machine with a Siberian Snake can be derived from fig. 1.
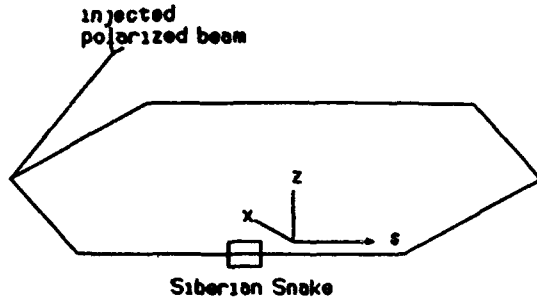
Fig. 1 The coordinate system. A spin manipulation system in the injector channel allows the injection of the beam in any polarisation direction. For the experiment a polarisation vector parallel to the vertical direction was chosen.

Using the coordinate system [x,s,z] def..ed in this figure and choosing $\psi(s)=0$ at the snake, the n-axis is

$$\vec{n} = (\sin(\psi(s)), \cos(\psi(s), 0) \qquad (3)$$

s is the path length of the trajectory and $\psi(s)$ is the spin precession angle. The spin rotation only takes place in the bending magnets. The expression $\psi(s)$ describes the non-uniform spin advance in the machine.

III. THE EXPERIMENT

A beam polarised along the s-axis is injected into the storage ring. The beam is cooled by an electron beam and stored for circa 10 seconds. After this time, the beam is directed towards the target of the polarimeter [10]. The target is a 4.5 mm thick graphite slab. The transverse tail of the bunch is scattered. During the next revolutions the center of the beam is brought gradually closer to the target until the whole beam intercepts with the target (fig. 2). Afterwards a new beam is injected and the measurement is repeated.

According to equation (3) the n-axis of the ring with the Snake is in the horisontal plane. The polarisation $\vec{P}$ of the injected vertically polarised beam oscillates therefore around the n-axis:

$$\vec{P} = P_0 (0, 0, (-1)^m) \qquad (4)$$

where m is the number of revolutions. For a moment energy oscillations are neglected.

A standard polarimeter integrating over many revolutions would find that the beam is unpolarized: in the time average the vertical spin direction cancels. In order to measure this time varying polarisation the polarimeter has to be gated in such a way that data are taken only

every second revolution (fig. 2). The gate is opened every second revolution for half a revolution. If there is no depolarisation, the polarimeter should measure a vertical polarisation.
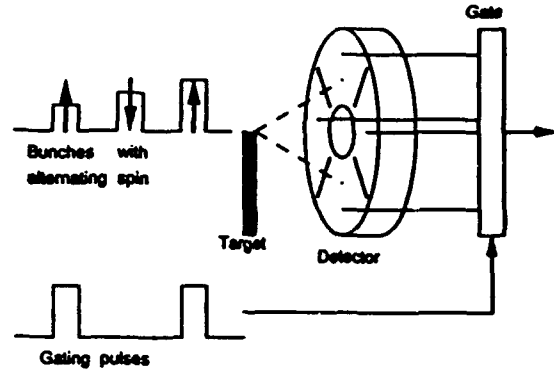
Fig. 2 The polarimeter and the gating system. The beam is directed to a carbon target and the asymmetry in the distribution of the scattered particles is measured [10]. Both the horizontal and the vertical polarisation are measured at the same time. The polarimeter is gated in such a way that data are taken every second revolution.

Synchrotron oscillations are energy oscillations around the nominal energy.

$$\left(\frac{\Delta\gamma}{\gamma}\right) = \left(\frac{\Delta\gamma}{\gamma}\right)_0 \sin(\omega_s t + \delta) \qquad (5)$$

where ω_s is the synchrotron frequency. Although the energy deviations are small these oscillations change the measurement in the following way:

The spin rotation in the solenoid for particles with energy deviation is no longer 180 degrees. Particles with higher (lower) energies then the nominal energy are rotated less (more) than 180 degrees according to equation (2).

This effect changes the results of the measurements significantly. Due to the energy oscillations the spin deviates from the vertical axis by

$$u = \frac{1}{n} \sum_n \sin(2\pi n + A \sin(2n\omega_s t_0 + \delta)) \qquad (6)$$

when the polarimeter only takes data every second revolution. t_0 is the revolution time and A is a measure for the magnitude of the energy deviations. As a result the energy oscillations reduce the degree of the measurable polarisation. The degree of reduction depends on the magnitudes of A and ω_s. The degree of the measurable polarisation increases with ω_s.

In the following the rotation angle of the solenoid is changed from 180 degrees to $180 + \beta/2$ degrees. For the same measurement as before, equation (6) has to be rewritten in the following way

$$u(\beta) = \frac{1}{n} \sum_n \sin(2\pi n + n\beta + A \sin(2n\omega_s t_0 + \delta)) \qquad (7)$$

33

β is changed by changing the current through the solenoid.

In fig. 3 the polarisation $u(\beta)$ is plotted as a function of β (=solenoid current). A current of 145.5 A corresponds to a spin rotation of 180 degrees. A lower current means less than 180 degrees rotation and a higher current more than 180 degrees rotation. It was assumed that the original polarisation of the injected beam was 80% parallel to the vertical direction (as in the experiment). The distance between the center frequency and the two sidebands corresponds to a synchrotron tune of $Q_s = 0.004$ (at which the machine operates).
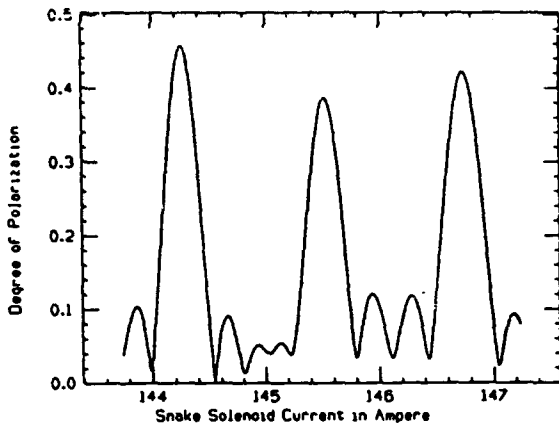
Fig. 3 Simulation of the measurement. The injected beam is 80% vertically polarised. The polarimeter measures the transverse component of the polarisation. The polarimeter is gated in such a way that data are taken only every second revolution of the beam. The two peaks centered around the main peak are caused by synchrotron oscillations.

Fig. 4 shows the results of the measurements. The position of the side peaks relative to the main peak is in excellent agreement with the simple assumptions developed in equations (6) and (7).
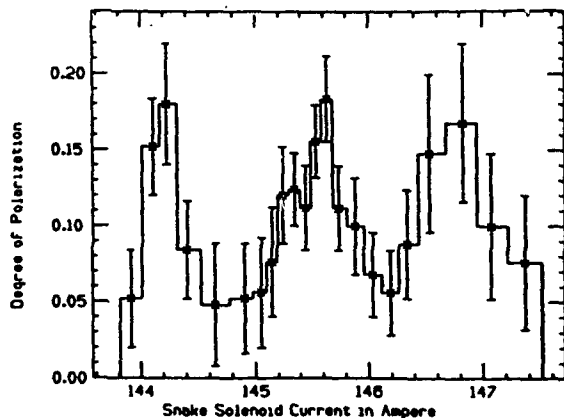
Fig. 4 The results of the measurements. The 3 peaks

are separated by the amount predicted in fig. 3. The absolute height is smaller by a factor of 2 compared with the calculations. This deviation has to be investigated in more detail in the future.

In summary, it was demonstrated for the first time that oscillations of the polarisation around the stable direction exist and can be measured.

V. REFERENCES

[1] N. Akchurin et al., Phys. Rev. Lett., 69,1753(1992).

[2] T. Niinikoski and R. Rossmanith, Nucl. Instrum. Methods A255,460(1987). Y. Onel, A. Penso and R. Rossmanith, Proc. VII International Symposium on High Energy Spin Physics, Protvino 1986.

[3] R. Schmidt, AIP Proc. 252, 1991 Accelerator Instrumentation Workshop, Newport News, Virginia, 1991.

[4] A. A. Sokolov and I. M. Ternov, Sov. Phys. Dokl. 8,1203(1964).

[5] A. D. Krisch et al., Phys.Rev.Lett.63,1137(1989).

[6] Y. Derbenev and A. M. Kondratenko, Sov. Phys. JETP 37, 968(1973).

[7] A. Chao, Nucl. Instrum. Methods 180,29(1981).

[8] M. Placidi et al., Proc. EPAC Conf., Nice 1990.

[9] P. Koutchouk, CERN Internal Note SL/AP Note 1991.

[10] B. von Przewoski et al., Proc. 9th Int. Symp. on High Energy Spin Physics, Bonn, Sept. 1990.

[11] V. Bargmann, L. Michel, and V. L. Telegdi, Phys. Rev. Lett. 2,435(1959).

[12] M. G. Minty, Studies of Siberian Snakes and Depolarizing Resonances at the Indiana University Cyclotron Facility Cooler Ring, Thesis, University of Indiana, July 1991.

A Clean Way to Measure Nonlinear Momentum Compaction Factor α_1

J.P. SHAN, I. KOURBANIS, D. MCGINNIS, K.Y. NG, and S. PEGGS

Fermi National Accelerator Laboratory, P.O. Box 500, Batavia, IL 60510

Abstract

α_1 is an important lattice parameter for transition crossing. There exist several ways to measure α_1, such as debunching near transition. The extraction of α_1 from debunching rate depends on the momentum spread of beam, which is hard to measure accurately. Here we report another way to bypass this difficulty. Instead of debunching, the beam is stored in a stationary bucket near transition. Since the bucket near transition is very small, the particles inside the bucket will fill the bucket and those outside will be lost if parameters are chosen properly. So the measured bunch length is equal to bucket length, which can be used to extract α_1. The nice thing about this mothed is that the measurement dose not depend on initial distribution of bunch as long as its initial emittance is big enough to fill the stationary bucket near transition. A test has been carried out in the Fermilab Main Ring (MR).

1 Introduction

In a synchrotron or a storage ring, the momentum compaction effect influences the longitudinal motion through the phase slip factor

$$\eta = \frac{1}{T_0}\frac{T - T_0}{\delta} = \eta_0 + \eta_1\delta + O(\delta^2), \qquad (1)$$

where $\eta_0 = \alpha_0 - \frac{1}{\gamma^2} \equiv \frac{1}{\gamma_T^2} - \frac{1}{\gamma^2}$, and

$$\eta_1 = \alpha_0\alpha_1 + \frac{3\beta^2}{2\gamma^2} - \frac{\eta_0}{\gamma^2}. \qquad (2)$$

Here T is the period of revolution for a particle with momentum offset $\delta = \frac{p-p_0}{p}$ and T_0 for a synchronous particle, β and γ follow usual relativistic kinematic notation, and γ_T is the transition gamma for a synchronous particle, α_0 and α_1 are defined in the expansion of orbit length

$$C - C_0 = C_0\alpha_0\delta\left[1 + \alpha_1\delta + O(\delta^2)\right], \qquad (3)$$

where C_0 is the orbit length for reference particle.

Near transition where η_0 vanishes, the nonlinear term

$$\eta_1 \approx \alpha_0(\alpha_1 + \frac{3}{2}) \qquad (4)$$

becomes very important. For a quasi-isochronous electron storage ring, $\eta_1 \approx \alpha_0\alpha_1$ since $\gamma >> \frac{1}{\sqrt{\alpha_0}}$. The first order

nonlinear compaction factor α_1 can be calculated analytically [1] for a FODO lattice or numerically from a lattice code such as MAD. But in a real machine, such as the Main Ring, there are a lot of unknown nonlinear components. So it is very important to be able to measure α_1.

There exist several ways to measure α_1, such as nonlinear dependence variation of revolution frequency on the momentum offset [2] or debunching near transition [3]. For a ring with big radius and small aperture, it's very difficult to apply the former method. The extraction of α_1 from debunching rate depends on the momentum spread of beam, which is hard to measure accurately. To bypass this difficulty, a new way to measure α_1 has been proposed [4], which uses a property of a stationary bucket near transition.

2 RF Bucket near Transition

The longitudinal Hamiltonian for stationay bucket ($\phi_s = 0$) including the nonlinear η_1 term can be written as

$$H(\phi,\delta) = \frac{eV}{\beta^2 E}\cos\phi + 2\pi h[\frac{1}{2}\eta_0\delta^2 + \frac{1}{3}\eta_1\delta^3] \qquad (5)$$

where V is RF voltage, h harmonic number, E beam energy.

The separatrix is a Hamiltonian contour through the unstable fixed point in the phase space. There are two sets of fixed points, one at $\delta = 0$ and another at

$$a = -\frac{\eta_0}{\eta_1} \approx -\frac{2\Delta\gamma}{\gamma_t(\alpha_1 + 3/2)} \qquad (6)$$

introduced by the nonlinearity and approximation in Eq. 6 is valid near transition. The nonlinear strength can be parameterized by a quantity

$$x = \sqrt{\frac{\pi h \beta^2 E|\eta_0|^3}{6eV_{rf}\eta_1^2}} \qquad (7)$$

When far away from transition ($x \gg 1$), the bucket around $\delta = a$ is way outside the momentum aperture. Near transition, a becomes smaller and the nonlinear contribution begins to make the bucket unsymmetric in the δ axis and the second set of bucket around $\delta = a$ moving close to the aperture as seen in the Fig. 1. Then comes a piont when the bucket height $\delta_+ = a$ under the critical condition $x = 1$. Even close to transition the bucket height does not depend on RF voltage and the bucket width begin to shrink. The properties of bucket can be summarized in the following

*Operated by the Universities Research Association Inc., under contract with the U.S. Department of Energy.

0-7803-1203-1/93$03.00 © 1993 IEEE

35
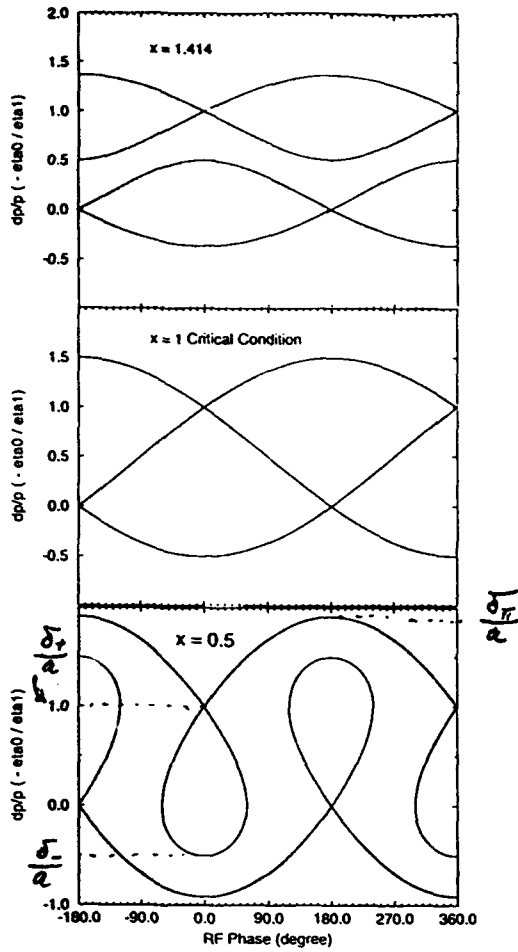
Figure 1: The stationary bucket near transition. The vertical axis is momentum offset normalized to $a = -\frac{\eta_0}{\eta_1}$.
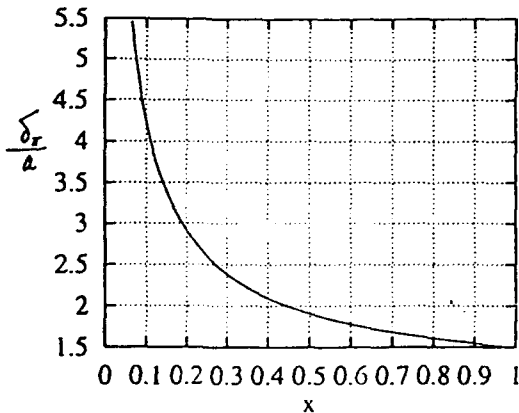
Figure 2: $\frac{\delta_\pi}{a}$ as a function of x

	regime	bucket height	width	type
table:	$x \gg 1$	$\delta_+ = \delta_- \propto \sqrt{V}$	2π	A
	$x > 1$	$\delta_+ > \delta_- \propto \sqrt{V}$	2π	B
	$x = 1$	$\delta_+ = 2\delta_- = a \propto \sqrt{V}$	2π	C
	$x < 1$	$\delta_+ = 2\delta_- = a$	$4\arcsin(x)$	D

In the table above, δ_+ and δ_- are respectively the bucket height in the upper and lower phase space as shown in Fig. 1. Another important parameter is the maximum momentum deviation in the separatrix. Since it's always at phase π, let's call this maximum momentum deviation δ_π. The ratio of δ_π over a depends only on x, as shown in Fig. 2. Here we assume $a > 0$.

For type D bucket, the bucket width depends on η_1. So if bucket width can be measured, x can be calculated. Then if know η_0 very accurately, η_1 (thus α_1) can be extracted.

3 Measurement Method and Parameter Choice

One way to measure the bucket length is to let beam fill the bucket. Then the measured bunch length will be the same as the bucket width. So if we can ramp the beam to a energy near transition, probably below trantion to avoid of complication of transition crossing. How far away from transition? The ground rule for choosing parameters is

$$1.5a < \delta_{aperture} < \delta_\pi \qquad (8)$$

to make sure that particles inside bucket are captured and those outside are lost to the momentum aperture. To get clean signal, the ratio of δ_π over a should be maximized. From Fig. 2, x should be less than 0.3 to get $\frac{\delta_\pi}{a} > 2.4$. On the other hand, the lower limit of x is set by the resolution of bunch length measurement. For the Fermilab Main Ring, the normal stationary bucket is 20 ns long. Bunch length shorter than 1 ns can not be measured accurately. The lower limit is $x > 0.1$. For a machine with lower RF frequency, such as the Brookhevan AGS, the lower limit could be even smaller.

4 Test in the Main Ring

4.1 Setup

The Main Ring is a synchrotron with following parameters

Radius	1000	m
γ_t	18.86	
f_{rf}	53	MHz
h	1113	

In the experiment, 20 bunches of beam with 1×10^{10} protons per bunch are accelerated from 8 Gev to a energy very close to transition energy at 0.44s. Then the RF voltage is lowered to less than 10 KV by using the technique of paraphasing at 0.47s. The bunch length is measured in the frequency domian by detecting the first (53 MHz) and third harmonic component (159 MHz)[5].
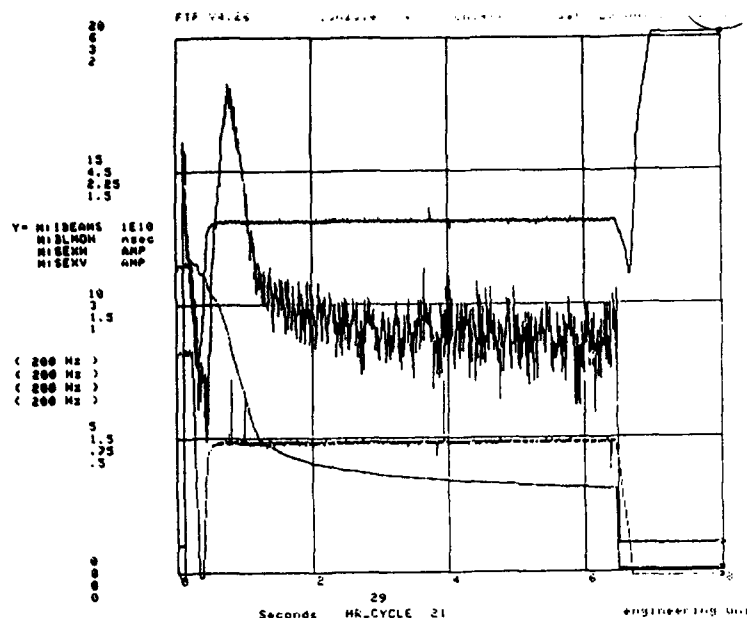
Figure 3: The beam accelerated to 17.63 Gev/c and stay at this energy for 6 s. with $I_h = 1.5$ A and $I_v = 1.6$ A.
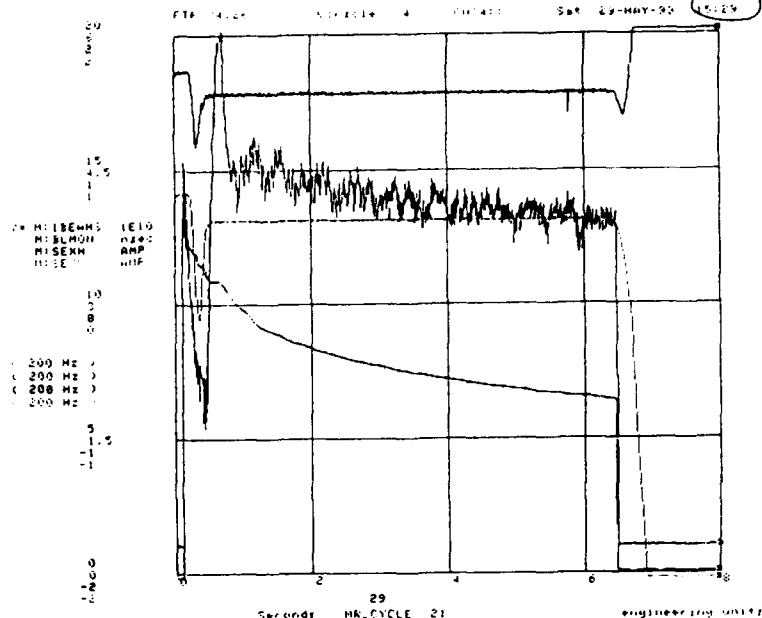
Figure 4: The same as the Fig. 4. with different sextupole currents $I_h = 2.0$ A and $I_v = 0.5$ A.

4.2 Observations

The experiment in the MR has just started. The preliminary measurement presented here was carried out at front porch momentem 17.63 Gev/c.

There are two sets of sextupoles in the Main Ring for correcting chromaticities. Far away from transition, the longitudinal dynamics should not be affected by sextupoles. Near transition we expect that the longitudinal dynamics is very sensitive to the setting of sextupoles. Fig. 3 and 4 are the observations of bunch length and beam intensity at front porch with different sextupole settings. It is obvious that the sextupole has very strong effect on the longitunal motion of beam.

5 Discussion

The preliminary data from the Main Ring are encouraging. The variation of longitudinal bucket width with sextupole strengths has been measured. For cleanest measurement of α_1, fine tuning of experimental parameters and careful isolation of transverse effect are needed. The forthcoming parametric scan are expected to confirm expexted scaling behavior.

Acknowledgements

Thank G. Jackson for the arrangement of beam time in the Main Ring . The stimulating discussions with K. Meisner, X. Lu, W. Gabella and P. Zhou are acknowledged.

References

[1] J.P. Shan, S. Peggs, and S. Bogacz. Fermilab pub92/124, to be published in Particle Accelerators, April 1992.

[2] E. Ciapala, A.Hofmann, S. Myers, and T. Risselada. *IEEE Nul.*, 26(3), June 1979.

[3] K.Y. Ng, C. Bhat, I. Kourbanis, J. Maclachlan, M. Martens, and J.P. Shan. In *Proc. XVth Int. Conf. on High Energy Accelerators*, 1992.

[4] J.P. Shan. Measuring α_1 by storing beam near transition with low rf volatge. Talk given at MIRF meeting, March 1992.

[5] G. Jackson and T. Ieiri. In *1989 IEEE Particle Accelerator Conference*, pages 863–, 1989.

Long-Term Tracking with Symplectic Implicit One-Turn Maps

Y. T. Yan, P. J. Channell,[1] M. Li, and M. J. Syphers

SSC Laboratory[2], 2550 Beckleymeade Ave., Dallas, TX 75237, USA

Abstract

Symplectic one-turn maps for long-term tracking of the Superconducting Super Collider (SSC) and its High Energy Booster (HEB) have been successfully used in dynamic aperture studies. We found that one-turn maps of about 5th order are sufficient for the SSC injection lattice, while for the HEB, slightly-higher-order (about 8th) one-turn maps are required. These results led to a tentative conclusion that the SSC is dominated by low-order resonances, that is, high-order (> 9) resonances do not play essential roles for the stability of the SSC.

Numerical particle tracking of circular accelerators, especially for a long term, has always consumed a great amount of computer time. In the past colleagues used scalar element-by-element accelerator tracking codes for such purposes. With such scalar tracking codes, only one particle can be tracked (advancement of phase-space coordinates) one element after another, then one turn after another, before another particle can be tracked. Therefore, most work was performed for short-term analyses, such as smear studies for predicting the linear aperture. However, after the SSC was proposed, it was realized that short-term studies alone were insufficient for deciding lattice issues, because the SSC is not as linear as the previous circular accelerators. Long-term stability and thus computational speed of particle tracking became critical issues for such a large nonlinear accelerator. The SSC contains more than 10,000 elements and needs to be operated for millions of turns. Therefore, long-term tracking studies with scalar element-by-element tracking codes are either not practical or virtually impossible. An improvement was then made to allow vectorized multi-particle tracking with the use of supercomputers [1]. Although the vectorized tracking speed was impressive (for a period of time) compared to scalar tracking, it still required more than 100 hours of Cray CPU time to obtain a survival plot up to 10^6 turns for the SSC. On the other hand, one-turn differential Lie algebraic maps had been attainable and used for order-by-order analysis [2]. It would be logical to consider using such one-turn maps for fast long-term tracking since

a circular accelerator, whether large or small, would be represented by a single element, the one-turn map. However, whether a one-turn map can be used for long-term tracking had always been a controversial issue although efforts to formulate one-turn-map tracking schemes had never been stopped (see reference [3] for a brief review).

In 1990, with the use of Zmap, an 11th-order Taylor map of the SSC was tested for advancing the phase-space coordinates of particles turn-by-turn via direct evaluation of the truncated 11th-order Taylor map (not exactly symplectic due to truncation) [4]. The survival plot obtained was found to be roughly the same as that obtained previously with element-by-element tracking [1]. This was the first time that the one-turn map showed some promise for long-term tracking of a practical accelerator lattice, although there were still some concerns about the non-exact symplecticity. The same one-turn map was also tested with 10th-order Taylor-map tracking, resulting in somewhat different survival plots. However, the 10th-order Taylor map—after it had been Lie-transformed (by Dragt-Finn factorization [6]) and re-expanded into an 11th- or 12th-order Taylor map to gain a higher degree of symplecticity—showed correct dynamic aperture up to 10^6 turns [7,8]. These results led us to conclude that a moderate-order (lower than 11th order), one-turn Taylor map is usually accurate enough, but its degree of symplecticity may not be enough for long-term tracking [8]. The wrong survival plots obtained with the direct Taylor-map tracking of 10th order are due not to inaccuracy of the map but to artificial diffusion of the particle orbits because of the lack of sufficient symplecticity. How to symplectify the Taylor map without imposing large spurious errors in the map becomes the key to success when using one-turn maps for long-term tracking.

To date, there have been several schemes developed for the purpose of symplectic one-turn-map tracking, most of which have not been tested for practical cases. There are Jolt factorization (Irwin factorization) [9], monomial factorization [10], integrable-polynomial factorization [11], fitted map [12], dynamical rescaling method [13], and the generating function method [14,15]. Based on the numerical procedure of [15] and with the use of Zlib [16], we have recently developed a program, called Zimaptrk, for performing symplectic implicit one-turn-map tracking of the SSC and the HEB. First, the one-turn map of the SSC or the HEB is separated into two maps, a symplectic linear

---

Figure 1. Survival plot

Legend
□ : 4th-order-map track
♦ : 5th-order-map track
✳ : 6th-order-map track

X = Y Initial Betatron Amplitude (mm)

Table 1: HEB Dynamic Aperture at 500,000 turns.

Seed Number	Rev 0 (mm)	Rev 1 (mm)
1	6.7	8.0
2	7.0	8.3
3	6.9	7.6
4	7.5	8.0
5	7.7	9.1
6	7.3	8.7
7	---	8.1
8	---	7.7
9	7.4	9.1
Average	(7.2)	8.3
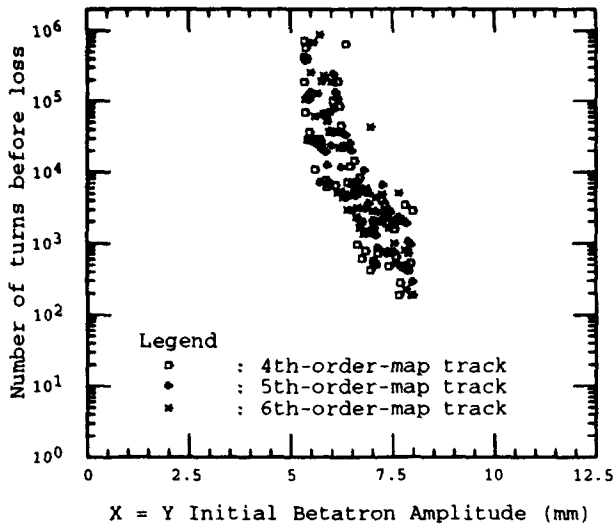
transfer matrix followed by a nonlinear Taylor map to enhance numerical stability. Then, the nonlinear Taylor map is converted into an implicit type of mixed-variable, vector-power-series map without imposing a certain form of generating function. (Of course, one of the four types of generating functions exists implicitly.) Because this method does not impose a predetermined form (not type) of generating function, it provides the same degree of accuracy as the explicit Taylor map at the same order. This method has shown much success in our long-term trackings for the SSC and the HEB and has saved us enormous amounts of computer time [15,17].

Shown in Figure 1 is a sample case of using Zimaptrk for symplectic one-turn-map long-term tracking of the SSC injection lattices where survival plots are shown for an SSC injection lattice with 4-cm diameter dipoles. Trackings with the 4th-, 5th-, 6th-, and 7th-order maps show roughly the same dynamic aperture. Table 1 shows dynamic apertures at 500,000 turns for many cases of the HEB lattice. That the average dynamic aperture (8.3 mm) over 9 random seeds of Rev-1 lattice is significantly larger than that of the Rev-0 lattice helps lead to the decision of replacing the previously designed HEB lattice (Rev 0) with the newly improved HEB lattice (Rev 1). That low-order one-turn maps work for both the SSC and the HEB also lead to a tentative conclusion that the SSC is dominated by low-order resonances, that is, high-order (> 9) resonances do not play essential roles for the stability of the SSC.

In summary, since one is interested only in phase-space regions where one-turn Taylor maps converge, it is fine to use one-turn maps not only for order-by-order analysis but also for turn-by-turn tracking. It is especially economical to use one-turn maps for long-term tracking of large circular accelerators.

References

[1] Y. Yan, "Supercomputing for the Superconducting Super Collider," *Energy Sciences Supercomputing 1990*, pp. 9–13 (1990), published by DOE National Energy Research Supercomputer Center, A. Mirin and G. Kaiper, eds. Y. Yan, G. Bourianoff, and L. Schachinger, "A Typical 'Ztrack' Long-Term Tracking Result," SSC Laboratory Report SSCL-303 (1990); also appears in *Proc. Workshop on Nonlinear Problems in Future Particle Accelerators*, Capri, Italy (April 1990), p. 297, W. Scandale and G. Turchetti, eds., published by World Scientific.

[2] E. Forest, M. Berz, and J. Irwin, "Normal Form Methods for Complicated Periodic Systems," *Particle Accelerators*, **24**, 91 (1989); M. Berz, "Differential Algebraic Description of Beam Dynamics to Very High Orders," *Particle Accel.* **24**, 109 (1989).

[3] Y. T. Yan, "Success in One-Turn Maps for Dynamic Aperture Studies—a Brief Review," SSCL-preprint-190 (1993), to appear in the AIP Conf. Proc. of the workshop held at BNL in October, 1992.

[4] Y. Yan, T. Sen, A. Chao, G. Bourianoff, A. Dragt, and E. Forest, "Comment on Round-off Errors and on One-Turn Taylor Maps," SSCL-301 (1990); also appears in *Proc. Workshop on Nonlinear Problems in Future Particle Accelera-*

tors, Capri, Italy (April 1990), p. 77, W. Scandale and G. Turchetti, eds., published by World Scientific; Y. Yan, "Zmap—A Differential Algebraic High-Order Map Extraction Program for Teapot Using Zlib," SSCL-299 (1990); A. Chao, T. Sen, Y. Yan, and E. Forest, "Applications of Zmap to the SSC," *Proc. of the 1991 IEEE Particle Accelerator Conference*, Vol. 1, p. 336 (1991); L. Schachinger and R. Talman, "Teapot: A Thin-Element Accelerator Program for Optics and Tracking," *Particle Accel.* **22**, 35 (1987).

[5] R. Kleiss, F. Schmidt, Y. Yan, and F. Zimmermann, "On the Feasibility of Tracking with Differential-Algebra Maps in Long-Term Stability Studies for Large Hadron Colliders," DESY HERA 92-01, CERN SL/92-02 (AP), and SSCL-564 (1992).

[6] A. Dragt and J. Finn, "Lie Series and Invariant Functions for Analytic Symplectic Maps," *J. Math Phys.* **17**, 2215 (1976);

[7] T. Sen, Y. Yan, A. Chao, and E. Forest, "Taylor Maps for Long-term Tracking at the SSC," SSCL-497 (1991).

[8] Y. T. Yan, "Applications of Differential Algebra to Single-Particle Dynamics in Storage Rings," SSCL-500 (1991); also appeared in *Physics of Particle Accelerators*, M. Month and M. Dienes, eds., *AIP Conf. Proc.* No. 249, Vol. 1, pp. 378–455 (1992); Y. Yan, "Brief Comment on One-turn Map for Long-term Tracking," *AIP Conf. Proc.*, No. 255, p. 305, A. Chao, ed. (1992).

[9] J. Irwin, "A Multi-kick Factorization Algorithm for Nonlinear Maps," SSCL-228 (1989); A. Dragt, "Methods for Symplectic Tracking," presented at Workshop on Nonlinear Problems in Future Particle Accelerators, Capri, Italy (1990); A. Dragt, I. Gjaja, and G. Rangarajan, "Kick Factorization of Symplectic Maps," Proc. IEEE Accel. Conf., p. 1621 (1991); A. Dragt and D. Abell, "Jolt Factorization of Symplectic Maps," Proc. of 15th International Conference on High-Energy Accelerators (to appear in 1993).

[10] I. Gjaja, "Monomial Factorization of Symplectic Maps," University of Maryland preprint 1-92 (1992); P.J. Channell, "Explicit Integration of Kick Hamiltonians in Three Degrees of Freedom", Los Alamos Internal Report AT-6: ATN-86-6 (1986).

[11] J. Shi and Y. T. Yan, "Symmetric ·ntegrable-Polynomial Factorization for Symplectic One-Turn-Map Tracking" in these proceedings.

[12] J. S. Berg, R. L. Warnock, R. D. Ruth, and E. Forest, SLAC-PUB-6037 (1992) and references therein.

[13] R. Kleiss, F. Schmidt, and F. Zimmermann, "Experience with a Simple Method to ·Symplectify' Differential Algebra Maps," Particle Acc. Vol. 41 (1992).

[14] D. Douglas and A. J. Dragt, "Lie Algebraic Methods for Particle Tracking Calculations," Proc. 12th Intl. Conf. on High-Energy Accelerators, F. T. Cole and R. Donaldson eds. (Fermilab 1983); A. J. Dragt et. al., *MARYLIE 3.0 User's Manual, U. of Maryland Physics Technical Report*; D. R. Douglas, E. Forest, and R. Servranckx, "A Method to Render Second Order Beam Optics Programs Symplectic," IEEE Tran. on Nucl. Sci. NS-32, No. 5, 2279 (1985); M. Berz, "The Description of Particle Accelerators Using High-Order Perturbation Theory Maps", AIP Conf. Proc. No. 184, p. 962, M. Month and M. Dienes eds. (1989).

[15] Y. T. Yan, P. J. Channell, and M. J. Syphers, "Performance of an Algorithm for Symplectic Implicit One-Turn Map Tracking,"SSCL-preprint-157 (1992) and references therein, submitted to J. Comp. Phys.

[16] Y. Yan and C. Yan, "Zlib—A Numerical Library for Differential Algebra," SSCL-300 (1990); Y. T. Yan, "Zlib 2.0—A Numerical Library for Differential Algebra and Lie Algebraic Treatment of Beam Dynamics," *Proc. of the 1991 IEEE Particle Accelerator Conference*, Vol. 1, p. 333 (1991); Y. T. Yan, "Zlib and Related Programs for Beam Dynamics Studies", to appear in Proc. of the 1993 Computational Accelerator Physics (CAP93) Conference.

[17] M. Li, D. Johnson, P. Kocur, R. Schailey, R. Servranckx, R. Talman, Y. T. Yan, R. York, and V. Yarba, "Modification of the Short Straight Sections of the High-Energy Booster of the SSC", in these proceedings.

Injection Method Using the Third Order Resonance at TARN II

M. Tomizawa, Y. Arakaki, K. Chida, S. Watanabe, T.Watanabe, T.Katayama and M.Yoshizawa
Institute for Nuclear Study, University of Tokyo,
3-2-1 Midori-cho, Tanashi-shi, Tokyo, 124, Japan
A. Noda
Institute for Chemical Research, Kyoto University,
Gokanosho, Uji-shi, Kyoto, 611, Japan

Abstract

The beam was successfully stored in the TARN II ring by an injection method using the third order resonance. Beam intensity obtained by the resonance injection is comparable with that by the multiturn injection. A new stacking method utilizing the resonance injection and the electron cooling is introduced.

I. INTRODUCTION

We studied an injection method utilizing the third order resonance. Resonance injection using the second order resonance was already performed in the electron ring[1]. We tried to apply the injection method utilizing the half-integer resonance to the ion ring. This injection mechanism is a reverse process of the slow extraction utilizing the third order resonance (in TARN II ring, the study of the slow extraction using the third order resonance was already done two years ago[2]). When the horizontal betatron tune is set near the third order resonance line, the beam from a transport line can be injected in the ring by a turn separation made by a sextupole field. The injection efficiency depends on the septum thickness of the inflector and the turn separation. The injected beam is stably stored in the ring by enlargement of the separatrix due to change of the horizontal betatron tune. Schematic drawing of this injection mechanism is shown in Fig.1. The resonance injection method is useful for the ring where the compact size is required, because this method does not need the fast-bump magnets.

On the basis of the resonance injection scheme, beam simulations were performed using the TARN II lattice. This result is described in section II. Beam tests using the resonance injection were performed at the TARN II ring. Beam was successfully injected in the ring. The injection procedure and results are described in section III. Finally, a new idea of the resonance injection utilizing an electron cooling is introduced in section IV.

II. BEAM SIMULATION

Beam simulation was performed to investigate the characteristics of the resonance injection. The tracking method with first order transfer matrices was used to calculate the beam behavior. Figure 2 shows the horizontal phase space at the injection point obtained by a single particle tracking. In the tracking, the unperturbed betatron tune was increased by about 2×10^{-6} per turn by changing the strength of the focusing quadrupole field. The sextupole strength $B''L/B\rho$ $(1/m^2)$ is set to 0.3015, which is the same as that used in the
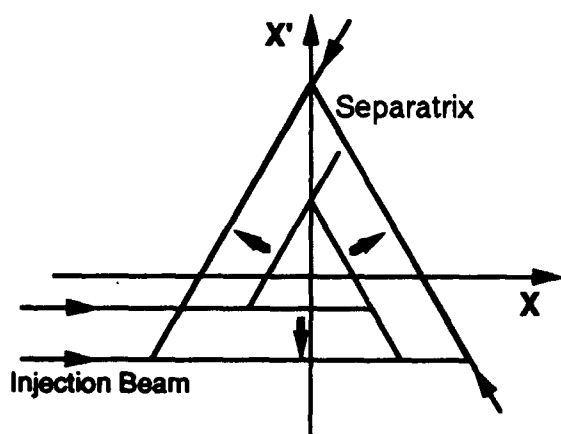
Fig.1 Schematic drawing of the injection mechanism
utilizing the third order resonance.
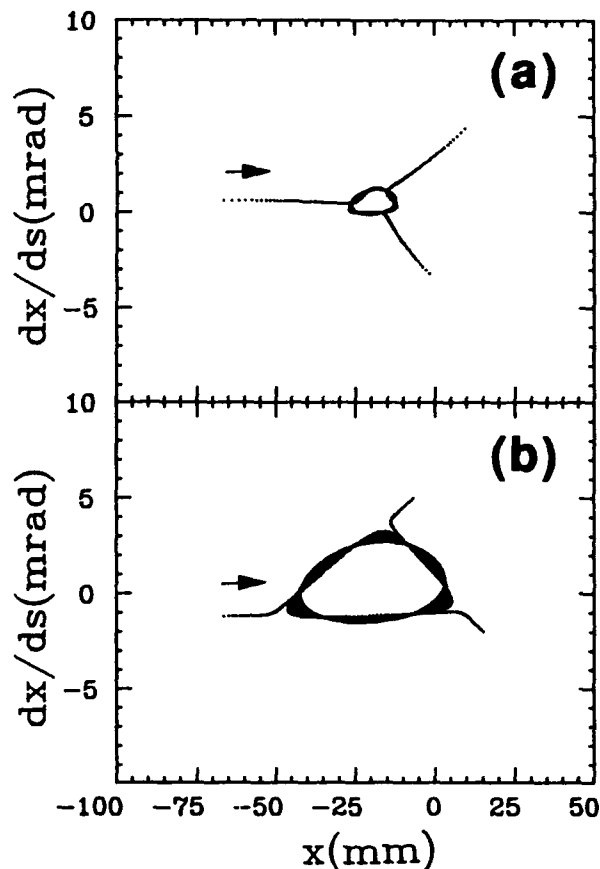
Fig.2 Phase space plot obtained a single particle tracking.

slow extraction study[2]. The starting point of the unperturbed betatron tune in (a) and (b) is 1.6650 and 1.6674, respectively. After 5000 turns, the particles shown in (a) and (b) are stably stored in the phase space corresponding to about 10π mm·mrad and 50π mm·mrad, respectively.

Figure 3 shows the phase space obtained by the muti-particle tracking calculation. (a) is the horizontal phase space at the injection point. Dots show particles stored in the ring. Solid line indicates injection beam emittance of 15π mm·mrad (design value). (b) is the phase space plot of the stored particles at a certain place in the ring. (a) shows that the acceptance to store particles in the ring can be covered with the emittance of the injection beam (in other words, injection efficiency is low). If the peak intensity of the beam from the transport line is equal, beam intensity stored by the resonance injection is the same as that by the multiturn injection.
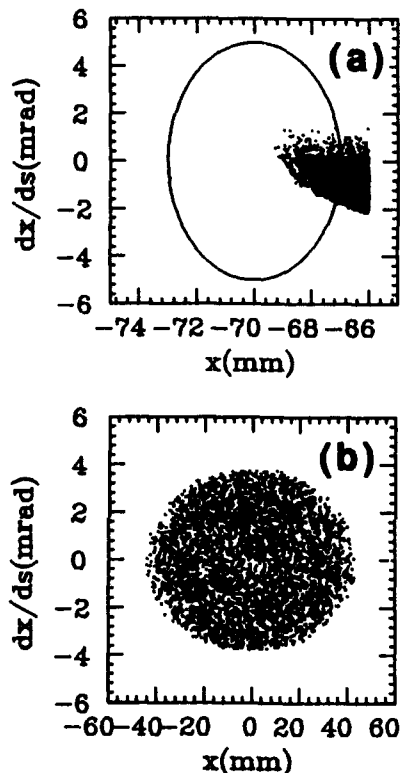
Fig.3 Phase space plot obtained multi-particle tracking.

III. BEAM TESTS

a) Procedure

The injection equipment consists of an electrostatic inflector, a sextupole magnet, and three correction coils of the lattice dipole magnets. Layout of the injection equipment in the TARN II is shown in Fig. 4. The same inflector as used in the multiturn injection was also used in the resonance injection. The sextupole magnet is placed at the same position as placed in the slow extraction. The beam tests were carried out with protons at the energy of 20 MeV from the SF cyclotron. The injection procedure is as follows.

1) The sextupole magnet is operated with dc operation. The horizontal betatron tune is shifted from 1.654 to 1.691 by increasing the strength of the field gradient of the radially focusing quadrupole magnets in the lattice.

2) At the beginning of the beam injection, the orbit bump-coils are excited in order to obtain the minimum beam aperture at the inflector. A bump of about 20 mm from the orbit center was made at the position where the inflector is placed.
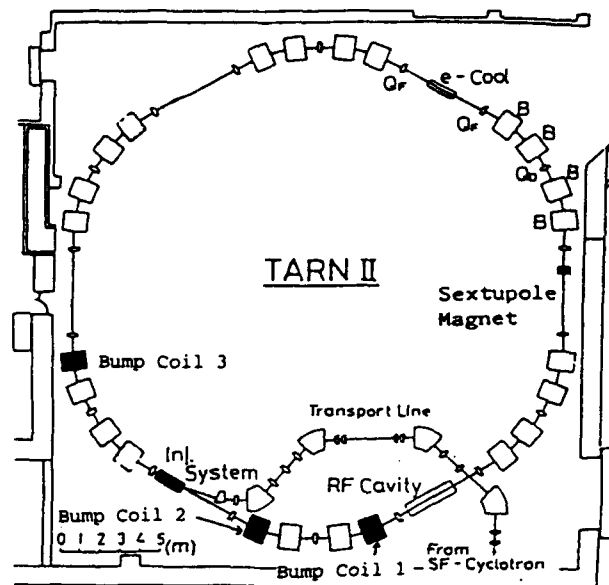
Fig.4 Layout of the resonance injection system of TARN II.
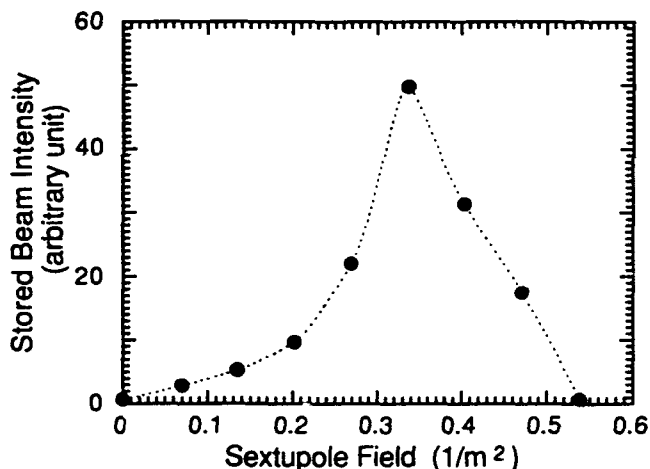
Fig.5 Dependence of the stored beam intensity on the sextupole field.

The pulse width of injection beam is set to about 500 msec with the repetition rate of about 0.2Hz. This width is rather longer than that with the multiturn method, which is determined by limit of the ramping rate of the power supplies of the lattice quadrupole magnets. All of the injection equipment was remotely controlled with a system using a CAMAC interface and a DAC board connected to a personal computer.

b) Results

Figure 5 shows stored beam intensity measured as a function of the sextupole strength. The intensity has a maximum

around B"L/Bρ=0.33. This reason is qualitatively interpreted as follows; the un-captured area in the phase space of the ring increases with the decrease of the sextupole strength. This decreases the stored beam intensity. On the other hand, when the sextupole field is too strong, the turn separation become too large. This decreases the injected beam intensity.
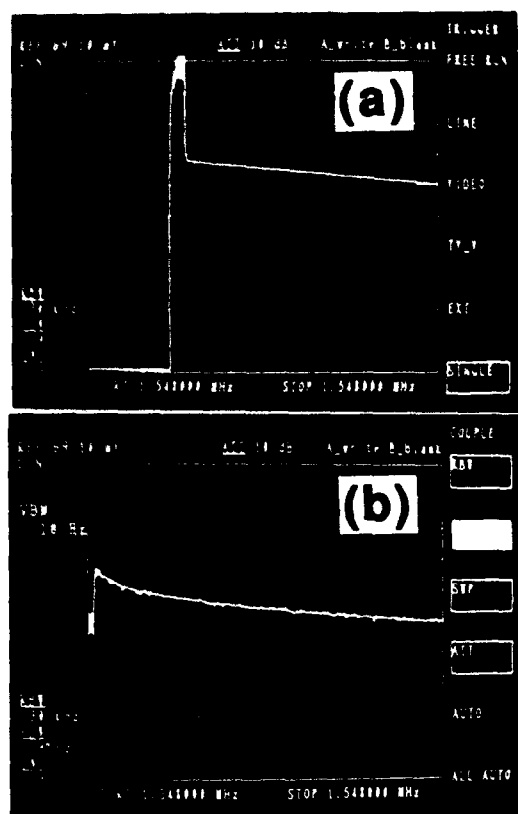
Fig.6 Stored beam intensity measured by the electrostatic
monitor. (a) and (b) are by the resonance injection
and the multiturn injection, respectively.

Next we measured the dependence of the stored intensity on the ramping rate of the betatron tune. This result shows that the stored intensity does not depend on the tune ramping rate in the range from 0.04/sec to 0.19/sec. Finally, beam intensity stored by the resonance injection was compared with that by the multiturn injection. Figures 6 (a) and (b) show beam intensity stored by the resonance and the multiturn injection, respectively. Beam intensity was measured by the electrostatic monitor. The obtained beam intensity for the resonance injection is comparable with that of the multiturn injection. The stored intensity amounted to about 6 μA corresponding to the multiplication factor of about 10, where the multiplication factor is defined as the ratio of the stored to the injected intensity. This multiplication factor is expected to be increased by optimization of the inflector position.

IV. PROPOSAL OF COOLED STACKING USING RESONANCE INJECTION

There is a stable region in the horizontal phase space for the third order resonance. Area of this stable region is

determined by strength of the sextupole field. If the captured beam in the ring is compressed in this stable region, the beam is kept in the stable region by the resonance crossing again (see Fig.7). An electron cooling is available to compress the beam emittance. For example, in the case of TARN II, injected proton beam is compressed up to less than 1π mm·mrad with typical cooling time of several seconds[3]. Therefore, the cooled stacking utilizing the resonance injection is possible by repeating the resonance crossing, just like that with the multiturn injection[4]. The stacked beam intensity depends on the beam life time. Therefore, the repetition rate of the stacking and the sextupole strength need to be adjusted so as to obtain the maximum intensity.
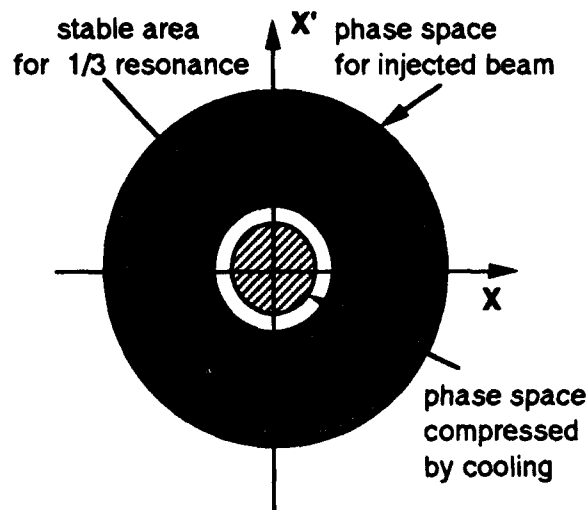
Fig.7 Schematic drawing of the cooled stacking mechanism
utilizing the resonance injection.

V. ACKNOWLEDGEMENT

VI. REFERENCES

[1] T. Takayama, Nucl. Instr. and Methods, B24(1987)420.
[2] M. Tomizawa et al., Nucl. Instr. and Methods, A326(1993)399.
[3] T. Tanabe et al., Nucl. Instr. and Methods, A307(1991)7.
[4] M. Grieser et al., 1991 IEEE Particle Accelerator Conference, San Francisco, p.2817.

Effects of Tidal Forces on the Beam Energy in LEP

L. Arnaudon, F. Bordry, W. Coosemans, B. Dehning, K. Henrichsen, A. Hofmann,
R. Jacobsen, J.P. Koutchouk, L. Lawson-Choroco, M. Mayoud, J. Miles, R. Olsen,
M. Placidi, G. Ramseier, R. Schmidt, J. Wenninger, (CERN, Geneva, CH),
A. Blondel, (Ecole Polytechnique, Paris), R. Aßmann, (Max-Planck-Institut, Munich, DE),
G.E. Fischer, C. Pan, (SLAC, Stanford, U.S.A.) and R. Olivier, (IGL, Lausanne University, CH).

Abstract

The e^+e^- collider LEP is used to investigate the Z particle and to measure its energy and width. This requires energy calibrations with ~20 ppm precision achieved by measuring the frequency of a resonance which destroys the transverse beam polarization established by synchrotron radiation. To make this calibration valid over a longer period all effects causing an energy change have to be corrected for. Among those are the terrestrial tides due to the Moon and Sun. They move the Earth surface up and down by as much as ~0.25 m which represents a relative local change of the Earth radius of 0.04 ppm. This motion has also lateral components resulting in a change of the LEP circumference (C_c=26.7 km) by a similar relative amount. Since the length of the beam orbit is fixed by the constant RF-frequency the change of the machine circumference will force the beam to go off-center through the quadrupoles and receive an extra deflection leading to an energy change given by $\Delta C_c/C_c \sim -\alpha_c \Delta E/E$. With the momentum compaction $\alpha_c = 1.85 \cdot 10^{-4}$ for the present LEP optics this gives tide-driven p.t.p. energy excursion up to about 220 ppm, corresponding to ~18.5 MeV for the Z energy. A beam energy measurement carried out over a 24 hour period perfectly confirmed the effects expected from a more detailed calculation of the tides. A corresponding correction can be applied to energy calibrations.

I. INTRODUCTION

A significant improvement in the precision of the measurements providing the absolute energy calibration of the LEP beam was registered during the 1991 physics run with the availability of transverse beam polarization [1] and the implementation of the resonant depolarization method for the precise determination of the mean beam energy [2]. In particular a systematic uncertainty of ~ 6.3 MeV in the Z mass and ~ 4.9 Mev in the Z width were quoted [3] for the LEP results. The Z mass error is dominated by the knowledge of the absolute energy scale, while the Z width error stems from uncertainties in the differences between the various center-of-mass energies. The analysis of the 1991 beam energy data suggested that effects other than temperature changes in the dipoles contribute to the overall LEP energy reproducibility and the hypothesis that tidal forces might be responsible for it was an-

ticipated in [4]. Fluctuations in the Energy Calibration data [2] were correlated to gravity variations in the Geneva area related to tidal forces. A rather strong correlation was found (Fig.1) despite the measurements having been taken over two months, [5]. Furthermore a tide related variation of the horizontal beam position was observed later [6], [7]. On the basis of this evidence the LEP Energy Working Group recommended the *TidExperiment* to be performed during the 1992 LEP run.
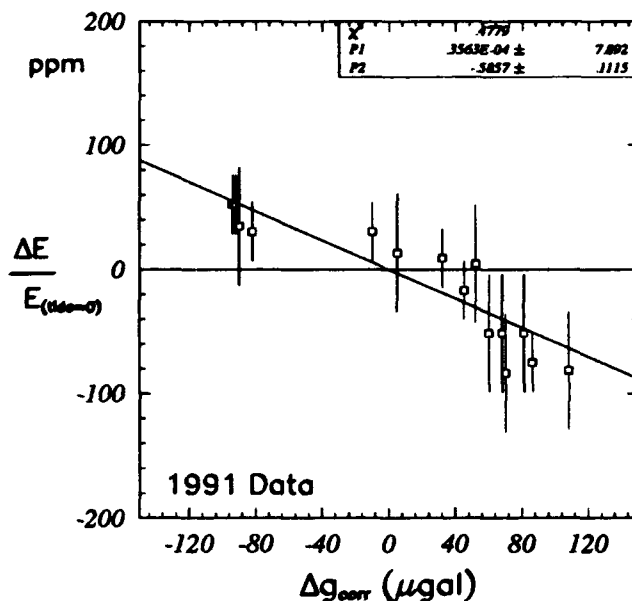
Figure 1: Correlation between relative beam energy deviations measured over the last two months of the 1991 LEP run and the corrections to the local gravity in the Geneva area ($1\,\mu$gal $= 10^{-6}$ cm s^{-2}).

II. GROUND MOTION AND ACCELERATORS

Alignment tolerances in modern and future accelerators have become more and more critical with the introduction of strong focusing magnetic elements to contain beam phase space and with increasing beam currents implying precise positional requirements to reduce interactions of wake fields with the beam environment [8],[9],[10]. Besides occasional motion from seasonal variations of water content in the soil, natural microseismic disturbances and other effects, Earth tides are the major example of *periodic ground motion*.

A. Earth Tides

The equilibrium between the gravitational attraction of Moon and Sun on Earth and the centrifugal forces results is a *quadrupolar* deformation of Earth's crust producing two daily bulges. Their amplitudes are modulated during the 29.53 days between two Moon-Earth-Sun conjunctions by the inclination to the ecliptic of the Earth rotational axis ($\epsilon = 23°26' \pm 1°20'$) and of the lunar orbital plane ($5°8' \pm 8'$) and by the 48 min 38 s difference between the periods of Lunar and Sun tides resulting in maxima at *full* and at *new* moon. These variations together with the ellipticities and oscillations of Earth's and Moon's orbits, equinox precession from Earth oblateness and other components result in a wide spectrum of periodicities which makes the picture more complex [11]. Two important observables related to the above phenomena, the *local gravity variations* and the *strain tensor* describing the lateral motion on Earth's crust associated to that in the vertical direction, can be calculated with computer codes [12], [13].

B. Effects on Accelerators

Due to the strain the horizontal position of the magnetic elements in an accelerator changes periodically with time. The *central orbit*, defined as the orbit passing in average in the magnetic center of the quadrupoles, and for which the energy information from magnetic measurements is valid, becomes *time-dependent*. The same occurs to the energy $E_{op}(t)$ of particles circulating on the orbit defined by the *operational* RF frequency f_{RF}^{op} used for the data taking, experiencing a time-dependent additional bending strength from off-axis passage in the quadrupoles and sextupoles. Beam energy changes $\Delta E(t) = E_{op}(t) - E_{tide=0}$ are related to strain-driven differences $\Delta C = C_{op} - C_{tide=0}$ between the lengths of the two orbits by the momentum compaction factor α_c :

$$\left(\frac{\Delta E(t)}{E_{tide=0}}\right)_{f_{RF}^{op}} = -\frac{1}{\alpha_c}\frac{\Delta C(t)}{C_c} \qquad (1)$$

where $E_{tide=0}$ is the energy of particles on the operational orbit of length C_c in absence of tides. The sign in Equ. (1) indicates that a positive strain (*expanding ring*) induces a *reduction* of the beam energy on the operational orbit with the usual notations. Monitoring of Earth's crust strain is quite complicated. A tidal effect simpler to measure is the time-dependent gravity variation $\Delta g(t)$ related to the strain via the coefficient

$$\alpha_{str} = \frac{\Delta C(t)/C_c}{\Delta g(t)/g_o} \quad < 0$$

which measures the fraction of gravity change coupling into strain. Here g_o is the unperturbed local gravity. A *positive strain* involves a *negative g−variation* and, from (1), a *negative E−variation*. Local gravity changes can be mon-

itored with gravity-meters or be calculated to good accuracy by Geophysics codes and correspondent corrections $\Delta g_{corr} = -\Delta g$ applied. Tidal energy variations (1) can then be related to gravity changes:

$$\frac{\Delta E(t)}{E_{tide=0}} = -\frac{\alpha_{str}}{\alpha_c}\frac{\Delta g(t)}{g_o} \qquad (2)$$

III. THE TIDEXPERIMENT

A. Resonant Depolarization

The *mean beam energy* is determined to great accuracy by measuring the spin tune ν_s of a polarized beam [2]. A time-varying radial magnetic field makes the spin to precess away from the vertical equilibrium position and a depolarizing resonance occurs at a frequency equal to the spin precession frequency :

$$f_{dep}^{res} = \delta\nu_s\, f_{rev}. \qquad (3)$$

The depolarizer frequency at the resonance gives the fractional part of the spin tune and the beam energy :

$$E_{beam} = \frac{m_e c^2}{a_e}\nu_s = 0.4406486\left(N_s \pm \frac{f_{dep}^{res}}{f_{rev}}\right) \qquad (4)$$

where f_{rev} is the beam revolution frequency, a_e the gyromagnetic anomaly and N_s an integer. An uncertainty $\Delta\delta\nu_s = \Delta f_{dep}/f_{rev}$ on the fractional part of the spin tune sets the accuracy on the beam energy to :

$$\frac{\Delta E}{E} = \frac{\Delta\delta\nu_s}{\nu_s}.$$

Offline data analysis provides a $\sim 2\cdot10^{-5}$ energy uncertainty (± 1 MeV at the Z resonance).

B. Quantitative predictions and Results

A strain amplitude $\Delta C/C_c \sim 4\cdot10^{-8}$ associated to a gravity variation $\Delta g/g_o \sim 2.5\cdot10^{-7}$ as predicted [12], [13] at LEP coordinates yields a strain coefficient $\alpha_{str} = -16\%$ and moves the Earth surface by up to about 25 cm. A similar relative change occurs in the transverse directions modifying the LEP circumference by $\Delta C \sim 1$ mm and producing, on a 90/60 lattice, ($\alpha_c = 1.85\cdot10^{-4}$) a relative beam energy variation of about 220 ppm ($\Delta E_{CM} \sim 18.5$ MeV at the Z resonance). A beam energy tidal dependence can be predicted from (2) where α_{str} is obtained by computer codes [12], [13] :

$$\frac{1}{\Delta g_{corr}(t)}\frac{\Delta E(t)}{E_{tide=o}} = -0.882 \text{ ppm}/\mu\text{gal}. \qquad (5)$$

First indications [5], [7] that the beam energy is influenced by tidal forces where spread over a long time span.
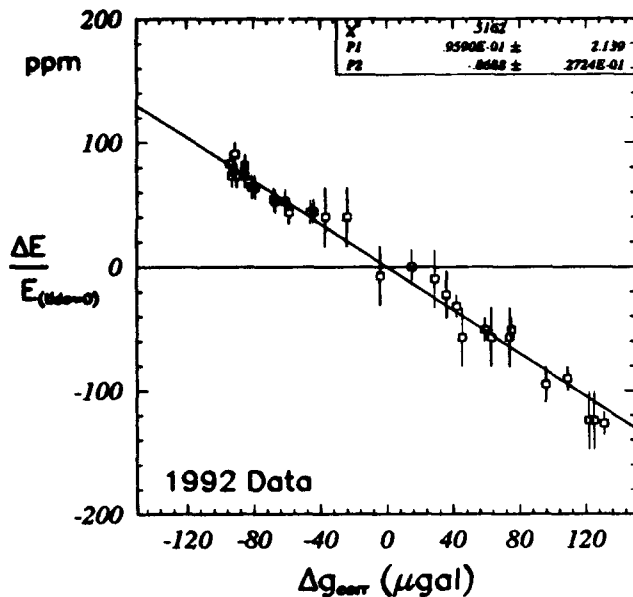
Figure 2: TidExperiment - Correlation between relative beam energy variations over the 24 hours measuring time and corrections to tide-induced local gravity changes. Fit: -0.869 ppm/μgal, expected: -0.882 ppm/μgal.
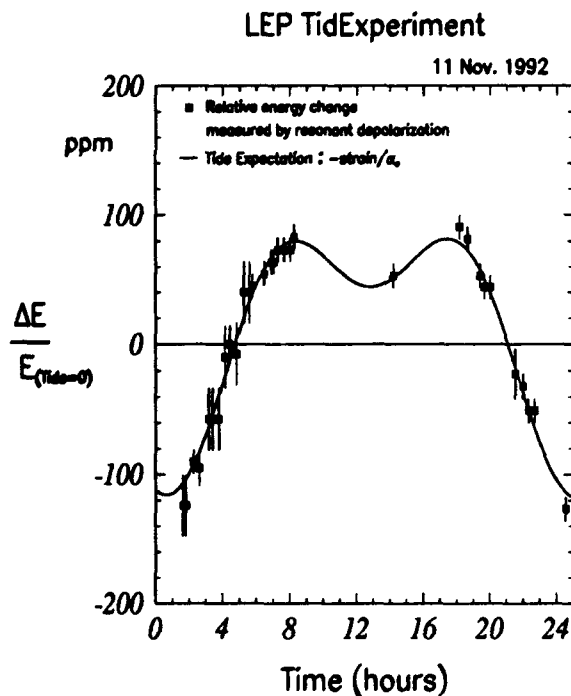
Figure 3: Beam energy variations measured over 24 hours compared to the expectation from the tidal LEP deformation.

To get a more accurate measurement of this correlation a dedicated experiment was carried out in which the beam energy was measured over a 24 hour time period of large tides. In Fig.2 the measured energy points are plotted against the calculated variation of the gravitational acceleration. The linear fit through these data agrees within the errors with the prediction (5). The time evolution of energy measurements over the 24 hours experiment is shown in Fig.3 and compared with the behavior predicted from strain evaluations (1).

IV. SUMMARY AND CONCLUSIONS

Fluctuations in the beam energy calibration data from the LEP 1991 run were correlated to local gravity variations from Earth tides. A dedicated experiment precisely measured the LEP electron beam energy over a 24 hour period to confirm the hypothesis of a dependence of the LEP beam energy on tidal Earth's crust deformations. The results agree well with the expected changes from detailed evaluations of tidal effects. This result provides a correction factor for past and future energy calibrations.

V. ACKNOWLEDGEMENTS

The success of the experiment was possible thanks to the fruitful collaboration of the Polarization team with the LEP physics community, the SL Division groups and the *Institut de Géophysique (IGL)* of the Lausanne University.

VI. REFERENCES

[1] L. Knudsen et al., "First observation of transverse polarization in LEP", Phys. Lett. B 270 (1991) 97.

[2] L. Arnaudon et al., "Measurement of LEP beam energy by resonant depolarization", Phys. Lett. B 284 (1992) 431.

[3] LEP Energy Working Group, "The Energy Calibration of LEP in 1991", CERN-SL/92-37(DI), July 1992. *Submitted to the XXVIth Int. Conf. on H. E. Physics, Dallas.*

[4] G. Fischer, A. Hofmann, Proc. Sec. Workshop on LEP Performance, J. Poole Editor, CERN SL/92-25, p. 337.

[5] M. Placidi, Proc. Third Workshop on LEP Performance, J. Poole Editor, CERN SL/93-19, p. 281.

[6] B. Richter, SLAC, private communication.

[7] R. Jacobsen, SL-MD Note 62, Nov. 1992.

[8] G.E. Fischer, SLAC-PUB-3392 Rev., July 1985.

[9] G.E. Fischer, Proc. First Int. Workshop on Accelerator Alignment, SLAC, July 1989. SLAC-375.

[10] G.E. Fischer, CAS School on Magnetic Measurements and Alignment, Montreux, Sept. 1992. CERN 92-05.

[11] P. Melchior, The Tides of the Planet Earth, 2nd Edition, Pergamon Press, 1983.

[12] Code by *Institut de Géophysique, IGL*, Lausanne.

[13] Code by J.C. Harrison, Univ. of Colorado.

The Appearance of Beam Lines

David C. Carey
Fermi National Accelerator Laboratory *
Batavia, Illinois 60510

Abstract

The combination of an existing graphics package with
a large program like TRANSPORT[1] has often resulted in
considerable modification to the large program. Use of
other graphics packages has resulted in essentially having
to repeat the work. This difficulty has been avoided in
a modification of TRANSPORT which produces layouts
of beam lines. Drawings of the reference trajectory and
three-dimensional images of all magnets are made by the
graphics package TOP DRAWER[2]. Nothing specific to
TOP DRAWER or any other graphics package has been
incorporated into TRANSPORT. If a user is familiar with
a different graphics package he or she can then begin usage
of this alternate package essentially immediately.

1 TRANSPORT Input Data

A section of a charged-particle optical system may be
represented in the input data for the computer program
TRANSPORT as:

```
DRIFT  0.5
QUAD   .25  5.0  .5, TYPE = PUCE  ;
DRIFT  0.25 ;
QUAD   .25  5.0  .5, TYPE = PUCE  ;
DRIFT  0.25
SBEND  .7405  9.  .5, TYPE = MAUVE   ;
DRIFT  0.25 ;
QUAD   .25  5.0  .5, TYPE = PUCE   ;
DRIFT  0.25 ;
```

The elements DRIFT, QUAD, and SBEND are listed in
the same order in the data as they occur in the beam line.
The element SBEND is a sector bending magnet including
the fringing fields at the entrance and exit. A rectangular
bending magnet, given the designation RBEND, is also
available in TRANSPORT.

The first number after each literal mnemonic (DRIFT,
QUAD, SBEND) is the physical length of that element.
The second number on the magnetic elements is the
strength of the magnetic field. Using the magnetic field
strength and the reference trajectory momentum (given

---

elsewhere in the data), one can now determine the floor
coordinates of the reference trajectory. The third number
on the QUAD elements is the aperture radius. The third
number on the SBEND element is the normalized field gra-
dient n.

The final item on the magnetic elements is the type spec-
ification. It can be used for reference to other specifications
about the magnet, as we shall see below.

2 Specifying a Plot

Using TRANSPORT, a plot may now be made of the
floor coordinates of the reference trajectory. This is done
by placing the instruction

```
PLOT, ZFLOOR, YFLOOR ;
```

in the input data before any of the physical elements. This
instruction produces a layout of the y and z coordinates.
The y coordinate is taken as vertical. The z coordinate is
taken as being along the initial direction of the reference
trajectory, unless another initial direction is specified in
the input data. Layouts may also be produced in the x
and z coordinates.

It is much more interesting and useful to be able to draw
the magnets with their physical dimensions as they sit on
the reference trajectory. For this purpose, it is essential
to know their dimensions. Here the type designation de-
scribed above allows the dimensions of a magnet to be
specified by type. Dimension specifications for the mag-
nets mentioned above might be given in the data as:

```
MAGNET, HEIGHT = .20, WIDTH = .30, TYPE = MAUVE ;
MAGNET, HEIGHT = .25, WIDTH = .25, TYPE = PUCE ·
```

There can be many different types of quadrupoles, bend-
ing magnets, sextupoles, and octupoles. The same set of
data could also have quadrupoles which are SAFFRON,
INDIGO, OCHRE, or AVOCADO. A type designation can
consist of any combination of letters and numerais up to

47

fifteen characters.

The illustrations with this article were made using the plotting package TOPDRAWER. However, there is nothing in TRANSPORT that is specific to TOPDRAWER. Similarly, there is nothing in TOPDRAWER that is in any way specific to TRANSPORT. If a TRANSPORT user is familiar with a different plotting package, he or she may switch over to that package without making any alterations in the TRANSPORT input or output or the program itself.

A skeleton data set for TOPDRAWER might look like:

```
SET LIMITS X -1.0 2.5
SET LIMITS Y -0.75 1.25
SET SCALE X LINEAR
SET SCALE Y LINEAR
TITLE TOP SIZE 2 'SECTOR BENDING MAGNET'
SET ORDER X Y
  DATA
  JOIN 1
STOP
```

The first six lines give the range of the coordinates, the type of scale, the title, and which cooordinate is horizontal and which vertical. The word DATA is not a TOP-DRAWER instruction. It indicates the location of the data to be plotted. The PLOT instruction in TRANSPORT produces an output file which is separate from the usual TRANSPORT output. A short auxiliary program exists which replaces the word DATA in the TOPDRAWER skeleton file with the contents of the TRANSPORT output file.

The execution of TRANSPORT, that of the short auxiliary program, and of TOP DRAWER can all be combined in a single procedure. The user need then only set up the TRANSPORT data set, including the PLOT instruction, and the TOP DRAWER skeleton data set, and then invoke the procedure. The TRANSPORT output will automatically be combined into the TOP DRAWER skeleton deck and plots will be produced.

The instruction JOIN 1 indicates that the points are to be joined by straight line segments. The instruction STOP indicates that there are no more instructions. Once the word DATA has been replaced by the file produced by TRANSPORT, the resulting set of data is a complete TOPDRAWER input data set.

TRANSPORT users will recall that several passes through a beam line or passes through several beam lines can be made in a single run of TRANSPORT. These multiple passes can all be plotted in the same job, either on the same plot or on several. The set of two commands DATA and JOIN 1 needs merely to be repeated as many times as there are passes in the job.

3 Simple Components

A quadrupole or an RBEND as seen from the side is a simple rectangle which is bisected by the reference trajec-

tory. It might look like:

From above an RBEND is still rectangular, but the bend can be seen in the reference trajectory. The sagitta correction is made automatically. The appearance would then be:
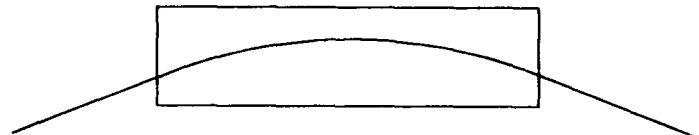
The elements can be rotated about the reference trajectory to give three-dimensional views. Such a view for an SBEND would be:
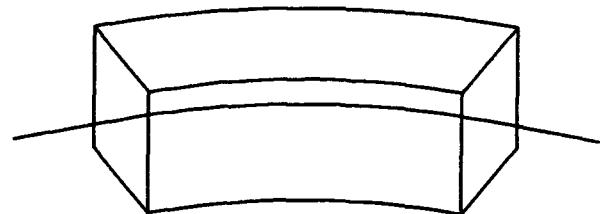
Two larger illustrations of sets of elements can be found on the next page.

[1] D.C. Carey, K.L. Brown, F. Rothacker, and Ch. Iselin, "TRANSPORT, A Computer Program for Designing Charged Particle Beam Transport Systems", SLAC Report SLAC91.

[2] R.B. Chaffee, "Introduction to Top Drawer", SLAC Computation Group Report CGTM No. 189.
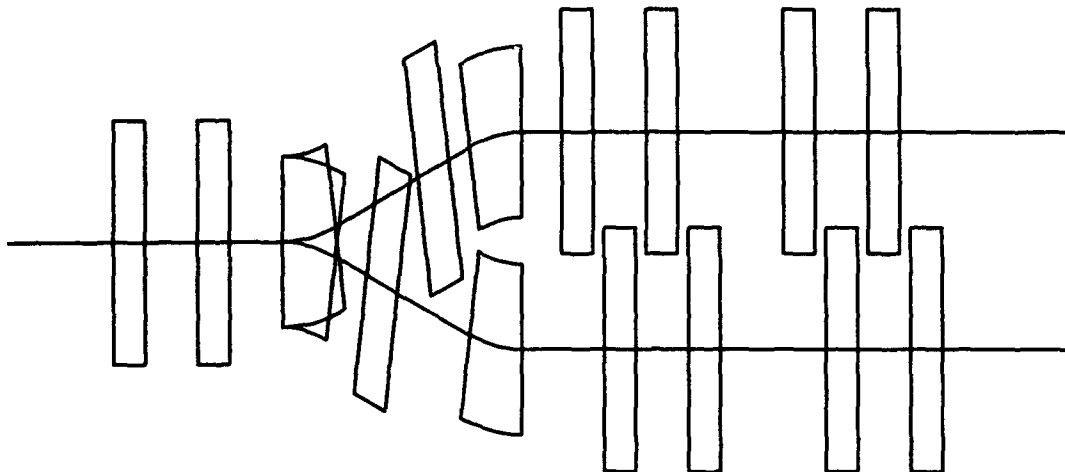
A switch in a beam line. Here the beam plots from two successive TRANSPORT runs are on the same plot. The beam lines have been designed so that the magnets do not collide.
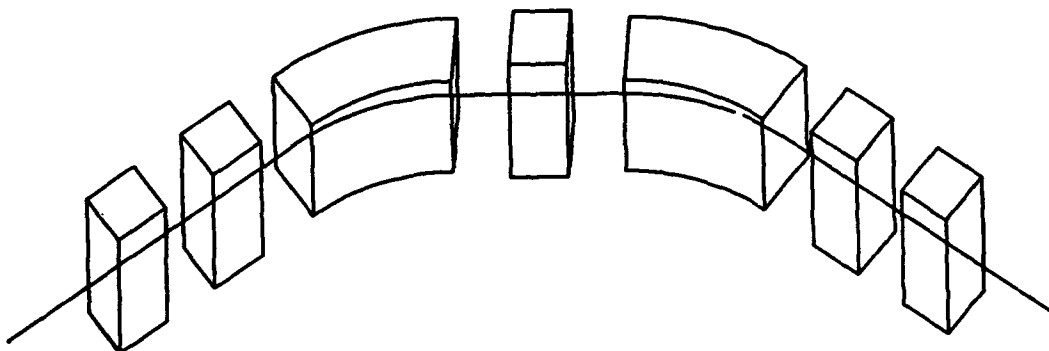
A view of a simple beam line. The reference trajectory is given an initial upward direction. The coordinate system is also rolled about the reference trajectory. The view then seems to be three-dimensional.

MULTIPOLE CHANNEL PARAMETERS FOR EQUALIZATION
OF BEAM INTENSITY DISTRIBUTION

Y.K.Batygin
Electrophysics Department
Moscow Engineering Physics Institute, 115409, Moscow, Russia

Abstract

A method of beam intensity redistribution in a transport channel containing linear and nonlinear elements to provide uniformed irradiation area at the target is discussed. Linear elements (quadrupoles) are used to prepare a large beam spot at the target and nonlinear elements (octupoles, dodecapoles, etc.) are used to improve the beam uniformity. A kinematic relationship between the final beam distribution vs. initial beam distribution and optics channel parameters is given. The flattening of a Gaussian beam is discussed.

Introduction

A uniformed irradiation zone at the target is often required when particle beams are applied. A particle distribution of an accelerated beam is usually approximated by Gaussian distribution. A useful method employing nonlinear optics to improve the beam distribution uniformity was considered [1-6]. The method is based on nonlinear transverse velocity modulation of particles which force the peripheral particles to move faster to the axis than the inner beam particles. During the drift after modulation the beam halo is eliminated and the boundaries of the beam become more pronounced. The method is applied sequentially to both transverse planes. A superposition of independent density transformations in transverse x and y directions results in a rectangular beam spot at the target with high uniformity (see fig. 1).

Equalization of a Gaussian Beam

The one dimensional problem of beam intensity redistribution was considered in ref. [8]. Modulation of transverse velocity of the beam at $z = 0$

$$v_x = v_{x0} + a_2 x_0 + a_3 x_0^2 + a_4 x_0^3 + \ldots + a_n x_0^{n-1} \quad (1)$$

transforms the initial distribution of particles $\rho(x_0) = dN/dx_0$ to distribution $\rho(x)$ at any z as

$$\rho(x) = \rho(x_0) \frac{1}{1 + \alpha_2 + 2\alpha_3 x_0 + \ldots + (n-1)\alpha_n x_0^{n-2}} \quad (2)$$

where $\alpha_n = a_n z/v_z$, v_z is a longitudinal beam velocity.
Particle distribution $\rho(x_0)$ of an accelerated beam is usually approximated by Gaussian function

$$\rho_0 \exp(-\frac{x_0^2}{2A^2}) = \rho_0 (1 - \frac{x_0^2}{2A^2} + \frac{x_0^4}{8A^4} + \ldots \frac{(-1)^k x_0^{2k}}{2^k k! A^{2k}}) \quad (3)$$

where the value of 2A is usually assumed to equal a transverse size (radius) of the beam. From eqs. (2) and (3) the modulation coefficients for uniform distribution
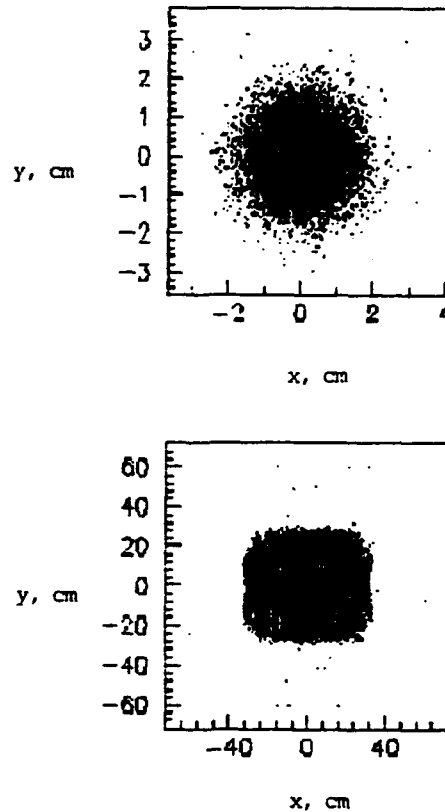
Fig. 1. Projections of computer simulation using code BEAMPATH [7] into real space (x-y) for an initial (upper) and final (lower) beam distribution in a nonlinear optics channel.

$$\rho(x) = P \quad (4)$$

at the target are:

$$\alpha_2 = \frac{\rho_0}{P} - 1 \, ,$$

$$\alpha_4 = -\frac{1 + \alpha_2}{6A^2} \, ,$$

$$\alpha_6 = \frac{1 + \alpha_2}{40A^4} \, , \quad (5)$$

$$\ldots \ldots ,$$

$$\alpha_{2k+2} = \frac{(-1)^k (1 + \alpha_2)}{2^k k! (2k+1) A^{2k}} \, .$$

50

To provide rectangular distribution the numerator and denominator in eq. (2) have to be the same function of x_0 and can be distinguished by constant value only. The number of lenses in a transport channel is limited that means the truncation of series in denominator. Let us see how the flattening of initial Gaussian beam depends on truncation of the series in equations (2) and (3).

The expansion (3) consists of the terms with even power of x_0 which correspond to optical elements with $2k+2$ ($k=1,2,...$) planes of symmetry or lenses with $4k+4$ poles (8-pole, 12-pole, 16-pole, 20-pole, etc.). Actually the pure octupole field, being proportional to x_0^3, corrects the second term in expansion (3), which is proportional to x_0^2. Similarly the field of ideal 12-pole lens, being proportional to x_0^5, corrects the third term in expansion (3), which is proportional to x_0^4, etc.

Assuming that the transport channel consists of quadrupoles to extend the beam and octupole to improve the uniformity of the beam. The final distribution is

$$\rho(x) = \frac{\rho_0 \exp(-x_0^2/2A^2)}{(1+\alpha_2)(1-x_0^2/2A^2)} \qquad (6)$$

The denominator of eq. (6) equals zero if $x_0 = \pm 2^{1/2}A$. It results in peaks at the boundaries of the final distribution (see fig. 2b). Adding a dodecapole gives the function

$$\rho(x) = \frac{\rho_0 \exp(-x_0^2/2A^2)}{(1+\alpha_2)(1-x_0^2/2A^2 - x_0^4/8A^4)} \qquad (7)$$

without any peculiarities because the denominator in eq. (7) is always positive (see fig. 2c). Expression (7) results in a more flattened distribution than eq. (6). Adding 16-pole lens results in peaks in the final distribution function as well because the denominator of the function

$$\rho(x) = \frac{\rho_0 \exp(-x_0^2/2A^2)}{(1+\alpha_2)(1 - x_0^2/2A^2 - x_0^4/8A^4 - x_0^6/48A^6)} \qquad (8)$$

equals zero if $x_0 = \pm 1.78555\ A$ (see fig. 2d).

The analysis shows that the final distribution is characterized by the peaks corresponding to zero values of denominator in eq. (2) if the highest multipole consists of $8k$ poles ($k=1,2,...$). On the contrary the final distribution is more flattened if the multipole series is truncated by a $8k+4$ pole element ($k=1, 2,...$). The portion of the flattened particles is increasing monotonously with the rise of the highest multipole number. In fig. 3 the number of flattened particles versus the highest multipole order is presented.

Parameters of multipole lenses

Eqs. (5) give the values of nonlinear optics coefficients to provide extended uniformed distribution. In ref. [9] the coefficients were determined via lenses parameters. It is convenient to use the definition of strength S_n of an n-th order multipole of length d_n for a beam with particle rigidity $(B \cdot \rho)[9]$:

$$S_n = \frac{E_0}{x} \frac{d_n}{(B\rho)} \qquad (5)$$

where B_0 is the pole-tip field, R is the pole-tip radius.

A simple combination of two magnetic quadrupoles at L distance between them results in an extended beam with the coefficient of linear modulation

$$\alpha_2 = S_2^2\ L\ z \qquad (10)$$

The strength of higher order multipoles which provide for a uniformed particle distribution is the following:

$$S_n = \frac{\alpha_n}{z} \qquad (11)$$

The equivalent electric pole-tip field of $2n$-pole lens is $E_0 = v_z B_0$.

The required number of ampere-turns MI at the pole of $2n$-pole magnetic lens is obtained using Stokes theorem:

$$\frac{1}{\mu_0} \oint \vec{B} \, \vec{dl} = \int \vec{j} \, \vec{dS} \qquad (12)$$

Selecting an integration loop along the circle between neighbouring poles and neglecting the magnetic field inside the core the left hand integral for the azimuthal component of magnetic field $B_\theta = B_0(r/R)^{n-1} \cdot \sin(n\theta)$ is

$$\frac{1}{\mu_0} \int_0^{\pi/n} B_\theta\ R\ d\theta = \frac{2}{\mu_0} \frac{B_0 R}{n} \qquad (13)$$

The right hand integral is equal to

$$\int \vec{j}\, \vec{dS} = 2\ MI \qquad (14)$$

From eqs. (13) and (14) it follows that

$$MI = \frac{B_0}{\mu_0} \frac{R}{n} \qquad (15)$$

The power consumption of the lens is

$$W = \frac{2}{n} \left(\frac{B_0 R}{\mu_0}\right)^2 \frac{g\ h}{S} \qquad (16)$$

where g is a specific resistance, h is an average length of one turn, S is a cross section of the winding at one pole.

Conclusion

The nonlinear optics method for improving the beam intensity distribution was discussed. The kinematic relationship between the initial and the final distribution via lenses parameters was given. The features of the Gaussian beam transformation into rectangular distribution were considered. Major considerations relating to selection of lens parameters to provide for a required distribution at the target were discussed.

<u>References</u>

1. C.H.Johnson, Nucl. Instr. Meth., 127, 1975, p.163.

2. Ph.F.Meads, Jr., IEEE Trans. Nucl. Science, NS-30, No. 4, 1983, p.2838.

3. E.Kashy and B.Sherrill, Nucl. Instr. Meth., B26, 1987, p.610.

4. B.Sherrill, J.Bailey, E.Kashy, C.Leakeas, Nucl. Instr. Meth. B40/41, 1989, p.1004.

5. A.Jason, B.Blind, E.Svaton, Proc. 1988 Linear Accel. Conference, CEBAF Report 89-001, p.192.

6. B.Blind, Nucl. Instr. Meth., B56/57, 1991, p.1099.

7. Y.Batygin, Proc.3rd Europ. Part. Accel. Conference, Berlin, 1992, p.822.

8. Y.Batygin, Beam Intensity Redistribution in a Non-linear Optics Channel, submitted at the 12th Int. Conf. on the Application of Accelerators in Research and Industry, Texas, 1992, to be published in Nucl. Instr. Meth.

9. K.L.Brown and R.V.Servranckx, AIP Conf. Proc. 127, p.32.
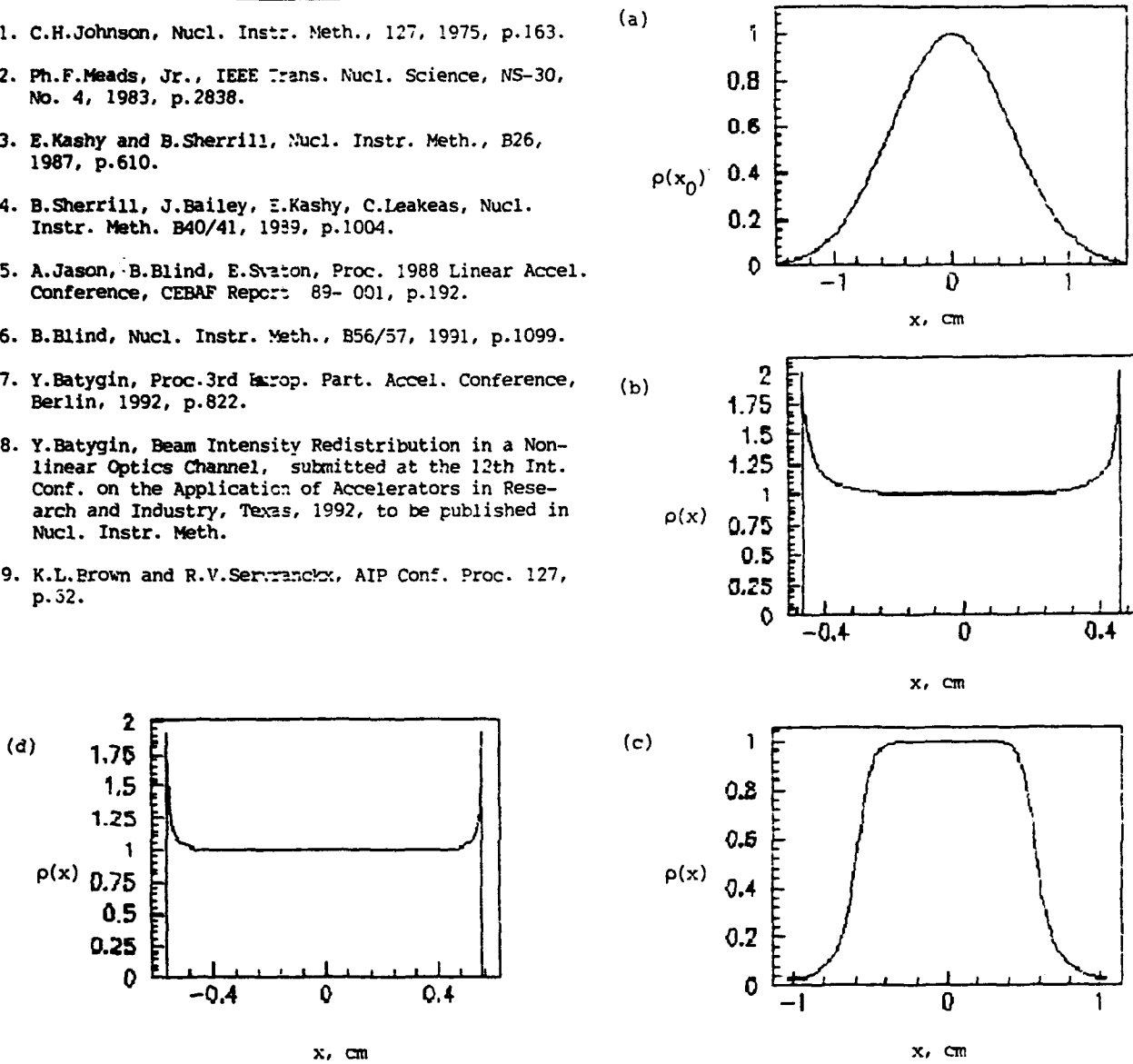
Fig. 2. Transformation of initial Gaussian distribution (a) into flattened distribution using different combinations of multipole lenses: (b) - octupole; (c) - octupole + dodecapole; (d) - octupole + dodecapole + 16-pole.(see eqs. (6), (7), (8)).
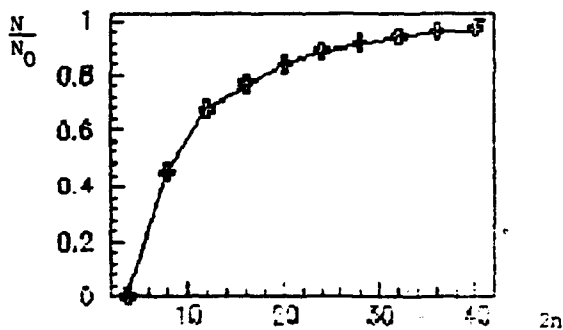
Fig. 3. Portion of flattened particles vs. number of poles of the highest multipole in transport channel.

Single Beam Effects due to Errors in Crab Compensation*

David Sagan

Laboratory of Nuclear Studies, Cornell University, Ithaca, NY 14853

Abstract

Errors in a crab compensation scheme such as betatron phase advance errors will lead to shape and orientation changes of a bunch. These changes can be computed in a systematic manner.

Introduction

The necessity of using a large number of bunches in the B-factories envisioned for the future necessarily aggravates the problem of separating the beams at the parasitic crossing points near the interaction point (IP). A possible solution is to use a crossing angle. The induced synchro-betatron coupling of an angle crossing can be completely eliminated in theory with 'crab' compensation in which the bunches of each beam would be tilted at the IP by an angle $\theta_{crb} = \theta_{cross}/2$ where θ_{cross} is the full crossing angle. In terms of the beam–beam interaction, the problems with a crab compensation scheme for a crossing angle are therefore caused by imperfections in the compensation. It is therefore important to understand the effect that crabbing errors will have on the beam in order to set tolerances on allowable errors. These errors can come from various sources. Possibilities include errors in the betatron phase advances from the crab cavities to the IP, the finite wavelength of the crab cavity RF, etc. It is the purpose of this paper to show how the effect of these errors can be analysed.

In general, the compensation errors can be divided into three groups: The first group comprises all zeroth order effects where the effect of the error on an individual particle is independent of the particle's coordinates. Errors in this group can result in transverse offsets between opposing bunches at the IP and/or longitudinal offsets of the IP itself. The second group comprises all first order effects where the effect of a compensation error on an individual particle is linear in the particle's coordinates. These errors result in crab angle errors and/or changes in the bunch's width and length. The final group comprises all higher order effects. These errors will cause distortion of the Gaussian shape of the bunch.

Several different types of crab compensation schemes have been proposed. In this paper 'transverse crabbing' — in which two RF cavities are used to give a time-varying sideways kick to a bunch as it passes through either cavity — will be considered[1]. An alternate scheme calls for using dispersion at the RF accelerating cavities to give the

correct crab angle at the IP[2]. In any case, the general analytic technique outlined in this paper will be applicable.

Zeroth Order Errors

Errors in a Crab cavity's RF phase (timing errors) will produce zeroth order effects. A phase error in one cavity will add a constant horizontal kick to the beam creating an orbit bump. At the IP the displacement Δx_{ip} due to a timing error Δt_{RF} in one cavity is [1]

$$\Delta x_{ip} = \frac{c\, \Delta t_{RF}}{2}\tan(\theta_{crb}). \qquad (1)$$

First Order Errors

First order errors in crab compensation lead to changes in the crabbing angle θ_{crb} and aspect ratio r_σ which is the ratio of the beam height (minor axis) to beam length (major axis). In order to be able to make the calculation of θ_{crb} and r_σ at the IP one needs to know two quantities[3]; namely, the one turn transfer matrix from IP to IP, $T_{ip \to ip}$, and the ratio of the emittances of normal modes $r_\epsilon \equiv \epsilon_a/\epsilon_b$. For the purposes of the analysis one need only consider the degrees of freedom in the plane in which the beam is being tilted. $T_{ip \to ip}$ will then be a 4×4 matrix. Using the idealised ring shown in Figure 1 $T_{ip \to ip}$ can be constructed as the product of seven matrices

$$T_{ip \to ip} = T_{c1 \to ip} \cdot T_{k1} \cdot T_{arc} \cdot T_{k2} \cdot T_{ip \to c2}, \qquad (2)$$

where $T_{c1 \to ip}$ and $T_{ip \to c2}$ are transport matrices between the crab cavities and the IP, T_{arc} is the transport matrix through the arc, and T_{k1} and T_{k2} are the kick matrices for crab cavities labeled C1 and C2 respectively.

The matrices on the right hand side of equation (2) are parametrised using a set of input parameters. The crabbing is taken to be in the horizontal plane with z being the longitudinal axis and x being the horizontal axis. For the purposes of this paper, the input parameters are denoted with a tilde to distinguish them from calculated quantities. For example, the input parameter $\tilde{\beta}_x(ip)$ is used in the construction of the matrices $T_{ip \to c2}$, and $T_{c1 \to ip}$ (see below) but once $T_{ip \to ip}$ is specified one can explicitly calculate the value of beta at the IP, $\beta_x(ip)$. Only in the case where there are no crab compensation errors will one be assured that $\beta_x(ip)$ will be equal to $\tilde{\beta}_x(ip)$. Explicitly, the matrices were constructed as follows: The transport matrices $T_{c1 \to ip}$, T_{arc}, and $T_{ip \to c2}$ are assumed to have the
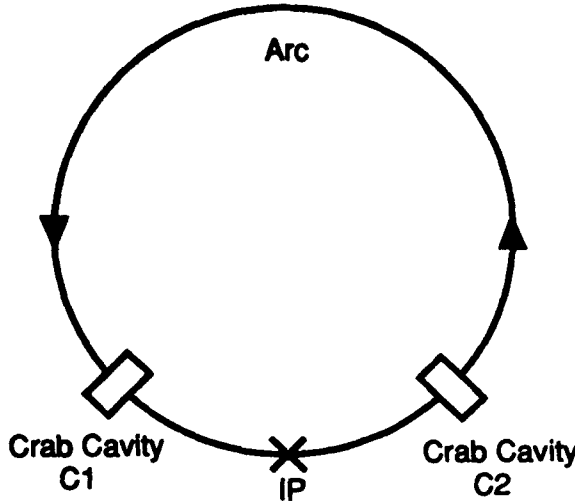
Figure 1: Model ring with 2 crab cavities.

Parameter	Nom. Value	Parameter	Nom. Value
$\tilde{\beta}_z(ip)$	1.0 m	$\tilde{\sigma}_z$	0.01 m
$\tilde{\beta}_z(crb)$	10.0 m	$\tilde{\sigma}_{p_z}$	$6.5 \cdot 10^{-4}$
$\tilde{\beta}_z(arc)$	10.0 m	$\tilde{l}_{c1 \to ip}$	0.0 m
θ_{crb}	0.012 rad	$\tilde{l}_{ip \to c2}$	0.0 m
$\tilde{Q}_{c1 \to ip}$	0.25	$\tilde{\eta}(c1)$	0.0 m
$\tilde{Q}_{ip \to c2}$	0.25	$\tilde{\eta}(c2)$	0.0 m
$\tilde{\epsilon}_z$	$1.3 \cdot 10^{-7}$ m	$\tilde{\eta}(ip)$	0.0 m
Q_z	0.682	$\tilde{\eta}'(c1)$	0.0 m
Q_s	0.085	$\tilde{\eta}'(c2)$	0.0 m
$\tilde{V}_{c1}$	1.0	$\tilde{\eta}'(ip)$	0.0 m
$\tilde{V}_{c2}$	1.0		

Table 1: Crab Compensation Input Parameters.

general form:

$$\mathbf{T}_{s1 \to s2} = \mathbf{T}_{\eta(s2)} \begin{pmatrix} \mathbf{R}_x & 0 \\ 0 & \mathbf{R}_z \end{pmatrix} \mathbf{T}_{\eta(s1)}^{-1}, \qquad (3)$$

where $\mathbf{T}_{\eta(s)}$ is used for putting in the dispersion η and dispersion derivative η' at a given point s:

$$\mathbf{T}_{\eta(s)} = \begin{pmatrix} 1 & 0 & 0 & \tilde{\eta}(s) \\ 0 & 1 & 0 & \tilde{\eta}'(s) \\ -\tilde{\eta}'(s) & \tilde{\eta}(s) & 1 & 0 \\ 0 & 0 & 0 & 1 \end{pmatrix}, \qquad (4)$$

and $\mathbf{R}_x$ is the 2 x 2 rotation matrix

$$\mathbf{R}_x = \begin{pmatrix} \sqrt{\frac{\tilde{\beta}_x(s2)}{\tilde{\beta}_x(s1)}} \cos(2\pi\tilde{Q}_x) & \sqrt{\tilde{\beta}_x(s1)\tilde{\beta}_x(s2)}\sin(2\pi\tilde{Q}_x) \\ \frac{-\sin(2\pi\tilde{Q}_x)}{\sqrt{\tilde{\beta}_x(s1)\tilde{\beta}_x(s2)}} & \sqrt{\frac{\tilde{\beta}_x(s1)}{\tilde{\beta}_x(s2)}} \cos(2\pi\tilde{Q}_x) \end{pmatrix} \qquad (5)$$

with $\tilde{Q}_x$ being the horizontal phase advance between $s1$ and $s2$. For $\mathbf{T}_{arc}$ the matrix $\mathbf{R}_z$ has the same form of equation (5) with $Q = Q_s$, the synchrotron tune, and $\beta(s1) = \beta(s2) = \sqrt{\sigma_z/\sigma_{p_z}}$ with $\sigma_{p_z} \equiv \sigma_E/E$. For $\mathbf{T}_{c1 \to ip}$ and $\mathbf{T}_{ip \to c2}$, $\mathbf{R}_z$ is given by

$$\mathbf{R}_z = \begin{pmatrix} 1 & -l \\ 0 & 1 \end{pmatrix}, \qquad (6)$$

where l in the above equation can be thought of as the local momentum compaction factor. $l = l_{c1 \to ip}$ for $\mathbf{T}_{c1 \to ip}$, $= l_{ip \to c2}$ for $\mathbf{T}_{ip \to c2}$.

The crab kick matrix $\mathbf{T}_{k1}$ for crab cavity C1 is given by

$$\mathbf{T}_{k1} = \begin{pmatrix} 1 & 0 & 0 & 0 \\ 0 & 1 & \tilde{V}_{c1}\kappa_t & 0 \\ 0 & 0 & 1 & 0 \\ \tilde{V}_{c1}\kappa_t & 0 & 0 & 1 \end{pmatrix} \qquad (7)$$

with a similar matrix for $\mathbf{T}_{k2}$. In the above equation the normalisation constant κ_t is given by

$$\kappa_t = \frac{1}{\sqrt{\tilde{\beta}_x(crb)\tilde{\beta}_x(ip)}}\tilde{\theta}_{crb}. \qquad (8)$$

The normalised voltage $\tilde{V}$ is such that with no errors in the compensation, $\tilde{V}_{c1} = \tilde{V}_{c2} = 1$ will result in the actual (i.e. calculated) crab angle at the IP, θ_{crb}, being equal to the value of the input parameter $\tilde{\theta}_{crb}$.

Once $\mathbf{T}_{ip \to ip}$ is specified the calculation of r_ϵ is obtained by assuming that all the emittance is generated uniformly in the arcs as outlined by Sagan[4]. The calculation of θ_{crb} and r_σ then follows from the general analysis for calculating rotation angles given by Orlov and Sagan[3].

Figure 2 shows the effect of varying $\tilde{Q}_{c1 \to ip}$ while keeping the other input parameters at their nominal values as shown in Table 1. The nominal values of the parameters were chosen to be similar to the current design of the Cornell B–factory CESR–B. There is a coupling resonance near $\tilde{Q}_{c1 \to ip} = 0.53$ where the normal mode tunes Q_a and Q_b satisfy $Q_a - Q_b =$ integer. Near the coupling resonance the normal mode emittance ratio r_ϵ blows up and is of order unity and there are large variations in θ_{crb} and r_σ. The sum resonance is near $\tilde{Q}_{c1 \to ip} = 0.70$ where $Q_a + Q_b =$ integer. Near the sum resonance there are also large variations in r_ϵ, θ_{crb} and r_σ. The difference between the sum and coupling resonances is that near the coupling resonance the beam is always stable while near the sum resonance there is a stop band where the one turn matrix displays an instability. In addition to the two mode coupling resonances there are also single mode resonances resonances near $\tilde{Q}_{c1 \to ip} = 0.12$ and near $\tilde{Q}_{c1 \to ip} = 0.62$ when one of the normal mode tunes passes through 0.5 and 1.0 respectively. Within the limits of the linear model used in the analysis, the single mode resonances have little effect upon θ_{crb}, r_σ, or r_ϵ. In fact the half-integer resonance is not detectable on the scale of figure.

As a practical matter, it is important to understand the variation of θ_{crb} near the operating point as a function of the various parameters. Figures 3 and 4 shows the effect of varying $\tilde{V}_{c1}$ and $\tilde{\eta}(C1)$ respectively upon θ_{crb} and r_σ while keeping the other input parameters at their nominal values. From Figure 3 one finds that $\Delta\theta_{crb}/\tilde{\theta}_{crb} \approx \Delta\tilde{V}_{c1}/2$. This is what one would naively expect since this change is 1/2 of what one would get if both cavity voltages where
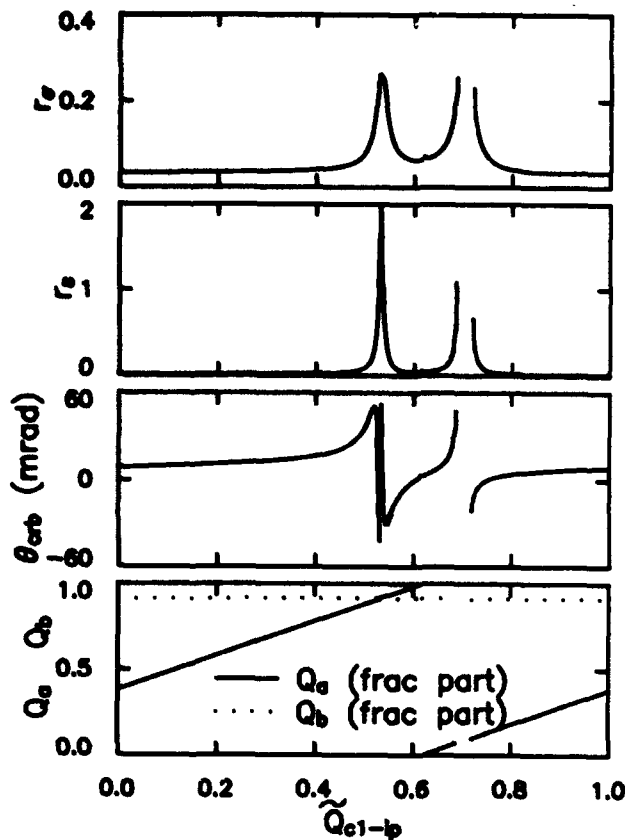
Figure 2: Eigen tunes crab angle, beam aspect ratio and normal mode emittance ratio verses $\widetilde{Q}_{c1\rightarrow ip}$.

Figure 3: Crab angle and beam aspect ratio as a function of voltage in crab cavity C1.
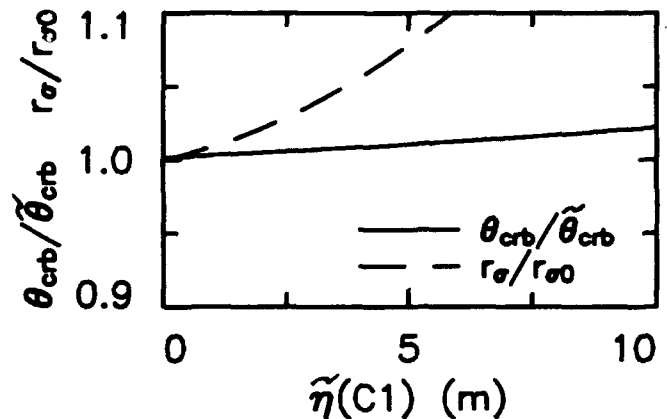
Figure 4: Crab angle and beam aspect ratio as a function of the dispersion at crab cavity C1.

changed in unison. With Figure 4 one sees that it takes a rather large dispersion to effect the crab angle by more than a few percent. This is to be expected since the kick at the crab cavities is, to first order, independent of the dispersion.

One can consider variations in the other parameters[4]. The General conclusion is that with the horizontal and longitudinal tunes far from a coupling resonance then θ_{crb} and r_σ are not 'overly' sensitive to errors in the crab compensation.

Higher Order Effects.

Higher order effects produce a distortion from a Gaussian profile. A systematic analysis is beyond the scope of this paper. These effects, however, are inevitably most significant near the extremities of the beam where the beam density is minimal. As an example of a higher order effect, consider the effect of finite crab cavity RF wavelength. A particle with displacement z will feel a kick in the crab cavity

$$\Delta x' \propto \sin(2\pi z/\lambda_{RF}) \approx \left(\frac{2\pi}{\lambda_{RF}}\right)\left(z - \frac{2\pi^2 z^3}{3\lambda_{RF}^2}\right). \quad (9)$$

For $\lambda_{RF} = 0.6$ m (500 MHz RF) a particle with a z of 0.023 m ($2.3\sigma_z$) will feel a kick which deviates 1% from

nonlinearity. Considering that only 1% of the particles have $z > 2.3\sigma_z$ the finite RF wavelength does not have a large effect on the overall beam shape. This is not to imply however that higher order effects are necessarily negligible since they induce synchrobetatron resonances for large amplitude particles.

References

[1] K. Oide and K. Yokoya, Phys. Rev. A, 40, p. 315, (1989).

[2] G. Jackson, AIP Conf. Proc. 214, p. 327, (1990).

[3] Y. Orlov, and D. Sagan, Cornell CBN 91-04, (1991).

[4] D. Sagan, Cornell CBN 91-01, (1991).

Lattice Design of the LANL Spallation-Source Compressor Ring*

Barbara Blind, Andrew J. Jason, and Filippo Neri
Los Alamos National Laboratory
AT-3, MS H811, Los Alamos, NM 87545, USA

Abstract

A new compressor ring for 790-MeV protons is proposed at Los Alamos National Laboratory to provide 1 MW of beam power for a spallation-neutron source. The design has unit-transfer-matrix achromatic arcs. Bunching, beam-control, and extraction elements reside in dispersionless straight sections. The arc symmetry and further high-order corrections maximize tune space available to the beam. The ring-injection scheme uses direct H^- injection and care is taken in disposing of the unstripped and partially stripped beams. The lattice design allows for transverse phase-space painting to maximize particle storage, as well as minimize stored-beam foil traversals.

I. INTRODUCTION

The ring is just one component of a proposed upgrade of the Los Alamos Meson Physics Facility (LAMPF) [1], designed to deliver 1 MW of beam power to two target stations operating at 40 Hz and 20 Hz, respectively. The 1.2-ms LAMPF pulse must be delivered to the ring in an irregular pattern 60 times per second; pulsed devices must hence operate at 120 Hz. Chopped beam (436 ns on, 235 ns off) is injected into the 671-ns-circumference ring for about 1790 turns. Beam bunches are superimposed by direct H^- injection. A gap is maintained by an rf system consisting of twelve cavities operating at first through fifth ring harmonic to produce a barrier bucket. At extraction the gap is 168 ns, sufficient for the fast ferrite kicker to rise and cleanly remove the 503-ns beam bunch from the ring in single-turn extraction.

A ring energy of 790 MeV was chosen, even though the LAMPF accelerator nominally delivers H^- of 800 MeV, because beam energy will be swept with the last 805-MHz side-coupled-linac tank by ±4 MeV during injection.

The ring circumference of 168.886 m was chosen so that the revolution frequency for 790-MeV protons is a subharmonic of 805 MHz; additionally, all five barrier-bucket rf harmonics are subharmonics of 805 MHz. A barrier bucket was chosen for its ability to keep the gap beam free, avoiding extraction losses as well as a possible e-p instability, and because it allows maximum beam capture and provides a bunching factor (average current/peak current) of 0.55, compared to 0.25 for a first-harmonic cavity. The beam emittance necessary to keep the space-charge tune depression below a certain value is inversely proportional to this bunching factor.

II. RING-DESIGN OVERVIEW

The ring is described in Table 1 and shown in Figure 1;

Table 1
Ring Design Parameters

Energy (MeV)	790
Circumference (m)	168.886
Repetition Rate (Hz)	40 + 20
Particles Per Pulse	$1.32 \cdot 10^{14}$
Number of Cells in Achromatic Arc	4
Number of Cells in Straight Section	5
Number of Superperiods	2
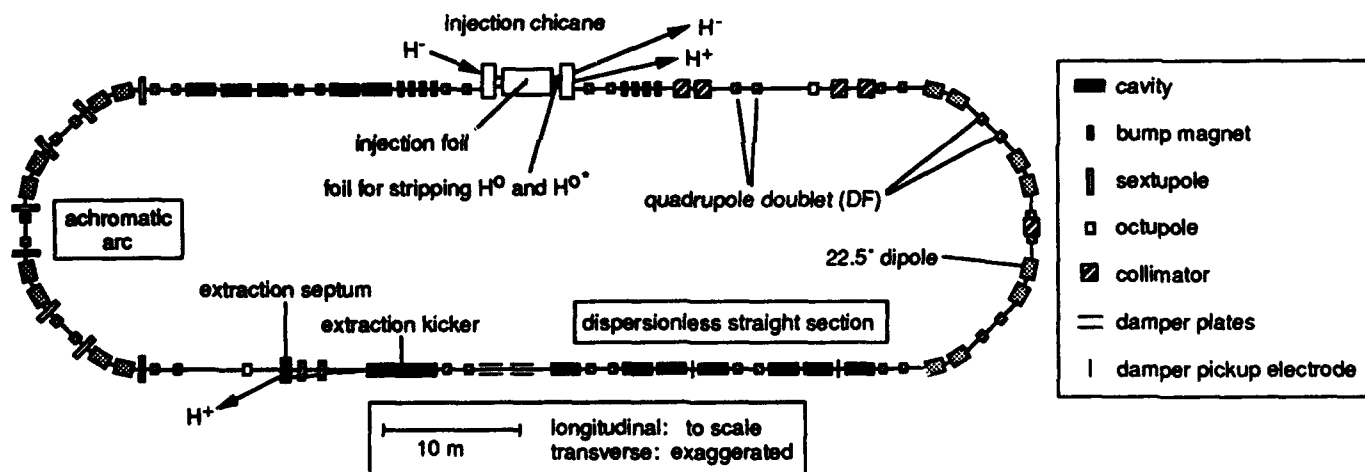
Figure 1. Ring layout.

it features dispersionless straight sections and arcs in the configuration of second-order achromats. Straight sections house the injection chicane, bump magnets for injection painting, collimators for beam-halo control, bunching cavities, a transverse-damper system, linear and nonlinear corrector elements, and the extraction kicker and extraction septum. One achromatic arc houses sextupoles, the other a dispersion collimator. Beam-position monitors and closed-orbit-correction steerers are located throughout the ring.

The desire to accomplish injection in a single drift mandated a minimum drift length of 8 m. This, together with arcs of the above-mentioned design, suggested a doublet, as opposed to a singlet, lattice. Five cells per straight section were chosen because of tune considerations, because for the required ring circumference the long drifts are adequately dimensioned (8.407 m), and because the five long drifts in low-loss areas (upstream of injection chicane and extraction kicker) can hold all rf cavities.

III. LINEAR LATTICE

The lattice functions of the ring, slightly different from those of one superperiod because of the injection chicane, are shown in Figure 2, the lattice parameters are given in Table 2. The machine tunes, $Q_x = 4.23$, $Q_y = 5.19$, correspond to phase advances per straight-section cell of $80.28°$ and $114.84°$, respectively, near the value of $90°$ that minimizes aperture requirements. Stored-beam emittances are $\varepsilon_x = \varepsilon_y = 110$ π-mm-mrad to limit space-charge tune shifts to -0.15, thus remaining in a stable region of tune space. Apertures are dimensioned for transverse acceptances of 420 π-mm-mrad and a momentum acceptance of $\pm$ 1% $\delta p/p$. Ring dipoles and quadrupoles are described in Table 3.
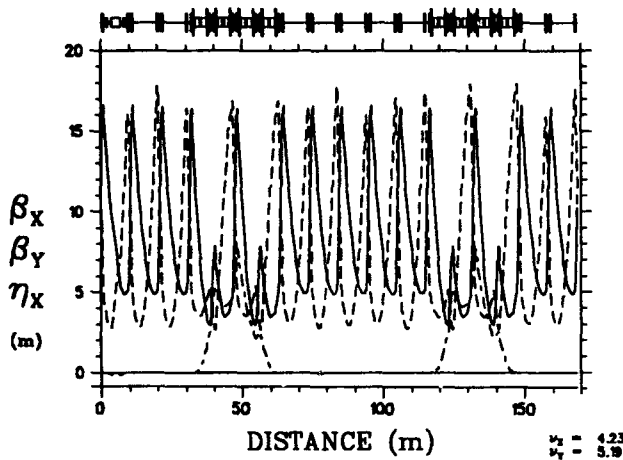
Figure 2. Ring lattice functions.

Table 2
Lattice Parameters

Q_x / Q_y	4.23 / 5.19
γ_T	3.34
$\beta_{x,max}$ (m) / $\beta_{y,max}$ (m)	16.62 / 17.93
$D_{x,max}$ (m)	7.70

Table 3
Magnet Description

Dipoles	
Arc Length (m)	1.600
Field (T)	1.188
Straight-Section Quadrupoles	
Effective Length (m)	0.500
Defocusing-Quadrupole Gradient (T/m)	-4.541
Focusing-Quadrupole Gradient (T/m)	3.990
Achromatic-Arc Quadrupoles	
Effective Length (m)	0.500
Defocusing-Quadrupole Gradient (T/m)	-3.687
Focusing-Quadrupole Gradient (T/m)	4.366

IV. NONLINEAR ISSUES

The first- and second-order chromaticities and the anharmonicities for the perfect ring, without either random or systematic errors in the magnetic elements, are given in Table 4. The beam will cover a large area in the tune diagram, both from the tune shift of the reference particle, due to space charge, and the tune spread around the central value, due to chromaticities and anharmonicities. Two families of four sextupoles each are placed in one arc to affect chromaticities. Two octupoles are placed at identical positions in the two ring straight sections to affect anharmonicities for control of tune spread.

Table 4
Nonlinear Ring Parameters

$\partial Q_x / \partial(\delta p/p)$	-4.86
$\partial Q_y / \partial(\delta p/p)$	-7.10
$\partial^2 Q_x / \partial(\delta p/p)^2$	182.07
$\partial^2 Q_y / \partial(\delta p/p)^2$	120.69
$\partial Q_x / \partial \varepsilon_x$ $(\pi$-m-rad$)^{-1}$	31.79
$\partial Q_y / \partial \varepsilon_y$ $(\pi$-m-rad$)^{-1}$	34.49
$\partial Q_x / \partial \varepsilon_y = \partial Q_y / \partial \varepsilon_x$ $(\pi$-m-rad$)^{-1}$	42.97

The widths of the resonance lines in the presence of ring imperfections, such as quadrupole-roll errors, and random and systematic higher-multipole errors in dipole and quadrupole fields, are a concern. Sets of Lambertson correctors are placed inside straight-section quadrupoles to affect the widths of the resonance lines. Skew-quadrupole correctors to affect $Q_x - Q_y = -1$, normal-octupole correctors to affect $4Q_x = 17$, and normal-decapole correctors to affect $Q_x + 4Q_y = 25$, $3Q_x + 2Q_y = 23$ and $5Q_x = 21$ have been identified.

V. RING INJECTION

The injection chicane, composed of two $5°$ septa and a $10°$ central dipole, moves the stored-beam orbit outward by 0.2 m. The injected H^- join the stored beam at the injection foil. Unstripped H^- are deflected away from the stored beam and disposed of in a beam dump, causing minimal activation in the ring.

Partially stripped H^{o*} (hydrogen atoms in excited states) have been identified as a source of activation in the Los Alamos Proton Storage Ring [2]. An H^{o*} loses its electron in a magnetic field of a strength that depends on quantum state. The H^{o*} thus may be stripped by a downstream magnet fringe field with consequent angular dispersion and particle loss. Placing the injection foil inside a dipole field can significantly reduce the problem by stripping higher states to remain within the stored-beam emittance. The field value is set so that lower states remain excited and can be disposed of in a beam dump after conversion to H^+ by a second foil. Optimization of this system indicates that a maximum loss of $<10^{-5}$ of the injected beam is in principle achievable.

Figure 3 illustrates the injection process. It shows the stored-beam ellipses of 110 π-mm-mrad area, and injected-beam ellipses of 3.2 π-mm-mrad (to 2σ) area. The injection point ($\bullet$), namely x, x', y, y' of the injected-beam centroid, is stationary (although beam energy is swept by $\pm 0.33\%$ $\delta p/p$). It is chosen such that those H^{o*} that are deflected by <2 mrad before conversion to H^+ (some 99.9% of them) lie inside the stored-beam ellipse, as indicated by the shaded area in Figure 3.
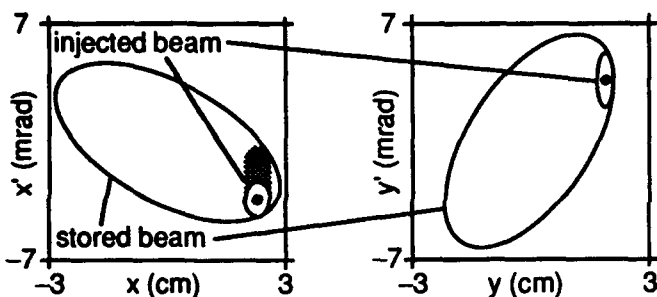
Figure 3. Transverse phase space at injection foil.

Injection painting is required to optimize the stored-beam distribution. Two sets of bump magnets relax the stored-beam centroid from near the injection point to the origin. Bumping is done such that emittance grows linearly with time. Because of the x-y correlation inherent in this bumping scheme, the distribution is rectangular and space-charge forces have octupolar components. This effect is magnified by an X-shaped beam pileup due to the particle motion in phase space. Figure 4 shows the transverse beam distribution at the end of injection, assuming accumulation in the perfect ring under neglect of space-charge forces. The foil is positioned so that its corner just covers the injected beam and injection painting keeps the number of foil traversals low, at an average of 10 per particle.

VI. PARTICLE TRACKING

The effects of space charge were assessed by first performing a fourth-order-polynomial fit to the potential of the distribution shown in Figure 4, and then tracking particles around the ring for 2000 turns including the forces derived from the potential. The beam-optics code Marylie

[3] was used. Beam size increases but remains smaller than the physical aperture.
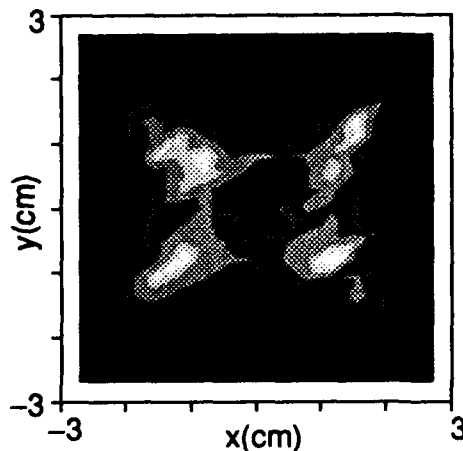
Figure 4. Beam distribution at end of injection.

The dynamic aperture of the machine was assessed by single-particle tracking to ninth order with the beam-optics code Tlie [4]. The machine was assumed to have random quadrupole-roll errors with a 10-mrad rms distribution, and random sextupole errors of 0.01 T/m^2 rms and decapole errors of 1.0 T/m^4 rms in the dipoles, as well as random octupole errors of 0.05 T/m^3 rms in the quadrupoles. The dynamic aperture as a function of particle momentum is shown in Figure 5. Improvements to the dynamic aperture will be made using first- and higher-order corrector elements.
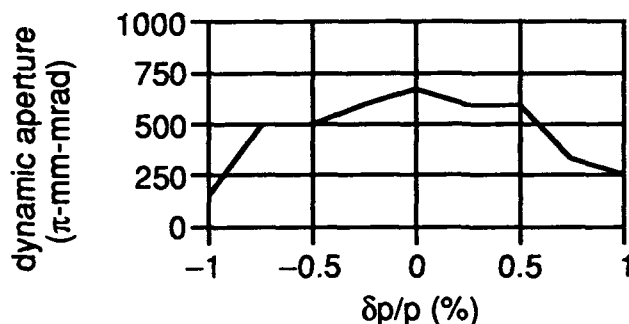
Figure 5. Dynamic aperture versus particle-momentum deviation.

VII. REFERENCES

[1] A. J. Jason, R. A. Hardekopf, R. W. Macek, H. A. Thiessen, and R. Woods, "A Los Alamos Design Study for a High-Power Neutron-Spallation-Source Driver," these proceedings.

[2] R. W. Macek, Los Alamos National Laboratory, private communication.

[3] A. J. Dragt, L. M. Healy, F. Neri, R. D. Ryne, D. R. Douglas, and E. Forest, "MARYLIE 3.0 – A Program for Nonlinear Analysis of Accelerator and Beamline Lattices," *IEEE Trans. Nucl. Sci.* 32(5), 2311 (1985).

[4] J. van Zeijts, "New Features in the Accelerator Design Code Tlie," to be published in the Proceedings of the Computational Accelerator Conference, Pleasanton, CA, Feb. 1993.

Optics Simulations of the 5 MeV NPBSE FOX Telescope

Michael F. Reusch and David L. Bruhwiler

Grumman Corporate Research Center

4 Independence Way, Princeton, NJ, 08540

Abstract

The far-field optics experiment (FOX) is a proposed design for the neutral particle beam space experiment (NPBSE) program. This 425 MHz straight beam line includes a 4.3 meter large-bore telescope. It is designed to deliver an 8 mA, 5 MeV neutral hydrogen beam with a transverse divergence of approximately 30 micro-radians to a target space vehicle (TSV) located up to 5 km away. We present zero current simulations, made with Grumman's TOPKARK code, of the telescope optics and the resulting 5 km target footprint. These simulations demonstrate the need for momentum compactation to minimize chromatic aberrations and for the careful use of octupoles to correct geometric aberrations. TOPKARK uses a novel line dipole model for the large-bore, combined function telescope objective lenses, constructed with rods of permanent magnet material, proposed for use in the FOX. We describe this model and its effect on the dynamics.

I. OVERVIEW OF FOX

The far-field optics experiment (FOX) design is largely due to the AT division at LANL [1]. It is a proposed design for the neutral particle beam space experiment (NPBSE) program.

It is a straight device, as seen in Fig. 1 approximately 11 meters long consisting of a 1 meter ion source, a 1.58 meter RFQ, a 1.74 meter DTL, a 4.31 meter telescope, a 0.25 meter WAFFOG and a 1.46 meter neutralizer. It operates at a frequency of 425 MHz and is designed to deliver an 8 mA, 5 MeV neutral hydrogen beam with a transverse divergence of approximately 30 micro-radians to a target located up to 5 km away.

The telescope section includes an RF cavity for momentum compactation. In the absence of any appreciable drift space, the RF phase is reversed in the last few cells of the DTL to longitudinally stretch the beam in preparation for this compactor.

The quadruplet eyepiece matches the beam from the DTL into the telescope objective. The objective itself is a quadrupole triplet. The last two quads of the eyepiece and the three objective quads control the beam focus and magnification in both transverse planes and match the maximum beam excursion in these planes in order to minimize
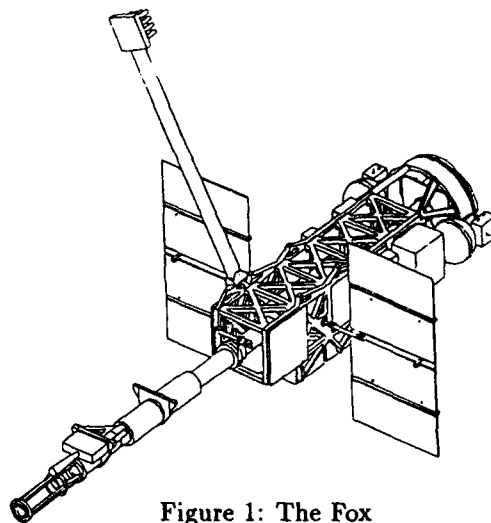
Figure 1: The Fox

the required beam pipe radius.

The large-bore objective lenses have a nominal diameter of 35 cm and are made of some 32 individual rods of suitably oriented permanent magnet material. Since each rod can be individually oriented, it is possible to control the multipole content of the objective, in particular the quadrupole and octupole content are thus determined. Still, because of the discrete nature of the rods, high order multipoles are seen by particles that approach them too closely.

II. THE TOPKARK CODE

The Topkark code is a Grumman reworking of a previous LBL-BNL-Grumman code developed for modeling a compact storage ring [10]. It exists in both a Taylor map version and a tracking version. Topkark incorporates both canonical [9],[11] and non-canonical integration techniques, automatic differentiation [7], and uses the LIELIB routines of Forest [8]. The code incorporates the usual array of iso-magnetic accelerator elements as well as a combined function bending element to dodecapole order. Topkark has been benchmarked against Marylie 3.0 [4] and TLIE [5].

Recent additions to the code include fitting routines for obtaining desired Taylor map coefficients and several space charge models which depend only on second moments of the distribution function [6]. The space charge models have been benchmarked against the TRACE3D code to linear

order and are discussed in more detail in this proceedings.

III. LARGE-BORE OBJECTIVE MODEL

The large-bore objective lenses are made of individual rods of suitably oriented permanent magnet material. In Topkark, each permanent magnet rod is modeled by a long, thin, rectangular loop of current carrying wire. The vector potential from each piece of straight wire is easily calculated analytically. These are added up and the limit of loop width d going to zero as the current I goes to infinity is taken so that the dipole moment Id remains constant. The resulting vector potential, equivalent to a line of equally oriented point dipoles, is obtained analytically.

$$A_z(x,y,z) = \frac{\mu_0 Id}{4\pi} \frac{(x-a)\cos\mu + (y-b)\sin\mu}{(x-a)^2 + (y-b)^2}$$
$$\left[\frac{z-z'}{\sqrt{(x-a)^2 + (y-b)^2 + (z-z')^2}} \right]_{z_1}^{z_2} \quad (1)$$

$$A_x(x,y,z) = \frac{\mu_0 Id}{4\pi} \cos\mu$$
$$\left[\frac{1}{\sqrt{(x-a)^2 + (y-b)^2 + (z-z')^2}} \right]_{z_1}^{z_2} \quad (2)$$

A_y is given by replacing $\cos\mu$ by $\sin\mu$ in Eq. 2. Here, $\mu + \pi/2$ is the angle of orientation of the dipole moment, while $Id \approx M\sigma$, where M is the magnitization and σ the cross sectional area of the rod. The variables a and b are the x, y coordinates of the rod. z_1 and z_2 are the longitudinal positions of its endpoints.

To obtain quadrupole symmetry, we choose N, the number of rods, to be a multiple of 4. Fox uses 32 rods spaced at angles a uniform distance apart. To obtain a desired multipole with quadrupole symmetry, we choose

$$\mu_i = (m+1)\,\theta_i + \pi/2 \quad (3)$$

Then $m = 2,4,6$ yields quadrupole, octupole and duode-capole respectively. Mixtures of multipoles may be obtained by suitable superposition of orientations. The first spurious multipole to appear is of order $N+m$. This model is a close analog of the REQ magnet design described by Halbach [12]

IV. OPTICS SIMULATIONS

The single particle Hamiltonian dynamics of the large-bore objective lenses incorporating the formula for the vector potential given above are integrated using a non-symplectic, adaptive Runge-Kutta technique since canonical integration is not an issue in the FOX.

The tracking code version of Topkark does not use a perturbative expansion but rather the exact form of the Hamiltonian. Thus, there is no limit to the perturbative order of the dynamics. The only errors made are related to the time step and order of integration.
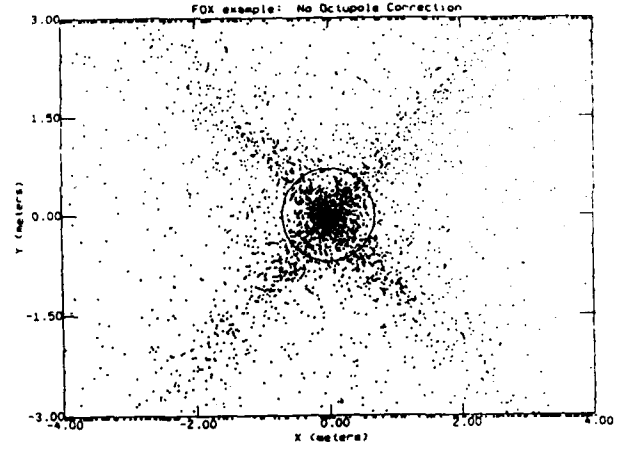
Figure 2: Uncorrected Fox design footprint at 5 km.
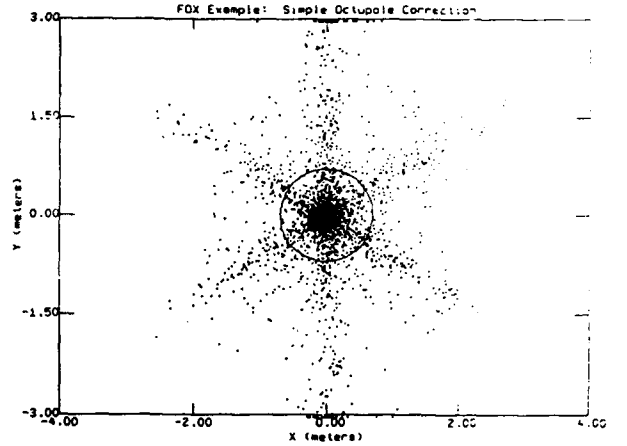
Figure 3: Simple Octupole correction Fox design footprint at 5 km.

However, the Taylor map version of the code is most useful in correcting aberrations. The fringe fields of quadrupole magnets directly feed third order geometric aberrations. These arise from a Lie polynomial of the form [2], [3],

$$f_4 = Ax^4 + Bx^2y^2 + Cy^4, \quad (4)$$

and generate the following kicks in the momentum,

$$p_x = \partial_x f_4 = 4Ax^3 + 2Bxy^2$$
$$p_y = \partial_y f_4 = 4Cy^3 + 2Bx^2y. \quad (5)$$

The coefficients A, B, C scale with telescope aspect ratio as radius over length to the third power. The uncorrected footprint is shown in Fig. 2

Simple octupole correction depends on the fact that A, B and C are linear in the strength of any octupole magnets. Then three octupole magnets can be used to zero all of A, B and C, dramatically reducing the third order geometric aberrations. However, this simple correction results in octupoles which feed up strongly into fifth order aberrations as shown in Fig. 3.

By using more than three independent octupoles (FOX uses seven), one can zero the third order coefficients while
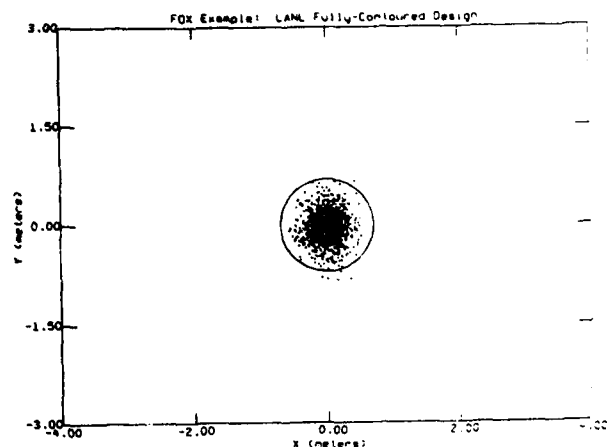
Figure 4: Contoured Fox design footprint at 5 km.

simultaneously minimizing the octupole strengths in the least squares sense. This greatly reduces feed-up to fifth order.

In the fully "contoured" LANL approach one explicitly minimizes the appropriate coefficients of the fifth order map with these extra octupoles, yielding a small but significant improvement over the least-squares approach. The footprint due to a fully contoured FOX objective is shown in Fig. 4

One further outcome of the FOX simulations was the necessity of increasing the objective bore diameter to 35 cm. Initial FOX designs used a bore diameter of 25 cm, while the beam had a nominal two sigma diameter of 20 cm. Reduced performance resulted because of the close approach of many particles to the permanent magnet rods. There, they were subject to the high order "spurious" multipoles due to the discrete number of the rods.

V. CONCLUSIONS

The particle tracking code Topkark, developed at Grumman, was used to simulate the beam optics of the FOX. These simulations demonstrated the following requirements, all of which are satisfied by the final optics design.

High order geometric aberrations must be carefully controlled through the use of "contoured" octupoles. Chromatic aberrations must be minimized through momentum compaction provided by an RF gap. The telescope objective bore must be significantly larger than the beam size in order to reduce the impact of very high multipole contributions from their 32 rod-like permanent magnets.

References

[1] A. Wadlinger et al., "FOX Optics Concept," NPBSE Interim System Design Review (ISDR) Data Package, pp. 86-126, (Grumman, Sept. 22, 1992).

[2] C.T. Mottershead, "NPB Telescope Design", Proccedings of the Fourth Neutral Particle Beam Technical Symposium, Chapter III, pp. 7-16 (Argonne National Laboratory, April 27 - May 1, 1992).

[3] A.J. Dragt and C.T. Mottershead, "Optimization of Multiple Octupole Strengths for Correction of Telescope Aberrations", Los Alamos National Laboratory technical note ATN:AT6-89-8 (1989).

[4] A.J.Dragt, L.M.Healy, F.Neri, R. Ryne, IEEE Trans. Nucl. Sci. 5, 2311 (1985).

[5] J. van Zeijts and F. Neri, "New Features in the Design code TLIE", to appear in Computational Accelerator Physics Conf. Proc. (Feb. 22-26, 1993).

[6] D.L. Bruhwiler and M.F. Reusch, "High-Order Optics with Space Charge", to appear in Computational Accelerator Physics Conf. Proc. (Feb. 22-26, 1993).

[7] M. Berz, Part. Accel. 24 , 91 (1989).

[8] E. Forest, M. Berz and J. Irwin, Part. Accel. 24, 91 (1989).

[9] E. Forest and R. D. Ruth, Physica D43, 105 (1990).

[10] M.F.Reusch, E.Forest and J. Murphy, IEEE Particle Accelerator Conf. Proc., San Francisco, 1651 (1991)

[11] H. Yoshida, Phys. Lett. A 150, 262 (1990).

[12] K. Halbach, Nucl. Inst. and Meth. 187, 109 (1981).

Longitudinal Kinetic Energy Spread from Focusing in Charged Particle Beams*

N. Brown, M. Reiser, D. Kehne, D. X. Wang, and J. G. Wang
Laboratory for Plasma Research
University of Maryland, College Park, Maryland 20742

Abstract

A charged particle beam can be given a longitudinal kinetic energy spread through focusing by magnetic solenoid lenses. Measurements of energy spread are reported and are compared with the results of computer simulations, which include several known sources of energy spread. These sources are discussed. The results of the measurements and the simulations agree, giving energy spreads which are two orders of magnitude larger than the initial thermal energy spread.

I. INTRODUCTION

Longitudinal kinetic energy spread can place limits on the operation of free electron lasers, the bunching of beams for heavy ion inertial fusion, radial focusing in accelerators, and other applications. The radial focusing of a beam by a magnetic solenoid lens creates energy spread in several ways, some of which are reversible and some of which are in practice irreversible. A reversible spread results from the linear focusing of a laminar beam; energy spreads which are in practice irreversible result from lens spherical aberrations and thermal motion of particles in the lens magnetic fields. Interparticle collisions can also cause an irreversible energy spread. We have measured the longitudinal energy spread of a 2.5-keV, 36-mA electron beam in a periodic channel, and we have done computer simulations of the same channel which include several known sources of energy spread.

Linear focusing of a laminar beam by a magnetic solenoid lens creates a reversible energy spread when the beam is focused to a waist radius which differs from the waist radius before the lens. Since a magnetic field changes only the directions of particle velocities, the change in radial potential energy with a change in waist radius is accompanied by an equal and opposite change in longitudinal kinetic energy. Lens spherical aberrations create additional energy spread, as particles at larger radii are focused more strongly. It has been shown [1] that the inclusion of nonlinearities of up to third order can result in a highly nonuniform density profile, and that particles near the edge of a laminar beam can be given enough energy to cross the axis. Any such change in transverse energy in a magnetic lens must be accompanied by an equal and opposite change in longitudinal energy. Initial transverse thermal velocities also play an important role in particle motion through a lens. In our case, even though the beam is space-charge dominated, initial transverse thermal velocities contribute significantly to the evolution of particles as they move through the lens magnetic fields, resulting in changes in the longitudinal kinetic energy which are much larger than the original transverse thermal energy.

II. EXPERIMENTAL RESULTS

The experimental setup consists of a short pulse electron beam injector [2] and a 5-m long periodic solenoid focusing channel [3]; the measurements of energy spread were made at 3.8-m along the channel. The electron beam is generated by a gridded electron gun with a generalized perveance of 4.3×10^{-3}. The channel, between the gun and the point of measurement, consists of three matching lenses followed by 24 channel lenses with a period of .136-m. The measurements were made with a parallel retarding grid energy analyzer. The first measurement was on a slightly mismatched beam, with a radius varying from 7.5-mm to 12-mm in the channel, a phase advance per period without space charge $\sigma_0 = 53^o$, and a space charge tune depression of .14. The second was on a mismatched beam with $\sigma_0 = 88^o$, a space charge tune depression of .22 and a radius varying from 4-mm to 8-mm in the periodic channel. The beam envelopes for the first and second measurements, obtained from the simulations, are shown in Figs. 1a and 1b, respectively.
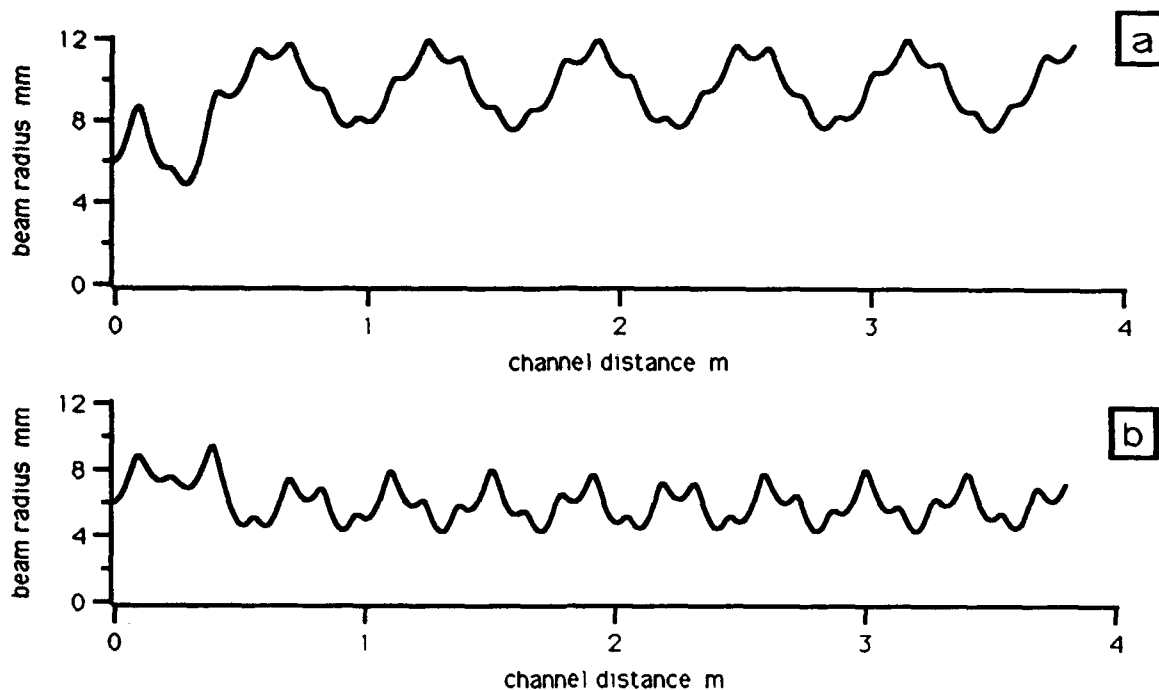
Fig. 1 Beam envelopes obtained from the simulations for the first (a) and second (b) cases. (a) has a tune depression of .13 with $\sigma_o = 53^\circ$; (b) has a tune depression of .22 with $\sigma_o = 88^\circ$.
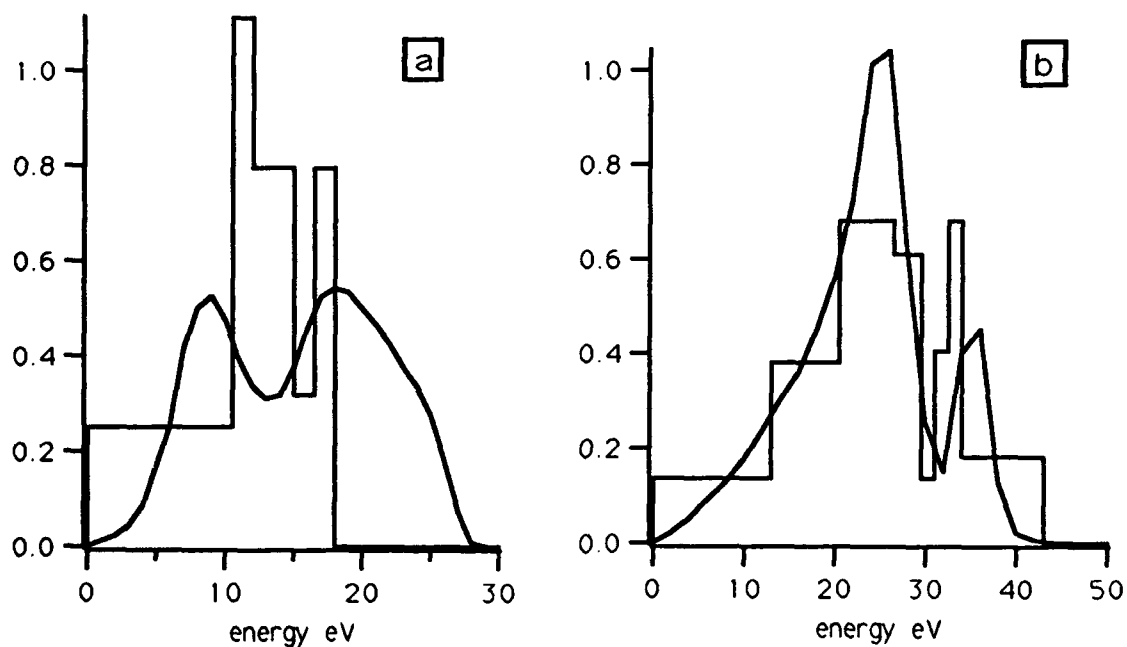
Fig. 2 Distributions in longitudinal kinetic energy for the first (a) and second (b) cases. The bar graphs are the experimental results. The solid lines are the simulation results. The zero points on the horizontal axes are set arbitrarily.

The measured energy distributions for the first and second cases are shown by the bar graphs in Figs 2a and 2b, respectively. The first has a full-width at half-maximum of about 10-eV; the second, with stronger focusing, has a FWHM of about 20-eV. The initial thermal FWHM energy spread is about .2-eV for both cases.

The zero point in Figs. 2a and 2b is arbitrarily set near one end of the distribution. Small variations in the alignment of the energy analyzer with respect to the direction of beam propagation do not change the measured energy distribution but do change the measurements of total energy. The beam energy at the end of the channel therefore cannot be found accurately with the parallel grid energy analyzer (the simulations show a drop in average longitudinal kinetic energy of about 30-eV, or slightly more than 1%, for both cases).

III. SIMULATION RESULTS

The basis for the computer simulation has previously been described [1]. It includes variations in the density profile and nonlinearities in the equations of motion of up to third order. The simulation calculates the evolution of the space charge field resulting from the motions of concentric rings of charge, assuming that the beam and the channel have circular symmetry. For this application we have added individual particles with transverse thermal velocities. The evolution of the particles is determined from the lens fields and from the calculated space charge field. Since the space charge field is found from the concentric rings of charge, the simulation is able to follow individual particle motions without having to calculate their interactions with each other. The distribution in longitudinal kinetic energy is found by keeping track of the longitudinal velocity of each particle throughout the channel. The resulting energy spreads are shown by the solid lines in Figs. 2a and 2b, corresponding to the first and second measurements, respectively.

IV. DISCUSSION

The energy distributions found from the measurements and the simulations in both cases differ from Gaussian distributions in that they have depressions near the center. This means simply that there is a particular energy range near the center of the distribution which few particles occupy. We do not yet have a physical explanation for this.

A source of longitudinal energy spread which is not included in the simulations is interparticle collisions. When a beam is accelerated from the cathode the longitudinal temperature becomes negligible compared with the transverse temperature. Coulomb collisions then redistribute the thermal velocities toward an isotropic equilibrium temperature, resulting in an increase in longitudinal energy spread. Ichimaru and Rosenbluth [4] have calculated this relaxation rate for a single-component plasma. While the time for relaxation to an isotropic temperature is much longer than the beam travel time, this effect can still produce a significant longitudinal energy spread in a relatively short distance. A more detailed discussion of this can be found elsewhere [5]. The FWHM energy spreads for the first and second cases are found to be 5-eV and 7-eV, respectively. Both give an increa between 5% and 15% in the FWHM energy s, from the simulations. When compared with results of the measurements, this difference is too small to conclude that transverse thermal collisions are contributing to axial energy spread in the beam. Work is in progress at the University of Maryland on an experiment in which thermal collisions are the dominant source of energy spread.

V. SUMMARY

Longitudinal kinetic energy spread induced by the focusing of an electron beam by magnetic solenoid lenses has been measured and simulated. Good agreement between the theory and experiment has been found.

VI. REFERENCES

[1] P. Loschialpo, W. Namkung, M. Reiser, and J. D. Lawson, J. Appl. Phys. **57**, 10 (1985).

[2] J. G. Wang, D. X. Wang, and M. Reiser, Nucl. Instr. & Meth. in Phys. Res. **A316**, 112 (1992).

[3] D. X. Wang, J. G. Wang, D. Kehne, and M. Reiser, accepted for publication in Applied Physics Letters.

[4] S. Ichimaru and M. Rosenbluth, Phys. Fluids **13**, 2778 (1972).

[5] M. Reiser, *Theory and Design of Charged Particle Beams* (John Wiley & Sons, New York, to be published in Fall 1993), Ch. 6.

Numerical and Experimental Studies of Halo Formation Due to Mismatch in a Space-Charge Dominated Electron Beam*

D. Kehne** and M. Reiser
Laboratory for Plasma Research
University of Maryland 20742

H. Rudd
6922 Nashville Rd.
Lanham, MD 20706

Abstract

Numerical and experimental studies of emittance growth and halo formation arising from beam mismatch have been performed. A mismatched 5 keV, 44 mA electron beam distribution passes through a 36-solenoid transport channel. Past studies have verified the agreement between experiment, simulation, and theory. Past simulation results show that a halo is responsible for emittance growth that results from the mismatch. Now simulation is used to find correlation between the initial distribution and the halo.

I. INTRODUCTION

Intense beams needed for applications such as FELs, electron-positron colliders, and Heavy Ion Inertial Fusion must maintain minimal emittance and size throughout the acceleration and transport region. Studies show that emittance growth arising from beam mismatch manifests itself in the form of a halo[1,2,3]. The halo is responsible for most of the emittance growth predicted by theory. Studies of multiple beams at the University of Maryland[3,4] provide a useful tool to explore halo formation.

II. BACKGROUND THEORY

Formulas predicting emittance growth due to conversion of free energy have been developed[5,6] and tested[3,4]. Theory predicts rms emittance growth of

$$\frac{\varepsilon_f}{\varepsilon_i} = \frac{a_f}{a_i}\left[1 + \frac{\sigma_o^2}{\sigma_i^2}\left(\frac{a_f^2}{a_i^2} - 1\right)\right]^{1/2} \tag{1}$$

where σ_i and σ_o are the phase advances per cell with and without space charge, a_i and a_f are the 2×rms radii of the equivalent initial stationary beam and the equivalent final stationary beam. For period length S, σ_i can be calculated as $\sigma_i^2/S^2 = \sigma_o^2/S^2 - K/a_i^2$ where $K=2(I/I_o)/(\beta\gamma)^3$, I is the beam current, $I_o=1.7\times10^4$ A, β and γ are the usual relativistic factors and a_f/a_i can be found using

$$\frac{a_f^2}{a_i^2} - 1 - \left(1 - \frac{\sigma_i^2}{\sigma_o^2}\right)\ln\frac{a_f}{a_i} = h. \tag{2}$$

For nonuniform charge distributions, the value of h is[5]

$$h = h_s = \frac{1}{4}\left(1 - \frac{\sigma_i^2}{\sigma_o^2}\right)\frac{U}{w_o}, \tag{3}$$

where U/w_o is a dimensionless parameter depending only on the geometry of the distribution. For mismatched beams[5],

$$h_m = \frac{1}{2}\frac{\sigma_i^2}{\sigma_o^2}\left(\frac{a_i^2}{a_o^2} - 1\right) - \frac{1}{2}\left(1 - \frac{a_o^2}{a_i^2}\right) + \left(1 - \frac{\sigma_i^2}{\sigma_o^2}\right)\ln\frac{a_i}{a_o}, \tag{4}$$

where a_o is the effective radius of the mismatched beam at the beginning of the channel. A waist is assumed here. In the presence of both effects, h_s and h_m add.

III. EXPERIMENTAL SETUP

The Electron Beam Transport Facility has been used to study the dynamics of multiple beam merging[3,4,7]. A 5-beamlet distribution of 44 mA and 5 keV is created by masking a 240 mA e⁻ beam. The 4×rms-emittance of the 5-beamlet distribution is estimated at 65π mm-mrad. This beam passes through 2 solenoids which mismatch the configuration to the 36 solenoid periodic (S=13.6 cm) channel that follows. The mismatch ratio(a_o/a_i) is 0.5. The values of σ_o and σ_i are 77° and 23° respectively and U/w_o was found to be 0.2656. A slit/pinhole device measures the emittance of the beam at the end of the channel. A movable phosphor screen is used to record pictures along the entire channel. Simulations were performed with the PIC code SHIFTXY described elsewhere[2]. In this paper, parameter z is defined as the distance from the aperture plate and N is the number of periods from the channel entrance.

IV. RESULTS

The two expected sources of emittance growth in this experiment are space-charge nonuniformity and mismatch. Previous studies[4] show that charge redistribution of the 5-beamlets causes the rms-emittance to grow by a factor of 1.5. This occurs in a quarter of a plasma wavelength, in agreement with theory, corresponding to a point midway between the two matching lenses. As the beam passes into the channel, the rms-emittance grows again as the free energy of the mismatch converts to kinetic energy, levelling off after 12 channel periods. A plot of emittance growth versus period number obtained from the computer simulation is shown in Fig. 1. Experimental pictures and simulated data revealed that, unlike for a matched beam, a halo forms around a

thermalized core. Elimnation of this halo via simulation resulted in a beam with no emittance growth past that due to the charge redistribution.
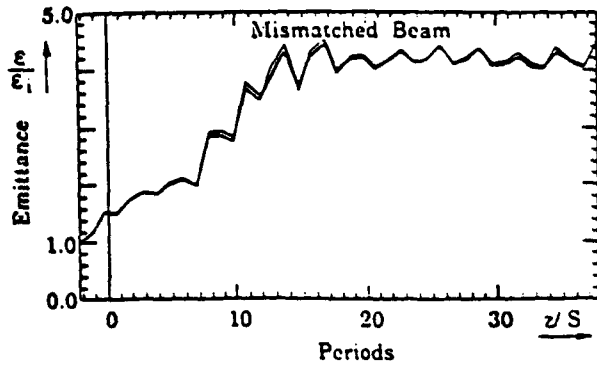
Fig. 1. Emittance growth plotted versus period number.

In this case, rms quantities do not reveal the details of the particle dynamics. Since the simulations are reliable, they are used to track the halo particles back to the initial phase space. The halo must first be defined. The x-y and x'-y' phase spaces of the beam at the beginning(N=-2.25) and end of the channel(N=36.3) are shown in Fig. 3a-d. The halo is clearly evident at N=36.3. We define halo particles somewhat arbitrarily as either having radial postion r greater than $r_{max}/2$ or slope r' greater than $r'_{max}/2$. By this definition, the halo is found to comprise 17% of the total beam current[3].

There is some question as to whether particles are swapped between the core and the halo. Comparision of halo particles at locations N=14, 22, 30, and 36 and shows that 80-90% recurrence of halo particles. The remnant mismatch causes the halo conditions to vary between these points and makes determination of the core/halo boundary difficult. The percentage of recurring halo particles could be much higher.

In order to determine correlations between halo particles and their position in the initial phase space, halo particles at N=36.3 are tracked back to the aperture plate. The problem is simplified by only considering particles originating from the inner beamlet and one outer beamlet. Phase space plots of core particles at N=36.3 originating from the inner beamlet are shown in Fig. 3e and f and from the outer beamlet in Fig 3g and h. The same plots of halo particles are shown in Figs. 3i-l. Note that the core of the outer beamlet is centered in the beamline while the halo is not. Substantial structure is evident in the halos of the beamlets while both cores are essentially thermalized. This inequity between the halo and core thermalization rates has also been noted by Wangler [2].

Phase space plots of particles in the initial distribution that will eventually enter the core are shown in Fig. 4m and n and the halo plots are in Figs. 3o and p. Several observations can be made from these plots. First, the inner beamlet contributes particles uniformly from its x-y phase space. Second, the outer beamlet contributes to the halo predominantly from the outer edge away from the beam center. Though core particles from the outer beamlet derive mostly from the edge facing the inner beamlet, many still lie on the outer edge. Fig. 3n shows that certain regions of the x-

x' phase space are excluded from the core entirely. These are particles with high velocities and high values of x.

The reason that particles are determined by both initial positon and velocity is simple. The electrostatic field set up by the 5-beamlet distribution exerts a force to either speed up or slow down each particle. This field is highest at the outer edge of the outer beamlet and lowest at the inner edge of the outer beamlet (and at the center of the center beamlet). Many halo particles come from the portion of the initial distribution that either gets the largest boost from the self-field or have large kinetic energy(KE) and are unaffected by the E-field. Likewise, core particles are genrerally determined by low KE, low E-field, or high velocity-cancelling E-field. This can be quantified by calculating the average KE of the various particles at z=0(the initial distribution) and after z=1 cm of propagation under the influence of the E-field. Table I summarizes these numbers. Despite these numbers, there are substantial numbers of particles that seem to gain energy later in the transport and hence enter the halo.

Table I. KE of core and halo particles at z = 0 cm.

KE	Core Particles		Halo Particles	
	inner	outer	inner	outer
(z=0)	0.43 eV	0.40 eV	0.63 eV	0.74 eV
(z=1 cm)	0.43 eV	0.40 eV	0.66 eV	0.79 eV

V. CONCLUSION

The analysis of the simulation data showing halo formation during the transport of a mismatched beam has led to several expected conclusions. First, most of the energy associated with the mismatch goes into the halo. Second, the beam core thermalizes much faster than the surrounding halo. Also, many of the particles that form the halo are determined by their position in the initial distribution. Though halo particles are found to be those particles of highest kinetic and potential energies, it is clear that subsequent dynamics play a part in the core/halo determination.

VI. REFERENCES

[1]O.A. Anderson and L. Soroka, Proc. of 1987 Part. Accel. Conf., Washington, DC, IEEE Cat. No. 87CH2387-9 1043, (1987).

[2]T. Wangler, Proc. of Symposium on High Brightness Beams for Advanced Accel. Appl., AIP Conference Proc. No. 253, 21 (1991).

[3]D. Kehne, M. Reiser, and H. Rudd, Proc. of Symposium on High Brightness Beams for Advanced Accel. Appl., AIP Conference Proc. No. 253, 47 (1991).

[4]I. Haber, D. Kehne, M. Reiser, and H. Rudd, Phys. Rev. A, 44 (6), 5194 (1991).

[5]M. Reiser, J. Appl. Phys. 70 (4), 1919 (1991).

[6]T. Wangler, K. Crandall, R. Mills, and M. Reiser, IEEE Trans. Nucl. Sci., NC-32 2196 (1985).

[7]D. Kehne, PhD Dissertation, Electrical Engineering Dept., Unviversity of Maryland, College Park, MD (1992).
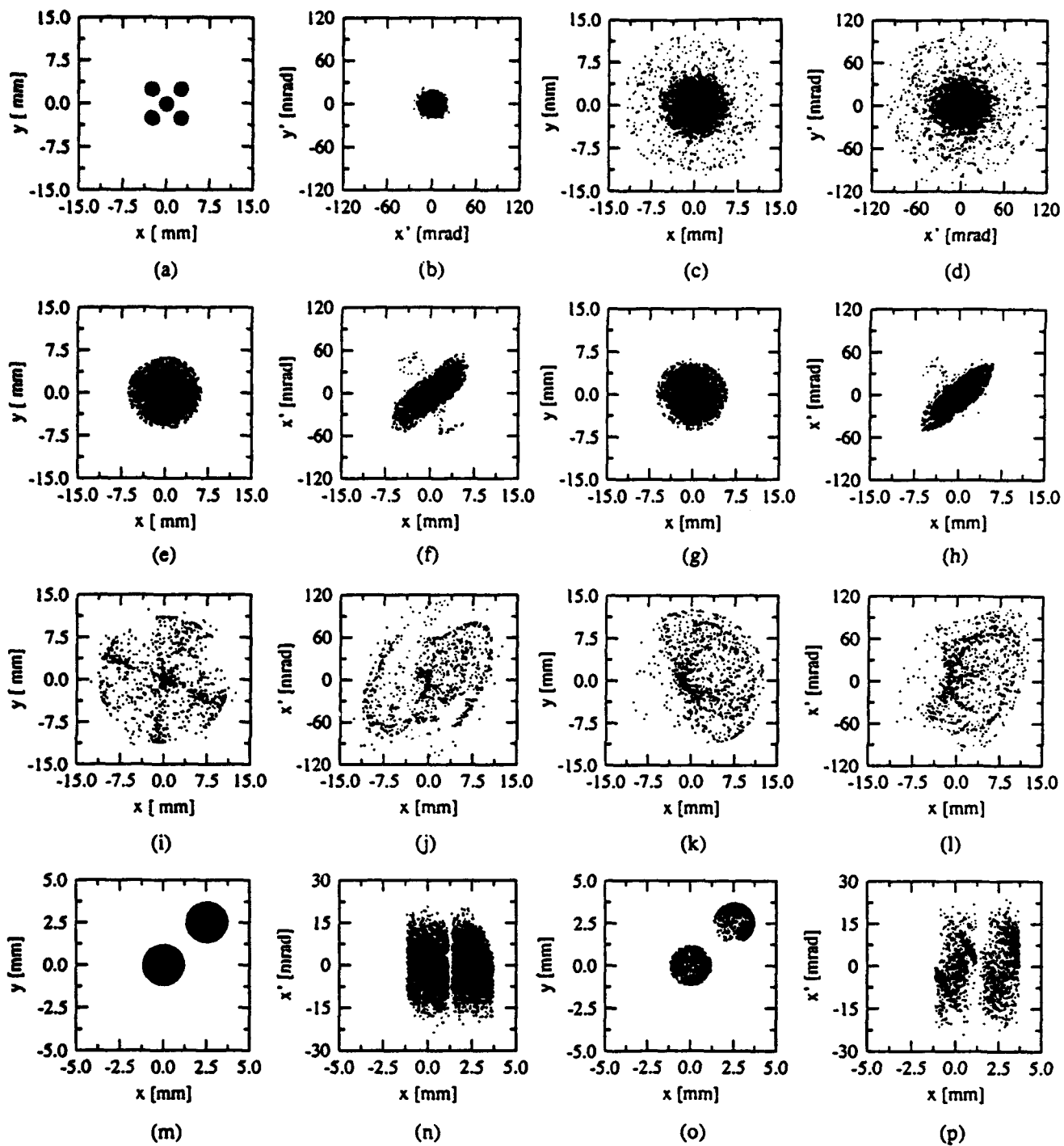
Fig.3. (a) and (b)x-y and x'-y' phase spaces for all particles at z=0 cm (N=-2.25); (c) and (d)x-y and x'-y' phase spaces for all particles at z=524 cm (N=36.3) showing diffuse halo; (e) and (f)x-y and x-x' phase spaces for core particles at N=36.3 that originate in the inner beamlet in Fig. 3a; (g) and (h)x-y and x-x' phase spaces for core particles at N=36.3 that originate in the upper right beamlet in Fig. 3a; (i) and (j)x-y and x-x' phase spaces for halo particles at N=36.3 that originate in the inner beamlet; (k) and (l) x-y and x-x' phase spaces for halo particles at N=36.3 that originate in the upper right beamlet; (m) and (n) x-y and x-x' phase spaces for particles in two beamlets of the initial distribution (z=0 cm, N=-2.25) that will be part of the core at N=36.3; and (o) and (p)x-y and x-x' phase spaces for particles in the two beamlets that will be part of the halo at N=36.3.

SUPPRESSION OF THE MAIN LEP COUPLING SOURCE

J. Billan, J.-P. Gourber, J.-P. Koutchouk, V. Remondino
CERN
CH-1211 Geneva 23

Abstract

An unexpected magnetisation of the thin nickel layer of the LEP dipole vacuum chamber has been identified as the main cause of the large horizontal to vertical optical coupling found during the LEP commissioning. Even though the betatron coupling could be much weakened by changing the difference between the tunes from 8 to 6, it was decided, after some tests, to suppress the source itself by demagnetising the nickel layer of every chamber. An "in situ" method avoiding a removal of the chambers has been developed. The coupling has been reduced by more than a factor 5. The demagnetisation suppresses a constraint on the betatron tunes and weakens the horizontal betatron spin resonances

I. INTRODUCTION

During the LEP injection test, in July 1988, an unexpected phase advance of $2°$ per cell was found to be due to the shielding effect of a thin nickel layer in the vacuum chamber. Most of this effect was cured by an appropriate shimming of the dipole magnets. But one year later, at the start-up of LEP, a strong betatron coupling was seen [1]. This effect was also due to the nickel layer. If the first effect is due to the permeability of the nickel layer, the second, as we will see below, is due to its large coercivity.

II. THE VACUUM CHAMBER AND ITS NICKEL LAYER
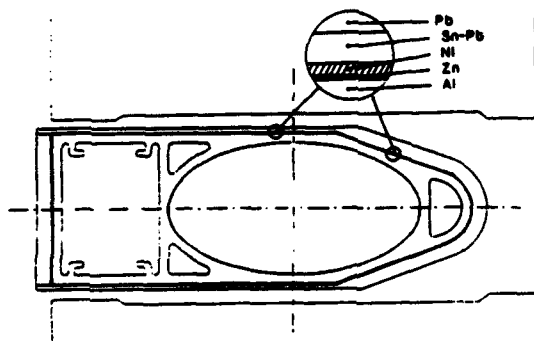
Figure 1: *The LEP dipole chamber and its nickel layer*

To limit synchrotron radiations effects, the aluminium chamber is shielded with lead plates and for corrosion reasons, these plates are tightly clad to the aluminium surface. The two metals are bonded using soft solder;

the aluminium surface having been prepared with electro-deposited layers of Zn, Ni and Sn-Pb eutectic (see Figure 1).

The magnetic characteristics of this $7\mu m$ nickel layer have been measured with a specially dedicated permeameter. Before applying any excitation field, we discovered on sample slices that this nickel was pre-magnetised at approximately 80% of the saturation field in the transverse direction of the chamber. The exact origin of this magnetisation is still unknown but it is sure that it occurred between the lead cladding and reception at CERN. After demagnetisation of the samples, we made the hysteresis cycles shown Figure 2.
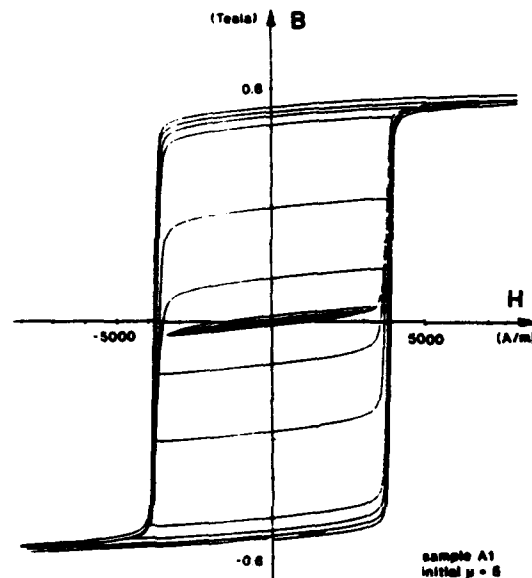
Figure 2: *Progressive hysteresis cycles of the nickel layer*

This Ni layer is a rather "hard" magnetic material $(\mu_0 H_c \approx 60.10^{-4}$ tesla$)$, with a nearly square hysteresis cycle. Once magnetised, a field larger than H_c is necessary to reverse its magnetisation. To demagnetise it the decrement of the applied alternating field should be small $(\approx 1\%)$. Inversely, once demagnetised, this layer remains insensitive to fields smaller than 80% of H_c.

III. THE ORIGIN OF THE COUPLING

For a thin magnetic layer, only the tangential component of an applied field has an influence on its magnetisation. For LEP dipoles, the maximum field on the 60 GeV cycle is 0.0715 tesla, and imposes the magnetisation of all but

the horizontal faces. Even on the 100 GeV cycle (B_{max} = 0.1080 tesla), the pre-magnetization of the two horizontal faces cannot be modified by the dipole field. Figure 3 shows the flux pattern calculated by POISSON generated by the remanent field in the two horizontal faces.
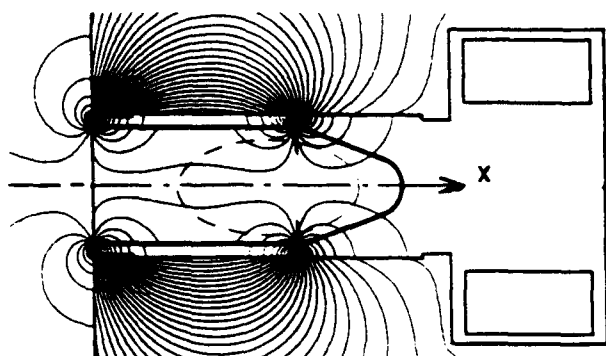
Figure 3: *The flux pattern created by the nickel layer*

An horizontal field gradient is clearly visible. Measurements of this field have been made on short samples of vacuum chamber, by sliding a 14 m² area and 40 cm long search coil along the median plane. The results are shown in Figure 4 on the curve labelled "before demagnetization".
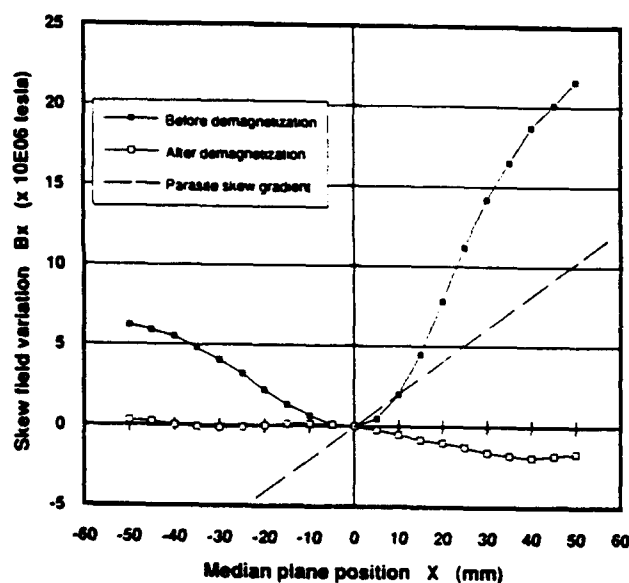
Figure 4: *Variation of the horizontal field measured on samples before and after demagnetization of the nickel layer. The skew gradient necessary for the maximum coupling (2.10^{-4} T/m) is also shown.*

As mentionned in [2], the parasitic source of the LEP coupling is: i) spread along the arcs of the machine, ii) independent of the energy level and, iii) due to a skew gradient of $\approx 2.10^{-4}$ T/m. All these criteria are quite consistent with the behaviour of the nickel layer which is definitely the main cause of the coupling.

IV. THE IN-SITU DEMAGNETIZATION

To reduce the limitations caused by this coupling, the first action was to compensate it with additional tilted

quadrupoles and optics changes [3]. But the parasitic field was not suppressed and some limitations still existed. For this reason, demagnetization of the nickel layer was studied. However, at that time all the chambers were installed in the machine and only a very few were available for sampling. Hence results from the laboratory samples were taken with caution and some margin was incorporated in the design of the method. The demagnetization effect was obtained from a 50 Hz, 0.05 tesla peak field tangential to the layer and decayed simply by slowly displacing the field generator away from the point to be demagnetized. Two systems: i) a solenoid passing along the chamber and ii) a C-shaped magnet sliding along the chamber, were first tested because they were directly powered by the mains but presented a serious drawback in requiring removal of the chamber from its magnet. These systems were used with success to test the efficiency of demagnetization in some places of the machine [4].

A third method not requiring the chamber to be dismantled was preferred for reason of cost and risk. The "in situ" demagnetization is performed by a one turn flat coil excited by a strong alternating pulsed current. This coil, inserted in the gaps between the chamber and the polefaces of the dipoles, is slid at 1 cm/s in the transverse direction to demagnetize the chamber. The current made by a dedicated power supply, is a 2000 A peak current, alternating at 50 Hz and with a pulse duration limited to 1ms in order not to burn the coil. The 20 km of the arcs were demagnetized in four weeks by four teams working in parallel.

Figure 5: *The operation of demagnetization. A set of coils is shown on the right and on the left, a coil, in place on each side of the chamber, is ready for demagnetization*

V. MEASUREMENT OF THE EFFICIENCY OF THE DEMAGNETIZATION

Figure 6 shows the result of an arc by arc analysis of vertical oscillations induced by forced horizontal betatron oscillations in a complete arc at a time. It shows a rather large dispersion of the parasitic gradient between arcs, indicating some variation in the production of the chambers

and a decrease of the mean value of this gradient by the demagnetisation to 19% of its initial value. Considering that 14% of the length of the chambers were not accessible to demagnetisation, it is clear that this operation has been an even greater success than expected from the partial tests.
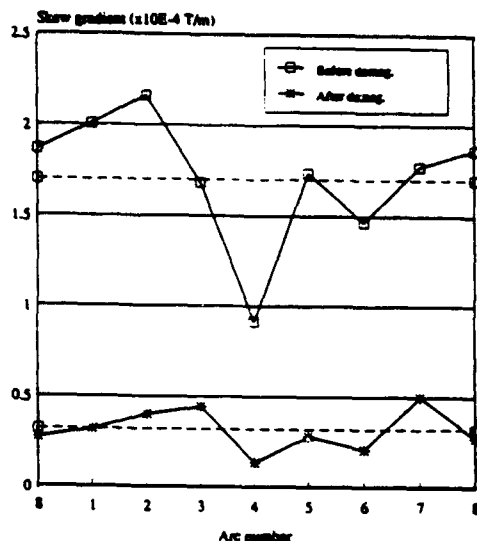
Figure 6: *The average parasitic skew gradient measured arc by arc, before and after demagnetisation*

VI. THE IMPROVEMENT OF THE MACHINE BEHAVIOUR

A. The betatron tunes

The 0th harmonics of the parasitic skew gradient is largely dominant and excites mostly betatron coupling resonances of the type $Q_x - Q_y = 8k$, $k \in \mathcal{R}$ [2]. The nominal betatron tunes of 70.3 and 78.2, chosen to maximise the luminosity, had to be changed, first to 71/77, and later to 70/76 to avoid a systematic resonance driven by the beam-beam forces. The betatron coupling was reduced in this way to its expected value from tolerances on magnetic fields and alignment and could be fully compensated using the available skew quadrupole scheme. However, the constraint on the tune difference makes it impossible to avoid simultaneously the tunes multiple of the machine periodicity in the two planes. Systematic defects were thus amplified in the vertical plane and created initial difficulties. To avoid having to constrain the tune difference, it was shown that the coupling can be minimised by splitting the betatron phase advances by 12° in the standard cell [5]. This however breaks the horizontal achromats, with a possible consequence for the dynamic aperture at very high energy.

The reduction by a factor of 5 of the spurious skew gradient decreases the strength of the strongest coupling resonance from 0.6 [2] to 0.12. This is still high for the skew compensation scheme, but can be combined with a split of the betatron phase advances less strict than in [5]. In 1993, LEP will be operated using an optics with phase advances of 90° and 60° in the horizontal and vertical planes which yields many advantages in addition to coupling compensation.

B. Polarization

The skew gradient was calculated to excite strongly a horizontal betatron spin resonance close to the Z^0 peak. The change of betatron tunes from 71/77 to 70/76 shifted the strongest resonance away from the Z^0 peak. The depolarising effect of the weaker resonances was minimised by changing the fractional part of the betatron tunes from .3 to .1. After demagnetisation (figure 7), the calculated depolarisation due to the spurious coupling becomes negligible compared to other sources.
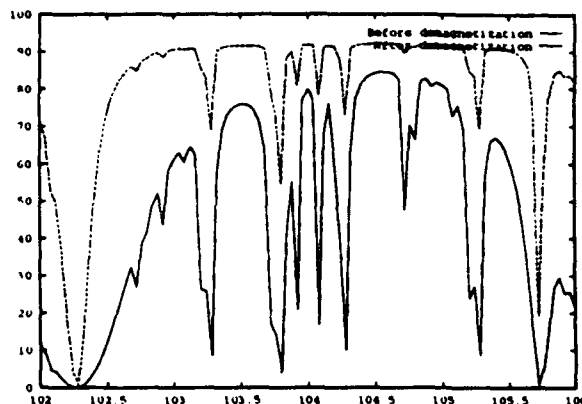
Figure 7: *Depolarisation due to the Ni alone before and after demagnetisation*

C. Decoupling of trajectories: injection and pretzel scheme

At injection, the skew gradient used to couple the large horizontal injection oscillation into the vertical plane with a compensation only after one turn. With the continuous increase in complexity, it was felt safe to reduce this oscillation. More important is the coupling of the horizontal pretzel separation into the vertical plane. Due to the different trajectories of the electrons and positrons, it results in miscrossings. The demagnetisation minimised this effect.

The additional skew quadrupoles which had been installed in the regular cells are now freed to be reconfigured as vertical dispersion correctors.

VII. REFERENCES

[1] A. M. Fauchet et al., 'Coupling in LEP: Characteristics of the source', LEP Commissioning Note 17 (1989).

[2] J. Billan et al., 'Measurement of the LEP coupling source', Proc. 2nd EPAC, Nice, (1990).

[3] J.P. Gourber et al., 'Compensation of linear betatron coupling in LEP', Proc. 2nd EPAC, Nice, (1990).

[4] J. Billan et al., 'Coupling in LEP: Influence of chamber demagnetisation in arc 2-3', SL-MD Note 52, (1992).

[5] J.P. Koutchouk, 'Self-compensation of the LEP distributed skew gradient', Proc. 3rd EPAC, Berlin, (1992).

Applications of Matrix Optics to Acceptance Studies in Low-beta Ion Linacs

K. Joh and J. A. Nolen
Argonne National Laboratory
Argonne, IL 60439, U. S. A.

Abstract

Four-gap superconducting resonators have been developed at Argonne for use in the low-beta positive ion injector (PII) for ATLAS [1]. These structures have been used successfully for ion velocities as low as 0.007c with q/m=0.1. First order matrix optics [2] and linear theory for the phase space transformations in accelerating systems [2], [3] are applied to the PII linac which includes low-beta heavy ion rf resonators and magnetic solenoids.

These provide a new method to match initial phase space ellipses when used with higher order transfer maps or ray-tracing calculations. And also we present a quantitative measure of nonlinearities using the concept of rms emittances and deviations of phase space coordinates between linear and nonlinear transformations. As a byproduct a way of identifying the dominant source of nonlinearity of system is indicated.

I. ACCEPTANCES

The maximum emittance of a beam that a system can accept is called the acceptance of the system; the particles within this acceptance will be transmitted without striking the wall. But only some part of the acceptance would transform linearly if there are aberrations.

A. Geometrical Acceptance

The geometrical acceptance of a system is defined as the acceptance calculated from linear phase space transformation. This is larger than the useful acceptance if nonlinearities are present.

The beam envelope at a position in a system with acceleration is given for an axially symmetric beam in n-dimensional phase space by [2]:

$$x_2 = \sqrt{(\det M)^{2/n} \beta_2 \epsilon_1} \,. \tag{1}$$

where det M is the determinant of the transfer matrix. And β_2, ϵ_1 are the beta-function at the position 2 and the initial beam emittance in one projected plane, respectively.

The beta-function at point 2 is found if the initial Twiss parameters of the phase space and the transfer map are known. Equation (1) is still valid for a nonaxially symmetric beam if n=2.

We define:

$$\beta^* = (\det M)^{2/n} \beta \,, \tag{2}$$

so that β^* is the effective beta-function.

Then the geometrical transverse acceptance of a system is limited by the maximum β^* and apertures of optical elements:

$$\text{GTacc} = \frac{R^2}{\beta^*_{\max}} \,. \tag{3}$$

where R is the aperture of the optical element at which the effective beta-function has maximum value $\beta^*_{\max}$.

For longitudinal phase space there is no physical aperture which limits acceptances, but to maintain the phase focusing aspect of the resonators phase excursions or time-of-flight deviations must be limited. For example if the rf phase offset is ϕ_0 for the reference particle, then the deviation of rf phase angle should not exceed ϕ_0 for any particle because at zero rf phase nonlinearity would be very important. Hence an estimate of the longitudinal acceptance is obtained by requiring:

$$\Delta t \leq \frac{\phi_0}{\omega} \equiv R_{\text{long}} \,. \tag{4}$$

where Δt is the deviation of the time-of-flight and ω is the angular rf frequency of a resonator.

Now R_{long} is analogous to the radial aperture for the transverse case, so we have for an estimate of the longitudinal acceptance:

$$\text{GLacc} = \frac{R^2_{\text{long}}}{\beta_{\max}} \,. \tag{5}$$

where R_{long} was defined above and $\beta_{\max}$ is the maximum value of the longitudinal beta-function.

In practice, we find that the longitudinal acceptance defined in this way is a good starting point for determining the linear acceptance as described below.

The geometrical acceptances can be found numerically by fitting the Twiss parameters of the phase spaces with an appropriate optimizer. The transverse or longitudinal

acceptance is calculated for an assumed initial set of Twiss parameters. Then the optimizer varies the Twiss parameters until the maximum values of the geometrical acceptances are determined.

B. *Linear Acceptance*

The nonlinearity of a system was not considered in the geometrical acceptance calculations described above. In practice only a fraction of the geometrical acceptance transforms linearly. To establish a quantitative measure of the degree of nonlinearity, a new quantity, called the deviation of the particle i, is defined:

$$\text{dev.} \equiv \frac{|x_l^i - x_n^i|}{x_{lm}} . \qquad (6)$$

where subscript l, n indicate linear and nonlinear transformations of the particle i, respectively, and x_{lm} means the maximum value of the coordinate x in the linear transformations of the geometrical acceptance.

We introduce a method to find linear acceptances by comparing linear and nonlinear transformations. As an example, let us find the transverse linear acceptance with dev. $\leq 1\%$:

• Find the geometrical acceptance using an optimizer.
• Find maximum values of position x_m and divergence x'_m from the linear transformation of the initial geometrical acceptance ellipse.
• Find deviations of phase space coordinates of individual rays with coordinates chosen on a grid bounded by the geometrical phase space ellipse from linear and nonlinear transformations.
• Discard all initial rays for which one of the deviations is greater than 1% to get the linear acceptance from the remaining rays.

Note that this deviation method gives the area and the orientation of a phase space ellipse. The degree of nonlinearity is controlled through the choice of the magnitude of dev. parameter.

II. NONLINEARITY OF A SYSTEM

For nonlinear systems the increase of rms emittance ("emittance growth") is often used as a quantitative measure of the nonlinearity. Here we examine the degree of correlation between the magnitude of the dev. parameter used above and the amount of emittance growth exhibited by the system.

The rms emittance is defined for a pair of phase space coordinates x and x' by [4]:

$$\epsilon_{rms} = 4\sqrt{< x^2 >< x'^2 > - < xx' >^2} . \qquad (7)$$

For linear systems the rms emittance is transformed in general [5]:

$$\epsilon_{rms2} = (\det M) \cdot \epsilon_{rms1} . \qquad (8)$$

where det M is the determinant of a transfer map of a system.

Thus $(\det M)^{-1} \epsilon_{rms}$ is constant of motion. And we use it to modify the usual definition of normalized emittance:

$$\epsilon_{nrms} = (\det M)^{-1} \cdot \epsilon_{rms} . \qquad (9)$$

Equation (9) would yield the common definition of the normalized emittance for the transverse case if ϵ_{rms} were multiplied by the initial value of $\beta\gamma$. Because of the invariance of the normalized emittance under linear transformations it might be used as a measure of the nonlinearity of a system by comparing its values between linear and nonlinear transformations.

We define differences of normalized emittances between linear and nonlinear transformations:

$$\delta\epsilon^{t,l} \equiv \epsilon_{nrms}^{t,l} - \epsilon_{nrms0}^{t,l} . \qquad (10)$$

where superscripts l, t indicate longitudinal and transverse phase spaces, respectively, and 0 indicates initial emittance.

Below we explore the correlation between the normalized rms emittance accepted by the system and the magnitude of the two maximum values of the dev. parameters. We also examine the relations between the rms emittance growth and the magnitude of the dev. parameters permitted in the transverse and longitudinal dimensions, including the effects of cross terms.

III. APPLICATION

We applied these concepts to the first section of the PII linac, which consists of three magnetic solenoids (s) and three low-beta rf resonators (I) as shown in Figure 1. The strengths of magnetic solenoids are adjusted to give beam waist conditions at the center of each resonator. Because of the low velocities the transfer maps are calculated analytically point-by-point through the system.

As an example a $^{238}U^{24+}$ beam with an incident velocity 0.0085c was used. The rf settings of field gradients and initial rf phase angles for the three resonators are:
I1: 4.5 MV/m (-10°), I2-1: 3.0 (-15°), I2-2: 3.0 (-15°).

The calculated geometrical transverse acceptance of the system is 263π mm·mr which is shown as the large ellipse in the Figure 2. The individual rays inside this ellipse are transformed nonlinearly with up to 3rd order off-axial fields of the rf resonators and magnetic solenoids to find linear acceptances for different deviations defined in the equation (6). In these raytracing calculations the initial longitudinal phase space area was assumed to be zero so that nonlinear coupling from transverse to longitudinal dimensions is emphasized.

Figure 2 shows the portion of the geometrical acceptance which transforms linearly with the dev. parameter limited to less than 0.01; the corresponding areas accepted are 263π mm·mr (geometrical) and 70π mm·mr (linear). A

calculation of the accepted rms emittance as a function of the maximum value of the dev. parameter over the range from dev. =0.01 to 0.10 shows a nearly linear relationship with the value of the linear rms acceptance increasing to 220π mm·mr at dev. =0.10. Figure 3 shows the details for dev. ≤ 0.05. Similarly, we evaluated the rms emittance growth of the transverse and longitudinal coordinates as a function of the dev. parameters in the transverse case. It was found, in agreement with previous experience with ATLAS calculations, that for very small nonlinearity in the transverse map, there are much more significant non-linearities appearing in the longitudinal dimension due to second-order cross terms. (The lowest order aberrations in transverse focusing are third order.) This is seen in Figure 2 where the distortion in the transverse ellipse is very small ($\delta\epsilon^t = 0.05\pi$ mm·mr) whereas the increase in longitudinal emittance is significant ($\delta\epsilon^l = 40\pi$ keV·nsec).

One interesting thing is the noticeable difference of the orientations of the geometrical and linear phase space el-lipses shown in Figure 2. To understand this the effective beta-functions for the two different orientations were plotted in the Figure 1. Qualitatively, these curves indicate that nonlinearities are minimized by keeping the effective beta-function small in I1 while allowing it to be larger in s1.

IV. CONCLUSIONS

The method to find linear acceptances and to scale non-linearites of a system by deviations of linear and nonlinear transformations seems to be well defined. Since this method is applicable to any accelerating or beam transport system it will provide a very easy and fast way to find linear acceptances and sources of nonlinearities, if higher order transfer maps are available.

This work was supported in part by the U.S. Department of Energy, Nucl. Phys. Div, under contract No. W-31-109-ENG-38

REFERENCES

[1] L.M. Bollinger et al. *Nuclear Physics*, A553, (1993) 859c-862c, and references therein.

[2] K. Joh, Michigan State University. *Ph.D. Dissertation*, (1993).

[3] D.R. Douglas, J. Kewisch. and R.C. York. *Proceedings of the 1988 Linear Accelerator Conference*, Williamsberg, Virginia, (1988) 328.

[4] P.M. Lapostolle. *IEEE Trans. Nucl. Sci.*, NS-18, No. 3, (1971) 1101.

[5] Alex J. Dragt, Filippo Neri, Govindan Rangarajan. *Physical Review A*, Vol.45, Number 4 (1991) 2572.
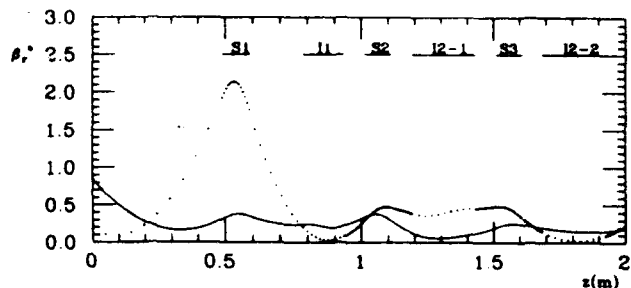
Figure 1: The system configurations and the effective beta-functions for Twiss parameters from the geometrical acceptance (solid) and the linear acceptance (dotted).
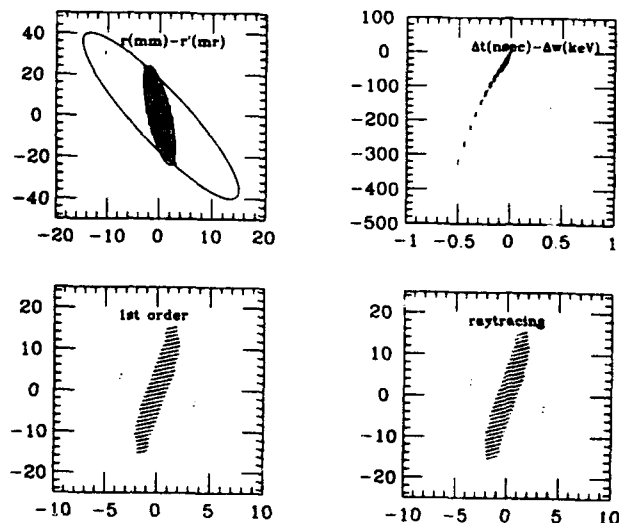
Figure 2: The phase space transformations of linear acceptance by linear (1st order) and nonlinear(raytracing) transformations with dev. =1%. The emittance induced in longitudinal phase space via nonlinear coupling with transverse coordinates is shown in the top right plot.
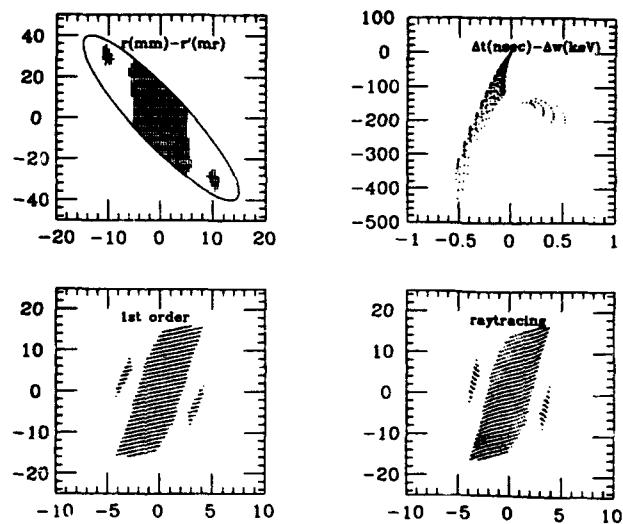
Figure 3: The phase space transformations of linear acceptance by linear (1st order) and nonlinear(raytracing) transformations with dev. =5%.

ANALYTICAL EVALUATION OF THE SECOND ORDER MOMENTUM COMPACTION FACTOR AND COMPARISON WITH MAD RESULTS

J.P. SHAN, S.G. PEGGS, S.A. BOGACZ

Fermi National Accelerator Laboratory *, P.O. Box 500, Batavia, IL 60510

Abstract

The second order momentum compaction factor α_1 is a critical lattice parameter for transition crossing in hadron synchrotrons and for the operation of quasi-isochronous storage rings, which have been proposed for free electron lasers, synchrotron light sources and recently for high luminosity e^+e^- colliders. First the relation between the momentum compaction factor and the dispersion function is established, with the "wiggling effect" included. Then an analytical expression of α_1 is derived for an ideal FODO lattice by solving the differential equation for the dispersion function. A numerical calculation using MAD is performed to show excellent agreement with the analytical result. Finally, a more realistic example, the Fermilab Main Injector, is shown not far away from the ideal lattice.

1 Introduction

In a synchrotron or storage ring, particles with different momenta have different closed orbits. The difference in the closed orbit length (ΔC) between a particle with momentum p and a reference particle with momentum p_0 may be expressed as an expansion in momentum offset δ

$$\Delta C = C_0 \alpha_0 \delta \left[1 + \alpha_1 \delta + O(\delta^2) \right], \quad (1)$$

where C_0 is the length of the reference orbit, and $\delta = \frac{p-p_0}{p_0} = \frac{\Delta p}{p_0}$. Such a dependence of orbit length on momentum is called momentum compaction, and α_0 is the linear momentum compaction factor. The second order momentum compaction factor α_1 is the focus of this paper.

Although rooted in the transverse motion, the momentum compaction effect influences the longitudinal motion through the phase slip factor

$$\eta = \frac{1}{T_0} \frac{T - T_0}{\delta} = \eta_0 + \eta_1 \delta + O(\delta^2). \quad (2)$$

where $\eta_0 = \alpha_0 - \frac{1}{\gamma^2} \equiv \frac{1}{\gamma_T^2} - \frac{1}{\gamma^2}$, and

$$\eta_1 = \alpha_0 \alpha_1 + \frac{3\beta^2}{2\gamma^2} - \frac{\eta_0}{\gamma^2}. \quad (3)$$

Here T is the period of revolution for a particle with momentum offset δ and T_0 is for a synchronous particle, β and γ follow usual relativistic kinematic notation, and γ_T is the transition gamma for a synchronous particle. Near transition η and η_0 are small and the contribution from the nonlinear term $\eta_1 \approx \alpha_0(\alpha_1 + \frac{3}{2})$ becomes very important. Nonzero η_1 leads to the fact that higher momentum particles and lower momentum particles can not agree when the synchronous phase should be switched [1], with transition timing spread (the so-called nonlinear time) proportional to $(\alpha_1 + \frac{3}{2})$. This intrinsic transition mistiming

is partly responsible for longitudinal emittance blow-up and beam loss for some machines. If we can set $\alpha_1 = -1.5$, the nonlinear effect will be suppressed and transition crossing will become much less harmful. For an isochronous electron storage ring, which was proposed for free electron laser [2], synchrotron light source [3] and recently for collider [4], α_1 determines the RF bucket height [5].

2 The Wiggling Factor

The closed orbit $x_{co}(s, \delta)$ of an off-momentum particle is described by the dispersion function

$$D(s, \delta) = \frac{x_{co}(s, \delta) - x_{co}(s, 0)}{\delta} = D_0(s) + D_1(s)\delta + O(\delta^2), \quad (4)$$

where $x_{co}(s, 0)$ is the reference orbit, and s is the azimuthal coordinate. Furthermore the effect of closed orbit offset on α_1 is negligible [6], therefore we can assume $x_{co}(s, 0) = 0$. For a span of $d\theta$, the orbit length

$$
\begin{aligned}
dl &= (\rho + D_0 \delta + D_1 \delta^2) d\theta \sqrt{1 + (D_0'\delta)^2} \\
&= ds \left[1 + \frac{D_0}{\rho} \delta + (\frac{D_1}{\rho} + \frac{1}{2} D_0'^2) \delta^2 \right], \quad (5)
\end{aligned}
$$

where $D_0' = \frac{dD_0}{ds}$. This relation is also valid for a straight sector if the limit $\rho \to \infty$ is taken in the appropriate way.

The difference in total closed orbit length of an off-momentum particle from that of a reference particle is simply

$$\Delta C = \oint (dl - ds) = \oint \alpha_0 (\delta + \alpha_1 \delta^2) ds. \quad (6)$$

Comparison of Eq.(6) and Eq. (6) yields

$$\alpha_0 = \frac{1}{C_0} \oint \frac{D_0}{\rho} ds \equiv \langle \frac{D_0}{\rho} \rangle \quad (7)$$

$$\alpha_1 = \frac{\langle D_1/\rho \rangle}{\alpha_0} + \frac{\langle D_0'^2 \rangle}{2\alpha_0}, \quad (8)$$

where $C_0 = \oint ds$ and $\langle ... \rangle$ means the average in the whole ring, and the last term in Eq. (8) $w = \frac{1}{2\alpha_0} \langle D_0'^2 \rangle = \frac{\langle D_0'^2 \rangle}{2\langle D_0/\rho \rangle}$ is called the wiggling factor [7].

Betatron oscillations may also contribute to the difference in orbit length [5], which provides a coupling mechanism between transverse and longitudinal motion. In general, this effect is very small.

3 Differential Equations For The Dispersion Function

The differential equations for dispersion function can be derived from the Hamiltonian, and expanded to the second order of δ

$$D_0'' + (\frac{1}{\rho^2} - K_1)D_0 = \frac{1}{\rho}, \qquad (9)$$

$$D_1'' + (\frac{1}{\rho^2} - K_1)D_1 = \frac{D_0'^2}{2\rho} - K_1 D_0$$

$$- \frac{1}{\rho}\left(1 - \frac{D_0}{\rho}\right)^2 - \frac{1}{2}K_2 D_0^2. \qquad (10)$$

where the prime represents the differentiation with respect to s, the azimuthal coordinate. Here $K_1 = \frac{e}{p_0 c}\frac{\partial B_y}{\partial x}$ and $K_2 = \frac{e}{p_0 c}\frac{\partial^2 B_y}{\partial x^2}$ are respectively the quadrupole and the sextupole strength for a reference particle.

These inhomogenous Hill equations could be solved in principle by using Green's function [8]. But it is not obvious to see how the dispersion function is related to other lattice parameters. In the next section we will solve Eq. (9) and Eq. (10) explicitly for an ideal FODO lattice, which is not far away from some realistic lattices, as shown later.

4 A Soluble Case: The Ideal FODO Lattice

The ideal FODO lattice that we consider is composed of N identical FODO cells, or 2N half cells. Each half cell starts at the center of a thin focussing quadrupole (QF) and ends at the center of a neighboring thin defocussing quadrupole (QD). The absolute integrated strength of half QF and QD is the same $q = |K_1|l_{hQ} = \frac{1}{f}$, where K_1 is the quadrupole gradient, and l_{hQ} focal length of the half quadrupole. The bending angle of each dipole is $\theta_0 = \frac{\pi}{N} = \frac{L}{R}$, where L is the half cell length, or the length of each dipole since $l_{hQ} \to 0$, and R is the radius of curvature for the reference particle. Another characteristic parameter is

$$s = qL \approx \sin\phi_{1/2}, \qquad (11)$$

which should not be confused with azimuthal coordinate s, where $\phi_{1/2}$ is the betatron phase advance per half cell.

It seems that one only needs to solve Eq.(9) and Eq.(10) in the dipole. Actually the necessary boundary conditions have also to be imposed by the thin quadrupoles.

In the dipole ($\rho = R$ and $K_1 = 0$), the general solution of Eq.(9) is

$$D_{0B}(\theta) = R(1 + c_1 \sin\theta + c_2 \cos\theta). \qquad (12)$$

The continuity of D and $\frac{dD}{dt} = (1 + \frac{x}{\rho})^{-1}D'$, combined with the symmetry condition $D_{0Q}' = 0$ at the center of the quadrupoles, can be solved to get

$$c_1 = \frac{c_2}{Q} = -\frac{Q}{(1 + Q^2)\cos\frac{\theta_0}{2}}. \qquad (13)$$

where $Q = Rq = \frac{s}{\theta_0} = \frac{Ns}{\pi}$. Substituting Eq.(12) into Eq.(8) and Eq.(2) gives

$$\alpha_0 = \frac{1}{\theta_0}\int_{-\frac{\theta_0}{2}}^{+\frac{\theta_0}{2}} d\theta \frac{D_{0B}}{R} = 1 - \frac{2tQ^2}{\theta_0(1 + Q^2)}, \qquad (14)$$

where $t = tan(\frac{\theta_0}{2})$, and the wiggling factor

$$w = \frac{\langle D_0'^2\rangle}{2\alpha_0} = \frac{Q^2\left[\theta_0(1 + t^2)(1 + Q^2) + 2t(1 - Q^2)\right]}{4(1 + Q^2)[\theta_0(1 + Q^2) - 2tQ^2]}. \qquad (15)$$
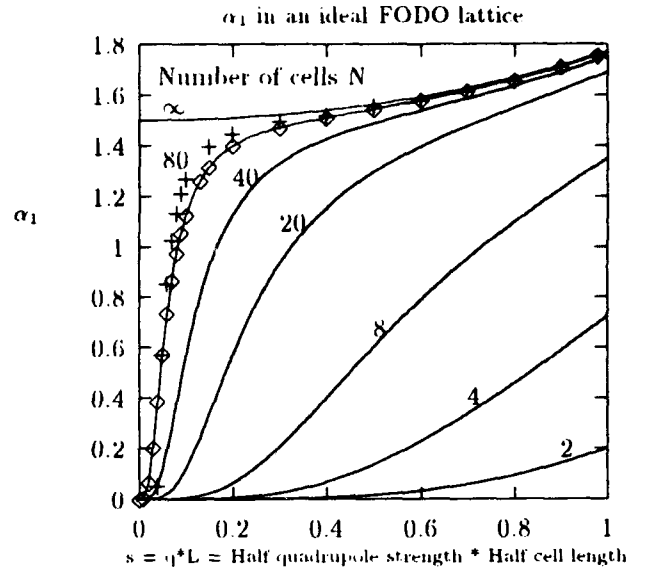
Figure 1: α_1 as a function of $s(\approx \sin\phi_{\frac{1}{2}})$ with different number of cells in an ideal FODO lattice. The solid line is the prediction from the analytical expression, which agrees excelently with MAD calculation with sector dipoles (diamond points). The plus points are MAD calculation with rectangular dipoles.

Following the same procedure, we now solve D_1. In the dipole

$$D_{1B}'' + \frac{1}{R^2}D_{1B} = -\frac{1}{R}(\frac{D_{0B}}{R} - 1)^2 + \frac{1}{R}\frac{D_{0B}'^2}{2} \qquad (16)$$

with the general solution

$$D_{1B}(\theta) = R[c_3 \sin\theta + c_4 \cos\theta] - \frac{1}{2R}\dot{D}_{0B}^2, \qquad (17)$$

which leads to a very simple closed result

$$\alpha_0\alpha_1 = \frac{1}{\theta_0}\int_{-\frac{\theta_0}{2}}^{+\frac{\theta_0}{2}} d\theta(\frac{D_{1B}}{R} + \frac{1}{2R^2}\dot{D}_{0B}^2) = c_4\frac{2\sin\frac{\theta_0}{2}}{\theta_0}. \qquad (18)$$

c_4 can be solved from the boundary conditions and substituted into Eq.(18) to get

$$\alpha_0\alpha_1 = \frac{Q^4 t(Q^2 t^2 + 3)}{\theta_0(1 + Q^2)^3}. \qquad (19)$$

Further substitution of Eq.(14) into Eq.(19) allows one to write

$$\alpha_1 = \frac{Q^4 t(Q^2 t^2 + 3)}{(1 + Q^2)^2[\theta_0(1 + Q^2) - 2tQ^2]}, \qquad (20)$$

which could alternatively be expressed as a function of s

$$\alpha_1 = \frac{s^4 t(s^2 t^2 + 3\theta_0^2)}{(\theta_0^2 + s^2)^2[\theta_0(\theta_0^2 + s^2) - 2ts^2]}. \qquad (21)$$

This result was also independently reached through a geometric approach[9].

Notice that both w and α_1 only depend on the strength of the quadrupoles and the number of cells. Fig. 1 is a plot of α_1 as a function of s with different number of cells. For a given N, w and α_1 increase as quadrupoles become stronger. The possible value of s is somewhere between 0 and 1 since $s \approx \sin\phi_{\frac{1}{2}}$. In the case $s = 0$ (cyclotron), from Eq. (14) and Eq. (20) we have $\alpha_0 = 1$ and $\alpha_1 = 0$ as expected. For real synchrotrons $\phi_{\frac{1}{2}}$ is usually between 30 and 45 degrees, and the operating range for s is $0.5 \sim 0.7$. Also notice that w and α_1 increase with N. Since N increases as ring size (roughly $N \propto \sqrt{R}$), w and α_1 are bigger for larger machines.

In the case $N \rightarrow \infty$, the centrifugal focussing of dipoles becomes negligible, and the analytical results reduce to

$$\alpha_0 = \frac{1}{Q^2}\left(1 - \frac{s^2}{12}\right), \qquad (22)$$

$$\alpha_1 = 3w = \frac{3\left(1 + \frac{s^2}{12}\right)}{2\left(1 - \frac{s^2}{12}\right)}. \qquad (23)$$

5 Comparison With MAD

In general, the differential equations cannot be solved analytically and numerical method has to be used. Unfortunately, α_1 is not directly available from the general codes such as MAD [10], which instead return the momentum compaction factor α_p. The value of α_1 has to be extracted from the dependence of α_p on δ. Care must be taken about which definition of α_p is used in a specific code. It may be

$$\alpha_{p1} = \frac{p}{C}\frac{dC}{dp} = \alpha_0\left[1 + 2(\alpha_1 + \frac{1}{2} - \frac{1}{2}\alpha_0)\delta\right] + O(\delta^2), \qquad (24)$$

or

$$\alpha_{p2} = \frac{p_s}{C_s}\frac{dC}{dp} = \alpha_0(1 + 2\alpha_1\delta) + O(\delta^2), \qquad (25)$$

or something else. It is also important to test these codes using some very simple lattices, for which an analytical solution is possible. If there is a good agreement, we can have confidence in numerical solutions of realistic lattices such as the Main Ring or the Main Injector, or an isochronous ring.

A lattice composed of 80 simplified FODO cells was set up as input to MAD. The length of a quadrupole was chosen as 1 micron. For every s, the momentum compaction factor α_p is calculated by MAD at three momentum offsets $\delta = -\delta_t, 0, +\delta_t$ with $\delta_t = 0.001$. Then α_1 was extracted from α_p as

$$\alpha_1 = \frac{\alpha_{p2}(\delta_t) - \alpha_{p2}(-\delta_t)}{4\alpha_0\delta_t}, \qquad (26)$$

if $\alpha_p = \alpha_{p2}$. The excellent agreement is achieved using the second definition, as shown in Fig. 1. The systematic discrepancy found in ref. [11] is now understood.

6 Deviation From the Ideal FODO Lattice

Taking the Main Injector ($N = 80, s = \sin\frac{\pi}{4} = \frac{1}{\sqrt{2}}[12]$, so $N \rightarrow \infty$ approximation valid) as an example, we will see how the deviations from an ideal FODO lattice affect α_1.

Sector Dipoles and Rectangular Dipoles: In the ideal lattice we assumed there was no dipole edge focussing, as with sector dipoles. In reality the Main Injector dipole is rectangular. How important is this? Fig. 1 shows that the difference between sector dipoles and rectangular dipoles is negligible in the case

of Main Injector. But as the cell phase advance and/or number of cells decreases the edge focussing becomes more important. So special care has to be taken with edge focussing in small accelerator rings.

Finite Length Quadrupole: For the simplicity of analytical solution, we have used a thin quadrupole approximation. What happens if quadrupole has finite length? From the model lattice, we see that α_1 changes from 1.545 to 1.550 by increasing the quadrupole length from 2 micron to 1 meter. This is not a surprise because the dominant source of momentum compaction comes from dispersion in dipoles, and the boundary conditions are dominated by the integrated strength of the quadrupoles.

Contribution from Sextupoles: If the sextupole strengths are set to make the net chromaticity $(1 - f)$ times the natural chromaticity, D_0 (and thus α_0 and w) will not change while D_1 will be modified, as shown in [11]

$$\langle D_1 \rangle \approx \frac{R}{Q^2}\left(1 - f + \frac{s^2}{12}\right). \qquad (27)$$

This approximation is true when the focussing from dipoles is negligible. Then

$$\alpha_1 = \frac{3 - 2f + \frac{s^2}{4}}{2\left(1 - \frac{s^2}{12}\right)}. \qquad (28)$$

So, when the net chromaticity is compensated to zero, or $f = 1$,

$$0.5 \leq \alpha_1 = \frac{1 + \frac{s^2}{4}}{2\left(1 - \frac{s^2}{12}\right)} \leq .68,$$ because $0 \leq s \leq 1$. For the Main Injector $s^2 = 0.5$, and we have $\alpha_1 = 0.587$. A value of $\alpha_1 = -1.5$ can be obtained in principle by setting $f \approx 3$ resulting in unpleasantly strong nonlinear fields.

References

[1] K. Johnsen. In *Proc. of the CERN Symposium on High Energy Accelerators and Pion Physics*, pages 106–109, CERN, 1956.

[2] D.A.G. Deacon. *Physics Report*, 76(5):349–391, 1981.

[3] S. Chattopadhyay et at. In *Proceedings of ICFA workshop on low emittance e^-, e^+ beams*, BNL 52090, 1987.

[4] C. Pellegrini and D. Robin. *Nucl.Instr.and Meth. A*, 301:27–36, 1991.

[5] Bruck et al. *IEEE Trans. Nul*, 20(3):822, June 1973.

[6] J.P. Shan, S. Peggs, and S. Bogacz. Fermilab pub92/124, April 1992.

[7] E. Ciapala, A.Hofmann, S. Myers, and T. Risselada. *IEEE Nul.*, 26(3), June 1979.

[8] J.-P. Delahaye and J. Jager. *Particle Accelerators*, 18:183–201, 1986.

[9] K.Y. Ng. Fermilab FN 578, December 1991.

[10] H. Grote and F.C. Iselin. *The MAD Program(Methodical Accelerator Design), User's Reference Manual.* CERN, 8.1 edition, September 1990.

[11] S.A. Bogacz and S. G. Peggs. In *Proceedings of the Fermilab III Instabilities Workshop*, pages 192–206, Fermilab, June 1990.

[12] Fermilab main injector Conceptual design report revision 2.3, appendum, Fermilab, March 1991.

Chromaticity Compensation Scheme for the Main Injector

S.A. Bogacz

Accelerator Physics Department, Fermi National Accelerator Laboratory
P.O. Box 500, Batavia, IL 60510 USA

Abstract

The current Main Injector lattice is studied in the context of full chromaticity compensation in the presence of the eddy current, saturation and the end-pack sextupole fields generated by the dipole magnets. Two families of correcting sextupole magnets are placed to compensate these fields and to adjust the chromaticity (in both planes) to some desired value. Variation of the dipole induced sextupole fields with the B-field (changing along a ramp) are modeled according to recent experimental measurements of the Main Injector dipole magnet. Analysis of the required sextupole strengths is carried out along two realistic momentum ramps. The results of our calculation give quantitative insight into the requisite performance of the sextupole magnets.

I. CHROMATICITY COMPENSATION

In addition to the dipoles and quadrupoles the Main Injector lattice includes two families of sextupole magnets (focusing and defocusing) located in the regular cells adjacent to the respective quadrupoles. The integrated strength, S, of an individual sextupole of length L (in geometric units of m^{-2}) is introduced as a thin element as follows

$$\Delta x' = S \, x^2 \qquad (1)$$

There is also additional sextupole field induced by each dipole magnet. This field combines the effect of eddy current as well as sextupole saturation and the geometric end-field effects. Here, one implements it by inserting a zero-length sextupoles at the middle of each dipole and at both ends (to mock-up the effects of the above fields). The integrated sextupole strengths corresponding to the 'body' and 'ends' effects are defined as follows

$$S_b = \theta_{dip} \, (b_2^{edd} + b_2^{sat}), \qquad (2)$$

$$S_e = \theta_{dip} \, b_2^{end},$$

where θ_{dip} is the bend angle of the dipole magnet.

The goal of this two families of sextupoles (f and d) is to compensate the natural chromaticity, $\underline{\chi}^o$, in the presence of the dipole sextupoles, S_b and S_e, to some desired value, $\underline{\chi}$, (both in the horizontal and vertical planes). One can describe the above compensation scheme in the following convenient notation (in terms of eight sensitivity coefficients)

$$\underline{\chi} = \underline{\chi}^o + M \begin{pmatrix} S_f \\ S_d \end{pmatrix} + S \begin{pmatrix} S_b \\ S_e \end{pmatrix} \qquad (3)$$

Here, the underlined symbols denote 2-dim column vectors and the bold face characters represent two-by-two matrices. These two dimensional objects correspond to the horizontal and vertical degrees of freedom. One can easily identify the eight sensitivity coefficients with the components of M and S matrices.

It is useful to express the sextupole strength in magnetic units of Tesla/m. Therefore, one introduces a column vector strength, $\underline{g}$. Its components describe the sextupole strength of both families as follows

$$\underline{g} = (B_o \rho) \begin{pmatrix} S_f \\ S_d \end{pmatrix} \qquad (4)$$

where ρ is a local curvature radius. Solving Eq.(3) with respect to $\underline{g}$ and applying Eqs.(2), yields the following formula

$$\underline{g} = (B_o \rho) \, M^{-1} \, [\underline{\chi} - \underline{\chi}^o - S \begin{pmatrix} S_b \\ S_e \end{pmatrix}] . \qquad (5)$$

The above expression is used to analyze the required sextupole strength as a function of changing B-field along two basic Main Injector ramps for different chromaticity compensations. The sensitivity coefficients for three families of sextupoles, S and M, are simulated for the Main Injector lattice using MAD tracking code[1]. The resulting coefficients along with the natural chromaticity, $\underline{\chi}^o$, are listed below

$$M = \begin{pmatrix} 8.28 & 0.901 \\ -1.82 & -4.43 \end{pmatrix} \times 10^2,$$

$$S = \begin{pmatrix} 1.49 & 3.50 \\ -1.39 & -3.00 \end{pmatrix} \times 10^3, \qquad (6)$$

$$\underline{\chi}^o = \begin{pmatrix} -33.6 \\ -32.9 \end{pmatrix} .$$

To complete the sextupole strength analysis, outlined by Eq.(5), one has to gain some insight into the sextupole content of a dipole magnet and its variation with B-field.

II. SEXTUPOLE CONTENT OF A DIPOLE MAGNET

First, we consider the sextupole field induced by the eddy current flowing in the dipole magnet lamination. Assuming that the field is proportional to the eddy current density, which in turn is linear in $\dot{B}_o$ one gets immediately the following relationship

$$b_2^{edd} \approx 8.128 \times 10^{-2} \frac{\dot{B}_o}{B_o} \quad [m^{-2}] , \qquad (7)$$

Here, the numerical proportionality coefficient was found[2] through numerical simulations.

Combined contributions of the saturation and static sextupole fields was found experimentally[3] via the flat and rotating coil measurements of the dipole magnet. The resulting sextupole strength variation with B-field is illustrated in Figure 1.
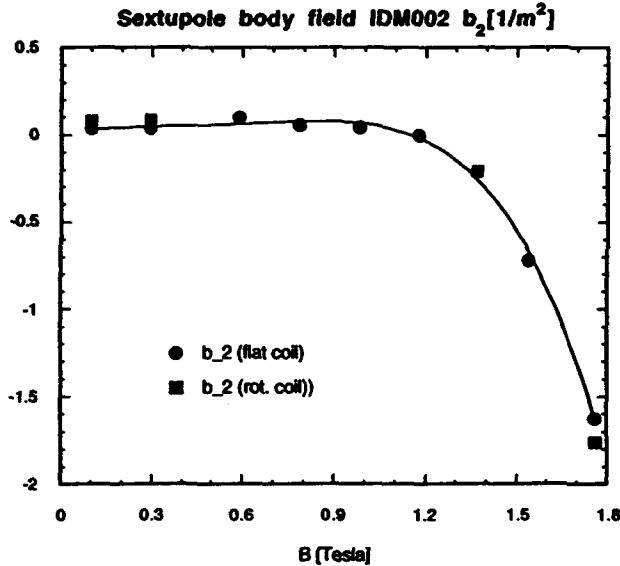
Figure 1

Finally, the end-field effect was measured for various geometries of the end-pack piece. They are collected in Figure 2. The end-pack #9 was selected as the design configuration for the dipole magnet end-pack.

Further analysis of the sextupole strength will be carried out for two realistic Main Injector ramps[4], namely the 150 GeV 'standard ramp' and the 120 GeV 'slow spill ramp'. To summarize the dipole content of the sextupole all three contributions are plotted as a function of momentum for 150 GeV 'standard ramp'. Figure 3 illustrates the above plots.
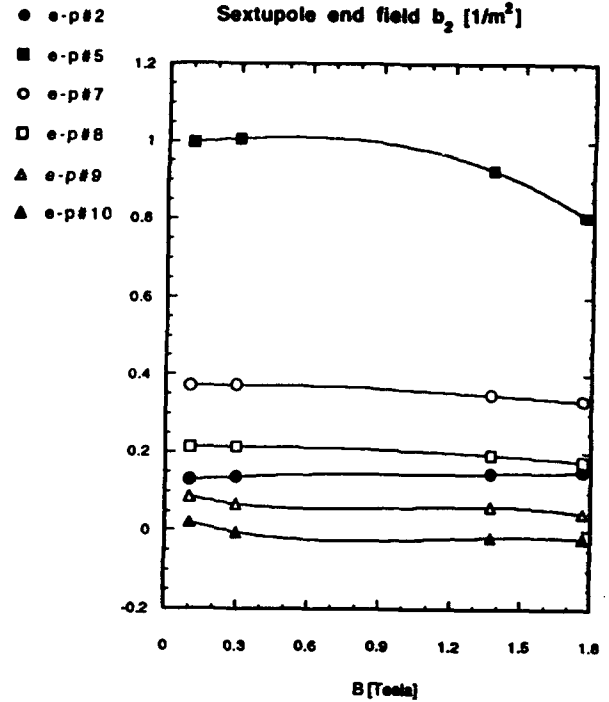
Figure 2

As one may have expected, the dipole sextupole at low B-fields starts at some static plateau and it is virtually dominated by the eddy current sextupole, while at higher B-fields the saturation components picks up and it eventually shapes up the sextupole field profile at the end of a ramp.
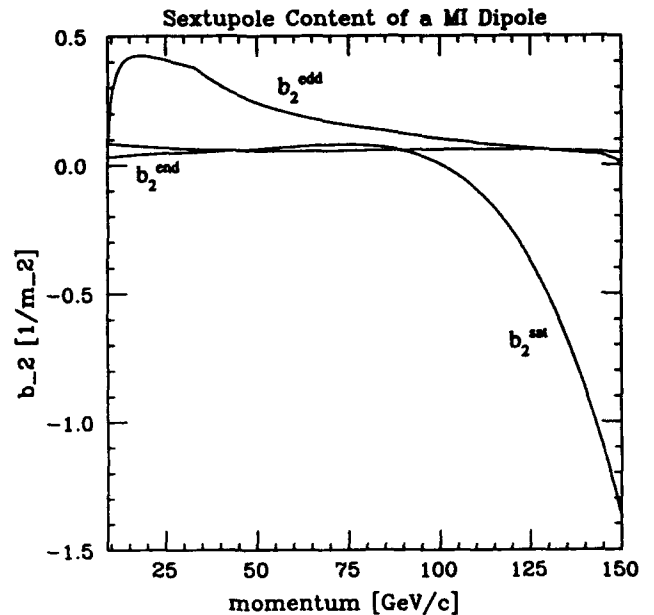
Figure 3

III. SEXTUPOLE STRENGTH – CONCLUSIONS

Now, one can evaluate the correcting sextupole strength, g, given by Eq.(5), for every point along a given momentum ramp (using values of b_2's taken from Figure 3). This procedure will generate the sextupole strength ramps for both families of correcting sextupoles (f and d). Figures 4 and 5 summarize final sextupole requirements for two model ramps. This assumes chromaticity flip at transition (from −10 units before transition to 10 units above transition, linearly, over a 20 msec time interval). The last condition is dictated by the head-tail instability assessment[5] carried out for the Main Injector.

Certain care is taken to maintain unipolarity of the power supplies for both families of correcting sextupoles (appropriate choice of the end-pack geometry). By convention, the focusing family carries positive and the defocusing one negative sign of the integrated sextupole strengths.

120 GeV 'slow spill ramp'

Chromaticity sextupole strengths

Figure 5

150 GeV 'standard ramp'

Chromaticity sextupole strengths
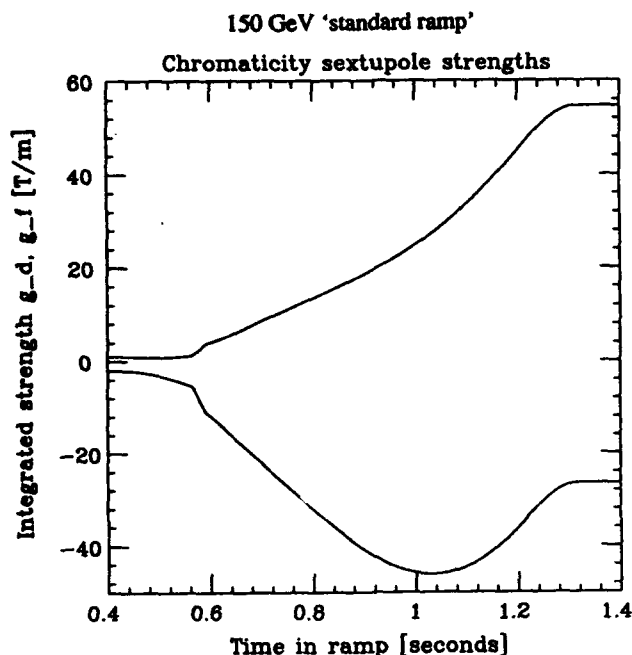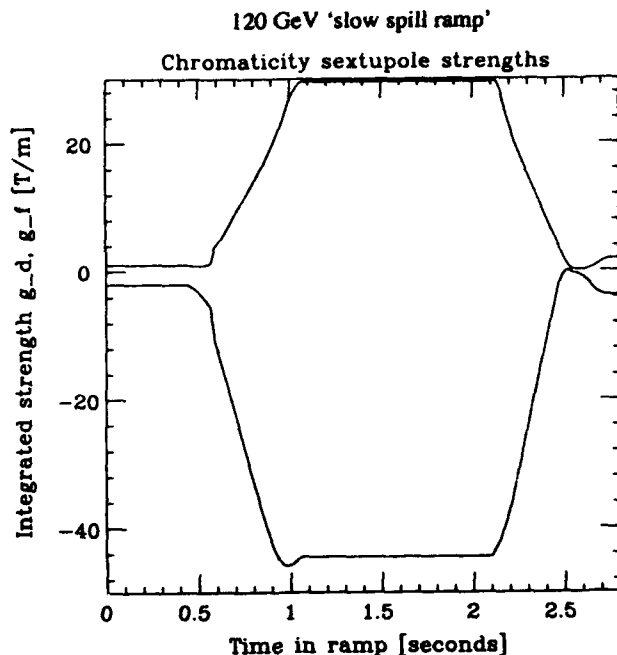
Figure 4

As one can see from Figures 4 and 5, the extreme value of the defocusing sextupole strength is bound by 45 Tesla/m for both ramps, while the maximum required strength of the focusing family in case of the regular 150 GeV ramp (55 Tesla/m) is much higher than the corresponding strength for the slow spill 120 GeV ramp (30 Tesla/m). This last feature is a result of smaller saturation sextupole component in case of the slow spill ramp (see Figure 3). The above extreme values of the sextupole strength for both families translate into the current/voltage requirements for the sextupole magnet design, which sets the standard for their power supplies performance.

REFERENCES

1. H. Grote and C. Iselin, The MAD program users reference guide, CERN/SL/90-13 (AP), 1990.
2. J-F. Ostiguy, Eddy current induced multipoles in the Main Injector, FERMILAB MI-0037, 1990.
3. H. Glass, Private Communication.
4. P. Martin, 150 GeV and revised 120 GeV Ramps, FERMILAB MI-0027A, 1990.
5. S.A. Bogacz, Coherent instability limits - Supplement, FERMILAB FN-507, 1989.

Accelerator Physics Analysis with Interactive Tools

J. A. Holt and L. Michelotti

Fermi National Accelerator Laboratory[†]
P. O. Box 500, Batavia, IL 60510, USA

Abstract

Work is in progress on interactive tools for linear and non-linear accelerator design, analysis, and simulation using X-based graphics. The BEAMLINE and MXYZPTLK class libraries, were used with an X Windows graphics library to build a program for interactively editing lattices and studying their properties.

I. INTRODUCTION

There are a number of general-purpose accelerator tracking codes in wide use such as SYNCH [1], MAD [2], or TEAPOT [3]. Each of these programs has an input format or language in which the user formulates the problem to be solved. This language is different from the language the code is written in. Frequently the accelerator physicist wants to solve a problem which does not fit within the constraints of the input language. The physicist must then duplicate the basic lattice handling functions which all codes must have as well as the special functions which solve the problem at hand. Also some problems can be solved more quickly when the input can be changed interactively and both the intermediate and final results be seen graphically. Most codes at present are a batch type operation; an input file is edited, the program is run and the final results are output.

We are developing a set of tools in which the input language is the same as the programming language. The code is written in C++ partly because of the ease in creating new "objects" that behave in every respect like fully functional variables of the language. We have integrated several types of class libraries to form applications customized to individual problems.[*] Different authors worked on different parts of the libraries. Because everything was encapsulated in objects, one author did not have to know any details of the objects created by another; only the interface to that object had to be known. As reported elsewhere [4], the MXYZPTLK [7] and BEAMLINE [8] class libraries were used to build a user-friendly, interactive, four-dimensional phase space tracker which, additionally, finds periodic orbits. The interface was based on the OSF/Motif widget toolkit and a C++ class library, MotifApp, written by Young [5]. The MotifApp class library is built upon to create tool classes. These widget classes reuse the beamline class by absorption; that is, they contain pointers to beamlines as part of their internal (private) data. The next section describes tools which have been written since writing [4].

II. BASIC TOOLS

Basic to any accelerator analysis program is the ability to edit an accelerator lattice, calculate twiss parameters and fit the tunes among other things.

A text-oriented lattice editor has been developed to interactively edit accelerator lattices. The editor consists of a scrollable list on which the user can insert and delete elements, by double-clicking on an element, the user is prompted for changes to that element by a dialog box. The lattice list can be filtered by element type. For example, one can list only the quadrupoles if so desired. The resulting lattice can be saved or recalled from a file. An additional command enables the user to "sectorize" (create a polynomial map) any portion of or all of the beamline.

A twiss parameter tool has been developed to display twiss parameters in several different formats which can be filtered by element type. There is a text format which can be saved to and recalled from disk, a list format where the user can double-click on a particular line and edit that element similar to the lattice editor and a graphics format where the twiss functions are plotted as a function of length along the beamline. Figure 1 show an example of the lattice editor and twiss tool. The parameter β_x is plotted [9] for the Tevatron low-beta lattice.

[†] Operated by the Universities Research Association Inc, under contract with the U.S. Department of Energy

[*]This is something in the spirit, if not substance, of LAMBDA [6] but without reference to data bases or specially formatted input files and with a better programming paradigm (object-oriented programming).
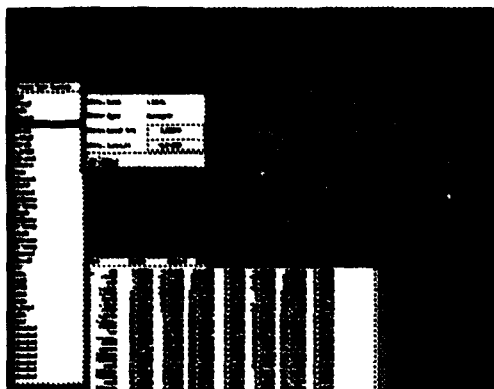
Figure 1: Lattice Editor and Twiss Tool Examples
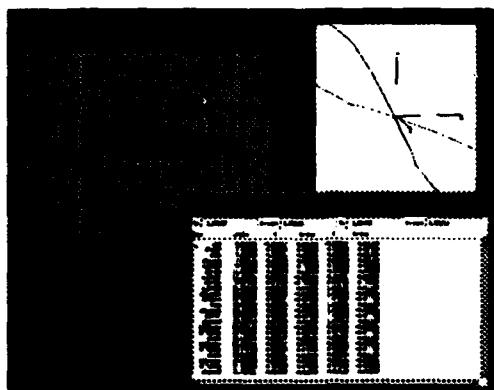
Figure 2: Tevatron Orbits using the Orbit Tool

There is an orbit tool which will receive points from the phase space tracker and plot/list the orbits along the lattice. There is also a 3D orbit plotter [10] which is useful for plotting the Tevatron's helical orbits. Figure 2 Shows the Tevatron antiproton orbit in 2D and both orbits at the D0 interaction region in 3D.

The circuit editor allows different elements to be grouped together in analogy to an electrical circuit. This is useful in the case of the Tevatron where different quadrupoles are connected to the same electrical bus.

With the tune fitter tool the the user interactively selects the focusing and defocusing circuits and is prompted for the desired tunes via a dialog box.

III. COMPOSITE TOOLS

All of the above tools can be used separately or can be combined together to make a more complicated analysis tool. As an example, the Tevatron collider has two low-beta regions for the two experiments CDF and D0. During the present collider run, it was discovered that the beams were not colliding at the center of the D0 detector and that there was a large beta-wave in the machine. A composite tool was developed to look at the perturbations in β when the values of various quadrupoles were changed. Figure 3
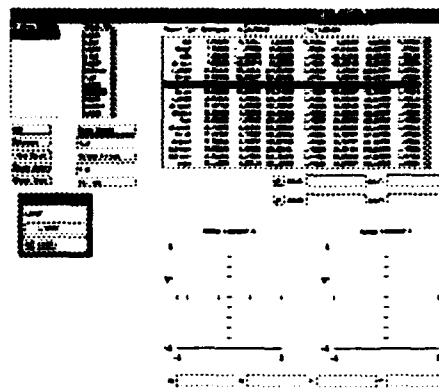
Figure 3: The $\Delta\beta/\beta$ calculation/plotting Tool

shows how the tool is laid out. In the upper right is the twiss tool. Next to it on the left is a circuit editor. Below that is the tune fitter. To the left of the ciruit editor is a list of quadrupoles to be perturbed. At the bottom is the vector plot of $\Delta\beta/\beta$ vs. $(\Delta\beta/\beta)'$ for both planes. The buttons on the far left control various functions such as choosing the reference point plotting control etc.

IV. FUTURE WORK

We plan to continue improving the prototype interactive tools developed so far and to add to the collection. The higher priority goals to be addressed include: (a) incorporating procedures into the phase space widgets so that orbit displays can toggle between "ordinary" or normal form coordinates; (b) interactively displaying the layout of the beamline using a three-dimensional graphics environment, such as Phigs; (c) tying that display to the lattice editor tools, so that beamline elements (or families of beamline elements) can be modified after picking them with a cursor; and (d) improving communication between the tools with persistent objects.

REFERENCES

[1] A. A. Garren, A. S. Kenney, E. D. Courant, A. D. Russell, and M. J. Syphers. *SYNCH: A Computer System for Synchrotron Design and Orbit Analysis. Users Guide*. Los Alamos Accelerator Code Group. Los Alamos National Laboratory.

[2] Hans Grote and F. Christoph Iselin. *The MAD Program (Methodical Accelerator Design). User's Reference Manual*. European Organization for Nuclear Research, Geneva, Switzerland. CERN/SL/90-13.

[3] L. Schachinger and R. Talman, *TEAPOT: A Thin Element Accelerator Program for Optics and Tracking*, Superconducting Super Collider Laboratory, SSC-52 December 1985.

[4] J. A. Holt, L. Michelotti and T. Satogata. *Accelerator Physics Analysis with an Integrated Toolkit* Int. J. Mod. Phys. A(Proc. Suppl.), 2b, 1007, 1993.

[5] Douglas A. Young. *Object-Oriented Programming with C++ and OSF/Motif.* Prentice Hall. Englewood Cliffs, NJ. 1992.

[6] Eric Barr, *et al.*, *Lattice Parameters Database and Operational Simulation at FNAL and SSCL.* IEEE Particle Accelerator Conference 1991, Proceedings. Vol.I pp.207-209.

[7] L. Michelotti. *MXYZPTLK: A practical users-friendly C++ implementation of differential algebra: User's Guide.* Fermi Note FN-535, Fermilab, January 31, 1990; *MXYZPTLK: A C++ Hacker's Implementation of Automatic Differentiation.* In *Automatic Differentiation of Algorithms: Theory, Implementation, and Application.* SIAM, Philadelphia, PA. 1991.

[8] L. Michelotti, *MXYZPTLK and Beamline: C++ Objects for Beam Physics.* In *Advanced Beam Dynamics Workshop on Effects of Errors in Accelerators, their Diagnosis and Correction.* (held in Corpus Christi, Texas, October 3-8, 1991) Published by American Institute of Physics, as Conference Proceedings No. 255. 1992.

[9] Peter Klingebiel and Gregory Bond, *Using the AthenaTools Plotter Wiget*, This plotter widget set was obtained via the Internet from a software archive site.

[10] Mark Edel, Jeff Kallenbach, Joy Kyriakopulos, Paul Lebrun and Donna Reid, *Visajet*, Fermilab, PU0136, 1992. The 3D widget was taken from the Visajet software which is part of the Nirvana Project.

The 50 MeV Beam Test Facility at LBL*

W. Leemans, G. Behrsing, K.- J. Kim, J. Krupnick, C. Matuk, F. Selph, and S. Chattopadhyay
Lawrence Berkeley Laboratory
1 Cyclotron Road, Berkeley, CA 94720 USA

Abstract

A new beam line, expected to be built by September 1993, will transport the 50 MeV electron beam from the ALS LINAC into an experimental area to support various R&D activities in the Center for Beam Physics at LBL. A variety of experiments are planned involving the interaction of such a relativistic electron beam with plasmas (plasma focusing), laser beams (generation of femtosecond X-ray pulses) and electromagnetic cavities (Crab cavities etc....). The beam line is designed using the measured emittance and Twiss parameters of the ALS linac. It accommodates the different requirements of the various experiments on the electron beam properties (charge, energy, pulse length) and on the handling of the beam before and after the interaction point. Special attention has also been given to incorporate diagnostics for measuring the beam properties (such as the electron energy, bunch length and charge) needed in the interpretation of the experiments.

I. INTRODUCTION

The Advanced Light Source (ALS) [1] at LBL has a 50 MeV linac, a booster ring which increases the electron energy to 1.5 GeV and a storage ring which is expected to need refilling every 6 - 8 hours. In between refills the 50 MeV electron beam will be transported into an experimental vault named the Beam Test Facility (BTF), to be operated under the auspices of the Center for Beam Physics at LBL in support of its experimental R&D program. We will conduct a variety of experiments involving the interaction of the relativistic electron beam with plasmas (plasma lens focusing), laser beams (beam diagnostic and generation of femtosecond X-ray pulses) and RF-structures. The main linac parameters are given in Table 1. The lay-out of the BTF-line is shown in Fig. 1.

Maximum Energy	50 MeV
Charge	1-2 nC/bunch
Bunch Length (σ_z)	10-15 ps
Emittance rms (unnorm)	0.3 mm-mrad
# bunches/macropulse @ 125 MHz	1 - 10 (max 100)
Macropulse rep. rate	1 - 10 Hz

Table 1: ALS Linac parameters

A first 108° bend uses a 22° dipole magnet (BX) to deflect the linac beam from its usual path towards the booster

ring, into the BTF-line, and two 43° dipole magnets (B1 and B2) to bend the beam into a transport tube through a concrete shielding wall. Three quadrupoles (Q1, Q2, Q3) located between BX and B2 are tuned to make the line achromatic after B2.
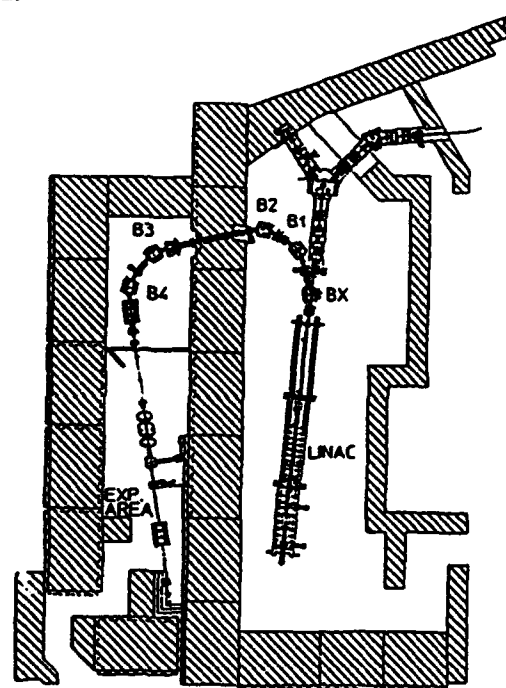
Figure 1: CAD lay-out of the BTF-line

A second 86° bend uses two 43° dipole magnets (B3 and B4) and a quadrupole doublet Q6. Using the Q4 and Q5 doublets upstream of this bend, the beam can be collimated and transported into this bend or focused onto a Cerenkov radiator, located in a diagnostic box, to measure the temporal bunch profile. The second bend is tuned to be achromatic after B4. A telescope consisting of two quadrupole triplets (Q7 and Q8) will allow a wide range of transverse beam sizes to be delivered to the experiments. Due to a slight non-isochronicity of the line, the electron bunch is expected to lengthen about 10 % for a momentum spread of 0.1 %. The vacuum chambers in the 43° bending magnets have been outfitted with a 1" diameter beam pipe tangential to the beam orbit to allow a laser beam to be brought onto the e-beam path.

II. MAGNETIC LATTICE DESIGN

The design of the magnetic lattice of the BTF-line has been done with the code TRACY [2], is based on the measured magnetic properties of the dipole and quadrupole magnets and uses the measured Twiss parameters and beam emittance of the linac. [3] The design goal was for the lattice to accommodate the different requirements set forth by the plasma lens and X-ray source experiments on the electron

beam, before and after the interaction point. Next we briefly discuss the experiments and the required electron beam parameters.

A. Plasma Lens Experiment

Aside from having the potential to enhance luminosity in future linear colliders, plasma lenses could be useful as small f-number lenses for tightly focusing relativistic beams of moderate energy. The scope of the plasma lens experiment is to study the properties of plasma lenses in both overdense and underdense (in particular the adiabatic lens) regimes.[4] Emphasis will be on resolving important issues such as time response of the lens, lens aberrations and shot-to-shot reproducibility. Using an envelope model, we have determined the plasma requirements (density, length and location) and the beam requirements (waist size, location, charge) which will allow us to study the different regimes. The plasma source will be isolated from the high vacuum transport line using Be-foils. The plasma will be created through multi-photon ionization. The plasma length will be varied from 10 to 35 cm, the density from 10^{11} - 10^{14} cm^{-3}. The e-beam will be focused to a spot with a β-function varying from 0.02 m to 0.4 m. The beam profile at different locations behind the lens will be measured by temporally and spatially resolving the Cerenkov light cone [5] produced when the electron beam hits a thin quartz radiator. The Q9 quadrupole triplet will transport the electron beam onto a beam dump. The optimized lattice is shown in Fig. 2. The graphics were generated with LATTICE. [6]
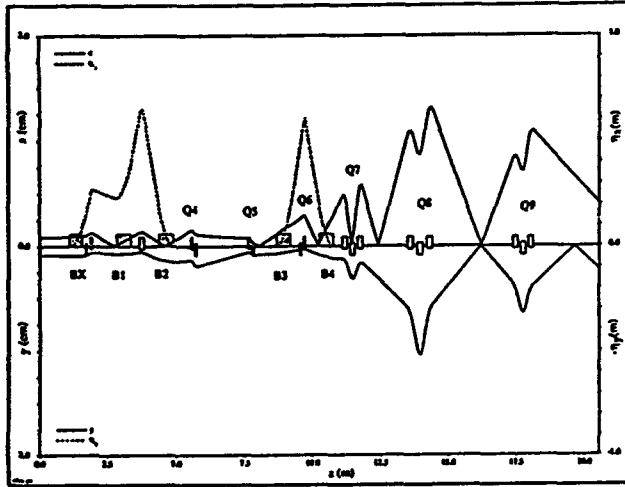
Figure 2: Optimized lattice for the plasma lens experiment.

B. Orthogonal Laser-Electron Beam Scattering Experiment

It is well known that when a photon beam collides with a relativistic electron beam, radiation upshifted in frequency by a factor proportional to γ^2 will be generated through a process named Thomson scattering.[7] Here γ is the Lorentz factor. The pulse duration in a head-on collision will be given by the longer of the laser or electron pulse duration. The electron pulse duration is at least a few ps ($\sigma_z = 10\text{-}15$ ps for our case) for typical accelerators. It has recently been proposed [8] to generate much shorter pulses of upshifted radiation by using

90° incidence. The optical pulse width is then determined by the longer of the incident optical pulse width and the transit time across the electron beam focus. In this orthogonal scattering geometry, the upshift of the radiation is given by 2 γ^2 and the divergence angle by $1/\gamma\sqrt{N}$. The laser beam acts as an electromagnetic undulator with N the number of electromagnetic oscillation cycles during the transit. In pricnciple, the electron beam size can be determined by measuring the divergence angle of the radiation.

The goals of the X-ray source experiment are twofold: 1) to develop technology towards measuring beam sizes relevant to future linear colliders and 2) to develop technology towards the generation of 1 Å, 30 fs pulses delivering 10^{12} photons/s for study of ultra-fast phenomena. In the present experiment we will collide, a high intensity (10^{16} - 10^{17} W/cm^2), ultra-short (200 - 300 fs) pulse from a Ti:Al$_2$O$_3$ laser (0.8 μm) at 90° with the electron beam. The lattice has been optimized to give an electron beam waist of 35 μm at the interaction point. This will generate a 0.4 Å X-ray pulse with 300 fs duration in a cone angle of 1.5 mrad, containing about 3 x 10^5 photons. A 90° C-magnet is utilized to separate the particle and photon beams after the interaction point. The optimized lattice is shown in Fig. 3.
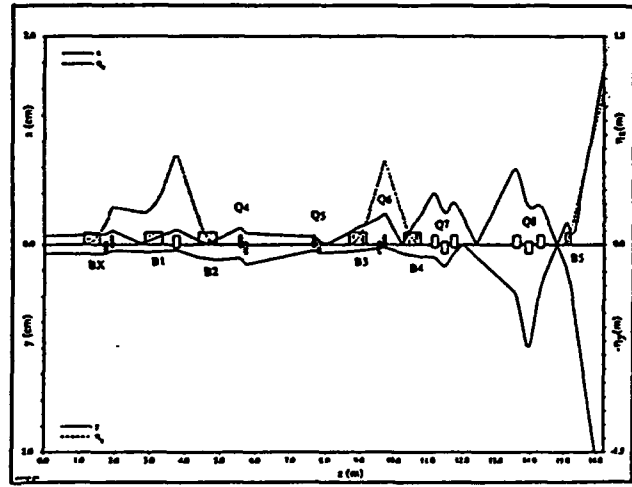
Figure 3: Optimized lattice for the X-ray source experiment.

III. Beam Line Diagnostics

The elecron beam energy, charge, bunch length and emittance are some of the important parameters which will be required for modeling the experiments. The beam energy can be measured using a variable dispersion in-line spectrometer which consists of the second bend and the triplet Q7. A horizontal collimator is located in the object plane and a fluorescent screen/TV module is located in the image plane. The charge will be measured non-destructively with an integrating current transformer. The bunch length will be measured by time resolving the Cerenkov light emitted when the electron beam transits a thin quartz plate. The beam emittance will be measured at two locations: 1) entrance to the BTF-line and 2) exit of the plasma lens. At the former locations the lens strength of an upstream quadrupole triplet is

varied while the beam size is monitored on a fixed fluorescent screen. At the latter location the Q8 triplet strength is fixed but a fluorescent screen or Cerenkov radiator is scanned along the beam direction.

The electron beam position along the beam path will be monitored non-destructively with beam position monitors made of high bandwidth pick-up buttons with a measured rise time of 16 ps. Fluorescent screens can be dropped into the beam path at 5 different locations for visual inspection of the beam profile and position, and to aid in the tuning of the achromatic sections. The spatial resolution with the present equipment has been measured to be about 20 μm.

IV. Power Supply Specifications and Timing Issues

The laser and e-beam alignment tolerances and the need for reproducibility in the plasma lens experiment put tight constraints on the shot-to-shot movement of the beam in the transverse and longitudinal directions. Current ripple in the supplies powering the bend magnets and the quadrupoles will respectively cause the beam to move in the horizontal plane and the focus to move back and forth around the optimum interaction point. A detailed study of the beam dynamics has determined that the critical supplies, those powering the dipole magnets and the quadrupole triplets Q7 and Q8 require a current stability of a part in 10^4. [9] With this power supply performance the main limitation stems from bunch-to-bunch energy variation due to beam loading in the 3 GHz accelerator structure. To increase the X-ray flux, we are considering colliding one single laser pulse with many electron bunches, separated by 8 ns, within the same macro-pulse. However, without beam loading compensation, the bunch to bunch energy variation is on the order of 0.8 %. This would cause the waist to move by as much as 10 Rayleigh ranges, thereby severely reducing the interaction efficiency. A beam loading compensation scheme based on phase adjustment of the RF signal fed to the 3 GHz accelerator structure will be tried out this spring and should reduce this an order of magnitude.

In addition, the orthogonal scattering experiment requires accurate synchronization between the laser and the electron beam. Since the linac utilizes a thermionic gun as opposed to a laser driven photocathode, synchronization is more difficult to achieve. An upper limit [10] for the timing jitter has been established at ± 10 ps, by triggering a Tektronix SCD5000 digitizing scope with the signal from a fast rise time (16 ps) pick-up button and monitoring the movement in time of the zero-crossing of the RF-signals which are fed to the first two subharmonic buncher cavities (125 and 500 MHz respectively) The laser can therefore be synchronized with respect to the 125 MHz RF-signal.

V. Status of Construction

The design of the BTF-line is nearing completion. Construction is progressing on schedule and is expected to finish September 1993. Commissioning will take place during Sept./Oct. 1993 with the first experiment scheduled for Nov. 1993.

VI.Summary

We have reported on the design of the Beam Test Facility which will utilize the 50 MeV ALS linac to conduct a variety of experiments in support of the experimental R&D for the Center for Beam Physics at LBL. The magnetic lattice was optimized for a plasma lens experiment and an experiment on orthogonal scattering of a laser beam off the electron beam to generate femto-second X-ray pulses. The optimization was carried out using the measured Twiss parameters and emittance of the linac and the measured magnetic properties of the beam line components. The stringent requirements set forth by both experiments on the transverse and longitudinal beam position necessitated a detailed analysis of power supply stability. Measurement of the bunch-to-bunch beam energy variation indicates that beam loading compensation will be required when attempting to increase the X-ray yield by colliding one single laser pulse with multiple bunches in a macro-pulse.

A variety of beam diagnostics will be implemented to allow measurement of the various beam parameters relevant in the interpretation of the experiments. Experiments are expected to commence during the fall of 1993.

VII. Acknowledgments

The authors want to thank J. Bengtsson for having made available the code TRACY, taking the time to teach one of the authors (W.L.) its power and elegancy and for his guidance in the design of the line and analysis of tolerances. We also thank Barry Bailey for coordinating all electrical work, the ALS operators for their help with the beam property measurements, J. Hinkson for his contributions to the evaluation of the beam line diagnostics, E. Wallace for helping with the design and construction of the plasma lens experiment and the Cerenkov diagnostic, Rick Donahue for having calculated the shielding requirements and L. Stout for his contributions to the initial lay-out.

VIII. References

[1] "1-2 GeV Synchrotron Radiation Source", Conceptual Design Report, LBL-PUB 5172 Rev., 1986.
[2] J. Bengtsson, E. Forest, and H. Nishimura, unpublished.
[3] J. Bengtsson, W. Leemans and T. Byrne, these proceedings.
[4] W. Leemans, A. Sessler, and S. Chattopadhyay, LBL-ESG Tech Note-199.
[5] Y. P. Chong et al., Proceedings 1989 PArt. Acc. Conf., 89CH2669-0, 1493 (1989).
[6] J. Staples, LBL - 23939, June 1987.
[7] See L. R. Elias, Phys. Rev. Lett. 42, 977 (1979) and references therein.
[8] K.-J. Kim, S. Chattopadhyay, and C. V. Shank, LBL-33074.
[9] W. Leemans and J. Bengtsson, LBL-ESG Tech Note-233.
[10]The actual timing jitter is probably smaller, as the measured value equals the manufacturer's specification of the internal scope trigger jitter.

KNOWLEDGE RULE BASE FOR THE BEAM OPTICS PROGRAM TRACE 3-D

George H. Gillespie, Peter K. Van Staagen and Barrey W. Hill
G. H. Gillespie Associates, Inc.
P. O. Box 2961
Del Mar, California 92014, U.S.A.

Abstract

An expert system type of knowledge rule base has been developed for the input parameters used by the particle beam transport program TRACE 3-D. The goal has been to provide the program's user with adequate on-screen information to allow him to initially set up a problem with minimal "off-line" calculations. The focus of this work has been in developing rules for the parameters which define the beam line transport elements. Ten global parameters, the particle mass and charge, beam energy, etc., are used to provide "expert" estimates of lower and upper limits for each of the transport element parameters. For example, the limits for the field strength of the quadrupole element are based on a water-cooled, iron-core electromagnet with dimensions derived from practical engineering constraints, and the upper limit for the effective length is scaled with the particle momenta so that initially parallel trajectories do not cross the axis inside the magnet. Limits for the quadrupole doublet and triplet parameters incorporate these rules and additional rules based on stable FODO lattices and bidirectional focusing requirements. The structure of the rule base is outlined and examples for the quadrupole singlet, doublet and triplet are described. The rule base has been implemented within the Shell for Particle Accelerator Related Codes (SPARC) graphical user interface (GUI).

I. Introduction

There are several applications of expert systems to accelerator problems, notably in the area of control systems [1,2]. Accelerator analysis software is another area where expert systems offer a profitable avenue of development. The application of expert system shells such as the Knowledge Engineering Environment (KEE) is one approach to developing expert systems for analysis codes [3]. However, the requirement to work within the SPARC GUI precluded the use of such environments. For ease of integration with SPARC it was also desirable to write the rules in C rather than LISP.

II. The Shell for Particle Accelerator Related Codes (SPARC) Environment

SPARC is a unique GUI environment developed to support accelerator simulation and analysis codes. The approach is similar to that suggested by Heighway [4]. Figure 1 shows a TRACE 3-D [5] SPARC application screen [6]. The SPARC interface has a number of important features which improve the speed and ease of setting up and defining a TRACE 3-D problem. The use of expert system type rules is the focus of this paper and several are discussed below.
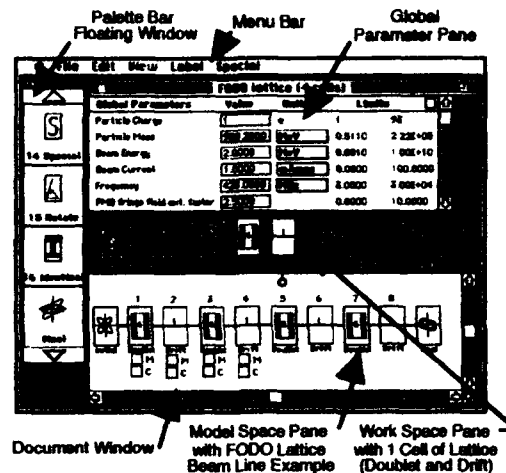
Figure 1. TRACE 3-D SPARC Application Screen.

III. Knowledge Rule Base Description

The primary objective of the expert system rules is to assist users in setting up beam line problems for TRACE 3-D. Both beginning and experienced users are intended to benefit. For novices the rules provide guidance. For advanced users the goal is to reduce the number of off-line calculations. In addition, the rules assist in the training of new users.

There are two classes of knowledge base rules in SPARC: (1) problem configuration rules and (2) input parameter rules. Problem configuration rules are concerned with the arrangement of components and are implemented in SPARC with rules defining the placement of graphical elements on the Model Space Pane of a Document Window (Figure 1). Input parameter rules are quantitative and are of two types: those specifying default values and those providing lower and upper limits for user guidance.

To facilitate development of the parameter rules, the TRACE 3-D input has been divided into four categories: (1) Global Parameters, (2) Piece Parameters, (3) Matching Parameters, and (4) User Preferences. The first two categories encompass the numerical input required to define a TRACE 3-D beam line. This work discusses rules developed for these parameters. The latter two categories are associated with the tasks that TRACE 3-D can preform once the beam line is defined. SPARC has special features to assist in their setup and are discussed elsewhere [6].

There are ten TRACE 3-D input parameters which have been assigned as SPARC Global Parameters. These include the five "top level" beam line parameters: particle charge (Q), particle

mass (ER), initial beam energy (W), beam current (XI) and radiofrequency (FREQ). Also included are two parameters which impact calculations for magnetic elements: the fringe field extension factor for permanent magnet quadrupoles (PQEXT) and a binary parameter which determines if chromatic aberrations are to be included (ICHROM). Two other Global Parameters set the maximum step sizes used in the TRACE 3-D beam dynamics: SMAX and PQSMAX. The last Global Parameter defines the initial beam setup (IBS) in terms of either emittances and Twiss parameters, or a sigma matrix.

The Piece Parameters include the transport parameters used by TRACE 3-D (arrays NT and A), the initial beam characteristics (arrays BEAMI, EMITI and SIGI), and the final beam characteristics used for matching (BEAMF array). These parameters are accessed by "double clicking" on the piece icons appearing in the Document Window. The transport parameters start with default values that can be modified by the user. The rules are applied to the parameters of a given piece, and a set of upper and lower limits for each parameter are displayed giving the user guidance. Several choices for units are available, often including a "smart units" option [6].

The limits for each of the Global and Piece Parameters are generated by a knowledge rule base developed specifically for the TRACE 3-D program. These rules are of three origins:

- TRACE 3-D driven,
- Particle beam optics utility, and
- Practical hardware constraints.

The first type includes constraints such as requiring the input parameter for any "identical element" (type 16) to lie between the first and last element numbers of the beam line model, and others based on step sizes (SMAX and PQSMAX) used in the beam dynamics calculations. Practical hardware constraints are derived from specific accelerator technology. Section IV describes rules for three TRACE 3-D transport elements, the quadrupole singlet, doublet and triplet, and illustrates examples from the three origins given above.

Guidelines have been developed in terms of what parameters can be used for rules relating to other parameters. For the baseline rules these guidelines limit the number of logic paths and eliminate circular paths and other conflicting requirements. Such conflicts can be handled in expert systems, but this was considered to be beyond the scope of the baseline rules. The guidelines assume that a "top-down" flow of information is the most important and they may be summarized as:

- Global limits may depend on Global Parameters,
- Global limits may not depend on Piece Parameters,
- Piece limits may depend on Global Parameters,
- Piece limits may use Piece Parameters of that Piece,
- Piece limits may not use Parameters from other Pieces,
- Default values must be constants and self-consistent.

As is apparent from the examples described below, these guidelines are not overly restrictive. It should be noted also that the

TRACE 3-D guidelines are not determined by SPARC limitations; other SPARC applications have different guidelines.

IV. Rules for Quadrupole Singlet, Doublet and Triplet Elements

A. Quadrupole Singlet (TRACE 3-D Element Type 3)

There are two input parameters for the TRACE 3-D quadrupole element. These are the magnetic field gradient, B', and the effective length, l. The limit rules and default values developed for these parameters are based on a water cooled, iron core, electromagnetic quadrupole, similar to the type discussed by Steffen [7]. A cross section is shown in Figure 2.
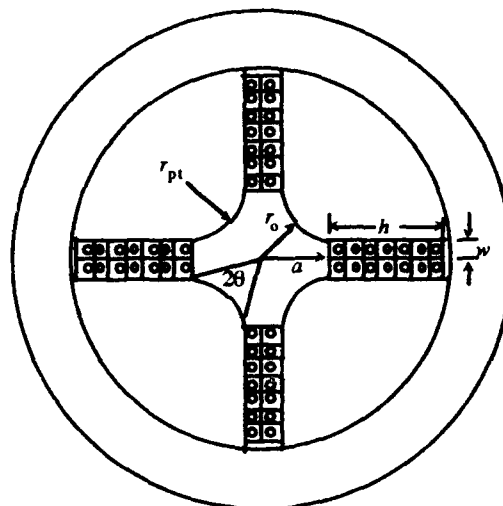
Figure 2. Electromagnetic Quadrupole Geometry.

The magnetic field gradient is

$$B' = 2\mu_o N I / r_o^2 \quad , \tag{1}$$

where I is the current in the windings, N is the number of turns per pole and r_o is the (radial) aperture. The guidance limits for the quadrupole field strength use a maximum estimate for NI consistent with a minimum estimate for r_o.

For low harmonic field content, Halbach suggests [8] that the radius of curvature of the pole tip, r_{pt}, be $1.15 r_o$ and that the half angle, θ, subtended by the pole tip be $\pi/6$. From these values and the geometry it can be shown that the distance a is $1.404 r_o$. Using $a = w/\tan[(\pi/4)-\theta]$ then gives $r_o = 2.658 w$. Characterizations [8] of hollow, water cooled, copper wire indicate that a good choice is square Anaconda wire of 3.665 mm. This is used to estimate a minimum practical radius:

$$r_{min} = 2.658 \, w. = 9.74 \text{ mm} \tag{2}$$

The maximum current density for such wire is typically 3×10^7 A/m^2, so the maximum current in the wire, I_{max}, is 201 A. The number of windings per pole, N, is set by the ratio h/w, generally about 4 [7,8]. We assume an aggressive upper design limit of 8, hence $N = 8$. The gradient limits are then:

$$B'_{max,min} = \pm 2\mu_o N I_{max} / r_{min}^2 = \pm 42.5 \text{ T/m} \tag{3}$$

The upper limit on the effective length, l_{max}, is determined by requiring that the focal point of the quadrupole be outside of the lens itself, i.e. that incoming parallel trajectories do not cross the axis inside the quadrupole, which would result in a lens that is defocusing in both transverse planes. If the length is less than this upper limit then the quadrupole will be focusing in one plane. This condition can be written as

$$l_{max} = (\pi/2)k^{-1} \quad , \tag{4}$$

where $k = [|B'|/B\rho]^{1/2}$ and $B\rho$ (in Tesla-meters) $= (1/300)[p / |Q|]$ is the particle rigidity. The lower limit on the quadrupole length is taken to be the maximum step size, SMAX, used in the TRACE 3-D beam dynamics calculations.

B. Quadrupole Doublet (TRACE 3-D Element Type 6)

The doublet transport element in TRACE 3-D is an antisymmetrical doublet [9] and consequently has three input parameters: the magnetic field gradient of the two quadrupoles, B', (the sign is that of the upstream quad), the effective length, l, of the two quadrupoles and the drift distance, d, between them. In TRACE 3-D the doublet subroutine calls the subroutines for the quadrupole and length elements. The limits and defaults for the quadrupole parameters in the doublet are adopted from those of the quadrupole (Section IV A). The rule for the upper limit on the drift distance between the quadrupoles is based on the zero-current stability condition for a FODO channel composed of drifts and these doublets (Figure 1). The stability condition for the channel can be written as [9]:

$$|\cos kl \cosh kl + (\cos kl \sinh kl - \sin kl \cosh kl)(kd) \\ - (\sin kl \sinh kl)(kd)^2/2| < 1 \quad . \tag{5}$$

This results in an upper limit on the drift spacing between the quadrupoles which can be expressed as a multiple of the quadrupole length, $d_{max} = Dl$, where:

$$D = [(\cos kl \sinh kl - \sin kl \cosh kl) + (\sinh kl + \sin kl)] \\ \times [(kl)(\sin kl \sinh kl)]^{-1} \quad . \tag{6}$$

The lower limit on the drift distance d is taken to be SMAX.

C. Quadrupole Triplet (TRACE 3-D Element Type 7)

The triplet transport element in TRACE 3-D is a symmetrical triplet [9] and has five input parameters. These are (1) the magnetic field gradient of the two outer quadrupoles B'_o, (2) the effective length of each of the two outer quadrupoles l_o (3) the drift distance between the inner and outer quadrupoles, (4) the magnetic field gradient of the inner quadrupole B'_i, and (5) the effective length of the inner quadrupole l_i. Figure 3 shows a schematic of the symmetrical triplet.

The limits for the parameters of the two outer quadrupoles are based on those of the quadrupole (Section IV A). For the inner quadrupole and drift spacing, the rules are based on the conditions for achieving bidirectional focusing. The conditions for bidirectional focusing can be written in terms of the parameter $s = d + (l_o + l_i)/2$ as:

$$l_o / [(k_o l_o) \sin(k_o l_o)] - 2l_i / [(k_i l_i) \sinh(k_i l_i)] < s \\ < l_o / [(k_o l_o) \sin(k_o l_o)] \quad , \tag{7}$$

and

$$s > 2l_i / [(k_i l_i) \sin(k_i l_i)] - l_o / [(k_o l_o) \sinh(k_o l_o)] \quad . \tag{8}$$

Here, the k's for the inner (i) and outer (o) quadrupoles are defined the same as for the singlet quadrupole (Section IV A). The constraints (7) and (8) are used to form the limit rules for the parameters of the inner quadrupole and drift length.
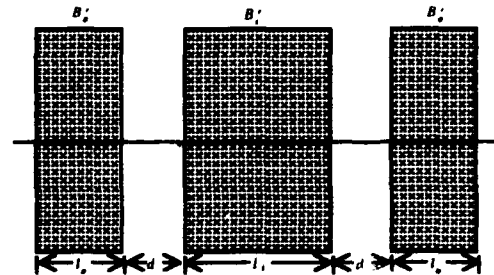
Figure 3. Schematic of Triplet Transport Element.

VI. Summary

An expert system type of knowledge rule base for the beam optics program TRACE 3-D has been developed. Limit guidelines for each input parameter incorporate constraints imposed by TRACE 3-D, beam optics utility and practical hardware experience. The rule base has been integrated into the SPARC interface for TRACE 3-D.

References

[1] D. E. Schultz and P. A. Brown, "The Development of an Expert System to Tune a Beam Line," Nuc. Instr. Meth. Phys. Res. A 293 (1990) 486-490.

[2] S. Kleban, M. Lee and Y. Zambre, "GENI: A Graphical Environment for Model-Based Control," Nuc. Instr. Meth. Phys. Res. A 293 (1990) 486-490.

[3] R. R. Silbar, "An Interactive Interface to the Beam Optics Code 'TRANSPORT'," AIP Conference Proceedings No. 177 (1988) 109-116.

[4] E. Heighway, "Magnetic Optics Design (A Designer's View of the Beam Transport Environment)," AIP Conference Proceedings No. 177 (1988) 181-203.

[5] K. Crandall and D. Rusthoi, "TRACE 3-D Documentation," Los Alamos National Laboratory Report LA-UR-90-4146 (1990) 92 pages.

[6] G. H. Gillespie and B. W. Hill, "A Graphical User Interface for TRACE 3-D Incorporating Some Expert System Type Features," 1992 Linear Accelerator Conference Proceedings (Ottawa) AECL-10728 (1992) 787-789.

[7] K. G. Steffen, High Energy Beam Optics, Interscience Publishers (1965).

[8] D. Liska, private communications (1993).

[9] E. Regenstreif, "Focusing with Quadrupoles, Doublets and Triplets," in Focusing of Charged Particles, Vol. 1, edited by A. Septier, Academic Press (1969) 353-410.

88

Beam Dynamics Studies of Four-gap Low-beta Superconducting Resonators

J. A. Nolen and K. Joh
Argonne National Laboratory
Argonne, IL 60439, U. S. A.

Abstract

The four-gap superconducting resonators which have been developed at Argonne for use in the low-beta positive ion-injector for ATLAS [1] have potential applications for ions with velocities less than 0.007c and q/m less than 0.1. It was previously observed that at low velocities these structures can be focussing in both longitudinal and transverse phase spaces due to an inherent alternating-phase-focussing property [2]. Studies are underway to determine the optimum combination of multi-gap structures and solenoids at low velocity and low q/m. In this paper we present the results of acceptance studies for the first three resonators at the front of the positive-ion injector linac, with and without the focussing solenoids. These studies include the effects of higher-order distortions in longitudinal and transverse phase spaces since minimising such aberrations is very important for most nuclear physics applications of such accelerators.

I. INTRODUCTION

The new positive-ion injector (PII) linac for ATLAS uses 18 4-gap superconducting niobium resonators [1] to accelerate ions as heavy as uranium from initial velocities of about 0.008c [3] [4]. The successful performance of this new linac has led us to investigate possible extensions of this technology to even lower velocities, with potential applications in the acceleration of radioactive beams. We are first investigating the details of the beam dynamics at the low velocity end of this linac, with special emphasis on the transverse and longitudinal acceptances and non-linearities. (see paper Ga9 of this conference [5].) Figure 1 is a schematic of the first two types of resonator at the entrance of the PII linac.
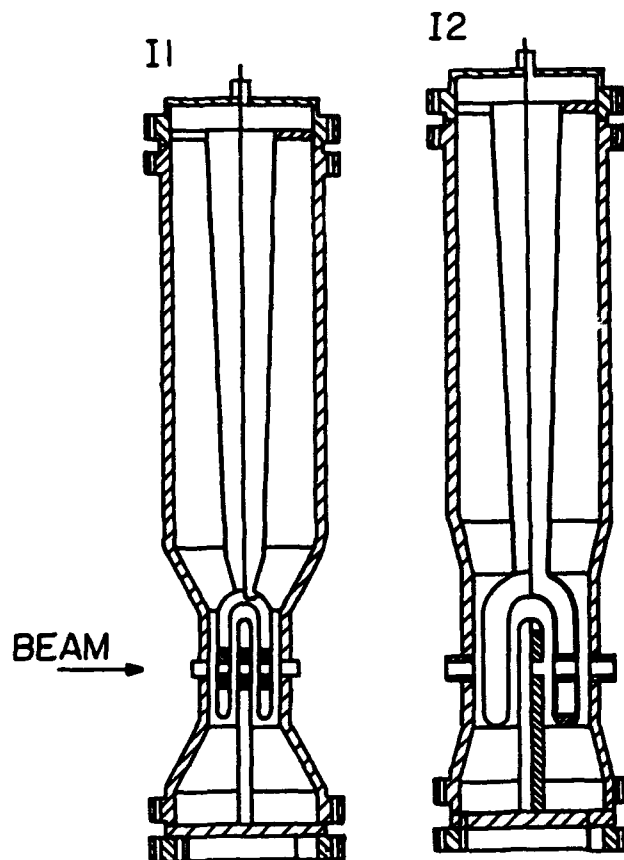
Figure 1: The first two of the four types of superconducting resonators in the PII linac; they are 48.5 MHz quarter-wave structures. The I1 type (left) has an effective length of 10 cm, in which the beam energy more than doubles.

II. ALTERNATING-PHASE FOCUSSING

Due to the rapid velocity increase in the first few gaps of this linac, as shown in Figure 2, there is an inherent alternating-phase focussing aspect to the beam dynamics [2] [6]. Figure 3 illustrates that the transverse focussing for an argon beam is so strong that an initially diverging beam is brought to a waist within the first 10 cm. Figures 4 and 5 illustrate more schematically the transverse and longitudinal focussing properties of the first two resonators for both argon and uranium beams.

Figure 3: The evolution of a transverse phase space ellipse through the I1 resonator. The beam is $^{40}Ar^{12+}$ and it is diverging slightly as it enters the the resonator, at the upper left box of the figure. (The beam is travelling left to right starting at the upper left and then from the top to bottom rows.) The very strong transverse focussing of the first gap is seen in the top row. In each box the vertical axis is divergence in mr and the horizontal is size in mm. The calculations are the results of raytracing with up to third order terms in the resonator electric field distribution.

Figure 2: The velocity, beta, of a uranium beam entering the I1 resonator at about 0.0086c and leaving at about 0.0134c. The gradient is 4.5 MV/m over the 10 cm effective length of the cavity.

III. NONLINEARITIES

The low velocity end of the PII linac consists of the following components: solenoid, I1 resonator, solenoid, I2 resonator, solenoid, second I2 resonator, etc. We have done calculations to compare the acceptances of the linac, in longitudinal and transverse phase spaces, for this standard configuration and for the case with the first three superconducting solenoids turned off. "Geometrical" and "Linear" acceptances were evaluated [5]. Although the acceptances are significantly greater with the solenoids, the results without look promising enough to search for more optimum configurations. Since the present calculations

Figure 4: Raytracing of initially parallel trajectories through I1 and I2. The upper plot is for a $^{40}Ar^{12+}$ beam, and the lower is for a $^{238}U^{24+}$ beam. In this case the vertical axis is the time deviation from the central partical. In both cases the rf phases are set for longitudinal focussing.
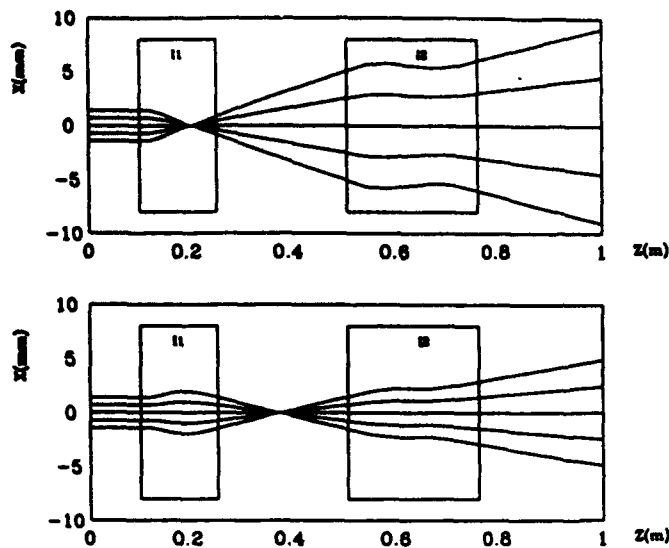
Figure 5: Plots similar to Figure 4, but in transverse phase space. The I1 resonator is stongly focussing for both beams, while I2 is only slighly focussing.

Figure 6: The shaded ellipse in the upper left box represents a transverse area of 11π mm·mr for a uranium beam entering the I1 resonator. The lower right box shows the particles transmitted, as calculated via raytracing. The lower left box shows the same particles calculated to first order only. The upper right shows the amount of emittance growth in the longitudinal coordinates in keV vertical axis and nsec horisontal axis. The initial longitudinal emittance was assumed to be sero to illustrate the coupling terms.

have been done with the actual linac configuration, it will be straightforward to test these predictions with actual beams in the near future. Figure 6 shows the predicted degree of distortion after three resonators for a uranium beam with no transverse focussing between them.

IV. FUTURE STUDIES

These studies will be continued, to develope the optimum combination of resonators and transverse focussing elements. Experimental studies will be done to test the predictions. As we gain experience with and understanding of the dynamics of these linac structures, more cost effective solutions will almost certainly evolve. For the first stages of acceleration of radioactive beams structures capable of accelerating ions with q/m values much less than the present 0.1 will be necessary. It appears that the PII technology will also be useful in this lower velocity, lower q/m regime.

REFERENCES

[1] K.W. Shepard, *et al.*, *Proc. 1989 IEEE Part. Accel. Conf.*, IEEE#89CH2669-0(1987)974.

[2] R.C. Pardo, *et al.*, *Proc. 1987 IEEE Part. Accel. Conf.*, IEEE#87CH2387-9(1987)1228.

[3] R.C. Pardo, *et al.*, paper Mc9 at this conference.

[4] L.M. Bollinger *et al.*, *Nuclear Physics*, A553, (1993) 859c-862c.

[5] K. Joh and J.A. Nolen, paper Ga9 at this conference.

[6] L. Sagalovsky and J.R. Delayen, *Proc. 1992 Linear Accel. Conf.*, C.R. Hoffmann, Ed., AECL-10728(1992)763.

Third-Order Corrections to the SLC Final Focus.*

N. J. Walker, R. Helm, J. Irwin, M. Woodley.

Stanford Linear Accelerator Center, Stanford University, Stanford, California 94309

Abstract

The minimum β achievable at the interaction point (β^*) with the current design of the SLC final focus is limited to ~5 mm by third order optical aberrations, most notably the U_{1266} and U_{3466} terms (using the notation of K. Brown). A new lattice is presented which effectively zeros these terms. The remaining third order terms which accrue from the interleaved sextupole pairs in the chromatic correction section (CCS) can be cancelled by the inclusion of five octupoles (two in the CCS, and three in the final telescope). The resulting final focus system is corrected to third order for any usable range of β^* (given the constraints on the beam divergence at the interaction point). The potential luminosity obtainable from such a system is also presented.

I. INTRODUCTION.

The current design of the SLC final focus essentially follows the design proposed by Brown[1]. It consists of two telescope sections, separated by a chromatic correction section (CCS) where two strong interleaved sextupole pairs (X and Y) are used to cancel the chromatic contribution to the beam size at the interaction point (IP)[2]. Although the design effectively cancels the second-order (chromatic) aberrations, the bandwidth of the system is limited by third-order effects. Analysis of these aberrations[3] has shown that they arise from two separate sources: (i) a small phase error between the sextupole pairs and the final triplet, and (ii) the interleaved X and Y sextupole pairs. The effect of the aberrations is to limit the minimum β^* at the IP to approximately 5 mm in both planes; a smaller β^* leads to a larger beam size as the aberrations begin to dominate over the linear optics. With the typical beam emittances seen in the final focus during the 1992 physics run (600 by 400 μmμr in the horizontal and vertical planes respectively), the smallest possible β^* was limited by SLD background considerations to give a beam divergence at the IP (θ^*) of ~300 μr in both planes, corresponding to a β^*_x of ~7 mm and a β^*_y of ~5 mm, which compare well to the optical optimum. For the current (1993) physics run, a "flat beam" is being used[4], where the vertical emittance in the final focus is of the order of 60 μmμr. The smallest vertical spot size (~0.8 μm) is now achieved with an IP beam divergence of approximately 100 μr, well below the SLD background limit. In order to increase the divergence (decrease the β^*), it is first necessary to identify and correct those aberrations which limit the beam

size. In this paper, a third-order correction scheme is proposed which effectively minimizes the third-order contributions to the beam size, enabling a vertical optimal β^* of ~1 mm, achieving a vertical spot size of ~0.3 μm at a divergence of 245 μr, given a vertical emittance of 60 μmμm. The decreased spot size gives a luminosity increase by a factor of 2.8 from the geometry alone, and an additional factor of ~1.4 from the beam-beam interaction (pinch effect), giving an overall luminosity gain of a factor of approximate ×4.

II. LIMITING THIRD-ORDER ABERRATIONS.

An analysis of the SLC final focus has shown[1] that the dominant vertical aberration is a high order chromaticity, U_{3466} (using the TRANSPORT[5] matrix notation). Using Lie Algebra techniques a complete analysis of the important third-(optical) order aberrations has been made in terms of monomials in the Hamiltonian[3]. The monomial corresponding to the afore mentioned chromaticity is $y'^2\delta^2$, where y' is taken to be the phase space coordinate at the IP. In all further discussions, it is assumed that the phase space coordinates (x,x',y,y') refer to those at the interaction point. Table 1 gives the results of the analysis (taken from [3]).

Monomial	TRANSPORT notation	Coefficient (meters)	% of total σ^2_y
$y'^2\delta^2$	U_{3466}	229.5	86
$x'y'^2\delta$	U_{1446}/U_{3246}	817.5	6
linear			3
$x'^2y'^2$	U_{1244}/U_{3224}	-2861.7	2.2
$x'y'\delta^2$	U_{1466}/U_{3266}	55.5	1.9

Table 1. Most significant aberrations to σ^*_y in order of contribution ($\theta^*_y = 245$ μr).

The vertical beam size is dominated by the $y'^2\delta^2$ term. Further analysis of this aberration[3] shows that it is almost entirely due to the interaction of the sextupoles and the triplet chromaticity. If the sextupole pair are at exactly the same phase as the triplet ($\pi/2$ out of phase with the IP), then the chromaticity from the sextupoles is simply given by $-K_s\eta_s R^2_{34}y'^2\delta$, where K_s is the integrated sextupole strength, η_s the dispersion function at the sextupoles, and R_{34} is the linear Green's function from the sextupole to the IP. The sextupole strength is then adjusted to exactly cancel the total chromaticity of the system. In the current SLC design, however, the sextupoles are not exactly at the correct phase, and the expression for the sextupole chromaticity (with respect to the IP) is given by:

$$-K_s\eta_s(R_{44}y - R_{34}y')^2\delta$$

$$= -K_s\eta_s R_{34}^2 y'^2\delta$$

$$+ 2K_s\eta_s R_{34}R_{44}yy'\delta$$

$$-K_s\eta_s R_{44}^2 y^2\delta \tag{1}$$

The first term in (2) is the desired chromaticity term which remains unchanged. The last term does not contribute to the vertical beam size at the IP. The contribution to the beam size from the second ($yy'\delta$) term is also small; however, this phase can interact with the triplet chromaticity ($\xi y'^2\delta$) to give the $y'^2\delta^2$ term, which can be estimated by taking the poisson bracket of the two monomials[3]:

$$\frac{1}{2}[2K_s\eta_s R_{34}R_{44}yy'\delta,\ \xi y'^2\delta] = 2K_s\eta_s R_{34}R_{44}\xi y'^2\delta^2. \tag{2}$$

Since the triplet chromaticity is approximately 60% of the total chromaticity of the final focus, we can replace ξ by $\xi \approx 0.6 \times K_s\eta_s R_{34}^2$, and the right hand side of (2) becomes

$$1.2 \times K_s^2\eta_s^2 R_{34}^3 R_{44}y'^2\delta^2 \tag{3}$$

For the current design final focus, equation 3 gives a coefficient for the $y'^2\delta^2$ term of ~200 m, which is within 15% of the total coefficient given in table 1.

III. CORRECTION OF $y'^2\delta^2$ (U_{3466}) TERM.

R_{34} and R_{44} are in effect the Y sine-like and cosine-like rays respectively, traced backwards from the IP. The sine-like ray drives the β functions and chromaticity of the final focus, and is the dominant (magnified) phase. The cosine-like ray is the demagnified phase. Equation 3 shows that the $y'^2\delta^2$ term depends on the value of the cosine-like ray at the Y sextupoles (R_{44}). By adjusting the optics of the final telescope using a new quadrupole placed close to the IP image point, it is possible to adjust the position of the cosine-like ray at the Y sextupoles, while leaving the sine-like ray (β functions) unchanged (figure 1).

An ideal location for the new quadrupole is exactly at the image point at the entrance to the final telescope: here, the sine-like ray passes naturally through zero and is unaffected by the quadrupole. Unfortunately, the image point is at the center of the B1 dipole, and a less optimal solution had to be found requiring the adjustment of the other magnets in the final telescope to correct the resulting perturbations to the β functions. In addition, it was also discovered advantageous to reflect the symmetry of the CCS optical functions (focusing magnets become defocusing and visa versa), to allow the new quadrupole to drive the cosine-like ray through zero at the Y sextupoles. Adjustment of the value of the cosine-like ray at the Y sextupoles (and hence the R_{44}), allows tuning of the $y'^2\delta^2$ term. The final solution does not have the cosine-like ray passing though the center of the Y sextupoles, but rather the ray is offset in order to cancel the remaining 15-20% of the aberration coming from other sources in the final focus. The solution also
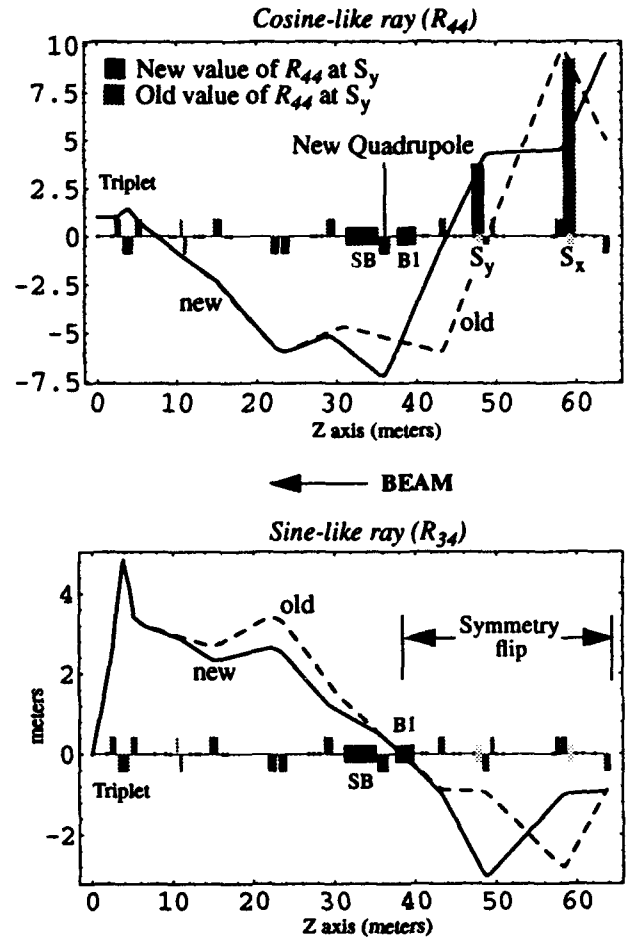
Figure 1. Sine- and cosine-like rays traced backwards from the IP through the final telescope and part of the CCS. Solid line represents the proposed (new) optics, while the dashed line represents the current (old) optics. On the top graph (cosine-like), the old and new values of the ray at the Y sextupole are indicated by the vertical bars. (Note: because of the symmetry exchange in the CCS, the X and Y sextupoles have interchanged).

minimizes the $x'^2\delta^2$ aberration (U_{1266}) to the horizontal IP beam size.

IV. OCTUPOLE CORRECTION.

Once the $y'^2\delta^2$ term has been cancelled, the minimum σ^*_y is achieved with a $\beta^*_y \sim 2$ mm ($\theta^*_y \sim 180\ \mu r$), with a reduction in beam size of approximately 1.8. The remaining aberrations are the octupole terms arising from the interaction of the interleaved sextupole pairs, and to some extent the long sextupoles themselves. Table 2 summarizes the remaining important aberrations for the new linear optics. These terms can be corrected by the addition of octupoles. The chromatic sextupole term ($x'y'^2\delta$) can be removed by placing a -I pair of octupoles in the CCS. This pair, when powered anti-symmetrically generate the required $x'y'^2\delta$ term, together with $x'^3\delta$ and $x'\delta^3$ terms which affect the horizontal IP beam size. When powered symmetrically, the pair generates pure geometric octupole terms (x'^4, $x'^2y'^2$, y'^4), together with the high order chromaticity terms $x'^2\delta^2$ and $y'^2\delta^2$ (the very terms that the final telescope modifi-

Monomial	TRANSPORT notation	Coefficient (meters)	% of total σ^2_y
$x'y'^2\delta$	U_{1446}/U_{3246}	-858.4	50
linear	-	-	21
$x'^2y'^2$	U_{1244}/U_{3224}	-3104.8	20
y'^4	U_{3446}	55.5	9

Table 2. Most significant aberrations to σ^*_y in order of contribution for new final telescope optics ($\theta^*_y = 245$ µr).
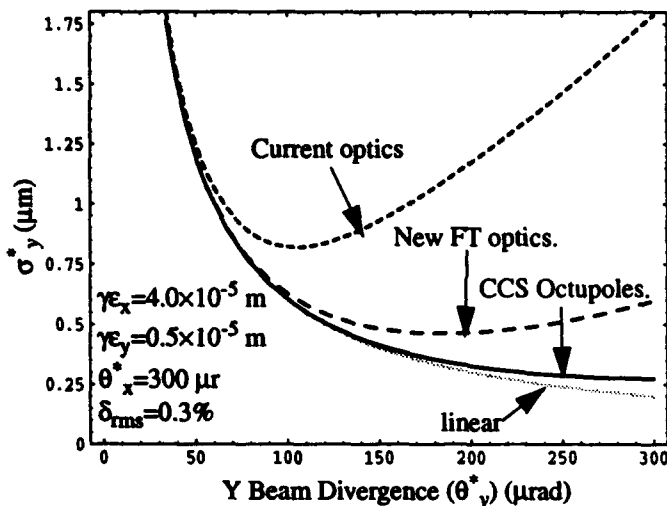
Figure 2. Vertical IP beam size (σ^*_y) as a function of vertical IP beam divergence (θ^*_y) for the current optics, final telescope modifications and CCS octupole compensation.

cations are designed to cancel). One possible solution is to place an anti-symmetric -I pair in the CCS to cancel the dominant $x'y'^2\delta$ term, and use three independent octupoles in the final telescope to exactly cancel the three pure geometric terms. The location of the -I CCS octupole pair is governed by (a) the maximum realizable octupole strength and (b) the tolerance on the $x'^3\delta$ term. The five octupole solution effectively reduces the vertical spot size to the linear limit with a divergence of 245 µr. A cheaper two octupole solution, which still uses a -I CCS pair, has been adopted with only a small loss in luminosity. The two octupoles are now run unequally, so as to reduce the RMS of the contributions of the various aberrations listed above. The solution was arrived at by first adjusting the octupole strengths anti-symmetrically to zero the $x'y'^2\delta$ term, and then symmetrically to minimize the pure geometric terms (the high order chromaticity terms generated being negligibly small). The solution obtained resulted in the downstream octupole having an integrated strength of ~900 m^{-3}, while the upstream octupole runs at approximately half that value, achieving a vertical beam size of 340 nm. Figure 2 shows σ^*_y as a function divergence for the proposed improvements.

V. NEW TUNING STRATEGY.

The current SLC final focus design utilizes two magnets in the upper telescope (UT), together with the final triplet and a small tuning quadrupole to adjust the β^*. To maintain a static

optics in the CCS and final telescopes (with the exception of small adjustments for fine tuning), it is proposed to move all the beam matching to the UT. To facilitate this, a new wire scanner capable of resolving a 1.5 µm vertical beam size will be installed at the IP image point at the entrance of the CCS. In addition, a new quadrupole will be installed in the UT to allow for a global tuning algorithm[6]. A new skew-quadrupole will also be installed to control the <xy> correlation in the beam. It is also proposed to include several new wire scanners throughout the UT and η suppression section to allow fast measurement of the incoming beam phase space[7].

VI. PROJECTED LUMINOSITY GAIN.

Table 3 gives the expected IP vertical beam size, luminosity (in units of Z particle production per hour) and beam-beam enhancement for the current final focus and the two proposed improvements. The enhancement factor (H_D) is calculated from scaling laws[8] and is strongly dependent on bunch length and bunch current. For all three scenarios, the horizontal beam size remains roughly constant at about 2 µm.

Table 3: Expected vertical beam size and luminosity for the current final focus and the two proposed improvements. Other beam parameters factored into the calculations are: $\varepsilon_x = 600$ µmµr, $\varepsilon_y = 60$ µmµr, $\theta^*_x = 300$ µr, $\sigma^*_z = 0.8$ mm, $\delta_{rms} = 0.3\%$, $N_b = 3.5 \times 10^{10}$ ppb.

	θ^*_y (µr)	σ^*_y (µm)	L (Z/hr)	H_D	$L^* = H_D L$
Current FF	104	0.839	66	1.16	76
FT Upgrade	190	0.462	122	1.41	171
FT Upgrade+ CCS Octupoles	245	0.340	170	1.44	245

REFERENCES.

[1] K. Brown, "A Conceptual Design of Final Focus Systems for Linear Colliders", SLAC-PUB-4159, (1987).

[2] J. Murray, K. Brown, and T. Fieguth, "The Completed Design of the SLC Final Focus System", SLAC-PUB-4219 (1987).

[3] N. Walker, J. Irwin, and M. Woodley, "Analysis of Higher Order Optical Aberrations in the SLC Final Focus using Lie Algebra Techniques.", these proceedings (1993).

[4] C. Adolphsen et al, "Flat Beams in the SLC", these proceedings (1993).

[5] K. Brown, "A First- and Second-Order Matrix Theory for the Design of Beam Transport Systems and Charged Particle Spectrometers", SLAC-75 or Advances in Particle Physics 1, 71 (1967).

[6] N. Walker, J. Irwin, and M. Woodley, "Global Tuning Knobs for the SLC Final Focus", these proceedings (1993).

[7] P. Emma, private communication.

[8] P. Chen, and K. Yokoya, Phys. Rev. D38, 987 (1988).

Global Tuning Knobs for the SLC Final Focus.[*]

N. J. Walker, J. Irwin, M. Woodley

Stanford Linear Accelerator Center, Stanford University, Stanford, California 94309

Abstract

The beam phase space at the exit of a given transport line generally depends on the incoming beam conditions, and thus in order to adjust the beam parameters at the exit of the line requires a prior knowledge of the initial beam parameters. The same is generally true for final focus systems. A tuning algorithm for β matching the SLC final focus is reported here in which no prior knowledge of the exact incoming phase space is required. Only a single beam size diagnostic located at either the interaction point (IP) or an image of the IP is required, together with a knowledge of the linear lattice from the quadrupoles to the tuning point. The algorithm is presented within the Lie Algebra framework. Although the algorithm is presented here is specific to linear collider final focus systems, the technique is generally applicable to any beamline.

I. INTRODUCTION.

The SLC final focus consists of two telescopes separated by a chromatic correction section (CCS)[1]. The demagnification of the final telescope (FT) is 5:1 in both planes, and approximately 8:1 horizontally and 3:1 vertically in the upper telescope (UT). Adjusting the focus at the interaction point (IP) is critical to achieving the maximum luminosity: the beam waist ($\alpha = 0$) must be at the IP, and the correct β function (β^*) is required to give the minimum possible beam size[2]. Given the dynamic range of the incoming beam conditions (especially emittance), it is necessary to be able to efficiently tune the final focus to acheve the required conditions at the IP. In general, beam matching in transport lines requires a prior knowledge of the initial beam phase space. These measurements are then given to a non-linear fitting algorithm that adjusts the quadrupoles in the line to achieve the desired results. In the following sections, an algorithm for achieving the correct β match in the SLC final focus is presented that requires only a single beam size diagnostic (wire scanner), and no prior knowledge of the incoming beam conditions. It is proposed to implement such an algorithm as part of the SLC final focus upgrade[3], where all the tuning will take place in the UT. To facilitate this, a new wire scanner will be positioned at the IP image point at the entrance to the CCS (exit of the UT). Although the algorithm is presented within the framework of the SLC final focus, the technique is generally applicable to any beamline.

II. β MATCHING ALGORITHM.

Figure 1 shows schematically the proposed tuning algorithm. For simplicity, only one plane will be considered. The

initial adjustment (figure 1a) brings the beam waist to the wire ($\alpha = 0$). This is achieved by applying an effective drift matrix:

$$R_d = \begin{pmatrix} 1 & s \\ 0 & 1 \end{pmatrix}. \tag{1}$$

In practice, the parameter s is scanned until a minimum in the beam size at the wire scanner is achieved. The next stage is to correct the beam size, *i.e.* adjust the β function (figure 1b), which is simply the application of a *magnifying* matrix of the form

$$R_m = \begin{pmatrix} m & 0 \\ 0 & \dfrac{1}{m} \end{pmatrix}. \tag{2}$$

In this case, the parameter m can either be scanned until the desired beam size at the wire is achieved, or it can be calculated and applied from the knowledge of the initial beam size at the wire. If there is no coupling in the beam (see section III), the beam is now matched to give the desired image at the IP (assuming that the demagnification and phase advance of the CCS and final telescope are correctly set).

The problem is now reduced to designing orthogonal control over the two parameters s and m (four when considering both X and Y planes). In the 2×2 matrices given in (1) and (2), there are three independent parameters; thus to generate the desired form of the matrix requires three (six) independent quadrupoles. It may at first seem strange that three independent variables are required to match two parameters (α and β); however the phase advance is also implicitly constrained, giving a total of three parameters. Because of the phase advance constraint, the solution arrived at may not be the optimum with respect to magnet strengths. A phase knob can be constructed which adjusts only the phase advance and leaves the β function unchanged and the waist at the wire. The corresponding matrix has the form

$$R_\phi = \begin{pmatrix} \sqrt{\beta} & 0 \\ 0 & \dfrac{1}{\sqrt{\beta}} \end{pmatrix} \begin{pmatrix} \cos\phi & \sin\phi \\ -\sin\phi & \cos\phi \end{pmatrix} \begin{pmatrix} \dfrac{1}{\sqrt{\beta}} & 0 \\ 0 & \sqrt{\beta} \end{pmatrix}. \tag{3}$$

which is more complicated than either (1) or (2), and requires a prior knowledge of the β function. The single parameter ϕ can be adjusted to relieve magnet power supplies which are at their maximum strength, without losing the β match.

III. CONSTRUCTION OF TUNING KNOBS.

To construct the orthogonal *knobs* to adjust the matching parameters, a perturbation technique is employed. The three matching quads need to be adjusted in such a way as to produce either a pure s, m, or ϕ. An elegant method for calculating

(a)   (b)   (c)

$$R = \begin{pmatrix} 1 & -s \\ 0 & 1 \end{pmatrix}$$ $$R = \begin{pmatrix} m & 0 \\ 0 & \dfrac{1}{m} \end{pmatrix}$$ Matched
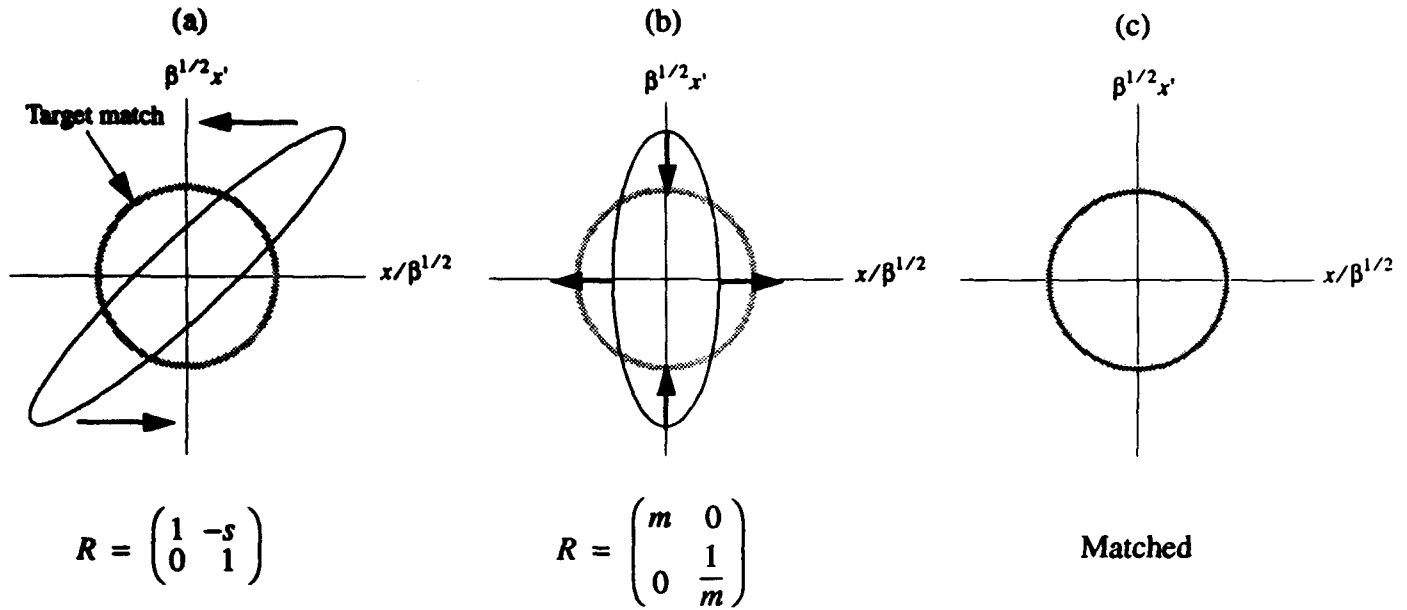
Figure 1. Figures (a), (b) and (c) represent the tuning stages involved in β matching (the phase space is normalized to the target β). First the waist is brought to the wire scanner by scanning the *s* parameter (a), then the required matching is achieved by adjusting the *m* parameter. All operations can be accomplished by measuring the beam size on the wire scanner.

the knobs is to use second-order Hamiltonians to represent the thin lens perturbations to the existing lattice, and then use them as generators in a Lie Algebra[4].

If the phase space coordinates at the wire scanner (matching point) are $x = (x, x', y, y')$, then the total perturbative Hamiltonian due to the three quadrupoles can be expressed as

$$H_{\Delta K} = ax^2 + bxx' + cx'^2, \quad (4)$$

where the coefficients are functions of the linear lattice (R matrix elements) between the quadrupoles and wire scanner, and the change in quadrupole strengths $\Delta K = (\Delta K_1, \Delta K_2, \Delta K_3)$. To first order, the coefficients in (4) can be expressed as linear functions of the ΔK_i's:

$$a = \frac{1}{2} \sum_{i=1}^{3} \Delta K_i R_{22}(i)^2$$

$$b = - \sum_{i=1}^{3} \Delta K_i R_{12}(i) R_{22}(i)$$

$$c = \frac{1}{2} \sum_{i=1}^{3} \Delta K_i R_{12}(i)^2 \quad (5)$$

where $R_{pq}(i)$ are the linear Green's functions from the ith quadrupole to the wire scanner. Over some small range, therefore, it is possible to have linear combinations of the quadrupole strengths which give independent control over the coefficients a, b and c.

When exponentiated, the Hamiltonian becomes a generator for a map[4]:

$$e^{:-H_{\Delta K}:} u = u + [-H_{\Delta K}, u] + \frac{1}{2!} [-H_{\Delta K}, [-H_{\Delta K}, u]] + \dots \quad (6)$$

where u can be any phase space coordinate. To see how the coefficients in $H_{\Delta K}$ relate to the required tuning matrices given in (1), (2) and (3), three cases are considered:

A. $a=0$, $b=0$.

The Hamiltonian given in (4) is now simply cx'^2. Applying (6) to x and x' gives:

$$x \to e^{:-cx'^2:} x = x + 2cx'$$

$$x' \to e^{:-cx'^2:} x' = x' \quad (7)$$

The equations in (7) can be represented as the matrix

$$\begin{pmatrix} 1 & 2c \\ 0 & 1 \end{pmatrix}, \quad (8)$$

which is the required drift matrix (1) with $s=2c$.

B. $a=0$, $c=0$.

Now $H_{\Delta K} = bxx'$, and the expansion given in (6) becomes

$$x \to e^{:-bxx':} x = (1 + b + \frac{b^2}{2} + \frac{b^3}{6} + \frac{b^4}{24} + \dots)x = e^b x$$

$$x' \to e^{:-bxx':} x' = (1 - b + \frac{b^2}{2} - \frac{b^3}{6} + \frac{b^4}{24} - \dots)x' = e^{-b} x' \quad (9)$$

In matrix form, the equations in (9) give the required magnification matrix (2), with $m = e^b$.

96

C. $a = (1/2)\phi/\beta$, $b = 0$, $c = (1/2)\phi\beta$.

The Hamiltonian is now given as:

$$H_{\Delta K} = \frac{1}{2}\frac{\phi}{\beta}x^2 + \frac{1}{2}\phi\beta x'^2. \tag{10}$$

The expansion (7) now generates the phase knob matrix (3), with the corresponding phase change ϕ.

Having equated the coefficients in the Hamiltonian to the desired tuning coefficients s, m and ϕ, it is a simple matter to calculate the required changes in quadrupole strengths to effect the knob. The linear equations given in (5) are only correct over a small range of the ΔK_i, and in order to make large corrections or scans of a given knob, it will be necessary to integrate through the change, i.e. take small steps in ΔK_i, recalculating the coefficients at each step. The size of the step has to be found empirically, although in simulations for the SLC tuning scheme, 9 or 10 steps have found to be sufficient. Figure 2 shows simulations of a waist (drift matrix) scan.
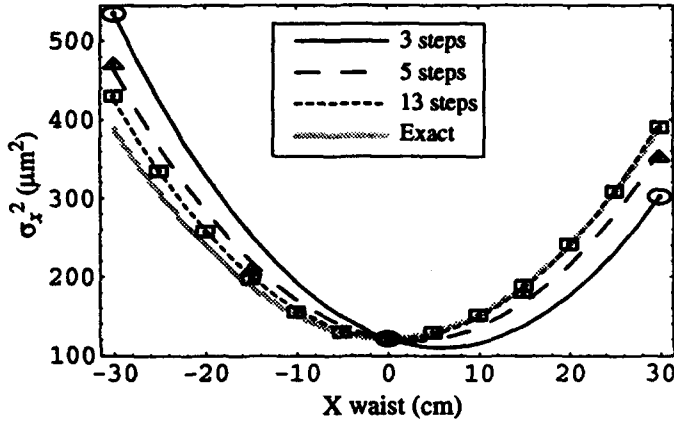
Figure 2. Simulations of an X waist (drift matrix) scan. The solid gray line represents a pure drift, while the other three lines represent scans using different step sizes.

IV. COUPLING CORRECTION.

A coupling correction can be formulated in exactly the same way as the β matching described in section II. In general four skew-quadrupoles are required to independently adjust the four skew parameters in the Hamiltonian:

$$H_{skew} = axy + bxy' + cx'y + dx'y'. \tag{11}$$

The associated coupled (now 4×4) matrix generated by this Hamiltonian is of the form

$$\begin{pmatrix} h & 0 & \zeta c & \zeta d \\ 0 & h & -\zeta a & -\zeta b \\ \zeta b & \zeta d & h & 0 \\ -\zeta a & -\zeta c & 0 & h \end{pmatrix}. \tag{12}$$

where $h = \cos(\theta)$, $\zeta = \sin(\theta)/\theta$, with $\theta^2 = ad-bc$ ($\theta^2 > 0$). In the case of $\theta^2 < 0$, then $h = \cosh(\theta)$, and $\zeta = \sinh(\theta)/\theta$. Because of the flat nature of the beam ($\sigma_x \gg \sigma_y$), only two of these coefficients are of interest in the SLC final focus: the b parameter adjusts the x-y tilt of the beam, while the d parameter increases

the small σ_y proportionally to the horizontal divergence. With the two skew-quadrupoles available in the UT, it is possible to independently control these two coefficients. The remaining coefficients, a and c, will be allowed to vary arbitrarily. Inclusion of the skew correction now necessitates the precise control of eight magnets (six normal- and two skew-quadrupoles), and the coefficients in (5) will in general contain the coupled Green's functions.

V. IMPLEMENTATION.

The beta matching algorithm (with coupling) will be implemented in FORTRAN as part of the SLC control system[5]. This system provides the necessary interface to the readback and control of the magnets which will be used, as well as a standardized user interface consisting of touch panels and displays. In addition, a Correlation Plot facility is provided which allows measurement of beam parameters as a function of magnet strengths[6]. Users will select a desired scan type (i.e. X-waist), scan range, and number of incremental steps from a touch panel. The beta matching software will compute quadrupole strengths for each step of the scan and then use the Correlation Plot facility to measure the beam size on a wire scanner as it steps the magnets through their precomputed setpoints. The user will be presented with the results of the scan graphically and will be allowed to select the optimum set of quadrupole strengths.

REFERENCES.

[1] J. Murray, K. Brown, and T. Fieguth, "The Completed Design of the SLC Final Focus System", SLAC-PUB-4219 (1987).

[2] N. Walker, J. Irwin, and M. Woodley, "Analysis of Higher Order Optical Aberrations in the SLC Final Focus using Lie Algebra Techniques.", these proceedings (1993).

[3] N. Walker, R. Helm, J. Irwin, and M. Woodley, "Third-Order Corrections to the SLC Final Focus.", these proceedings (1993).

[4] J. Irwin, "The Application of Lie Algebra Techniques to Beam Transport Design", Nuc. Inst. and Methods, A298, 460 (1990).

[5] N. Phinney and H. Shoaee, "The SLC Control System: Status and Development", SLAC-PUB-4215 (1987).

[6] L. Hendrickson, N. Phinney, and L. Sanchez-Chopitea, "Correlation Plot Facility in the SLC Control System", SLAC-PUB-5685 (1991).

Sigma Matrix Reconstruction in the SLC Final Focus*

Stanford Linear Accelerator Center, 2575 Sand Hill road, CA94305 USA

P.RAIMONDI, P.J.EMMA, N.TOGE, N.J.WALKER and V.ZIEMANN

Abstract

The knowledge of the Beam Parameters at the entrance of the SLC final focus is important for modeling the final focus optics and predicting spot sizes and angular divergences at the interaction point (IP). It is also an important diagnostic for measuring possible anomalous emittance growth in the SLC Arcs. Reported here is a technique for measuring all the independent beam parameters at the beginning of the final focus. Use is made of the spot size measurements at wire scanners as a function of quadrupole strengths. Results for the SLC 1993 run are presented.

I. INTRODUCTION

The determination of all the independent beam parameters at the entrance of the SLC Final Focus has become a necessary task in order to understand anomalous emittances growth and beta-mismatch in the last two sections of the 50 GeV Linac and the Arcs. A full 4x4 sigma matrix reconstruction is required to determine the X-Y coupling terms which arise from the Arcs. In addition to the coupling, anomalous emittance growth due to Synchrotron radiation and beam mismatch effects can be present [1], so a technique for measuring the uncoupled intrinsic emittances in the final focus is highly desirable.

II. DESCRIPTION OF THE TECHNIQUE

The sigma matrix reconstruction is performed by means of spot size measurements using a wire scanner (WS4) immediately upstream of the Superconducting final focus triplets.

This is normally a high "beta" point, but by retuning the beta matching section it is possible to bring both waists to the wire location and obtain spot sizes of the order of 100 μm. Next, by varying two normal quads and one skew quad and measuring the X, Y and U (45° wire) spots at the different quad settings, it is possible to extract all the beam parameters. Fig.1 shows an example of the σ_x^2, σ_y^2 and σ_u^2 as a function of a x-focusing quad.
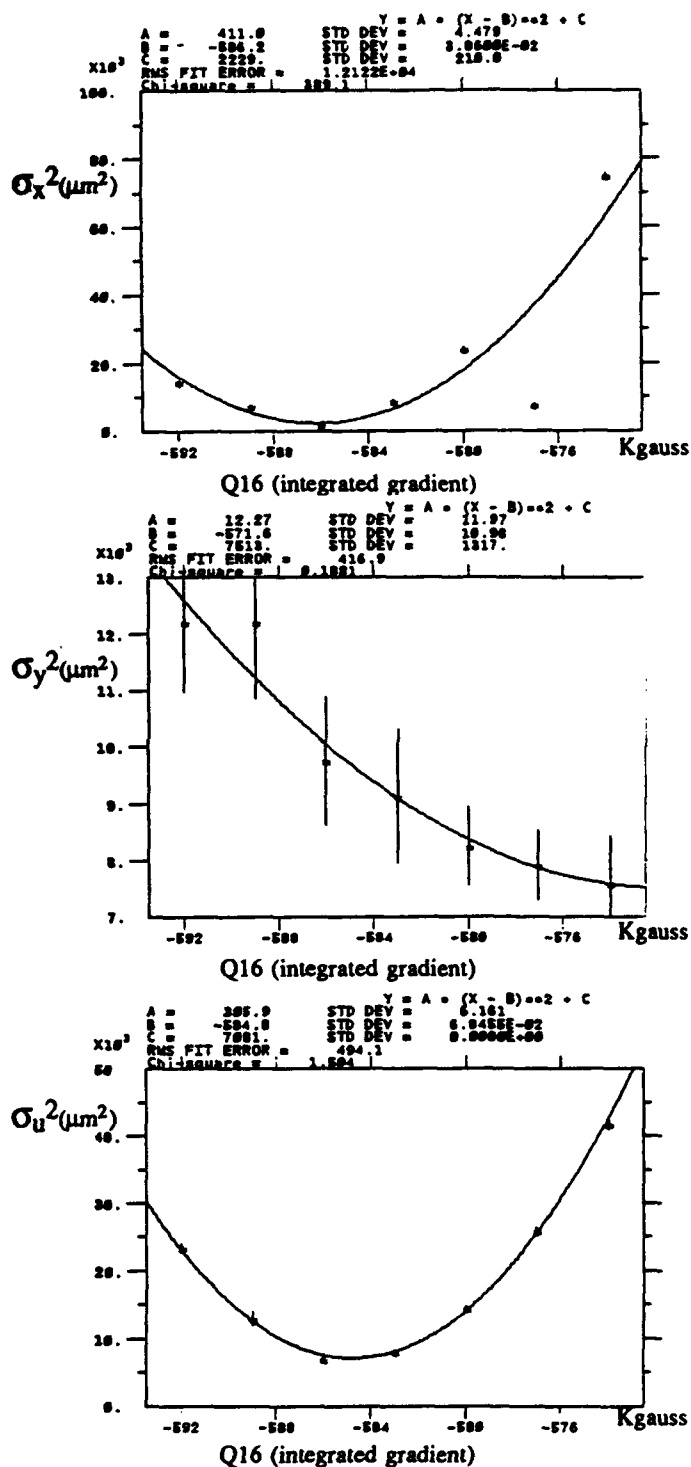
Figure 1. X, Y and U spot sizes as function of one of the measurement (Q16) quads.

In an uncoupled treatment just the X and Y plots shown in Fig.1 are sufficient to determine the beam twiss parameters. With the addition of the coupling however, it is necessary to use three different quad scans and a non-linear fitting algorithm to extract the off-diagonal elements.

The 4x4 beam sigma covariance matrix σ^2 is parametrized as follows:

$$\sigma^2 = B \cdot C \cdot E \cdot C^t \cdot B^t$$

where:

$$E = \begin{bmatrix} \varepsilon_x & 0 & 0 & 0 \\ 0 & \varepsilon_x & 0 & 0 \\ 0 & 0 & \varepsilon_y & 0 \\ 0 & 0 & 0 & \varepsilon_y \end{bmatrix}$$

$$C = \begin{bmatrix} h & 0 & g \cdot c & g \cdot d \\ 0 & h & -g \cdot a & -g \cdot b \\ g \cdot b & g \cdot d & h & 0 \\ -g \cdot a & -g \cdot c & 0 & h \end{bmatrix}$$

$$B = \begin{bmatrix} \sqrt{\beta_x} & \alpha_x \cdot \sqrt{\beta_x} & 0 & 0 \\ 0 & \dfrac{1}{\sqrt{\beta_x}} & 0 & 0 \\ 0 & 0 & \sqrt{\beta_y} & \alpha_y \cdot \sqrt{\beta_y} \\ 0 & 0 & 0 & \dfrac{1}{\sqrt{\beta_y}} \end{bmatrix}$$

$$g = \frac{\sin(\sqrt{\Delta})}{\sqrt{\Delta}} \ , \ h = \cos(\sqrt{\Delta}) \ , \ \Delta = a \cdot d - c \cdot b$$

ε_x, β_x, α_x, ε_y, β_y and α_y are the usual twiss parameters, while a, b, c and d, represents the coupling terms. This parametrization has the advantages to get immediately the intrinsic beam emittances and to let the coupling parameters range between +/- oo, having always the sigma matrix positive defined.

The fitting is performed by minimizing the χ^2 sum:

$$\chi^2 = \sum_{i=1}^{n} \left(\frac{\sigma_i^{exp} - \sigma_i^{theo}(\varepsilon_x, \beta_x, \alpha_x, \varepsilon_y, \beta_y, \alpha_y, a, b, c, d)}{\Delta\sigma_i^{exp}} \right)^2$$

where ε_x, β_x, α_x, ε_y, β_y, α_y, a, b, c and d are the fitted parameters, and σ_i^{exp} are the measured X, Y and U spot sizes.

III. RESULTS

Table 1 shows the results for two particular measurements of the positron σ^2 during the 1993 run. The first measurement was made with the round beam configuration ($\varepsilon_x \sim \varepsilon_y$ at the end of the Linac), the second one was made in the flat beam configuration ($\varepsilon_x \gg \varepsilon_y$). The agreement with the predicted emittance growth from the Arcs is very good and the residual coupling is small.

Table 1

Measured positron beam parameters a the entrance of the final focus in the "round" and "flat" beam cases.

	Round beam		Flat beam	
	Theoretic	Measured	Theoretic	Measured
β_x(mt)	8.70	12.09 ± 1.06	8.70	6.99 ± 0.69
α_x	0.00	1.09 ± 0.16	0.00	1.50 ± 0.18
ε_x(E-10)	7.20	7.44 ± 0.77	9.60	10.46 ±1.23
β_y(mt)	1.14	1.38 ± 0.27	1.14	1.44 ± 0.48
α_y	0.00	0.10 ± 0.18	0.00	0.80 ± 0.07
ε_y(E-10)	3.50	3.59 ± 0.45	0.65	0.60 ± 0.12
a	0.00	0.19 ± 0.20	0.00	0.32 ± 0.17
b	0.00	0.42 ± 0.21	0.00	0.41 ± 0.13
c	0.00	-0.30 ± 0.15	0.00	0.30 ± 0.12
d	0.00	-0.11 ± 0.13	0.00	0.50 ± 0.12

Using these value we have been able to successfully predict the values for the beta-matching quads in order to cancel the residual coupling and to set to optimal beta functions at the interaction point .

IV. CONCLUSIONS

The knowledge of the incoming sigma matrix in the final focus is a useful beam diagnostic and has been successful used in optimizing the first order final-focus optic during the 1992 and in the course of the 1993 SLC runs.

V. REFERENCES

[1] Phase Space and Synchrotron Radiation Emission in High Energy Electrons Transport lines. W.SPENCE, P.EMMA, N.WALKER: IEEE-PAC93 proceedings.

Beam Based Alignment of the SLC Final Focus Superconducting Final Triplets*

P.RAIMONDI, P.J.EMMA, N.TOGE, N.J.WALKER and V.ZIEMANN

Stanford Linear Accelerator Center, 2575 Sand Hill road, CA94305 USA

Abstract

The strong demagnification inherent in final focus systems requires very high gradients for the final quadrupoles. Alignment of these magnets is critical in order to minimize the dispersion at the interaction point and backgrounds in the detector due to synchrotron radiation. Reported here is a technique for aligning the final quadrupoles with respect to the beam centroid, which makes use of measurements of the beam position downstream of the quadrupoles when their fields are varied. Results for the SLC final focus final superconducting triplets are presented, where a resolution of <20 μm is achieved.

I. DESCRIPTION OF THE TECHNIQUE

The basic idea to perform the alignment is that the beam trajectory is steered by a misaligned quadrupole in proportion to the quad strength and to the misalignment itself. The developed procedure can be summarized in four different steps:

1) Establish the reference orbit to which the quadrupoles are to be aligned.

2) Measure the BPM scale-factors variing the beam orbit using beam "bumps", with all the magnetic elements in the section off.

3) Evaluate the misalignment by changing the quadrupole field-strength and recording the orbit distortions.

4) Apply alignment correction with magnet movers and repeat step (3).

The first step is performed by turning off the triplets and centering the beam in the BPMs in the IP region using correctors upstream of the triplets (fig.1).

In the second step the BPM scale-factors are evaluated considering that between the correctors used to generate the bumps and the BPMs there are only drift spaces. In fig.2 is shown typical behavior of the BPM readings when we apply bumps of different amplitudes. Particularly the orbit between

the [NBP06,SBP06] should be a straight line, it is therefore very easy to extract the scale factors.

This "calibration" is crucial to avoid relative and systematic errors in the evaluation of the misalignments.
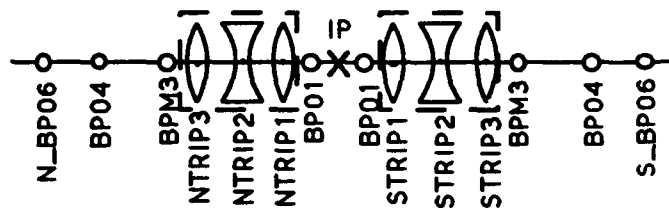
Figure 1. Schematic layout of the beam line in the IP region.
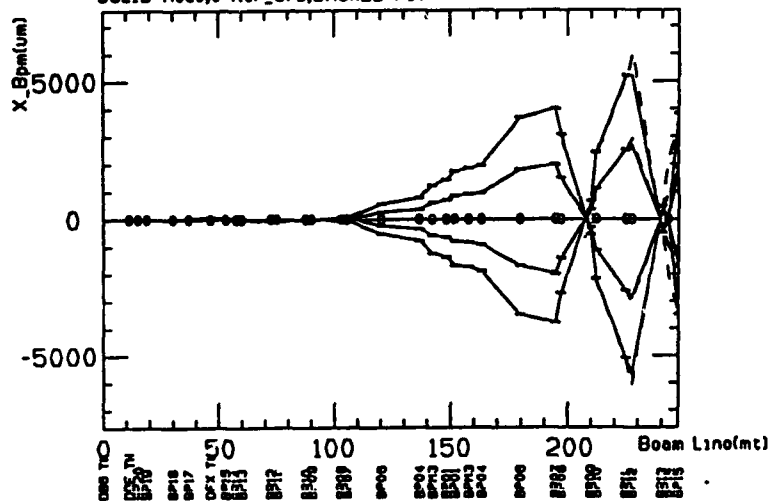
Figure 2. Beam orbit at different corrector values in the IP region as read from the BPMs with all the magnetic elements in the region [NBP06,SBP06] turned off.

Successively the triplet field is varied and the relative orbit distortions are measured using BPMs upstream and downstream of the triplets. As a further complication, it is not possible to act on the single quads independently, however it can be shown that the beam centroid variation "x" downstream of three quads Q1, Q2 and Q3 excited at a field strength "q" is a linear combination of the three misalignments m_1, m_2 and m_3 according to:

$$x = q^3 a_{31} m_1 + q^2 (a_{21} m_1 + a_{22} m_2) + q(a_{11} m_1 + a_{12} m_2 + a_{13} m_3)$$

Presented at the Particle Accelerator Conference (PAC 93), Washington, D.C., May 17-20, 1993.

where a_{ij} are coefficient depending only on the optics of the system. Hence, given a sufficient number of "x" measurements at different triplet strengths, it is possible to build an over determined linear system in terms of the unknown misalignments. The situation in slightly more complex if we want to take into account the incoming beam centroid jitter to improve the accuracy of the method, therefore the algorithm has been generalized to fit for these additional unknowns.

II. RESULTS

In fig.3 is shown a typical output from the data analysis and table 1 summarizes the evaluated triplet misalignments before and after a move showing residual misalignments of the order of 30 μm (1992 data). The misalignments are expressed in terms of average offset and tilt of the whole triplets since is possible to move them as a whole unit (see fig.1).

Table 1

Measured triplet misalignments before and after movement.

	North Triplet		South Triplet	
	before	after	before	after
X_offset (μm)	-357.4	3.0	303.7	-44.0
X'_offset(μrad)	-78.0	0.7	-66.2	9.7
Y_offset (μm)	93.8	29.3	10.5	-13.5
Y'_offset(μrad)	20.5	6.4	-2.3	2.9

The overall steering turning then on/off due to the residual triplets misalignments after correction is typically of the order of 30 μrad, causing orbit distortions easily compensated with correctors with negligible contribution to the IP-dispersion and to detector backgrounds.

III. CONCLUSIONS

The procedure has been successfully used in the SLD-SLC 1992 and 1993 runs. In this last run in particular, since an upgrade in the BPM resolutions in the Final Focus, it has been possible to reach a resolution better than 10 μm. With this improvement, the electrons and positrons beams are steered so little from the reference orbit that they are usually colliding immediately after the triplet alignment.

NTRIP3 X-Misal.:   160.5 um +/-   7.2 um
NTRIP2 X-Misal.:   149.9 um +/-   9.9 um
NTRIP1 X-Misal.:   128.7 um +/-   9.1 um

SOLID-Meas,o-Ref_Orb,DASHED-Fit,POINTS-After_Correction

STRIP1 X-Misal.:   -475.3 um +/-   10.1 um
STRIP2 X-Misal.:   -450.9 um +/-   12.3 um
STRIP3 X-Misal.:   -368.1 um +/-   10.4 um

SOLID-Meas,o-Ref_Orb,DASHED-Fit,POINTS-After_Correction
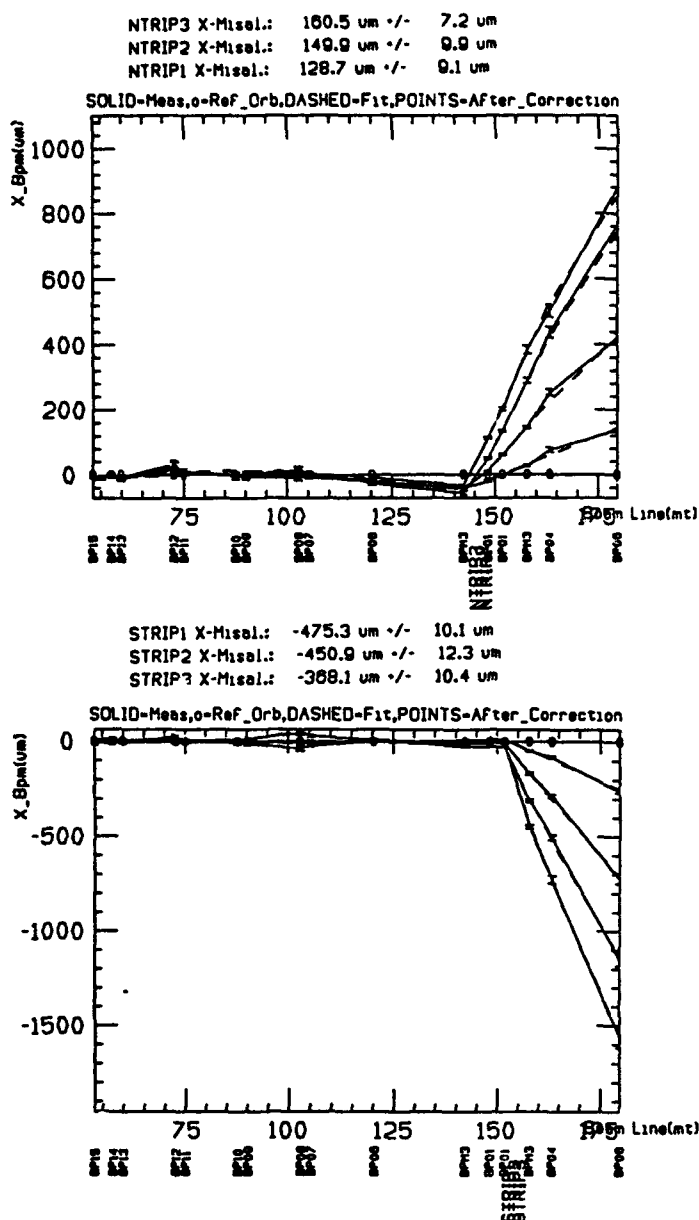
Figure 3. Fit of the X-beam-orbits at different triplet strengths for the north and south triplets with respect to the same reference orbit. The increased steering for increased strengths is clear.

A Design of a Quasi-Isochronous Storage Ring

S.Y. Lee[a], K.Y. Ng[b], and D. Trbojevic[c]
[a]Department of Physics, Indiana University, Bloomington, IN 47405
[b]Fermi National Accelerator Laboratory, P.O. Box 500, Batavia, IL 60510
[c]Brookhaven National Laboratory, Upton, Long Island, NY 11973.

Abstract

Isochronous electron storage rings may offer advantages for future high luminosity meson facotries. A Quasi-isochronous lattice based on the design principle of flexible γ_T lattice is studied. The emittance and chromatic properties of such a lattice are studied. Applications of this design technique for electron storage rings will be discussed.

1 INTRODUCTION

Shorten the bunch length is an effective way of increaing the brightness and luminosity of the electron storage rings. A possiblility of reducing the bunch length is to operate the electron storage ring near to the transition energy, where nonlinear synchrotron motion [1-3] determines the equilibrium geometry of the bunch distribution.

Driven by the demand of high energy physics experiments and a possibility of high brightness synchrotrons or damping rings, UCLA group has proposed a quasi-isochronous (QI) Φ-factory design by using reverse bends in the lattice, which will result large dispersion function values.

On the other hand, the QI can easily be achieved from the flexible γ_T design principle. Teng [4] had advanced the flexibile γ_T lattice design by introducing the π insertion. The combination of the FODO cells with π insertion was applied successfully and studied extensively by Trbojevic et al. [5] The transverse beam dynamics of these lattice is well understood. In this paper, we apply the design principle to achieve QI condition without using the reverse bend. Section 2 reviews the basic module of the flexible γ_T lattice. Section 3 discusses the QI condition. Section 4 evaluate the emittance of the electron storage ring. The conclusion is given in section 5.

2 THE BASIC MODULE

The basic module for a variable γ_T lattice is given by [5]

$$M_a\left\{\frac{1}{2}Q_F B Q_D B \frac{1}{2}Q_F\right\} M_b\left\{Q_{F_1} O_1 Q_{D_2} O_2\right\} M_c + \text{ref. sym.}$$

where $M_{a,b,c}$ are marker locations, Q's are quadrupoles, O's are drift spaces, and B's stand for dipoles. The horizontal betatron transfer matrix of the FODO cell is given by

$$M_{FODO} = \begin{pmatrix} \cos\mu & \beta_F \sin\mu & D_F(1-\cos\mu) \\ -\frac{1}{\beta_F}\sin\mu & \cos\mu & \frac{D_F}{\beta_F}\sin\mu \\ 0 & 0 & 1 \end{pmatrix}, \quad (1)$$

where μ is the horisontal phase advance in the FODO cell. We have assumed symmetry in the Courant-Snyder parameters at the center of the focusing quadrupole, i.e., $\beta'_F = 0$ and $D'_F = 0$.

In the thin-lens approximation with equal focusing and defocusing strengths, the Courant-Snyder parameters are given by $\sin\frac{\mu}{2} = \frac{L_F}{2f}$, $\beta_F = \frac{2L_F(1+\sin\frac{1}{2}\mu)}{\sin\mu}$, $D_F = \frac{L_F\theta(2+\sin\frac{1}{2}\mu)}{2\sin^2\frac{1}{2}\mu}$, where L_F is the length of the half FODO cell, f is the focal length of quadrupoles in the FODO cell, and θ is the bending angle of the dipole B. However it is worth pointing out that the applicability of Eq. (1) is not limited to thin-lens approximation. In the normal FODO lattice, the dispersion function is assumed to be periodic in each FODO cell. In this case, the dispersion function at the center of the focusing quadrupole is D_F with $D'_F = 0$.

Since the momentum compaction factor is given by

$$\alpha = \frac{1}{\gamma_T^2} = \frac{1}{L_m}\sum_i D_i\theta_i, \quad (2)$$

the flexible γ_T lattice can be achieved by prescribing the dispersion function at the beginning of the FODO cell with values D_a and D'_a. The value $D'_a = 0$ is usually chosen for convenience in the lattice function matching.

Depending on the initial dispersion value at marker M_a, the dispersion function at marker M_b is given by

$$D_b = D_F - (D_F - D_a)\cos\mu, \quad D'_b = \frac{D_F - D_a}{\beta_b}\sin\mu, \quad (3)$$

where β_b is the betatron amplitude function at marker M_b with $\beta_b = \beta_F$. In the matching section (assuming that there is no dipole or negligible dipole contribution to dispersion), the dispersion action is invariant, i.e.,

$$2J_c = 2J_b = \frac{D_b^2}{\beta_b} + \beta_b D_b'^2 = 2J_F[1-2(1-\zeta)\cos\mu + (1-\zeta)^2],$$

with $\zeta = \frac{D_a}{D_F}$ as the ratio of the desired dispersion at marker M_a of the FODO cell and J_F is the dispersion action for the regular FODO cell at the focusing quadrupole location.

The dispersion functions and other Courant-Snyder parameters are then matched at the symmetry point at marker M_c with a doublet (or triplet). The betatron transfer matrix is given by

$$M_{b\rightarrow c} = \begin{pmatrix} \sqrt{\frac{\beta_c}{\beta_b}}\cos\psi & \sqrt{\beta_b\beta_c}\sin\psi & 0 \\ -\frac{1}{\sqrt{\beta_b\beta_c}}\sin\psi & \sqrt{\frac{\beta_b}{\beta_c}}\cos\psi & 0 \\ 0 & 0 & 1 \end{pmatrix}, \quad (4)$$

where we have also assumed a symmetry condition at marker M_c for the Courant-Snyder parameters, i.e., $\beta'_b = 0$ and $\beta'_c = 0$. Here, β_b and β_c are the betatron amplitudes at, respectively, markers M_b and M_c, while ψ is the betatron phase advance between markers M_b and M_c.

The required dispersion matching condition at marker M_c is $D'_c = 0$. Using Eq. (3), we obtain then

$$\tan\psi = \frac{(1-\zeta)\sin\mu}{1-(1-\zeta)\cos\mu} . \tag{5}$$

This means that the phase advance of the matching section is not a free parameter, but is determined completely by the initial dispersion value D_a at marker M_a and the phase advance of the FODO cell. This condition is independent of whether we use a doublet or a triplet for the betatron-parameter matching. However, it is preferable to use a doublet matching section. The total phase advance of the whole basic module is then given by $2(\mu + \psi)$, which is a function of only the desired dispersion function at marker M_a and the phase advance μ in the FODO cell.

Quadrupoles Q_{F_1} and Q_{D_2} in the matching section are then adjusted to achieve the required phase advance ψ given by Eq. (5). A low betatron amplitude function at marker M_c is desired so that D_C will be small. Care should also be taken in the arrangement and choices of quadrupoles Q_{F_1} and Q_{D_2} in order to achieve reasonably small vertical Courant-Snyder parameters. Then, the matching becomes relatively simple. [5]

The dispersion values at the midpoints of dipoles in the FODO cell are given by $D_{B_1} = D_a(1 - \frac{1}{2}\sin\frac{1}{2}\mu)$, $D_{B_2} = D_a(1 - \frac{1}{2}\sin\frac{1}{2}\mu) + (D_F - D_a)\sin^2\frac{1}{2}\mu$. In the thin-element approximation, the momentum compaction becomes

$$\alpha = \frac{1}{L_m}\sum_{\text{modules}} (D_{B_1} + D_{B_2})\theta , \tag{6}$$

where θ is the bending angle of each dipole and L_m is the length of the half-module. In comparison with the momentum compaction factor of lattice made from conventional FODO cells, we obtain

$$\frac{\alpha}{\alpha_{\text{FODO}}} = \frac{L_F}{L_m}\left[\zeta + (1-\zeta)\frac{\sin^2\frac{1}{2}\mu}{2(1 - \frac{1}{2}\sin\frac{1}{2}\mu)}\right] , \tag{7}$$

which agrees well [5] with that obtained from realistic lattice design by using the MAD or the SYNCH programs. Note here that the momentum compaction factor is a linear function of the initial dispersion function if the module length is a constant. Although the thin-lens approximation has been used for the quadrupoles and dipoles, it is easy to see that this linear relationship is exact even for thick elements.
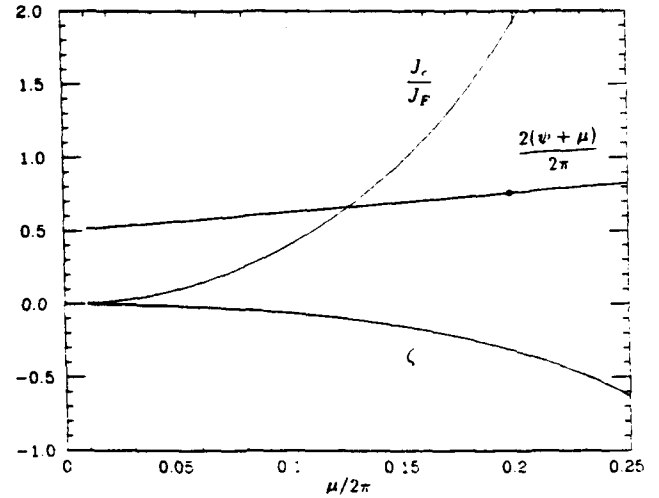
Figure 1: The dispersion function parameter ζ at M_a, the total phase advance of the QI module and the dispersion action in the straight section are plotted as a function of the phase advance of the FODO cell component

3 QUASI-ISOCHRONISM CONDITION

A basic module with isochronous condition is given by the condition $\alpha = 0$. Using Eq. (7), we obtain

$$\zeta = -\frac{\sin^2\frac{\mu}{2}}{2 - \sin\frac{\mu}{2} - \sin^2\frac{\mu}{2}}, \tag{8}$$

for the basic module. The parameter ζ, the phase advance, $2(\psi + \mu)$, and $\frac{J_c}{J_F}$ of the isochronous module is shown in Fig. 1 as a function of μ of the FODO cell. Thus the accelerator made of modules which satisfies the above condition will be a QI storage ring. These QI storage rings are tunable by adjusting the ζ through the phase advance μ of the FODO cell.

A special class of these QI storage rings are composed with module having odd multiple of the 90° betatron phase advance, which is usually prefered by beam dynamics consideration. The 270° phase advance QI module can be achieved with the condition $\mu = 69°$ shown as a dot in Fig. 1. Such module have the dispersion action in the straight section given by $J_c \approx 1.75J_F$. The maximum positive dispersion function at the symmetry point, M_c is then given by

$$D_c \approx \sqrt{1.75\frac{\beta_c}{\beta_F}}|D_a| \approx 0.38\sqrt{\frac{\beta_c}{\beta_F}}|D_F(69°)|$$

Thus the dispersion function of such a module is smaller than the corresponding FODO cell at 90° of phase advance.

4 EMITTANCE OF ISOCHRONOUS CELLS

The emittance of electron storage ring is an important quantity in the performance of the electron storage ring
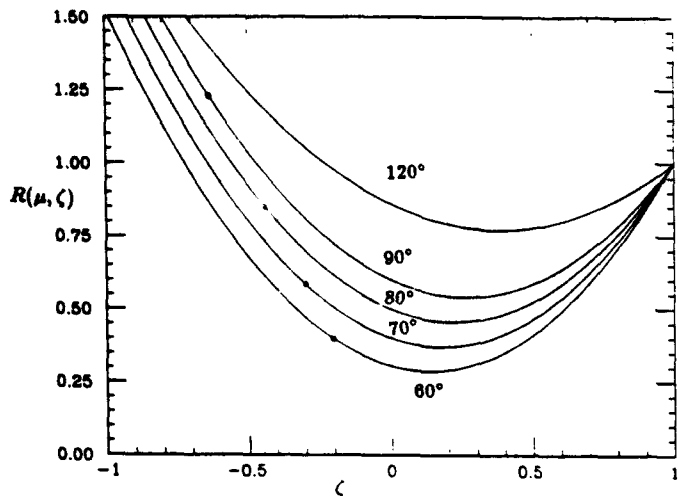
Figure 2: The ratio of the average H-function in the dipole is plotted as a function of ζ, the initial dispersion function at QF location for phase advance $\mu = 60°, 70°, 80°, 90°$ and $120°$. Here a QI lattice is given by a relation between ζ and μ shown in Fig. 1

design. For the isochrounous storage ring, the emittacne is given by

$$\epsilon = C_q \frac{\gamma^2 \langle H \rangle}{J_s \rho}$$

where $C_q = 3.84 \times 10^{-13}$ m and the dispersion action, H, is given by $H = \frac{1}{\beta_s}[D_s^2 + (\beta_s D_s' - \frac{\beta_s'}{2} D_s)^2]$. Using the thin lense approximation by dividing each dipole in FODO cell into two sections, we obtain

$$\frac{D_{B1}}{D_F} = \zeta(1 - \frac{1}{2}\sin\frac{\mu}{2}) + \frac{1}{4}\frac{\sin^2\frac{\mu}{2}}{2 + \sin\frac{\mu}{2}},$$

$$\frac{D_{B1}'L}{D_F} = -\zeta\sin\frac{\mu}{2} + \frac{\sin^2\frac{\mu}{2}}{2 + \sin\frac{\mu}{2}},$$

$$\frac{D_{B2}}{D_F} = \zeta(1 - \frac{1}{2}\sin\frac{\mu}{2} - \sin^2\frac{\mu}{2}) + \frac{\sin^2\frac{\mu}{2}}{2 + \sin\frac{\mu}{2}}(\frac{9}{4} + \sin\frac{\mu}{2}),$$

$$\frac{D_{B2}'L}{D_F} = \zeta\sin\frac{\mu}{2}(1 - 2\sin\frac{\mu}{2}) + \frac{\sin^2\frac{\mu}{2}}{2 + \sin\frac{\mu}{2}}(3 + 2\sin\frac{\mu}{2}),$$

$$\beta_{B1} = \beta_{B2} = \frac{L}{\sin\mu}(2 - \sin^2\frac{\mu}{2}), \quad \frac{\beta_{B1}'}{2} = -\frac{\beta_{B2}'}{2} = -\frac{1}{\cos\frac{\mu}{2}}.$$

The H-function can then be expressed as

$$\langle H \rangle = \rho\theta^3 F_{FODO}(\mu) R(\mu, \zeta), \qquad (9)$$

where

$$F_{FODO} \approx \frac{1 - \frac{3}{4}\sin^2\frac{\mu}{2}}{\sin^3\frac{\mu}{2}\cos\frac{\mu}{2}},$$

in the thin lense approximation. By definition, we have $R(\mu, \zeta = 1) = 1$. The ratio function R of the variable γ_T lattice is shown in Fig. 2, where the QI lattice corresponds to points marked on the figure. The particularly interesting

QI lattice with $\zeta \approx -0.3$ and $\mu = 70°$ has an emittacne of about 60% of that of the corresponding regular FODO cell lattice. Since the emittance of FODO cell lattice is proportional to $\frac{1}{\mu^3}$, the QI lattice at the phase advance of $70°$ is equivalent to that of a regular $90°$ FODO cell lattice. Although the emittance of a QI lattice is still about two orders of magnitude larger than the minimum emittance Chasman-Green lattice with $\langle H \rangle|_{MBOG} = \frac{1}{4\sqrt{15}}\rho\theta^3$, [6] the QI lattice has the simplicity of tunability of the momentum compaction factor α.

5 CONCLUSION

Lattice, which is made of QI modules are QI lattice. For a low energy accelerator, such as the Φ-factory, with $B\rho \approx 1.7$ Tm, race track with two module can be considered. Such lattice does not have dispersion free straight sections. For higher energy accelerators, dispersion free straight sections discussed in ref. [5] can be incooporated into the lattice.

We have made an extension of the flexible γ_T lattice to the regime of the quasi-isochronism. We found that the resulting emittance is better than that of the corresponding FODO cell lattice. The simplicity of the FODO cell remains to be the key feature of the QI lattice. The longitudinal phase space can however be controlled by the momentum compaction factor in proper balance between the microwave instability and the synchrotron radiation damping. Possible applications of the QI lattices are Φ-factory, small damping ring, or synchrotron radiation sources. It might offer advantages in offering a smaller equilibrium longitudinal phase space area without resorting to high rf voltage consideration.

6 REFERENCES

[1] H. Bruck, J.P. Bardin, J.F. Gournay, J.L. Laclare, G. Leleux, IEEE Trans. NS-20, 822 (1973)

[2] C. Pellegrini and D. Robin, NIM A301, 27 (1991); Proc. IEEE PAC, 398 (1991).

[3] S.Y. Lee and J. Wei, Proc. EPAC, p.764 (1988).

[4] L.C. Teng, Infinite Transition-energy Synchrotron Lattice using π-straight Section, Part. Acc. 4, pp. 81-85 (1972).

[5] D. Trbojevic, D. Finley, R. Gerig, and S. Holmes, Design Method for High Energy Accelerator without Transition Energy, Proc. of Second European Particle Accelerator Conference, Nice, France, June 1990, pp 1536-1538. K.Y. Ng, D. Trbojevic, and S.Y. Lee, A Transitionless Lattice for the Fermilab Main Injector, Proc. of 1991 IEEE Part. Accel. Conf., May 6-9, 1991, San Francisco, California, pp 159-161. S.Y. Lee, K.Y. Ng and D. trbojevic, FN-590 (1993).

[6] S.Y. Lee and L. Teng, Proc. IEEE PAC, p.2679 (1991).

Optimization Method for Orbit Correction in Accelerators*

Eva Bozoki and Aharon Friedman

National Synchrotron Light Source,

Brookhaven National Laboratory, Upton, NY 11973

Abstract

We present a method to minimize the corrector strengths required to reduce the rms beam orbit. Any least square correction method will usually lead to undesirably strong corrector settings. The method, we are presenting, minimizes the total kick vector by finding the eigen solutions of the equation $\vec{X} = A\hat{\theta}$, where $\vec{X}$ is the orbit change vector $\hat{\theta}$ is the kick vector and A is the response matrix. Since A is not necessarily a symmetric or even square matrix we symetrize the matrix by using $A^T A$ instead. Eigen vectors with corresponding small eigen values generate negligible orbit changes. Hence, in the optimization process the kick vector is made orthogonal to the eigen vectors.

The physical interpretation of the eigenvectors will be discussed. We will illustrate the application of the method to the NSLS X-ray and UV storage rings. From this illustration it will be evident, that the accuracy of this method allows the combination of the global orbit correction and local optimization of the orbit for beamlines and insertion devices.

1 Introduction

In circular machines, the beam orbit is usually very important to the output of the machine. A good example is synchrotron radiation facilities where the source point and direction of the photon beams depend on the beam position and angle. In addition the lifetime of the beam in the machine, the maximum current, and sometimes the ability of the machine to store a beam at all depends on an accurate beam orbit.

2 The response matrix and its eigen states

Usually in a circular machine, the beam position is monitored by a set of pickup electrodes (PUE), distributed around the machine and orbit correction is performed using a set of distributed dipoles (correctors). The relationship between a change in the strength of a corrector and the corresponding change of the beam position at the PUEs, is expressed by the response matrix. In this section we define and analyze the response matrix.

2.1 Definition of the response matrix

It is well known that the orbit change due to a change in the corrector strengths (orbit kick) can be expressed as [1]:

$$\vec{X} = A\vec{\Theta} \qquad (1)$$

where $\vec{\Theta} = [\Theta_j]$, $1 \leq j \leq N_c$ is the kick vector, $\vec{X} = [X_i]$, $1 \leq i \leq N_m$ is the orbit vector and $A = (A_{i,j})$ is the response matrix. The element $A_{i,j}$ of the response matrix is the orbit change on the i-th orbit monitor due to a unit kick from the j-th corrector. In this paper, unless otherwise specified, the beam position and the orbit kick are expressed in mm and Kdigit[1], respectively.

2.2 Eigen solutions of the response matrix

In general, the number of correctors and monitors are different, consequently the response matrix A is rectangular and Eq. (1) is over or under constrained. To solve Eq. (1), we left-multiply it by A^T, the transpose of the response matrix A:

$$A^T \vec{X} = A^T A\vec{\Theta} \qquad (2)$$

The solution of Eq. (2) is the least-square approximation of a solution of Eq. (1). The matrix $A^T A$ is symmetric and non negative. The eigen solutions of Eq. (2) can be found by diagonalyzing the matrix $A^T A$, resulting in the eigen values $[\lambda_j]$ and the corresponding eigen vectors $[\hat{\theta}_j]$. An eigen vector $\hat{\theta}_j$ represents a set of corrector values. The orbit change corresponding to the j-th eigen vector is:

$$\vec{x}_j = A\hat{\theta}_j \qquad (3)$$

It can be shown that

$$(\vec{x}_j \cdot \vec{x}_j) = \lambda_j \qquad (4)$$

The physical meaning of the eigen values becomes clear from Eq. (4). An eigen value λ_j is a quantitative measure of the orbit response (of the machine) to the j-th eigen vector. A small eigen value λ_j corresponds to a small x_j orbit change ($< x_j^2 >_{rms} = \lambda_j / N_m$). This property of the eigen solutions will be used later in the paper for reducing the corrector strengths without significantly changing the resulting orbit.

3 The representation of a circular machine

In order to give physical interpretation to the response matrix and its eigen solution one has to look at the dynamics of the beam orbit in a circular machine. In this section we lay out the dynamics that lead to the response matrix and show the physical meaning of its eigen solution in one case.

---

[1]digits - Digitized voltage of the computer controlled corrector power supply.

3.1 Courant-Snyder equation

For a given set of discrete PUEs and correctors, the beam position at the j-th PUE is:

$$\frac{x_i}{\sqrt{\beta_i}} = \frac{1}{2\sin\pi\nu}\sum_{j=1}^{N_c}\theta_j\sqrt{\beta_j}\cos\nu\left(|\phi_i' - \phi_j| - \pi\right) \quad , \quad (5)$$

where β_i is the β function value at the PUE in which x_i is observed, ϕ_i' is the phase location of that PUE, θ_j is the angular kick introduced to the beam by the corrector located at phase ϕ_j, β_j is the β function value at ϕ_j, ν is the tune (number of betatron oscillations) of the machine, and N_c is the total number of correctors.

It is easy to see from Eq. (5) that the elements of the response matrix A are:

$$A_{ij} = \frac{\sqrt{\beta_i\beta_j}}{2\sin\pi\nu}\cos\nu\left(|\phi_i' - \phi_j| - \pi\right) \quad . \quad (6)$$

Note, that in most practical cases the numerical value of the matrix element A_{ij} cannot be theoretically evaluated to a satisfactory accuracy, since the values of β_i and β_j are not known. It was actually suggested [4] to use the measured value of the response matrix elements in order to estimate the values of the β function.

3.2 Equidistant correctors and monitors

Consider the case, when there are equal number of PUEs and correctors ($N_m = N_c = N$) and they are positioned at equal intervals around the ring. Furthermore, for the sake of simplicity, we assume that the β function has the same value for any PUE ($\beta_i = \beta_M$), and that it has the same value for any corrector ($\beta_j = \beta_C$). Clearly the response matrix in such a case is cyclic [2] since the symmetry is such that the point $i = 0$ can be chosen arbitrarily to be any PUE. It is indeed, easy to prove, by way of mathematical induction that Eq. (6) yields a cyclic matrix whose first line is

$$A_{1j} = \frac{\sqrt{\beta_M\beta_C}}{2\sin\pi\nu}\cos\nu\left[\frac{2\pi}{N}\left(j - \frac{1}{2}\right) - \pi\right] \quad . \quad (7)$$

The i-th element of the j-th eigen vector and the j-th eigen value of a cyclic matrix A are:

$$\hat{E}_j(i) = \frac{1}{\sqrt{N}}\exp\left(i\frac{2\pi}{N}j2\right) \quad , \quad (8)$$

$$\lambda_j = \sum_{k=1}^{N}A_k\exp\left[i\frac{2\pi}{N}j(k-1)\right] \quad . \quad (9)$$

Thus the eigen vectors of the response matrix are those expressed by Eq. (8), namely they are the harmonics of

---

[2] A cyclic matrix is a matrix where the lines are arranged so that the first element of a line is the last element of the previous line and the other elements are copies from the previous line.

---

the ring. Substituting Eq. (7) in Eq. (9) results in

$$\lambda_j = \frac{1}{2}\exp\left[i\pi j\left(1 - \frac{1}{N}\right)\right]\frac{\sin\pi(j+\nu)}{\sin\frac{\pi}{N}(j+\nu)}$$
$$+\frac{1}{2}\exp\left[-i\pi j\left(1 - \frac{1}{N}\right)\right]\frac{\sin\pi(j-\nu)}{\sin\frac{\pi}{N}(j-\nu)} \quad . \quad (10)$$

As it is expected [1], the orbit response to the j-th harmonic (λ_j) gets larger as j gets closer to the tune ν.

It can be shown [5], that for the most general case of non symmetric rings with non equidistant and non equal number of correctors and monitors, the eigenvectors represent the harmonics, the local bumps and the errors in the ring.

4 Corrector strengths reduction

As mentioned earlier, the property of the eigen solutions that a small eigen value corresponds to a small orbit change can be used for reducing the corrector strengths without significantly changing the resulting orbit.

Let $\vec{X}_o$ be the orbit to be corrected and $\vec{\Theta}$ its corresponding kick vector, calculated by any method (e.g. least square). The RMS of the residual orbit is:

$$X_{rms}^2 = \frac{1}{N_m}|A\vec{\Theta} - \vec{X}_o|^2 \quad . \quad (11)$$

As long as the λ_j eigenvalue is small, the corresponding $\vec{x}_j$ orbit is small and one can reduce the $\vec{\Theta}$ kick vector by the j-th eigenvector without significantly modifying the orbit. The reduced kick vector is:

$$\vec{\Theta}_{red} = \vec{\Theta} - \sum_{j=1}^{M}(\vec{\Theta}\cdot\hat{\theta}_j)\hat{\theta}_j \quad , \quad (12)$$

$$\Delta\vec{X}_{rms}^2 = \vec{X}_{rms}^2 - (\vec{X}_{red}^2)_{rms} < \epsilon \quad . \quad (13)$$

The $\vec{\Theta}_{red}$ reduced kick vector is 'equivalent' to the original $\vec{\Theta}$ vector to ϵ accuracy. It is important, that both, the norm of the vector and its largest component is reduced:

$$|\vec{\Theta}_{red}|^2 < |\vec{\Theta}|^2 \quad and \quad (\Theta_{red})_{max} < \Theta_{max} \quad . \quad (14)$$

This method was implemented in the NSLS resulting in reduction of up to 70% in the average corrector strength and up to 90% in the maximum corrector strength. In addition the accuracy of orbit correction was significantly improved since the elimination of the small eigenvalue states reduces the error in orbit calculation.

5 Correction by decomposition

In the previous Section, we made use of the eigensolutions to reduce a given $\vec{\Theta}$ kick vector, obtained by any method of orbit correction. However, one can directly use an eigenvector decomposition based orbit correction method, thus avoiding the need for reduction. This method will yield the 'minimum' kick vector for a desired accuracy of orbit correction.

5.1 Global orbit correction

Let $\vec{X}_o$ be the orbit to be corrected and let us decompose it in terms of the $\vec{x}_j$ 'eigen'[3] orbits:

$$c_j = \vec{X}_o \cdot \vec{x}_j \quad , \tag{15}$$

That is, each $\vec{x}_j$ vector is represented in $\vec{X}_o$ by the c_j coefficient.

Let us next define an orbit vector, $\vec{X}_{\epsilon_o}$ as:

$$\vec{X}_{\epsilon_o} = \sum_{j=1}^{N_c} c_j \cdot \vec{x}_j \quad . \tag{16}$$

The norm of this vector is $|\vec{X}_{\epsilon_o}|^2 = \sum_{j=1}^{N_c} c_j$ and $|\vec{X}_{\epsilon_o}|^2 \leq |\vec{X}_o|^2$. Actually, the uncorrectable part of the orbit is: [4]

$$\Delta \vec{X}_{rms}^2 = \frac{1}{N_m}(|\vec{X}_o|^2 - |\vec{X}_{\epsilon_o}|^2) = \epsilon_o^2 \quad . \tag{17}$$

Substituting Eq. (3) into Eq. (16) we obtain

$$\vec{X}_{\epsilon_o} = A \sum_{j=1}^{N_c} c_j \hat{\theta}_j \quad , \tag{18}$$

that is, the kick vector which corrects the $\vec{X}_o$ orbit to to ϵ_o accuracy can be obtained from the eigenvector decomposition of this orbit as:

$$\vec{\Theta} = \sum_{j=1}^{N_c} c_j \hat{\theta}_j / \sqrt{\lambda_j} \quad . \tag{19}$$

This method already assured that we are using only the minimum contribution from each eigenvector, thus the $\vec{\Theta}$ kick vector is 'minimized'. If, however, one can allow an $\epsilon > \epsilon_o$ tolerance in the orbit correction, then some eigenvectors (or part of it) with the smallest eigen values can be omitted, further reducing the $\vec{\Theta}$ kick. Actually, we can skip the eigenvectors until the corresponding decomposition coefficients satisfy:

$$\sum_{j=1}^{J} c_j^2 \leq E \quad where \quad E \equiv N_m \epsilon^2 \quad . \tag{20}$$

In reality, there is no such J, for which the equality would be exactly satisfied. Generally, the sum for the first $J-1$ eigenvector is E' < E and for the J-th eigenvector the sum will be greater then E:

$$\sum_{j=1}^{J-1} c_j^2 + c_J^2 = E' + c_J^2 \quad . \tag{21}$$

---
[3] The $\vec{x}_j$ vectors are defined in Eq. (3), they represent the orbit change corresponding to the $\hat{\theta}$ eigenvectors. They comprise an orthogonal but not a complete ortoganal set, and they are not unit vectors.

[4] This part of the orbit cannot be corrected by any method with the given set of orbit correctors.

Therefore to achieve an ϵ accuracy in the orbit correction, we can omit the first $J-1$ eigenvectors and a part of the J-th. The remaining terms will be:

$$c_J'^2 + \sum_{j=1}^{J+1} c_j^2 \quad , where \quad c_J' = c_J - \Delta \quad and \quad \Delta = \pm \sqrt{E - E'} \tag{22}$$

and the sign of Δ is the same as the sign of c_J.

The implementation of this method in the NSLS resulted in orbit correction to an accuracy of $X_{rms} = 15 \mu m$ with very small changes in corrector strength (sometimes the average corrector strength was in the single digits).

5.2 Including local bumps

The tolerance on the global RMS orbit, even though very stingent, is usually larger then the tolerance on a few selected PUE's, usually at the ends of insertion devices. In case of the NSLS X-ray ring, for example, the requirement on the global RMS orbit is 100 μ, while before/after the insertion devices 20 μ. During operation, for each fill of the ring, first the global orbit was corrected using harmonic or least-square method then local bumps were implemented to position the orbit more accurately at the insertion devices.

With the decomposition method we implemented the global and local orbit correction at the same time by assigning different weight factors at those PUE's in sensitive positions before/after the insertion devices.

6 Other uses of eigen vectors

One can use the Eigen vectors to measure the Response Matrix. Instead of the usual method of kicking with one corrector at a time and measuring the orbit response of the ring, the excitation of the Eigen vectors yield better results with higher accuracy [5].

We are also using the Eigen vector decomposition method in Digital Feedback in the storage rings (see [6]).

I. REFERENCES

[1] G. Guinard, CERN 77-10 ISRD, 6 June (1977).

[2] A. Jackson, SRS/NSS/75/103 (1975).

[3] E.D. Courant and H.S. Snyder, Annals of Phys., **3**, No. 1, p. 1–48, (1958).

[4] E. Bozoki, Proc. of the Workshop on Modeling Based Accelerator Controls, p. 5, (1987).
E. Bozoki, NSLS Tech Notes #291 and #296, (1987).

[5] A. Friedman and E. Bozoki, In preparation.

[6] A. Friedman, E. Bozoki, O. Singh, J. Smith, In this Proceedings.

A Fast Model-Calibration Procedure for Storage Rings[*]

W. J. Corbett, M. J. Lee, V. Ziemann

Stanford Linear Accelerator Center

Stanford, CA 94309 USA

Abstract

The ever-increasing demand for better performance from circular accelerators requires improved methods to calibrate the optics model. We present a linear perturbation approach to the calibration problem in which the modeled BPM-to-corrector response matrix is expanded to first order in quadrupole strengths. The result is numerically fit to the measured response matrix yielding quadrupole strength errors, corrector strength errors, and BPM linearity factors. The large number of degrees of freedom in the fit allows a comprehensive error analysis, including the determination of BPM resolutions. In this way, a self-consistent first order optics model of SPEAR was generated which reproduces the measured tunes.

I. INTRODUCTION

In the course of developing an optics model for storage rings, a series of corrector kicks is typically applied to the beam and the resulting orbit shift is measured. Then, by simultaneously analyzing the horizontal and vertical orbit perturbations (and perhaps a measurement of dispersion), the *on-line model is numerically verified, or updated if necessary.* In the analysis procedure, the fitting parameters can include quadrupole strengths, corrector strengths, or beam energy errors, for instance. Although this multi-track analysis method improves the agreement between model and measurement, it is a manual process restricted to a limited set of measurements and fitting variables.

Recently however, a method for fast calibration of the optics model (CALIF) has been developed which automates the fitting procedure to include the full set of horizontal and vertical response matrix measurements. This method was originally based on a linear perturbation approach used for phased-array antenna design [1], but with re-interpretation for the application to accelerators. The matrix formalism allows us to expand the set of variable quadrupole strengths, solve for corrector strength and BPM linearity calibration factors, and estimate the BPM resolutions for the measured data set. The updated optics model, including statistically correlated error bars for all fitted quantities, can then be used to predict Twiss parameters at every element in the storage ring.

II. THE CALIF ALGORITHM

The objective of the CALIF algorithm is to obtain a consistent computer model of the as-built machine based on a set of difference orbit measurements. Using a first-order perturbation approach, we seek modeling errors in the following parameters

- Quadrupole gradients
- Corrector scale factors
- BPM scale factors
- BPM resolution errors

including a comprehensive error analysis of the results. From the difference orbit measurements, we first determine the BPM-to-corrector response matrix coefficients

$$\overline{C}^{ij} = \frac{\Delta x \text{ at BPM } i}{\Delta x' \text{ at corrector } j} \qquad (1)$$

which are then compared to the perturbed expression for the computer model prediction, namely,

$$\overline{C}^{ij} = C^{ij} + \sum_q \frac{\partial C^{ij}}{\partial k_q} \delta k_q \qquad (2)$$

where C^{ij} and $\partial C^{ij}/\partial k_q$ are the computer-model response-matrix coefficients and their derivatives with respect to the gradient of a particular quadrupole or quadrupole family, respectively. The C^{ij} and $\partial C^{ij}/\partial k_q$ are easily calculated with accelerator modeling codes such as COMFORT [2]. The δk_q are the sought-after gradient errors needed to explain the measured response-matrix coefficients $\overline{C}^{ij}$.

The solution of Equation 2 is strongly affected by errors in the linear-scale factors for both the correctors and BPMs. To take these affects into account, we augment the left-hand side of Equation 2 by variable corrector-scale factors, x^j, and BPM scale factors, y^i, to arrive at a relation among the unknown quadrupole-gradient errors, corrector scales, and BPM scales,

$$C^{ij} = y^i \overline{C}^{ij} x^j - \sum_q \frac{\partial C^{ij}}{\partial k_q} \delta k_q \qquad (3)$$

Furthermore, each $\overline{C}^{ij}$ has an intrinsic measurement error due to the limited resolution of the BPMs which is given by

$$\sigma\left(\overline{C}^{ij}\right) = \frac{\sigma(\text{BPM } i)}{\Delta x' \text{ at corrector } j}. \qquad (4)$$

We initially assume the same value of σ for all BPMs.

Now we are in a position to use Equation 3 in a linear least-squares fit, either for the corrector scales x^j and the gradient errors δk_q while keeping the BPM scales fixed, or for the BPM scales and the gradient errors while keeping the corrector scales fixed. In SPEAR eight quadrupole families, thirty correctors (x and y, respectively) and twenty-six BPMs yield up to a maximum of 1560 measured $\overline{C}^{ij}$. Since only about sixty parameters are fitted, we have a huge number of degrees of freedom which allows a careful error analysis.

The organization inside the CALIF code is as follows: first a setup file is read that contains status bits of the variable parameters to be included in the fit, the filenames of the measured difference orbits, and the computer model C^{ij} files.

Then, according to Equation 3, a matrix A is constructed in which the columns are related to the fitting parameters x^j and δk_q, and the rows are related to the $\overline{C}^{ij}$. Each row is weighted according to its associated measurement error, given by Equation. 4. In the next step, this over-determined set of linear equations is inverted. Using informal, but obvious notation, we get

$$(x^j : \delta k_q)^T = \left(\frac{A^T}{\sigma} \frac{A}{\sigma} \right)^{-1} \left(\frac{A^T}{\sigma} \right) \left(\frac{C^{ij}}{\sigma} \right), \qquad (5)$$

where $(A^T/\sigma \ A/\sigma)^{-1}$ is the covariance matrix from which the fit errors on $(x^j : \delta k_q)^T$ are deduced. The colon in Equation 5 indicates partitioning of the corrector scale and quadrupole-strength error vectors.

Next, the BPM resolution errors are deduced by calculating the contribution of each BPM to the total χ^2 for the problem. The BPM resolutions are then rescaled so that each BPM contributes equally, and the χ^2 is forced to unity. Inconsistent (noisy) BPMs are rejected at this stage. This procedure is iterated until the χ^2 remains close to unity, which typically takes one to three iterations.

In a final step, the updated solution for the corrector scales remains constant, and an iterative procedure similar to the one just described is launched in order to fit the BPM scale factors y^i and the quadrupole gradient errors.

The procedure for alternately fitting the corrector scales and the BPM scales is iterated typically four times until a self-consistent set of gradient errors, corrector scales, BPM scales, and BPM resolution errors is found. A normal run for SPEAR usually involves a total of about fifteen fits, where each fit takes about one minute on a VAX8700. The bulk of this time is spent inverting the matrix needed for the calculation of the covariance matrix.

Recently, the CALIF program and associated drivers used to compute 4 × 4 response matrix elements have been updated to include arbitrary numbers of quadrupole, corrector, and BPM elements. These modifications make it possible to apply the CALIF program to most storage rings. For machines with strong focusing, the linearity of the partial derivatives may be valid only in a restricted range. In this case, the step size used

for the quadrupole strengths in each iteration of the fitting procedure can be adjusted to achieve faster convergence.

III. EXPERIMENTAL RESULTS

The first application of the CALIF program was carried out using measurements of the bare SPEAR lattice, with all insertion devices and skew quadrupoles turned off. The 4 × 4 corrector response matrix $\overline{C}^{ij}$ was measured relative to a flat-orbit configuration where the beam was steered to the center of the BPMs. Due to the long time required to measure the response matrix, only one measurement was made for each horizontal and vertical corrector. The peak closed-orbit perturbations were about 2–3 mm in SPEAR, and the tune shift produced by the corrector kicks was within the frequency line width as measured by the spectrum analyzer.

Next, we extracted the on-line optics model for computation of the theoretical corrector-response matrix, and its derivatives with respect to the quadrupole family strengths. The derivatives were computed with COMFORT [2] by evaluating $\Delta C^{ij}/\Delta k_q$ for values Δk_q on the order of 1×10^{-3}. Finally, a set-up file was compiled directing CALIF to the measured data and computed response matrices.

The results of the CALIF computation are listed in the following table. Only a few of the horizontal correctors and BPMs are shown as examples:

Quadrupole	Initial Value	Final Value	Error (+/-)
Q3	-0.9316 (m^{-2})	-0.9293	0.188E-03
Q2	0.3700 (")	0.3713	0.135E-03
Q1	-0.2543	-0.2651	0.843E-03
QFA	0.7711	0.7701	0.102E-02
QDA	-0.7214	-0.7314	0.442E-03
QFB	0.4714	0.4730	0.538E-03
QF	0.4301	0.4266	0.218E-03
QD	-0.6651	-0.6685	0.157E-03

Corrector (x)	Initial Value	Final Value	Error (+/-)
HCORR1	1.0	0.839	0.023
1BB2T	1.0	1.051	0.025
2BB2T	1.0	1.156	0.029

BPM (x)	Initial Value	Final Value	Error (+/-)
WIS1	1.0	1.033	0.017
1S2	1.0	1.074	0.031
2S3	1.0	1.037	0.026

Tune	Initial Value	Final Value	Measurement
Q_x	6.864	6.834	6.838
Q_y	6.635	6.753	6.749

From the table, we find that the tunes of the calibrated model agree in both planes to within 0.004 with the measured tunes. Since the tunes were not part of the fitting procedure, this result gives us confidence in the fidelity of the calibrated model. For the quadrupole strengths, we found deviations of less than $0.01 \, \text{m}^{-2}$, with error bars of less than ±0.001. The

corrector scale errors were in the range of <10 percent, with 3 percent accuracy. These results indicate that the matrix "A" discussed in Section II was well conditioned.

For the BPM resolutions, we found the average vertical value of σ was about 100 microns, which is a plausible result for SPEAR. In the horizontal plane, the resolutions were larger, about 200–250 microns, possibly due to the button geometry or longitudinal misalignment of components in SPEAR. Following the installation of new BPMs and re-alignment of SPEAR, we will repeat the process and compare results. The entire process, including measurement and data analysis, takes only about two hours.

IV. CONCLUSION

A conceptually simple and fast way to calibrate the linear optics model for storage rings was developed and tested on SPEAR with great success. One of the primary advantages of this technique is that the problem has a large number of degrees of freedom that allow a careful error analysis of the solution. When applied to SPEAR, for instance, the eight quadrupole magnet strength errors were found to generally be less than $0.01\,\mathrm{m}^{-2}$, with error bars less than ± 0.001. With these errors corrected, the model tunes now agree to within 0.004 with the measured tunes in both the horizontal and vertical planes. This calibrated model for SPEAR now gives us excellent agreement between simulated orbits and the measured orbit data, and accurately computes the Twiss parameters at every element in SPEAR.

V. REFERENCES

[1] R. S. Elliott, *Antenna Theory and Design*, 1981, Prentice-Hall, Inc., Englewood Cliffs, N. J. 07632.

[2] M. D. Woodley, et al., "Control of Machine Functions, or Transport Systems," SLAC–PUB–3086, March 1983.

Dynamic Accelerator Modeling*

H. Nishimura

Lawrence Berkeley Laboratory, University of California, Berkeley, California 94720

Abstract

Object-Oriented Programming has been used extensively to model the LBL Advanced Light Source 1.5 GeV electron storage ring. This paper is on the present status of the class library construction with emphasis on a dynamic modeling.

I. INTRODUCTION

The Advanced Light Source (ALS) at Lawrence Berkeley Laboratory represents one of the new generation of electron storage rings being developed for high brightness synchrotron radiation experimentation [1]. These low emittance storage rings require high accuracy, multi-parameter accelerator models for trajectory calculations and model-based control systems. During the lattice design phase, computer-intensive off-line modeling and simulation programs were developed to study magnet structures and tolerances [2]. The models were later made more flexible and interactive by taking advantage of Object-Oriented Programming(OOP) languages and techniques [3]. This paper describes the next logical step to integrate the modeling software with the accelerator control system in order to provide model-based control and automated analysis of the accelerator.

II. DYNAMIC MODELING AND OOP

A. Dynamic Modeling

Traditionally, a tracking or modeling code supports only one accelerator configuration and it is tightly coupled to a particular approximated Hamiltonian and its integrator. **Dynamic Modeling** [4] is a new modeling technique that supports multiple accelerator configurations at run time. It also isolates the simulation code framework from the detail of its numerical integrator. These tasks can be supported quite naturally using an OOP concept. The general software requirements that include correctness, robustness, extendibility, reusability and compatibility [3] are all supported by OOP. Additional specific requirements for the accelerator control system described in the reference [5] also requires OOP.

Dynamic Modeling is just one of the merits we can get from **OOP**. Instead of creating a virtual accelerator using all the lines of a code, we can construct a class of accelerators and create, manipulate and annihilate multiple virtual accelerators at run time. It makes the calibration of the model efficient because virtual machines behave like *dynamic* variables. It also makes the modeling of operations with undulators easier by keeping many configurations with different undulator settings.

B. Class Libraries

Our effort has been focused on the development of class libraries which serve as building blocks of various kinds of applications. There are three kinds of class libraries: modeling, hardware access and applications. A class for modeling and simulation is called **Goemon** [6] and supports **Dynamic Modeling**.

C. Modeling on the ALS Control System

The programs we used in the lattice design phase [2] were developed on VAX/VMS and written in VMS Pascal. The first step to create **Goemon** was to extract a linear modeling engine from them. Then it was rewritten in ANSI C for the use on Unix workstations and IBM PC clones that have on-line access to the hardware of the accelerator [7]. We used **Eiffel** (v2.3) [8] on Unix to construct a class library at a very high level, keeping the numerical engine in C [4]. Now it has been completely rewritten in C++ on PC clones running Microsoft Windows 3.1 or NT and is being ported to Unix. This version covers the range from the lower level numerical engine to the higher level optics calculations and fittings.

D. Design and Analysis

The Object-Oriented Approach was applied not only for programming but also for design and analysis. We used the

Class Name
attribute
operation

Object Modeling Technique [9] with OMTool [10] for object design and analysis. In this notation, a class is represented as shown. (We may omit names of attribute and operation in this paper.)

The physics part (**Goemon**) was designed to have:
1. Simplicity
2. Distinction between Component and Machine.
3. Separation from Hardware Layer
4. Separation from Graphics
5. Separation from Machine Operation

Simplicity is important in the class library construction. The choice of inheritance or aggregation was the main issue for us. Component and Machine corresponds to magnets in a warehouse and an accelerator assembled from them. But the term *Machine* is usually used for the hardware, therefore we will call it *Accelerator*. Separation is to keep the model portable. Since the low level machine access can be performed without modeling, a model layer should be independent from it. Graphics heavily depend on the development environment, therefore the model should be separated from them. Machine operation means various kind of parameter fitting and machine study. Since it accesses the hardware and requires graphics, it must not be a part of the model. These requirements on separation can be well described as follows: Model, hardware access and graphics should be supported independently by their own class libraries and serve as suppliers to the client classes that include machine operations and studies. This is again the matter of *has-a* and *is-a* relationship.

III. CLASS LIBRARIES

Currently, we classify as follows:
    Physics (Goemon)
  Component Class
  Accelerator Class
    Hardware
  Device Class
    Client
  Graphics Class
  Operation Class
We describe the structure of 5 classes mentioned above.

A. *Component Class*

A beam line is a series of elements like drift spaces, magnets and monitors. The class **Element** serves as a base class for these elements. **Drift** is a class for drift spaces and a base for thick linear elements like quadrupole and bending magnets. **Marker** is a base class for markers and thin elements that cover multipole magnets. **Wiggler** is treated as a special quadrupole which will be enough for elementary linear optics calculation. When a better model for a wiggler/undulator is required, it will be a derived class of it.
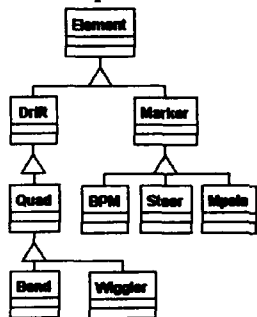
The most important method of **Element** is *pass* that transfers a particle $v=(x,p_x,y,p_y,\delta p/P_0)$ through it. Here (x,y) is a transverse coordinate, (p_x,p_y) is the canonical momentum, δp=momentum deviation, P_0=nominal momentum. The stan-

dard 4x5 matrix formalism is used as the integrator but it can be easily replaced with another formula making use of the inheritance mechanism without influencing other parts.

B. *Accelerator Class*

This is a class for virtual machines. **BeamLine** represents a beam transfer line that is a list of **Component Class** objects. It has an array of **Celement**. **Celement** class has an **Element**, path and Twiss functions at each position. **Ring** is a circular **BeamLine**. It has a collection of **Element** objects to

assemble a beam line. **Ring** is the class that directly supports dynamic modeling. An instance of **Ring** is a virtual accelerator. The figure (right) shows the relationship between Component and Accelerator classes.

The **ALS** storage ring classes are derived from **Ring**. **ALSSR0** is the ideal ring with full symmetry, **ALSSR** for full lattice and **ALSSRW** with wigglers/undulators. **ALSSR** has knobs to manipulate any magnets around the ring freely. Then it calculates all the linear optics, synchrotron integrals and related parameters.

C. *Graphics Class*

A graphical user interface library should support both windows environment on Unix workstations and PC running MS Windows. We use **zApp** [11] on PC to cover Windows 3.1 and NT. We will be using **zApp** when OSF/Motif version is released. A customized graphics class for **ALS** is being developed using **zApp**.

D. *Device Class*

Layered on top of the **ALS** control system, **Device** provides virtual devices. **Channel** corresponds to each hardware access channel (**DMM** database entry [7]). The figure shows that **Device** has one or more channels.

PSMagnet is a base class for magnet power supplies. Since there are many quadrupoles, steering magnets and BPMs and are frequently used by application classes, dedicated access is provided.

Previously, **Device** was a descendent of **Channel** and served in the commissioning phase for process

112
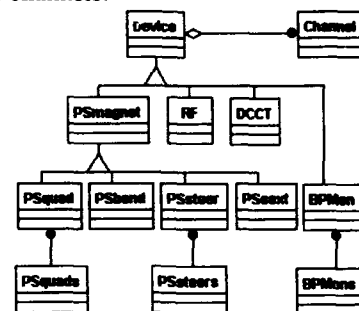
controls. But this design turned out to be inadequate to handle devices that have many channels and is being rewritten as described above. This is also a matter of *is-a* and *has-a* relationship.

PSmagnet is for the magnet power supplies and contains subtasks to perform slow settings of currents. **PSquads** and **PSsteer** are for ganged operation that synchronizes subtask objects. **DCCT** is a class for a beam current monitor that keeps track of beam current intensity. **BPMons** handles 96 beam position monitors and have been used intensively during the commissioning period.

E. Operation Class

This supports various kinds of parameter fitting operations on the **Accelerator** object which covers tune fitting, orbit correction and undulator compensation. This class is a client of all other classes mentioned above and is specific to the **ALS**. The construction of this class has just started. Currently we have **Smatrix** and **Bump**.

Smatrix is for the sensitivity matrix manipulation including file access. An on-line data taking application and **Goemon** both use this class to have a common data format.

Bump is for local orbit bumps with 3 steering magnets. It can be associated with **ALSSR** or **Smatrix**, which makes both model-based and model-free local orbit corrections possible. As **Bump** is not a part of the model, it is possible to pass its objects to the real-time control layer for fast orbit corrections.

IV. FUTURE PLAN

The following items are on the list.

A. Persistency

As **OOP** itself does not support persistency, device objects must read and write the values of their internal parameters including the nominal current settings from/to files. There is a need for a database management system to administer these values with access to the objects. We are evaluating the Object-Oriented Database Class Library **Raima Object Manager** [12] for this purpose. It gives persistency to objects by using multiple inheritance.

B. Model-based Control

The effort to implement a model-based control layer on top of the existing control system has just been started for the operation with undulators. The migration of **Goemon** to the control system will be done by providing the server-client mechanism over the network. **OOP** in this area has not yet been well investigated.

C. Data Analysis

The **ALS** storage ring was operated for 6 weeks with RF. During that period, most of the machine studies were to measure fundamental parameters (closed orbit, tunes, chromaticities and sensitivity matrices) and they have not yet been fully analyzed. Several application programs based on the class libraries are being used, but there should be an effort to construct a class for data analysis.

VI. REFERENCES

[1] "1-2 GeV Synchrotrons Radiation Source, Conceptual Design Report", LBL PUB-5172 Rev. LBL, 1986; A. Jackson, "Commissioning and Performance of the Advanced Light Source", these proceedings.

[2] H. Nishimura, "Tracy, A Tool for Accelerator Design and Analysis", European Part. Accel. Conf., 803 (1988). E. Forest and H. Nishimura, "Vertically Integrated Simulation Tools for Self-Consistent Tracking and Analysis," Proc. Part. Accel. Conf., CH2669, 132(1989). J. Bengtsson, E. Forest and H.Nishimura, "Tracy2 Users Manual", unpublished.

[3] B. Meyer, "Object-Oriented Software Construction" (Prentice-Hall, NJ, 1988).

[4] H. Nishimura, "Dynamic Accelerator Modeling Uses Objects in Eiffel", Computers in Physics 6, 456 (1992).

[5] C. Cork and H. Nishimura, "Framework for Control System Development", Proc. of ICALEPCS '91, Tsukuba, Japan, 1991.

[6] H. Nishimura, "Object-Oriented Accelerator Modeling in C++", to be published.

[7] S. Magyary et al., "Advanced Light Source Control System", IEEE Part. Accel.. Conf., 87CH23879, 532 (1987);.S. Magyary, "Anatomy of a Control System: A System Designer's View," these proceedings.

[8] Eiffel 2.3 (Interactive Software Engineering, CA).

[9] J. Rumbaugh et al.., "Object-Oriented Modeling and Design" (Prentice Hall, NJ, 1991)

[10] OMTool (GE Advanced Concepts Center, PA)

[11] zApp (Inmark Development Corporation, CA)

[12] Raima Object Manager (Raima Corporation, WA)

Procedure for Determining
Quadrupole and BPM Offset Values in Storage Rings*

W. J. Corbett, V. Ziemann
Stanford Linear Accelerator Center
Stanford, CA 94309 USA

Abstract

One of the most elusive problems in storage-ring commissioning has historically been the determination of quadrupole and BPM offset values. We present a simple linear solution based on the principle that the element offset values are independent of lattice configuration.

I. INTRODUCTION

The conversion of SPEAR from a collider facility to a synchrotron radiation source lead to an increased emphasis on understanding the absolute beam orbit in the storage ring. The new goal, of course, is to steer the photon beams down the beamlines with minimum electron-beam offset in the quadrupoles and sextupoles, and minimum corrector strengths [1]. This condition requires both precision quadrupole alignment and minimum DC readback errors on the beam position monitors (BPMs).

At present, a number of quadrupoles in SPEAR are known to be misaligned by several mm horizontally, and the estimated BPM readback offsets are in some cases also several mm. The combined errors complicate both beamline steering and analysis of the electron beam orbit. For this reason, we have formulated a general procedure for determining quadrupole and BPM offset values in storage rings.

II. THEORY

The first step of any beam-based alignment procedure is experimental verification of the first-order optics model [2]. In this context, the model refers to quadrupole and corrector strengths, and BPM linearity factors.

Once the model is established, the component of the closed orbit distortion (COD) induced by correctors can be computed,

$$x_c^i = C^{ij}\Delta\theta^j \qquad (1)$$

where C^{ij} is the corrector response matrix (units mm/mrad), $\Delta\theta^j$ are the corrector strengths, and x_c^i is the orbit displacement evaluated at each BPM. The model can also be used to predict the COD induced by quadrupole displacements,

$$x_q^i = Q^{ij}\Delta x_q^j, \qquad (2)$$

where Q^{ij} has units (mm/mm) and Δx_q^j is the column vector of quadrupole misalignments.

In general, the errors could be due to quadrupole angle errors, bend roll errors, etc., or sector errors where a group of magnets is mounted to a common (misaligned) support. For this analysis, we assume the kicks generating COD to emanate from offset errors at the quadrupoles.

Superposition of (1) and (2) yields the total COD:

$$x_{cod}^i = x_c^i + x_q^i = C^{ij}\Delta\theta^j + Q^{ij}\Delta x_q^j. \qquad (3)$$

Isolating the quadrupole contribution,

$$Q^{ij}\Delta x_q^j = x_{cod}^i - C^{ij}\Delta\theta^j, \qquad (4)$$

we can solve for the quadrupole offset vector Δx_q^j using standard techniques:

1. Q-Matrix Inversion (e.g., Singular Value Decomposition [3])
2. Most Effective Quadrupole (MICADO [4])
3. GOLD Method (Piecewise Solution [5])

In SPEAR, however, the problem is complicated by constant but unknown BPM readback errors, and an unknown energy offset of the beam. Thus, we have,

$$x_{cod}^i + \Delta x_b^i = C^{ij}\Delta\theta^j + Q^{ij}\Delta x_q^j + \eta^i\frac{\Delta p}{p}, \qquad (5)$$

where Δx_b^i is the column vector of BPM readback errors, and η^i is the dispersion function evaluated at each BPM.

In matrix form, the COD equation reads

$$\bar{x}_{cod} - \bar{C}\Delta\bar{\theta} = \left[-\bar{I}:\bar{Q}:\bar{\eta}\right]\left[\Delta\bar{x}_b:\Delta\bar{x}_q:\frac{\Delta p}{p}\right]^T \qquad (6)$$

where I is the identity matrix, and the colons indicate partitioning of vectors and matrices. With the set of unknowns expanded to $\bar{S} = \{\Delta\bar{x}_b:\Delta\bar{x}_q:\Delta p/p\}$, use and interpretation of techniques 1-3 outlined above is complicated.

One way to find the set of unknowns $\bar{S}$ is the following. By changing quadrupole strengths, we can experimentally generate a linearly independent set of Eq. 6 with different response-matrix coefficients C^{ij}, Q^{ij}, and η^i, and least-squares fit the expanded set of equations to solve for the quadrupole offsets, BPM offsets and energy error.

The error bars associated with the solution vector $\bar{S} = \left\{ \Delta \bar{x}_b : \Delta \bar{x}_q : \Delta p / p \right\}$ are the diagonal elements of $[A^T A]^{-1}$, where A is the response matrix

$$A = \begin{bmatrix} -\bar{I} & \bar{Q}_1 & \bar{\eta}_1 \\ \cdots & \cdots & \cdots \\ -\bar{I} & \bar{Q}_n & \bar{\eta}_n \end{bmatrix}$$

Note that a set of n measurements based on n different lattice configurations fill the rows of A, that is, Eq. 6 repeated n times to fill the rows of A.

Unfortunately, if we try to determine the entire solution vector $\bar{S}$ for the storage ring in one pass, the error bars are large. Three alternatives are possible:

1. Compute the difference between the COD Eq. 6 evaluated for each new lattice relative to the reference configuration. The result is elimination of BPM offset errors from the solution vector $\bar{S}$. Once the reduced solution vector $\bar{S} = \left\{ \Delta \bar{x}_q : \Delta p / p \right\}$ is found, computation of the BPM offset errors $\Delta \bar{x}_b$ is straightforward.
2. Solve the set of Eq. 6 for the n configurations simultaneously in a piecewise fashion along sections of the ring, and reconstruct the entire solution from the separate parts. The advantage is reduction of the set of variables, and more control over the fitting procedure.
3. Combination of methods 1 and 2.

III. APPLICATION TO SPEAR

A FORTRAN program (ALIGN) was written to simultaneously solve the set of Eqs. (6) for a multiplicity of lattice configurations in SPEAR. The code structure is straightforward. First, we read the measured COD, corrector strengths, and the response matrices C^{ij}, Q^{ij} and η^i. Next, we subtract the (n-1) orbit Eqs. (6) evaluated with perturbed quadrupole values from the initial reference orbit, form the matrix A, and solve for the quadrupole offset values $\Delta \bar{x}_q$ and energy error $\Delta p / p$. Intrinsic BPM measurement errors can be included in the calculation. In the last step, the quadrupole offsets are held constant, and the fitting procedure is repeated to calculate BPM offsets, with error estimates.

Numerically, we found convergent solutions for test cases using known seeds for quadrupole and BPM offset values in the SPEAR lattice. The solutions had error bars approaching 10 mm which indicated problems with measurement sensitivity (ill-conditioned response matrix A).

Experimentally, the SPEAR data was measured by first moving individual quadrupole family strengths until the tune approached either the integer or 1/3

integer resonance ($\nu_x=6.820$, $\nu_y=6.720$, nominally). The typical excursion in magnet strength was ~1%. Later, pairs of horizontal (or vertical) focussing magnets were moved in opposite directions to obtain up to 15% excursions in strength.

Analysis of the measured data has been limited to piecewise solutions across the collider-interaction regions, where six quadrupole families were varied. The solutions have not converged, however, probably due to the combined effect of small orbit perturbations and inadequate BPM resolution. To increase the measurement sensitivity, one must generate large differences in the beta functions that are used to compute the response-matrix elements C^{ij} and Q^{ij}.

IV. DISCUSSION

This procedure for determining quadrupole and BPM offset values is in some respects similar to the common magnet-shunt technique used to center the beam in optical components which dates back at least to CEA [6]. In the present development, however, the ideas are extended to include use of a beam-calibrated optics model and statistical analysis of the percieved offset errors. Analysis of the true source of errors (i.e., quadrupole offsets versus bend rotations) is extremely complicated and probably not possible for most accelerators. But by determining the most likely locations of kicks and BPM offsets, these points can be checked for error, and a working model of the absolute beam orbit can be defined. The same procedures can be applied to; either circular c near accelerators.

Acknowledgments

V. REFERENCES

[1] W. J. Corbett, et al., "Optimum Steering of Photon Beams in SPEAR," these proceedings.

[2] W. J. Corbett, M. J. Lee, and V. Ziemann, "A Fast Model-Calibration Procedure for Storage Rings," these proceedings.

[3] W. Press, et al., Numerical Recipes, Section 2.9, Cambridge University Press, Cambridge, 1986.

[4] M.H.R. Donald, et al., 1981 PAC, Washington, DC, March 11–13, 1981, SLAC–PUB–2666.

[5] M. J. Lee, et al., Euro. Conf. on Control Systems for Exp. Physics, Villiars, Switzerland, Sept. 28–Oct. 2, 1987. SLAC–PUB–4411 (A).

[6] A. Hofmann, private communication.

Beam Based Alignment of the SLC Final Focus Sextupoles*

P. Emma, J. Irwin, N. Phinney, P. Raimondi, N. Toge, N.J. Walker, V. Ziemann
Stanford Linear Accelerator Center
Stanford, California 94305

ABSTRACT

The strong demagnification inherent in final focus systems requires local cancellation of the resulting chromaticity. Strong sextupole pairs separated by a $-I$ transform are positioned $\pi/2$ in betatron phase away from the Interaction Point (IP) in order to cancel chromatic aberrations primarily due to the final quadrupoles. Sextupole alignment is critical in order to provide orthogonal tuning of the chromaticity and, in the case of the SLC, to limit the third and higher order optical aberrations generated from misaligned and 'nested' horizontal and vertical sextupole pairs. Reported here is a novel technique for aligning the beam centroid to the sextupole centers, which uses measurements of *the* critically dependent parameter — the beam size at the IP. Results for the SLC final focus sextupoles are presented, where a resolution of <50 μm is achieved.

I. MOTIVATION

The motivation for achieving good static [1] sextupole alignment is actually two-fold in the SLC final focus. Tuning time is minimized by orthogonalizing chromaticity control with respect to IP beam waist adjustments ($\beta^{*\prime}$), dispersion control, and coupling correction. Furthermore, due to space requirements, the SLC final focus chromatic correction sections employ 'nested' horizontal and vertical sextupole pairs — four per final focus [2]. The linear optics between the two sextupole pairs are designed to provide a $-I$ transform to cancel geometric and chromatic dispersion aberrations. Misaligned sextupoles within the nested system generate skew and normal quadrupole fields which distort the $-I$ transform and so generate higher order optical aberrations which are not all correctable. Therefore, it is critical to achieve static alignment of these sextupoles to within ~200 μm for present SLC beam parameters.

II. THE ALIGNMENT METHOD

The sextupole pairs are placed $\pi/2$ in phase from the IP at points of large horizontal dispersion. Therefore, a horizontal sextupole offset will introduce a normal quadrupole field and generate horizontal IP dispersion and both horizontal and vertical waist shifts. A vertical offset will introduce a skew quadrupole field and generate vertical IP dispersion and coupling. The SLC final focus design provides orthogonal correction for each of these effects. By measuring the amount of IP waist, dispersion, and coupling change as a function of each sextupole strength, the horizontal and vertical sextupole

offsets with respect to the final focus orbit are calculated. Alignment correction is implemented by closed orbit bumps with horizontal and vertical dipole corrector magnets within the final focus. A desirable quality of the technique is that the measurement tolerances are consistent with the alignment goals — if there are no measurable waist, dispersion, or coupling changes in the IP beam given significant sextupole strength changes, then the necessary alignment is achieved.

For SLC, there are just two power supplies for the four sextupoles per final focus. The two X-sextupoles (horizontal chromaticity correction) are in series on one supply, while the Y-sextupoles are in series on a second supply. Fortunately, due to the $-I$ transform between pairs, this is ideal — the waist, dispersion, and coupling changes at the IP can be independently separated into symmetric and anti-symmetric components of sextupole pair misalignment in X and Y. Figure 1 illustrates the eight different observable misalignment components. The individual sextupole misalignments are simply linear combinations of these eight components.
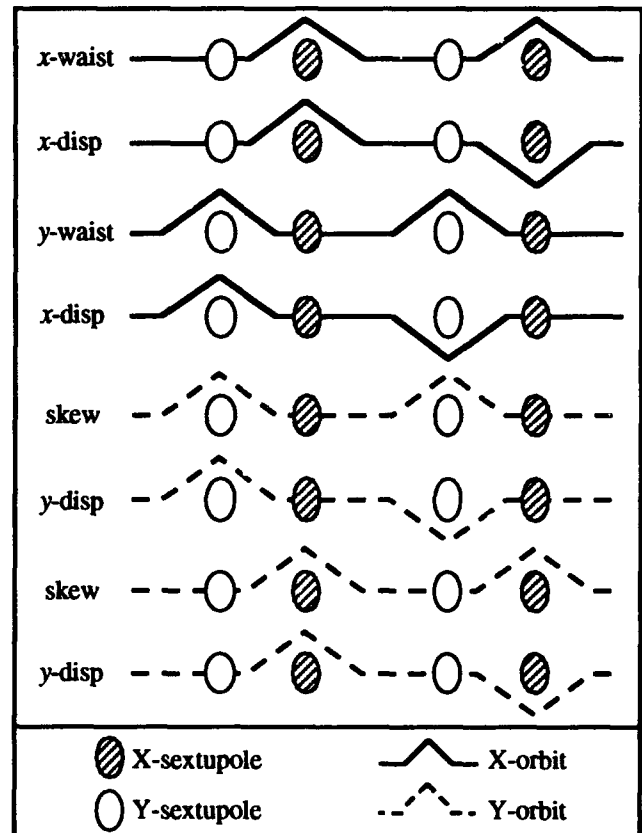
Fig 1. The eight measured sextupole misalignment combinations (4 per plane) and the dominant generated optical effect observed at the IP (waist shift, dispersion, and coupling or 'skew').

In order to illustrate the connection between misalignment components and generated optical effects suppose the sextupole is misaligned (x_0, y_0) with respect to the beam centroid. The sextupole kick angles, ($\Delta x'$, $\Delta y'$), of a particle with centroid position deviation ($x + \eta\delta, y$) in one sextupole of strength Δk then become

$$\Delta x'(x, y, \eta, \delta, x_0, y_0) = \frac{1}{2!}\Delta k\{(x + x_0 + \eta\delta)^2 - (y + y_0)^2\} ,$$

$$\Delta y'(x, y, \eta, \delta, x_0, y_0) = \Delta k(x + x_0 + \eta\delta)(y + y_0) . \quad (1)$$

Here δ is the fractional energy deviation ($= \delta E/E_0$) and η is the nominal horizontal dispersion at each sextupole per pair. Note, the final focus dispersion must first be corrected to fairly loose tolerances before the alignment procedure begins.

Each optical effect is labeled below in (2) and (3) after summing the two kicks due to misalignments of one sextupole pair and using the $-I$ transform between sextupoles. These kicks become positions at the IP through the R_{12} and R_{34} transfer matrix elements from relevant sextupole to IP.

$$\Delta x_1'(x, y, \eta, \delta, x_{01}, y_{01}) - \Delta x_2'(-x, -y, \eta, \delta, x_{02}, y_{02}) = \quad (2)$$

$2\Delta k x \eta\delta +$	(x-chromaticity)
$\Delta k x (x_{01} + x_{02}) +$	(x-waist)
$\Delta k \eta\delta(x_{01} - x_{02}) -$	(x-dispersion)
$\Delta k y (y_{01} + y_{02}) +$	(skew)
$\Delta k[(x_{01}^2 - x_{02}^2) - (y_{01}^2 - y_{02}^2)]$	(x-steering)

$$\Delta y_1'(x, y, \eta, \delta, x_{01}, y_{01}) - \Delta y_2'(-x, -y, \eta, \delta, x_{02}, y_{02}) = \quad (3)$$

$2\Delta k y \eta\delta +$	(y-chromaticity)
$\Delta k y (x_{01} + x_{02}) +$	(y-waist)
$\Delta k \eta\delta(y_{01} - y_{02}) +$	(y-dispersion)
$\Delta k x (y_{01} + y_{02}) +$	(skew)
$\Delta k(x_{01}y_{01} - x_{02}y_{02})$	(y-steering)

With measurements of waist, dispersion, and skew changes at the IP as a function of sextupole pair strength changes, the symmetric, ($x_{01}+x_{02}$) and ($y_{01}+y_{02}$), and the asymmetric, ($x_{01}-x_{02}$) and ($y_{01}-y_{02}$), misalignment components are calculated per pair. For example, the horizontal symmetric misalignment of the X-sextupole pair is calculated by measuring the x-waist shift, Δw_x, per strength change, Δk, using the large R_{12} (3.3 m) from these sextupoles to IP.

$$\frac{1}{2}(x_{01} + x_{02}) = \frac{\Delta w_x}{2R_{12}^2 \Delta k} \quad (4)$$

Figure 2 shows two 'waist-scans' done at different X-sextupole strength settings. The waist positions have shifted with respect to each other by $\Delta w_x = 1.49 \pm 0.09$ cm for a sextupole strength change of $\Delta k = 1.97$ m^{-2} and indicate the symmetric horizontal misalignment is 354 ± 21 μm.

III. ALIGNMENT CORRECTION

After measurement of a specific misalignment component, an orbit bump is introduced with dipole corrector magnets which removes only that component. Figure 3 shows a large horizontal symmetric bump introduced at the Y-sextupoles to

remove the y-waist dependence on Y-sextupole strength (shown is an extreme case of 1 mm to test bump closure).
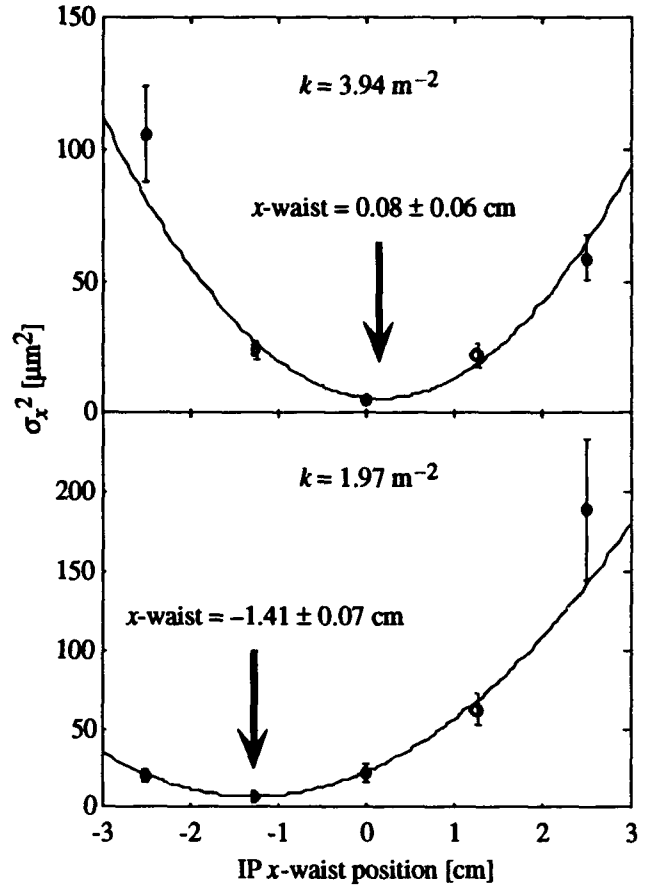
Fig 2. Two x-waist scans (IP beam size vs. waist position) done at different X-sextupole strengths, k, reveal a horizontal symmetric component of sextupole misalignment of 354 ± 21 μm.
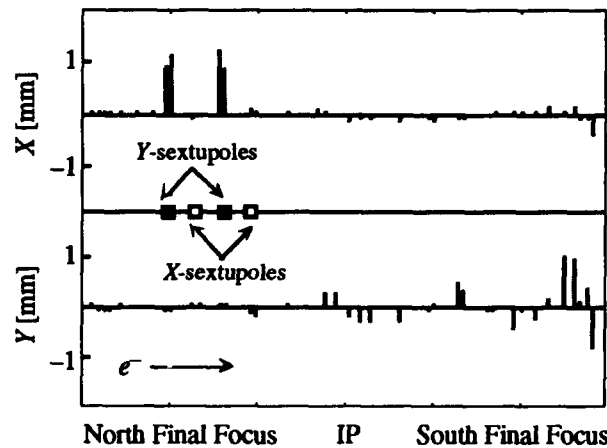
Fig 3. A horizontal symmetric e^- orbit bump introduced with dipole correctors to remove y-waist dependence on Y-sextupole strength (shown is an extreme case of 1 mm to test bump closure).

There are sufficient dipole correctors in the final focus to orthogonally correct all eight misalignment components per side (North e^- and South e^+). A second iteration is always performed to verify the sign and magnitude of correction. With large corrections (>400 μm), a second smaller correction is usually necessary to align to near measurement precision.

With the sextupoles detuned, uncorrected chromaticity causes the minima of these scans to increase. A practical approach is to run the two scans on either side of the nominal sextupole setting. This optimizes the waist measurement precision by reducing the chromatic increase.

To further optimize measurement precision, the IP beam size measurements are made at low beam current (0.5×10^{10}) with the existing 4 μm diameter Carbon filament wires near the IP [3]. The measurement is corrected for the large wire diameter and clean, reproducible results for the single beam of interest have been achieved down to 1.3 μm beam sizes [4].

When the alignment is complete and all corrections have been verified, two linear combinations of the two sextupole pair strengths are scanned to minimize the IP beam size per plane. The linear combinations are intended to orthogonally control horizontal and vertical IP chromaticity [5]. With the sextupoles aligned, these scans will now reliably minimize chromaticity and achieve the optimal IP beam sizes. Figure 4 shows a vertical chromaticity scan done after alignment which achieves a 1.55 μm vertical IP e^- beam size.
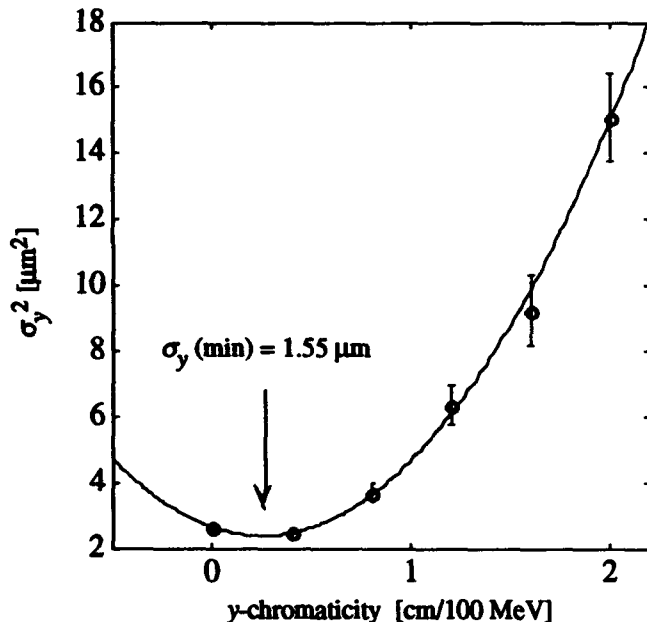
Fig 4. A vertical IP chromaticity scan after alignment which now truly minimizes chromaticity. The y-chromaticity control is a linear combination of sextupole pairs calibrated in centimeters of IP waist shift per 100 MeV energy deviation. A minimum spot of 1.55 μm is achieved.

Care must be taken during normal operations to maintain each final focus orbit over the duration of the run. Occasionally orbit distortions appear which may be traced to beam position monitor (BPM) offset drifts or actual trajectory changes within the final focus. These changes must be verified and, if necessary, corrected with some subset of the alignment techniques described above. No steering is done within the final focus chromatic correction sections without verification of the sextupole alignment.

IV. CONCLUSIONS

This sextupole alignment technique has been used successfully before each of the 1992 and 1993 SLC/SLD luminosity runs during initial machine setup. Immediate impact was seen on IP beam sizes obtainable and overall final focus tuning time. The dramatic increase in SLC luminosity over the last two years owes, in part, to careful initial final focus sextupole alignment.

V. ACKNOWLEDGMENTS

The authors are grateful to the SLC operations staff for the many hours of machine stability necessary to complete the alignment.

VI. REFERENCES

[1] In this case 'static' refers to a time scale of many hours. Small diurnal variations are compensated with normal daily tuning.

[2] The original SLC final focus design used eight sextupoles per side. Subsequent investigations showed that only four were useful. Presently only four are powered which improves alignment tolerances.

[3] C. Field, "Problems in Measuring Micron Size Beams", *Proc. Particle Accelerator Conference*, Chicago, Illinois (March 1989).

[4] IP wire measurements are made in 'round-beam' mode where the horizontal and vertical emittances are nearly equal. In 'flat-beam' mode — decoupling the damping ring tunes — the optimized vertical IP beam size is ~0.8 μm.

[5] N. Toge, *et al.*, "Chromaticity Corrections in the SLC Final Focus System", *Proc. Particle Accelerator Conference*, San Francisco, California (May 1991).

Analysis of Higher Order Optical Aberrations in the SLC Final Focus using Lie Algebra Techniques.*

N. J. Walker, J. Irwin, M. Woodley

Stanford Linear Accelerator Center, Stanford University, Stanford, California 94309

Abstract

The SLC final focus system is designed to have an overall demagnification of 30:1, with a β at the interaction point (β*) of 5 mm, and an energy band pass of ~0.4%. Strong sextupole pairs are used to cancel the large chromaticity which accrues primarily from the final triplet. Third-order aberrations limit the performance of the system, the dominating terms being U_{1266} and U_{3466} terms (in the notation of K. Brown). Using Lie Algebra techniques, it is possible to analytically calculate the size of these terms, in addition to understanding their origin. Analytical calculations (using Lie Algebra packages developed in the *Mathematica* language) are presented of the bandwidth and minimum spot size as a function of divergence at the interaction point (IP). Comparisons of the analytical results from the Lie Algebra maps and the results from particle tracking (TURTLE) are also presented.

I. INTRODUCTION.

The SLC final focus design consists of two telescopes, each with point to point focusing (phase advance of π radians), separated by a 2π radian identity module with a large dispersion function which facilitates the second (optical) order chromaticity correction using strong sextupoles: figure 1 shows the optics. The chromatic correction scheme and overall telescopic
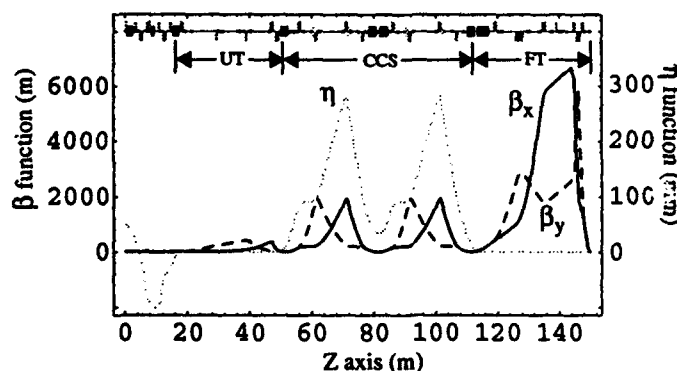
Figure 1. Optics functions for the SLC final Focus

design are essentially that proposed by Brown[1] and is well documented in the literature[2]. The predominant source of chromaticity is the final triplet, for which the correction scheme consists of two -I pairs of sextupoles placed in such a position that the dispersion function is symmetric: such an arrangement exactly cancels the unwanted geometrics, leaving

only the desired chromatic terms.

Although the second order optical aberrations are exactly cancelled, the bandwidth of the system is still limited by third (optical) order aberrations. Brown[1] showed that the dominant remaining aberration is a high order chromaticity (U_{1266} and U_{3466} in the TRANSPORT[3] notation). Using powerful Lie Algebra techniques, it is possible to analyze the individual aberrations and understand their origins. In this report, an analysis of the important aberrations using Lie Algebra tools developed in the *Mathematica*[4] language is presented.

II. LIE ALGEBRA TECHNIQUES.

Lie Algebra techniques as applied to charged particle optics have been extensively covered elsewhere[5,6,7]. Here extensive use of Lie Algebra methods developed by Irwin[6] is made, of which a good review can be found in the thesis by Roy[7]. Only a brief introduction to the terminology and general philosophy of the methods is given here: the reader is referred to the literature for a more detailed description of the subject.

In the following subsections the important Lie Algebra tools are introduced which will later be used to analyze the aberrations. In the following discussions, $x' \equiv \partial x / \partial s$, is used rather than the conjugate momentum p_x, as this is more in keeping with the traditional matrix theory of Brown[2].

A. Hamiltonians.

The starting point of the calculation is the formulation of the perturbed Hamiltonian for the elements (magnets) of concern, and evaluating them at the non-perturbed, linear phase space coordinates at that element; this type of calculation is referred to as an *interaction representation*.

For the present analysis, two elements are of interest:

$$\text{Chromatic Quadrupole:} \quad -\frac{1}{2} K_Q \bar{\delta}(x^2 - y^2) \qquad (1)$$

$$\text{Sextupole:} \quad \frac{1}{3!} K_S(x^3 - 3xy^2) \qquad (2)$$

where K_Q and K_S are the integrated quadrupole and sextupole strength respectively, $\bar{\delta}$ is given by $\delta/(1+\delta)$, where δ is the fractional momentum deviation $\Delta P/P_0$, and x and y are the *local linear* phase space coordinates. The Hamiltonians given in (2) and (3) represent thin lens kicks. To include the effects of thick (lumped) elements, it is necessary to integrate the Hamiltonian over the length (L) of the magnet:

$$H_{thick}(x_c, x'_c, y_c, y'_c) = \int_{-L/2}^{L/2} H_{thin}(x(s), y(s)) \, ds \qquad (3)$$

where (x_c, x'_c, y_c, y'_c) represent the coordinates at the center of the magnet. $x(s)$ and $y(s)$ are given by the linear optics of the element[5].

B. Poisson Brackets

At the heart of the Lie Algebra approach is the *Poisson Bracket* (PB). The PB of any two functions of phase space f and g is given by

$$[f, g] = \frac{\partial f}{\partial x} \frac{\partial g}{\partial x'} - \frac{\partial f}{\partial x'} \frac{\partial g}{\partial x} \qquad (4)$$

Hamilton's equations of motion can be represented using PB as

$$\frac{\partial x}{\partial t} = [-H, x]$$
$$\frac{\partial x'}{\partial t} = [-H, x'] \qquad (5)$$

where H is the Hamiltonian.

One important property of poisson brackets is that they remain invariant under a symplectic transformation; this property allows the transformation of the local coordinates in the Hamiltonians to any point in the lattice using the linear Green's functions (R matrix elements). In the beam optics calculations that follow, use is made of the invariance property to transform all the coordinates to the interaction point (IP) of the final focus.

C. Beam line Representation: CBH theorem.

If H_i represent the Hamiltonians for the magnetic elements in the beam line, then the line can be represented in the exponential Lie notation as

$$e^{:-H_1:} e^{:-H_2:} e^{:-H_3:} \ldots e^{:-H_N:} \qquad (6)$$

where the H_i are placed in the order they appear in the beamline. The total effective Hamiltonian for the system can be calculated using the Cambell-Baker-Hausdorf (CBH) theorem:

$$H_T = \sum_{i=1}^{N} H_i - \frac{1}{2} \sum_{i=1}^{N} \sum_{j=1}^{i} [H_j, H_i] + \ldots \qquad (7)$$

Each PB term in (7) represents higher and higher orders in the Hamiltonian. In the work reported here, the H_i are the third-order Hamiltonians given in (1) and (2), so the first PB in the CBH theorem generates fourth order terms; this is sufficient for the analysis of the SLC final focus.

In the exponentiated form, the Hamiltonian becomes a generator for a map:

$$x \rightarrow e^{:-H_T:} x = x + [-H_T, x] + \frac{1}{2}[-H_T, [-H_T, x]] + \ldots \qquad (8)$$

For the analysis of the final focus, H_T is a polynomial expressed in the linear phase space coordinates at the IP. Each monomial in H_T represents a unique aberration, the effect of which can be approximated independently by taking the first PB term in (8):

$$\Delta x \approx [-H_T, x] = \frac{\partial H_T}{\partial x'} \qquad (9)$$

Equation 9 can be used to estimate the effect of each individual monomial in the Hamiltonian on the IP spot size. It is important to note, however, that when making an exact third- (optical) order calculation, it is important to also include the second PB term in (8), as this will contribute to third-order terms in the map.

III. *Mathematica* TOOLS.

Mathematica[4] is a powerful language for doing symbolic computations. Since the Lie Algebra techniques presented in the previous section involve the manipulation of polynomials, *Mathematica* is ideally suited to the task. Several *Mathematica* packages have been developed to enable Lie Algebra analysis of beamlines, collectively referred to as *LAMA* (*Lie Algebra Mathamatica Analysis*) packages: they are

LAMA`TransportDefinition`.
A package containing a framework for the definition of magnetic elements and beamlines, together with tools for manipulating and modifying them.

LAMA`LinearOptics`.
A package for doing simply linear optics, such as calculation of tables of R matrices for a given beamline.

LAMA`PoissonBracket`.
Implements PB of predefined phase space coordinates.

LAMA`HamiltonianOptics`.
Contains all the definitions of the Hamiltonians for known magnetic elements, and performs thick lens integration (equation 3). Also contains definitions for Lie algebra tools and several high level analysis tools and manipulation tools for polynomials.

LAMA`ExpectationValue`.
A package for calculating high order moments, and expanding them in terms of second order moments of given distributions.

Since *Mathematica* is a symbolic language, parameters such as magnet strengths can be left as symbols to allow fitting.

IV. RESULTS OF SLC FINAL FOCUS ANALYSIS.

Figure 2 shows a curve of σ^*_x and σ^*_y as a function of linear beam divergence at the IP (θ^*). The solid curve is the result of a symbolic third (optical) order map generated using the *Mathematica* Lie Algebra tools (essentially equations 7 and 8), while the dots represent the results of TURTLE[8] simulations: the analytical results generated by *Mathematica* are in good agreement with the simulations. It is important to emphasize the difference between *simulation* and *symbolic* calculations:

120
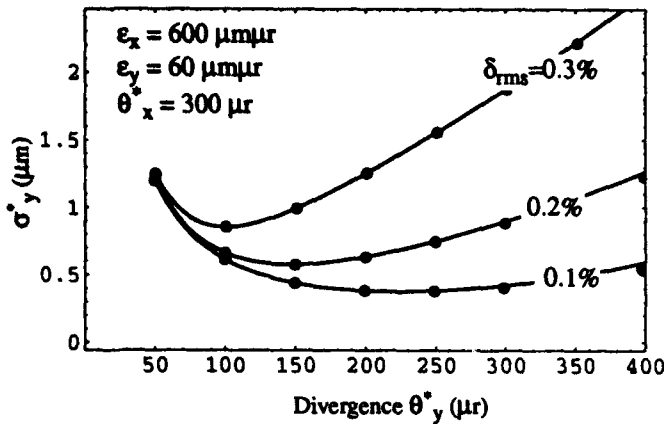
Figure 2. Vertical IP spot size as a function of divergence for various beam energy spreads (δ_{rms}). Solid lines represent symbolic *Mathematica* calculation, dots represent TURTLE simulations.

the *Mathematica* results are analytical (symbolic) formulae of the from $\sigma^*_y = \sigma^*_y(\varepsilon_x, \varepsilon_y, \theta^*_x, \theta^*_y, \delta_{rms})$, and can be manipulated accordingly.

Table 1 gives the results of a term by term analysis of the total Hamiltonian with respect to the vertical IP spot size (σ^*_y).

Table 1. Most significant aberrations to σ^*_y in order of contribution.

Monomial	TRANSPORT notation	Coefficient (meters)	% of total σ^2
$y^{\prime 2}\delta^2$	U_{3466}	229.5	86
$x'y^{\prime 2}\delta$	U_{1446}/U_{3246}	817.5	6
linear			3
$x^{\prime 2}y^{\prime 2}$	U_{1244}/U_{3224}	-2861.7	2.2
$x'y'\delta^2$	U_{1466}/U_{3266}	55.5	1.9

By far the most dominant aberration is the $y^{\prime 2}\delta^2$, which in TRANSPORT notation is the afore mentioned U_{3466} term. One possible method of determining the origin of such a term is by identifying which PBs in the second term of the CBH contribute to the total coefficient. Replacing the double sum in (7) by a matrix $A_{ij} = [H_i, H_j]$ of polynomials, whose upper diagonal elements are zero, one can easily extract the coefficient of the $y^{\prime 2}\delta^2$ term in each of the polynomials in A. Figure 3 shows a three dimensional bar chart representing the contributions from the A_{ij} polynomials to the total $y^{\prime 2}\delta^2$ term.

Figure 3 immediately reveals that the largest source of the $y^{\prime 2}\delta^2$ aberration comes directly from an interaction of the sextupoles and the triplet. Further investigation shows that the Y sextupoles are not exactly π radians in phase away from the triplet, and that this phase error gives rise to a small chromaticity term $\xi yy'\delta$. Interaction of the $yy'\delta$ aberration with the strong chromaticity of the triplet ($\alpha y^{\prime 2}\delta$) results in the $y^{\prime 2}\delta^2$ term:

$$[\xi yy'\delta, \alpha y^{\prime 2}\delta] = 2\alpha\xi y^{\prime 2}\delta^2 \tag{10}$$

Having identified the source of the aberration, it is now possible to design a modification to the linear optics to correct the phase error of the sextupoles, and thus reduce the magni-
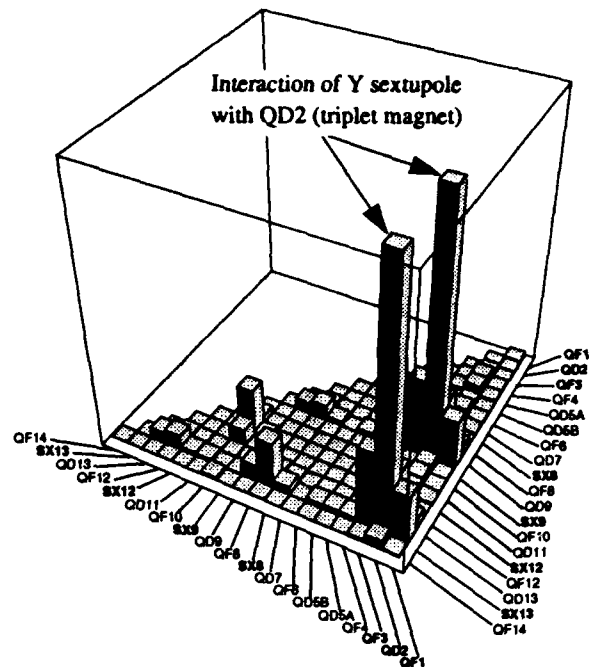
Figure 3. Coefficient of $y^{\prime 2}\delta^2$ monomial (arb. units) in the interaction polynomial $[H_i, H_j]$ for the CCS and final telescope magnets.

tude of the aberration [9].

REFERENCES

[1] K. Brown, "A Conceptual Design of Final Focus Systems for Linear Colliders", SLAC-PUB-4159, (1987).

[2] J. Murray, K. Brown, and T. Fieguth, "The Completed Design of the SLC Final Focus System", SLAC-PUB-4219 (1987).

[3] K. Brown, "A First- and Second-Order Matrix Theory for the Design of Beam Transport Systems and Charged Particle Spectrometers", SLAC-75 or Advances in Particle Physics 1, 71 (1967).

[4] S. Wolfram, "*Mathematica*: A System for Doing Mathematics by Computer", Second Edition, Addison-Wesley Publishing Company (1991).

[5] A. Dragt, F. Neri, G. Rangarajan, D. Douglas, L. Healy, and R. Ryne, "Lie Algebaic Treatment of Linear and Nonlinear Beam Dynamics", Ann. Rev. Nucl. Part. Sci. 38, 455 (1988).

[6] J. Irwin, "The Application of Lie Algebra Techniques to Beam Transport Design", Nuc. Inst. and Methods, A298, 460 (1990).

[7] G. Roy, "Analysis of the Optics of the Final Focus Test Beam using Lie Algebra based Techniques", PhD thesis, SLAC, (1992).

[8] D. Carey, K. Brown, and C. Iselin, "TURTLE, A Computer Program for Simulating Charged Particle Beam Transport Systems, Including Decay Calculations", SLAC-246, and Fermilab PM-31 (1982).

[9] N. Walker, J. Irwin, R. Helm, and M. Woodley, " Third-Order Corrections to the SLC Final Focus", these proceedings (1993)

Simulation Support for Commissioning and Operating the SSC Linac*

F.W. Guy, J.W. Hurd, C.R. Chang, D.Raparia, C.Y.Yao
Superconducting Super Collider Laboratory
2550 Beckleymeade Avenue, Dallas, Texas 75237

Abstract

Many different beam dynamics simulation techniques and codes will be used during commissioning of the SSC Linac. As commissioning progresses, these techniques and codes will be developed, improved, tested and integrated into the linac control system. When the initial commissioning is finished, the control system will include a solid basis of simulation capability for normal operational use and periodic tuneup. For instance, some of the procedures that must be supported during both commissioning and normal operation are matching, steering, acceptance scanning, RF tuneup and emittance measurements. These all require simulation capability that should be easily available to the operator in a form that: 1) takes its input directly from linac diagnostics; 2) is immediately useful without sophisticated analysis; and 3) produces whatever output is best suited for the task at hand, be it a graphic on a screen or a control signal to an actuator. We discuss the various approaches that are being pursued to ensure that the necessary beam dynamics simulation capability will be available as needed.

I. INTRODUCTION

Beam dynamics simulation of the SSC Linac can be divided into two major categories. These are on-line and off-line simulation, with some overlap between them. On-line simulation uses capabilities built into the accelerator control system. Its main purpose is to monitor, test and adjust the accelerator during actual operation. Off-line simulation, using computers separate from the control system, has several purposes. It is used for design, parameter and error studies. Another important function is to generate performance predictions that can be compared with experimental measurements to verify both the beam dynamics codes and accelerator models that have been used in those codes. Off-line simulation is also an essential tool to track down and correct errors in design, manufacture, installation, adjustment and operation, and to generate simulated "data" to develop and check on-line simulation capability.

No beam-dynamics code can do a good job unless its model of the accelerator is reasonably accurate. Our models start with the SSC Linac design configuration, are modified within or outside the specified tolerances for error studies, and will be corrected by measurements of the actual as-manu-factured assemblies as these measurements become available. There are many beam dynamics codes available of widely varying complexity, physics capability, user-friendliness and computer requirements. Given limited time and resources, how does one choose the "best" beam dynamics code for a particular simulation need? An important criterion is familiarity. It takes time and practice to learn the correct use of complicated codes, to understand their physics and to know their limitations. The codes mentioned in this paper are those we presently anticipate using; we believe they will do the job and we have experience with them. Many other good codes are available to us and no doubt we will add some of these to our arsenal as we perceive the requirements.

II. BEAM DYNAMICS SIMULATION CODES FOR ON- AND OFF-LINE ANALYSIS

A. Matrix Codes

These codes are fast and easy to use, but usually cannot calculate second-order effects or those due to non-uniform, non-elliptical or non-symmetric beam charge distributions. The well-known user-friendly matrix optics codes TRACE2D and TRACE3D [1] are used for preliminary design, for instance to set up beamline geometry in matching sections or LEBTs. They provide quick calculations of focusing, matching, phase advances, beam parameters, etc. TRACE physics is used in two specialized codes, PARTRACE [2] and CCLTRACE [3], used for error studies in, respectively, the DTL (Drift-Tube Linac) and the CCL (Coupled-Cavity Linac). TRACE has proven quite useful in our work. We plan to integrate the TRACE physics and user interface into many of our on-line simulation and control functions.

B. Ray-tracing Codes

AXCEL [4] has been used for design and analysis of the einzel lens LEBT (Low-Energy Beam Transport) between the ion source and the RFQ (Radio Frequency Quadrupole). The code has axial symmetry and a limited set of input beam parameters. It calculates space-charge effect.

C. "Particle-pushing" codes

SSCL is using several codes in the PARMTEQ [5]—PARMILA [6] family. These codes transport particles through elements of a beamline, such as RFQ or DTL cells. A similar code, CCLDYN [7], is used to simulate CCL beam dynamics. Most of these codes have been modified in one way or another to model unique features of the SSC Linac. Other particle-transport codes used at SSCL for certain special problems are HESQT [8], BUCKSHOT [9], and ARGUS [10]. Multiparticle codes usually have long running times and are not suitable for integration into the on-line system except in a few special cases such as a single-particle version of

PARMILA used for some steering and RF power setting algorithms.

D. Beam Analysis Codes

These are included here for completeness although they are not strictly simulation codes. We use two codes to analyze experimental data from the slit-and-collector beam emittance diagnostics. They are a code that resides in the TACL accelerator control system [11] and gives a preliminary on-line analysis of the collected data so that the operator may judge its quality; and REANE [12], an off-line analysis code with many special features. REANE has been modified by the SSC Linac Group to allow more flexibility in data analysis and to enable it to run on any UNIX platform with X11 X-Window capability. REANE input files generated by the TACL-based analysis code can be used to produce a file of particle coordinates for use in the PARMTEQ—PARMILA codes; thus these beam analysis codes have become part of the simulation support effort.

E. Codes for Setting RF Phase and Amplitude

Accurate setting of RF power phase and amplitude in each tank is essential to maintain beam quality. Procedures for achieving this include the absorber-collector phase-scan, and the Δt [13] method. Both of these have proven very useful in other accelerators, and we will try a new method [14] called "least-squares" that calculates correct RF setting and actual input beam energy by minimizing the difference between measured and calculated beam output phase over a range of input beam energy and RF parameters. In preparing for commissioning, we are simulating each of these methods [15] off-line and intend to have them available in the control system. Phase scans and Δt are inherently on-line methods. Least-squares requires more computation and may be done "semi-off-line" on a separate computer, but is reasonably fast.

F. Special-Purpose Codes

A number of small codes, both on- and off-line, will be available for purposes such as steering, emittance calculations from beam envelope measurements, and so forth.

III. CODES FOR SPECIFIC LINAC SECTIONS

A. Ion Source

Ab-initio calculations of ion source output have not been used at SSCL because our sources are designed and built at other institutions. We have relied on beam measurements (which have certain complications and difficulties) or standard types of inputs such as waterbag, gaussian, etc. to provide the LEBT input in our calculations. SSCL has two types of H⁻ sources, magnetron and volume. The magnetron source [16] produces a divergent ion beam from a small aperture; the beam is fairly well characterized by a uniform angular distribution. The volume source [17] has a larger aperture and a more parallel beam. The distribution of ions across the aperture may not be uniform. There is a large electron component that must be removed by a spectrometer magnet a few centimeters from the aperture, which complicates the space-charge calculation and bends the ion beam slightly. The result is a non-uniform, non-symmetric beam. Eventually we expect to improve the extraction aperture and spectrometer design through beam-dynamics calculations, but for now we randomly sample the REANE input experimental data file to construct a file of input particle coordinates for the particle-following codes.

B. Low Energy Beam Transport

An einzel lens LEBT is presently being used in the SSC Linac and is producing a beam that is quite satisfactory for near-term goals [18]. The AXCEL code has been used for design and calculation of this lens. AXCEL has axial symmetry and therefore cannot accommodate input beams generated from experimental volume-source data, but it has been useful in showing how various symmetric beams respond to changes in electrode voltage. Transport of volume-source beams through the einzel lens could be calculated with a particle-following code such as BUCKSHOT or ARGUS, but because of time constraints this has not yet been done. The main purpose of LEBT beam-dynamics calculations is to provide the RFQ with a beam that will result in maximum transmission of accelerated beam. For the einzel lens, this goal can easily be realized during RFQ operation by trial-and-error adjustment of two high-voltage DC power supplies for the focusing electrodes, and four power supplies for steering; steering and focusing are weakly coupled as long as steering is small.

Two other candidates for the SSC LEBT are the Electrostatic Quadrupole (ESQ) [19] and Helical Electrostatic Quadrupole (HESQ) [20] geometries. These are more complicated than the einzel lens, but are expected to provide better quality beams to the RFQ. Beam dynamics of these lenses can be calculated by TRACE, PARMILA, ARGUS and (for the HESQ) by DEEPRAP. Calculations are essential to determine proper steering and focusing voltages for these LEBTs because of the large number of power supplies; the HESQ, for instance, requires twelve DC power supplies, of which eight are used for both steering and focusing and four for focusing only. Optimizing the beam by trial-and-error would be a difficult (if not impossible) task; on-line simulation will be required.

C. RFQ

RFQ simulation at SSCL is handled almost entirely by variations of the PARMTEQ code and its associated support codes. The main exception is matching, done with TRACE. The code used at SSCL is adapted from an older Los Alamos National Laboratory version. SSCL's code was revised to include the higher-order multipole expansion of the vane tip field; the older LANL version had only the original "two-term" field. This revision was done so that the SSCL version can accurately simulate the SSC RFQ, which was designed at LANL using a similar multipole treatment. These codes are based on a "z-dependent" treatment of the particle dynamics; there is also a "t-dependent" version of PARMTEQ that was

furnished to SSCL by Chalk River Laboratories. The latter code also has a version of the multipole treatment. Both versions give approximately the same results on test problems.

Further extensions of RFQ simulation physics include 3-D space-charge and image charges. A version of PARMTEQ with these physics additions, including the multipole treatment, has been developed at SSCL. A previous 3-D space-charge, image-charge code has been reported in Reference [21]; 2-D vs. 3-D space-charge seems to make very little difference on any of the runs, but there are definite differences on some RFQs when image charges are used in the simulations. For the SSC RFQ, however, image charge effects are minimal.

D. DTL and Matching Sections

TRACE3D and PARMILA are the codes most used for beam-dynamics design and calculation of the drift-tube linac, the RFQ-DTL matching section, and the DTL-CCL matching section. Error studies generally use PARTRACE. Specialized versions of single- and multi-particle PARMILA are used in off-line steering, matching and RF power setting simulations; TRACE will be the principal physics package for on-line simulations of these sections. PARMILA has been modified to include focusing-magnet high-order multipoles.

Phase-scan will be used for setting the RF phase and amplitude in the matching section bunchers. Phase-scan on bunchers requires no simulation capability because the 90° phase point and voltage can be determined directly from beam phase measurements. This technique is also good for preliminary RF adjustment on DTL tanks but requires longitudinal beam-dynamics simulation. This has been done for the SSC DTL. Results indicate that (assuming an accurate model) phase-scan can get "in the ballpark" but a more sophisticated technique is required for final adjustment of RF power. The Δt method is one such; simulation capability for Δt will be provided in the control system. Δt will not work on the first DTL tank, because this method requires measurement of the beam throught the tank with the RF off, and the beam not only debunches but goes unstable. The least-squares method has been tested repeatedly with simulated noisy "data" and has worked very well with all SSC DTL tanks. This method provides a direct calculation of measurement errors in RF phase and amplitude and in input beam energy.

E. CCL

For the coupled-cavity linac, we use TRACE3D, CCLDYN and CCLTRACE. Steering and matching off-line simulations will be done with both TRACE and single- and multi-particle CCLDYN, error studies mostly with CCLTRACE, and on-line simulations by TRACE. The Δt method will be used for RF settings. The least-squares method will probably be used as well; however, it has not yet been simulated for the CCL. CCLDYN has been modified to include focusing-magnet high-order multipoles and the "Yurij Effect" [22].

IV. CONCLUSIONS

A variety of beam-dynamics simulation codes (and the expertise for their use) are available at the SSCL. Some codes will need to be modified and others created to satisfy the particular requirements of the SSCL. Altogether, we expect to have quite effective simulation capability and support for commissioning and operation of the SSC Linac.

VI. REFERENCES

[1] K.R.Crandall, "TRACE, an Interactive Beam Dynamics Program," *AIP Conference Proceedings 177, Linear Accelerator and Beam Optics Codes*, La Jolla Institute, pp. 29-36 (1988).

[2] K.R. Crandall, "Error Studies Using PARTRACE, A New Program that Combines PARMILA and TRACE 3D," *Proc 1988 Linear Accelerator Conference*, pp. 335-337.

[3] CCLTRACE, K.R. Crandall, private communication.

[4] E.F. Jaeger and I.C. Whitson, "Numerical Simulation for Axially Symmetric Beamlets in the Duopigatron Ion Source," ORNL/TM-4990, Oak Ridge, TN (1975).

[5] K.R. Crandall, "PARMTEQ—A Beam-Dynamics Code for the RFQ Linear Accelerator," *AIP Conference Proceedings 177, Linear Accelerator and Beam Optics Codes*, La Jolla Institute, pp. 22-28 (1988).

[6] G.P. Boicourt, "PARMILA An Overview," ibid., pp1-21; Los Alamos National Laboratory Report LA-UR-88-1544.

[7] CCLDYN, K.R. Crandall, private communication.

[8] HESQT, D. Raparia, private communication.

[9] J.S. Wagner, "BUCKSHOT, A 3-D Gridless Magnetostatic Particle Code," Sandia National Laboratory Report SAND87-2019.

[10] *ARGUS Code Manual*, Science Applications International Corporation (1991).

[11] J. Sage, private communication.

[12] H.D. Holt, "Analyzing GTA Emittance Data," Los Alamos National Laboratory AT-10 Technical Note 91-01 (1991).

[13] K.R. Crandall, R.A. Jameson, D. Morris, and D.A. Swenson, "The Δt Turn-On Procedure," *Proc. 1972 Proton Linear Accelerator Conf.*, Los Alamos, NM, Oct 10-13, 1972, Los Alamos Scientific Report LA-5115, Nov. 1972, pp 122-125.

[14] F.W. Guy and T.P. Wangler, "Least-Squares Fitting Procedure for Setting RF Phase and Amplitude in Drift-Tube-Linac Tanks," *Proc. 1991 IEEE Particle Accelerator Conference*, Vol. 5, pp. 3056-3058.

[15] F.W. Guy and J.W. Hurd, "Procedures for Setting RF Phase and Amplitude in SSC Drift-Tube-Linac Tanks," *Proc. 1992 Linear Accelerator Conference*, Vol. 1, pp. 196-198.

[16] K. Saadatmand et. al., "Performance of the SSC Magnetron Ion Source and LEBTs," ibid., pp. 94-96.

[17] K. Saadatmand and N.C. Okay, "Performance of the SSC RF-Driven Volume Source," ibid., pp. 97-99.

[18] J. Lenz et. al., "Comparison of Experimental and Simulated Results for the SSC LEBT," these proceedings.

[19] S. Guharay et.al., "An ESQ Lens System for Low Energy Beam Transport Experiments on the SSC Test Stand," ibid.

[20] D. Raparia, "Beam Dynamics of the Low Energy Beam Transport and Radio Frequency Quadrupole," Ph.D. Thesis, University of Houston, Houston, TX (1990).

[21] F.W. Guy, "Three-Dimensional Space Charge and Image Charge Effects in Radio-Frequency-Quadrupole Accelerators," *Proc. 1991 IEEE Particle Accelerator Conference*, Vol. 5, pp. 3032-3034.

[22] Yu. Senichev et. al., "Beam Loading Effect in SSCL Coupled Cavity Linac," these proceedings.

The Provision of IP Crossing Angles for the SSC

Y. Nosochkov

Superconducting Super Collider Laboratory *
Dallas, TX 75237

D.M. Ritson

SLAC, Stanford University, Stanford, CA 94309

Abstract

Luminosity is to be produced at the SSC collider by crossing with finite angle the counter circulating proton beams at each interaction point (IP). Such a crossing angle introduces unwanted dispersion in the high beta triplet quadrupoles adjacent to the IPs which must be corrected out. We propose to produce variable crossing conditions at each IP with local steering dipoles adjusted to give required slopes and displacements for each IP. The anomalous dispersion introduced by these orbit displacements will be corrected in the arcs (dispersive region) just prior to entry and exit into the IRs with opposite polarity quadrupole pairs separated by 90° in phase, a "late" correction scheme. Such pairs cause minimal change to the betatron functions but produce dispersion that can be set to cancel the anomalous dispersion. The IR design is such that the phase advance between correctors and the IP triplet gives efficient full local anomalous dispersion cancellation. The proposed system is to be formed from standard SSC corrector elements and will provide the range of crossing conditions required for collision optics and for separating the beams at injection.

I. INTRODUCTION

There are four interaction regions in the SSC, two in the East cluster and two in the West. Vertical schematic view of the baseline IR optics is shown in Figure 1 [1]. The beams are brought into collision in the middle of the IR by use of a set of vertical dipoles. The central region containing the space for detector and adjacent final triplets is common for both rings, thus the beams share the same beam pipe in it. At the SSC collider the nominal bunch spacing will be $5\,m$. An ideal IR optics does not provide any beam separation in the common central region. Therefore, besides the IP, the counter circulating beams would have about seventy satellite head-on collisions in each IR before separation into separate vacuum chambers. This is not allowed from both beam stability and experimental points of view.

To avoid unwanted head-on collisions the beams must be separated everywhere other than at the main IP. To ensure that the achievable luminosities are not substantially degraded by the long range beam-beam interactions at the satellite crossings the beams must be separated by $> 10\,\sigma$
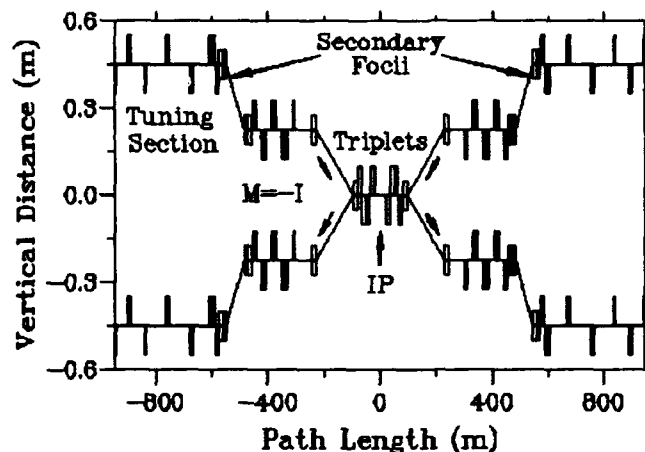
Figure 1. Vertical view of an IR.

at these points. This separation can be achieved by introducing the finite crossing angle at the IP of $\sim 100\,\mu rad$. The crossing angle requirements vary widely for injection and collision conditions and should further permit either horizontal or vertical crossings. Too large values of the crossing angle, however, should be avoided in order to prevent a significant reduction of the luminosity, and to minimize the orbit displacements in the final triplet quadrupoles and the effect of synchro-betatron resonances induced at the IP (cf for instance Reference [2]).

The crossing angle and/or the orbit displacement at the IP can be produced by a set of properly adjusted local steering dipoles. This, however, causes the beams go offset the center of the quadrupoles, thus creating an anomalous dispersion. Mostly this dispersion is generated by the orbit changes in the final triplet quadrupoles where the β function at nominal collision conditions reaches the value of $9\,km$. A crossing angle in one IR at collision may create an anomalous dispersion of up to 20% in magnitude of the nominal dispersion in the collider. Therefore, it should be corrected locally.

The scheme previously proposed by the SSC Central Design Group in Reference [3] was to correct the anomalous dispersion locally by inducing a large orbit bump in the quadrupoles prior to the triplets. This scheme required substantial strengths of steering dipoles and large deflections. In this paper we propose to produce variable crossing conditions at each IP with local steering dipoles and
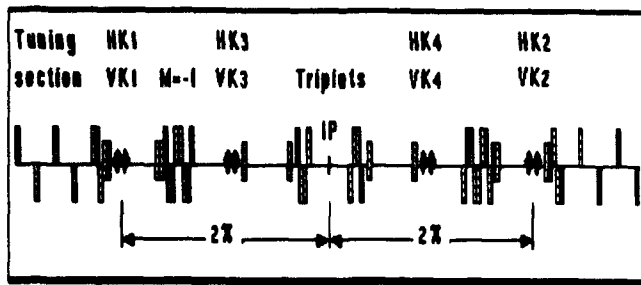
Figure 2. Location of the steering dipoles in the IR.

to correct an anomalous dispersion by generating a cancelling dispersion wave in the arcs with opposite polarity trim quadrupoles separated by 180° in phase. This scheme provides a wide range of values for the crossing angles and displacements at the IP with modest strengths of local correctors. The details of the scheme are given below.

II. LAYOUT OF THE PROPOSED CROSSING ANGLE SCHEME

A. Crossing Conditions at the IP

Crossing conditions at the IP can be achieved with a set of local steering dipoles. Each of them will generate a wave of the orbit deviation which has the following form:

$$x(s) = \theta\sqrt{\beta(s)\beta_\theta}\,\sin(\mu(s) - \mu_\theta)\,, \qquad (1)$$

$$x'(s) = \theta\sqrt{\frac{\beta_\theta}{\beta(s)}}[\cos(\mu(s)-\mu_\theta)-\alpha(s)\sin(\mu(s)-\mu_\theta)]\,, \quad (2)$$

where θ is the angular kick produced by a steering dipole, and β, α and μ are the Twiss parameters and a phase advance respectively. In general, two steering dipoles per each half IR are required to provide specific values of the orbit slope and displacement at the IP and to put the beam back on its equilibrium orbit on the other side of the IP. This number, however, can be reduced by appropriate choice of the phase advance between the kickers and the IP. The present optics of the IR [1] has two secondary focal points located 2π apart in phase from the IP symmetrically on each side of the IP. This is shown in Figure 2.

According to the above equations a horizontal dipole kicker placed exactly at the secondary focus will provide at the IP a horizontal angular deflection without affecting the position of the IP, and propagation of this orbit wave can be completely cancelled by a kicker placed at the second focus on the other side of the IP. These kickers are labeled HK1 and HK2. Vertical kickers VK1 and VK2 to produce vertical angular deflections are also provided. In practice, however the above correctors will be placed next to adjacent vertical dipoles at some small distance from the secondary focus. This would cause a small residual orbit displacements at the IP and at the position of the second kicker. Therefore, to provide a complete orbit

bump another pair of steering dipoles is necessary. These additional kickers labeled HK3, HK4 and VK3, VK4 are placed approximately $\pi/2$ in phase from the IP. They become important if a displacement at the IP is required.

B. Correction of the Anomalous Dispersion

The main sources of the anomalous dispersion at collision conditions are the final triplet quadrupoles where the orbit is displaced by a maximum of 4.6 mm for the crossing angle of 135 μrad, and the β_{peak} is 9 km at a nominal luminosity. To correct a horizontal dispersion associated with horizontal crossing conditions at the IP we propose to use a few families of quadrupole pairs located in the adjacent to the IR standard collider cells. Each quadrupole will generate an additional dispersion wave which is proportional to the natural horizontal dispersion η_{qx} at the quadrupole location

$$\eta_x(s) = -\eta_{qx}\sqrt{\beta(s)\beta_q}\,\frac{G_q l_q}{B\rho}\sin(\mu(s) - \mu_q)\,. \qquad (3)$$

The phase advance across the standard cell is 90°. Thus, if the quadrupoles in each pair are separated by 180° in phase and have equal strengths and opposite polarities, then they generate a net wave of dispersion without affecting the betatron motion. The IR optics provides a horizontal (vertical) phase advance of 90° × integer between the IP and any F (D) quadrupole in the collider cells. On the other hand, the triplets generating most of the anomalous dispersion are located also approximately 90° from the IP. Therefore, the above quadrupole correctors can be placed next to the F quadrupoles with almost right phase shift of $n\pi$ from the triplets to generate a cancelling wave of horizontal dispersion.

Two quadrupole pairs HQ1 and HQ2 one on either side of the IP will in practice provide quite satisfactory dispersion cancellation. As an example, Figure 3 shows schematically the phase positions of the above correctors in the vicinity of the East North IR. The first pair HQ1 corrects primarily for the effect of the left triplet, thus cancelling the dispersion at the IP. The second one corrects for the dispersion produced by the triplet on the right side. In the real configuration the above correctors only approximately satisfy the ideal phase advances shown in Figure 3. This would result in a small residual dispersion in the collider which in real cases would be less than 7 cm. This seems to be not a problem for machine operation. To provide full cancellation of the dispersion a third quadrupole pair HQ3 located 90° away from HQ2 is required. A typical example of the horizontal crossing angle at the North East IP is given in Figure 4. It shows the horizontal closed orbit and dispersion associated with the crossing angle of 135 μrad at collision conditions with $\beta^* = 0.5\,m$ for the baseline IR optics. Large dispersion shown in the adjacent to the IR arc cells and in the Hinge region is the natural dispersion of the machine. The strengths of the kickers $B_k l_k$ (Tm) and quadrupoles $G_q l_q$ (T) in this case are given in the fol-
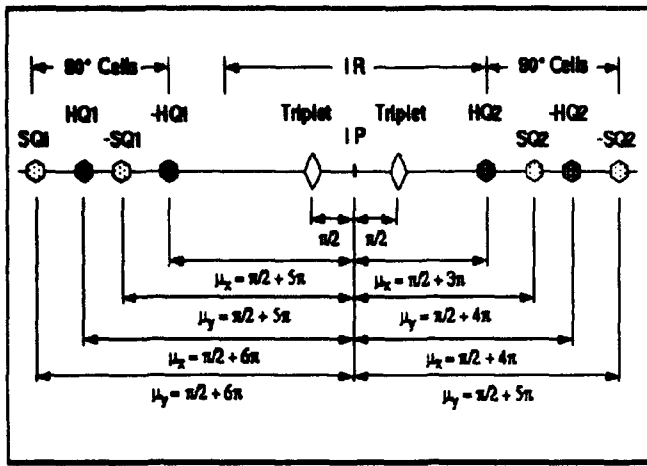
Figure 3. Phase positions of the quadrupole correctors with respect to the East North IP.
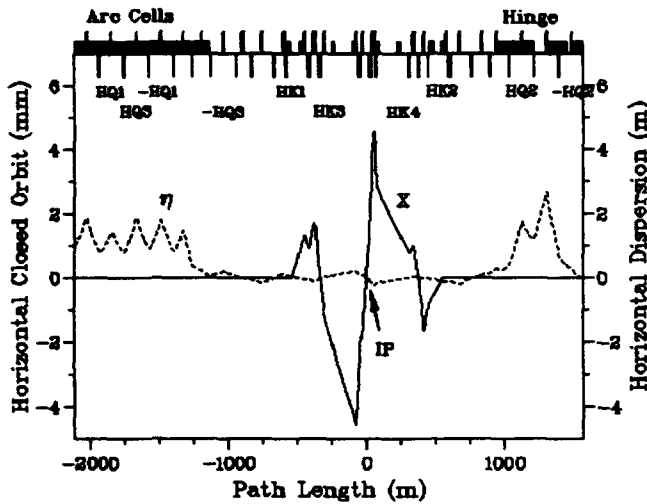
Figure 4. Horizontal crossing angle at the IP.

lowing table. All the values do not exceed the maximum strengths specified for standard SSC collider correctors.

HK1	HK2	HK3	HK4	HQ1	HQ2	HQ3
0.957	-0.584	-0.013	0.015	-18.1	-27.2	0.9

To correct a vertical dispersion associated with vertical crossing conditions a set of skew quadrupole pairs are required instead of normal quadrupoles. The requirements for these correctors are identical to those in the horizontal scheme. Similarly to formula (3), a skew quadrupole generates a wave of vertical dispersion proportional to the natural horizontal dispersion η_{qx} at its location. The skew quadrupoles now are located next to D quadrupoles in the cells adjacent to the IR. Positions of the primary pairs SQ1 and SQ2 are shown schematically in Figure 3. To compensate slight difference between real phase locations of the above pairs and theoretical positions shown in Figure 3,
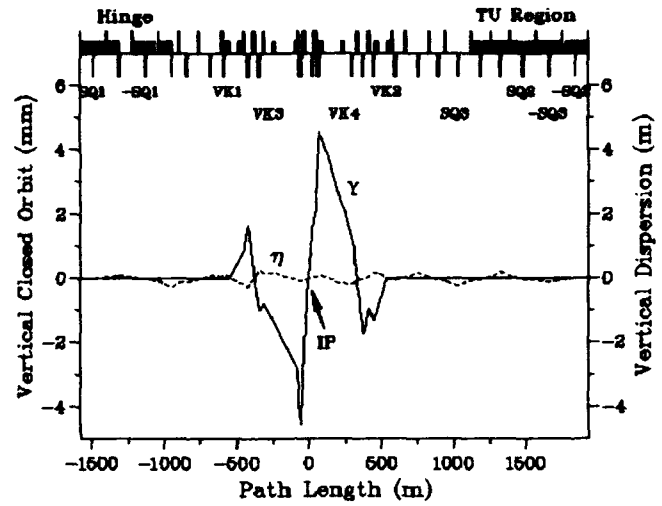
Figure 5. Vertical crossing angle at the IP.

a third pair SQ3 shifted by 90° from SQ2 is required. In practice, again, running only with first two pairs would not be a problem. Figure 5 shows an example of vertical crossing angle of $135\,\mu rad$ at the East South IP for the baseline collision optics with $\beta^* = 0.5\,m$. The strengths of the correctors $B_k l_k\,(Tm)$ and $G_q l_q\,(T)$ are given in the next table.

VK1	VK2	VK3	VK4	SQ1	SQ2	SQ3
0.584	-0.957	-0.015	0.013	-58.7	-29.4	-5.2

III. CONCLUSIONS

The design for a crossing angle system described above appears to be both satisfactory and a substantial improvement of the previous SSC designs based on "early" not "late" correction of the associated anomalous dispersion. The scheme was checked for different crossing conditions at the IPs including a crossing angle and a beam separation for both injection and collision lattice configurations. It provides both horizontal and vertical crossing conditions at the IPs with modest corrector strengths.

IV. REFERENCES

[1] Y. Nosochkov et. al., "Current Design of the SSC Interaction Regions", these proceedings.
[2] W. Chou and A. Piwinski, "Synchro-Betatron Resonances Excited by the Beam-Beam Interactions at a Crossing Angle in the SSC", SSCL-Preprint-119 (1992).
[3] A.A. Garren and D.E. Johnson, "Controlling the Crossing Angle in the SSC", 1989 IEEE Particle Accelerator Conference, pp. 1334-1336.

Interactive Simulation of LEB Commissioning Procedure on a Hypercube Parallel Computer

G. Bourianoff, M. Botlo, B. Cole, S. Hunt, N. Malitsky, A. Romero

SSC Laboratory*
2550 Beckleymeade Avenue
Dallas, Texas 75237

Abstract

It is desirable that an interactive simulation of accelerator operation be developed in order to write and test commissioning, correction, supervisory control, closed loop control, optimization and automation code prior to machine construction. The simulator should produce realistic diagnostic information, analyze and display the information at a workstation, accept operator input, and react appropriately. Such a system has been developed by the Accelerator System Control Simulator Collaboration to model the Low Energy Booster (LEB). The system is implemented on a 64 node INTEL ISPC/860 parallel computer which operates at approximately 600 Mflops. The simulator can track 512 particles on 32 nodes at 1 turn per second using an element by element symplectic integrator based on the TEAPOT algorithm. An operator interface has been implemented on a SUN Sparc 2 workstation operating as a client to a VME based 68040 processor board running VxWorks real time operating system. Data display and operator input utilize the operator interface routines in the EPICS control system. Data access between the SPARC Card and the HYPERCUBE is accomplished currently with an interprocess socket connection. Simulation of the interactive closed orbit smoothing process will be shown.

INTRODUCTION

Because of its raw processing power, the parallel processor is being used as the engine in an interactive simulator of the Low Energy Booster (LEB). This simulator is being developed for two purposes. The first is to develop a platform on which high level correction code can be developed and from which an operator can control the simulator with the same look and feel he or she will experience in the control room. The second purpose is to test the data handling characteristics of the EPICS control system.
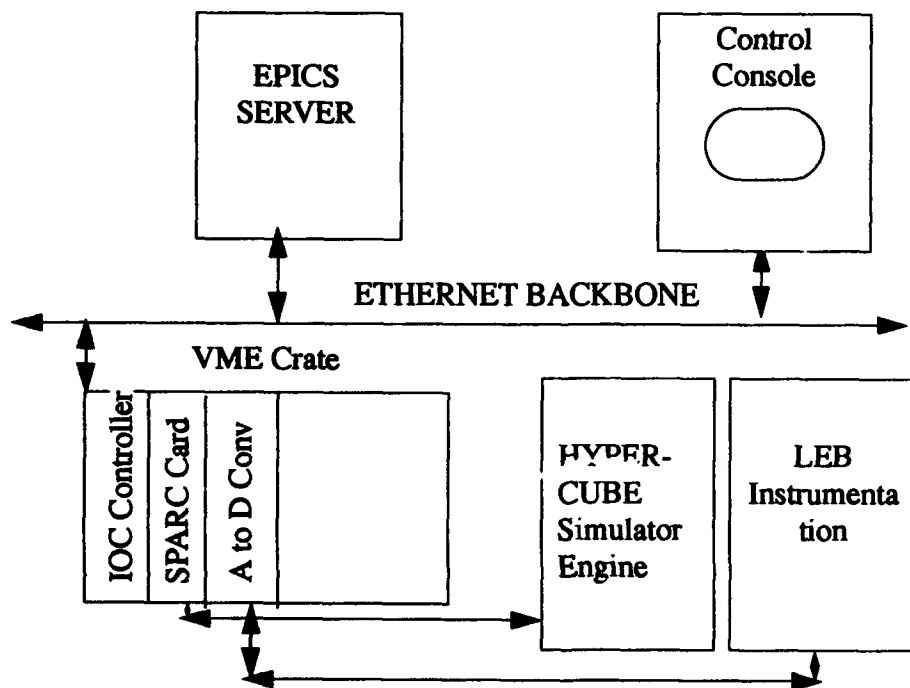
Figure1 Schematic Diagram of LEB Simulator

Simulator Architecture

The architecture of the simulator is shown in figure 1. The computational model running on the Hypercube is shown in the lower right hand corner adjacent to a box showing LEB instrumentation. The simulation results produced on th Hypercube are transferred over an Ethernet connection to a rack mounted SPARC card which formats the data into the same form produced by the A to D converter which actually receives the data from the LEB instrumentation. A software driver for the SPARC card then reads or writes the data into the EPICS control system where it is handled in the same manner that data produced by the actual accelerator instrumentation.

The LEB and its instrumentation do not exist at the present time. The propose of showing it in figure 1 is to emphasize the simulator engine is interchangeable with the actual instrumentation form the viewpoint of the high level control code.

The communication between the hardware components shown in Fig. 1 use a collection of hardware links and software protocols that closely resemble those that will be found in the SSC control system. The heart of the communication between the application code running in the Unix environment and the instrumentation hardware (modeled here by the Hypercube) is the EPICS database that physically resides in the Input Output Controller (IOC). The IOC itself is a Motorc.a 68040 based processor in a VME crate. The EPICS database has a set of pointers that connect variables that can be accessed from the UNIX world (channel access variables) to actual hardware addresses that connect to the low level instrumentation. The database also contains the information on data format, refresh frequency, error codes, etc. that are required to interpret the raw instrumentation signals.

In the simulator, data is produced asynchronously by the simulator engine. This is passed over an Ethernet connection directly to VME memory space. Event flags are posted when new data has been produced by the Hypercube. Similarly, when the high level application code has calculated some corrector settings, an event flag is posted and corrector settings are passed from VME memory to the appropriate elements in the simulation code running on the Hypercube. All data input and output operations in the application code are handled by channel access calls and therefore the code should run intact on the control room console when the accelerator is commissioned.

SIMULATOR ENGINE

The simulator engine consists of an 64 node Intel IPSC/ 860 Hypercube parallel processor running a powerful simulation code based on the TEAPOT tracking algorithm described in Ref. 1. The Hypercube is a 64 node, distributed memory, MIMD computer. It utilizes the I860 RISC processor on each node. Each node executes the tracking code at approximately 8 MFLOPS in double precision. All 64 nodes therefore constitute a dedicated facility operating at approximately 0.5 GFLOPS. The nodes operate with NX, a subset of UNIX. It is a single process operating system with significantly reduced capabilities relative to the full UNIX implementation. It does however allow socket connections to individual nodes. Communications internal to the engine are done using a proprietary message passing library

The simulation code in an element by element tracking code which exactly integrates the equations of motion in a symplectic manner. The code models a real accelerator lattice with assigned errors in virtually all the lattice components. The code also simulates the operational correction process whereby lumped element correctors are set to compensate for assigned random and systematic errors. The simulation model includes various diagnostic devices, most notably BPMs.

The operational mode of the simulation code has been modified to more closely resemble an operating accelerator. Particles can be injected and tracked for a predetermined number of turns, until the are lost or tracked until an event is posted on the control console signaling additional information is to be transferred During the tracking, the system of BPM's is measuring the beam centroid position at all locations on a turn by turn basis, and sending this information to the EPICS control system. For most applications, it is sufficient to track between 16 and 64 particles in an ensemble.

OPERATOR INTERFACE

The simulator uses the graphical user interface that is integral to EPICS. Thus, the simulator has the same look and feel as the actual operating software. The graphical user interface executes on the Control Console and communicates with the UNIX world through channel access calls.

At the present time, several high level correction modules have been written that deal with first turn injection into the LEB. Eleven modules have been written thus far as prototypes which exercise the simulator's capabilities. Figure 2 shows a screen from the operating simulator

The screen demonstrates some of the capabilities and limitations of the OPI interface. The column of buttons on the right show the individual correction modules which may be invoked from the main control screen. The general procedure is to execute the subroutines in the order they appear on the screen. The text windows to the left of the cartesian plot indicate the operation taking place and wether or not it is complete. The upper plot indicates the particle trajectory after the corrector settings shown in the bottom plot have been implemented. The correction operations require 10 to 30 seconds to execute on the simulator which is similar to the actual production code.

The text window pair associated with the top graph show maximum displacement of the horizontal and vertical trajectories in mm. The text window pair associated with the lower graph shows the maximum corrector strengths in radians.

First experience with the simulator has already yielded useful infor nation on various features of the OPI. For

example, the scale size can be set only at compile time and the caption size cannot be set by the user at all. This is in no sense a serious problem but it does indicate the utility of the simulator in identifying inadequate or undesirable features of EPICS in general and the OPI in particular.
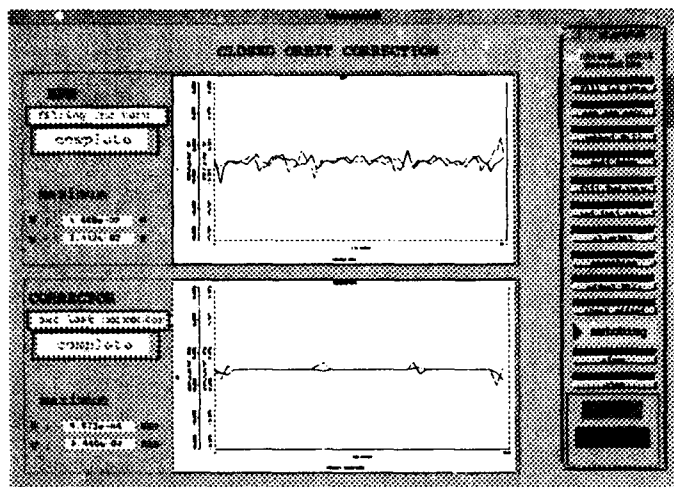
Figure 2 Typical Simulator Screen

CORRECTION MODULES

The operation of the simulator begins with an operator sitting in front of the control console workstation shown in figure 1. He or she starts initiates the simulation code on the hypercube and initiates the simulator process on the workstation. A screen as shown in figure 2 appears at the work station and the operator pushes one of the buttons shown on the right of the screen. The simulator process reads the required information from the EPICS database, performs the required calculations and writes out modified corrector settings to the Hypercube code by way of the EPICS database.

At the present time there are two general classes of operational code that have been developed for the simulator. The first is a set of modules that deal with establishing a smooth closed orbit starting from injection into a completely uncorrected lattice with an unknown beam offset and unknown calibration of the main dipole field. The second is a tune measurement module.

The first class of code consists of eleven separate modules. The operator interface for this class is shown in Fig. 2. The individual modules are listed in table 1.

Table 1: Correction Modules

Module Name	Function
fill 1st turn	inject a beam and track 1 turn
set 1st corr	set the first 4 correctors to zero injection offset and injection angle at entry.
adjust B_o	adjust dipole field based on 2 BPM's

Table 1: Correction Modules

Module Name	Function
pull beam	set 4 additional correctors at beginning of super-periods
fill 2nd turn	inject and track 2 turns, save trajectory from 2nd turn.
set last corr	set last4 correctors to zero beam offset and angle at entry of 2nd turn.
closed orbit	Find closed orbit by averaging particle trajectories over 128 turns.
smoothing	smooth closed orbit
adjust B_o	adjust Bo field so average corrector strength is zero
check offset	find injection offset by observing trajectory oscillations about closed orbit.
Matching	Correct injection offset

FUTURE PLANS

The simulator will also serve as a realistic environment in which to determine data handling overheads and operational bandwidth within the EPICS control system. The simulator will be extended to include a data buffer which will record data produced by the Hypercube and subsequently write it out in a "burst" mode which will equal the rate at which data is produced by the actual instrumentation.

The simulator will also accurately represent the hardware configuration that will be encountered in the LEB. Specifically, the current LEB control system plan calls for one IOC in each of the 12 sector houses and one concentrator IOC that communicates with the low level IOCs. The high level application code will access information from the concentrator and the lower level IOCs will be invisible except for the added delay in transferring data. The actual delays in this kind of configuration are not known at the present time and their determination is vital to predicting closed loop response times. It is anticipated that this work will be completed in the next few months.

REFERENCES

1. L. Schachinger and R. Talman, Teapot: Thin-Element Accelerator Program for Optics and Tracking, *Particle Accelerators*, 1987, Vol. 22, pp. 35-56.

Localized Chromaticity Correction of Low-Beta Insertions in Storage Rings*

M. Donald, R. Helm, J. Irwin, H. Moshammer
Stanford Linear Accelerator Center, Stanford, CA 94309
E. Forest, D. Robin, A. Zholents
Lawrence Berkeley Laboratory, Berkeley, CA 94720
M. Sullivan
University of California Intercampus Institute for Research at Particle Accelerators,
Stanford Linear Accelerator Center, Stanford, CA 94309

Abstract

The correction of the chromaticity of low-beta insertions in the storage rings is usually made with sextupole lenses in the ring's arcs. When decreasing the beta functions at the insertion point (IP), this technique becomes fairly ineffective, since it fails to properly correct the higher order chromatic aberrations. Here we consider the approach where the chromatic effects of the quadrupole lenses generating low beta functions at the IP are corrected locally with two families of sextupoles, one family for each plane. Each family has two pairs of sextupoles which are located symmetrically on both sides of the IP. The sextupole-like aberrations of individual sextupoles are eliminated by utilizing optics forming a -I transformation between sextupoles in the pair. The optics also includes bending magnets which preserve equal dispersion functions at the two sextupoles in each pair. At sextupoles in one family, the vertical beta function is made large and the horizontal is made small. The situation is reversed in the sextupoles of the other family. The betatron phase advances from the IP to the sextupoles are chosen to eliminate a second order chromatic aberration. The application of the localized chromatic correction is demonstrated using as an example the lattice design for the Low Energy Ring of the SLAC/LBL/LLNL PEP-II B Factory.

I. INTRODUCTION

Chromatic correction is a common requirement in many optical and electronic systems as well as charged particle beam lines. It has been noted in several contexts that local chromatic correction is preferable. In storage rings, it is usual to correct chromatic aberrations with sextupole families in the FODO arrays of the arcs. For colliding rings with very small β-function values at the interaction point (IP), large values of chromaticity are generated in the final focusing quadrupoles. Attempts to correct this with arc sextupole families can fail for two reasons: i) the transport of chromaticity through a lattice gives rise to higher order chromaticity which remains uncompensated, and ii) the arc sextupoles, which typically are interleaved, create unacceptable amounts of octupole aberration when they are strengthed to compensate for additional chromaticity.

This paper describes the adaptation of a scheme used in the final focus systems of linear colliders to locally compensate chromatic aberrations of final
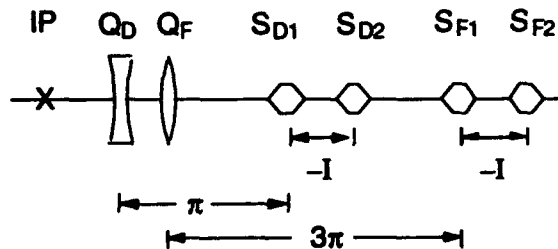
Figure 1. A schematic for a typical final focus chromatic correction system

doublets [Ref 1]. It consists of two pairs of non-interleaved sextupoles in the interaction region (IR) on either side of the IP.

A. Description of Typical Chromaticity Correction Scheme

The typical final focus chromatic correction system, shown in Fig. 1, consists of two pairs of sextupoles. Each sextupole of a pair is placed -I from the another, so that the sextupole aberration is cancelled, and at $n\pi$ phase difference from the quadrupole whose chromaticity is being compensated. Typically the vertical plane is more strongly focused than the horizontal, so the vertical compensation is closest to the IP. At this pair of sextupoles, the vertical β-function is large, and the horizontal β-function is small. The linear transformer between the first and second pairs of sextupoles reverses this β-function ratio so that the second sextupole pair primarily compensates the horizontal chromaticity of the final doublet. Beyond the second sextupole pair is a β-matching section. From the begining of the β-match through the IP, the system has only a small residual chromatically, and so is chromatically transparent when placed in a storage ring. Of course, in a storage ring there needs to be an identical system on the other side of the IP.

The dispersion function is an important feature of the compensation scheme described above. There must be dispersion at the sextupoles, usually equal at both sextupoles of a pair, so that the sextupole strengths are at a minimum, and certain other aberrations, such as high-order dispersion arising in the -I section, are cancelled. Typically there is a bend in the β-match section $\pi/2$ from the first sextupole, to launch a dispersion function, a bend at the middle of each -I to symmetrize the dispersion function, and a bend in the final telescope $\pi/2$ from the final sextupole to terminate the dispersion.
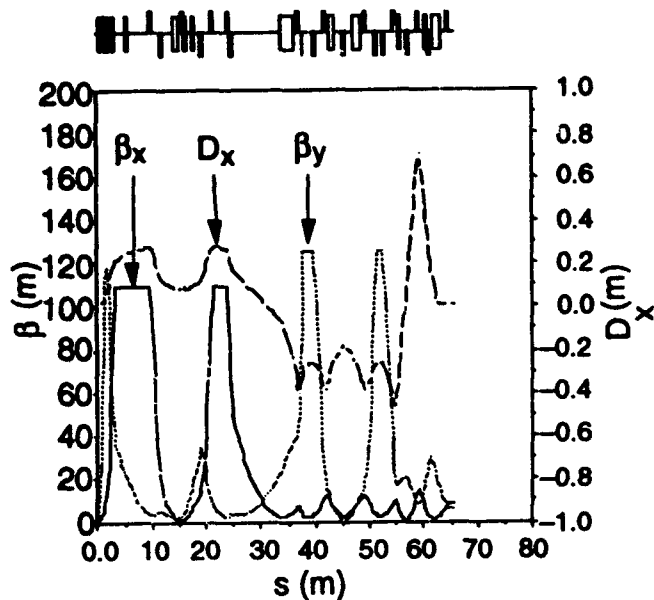
Figure 2. The lattice functions for the LER IR chromatic correction system.

Figure 4. The horizontal and vertical β-function at the RF cavity in the LER as a function of energy.

Figure 3. The horizontal and vertical tune shift of the LER as a function of energy.

B. Compensation of Second-Order Chromatic Terms

The second-order chromatic terms in the one-turn nonlinear generator arise from the first Poisson bracket $1/2$ $[H_i,H_j]$ in the CBH theorem expansion, where H_i is the chromatic-aberration Hamiltonian coming from a quadrupole or from a sextupole at a location with horizontal dispersion. For a quadrupole, $H_i = -1/2$ $k_{Qi}\delta$ (x_i2-y_i2). For a sextupole, k_{Qi} is replaced by k_{Si} η_i. In other words, the higher-order chromatic term arises from chromaticity in one quadrupole (or sextupole) modifying the chromatic contribution of another

quadrupole (or sextupole). This Poisson bracket can be evaluated to yield $1/2[H_i,H_j]=1/2$ k_{Qi} k_{Qj} δ^2 $([x_i,x_j]$ x_ix_j $+$ $[y_i,y_j]$ $y_iy_j)$. The factor $[x_i,x_j]$ $([y_i,y_j])$ is just the $(1,2)$ $[(3,4)]$ element of the linear transfer matrix between quadrupoles i and j. If these elements are separated by $n\pi$, their interaction is zero, and away from $n\pi$ this term can take one sign or the other. This feature of the source of second-order terms can be used to advantage within the framework of the chromaticity compensation scheme we have described above [Ref 4]. By slightly varying the phase shift between the sextupole pair and the chromatic source, it is possible to vary the sign of the second-order chromatic term and compensate, for example, any second-order tune shift term that remains in the full ring.

C. Description of the PEP-II LER Chromaticity Correction Scheme

The scheme described above was studied for PEP-II LER [Ref 3]. This effort was unsuccessful because space constraints required strong intermediate quadrupoles which generated unacceptable chromaticty between sextupole pairs. A solution for the PEP-II low energy ring was achieved by placing a sextupole at the final doublet. As a result of this bend and an offset-quadrupole [Ref 4] near the IP, large dispersion and a large horizontal β–function exist at the F quadrupole of the doublet. By beginning compensation immediately, additional space becomes available, and the strong quadrupole problem mentioned above is resolved. Figure 2 shows the lattice functions for the completed design. The sextupole near the first F quadrupole is placed where β_y is small. The interchange of the vertical and horizontal compensation, with the horizontal compenstions closest to the IP, is acceptable because the

situation is less extreme than in the FFTB where $\beta_y^* = 0.1$ mm.

Because the correction is local, precisely $n\pi$ (n=0 or n=2) from the source, both the tune-shift with energy and variation of the β-function with energy $(d\beta/d\delta)$ are compensated. Since uncompensated first-order terms give rise to higher-order terms, we have also reduced higher-order chromatic terms. Figure 3 shows the tune-shift as a function of energy. Little first- or second-order dependence on δ remains in the PEP-II LER lattice. Figure 4 shows β_x (δ) and β_y (δ) at the RF cavity, where a δ-dependent β-function could drive synchro-betatron resonances. β_x (δ) and $\beta_y(\delta)$ are well behaved here and at other locations throughout the ring.

A local chromatic correction scheme with sextupoles near the IP was previously used in VEPP-4 [Ref 3]. In this case there was dispersion at the final doublet due to the choice of a vertical solenoidal magnetic field. However, in VEPP-4 there were only one SD and one SF on each side of the IP. A scheme similar to VEPP-4 was also considered for designs of storage rings with monochromator optics [Ref 6].

REFERENCES

[1] Oide, SLAC-PUB-4953, 1989.
[2] Private Comm. K. Brown and R. Helm compensated 2nd-order chromaticty in their FFTB designs.
[3] E. Forest, et al, LBL-33479, Jan 1993, Submitted to KEK B-factory workshop.
[4] PEP-II B-factory CDR.
[5] VEPP-4 report on All Union Conf. for Charged Particle Accelerators.
[6] A. Zholentz, CERN-CL-92-27(AP).

Amplitude Function Mismatch

M.J. Syphers, T. Sen
Superconducting Super Collider Laboratory*
2550 Beckleymeade Ave., Dallas, TX 75237
and
D. A. Edwards
DESY/Fermilab*
P. O. Box 500, Batavia, IL 60510

Abstract

We develop the general equation of motion of an amplitude function mismatch in an accelerator lattice and look at its solution for some interesting cases. For a free β-wave oscillation the amplitude of the mismatch is written in terms of the determinant of a single matrix made up of the difference between the new Courant-Snyder parameters and their ideal values. Using this result, once one calculates the mismatch of the amplitude function and its slope at one point in the lattice (at the end of a *nearly* matched insertion, for example), then the maximum mismatch downstream can be easily computed. The formalism is also used to describe emittance growth in a hadron synchrotron caused by amplitude function mismatches at injection.

While most of the content of this paper is not new to the accelerator physics community, we thought it would be useful to place this important, basic information all in one place. *Besides the classic work of Courant and Snyder, our sources include other papers, internal reports, and numerous discussions with our colleagues.* More details may be found in a related paper.[1]

I. A STARTING POINT

The general solution for linear betatron oscillations in one transverse degree of freedom can be written as[2] $x(s) = A\sqrt{\beta(s)}\cos[\psi(s) + \delta]$ where A and δ are constants given by the particle's initial conditions. The phase advance $\psi(s)$ and the amplitude function $\beta(s)$ satisfy the differential equations $\psi' = \frac{1}{\beta}$, $2\beta\beta'' - \beta'^2 + 4\beta^2 K = 4$, where $K = e(\partial B_y/\partial x)/p$, with e = charge, p = momentum, $\partial B_y/\partial x$ = magnetic field gradient, and $\beta' = d\beta/ds$, etc. When one considers the periodic solution of the amplitude function, the motion through a single repeat period can be described in terms of the Courant-Snyder parameters $\beta(s)$, $\alpha(s) \equiv -(d\beta(s)/ds)/2$, and $\gamma(s) \equiv (1 + \alpha^2)/\beta$, using the matrix

$$\begin{pmatrix} \cos\psi_C + \alpha\sin\psi_C & \beta\sin\psi_C \\ -\gamma\sin\psi_C & \cos\psi_C - \alpha\sin\psi_C \end{pmatrix} \quad (1)$$

which operates on the state vector X, with $X = (x, x')^T$. Here, the phase advance is $\psi_C = 2\pi\nu = \int_{s_0}^{s_0+C} \frac{ds}{\beta(s)}$, where

C is the repeat distance of the hardware, which may be the circumference of the accelerator, and ν is the *tune* of the synchrotron.

The matrix of Equation 1 is often written in compact form as $M = I\cos\psi_C + J\sin\psi_C$ where

$$J \equiv \begin{pmatrix} \alpha & \beta \\ -\gamma & -\alpha \end{pmatrix}. \quad (2)$$

The amplitude function and its slope propagate through an accelerator section according to

$$J_2 = M(s_1 \to s_2)J_1 M(s_1 \to s_2)^{-1}, \quad (3)$$

where J_1 and J_2 contain Courant-Snyder parameters corresponding to points 1 and 2, and $M(s_1 \to s_2)$ is the transport matrix between these two points.

II. PROPAGATION OF A THIN GRADIENT ERROR

We wish to see how the amplitude function downstream of a thin gradient error is altered. If $J_0(s_0)$ is the matrix of unperturbed Courant-Snyder parameters at the location of the error and $J_0(s)$ contains the unperturbed parameters at a point downstream, then, using Equation 3,

$$\Delta J(s) = M(s_0 \to s)\Delta J(s_0)M(s_0 \to s)^{-1}, \quad (4)$$

where

$$\Delta J(s) = J(s) - J_0(s) = \begin{pmatrix} \alpha - \alpha_0 & \beta - \beta_0 \\ -(\gamma - \gamma_0) & -(\alpha - \alpha_0) \end{pmatrix}; \quad (5)$$

β is the new value of the amplitude function at s, β_0 is the unperturbed value, etc. Through a thin quad, $\Delta\alpha = q\beta_0$, $\Delta\beta = 0$, and $\Delta\gamma = 2\alpha q + \beta q^2$ and so

$$\frac{\Delta\beta(s)}{\beta_0(s)} = -(\beta_i q)\sin 2\psi_0(s - s_0)$$

$$+ \frac{1}{2}(\beta_i q)^2 [1 - \cos 2\psi_0(s - s_0)] \quad (6)$$

where $\psi_0(s-s_0)$ is the unperturbed phase advance between points s_0 and s and $\beta_i \equiv \beta_0(s_0)$. The amplitude function perturbation oscillates at twice the betatron frequency and for $(\beta_i q)$ sufficiently small, the perturbation describes simple harmonic motion. The change in α also propagates at

twice the betatron frequency, it being given by

$$\Delta\alpha(s) = \beta_i q \left[\cos 2\psi_0(s - s_0) - \alpha_0(s)\sin 2\psi_0(s - s_0)\right]$$
$$-\frac{1}{2}(\beta_i q)^2[\sin 2\psi_0(s - s_0)$$
$$-\alpha_0(s)(1 - \cos 2\psi_0(s - s_0))] \quad . \quad (7)$$

Introducing this quad error also changes the phase advance across the lattice. The new phase advance $\psi(s - s_0)$ across this section may be calculated using $\sin\psi(s - s_0) = \bar{M}(s_0 \to s)_{12}/\sqrt{\beta_i \beta(s)}$ where $\bar{M}(s_0 \to s)_{12}$ is the (1,2) element of the new ring matrix and $\beta(s)$ is the new amplitude function at s. Using Equation 6, we obtain

$$\sin\psi(s - s_0) = [1 - \beta_i q \sin 2\psi_0(s - s_0)$$
$$+ (\beta_i q)^2 \sin^2\psi_0(s - s_0)]^{-1/2}\sin\psi_0(s - s_0) \quad . \quad (8)$$

An explicit result for the change in the phase advance may be obtained perturbatively in orders of the quad error q from the above exact expression. To second order in q, we find that the change $\Delta\psi \equiv \psi(s - s_0) - \psi_0(s - s_0)$ is

$$\Delta\psi = \beta_i q \sin^2\psi_0(s - s_0)$$
$$- (\beta_i q)^2 \sin 2\psi_0(s - s_0)\sin^2\psi_0(s - s_0) + O(q^3) \quad . \quad (9)$$

To first order in q, at a point $\pi/2$ away from the location of the error, there is no change in the β function while the change in phase advance is at its maximum value of $\beta_i q$.

III. EQUATION OF MOTION OF β-WAVE

The equation of motion for an amplitude function mismatch is nonlinear when s is taken as the independent variable. A more congenial equation can be developed by using the the reduced phase $\phi \equiv \psi/\nu$ as the independent variable. For betatron oscillations the Floquet transformation, where the other variable is $\zeta = x/\sqrt{\beta}$, produces the equation of motion $\frac{d^2\zeta}{d\phi^2} + \nu^2\zeta = 0$ which is pure simple harmonic motion with frequency (tune) ν. For the amplitude function mismatch, we need to define the reduced phase in terms of the unperturbed functions. That is, let $\phi \equiv \psi_0/\nu_0$, where $d\psi_0/ds = 1/\beta_0$, and ν_0 is the unperturbed tune. The equation of motion for $[\beta(\phi) - \beta_0(\phi)]/\beta_0(\phi) \equiv \Delta\beta/\beta_0$ in the absence of gradient errors is then

$$\frac{d^2}{d\phi^2}\frac{\Delta\beta}{\beta_0} + (2\nu_0)^2\frac{\Delta\beta}{\beta_0} = -2\nu_0^2 \det\Delta J$$
$$= 2\nu_0^2[\Delta\alpha^2 - \Delta\beta\Delta\gamma] \quad (10)$$

where $\Delta\alpha = \alpha(\phi) - \alpha_0(\phi)$, etc. The quantity $\det\Delta J$ is an invariant in portions of the lattice without gradient perturbations as can be seen with the aid of Equation 3.

So, the free amplitude function distortion oscillates with twice the betatron tune and with a constant offset given by the determinant of the ΔJ matrix at any point. This offset must be there since $\beta > 0$ and hence $\Delta\beta/\beta$ must always be greater than -1.

Rewritten in terms of the Courant-Snyder parameters,

$$\det\Delta J = -\frac{\left(\frac{\Delta\beta}{\beta_0}\right)^2 + \left(\Delta\alpha - \alpha_0\frac{\Delta\beta}{\beta_0}\right)^2}{1 + \Delta\beta/\beta_0} < 0. \quad (11)$$

Thus, $|\det\Delta J|^{1/2}$ can be interpreted as the amplitude of the β mismatch for small perturbations.

The solution to Equation 10 is just simple harmonic motion with a constant term added:

$$\frac{\Delta\beta}{\beta_0}(\phi) = A\cos 2\nu_0\phi + B\sin 2\nu_0\phi + \frac{1}{2}|\det\Delta J|. \quad (12)$$

The constants A and B are found from the initial conditions:

$$A = \frac{\Delta\beta}{\beta_0}(0) - \frac{1}{2}|\det\Delta J|, \quad (13)$$

$$B = \alpha_0\frac{\Delta\beta}{\beta_0}(0) - \Delta\alpha(0). \quad (14)$$

Thus, the maximum value of $\Delta\beta/\beta_0$ downstream of our starting point $\phi = 0$ is given by

$$\left(\frac{\Delta\beta}{\beta_0}\right)_{max} = \sqrt{A^2 + B^2} + \frac{1}{2}|\det\Delta J|$$
$$= \frac{|\det\Delta J|}{2} + \sqrt{|\det\Delta J| + \left(\frac{|\det\Delta J|}{2}\right)^2} \quad (15)$$

where use has been made of Equation 11. The maxima occur at phases where

$$\tan 2\nu_0\phi = \left(\frac{\alpha_0\frac{\Delta\beta}{\beta_0} - \Delta\alpha}{\frac{\Delta\beta}{\beta_0} - |\det\Delta J|/2}\right)_0. \quad (16)$$

The usefulness of the above result is, of course, that once one calculates the mismatch of the amplitude function and its slope at one point in the lattice (at the end of a *nearly* matched insertion, for example), then the maximum mismatch downstream can be computed immediately.

If we look once again at the perturbation downstream of a thin quadrupole error, we see that just after the quad,

$$\det\Delta J = \begin{vmatrix} q\beta_i & 0 \\ -\Delta\gamma & -q\beta_i \end{vmatrix} = -(q\beta_i)^2 \quad (17)$$

where $\beta_i = \beta_0$ at the location of the quadrupole. Then,

$$\left(\frac{\Delta\beta}{\beta_0}\right)_{max} = q\beta_i\sqrt{1 + (q\beta_i)^2/4} + \frac{1}{2}(q\beta_i)^2 \quad (18)$$
$$\approx q\beta_i = \sqrt{|\det\Delta J|} \quad (19)$$

where the last line is valid for small perturbations.

IV. GENERAL EQUATION OF MOTION

To include the driving terms due to gradient errors in the equation of motion for $\Delta\beta/\beta_0$, we let β_0 satisfy the differential equation $K\beta_0 = \gamma_0 + \alpha_0'$, and let β satisfy $(K + k)\beta = \gamma + \alpha'$, where $\beta = \beta_0 + \Delta\beta$, etc. Then, the relative β error satisfies

$$\frac{d^2}{d\phi^2}\frac{\Delta\beta}{\beta_0}(\phi) + (2\nu_0)^2 \frac{\Delta\beta}{\beta_0}(\phi)$$

$$= -2\nu_0^2 \left[\beta_0^2(\phi)\,k(\phi)\left(1 + \frac{\Delta\beta}{\beta_0}(\phi)\right) + \det\Delta J(\phi)\right]. \quad (20)$$

Here, in general, $\det\Delta J(\phi)$ is not invariant as it is altered by gradient perturbations:

$$\frac{d}{d\phi}\det\Delta J(\phi) = \beta_0^2 k \frac{d}{d\phi}\frac{\Delta\beta}{\beta_0} \quad (21)$$

For small perturbations we can drop quantities which are second order in the small quantities, e.g. $k\Delta\beta$. This reduces the above equation to

$$\frac{d^2}{d\phi^2}\frac{\Delta\beta}{\beta_0}(\phi) + (2\nu_0)^2\frac{\Delta\beta}{\beta_0}(\phi) = -2\nu_0^2\,\beta_0^2\,k(\phi) \quad (22)$$

as appears in Courant and Snyder.[2]

Noting that $\Delta\alpha - \alpha_0(\Delta\beta/\beta_0) = -(1/2\nu_0)d(\Delta\beta/\beta_0)/d\phi$, one can easily exhibit Equation 20 entirely in terms of $\Delta\beta/\beta_0$ and its derivatives with respect to ϕ. Differentiating this resulting equation one obtains a *linear* differential equation for $\Delta\beta/\beta_0$:

$$\frac{d^3}{d\phi^3}\frac{\Delta\beta}{\beta_0} + (2\nu_0)^2(1 + \beta_0^2 k)\frac{d}{d\phi}\frac{\Delta\beta}{\beta_0}$$

$$+ 2\nu_0^2\frac{d}{d\phi}[\beta_0^2 k](1 + \frac{\Delta\beta}{\beta_0}) = 0. \quad (23)$$

V. INJECTION MISMATCH

It is also of interest to look at the effects of mismatches of amplitude functions upon entrance to an accelerator. The treatment below may be followed in more detail in [3] and [4]. A beam which is described by Courant-Snyder parameters that are not the periodic parameters of the accelerator into which it is injected will tend to filament due to nonlinearities and hence have its emittance increased. Suppose β and α are the Courant-Snyder parameters as delivered by the beamline to a particular point in an accelerator, and β_o, α_o are the periodic lattice functions of the ring at that point. A particle with trajectory (x, x') can be viewed in the $(x, \beta x' + \alpha x) \equiv (x, \eta)$ phase space corresponding to the beamline functions, or in the $(x, \beta_0 x' + \alpha_0 x) \equiv (x, \eta_0)$ phase space corresponding to the lattice functions of the ring. If the phase space motion lies on a circle in the beamline view, then the phase space motion will lie on an ellipse in the ring view. The equation of the ellipse in the "ring" system will be

$$\frac{(1 + \Delta\alpha_r^2)}{\beta_r}x^2 + 2\Delta\alpha_r\,x\eta_0 + \beta_r\eta_0^2 = \beta_0 A^2. \quad (24)$$

where $\beta_r \equiv \beta/\beta_0$ and $\Delta\alpha_r \equiv \alpha - \alpha_0(\beta/\beta_0)$.

If the phase space coordinate system were rotated so that the cross-term in the equation of the ellipse were eliminated, the ellipse would have the form $x_e^2/b_r + b_r\eta_{oe}^2 = \beta_0 A^2$ where $b_r \equiv F + \sqrt{F^2 - 1}$ and F is given by

$$F \equiv \frac{1}{2}\left[\beta_0\gamma + \gamma_0\beta - 2\alpha_0\alpha\right]. \quad (25)$$

Note that if $\Delta\alpha_r = 0$, then $b_r = \beta_r$

There is a physical significance to the quantity b_r; it is the ratio of the areas of two circumscribed ellipses which have shapes and orientations given by the two sets of Courant-Snyder parameters found in the matrices J and J_0. This might suggest that a beam contained within the smaller ellipse upon injection into the synchrotron (whose periodic functions give ellipses similar to the larger one) will have its emittance increased by a factor b_r. However, this would be an over-estimate of the increase of the average of the emittances of all the particles.

If in the beamline view the new phase space trajectory is $x^2 + \eta^2 = b_r R^2$, then in the synchrotron view, the equation of the ellipse would be $\frac{x^2}{b_r R^2} + \frac{\eta_0^2}{R^2/b_r} = 1$. A particle with initial phase space coordinates x_i and η_{oi} will commence describing a circular trajectory of radius a in phase space upon subsequent revolutions about the ring. The equilibrium distribution will have variance in the x coordinate

$$\sigma^2 = \langle x^2 \rangle = \frac{\langle a^2 \rangle}{2} = \frac{b_r^2 + 1}{2b_r}\sigma_0^2 = F\,\sigma_0^2, \quad (26)$$

where σ_0^2 is the variance in the absence of a mismatch. This expression can be rewritten in terms of $\det\Delta J$ which we found in Section III.:

$$\frac{\sigma^2}{\sigma_0^2} = 1 + \frac{1}{2}\left|\det(\Delta J)\right|. \quad (27)$$

For the case where the slope of the amplitude function is matched and equal to zero, we have

$$\frac{\sigma^2}{\sigma_0^2} = 1 + \frac{1}{2}\left(\frac{\Delta\beta/\beta_0}{\sqrt{1 + \Delta\beta/\beta_0}}\right)^2. \quad (28)$$

This says that a 20% β mismatch at injection, for example, would cause only a 2% increase in the rms emittance.

VI. REFERENCES

[1] T. Sen, M. J. Syphers, "Notes on Amplitude Function Mismatch," SSC Report SSCL-604, October 1992.

[2] E.D. Courant and H.S. Snyder, "Theory of the Alternating-Gradient Synchrotron," Annals of Physics, vol. 3, No. 1, p.26 (1958).

[3] M. J. Syphers, "Injection Mismatch and Phase Space Dilution," Fermilab FN-458, June 1987.

[4] D. A. Edwards and M. J. Syphers, *An Introduction to the Physics of High Energy Accelerators*, John Wiley, and Sons, New York, 1993.

SSC Collider Arc Lattice

M.J. Syphers, E. D. Courant, A. A. Garren, S. K. Kauffmann, T. Sen
Superconducting Super Collider Laboratory*
2550 Beckleymeade Ave., Dallas, TX 75237

Abstract

The new configuration for the SSC collider-ring arcs will be discussed. This design provides magnet-free spaces for future needs by omitting a fraction of the dipoles in the regular cell lattice. Previously, no space was available in either of the two 35 km long arcs for equipment that might be desirable at some future time. The placement of the new straight sections was based on usefulness for future upgrades such as beam scraping, beam polarization, transverse dampers, and correction magnet schemes, as well as on location of service shafts and on perturbations of the ring geometry.

I. DESCRIPTION OF A COLLIDER ARC

The main 20 TeV Collider ring for the SSC Laboratory is composed of a North Arc and a South Arc joined by East and West Cluster Regions. The Cluster Regions each contain a Utility Straight Section (UT) and two Interaction Straight Sections (IR); for the most part, these areas are made up of quadrupoles and are generally free of bending. Each arc contains 392 half cells; in its 1990 configuration[1], each half cell consisted of a quadrupole magnet, a spool piece, and five dipole magnets. Of these, 32 half cells contained 4 standard-length dipole magnets (15.165 m magnetic length) plus one short dipole magnet (12.6375 m magnetic length), while the remaining half cells contained 5 standard length dipole magnets. The space provided by the shorter dipoles is used for cryogenic section isolation, cryogen and power feed, and turn-around locations. This scheme thus results in an extra 2.5 m of straight section at six-cell intervals. In the lower ring, these extra straight sections were located next to horizontally focusing quadrupoles and therefore were next to defocusing quadrupoles in the upper ring. Throughout the entire 35 km of each arc, there was no free space to put in any future equipment, should that ever be desirable, nor was there any place where the beam pipe could be directly accessed.

II. POSSIBLE USES FOR SPACE IN THE ARCS

As the design of the Collider matured and implications of the baseline design were studied, it became apparent that free space in the arcs of the Collider was desirable. This was viewed as a relatively small perturbation in the overall design of the accelerator; the philosophy of the modular lattice design would be retained – arc modules, IR modules, UT modules, with dispersion-matched bending regions in between. It was felt that free space in the 35 km arcs would greatly enhance the potential uses of the Collider as well as be contingency for meeting design requirements by providing space for equipment which could be added at a later time.

Examples for possible uses of free space in the arcs include room for beam scrapers to handle beam halo and emittance control. The present design calls for a few such devices located in the Utility Straight Sections, but one might envision the need to have a more global system, especially if the beam current were increased in the future. Room for these devices in the arc might also be desirable for scraping particles at regions of non-zero dispersion (the present design has zero dispersion nearly everywhere outside of the arcs). Other possible future uses for space in the arcs might include beam damping systems for handling beam instabilities, beam emittance cooling systems for maintaining or reducing the emittance of stored beams, and other special beam diagnostic equipment. Another feature which the overall SSC design has tried to maintain is the ability of the Collider to support polarized beams. Each of the booster accelerators as well as their interconnecting beamlines provide sufficient free space for insertion of devices which would permit them to transport and accelerate polarized beams. Once in the Collider, however, "Siberian snakes" must be provided in the arcs to maintain polarization. It has been estimated that a number of such devices, each roughly 10 meters long, are necessary in each arc[2]. Though it is hoped that none of the devices mentioned above will be required to meet the baseline design, it is hard to tell what devices might be needed in the event that certain baseline parameters are not met, or if one wishes to maintain upgrade potential.

It should be noted that the Fermilab Tevatron (and Main Ring) has 12 m of "free space" in each of its six arc sectors; each of these straight sections now contains equipment vital to the operation of the accelerators.

137
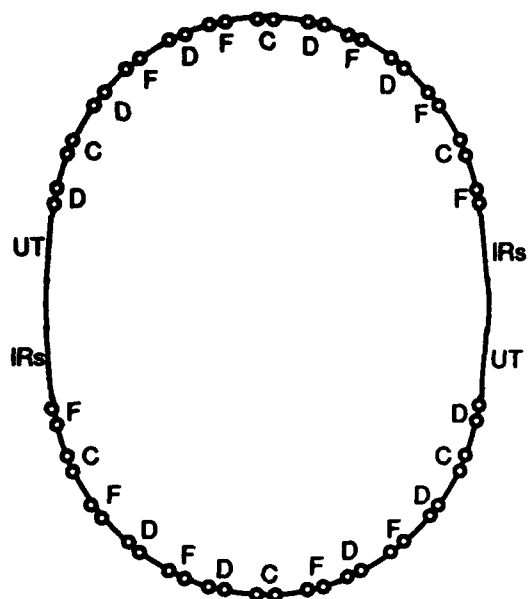
Figure 1. Sketch showing the approximate layout of the 15 m free spaces in the arcs of the Collider; the polarities shown are of the nearest quad in the upper ring.

Figure 2. (a) 1990 design of bending region between two IRs within a cluster. (b) New design of this region, generating a high dispersion point in the middle half cell. The number of 13 m (s) and 15 m (L) dipole magnets in each half cell are indicated.

III. DEVELOPMENT AND DESCRIPTION OF THE NEW DESIGN

For straight sections to be introduced into the Collider arcs, care had to be taken to place them at locations favorable for a variety of possible future applications. In addition, attempts were made to allow for placing utility shafts on the properties being offered by the state of Texas, a feature that the 1990 lattice could not accommodate without extra tunneling costs.

Over 30 different lattices were examined between February 1991 and August 1991. The new adopted design, referred to internally as SSC10F, is one in which dipoles are removed from the lattice in a pattern such that a pair of "holes" have 180° phase difference for dispersion matching, with some of these pairs displaced 90° in phase from other such pairs. The pairs come in three types: ones next to focusing quadrupoles("F"), ones next to defocusing quadrupoles("D"), and ones at mid-half cell locations("C"). The distribution of pairs is nearly uniform, so that the bend center of an arc sector was left nearly unchanged, thus keeping the geometrical layout of the Collider close to that of the original design. A sketch showing the approximate layout of the 15 m free spaces is found in Figure 1.

The introduction of pairs of "missing bends," 180° apart in betatron phase, generates local perturbations of the dispersion function. The maximum perturbation is roughly 0.45 m when the pairs are next to focusing quadrupoles, and only 0.07 m when next to defocusing quadrupoles.

In the new design, the total number of 2.5 m spaces and 15 m spaces is greater than the total number of 2.5 m

spaces found in the 1990 design. The extra spaces are put in for two reasons. Firstly, they ensure that the largest distance between cryo-isolation points is six cells, the standard distance found in the baseline design. Secondly, the larger number of isolation points allows the design to conform more easily to the land acquisition strategy of the laboratory and the state of Texas; the positioning of the smaller and larger free spaces permitted choices of where to construct shafts to bring utilities into the Collider. In this way, the lattice contains either a 15 m space or a 2.5 m space, necessary for feed or turn-around spool pieces, within the boundaries of each service area site offered by the state of Texas.

Changes to the horizontal bending were also made in the cluster region. The configuration of bending magnets between the Interaction Regions (IRs) and Utility Region (UT) has been slightly altered from the 1990 design in order to reduce the maximum geometric excursions from the original footprint. The new configuration keeps the ratio of bending in the arc to bending in the cluster roughly the same as in the baseline design.

In addition, the bending region between the two IRs within a cluster has also been reconfigured. Originally, this region contained mostly short dipoles with bending in every one of the seven half cells. The new design calls for mostly long dipoles, with the middle half cell free of bending. This provides a straight section where the dispersion function will be larger than that found in the arcs (2.85 m as opposed to 1.85 m). This region can be useful for diagnostics, and may be suited for scraping off-energy beam particles. The total integrated length of bending in this region is the same as in the 1990 design, and the change to the quadrupole count is minimal. A comparison of this region redesigned region with the 1990 design is shown in Figure 2.

Table 1 shows some of the relevant parameter changes introduced by the new design, which was officially adopted

Table 1. Changes of Relevant Parameters for One Ring

	Baseline	New Lattice
15m free spaces (arc)	0	26
2.5m free spaces (arc)	34	26
15m spaces (cluster)	0	2
2.5m spaces (cluster)	2	0
Long Dipoles (15m)	3978	3972
Short Dipoles (13m)	252	196
Stand. Quads	832	848
Disp. Suppr. Quads	60	40
Bend Field Increase	0	1.27%
Max. Dispersion in arc		
Top ring	1.87 m	2.26 m
Bottom ring	1.81 m	2.26 m
Max. Dispersion in ring		
Top ring	1.87 m	2.85 m
Bottom ring	1.81 m	2.85 m

in March, 1992. The required bend field is raised by 1.27%, assuming the same magnetic length for the dipole magnets.

IV. DESIGN IMPLICATIONS

The new lattice slightly alters the bend center of each half sector, thereby changing the geometry of the Collider rings. One of the constraints in the exercise was that the west utility straight section, where the High Energy Booster connects to the Collider accelerators, be held fixed to its location and orientation as of April 29, 1991. The original "footprint," used for land acquisition, was based on the 1989 lattice and featured a 1000 ft band with the ring center line located 250 ft from the inside of the band, and 750 ft from the outside of the band. The ring design could move radially by as much as ±65 ft and still satisfy shielding requirements. The new design satisfies this criterion. Muon vectors associated with a point loss around the ring, scraping in the utility straight sections as well as in the new straight sections near the ends of the arcs, IP interactions, and beam backstops, all fell within existing site boundary definitions.

The free space generated by the removal of a dipole in the arc could be filled by either an empty magnet cryostat or a warm beam pipe with a cryogenic bypass section. While it is assumed that a cryogenic bypass element could be designed to fit within the existing tunnel tolerances, the plan is to use empty cryostats in the new 15 m spaces. Warm bypasses would only be developed if and when future uses of the 15 m spaces dictate such action.

With the new arrangement of short dipoles and long free spaces, the cryogenic loops encountered within an arc are of the same order in length as those found in the original arc design.

The power supply system is the one most affected by the relocation of shafts. In the new design, some power loops between shafts are longer and others shorter than in the original 1990 design[1]. The furthest departure from the baseline occurs in the South Arc, where one shaft is 3 cells from its original location. The resulting inductive imbalance in the two legs of the power circuit raised the maximum voltage-to-ground difference to an uncomfortable level (larger than 1 kV). However, a decision was independently made to increase the number of energy dump switches in the power circuit by a factor of two, decreasing the maximum voltage-to-ground by the same factor. This makes the voltage level tolerable, even with the new lattice.

V. CONCLUDING REMARKS

The lattice design presented here was developed in 1991 in order to settle definitively the geometry of the Collider rings so as to permit land acquisition and the beginning of civil construction of the Collider tunnel. With the exception of a minor modification in the cluster regions, quadrupole magnet locations did not change with respect to the 1990 lattice; only the numbers and placement of dipole magnets were adjusted.

Already a use has been found for part of the new free space generated in the arcs[3]. By placing skew quadrupole correctors in these locations, stronger correctors could be used, and the need for skew quadrupoles in the middle of half cells, supported on the ends of a 15 m dipole magnet, has been obviated.

It should be pointed out that designs of the cluster regions continue to be studied[4, 5]. Possible future modifications to these regions affect only the numbers and positioning of quadrupoles, and perhaps vertical bending magnets, in or near the interaction regions. The horizontal geometry of the Collider arcs would not be affected.

VI. ACKNOWLEDGMENTS

The authors would like to thank the many members of the SSCL staff who contributed to the development of this design, with special thanks to Don Edwards, Helen Edwards, and Paul Reardon.

VII. REFERENCES

[1] *Site-Specific Conceptual Design Report of the Super-conducting Super Collider*, SSCL, ed. J. R. Sanford, SSCL-SR-1056, July, 1990.

[2] E. Courant, internal SSCL memo dated January 17, 1991.

[3] Y. Cai, et al., "Decoupling Correction for the SSC Collider," these proceedings.

[4] Y. Nosochkov, et al., "Current design of the Interaction Regions at the SSC," these proceedings.

[5] B. Parker, "Design Status Report on the Collider Utility Straight Insertions," these proceedings.

Second Order Chromaticity of the Interaction Regions in the Collider

T. Sen and M.J. Syphers
Superconducting Super Collider Laboratory *
Dallas, TX 75237

Abstract

The collider in the SSC has large second order chromaticity (ξ_2) with the interaction regions (IRs) contributing substantially to it. We calculate the general expression for ξ_2 in a storage ring and find that it is driven by the first order chromatic beta wave. Specializing to the interaction regions, we show that ξ_2 is a minimum when the phase advance ($\Delta\mu_{IP-IP}$) between adjacent interaction points is an odd multiple of $\pi/2$ and both IRs are identical. In this case the first order chromatic beta wave is confined within the IRs. Conversely, ξ_2 is large either if $\Delta\mu_{IP-IP} = (2n+1)\pi/2$ and the two IRs are very far from equality or if the two IRs are equal but $\Delta\mu_{IP-IP} = n\pi$.

I. TUNE SHIFT AND CHROMATICITY TO 2ND ORDER

Consider a storage ring and label two points on it as 1 and 2. Let μ_0 be the global phase advance around the ring and (β_1, α_1, γ_1) the Twiss functions at point 1. The periodic transfer matrix at point 1 can be written as

$$M_1 = M(2 \to 1) \cdot M(1 \to 2) \qquad (1)$$

where $M(2 \to 1)$ is the transfer matrix from point 2 to 1 etc. Let μ_1 and μ_2 be the phase advances at points 1 and 2 respectively with respect to an arbitrary reference point and $\mu_{21} = |\mu_2 - \mu_1|$. We now introduce two infinitesimally thin quads of strengths $q_1 = k_1\Delta s_1$ and $q_2 = k_2\Delta s_2$ at points 1 and 2 respectively. Their perturbations to the transfer matrix are described by the matrices P_1 and P_2 where P_i is

$$P_i = \begin{bmatrix} 1 & 0 \\ -k_i\Delta s_i & 1 \end{bmatrix} \qquad (2)$$

These quad errors change the cyclic transfer matrix at point 1 to $\bar{M}_1$

$$\bar{M}_1 = M(2 \to 1) \cdot P_2 \cdot M(1 \to 2) \cdot P_1 \equiv M_1 + \Delta M_1 \quad (3)$$

Let $\Delta\mu$ be the change in the global phase advance around the ring. We scale the quad errors by an arbitrary parameter ϵ i.e. $k_1 \to \epsilon k_1$, $k_2 \to \epsilon k_2$ and expand $\Delta\mu$ as a power series in ϵ,

$$\Delta\mu = \epsilon\Delta\mu_1 + \epsilon^2\Delta\mu_2 + \ldots \qquad (4)$$

The new global phase advance $\bar{\mu}_0 = \mu_0 + \Delta\mu$ is to be found from

$$\cos\bar{\mu}_0 = \frac{1}{2}\mathrm{Tr}\,\bar{M}_1 = \cos\mu_0 + \frac{1}{2}\mathrm{Tr}\,\Delta M_1 \quad . \qquad (5)$$

We also have

$$\cos\bar{\mu}_0 = \cos\mu_0\cos\Delta\mu - \sin\mu_0\sin\Delta\mu \quad .$$

Substituting Equation (4) into the above and equating it to the expression for $\cos\bar{\mu}_0$ given by Equation (5), we have

$$\frac{1}{2}\mathrm{Tr}\Delta M_1 = -\epsilon\sin\mu_0\Delta\mu_1 - \epsilon^2[\sin\mu_0\Delta\mu_2 + \frac{\cos\mu_0(\Delta\mu_1)^2}{2}]$$
$$+O(\epsilon^3). \qquad (6)$$

To obtain the corrections to μ_0 order by order, we equate the coefficients of like powers of ϵ on both sides of the above equation. We can generalise to N quad errors in the ring and then take the limit of infinitesimally thin quads distributed around the ring of circumference C. In this limit, the 1st and 2nd order terms are,

$$\Delta\mu_1 = \frac{1}{2}\int_0^C k(s)\beta_0(s)ds$$

$$\Delta\mu_2 = \frac{1}{4\sin\mu_0}\int_0^C k(s)\beta_0(s)ds\int_s^C k(s')\beta_0(s')$$
$$\times\,[\cos\mu_0 - \cos(\mu_0 - 2|\mu(s') - \mu(s)|)]\;ds'$$
$$-\frac{1}{2}\cot\mu_0(\Delta\mu_1)^2 \qquad (7)$$

Here we have let $\beta_0(s)$ denote the unperturbed β function at the point s. In the equation for $\Delta\mu_2$, we convert the integral over part of the ring to one over the complete ring and obtain

$$\Delta\mu_2 = -\frac{1}{8\sin\mu_0}\int_0^C k(s)\beta_0(s)ds\int_s^{s+C} k(s')\beta_0(s')$$
$$\times\,\cos[\mu_0 - 2|\mu(s') - \mu(s)|]\;ds' \qquad (8)$$

Recognizing that the integral over s' is related to the expression for the 1st order change in the β function [1], we obtain

$$\Delta\mu_2 = \frac{1}{4}\int_0^C k(s)\Delta\beta_1(s)ds \quad . \qquad (9)$$

This important relation tells us that the first order distortion in the β function propagating around the machine gives rise to the second order tune shift. The total phase

shift to second order in the gradient errors is (after putting the arbitrary parameter ϵ to unity),

$$\Delta\mu = \frac{1}{2}\int_0^C k(s)\beta_0(s)ds + \frac{1}{4}\int_0^C k(s)\Delta\beta_1(s)ds + O(k^3) \ .$$ (10)

The gradient perturbations of interest here are those seen only by particles off the design momentum. The chomatic error introduced by the quads is then corrected by placing sextupoles at places of non-zero dispersion. Assuming that only the horizontal dispersion D_x is non-zero, the effective quadrupole strengths in the horizontal and vertical planes for a particle with relative momentum deviation $\delta = \Delta p/p_0$ are respectively,

$$\begin{aligned}
K_x^{eff} &= K_x(s,\delta) + S(s,\delta)D_x(s,\delta)\delta \\
K_y^{eff} &= K_y(s,\delta) - S(s,\delta)D_x(s,\delta)\delta
\end{aligned}$$ (11)

As functions of δ, $K(s,\delta) = K_0(s)/(1+\delta)$ and $S(s,\delta) = S_0(s)/(1+\delta)$, where K_0 and S_0 are the nominal quad and sextupole strengths experienced by a particle on momentum. We expand D and β as power series in δ,

$$\begin{aligned}
D(s,\delta) &= D_0(s) + \Delta D_1^C(s)\delta + \Delta D_2^C(s)\delta^2 + \ldots \quad (12)\\
\beta(s,\delta) &= \beta_0(s) + \Delta\beta_1^C(s)\delta + \Delta\beta_2^C(s)\delta^2 + \ldots \quad (13)
\end{aligned}$$

where the superscript C denotes a chromatic expansion. Hence the gradient error in the horizontal plane for the off-momentum particles is

$$k(s) = [S_0 D_0 - K_0]\delta + [K_0 + S_0(\Delta D_1^C - D_0)]\delta^2 + O(\delta^3) \quad (14)$$

Substituting into Equation 10 and writing the tune shift in terms of the first and second order chromaticity ξ_1 and ξ_2 respectively,

$$\Delta\nu \equiv \frac{1}{2\pi}\Delta\mu = \xi_1\delta + \xi_2\delta^2 + O(\delta^3) \quad (15)$$

we obtain

$$\begin{aligned}
\xi_1 &= \frac{1}{4\pi}\int_0^C \beta_0(s)[S_0(s)D_0(s) - K_0]\,ds \\
\xi_2 &= \frac{1}{8\pi}\int_0^C [S_0(s)D_0(s) - K_0]\Delta\beta_1^C(s)\,ds \\
&\quad + \frac{1}{4\pi}\int_0^C \beta_0(s)S_0(s)\Delta D_1^C(s)\,ds - \xi_1 \quad (16)
\end{aligned}$$

The first order changes in β and D are given by

$$\begin{aligned}
\frac{\Delta\beta_1^C(s)}{\beta_0(s)} &= \frac{-1}{2\sin\mu_0}\int_s^{s+C}[S_0(s')D_0(s') - K_0(s')]\beta_0(s') \\
&\quad \times \cos[\mu_0 - 2|\mu(s') - \mu(s)|]\,ds' \\
\Delta D_1^C(s) &= -\sqrt{\beta_0(s)}\int_s^{s+C}\frac{\sqrt{\beta_0(s')}}{\sin(\mu_0/2)}[S_0(s')D_0(s') - K_0(s')] \\
&\quad \times D_0(s')\cos[\frac{\mu_0}{2} - |\mu(s') - \mu(s)|]\,ds' \quad (17)
\end{aligned}$$

Ignoring the phase factors for the moment, we see that $\Delta\beta_1^C$ which contains factors of $\beta(s)$ rather than $\sqrt{\beta(s)}$ (as occurs in ΔD_1^C) will dominate the contribution to the second order chromaticity. This situtation can change if we choose the phase advances between the major chromatic error sources appropriately. For example, two sources of equal strength $\pi/2$ apart in phase will produce β waves exactly out of phase so there will be no resultant β wave. The dispersion waves produced by the same two sources will add in quadrature. Alternatively, if we want to cancel the net dispersion wave, the two sources should be π apart in phase. In this case the β waves will add exactly in phase.

Hence to reduce the second order chromaticity, the first order changes in β and also in the dispersion D should be minimized. Conversely, the regions where $\Delta\beta_1$ is large (e.g. the triplets in the IRs) will contribute the most to the second order chromaticity. The above expression also exhibits the variation of ξ_2 with the global tune. Since the first order β wave diverges at integer and half-integer tunes, ξ_2 will be amplified as ν_0 approaches 0 or 0.5 and will be a minimum at $\nu_0 = 0.25$.

II. CHROMATICITY DUE TO IR TRIPLETS

The total chromaticity of an IR includes contributions from the triplets, the quads in the $M = -I$ section and the variable strength quads in the tuning section [2]. The triplets alone contribute 76% of this chromaticity at collision. Consequently we will consider the tune shift due to the chromatic error of the 4 IR triplets only and ignore the effect of other quadrupoles and sextupoles. Let

$$Q_i\beta_i \equiv \int_{ith\ triplet} K\beta\,ds \ .$$

Then to 2nd order in the momentum deviation δ, the phase shift due to these 4 triplets is

$$\Delta\mu = \Delta\mu_1\delta + \Delta\mu_2\delta^2 + O(\delta^3) \quad (18)$$

where $\Delta\mu_1 = -1/2\sum_{i=1}^4 Q_i\beta_i$ and

$$\begin{aligned}
\Delta\mu_2 &= \sum_{i=1}^3\sum_{j=i+1}^4 \frac{Q_i\beta_i Q_j\beta_j}{4\sin\mu_0}[\cos\mu_0 - \cos(2\mu_{ji} - \mu_0)] \\
&\quad -\Delta\mu_1 - \frac{1}{2}\cot\mu_0(\Delta\mu_1)^2 \quad (19)
\end{aligned}$$

μ_{ji} is the phase advance from the ith triplet to the jth triplet and $\nu_0 = \mu_0/2\pi$ is the global tune of the ring. The first order chromaticity is independent of phase advances between the triplets. However the second order chromaticity depends crucially on the relative phase advances between the triplets. If the phase advance between the IPs is $\Delta\mu_{IP-IP}$, then the relative phase advances have the following values,

$$\begin{aligned}
\mu_{21} &= \pi, \quad \mu_{31} = \Delta\mu_{IP-IP}, \quad \mu_{41} = \Delta\mu_{IP-IP} + \pi \\
\mu_{32} &= \Delta\mu_{IP-IP} - \pi, \quad \mu_{42} = \Delta\mu_{IP-IP}, \quad \mu_{43} = \pi \quad (20)
\end{aligned}$$

With these values, the second order contribution reduces to

$$\Delta\mu_2 = \Delta\mu_{2Q} + \frac{1}{2}(Q_1\beta_1 + Q_2\beta_2 + Q_3\beta_3 + Q_4\beta_4) \quad (21)$$

where $\Delta\mu_{2Q}$ is the contribution from terms second order in the quad strengths,

$$4\tan\mu_0\Delta\mu_{2Q} = (Q_1\beta_1 + Q_2\beta_2)(Q_3\beta_3 + Q_4\beta_4)$$
$$\times\left\{1 - \frac{\cos(2\Delta\mu_{IP-IP} - \mu_0)}{\cos\mu_0}\right\}$$
$$-\frac{1}{2}(Q_1\beta_1 + Q_2\beta_2 + Q_3\beta_3 + Q_4\beta_4)^2 \quad (22)$$

For arbitrary μ_0, the term in curly braces is a maximum and hence $\Delta\mu_{2Q}$ is a minimum if $2\Delta\mu_{IP-IP} = (2n+1)\pi$. Conversely $\Delta\mu_{2Q}$ is a maximum if $2\Delta\mu_{IP-IP} = 2n\pi$. The large β functions in the triplets ensures that $\Delta\mu_{2Q}$ completely dominates the contribution to $\Delta\mu_2$. Hence choosing $\Delta\mu_{IP-IP} = (2n+1)\pi/2$ minimizes the 2nd order chromaticity of the IRs. This is due to the fact that the chromatic β waves from the IRs are exactly out of phase and interfere destructively. The following discussion will assume this choice of $\Delta\mu_{IP-IP}$.

An exact cancellation of the β waves occurs if the two IRs have the same β_{peak}. In this configuration, the repetitive symmetry across the two IRs implies $Q_3\beta_3 = Q_1\beta_1$, $Q_4\beta_4 = Q_2\beta_2$. $\Delta\mu_{2Q}$ vanishes as a consequence of the fact that the β wave is zero outside the triplets. The entire 2nd order phase shift is

$$\Delta\mu_2 = (Q_1\beta_1 + Q_2\beta_2) \quad . \quad (23)$$

For this case alone, $\Delta\mu_2$ is independent of the global tune ν_0.

In the following table, we evaluate the 2nd order chromaticity due to the triplets in three different configurations and at two tunes.

Table 1 : 2nd order chromaticity due to the triplets

Case	ξ_2	
	$\nu_0 = 0.285$	$\nu_0 = 0.4$
I) Equal IPs		
β^*=0.25m	154.0	154.0
β^*=0.50m	77.0	77.0
II) Unequal IPs		
β^*=0.25m, β^*=0.50m	1156.4	6524.8
III) One IP		
β^*=0.25m, β^*=8.00m	3977.5	24132.6

For all cases except the first, the second order chromaticity is a minimum at $\nu_0 = 0.25$ and will be significantly amplified as $\nu_0 \rightarrow 0.5$.

The chromaticity correction scheme proposed for the IRs is discussed in [3]. Briefly, sextupoles are placed in 24 arc cells adjacent to the cluster containing the two IRs. The third case in Table 1 at tunes (123.435,122.416) has large ξ_2 and requires nonlinear correction. For this configuration, Figure 1 shows the chromatic β wave (at δ=0.0003) through the cluster and adjacent cells without the nonlinear correction. Figure 2 is the corresponding figure after the nonlinear chromaticity is corrected. The β beat in the
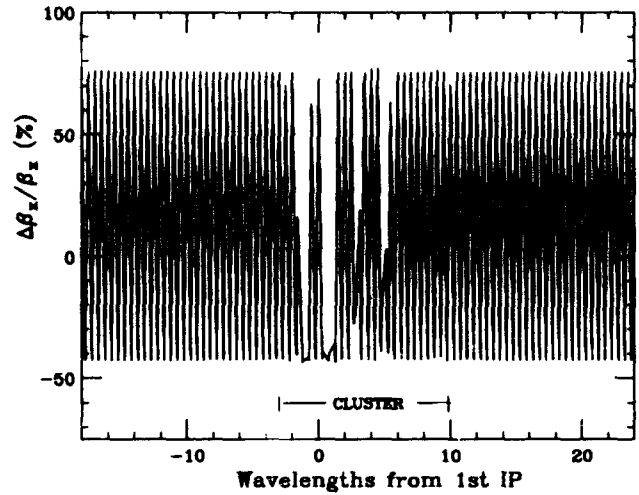
Figure 1. Horizontal Chromatic β beat without nonlinear chromaticity correction
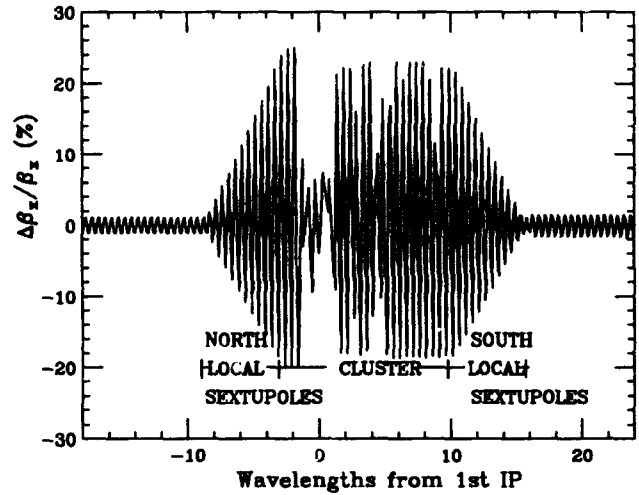
Figure 2. Horizontal Chromatic β beat with nonlinear chromaticity correction

arcs is reduced from 75% in Figure 1 to 2% in Figure 2. This clearly illustrates the connection between the chromatic β wave and the nonlinear chromaticity.

III. REFERENCES

[1] E.D. Courant and H.S.Snyder, *Annals of Physics*,3, 1 (1958).

[2] Y. Nosochkov et.al., "Current Design of the SSC Interaction Regions", these proceedings.

[3] T. Sen et.al., "Chromaticity Correction for the SSC Collider Rings", these proceedings.

Chromaticity Correction For The SSC Collider Rings

T. Sen, Y. Nosochkov, F. Pilat, and R. Stiening
Superconducting Super Collider Laboratory *
Dallas, TX 75237
D.M. Ritson
SLAC, Stanford University, Stanford, CA 94309

Abstract

We address the issue of correcting higher order chromaticities of the collider with one or more low β insertions. The chromaticity contributed by the interaction regions (IRs) depends crucially on the maximum value of β in the two IRs in a cluster, the phase advance between adjacent interaction points (IPs), and the choice of global tune. We propose a correction scheme in which the linear chromaticity is corrected by a global distribution of sextupoles and the second order chromaticity of each IR is corrected by a more local set of sextupoles. Compared to the case where only the linear chromaticity is corrected, this configuration increases the momentum aperture more than three times and also reduces the β beat by this factor. With this scheme, the tune can be chosen to satisfy other constraints and the two IRs in a cluster can be operated independently at different luminosities without affecting the chromatic properties of the ring.

I. INTRODUCTION

The racetrack shaped collider lattice consists basically of 2 arcs located on the North and South sides and 2 clusters placed on the West and on the East. Each arc contains 196 identical FODO cells with the phase advance across a cell being 90 degrees and the length of each cell is 180 m. The lattice of each cluster includes 2 IRs, the utility section and the interconnect sections between them. The arcs occupy about 81% of the lattice and therefore contribute significantly to the chromaticity of the machine. They dominate the collider chromaticity at injection. However, in the collision mode, the IRs have a larger chromaticity than the arcs because of the very high values of the β functions in the final focussing quadrupoles.

The linear chromaticity contributed by major sources is shown in Table 1. L^* denotes the free space reserved on either side of each IP for the detectors. (ξ_x, ξ_y) denote the horizontal and vertical chromaticities respectively. The total chromaticity of an IR includes contributions from the triplets, the quadrupoles in the M= -I section and the variable strength quadrupoles in the tuning section. At collision, the triplets contribute about 76%, the M= -I section about 19% and the the tuning section accounts for the rest. A description of the different modules in each IR can be seen elsewhere in these proceedings [1].

Table 1: Major sources of chromaticity in the collider lattice

SOURCE	ξ_x	ξ_y
Two arcs	-124	-123
1 low β IR, L^*=20.5m, β^*=0.50m	-51	-51
1 medium β IR, L^*=90m, β^*=1.95m	-45	-45
Max. sextupole component in dipoles ($b_2 = 0.8 \times 10^{-4} m^{-2}$)	160	-136
Complete collider lattice: 2 low β IRs (β^*=0.50m) 2 medium β IRs (β^*=1.95m) $b_2 = 0.8 \times 10^{-4}$ m^{-2} in dipoles	-171	-469

II. 2nd ORDER CHROMATICITY

The tune shift $\Delta\nu$ due to chromatic errors can be expanded in powers of the relative momentum deviation $\delta = \Delta p/p_0$ as

$$\Delta\nu = \xi_1\delta + \xi_2\delta^2 + \ldots$$

The 2nd order chromaticity ξ_2 is given by [2]

$$\xi_2 = \frac{-1}{8\pi} \int_0^C K_0 \Delta\beta_1 \, ds - \xi_1$$

K_0 denotes the nominal gradients and $\Delta\beta_1$ is the 1st order chromatic β wave,

$$\Delta\beta_1(s) = \frac{\beta_0(s)}{2\sin 2\pi\nu_0} \int_s^{s+C} K_0(s')\beta_0(s') \times \cos\left[2\pi\nu_0 - 2|\psi_0(s') - \psi_0(s)|\right] ds'$$

From the above expression we deduce that the β wave depends on the global tune ν_0, and on the phase advance between sources of the chromatic gradient errors and that it propagates at twice the betatron frequency. This in turn implies the following : i) ξ_2 is large as the fractional part of the tune $[\nu_0]$ approaches 0.0 or 0.5 and it is a minimum when $[\nu_0]$=0.25. ii) the largest source of ξ_2 are the triplets. ξ_2 is smallest when the phase advance between IPs in a cluster, $\Delta\Psi_{IP-IP}$, equals $(2n + 1)\pi/2$ and a maximum when $\Delta\Psi_{IP-IP} = n\pi$.

The IRs have been designed so that the phase advance between adjacent IPs is an odd multiple of $\pi/2$. With this configuration, there is an exact cancellation of β waves from the two IRs in a cluster when the β peaks in both IRs are equal. Larger the difference in the β peaks between the two IRs, greater is ξ_2 of the cluster. The most need for higher order chromaticity correction thus arises when only one IR is at collision optics and $[\nu_0]$ close to 0.5.
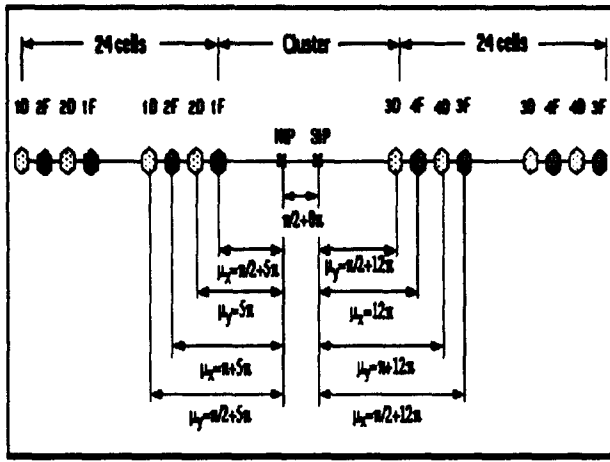
Figure 1. Local Sextupole Distribution

Figure 2. 2Ψ Phasor Diagram for the horizontal chromatic β wave

III. CHROMATICITY CORRECTION SCHEME

The collider has two low-β IRs in the East cluster and two medium-β IRs in the West. Our proposed scheme requires placing sextupoles in 24 cells in each arc adjacent to the cluster, for correcting the higher order chromaticity of the East cluster, and, if necessary, the same for the West cluster. In the remaining cells, two families of sextupoles are placed to correct the linear chromaticity of the collider. The linear correction scheme is called "global" and the higher order scheme "local", since the local scheme corrects for only the IRs. The distribution of local sextupoles spanning 6 wavelengths is shown in Figure 1. The North and South IPs are labelled NIP and SIP respectively.

The families (1F,1D) are $\pi/2$ (mod 2π) in (horizontal, vertical) phase from NIP and hence correct primarily for the (horizontal,vertical) chromaticity of the North IR. The families (3F,3D) do the same for the South IR. The local scheme must contribute zero linear chromaticity for it not to disturb the compensation done by the global scheme. The families (2F,2D) therefore have opposite polarities to the families (1F,1D) respectively and (4F,4D) are opposite to (3F,3D). When members of a family are exactly π apart in phase, the β waves produced by them are in phase and second order geometrical aberrations are removed [3]. However, here with this choice the β waves in both planes are not exactly cancelled. There is a residual β wave in the horizontal plane of relative amplitude β_{min}/β_{max} from the D sextupoles and similarly in the vertical plane from the F sextupoles. An exact cancellation is obtained by introducing a phase slip Δ between the local sextupoles. Trim quads placed in these 24 cells provide the following phase advances per cell :

NORTH ARC : $\mu_x = \pi/2 - \Delta$, $\mu_y = \pi/2 + \Delta$

SOUTH ARC : $\mu_x = \pi/2 + \Delta$, $\mu_y = \pi/2 - \Delta$

where $\Delta = (2/(2N+1))\tan^{-1}(\beta_{min}/\beta_{max})$. With $N = 24$, we get a phase slip of $0.40°$ per cell.
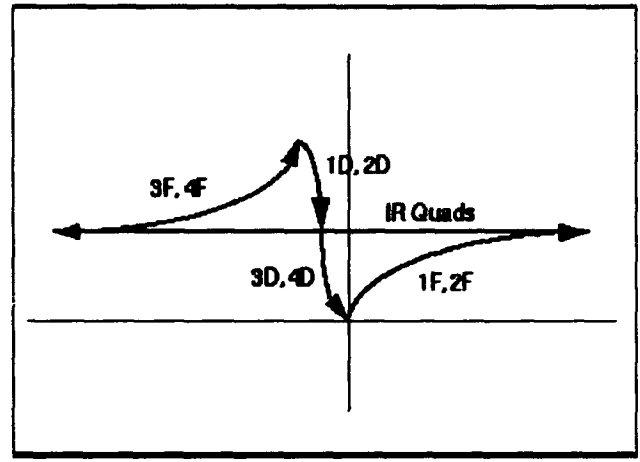
The local correction scheme can be understood by representing the beta waves from each source in a 2Ψ phasor diagram. The angle between any two vectors in this diagram is twice the phase advance between the corresponding sources. Figure 2 shows that with the phase slip, the horizontal chromatic β wave from all sources in the IR is cancelled. A similar diagram can be drawn for the vertical β wave by interchanging the F and D labels.

In what follows, we consider only the configuration of the East cluster with the largest ξ_2 i.e. one IR at $\beta^* = 0.25$m, the other at $\beta^* = 8.0$m and the tunes to be (123.435,122.415). An advantage of correcting this configuration is that we do not need to rely on the chromatic cancellation of one IR by another. This is important in practice since the detectors at the two IPs might well be operating at different luminosities.

First, the chromatic behaviour with only the linear chromaticity corrected is examined. Figure 3 shows the variation of the tune shift with the relative momentum deviation δ and Figure 4 shows how the relative β^* at the IP varies with δ. The standard deviation σ_p for δ is $\approx 6\times10^{-5}$ at 20 TeV. For stable operation of the beam we require the tune shift $\Delta\nu < 0.002$. Only linear correction gives a momentum aperture of approximately 2.5 σ_p which is inadequate. The relative variation in β^* is also large, reaching 10% at $1\sigma_p$. Clearly, higher order chromaticity correction is needed.

The nonlinear correction was done by minimizing the tune shift as a function of δ to the 2nd and 3rd order using the module HARMON in MAD [4]. The variation of tune with δ, shown in Figure 5, is significantly improved. The tune variation is flat over $\pm2\sigma_p$ and the momentum aperture is increased to approximately $8\sigma_p$ for $\Delta\nu < 0.002$. The relative β^* variation (shown in Figure 6) is less than 2% at $1\sigma_p$. These improvements in the chromatic behaviour may be sufficient for the stable operation of the collider.
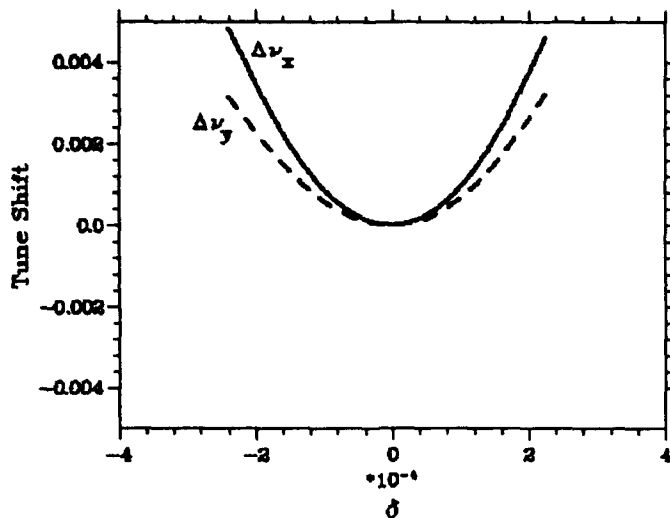
Figure 3. Tune variation with δ : Global correction
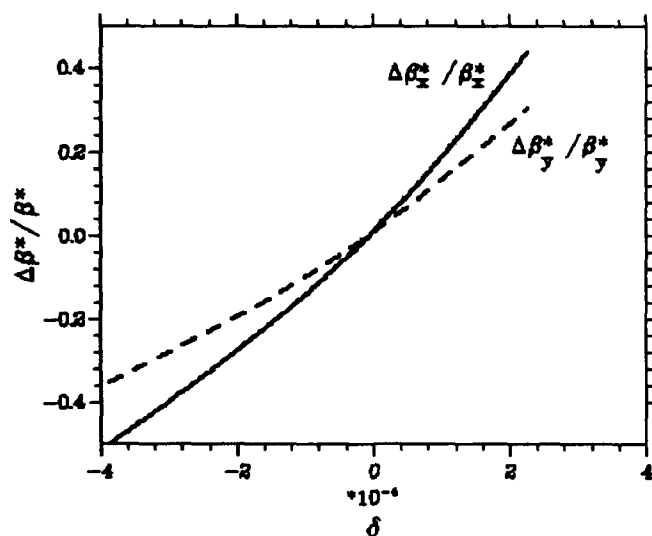
Figure 4. Variation of β^* with δ : Global correction
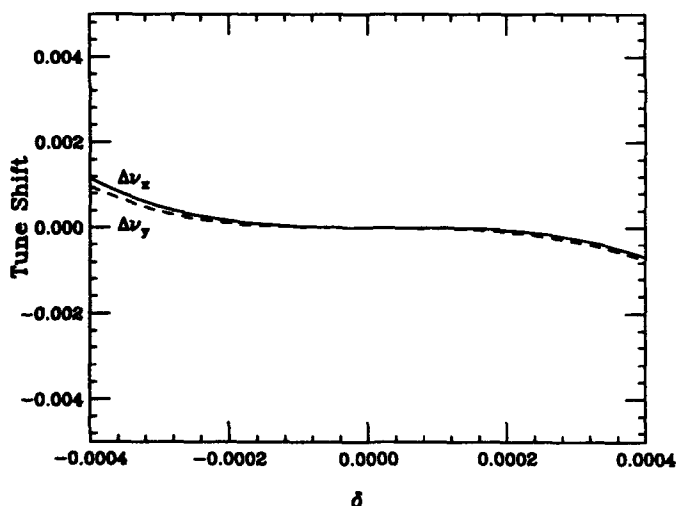
Figure 5. Tune variation with δ : Local correction
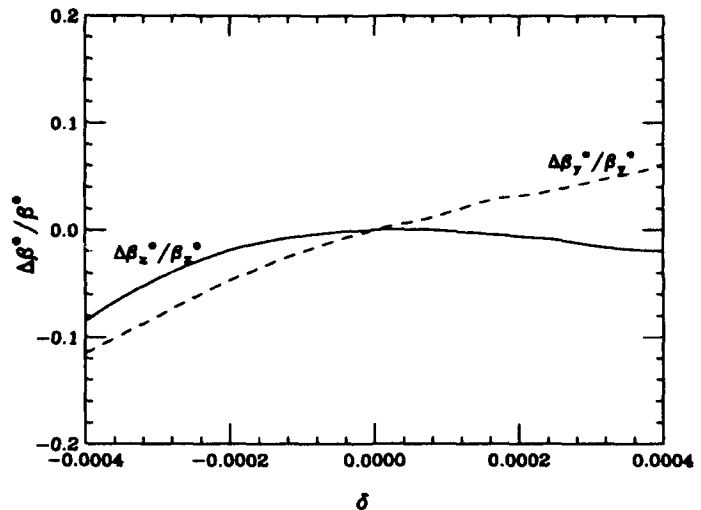
Figure 6. Variation of β^* with δ : Local correction

A simpler method of setting the sextupole strengths also gives similar results. All the local D sextupoles have the same absolute strength $|S_D|$ and the local F sextupoles are set to the absolute strength $|S_F| = (\eta_x^{min}/\eta_x^{max})|S_D|$, η_x being the horizontal dispersion in the standard cell. The strength S_D is chosen to be the value that minimizes the chromatic β beat in the arcs. The polarities and phase advances between the sextupoles are the same as before. With this method we have only a one parameter family of sextupoles. The fact that the chromatic behaviour is similar to that obtained by optimizing with HARMON shows that this scheme is quite robust. The local sextupoles used in either of the two methods mentioned here have strengths of the same order of magnitude as the global sextupoles, which correct the linear chromaticity of the lattice with all four IRs.

The effect of the local sextupoles on the dynamic aperture has also been examined. It is found [5] that when all field errors are included, specially those in the IR triplets, the dynamic aperture for particles off the design momentum is improved and that for particles on momentum is not affected. This improvement in both the momentum aperture and dynamic aperture is seen for other configurations of IRs as well.

IV. REFERENCES

[1] Y. Nosochkov et. al., "Current Design of the SSC Interaction Regions", these proceedings.
[2] T. Sen and M. Syphers, "2nd Order Chromaticity of the Collider", these proceedings.
[3] K.L. Brown, SLAC-PUB-2257 (1979)
[4] H.Grote and F.C. Iselin, MAD, CERN/SL/90-13(AP), 1990.
[5] F. Pilat et. al., "Dynamic Aperture of the Chromatically Corrected Collider Lattice", these proceedings.

Effect of Power Supply Ripple on Emittance Growth in the Collider.

T. Sen and M.J. Syphers
Superconducting Super Collider Laboratory*
Dallas, TX 75237

Abstract

Power supply ripple at frequencies of 720 Hz and its harmonics is expected to affect the motion of particles in the collider. These ripple frequencies are nearly resonant with the betatron frequencies. To estimate the tolerable ripple levels, we have tracked particles through the complete nonlinear lattice for 10^4 turns with ripple fed from 10 different power stations and including up to 7 different ripple frequencies. We presently estimate that relative ripple amplitudes must be below the 10^{-8} level for there to be no significant impact on the emittance over the short term.

I. INTRODUCTION

Experience at the CERN SpS and other colliders has shown that power supply ripple affects the long term dynamic aperture through modulation of the tune. A problem specific to the SSC is that betatron frequencies may be nearly resonant with ripple frequencies, due to the relatively low orbital frequency. This can lead to emittance growth through driven betatron oscillations. Since the working tune may not be known precisely till commissioning, it is important to set tolerance levels for ripple amplitudes at or near betatron frequencies. In this paper we present a preliminary estimate by tracking particles for 10^4 turns through the complete nonlinear lattice with a reasonably realistic ripple distribution.

II. DESCRIPTION OF POWER SUPPLY RIPPLE

The 87 km long collider is powered by 10 power supply stations. One station will feed approximately 480 dipoles and 96 quadrupoles. Each string of magnets is connected to a power supply through a low pass filter. Voltage ripple in the power supply will lead to a ripple in the magnetic field in the dipoles and quads. The string of magnets can be modelled as a damped transmission line which attenuates the ripple as it propagates. The ripple field behaves as an exponentially decaying sinusoid, i.e.

$$B_{rip}(s,t) = \sum_j \Delta B^0(\omega_j)\cos(\omega_j t - k_j s)e^{-\alpha_j |s|} \quad (1)$$

The attenuation length $1/\alpha$ is a function of the ripple frequency, decreasing for high frequencies. Assuming that 12-

pulse SCR power supplies are used as planned, the largest ripple field will be at 720 Hz. The attenuation length at 720 Hz is about 13 dipoles.

Ripple in the beam tube will be reduced by a combination of factors, i) appropriate choice of the low pass filter, ii) eddy current losses in the shielding of the beam tube and in the proposed copper liner and iii) by a damping resistor placed in parallel with the magnets. According to present estimates [1], the magnetic field ripple at 720 Hz can be reduced to 1 part in 10^{10} at 20 Tev and smaller for other ripple frequencies.

III. EFFECTS OF RIPPLE

The modulating dipole field changes the closed orbit and makes it time dependent while the ripple in the quads causes a modulation in the tune. More importantly, the changes in the fields can also cause a growth in emittance and the tune modulation can reduce the long term dynamic aperture.

Analytic calculations of both the tune shift and the orbit shift show that they oscillate with the ripple frequency but with very small amplitudes. For example, a ripple field at 720 Hz with relative amplitude 10^{-7} leads to a maximum orbit shift of 1 micron and a tune shift of less than 5×10^{-7}. We conclude that a distribution of ripple frequencies with maximum relative amplitude of 10^{-10} will have negligible impact on the closed orbit and tune.

The primary concern with ripple is emittance growth due to resonantly driven betatron oscillations arising either from dipole kicks at the betatron frequency or quadrupole kicks at twice the betatron frequency. One choice of working tunes for the collider has been (123.765, 122.791) which correspond to betatron frequencies of (808 Hz, 719 Hz) in the horizontal and vertical planes respectively. In this case, the core of the beam will have its dipole mode driven resonantly in the vertical plane by the ripple at 720 Hz and the higher order modes by the superharmonics of 720 Hz. Substantial emittance growth is expected in this case. Even though this is easily avoided by shifting the tune, some particles in the beam might still be resonantly driven if there is sufficient tune spread. In the collision mode, the major sources of tune spread are i)the beam-beam interaction, ii)multipole fields in the magnets and iii)uncorrected chromaticity. The total tune spread might be as large as 0.02 leading to a frequency spread of about 69 Hz.

In order to provide the tightest tolerance on allowable ripple levels, we study the emittance growth when the rip-

ple frequency is resonant with the betatron frequency. If the filters and damping mechanisms can be designed to meet this tolerance, then power supply ripple will not be a significant factor in the choice of tune.

IV. LINEAR LATTICE

Preliminary studies were done with a linear lattice to study the relative effects of dipoles and quads at a ripple frequency of 720 Hz. For this simplified linear lattice the betatron frequency in both planes was 743 Hz. A beam of 1000 particles with a gaussian distribution in all six dimensions was tracked through the lattice. The natural chromaticity was not corrected resulting in a large frequency spread of about 90 Hz. With relative ripple amplitudes of up to 10^{-4} in only the quads, there was no emittance growth over a period of 1000 turns. However there was substantial emittance growth over the same period with ripple in only the dipoles. This is expected since the quads do not cause a resonant growth at the betatron frequency but they do cause a parametric resonance at twice the frequency. The ripple distribution shows that ripple frequencies above 1 kHz are attenuated by an order of magnitude compared to the amplitude at 720 Hz. Hence we expect that dipole ripple will dominate the effects on the beam emittance.

V. NONLINEAR LATTICE

The cycle time intended for the collider at collision energy of 20 Tev is 24 hours. A variety of processes such as beam–gas scattering, intra–beam scattering, power supply ripple, and noise can lead to substantial emittance growth over this interval. Since it is not practical to track particles for this length of time through the complete non-linear lattice, simulations alone cannot provide accurate tolerances for all these effects. However, simulations can be used as a guide to understand the effects over shorter time periods. We have this purpose in mind.

The lattice used for tracking has as complete a description of all magnets as presently available. It includes the field errors in all the dipoles and quadrupoles in the arcs and straight sections, particularly those in the Interaction Regions where the β function is very large. The linear chromaticity and coupling has also been corrected with an appropriate set of sextupoles and skew quadrupoles. The tracking routine is a modified version of "Ztrack" which uses the tracking algorithm of Teapot [2]. Ripple, with the spatial and temporal distribution given in Equation (1), was propagated from ten feedpoints. 100 particles with a gaussian distribution in all six dimensions were tracked through the lattice. No beam-beam effects were included in the simulation so the tune spread resulted from the non-linearity and residual chromaticity. Since the study with the linear lattice had shown that dipoles cause the dominant emittance growth at the ripple frequencies of interest, ripple in the quads was not included in the results reported here.

We report first the results of a study with the ripple not resonant with the betatron frequencies in a distribution of 100 particles. Two lattices were used, one with the nominal betatron frequencies (749Hz, 771Hz), the other with (981Hz, 909Hz). The frequency spread in either case was less than 15Hz. Two runs were done at a ripple frequency of 720 Hz, one at a relative amplitude of 10^{-5}, the other at 10^{-4}. In both cases there was no evidence of emittance growth over 10^4 turns.

The resonant case has been studied in more detail. The lattice was tuned to betatron frequencies (808Hz, 719Hz). Frequencies with the 7 largest amplitudes were chosen from the ripple distribution.

First, particles were tracked with only one of these frequencies at a time to determine the relative effects of each on the emittance. The rms, normalized emittance for these particles was specified to be the nominal beam emittance of 1πmm–mrad. The relative amplitude of ripple in each case was the same at 10^{-6}. The average emittance growth at the end of 10^4 turns due to each of these frequencies is shown in Table 1.

Table 1 : Emittance growth ($\epsilon_0 = \pi$ mm-mrad) after 10^4 turns, with individual ripple frequencies.

f (Hz)	k (m^{-1})	$1/\alpha$ (m)	$\Delta\epsilon_x/\epsilon_x$(%)	$\Delta\epsilon_y/\epsilon_y$(%)
60.	0.002	925	0.45	−0.04
120.	0.002	561	0.68	0.17
240.	0.003	364	1.56	0.27
720.	0.005	175	58.92	221.57
1440.	0.007	136	0.00	2.21
2160.	0.009	106	0.12	0.09
2880.	0.010	91	−0.06	−0.04

As expected, the ripple at 720 Hz causes the largest emittance growth by orders of magnitude. In the next study we included all 7 frequencies with the ripple at 720 Hz having the largest amplitude and the amplitudes of the others scaled appropriately from the ripple distribution. The emittance was also increased to 5πmm–mrad so that the tune spread would be larger due to the nonlinearity. Two tracking runs were done, one with relative amplitude ($\Delta B_{max}/B$) of the 720Hz ripple set to 10^{-6} and the other with $\Delta B_{max}/B$ equal to 10^{-7}. Figures 1 and 2 show the growth in emittance in the two planes at these amplitudes. With fewer particles resonant at 720 Hz for these cases, the average vertical emittance growth has dropped to 63% at $\Delta B_{max}/B_0 = 10^{-6}$ compared to the 222% growth (shown in Table 1) when the beam emittance was five times smaller. Figure 2 also shows that the emittance after an initial linear increase settles down to an oscillatory behaviour about a larger equilibrium value. This is exactly the behaviour shown by a harmonic oscillator driven by a sinusoidal force whose frequency changes in time and which passes through resonance at some instant. In our case, the initially resonant particles get driven to larger amplitudes where they get detuned from resonance. In the
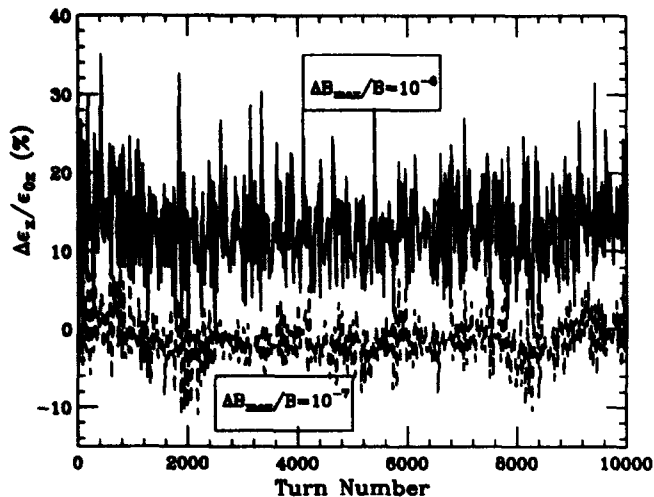
Figure 1. Growth in Horizontal Emittance ($\epsilon_0 = 5\pi$mm-mrad) with 7 ripple frequencies.
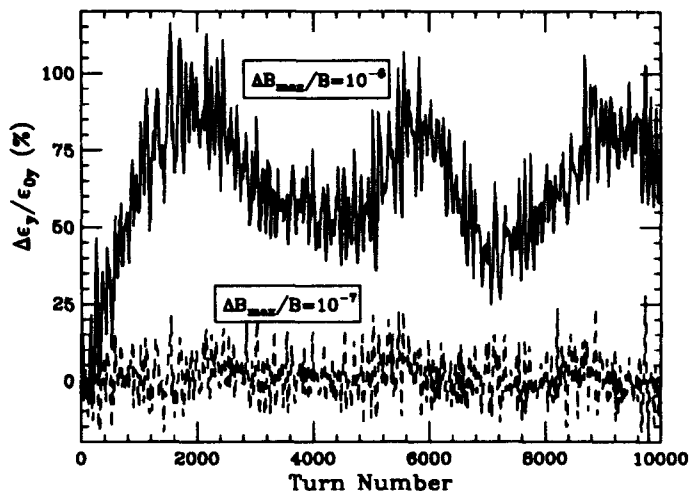
Figure 2. Growth in Vertical Emittance ($\epsilon_0 = 5\pi$mm-mrad) with 7 ripple frequencies.

absence of other mechanisms driving particles whaich are off–resonance into resonance with the ripple frequency, no systematic growth of emittance will occur after this initial increase due to the ripple. Decreasing the ripple amplitudes by one order of magnitude to $\Delta B_{max}/B_0 = 10^{-7}$ reduces the average growth in vertical emittance to 0.8%.

The vertical emittance growth seen here is due to the residual coupling in the lattice since the ripple in the dipoles kicks the beam only horizontally. We expect greater sensitivity to ripple frequencies resonant with the horizontal betatron frequency. A single ripple field with frequency 808Hz at $\Delta B/B_0 = 10^{-7}$ with the same transverse beam size as above gives rise to an average growth of 61% in the horizontal emittance and -1% in the vertical emittance over 10^4 turns. At $\Delta B/B_0 = 10^{-8}$, the horizontal emittance growth drops to 0.01%.

VI. NOISE TOLERANCES

The required tolerances on noise levels can be estimated using the expressions given, for example, in [3]. The growth in the normalized emittance due to noise in dipoles is given by

$$\frac{d\epsilon_N}{dt} = \pi(\beta\gamma)f_0\beta_d\langle(\delta\theta)^2\rangle \qquad (2)$$

f_0 is the revolution frequency, β_d is the beta function at the dipole and $\langle(\delta\theta)^2\rangle$ is the average of the square of the angular kick. We assume that the noise also attenuates with distance from each power supply, that the 10 power stations are uncorrelated and set

$$\langle(\delta\theta)^2\rangle \approx \sqrt{10}N_d(\Delta B/B)_{noise}\theta \qquad (3)$$

where $N_d \approx 30$ is the number of dipoles next to each station with significant noise and θ is the bend angle per dipole. Requiring that the emittance growth not exceed 10% over the cycle time of 1 day leads to $(\Delta B/B)_{noise} < 7 \times 10^{-11}$.

Noise in quadrupoles leads to an emittance growth given by

$$\frac{d\epsilon_N}{dt} = \frac{1}{2}f_0\beta_q^2\langle(\Delta K)^2\rangle\epsilon_N \qquad (4)$$

β_q is the beta function at a quadrupole and K is the inverse focal length of the quadrupole. We assume that noise from each station will propagate with sufficient amplitude into 4 focussing quadrupoles. Requiring that emittance growth not exceed 10% leads to a more relaxed tolerance of $(\Delta B'/B')_{noise} < 4\times10^{-7}$, where B' is the gradient field.

VII. CONCLUSIONS

Taking into account only the ripple in the dipole fields we have found that the relative amplitude of the ripple must be at or below the 10^{-8} level for there to be no emittance growth over 10^4 turns, if the main ripple field is resonant with the betatron frequency. Another possible source of significant emittance growth is ripple in the Interaction Region quadrupoles, a subject now under study. Present power supply designs call for the ripple fields to be damped to the 10^{-10} level. With the proper choice of tune, this may be sufficient to not cause any significant emittance growth over the time scale of collider operation.

VIII. REFERENCES

[1]R.E. Shafer and K.M. Smedley,"Electrical Characteristics of Long Strings of SSC Superconducting Dipoles", *HEACC 1992*, Hamburg.
[2]L. Schachinger & R.T. Talman, *Part. Acc.*, 22, 35 (1987).
[3] G. Jackson et.al.,"Luminosity lifetime in the Tevatron",*Proceedings of the 1st European Particle Accelerator Conference*, 1988, pp. 556-558

The QBA Optics for the 3.2 GeV Synchrotron Light Source ROSY II

D.Einfeld [#] and M.Plesko [+]

[#] Research Center Rossendorf e.V.,B.O. 19 D - 8051 Dresden
[+] Sincrotrone Trieste, Padriciano 99,I - 34012 Trieste

Abstract

ROSY, a synchrotron light source dedicated to material research has been proposed to be built at the reseach Center Rossendorf in the Dresden region of Germany. At a early stage of the project the idea was to built ROSY in two steps: ROSY I as an compact light source and as an injector for ROSY II. ROSY II shall be a high brillance light source (3rd generation) serving photons with energies up to 30 keV. For the design of ROSY II a modified QBA-lattice was taken. With an energy of 3.2 GeV and a magnetic field of 1.33 T in the bendings magnets the critical photon energy is 9.0 keV. With 12 achromats and a circumference of 310 m, the emittance yields 3 nm rad. The dynamic aperture is +/- 10 mm in both directions .

I. INTRODUCTION

Synchrotron light sources of the 3rd generation have been built for an energy range between 1.5 - 2.0 GeV and 6.0 - 8.0 GeV [1]. A gap exist around the energy region 3 to 4 GeV. In this region there are at present only the sources DORIS, IHEP and SPEAR [1] which are running mostly as dedicated light sources, but from the machine point of view they are first generation machines. Therefore ROSY II should be a 3rd generation light source with an energy of at least 3 GeV. As a lattice the modofied QBA-Optic, which showed very promising results for LISA [2], has been choosen. At the "Workshop on Fourth Generation Light Sources" [3] the QBA - lattice has been recognized as one structure which could meet the requirements of the next generation of light sources.

II. MINIMIZING THE EMITTANCE

The most important factor for synchrotron radiation users is the brilliance which is mainly determined by the cross-section of the beam and given by the square root of the emittance multiplied with the betatron function. The emittance scales in general with the square of the energy and the third power of the bending magnet´s deflection angle. The optics influence the emittance via the H-function, which is determined by the shape of the horizontal betatron (β) and dispersion (η) functions within the dipole magnets only. Low emittances can be reached if the $\beta(s)$ and $\eta(s)$ have a minimum there. Two extrem cases are shown in Figure 1. Figure 1a represents the two dipoles of the double bend achromat (DBA) structure [4] and Figure 1b represents the central dipole of the triple bend achromat (TBA) structure[4]. In both cases the formula

Fig. 1a

$$S^* = 3\,L/8, \qquad \beta_m = \sqrt{\frac{3}{320}} \cdot L$$

$$\varepsilon_{xo} = Cq \cdot \gamma_o^2 \cdot \frac{1}{J_x} \cdot \varphi^3 \cdot \frac{1}{4\sqrt{12}}$$

Fig. 1b
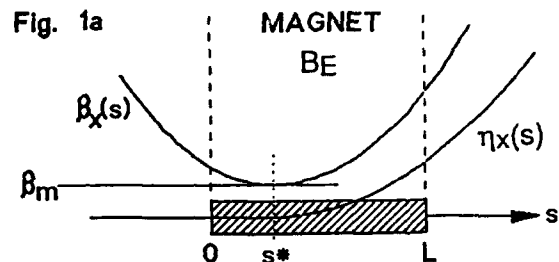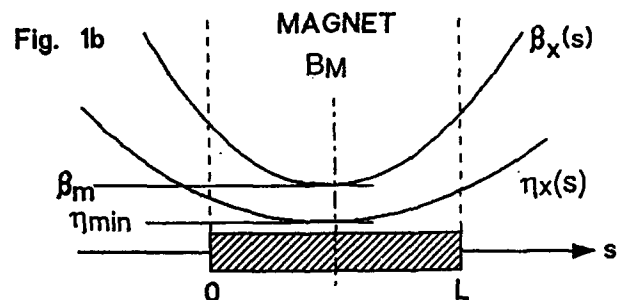
$$\beta_m = \frac{1}{2\sqrt{15}} \cdot L, \qquad \eta_m = \frac{1}{24\,\rho} \cdot L^2$$

$$\varepsilon_{xo} = Cq \cdot \gamma_o^2 \cdot \frac{1}{J_x} \cdot \varphi^3 \cdot \frac{1}{3.4\sqrt{12}}$$

Figure 1. Twiss functions in a bending magnet which ninimize the H - function for a nondispersive entrance (a) and in the general case (b). The expressions for the optimal values of the Twiss function and the minimal emittances are shown.

for the smallest emittance and also the conditions to reach this are given. ε(Fig. 1b) is roughly one third of ε (Fig. 1a) The smallest emittance can be reached with the case represented in Figure 1b. Hence to get the smallest emittance, a storage ring should have a lattice which provides a shape of the horizontal betatron and dispersion functions as represented in Fig. 1b in all dipole magnets. However, other design considerations forbid this. A light source includes undulators and wigglers and at the position of these insertion devices, in the long straight sections, the dispersion has to be zero. This requires a matching of the twiss functions to the desired values within the straight sections.
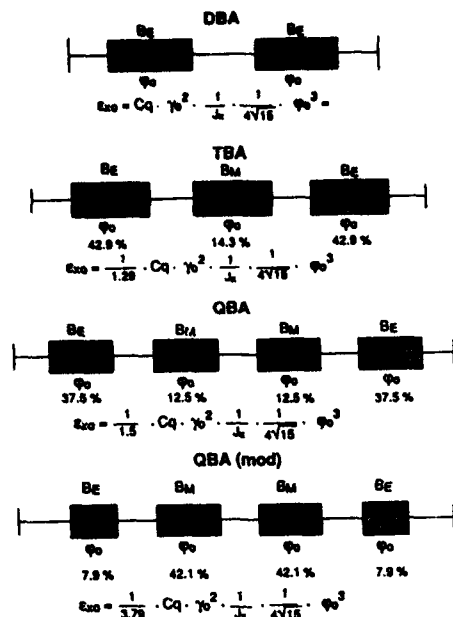
Figure 2. A comparison of theoretical minimal emittances obtained by different bending magnet structures. The persentages under the magnets indicate their relative contributions to the H - function average.
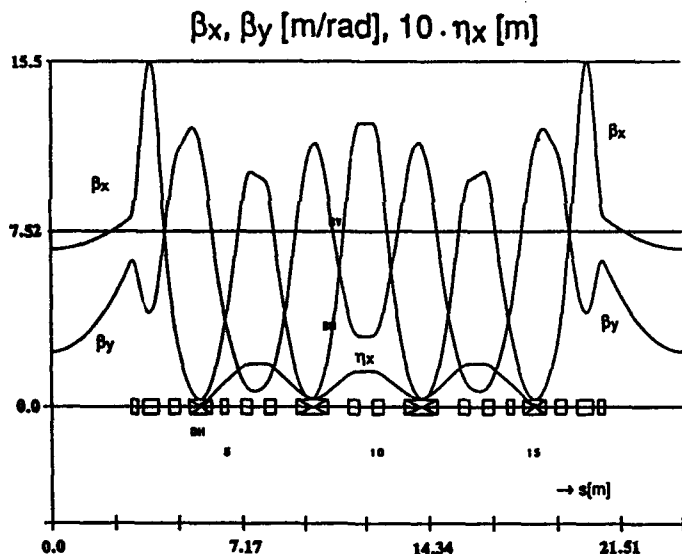
Figure 3. The lattice of a 3 GeV, 3 pi nm rad emittance light source ROSY II. The positions of the chromatic sextupoles are indicated with vertical bars.

The zero dispersion can be matched only in the case the straight section is on the left side of the dipole in Fig. 1a. Two of these dipoles with one quadrupole in between form the well known DBA structure [6]. Implicit to the DBA structure is the requirement that the phase advance from the beginning of the first to end of the second dipole has to be π. This is only possible if the distance between both dipoles is very large [7] or there are at least two more quadrupoles in between the dipoles, as for the ELETTRA design [8]. In most DBA designs the minimal emittance has not been attained.
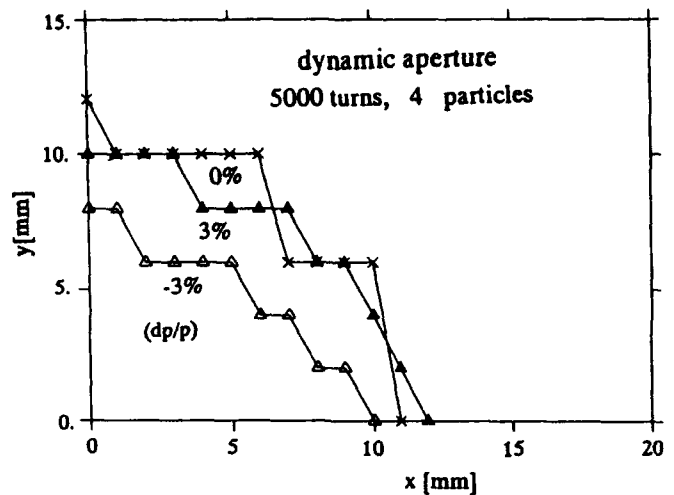
Figure 4. The dynamic aperture of ROSY II with optimized chromatic sextupoles.
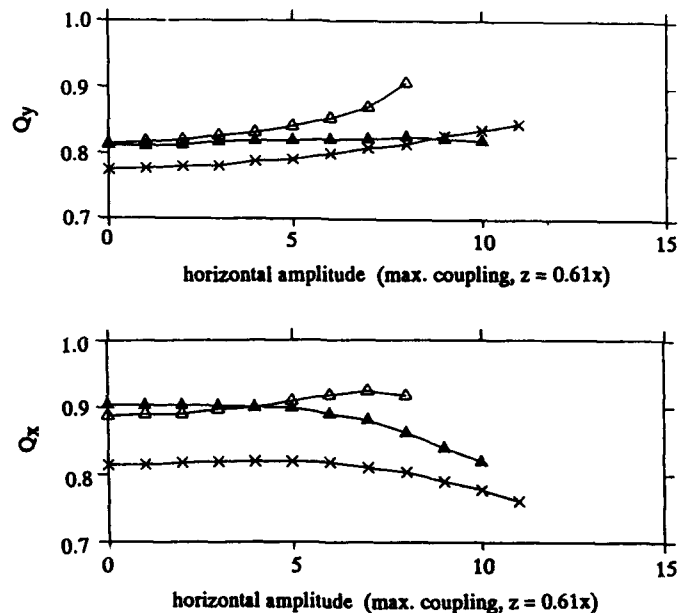
Figure 5. The fractional tune of ROSY II as a function of the initial particle amplitude for on energy particles (crosses), and dp/p = -3% (open triangles), and + 3 % (full triangles), respectively.

Inserting a further dipole between the two DBA dipoles and providing there a shape of the Twiss functions as given in Fig. 1b represents a TBA structure. Such an arrangement would have a lower emittance if the Twiss functions reached the optimal values both in the central and in the outer dipoles. However, it has been proved that this is not possible [9]. Even if it was possible, the ideal emittance of the TBA lattice would be smaller than the ideal DBA emittance by only a factor 1.3 because of the relatively high contributionof the outer magnets to the total emittance (85.5%, see Fig. 2). In conclusion, it can be said that the TBA - structure is DBA dominated.

150
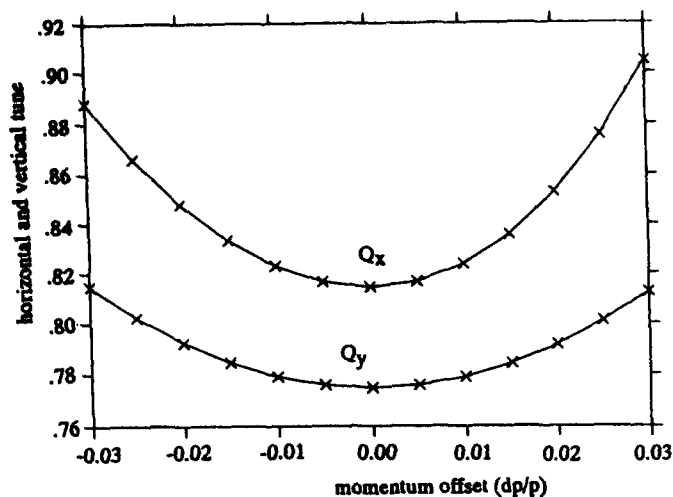
Figure 6. The fractional tune of ROSY II as a function of particle energy deviation

STORAGE RING PARAMETERS

Achromatic structure	QBA
Normal energy (GeV)	3
Superperiod	12
Circumference (m)	292.8
Mean radius (m)	46.6
Max. current (mA)	300
R.F. Frequency (MHz)	500
Harmonic number	488
Quantum lifetime (h)	10
Natural emittance (π mm rad)	3
Natural energy spread (%)	0.1
Betatron tunes Q_x/Q_y	21.90/14.80
Natural chromaticities ξ_x/ξ_y	-51/-30
Momentum compaction factor	$0.75 \cdot 10^{-3}$
Beta functions	
Horizontal (max/min)	13.3/0.3
Vertical (max/min)	12.1/0.6
Straight section (max/min)	7.18/2.29
Maximum dispersion (m)	0.18
Number of dipole magnets (5/10)	24/24
Dipole length (m) (5/10)	0.84/1.62
Bending radius (m)	8.00
Bending field (T)	1.25
Gradient (T/m) / field index	7.5/48.00
Number of quadrupoles	18/96/24=168
Length of quadrupoles (m)	0.25/0.40/0.6
Quadrupole families	6
Gradient (T/m) / strength (m⁻²)	17
Number of sextupoles	132
Length of sextupoles (m)	0.2
Sextupole families	3
Sextupol parameter,$S=B/R2(T/m^2)$	750

Table 1. Parameters of the storage ring ROSY II designed with a modified QBA - optic

[1] J.Murphy,"Synchrotron Light Source Data Book",BNL 4233, Brookhaven National Laboratory
[2] D.Einfeld, D.Husmann, M.Plesko,"Dynamic Aperture of the 2.5 GeV Synchrotron Radiation Source Lisa", This Proceedings
[3] M.Cornacchia and H. Winick,"Workshop on Fourth Generation Light Sources",SSRL 92/02, Stanford, February 1992
[4] R.Chasmann and K. Green,"Preliminary Design of a Dedicated Synchrotron Radiation Facility",IEEE Trans. Nucl. sci.,NS - 22, 1765 (1975)

III THE MODIFIED QBA - LATTICE

The QBA structure is obtained by inserting two dipoles between the two DBA bending magnets. Also in this arrangement the highest contribution to the emittance is given by the outer magnets (Fig. 2, 37.5 %). The investigation of a QBA structure for the 6 GeV Riken storage ring [10] has shown that this structure has no merits with respect to the DBA or TBA structures.

Quite different is the behavior of a modified QBA structure which we firstly proposed for a planned synchrotron light source LISA [2]. As mentioned above, the emittance of the TBA structure is not ideal because of the unsatisfactory matching of the twiss functions from the straight sections to the central dipole. Matching the twiss functions to an outer dipole with a deflection angle φ/2 should force a smaller increase in the emittance with respect to the ideal one, because the differences between the existing and the matching conditions are not so large. The second advantage of the halved deflection angle in the outer dipole is that its contribution to the emittance is small. According to Figure 2 the contribution of the outer magnets to the emittance in the ideal case is reduced to 15 %. Consequently, this structure is really determined by the dipole of Figure 1b, which gives the smallest emittance.

IV THE SYNCHROTRON LIGHT SOURCE ROSY II

The lattice of ROSY II is shown in Figure 3. The bending magnets in the middle of the achromat perform a deflection of 6 degree and the magnets in the matching section of 3degree. With this ratio one gets the smallest emittance. The space for the insertion devices is 6 m. The main parameters of the storage ring ROSY II are summarized in Table 1. The dynamical aperture is given in Figure 4 and the tuneshifts with amplitude as well as momentum are presented in the Figures 5 and 6

All dynamic properties of the lattice behave sufficiently well. The low emittance of 3 nm rad indicates that with such kind of lattices performances in the direction of fourth generation light sources are feasible indeed.

[5] D.Einfeld and G. Mülhaupt,"Choice of the Principle Parameters and Lattice of BESSY",Nucl. instr. Meth. 172 (1980)
[6] see [4]
[7] A.Jackson,"A Comparison of Chasmann - Green and Triple Bend Achromat",Particle Accelerators, Vol 22,111 (1987)
[8] "ELETTRA Conceptional Design Report",Sincrotrone Trieste, April 1989
[9] G. Wüstefeld," The Minimization of the Natural Emittance in the Triple Bend Achromat", BESSY TB 108/87, March 1987
[10]K.Tsumaki, R. Nagaoka, H. Tanaka, K. Yoshida, M. Hara, "Lattice Comparison for the 8 GeV Synchrotron Radiation Source", 1989 Particle Acc. Conf., Chicago
[11] see [2]

Dynamic Aperture of the 2.5 GeV Synchrotron Radiation Source LISA

D.Einfeld #), D.Husmann +) , M.Plesko $)

#) Fachhochschule Ostfriesland, Constantiaplatz 4, D - 2970 Emden
+) Physikalisches Institut der Univ. Bonn, Nußallee 12, D - 5300 Bonn 1
$) Sincrotrone Trieste, Padriciano 99,I - 34012 Trieste

Abstract

LISA, a Light Source for Industrial and Scientific Application, has been proposed to be built in the Bonn region of Germany. For the lattice a modified "Quadrupole Bend Achromat " (QBA) will be used. The novel feature of this lattice is the application of two types of bending magnets with a vertical focusing component and different deflection angles to keep the radiation integrals small. The long bending magnets (20°) will be used in the arc of the achromat and the small (10°) are foreseen to perform the matching of the twiss functions from the arc to the straight sections without blowing up the emittance determined by the magnets in the arcs. With a sixfold symmetry, a circumference of 125 m an emittance smaller than 20 nm rad can be obtained. The natural chromaticities and the sextupole strength are moderate, the dynamic aperture is +/- 30 mm (100 σ_x and 170 σ_y), the momentum acceptance is more than +/- 9 % and the tune shift with amplitude is very promising.

I. INTRODUCTION

The synchrotron radiation source LISA, which has been presented first at the EPAC 1992 [1], is primarily foreseen for industrial applications. There is a strong demand to utilize synchrotron radiation for microlithography on thick layers in connection with the LIGA process [2], which needs a radiation spectrum around a critical wavelenght of 0.2 nm. This spectrum is being produced by 2.5 GeV electrons deflected in a magnetic field of 1.5 Tesla. For LISA a new lattice , the modified QBA-Optics, has been worked out. This lattice results in a compact storage ring with a quite low emittance. The complete LISA ring is composed of six achromats and straight sections of 4.6 m in lenght between them. The total circumference adds up to 124.8 m. The ring emittance at the energy of 2.5 GeV is calculated to be 20 nm rad which is a rather low value for such a machine and is due to the new QBA-lattice.

The small emittance is certainly not absolutely necessary for the industrial application for LIGA, however, it makes this machine attractive for fundamental research as well.

II. LATTICE OF THE QBA-STRUCTURE

The LISA magnet ring consists of 6 achromats and a long straight sections between them. Each achromat is combined of 2 unit cells (as shown in Fig.1) and matching cells on both sides to match the optical functions to the conditions of the straight sections. The unit cell contains the bending magnet B_2 (20°) and the adjacent quadrupoles Q_M; the matching section contains the dipole

B_1 (10°) and the 4 adjacent quads too.The dipoles B_2 bend the orbit by an angle φ while those (B_1) in the matching cells bend the beam only by half of the angle φ. The curves of the twiss functions within an achromat are given in Figure 2.
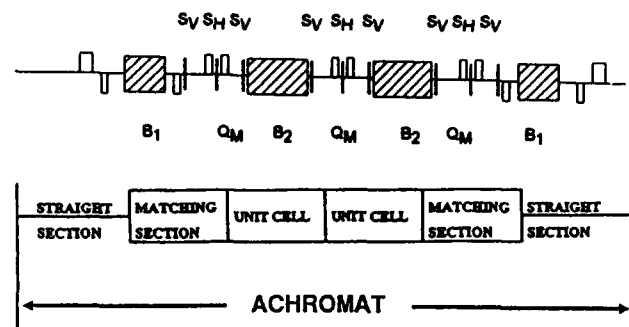
Figure 1. Composition of a QBA - achromat and the arrangement of magnets within a unit cell
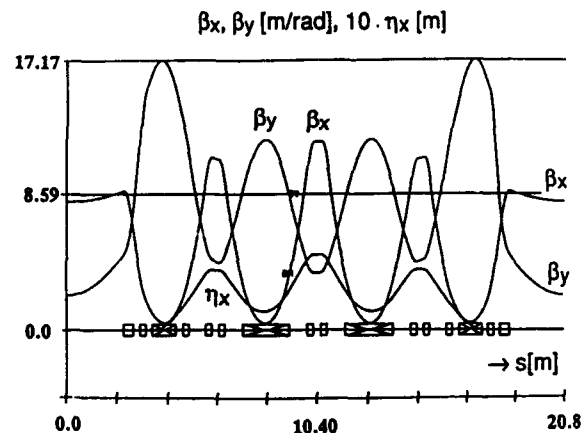
Figure 2. The Twiss functions and the lattice of the proposed LISA storage ring

The performance of the storage ring is characterized by the parameters: emittance, betatron tunes, chromaticities, partition numbers and the momentum compaction factor. The emittance of the QBA-structure is mainly determined by the unit cell, which has for a certain strength k_M^* the minimized value $\varepsilon_{x0} = 20$ nm rad. For k_M-values larger than k_M^* the emittance increases drastically and for k_M-values smaller than k_M^* it increases slowly . The detailed results are given in the report [3].

The chromaticity in the vertical direction is moderate, but in the horizontal direction it increases significantly with k_M-values larger than k_M^* (which yields the lowest emittance).

152

The chromaticities at the lowest emittance are moderate and it should be possible to operate the unit cell at this value of k_M^*. An advantage of the lattice is that together with a reduction of the chromaticity by a factor of 2 the emittance only increases by a factor of 1.5.

The betatron tune Q_x in the horizontal plane is almost exclusively determined by the strenght of the horizontal focusing quad Q_M of the unit cell. The vertical betatron tune Q_y is mainly determined by the strenth of the gradient in the bending magnets (B_1 and B_2)and only slightly dependent on the one of the quad Q_M. Therefore Q_x and Q_y are more or less independently controlled by either the k_M-value of the quad Q_M or the gradient of the bending magnets B_2 and B_1. Some working points are shown in the tune diagram in Fig.3. As the vertical tune of one achromat is close to 0.5 it was difficult to find both, the working point of the ring and that of the single achromat, far from half integer and third integer resonances. Several lattices with acceptable working points and chromaticities were tested in further optimization studies. The position of the chromaticity correcting sextupoles were optimized by use of the computer code CATS [4]. There are only two families of sextupoles but there is more than one sextupole of each family in an achromat. Thus a partial cancelling of higher order terms has been achieved. A sufficiently large dynamic aperture for almost all lattices studied has been obtained by a proper positioning of the chromatic sextupoles.
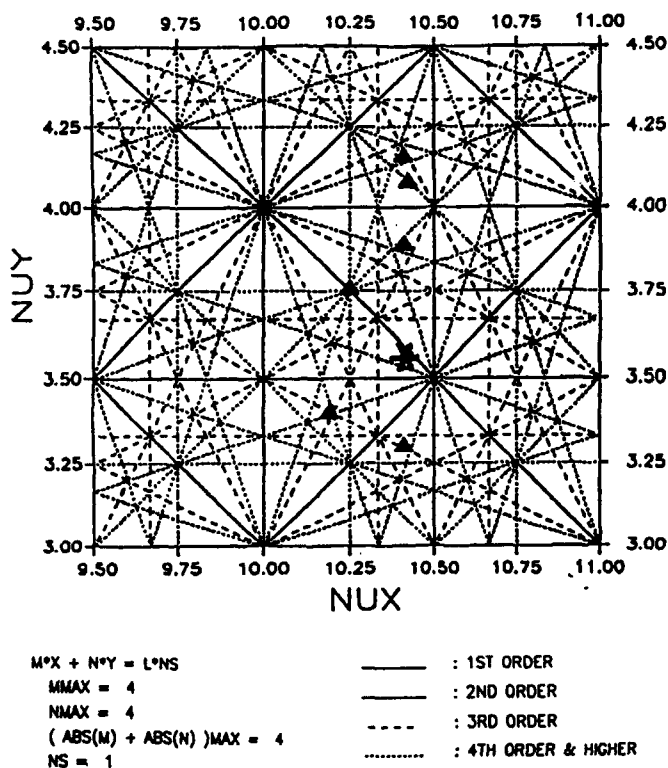
Figure 3. Tune diagramm of the modified QBA-optics with investigated working points. The choosen point Qx=10.413 and Qy=3.559 is indicated by a star

III. DYNAMIC APERTURE

The dynamic aperture calculated for the optimized chromatic sextupole layout (Figure 1) is shown in Figure 4 for energy deviations from -9 % to +9 %. The tracking has been performed with 1 particle for 100 turns. To confirm the results 4 particles were tracked for 5000 turns. The calculations have been carried out with the code RACETRACk [5] and checked with the codes CATS [4], MAD [6] and BETA [7].
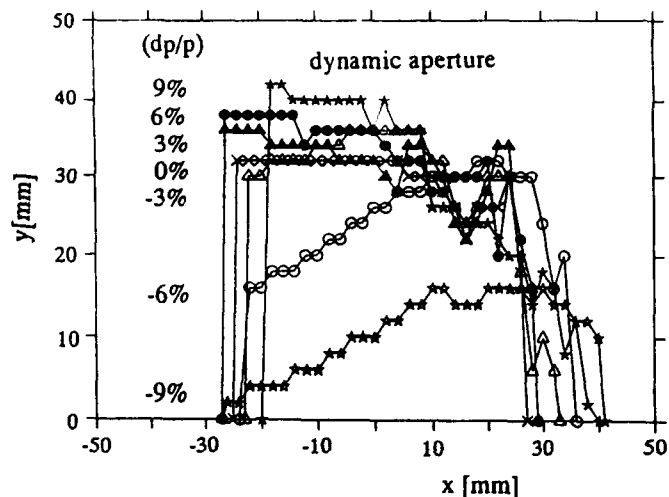
Figure 4. Results of tracking calculations of the dynamic aperture of the modified QBA-structure for 1 particle and 200 turns

For particles at nominal energy the dynamic aperture extends from -27mm to +27 mm in the horizontal direction (100 σx) and stays constant about 30 mm in the vertical direction (170 σy, coupling 0.5 at about within the entire range). This gives sufficient space for the injection process and for a long beam lifetime. There is no reduction of the phase space at energy deviations of +/- 3 %. A reduction only occurs at energy deviations below - 6 %. But even at - 9 % the dynamic aperture is still surprisingly large. Compared to other 3rd generation light sources the dynamic aperture of this QBA-lattice is very large.

The betatron tunes are only weakly dependent on the corresponding oscillation amplitudes only as is shown in Figure 6 . The tune increases quadratically with the amplitude to the upper limit of the dynamic aperture, indicating that the second order approximation which is used in CATS is valid within the entire range.

The dependence of the tune shift on the momentum is shown in Figure 6. It is remarkable that a closed solution still exists up to a momentum deviation of +/-9 %. According to the design of the rf-system only particles with a momentum offset of +/- 3 % in the maximum will be captured. Therefore only this momentum interval is important and the tune within this range is almost constant.
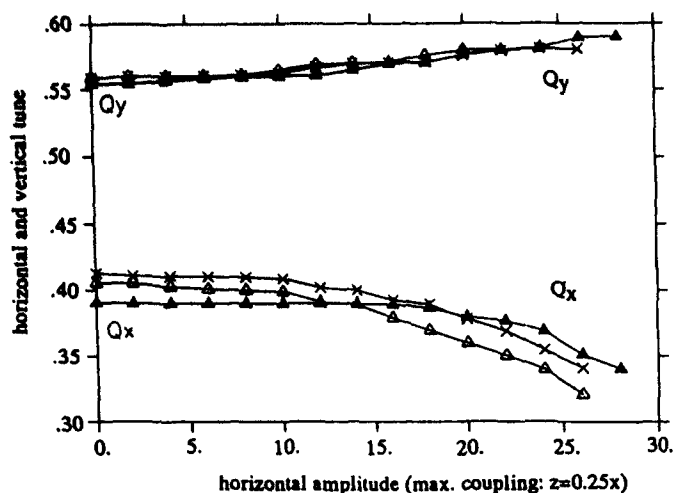
Figure 5. The fractional tune of LISA as a function of the initial amplitude for on energy particles (crosses), and dp/p = 3 % (open triangles), and + 3 % (full triangles), respectively.
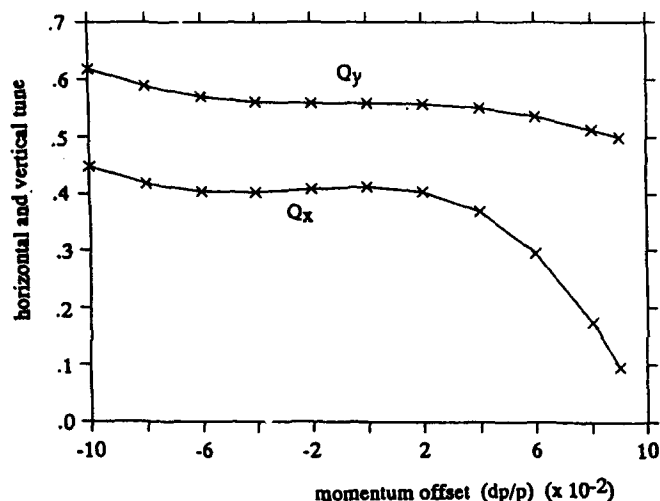
Figure 6. The fractional tune of LISA as a function of particle energy deviation
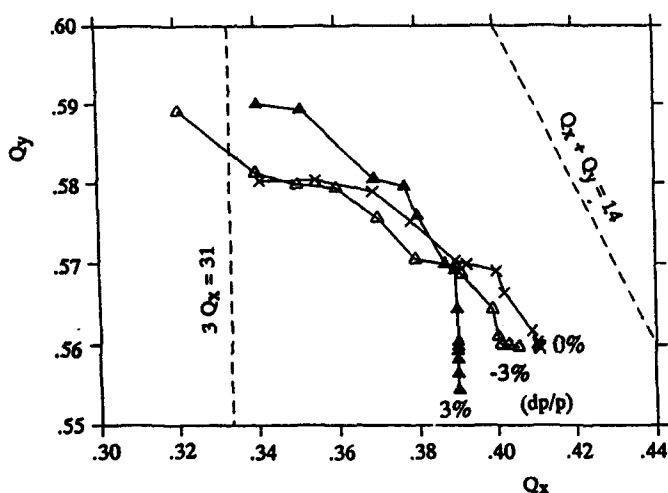
Figure 7. Working point shift with amplitude and momentum offset. Indicated are second and third order resonances.

Figure 7 shows the tune shift with increasing amplitude at the nominal energy and for a +/- 3 % momentum deviation. Each point represents an increase of 2 mm in the horizontal and of 1.4 mm in the vertical amplitude. No dangerous lines are crossed.

IV. COMPARISON WITH OTHER MACHINES

There are 2 machines of the 2nd generation running at roughly the same energy: the Daresbury machine "SRS2" at a nominal energy of 2 GeV and the "NSLS XRAY" ring with an energy of 2.5 GeV. SRS2 has a FODO-structure, $22.5°$ bending magnets, a circumference of 96 m and an emittance of 100 nm rad. Scaling SRS2 to the same energy and deflection angles as for LISA the emittance increases to 110 nm rad, which is larger by a factor of 5.5 compared to LISA. The "NSLS XRAY" source has a DBA-structure with $22.5°$ bending magnets, a circumference of 172.8 m and an emittance of 100 nm rad. Using $20°$ bending magnets would reduce the emittance to 70 nm rad, which is a factor of 3.5 larger than for LISA. According to the criteria LISA is a 3rd generation light source.

Furthermore LISA can be compared to the machines of the 3rd generation: ALS, ELETTRA and the POHANG Light Source. They are all designed to run at an energy of 2 GeV and have an emittance around 6 to 9 nm rad at this energy. Scaling this value to the energy and the bending angle of LISA results in 40 to 65 nm rad which is more than twice the LISA emittance.

The low emittance of the modified QBA-lattice has been observed even more evidently at larger rings, which has been demonstrated in another contribution to this conference [8].

[1] D.Einfeld,J.Hormes,D.Husmann and F.Anton, "The Low Emittance 2.5GeV Synchrotron Light SAource LISA" , Proceedings EPAC92, Vol. 2,pp 1693-1695

[2] E.W.Becker and W.Ehrfeld, "Das LIGA-Verfahren-Mikrofertigung durch Röntgentiefenlithographie mit Synchrotronstrahlung, Galvanoformung und Kunststoffabformung", Phys. Bl. 44, 166, 1988

[3] D.Einfeld,D.Husmann,M.Plesko,"An Investigation of the QBA-optics for the Storage Ring LISA", BONN-ME-92-02, Bonn University, August 1992

[4] R.Nagaoka, "CATS - A Computer Code for the Optimization of Sextupoles and Linear Optics in Circular Accelerator", Sincrotrone Trieste,ST/M-91/3, February 1991

[5]F.Iazzourene,C.J.Bocchetta,R.Nagaoka,L.Tosi, A.Wrulich, "RACETRACK User's Guide", Sincrotrone Trieste, ST/M - 91/11,July 1991

[6] U.Grote, F.C.Iselin,"MAD, User's Reference Manuel" CERN/SL/90 - 13 (AP)

[7] L.Farvacque, A.Robert,"BETA User's Guide",ESRF-SR/LAT 88-08

[8] D.Einfeld,M.Plesko,"The QBA-Optics for the 3.2 GeV Synchrotron light Source ROSY II", This Proceedings

Four Cell Third Order Achromats
and Their Application to Multi-Pass Time-of-Flight Spectrometers

Weishi Wan and Martin Berz
Department of Physics and Astronomy, and
National Superconducting Cyclotron Laboratory
Michigan State University, East Lansing, MI 48824

θ_x	$\theta_y = 0$	$\theta_y = 90$	$\theta_y = 180$	$\theta_y = 270$
0	F R S C	F R S C	F R S C	F R S C
90	F R F R	F R F R	F R F R	F R F R
180	F R S C	F R S C	F R S C	F R S C
270	F R F R	F R F R	F R F R	F R F R

Table 1: Achromatic systems with $(a|\delta) = 0$ after the first cell. In case $(x|\delta) = 0$, exchange R and C.

Abstract

A repetitive third order achromatic system was designed. As an example, we chose the ESR storage ring at GSI. Instead of repetition of cells, which is widely used in achromat design based on normal form theory, we utilize cells which are obtained from the the original ones through mirror imaging about the x-y plane, which corresponds to a reversion. In our design, the second half of the ring is the reversion of the first one, and two turns make a third order achromat. The dynamical aperture was determined by tracking with 11th order maps using COSY INFINITY [4]. The 9th order time-of-flight resolution was calculated statistically with beams of different emittances.

I. INTRODUCTION

In the past few years, various third order achromatic systems containing at least five repetitive identical cells have been found using normal form theory [1] [2] [3]. The number of bending magnets needed ranges from 5 to 150. By introducing mirror symmetry into the consideration, we developed a new theory which requires only four cells and one bend per cell to get a third order achromat [4] [5] [6]. According to the theory, the linear map of every cell should be a rotation with the phase advance $\mu_{x,y} = n * 90deg$ ($n = 0, 1, 2, 3$) plus no more than one nonzero chromatic term. Based on this, a family of achromatic systems which demand the fewest conditions on the first cell (10 for second order 15 for third order) were found and are listed in table 1. Here F (Forward) stands for the base cell of a system, R is the reversed cell which reverses the order of the elements in the forward cell, S is the switched cell which flips the bending direction of the forward cell, and C is the combined cell which switches the bending direction and reverses the order of elements simultaneously.

Inspired by the fact that due to symplecticity, the only aberrations left in an achromat are $(t|\delta^n) = 0$ ($n = 0, 1, 2, \cdots$), we adopted the idea of making ESR a high resolution

time-of-flight energy spectrograph by redesigning it as a third order achromat. The designing process is presented in section II., where the strengths of the multipoles are found quite feasible. Section III. shows our analysis of the system which includes the long term stability of the system and the resolution it can achieve.

II. DESIGN OF THE ACHROMAT

A. First Order Design

In order to design a circular machine as a third order achromat, no switched (S) or scwitched-reverse (C) sections can be used, and so we use the patten FRFR. This means that the first order map of the forward cell has to have $\mu_x = 90deg$ or $270deg$. The ESR ring contains six dipoles, twenty quadrupoles, eight sextupoles as well as RF cavities, beam cooling devices, and the injection-extraction system. Two long straight sections divide it into two identical parts, each of which is symmetric about its center. (Figure 1) [7]. It is much easier to take half rather than a quarter of the ring as the forward cell. Consequently, the other half should be the reversed cell, and an achromat corresponds to two turns of the ring. Since there are five conditions for a symmetric cell to meet [6], it is sufficient to fit only the quad strengths to find a desired solution. Thus the first order layout of the existing ESR ring is preserved. Also because of the symmetry, the forward cell is a first order achromat. The field gradients of the quads are displayed in Table 2.
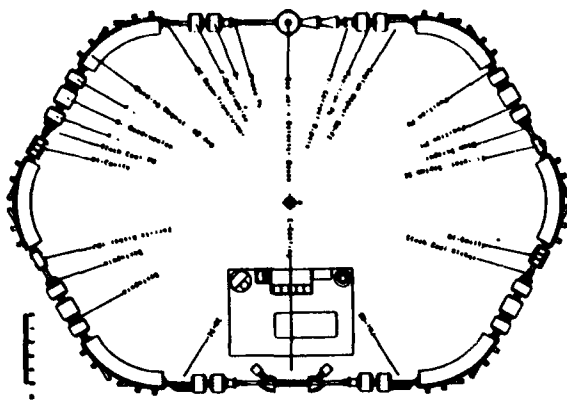
Figure 1: The original ESR

Element	Field Gradient(T/m)
Quadrupole1	5.2141708710097464
Quadrupole2	-3.7780943756357911
Quadrupole3	-0.2757583566872618
Quadrupole4	-1.0861967098567489
Quadrupole5	2.1018617072758571

Table 2: The field gradient of the quads

Element	Field Gradient (T/m^3)
Octupole1	-285.07749404229136
Octupole2	368.94910085314347
Octupole3	614.99793829516426
Octupole4	680.30311596846740
Octupole5	-5442.7323531935168
Octupole6	4250.2409995782432
Octupole7	-837.91940849587759
Octupole8	-1920.2296769772195
Octupole9	3595.6586358546853
Octupole10	-2187.7620170696497
Octupole11	2622.2366537113714
Octupole12	-1494.9597751428264
Octupole13	-757.00955057500670
Octupole14	305.17394857470414
Octupole15	-146.44242626707558

Table 4: The field gradient of the octupoles

B. *Second and Third Order Achromat*

Ten sextupoles were placed symmetrically in the forward cell. The values of the field satisfying the conditions for the second order map were found using the nonlinear optimizer in COSY INFINITY (Table 3). The same was done with the third order correction except that there are more octupoles after the third bend than before the first one. The positions of some of the multipoles were carefully chosen to limit the required field strengths. (Figure 2), and the results are quite realistic (Table 4).

Element	Field Gradient(T/m^2)
Sextupole1	-12.655855454352217
Sextupole2	8.0550942902064335
Sextupole3	-14.549046698823922
Sextupole4	15.697993340520378
Sextupole5	0.8844613366417970
Sextupole6	-53.905125612548678
Sextupole7	66.273372392466883
Sextupole8	-16.648568962020669
Sextupole9	-0.1067654043405714
Sextupole10	3.4540652334940187

Table 3: The field gradient of the sextupoles

Figure 2: The upgraded ESR, the long multipoles are quads and the short ones are sextupoles and octupoles

156
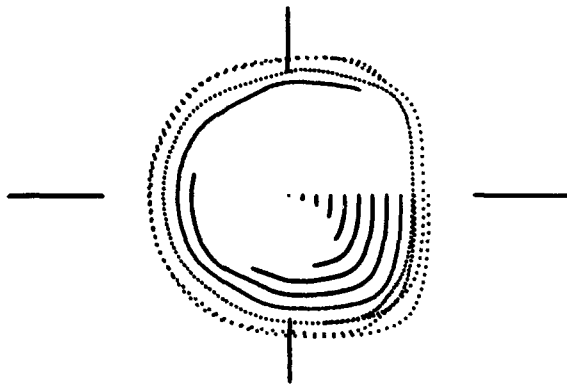
Figure 3: 200 turn tracking of the x-a motion of on-energy particles

Figure 4: Resolution vs number of turns at different emittances

III. ANALYSIS OF THE RING

A. *Dynamical Aperture*

Since our goal is to make ESR a multi-pass time-of-flight spectrograph, the long term behavior becomes of vital importance. It was studied with an 11th order one turn map which was generated by COSY INFINITY and used for non-symplectic tracking. The 200 turn dynamical apertures for both horizontal and vertical motion were determined by analyzing phase space plots. For particles of momentum spread ±0.5% to survive 200 turns, they are roughly 100 π mm mrad horizontally and 15 π mm mrad vertically. As an example, Figure 3 shows the horizontal motion of on-energy particles up to 200 turns.

B. *Resolution*

The resolution of this machine was determined in a statistical way. First, the 9th order one turn map was computed. Secondly, a large number of particles (1000) inside a certain phase space area were produced randomly by COSY. Then these particles were sent through the one turn map n times, therefore the n-turn time-of-flight of each particles were computed. Considering the random errors of the detector, which was assumed to be about 100 ps), the predicted energy deviations of every particle were calculated. Finally the difference between the predicted and initial energy deviations was obtained and the resolution of the ring was determined by calculating the inverse of the average differences. The dependence of the resolution on the number of turns and the emittance is presented in Figure 4 .

IV. CONCLUSION

A multi-turn third order achromat has been designed based on the layout of the ESR. The strengths of the magnetic multipoles are feasible and the dynamical aperture seems realistic for operation. For a rather large phase space, the resolution can be impressively high.

REFERENCES

[1] A. J. Dragt, *Nucl. Instr. Methods* A258, 339 (1987).

[2] F. Neri, in *Proc. Workshop on High Order Effects.* M. Berz and J. McIntyre (Eds.), Technical Report MSUCL-767 (1991).

[3] F. Neri, private communication.

[4] M. Berz, *COSY INFINITY Reference Manual Version 6*, Technical Report MSUCL-869 (1993).

[5] W. Wan, E. Goldmann and M. Berz, *Proc. Workshop on Nonlin. Effects Accel. Phys.*, Berlin (1992). M. Berz, S. Martin and K. Ziegler (Eds.), IOP Publishing, Bristol.

[6] W. Wan, E. Goldmann and M. Berz, *Proc. Comput. Accel. Phys. Conf.* (1993). To be published.

[7] B. Franzke *Nucl. Instr. Methods* B24/25, 18 (1987).

An automatic finder of field defects in a large A.G. machine

André VERDIER, Jean-Cédric CHAPPELIER(VSNA)
CERN CH1211 Geneva 23

Abstract

A series of program modules has been written in C, which can perform various tasks to analyse closed orbit measurements. They have been grouped into a software package which can be used by an operator to find field defects from orbit measurements. The basic algorithms used are well known and simple, based on fitting betatron oscillations. The effort has been put in the execution speed and ease of use.

New algorithms have been introduced to detect wrong measurements and check the relevance of the kick calculation, which are a decisive step towards automatization. It is presently possible to localise all relevant dipole field defects in a machine as large as LEP within less than one hour, including the check of the orbit readings.

I. THE PRINCIPLES

The essential part of the orbit treatment is the so-called fitting method. In a defect-free region, the on-momentum orbit measurements are expected to follow a betatron oscillation like :

$$y_i = a \cdot \sqrt{\beta_i} \cos(\mu_i) + b \cdot \sqrt{\beta_i} \sin(\mu_i) + c + \eta_i$$

where y_i stands for the ith measurement of the orbit, β_i and μ_i for the corresponding TWISS parameters and η_i for a realisation of a null-mean additive noise. Given this definition of η_i, we must put in the equation the average of the noise which is c. This parameter can be interpreted also as an offset of the measurements.

The values of a, b and c, are computed by means of the least-squares method. In fact what is interesting is not the values of a, b or c themselves, but how relevant is the fit, i.e. whether the measurements follow a betatron oscillation or not. To answer this question, we compute the residual $F_{n,j}$ of the fit :

$$F_{n,j} = \sqrt{\frac{1}{n-3} \sum_{i=j}^{j+n-1} (\tilde{y}_i - y_i)^2}$$

where $\tilde{y}_i$ is the estimation of y_i on the interval $[j, j+n-1]$. In practice the fitting width n varies between 4 (the minimum width since we fit 3 parameters) and a given maximum

fitting width we will call M. j denotes the position of the current measurement. The sums are here expressed from j to $j+n-1$ for sake of clarity. In practice we do not take into account the measurements considered as bad, so that the sums are done over n "good" measurements starting from position j (which can go further than $j+n-1$ if bad measurements are in between). The bad measurements are merely skipped.

Since $F_{n,j}$ is obviously related with the r.m.s. of η, we decided to normalise it in order to deal with numbers of the order of unity :

$$F_{n,j} = \sqrt{\frac{1}{n-3} \sum_{i=j}^{j+n-1} (\frac{\tilde{y}_i - y_i}{\sigma})^2}$$

with σ the r.m.s. of η. So a large value of $F_{n,j}$ indicates a bad fit, i.e. a defect inside the fitting range, whereas a value around unity indicates a good fit, i.e. a piece of closed orbit behaving like a betatron oscillation.

Thus if there is a defect between $i-1$ and i, all the values $F_{n,i-n+1}, \cdots, F_{n,i}$ will be large. If the $F_{n,j}$ values are displayed in array tables, n being the column index and j the line index, we observe typical patterns associated with defects. To a single measurement wrong at position j correspond n large values of $F_{n,j}$ at positions $j-n, j-n+1, \dots, j$. To a discontinuity in the orbit between positions $j-1$ and j, correspond n-1 large values of $F_{n,j}$ at positions $j-n, j-n+1, \dots, j-1$. As it is easy to recognise such patterns in a residue table, they were called "signature" in previous studies [2]. A common feature of the two examples above is the appearance of large values of $F_{n,j-n}$ following small values of $F_{n-1,j-n+1}$. This looks like a stair in the table and can be easily detected. This is what is used to locate defects.

II. NEW ALGORITHMS

A. Defect searching

The defect detection in A.G. machines was previously done by looking at the above defined signatures. But it appeared, after many orbit treatments, that simple signatures are not frequent and that it is much more efficient to look for "stairslike pattern" to find the defects. There-

fore this was the criterion chosen to be implemented in the automatic system. The algorithm to find a defect is the following : We compute the fit residues for the current measurement –let us say j– for different width : $F_{4,j}, \ldots, F_{M,j}$, where M stands for the maximum fitting width. If $F_{4,j}$ is "large" (with respect to a given threshold experimentally set to 1.1), the algorithm begins to search for a stair, i.e. it looks if $F_{5,p(j)} > F_{4,p(j)}$ where $p(j)$ is the previous measurement strictly before j which is not disabled (usually $j-1$). The algorithm carries on until it reaches the maximum fitting width M : for a current width n it tests whether $F_{n,p^{n-4}(j)} > F_{n-1,p^{n-4}(j)}$. If it as been the case for all n from 4 to M, then a defect is detected between measurement $j+3$ (excluded) and $j+4$ (included).

When such a defect has been detected, a penalty parameter is computed to in order to evaluate its importance. Since a defect between pick-up $i-1$ (excluded) and pick-up i (included) affects $N-1$ fits earlier (i.e. from measurement $i - N + 1$ to measurement $i - 1$ at least), N being the fitting-width, we decided to introduce :

$$f(i) = \sqrt{\frac{1}{(M-1)\cdot(M-3)}\sum_{n=4}^{M}\sum_{k=i-M+1}^{i-1} F_{n,k}{}^2} \quad (1)$$

The smaller (or at least the closer to 1) this number is the better all the concerned fits are and then the less important is the detected defect.

B. Relevance of an action performed on orbit measurements

In order to test the relevance of actions made on orbit measurements (like deletion of one measurement, addition of a field defect or their opposite), we introduce a measure of its efficiency as follows :

$$efficiency = 100\cdot\frac{f(i) - \bar{f}(i)}{f(i)} \quad (in \%)$$

where $\bar{f}$ denote the value of f, defined in (1), after the action has been performed. So if this action is relevant, the fits will be better after it and therefore $\bar{f}$ will be smaller than f and the above efficiency will be positive. If the action performed is not relevant the efficiency will be around 0 or even worse : negative.

C. The automatic system

With the detection and evaluation of defects and with the measure of the efficiency of a performed action, we now have the tools to built up an automatic treatment of orbit measurements. The algorithm we developed is described by figure 1. At first the expected noise r.m.s. is adjusted in order to deal with fit residues around 1. To this end the
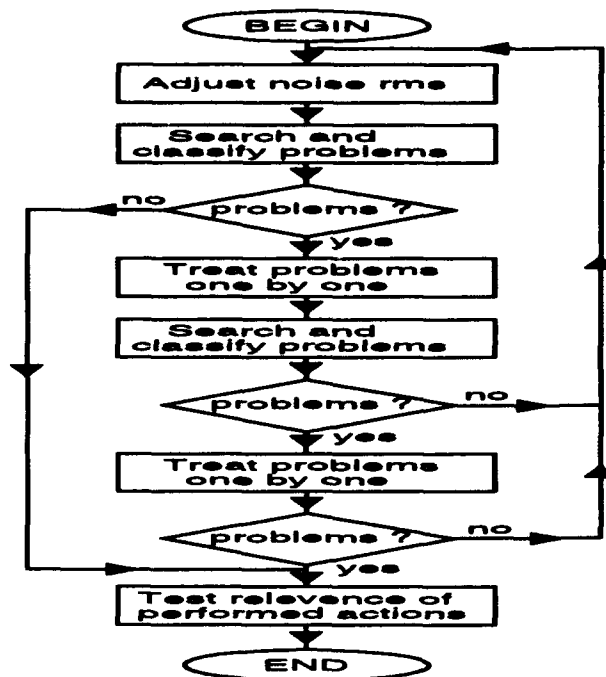
Figure 1: Automatic orbit treatment algorithm

fit residues are computed for the whole machine and for all fitting width from 4 to M. Since those residues must be around 1 if no defect occurs and if the noise r.m.s. is the one expected, this r.m.s. is s . .. a value such that the mean of all residues is 1.

Then a search for defects is done all around the machine, as explained in subsection A., and the defects are classified according to their penalty parameter in order to deal we most important ones first. Treating minor defects before major ones can bring severe errors and misunderstandings of the actual defects. Defects with a penalty less than a given threshold (which can be adjust by the user) are neglected in order not to treat to many defects at the same time.

Then for each defect detected, we analyse it as follows :

a - first test the suspected measurement by removing it and looking at the efficiency of the removal. If this efficiency is greater than 7.5%, the measurement is labeled as faulty.

b - if the measurement is not found faulty, then search for a field defect, i.e. a kick, between i and $i - 1$ (for a defect occurring in i). The kick calculation is done by minimising the error between the downstream measurements and the upstream measurements extrapolated with the effect of the kick.

c - if no field defect is found between i and $i-1$ test both

adjacent measurements of i : $i - 1$ and $i + 1$ as in a)

d - if no bad measurement if found within those neighbors, search for a field defect between $i - 1$ and $i + 1$

e - if nothing found, look for a field defect between $i - 2$ and i

f - if nothing found, search for field defect between $i - 2$ and $i + 1$

g - if there is still nothing found, give up here and let the problem unsolved. It will either be solvable afterwards or solved by the human user.

As described in the organigram (fig. 1) either the automatic system is run as a loop if all the detected defects have been treated, or the treatment is tried once again because the change of the situation can have made solvable problems which were not before. If after this second trial there are still remaining problems, the relevance of all the performed actions is checked by looking at the efficiency of their opposite. For example, if a measurement has been disabled, it is enabled and the efficiency of this action is tested. If the efficiency is negative the measurement is kept disabled otherwise it is enabled. The same treatment is applied to the field defects found. Then the process is stopped and the hand is given back to the user. If no problem remains after the second trial, the automatic process is run as a loop.

III. RESULTS

The automatic system was used at the end of 1992 to help the search of defects in coordination with the survey. Almost all large misalignments were found, the detailed report can be found in [3].

However the LEP machine was too much misaligned and this effort did not pay. In particular an important defect consisting of a common misalignment of seven quadrupoles was missed because it did not appear on the measurements done with a 90° optics. The pattern of the misalignment is shown on figure 2. In fact this defect was identified with the 60° optics. It was simply not considered relevant because it disappeared on the 90° optics. This experience was useful as it leads us to the right procedure, i.e. choosing the lowest possible phase advance per cell for the closed orbit analysis with the fitting method.

IV. CONCLUSION

An automatic system to find field defects in a large A.G. machine is available. It allows to locate defects in an orbit made of about 500 measurements in about one hour.
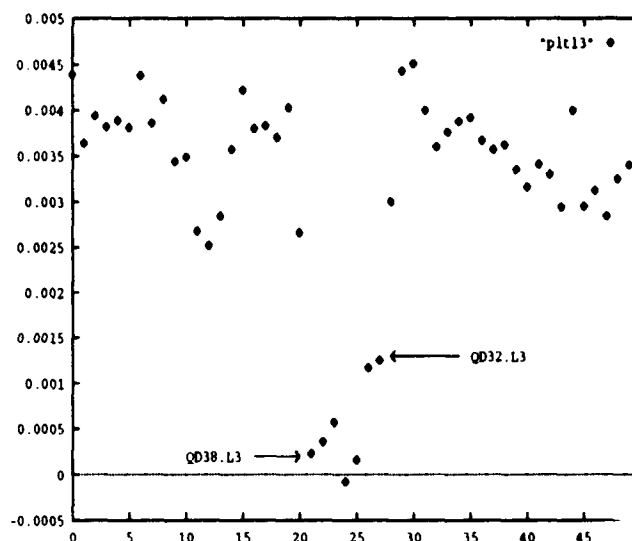
Figure 2: Misalignment missed by the fitting method. This misalignment makes a series of π-bumps if the phase advance per cell is 90°, which is the case for the named quadrupoles.

Using in the analysis of orbits for helping the LEP realignment in 1993, made it possible to identify problems related with its use. A positive outcome of this exercise was that the sampling of the orbit in term of betatron phase advance is critical. With one BPM at each D quadrupole, as in LEP, it is necessary to use an optics with a phase advance per cell below 60° in order not to miss defects.

V. REFERENCES

[1] G. GUIGNARD
The closed orbit measurement as a diagnostic tool for localization and correction of misalignments in the ISR, 11TH International Conference on High Energy Accelerators , held at CERN, July 1980. Also CERN ISR-BOM/80-21.

[2] D. BRANDT, A. VERDIER
Exhaustive search of field defect compensation and reading errors in A.G. machines, First EPAC in Rome, June 1988. Also CERN/LEP-TH/88-25.

[3] J.C. Chappelier and A. Verdier
Bare orbit analysis before the 92/93 shutdown. SL-MD Note 73 (January 27, 1993).

Automatic and expert systems for orbit analysis

André VERDIER,Jean-Cédric CHAPPELIER(VSNA)
CERN CH1211 Geneva 23

Abstract

In alternating gradient machines, the analysis of closed orbit or trajectory measurements in terms of betatron oscillations is useful to detect field defects. This has been used for long to help realignment.

In a large machine like LEP it is not practical to launch a survey check without making sure of the existence of the defects. In order to improve the reliability of their detection, it is extremely useful to have a fast system which makes it possible to cross-check several measurements.

For treating a large quantity of information in an empirical way, the use of an expert-system was proposed. In fact the numerical content of accelerator orbit measurements as well as the good knowledge of the modeling of such a machine makes such a system useless. The experience gained on the analysis of closed orbit measurements done at CERN shows that a simple algorithmic process is more efficient to analyse closed orbit measurements.

I. HISTORICAL INTRODUCTION

The search for field defects by fitting closed orbit measurements with betatron oscillations has been used for a long time [1]. The principle is that, in a part of a machine without any field error, the closed orbit is merely a betatron oscillation. As the modeling of these oscillations is well known, it is easy to determine whether a given closed orbit measurement behaves like a betatron oscillation or not by means of the very common technique of the least-squares fits. If the fit residue is large with respect to the expected r.m.s error of the measurements, a defect has been detected.

What is useful for a circular machine is to detect field defects and especially to distinguish them from orbit measurement errors. This last point is very important as it avoids a displacement of personals towards a place without any interest. For this analysis many tests have to be done. As we wanted to make an automatic system to perform those tests for LEP, a first feasibility study was done on the accumulation ring EPA at CERN [2]. It made it possible to determine exactly the location of the main dipole error in this machine.

At this time a Fortran program was written to compute the fits. The test of measurement relevance was done by looking for special patterns on the printout constituted of tables of residues associated with fit done with four to eight or more measurements downstream each Beam Position Monitor (BPM). Then removing the effect of detected field defects and disabling bad measurements was done by editing the input of the Fortran program. Thus the feasibility of the method was shown but the procedure was very much time consuming. Therefore it was decided to launch a further study to make a faster system.

It was felt that the patterns observed by printing tables of fit residues [3, 7] were symbolic quantities and that many rules were applied systematically in the course of the analysis. As we thought that we could do a more efficient analysis by increasing the number of rules, the approach of expert-system was attempted [4]. About half a man-year was spent on this. We obtained a system which was able to analyse the EPA orbit in some minutes whilst it took about some hours to do it with the Fortran program. However when we tried to apply this system to a larger machine like SPS (LEP was not built yet), we observed that it was no longer faster than the old procedure based on the Fortran program : it took some days to do the analysis. This was due to weaknesses in the organisation of the system and also to the fact that we were not able to find efficient rules nor to identify a large number of typical patterns in the residue tables.

When LEP was in operation, we decided to launch again the study with a new mind. Drawing lessons from the past, the expert-system approach was dropped. In what follows, we show why this approach was not the right thing to do.

II. WHAT EXPERT-SYSTEMS ARE AND ARE NOT

A general definition of what is an expert-system could be "a system for representing large quantities of knowledge" [5]. More precisely an expert-system is "a computer program that has a lot of knowledge in a specific field and is able to reach human-expert results in that field" [6]. But this definition does not take into account the methodological aspect of expert-systems, which consists of putting apart the knowledge of a specific field on one side (men-

tioned as "facts" and "rules" on figure 1) and the 'reasoning' mechanisms on the other side ("inference engine" on figure 1).
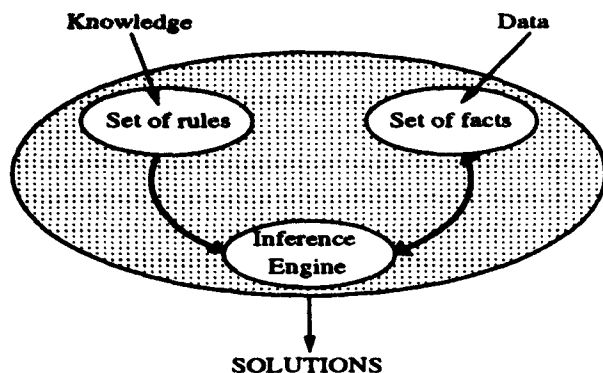
Figure 1: Expert-system architecture

The main applications of such systems are : symbolic knowledge manipulation, 'reasoning' in a fussy and incomplete domain, natural communication with humans [5]. More generally, any problem for which no algorithmic solution [1] is known, i.e. problems which need heuristics[2] belong to expert-systems (and more generally Artificial Intelligence) domain [5][6]. All those domains have two common characteristics :

- the informations used are symbolic,

- some choices have to be made, choices without certainty between many possibilities.

The expert-system field is even more precisely defined in [6] with the list of the seven kinds of problems which can be treated by such systems : "static" and "dynamic" diagnostic, task ordering and resource assignment, intelligent filtering, computer-aided design, conceptualization and computer-assisted instruction.

III. ANALYZING A CLOSED-ORBIT MEASUREMENT

It appears, from the above considerations, that the "expert-system" approach is not appropriate for analyzing closed-orbit measurements for several reasons :

- what previously gave us the idea of expert-system was these patterns we called "signatures" [2]. For instance,

---

[1] set of well defined operations which can be run in a finite time on a computer.

[2] rules with which one can find a solution without reliable theoretical background.

we consider fits done over four successive measurements and we list the residues of these fits done at each BPM. A single bad measurement results in a sequence of 4 large residues (signature of a bad measurement) whereas a single field defect results in a sequence of only 3 large residues (signature of a field defect). However when the situation becomes more complicated than those simple cases (mixing of bad measurements and field defect) these signatures disappear. This is precisely the case where a computer program is needed. On the other hand the number of symbols ("signatures") and rules used is very limited : except for the above simple signatures, it was never possible to determine other more complicated patterns to deal with any complicated case. This small number of patterns and empirical rules is a good indication for trying algorithmic processes. It shows that this problem does not need the power of expert-systems : building such a system is really time consuming (in our first try : half a human-year was not enough to obtain an operational system) and is justified only for big amount of rules.

- we know a precise mathematical model for betatron oscillations and closed orbit distortions. There is no symbol in that problem the expression of which cannot be fully calculated. It is more a computable input-output relation than a "reasoning tree" : it is a "low-level" problem. Furthermore the symbolisation reduces information, but in this case without simplifying the problem. Symbolisation is only useful when the reduction of information is sensible and induces simplifications without which no solution can be found.

- we wanted a fast treatment, whereas expert-systems are more often very slow to conclude, as it was the case in our first trial.

We then developed an algorithmic program which solves most of the situations [7]. It can certainly be improved by including solutions to more situations in which the human-expert empirical rules are still very simple. But one should keep in mind that in such a system there will always be a point at which the program should ask "what to do" or "how to continue" to the human-expert. This point has to be well defined, considering an equilibrium between programming cost (time and money) and convenience of use. In our case, where we have to process about 500 measurements, the number of cases left to the operator decision is of the order of one tenth. This number is small enough to let the analysis be completed within one hour.

IV. CONCLUSION

The numerical content of accelerator orbit measurements as well as the good knowledge of the modelling

of such a machine makes expert-systems useless for orbit analysis. The experience gained on the analysis of closed orbit measurements we have done shows that a simple algorithmic process is more efficient to analyse closed orbit measurements. We built up an automatic procedure which is able to find the field defect of LEP in less than one hour, which is a considerable improvement compared with the methods previously used. Notice that with this algorithmic approach all possible solutions at one step can be tested in a short time, showing, if still necessary, that the expert-system approach was for sure not appropriate. As mentioned in [6] : *"The expert-system approach is not justified for all kinds of problems. For example, in cases where all possible solutions can be exhaustively tested in a reasonable time (...) there is no need searching for another method"*.

ACKNOWLEDGMENTS

V.   REFERENCES

[1] **G. GUIGNARD**
The closed orbit measurement as a diagnostic tool for localization and correction of misalignments in the ISR, 11TH International Conference on High Energy Accelerators , held at CERN, July 1980. Also CERN ISR-BOM/80-21.

[2] **D. BRANDT, A. VERDIER**
Closed orbit correction with the fitting method, LEP Note 596, November 1987.

[3] **D. BRANDT, A. VERDIER**
Exhaustive search of field defect compensation and reading errors in A.G. machines, First EPAC in Rome, June 1988. Also CERN/LEP-TH/88-25.

[4] **D. BRANDT, F. VARLOT, A. VERDIER**
Première version d'un système expert pour la recherche des défauts de champ, LEP Note 624, April 1989.

[5] **J.L. LAURIERE**
Intelligence Artificielle, Résolution de probl'emes par l'Homme et la machine, Eyrolles 1987.

[6] **A. BONNET, J.-P. HATON, J.M. TRUONG-NGOC**
Systèmes Experts, Vers la maîtrise technique, InterEditions 1986.

[7] **A. VERDIER, J.-C. CHAPPELIER**
An automatic finder of field defects in a large A.G. machine, this Conference, May 1993.

Symplectic Scaling, a DA Based Tool

G. H. Hoffstätter and M. Berz
Department of Physics and Astronomy and
National Superconducting Cyclotron Laboratory
Michigan State University, East Lansing, MI 48824

Abstract

Maps of magnetic particle optical elements written in geo-metric coordinates have two scaling properties. These are connected to the fact that the maps depend only on the ra-tio of field strength to magnetic rigidity and on the product of field strength to the size of the element. Once the map of an element is known for a given type of beam particles as a function of the magnetic field strength at the pole tip, the first scaling property can be used to compute the map for any particle type. With the second scaling property, the map can be computed for any similar element which differs in size. Usually the map is not known as a function of the magnetic field. With DA based programs, however, one can obtain the Taylor expansion of that function.

The expansion can serve to approximate maps which could otherwise only be calculated by very time consuming numerical integration. To make this method applicable to cases where the symplectic structure is important, canon-ical maps have to be approximated. The approximated maps still have to be completely symplectic up to their ex-pansion order. To meet this requirement, we have exam-ined how the scaling properties can be used in connection with the symplectic representations of Lie transformations and generating functions. Useful examples of the result-ing symplectic scaling method include maps of fringe fields, as well as solenoids. Speed and accuracy of the method, which was implemented into version 6 of COSY INFIN-ITY, will be demonstrated and a guide given how to apply this method most efficiently.

I. Introduction

Computer codes which can manipulate and differentiate truncated power series of functions, differential algebra (DA) codes, can be used to integrate coupled autonomous differential equations $d\vec{z}/ds = \vec{f}(\vec{z})$ very efficiently by us-ing the Lie derivative $L_f = \vec{f}\vec{\nabla} + \partial_s$ [1]. This entails the

possibility to obtain transfer maps of main–field regions, where the equation of motion does not depend on the in-dependent variable s. The transfer map after a main field of length l_0 is obtained by evaluating $\vec{M}(\vec{z}) = \exp(l_0 L_f)\vec{z}$.

This method can not be applied when the equation of motion is governed by fields which depend on the path length s of the reference trajectory. Such nonautonomous differential equations are usually solved by some means of numerical integration. Evaluating this integration in DA automatically yields the transfer map [1, 2]. However, this integration is extremely time consuming compared to the method for the main field, which is faster by up to three orders of magnitude [3].

We look for an alternative which should not compro-mise much accuracy but work much faster. Since we want to implement the algorithm into an arbitrary order code, it should work to all orders. The obtained maps have to be completely symplectic up to their evaluation order. For repetitive systems this need is obvious. The destructive effect of symplecticity violation on phase space would be magnified with every turn [4]. The symplectic condition can also be important in single pass systems, for instance when the spherical aberration of solenoids is of interest or when an achromat is designed [6, 5], since the symplec-tic condition enforces certain relations between aberration coefficients.

In the past, a variety of approximations have been used which speed up the process of obtaining the desired maps, in particular for the simulation of fringe fields:

- Low accuracy numerical integration – is not accurate and not symplectic.

- Fringe field integrals, which are for instance used in the codes TRANSPORT [8] and GIOS – can not be used for solenoids, is in general not symplectic and so far only available to third order although attempts are being made to extend it to fifth order [7].

- The Impulse approximation, which is used in TRANS-PORT – can not be used for solenoids and works only to second order.

Here we present an approximation without those draw-backs, which has been implemented in version 6 of the DA code COSY INFINITY.

II. Symplectic Scaling

A. Scaling

In geometric coordinates $\vec{z} = (x, x', y, y', \delta_l, \delta_p)$, which are used in TRANSPORT [8], the transfer map has two scaling properties. Those properties are made obvious by the Lorentz force equation

$$\frac{d(\gamma m \frac{d\vec{r}}{dt})}{dt} - q\frac{d\vec{r}}{dt} \times \vec{B}(\vec{r}) = \vec{f}(\vec{r}, t) = 0 \qquad (1)$$

with relativistic γ, mass m, time t, charge q, magnetic field $\vec{B}$, and coordinate vector $\vec{r}$. Let $\vec{r}(\vec{r}_0, \dot{\vec{r}}_0, t)$ be a solution of the Lorentz equation. When the field is now changed to $\alpha\vec{B}(\alpha\vec{r})$, we get a new equation of motion. This equation can be obtained by substituting $\alpha\vec{r}$ for $\vec{r}$, αt for t, and leaving $\dot{\vec{r}}$ unchanged. Therefore, a field $\alpha\vec{B}(\alpha\vec{r})$ leads to the equation

$$\vec{f}(\alpha\vec{r}, \alpha t) = 0 \quad , \qquad (2)$$

which has the solution $\frac{1}{\alpha}\vec{r}(\alpha\vec{r}_0, \dot{\vec{r}}_0, \alpha t)$. This we call geometric scaling: magnifying a magnetic element and ray coordinates by a factor of α yields a possible particle ray if at the same time the field strength is reduced by the same factor.

The second scaling property, rigidity scaling, is also obtained from equation (1) and states that the particle ray does not change whenever the ratio qB/p does not change; B denotes the pole tip field.

Suppose we knew the function $\vec{z}_f = \vec{F}(\vec{z}_i, B)$, the transfer function from one plane in the accelerator to another as a function of the magnetic field at the pole tip. With geometric scaling we could find all maps for similar elements which differ in size, and with rigidity scaling all maps which differ in properties of the particle could be obtained. However, since we are interested in canonical maps, which do not scale via the above method, it is necessary to use a momentum dependent transformation $\vec{z} = T(\vec{z}, p)$ to transform from geometric coordinates $\vec{z}$ to canonical coordinates $\vec{z} = (x, a, y, b, \delta_\tau, \delta_E)$ [2].

Once a transfer map is obtained at a field B_0 in canonical coordinates by means of numerical integration in DA, it can be transformed into geometric coordinates. The transfer function in geometric coordinates contains the dependence of motion on the momentum. The required transfer function, which depends on the pole tip strength B, can therefore be created using rigidity scaling. Computing this function once for a certain particle and an element of a certain size is enough to calculate the transfer map of all kinds of particles through similar elements of any size, and hence this map contains complete information. Using DA, the Taylor expansion in the quantity $\delta_B = (B - B_0)/B_0$ around the reference field B_0 is obtained automatically. Saving this Taylor expansion gives us a reference file to approximate all kinds of maps which can be obtained by scaling. The approximation will be as accurate as the Taylor expansion approximates the function, which is very accurate for several reasons:

- The Taylor expansion in respect to δ_B can be of higher order than the order in which the map is computed.
- There are several methods which yield aberration coefficients as multiple integrals over powers of derivatives of the field and the fundamental rays [?, 6, ?]. Since the rays do not change much in fringe fields, those integrals are very close to power series in respect to B. For solenoids this is not the case since the fundamental rays in a solenoid strongly depend on B.

- The deviation of the magnetic field from the reference magnetic field is often quite benign, especially when the approach described in the next chapter is used.

This direct route yields approximate maps, which however would not be exactly symplectic. As mentioned in the introduction, this can not be tolerated. We therefore compute a symplectic representation, which depends on B, and store the Taylor expansion of this symplectic representation. Evaluating the expansion gives an approximate symplectic representation, which in turn yields a fully symplectic map.

B. Symplectic representation

As representation we choose the single Lie exponent, which has speed advantages compared to the other five representations that are implemented in COSY INFINITY: [9].

$$\vec{M}(\vec{z}) = M_1(B)e^{:P(B): \vec{z}} \qquad (3)$$

with the usual notation $: f : g$ of the Poisson bracket of f with g, the linear matrix $M_1(B)$, and the Lie exponent $P(B)$ which is a polynomial of orders higher or equal to three in the map coordinates. The coefficients of the matrix and of the polynomial are functions of B. Therefore the map

$$M_1^{-1}(B)\vec{M}(\vec{z}, B) = \vec{z} + \vec{N}(\vec{z}, B) \qquad (4)$$

has to be represented by a Lie exponent. Evaluating the symplectic condition

$$(I + \partial_{\vec{z}}\vec{N})J(I + \partial_{\vec{z}}\vec{N})^T = J \qquad (5)$$

order by order shows that this representation always exists for symplectic maps and that it is unique. Here I describes the unity matrix and J the symplectic matrix.

Often there are a variety of generating functions which can represent the matrix $M_1(B)$, but it can not be guaranteed that there always exists a generating function of the classical type. For the cases of fringe fields and for solenoids, however, there is always at least one possible choice. We choose an appropriate generating function according to the greatest determinant of the submatrix which has to be inverted [1].

C. Application

The whole process of using the symplectic scaling (SYSCA) procedure is contained in the flow diagram in figure 1. The

left part refers to the creation of a reference representation by creating a canonical reference map that contains the dependence of the map on energy and computing the dependence of the map on the magnetic field via rigidity scaling. Then the symplectic representations are computed as functions of the field strength and saved to a file. The right part refers to reading the representation and inserting δ_B suitably to describe a map $\vec{M}^s$ which can be scaled to the desired map $\vec{M}^*$. From this representation the canonical map is computed and transformed to a geometric map which is used for scaling. The scaled geometric map is finally transformed back to a canonical map.

Order	Solenoid	Dipole	Quadrupole
1	6	184	30
2	8	110	21
3	14	80	16
4	20	74	12
5	33	55	11
6	35	65	10
7	39	60	11

Table 1: Speed advantage of SYSCA over numerical integration.

$\vec{M}(\vec{z})$ $\vec{M}^*(\vec{z})$
(1) $\vec{T}(p^*)$
$\vec{R}^*(\vec{z})$
(1)
$\vec{R}^s(\vec{z})$
$\vec{M}(B)$
(3) $\vec{T}^{-1}(p^s)$
$\vec{M}^s(\vec{z})$
$F(B), \; P(B)$
(3)
$F^s, \; P^s$
reference file   reference file
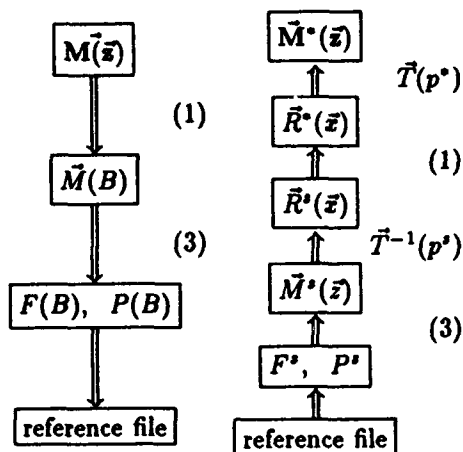
Figure 1: A map for arbitrary beam parameters, element size, and field strength can be computed from the map of a similar element using symplectic scaling.

For the reasons explained above, this approximation is very accurate for a wide range of the scaling factor δ_B. For fringe fields it can range up to 100, whereas for circular elements the tolerance is smaller for the given reasons and is usually limited to about 10%. The most efficient use of symplectic scaling does not require a great range for δ_B at all. A typical problem in the design of accelerating structures, storage rings or imaging structures is to:
- fit system parameters according to some optical conditions.
- evaluate a system with small deviations from the optimized parameters to determine the system's sensitivity to construction errors.

Both applications have in common that the map of a system has to be computed very often with slightly changed parameters. The way to tackle those problems with a gain of speed and practically no loss of accuracy is to optimize the system neglecting fringe fields. Reference files can now be created which correspond to this crude approximation as basis for the approximation of other elements. A new optimization run using SYSCA will now yield a final optimized result. The saved files can also be used as basis for the error analysis. The results will again be very accurate since the changes considered will not cause big deviations from the reference map.

D. *Speed and Accuracy*

Reference [3] contains several example results of SYSCA. From this and other experiences, an estimate on the speed is given in table 1 as function of the evaluation order. The accuracy depends on the order of evaluation of the expansion in δ_B and the value of δ_B. When the approximation is performed according to the procedure given above, the results are usually of an accuracy comparable to the COSY standard integrator, which is a Runge–Kutta of 8th order with accuracy of about 10^{9-n} for coefficients of order n.

REFERENCES

[1] M. Berz. Arbitrary order description of arbitrary particle optical systems. *Nucl. Instr. and Meth.*, A298:426–440, 1990.

[2] M. Berz. New Features in COSY INFINITY. *Proc. to Conp. Accel. Phys. 93.*, 1993.

[3] G. H. Hoffstätter, M. Berz. An Efficient Symplectic Approximation for Fringe–Field Maps. *Proc. to Conp. Accel. Phys. 93.*, 1993.

[4] I. Gaja, A. J. Dragt, D. T. Abell. A comparison of Methods for Long-Term Tracking Using Symplectic Maps. *Proc. to Workshop on Nonlin. Effects in Accel. Phys., Berlin, IOP Publishing.*, 1992.

[5] W. Wan, Eyal Goldmann, M. Berz. The Design of a Four Cell Third Order Achromat *Proc. to Conp. Accel. Phys. 93.*, 1993.

[6] H. Rose. Hamiltonian magnetic optics. *Nucl. Instr. and Meth.*, A258:374–401, 1987.

[7] B. Hartmann and M. Berz and H. Wollnik. The computation of fringing fields using Differential Algebra. *Nucl. Instr. and Meth.*, A297:343–353, 1990.

[8] K. L. Brown, F. Rothacker, D. C. Carey, and Ch. Iselin, TRANSPORT User's Manual. *SLAC-91.*, 1977.

[9] M. Berz. COSY INFINITY Version 6 Reference Manual. *MSUCL-869.*, 1991.

New Features in DIMAD

R.V. Servranckx

TRIUMF, 4004 Wesbrook Mall, Vancouver, B.C. V6T 2A3

Abstract

This paper presents the new features that have been introduced recently in DIMAD. [1]

The first is a simplified (not self consistent) simulation of transverse space charge effects. This simulation can be used in conjunction with all the tracking operations of DIMAD.

The second is a new accelerating cavity, in which the accelerating field can be a function of the longitudinal coordinate.

The third is the translation capability of the MAD input format to a COSY compatible input.

The fourth is the creation of a COSY input file for lattices with alignment and field errors and subsequent corrections.

I. SPACE CHARGE SIMULATION FEATURE

The space charge effect simulated is that of the transverse distribution only. The distribution is assumed to remain elliptical in the transverse plane x-y. It is also assumed to remain Gaussian. Results provided by the program indicate if these assumptions are reasonable.

The simulation installed in DIMAD is a derivation inspired from the approach of G. Parzen [4]. U. Wienands and G. Wellman [5] improved the method introduced by Parzen. However some problems occurred in the fitting procedure of the matched beam under space charge conditions. The solution we adopted uses only one reference particle instead of 4 (G. Parzen) or 8 (U. Wienands). This avoids introducing some incorrect geometrical assumptions about the shape of the matched beam.

The simulation is first run for some number of turns to allow the distribution to stabilize around an elliptical shape. Then any other tracking routine of DIMAD can be used. All particles are subjected to the space charge forces defined by the reference particle. At all times the reference particle continues to be tracked and the space charge distribution is updated regularly.

II. CEBAF TYPE ACCELERATING CAVITY

David Douglas of CEBAF developed a formalism for simulating the tracking of particles through an accelerating cavity whose longitudinal accelerating electric field varies with the longitudinal coordinate. [6] This option was used successfully in simulating the behaviour of the CEBAF superconducting cavities. The simulation results agreed reasonably well with the measurements on the CEBAF linac.

Those interested in using this feature for other types of cavities should contact David Douglas at CEBAF.

III. COSY INPUT FORMAT GENERATION

Two COSY input generations have been implemented in DIMAD. The first one is within the standard input reading modules. It simply translates the Standard (Mad) input [3] into a COSY compatible format. [2] Only the element and beam line definitions are translated. The variable links used in the standard input are lost. Only the resulting numerical values are translated.

The second input is within the DIMAD operation stream. It can appear at any position in that stream. The currently used lattice, in its final status when the translation is required, is translated. The translation thus will include any misalignement and field errors and also corrector values as set by DIMAD. Since COSY operates in canonical variables, the symplectic option of DIMAD has to be set before invoking the translation.

IV. REFERENCES

[1] R. Servranckx, K. Brown, L. Schachinger, D. Douglas, *Users Guide to the Program DIMAD*, SLAC report 285 UC-28 May 1985.

[2] M. Berz, *COSY INFINITY Version 5 , User's Guide and Reference Manual*, Technical report MSUCL-811, December 1991.

[3] D.C. Carey, F.C. Iselin, *Standard input Language for Particle Beam and Accelerator Computer Programs*, 1984 Summer Study on the Design and Utilization of the Superconducting Super Collider, (Snowmass, Colorado, 1984).

[4] G. Parzen, *Space Charge Limits in Proton Synchrotrons*, (submitted to Nucl. Instrum. and Methods)

[5] G.F. Wellman, Transverse Space Charge Simulation in DIMAD, In collaboration with U. Wienands. TRI-DN-89-K84.

[6] D. Douglas (private communication).

A First Order Matched Transition Jump at RHIC

S. Peggs, S. Tepikian, D. Trbojevic

Brookhaven National Laboratory*, Upton, New York 11973

I INTRODUCTION

RHIC, the Relativistic Heavy Ion Collider at Brookhaven National Laboratory, will be the first superconducting accelerator to cross transition, when ramping begins in 1998. All ion species except for protons will cross transition. Simulations show gold ion losses of 70%, and longitudinal emittance growth of 60%, if nothing is done to ameliorate the crossing [1,2,3]. RHIC will also be the first accelerator to use a *matched first order* transition jump to modify γ_T for a short time, by pulsing a set of quadrupoles, so as to cross transition rapidly, with little beam disturbance. "First order" means that the change in γ_T is proportional to the pulse current. "Matched" means that the quadrupole arrangement minimizes optical distortions. Crucially, the maximum dispersion is only 2.30 meters, compared to the unperturbed value of 1.84 meters. This paper describes the transition jump design, and reports on its performance in the lattice RHIC92.3 [4].

II PERFORMANCE PARAMETERS

Transition comes when the differential of circulation time with respect to $\delta = \Delta p/p_0$, the off momentum parameter, is zero. This happens when the relative rate of change of speed β equals the relative increase in path length - when

$$\frac{1}{\beta}\frac{d\beta}{d\delta} = \frac{1}{\gamma_T^2} = \frac{2\pi}{C_0}\langle\eta\rangle \qquad (1)$$

Here C_0 is the circumference of RHIC, and $\langle\eta\rangle$ is the dispersion function averaged over bend angle (in dipoles), leading to a value $\gamma_T = 22.8$ that is a property of the lattice optics. See Table 1 for these and other parameters.

Two time scales characterize transition crossing. The *non-adiabatic* time T_c, given by

$$T_c = \left(\frac{AE_T}{Z e V |\cos(\phi_s)|} \cdot \frac{\gamma_T^3}{h\gamma'} \cdot \frac{C_0^2}{4\pi c^2}\right)^{1/3} \qquad (2)$$

with a nominal value of 0.041 seconds, represents the time during which the longitudinal motion of the synchronous particle ($\delta = 0$) is not well represented by a slowly varying Hamiltonian [5]. The *nonlinear* time T_{nl},

$$T_{nl} \doteq \frac{(\alpha_1 + \frac{3}{2}\beta_T^2)\,\delta_{max}\,\gamma_T}{\gamma'} \qquad (3)$$

has a nominal value of 0.129 seconds. It parameterizes the Johnsen effect, in which particles with different momenta cross transition at different times [6,7]. Transition is delayed or advanced by $\pm T_{nl}$ for a particle with $\delta = \pm\delta_{max}$ at the edge of the beam. A subsidiary advantage of first order schemes over second order schemes is that the "nonlinear parameter" α_1, defined through

$$\frac{C}{C_0} = 1 + \frac{\delta}{\gamma_T^2}[1 + \alpha_1\delta + O(\delta^2)] \qquad (4)$$

is almost constant during the jump [8].

RHIC is unusual in that $T_{nl} \gg T_c$ - the nonlinear time is much longer than the non-adiabatic time. This is mainly because $\gamma' = d\gamma/dt = 1.6\ s^{-1}$ is relatively small - superconducting accelerators ramp slowly. For comparison, $\gamma' = 162\ s^{-1}$, $T_{nl} = 1.5$ msec and $T_c = 3.5$ msec in the normal conducting Fermilab Main Ring. The nominal bipolar jump illustrated in Figure 1 maintains a clearance of

$$|\gamma - \gamma_T| > 0.4 \approx 2\gamma' T_{nl} \qquad (5)$$

except for about 60 milliseconds. Transition is crossed at about $d(\gamma-\gamma_T)/dt = 14.9\ s^{-1}$, almost ten times faster than without a jump. Longitudinal simulations predict that these jump parameters lead to no particle loss, and reduce the longitudinal emittance blow up to only about 10%.

Non-adiabatic time	T_c [s]	0.041
Nonlinear time	T_{nl} [s]	0.129
Transition gamma	γ_T	22.8
Transition jump step	$\Delta\gamma_T$	−0.8
Transition jump time	ΔT [s]	0.060
Acceleration rate, $d\gamma/dt$	γ' [s^{-1}]	1.6
Jump rate, $d\gamma_T/dt$	γ_T' [s^{-1}]	−13.3
Max off-momentum parameter	δ_{max}	0.0043
Max. jump dispersion	η_{Jmax} [m]	2.30
Circumference	C_0 [km]	3.834
Atomic number	Z	79
Atomic weight	A	196.97
Ions per bunch	N	10^9
Transition energy per nucleon	E_T [GeV]	21.4
Peak RF voltage	V [MV]	0.3
Stable phase	ϕ_S	0.16
Harmonic number	h	342
Longitudinal emittance (95%)	ϵ [eV-s]	0.3
Nonlinear parameter	α_1	0.6

Table 1 Nominal RHIC operating parameters for gold ions.

γ

Bipolar jump

Δγ = 0.8

γ_T

Stay clear zone

60 msec

ΔT = 4T_nl ≈ 516 msec

dγ/dt ≈ 1.6 (s⁻¹)

t, ramp time
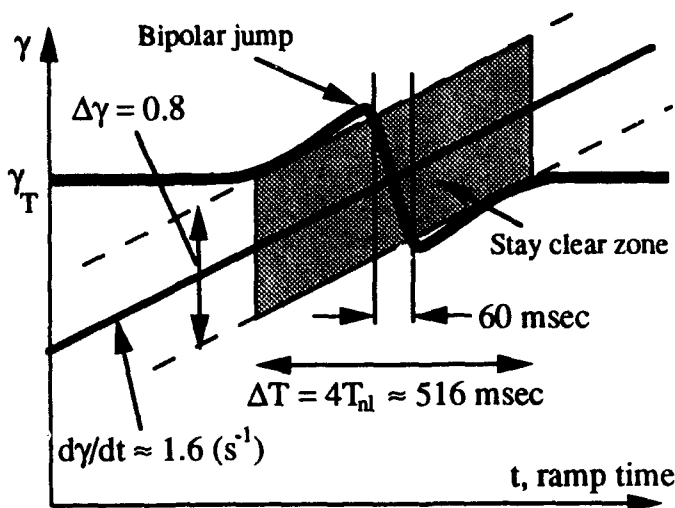
Figure 1 Transition is crossed almost 10 times faster with the nominal RHIC bipolar transition jump than without. Not to scale.

III THE TWO FAMILY DESIGN

When a quadrupole i is perturbed by strength q_i, the horizontal tune shifts to first order by

$$\Delta Q_H = \frac{1}{4\pi} \sum_i q_i \beta_{Hi} \qquad (6)$$

Risselada derives the elegant result, valid to all orders, that

$$\Delta \frac{1}{\gamma_T^2} = -\frac{1}{C_0} \sum_i q_i \eta_i^* \eta_i \qquad (7)$$

where η_i^* is the perturbed dispersion function [9]. All of the existing transition jump schemes at other accelerators (that the authors are aware of) are *second order unmatched* schemes. Most such schemes [9] have only one family of quadrupoles of strength q so that, to first order in q,

$$\eta_i^* = \eta_i + \frac{d\eta_i}{dq} q \qquad (8)$$

ready for substitution into equation (7). Usually all perturbed quads have the same periodic value for η_i and β_i, while their polarities are regularly flipped, so that the first order sums in equations (6) and (7) are identically zero [10]. In all cases, second order schemes deliberately rely on large changes in the dispersion function. This is a major disadvantage, since it intrinsically leads to large beam sizes at transition [11]. However, in the first order analysis that follows, $\eta^* = \eta$, so that the change in γ_T from a single perturbed quad goes like η_i^2, its dispersion squared, while the change in the tune is proportional to β_{Hi}, its beta function.

The lattice of each RHIC ring consists of six arcs connected by six interaction regions. Each of the 12 matched FODO cells in an arc has a phase advance of slightly less than 90 degrees. The crossing point telescope optics at the center

of an interaction region are matched to a neighboring arc through 5 half cells, in which the beta functions are very close to arc FODO cell values, but which are (almost) dispersion free. Immediately next to every quadrupole in the arcs and in the interaction regions is a small superconducting correction magnet. Most correctors have one dipole winding, but some have four concentric windings.

There are two families of 24 γ_T quads in each of RHIC's two rings, in the second layer of some four layer correction magnets. The "G" family is at locations next to focussing quadrupoles where η, β_H and β_V are all close to their matched FODO cell values. This family has a strong effect on γ_T, and also on the horizontal tune, according to equations (6) and (7). The "Q" family is located next to the 4 focussing quads in every interaction region where the dispersion η is almost zero, but where β_H and β_V are still close to their FODO cell values. This second family is used to null out the horizontal tune shift (and also the much smaller vertical shift), with only a minor effect on γ_T. The two family strengths have opposite signs, and only a small difference in absolute value - 6% for the nominal jump - so that $q_G \approx -q_Q$.

Figure 2 shows how lattice parameters of interest vary as a function of q_G, the strength of the G family. The inner pair of vertical dashed lines are drawn through $\Delta\gamma_T = -0.4$ and 0.4, requiring $q_G = -0.0036$ and 0.0043 m⁻¹, respectively. This is well inside the extreme performance obtained when the power supplies are run at their nominal maximum current of 50 Amps, when $q_G = \pm 0.0084$ m⁻¹, as shown by the outer pair of vertical dashed lines. Although some curvature is visible on the $\Delta\gamma_T$ line, this jump scheme is very linear. Extended performance is available, if necessary.

β_Hmax/100

η_max

Δγ_T

η_min

Lattice parameters [m]

Perturbation strength of family G, k_G [1/m]
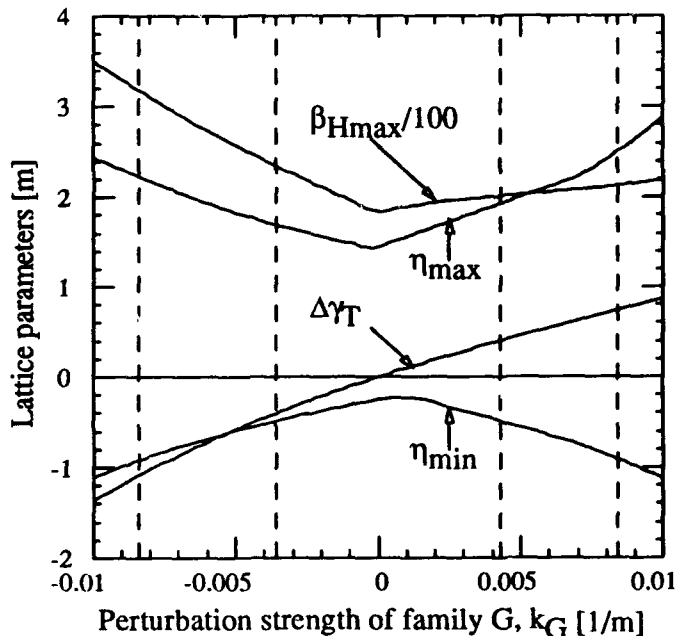
Figure 2 Change in γ_T and optical distortions versus the strength of the transition jump perturbation. Dashed lines show nominal and extreme excitation strengths.
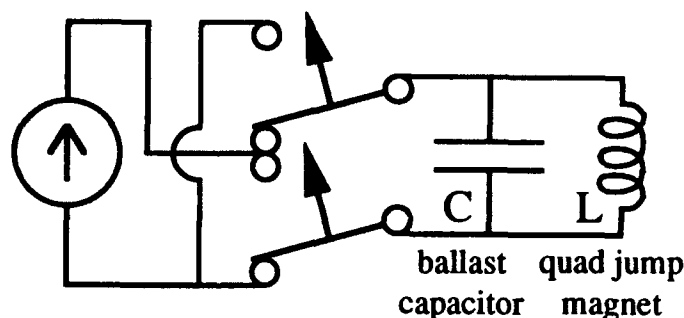
Figure 3 Equivalent circuit of the transition jump quadrupole families. There is a total of 12 power supplies per RHIC ring.

Figure 3 shows the equivalent circuit of the bipolar switching power supplies. The magnet current profile has the same shape and timing as the γ_T curve shown in Figure 1 (since the response is linear). That is, the excitation current slowly ramps up to a value of about 24 Amps over about 0.23 seconds, according to a programmable curve pre-loaded into a function generator table. Then the solid state switches open, so that the current in the magnet reverses polarity in half the natural period of the LC combination of the correction winding and the ballast capacitor, about 0.06 seconds. The switches close with reversed polarity when the voltages across them are near zero. Finally, the current again follows a function generator table as it ramps down to zero.

IV OPTICAL PERTURBATIONS

The RHIC FODO cell phase advance, nearly 90 degrees, is very favorable for reducing unwanted optical perturbations - beta waves and dispersion waves. Downstream from one of the γ_T quads there is a free horizontal beta wave

$$\frac{\Delta\beta}{\beta} = -q\,\beta_q\,\sin[2(\phi-\phi_q)] \qquad (9)$$

with a phase advancing twice as fast as the betatron phase. There is also a free horizontal dispersion wave, given by

$$\frac{\Delta\eta}{\sqrt{\beta}} = -q\,\eta_q\,\sqrt{\beta_q}\,\sin(\phi-\phi_q) \qquad (10)$$

advancing in step with the betatron phase. If two γ_T quads with the same strength are arranged in a doublet, at focussing quadrupoles one cell apart, their free beta waves are launched almost 180 degrees out of phase. That is, although the beta function is significantly perturbed between the two quads, very little of the wave escapes into the rest of the ring. Further, if two doublets in a dispersive region are placed next to each other in a quadruplet, so that γ_T quads are next to four focussing quadrupoles in sequence, then the dispersion wave will also be almost completely confined within the four quads.

The G family is arranged as six quadruplets, one at the beginning of each of the six arcs. By contrast, the Q family is arranged as twelve isolated doublets, one on either side of each of the six interaction points. These do not generate a significant dispersion wave, because they are at almost non-dispersive locations. Some global optical distortions do exist in practice, since the phase advance is somewhat less than 90 degrees, and since the γ_T quads do not have perfectly matched values (even by design). Figure 2 shows how the ring wide values for $\beta_{H\,max}$, η_{max}, and η_{min} vary as a function of q_G, the G family strength. The variation of $\beta_{V\,max}$ is less than 4% over the entire range, and so it is not shown.

An alternative arrangement, that was also investigated for RHIC, is to place one G family doublet on either side of an interaction point. This generates a dispersion wave across the interaction region, but because the unperturbed dispersion is almost zero there, anyway, this is not a problem. The phase advance between doublets still must be 180 degrees (plus an integer times 360 degrees) if the dispersion wave is to be canceled before it reaches the arcs. This is more difficult to guarantee when the doublets are far apart, than when the doublets are close together in neighboring FODO cells.

V CONCLUSIONS

Transition is the time when the momentum spread of the beam is at its largest. Since $\delta_{max} = .0043$ and $\eta_{max} = 2.3$ meters for the jump presented here, the displacement of the momentum edge of the beam is 9.9 mm, much larger than the betatron root mean square beam size of about 1.6 mm. The total beam size is well within the available aperture.

Although RHIC is unfortunate in being the first superconducting accelerator to cross transition, it is fortunate in being the first accelerator to support a matched first order transition jump. This jump is expected to prevent particle losses, and to almost entirely eliminate emittance growth. RHIC can support such a jump, while other accelerators cannot, because it has relatively many dispersion free quadrupoles with standard FODO cell beta functions, and because the phase advance per cell is close to 90 degrees.

VII. REFERENCES

[1] S.Y. Lee and J. Wei, Proc. EPAC, Rome, (1988), p. 764
[2] J. Wei, Ph.D. thesis, State Univ. NY at Stony Brook, (1990)
[3] J. Wei, Proc. European Part. Acc. Conf., Berlin, (1992)
[4] RHIC Design Manual, RHIC, BNL, Upton NY 11973
[5] A. Sorenssen, Particle Accelerators, 6, 141, (1975)
[6] K. Johnsen, Proc. CERN Symposium on HE Accelerators and Pion Physics, Geneva, (1956)
[7] K. Takayama, Particle Accelerators, 14, 201, (1984)
[8] S.A. Bogacz, S. Peggs, IEEE PAC, San Francisco (1991), p. 1657
[9] T. Risselada, CERN PS/90-51, Geneva, (1990)
[10] W. Merz, C. Ankenbrandt, K. Koepke, IEEE PAC, Washington, (1987), p. 1343
[11] S. Peggs, S.A. Bogacz, F. Harfoush, IEEE PAC, San Francisco (1991). p. 1160

Comparison of Aperture Determinations on RHIC for Single Particles Tracked 10^6 Turns and 100 Particles, Having Randomly Generated Initial Coordinates, Tracked for 1000 Turns*

George F. Dell

Brookhaven National Laboratory
Upton, NY 11973, USA

Abstract

Aperture determinations from 100 particles tracked for 1000 turns using randomly selected initial coordinates are compared with results from 10^6 turn runs when initial coordinates are defined by $\epsilon_x = \epsilon_y$ and $X_i' = Y_i' = 0$. Measurements were made with ten distributions of magnetic field errors. The results from tracking 100 particles for 10^3 turns are equivalent to those from 10^6 turn runs, have a distribution of considerably less width, and require only one tenth the computer time.

I. INTRODUCTION

Aperture determinations are made by probing phase space in a direction defined by the initial coordinates. Tracking on lattices, such as RHIC at BNL and various SSC lattices, indicates there is repetitive transfer of emittance between the horizontal and vertical planes. This transfer can be complete to either plane and depends upon the random field errors as well as the sextupoles used for chromaticity correction. This is illustrated in Figure 1 for the configuration that defined the aperture. The resulting time dependence of ϵ_x and ϵ_y causes the particle to probe in directions other than that defined by its initial coordinates.

Most frequently investigators have used initial coordinates defined by $\epsilon_{x(i)} = \epsilon_{y(i)}$ and $X_i' = Y_i' = 0$. In this paper a method that is patterned after the observed time dependence of ϵ_x and ϵ_y in Fig. 1 is used for selecting the initial coordinates of the test particles. The total emittance $\epsilon_{t(0)}$ is distributed in any way that satisfies the relation $\epsilon_{t(0)} = \epsilon_{x(i)} + \epsilon_{y(i)}$, and X' and Y' can be nonzero. One hundred particles having randomly selected $\epsilon_{x(i)}, \epsilon_{y(i)}, X_i, X_i', Y_i$, and Y_i' are tracked for 1000 turns.

The study has been made using the rhic92(0.0) lattice when $\beta^* = 2m$ as well as $\beta^* = 6m$. The tunes are $\nu_x = 28.827$ and $\nu_y = 28.823$. The effects of nonlinear fields are represented by thin lens kicks located at the center of all quadrupoles and at both ends and the center of all dipoles, where they are given the weights of 1/6 and 2/3, respectively. Multipole expansions of random field errors are generated from the rms errors $(\sigma a_n, \sigma b_n)$ of Herrera etal[1] according to a Gaussian distribution that is truncated

at $\pm 3\sigma$. The expansion is made with $2 \leq n \leq 16$ for dipoles and $2 \leq n \leq 10$ for quadrupoles. Aperture determinations were made for ten sets of random field errors generated by using different seeds to initialize the random number generator. No systematic errors were included. Tracking was performed on the NERSC CRAY.C computer at LLNL using a special version of PATRICIA.[2] Measurements were made at $\Delta P/P = 0$. The test particles were always launched at the beginning of an inner arc of RHIC. The amplitude of the test particle was checked at every element to assure it remained within the vacuum chamber.

II. TRACKING

1. Generation of initial coordinates – The steps used in generating the coordinates for multiparticle launching are:
    1. Define the initial total emittance $\epsilon_{t(0)}$.
    2. Select the initial horizontal emittance randomly:
       $$\epsilon_{x(i)} = \epsilon_{t(0)} * \text{RANF}$$
    3. Determine the initial vertical emittance $\epsilon_{y(i)}$:
       $$\epsilon_{y(i)} = \epsilon_{t(0)} - \epsilon_{x(i)}$$
    4. Select the initial coordinate X_i randomly:
       a). $X_{\max} = \sqrt{\left(\epsilon_{x(i)} * \beta_x\right)}$
       b). $X_i = X_{\max}(1. - 2. * \text{RANF})$
    5. Determine X' from the Courant-Snyder relation:
       a). $X_i' = \left(-\alpha_x * X_i \pm \sqrt{\left(\epsilon_{x(i)} * \beta_x - X_i\right)}\right)/\beta_x$
       b). Select the sign of $\sqrt{\left(\epsilon_{x(i)}\beta_x - X_i^2\right)}$ randomly
    6. Repeat step 4 and 5 with X replaced by Y.

2. Multiparticle Tracking – One hundred particles having randomly generated initial coordinates were launched and tracked in sequence. If any particle failed, the motion was considered unstable, and the run was terminated. The total emittance $\epsilon_{t(0)}$ was decreased in steps from a large value until all particles survived for 1000 turns. The results are expressed in terms of an equivalent X defined as $X_i = \sqrt{\epsilon_{t(0)} * \beta_x/2}$ and are thus consistent with the convention used for the standard launch when $\epsilon_{x(0)} = \epsilon_{y(0)}$.

3. Single particle tracking for 10^6 turns – With $\epsilon_{x(0)}$ and $\epsilon_{y(0)}$ always equal, X_i was decreased from a large amplitude at which the particle was lost to an amplitude where the test particle first stayed within

---

the vacuum chamber for 10^6 turns. The smallest of the ten measurements was used as the aperture.

III. DISCUSSION

The aperture measurements at $\beta^* = 2m$ for multiparticle and 10^6 turn runs are shown as histograms in Figure 2. The number in each bin indicates the set of random errors used for the determination. The test particle survived at the amplitude corresponding to the left side of the bin and failed at the amplitude corresponding to the right side of the bin. Measurements were also made when $\beta^* = 6m$. These are included in Table 1 and are reported elsewhere[3]. It is noted that:

1. The apertures defined by the worst case from 10^6 turn and multiparticle runs are essentially equal.

2. The spread in the distribution of results is smaller for multiparticle than for single particle tracking.

3. The computer time required for the multiparticle studies is one tenth that for the 10^6 turn studies.

Analysis of results from the single particle tracking of Figure 2(a) shows a correlation between the degree of emittance transfer and the worst and best case apertures. The worst case shows large emittance transfer; the best case shows modest emittance transfer The smear plots generated from the first 300 turns and the last 300 turns of these 10^6 turn runs are essentially identical. Hence there is little emittance growth with time. It is also found that the shape of smear plots, generated from 300 turn runs, has only a weak dependence on initial emittance at initial amplitudes for which the particles remain within the vacuum chamber for at least 1000 turns. Hence there is a weak dependence of emittance growth on initial amplitude. Since runs stable for 10^6 turns are not in the region of rapid emittance growth, it seems justifiable to conclude that the best and worst case apertures are determined by emittance coupling, rather than emittance growth. This assertion has been at least qualitatively verified by tracking with initial coordinates defined by $\epsilon_x = \epsilon_t$ and $\epsilon_y = X' = Y' = 0$ – a configuration achieved in multiparticle tracking as well as in single particle tracking with total emittance transfer between the horizontal and vertical planes.

Table 1: Aperture Determinations for RHIC92
$X_i mm = \sqrt{\epsilon_{t(0)} * \beta_x/2}$ where $\beta_x = 50m$

β^*	SINGLE PARTICLE TURNS		MULTIPARTICLE TURNS
	1000	10^6	1000
2	8.3 ± 0.1	6.7 ± 0.1	6.5 ± 0.1
6	16.3 ± 0.1	14.3 ± 0.1	13.7 ± 0.1

IV. REFERENCES

1. PATRICIA, 1980 version by H. Wiedemann, SLAC, modified for multipoles by S. Kheifets, SLAC; further modifications at BNL by G.F. Dell.

2. J. Herrera, R. Hogue, A. Prodell, P. Thompson, P. Wanderer, and E. Willen, IEEE PAC, Washington D.C., March 16-19, 1987, pp 1477-1479.

3. G.F. Dell, Proceedings on the Stability of Particle Motion in Storage Rings, Brookhaven National Laboratory, Oct. 19-24, 1992.
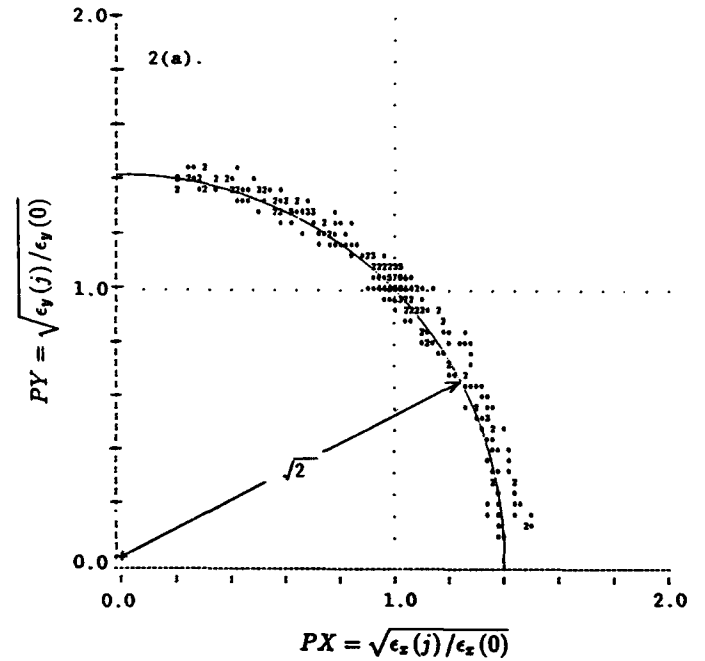
Figure 1: Normalized smear plot showing emittance transfer during the first 300 turns of a 10^6 turn run at $\beta^* = 2m$ with seed #9.

a) One particle (10^6 turns)
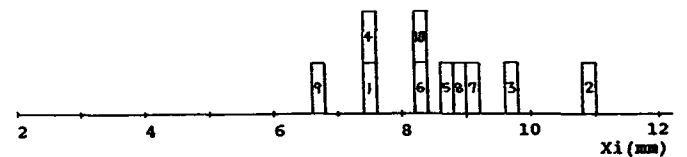
b) Multipart (100 x 10^3 turns)
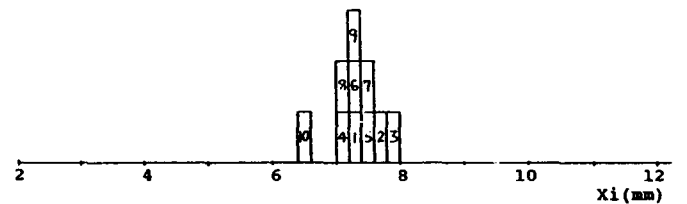
Figure 2: RHIC92, $\beta^* = 2m$. Aperture determinations for: a) one particle/seed tracked 10^6 turns, and b) 100 particles/seed tracked 1000 turns.

STATUS OF THE VARIABLE MOMENTUM COMPACTION STORAGE RING EXPERIMENT IN SPEAR*

P. TRAN, A. AMIRY, C. PELLEGRINI, University of California, Los Angeles, Los Angeles, CA 90025, USA
J. CORBETT, M. CORNACCHIA, M. LEE, H.-D. NUHN, H. WINICK, D. WU
Stanford Linear Accelerator Center, Stanford, CA 94309 USA
A. HOFMANN, CERN, CH-121 Geneva 23, Switzerland
D. ROBIN LBL, Berkeley, CA 94720, USA

Abstract

Variable momentum compaction lattices have been proposed for electron-positron colliders and synchrotron radiation sources to control synchrotron tune and bunch length. To address questions of single particle stability limits, a study has been initiated to change the SPEAR lattice into a variable momentum compaction configuration for experimental investigation of the beam dynamics. In this paper, we describe a model-based method used to transform SPEAR from the injection lattice to the low momentum compaction configuration. Experimental observations of the process are reviewed.

I. INTRODUCTION

The recent interest in low-momentum compaction electron-beam colliders and storage rings arises from their inherent short-bunch characteristic. The short bunches translate directly to higher luminosity, in the case of colliders, or brighter and potentially coherent synchrotron radiation in the case of storage rings.[2,3]. Hence, the performance of future accelerators and synchrotron light sources may be enhanced by operating in the low momentum compaction regime. The potential gain in performance has motivated a collaboration between SLAC/SSRL and UCLA to investigate the possibility of modifying SPEAR to operate in the low momentum compaction regime and to experimentally study the single-particle dynamics in this regime. Similar experiments are being conducted at UVSOR[4] and NSLS.[5]

The current SPEAR lattice configuration, designed for low emittance and high brightness operation, has tunes of 6.818 and 6.721, respectively in the x and y planes, respectively, and a momentum compaction of 0.017. The natural one-sigma bunch length is approximately 5 cm long. Some future light sources and colliders will likely have bunch lengths in the millimeter to sub-millimeter range. To simulate the short-bunch dynamics of these machines, the SPEAR bunch length must be reduced by a factor of 10 or more. Consequently, the momentum compaction value must be reduced by a factor of at least 100, since the bunch length is proportional to the square-root of the momentum compaction. We expect, however, that the effects of reducing the momentum compaction on either dynamic aperture or bunch stability to manifest themselves even before this is achieved. One of the main goals of our experiment is to study these effects.

II. LOW MOMENTUM COMPACTION LATTICE FOR SPEAR

a. Single-Configuration Approach: Direct Injection

To achieve low momentum compaction without significant hardware changes, the designers have shaped the dispersion function around the ring so as to yield a low average dispersion value. Since SPEAR was originally designed as a collider, and is now operated as a synchrotron light source, the current lattice inherits two low-beta insertions. The forced oscillation of the dispersion function and the quadrupole geometry in the low-beta insertions produce a relatively large mismatch in the beta-functions. Thus, the physical aperture is a concern for our low momentum compaction lattice. A low momentum compaction magnetic lattice has been developed for SPEAR for direct injection testing by carefully matching the dispersion function along the arcs to that of the low-beta insertions.[6] This lattice has a relatively small dynamic aperture, approximately +/-10 sigma, with full transverse coupling. The beam stay-clear for this lattice is acceptable for testing, despite the beta-function mismatch. The tunes are 4.42 and 7.28 for x and y, respectively.

Even though the lifetime of stored beam in this lattice was short (on the order of minutes), the maximum stored current reached 0.5 mA. Unfortunately, the current was below the detection limit of the BPM system, so orbit measurements and corrections were not possible. One cause of the short lifetime could have been modelling errors in setting up the configuration. Calculations have shown low momentum compaction lattices to be very sensitive to quadrupole strength values (See below). Small discrepancies between the machine and its model could mean the difference between a positive momentum compaction value and a negative one.

b. Multiple-Configuration Approach: Magnet Ramping

An alternative to direct application of the single-configuration approach is the multiple-configuration procedure. Here, we apply small changes in the strength of the quadrupoles to take SPEAR slowly from its operating low emittance configuration to a final low momentum compaction lattice. The incremental changes in the quadrupole strength are accomplished through a series of configuration ramps between intermediate lattices. This method avoids the complications associated with a direct application and allows the opportunity to study effects that may occur during the process of reducing the momentum compaction. We have produced 100 intermediate lattices for the purpose of testing this approach. The lattices were created by
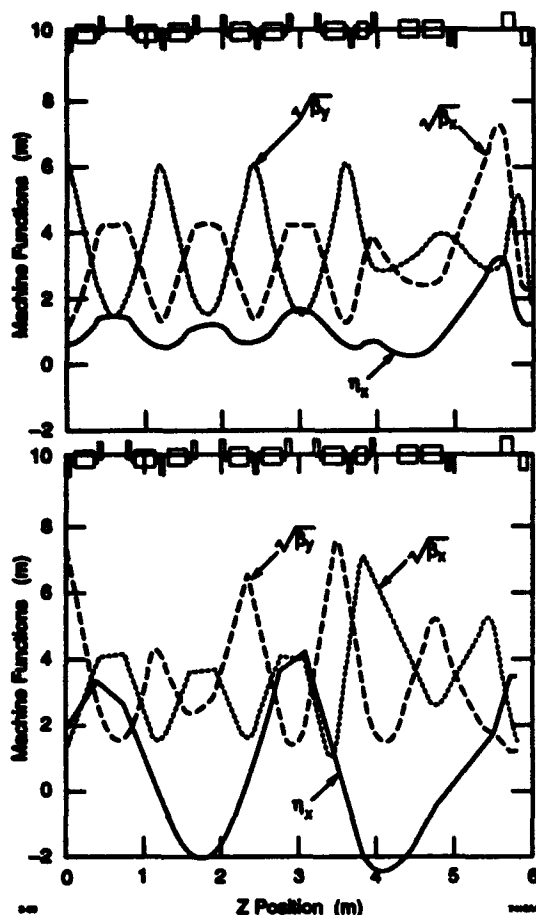
Figure 1. Machine functions of (a) SPEAR low emittance lattice, (b) lattice at the end of the multi-configuration path.
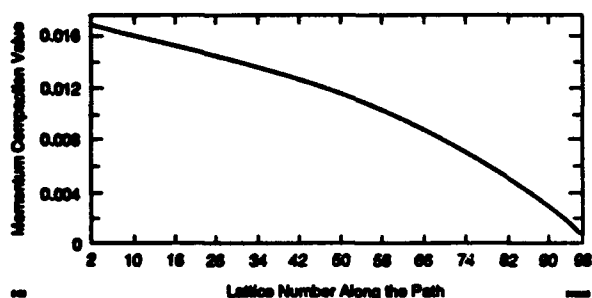
Figure 2. Calculated momentum compaction values along the multi-configuration path.

MAD[7] with local constraints placed on the machine functions and tunes. A total of eight contraints were used, corresponding to eight families of quadrupoles in SPEAR. Figures 1a and b show the machine functions for two of these lattices. Figure 2 shows the variation of the momentum compaction value along this path. Notice the sensitivity of the lattices to quadrupole strength near the end point. The end lattice has characteristics similar to those of the low momentum compaction lattice used in the direct injection test. The

tunes, however, are held constant at the injection tunes of 6.818 and 6.721 in the x and y planes, respectively.

A magnet ramp test of SPEAR through these intermediate lattices was conducted recently. Initially , a current of 3.5 mA was stored at 2.3 GeV in the low emittance configuration. To gain aperture, the energy was then reduced to 1.8 GeV to decrease emittance. Next, we down loaded the quadrupole strength values for each new configuration and slowly ramped through successive lattices. This process was successful until we reached intermediate lattice number 25. At this point, partial beam loss occurred due to head-tail instantiability, caused by the y-chromaticity becoming negative. As we continued ramping along the path with 0.23 mA current (below the head-tail threshold), the beam was completely lost at intermediate lattice number 30. This time, we believe the beam was lost because of the dynamic aperture limitations, as confirmed by simulations using the KRAKPOT[8] tracking code.

III. WORK IN PROGRESS

a. SPEAR Model Upgrade

Thus far, we have explored limits that may impact future low momentum compaction experiments in SPEAR. In particular, both the direct injection and multi-configuration tests have indicated the need for a more accurate model. Since our initial tests, progress has been made toward in-situ calibration of the SPEAR model.[9]

b. Dynamic Aperture Improvement

Another problem apparent from the simulations is the limit on dynamic aperture. Since the lattices used in the injection test as well as the final lattice in the multi-configuration path experiment have a relatively small dynamic aperture (+/- 10 and 6 sigma, respectively), we are planning to employ octupoles to redue the amplitude-dependent tuneshift. The effect on dynamic aperture is shown in Figs 3a and b. Simulations show that octupoles can increase the dynamic aperture significantly. we also continue to explore other multi-configuration paths. To aid this effort we have developed a multi-step path design program which can automate this process by fitting the momentum compaction value directly.[10]

c. 6-D PLM System

To enhance our on-line lattice diagnostic capability, a six-dimensional Phase-space Linearity Monitor (PLM)[11] has been developed and is being tested in SPEAR. This system enables us to investigate resonances that develop along the multi-configuration path by measuring the beam centroid coordinates (x,x',y,y',dE/E,t) at every turn. The PLM will be used to characterize and verify the dynamic aperture and to study nonlinear effects[12,13] in future experiments. A schematic diagram of the PLM system is shown in Fig. 4.
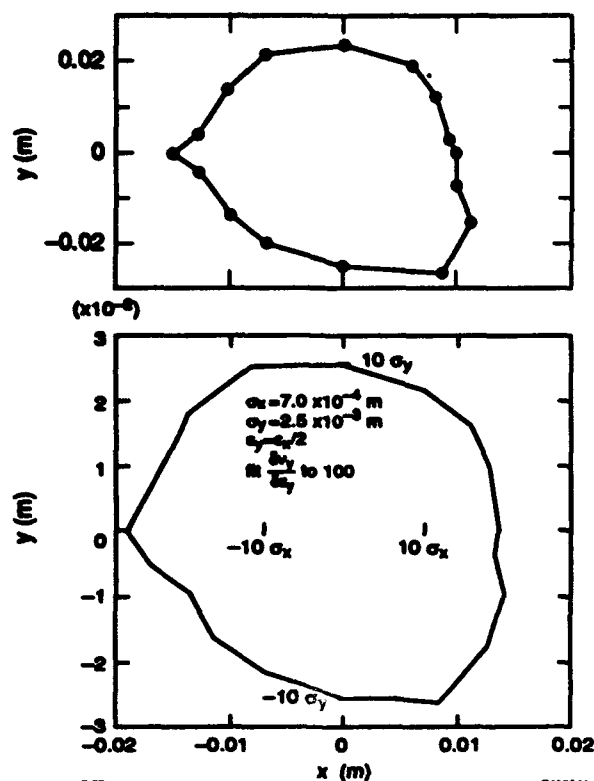
Figure 3. Dynamic aperture of the low momentum compaction lattice used in the direct injection test, (a) tracking without octupoles, and (b) tracking with octupoles.

Figure 4. Block diagram of the 6-D PLM system.

4. CONCLUSION

The complicated task of developing a low momentum compaction lattice for SPEAR with the current hardware configuration has led us to explore alternatives. The experience gained from these initial tests has helped to determine the limitations of the storage ring and to prepare the necessary tools and procedures for performing future experiments including a SPEAR model upgrade, study of octupoles for dynamic aperture improvement and the PLM monitor system for on-line lattice diagnostics. We hope that these new tools and procedures will aid in achieving the goal of operating SPEAR in a low momentum compaction regime.

REFERENCES

[1] C. Pellegrini and D. Robin, "Isochronous Storage Rings and High-Luminosity Electron-Positron Colliders," CP Violation and Beauty Factories and Related Issues in Physics, Annals of the New York Academy of Sciences, Vol 619, 1991.

[2] D. Robin, UCLA Ph.D. Thesis (1991)

[3] H. Hama, S. Takano and G. Isoyama, "Control of bunch length of the UVSOR storage ring", UVSOR Activity Report 1991, ISSN 0911-5730 (1992).

[4] S. Krinsky, J.B. Bittner, A.A. Fauchet, E.D. Johnson, J. Keane, J.B. Murphy, R.J. Nawrocky, J. Rogers, O.V. Singh and L.H. Yu, "Storage ring Development at the National Synchrotron Light Source," AIP Conference Proceedings 249, page 762 (1992).

[5] A. Hofmann, CERN, Private Communication

[6] H. Grote and F. C. Iselin, MAD, Version 8.1 CERN/SL/90-13 (1990)

[7] E. Forest, LBL, private communication

[8] W.J. Corbett, M.J. Lee, V. Ziemann, A Fast Model Calibration Procedure for Storage Rings, these proceedings.

[9] V. Ziemann, SLAC, private communication.

[10] J.-L. Pellegrin, SLAC, J. Yang, SLAC/SSRL, and C. Wermelsk, GMD, private communication.

[11] P. L. Morton, J.-L. Pellegrin, T. Raubenheimer, M. Ross, SLAC-PUB-4230 (1987).

[12] D. D. Caussyn et al., Phys. Re. 46A, No. 12 (1992) 7942.

SSC High Energy Booster Resonance Corrector and Dynamic Tune Scanning Simulation

Peilei Zhang and Shinji Machida
Superconducting Super Collider Laboratory*
2550 Beckleymeade Ave., Dallas, TX 75237

Abstract

A resonance correction system for the High Energy Booster(HEB) of the Superconducting Super Collider (SSCL) was investigated by means of dynamic multiparticle tracking. In the simulation the operating tune is scanned as a function of time so that the bunch goes through a resonance. The performance of the half integer and third integer resonance correction system is demonstrated.

I. INTRODUCTION

The 2 TeV superconducting High Energy Booster is the last synchrotron ring in SSC injection chain, which consists of 512 dipole and 318 quadrupole magnets. It appears as an oval ring with two long strait sections, two short strait sections and six arcs. Because of the multi-pole errors in these magnets, betatron resonances of several orders are exited. Local non 0th-order-effect correctors are designed to compensate the resonance for this large synchrotron [1]. Correcting these resonances can be done by calculation the bandwidth of a resonance. For a real machine, not all the error information, especially random errors, is obtainable, therefore one must adjust the corrector interactively by looking at beam behavior. The corrector schemes described in this article are tested with a dynamic simulation study that looks at the emittance growth and beam loss using macro particles in the lattice with and without the resonance correction system.

II. RESONANCE CORRECTION SCHEME

The working point of the HEB is (39.42, 38.41) in tune space, which is between half integer and third integer resonance lines (see Figure 1). Therefore a half integer and third integer resonance corrector are needed to compensate the strong half and third integer resonance lines.

The correctors are placed in the arcs of HEB. The arcs consist of 90° FODO cells. Figure 2 shows two cell layout and the betatron functions. The correctors are inside spool pieces that are close to each quadrupole magnet.
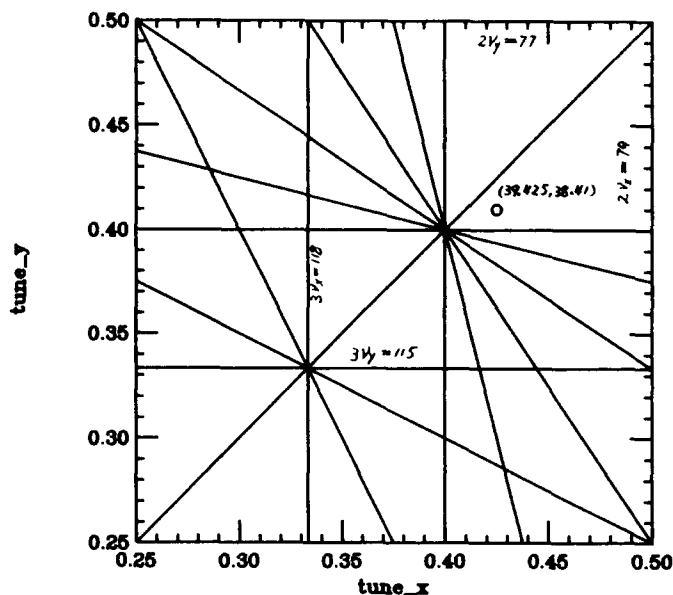
Figure 1. HEB working point in tune diagram.

A. The half integer correction scheme

The half integer corrector consists of eight quadrupole magnets, four of them for resonance line $2\nu_x = 79$ and the other four for resonance line $2\nu_y = 77$, respectively. Each of the four magnets is assigned into two groups, powered by two adjustable power supplies, and those groups of magnets form two orthogonal vectors in phase space to generate harmonics with the desired magnitude and phase. To avoid generating 0th harmonics or tune shifts, two magnet sets in each group are wired in series with opposite polarity and placed in the positions with 90° betatron phase advance or 180° for 2nd harmonic. The driving force is $\int B'\beta_x exp(2i\phi_x)ds$ for $2\nu_x = 79$. The quadrupole magnets are placed in high β_x regions and the scheme is shown in Figure 3. 45° betatron phase advance or 90° for 2nd harmonic between the two sets of magnets is needed to form a pair of orthogonal vectors, which is achieved by using straight section phase advance.

A similar scheme for $2\nu_y = 77$ is shown in Figure 3. The quadrupole magnets are placed in a high β_y region for this case.

176
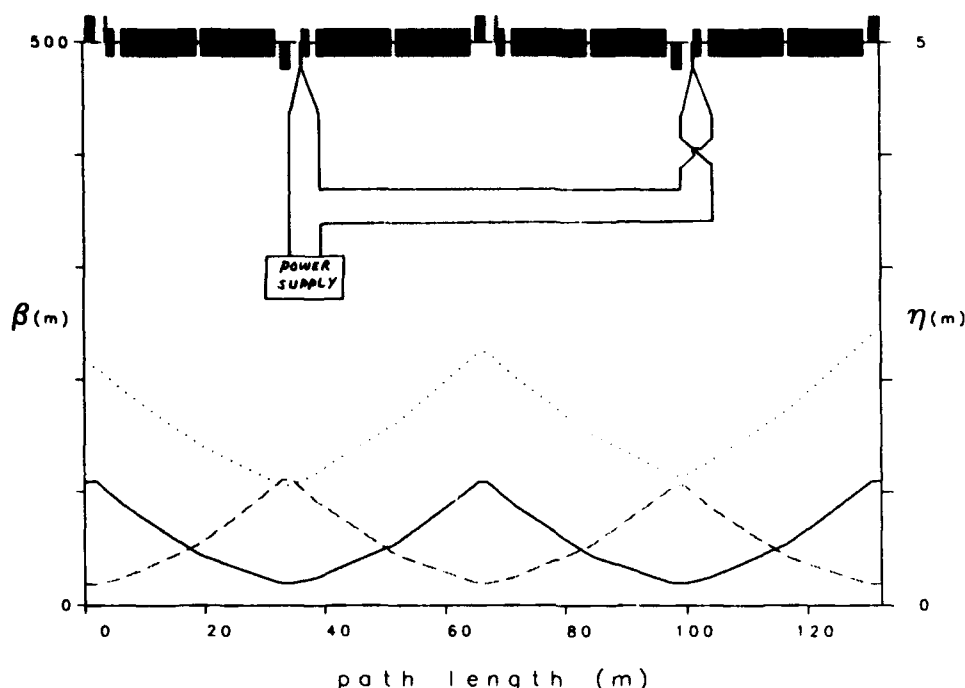
Figure 2. Two FODO cells and the betatron functions. Magnets in series with opposite polarity.
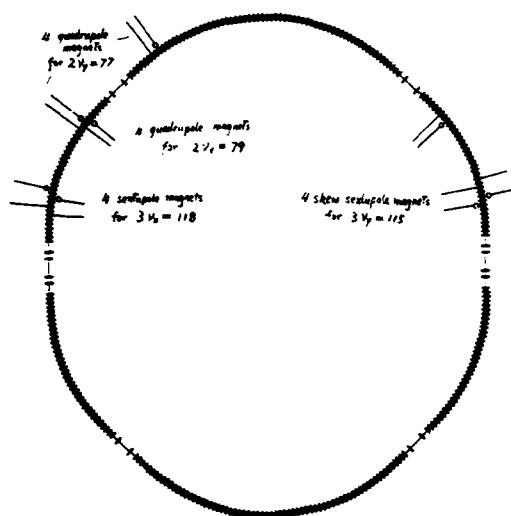
Figure 3. The correction scheme in half HEB ring. The little circles represent reversed polarity.

B. The 3rd integer correction scheme

The working point of HEB is close to $3\nu_x = 118$ and $3\nu_y = 115$ resonance lines. The driving force for $3\nu_x = 118$ resonance lines is $\int B'' \beta_x^{3/2} exp(3i\phi_x) ds$ and four sextupole magnets are used to compensate the line. Two sextupole magnets are placed where the betatron phase difference is 180° and they are wired in series with opposite polarity to avoid generating the 0th harmonic or chromaticity (see Figure 3).

Four skew sextupole magnets are used to compensate $3\nu_y = 115$.

III. DYNAMIC TUNE SCANNING SIMULATION

A modified version of Simpsons code is used to evaluate the performance of the resonance correction system. This code is a fully 6-D multiparticle tracking program with acceleration [2]. In the simulation, time is the independent variable instead of the longitudinal position that can dynamically change machine parameters, such as tune and chromaticity as a function of time just like real machines. This feature makes the simulation of resonance crossing much easier. The table of quadrupole magnet strength at several times, for instance, is read into the code and interpolated at the time when a tracking particle passed the element. We observed the rms emittance and beam loss, due to the resonance crossing, to check the performance of the proposed resonance correction system. The bandwidth of the individual resonance is estimated, and the needed strength of correctors is then calculated so that the bandwidth is reduced to near zero. The simulation of both lattices with and without correction is performed and a comparison is made to check the effect of the correction.

In the dynamic tune scanning simulation for half integer correction, the working point is linearly moving from (39.424, 38.414) to (39.543, 38.533) in 10 msec. At about 6 msec, the working point crossed the half integer. 1024 particles are used to calculate emittance. Emittance growth is occurring at a half integer crossing, while corrector circuits are turned off. A smooth half integer crossing is also shown in Figures 4 and 5 for a well corrected HEB.

177

The results for horizontal and vertical planes are shown in Figures 4 and 5 respectively.
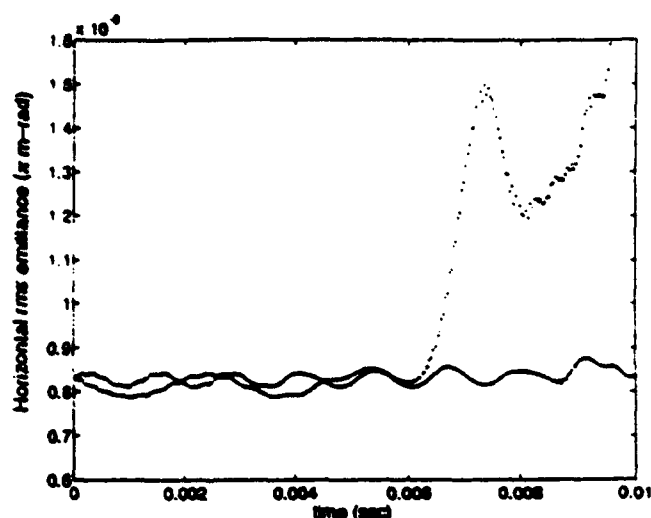
Figure 4. Horizontal emittance with and without half integer correction.
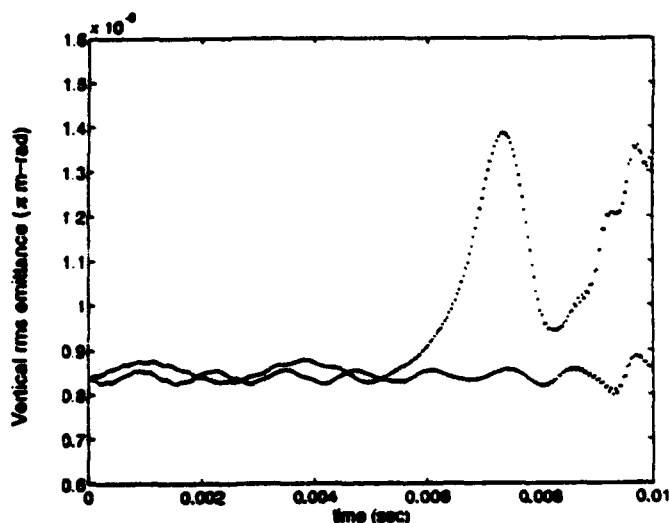
Figure 5. Vertical emittance with and without half integer correction.

In the dynamic tune scanning simulation for third integer correction, the working point is linearly moving from (39.398, 38.261) to (39.252, 38.095) in 40 msec. Figure 6 shows the correction effect with the comparison of emittance growth with and without corrector. Without correction, the emittance grows quickly since some particles under resonance move off the bunch center. These particles finally lose, and the calculated emittance temporary drops. Then some particles move outwards and emittance grows again. As a result, a saw tooth like emittance growth picture has been seen.
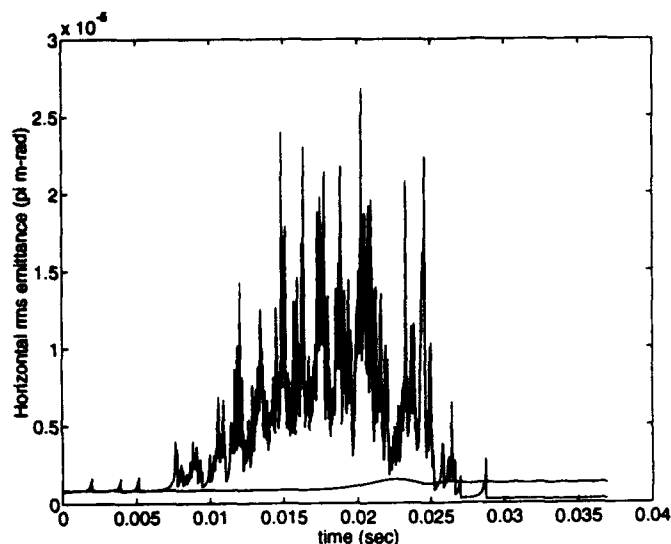
Figure 6. Horizontal emittance with and without 3rd integer correction.

IV. SUMMARY

Local non 0th-order-effect half integer and third integer correction schemes work well with large synchrotrons. A dynamic tune scanning simulation is close to real machine operation.

V. REFERENCES

[1] P. Zhang, 'A Study of Tunes near Integer Values in Hadron Colliders' *Fermi National Accelerator Laboratory, FN-577.*

[2] S. Machida, *Computational Accelerator Physics Conference 1993.*

Transport Properties of the CEBAF Cavity*

Zenghai Li

Dept. of Physics, The College of William and Mary, Williamsburg, VA23187,
and CEBAF, 12000 Jefferson Avenue, Newport News, VA 23606

J. J. Bisognano and B. C. Yunn

CEBAF, 12000 Jefferson Avenue, Newport News, VA 23606

Abstract

The transport properties of the CEBAF 5-cell cavity are studied. The 3-D cavity fields are calculated by use of the 3-D program MAFIA and are incorporated in a modified PARMELA. Numerical simulation results show that the cavity has finite dipole, quadrupole and skew quadrupole field components, which are due to the asymmetric field in the fundamental and the higher-order-mode couplers. The azimuthal focusing of the cavity disappears for high energy particles as $\frac{1}{\gamma}$. The dependence on the initial energy and cavity phase is given. The cavity-steering effects were measured on the CEBAF 45 MeV injector and are in good agreement with the numerical simulation.

I. Introduction

The CEBAF superconducting cavity has five cylindrical symmetric cells and two end-couplers as shown in Figure 1. One is the fundamental-power(FP) coupler which couples RF power to the cavity. The other is the higher-order-mode (HOM) coupler which is designed to couple the higher-order-mode field, generated by the beam, to an RF load. The FP and HOM couplers do not have cylindrical symmetry, and these asymmetric structures generate asymmetric fields at their adjacent regions. The deflecting fields on the axis are no longer zero. Cavity-steering effects are important issues in nominal linac operation, and they are also a concern in a proposed CEBAF FEL, where two beams share the linac. In the proposal [1], both FEL and physics beams are injected into the cavity with different energies and are accelerated in the cavity at different phases. Since the steering effect of the cavity depends on both the phase of the RF field and the energy of the particle, the steering effect must be understood to successfully transport the two beams. To study these issues, a full 3-D modeling of the cavity is required, which is the motivation for this paper.
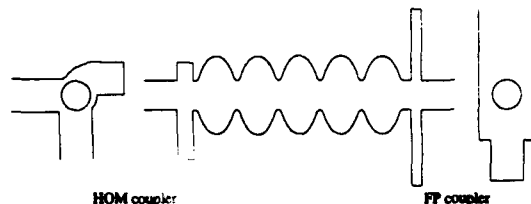
Figure 1. CEBAF 5-cell Cavity.

The 3-D fields of the CEBAF 5-cell cavity are calculated by use of MAFIA [2]. A particle tracking program PARMELA [3] is modified to take the full MAFIA fields into the calculation. The properties of the 5-cell cavity are studied by use of PARMELA and are compared with the experimental results. A more detailed account can be found in a CEBAF report [4]. PARMELA simulations of CEBAF cryomodules can be found in reference [5].

II. Field Distribution of the CEBAF Cavity

The CEBAF cavity is a 3-D structure (Figure 1). The maximum radius of the cell is 9.4 cm and the beam pipe radius is 3.5 cm. In this paper, we are interested only in the transverse effects of the fundamental mode field. The frequency of this mode is 1497 MHz, which is well bellow the cutoff frequency of the 3.5 cm beam pipe. To have a good boundary condition, the 3.5 cm pipe is extended up to 10 cm beyond the couplers on each side of the cavity where the field of the fundamental mode has vanished. The FP coupler has two ends. One end is terminated by the superconducting material while the other end is a waveguide leading to the RF power system. The length of the waveguide is taken as 20.7 cm in the calculation, which is a short position [6] for the fundamental mode. The HOM coupler is used to transfer the HOM field to a load, and the actual length of the two arms is more than 30 cm. Since it only perturbs the field distribution in the beam pipe region and does not propagate the fundamental mode, the length of the two arms is shortened to 15.5 cm in the calculation. Figure 2 shows the E and the B fields on the axis. The E_z
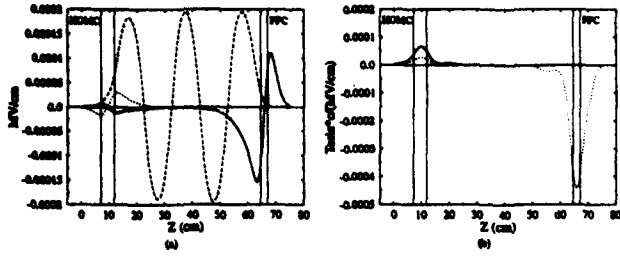
Figure 2. Field distribution on the axis (cav503f). Downstream FPC.
a) Electric field, solid line: E_z; dotted line: E_y; dashed line: $E_x/100$.
b) Magnetic field, solid line: B_x ; dotted line: B_y.

Figure 3. Energy gain vs. initial cavity phase for the particles with different initial energies. Gradient = 5 MV/m. From the left to the right: 0.5, 1.0, 1.5, 5.0, 1000.0 MeV (cav503f, downstream FPC).

field shown in the figure is scaled by 0.01. The flatness of the E_z field is about 2.5% in the 5 cells.

III. NUMERICAL SIMULATION OF THE BEAM TRANSPORT IN THE CAVITY

A new subroutine CBFCAV3D is incorporated into PARMELA for the CEBAF 3-D cavity simulation. This subroutine takes the MAFIA result of the previous section as the field distribution in the cavity. In PARMELA, the particle advances step by step in the cavity under the Lorenz force given by

$$\mathbf{F} = e(\mathbf{E}\sin(\omega t(z) + \phi_0) + \mathbf{v} \times \mathbf{B}\cos(\omega t(z) + \phi_0)) \quad (1)$$

where ϕ_0 is the initial phase of the cavity. The momentum change of the particle after passing through the cavity is given by

$$\Delta \mathbf{P} = \int_{z=0}^{z=L} \mathbf{F}\frac{dz}{v_z} \quad (2)$$

A. Acceleration of the cavity

First we want to know the energy gain and the maximum acceleration phase for the particles with different initial energies. For a given momentum change ΔP, the energy change of the particle is

$$\Delta E = \gamma m_0 c^2 \left(\sqrt{1 + \frac{2P_0\Delta P + \Delta P^2}{(\gamma m_0 c)^2}} - 1 \right) \quad (3)$$

where P_0 is the initial momentum. Figure 3 shows the energy gain of the particles with different initial energies as functions of the initial phase of the cavity. The gradient of the cavity is 5 MV/m. As one can see, 1) the maximum energy gain is different for different initial energy particles, 2) the phase for the maximum energy gain (on-crest phase) is different for different initial energy particles and 3) the acceleration is not symmetric about the crest for low-energy particles. At 5 MeV, the electrons are quite relativistic, and the acceleration curve is almost the same as that of the 1 GeV electrons.

B. Multipole components of the cavity deflection

The transverse momentum changes, ΔP_x and ΔP_y, determine the deflection of a particle by a cavity. The deflection angles corresponding to the momentum changes are $\Delta \alpha_x = \frac{\Delta P_x}{P}$ and $\Delta \alpha_y = \frac{\Delta P_y}{P}$. Generally, ΔP_x and ΔP_y are functions of (x, y), and can be expanded as Taylor expansions of x and y. The coefficients of the expansion are related to the multipoles and can be obtained by means of the Fourier transform.

The z Fourier component of the electric field E_z can generally be expressed by [7]

$$E_z(r, \theta, z, \beta_z) = \sum_{n=0}^{\infty} A_n J_n(\gamma_r r)\cos(n\theta)e^{-i\beta_z z}$$

$$+ \sum_{n=0}^{\infty} B_n J_n(\gamma_r r)\sin(n\theta)e^{-i\beta_z z} \quad (4)$$

where $\gamma_r^2 + \beta_z^2 = k^2 = \frac{\omega^2}{c^2}$, $J_n(\gamma_r r)$ is the Bessel function. Assume $\beta \approx 1$ and that the trajectory is a straight line. From Panofsky-Wenzel theorem we have, to order of r, a transverse momentum change of the form

$$\Delta \mathbf{P}_t = \frac{ie}{\omega}\left(\frac{\gamma_r A_1}{2}\mathbf{x}_0 + \frac{\gamma_r B_1}{2}\mathbf{y}_0 - \frac{\gamma_r^2 A_0}{2}(x\mathbf{x}_0 + y\mathbf{y}_0) \right)$$

$$+ \frac{ie}{\omega}\left(\frac{\gamma_r^2 A_2}{4}(x\mathbf{x}_0 - y\mathbf{y}_0) + \frac{\gamma_r^2 B_2}{4}(y\mathbf{x}_0 + x\mathbf{y}_0) \right)$$

$$= D_x\mathbf{x}_0 + D_y\mathbf{y}_0 + F(x\mathbf{x}_0 + y\mathbf{y}_0)$$

$$+ Q(x\mathbf{x}_0 - y\mathbf{y}_0) + S(y\mathbf{x}_0 + x\mathbf{y}_0) \quad (5)$$

F is the azimuthal-focus strength, D_x and D_y are the dipole strengths in the x and y planes, and Q and S are the quadrupole and the skew quadrupole strengths respectively. The synchronous condition requires that $\gamma_r^2 = k^2 - \beta_z^2 = \frac{\omega^2}{c^2} - \frac{\omega^2}{v^2} = -\frac{\omega^2}{v^2\gamma^2}$, which goes to zero as γ goes to infinity. From Eq.(4), if E_z is to have finite acceleration, dipole and quadrupole components, the coefficients of the expansion must satisfy

$$A_0 = \text{const.} \qquad A_1, B_1 \propto \frac{1}{\gamma_r} \qquad A_2, B_2 \propto \frac{1}{\gamma_r^2}$$
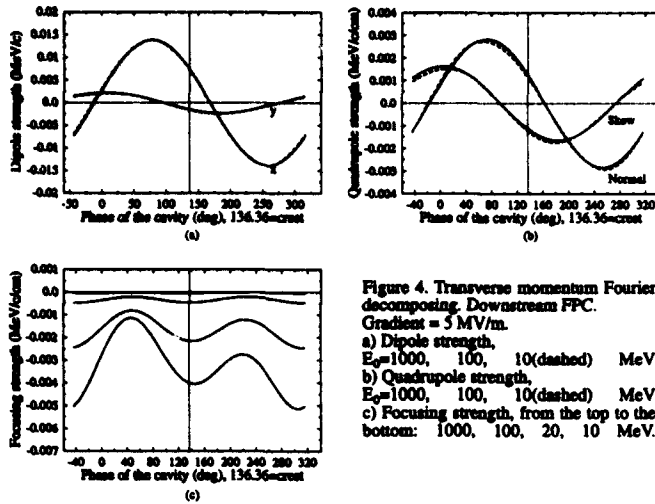
Figure 4. Transverse momentum Fourier decomposing. Downstream FPC. Gradient = 5 MV/m.
a) Dipole strength,
E_0=1000, 100, 10(dashed) MeV
b) Quadrupole strength,
E_0=1000, 100, 10(dashed) MeV
c) Focusing strength, from the top to the bottom: 1000, 100, 20, 10 MeV.

Figure 5. Experiment results of cavity-steering effect.
a) measured on 4/30/92, b) measured on 5/7/92.

Figure 6. Symmetrized Figure-5 results. a) measured on 4/30/92, b) measured on 5/7/92. Solid=experiment; Dashed=PARMELA.

For large γ, D_x, D_y, Q and S become finite while F vanishes as $\frac{1}{\gamma^2}$. If the trajectory change is taken into account, F varies as $\frac{1}{\gamma}$ [8] instead of $\frac{1}{\gamma^2}$.

To calculate the coefficients of Eq.5, we first calculate the ΔP_x and ΔP_y for a number of particles initially distributed on a circle of radius a at $z = 0.0$ with certain energy and zero transverse momentum, and then do Fourier transforms of ΔP_x and ΔP_y. The coefficients are shown in Figure 4. The cavity gradient in Figure 4 is 5 MV/m.

IV. EXPERIMENTAL RESULTS

Experiments were conducted to measure the steering effect of the CEBAF cavity on the 45 MeV CEBAF injector. In these experiments, we run the injector at about 20 MeV. The cavity measured is the second last cavity in the second cryomodule, and the results are shown in Figure 5, as a function of RF phase. The beam position is relative to the position of the particle on crest and is measured at about 17 m downstream from the cavity. Figure 5a is for a case with 18.42 MeV initial energy and 5.26 MV/m cavity gradient. Figure 5b is for a case with 17.28 MeV initial energy and 5.106 MV/m cavity gradient.

The data shown in Figure 5 contain both cavity steering effects and transverse kicks from the tilt misalignment of the cavity. They are functions of the RF phase. The maximum coupler kicks are about 50^0 off crest in both the x and y directions, which are not symmetric about the crest phase, while the kicks from the misalignment of the cavity have maximums on the crest phase and are symmetric about the crest (cosine-like). They can be removed by symmetrizing the data shown in Figure 5 about the crest phase. The differences of the symmetrizing are only from the coupler steering, which is shown in Figure 6. To compare with the PARMELA simulation, the position displacement is converted to transverse momentum. Agreement of the experiment with the simulation is very good.
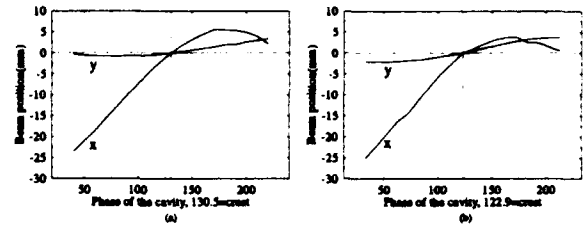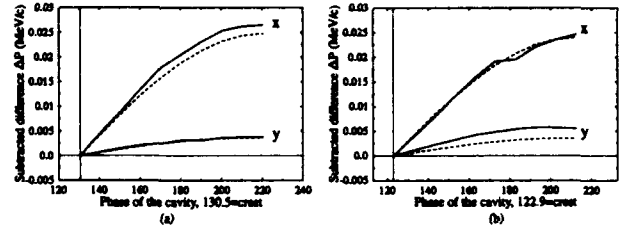
V. CONCLUSION

Cavity steering and focusing studied in this paper is from the fundamental mode field only. The modified PARMELA reveals that the cavity fundamental mode has finite multipoles which are due to the asymmetric HOM and FP couplers. Experimental results agree with the steering effects calculated.

REFERENCES

[1] *Proposal: High-Power UV and IR Free Electron Lasers Using the CEBAF Superconducting Accelerator*, Vol. 1, May 1992.

[2] R. Klatt *et al.*, "MAFIA - A Three-Dimensional Electromagnetic CAD System for Magnets, RF Structures and Transient Wake-Field Calculation," *Proc. 1986 Linear Accelerator Conference, p. 276.*

[3] *PARMELA: A Particle Dynamics Code for Electron Linacs (manual).*

[4] Z. Li *et al.*, "Transport Properties of the CEBAF Cavity," CEBAF preprint, to be published.

[5] M. G. Tiefenback *et al.*, "Emittance Measurements and Transverse Cavity Transfer Matrix in the CEBAF Nuclear Physics Accelerator," These proceedings.

[6] Z. Li *et al.*, "Numerical Simulation of the CEBAF 5-Cell Cavity," to be published.

[7] Curtis C. Johnson, *Field and Wave Electrodynamics*, (McCraw-Hill Inc., 1965).

[8] G. Krafft, "More on the Transfer Matrix of a Cavity," CEBAF-TN-91-069.

Global Coupling and Decoupling of the APS Storage Ring *

Y.C. Chae† J. Liu‡ L. C. Teng
Argonne National Laboratory, 9700 So. Cass Ave., Argonne, IL 60439

Abstract

This paper describes a study of controlling the coupling between the horizontal and the vertical betatron oscillations in the 7-GeV Advanced Photon Source (APS) storage ring. First, we investigate the strengthening of coupling using two families of skew quadrupoles. Twenty skew quadrupoles are arranged in the 40 sectors of the storage ring and powered in such a way so as to generate both quadrature components of the required 21st harmonic. The numerical results from tracking a single particle are presented for the various configurations of skew quadrupoles. Second, we describe the global decoupling procedure to minimize the unwanted coupling effects. These are mainly due to the random roll errors of normal quadrupoles. It is shown that even with the rather large rms roll error of 2 mrad, the coupling effects can be compensated for with 20 skew quadrupoles each having maximum strength one order of magnitude lower than the typical normal quadrupole strength.

I. GLOBAL COUPLING

A. Introductory Remarks

For a given skew quadrupole distribution, $m(\theta) = \frac{1}{(B\rho)} \frac{\partial B_x}{\partial x}$, we can show that the ratio of the horizontal (x) and vertical (y) oscillation amplitude can be expressed as [1]

$$\frac{y_{amp}}{x_{amp}} \cong \frac{\frac{1}{2}\sqrt{a_k^2 + b_k^2}}{\nu_y^2 - (\nu_x - k)^2},$$ (1)

where a_k and b_k are the kth harmonic coefficients defined by

$$m(\theta) = \sum_{p=-\infty}^{p=+\infty} (a_p \cos p\theta + b_p \sin p\theta),$$

where θ is the azimuthal angle around the ring. Deriving Eq. (1), we assumed that the tunes are near the coupling resonance, namely, $|\nu_x - \nu_y| \cong k$. For the APS storage ring, since the design tunes are $\nu_x = 35.22$ and $\nu_y = 14.30$, the above equation clearly shows that we need to excite the $k = 21$ harmonic to cause the coupling most efficiently. In the next sections, the arrangement of skew quadrupoles to excite the 21st harmonic is discussed and some numerical results are presented.

B. Arrangement of Skew Quadrupoles

Consider N skew quadrupoles with the same strength evenly distributed around the ring with period $\frac{2\pi}{N}$ as shown in Fig. 1(a). Then Fourier harmonic numbers are $k = nN$ where n is an integer. In order to obtain the harmonic number k such that $k = nN + mM$, we may impose on top of Fig. 1(a) the square wave function with period $\frac{2\pi}{M}$. Such a function is shown in Fig. 1(b) and the corresponding modulated function can be

expressed as a Fourier series by

$$f(\theta) = \frac{2N}{\pi^2} \sum_{m=1,odd} \frac{\sin(mM\theta)}{m} +$$ (2)

$$\frac{2N}{\pi^2} \sum_{n=1} \sum_{m=1,odd} \frac{\sin(nN + mM)\theta - \sin(nN - mM)\theta}{m}.$$

Hence we show that we can generate an arbitrary harmonic by changing the period of the square wave function.

In the APS storage ring[1], the spaces available for the skew quadrupoles are between Q3 and S2 in the upstream half of a sector (half sector A), which we will call the A:QS family, and between Q4 and S3 in the downstream half of a sector (half sector B), which we will call the B:QS family. The number of skew quadrupoles considered is ten for each family. We may install the focusing A:QS in every fourth cell, say cell numbers 1, 5, 9, 13 and 17, and the defocusing A:QS in cells 21, 25, 29, 33 and 37. This family alone can adequately generate the desired 21st harmonic. Using Eq. (2), with $N = 10$ and $M = 1$ for the A:QS family, we find the coefficient of the 21st harmonic to be $b_{21} \equiv c = \frac{20}{\pi^2}$ which is greater than unity. The B:QS family adds to the quadrature components because A:QS and B:QS are not in phase. For the arrangement shown in Fig. 1(c) which we will call the "normal" arrangement, we may write

$$m(\theta) = c(a \cos 21\theta + b \sin 21\theta),$$ (3)

where $a = -\sin 21\Delta\theta_o$, $b = 1 + \cos 21\Delta\theta_o$, and $\Delta\theta_o$ is the shift of the origin of the B:QS family with respect to the origin of the A:QS family which is the middle of the A:QS skew quadrupole in cell number 1. In the APS storage ring $\Delta\theta_o$ is $\frac{\pi}{8}$. We note that, if A:QS and B:QS are exactly in phase, $a = 0$ and $b = 2$.

In the next section, we present numerical results of the coupling coefficient obtained by tracking a single particle. We first use the "normal" arrangement as the basis and then we attempt to find the optimum arrangement for obtaining full coupling.

C. Numerical Results

For single particle motion the Courant-Snyder invariant is

$$\epsilon_x = \frac{x^2 + (\alpha_x x + \beta_x x')^2}{\beta_x}.$$

The coupling ratio in this report is defined as

$$\kappa = \frac{(\epsilon_y)_{max}}{(\epsilon_x)_{max}}.$$

This definition is consistent with the ratio of emittances of a group of particles (a beam), because the emittance is the phase space area enclosed by the envelope of the beam. However, since the linear optical parameters, $\beta_{x,y}$ and $\alpha_{x,y}$, are ill-defined in the coupled lattice, our definition of the emittance is not the true projection of the four-dimensional phase space volume onto the (x, x') or (y, y') plane as defined in [3]. But for our application it is an adequate approximation to the real projected emittance.

---

*Work supported by U.S. Department of Energy, Office of Basic Energy Sciences under Contract No. W-31-109-ENG-38.
†On leave from University of Houston.
‡On leave from University of Wisconsin, Madison.

---

[1] For the arrangement of lattice elements and the nomenclature rules used in the APS project, see Ref. [2]

0-7803-1203-1/93$03.00 © 1993 IEEE

In order to estimate the coupling ratio with the intentional insertion of skew quadrupoles in the otherwise uncoupled APS storage ring lattice, we used the program MAD [4]. For "normal" configuration, we achieved full coupling with the integrated skew quadrupole strength of $B'l =0.25$ T which is larger than the 0.2 T of the design normal operating strength.

In order to achieve full coupling at the skew quadrupole strength 0.2 T, we optimized the skew quadrupole arrangement. One optimization procedure is to rotate the B:QS family by $n\frac{2\pi}{10}$ in a clockwise direction while A:QS is fixed at the original place. With $n = 1$, B:QS in cell 3 goes to cell 7 and B:QS in cell 7 to cell 11 and so on. This operation is shown in Fig. 1(d). By using this shifting operation, we control the a and b coefficients in Eq. 3 which can be written

$$a = a(A:QS) + a(B:QS), \quad b = b(A:QS) + b(B:QS),$$
$$a(A:QS) = 0, \quad b = b(A:QS) = 1,$$
$$a(B:QS) = -sin21\Delta\theta_n, \quad b(B:QS) = cos21\Delta\theta_n,$$

where $\Delta\theta_n = \Delta\theta_0 + \frac{2\pi}{10}n$ and $\Delta\theta_0 = \frac{\pi}{8}$. The coefficients $a(B:QS)$ and $b(B:QS)$ for different n values are plotted in the polar coordinate system as in Fig. 2. We notice that two skew families are almost in phase when $n = 7$ and the amplitude of the 21st harmonic is

$$|c_{21}| = \sqrt{a_{21}^2 + b_{21}^2} \cong 2,$$

which is the desired result.

The tune separation and the coupling ratio for various arrangements of the B:QS family of the skew quadrupoles with the integrated strength $B'l = 0.2\ T$ are listed in Table 1. The tune separation data, an indication of coupling, clearly shows that the $n = 7$ arrangement is the most efficient way of coupling the lattice. However, the coupling ratio doesn't show a clear advantage of the $n = 7$ over the $n = 8$ arrangement. This is because once the beam is close to full coupling, the coupling ratio is saturated, i.e. not much advantage is gained from the optimized arrangement over a less optimized one.

Table 1
Coupling Effects of Various Skew Quadrupoles Arrangement

Arrangement No.	$|\nu_x - \nu_y|$	$\kappa = \epsilon_{ymax}/\epsilon_{xmax}$
n=0 (normal)	0.104	0.797
n=1	0.080	0.403
n=2	0.087	0.542
n=3	0.115	0.798
n=4	0.145	0.891
n=5	0.171	0.888
n=6	0.185	0.936
n=7	0.186	0.952
n=8	0.172	0.963
n=9	0.145	0.936

II. GLOBAL DECOUPLING

A. Treatment of Weak Coupling Using Matrix Formalism

Following S. Peggs [5], we may write the normalized transfer matrix for the ring as

$$T = \begin{pmatrix} M & m \\ n & N \end{pmatrix}. \tag{4}$$

This normalized transfer matrix is the similarity transformation of the Edwards and Teng matrix [6], T'. We further define a "fundamental" coupling matrix as

$$H = m + n^+. \tag{5}$$

Then, on the coupling resonance $\nu_x = \nu_y$, the tune separation becomes

$$\delta\nu \cong \frac{\sqrt{det(H)}}{2\pi sin\pi(\nu_x + \nu_y)}. \tag{6}$$

The procedure to minimize $\delta\nu$ is often called "global decoupling."

According to M. Billing [7], H can be written

$$H = H_+ sin\pi(\nu_x + \nu_y) + H_- sin\pi(\nu_x - \nu_y). \tag{7}$$

$H_\pm$ are defined as

$$H_\pm = \sum_{SQ} q_m \begin{pmatrix} cos\omega_\pm(s_m) & sin\omega_\pm(s_m) \\ -sin\omega_\pm(s_m) & cos\omega_\pm(s_m) \end{pmatrix},$$

where $q_m = \frac{\sqrt{\beta_x\beta_y}}{f}$ is the dimensionless skew quadrupole strength of focal length f and

$$\omega_\pm(s_m) = (\pm\phi_y(s_m) - \phi_x(s_m)) + \pi(\pm\nu_y - \nu_x),$$

where $\phi_{x,y}(s_m)$ is the betatron phase at the skew quadrupole measured from the reference point. These expressions are convenient because all the quantities used in the formula are those of the uncoupled lattice. Defining $p = \sum q_m cos\omega_+$ and $r = \sum q_m sin\omega_+$, and noting that the contribution of the H_- term in Eq. (7) vanishes on the coupling resonance, we rewrite Eq. (6) as

$$\delta\nu = \frac{\sqrt{p^2 + r^2}}{2\pi}, \tag{8}$$

which we want to minimize.

B. Decoupling Procedure and Its Application

A routine procedure to decouple the lattice by the operator is simulated using the MAD program interactively. In the simulation, Q1s (see Ref. [2] for locations) are chosen as the trim quadrupoles.

Rewriting p and r,

$$p = \sum_{A:QS} q_m cos\omega_+ \sum_{B:QS} q_m cos\omega_+ + p_o$$

$$r = \sum_{A:QS} q_m sin\omega_+ \sum_{B:QS} q_m sin\omega_+ + r_o \tag{9}$$

where p_o and r_o are from the random roll errors of normal quadrupoles in the ring, we can see that it is convenient to use A:QS to control r, and B:QS to control p, or vice versa. With

the midpoint of the straight section of cell 0 as the reference point, we found that A:QS mainly controls r. With the ten skew quadrupoles of the A:QS family, we get

$$p(A : QS) = 0.2\,|g_m|, \quad r(A : QS) = 6.0\,|g_m|.$$

For optimal control of p using the B:QS family, we consult Fig. 2 in order to find the most efficient arrangement. There we find that the phase of $n = 4$ or $n = 9$ arrangement is almost orthogonal to that of A:QS.

In the simulation, we used the $n = 0$ arrangement of B:QS. Coupling is caused by the random roll errors of normal quadrupoles. The minimum tune separations before and after decoupling are summarized in Table 2 with the same seed number for the assignment of random errors. We note that $\delta\nu$

Table 2
Effect of Decoupling Procedure on the Tunes

Error level	$\delta\nu$ (before)	$\delta\nu$ (after)	A:QS (B'l)	B:QS (B'l)
0.5 mrad	0.0186	0.00133	0.019 T	0.055 T
1.0 mrad	0.0353	0.00465	0.031 T	0.100 T
2.0 mrad	0.0714	0.0282	0.019 T	0.140 T

before decoupling is linearly proportional to the magnitude of rms errors, as expected.

The effects of decoupling on the phase motion at the normal tunes was found to reduce the coupling ratio significantly. For the error level of 2 mrad, the coupling ratio reduced down to 0.1 from 0.65.

III. CONCLUSION

In this report we investigated the coupling procedure to put a beam in the fully coupled state and the decoupling procedure to cancel the coupling effects due to the random roll errors of normal quadrupoles. The harmonic analysis of skew quadrupole distribution provides the common ground for finding the optimum arrangement of skew quadrupoles. We achieved full coupling at the integrated skew quadrupole strength of 0.2 T and we succeeded in reducing the coupling down to below 10 percent even with the rather large lattice quadrupole rms roll error of 2 mrad.

IV. REFERENCES

[1] Y.C. Chae, "Global Coupling and Decoupling in the APS Storage Ring," ANL/APS/LS-207, May, 1992.

[2] G. Decker, "Nomenclature and Name Assignment Rules for the APS Storage Ring," ANL/APS/LS-196, March, 1992.

[3] K.L. Brown and R.V. Servranckx, "Cross-Plane Coupling and Its Effects on Projected Emittance," SLAC-PUB-4679, August, 1989.

[4] H. Grote and F.C. Iselin, "The MAD Program Version 8.1," CERN/SL/90-13(AP), May, 1990.

[5] S. Peggs, "Coupling and Decoupling in Storage Rings," IEEE NS-30, No. 4, August, 1983.

[6] D. Edwards and L.C. Teng, "Parameterization of Linear Coupled Motion in Periodic Systems," IEEE NS-30, No. 3, June, 1973.

[7] M. Billing, "Controls in Use at CESR for Adjusting Horizontal to Vertical Coupling," IEEE NS-32, No. 5, October, 1985.
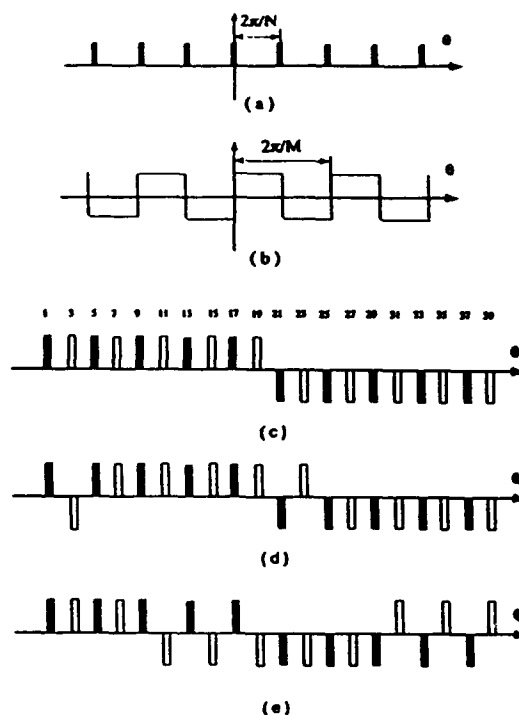
Figure 1

(a) Periodic delta function. (b) Square wave function. (c) Skew quadrupole arrangement where a solid block represents the A:QS family and a blank block represents the B:QS family. The number on the block indicates the cell number in the APS storage ring and we will call this arrangement the "normal" arrangement. (d) Shift of B:QS by an amount of $2\pi/10$, namely $n=1$. (e) Shift of B:QS by an amount $7\frac{2\pi}{10}$, namely $n=7$ (the optimized arrangement achieving full coupling).
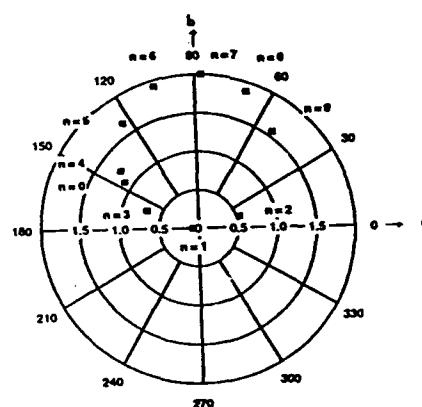
Figure 2

a(B:QS) and b(B:QS) coefficients from the B:QS skew quadrupole family. Note that since a(A:QS)=0 and b(A:QS)=1.0, this figure shows that two families are almost in phase with n=7.

Conventional Collimation and Linac Protection

J. Irwin, R. Helm, W. R. Nelson and D. Walz
Stanford Linear Accelerator Center
Stanford, CA 94309

Abstract

We describe linac protection and a conventional collimation system appropriate for a next linear collider. The linac accelerating structure can be protected from "worst credible failures" by a system of sacrificial spoilers. For the collimation system we consider the effects of transverse wakefields and the transmission, heating, mechanical stress, and edge-scattering properties of scrapers. We require local chromatic correction, scraper survival for two pulses of a mis-steered beam containing 0.5×10^{12} particles per pulse, average interception capability of 1% of the beam at any scraper, and zero particles incident on the final doublet in the final focus system. We describe emittance dependent limitations of this system and present formulae which determine scraper gaps. Conventional collimation systems appear adequate to collimate the beams of next generation 0.5 and 1.0 TeV c.m. linear colliders. Though we have combined functional units where possible to reduce total length, the length of our lattices for these systems are longer than 1 km per linac.

INTRODUCTION

There are many known sources of halo particles in electron linacs [Ref. 1], halos which: i) are present upon extraction from the damping ring, ii) are created in the bunch compressor, iii) are generated by wakefields within the linac, especially as a consequence of tails in bunch length, iv) are created by mismatches, misalignment and steering errors in the linac, v) result from injection jitter into the linac, vi) come from acceleration of dark current, and vii) are produced by hard Coulomb scattering within the linac. Sources i) through vi) can be ameliorated by a variety of strategies, whereas vii) places an irreducible lower limit on halos. An estimate of the fraction of particles scattered into a halo beyond "$n\sigma$" is [Ref. 2] $\Delta N/N \approx (5 \times 10^5)/n^2$ for a 5 km linac with gas pressure of 10^{-8} Torr. For $N = 0.5 \times 10^{12}$ and $n = 5$, $\Delta N \approx 10^6$. Since it may be true that even one particle hitting the final doublet can blind the detector [Ref 3], and substantial tails beyond $7\sigma_x$ or $35\sigma_y$ can cause synchrotron radiation incident on the final doublet, a collimation system for the next linear collider will be mandatory.

At the end of a 1 TeV/cm energy X-band linac the beam will have a $\sigma_x\sigma_y$ product of 5 μm^2 and each pulse will contain more than 0.5×10^{12} particles with an energy of 40 kJ. The time averaged power will be 8 MW [Ref 4]. One pulse of such a beam hitting any known solid material would vaporize and likely shatter it. Moreover, wakefields from jaws attempting to collimate micron-sized low-emittance beams could destroy the emittance. Potential radiation damage, absorber heat loads, detector backgrounds, and edge scattering further complicate

this problem. We begin by describing the collimation system we propose, and then show how it meets projected operating requirements for an X-band linear collider.

Conventional Collimation System

We symbolically represent a four-phase collimation system as follows:

IP phase: mai..h/e.v.H/E__h/e.V.H/E..π/2..
FD phase: h/e.v.H/E__h/e.V.H/E..π/2..
IP phase: H/E.V__H/E.V..π/2..
FD phase: H/E.V__H/E.V..mao

where IP (FD) phase indicates that particles in phase with the interaction point (final doublet) are being collimated. mai stands for the incoming match to the first phase of scraping, and mao stands for the match from the last FD phase into the next lattice section. "π/2" represents a lattice section which advances the phase of both the horizontal and vertical betatron motion by π/2. A long underline indicates that the joined symbols are part of a -I section. The small letters h,v, and e represent thin 0.25 radiation length (r.l.) pyrolytic carbon spoilers, which are designed to withstand a pulse or two of a mis-steered beam, while creating a divergent angle in the beam sufficiently large that downstream absorbers are not harmed. The large letters H, V, and E represent absorbers which are 20 r.l. long, made either of water-cooled copper where a large flux is expected, or a higher-Z material such as tungsten, in low flux situations.

The combination h/e or H/E indicates a position where energy and the horizontal plane are being collimated together. Two of these at -I with a symmetric dispersion function combine to collimate a triangle in (x,δ) space.

The β-functions must be large at the scrapers so that: i) the beam, if mis-steered, is sufficiently large when in hits the spoiler, and ii) the beam and collimator gap are large enough to make the wakefields small. Chromaticity is created because of the large β-functions. A large dispersion function is required for energy collimation, and this can be used in conjunction with sextupole pairs at -I for chromaticity correction. Sextupole pairs have been placed at all spoilers and absorbers represented above. Lattice functions for a 3-phase collimation system are shown in Fig. 1. Overall system length could likely be reduced by redesigning the third and fourth phases, since these have no requirements based on spoiler survival, and absorbers will receive far less flux.

We have not attended to the ultimate fate of all secondary particles created at the spoilers. Absorbers other than those specifically called out will certainly be required.

Because of the large dispersion function and large β-functions, the whole system must be protected against beams that are very badly mis-steered or are far off-energy. We propose to accomplish this with sacrificial tungsten spoilers at the entrance to the collimation system set at 35 σ_x and 280 σ_y.
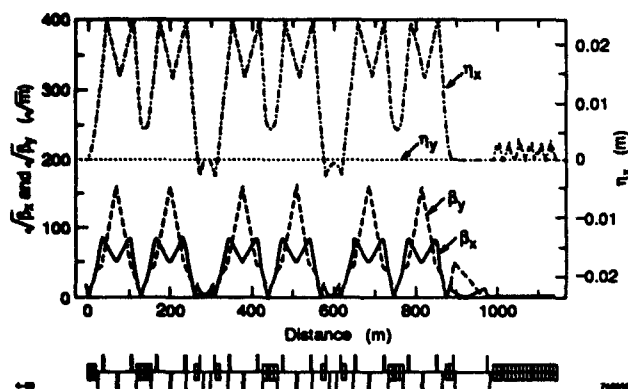
Figure 1. Lattice functions for three-phase collimation systems.

Energy Deposition in Spoilers

Figure 2. The energy deposited in several materials by a 500 GeV beam of 10^{12} particles incident with a $\sigma_x\sigma_y$ product equal to 2000 μm^2.

Limitations of Conventional Collimation Systems

To minimize wakefields, scrapers must be tapered. The optimum taper angle is given by:

$$\Theta_T{}^{opt} = 1.6 \, (\lambda\sigma_z/g^2)^{1/4}$$

where g is the scraper gap, λ is the skin depth, and σ_z is the rms bunch length [Ref 5]. Taken together, the wake from the taper, which prefers a small gap, and the resistive wall wake which requires a large gap, yield the following condition [Ref 6]:

$$2 u^3 - 3 a u^2 + 1 \leq 0$$

where $u = (g/g_1)^{1/2}$ and $a = (n/n_{min})^2$, where

$$g_1 \approx 0.9 \, (\Sigma n_i L_{Fi}\lambda_i{}^{1/2})^{2/3} \, \sigma_z{}^{1/6} \, / \, (\Sigma n_i \, \lambda_i{}^{1/4})^{2/3}$$

and

$$n_{min}{}^2 \approx 0.8 \, t/t' \, Nr_e/(\epsilon_N\sigma_z) \, (\Sigma n_i L_{Fi}\lambda_i{}^{1/2})^{1/3} \, (\Sigma n_i \, \lambda_i{}^{1/4})^{2/3} \, \sigma_z{}^{1/3}$$

Here, n_i is the number of scrapers at the phase being considered with length L_{Fi} and resistive skin depth λ_i. ϵ_N is the normalized emittance, N is the number of particles per bunch, and r_e is the classical electron radius. In other words, for a = 1, which occurs at n = n_{min}, where n is the number of sigmas being collimated, the cubic equation has one positive root at u = 1 (g = g_1). Corresponding to this gap and n we have a β-function $\beta_1 = g_1{}^2/(n_{min}{}^2\epsilon)$. The jitter amplification deemed acceptable is t'/t. The outgoing jitter strength t' is perpendicular in phase space to the incoming jitter strength.

For n > n_{min} the cubic equation has two positive roots and any u between the roots satisfies the equation. For n/n_{min} = 1.1 the roots are u =0.66 and u=1.6, hence g may take any value in the range $0.37g_1 < g < 2.6g_1$, and β can take any value in the range $0.16\beta_1 < \beta < 5.6\beta_1$. For n/n_{min} = 5/3 the roots are u = 0.5 and u = 2.4. Hence g may take any value in the range $0.25g_1 < g < 5.8g_1$, and β can take any value in the range $0.02\beta_1 < \beta < 12\beta_1$. We see that n_{min} is tightly set by the equation, but that for n only slightly larger than n_{min}, rather broad ranges of g and β are possible.

Bunch-to-bunch and pulse-to-pulse energy jitter can also be a problem. However, because of the symmetric dispersion function in the -I sections, the wakes from scrapers at -I will have opposite polarity and could be designed to cancel one another.
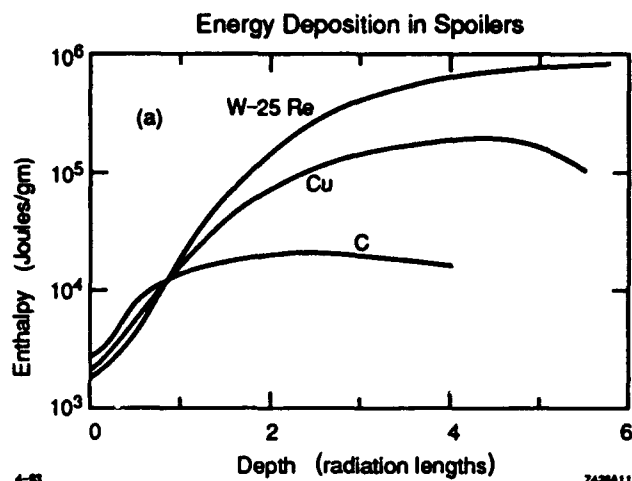
Required Collimation Cuts

The transverse collimation cut is determined by the final focus design together with the maximum divergent angle expected at the IP. The final doublet apertures are primarily determined by wakefield criteria. We take $6\sigma_x$ and $35\sigma_y$ as acceptable collimation cuts to avoid any particle hitting the final doublet and to minimize synchrotron radiation flux incident on the doublet.

The acceptable energy cut is determined by the bandwidth of the transport system from the collimation system to the final doublet. Studies show that the bandwidth is about 5.5%, so we have taken 4% as an acceptable energy cut.

Spoiler Survival

Within the constraints dictated by the beam dynamics described above, the β–functions must be large enough that the energy density deposited by a full beam pulse incident on a spoiler will not destroy it. The spoiler should withstand two beam pulses to allow for data acquisition in puzzling circumstances. Figure 2 shows the energy deposited per gram for three materials for $\sigma_x\sigma_y$ = 2000 μm^2 and $Nn_B=10^{12}$ particles per bunch. Energy density can be translated into temperature rise using enthalp vs. temperature data for the material. Carbon is thermally very rugged. It may be coated and plated to reduce resistive wall wakefields.

Post-Spoiler Particle Distributions

Figure 3 shows the angular distribution of particles exiting the spoilers. Each curve represents particles in a 1 GeV bin at energies indicated. These show that angular distributions are independent of energy. At the scrapers, $\sigma_x' \approx 30$ nr so the scattering angles represent $10^3\sigma$ horizontally. The great majority of these particles will be intercepted by absorbers in the same-phase beamline section where they were produced. Those with very small angles, $\leq 35 \, \sigma_x$, about 1μr at the spoiler, will be
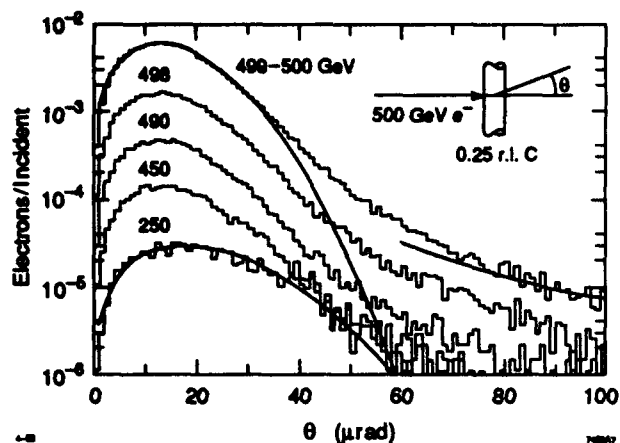
Figure 3. The angular distribution for particles exiting a 0.25 r.l. pyrolytic carbon spoiler. Solid lines correspond to a single scattering ansatz.

Figure 4. The probability of rescattering into the beam with energy degradation less than 4% as a function of initial position from the scraper edge.

transported to the next-phase beamline. This fraction is about 2×10^{-3}. Hence one would expect about 1 particle in 10^4 to hit the next spoiler within 1 σ of the edge of the scraper.

Edge Scattering

After the two collimation phases with thin carbon spoilers, the re-population of the beam halo comes from edge scattering. The angular distribution for these particles is similar to that shown in Fig. 3. Figure 4 shows the number that reenter the halo with energies above the 4% cut. Ten percent of those particles hitting within 0.3 μm from the edge will re-emerge in the beam. For incident particles spread over a width of 1 $\sigma \approx 700$ μm, 0.5×10^{-4} re-emerge in the beam. The number of edge-scattered particles in the beam after the third phase of collimation will be at least 10^{-8} of those incident on the first carbon spoiler. These will be intercepted in the final FD phase collimation.

Tail Repopulation

There is about a kilometer of beam-line from the last collimator to the IP, including a possible "big fork" to allow switching between two detectors, a 200-m long "big bend" for muon protection (and to accommodate two detectors and a crossing angle independent of linac orientation), and the final focus system. In order to insure that less than one particle per beam-pulse impacts the final doublet as a result of being hard scattered by a gas nucleus, it is necessary to have gas pressures of 10^{-9} Torr in the "big fork" and "big bend" [Ref 6]. Collimators should be placed in the final focus system at the first large β-function location.

Linac Protection System Issues

A badly mis-steered beam in the linac could destroy a long length of accelerator by destroying the edge of an iris, executing a betatron oscillation, destroying the edge of another iris, and so on down the machine. The destructive capability of an
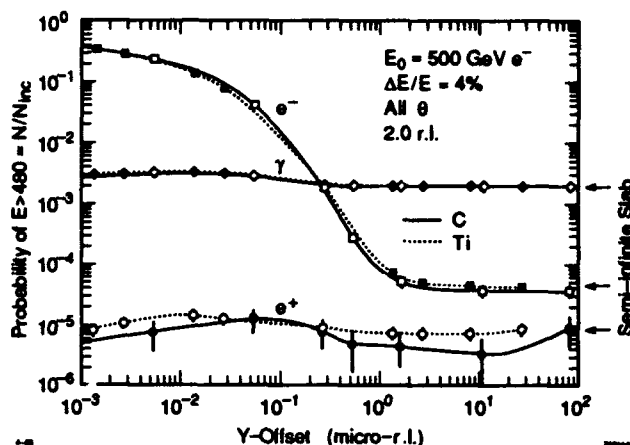
8 MW beam having a cross-sectional area of a few square microns is awesome.

The worst credible failure that we have identified is a simultaneous short in the windings of two poles of a quadrupole. We assume that a system designed to detect magnet problems failed, and that continuous beam-position monitor (BPM) analysis also failed to identify the errant beam. While the resultant field on the quadrupole axis is not large enough that the beam will hit the accelerator structure before the next quad, it can hit the structure in the accelerator section after that [Ref 6].

Our proposal for protecting the linac from this and similar failures is to insert a "sacrificial spoiler" immediately before each quadrupole. The word "sacrificial" indicates that we expect to have to replace this element if ever the full beam is incident upon it. The inner radius of the "sacrificial spoiler" must be such that a mis-steered beam passing through it cannot hit the accelerating irises before reaching the next quadrupole. For a structure iris radius of 4.4 mm, the spoiler radius must be about 1 mm. The wakefield induced emittance growth from a linac filled with such spoilers is acceptably small ([Ref 6]).

References

1. J. Seeman, SLAC, Private communication.
2. K. Yokoya and V. Telnov at the LC91 workshop.
3. G. Punkar, SLAC, is currently studying this problem. Private communication.
4. Working Parameter List, SLAC Parameter Working Group, April 1993.
5. J. Irwin, N. Merminga, R. Helm, and R. Ruth, *Optimizing a Nonlinear Collimations System for Future Linear Colliders*, SLAC-PUB-5507 (March 1991).
6. J. Irwin, R. Helm, W.R. Nelson, and D. Walz, *Conventional Collimation and Linac Protection for Future Linear Colliders*, to be published.

Measurement of Beta-Function and Phase Using the Response Matrix*

Y. Chung, G. Decker and K. Evans, Jr.
Argonne National Laboratory, Argonne, IL 60439

Abstract

A new method for extracting the beta-function and phase for the beam position monitors (BPMs) and the corrector magnets from the measured response matrix is presented. The response matrix relates beam motion at the BPM locations to changes in corrector magnet strengths. Using the model beta and phase as the initial values, new values are obtained by iteration. The accuracy of beta and phase thus calculated is limited by the accuracy of response matrix measurement and calibration of BPMs and correctors. The scaling ambiguity in the beta-function is resolved by matching the beta product and phase advance across a drift region. A by-product of this technique is an accurate determination of the betatron tune, and in principle, quadrupole strengths can be calculated from the betas and phases. This method is applied to data obtained from the X-ray ring at the National Synchrotron Light Source at Brookhaven. The possibility of applying the results to lattice-debugging will also be discussed.

I. INTRODUCTION

In the past, several methods for the measurement of accelerator beta functions and betatron phase have been suggested and applied. Accelerators having independently controllable quadrupole magnets can make use of the variation of tune with quadrupole magnet strength to extract the value of beta at the location of the quad, as is done at the Cornell Electron Storage Ring [1]. A technique was suggested by Harrison and Peggs [2] whereby betas and phases could be determined from closed orbit measurements resulting from varying two steering correctors in turn, provided that the values of beta and phase at those two correctors could be found from some other technique. The beta function and phase at the locations of all beam position monitors (BPMs) could in principle be found in this way.

In this paper, a technique is presented for determining the best fit betas and phases at all BPMs and all steering correctors from measured response matrix data. The response matrix relates beam motion at the BPM locations to changes in steering corrector strengths. This technique is similar to that of Ref. [2], but makes use of all steering correctors rather than just two. Because the problem is severely over-constrained, the method of singular value decomposition (SVD) of a matrix is used to minimize the difference between the resulting ring model and the measured response matrix data. One by-product of this technique is an accurate

determination of the betatron tune. The technique is applied to data obtained from the X-ray ring at the National Synchrotron Light Source at Brookhaven. Results are obtained which agree qualitatively with measurements made there two and a half years ago using the technique of Ref. [2], together with the least squares fitting, by Decker and Swenson. [3]

II. THEORY

Suppose that there are M BPMs and N correctors in the storage ring. Both M and N are larger than 1. Let β_i and ψ_i be the amplitude and phase functions at the location of the i-th BPM. β_{cj} and ψ_{cj} are similarly defined for the j-th corrector. The response matrix R_{ij} corresponding to the beam motion at the i-th BPM per unit angle of kick by the j-th corrector is then given by [4]

$$R_{ij} = \frac{\sqrt{\beta_i \beta_{ci}}}{2 \sin \pi \nu} \cos (\psi_i - \psi_{cj} \pm \pi \nu). \quad \begin{cases} +: \psi_i < \psi_{cj} \\ -: \psi_i > \psi_{cj} \end{cases} \quad (1)$$

ν is the betatron tune of the machine. The response matrix R_{ij} can be obtained from measurements, and we will develop in the following a method to extract the beta function and phase from the measured data using Eq. (1).

A. Calculation of Beta and Phase Functions

Let us define

$$\psi_{cij} = \begin{cases} \psi_{cj}, & \psi_{cj} < \psi_i \\ \psi_{cj} - 2\pi\nu. & \psi_{cj} > \psi_i \end{cases} \quad (2)$$

Then it can be shown that β_i and ψ_i are given by

$$\beta_i = (c_i^2 + s_i^2) \sin^2 \pi\nu,$$

$$\psi_i = \tan^{-1}\left(\frac{s_i}{c_i}\right) + \pi\nu, \quad (0 < \psi_i < 2\pi\nu \text{ and } \psi_{i+} \cdot \psi_i) \quad (3)$$

where c_i and s_i are solutions of

$$c_i \cos \psi_{cij} + s_i \sin \psi_{cij} = \frac{2}{\sqrt{\beta_{cj}}} R_{ij}. \quad (1 \le j \le N) \quad (4)$$

In matrix form, Eq. (4) can be written as

$$\mathbf{A} \cdot \mathbf{x} = \mathbf{a} \quad (5)$$

where

$$A = \begin{pmatrix} \cos \psi_{ci1} & \sin \psi_{ci1} \\ : & : \\ \cos \psi_{ciN} & \sin \psi_{ciN} \end{pmatrix}, \quad x = \begin{pmatrix} c_i \\ s_i \end{pmatrix}, \quad (6)$$

and

$$a = \begin{pmatrix} \dfrac{2R_{i1}}{\sqrt{\beta_{c1}}} \\ : \\ \dfrac{2R_{iN}}{\sqrt{\beta_{cN}}} \end{pmatrix}. \quad (7)$$

The functions β and ψ for the correctors can be similarly obtained. With the definition

$$\psi_{ij} = \begin{cases} \psi_i, & \psi_i < \psi_{cj} \\ \psi_i - 2\pi v, & \psi_i > \psi_{cj} \end{cases} \quad (8)$$

beta and phase functions for the correctors can be obtained from

$$\beta_{cj} = (c_{cj}^2 + s_{cj}^2) \sin^2 \pi v,$$

$$\psi_{cj} = \tan^{-1}\left(\frac{s_{cj}}{c_{cj}}\right) + \pi v. \quad (0 < \psi_{cj} < 2\pi v \text{ and } \psi_{cj+1} > \psi_{cj}) \quad (9)$$

c_{cj} and s_{cj} are solutions of

$$B \cdot y = b, \quad (10)$$

where

$$B = \begin{pmatrix} \cos \psi_{1j} & \sin \psi_{1j} \\ : & : \\ \cos \psi_{Mj} & \sin \psi_{Mj} \end{pmatrix}, \quad y = \begin{pmatrix} c_{cj} \\ s_{cj} \end{pmatrix}, \quad (11)$$

and

$$b = \begin{pmatrix} \dfrac{2R_{1i}}{\sqrt{\beta_1}} \\ : \\ \dfrac{2R_{Mi}}{\sqrt{\beta_M}} \end{pmatrix}. \quad (12)$$

In Eq. (5), A is an $N \times 2$ matrix which is a function of the phases of both the BPMs and correctors. x and a depend on the BPMs and the correctors, respectively. Similarly, in Eq. (10), B is an $M \times 2$ matrix which is a function of the phases of both the BPMs and correctors. y and b depend on the correctors and the BPMs, respectively. In addition, v is also an unknown parameter to be determined.

In order to obtain a self-consistent set of solutions, we will use iteration. We start with a set of initial values for $\{\beta_i, \psi_i\}$, $\{\beta_{cj}, \psi_{cj}\}$, and v, which we use to obtain the matrices A and B and the vectors a and b. Since the number of equations is larger than the number of unknowns, the problem is overdetermined, and therefore, the exact solution does not exist in general. However, approximate solutions can still be obtained such that $| A \cdot x - a |$ and $| B \cdot y - b |$ have the minimum values possible. These are the closest solutions for Eqs. (5) and (10), and can be obtained using the technique of singular value decomposition (SVD). [5] The solutions thus obtained will best fit the measured response matrix and are used as the initial guess for the next iteration. This process continues until the solutions converge for a given v.

B. Error Analysis and Determination of Tune

With the solutions for β and ψ, the response matrix R' is reconstructed using Eq. (1) and the r.m.s. error

$$\Delta R = \sqrt{\frac{1}{MN} \sum_{i,j} (R'_{ij} - R_{ij})^2} \quad (13)$$

is calculated. The error function ΔR represents the accuracy of the tune v used for iteration. The correct tune corresponds to the minimum ΔR, which again can be used to estimate the error in the β-function. Let us assume that the relative error in β is constant. That is,

$$\frac{\delta \beta_i}{\beta_i} \approx \frac{\delta \beta_{cj}}{\beta_{cj}} = \delta a = \text{constant} \quad \text{for all } i, j. \quad (14)$$

Then from Eq. (1), it can be shown

$$\delta a \leq 4 \sin (\pi v) \Delta R <\beta_i \beta_{cj}>^{-1/2}. \quad (15)$$

$<\cdots>$ denotes the average value. This analysis, however, does not include the calibration errors in the BPMs and correctors, which could actually dominate the measurement error.

C. Resolution of Beta-Scaling Ambiguity

Inherent in the preceding analysis are the ambiguities in the scaling of beta functions and the offset of the phase function. The phase offset has no physical meaning and we will concentrate on the resolution of beta-scaling ambiguity.

In Eq. (1), R_{ij} remain unchanged when β_i is multiplied and β_{cj} is divided by a constant. Therefore, an extra constraint is necessary to determine the beta functions for BPMs and correctors. Consider a drift region of length L which has beta functions β_1 and β_2 at the end points and phase difference of $\Delta\psi$. Then we have

$$\sqrt{\beta_1 \beta_2} \sin \Delta\psi = L. \quad (16)$$

If a pair of BPMs or correctors can be found which have drift region between them, the scaling constant for the beta functions can be determined using Eq. (16). Multiple such pairs could be used to check for errors.

D. Measurement of Quadrupole Strength

The strength of a quadrupole magnet can be determined if beta and phase functions are known at points on both sides as shown in Fig. 1. The point 1 is at a distance l_1 from the quadrupole magnet and has β_1 and ψ_1; similarly for point 2 on the other side. The quadrupole has length l_q.
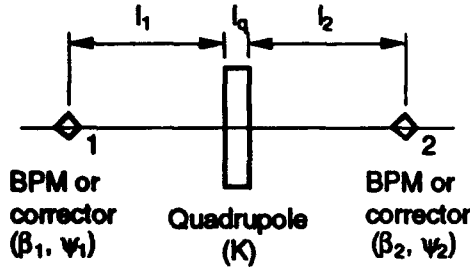
Fig. 1: Determination of quadrupole strength using β and ψ.

The quadrupole strength K is then determined from

$$\sqrt{\beta_1 \beta_2} \sin |\psi_2 - \psi_1| = \qquad (17)$$

$$\begin{cases} \left(\dfrac{1}{q} - l_1 l_2 q\right) \sin(q l_q) + (l_1 + l_2) \cos(q l_q), & K > 0 \\[2ex] \left(\dfrac{1}{q} + l_1 l_2 q\right) \sinh(q l_q) + (l_1 + l_2) \cosh(q l_q), & K < 0 \end{cases}$$

where $q = \sqrt{|K|}$. In case the right-hand side of Eq. (17) is not very sensitive to changes in q, the accuracy of the solution depends largely on that of the β and ψ functions.

III. ANALYSIS OF NSLS X-RAY RING

In this section, we analyze the response matrix in the vertical plane of the X-ray ring of the National Synchrotron Light Source (NSLS) at Brookhaven National Lab. [6] Forty-eight BPMs and 39 correctors were used.

With ~0.005 mm error of BPM reading and corrector kick of ~0.16 mrad for measurement of the response matrix, the measurement error δR is estimated to be $\delta R \approx 0.005 / 0.16 \approx 3 \times 10^{-2}$ (m/rad). Figure 2 shows the plot of ΔR as a function of v. The minimum point is $v = 6.184$, where $\Delta R = 2.4 \times 10^{-2}$ m/rad. This is in good agreement with the estimated error δR.

The β-functions obtained from the measurement ($v = 6.184$) and the ring model ($v = 6.2$) are shown in Fig. 3. From Eq. (15), the relative error δa in calculation of the β-functions is less than 2.3×10^{-3}.

When the results were applied to obtain the strengths of the quadrupoles, significant deviations (~40%) from the nominal values were observed. This is largely attributable to (1) calibration error in the BPMs and correctors and (2) the fact that K is very sensitive to the resulting error in β-functions ($\Delta K/K \approx 0.3\, \Delta \beta$ (m)). Considering the proximity of adjacent magnets to the correctors in the ring, sensitivity calibration of the correctors seems to be the dominant error source.
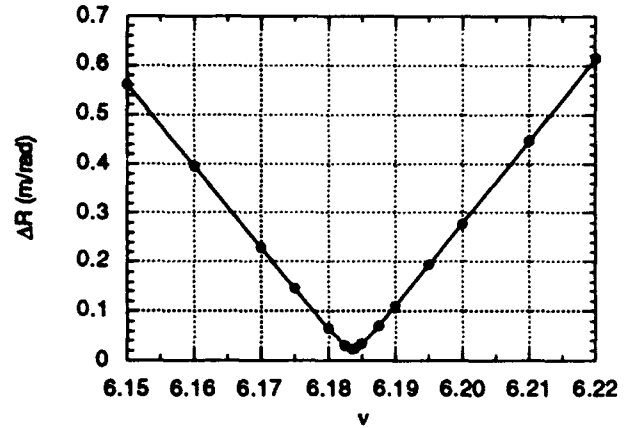
Fig. 2: Response matrix error to determine the vertical tune of the NSLS X-ray ring. The minimum point is: $v = 6.184$, $\Delta R = 2.4 \times 10^{-2}$ m/rad. The nominal tune is 6.2.
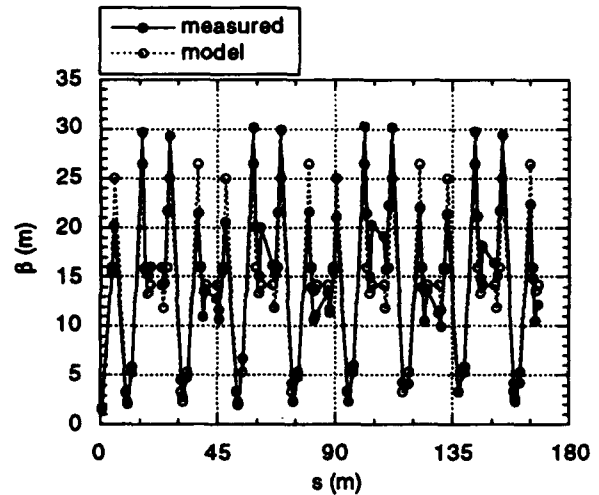
Fig. 3: The model and measured β-functions of the NSLS X-ray ring in the vertical plane.

IV. REFERENCES

[1] G. Decker, "Operational Aspects of Experimental Accelerator Physics," LS-182, Argonne National Lab, 1992.

[2] M. Harrison and S. Peggs, "Global Beta Measurement from Two Perturbed Closed Orbits," Proc. 1987 Particle Accelerator Conference, IEEE CH2387-9/87/0000-1105

[3] G. Decker and C. Swenson, unpublished.

[4] M. Sands, "The Physics of Electron Storage Rings - An Introduction," SLAC-121, 1970.

[5] W. Press et al., Numerical Recipes in C, Cambridge University Press, p. 60, 1989.

[6] J. Safranek, private communication.

MATCH 1.0 – The Program for Analytical Matching of Insertion

Ivan P. Yudin

Joint Institute for Nuclear Research

141980, Dubna, Moscow Region, Russia

Abstract

An algorithm and a program for investigation of a matched straight insertion has been proposed. Formulae have been derived for analytic computation of the insertion parameters in a "thick" lenses aproximation. The results of matching of the synchrotron straight section are presented.

I. INTRODUCTION

Beam Matching

For the beam transport of charged particles, there is the solve often an inverse problem of beam dynamics, the matching of phase volumes of the beam [3-6]. We assume the detection of parameters for the elements of the magnetic optics (such as geometry, fields) of a facility realizing the beam transport with a phase volume of $V_1 = (x_1, x_1', y_1, y_1')$ from point s_1 (beginning of the mathing section of the transport channel, see fig.1) to point s_2 (end of the mathing section) with a phase volume of $V_2 = (x_2, x_2', y_2, y_2')$ to be the solution of this matching problem. We shall assume the betatron functions $\alpha_1^x, \beta_1^x, \alpha_1^y, \beta_1^y$ for horisontal and vertical motion at the beginning of the matching section and $\alpha_2^x, \beta_2^x, \alpha_2^y, \beta_2^y$ at the end to be well-known quantities. Under certain circumstances, only some of above mentioned quantities or their combinations, such as $\sqrt{\beta_2^x/\beta_1^x}$, $\sqrt{\beta_2^y/\beta_1^y}$, $\alpha_1^x = \alpha_1^y = 0$, etc. might be known, whereas the remaining quantities will be arbitrary ones. In order to solve the matching problem, it is necessary to establish the required phase leading on the matching section (s_1, s_2), to dispose of applicable chromaticity or even to match the dispersion function $D_{x,y}$ $D_{x,y}'$ totally, or sometimes we must take care of the matching of direction and polarization degree of the beam and, possibly, of other characteristics.

Optimization

The problem of optimizing parameters of such a facility is connected closely to the matching problem. Its solution will be carried out by taking into account the limitations on all possible values of the parameters for elements of magnetic optics of the projected facility.

Sometimes, it is impossible or objectionable during the projection period to have lengths of lenses and single gaps different from those, which were selected during preliminary

designing. In experiments with colliding beams [7] for instance, one strives to provide for an interaction point: the cross-over in some free gaps, where $\beta_{min}^{x,y}$ does not surpass a certain taken value. The solution of the optimization problem as a whole tends to increase the planning and operation economy of the transport channel under investigation.

Usually (see ref.[8,9]), the matching is not separated from the general optimization problem and their solution occurs commonly and simultaneously. In the proposed method, the matching and optimization functions were separated. The optimization was carried out on the basis of a transport channel, which was developped and matched already. In order to solve the matching problems, we propose analytical expressions, which will be compiled below.

II. MATCHING METHOD

We shall present a solution of the matching problems in linear approximation by means of a minimum number of magneto-optical elements: a doublet of "thick" magnetic quadrupole lenses. For the chosen matching section (see fig.1), we shall whrite the matrix equation of matching as follows:

$$\hat{L}_3 \cdot \hat{F} \cdot \hat{L}_2 \cdot \hat{D} \cdot \hat{L}_1 = \hat{M}(2/1), \qquad (1)$$

where $\hat{L}$, $\hat{F}$, $\hat{D}$ are matrices of linear optics of 2×2 size, the shape of which is well-known, ref.[3,10]. For instance, the matrix elements (m.e.) $L_{12}^x = L_{12}^y = L$, $F_{11}^y = \varphi_F$, $D_{12}^y = (1/k_D) \cdot \sin\varphi_D$, $F_{11}^x = \cos\varphi_F$, $\varphi_F = k_F \cdot l_F$, $k_F = \sqrt{G_F/B_\rho}$; G_F is the gradient and l_F is the effective length of the lens; L indicates the length of a free path, and B_ρ - the magnetic particle rigidity of transported particles. $\hat{M}(2/1)$ can be expressed (see e.g. [10]) by betatron functions $\alpha_1^{x,y}$, $\beta_1^{x,y}$, $\alpha_2^{x,y}$, $\beta_2^{x,y}$ and phase leading $\Delta\psi^{x,y} = \psi^{x,y}(s_2) - \psi^{x,y}(s_1)$:

$$\hat{M}(2/1) = \begin{pmatrix} M_{11} & M_{12} \\ M_{21} & M_{22} \end{pmatrix}, \qquad (2)$$

where

$M_{11} = \sqrt{\beta_2/\beta_1}(cos\Delta\psi + \alpha_1 \cdot sin\Delta\psi)$

$M_{12} = \sqrt{\beta_1 \cdot \beta_2}sin\Delta\psi$

$M_{21} = -\frac{(1+\alpha_1\alpha_2)\cdot sin\Delta\psi + (\alpha_2-\alpha_1)\cdot cos\Delta\psi}{\sqrt{\beta_1\cdot\beta_2}}$

$M_{22} = \sqrt{\frac{\beta_1}{\beta_2}}(cos\Delta\psi - \alpha_2 \cdot sin\Delta\psi)$
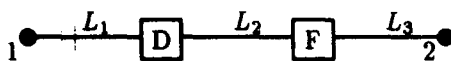
Fig.1 Section of matching by lens doublet.

After having determined the m.e. in (1), we can write eq. (1) as a system of 6 equations:

$$\begin{cases} T_{11}^x = M_{11}^x & T_{21}^x = M_{21}^x & T_{22}^x = M_{22}^x \\ T_{11}^y = M_{11}^y & T_{21}^y = M_{21}^y & T_{22}^y = M_{22}^y \end{cases} \quad (3)$$

where the matrix T is the result of the matrix product on the left side of (1). We should note that the equation of $T_{12} = M_{12}$ is fulfilled automatically due to the Lousville theorema on the concervation of the phase volume: $det|T| = det|M| = 1$. The problem of matching phase volumes of the transported beam is solved usually by nonlinear programming methods [8,9]. If we have written the matching equation system of (1), which is transcendental, we are able to proceed with the following stage: its solution by direct numerical methods. We are able to reduce the composed matching equation system (3) in the present paper by means of successive analitical transformations to one equation with one unknown quantity, that is $\Delta\psi^x$. After having solved this equation on a computer, we can write the characteristics of the matching section: the lengths of fieldless paths, the effective lengths and the gradients of magnetic lenses analitically as a function of the chosen vector of the parameters: $\bar{P} = (\alpha_1^x,\ \beta_1^x,\ \alpha_2^x,\ \beta_2^x,\ \alpha_1^y,\ \beta_1^y,\ \alpha_2^y,\ \beta_2^y,\ \varphi_F,\ \varphi_D,\ \Delta\psi^y)$ and the free parameter $\Delta\psi^x$.

We shall introduce a series of notations, which are helpful for solving the equation system (3):

$$\Delta_{12} = a_{11} \cdot a_{22} - a_{12} \cdot a_{21},$$

$$\Delta_{12}' = b_{11} \cdot L_3 \cdot b_{12} \equiv (a_{22} \cdot a_{13} - a_{12} \cdot a_{23}) +$$

$$+ L_3 \cdot (a_{22} \cdot a_{14} - a_{12} \cdot a_{12} \cdot a_{24}),$$

$$\Delta_{12}'' = b_{21} + L_3 \cdot b_{22} \equiv (a_{11} \cdot a_{23} - a_{21} \cdot a_{13}) +$$

$$+ L_3 \cdot (a_{11} \cdot a_{24} - a_{21} \cdot a_{14}),$$

$$\Delta_{34} = a_{31} \cdot a_{4n} - a_{41} \cdot a_{32},$$

$$b_{31} + b_{32}/k_F) \equiv (a_{33} \cdot a_{42} - a_{32} \cdot a_{43}) +$$

$$+ (1/k_F) \cdot (a_{34} \cdot a_{42} - a_{44} \cdot a_{32}),$$

$$b_{41} + b_{42}/k_F \equiv (a_{31} \cdot a_{43} - a_{33} \cdot a_{41}) +$$

$$+ (1/k_F) \cdot (a_{31} \cdot a_{44} - a_{34} \cdot a_{41}),$$

$$\Delta = \Delta_{12} \cdot \Delta_{34} \cdot (b_{22} \cdot b_{32} - b_{12} \cdot b_{42}),$$

$$\Delta_1 = \Delta_{12} \cdot [\Delta_{12} \cdot (b_{32} \cdot b_{41} - b_{31} \cdot b_{42}) +$$

$$+ \Delta_{34} \cdot (b_{11} \cdot b_{42} - b_{21} \cdot b_{32})],$$

$$\Delta_2 = \Delta_{34} \cdot [\Delta_{12} \cdot (b_{12} \cdot b_{41} - b_{22} \cdot b_{31}) +$$

$$+ \Delta_{34} \cdot (b_{11} \cdot b_{22} - b_{12} \cdot b_{21})],$$

where

$$\begin{array}{ll} a_{11} = \tilde{s}_1 \cdot c_2, & a_{12} = \tilde{s}_1 \cdot s_2, \\ a_{21} = -s_1 \cdot \tilde{c}_2, & a_{22} = -s_1 \cdot \tilde{s}_2, \\ a_{31} = \tilde{s}_1 \cdot s_2, & a_{32} = -\tilde{s}_1 \cdot c_2, \\ a_{41} = s_1 \cdot \tilde{s}_2, & a_{42} = s_1 \cdot \tilde{c}_2, \\ a_{51} = -\tilde{c}_1 \cdot s_2, & a_{52} = -\tilde{s}_1 \cdot s_2, \\ a_{61} = c_1 \cdot \tilde{s}_2, & a_{62} = s_1 \cdot \tilde{s}_2, \\ a_{13} = M_{11}^x - \tilde{c}_1 \cdot c_2, & a_{14} = -M_{21}^x, \\ a_{23} = M_{11}^y - c_1 \cdot \tilde{c}_2, & a_{24} = -M_{21}^y, \\ a_{33} = -\tilde{c}_1 \cdot s_2, & a_{34} = -M_{21}^x, \\ a_{43} = c_1 \cdot \tilde{s}_2, & a_{44} = -M_{21}^y, \\ a_{53} = M_{22}^x - \tilde{c}_1 \cdot c_2, & a_{54} = -M_{21}^x, \\ a_{63} = M_{22}^y - c_1 \cdot \tilde{c}_2, & a_{64} = -M_{21}^y, \\ c_1 = cos\varphi_D, & c_2 = cos\varphi_F, \\ \tilde{c}_1 = ch\varphi_D, & \tilde{c}_2 = ch\varphi_F, \\ s_1 = sin\varphi_D, & s_2 = sin\varphi_F, \\ \tilde{s}_1 = sh\varphi_D, & \tilde{s}_2 = sh\varphi_F. \end{array}$$

After a series of transformations and using this notation, we are able to express the unknown values of

$$\begin{cases} k_F = \Delta/\Delta_2, \\ k_D = k_F \cdot \Delta_{32}''/\Delta_{12}, \\ L_3 = \Delta_1/\Delta, \\ L_2 = (1/k_D) \cdot \Delta_{12}'/\Delta_{12}, \\ L_1 = (L_2 \cdot k_F \cdot a_{51} + a_{52} \cdot k_F/k_D - a_{53})/a_{54} \end{cases} \quad (4)$$

Each of this $(L_1,\ L_2,\ L_3,\ k_F,\ k_D)$ is a function of the parameters $\alpha_{1,2}^x,\ \beta_{1,2}^x,\ \varphi_F,\ \varphi_D,\ \Delta\psi^y,\ \Delta\psi^x$ (one of which may be free, for instance $\Delta\psi^x$). It follows from solving system (3) by taking into account (4) and above notation that these parameters are coupled by the equation:

$$\Phi \equiv L_2 \cdot k_F \cdot a_{61} + a_{62} \cdot k_F/k_D - a_{63} - L_1 \cdot a_{64} = 0, \quad (5)$$

from which we derive the value of the given free parameter, in this case $\Delta\psi^x$. For the matching section of the beam injection channel into the synchrotron SPIN, which we shall investigate below, the function $\Phi(\Delta\psi^x)$ is plotted in the fig.2, where the solution of eq.(5) corresponding to

physical requirements is denoted by the symbol (*). The value of φ_F, φ_D determines the length of lenses.
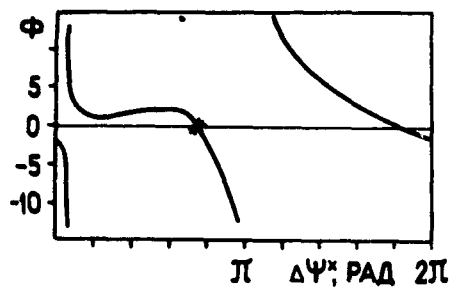
Fig.2 Function $\Phi(\Delta\psi^x)$. (*) denoted the physical solution of $\Phi(\Delta\psi^x) = 0$.

The range of permissible values for these quantities are illustrated in fig.3.

III. PROGRAM MATCH 1.0 and RESULTS

The described matching algorithm was realized as FORTRAN-program MATCH 1.0 on the VAX, IBM, CDC-6500 and IBM PC computers at Dubna JINR. As user's interactive mode with computer, this program allows to look quickly over the spase of the parameters $\bar{P}$ and to select the most economical version of calculated structure.

The matching of the channel [11] for beam injection into the ring of the superconducting synchrotron SPIN [1,2] was carried out by the proposed method for an energy of 0.600 MeV with $B_\rho = 0.111945\ T \cdot m$. The beam envelopes X_{max} and Y_{max} along the injection channel are plotted. We obtained the betatron functions α_1^x, α_1^y and β_1^x, β_1^y by means of MATCH1.0, calculating the betatron motion on the transport section from the entrance into the regular synchrotron structure. At the entrance point $\alpha^x = \alpha^y = 0$, $\beta^x = 2.434\ m$ and $\beta^y = 0.685\ m$. The values of β_2^y, β_2^y and α_2^x, α_2^y were obtained in beam transport matching section. At the beginning of this section
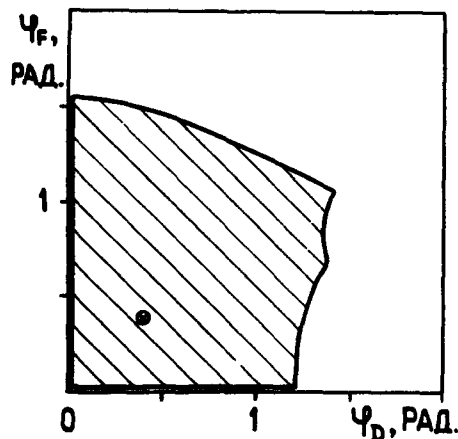
Fig.3 Range of values of the parameters φ_F and φ_D. The symbol $\odot$ denoted the chosen value of $\varphi_F = 0.559$ rad and $\varphi_D = 0.488$ rad.

$\beta_x = \beta_y = 1.500\ m$ and $\alpha_x = \alpha_y = 0$. The values of $\beta_{1,2}^{x,y}$ and $\alpha_{1,2}^{x,y}$ which have been obtained at the ends of the matching section follows:

$$\beta_1^x = 2.1327\ m \quad \alpha_1^x = 2.51607$$
$$\beta_1^y = 1.3168\ m \quad \alpha_1^y = -2.56981$$
$$\beta_2^x = 3.5482\ m \quad \alpha_2^x = 0.38639$$
$$\beta_2^y = 1.2876\ m \quad \alpha_2^y = -0.25838$$

For the quantities $\varphi_F = 0.559$ rad, $\varphi_D = 0.488$ rad and $\Delta\psi^y = 0.8855$ rad we have $\Delta\psi^x = 2.02296$ rad. Here is $L_1 = 0.5276\ m$,

$$l_D = 0.1529\ m, \quad k_D = 3.1919 m^{-1}, \quad L_2 = 0.8268\ m,$$
$$l_F = 0.3096\ m, \quad k_F = 1.8056 m^{-1}, \quad L_3 = 0.2096\ m.$$

IV. CONCLUSION

Analytical expressions have been found, which offer a solution for the matching problem of a doublet of magnetic quadrupole lenses in "thick" lens approximation. For the given beam profile, it is easy to chose the most economical version of the matching structure, which fulfills the given requirements. The mathing of phase volume of a beam, which was injected and captured in the accelerating cycle for the injection channel of the superconducting synchrotron at Dubna JINR, was achieved by means of the given method.

References

[1] I.A.Shelaev, et al. Dubna JINR, **P9-83-582**, 1983; see, too: I.A.Shelaev et al. *In Proc. 12 Intern. Conf. on High-Energy Accelerators*, Fermilab, 11-16 Aug. 1983, Batavia, Illinois, 1983, p.416.

[2] I.A.Shelaev, I.P.Yudin. Dubna JINR, **P9-12346**, 1979.

[3] H.Bruck, Cyclic Particle Accelerators, Atomizdat, Moscow, 1970.

[4] P.F.Meads, jr., Nucl. Inst. and Meth., 1971, **96**, p.351.

[5] P.F.Meads, jr.,IEEE Trans.on Nucl.Sci.,1973,20, p.875.

[6] I.A.Shelaev, I.P.Yudin. Dubna JINR, **9-11745**, 1978.

[7] V.V.Anashin, et al. VEPP-4: Status and plans. In: Proc. of the 9th All-Union Conf. on Particle Accelerators, Dubna, Oct.16-18th,1984,vol.II,p.233,1985.

[8] S.N.Andrianov et al. In: Conf. on Programming and Mathematical Methods to Solve Physical Problems. Dubna JINR, Sept.20-23rd,1977,D10, 11-11264,1978.

[9] F.C.Iselin. CERN-LEP-TH/85-15, Geneva, May 1985.

[10] C.Bovet et al. A Selection of Formulae and Data Useful for Design of A.G.Synchrotrons. CERN/MPS-SI/Int, DL/70/4. Geneva, 1970.

[11] E.A.Matyushevsky, I.A.Shelaev, I.P.Yudin. Dubna JINR, **P9-83-817**, 1983.

[12] I.P. Yudin. Dubna JINR, **P9-86-601**, 1986.

The application package DeCA for calculating cyclic accelerators.

P.I. Gladkikh. A.Yu. Zelinsky. M.A. Strelkov

Kharkov Institute of Physics and Technology, 310108,Kharkov, Ukraine

Abstract.

The application package DeCA (Design Cyclic Accelerator) is offered to solve a set of problem which arise on designing electron storage ring. The package is based on the block principle. This makes it extremely flexible in designing storage rings and investigating beam dynamics in them. The package is intended for a user not familiar with programming languages, it is arranged so that the user familiar with FORTRAN-77 can easily extend the package functions. This is of particular interest, when the input data are the storage ring or electron bunch parameters. The code allows operation in both the batch and interactive modes. The programming language is FORTRAN-77. The capacity of the total package is 40 000 code lines. The necessary main storage capacity for the total version is 4 Mbytes.

1.INTRODUCTION.

In recent years the application package DeCA [1,2] is in wide use in Kharkov Institute of Physics and Technology for design and modernization of storage rings and numerical experiments. The package was used for elaboration of such projects as: electron pulse stretcher ring PSR-2000 [3] with an operating energy 3 GeV, the source of synchrotron radiation ISI-800 [4] with an operating energy 0.8 GeV. the source of synchrotron radiation with an operating energy 2.5 GeV for the Nuclear Research Center in Karlsruhe, Germany. Calculations for the Amsterdam Pulse Stretcher Ring (AmPS) also have been carried out. The computer simulation of the chromatic beam extraction was performed for the PSR-2000 lattice using DeCA [5]. The package includes the following accelerator physics features: calculations of lattice functions and integral characteristics of the beam taking into account the installation errors and energy loss due to synchrotron radiation, reference orbit correction, Hamiltonian formalism for investigation of resonance effects, optimization of lattice parameters. investigation of dynamic aperture by both an analytical and numerical methods taking into account the high order components of magnetic field, numerical simulation of particles motion in 6-dimensional phase space, investigation of spin-orbit motion. The package has rich possibilities for information reflections. The organization of the DeCA code allows to carry out calculations with several input lattice and command files simultaneously. The last version of the DeCA code is realized at the IBM 360/370 like computer and may be accommodate at VAX VMS system and personal computer.

2. PACKAGE STRUCTURE

All program modules of the DeCA package (except the main and standard modules) are unified by the functional principle into several blocks. According to their assignment. these blocks are subdivided into system units (which provide all service functions) and functional units (which directly implement the code functions). Among the system units we mention the following: DIAG - printing of diagnostic messages of the code. FILES - data file handling, COMM - code control (commands block). REFLI - digital and graphic display of information, data display in the plotter.

The functional units of code version 3.3 include: IMOS - description of lattice elements and structures, GAC - calculation and mapping of the geometry of the machine. BEAM - assignment of initial beam parameters. REFTL - calculation of machine functions and parameters. SR - calculation and mapping of synchrotron radiation parameters. MDP - simulation of beam dynamics with nonlinear elements. SOM - simulation of spin-orbital motion of the beam.

All functional blocks and the system part of the package may be combined in various versions of the package depending on user requirements.

3. INPUT DATA.

All data files used in the DeCA package are described in the table arranged in the file of the FIDEF (FIle DEFine) type in the fixed format [6]. Files of following types are necessary described in this table: CODEF - file containing the definitions of all control commands in the text form, COMM - control commands specifying instruction for action, COMMT - control commands introduced from a terminal in the interactive mode, ELDEF - file containing the definition of lattice elements. EDEF - file containing the definition of graphic pictures of lattice elements. MOS - file containing the description of the lattice, IBEAM - file containing the initial particle coordinates.

4. DESCRIPTION OF THE STORAGE-RING LATTICE

All lattice elements are assumed to be located along the reference orbit: the orbit of the particle with energy E_0 in ideal field in all magnet elements. The geometric axis of magnet elements is coincident with this orbit. The reference orbit consists of a number of straight sections and arcs formed by bending magnets. The moving set of three vectors forms the right-hand frame of coordinates X,Z,S. The instantaneous direction of the axis S is coincident with the direction of the tangent to the reference orbit, the axes X and Z lie in the radial and vertical planes, respectively.

All lattice elements that have been realized in DeCA code are described in the file of the ELDEF type, where the

formats of the element definition in the lattice are fixed. The following lattice elements are realized in the code version 3.3:

NULL - empty element.
DS - drift space.
PICK - pick-up station.
BM - bending magnet.
BMR - bending rectangular magnet,
PFR - pole face rotation.
KICX - kicker magnet in XS plane.
KICZ - kicker magnet in ZS plane.
COR - correction magnet,
QL - quadrupole magnet,
QLP - pulse quadrupole magnet,
SOL - solenoid.
ROT - rotation of coordinate frame around axis "S"
RFC - thin RF-cavity:
RFCN - RF-cavity:
SL - sextupole magnet,
SLP - pulse sextupole magnet,
OL - octupole magnet,
OLP - pulse octupole magnet,
MLP - multipole magnet.
INJ - injection point,
ESX - electrostatic X-septum,
ESZ - electrostatic Z-septum.
MSX - magnetic X-septum,
MSZ - magnetic Z-septum.
APRL - local rectangular aperture,
APEL - local elliptic aperture,
APRG - global rectangular aperture
APEG - global elliptic aperture,
INCR - increment/decrement.

To describe the machine lattice, we use the input files of MOS type (Magnetic Optical Structure). The description is the sequence of sentences, each specifying one element or a group of elements in the particular place of the lattice. Sentences of the following types are used at the language of lattice description:

- explicit assignment of the lattice element;
- a copying of a previously defined element;
- explicit assignment of the substructure (group of elements);
- direct or inverse copying of a previously defined substructure.

For example a description of the element in the lattice of the source of synchrotron radiation for Karlsruhe Nuclear Research Center are presented below:

```
SUP(1): LINE;
  DS1: DS   L=1.45548;
  QF1: QL   L=0.30  K1=1.87;
  DS2: DS   L=0.30;
  QD1: QL   L=0.30  K1=-1.25;
*** FIRST BEND
  CELL(1): LINE;
  B(1): BMR L=1.468 ANG=15. K1=-0.09541;
  DS3(1): DS   L=0.35;
  DS3(2): ;
```

```
  B(2): ;
  DS4: DS   L=0.60;
  QF2: QL   L=0.30  K1=2.35758;
  DS5: DS   L=0.80;
  B(3): ;
  DS5:  DS   L=0.25;
 CELL(1): ENDLINE;
 -CELL(2): ;
SUP(1): ENDLINE;  .
SUP(2):; SUP(3):; SUP(4): ;
```

Commands of the package control are defined in the file of the CODEF type where the command formats are determined [6]. The code can work both in the interactive and in the batch calculation modes. The file of the COMM type is formed to work in batch mode. Then the control of the code is passed to this file.

About 70 commands are realized in the DeCA code. These commands provide the execution of all necessary functions.

For example we present the fragment of the COMM file:

```
IMOS DECKRL3;  ENER E=2.5;
TOLS X=0.0001 Z=0.0001 S=0.0001;
IRL LONG; MTEL CYC;
FFSL ICH CHR;
GRFL BETX BETZ PSIX EL1=QF1; PRFL;
DAP SL PRX PRC Z=0.0 AZIM=QF1;
```

4. FUNCTIONAL POSSIBILITIES OF THE PACKAGE.

The package DeCA uses 5x5 matrix (matrix elements that describe the perturbations of the magnetic field due to errors in the installation of lattice elements and their imperfections are recognized in fifth column of the matrix) and the coordinate vector $(x,x',z,z',1)$ for description of particle motion without taking into account the energy spread in the beam ($p=p_0=const$); 7x7 matrix and the coordinate vector $(x,x',z,z',1,s,\Delta E/E)$ are used for description of particle motion taking into account the energy spread in the beam ($p=p_0+\Delta p)$ (following A.W.Chao [7], we included elements that describe the energy losses due to synchrotron radiation into fifth column of the bending magnet matrix); 8x8 matrix and the coordinate vector $(x,x',z,z',s,\Delta E/E,\alpha,\beta)$ for description of spin-orbit motion of particles and 3x3 matrix and coordinate vector (S_x,S_z,S_s) for description of spin motion of particles. The numerical simulation taking into account the influence of nonlinear magnetic fields on particle motion is carried out in the 6 dimensional phase space $(x,x',z,z',s,\Delta E/E)$.

4.1 Lattice functions and integrals characteristics of the beam.

The algorithms for calculations of lattice functions, integral characteristics of the beam, analytical treatment of the dynamic aperture are based on the following model of the ring lattice. The orbit in the storage ring is assumed to be plane, i.e., there is no pitch to the vertical plane, the vertical

dispersion is zero. no twisting occurs. The curvature radius ρ and the field index n are regarded to be constant inside the bending magnet. The magnetic field boundaries in the magnets are assumed to be sharp.

The code allows to calculate amplitude and dispersion functions of the lattice. coordinates of the reference orbit. betatron oscillations tunes. integral characteristics of the beam such as: emittance. energy spread. chromaticity of the system, energy losses per turn. momentum compaction factor, equilibrium beam size and divergence etc. The detail description of package possibilities and algorithms used can be find in [8]. Calculations are based on analytical equations. The tune shift and dynamic aperture that have been caused by sextupole and octupole components of magnetic field can be calculated by using the Hamiltonian formalism. The correction of the reference orbit is carried out by the method of Herrevard-Baconierry.

4.2.Numerical simulation.

The block of numerical simulation is organized thus that we can observe practically all single particle effects that are known in accelerator physics. The 10-th pole thin lens is used at the block for simulation of nonlinear effects. The chromatic aberrations are taken into account in this model. Lens parameters may be changed according to some definite low. It allows to simulate the pulse elements. The wide possibilities of input beam parameter setting (the setting of particle distribution on the bunch, the setting of fixed particle coordinates and combination of both these methods) in combination with the convenient displaying output information allows to investigate resonance processes such as. multiturn injection and slow beam extraction.

4.3 Spin-orbit motion and equilibrium degree of polarization.

The SOM block allows to simulate the spin motion of particles and to calculate the equilibrium degree of polarization. The calculations are based on matrix formalism and linear beam dynamics. We use the algorithm which was designed by A.W.Chao [9] and H.Mais [10] and is based on analyzing of the eigenvectors and eigenvalues of the cyclic matrix of spin-orbit motion. Unlike the SLIM code by A.W.Chao, in the DeCA code the thick matrix models of magnet elements for the description of spin-orbit motion are used. The programmed connections between code modules allow to calculate the equilibrium degree of polarization as a function of coordinates of the reference orbit.

4.4 Lattice parameter optimization.

The universal mechanism of the choice and optimization of lattice parameters which allows to optimize any lattice parameter is used in the DeCA package. The code has got the following possibilities:
- setting the space of lattice parameters being varied (any parameters of lattice elements: element lenght, lense strenght

etc.). The method of variation for every parameter is set independently:
- setting the list of parameters which are optimize (any characteristics and lattice functions: beta function, dispersion function. emittance etc.). Criteria of optimization has a follow form:

$$\text{form:} \quad \sum_i^N w_i p_i \longrightarrow \text{min. where } p_i - \text{parameters which are}$$

optimize. w_i - weight coefficients. ;
- multiple calculation of parameters under optimization and selection of variants which satisfy the given criteria.

5.REFERENCE

[1] P.I.Gladkikh.M.A.Strelkov,A.Yu.Zelinsky. DeCA - code for analyzing and design of cyclic accelerators. Proc. of the Second European Part. Accel. Conf. EPAC-90, Nice 12-16 June, 1990, v.2, pp. 1688-1691.

[2] P.I.Gladkikh,M.A.Strelkov,A.Yu.Zelinsky. New version 3.3 of the DeCA code. Proc. Third European Part. Accel. Conf.. EPAC-92. Berlin 24-28 march. 1992. v.1, pp. 685-687.

[3] S.V.Efimov.P.I.Gladkikh,A.Yu.Zelinsky et al. The Pulse Stretcher Ring PSR-2000. Current Status. Proc. Third European Part. Accel. Conf.. EPAC-92, Berlin 24-28 march. 1992. v.1, pp. 453-455.

[4] I.Karnaukhov,V.Androsov,E.Bulyak et al. The Synchrotron Light Source for the Ukrainian Research Center. This Proceeding.,PAC-93.

[5] S.V.Efimov.P.I.Gladkikh,I.S.Guk et al. The PSR-2000. Current Status. Proc. XIII Particle Accel. Conference, Dubna 13-15 october, 1992, to be published.

[6] P.I.Gladkikh,M.A.Strelkov,A.Yu.Zelinsky. Application package DeCA. Version 3.3. User.s guide. Part 1. Preprint KhPTI 1993, to be published.

[7] A.W.Chao. Evaluation of beam distribution parameters in an electron storage ring. J.Appl.Phys.. v.50(2), February 1979y,pp. 595-598.

[8] P.I.Gladkikh,M.A.Strelkov,A.Yu.Zelinsky. Calculation of integral electron storage ring beam characteristics in the application package DeCA. Version 3.3. A physical model. Preprint KhPTI 1993. to be published.

[9] A.W.Chao. Evaluation of radiative spin polarization in an electron storage ring. Nucl. Instr. & Meth., 180(1981), pp.29-36.

[10] H.Mais, G.Ripken. Theory of spin-orbit motion in electron-positron storage rings. DESY 83-062

Echo Effect in Accelerators

G. V. Stupakov and S. K. Kauffmann
Superconducting Super Collider Laboratory*
2550 Beckleymeade Ave., Dallas, TX 75237

I. INTRODUCTION

The echo effect has been known for many years in different fields of physics. Examples are the spin echo in solids [1], photon echo in solids and gases [2], plasma wave echo [3], and the echo in a liquid with gas bubbles [4]. The media that exhibit the echo characteristically consist of (or contain in them) an ensemble of oscillators with different eigenfrequencies and negligibly small dissipation. An initial perturbation applied to such a medium excites oscillations (or waves) that slowly damp due to dephasing. This kind of damping differs essentially from that which would result from a dissipative mechanism; in particular, dephasing does not increase the entropy of the medium. It has the remarkable feature that even after the oscillations are completely damped out, the system keeps a "recollection" about them, and a special kind of a disturbance applied to the medium can transiently restore the oscillations in the form of an echo signal.

The betatron echo in a hadron accelerator [5,6] can be observed in a situation where the beam is injected off-center into the ring at time $n = 0$ (n is the time measured in the number of turns), causing its centroid to undergo betatron oscillations. After these oscillations have completely damped out due to beam decoherence, the beam is excited by a quadrupole kick at time $n = n_1$. This kick does not produce any visible displacement of the beam at that time, but it turns out that close to time $n = 2n_1$ the beam centroid undergoes transient betatron oscillations with an amplitude which is a fraction of the initial beam offset.

A manifestation of echo effect is illustrated by Figures 1 and 2. Figure 1 shows the amplitude of betatron oscillation of an offset beam that damps to extinction due to decoherence. If, however, a quadrupole kick is performed at $n = 20$, one observes an echo that recoheres back (and then decoheres again) with the maximum around $n = 40$, as shown in Figure 2.
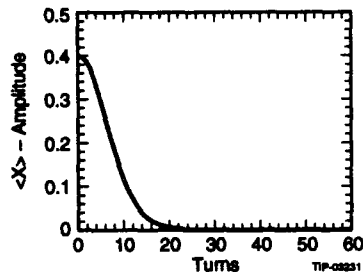
Figure 1. Damping of amplitude of the betatron oscillations of an offset Gaussian beam.
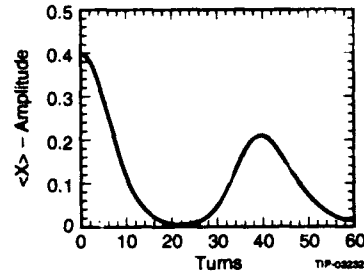
Figure 2. Echo response of the betatron amplitude after a quadrupole kick at $n = 20$.

II. THEORY OF ECHO

To describe one-degree-of-freedom transverse motion of a beam particle in an accelerator ring we choose to work with the normalized phase space coordinates

$$x = \frac{X}{\sqrt{\beta}}, \qquad p = \beta \frac{d}{s} \frac{X}{\sqrt{\beta}}, \tag{1}$$

where X is the particle deviation with respect to the closed orbit, β is the beta function and s is the path along the orbit. We also define the vector z,

$$z = \begin{pmatrix} x \\ p \end{pmatrix}. \tag{2}$$

and the action J and the angle ϕ according to

$$J = \tfrac{1}{2}|z|^2 = \tfrac{1}{2}\left(p^2 + x^2\right), \qquad \phi = -\arctan\frac{p}{x}. \tag{2.1}$$

According to Courant-Snyder theory, in a perfectly linear accelerator, particles are simply rotated clockwise in this normalized phase space at a fixed radius through angle $2\pi\nu$ on each turn, where ν is the accelerator tune. Thus,

$$z_n = R_n(\nu)z_{n=0}, \tag{3}$$

where the subscript n indexes the turn number, and $R_n(\nu)$ is represented as the clockwise rotation matrix,

$$R_n(\nu) = \begin{pmatrix} \cos 2\pi n\nu & \sin 2\pi n\nu \\ -\sin 2\pi n\nu & \cos 2\pi n\nu \end{pmatrix}. \tag{4}$$

Offset particle beams decohere, if the tune itself depends on the particle amplitude $|z|$, due to systematic non-linearities present in the accelerator. For a monochromatic beam, the presence of systematic sextupole or octapole non-linearities generates a quadratic dependence of tune on amplitude $|z|$, i.e.,

$$\nu(|z|) = \nu_0 + \Delta\nu\frac{|z|^2}{\sigma^2}, \tag{5}$$

where v_0 is the nominal tune, Δv has the interpretation of a tune spread and σ is the rms beam radius. In realistic situations, $\Delta v \ll v_0$.

As stated previously, the beam is assumed to be injected off center into the ring at $n = 0$. Let $\psi(z) \equiv \psi(x,p)$ denote its initial particle distribution function. After the injection, the beam experiences free betatron oscillations and at $n = n_1$, just before the quadrupole kick, the vector $z_{n=n_1-\varepsilon}$ can be obtained by the linear transformation of the initial z,

$$z_{n=n_1-\varepsilon} = R_{n_1}(v_1)z, \qquad (6)$$

where $v_1 = v(|z|)$ is given by Eq. (5) with z being given by the initial values of the particle's coordinate and momentum.

The quadrupole kick produces a transformation of z that is characterized by the following matrix:

$$Q = \begin{pmatrix} 1 & 0 \\ -q & 1 \end{pmatrix}, \qquad (7)$$

where q is equal to the ratio of β at the quad location to the focal length of the quad. After the quadrupole kick, betatron oscillations, proceed with a different frequency, because the kick changes the amplitude $|z|$ and therefore the tune. Before writing down the matrix that describes oscillations after the kick, we have to express the new value of $|z_{n=n_1+\varepsilon}|$ just after the quad kick in terms of the old one $|z|$. Straightforward calculations yield,

$$|z_1|^2 \equiv |z_{n=n_1+\varepsilon}|^2 = |QR_{n_1}(v_1)z|^2 =$$
$$= |z|^2 \left(1 + q\sin 2(\phi_1 - \theta) + q^2 \cos^2(\phi_1 - \theta)\right), \qquad (8)$$

where θ is the polar angle in the phase space, $\theta = \arctan(p/x)$, and

$$\phi_1 = 2\pi n_1 v_1. \qquad (9)$$

Now, free oscillations after the quadrupole kick, $n > n_1$, generate a transformation given by $R_{n-n_1}(v_2)$, with the tune,

$$v_2 = v_0 + \Delta v \frac{|z_1|^2}{d^2}, \qquad (10)$$

so that a complete transformation, casting the initial z into the final z_n ($n > n_1$), is the product of the three matrices,

$$z_n = R_{n-n_1}(v_2)QR_{n_1}(v_1)z =$$
$$= \begin{pmatrix} \cos(\phi_1 + \phi_2) & \sin(\phi_1 + \phi_2) \\ -\sin(\phi_1 + \phi_2) & \cos(\phi_1 + \phi_2) \end{pmatrix}\begin{pmatrix} x \\ p \end{pmatrix} -$$
$$-q\begin{pmatrix} \cos\phi_1 \sin\phi_2 & \sin\phi_1 \sin\phi_2 \\ \cos\phi_1 \cos\phi_2 & \sin\phi_1 \cos\phi_2 \end{pmatrix}\begin{pmatrix} x \\ p \end{pmatrix}, \qquad (11)$$

where,

$$\phi_2 = 2\pi(n - n_1)v_2. \qquad (12)$$

Thus, after n turns $(n > n_1)$, the averaged displacement of the beam is,

$$\bar{z}_n = \iint z_n \psi(z)d^2z =$$
$$= \iint dxdp\,\psi(x,p)x\begin{pmatrix} \cos(\phi_1 + \phi_2) & -q\cos\phi_1 \sin\phi_2 \\ -\sin(\phi_1 + \phi_2) & -q\cos\phi_1 \cos\phi_2 \end{pmatrix} +$$
$$+ \iint dxdp\,\psi(x,p)p\begin{pmatrix} \sin(\phi_1 + \phi_2) & -q\sin\phi_1 \sin\phi_2 \\ \cos(\phi_1 + \phi_2) & -q\sin\phi_1 \cos\phi_2 \end{pmatrix}. \qquad (13)$$

Based on this formula, further analysis developed in Reference 6 shows that an echo signal appears around the time $n = 2n_1$ with an amplitude that depends on the initial beam offset a, the strength of the quadrupole kick q and time n_1 of this kick. Moreover, in principle, multiple echoes with diminishing amplitudes can be observed at times equal to even multiples of n_1.

A simplified perturbation theory of the echo, based on a slightly different approach, can be found in Reference 5.

Using Eq. (13), we performed the integration for a Gaussian distribution function,

$$\psi(z) = \frac{1}{2\pi\sigma^2}\exp\left(-\frac{|z - a\hat{x}|^2}{2\sigma^2}\right), \qquad (14)$$

where $\hat{x} = (1,0)$ is the unit vector in the x-direction, in which the initial Gaussian beam has been offset by a. The following values of parameters have been chosen, $v_0 = 0.285$, $\Delta v = 2.18\cdot10^{-3}$, $a/\sigma = 5.84$ and $q=-0.16$. The result is shown in Figure 2.

III. PHASE SPACE PORTRAITS AND THE OPTIMAL KICK

A deeper insight into the physical nature of the echo can be obtained by examining successive phase space portraits of the distribution of particles. We performed computer simulations by tracking 32,000 particles from an initial Gaussian distribution, each of which was advanced in time in accordance with the equations of the previous section. The results are shown in Figure 3.

An initially offset Gaussian beam is displayed in Figure 3a. It decoheres into a spiral-like structure (Figure 3b) until, at $n=20$, a quadrupole kick is applied to the beam. This kick produces elliptical flattening of decoherence spiral, as shown in Figure 3c. The subsequent evolution of the beam (see Figures 3d and 3e) shows development of sharp tips which interrupt the smooth shape of the spiral. These tips come into confluence near where our original off-center beam was launched in the first instance, as is seen in Figure 3f. This tends to occur at approximately $2n_1$ turns, where n_1 is the number of turns from the launch of the offset beam to the quad kick. This confluence of the phase reversal tips is what causes the "echo" of the original beam offset.

IV. SUMMARY

The transverse echo effect is a consequence of reversibility of the particle motion in an accelerator. Investigation of the echo requires special hardware in the form of a pulsed quadrupole, that has to be able to produce a kick, having duration less than the revolution period.

Any dissipative mechanism that breaks the reversibility (such as synchrotron radiation, intrabeam scattering or collisions with the residual gas) will attenuate the echo, eventually destroying it completely. A more detailed theory should account for these additional effects. On the other hand, sensitivity of the echo to these kinds of effects could possibly be used as a diagnostic tool.

Note that the echo which we are discussing should not be confused with the recoherence due to machine chromaticity and RF-induced synchrotron motion studied in Reference 7.

The result of the present paper can be also applied to longitudinal dynamics to demonstrate the existence of an analogous echo in synchrotron oscillations [8].

V. REFERENCES

[1] E. L. Hahn, *Phys. Rev.* **80**, 580 (1950).

[2] N. A. Kurnit, I. D. Abella and S. R. Hartmann, *Phys. Rev. Lett.* **13**, 567, (1964).

[3] Hill R. M. and Kaplan D. E. *Phys. Rev. Lett.* **14**, 1061, (1965).

[4] I. A. Kotel'nikov. *Izvestija visshikh uchebnich zavedenij. Radiofizika.* **26**, 1227, (1983).

[5] G. V. Stupakov. Echo Effect in Hadron Colliders. SSC Report SSCL-579, July 1992.

[6] G. Stupakov and S. Kauffmann. Echo Effect in Accelerators. SSC Report SSCL-587, September, 1992.

[7] I. C. Hsu. *Particle Accelerators*, **34**, 43, (1990).

[8] N. Mahale, J. Palkovich, S. Kauffmann, S. Dutt and T. Ellison, in preparation.

Figure 3. Phase portraits of an evolving Gaussian beam, showing the echo effect.

An important question, concerning the echo, is what values of parameters generate the maximal echo. Based on Eq. (13), a perturbation theory can be developed, assuming that the initial offset is small, $a \ll \sigma$, and the kick is weak, $q \ll 1$. It predicts the following form of the echo signal,

$$\left|\bar{z}_n\right| = aq \left| \frac{4\pi\Delta v(n-n_1) + \frac{1}{2}\left[1+4\pi i\Delta v(n-2n_1)\right]}{\left\{\left[1+4\pi i\Delta v(n-2n_1)\right]^2 + \left[4\pi q\Delta v(n-n_1)\right]^2\right\}^{3/2}} \right| \qquad (15)$$

(this formula is valid in the vicinity of the echo peak, $n = 2n_1$). A simple investigation shows that the maximum echo is attained for

$$q = 0.056\left(\Delta v n_1\right)^{-1} \qquad (16)$$

and is equal to $\left|\bar{z}_n\right|_{max} = 0.38a$. As shown in Figure 2, for a relatively large initial offset (for which Eq. (15) is not applicable), more exact model calculations show an even larger echo, which can reach about 50% of the initial displacement.

Tune Shift Effect Due to the Sextupole Longitudinal Periodic Structure in the Superconducting Dipole Magnets

G. López and S. Chen

Superconducting Super Collider Laboratory*

2550 Beckleymeade Ave., Dallas, TX 75237 USA

Abstract

Using the standard Hamiltonian perturbation theory, the tune shift due to the sextupole periodic pattern in the superconducting dipole magnets is estimated for the Superconducting Super Collider (SSC) machine. The result indicates that this effect is of the order of 10^{-9}. Therefore, this effect can be neglected in the dynamics of the beam.

I. INTRODUCTION

The discovery of the sextupole, dipole, and quadrupole longitudinal periodic structure due to the persistent-current field in the HERA superconducting magnets at Deutsches-Elektronen-Synchroton Laboratory (DESY) [1] has raised questions about the possible effects of this pattern on the dynamics of the beam. Experiments carried out suggest that this periodic pattern is due to the strand pitch in the superconducting cable (s.c.), and measurements indicate that its wavelength is approximately equal to this strand pitch (9.1 ± 0.5 cm for the outer coil of the Superconducting Super Collider (SSC) s.c. dipoles). The sextupole pattern has already been confirmed in a short 50-mm R&D dipole magnet [2], and the effect in the dynamic of the beam in the SSC requires a confident estimate, even if it is known already that the effect must be small. It is possible to see this effect by calculating the tune shift through the Hamiltonian formalism. To calculate the tune shift, the superconvergent Hamiltonian perturbation method [3] is used, applying the standard canonical transformations and averaging [4].

II. HAMILTONIAN FORMALISM

The Hamiltonian for a synchronous relativistic charged particle traveling around an accelerator ring can be written as:

$$H = \frac{1}{2}(P_x - \frac{e}{cp}A_x)^2 + \frac{1}{2}(P_y - \frac{e}{cp}A_y)^2 - \frac{e}{cp}A_s +$$
$$+ \frac{1}{2}K_1(s)y^2 - \frac{1}{2}\left(K_1(s) - \frac{1}{\rho^2}\right)x^2 , \quad (1)$$

where p is the longitudinal momentum of the particle, $P_x = p_x/p$ and $P_y = p_y/p$ are its normalized transversal momenta, e is the charge of the particle, c is the

speed of light, $\rho(s)$ is the curvature of the accelerator ring, $K_1(s)$ describes the linear lattice of the machine (without longitudinal oscillation pattern), and A's are vector potential components. This Hamiltonian can be written as $H(x, y, s) = H_o(x, y, s) + V(x, y, s) + U(x, y, s)$, where H_o, $V = V^{(1)} + V^{(2)}$, and U are defined by

$$H_o(x, y, s) = \frac{1}{2}\left(P_x^2 + K_x(s)x^2\right) + \frac{1}{2}\left(P_y^2 + K_y(s)y^2\right) ,$$
$$(2a)$$
$$V^{(1)}(x, y, s) = -(e/cp)A_s , \quad (2b)$$
$$V^{(2)}(x, y, s) = -(e/cp)(P_xA_x + P_yA_y) , \quad (2c)$$

and

$$U(x, y, s) = (e/cp)^2(A_x^2 + A_y^2)/2 . \quad (2d)$$

The longitudinal periodic structure of the magnetic field induces a longitudinal field component which, in turns, requires the three components of the vector potential. For tune shift calculations, it is more convenient to express the Hamiltonian in the canonical variable (J, ϕ), where J and ϕ are the vectors $J = (J_1, J_2)$ and $\phi = (\phi_1, \phi_2)$. This can be accomplished through the generating function

$$F(s, x, y, \phi) = -\sum_{i=1}^{2} x_i \left(\tan\phi_i - \dot{\beta}_i/2\right)/\beta_i(s) , \quad (3)$$

where $\beta_i(s)$ is the beta function associated with the motion of the particle in the i (x for $i = 1$, y for $i = 2$) direction; $\dot{\beta}_i$ is its derivative with respect to s, and $\phi_i(s)$ is the betatron phase, which is related to the beta function through $\phi_i(s) = \phi_i(0) + \int_0^s d\sigma/\beta_i(\sigma)$. The action, J_i, the coordinates and the canonical momenta are given by $J_i = -\partial F/\partial \phi_i = \left[x_i^2 + (\beta_i\dot{x}_i - \dot{\beta}_ix_i/2)^2\right]/2\beta_i$,

$$x_i = \sqrt{2J_i\beta_i}\cos\phi_i , \quad (3a)$$
$$P_i = -\sqrt{2J_i/\beta_i}\left(\sin\phi_i - \frac{1}{2}\dot{\beta}_i\cos\phi_i\right) , \quad (3b)$$

for $i = 1, 2$, i.e., $i = x, y$. Furthermore, the expression (2a) becomes

$$\mathcal{H}_o = \sum_{i=1}^{2} \frac{J_i}{\beta_i(s)} , \quad (4)$$

and the other expressions also become functions of the action-angle variables. To calculate the tune shift, the

average of the Hamiltonian along the whole machine, $\mathcal{C}$, and all over the betatron phases must be determined:

$$< \mathcal{H} >= \frac{1}{2\pi} \int_0^{\mathcal{C}} ds \frac{1}{(2\pi)^2} \int_0^{2\pi} \int_0^{2\pi} d\phi_1 d\phi_2 \, \mathcal{H}(s,\phi,J) \; . \tag{5}$$

Hence, the partial derivation of this quantity with respect to the action brings about the tune of the machine, $\nu_i = \partial < \mathcal{H} > /\partial J_i$, $i = 1, 2$, which is mainly given by the average of the term (4). The other terms, (2b) to (2d), give the tune shift of this value. This expression represents the first order in perturbation strength. The sextupole component of the magnetic field does not induce tune shift of a first order in perturbation strength. To calculate its tune shift effect, it is required to go to the second order in perturbation.

To go to a second-order perturbation theory, a new canonical transformation must be made, (Φ, K). This canonical transformation is close to the identity (the original action-angle transformation (3)) and is characterised by the generating function

$$F_{new}(s,\phi,K) = \sum_{i=1}^{2} K_i \phi_i + G(s,\phi,K) \; , \tag{6}$$

where G is a function to be determined. The relation between the new variable (Φ, K) and the old ones (ϕ, J) is given by the expressions $J_i = \partial F_{new}/\partial \phi = K_i + G_{\phi_i}$ and $\Phi_i = \partial F_{new}/\partial K_i = \phi_i + G_{K_i}$, where the subindex means partial differentiation. In addition, the new Hamiltonian, $\widehat{\mathcal{H}}(s, \Phi, K)$, is given by

$$\widehat{\mathcal{H}} = \sum_{i=1}^{2} K_i/\beta_i(s) + \sum_{i=1}^{2} (\partial G/\partial \phi_i)/\beta_i(s) + \partial G/\partial s +$$
$$+ \mathcal{V}(s, \Phi - G_K, K + G_\phi) + U(s, \Phi - G_K, K + G_\phi). \tag{7}$$

Doing a Taylor expansion of the last two terms on the right hand side of (8), it follows

$$\widehat{\mathcal{H}} = \sum_{i=1}^{2} K_i/\beta_i(s) + \mathcal{V}^{(1)}_{m=2}(s, \Phi, K) +$$
$$+ \sum_{i=1}^{2} (\partial G/\partial \phi_i)/\beta_i(s) + \partial G/\partial s + \mathcal{V} +$$
$$+ \sum_{i=1}^{2} [\mathcal{V}_{K_i} G_{\phi_i} - \mathcal{V}_{\phi_i} G_{K_i}] + \mathcal{U}(s, \Phi, K) + \dots \; , \tag{8}$$

where a possible quadrupole term in (2) has been extracted from $\mathcal{V}$ and put together with the first-order zero average terms, first line in (8), and the term $\mathcal{U}$ has been put together with the second-order terms, third line in (8). In this expression, it is possible to make

$$\sum_{i=1}^{2} \frac{1}{\beta_i(s)} \frac{\partial G}{\partial \phi_i} + \frac{\partial G}{\partial s} + \mathcal{V} = 0 \; , \tag{9}$$

"legally" deleting the term $\mathcal{V}$ from the Hamiltonian. The soluion of this partial differential equation brings about the following expression for G (see Reference [5]):

$$G(s,\phi,K) = -\int_0^s \mathcal{V}(\xi, \phi - \psi(s) + \psi(\xi), K) \, d\xi \; , \tag{10}$$

where the components of the function ψ are defined by $\psi_i(s) = \int_0^s d\sigma/\beta_i(\sigma)$. Using this expression in (8), the full second-order approximation can be solved, neglecting higher-order terms. Consequently, the second order in perturbation Hamiltonian can be written as

$$\widehat{\mathcal{H}} = \sum_{i=1}^{2} \frac{K_i}{\beta_i(s)} + \mathcal{V}^{(1)}_{m=2}(s, \phi, K) + \mathcal{H}_{11} + \mathcal{H}_{12} + \mathcal{H}_{22} \; , \tag{11}$$

where $\mathcal{H}_{11}$, $\mathcal{H}_{12}$, and $\mathcal{H}_{22}$ are given by

$$\mathcal{H}_{11} = \sum_{i=1}^{2} \left[\mathcal{V}^{(1)}_{K_i} G^{(1)}_{\phi_i} - \mathcal{V}^{(1)}_{\phi_i} G^{(1)}_{K_i} \right] \; , \tag{12a}$$

$$\mathcal{H}_{12} = \sum_{i=1}^{2} \left[\mathcal{V}^{(1)}_{K_i} G^{(2)}_{\phi_i} - \mathcal{V}^{(1)}_{\phi_i} G^{(2)}_{K_i} \right] + \sum_{i=1}^{2} \left[\mathcal{V}^{(2)}_{K_i} G^{(1)}_{\phi_i} - \mathcal{V}^{(2)}_{\phi_i} G^{(1)}_{K_i} \right] \; , \tag{12b}$$

and

$$\mathcal{H}_{22} = \sum_{i=1}^{2} \left[\mathcal{V}^{(2)}_{K_i} G^{(2)}_{\phi_i} - \mathcal{V}^{(2)}_{\phi_i} G^{(2)}_{K_i} \right] + \mathcal{U} \; , \tag{12c}$$

where, using (2b) and (2c), the decomposition $\mathcal{V} = \mathcal{V}^{(1)} + \mathcal{V}^{(2)}$ has been made, and $G^{(i)}$ for $i = 1, 2$ is defined as $G^{(i)} = -\int_0^S \mathcal{V}^{(i)}(\xi, \phi - \psi(s) + \psi(\xi), K) \, d\xi$.

III. SEXTUPOLE TUNE SHIFT

The components of the vector potential resulting from the sextupole longitudinal oscillation pattern in an s.c. dipole is given by [7]:

$$A^{(3)}_x = -(3x^2 y^2 - y^4)\dot{v}/5 \; , \tag{13a}$$

$$A^{(3)}_y = +(3x^3 y - xy^3)\dot{v}/5 \; , \tag{13b}$$

$$A^{(3)}_s = -(x^3 - 3xy^2)v \; , \tag{13c}$$

where $v(s)$ is the function responsible for the longitudinal oscillation pattern ($\dot{v}$ is its differentiation) and is given by $v(s) = (b_3 + a \sin \kappa s)/3$, where b_3 represents the systematic component, a represents the amplitude of the oscillation pattern, and κ denotes the wavelength number of the longitudinal periodic pattern. The contribution of the systematic sextupole component average value, b_3, is well known, and it will be ignored in the calculations.

It is not difficult to see from (13), (2), (3a), (10), and (12) the following order of dependence in the action for the second-order terms of the Hamiltonian, $\mathcal{O}(\mathcal{H}_{11}) \sim K^2$, $\mathcal{O}(\mathcal{H}_{12}) \sim K^3$, and $\mathcal{O}(\mathcal{H}_{22}) \sim K^4$. Therefore, the terms (12b) and (12c) are expected to be very small, and they

will not be presented here. From the expressions (13c), (2b), (3b), and (10), the following expressions are obtained

$$\mathcal{V}^{(1)} = (e/pc)\, 2^{3/2} v \left[(K_1\beta_1)^{3/2} \cos^3 \phi_1 \right.$$
$$\left. -3(K_1\beta_1)^{1/2} K_2\beta_2 \cos\phi_1 \cos^2\phi_2 \right] \text{, and} \qquad (14a)$$

$$G^{(1)} = -(e/cp)\, 2^{3/2} \left\{ K_1^{3/2} \sum_{\rho=0}^{3} \binom{3}{\rho} \cos^{3-\rho}\phi_1 \sin^\rho \phi_1\, g_{11}^\rho(s) \right.$$
$$\left. -3K_1^{1/2} K_2 \sum_{\rho=0}^{1}\sum_{\dot\rho=0}^{2} \binom{2}{\dot\rho} \cos^\sigma \phi_1 \sin^\rho \phi_1 \cos^\delta \phi_2 \sin^{\dot\rho}\phi_2\, g_{12}^{\rho\dot\rho}(s) \right\},$$
$$(14b)$$

where $\sigma = 1-\rho$, $\dot\sigma = 2-\dot\rho$, and the functions g_{11}^ρ and $g_{12}^{\rho\dot\rho}$ are given by

$$g_{11}^\rho(s) = \int_0^s v(\xi)\beta_1^{3/2}(\xi) \cos^{3-\rho}\delta_1 \sin^\rho \delta_1\, d\xi \qquad (15a)$$

and

$$g_{12}^{\rho\dot\rho}(s) = \int_0^s v(\xi)\beta_1^{1/2}(\xi)\beta_2(\xi) \cos^\sigma \delta_1 \sin^\rho \delta_1 \cos^\delta \delta_2 \sin^{\dot\rho}\delta_2\, d\xi$$
$$(15b)$$

where δ_i is defined as $\delta_i(s,\xi) = \psi_i(s) - \psi_i(\xi)$, $i = 1,2$. Doing the partial differentiations of (14s), calculating the obtained average values, and making some rearrangements, it follows that

$$< \mathcal{H}_{11} > = -\left(\frac{e}{cp}\right)^2 \left\{ K_1^2 \left[27q_{11;1}^1 - 9q_{11;1}^3 \right] \right.$$
$$+K_1K_2 \left[-9Q_{12;1}^{10} + 18Q_{12;1}^{12} - 9q_{11;2}^1 - 9q_{11;2}^3 + 108Q_{12;2}^{01} \right]$$
$$\left. +K_2^2 \left[27Q_{12;2}^{10} - 9Q_{12;2}^{12} \right] \right\}, \qquad (16)$$

where the following definitions have been used:

$$q_{11;1}^\rho = \frac{1}{2\pi} \int_0^C v(s)\beta_1^{3/2}(s) g_{11}^\rho(s)\, ds , \qquad (17a)$$

$$q_{11;2}^\rho = \frac{1}{2\pi} \int_0^C v(s)\beta_1^{1/2}(s)\beta_2(s) g_{11}^\rho(s)\, ds , \qquad (17b)$$

$$Q_{12;1}^{\rho\dot\rho} = \frac{1}{2\pi} \int_0^C v(s)\beta_1^{3/2}(s) g_{12}^{\rho\dot\rho}(s)\, ds , \qquad (17c)$$

and

$$Q_{12;2}^{\rho\dot\rho} = \frac{1}{2\pi} \int_0^C v(s)\beta_1^{1/2}(s)\beta_2(s) g_{12}^{\rho\dot\rho}(s)\, ds . \qquad (17d)$$

Thus, the tune shift is given by the partial derivation of this expression with respect to the action variables:

$$(\Delta\nu_j)_{K_i=\epsilon_N/2\gamma} = r_p\epsilon_N\lambda_j/mc^2\gamma^3, \quad j=1,2, \qquad (18)$$

where λ_1, λ_2 are defined as $\lambda_1 = -27q_{111}^1 + 9q_{111}^3 + \frac{9}{2}Q_{121}^{10} - 9Q_{121}^{12} + \frac{9}{2}q_{112}^1 + \frac{9}{2}q_{112}^3 - 54Q_{122}^{01}$, $\lambda_2 = 9Q_{121}^{10} -$

Table 1
Numerical Integration

$25\times$	COLLIDER	HEB
$q_{11;1}^1$	-1.546×10^{15}	-5.555×10^{12}
$q_{11;2}^1$	-8.926×10^{14}	-1.734×10^{12}
$q_{11;1}^3$	-8.500×10^{14}	$+11.477 \times 10^{15}$
$q_{11;2}^3$	-3.363×10^{14}	$+8.616 \times 10^{15}$
$Q_{12;1}^{10}$	-9.072×10^{14}	-1.719×10^{12}
$Q_{12;1}^{12}$	-2.057×10^{11}	$+2.141 \times 10^{10}$
$Q_{12;2}^{10}$	-1.546×10^{15}	-5.479×10^{12}
$Q_{12;2}^{12}$	-7.227×10^{10}	$+1.158 \times 10^{10}$
λ_1	$+5.660 \times 10^{17}$	$+1.422 \times 10^{17}$
λ_2	$+1.895 \times 10^{17}$	$+7.805 \times 10^{16}$
$\Delta\nu_1/a^2$	2.7×10^{-11}	6.82×10^{-9}
$\Delta\nu_2/a^2$	9.1×10^{-13}	3.74×10^{-9}

$18Q_{121}^{12} + 9q_{112}^1 + 9q_{112}^3 - 108Q_{122}^{01} - 27Q_{122}^{10} + 9Q_{122}^{12}$. Table 1 shows the results of these integrations along the Collider and High Energy Booster (HEB) machines of the SSC.

As can be seen from these numerical values, the dynamics of the beam are not affected by the longitudinal sextupole oscillation patter in the s.c. magnets. It is pointed out that the values shown in the table can change by one order of magnitude, since the integration depends on the wavelength of the longitudinal oscillation pattern.

Higher-order multiples have smaller contributions than the sextupole and can be neglected as well. However, there is also a longitudinal quadrupole oscillation pattern in the s.c. dipole magnets, but since the quadrupole multiple is not a symmetry allowed in the dipole magnets, the amplitude, a, of this oscillation is expected to be random from magnet to magnet. To calculate the contribution to the tune shift of the quadrupole longitudinal oscillation pattern, a simple first order in perturbation theory can be done obtaining a contribution $\Delta\nu/a = \pm 10^{-5}$, where a must be given in Gauss/cm.

IV. CONCLUSIONS

The expected tune shift due to the longitudinal oscillation sextupole component pattern is of the order of 10^{-9}. Therefore, this pattern is not relevant for the dynamics of the particles for the SSC Collider or the HEB machines.

V. REFERENCES

[1] H. Brück et al., DESY HERA 91-01, January 1991.

[2] M. Wake et al., TS-SSC-91-32, February 1991.

[3] A. N. Kolmogorov, *Dokl. Akad. Nauk SSSR* **96**, 527 (1954).

[4] E. D. Courant et al., *AIP Com. Proc. Series*, No. 127, 295 (1985).

[5] G. López and S. Chen, SSCL-550 (1991).

Decoupling Schemes for the SSC Collider

Y. Cai, G.Bourianoff, B.Cole, R.Meinke, J. Peterson, F. Pilat, S. Stampke, M.Syphers and R.Talman

SSC Laboratory, 2550 Beckleymeade Avenue, Dallas, Texas 75237 USA*

Abstract

A decoupling system is designed for the SSC Collider. This system can accommodate three decoupling schemes by using 44 skew quadrupoles in the different configurations. Several decoupling schemes are studied and compared in this paper.

I. INTRODUCTION

The SSC Collider consists of two arcs and two clusters and has two-fold symmetry. There are three insertions, two interaction regions and one utility region in each cluster. Two approved experiments, SDC and GEM, are located in the east cluster. Injection lines from the high energy booster, the beam abort system and RF system reside in the west utility. Other than some small bending regions between the insertions to deflect neutral particles from experiments, most bending is accomplished in arc. There are 196 FODO (90 degree) cells in each arc.

In an ideal synchrotron accelerator containing dipoles, quadrupoles and sextupoles with no alignment errors or multipole errors, motion of a particle in the horizontal plane is decoupled from its motion in vertical plane. This fact makes an ideal accelerator very simple to understand, therefore, easy to operate. In a real accelerator, the linear motions are always coupled due to skew quadrupole (a_1) errors. In the case of the SSC Collider, there are three major sources of skew quadrupole errors. Main superconducting dipole magnets produce a skew quadrupole component when up-down symmetry is broken during a manufacturing process. Even with perfect symmetry, there are still sextupole (b_2) errors due to persistence current in superconductors. These sextupole errors will feed down to skew quadrupole if particles do not pass the center of the dipole vertically. The second source is roll of main quadrupole magnets when aligned or fabricated. The last one is due to

Table 1
Sources of Linear Coupling

a_1 in dipole	sys.	0.10 unit	0.5 T
	rms.	1.25 unit	2.8 T
roll of quads	rms.	0.5 mrad	1.1 T
Vertical disp. sexts.	rms_corr	0.33 mm	1.2 T
	rms_b_2	1.00 mm	0.9 T

sextupole corrector magnets when misaligned vertically. The total skew quadrupole errors in a half cell at collision energy are tabulated in the last column (GL in Tesla) of Table 1.

Table 1 shows that dipole magnets are the dominant sources of linear coupling simply because of the number of dipole magnets in the Collider. Those errors are used in simulations in later sections.

II. DECOUPLING SCHEMES

In a coupled circular accelerator, fractional tunes of horizontal and vertical betatron motions can not be operated closely. Two families of skew quadrupoles are needed to reduce the band width (difference resonance) between fractional tunes so that fractional tunes can be operated closely to avoid other resonances. For this reason, almost all circular accelerators use this scheme to decouple vertical and horizontal motions. Operationally, this scheme is also very simple since changing and measuring tunes required in this scheme are routine operations. We will adopt it as a basic operation in the decoupling system because it is a proven scheme.

A two family decoupling scheme only reduces the width of difference resonance caused by skew quadrupole errors. It is known that skew quadrupole errors also contribute to a sum resonance. For a strongly coupled machine, the linear sum resonance can also cause some secondary effects, for example distorted beta function and residual tune split. To correct the secondary effects, an additional two families of skew quadrupoles are needed. Operationally, sum resonances can be minimized in the same way as the difference resonance. However, there is another way to use four families of skew quadrupoles by minimizing four independent coupling matrices elements in the one-turn matrix at a selected location. In this scheme two kickers with difference of 90^0 in betatron phase are needed in each plane to measure the coupling matrix. It can be shown that these two methods of using four families are nearly equivalent. The second one is used in our simulations.

Transverse linear betatron motion can be described by a four by four symplectic matrix. This matrix always can be block diagonalized into two by two matrices[1][2]. The motion described by the diagonalized matrix is called eigen motion. The planes defined by the eigen motion with a small amplitude are called the eigen planes. The angles between the eigen planes and the horizontal or vertical planes can be measured by analyzing the reading of beam position monitors (BPMs) while the beam is excited horizontally or vertically. Therefore, the eigen angles at a beam position monitor location can be minimized by adjusting nearby skew quadrupole magnets accordingly[3]. This scheme requires that every skew quadrupole magnet have its own power supply and be controlled independently.

III. DECOUPLING SYSTEM

The SSC collider is very different from any other accelerators because its size. In particular, it has very long arcs. Coupling can be built up gradually in the 196 cells to intolerable levels. For instance, to the point where eigen angle approaches 45^0 so that there is no way to distinguish the horizontal motion from the vertical. Due to this fact, some skew quadrupoles in arcs are needed to reduce the build up of coupling. In the Collider decoupling system, there are five evenly distributed pairs of skew quadrupole magnets at missing dipole locations[4] in each arc. They will be used to minimize eigen angles of BPMs locations in the arcs.

Betatron tune adjustment will be made by two families of trim quadrupoles in the arcs. Therefore, differences in phase among skew quadrupoles in arcs will not be kept in constant when the Collider is tuned. As a result, skew quadrupoles in the arcs cannot be grouped into families because the final operating tunes for the Collider will be determined only after its commissioning. The correction systems have to accommodate a range of ±3 unit in tunes.

On the other hand, phase advances in each cluster will be fixed as the Collider is tuned. This is crucial for many interaction region correction schemes. For example, non-linear chromatic effects from triplets near an interaction point can be corrected by sextupoles at ends of arcs. To take advantage of this fact, four skew quadrupole magnets are placed inside or near each insertion in the clusters so that they can be grouped into four families based on their phases. Two families of skew quadrupoles for the difference resonance correction are at the middle of an empty half cell to maximize the difference of phases between horizontal and vertical betatron oscillations. The skew quadrupole magnets near interaction regions are located outside the tuning quadrupole magnets so that the phase relationship among skew quadrupoles will not be changed during a beta squeeze. This makes the decoupling sequence orthogonal to the beta squeeze sequence during the Collider operation.

These families are formed in control software, and can be rearranged in different clusters if the tunes of the Collider are changed.

IV. RESULTS

The different decoupling schemes described above have been simulated by using the tracking code TEAPOT on the same lattice and with the same set of alignment errors and multipole errors so that the comparison can be made directly. Betatron tunes in simulations are $v_x = 123.785$, and $v_y = 122.765$. The selection of the difference of one unit in integer part of tunes is to suppress the effects from systematic a_1 in main dipole magnets. Because the Collider has two fold symmetry, systematic errors only contribute to even integer resonances. A summary of simulation results is tabulated in Table2.

Table 2 shows that 24 skew quadrupoles in four families are adequate to minimize tune separation. However, controlling eigen angles within ±10 degree is also very important for simple operation of the Collider. The next four figures show that only one scheme can achieve the control of eigen angles with 44 individually set skew quadrupoles by using the eigen angle minimization scheme. Schemes based on families only can control eigen angles in a very limited way. Eigen angles accumulate in arcs and exceed 10^0 when no skew quadrupole magnets are in the arcs.

Table 2

Minimum Tune Separation

Decoupling Schemes	Number of skew quads	Minimum tune separation
No correction	0	0.024
Two families	12	0.010
Four families	24	0.003
Minimizing eigen angles	44	0.0005
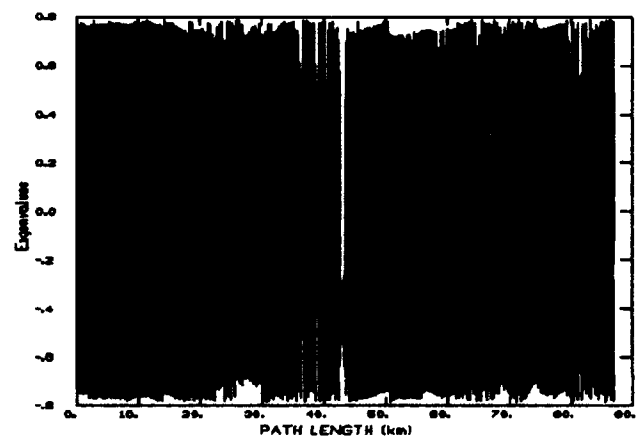
Figure 1. Eigen angles in radian with no coupling correction. It shows that eigen angles reach 45 degree at many locations in the Collider and the motions in different planes are coupled very strongly.
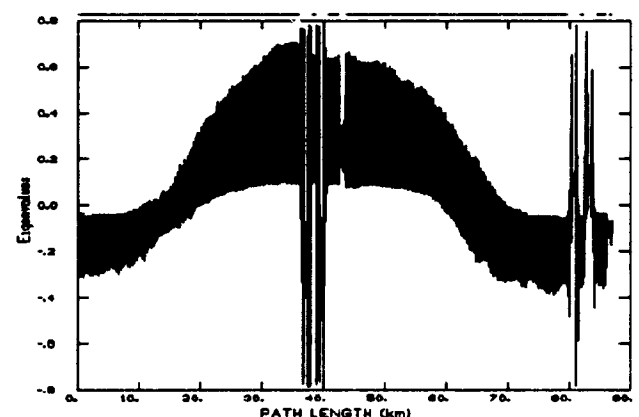
Figure 2. Eigen angles in radians with two families of 12 skew quadrupoles in clusters. It shows that eigen angles have been brought under control. However, eigen angles accumulate in arcs and reach 45^0 at the end of arcs.
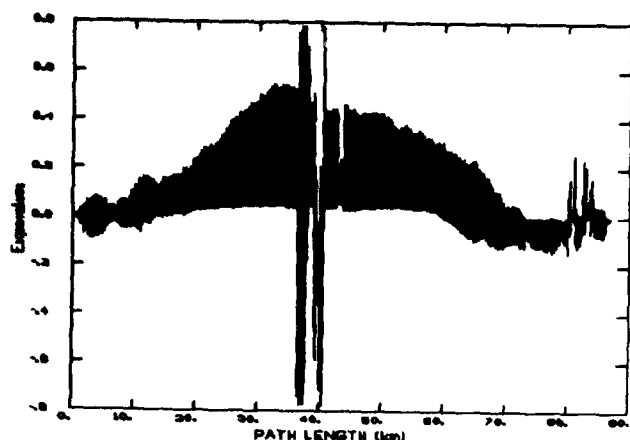
Figure 3. Eigen angles in radians with four families of 24 skew quadrupoles in clusters. It shows that maximum eigen angles are reduced by factor of two compared to two family scheme.
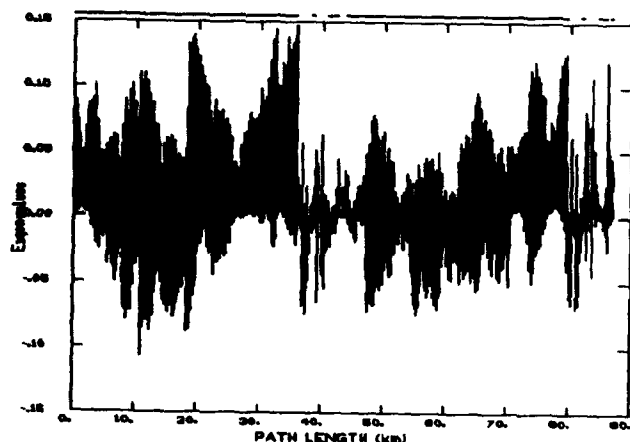
Figure 4. Eigen angles in radians with 44 independently set skew quadrupoles. It shows that maximum eigen angles is less than 10^0.

Other multipole errors and alignment errors in magnets are included in the simulations. The difference in dynamic aperture and linear aperture is the within 10% for all cases listed.

The integrated strength of skew quadrupole magnets required in these studies is 150 Tesla in the clusters and 80 Tesla in the arcs. The difference in strength is largely due to the large coupling caused by triplet quadrupoles inside the interaction regions.

V. CONCLUSIONS

The decoupling system with 44 skew quadrupoles, among them 20 in arcs and 24 in clusters, is very flexible and can be used in many different ways. At the early stage of operations, the simple two family scheme is likely to be used. Skew quadrupoles may be set individually when the Collider is better understood.

VI. REFERENCES

[1] D. Edwards and L. C. Teng, "Parameterization of linear coupled motion in periodic systems," *IEEE Trans. Nucl.Sci.* NS-20, No.3, 1973

[2] S. Peggs, "Coupling and decoupling in storage rings,"*IEEE Trans. Nucl. Sci.* NS-30, No4, August 1983

[3] R. Talman, "Single particle motion," Notes for joint US-CERN school, Capri, Ita¹v, October, 1988

[4] M. Syphers, E. Courant, A. Garren, K. Kauffmann, T. Sen, "SSC Collider arc lattice," these proceedings

MATRIX NONLINEAR BEAM DYNAMICS IN CURVILINEAR SPACE-TIME

Alexander Dymnikov
Institute of Computational Mathematics
University of St. Petersburg
Stary Petergof 198904
St. PETERSBURG, Russia

Ragnar Hellborg
Department of Physics
University of Lund
Sölvegatan 14
S-223 62 LUND, Sweden

ABSTRACT

A general relativistic matrix theory of charged particle beam motion along an arbitrary curved optical axis in 4-space-time has been developed. This theory uses three basic matrix functions: the reference frame matrix, the curvature matrix and the electromagnetic matrix. The Cartan method of the moving 3-vector is generalized as the method of the moving 4×4 reference matrix. The curvature matrix function consists of the normal curvature, the geodesic curvature and torsion and three components of the gravitational force acting on the reference particle. The matrix equations of the beam motion and of the electromagnetic field are written.

The nonlinear equations in phase space are reformulated as linear equations in phase moment space. A new compact recursive method is proposed for integrating these linear equations. Using this method the phase volume of the beam will be strictly conserved in each step of the numerical integration.

1 INTRODUCTION

A general relativistic theory of charged particle beam motion along a curved optical axis, including the gravitational field, is important for designers of optimal beam control systems. Some basic publications on this topics can be found in [1] − [4]. In these references the scalar and tensor methods are used and usually a nonrelativistic theory is developed. In this paper a new matrix approach is presented which is based on some previous papers [5] − [7]. This approach gives the possibility to develope a matrix relativistic theory of charged particle beam motion in the most general case of curved reference trajectory, including the gravitational force and space charge. Two detailed reports on this purpose have just recently been published [8]. Some earlier papers have been devoted to the special problem of the effect of space charge. Both for the general case [9] and for a special case with an infinitely long beam and with an elliptical beam cross-section in a static electromagnetic field [10] and [11].

2 THE EQUATIONS OF A PARTICLE BEAM MOTION AND THE EQUATIONS OF AN ELECTROMAGNETIC FIELD.

We understand the motion of any material body as a motion relative to other material bodies. The motion of any particle Q of the beam is described in the form of a motion relative to a single particle M of the beam. The particle M is called *the reference particle*. The trajectory of the reference particle is called *the reference trajectory* or *the optical axis* of the beam. We assume that the reference trajectory is known and the motion of the reference particle is described relative to any material body. The position of an arbitrary particle Q in the moving reference frame is determined by the 4-vector $L = \tilde{e}x$, where e is the reference frame matrix, attached to the reference particle M, x_1 and x_2 are the transverse coordinates, x_3 is the longitudinal coordinate and $x_4 = cst$. All quantities used are either dimensionless or expressed in terms of units of length of the beam motion or of the inverse length.

The complete motion of an arbitrary particle Q can be decomposed in the following way:

$$dQ = dM + dL = \tilde{e}dz_m + d(\tilde{e}x)$$

The motion of the reference frame is determined by the equation:

$$\frac{de}{ds} = e' = P(k, l)e, \quad e(s_0) = e_0$$

where:

$$P(k,l) = \begin{pmatrix} 0 & k_3 & -k_2 & l_1 \\ -k_3 & 0 & k_1 & l_2 \\ k_2 & -k_1 & 0 & l_3 \\ l_1 & l_2 & l_3 & 0 \end{pmatrix}$$

$$e\tilde{e} = G = \begin{pmatrix} -1 & 0 & 0 & 0 \\ 0 & -1 & 0 & 0 \\ 0 & 0 & -1 & 0 \\ 0 & 0 & 0 & 1 \end{pmatrix}$$

For the Darbou reference frame k_1 is the normal curvature, k_2 is the geodesic curvature, k_3 is the geodesic torsion. The 3-vector l is the vector corresponding to the gravitational force F, acting on the reference particle, *i.e.* $F = -pl$. The coordinates z_m are chosen such that $z_{m1} = z_{m2} = 0$, $z_{m3} = s$, $z_{m4} = ct_m$, $ds = pd\tau_m$, $dz_{m4} = \gamma d\tau_m$, $d\tau_m^2 = d\tilde{M}dM$, where p is the reference momentum and γ is the reference energy. We assume that the observer is located in the plane $x_3 = 0$, *i.e.* that all particles Q reaching this plane at different times are detected. We will study the dynamics of particles in the plane $x_3 = 0$, and therefore we have four independent variables x_1, x_2, x_4 and s.

The equations of motion for an arbitrary particle Q can be written as:

$$\left(\frac{z'}{\tau'}\right)' = \frac{1}{\tau'}P\left(\hat{B},\hat{E}\right)z' \qquad (1)$$

where:

$$\tau' = \sqrt{\tilde{z}'Gz'}, \quad \hat{B} = B\tau' + k, \quad \hat{E} = E\tau' - l$$

$$z' = z'_m + x' + \tilde{P}(k,l)x$$

$$z'_{m1} = z'_{m2} = 0, \quad z'_{m3} = 1, \quad z'_{m4} = \frac{\gamma}{p}$$

$$z_{m4} = \int_{s_0}^{s}\frac{\gamma}{p}ds + z_{m40}$$

The fields B and E are functions of x_1, x_2, x_4 and s. The 3-vectors k and l and the scalars γ and p are functions of s.

The Maxwell equations of electromagnetic field may be written in the following matrix form:

$$\underset{\uparrow}{P}(B,E)G\underset{\downarrow}{\nabla}(z) + [P(B,E)GP(k,l)]\frac{1}{a_3}i(3) +$$

$$+ [P(-k,l)P(B,E)G]\frac{1}{a_3}i(3) + \rho\frac{dz}{d\tau} = 0 \qquad (2)$$

$$\underset{\uparrow}{P}(-E,B)G\underset{\downarrow}{\nabla}(z) + [P(-E,B)GP(k,l)]\frac{1}{a_3}i(3) +$$

$$+ [P(-k,l)P(-E,B)G]\frac{1}{a_3}i(3) = 0$$

where:

$$\bar{i}(3) = (0,0,1,0), \quad \bar{\nabla}(z) = (\nabla_1(z)...\nabla_4(z))$$

$$\nabla_i(z) = \frac{\partial}{\partial z_i}, \quad \nabla_i(z) = \nabla_i(x), \quad i = 1,2,4$$

$$\nabla_3(z) = -\frac{a_1}{a_3}\nabla_1(x) - \frac{a_2}{a_3}\nabla_2(x) + \frac{1}{a_3}\nabla(3) - \frac{a_4}{a_3}\nabla_4(x)$$

$$\nabla(s) = \frac{\partial}{\partial s}$$

$$a_1 = -k_3x_2 + l_1x_4, \quad a_2 = k_3x_1 + l_2x_4$$

$$a_3 = 1 - k_2x_1 + k_1x_2 + l_3x_4, \quad a_4 = \frac{\gamma}{p} + l_1x_1 + l_2x_2$$

3 THE METHOD OF EMBEDDING IN PHASE-MOMENT SPACE FOR SOLVING THE NONLINEAR EQUATIONS OF THE MOTION OF A PARTICLE BEAM

The analysis and calculation of the nonlinear systems of equations for beam formation are considerably simplified by a transformation from the nonlinear differential equations of motion in the phase space (x, x') to the system of linear equations in extended phase space, the phase moment space. This is the essence of the method of embedding in phase moment space. In this method the ideas that were originally presented in ref. [12] have been developed further in ref. [7].

We define recursively the rth power of the vector x as:

$$x^r = \begin{pmatrix} x_1 & ... & x^{r-1}(1) \\ ... & & ... \\ x_n & ... & x^{r-1}(n) \end{pmatrix}, \quad x^l(j) = \begin{pmatrix} x_jx^{l-1}(j) \\ ... \\ x_nx^{l-1}(n) \end{pmatrix}$$

$$x^0(j) = 1, \quad j = 1,...,n, \quad l = 1,...,r$$

This is called the r-moment of the vector x or in short, the r-moment, which has $\alpha(n,r)$ scalar elements, where:

$$\alpha(n,r) = \frac{(n-1+r)!}{(n-1)!r!}$$

Let us introduce the 6-vector h, given by:

$$h_i = x_i, \quad i = 1,2,3, \quad h_4 = \frac{p}{p(0)}x'_1$$

$$h_5 = \frac{p}{p(0)}x'_2, \quad h_6 = \frac{p^3}{p^3(0)}x'_4$$

It is possible to show that in the phase space $\backslash\dot{}j$ the phase volume remains constant during the motion.

Using the Taylor expansion of the functions $B(h)$, $E(h)$ and $\tau'(h)$ to transform them into a finite series, the equations of motion can be written as:

$$h' = F(s)\langle h^r \rangle \qquad (3)$$

where the vector is given from $\langle \vec{h}^r \rangle = (h^1, h^2, ..., h^r)$.

The equations for the phase moments h^s, where $s = 2, ..., r$, can be obtained with the same accuracy as eq. (3). Therefore it is possible to write the linear equation for the vector $\langle h^r \rangle$ in the following way:

$$\langle h^r \rangle' = P(s)\langle h^r \rangle \qquad (4)$$

We call the matrix $P(s)$ the coefficient matrix. The solution of the linear equation for h, given by eq. (4), coincides with the solution of eq. (1), which has been obtained by the successive-approximation method. The method of reducing eq. (3) to the form of eq. (4) is reffered to as the method of embedding in phase moment space.

The solution of eq. (4) is written in terms of a matrizant in the form:

$$\langle h^r \rangle = \begin{pmatrix} h^1 \\ ... \\ h^r \end{pmatrix} = \begin{pmatrix} R^{11} & ... & ... & R^{1r} \\ 0 & R^{22} & ... & R^{2r} \\ ... & ... & ... & ... \\ 0 & 0 & ... & R^{rr} \end{pmatrix} \begin{pmatrix} h^1 \\ ... \\ h^r \end{pmatrix} =$$

$$= R(P, s/s_0)\langle h_0^r \rangle$$

The matrizant R has, in the same way as the coefficient matrix P, the form of an upper triangular block.

A continuous generalized analogue of the Gauss brackets [6] and [13] can be used to calculate the matrizant for an arbitrary coefficient matrix. In this method there is rigorous conservation of the phase volume of the beam at each stage of the calculations. An effective computer code, based on this method, has been written for studying the beam dynamics for an arbitrary axial distribution through fifth order in the nonlinearity [14].

4 SUMMARY

A new matrix and recursive approach has been outlined for treating nonlinear optics of charged particle beams. This approach is a new analytical and computational tool for designers of optimal beam control systems. This relies on three basic matrix functions: the reference frame matrix, the curvature matrix and the electromagnetic matrix. The nonlinear equations in phase space are reformulated as linear equations in phase moment space. A compact, conservative, recursive method of integrating the equations of motion is proposed. All quantities in the equations of motion and in the field equations are either dimensionless or expressed in terms of units of length or inverse length.

REFERENCES

1. Cotte M., Recherches sur l'optique électronique. Annales de Physique, 10 (1938), 333-405.
2. G.A. Grinberg, Selected Problems of Mathematical Theory of Electrical and Magnetic Phenomena, Press of Academy Sciences USSR, Moscow, Leningrad (1948), 507-535 (in Russian).
3. K.G. Steffen, High Energy Beam Optics, (Wiley 1965), p. 94-97.
4. Zhou Liwei, Ni Guoqiang and Qiu Baicang, Optic, 79, No. 2 (1988) 53-66.
5. A.D. Dymnikov, Deposited Report B1-10427 (in Russian), JINR, Dubna (1977).
6. A.D. Dymnikov, Problems in Mechanics and Control Processes, No. 2, Control of Dynamical Systems (in Russian) (Leningrad State University, Leningrad, 1978), p64.
7. A.D. Dymnikov and G.M. Osetinskii, Sov. J. Part. Nucl. 20, No.3 (1989), 293-310.
8. A. Dymnikov and R. Hellborg, Matrix theory of the motion of a charged particle beam in curvilinear space-time. Part I and II, Nucl. Instr. Meth. part A in press.
9. A. Dymnikov and R. Hellborg, The influence of space charge on the motion of a bunch of articles in an ion optical system, submitted to Nucl. Instr. Meth. part B.
10. A. Dymnikov, R. Hellborg, J. Pallon, G. Skog, c. Yang and G. Ohlén, Nucl. Instr. Meth. A 328 (1993) 164.
11. A. Dymnikov, R. Hellborg, J. Pallon, G. Skog and C. Yang, Calculation of the beam transport through the low energy side of the Lund Pelletron accelerator, Accepted for publication in Nucl. Instr. Meth. part A.
12. K.L. Brown, R. Belbeoch and P. Bounin, Rev. Sci. Instr. 35, 481 (1964).
13. V.Yu. Vasilev and A.D. Dymnikov, Sov.At. Energy (English translation), 374, 1091 (1974).
14. M.F. Galochkina and A.D. Dymnikov, Proc. Int. Symp. and Summer School Math. Modelling and Sci. Comp., Albena, Bulgaria 1990.

A Numerical Check of the Thermal Wave-Model for Particle-Beam Dynamics

R. Fedele, G. Miele

Dipartimento di Scienze Fisiche, Università di Napoli "Federico II",

Mostra D'Oltremare, Pad. 19, I-80125 Napoli, Italy

F. Galluccio

Istituto Nazionale di Fisica Nucleare, Sezione di Napoli,

Mostra D'Oltremare, Pad. 20, I-80125 Napoli, Italy

Abstract The recently proposed *thermal wave model for transverse particle-beam dynamics* is tested numerically in the case of propagation through a quadrupole lens with sextupole deviations. This check is performed by comparing the model predictions, obtained analytically using perturbation theory at first order, with the results of a conventional tracking code. The results of this comparison are shown here: a remarkable agreement between the prediction of the wave model and the output of the standard treatment is found, which opens up the possibility of studying transverse beam-dynamics from a novel and, hopefully, very powerful point of view.

1 Introduction

Transverse beam-dynamics in particle accelerators is generally approached by means of single-particle tracking. This allows the characteristic parameters of the machine such as tunes, chromaticities or Twiss parameters to be determined, and the stability region of phase-space, the so-called 'dynamic aperture', to be identified; this last one can only be evaluated at the cost of often very long and CPU-time consuming tracking-simulation procedures. The recently proposed *thermal wave model for relativistic charged particle beam propagation* [1] allows us to represent the beam as a whole, by means of a complex function, the so-called beam wave function (bwf), whose squared modulus is interpreted as the transverse distribution function: the response of the beam to the different linear and non-linear elements throughout the machine can then be described in terms of the evolution of the above bwf.

This model assumes that the transverse particle-beam dynamics is governed by a Schrödinger-like equation for the bwf which is analogous to the equations holding in non-relativistic quantum-mechanics and electromagnetic beam-optics, as it has been recently pointed out [1]. The thermal wave-model has already been applied successfully to the treatment of an ideal quadrupole-like lens with octupole deviations [2], as well as to the description of the nonlinear beam-plasma interaction [3].

In this paper, after a brief review of the main properties of the thermal wave model, we apply the standard perturbation theory generally used in solving Schrödinger equation to determine the momentum distribution of a purely Gaussian incoming beam at the end of a quadrupole lens with a small sextupole deviation. The calculation is performed in thin lens approximation, up to first order in the sextupole strength. The theoretical predictions are then compared with the results of a standard tracking code.

2 The Thermal Wave Model

According to this model, the transverse dynamics of a relativistic particle-beam which travels along the z-axis with velocity βc ($\beta \approx 1$), interacts with the surrounding medium through a potential $u(\vec{r}, z)$, and suffers the thermal spreading (emittance spreading), is governed by a Schrödinger-like equation for a complex wave function $\Psi(\vec{r}, z)$ called the *beam wave function* (bwf). In this equation, the role of the diffraction parameter is played by the transverse emittance ϵ and the analogous of time is represented by the longitudinal coordinate z. Without lack of generality, we can consider only one transverse dimension, say x. In this case, the beam wave equation of Ref. [1] becomes

$$i\epsilon \frac{\partial \Psi}{\partial z} = -\frac{\epsilon^2}{2} \frac{\partial^2}{\partial x^2} \Psi + U(x, z)\Psi \quad , \qquad (1)$$

where $U(x, z)$ is a dimensionless potential, which, in general, should be obtained by integrating the field force equation

$$F = -m_0 \gamma \beta^2 c^2 \frac{\partial}{\partial x} U \quad ; \qquad (2)$$

m_0 and $\gamma = (1 - \beta^2)^{-1/2}$ are the particle rest mass and the relativistic gamma factor, respectively.

Denoting with $\Sigma(x, z)$ and N the transverse density and the total number of particles, respectively, the physical meaning of Ψ is given by the following relationship:

$$\Sigma(x, z) = N |\Psi(x, z)|^2 \qquad (3)$$

where the following normalization for Ψ has been provided:

$$\int_{-\infty}^{+\infty} |\Psi|^2 \, dx = 1 \qquad (4)$$

According to (3), the squared modulus of Ψ provides the transverse density profile of the beam, whilst the squared modulus of its Fourier transform, $\tilde{\Psi}$, provides the corresponding momentum distribution.

The pair of coupled equations (1) and (2) describes the evolution of the particle beam and also represents a *wave description* for the charged particle beam optics in paraxial approximation.

Given the beam distribution in the configuration space, it is possible to define in complete analogy with quantum mechanics, the effective transverse beam size (r.m.s.)

$$\sigma(z) = \left[\int_{-\infty}^{+\infty} x^2 |\Psi|^2 \, dx \right]^{1/2} , \qquad (5)$$

and the average transverse beam momentum:

$$\sigma_p(z) = \left[\frac{\epsilon^2}{2} \int_{-\infty}^{+\infty} \left|\frac{\partial}{\partial x}\Psi\right|^2 dx\right]^{1/2} . \qquad (6)$$

An *uncertainty principle*, fully similar to the uncertainty principle known in quantum mechanics, holds:

$$\sigma \sigma_p \geq \frac{\epsilon}{2} . \qquad (7)$$

Note that the definition of ϵ commonly used in accelerator physics differs from this one by a factor 2.

In the following we solve (1) in the case of a purely Gaussian initial beam, with the transverse potential given by

$$U(x,z) = \frac{1}{2}k_1 x^2 + \frac{1}{6}k_2 x^3 : \qquad (8)$$

this corresponds to a quadrupole lens of focusing strength k_1 with sextupole aberrations of strength k_2. To this end, we start considering the simplest case of a beam passing through a pure quadrupole.

3 Beam propagation in a quadrupole

Let us consider a relativistic charged-particle beam crossing a quadrupole lens. The stationary configurations for the density profile are obtained by solving the following equation

$$i\epsilon \frac{\partial \Psi}{\partial z} = -\frac{\epsilon^2}{2}\frac{\partial^2}{\partial x^2}\Psi + \frac{1}{2}k_1 x^2 \Psi . \qquad (9)$$

Fixing at $z = 0$ the dimension of the beam σ_0 and its dispersion $\alpha = -\sigma_0^2/(\epsilon\rho_0)$, we get as solutions the following discrete modes

$$\Psi_n^0(x,z) = \frac{1}{[2\pi\, 2^{2n}\, (n!)^2]^{1/4}} H_n\left(\frac{x}{\sqrt{2}\sigma(z)}\right)$$

$$\times \exp\left[-\frac{x^2}{4\sigma^2(z)} + i\frac{x^2}{2\epsilon\rho(z)} - i(2n+1)\phi(z)\right] \qquad (10)$$

where H_n are Hermite polynomials, and the functions $\sigma(z)$, $\rho(z)$ and $\phi(z)$ are defined as follows

$$\sigma(z) \equiv \sigma_0 \left[\left(\cos\sqrt{k_1}z + \frac{1}{\sqrt{k_1}\rho_0}\sin\sqrt{k_1}z\right)^2\right.$$

$$\left. + \frac{\epsilon^2}{k_1\sigma_0^4}\sin^2\sqrt{k_1}z\right]^{1/2} , \qquad (11)$$

$$\frac{1}{\rho(z)} \equiv \frac{1}{\sigma(z)}\frac{d\sigma(z)}{dz} , \qquad (12)$$

$$\phi(z) \equiv \left\{\arctan\left[\left(\frac{\sigma_0^2}{\epsilon\sqrt{k_1}\rho_0^2} + \frac{\epsilon}{\sqrt{k_1}\sigma_0^2}\right)\right.\right.$$

$$\left.\left. \times \tan(\sqrt{k_1}z) + \frac{\sigma_0^2}{\epsilon\rho_0}\right] - \arctan\left(\frac{\sigma_0^2}{\epsilon\rho_0}\right)\right\} \qquad (13)$$

In the simple case of $|\rho_0| = \infty$ and for a thin lens $\sqrt{k_1}l$, with l the length of the lens, we get the approximated results: $\sigma(l) \approx \sigma_0$, and $\rho(l) \approx -1/(k_1 l)$.

4 Sextupole aberrations

If we consider a quadrupole lens with sextupole deviations, the equation to solve is (1) with the potential (8). Unfortunately exact solutions of this equation are not known, thus we adopt a standard perturbative technique [2]. We denote with $V(x,z) = (1/6)k_2 x^3$ the sextupole potential, and treat its effect as a perturbation term with respect to the aberrationless hamiltonian contained in the r.h.s. of (9). Provided that $\sigma_0 k_2/3k_1 \ll 1$, it is easy to show that the non-normalized bwf at the exit of the lens is given by

$$\Psi(x,l) = \left(1 - i\frac{l}{6\epsilon} k_2 x^3\right)\Psi_{in}(x,0) , \qquad (14)$$

where Ψ_{in} is the initial condition for the bwf, fixed at the beginning of the lens. If we assume as initial condition a pure Gaussian beam-density profile, (10) for $n = 0$, with vanishing initial dispersion and dimension σ_0

$$\Psi_{in}(x,0) = \frac{1}{[2\pi\,\sigma_0^2]^{1/4}} \exp\left[-\frac{x^2}{4\sigma_0^2}\right] . \qquad (15)$$

In order to obtain the momentum distribution of the beam (not normalized), we Fourier transform (14), and we get

$$\overline{\Psi}(p,l) = \left[1 + \frac{k_2\sigma_0^3 l}{6\epsilon}\frac{1}{\xi^3}H_3\left(\frac{p\sigma_0}{\epsilon}\frac{1}{\xi}\right)\right]$$

$$\times \exp\left[-\frac{p^2\sigma_0^2}{\epsilon^2}\frac{1}{\xi^2} + i\phi(l)\right] , \qquad (16)$$

with $H_3(x) = 8x^3 - 12x$

and $\xi \equiv \sqrt{\left(1 + i\frac{2K_1\sigma_0^2}{\epsilon}\right)} \equiv \sqrt{1 + i\delta} . \qquad (17)$

where $K_1 \equiv k_1 l$ is the integrated focusing strength. We now denote with $\tau = K_2\sigma_0^3/(6\epsilon)$ ($K_2 \equiv k_2 l$), and with $y = p\sigma_0/\epsilon \equiv x'/2\sigma_{p0}$; the squared modulus of the normalized bwf can then be written in momentum space

$$|\overline{\Psi}(y)|^2 = \left[1 + \frac{144\tau^2}{(1+\delta^2)^2}y^2 - \frac{192\tau^2}{(1+\delta^2)^3}y^4\right.$$

$$+ \frac{64\tau^2}{(1+\delta^2)^3}y^6 - \frac{24\tau(1-\delta^2)}{(1+\delta^2)^2}y + \frac{16\tau(1-3\delta^2)}{(1+\delta^2)^3}y^3\right]$$

$$\times \frac{2\sigma_0}{\epsilon}[2\pi(1+\delta^2)(1+15\tau^2)^2]^{-1/2} \exp\left[-\frac{2y^2}{(1+\delta^2)}\right] ; \quad (18)$$

note that $|\overline{\Psi}|^2$ is the product of a gaussian function times a polynomial function of order 6, where the term of order 5 is missing.

5 Numerical Check

A numerical experiment has been carried out, and the theoretical probability distribution of (18) has been compared with the one produced by a standard tracking technique.

A simple magnetic system has been considered, made of two thin multipoles, a quadrupole of integrated strength K_1, and a sextupole of integrated strength K_2, whilst
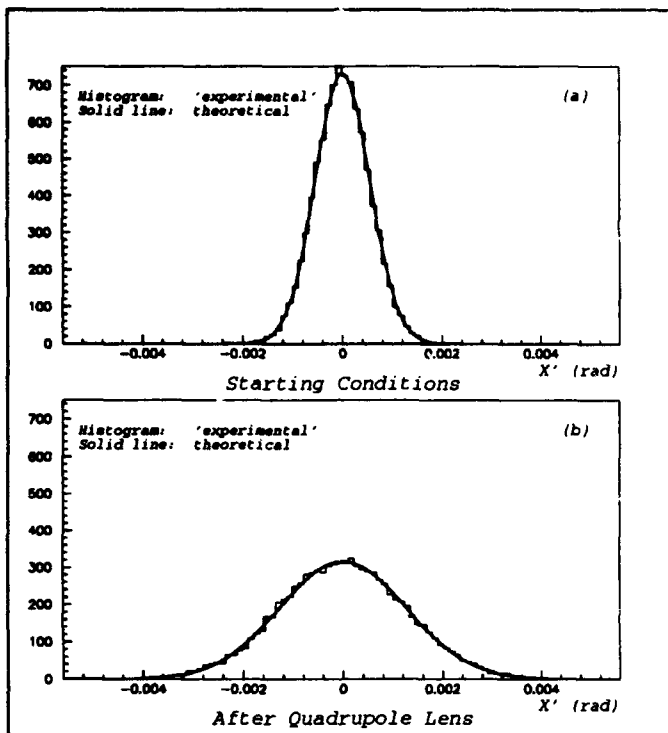
Figure 1: Simulated and Theoretical x' Distributions

Figure 2: Simulated and Theoretical x' Distributions

30000 particles with starting coordinates x and x' randomly distributed on a 2-dimensional Gaussian have been used to simulate the beam. A tracking simulation of these particles through the device has been done by means of a simple 'kick' code: this is generally more than adequate when thin lens approximation can be applied; the coordinates of all particles have been recorded at the exit of each lens. For the sake of simplicity, it has been chosen to perform the test comparing the distributions of the x' coordinate of the phase-space $(x - x')$; comparing the x distribution would have required the addition of a drift space at the end of the apparatus.

In Fig. 1a the starting distributions of x' are displayed: the histogram, properly normalized to take into account the total number of particles and the bin width, represents the 'experimental' data, whilst the continuous curve is the theoretical starting distribution according to (18) with $K_1 = 0$ and $K_2 = 0$, i.e. $\delta = 0$ and $\tau = 0$: the agreement between the two makes us feel confident that the description of the beam by means of its σ_0 and σ_{p_0}, and the two normalizations, are done consistently.

The simulated beam distribution and the theoretical one after passing through the quadrupole, (18) with $\tau = 0$, are shown in Fig. 1b. Also here, a complete agreement is noticeable: the distributions are much wider, but they both keep purely Gaussian with same σ's and heights.

In Fig. 2 the distributions at the exit of the full device are shown for two different strengths of the sextupole: here the histogram, as usual, represents the experimental distribution, and the solid line is its best fit with a Gaussian function times a polynomial of order 6; the distribution predicted by the thermal wave model is, instead, represented by a dashed line in Fig. 2; the agreement between the predictions of the model is quite impressive: indeed only in Fig. 2b, where the sextupole strength becomes very large and the inequality $\sigma_0 k_2/3k_1 \ll 1$, is not strictly sat-

isfied any more, the dashed line is barely visible, whilst in Fig. 2a it overlaps perfectly with the best fit curve and the only sign of its presence is the slight thickening of the line.
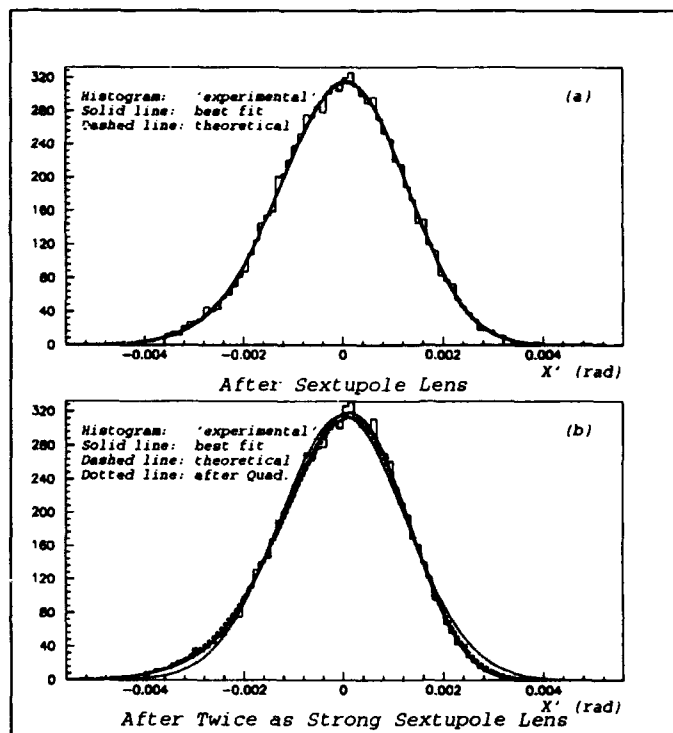
It should be also said that, in order to produce a detectable effect after a single pass, the sextupole strengths used exceed by far the values typical of circular accelerators.

Finally the dotted line in Fig. 2b reminds the probability distribution of the beam at the exit of the quadrupole, before undergoing the non-linear force.

6   Conclusions

This simple, but very significant numerical experiment has proved the capability of the recently proposed *thermal wave model* to describe the charged-particle beam-dynamics quite accurately.

Much remains to be done — like, for instance, the extension to 2- or even to 3-D, or the development of an iterable formulation — to make this model really interesting for the study of the typical, still unsolved, beam-dynamics problems. Nevertheless, its very innovative feature of allowing the treatment of the whole beam at the same time, makes it look extremely promising for a new, and more complete, approach to the subject.

References

[1] R. Fedele and G. Miele, *A Thermal-Wave Model for Relativistic Charged-Particle Beam Propagation*, Nuovo Cimento D **13**, 1527 (1991)

[2] R. Fedele and G. Miele, *Spherical Aberrations in the Thermal Wave Model for Luminosity Estimates in Particle Accelerators*, Phys.Rev. A **46**, 6634 (1992)

[3] R. Fedele and P.K. Shukla, *Self-Consistent Interaction between the Plasma Wake Field and the Driving Relativistic Electron Beam*, Phys.Rev. A **44**, 4045 (1992)

Longitudinal Dynamics for Electrons in the Thermal Wave Model for Charged Particle Beams

R. Fedele[1],   G. Miele[1],   and   L. Palumbo[2]

[1] *Dipartimento di Scienze Fisiche, Università di Napoli "Federico II", and INFN Sezione di Napoli, Italy*

Mostra d'Oltremare Pad.20, I-80125 Napoli, Italy

[2] *Dipartimento di Energetica, Università di Roma "La Sapienza", and INFN-LNF, Italy*

Via A. Scarpa,14, Roma, Italy

Abstract An extension of the longitudinal thermal wave model, including both radiation damping and quantum excitation (stochastic effect) is presented here. We show that, in the presence of the RF potential well, the longitudinal dynamics is governed by a 1-D Schrödinger-like equation for a complex wave function whose squared modulus gives the longitudinal bunch profile. Remarkably, the appropriate emittance scaling is naturally recovered, and the asymptotic equilibrium condition for the bunch length is found. These results open the possibility to apply the thermal wave model, already tested for protons, in a more accurate way to electrons.

1 Introduction

In the study of charged particle beam dynamics for accelerators and plasma physics, a number of nonlinear and effects are relevant [1]. Due to the electromagnetic interactions between the particles and their image charges induced in the surroundings, these nonlinear effects also acquire collective nature [1]. This property is enhanced for very intense beams, which are employed in very high luminosity colliders. In addition, radiation damping and quantum electromagnetic fluctuations (quantum excitations) are generally present in the beam longitudinal dynamics especially for electron bunches.

Recently, a *thermal wave model for charged particle beam dynamics* has been formulated [2] and successfully applied to a number of linear and nonlinear problems in beam physics [3]-[7]. In this approach, the beam transverse (longitudinal) dynamics is formulated in terms of a complex function, the so called beam wave function (bwf), whose squared modulus is proportional to the bunch density. This wave function satisfies a Schrödinger-like equation in which Planck's constant is substituted with the transverse (longitudinal) bunch emittance [2],[7]. In particular, this model is capable of reproducing the main results of the conventional theory about transverse beam optics and dynamics (in linear and nonlinear devices) [2]. Moreover, it represents a new approach to estimate the luminosity in particle accelerators [4], [5], as well as to study the self-consistent beam-plasma interaction [3]. Remarkably, this model, if applied to the longitudinal bunch dynamics, allows us to describe, in a simple way, the synchrotron motion when both self-interaction and the radio frequency (RF) potential well are taken into account. In particular, the right conditions for the coherent instability in circular machines have been recovered [6],[7] and new interesting soliton-like solutions for the beam density have been discovered [6],[7].

In this paper we improve the thermal wave model for longitudinal bunch dynamics given in [6], [7]. By starting from the conventional longitudinal single-particle dynamics in circular accelerators, the problem that we want to solve is formulated in terms of an appropriate wave model which describes the evolution of the beam, when the RF potential well is taken into account together with radiation damping and quantum excitation. We show that the longitudinal beam dynamics is still correctly governed by a Schrödinger-like equation for the bwf. The envelope description is straightforwardly obtained from the wave solution and, correspondingly, the results are compared with those that are given in the conventional theory. In particular, an asymptotic time-limit for the bunch length and the emittance time-scaling law are obtained.

2 Definition of the problem

It is well known that the motion of a single particle within a stationary bunch travelling in a circular accelerating machine with velocity βc ($\beta \approx 1$), with radius $R_0 = cT_0/2\pi$ (T_0 being the revolution period), if both radiation damping and quantum excitation are taken into account. is governed by the following coupling equations:

$$\frac{dx}{ds} = \eta \mathcal{P} \quad, \tag{1}$$

$$\frac{d\mathcal{P}}{ds} = -\frac{q\Delta V}{cT_0 E_0} - \frac{D}{cT_0}\mathcal{P} - \frac{1}{E_0}\frac{dR}{ds} \quad, \tag{2}$$

where $\mathcal{P} \equiv \frac{\Delta E}{E_0}$ is the relative longitudinal energy spread of the particle with respect to the synchronous particle ($\Delta E = 0$), and $U(x,s) \equiv (1/cT_0 E_0)\int_0^x q\Delta V\, dx'$ is the effective potential energy that the particle sees after a turn in the ring (ΔV being the corresponding total voltage variation seen by the particle). x is the longitudinal displacement of the particle in the bunch with respect to the synchronous one and $s \equiv ct$ (t being the time). E_0 and q

212

stands for the synchronous particle energy and charge, respectively. $\eta \equiv \alpha - 1/\gamma^2$ are the phase slip factor, where α and $\gamma = (1 - \beta^2)^{-1/2}$ the momentum compaction and the relativistic gamma factor, respectively. D is the damping coefficient [8] and dR/ds accounts for the quantum excitation effect (noise) (R being the difference between the energy effectively radiated by the particle during a time interval t and the average of this energy). It is easy to see that (1) and (2) are the usual equations for the longitudinal motion [8] under the substitution $s = ct$ and $\mathcal{P} = \Delta E/E_0$. By denoting with $< u^2 >^{1/2}$ the quantum fluctuations associated to the noise, the term dR/ds can be written in the following way:

$$\frac{dR}{ds} = \frac{\Gamma}{c} < u^2 >^{1/2} \quad , \qquad (3)$$

where Γ is the mean rate of photon emission.

By considering a linearised RF-voltage only ($U_{RF} \equiv \frac{1}{cT_0 E_0} \int_0^s \Delta V ds' \approx \frac{1}{2}\frac{K}{\eta}x^2$, where K is the RF cavity strength), it is easy to prove that the Lagrangian associated to (1) and (2) is given by

$$\mathcal{L}(x, x', s) = \left[\frac{1}{2\eta}x'^2 - \frac{1}{2}\frac{K}{\eta}x^2 - \left(\frac{1}{E_0}\frac{dR}{ds}\right)x\right]e^{\gamma s}, \quad (4)$$

where $x' \equiv dx/ds$ and $D/(cT_0)$ is the damping rate. Consequently, the corresponding Hamiltonian is defined as $H(x, p, s) = x'p - \mathcal{L}(x, x', s)$, with $p \equiv \frac{\partial \mathcal{L}}{\partial x'} = \frac{x'}{\eta}e^{\gamma s}$, and it can be put in the following form:

$$H(\tilde{y}, \tilde{p}, s) = \frac{\eta}{2}\tilde{p}^2 + \frac{1}{2}\frac{K}{\eta}\tilde{y}^2 - \frac{1}{2}\frac{K}{\eta}\tilde{x}_0^2(s) \quad . \qquad (5)$$

where $\tilde{x}_0(s) \equiv -\frac{\eta e^{\frac{\gamma}{2}s}}{KE_0}\frac{dR}{ds} \equiv x_0 e^{\frac{\gamma}{2}s}$, $\tilde{p} \equiv p\, e^{-\frac{\gamma}{2}s}$, $\tilde{x} \equiv x\, e^{\frac{\gamma}{2}s}$, and $\tilde{y} = \tilde{x} - \tilde{x}_0$. It is interesting to observe that H, in the variable $\tilde{y}$ and $\tilde{p}$, looks like the Hamiltonian of an undamped harmonic oscillator. In order to write a Schrödinger-like equation for the bwf, which describes the longitudinal dynamics of a short bunch ($\sigma << R_0$) in the presence of both radiation damping and quantum excitation, we have to write the following quantization rules, in complete analogy with our previous works [2]-[7] $\tilde{p} \to \hat{\tilde{p}} \equiv -i\epsilon\frac{\partial}{\partial \tilde{x}}$, and $H \to \hat{H} \equiv i\epsilon\frac{\partial}{\partial s}$. Consequently, (5) gives (for $\eta \neq 0$)

$$i\epsilon\eta\frac{\partial\tilde{\Psi}}{\partial s} = -\frac{\epsilon^2\eta^2}{2}\frac{\partial^2\tilde{\Psi}}{\partial\tilde{y}^2} + \frac{1}{2}K\tilde{y}^2\tilde{\Psi} + \frac{1}{2}K\tilde{x}_0^2\tilde{\Psi} \quad , \qquad (6)$$

where $\tilde{\Psi} = \tilde{\Psi}(\tilde{y}, s)$ satisfies the normalisation condition $\int_{-\infty}^{\infty} |\tilde{\Psi}(\tilde{y}, s)|^2\, d\tilde{y} = 1$.

3 Solutions

In order to solve (6), we introduce the following transformation for the bwf: $\tilde{\Psi}(\tilde{y}, s) = \Psi(\tilde{y})\exp\left[i\frac{K}{\epsilon\eta}\int_0^s \tilde{x}_0^2(s')ds'\right]$. Thus, we easily obtain

$$i\epsilon\frac{\partial\Psi}{\partial s} = -\frac{\epsilon^2\eta^2}{2}\frac{\partial^2\Psi}{\partial\tilde{y}^2} + \frac{1}{2}K\tilde{y}^2\Psi \quad . \qquad (7)$$

Solutions of (7) are well known in terms of Hermite-Gauss modes [7]:

$$\Psi_m(\tilde{y}, s) = \frac{\exp\left[-\frac{\tilde{y}^2}{4\tilde{\sigma}_y^2(s)}\right]}{\left[2\pi 2^{2m}(m!)^2\tilde{\sigma}_y^2(s)\right]^{1/4}} H_m\left(\frac{\tilde{y}}{\sqrt{2}\tilde{\sigma}_y(s)}\right)$$
$$\times \exp\left[i\frac{\tilde{y}^2}{2\epsilon\eta\tilde{\rho}_y(s)} + i(1 + 2m)\tilde{\phi}_y(s)\right] \quad . \quad (8)$$

where the H_m's are the Hermite polynomials ($m = 0, 1, 2, ...$), and the function $\tilde{\sigma}_y(s)$ satisfies the following differential equation:

$$\frac{d^2\tilde{\sigma}_y}{ds^2} + K\tilde{\sigma}_y - \frac{\epsilon^2\eta^2}{4\tilde{\sigma}_y^3} = 0 \quad . \qquad (9)$$

with $\frac{1}{\tilde{\rho}_y} = \frac{1}{\tilde{\sigma}_y}\frac{d\tilde{\sigma}_y}{ds}$, and $\frac{d\tilde{\phi}_y}{ds} = -\frac{\epsilon\eta}{4\tilde{\sigma}_y^2}$.

Note that $\tilde{\sigma}_y(s) = \left[\int_{-\infty}^{\infty} \tilde{y}^2|\Psi(\tilde{y}, s)|^2\, d\tilde{y}\right]^{1/2} \equiv < \tilde{y}^2 >^{1/2}$ (quantum-like expectation value of $\tilde{y}$). Thus, Eq.(9) is the bunch envelope equation. We observe that $\tilde{\sigma}_y^2 =< (\tilde{x} - \tilde{x}_0)^2 >=< (x - x_0)^2 > e^{\gamma s}$. Consequently, we can write both the solution for the b.w.f. in terms of x and s, and the envelope equation for the quantity $\overline{\Delta x} \equiv < (x - x_0)^2 >^{1/2}$ simply from (8) and (9). We easily get:

$$\Psi_m(x, s) = \frac{\exp\left[-\frac{(x-x_0)^2 e^{-\gamma s}}{4\overline{\Delta x}^2(s)} + i\theta(x, s)\right]}{\left[2\pi 2^{2m}(m!)^2\overline{\Delta x}^2(s)\right]^{1/4}} \times$$
$$H_m\left(\frac{(x - x_0)e^{-\frac{\gamma}{2}s}}{\sqrt{2}\,\overline{\Delta x}}\right) \qquad (10)$$

$$\frac{d^2\overline{\Delta x}}{ds^2} + \gamma\frac{d\,\overline{\Delta x}}{ds} + \left(K + \frac{\gamma^2}{4}\right)\overline{\Delta x} - \frac{\epsilon^2\eta^2 e^{-2\gamma s}}{4\,\overline{\Delta x}^3} = 0 \quad , \quad (11)$$

with $\frac{1}{\rho_x} = (1/\overline{\Delta x})\frac{d\,\overline{\Delta x}}{ds}$, $\frac{d\phi_x}{ds} = -\frac{\epsilon\eta}{4\,\overline{\Delta x}^2}$, and $\theta(x, s) \equiv \frac{(x-x_0)^2}{2\epsilon\eta/\left(\frac{\gamma}{2}+\frac{1}{\rho(s)}\right)} + i(1+2m)\int_0^s \frac{d\phi_x}{ds'}e^{-\gamma s'}ds'$. In particular, from the (10) we can obtain the longitudinal bunch profile, for $m = 0$ (fundamental mode), which is a pure Gaussian distribution:

$$|\Psi_0(x, s)|^2 = \frac{\exp\left[-\frac{(x-x_0)^2 e^{-\gamma s}}{2\,\overline{\Delta x}^2(s)}\right]}{\left[2\pi\,\overline{\Delta x}^2(s)\right]^{1/2}} \quad . \qquad (12)$$

We note that, when radiation damping and quantum excitation can be neglected, i.e. $\gamma = 0$ and $x_0 = 0$, respectively, (11) becomes:

$$\frac{d^2\sigma_x}{ds^2} + K\sigma_x - \frac{\epsilon^2\eta^2}{4\sigma_x^3} = 0 \quad , \qquad (13)$$

with $\sigma_x \equiv < x^2 >^{1/2}$ (the bunch length), which recovers the envelope equation associated to the undamped synchrotron oscillations [7].

213

In general, (11) shows that: (a) a friction-like term, which is in competition with the quantum excitation effect, is introduced; (b) a synchrotron frequency shift, due to the damping effect, is introduced as well; (c) the emittance scaling law can be extrapolate, which results to be:

$$\epsilon_x(s) = \epsilon \, e^{-\gamma s} \quad . \tag{14}$$

However, we will go back to discuss on the point (c) in the next Section, where we start from the r.m.s. emittance definition and give straightforwardly the emittance scaling law. We now observe that the asymptotic limit for $\overline{\Delta x}$ can be obtained from (11). In fact, in the limit $s \to \infty$, the equilibrium solution gives $\left(\overline{\Delta x}\right)_{eq} = <(x - x_0)^2>_{eq} = 0$. However, observing that $<(x-x_0)^2> = \sigma_x^2(s) - x_0^2(s)$, we have $(\sigma_x)_{eq} \equiv \sigma_x(s = \infty) = \frac{|\eta|}{|K|E_0}\left(\frac{dR}{ds}\right)_{s=\infty}$. On the other hand, from (3) follows that $\frac{1}{\sqrt{K}E_0}\frac{dR}{ds} = \frac{\Gamma}{\Omega_s}\frac{<u^2>^{1/2}}{E_0} \equiv \sigma_p^N(s)$, where $\Omega_s = c\sqrt{|K|}$ is the synchrotron frequency and σ_p^N stands for the bunch energy spread due to the quantum fluctuations (quantum noise). Consequently, $(\sigma_x)_{eq} = \frac{|\eta|}{\sqrt{|K|}}\left(\sigma_p^N\right)_{eq}$, where $\left(\sigma_p^N\right)_{eq} \equiv \sigma_p^N(s = \infty)_{eq}$. By introducing the synchrotron number $\nu_s \equiv \Omega_s/\omega_0 = (c\sqrt{|K|})/\omega_0$ [1], (10) easily becomes $(\sigma_x)_{eq} = \frac{|\eta|R_0}{\nu_s}\left(\sigma_p^N\right)_{eq}$, where $\omega_0 = 2\pi/T_0 = 2\pi R_0/c$ is the revolution angular frequency.

4 Emittance scaling law

First of all, it is easy to prove that, under the transformation $\tilde{p} \equiv p\, e^{-\frac{\gamma}{2}s}$, and $\tilde{x} \equiv x\, e^{\frac{\gamma}{2}s}$, the quantity $A = <\tilde{x}^2><\tilde{p}^2> - <\tilde{x}\tilde{p}>^2$, is conserved, i.e. $<\tilde{x}^2><\tilde{p}^2> - <\tilde{x}\tilde{p}>^2 = <x^2><p^2> - <xp>^2$, where $<...>$ stands for the quantum-like average value. Thus, by observing that $<\tilde{p}^2> = <p^2> e^{-\gamma s}$, $<\tilde{x}^2> = <x^2> e^{\gamma s}$ and $<\tilde{x}\tilde{p}> = <xp>$, and, using (10) for $m = 0$, we easily obtain $A = \frac{\epsilon^2}{4} = constant$, which shows that the diffraction parameter of our model, i.e. the longitudinal emittance, is one of the Courant-Snyder invariants.

We now show the connection between this invariant and the r.m.s. emittance $\overline{\epsilon}^2_{th}$, defined in the following way, which is similar to the definition given by Lapostolle [1]:

$$\overline{\epsilon}^2_{th}(s) = 4\left[<x^2><x'^2> - <xx'>^2\right] \quad . \tag{15}$$

Substituting $x' = \eta p\, e^{-\gamma s}$, we find:

$$\overline{\epsilon}^2_{th}(s) = 4\left[<x^2><\hat{p}^2> - <x\hat{p}>^2\right]e^{-2\gamma s} \quad , \tag{16}$$

which is the same emittance scaling law predicted by (14):

$$\overline{\epsilon}^2_{th}(s) = \epsilon^2 e^{-2\gamma s} \quad . \tag{17}$$

Eq.(17) shows that ϵ is just the initial ($s = 0$) value of the r.m.s. emittance, namely the value produced by the bunch source at a given temperature.

5 Remarks and conclusions

In this paper we have presented an extension of the recently proposed *thermal wave model for particle dynamics* [2] to the longitudinal motion in circular accelerators when both radiation damping and quantum excitation are taken into account. We have shown that the particle dynamics in the presence of a RF potential well is governed by a 1-D Schrödinger-like equation for a complex wave function, whose squared modulus gives the longitudinal bunch profile. We have proved that the solutions for the bwf of this problem are given in terms of the well known Gauss-Hermite modes. In particular, the fundamental mode (lowest-energy mode) gives a pure Gaussian space-distribution for the particles, and the corresponding envelope equation gives an asymptotic value for the bunch length, which is expressed in terms of the quantum fluctuations (noise). In addition, the emittance scaling law has been recovered. We would like to stress that (15) is similar to the Lapostolle's definition of the r.m.s. emittance [1], but here the averages are defined in a way which is formally identical to the Quantum Mechanics. In conclusion, the above results allow us to apply the thermal wave model, already successfully applied to the undamped longitudinal dynamics (protons) [7], to the synchrotron electron motion in a more accurate way, since in this case both radiation damping and quantum excitation are not negligible.

References

[1] J.Lawson *The physics of charged-particle beams*, Clarendon Press, 2nd edition, Oxford(1988)

[2] R. Fedele and G. Miele, *A Thermal-Wave Model for Relativistic-Charged-Particle Beam Propagation*, Nuovo Cimento, **13D**, 1527 (1991)

[3] R. Fedele and P.K. Shukla, *Self-Consistent Interaction between the Plasma Wake Field and the Driving Relativistic Electron Beam*, Phys.Rev.**A44**, 4045 (1992)

[4] R. Fedele and G. Miele, *Spherical Aberrations in the Thermal Wave Model for Luminosity Estimates in Particle Accelerators*, Phys.Rev.**A46**, 6634 (1992)

[5] R. Fedele, F. Galluccio, and G. Miele *A Numerical Check of the Thermal-Wave Model for Charged Particle-Beam Dynamics*, these proceedings (1993)

[6] R. Fedele, L. Palumbo, and V.G. Vaccaro *A Novel Approach for Nonlinear Longitudinal Dynamics in Particle Accelerators*, Proc. EPAC 92 (Berlin, 24-28 March 1992) H. Henke, H. Homeyer and Ch.Petit-Jean-Genaz Ed.s, Editions Frontieres (1992), p.762

[7] R. Fedele, G. Miele, L. Palumbo, and V.G. Vaccaro *Thermal-Wave Model for Nonlinear Longitudinal Dynamics in Particle Accelerators*, Dipartimento di Scienze Fisiche, Universitá di Napoli, Rep. DSF-T-93/15 (1993), submitted to Phys. Lett. A

[8] J. Haissinski, *Exact Longitudinal Equilibrium Distribution of Stored Electrons in the Presence of Self-Fields*, Il Nuovo Cimento **18 B**, 72 (1973)

Experimental Measurement of Dynamic Aperture
at the Photon Factory Storage Ring

Y. Kobayashi, T. Mitsuhashi, A. Ueda, and T. Yamakawa[1]
Photon Factory, National Laboratory for High Energy Physics,
1-1 Oho, Tsukuba, Ibaraki 305, Japan

Abstract

The transverse dynamic apertures were measured as a function of the octupole strength at the Photon Factory Storage Ring (PF-Ring). A remarkable octupole dependence did not appear in the vertical aperture. On the other hand, the horizontal aperture was clearly dependent on the octupole strength. This result agreed well with a prediction of the computer simulation.

I. Introduction

The nonlinear beam dynamics of the transverse betatron oscillation in circular accelerators has been studied using analytical and numerical methods. In the design of low emittance rings for a high brilliant synchrotron radiation or large colliders with superconducting magnets, the nonlinear dynamics has been important, especially the problem of a dynamic aperture has been serious in such new rings. For the strong sextupole fields used to compensate the large chromaticities or the higher order multipole fields produced by the superconducting magnets, the dynamic apertures tend to be rather smaller than those of the previous rings. Much effort, therefore, has been devoted to develop various correction methods for nonlinear effects and to enlarge the dynamic apertures [1].

The 2.5 GeV PF-Ring, which is a dedicated synchrotron radiation source, has been stably operated for a decade. Recently, we are planning to reform this ring toward much lower emittance ring that can supply a higher brilliant synchrotron radiation [2]. Then, one of the most serious issues in this plan is that the dynamic aperture becomes small due to the strong sextupole fields. From a prediction of the computer simulation using a model of an ideal machine without any errors, the dynamic aperture is still larger than the physical aperture. Since the real machine has various imperfections, however, we need to estimate the quantitative difference of the dynamic aperture between the experimental measurement and the computer simulation.

At the PF-Ring, the dynamic aperture can be reduced by existing octupole magnets employed to suppress the transverse instabilities in usual operation mode. As the first step, therefore, we experimentally measured the dynamic aperture as a function of the octupole strength and compared the result with a prediction of the computer simulation.

II. Experiment

The basic procedure of this experiment was to measure a beam loss after providing beam with a single kick. The kicked beam circulates with a large coherent betatron oscillation, and then the beam will be lost when the amplitude of the coherent oscillation is near the dynamic or the physical aperture. Thus, the aperture will be estimated by the relation between the beam loss and the coherent betatron oscillation amplitude. Here, the distinction between the dynamic and the physical aperture is made according to whether the aperture is dependent on the octupole strength.

A. Ring Condition

The experiment was made under the almost same condition as a usual operation. The single-bunch positron beam was used, and the initial stored current was always set to be about 5 mA to make the collective effects small as possible. In this experiment, betatron tunes were fixed, chromaticities were compensated by sextupole magnets and set to be near zero, and closed orbit distortions were corrected by steering dipole magnets. The insertion devices were set to be maximum gap or turned off to remove the complex effects on beam. The physical apertures of this ring are determined by the ducts of insertion devices in both horizontal and vertical planes. The relevant orbit parameters are listed in Table 1.

Table 1. Relevant orbit parameters of the PF-Ring

Beam Energy	2.5 GeV
Circumference	187 m
Natural Emittance [H/V]	128/2.5 nm·rad
Energy Spread	7.3×10^{-4}
Revolution Period	625 nsec
Betatron Tune [H/V]	8.468/3.325
Corrected Chromaticity [H/V]	0.77/0.23
Transverse Radiation Damping Time	7.8 msec
Beta Function at Fast Kicker [H/V]	15.2/9.0 m
at Scraper [H/V]	16.5/8.0 m
at MPW#13 [H/V]	14.0/12.0 m
at VW#14 [H/V]	8.0/7.0 m
Beam Size at Scraper [H/V]	1.6/0.14 mm
Predicted Physical Aperture (Half width)	
at VW#14 / at Scraper [H]	21.0/ 30.2 mm
at MPW#13/ at Scraper [V]	12.0/9.8 mm

B. Hardware Description

The fast kicker magnet system was installed to provide beam with a large coherent oscillation by only a single kick. This system consists of a horizontal and a vertical kicker magnet, a pulser of the pulse forming network (PFN) type with thyratron switchings and a charging high voltage power supply controlled by trigger and timing circuits. The kicker magnets were designed with the conventional type, which has a window frame ferrite core with a double turn coil. The field strength of the kicker magnets was measured as a function of a charging high voltage using a long search coil. The strength increases linearly with the high voltage. The ceramic duct with Ti coating of 2μm is used for these kicker magnets. The

overall field reduction from the duct was less than 6%. The specification of the fast kicker magnet system is listed in Table 2.

The eight octupole magnets are now used in the usual operation to suppress the transverse beam instabilities. Each magnet can be excited by the independent bipolar power supply within currents of ±3A. The detail about the octupole magnets was described in the previous paper [3].

Table 2. Specification of the fast kicker magnet system

Magnet Core Material	Ferrite
Coil Turn Number	2
Core Gap [H/V]	56/96 mm
Core Length	150 mm
Magnet Inductance [H/V]	2.2/1.1 μH
Maximum Charging Voltage	40 kV
Maximum Repetition Rate	0.5 Hz
Pulse Width [H/V]	425/335 nsec

C. Measurement procedure

First, we adjusted the discharging trigger timing so that we fit the circulating beam to the peak of the pulse in the kicker magnets. The signal of the circulating beam was picked up from one electrode of the button type position monitors (BPM) in the ring. Since a distance between the kicker magnets and the BPM is fixed, the timing adjustment was made by delaying the trigger signal for pulsing the kicker magnet within the revolution period. The best timing was determined by estimating the trigger delay time to give maximum beam loss when the beam was kicked with a constant charging high voltage.

Next, the amplitude of the coherent betatron oscillation produced by a single kick was calibrated using a beam scraper already installed in the ring. Since the coherent oscillation

amplitude increases linearly with a charging high voltage, it is accurate to calibrate the amplitude at two positions of the scraper. Figures 1 show the beam loss rate as a function of the high voltage set value V_k, which is proportional to the charging high voltage. The coherent oscillation amplitude Z is indicated as the following equation,

$$Z = \frac{\Delta Z}{\Delta V_k} \times V_k \qquad (1)$$

where Z represents both horizontal and vertical amplitudes (X and Y). Then, ΔZ is the relative difference between two positions at the scraper, and ΔV_k the relative difference of the high voltage set values corresponding to ΔZ. The ΔV_k is estimated from the figures 1. Therefore, the amplitude of the coherent oscillation at the scraper could be obtained until the maximum V_k through eq. (1). The overall accuracy of the amplitude would be about 10%.

After finishing the timing adjustment and the calibration, the aperture was evaluated as follows. All octupole magnets are excited with a desired current. Then, with increasing the high voltage set value by a proper step, we measured the beam loss after kick and calculated the rate of the beam loss to the initial stored current. Whenever the beam was lost, it was restored for keeping the same condition. This measurement was repeated, and the high voltage was increased until that the beam loss rate reached to 100%. Furthermore, the measurements were made in several octupole excitation currents.

III. Computer Simulation

The simulation was performed using the computer code similar to the program PATRICIA [4] in which the multipole

Figure 1. Calibration of the coherent oscillation amplitude at the scraper. (a) is in horizontal plane and (b) in the vertical plane.
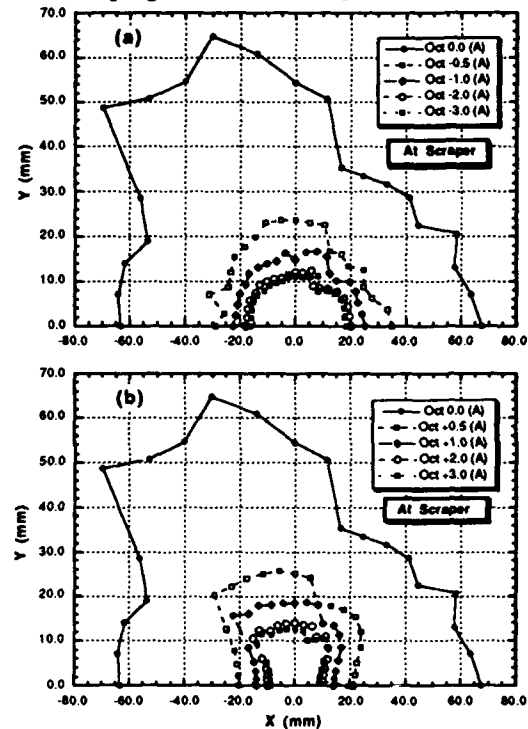
Figure 2. Results of the computer simulation using on-momentum particles. (a) is the result in the negative excitation currents of the octupole magnets and (b) in the positive ones.

field was treated as a kick using thin lens approximation to transform the particle trajectories. The simulation model was an ideal lattice without any errors, but with the same betatron tunes as the usual operation. The dynamic aperture is defined as a maximum initial amplitude to give the circulation of 1000 turns in the particle tracking. Figures 2 show the dynamic aperture surveyed on the two-dimensional x-y plane at the scraper. We see that the dynamic aperture rapidly shrinks with increase of the octupole strength.

IV. Measurement Result and Discussion

A. Horizontal plane

The measurements were made at six different excitation currents of the octupole magnets. Figure 3 shows the beam loss rate as a function of the coherent oscillation amplitude at the scraper. Because the beam has some sizable distribution and circulates more than 10000 turns until that the coherent oscillation damps after kick, the inevitable spread of the amplitudes corresponding to several times beam size from the beginning of the beam loss to 100% exist. For this reason, we defined the aperture as the spread amplitude from 10% to 90% in this experiment. This situation is quite different from the case of the computer simulation using a single particle tracking. Nevertheless, we tried to compare the experimental result with a prediction of the computer simulation. Figure 4 shows the coherent oscillation amplitude with three cases, 10%, 50% and 90% loss, as a function of the octupole excitation currents and includes the tracking result at the scraper in the horizontal plane. It is clearly understood that the aperture is physically determined without the octupole excitation. In fact, the effective physical aperture at the scraper is about 30mm that is calculated from the duct size of VW#14. On the other hand, when the octupole magnets are excited, we see that the aperture is dynamically limited because it is dependent on the octupole strength. Furthermore, the measurement result agrees with the prediction of the computer simulation under the different definition of the dynamic aperture. This is almost consistent with the result at Aladdin [5].

B. Vertical plane

The measurements were made at nine different excitation currents. Figure 5 shows the same as figure 4, but in the
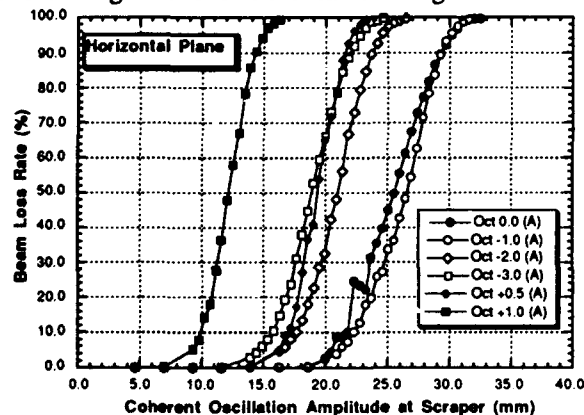
Figure 3. Beam loss rate as a function of the coherent oscillation amplitude at the scraper in the horizontal plane.

vertical plane. A remarkable octupole dependence is not observed. It suggests that the vertical aperture is physically determined in this experimental condition even if the octupole magnets are strongly excited. The effective physical aperture at the scraper becomes about 8.0mm that is estimated from the measurement. However, since it is smaller than the predicted one from the duct size of MPW#13 (about 9.8mm), we are now investigating the vertical physical aperture by another method.
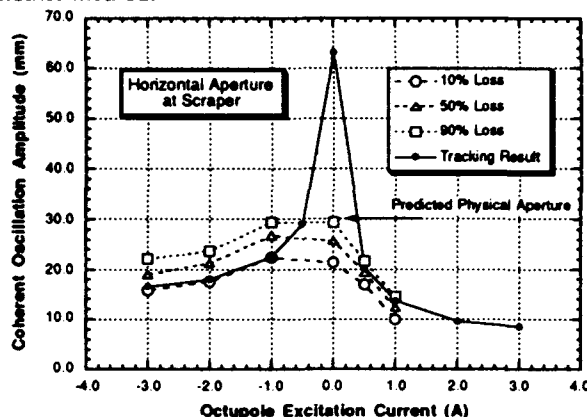
Figure 4. Coherent oscillation amplitude at the scraper as a function of the octupole excitation current in the horizontal plane.
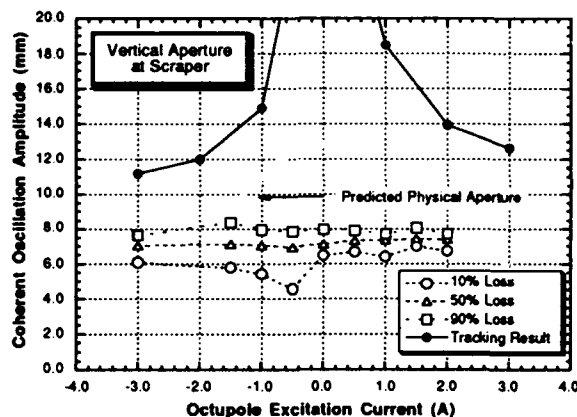
Figure 5. Coherent oscillation amplitude at the scraper as a function of the octupole excitation current in the vertical plane.

V. Acknowledgment

We would like to thank Prof. H. Kobayakawa, the director of the Light Source Division of the Photon Factory, and other staff for their supports. We also thank Prof. Y. Kamiya of ISSP for his suggestion in this experiment.

VI. References

[1] See, for example, "Proceedings of the Second Advanced ICFA Beam Dynamics Workshop", Lugano, CERN 88-04, 1988

[2] M. Katoh and Y. Hori, "Report of the Design Study on a High Brilliance Configuration of the PF Storage Ring", KEK Report 92-20, 1993, in Japanese.

[3] M. Katoh et al., "Dynamic Aperture of the Photon Factory Storage Ring", Particle Accelerators, Vol.28, p.17, 1990

[4] H. Wiedemann, PEP Note-220, 1976

[5] J. Bridges et al., "Dynami   rture Measurement on Aladdin", Particle Acc   Vol.28, p.1, 1990

Lattice and Dynamic Aperture of the
Duke FEL Storage Ring*

Y. Wu, V. N. Litvinenko, J. M. J. Madey
Duke University Free Electron Laser Laboratory
Box 90319, Duke University Durham, NC 27708-0319

Abstract

A low emittance lattice of the Duke FEL (Free Electron Laser) storage ring dedicated to drive UV-VUV FELs is presented. The second order geometrical aberration is compensated to increase the dynamic aperture. The 6-D dynamic aperture study has been performed on this lattice using symplectic tracking codes, which demonstrates a large energy aperture. The influences of higher-order multipoles (HMs), RMS errors and 6.8-m OK-4 undulator on dynamic aperture are studied. The transverse dynamic aperture is mainly limited by HMs in the straight section quadrupoles.

For future FEL operations, we have designed a new straight section lattice for a 26-m long FEL undulator. The dynamic aperture for this lattice is discussed.

I. New Lattice Design

The original design of the FEL storage ring in Stanford [1] had problems with the sextupole saturation from closely placed dipole magnets and asymmetric dipole fields due to parabolic endpieces needed to create sextupole moments. We have eliminated these problems in the new lattice design by removing sextupole magnets and dipole endpieces. To create sextupole moments we have used combined function magnets: asymmetrically excited quadrupoles and dipoles with thin steel shims installed in the center of the magnets [2,3].

The Duke storage ring [4] has a racetrack configuration with two identical arcs and two long straight sections. Each arc is made up of ten FODO cells. The north straight section provides space for injection, RF cavity and 3.64-m NIST undulator; the south straight section is flexible to contain undulators with a maximum length of 26-m. The storage ring layout is shown in Figure 1 and the lattice parameters are given in Table 1.

Table 1. Duke storage ring lattice parameters.

Circumference [m]	107.46
Number of dipoles and quadrupoles	40, 64
Number of FODO cells	20
Length of straight section, and arc [m]	34.21, 19.52
Momentum compaction	0.0086
Operation energy [GeV]	0.25 - 1.0
RF frequency [MHz] (RF voltage 850 kV)	178.547
Energy Acceptance (limited by RF)	$\pm 3.0\%$
Horizontal emittance [mm-mrad]	0.018
Nominal tunes, v_x and v_y	9.1107, 4.1796
Natural chromaticities, C_x and C_y	-10.0, -9.78
Maximum FEL undulator length [m]	26.0

To minimize the second-order geometric aberrations due to strong sextupole moments, we design arc cells with a structure similar to the second-order achromat. The phase advance per cell is chosen as $\Delta\Psi_x = (3/10)\,2\pi$ and $\Delta\Psi_y = (1/10)\,2\pi$. The last two cells are modified to match (η_x, η_x') functions to zero in the straight sections. Finally, we redistribute sextupole moments in the modified cells to cancel horizontal second-order geometric aberrations and minimize the cross-talk aberrations of the two transverse planes [3].

II. Dynamic Aperture of Duke Storage Ring

The tracking codes used for dynamic aperture study are Tracy [5] and Despot [6], which employ fourth-order symplectic integrators for magnets. To study the influence of undulators, a second-order symplectic integrator is added to both codes.
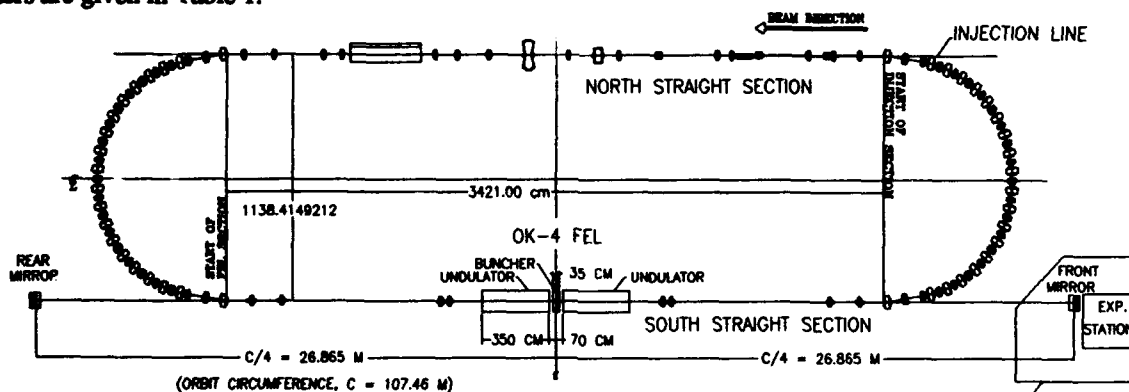
Figure 1. Layout of Duke FEL storage ring with OK-4 optical klystron.

A. Influence of higher-order multipoles (HMs) and RMS errors

HM strengths are extracted from magnetic measurement data [2,3]. The strong HMs in straight section quadrupoles ($K_5/K_1 = -1.576 \times 10^4 \, \text{m}^{-4}$ and $K_9/K_1 = -2.62 \times 10^{10} \, \text{m}^{-8}$) caused by imperfect design are used in the tracking codes. Much weaker HM moments in arc quadrupoles are neglected.

Reasonable RMS errors are assumed in our simulations: $dB/B = 0.0005$ in dipoles, $dK_1/K_1 = 0.001$ in quadrupoles and $dK_2/K_2 = 0.01$ in sextupole strengths; transverse position errors $dX = dY = 0.1 \, \text{mm}$ and longitudinal rotation errors $dT = 0.5 \, \text{mrad}$ in all magnets. All beam position monitors (BPMs) have RMS displacement errors of 0.2 mm. The closed orbit is corrected by 51 horizontal and 31 vertical correctors. A statistical study has been done using eight different seeds to generate RMS errors [3].

In Figure 2, we have shown that the transverse aperture is mainly limited by the HMs in straight section quadrupoles. RMS errors do not significantly reduce the aperture.
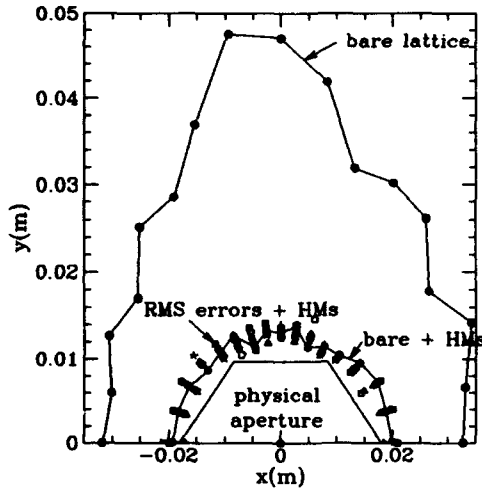
Figure 2. Comparison of Transverse dynamic apertures for two kinds of lattices: (1) Lattice with RMS errors and HMs; (2) Lattice with only HMs. In these calculations, radiation is turned on, particles are tracked for 1000 turns and apertures are plotted after the septum magnet. (The same as in Figure 3.)

B. Energy aperture of lattice

High efficiency FELs and long Touchek life time require a large energy aperture. By performing a tracking study on the bare lattice (containing only dipole, quadrupole and sextupole components), we find that the energy aperture is ±3.0%, only limited by RF voltage of 850 kV (at this voltage, the RF system has an energy acceptance ±3.1%). Using an advanced RF system with peak voltage of 3.4 MV, ±5.0% energy aperture is achievable according to the tracking study [3].

The energy dependence of transverse aperture is plotted in Figure 3 for a realistic lattice with HMs and RMS errors described in section II.A. At the largest energy deviations ±3.0%, the transverse apertures are comparable to the physical aperture.

C. Influence of a FEL undulator

The first FEL to be operated in the Duke storage ring is OK-4 optical klystron [7]. OK-4 is provided by our collaborators from the Budker Institute for Nuclear Physics at Novosibirsk in Russia [4]. We summarize the OK-4 parameters in Table 2.
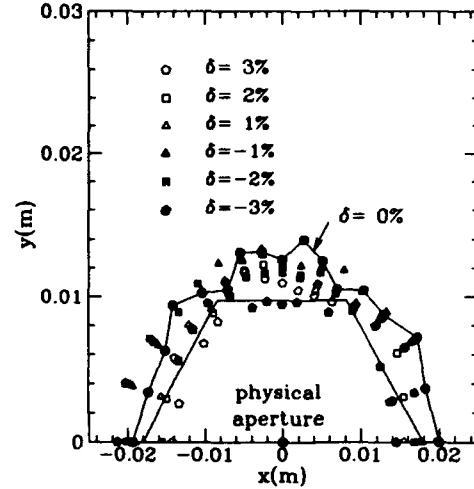
Figure 3. Dynamic apertures for electrons with seven different energies in a realistic lattice (RMS + HMs).

Table 2. OK-4 undulator parameters.

Number of undulators	2
Length of each undulator [m]	3.4
Number of periods	33.5
Undulator period and gap [cm]	10.0, 2.2
Max. magnetic field along the axis [kGs]	5.3

The magnetic filed in this planar undulator is described by the vector potential $\vec{A} = A_x \hat{x} = (B_w / k_w) \cosh(k_w y) \sin(k_w z) \hat{x}$, where $k_w = 2\pi / \lambda_w$, λ_w is the undulator period and B_w is the peak magnetic field. The normalized Hamiltonian of an undulator is

$$K(x, y, \delta; \overline{p_x}, \overline{p_y}, l; z) = -\sqrt{(1+\delta)^2 - (\overline{p_x} - eA_x / cp_0)^2 - \overline{p_y}^2},$$

where l is the path length, p_0 is the design momentum and p is the momentum of the electron $p = p_0(1+\delta)$; $\overline{p_x}$ and $\overline{p_y}$ are normalized canonical momenta $\overline{p_{x,y}} = (p_{x,y} / p_0)$.

Averaging the Hamiltonian for one period, and expanding to the order of $\overline{p_{x,y}}^2$, we obtain

$$\langle K(x, y, \delta; \overline{p_x}, \overline{p_y}, l; z) \rangle = \left\{ -\delta + \frac{\overline{p_x}^2 + \overline{p_y}^2}{2(1+\delta)} \right\} + \frac{(\cosh(k_w y))^2}{4(1+\delta)} \left(\frac{B_w e}{cp_0 k_w} \right)^2.$$

This average Hamiltonian is implemented in Tracy and Despot using a second-order symplectic integrator.

In Figure 4, we compare the dynamic apertures for three lattices: a lattice with OK-4 undulators; a lattice with HMs and a lattice with both OK-4 and HMs. Clearly, while the dynamic aperture remains much larger than the physical aperture after the installation of OK-4, HMs reduce the aperture dramatically. Introducing OK-4 to the lattice with HMs does not further reduce the aperture. By analyzing the tracking data, we find that particle losses are caused by strong

high order resonances introduced by HMs. To increase the aperture, we propose to install steel shims in straight section quadrupoles at locations of large β functions to reduce HM strengths. The improved dynamic apertures with HM strengths 0.5 and 0.1 times of the uncompensated values are also shown in Figure 4.
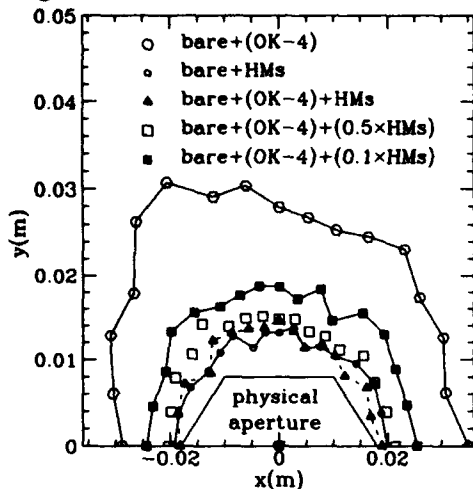
Figure 4. Influence of OK-4 on the dynamic aperture. The HMs are the main limitation of the dynamic aperture. The aperture can be enlarged by reducing the HM strengths. (The plot is made after the septum magnet, particles are tracked for 1000 turns without radiation. The same as in Figure 6).

III. Lattice Design for 26-m FEL Undulator

In order to reach shorter wavelengths (VUV and X-ray) and increase the FEL gain, we design a lattice to accommodate a 26-m FEL undulator with 10 cm period and 5.5 kGs peak magnetic field.
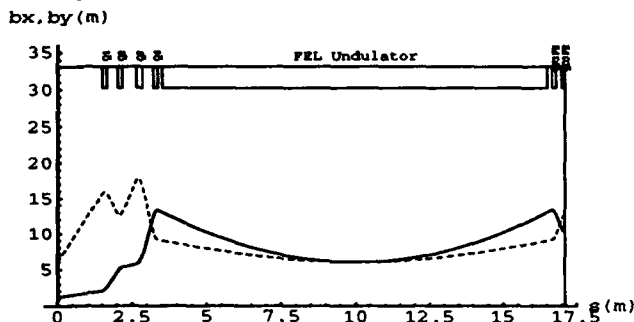
Figure 5. Beta functions in the south straight section with 26-m FEL undulator. The solid line is β_x; the dashed line is β_y.

In this design, we provide two 13-m spaces for undulators in a bilaterally symmetric structure in the south straight section. We use a triplet at the center of the section to match $\beta_x = \beta_y = 6$ m and $\alpha_x = \alpha_y = 0$ in the middle of each undulator. Four quadrupoles are then used to match twiss parameters from the end of arc to the center of undulator. We plot the β-functions in Figure 5 for the first half of this straight section. Finally, the north straight section is used to fit the tunes to nominal values ($v_x = 9.1107, v_y = 4.1796$).

The dynamic aperture of this lattice has been computed and plotted in Figure 6. Similar to the lattice with

OK-4, a large reduction of the dynamic aperture is caused by HMs.
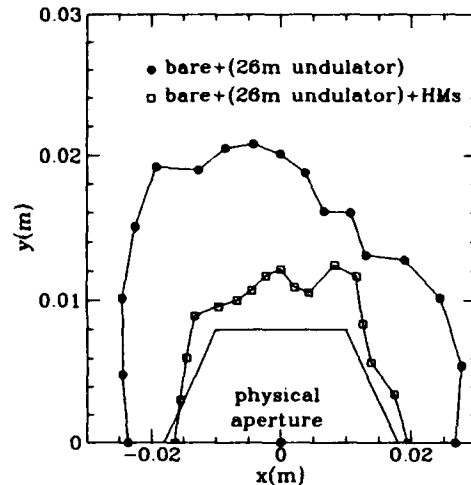
Figure 6. Dynamic aperture of the Duke storage ring with a 26-m undulator.

IV. Conclusion

In this study we find that the major limitation of dynamic aperture for the Duke FEL storage ring is higher-order multipoles in straight section quadrupoles due to an imperfect design of the magnets. The undulators (the 6.8-m OK-4 undulator or the 26-m long undulator) play a less important role in reducing the aperture. The overall dynamic aperture of a realistic lattice for the Duke storage ring is larger than the physical aperture.

V. Acknowledgments

VI. REFERENCES

[1] L. Emergy et al., "1.2 GeV High Brightness Photon Source at the Stanford Photon Research Laboratory", IEEE CH 2387-9, 1496 (1987).

[2] B. Burham et al., "Specific Features of Magnet Design for the Duke FEL Storage Ring", these proceedings.

[3] Y. Wu et al., "Dynamic Aperture Study for the Duke FEL Storage Ring", (14th Int. Free Electron Laser Conf., Kobe, Japan, 1992) Nucl. Instr. Meth.

[4] V. N. Litvinenko et al., "UV-VUV FEL Program at Duke Storage Ring with OK-4 Optical Klystron", these proceedings.

[5] TRACY, J. Bengtsson and H. Nishimura, Lawrence Berkeley Lab, private communication.

[6] DESPOT, E. Forest, Lawrence Berkeley Lab, private communication.

[7] I. B. Drobyazko et al., "Lasing in Visible and Ultraviolet Regions in an Optical Klystron Installed on the VEPP-3 Storage Ring", Nucl. Ins. and Meth. in Phys. Res. A282 (1989) 424-430.

SYNCHROBETATRON COUPLING EFFECTS IN ALTERNATING PHASE FOCUSING*

Wen-Hao Cheng, Robert L. Glucksrern and Hiromi Okamoto
Department of Physics, University of Maryland
College Park, MD 20742-4111

Abstract

In the alternating phase focusing linac with a symmetric synchronous phase sequence, the lowest order resonance ($\sigma_l - 2\sigma_t = 0$) due to the synchrobetatron coupling occurs naturally, causing significant emittance transfer between the longitudinal and transverse motions. A model for the coupled motion including the amplitude dependent tune shift is proposed. Two approximate invariants are derived. Results from computer simulations of a bunched beam yield good agreement with the formula for the invariant derived from the theory. We provide, moreover, a way to move the parameters away from the lowest order resonance, and thus lower the emittance exchange due to the resonance.

I. Introduction

It is well known that longitudinal stability can be obtained in a non-relativistic drift tube accelerator by traversing each gap as the rf accelerating field rises. However, the rising accelerating field leads to a transverse defocusing force which is usually overcome by the use of magnetic focusing elements inside the drift tubes. Alternating the sign of the synchronous phase is a way to provide both longitudinal and transverse focusing without the use of focusing magnets. Exploration of this idea [1] shows that the stable longitudinal phase space area which is related to the current carrying capacity is smaller than for the Alvarez type DTL. In an earlier paper [2], we tested the current carrying capacity of an APF linac by adapting the simulation code PARMILA, which includes space charge, to the APF structure. We found, however, that significant emittance growth arose even in a low intensity beam for which phase space matching was approximately achieved. In the present paper, we show that the emittance growth for a matched beam without space charge is a response to the lowest order resonance ($\sigma_l = 2\sigma_t$) which naturally occurs in symmetric APF [3].

In the following study, we assume a synchronous phase configuration of the periodic length $N\beta\lambda$ where the synchronous phase pattern is

$$\phi_{s(i)} = -\phi_0 - \phi_1, \quad i = 1, 2, \cdots, N/2,$$

$$\phi_{s(i)} = -\phi_0 + \phi_1, \quad i = N/2+1, \cdots, N.$$

Here, both ϕ_0 and ϕ_1 are positive, with ϕ_0 representing a small asymmetric offset to accompany the large alternating ϕ_1. The desired synchronous phase configuration can be obtained by choosing drift tube lengths which alternate appropriately. In previous work [2], where no synchrobetatron coupling was considered, we concluded that, to achieve simultaneous beam matching in both directions while still keeping the phase acceptance and transverse beam size constant, we must separately keep ϕ_0, $K\cos\phi_1$, $KN\sin\phi_1$ continuous across any transition, where K is a dimensionless parameter defined by

$K \equiv 2\pi ZeE_0T\lambda/Amc^2\beta\gamma^3$. We then have to increase the average accelerating field E_0T as $\beta\gamma^3$ to keep K as well as ϕ_0, ϕ_1 and N constant. Another possibility is to modulate the synchronous phase ϕ_1 continuously such that the effective N increases continuously as $\beta\gamma^3$, keeping ϕ_0 and E_0T constant. Here we study the first scheme only.

II. Analysis and Simulation

We assume that the change of $\beta\gamma$ is small over a focusing period and adopt the E_0T-ramping scheme which makes K constant. For an APF structure, the equations for the transverse and longitudinal motions can be derived by a Fourier expansion of the step functions [1]. Let us consider the smoothed version of the equations of motion containing the coupling terms $O(x^2)$ and $O(x\psi)$, and the terms $O(\psi^2)$ and $O(\psi^3)$ which yield the longitudinal amplitude dependent tune shift:

$$x'' + \sigma_t^2 x = -\sigma_a^2 x\psi, \tag{1.1}$$

$$\psi'' + \sigma_l^2\psi = \sigma_b^2\psi^2 + \sigma_d^2\psi^3 - \frac{k_w^2}{2}\sigma_c^2 x^2, \tag{1.2}$$

where $\psi = \phi - \phi_s$, $k_w = 2\pi/\beta\gamma\lambda$, $\tau = s/N\lambda\beta$, $' = d/d\tau$. Here

$$\sigma_t^2 = B_s + \frac{1}{8\pi^2}\sum_{n=1}^{\infty}\left[\frac{C_{s(n)}}{n}\right]^2, \tag{2.1}$$

$$\sigma_l^2 = -2B_s + \frac{1}{2\pi^2}\sum_{n=1}^{\infty}\left[\frac{C_{s(n)}}{n}\right]^2, \tag{2.2}$$

$$\sigma_a^2 = B_c\left\{1 - \frac{1}{16\pi^4}\sum_{n=1}^{\infty}\left[\frac{C_{s(n)}}{n^2}\right]^2\right\} - \frac{1}{8\pi^2}\sum_{n=1}^{\infty}\frac{C_{s(n)}C_{c(n)}}{n^2}, \tag{2.3}$$

$$\sigma_b^2 = B_c\left\{1 + \frac{1}{8\pi^4}\sum_{n=1}^{\infty}\left[\frac{C_{s(n)}}{n^2}\right]^2\right\} - \frac{1}{2\pi^2}\sum_{n=1}^{\infty}\frac{C_{s(n)}C_{c(n)}}{n^2}, \tag{2.4}$$

$$\sigma_c^2 = B_c\left\{1 + \frac{1}{32\pi^4}\sum_{n=1}^{\infty}\left[\frac{C_{s(n)}}{n^2}\right]^2\right\} + \frac{1}{4\pi^2}\sum_{n=1}^{\infty}\frac{C_{s(n)}C_{c(n)}}{n^2}, \tag{2.5}$$

$$\sigma_d^2 = -\frac{B_s}{3} + \frac{1}{4\pi^2}\sum_{n=1}^{\infty}\left[\frac{C_{s(n)}}{n}\right]^2$$

$$- \frac{1}{8\pi^4}\sum_{n=1}^{\infty}\left[\frac{C_{s(n)}}{n^2}\right]^2 - \frac{1}{64\pi^6}\sum_{n=1}^{\infty}\left[\frac{C_{s(n)}}{n^3}\right]^2. \tag{2.6}$$

The dimensionless parameters in Eqs. (2) are

$$B_s = \frac{KN}{2}\sum_{i=1}^{N}\sin\phi_{s(i)},$$

$$B_c = \frac{KN}{2}\sum_{i=1}^{N}\cos\phi_{s(i)},$$

$$C_{s(n)} = KN\sqrt{\left[\sum_{i=1}^{N}\cos 2n\pi\tau_i\sin\phi_{s(i)}\right]^2 + \left[\sum_{i=1}^{N}\sin 2n\pi\tau_i\sin\phi_{s(i)}\right]^2},$$

221

$$C_{\alpha(\omega)} = KN\sqrt{\left[\sum_{i=1}^{N}\cos 2n\pi\tau_i \cos\phi_{\alpha(i)}\right]^2 + \left[\sum_{i=1}^{N}\sin 2n\pi\tau_i \cos\phi_{\alpha(i)}\right]^2},$$

where the τ_i coordinate is

$$\tau_1 = 0, \quad \tau_i(i \neq 1) = \sum_{j=1}^{i-1}(2\pi + \phi_{s(j+1)} - \phi_{s(j)})/2\pi N.$$

The nonlinear coupling between x and ψ motions can easily be seen here. The second order solutions for Eqs. (1) include the resonance terms, containing the factor $\Delta_- = 2\sigma_t - \sigma_\ell$ in the denominator. When $\phi_0 = 0$, we have $B_s = 0$ and thus $\Delta_- = 0$, because of Eqs. (2.1) and (2.2). Thus the resonance due to the synchrobetatron coupling, which will cause rapid emittance exchange, is expected to occur when a symmetric phase sequence is chosen. Other higher order resonances can also exist when taking the higher order coupling terms into account. However, the (2,1) difference resonance described above is the lowest order and the most severe one, as long as there is no troublesome sum resonance.

Upon treating the coupling and nonlinear oscillation terms on the right hand sides of Eqs. (1) as the forcing terms that drive the linear oscillations close to resonance, we may try the solutions of Eqs. (1) similar to the solutions of the linear system, but with slowly varying amplitudes and phases. Specifically, we write

$$x(\tau) = X(\tau)\cos(\sigma_t\tau + \alpha(\tau)),\qquad (3.1)$$

$$\psi(\tau) = \Phi(\tau)\cos(\sigma_\ell\tau + \beta(\tau)),\qquad (3.2)$$

with the conditions:

$$x'(\tau) = -\sigma_t X(\tau)\sin(\sigma_t\tau + \alpha(\tau)),\qquad (4.1)$$

$$\psi'(\tau) = -\sigma_\ell\Phi(\tau)\sin(\sigma_\ell\tau + \beta(\tau)).\qquad (4.2)$$

The first order derivatives of $X(\tau)$, $\Phi(\tau)$, $\alpha(\tau)$ and $\beta(\tau)$ can be obtained by substituting Eqs. (3) into Eqs. (1) under the assumptions of Eqs. (4), and can be approximated by taking their averages over one cycle of rapid variation, according to the KBM (Krylov-Bogoliubov-Mitropolsky) method. The high frequency modes are averaged out and only the low frequency Δ_- part near resonance is kept. Implementation of the KBM averaging transforms the two second order equations into four first order equations, and two integrals of motion can then be derived. We relate the averaged maximum amplitudes $X(\tau)$ and $\Phi(\tau)$ to the normalized emittances for particle beams with uniform distributions in both the longitudinal and transverse directions: $X^2(\tau) = \varepsilon_x N\lambda/\sigma_t$ and $\Phi^2(\tau) = \varepsilon_z k_w^2 N\lambda/\sigma_\ell$, where ε_x is the normalized transverse effective emittance in x-p_x phase space, and ε_z is the normalized longitudinal effective emittance in z-p_z phase space. Here we define the effective emittance as four times of the rms emittance for the upright ellipse and treat $\gamma \approx 1$ as the non-relativistic approximation. The two adiabatic invariants E_1 and E_2 thereby are

$$E_1 = \sigma_t X^2(\tau)/\sigma_a^2 + 2\sigma_\ell\Phi^2(\tau)/k_w^2\sigma_c^2$$

$$= N\lambda(\varepsilon_x/\sigma_a^2 + 2\varepsilon_z/\sigma_c^2),\qquad (5.1)$$

$$E_2 = \Delta_- J + \eta_2 J^2/2 - \eta_1(1-J)\sqrt{J}\cos\Psi,\qquad (5.2)$$

where

$$J(\tau) = 2\sigma_\ell\Phi^2(\tau)/\sigma_c^2 k_w^2 E_1 = 2N\lambda\varepsilon_z/\sigma_c^2 E_1,\qquad (6.1)$$

$$\Psi(\tau) = \Delta_-\tau + 2\alpha(\tau) + \beta(\tau),\qquad (6.2)$$

$$\eta_1 = (k_w\sigma_a^2/2\sigma_t)\sqrt{\sigma_c^2 E_1/2\sigma_\ell},$$

$$\eta_2 = \left(\frac{\sigma_c^2 k_w^2 E_1}{2\sigma_\ell}\right)\left(\frac{3\sigma_d^2}{8\sigma_\ell} + \frac{5\sigma_b^4}{12\sigma_\ell^3}\right),$$

where the term in σ_b^4 has been carried to 2nd order for consistency in obtaining the J dependence of the tune shift. Note that the second invariant E_2 can be determined from the initial conditions of the variables J and Ψ at the injection point of a linac, and is derived with the assumption of constant β to treat the parameters η_1 and η_2 as constant. The simulation results in Fig. 1 show the transfer of normalized rms emittance between the longitudinal and transverse motions and also confirm the validity of Eq. (5.1). The saturation of emittance exchange, i.e., de-coupling of the coupled oscillation, is due to the effect of acceleration which reduces the coupling strength. A plot of $\cos\Psi$ as a function of J gives a qualitative description of the behavior of the system. Fig. 2 shows an example of the configuration diagram for Eq.(5.2). The stable zone of the diagram shown is within the region $-1 \leq \cos\Psi \leq 1$ and $0 \leq J \leq 1$. The coupled oscillations are bounded due to the fact that the first invariant is the sum of square of amplitudes, which is, per se, the property of a difference resonance. In Fig. 2, all initial coupling phase angles $\Psi(0)$ are employed equally from 0 to 2π when considering the particle beam with a uniform distribution of amplitudes X and Ψ in the trace space. The rise or fall of an emittance oscillation at the beginning depends upon the initial amplitude J(0).
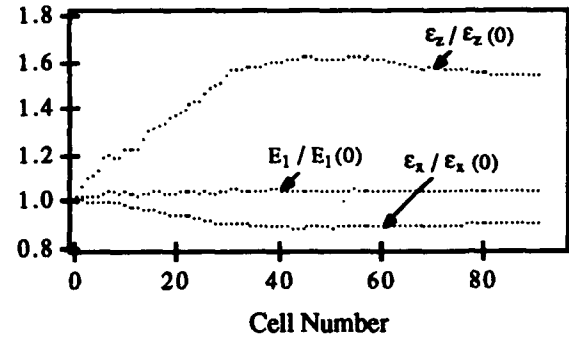
Fig. 1 Simulation results for the emittance transfer between longitudinal and transverse motion, and the first invariant from Eq. (5.1). The parameters are K=0.556, N=4, $\phi_1 = 70$, $\phi_0 = 0$. The injection emittances are: $\varepsilon_X = 0.5242$ cm-mrad, $\varepsilon_z = 0.0758$ cm-mrad.
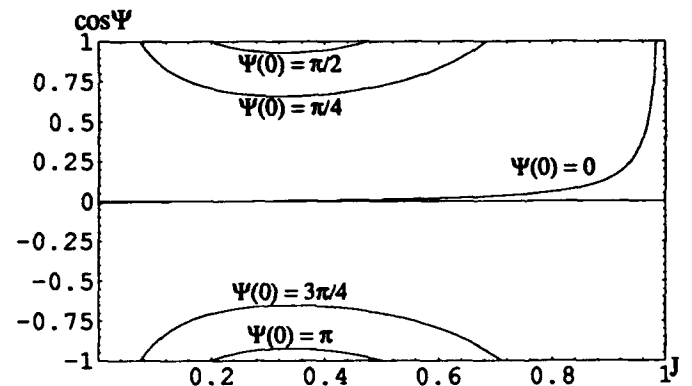
Fig. 2 Configuration diagram for $\cos\Psi$ vs. J.
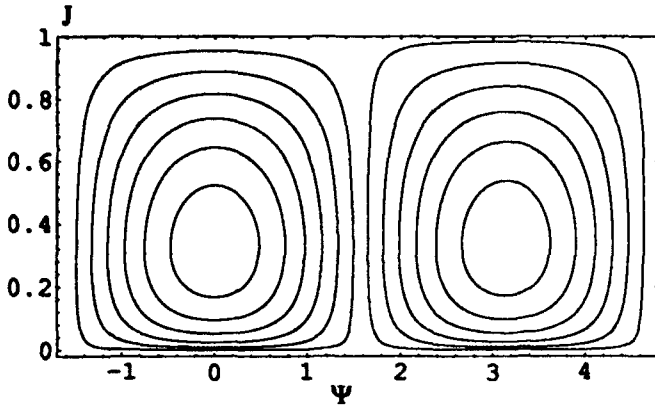
Fig. 3 Poincare mapping of J-Ψ space, when $\phi_0 = 0$.

Cell Number
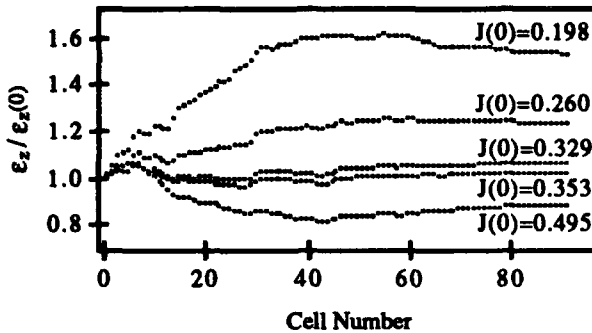
Fig. 4 Simulation results for the longitudinal emittance growth with different initial scaled emittance J(0), where the system is on resonance.

The existence of the first invariant enables us to easily reduce the four differential equations to two with the help of the function J:

$$J'(\tau) = -\eta_1(1 - J(\tau))\sqrt{J(\tau)} \sin \Psi(\tau), \qquad (7.1)$$

$$\Psi'(\tau) = \Delta_- + \eta_2 J(\tau) + \eta_1\left(\frac{3J(\tau)-1}{2\sqrt{J(\tau)}}\right)\cos \Psi(\tau). \qquad (7.2)$$

It is worthwhile to note that the result of the second invariant can also be obtained by the Hamiltonian equations of motion, with $J(\tau)$ and $\Psi(\tau)$ treated as a pair of conjugate canonical variables. The Hamiltonian $H(\Psi,J)$ is then just identical to the second invariant E_2.

The phase space of the Hamiltonian flow for system (5.2) at resonance, i.e. when $\Delta_- = 0$, is plotted in Fig. 3. The two fixed points on the resonance manifold can be found via the conditions: $J' = 0$ and $\Psi' = 0$. Numerically, the term involving the amplitude dependent tune-shift η_2 contributes only as a small modification of the value of J at the fixed point. The fixed points of the system at resonance are then approximately equal to $J \approx 1/3$, $\Psi = 0$ and π. According to Eqs. (5) and (6), when $J = 1/3$, the ratio of longitudinal and transverse emittances have a following relationship:

$$\varepsilon_x/\varepsilon_z = (\sigma_c/\sigma_a)^2/4 \approx 1/4.$$

Therefore, if we inject a beam with the emittance ratio $\varepsilon_x/\varepsilon_z$ near 1/4, such that the initial J is near 1/3, which is close to the fixed point of the resonance Hamiltonian when $\phi_0 = 0$, the variation of J on average will then increase only a small

amount, due to the asymmetric shape of phase space [cf. Fig. 3], until it reaches equilibrium [cf. Fig. 4]. For the particles with initial J smaller (larger) than 1/3, the average variation of J for particles with different phases will then tend to grow (decrease). Simulations of the bunched beam for different scaled emittance ratio shown in Fig. 4 confirm this prediction. The domain of resonance can be found from the stationary solution of Eqs. (7.2) when $\Psi' = 0$, $\Psi=0$ or π and the η_2 term is neglected: $|\Delta_- (\text{band})| \leq |\eta_1(3J - 1)/2\sqrt{J}|$. Therefore, when the initial J is not near 1/3, the design of an APF linac requires as large a non-zero phase offset as possible such that the detuning Δ_- is away from the resonance band, reducing the emittance exchange to as low a level as possible. Results of simulations for $J(\tau)/J(0)$ with different ϕ_0 are shown in Fig. 5.

Cell Number
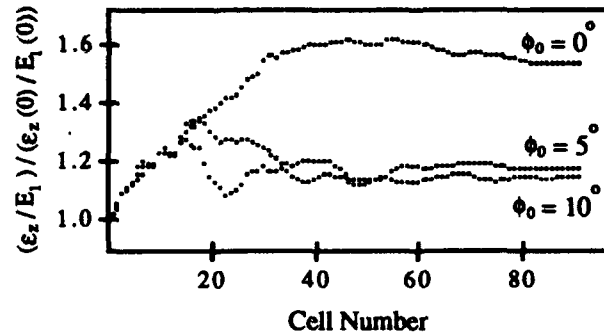
Fig. 5 Simulation results for the longitudinal emittance growth with different phase offsets.

We note that the constant-β ansatz is not physically realistic, since the acceleration rate is usually higher than the emittance exchange rate. When considering the acceleration, where the parameters η_1 and η_2 are τ dependent, the second invariant E_2 in Eq. (5.2) can no longer be achieved by integration of Eqs. (7.1) and (7.2). However, Figs. 2 and 3 can still give a qualitative description of the dynamics of synchrobetatron coupling.

III. Summary

The equations of coupled motion for an APF linac are truncated, smoothed and averaged. We have shown that in both the simulations and the analysis, the emittance exchange between the longitudinal and transverse motions due to the coupling resonance can be decreased by either choosing an emittances ratio such that the system is close to the fixed points of the resonance manifold; or by introducing a non-zero phase offset in the synchronous phase sequence of the APF linac.

References

[1] H. Okamoto, " Beam Dynamics of Alternating Phase Focused Linacs ", Nucl. Instr. Meth., A284, 23, 1989.

[2] Wen-Hao Cheng, Robert L. Gluckstern, Subrata Nath and Thomas P.Wangler, " Alternating Phase Focusing Including space charge ", Proceedings of the Linac Conference , Ottawa, Ontario, Canada, p.193, August 1992.

[3] H. Okamoto, " Coupled Motion in Alternating Phase Focused Linacs ", Bulletin of the Institute for Chemical Research, Kyoto University, Vol. 69, No.1, 1991.

Experimental Determination of a Betatron Difference Resonance *

M. Ellison[a], M. Ball[a], B. Brabson[a], J. Budnick[a], D.D. Caussyn[a], A. W. Chao[b], J. Collins[a],
V. Derenchuk[a], S. Dutt[b], G. East[a], T. Ellison[a], D. Friesel[a], B. Hamilton[a], H. Huang[a],
W.P. Jones[a], S.Y. Lee[a], D. Li[a], M. Minty[c], S. Nagaitsev[a], K. Y. Ng[d], X. Pei[f],
T. Sloan[a], M. Syphers[b], L. Teng[e], Y. Wang[a], Y. T. Yan[b], P.L. Zhang[b]

Abstract

The betatron difference resonance, $Q_s - 2Q_x = -6$, where $Q_{s,x}$ are the number of betatron oscillations per turn, was studied at the Indiana University Cyclotron Facility (IUCF) cooler ring. The position of the beam was measured in both the horizontal and vertical planes of oscillation after a pulsed kicker magnet was fired to produce coherent motion. The effect of the coupling resonance was clearly observed and it was found that the subsequent particle motion could be described by a simple Hamiltonian. The resonance strength and tune shift as a function of betatron amplitude were measured.

I Introduction

For particle motion in a circular accelerator, the betatron positions $x(s)$ and $z(s)$, around the closed orbit, in the presence of magnetic field errors $\Delta B_{s,x}$ are given by Hill's equation [1]:

$$\frac{d^2x}{ds^2} + K_s(s)x = \frac{\Delta B_x}{B\rho}; \quad \frac{d^2z}{ds^2} + K_x(s)z = -\frac{\Delta B_s}{B\rho}, \quad (1)$$

with $\quad \Delta B_x + i\Delta B_s = B_o \sum_{n \geq 2}(b_n + ia_n)(x + iz)^n,$

where b_n and a_n are the normal and the skew multipole components, respectively. The $K_{s,x}(s)$ are functions of the quadrupole strength, $B\rho = pc/e$ is the magnetic rigidity, and s is the longitudinal particle coordinate which advances from 0 to C, the circumference, as the particle completes one revolution. Both $K_{s,x}(s)$ and the field error term $\Delta B_{s,x}/B\rho$ are periodic functions of s with period C. The field error term $\Delta B_{s,x}/B\rho$, which arises from higher-order multipoles, is normally small. However when the resonance condition, $mQ_s + nQ_x = l$, with m, n, l integers, is approached, particles will encounter coherent kicks from the multipoles. This coherent perturbation can have a profound effect on particle motion.

Based on the theory of betatron motion, the betatron amplitude of particle motion is given by, $x, z = \sqrt{2\beta_{s,x}J_{s,x}}\cos(\phi_{s,x})$, where $J_{s,x} = (x^2, z^2 + p_{s,x}^2)/2\beta_{s,x}$

are the actions, β is the beta function and ϕ is the betatron phase advance. Assuming a single resonance, the Hamiltonian can be written as [2],

$$H \approx H_o(J_s, J_x) + gJ_s^{\frac{|m|}{2}} J_x^{\frac{|n|}{2}} \cos(m\phi_s + n\phi_x - l\theta + \chi) \cdot (2)$$

where g and χ are determined by the nonlinear multipoles which drive the resonance,

$$H_o = Q_{so}J_s + Q_{xo}J_x + \frac{\alpha_{ss}}{2}J_s^2 + \alpha_{sx}J_sJ_x + \frac{\alpha_{xx}}{2}J_x^2$$

θ is the azimuthal angle, and $\alpha_{ij} = \partial Q_i/\partial J_j$. This Hamiltonian can be integrated after performing a canonical transformation with the generating function,

$$F_2(\phi_s, \phi_x, J_1, J_2) = J_1(m\phi_s + n\phi_x - l\theta + \chi) + J_2\phi_x. \quad (3)$$

The new coordinates are, $\phi_1 = (m\phi_s + n\phi_x - l\theta + \chi)$, $\phi_2 = \phi_x$, $J_1 = J_s/m$, and $J_2 = J_x - nJ_s/m$. The new Hamiltonian, $\tilde{H}$, is given by,

$$\begin{aligned}\tilde{H} &= \delta_1 J_1 + \frac{\alpha_{11}}{2}J_1^2 + [Q_{xo}J_2 + \frac{\alpha_{xx}}{2}J_2^2] \quad (4)\\ &+ g(mJ_1)^{\frac{|m|}{2}}(nJ_1 + J_2)^{\frac{|n|}{2}}\cos(\phi_1)\end{aligned}$$

where $\delta_1 = mQ_{so} + nQ_{xo} - l + (m\alpha_{sx} + n\alpha_{xx})J_2$ and $\alpha_{11} = \alpha_{ss} + 2n\alpha_{sx} + n^2\alpha_{xx}$. This new Hamiltonian is independent of θ and ϕ_2, thus $\tilde{H}$ and J_2 are constants of motion which determine the particle motion completely.

If there is only a horizontal kick, $(J_{xo} = 0)$ then for the resonance considered here where $m = 1$ and $n = -2$ Eq. 4 becomes,

$$(2J_1 - J_2)[\frac{\alpha_{11}}{4}J_1 - g\sqrt{J_1}\cos\phi_1 + \frac{\delta_1}{2} + \frac{\alpha_{11}}{8}J_2] = 0 \quad (5)$$

The particle trajectory can be seen to follow the path of two intersecting circles in the map of $(\sqrt{J_1}\cos\phi_1, \sqrt{J_1}\sin\phi_1)$. The circle $2J_1 - J_2 = 0$ is called the "launching" circle, while the circle

$$\frac{\alpha_{11}}{4}J_1 - g\sqrt{J_1}\cos\phi_1 + \frac{\delta_1}{2} + \frac{\alpha_{11}}{8}J_2 = 0$$

is the nonlinear "coupling" circle. Matching the measured particle trajectories with the contours of constant $\tilde{H}$ can determine g, α_{11} and δ_1 only to an arbitrary multiplicative constant. If any one parameter is known then the "scale" is fixed and the other two parameters can also be uniquely determined.

II Experimental Method
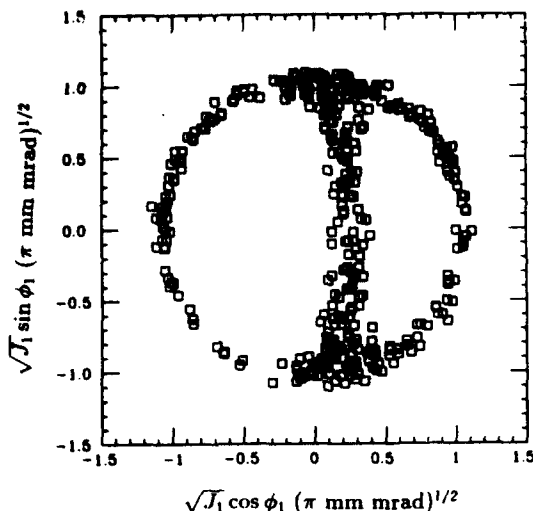
Figure 1: Plot of data obtained after a horizontal kick, displayed without averaging. The same kick is displayed in Fig. 2 with averaging (the data set with the largest J_2).

Figure 2: Plot of data (symbols) and fit (solid lines) to the Hamiltonian Eq. 5 for three different values of J_2. There was no vertical kick and both the launching and coupling circles are shown.

Protons were injected into the IUCF cooler ring at 45 MeV on a ten second timing cycle. The beam was bunched at harmonic number 1, with the rf cavity operating at 1.03168 MHz. The bunched beam was electr... cooled for several seconds reducing its unnormalized rms emittance to < 0.3 π mm mrad. The motion of a beam bunch with this small an emittance can closely simulate single particle motion. Since $J_2 = J_z - nJ_s/m$ is invariant, the difference resonance considered here is stable since the action in both planes of oscillation is bounded. Thus, it was possible to store beam with the betatron tunes on the resonance.

A coherent transverse oscillation was imparted to the bunch by firing pulsed kicker magnets. The subsequent motion was recorded on a turn-by-turn basis [3] for a complete grid of horizontal and vertical kicker strengths. The conversion from two position measurements (x_1, x_2) in each plane to normalized position and momentum coordinates (x_1, p_s) is described elsewhere in these proceedings [4]. The gain of the data acquisition system was calibrated against the beam position monitoring system in the cooler ring which itself was calibrated against a wire scanner. The uncertainty in position gain is estimated to be $\pm 10\%$.

III Data and Analysis

A. Data Reduction

The two position measurements, in each plane of oscillation, were converted to normalized coordinates and both $\phi_{s,z}$, from which ϕ_1 was derived, and J_s were computed for each turn. So that the features of the nonlinear coupling resonance could be seen more clearly a 10-turn running average was used in all cases except for ϕ_1 when only a horizontal kick was applied and no coherent motion had yet developed in the vertical plane. With no coherent motion the measurement of ϕ_z was not meaningful. An example of the data displayed without averaging is shown in Fig. 1.

It was thought that measurements of the tune shift with
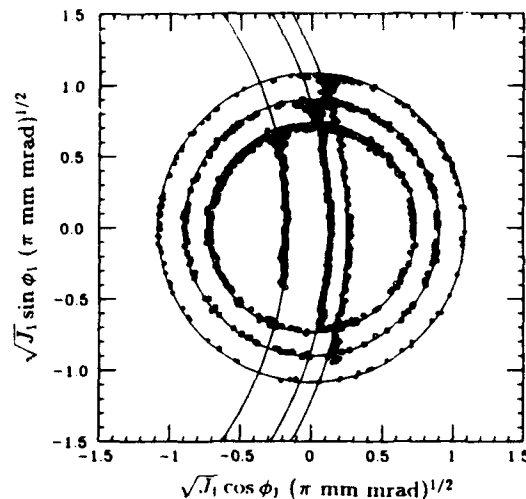
amplitude parameters α_{ss}, α_{sz} and α_{zz} could be made directly. With α_{11} known both g and δ_1 could then be determined. To measure the α parameters one need only find the slope of the measured tune verses J. However, our measurements were complicated by two factors. Firstly, the unperturbed tunes are not stable in the cooler ring. If one tracks the phase in $(x, z ; p_{s,z})$ phase space it is possible to measure the tune, assuming a pure tone, in as few as 50 turns. Using this method of tracking the tune a 60 Hz modulation was observed in Q_s of ± 0.0005 and in Q_z of ± 0.002. This uncertainty in the tune prior to the kick resulted in a large scatter of the measured tunes after the kick. Secondly, the resonance stop band was larger than anticipated so that even with $|Q_s - 2Q_z + 6| > 0.05$ the effect of the resonance was evident.

It was latter found that a two-kick procedure allows for the measurement of the α parameters even when the base tunes are not stable. The bunch is first given a small coherent oscillation by using the rf knock out system. This coherent motion allows the phase of the betatron oscillation to be tracked and thus, the base tune to be measured. The bunch is then given a larger kick with one of the pulsed kicker magnets 500 turns later. In this way the tune change resulting from the change in J can be accurately measured. The α parameters were measured using the two-kick proceedure when $Q_s - 2Q_z + 6 \approx -0.08$. While the value of α_{11}, determined at this tune location differed from the value of α_{11} determined from the resonance data the measurements will be useful when modeling the nonlinear elements in the cooler ring.

B. Fitting the Measured Tune

While the contours of constant $\tilde{H}$ are invariant if g, α_{11} and δ_1 are each multiplied by the same constant, the phase advance per turn, $\Delta\phi_1$, is not invariant. By differentiating
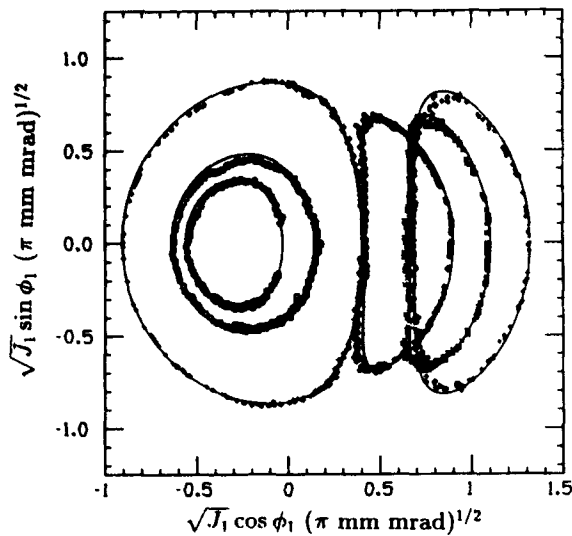
Figure 3: Plot of data (symbols) and fit (solid lines) to the Hamiltonian Eq. 4. The vertical kick was held constant and strength of the horizontal kick was varied.

Figure 4: Plot of measured (symbols) and predicted (solid lines) tune for five of the six kicks shown in Fig. 3.

the Hamiltonian one finds,

$$\frac{\partial \tilde{H}}{\partial J_1} = \frac{d\phi_1}{d\theta} \approx \frac{\Delta\phi_1}{2\pi} \tag{6}$$

$$\frac{\partial \tilde{H}}{\partial J_1} = \delta_1 + \alpha_{11}J_1 + g\cos\phi_1\left(-3J_1^{1/2} + \frac{J_2}{2J_1^{1/2}}\right).$$

Using δ_1 and g as adjustable parameters with χ fixed at -1.01 radians, the measured phase advance of ϕ_1 was fit to Eq. 6. Fitting 25 different kicks the mean resonance strength was -493×10^{-6} $(\pi$ mm mrad$)^{-1/2}$ with a standard deviation of $\pm 52 \times 10^{-6}$. Since the phase advance of ϕ_1 was not very sensitive to the value of α_{11}, the value of α_{11} was found instead by matching the curvature of the nonlinear coupling circle, when only a horizontal kick was applied, to the experimental data. The parameter α_{11} was found to be 350×10^{-6} $(\pi$ mm mrad$)^{-1}$ with the uncertainty estimated at $\pm 50 \times 10^{-6}$.

There was also a systematic variation in δ_1 with J_2. From the slope of δ_1 vs. J_2 the quantity $\alpha_{sz} - 2\alpha_{ss}$ was found to be $(-160 \pm 25) \times 10^{-6}$ $(\pi$ mm mrad$)^{-1}$. The values of g, α_{11} and χ were held constant when fitting the Hamiltonian to the experimental data.

C. Fitting the Hamiltonian

When only a horizontal kick was applied Eq. 5 was used to draw both the launching and coupling circles. The data was inspected to find $J_2 = J_z + 2J_s$ and δ_1 was adjusted for each kick. Three data sets with different values of J_2 are shown in Fig. 2. It was by fitting the curvature of the coupling circle to this data that the value of α_{11} was determined.

When there was both a horizontal and a vertical kick the data was fit to Eq. 4. The values of g, α_{11} and χ were again held constant, the value of δ_1 was adjusted for each kick and the data was inspected to find the maximum of J_1.

The value of J_2 used was the sum of the maximum of $2J_1$ and the minimum of J_z. The sharpness of the transition from the launching to the resonance circle is sensitive to the minimum value of J_z. By using the value of J_2 obtained by this prescription the minimum value of J_z was not overestimated. The value of the constant $\tilde{H} - [Q_{zo}J_2 + \alpha_{zz}J_2^2/2]$ was determined by the requirement that $\cos\phi_1$ was equal to ± 1 when J_1 was a maximum. Whether $\cos\phi_1$ was set to $+1$ or to -1 depended upon which side of the separatrix the particle was on. In Fig. 3 six data sets are shown for which the strength of the vertical kick was held constant while the strength of the horizontal kick was incremented, along with the fits to Eq. 4. For five of the kicks shown in Fig. 3 the measured and predicted tunes are shown in Fig. 4.

IV Conclusion

The betatron difference resonance, $Q_s - 2Q_z = -6$, was investigated at the IUCF cooler ring. It was found that a single resonance Hamiltonian accurately described the coupled motion. It was possible to match both the phase advance per turn of ϕ_1 and the contour traced in the map of $(\sqrt{J_1}\cos\phi_1, \sqrt{J_1}\sin\phi_1)$ with the predictions from the Hamiltonian Eq. 4. The values of the resonance strength g, and of the tune shift with amplitude parameters, α_{11}, and $\alpha_{sz} - \alpha_{zz}$ were determined. The agreement with the predicted values of these quantities is under investigation.

References

[1] E.D. Courant and H.S. Snyder, Ann. Phys. (NY) vol. 3, p. 1 (1958).

[2] R. Ruth, in *Physics of Particle Accelerators*, AIP Conf. Proc. No. 153 p. 150 (1987).

[3] S.Y. Lee, *et al.*, Phys. Rev. Lett. 67, 3768 (1991); D.D. Caussyn, *et al.*, Phys. Rev A bf 46, 7942 (1992).

[4] Y. Wang, *et al.*, "Experimental Results of the Sum Resonance", in these proceedings.

Experimental Results of the Betatron Sum Resonance *

Y. Wang[a], M. Ball[a], B. Brabson[a], J. Budnick[a], D. D. Caussyn[a], A. W. Chao[b], J. Collins[a],
V. Derenchuk[a], S. Dutt[b], G. East[a], M. Ellison[a], D. Friesel[a], B. Hamilton[a], H. Huang[a],
W. P. Jones[a], S. Y. Lee[a], D. Li[a], M. Minty[c], S. Nagaitsev[a], K. Y. Ng[d], X. Pei[f],
T. Sloan[a], M. Syphers[b], L. Teng[e], Y. T. Yan[b], P. L. Zhang[b]

Abstract

The experimental observations of motion near the betatron sum resonance, $\nu_x + 2\nu_z = 13$, are presented. A fast quadrupole (Panofsky-style ferrite picture-frame magnet with a pulsed power supplier) producing a betatron tune shift of the order of 0.03 at rise time of 1 μs was used. This quadrupole was used to produce betatron tunes which jumped past and then crossed back through a betatron sum resonance line. The beam response as function of initial betatron amplitudes were recorded turn by turn. The correlated growth of the action variables, J_x and J_z, was observed. The phase space plots in the resonance frame reveal the features of particle motion near the nonlinear sum resonance region.

I. INTRODUCTION

For particle motion in a circular accelerator, the betatron oscillation $x(s)$ and $z(s)$, around the closed orbit is given by the Hill's equation [1]:

$$\frac{d^2 x}{ds^2} + K_x(s)x = \frac{\Delta B_z}{B\rho}; \quad \frac{d^2 z}{ds^2} + K_z(s)z = -\frac{\Delta B_x}{B\rho}, \quad (1)$$

with

$$\Delta B_z + i\Delta B_x = B_o \sum_{n \geq 2}(b_n + ia_n)(x + iz)^n,$$

where b_n and a_n are the normal and the skew multipole components, respectively. The functions $K_x(s)$, $K_z(s)$ are the functions of the quadrupole strength, $B\rho = p/e$ is the magnetic rigidity, and s is the particle longitudinal coordinate, which advances from 0 to C, the circumference, as the particle completes one revolution of the cyclic accelerator. Both $K_{x,z}(s)$ and the anharmonic term $\frac{\Delta B_{x,z}}{B\rho}$ are periodic functions of s with period C. The number of oscillation periods in one revolution are betatron tunes, ν_x and ν_z, which can be adjusted by varying the quadrupole strength $K_{x,z}(s)$. The anharmonic term $\frac{\Delta B_{x,z}}{B\rho}$, which arise from higher-order multipoles, is normally small. However

when the condition, $m\nu_x + n\nu_z = l$, with m, n, l as integers is satisfied, the particle can encounter coherent perturbative kicks from the multipoles. These nonlinear resonances usually lead to beam diffusion, halo, and beam loss. The experimental studies of the betatron sum resonances will aid in the understanding of these nonlinear effects.

Based on the theory of betatron motion [1], the betatron amplitude of particle motion is given by,

$$x = \sqrt{2\beta_x J_x}\cos(\phi_x); \quad z = \sqrt{2\beta_z J_z}\cos(\phi_z) \quad (2)$$

with J_x, J_z as invariant actions for unperturbed motion. The Hamiltonian based on perturbation expansion of action-angle variables, and assuming a single dominant resonance can be written as [2]

$$H \approx H_o(J_x, J_z) + gJ_x^{\frac{|m|}{2}} J_z^{\frac{|n|}{2}} \cos(m\phi_x + n\phi_z - l\theta + \chi)$$

where g, χ are determined by the nonlinear multipole denoted by (m, n). Using the generating function, [2]

$$F_2(\phi_x, \phi_z, J_1, J_2) = J_1(m\phi_x + n\phi_z - l\theta + \chi) + J_2\phi_z,$$

the Hamiltonian in the resonance frame, with the new coordinates $\phi_1 = (m\phi_x + n\phi_z - l\theta + \chi)$, $\phi_2 = \phi_z$, $J_1 = \frac{J_x}{m}$, and $J_2 = J_z - \frac{n}{m}J_x$, is given by

$$\tilde{H} = \bar{H}_o(J_1, J_2) + g(mJ_1)^{\frac{|m|}{2}}(nJ_1 + J_2)^{\frac{|n|}{2}}\cos(\phi_1).$$

This new Hamiltonian is independent of θ and ϕ_2, thus $\tilde{H}$ and J_2 are the constants of motion and with the boundary conditions they should determine particle orbit completely. For the resonance given by the condition $\nu_x + 2\nu_z = 13$, the constant of motion J_2 is $J_z - 2J_x$, which implies the motion is unbounded and that this resonance is unstable. In the phase space plot $(\sqrt{J_x}\cos\phi_1, \sqrt{J_x}\sin\phi_1)$, particle motion which are outside of the stop-band of the sum resonance will form a circle and reach outward when they are on the resonance. The experimental results for motion near the betatron sum resonance at $\nu_x + 2\nu_z = 13$ are presented in this paper. The Sec. II describes the experimental method, the data and analysis are presented in Sec. III, and Sec. IV is the summary.

II. EXPERIMENTAL METHOD

This experiment was performed using Indiana University Cyclotron Facility (IUCF) cooler ring which is hexagonal with a circumference of 86.82 m. A 45 MeV proton

beam injected, electron cooled and stored in a 10 second cycle. The stored beam is consisted of a single bunch with typically 3×10^8 protons and the bunch length of about 5.4 m(or 60 ns) spread full width at half maximum (FWHM). The revolution period in the accelerator was 969 ns with bunching produced by operating a rf cavity with frequency 1.03168 MHz with a harmonic number h of 1. The stability of the horizontal and vertical closed orbits were estimated to be better than 0.2 mm FWHM, respectively. To excite a betatron oscillation, a pulsed deflecting magnets having a time width of 600 ns FWHM were used. In this measurement, the beam was kicked by the deflecting magnets in both the horizontal and vertical directions simultaneously. In order to reach the betatron sum resonance, a betatron tune jump quadrupole, which is a Panofsky-style ferrite picture-frame magnet with pulsed power supply, was used [3]. This quadrupole is capable of producing a tune shift of the order of 0.03 with a rise time of 1 μs. The tune shift then decreases exponentially with a time constant of 3 ms due to the time constant of the pulsed power supply. The quadrupole was used to jump the betatron tunes onto the sum resonance or alternatively the tunes jumped over the sum resonance line which then cross through the resonance due to the pulsed power supply used for the fast quadrupole. The tune diagram for IUCF cooler ring is shown in Fig. 1, where the points A(3.7758,4.6374) and B(3.7988,4.5829) refer to the tunes before and after the tune jump quadrupole were turned on, respectively. After the tunes were jumped (with a rise time of 1μs), the tunes change from B to A crossing the resonance line due to the pulsed power supplier. The relative time between the kick
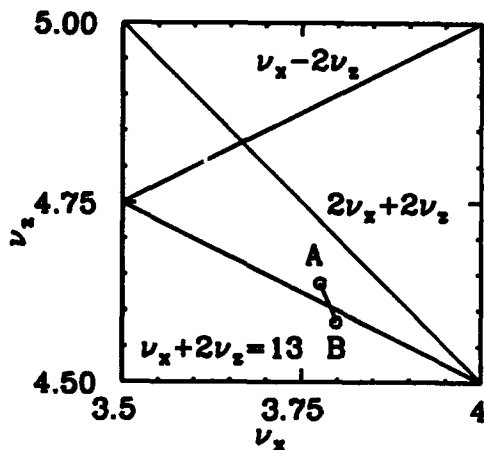
Fig. 1 Tune diagram

and the tune jump was adjustable. The data presented here was obtained for this case in which the kick magnet and the tune jump quadrupole had been turned on at the same time. The horizontal and vertical betatron motion of the beam centroid was tracked using four beam-position monitors (BPM's), two for each direction. The right (R) and sum (Σ) signal from each BPM were recorded turn by turn (up to 16000 turns) using our digitizing system

[4]. The normalised position then was deduced from the relation $\frac{2R-\Sigma}{\Sigma}$. The position calibration for the BPM was determined by calibrating a BPM identical to those used in the experiment and with amplifiers that were carefully matched to have the same gain as those used for the experiment, against a nearby wire scanner. The position signal at two different positions around the ring is used to locate the beam in the phase space x-p_x.

III. DATA AND ANALYSIS

The measured beam position spectra, $x_1(n)$ and $z_1(n)$, around closed orbit are shown in Fig. 2 as functions of
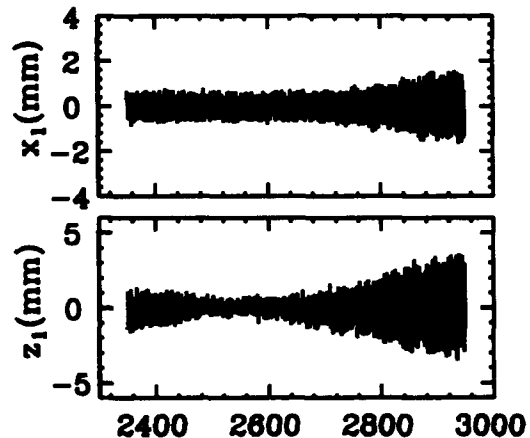
Fig. 2 Betatron oscillation amplitudes as function of turns

turns. The data shown are the betatron oscillation amplitudes from the turn numbers 2350 to 2950, which is in the time period 2.28 to 2.86 ms after the kick and the tune jump quadrupole were turned on. The measured betatron oscillation amplitudes reach a maximum near the turn number 2950 and these data after it is not shown here. The normalised momentum p_{x1} and p_{z1} which are defined as the conjugate variables of those in Eq. (2) can be evaluated from the measured quantities (x_1, x_2) and (z_1, z_2), respectively. The p_{x1} becomes [4]

$$p_{x1} = -x_1 cot\phi_{12} + \frac{\sqrt{\beta_{x1}/\beta_{x2}}}{\sin\phi_{12}}x_2, \qquad (3)$$

where the ϕ_{12} is the betatron phase advance between the two BPM's. The equation for a circle in x_1, p_{x1} is an equation for an ellipse in the variables x_1 and x_2, given by

$$\left(-x_1 cot\phi_{12} + \frac{\sqrt{\beta_{x1}/\beta_{x2}}}{\sin\phi_{12}}x_2\right)^2 + x_1^2 = 2\beta_{x1}J. \quad (4)$$

The values of ϕ_{12} and β_1/β_2 were determined by fitting experimental data, taken where it is known the motion is linear, to this equation of an ellipse. The normalised momentum p_{z1} was evaluated as the same way by replacing the x_1, x_2 by the z_1, z_2. The action variables J_x and J_z

were evaluated by

$$J_s = \frac{p_{s1}^2 + x_1^2}{2\beta_{s1}}, \quad J_z = \frac{p_{z1}^2 + z_1^2}{2\beta_{z1}}. \quad (5)$$

They are plotted, in unit of (π mm $mrad$), in Fig. 3 as a function of the turns. Also in the Fig. 3, the J_z is plotted as function of the J_s. Correlated growth of the action variables J_s, J_z can be seen from this data. The solid line in Fig. 3 is the $J_z - 2J_s = J_2$ relation. The
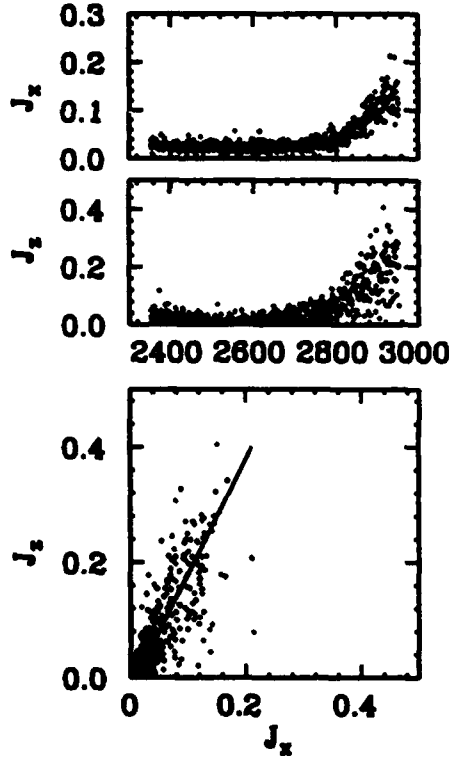
Fig. 3 Action variables J_x and J_z

particle motion is also plotted in phase space ($\sqrt{J_s}\cos\phi_1$, $\sqrt{J_s}\sin\phi_1$), which is shown in Fig. 4. The particle motion at initial 450 turns are denoted by the point in the Fig. 4, and the crosses are refer to the last 150 turns where the particle motion is moving outward.

It is certainly useful to monitor the betatron tunes and it can be an alternative way to check whether the particle motion is on the sum resonance or not. However the conventional method, to do FFT, is not practical because of the nature of the sum resonance and the fast quadrupole which makes the tunes change continously. To measure the tunes, the betatron tunes were tracked using the action angle advance $\Delta\phi$ at each turn, $\nu(n) = \frac{\Delta\phi(n)}{2\pi}$, where the n is the turn number, and a running average (± 10 turns) was used in average. The effect of the tune jump quadrupole was shown in Fig. 5. The upper and lower curves are the horizontal tune, ν_s, while the tune jump quadrupole was off and on, respectively, and the solid line is the calculated tune, ν_s, from the parameters of the tune jump quadrupole [3]. The motion of the tune across the resonance line as indicated in Fig. 1 was verified by this

tune tracking method.
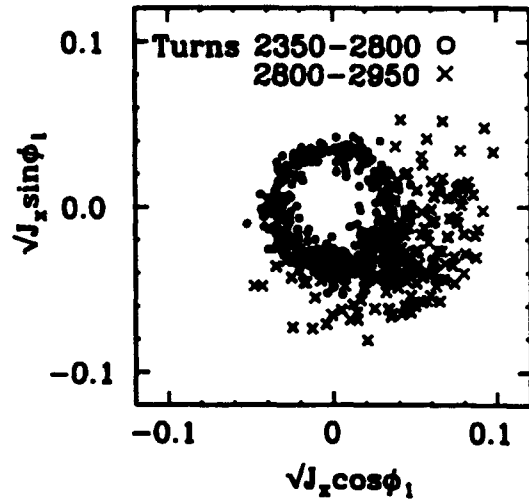
Fig. 4 Phase space plot on resonance frame
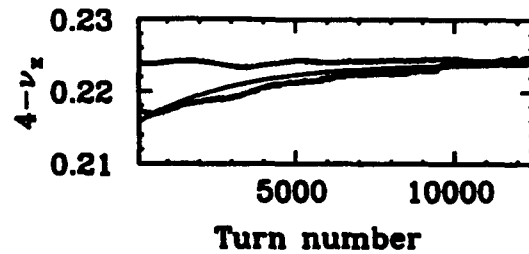
Fig. 5 The effect of the fast quad. on the betatron tune

IV. SUMMARY

The betatron sum resonance has been observed experimentally. The fast quadrupole which can produce a tune shift of 0.03 with a rise time of 1 μs certainly was an important tool for the success of this experiment. The data show the correlated growth of the action variable J_s and J_z. The phase space plot in the resonance frame reveal the expected outward motion when the sum resonance is encountered. Further study of the dynamics at this sum resonance is underway.

REFERENCES

[1] E.D. Courant and H.S. Snyder, Ann. Phys. (NY) vol. 3, p. 1 (1958).

[2] S.Y. Lee (unpublished).

[3] J. Budnick, T. Hall, D. Li, and S.Y. Lee, in this proceeding.

[4] S.Y. Lee et al., Phys. Rev. Lett. 67, 3768 (1991); D.D. Caussyn, et al., Phys. Rev. A46, 7942 (1992).

Chromaticity Compensation and Dynamic Aperture Limitation of SIBERIA-2

V.Korchuganov, E.Levichev and V.Sajaev,
Budker Institute of Nuclear Physics,
630090 Novosibirsk, Russia

Figure 1: Schematic desing of one half of SIBERIA-2 cell and the optical function

Abstract

Nonlinear beam dynamics studies of the 2.5 GeV dedicated SR source SIBERIA-2 are described. The effect of chromatic sextupoles and measured multipole field errors are taken into account. The influence of high order resonances is considered. The technique for finding the alternative operation point with an extended nonlinear stable region is described.

I. INTRODUCTION

The dedicated SR source SIBERIA-2 [1] is intended for experiments with photon beams of high brightness from both dipoles and insertion devices. The requirements for horizontal emittance minimization together with the matching of lattice functions in the insertion device regions determine the lattice quite unambiguously [2]. The intrinsic feature of low-emittance lattices is rather large chromatic aberrations due to the strong horizontal focusing needed to achieve the minimal emittance.

To compensate the chromatisity, strong sextupoles are in use. Due to the presence of sextupoles the nonlinear effects become of great importance for the transverse particle motion and nonlinear perturbation may lead to a severe reduction of dynamic aperture and beam lifetime limitation.

II. NATURAL CHROMATICITY COMPENSATION

SIBERIA-2 has a six fold symmetry lattice with 12 three meter long straight sections to accommodate insertion devices, rf and injection equipment. The horizontal emittance at 2.5 GeV is equal to $\epsilon_x = 76$ nm-rad. Fig. 1 shows one half of the cell together with the optical functions for the operation point $\nu_x = 7.717$ and $\nu_z = 7.694$. For this mode the produced natural chromaticities are equal to $\xi_x = -23.9$ and $\xi_z = -23.8$.

Two families of chromatic sextupoles are introduced in the dispersive straight section in a way to conserve both lattice
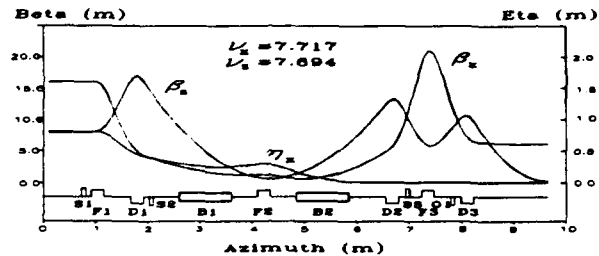
symmetry and cell mirror symmetry.

The betatron tune region was chosen far from the sextupole structure resonances $3\nu_x = 24$, $\nu_x + 2\nu_z = 24$, $-\nu_x + 2\nu_z = 6$, as well as the resonances $\nu_x = 7.5$ and 8. The other first order sextupole resonances which are closer to the working point are suppressed due to the lattice symmetry.

Fig. 2 illustrates the dependences of the tunes and lattice functions at the cell middle point on the momentum deviation while the linear chromaticities are corrected.
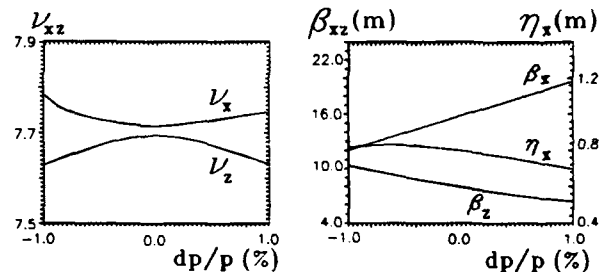
Figure 2: The dependences of the tunes and optical functions on momentum deviation with corrected chromaticity

III. REQUIRED APERTURE

The required aperture was estimated bearing in mind:
i) *Injection efficiency.* The 450 MeV electrons will be injected in one turn into the horizontal phase space using a bump orbit which is produced by a nanosecond kicker and a prekicker [3]. Taking into account the injected beam
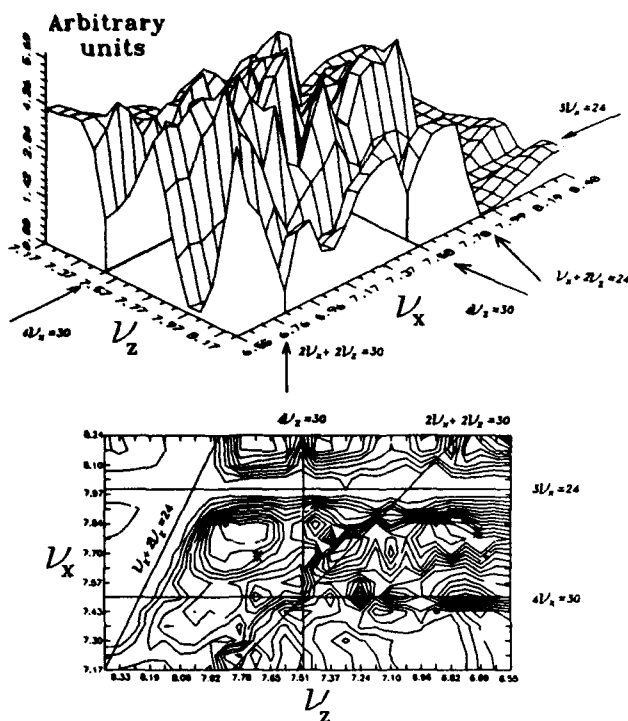
Figure 3: Dynamic aperture versus betatron tunes

emittance, septum leak field, injection orbit errors, etc. the required aperture is 2.6 cm in horizontal direction. The vertical aperture is determined by the injected beam emittance and should not be less than ±0.8 cm.

ii) *Beam lifetime.* For SR experiments with high time resolution the single bunch operation mode is required. The computation results have shown that for the $\sim 0.1 - A$-single bunch the beam lifetime is determined by Touschek effect in the whole energy range of SIBERIA-2. To provide good lifetime at 2.5 GeV with 0.1 A electron current, average pressure ≤ 2 nTorr and betatron oscillations coupling $\varepsilon_z = 0.01\varepsilon_x$ the following aperture sizes are needed: $A_x = \pm 2.4$cm, $A_z = \pm 1.3$cm (the possible rms closed orbit errors $\sigma_{x,z} = \pm 0.3$ cm were included into consideration). The vacuum chamber and the "good" field area in dipoles and quadrupoles do not restrict the aperture size.

IV. TRACKING

The simulation has been carried out using the FORTRAN 77 code MAcSim, developed by the authors [4] and run on MicroVAX-3.500 under VAX/VMS-5.2. As is standard, the code is double precision.

The code tracks the particles through the sequence of magnet elements in finite-length or thin-length approximation. To economize the CPU time for the linear part of the lattice the matrices are prepared before tracking and the structure is composed into a block structure. For finite length nonlinearity the 4-order Runge-Kutta integration is used while for thin element a nonlinear kick is performed. Systematic and/or random multipole errors can be intro-

duced in any element.

At each turn, phase coordinates are accumulated. After the tracking performed, the graphics or other outputs can be done in any canonical variables set: $J - \psi$, $x - p$ or $x - z$.

Options include: spectral analysis, the computation of the amplitude dependent tune shift, harmonic correction, distortion functions, Courant-Snyder invariant deviation, etc.

V. TRACKING RESULTS

A. Operation point

In order to test the sensitivity of the lattice to the operation point, the dependence of the dynamic aperture on betatron tunes was investigated. The tunes were changed by the quadrupoles in nondispersive straight section in the ranges: $\nu_x = 7.15 \div 8.25$ and $\nu_z = 6.55 \div 8.35$ with the step equal to $\Delta\nu = 0.05$. After the linear chromaticity correction, the dynamic aperture was calculated for 500 revolutions in each point.

To have a convenient figure of merit, which combines horizontal and vertical dimensions of the dynamic aperture and its shape, in a boundary curve $A_z = f(A_x)$ an ellipse whose area as large as possible was inscribed. Then the only quantity (ellipse area S_m) characterizes the aperture "quality". This criterion allowes us to avoid apertures which are large, but irregular in shape.

The results of the simulation are demonstrated in Fig. 3. The following structure sextupole resonances are close to the initial operation point $\nu_x = 7.717, \nu_z = 7.694$:
$3\nu_x = 24$, $\quad \nu_x + 2\nu_z = 24$ (first order);
$4\nu_x = 30$, $\quad 2\nu_x + 2\nu_z = 30$, $\quad 4\nu_z = 30$ (second order).
The most powerful among them are $3\nu_x = 24$ and $\nu_x + 2\nu_z = 24$: in our case, strong nonlinenear coupling is present in transverse motion.

Fig. 4 illustrates the dynamic aperture for the initial operation point ($S_m \simeq 3.6$, arbitrary units). The alternative operation point $\nu_x = 7.763, \nu_z = 6.698$ was chosen to increase the dynamic aperture: at this point $S_m \simeq 9.5$ whereas the parameters which determined the machine performance (emittance, amplitude functions, etc.) are almost the same.
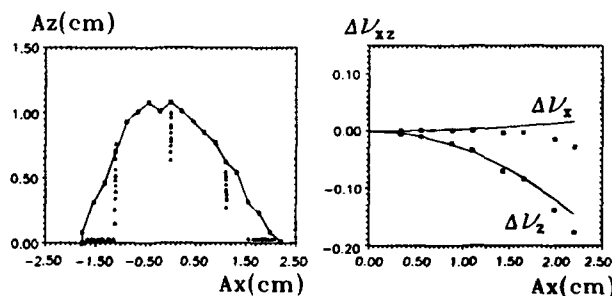
Figure 4: Dynamic aperture without/with multipole errors and amplitude dependent tune shift (initial point).

B. Tracking at the initial operation point

Phase trajectories for the initial operation point in $J_x - \psi_x$ space are shown in Fig. 5. These plots are taken in the middle of the nondispersive straight section, where $\alpha_{x,z} = 0$.

Near the limit of the stable area ($A_x \simeq 2.4$cm) one can see
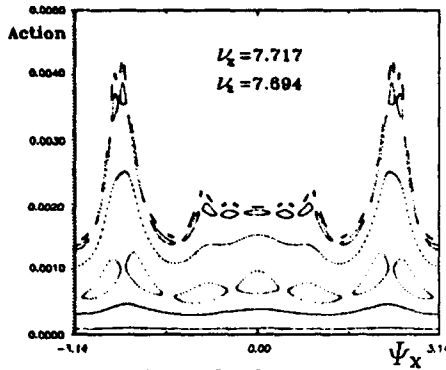
Figure 5: Horizontal phase space trajectories (initial point).

the resonances $18\nu_x = 138$ and $29\nu_x = 222$ (the last looks like the island chain in the stochastic region). At $A_x \simeq 1.4$ cm there is strong enough (the width ΔJ_x is large) resonance $7\nu_x = 54$. In spite of the fact that this resonance is isolated by invariant surfaces, these surfaces can expect to be destroyed due to the breaking of the lattice symmetry (for example, by the multipole errors) and the stable area limit will be shrinked.

The distortion of the invariant curves is explained by the combined effect of the resonances $3\nu_x = 24$ and $4\nu_x = 30$. The vertical plane tracking was plotted as well and the nonlinear coupling effects were investigated.

Fig. 4 plots the tune versus the amplitudes obtained by tracking and calculated according to the second order perturbation theory. The discrepancy between them suggests that the higher orders should be taken into account.

To find the influence of multipole errors on the dynamic aperture the tracking for 10 lattices with systematic and random multipole errors was performed. The results of magnetic mapping of the lattice elements provide us with the errors amplitudes.

The plot of tracking results in Fig. 4 shows the shrinking of the stable area. It is worth noting that the resonance $7\nu_x = 54$ has an essential effect on the dynamic aperture limitation in horizontal plane.

C. Alternative Operation Point

The following conditions were taken into account to chose alternative tunes:

i) the experimental capability of the machine, which depends on such parameters as emittance, lattice functions, etc., should not be restricted;

ii) the dynamic aperture has to be increased;

iii) the sensitivity of the lattice to multipole errors should
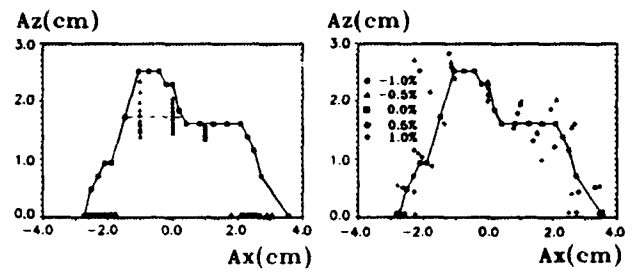
Figure 6: Dynamic aperture without/with multipole errors and momentum dependence of the dynamic aperture for the alternative point.
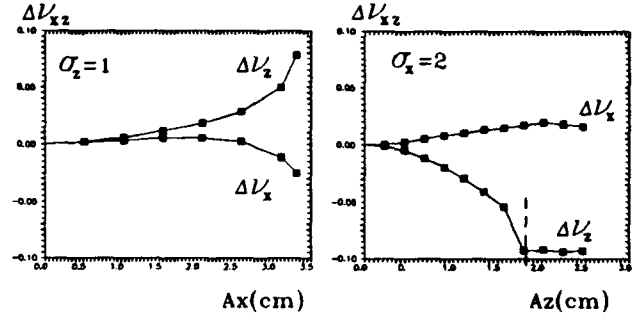
Figure 7: Amplitude dependent tune shift (alternative point).

reduce.

From the above, $\nu_x = 7.763$ and $\nu_z = 6.698$ were chosen as the tune values for the alternative point. The dynamic aperture with/without multipole errors for the detuned version is given in Fig. 6, the amplitude dependent tune shifts are depicted in Fig. 7. The motion behind the dashed line in both Figures cannot be considered as unambiguously stable, because the studies evidence that this region ($A_z \geq 1.8$cm) is inside the resonance $2\nu_z - \nu_x = 6$ and any symmetry break will distort the stability.

The horizontal phase curves demonstrate the absence of strong resonances inside the aperture. Fig. 6 gives the numerical results for the off-momentum particle at $\pm 1\%$ momentum deviation for the alternative operation point.

REFERENCES

[1] V.Anashin, A.Valentinov et al, "The dedicated SR source SIBERIA-2", *The Proceedings of the 11-th Russian Particle Conference*, Dubna 1989, p.277-280 (in Russian)

[2] V.N.Korchuganov et al, NIM208(1983), p.11-18.

[3] G.Erg et al. "Injection system for the SIBERIA-2 storage ring", these proceedings.

[4] V.Korchuganov, E.Levichev and V.Sajaev, "Dynamic aperture of SIBERIA-2 storage ring", *Preprinp INP 93-27*, Novosibirsk 1993 (in Russian).

RF Voltage Modulation at Discrete Frequencies, for Application to Proton Extraction using Crystal Channeling

W. E. Gabella[a], J. Rosenzweig[a], R. Kick[b], and S. Peggs[c]

[a]University of California Los Angeles, Physics Department

405 Hilgard Ave., Los Angeles, CA 90024

[b]Illinois Mathematics and Science Academy, Aurora, IL 60506

[c]Brookhaven National Laboratory, Upton, Long Island, NY 11973

Abstract

RF voltage modulation at a finite number of discrete frequencies is described in a Hamiltonian framework. The theory is applied to the problem of parasitic extraction of protons from a circulating beam in a high energy hadron collider, using a bent crystal as a thin "septum" extraction element. Three modes of employing discrete resonances are discussed: a strong, single drive resonance which may be used to excite protons to hit deep within the crystal; a single resonance ramped in such a manner that the island can carry trapped particles from low to high amplitudes; and overlapping resonances to create a chaotic band for separating the moving island and the large amplitude island. Simulations are used to confirm the expected dynamics, and finally a prototypical extraction scheme is described.

I. Introduction

We explore using RF voltage modulation to affect the flux of protons onto a bent crystal being used to extract the protons from a storage ring. A low flux, high energy proton beam would be useful for both a test beam and for fixed target B-physics experiments at the next generation of hadron colliders [1]. RF noise has also been considered to enhance the flux on the crystal [2].

RF modulation is used to affect the longitudinal phase space dynamics while keeping the beams relatively unaffected at the interaction regions, which are presumed to have zero dispersion [3]. At the crystal, the dispersion would be large relative to the betatron amplitude, so the longitudinal motion affects the beam distribution significantly. This leaves open the possibility of extracting beam (from the halo) while beam collisions occur.

Channeling in a bent crystal could provide an economical way to extract a small flux of protons from a storage ring. Extraction of circulating beam has recently been demonstrated at the CERN SPS [4]. For appropriate beam parameters, a significant fraction of impinging protons channel between the planes of symmetry in the crystal, executing "betatron" oscillations in the effective focusing force. If the crystal is adiabatically bent then channeled protons follow the bend [5, 6] and are extracted from the storage ring. For the Tevatron experiment 853 [7], 7 meters of pulsed kicker magnets are replaced by a 3 centimeter long bent crystal to send 900 GeV protons down an abort beam line.

Using voltage modulation islands can be placed and manipulated in the RF bucket. The position, width and island tunes are well described by analytic theory. These islands will be used to affect the dynamics of single particles. A large island near the RF separatrix gives particles a large step into the crystal, an island with a ramped modulation frequency moves particles from smaller amplitudes to larger, and many overlapping islands form a stochastic layer that buffers between any ramped islands and large outer islands.

II. Islands in the RF Bucket

The longitudinal dynamics of a proton stored in a ring can be described by an effective Hamiltonian. This form for the Hamiltonian relies on the energy gain from a cavity being small relative to the particle energy, so the discrete system can be approximated by a continuous one. This is equivalent to requiring that the synchrotron tune, Q_{s0}, is small, then the longitudinal dynamics for a single proton is described by

$$H(q, p, t) = 2\pi Q_{s0}\left(\frac{p^2}{2} + 1 - \cos\phi\right) \quad , \qquad (1)$$

where $p = 2\delta_p/\delta_{sep}$ gives the relative momentum offset, δ_{sep} is the offset at the separatrix, ϕ is the phase, or timing, of the proton at the RF cavity, and t is time measured in turns around the ring. We do not discuss the above in much greater detail, but refer the reader to a standard treatment of RF phase stability [8]. The synchrotron tune given in terms of other RF parameters is $Q_{s0}^2 = h\eta e V_0/(2\pi\beta^2 E_0)$, and the momentum offet at the separatrix is $\delta_{sep} = 2Q_{s0}/(h\eta)$, where h is the harmonic number and η is the phase slip factor.

If the RF voltage is modulated at frequencies near twice the synchronous frequency, resonant islands appear in the RF bucket. Since the tune of a single particle in the RF

bucket depends on its amplitude in the bucket, choosing the frequency of the modulation sets the position in the bucket where the modulation has the most effect. Defining the amplitude of a particle as $2a^2 = p^2/2 + 1 - \cos\phi$, or in terms of the off-momentum parameter $a = \delta_{max}/\delta_{sep}$, the synchrotron tune is to a good approximation $Q_s(a)/Q_{s0} = 1 - a^2/4$. Since the pendulum system is solvable, it should come as no surprise that there is an exact expression for the tune shift with amplitude in terms of elliptic integrals [9].

The width of the island depends on the strength of the modulation. For a voltage modulation of the form $V(t) = (1 + \epsilon \cos(2\pi Q_m t + \alpha))V_0$, the effective Hamiltonian is

$$H(q,p,t) = 2\pi Q_{s0}\left(\frac{p^2}{2} + \left(1 + \epsilon\cos(2\pi Q_m t + \alpha)\right)\left(1 - \cos\phi\right)\right).$$

$$(2)$$

The width of the island is $\Delta a_{1/2} = \sqrt{\epsilon}$, and the island is centered at an amplitude of a_R satisfying $Q_s(a_R) = Q_m/2$. The tune with which particles circulate inside the island, the island tune, is given by $Q_I/Q_{s0} = a_R\sqrt{\epsilon}/2$. A relatively small RF modulation can create a relatively large island and island tune.

III. ADIABATIC RAMPED ISLANDS

Islands that are slowly moved from small amplitudes to large ones can be used to re-populate the large amplitude regions of phase space after those particles there have been extracted. It can be moved by ramping the modulation tune from Q_{m1} centered at an amplitude of a_1 to Q_{m2} centered on a_2. If this ramping is slow enough compared to the time scale of the particle circulation in the island, there remains a stable area in the island and particles may trap and be carried from small to large amplitudes [10]. The precise formulation of the adiabatic condition gives

$$\left|\frac{dQ_m}{dt}\right| < 2\pi Q_i^2 = \frac{\pi}{2}\epsilon a^2 Q_s(a) \quad , \qquad (3)$$

where Q_s is the synchrotron tune at the current position of the island a.

In Fig. 1, five trajectories are launched around the initial positions of the island and tracked while the island is ramped; one of the trajectories is launched at the island center. This shows that ramped islands in phase space can move particles from small amplitudes to large albeit with some time structure superimposed. For instance, in the case of the Tevatron example shown in Fig. 1, the time to reach the large amplitude, 500,000 turns, corresponds to about 10 seconds of real time.

IV. STOCHASTIC REGION

The time structure for particles that are brought up from low amplitudes can be alleviated by first passing them through a stochastic layer. This layer can be formed
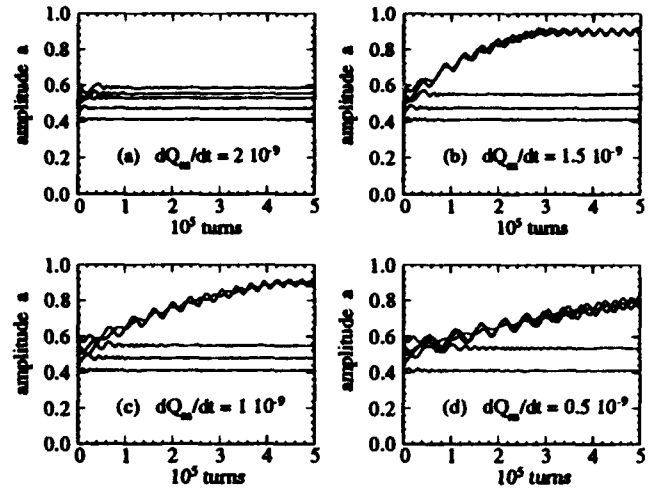
Fig. 1. Effect of ramped island on neighboring trajectories.

by overlapping several "islands". Then particles move through this layer and into the large, outer island. In Fig. 2(a), 12 trajectories with initial conditions very close to each other and in the stochastic layer, formed by 9 overlapping islands, are tracked. Fig. 2(b) shows that the variance of the amplitude for the trajectories grows exponentially with the time, filling the layer.

V. PROTOTYPE SCHEME

In Fig. 3, a prototypical extraction scenario is used and a trajectory that is initially trapped in the ramped island is shown. For the first 2×10^6 turns the proton is trapped in the moving island, then it enters the stochastic layer, here formed by 5 overlapping islands. It meanders until it is caught in the large island, in which it executes an oscillation out to $a = 0.8$, where the crystal would be placed to extract the proton. Later, the proton detraps from the large island and moves back into the stochastic layer.

VI. CONCLUSION

It is possible using discrete RF voltage modulation to control and enhance the flux of circulating protons onto the face of a bent crystal used for extraction. It is thought, but remains to be demonstrated that these techniques give a bigger step size into the crystal resulting in more efficient channeling than RF noise diffusion of the beam. A big, large amplitude island, a ramped island, and a stochastic layer formed from islands make-up a toolbox for controlling the flux of particles and the extraction rate using bent crystals.

Fig. 2(a). Trajectories tracked in the stochastic layer formed by 9 overlapping islands.

Fig. 2(b). The variance of the amplitudes for the 12 trajectories shown in Fig. 2(a).

Fig. 3. Amplitude of a proton initially trapped in a moving island, carried to a stochastic layer, and "inserted" into a large amplitude island.

REFERENCES

[1] The SFT Collaboration, "An Expression of Interest in a Super Fixed Target Beauty Facility at the SSC", EOI-14, submitted SSC Program Advisory Committee, (1990).

[2] Barry S. Newberger and H.-Jeng Shih, "Low Intensity Beam Extraction at the SSC", in *Proceedings of the U. S.-Japan Workshop on Nonlinear Dynamics and Particle Acceleration, Tsukuba, Japan, October, 1990*, edited by T. Tajima and Y. Ichikawa.

[3] W. Gabella et. al., "RF Voltage Modulation at Discrete Frequencies, with Applications to Crystal Channeling Extraction", submitted to Part. Accelerators, also Fermilab-TM-1783, May, 1992; G. Jackson, "Extraction from the Fermilab Tevatron using Channeling with a Bent Crystal", in these proceedings.

[4] S. Weisz, et. al., "Proton Extraction from the CERN-SPS by a Bent Crystal", in these proceedings.

[5] J. S. Forster, et. al., "Deflection of GeV Particle Beams by Channeling in Bent Crystal Planes of Constant Curvature", Nucl. Physics, **B 318** (1989) 301-308.

[6] S. P. Moller, "High Efficiency Bending of 450 GeV Protons using Channeling", Phys. Letters, **B 256** (1991) 91-96.

[7] R. A. Carrigan, et. al, "Proposal for a Test of Low Intensity Extraction from the Tevatron Using Channeling in a Bent Crystal", P-853 submitted to the Fermilab Program Advisory Committee, (1991).

[8] W. T. Weng and S. R. Mane, "Fundamentals of Particle Beam Dynamics and Phase Space", in *The Physics of Particle Accelerators* AIP **249**, (American Institute of Physics, New York, 1992).

[9] A. J. Lichtenberg and M. A. Lieberman, *Regular and Stochastic Motion*, (Springer, New York, 1983).

[10] S. Peggs, "Proton Mining—Dual Frequency Amplitude Modulation", Fermilab-AP-91-001, (1991).

Modification of the Short Straight Sections of the High Energy Booster of the SSC*

M. Li, D. Johnson, P. Kocur, R. Schailey, R. Servranckx, R. Talman, Y. Yan, R. York, and V. Yarba

Superconducting Super Collider Laboratory* 2550 Beckleymeade Ave., Dallas, TX 75237

Abstract

The tracking analysis with the High Energy Booster (HEB) of the Superconducting Super Collider (SSC) indicated that the machine dynamic aperture for the current lattice (Rev 0 lattice) was limited by the quadrupoles in the short straight sections. A new lattice, Rev 1, with modified short straight sections was proposed. The results of tracking the two lattices up to 5×10^5 turns (20 seconds at the injection energy) with various random seeds are presented in this paper. The new lattice has increased dynamic aperture from ~7 mm to ~8 mm, increases the abort kicker effectiveness, and eliminates one family (length) of main quadrupoles.

The code DIMAD [1] was used for matching the new short straight sections to the ring. The code TEAPOT [2] was used for the short term tracking and to create a machine file, zfile, which could in turn be used to generate a one-turn map with the use of ZLIB [3] for fast long-term tracking using a symplectic one-turn map tracking program ZIMAPTRK [4].

I. INTRODUCTION

The HEB lattice is designed to operate in the energy range of 0.2-2 TeV. The HEB is a bipolar machine, that alternately injects beam to the top and bottom collider ring. A geometry compatible with easy injection from a monopolar Medium Energy Booster (MEB) is required. The basic overall design consists of two nearly semicircular arcs connected by long straight sections. One long straight section is used for fast ejection of the beams in opposite directions for transfer to the two collider rings as well as for the resonantly-extracted test beams; in addition, it contains the RF acceleration system. The other long straight section contains the electrostatic septa for extraction of the test beams (Future requirement). The two semicircular arcs each contain two short straight sections. The two in the south are used for beam injection from the MEB, and the two in the north arc are used for the two beam aborts. The HEB geometry is shown in Figure 1.

The HEB normal operation cycle begins at the injection of proton bunches from the MEB at 200 GeV, which lasts about 20 seconds, or 5.5×10^5 turns. Simulation of Rev 0 lattice up to 10^5 turns indicated that the quadrupoles in the short straight sections dominated the nonlinearities of the HEB ring and limited its dynamic aperture [5]. The dynamic aperture can be increased from 7 mm to 9 mm when the multipole errors are set to zero in the short straight section quadrupoles. Further simulation work, using various random number seeds, even failed to find the closed orbit correctly after the multipole errors of the quadrupoles in short straight sections were included. This motivated us to change the Rev 0 lattice.

Efforts were exerted to decrease the beta-functions in short straight sections and shorten the lengths of the quadrupoles in same region, such that the $\Sigma k\beta l$ would be reduced. Since the civil design work for the tunnel already started, we decided to limit any geometrical changes to the short straight sections. The new Rev 1 lattice keeps the length of each short straight section unchanged, but decreased the central clear drift region from 112.7 m to 102.5 m. The 102.5 m was necessary to allow MEB to HEB injection within the central drift area. On the other hand, the abort line located in the north short straight sections preferred higher vertical β-functions to increase the abort kicker effectiveness. Rev 1 lattice achieved this, which seems to be contrary to the goal of reducing the $\Sigma k\beta l$. Since the quadrupoles in short straight sections are shortened significantly, we are able to replace one family of quadrupoles with the main arc quadrupole supplemented by adding corrector trim quadrupoles. This should reduce the overall cost of the HEB.
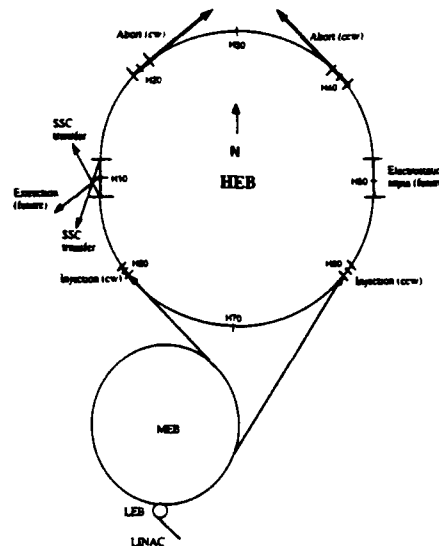
Figure 1. HEB ring layout.

II. REV 1 LATTICE

Figure 2 shows the schematic view of half short straight section of Rev 0 and Rev 1 lattices. First of all, by separating the doublet quadrupoles, Qs2 and Qs3, we succeeded in reducing the lengths of each quadrupole, as well as the β-functions in short straight sections. Spool 1 has been moved in between Qs2 and Qs3 in north short straight sections (H20, H40). This allowed the abort kickers to be shifted closer to the quadrupole and in a region with higher vertical β functions; This increased the kicker effectiveness. By separating Qs2 and Qs3 by the exact slot length of the spool piece plus standard interconnect, the need for a special length empty cryostat is eliminated.

For the injection straight sections (H60, H80) spool 2 has been moved to between Qs2 and Qs3. By doing this, enough

clear drift is provided in the center of the straight section to accommodate the injection beamlines from the MEB.

Fitting showed that the Qs1 length needed was close to the main quadrupole effective magnetic length of 1.6 m. In order to use the main quadrupole for Qs1 and eliminate one family of quadrupoles, we used two correction quadrupoles to compensate for the slight length difference. Fitting was performed using the code DIMAD.

The β and η functions of Rev 0 and Rev 1 short straight sections are shown in Figure 3 and Figure 4. The $\Sigma k\beta l$ of the two short straight sections are presented in Table 1.
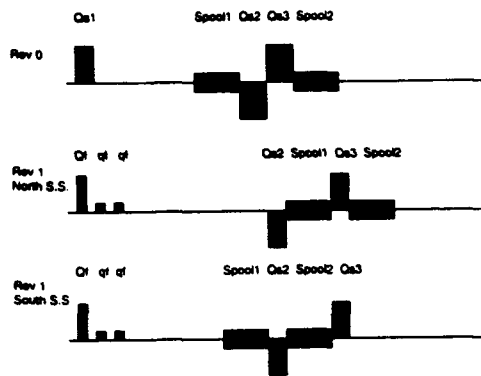
Figure 2. Comparison of the short straight section in Rev 0 and Rev 1 lattices.
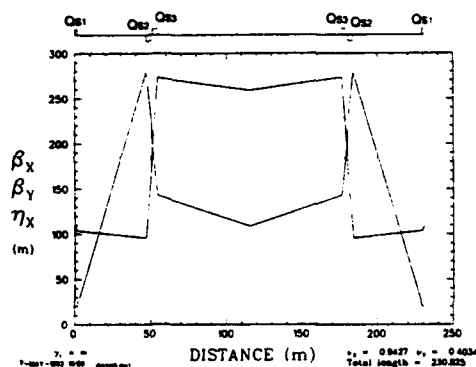
Figure 3. β and η functions of Rev 0 short straight section.
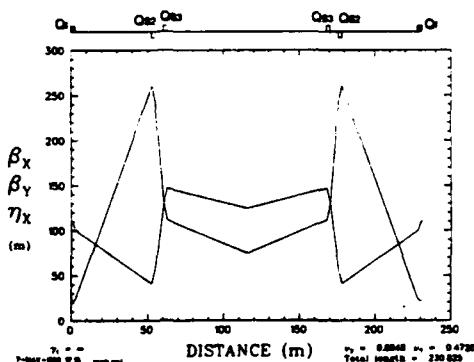
Figure 4. β and η functions of Rev 1 short straight section.

Table 1
The Sum of k*l*β in short straight sections

Quads	k(m^{-2})	l (m)	β_x (m)	β_y (m)	lkl lβ_x	lkl lβ_y
Rev 0						
Qs 1	0.0276	2.2578	103.8	20.4	6.48	1.27
Qs 2	−0.0276	3.3465	164.3	228.2	15.20	21.11
Qs 3	0.0276	3.3465	273.4	143.0	25.29	13.23
Total					46.97	35.61
Rev 1						
Qf	0.0276	1.6	113.2	19.5	5.00	0.86
qf	0.009	0.26	107.3	20.8	0.25	0.05
qf	0.010	0.26	105.6	21.2	0.27	0.06
Qs2	−0.0276	2.228	57.0	257.9	3.51	15.86
Qs3	0.0276	2.228	149.0	120.3	9.16	7.40
Total					18.19	24.23

III. LONG TERM TRACKING

To perform long term tracking we use TEAPOT to convert each magnet into one or more thin lenses and concatenate them to a machine file. All misalignment and multipole errors are included, and then the correction scheme is used to compensate for errors. This machine file is then used to get a one-turn map by using a ZLIB related program ZMAP. Finally, the symplectic one-turn map tracking code ZIMAPTRK is used for fast long-term tracking of up to 5×10^5 turns to determine the dynamic aperture.

Rev 1 lattice has a $\pm 3\%$ β-function mismatch in arc cells in order to maintain 102.5 m clear space at the middle of the south short straight section. This mismatch is ...gible compared with greater mismatch introduced by ...alistic nonlinearities. The misalignment of magnets and Beam Position Monitors (BPM), and multipole errors of magnets we are using for simulation are shown in Table 2 and Table 3 separately. For correction quadrupoles each multipole error of main quadrupoles multiplied by 10 is used. After correction the maximum deviation of closed orbit is less than 1 mm, the chromaticity is fit to zero, the coupling effect is minimized, and the machine is tuned to the nominal tunes ($v_\chi = 39.425$, $v_y = 38.415$).

The final results of the dynamic apertures are shown in Table 4. Rev 0 lattice failed to get a closed orbit with two of nine random number generation seeds. A mini study was conducted on the Rev 1 lattice by doubling each multipole error of the quadrupole in short straight section only and of all magnets with the seed number 7. The closed orbit exists in both cases, and the dynamic aperture is 7.5 mm (double error of quadrupole in short straight sections only) or 6.0 mm (double error of all magnets) respectively. This indicated that the quadrupoles in short straight sections are no longer dominating the nonlinearities of the HEB ring and the Rev 1 lattice is more reliable.

Table 2
HEB Magnet and BPM Alignment Tolerances

Element	Component	Tolerance
Dipole	Horizontal σ_x (mm)	1.1
	Vertical σ_y (mm)	1.1
	Field Angle σ_Θ (mrad)	1.01
	Sigma b_0	0.001
Quadrupole	Horizontal σ_x (mm)	0.4
	Vertical σ_y (mm)	0.4
	Field Angle σ_Θ (mrad)	0.56
BPM	Horizontal σ_x (mm)	0.3
	Vertical σ_y (mm)	0.3

Table 3
Limit of HEB Magnet Multipoles

Multipole	Dipole Random RMS ($\times 10^{-4}$ @ 1 cm)	Quadrupole Random RMS ($\times 10^{-4}$ @ 1 cm)	Dipole Systematic ($\times 10^{-4}$ @ 1 cm)	Quadrupole Systematic ($\times 10^{-4}$ @ 1 cm)
a1 / b1	1.25 / 0.50	4.80 / 0.00	0.04 / 0.04	2.00 / 0.00
a2 / b2	0.35 / 1.15	1.77 / 1.77	0.032 / −2.00	0.184 / 0.184
a3 / b3	0.32 / 0.16	0.81 / 0.81	0.026 / 0.026	0.085 / 0.085
a4 / b4	0.05 / 0.22	0.22 / 0.22	0.02 / 0.08	0.078 / 0.078
a5 / b5	0.05 / 0.02	0.206 / 0.103	0.02 / 0.02	0.072 / −0.57
a6 / b6	0.02 / 0.02	0.032 / 0.032	0.02 / −0.02	0.033 / 0.033
a7 / b7	0.02 / 0.02	0.029 / 0.029	0.02 / 0.02	0.03 / 0.03
a8 / b8	0.02 / 0.02	0.02 / 0.02	0.02 / 0.02	0.02 / 0.02

Table 4
HEB Dynamic Aperture at 500,000 Turns

Seed Number	Rev 0 (mm)	Rev 1 (mm)
1	6.7	8.0
2	7.0	8.3
3	6.9	7.6
4	7.5	8.0
5	7.7	9.1
6	7.3	8.7
7	failed	8.1
8	failed	7.7
9	7.4	9.1
Average	(7.2)	8.3

IV. SUMMARY

ZIMAPTRK succeeded in long term tracking of the HEB up to the million turn level. It will be used for tracking the HEB with ramping of the energy in the future.

V. REFERENCES

[1] R. Servranckx, K. Brown, et al., *Users Guide to the Program DIMAD*, SLAC report 285 UC–28(A), May 1985.

[2] L. Schachinger and R. Talman, *TEAPOT: A Thin-Element Accelerator Program for Opticsand Tracking*, Particle Accelerators 22, 35 (1987).

[3] Y. Yan and C. Yan, *Zlib: A Numerical Library for Differential Algebras*, SSC report, SSCL-300 (1990); Y. T. Yan, *Applications of Differential Algebra to Single-Particle Dynamics in Storage Rings*, Physic of Particle Accelerators, M. Month and M. Dienes eds, AIP Conf. Proc. No. 249, p. 378 (1992).

[4] Y. Yan, M. Li, M. Syphers and P. Channell, *Long-Term Tracking with Symplectic Implicit One-Turn Taylor Maps*, Particle AcceleratorConference, Washington D.C., May 1993.

[5] M. Li and D. Johnson, *Dynamic Aperture Study of High Energy Booster of SSC*. 1992 Joint April Meeting of the APS and the AAPT, Washington, D.C., 20–24 April 1992.

Dynamic Aperture of the Chromatically Corrected Collider Lattice

F.Pilat, Y.Nosochkov, T. Sen and R.Stiening

Superconducting Super Collider Laboratory*
2550 Beckleymeade Avenue, Dallas, TX 75237

Abstract

A scheme for correcting the second order chromatic effects generated by the Interaction Regions (IRs) has been designed for the SSC Collider ring, where four families of sextupoles are located in the arc sectors next to the East Cluster. The effect of these sextupoles on the dynamic and momentum aperture of the machine has been evaluated with a simulation model in which alignment, field errors and operational corrections are realistically represented. Several optics configurations with different values of β^* at the Interaction Points (IPs) have been studied for different sets of field error specifications in the IR quadrupoles. The local chromaticity correction system improves the momentum aperture of the Collider for every configuration studied with no relevant loss of dynamic aperture on momentum, when the effect of errors are taken into consideration.

I. INTRODUCTION

The dynamic and momentum aperture of the Collider ring in the presence of the local sextupole scheme [1] has been studied in detail in order to establish the performance as well as the feasibility of the scheme itself. Sextupoles, as nonlinear elements, can potentially reduce the dynamic aperture of the machine, so the behavior of the Collider lattice has been checked with a realistic simulation model. For every configuration of the optics and setting of the local sextupoles correction scheme we determined the dynamic aperture, identified with the largest amplitude surviving 1024 turns. The choice of the *short term* dynamic aperture as a figure of merit is justified by the fact that the main aim is to compare different machine configurations and not to investigate its long term stability. Selected cases have been tracked for 100000 turns and the comparison with the short term results will be discussed in the following.The behaviour of different configurations of the Interaction Region optics and of the sextupole scheme has been studied first for the *ideal lattice*, i.e. the first order lattice plus the sextupoles as the only source of nonlinearity. The ideal lattice has then been compared with a realistic model of the lattice where the effect of *errors* and their operational *corrections* is taken into consideration. The initial conditions for the amplitudes of the particles tracked have been selected as follows:

$x_n = n * \sigma_x$ where $\sigma_x = (\beta_x \, \varepsilon_x)^{1/2}$ and $(\beta\gamma)_{rel} \, \varepsilon_x = 1$ mm mrad
$y_n = n * \sigma_y$ where $\sigma_y = (\beta_y \, \varepsilon_y)^{1/2}$ and $(\beta\gamma)_{rel} \, \varepsilon_y = 1$ mm mrad
At the beginning of the lattice $\beta_x \sim \beta_y \sim 460$m, $\alpha_x \sim \alpha_y \sim 0$ and $D_x = 0$, so that at this location $\sigma_x \sim \sigma_y \sim 1.47 * 10^{-4}$ m at 20 TeV

II. IDEAL LATTICE

The β^* at the collision point of the collider low-beta IRs can be tuned between 0.25m and 8m, the latter value corresponding to the injection optics; the nominal value at collision is 0.5m. Each IR, 2 in the East Cluster and 2 in the West Cluster, can be tuned independently to a value of β^* in this range. The optical configurations simulated have always the injection optics in the West Cluster and several combinations of β^* in the East Cluster, i.e. in the north low beta IR (ENLB) and in the south low beta IR (ESLB). The configuration studied are labeled as follows:
N50-S50 : baseline symmetric, $\beta^*_{ENLB} = 0.50$m, $\beta^*_{ESLB} = 0.50$m
N25-S25 : low β^*symmetric, $\beta^*_{ENLB} = 0.25$m, $\beta^*_{ESLB} = 0.25$m
N25-S50 : low β^*asymmetric , $\beta^*_{ENLB} = 0.25$m, $\beta^*_{ESLB} = 0.50$m
N25-S800: asymmetric , $\beta^*_{ENLB} = 0.25$m, $\beta^*_{ESLB} = 8$m
The last configuration, where one East IR is tuned for maximum luminosity and the other is tuned to the injection optics, is expected to be the most sensitive to chromatic effects [2]. The first configuration is the baseline optics for the Collider and it is the least sensitive to chromatic effects. In order to enhance the effect of higher order chromaticity, the fractional tune of the lattice for this simulation has been chosen reasonably close to the half integer ($\nu_x=123.435$, $\nu_y=122.415$).

Table 1: Dynamic and momentum aperture(σ) of the ideal lattice

$\frac{\Delta p/p}{10^{-4}}$	N50 S50	N50 S50	N25 S25	N25 S25	N25 S50	N25 S50	N25 S800	N25 S800
	glb	lcl	glb	lcl	glb	lcl	glb	lcl
0	100	70	100	40	100	50	100	50
1	100	70	100	40	100	50	100	50
2	100	70	100	40	100	50	100	50
3	100	70	100	40	100	50	90	50
4	100	70	100	40	100	40	50	50
5	100	70	100	40	80	40	20	50
6	100	70	80	30	70	40	0	50
7	100	70	70	30	50	40	0	50
8	100	70	50	30	40	40	0	50
9	100	70	0	30	20	40	0	50
10	100	70	0	30	0	40	0	50

Studies of beam-beam effects also suggest a working point close

to 0.4. Table 1 summarizes the results for the ideal lattice: for each configuration described above, the dynamic and momentum aperture for the lattice with the total linear chromaticity compensated by the sextupoles in the arcs only (global), is compared to one (local) where the linear and second order chromatic effects arising from the IRs are corrected by the local sextupole scheme and the linear chromaticity from the rest of the machine is corrected by the arc sextupoles.

The local sextupoles cause a significant increase of the momentum aperture, in particular for the asymmetric optics configurations. This confirms the improvement in machine performance expected, given the better tune versus momentum curves and beta beat in the presence of the local scheme [1]. The strong local sextupoles cause however a reduction of the dynamic aperture on momentum. This effect, together with the strength requirement on the local sextupoles, led us to limit the use of the local system only to compensating the *higher order* chromaticity of the IRs a d to correct the linear chromaticity, caused by both the arcs a' d the IRs, with the arc sextupoles.

III. LATTICE WITH ERRORS

The investigation of performance of the local sextupole scheme done for the ideal lattice has been repeated and extended to a realistic model of the machine where the effect of errors and their corrections are accurately simulated. This study allows us to establish whether the benefits of the local scheme demonstrated for the ideal lattice still holds in the presence of errors that could potentially mask the effectiveness of sextupoles, and to investigate more thoroughly the issue of loss of dynamic aperture on momentum.

The model used for the simulation, and implemented in the code TEAPOT [3], describes realistically the single particle dynamics of the Collider as far as errors and corrections are concerned. Collective and beam beam effects are not included in the model. Every relevant element in the lattice such as a bend, quadrupole, sextupole, beam position monitor, etc., is assigned random *alignment errors* and roll errors; main dipoles and quadrupoles also have systematic and random *field errors* associated with them, where normal and skew multipoles are specified up to the order 9. The issue of the error specifications for the Collider is a matter of continuing study and will not be discussed here in detail: except where otherwise specified, the assumptions for the alignment and field errors reflect the so called Collider 3B Specifications Document [4]. We did not include alignment errors in the IR triplets: the triplets are extremely sensitive to these errors and the correction of their effects on the collider dynamics is the topic of an ongoing independent study. Also, the effect of the crossing angle at the interaction point is not generally included in the discussion that follow. The effect of the crossing angle and triplet specifications for the baseline collider optics will be discussed at the end.

The operational corrections necessary to operate the machine with imperfections are also accurately described in the model: the *closed orbit* is found by a steering algorithm, the lattice is retuned to the original fractional *tune* by means of trim quadru-

poles and the *local* compensation of *coupling* is achieved by a set of 44 skew quadrupoles, 24 of them placed in the clusters and 20 in the arcs [5].

Several configurations have been studied with the above described set of errors and corrections: N25-S800, N50-S800 and the baseline collider optics N50-S50. We will limit the detailed discussion to the former one.

A. Configuration N25-S800

As already remarked, this optical setting has been studied in more detail since it represents a worst case scenario as far as chromatic effects from the IRs are concerned. The low beta IR tuned at 0.25m contributes about 100 units of chromaticity. We compared the following sextupole correction schemes:

global : Linear chromaticity ξ from arcs *and* IRs corrected with the arc sextupoles

local : All the linear chromaticity ξ is corrected with the arc sextupoles. The local sextupole system minimizes the 2nd and 3rd order tune shift with momentum.

For every correction scheme the dynamic aperture as a function of momentum has been determined for different error sets.
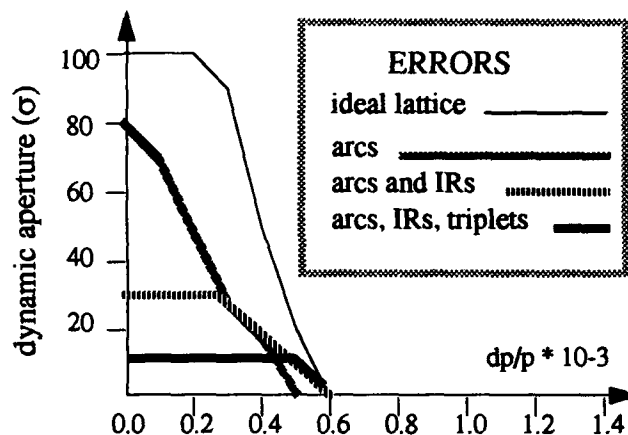
Figure 1. Aperture for the *global* correction scheme

Figure 1 describes the aperture in presence of the *global* chromaticity correction scheme, for different field error assignments: when field errors are added to the arc dipoles and quadrupoles, the dynamic aperture decreases. The assignment of field errors to the IR quadrupoles and successively to the triplets further reduces the dynamic aperture of the machine, verifying that the dynamics at collision energy is dominated by the IRs. Figure 2 summarizes the results relative to the *local* chromaticity correction scheme. One can notice the same reduction of dynamic aperture caused by the field errors in the IR quadrupoles. The momentum aperture for all the error configurations clearly improves with the local sextupole scheme. The apparent reduction of aperture of the ideal lattice for $\Delta p/p=0$ for the local scheme versus the global one is no longer relevant when the realistic field errors in the IR quadrupoles are added.

Lattice performance in the presence of errors led us to select the local scheme as the most effective way of correcting the chromatic effects of the IRs. The local scheme adopted here is also

preferred because of the minimum strength of the local sextupoles.
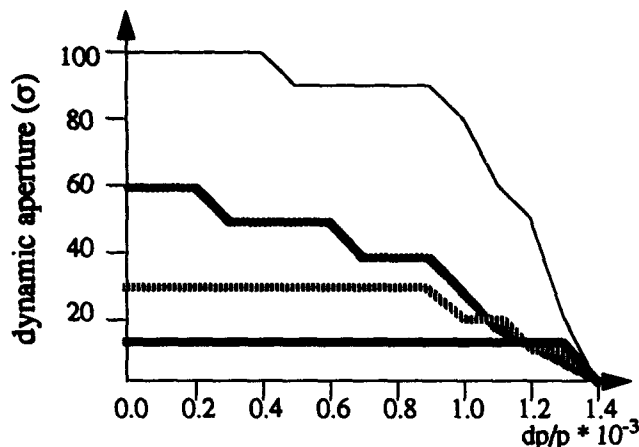
Figure 2. Aperture for the *local* correction scheme

B Effect of the crossing angle and field quality in the IR triplets.

As previously remarked, the former results about the collider dynamic aperture at collision energy do not take into consideration the effect of the crossing at the IPs and assume the 3B specifications for the field quality in the IR quadrupoles. Both assumptions have important consequences as far as the effect of the IR triplet quadrupoles on the dynamics is concerned. Work is presently in progress that specifically addresses IR triplet issues: some results will be summarized here for the N50-S50 baseline optics configuration.

The dynamic aperture for this optics, without crossing angle and assuming the standard 3B specifications for the IR triplets is 10 sigma. The global sextupole correction scheme is used here since the optical symmetry makes this optics less sensitive to chromatic effects.

A horizontal (vertical) *crossing angle* of 135 µrad between the two beams at the 2 East Cluster IPs is achieved with a system of 4 horizontal (vertical) kickers per IP. [6] The residual horizontal (vertical) dispersion produced by the system is corrected with a set of 6 normal (skew) quadrupoles per IP. The effect of the crossing angle is to make the beam pass off axis through the triplets, increasing the effect of the higher order multipoles in the quadrupoles. For a crossing angle of 135 µrad the maximum closed orbit offset in the triplets is ~5 mm: this effect has been simulated and the reduction of the aperture at collision found to be at the 1-2 sigma level.

The multipoles assumed so far for the triplets have been derived from the specifications for the 40mm aperture arc quadrupoles by appropriately scaling the values to an aperture of 50mm in the IR quadrupoles. A study is now in progress towards the exact determination of the field quality required for the IR triplets, in particular the higher order multipoles responsible for aperture reductions. Recent results show that the *systematic* b_5 *multipole* in the triplets, the first multipole allowed by symmetry in a quadrupole, has a significant effect on the aperture. Lowering b_5 from $0.534 * 10^{-4}$ (at 1cm) to $0.1 * 10^{-4}$

increases the dynamic aperture by 3-4 sigma. The typical value range for the dynamic aperture at collision for the baseline optics, taking into consideration the effect of the crossing angle, the b_5 multipole and the misalignment of the triplets is 11-12 sigma.

C. Long term tracking

As previously remarked, all the aperture results previously presented are based on short term tracking (1024 turns) that is adequate for comparative purposes. Also, synchrotron oscillation were not included as non relevant on the 1000 turns scale (~2 synchrotron oscillations). The baseline collision optics configuration (with crossing angle and the present specifications for triplet alignment and field quality) has been tracked for 100000 turns with synchrotron oscillations up to a momentum deviation of $4*10^{-4}$ [6]. The 100000 turns dynamic aperture is found to be 9 sigma, to be compared to the 11 sigma of stability at 1000 turns.

IV. CONCLUSIONS

Our scheme for correcting the nonlinear chromaticity of each IR consists of placing sextupoles in 4 families in the regular cells adjacent to the IRs and spread out over 6 betatron wavelengths into the arcs on each side of a cluster. These 'local' sextupoles correct primarily for the second and to a lesser extent the third order chromaticity of the IRs while contributing net zero linear chromaticity. The linear chromaticity of the entire Collider ring is removed by two families of sextupoles in the remai : ng cells in the arcs.

We have tested the above scheme with different configurations of IRs. It improves the chromatic and dynamic behaviour for every configuration studied. Even for the worst case with one IP at β^*=0.25m and the other at β^*=8m, the nonlinear correction scheme increase the momentum aperture more than two times. This increased momentum aperture is obtained at the expense of a slight reduction in the dynamic aperture for particles on momentum, when no field errors in the magnets are included. When we add a realistic set of errors, specially the field errors in the IR triplets, the local sextupoles do not affect the dynamic aperture on momentum.

V. REFERENCES

[1] T.Sen, Y.Nosochkov, F.Pilat, D.Ritson, R.Stiening, "Chromaticity Correction for the SSC Collider Ring", These Proceedings.

[2] T.Sen, M.Syphers, "Second Order Chromaticity of the Interaction Regions in the Collider", These Proceedings

[3] L. Schachinger and R.Talman, TEAPOT, *Part. Acc.*, **22**, 35

[4] Specification (Level 3B) Collider Arc, SSCL, E10-000027

[5] Y.Cai, B.Cole, R.Meinke, J.Peterson, F.Pilat, S.Stampke, M.Syphers, R.Talman, "Decoupling schemes for the SSC Collider", These Proceedings

[6] Y.Nosochkov, D.Ritson, "The Provision of the IP Crossing Angles for the SSC", These Proceedings

[7] B.Cole, J.Greene, Private Communication

An Optimized Formulation for Deprit-Type Lie Transformations of Taylor Maps for Symplectic Systems

Jicong Shi[1]

Department of Physics, University of Houston, Houston, TX 77204-5506, USA

Yiton T. Yan

SSC Laboratory[2], 2550 Beckleymeade Ave., Dallas, TX 75237, USA

Abstract

We present an optimized iterative formulation for directly transforming a Taylor map of a symplectic system into a Deprit-type Lie transformation, which is a composition of a linear transfer matrix and a single Lie transformation, to an arbitrary order.

For a sympletic system, a one-turn map can be written as a composition of a linear transfer matrix and a nonlinear Taylor map M of the form [1]

$$M\vec{z} = \vec{z} + \vec{U}_2(\vec{z}) + \vec{U}_3(\vec{z}) + \dots \quad (1)$$

which can be converted order-by-order into Lie transformations in the form of Dragt-Finn factorization [2]:

$$M\vec{z} = e^{:f_3(\vec{z}):}e^{:f_4(\vec{z}):}\dots\vec{z}, \quad (2)$$

where $\vec{z}$ represents the canonical phase-space coordinates; $f_i(\vec{z})$ and $\vec{U}_i$ are the homogeneous polynomial and the vectorial homogeneous polynomial of degree i, respectively; $: f_i(\vec{z}) :$ is the Lie operator associated with the function $f_i(\vec{z})$, which is defined by the Poisson bracket operation $: f_i(\vec{z}) : \vec{z} = [f_i(\vec{z}), \vec{z}]$. By means of the Campbell-Baker-Hausdorff (CBH) formula [2], the product of Lie transformations in Eq. (2) can be combined to form a single Lie transformation:

$$M\vec{z} = e^{:g(\vec{z}):}\vec{z}, \quad (3)$$

where

$$g(\vec{z}) = g_3(\vec{z}) + g_4(\vec{z}) + \dots, \quad (4)$$

and $g_i(\vec{z})$ is a homogeneous polynomial of order i. Note that except $g_3(\vec{z}) = f_3(\vec{z})$, $g_i(\vec{z})$ is generally different from $f_i(\vec{z})$. Since obtaining a single Lie transformation from Eq. (2) via CBH formula is pretty tedious and one may need such a single Lie transformation under certain circumstances [3], we have worked out an optimized algorithmic formulation for obtaining this single Lie transformation directly from the Taylor map of Eq. (1) [4]. It should be noted that we are not claiming that we are the first to try such a direct single Lie transformation. It is very likely that others may have different approach. The purpose of this note is to share with colleagues the simple and optimized algorithm we have obtained. The algorithm is described as follows.

Let us define, for each order n, a set of auxiliary vector homogeneous polynomials of degree n, $\{\vec{W}_n^{(m)}(\vec{z}), m = 1, 2, \dots, n\}$. $g_{n+1}(\vec{z})$ for $n = 2, 3, \dots$ are then obtained through order-by-order iteration given by the following steps:

$$g_{n+1}(\vec{z}) = -\frac{1}{n+1}\vec{z}^T S \vec{W}_n^{(1)}(\vec{z}), \quad (5)$$

where

$$\vec{W}_2^{(1)}(\vec{z}) = \vec{U}_2(\vec{z}), \quad (6)$$

and for $n \geq 3$,

$$\vec{W}_n^{(1)}(\vec{z}) = \vec{U}_n(\vec{z}) - \sum_{m=2}^{n-1} \vec{W}_n^{(m)}(\vec{z}), \quad (7)$$

where $\vec{W}_n^{(m)}$ for $2 \leq m \leq n$ is given by

$$\vec{W}_n^{(m)}(\vec{z}) = \frac{1}{m}\sum_{i=1}^{n-m} : g_{i+2}(\vec{z}) : W_{n-i}^{(m-1)}(\vec{z}). \quad (8)$$

In Eq. (5), S is the antisymmetric matrix [1] and the superscript T denotes the transpose.

This optimized algorithm is planned to be implemented in Zlib [5], a differential Lie algebraic numerical library.

REFERENCES

[1] Y.T. Yan, *AIP Conf. Proc. No. 249*, edited by M. Month and M. Dienes (AIP, 1992), p. 378.

[2] A. Dragt and J. Finn, J. Math. Phys. **17**, 2215 (1976).

[3] J. Shi and Y. T. Yan, "Symmetric Integrable-Polynomial Factorization for Symplectic One-Turn-Map Tracking" in these proceedings.

[4] J. Shi and Y. T. Yan, preprint (1993).

[5] Y.T. Yan and C. Yan, SSCL-300 (1990).

242

Symmetric Integrable-Polynomial Factorization for Symplectic One-turn-Map Tracking

Jicong Shi[1]
Department of Physics, University of Houston, Houston, TX 77204-5506, USA

Yiton T. Yan
SSC Laboratory[2], 2550 Beckleymeade Ave., Dallas, TX 75237, USA

Abstract

It was found that any homogeneous polynomial can be written as a sum of integrable polynomials of the same degree by which Lie transformations can be evaluated exactly. By utilizing symplectic integrators, an integrable-polynomial factorization is developed to convert a symplectic map in the form of Dragt-Finn factorization into a product of Lie transformations associated with integrable polynomials. A small number of factorization bases of integrable polynomials enables one to use high-order symplectic integrators so that the high-order spurious terms can be greatly suppressed. A symplectic map can thus be evaluated with desired accuracy.

I. INTRODUCTION

In large storage rings, high-intensity beams are required to circulate for many hours in the presence of nonlinear perturbations of multipole errors in magnets. Extensive computer simulations are thus necessary to investigate the long-term stability of beams. The conventional approach in which trajectories of particles are followed element by element through accelerator structures is, however, very slow in these situations. A substantial computational as well as conceptual simplification is to study the stability of particles by using one-turn maps.

While finding a closed analytical form of a one-turn map is impossible for a large-storage ring with thousands of elements, a truncated Taylor expansion of one-turn map—the Taylor map—can be easily obtained. Even though some successes have been reported using the Taylor maps, the truncation inevitably violates the symplectic nature of systems and consequently leads to spurious effects if the maps are used to study the long-term stability [1]. A reliable long-term tracking study with the Taylor map is therefore possible only if its nonsymplecticity effect can be eliminated without much reduction in the tracking speed.

In order to eliminate the nonsymplecticity, the Taylor map is usually converted into Lie transformations with

Dragt-Finn factorization [2]. A map in the form of Lie transformations is guaranteed to be symplectic, but generally cannot be used for tracking directly because evaluating a nonlinear map in such a form is equivalent to solving nonlinear Hamiltonian systems which cannot be done in general. Several methods, such as jolt factorization [3] and monomial factorization [4], have been proposed to deal with this difficulty by converting the Lie transformation from its general the form into special forms that can be evaluated directly. While these methods seem promising, their applications lead to considerable theoretical and computational complexities, chief of which is unpredictability of high-order spurious terms that may lead to a less than accurate evaluation of the map.

Since a general Lie transformation corresponds to a nonintegrable system that cannot be evaluated exactly, the challenge here is how to evaluate a Lie transformation approximately without violating the symplecticity and with a controllable accuracy. One way is to divide the nonintegrable system into subsystems that are integrable individually. The set of subsystems of minimum number is the most promising one to serve as the zeroth-order approximation because it would generate less high-order error and be a better starting point for higher-order treatments. For Lie transformations associated with homogeneous polynomials, we have shown [5] that any polynomial can be written as a sum of integrable polynomials by which Lie transformations can be evaluated exactly. Since the number of integrable polynomials can be much smaller than the number of monomials, a factorization based on the integrable polynomials will have many fewer terms so that a higher order factorization becomes practical. In order to achieve an optimization between a desired accuracy and a fast tracking speed, we have proposed a factorization on the integrable polynomials with symplectic integrators [5]. The advantage of the factorization with symplectic integrators is the suppression of high-order spurious terms to a desired accuracy [6–8].

II. INTEGRABLE POLYNOMIAL IN LIE TRANSFORMATION

A polynomial in $\vec{z}$ is called an integrable polynomial if

its associated Hamiltonian system is integrable, i.e., its associated Lie transformation can be evaluated exactly. Let $\{g_i^{(k)}|k = 1, 2, ..., N_g\}$ denote a set of integrable polynomials of degree i. In what follows, we shall show that any polynomial in $\vec{z}$ can be expressed as a sum of integrable polynomials of the same degree, i.e.,

$$f_i(\vec{z}) = \sum_{(\sum \sigma_j)=i} a(\vec{\sigma}) z_1^{\sigma_1} p_1^{\sigma_2} z_2^{\sigma_3} p_2^{\sigma_4} z_3^{\sigma_5} p_3^{\sigma_6} = \sum_{k=1}^{N_g} g_i^{(k)}, \quad (1)$$

where f_i is any homogeneous polynomial of degree i in phase-space vector $\vec{z} = (z_1, p_1, z_2, p_2, z_3, p_3)$ and $a(\vec{\sigma})$s are constant coefficients. After factorizing it as a product of Lie transformations associated with integrable polynomials, $\exp(: f_i :) \vec{z}$ can be therefore evaluated directly. Since the minimum number of integrable polynomials N_g is much smaller than the number of monomials, the accuracy of factorization with $\{g_i^{(k)}\}$ as bases can be carried to a desired order with the use of symplectic integrators.

Homogeneous polynomials of degree 3 in 6-variables consist of 56 monomials, which can be grouped under 8 integrable polynomials of degree 3, $\{g_3^{(n)}|n = 1, 2, ..., 8\}$:

$$g_3^{(1)} = c_1^{(1)} z_1^3 + c_2^{(1)} z_1^2 p_1 + c_3^{(1)} z_2^3$$
$$+ c_4^{(1)} z_2^2 p_2 + c_5^{(1)} z_3^3 + c_6^{(1)} z_3^2 p_3, \quad (2)$$

$$g_3^{(2)} = c_1^{(2)} p_1^3 + c_2^{(2)} p_1^2 z_1 + c_3^{(2)} p_2^3$$
$$+ c_4^{(2)} p_2^2 z_2 + c_5^{(2)} p_3^3 + c_6^{(2)} p_3^2 z_3, \quad (3)$$

$$g_3^{(2+i)} = z_i h_2^{(2+i)}(z_j, p_j, z_k, p_k), \quad (4)$$

$$g_3^{(5+i)} = p_i h_2^{(5+i)}(z_j, p_j, z_k, p_k), \quad (5)$$

where (i, j, k) goes over all cyclic permutations of $(1, 2, 3)$, $h_2^{(n)}$s are homogeneous polynomials of degree 2 in 4-variables, and $c_m^{(n)}$ is the coefficient of the corresponding monomial in f_3. It should be noted that the decomposition of f_i into integrable polynomials is not unique. $g_3^{(1)}$ and $g_3^{(2)}$ can be further combined into a single integrable polynomial since the Hamiltonian system with $H = -(g_3^{(1)} + g_3^{(2)})$ is integrable. We chose two separate integrable polynomials instead of the combined one because the solution for the later cannot be written in a closed form and directly used in tracking.

The Lie transformations associated with integrable polynomials can be converted into simple iterations [5]:

$$e^{:g_3^{(1)}:} z_i = \frac{z_i}{1 + c_{2i}^{(1)} z_i}, \quad (6)$$

$$e^{:g_3^{(1)}:} p_i = -\frac{(c_{2i-1}^{(1)} z_i + c_{2i}^{(1)} p_i)(c_{2i}^{(1)} z_i + 1)^3 + c_{2i-1}^{(1)} z_i}{c_{2i}^{(1)}(1 + c_{2i}^{(1)} z_i)}, \quad (7)$$

$$e^{:g_3^{(2)}:} z_i = \frac{(c_{2i-1}^{(2)} p_i + c_{2i}^{(2)} p_i)(c_{2i}^{(2)} p_i - 1)^3 - c_{2i-1}^{(2)} p_i}{c_{2i}^{(2)}(1 - c_{2i}^{(2)} p_i)}, \quad (8)$$

$$e^{:g_3^{(2)}:} p_i = \frac{p_i}{1 - c_{2i}^{(2)} p_i}, \quad (9)$$

$$e^{:g_3^{(2+i)}:} z_i = z_i, \quad (10)$$

$$e^{:g_3^{(2+i)}:} p_i = p_i + h_2^{(2+i)}(z_j, p_j, z_k, p_k), \quad (11)$$

$$e^{:g_3^{(5+i)}:} z_i = z_i - h_2^{(5+i)}(z_j, p_j, z_k, p_k), \quad (12)$$

$$e^{:g_3^{(5+i)}:} p_i = p_i, \quad (13)$$

$$e^{:g_3^{(2+i)}:} \vec{r} = U_{2+i}^{-1} \exp(z_i \Lambda_{2+i}) U_{2+i} \vec{r}, \quad (14)$$

$$e^{:g_3^{(5+i)}:} \vec{r} = U_{5+i}^{-1} \exp(p_i \Lambda_{5+i}) U_{2+i} \vec{r}, \quad (15)$$

where (i, j, k) goes over all cyclic permutations of $(1, 2, 3)$.

$$\vec{r} = (z_j \quad p_j \quad z_k \quad p_k)^T,$$

$$\frac{\partial}{\partial \vec{r}} = \left(\frac{\partial}{\partial z_j} \quad \frac{\partial}{\partial p_j} \quad \frac{\partial}{\partial z_k} \quad \frac{\partial}{\partial p_k}\right)^T,$$

$$\Lambda_n = U_n \left[\Gamma \frac{\partial}{\partial \vec{r}} \left(\frac{\partial}{\partial \vec{r}}\right)^T h_l^{(n)}\right] U_n^{-1}$$

$$= \begin{pmatrix} \lambda_1^{(n)} & 0 & 0 & 0 \\ 0 & \lambda_2^{(n)} & 0 & 0 \\ 0 & 0 & \lambda_3^{(n)} & 0 \\ 0 & 0 & 0 & \lambda_4^{(n)} \end{pmatrix}, \quad (16)$$

where superscript T denotes the transpose and Γ is a 4-dimensional antisymmetric matrix:

$$\Gamma = \begin{pmatrix} 0 & -1 & 0 & 0 \\ 1 & 0 & 0 & 0 \\ 0 & 0 & 0 & -1 \\ 0 & 0 & 1 & 0 \end{pmatrix}. \quad (17)$$

Similarly, 126, 252, and 462 monomials of homogeneous polynomials of degree 4, 5, and 6 in 6-variables can be grouped into 20, 42, and 79 integrable polynomials of degree 4, 5, and 6, respectively [5].

III. SYMMETRIC INTEGRABLE-POLYNOMIAL FACTORIZATION

With integrable polynomials, a symplectic map in the form of the Dragt-Finn factorization can be rewritten as

$$\vec{U}_s(\vec{z}) = R \prod_{i=3} \exp\left(\sum_{n=1}^{N_i} : g_i^{(n)} :\right) \vec{z}, \quad (18)$$

where R denotes the linear transformation and N_i is the number of integrable polynomials of degree i. By means of Campbell-Baker-Hausdorff (CBH) formula [2], one can, in principle, convert the Lie transformation associated with a sum of integrable polynomials into a product of Lie transformations associated with integrable polynomials. Since those integrable Lie transformations of the same order are,

in general, not commutable, such nonsymmetric separation will cause spurious errors on the next and higher orders. We therefore propose that symplectic integrators [6-8] be properly used to achieve symmetric seperation of integrable Lie transformations so that spurious errors can be as much suppressed as desired.

For $i \geq 5$, since $\left(: g_i^{(n_1)} : g_i^{(n_2)}\right)$ is a homogenous polynomial with degree higher than 7, a factorization with up to the 7th order is easily obtained by directly using the first-order integrator,

$$\exp\left(\sum_{n=1}^{N_i} : g_i^{(n)} :\right) = \prod_{n=1}^{N_i} \exp\left(: g_i^{(n)} :\right) + \epsilon(2i-2), \quad (19)$$

where $i \geq 5$ and $\epsilon(2i-2)$ represents the truncated terms, which are homogeneous polynomial with degree higher than $2i - 3$. For $i = 5$ and 6, the lowest-order truncated term is a homogeneous polynomial of degree 8 and 10, respectively.

For homogeneous polynomials of degree 4, we use the 2nd-order integrator and obtain a 7th-order symplectic map

$$\exp\left(\sum_{n=1}^{20} : g_4^{(n)} :\right) = \left(\prod_{i=1}^{20} e^{: \frac{1}{2} g_4^{(n_i)} :}\right) \prod_{i=1}^{20} e^{: \frac{1}{2} g_4^{(21-n_i)} :} + \epsilon(8), \quad (20)$$

where $(n_1, n_2, ..., n_{20})$ is any permutation of $(1, 2, ..., 20)$. The lowest-order truncated term in Eq. (20) is a homogeneous polynomial of degree 8.

In order to obtain a 6th-order symplectic map, we have to use the 4th-order integrator [6-8] to factorize $\exp(: f_3 :)$, which yields a product of $7^3 = 343$ Lie transformations associated with integrable polynomials:

$$\exp\left(\sum_{n=1}^{8} : g_3^{(n)} :\right) = \prod_{i=1}^{7}\prod_{j=1}^{7}\prod_{k=1}^{7} \exp\left(: d_i d_j d_k D_{ijk} :\right) + \epsilon(7). \quad (21)$$

$$d_1 = d_7 = \frac{1}{2(2 - 2^{1/3})}, \quad d_2 = d_6 = \frac{1}{2 - 2^{1/3}},$$

$$d_3 = d_5 = \frac{1 - 2^{1/3}}{2(2 - 2^{1/3})}, \quad d_4 = \frac{-2^{1/3}}{2 - 2^{1/3}}. \quad (22)$$

D_{ijk} is an integrable polynomial of degree 3 that can be chosen according to following pattern,

$$i = \text{even}\begin{cases} j = \text{even}\begin{cases} k = \text{even}, & D_{ijk} = g_3^{(n_1)} \\ k = \text{odd}, & D_{ijk} = g_3^{(n_2)} \end{cases} \\ j = \text{odd}\begin{cases} k = \text{even}, & D_{ijk} = g_3^{(n_3)} \\ k = \text{odd}, & D_{ijk} = g_3^{(n_4)} \end{cases} \end{cases}$$

$$i = \text{odd}\begin{cases} j = \text{even}\begin{cases} k = \text{even}, & D_{ijk} = g_3^{(n_5)} \\ k = \text{odd}, & D_{ijk} = g_3^{(n_6)} \end{cases} \\ j = \text{odd}\begin{cases} k = \text{even}, & D_{ijk} = g_3^{(n_7)} \\ k = \text{odd}, & D_{ijk} = g_3^{(n_8)} \end{cases} \end{cases}$$

where $(n_1, n_2, n_3, n_4, n_5, n_6, n_7, n_8)$ is any permutation of the first eight digits, (1, 2, 3, 4, 5, 6, 7, 8). The lowest-order truncated term in Eq. (21) consists of homogeneous polynomials of degree 7.

IV. CONCLUSION

We have shown that any polynomial can be written as a sum of integrable polynomials of the same degree. The number of optimized integrable polynomials is much smaller than the number of monomials. For homogeneous polynomials of degree 3 to 6, we were able to group 56, 126, 252, and 462 monomials into 8, 20, 42, and 79 integrable polynomials, respectively. All Lie transformations associated with these integrable polynomials were translated into simple iterations that can be directly used in tracking. By utilizing the symmetric symplectic-integrators, we have developed a factorization scheme based on the integrable polynomials in which Lie transformations associated with homogeneous polynomials are converted into a product of Lie transformations associated with integrable polynomials. A much smaller number of integrable polynomials not only serves a more accurate set of factorization bases but also enables us to use high-order factorization schemes so that the truncation error can be greatly suppressed. The map in the form of Lie transformations associated with integrable polynomials could therefore be a reliable model for studying the long-term behavior of symplectic systems in the phase space region of interest.

REFERENCES

[1] Y. T. Yan, *AIP Conf. Proc. 249*, edited by M. Month and M. Dienes (AIP, 1992), p. 378, and references therein.

[2] A. Dragt and J. Finn, J. Math. Phys. **17**, 2215 (1976).

[3] J. Irwin, SSCL Report SSCL-228, (1989); A. Dragt, I. Gjaja, and G. Rangarajan, *Proc. IEEE Accel. Conf.*, p. 1621 (1991).

[4] I. Gjaja, preprint, (1992).

[5] J. Shi and Y. T. Yan, preprint, (1993).

[6] E. Forest and R. D. Ruth, Physica D **43**, 105 (1990).

[7] F. Neri, "Lie algebras and canonical integration," Dept. of Phys., Univ. of Maryland, preprint (1988).

[8] H. Yoshida, Phys. Lett. **150**, 262 (1990).

Recent Results from the Dynamic Aperture Experiment at the SPS

W. Fischer, J. Gareyte, M. Giovannozzi, T. Risselada, W. Scandale and F. Schmidt
CERN
CH 1211 - Geneva 23

Abstract

Since 1986 dynamic aperture studies [1, 2, 3, 4] have been performed at the SPS in view of the LHC, the projected superconducting proton accelerator in the LEP tunnel. The aim of these experiments is to understand the aperture limiting effects of non–linearities and to define a model which allows the prediction of these effects in tracking studies. To this end the SPS, which is a very linear machine, is made non–linear in a controlled manner by 8 strong sextupoles powered in such a way that high order effects prevail. In this machine the short–term particle losses after seconds are well understood and in agreement with simulations. It has also been shown previously that power supply ripple in conjunction with the non–linearities can cause long–term losses after minutes. The 1992 experiment was aimed at providing enough data to allow a more quantitative comparison with a simulation model. Much care had to be taken to achieve stable and reproducible machine conditions and to perfect the instrumental tools needed for these delicate investigations.

1 Introduction

After a series of technical failures we finally managed to have one successful experimental session in 1992 which allowed some data taking with good machine conditions. Last year numerous 8 hours shifts, which are now reserved each week at the SPS, were used to test and commisson two instruments: BOSC, the turn–by–turn data acquisition system [5] and the linear wire scanners [6]. The progress of our experiment was set back by the fact that at first we did no longer recover the agreement between tracking results and experimental data which we had found in previous years. In the second section we will report on a new calibration of several of our instruments to resolve this problem. The disagreement could finally be attributed to an aging of the kicker. In the third section we will present the measurements done in the experiment of November 1992. And finally, in section four, we will present results and compare them with tracking simulation. As we were looking for precise quantitative agreement we made every effort to include detailed knowledge of the real machine in the tracking model.

2 Calibration of the Equipment

The kicker calibration done in 1988 proved no longer valid. Therefore we made an effort to do this calibration again and relate it to other instruments, namely horizontal and vertical scrapers and one rotational and two linear wire scanners.
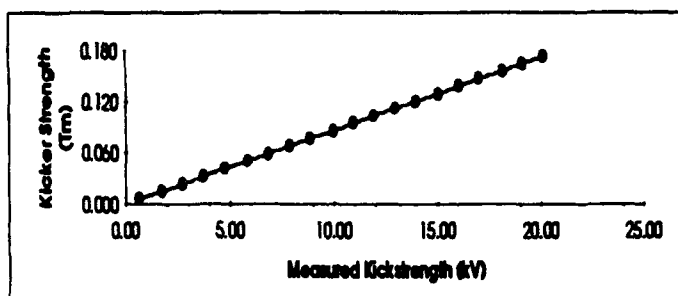
Figure 1: Kicker Calibration

Firstly we measured the current through the kicker magnet as a function of demanded kicker strength in kV. We found a good linear behavior down to small kick strengths (see Fig. 1).

Secondly we tried to relate the different instruments. The rotational wire scanner shows a rather linear behavior up to 60% of the kick strength that we use in our experiment. The linear wire scanners have a satisfactory linear response over a wide range of kick amplitudes. However, the later seem to underestimate the calibrated kick strength by 15%. The different scraping experiments also show the same discrepancy of 15% with the wire scanners. All measurements are consistent with the exception of an apparent difference of calibration factors between the wire scanners and the other instruments. This difference still needs to be resolved.

Thirdly we evaluate the error introduced in the tune measurement by the fact that we kick a beam of finite emittance instead of a single particle. At maximum kick strength this introduces in our case a tune shift of only 1.3×10^{-4}. However, due to nonlinear (mainly quadratic) chromaticity there is also a tune shift due to momentum deviation which amouts to 6×10^{-4} and is only marginally dependent on transverse kick strength.

3 Measurements

The experiment demands a very careful setting up of the SPS. The closed orbit is corrected in both planes below 0.4mm rms, the linear coupling is compensated so that the closest tune approach is 2×10^{-3}, the linear chromaticity is well compensated (Q' below 1). The energy is set to

120GeV where the linearity is neither disturbed by space charge effects nor by saturation of magnets. The machine is made nonlinear in a controlled manner by 8 sextupoles in a way which leaves chromaticity unchanged to first order and the neighboring third order resonance only weakly excited. We work at a small intensity of 2×10^{12} protons and normalised r.m.s. emittances of $2.5\pi \times 10^{-6}$m.

After recalibrating our kicker we could achieve a sufficiently good agreement between experiment and tracking. In the tracking we introduced meticulously every detail observed in the experiment: a residual linear coupling corresponding to the observed closest tune approach of 2×10^{-3}, the measured horizontal and vertical emittances and the measured closed orbit.
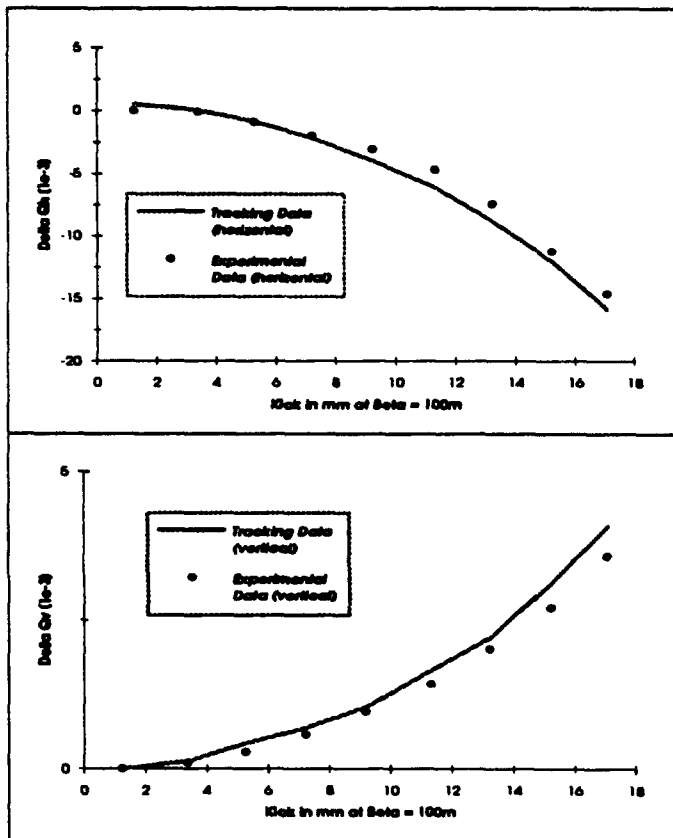
Figure 2: Horizontal and vertical detuning

In Fig. 2 the measured horizontal and vertical tunes are plotted as a function of amplitude and compared with the tracking results. One observes a very good agreement, the discrepancy reaching only 1×10^{-3} in the horizontal and 5×10^{-4} in the vertical plane. By comparison a similar measurement done in absence of the 8 strong sextupoles shows a 10 times smaller detuning. The natural ripple in the horizontal and vertical plane was measured with the continous Q-measurement to be 2.2×10^{-4} peak to peak. A Fourier analysis up to 1000Hz shows seven relevant lines whose added amplitudes account for a total ripple depth of 1.2×10^{-4}. The discrepancy between the total depth and our seven major ripple lines is probably due to very

low and/or high frequency components (to be clarified). These seven lines were always considered in the tracking simulations.
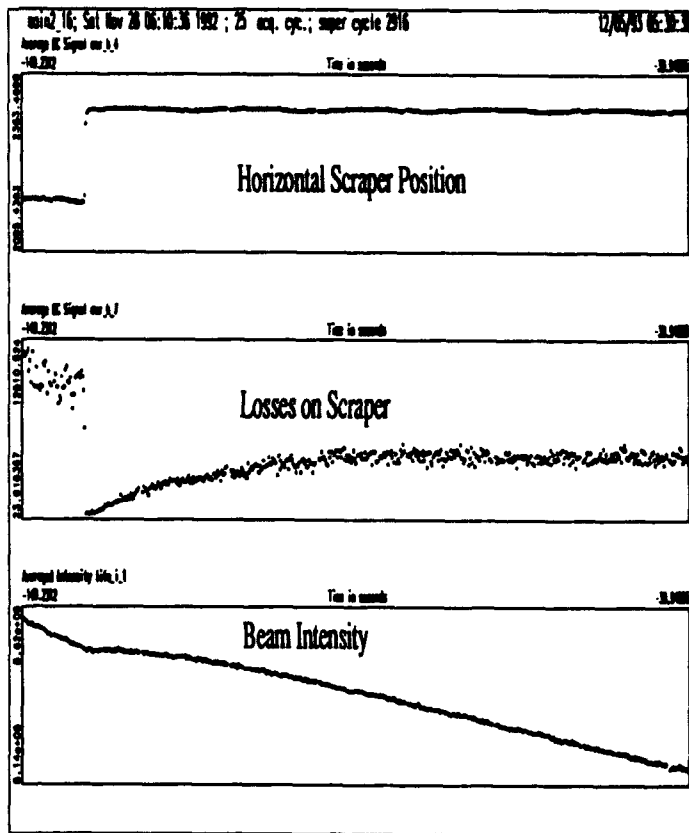
Figure 3: Measurement procedure

For observing the long term stability under the influence of sextupole nonlinearities and tune modulation the following procedure (see Fig. 3) was used: the beam was kicked to obtain a hollow distribution with enough particles at the required amplitude and scraped verticaly and horizontaly to have well defined edges. Then, the vertical scraper was retracted by 10mm and the horizontal by 1mm, and beam intensity and particle loss at the scraper observed. After a sufficiently long period the particles have diffused to reach one or both scrapers. The losses observed when moving the scrapers back to their original position teaches us in which plane the diffusion has preferentially occurred.

The parameters are varied in the experiment:

- Tunes (Q_H, Q_V): (26.0637, 26.5316), (26.605, 26.537)

- Hor. kicks [mm] at $\beta_H = 100$m: 12.8, 14.7, 16.6

- Added ripple frequency [Hz]: 9, 40, 180

- Frequency pairs [Hz]: (9, 40), (9, 180)

- Ripple depths ΔQ peak to peak [10^{-3}]: 0.55, 1.1, 1.87

and in the tracking:

- Turns: 2×10^6, about 46s storage time.

- Amplitudes: that corresponds to the scraper in-position minus 0, 0.5 and 1mm.

- Apertur: the scraper in the out-position.

- Momenta: $\pm 0.75 \times 10^{-3}$ in 5 steps.

4   Results

The first working point is carefully placed so as to avoid 5th and 7th order resonances. Due to non-linear detuning, the particles are distributed along a working line in the tune diagram, which straddles an 8th order resonance. At the other working point the working line crosses stronger 5th and 7th order resonances.

At the first point and for a kick of 14.7mm there was no sign of particles reaching the retracted scrapers over a period of more than 200s when ripple was absent or for the smaller ripple depth. For the medium and larger depth the particle loss sets in after about 200s and (35-60)s respectively. Like in previous years we find that the effect of tune modulation increases more than linearly with the ripple depth.

In the tracking we see that with no added ripple almost all particles are regular and thereby stable, while in all cases with ripple the motion is chaotic and therefore potentially unstable. This holds also for the second working point. Though chaotic, it needs the largest depth in the tracking to barely see some loss which is in good agreement with the experiment (the number of turns is also just marginally sufficient).

For the situation with two frequencies the results can not be compared directly because by accident the medium depth was used in the tracking instead of the small one as in the experiment. Nevertheless in both cases the differences with respect to the case with only one frequency (but same total depth) were not large, though more pronounced in the tracking. The strong effect found previously [4] apparently requires the vicinity of some stronger resonances.

When reducing the kick (small kick, large ripple depth) an immediate particle loss sets in, both in the experiment (too fast to be measured with precision) and in the tracking (in about 2s). The reason for this unstable behavior is that the 8th order resonance is crossed right at this amplitude. This could be seen clearly as a dip in the tune distribution taken with the Schottky system. The presence of this resonance is also responsible for the large losses at larger amplitude (see above).

At the second working point we applied the largest kick, but as we scraped down to the same positions the results are comparable. For the small depth the loss sets in after 17, 14 and 10s for 9, 40 and 180Hz respectively. In the tracking the tune modulation was also much more effective at that second working point. It became however clear that tracking only one or two particles is insufficient, because the loss times can vary by large factors (values up to 40 have been observed) even for close-by particles. We have therefore launched a massive tracking study with 60 particles over 10 million turns (200s storage time in the SPS) for some well choosen cases.

5   Conclusions

Even though the tracking results are still preliminary they seem to agree with the experiment within the limit of our knowledge of the SPS (about 5-10%). We feel therefore confident that tracking studies allow indeed very good predictions provided the non-linearities are considered in conjunction with tune modulation. These studies will be pursued since we are still far from understanding the actual mechanism that leads to slow particle loss.

6   Acknowledgements

References

[1] L. Evans et al., *The non-linear dynamic aperture experiment in the SPS*, 1st European Conference on Particle Accelerators, Rome, 7-11 June, 1988, CERN SPS/88-22 (AMS).

[2] J. Gareyte, A. Hilaire and F. Schmidt, *Dynamic aperture and long-term particle stability in the presence of strong sextupoles in the CERN SPS*, Particle Accelerator Conference, Chicago, 20-23 March, 1989, CERN SPS/89-2 (AMS).

[3] D. Brandt et al., *Influence of power supply ripple on the dynamic aperture of the SPS in the presence of strong non-linear fields*, 2nd European Conference on Particle Accelerators, Nice, 12-16 June, 1990, CERN SL/90-67 (AP).

[4] X. Altuna et al., *The 1991 dynamic aperture experiment at the CERN SPS*, Particle and Field Series 48, Conf. Proc. No. 255, Corpus Christi (1991), pp. 355-369, CERN SL/AP 91-43, LHC Note 171.

[5] A. Burns et al., *The Million Turn Data Acquisition System BOSC*, see this conference.

[6] W. Fischer, M. Giovannozzi and F. Schmidt, *Instrumentation and equipment for the diffusion experiment*, CERN SL-MD Note 42.

Higher order tune derivatives due to low-β insertions.

André VERDIER

CERN CH1211 Geneva 23

Abstract

In an electron machine the adjustment of the first order derivatives of the tunes with respect to momentum is important to counteract the dipole mode head-tail instability. In the case where low-β insertions are included in the lattice, this first order correction is not sufficient because important higher order tune derivatives appear. The associated strong quadratic variation of the tunes with momentum, results in a linear betatron instability for a small number of standard deviations in energy. This makes the life-time unacceptably small. The origin of tune derivatives of order larger than one is explained. The principle of their correction is recalled.

I. INTRODUCTION

The chromaticity problem is approached here as a particular case of a general treatment of gradient perturbations which had been developed for optimising an imperfect matching [1]. This treatment, which deals with a one-degree of freedom motion, will first be recalled. Then its application to the higher order chromaticity due to a low-β insertion will be done. The compensation with sextupole families will then be shortly examined. These matters had been developed in a course given by the author [2]. The aim of this paper is to explain more clearly the formula for Q″ which is the key point of the treatment and to correct some minor mistakes.

II. GLOBAL ESTIMATION OF A GRADIENT PERTURBATION

We consider a perfect machine at the end of which the betatron-functions have the values β and α. By definition the betatron functions have also the values β and α at the beginning of the machine.

We introduce in this machine a certain gradient perturbation. The effect of this perturbation can be computed exactly by means of the transforms of β and α through the perturbed machine, which are β^t and α^t, and the associated phase advance μ^t defined by :

$$\mu^t = \int_0^C \frac{ds}{\beta^t} \tag{1}$$

These quantities are indeed enough to obtain the perturbed one turn matrix [3], the elements of which are:

$$m_{11} = \sqrt{\frac{\beta^t}{\beta}}(\cos \mu^t + \alpha \sin \mu^t)$$

$$m_{12} = \sqrt{\beta \beta^t} \sin \mu^t$$

$$m_{21} = \frac{1}{\sqrt{\beta \beta^t}}\left((1 + \alpha \alpha^t)\sin \mu^t + (\alpha^t - \alpha)\cos \mu^t\right)$$

$$m_{22} = \sqrt{\frac{\beta}{\beta^t}}(\cos \mu^t - \alpha_t \sin \mu^t)$$

It is important to note that β^t and α^t are not true Twiss-functions : they have the same meaning as Twiss-functions in a transfer line. The true β-function β^* at the end of the perturbed machine can be obtained from the second element of the first line of this matrix :

$$\beta^* = \sqrt{\beta \beta^t} \sin \mu^t / \sin \mu^*$$

The new tune μ^* can be computed from the trace of the perturbed matrix :

$$2\cos \mu^* = \left(\sqrt{\frac{\beta^t}{\beta}} + \sqrt{\frac{\beta}{\beta^t}}\right)\cos \mu^t + \left(\alpha\sqrt{\frac{\beta^t}{\beta}} - \alpha^t\sqrt{\frac{\beta}{\beta^t}}\right)\sin \mu^t \tag{2}$$

Putting :

$$\theta = \arctan \frac{\alpha\sqrt{\frac{\beta^t}{\beta}} - \alpha^t\sqrt{\frac{\beta}{\beta^t}}}{\sqrt{\frac{\beta^t}{\beta}} + \sqrt{\frac{\beta}{\beta^t}}} = \frac{\beta^t\alpha - \alpha^t\beta}{\beta + \beta^t}$$

We can transform equation (2) into :

$$\cos \mu^* = \cos(\mu^t + \theta) \times$$

$$\sqrt{1 + \frac{1}{4}\left(\sqrt{\frac{\beta^t}{\beta}} - \sqrt{\frac{\beta}{\beta^t}}\right)^2 + \frac{1}{4}\left(\alpha\sqrt{\frac{\beta^t}{\beta}} - \alpha^t\sqrt{\frac{\beta}{\beta^t}}\right)^2} \tag{3}$$

In order to obtain this expression, there is a trick consisting of adding 4 to the sum of the squares of the coefficients of the trigonometric functions in equation (2), so that the sign plus in the first one can be changed to minus. As the term under the square root is always larger than 1, there are values of $\mu^t + \theta$ for which $\cos \mu^*$ is larger than 1, even if

the unperturbed $\cos \mu$ is smaller than 1 : the gradient perturbation has opened 'gradient stopbands'. An illustration of this effect can be found in ref [1].

It is worth noting that the expression under the square root can be used as a measure of mismatch when trying to match an insertion. In the case of an imperfect matching, minimising this expression guarantees that the stopbands associated with the mismatch have the minimum width.

III. Chromatic perturbation

We expand μ^t and μ^* in power series of the relative momentum deviation δ. μ^* is then $2\pi Q(\delta)$, Q being the tune of the machine, which is a function of the momentum deviation.

$$\mu^t = \mu + \mu^{t\prime}\delta + \frac{1}{2}\mu^{t\prime\prime}\delta^2 + ...$$

$$\mu^* = \mu + \mu'\delta + \frac{1}{2}\mu''\delta^2 + ...$$

We expand also β^t and α^t :

$$\beta^t = \beta + \beta'\delta + ... , \quad \alpha^t = \alpha + \alpha'\delta + ...$$

β and α being the on-momentum values. α' and β' are not the derivatives of α and β with respect to momentum, but the derivative of the transforms of the on-momentum functions through the machine. The computation of this β' can be found in [4]. For instance the contribution to this derivative of a thin quadrupole of length l and normalized gradient k is :

$$\frac{\beta'}{\beta} = -kl\beta_0 \sin 2[\mu - \mu_0] \qquad (4)$$

where the unlabeled optics parameters refer to the point of longitudinal coordinate s where the derivative is computed and the quantities labeled 0 refer to the quadrupole location. Taking the derivative of 4 with respect to s :

$$\alpha\frac{\beta'}{\beta} - \alpha' = kl\beta_0 \cos 2[\mu - \mu_0] \qquad (5)$$

Now we carry on with the identification of the terms with the same power of δ in the LHS and RHS of equation (3) after expansions in power of δ. The terms in δ give:

$$\mu' = \mu^{t\prime} + \frac{1}{2\beta}[\alpha\beta' - \beta\alpha']$$

μ' is the first derivative of the tune of the perturbed machine multiplied by 2π , $\mu^{t\prime}$ is obtained from 1.

Then, identifying the terms in δ^2, we obtain :

$$\mu'' = \mu^{t\prime\prime} + \left[\frac{\alpha\beta'}{\beta} - \alpha'\right]' + \mu^{t\prime}\left[\frac{\alpha\beta'}{\beta} - \alpha'\right]\cot\mu$$

$$- \frac{1}{4}\cot\mu\left[\left(\frac{\beta'}{\beta}\right)^2 + \left(\frac{\alpha\beta'}{\beta} - \alpha'\right)^2\right] \qquad (6)$$

In this expression the last term is much larger than the other ones as long as the first derivative $\mu^{t\prime}$ is some units. It describes the effect of the first order off-momentum mismatch of the β-function due to the low-β insertion. The numerical support of these statements is given below.

Identifying the terms in δ^3 leads to a similar result. The large term is still there, as well as its derivative with respect to momentum.

IV. Q" due to a low-β insertion

We consider the case of a machine composed of $\mathcal{N}_s$ superperiods with one symmetric low-β insertion per superperiod. All machine quadrupoles contribute to the chromatic effects but there is at least a strong one, close to the crossing point, which has a dominant effect on the second order tune derivative. In order to give an idea of the order of magnitude of this effect, we can consider the case of LEP under physics conditions, in the vertical plane. The β-value at the interaction point β^* is 5cm. The closest quadrupole is at 3.7m, it has a length of 2m and a strength k of $0.164m^{-2}$. The β-value at the quadrupole centre is about 400m, and the expression $kl\beta_0$ has a value of about 130. For the other lattice quadrupoles of length 2m, k is always below 0.03 and the β-value below 140m, resulting in $kl\beta_0$ smaller than 8. In equation 6 all contributions add-up linearly with phase terms as given by formulae 4 and 5, so that the effect of the low-β quadrupole dominates.

Keeping only the effect of the off-momentum mismatch due to two low-β quadrupoles in phase (they are π apart) per insertion, formula 6 takes the form :

$$Q'' \simeq -\frac{\mathcal{N}_s}{2\pi}(kl\beta)^2 \cot\frac{2\pi Q}{\mathcal{N}_s} \qquad (7)$$

Q being the tune of the machine, Q'' its second derivative with respect to momentum and $\mathcal{N}_s$ the number of superperiods.

The cotangent of the tune per superperiod is an important factor. If it is close to a half integer, the cotangent becomes very large. This is precisely a condition favorable for the beam-beam effect, because of the associated reduction of the beam size at the crossing point.

With the above mentioned LEP parameters of the low-β quadrupoles, Q'' given by formula 7 is 3.3×10^4. A tune shift of -0.2 is enough to produce a betatron instability since the fractional part of the vertical tune is 0.2. This tune shift is obtained with a momentum deviation of 3.5×10^{-3} with this value of Q''. The actual variation of the tunes with momentum of LEP with two sextupole families, for the physics optics, is shown on fig 1. We observe that the betatron instability occurs indeed at about 3×10^{-3} in the vertical plane. This shows the dominant

effect of the off-momentum mismatch on the second order tune derivative for this plane. In the horizontal plane the variation of the tune with momentum has a much smaller curvature. This is because the $kl\beta$ value is smaller than that for the vertical plane by a factor of about five. A similar situation occurs in the vertical plane for the injection optics where $\beta_y{}^*$ is reduced by a factor three, which reduces the contribution to Q'' by one order of magnitude.

If the tune per superperiod is close to a quarter integer modulo one half, the cotangent becomes small and tunes satisfying this condition avoid taking care for the compensation. This is for instance what has been done to test LEP with 90° cells. Choosing the tunes:
$$Q_h = 91.30 \quad Q_v = 97.20$$

makes it possible correct the chromaticity with two sextupole families for a β^* of 5cm [5], one order of magnitude being gained on $\cot \frac{2\pi Q}{N_s}$.

The machine parameters making $kl\beta$ large are mainly β^* and the distance L between the crossing point and the centre of the low-β quadrupole. $kl\beta$ is determined by the necessity of changing the sign of the derivative of β after the low-β quadrupole. For a thin lens model, we have :
$$kl\beta = -2\alpha = 2L/\beta^*$$

We can check for the LEP parameters given above that this expression gives 190, which is quite close to the actual value of 130. Putting this expression in 7, we see that Q'' scales with $(L/\beta^*)^2$.

V. COMPENSATION OF THE OFF-MOMENTUM MISMATCH

An obvious solution is to use sextupoles to match the first derivative of the β-function. As there are already such elements to adjust the first derivative of the tunes, the best procedure is to split them into families in order to make "off-momentum cells" which match the first derivative of the tune with respect to momentum. A variety of such arrangements has been tried. A review can be found in ref [2]. The experience shows that the best procedure consists in splitting the sextupoles into families as regular as possible with a phase advance per cell close to a simple fraction of π. This phase constraint guarantees both that the correction is possible, as two sextupoles separated by a π phase advance act in phase for the correction of β' (see equations 4 and 5), and that the non-linear transverse oscillations have the least detrimental effect.

VI. CONCLUSION

Increasing a lepton storage ring luminosity by decreasing the value of the β-function at the crossing point is lim-
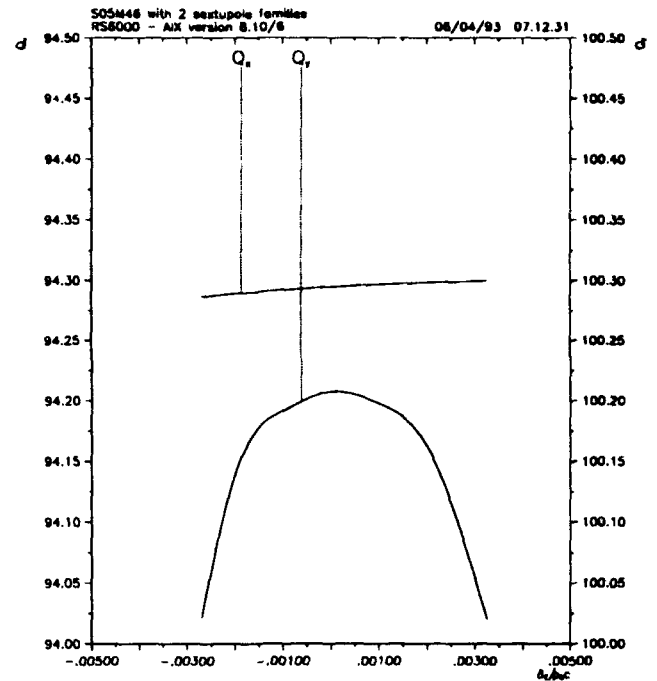
Figure 1: Variation of the tunes with relative momentum deviation for the LEP optics used in 1992. Qx=94.3, Qy=100.2 on the central orbit. There are four superperiods with one low-β insertion per superperiod. The first derivatives of the tunes have been set to about 2.5 with two sextupole families

ited by the non-linear chromaticity produced by the low-β insertion. The essential part of this effect is due to the second tune derivative with respect to momentum. When β^* is decreased below a certain threshold, this contribution to the non-linear chromaticity has to be compensated by splitting the sextupoles into families.

VII. REFERENCES

[1] A. Verdier, Linear optics design of the superconducting low-β insertion in the Intersecting Storage Rings at CERN,Nuclear Instruments and Methods, 207 (1983) 301-307.

[2] A. Verdier, Chromaticity. In CERN Accelerator School in Noordwijkerout, Netherlands (16-27 September 1991).

[3] K.G. Steffen, H. Hultschig and W. Kern, Use of generalised amplitude and phase functions in designing beam transport systems, DESY/A 2-70 (1960).

[4] B. Autin and A. Verdier, Focusing perturbations in alternating gradient structures, CERN ISR-LTD/76-14, (1976).

[5] T. Bohl et al. Ramp squeeze and collisions with the 90° lattice. LEP Performance Note 76 (8 January 1992).

A Quasi-Isochronous Operation Mode for the LNLS UVX Storage Ring

Liu Lin* and C.E.T. Gonçalves da Silva, Unicamp and LNLS
Laboratório Nacional de Luz Síncrotron - LNLS/CNPq
Caixa Postal 6192 - 13081-970 Campinas - SP - Brazil.

Abstract

We present an operation mode with very small momentum compaction factor for the LNLS UVX electron storage ring under construction in Campinas, Brazil. We establish conditions for longitudinal single particle stability in this quasi-isochronous mode including second order longitudinal and transverse effects. The results indicate that it is possible to operate this ring with the momentum compaction reduced by a factor of 100 with respect to the normal operation mode.

INTRODUCTION

The growing interest in very short electron and photon bunches provided by quasi-isochronous storage rings makes both the proposal of such rings for experiments and the analysis of higher-order longitudinal dynamics of considerable importance. The condition of quasi-isochronicity requires a momentum compaction factor α several orders of magnitude smaller than the values normally found in storage rings used for synchrotron light sources. This leads to an orbit length which is nearly independent of the particle energy deviation. This is a necessary condition to produce ultra-short electron bunches as the bunch length scales with $\sqrt{\alpha}$. The expected problems with quasi-isochronous rings are mainly related to higher order longitudinal dynamics and beam instabilities. When the zeroth-order (energy independent) momentum compaction factor approaches zero, its higher order terms in energy deviation can become dominant and introduce new features in the longitudinal dynamics. In addition, several beam instabilities have thresholds which depend on α. These problems, however, can be overcome as indicated theoretically by C.Pellegrini and D.Robin[1], H.Wiedemann[2] and L.Lin and C.E.T. Gonçalves da Silva[3] and demonstrated experimentally by Hama *et al.* [4] for the UVSOR ring.

In this paper we present a small momentum compaction operation mode for the LNLS UVX electron storage ring[5] under construction in Campinas, Brazil. We study the single particle dynamics of this quasi-isochronous mode using a general form for the momentum compaction factor which includes the effect of second order terms and the transverse betatron oscillations. Tracking studies are also presented.

OPTICAL FUNCTIONS FOR UVX QUASI-ISOCHRONOUS MODE

The LNLS UVX lattice consists of six long straight sections matched to six arcs with two dipoles and two quadrupoles between the dipoles. In the standard operation mode each arc is made achromatic and, as a consequence, the dispersion function η_x is always positive. To lower the momentum compaction we combine two standard superperiods

into one with four dipoles and we force the dispersion function to negative values at the two central ones. Thus, we obtain a three-fold symmetric quasi-isochronous ring preserving three first-order dispersion free straight sections.

We set the betatron phase advance so that the horizontal and vertical tunes in this mode are the same as in the standard mode. This allows continuous transference from the standard to the quasi-isochronous mode without crossing resonance lines during the process. This scheme has the advantage of avoiding the need to establish new injection conditions in this mode relaxing, therefore, the requirements for dynamic aperture.

The zeroth-order momentum compaction factor α_0 can be controlled by adjusting the negative part of the dispersion. In this particular quasi-isochronous mode for UVX we have reduced α_0 by a factor of 100 as compared to the standard operation mode. This reduces the bunch length by a factor of 10, in this case from 8 mm (27 ps) to 0.8 mm (2.7 ps).

Figure 1 shows the optical functions and the magnet lattice for one quasi-isochronous superperiod in UVX. We have 4 families of sextupoles in the dispersive section and two families in the non-dispersive section. We use the dispersive sextupoles to simultaneously correct the chromaticities and set the first order momentum compaction to a desired value. The non-dispersive sextupoles are used to optimize the dynamic aperture.
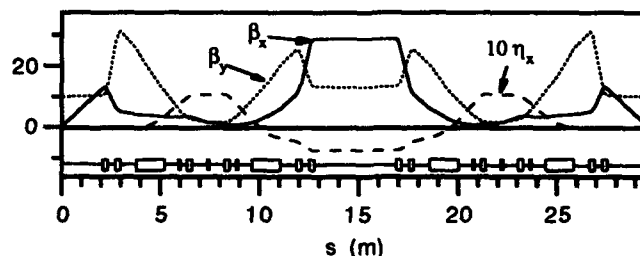
Figure 1: Optical functions and magnet lattice for one UVX quasi-isochronous superperiod.

NON-LINEAR SYNCHROTRON OSCILLATIONS

In order to describe the longitudinal motion of the electrons considering higher order and transverse motion effects we need to include them into the expression for the momentum compaction factor. The path difference for one revolution around the ring for an arbitrary particle with respect to the ideal one can be derived by geometric considerations:

$$\frac{\Delta L}{L_0} = \frac{1}{L_0} \oint ds \left(\frac{1 + x/\rho}{\cos(\theta)} - 1 \right) \qquad (1)$$

where $\theta^2 = x'^2 + y'^2$. We expand (1) keeping terms up to second order and express the particle amplitudes x and y as

$$x = x_\beta + \eta_0 \delta + \eta_1 \delta^2$$
$$y = y_\beta \qquad (2)$$

*Graduate student at IFQSC - Universidade de São Paulo.

where δ is the relative energy deviation. Noticing that the integrals containing terms which are linear with x_β and y_β vanish due to their oscillatory character, we have

$$\Delta L/L_0 = k_0 + \alpha_0 \delta + \alpha_1 \delta^2 \qquad (3)$$

where

$$\alpha_0 = \frac{1}{L_0} \int_0^{L_o} \frac{\eta_o}{\rho} ds \qquad (4)$$

$$\alpha_1 = \frac{1}{L_0} \int_0^{L_o} \left(\frac{\eta_1}{\rho} + \frac{\eta_0'^2}{2} \right) ds \qquad (5)$$

$$k_0 = \frac{1}{2L_0} \int_0^{L_o} ds \left(x_\beta'^2 + y_\beta'^2 \right) \qquad (6)$$

α_0 and α_1, respectively the zeroth and first order momentum compaction, are of chromatic nature and k_0 is of geometric nature. k_0 represents the effect of transverse oscillations on the orbit length. It can be estimated by using the smooth approximation for the betatron oscillations:

$$k_0 \approx \frac{\pi}{2L_0} \left(\varepsilon_x v_x + \varepsilon_y v_y \right) \qquad (7)$$

The first order dispersion η_0 is determined only by the first order magnetic elements whereas the second order term η_1 is affected not only by those elements but also by the sextupoles. This makes the sextupole the natural 'knob' to vary the first order momentum compaction in a controlled way without changing the zeroth order value.

The longitudinal equations of motion are:

$$\dot{\varphi} = \omega_{rf} \left(k_0 + \alpha_1 \delta + \alpha_2 \delta^2 \right) \qquad (8)$$

$$\dot{\delta} = \frac{e\hat{V}_0}{E_0 T_0} \left(\sin\psi - \sin\psi_s \right) - \frac{U_0 J_\varepsilon \delta}{E_0 T_0} \qquad (9)$$

where ω_{rf} is the angular frequency of the rf cavity, $\hat{V}_0$ is the peak voltage in the cavity, T_0 is the revolution period, U_0 is the energy radiated in one turn by the ideal particle and J_ε is the radiation damping partition number. In deriving eq.(9) we have expressed the accelerating voltage by a sinusoidal wave form $V(\psi) = \hat{V}_0 \sin\psi$. The ideal particle arrives at the accelerating cavity exactly at the synchronous phase ψ_s.

The last term on the right hand side of equation (9) represents the damping of the longitudinal oscillations. In our analysis we will neglect this damping term. In this case the equations of motion can be derived directly from the Hamiltonian:

$$H = \omega_{rf} \left(k_0 \delta + \frac{\alpha_0}{2} \delta^2 + \frac{\alpha_1}{3} \delta^3 \right) + \frac{e\hat{V}_0}{E_0 T_0} \left(\cos\psi + \psi \sin\psi_s \right)$$

which is the Hamiltonian for the dynamics of longitudinal phase motion including sextupoles and transverse effects.

We consider firstly the case where $k_0=0$. In the usual case ($\alpha_1=0$) the longitudinal phase space (ψ,δ) presents just one stable and one unstable fixed point at $(\psi_s,0)$ and $(\pi-\psi_s,0)$, respectively. The second-order term ($\alpha_1 \neq 0$) creates additional stable and unstable fixed points at, respectively, $(\pi-\psi_s, -\alpha_0/\alpha_1)$ and $(\psi_s,-\alpha_0/\alpha_1)$. We call attention to the existence of this new stability zone on the other flank of the rf wave, centered at $\delta = -\alpha_0/\alpha_1$, which does not appear in the linear theory. We will call the stable phase region around the usual

stable fixed point a normal bucket and the stable phase region around this new stability point an anomalous bucket.

We define a critical α_1:

$$\alpha_{1C} = \sqrt{\frac{E_0 T_0 \omega_{rf} |\alpha_0|^3}{12 e\hat{V}_0 \left(-\cos\psi_s + (0.5\pi - \psi_s)\sin\psi_s \right)}}$$

According to the value of α_1, the phase diagram will assume a different aspect. For $|\alpha_1|<\alpha_{1C}$ the normal buckets are very similar to the buckets in the linear theory, but with a great asymmetry between the two branches of the separatrix. In this case, the energy aperture is very large, as well as the separation between the normal and anomalous buckets. As $|\alpha_1|$ increases the buckets approach each other. For $|\alpha_1|>\alpha_{1C}$ the buckets change their form and the stable region decreases very rapidly reducing the energy and phase aperture. For $|\alpha_1|=\alpha_{1C}$ we have just the transition between the two cases as can be seen in figure 2.
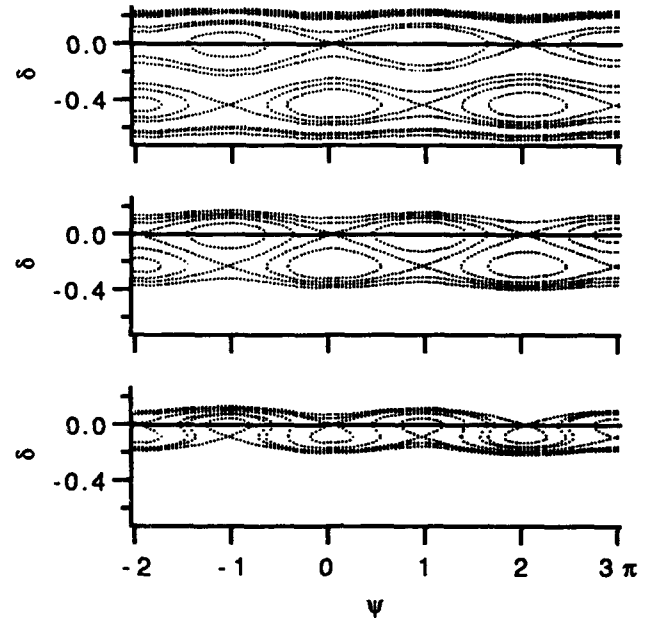
Figure 2: Effect of α_1 onto phase space separatrix. When $|\alpha_1|$ is small (top), the buckets are large and well separated. As $|\alpha_1|$ increases, the buckets approach each other and for $|\alpha_1|>\alpha_{1C}$ (bottom) their size decrease rapidly. The middle diagram shows the transition when $|\alpha_1|=\alpha_{1C}$.

We have seen that when the first order momentum compaction factor becomes dominant the anomalous bunches approach the normal bunches. Eventually, the anomalous bunches move within the physical energy acceptance of the storage ring. In this situation, it might be possible to observe the anomalous extra bunches intercalated in phase with the normal ones, doubling the number of bunches. It is interesting to see qualitatively what happens at this new point of stability. From the equation for the longitudinal phase, $\dot{\varphi} \propto \alpha\delta$, we see that a necessary condition for a stable solution (oscillatory phase) is that $\alpha\delta$ changes sign periodically. In the usual case, we have a constant α and δ oscillates around zero changing sign periodically. In the anomalous case, the term which periodically changes sign is α while δ has always the same sign. This is possible only

253

because the nonlinearity introduces the energy dependence of the momentum compaction factor. Expressing $\alpha = \alpha_0 + \alpha_1 \delta$, we see that the momentum compaction will oscillate around zero for values of δ in the neighborhood of $\delta = -\alpha_0/\alpha_1$, which is exactly the energy of the anomalous stable point. In this situation, the anomalous bucket is entirely confined to the negative δ half-plane (α_0 and α_1 of the same sign) or to the positive δ half-plane (α_0 and α_1 of opposite sign).

We consider now the effect of the term k_0, from transverse oscillations, to the longitudinal buckets. We expand δ for small k_0 and analyze the variation of the fixed points with the introduction of the transverse motion:

$$\delta_{fp} \approx \begin{cases} -\dfrac{1}{2}\dfrac{k_0}{\alpha_0} \\[2ex] -\dfrac{\alpha_0}{\alpha_1} + \dfrac{1}{2}\dfrac{k_0}{\alpha_0} \end{cases} \qquad \psi_{fp} = \begin{cases} \psi_s \\[1ex] \pi - \psi_s \end{cases}$$

Since k_0 is always positive, we conclude that if α_0 has the opposite sign to α_0/α_1 the fixed points move in such a way that the stable phase space area increases with k_0. In the other case, α_0 with the same sign as α_0/α_1, the stable area decreases with k_0. The transverse motion has thus introduced a distinct behavior depending on the sign of the zeroth and first order momentum compaction values.

For UVX the critical value of α_1 is $\alpha_{1C} = 3 \times 10^{-4}$. We study the case when the anomalous bunches are within the physical acceptance of the ring, $\delta_{phys.acc} = 3\%$. The rf bucket will just fill the physical acceptance for $|\alpha_1| = 4.4 \times 10^{-3}$. Regarding the sign of α_0 and α_1 we choose positive α_0 to keep the normal bunches at the same phase as in the standard operation mode, and negative α_1 to have the phase space increased with k_0. We estimate the contribution from transverse motion, considering 10 % emittance coupling, to be $k_0 = 2.5 \times 10^{-8}$. Figure 3 shows the normal and the anomalous buckets in this case. There are no noticeable perturbations to the buckets due to transverse motion.
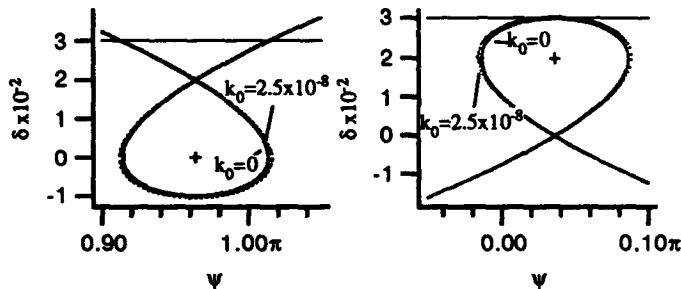
Figure 3: Normal (left) and anomalous (right) buckets for UVX (full line) and the effect of transverse motion on the buckets (dotted). Straight lines are physical limits of the ring.

DYNAMIC APERTURE CALCULATIONS

Tracking studies have been performed to determine the dynamic aperture of this UVX quasi-isochronous mode using the codes Patpet[6] and Teapot[7]. Both codes provided similar results. Two families of sextupoles in the non-dispersive region are used to minimize the tune shift with amplitude. We recall that these sextupoles do not affect either the chromaticities or the momentum compaction of the ring. The dynamic aperture simulations include effects of systematic multipole errors and synchrotron oscillations for 1% energy deviation. The results are shown in figure 4.
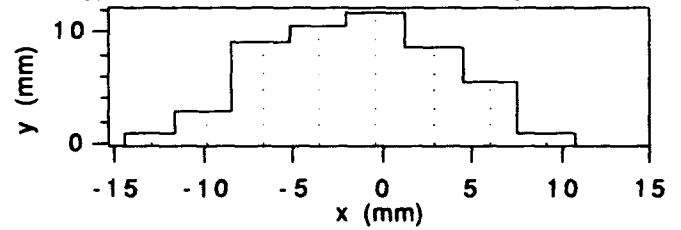
Figure 4: Dynamic aperture for UVX quasi-isochronous mode with dispersive sextupoles adjusted to set chromaticies to zero and α_1 to -4.4×10^{-3}; and non-dispersive sextupoles set to minimize the tune shift with amplitude. Systematic multipole errors and synchrotron oscillations for $\delta = 1\%$ are also included. The off-energy orbit has been subtracted.

CONCLUSIONS

We have analyzed the longitudinal phase space in quasi-isochronous storage rings including second order terms and the effect of betatron oscillations on the momentum compaction factor. The presence of the second order term introduces a new set of stable buckets displaced in energy and intercalated in phase with respect to the original set of stable buckets. When transverse betatron motion is considered, the stable phase region will depend on the particle amplitude. We have shown that this dependence will tend to enlarge the stable region when the signs of α_0 and α_0/α_1 are opposite.

We have also proposed a quasi-isochronous operation mode for the LNLS 1.15 GeV UVX electron storage ring where α_0 is 100 times smaller than in the standard mode. The chromaticities and the first order momentum compaction can be tuned by means of the sextupoles. The mode can be achieved by a continuous transfer from the standard operation mode, avoiding setting new injection conditions. This scheme could not be used for observing the new anomalous bunches since they do not exist in the standard mode. Dynamic aperture calculations show that we can have long lifetimes in this mode although injection is still difficult.

We note that the natural emittance of the beam in this quasi-isochronous mode has increased by a factor of approximately 4 with respect to the standard mode. We plan to continue exploring the condition of simultaneous small emittance and short bunches as well as questions related to beam instabillities which were not addressed in this report.

ACKNOWLEDGMENTS

We wish to thank J. Le Duff, H. Wiedemann and A. R. D. Rodrigues for many interesting discussions.

REFERENCES

[1] C. Pellegrini and D. Robin, *NIM* A301 (1991) 27-36.
[2] H. Wiedemann, SSRL ACD Note 125, August 21, 1992.
[3] L. Lin and C.E.T. Gonçalves da Silva, accepted by *NIM*.
[4] H. Hama *et al*, *Proc. of the Workshop on Fourth Generation Light Sources*, SSRL 92/02 (1992).
[5] See, for instance, Liu Lin, L. Jahnel and P. Tavares, *Proc. of the 3rd European Particle Accelerator Conference* (1992).
[6] L.Emery *et al*, *SSRL ACD Note* 36, 1988.
[7] L.Schachinger, R.Talman, *Part. Acc.* 22 (1987) 35-56.

Tracking Studies and Machine Performance Simulation of the SSC Low Energy Booster

X. Wu, R. York, R. Servranckx, S. Machida, J. F. Knox-Seith and U. Wienands
Superconducting Super Collider Laboratory*
2550 Beckleymeade Ave., Dallas, TX 75237

Abstract

The features of the SSC Low Energy Booster (LEB) lattice design include a high transition γ_t to avoid transition crossing during acceleration, dispersionless straight sections and moderate peak dispersion in arc sections. It has a three-fold symmetry with separate arcs and long straight sections to provide adequate azimuthal space for the required hardware. We have done tracking studies and machine simulations to verify the optical stability and performance of the LEB lattice. The results of these studies including misalignment, closed orbit correction and simulation of magnetic field errors are presented in this paper. Linear coupling resonances and 3rd order structure resonances have been analyzed and correction schemes have been developed to minimize their effect.

Figure 1. Lattice Funct· is of the LEB Superperiod

I. INTRODUCTION

The Low Energy Booster (LEB) of the SSC will accelerate protons from an injection momentum of 1.22 GeV/c to a final momentum of 12 GeV/c in 50 ms. It will operate in two different modes, the collider fill mode and the test beam mode with a normalized transverse beam emittance (rms) of 0.6 π mm-mrad and 4.0 π mm-mrad, respectively. The overview of the lattice and status of the LEB are included in these proceedings and elsewhere.[1,2] Figure 1 shows the lattice functions of a superperiod of the LEB at the nominal working tune point of (11.65, 11.60) calculated using the code DIMAD.[3]

The main goal of this study is to explore the optical stability and the machine performance of the LEB lattice. It consists of evaluating the effects of misalignment and field errors of the magnet elements and providing schemes for closed orbit and resonance corrections. The procedure begins by tracking and analyzing the performance of the "ideal" LEB lattice for which the only nonlinear magnet element is the chromaticity sextupole. Then the misalignment, closed orbit correction and the field errors of the magnet elements are included. Finally, the resonance corrections have been performed and similar tracking studies done to verify their effects. The lattices have been tracked for 1000 turns at the injection momentum of 1.22 GeV/c. No acceleration and space charge effects are included.

II. TRACKING STUDIES AND SIMULATION

A. The "Ideal" LEB Lattice

The linear LEB lattice has a natural chromaticity of about -15 in both horizontal and vertical planes. A total of 48 chromaticity sextupoles belonging to three families are positioned in 16 short straight sections inside the arcs. They are used to correct the chromatic aberrations. Protons with different initial amplitudes are tracked using the "ideal" LEB lattice where the only source of nonlinearity is the chromaticity sextupoles. Figure 2 shows the transverse phase space plot and the resonance spectrum of the tracking result of a proton at $\epsilon^* = 36$ π mm-mrad. The dynamic aperture of the "ideal" lattice, determined by those particles surviving 1000 turns of tracking, is larger than 800 π mm-mrad. The horizontal and vertical smear (rms) for the proton beam are 2.01% and 3.67% in collider fill mode, 6.23% and 9.52% in the test beam mode, respectively. The dominant resonance causing smear is the 3rd order structure resonance $\nu_x - 2\nu_y = -12$, which arises due to the presence of second-order geometric aberrations in the arcs.

B. Misalignment, Closed Orbit Correction and Magnetic Field Errors

The LEB lattice elements were misaligned assuming a Gaussian distribution with position errors of $\sigma_{x,y} = 0.4$ mm, $\sigma_z = 5$ mm and yaw errors of $\sigma_{z'} = 1$ mrad in our

Figure 2. Transverse Phase Space and Resonance Spectrum of the "ideal" LEB lattice

Table 1
Uncorrected rms and Peak Orbit Excursion

Random Seed	$x(rms)$ (mm)	$y(rms)$ (mm)	$x(peak)$ (mm)	$y(peak)$ (mm)
Uncorrected				
1	3.91	3.82	12.75	11.34
2	4.30	4.98	15.75	11.56
3	5.10	4.92	17.76	12.58
4	3.17	3.15	14.54	9.30
5	4.12	3.43	14.58	10.88
Corrected				
1	0.87	1.06	4.48	5.28
2	0.95	1.02	3.55	4.48
3	0.89	0.86	4.42	3.83
4	0.87	1.06	4.08	.06
5	1.11	0.90	4.86	.24

has been reduced to about 60 π mm-mrad. Our tracking studies indicate very little dependence on the random seed. The dynamic aperture is, however, well beyond the LEB vacuum chamber admittance of 40 π mm-mrad. Although resonance corrections are certainly required to minimize the resonances, and in turn, reduce the the smear and increase the dynamic aperture, the specifications for the LEB element alignment tolerances and magnetic field error multipoles appear to be quite adequate.

C. Resonance Corrections

Third order structure resonances are generated mainly by the 48 relatively strong chromaticity sextupoles in the arc sections. The magnetic field error multipoles and misalignment also contribute to these resonances. Corrections can be made by adding new sextupoles or by adjusting the strength of existing sextupoles in the LEB lattice. Previous tracking studies indicate that the dominant 3rd order resonances have little influence on the dynamic aperture. However, they do cause significant smear for the protons with large amplitudes. We have developed a resonance correction procedure using the basic lattice code DIMAD to transfer a complete LEB lattice description with imperfections, including field and alignment errors, to the differential-algebra (DA) code COSY INFINITY[4] and obtain a high order Taylor series map of the LEB lattice. The DA tools available in COSY INFINITY are then used to analyze the Taylor series map, evaluate the high order resonances and then perform the resonance correction using the proposed correction scheme.

The current 3rd order structure resonance correction scheme is to adjust the strength of existing chromaticity sextupoles in 8 families in each arc section since each of the LEB sextupoles has its own independent power supply. The zero chromaticity requirement is satisfied by having a pair of sextupoles with the opposite polarities located at symmetric positions of the lattice. Any specific 3rd order

simulation. Ninety beam position monitors adjacent to all main quadrupoles with an overall error of 1 mm were used to read the beam x and y positions. The dipole orbit correctors adjacent to quadrupoles focusing in the plane were then used to minimize the beam position monitor readings in that plane using a least square fit procedure. Table 1 shows the resultant uncorrected and corrected rms and peak closed orbit excursions.

Two prototype quadrupoles have been built at LBL and INP. The magnetic field multipoles were measured using a rotating coil device and used to provide the systematic and random magnetic field error multipoles for main quadrupoles in our simulation. Similar prototype dipoles are also being built at SLAC and INP. Meanwhile, field multipoles calculated using POISSON were used in our simulation for LEB bending dipoles and chromaticity sextupoles to determine their effects on the machine performance of the LEB lattice.

Figure 3 shows the transverse phase space plot and the resonance spectrum of the tracking result of a proton at $\epsilon^* = 36$ π mm-mrad using the LEB lattice with magnetic field errors, misalignment and closed orbit correction. In addition to the dominant 3rd order structure resonance, strong linear coupling resonances have been generated by the misalignment and magnet field error multipoles. Much larger smear has been generated for the protons with larger amplitudes, and the dynamic aperture of the LEB lattice

Figure 3. Transverse Phase Space and Resonance Spectrum of the LEB lattice with Magnetic errors, Misalignment and Closed Orbit Correction

Figure 4. Transverse Phase Space and Resonance Spectrum of the LEB lattice after the Resonance Correction

resonance can be completely cancelled using the current scheme. However, the resultant sextupole settings will affect the amplitudes and phases of the other resonances. The goal is to reduce the dominant resonances and at the same time keep the others undisturbed as much as possible.

The coupling resonances $\nu_x + \nu_y = 23$ and $\nu_x - \nu_y = 0$ are mainly caused by the skew quadrupole terms of the field error multipoles and the misalignment. Four skew quadrupoles similar to the regular trim quadrupole in the lattice have been added in the injection straight section to correct these coupling resonances. The complex coefficients of the coupling resonances were calculated using a resonance analysis code[5] and four independent knobs were then defined which are the linear combinations of the four skew quadrupole strengths. Each can be used to correct the amplitude or phase of a certain coupling resonance with little influence on the others. The correction procedure consists of iterating back and forth between skew quadrupole strength adjustment and tracking with DIMAD in order to simulate the correction process in a real machine scenario. Different random seeds and LEB working points were used in the process, and another code SIMPSONS[6] was also used to compare the tracking results.

Figure 4 shows the transverse phase space plot and the resonance spectrum of the tracking result of a proton at $\epsilon^* = 36\pi$ mm-mrad using the LEB lattice after the resonance correction. One can clearly see the improvement of the LEB lattice linearity and the effects of the resonance correction. The horizontal and vertical smear (rms) for the proton beam after resonance correction are 2.93% and 2.54% in collider fill mode, 5.64% and 4.07% in the test beam mode, respectively.

III. REFERENCES

[1] U. Wienands, et. al. "Status of the SSC Low Energy Booster", these proceedings.

[2] U. Wienands, et. al. "The H-γ_t Lattice of the SSC Low Energy Booster", *Conference Record of the XVth International Conference on High Energy Accelerators*, (Hamburg, 1992).

[3] R. V. Servranckx, et. al. "User's Guide to the Program DIMAD", SLAC Report 285 UC-28, May 1985.

[4] M. Bertz, "User's Guide and Reference Manual for COSY INFINITY", MSUCL-811, December 1991.

[5] R. V. Servranckx, et. al. "Resonance Analysis Program for Circular Machines", private communications.

[6] S. Machida, "The SIMPSONS Program, 6-D Phase Space Tracking with Acceleration", *Conference Record of Computational Accelerator Physics*, (February, 1992).

Magnetic Correction of RHIC Triplets

J. Wei, R. Gupta, S. Peggs

Brookhaven National Laboratory*, Upon, New York 11973

I INTRODUCTION

Triplets of large bore quadrupoles will be antisymmetrically placed on either side of all six intersection points of the Relativistic Heavy Ion Collider (RHIC) [1]. In RHIC collision optics, the triplets at the two experimental detectors are intended to enable the collision beta function to be reduced to the design goal of $\beta^* = 1.0$ meter in both planes, in order to minimize the spot size and maximize the luminosity. This requires running with $\beta_{max} \sim 1400$ meters in the triplet, where the beams will have their largest size, both absolutely and as a fraction of the available aperture. Hence, the ultimate performance of RHIC rests on achieving the highest possible magnetic field quality in the triplets.

Figure 1 shows the layout of a triplet, with the quadrupoles moved as close together as possible. Table 1 lists some triplet parameters, such as the different lengths of quadrupoles Q1, Q2, and Q3, and the 5σ beam size - about 71% of the 6.5 cm coil radius. All three quadrupole models have the same coil and iron cross-section in the main body, and all have the same coil "saddle" ends and electrical lead geometry. Lumped correctors, labeled C1, C2, and C3 in the Figure, carry three nonlinear windings to compensate for measured multipoles, in addition to carrying dipole corrector windings. This paper discusses the correction of magnetic errors expected in the quadrupole bodies and ends, using both these lumped correctors and also quadrupole body tuning shims.

◄— towards the interaction point

towards the arc —►
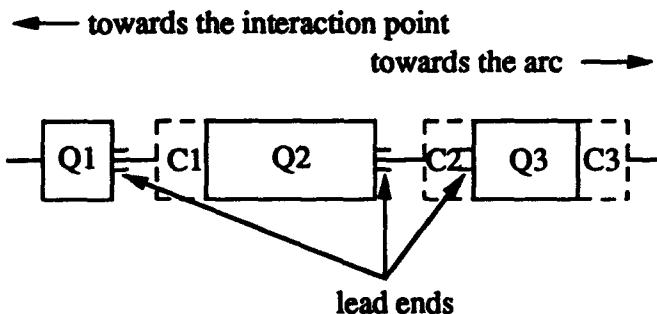
lead ends

Figure 1 Schematic layout of the RHIC triplet, showing the quadrupoles, the orientation of the quadrupole lead ends, and the local correctors C1, C2, and C3 .

Number of triplet quads in RHIC	72	
Magnetic length of Q1, Q2, Q3	1.44, 3.40, 2.10	[m]
Operating temperature	4.35	[K]
Design gradient	48.1	[T/m]
Design current	5.0	[kA]
Maximum triplet beta function	1.40	[km]
Maximum transverse beam size (5σ)	0.047	[m]
Coil inner diameter	0.130	[m]
Coil outer diameter	0.154	[m]
Iron inner diameter at midplane	0.174	[m]
Iron inner diameter at pole	0.184	[m]
Iron outer diameter	0.350	[m]
Minimum beam spacing at Q1	0.424	[m]

Table 1 Some basic triplet design parameters

II QUADRUPOLE BODY AND END HARMONICS

A detailed description of the triplet quadrupole design and construction can be found elsewhere [2,3]. To summarize, design or construction errors in the placement of the single layer coil are the strongest potential source of unwanted field harmonics. These harmonics are independent of excitation. By contrast, error harmonics generated from mislocation of the iron yoke are weaker - but still dangerous - and depend on the excitation level because of saturation effects. Almost negligible is the weak magnetic coupling of side-by-side triplets in RHIC's two horizontally separated rings. Two Q1 magnets lie in a common cryostat because the reference orbits are not fully separated this close to the intersection point.

All harmonics are optimized at 5,000 Amps, the maximum operating current, and so careful attention has been paid to locations in the yoke where the iron tends to saturate. In particular, the inner surface of the yoke makes a smooth transition from an arc of radius 87 mm to an arc of radius 92 mm. The angle that this transition makes with the midplane, and the corresponding transition angle of the RX630 plastic spacer that separates the coil and the yoke, are slightly different. This leaves eight symmetrically placed 7 millimeter holes between the spacer and the iron, where composite tuning shims will be installed. The nominal mix of 50% iron, 50% brass, will be varied for field harmonic correction.

Table 2 shows the tentatively expected values for the mean and standard deviation of normal and skew quadrupole harmonics, b_n and a_n, in triplet quadrupoles. Only significant harmonics with absolute systematic or random values greater than 0.1 are listed. The mean or "systematic" values are based on measurements of two prototype

quadrupoles, reported elsewhere [3,4], but they have been modified to reflect the predicted effect of a modest design iteration on future magnets. This iteration will remove most of the differences between predictions and measurements in the prototypes, so that the allowed multipoles b_5, b_9 and b_{13} come closer to zero. Random errors in the Table come from the copious measurements of 8 cm aperture RHIC arc quadrupoles. The standard notation used is defined by

$$(B_y + iB_x) = G(x + iy) .$$ (1)

$$\left(1 + 10^{-4} \sum_n (b_n + ia_n) \left(\frac{x + iy}{R}\right)^{n-1}\right)$$

where G is the nominal gradient in the center of the quadrupole body, and R = 4.0625 cm is the reference radius.

ORDER, n	NORMAL		SKEW	
BODY	$<b_n>$	$\sigma(b_n)$	$<a_n>$	$\sigma(a_n)$
1		10.0	.8	.4
2	.5	1.4	.1	1.2
3	(.0)	.6	.3	.7
4	.3	.6	.1	.5
5	1.5	.5	-.4	.1
9	-.2	.1	.0	.1
LEAD END	$<B_n>$	$\sigma(B_n)$	$<A_n>$	$\sigma(A_n)$
1			5.6	2.4
2	-.1	.7	-2.5	1.1
3	-.3	.3	.4	.1
5	2.8	.3	-1.6	.2
9	.3	< .1	.2	< .1
RETURN END	$<B_n>$	$\sigma(B_n)$	$<A_n>$	$\sigma(A_n)$
1			-.4	.4
2	.3	1.8	1.4	.5
3	-.1	.2	-.1	.3
4	.0	.1	.2	.2
5	1.4	< .1	-.1	< .1

Table 2. Expected mean and standard deviation for triplet quadrupole harmonics at 5,000 Amps, derived from prototype magnet measurements plus a minor design iteration.

The four quadrupole coils are electrically interconnected at the "lead end" of the quadrupole, by carrying two leads from each coil beyond the body of the magnet to a splice plate. These eight leads generate allowed field harmonics - b_1, b_5, b_9, .. and a_1, a_5, a_9 .. - both inside and outside the iron. The leads go through a 90^0 rotation once they are out of the magnet, effectively changing the sign of the current in the lead, and the sign of the multipoles generated. Each coil is also bent around a saddle at both the lead end and the "return end" of its pole piece. These saddles are designed to give near zero allowed harmonics b_5 and b_9. Table 2 also lists the

expected *integrated* quadrupole end harmonics, B_n and A_n, where, for example,

$$B_n = \int_{end} b_n \, dl$$ (2)

Body and end harmonics in Table 2 may be directly compared after multiplying the body value with the magnetic length of the appropriate quadrupole. This shows that only the b5 (dodecapole) end harmonics are of real concern.

Triplet quadrupoles are measured with the lead end away from an observer who is looking along the s-axis, through the magnet. The x-axis points to the left, and the y-axis points vertically upwards, in a right handed (x,y,s) measurement coordinate system. Table 3 indicates how to get from the sign of a measured harmonic to the sign of the actual harmonic, when a magnet has been rotated about a vertical axis between measurement and installation, so that the lead end is nearest the observer. Note that the sign of a harmonic is independent of the polarity of the magnet power supply.

dipoles:	$b_n \to (-1)^n \, b_n,$		$a_n \to (-1)^{n+1} \, a_n$	
quads:	$b_n \to (-1)^{n+1} \, b_n,$		$a_n \to (-1)^n \quad a_n$	

Table 3 After rotating by 180 degrees about the vertical axis.

III TRIPLET CORRECTION STRATEGY

The nominal horizontal and vertical tunes, 28.190 and 29.180, lie between 5th and 6th order resonances. Tune shifts from all contributions must be kept well below 0.033 in order for the beam to remain well within the tune plane triangle defined by these resonances and the coupling diagonal. The triplet errors shown in Table 2 dominate the tune shift contribution at storage - with two interaction regions operating at $\beta^* = 1$ m and four at $\beta^* = 10$ m - if they are uncorrected by shimming or by local correctors.

ORDER, n	NORMAL, b_n	SKEW, a_n
0	C1 or C3	C3 or C1
1	-	C2
2	S, (C2)	S
3	S, C1, C3	S, (C2)
4	S, C1, C3	S
5	S, C1, C3	S, (C2)
6+	-	-

Table 4 The triplet quadrupole correction strategy.

Table 4 shows which correction methods will be used for each harmonic - 'S' indicates that a multipole is corrected by shimming, while 'C1' indicates, for example, that a winding in

local corrector C1 is independently powered. An entry in parentheses means that a winding is present on a contingency basis - a power supply is not expected to be connected to it. Live correction might also be possible, by adjusting the lumped corrector excitations according to operational beam dynamics measurements. This is not proposed here, however, since this is not a conventional procedure at existing colliders.

The nominal thickness of the iron part of a tuning shim is 3.3 mm, but this can vary from 0.0 to 6.6 mm, easily sufficient to correct for the expected harmonics. After magnetic measurements on an individual magnet, the shim vector representing the 8 thicknesses is found [5] such that

$$\int_{body} (b_n + Db_n)\, dl + B_{n\ lead} + B_{n\ return} = 0 \qquad (3)$$

for the 8 goal harmonics, $n = 2$ through 5, normal and skew. Unfortunately the shims also cause feed up and feed down harmonics. Feed down to orders 0 and 1 is unimportant, since these harmonics are readily compensated by dipole and quadrupole correctors. Most prominent is feed up to b_9, caused by the shimming correction of b_5.

These effects are best described by taking the harmonic change vector as the independent variable. The changes in harmonics for multipole orders displaced by $4I$ from the original, where I is an integer, are then given by

$$\begin{pmatrix} \Delta b_{3+4I} \\ \Delta b_{5+4I} \\ \Delta b_{2+4I} \\ \Delta b_{4+4I} \end{pmatrix} = \begin{pmatrix} A_I & 0 & 0 & 0 \\ 0 & B_I & 0 & 0 \\ 0 & 0 & C_I & D_I \\ 0 & 0 & E_I & F_I \end{pmatrix} \begin{pmatrix} \Delta b_3 \\ \Delta b_5 \\ \Delta b_2 \\ \Delta b_4 \end{pmatrix} \qquad (4)$$

and

$$\begin{pmatrix} \Delta a_{3+4I} \\ \Delta a_{5+4I} \\ \Delta a_{2+4I} \\ \Delta a_{4+4I} \end{pmatrix} = \begin{pmatrix} G_I & 0 & 0 & 0 \\ 0 & H_I & 0 & 0 \\ 0 & 0 & J_I & K_I \\ 0 & 0 & L_I & M_I \end{pmatrix} \begin{pmatrix} \Delta a_3 \\ \Delta a_5 \\ \Delta a_2 \\ \Delta a_4 \end{pmatrix} \qquad (5)$$

Normal and skew harmonic changes are completely independent, as are even and odd multipole order changes, because the shim locations have quadrupole symmetry. The ratios between the odd harmonics generated at orders 1, 5, 9, et cetera, are fixed and constant, as are the ratios between those generated at orders 3, 7, 11, et cetera. By contrast, the change in an even order harmonic depends on the changes in both harmonic 2 and harmonic 4.

An analytical calculation based on first order perturbation theory is used to dead reckon the local corrector excitations in a single triplet, based on measurements of its three constituent quadrupoles [6]. Local correction is necessary even after adjusting the integrated goal harmonics to zero according to equation (3), because the beta functions vary rapidly in the triplet, and multipole errors in the ends of the quadrupoles can not be completely compensated by those from the body.

IV CONCLUSION

Figures 2a and 2b shows the tune footprint for on-momentum particles before and after triplet correction. The only magnetic errors present in the perturbation theory model used to get these results are the systematic errors listed in Table 2. All random harmonics are dropped, a simplifying approximation that makes little quantitative difference. In more realistic simulations it is assumed that there is a 10% error in the accuracy of measurement of individual quadrupole harmonics. Here, however, perfect knowledge of the quadrupoles is assumed. Each mesh of points represents a spectrum of particles launched with initial amplitudes between 0σ and 5σ in each plane individually, or along several contours of constant total action, $J_h + J_v$, where the ratio of horizontal and vertical actions, J_h/J_v, is smoothly varied. Chromatic tune spread (not shown) is dominated by the net positive linear and nonlinear chromaticities from the bare lattice, and not by the triplet quadrupoles, because the dispersion function is so small in the triplets.

Before correction, the tune footprint is unacceptably broad. Tuning and shimming are predicted to be very effective in reducing the spread of the footprint to a level that is negligible compared to the chromatic spread that is inevitably present. The results of the perturbation theory model shown here are consistent with more complex models that are numerically simulated, using tracking programs.
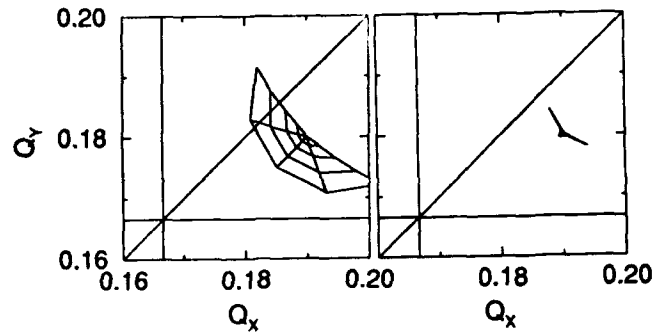
Figure 2 The tune footprint before and after correction, by shimming and excitation of the local correctors. The tune spread after correction is negligible compared to the tune spread due to linear chromaticity.

VI REFERENCES

[1] RHIC Design Manual, RHIC, BNL, Upton NY 11973
[2] R. Gupta et al, IEEE PAC, San Francisco (1991), p. 2239
[3] R. Gupta et al, these proceedings
[4] A. Jain and P. Wanderer, RHIC-MD-187, BNL, (1993)
[5] R. Gupta, code SHIMCAL, RHIC-MD-185 , BNL, (1992)
[6] J. Wei and M. Harrison, Int. Conf. on High Energy Accelerators, Hamburg, (1992)

Beam-Beam Modulational Diffusion in 2 1/2 Dimensions

T. Satogata and S. Peggs
Brookhaven National Laboratory[†]
Building 1005-3, Upton, NY 11973, USA

Abstract

Qualitative theoretical predictions for single particle modulational diffusion in 2 1/2 dimensions are compared with simulation results. Typical Fermilab Tevatron parameters are used for two beam-beam interactions under the influence of tune modulation created by synchrotron oscillations. When sideband overlap occurs on a pure one-dimensional resonance, diffusive growth is predicted and observed in the other transverse dimension. However exponential amplitude growth is observed in simulation instead of classically predicted root-time diffusive growth. Exponential growth rates are measured in particle tracking and possible impact on Tevatron luminosity upgrades is mentioned.

I. INTRODUCTION

Tune modulation is well known to have important effects on the dynamical response of particles to nonlinearities within an accelerator. In particular, theory, simulation and experiment investigating high order beam-beam resonances only agree qualitatively once tune modulation is incorporated[1,2]. Some recent investigation has concentrated on the phenomenon of modulational diffusion [3,4,5]. Salient features of this amplitude growth mechanism relevant to this study are:

- No external noise is present.

- Primary driving resonance overlap from tune modulation creates a thick layer of stochasticity in one dimension of motion.

- Weak coupling drives random-walk amplitude growth in the nonresonant plane. The diffusion rate is highly dependent on the proximity of this coupling resonance.

- Amplitude growth is diffusive, i.e. proportional to the square root of time.

Timescales of modulational diffusion are tens to tens of thousands of modulation periods; in a collider such as the Tevatron these timescales can range up to minutes. This mechanism is therefore a source of emittance growth and luminosity degradation that would significantly impact operations yet be difficult to diagnose.

Since modulational diffusion requires sideband overlap, it is present only in a region of the tune modulation parameter space where such overlap creates a thick layer of stochasticity. We assume tune modulation of the form

$$Q \to Q + q \sin(2\pi Q_M t) \, , \qquad (1)$$

where the time t is measured in turn number. For a one-dimensional primary resonance (with a strength characterized by the small-oscillation tune, or "island tune", Q_I), the region of parameter space that gives thick layer stochasticity is labeled by "Chaos" in Figure 1. This diagram has previously been investigated in part of experiment E778 at Fermilab [6,7]. The parameter diagram approach is powerful: given knowledge of the tune modulation strengths and frequencies in a particular machine (say, from chromaticity and typical momentum spread) one can set limits on Q_I and resonance strengths such that the chaotic region is never sampled and no modulational diffusion can exist.
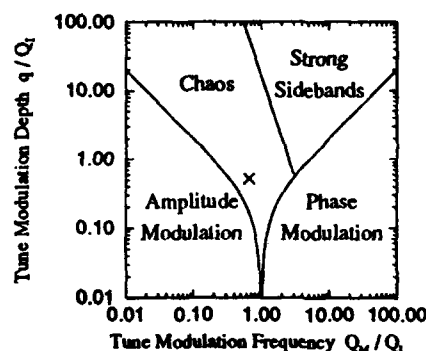
Figure 1. The (q, Q_M) parameter plane. The cross marks the point where simulations were performed.

Parameter	Symbol	Value
Horizontal base tune	Q_{x0}	20.597
Vertical base tune	Q_{y0}	20.580
Synchrotron tune	$Q_s = Q_M$	$7.8 \cdot 10^{-4}$
Chromaticity	$\xi_{(x,y)}$	3
Momentum offset	σ_p/p	$3 \cdot 10^{-4}$
Linear beam-beam tune shift	ξ	$5 \cdot 10^{-3}$
Tune modulation depth	q	10^{-3}
Beta function at IP	β^*	0.5 m

Table 1: Simulation parameters for 1992 Fermilab Tevatron collider run.

II. Simulation Parameters

We use a model of the Tevatron with two offset beam-beam kicks in an otherwise linear machine. All parameters used in the simulation are realistic except the base tunes, which are adjusted as described below. In this model all amplitudes are reported in units of the (round) transverse beam size σ; the beam-beam kick is then given in each plane by

$$\frac{\Delta x'}{\sigma} = \frac{-4\pi\xi}{\beta^* R^2}\left[1 - e^{-R^2/2}\right]\frac{x}{\sigma}, \qquad (2)$$

where $R = \sqrt{x^2 + y^2}/\sigma$, β^* is the linear beta function at the interaction point, and ξ is the linear beam-beam tune shift parameter.

Typical collider operations during the Fermilab 1992–3 collider startup used tunes of $Q_x = 20.586$ and $Q_y = 20.575$, with other relevant parameters listed in Table 1. This operating point lies between the $12Q_x$ and $5Q_x$ resonances, allowing a maximum beam-beam tune shift of $\xi = 9 \cdot 10^{-3}$ at each of the two low-beta crossing points before significant portions of the beam are affected by these low order resonances. A typical beam-beam tune shift per crossing is presently $5 \cdot 10^{-3}$, but luminosity upgrades such as the Main Injector will undoubtedly make this value even larger.

This study concentrates on the effects of the primary $5Q_x$ resonance, using this resonance as the source of stochasticity to drive modulational diffusion. Coupling is provided by the $4Q_x + Q_y$ resonance which is also driven by the beam-beam interaction. Moving the horizontal base tune from its nominal operations value to $Q_{x0} = 20.597$ produces a resonance island chain at $a_x = 2.2\sigma$ with $Q_I = 1.51 \cdot 10^{-3}$. This motion turns into a thick stochastic layer suitable for driving modulational diffusion in the vertical plane when realistic tune modulation from synchrotron oscillations and chromaticity is introduced, as shown in Figures 1 and 2. The tune modulation strength and tune used here are $q = 10^{-3}$ and $Q_M = 7.8 \cdot 10^{-4}$, for the Tevatron lattice in collider mode.

Because the beam-beam interaction couples strongly at large amplitudes, particles were launched at an initial vertical amplitude of 0.1σ. This amplitude was allowed to grow up to 1σ, where vertical motion starts to couple back to the horizontal stochastic motion, before tracking was stopped. Although not reported here, other simulations showed a similar growth mechanism operating at larger, more realistic, vertical amplitudes.

III. Simulation Results

Modulational diffusion theory predicts a strong dependence of diffusion rate on the proximity of the coupling resonance to the main driving resonance in the tune domain. This proximity is described by the quantity α,

$$\alpha \equiv \frac{\Delta Q_x}{q}. \qquad (3)$$

For the resonances of interest here, this quantity is given by the vertical base tune and the tune modulation strength q:

$$\alpha \equiv \frac{20.6 - Q_{y0}}{4q}. \qquad (4)$$

For values of α ranging from zero to about two, the diffusion is expected to be very strong [5]; the presence of the linear coupling resonance $Q_x - Q_y$ also complicates matters. A region with weaker diffusion, from $\alpha \approx 2$ to $\alpha \approx 5$, was investigated with vertical base tunes ranging from $Q_{y0} = 20.5820 - -20.5920$.

Figure 3 shows typical vertical amplitude growth over a long timescale, approximately 3500 synchrotron periods or $4 \cdot 10^6$ machine turns. This represents over one minute of actual machine operation in the Tevatron. Both log-log and log-linear scales are plotted, and it is apparent that the amplitude growth is exponential (linear on the log-log plot), not root-time as is classically predicted by standard modulational diffusion models. This type of growth was seen over several orders of magnitude of growth rate.

We quantify the exponential amplitude growth rate by the parameter γ:

$$a_y(t) = a_{y0}e^{\gamma t}. \qquad (5)$$

This rate was measured from a linear fit of $\log a_y$ versus time for approximately fifty particles launched over the base tunes mentioned above. This rate is plotted on a log-linear scale versus the coupling resonance proximity α in Figure 4, and shows structure similar to that of the diffusion rate in the diffusive growth case of [5]. No amplitude growth is evident over ten thousand synchrotron periods at these base tunes when tune modulation is removed, indicating that modulational diffusion is indeed responsible for this amplitude growth.
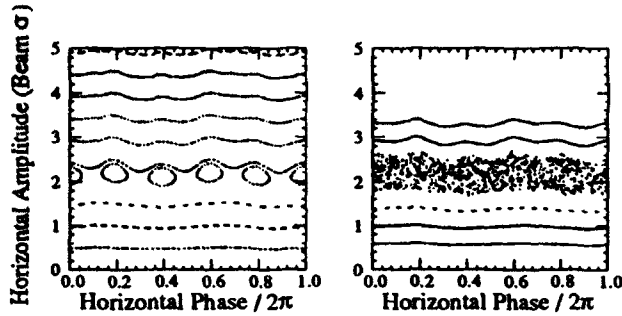
Figure 2: One-dimensional phase space motion at $Q_x = 20.597$, influenced by a strong $5Q_x$ resonance. The left figure is unmodulated; the right figure is influenced by tune modulation as listed in Table 1 and Figure 1.
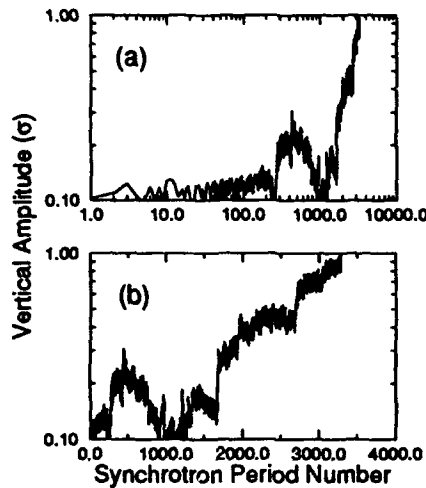
Figure 3: Vertical amplitude growth versus synchrotron period number on log-log and log-linear scales. The vertical tune is $Q_y = 20.5871$, or $\alpha = 3.225$
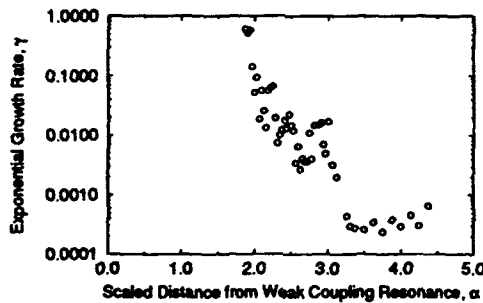
Figure 4: Exponential growth rate measured from simulation as a function of α, the proximity to the $4Q_x + Q_y$ coupling resonance.

IV. CONCLUSIONS

Under current operating conditions in the Tevatron, the beam is not expected to be affected by the $5Q_x$ resonance this strongly. However with future luminosity upgrades which will increase the beam-beam tune shift per crossing and the presence of higher-order resonances (in particular $17Q_x$ and $22Q_x$) that may serve as sources of emittance growth [2], modulational diffusion may provide a mechanism for slow luminosity degradation in hadron colliders and storge rings. Because modulational diffusion only occurs when thick-layer stochasticity is present, the tune modulation parameter diagram of Figure 1 may be used to place constraints on acceptable resonance strengths for operations in these machines.

Present work includes a concrete theoretical prediction of exponential growth rates in the case of an amplitude-dependent coupling strength. It has been suggested that the exponential growth observed in this simulation is due to the amplitude dependence of the coupling resonance strength, increasing the coupling strength as the vertical amplitude grows [8]. The collective nature of amplitude growth in the beam-beam modulational diffusion system is also under investigation to see what observable changes in beam emittance this mechanism produces.

REFERENCES

[1] S. Peggs and R. Talman, *Nonlinear Problems in Accelerator Physics*. Ann. Rev. Nucl. Part. Sci. **36**, 287–325 (1986).

[2] S. Tepikian and S. Y. Lee, *Beam-Beam Interaction and Higher Order Resonances*. Proceedings of the 1991 IEEE Particle Accelerator Conference, Vol. 3, 1639, March 1991.

[3] M. Month and J. Herrera, editors, *Nonlinear Dynamics and the Beam-Beam Interaction*. AIP Conf. Proc. **57**, 1979.

[4] A. J. Lichtenberg and M. A. Lieberman, *Regular and Stochastic Motion*. Springer-Verlag, New York, NY (1983).

[5] B. V. Chirikov, et al., *A Theory of Modulational Diffusion*. Physica **14D**, 289–304 (1985).

[6] T. Satogata, et al., *Driven Response of a Trapped Particle Beam*. Phys. Rev. Lett. **68**, 1838–41 (1992).

[7] T. Satogata, *Nonlinear Resonance Islands and Modulational Effects in a Proton Synchrotron*, Ph. D. Thesis, Northwestern University, 1993.

[8] Oliver Brüning, private communication.

Preparation of an Experiment to Investigate Nonlinear Beam Dynamics at the Storage Ring DELTA

Michael Schürmann

Institute of Acceleratorphysics and Synchrotronradiation, DELTA

University of Dortmund, 44221 Dortmund, Germany

Abstract

The investigation of nonlinear beam dynamics is one of the research fields at the electron storage ring DELTA [1] [2]. Optimisation of strength and distribution of the sextupole magnets in the ring and dynamic aperture needs knowledge about phasespace structure and nonlinear resonances. For this purpose measurements of the beam position turn by turn are a very suitable.

1 The Tracking Method

Since both rings of the DELTA facility, the booster BoDo and DELTA itself are under construction at the moment, there is no possibility to use experimental data so far. All considerations are based on simulation results of measurements mainly performed with the program MAD [3]. First of all we compare the different tracking methods TRANSPORT, LIE3 and LIE4 with optical data of the BoDo ring.
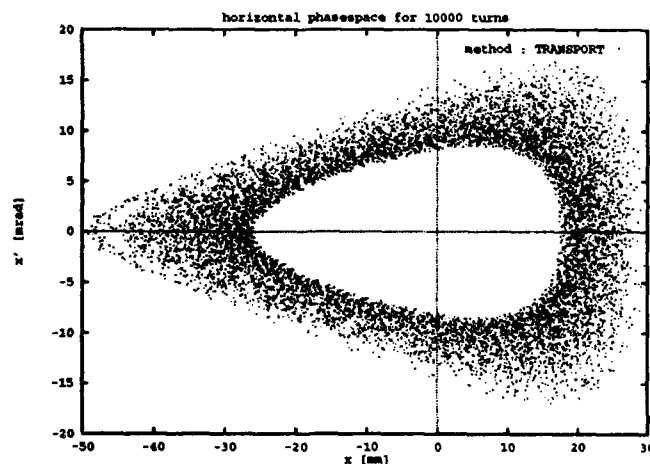
Figure 1: Horizontal phasespace with TRANSPORT

Figure 1 and 2 show the horizontal phasespace for 10000 turns with the same start parameter nearly at the limit of the dynamic aperture. The lattice contains only the separate sextupoles as nonlinear elements, but no higher multipoles due to fringe fields of the magnets. Figure 1 shows the result of the tracking method TRANSPORT. The disadvantage of the non symplectic matrix formalism is visible. The violation of Liouville's theorem produces an unphysically damping of the betatron oscillation. To get a more physical result the Lie algebra method up to third

order in nonlinearities (LIE3) was used (fig. 2). The results of the phasespace calculation with the LIE4 method are the same as with LIE3 but they need a faktor three more in time.
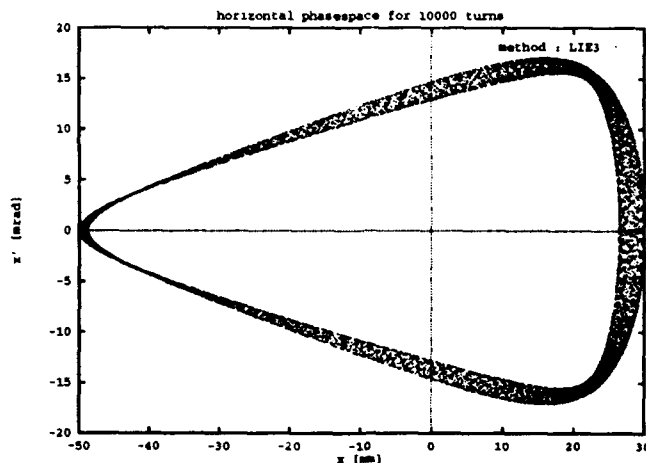
Figure 2: Horizontal phasespace with LIE3

2 Phasespace for Different Betatron Oscillations

Both the simulation and the measurements use the firing of a feedback kicker to excite a betatron oscillation. For the simulation the electron bunch is represented by 20 particles, forming a gaussian distribution with 3 σ standard deviations. The perturbation is simulated by a simple kick. The optical data of DELTA used for this simulations contain all known nonlinearities, the separated sextupole magnets, the measured multipoles in the quadrupole and dipole magnets and their fringe fields. Figure 3 and 4 show the position of the bunch for the first 10 turns at the location of BPM 1 and for the last 10 of 10000 turns. For the moderate perturbation with a 2.5 mrad kick the deformation of the bunch is small and it is clearly visible which particle belongs to which turn. After 10000 turns all the particles are distributed all over the phasespace ellipse because of Landau damping and a separation of turns is no longer possible. With a 4 mrad stimulation the first 10 turns look something different (fig. 5). The influence of nonlinearities distort the structure of the bunch after a few turns. The phasespace for the last turns

similar to figure 3. You have more or less an homogeneous distribution over the ellipse.
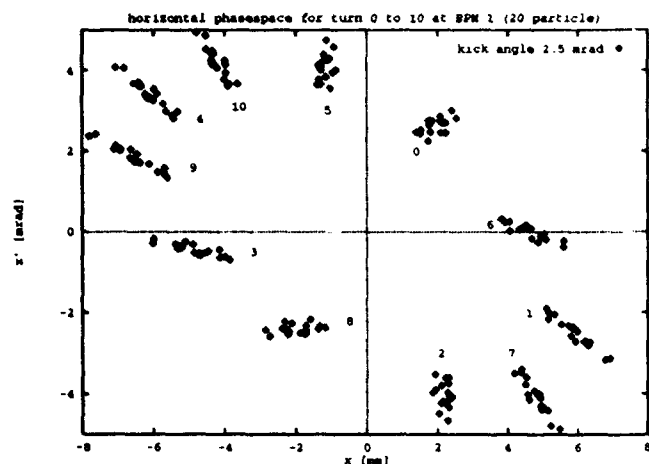
Figure 3: First 10 turns with 2.5 mrad kick
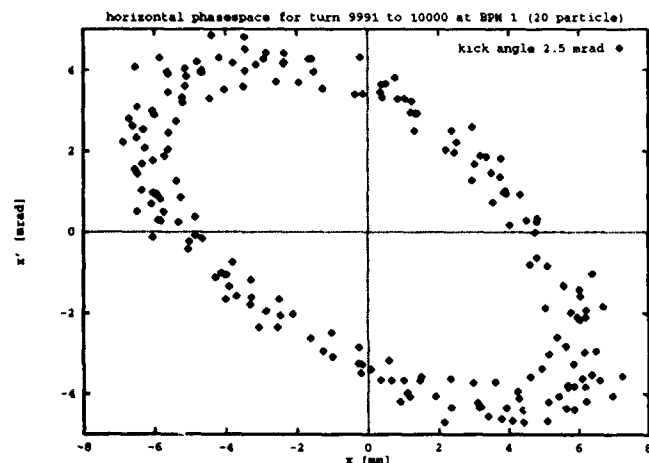
Figure 4: Last 10 turns with 2.5 mrad kick
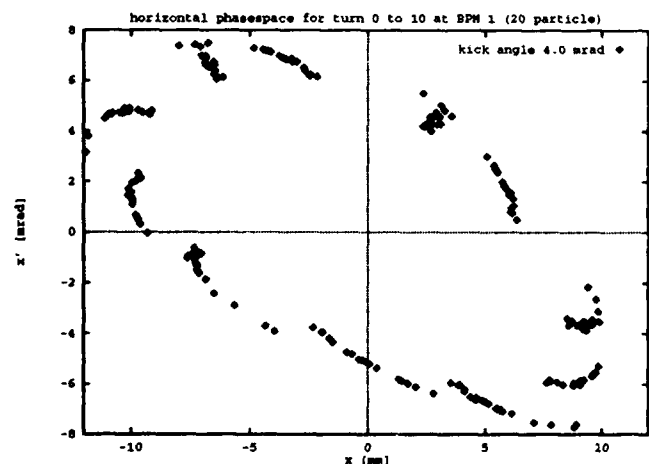
Figure 5: First 10 turns with 4.0 mrad kick

The only parameters one can get from the BPM's are are the horizontal and vertical displacement of the center of charge. It is obviously that the displacement decreases if the particles of one bunch are distributed over the ellipse more or less homogeneous. This distribution is an effekt of Landau damping. The influence of synchrotron damping is neglectible. One damping time of the DELTA storage ring at 1.5 GeV is about 10 ms and 270 ms at an energy of 0.5 GeV. As 270 ms corresponds to 675000 turns the damping for the first 10000 turns can be neglected. As one can see in figure 6 the damping is not the only effekt.
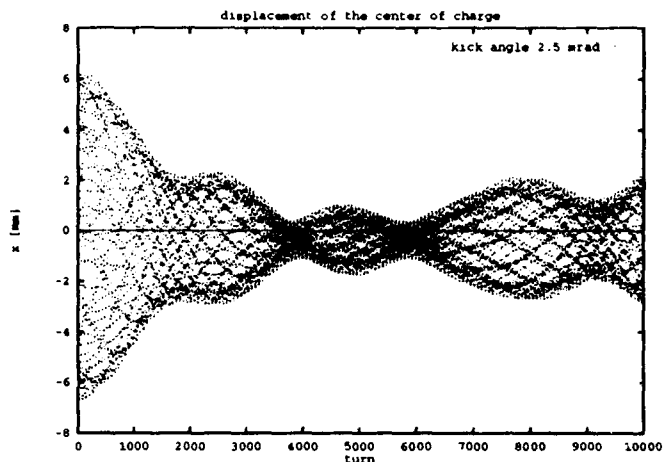
Figure 6: Displacement of the center of charge versus turn for 2.5 $mrad$ kick

For moderate beam perturbation a periodic damping and excitation of the center of charge is visible. Damping to a minimum means that the particles are more or less equal distributed all over the ellipse. Excitation means a concentration of the particles in one part of the ellipse. With a 4 $mrad$ perturbation every structure and every damping and stimulation mechanism is lost.
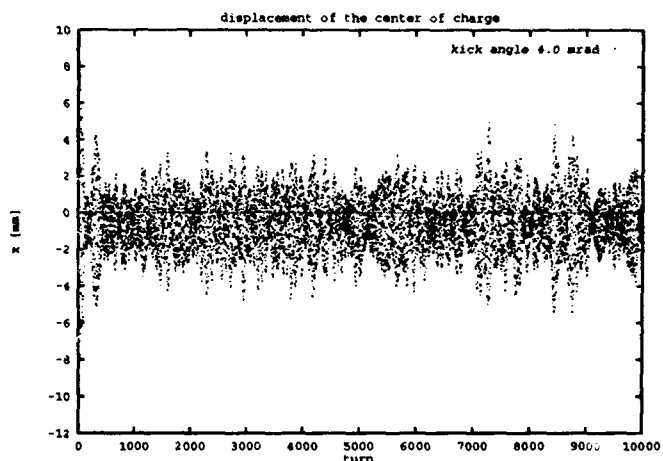
Figure 7: Displacement of the center of charge versus turn for 4 $mrad$ kick

The monitor signal looks like electronic noise but nev-

265

ertheless it contains information about the optics. If one looks at the fourier spectrum of the displacement (fig. 8,9) one can see in case of linear optics small peaks at the location of the horizontal tune Q_x and at $2*Q_x$. In the nonlinear case the main peaks are broader and have many additional small peaks. One can also detect a tune shift depending on the stimulation kick.
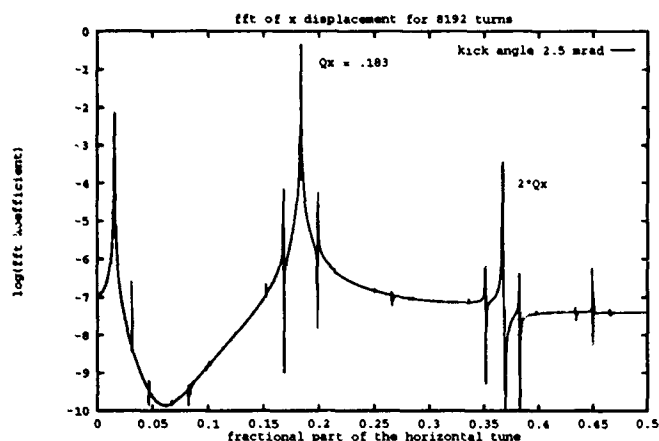
Figure 8: fft of the displacement with 2.5 *mrad* kick
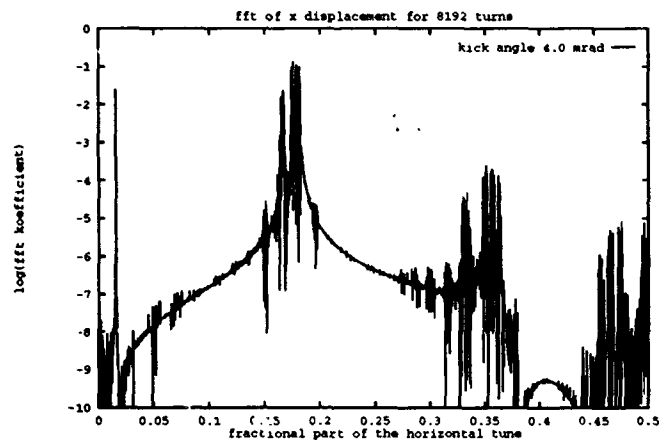
Figure 9: fft of the displacement with 4 *mrad* kick

3 Reconstruction of the Phase-space

To calculate the phasespace from the monitor signals which can only measure the displacement of the beam but not the derivative, one has two possibilities. First you can use the betafunctions, the gradient of the betafunctions at the location of the two beam position monitors and the phase advance between them from other measurements to calculate the derivatives with the help of the matrix-formalism. This method has disadvantages. The optics

parameter are only known with an accuracy of about a few percent and that is not enough for precise statements about the phasespace. Furthermore the matrixformalism takes into account only linear elements of the optics and neglects all nonlinearities. Therefore it is better to use the measured magnetic field distribution between the monitors with all higher multipoles. Doing this it is possible to solve the Lorentz equation using a series expansion of the magnetic field. At this X_1 at BPM 1 is a fix parameter and X_1' will be vary til X_2 at BPM 2 is matched. X_2' is fixed automatically by this 'shooting' method.
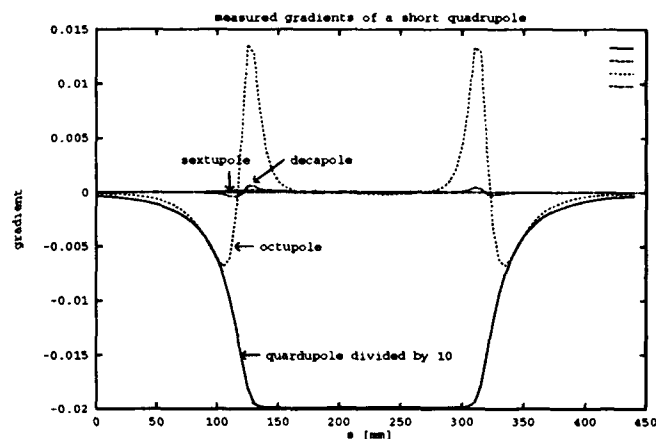
Figure 10: Example of measured gradients of a short quadrupole [4]

4 Conclusion

Measurements of the pasespace turn by turn are useful to study damping mechanisms, tuneshifts due to nonlinearities and resonace widths as one can see before. Before an experiment can be designed some theoretical considerations are nessesary. Therefore, tracking programs are very helpfull. The influence of magnet misalignments, accuracy of BPM monitors will take into account next. The analysis of the monitor data will be improved to extract informations as most as possible.

References

[1] N. Marquardt, Report on DELTA One Year Before Routine Operation, This Conference.

[2] DELTA Group, DELTA Status Report (August 1990), unpulished

[3] F. C. Iselin, H. Grote, The MAD Programm Version 8.4, CERN/SL/90-13

[4] F. Brinker, Phd. Thesis, to be published

Statistics of the Half-Integer Stopband

S. Dutt, F. Chautard, R. Gerig, and S. Kauffmann

SSC Laboratory*

2550 Beckleymeade Avenue

Dallas, TX 75237-3997, USA

Abstract

We consider the statistical nature of the stopband set up in the vicinity of a half-integer tune when a linear lattice is subjected to quadrupole errors distributed according to gaussians. The probability density function of the stopband, treated as a complex number, is found to be a correlated bivariate gaussian in the real and imaginary parts. The mean magnitude of the stopband is calculated in terms of the complete elliptic integral of the first kind, and the conditional probability density of its magnitude is obtained in closed form. A number of limiting conditions are studied. Finally, we estimate the requirements on a correction system for neutralizing the stopband with a given probability of success.

I. INTRODUCTION: PHYSICS

Consider a linear lattice subjected to small quadrupole errors. Fig. 1(a) displays the eigenvalues of the one-dimensional transfer matrix in the complex plane [1]. If the unperturbed tune ν lies close to a half-integer, the eigenvalues $e^{\pm i\mu}$, $\mu = 2\pi\nu$, will lie on either side of the negative real axis, as shown. The influence of the quadrupole errors will be either (i) to rotate the eigenvalues away from the negative real axis, or (ii) toward it. If the effect is the latter, then as the strength of the perturbation increases, the eigenvalues will coincide on the negative real axis at some point. At this stage, further increasing the strength of the perturbation will either (i) move the eigenvalues past each other on the unit circle, or (ii) cause them to move onto the real axis, thereby making the lattice unstable. Lattice configurations corresponding to these two possibilities are displayed in Figs. 1(b) and 1(c), where we assume that the unperturbed lattice has a superperiod of two, and the perturbing quadrupoles, of equal strength, to be separated by a superperiod. In the first case, Fig. 1(b), the eigenvalues would rearrange themselves on the unit circle. In the second case, Fig. 1(c), the eigenvalues would move onto the real axis if the perturbation is sufficiently strong. It is customary to attribute the resulting instability to the *half-integer stopband*. Note that there is no stopband for the perturbed lattice, in the sense that the tune must reach the half-integer before the lattice becomes unstable [3]. One can, however, speak of a stopband for the *unperturbed* lattice, Fig. 2. The tune shift caused by the perturbing
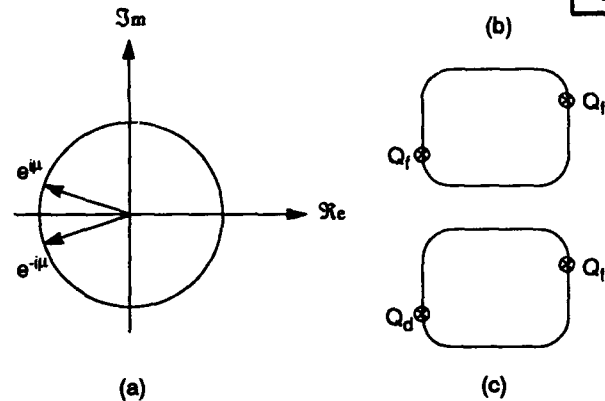
Figure 1: (a) Eigenvalues of one-dimensional transfer matrix near half-integer tune. (b) Stable, and (c) possibly unstable lattice configurations near half-integer with perturbing quadrupoles separated by a superperiod.
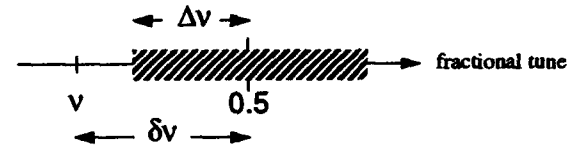
Figure 2: The half-integer stopband as seen by the unperturbed lattice.

quadrupoles in Fig. 1(c) is

$$\text{tune shift} \approx \delta\nu \times \left[1 - \sqrt{1 - \left(\frac{\Delta\nu}{\delta\nu}\right)^2} \right], \qquad (1)$$

where $\Delta\nu$, called the *stopband halfwidth*, is [2]

$$\Delta\nu = \left| \frac{1}{4\pi} \oint ds\, Q(s)\beta(s)\, e^{i(2W + ps/R)} \right|, \qquad (2)$$

and

$$W(s) = \mu(s) - \nu\frac{s}{R}, \quad \mu(s) = \int_0^s \frac{ds'}{\beta(s')}.$$

$Q(s)$, the distribution of quadrupole errors, is the gradient error normalized by the nominal rigidity, p the $2\nu^{\text{th}}$ harmonic, s the longitudinal coordinate, and R the average machine radius. Lattice functions in (2) correspond to the unperturbed lattice. In this view, the unperturbed tune must lie outside the shaded region set up by the perturbing quadrupoles, i.e., $\delta\nu \geq \Delta\nu$, or the tune shift given by (1) becomes complex, and the lattice becomes unstable. Hence, the shaded region about the half-integer is referred to as a stopband.

267

II. STATISTICS

The half-integer stopband $\Delta\nu$ is the magnitude of the complex integral in (2), which we denote by $\Delta\nu_c$. The only statistical element which appears in (2) is the factor of $Q(s)$, the distribution of quadrupole errors in the lattice elements. If $\beta(s)$ varies slowly in the lattice elements, we can make the approximation

$$\Delta\nu_c \approx \frac{1}{4\pi} \sum_k Q_k \beta_k \ell_k \, e^{i(2W_k + p s_k/R)}, \qquad (3)$$

where the index k runs over the lattice elements, with ℓ_k the length of the kth element. Given that Q_k is a gaussian random variable with zero mean and RMS variation of σ_k, we are required to compute the mean and variance of $\Delta\nu = |\Delta\nu_c|$.

We recast the problem in more abstract form. Let $Z = (X, Y)$ be a complex number made up as

$$X = \sum_k c_k \, x_k, \quad Y = \sum_k d_k \, x_k, \qquad (4)$$

where $c_1, \ldots, c_n, \; d_1, \ldots, d_n$ are real constants, and $x_1, \ldots, x_n$ are independent gaussian random variables with

$$< x_k > = 0, \quad < x_k^2 > = \varsigma_k^2. \qquad (5)$$

We are required to compute

$$\left\langle \sqrt{X^2 + Y^2} \right\rangle, \text{ and } \left\langle X^2 + Y^2 \right\rangle.$$

We state without proof a lemma used to calculate the joint PDF of X and Y:
■ Let $x_1, \ldots, x_n$ be independent random variables with PDF's $p_1, \ldots, p_n$ respectively. Let X, Y be functions of the independent variables, or

$$X = F(x_1, \ldots, x_n), \quad Y = G(x_1, \ldots, x_n).$$

If $P(X, Y)$ denotes the joint PDF of X and Y, then

$$P(X, Y) = \int dx_1 \cdots dx_n \, p_1 \times \ldots p_n \delta(X - F) \, \delta(Y - G)$$

where δ denotes the Dirac delta function. In other words, the joint PDF of X, Y is the average over $x_1, \ldots, x_n$ of $\delta(X - F(x_1, \ldots, x_n)) \times \delta(Y - G(x_1, \ldots, x_n))$.
■ The joint PDF of X and Y in (4), works to be

$$\hat{P}(X, Y) =$$
$$\frac{1}{2\pi\sqrt{\sigma_X^2 \, \sigma_Y^2 - <XY>^2}} \times$$
$$\exp\left[-\frac{X^2 \sigma_Y^2 + Y^2 \sigma_X^2 - 2XY <XY>}{2(\sigma_X^2 \sigma_Y^2 - <XY>^2)} \right],$$
$$(6)$$

where

$$\sigma_X^2 \equiv \langle X^2 \rangle - \langle X \rangle^2, \quad \sigma_Y^2 \equiv \langle Y^2 \rangle - \langle Y \rangle^2,$$

$$\langle X \rangle = \langle Y \rangle = 0,$$

$$\langle X^2 \rangle = \sum_k c_k^2 \, \varsigma_k^2, \quad \langle Y^2 \rangle = \sum_k d_k^2 \, \varsigma_k^2,$$

$$\langle XY \rangle = \sum_k c_k \, d_k \, \varsigma_k^2.$$

From (6) we see that if $\langle XY \rangle = 0$, X and Y become uncorrelated gaussian random variables.
■ The average of $\sqrt{X^2 + Y^2} \equiv r$ works out to be

$$\langle r \rangle = \left(\frac{\pi}{2}\right)^{\frac{1}{2}} \left[\sigma_X^2 \, \sigma_Y^2 - \langle XY \rangle^2 \right]^{\frac{1}{4}} P_{\frac{1}{2}}(\zeta), \qquad (7)$$

where

$$\zeta = \frac{\sigma_X^2 + \sigma_Y^2}{2\sqrt{\sigma_X^2 \, \sigma_Y^2 - \langle XY \rangle^2}}. \qquad (8)$$

$P_{\frac{1}{2}}$ is the Legendre function of index half[4]. It is easily established that ζ, the argument of $P_{\frac{1}{2}}$, is greater than or equal to 1. For values of $\zeta \geq 1$, $P_{\frac{1}{2}}$ can be expressed as

$$P_{\frac{1}{2}}(\zeta) = \frac{2}{\pi} \left[\zeta + \sqrt{\zeta^2 - 1} \right]^{\frac{1}{2}} E(m),$$

where

$$m = \left[\frac{2\sqrt{\zeta^2 - 1}}{\zeta + \sqrt{\zeta^2 - 1}} \right]^{\frac{1}{2}}, \text{ and } E(m) = \int_0^{\frac{\pi}{2}} d\theta \, \sqrt{1 - m \sin^2\theta}$$

is a complete elliptic integral of the first kind [4]. Combining these results, we obtain

$$\langle r \rangle = \sqrt{\sigma_X^2 + \sigma_Y^2} \, f(\zeta), \qquad (9)$$

where

$$f(\zeta) = \left[\frac{1}{\pi} \left(1 + \sqrt{1 - \zeta^{-2}} \right) \right]^{\frac{1}{2}} E(m).$$

The average of r^2 can be obtained directly from (4) and (5)

$$\langle r^2 \rangle = \langle X^2 + Y^2 \rangle = \sigma_X^2 + \sigma_Y^2 \equiv \sigma^2. \qquad (10)$$

■ From the properties [4] of $E(m)$ we obtain

$$0.8 \, \sigma \leq \langle r \rangle \leq 0.9 \, \sigma. \qquad (11)$$

A simple and robust approximation is thus obtained

$$\langle r \rangle \approx \sigma. \qquad (12)$$

Also, from (11) we have

$$0.19 \, \sigma^2 \leq \text{var}(r) \leq 0.36 \, \sigma^2.$$

■ The significance of the variable ζ, defined in (8), requires comment. The smallest value ζ can have is unity. It obtains when $<XY> = 0$ and $\sigma_X = \sigma_Y$, i.e., when X and Y are uncorrelated and have the same variance. However, a value of ζ larger than unity does not necessarily signify
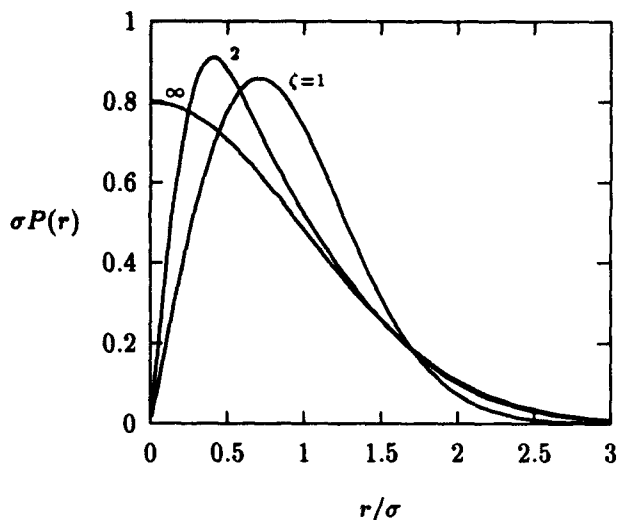
Figure 3. Conditional probability density function of the magnitude of the stopband, for $\zeta = 1$, $\zeta = 2$, and $\zeta \to \infty$.

Figure 4. Probability of finding r between 0 and some prescribed limit, for $\zeta = 1$ and $\zeta \to \infty$. For intermediate values of ζ, the curve will lie within the envelope defined above.

an increasing degree of correlation. This can be seen from (6), which requires only that $< XY > = 0$ for X and Y to be uncorrelated variables, in which case

$$\zeta \to \frac{1}{2}\left(\frac{\sigma_X}{\sigma_Y} + \frac{\sigma_Y}{\sigma_X}\right).$$

Accordingly, if $\sigma_X \neq \sigma_Y$, ζ will be greater than unity, and will become large if $\sigma_X \ll \sigma_Y$, or vice versa. Another way for ζ to become larger than unity is when X and Y are correlated, which requires $< XY > \neq 0$. The degree of correlation between X and Y is measured by how close the value of $| < XY > |$ comes to $\sigma_X \sigma_Y$. For example, if the constants $c_1, \ldots, c_n$ and $d_1, \ldots, d_n$ in (4) are identical, then X is identical to Y, which represents perfect correlation. In this case one obtains $\sigma_X \sigma_Y = < XY >$. This is sufficient to make the value of $\zeta \to \infty$, as in the case of uncorrelated variables with grossly different variances.

■ The conditional probability density function $P(r)$ of the magnitude of the stopband r is

$$P(r) = 2\frac{\zeta r}{\sigma^2}\exp\left(-\frac{\zeta^2 r^2}{\sigma^2}\right)I_0\left(\sqrt{1 - \zeta^{-2}}\,\frac{\zeta^2 r^2}{\sigma^2}\right). \quad (13)$$

Fig. 3 displays $\sigma P(r)$ as a function of r for three different values of ζ.

■ The limiting cases $\zeta = 1$ and $\zeta \to \infty$ can be worked out explicitly, and provide some insight into the behavior of $P(r)$ as a function of ζ. In the first case, $\zeta = 1$, one obtains from (13)

$$P(r) = 2\frac{r}{\sigma^2}\exp\left(-\frac{r^2}{\sigma^2}\right).$$

This is precisely the conditional PDF in the radial variable for a bivariate gaussian with equal variances. In the second limiting case, $\zeta \to \infty$, we use the asymptotic form [4] of $I_0(z)$ to obtain

$$P(r) \sim \sqrt{\frac{2}{\pi\sigma^2}}\,\exp\left(-\frac{r^2}{2\sigma^2}\right).$$

This is a "half" gaussian, as can be seen in Fig. 3. Since $\zeta \to \infty$ represents (i) the case of perfectly correlated variables, or (ii) the case when the individual variances of X and Y are grossly different, we expect r to be determined by a single variable. In this case, the resulting distribution should remain gaussian, except that it must be positive. Hence, a half-gaussian. For intermediate values of ζ, the peak of the PDF moves closer to the origin, and the tail decays more rapidly, i.e., it approaches the half-gaussian case.

■ The probability

$$p(r) = \int_0^r d\bar{r}\, P(\bar{r})$$

of finding r between 0 and an arbitrary multiple of σ up to 3σ is shown in Fig. 4 for the limiting values of $\zeta = 1$ and $\zeta \to \infty$. Probability curves for intermediate values of ζ will lie within the envelope defined by the limiting cases.
■ Finally, we illustrate the use of these results. Say we would like to design a correction system for the stopband with a 0.95 probability of being sufficiently strong. Fig. 4 tells us that the correction system must have a driving term (2) equal to 1.7σ for $\zeta = 1$, and 2.0σ for $\zeta = \infty$. σ and ζ would have to be computed from the correspondence between (3) and (4), and knowledge of the machine lattice and its error distribution.

III. REFERENCES

[1] E. Courant and H. Snyder, Ann. Phys. 3, 1 (1958).

[2] S. Dutt, et al., "The Half-Integer Stopband: Physics and Statistics," SSC-PMTN-56M (1992).

[3] R. M. Talman, private communication.

[4] M. Abramowitz and I. A. Stegun (Eds.), "Handbook of Mathematical Functions," Dover, New York (1972).

269

Stochastic Dynamics for Accelerators

A. Pauluhn

Deutsches Elektronen-Synchrotron DESY, Notkestr. 85

2000 Hamburg 52, Germany

Abstract

In this report we introduce several approaches to stochastic problems in accelerator physics. The first part of the present work treats the concepts of stochastic differential equations (SDEs) and of Fokker-Planck equations (FPEs), whereas in the second part we concentrate on discrete models and investigate a method of calculating density functions via stochastic mappings.

I. INTRODUCTION

The motion of particles in an accelerator is strongly influenced by various stochastic effects such as ground motion, power supply ripples, noise caused by the quantum emission of synchrotron radiation and explicit noise in the rf system. A good description of external noise, i.e. of the influence of a great number of nearly uncorrelated, rapidly fluctuating random effects on a system, is the Gaussian white noise process (GWN) $\xi(t)$. This process has the properties $< \xi(t) >= 0$ and $< \xi(t)\xi(t') >= \delta(t - t')$. Another advantage of using the white noise concept is the fact, that for such noise "inputs" the resulting process is a Markovian process. Markovian processes are those, whose future depends only on the present and not on the past ("without memory"). We present some methods of treating differential equations which include stochastic quantities and calculate moments and density functions. In the case of nonlinear, time dependent coefficients in the describing equations very few results exist, and good numerical tools become necessary. We investigate integration schemes for SDEs and apply them to several examples like a simple model of the beam-beam interaction and the synchrotron motion. For the study of the synchrotron motion we also chose a kind of complementary access to stochastic systems as opposed to stochastic differential equations, the Fokker-Planck equation.

The second part of this study is concerned with a discrete approach to a nonlinear damped stochastically excited system like particle motion in an e^--storage ring. We present an algorithm for computing the density function and follow its evolution in time. By tracking particles in a discretized phase space we compute a stochastic matrix as a time propagator for the density function, again making use of the fact that we describe a Markov process. We study simple models of the beam-beam effect and compare our results with results obtained via usual tracking techniques.

II. MODELLING STOCHASTIC EFFECTS WITH SDES

Including stochastic effects in the equations of motion of a dynamical system, the system variables become stochastic processes, i.e. time dependent random variables. In our investigations we start from equations of the form

$$\dot{\vec{x}} = \vec{f}(\vec{x}) + \underline{g}(\vec{x})\vec{\xi}(t) \quad ,$$

where $\vec{\xi}(t)$ describes the noise process and has the properties of the GWN. The first term of the right hand side gives the deterministic part of the equation, and the second introduces a diffusion component.

A. Numerical Solution

For a numerical approach to SDEs, one performs the following steps:

i) Taylor expansion of the approximate solution in the stepwidth h

ii) model the noise process and, if necessary, functionals of it

iii) simulate lots of realizations for averaging.

Difficulties in the simulation procedures are for example contained in the second point of the listing: how can such an irregular process as WN, or higher order functionals of it be modelled? In simulations these expressions have to be substituted by simple functions of random vectors, so that they yield the same moments up to a given order, which is often quite CPU-time consuming. Therefore one is limited to algorithms of low order [1],[2].

B. Examples:

a. Beam-Beam Model:

As an example for a time-dependent potential we made calculations for a one-dimensional SDE with beam-beam kick, damping and noise for a simple beam-beam interaction model (round beams, weak-strong approximation).

The equation reads:

$$\ddot{x} + \alpha\dot{x} + \omega^2 x + f(x,s) = \sqrt{d} \cdot \xi(s),$$

with

$$f(x,s) = -8\pi\xi_{bb}(\frac{1 - e^{-\frac{1}{2}x^2}}{x})\delta_p(s),$$

where $\delta_p(s) = \sum_{n=-\infty}^{\infty} \delta(s - nL)$ and $\sqrt{d} = \sigma\omega\sqrt{2\alpha}$. We used a ring of length $23.25m$ with a Q-value of 3.7 and a strong beam-beam parameter of $\xi_{bb} = 0.07$. The damping time was taken to be 1000 turns. We chose the weight of
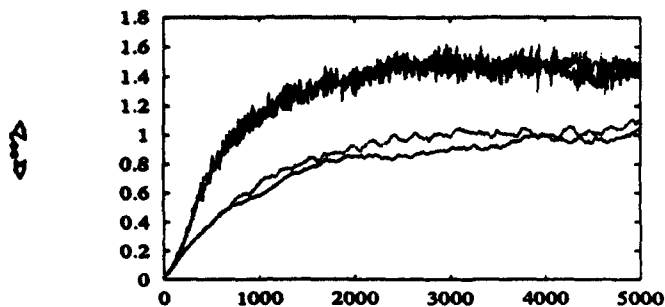
Figure 1: $< x^2 >$ vs. no of turns, linear case (lower curves) and with beam-beam kick force (upper curves).

Figure 2: $< J >= \pi < \epsilon >, \phi_0 = 0.1deg, W_0 = 0.001eVs$, strong stochastic perturbation $d = 0.01$.

the noise such as to have the equilibrium value of $< x^2 >$ for the harmonic oscillator normalized to 1. These parameters have been chosen in a way to make the effect of the periodic kick force easily visible. In the SDE simulation we took 500 samples for the averaging over the noise process. We made calculations with the corresponding transfer map for the same two systems, using 1000 samples for the averaging process, and compared the mapping results with the SDE results. In figure 1 we show the second moment of x, which measures the bunch size in x-direction. The two lower curves are the results for the unperturbed harmonic oscillator, the two upper curves give the results for the same system being periodically kicked by the beam-beam force. We suppressed the errorbars in this plot for clarity. In both cases, unperturbed (= noisy harmonic oscillator, linear system, $f(x,s) = 0$) and perturbed (= noisy HO plus beam-beam kick force), an equilibrium value is reached. The good agreement of the curves is obvious, although we had "continuous" damping and noise all around the ring in the continuous (within stepwidth h) SDE algorithm, compared to the mapping scheme with already integrated noise and damping applied once, at the interaction point, where the kick is also invoked. Apart from that, the SDE simulation was much more CPU-time consuming. The calculations were performed on an HP730/9000.

b. Double Rf System with Stochastic Excitation

Noise in the accelerating facilities can lead to significant emittance growth and limit the lifetime of a bunched proton beam [3]. Here we study the influence of phase noise in a double rf system, which is an example of a nonlinear undamped system perturbed by fluctuating forces. J. Wei investigated a double rf system in combination with stochastic cooling [4]. Let ϕ describe the phase deviation of a circulating particle relative to the synchronous particle and $W = \frac{\Delta E}{\omega_{rf}}$ its canonically conjugated variable, the relative deviation in energy from that reference particle. The corresponding differential equation reads:

$$\ddot{\phi} = -C_W C_\phi \sin(\phi) + \frac{1}{m} C_W C_\phi \sin(m\phi) + 2C_W \sqrt{d}\xi(t).$$
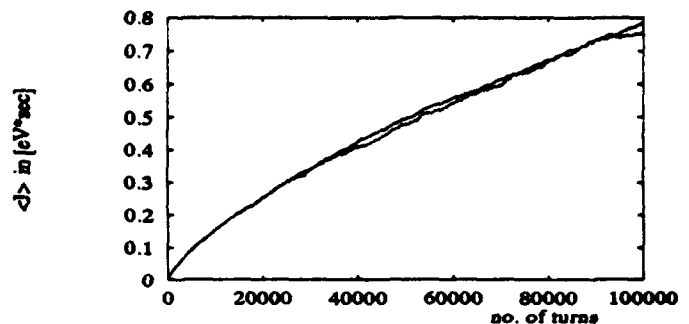
where $C_W = \frac{h^2\omega_0^2\eta}{2E\beta^2}, C_\phi = \frac{qe\hat{V}}{\pi h}$, qe=electric charge of the particle, h= harmonic number, γ_t= transition energy, $\eta = \frac{1}{\gamma_t^2} - \frac{1}{\gamma^2}$, ω_0=revolution frequency of the synchronous particle, βc=velocity of the synchronous particle, $E = m_0c^2\gamma =$ synchronous energy, $\sqrt{d}$= scaling diffusion parameter for the noise term, $\xi(t)$= noise process .

For the action variable $J = \oint W d\phi$, which is related to the emittance via $\epsilon = \frac{1}{\pi}J$, we get the approximation [4],[2]: $< J >= const < (C_W W^2 + \frac{1}{2}C_\phi[(1 - \cos(\phi)) - \frac{1}{4}(1 - \cos(2\phi))])^{\frac{3}{4}} >$, which was used to simulate the growth of the action variable. The parameters used were: $q = 1, \hat{V} = 60kV, h = 1100, m = 2, \eta = 5.75 \cdot 10^{-4}, \omega_0 = 47kHz \cdot 2\pi, \beta = 1.0, E = 40GeV$.

Another way to study the synchrotron dynamics is to calculate the FPE in the action variable. Using perturbation theory techniques [3] we get the Fokker-Planck equation:

$$\frac{\partial\rho}{\partial t} = \frac{3}{8}d2C_W const^{\frac{3}{2}}\frac{\partial}{\partial J}(J^{\frac{3}{2}}\frac{\partial}{\partial J}\rho(J)).$$

and can derive the SDE in the action variable J [2]:

$$\dot{J} = \frac{1}{3}BJ^{-\frac{1}{3}} + \sqrt{2B}J^{\frac{1}{3}}\xi(t),$$

with $B = \frac{3}{8}d2C_W const^{\frac{3}{2}}$. Figure 2 shows the results for the emittance growth $< J(t) >$. In this plot we compare the simulations of the ϕ-SDE with those for the J-SDE (500 particles). Both curves agree very well, even on long time scales.

III. COMPUTING DENSITY FUNCTIONS VIA STOCHASTIC MAPPINGS

A quantity of fundamental significance for the description of particle motion in a storage ring is the density function and its evolution in time. It holds the information about beam sizes and lifetimes. In general the density is obtained via tracking many particles over a large number of turns (a few damping times). In what follows we describe a discrete model for calculating the phase space density function $\rho(x,p,t)$ of an electron storage ring in the presence of damping, external noise and nonlinearities
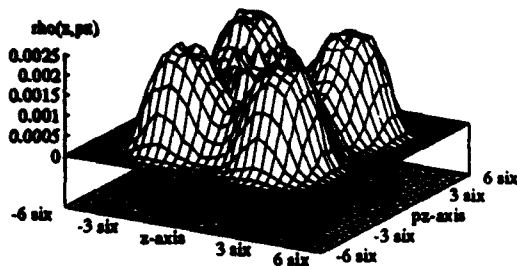
Figure 3: $\rho(z,p_z)$ 1852 turns=τ_d,$Q = 5.24, \xi = 0.029, \alpha = 5.4 \cdot 10^{-4}$, 30×30-grid, absorbing boundaries at 6σ.

Figure 4: $\rho(z,p_z)$, z-proj., mapping alg.(200p/bin) and tracking (10p/bin), after $\frac{1}{4}\tau_d, \frac{1}{2}\tau_d, 20\tau_d$, $Q = 5.14$.

(here: beam-beam force). The idea of the presented algorithm mainly goes back to A. Gerasimov [5]. It consists of the construction of a time propagator (two-time transition probability) for a discrete Markov process, see also [6].

A. The Time Propagator Matrix

We consider a one-dimensional beam-beam model for the interaction of two round beams. The transformation for one turn consists of the kick at the IP and of the linear part, given by the transfer matrices. The phase space is partitioned into discrete states i ($n \times n$-grid), where a particular state is identified with a position on the grid. For a transition probability having the Markov property, the following holds: $P(x_{n+1} = j|x_n = i; h) = P(x_{n+1} = j|x_n = i) = p_{ij}(n)$. $P(x_{n+1} = j|x_n = i; h)$ is the probability of being in state j at time $n + 1$, after having been in state i at time n and having the "history" h. For the two-time transition probability this yields: $p_{ik}^{(2)} = \sum_{j \in I} p_{ij} p_{jk}$. One arranges the probabilities for all possible transitions between the different states as a matrix $A_{ij} = p_{ij}$ (stochastic matrix). Tracking many particles for a certain number of turns, we compute A as the matrix of the relative frequencies of transitions between the different bins of the phase space grid. The number of turns in the tracking can be chosen in different ways, for example such as to have still enough particles in the tails of the distribution. In general one takes one half of the damping time. After we have evaluated the time propagator matrix A, we apply it successively to the initial density ρ_0 and simulate the time evolution of ρ : $\rho_1 = A\rho_0$, $\rho_n = A^n \rho_0 = A\rho_{n-1}$.

In figure 3 we see a calculation of the vertical density after one damping time, starting from a homogeneous initial density.
Figure 4 shows a comparison between direct tracking (10 particles/bin) and the mapping algorithm (200 p/bin). The agreement is very good, although after 40000 turns the "mapped density" curve is slightly below the "direct one". The mapping needed about two orders of magnitude less CPU-time.

B. "Macrostates" and Higher-Dimensional Systems

Instead of calculating the transition probability operator for every two gridpoints (or "microstates"), we now search for a partition of the phase space into larger structures ("macrostates") in order to reduce the computing
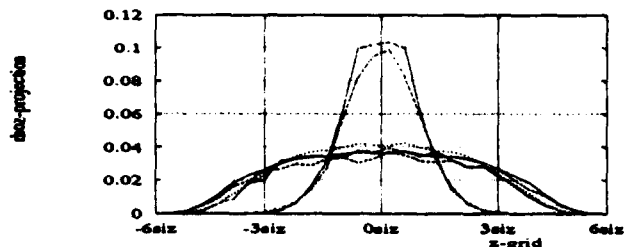
effort and handle higher-dimensional systems. We then compute the transition matrix for these larger units. For two-dimensional systems, it is necessary to find a partition of an $n \times n \times n \times n$-phase space grid. The iteration time parameters therefore have to be chosen in such a way as to get a sufficient small number of macrostates to keep the matrices treatable, but nevertheless the macrostates should still represent the structure of the phase space.

IV. CONCLUSIONS

We introduced several numerical integration algorithms for SDEs and applied them to examples in accelerator physics. Although the results are good, the methods are very CPU time consuming. By making a combined analytical and numerical analysis of a nonlinear rf system with phase noise we could show that simulations with SDEs and analytical perturbation theory were in excellent agreement.

In the second part of the presented work we have introduced and tested an algorithm to investigate the motion of ultrarelativistic charged particles under the influence of damping, noise, and certain non-linear forces. Via a stochastic mapping we calculated a time propagator and computed a "numerical Markov chain" for the probability density on the phase space. By using this method one gets a very good impression of the time evolution of the density function. Resonance structures on the phase space can be made easily visible. Besides, the algorithm is by 2-3 orders of magnitude faster than direct tracking methods.

V. REFERENCES

[1] Honerkamp,J., Stochastische dynamische Systeme, VCH, Weinheim, (1990)

[2] Pauluhn,A., Stochastic Beam Dynamics with Special Applications to a Double Rf System, DESY HERA 93-02, (1993)

[3] Krinsky,S.,Wang,J.M., Bunch Diffusion due to RF Noise, Part. Acc., 12, 1982

[4] Wei,J., Stochastic Cooling with a Double RF System, BNL-46792, AD/RHIC-105, Informal Report, (1991)

[5] Gerasimov,A., Private communication

[6] Pauluhn,A., Gerasimov,A., Mais,H., A Stochastic Map for the One-Dimensional Beam-Beam Interaction, in the Proc. of the 15th Int. Conf. on High Energy Accelerators, Hamburg, (1992)

DIFFUSION PHENOMENA IN SIMPLE HAMILTONIAN SYSTEMS: SOME ANALYTICAL AND NUMERICAL RESULTS

A.Bazzani[†,∗], M Giovannozzi[◦,∗], S. Rambaldi[△,∗], G. Turchetti[△,∗]

Dip. di Fisica Univ. di Bologna[△], INFN Sezione di Bologna ITALY[∗]

Dip. di Matematica Univ. di Bologna[†], CERN- SL Division[◦]

Abstract

We study both numerically and analytically some simple Hamiltonian systems perturbed by a random noise or by a periodic (or quasi-periodic) noise. In this way we simulate the effects of the ripple in the power supply on the betatronic motion in a particle accelerator. We consider the dependence of the diffusion in the phase space on the relevant parameters of our system like the nonlinear terms, the strength of the noise and, in the deterministic case, its modulation frequency. We discuss also the possibility of describing the evolution of a distribution function for an integral of motion of the unperturbed system, like the action or the energy, by means of a Fokker–Plank equation. The results are compared with numerical simulations.

I. INTRODUCTION

Recent experiments in high energies hadron colliders have shown that the beam lifetime is substantially decreased when the nonlinear effects due to the multipolar errors are combined with the fluctuations of current (ripples) [1]. At present no satisfactory interpretation of the experimental results has been found and no simple models have been extensively investigated. In the experiments the slow periodic modulation is enhanced but it is not evident that the effects of a stochastic modulation can be a priori neglected; on the other hand when the dynamics is almost linear, no appreciable diffusion is observed and the beam is stable. This suggests that, if a stochastic modulation is present it affects the phase rather than the amplitude of the betatronic oscillations; the diffusion would then depend uniquely on the coupling with the nonlinear terms. We analyse here a simple model of a nonlinear integrable hamiltonian system where, the frequency is modulated with a stochastic perturbation or periodic perturbation. The phase space of the unperturbed hamiltonian has a separatrix which corresponds to the dynamic aperture. The presence of modulation allows the orbits to reach the separatrix and escape to infinity in a finite time interval. We look for the time evolution of the distribution function for a given initial population. Even in this oversimplified model the numerical simulations are extremely heavy and it is hard to investigate the dependence on the parameters. The behaviour of the stochastic and periodic modulation is radically different. In the first case we justify theoretically the description of the diffusion in the nonlinear invariant of motion, by a Fokker-Planck equation [2] with a variable diffusion coefficient. The presence of the separatrix (dynamic aperture) is taken into account with an absorbing barrier, whereas a reflecting boundary condition (flux conservation) is imposed at the origin. The presence of a sextupole leads to a cubic diffusion coefficient which makes the diffusion extremely slow close to the origin, whereas it becomes significant in the vicinity of the separatrix where the absorption by the barrier simulates the escape to infinity.

The slow periodic modulation is analyzed in the framework of the adiabatic theory [3]. The origin is surrounded by invariant domains which are swept by any orbit when the frequency is slowly varied. On the contrary the region swept by the separatrix is chaotic and once the outer boundary is reached the escape to infinity still occurs. Compared to the stochastic modulation, there is a region defined by the inner boundary of the pulsating separatrix which is stable and the evolution of the distribution function in the chaotic region is not of diffusive type.

II. MODEL AND RESULTS

We consider the Hamiltonian

$$H = \omega \frac{p^2 + x^2}{2}(1 + \epsilon \xi(t)) - \frac{x^3}{3} \qquad (1)$$

which models the betatronic motion in the horizontal plane in the presence of sextupoles using normalized coordinates. In (1) $\xi(t)$ denotes continuous realization of a random stationary process with zero average $\langle \xi \rangle = 0$ and correlation $G(t - t') \equiv \langle \xi(t)\xi(t') \rangle$ and ϵ is a small parameter. We will then consider the limit case in which the correlation length vanishes and the process becomes δ correlated; such a limit describes the increments of a Wiener process.

Introducing the action angle variables for the harmonic oscillator $x = \sqrt{2j}\sin\theta$ and $p = \sqrt{2j}\cos\theta$ we have

$$H = \omega j - \frac{2^{3/2}}{3}j^{3/2}\sin^3\theta + \epsilon\omega j\xi(t) \equiv h_0(j,\theta) + \epsilon\omega j\xi(t) \quad (2)$$

By solving exactly the Hamilton's Jacobi equation for the hamiltonian h_0 or approximately by perturbation theory we determine a unique transformation $j = V(\theta, J)$ close to identity such that $h_0(j, \theta) = H_0(J)$ and

$$H = H_0(J) + \epsilon V(J, \theta) \xi(t) \qquad (3)$$

We remark that we have chosen to work with the initial angle since the simulations are carried out choosing a uniform distribution in the initial angle θ.

Following a procedure introduced by Gurievich et al. [4] in plasma physics, we separate the phase space density, which satisfies Liouville's equation, into an average and a fluctuating part

$$\rho = \rho_0 + \epsilon \rho_1, \qquad \rho_0 = \langle \rho \rangle \qquad \langle \rho_1 \rangle = 0 \qquad (4)$$

Choosing an initially uniform distribution in the angle or for t large enough that a uniform distribution is attained, ρ_0 will remain independent of Θ and will satisfy the Fokker-Planck equation

$$\frac{\partial \rho_0}{\partial t} = \frac{\epsilon^2}{2} \frac{\partial}{\partial J} \langle V_\theta^2 \rangle \frac{\partial \rho_0}{\partial J} + O(\epsilon^3) \qquad (5)$$

which is the diffusion equation for the action. The diffusion coefficient

$$D_J = \frac{\epsilon^2}{2} \langle V_\theta^2 \rangle \qquad (6)$$

depends on the action itself and agrees with the quasilinear approximation.

The derivation is based on the Liouville equation and an expansion for ϵ small; the hypothesis of a δ correlated noise is crucial to obtain a differential equation like (5) rather than an integro-differential equation. Even limit theorems in the theory of stochastic processes do not allow to recover a Fokker-Planck equation if the δ correlation hypothesis is dropped.

Even though the exact computation of $H_0(J)$ and $V(J, \theta)$ could be carried out we preferred to compute the second order in perturbation theory since this is the only available way of determining $D(J)$ in more realistic models. According to the canonical perturbation theory we have:

$$H(J) = \omega J - \frac{1}{\omega} \frac{5}{12} J^2 \qquad (7)$$

and the diffusion coefficient reads

$$D = \frac{\epsilon^2}{2} \langle V_\theta^2 \rangle = \frac{\epsilon^2}{2} \left[J^3 + \frac{21}{8} \frac{J^4}{\omega^2} \right] \qquad (8)$$

The position of the absorbing barrier $J = J_s$ is computed by imposing $H_0(J_s) = E_s$ where $E_s = \omega^3/6$ is the energy of the separatrix. A simple computation gives

$$J_s = \omega^2 \frac{6 - \sqrt{26}}{5} \qquad (9)$$

Introducing a normalized time and action

$$y = \frac{J}{J_s}, \qquad \tau = \epsilon^2 \frac{J_s}{4} t \qquad (10)$$

the Fokker-Planck equation reads

$$\frac{\partial \rho_0}{\partial \tau} = \frac{\partial}{\partial y} y^3 \left[1 + \frac{21}{8} \frac{J_s}{\omega^2} y \right] \frac{\partial \rho_0}{\partial y} \qquad (11)$$

In figures 1 we compare the distribution function of the energy, computed by numerical simulation with the solution of the Fokker-Planck equation at $\tau = .01$. The initial condition was a narrow gaussian in the energy centered at the middle of the dynamic aperture, the number of particles in the numerical simulation was 40,000. In figure 2 we show the same distribution function as in fig. 1, but after a longer time ($\tau = .05$). The first order perturbative calculation of the diffusion coefficient gives an agreement of $\sim 20\%$ while the second order gives almost a best fit (remark that we had no adjustable parameters).
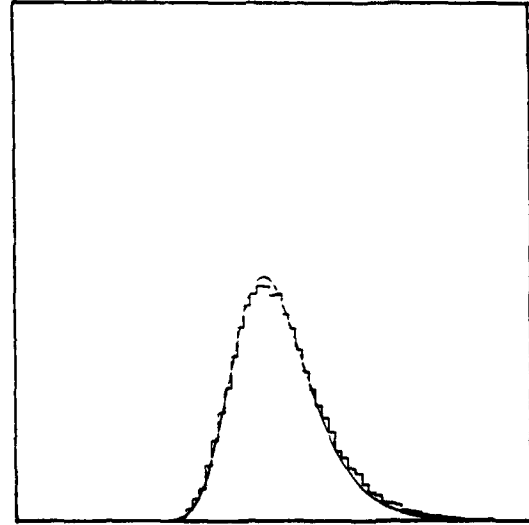
Figure 1: The distribution function for the energy when the linear frequency is stochastically perturbed: comparison between the numerical simulation and the solution of the Fokker-Planck's equation (smooth curve) at $\tau = .01$

We have considered the same hamiltonian system with a slow periodic modulation $\xi(t) = \cos \Omega t$ with $\Omega \ll \omega$. According to the adiabatic theory the separatrix is slowly pulsating with the same frequency Ω. We have distributed the particles uniformly half way on the ring swept by the separatrix along an unperturbed trajectory. The population has a low spread due to the modulation; when the separatrix crosses a particle then the particle is kicked off towards infinity. According to this picture, which becomes exact in the limit $\Omega \to 0$, the population remains constant until the encounter with the separatrix occurs after a quarter of period $T = \pi/(2\Omega)$, and afterwards it vanishes in a very short time interval. When Ω is rather small $\Omega/\omega = 5 \times 10^{-4}$ this phenomenon is observed with a good accuracy (Fig. 3). When Ω/ω is increased to 10^{-1} the adiabatic theory is no longer applicable and after a first rapid decrease, a long queue is observed (Fig. 4) due to the chaotic region generated by the separatrix.
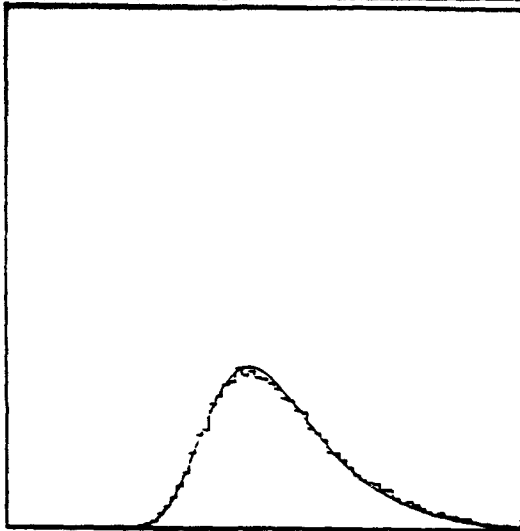
Figure 2: The distribution function for the energy when the linear frequency is stochastically perturbed: comparison between the numerical simulation and the solution of the Fokker-Planck's equation (smooth curve) at $\tau = .05$

III. CONCLUSIONS

Certainly the proposed model is a very crude description of the ripple induced diffusion in particle accelerator however this can be certainly useful to understand the effect of a stochastic or periodic perturbation of the linear frequency of a non-linear Hamiltonian systems. The main defect is the absence of resonances, which are taken into account when a discrete description of the lattice is given by an area preserving map. An extension of the previous results to a discrete model is perhaps possible but mathematically much more difficult to be justified. Certainly simulations can be carried out and the present analysis will be helpful in interpreting them.

REFERENCES

[1] Altuna A. et al., "The 1991 Dynamics Aperture experiment at the CERN SPS", AIP Conf. Proc., No 255 (1991).

[2] Risken H. "The Fokker-Planck equation", Springer-Verlag 1989 2nd ed.

[3] Neishtadt A.I., "Change of the adiabatic invariant at the separatrix", Sov. J. of Plasma Phys., No 12, 568 (1986).

[4] Gurievich A.V., Zybin K.P. and Luk'yanov A.V. "Relaxed turbulent state and anomalous transport processes", Sov. Phys. JEPT, No 71, 261 (1990).
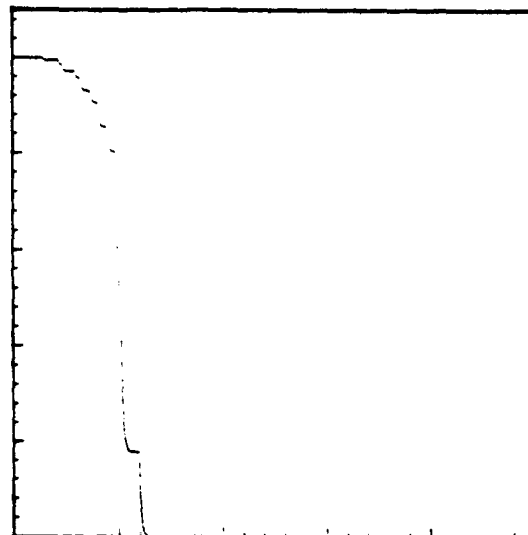
Figure 3: Number of particles versus time: the initial population is 10.000, the ratio Ω/ω is .0005 and each unity on the x-axis corresponds to 5000 time unities
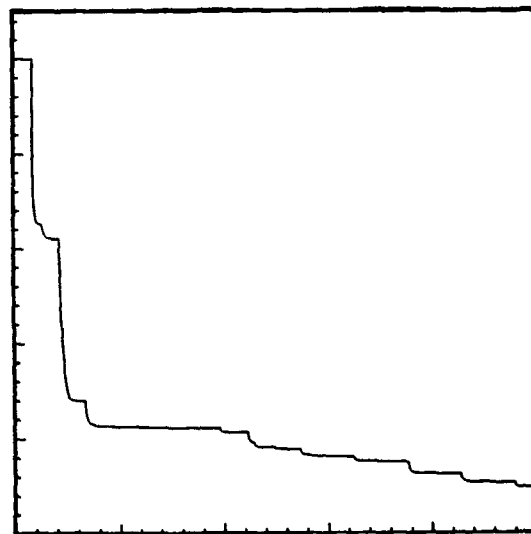
Figure 4: Number of particles versus time: the initial population is 10.000, the ratio Ω/ω is .1 and each unity on the x-axis corresponds to 5000 time unities

Particle Acceleration in Extremely Strong Electromagnetic Wave Fields

K.O Thielheim
Institut für Reine und Angewandte Kernphysik
Abteilung Mathematische Physik
University of Kiel, Germany

1. Particle Motion in Plane Monochromatic Wave Fields

The dynamics of electrically charged particles in electromagnetic wave fields is of relevance for a large variety of physical phenomena. Therefore this topic is dealt with more or less extensively in many text books on classical electrodynamics.

The present paper can be seen in the context of recent work on the origin of high energy cosmic ray particles [1,2,3]. Plane-wave formalism without radiation reaction based on the *Lorentz* equation is adequate for the description of particle dynamics if the wave amplitude is of moderate strength. Particle motion then is periodic in velocity space so that there is an upper limit to particle energy.

We have shown that plane-wave formalism without radiation reaction also is a powerfull tool to define and to calculate important features of particle dynamics in spherical wave fields. Among these features are the acceleration boundary [4], the plasma border [5] and the $1/r_0^2$ - law of asymptotic energy [1].

But in extremely strong wave fields the influence of radiation forces has to be taken into account. Motion under the influence of radiation reaction no longer is periodic in velocity space. Particles, at least in principle, can achieve unlimited values of energy [6-15]. This mechanism, therefore, may be relevant for the understanding of cosmic particle acceleration to extremely high energies as, for example, in cosmic jets associated with rotating magnetized configurations. One may also think of man made jets constituted of laser beams connecting natural or artificial satellites [16-18].

It is the intention of this paper to present and to discuss some results, which may be of interest in the above mentioned context.

2. Equations of Motion

Momentum transfer between a particle of mass m and electric charge e and all other electromagnetically charged particles around, represented by an external electromagnetic field and described by a field tensor F_{jk} may, in classical electrodynamics, be described by

(1) $du_j / d\tau = \eta_0 F_{jk} u^k + \tau_0 G_{jk} u^k$

with $\eta_0 = e/mc$.

The first term on the right side of this equation of motion is constructed from the *Lorentz* derivative $u^L_j = \eta_0 F_{jk} u^k$ of the particle velocity u_j, representing the *Lorentz* force. The *Lorentz* term contains the first order contributions in the interaction constant e to the total force acting on the particle under consideration.

In the second term on the right side represents the radiation force. $\tau_0 = 2e^2/3mc^3$ is the radiation constant and G_{jk} is the radiation force tensor.

Both, the field tensor F_{jk}, as well as the radiation force tensor G_{jk} are antisymmetric tensors thus allowing for the conservation of the norm of particle velocity $u_j u^j = c^2$ or, as one may take it, for the particle to stay on its mass shell $p_j p^j = m^2 c^2$.

Dirac in his early work [19] has suggested

(2) $G_{jk} = (\{ d^2u_j / d\tau^2 \} u_k - u_j \{ d^2u_k / d\tau^2 \}) / c^2$.

The *Lorentz-Dirac* equation (L-D equation), unfortunately, also describes run-away solutions: For vanishing external fields, $F_{jk} = 0$, by multiplication with $du_j / c^2 d\tau$ equation (1) with (2) reduces to

(3) $d \{(du_j/d\tau)(du^j/d\tau)\} / d\tau = 2 \{(du_j/d\tau)(du^j/d\tau)\} / \tau_0$

with the (unphysical) solution

(4) $d \log \gamma / d\tau = (d \log \gamma / d\tau)_{\tau=0} \exp(\tau / \tau_0)$.

These difficulties have widely been discussed in literature. Obviously, they arise, since in the radiation force tensor (2) the kinematic acceleration $du_j / d\tau$ has been introduced instead of the *Lorentz* acceleration $u^L_j = \eta_0 F_{jk} u^k$. But there are strong arguments in favour of the

Lorentz acceleration, because in self-consistent *Maxwell* theory the only forces available are the electromagnetic forces.

Therefore, instead of (2), one may introduce the radiation force tensor

(5) $G_{jk} = (u^{LL}_j u_k - u_j u^{LL}_k) / c^2$

constructed from the second *Lorentz* derivative $u^{LL}_j = \eta_0^2 F_{jk} F^{kl} u_l$. The radiation force constructed with the help of the radiation force tensor (5) contains fourth order contributions in the interaction constant e to the total force acting on the particle.

The second part of this radiation force, $\tau_0 u^{Lk} u^L_k u_j / c^2$, the *Larmor* term, can be deduced through *Lorentz* transformation from *Larmor*'s radiation formula for the rate of energy at which the particle emits electromagnetic waves in the momentary rest frame MRS, $P = (\tau_0 / m)(e E)_{MRS}^2$, where E is the electric vector.

Thus, in the MRS, the *Larmor* term characterizes the particle as a source of electromagnetic waves while, at the same time, the first part of the radiation force characterizes the particle as a sink of electromagnetic waves. This characterization corresponds to the fact that the second part of the radiation force, the *Larmor* term, can be related to a retarded *Green*'s function, while the first part of the radiation force can be related to an advanced *Green*'s function, as has already been considered by Dirac [19].

In the MRS, non relativistic kinematics and dynamics applies: Under the action of a force F (any force) during some interval of the time coordinate δt a momentum F δt = δp is transferred to the particle. But in the same time interval δt the energy transferred to the particle vanishes: $(F, \delta x) = (F, v) \delta t = \delta T = 0$.

Correspondingly, the zeroth component of the radiation force (as of any force) vanishes in the MRS: the particle can be said to function as a relay for wave energy, which is emitted at the same rate as it is absorbed, it actually mediates the transfer of energy from incoming to outgoing waves.

In the MRS, the equation of motion (1) with (5) may be written

(6) $dv / dt = \eta_0 E + \tau_0 \eta_0^2 [E, H]$.

where v is the velocity vector and H is the magnetic field vector. The first term on the right side of this equation of motion represents the static *Coulomb* force, which is proportional to the electric vector, while the last term,

which is proportional to *Poynting*'s vector, represents the radiation force (often referred to as radiation pressure).

Instead of (5), *L.D. Landau and E.M. Lifschitz* [20] have suggested the radiation force tensor

(7) $G_{jk} = \eta_0 (dF_{jk} / d\tau) + (u^{LL}_j u_k - u_j u^{LL}_k) / c^2$,

leading to the *Lorentz-Dirac-Landau* equation (L-D-L equation)

(8) $du_j /d\tau = \eta_0 F_{jk} u^k + \eta_0 \tau_0 (dF_{jk} / d\tau) u^k$
        $+ \tau_0 (u^{LL}_j u_k - u_j u^{LL}_k) u^k / c^2$,

which incorporates an additonal third oder contribution in the interaction constant e, $\eta_0 \tau_0 (dF_{jk} / d\tau) u^k$.

In the MRS, the L-D-L equation has the form

(9) $dv / dt = \eta_0 E + \tau_0 \eta_0 dE / dt + \tau_0 \eta_0^2 [E, H]$.

In general, within a given inertial frame of reference S, the particle is expected to loose energy through the emission of electromagnetic waves and, at the same time, to gain energy through the absorption of electromagnetic waves in addition to the change of energy caused through the work done by the *Lorentz* force.

In many examples the radiative loss of energy is known to exceed the radiative gain of energy, as e.g. for particle motion within a plane perpendicular to an external homogeneous, constant magnetic field when the particle moves in on the narrowing windings of a spiral, while dissipating energy in the form of synchrotron radiation.

In other examples the radiative loss and gain of energy compensate, as for particle motion on a straight line parallel to an external homogeneous, constant electric field. While dissipating energy in the form of electromagnetic waves through longitudinal acceleration the increase of kinetic particle energy through the work done by the *Coulomb* force occurs at the same rate it would do without radiation being produced.

Still there are examples in which the radiative gain of energy exceeds the radiative loss of energy. This is the case, e.g., for particle motion in an external plane, monochromatic wave field. Actually this can already be expected to happen from the appearance of the *Poynting* vector in the equation of motion (1) with (5) or with (7) within the MRS.

3. Asymptotic Behaviour of Energy Development

In view of possible applications to cosmic particle acceleration we have studied the asymptotic behaviour

277

of solutions of the L-D-L equation for sufficiently large values of particle phase $\Phi = x^0 - x^1$, where $x^0 = x^0 / r_L$ with $x^0 = ct$ is the dimensionless time coordinate, $r_L = c/\omega = \lambda / 2\pi$ is the light radius and λ is the wave length, while $x^1 = x^1 / r_L$ is the spatial, cartesian coordinate in the direction of wave propagation. The conditions for the asymptotic regime are

(10) $\Phi \gg 1$

and

(11) $w_0 \, l_0 \, f_0^2 \, \Phi / 2 \gg 1$,

where $w = d\Phi / ds$ with $(ds)^2 = dx^i \, dx_i$ and the initial value $w_0 = w (\Phi_0)$. Especially, $w_0 = 1$ for particles initially at rest. $l_0 = c \, \tau_0 / r_L$ is the dimensionless radiation constant and $f_0 = (e / mc^2) \, r_L \, E_0$ is the dimensionless field amplitude.

Under these premises

(12) $\gamma \to u^1$
        $\to l_0 \, (f_0^2 / 4)$
        $[1 + f_0^2 \, (\sin^2\alpha \, \sin^2\Phi + \cos^2\alpha \, \cos^2\Phi)] \, \Phi$,

where α ist the polarization parameter with $\alpha = 0$ for linear polarization and $\alpha = \pm \, \pi / 4$ for circular polarization, furthermore

(13) $x^1 \to (1/24) \, l_0^2 \, f_0^4 \, [1 + f_0^2 / 2] \, \Phi^3 + (1/32) \, l_0^2 \, f_0^6$
        $[\Phi^2 \sin(2\Phi) + \Phi \cos(2\Phi)] \cos(2\alpha)$.

Therefore, in the special case of circular polarization,

(14) $\gamma \to u^1 \to l_0 \, (f_0^2 / 4)[1 + f_0^2 / 2] \, \Phi$

and

(15) $x^1 \to (1 / 24) \, l_0^2 \, f_0^4 \, [1 + f_0^2 / 2] \, \Phi^3 + const$

so that

(16) $\gamma \to u^1 \to (3^{1/3}/2) \, l_0^{1/3} \, f_0^{2/3} [1 + f_0^2/2]^{2/3} \, (x^1)^{1/3}$.

Obviously, there are the following two regimes which can be distinguished

(17) $\gamma \to u^1 \to (3^{1/3}/2) \, l_0^{1/3} \, f_0^{2/3} \, (x^1)^{1/3}$,
            for $f_0^2 \ll 1$

and

(18) $\gamma \to u^1 \to (3^{1/3}/2^{5/3}) \, l_0^{1/3} \, f_0^2 \, (x^1)^{1/3}$
            $= (4\pi)^{-4/3} \, e^{6/3} \, m^{-7/3} \, c^{-3} \, H_0^2 \, t^{1/3} \, v^{-4/3}$,
            for $f_0^2 \gg 1$.

4. References

[1]   K.O. Thielheim
Fundamentals of Cosmic Physics, 13, 357-399 (1989)

[2]   K.O. Thielheim
in: P.R. Blake and H.F. Nash, eds.
Proc. 12th ECRS, Nottingham
Nucl. Phys. B (Proc. Suppl.), 22B, 60-79 (1991)

[3]   K.O. Thielheim
in: P. Bosetti, ed.
Trends in Astroparticle Physics
Proc. 2nd Int. Symp., Aachen
Teubner Verlag, in press (1992)

[4]   K.O. Thielheim
J. Phys. A: Math. Gen., 20, L203-L206 (1987)

[5]   K.O. Thielheim
in: N.M. Shapiro and J.P. Wefel, eds.
NATO ASI series 270, 523-536 (1989)

[6]   J.J. Sanderson
Phys. Lett., 18, 114-115 (1965)

[7]   T.W.T. Kibble
Phys. Lett., 20, 627-628 (1966)

[8]   E.S. Sarachik and G.T. Schappert
Phys. Rev. D, 1, 2738-2753 (1970)

[9]   A.D. Steiger and C.H. Woods
Phys. Rev. D, 6, 1468-1473 (1972)

[10]   H. Heintzmann and M.Grewing
Z. Physik, 251, 77-86, (1972)

[11]   M. Grewing, E. Schröfer and H.Heintzmann
Z. Physik, 260, 375-384 (1973)

[12]   J. Krüger and M. Bovyn
J. Phys. A: Math. Gen., 9, 1841-1846 (1976)

[13]   H. Stöckel
Fortschr. d. Physik, 24, 417-475 (1976)

[14]   D.M. Fradkin
Phys. Rev. Lett., 42, 1209-1212 (1979)

[15]   D.M. Fradkin
Phys. Rev. D, 22, 1018 - 1023 (1990)

[16]   K.O. Thielheim
in: W. Scandale, G. Turchetti, eds
Proc. Int. Symp., Capri
World Scientific, 255-269 (1990)

[17]   K.O. Thielheim
in: P. Grieder, ed.
Proc. 13th ECRS, Genf
in press (1992)

[18]   K.O. Thielheim
Ap. J., May (1993)

[19]   P.M.A. Dirac
Proc. Roy. Soc. (London) A, 167, 148-169 (1938)

[20]   L.D. Landau and E.M. Lifschitz
Klassische Feldtheorie
Akademie-Verlag, Berlin (1961)

Laser Powered Beam Conditioner for Free-Electron Lasers and Synchrotrons[*]

Hongxiu Liu and George R. Neil

CEBAF, 12000 Jefferson Ave., Newport News, VA 23606

Abstract

A new method of using an additional laser for electron beam conditioning in free-electron lasers (FELs) and synchrotrons is proposed. Theoretical analysis and calculations are presented, showing that the axial energy spread of electrons due to their betatron motion in undulators can be dramatically reduced by interacting with a quasi-TEM_{10} Gaussian mode optical beam. It is required that the electrons be pre-bunched over half an optical cycle in advance.

I. INTRODUCTION

As is well known, *emittance* of an electron beam is one of several major limitations to the performance of free-electron lasers (FELs) and synchrotrons. It causes an axial velocity spread owing to the electrons' betatron motion in undulators. This axial energy spread severely affects the interaction between electrons and optical waves in the form of phase spreading in FELs or degradation of the spectral purity of radiation in the form of non-homogeneous broadening in synchrotrons. Therefore, *beam conditioning* using rf standing waves or traveling waves has been proposed as an attempt to reduce this axial velocity spread for improving the performance of coherent radiation sources [1,2].

In this paper, we propose another new method of beam conditioning using a conventional laser as the conditioning power for the first time. It is of significance to explore the new features and possibilities that a laser powered beam conditioner can provide especially for ultraviolet and x-ray coherent radiation, since a difference of several orders of magnitude in frequency exists from microwave to optical waves. This tremendous difference may result in new features and alter scaling relationships.

Before describing and analysing the laser powered beam conditioner, the idea is placed in context with previous research in three different areas: the research of Sessler, et al. [1] which uses a set of cavities operating in the TM_{210} mode before the undulator, of Sprangle, et al. [2] which uses a slow TM waveguide mode internal to the undulator, and a new scheme of emittance compensation for FELs using a conventional laser the authors are pursuing [3,4]. The possibility of conditioning an electron beam using the axial electrical component of a TEM_{10} mode Gaussian beam *in vacuum* occured when we noticed that such an axial electrical component has been considered for laser acceleration [5,6]. The basic argument is that if the axial component works for laser acceleration, it may work easily for beam

conditioning, since in the latter case, much smaller energy exchange is needed.

II. CONDITIONING MECHANISM

First, let us examine the axial velocity spread introduced when an electron moves through a common magnetostatic undulator. We assume that the undulator is linearly polarised in the y (vertical) direction and provides a natural focusing. In this case, in the absence of external focusing, the normalised mean axial velocity of an electron, averaged over one undulator period, is

$$\beta_z = 1 - \frac{1}{2\gamma^2}(1 + a_u^2) - \frac{1}{2}(k_\beta^2 y_0^2 + \theta_{x0}^2 + \theta_{y0}^2), \quad (1)$$

where γ is the relativistic energy factor of the electron, $a_u = |e|B_0/\sqrt{2}mck_u$ is the rms undulator strength parameter in mks units, e is the charge of an electron, m is the rest mass of an electron, c is the speed of light, B_0 is the peak magnetic field of the undulator, $k_u = 2\pi/\lambda_u$, λ_u is the undulator period, $k_\beta = 2\pi/\lambda_\beta = a_u k_u/\gamma$ is the betatron wavenumber, and y_0, θ_{x0} and θ_{y0} are the initial conditions of the electron's position and divergence angles, respectively. The beam conditioning is made possible due to the fact that, as has been noted in Ref. [7], this axial velocity depends only on the initial conditions for each individual orbit and is constant along any given betatron orbit. Therefore, we conclude that the ideal case is to condition an electron beam at the beginning part of an undulator so that the benefit of conditioning can be fully utilised during the remaining greater part of the undulator.

Next, we discuss the axial electrical field component of a Gaussian mode laser beam *in vacuum*. It is clear that there is no longitudinal field components as far as an infinite plane electromagnetic wave is concerned. As has been proved theoretically and experimentally [8,9], however, axial field components do exist when there is a transverse gradient associated with the transverse field components. Based on such a fact, the axial electrical field component associated with a TEM_{10} mode Gaussian beam in vacuum was proposed for laser acceleration [5]. Here we turn this axial electrical field component for beam conditioning by using its transverse gradient.

Assuming that a Gaussian beam in a TEM_{10} mode, or quasi-TEM_{10} mode, as suggested in Ref. [5], is linearly polarised in the y direction, we can write its electrical and magnetic field components to first order in θ_d in mks units as follows

$$E_y = E_0(\frac{w_0}{w})(\frac{\sqrt{2}y}{w})e^{-\rho^2/w^2}\cos\psi, \qquad (2.1)$$

$$B_x = -E_y/c, \qquad (2.2)$$

$$E_z = \frac{E_0\theta_d}{\sqrt{2}}(\frac{w_0}{w})^2 e^{-\rho^2/w^2}[(1-\frac{2y^2}{w^2})^2 + s^2]^{1/2}\sin(\psi + \theta), \qquad (2.3)$$

where E_0 is the electrical field amplitude, w_0 is the minimum optical beam spot size defined by $\pi w_0^2 = \lambda Z_R$, λ is the optical wavelength, Z_R is the Rayleigh range, $w(s) = w_0(1+s^2)^{1/2}$ is the beam radius at a longitudinal position z normalized to $s = z/Z_R$, $\rho = \sqrt{z^2 + y^2}$, $\theta_d = w_0/Z_R$ is the diffraction angle, and ψ and θ are defined as follows

$$\psi = \omega t - kz + 2\arctan(s) - s(\frac{\rho^2}{w^2}), \qquad (2.4)$$

$$\theta = \arctan(\frac{sw^2}{2y^2 - w^2}), \qquad (2.5)$$

where ω is the angular optical frequency, and $k = 2\pi/\lambda$ is the optical wavenumber. The longitudinal magnetic field component, B_z, is neglected for its trivial effect on the transverse particle dynamics. The third term on the right-hand side of Eq. (2.4) represents the so-called Guoy phase shift associated with the TEM_{10} Gaussian mode [10]. The variable θ is an additional phase shift introduced into the axial electrical field component, resulting from the transverse variation of both amplitude and phase front of the transverse electrical field component.

As can be seen from Eqs. (2.3) and (2.5), there exists a turning point vertically around which the axial electrical field vector reverses its direction. This provides a mechanism for accelerating and decelerating electrons according to their betatron amplitude. By further examing the expression for the axial electrical field component, it can be found that the optimum conditioning is reached when the condition $y \simeq w$ is fulfilled. This indicates that the electron beam should possess about the same size as the conditioning laser beam does.

In general, an electron can never be steadily accelerated or decelerated along its propagation with the conditioning wave. Instead, it will experience an oscillatory process of being accelerated and decelerated, and there will be no net energy exchange between the electron and the conditioning wave. However, if we have the beam waist of the conditioning wave located around the entrance of an undulator longitudinally, there will be a net energy exchange between the electron and the conditioning wave owing to the natural divergence of a Gaussian beam.

III. NUMERICAL CALCULATIONS

The impact of the laser powered beam conditioner is demonstrated by computer simulation with two numerical examples. In the first example, a CO_2 laser is used.

The energy and the 4σ normalised emittance of the beam are 101.7 MeV and 26 π mm mrad, respectively. The undulator period is arbitrarily chosen to be 2 cm, and the peak magnetic field strength is 7.57 kG, corresponding to $a_u=1$. The conditioning laser has the following parameters: wavelength $\lambda=10.6$ μm, Rayleigh range $Z_R=6$ cm, and field strength parameter $a_c=0.01$. The starting point where the interaction between the electrons and the conditioning laser begins is $s_0=0$, i.e., the laser beam waist is located exactly at the entrance to the undulator. The initial phase $\psi_0=155°$. With the above parameters, the fundamental undulator radiation wavelength is 0.5 μm. In the computer simulation 500 particles were used. As is shown in Fig. 1, the rms axial energy spread is reduced from 0.29% to 0.12% within a conditioning range of 12 cm or so, corresponding to a factor of 2.4 reduction of the axial energy spread.
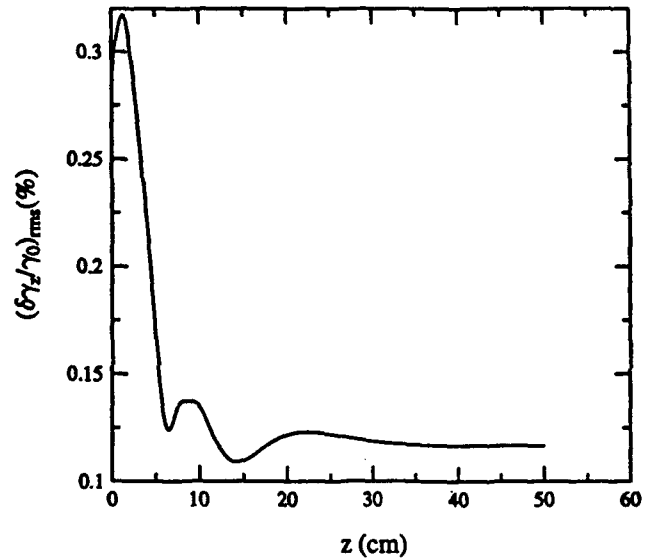
Fig.1 Variation of rms axial energy spread of an electron beam (101.7 MeV, $\epsilon_n=26$ π mm mrad) along the beginning part of the undulator, conditioned with a CO_2 laser ($\lambda=10.6$ μm, $Z_R=6$ cm) for 0.5 μm radiation.

In the second example, a Neodymium glass laser is used as the conditioning source. The electron beam energy is raised to 320 MeV. The undulator period remains 2 cm. With a peak magnetic field strength of 6.6 kG, the fundamental undulator radiation wavelength is 0.045 μm. The parameters for the conditioning laser are: $\lambda=1.06$ μm, $Z_R=20$ cm, $a_c=0.0035$, and conditioning starting position $s_0=0.1$, i.e., the optical waist is 2 cm inside the undulator. The 4σ normalised beam emittance is 9 π mm mrad. The init. phase is $\psi_0=150°$. As is shown in Fig. 2, the beam is conditioned within a distance of about 42 cm inside the undulator, and the axial energy spread is reduced from 0.076% to 0.032%, a reduction by a factor of 2.4. Note

that the conditioning length is about twice the Rayleigh range in both examples.
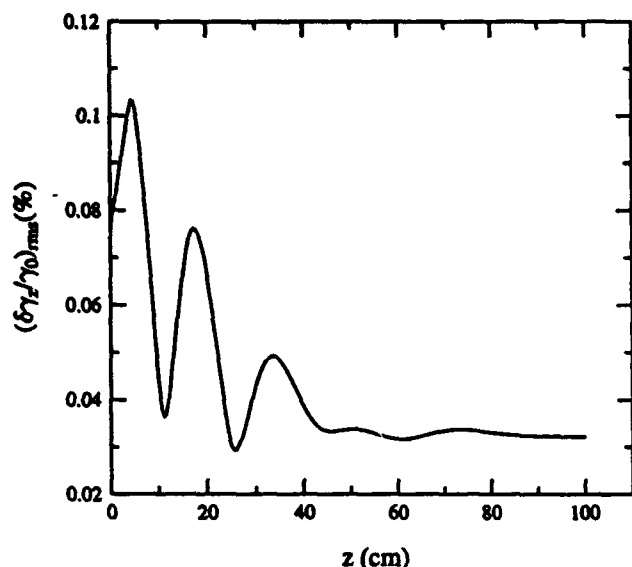
Fig.2 Variation of rms axial energy spread of an electron beam (320 MeV, $\epsilon_n=9 \pi$ mm mrad) along the beginning part of the undulator, conditioned with a Neodymium glass laser ($\lambda=1.06$ μm, $Z_R=20$ cm) for 0.045 μm radiation.

IV. DISCUSSIONS

One attractive feature of a laser powered beam conditioner is the relatively modest laser requirement. The optical power required for conditioning can be estimated according to the following formula [3]

$$P(\text{GW}) = 3.4 a_c^2 Z_R/\lambda. \qquad (3)$$

For the CO_2 laser in the first example, the corresponding optical power is about 2 GW; for the Neodymium glass laser in the second example, the required optical power is about 8 GW. Both of them are readily achieved.

The laser powered beam conditioner may have some potential advantages. Among them are the elimination of rf structures, that may cause beam breakup instability as well as wakefields, and relatively less severe transverse kick effects due to the fact that the conditioning wave is diffraction limited.

Next, note that there are two kinds of sources of constraints on the beam emittance: one is the overlap requirement, the other is the synchronism requirement [11]. In general, the second constraint is more restrictive than the first one for long undulators, which is the case the "conditioning" is mainly for. In this case, it is advantageous to have the electrons well conditioned just within the very beginning part of an undulator so that the full benefit can

be realised. Further, there is no possibility of beam degradation between the conditioner and undulator as would be the case for separate systems.

We found that the conditioning is dependent on the initial phase from one half optical cycle to the other. Therefore, it is required that the electrons be pre-bunched over half an optical cycle in advance. This pre-bunching can be realised at a lower electron beam energy using the identical laser wave [6] or using a segment of undulator as for an optical klystron [11]. The latter method has been experimentally verified. This may finally determine the easy implementation of the laser powered beam conditioner.

ACKNOWLEDGEMENT

REFERENCES

[1] A. M. Sessler, D. H. Whittum and L. H. Yu, *Phys. Rev. Lett.* 68, 309 (1992).

[2] P. Sprangle, B. Hafizi and G. Joyce, *Proc. of the 14th Int. FEL Conf.*, Kobe, 1992.

[3] G. R. Neil and H. Liu, CEBAF TN-92-035.

[4] G. R. Neil, H. Liu and B. Yunn, this conference.

[5] F. Caspers and E. Jensen, in *Laser Interaction and Related Plasma Phenomena*, Vol. 9, edited by H. Hora and G. H. Miley (Plenum Press, New York, 1991), pp. 459-466.

[6] E. J. Bochove, G. T. Moore, and M. O. Scully, *Phys. Rev. A*, 46, 6640 (1992).

[7] D. C. Quimby, *Nucl. Instrum. Methods* A250, 456 (1986).

[8] M. Lax, W. H. Louisell and W. B. McKnight, *Phys. Rev. A*, 11, 1365 (1975).

[9] L. Cicchitelli, H. Hora and R. Postle, *Phys. Rev. A*, 41, 3727 (1990).

[10] A. E. Siegman, *Lasers* (University Science Books, Mill Valley, CA, 1986).

[11] C. A. Brau, *Free-Electron Lasers* (Academic Press, San Diego, CA, 1990).

Tracking Studies of Insertion Device Effects on Dynamic Aperture in the APS Storage Ring*

Yong-chul Chae† E. A. Crosbie
Argonne National Laboratory, 9700 So. Cass Ave., Argonne, IL 60439

Abstract

We studied the effects of an insertion device (ID) on the dynamic aperture in the 7-GeV Advanced Photon Source (APS) storage ring using the program RACETRACK [1]. We found that the nonlinear effect of the ID is the dominant effect on the dynamic aperture reduction compared to the other multipole errors which exist in the otherwise ideal lattice. The previous study of dynamic aperture [2] was based on the assumption that the effect of the fast oscillating terms in L. Smith's Hamiltonian [3] is small, and hence can be neglected in the simulation. The remarkable agreement between the previous study and the current results using RACETRACK, including all effects of the fast oscillating terms, justified those assumptions at least for the APS ring.

I. INTRODUCTION

The Advanced Photon Source (APS) storage ring is a 7-GeV *third generation* light source with forty straight sections. Intense x-ray beams will be delivered by thirty-four undulators and wigglers. Thus the effects, linear and nonlinear, of the insertion devices on the beam dynamics becomes important. In this report we present the numerical tracking studies of the effect of IDs on the dynamic aperture.

II. PLANAR INSERTION DEVICES

A. Motivation for Using RACETRACK

The field components for a planar insertion device (ID) suggested by K. Halbach [4] are given by:

$$B_y = B_o \cosh k_x x \cosh k_y y \cos kz$$

$$B_x = \frac{k_x}{k_y} B_o \sinh k_x x \sinh k_y y \cos kz \qquad (1)$$

$$B_z = -\frac{k}{k_y} B_o \cosh k_x x \sinh k_y y \sin kz$$

where

$$k_x^2 + k_y^2 = k^2 = \left(\frac{2\pi}{\lambda_w}\right)^2$$

and λ_w is the period length.

The Hamiltonian with respect to the oscillating equilibrium orbit suggested by L. Smith [3] is given by:

$$H = \frac{1}{2}(p_x^2 + p_y^2) + \qquad (2)$$

$$\frac{1}{4k^2\rho^2}\left[\cosh^2 k_x x \cosh^2 k_y y + \frac{k_x^2}{k_y^2}\sinh^2 k_x x \sinh^2 k_y y\right]$$

$$-\frac{\sin ks}{k\rho}[p_x(\cosh k_x x \cosh k_y y - 1)$$

$$-\frac{k_x}{k_y}p_y \sinh k_x x \sinh k_y y]$$

Expanding to fourth order in x and y, and assuming $k_x = 0$, i.e. an ID with infinite width in the horizontal direction, Eq. 2 becomes

$$H = \frac{1}{2}(p_x^2 + p_y^2) + \frac{1}{2}\left(\frac{1}{2\rho^2} - \frac{p_x k}{\rho}\sin ks\right)y^2 + \frac{k^2}{12\rho^2}y^4, \qquad (3)$$

where ρ is the radius of curvature in the peak field in the ID, B_0. We note that this Hamiltonian has a constant linear focusing term and an octupole-like term in the vertical direction if we neglect the fast oscillating (compared to betatron oscillation) term contained in $\sin(ks)$ for the moment. Neglecting the $\sin(ks)$ term, we may treat the ID as a long quadrupole with a lumped nonlinear element at the center. The equations of motion may be written as

$$\frac{d^2 y}{ds^2} = \frac{-\sinh(2ky)}{4k\rho^2}, \quad \frac{d^2 x}{ds^2} = 0,$$

where s is the equilibrium orbit length. The previous tracking study based on this approach was done using the PACMAN code [2]. We found that the dynamic aperture was larger than the physical aperture at the ID section.

As a continuation of this effort, including the effects of fast oscillating terms, we decided to use RACETRACK for dynamic aperture study. The program, developed at Sincrotrone Trieste, has a unique ability to perform second-order symplectic integration for motion in the insertion device [5, 6].

B. Effects of an ID on Dynamic Aperture

One of the major insertion devices in the APS project is the Type-A undulator with peak field B_0=0.85 T, undulator period λ_w=3.3 cm, total ID length L_{ID}=2.31 m. The constant linear vertical focusing strength for this ID is

$$\frac{L_{ID}}{2\rho^2} = 0.0015(m^{-1}) << K_Q = 0.51147(m^{-1})$$

where K_Q is a typical quadrupole strength in the APS ring. Hence the linear effect of the ID considered here will be very small. In order to investigate the effect of oscillating terms, we first note that p_x is constant for each pass of the particle through the ID. The equation of motion is therefore a Mathiew equation. Examination of this equation shows that the focusing effect of the oscillating

term was negligible for acceptable values of p_x. This is verified by comparing the linear tune shifts obtained from the analytic estimation and the numerical result of RACE-TRACK. Thus, the linear effect of the ID on the dynamic aperture reduction is very small. This is clearly seen in Fig. 1 which shows that dynamic aperture reduction is mainly due to the nonlinear effect of the ID.

Since the lattice elements in the ring have error fields due to imperfect construction, the effects of the multipole errors in the lattice were investigated. For this purpose, the random normal sextupole and octupole field errors based on the APS magnetic field tolerance budget were included in the dipole and quadrupole magnets. The rms values of these multipole errors are $b_{2D} = 5 \times 10^{-5}$, $b_{3D} = 1 \times 10^{-5}$, $b_{2Q} = 1 \times 10^{-4}$ and $b_{3Q} = 5 \times 10^{-5}$ where b_{nD} and b_{nQ} are the normal $2(n+1)$-pole field coefficients in the dipole and quadrupole magnets, respectively. Field error coefficients are defined as

$$B_y + iB_x = B_0 \sum_{n=0} (b_n + ia_n)(x + iy)^n,$$

where b_n and a_n indicate the normal and skew components, respectively. Although these error fields reduce the dynamic aperture of an ideal lattice without an ID, we expected that, because ID effects on dynamic aperture reduction are so dominant, the inclusion of the multipole errors in the ordinary lattice would not cause much additional change to a dynamic aperture already reduced by the presence of the ID. This is verified in Fig. 2.

The results for multiple IDs are also shown in Fig. 1. As expected, the dynamic aperture is further reduced as the number of IDs around the ring increases. However, the aperture reduction for 20 IDs is no worse than that for 10 IDs. The dynamic aperture is still larger than the physical aperture.

Although not shown here, we investigated the effect of the non-zero horizontal wave number (k_x). Depending on whether k_x is real or imaginary, such an ID will provide additional horizontal focusing and defocusing, respectively. We found the tracking results were essentially the same in the realistic variation of k_x values.

Finally, we want to mention that when we compare the tracking results from the programs PACMAN and RACE-TRACK the phase space as well as dyanamic aperture show remarkable agreement (see Fig. 3 for the comparison of dynamic aperture). Thus, we may tentatively conclude that the effect of the fast oscillating terms which appeared in L. Smith's Hamiltonian will be small for the IDs in the APS storage ring.

III. HELICAL INSERTION DEVICES

There is an increasing interest in the utilization of circularly or elliptically polarized light for some types of experiments. Such a light will be delivered by helical IDs. One type of helical ID considered in the APS project is the crossed insertion device originally conceptualized by Onuki [7]. The magnetic fields of crossed IDs are the superposition of the horizontal and vertical planar IDs whose field expressions, in simplified form, may be written as

$$B_x = B_0' sin(kz), \quad B_y = B_0 sin(kz - \alpha), \quad B_z = 0, \quad (4)$$

where B_0' and B_0 are the peak field in the x- and y-directions, respectively, k is the usual wave number, and α is the longitudinal phase slip between the horizontal and vertical planar IDs. By adjusting α, the field projected onto the x-y plane will be either circular or elliptic. For instance, if B_0' is equal to B_0, the field will look circular if $\alpha = \frac{\pi}{2}$ or $\frac{3\pi}{2}$ and elliptic if $\alpha = \frac{3\pi}{4}$ or $\frac{7\pi}{4}$.

In the APS, such a helical ID has the parameters $B_0 = 1\ T$, $B_0' = 0.07\ T$, $\lambda_w = 15\ cm$, and total length of device $L_{ID} = 3\ m$. Since the deflection parameter K, defined by

$$K = 0.934\ \lambda_w(cm)\ B_0(T),$$

is equal to 14 for this device, it has the focusing characteristics of a wiggler. In general, the dominant effect of a wiggler is conceived as linear because it usually requires a higher peak field and a longer period length than an undulator. Such a linear effect results in dynamic aperture reduction through breaking the symmetry of the lattice. Thus, a sophistiscated matching scheme may be required to restore the linear optics. However, for the APS helical ID, the distortion of linear optics is found to be very small mainly because the beam energy is high and the peak field is relatively low comparable to the planar Type-A ID considered in the previous section.

Also, the nonlinear effect of the helical ID will be small compared to the effect of the Type-A ID since the helical ID has a longer period length than the Type-A ID. We may expect that the dynamic aperture reduction due to the single helical ID should not be worse than that for the single Type-A ID. This is seen in Fig. 4 which shows the tracking results from RACETRACK for the various values of the B_0' field.

IV. CONCLUSION AND DISCUSSION

A study of the effects of an insertion device on the dynamic aperture is presented in this report. We found that, for Type-A and helical insertion devices considered for the APS project, the nonlinear effect was the dominant cause of dynamic aperture reduction. Also, with up to 20 IDs in the ring, stable amplitude of the beam oscillation is still outside of the physical vacuum chamber.

We also found that when we compared the numerical results from RACETRACK with the one from Ed Crosbie's PACMAN, the agreement between the two were remarkable. Hence, we may tentatively conclude that the effects of the fast oscillating terms contained in the ID Hamiltonian are negligible.

V. ACKNOWLEDGEMENTS

from Sincrotrone Trieste, was most helpful to us in this study.

VI. References

[1] F. Iazzourene, et al., "RACETRACK USER'S GUIDE VERSION 4," Sincrotrone Trieste, July, 1991.

[2] "7-GeV Advanced Photon Source Conceptual Design Report," ANL-87-15, 1987.

[3] L. Smith, "Effects of Wigglers and Undulators on Beam Dynamics," LBL ESG TECH NOTE-24, September, 1986.

[4] K. Halbach, "Physical and Optical Properties of Rare Earth Cobalt Magnets," NIM, Vol 187, 1981.

[5] R. Nagaoka and L. Tosi, "An Improved Scheme for Integrating the Particle Motion through the Insertion Device in RACETRACK," ST/M-90/6, Sincrotrone Trieste, March, 1990.

[6] R. Nagaoka and L. Tosi, "An Extended Scheme of the New Tracking Routine for Nonplanar Insertion Devices," ST/M-91/4, Sincrotrone Trieste, May, 1991.

[7] H. Onuki, "Elliptically Polarized Synchrotron Radiation Source with Crossed and Retarded Magnetic Fields," NIM, Vol. 246, 1986.

Figure 2
Dynamic aperture reduction due to a single ID with and without the multipole errors in the lattice.
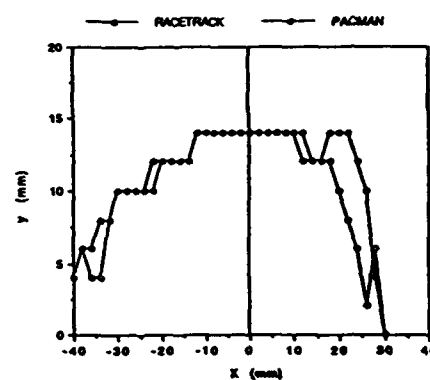
Figure 3
Dynamic aperture reduction due to a single ID (Comparison of results from the PACMAN and RACETRACK programs).

Figure 1
Dynamic aperture reduction due to a single ID (linear effect vs. total effect) and due to multiple IDs.
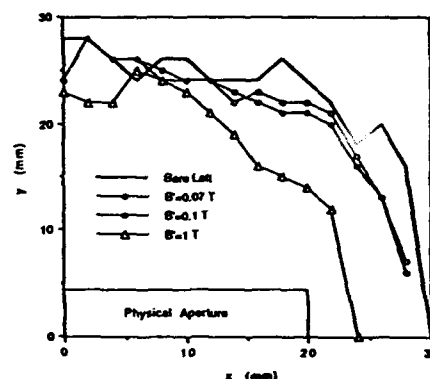
Figure 4
Dynamic aperture reduction due to a single helical ID $(B_0 = 1.0\,T$ and $B_0' = 0.07\,T,\ 0.1\,T,\ 1.0\,T)$.

Particle Diffusion from Resonance Islands in Aladdin at SRC*

J. Liu, E. Crosbie, L. Teng, J. Bridges, D. Ciarlette
R. Kustom, D. Voss, F. Mills, M. Borland
APS, Argonne National Laboratory, Argonne, IL 60439, USA
K. Symon
Dept. of Physics, University of Wisconsin-Madison, Madison, WI 53706, USA
W. Trzeciak
Synchrotron Radiation Center, Stoughton, WI 53589, USA

Abstract

The dynamics of the beam in the resonance islands was studied on the electron storage ring Aladdin at the Synchrotron Radiation Center(SRC). We especially studied the horizontal third- and fourth-integral resonances driven by sextupole fields in the first and second order. A fast kicker was fired to kick the beam into one of the outboard stable islands. The beam took on a quasi-Gaussian distribution and slowly diffused out of the island. The diffusion rate and its dependence on the strengths of the driving sextupoles and the chromaticity sextupoles were measured by tracing the resonance peak of the betatron oscillation on the spectrum analyzer. Beam positions were also recorded through the data acquisition device which was clocked by a pulse-delay circuitry. Interesting results are shown and compared with numerical calculations.

I. INTRODUCTION

Aladdin is a 1-GeV electron storage ring composed of four arc and four straight sections. In normal operation it stores 15 beam bunches with horizontal beam sizes $\sigma_x \simeq 0.82$ mm. In our nonlinear beam dynamics experiment, only one beam bunch is used at an average current of 10 mA. Four pairs of unused horizontal and vertical chromaticity correcting sextupoles are optionally employed to excite desired resonant harmonics, and a fast kicker is fired to drive the coherent betatron oscillation. The details of measurements of the horizontal third- and fourth-integral resonance can be found in Ref [1] and [2]. During the measurement of the horizontal fourth-integral resonance $4\nu_x = 29$, we found that the particles initially captured into the resonance islands did not remain in islands but diffused back to the origin in a few seconds.

The beam lifetime in the resonance island is determined by such transverse diffusion process as quantum fluctuations due to synchrotron radiation, multiple scattering from residual gases, and intrabeam scattering. The purpose of the experiment was to measure the diffusion rates between the islands and the central region as a function of resonance island size.

II. EXPERIMENTAL MEASUREMENT

The third-integral resonance $3\nu_x = 22$ was chosen for
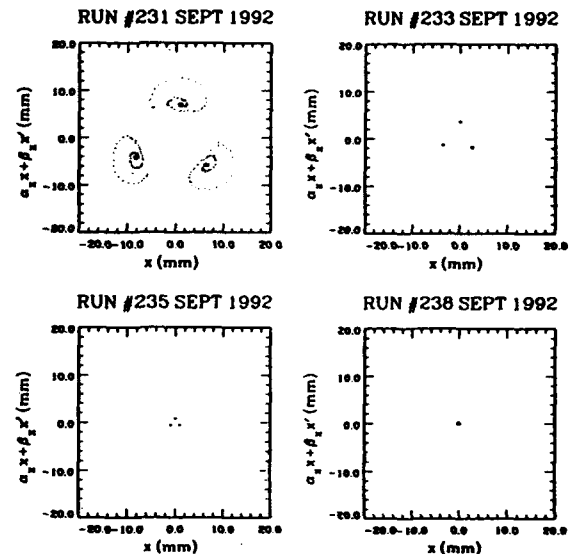
Figure 1
Third-integral resonance measurement at $\nu_x = 7.328$

measurement since the island size is relatively easily controlled with driving sextupoles. Figure 1 is a series of typical results from the BPM measurement of the beam centroid, showing the diffusion process. The first plot clearly shows the resonance island pattern with decoherent damping due to the nonlinear detuning. The beam centroids are damped to the island centers in about 300 turns. As more particles diffuse back to the central region, the amplitude of the beam centroid gradually decreases and finally becomes zero.

An efficient way to measure the diffusion rate is to trace the coherent signal on the spectrum analyzer. Right after the beam is kicked into one of the islands, a coherent betatron signal immediately appears at the resonant tune. Sometime later particles slowly leak out of the island while the signal exponentially decreases at a certain rate.

Figure 2 (a) shows an early measurement of the diffusion time versus the driving sextupole, taken at $\nu_x = 7.325$ with chromaticity $\xi_x = 0.808$. The driving sextupole SF1 is powered to control the island size, while chromaticity-correcting sextupole SFs are adjusted to keep chromaticity constant. Figure 2 (b) plots the diffusion time τ versus I_{SF}. The SF1 was set at $I_{SF1} = 45$ A, and the SFs are adjusted from $I_{SF} = 33.3$ to 35.5 A, which results in the chromaticity changing from 0.500 to 1.664. The diffusion

Figure 2

DIFFUSION TIME   **CHROMATICITY EFFECT**

(a) τ vs. I_{SF1} (b) τ vs. I_{SF}

Figure 2

Diffusion time measurement at $\nu_x = 7.325$

DIFFUSION TIME   **DIFFUSION TIME**

(a) $\xi_x = 0.160$ (b) $\xi_x = 1.083$
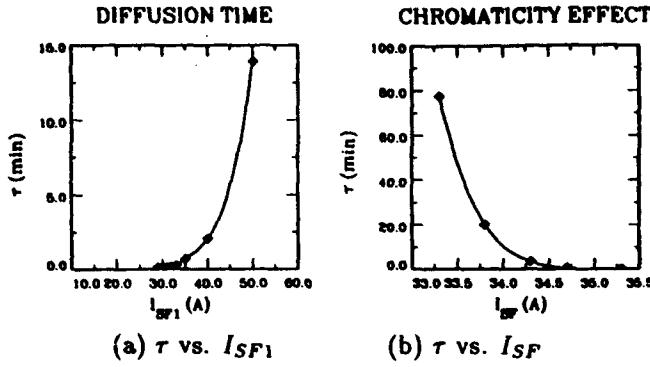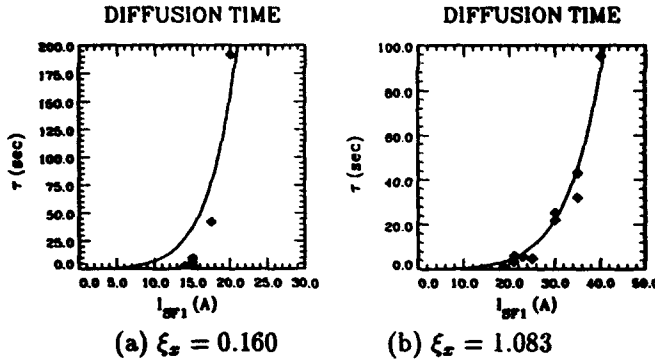
Figure 3

Diffusion time measurement at $\nu_x = 7.327$

time is exponentially decreased. This indicates that when ξ_x is large, the beam emittance is increased.

A recent measurement illustrates a shorter diffusion time. In Figure 3, we plot the τ against I_{SF1} at $\nu_x = 7.327$ with chromaticities $\xi = 0.16$ and $\xi_x = 1.083$. The solid curves are results fitted with the function,

$$\tau = \frac{\tau_x}{\gamma I_{SF1}^{1/2}} e^{\gamma I_{SF1}^{1/2}}, \tag{1}$$

where γ is a fitting parameter depending upon the chromaticity and the details of the diffusion process and τ_x is the damping time given by $\tau_x = 0.022$ seconds. We obtain $\gamma = 2.617$ and $\gamma = 2.128$ for $\xi_x = 0.160$ and $\xi_x = 1.083$ respectively, which predicts a beam size about double that expected from quantum emission. Eq. (1) follows from the Sands formula [3] for τ, assuming island size is proportional to $I_{SF1}^{1/2}$. As we see, the Sands formula does not agree with the measurement for the small island size.

The outward diffusion was also measured with the laser beam analyzer. At specified time intervals, the analyzer takes frames of a synchrotron light spot through a camera mounted at a beamline port. Our camera was focused on the central region and one of the islands. By appropriately choosing an aperture to include one of the synchrotron light images, we obtained beam intensity in arbitrary units.

We first set the driving sextupole $SF1$ to $I_{SF1} = 50A$, and then decreased the central stability region by jumping

CENTER DIFFUSION RATE   **ISLAND GROWTH RATE**

(a) Central intensity   (b) Island intensity
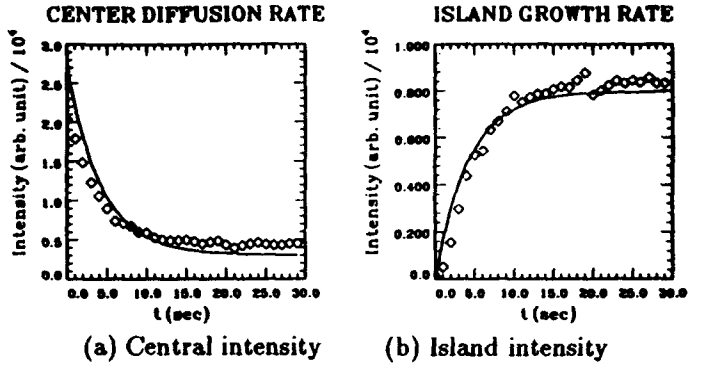
Figure 4

Measurements of the intensities in the center and islands

the betatron tune close to the resonance $3\nu_x = 22$. The TV monitor clearly showed the diffusion process as particles gradually diffused into islands, and 25 seconds later the beams in the center and islands reached an equilibrium. As one can see from Figure 4, the beam intensity in each region approaches its equilibrium value exponentially.

Assume C and I are beam intensities in the central region and islands, respectively. By solving equations

$$\frac{dC}{dt} = -\frac{C}{\tau_c} + \frac{I}{\tau_i}, \qquad \frac{dI}{dt} = -\frac{I}{\tau_i} + \frac{C}{\tau_c}, \tag{2}$$

one can obtain

$$C = \frac{C_0}{1+\alpha}[1 + \alpha e^{-\frac{t}{\tau}}], \qquad I = \frac{C_0\alpha}{1+\alpha}[1 - e^{-\frac{t}{\tau}}], \tag{3}$$

where C_0 is the initial intensity in the central region; $\alpha = \frac{\tau_i}{\tau_c}$ and τ is the effective diffusion time defined by $\frac{1}{\tau} = \frac{1}{\tau_c} + \frac{1}{\tau_i}$, and τ_c and τ_i are diffusion times for the central beam and for the island beam, respectively

Using Eq. (3) to fit the intensity measurements simultaneously with the least squares method, we obtain $C_0 = 26972$, $\alpha = 7.83$ and $\tau = 4.24$ seconds which give $\tau_c = 4.78$ seconds and $\tau_i = 37.41$ seconds. The fit is shown as the solid curves in Figure 4.

III. NUMERICAL SIMULATION

When an electron passes through a bending magnet, it losses its energy by releasing photons in a random Poisson process. The photon energy is randomly chosen from the appropriate distribution [4]. For reasonable statistics, at least 100 particles should be included and tracked up to 10^8 turns (30 seconds). To speed the simulation, the total effect of the quantum emission and RF acceleration damping is replaced with a Gaussian distribution,

$$P(\Delta x) = \frac{1}{\sqrt{2\pi}\sigma} e^{-\frac{\Delta x^2}{2\sigma^2}}, \qquad P(\Delta p_x) = \frac{1}{\sqrt{2\pi}\sigma} e^{-\frac{\Delta p_x^2}{2\sigma^2}}, \tag{4}$$

where $\sigma = \frac{1}{2}\overline{\Delta x^2}$, based on the central limit theorem [5]. One can then choose Δx and Δp_x once a turn from the random generator and add them to the betatron amplitude. At $\nu_x = 7.327$, typically $\sigma = 3.9860 \times 10^{-6}$ m for
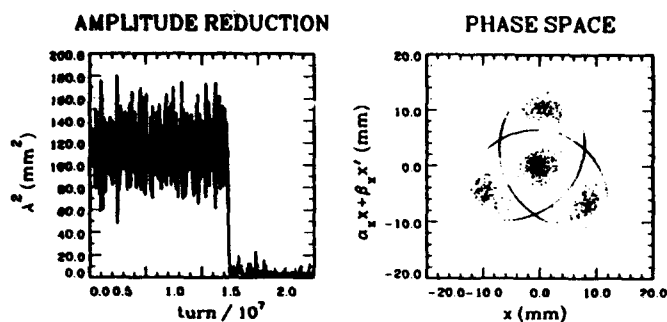
Figure 5
A single particle diffuses into the central region from
resonance island at $\nu_x = 7.327$

(a) At the 4 msecond   (b) At the 7.5 second
Figure 7
Simulation of the outward diffusion process

Figure 6
A simulation of the particle diffusion from the resonance
island; $\nu_x = 7.327$ and $\xi_x = 0.16$
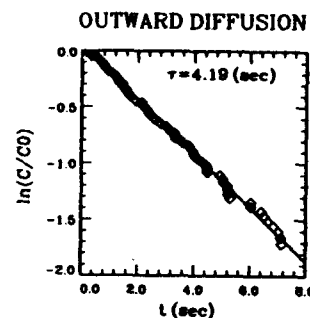
Figure 8
The outward diffusion of the central particles

Aladdin. Figure 5 illustrates that a single particle, initially located at the stable fixed point in the resonance island, diffuses into the central region from the resonance island.

The particle diffusion from resonance islands is first simulated. Figure 6 shows the simulation results corresponding to the case $\xi_x = 0.16$ as shown in Figure 3 (a). A total of 100 particles are initially located at the fixed point in one of the islands. Some time later particles take on a quasi-Gaussian distribution and slowly diffuse out of the island. If particles pass across the separatrix, they are lost from the island. In this way the diffusion rates are obtained by fitting the number of lost particles. The simulation results (rhombus) are consistent with the experimental results (circles).

In the simulation of particle diffusion from the central region to the island, the linear lattice parameters at the beamline port are used, where $\beta_x = 0.9354$ m and $\epsilon_{x0} = 8.5377 \times 10^{-7}$ (π rad-m). A total of 100 particles are tracked, starting at zero amplitude. Two frames of particle distributions at different times are selected to demonstrate the outward diffusion process as shown in Figure 7. The diffusion rate from simulation is also shown in Figure 8 plotted as $ln(C/C_0)$ against time. The fitting gives the diffusion time $\tau_c = 4.193$ seconds which is rather consistent with the measured τ_c.

IV. CONCLUSION

The particle diffusion from the resonance island and the inverse process are studied experimentally and numerically. Experimental measurements have partially verified the stochastic diffusion theory applying to the resonance phase map, and reveal the dependence of diffusion time on the machine chromaticity. To completely understand the experiment, we are continuing studies of the beam dynamics in the resonance island.

V. REFERENCES

[1] E. Crosbie, et al. "Non-linear Resonance Studies at the Synchrotron Radiation Center, Stoughton, Wisconsin," *Conference Record of the 1991 IEEE Particle Accelerator Conference*, Vol. 3, pp. 1624-1626, 1991.

[2] J. Liu, et al. "Fourth-Integral Resonance Study on ALADDIN at SRC," Argonne Lab, Light Source report, LS-214, 1992.

[3] M. Sands, "The Physics of Electron Storage Rings-An Introduction," SLAC-121, May, 1979.

[4] E. Crosbie, "Effect of Synchrotron Radiation in the Proposed 4 GeV Argonne Microtron," *IEEE Trans. Nucl. Sci.*, NS-30, No. 4, 3218, 1983.

[5] Keith R. Symon, private communication.

ALTERNATING-PHASE FOCUSING
WITH AMPLITUDE MODULATION

L. Sagalovsky, J. R. Delayen

Engineering Physics Division, Argonne National Laboratory

Argonne, Illinois 60439 USA

Abstract

We have previously developed a model of alternating-phase focusing (APF) applicable to ion linacs comprised of short independently controlled cavities. The main beam dynamical aspects of APF are adequately described by four parameters: equilibrium synchronous phase, phase modulation amplitude, length of APF period, and incremental energy gain. In this paper we report on an extension of the analysis to include simultaneous modulation of the accelerating field amplitude. Two additional parameters are included: relative phase between the amplitude and phase modulation and magnitude of the amplitude modulation. The effects of amplitude modulation on the stable regions and longitudinal acceptance are discussed.

I. INTRODUCTION

In our previous paper [1], we developed an analytical model suitable for studying APF beam dynamics in low-energy superconducting linacs. We derived equations of motion for the electric field described by a cylindrically symmetric travelling wave with a continuous phase modulation and obtained approximate analytical solutions for both the regions of linear stability and the nonlinear longitudinal acceptance. In this paper, we generalize the model to include a simultaneous modulation of the acceleration amplitude. Early works in the field [2] suggested that the amplitude modulation may increase the effectiveness of APF. We show how the effect can be quantified in the context of our model.

II. APF BEAM DYNAMICS

A. Equations of Motion

We choose a sinusoidal modulation for both the phase and the amplitude of the electric field:

$$E_z = E_0 \left[1 + \epsilon \sin \left(\int_0^z \frac{2\pi}{\Lambda} dz' + \delta \right) \right] \quad (1)$$
$$\times \cos \left[\omega t - \int_0^z k(z') dz' + \phi_0 + \phi_1 \sin \left(\int_0^z \frac{2\pi}{\Lambda} dz' \right) \right],$$

where ω is the angular velocity and k is the wave number of the rf field, ϕ_0 is the equilibrium phase, Λ and ϕ_1 are the APF period and phase modulation amplitude respectively, and ϵ and δ are the amplitude modulation strength and relative phase respectively. For the central reference trajectory z_c, we take

$$\omega t - \int_0^{z_c} k(z') dz' = 0. \quad (2)$$

We will use the following dimensionless variables to analyze APF throughout the paper,

$$\Delta\phi \equiv -k\Delta z, \quad \tau \equiv \int_0^{z_c} \frac{dz}{\Lambda}, \quad \nu \equiv \frac{\Lambda}{\beta\lambda}, \quad (3)$$

and

$$\eta \equiv \frac{qE_0\beta\lambda}{m\beta^2 c^2/2}, \quad \langle\eta\rangle \equiv \frac{q\langle E\rangle\beta\lambda}{m\beta^2 c^2/2}, \quad (4)$$

where $\langle E \rangle$ is the accelerating gradient obtained by averaging E_z given by eq. 2 over one APF period,

$$\langle E \rangle = E_0 \left[J_0(\phi_1) \cos\phi_0 - \epsilon J_1(\phi_1) \sin\phi_0 \cos\delta \right]. \quad (5)$$

Following derivations in ref. [1], we get the equation of motion for the longitudinal coordinate $\Delta\phi$,

$$\frac{d^2\Delta\phi}{d\tau^2} = -\pi\eta\nu^2 \Big[\big(c(\Delta\phi) - c(0) \big) $$
$$+ \epsilon \big(c(\Delta\phi)s(\Delta\phi) - c(0)s(0) \big) \Big], \quad (6)$$

where

$$c(\Delta\phi) = \cos \left[\phi_0 + \Delta\phi + \phi_1 \sin\left(2\pi\tau - \frac{\Delta\phi}{\nu} \right) \right], \quad (7)$$

$$s(\Delta\phi) = \sin \left[\sin\left(2\pi\tau - \frac{\Delta\phi}{\nu} + \delta \right) \right]. \quad (8)$$

In the transverse direction, we confine our attention to the linear motion only. The linear equation in the radial coordinate r will be given in the next section. It is obtained from using Maxwell's equations which to the first order in r relate the transverse and the longitudinal field component, $E_r(r, z; t) = -r/2 \quad \partial E_z / \partial z$.

B. Regions of Linear Stability

Linearized equations of motion can be written as follows,

$$\frac{d^2 \Delta \phi}{d\tau^2} = \pi \eta \nu \left[(\nu - \phi_1 \cos 2\pi\tau) \sin (\phi_0 + \phi_1 \sin 2\pi\tau) \right] \Delta\phi, \tag{9}$$

$$\frac{d^2 r}{d\tau^2} = -\frac{\pi}{2} \eta \nu \left[(\nu - \phi_1 \cos 2\pi\tau) \sin (\phi_0 + \phi_1 \sin 2\pi\tau) \right] r. \tag{10}$$

Keeping only the $n = 1$ term, we obtain the well-known Mathieu equations

$$\frac{d^2 \Delta \phi}{d\tau^2} - 2 \left[B + C_1 \sin (2\pi\tau + \theta_1) \right] \Delta\phi = 0, \tag{11}$$

$$\frac{d^2 r}{d\tau^2} + \left[B + C_1 \sin (2\pi\tau + \theta_1) \right] r = 0, \tag{12}$$

for which we can compute stable region boundaries. The coefficients B and C_1 can be computed explicitly in terms of the APF parameters,

$$B = \frac{\pi}{2} \eta \nu^2 \left[J_0(\phi_1) \sin \phi_0 + \epsilon J_1(\phi_1) \cos \phi_0 \cos \delta \right], \tag{13}$$

$$C_1 = -\pi \eta \nu |J_1(\phi_1)| \cos \phi_0 \sqrt{\nu^2 + \tan^2 \phi_0} \, \xi(\epsilon), \tag{14}$$

where

$$\xi(\epsilon) = 1 - \frac{\epsilon}{\phi_1} \frac{(1 - \nu^2) \sin 2\phi_0 \cos \delta + 2\nu \sin \delta}{2 (\sin^2 \phi_0 + \nu^2 \cos^2 \phi_0)} + O(\epsilon^2). \tag{15}$$

Fig. 1 (a) shows stability boundaries in the $\phi_1 - \nu$ plane for $\phi_0 = 5°$, $\langle \eta \rangle = 0.25$ (parameter $\langle \eta \rangle$ represents the relative energy change over $\beta\lambda$) with no amplitude modulation. Figs. 1 (b), (c), (d) show the effect of modulating the field amplitude with $\epsilon = 0.1$ and the relative phase δ of $0°$, $90°$, and $180°$. The shift of the stable region to lower values of ϕ_1 is desirable because it allows to use smaller electric field strength E_0 to achieve the same accelerating gradient in the APF cell (cf. eq. 5).

C. Calculation of Longitudinal Acceptance

Eq. 6 can be expanded in a Fourier series and written in the most general form as follows,

$$\frac{d^2 \Delta \phi}{d\tau^2} = -\frac{\partial U_0}{\partial \Delta\phi} + \sum_{n=1}^{\infty} \left[u_n \sin(2\pi n\tau) + v_n \cos(2\pi n\tau) \right]. \tag{16}$$

Solution to eq. 16 can be expressed as a sum of two components,

$$\Delta\phi(\tau) = \langle \Delta\phi(\tau) \rangle + \delta (\Delta\phi(\tau)), \tag{17}$$
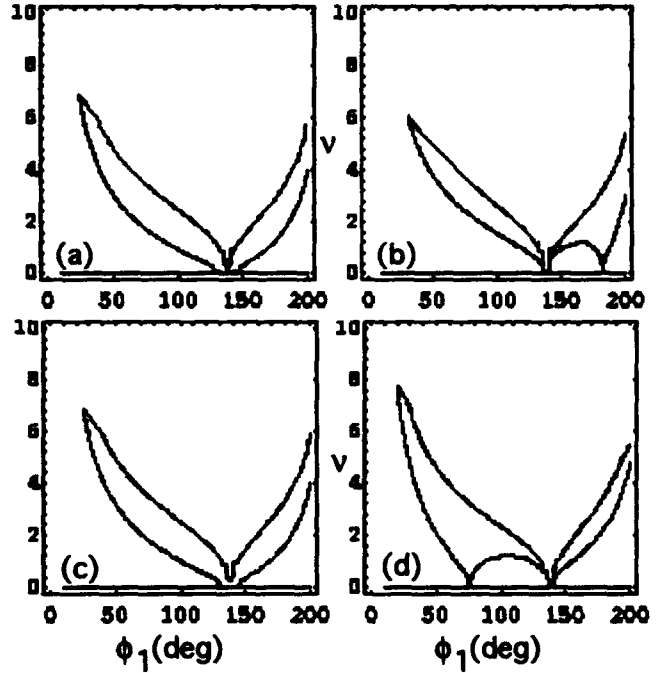
Figure 1: Stability boundaries for trajectories not exceeding 90° in either transverse or longitudinal phase advance with $\phi_0 = 5°$ and $\langle \eta \rangle = 0.25$ for (a) $\epsilon = 0$, (b) $\epsilon = 0.1$, $\delta = 0$, (c) $\epsilon = 0.1$, $\delta = \frac{\pi}{2}$, (d) $\epsilon = 0.1$, $\delta = \pi$.

where $\langle \Delta\phi(\tau) \rangle$ represents the average motion and $\delta (\Delta\phi(\tau))$ represents the fluctuations caused by the rapidly oscillating force (from here on we will drop the $\langle \rangle$ when denoting the slowly varying solution). Following the prescription given in ref. [3] and applied to the problem of longitudinal acceptance in ref. [4], we can obtain the time-averaged equation of motion as

$$\frac{d^2 \Delta \phi}{d\tau^2} = -\frac{dU_{\text{eff}}}{d\Delta\phi}, \tag{18}$$

where

$$U_{\text{eff}} = U_0 + \frac{1}{16\pi^2} \sum_{n=1}^{\infty} \frac{u_n^2 + v_n^2}{n^2}. \tag{19}$$

The potential function U_0 and the Fourier coefficients u_n, v_n can be written as follows,

$$U_0 = U_0^0 + \epsilon U_0^1, \quad u_n = u_n^0 + \epsilon u_n^1, \quad v_n = v_n^0 + \epsilon v_n^1, \tag{20}$$

where U_0^0, u_n^0, v_n^0 were given explicitly in ref. [1] and

$$U_0^1 = \pi \eta \nu^2 J_1(\phi_1) \cos \delta (c_1 + s_0 \Delta\phi - c_0), \tag{21}$$

$$u_n^1 = -\pi \eta \nu^2 \begin{cases} \frac{2n}{\phi_1} J_n(\phi_1) \left(c_1 c_{-1}^\delta - c_0 c_0^\delta \right) & \text{if } n \text{ odd} \\ -J_{n-1}(\phi_1) \left(s_1 s_{-1}^\delta - s_0 s_0^\delta \right) \\ -J_{n+1}(\phi_1) \left(s_1 s_{+1}^\delta - s_0 s_0^\delta \right) & \text{if } n \text{ even} \end{cases}, \tag{22}$$

$$v_n^1 = -\pi \eta \nu^2 \begin{cases} \frac{2n}{\phi_1} J_n(\phi_1) \left(c_1 s_{-1}^\delta - c_0 s_0^\delta \right) & \text{if } n \text{ odd} \\ J_{n-1}(\phi_1) \left(s_1 c_{-1}^\delta - s_0 c_0^\delta \right) \\ -J_{n+1}(\phi_1) \left(s_1 c_{+1}^\delta - s_0 c_0^\delta \right) & \text{if } n \text{ even} \end{cases}, \tag{23}$$

289

$$c_0 = \cos\phi_0, \quad c_1 = \cos(\phi_0 + \Delta\phi),$$

$$s_0 = \sin\phi_0, \quad s_1 = \sin(\phi_0 + \Delta\phi),$$

$$c_0^\delta = \cos\delta, \quad c_{\pm 1}^\delta = \cos\left(\delta \pm \frac{n}{\nu}\Delta\phi\right),$$

$$s_0^\delta = \sin\delta, \quad s_{\pm 1}^\delta = \sin\left(\delta \pm \frac{n}{\nu}\Delta\phi\right).$$

Given the effective potential, we can calculate the width of the separatrix in the $(\Delta\phi, \frac{\Delta W}{W})$ space and the longitudinal acceptance. The equations are found in ref. [1]. Below we examine the solution accurate to $O(\Delta\phi^2)$.

1) *Second-Order Solution:* The effective potential U_{eff} can be expanded to $O(\Delta\phi^3)$ to yield

$$U_{\text{eff}}(\Delta\phi) = \frac{a}{2}\Delta\phi^2 - \frac{b}{3}\Delta\phi^3 + \cdots, \tag{24}$$

where a is the square of the linear phase advance σ_L,

$$a = \sigma_L^2 \simeq 2B + \frac{1}{2\pi^2}C_1^2 \tag{25}$$

and b is given by

$$b \simeq \frac{\pi}{2}\eta\nu^2\left[J_0(\phi_1)\cos\phi_0 - \epsilon\cos\delta J_1(\phi_1)\sin\phi_0\right]$$
$$+ \frac{3}{8}\eta^2\nu^2\left(1 - \nu^2\right)J_1^2(\phi_1)\sin 2\phi_0 \tag{26}$$
$$\times \left[1 + 2\epsilon\frac{\cot 2\phi_0}{\phi_1}\cos\delta + O\left(\epsilon^2\right)\right].$$

The width of the separatrix Ψ and the acceptance α_L are calculated to be

$$\Psi = \frac{3}{2}\frac{a}{b}, \quad \alpha_L = \frac{6}{5\pi\nu}\frac{a^{5/2}}{b^2}. \tag{27}$$

We have kept only the $n = 1$ terms in eqs. 25, 27.

Figs. 2(a) and 2(b) show the effect of varying the relative phase δ on the separatrix width and the acceptance respectively for different values of ϵ. The calculations were performed for $\langle\eta\rangle = 0.25$, $\phi_0 = 5°$, $\phi_1 = 60°$, and $\nu = 4$. For $\epsilon = 0.1$ the separatrix can be widened by 20% with a corresponding 67% increase in the acceptance; for $\epsilon = 0.2$ the respective numbers are 33% and 147%.

III. CONCLUSIONS

The enhanced model of the traveling wave with continuous phase and amplitude modulation presented in this paper gives quantitative predictions to the problem of longitudinal stability in APF linacs. The model describes the physics of APF with six parameters and yields analytic solutions for the stable regions and the longitudinal acceptance.

Effects of modulating accelerating field amplitude can be computed explicitly keeping only quadratic terms in the expression for the time-averaged APF force. Relative
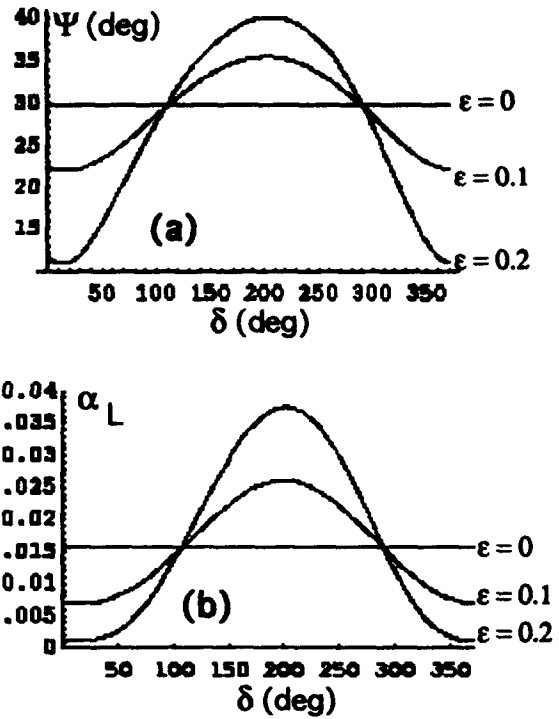
Figure 2: Plots of (a) the separatrix width Ψ and (b) the longitudinal acceptance α_L for $\langle\eta\rangle = 0.25$, $\phi_0 = 5°$, $\phi_1 = 60°$, $\nu = 4$ as a function of the relative phase δ for various values of the strength parameter ϵ.

phase between the amplitude and phase modulations determines the degree of the acceptance enhancement (or reduction). Many different scenarios can be investigated in the context of the model.

Future work will focus on investigations of practical limits of APF in linacs with independent superconducting cavities and space-charge current limits.

REFERENCES

[1] L. Sagalovsky, J. R. Delayen, *Proc. 1992 Linear Accelerator Conf.*, **AECL - 10728**, 763 (1992).

[2] V. V. Kushin, V. M. Mokhov, *Atomnaya Energiya* **35** (3) (1973).

[3] P. L. Kapitsa, *Zh. Eksper. Teor. Fiz.* **21**, 588 (1951).

[4] H. Okamoto, *Nucl. Instrum. Methods* **A284**, 233–247 (1989).

FULL-TURN SYMPLECTIC MAP
FROM A GENERATOR IN A FOURIER-SPLINE BASIS*

J. S. Berg, R. L. Warnock, and R. D. Ruth

Stanford Linear Accelerator Center, Stanford University, Stanford, CA 94309

É. Forest

Lawrence Berkeley Laboratory, University of California, Berkeley, CA 94720

Abstract

Given an arbitrary symplectic tracking code, one can construct a full-turn symplectic map that approximates the result of the code to high accuracy. The map is defined implicitly by a mixed-variable generating function. The generator is represented by a Fourier series in angle variables, with coefficients given as B-spline functions of action variables. It is constructed by using results of single-turn tracking from many initial conditions. The method has been applied to a realistic model of the SSC in three degrees of freedom. Orbits can be mapped symplectically for 10^7 turns on an IBM RS6000 model 320 workstation, in a run of about one day.

I. INTRODUCTION

Long term stability of orbits in circular accelerators is usually studied by tracking codes, which integrate the equations of motion through the lattice by some symplectic integration algorithm, proceeding element-by-element. There have been various attempts to summarize the full-turn evolution defined by a tracking code in an analytic formula, a *full-turn map*. If the map represented the code to sufficient accuracy, and could be evaluated in substantially less time than the time for tracking one turn, it could be used for economical studies of long-term evolution.

The method of automatic differentiation [1] allows one to differentiate the tracking algorithm, so as to generate a large number of Taylor coefficients of the corresponding map. The resulting map, given as a truncated Taylor series, cannot be exactly symplectic. In a region of phase space close to the dynamic aperture, the failure of symplecticity may be so large as to raise doubt about the usefulness of the map. This is the case for the highest order Taylor maps generated for the SSC (Superconducting Super Collider).

One possibility is to symplectify the map by producing a mixed-variable generating function that induces an exactly symplectic map that closely approximates the underlying map. This can be done by using formal power developments in Cartesian coordinates to solve the nonlinear equations that define the generator in terms of the map. This method was proposed and carried out long ago [2]. Because of convergence difficulties it proved not to be very useful for some accelerators (for instance the

Berkeley Advanced Light Source and the Tevatron), but recently Yan, Channell, and Syphers have reported some success with an application to the SSC [3].

We describe a different way to construct a symplectic full-turn map from a tracking code or other "source map". We again define the map through a mixed-variable generating function, but given as a function of action-angle coordinates rather than Cartesian coordinates. We avoid the use of Taylor series in favor of methods based on Fourier developments and spline interpolation. We believe that these methods are more appropriate at large amplitudes, since they use information on the function to be represented at many points in the region of interest.

This paper is a brief summary of our mapping method. Details and associated references can be found in [4].

II. CONSTRUCTING THE MAP

The map is defined to be a transformation from the "old" variables $(\mathbf{I}, \mathbf{\Phi})$ to the "new" variables $(\mathbf{I}', \mathbf{\Phi}')$. The generating function in this case will be in terms of old action and new angle variables:

$$G(\mathbf{I}, \mathbf{\Phi}') = \sum_{\mathbf{m}} g_{\mathbf{m}}(\mathbf{I}) e^{i\mathbf{m}\cdot\mathbf{\Phi}'}. \qquad (1)$$

The transformation equations are then

$$\mathbf{I}' = \mathbf{I} + G_{\mathbf{\Phi}'}(\mathbf{I}, \mathbf{\Phi}'), \qquad \mathbf{\Phi} = \mathbf{\Phi}' + G_{\mathbf{I}}(\mathbf{I}, \mathbf{\Phi}'). \qquad (2),(3)$$

We start with a "source map," which gives the final variables as an explicit function of the initial variables:

$$\mathbf{I}' = \mathbf{I} + \mathbf{R}(\mathbf{I}, \mathbf{\Phi}), \qquad \mathbf{\Phi}' = \mathbf{\Phi} + \mathbf{\Theta}(\mathbf{I}, \mathbf{\Phi}). \qquad (4),(5)$$

This map will usually be defined as the result of tracking over one turn, but in the numerical work reported here it was a 12th order Taylor series map.

The Fourier coefficients are obtained from (2) and (4) as

$$g_{\mathbf{m}}(\mathbf{I}) = \frac{1}{(2\pi)^d i m_\alpha} \int_0^{2\pi} d\mathbf{\Phi}' G_{\Phi'_\alpha}(\mathbf{I}, \mathbf{\Phi}') e^{-i\mathbf{m}\cdot\mathbf{\Phi}'}$$

$$= \frac{1}{(2\pi)^d i m_\alpha} \int_0^{2\pi} d\mathbf{\Phi}' R_\alpha(\mathbf{I}, \mathbf{\Phi}(\mathbf{I}, \mathbf{\Phi}')) e^{-i\mathbf{m}\cdot\mathbf{\Phi}'}. \qquad (6)$$

Presented at the Particle Accelerator Conference (PAC 93), Washington, DC, May 17-23, 1993.

Since we do not know R as a function of Φ', we perform a change of variables in the integral to get an integral over Φ:

$$g_m(I) = \frac{1}{(2\pi)^d \, i m_\alpha} \int_0^{2\pi} d\Phi \, R_\alpha(I, \Phi) \, e^{-i m \cdot \Phi} \cdot$$

$$e^{-i m \cdot \Theta(I, \Phi)} \det(1 + \Theta_\Phi(I, \Phi)). \tag{7}$$

The integral is then discretized to obtain

$$g_m(I) = \frac{1}{i m_\alpha \prod_\beta J_\beta} \sum_j R_\alpha(I, \Phi_j) \, e^{-i m \cdot \Phi_j}$$

$$e^{-i m \cdot \Theta(I, \Phi_j)} \det(1 + \Theta_\Phi(I, \Phi_j)), \tag{8}$$

where J_β is the number of Φ_β mesh points in the β dimension, and the summation is over integer vectors j such that $j_\beta \in \{0, \ldots, J_\beta - 1\}$.

The $m = 0$ mode must be handled differently. We instead must use Θ values. The resulting summation is

$$g_0(I) = -\frac{1}{\prod_\beta J_\beta} \sum_j \Theta(I, \Phi_j) \det(1 + \Theta_\Phi(I, \Phi_j)). \tag{9}$$

To increase the speed of evaluation of the map, Fourier modes that are smaller than the expected or desired accuracy of the map can be removed from the generating function.

We obtain values of $g_m(I)$ for values on a mesh in I. We then choose a set of basis functions $B_j^{(\alpha)}(I)$ to use in interpolating the coefficients such that

$$g_m(I) = \sum_j g_{m,j} \prod_\alpha B_{j_\alpha}^{(\alpha)}\left(I^{(\alpha)}\right). \tag{10}$$

The index α labels the different degrees of freedom. For the $m \neq 0$ modes, the interpolation is straightforward. For the $m = 0$ mode, one must be careful to consider the fact that the derivatives of the basis functions are linearly dependent. Details of this can be found in [4]. It is advantageous to choose B-splines for the basis functions. Because they have a small region where they are nonzero, their use greatly increases the speed of evaluation of the map.

III. EVALUATING THE MAP

The map is evaluated by performing a Newton iteration to obtain Φ' and then substituting into (2) to get I'. An initial guess for the Newton iteration is provided by an explicit map with a small number of modes retained.

IV. THREE DIMENSIONS

The method can be used in any number of dimensions. In a three dimensional accelerator problem, however, it is not advantageous to do the third dimension in action-angle variables. Instead, note that most of an accelerator ring is time independent. One can construct a map for the time independent part that has the energy deviation as an additional parameter, which is treated on equal footing with the actions. The time-dependent parts (usually r.f. cavities) can then be treated separately as the user chooses. Time-of-flight information is obtained by taking a derivative of the generating function with respect to energy deviation.

V. PRECONDITIONING THE SOURCE MAP

Finally, note that since one wants to perform the action interpolation over a finite domain that does not include the origin in each phase space plane, the plain source map is sometimes not well-suited for direct application of this method. This can be overcome by performing a preliminary canonical transformation on the source map so as to have the new source map take an annulus of initial conditions into a similar (larger) annulus. This can be done easily by a linear transformation or a low-order Taylor series mixed-variable generating function.

VI. RESULTS

As an example, we take the source map to be a 12th order Taylor series map for a realistic model of the SSC. Results for accuracy (agreement with the source map) and iteration time for a three dimensional map are shown in figures 1 through 2. The "mode cutoff" is a measure of the maximum size of the Fourier modes that are being removed from the generating function. The number of actions indicates the number of mesh points in each dimension of action interpolation. The order refers to the order of B-splines used in action interpolation. The curves have approximately slope 1 when the error is dominated by the number of Fourier modes being thrown away. They begin to level off when the error is dominated by the action interpolation (low actions) or failure of symplecticity of the source map (high actions).

We have constructed maps at amplitudes near the dynamic aperature, and have found that we can track stable trajectories for 10^7 terms in about a half a day in two dimensions and about a day in three dimensions. Times are on an IBM RS6000 320H workstation.

Finally, in figure 3 we show "survival plots," and see that our map gives a similar long-term dynamic aperatures to the map it is trying to approximate.

VII. REFERENCES

[1] M. Berz, Particle Accelerators **24**, 109 (1989).

[2] D. R. Douglas and A. J. Dragt, *Proc. 12th International Accelerator Conf.*, edited by F. T. Cole and R. Donaldson, p. 139 (FNAL, Batavia, 1983).

[3] Y. Yan, P. Channell, M. Syphers, SSCL-Preprint-157 (1992).

[4] J. S. Berg, R. L. Warnock, R. D. Ruth, É. Forest, SLAC-PUB-6037 (1993).
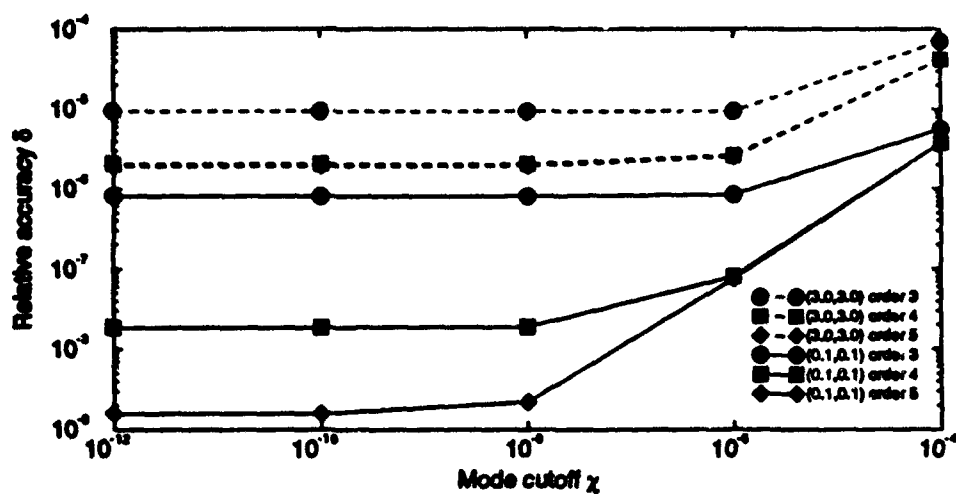
Figure 1: Relative accuracy of 3-D map
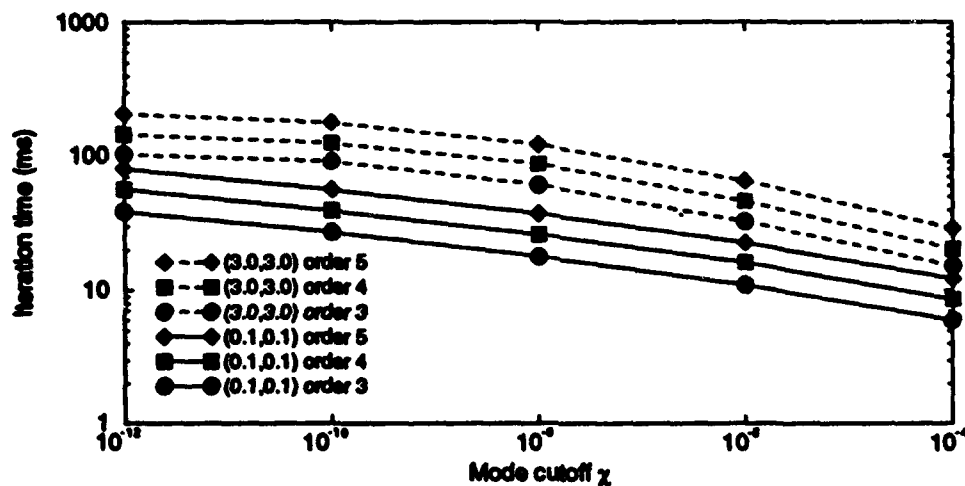
Figure 2: Iteration time of 3-D map.
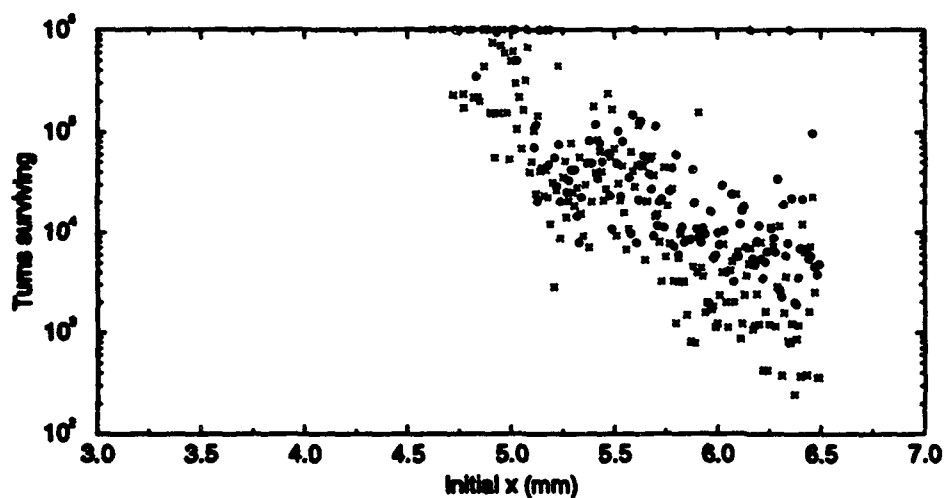
Figure 3: Survival plot. Circles are Taylor series, crosses are the map.

Synchrobetatron Resonances Due to Crab Cavities

S. Kurokawa and D. Pestrikov[1]
KEK, National Laboratory for High Energy Physics,
1-1 Oho, Tsukuba-shi, Ibaraki, 305, Japan

Abstract

Perturbation of the particle motion by a crab-cavity can excite the synchrobetatron resonances. We estimate the the tolerances of the residual dispersion function in the crab-cavity as well as of the chromatic distortion of the phase advance between cavities due to these resonances.

I. INTRODUCTION

An important option of the B-factories with close by spacing bunches inside the beam is the use of a large crossing angle collision schemes [1,2]. In order to avoid the loss of the luminosity and synchrobetatron resonances, which are specific to the conventional crossing angle schemes [3], it was suggested [4] to use the so-called crab-crossing scheme, which initially was invented for linear colliders [5]. In this report we discuss the tolerances for the ring imperfections, related to synchrobetatron resonances due to crab-cavity. We assume the scheme, where bunches are tilted in the horizontal plane by RF-kickers, placed at points, with $\mp\pi/2$ phase advances of the horizontal betatron oscillations from the collision point. For numerical estimations we use the parameters reported in [2].

II. DISPERSION IN A CRAB-CAVITY

TM110-mode with a transverse deflecting voltage

$$V = \frac{cE\phi}{\Omega\sqrt{\beta_x^*\beta_{crab}}} \qquad (1)$$

can give a necessary kick. Here, E is the particle energy, 2ϕ crossing angle, Ω RF-frequency of the cavity, β_x^* β-function at the IP and β_{crab} β-function at the crab-cavity. To produce the crossing angle of 50 mrad, the deflecting voltages must be 0.82 MV for LER and 1.9 MV for HER. For the sake of simplicity we neglect the effect of the edge fields of the crab-cavity and assume that a vector potential of the deflecting TM110-mode is

$$\mathbf{A}_\perp = 0, \quad A_\parallel = -V\frac{2x}{k_1 r}J_1(k_1 r)\Delta(s)\sin(\Phi). \qquad (2)$$

Here, $\Phi = \Omega t + h\varphi_0$, φ_0 is the phase of the synchronous particle, h the RF-harmonic number, $J_1(x)$ the Bessel function of the 1st order, γ_1 its first root ($\gamma_1 \simeq 3.832$), $k_1 = \gamma_1/b$, b

the radius of the cavity; $r^2 = x^2 + z^2$;

$$\Delta(s) = \delta(s + L/2) + \delta(s - L/2), \qquad (3)$$

where L is the distance between cavities. We take that the oscillations of a particle near the closed orbit are described by the following equations ($\tau = \omega_0 t$ is taken as an independent variable, $\gamma\alpha \gg 1$)

$$
\begin{aligned}
&x = x_b + \eta\frac{\Delta p}{p}, \quad x_b = a_x\cos\psi_x, \quad z = a_z\cos\psi_z \\
&\theta = \tau + \varphi, \quad \varphi = \varphi_s\cos\psi_s, \quad \varphi' = \nu_s\varphi_s\sin\psi_s, \\
&I_{x,z} = \frac{p(\nu a^2)_{x,z}}{2R_0} = \frac{pJ_{x,z}}{2}, \quad \psi'_{x,z} = \nu_{x,z}, \\
&I_s = \frac{pR_0\nu_s\varphi_s^2}{2\alpha} = \frac{pJ_s}{2}, \quad \psi'_s = -\nu_s.
\end{aligned} \qquad (4)
$$

The hamiltonian part of equations of motion of a perturbed particle is generated by the following Hamiltonian

$$
\begin{aligned}
&H = \nu_x J_x + \nu_z J_z - \nu_s J_s + U_{bb} - W\Delta(s)\sin(\Phi), \\
&W = W_0\frac{2x}{k_1 r}J_1(k_1 r), \quad W_0 = \frac{2eVR_0}{E},
\end{aligned} \qquad (5)
$$

where U_{bb} describes the beam-beam interaction. Provided that the dispersion function in the cavities is zero, and the betatron phase advance between the tilting and restoring cavities is π, the Hamiltonian in Eq.(5) predicts only resonances due to the beam-beam interaction. We assume that the working point of the ring is chosen outside the stopbands of the beam-beam instability. Then, the term U_{bb} describes only the beam-beam tune shifts. For a bunch with a very flat, Gaussian distribution in transverse coordinataes the tune shift of the horizontal betatron oscillations is

$$\Delta\nu_x = \xi_x\frac{1 - \exp(-J_x/2\epsilon_x)}{J_x/2\epsilon_x}, \quad \xi_x = \frac{Ne^2}{2\pi E\epsilon_x}. \qquad (6)$$

Assuming $r \ll b$ and using a Taylor expansion of the Bessel function, we write

$$\delta W = W - W_0 x = -W_0 x\left(1.83\frac{r^2}{b^2} - 1.121\frac{r^4}{b^4} + \ldots\right). \qquad (7)$$

The lowest synchrobetatron resonances due to the residual dispersion are made by $\delta W_1\Delta(s)\sin(\Phi)$, where

$$\delta W_1 = -1.83 W_0\eta\frac{\Delta p}{p}\frac{3x_b^2 + z^2}{b^2}. \qquad (8)$$

These resonances correspond to combinations $2\nu_x + m_s\nu_s = n - \Omega/\omega_0$ and $2\nu_z + m_s\nu_s = n - \Omega/\omega_0$, where $m_s = 2l$, l

and n are integers. If we take $\Omega/\omega_0 = h$, the averaging of the Hamiltonian (5) near, for instance, the resonance $2\nu_x = m_s\nu_s$, results in

$$H = H_0 + \xi_x F + \Lambda|\eta m_s J_{m_s}(h\varphi_s)|J_x \cos\chi,$$

$$H_0 = \nu_x J_x - \nu_s J_s, \quad F = 2\epsilon_x \int\limits_0^{J_x/2\epsilon_x} dt\,\frac{1 - e^{-t}}{t}, \qquad (9)$$

$$\Lambda = 5.5\frac{eV\nu_s\beta_{crab}}{\pi b^2 Eh\alpha}, \quad \chi = 2\psi_x - m_s\psi_s.$$

Due to $J_m(x) \simeq x^m/(2^m m!)$, when $x < 1$, this instability mainly affects the particles with large amplitudes of synchrotron oscillations.

Since H in Eq.(9) depends only on one phase variable χ, we can use an additional integral of motion $C = (J_s/m_s) - (J_x/2)$ to reduce the study of a 4-dimensional problem described by H to the study of an equivalent two-dimensional problem, described by the Hamiltonian $H'(J_x, \chi) = H[J_x, m_s(J_x/2 + C), \chi]$. The character of the trajectories in the phase-space (J_x, χ) can be figured out inspecting the behaviour of the curves $H^{\pm}(J_x) = H'(J_x, \cos\chi = \pm 1)$. The oscillations are stable, if the horizontal line $H' = const$ starting, for instance, from the curve $H^+(J)$ crosses the curve $H^-(J)$, or crosses the curve $H^+(J)$ again. Otherwise, the Hamiltonian $H'(J_x, \chi)$ describes unstable oscillations(see, for instance, Ref.[6]).

From Eq.(9), we obtain ($\Delta = \nu_x - m_s\nu_s/2$)

$$H^{\pm} = \Delta \pm \Lambda|\eta m_s J_{m_s}(h\varphi_s)| + \xi_x F,$$
$$\varphi_s^2 = (\varphi_s)_{in}^2 + \frac{\alpha\epsilon_x m_s}{2R_0\nu_s}\left(\frac{J_x - J_{xin}}{\epsilon_x}\right), \qquad (10)$$

where φ_{sin} is initial amplitude of synchrotron oscillations and J_{xin} initial value of J_x. As far as $F \simeq 2\epsilon_x \ln(J_x/\epsilon_x)$, when $J_x \gg \epsilon_x$, the Hamiltonians $H^{\pm}$ describe unstable oscillations provided that

$$|\Delta| \leq \Delta_{th} = \Lambda|\eta m_s J_{m_s}(h\varphi_s)|. \qquad (11)$$

In the colliding beam mode the instability at small amplitudes is suppressed by a nonlinearity of the beam-beam kick. At large amplitudes of betatron oscillations the beam-beam nonlinearity becomes too weak to suppress the instability. The balance between excitation and suppression effects determines the dynamic aperture of the ring. As can be seen from Fig.1, on exact resonance $2\nu_x = 2\nu_s$ the instability limits dynamic aperture of tail particles at $a_x \simeq 20 \div 30\sigma_x$. However since the value Δ_{th} indeed is very small ($\Delta_{th} = 10^{-4}$), this resonance is very narrow and can be easily avoided by a small variation of either ν_x, or ν_s.

For KEK B-factory $(\beta_{crab})_x \simeq 2(\beta_{crab})_z$ [2] and, therefore the strengths of the vertical synchrobetatron resonances are 6 times smaller then the strengths of the corresponding horizontal resonances. However, since this instability determines vertical dynamic aperture in terms of σ_z, due to small aspect ratio $(\sigma_z \ll \sigma_x)$ the limitation of the vertical dynamic aperture due to this instability can be more severe.
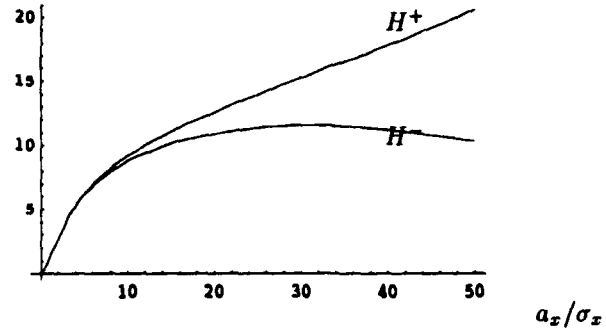
Figure 1: Hamiltonians $H^{\pm}$; $\eta = 10cm$, $m_s = 2$, $A_s = 20\sigma_s$, $a_{xin} = 20\sigma_x$, $\Delta = 0$.

III. CHROMATIC DISTORTIONS

Stronger perturbations can be caused by the dependence of the phase advance of the horizontal betatron oscillations

$$\Delta\psi = \int\limits_{-L/2}^{L/2} \frac{ds}{\beta(s)} \qquad (12)$$

on the particle momentum $\beta(s, \Delta p) \simeq \beta(s)(1 + \zeta\Delta p/p)$, where $\zeta = (\partial\ln\beta/\partial\ln p)$. Assuming that $|\zeta\Delta p/p| \ll 1$ and that $\zeta = const$ between the tilting and restoring cavities, the additional phase advance $(\Delta\psi = \pi + \delta\psi)$ becomes $\delta\psi \simeq -\pi\zeta(\Delta p/p)$. Then, a combination $W\Delta(s)\sin(\Phi)$ excites the following set of resonances: $\nu_x + m_s\nu_s = n$, $3\nu_x + m_s\nu_s = n$, $\ldots$, $m_s = 2l$. The lowest family $(\nu_x + m_s\nu_s = n)$ is described by the perturbation $(\vartheta = \sqrt{\beta_{crab}/\epsilon_x})$

$$\delta H = \Lambda_1\sqrt{\frac{J_x}{\epsilon_x}}\cos(\chi), \quad \Lambda_1 = \zeta\frac{eVm_s\nu_s|J_{m_s}(h\varphi_s)|}{Eh\alpha\vartheta}. \qquad (13)$$

Due to $\delta H \sim \sqrt{J_x}$, this perturbation can open Hamiltonians $H^{\pm}$ for resonant particles $(\Delta = \nu_x + m_s\nu_s - n < 0)$ in the region $J_x \sim \epsilon_x$ (see Fig.2). Fig.3 shows examples of the trajectories for such particles in the slow phase-space $(x = \sqrt{J_x/\epsilon_x}\cos\chi$ and $p = -\sqrt{J_x/\epsilon_x}\sin\chi)$. These
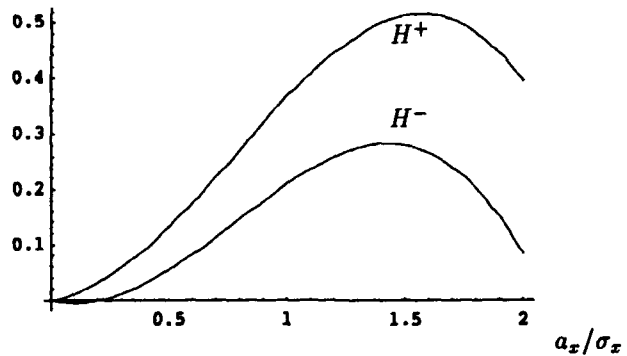
Figure 2: Hamiltonians $H^{\pm}$; $\zeta = 1$, $m_s = 2$, $A_s = 5\sigma_s$, $a_{xin} = \sigma_x$, $\Delta = -.6\xi$, $\xi = .05$.

curves were calculated taking into account the synchrotron radiation damping and neglecting the variation of φ_s due
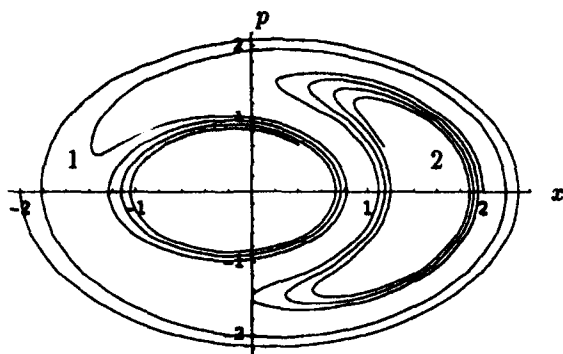
Figure 3: Phase trajectories corresponding to the Hamiltonians $H^{\pm}$ shown in Fig.2; $\lambda_{sr} = 10^{-4}\omega_0$; $p_{in} = 0$; 1. $x_{in} = -2, 2.$ $x_{in} = 2.$
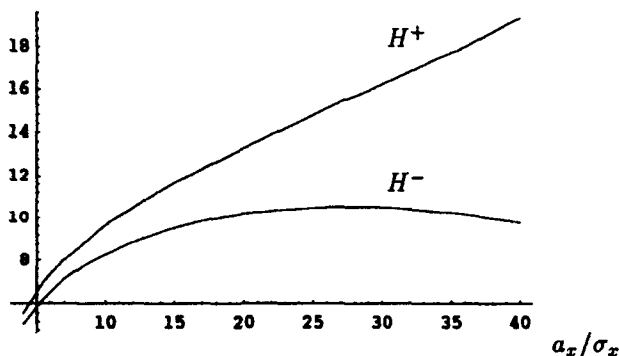
Figure 4: Hamiltonians $H^{\pm}$; $\zeta = 1$, $m_s = 2$, $A_s = 5\sigma_s$, $a_{xin} = 20\sigma_x$, $\Delta = 0$, $\xi = .05$.
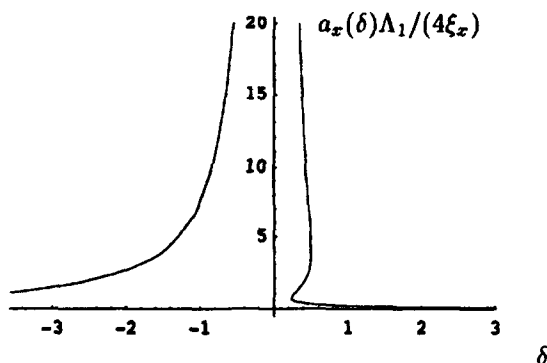
Figure 5: Resonance curve for horizontal oscillations; $\delta = 16\Delta\xi_x/\Lambda_1^2$, $\zeta = 1$, $m_s = 2$.

to the variation of J_x. At large amplitudes $(J_x \gg \epsilon_x)$ and $\Delta = 0$ Hamiltonian in Eq.(13) describes instable oscillations (see Fig.4) which can limit the dynamic aperture of the ring. As seen from Fig.5, the width of unstable region is $\Delta < \Lambda_1^2/(16\xi_x)$. For KEK B-factory [2] and $\zeta = 1$ this gives $\Delta < 0.01$.

IV. CONCLUSION

In this paper we showed that without special efforts the perturbations due to residual dispersion in a crab-cavity and chromatic distortions limit the dynamic aperture of the ring, if the working point approaches the lines of the synchrobetatron resonances. Since the value of the dynamic aperture essentially depends on the nonlinearity of the beam-beam deflecting force, one can expect the decrease of the dynamic aperture when ξ decreases (such a decay may occur due to, say, the loss of the bunch intensity). Since the strength of these resonances is proportional to $J_{m_s}(h\varphi_s)$, they mainly disturb the particles with large amplitudes of synchrotron oscillations $(A_s \gg \sigma_s)$.

The perturbation due to residual dispersion in crab-cavities causes rather nerrow resonances, which can be avoided by small variations of tunes.

Chromatic distortions seems to be more dangerous due to the possibility of the excitation of the synchrotron satelites near integer resonance $(\nu_x + m_s\nu_s)$. Since these resonances are not suppressed by the synchrotron radiation damping, they must be avoided by the proper choice of the working point in the tune diagram.

In both cases the strengths of resonances are proportional to the ratio $\nu_s/\alpha \propto 1/\sqrt{\alpha}$. This fact can cause an additional limitation on the use of the low-α lattices in the rings with crab-crossing.

V. REFERENCES

[1] An Asymmetric B-Factory Based on PEP. Conceptual Design Report. LBL PUB-5303, SLAC-372, CALT-68-1715, UCRL-ID-106426, UC-IIRPA-91-01, 1991.

[2] Accelerator Design of the KEK B-factory. Ed. by S. Kurokawa, K. Satoh and E. Kikutani. KEK Report 90-24, 1991.

[3] A.Piwinski. IEEE Trans on Nucl. Sci. NS-24, 1408, 1977.

[4] K. Oide, K. Yokoya, Phys. Rev. A-40, p. 315, 1989.

[5] R.B. Palmer, SLAC-PUB-4707, 1988

[6] N.S.Dikansky, D.V.Pestrikov. Physics of Intense Beams in Storage Rings. Nauka, Novosibirsk, 1989.

Andreev V.V., Yudin I.P.
Joint Institute for the Nuclear Research, Dubna,141980, Russia

A thorough analisys of the charged particles dynamics on the basis of the matrix formalism up to the 3-rd order inclusve for the sector dipole magnets is usually held in a curvelinear coordinate system. In those cases, whenever the dipole is not a sectoral one, transformation to the curvelinear coordinates, associated with the trajectory of the central particle of the beam, doesn't proove itself, because of the difficulty of the physical interpretation of the obtained results.That makes necessary to analyse the dynamics of the beam in the bending magnet in the cartesian (rectangular) coordinate system.

1. Motion Equation in the Rectangular (Cartesian) Coordinates . Linear Approximation

It is well known that the motion of the charged particle with the charge q and mass m in a magnetic field with the induction $\vec{B}$ is determined by the Lorentz force:

$$\frac{d}{dt}(\gamma m \vec{v}) = -q/c \cdot [\vec{v} \times \vec{B}], \qquad (1.1)$$

where $\vec{v}$ - speed of a particle, $\gamma = (1-\beta^2)^{-1/2}$, $\beta = v/c$, c - light speed. We examine the rectangular (Cartesian) coordinate system XYZ with the axis OZ, directing stright alone the motion of a particle. In the linear approximation the magnetic field $\vec{B} = (0, B_0, 0)$ we would obtain the non-linear differential equation of the plane trajectory $x(z)$

$$x'' = -\frac{1}{\rho_0} \cdot (1 + x'^2)^{3/2}, \qquad (1.2)$$

where $1/\rho_0 \equiv h = qB_0/(\gamma pc)$ - the curvature of the trajectory, $p = mv$ - the particle momentum. The analytic solution of Eq. (1.2) with the initial conditions of $x(0) = x_0$, $x'(0) = x'_0$, is well known[1]

$$\begin{cases} x(z) = \sqrt{\rho_0^2 - (z - c_1)^2} + c_2, \quad x'(z) = \dfrac{z - c_1}{\sqrt{\rho_0^2 - (z - c_1)^2}}, \\ c_1 = x'_0 \cdot \dfrac{\rho_0}{\sqrt{1 + x'^2_0}}, \quad c_2 = x_0 - \dfrac{\rho_0}{\sqrt{1 + x'^2_0}}. \end{cases} \qquad (1.3)$$

The determination of the higher order optics for the Eq. (1.1) in Cartesian coordinates is more complicated. It is easier to determine the higher than the first order optics in curvelinear coordinate system with furter transformation back to XYZ. Such transformation is adequally described by changing of the 2-d and 3-rd order abberation coeffs only.

Let $\vec{X}^0 = (x_0, x'_0, y_0, y'_0, l, \delta)$ be the initial conditions vector. $\vec{X}(z)$ we would perform in the form of the decomposition on the initial parameters X^0_i $(i = 1, 2)$

$$X_i(z) = R_i(z, \vec{X}) + \sum_{j=1}^{6} \sum_{k=j}^{6} T^c_{ijk}(z) X^0_j X^0_k +$$

$$+ \sum_{j=1}^{6} \sum_{k=j}^{6} \sum_{l=k}^{6} U^c_{ijkl}(z) X^0_j X^0_k X^0_l \qquad (1.4)$$

The index "c" shows that the coeffs were obtained in rectangular (Cartesian) coordinate system. With $i=3,...,6$ functions $R_i(z, \vec{X})$ are linear on $\vec{X}$ and correspond with the general type (TRANSPORT-type). We define the decomposition coeffs (1.4) following the formalism [2].

2. The 3-rd Order Beam Optics of a Dipole Magnet

The solution of the Eq. (1.1) in the curvelinear coordinates (especially in its linear approximation) is well known. That's why we would review general parts briefly.

The right-oriented curvelinear coordinate system XYS is chosen so, that the ort $\vec{s}$ should be aimed on a tangent to some, chosen before, respondent to the predifined specific initial conditions, of the arbitrary (relative) trajectory.

Because of the well known symmetry relation of the scalar magnet potential, in relation to the mid-plane, a particle, that starts in that plane won't leave it.

$$\varphi(x, y, s) = -\varphi(x, -y, s) \qquad (2.1)$$

We would decompose Eq. (1.1). To obtain the abberation coeffs of the decomposition (1.4), it is necessary to carry out the following procedures:

1. Decompose $B(x, y, s)$ close to the arbitrary trajectory, taking into account the symmetry relation (2.1).
2. Decompose Eq. (1.1) up to the necessary order.
3. Carry out the substitution of (1.3) into the obtained equation.
4. Generate the differencial equations, by equating the coeffs of the identical members.
5. Find out the linear independent solutions of the obtained equations, Green function, after what integrate it order after order, with the right parts of the mentioned above equations.

2.1 Decomposition of the B(x,y,s) Field.

To decompose the $B(x, y, s)$ we would use the Maxwell equation and the symmetry relation.

We rewrite the scalar potential in the form, correspondent with Eq. (2.1). To obtain the recurrent equations between the coeffs in φ- decomposition we would use the Laplas equation. Further by identifying the decomposition coeffs with a well known decomposition of the central field $B_y(x, 0, s)$, we wuold perform those coeffs in terms of the valueless coeffs of the so called "multiplicative force" $k_1(s)$, $k_2(s)$ и $k_3(s)$

$$B_y(x, 0, s) = B_y(0, 0, s) \cdot [1 - k_1 hx + k_2 h^2 x^2 + k_3 h^3 x^3 + ...],$$

$$\begin{cases} k_1 = -\left[1/hB_y \; \partial B_y/\partial x \right]_{x=y=0} \quad (quadrupole), \\ k_2 = \left[1/2h^2 B_y \; \partial^2 B_y/\partial x^2 \right]_{x=y=0} \quad (sextupole), \\ k_3 = \left[1/6h^3 B_y \; \partial^3 B_y/\partial x^3 \right]_{x=y=0} \quad (octupole). \end{cases} \qquad (2.1.1)$$

Then the decomposition of the field components up to the 3-rd order are the following:

$$B_x(x, y, s) = p_0 c/q \; [-h^2 k_1 y + 2 h^3 k_2 x y + 3 h^3 x^2 y + (-h^4 k_3 - h^4 k_2/3 + 2hh'k'_1/3 + h^2 k''_1/6 + h'^2 k_1/3 + h h'' k_1/3 - h^4 k_1/6 + h'^2/6 + h h''/3) y^3 + ...],$$

$$B_y(x, y, s) = p_0 c/q \; [h - h^2 k_1 x + h^3 k_2 x^2 + h^4 k_3 x^3 + (-h^3 k_2 + h^3 k_1/2 - h''/2) y^2 + (-3h^4 k_3 - h^4 k_2 + 2hh'k'_1 + h^2 k''_1/2 + h'^2 k_1 + hh'' k_1 - h^4 k_1/2 + h'^2/2 + hh'') xy^2 + ...],$$

$$B_s(x, y, s) = p_0 c/q \; [h' y + (-h^2 k^2_1 - 2 h h' k_1 - hh') xy + (-h^3 k'_2/3 - h^2 h' k_2 + h^3 k'_1/6 + h^2 h' k_1/2) y^3 + (h^3 k'_2 + 3h^2 h' k_2 + h^3 k'_1 + 2h^2 h' k_1 + h^2 h') x^2 y + ...]. \qquad (2.1.2)$$

2.2 Decomposition of the Motion Equation.

The result form of the motion equation in the X- and Y-plane is the following

$$x'' - (1 - k_1) h^2 x = h \delta - (1 - 2 k_1 + k_2) h^3 x^2 + h' x x' +$$
$$+ (2 - k_1) h^2 x \delta + h x'^2/2 + (h'' - h^3 (k_1 - k_2)) y^2 +$$
$$+ h' y y' - h y'^2/2 - h \delta^2 + (k_1 - 2 k_2 - k_3) h^4 x^3 -$$
$$- h h' x^2 x' + (1 - 2 k_1 + k_2) h^3 x^2 \delta - (2 - 2 k_1/3) h^2 x x'^2 -$$
$$- (h'^2/2 + k_1 (h^4/2 + h h'' + h'^2) + 2 h h' k'_1 + h^2 k''_1 -$$
$$- 3 h^4 (k_2 + k_3)) x y^2 - (h k'_1 + 2 h' k_1) h x y y' +$$
$$+ h^2 k_1 x y'^2/2 - (2 - k_1) h^2 x \delta^2 + 3 h x'^2 \delta -$$
$$- h^2 k_1 x' y y' - (h'' - h^3 k_1 + 2 h^3 k_2) y^2 \delta/2 - h' y y' \delta +$$
$$+ h y'^2 \delta/2 + h \delta^3), \tag{2.2.1}$$

$$y'' + h^2 k_1 y = 2(k_2 - k_1) h^3 x y + h' x y' - h' x' y + h x' y' +$$
$$+ h^2 k_1 y \delta - (k_1 - 4 k_2 - 3 k_3) h^4 x^2 y - h h' x^2 y' + (2 h' k_1 +$$
$$+ h k'_1) h x x' y - (2 - k_1) h^2 x x' y + 2 (k_1 - k_2) h^3 x y \delta -$$
$$- h^2 k_1 x'^2 y/2 + h' x' y \delta + h x' y' \delta + (h h' '/3 + h'^2 -$$
$$- (h^4/6 - h h''/3 - h'/3) k_1 + + 2 h h' k'_1 + h^2 k''_1/6 -$$
$$- h^4 k_3) y^3 - 3 h^2 k_1 y y'^2/2 - h^2 k_1 y \delta^2 + \ldots \tag{2.2.2}$$

2.3 The Differencial Equations of the Matrix Elements.

The further algorithm of soluting the Eqs. (2.2.1)-(2.2.2) is evident. To determine the linear independent solutions we examine the linear parts of those equations:

$$\begin{cases} x'' - (1 - k_1) h^2 x = h \delta, \\ y'' + k_1 h^2 y = 0. \end{cases} \tag{2.3.1}$$

Each of the mentioned above equations has at least two linear independent solutions. The general solution of the equations, as it is well known, is the linear combination of the linear independent solutions with the arbitrary coeffs. Besides all the equation for the determination of the $x(s)$ with the right part has also a private solution, that is one of the components of the general one. Let's define the most general form of the mentioned solutions in the bending plane as:

1. *Sine-like function* $s_x(s): s_x(0) = 0, s'_x(0) = 1, \delta = 0$.
2. *Cosine-like function* $c_x(s): c_x(0) = 1, c'_x(0) = 1, \delta = 0$.
3. *Dispersion function* $d_x(s): d_x(0) = 0, d'_x(0) = 0, \delta = 1$.
4. *Sine-like function* $s_y(s): s_y(0) = 0, s'_y(0) = 1, \delta = 0$.
5. *Cosine-like function* $c_y(s): c_y(0) = 1, c'_y(0) = 1, \delta = 0$.

Those functions define the so-called *characteristic rays* of the arbitary magnetic system and all of it's abberation coeffs. The common solutions of the Eq. (2.3.1) with the initial conditions (ch. 1) is the following:

$$\begin{cases} x(s) = c_x(s) \cdot x_0 + s_x(s) \cdot x'_0 + d_x(s) \cdot \delta, \\ y(s) = c_y(s) \cdot y_0 + s_y(s) \cdot y'_0. \end{cases} \tag{2.3.2}$$

That common form of the generated solutions makes evident that the Green function $-G(s, \xi) = s(s) c(\xi) - c(s) s(\xi)$, and the private solution of the nongomogenius equation $q'' + k^2 q = f$ should be generated by means of the integral

$$q = \int_0^s G(s, \xi) f(\xi) \, d\xi. \tag{2.3.3}$$

2.4 Differential Equations of the Abberation Coeffs.

The abberation coeffs of the matrices $R_{ij}(s)$, $T_{ijk}(s)$, $U_{ijkl}(s)$ are the solutions of the nonhomogenius garmonic oscillation differential equations of the Eq. (2.3.3) form with the null initial conditions. We would state that the right parts of the equations for obtaining the elements T_{ijk} - are the square

forms of the 1-st order coeffs. The driving forces of the 3-rd order coeffs $U_{ijkl}(\xi)$ have a more complicated form. We notice that the "angle" elements of the matrix $(i=2,4)$ are calculated by differentiating on s of the "coordinate" elements $(i=1,3)$.

3. Linear Approximation

Magnetic field of the "pure" dipole $\vec{B} = B(0, B_0, 0)$, $h(s) = 1/\rho_0 = const$, $k_1 = k_2 = k_3 = 0$.

$$\begin{cases} s_x = \rho_0 \sin s/\rho_0, c_x = \cos s/\rho_0, \\ s_y = y, c_y = 1. \end{cases} \tag{3.1}$$

Green functions on projections $(s \geq \xi)$

$$\begin{cases} G_x(s, \xi) = \rho_0 \sin((s - \xi)/\rho_0), \\ G_y(s, \xi) = s - \xi. \end{cases} \tag{3.2}$$

Dispersional function $d_x(s) = \rho_0 (1 - c_x(s))$.

The non-zero matrix elements R_{ij}

$$R_{11} = c_x, R_{12} = s_x, R_{16} = \rho_0 (1 - c_x), R_{21} = -s_x/\rho_0^2,$$
$$R_{22} = c_x, R_{26} = s_x/\rho_0, R_{33} = 1, R_{34} = s, R_{44} = 1,$$
$$R_{51} = s_x/\rho_0, R_{52} = \rho_0 (1 - c_x), R_{55} = 1, R_{56} = s - s_x,$$
$$R_{66} = 1.$$

4. Nonlinear Abberation Coeffs

The non-zero coeffs of the 2-d order:

$$T_{111} = -(1 - c_x^2)/2\rho_0, T_{112} = s_x c_x/\rho_0, T_{116} = s_x^2,$$
$$T_{122} = \rho_0 s_x (1 - c_x), T_{126} = s_x (1 - c_x),$$
$$T_{144} = -\rho_0 (1 - c_x), T_{166} = -s_x^2/2\rho_0, T_{314} = s s_x/\rho_0,$$
$$T_{324} = \rho_0 s (1 - c_x), T_{346} = s - s_x.$$

The 3-rd order:

$$U_{1111} = c_x^3 h^4/8 - c_x h^4/8 + c_x^5 h^2/8 - c_x^3 h^2/4 + c_x h^2/8,$$
$$U_{1112} = c_x^2 h^4 s_x/8 + c_x^4 h^2 s_x/8 - c_x^2 h^2 s_x/8,$$
$$U_{1116} = h^3 s_x s/2 - h s_x s/2 - 11 c_x h^5 s_x^4/8 - h^5 s_x^4/2 +$$
$$+ c_x^5 s_x^4/2 + c_x h^3 s_x^4 + 5 c_x h^5 s_x^2/8 - c_x^3 h^3 s_x^2/2 +$$
$$+ h^3 s_x^2 + c_x^3 h s_x^2/2 + c_x^5/h/4 + c_x^4 h/2 - c_x^2 h/2 - c_x h/4,$$
$$U_{1122} = -h^2 s_x s/4 - 3 c_x^2 h^2 s_x/8 - 3 c_x^4 s_x/8 - c_x^3 s_x/8 -$$
$$- c_x s_x + 3 s_x/2 - c_x^3 h^2/8 + c_x h^2/8 - c_x^5/8 + c_x^3/3 +$$
$$+ c_x^2 - 11 c_x/8,$$
$$U_{1126} = -c_x h s/2 + c_x s/2h + c_x^2 h^3 s_x/4 + c_x^4 h s_x/4 -$$
$$- c_x^4 s_x/4h - c_x^2 s_x/4h,$$
$$U_{1144} = -h^2 s_x s^2/4 + h^2 s_x s/2 + c_x s/4 - s_x/4 + c_x^2/2 - 1/2,$$
$$U_{1166} = -h^2 s_x s/2 + s_x s/2 + c_x h^4 s_x^4 + h^4 s_x^4 - c_x h^2 s_x^4 -$$
$$- c_x h^4 s_x^2/2 + + c_x^3 h^2 s_x^2/2 + c_x h^2 s_x^2/2 - 2 h^2 s_x^2 -$$
$$- c_x^3 s_x^2/2 - c_x^4 + c_x^2,$$
$$U_{1222} = c_x s/4 + c_x^2 h^2 s_x/4 + c_x^4 s_x/4 - s_x/2 - 3 c_x^5/8h^2 +$$
$$+ 5 c_x^3/4h^2 - c_x^2/h^2 + c_x/8h^2 - 3 c_x^3/8 + 3 c_x/8,$$
$$U_{1226} = h s_x s/4 + 3 c_x^2 h s_x/8 + 3 c_x^4 s_x/8h + c_x^2 s_x/8h -$$
$$- c_x s_x/h + s_x/2h + c_x^3 h/8 - c_x h/8 + c_x^5/8h - c_x^3/2h -$$
$$- c_x^2/2h + 7 c_x/8h,$$
$$U_{1244} = s_x s^2/4 - c_x s/4h^2 - c_x s/2 + s_x/4h^2 + c_x s_x/2 +$$
$$+ c_x/h^2 - 1/h^2,$$
$$U_{1446} = c_x/2h - c_x^2/2h, U_{1666} = (1 - c_x^2)/2h,$$
$$U_{3114} = -h^2 s^2/4 + c_x h^2 s_x s/4 + h^2 s_x s + h^2 s/4 -$$
$$- c_x h^2 s_x/4 - h^2 s_x,$$
$$U_{3124} = h^2 s^3/12 + s^2/4 - c_x s_x s/4 - 2 s_x s - c_x^2 s/4 +$$

$+5s/4 + s_x + c_x^2/2 + 2c_x - 5/2,$

$U_{3146} = h s^2/4 - c_x h s_x s/4 - 3hs/4 + s/2h + 3c_x h s_x/4 - c_x s_x/2h,$

$U_{3224} = -s^3/12 + c_x^3 s/4h^2 - s/4h^2 - s/2 + c_x s_x/2 + c_x^2/2h^2 - 2c_x/h^2 + 3/2h^2,$

$U_{3246} = -h s^2/4 - s^2/4h + c_x s_x s/4h + s/h - s_x/h - c_x^2/4h - c_x/h + 5/4h,$ $U_{3444} = -s_x/2 - s/2.$

Nine elements T_{5jk} and nineteen elements U_{5jkl} are not listed.

5. The Cartesian Coordinates

To gain the physically trustworthy results it is necessary to transform the data to the rectangular (Cartesian) coordinate system XYZ. We would agree on the following designations:

$$\begin{cases} x_1 = x, \; x_2 = dx/dz = x'/(1+hx), \; x_3 = y, \\ x_4 = dy/dz = y'/(1+hx), \; x_5 = l, \; x_6 = \delta. \end{cases} \quad (5.1)$$

It is important to notice that results obtained in different coordinate systems differ only with the non-linear members. It won't be difficult to obtain the Cartesian elements T_{ijk} and U_{ijkl} of the matrix, having marked them with the "c". Here we discuss only those elements that differ from one system to another.

$T^c_{112} = T_{112} + h s_x, \; T^c_{211} = T_{211} - h c_x c'_x,$

$T^c_{212} = T_{212} + h s'_x - h(c_x s'_x - c'_x s_x),$

$T^c_{216} = T_{216} - h(c_x d'_x + c'_x d_x), \; T^c_{222} = T_{222} - h s_x s'_x,$

$T^c_{226} = T_{226} - h(s_x d'_x + s'_x d_x),$

$T^c_{266} = T_{266} - h d_x d'_x, \; T^c_{314} = T_{314} + h s_y,$

$T^c_{413} = T_{413} - h c_x c'_y, \; T^c_{414} = T_{414} + h s'_y - h c_x s'_y,$

$T^c_{423} = T_{423} - h s_x c'_y, \; T^c_{424} = T_{424} - h s_x s'_y,$

$T^c_{436} = T_{436} - h c'_y d_x, \; T^c_{446} = T_{446} - h s'_y d_x,$

$T^c_{512} = T_{512} + h R_{52}.$

The 3-rd order:

$U^c_{1112} = U_{1112} + T_{112} h, \; U^c_{1122} = U_{1122} + 2 T_{122} h,$

$U^c_{1126} = U_{1126} + T_{126} h, \; U^c_{1134} = U_{1134} + T_{134} h,$

$U^c_{1144} = U_{1144} + 2 T_{144} h,$

$U^c_{2111} = U_{2111} + c_x^2 c'_x h^2 - (T_{111} c'_x + T_{211} c_x) h,$

$U^c_{2112} = U_{2112} + ((c_x^2 - c_x) h^2 - T_{111} h) s'_x + ((2c_x - 1) c'_x h^2 - T_{211} h) s_x - (T_{112} c'_x - T_{212} c_x - T_{212}) h,$

$U^c_{2116} = U_{2116} + (c_x^2 d'_x + 2 c_x c'_x d_x) h^2 - (T_{111} d'_x + T_{211} d_x + T_{116} c'_x + T_{216} c_x) h,$

$U^c_{2122} = U_{2122} + ((2c_x - 2) h^2 s_x T_{112} h) s'_x + c'_x h^2 s_x^2 - T_{212} h s_x - (T_{122} c'_x + T_{222} c_x - 2 T_{222}) h,$

$U^c_{2126} = U_{2126} + ((2c_x - 1) h^2 d_x - T_{116} h) s'_x + (((2c_x - 1) d'_x + 2 c'_x d_x) h^2 - T_{216} h) s_x - (T_{112} d'_x + T_{216} d_x + T_{126} c'_x + T_{216}) h,$

$U^c_{2133} = U_{2133} - (T_{133} c'_x - T_{233} c_x) h,$

$U^c_{2134} = U_{2134} - (T_{134} c'_x + T_{234} c_x - T_{234}) h,$

$U^c_{2144} = U_{2144} - (T_{144} c'_x + T_{244} c_x - 2 T_{244}) h,$

$U^c_{2166} = U_{2166} + (c_x d_x d'_x + c_x d_x^2) h^2 - (T_{116} d'_x + T_{216} d_x + T_{166} c'_x + T_{266} c_x) h,$

$U^c_{2226} = U_{2226} + (2 d_x h^2 s_x - T_{126} h) s'_x - d'_x h^2 s_x^2 - T_{226} h s_x - (T_{122} d'_x + T_{222} d_x) h,$

$U^c_{2233} = U_{2233} - (T_{133} s'_x + T_{233} c_x) h,$

$U^c_{2234} = U_{2234} - (T_{134} s'_x + T_{234} c_x) h,$

$U^c_{2244} = U_{2244} - (T_{144} s'_x + T_{244} c_x) h,$

$U^c_{2266} = U_{2266} + (d_x^2 h^2 - T_{166} h) s'_x - (2 d'_x d'_x h^2 - T_{266} h) s_x - (T_{126} d'_x + T_{226} d_x) h,$

$U^c_{2336} = U_{2336} - (T_{133} d'_x + T_{244} d_x) h,$

$U^c_{2346} = U_{2346} - (T_{134} d'_x + T_{234} d_x) h,$

$U^c_{2446} = U_{2446} - (T_{144} d'_x + T_{244} d_x) h,$

$U^c_{2666} = U_{2666} + d_x^2 d'_x h^2 - (T_{166} d'_x + T_{266} d_x) h,$

$U^c_{3114} = U_{3114} + T_{314} h, \; U^c_{3123} = U_{3123} + T_{323} h,$

$U^c_{3124} = U_{3124} + 2 T_{324} h, \; U^c_{3146} = U_{3146} + T_{346} h,$

$U^c_{4113} = U_{4113} + c_x^2 c'_y h^2 - (T_{111} c_y^2 + T_{413} c_x) h,$

$U^c_{4114} = U_{4114} + ((c_x^2 - c_x) h^2 - T_{111} h) s'_y + (T_{414} - T_{414} c_x) h,$

$U^c_{4123} = U_{4123} + ((2 c_x - 1) c'_y h^2 - T_{413} h) s_x - (T_{112} c'_y + T_{423} c_x - T_{423}) h,$

$U^c_{4124} = U_{4124} + ((2 c_x - 2) s_x h^2 - T_{112} h) s'_y - (T_{414} s_x + T_{424} c_x - 2 T_{424}) h,$

$U^c_{4136} = U_{4136} + 2 c_x c'_y d_x h^2 - (T_{413} d_x + T_{116} c'_y + T_{436} c_x) h,$

$U^c_{4146} = U_{4146} + ((2 c_x - 1) d_x h^2 - T_{116} h) s'_y - (T_{414} d_x + T_{446} c_x - T_{446}) h,$

$U^c_{4223} = U_{4223} + c'_y s_x^2 h^2 - (T_{112} c'_y + T_{423} s_x) h,$

$U^c_{4224} = U_{4224} + (s_x h^2 - T_{122} h) s'_y - T_{424} h s_x,$

$U^c_{4236} = U_{4236} + (2 c'_y d_x h^2 - T_{436} h) s_x - (T_{423} d_x + T_{126} c'_y) h,$

$U^c_{4246} = U_{4246} + (2 s_x d_x h^2 - T_{126} h) s'_y - (T_{446} s_x + T_{424} d_x) h,$

$U^c_{4333} = U_{4333} - T_{133} c'_y h,$

$U^c_{4334} = U_{4334} - (T_{133} s'_y - T_{134} c'_y) h,$

$U^c_{4366} = U_{4366} + c'_y d_x^2 h^2 - (T_{166} c'_y + T_{436} d_x) h,$

$U^c_{4444} = U_{4444} - T_{144} s'_y h,$

$U^c_{4466} = U_{4466} + (d_x^2 h^2 - T_{166} h) s'_y - T_{446} d_x h,$

$U^c_{5112} = U_{5112} + T_{512} h, \; U^c_{5122} = U_{5122} + 2 T_{522} h,$

$U^c_{5126} = U_{5126} + T_{526} h, \; U^c_{5134} = U_{5134} + T_{534} h,$

$U^c_{5144} = U_{5144} + 2 T_{544} h.$

We notice that such algorithm might be applied to the research of any multipoles of the higher order.

6. The Realisation of the Method

The model described above was used as a basis of it's program realisation on IBM PC/AT. The main problem, as we stated before, was that the decomposition of the motion equation and field components was held within the arbitrary trajectory (in the curvelinear coordinates XYS), though the results had to be represented in a Cartesian coordinates XYZ. The correction of the 2-d and 3-rd order abberation coeffs eliminates only part of the problem. The transformation to the Cartesian coordinate system involves the difinition of the equation of the arbitrary trajectory, thus the solution Eq. (1.2) was found with the substitution of the linear part of the decomposition $\bar{X}(z)$ (1.4). Such substitution is prooved with the fact, that the generated relative trajectories of the beams with the momenta of more than 1 GeV/c are of a low difference with the geometrical axis of a magnet.

Referencies

1. Gerdt V.P. etc. Algebraic-Numeric Caculations of Proton Trajectories in Bending Magnets of Synchrotron Accelerator. JINR Comm., E11-89-755, Dubna, 1989.

4. Sagalovsky L. Private message.

EFFECTS OF PLANE UNDULATOR (WIGGLER) FIELDS ON BEAM DYNAMICS AT LARGE ORBIT DISTORTION

S.Efimov, E.Bulyak
Kharkov Institute of Physics and Technology,
310108 Kharkov, Ukraine

Abstract

Effects of plane undulator sine-lake fields on beam dynamics in Storage Rings are investigated. Expressions for tune shifts of betatron oscillations versus their amplitudes are obtained for the case, where the orbit curvature inside the undulator is rather large. It takes place in compact synchrotron light sources with undulator insertions. In the limiting case these expressions for small orbit deflections are coincident with the known relations. Discussion of the results obtained is presented.

I. INTRODUCTION

Previously [1], we have considered the nonlinear effects of a plane undulator, and have derived the expressions for linear and nonlinear vertical tune shifts. Those results were based on using the expressions for the tune shift caused by the frigning fields of the dipole magnet [2]. where the vertical field component was described by a sine curve. The problem was solved to the $\sin \alpha = \alpha$ approximation (α is the angle of particle deflection in the undulator field), this being quite sufficient in the majority of case. However, validity of this approximation has not been investigated for the storage rings of relatively low energies (about several hundred MeV) comprising inserts (undulators and wigglers). The aim of this report is to analyze the effect of plane- insert fields on beam dynamics for significant orbit distortions within these inserts.

II. THE FIELD IN THE FIXED COORDINATE SYSTEM

The field in a fixed coordinate system we investigate the plane undulator with parallel poles , infinitely extended in the transverse (horizontal) direction (figure 1).

The magnetic field components of this undulator are written in the known form (e.g.,[3]):

$$B_s = B_0 \sinh(k_u z) \sin(k_u s);$$

$$B_x = 0;. \qquad (1)$$

$$B_z = B_0 \cosh(k_u z) \cos(k_u s),$$

where $k_u = \lambda / 2\pi$ is the undulator parameter, λ being is period.

This field can be described by one component of the magnetic vector potential:

$$A_x = -\frac{B_0}{k_u}\cosh(k_u z)\sin(k_u s). \qquad (2)$$
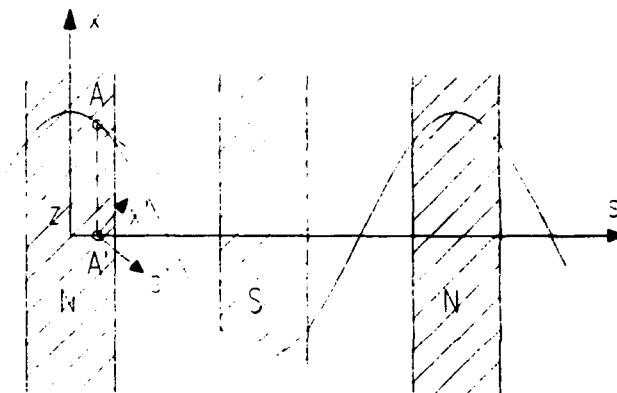
Figure 1. A schematic model for calculations.

III. THE FIELD IN THE NATURAL COORDINATE SYSTEM

To analyze the motion in the vicinity of the equilibrium orbit. we shall go over to the natural coordinate system (σ, χ, z) , the origin of which moves along the trajectory

$$x = \frac{1}{k_u^2 \rho}\cos(k_u s), \qquad (3)$$

ρ is the trajectory curvature radius, which is dependent on the effective length of the pole, the field in the gap and the particle energy.

Taking into consideration the infinite extension of poles in the transverse direction. we may go over to the s', x', z' coordinate frame, which moves along the S axis but is turned by an angle

$$\alpha(s) = -\arctan\left(\frac{1}{k_u \rho}\sin(k_u s)\right)$$

in reference to the fixed system. in terms on which the expressions for fields (1),(2) are written. Proceeding from the expression for the increment $d\sigma$ over the length ds,

$$d\sigma = ds\sqrt{\frac{1}{k_u^2\rho^2}\sin^2(k_u s) + 1},$$ the trajectory

extension is written as:

$$\sigma(L_u) = \frac{2L_u}{\pi}\sqrt{1+p^2}\,E\left(\frac{p}{\sqrt{1+p^2}}\right). \qquad (4)$$

where L_u is the undulator length;

$p = \lambda / 2\pi\rho$;

$E(k)$ is the second-kind complete elliptic integral.

The magnetic vector potential components $\bar{A}$ are written in the s', x', z' system as:

$$A_{s'} = \frac{B_0^2}{Bk_u}\cosh(k_u z)\sin^2(k_u s)\frac{p}{\sqrt{1+p^2\sin^2(k_u s)}}$$

$$A_{x'} = \frac{B_0^2}{Bk_u}\cosh(k_u z)\sin(k_u s)\frac{1}{\sqrt{1+p^2\sin^2(k_u s)}}$$

$$A_{z'} = 0. \qquad (5).$$

IV. ANALYSIS OF THE MOTION

In the natural coordinate system employed. the longitudinal momentum of the particle is well in excess of the transverse momentum and this allow us to use the methods of the perturbation theory. It is known[4], that the stabilizing part of the perturbation Hamiltonian leading to the tune shift has the form

$$H_{st} = -\frac{A_{g'}R^2}{B\rho}, \qquad (6)$$

where R is average radius of the machine;
$\vartheta = s / R$ is the azimutal angle;
$B\rho$ is the particle magnetic rigidity.

Using expression [4] for the tune shift

$$v_z - v_{z0} = \frac{1}{2\pi}\int_0^{2\pi}\frac{\partial H_{st}}{\partial|a_z|^2}d\vartheta$$ where $|a_z|$ and z are

related by $|a_z|^2 = z^2\left(|V'|^2 - v_{z0}^2|V|^2\right)$, and averaging the Hamiltonian over the whole perimeter of the setup, we obtain the following expression for the tune shift

$$v_z - v_{z0} = \frac{B_0^2 p L_u R}{\pi^2 B^2 \rho}\left[\frac{1}{kp}E(k) - \frac{k}{p^3}K(k)\right]\times$$

$$\sum_{j=1}^{\infty}\frac{1}{j!(j-1)!}|a_z|^{2(j-1)}|V|^{2j}k_u^{2j-1}, \qquad (7)$$

where $k = \frac{p}{\sqrt{1+p^2}}$:

$K(k)$ is tte first-kind complete elliptic integral;

$|V|$ is the modules of the Floquet function averaged over the undulator length.

It should be noted that at $p\to 0$ the term in square brackets $\to \pi/4$, and after substitution of $|V|^2 = \beta_z/2R$, where β_z is the vertical amplitude function. we obtain from (7) the expression for tune shifts given in [1]:

-linear shift

$$v_z - v_{z0} = \frac{L_u\beta_z}{8\pi\rho^2}: \qquad (8a)$$

-nonlinear shift

$$v_z - v_{z0} = \frac{\pi L_u|a_z|^2\beta_z^2}{8\rho^2\lambda^2 R}. \qquad (8b)$$

For practical applications. it appears more convenient to use in expression (8b) the betatron oscillation amplitude $a_z^* \approx \sqrt{\beta_z\varepsilon_z}$, (where ε_z is the vertical beam emittance) which is related to $|a_z|$ by $|a_z|^2 = a_z^{*2}R/2\beta_z$. If we

restrict ourselves to the first two terms of the series expansion in k $E(k)$ and $K(k)$, then the expression for the tune shift, which are suitable for their practical use, take the form:

-linear shift

$$v_z - v_{z0} = \frac{L_u p\left(2 + 3p^2\right)\beta_z k_u}{16\pi\rho\sqrt{1 + p^2}\left(1 + p^2\right)};$$ (9a)

-nonlinear shift

$$v_z - v_{z0} = \frac{L_u p\left(2 + 3p^2\right)a_z^{*2}\beta_z k_u^3}{128\pi\rho\sqrt{1 + p^2}\left(1 + p^2\right)}.$$ (9b)

The tune shift due to the trajectory extension in the undulator (see expression (4)) is given by

$$v_y - v_{y0} = \frac{L_u\left(\sqrt{1 + p^2}\left(1 - \frac{p^2}{4\left(1 + p^2\right)}\right) - 1\right)}{2\pi\beta_y}$$

(10)

where y=x,z.

V. CONCLUSIONS

We have derived here the expressions for the tune shift caused by the fields of a plane undulator (wiggler) in the case of a significant orbit distortion. Numerical estimates show that in most cases, in practice, it suffices to use expression (8) because even in the consideration of the effects of caused superconducting inserts in compact storage rings the difference between the results obtained by the use of expressions (8) and (9) is not greated than 10...15%. Yet, the effects by themselves are rather significant and their compensation by means of, for example, magnetic-lens systems is a serious problem.

VI. REFERENCES

[1] S. Efimov "Fringing Field Effects of the Plane Undulator on Beam Dynamics in Storage Ring", Proc. EPAC-92, vol.1, p.664-666.
[2] E.Bulyak, S Efimov "Nonlinear effects occurring due to fringe fields of cyclic accelerator dipoles". Proc. EPAC-90, vol.2, p.1455-1457.
[3] Thomas C. Marshall "Free-electron lasers".1985.
[4] G. Guignard. "A general treatment of resonances in accelerators",CERN 78-11, Geneva, 1978.

302

BUNCHING PROPERTY OF HIGH CURRENT INJECTOR WITH SUBHARMONIC PREBUNCHER IN LINAC

Zhang Zhenhai, Chen Yinbao

China Institute of Atomic Energy
P.O.Box 275(17), Beijing 102413, China

ABSTRACT

The electron beam bunching property in the high current injector with a prebuncher operating at the twelfth subharmonic(SHB) of the accelerator frequency 1300Mhz has been studied in this paper. The longitudinal compression of the pulse varying with the beam current and the voltage excited by the prebuncher is discussed in detail. Finally, some numerical results taking account of the beam current distribution are given for L-band linac by using of the modified dynamical simulating code PARMELA.

1. Introduction

There are alternative schemes of the injectors of RF free-electron laser (FEL) facility. The first one is microwave-electron gun or photo emission electron gun. It is expected to acquire high quality electron beam, but difficult to develop; The second one is composed of a DC electron gun and a subharmonic buncher(SHB). It is rather easy to do but has difficulty in improving the electron beam quality. We prefer the later to the former in our FEL facility according to our technology limits. The bunching property of RF linac with SHB is discussed in detail in this paper. The prebuncher with SHB often consists of the following parts: high current DC-gun, one or two SHBs, a RF buncher, an accelerating section. The solenoid magnetic field must be used to overcome the space charge influence and BBU effect [1] . The high intensity injector in CIAE consists of a 80KV DC gun, one SHB with the frequency of 108.3MHz which is the twelfth subharmonic of the 1300 Mhz, a RF buncher with 7 cells accelerating the electron beam to 2 MeV and an accelerating segment. The drift distance between the SHB and RF buncher is 140 mm. The bunching properties of the SHB and RF bunhcher and the matching property between them are the main tasks of particle dynamics in high current injector.

2 Bunching property of the SHB

Suppose that the beam emitted by the DC gun is a Gaussian distribution bunch in longitudinal direction and uniform in the transvers phase space (x-x'-y-y'). According to the reference [2], it is convenient to produce the simulating beam which corresponds to that distribution in longitudinal as shown in Fig.1. PARMELA code is adapted to simulate this special beam. When particles pass through the SHB, their velocities are modified and the beam length is compressed in the drift space.

2.1 The influence of the beam current

Keeping the modified voltage(45KV) and beam length (2.8ns) constant, we made simulating calculations when the beam current is 2A, 4A, 5A respectively. It is interesting to find that bunching efficiency decreases rapidly with the beam current increasing but the location of longitudinal beam focus change a little as shown in Fig.2. By this virtue, we can expec the facility operating at great range of the beam current

2.2 The influence of modifed voltage

When modifed voltage of SHB increases, the bunhching efficiency decreases and the longituidinal beam focus moves forward as shown Fig.3; the oscillating amplitude of the beam transverse envolope damps with time. Beam transverse emittance increases because of the space charge effect. The beam longitudinal focus is in agreement with the peak of the transvers emittance as shown in Fig.4. This implies that transverse motion is coupled with the longitudinal motion.

2.3 Bunching property of the RF buncher

The beam transverse emittance increases rapidly in the RF buncher because of the drammatically longitudinal phase motion and the intensively coupling between the transverse and longitudinal motion. To avoid the excessive phase oscillating and constrain the increase of the transverse emittance,the phase velocity of RF buncher often rise rapidly to that of light with the pay of lower traawing efficiency.

2.4 Matching property between SHB and RF buncher

In order to obtain high quality beam, the matching property between SHB and RF buncher must be studided carefully. The two aspects interact with each other and have great influence in the quality of output beam. A set of parameters of the calculating results of the injector in CIAE are given as shown in Fig5 and Fig 6.

The solenoid magnectic field must be used to restrain the motion of the transvers and BBU effect. the magnectic field have great influence on the transvers emittance and envelope of beam.

3 Conclusion

In the high current injector with subharmonic prebuncher, many conditions shound be took into considration to aquire high qulity beam such as beam current, the modified voltage of SHB, and the drift space length etc. There are some methods can be took to improve the beam quality : increasing the injecting energy of the DC gun , discreasing the longitudinal length of pulse emitted by the DC gun and using two SHBs and so on . Because of high beam current, the compressing ratio is about 3 when only one SBH is used; when two SHBs are used; one can get high compressing rate but it is more complicated and the its cost will increase . Finally, no matter wihch methods you take , the matching problem is very important if you want to obtain high quality beam.

Reference
[1] P.M. Lapostolle et al .
        Linear Accelerator, North
        Holland Publ.
        Co.,Amsterdam,1970.
[2] Zhang Xiaozhe, "Application
        of Marte Carlo Methods in
        Particle Transport",
        Beijing,
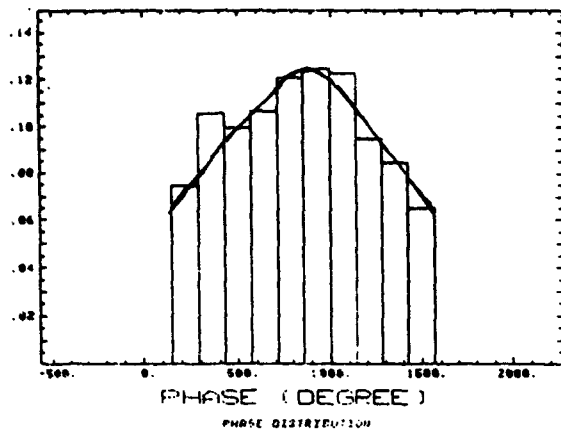
Fig 1. beam longitudinal distribution.
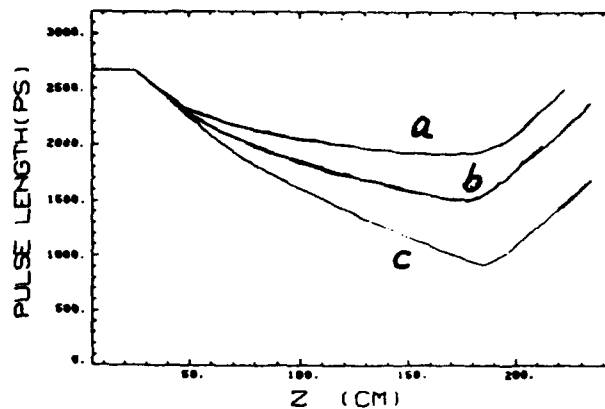
Fig 2. bunching efficiency varing with the beam current a) I= 5A, b)I= 4 A,c) I= 2.5 A.
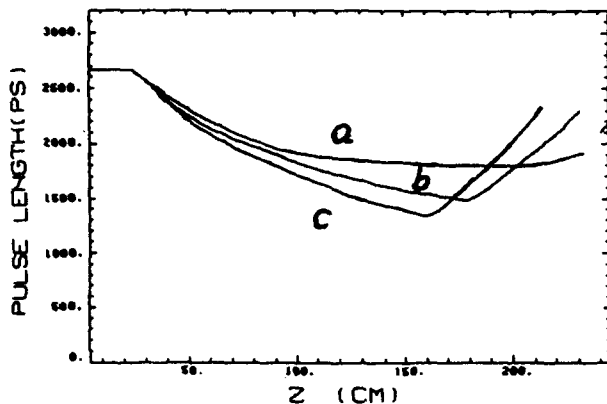
Fig 3. bunching efficiency varing with the modified voltage (a)V=40KV,(b)V=45KV,(C)V=50KV.
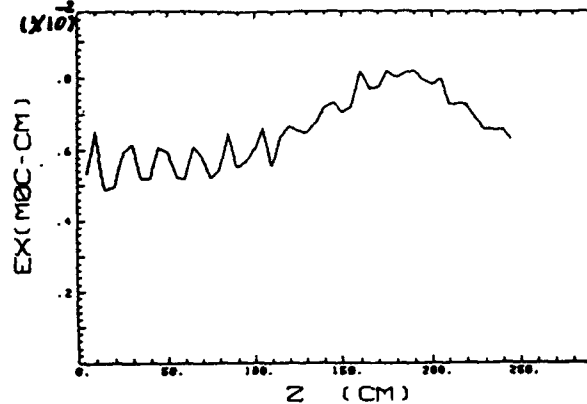
Fig 4. transverce emittance varing with the distance (no RF buncher) Egun=100 KeV, I= 2.5 A t = 3.0 ns.
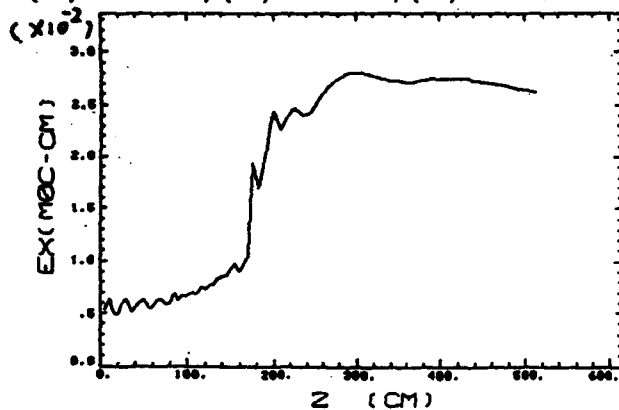
Fig.5 transvers emittance varing with the distance Egun = 100KeV I=2.5 A, t = 3.0 ns .
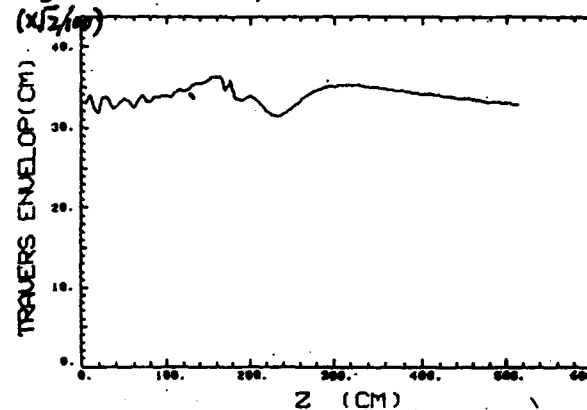
Fig.6 beam transvers envelope varing with the distance.

Beam Transport Line of CIAE Medical Cyclotron

and Its Magnetic Elements Design Studies

Tianjue ZHANG   Chenjie CHU   Mingwu FAN

China Institute of Atomic Energy
P.O. 275(3),   Beijing, 102413,   PRC

Abstract

More than 300 μA proton beam has to be transported from exit of a cyclotron to target. The final beam spot less than $\Phi 8$ mm in diameter was asked. To reduce the cost of the system the beam aperture is limited to 50 mm in diameter and the magnetic elements are carefully designed with easier fabrication and loose tolerance. For example, the cross section of the pole faces of the quadrupoles are broken line shaped instead of hyperbola. And the two steering magnets have been added to control the vertical and hozizontal position of the beam on the target.

I . INTRODUCTION

CIAE Medical Cyclotron is a fixed-field, fixed-frenquency cyclotron. It is built to produce short-lived radioisotopes. Its vault and target room is showen in fig. 1. More than 300 μA proton beam has to be transported from exit of the cyclotron to target for isotopes production. The beam line for this purpose is being built in CIAE.
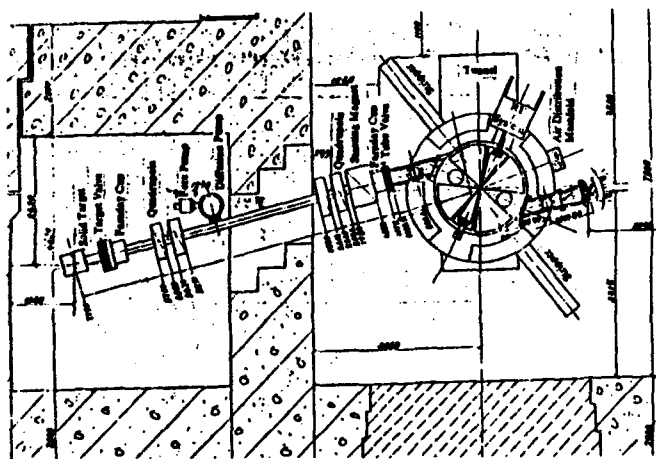
Fig. 1 The vault and target room

II . BEAM LINE DESIGN

The beam is able to be extracted form the cycltron after H^- ion stripped cross a thin carbon foil. The proton is bent out of the cyclotron by the edge field. The stripper is radially and azimuthally adjustable, that make the extracted beams at different energies are directed towards the centre of the switching magnet. To reduce the cost of the system the beam aperture is limited to 50 mm in diameter. In order to meet the requirement of the final beam spot less than $\Phi 8$ mm, two pairs of quadrupole are used instead of a triplet or a pair of quadrupole [1,2]. Two steering magnets are used to control the vertical and horizontal position of the beam on the target. The bending angle is more than 2 $^\circ$.

After stripper, the beam emittance is provied as:
$$\varepsilon_x = 8.4 \times 6.38 \times 10^{-6} \text{m.rad}$$
$$\varepsilon_y = 2.7 \times 6.25 \times 10^{-6} \text{m.rad}$$

The beam line is designed based on the code TRANSPORT.

For 30MeV beam , the results are:

1. The maximum of envelope in X direction is limited in 24.87 mm, in Y direction 17.77 mm.

2. Position of the elements is showen in fig. 1.

3. In the working condition ,the magnetic field gradients are:
$$K_1 = -0.57605\text{kG} / \text{cm}$$
$$K_2 = 0.57308\text{kG} / \text{cm}$$
$$K_3 = -0.66457\text{kG} / \text{cm}$$
$$K_4 = 0.72957\text{kG} / \text{cm}$$

For 20MeV beam , the results are:

1. The maximum of envelope in X direction is limited 24.40 mm, in Y direction 21.19 mm.

2. Position of the elements is the same as above.

3. The magnetic field gradients are :

$$K_1 = -0.44126 kG/cm$$
$$K_2 = 0.45866 kG/cm$$
$$K_3 = -0.57052 kG/cm$$
$$K_4 = 0.63962 kG/cm$$

The envelope of different energy ion are showen in Fig. 2.1 and Fig 2.2.

Fig. 2.1 30MeV beam envelope

Fig. 2.2 20MEV beam envelope

III. Quadrupole Design

In order focus the bean successfully ,the magnetic field distribution in quadrupole should be:

$$\frac{dB_x}{dy} = \frac{dB_Y}{dx} = const.$$

Therefore, the cross section of the pole surface should be hyperbola supposing $\mu \to \infty$. To avoid the different in the fabrication , the cylinder face is usually used instead of hyperbola in many cases. Based on the precise results of the magnetic field computation code, the broken line shaped can be used instead of hyperbola for the quadrupole. One eighth dimension of the quadrupole is showen in fig 3. The magnetic field distribution from DE2D software package are showen in fig. 4 . Three dimensional results of magnetic field computation (by DE3D) are showen in fig. 5 and fig. 6. It can be seen that the magnetic field gradients dB_Y/dx are close to const. in region [0,3]. Fig. 7 and fig. 8 show the mapping results. The different gradient can be obtained from -1 kG/cm to 1 kG/cm useing adjustment near of the current. Fig. 9 shows the quadrupole .

Fig. 3 The one-eighth of the quadrupole
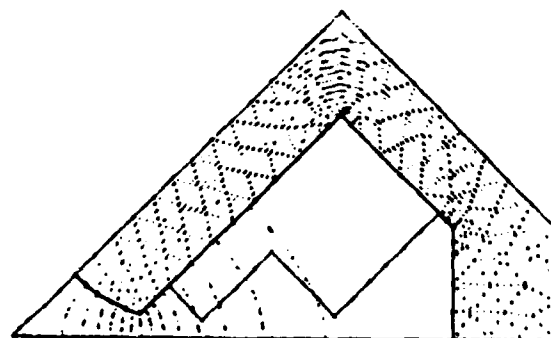
Fig. 4 The magnetic field distribution computed by DE2D
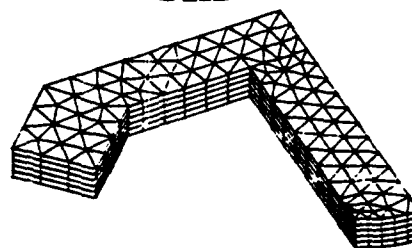
Fig. 5 The three dimensional mesh of the iron region
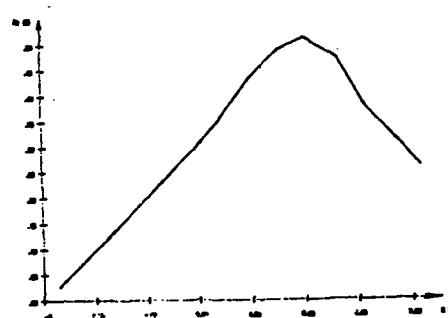
Fig. 6 The magnetic field gradient computed by DE3D
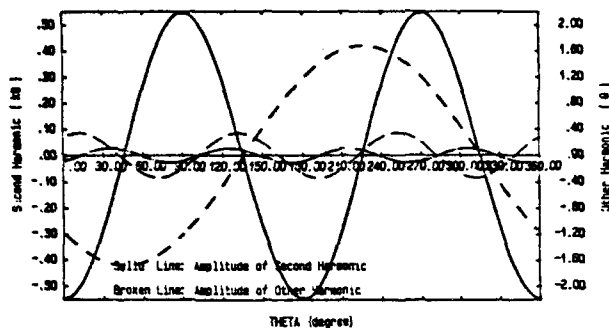
Fig. 7 The mapping results —— harmonic field
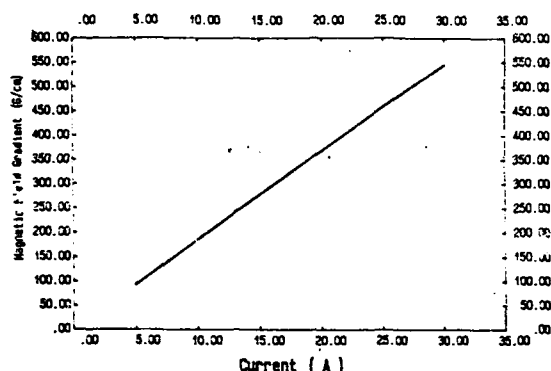
Fig. 8 The mapping results —— magnetic field gradient

Fig. 9 The quadrupole

IV. STEERING MAGNET DESIGN

In order to adjust the the vertical and horizontal position of the beam on the production target, two steering magnet are designed. The central the beam position ± 20 cm in the target.

The structure of steering magnet showed in fig. 11 The pole breadth of steering magnet is 12 cm. The gap

height is 7.2 cm.and the effective length will be approximately equal to:

$$L_{eff} = 12 + 2 \times 0.65 \times 7.2 = 21.36 \ (cm)$$

The computation results of magnetic field distribution is showed in fig. 12. The field indensity in the gap is 1521 G given by computation and measurement. With the beam energy 30 MeV, the rotated angle is

$$R = \frac{m_0 c}{qB} \sqrt{(2 + \frac{K}{E_0})\frac{K}{E_0}} = 5.2448(m)$$

Where K is kinetic energy. E_0 is rest mass. Then the beam bending angle is 2.3331 ° and the movement on target is 22.26 cm. magnet .
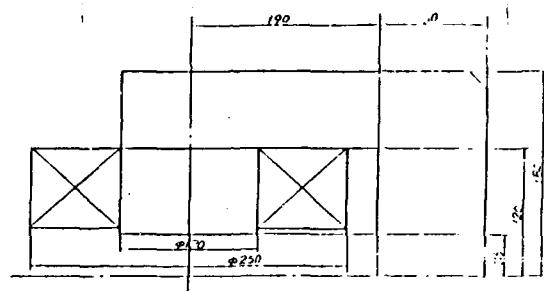
Fig. 10 The structure of steering magnet
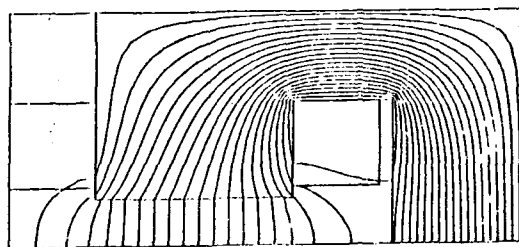
Fig. 11 The magnetic field distribution of steering magnet

V. CONCLUSION

The beam transport line is designed according to the requirements.

All magnetic elementsc possess same common characteristics: easier to machine, loose tolerance and lower power consumption et al.

Resonant Beam Extraction with Constant Separatrix

K. Hiramoto, M. Tadokoro, J. Hirota and M. Nishi
Energy Research Laboratory, Hitachi, Ltd.
2-1, Omika-cho, 7-chome, Hitachi-shi, Ibaraki-ken, 319-12, Japan

Abstract

A new scheme for slow beam extraction using nonlinear resonance is presented to realize small emittance. In the scheme, the amplitude of the betatron oscillations is increased by perturbations, while keeping the separatrix constant. As a measure of perturbation, the transverse filtered noise is studied in computer simulations. It is shown that the emittance of the extracted beam is vanishngly small. It is also shown that the time structure of the extracted current is not affected by the ripple in the magnet current.

I. INTRODUCTION

In a circular accelerator such as a synchrotron for physical experiments or medical use, a charged particle beam is slowly extracted by using nonlinear resonance of the betatron oscillations[1][2]. The separatrix of the nonlinear resonance of the betatron oscillations is defined as the boundary in the phase space between stable and unstable betatron oscillations. In order to excite the nonlinear resonance to the beam having not only large betatron amplitudes but also small ones, conventional slow extraction methods gradually make the separatrix shrink and finally vanish by varying the betatron tune, defined as the number of the betatron oscillations per one revolution. This tune change is realized by controlling the quadrupole magnets or the radio frequency of the acceleration.

Changing of the separatrix size generally varies the orbit gradient and turn separation of the extracted beam at the deflector position. As a result, it is expected that the position and size of the extracted beam change, that is, the emittance of the extracted beam becomes larger. Some countermeasures have been taken to keep the beam characteristics constant during the extraction[3][4]. These countermeasures, however, require rather complicated design and control. Then, we have proposed a new, simpler nonlinear resonant extraction scheme[5] in which the beam is ejected with a constant orbit gradient and turn separation by perturbing only the beam to increase the betatron amplitudes while maintainig steady operation of other components. In the paper, we showed that the tranverse filtered noise and monochromatic perturbation are potentially good measures of the increase in the betatron amplitudes.

Another concern in the slow beam extraction is preventing an intermittent time structure of the extracted beam current due to current ripple of the magnet power supply. In the present scheme using the transverse filtered noise, it is expected that the intermittent extraction can be prevented by the effect of random motion due to the applied noise[6]. Then, the time structure of the extracted current is evaluated for the scheme applying the filtered noise and compared with that by the conventional scheme.

II. EXTRACTION SCHEME

The present extraction scheme is characterized by keeping the separatrix constant for nonlinear resonance of the betatron oscillations and increasing the amplitude of the betatron oscillations to excite the resonance (Fig.1). Since the separatrix is kept constant, the orbit gradient and turn separation at the deflector position are almost constant. Therefore, the emittance of the extracted beam can be reduced to a negligibly small value. The following methods can be used to increase the amplitude of the betatron oscillations:

(1) transverse perturbation by a high frequency electromagnetic field,

(2) longitudinal perturbation by a high frequency electromagnetic field, from the position of a non-zero dispersion function, and

(3) scattering of the beam by other neutral or charged particles.

Amplitude Growth of the Betatron Oscillations
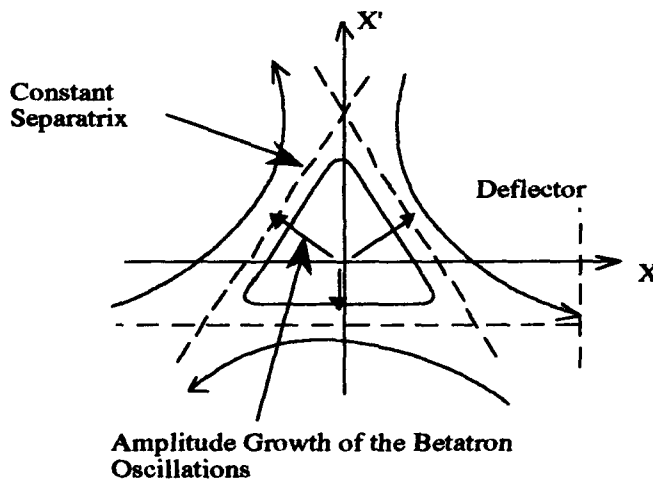
Fig.1 Phase Space of the Extraction Scheme with Constant Separatrix

Generally, the betatron tune varies with the betatron amplitude under the nonlinear magnetic field. Then, the tune spectrum of the beam at the resonant extraction spreads. Therefore, in order to eject the beam having the spread tune spectrum, it is effective for the transverse perturbation in method (1) to have wide band frequency components synchronous with the spread betatron tunes. A single frequency perurbation for the same purpose was also proposed[5][7].

The applied tranverse noise is expected to cause the circulating beam to diffuse in the transverse phase space. This diffusion makes the amplitude of the betatron oscillations increase slowly with relatively fast, but small fluctuations. Because of the fluctuations, the effect of the low frequency ripple of the magnet currents is expected to be overcome. This effect for longitudinal diffusion has been confirmed in the

ultra slow extraction scheme developed in CERN[6]. In the following section, the wide band perturbation with filtered noise is studied through computer simulations.

III. COMPUTER SIMULATION METHOD

In the computer simulations, a coasting beam is assumed with the design momentum. The coasting beam is divided into N_s bins having an equal size along the circulating direction. It is assumed that the beam in each bin has an equal emittance and consists of N_p super particles. The initial particle distributions in the normalized phase space are assumed to be Gaussian with an rms value of σ for both X and X' directions. The emittance is defined as the phase space area including 3σ for both X and X'. The betatron oscillations and nonlinear resonance of the beam are analyzed in the normalized phase space with one degree of freedom. Thin lens approximations are applied to the treatments of the effects of the nonlinear magnetic field and the high frequency perturbation field:

$$\begin{vmatrix} X_{i,j,new} \\ X'_{i,j,new} \end{vmatrix} = \begin{vmatrix} \cos\phi, -\sin\phi \\ \sin\phi, \cos\phi \end{vmatrix} \begin{vmatrix} X_{i,j,old} \\ X'_{i,j,old} + f(X_{i,j,old}) \end{vmatrix} + \begin{vmatrix} C_1\delta_i \\ C_2\delta_i \end{vmatrix} \quad (1)$$

where X and X' are the position and orbit gradient normalized by the Twiss parameters: i $(=1,\cdots N_s)$, the bin number in the s direction; j $(=1,\cdots N_p)$, the particle number in the i-th bin; ϕ, the phase advance of the betatron oscillations per one revolution in the accelerator; f $(X_{i,j,old})$, the transverse kick by the nonlinear magnetic field with thin lens approximation; δ_i, the transverse perturbation for an increase of the betatron amplitude; and C_1 and C_2 are constants determined by the lattice elements between the nonlinear magnetic field f(x) and the transverse perturbation δ_i. Then, the nonlinear resonance can be analyzed by successive calculation of Eq.(1) for each particle. δ_i by the filtered noise is approximated by superposing perturbation signals of multi frequency components having respective random phases. In the following, the perturbation intensity $\overline{A}$ is defined by rms value of δ_i.

For comparison, the conventional scheme varying the tune is analyzed with the assumption that the phase advance of the betatron oscillations per one revolution is decreased monotonically from the initial value of ϕ_{init} to the final value of ϕ_{end}:

$$\phi = \phi_{init} + (\phi_{end} - \phi_{init}) N_{rev}/N_{tot} , \quad (2)$$

where N_{rev} is the revolution number after initiation of the extraction and N_{tot} is the total revolution number during the extraction. For both the present extraction scheme and the conventional one, the effect of the ripple of the magnet current is considered through the following relationship:

$$\phi = \phi_0 + \Delta\phi \sin(N_{rev} / N_{rip}) \quad (3)$$

where ϕ_0 is the phase advance without the ripple, $\Delta\phi$ is the ripple amplitude of the phase advance, and N_{rip} is the ripple period in a unit of the revolution number.

IV. SIMULATION R℠ ULTS

The above computer simulation technique was applied

to analysis of the second order resonant extraction by the present scheme. The fractional part of the betatron tune was assumed to be 0.505. The beam was divided into 20 bins, each of which consisted of 1000 super particles. The beam emittance was assumed to be 10 $\pi mm \cdot mrad$. The nonlinear magnetic field was defined to make the separatrix larger than the beam emittance of 10 $\pi mm \cdot mrad$. For simplicity, it was assumed that the filtered noise and the nonlinear magnetic field were applied to the beam at the same position. It was assumed that the filtered noise has spread frequency components equivalent to the tune range from 0.495 to 0.505 and the power of each frequency component was equal. The deflector for the extraction is assumed to be at $Xd = 10 \times 10^{-3}$.
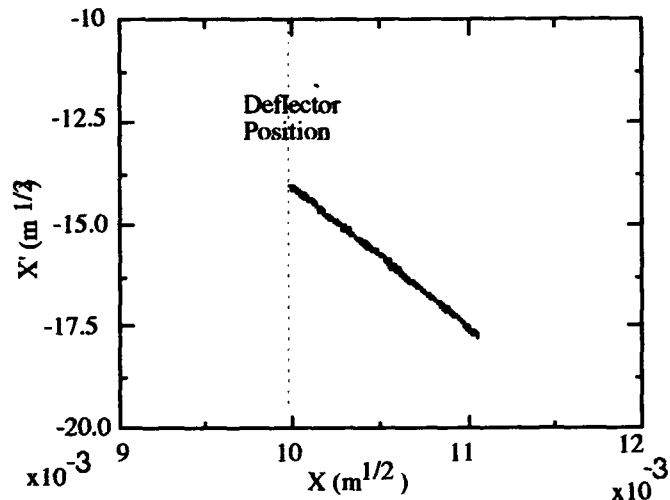
Fig.2 Phase Space Positions of the Extracted Particles
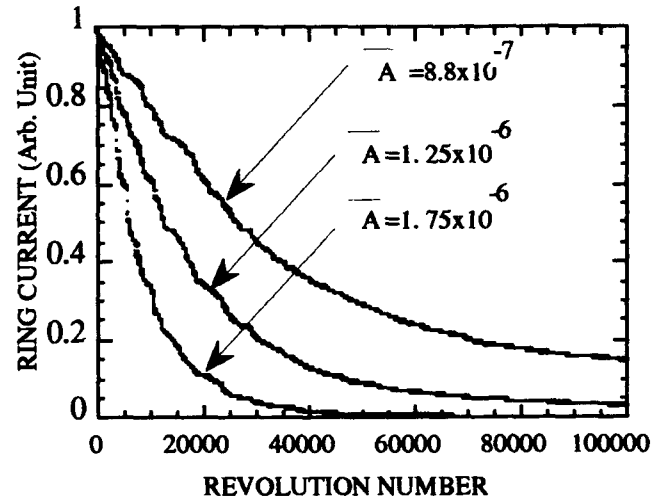
Fig.3 Relationship between Revolution Number and Ring Current

Figure 2 shows the phase space plots for the particle inside the separatrix. The rms value of the perturbation $\overline{A}$ was assumed to be 1.25×10^{-6}. It was confirmed in the simulations that the orbit gradient is kept constant and the emittance of the extracted beam is smaller than 0.5 $\pi mm \cdot mrad$. For comparison, the resonant extraction was analyzed next by varying the separatrix size. The betatron tune was reduced

linearly from 0.505 to 0.500 so that the separatrix shrank and finally vanished. The results showed that the orbit gradient changes significantly in comparison with the present scheme.

The change in the fraction of super particles in the separatrix, i.e. the accelerator ring current, is shown in Fig.3. Results for three perturbation intensities of $\bar{A}$ = 8.8 x10^{-7}, 1.25x 10^{-6} and 1.76 x10^{-6} are shown. The ring currents decrease more rapidly when increasing the noise intensity. The behavior of the particles in the phase space under transverse noise can be written by a diffusion equation and the diffusion constant is proportional to the square of the perturbation intensity $\bar{A}$. In a typical slow extraction, it is necessary to eject the beam during about 10^{6} revolutions. Since the required diffusion coefficient is inversely proportional to the extraction period, the necessary noise intensity $\bar{A}$ is reduced to about 5.0x10^{-7} for the above extraction time. Assuming that the beam is a proton beam of 250 MeV and the tranverse perturbation is added by a kicker of 0.5 m length at a point where the betatron function is 10 m , the necessary noise voltage is lower than about 50 V.
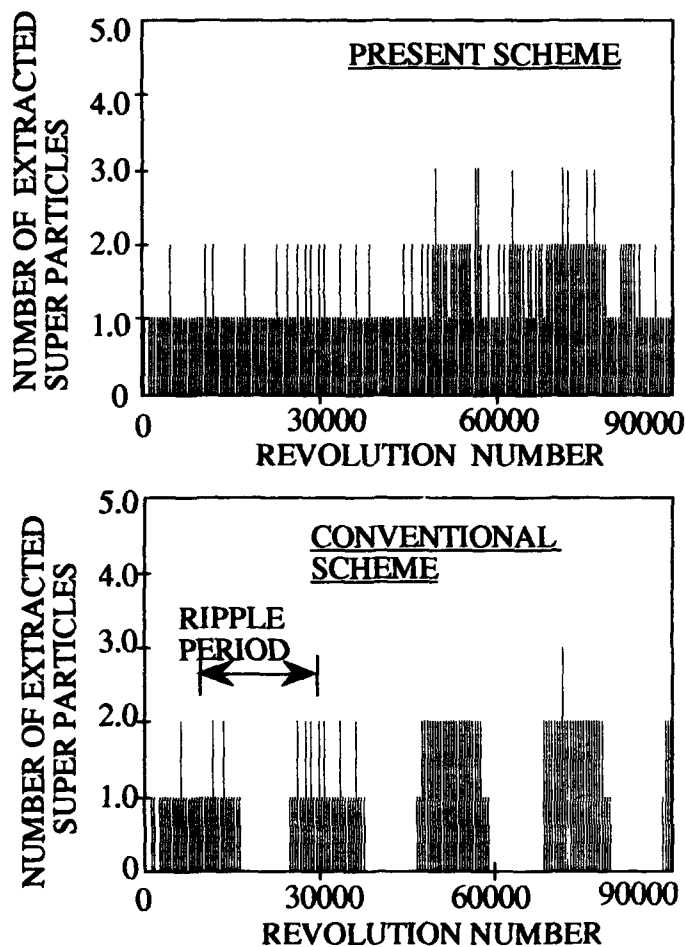
Figure 4 shows the time (revolution number) dependences of number of the extracted super particles for the present and conventional extraction schemes. It was assumed for both schemes that the ripple of the phase advance, that is, $\Delta\phi/\phi_0$ was 10^{-4} and N_{rip}, the period of the ripple was the revolutin number of 20000. For the present extraction scheme, the rms intensity of tht pertubation noise was 5.0x10^{-7}. It is seen that extraction by the conventional scheme occurs intermittently. The time structure of the extraction by the present scheme is less affected by the ripple because of the random motion of the particles due to the applied filtered noise.

V. CONCLUSIONS

A new scheme for resonant extraction was presented to realize beam extraction with small emittance and constant characteristics of the position and size. The present extraction scheme is characterized by keeping the separatrix constant and increasing the amplitude of the beatatron oscillations to excite the resonance. This scheme was studied for a second order resonant extraction by computer simulations. As a measure for the perturbation, the transverse filtered noise were studied. It was shown that the emittance of the extracted beam could be reduced to a negligibly small value. It was also shown that the time structure of the extracted current was less affected by the ripple of the magnet current in comparison with that by the scheme varying the separatrix size.

References

[1] A. Itano et al., Proc. of 7th Symp. on Accel. Sci. and Technol., p42, Osaka, Japan, 1989

[2] M. Yoshizawa et al., Proc. of the 1991 Particle Accelerator Conference, p875, San Francisco, U.S.A., 1991

[3] W. Hardt, CERN/PS/DL/LEAR Note 81-6, 1981

[4] F. Soga et al., Proc. of 6th Symp. on Accel. Sci. and Technol., p268,Tokyo, Japan, 1987

[5] K. Hiramoto et al., Nucl. Instrum. Meth. A322, p154 (1992)

[6] R. Cappi et al., CERN/PS/OP/DL 80-16,1980

[7] M. Tomizawa et al., Nucl. Instrum. Meth. A326, p399 (1993)

Fig.4 Number of Extracted Super Particles

The On-line Control Software For BEPC Beam Transport Lines

Xiaolong Zhang, Kaiyu Wei, Chuang Zhang
Institute of High Energy Physics, Chinese Academy of Sciences
P.O. Box 918, Beijing 100039, China

Abstract

The on-line control software for BEPC beam transport lines are developed and incorporated in the BEPC control system. The polynomial fitting for the excitation curves of the transport line magnets are carried out, and the polynomials are loaded into the BEPC database. The programs TRANSPORT, MAGIC, COMFORT serving as the tool for the beam transport line computation are compared in the point of on-line control. The design and debugging of the software are accomplished and the operation results are analyzed. As a result, the development of the on-line software provides a powerful tool for BEPC commissioning and operation.

I. GENERAL DESCRIPTION

The beam transport lines of BEPC are designed elaborately in order to obtain high efficiency and enhance the integral luminosity. Fig.1 illustrate their layout.
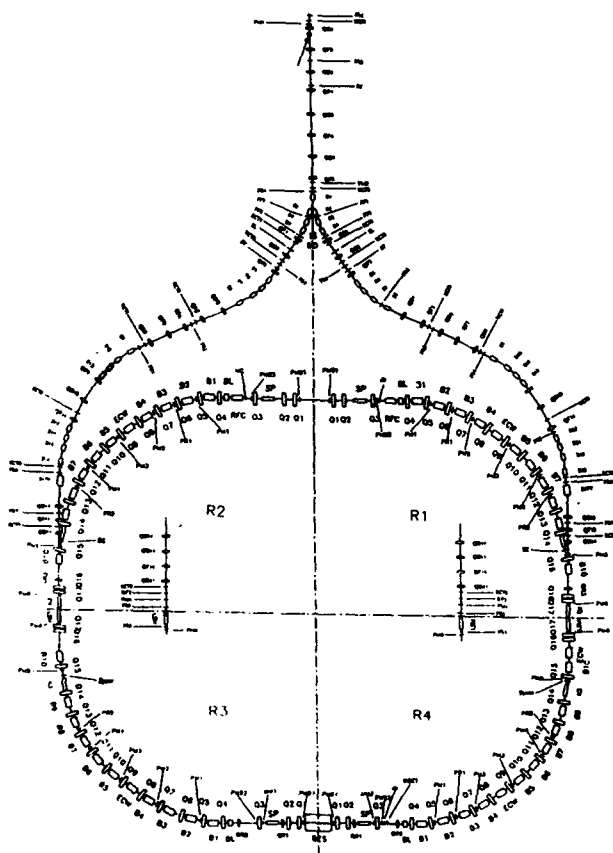
Fig. 1 The layout of BEPC

The beam coming from the linac end is fitted as an upright ellipse at the exit of the common line by TCQ5-8, so that we need not to change the polarity of the quad-magnets when the beam is switched between electron and positron. At the end of the common line, a switch magnet branches off the beams according to the charges it bearing. The two branches of TE and TP are symmetrically designed to transport the electron beam and positron beam to the injection points respectively. In each branch, the beam is bent 60° out and then -60° in and at last 8.015° up to the injection point on the plane of the storage ring. In each horizontal bend region, there is an achromatic section. And in the last vertical bend section, the beam is anchromatized vertically[1]. The efficiency of this transport line running under the optimized model reaches about 80%. But this is only for the primary control, it would be different and inflexible when the conditions of the linac or the ring are changed.

Therefore, for pursuing the high efficiency, the control software are needed to set the operation models of the transport lines on-line so that the variations of the linac exit parameters and the changes of the injection model of the storage ring can easily be fitted. Furthermore, the upgrades of the running models will be carried out much more conveniently and more researches will be done by the means. But on the contrary, we must search the models fitting for the linac and the ring and key the transformed numbers of the corresponding currents of each magnet to the database off-line under the primary control mode. After a deep insight of the primary control of the BEPC transport lines, the on-line control software which resembled the ones of the BEPC storage ring have been developed on the basis of the present operation mode of the beam transport lines.

The tasks of developing and implementing the on-line control software include three broad categories: (A) the study of the computation programs and the off-line analyzing of the transport lines. (B) the study of the polynomial fitting of excitation curves of the magnets. (C) the debugging of the programs and operation study.

II. EXCITATION CURVES FITTING OF MAGNETS

Since magnets are the primary elements of the accelerator, the excitation currents of the magnets are the main parameters for control. The measured data of a magnet are series of separated points, so the curve fitting of these points is needed.

After carefully processing the measured data of magnets, it was found that the magnets of the same group

312

have a good consistence, so the sequence of average all fields first or fitting every single magnet first then average them seems not much different. After a meticulous studying of the polynomial fitting, we choose integral field B as a function of excitation current I and zero offset for it does not cause any problem. We selected to fit them to the sixth order and obtain a precision about 0.1% which is about the measurements. The BEPC revised version of fitting program POLYA, which was transplanted from FNAL, was used in this procedure.

As soon as all the polynomials were obtained, we had them loaded into the BEPC database by running a program.

III. THE SOFTWARE ACHITECTURE

The software can be divided into two main processes according to the functions they perform: TMODEL to fit for the models, TRLIN to do graphic displays (see Table 1). The on-line control procedure is shown in Fig.2.

Table 1.
The Main Functions of TMODEL and TRLIN

Process	Subtask	Functions
TMODEL	TCOMFWRT	Preparing input data file, spawning COMFORT, processing output file and putting the results into database
	TCOMFPT	Print out the output file of COMFORT
TRLIN	TRDSP	Read the output file of COMFORT and display curves on the screen
	TRPRT	Print out the Twiss parameters whole line

TMODEL manages two programs: TCOMFWRT and TCOMFPT. The first program TCOMFWRT fetches the data of the currents for every main magnet at present from database and turns them into the strength and then writes a COMFORT input data deck to spawn COMFORT running. If it goes without any error, TCOMFWRT reads its output file and transforms the strength to currents of the corresponding magnets and put them into the datbase for updated model. If it is satisfying, this model can be put into running. In this procedure, the branch to be fitted is also specifies . The second program TCOMFPT is used to print out the COMFORT output file for the off-line analysis.

The process TRLIN includs two programs: TRDSP and TRPRT. TRDSP displays the horizontal or vertical β, η and σ functions and relevantly TRPRT prints out the twiss parameters of the current model graphically along

the transport line. All the communications among them and database are enactivated via the touch panel and dispatched by the task control process AVTX. The touch pannel programs are written in FORTH language.
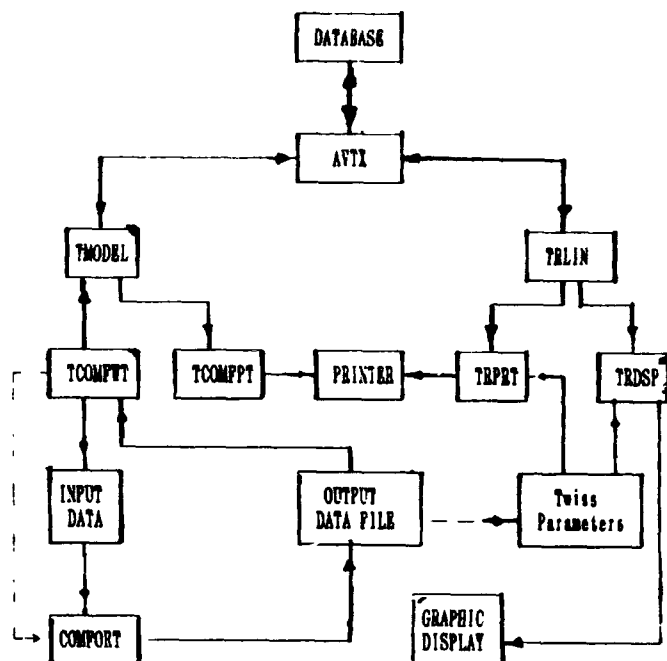
Fig.2 On-line Controll Procedure

This on-line control software has been accomplished and put into operation. The results seem satisfying and promising.

IV. THE SOFTWARE DEVELOPING AND IMPLEMENTING

The wellknown programs as TRANSPORT, MAGIC and MAD are powerful for optical calculation and accelerator design, but for the purpose of on-line control, they are too slow and memory intensive for the control system from our study, which is in agree with other results [2,3]. We take the advantage of COMFORT as the main on-line fitting program, and that also matches with the storage ring. (see Table 2)

Table 2.
A Brief Comparision of The Computer Codes

Program	Size (blocks)	Speed (seconds)
COMFORT	450	12
MAGIC	500	94
TRANSPORT	1120	25

The positions and the number of the fitting points, the variables a   rget parameters and others used for the

on-line control software are also carefully analyzed and calculated. We selected three key positions as fitting points: the exit of the common line, the end point of horizontal bend section and injection point. These are enough based on the off-line studies and the design catalog[1]. The initial parameters of the beta functions are computed and loaded into the database according to every operation mode. The debugging of the programs are categories into three steps: off-line progressing, debugging and on-line commissioning. After all these being finished, the software is put into real application. Fig.3. shows the Twiss parameters along the transportline fitted on-line.
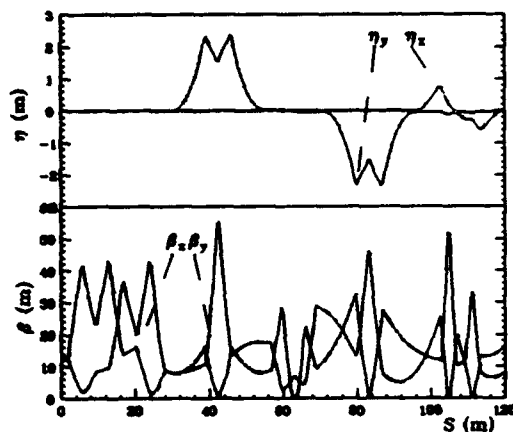
Fig.3 β and η Functions Along the Line

For the perfect on-line control of the BEPC beam transport system, the beam diagnostic devices needed. A beam emittance measurement system in the common line is installed, which uses the three-kick method to vary the

appropriate quad-magnet gradient three times and to measure the sizes of the spot on the profile monitor downstream and calculates the twiss paremeters and emittance at linac exit. Besides the acquired design theoretical values that the linac must fit, we can also take out the real measured parameters to fit for initial values.

V. CONCLUSION

The software serves as a useful means for fully bringing out latent potentialities of BEPC transport line and storage ring, raising the efficiency of the beam transportation and injection, as well as the integral luminosity of the collider. It is also a good tool for the researches of theories and experiments of the beam transportation and injection in order to carry on further studies of the occasional injection problem of BEPC. And it has taken a important role in the experiment of the current limitation of the ring versus injection energy.

VI. ACKNOWLEDGEMENT

VII. REFERENCES

[1] K. Wei and J. Lu, "The Design of BEPC Transport Lines," *IHEP Internal Report*, (1986)

[2] M.D. Woodley et al. "Control Of Machine Functions Or Transport Systems," SLAC PUB-3086, (1983)

[3] M.J. Lee et al. "On-line Control Models For the Stanford Linear Collider," SLAC-PUB-3072, (1983)

[4] K. L. Brown et al. "TRANSPORT, A Computer Program for Designing Charged Particle Beam Transport System," SLAC-91, Rev. 2, (May 1977)

[5] A.S. King et al. "MAGIC, A computer Code for Design Studies of Insertions and Storage Rings," SLAC-183, RL-75-110

ABOUT EXTRACTION OF 70-GEV PROTONS
BY A BENT CRYSTAL
FROM THE IHEP ACCELERATOR TO THE PROZA SETUP

A.A.Asseev, A.N.Vasil'ev, E.A.Ludmirsky, V.A.Maisheev,
S.B.Nurushev, Yu.S.Fedotov
Institute for High Energy Physics
142284, Protvino, Moscow region, Russia

1 INTRODUCTION

In 1987, during investigation the polarization effects on the experimental setup PROZA, an indication on a possible discovery of an unknown phenomenon, the scaling asymmetry [1], was obtained. The interval of the investigated energies was not large: from 13 GeV at BNL [2] to 40 GeV at IHEP. It was very desirable to extend this region to the maximum of the IHEP accelerator energy – 70 GeV by extracting the accelerated proton beam onto the target of the experimental setup.

The extraction methods used before [3] could not ensure the required beam parameters. It was decided to investigate a possibility of the A-70 primary beam extraction by a bent crystal. For the first time an attempt to realize such extraction was made in Dubna (1984) with the 4.2, 6.0 and 7.5 GeV beam [4].

The first results of the 70 GeV proton extraction from the IHEP accelerator made in 1989 with the crystal of Si, istalled into the vacuum chamber of magnetic block 25 and bent by 80 mrad, were reported in [5]. Since 1990 the physical use of the new method of extraction was started and a few runs of polarization experiments on the PROZA setup were done.

The results of investigation both the regime of proton extraction to the PROZA setup and work of it simultaneously with extraction of the secondary particles from internal targets (IT) to other beam lines are reported in the article.

2 PECULIARITIES OF USING THE CRYSTAL

One of the peculiarities of using a crystal for the beam extraction to experimental setup is the position of it, $\sim 55 - 60$ mm from the central orbit (in the region of the beam envelope), that is more distant than the IT working coordinates (± 40 mm). To steer an A-70 primary beam onto the crystal a local distortion (bump) of the closed orbit was required. The bump is formed with an additional field ΔH generation into the magnetic gaps of four blocks 20, 22, 26, 28 [5,6]. Such an orbit bump gives a required beam deflection on the crystal asimuth and makes no aperture limitations through the accelerator.

Another peculiarity of the new method of ejection was the requirement to arrange a possibility of simultaneous work with the PROZA setup experimental setups of other beam lines (e.g. 4 and 18) with the secondary beams: on A-70, as a rule, 4-5 experimental setups use simultaneously beams from IT.

It should be noted, that for a beam steering onto the crystal one can also use a bump which is formed with blocks 20, 21, 26, 27. Such a bump in some regimes (e.g. at the simultaneous work with nonresonant slow extraction [7,8]) is more preferable.

We give here some parameters of the IHEP accelerated beam which allow one to estimate possible efficiency of extraction under direct steering of the beam onto the crystal 0.5 mm thick. For the intensity $\leq 10^{13}$ ppc[1] the beam emittance equals 1 mm·mrad and its angular divergence is about ± 0.2 mrad. For higher intensity of the beam its emittance reaches 2 mm·mrad and angular divergence of about ± 0.3 mrad. The critical channeling angle of the crystal is $\psi_c \sim \pm 25$ μrad.

3 EXPERIMENTAL RESULTS

The most important dependencies characterizing the efficiency of proton extraction by the bent crystal of block 25 of A-70 are shown in fig.1. Curves 1 and 2 show the number of particles extracted into the beam line versus the intensity of the beam interacting with the crystal for two cases mentioned above: when the bumps for steering the beam onto the crystal are formed with blocks 22, 28 or blocks 21, 27 respectively in addition to blocks 20, 26.

Curves 3 and 4 of fig.1 show respectively the extraction efficiency for the cases 1 and 2. It is seen that in the best case the extraction efficiency reaches $\sim 1.5 \cdot 10^{-4}$ that is in agreement with results reported in [9].

Possible explanation for different extraction efficiencies (see fig.1):

– decrease of the efficiency (both curves 3 and 4) can be explained with increase the beam divergence when the crystal goes deeper ito the beam,

– increase of the extraction efficiency (curve 4) is due to variations of the input angles of particles captured into channeling mode under steering a beam onto the crystal. Since the bump used in this case is not equivalent to the case of curve 3, the extracted intensity increases. But it takes place only when the crystal goes from the halo into the densed part of a beam and only till an angular beam divergence becomes much more than the critical channeling angle ψ_c.

---

[1] ppc – protons per cycle.
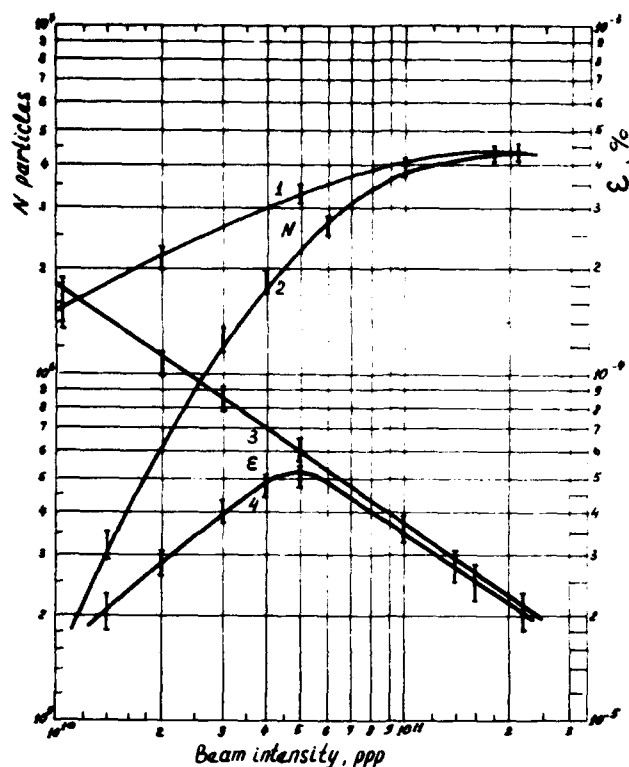
Figure 1: Number of particles into the beam line and extracting efficiency versus intensity of a beam interacting with the crystal for two regimes: 1,3 - c.o. bump is formed with blocks 22,28; 2,4 - with blocks 21,27 in addition to blocks 20,26.

Figure 2: The oscillograms of simultaneous extraction from the accelerator different particles for different experiments. a) and d) – extraction of 70-GeV protons by the bent crystal and nonresonant slow extraction, respectively; b) and c) – extraction of 40-GeV secondary beams from the IT. Time scale – 200 ms/div.

Fig.2 gives an impression about duration and quality of the beams when accelerated protons and secondaries are extracted simultaneously from the accelerator to different beam lines for the different experiments. The traces a) and d) of the oscillograms – a time structure of the 70-GeV proton beam extracted to the PROZA (beam line 14) by the bent crystal and to FODS-2 (beam line 22) in the nonresonant slow extraction mode [7,8]. The traces b) and c) – a time structure of the 40 GeV secondary particle beams extracted to the setups GAMS, MIS JINR (beam line 4) and GIPERON (beam line 18) from IT installed respectively into magnetic blocks 27 and 35 of A-70. Fig.2 confirms an investigated earlier possibility of proton extraction to the PROZA facility by the bent crystal of block 25 simultaneously with extraction of particles for different experiments by other methods of extraction in the same accelerator cycle. A high quality of the extracted beam time structure is reached due to use of the thin IT [10] preliminary scattering beam before steering it on the crystal.

A proton beam was formed with the existing focusing elements of beam line 14 forming negative hadron beams (mainly the π^--mesons) with the momentum $\leq$ 40 GeV/c.

Possibility to compare, in the target region of the experimental setup PROZA, spatial and angular distributions of the 70-GeV proton beam extracted by the bent crystal and π^--mesons of the 40 GeV energy from the IT of block 24 is presented on figs.3 and 4. Fig.3 gives a spatial distribution, fig.4 – an angular one in horizontal and vertical planes (a and b, respectively).
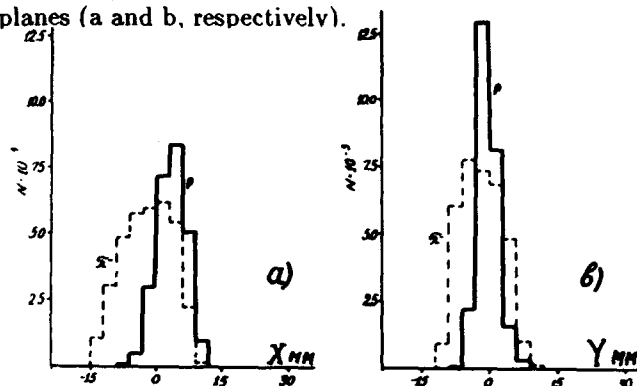
Figure 3: The spatial distributions of the 70-GeV protons and 40-GeV π^--mesons at 3.1 m before the target of the experimental setup.
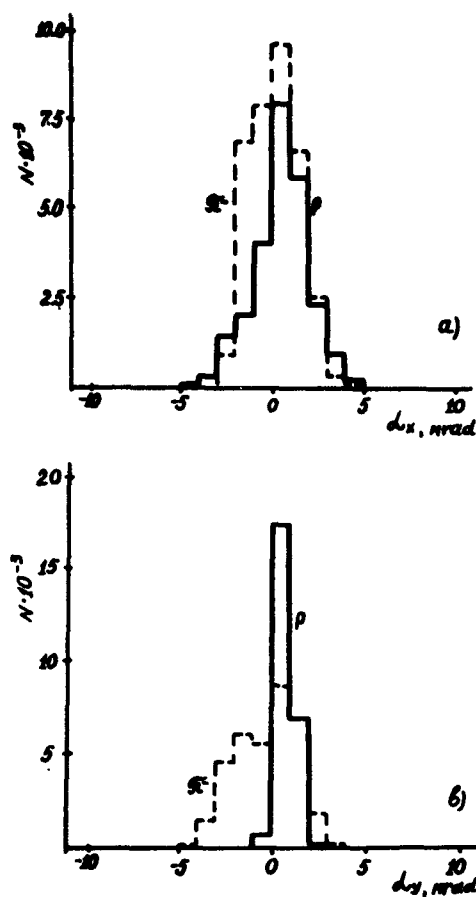
Figure 4: The angular distribution of the proton and π^--meson beams on target of the experimental setup.

It is seen that the transverse distribution of the proton beam is about 2 times narrower than that of the pion beam, the proton beam has as well less angular divergence. Fig.5 shows the phase ellipses of the 70-GeV proton beam and the 40-GeV π^--mesons in two planes (a and b, respectively) at about 3.1 m before a target of the experimental setup. A percentage of the beam contained into ellipses and the appropriate area in $mm \cdot mrad$ are shown there also. One can see that in this case there is a substantial improvement of the proton beam parameters comparing to the π^--meson beam parameters. So, the phase space area of the proton beam is 2 times smaller in XX'-plane and about 4 times – in YY'-plane. Such parameters of the formed beam satisfy well the requirements of the polarization research on the experimental setup PROZA.

4   CONCLUSION

Experience during a long time (a few runs in 1990-1992 more than a month each) of the new method of the maximum energy protons extraction by a bent crystal for the physical experiments gained for the first time at the IHEP allows us to make conclusion about its reliability, high stability of the beam parameters, compatibility of it with other methods and modes of particle extraction. Simplicity of using bent crystals, possibility of mounting them in any re-gion of the accelerator vacuum chamber as well as possibility of using the existing beam lines suggest an expedience of their wide use for beam extraction both on the IHEP accelerator and on other machines of higher energies.
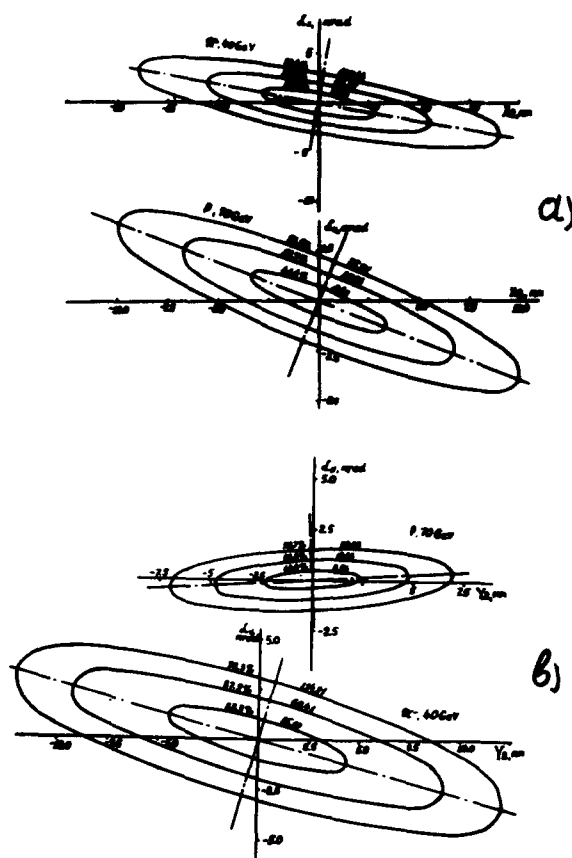
Figure 5: Phase ellipses of the proton and π^--meson beams at 3.1 m before a target of the experimental setup: a) – in horizontal plane, b) – in vertical plane.

5   REFERENCES

[1] V.D.Apokin et al. Phys. Lett. B243 (1990) 461.

[2] S.Saroff et al. Phys. Rev. Lett., v. 64, 1990, p. 995.

[3] J.C.Raoul et al. Nucl. Instr. and Meth., v.125, 1975, p. 6585.

[4] V.V.Avdeichikov et al. JINR Communications N1-84, Dubna, 1984.

[5] A.A.Asseev et al. IHEP 89-57, Serpukhov, 1989.

[6] A.A.Asseev et al. Nucl. Instr. and Meth. A309 (1991) 1-4.

[7] A.A.Asseev et al. J. of Tech. Phys. 60 (1990) 70, Leningrad.

[8] A.A.Asseev et al. Proceedings of the 2-nd European particle accelerator conference, v. 2, p.1604, Nice, 1990.

[9] R.A.Carrigan, Jr., Nucl. Instr. and Meth, B33 (1988) 42.

[10] Yu.M.Ado et al. IHEP 88-9, Serpukhov, 1988.

INCREASE A BENT CRYSTAL EXTRACTION EFFICIENCY BY MEANS OF THIN INTERNAL TARGET

A.A.Asseev, E.A.Myae, S.V.Sokolov, Yu.S.Fedotov
Institute for High Energy Physics
142284 Protvino, Moscow region, Russia

Abstract

Results of the new regime tuning are reported. The efficiency estimates for different particle distributions on a bent crystal input for a concrete scheme of the IHEP accelerator proton beam extraction were made.

1 INTRODUCTION

The extraction efficiency for the protons extracted during direct steering of a proton beam on the bent crystal, istalled in the vacuum chamber of A-70, reaches $\sim 1.5 \cdot 10^{-4}$ [1]. It goes down noticeably if the intensity of the particles interacting with the crystal increases. Maximum number of particles that reach the experimental setup is $\sim 4.5 \cdot 10^6$ ppc and practically does not increase at steering $> 10^{11}$ ppc onto the crystal. But the extraction efficiency may be increased significantly by elastic scattering of the accelerated protons on the thin internal target (IT) [2] installed upstream of the crystal. The number of particles in the beam line is doubled and reaches 10^7 ppc.

2 EXPERIMENTAL RESULTS

The number of particles extracted from the accelerator by a bent crystal to one of the experimental setups (PROZA [3]) versus the coordinate of the thin IT preliminarily scattering the primary beam is shown in fig.1. The scheme of extraction as well as mutual disposition of the extracting elements (targets, crystals, etc.) are given somewhere else [1,4,5]. Curves 1,2,3 of fig.1 show how the extracted protons intensity depends on the closed orbit position on the target asimuth (coordinates 52, 54 and 56 mm, respectively). Curve 4 is the dependence of intensity of the accelerated beam interacting with the target versus its coordinate (i.e. on the beam-target depth intersection) under constant feedback loop gain of the steering system.

The dashed horizontal line shows the maximum number of particles extracted to the PROZA setup during direct steering the beam on the crystal, i.e. without preliminary scattering.

It follows from the presented data that the number of particles extracted to the beam line by a bent crystal increases two times if the beam is scattered by a thin IT.

The presence of the second maxima of the extracted intensity when moving the IT to the outside can possibly be explained by changing the beam particles density on the input of the crystal. There is also difference between
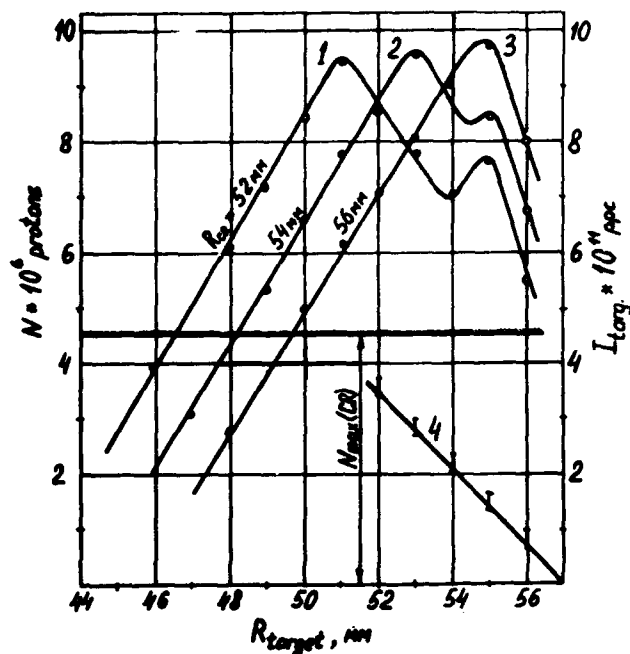
Figure 1: Number of particles extracted from the accelerator by bent crystal after scattering in a thin internal target. Curves 1, 2 and 3 correspond to different crystal coordinates from the central orbit. $N_{max}(CR)$ – the maximum number of particles extracted by the crystal without target. $4 - I_{targ.} = f(R_{targs.})$.

the target and crystal coordinates of 2 mm, when the conditions of the maximum intensity extraction are realized.

The reported extraction mode was realized in the IHEP accelerator for the first time in January 1991 and after that it is continuously used [6].

Let us evaluate an extraction efficiency by using the experimental beam characteristics [7,8] and the concrete extraction conditions shown in fig.2.

Two cases are considered:

– direct steering of the beam onto the crystal (phase ellipses of r-plane are marked as 1' and 1), and

– preliminary steering of the beam onto the target (phase ellipses are 2 and 2') with the following hitting the

318

crystal by the particles with large amplitudes.

The phase ellipses are shown for accelerator blocks 24 and 25 where the target and crystal are installed. The functions $\Phi(r)$ of the beam particle distribution normalized to 10^{12} protons are given also. The coordinates of the crystal and thin target can be seen on fig.2.
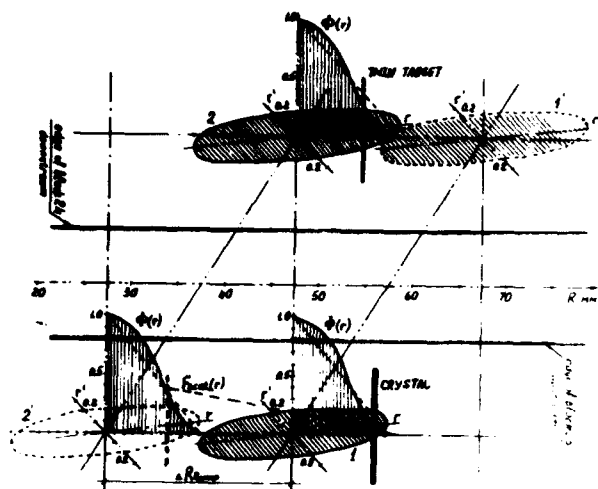
Figure 2: Geometry of the experiment on scattering particles by the thin target before extraction through the crystal of magnet block 25, and some of the beam characteristics. All the explanations are in the text.

To estimate the extraction efficiency, the $\sim 1.5 \cdot 10^{11}$ ppc intensity of the particles interacting with the thin target was taken. In order to simplify the estimates the curve $\Phi(r)$ has been changed by a linear function (shown with the broken lines). The shadows of the beam and scattering target on the crystal asimuth in block 25 for the second case are shown as ellipse 2' and broken and dashed vertical lines. The line $F_{scat}(r)$ is an approximation of the radial distribution dependence for the particles underwent the multiple coulomb and nuclear elastic scatterings after interaction with the target. The data on the scattering amplitudes are taken from [2,9]. At the major semiaxis of an ellipse ~ 10 mm in case of a direct beam steering onto the crystal a linear particle density on it is $5 \cdot 10^{10}$ protons/mm, and the maximum value of the extraction efficiency is $\sim 1.5 \cdot 10^{-4}$ [1].

In the case of preliminary scattering of $\sim 1.5 \cdot 10^{11}$ protons by the thin target we will get accordingly $3 \cdot 10^{9}$ protons/mm which implies a decrease of particles density on the crystal ~ 17 times. Taking into account that the extracted intensity increases twice we will get the extraction efficiency value $\sim 0.5\%$.

The confirmation of the estimates one can get from the direct comparison of the extraction efficiencies for both cases mentioned above.

a) extraction by the crystal without target.

The extraction efficiency is $\sim 1.5 \cdot 10^{-4}$ which corresponds to steering $\sim 1.5 \cdot 10^{10}$ onto the crystal or the beam linear density $\sim 3 \cdot 10^{10}$ protons/mm by the crystal thick-

ness ~ 0.5 mm. On the whole, taking into account that particle density is lowered to the edge of a distribution function, the data of the above mentioned estimations are in a satisfactory agreement obtained with experiment.

b) extraction during scattering the beam by thin target.

With the number of protons hitting the crystal $\sim 1.5 \cdot 10^{9}$, the extraction efficiency equals $\sim 0.7\%$ that is also close to the value a obtained above. The real extraction efficiency is expected to be noticeably higher with optimising the construction of the accelerator vacuum chamber and a head part of the beam line.

It seems to be the right time to already speak about using the considered slow extraction mode up to intensities $\sim 10^{8}$ protons/sec.

3   REFERENCES

[1] A.A.Asseev et al. IHEP 91-25, Protvino, 1991.

[2] Yu.M.Ado et al. IHEP 88-9, Serpukhov, 1988.

[3] V.D.Apokin et al. Nucl. Phys. B255 (1985) 253.

[4] A.A.Asseev et al. Nucl. Instr. and Meth. A309 (1991) 1-4.

[5] A.A.Asseev et al. Proceedings of the IEEE particle accelerator conference, San Francisco, 1991, v. 1, p. 189.

[6] A.A.Asseev et al. IHEP 91-46, Protvino, 1991.

[7] V.I.Gridasov et al. IHEP 70-58, Serpukhov, 1970.

[8] A.A.Asseev et al. IHEP 91-154, Protvino, 1991.

[9] V.I.Gridasov et al. IHEP 73-78, Serpukhov, 1973.

INFLUENCE OF THIN INTERNAL TARGET
ON THE BENT CRYSTAL EXTRACTION EFFICIENCY

A.A.Asseev, S.V.Sokolov

142284, Protvino, Moscow region, Russia

Abstract

An attempt to explain the effect of extraction efficiency increase due to thin internal target during extraction of proton beam by a bent crystal was made, and results of computer simulation of the thin target influence on the beam parameters in our experiment are given.

1 INTRODUCTION

Using the thin internal target (TIT) of a carbonic cloth ~ 50 mg/cm^2 thick [1] allowed one to significantly increase the extraction efficiency of a Si bent crystal installed into the IHEP accelerator vacuum chamber [2,3,4]. Due to scattering some part of the primary beam on the internal target, the intensity of protons transported to the experimental setup was increased 2 times. Preliminary estimates of the extraction efficiency, which were made with account of conditions of the experiment, showed that the extraction efficiency could reach $\sim 0.5 - 0.7\%$ [5]. In the work on computer simulation of multi-turn accelerated proton dynamics during interaction of the beam with TIT installed before the crystal is reported. It is shown that in case of positive working coordinates of TIT one can get higher bent crystal extraction efficiency as compared to the case of direct steering of the accelerated beam onto the crystal.

2 RESULTS OF COMPUTER SIMULATION

The following main processes are taken into account in the program simulating accelerated proton beam interaction with TIT:

- decrease of a proton beam intensity due to nuclear interaction of particles with the target,
- increase of betatron amplitudes due to multiple Coulomb scattering of particles into the target material
- decrease of the particle momentum due to ionization beam losses, and the closed orbit shift toward the accelerator center.

Two cases of placing the target relatively to the central orbit were considered: on positive and on negative coordinates, as dynamics of beam-target interaction in both cases is different [6]. Simulation of the above mentioned processes was made by Monte-Carlo method, taking into account concrete conditions existing in the IHEP accelerator.

---

[1] ppc – protons per cycle.

Initial distribution of the beam particles over the amplitudes of betatron oscillations was given by Reley law, and $\Delta p/p_o$ distribution was governed by the normal law. The time of beam-target interaction during which one should keep constant spill, was taken equal to 1s.

The calculation results are presented in figs.1 and 2. Fig.1 shows transformation of the beam particles distribution function for different variants of TIT placing. Here the dependencies of $F(x)$-particle distribution function versus their maximum coordinates are given. As a maximum coordinate of particle relatively to the equilibrium orbit was taken the value:

$$x = A_r + \psi \cdot \frac{\Delta p}{p_o}, \qquad (1)$$

where A_r - a horizontal betatron amplitude, ψ is a dispersion function, $\Delta p/p_o$ - momentum deviation. Curve 1 of this figure corresponds to the initial beam of the accelerator, curve 2 - to the case of TIT on negative coordinates, curve 3 - to the positive coordinates of TIT. One can see a substantial difference of the distribution functions that is determined by influence of the TIT.
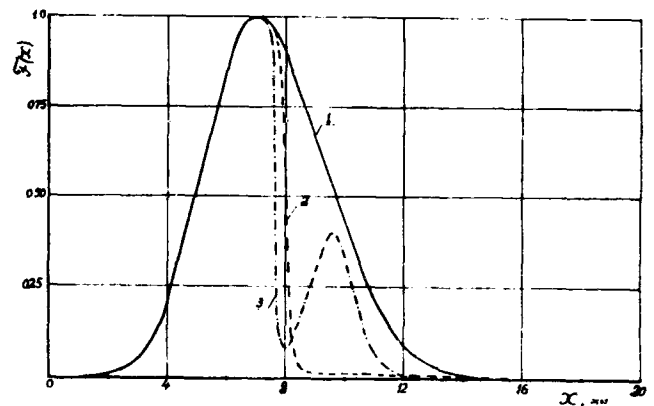
Figure 1: Particle distribution function on maximum coordinate under steering beam onto the thin target. Curve 1 - initial beam into accelerator, 2 - target on negative coordinates, 3 - thin target on positive coordinates.

One should point out that initial distribution function (curve 1 of fig.1) is normalized to the intensity 10^{12} ppc[1], and on large coordinates ($x > 16$ mm) there are so many particles (by our estimates $\geq 10^9$ protons [5,7]) that after

channeling and extraction one still has enough of them, even taking into account the attained efficiency, to guarantee interesting physical experiments.

Further, on receiving the shown dependencies, the width of the angular distribution for the particles having coordinates more than the given one was calculated. Su··h distributions are shown in fig.2. Curve 1 corresponds to the initial beam, curves 2 and 3 - to the cases of TIT placing on negative and positive coordinates, respectively. It should be noted that curves 2 and 3 on both figs.1 and 2 refer to the time instant of 300 ms from the beginning of steering the beam onto the target, i.e. when equilization of the particles asimuthal density into the accelerator due to TIT is occured [6].
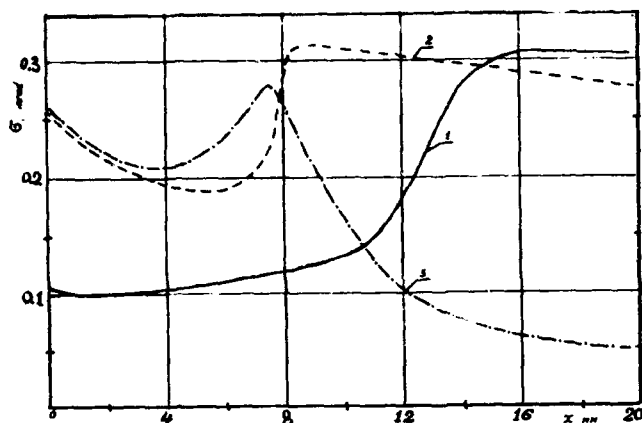
Figure 2: Dependence of the particles anglo̅rdistribution width on coordinate at steering of the beam onto the thin target. Curves 1,2,3 – as on fig.1.

One can see from fig.2 that the most favourable for particle capturing into channeling is the case of TIT placing on positive coordinates, as the angular divergence of the

beam particles having large amplitudes significantly decreases, approaching the critical crystal channeling angle value at 70 GeV $\psi_c \sim \pm 25$ μrad.

So, two functions exert influence on the bent crystal extraction efficiency:
- distribution of proton beam intensity over coordinates, and
- character of the angular distribution of this particles over different coordinates.

Analysis of figs.1 and 2, and comparison of the given dependencies with experimental results [5] confirm the TIT influence on increase the bent crystal extraction efficiency. Using this method of beam blowing up at the IHEP accelerator allowed one to get the efficiency during extraction of particles by a bent crystal $\sim 1\%$ as well as to transport $\geq 10^7$ of protons to experimental setup.

The merit of the given method of beam diffusing is that the core of the beam is not touched, a target slowly goes into beam, interacting with it during the time defined by the steering rate.

3   REFERENCES

[1] Yu.M.Ado et al., Proc. of the X1-th Particle Accelerator Conference, Dubna, 1989, v II, p. 315.

[2] A.A.Asseev et al., IHEP 89-57, Serpukhov, 1989.

[3] A.A.Asseev et al., Nucl. Instr. and Meth. A309(1991)1.

[4] A.A.Asseev et al., Proc. of the IEEE Particle Accelerator Conference, San Francisco, 1991, v. 1, p. 189.

[5] A.A.Asseev et al., IHEP 91-182, Protvino, 1991. To be published in Nucl. Instr. and Meth., Sect. A.

[6] A.A.Asseev, S.V.Sokolov, Proc. of the 2-nd European Particle Accelerator Conference, Nice, 1990, v. 2, p. 1725.

[7] A.A.Asseev et al., IHEP 79-91, Serpukhov, 1979

EXTRACTION OF 50 GeV PROTONS
FROM IHEP ACCELERATOR BY BENT CRYSTAL

A.A.Asseev, V.A.Maisheev, E.A.Myae
142284, Protvino, Moscow region, Russia

Abstract

The increase of the bent crystal extraction efficiency due to thin internal target at extraction of 70-GeV protons has been confirmed at 50 GeV. The experimental results as well as the efficiency estimates are given.

1 INTRODUCTION

During one of the runs in 1992 the IHEP accelerator (A-70) was working part of the time with the accelerated beam of reduced energy – 50 GeV. In such regime extraction of 50 GeV protons by a bent crystal of Si, installed earlier in block 25 of A-70 [1], was realized. The beam was extracted to one of the experimental setups (SIGMA [2]) for methodical experiments. In the article main results of setting up the regime of proton extraction from A-70 at 50 GeV energy level are reported.

2 EXPERIMENTAL RESULTS

Protons were extracted to beam line 2 by the same bent by 80 mrad crystal which is used for 70 GeV proton extraction to beam line 14 for the experimental setup PROZA [3]. The beam lines scheme is shown in fig.1. Beam lines 2 and 14 have a common head part, but strength of the magnet M1 used to deflect the beam to setup SIGMA direction is not enough to deflect 70-GeV protons to beam line 2. Strength of M1 allows one to use a 50-GeV beam. The scheme of beam steering onto the crystal where blocks 20, 26 and 21, 27 of A-70 are used for forming the orbit bump is similar to the described earlier one [1,4].
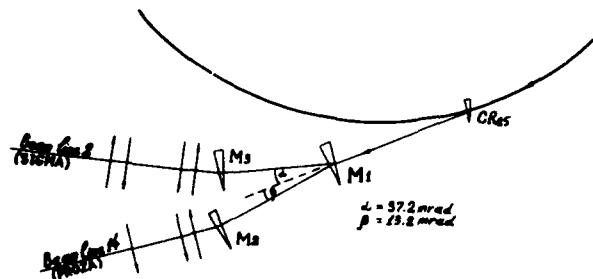
Figure 1: Scheme of beam extraction to the experimental setups SIGMA (50 GeV) and PROZA (70 GeV).

2.1 Direct steering of the beam onto the crystal

In such a mode the intensity of $4.6 \cdot 10^6$ protons was fixed on the setup SIGMA, when $\sim 10^{11}$ particles were steered onto the crystal, i.e. extraction efficiency was $\sim 4.6 \cdot 10^{-5}$. It corresponds to the efficiency value obtained before [1] and confirmes keeping the geometrical conditions of beam extraction from A-70 at 50 GeV. As before [5], the extraction efficiency goes down noticeably if the intensity of the primary beam interacting with crystal increases. It is supposed, that it depends on the beam steering dynamics together with the thermal, radiation and other effects at high intensity of a primary beam.

2.2 Using the thin internal target

Preliminary beam scattering by a thin target to throw the protons onto the crystal gives the extraction efficiency increase at 50 GeV energy level. But, on comparing to the case of intensity doubling under extraction of 70-GeV protons to beam line 14 [6], we fixed an increase of the intensity into beam line 2 only by 30%.

The dependence of particles number extracted from the accelerator by a bent crystal versus the thin target radial coordinate is given in fig.2 (curve 2). A thin target [7] – a carbonic cloth of thinckness ~ 50 mg/cm^2 is used in the IHEP accelerator for the secondary particle generation and allows one to improve significantly the extracted beams quality. Curve 1 in fig.2 (see, e.g. [6]) shows analogous dependence at a primary beam energy of 70 GeV. Both of the curves were obtained under equal geometric conditions. $N_{max}(CR)$, which is approximately the same in both cases, means the maximum number of particles extracted from the accelerator under direct steering of the beam onto the crystal.

Analysis of fig.2 data shows that numerical values of main beam characteristics of the 50- and 70-GeV protons (maxima of intensity, its "initial" levels $(N_{in})_E$ and gradients of increase) are approximately proportional to the primary beam energy. One can get estimates of efficiency of extraction by a bent crystal at 50 GeV energy, using the approach taken in [6]. In the particular case, $\sim 3 \cdot 10^{11}$ ppc[1] interacted with a thin target which corresponds to the intensity $\sim 3 \cdot 10^9$ protons hitting the crystal of thickness ~ 0.5 mm during extraction. It follows from fig.2 that maximum intensity extracted into the beam line at 50 GeV

---

[1]ppc – protons per cycle.

is $\sim 6 \cdot 10^6$ protons. It corresponds to the extraction efficiency 0.2%.
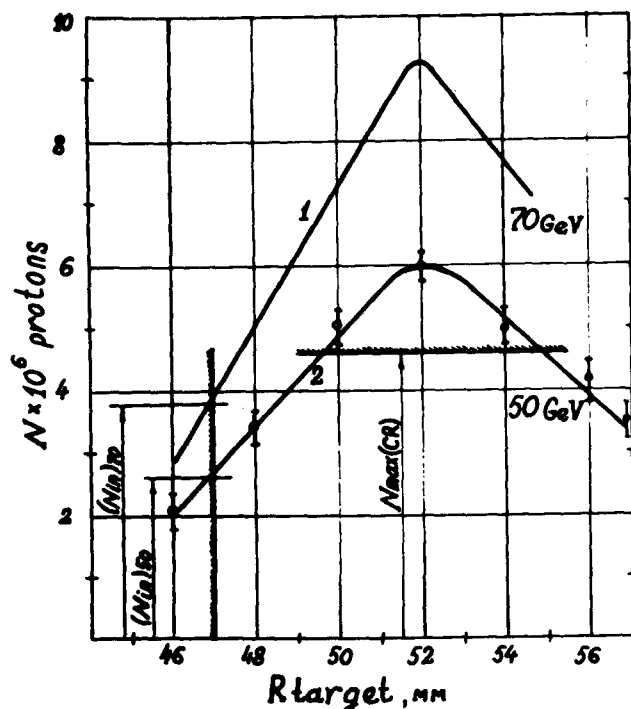
Figure 2: Dependence of particles number extracted from the accelerator by bent crystal under preliminary beam scattering by a thin internal target versus its coordinate. Curve 1 – the energy 70 GeV, 2 - 50 GeV.

3 CONCLUSION

The data given above confirm the received earlier (see [6]) result of increasing the efficiency of beam extraction by a bent crystal under preliminary scattering of the beam by a thin internal target. The extraction efficiency obtained by this method can significantly exceed the extraction efficiency in the case of direct steering of the beam onto the crystal.

The estimates show that, for example, at the Tevatron energy (800 GeV), taking into account the factor of extracting efficiency change with energy, one can extract $\sim 10^8$ protons by bent crystal which satisfies the new experiment requirements (see, e.g. [8]).

4 REFERENCES

[1] A.A.Asseev et al., Nucl. Instr. and Meth. A309 (1991) 1.

[2] Yu.B.Bushnin et al., Phys. Lett. 29B (1969) 48.

[3] V.D.Apokin et al., Nucl. Phys. B255 (1985) 253.

[4] A.A.Asseev et al., IHEP 91-25, Protvino, 1991.

[5] A.A.Asseev et al., Proc. of the IEEE Particle Accelerator Conference, San Francisco, 1991, v. I, p. 189.

[6] A.A.Asseev et al., IHEP 91-182, Protvino, 1991. To be published in Nucl. Instr. and Meth., Sect. A.

[7] A.A.Asseev, S.V.Sokolov, Proc. of the 2-nd European Particle Accelerator Conference, Nice, 1990, v. 2, p. 1725.

[8] R.A.Carrigan, Jr. et al., FNAL proposal P-583 (1991).

ON USING THE THIN TARGET AT EXTRACTION OF PROTONS FROM THE ACCELERATORS BY BENT CRYSTAL

A.A.Asseev

Institute for High Energy Physics

142284 Protvino, Moscow region, Russia

Abstract

The influence of the thin target on the bent crystal extraction efficiency at 70 GeV is discovered in the IHEP accelerator. This effect was confirmed also at 50 GeV. It is supposed that the effect can be used under a beam extraction from the higher energy accelerators.

1 INTRODUCTION

The effect of increasing the bent crystal extraction efficiency [1,2] may be used for extraction of a beam from the high energy accelerators (e.g. Tevatron and SPS) for the new planned experiments [3,4].

The estimates of results expected, due to use of thin targets, in other accelerators under extraction of protons by a bent crystal, and based on the experimetal data obtained in the 70-GeV IHEP accelerator are given in this article.

Figure 1: Number of particles extracted from the accelerator by bent crystal under preliminary beam scattering by a thin internal target versus its coordinate. Curve 1 – the energy 70 GeV, 2 – 50 GeV. $N_{max}(CR)$ is a maximum number of particles extracted by bent crystal without a thin target.

2 EXPERIMENTAL RESULTS

As it was reported in [1], there is a doubling of the extracted beam intensity under extraction by the bent crystal of the 70-GeV protons having been preliminary scattered by a thin target.

Preliminary scattering of a beam by the thin target with the following hitting the crystal by scattered particles also gives at the energy 50 GeV an increase of extraction efficiency. However, on comparing the case of intensity doubling at extraction of the 70-GeV protons into the beam line 14, the increase of intensity in the beam line 2 only by 30% was fixed [2]. Both of the experiments were carried out under the same geometric conditions.

Fig.1 shows the number of particles extracted from the accelerator by bent crystal versus the thin target coordinate for two levels of the primary bean energy: 70 GeV (curve 1) and 50 GeV (curve 2).

Analysis of the data [1,2] shows that the quantitative value of the main characteristics of the proton beam extracted at 50 and 70 GeV energy, i.e. maxima of intensity, it's "initial" levels $(N_{in})_E$ and gradients of increase $(\frac{dI}{dR})_E$, are approximately proportional to the coefficient $\gamma_E = \frac{70}{50}$ that expresses the primary beam energies relation.

3 EVALUATION OF USING THE METHOD ON OTHER ACCELERATORS

3.1 FNAL

Let us suppose, that the relations shown above will be valid also under analogous experiments at higher energies. Then, e.g. for the Tevatron, we would have ($\gamma_E = 800/70 \approx 11.4$):

– initial level of intensity

$(N_{in})_{800} = \gamma_E \cdot (N_{in})_{70} \approx 4.7 \cdot 10^7$ particles,

– gradient of intensity increase

$(\frac{dI}{dR})_{800} = 11.4 \cdot (\frac{dI}{dR})_{70} \approx 1.1 \cdot 10^7$ particles/mm.

Therefore, the maximum number of particles extracted by bent crystal may be

$(N_{max})_{800} = (N_{in})_{800} + (\frac{dI}{dR})_{800} \cdot \Delta R = 9.8 \cdot 10^7$ particles, where $\Delta R = 5$ mm (see fig.1).

This value of intensity nearly corresponds to the required one for the SFT experiment in SSC and is enough for a scaling experiment on proton extraction by bent crystal which is being prepared in Tevatron [3] and SPS [4].

3.2 JINR

Let us give analogous estimates for the well known experiment at Dubna [5], where protons with energies 4.2, 6.0 and 7.5 GeV were extracted for the first time. Results of estimates for the energies 4.2 and 6.0 GeV are given in Table. Data for the 7.5 GeV energy are not analyzed because the beam line, calculated for the 6 GeV beam, was not able to transport to the experimental hall 7.5 GeV particles.

Table 1: Estimates of possible intensity under using the thin target.

	E, GeV	Intensity under direct extraction by crystal [5]	γ_E	Possible intensity $N_{max} = \gamma_E \cdot (N_{max})_{IHEP}$
JINR	4.2	$(2-5) \cdot 10^5$	0.06	$\sim 6 \cdot 10^5$
	6.0	$\sim 5 \cdot 10^5$	0.085	$\sim 8.5 \cdot 10^5$
IHEP [1]	70.0	$\sim 4.5 \cdot 10^6$	1	10^7

It is seen that, in case of a thin target use, extracted intensity could be higher, but an influence of scattering effect is expressed weakly. Apparently, this is explained by both large dimensions of a beam at low energy and weak focusing and a small angular divergence of particles of large amplitudes. Additional scattering renders only weak influence on amplitudes and angular divergence of such a beam. At high energies and strong focusing, effects of particle scattering before steering them onto the crystal are expressed more distinctly.

The results of the above made estimates for graphic reason are presented in Figs.2 and 3. Curve 2 of Fig.2 shows the experimental dependence of intensity of the 70-GeV proton beam extracted into a beam line by the bent crystal under the particles scattering with a thin target, while curves 1 and 3 present the prognosis of possible dependencies for the JINR (Dubna) and FNAL accelerators. In Fig.2 $N_{max}(CR)_{6,70}$ are the levels of maximum intensity extracted from the accelerators JINR and IHEP under the direct steering a beam onto the crystal with the energy 6 and 70 GeV (experiment), respectively.
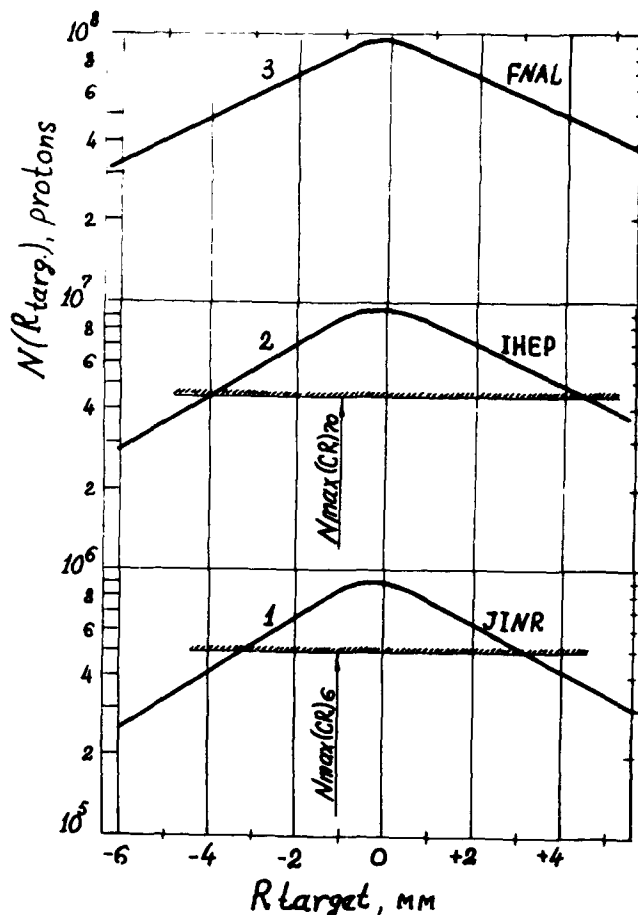
Figure 2: Intensity of the proton beam extracted by bent crystal with use of thin target versus its coordinate. 2 – IHEP experiment [1], 1,3 – the estimates for the JINR accelerator (Dubna) and Tevatron (FNAL), respectively.

Fig.3 illustrates dependence of maximum intensity extracted by a bent crystal versus accelerated beam energy both for the case of direct steering a beam onto the crystal (curve 1) and after scattering it with the thin target (curve 2). The experimental values are marked with a cross.

[1] The experimental data.

Figure 3: Maximum intensity of the beam extracted by bent crystal versus an energy. 1 – under direct steering a beam onto the crystal, 2 – after scattering with a thin target. The experimental values are marked with a cross.

4 CONCLUSION

The data given in [1,2] confirm that the preliminary scattering of particles with a thin target stimulates an increase of the bent crystal extraction efficiency. Extraction efficiency could be obtained with this method may significantly surpass the efficiency attainable under direct steering the beam onto the crystal. Estimates of the extracted beam intensity, that one can suppose in the scaling experiments on the higher energy accelerators, may be checked experimentally.

5 REFERENCES

[1] A.A.Asseev et al., IHEP 91-182, Protvino, 1991. To be published in Nucl. Instr. and Meth., Section A.

[2] A.A.Asseev et al., IHEP 92-137, Protvino, 1992.

[3] R.A.Carrigan, Jr. et al. FNAL proposal P-853 (1991).

[4] B.N.Jensen et al. CERN proposal CERN/DRDC 91-25 (1991).

[5] V.V.Avdeichikov et al., JINR Communication 1-84, Dubna, 1984. English translation Fermilab FN-429 (1986).

A Digital Computer Program for the Simulation of Positive or Negative Particle Beams on a PC.

Jack E. Boers

Thunderbird Simulations

626 Bradfield Drive, Garland, TX 75042-6005 USA

Abstract

PBGUNS, an expanded and improved version of the SNOW2D code for extracted ion beams will be described and demonstrated. The new code includes the electrode description and electron beam capabilities of the SPEED code. The new version includes positive and negative ion beam extraction systems and may include skew[1] (azimuthal energy particles) permitting the simulation of thermal effects in high energy plasmas, thermal effects in low energy electron beams, and the computation of x-x' emittance plots from axisymmetric simulations. Plasma electrons (and positive ions for negative ion beams) are simulated with background Boltzmann distributions. Electrodes are described with quadratic equations while potentials are solved by basic relaxation techniques on a rectangular array of squares. Smooth electrodes are created by extending fields into electrodes. A fine mesh covers the cathode and/or plasma-extraction region to furnish the additional accuracy required for the calculations near the particle emission surface. Axisymmetric and rectangular magnetic fields can be included in the trajectory calculations. It is written in FORTRAN 77, employing Calcomp-Versatec type plotting routines and is run on 386 or 486 IBM PC's with DOS Extenders. Generic FORTRAN 77 is used to facilitate the transfer of the program to other computers with only minor modifications.

I. INTRODUCTION

PBGUNS was originally developed from the SNOW2D and SPEED codes for the simulation of negative, sputter-source, ion beams and was then expanded to include regular plasma sources as well as thermionic and field emission relativistic and non-relativistic electron beams. The need to simulate the smooth curved emitter required for sputter ion sources required the smooth cathode routines used for electron beam simulations as well as a method of simulating the background plasma of positive ions and electrons. It was determined some time ago that a finer mesh was needed over the plasma region of an ion beam source, and recently the fine mesh was added to the SPEED program adding greater accuracy in the cathode region. The combined program is superior in accuracy and capabilities to either of its predecessors.

The 15,000 line FORTRAN program currently runs on an 80386 or 80486, IBM PC or clone, with at least 16 MBytes of memory, using DOS extenders. NDP-FORTRAN and NDP-PLOT (from Microway) are used for the compiler and the plotting capability. It will run small problems (100x50 arrays) in as little as 10 minutes, but may require several hours for very large problems (450x200) arrays, (about the limit for 16 MBytes of memory). Obviously larger memories would permit larger simulations and faster processors would require less time. All calculations are done in double precision (8 byte) arithmetic.

The potentials are solved on a two dimensional array using Poisson's equation in rectangular or axisymmetric configurations. The beam is simulated by computing representative trajectories (up to 7000) through the device. Space charge is computed from the trajectories and stored on a matrix identical to the voltage array. The cathode or plasma region for extraction problems is simulated on a second (and usually finer) matrix so that greater accuracy and resolution can be obtained, most importantly at the cathode or plasma surface. Thermal effects, which can be very important for either electron or ion extraction, can be simulated including skew (azimuthal) angular distributions.

II. THEORY

The voltages are computed by iteratively solving Poisson's Equation;

$$\nabla^2 V = \frac{-\rho}{\epsilon_0} \qquad (1)$$

where V is the voltage, ρ the space-charge density, and ϵ_0 the permittivity of a vacuum (all in SI units). This is expressed in (second order) difference form for solution. For plasmas the space-charge term takes on the form;

$$\rho = \rho_e + \rho_{ni} + \rho_{pi} \qquad (2)$$

where ρ_e is the electron space charge density and ρ_{ni} and ρ_{pi} represent the negative and positive ion space charge densities.

$$\rho = \rho_i + \rho_{eo} e^{\left(\frac{-eV}{kT_e}\right)} \qquad (3)$$

Where k is the Boltzmann constant, T_e is the electron temperature and ρ_{eo} is the ion space-charge density at the injection plane. Solution of this very non-linear, and somewhat unstable problem, consists of repetitively solving Eq. 1 using the new values computed for the voltage on the left to upgrade the

voltage used in the space-charge density term on the right. For negative ion beams the method of solution is similar but both the electrons and positive ions are represented by Boltzmann distributions.

The Lorentz force equation (4) or the relativistic Lagrange equation (5) can be solved in either cartesian coordinates (for rectangular configurations) or in axisymmetric-cylindrical coordinates for axisymmetric configurations.

$$F = -e(E + v \times B) \tag{4}$$

$$L = eV - e(A \cdot v) - m_0 \left(1 - \frac{v^2}{c^2}\right) \tag{5}$$

Where e is the electronic charge, m_0 the rest mass of the particle, B the applied magnetic field, A the magnetic vector potential, v the velocity of the particle, and c the velocity of light. These equations are expressed in difference form and solved for the successive points as a function of the preceding points and the electric and magnetic fields. All derivatives are expressed to second order in the equations and this seems to furnish sufficient accuracy.

Space charge limited emission is computed using Child's Law as modified by the Langmuir-Blodgett correction

$$J = \frac{4e_0}{9} \sqrt{\frac{2e}{m}} \frac{v^{\frac{3}{2}}}{x^2 \beta^2} \tag{6}$$

where x is two fine matrix square lengths in front of the cathode and β^2 Langmuir-Blodgett correction for curvature of the surface. Field emission current is calculated with the Fowler-Nordheim equation

$$J = 1.54e-6 \frac{E^2}{W} e^{9.32\sqrt{W}} e^{\frac{6.36e9W^{1.57}}{E}} \tag{7}$$

where W is the work function in eV and E the electric field at the emission surface.

At the sputter surface a uniform emission of secondary ions in a cosine angular distribution and a sheath of several hundred Volts is assumed. The angular distribution is transformed through the sheath so that the energy distribution (normal and transverse to the surface) is preserved with the sheath voltage added. The voltage difference between the source of ions and the plasma potential is specified and is used in the transformation, but is not simulated in the voltage relaxation.

III. THE PROGRAM

PBGUNS is capable of simulating virtually any type of electron or ion beam. Ion beams can be extracted from plasma sources for positive or negative ions and sputter sources for negative ions as well as space charge limited ion sources.

The electrode configuration is described by quadratic equations which can consist of as few as 2 equations for a simple field emitter or as many as 60 equations for complex electrodes used in image intensifiers. The equations are defined by their endpoints and/or radius and center of curvature. The program relies on the fineness of the mesh to provide adequate resolution and requires electrodes to be at least one matrix square thick. The fine matrix covering the cathode or plasma region is automatically defined by the program with a resolution defined by the user.

Plots of the trajectories and equipotentials can be obtained either separately or overlaid on the same plot. Reduced annotation plots can be produced for show and tell. Current density distributions of the cathode and target are available and emittance plots can also be plotted.

IV. RESULTS

Results are in good agreement with experimental data or theory where available for comparison. The trends with negative ions have been to agree better with the data that is available as the beams seem to be more divergent than was obtained before the negative ion capability was added. The additional terms in the space charge calculation have pushed the plasma surface significantly forward over what was obtained with the positive ion simulation.

Significant efforts have been made to compare results with the experimental and theoretical data presented in the Chan[1], et al, paper. Their results indicate a beam larger than the experimental data do to their assumption of the flat emission surface from the plasma. PBGUNS yields quite similar results to their theoretical results if the parameters are adjusted so that a nearly flat emission surface is formed on the plasma. Their experimental emittance plot seems to indicate a significantly smaller beam than their experimental data. Reducing the background positive ion density (making the plasma surface concave) and lengthening the simulation has produced results, Figs. 1, 2, and 3 more similar to their experimental data. Figure 1 is the trajectory plot for a concave plasma surface. Figure 2 is the emittance plot obtained with a total of 25 particles injected at each point along the injection plane with 4.5 eV thermal energy in 14 degree increments. Figure 3 is the x-x' emittance computed using the same data with a technique similar, but not identical to Chan[1], et al. The results suggest that the ion temperature must be still higher and the emission may not be uniform.

V. REFERENCES

[1] Chan, C.F., et al.,"Dynamics of Skew Beams and the Projectional Emittance", *NIMPR*, A309, 112 (1991)

TRAJECTORIES AND EQUIPOTENTIALS
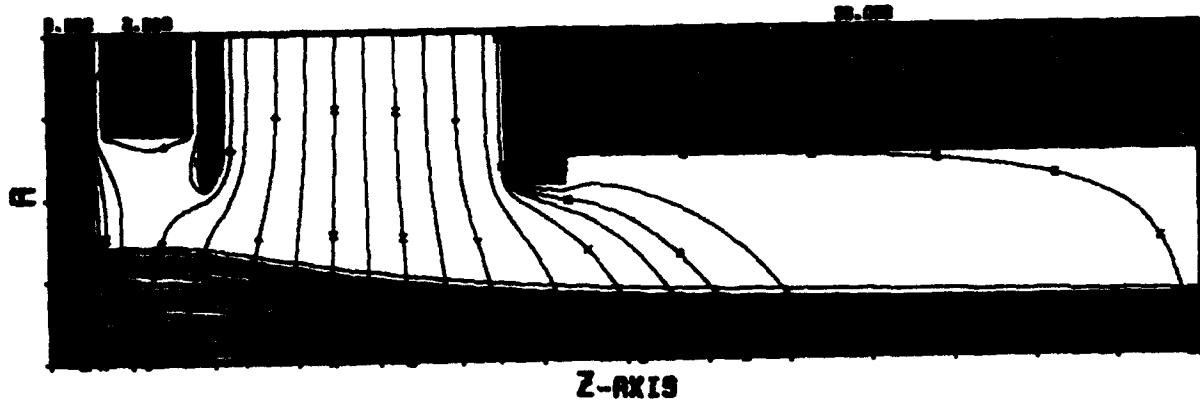
Figure 1. Sampled thermal trajectories for Chan's example with concave plasma surface.
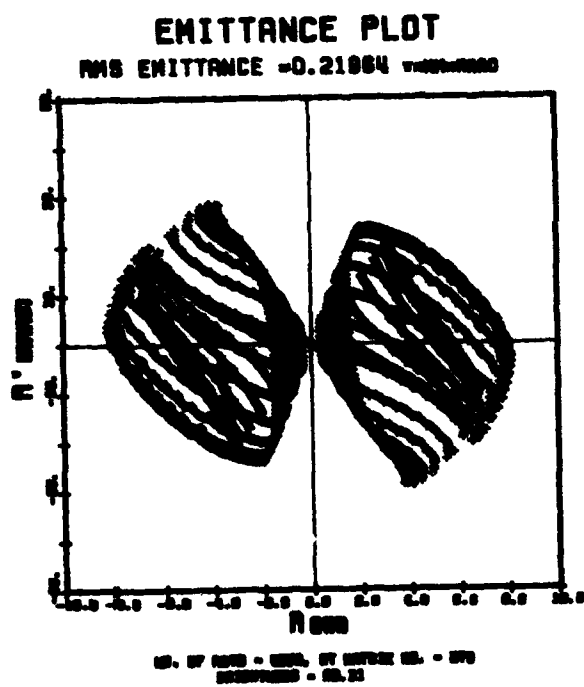
Figure 2. r-r' Emmitance plot for Example above.
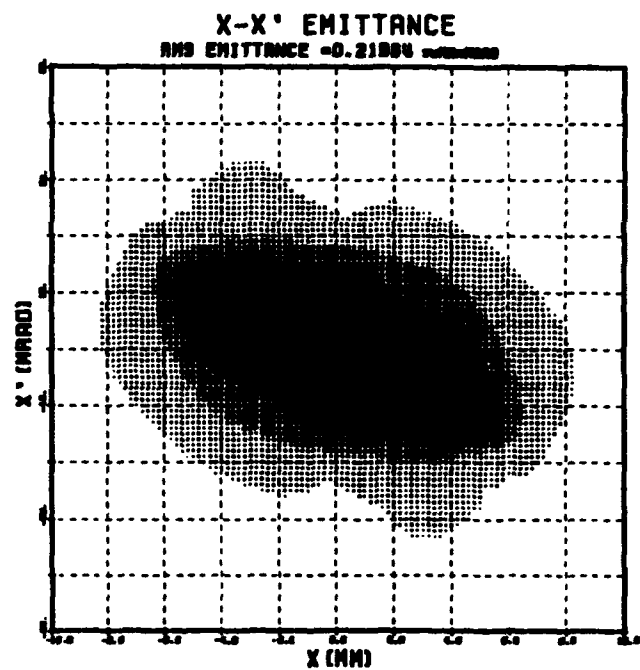
Figure 3. x-x' Emittance plot for same example.

Antiproton Extraction in the Fermilab Antiproton Accumulator*

Mike Church, Stephen O'Day
Fermi National Accelerator Laboratory
P.O. Box 500, Batavia, Illinois 60510, USA

Abstract

The RF and other manipulations required to extract antiprotons from the Accumulator core for Collider operation are described. ESME simulations of the motion in longitudinal phase space are shown. Measurements of the emittances of the extracted antiprotons are presented. The effect of the unstacking process on the core longitudinal and transverse emittances is examined and recent performance is also presented.

I. INTRODUCTION

In order to maximize the initial luminosity of proton-antiproton collisions in the Tevatron, as many antiprotons as possible must be extracted from the Accumulator core in a phase space volume small enough to be efficiently transferred to the Main Ring and there accelerated from 8.9 Gev/c to 150 Gev/c before injection into the Tevatron. The process of transferring antiprotons from the Accumulator core to the Fermilab Main Ring has been previously described [1]. However, increased antiproton stack (core) sizes, upgrades to the Accumulator stochastic cooling systems, and additional operational experience in the current Collider run have all led to refinements in this process. The increase in antiproton stack size by approximately a factor of two over the 1988 Collider run has led to beam loading in one of the rf cavities and beam instabilities due to trapped positive ions [2] [3]. Improvements to the Accumulator stochastic cooling systems have led to much denser antiproton cores, which in turn contributes to the two problems mentioned above, but also allows for a much greater fraction of the antiproton core to be transferred to the Main Ring.

II. PROCEDURE

Antiprotons are rf unstacked from the core by an H=2, 1.26 MHz suppressed bucket rf system (ARF2). 10-15% of the antiproton core is (pseudo)adiabatically captured in a single bucket of size 1.25 ev-sec which is 12 volts on the cavity. This bunch is then accelerated across the Accumulator momentum aperture by about 140 Mev/c in an rf bucket of constant size. On the extraction orbit a second H=2 rf system (ARF3) is then turned on to 810 volts to narrow the single bunch to 210 nsec. This is followed by adiabatic bunching by an H=84, 53 MHz rf system (ARF1) which produces 11 bunches, separated by 19 nsec, under a parabolic envelope. At this point the 11 bunches are simultaneously extracted from the Accumulator by a kicker magnet. After acceleration to

---

150 Gev/c these 11 bunches are coalesced into one bunch in the Main Ring [4]. This entire process is repeated 6 times to produce the 6 antiproton bunches in the Tevatron. The voltage and frequency curves of the 3 rf systems are shown in Figure 1. Figure 2 shows the phase space distribution of particles in the rf buckets just before extraction as generated by ESME [5] using the rf curves in Figure 1.

Since the ARF2 bucket is entirely full with an almost uniform density of antiprotons, and since the synchrotron frequency at the center of the bucket is only a few hertz, it was found that slowing the entire process down as much as possible minimized the amount of beam that fell out of the bucket on its trip from the core to the extraction orbit. It was also found that by varying the precise location in the core from which beam is unstacked, the fraction of the core unstacked over the 6 shots could be maximized. This is due to phase displacement by the moving rf bucket which displaces the centroid of the remaining antiproton core.
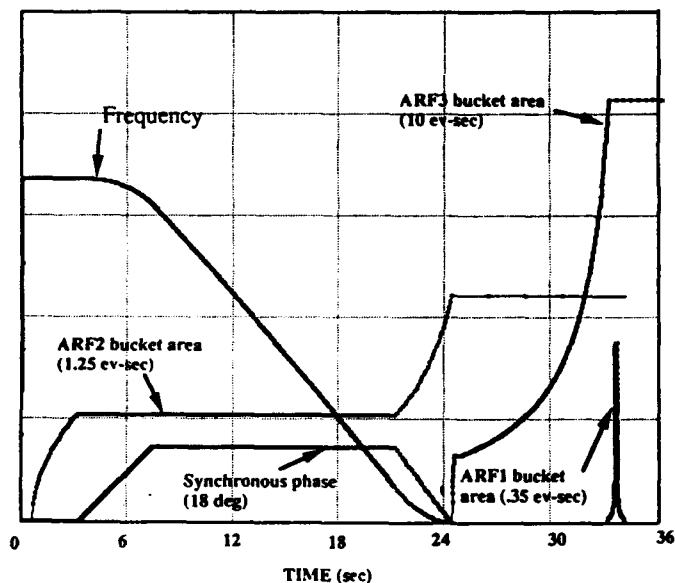
Figure 1. Frequency, synchronous phase, and bucket area for the 3 rf cavities as a function of time during the unstacking process.

III. ANTIPROTON CORE

The Accumulator core cooling systems have recently been upgraded from 2-4 GHz bandwidth cooling to 4-8 GHz bandwidth cooling [6]. This has allowed much larger stacks to be cooled to much smaller emittances. Typical horizontal and vertical emittances are .9 π mm-mrad and .6 π mm-mrad respectively. A typical momentum width is 2.5 Mev/c (σ). For an antiproton stack size of 100 mA (10^{12} particles) this corresponds to a peak density of .12 x 10^{12} particles per 1.25
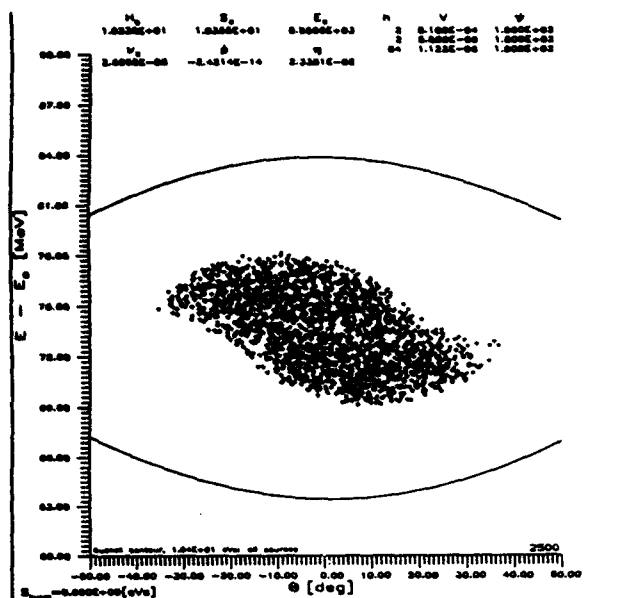
Figure 2. Longitudinal phase space distribution of particles after complete bunching with ARF3 (H=2) but before bunching with ARF1 (H=84); and after complete bunching with ARF1.

ev-sec. Figure 3 shows a typical core longitudinal density measurement just before antiproton extraction. The largest stack obtained to date is 155 mA.

Instability due to trapped positive ions in these large stacks was initially effectively eliminated by increasing the clearing electrode voltage from 100 V to 1kV. However, for stacks over about 110 mA it has become necessary to slightly bunch the antiproton core with ARF2 at about 5 V to stabilize the beam prior to extraction. This technique for beam stabilization is well known in electron storage rings [7] and it has been found to be effective here also.
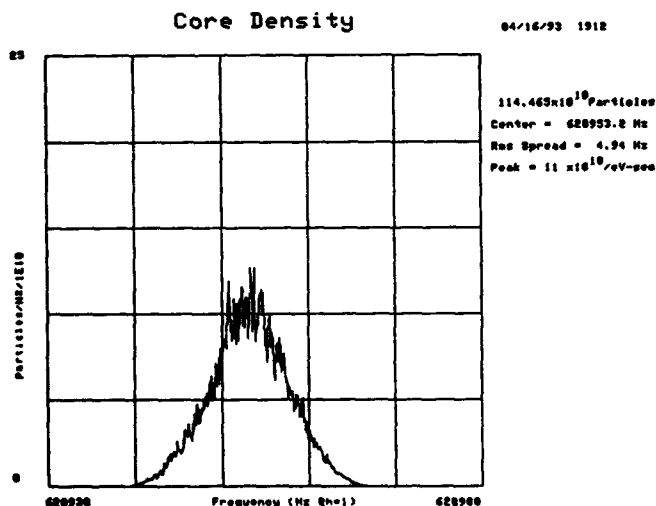
Figure 3. Antiproton core frequency spectrum. Momentum is given by $\eta * dP/P = dF/F$ where η is -.023.

The procedure for extracting the 6 antiproton bunches has been tailored to match the increased core cooling power. The 4-8 GHz cooling systems have a fast enough cooling rate such that a short wait (40-120 seconds) between antiproton extractions is enough to allow the core to cool down to smaller emittances in all 3 dimensions after each extraction. The transverse emittance of the 6th extraction is typically 10% smaller than for the 1st extraction.
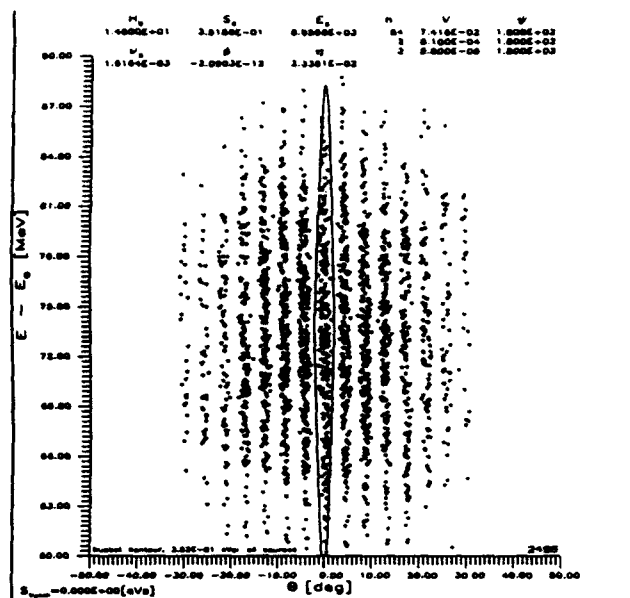
IV. BEAM LOADING

Increased antiproton core densities have also produced a deleterious beam loading [8] effect in ARF3. The ARF3 cavity has a shunt impedance of about 1000Ω. If 10 mA is unstacked from the core, this will produce a voltage of .01 x 1000 / 2 = 5V which is 90° out of phase with the 12V being driven by the generator on ARF2. In practice this causes large dipole oscillations within the rf bucket during unstacking, which in turn causes much of the beam to fall out of the bucket before reaching the extraction orbit. Without some remedy, the maximum amount of beam that could be extracted in a single shot was about 7 mA. The solution used involved shorting the ARF3 cavity during the extraction process until the beam reached the extraction orbit, and then quickly unshorting the cavity. This appears to cause some quadrupole oscillations within the bucket, causing some longitudinal emittance growth. However as much as 14 mA has been extracted in a single shot using this technique. Figure 4 shows the longitudinal bunch structure with ARF3 shorted and unshorted.

V. RECENT PERFORMANCE

The transverse emittances of the extracted beam, as measured from a SEM profile in the beam transfer line between the Accumulator and Main Ring, range from .5 π mm-mrad to 1 π mm-mrad depending on stack size. The longitudinal profile is measured from a Schottky pickup in the Accumulator. Figure 5 shows the stack profile before and

after extracting 6 bunches. Note that the core is displaced slightly after the extractions, and that about 10% of the beam that is unstacked from the core is scattered along the momentum aperture. ESME simulations also predict that 10% of the beam should fall out of the bucket during acceleration to the extraction orbit. The transfer efficiency from Accumulator to Main Ring is typically 95% if the transverse emittances are less than 1 π mm-mrad. Above this, the transfer efficiency drops rapidly due to aperture restrictions in the Main Ring and transfer line. Typically about 50% of the antiproton core can be extracted in 6 shots.

1.38 ev-sec rf buckets were tried but found to be inefficient in acceleration in the Main Ring. The longitudinal emittance of the extracted beam is measured with a resistive wall monitor and bunch length monitor in the Main Ring. These show that there is about a 35% longitudinal emittance blowup in the extraction process. Simulations with ESME also predict an emittance growth of 35%, primarily due to the ARF3 non-adiabatic bunching previously mentioned.
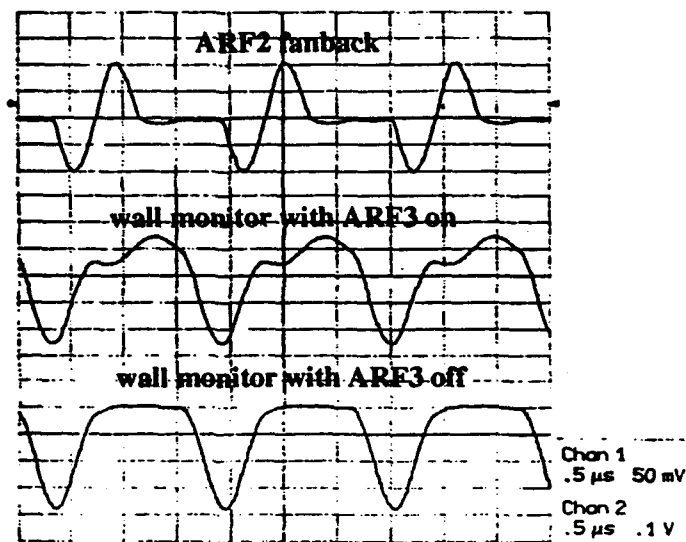
Figure 4. Top trace is ARF2 voltage waveform. Bottom two traces show the effect of beam loading on bunch structure.

VI. CONCLUSIONS

Antiproton extraction from the Accumulator has improved dramatically during the present Collider run. Figure 6 is a plot of the number of antiprotons per bunch in the Tevatron at 900 Gev/c as a function of stack size. Although the curve is beginning to flatten at large stack sizes, we expect that larger antiproton stacks will continue to contribute to greater luminosities in the Tevatron.

VII. REFERENCES

[1] Bharadwaj V, et al. In Proc. IEEE 1987 Part. Acc. Conf., Washington DC. 2:1022-24. New York: IEEE (1987)
[2] Fullett K, Werkema S, Zhou P. This conference.
[3] Alves-Pires R, et al. In Proc. IEEE 1989 Part. Acc. Conf., Chicago. 2:800-2. New York: IEEE (1989)
[4] Martin P, et al. In Proc. IEEE 1989 Part. Acc. Conf., Chicago, 3:1827-28. New York: IEEE (1989)
[5] MacLachlen J, Stahl S. Fermilab Technical Memo TM-1650 (1990)
[6] Marriner J, et al. In Proc. IEEE 1989 Part. Acc. Conf., Chicago, 2:648-50. New York: IEEE (1989)
[7] Rowe EM. In AIP Conf. Proc. 171: Vacuum Design of Advanced Compact Synchrotron Light Sources, ed. HJ Halama, JC Schuchman, PM Stefan, pp193-206. New York: AIP (1988)
[8] Raka E. In AIP Conf. Proc. 184: Physics of Particle Accelerators, ed. M Month, M Dienes, 1:288-342. New York: AIP (1989)
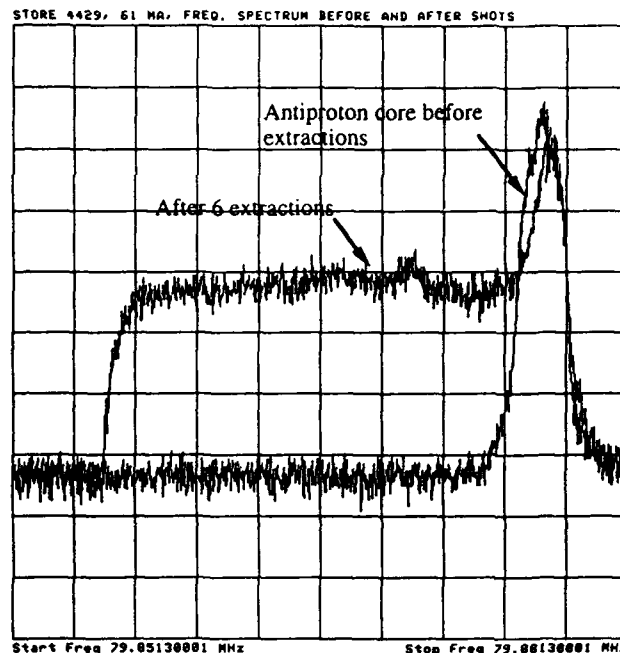
Figure 5. Antiproton frequency spectrum before and after 6 extractions.
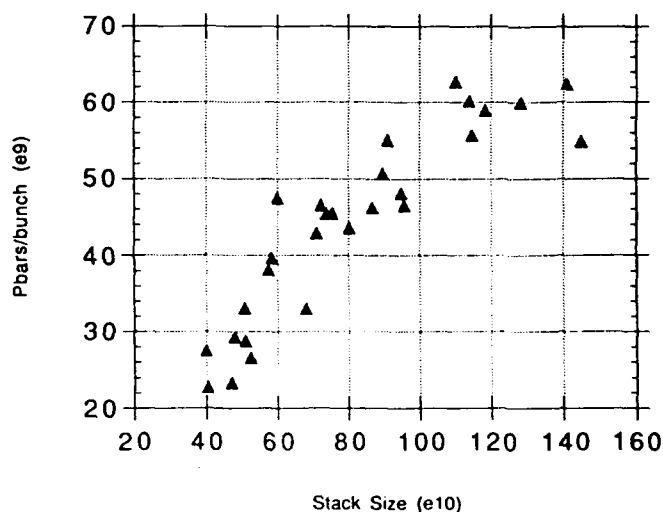
Figure 6. Number of antiprotons/bunch at 900 Gev/c in the Tevatron as a function of antiproton stack size.

332

Beam Optics of LEB-MEB Transfer Line
for Superconducting Super Collider

Naifeng Mao, John A. McGill, Karl L. Brown and Rodney E. Gerig
Superconducting Super Collider Laboratory*
2550 Beckleymeade Ave., Dallas, TX 75237

Abstract

The beam optics of the transfer line between the Low Energy Booster (LEB) and the Medium Energy Booster (MEB) at the Superconducting Super Collider Laboratory is presented. The 12 GeV/c proton beam is extracted from the LEB and injected into the MEB at strictly defined extraction and injection points. The beamline has a high flexibility for β and η function matchings. Effects of various errors are studied, and a beam position correction scheme is proposed.

I. INTRODUCTION

The LEB-MEB transfer line at the Superconducting Super collider Laboratory transports 12 GeV/c proton beam from the Low Energy Booster (LEB) to the Medium Energy Booster (MEB). The two boosters are at different elevations, and the extraction and injection points on these two rings are strictly defined. The tune point of the LEB may vary to a certain extent, and six tune points are selected to represent the possible range of tuning. The lattice functions of these two boosters may also vary because of various errors in these two boosters. Therefore, the optics design of the LEB-MEB transfer line must consider the basic optical problems, such as beam centroid matching, β function matching, and η function matching.

The misalignments and field errors of the transfer line magnets are sources of beam centroid, β function and η function mismatchings, all of which can cause emittance growth. In order to obtain a high luminosity in the collider, the emittance growth has to be minimized. The effects of different kinds of errors along the transfer line are studied, and a beam position correction scheme is proposed.

Relating to the transfer line, there is also an absorber (beam dump) line, which transports the proton beam extracted from the LEB to the absorber during the LEB commissioning. This line will not be discussed in this paper.

II. LAYOUT AND MATCHINGS

The elevation difference between the LEB extraction point and the MEB injection point is about 0.46 m and the total length from the extraction point to the injection point is about 249 m. The general layout of this transfer
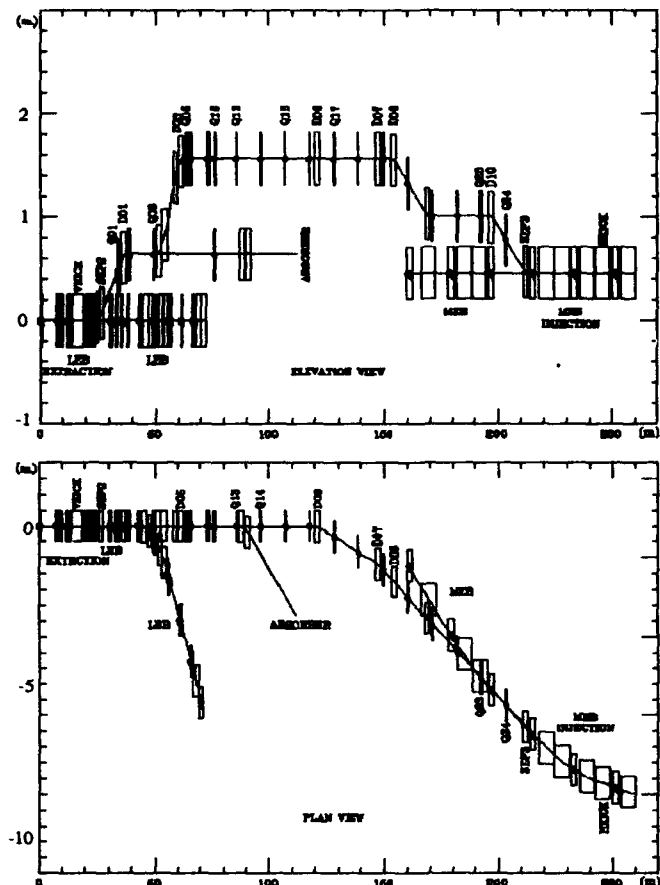
Figure 1. Layout of the LEB-MEB transfer line.

line is shown in Figure 1, including the elevation view and plan view.

The LEB extraction straight, which consists of a vertical kicker (VKICK, Figure 1), five bump magnets and two septum magnets (SEP1 and SEP2), extracts the beam vertically from the LEB. The MEB injection straight, including a Lambertson septum magnet (SEP3) and a horizontal kicker (HKICK), injects the beam into the MEB at the injection point.

The transfer line itself has ten dipoles (each 2 m in length) and twenty-four quadrupoles (each 0.5 m in length) to transport the beam from the LEB to the MEB, and complete the beam centroid matching, β function matching and η function matching. The twenty-four quadrupoles are separated into three sections, an η_y matching section
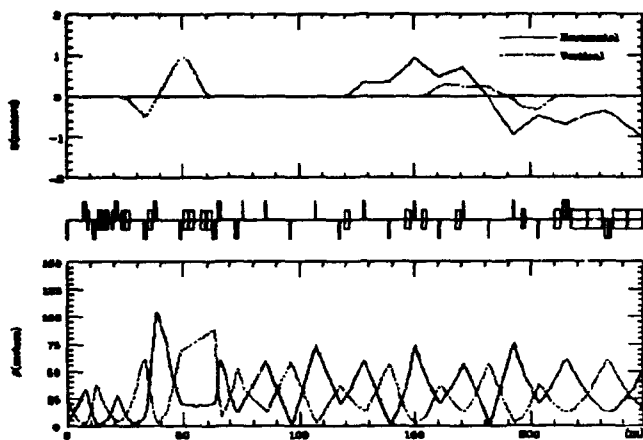
Figure 2. β and η functions of the LEB-MEB transfer line.

(five quadrupoles, Q01 through Q05), a β matching section (seven quadrupoles, Q06 through Q12), and a FODO section (twelve quadrupoles, Q13 through Q24). The FODO section also plays a role of η function matching while lattice functions of these two boosters vary.

A. Centroid Matching

The layout is the result of the beam centroid matching. This matching is completed by the ten dipoles with suitable positions and bending angles. The first five vertical dipoles (D01 through D05, Figure 1) separate the transfer line from the LEB ring entirely in the vertical direction, and raise the beam center line to an elevation of about 1.57m. On the MEB side, the last three vertical dipoles (D08 through D10) and the Lambertson septum magnet (SEP3) lower the beam line to the MEB elevation, and make the beam move in the horizontal plane.

The centroid matching in the horizontal plane is mainly accomplished by the two horizontal dipoles (D06 and D07). By adjusting the positions of these two dipoles and setting their total bending angle to 4.59^0, the beam after passing through these two dipoles has the required position and direction, and therefore can be precisely injected into the MEB by the horizontal kicker.

B. β Function Matching

The required β and η matchings of the transfer line are performed by adjusting the parameters of the dipoles and quadrupoles. The β and η functions along the transfer line for one LEB tune point (TUNE E) are shown in Figure 2. The β functions have a maximum value of 103 m, and in most of the transfer line are only 75 m or less. This means that the transfer line has a low sensitivity to errors in the magnets.

The β matching is performed by the β matching section of seven quadrupoles, but because three pairs of adjacent quadrupoles are powered in series, the seven quadrupoles have just four adjustable quadrupole components necessary to complete the β_x, β_y, α_x and α_y matchings. In

addition, the β function variations due to the errors of these two boosters are also considered. The analysis results show that this section can complete the matching for 20% β variation of the LEB and 10% β variation of the MEB, as required.

Since this β matching section is located in the region where the η functions are zero, the β function matching has no effect on the η functions.

The FODO section, downstream of the β matching section, transports the beam for more than 120 m, through a set of dipoles, to the MEB injection straight. Because of the space limitation in the transfer line, the parameters of the FODO array are slightly different from the MEB lattice, and a small but unimportant β function beating within this section appears.

C. η Function Matching

The η functions in the horizontal plane are $\eta_x = \eta_x' = 0$ at the LEB extraction point and $\eta_x = -1.063$ m, $\eta_x' = -0.049$ at the injection point (Figure 2). The η_x function matching is completed by adjusting the positions and relative bending angles of the two horizontal dipoles (D06 and D07), while meeting the requirement of the horizontal centroid matching.

If the horizontal η functions of these two boosters vary, ·the matching can be regained by adjusting the gradients of one or two pairs of quadrupoles in the FODO section in an orthogonal way [1]. The two quadrupoles of each pair are separated by 180^0 phase advance and the transfer matrix between them is -1. For η_x matching, a phase advance approximate to $(n+1/2)$ x 180^0 between this pair and MEB injection point is required; and for η_x' matching, a phase advance approximate to n x 180^0 is required. To achieve matching, the η_x functions at the positions of the paired quadrupoles should be different. This occurs if a horizontal dipole is located between the paired quadrupoles. In the LEB-MEB transfer line, quadrupoles Q15 and Q19 are chosen for η_x matching, Q13 and Q17 for η_x'. The gradient adjustment for the two paired quadrupoles is of opposite sign. A gradient adjustment of about 5% is needed for an LEB horizontal dispersion variation of $\Delta \eta_x = 0.1$ m.

In the vertical plane, this transfer line is an achromatic transport system. η_y matching is performed by the η_y matching section (Q01 through Q05). Because multiple power supplies are used, this section has only three adjustable components, two for η_y and η_y' matchings, and the other for producing a horizontal waist. If the η_y functions of these two boosters vary, the rematching can also be achieved by adjusting the gradients of one or two pairs of quadrupoles in the FODO section, as discussed for η_x matching. Obviously, this transfer line has a high flexibility to match different conditions.

The beam optics is calculated with program TRANSPORT [2].

III. ERROR EFFECTS AND POSITION CORRECTION SCHEME

The magnet misalignments and field errors in the transfer line cause beam centroid, β function, and η function mismatchings. The tolerance to the misalignments and field errors are mainly constrained by two factors, one is the limited magnet aperture, and the other is the allowed emittance growth. The latter is more stringent, as the allowed emittance growth is only a few percent.

The transverse emittance dilution due to mismatching has been studied in detail [3]. For beam centroid mismatching Δx and $\Delta x'$, the transverse emittance dilution factor

$$F_x \sim \frac{\epsilon}{\epsilon_0} = 1 + \frac{1}{2}[\frac{\Delta x_{eq}}{\sigma_0}]^2, \qquad (1)$$

where

$$\Delta x_{eq} = \sqrt{(\Delta x)^2 + (\beta \Delta x' + \alpha \Delta x)^2}. \qquad (2)$$

The rms transverse beam sizes σ_0 at the MEB injection point are 1.5 mm and 0.8 mm in the horizontal and vertical planes, respectively. If an emittance growth of less than 1% is required for centroid mismatching, Δx_{eq} should not exceed 0.1 mm. In practice, beam position corrections are necessary. In order to study the effects of various errors on the beam centroid, β and η, and to develop a position correction scheme, a program, EAC, has been developed [4] and used in the LEB-MEB transfer line design. Errors causing beam centroid mismatching can be divided into two types. One type includes the magnet field instabilities, and the other includes all the systematic errors, such as dipole rotations and field setting errors, quadrupole transverse displacements, centroid displacement and angular deviation of the LEB extracted beam and so on.

An analysis has been made on the beam centroid mismatching caused by the field instabilities. The fractional errors assumed in the analysis are as follows: 1×10^{-2} for LEB extraction and MEB injection kickers, 2×10^{-3} and 1×10^{-3} for the first and second LEB extraction septum magnets respectively, $(1-2) \times 10^{-4}$ for the MEB injection Lambertson septum magnet and the ten dipoles of the transfer line itself. The analysis shows that the centroid mismatching in the vertical plane $\Delta y_{eq} = 1.0$ mm, if the field errors of the injection septum magnet and the ten dipoles are 1×10^{-4}; and $\Delta y_{eq} = 1.5$ mm, if the field errors are 2×10^{-4}. These mismatchings correspond to 76% and 167% emittance growths. An injection damping system in the MEB is needed to correct this effect.

As for the beam centroid mismatching due to systematic errors (say, a dipole rotation angle of 1.0 mrad, a field setting error of 5×10^{-4}, a quadrupole transverse displacement of 0.25 mm, an LEB extracted beam centroid displacement of 0.5 mm, and a beam angular deviation of 0.1 mrad), it can be corrected by using a correction scheme, consisting of correctors and beam position monitors in the transfer line. The scheme is designed through statistical simulation; that is, randomly choosing field errors, then
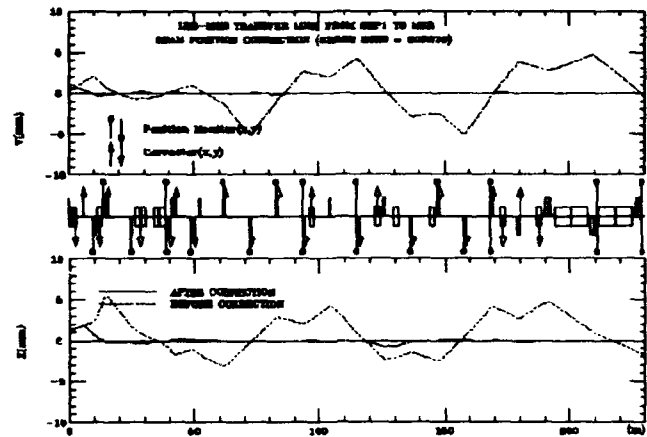
Figure 3. Position correction scheme.

calculating the necessary corrector strengths and the centroid displacement along the transfer line. One thousand seeds are normally used in the simulation. Figure 3 shows a correction scheme for the LEB-MEB transfer line, which uses fewer correctors and lower corrector strengths, and has an optimal correction result. In most of the transfer line, "one (corrector) to one (downstream monitor)" correction mode is used. It means that each corrector corrects the beam centroid displacement where the monitor is located. But at the end of the transfer line, "two to two" correction mode needs to be used normally. This mode corrects both beam centroid displacement and angular deviation. After correction, the maximum transverse centroid displacement along the transfer line is about 2.1 mm; and at the end of the transfer line Δx_{eq} and Δy_{eq} are less than 0.02 mm, corresponding to an emittance growth of less than 0.1%. The maximum corrector strength required is less than 0.7 mrad.

The β function and η function mismatchings caused by rms quadrupole gradient error of 1×10^{-3} will lead to an emittance growth of less than 0.1%.

IV. REFERENCES

[1] Karl L. Brown and Roger V. Servranckx, "First- and Second-order Charged Particle Optics", SLAC-PUB-3381, SLAC, 1984.

[2] Karl L. Brown et al., "TRANSPORT, A Computer Program for Designing Charged Particle Beam Transport System", SLAC-91, Rev. 2, SLAC, 1977.

[3] Michael J. Syphers, "An Improved 8 GeV Beam Transport System for the Fermi National Accelerator Laboratory", FNAL-TM-1456, FNAL, 1987.

[4] Fuhua Wang and Naifeng Mao, "Beam Line Error Analysis, Position Correction and Graphic Processing", Proceedings, Computational Accelerator Physics Conference, 1993.

Acceleration and Bunching by a Gap

S. Kulinski

INFN, LNF, P.O. Box 13, 00044 Frascati (Italy)

Abstract

The relativistic equations of axial motion of a charged particle in an RF electric field inside a gap are analysed.The solution to these equations can be expressed as the incomplete elliptic integrals of the first and third kinds. The approximate solutions based on the average particle velocity in the gap are also found. The bunching by a gap is analysed by considering the phase ϕ_e after the drift as a function of the entrance phase ϕ_i: $\phi_e=\phi_i+\phi_t+\phi_d$, ϕ_t is the transit angle in the gap, ϕ_d drift angle. Starting from the general condition for bunching $d\phi_e/d\phi_i \leq 1$ it is shown that bunching begins with the input phase ϕ_{ipm} corresponding to the minimum of the momentum p_m at the exit of the gap and ends at phase ϕ_{ipM} when the momentum attains its maximum p_M. The width of the bunched phases $\Delta\phi_e$ is analysed as a function of different parameters and can be optimized according to the imposed conditions.

I. INTRODUCTION

Bunching is the basis of many microwave devices in which the interaction between the beam of particles and an electromagnetic wave plays an essential role as for instance in klystrons or linear accelerators. Consequently the problem of bunching was analysed by many authors [1-3]. Usually this analysis is based on some simplifying assumptions. The most important are: i) The transit time of a particle through the interaction gap is negligible in comparison with the field period. ii) The AC voltage V_g in a gap is small in comparison with the DC voltage V_0. iii) Space charge effects are ignored.

In the present paper the analysis will be made without the first two of above restrictions. To take properly into account these effects the relativistic equations of motion of particles in a gap are solved.Spatially constant field in a gap is assumed, since then the analytical solutions are possible. However, as it was shown by numerical calculations [3], the results for other field distributions e.g. gaussian are similar. The analysis is made for electrons, but the results can be used also for other charged particles.

II. AXIAL MOTION IN A GAP

A. Equations of Motion

Equations of motion are

$$d\gamma/ds = A \cos\phi \qquad (1)$$

$$d\phi/ds = 2 \pi \gamma/(\gamma^2 - 1)^{1/2} \qquad (2)$$

where, γ is the relativistic energy factor, $s = z/\lambda$, z-axial distance, λ- wave-length, ϕ- electric field phase in a gap, A =

$q\lambda E/W_0$, q-charge, E- electric field intensity, $W_0 =m_0c^2$- particle rest energy.

In the case of E = const. an analytical solution to Eqs (1) and (2) can be found. First by elimination of ds we find equation for the normalized momentum $p=mv/m_0c=\gamma\beta$, ($\beta=v/c$)

$$p = p_0 + A_1 (\sin\phi - \sin\phi_0) = \gamma\beta \qquad (3)$$

Here subscript o denotes the initial values. Eq. (3) defines the phase trajectories in the phase space (p,ϕ), however, it does not give the dependences $\gamma = \gamma(s)$ and $\phi = \phi(s)$. To obtain these relations using Eq.(3) we express γ and $\cos\phi$ as functions of momentum p. Inserting these relations into Eq. (1) and integrating we get

$$s = \pm\frac{1}{2\pi}\int_{p_o}^{p}\frac{pdp}{\sqrt{(1+p^2)(A_1^2-(p-p_o+A_1\sin\phi_o)^2)}} \qquad (4)$$

The integral (4) can be expressed in terms of the incomplete elliptic integrals of the first and third order [3]. Since the expressions with these integrals are rather complicated, for numerical calculations it could be preferable to integrate directly Eqs. (1) and (2) or (4). However, it would be more effective if one could solve analytically, even approximately, Eqs (1,2) without the necessity to calculate the integral (4).

B. Approximate Solutions to the Equations

The phase ϕ as seen by a particle can be written as $\phi = \phi_0 + \phi_t (s)$, where ϕ_0 is the initial phase and $\phi_t(s)$ is the transit phase given by

$$\phi_t(s) = 2 \pi \int_{s_o}^{s} \frac{ds}{\beta(s)} = \frac{2\pi(s-s_o)}{\beta_{av}} \qquad (5)$$

β_{av} is the average particle velocity in the gap as defined by (5). To find β_{av} we will average the Eq. (3) for p over the changes of phase $(\phi_0,\phi_0 + \phi_t(s))$

$$p_{av} = p_0 +A_1((\sin\phi)_{av} - \sin\phi_0)= 1/(1/\beta_{av}^2-1)^{1/2} \qquad (6)$$

where

$$(\sin\phi)_{av}=1/\phi_t \int_{\phi_o}^{\phi_o+\phi_t} \sin \phi d\phi = (\cos\phi_0 - \cos(\phi_0 +\phi_t)/\phi_t \qquad (7)$$

Inserting (7) into (6) we will get equation for β_{av}

$$p_0 - (1/(\beta_{av})^2 - 1)^{-1/2} = \qquad (8)$$

$$A_1(\sin\phi_0 -(\cos\phi_0 - \cos(\phi_0+\phi_t))/\phi_t)$$

In the case of small changes of the velocity in a gap $\Delta\beta/\beta<<1$ equation (8) can be reduced to quadratic equation for the small quantity proportional to $\Delta\beta/\beta$. To obtain this equation we put

$x_0 = 1/\beta_0$, $x = 1/\beta_{av} = x_0(1 + y)$, $\phi_t = 2\pi s x = \phi_{t0}(1 + y)$, $\phi_{t0} = 2\pi s x_0$ is the transit angle of the particle with the input velocity β_0. Assuming that $y \ll 1$, valid surely for small signal bunching, we can expand functions of Eq.(8) into series up to the second order in y in the vicinity of x_0 to obtain quadratic eqution for y with the aid of which β_{av} is found.

III. BUNCHING

A. Central Particle

In the process of bunching by the velocity modulation a special role plays the central particle. Usually this is the particle which passes an interaction gap without the change of energy. We should then find such a phase ϕ_0 for which a particle leaves the gap without changing its momentum p_0. Using Eq. (3) we obtain the obvious relation

$$\sin\phi_{0c} = \sin(\phi_{0c} + \phi_{tc}) = \sin(\phi - \phi_{0c}) \quad (9)$$

and

$$\phi_{0c} = (k + 1/2) \pi - 0.5 \phi_{tc} \quad (10)$$

where ϕ_{tc} is the transit angle of the central particle. Assuming that $\phi_{tc} < \pi$ (narrow gap not to large signals) we will have for electrons $k = 0$ and $\phi_{0c} = (\pi - \phi_{tc})/2$.

The precise solution for ϕ_{0c} can be now obtained with the aid of Eq. (4) where the limits of the integral should be (p_{min}, p_0) and p_{min} is given by (for electrons $A_1 < 0$)

$$p_{min} = p_0 + A_1(1 - \sin\phi_0) \quad (11)$$

The approximate solutions can be obtained from Eq. (8) inserting , according to Eq. (10), $\phi_0 = \phi_{0c} = (\pi - \phi_{tc})/2$ to get

$$p_0 - (x^2 - 1)^{-1/2} + A_1 (\sin\alpha/\alpha - \cos\alpha) \quad (12)$$

where $x = 1/\beta_{av}$, $\alpha = \phi_{tc}/2 = \pi s x$

B. General Relations for Bunching

In the case of a bunching system composed of a gap of length L and a drift D, the exit angle is given by

$$\phi_e = \phi_i + \phi_t + \phi_d = \phi_i + F/\beta \quad (13)$$

where ϕ_i -input phase, $\phi_t = 2 \pi L/(\lambda \beta_{av})$ is the transit angle in the gap, $\phi_d = 2\pi D/(\lambda \beta)$ is the drift transit angle and β is the exit velocity. Putting $\beta_{av} = h\beta$, where h is usually close to 1, F is equal to

$$F = 2 \pi D/\lambda (1 + L/hD) \quad (14)$$

General condition for bunching is

$$d\phi_e/d\phi_i \leq 1 \quad (15)$$

Taking into acount (13) and (14) Eq. (15) becomes

$$d\phi_e/d\phi_i = 1 - F/(p^2(1 + p^2)^{1/2})dp/d\phi_i \leq 1 \quad (16)$$

We begin with some general conditions for bunching, which can be obtained from the relation (16). Generally, since $F > 0$ then the condition (16) requires that $dp/d\phi_i \geq 0$. It means that bunching starts with phase $\phi_i = \phi_{ipm}$ corresponding to p_{min} at the exit and ends with the phase ϕ_{ipM} for which $p=p_{max}$. The range of bunched input phases is

$$\Delta\phi_i = \phi_{ipM} - \phi_{ipm} \quad (17)$$

Then to define the starting conditions for bunching we should find the extrema of the momentum p as a function of ϕ_i. For $\Delta\phi_e$ we should find extrema of ϕ_e using the equation $d\phi_e/d\phi_i = 0$. Generally, depending upon the parameter F and momentum p_0 this equation can have 0, 1 or two solutions. In the case of 0 or one solution we have $0 \leq d\phi_e/d\phi_i \leq 1$. The bunched output phase ϕ_e is a monotonic function of the input phase ϕ_i. $\Delta\phi_e$ is equal to $\Delta\phi_e = \phi_{epM} - \phi_{epm}$, where ϕ_{epM} and ϕ_{epm} are the output phases after the drift corresponding to p_{max} and p_{min} at the exit of the gap.

In the case of two solutions we have four characteristic points on the curve $\phi_e = \phi_e(\phi_i)$ on which depends the width $\Delta\phi_e$. The bunching starts with $p = p_m$ and $\phi_i = \phi_{ipm}$. For $\phi_i > \phi_{ipm}$ $dp/d\phi_i > 0$ and $d\phi_e/d\phi_i > 0$ up to the point where $d\phi_e/d\phi_i = 0$ and $\phi_e = \phi_{eM}$. Beyond this point $dp/d\phi_i > 0$ but $d\phi_e/d\phi_i < 0$ until the point where $d\phi_e/d\phi_i = 0$ and $\phi_e = \phi_{em}$ is reached. After that ϕ_e begins to increase again and bunching stops when $dp/d\phi_i = 0$, $p = p_M$ and $\phi_e -- \phi_{epM}$. The width $\Delta\phi_e$ is equal now

$$\Delta\phi_e = \max (\phi_{eM}, \phi_{epM}) - \min (\phi_{em}, \phi_{epm}) \quad (18)$$

Further analysis will be possible when the extrema of the momentum p and the extrema of ϕ_e are found.

C. Extrema of the Momentum P

At the end of the gap the momentum p is given by

$$p = p_0 + A_1 (\sin(\phi_i + \phi_t) - \phi_i) \quad (19)$$

It can be shown that $dp/d\phi_i$ is equal to

$$dp/d\phi_i = \frac{p^2\sqrt{1 + p^2} A_i (\cos(\phi_i + \phi_t) - \cos\phi_i)}{p^2\sqrt{1 + p^2} + A_i g \cos(\phi_i + \phi_t)} \quad (20)$$

Here $g = 2 \pi L/(h \lambda)$. Then from $dp/d\phi_i = 0$ follows

$$\cos(\phi_i + \phi_t) - \cos\phi_i = 0 \quad (21)$$

Eq. (21) has two principal solution in the range ($-\pi, \pi$)

$$\phi_i = -\alpha, \qquad p_{extr} = p_0 + 2 A_1 \sin\alpha$$

$$(22)$$

$$\phi_i = \pi - \alpha, \qquad p_{extr} = p_0 - 2 A_1 \sin\alpha$$

where $\alpha = \phi_t/2$. For electrons $A_1 < 0$ and the first solution is for p_{min} the second for p_{max}. The range of bunched input phases is

$$\Delta\phi_i = \phi_{ipM} - \phi_{ipm} = \pi + \alpha_{ipm} - \alpha_{ipM} \qquad (23)$$

Since $\alpha_{ipm} > \alpha_{ipM}$ then $\Delta\phi_i > \pi$. Usually for small signal bunching $p_0 \gg 2 A_1$, the difference between p_M and p_m is small so that $\Delta\phi_i$ is close to π. For large signal, when A_1 can be comparable with p_0 $\Delta\phi_i$ can substatially differ from π. To solve completely the problem we should find the transit angles ϕ_{tpm} and ϕ_{tpM}. The precise solution can be obtained with the aid of equation (4). Approximate solution is obtained inserting relations (22) and (23) into (8) to get the equation for $x = 1/\beta_{av}$

$$p_0 - (x^2 - 1)^{-1/2} + A_1 \sin\pi s x = 0 \qquad (24)$$

D. Extrema of the Bunched Output Phase Φ_e

The extrema of ϕ_e are given by $d\phi_e/d\phi_i = 0$. Using (16) and (20) we get

$$(25)$$

$$p^2(1 + p^2)^{1/2} - (2\pi D/\lambda)A_1(\cos(\phi_i + \phi_t) - (1 + L/hD)\cos\phi_i) = 0$$

In this equation the transit angle ϕ_t is a function of ϕ_i so that in principle it is an equation for ϕ_i. However, since we do not know explicitly the functional dependence $\phi_t = f(\phi_i)$, we should use some iterative procedure to solve Eq. (25). For a given value of ϕ_i, ϕ_t can be found either precisely with the aid of Eq. (4) or approximately using equation (8). Usually for small signal bunching the simpler approximate solution is sufficiently accurate. Generally, as it was already mentioned above Eq. (25) can have 0, 1, or 2 solution for ϕ_i in the range $(-\pi, \pi)$. The number of solutions depends on the parameters of the bunching system: Vo, Vb, D, L and λ. Solution of Eq. (25) defines the type of bunching and $\Delta\phi_e$. This, together with previously found quantities : $\Delta\phi_i$, p_{min}, p_{max} defines completely the bunching system giving not only the effectiveness of phase bunching $\Delta\phi_i/\Delta\phi_e$, but also the energy dispersion introduced by the system $\Delta p = p_{max} - p_{min}$.

Up to now we used a general definition of the bunching factor $R = \Delta\phi_i/\Delta\phi_e$ with $\Delta\phi_i$ and $\Delta\phi_e$ defined by Eqs (17) and (18) correspondingly. However, in practice e.g. for positron production or injection into superconducting cavities, where both small phase and energy dispersion is essential, we often would like to have rather narrow well bunched output phases. It means that in the vicinity of the central particle the changes of ϕ_e should be small for sufficiently large variations of ϕ_i. This can be done by choosing the bunching parameter in such a way as to have two extrema of ϕ_e close to each other, since then $d\phi_e/d\phi_i \approx 0$, variations of ϕ_e are small and given by

$$\phi_e \approx \phi_{ee} + 0.5 (\phi_i - \phi_{ie})^2 d^2\phi_e/d\phi_i^2 \qquad (26)$$

where ϕ_{ee} corresponds to the extremum of ϕ_e and ϕ_{ie} the value of ϕ_i in this point. We can now define the effective value of bunching as

$$R_{eff} = (\phi_{iM} - \phi_{im})/(\phi_{eM} - \phi_{em}) \qquad (27)$$

where ϕ_{eM} and ϕ_{em} are the extrema of ϕ_e , ϕ_{iM} and ϕ_{im} are the values of the input phase ϕ_i corresponding to the points in which ϕ_e is equal to ϕ_{em} and ϕ_{eM}, outside the points of extrema of ϕ_e. These values can be found from Eq. (26) . The second derivative $d^2\phi_e/d\phi_i^2$ is found by differetiating once again Eq. (16)

C. Numerical Example

The program GAPAC (GAP ACceleration) has been written to make the numerical calculations and to check the validity of approximations. As an example we have chosen the prebuncher made for the SC accelerator LISA of Frascati Laboratories. The main parameters of this prebuncher are: $V_0 = 100$ kV, $\lambda = 0.6$m, gap length $L = 0.1 \lambda = 0.06$m, drift length $D = 1.36$m, gap RF voltage $V_g \approx 10$kV. Two kinds of calculations have been made. First the value of classical bunching parameter $B_{po} = D V_g \pi/(V_0 \lambda \beta_0)$ was found for which $R = \Delta\phi_i/\Delta\phi_e$ is maximum. $\Delta\phi_i$ and $\Delta\phi_e$ are given by Eqs. (17) and (18) correspondingly. The calculation has shown that the maximum is $R_M \approx 7$ and is obtained for $B_{po} \approx 1.81$. In fact these values seems to be common for small signal bunching. In the second case we were looking for the solution giving $\Delta\phi_i$ greater than 60 degrees and $\Delta\phi_e$ of the order of one degree. The solution chosen was $B_{po} = 1.45$, $\Delta\phi_i \approx 82°$, $\Delta\phi_e = \phi_{eM} - \phi_{em} \approx 1.2°$ and $R_{eff} \approx 70.5$. Theoretically there was no problem to get $Re\phi\phi$ an order of magnitude larger e.g. $\Delta\phi_i \approx 45°$ and $\Delta\phi_e \approx 0.1°$.

In both cases the difference between the precise and approximate solutions was below 1%. Only in the case when the extrema of ϕ_e were very close to each other the precise solution of Eq. (25) was necessary.

IV. REFERENCES

[1] D.R. Hamilton et al. Klystrons and Microwave Triodes. Dover Publications , N. York , 1966.

[2] V.N. Shevtchik Osnovy Elektroniki Sverkhvysokikh Tchastot, Moscow 1959.

[3] S. Kulinski Large Signal Electron Bunching. PS/LPI/Note 85 - 11, CERN, Geneve 1985.

THE NEW SLOW EXTRACTION SYSTEM OF THE CERN PS

Ch. Steinbach, H. Stucki, M. Thivent

CERN, CH 1211 Geneva 23

Abstract

The slow extraction from the CERN PS to the East Area was completely rebuilt in March 1992. The new layout benefits from several improvements. The losses on the magnetic septa are suppressed by means of a novel concept applied to the third-integer resonance optics. The vacuum has been improved (in view of future lead ion acceleration) by means of a reduction in the number of septa and a change in their technology. Synchrotron radiation damage during lepton cycles is avoided by installing the septa on the inner side of the machine aperture. Maintenance is simplified, servicing eased and personnel radiation doses reduced by the use of modular plug-in units. The beam dynamics, the layout, the main characteristics of the hardware and the resultant performance are presented.

I. INTRODUCTION

The extracted beam from the CERN PS to the East experimental Area is used by numerous physics teams for the development of detectors. The proton momentum is 24 GeV/c and the intensity moderate (usually $3\ 10^{10}$ protons per cycle). The extraction system used until the end of 1991 had been installed 20 years ago [1]. Besides the obsolescence of some of the equipment, there were several reasons for replacing it. The acceleration of leptons for the LEP machine creates synchrotron radiation causing outgassing and damage to the magnetic septa, and severe sparking from the cathode of the electrostatic septum. The decision to accelerate heavy ions (lead) in the near future requires an improvement of the vacuum (10^{-9} torr). Finally, it was desirable to lower the number of elements in the ring to reduce maintenance and gain space for new equipment necessary for the numerous tasks of the PS, including operation for LHC in the future.

II. EXTRACTION LAYOUT

A. The resonance

The new system uses the third integer resonance 6 1/3, as did the previous extraction. The resonance is closer to the standard working point and the beam envelope fits better in the machine acceptance than for the half integer resonance.

To protect the extraction hardware from synchrotron radiation during the lepton cycles, it was decided to place the electrostatic and the thin magnetic septa on the inner side of the machine aperture, towards the machine centre.

On the 24 GeV/c flat top, the beam is brought near to the resonance from a horizontal tune of about 6.2 by pulsing two quadrupoles. RF debunching is then performed and the momentum dispersion is enlarged. Since the chromaticity is negative and the first septum is on the inside of the ring, the beam is pushed through resonance by a slowly increasing field in the main magnets of the PS.

B. The quadrupoles

The two quadrupoles have three purposes:
- increase Q_h as already mentioned,
- increase β_h at both electrostatic and thin magnetic septa to enhance the beam deflection,
- decrease the horizontal dispersion at the electrostatic septum and increase it at the thin magnetic one to adapt the extraction to the momenta of the particles belonging to different separatrices, as will be seen in II.E.

The effect of the quadrupoles is summarized in table 1.

Table 1: Lattice parameters at the positions of the septa

Location	Unperturbed machine		Machine with 2 quads	
	β horiz.	Dispersion	β horiz.	Dispersion
Electrostatic septum	22.2 m	3.04 m	36.2 m	1.27 m
Magnetic septum	22.6 m	3.04 m	35.5 m	5.01 m

C. The Sextupoles

Two sextupoles are installed to meet three requirements:
- the phase of the 19th harmonic determines the phase plane angle of the separatrix at the electrostatic septum,
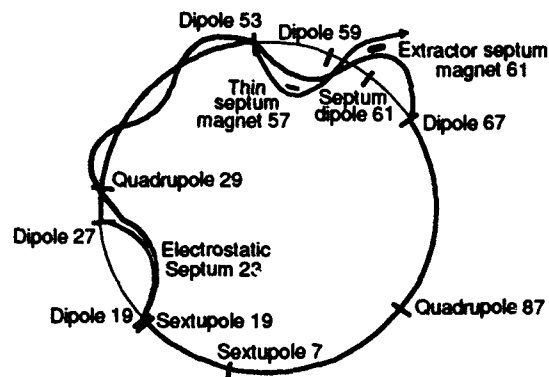
Fig.1: Schematic view of the extraction and its elements

- the amplitude of the 19th harmonic drives the resonance to give 10 mm spiral pitch at the electrostatic septum,
- the zero harmonic helps to reduce the absolute value of the chromaticity to satisfy equation (1) (see section E).

D. The septa

The electrostatic septum is almost an integer number of betatron wavelengths away from the equivalent sextupole. The deflection is 0.28 mrad. A $\lambda/2$ bump pushes the beam inside towards it. It has not been possible to superimpose the separatrices of various momenta [2] (Fig.2). The cost in efficiency is of the order of 0.5% which is quite acceptable.

The thin septum magnet is located 2.17 betatron wavelengths further downstream. The separation between extracted and circulating beam is 8 mm, amply sufficient to house the septum in spite of its outwards deflection.

The extraction septum is situated 1/4 betatron wavelength further downstream, outside the vacuum after the separation of the extraction channel from the machine chamber. The local bump is common to both magnetic septa and gives angle as well as displacement at the extractor septum magnet. It is created by 4 dipoles, one of them being a septum magnet.
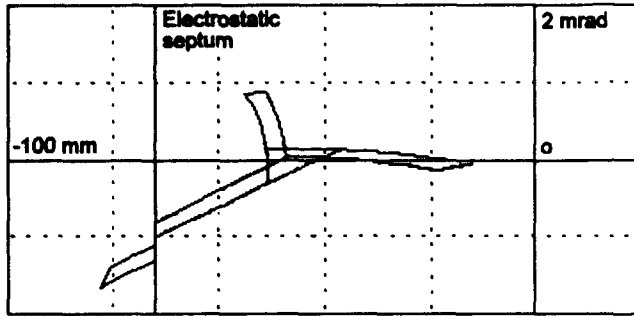
Fig.2: Phase plane at the exit of the electrostatic septum

The extracted beam crosses the fringe field of two PS standard C-shaped combined function magnets before reaching the first transfer quadrupole. The vertical emittance is doubled due to the non-linearity of the fringe field.

E. Chromatic effect at the thin septum magnet

The kick given by the electrostatic septum to the extracted beam transforms into a jump at the thin magnetic septum. In general, however, the position of this jump depends on the momentum of the particles.

This effect is corrected (Fig.3) by a proper choice of the dispersion at the septa [3], the condition to satisfy being:

$$D_{n2} \sin\varphi_1 - D_{n1} \sin\varphi_2 = \frac{8\pi Q'_x}{S}\sin(\varphi_2 - \varphi_1) \qquad (1)$$

where φ_1 and φ_2 are the betatron phase angles between the sextupole and the electrostatic and thin magnetic septa, D_{n1} and D_{n2} the normalized dispersion coefficients at these septa, Q'_x the horizontal chromaticity and S the normalized strength of the 19th harmonic of the sextupolar perturbation.
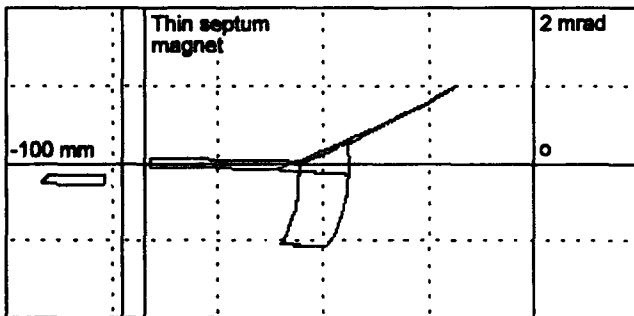
Fig.3: Phase plane at the entrance of the thin magnetic septum

We choose S = 0.13 which leads to Q'_x = -3.2
The instantaneous momentum spread of the extracted beam is given by [3]:

$$\frac{\Delta p}{p} = \frac{S\sqrt{\pi\varepsilon_o\sqrt{3}}}{24\pi Q'_x} \qquad (2)$$

For the nominal horizontal circulating beam emittance ε_o (at 2σ) of 0.5π μm at 24 GeV/c, the result is $\Delta p/p = 8 \ 10^{-4}$.

III. THE ELECTROSTATIC SEPTUM

The septum itself is made up of a 0.1 mm Molybdenum foil stretched on an "Anticorodal" frame which matches the inside dimensions of the accelerator vacuum chamber to avoid impedance discontinuities for the circulating beam. The high voltage cathode is of aluminum with an 8μm thick surface oxidation obtained in a chromic acid bath. The operating voltage is 150 kV and the gap is 17 mm.
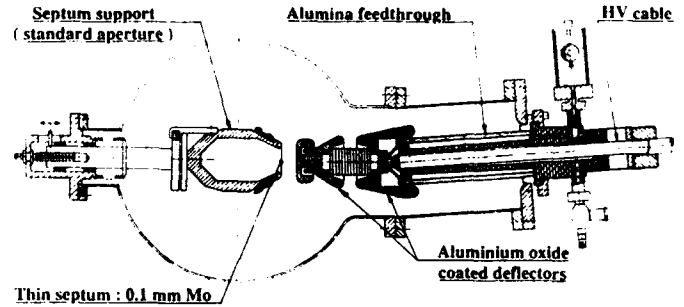
Fig.4: Drawing of the electrostatic septum

The holders and the HV feed-through are made of inorganic material: aluminum oxide brazed to metal parts. Grounded deflectors are made of stainless steel, and HV deflectors of oxidized aluminum as the cathode. A 200 Ω damping resistor is connected between the power supply and the electrode to absorb the energy in case of sparking.

IV. THE THIN SEPTUM MAGNET AND ITS TANK

The thin magnetic septum is equipped with a single-turn coil. It is slowly pulsed with 10 kA during a 600 ms flat top. The gap is 25 mm and the induction 0.7 T. The 4 mm septum is cooled by 5 water pipes of 2mm x 2mm cross section.
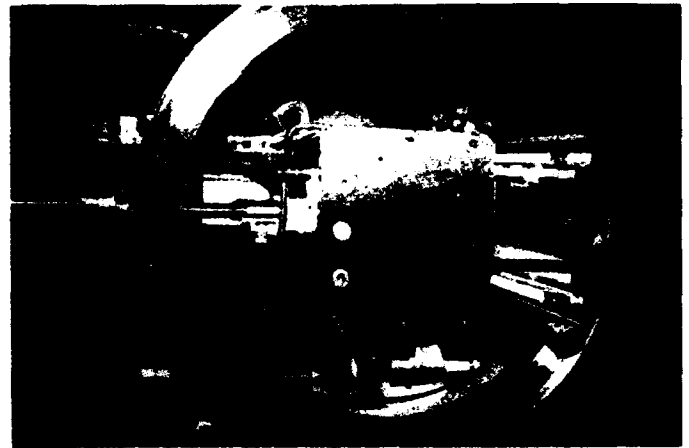
Fig.5: The thin septum magnet in the open tank before installation

The newly developed coaxial current feed-through is insulated with brazed alumina. The magnet yoke iron laminations are insulated with polyimide film every 3 mm. It can be baked at 180°C with 4 infrared lamps fitted with reflectors to keep the tank below 50°C since conventional aluminum vacuum joints are used. The power connection

consists of 26 copper foils each of 0.5mm x 200 mm cross section to allow radial and angular adjustment of the magnet.

The power supply safety interlocks take into account the vacuum level and the cooling water flow.

The vacuum tank is a longitudinal stainless steel cylinder of 420 mm inside diameter and 10 mm wall thickness. All components such as septum magnet, positioning system, vacuum pump, alignment pads and beam observation system are mounted directly on the tank. Ion pumps are placed below and sublimation pumps on top of the tank. Fixed inside the tank, a gutter-shaped sheet surrounds the circulating beam aperture to lower the tank impedance as seen by the beam and avoid instabilities of high intensity beams. This constitutes a compact, easily transportable and modular plug-in unit which simplifies maintenance, eases servicing and reduces the personnel radiation dose.

Fig.8: The extraction magnet and the septum bumper
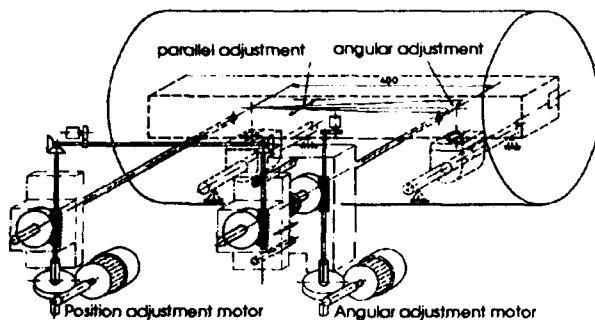
Fig.6: Sketch of the thin septum magnet position adjustment

Fig.6 shows the positioning principle of the magnet which is supported inside the tank by titanium-carbonate-coated linear stainless steel bearings. The magnet is positioned by two rods moved by a parallel adjustment motor. A second motor provides the angular positioning by moving one of the parallel drive gear boxes. The available adjustment is ±15 mm in position and ±5 mrad in angle.
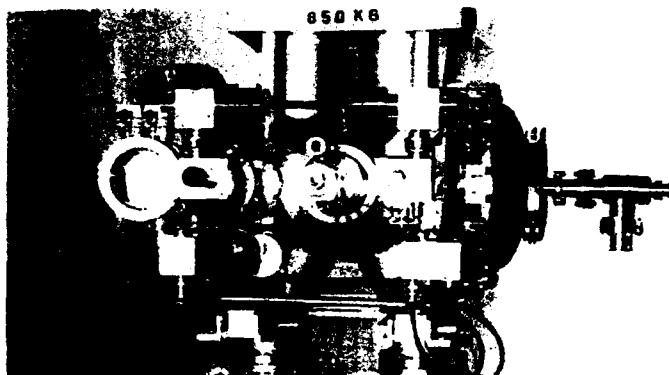
Fig.7: The thin septum tank with the positioning system

V. THE EXTRACTION AND BUMPER SEPTUM MAGNETS

These septum magnets are multiturn and placed outside the vacuum. The bumper has a 10-turn coil and the extractor a 4-turn one. They are slowly pulsed to avoid eddy currents in the chambers. Cooling is provided to each half turn of the coils and thermostats protect against possible corrosion-induced blockage.

VI. BEAM MONITORING

Tuning the extraction makes use of the general purpose measurement devices for orbit, betatron tune and losses. Dedicated monitors have also been installed: a secondary emission grid monitor and a TV screen at the thin septum magnet, another screen and a secondary electron chamber in the channel at the exit of the machine fringe field. The latter is calibrated by comparison with a beam transformer in a specially implemented fast extraction mode.

VII. PERFORMANCE

For the standard beam intensity of 3×10^{11} protons per cycle, the measured efficiency is about 95%, the horizontal and vertical extracted beam emittances are respectively 0.1 and 0.8 $\pi\mu$rad, the instantaneous $\Delta p/p$ being 0.08% for a total $\Delta p/p$ of 0.3% after debunching. Losses are essentially concentrated at the electrostatic septum. The maximum spill length is 500 ms, limited by the main magnet dissipation.

VIII. CONCLUSION

The PS slow extraction has been upgraded to answer the foreseeable needs. The septa and tanks are compatible with the vacuum quality required by the future acceleration of lead ions, they are shielded from the synchrotron radiation emitted during lepton cycles and their maintenance is easier. These improvements have been obtained while keeping the same performance in energy and efficiency.

IX. ACKNOWLEDGEMENTS

XI. REFERENCES

[1] W. Kubischta, Multiple target extraction sharing scheme at the CPS, Proc. of the VIIIth Int. Conf. on High Energy Accelerators, CERN, Geneva, 1971, p. 110.

[2] W. Hardt, Ultraslow extraction out of Lear (transverse aspects), CERN internal report PS/DL/LEAR Note 81-6.

[3] Ch. Steinbach, Beam optics at resonant extraction septa, Proc. of EPAC, Berlin, 1992, p. 857.

Simulation of Slow Extraction in the Main Injector

C. S. Mishra, F. A. Harfoush, and J. Johnstone
*Fermi National Accelerator Laboratory**
Batavia, Illinois 60510

Abstract

Recent modifications to the tracking code TEAPOT have allowed us to simulate both ramp and slow extraction in the Fermilab Main Injector at 120 GeV/c . This calculation includes all the magnetic field and alignment errors. Preliminary results from this calculation are presented here and compared with other calculations. Further studies to optimize the strength and ramp of the extraction elements are in progress.

I. INTRODUCTION

The Fermilab Main Injector (FMI) is designed to provide high intensity slow extracted beam, 3×10^{13} protons every 2.9 sec with 33% duty factor. This 120 GeV/c beam will be used for the studies of CP violation and rare Kaon decays and detector R&D. The new FMI will enable a state of the art Kaon experiment, in a similar amount of running time, to improve the upper limits of rare Kaon decays by two orders of magnitude.

The slow extraction in FMI is planned by exciting the half-integer resonance. The half-integer resonance is a linear resonance and can be induced by a quadrupole field. The beam in this case is either entirely stable or entirely unstable. The extraction rate is controlled by using an octupole field, which splits the beam phase space into stable and unstable region. In this paper we describe the simulation of slow extraction in FMI. The FMI lattice we have used contains all errors and appropriate extraction elements. Due to CPU limitations, ramping is done in few hundred turns. In all these calculations a modified version of the thin element tracking code TEAPOT [1], and MAD [2] are used.

II. EXTRACTION CONDITIONS

The FMI lattice used in these calculations has the dipole body and end multipoles, both normal and skew, calculated by using the method described in [3]. The values of the systematic and random errors of the quadrupoles are calculated using the Main Ring quadrupole measurements. All skew quadrupole field errors are turned off,

for the convenience of the simulation. Tables 1 and 2 of [3] summarize all of the multipoles. The misalignment of all the magnetic elements and beam position monitors has been included in this calculation. The rms of the alignment error with respect to the closed orbit is 0.25mm in both horizontal and vertical planes. In addition dipole magnets have an rms roll angles of 0.5 mrad. In the lattice there are 18 RF cavities, each operating at $V_{rf} = 0.0555$ MV at 120 GeV. The RF frequency is set to 53 MHz corresponding to a harmonic number of 588. Synchroton oscillation was included in the simulations by launching all particles with an amplitude of $\delta_{max} = (\Delta p/p)_{max} = 0.3\text{E-3}$ at 120.0 GeV.

The base tune of FMI is $(Q_x, Q_y) = (26.425, 25.415)$. Before the extraction process the FMI is corrected by the methods described in [4]. The extraction process begins by changing the main quadrupole power in order to raise the horizontal tune closer to the half integer 26.485. Using the 32, 0th-harmonic octupoles, placed in the ring an amplitude-dependent tune shift and consequently a tune spread in the beam is induced. The existing octupole component of the Main Ring quadrupoles adds up to the 0th-harmonic octupoles and help this process. The 0th-harmonic octupoles are not used as correctors during slow extraction. The 53rd harmonic quadrupoles are turned on to achieve a desired orientation of the phase space. Sixteen of these recycled Main Ring quadrupoles are distributed around the ring, separated into two orthogonal families (cosine and sine). One family alone excites the 53rd harmonics for resonant extraction, while both families are used to cancel the natural half-integer stopband of the machine. The strength of the quadrupoles and octupoles are chosen so that at the end of the initial ramp the stable phase-space area is as large as the emittance of the circulating beam.

The 53rd harmonic quadrupoles are further ramped to increase the width of the half-integer stopband and start moving the stopband through the beam. Small amplitude (smaller tune) particles remain stable, with their phase-space motion on subsequent turns oscillating between the fixed points. Every turn the stable phase-space area shrinks and the large amplitude particles enter the stopband and become unstable. The unstable particles

streams out along the separatrix until they jump across the wires of electrostatic septum. The particles with horizontal amplitude larger than the horizontal location of the septum are kicked to provide enough separation between the circulating and extracted beams at the lambertson.

III. EXTRACTION SIMULATIONS

The FMI extraction will take place over 1.0 sec or 100k turns for 3×10^{13} protons. A real simulation of this process will require a considerable amount of CPU time. Simulations of the quadrupole and octupole ramp and final extraction process have been done in several hundered turns by using the modified TEAPOT and MAD. The new modified TEAPOT code can do both the tracking calculations and model the extraction. The added feature of this code is that it allows one to ramp the magnetic elements, by adding the addtional strength to a particular magnetic element as error, after a certain number of particle turns. This simulation in reality corresponds to fast resonant extraction, in which the beam is fully extracted within a few milliseconds. The extension of this simulation and extraction process to longer time spans is a straight forward procedure.

Initial particle positions and transverse momenta were generated randomly from uncoupled, gaussian distribution in both planes. 1000 particles were tracked in these simulations. Before launching these particle the FMI lattice is corrected by the method described in [4]. The simulation begins by increasing the horizontal tune of the machine from the nominal value of .425 to .485 using the main quadrupole circuits. During the first hundred turns the desired orientation of the phase-space at the septum is achieved by slowly energizing the appropriate 53rd harmonic quadrupole and 0th harmonic octupole circuits. In the present simulation the strength of these elements is increased every turn of particle tracking. At this stage the stable phase space region is just large enough to enclose the emittance of the beam as shown in 1.

The extraction septum is turned on for subsequent tracking. This provides a horizontal kick to the particle whose amplitude is larger than 16 mm, the location of the septum wire. The 53rd harmonic quadrupoles are slowly ramped over several hundred turns. This makes the particles move along the separatrix with their amplitude growing exponentially every turn until they ultimately jump the electrostatic septum wire. Figs 2,3 show the phase space of these particles after 50 turns at the electrostatic septum and lambertson. One can clearly observe the separation between the circulating and extracted beam is achieved. These calculations are done using the modified version of the TEAPOT code. The location of the septum and lambertson are choosen such that there is about 83 deg of phase advance between them. Figs 4,5 show the same after 150 turns, where most of the particles are already extracted. During this process of ramping and extraction only 2% of the particles were lost. 1% were lost when their amplitude became so large that they hit the aperture of the

machine, while the other 1% were lost by particles hitting the septum wire. At present the extraction rate simulated by TEAPOT is not quite uniform. More study is needed to control the rate of extraction, which can be done by changing the rate of the two ramps.

In an independent study tracking with the code MAD was performed. In this simulation similar input and ramp were also used. Figs. 6,7 show the phase space distribution of the particle after 500 turns. In this calculation a local orbit bump provides the angular offset at the septa, and ensures that the extracted beam is consistent with the trajectory and aperture of the 120 GeV/c beamline to switchyard.

IV. CONCLUSION

The simulations described in this paper show that the proposed slow extraction scheme for the FMI will work with high efficiency. Further details of the strength of the extraction elements and speed of ramp for uniform extraction is being worked out. Results obtained with the modified TEAPOT version seem to be in agreement with MAD results.

V. ACKNOWLEDGMENTS

V. REFERENCES

[1] L. Schachinger and R. Talman, Particle Accl. 22, 35(1987).

[2] H. Grote and F. C. Iselin, "The MAD program" CERN/SL/90-13.

[3] F. A. Harfoush and C. S. Mishra, "Systematic and Random Errors for Main Injector Tracking," Fermi Internal Notes, *MI-0066*,in PAC93 proceedings.

[4] C. S. Mishra and F. A. Harfoush, "Correction Schemes to Improve the Dynamical Aperture of the Main Injector," in PAC93 proceedings.
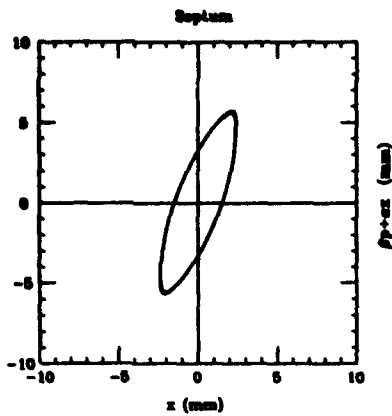
Figure 1: Stable phase space region of the beam

Figure 2: Phase space at electrostatic septum for turn=50

Figure 3: Phase space at lambertson for turn=50
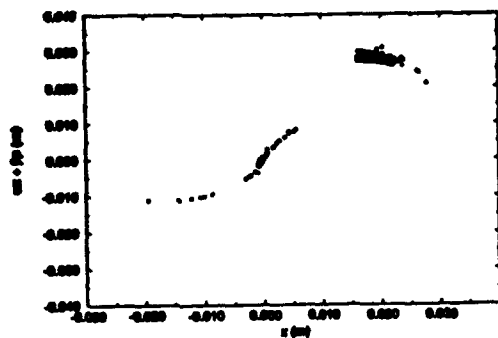
Figure 4: Phase space at electrostatic septum for turn=150

Figure 5: Phase space at lambertson for turn=150
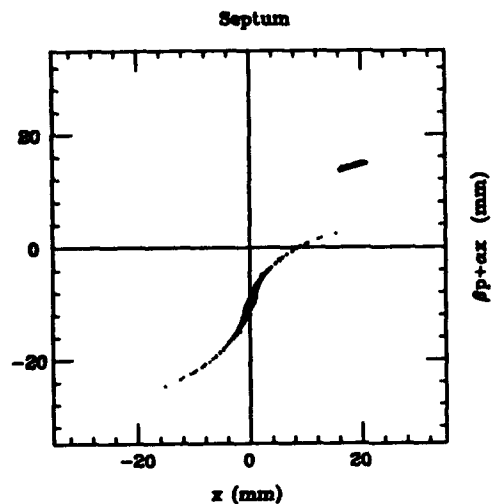
Figure 6: Phase space at electrostatic septum for turn=500 using MAD
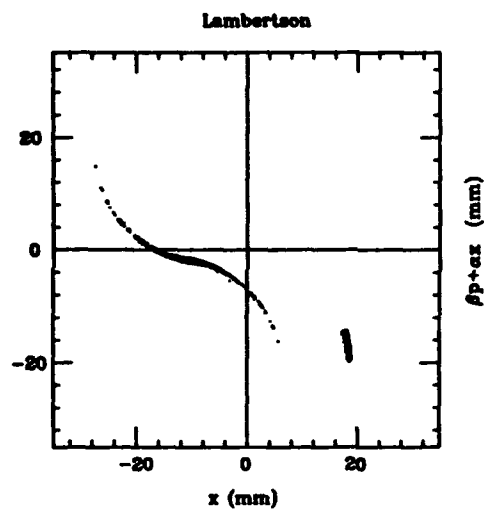
Figure 7: Phase space at lambertson for turn=500 using MAD

344

Stability of Beam in the Fermilab Main Injector

C. S. Mishra and F. A. Harfoush
*Fermi National Accelerator Laboratory**
Batavia, Illinois 60510

Abstract

The Fermilab Main Injector is a new 150 GeV protron synchrotron, designed to remove the limitaions of the Main Ring in the delivery of high intensity proton and antiproton beams to the Tevatron. Extensive studies has been made to understand the performance of the Main Injector. In this paper, we present a study of the Main Injector lattice, which includes magnetic and misalignment errors. These calculations shows the Main Injector's dynamical aperture is larger than its design value of 40π mm mradian at injection.

I. INTRODUCTION

The Fermilab Main Injector (FMI) will be constructed using a newly designed conventional dipole magnets and mostly recycled quadrupoles from the Main Ring. The FMI lattice has two different types of cells, the normal FODO cells in the arcs and straight sections and the dispersion-suppressor FODO cells adjacent to the straight sections to reduce the dispersion to zero in the straight sections.

Simulations results of the FMI at its two most critical times, injection and slow extraction are presented in this paper. The FMI lattice includes the magnetic field errors, both systematic and random, and misalignment errors. Studies of closed orbit errors, betatron function errors, tune versus amplitude and dynamical aperture are presented in this paper. Results shows that the dynamical aperture meet the design specifications. A thin element tracking program TEAPOT[1] has been used for these simulations.

II. TRACKING CONDITIONS

The Main Injector lattice has two different sizes dipole magnets, there magnetic lengths are 6.096 and 4.064 meters at 120 GeV. The magnetic length of these dipoles changes with energies due to the saturation of ends, and at 8.9 GeV their length is 2.46 mm larger than the nominal at 120 GeV[2]. This change in length introduces a non

zero dipole multipole at each end of the magnet. This additional bending of the particle, is corrected by decreasing the dipole excitation.

The ends of the magnet have different magnetic multipoles than the body of the magnet. For the tracking calculation the two ends and the body are treated as separate magnets . The dipole body and end multipoles, both normal and skew, are calculated by using the method described in[3]. At present we have only two prototype Main Injector dipoles, so the random errors of the body multipoles are calculated by using the measurements of the B2 dipoles at 210 Amps for 8.9 GeV.

The values of the systematic and random errors of the quadrupoles are calculated using the Main Ring quadrupole measurements. There are a very limited number of measurements available for MR Quads. The Main Ring quadrupoles have a large octupole component and random error. The variation of the octupole strength and random errors with current are small. All skew quadrupole field errors are turned off, for the convenience of the simulation. Using a coupling compensation scheme any linear coupling effects due to the presence of skew quadrupole can be removed. Table 1 and 2 of ref [3] summarizes all of the multipoles as used in the input file to TEAPOT. Multipole field errors are quoted in units of 10^{-4} at a displacement of one inch.

The misalignment of all the magnetic elements and beam position monitors has been included in this calculation. The RMS of the alignment error with respect to the closed orbit is 0.25 mm in both horizontal and vertical direcJions. In addition dipole magnets have an RMS roll angle of 0.5 mrad.

Base tune of $(Q_x, Q_y) = (26.425, 25.415)$ were used in all the simulations. This tune is different than (26.407, 25.409) which was used in earlier calculations. This change in tune was necessary to increase the dynamic aperture, with all magnetic and misalignement errors turned on, the presence of RF, and with chromaticity set to desired value. In the lattice there are 18 RF cavities, each operating at $V_{rf} = 0.0218$ MV and 0.0555 MV at 8.9 and 120 GeV respectively. The RF frequency is set to 53 MHz corresponding to a harmonic number of 588.

III. TRACKING RESULTS

A. Closed orbit and Betratron Function Errors

In the Main Injector lattice there are 208 quadrupoles, 128 are recycled Main Ring quadrupoles, rest are newly designed. Located inside these quadrupoles are the beam position monitors. The vertical and horizontal beam position are measured at the focusing and defocusing quadrupoles respectively. The vertical and horizontal displacement of the particles are corrected by applying corresponding kicks just after these position monitors.

The average RMS closed orbit deviation before correction is 5.9 mm horizontal and 4.4 mm vertical for the selected seed. After three iterations of the orbit corrections the average RMS closed orbit deviation is reduced to 2.3×10^{-4} mm (H) and 7.2×10^{-7} mm (V). Most of the close orbit deviation is due to dipole random and misalignment errors . Figs 1a and 1b show the distribution of uncorrected horizontal and vertical RMS closed orbit errors for 20 different seeds at 8.9 and 120 GeV. The average RMS deviation of each seed is 5.0 mm and 3.9 mm in the horizontal and vertical planes respectively.

The maximum corrector strength required to correct these orbit deviations is 100 $\mu radians$ in both planes at these energies. In the Main Injector we plan to recycle Main Ring dipole correctors and also use newly build dipole correctors. At 8.9 GeV the Main Injector dipole correctors can provide 2000 μ radian and 1300 μ radian of horizontal and vertical corrections respectively.

Due to the presence of the dipole and quadrupole random errors and magnet alignment errors there is a variation of the β function around the FMI from an ideal lattice. Figs 2a and 2b show the distribution of the horizontal and vertical $\Delta\beta/\beta$ when all the errors are included. The sigma of these deviations is about 5%. The variation in β can be further reduced by using correction scheme utilizing extraction quadrupoles in the lattice. Since all the Main Ring quadrupoles will be measured before their placement in the FMI we can develop a shuffling scheme of quadrupoles for their placement in FMI.

B. Dynamical Aperture

We have studied the survival of particles launched at different amplitudes in the Main Injector at the injection energy. A single particle will go around 35000 turns at the injection energy of 8.9 GeV during any operation that involves filling the ring with six Booster bunches. At 120 GeV where slow extraction of the proton beam is planned the beam will stay in the ring for a maximum of 1.0 sec (flattop). At 120 GeV we have simulated this but 100k turns. A particle is launched with a maximum horizontal displacement "A" defined at a location where the horizontal beta function is at its maximum of 75 meters. The maximum vertical displacement of the same particle is 0.4A (x/y=2.5) also at a beta of 75 meters. Synchroton oscillation were included in the simulation by launching all particles with an amplitude of $\delta_{max} = (\Delta p/p)_{max} = 2.0 \times E - 3$.

Particles were launched from 15 mm to 35 mm amplitude. Simulations were performed for five different seeds. Figs 3a and 3b are survival plots, displaying how many turns a particle survives in the Main Injector at 8.9 and 120 GeV, as a function of initial amplitude. If the dynamical aperture of the machine is defined as the smallest amplitude particle that did not survive, then the dynamical aperture for the Main Injector at the injection energy is predicted to be 34.4±0.8 mm, corresponding to a normalized emittance of $96.8 \pm 4.5\pi$ mm-mradians.

C. Other Studies

We have studied the effect of power supply ripples on the FMI performance. It is expected that the FMI power supply will achive similar regulation as Main Ring power supply, i.e. $\pm$ 300 ppm and $\pm$ 60 ppm at injection and extractions respectively. This ripple causes a shift in tune-tune plane of about $\pm$ 0.017(h) and $\pm$ 0.019(v) at injection and $\pm$ 0.008(h) and $\pm$ 0.005(v) at 120 GeV. This does not seem to be a serious problem.

We have also studied the alignment tolerance of the magnetic element and have concluded that it is important and feasible to achieve the alignement tolerance described in this paper.

IV. CONCLUSION

These calculations show that the Main Injector design exceeds the design specification of 40π mm mradians normalized emittance at injection. The larger octupole and the random variation of the quadrupole strengths are the limiting factor for this dynamical aperture. A correction scheme has been developed to increase this dynamical aperture which is not necessary at 8.9 GeV but will be desired for 120 GeV slow extraction.

V. ACKNOWLEDGMENTS

V. REFERENCES

[1] L. Schachinger and R. Talman, Particle Accl. 22, 35(1987).

[2] C. S. Mishra, H. D. Glass and F. A. Harfoush, "Effective Length of the Main Injector Dipole and its Effect on Main Injector," Fermi Internal Notes *MI-0072* and H. D. Glass et al, FERMI-TM-1815,1992.

[3] F. A. Harfoush and C. S. Mishra, "Systematic and Random Errors for Main Injector Tracking," Fermi Internal Notes, *MI-0066*,in PAC93 proceedings.

[4] C. S. Mishra and F. A. Harfoush, "Simulation of the Dynamical Performance of the Main Injector," Fermi Internal Notes *MI-0070* and FERMILAB-CONF-92/075.
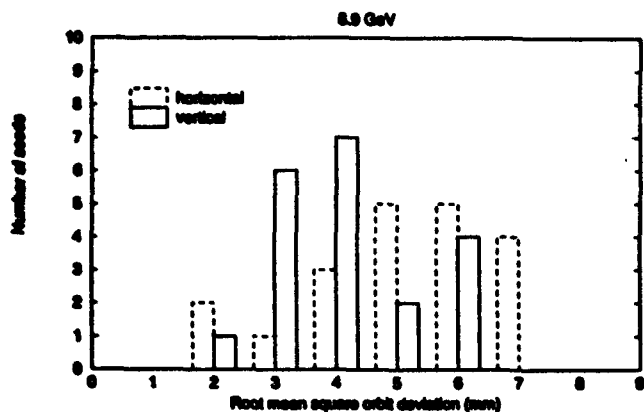
Fig. 1a Histogram of Closed orbit errors before correction
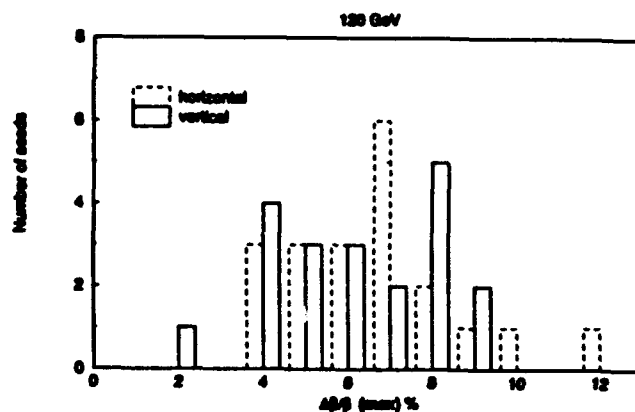
Fig. 2b Histogram of Maximum ($\Delta\beta/\beta$)
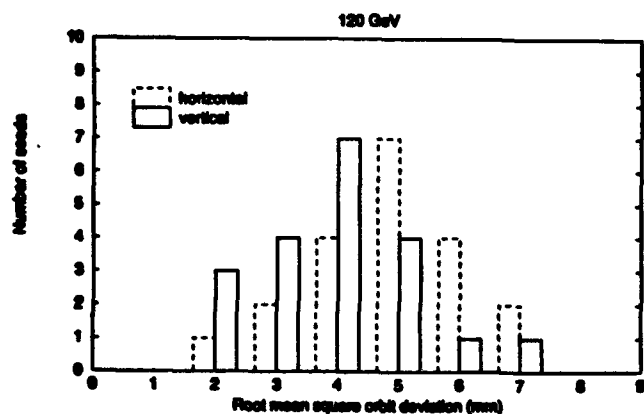
Fig. 1b Histogram of Closed orbit errors before correction
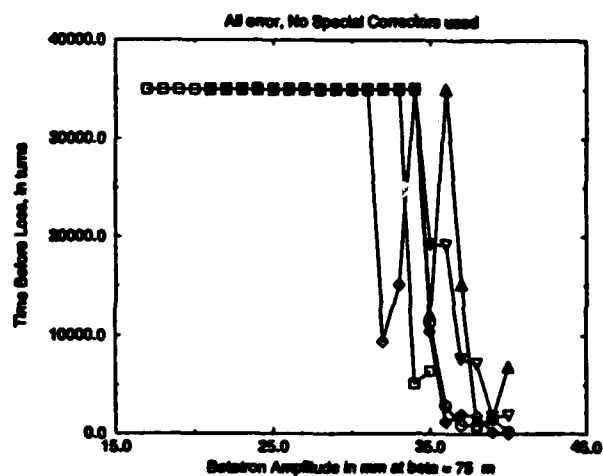
Fig. 3a Survival Plot at 8.9 GeV
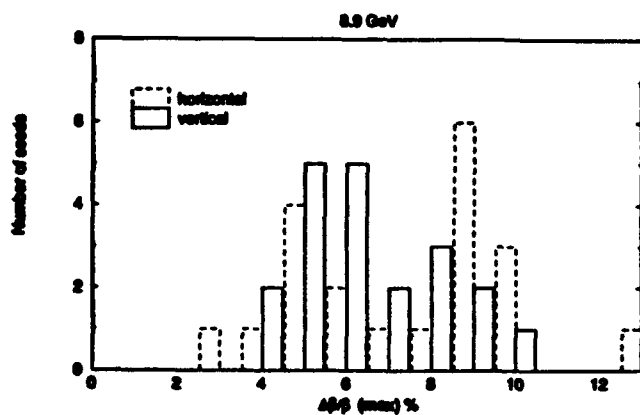
Fig. 2a Histogram of Maximum ($\Delta\beta/\beta$)
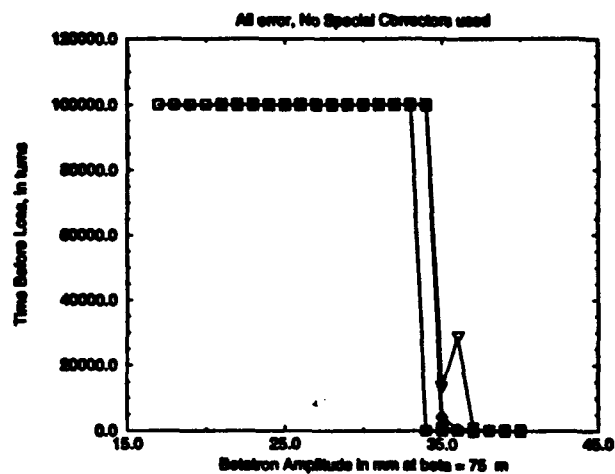
Fig. 3b Survival Plot at 120. GeV

347

Correction Schemes to Improve the Dynamical Aperture of the Main Injector

C. S. Mishra and F. A. Harfoush
*Fermi National Accelerator Laboratory**
Batavia, Illinois 60510

Abstract

Tracking simulations have revealed that the dominant factor limiting the dynamical aperture of the Main Injector are the large octupole component and the random errors in the recycled Main Ring quadrupoles. This paper describes a correction scheme that reduces the effect of these errors on the performance of the Fermilab Main Injector, specially for the slow extraction operation.

I. INTRODUCTION

The Fermilab Main Injector (FMI) is designed for multipurpose operation. At present four modes of operations for the FMI are planned. These correspond to antiproton production and slow or fast spill at 120 GeV/c, fixed target and collider operation at 150 GeV/c. Combinations of the above operational modes are also anticipated. It is important to understand the limitations of the lattice design and find new schemes which will improve the performance of the FMI. Simulations [1] of the FMI lattice, which includes the magnetic field errors, both systematic and random, misalignment errors, show that the dynamical aperture is larger than the design value of 40π mm-mradians at injection. The dynamic aperture can become a limiting factor at slow extraction and therefore requires a closer study. Here the base tune is slowly increased to half integer resonance, before the extraction elements are turned on.

In this paper we discuss the limitations and correction schemes which utilizes the octupole and trim quadrupoles already placed in the lattice to increase the dynamic aperture.

II. TRACKING CONDITIONS

The FMI lattice has two different sizes dipole magnets. For tracking calculations each dipole magnet is cut in three pieces, two ends and one body. The dipole body and end multipoles, both normal and skew, are calculated by using the method described in [2]. To this date only two prototype dipoles have been built, so the random body errors are calculated from the available measurements of the B2 dipoles in the Main Ring (MR). Systematic and random errors of the quadrupoles are calculated using the MR quadrupole measurements. These quadrupoles have a large octupole component and random error. The large random error in dipole and quadrupole field strength can be attributed to the limited number of available measurements. All skew quadrupole field errors are turned off for the convenience of the simulation. Tables 1 and 2 of [2] summarize all of the multipoles used in the input file to the thin element tracking program TEAPOT [3].

The misalignment of all the magnetic elements and beam position monitors has been included in our calculations. The rms of the alignment error with respect to the closed orbit is 0.25 mm in both horizontal and vertical planes. In addition dipole magnets have an rms roll angle of 0.5 mrad.

Base tune of FMI is $(Q_x, Q_y) = (26.425, 25.415)$. This base tune has been used in our studies of the dynamic aperture except at slow extraction where the horizontal tune is changed to 26.485. This is further discussed in this paper. In the lattice there are 18 RF cavities, each operating at $V_{rf} = 0.0218$ MV and 0.0555 MV at 8.9 and 120 GeV respectively. The RF frequency is set to 53 MHz corresponding to a harmonic number of 588. Synchrotron oscillation was included in the simulations by launching all particles with an amplitude of $\delta_{max} = (\Delta p/p)_{max} = $ 2.0E-3, 0.3E-3 at 8.9 and 120.0 GeV respectively.

III. TRACKING RESULTS

We have studied the variation of the horizontal and vertical tunes as the amplitude of motion is increased. A particle is launched with a maximum horizontal displacement of "A" at a location where the horizontal beta function is at its maximum of 75 meters. The maximum vertical displacement of the same particle is 0.4A (x/y = 2.5) also at beta of 75 meters. Synchroton oscillation were included in the simulation by launching the particles with the proper non zero $\Delta p/p$. Figs 1a and 1b show the tune-tune plot at 8.9 and 120 GeV/c respectively. The particle labels on the tune plot corresponds to the initial amplitude "A" of a test particle in millimeters. Plot of tune versus amplitude is very close to a straight line for amplitudes less than 28

mm at 8.9 GeV/c, and less than 31 mm at 120 GeV/c. The nonlinear detuning at larger amplitudes is dominated by a combination of systematic octupole error in the recycled MR quadrupoles, and second order sextupole effects. Half of this detuning is due to the octupole component.

The presence of the dipole and quadrupole random errors and magnet alignment errors contribute to a variation of the β function around the FMI away from the error free lattice, as discussed in [1]. The average $\Delta\beta/\beta_{max}$ is about 6.4%. Fig. 2a is sample β function variation around the ring at a given seed with all the errors described earlier included.

The dynamical aperture of the FMI at 8.9 GeV and 120 GeV has been discussed in [1]. At 120 GeV, close to the half integer resonance extraction, the horizontal tune is changed from $Q_x = 26.425$ to 26.485. This is achieved by ramping the main quadrupoles in 0.1 sec. The detuning of the particle will remain the same at this setting and will result in loss of large amplitude particle. The slow extraction septum is placed at 16mm. We have studied the dynamical aperture of the FMI for slow extraction. In this regime particles remain in the FMI for 1.0 sec equivalent to about 100k turns. A survival plot is shown in Fig. 3. The dynamical aperture at 120 GeV is reduced from 34.6 ± 0.5 to 20.67 ± 1.25 mm . These calculations have not been taken into account other effects like power supply ripples, and space charge. If included we expect a further reduction in the dynamical aperture. Because the beam behaviour is more unstable at slow extraction a bigger dynamical aperture is needed.

III. IMPROVEMENTS

The focusing and defocusing quadrupoles are powered by two separate buses, and the current in each bus can be different. All the recycled MR quadrupoles will be measured for field quality and retuned if necessary before they are placed in the FMI. A smart shuffling scheme can be worked out that reduces the rms error in quadrupole field strength around the ring. A simple scheme is to divide the quadrupoles into two groups. One group will contain the quadrupoles with a strength higher than the total mean value and another group will contain the lower strength. This separation into two groups will reduce the rms error of quadrupoles by creating two non gaussian distributions. This has the equivalent effect of dividing the rms error by $2\sqrt{2}$. To simulate this process in our tracking we have reduced the rms error of quadrupoles from 24.0E-4 $(1/in^2)$ to 8.0E -4 $(1/in^2)$.

The FMI lattice has 32 octupoles and 16 trim quadrupoles placed around the ring for extraction. There are also 8 corrector octupoles in the ring. We are evaluating the possibilities of adding 8 more similar octupoles. The MR quadrupoles have a positive octupole component almost invariant with energy. The extraction and corrector octupoles will be used to zero the total octupole component in the ring. The bipolar power supply on these mag-

nets will enable us to use them for slow extraction, and as correctors at all other energies.

Fig. 4 shows the detuning of the particles at 120 GeV with the quadrupole random error reduced by $\frac{1}{3}$, and with the octupole correction elements turned on. Detuning of particles with large amplitude is reduced by about 30%. Fig. 5, is the survival plot before and after correction for one seed at the slow extraction tune of (Q_x, Q_y) = (26.485,25.425). The dynamical aperture increases by about 7mm. This is due mainly to the reduced $\Delta\beta/\beta$, and to the smaller total octupole in the FMI.

The variation in $\Delta\beta/\beta$ can be further reduced by canceling the natural half-integer stopband of the FMI. This is achieved by using the trim quadrupoles placed in the ring for slow extraction. Just like octupoles these trim quadrupoles can be used as extraction element for slow extraction, and as correctors at all other energies. Fig. 2(b) shows the $\Delta\beta/\beta$ of the FMI after the quadrupole random error, octupole, and half-integer stopband corrections have been included. Fig. 5, shows that the dynamical aperture does not increase when the half-integer stop band correction is added to the two other corrections.

IV. CONCLUSION

Using the correction schemes described in this paper our studies have shown that it is possible to reduce the effect of the quadrupole random error, and octupole multipole. This correction scheme provides us with additional aperture at all energies, especially for the 120 GeV slow extraction.

V. ACKNOWLEDGMENTS

V. REFERENCES

[1] C. S. Mishra and F. A. Harfoush, "Simulation of the Dynamical Performance of the Main Injector," Fermi Internal Notes *MI-0070*, FERMILAB-CONF-92/075 and in PAC93 proceedings.

[2] F. A. Harfoush and C. S. Mishra, "Systematic and Random Errors for Main Injector Tracking," Fermi Internal Notes, *MI-0066*,in PAC93 proceedings.

[3] L. Schachinger and R. Talman, Particle Accl. 22, 35(1987).
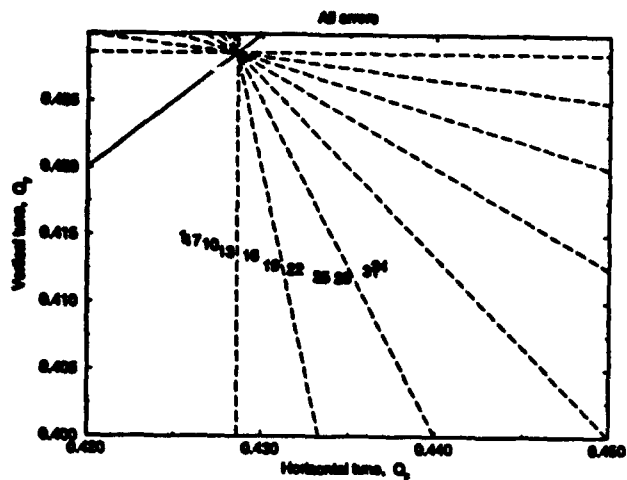
Fig. 1a Tune Tune plot for 8.9 GeV
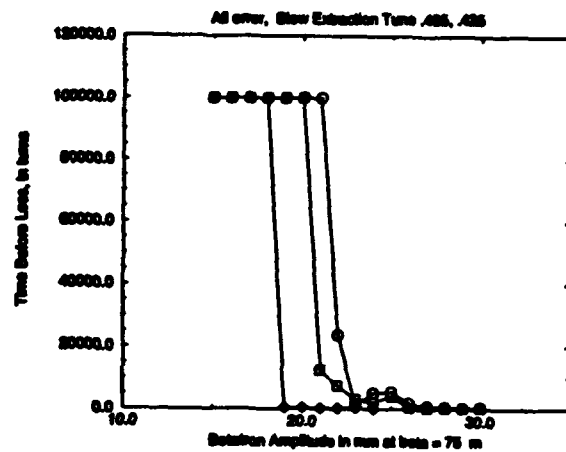
Fig. 3. Survival Plot at 120. GeV
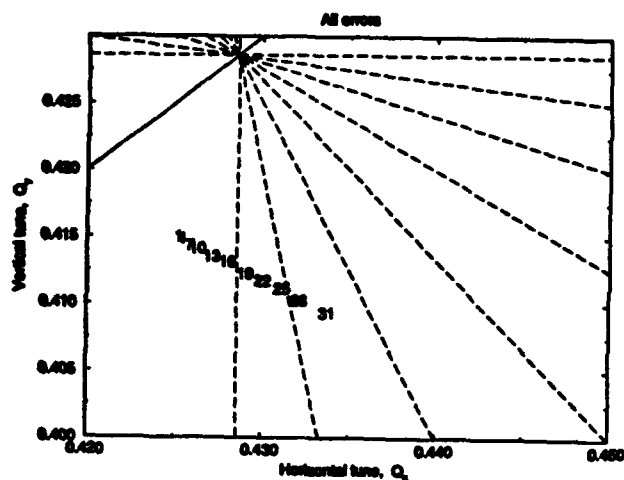
Fig. 1b Tune Tune plot for 120.0 GeV
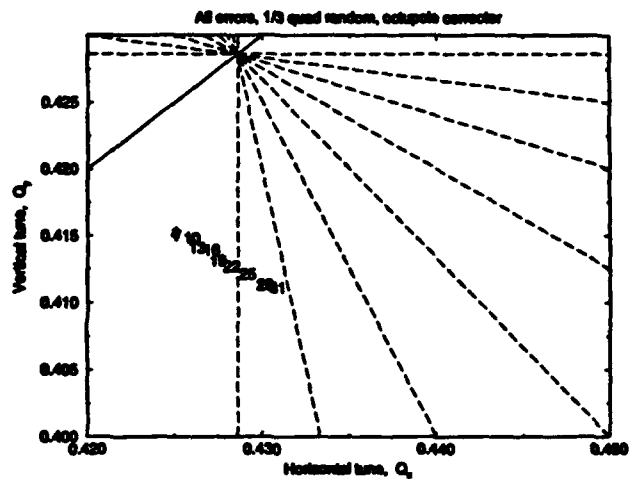
Fig. 4 Tune Tune plot for 120.0 GeV
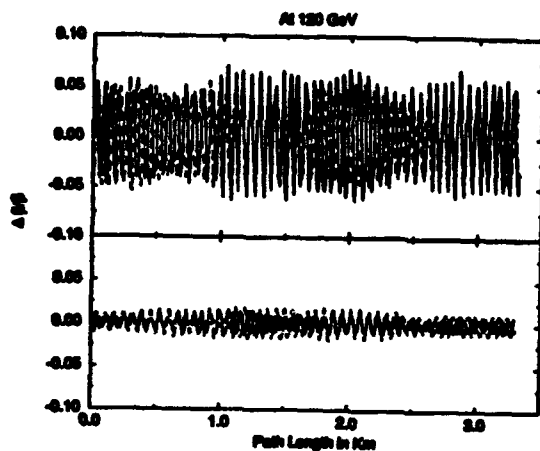
Fig. 2a Variation in Beta Function

Fig. 2b Variation in Beta Function with corrections
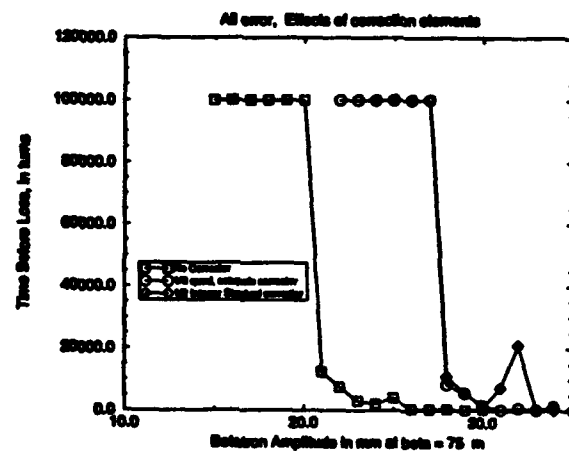
Fig. 5 Survival Plot at 120. GeV

Defining the Systematic and Random Multipole Errors For Main Injector Tracking

F. A. Harfoush, B. C. Brown, H. D. Glass, C. S. Mishra and S. Peggs

Fermi National Accelerator Laboratory*

Batavia, Illinois 60510

Abstract

At the Fermilab Magnet Test Facility (MTF) measurements of magnet field shape and strength have been performed. The tracking of the Fermi Main Injector (FMI) lattice requires a detailed knowledge of the magnetic field quality and its variation from magnet to magnet. As of this date only two prototype dipole magnets have been built, not enough to do a statistical analysis. For this purpose we have used old Main Ring dipole measurements. Measurements on a subset of Main Ring (MR) quadrupoles are also available. From the different sets of measurements available to us we have separated in our simulation the end multipoles from the body multipoles. Such a dissection of the magnet enables us to study more closely the effects of the end multipoles on the performance of the Main Injector. In particular we have studied the closed orbit errors due to variations in effective length of the long and short type dipoles. Tables of multipole errors are presented at both injection (8.9 GeV/c) and slow extraction (120 GeV/c) energies.

I. INTRODUCTION

Data from the Main Ring B2 dipole measurements are carefully selected to derive statistical information that can be applied to the MI dipoles. The data were obtained with a rotating coil and measured at 97A, 210A, and 1700A. The B2 dipole strength was obtained from a stretched wire probe 1" wide. The new MI prototype dipoles have been measured by a Hall probe, NMR probe, rotating coil, and flat coil probe. The Hall and NMR probe measures field at any (x, y, z) location in the magnet. The rotating coil is a cylindrical probe of radius 0.86" with wire windings on the surface and measures the integrated (over the length of the probe) multipoles of the magnet. These measurements are analyzed with a 1" reference radius. The flat coil is a probe with several coil windings around a rectangular frame. The probe measures the integrated relative flux as a function of position by translation of the probe. It can also measure the integrated relative flux as a function of magnet current.

II. SYSTEMATIC AND RANDOM ERRORS

A. Case of Dipoles

The Main Injector lattice has both a long and a short type dipole magnets. Their magnetic lengths at 120 GeV/c have a ratio equal to $\frac{2}{3}$, and their respective lengths are 6.096 and 4.064 meters. The magnetic length of these dipoles varies with energy due to saturation of ends. Because the end pack design is the same for both types of magnets the absolute change in effective length for each magnet will be the same. However the relative change in each case will be different. To study what effect this might have on the closed orbit of FMI the field errors due to the end dipole are separated from the body field errors. Multipoles due to dipole end are defined . TEAPOT in a separate element called MULTIPOLE. Because a dipole component in MULTIPOLE has the undesired effect of changing the reference orbit of the machine it is represented by a horizontal kick HKICK equal to

$$H_{kick} = \frac{\Delta L}{2 L_{ref}} \times \left(\frac{2\pi}{904/3} \right) \qquad (1)$$

where ΔL is the absolute change in effective length and L_{ref} is the reference length at 120 GeV/c. An increase or decrease in bending angle of the particles is corrected by changing the dipole field strength. In TEAPOT this is taken into account by adding a systematic field error to the dipoles. The multipoles at each end, both normal and skew, are calculated from the following equation:

$$\int B_n dl = \int_{-\infty}^{\infty} B_n dl - \int_{L_o} B_n dl \qquad (2)$$

where L_o is the physical length of the magnet, and B_n is the n-th field multipole. In our case $L_o = 240''$. Details of the calculations are given in [1,2]. The integrated end multipoles quoted in Tables 1,2 are in units of 10^{-4} at a 1" radius, and normalized to the integrated body dipole. They represent the latest end pack design. Body multipoles and end multipoles can be directly added to obtain the total integrated multipole. The random errors of the body multipoles are calculated, as mentionned earlier, from the B2 dipole measurements. A conservative estimate of dipole strength variation has been used since measurements on

the available sample have been limited by measurement errors. A small sample measured over a short period of time shows a variation of 2.5 units. No random errors are added to the end dipole.

B. Case of Quadrupoles

The values of the systematic and random errors of the quadrupoles are calculated using the Main Ring quadrupole measurements. The available measurement system provides limited information on quadrupole strength. A conservative assumption is made. It is observed that the variation of the octupole strength with current is very small suggesting a geometric effect. All skew quadrupole field errors are turned off for the convenience of the simulation. Using a coupling compensation scheme any linear coupling effects due to the presence of skew quadrupole can be corrected for.

Results are again summarized in Tables 1,2 at both injection and slow extraction energies.

II. RESULTS

A. Closed Orbit Errors

In the Main Injector lattice there are 208 quadrupoles. Located inside these quadrupoles are the beam position monitors. The vertical and horizontal beam positions are measured at the focussing and defocussing quadrupoles respectively. The vertical and horizontal displacement of the particles are corrected by applying corresponding kicks just after these position monitors. A typical uncorrected closed orbit for a given seed in both the horizontal and vertical plane at 8.9 GeV/c is shown in Fig. 2. The maximum corrector strength necessary to correct the orbit deviations in both planes is within the range of available corrector bend strength.

B. Betatron Function Errors

Fig. 1 is a sample plot of the horizontal and vertical beta function with all errors included and for a given seed. Variation in beta function from seed to seed is quite noticeable. The rms of these variations is in good agreement with what analytical formula predicts due simply to random quadrupole errors. This implies, and not surprisingly, that the major source of error contributing to the beta variations is the quad random error. More results on the closed orbit errors and betatron errors are presented in [3].

IV. CONCLUSION

The separation of the end dipole field errors from the body field errors made it possible to analyze how important the variations in effective length of the long and short dipoles in the FMI are. Effects on closed orbit and beta function variations were found to be negligible. Studies have also shown that the two source of field errors dominating the performance of the FMI are the assumed
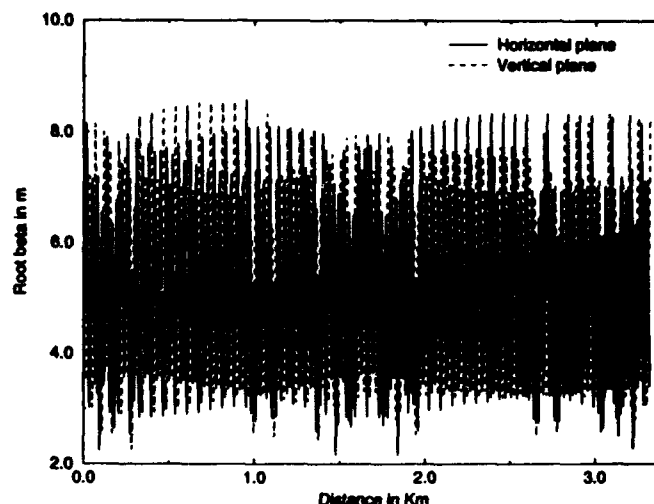
Figure 1: Sample beta function with all errors included

quadrupole random errors and the octupole error in the recycled Main Ring quadrupoles. A shuffling scheme of the quadrupoles supplemented by an octupole correction scheme greatly improves the characteristics of the machine. This is explained in more details in [4].

V. REFERENCES

[1] F. A. Harfoush and C. S. Mishra, "Systematic and Random Errors for Main Injector Tracking," Fermi Internal Notes, *MI-0066*.

[2] C. S. Mishra, H. D. Glass and F. A. Harfoush, "Effective Length of the Main Injector Dipole and its Effect on Main Injector," Fermi Internal Notes *MI-0072*.

[3] C. S. Mishra and F. A. Harfoush, "Stability of Beam in the Fermilab Main Injector," *Proceedings of this Conference.*

[4] C. S. Mishra and F. A. Harfoush, "Correction Schemes to Improve the Dynamic Aperture of the Main Injector," *Proceedings of this Conference.*
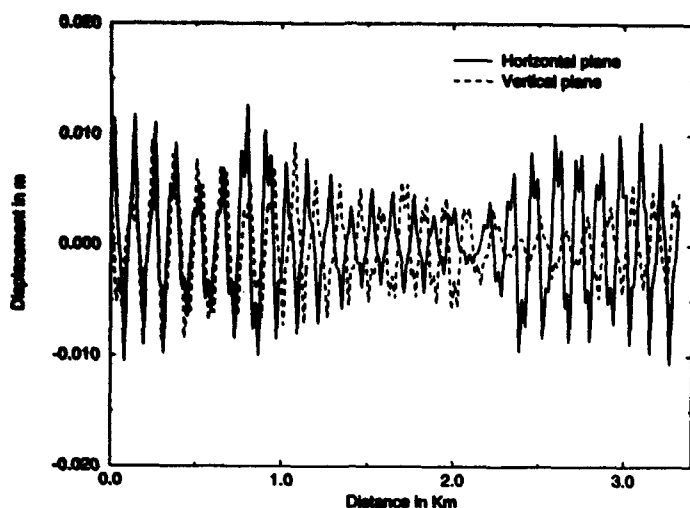
Figure 2: Uncorrected closed orbit at 8.9 GeV/c

Magnet Type	Multipole Order	Normal Errors		Skew Errors	
		$< b_n >$	σb_n	$< a_n >$	σa_n
Dipole Body	dipole	-4.68	10.0	–	–
	quad	-0.13	0.45	–	–
	sext	0.43	0.61	-0.04	0.22
	8	0.09	0.13	0.00	0.41
	10	0.18	0.32	0.03	0.15
	12	-0.03	0.10	0.00	0.19
	14	-0.01	0.23	-0.05	0.08
Dipole End	dipole	2.02	–	0.00	–
	quad	0.03	–	–	–
	sext	0.256	–	0.03	–
	8	-0.021	–	0.02	–
	10	-0.095	–	0.00	–
	12	0.009	–	-0.03	–
	14	0.002	–	0.00	–
MR Quads (Recycled)	quad	–	24.0	–	–
	sext	0.50	2.73	0.12	1.85
	oct	5.85	1.02	-1.16	2.38
	10	-0.10	1.12	0.42	0.47
	12	-1.82	0.63	0.40	0.70
	14	0.21	0.64	-0.55	0.44
	16	1.41	0.64	–	–
	18	-0.03	0.12	0.14	0.16
	20	-0.80	0.06	0.02	0.07
MI Quads (Newly built)	quad	–	24.0	–	–
	sext	–	2.73	–	–
	oct	-0.39	1.02	–	–
	10	–	1.12	–	–
	12	-1.39	0.63	–	–
	14	–	0.64	–	–
	16	1.29	0.64	–	–
	18	–	0.12	–	–
	20	-0.73	0.06	–	–

Table 1: Magnetic errors used in the 8.9 GeV simulation (see text for details & units)

Magnet Type	Multipole Order	Normal Errors		Skew Errors	
		$< b_n >$	σb_n	$< a_n >$	σa_n
Dipole Body	dipole	0.00	10.0	–	–
	quad	-0.30	0.21	–	–
	sext	-1.16	0.49	-0.03	0.17
	8	0.02	0.06	-0.02	0.29
	10	-0.09	0.25	-0.04	0.07
	12	-0.04	0.06	-0.01	0.21
	14	-0.08	0.25	-0.05	0.08
Dipole End	dipole	0.00	–	0.00	–
	quad	0.08	–	–	–
	sext	-0.52	–	0.05	–
	8	-0.012	–	0.02	–
	10	0.084	–	0.05	–
	12	0.008	–	-0.03	–
	14	-0.021	–	0.01	–
MR Quads (Recycled)	quad	–	24.0	–	–
	sext	1.69	2.29	-0.47	3.14
	oct	5.29	1.29	0.68	0.43
	10	-0.72	0.90	0.41	0.34
	12	-1.71	0.16	-0.31	0.14
	14	-0.25	0.92	-0.02	1.11
	16	1.37	0.92	–	–
	18	-0.22	0.92	0.06	0.25
	20	-0.82	0.33	-0.05	0.08
MI Quads (Newly built)	quad	–	24.0	–	–
	sext	–	2.29	–	–
	oct	-0.10	1.29	–	–
	10	–	0.90	–	–
	12	-1.41	0.16	–	–
	14	–	0.92	–	–
	16	1.32	0.92	–	–
	18	–	0.92	–	–
	20	-0.74	0.33	–	–

Table 2: Magnetic errors used in the 120 GeV simulation (see text for details & units)

353

Experience with the New Reverse Injection Scheme in the Tevatron

S.SARITEPE* G.GODERRE, G.ANNALA, B.HANNA, A.BRAUN
Fermilab† P.O. Box 500, Batavia, IL 60510

Introduction

In the new injection scenario the antiproton beam is injected onto a helical Tevatron orbit to avoid the detrimental effects of the beam-beam interaction at 150 GeV. The new scenario required changes in the tuning procedures. Antiprotons are too precious to be used for tuning, therefore the antiproton injection line has to be tuned with protons by reverse injecting them from the Tevatron into the Main Ring.

Previously, the reverse injection was performed in one supercycle. One batch of uncoalesced bunches was injected into the Tevatron and ejected after 40 seconds. The orbit closure was performed in the Main Ring. In the new scheme the lambertson magnets have to be moved, separator polarities have to be switched, activities that cannot be completed in one supercycle. Therefore, the reverse injection sequence was changed. This involved the redefinition of TVBS (Tevatron Beam Synchronized Clock) event $D8 as MRBS (Main Ring Beam Synchronized Clock) $D8 [1] thus making it possible to inject 6 proton batches (or coalesced bunches) and eject them one at a time on command, performing orbit closure each time in the Main Ring.

Reverse (Antiproton) Injection Line

The details of the reverse injection line can be found in reference [2]. Here we present the injection line sketch and the circuit diagram showing the reverse injection shunt (Fig.(1) and Fig.(2)).

Tuning Procedure

There are basically four modes of tuning for the reverse injection.

* current address: SSCL, MS 1040, 2550 Beckleymeade Ave. Dallas, TX 75237

† Operated by the Universities Research Association, Inc., under contract with the U.S. Department of Energy.
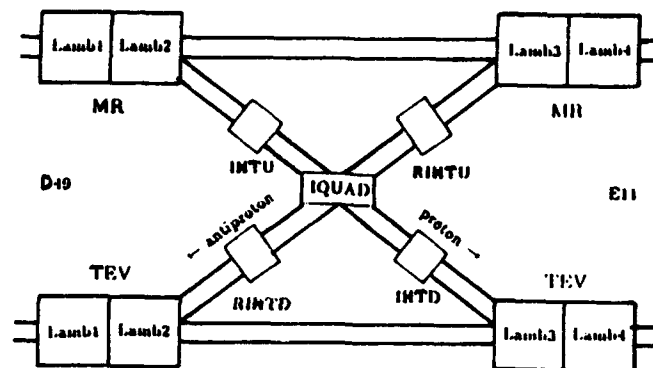
Figure 1: Proton and Antiproton injection lines.

(1) Routine tuning, i.e. orbit closure before each shot
(2) Adjustments after orbit smoothing
(3) Adjustments after helix amplitude changes
(4) Reverse Injection checkout. This is done during startup after long shutdowns

Routine Tuning:

In the new reverse injection scheme, 6 proton bunches are injected onto the injection orbit. Proton lambertsons are moved out, the injection bump at E0 is removed, the separator polarities are switched, then finally the separators are powered. The resultant orbit is the same one that the antiproton beam would be launched onto. Ejecting proton bunches from this orbit is equivalent to injecting antiprotons onto the same orbit.

Adjustments after orbit smoothing:

If the position and angle differences resulting from orbit smoothing are small, a simple orbit closure would be sufficient. If the orbit differences around E0 (injection location) are substantial then one has to adjust the reverse injection time bump. In principle a reverse injection time bump in the vertical plane is not needed. One may heve to create one if it helps the kicker or the shunt. The goal in this tuning is to find the comprimise between the kicker strength,

0-7803-1203-1/93$03.00 © 1993 IEEE

354
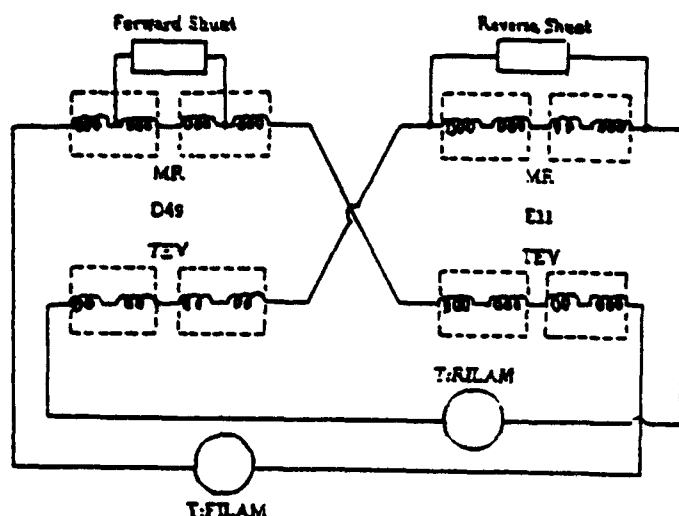
Figure 2: Circuit diagram showing the shunt connections. This diagram was drawn from tunnel observations by J.Annala. If the forward shunt and the reverse shunt both remove , for instance, 5 Amps from the circuit, the angle adjustment provided by the reverse shunt will be twice as big as that provided by the forward shunt.

---

shunt current and the losses.

Adjustments after helix amplitude changes:
Helix amplitude is subject to change during the collider run. Again a simple orbit closure will be sufficient in most cases. If the change in the helix amplitude is big then one must perform orbit closure in small steps. As the helix amplitude is changed in steps orbit closure is performed each time. Once the final closure values are obtained they must be entered in the Sequencer file #13.

Reverse Injection checkout:
A complete checkout of the reverse injection may be necessary after long shutdowns. The details are explained in ref [3]

Orbits

It is paramount to have hardcopies of the Tevatron and Main Ring orbits for the reverse injection. One needs the closed orbit and the last turn orbit in the Tevatron and the closed orbit and the first turn orbit in the Main Ring. Some of the orbits are shown in ref [3].

January 1992 studies

During the January 1992 studies. the reverse injection time bump had to be recreated since we did not know the best last turn Tevatron orbit that would allow a loss-free ejection. The closed orbit positions and angles had to changed also.

After the January studies. during the shutdown the D49 Tevatron lambertsons were raised by 8 mm. The closed orbit and the time bump changed during collider commissioning. Since the closed orbits and the time bump may change again in the future. the orbits shown in ref [3] should be taken as hints for future adjustments.

Problems during January 1992 studies

In the beginning there were hardware problems. One should be vigilant about the T:IQUAD reversing switch since it may get stuck in the reverse polarity and do not switch back to the forward polarity. Another problem area was the D48 kicker. We discovered that the D48 kicker was shorted. Diagnosis and replacement of this magnet cost us 5 shifts.

We learned to be careful about the "prepare for beam" and other timers in the Main Ring BPM system. For instance, the Main Ring BPM readings for the $20 cycles were being overwritten by the $29 cycles in the absence of proper precautions. In the current setup "prepare for beam" in the Main Ring is taken care of by the Sequencer.

The new closed orbit positions at D49 and E11 made it necessary to change the horizontal time bump angle between D49 and E11. The initial solution was to have 21 mm at D49 and 6 mm at E11 when the time bump was playing. This worked fine. however. when the proton helix was opened. beam was scraping on something that looked like the backend of the field-free region of the D49 lambertsons. It may have been the flange instead of the backend. Nevertheless. the time-bump at D49 was reduced to 11 mm. the "stored beam" positon for the lambertsons was changed from -930 mils to -600 mils. This solved the horizontal aperture problem.

There was a vertical aperture problem at D49 as well. We could not open the proton helix to 100%. We lowered the closed orbit position by 3 mm. we wanted to lower it

further by 8 mm. but the shunt was running at 0 Amps so we could not do it. This limited the helix amplitude at 150 GeV to 60% of the design value. At 900 Gev the helix could be opened to 100% percent since the helix amplitude shrinks with energy.

Conclusion

A record of the previous injection (ejection) orbits is the most important information during commissioning. The next piece of important information is the kicker traces. The correct waveforms must be archived and compared to the observed waveforms. Here we show the correct kicker waveforms for the kickers involved in the reverse injection (Fig.(3) and Fig.(4)). Any deviation from the waveforms shown in these figures indicate kicker hardware problems.

Figure 4: Waveform for the Tevatron D48 Kicker. This kicker ejects the proton beam from Tevatron during reverse injection.

References

[1] R.J.Ducar, "Why TVBS SD8 Became MRBS SD8", Unpublished Note (July 1991).

[2] S.Saritepe and G.Annala; "Beam Transfer at E0: An Overview", FERMILAB-TM-1790 (1992).

[3] S.Saritepe and G.Annala; "Tevatron Reverse Injection", FERMILAB-TM-1791 (1992).

[4] S.Saritepe and G.Annala; "Tevatron Injection Timing", FERMILAB-TM-1792 (1992).

Figure 3: Waveform for the Main Ring E17 Kicker. This kicker places the reverse injected (ejected) Tevatron beam onto the Main Ring orbit.

The kicker timing issues are also crucial during commissioning. The reverse injection timing for the Tevatron are discussed in detail in reference [4].

Acknowledgements

Injection and Extraction-Performance at the SIS/ESR-Facility

H. Eickhoff, K. Blasche, U. Blell, B. Franzke, J. Pinkow
GSI, Gesellschaft für Schwerionenforschung mbH
D-64220 Darmstadt

Both the "Heavy-Ion Synchrotron" (SIS) [1] and the "Experimental Storage Ring" (ESR) [2] are designed for beam accumulation and beam extraction. The concepts are different in each machine according to the specific beam-properties and requirements. In this article a summary of the technical realisation of the injection and extraction systems and the operation results are given.

	type	duration
		(s)
SIS		
Injection	Multi-turn	1×10^{-6} - 5×10^{-4}
	fast	2×10^{-7} - 3×10^{-6}
Extraction	fast	2×10^{-7} - 3×10^{-6}
	slow	2×10^{-2} - 10
	stochastic	2 - 10
ESR		
Injection	fast	2×10^{-7} - 3×10^{-6}
Extraction	fast	2×10^{-7} - 3×10^{-6}
	slow	2×10^{-2} - 10 (*)
	stochastic	10 - 1000 (*)
	charge ch.	10 - 1000 (*)

(*) = estimated

SIS - MULTITURN-INJECTION

Figure 1: Multiturn-Injection at SIS
The upper trace shows the beam-transformer signal in the injection beam-line; the lower shows the beam accumulation in SIS over 20 turns.

The maximal achieved accumulation factor is near 30, which is close to the theoretical one, if the theoretical losses during the process are taken into account.

1 INJECTION MODES

1.1 Multiturn-Injection (SIS)

The UNILAC, the injector for the SIS, delivers the ion beam with a macropulse-length between 0.5 and 5 ms. In the SIS the beam is accumulated by stacking in the horizontal phase space ("Multiturn-injection") with 4 fast ramped bump-magnets.

The injection-line, designed for ions with a magnetic rigidity between 0.5 and 4.5 Tm, consists of an electrostatic "chopper", matching quadrupoles, an inflector magnet, and an electrostatic wire-septum.
The injected emittances are near 5π mm mrad both in hor. and vert. phase space; the SIS hor. acceptance is calculated to be about 200π mm mrad, corresponding to a maximal accumulation factor of 40.

1.2 Fast Injection (ESR, SIS)

After fast extraction at SIS the ion beam is injected into the ESR by means of "fast injection" with "bunch-to-bucket" transfer. The incoming beam is deflected to a stable injection orbit by a C-shaped kickermagnet, consisting of 3 modules in one vacuum vessel. The "double-shot" operation mode allows a rapid transfer of two times 2 bunches, that can be accepted by the ESR, within one SIS-cycle (see Fig. 2). Beam accumulation is done in the longitudinal phase-space by the RF-stacking method; during this injection process beam cooling by means of the electron-cooler is performed on the accumulation-orbit. Cooling on the injection orbit is possible as well, either with the electron-cooler and/or in the near future by stochastic cooling. This injection procedure has become a routine operation mode; improvements of the injection- and accumulation efficiency are necessary.
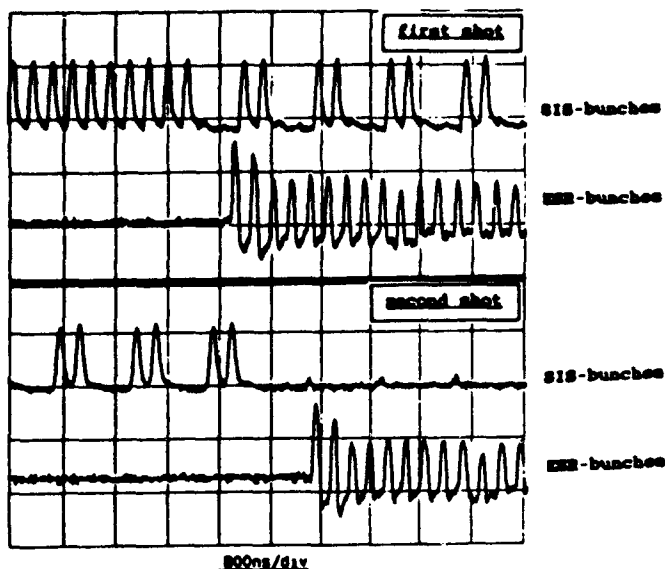
Figure 2: Fast Injection into the ESR.
Two times 2 out of 4 SIS bunches are injected.

For the SIS Reinjection mode the ESR serves as the Injector for the SIS. The cooled ion beam with a maximal magn. rigidity of 10 Tm is fast extracted from the ESR and injected ("bunch-to bucket transfer") into SIS for postacceleration up to 18 Tm and delivered to the experimental areas by means of fast or slow extraction. The fast inflecting device in SIS is the kickermagnet, that is also used for fast extraction; 4 auxiliary coils within special bending magnets create a local closed orbit bump to minimize the required kick-strength; the 3 magnetic injection septa are switched in series and connected to a special designed pulsed power supply.

2   EXTRACTION MODES

2.1   Fast-Extraction (SIS, ESR)

The fast extraction mode is used for beam transfer to the ESR and for experiments, which need high-intense pulse currents. The main device for this operation mode is the kickermagnet (also used for Reinjection), which is housed in two vacuum vessels. In total 9 parallel switched kicker modules can be excited sychronously at maximal beam rigidity, in order to deflect the beam into the extraction channel. The deflection time can be varied continously between 200 and 3000 ns; thus, a various number of bunches can be extracted. Due to the special power-supply design a second extraction is possible after at least 30 ms ("double-shot").

In the extraction channel the beam is deflected by 3 septum-magnets, which are switched in series and connected to the power-supply of the main dipoles; this extraction channel is used both for fast a slow extraction.

The extraction efficiency can be estimated to be around 90%.

At the ESR a cooled ion beam with a magnetic rigidity between 1 and 10 Tm can be fast extracted to the SIS (SIS-Reinjection) with the ESR injection kicker. This mode was already successfully tested.

2.2   Slow-Extraction modes (SIS,ESR)

At SIS the Resonance-Extraction mode is used for most high energy experiments within a wide energy-range up to a maximum magnetic rigidity of 18 Tm. After acceleration the beam is gradually driven into a horizontal 1/3-order resonance by means of 6 sextupoles and two fast quadrupoles. The unstable particles are deflected into the extraction channel by an electrostatic wire septum.
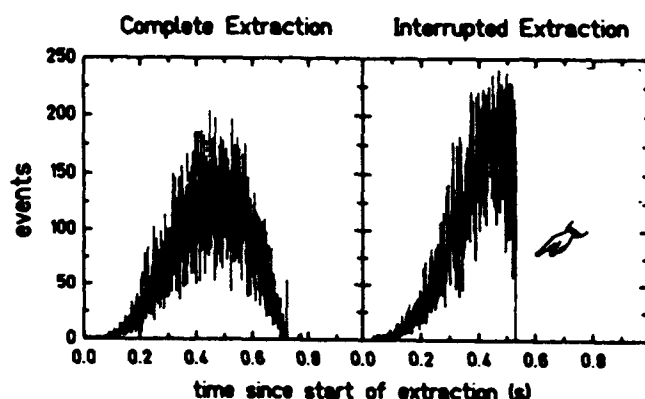
Figure 3: Slow (resonant) extraction at SIS with rapid spill interruption

Due to the quality of the magnet power-supplies, a spill duration of up to 7 s with moderate time structure on the spill is achieved. Extraction efficiencies around 85% were reached; beam emittances of $2\ \pi$ mm mrad (horizontal) and $4\ \pi$ mm mrad (vertical) were measured at high energies (1000 MeV/u) [3].

Fast interruption (about 200 μs) of the extracted beam is possible by the request of the experimentalists [4] (see Fig. 3).

Beside the 1/3-order resonance-extraction 2 additional slow extraction modes are under investigation at the ESR. The first mode is the beam extraction, which takes advantage from electron capture- and electron stripping-processes by the electron cooler and the internal gas-target, leading to a change of the magnetic rigidity of the circulating ions. Beam simulations show (see Fig. 4), that due to the different orbits these ions can be deflected into the extraction channel MS by 2 deflecting devices: one small septum magnet ESM for the ions having captured an electron and the electrostatic septum ES (that is also used

for the resonant extraction) for the stripped ions. (Fig. 4) The advantage of this type of extraction is the preservation of the excellent beam quality (emittance, momentum spread), that is achieved by the electron-cooling. The extraction time, which depends on the stripping- and capture cross-sections that can be reached, are estimated between some seconds up to several minutes.
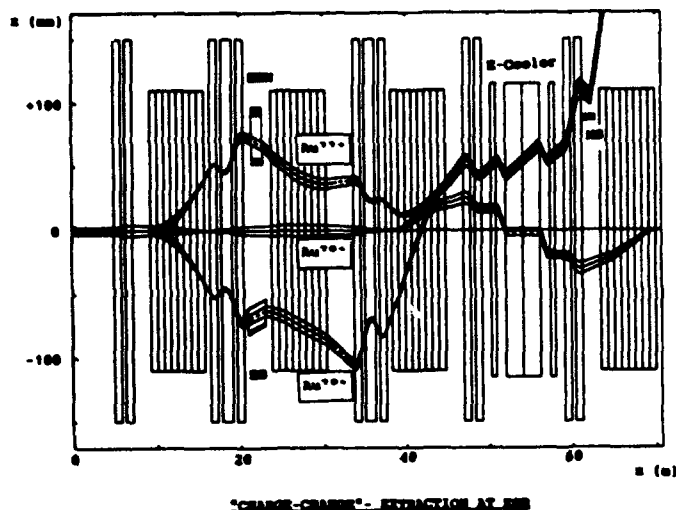
Figure 4: Different Orbits for Charge-change-Extraction Au+77 (electron capture in electron-cooler), Au+78 (injected beam), Au+79 (electron stripping in the gas-target)

A third slow extraction mode under investigation is the 'stochastic' extraction, that is used at LEAR for spill durations up to 1 hour. Within a thesis at GSI [5] experiments of this type of extraction have been performed at SIS in order to examine the spill performance for extraction times of some seconds.
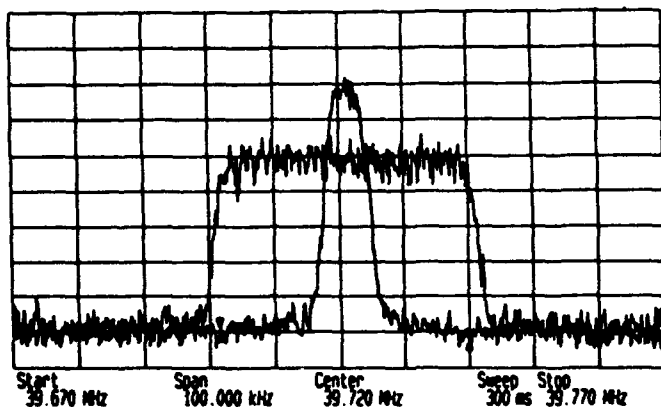
Figure 5: Shaping of an $^{18}O^{8+}$-beam at 697 MeV/u
Both the momentum-distribution before (gaussian) and after shaping with a noise of 4 kHz bandwidth, applied during 1 s with a voltage of U = 750 V, are shown.

Both low-frequency noise amplitudes used for the beam-

shaping and the diffusion process to the 1/3 order resonance are created by means of a digital noise-generator connected via a mixer to one of the SIS accelerating cavities. Comparisons between the resonant- and stochastic extraction showed, that the spill-modulation is similar for extraction-times in the order of a few seconds; emittance measurements of the extracted beam indicate identical transverse emittances, but, as expected, in contrary to the resonant extraction a constant momentum of the spill for the stochastic extraction mode. It was also shown, that the influence of a power-supply ripple on the spill modulation is much poorer for the stochastic extraction. This extraction mode is intended especially for the ESR-operation in the stretcher mode for spill durations from a few seconds up to several minutes.
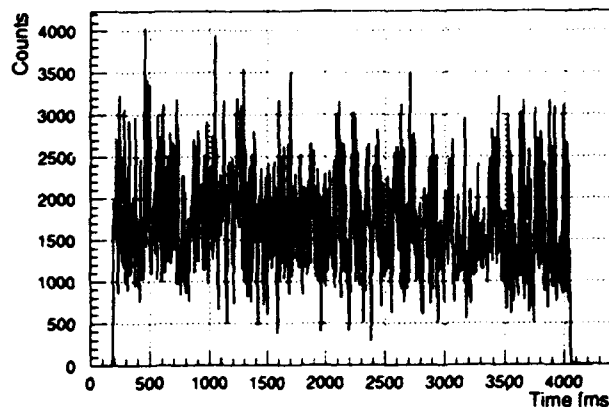
Figure 6: Stochastic extraction from SIS
The spill, measured by a scintillator in the extraction line, is shown

3 REFERENCES

[1] K.Blasche et al.; The Heavy Ion Synchrotron SIS: A Report on New Design Features and on the Machine Improvement Program; this conference

[2] B. Franzke et al.; Results from Heavy Ion Beam Accumulation, Cooling, and Experiments at the ESR; this conference

[3] M. Steiner et al.; Preliminary measurements of SIS18 beam parameters; Nucl. Instr. and Meth. in Phys. Res. A312, p. 420-424

[4] Haberer et al.; to be pubished in Nucl. Instr. and Meth.

[5] J. Pinkow; Thesis; to be published

The AGS-Booster Complex for the g-2 Experiment and RHIC Injection*

Mitsuyoshi TANAKA and Yong Y. Lee
Brookhaven National Laboratory
Upton, NY 11973

Abstract

The delivery of a beam with characteristics appropriate for the g-2 muon storage ring and the filling of the RHIC heavy ion collider from the AGS main ring requires a new fast extracted beam (NewFEB) system. The NewFEB system must be capable of performing single bunch multiple extraction of a heavy ion beam, as well as a high intensity proton beam at a time interval of 25 ms up to 12 times per AGS cycle. The new system will consist of a fast multi-pulsing kicker and an ejector septum magnet with local orbit bumps.

I. INTRODUCTION

Since the present fast extraction beam (FEB) and single bunch extraction (SBE) systems [1] are no longer available for the post-Booster era, the NewFEB system [2] will serve as the AGS extraction system not just for the muon g-2 experiment [3] but also for RHIC [4] and the recently approved long baseline neutrino oscillation experiment [5] at AGS as well. The AGS Booster, recently completed, allows the AGS to accelerate heavy ions (HI) beyond Si^{28} up to Au^{197} and will increase the proton intensity in the AGS by a factor 4 [6].

For the g-2 experiment, which is now constructing a 14 m diameter superferric muon storage ring with B=1.5 T in order to improve the previous CERN measurement of the anomalous magnetic moment (a_μ) by a factor of 20, NewFEB must meet the following requirements: (1) extract the bunched proton beam up to full energy and intensity to the new V-target through the existing U-line for 3.1 GeV/c pion production, and (2) perform single bunch multiple extraction (SBME) at 25 ms intervals up to 12 times per AGS cycle. The remaining bunches, if any, have to be debunched and go though the slow extraction beam (SEB) channel for AGS HEP experiments.

With the NewFEB system the AGS will also serve as an injector for the RHIC, which is under construction. The circumference of the RHIC ring is 19/4 times larger than the AGS and its harmonic number at injection is 342 compared to 12 of the AGS. The present RHIC design assumes that the AGS will accelerate three bunches per pulse and transfer individual bunches one by one into the waiting rf buckets in RHIC (SBME). Each RHIC ring will be filled with 57/114 bunches one after another in a few minutes every 10 hours or so and accelerate heavy ions to energies of 250·(Z/A) GeV/N.

The schematic layout of the AGS-Booster complex is shown in Figure 1.
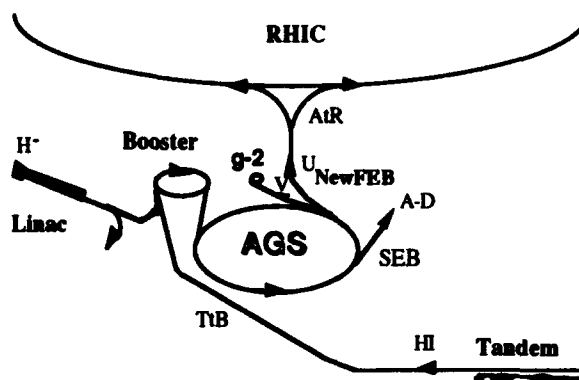
Figure 1. Schematic view of the AGS-Booster complex.

II. DESIGN OF THE NewFEB

A. Machine and Beam Parameters

Due to its high intensity operation for the g-2 experiment and the neutrino experiment, it is important that the NewFEB system can achieve a high extraction efficiency (>99%). On the other hand, for RHIC injection, the beam intensity is low but pulse-to-pulse and cycle-to-cycle modulations in the extracted bunch beam parameters must remain within acceptable levels since any excess will directly influence RHIC performance. Therefore, stability and reproducibility of the extracted beam parameters are crucial for RHIC injection.

For design purposes, we may assume that the operational NewFEB proton momentum range is (1) 22 < p < 30 GeV/c, (2) the 95 % normalized transverse emittance of the high intensity beam should be $\varepsilon^n_{h,v}(95\%) = 6 \cdot \sigma^2/\beta \cdot (p/m) \leq 50 \pi$ mm-mrad, where σ is the standard deviation of the beam size due to the transverse emittance, and (3) the maximum total momentum spread allowed is $(dp/p)_{full} \leq \pm 0.2 \%$. The actual measured values of ε^n and dp/p for the AGS beam are strongly dependent on the machine condition, especially the beam intensity. However, under the normal running conditions it is generally agreed that $\varepsilon^n(95\%) = (20 - 40) \pi$ mm-mrad, and $(dp/p)_{full} = \pm (0.05 - 0.12) \%$. The high intensity values with the Booster have not yet been established.

For RHIC injection, the expected values of ε^n and dp/p for both protons and heavy ions are substantially lower than the current values since the AGS Booster can deliver much more intensity than that assumed for the RHIC design parameters.

It should be noted that a fast kicker and an ejector septum magnet must be located at straight section G10 and at straight section H10, respectively, in order to utilize the existing U line and due to limited availability of straight sections. At 10-foot straight section (G10, H10), β_h and β_v are rapidly

changing as well as D_x. The parameters and performance of the present AGS machine are summarized as follows:

Table 1. AGS parameters.

Circumference	$C = 2\pi R = 807.075$	[m]
Curvature	$\rho = 85.17$	[m]
Revolution Time	$t_{rev} = 2.692$	[ms]
Tune	$Q_h \cong Q_v \cong 8.7$	
Beta Functions	$\beta_{h,v} = 22.5 \, (10.5)$	[m]
Dispersion Function	$D_x{}^{max} = 2.20$	[m]
No. of Bunches	$N_b = 12$, (3 for HI)	
Full Bunch Length	$t_b = 35\pm5$	[ns]
Gap bet. Bunches	$t_s = 224$ (peak-to-peak)[ns]	
Typical Intensity	$1.6 \cdot 10^{13}$	[ppp]
	$3.0 \cdot 10^8$	[Si/p]
	$1.0 \cdot 10^8$	[Au/p]
Typical AGS Cycle	2.0 (FEB), 3.4 (SEB) [s]	
Typical Momentum	$p = 24.5, 28.5$ (p) [GeV/c]	
	29.0·(Z/A) [GeV/c/N]	
Emittance	$\varepsilon^n{}_{h,v}(95\%) \cong 35 \, \pi$ [mm-mrad] (p)	
Momentum Spread	$(dp/p)_{full} \cong \pm 0.12$ [%]	

The following tables lists the expected beam parameters and performance of the AGS Complex for its NewFEB operation:

Table 2. NewFEB beam parameters.

Units:	g-2	RHIC	RHIC	
Particles =	Protons	Protons	Heavy ions	
p =	22-29	29.0	29.0·(Z/A)	[GeV/c/N]
			$(29.75 \cdot (Z/A)$ for $_{197}Au^{77+})$	
N_{SBE} =	1,3,(12)	3	(19-2(·2)) for 2 rings	
N_p/Bunch =	< 4000	100	1 - 6	[10^9]
$\varepsilon^n{}_h(95\%)$ =	< 50 π	< 20 π	< 10 π	[mm-mrad]
$(dp/p)_{full}$ =	< $\pm$ 0.2	< $\pm$ 0.06	< $\pm$ 0.10	[%]
A_{bunch} =	1.0	0.3	0.3	[eV-s/N]
L_{bunch} =	< 40	< 17	< 17	[ns]
Oper. Mode: (with SEB)filling two rings every 10 hr.				

B. Extraction Scheme

The new system will consist of a fast multi-pulsing kicker at s.s.G10 followed by a thick septum ejector magnet at s.s.H10. To minimize the required voltage on pulsing the fast kicker we designed a C-type open ferrite magnet with a pole tip. The kicker will be placed about 50 mm from the central orbit. A few ms before the extraction two extraction bumps are created to bring the beam in to the aperture of the kicker and adjacent to the septum of the ejector. At extraction, the kicker is triggered every 25 ms to send one bunch at a time into the ejector, which gives an additional kick to extract the bunch out of the ring. In Figure 2, we show a schematic layout of the NewFEB extraction components and the particle trajectories.
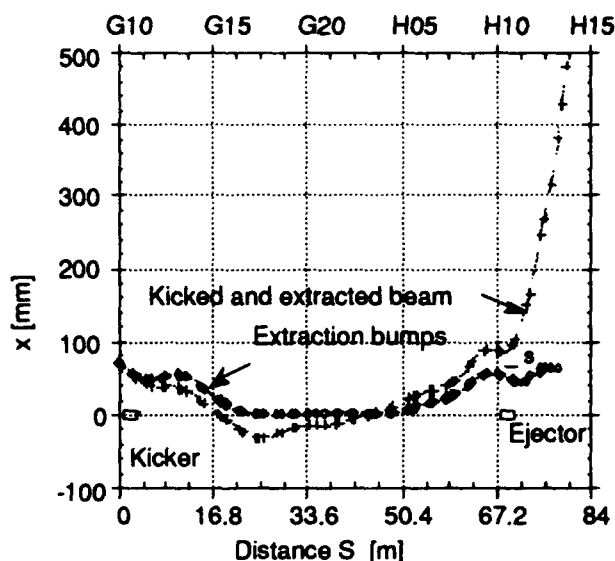
Figure 2. Layout of the NewFEB components.

C. Fast Kicker, Ejector and Orbit Bumps

Using the 99% emittance at p=29 GeV/c, we have the full horizontal beam width $w_f \leq 16.4$ mm at both G10 and H10. Assuming that we need 2 mm clearance at both sides of the septum of the ejector magnet, and 10 mm septum thickness, then the required separation of the circulating beam and the beam kicked by the fast kicker is $\Delta x = 30.4$ mm at H10. The kicker must deflect the beam by

$$\theta(G10) = \Delta x / \sqrt{\beta(G10) \cdot \beta(H10)} \cdot \sin(\Delta\mu) = -1.80 \text{ mrad},$$

where $\Delta\mu$ is the betatron phase advance from the kicker to the septum calculated from the AGS lattice. This corresponds to $\int Bdl = B_0 \cdot l_{eff} = -0.18$ T-m. Since it is desirable to keep the maximum pulse voltage less than 40 kV, the kicker magnet will be subdivided into four modules and powered in parallel. The kicker has a limited aperture, 32 mm x 22 mm (w x g) and a pole tip which is shaped to maximize the good field region while keeping a gap as large as possible as shown in Figure 3.
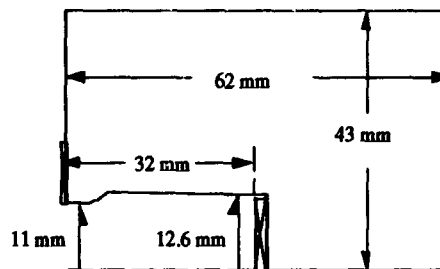
Figure 3. Geometry of the fast kicker.

For NewFEB operation, the ejector magnet also has to pulse every 25 ms up to 12 times per AGS cycle. As a result, the temperature of the copper septum will rise significantly,

361

causing wear of the insulation. Therefore, the septum needs 10 mm thickness and must be water-cooled.

Two 1 λ rather than standard 3/2 λ local orbit deformations are created to avoid the kicked beam hitting the vacuum chamber wall around at s.s.G17. These bumps are generated by powering backleg windings on selected AGS main magnets so arranged that the tune shifts and stopbands at Q_h =8.5 are minimized. The basic design parameters of the kicker, ejector and extraction bumps are summarized in Table 3.

Table 3 . NewFEB magnet parameters.

	Kicker	Ejector	Bumps
Aperture[mm]	32 x 22	72 x 25	Full
θ_{max} [mrad]	2.0	22.0	2.0/pair
wave form	half since	half sine	half sine
t_{base}	360 ns	2 ms	5 ms
I_{max}	2.0 kA	23 kA	1.0 kA
I_{max}	2.0 kA	23 kA	1.0 kA
Tolerance	< 0.9 %	< 0.09 %	< 0.8 %

D. Beam Instrumentation

In order to observe possible bunch-by-bunch beam scraping during the NewFEB e.;traction, the new fast beam loss monitors will be installed at key extraction points. The present beam position monitor (PUE) system will be upgraded with a universal bunch-by-bunch digitizer so that we can take orbit data at the rf rate, allowing tracking over many orbits. It should also improve absolute beam position measurement capabilities.

III. SIMULATION

To find out the circulating and the extracted beam parameters at the middle of s.s.H13 (the entrance of the existing U-line), simulation studies are performed with a model of the AGS, using the accelerator modeling program MAD. We run MAD to obtain the desired orbit at the kicker and at the ejector, making adjustments of the extraction bumps at the tune $Q_h \cong 8.75$. Then, the particle with initial conditions {x, x'} at the beginning of s.s.G10 is traced through the lattice and receives an appropriate kick (1.6 mrad) at the kicker and an additional kick (21 mrad) at the ejector up to the middle of s.s.H13, where the beam should be about 43 cm away from the central orbit, free from the fringe field of the ring magnets as shown in Figure 2.

The simulation results show that the optical parameters ($\beta_{h,v}$, $\alpha_{h,v}$, D_x, D_x') at s.,s.H13 are sensitive to fine bump tunings and fringe field effects from the septum to s.s.H13. Therefore, tracking studies using the AGSBEAM code which has a complete main magnet field map [7] and TOSCA 3D program [8] are also being performed to confirm the MAD results at s.s.H13 for the proper optical design for the U-line and its optical matching with the AtR line.

VI. CONCLUSIONS AND OUTLOOK

The basic engineering design is made on the NewFEB system at the AGS, which is capable of performing single bunch multiple extraction every 25 ms up to 12 times per AGS cycle for g-2 experiment and RHIC injection. It is expected that the g-2 muon storage ring and RHIC are expected to be completed in 1994 and in 1997, respectively. Due to its high intensity operation for the g-2 experiment, it is important that the NewFEB system can achieve a high extraction efficiency. On the other hand, for RHIC injection, stability and reproducibility of the extracted bunched beam parameters are crucial since any change of the extracted beam parameters will directly influence RHIC performance. Further simulation studies of the NewFEB extraction and machine studies with the Booster will be needed to specify the NewFEB extraction performance as well as the overall required AGS capability as the injector for RHIC and the high intensity proton machine.

VI. REFERENCES

[1] W.T. Weng, "The AGS New Fast Extraction System and the Single Bunch Extraction", *IEEE Trans. Nucl. Sci.* NS-30, No. 3 (1983).

[2] M. Tanaka and Y.Y. Lee, "The AGS New Fast Extraction System for the g-2 Experiment and RHIC Injection", *1991 IEEE Part. Accel. Conf.* (Sn. Francisco), p. 9589.

[3] AGS Experiment 821, "A New Precision Measurement of the Muon g-2 Value at the Level of o.35 ppm".

[4] BNL-52195, "Conceptual Design of Relativistic Heavy Ion Collider", May 1989.

[5] AGS Experiment 889, "Proposal for a Long Baseline Neutrino Oscillation Experiment at the AGS".

[6] W.T. Weng, "Operation of the Brookhaven AGS with the Booster", this conference.

[7] H.W. Foelsche and N. Tsoupas, private communication.

[8] W. Meng, private communication.

First-Turn Losses in the LAMPF Proton Storage Ring (PSR)

R. Hutson and R. Macek

Medium Energy Physics Division, Los Alamos National Laboratory, Los Alamos, New Mexico 87545 USA

Abstract

Beam-loss measurements indicate that 0.2 - 0.3% of the protons injected into the PSR are lost during the first turn. We describe a plausible mechanism, involving field stripping of excited hydrogen atoms, for these losses. Protons are injected into the PSR by transporting a neutral hydrogen beam through a hole in the yoke of one ring bender and then through a carbon foil on the ring axis. The foil strips roughly 93% of the beam atoms to protons. Although the original PSR design assumed that all unstripped atoms would pass through a hole in the yoke of the next downstream bender and on to a beam stop, recent calculations [1] indicate that about 6% of these unstripped atoms will emerge from the foil in an excited state with principle quantum number $n \geq 3$. These calculations also indicate that atoms in excited states with $n \geq 3$ will be stripped quickly to protons in the 1.2-Tesla field of the downstream bender. The trajectories of these protons will be outside the phase-space acceptance of the ring and will be quickly lost by collision with the beam pipe, thereby giving rise to first-turn losses. The estimated numbers of protons that would be lost by this mechanism are consistent with the observed first-turn loss rates. This mechanism has important consequences for the design of future storage rings that use neutral atom or negative ion stripping for injection.

I. INTRODUCTION

Minimization of beam losses is a major goal at the PSR. At the present time the PSR operates with beam loss rates in the range 0.35–0.45 μA, just below 0.50 μA, at which level radioactivation of ring components by the 800-MeV beam begins to make hands-on maintenance unreasonably difficult. Therefore, any reduction of loss rates is highly desirable for mitigation of maintenance problems, and because it would permit raising the average beam current injected into the ring.

Many of the development experiments done at the PSR have been aimed at furthering understanding of the mechanisms that cause beam loss. Two major classes of loss occur: slow losses that would, if acting alone, result in a circulating beam lifetime of thousands of turns; and first-turn losses in which a significant fraction of the injected beam is lost before making one complete revolution around the ring. Slow losses have been understood for some time [2]. They represent the loss of a small fraction of the total circulating beam for each revolution around the ring. Only recently has there emerged a convincing hypothesis to explain the cause of first-turn losses. This paper discusses the new hypothesis.

II. MEASUREMENT OF BEAM LOSS

Beam losses in the PSR are measured with a system of ten loss monitors located around the outer periphery of the PSR tunnel. The loss monitors are liquid-scintillator-filled cans coupled to photomultiplier tubes. Figure 1 shows a typical beam loss rate pattern recorded during an interval spanning approximately 600 μs of beam injection followed by a 100-μs period during which the beam is allowed to coast without injection of additional beam. There are two components to this loss signal. One is a measure of the slow loss rate. It is proportional to the amount of beam circulating in the ring and increases linearly with time. The other component is a measure of the first-turn loss rate, and is constant during injection because protons are being injected at a constant rate. This component drops to zero at the end of injection.

The total beam loss is proportional to the total area under the curve while the first-turn loss is proportional to the area under constant-width band at the top of the curve. There is a short spike in the loss rate associated with the extraction of the circulating beam from the ring.

Total beam losses are typically 0.6 - 0.7% of the amount of beam injected into the PSR with first-turn losses contributing 0.2 - 0.3 % to this total.
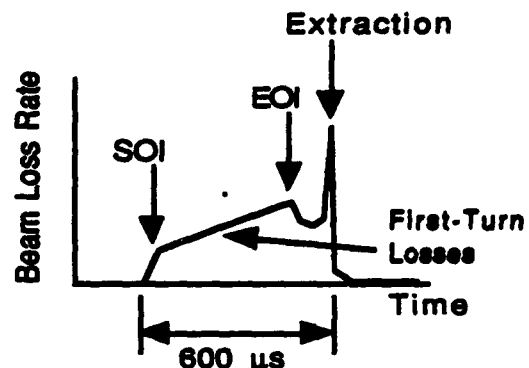
Figure 1. Beam Losses as a Function of Time During and for 100 μs After the End of Injection (SOI = start of injection; EOI = end of injection)

III. H⁺ INJECTION INTO THE RING

An understanding of the new hypothesis about the origin of first-turn losses is helped by a brief description of the process by which protons are injected into the PSR. As illustrated in Figure 2, 800-MeV H^- ions are stripped to H^0s in a 1.8-Tesla stripper magnet upstream of the ring. The H^0s then enter the ring through a hole in a ring dipole magnet. In the ring, H^0s are stripped to protons by a 200-μg/cm² carbon foil located on the ring axis, and the protons then circulate in the ring.
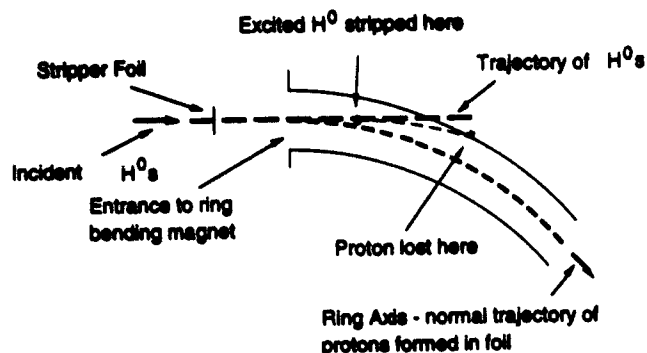
Figure 4. Schematic Illustration of the Process by which Excited H^0s Give Rise to First-turn Losses

Table 1. Angular displacement and loss location in ring of protons from stripping of various n states of H^0 and estimated yield of the n states

n	$\Delta\theta$ range (mradians)	Loss location in the ring	Estimated yield from 200-μg/cm^2
3	22 - 50	in first dipole	0.30% *
4	6.1 - 12	after first dipole but in the next 3 ring sections	0.20%
5	1.8 - 4.4	small fraction lost on ring limiting aperture	0.15%

* 1/2 of measured yield from H^- on 200-μg/cm^2 carbon foil

Figure 5 shows the horizontal-plane ring phase-space acceptance ellipse and the H^0 beam ellipses at the entrance to the dipole downstream of stripper foil. As an example, the range of angles, taken from Table 1, over which protons from stripped n=4 states are distributed is indicated.
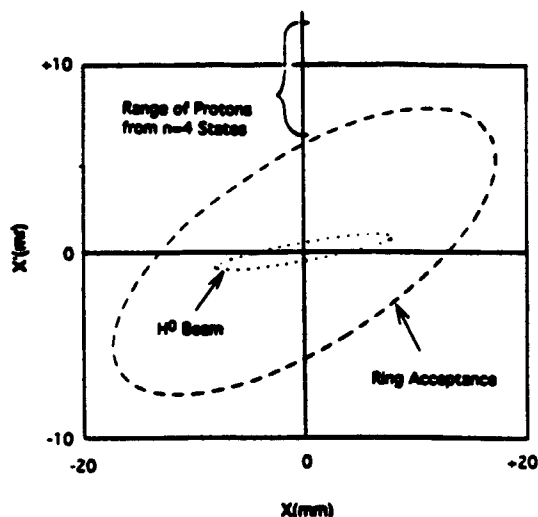
Figure 5. Horizontal-plane Ring Acceptance and Incident H^0 Beam Phase-space Ellipses at the Entrance to the Dipole Magnet Downstream of the Stripper Foil

For high n states, lifetimes are short and stripping occurs so early in fringe field of the magnet that the resulting protons follow essentially the same trajectories that protons formed in the foil do. For n=1 and n=2, H^0 states are not stripped and continue on to the H^0 beam stop.

V. DISCUSSION OF RESULTS

A. Comparison of Measured and Estimated First-Turn Losses

Experiments [7] have shown that approximately 0.50% of 800-MeV H^-s incident on a 200-μg/cm^2 PSR stripper foil are converted to H^0s in the n=3 state. Following the plausibility argument of section IV.A., we estimate that approximately 0.25% of the ground-state H^0s incident on the foil are converted to H^0s in the n=3 state. Assuming that first-turn losses originate primarily from n=3 and n=4 states, and using the yields presented in Table 1, we estimate that the first-turn losses should be approximately 0.4% of the total H^0 beam incident on the foil. This is somewhat larger than the 0.3% observed with the loss monitors. However, since a large fraction of the first-turn losses occur inside the first dipole downstream of the foil, the loss monitors will be shielded from the beam spill point by the steel of the magnet, and will provide an underestimate of the actual losses.

B. Conclusions and Discussion

We conclude that the estimated losses are consistent with the measured values, and interpret this fact as support for the hypothesis that excited-state H^0s are the cause of the losses.

Since new high-intensity proton storage rings being designed or contemplated involve H^- ion injection through stripper foils, recognition and careful consideration of the consequences of the formation of excited H^0s is important for the understanding and control of beam losses.

VI. REFERENCES

[1] J. Macek, private communication.
[2] R. Macek *et al*, "Analysis of beam losses at PSR," *Conference record of the 1988 EPAC Conference*, Vol. 2, pp. 1252-1254.
[3] A. Mohagheghi *et al*, "Interaction of relativistic H^- ions with thin foils," *Phys. Rev. A*, Vol. 43, No. 3, pp. 1345 - 1365 (1991).
[4] T. Bergeman *et al*, "Shape resonances in the hydrogen Stark effect in fields up to 3 MV/cm," *Phys. Rev. Let.*, Vol. 53, No. 8, pp. 775 - 778 (1984).
[5] Chihiro Ohmori, private communication.
[6] R. Damburg and V. Kolosov, "Theoretical studies of hydrogen Rydberg atoms in electric fields'" in Rydberg states of atoms and molecules, edited by R. Stebbings and F. Dunning (Cambridge University Press, Cambridge, 1983), pp. 31 - 71.
[7] J. Donahue *et al*, "Measurement of H^0 excited states produced by foil stripping of 800-MeV H^- ions," these proceedings.

For each PSR pulse, protons are injected at a constant rate for typically 1675 turns or 600 μs. At the end of injection the circulating proton bunch is extracted and transported to the spallation neutron target at the Los Alamos Neutron Scattering Center (LANSCE).

Approximately 7% of the incident H^0s that hit the 200-μg/cm^2 foil pass through without being stripped to H^+s. Most continue undeflected by magnetic fields, and pass out through a hole in the yoke of the downstream dipole magnet and on to a beam stop. However, some exit the foil in excited atomic states and are stripped to H^+ in the downstream dipole.
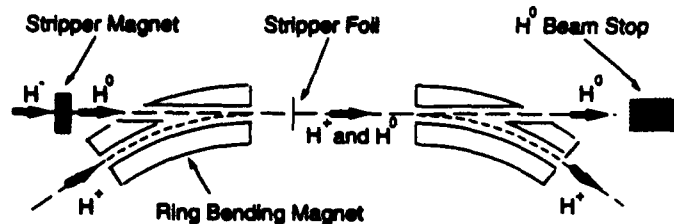
Figure 2. Beam Injection into the PSR

IV. THE MECHANISM OF EXCITED H^0 FORMATION AND PSR FIRST-TURN LOSSES

A. Introduction

Our conjecture is that the presence of excited state H^0s emerging from the stripper foil is the root cause of first-turn losses in the PSR. Other work [3] has shown that when 800-MeV H^-s pass through thin carbon foils, there are significant numbers of H^0s that emerge from the foil in an excited atomic state. In these H^0s the electron is relatively weakly bound, and some higher states will be susceptible to field stripping from the atom in the 1.2-Tesla field of the ring dipole magnet downstream of the stripper foil. Field stripping of 800-MeV excited-state H^- ions in magnetic fields was demonstrated in earlier experiments [4]. The same processes will occur when ground-state H^0s pass through foils.

B. Simple Theory of Excited-State H^0 Formation and Field Stripping

In a simple picture of excited H^0 formation, when an 800-MeV ground-state H^0 or H^- enters a foil, the electron (or electrons) is stripped from the proton, but continue in near proximity to and at the approximately same speed as the resulting proton. There is a significant probability that an electron will be recaptured into an excited H^0 state because the electron(s) and the proton remain relatively near each other in their passage through the remaining thickness of foil. Since, in the case of H^0 stripping, there is only one electron following the proton, instead of two as in the case of H^- stripping, it is plausible to assume that the number of excited-state H^0s formed from H^0 beams will be about half the number formed from H^- beams.

Field stripping of the excited-state H^0s can occur because, in the rest frame of the H^0, the magnetic field is transformed

in part to an electric field that distorts the atomic potential well. If the distortion is large enough, electrons in the higher excited states escape. Simple calculations [1,5] indicate that electrons in energy levels with principle quantum numbers of about three and above are unbound and will be stripped in a 1.2-Tesla field. Figure 3 is an approximate representation of the potential well for an 800-MeV H^0, both in zero field and in a 1.2-T magnetic field.
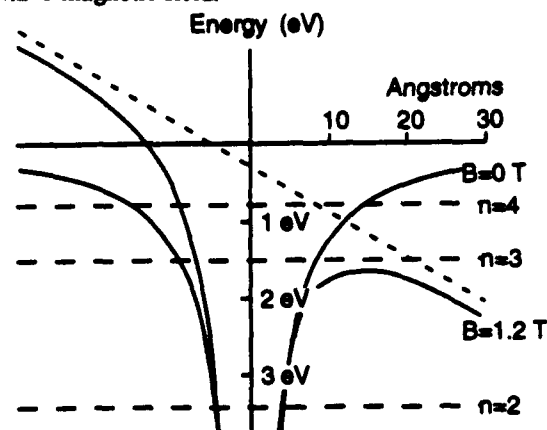
Figure 3. Hydrogen Atom Potential Well Distortion for 800-MeV H^0s in a 1.2 -Tesla Magnetic Field

C. More Detailed Theory of Excited-State H^0 Formation and Field Stripping

Damburg and Kolosov [6] give a more precise treatment of the Stark splitting of atomic levels for atoms in electric fields (or, equivalently, energetic atoms moving through magnetic fields). This approach allows one to calculate the energy levels and widths, and therefore the lifetimes, of excited H^0s that emerge from the stripper foil. These more precise calculations indicate that there are electrons in states with $n \geq 3$ that will be stripped in the dipole magnet downstream of the foil.

The excited H^0s entering the first 1.2-tesla dipole downstream of the PSR foil will have finite lifetimes in the field and will, therefore, penetrate part way into the field region before being stripped to protons. Until they are stripped, the H^0s will not follow the same trajectories as will protons. Therefore, if an excited H^0 progresses far enough into the magnet before stripping, it will not be within the phase space acceptance of the ring, and will be lost on the sides of the ring vacuum pipe within one revolution of the ring, which will cause first-turn losses. This process is illustrated schematically in Figure 4.

Following the treatment of Damburg and Kolosov [6], we find that there are H^0 states with principle quantum numbers $n=3$ and $n=4$ that strip in the dipole field, but that live long enough so that the resulting proton finds itself outside the phase space acceptance of the ring.

Table 1 summarizes some results of calculations of the fields at which various n states strip. The table also indicates the FWHM range of angles over which the resulting proton trajectories deviate from the center of the ring acceptance ellipse, and indicates yields and proton loss locations.

365

Stripper-Foil Scan Studies of the First-Turn Beam Loss Mechanism in the LAMPF Proton Storage Ring (PSR)

R. Hutson, D. Fitzgerald, S. Frankle, R. Macek, M. Plum, and C. Wilkinson

Medium Energy Physics Division, Los Alamos National Laboratory, Los Alamos, NM 87545 USA

Abstract

First-turn beam losses in the LAMPF Proton Storage Ring were measured as a function of the left-right position of the carbon foil used to strip neutral hydrogen atoms to H^+ for proton injection into the PSR. Two foil thicknesses, 200 and 300 $\mu g/cm^2$, were tested. Results indicated that first-turn loss is caused predominately by magnetic field stripping of a small fraction of the H^0 atoms that pass through the stripper foil without being stripped to protons, and the results were not consistent with a mechanism involving protons originating from atoms in the halo of the neutral beam incident on the stripper foil.

I. INTRODUCTION

A significant fraction of beam losses in the PSR are presently due to protons being lost before completing one turn around the ring. The cause of these first-turn losses has not been understood until now. Earlier hypotheses hinged on the idea that first-turn losses constituted loss of protons in the halo of the injected beam, but measurements of the extent of beam halos did not conclusively support this idea.

In an accompanying paper [1], a new hypothesis about the cause of first-turn beam losses in the PSR is proposed. It is suggested that unstripped H^0s emerge from the foil in excited states, are subsequently field stripped to H^+s in the first bending magnet downstream of the stripper foil, and are then lost before completing the first turn around the ring because they were stripped to H^+ outside the acceptance phase space of the ring.

The present paper describes the measurements made to search for evidence that would distinguish between these two mechanisms for first-turn losses over the other.

II. BEAM INJECTION INTO THE PSR

Protons are injected into the PSR by magnetic field stripping 800-MeV H^- ions to H^0s and then stripping the H^0s to protons in a 200-$\mu g/cm^2$ carbon foil placed on the ring axis. Roughly 5% of the injected H^0s that hit the foil are not stripped to H^+s and are transported through the field of the downstream ring bender and out through a hole in the magnet yoke to a beam stop. This arrangement is illustrated schematically in Figure 1,

which shows the injection section of the PSR. For each PSR pulse, protons are injected at a constant rate for typically 600 μs, and at the end of injection they are immediately extracted.
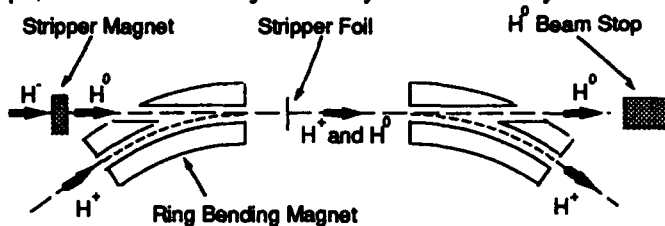
Figure 1. Beam Injection into the PSR

III. POSSIBLE ORIGINS OF FIRST-TURN LOSSES AND THEIR CONSEQUENCES

A. Beam Halos

If the halos of the injected beam are too large, protons originating from stripped H^0s in the halos will fall outside the phase space acceptance of the ring, and will be lost quickly by collisions with the walls of the ring vacuum pipe. Because, in the horizontal plane, the injected beam has a significantly larger emittance than in the vertical plane, and because there is a large mismatch between the injected beam horizontal-plane phase space ellipse and the ring lattice ellipse, protons from beam halos in the horizontal beam profile are more likely to cause first-turn losses than are halos in the vertical profile.

B. Magnetic Field Stripping of Excited H^0s

A recent suggestion [1] about the cause of first-turn losses is that a small fraction of unstripped H^0s exit the stripper foil in relatively loosely bound excited states that can be field stripped to H^+s in the magnetic field of the first downstream ring bending magnet. However, since an excited H^0 has a finite lifetime in a magnetic field, it will not be immediately stripped to a proton when it enters the fringe field of the magnet, and, as a consequence, its trajectory in the magnet before being stripped will not be exactly the same as that of a proton. A significant number of the protons resulting from excited H^0 stripping will, then, find themselves outside the acceptance phase space of the ring, and will be lost by collisions with the beam pipe wall before making a full revolution around the ring.

IV. THE MEASUREMENTS

A. *Methods*

Our approach to gathering evidence in support of a particular first-turn loss mechanism hinged on two comparisons. The first was to look at the change in first-turn losses vs. the change in ring beam as the stripper foil was scanned horizontally across the injected H^0 beam. The relationship between the amount of ring beam and the first-turn losses was then compared with the patterns expected for each of the two mechanisms described above.

The second comparison was between the magnitude of first-turn losses for two different stripper foil thicknesses. If field stripping of excited H^0s is the primary cause of losses, then the losses should be less for thicker foils since the stripping efficiency is greater, leaving fewer excited H^0s to be field stripped in the bending magnet.

Both the foil-scan and the foil-thickness comparisons involved measuring two quantities, ring beam and first-turn losses. A toroidal current monitor in the ring was used to measure the ring beam current while beam losses were measured with a system of ten loss monitors spaced uniformly around the periphery of the ring tunnel.

B. *Stripper Foil Scan Studies*

Three different foils, 200 $\mu g/cm^2$ thick and 10 mm wide, 200 $\mu g/cm^2$ thick and 16 mm wide, and 300 $\mu g/cm^2$ thick and 16 mm wide, were scanned across the beam. Each foil was moved in 1-mm horizontal steps across the injected H^0 beam whose horizontal rms width at the foil was 6 mm.

At each foil position we measured both the ring beam current and the first-turn losses. The amount of beam injected into ring varied as the foil was moved to cover different amounts of the incoming H^0 beam.

If the beam-halo mechanism is the cause of first-turn losses, then the loss rate will be directly proportional to the amount of beam halo that is covered by the stripper foil. If one uses a stripper foil wide enough to completely cover the injected beam, then, as the stripper foil is moved from a position completely outside the bounds of the beam to where it starts covering the beam halo on one side, one would see a rapid rise of the loss rate. After the halo on one side is completely covered by the stripper foil, moving the foil to cover more of the injected beam would result in more ring beam, but it would not cause a significant increase in the amount of first-turn loss. As the foil is moved farther to also cover the beam halo on the other side, the loss rate would again increase until the halos on both sides are covered, at which point first-turn loss rate would be a maximum.

There is evidence, from beam steering in the horizontal plane, that the injected beam very nearly fills the accepted phase space of the ring, and that beam halos can contribute to first-turn losses if the injected beam is not steered properly on the ring axis [2]. However, there is no conclusive evidence that, when the beam is properly steered, beam halos contribute significantly to first-turn losses.

On the other hand, consider the case in which losses are caused by field stripping of excited H^0s. Since both the number of H^+s and H^0s are directly proportional to the number of H^0s incident on the foil one would expect to find that the amount of first-turn loss is linearly related to the ring beam current.

Figure 2 illustrates, for the two mechanisms described above, the expected qualitative relationship between the first-turn losses and the ring beam as the foil is moved from a position where none of the injected H^0 beam is being intercepted by the foil to a position where the foil is centered on and completely covering the beam.
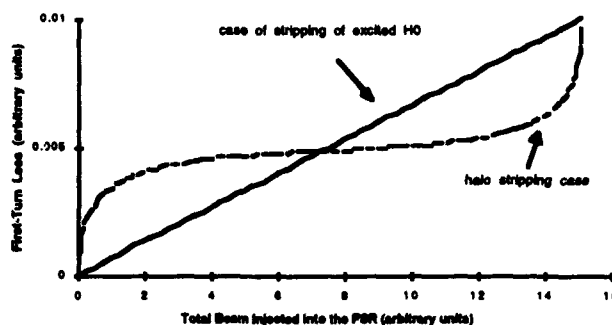
Figure 2. Expected Patterns of First-Turn Beam Loss vs. Beam Injected into the PSR for the Two Loss Mechanisms

C. *Foil Thicknesses Studies*

Also of interest is the difference between first-turn losses for stripper foils of different thicknesses. Thicker foils will strip more of the injected beam, leaving fewer H^0s and correspondingly fewer excited H^0s. If excited H^0s are the cause of first-turn losses, then thicker foils should result in the production of fewer excited H^0s. In this case losses will be proportional to the amount of beam injected into the ring. If, on the other hand, protons originating from the injected beam halos cause first-turn losses, the ratio of losses to ring beam will be largely independent of foil thickness. We base our comparison of first-turn losses vs. foil thickness on the data for the two 16-mm wide foils of 200 $\mu g/cm^2$ and 300 $\mu g/cm^2$ thickness.

V. RESULTS AND CONCLUSIONS

A. *Stripper Foil Scan Studies*

Results of the foil scan studies are summarized in Figure 3. The plots show, for each of the three foils used, the magnitude of first-turn losses vs. ring beam current as the foil is scanned across the beam. The plots trace out the first-turn loss history as the foils are scanned from the far left side of the

beam (negative x values), to the beam center, and finally to the far right side (positive x values).

The 10-mm-wide foil results in Figure 3a show an almost linear relationship between first-turn losses and ring beam both as the foil is moved from the far left side of the beam to the center of the beam and continuing to the right where most of the beam once again misses the foil. This result is exactly what would be expected if first-turn losses are caused by field stripping of H^0s.
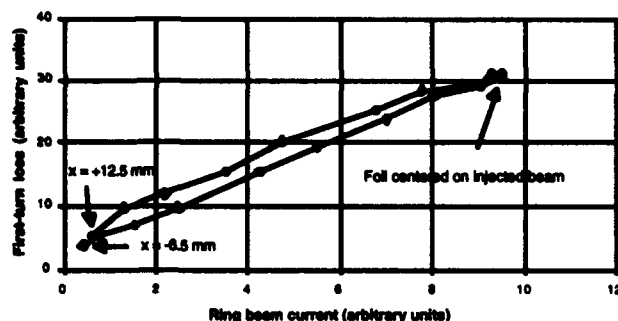
Figure 3a. First-turn loss vs. Ring Beam for 200 μg/cm^2, 10-mm-wide Carbon Stripper Foil
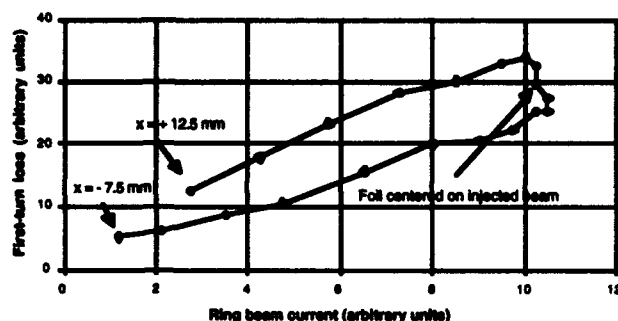
Figure 3b. First-turn loss vs. Ring Beam for 200 μg/cm^2, 16-mm-wide Carbon Stripper Foil
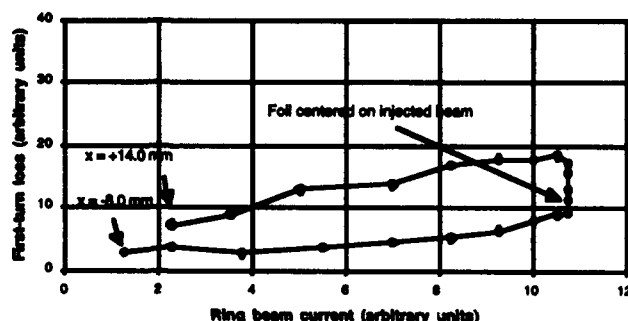
Figure 3c. First-turn loss vs. Ring Beam for 300 μg/cm^2, 16-mm-wide Carbon Stripper Foil

Results shown in Figure 3b and 3c for the 16-mm-wide foils also show a generally linear relationship between beam loss and ring beam as the foil is scanned toward and away from the injected beam center. However, in these two wide-

foil cases there is a range of foil positions near beam center for which most of the injected beam is covered resulting in an essentially constant ring beam current for several adjacent foil positions. An unexpected feature of the results for these two wider foils is that first-turn losses change significantly over the range of positions for which the foil is roughly centered on the beam. We believe that this asymmetry in the pattern of the first-turn vs. beam current relationship is probably due to some combination of an asymmetry in the phase space acceptance of the ring and/or a spill-location sensitivity of the loss monitors, although we have not yet made detailed studies or calculations to verify this idea.

B. Foil Thicknesses Studies

Figures 3b and 3c indicate that, for the same amount of ring beam current, first-turn losses with the 300 μg/cm^2 foil are about 45% of the losses with the 200 μg/cm^2 foil. Assuming that field stripping of excited H^0s is the cause of first-turn losses, and estimating the fraction of the injected H^0s that survive unstripped after passing through a foil, we predicted that losses with the 300 μg/cm^2 foil would be roughly 30% of the losses with the 200 μg/cm^2 one. This prediction is significantly lower than was observed. However, there is considerable uncertainty about the effect of foil thickness on in the energy level distribution of excited H^0 states. The number of H^0s that are field stripped is sensitive to this distribution so the observed discrepancy between measurement and prediction is not surprising. If protons from the halos of the injected beam were the cause of first-turn losses, the losses would be the same fraction of the injected beam independent of foil thickness.

Therefore, we conclude that the results of the foil thickness studies are consistent with the hypothesis that field stripping of excited H^0s is the cause of first-turn losses.

VI. REFERENCES

[1] R. Hutson and R. Macek, "First-Turn Losses in the LAMPF Proton Storage Ring (PSR)", these proceedings.
[2] R. Macek, et al , "Analysis of beam losses at PSR", Conference record of the 1988 EPAC Conference, Vol. 2, pp. 1252-1254.

Measurement of H^0 Excited States Produced by Foil Stripping of 800-MeV H^- Ions[*]

J. Donahue, D. Clark, S. Cohen, D. Fitzgerald, S. Frankle, R. Hutson,
R. Macek, E. Mackerrow, O. van Dyck, and C. Wilkinson
Los Alamos National Laboratory
Los Alamos, NM 87545 USA

H. Bryant, M. Gulley, M. Halka, P. Keating, and W. Miller
University of New Mexico
Albuquerque, NM 87131 USA

Abstract

Foil stripping of H^- directly to H^+ is being considered for proton injection in the next generation of high-current proton storage rings. This technique can result in significant losses because excited states of H^0, which are also produced in the foil, are field stripped in the downstream bending magnets. Without due care in the injection system design, many of the resulting protons will be outside the acceptance of the storage ring and will be quickly lost. We measured the production of such H^0 excited states at the LAMPF High Resolution Atomic Beam Facility. An 800-MeV H^- beam was passed through carbon foils of thicknesses 70, 100, 200, and 300 $\mu g/cm^2$, and the excited states were analyzed by a special magnet downstream of the foil. The magnet had a linear field gradient so that the trajectories of the outgoing protons could be used to reconstruct the field values at which the various H^0 stripped. We found that about 1% of the H^0 emerge in excited states which can be stripped to protons by ring-bending magnets.

I. INTRODUCTION

We have measured the production of excited neutral hydrogen atoms in a foil by studying their subsequent field ionization in a magnet. The foil thicknesses were comparable to those being used for injection into existing storage rings and to those being considered for storage rings at the next generation of spallation neutron sources. The linear field gradient magnet had a field shape similar to the fringe field in a ring-bending magnet. This experiment combined the efforts of the Proton Storage Ring (PSR) development group and a basic research group that has been doing accelerator-based atomic physics research at Los Alamos using laser-ion colliding beams for the past twenty years [1].

The experiment took place at the High Resolution Atomic Beam Facility at LAMPF where a "laser-quality" external H^- beam is available. The beam kinetic energy can be varied from 100 MeV to 800 Mev with typical beam parameters of 2-mm spot size, 100-μrad divergence, and 0.05% $\delta p/p$. With special tuning, these parameters can be improved to <0.5-mm spot size, <10-μrad divergence and $\approx$0.01% $\delta p/p$ [2].
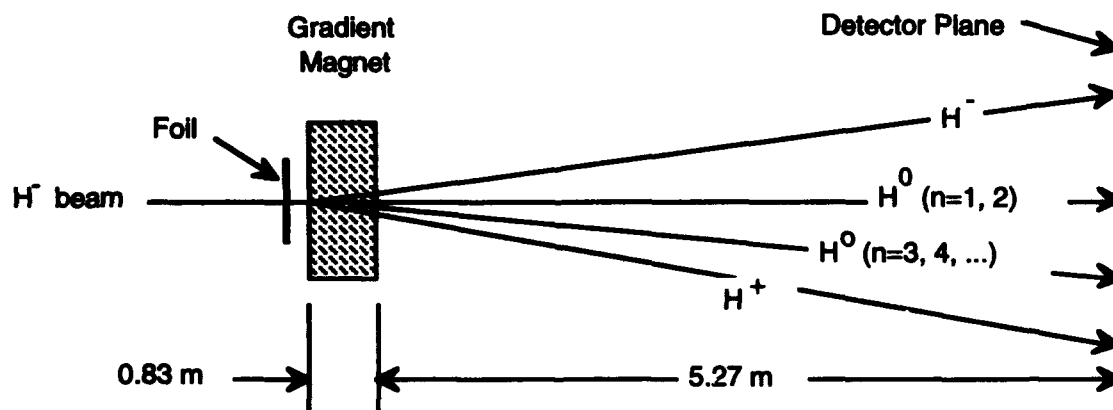
Figure 1. Layout of experiment to measure production of excited states.

369

When a beam of H$^-$ ions strikes a foil, some ions are stripped of both electrons to become protons (H$^+$), some are stripped of one electron to become hydrogen atoms (H^0), and some pass through the foil unscathed. At the foil thickness of interest for injection, most will be H$^+$. Some of the H^0 will be produced with the bound electron in an excited state. The distribution of these excited states was the quantity to be determined by this experiment.

When the H^0 enter a magnetic field, they are subjected to a motional electric field in their rest frame. This field is given by

$$F = (3 \times 10^6)\, \gamma\beta \times B, \qquad (1)$$

where F is in V/m and B is in tesla. The symbols γ and β are the usual relativistic parameters of the beam. For an 800-MeV atom, $\beta = 0.842$ and $\gamma = 1.85$. Thus a magnetic field of 1 T transforms to an electric field of 4.7 MV/m in the rest frame of the atom.

This intense electric field causes the atom to become unstable since the electron can tunnel out through the potential barrier. Ionization will proceed rapidly at a critical field given, to first order, by

$$F_c\,[V/m] = \frac{5.142 \times 10^{11}}{9n^4}, \qquad (2)$$

where n is the principal quantum number of the spherical states.

In the presence of a field, the states with definite lifetime are parabolic states represented by the quantum numbers (n1, n2, m) [3]. These are related to the spherical states (n, l, m) through the Clebsch-Gordon coefficients.

The principal quantum number is related to the parabolic quantum numbers by

$$n = n_1 + n_2 + m + 1. \qquad (3)$$

II. TECHNIQUE

We studied the excited states using a gradient magnet with a field that increases linearly with distance along the beam line. When a given H^0 state reaches the critical field, given by equation (2), it is stripped and the resulting H$^+$ is bent in the downstream magnetic field. The magnet is followed by a drift region and then a detector system. Knowing the field map of the magnet, we can then reconstruct the field at which a particular H^0 ionized. This technique and this same magnet have been used previously to study the ionization probability of the H$^-$ ground state as a function of field [4].

The apparatus consisted of the foil box, the gradient magnet, a 5.27-m flight path and a detector system. The floor layout is shown in Fig. 1. The detector system consisted of a scintillator telescope, a multi-wire proportional chamber (MWPC), and a scanning scintillator. The scintillator telescope covers the entire beam so that the experiment can be properly normalized. Standard beam diagnostics and phase-space tailoring apparatus are not shown.

The gradient magnet is a half quadrupole turned sideways to the beam. The beam enters through a hole in the return yoke and then encounters a vertical magnetic field whose strength increases linearly with distance. The maximum field available is 1.9 T and the length of the gradient region is 0.2 m.
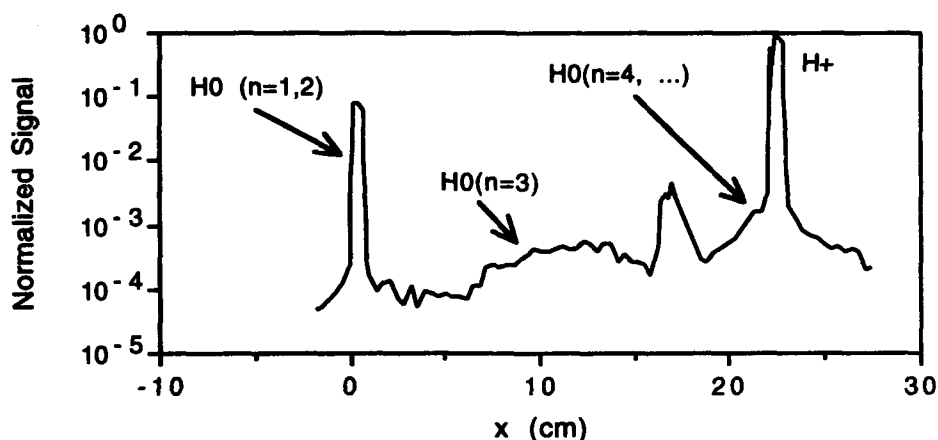
Figure 2. Typical data taken with the scanning scintillator and normalized to incident ions. The data shown are for a peak field of 1.3 Tesla and a foil thickness of 200 µg/cm^2. The sharp peak near 17.5 cm is believed to be spurious and will be investigated further during the 1993 run.

The data are analyzed using the Damburg-Kolosov (DK) formalism [5]. DK represent the unstable states as Breit-Wigner resonances and give a formula for the widths in terms of the field, the Stark-shifted energy of the state, and the parabolic quantum numbers. The Stark energy of the state are calculated from fifth-order perturbation theory.

We have tested the DK formalism by comparing to exact numerical calculations. These numerical calculations were verified in a previous experiment where we used a laser to excite the Stark states [6]. We found that the DK energies are accurate to 0.05% and the DK widths are accurate to better than 20% in the region of interest.

Our analysis code starts with a given distribution of excited states, finds out where they ionize using the DK formalism, and then traces the H^+ trajectories through the magnet and into the detector. The input parameters are then varied using a non-linear optimization code until a best fit is obtained. Many of the software subroutines were developed in a previous series of foil experiments [7].

III. RESULTS

The analysis program is still being tuned up, so precise numbers for the distribution of states are not yet available. We can see that the excited states that can be stripped in the downstream magnet are about 1% of the incident beam. This is enough to cause serious first-turn losses in high-current storage rings.

A typical data set is shown in Fig. 2. At this time, we believe that the sharp peak near x=17.5 cm is spurious and not an excited H^0 state. After subtracting this peak, the excited states are consistent with a statistical distribution in which sub-states are populated equally.

IV. FUTURE WORK

We are planning an improved experiment for the fall of 1993. The next experiment will have a MWPC detector with larger aperture and capable of higher rates. An upstream laser beam will be used to produce H^0 in a well-defined state so that we can track them through the magnet. This will allow us to verify the analysis code and look for systematic effects.

VI. REFERENCES

[1] H.C. Bryant, et al., "Atomic Physics with Relativistic Beams," in Atomic Physics 7, Daniel Kleppner and Francis M. Pipkin, Eds. (Plenum Press, 1981).

[2] P.G. Harris, et al., "Measurement and Reduction of Momentum Spread in the LAMPF Linac Beam," Nucl. Instrum. Methods A292, 254 (1990).

[3] Hans A. Bethe and Edwin E. Salpeter, Quantum Mechanics of One- and Two-Electron Atoms, (Plenum, 1957).

[4] A.J. Jason, D.W. Hudgings, and O.B. van Dyck, "Neutralization of H⁻ Beams by Magnetic Stripping," Los Alamos National Laboratory report LA-UR-81-831 (1981).

[5] R.J. Damburg and V.V. Kolosov, "Hydrogen Rydberg Atoms in Electric Fields," in Rydberg states of atoms and molecules, R.F. Stebbings and F.B. Dunning, Eds. (Cambridge University Press, 1983).

[6] T. Bergeman et al., "Shape Resonances in the Hydrogen Stark Effect in Fields up to 3 MV/cm," Phys. Rev. Lett. 53, 775 (1984).

[7] A.H. Mohagheghi et al., "Interaction of relativistic H⁻ ions with thin foils, Phys. Rev. A43, 1345 (1991).

REDUCING PHASE-DEPENDENT EMITTANCE GROWTH WITH LOCAL FLATTOPPING

R.E. Laxdal, T. Kuo, G.H.Mackenzie, L. Root
TRIUMF, 4004 Wesbrook Mall, Vancouver, B.C., Canada V6T 2A3
A. Papash
INR, Kiev, Ukraine

Abstract

The efficiency of the proposed H^- extraction in the TRIUMF cyclotron is improved by inducing a precessional component to the radius gain per turn by exciting a coherent radial betatron oscillation at $\nu_r = 3/2$. Beam test and computer simulation results show that accompanying this improvement is a growth in the transverse emittance of the extracted beam. The growth is, in part, due to phase-dependent mixing of the perturbed beam. This phase-dependence can be greatly reduced by flattopping the local energy gain per turn with the addition of a higher harmonic accelerating field in phase opposition to the fundamental. A 92 MHz, 4th harmonic, $\lambda/4$ cavity installed in the TRIUMF cyclotron has been used for such a purpose. Results of both computer simulations and beam tests will be presented.

I. INTRODUCTION

A general description of the method proposed to extract H^- ions from the TRIUMF cyclotron, including a layout of the extraction hardware, has been given previously. [1] An .. deflecting device (RFD), already installed, will improve the extraction efficiency by adding a precessional component to the radius gain per turn. The RFD generates a large coherent oscillation by exciting particles crossing the $\nu_r = 3/2$ resonance at 428 MeV (~292 in.) with a radial rf electric field. At higher energies, as ν_r increases, the oscillation precesses generating modulations in beam density. Several precession cycles (~100 turns) later at 452 MeV (~305 in.) an increase in the radius gain per turn of a factor of four is produced. A typical beam density plot from a differential probe is shown in Fig. 3. The extraction point coincides with the third density minimum (304 in. at the azimuth of the probe). An electrostatic deflector, or in the present study, a wide foil is positioned at this point to select the beam for extraction.

The present RFD has been found to stretch the vertical emittance [2]. The growth occurs due to vertical fields $\mathcal{E}_z$, associated with the $d\mathcal{E}_r/dr$ gradient in the RFD field that happen to coincide with the $\nu_z = 1/4$ resonance at 419 MeV. The resulting mismatch precesses in vertical phase space.

Both the radial coherent amplitude and the amount of vertical stretching induced by the RFD is proportional to the product of the average radial kick and the number of turns in the resonance region and varies with particle phase as $\cos(\phi/2)/\cos(\phi)$, while the rate of radial advance of the center of precession (accelerated equilibrium orbit) varies as $\cos(\phi)$. This phase-dependence leads to increases in the both the extracted radial and vertical emittances.

II. LOCAL FLATTOPPING

In some cyclotrons a small amplitude of a higher harmonic accelerating field is added for most or all of the acceleration to equalize, or 'flattop' the energy gain for a finite phase band to achieve separated turn extraction. In general all higher harmonic cavities can combine with the fundamental to flattop the energy gain, however as the harmonic m increases, the useful phase width of the flattop is reduced to π/m. In this paper we report how a relatively small fourth harmonic cavity can be used to locally flattop the energy gain per turn and reduce the phase-dependent emittance growth from precessional extraction or from stretching from resonances prior to extraction.

A 4th harmonic $\lambda/4$ auxiliary accelerating cavity [3] [4] (AAC), installed in the TRIUMF cyclotron, spans the energy range from 370–500 MeV (278–310 in.) with the voltage rising sinusoidally from inner to outer radius. The cavity can be used to flattop the local energy gain per turn, initially 340 keV, in the precessional extraction region from 420 MeV to 450 MeV. Simulations show that a voltage of 20 kV is sufficient for this purpose.

III. COMPUTER SIMULATIONS

A. Radial

A computer study was initiated to investigate the benefits of local flattopping. The beam arriving at the RFD was assumed to be homogenous (i.e. lacking turn structure) and matched to the cyclotron acceptance. A set of particles on the boundary of a matched radial phase ellipse were tracked using GOBLIN through the precessional extraction process for various initial particle phases. The results, summarized in Fig. 1(a), show the particle ellipses in radial phase space in the extraction region for two different initial phases, 0° and 20°. Part of the previous precession cycle is also shown, as is an extraction septum to illustrate the details of the extraction process. The radius of the septum corresponds to 452 MeV for the azimuth used in the study. The hatched region represents the area in radial phase space occupied by the extracted beam.

The particle ellipses are displaced from, and rotate about, the equilibrium orbit generating an increased radius gain per turn. Since extraction, in most cases[1], takes place over more than one turn the extracted emittance for a narrow phase band is broadened by the rotation of the ensemble . The 20° particles follow a slightly different precession path in phase space than the 0° particles. This will lead to further increases in the extracted radial emittance as different phases are injected into different regions of phase space. In Fig. 1(b) a small fourth harmonic is added in opposition to the main accelerating field in the GOBLIN simulation. In this case different phases follow more closely the same precession trajectory and hence occupy a smaller phase space area once extracted.

Monte-Carlo simulations were done to estimate the extracted radial emittance using the RFD with and without flattop. For an RFD voltage of 110 V/mm·m, a circulating radial emittance of $1\pi\mu m$ and a phase band of 40°, the extracted emittance is $4\pi\mu m$. The addition of a fourth harmonic flattop voltage reduced the extracted emittance to $3\pi\mu m$.

B. Vertical

GOBLIN was also used to track particles on the boundary of a matched vertical ellipse through the RFD. The results are

---

[1] Depending on septum positioning some phases will be extracted in one turn but since the beam density is uniform most will not be extracted cleanly.
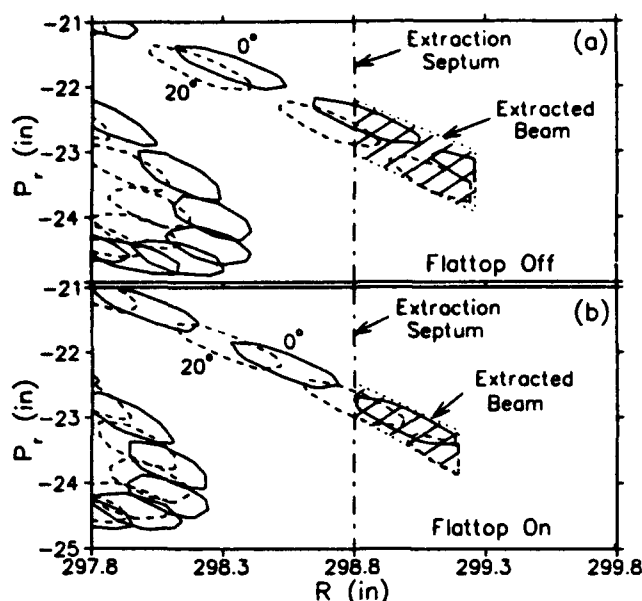
Figure 1: Result from a GOBLIN tracking study. Shown is the position in radial phase space of a matched beam ellipse undergoing precessional extraction for two different starting phases, 0 and 20°. In (b) a 4th harmonic flattopping voltage has been added to the accelerating field reducing the variation in precession between the two phases. The hatched regions represent the area in radial phase space occupied by the extracted, 20° wide, beam.

Figure 2: Result of a GOBLIN tracking study showing vertical phase ellipses for turns in the extraction region for rf phases of 5 and 15°. The phase dependence in the orientation of the stretched ellipse evident in (a) is reduced in (b) by the addition of a flattopping voltage.

summarized in Fig. 2(a). The orientations of the stretched vertical ensemble in the extraction region are plotted for two different initial phases, 5 and 15°. For a single phase the orientation changes as the stretched ellipse rotates from turn to turn. At any one radial position the two phases have different orientations. This will increase the extracted vertical emittance for a wide phase band as the various ellipses superimpose in the deflector. In Fig. 2(b) the flattop voltage reduces the phase-dependence in the orientation of the stretched vertical emittance.

Monte-Carlo calculations show that for an RFD voltage of 110 V/mm·m and a phase band of 40° the extracted vertical emittance is three times larger than that from a narrow 5° phase band. By adding a fourth harmonic flattop voltage the extracted emittance of the 40° case is only slightly bigger than the small phase band result.

IV. BEAM TESTS

Several experiments were made to investigate the possible benefits of the use of local flattopping in the TRIUMF cyclotron. Flags and slits were used to select a narrow phase band of ∼5° FWHM. The small phase band is useful for studying phase dependent effects since the central phase of the bunch can be varied by altering the main rf frequency. A variation of ±200 Hz results in a phase shift of ±20° at the extraction region. In a typical study five different central phases, 0, ±10°, ±20° are each sampled and then the results are compared to test for phase-dependent effects.

The local flattopping condition is found by setting the AAC to the estimated voltage and altering the phase until the RFD induced beam density modulation pattern is stable at the extraction point over the required phase range. A comparison for a ±20° phase variation for flattop off (a) and flattop on (b) is shown in Fig. 3. In practice the differential finger of a radial probe is positioned just beyond the fourth peak of the density plot (at point 'P' in Fig. 3(b)) and the frequency is scanned while noting the stability of the current on the finger.
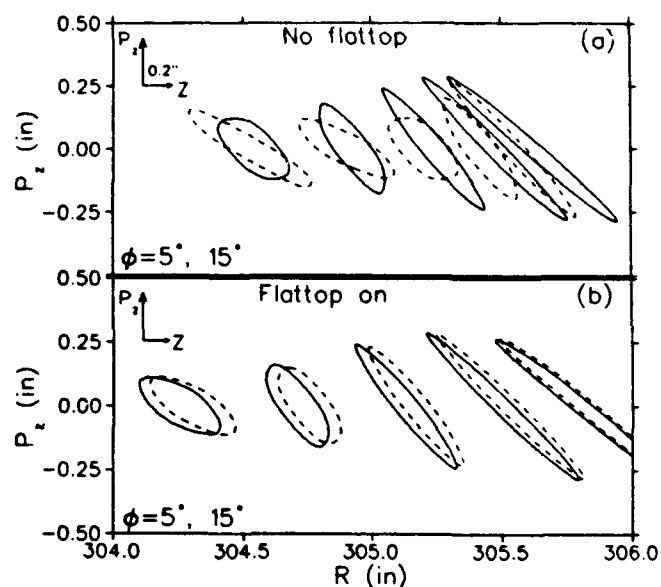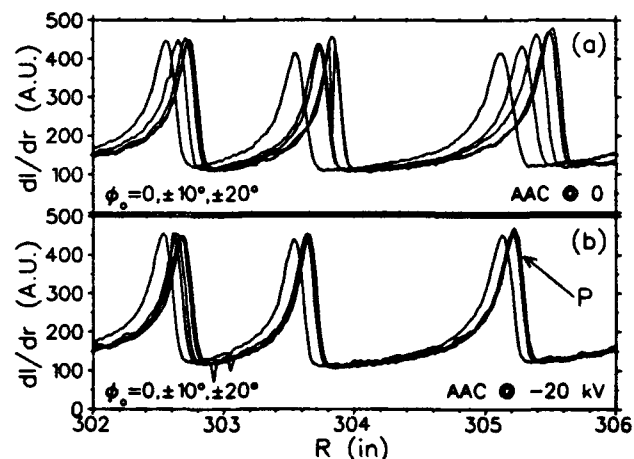
Figure 3: The signal from the differential finger of a radial probe showing the modulation in beam density produced by the RFD for various phases spanning ±20°. In (a) the AAC cavity is off while in (b) the cavity is on and set for local flattopping.

A. Vertical Measurements

A probe with five, 6.2 mm tall, horizontal fingers placed one above the other was scanned to measure the vertical width of the beam over the full extraction region for various central phases. A summary of the width scans is shown in Fig. 4. In (a) the AAC is off while in (b) flattopping is used. The scans clearly show evidence of the vertical stretching initiated at the RFD (R=292 in.) and the subsequent precession of the stretched vertical ensemble. At the azimuth of this probe the extraction point occurs near 302 in. The top scans show the phase dependence in the precession of the stretched phase space that develops leading up to this radius. In (b) the phase dependence is eliminated by the addition of the local flattopping.

The vertical width can also be measured by dipping a carbon stripping foil into the beam vertically and measuring the beam
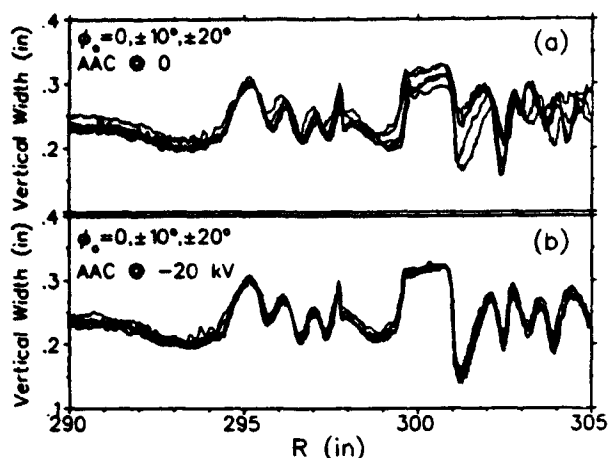
Figure 4: Experimental result showing the vertical beam width in the extraction region for various rf frequencies covering the phase range ±20°. The phase dependence evident in (a) is cancelled in (b) by adding a flattopping voltage to the AAC.

transmission as a function of foil position. A foil dip with a foil much narrower than the radius gain per turn will give a measure of the full width of the beam. However, if large coherent radial oscillations are present (eg during precessional extraction), a shadowing probe must be used to eliminate higher energy particles coming back through the foil. We use a wide foil shadowed by a probe one radial betatron cycle upstream, positioned to take 80% of the circulating beam with the foil fully down. Beam width plots for rf frequencies covering the phase range ±20° are shown in Fig. 5(a). Phase dependent variations in the vertical width at the position of the foil are evident. With the local flat-topping on (Fig. 5(b)) the phase dependence is eliminated. The width difference between flattop on and flattop off is caused by a change in the number of turns from the onset of the vertical stretching caused by the extra decelerating field.
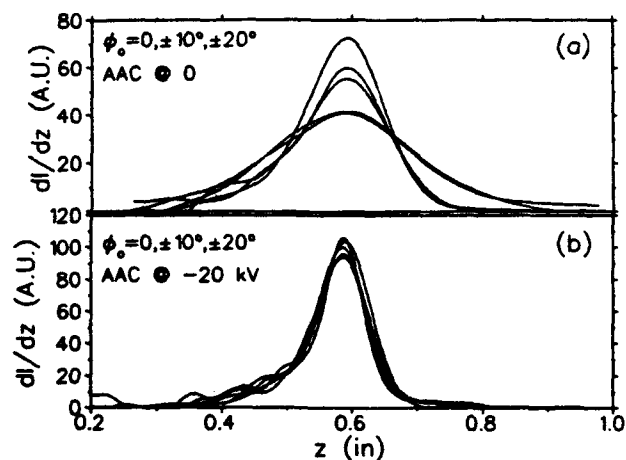
Figure 5: In (a) the vertical beam width at the point of extraction is plotted for beams of central phase 0, ±10°, ±20° indicating a phase dependent behavior. In (b) the phase dependence is eliminated with the addition of a local flattop to the energy gain per turn.

B. Horizontal Measurements

One measure of the phase dependence of the radial emittance of the extracted beam is to measure the radial width of the

beam on a totally intercepting blocking probe placed at the extraction point for various phases. This can be done by scanning, radially, a shadow probe one betatron cycle upstream from the 'blocker', and measuring the current on the 'blocker' as a function of 'shadow' position. Several scans were taken for different incoming beam phases and the results were differentiated to produce the radial width of the beam on the blocking probe, in this case a wide stripping foil. The variation of the radial width with respect to incoming beam phase is shown in Fig. 6 for no flattopping and for the flattopping turned on. The larger radial width in the 'AAC on' case is due to a slight radial shift in the extraction foil to a position with a higher radius gain per turn.
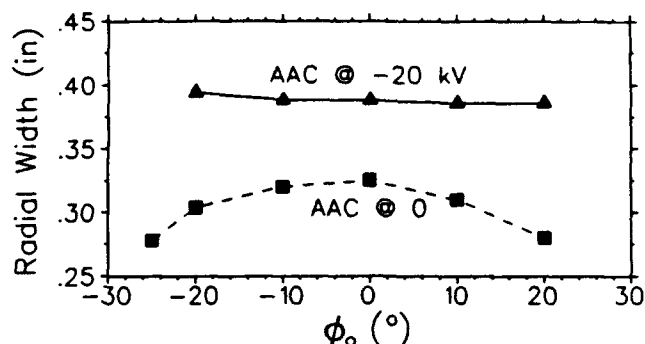
Figure 6: The radial width of the beam on a wide extraction foil as a function of beam phase for flattopping off (dashed curve) and flattopping on (solid curve).

C. Emittance Measurements

A wide foil was used to extract the beam into a beam line where three wire monitors separated by drift spaces were used to measure the transverse emittance. The phase dependence in the extracted beam was estimated by measuring the horizontal and vertical beam spot on the monitors for various beam phases. Although the monitors have inadequate resolution to calculate the absolute emittance accurately it was clear that the beam spot on the monitors did vary with beam phase. The addition of the flattopping reduced this phase dependent effect. New scanning wire monitors have been designed which will improve this measurement.

V. REFERENCES

[1] M. Zach, et al., "Status of the H⁻ Extraction Program at TRIUMF", Proc. 12th Conf. on Cyc. and their Applic., Berlin 1989, p. 368.

[2] R.E. Laxdal, et al., "Beam Quality Investigations for H⁻ Extraction at TRIUMF", Proc. 13th Intl. Conf. on Cyc. and their Applic., Vancouver, 1992, p. 415.

[3] R.E. Laxdal, "Initial Operating Experience with the Auxiliary Accelerating Cavity for the TRIUMF Cyclotron", Proc. IEEE Part. Accel. Conf., San Francisco, 1991, p. 810.

[4] R.E. Laxdal, et al., "Beam Test Results using the Auxiliary Accelerating Cavity", Proc. 13th Intl. Conf. on Cyc. and their Applic., Vancouver, 1992, p. 442.

An Ion-Source Model for First-Order Beam Dynamic Codes

C. L. Fink, and B. P. Curry
Argonne National Laboratory
9700 S. Cass Avenue
Argonne, IL 60439

Abstract

A model of a plasma ion source has been developed that approximates the system of Poisson and Boltzman-Vlasov equations normally used to describe ion sources by an external electric field, a collective electric field due to the charge column, and the starting boundary conditions. The equations of this model can be used directly in the Lorentz force equation to calculate trajectories without iteration.

INTRODUCTION

The physics of a plasma ion-source is usually described in terms of a system of Poisson and Boltzman-Vlasov equations for each of the ion species involved[1]. This system is usually solved numerically after various levels of approximation are made to make the problem tractable. In general, this procedure gives reasonable agreement with experiment, especially for positive ion codes. The problem, however, is that the effects of various approximations and/or source components on source performance are difficult to separate and thus optimization of source performance is difficult.

In this paper, we develop a model of an ion source that consists of an external electric field due primarily to the source geometry, a collective electric field due to the charge column, and a set of initial boundary conditions on the ions as they are injected into the external and collective fields. Since the charge column is not infinitely long, there will be axial component to the collective electric field[2]. Because this model separates out the external and collective fields, it should be relatively easy to trace particle trajectories or incorporate the model into codes like TRACE2D[3]. In this paper, we will discuss the key features and assumptions of the model. We will provide a more detailed comparison of the model predictions with those of standard source codes such as SNOW[4] in a later paper.

OVERVIEW OF A TYPICAL POSITIVE-ION SOURCE MODEL

Figure 1 shows the simple positive-ion source geometry to be modeled. The plasma to extractor electrode distance D is 8 mm, the aperture radius is 2.5 mm, and the sheath to plasma electrode distance L varies between 1 and 4 mm. Note that the usual hole in the extraction electrode has been eliminated for simplicity.

In source codes like SNOW, the initial ion beam is injected into the plasma with an energy of 5 to 10 eV in a direction parallel to the axis with a current density Jo. These positive ions are neutralized within the plasma by a Boltzman distribution of electrons with an electron temperature typically of 2 to 10 eV. As the ions approach the plasma electrode, a sheath forms at the edge of the plasma, which has the effect of reflecting the electrons and accelerating the positive ions out of the plasma. Usually, the width of the sheath is approximately 0.1 to 0.001 mm with an electric field on the order of a MV/m. After being extracted from the sheath the ions are further accelerated by the electric field from the extraction electrode.
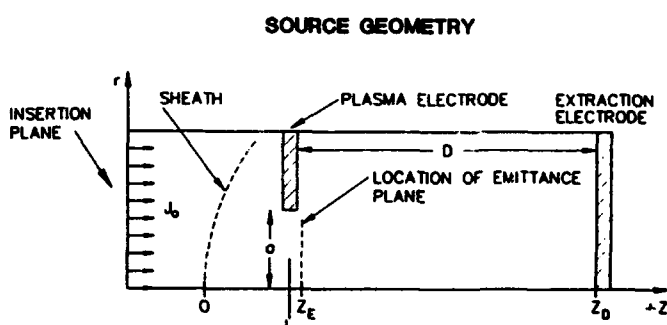
SOURCE GEOMETRY

Figure 1. Definition of Source Geometry

The Poisson and Boltzman-Vlasov equations are solved iteratively by calculating an initial potential distribution, ray-tracing the ion trajectories to obtain a new charge density, and then solving the Poisson equation until consistency is achieved. This final potential is then used to ray-trace the ions to obtain current densities and two-dimensional phase space distributions at the location Z_E.

CALCULATION OF EXTERNAL FIELD

The external field is determined by solving Laplace's equation for the source geometry using a code such as SIMION or by using the technique of aperture superposition[5]. The problem in determining the external fields arises from the fact that the this field depends on the unknown position and shape of the sheath formed in extracting the plasma.

In our model we approach this problem by assuming that the position of the sheath has the dominant effect on determining the external fields and that the shape of the sheath is less important. The top half of Fig. 2 shows calculations[6] of the phase-space distribution from SNOW for a range of current densities using the geometry of Fig. 1. The bottom half shows phase-space distributions calculated using

375

external fields for a planar plate located at various values of L relative to the plasma electrode. The key observation from these calculations is that the shape of the phase-space distributions does not appear to be strongly dependent on the space-charge forces, and that the current density Jo is closely related to the sheath position.
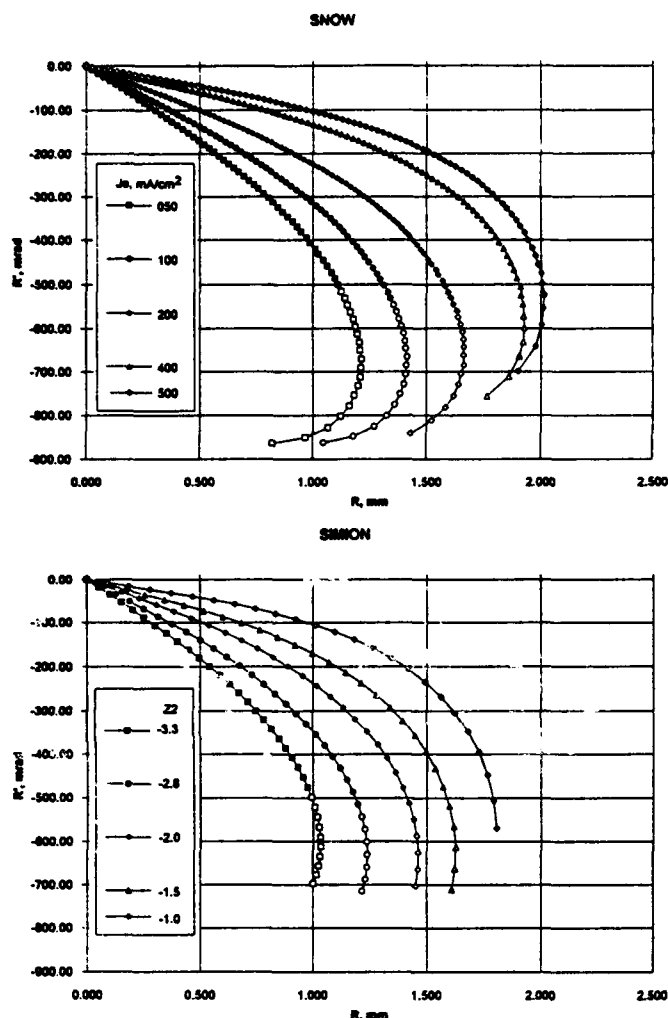
Figure 2. Phase-Space Distributions

The preceding observations suggest that a good first approximation in calculating the external fields is to simply replace the sheath by a planar plate and to choose the position of the plate to provide the desired current density. Using a sheath shape that is not planar does not complicate the analytical determination of the external fields. The complication is in devising a method to determine the sheath shape.

The key is to determine the functional relationship between Jo and the plate position without solving the Poisson-Boltzman equations. We propose that this relationship can be determined by requiring that the axial electric field due to the charge column be equal to the

negative of the Laplacian electric field when the sheath is replaced by a conducting surface. Figure 3 shows a plot of the current density versus sheath-to-plasma electrode distance L. The solid line shows the sheath position (5-eV equipotential) from the SNOW calculation. The open symbols show the current densities required to match the Laplacian and column electric fields at a particular L using a planar emission electrode. The column electric fields were calculated using the formulas for a column of charge of constant radius a as described in the following section. The data suggest that the exact current density for a particular L is not a sensitive function of a. The use of the experimental aperture size of 2.5 mm appears to be a good initial choice to reproduce the SNOW data. The solid symbols correspond to a concave emission electrode and appear to give a better fit to the data over the range of L. The problem in concave calculations is in determining the radius of curvature of the emission electrode.
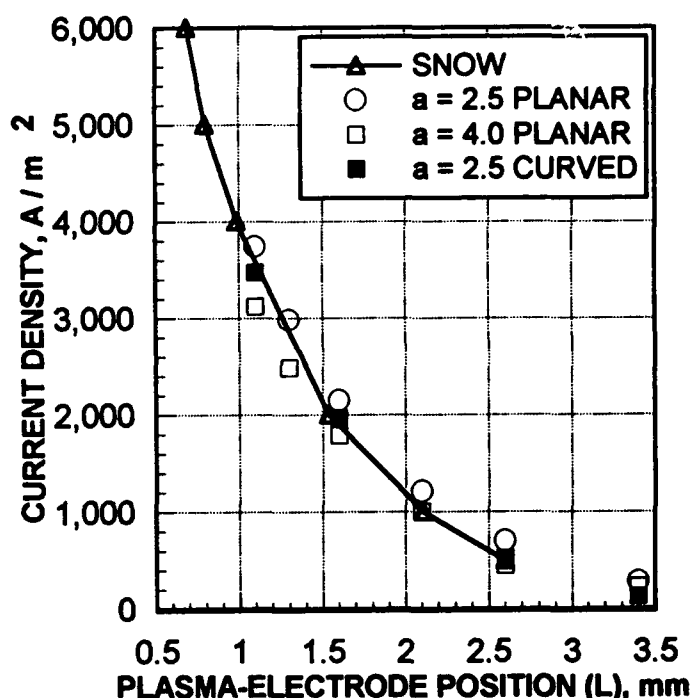
Figure 3. Current Density Versus Sheath Position

BOUNDARY CONDITIONS

One of the most uncertain features of this model is the boundary conditions to use at the emission electrode. Since the sheath region is relatively thin and since the sheath shape is approximately planar, it would not be unreasonable to expect that the ions would not be significantly bent in the sheath region and that the amount of energy gain would be limited. Thus a first approximation is simply to assume that the ions have the same direction and energy at the sheath as at the insertion plane. Note, however, that if the ions are not emerging perpendicular to the emission surface, then the energy of the emitted ions can have a significant effect on the resulting beam optics.

376

ELECTRIC FIELD FROM A COLUMN OF CHARGE

The potential due to a distribution of space charge is given by Kirstein et. al[7]. This potential vanishes at z = 0, but not at z_D. If we add a potential that is a linear function of z, and that varies from 0 to the negative of Kirstein's potential at z_D, then it will also satisfy the requirement of zero potential at the end of the column. Differentiating this modified potential gives the space charge field.

$$Ez(0,z) = \frac{1}{2\varepsilon_0}\left\{ \int_0^z \rho(z')\left[\frac{z+z'}{\sqrt{a^2+(z+z')^2}} - \frac{z-z'}{\sqrt{a^2+(z-z')^2}} \right]dz' \right.$$

$$+ \int_z^{z_D} \rho(z')\left[\frac{z+z'}{\sqrt{a^2+(z+z')^2}} - \frac{z-z'}{\sqrt{a^2+(z-z')^2}} - 2 \right]dz' \qquad (1)$$

$$\left. + \frac{1}{z_D}\int_0^{z_D} \rho(z')\left[\sqrt{a^2+(z_D-z')^2} - \sqrt{a^2+(z_D+z')^2} + 2z' \right]dz' \right\}$$

where a is the column radius and z_D is its length. In this equation we have assumed the charge density is uniform in the radial direction and a is constant.

We can use the above expression to obtain the radial and axial field components off the axis, using the paraxial approximation:

$$Er(r,z) = \frac{r}{2}\left[\frac{\rho(z)}{\varepsilon_o} - \frac{\partial}{\partial z}Ez(0,z) \right] \qquad (2)$$

$$Ez(r,z) = Ez(0,z) - \frac{r^2}{2}\left[\frac{\partial^2}{\partial z^2}(Ez(0,z)) - \frac{1}{\varepsilon_o}\frac{\partial}{\partial z}(\rho(z)) \right] \qquad (3)$$

Inserting the axial space charge field (eq. (1)) into eqs (2) and (3) yields the entire space charge field in the paraxial approximation., provided the charge density is known.

The charge density is related to the ion beam current density by

$$\rho(z') = \frac{4}{9}\frac{J_0}{\chi}\frac{\varepsilon_o}{\sqrt{T_o+\varphi(z')}} \qquad (4)$$

where T_0 is the ions' initial kinetic energy, $\chi = (4/9)\varepsilon_0\sqrt{2e/m_{ion}}$, J_0 is the beam current density, and ϕ is the total potential (solution of Poisson's equation) on axis. We approximate this potential with the space charge limited planar diode potential given by

$$\phi(z') = \left(\frac{J_0}{\chi}\right)^{2/3} z'^{4/3} \qquad (5)$$

Now we can relate the sheath position to the beam current density. Since the sheath is an emitting surface, the total field (applied plus space charge) must vanish at z = 0. The space charge field is obtained from eq. (1).

$$Ez(0,0) = \frac{1}{\varepsilon_0}\int_0^{z_D}\rho(z')\left\{ \frac{z'}{z_D}-1+\frac{z'}{\sqrt{a^2+z'^2}} \right.$$

$$\left. -\frac{1}{2z_D}\left(\sqrt{a^2+(z_D+z')^2} - \sqrt{a^2+(z_D-z')^2} \right) \right\}dz' \qquad (6)$$

Equating this field to the negative of the field resulting from Laplace's equation, using eqs. (4) and (5), gives the beam current density as a function of the applied voltages, the sheath location, and the extraction geometry.

DISCUSSION

Using the assumptions and formulas presented in this paper, it is relatively easy to calculate ion trajectories from an ion source without having to solve iteratively a complicated system of Poisson and Boltzman-Vlasov equations. In addition the physics of the problem is more readily apparent. We are currently in the process of developing a code using the model described in this paper to calculate phase-space distributions for comparison with SNOW calculations. It is expected that by varying the various parameters and assumptions in our model to obtain agreement with the SNOW data, we will obtain additional information on which source parameters are limiting source performance.

REFERENCES

[1] J. H. Whealton, et al., "Computer Modeling of Negative Ion beam Formation," J. Appl. Phys. 64, 6210 (1988)

[2] D. A. De Wolf, "Basics of Electron Optics," John Wiley&Sons, Inc. 1990.

[3] K. R. Crandall and D. P. Rusthoi, "Documentation for TRACE: An Interactive Beam-Transport Code," Los Alamos Report LA-10235-MS, (1985)

[4] J. E. Boers, "SNOW", Thunderbird Simulations, 626 Bradsfield Drive, Garland Texas, 75042-6005

[5] P. W. Hawkes, E. Kasper, "Principles of Electron Optics," Academic Press, Volume 1, 143 (1989)

[6] C. L. Fink, and B. P. Curry, "Simple Optics Description of The Plasma Sheath and Plasma Electrode Region," Sixth Intern. Symp. on Production and Neutralization of Negative Ions and Beams, Brookhaven , Nov. 1992, to be published.

[7] P. T. Kirstein, et al., "Space-Charge Flow," p. 405, McGraw-Hill, New York 1967

Lattice Design and Injection Issues for the 2 TeV SSCL High Energy Booster to Collider Injection Lines

Fuhua Wang , Ron Schailey, John McGill, David Johnson

Superconducting Super Collider Laboratory*, 2550 Beckleymeade Avenue, Dallas TX 75237 USA

Karl L. Brown

Stanford Linear Accelerator Center, Stanford University, Stanford, CA 94309

Abstract

An intensive and systematic lattice design study for the 2 TeV injection lines from the High Energy Booster (HEB) to the Collider rings has led to a compact resistive magnet solution which is a one piece achromat having beta function transitions on both ends and a pseudo-periodic structure in between. A comparison between several possible solutions concentrated on the desired optical flexibility and major technical problems associated with the huge amount of beam energy (6.55MJ) in the HEB and mechanical interferences. The HEB extraction and Collider injection schemes were designed with kicker misfire control and aperture limits on both the HEB and the Collider sides.

I. INTRODUCTION

The High Energy Booster (HEB) ring is the last booster of the 20 TeV Superconducting Super Collider. The HEB west long straight section where extraction takes place, is directly over the two Collider rings, in the west utility straight section, where injection occurs. The vertical separation between HEB and the bottom Collider is 14 m, which is determined by radiation safety requirements. The elevation separation between the two Colliders is 0.9 m.

There are two beam lines to transfer both the clockwise (CW) and counterclockwise (CCW) extracted HEB beams to top Collider and bottom Collider, respectively. Most of the difficulties of lattice design for these lines come from the very confined space limits. In 1991, a resistive magnet solution was proposed [1]. However, the use of iron-dominated magnets, limited to 1.8 T, basically filled about 1/2 of the length of the transfer line with dipoles. The consequent restrictions on the placement of quadrupoles resulted in an irregular beta function and limited tuning flexibility. An intense study of lattice design was performed in 1992 [2], which resulted in several different designs: a lattice with two "M=-I" achromats; a hybrid solution (using superconducting and resistive magnets); and a compact resistive magnet solution. The compact "one piece" resistive solution has been adopted for its optical flexibility, few problems of physical interference, operational reliability, and cost saving.

Operational reliability and safety is a major concern of this transfer system design. The HEB extraction and Collider injection aperture limits have been carefully examined to avoid quenching of magnets by mis-steered beam and beam halos.

HEB extraction and Collider injection kickers have been carefully segmented to reduce the strength of a single kicker unit so to prevent equipment damage, especially Collider elements, by mis-steered beam due to single kicker misfire or pre-fire, which will likely happen once in a while. A bump scheme is also incorporated for HEB extraction serving the same purpose. Since all magnets in the transfer line are warm, one can consider implementation of a collimator system to further protect Collider elements from HEB kicker misfires [3].

II. LATTICE DESIGN STUDY

The design study here in many ways is an effort to solve inter-accelerator transfer line optical problems dealing with an insufficient length (phase advance) and strict matching requirements. The basic optical design goals of these lines are (a) Centroid matching, *i.e.*, closed orbit matching; (b) β matching; and (c) Dispersion function matching. By dealing with η and β matching differently, one can work as follows: (1) η matching first, β matching second; (2) β matching first, η matching second; or (3) simultaneous η and β matching.

The compact resistive lattice is a one piece β & η matching lattice with mixed η and β matching to overcome the shortage of phase advance. Instead of making "Optical Insults" (highly irregular β matching section), two quadrupoles are used at each end to reduce the maximum β amplitude, and to present reasonable β functions to start a periodical oscillation. A pseudo-periodic structure is created in the middle part to provide optical flexibility of the lattice. Figure 1 shows the lattice functions of the compact resistive design. It is easy to count how many variables are needed to match the HEB to Collider directly: two for η, four for Twiss parameters. Practically, one quadrupole on each side is added to have some preliminary control of β amplitudes which are the extensions of β oscillation in straight sections of these rings.

To cancel dispersion more naturally, one has to pay attention to the 2π phase shift between the two major bending centers. On one hand, one has to push bends to both ends to save total bending power, on the other hand, one has to maneuver "tails" of each bending group (parts close to center) to balance the group bend center position. The final matching of six parameters in most cases is accomplished by varying gradients of the "six quadrupoles" in the middle of the line. However two quadrupoles, one at each end play an important role in shaping the β oscillation wave forms in the center part. Itera-

tions usually are carried on to make β oscillation in the middle part more nearly a periodical structure.

For comparison, the two, -I achromats lattice is depicted in Figure 2. This lattice has the advantage of separating η and β matching. However, study shows, due to the insufficient length of the line, that orthogonal control of η and β is limited to a small range. Spatial interference problems, cost increases and the difficulty to collimate the beam in the lines using superconducting magnets brought the abandonment of this approach.

III. OPTICAL FLEXIBILITY

In actual machine operation, the matching conditions on both the HEB and Collider sides may change to what may be good for the machine tuning. It is ideal to fit these tuning processes without moving quadrupoles around in beam lines. In our case, the lattice structures are irregular, and in most of the designs there are no orthogonal controls on β & η. Matching or tuning totally depends on computer fitting. Therefore we must ask what is the tuning flexibility?

The optical or tuning flexibility of the beam line may be defined as: "the matching range of HEB & Collider operating points which the beam line can accommodate." The criterion set for matching is the maximum allowed emittance dilution in the following machines (here, Collider rings), when a perfect matching is not possible. The limits for beamline tuning are: (a) Quadrupole gradient strength limit, which is a technical limit; and (b) Maximum betatron amplitude along the line, a

consideration from beamline aperture and error sensitivity requirements. Figure 3 illustrates the above conceptions. We have to link changes on β or η values to emittance dilution properly. The allowed maximum fractional emittance dilution is <10%. This roughly corresponds in one transverse direction to +50% β mismatching, or to 1m η mismatching at the Collider input [2].

Results of fitting calculations for various designs have been compared. Fitting has been made to deal with mathematical problems, quadruples can be grouped in different ways or in different fitting order etc. An amazing result is the one piece solution always allows good matching while the other solutions may result in some degree of dilution. It is believed the pseudo-periodical structure helps to accommodate a wide range of matching conditions, by allowing β amplitudes up and down in the central part of the line. For example, a 0.3m η error initiated in HEB side will result in -0.8m η at Collider side. Now if a +1m η value is required to be matched at the Collider side, this will be a much more difficult condition. It is observed that the pseudo-periodical structure allows the β amplitude to blow up in the middle so as to meet the matching requirements. In the example shown in Figure 4, different β match conditions are imposed as well. This represents one of the worst cases. The peak β amplitude increases from ~200m to 600m, one quadrupole field gradient is tuned up to 40T/m (27% more than design value). But the matching is good, while β and gradient values are still within beamline "tuning limits".
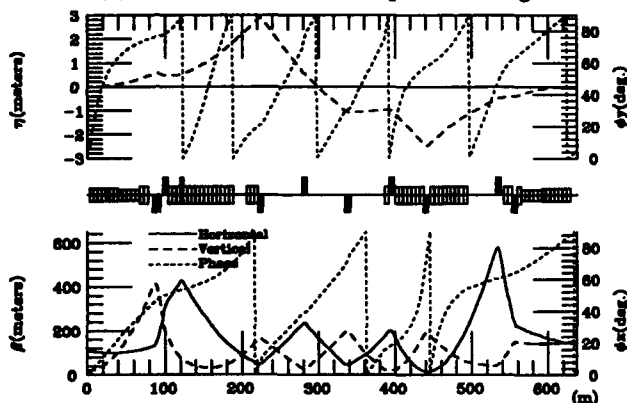
Figure 1 Lattice Functions of Compact Resistive Solution
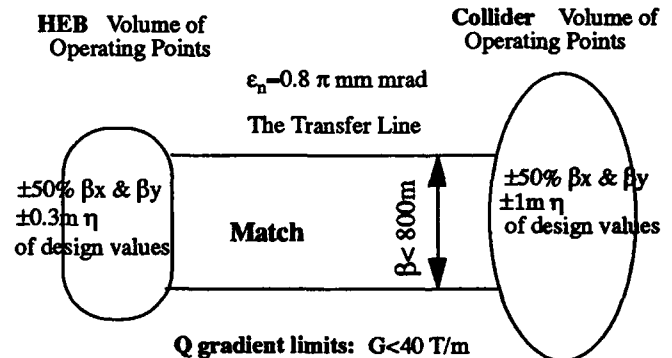
Figure 3 Optical Flexibility for Compact Resistive Solution

Figure 2 β & η Functions of -I Lattice
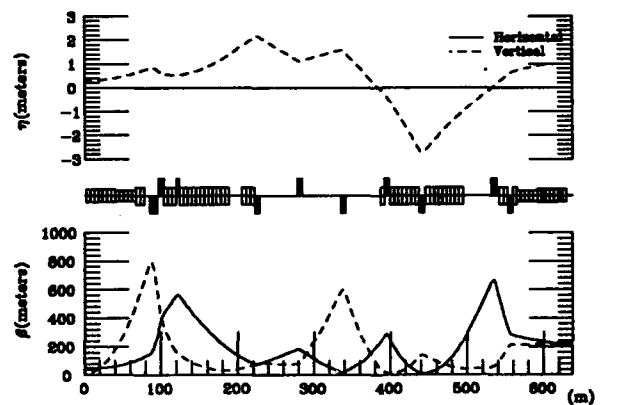
Figure 4 0.3m η & -50%β at HEB matching to 1m η & +50%β at Collider(Nine Gradients varied)

IV. HEB KICKER EXTRACTION SCHEME

The HEB extraction is performed by a combination of a local "three" bump scheme, Figure 7, and a set of fast pulsed kicker magnets, Figure 6, for clockwise (CW) and counter-clockwise (CCW) extraction to the HEB to Collider (HTC) transfer line. The local bump scheme moves the HEB closed orbit towards the magnetic septum of the Lambertson magnets[3], Figure 3. The horizontal "three" bump magnets are found in standard superconducting spools along with other HEB correction elements. Their strengths are: BMP1 -0.250T-m, BMP2 +0.515 T-m, and BMP3 -0.432 T-m. The CW extraction kickers then move the extracted beam into the field region of the Lambertson magnets, and beam bends downward towards the top Collider, and similarly for CCW extraction. The extraction kickers (6, CW) and (8, CCW) are chosen such that their kick/module is 25 μr. This segmentation of the kickers, along with 3.8mm bump, serves to mute the effect of a single kicker mis/prefire and minimize the effect of a two kicker mis/prefire in terms of the resultant "free" β oscillations of beam centroid. These mis/prefires are treated elsewhere [3]. The extraction kickers have a rise time of 1.7 μs and flat top time of 36 μs. The nominal 1% total output deviation (TOD) on flat top ripple, droop, pulse to pulse reproducibility, will require a transverse damper in the Collider to compensate this effect. Other extraction kicker parameters are as follows: magnet field length of 1.0m, and slot length of 1.5m, and nominal magnetic field of 1.67 KG. It should be noted that the first Lambertson magnet is "rolled", or rotated, so that any residual horizontal angle from kickers is canceled.

V. COLLIDER KICKER INJECTION SCHEME

The Collider injection is performed as follows. The beam in the HTC transfer line is moved towards the Collider closed orbit by the quadrupole "steering", due to off axis beam centroid through Collider quadrupoles QU3B and QU4B just downstream of the injection Lambertsons. The injection kickers, then bend the injected beam on axis. The last Lambertson is "rolled" to cancel any residual angle of kicker and quadrupole steering. The injection kicker parameters are given in Figure 8. The beam positions at injection Lambertson and QU3B interface are given in Figure 5, with care to consider kicker mis/prefire from HEB extraction kickers as well as from Collider injection kickers, and timing errors[3].

Figure 6. HEB Kicker Extraction Scheme
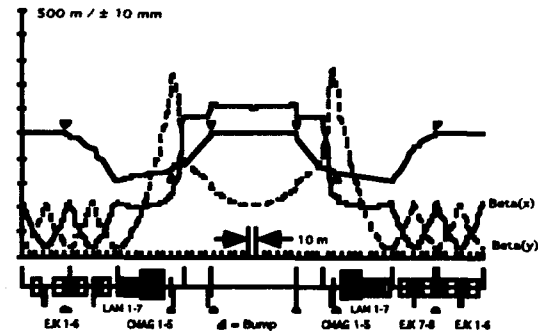
Figure 7. HEB Local Bump Scheme for Extraction
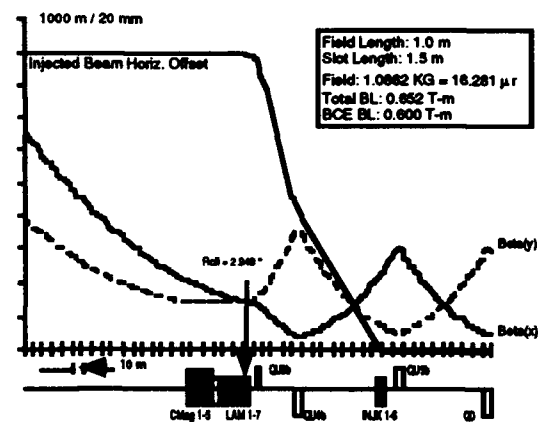
Figure 8. Collider Kicker Injection Scheme

Figure 5. Collider Injection Lambertson Magnet and Quadrupole QU3B Interface Section

VII. REFERENCES

[1] F. Wang, R. Schailey "HEB to Superconducting Super Collider Transfer Lines," IEEE Particle Accelerator Conference 91CH3038-7 p.985 1991.

[2] F. Wang, K. Brown, J. McGill, D. Johnson "Lattice design Study for the HEB to Collider Transfer Lines," SSCL numbered publications (to be published) May 1993.

[3] R. Soundranayagam et al. "Consequences of Kicker Failure During HEB to Collider Injection and Possible Mitigation," these proceedings.

Detailed Studies on the Beam Transfer Line from Linac to Low Energy Booster Synchrotron for the SSC

R. Bhandari, J. McGill, F. Wang and S. Penner

Superconducting Super Collider Laboratory*, 2550 Beckleymeade Avenue, Dallas, TX 75237, USA

Abstract

Ion optical and engineering aspects of the Linac to LEB transfer line [1] are described. This 210 m long line will transport a 600 MeV H⁻ beam between the two accelerators. Emittance growth expected at injection due to errors on various components in the line has been estimated. Some design details of the LEB injection girder are presented.

I. INTRODUCTION

A 600 MeV H⁻ Linac [2] is the first accelerator in the chain of four injectors for the Collider. It is presently under construction and scheduled to be operational by summer 1995. Simulation studies show that the linac beam emittance is expected to be $0.23 \, \pi$ mm-mrad, rms, normalized, in each transverse plane. In order to limit the emittance to $1 \, \pi$ mm-mrad at 20 TeV in the Collider, it is necessary to restrict the emittance growth at successive injection and acceleration stages. As per the overall emittance growth budget, final emittance after completion of the LEB injection cycle should not exceed $0.4 \, \pi$ mm-mrad. This growth results due to various injection errors and scattering in the carbon foil used for charge exchange injection. Several beam diagnostic elements have been provided on the line to meet the emittance growth requirements. Beam halos will be scraped and dumped on the absorbers in a controlled manner in order to minimize activation of the accelerator components and surroundings

II. STATUS AND DETAILS OF THE TRANSFER LINE

First half of this transfer line (figure 1a) is primarily a FODO array with 90° phase advance. It utilizes quadrupoles with 23 mm aperture diameter. These quadrupoles are identical to those used in the Coupled Cavity Linac (CCL), which accelerates the beam from 70 to 600 MeV. Two prototypes have been fabricated and field measured. The measured and calculated field properties compare very well. Industrial production of 106 quadrupoles will begin in the summer of this year. All these magnets have built-in steering coils which will be selectively energized. Four picture frame type steering magnets have been provided at the beginning of the line to align the CCL beam onto the optic axis with the help of four position monitors. The diagnostic elements e.g. position monitors, toroids, wire scanners etc. are the same as those on the CCL. Wire scanners will, primarily, be used to tune first four matching quadrupoles which are independently excited. We plan to use the least square fitting technique with deviations in
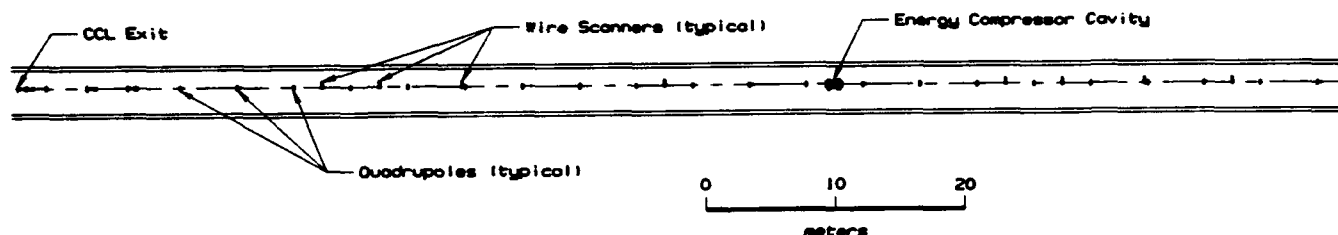
Figure 1a. First half of the Linac to LEB transfer line. Beam is transported by a FODO array over 80% of the length of this half.
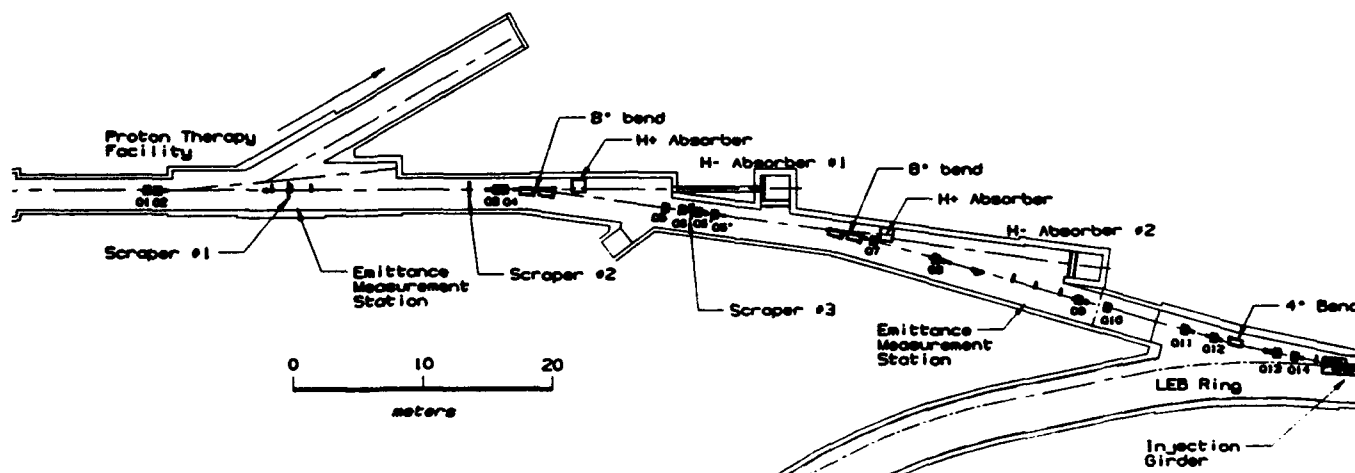
Figure 1b. Second half of the Linac to LEB transfer line. Q: Quadrupole magnets. Scrapers are about $500 \, \mu g/cm^2$ thick carbon foils. Provision has been kept in the building to switch the beam toward a future proton therapy facility.

the beam sizes from matched values as dependent and quadrupole currents as independent variables. Nineteen quadrupoles, which actually form the FODO array, are energized using two power supplies. Last two quadrupoles on this half are also used for phase space matching. In order to improve the pumping efficiency, larger beam pipe sections (75 mm) have been provided between the quadrupoles which are 4.3 m apart. There will be one ion pump on each of these sections.

Second half of the transfer line (figure 1b) has larger cross section, in general. It uses quadrupoles with aperture diameter of 75 mm. Engineering drawings for these quadrupoles and the steering magnets have been prepared and industrial prototypes will be ready for measurements in July 1993. There are two 8° and one 4° bends on this line. Each 8° bend consists of two 4° dipole magnets 0.5 m apart. We are, therefore, building five identical 4° dipoles, each being a 1 m long rectangular magnet. Maximum bending field has been restricted to 4 kG at 1 GeV to limit losses due to Lorentz stripping in the beamline to 0.1% [3]. Splitting the 8° bends offers another advantage i.e. the scraped beam is diverted toward H^+ absorbers without experiencing strong edge defocussing effects. Dipole magnets have been designed to keep $\Delta B/B$ due to sextupole component below 1×10^{-4} at 1 cm from the central ray. This eliminates the need for sextupole magnets which were earlier provided to minimize the phase space distortion at dispersive location at the center of the achromat formed by two 8° bends. A prototype dipole will be assembled in-house by September 1993. All the magnets are designed for operation upto 1 GeV energy.

Injection Girder

Figure 2 shows the injection girder assembly. Four identical bump magnets, excited by one power supply in series, will bump the circulating beam by 47.2 mm from the LEB axis during injection. Each bump has a magnetic length of 0.6 m. A 1.4 m long septum magnet separates the injected beam from the circulating beam. Figure 3 shows cross sections of the first bump and the septum magnets at their exit ends, and relative positions of the injected, bumped and circulating beams. An iron shield between the two magnets minimizes the magnetic field interaction. Bump magnets have a flattop time of 35 μs. While the rise time is not so critical, the fall time should be shortest possible (section III). Excitation waveform for the septum magnet is a 1.5 ms half sine wave. The magnets will be made using thin (0.05 mm) laminations in form of a tape wound core (figure 3). All these magnets have been designed to operate at 4 kG peak field at 1 GeV. Mechanical designs have been completed and the prototypes are expected to be supplied by industry in October 1993. Bump magnets have ceramic vacuum chambers to eliminate eddy current effects.

The H^- beam will be stripped to H^+, with 95 % efficiency, using a 200-250 μg/cm^2 thick carbon foil placed midway between bump 2 and bump 3 magnets [3]. Over 4% of the incoming beam will be converted into H^0 and the rest remains H^-. The H^0 beam travels undeflected to a beam stop at the exit of bump 4. The H^- beam, bent to the left by bump 3, comes out into the air through a thin window to fall on the same beam stop. Intensity of this beam will be monitored. Its unusual rise will indicate foil rupture. Two position monitors, downstream of bump 4, on the LEB ring will be used to align the injected beam. A foil positioning mechanism holds spare foils, and TV viewed flag, and changes them without breaking the vacuum.
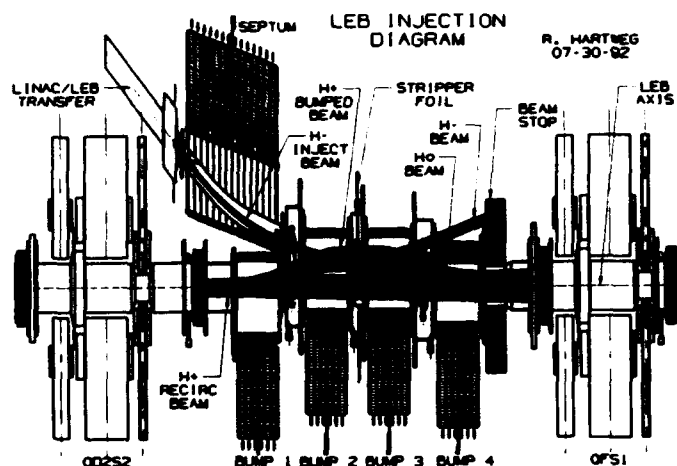
Figure 2. LEB injection girder assembly. Quadrupoles QD2S2 and QFS1 belong to the LEB lattice. Wire scanners between bumps 1 & 2 and bumps 3 & 4 will scan both injected and circulating beams. Vertical scale has been blown up for clarity.
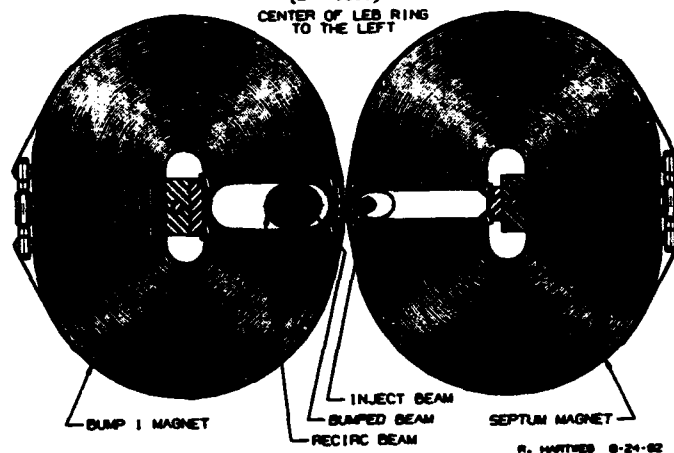
Figure 3. Cross section at the exit ends of the bump1 and the septum magnets.

Energy Compressor Cavity

No. of cells has been reduced to 11, from earlier 20, to keep phase shift for the RF drive low at the onset of the beam loading. At the same time, total power requirement was also kept low. Primary function of this cavity is to reduce energy spread of the beam. However, it also corrects for the energy jitter due to CCL instabilities. The energy correction is given by:

$$\Delta T_c = q . (E_o T)L . \cos (\Delta\phi + \Delta\theta - \pi/2)$$

where, $E_o T$ is the average accelerating gradient, L is cavity length, $\Delta\phi$ is phase difference between the ideal particle and a particle with energy error and $\Delta\theta$ is the RF phase fluctuation. Ideal particle undergoes no energy change if $\Delta\theta=0$.

Beam Scraping

Two scrapers, installed upstream of the first 8° bend, will scrape particles which are very much off in position and angle

in each transverse plane. Ray tracing calculations, using TURTLE, show that a majority of scraped particles (H⁺) can be transported to the absorbers without hitting the beamline components. Similar results were obtained for the off momentum particles scraped at the center of the achromat. In both case, these particles do not enter the second 4° dipole of the 8° bends. Instead, they come out of the exit edge of the first 4° dipole and travel straight to the absorber.

Beam Steering

In the first half of the line, there are three beam alignment systems in each plane. Each system consists of two steerers and two position monitors. In the second half, a position monitor is provided near every quadrupole cluster and a steerer is placed upstream. Last two steerers in each plane allow near orthogonal control of position and angle at the injection point.

III. EMITTANCE GROWTH

Magnetic field instabilities, phase space and dispersion mismatches and scattering in the stripper foil are the major sources of emittance growth. We have used Sypher's formalism [4] to estimate emittance growth due to first two sources. In this formalism, time average distribution under the effect of the errors is calculated. By comparing it with the initial distribution, emittance dilution factor is obtained. Emittance growth (rms, nc ''zed) due to dipole field instability is given by:

$$\Delta\varepsilon_n = 0.5 \, \pi \, \beta_1 \, (\Delta\alpha)^2 (\beta\gamma)_{Lorentz}$$

where, β_1 is the lattice beta function at the dipole and $\Delta\alpha$ is deviation in the bending angle due to field change. Normalized emittance growth values (rms) expected due to field instability in various dipole magnets are as follows:

Bump (Stability 0.1%)   : 0.0153 π mm-mrad

Septum (Stability 0.04%)   : 0.0082 π mm-mrad

D2 Dipole (Stability 0.01%): 0.0013 π mm-mrad

Since, all 4 magnets of the achromat are excited by one power supply in series, there is, ideally, no net effect due to field instability. The stability of this power supply is also 0.01% because first 8° bend will be used to determine the beam energy. Emittance growth due to dispersion mismatch at injection is proportional to $(\Delta p/p)^2$. It is negligible in our case because the acceptable $\Delta p/p$ is 1×10^{-4} to maximize capture in the LEB. Nominal values of η and η' are zero at injection.

The quadrupole magnet power supplies have been specified to have a stability of 0.1% of the full scale current. With this range of error, we used a slightly modified TRANSPORT code to simulate 250 beamlines corresponding to different sets of random errors on the quadrupole fields. Each set of errors produces β mismatch at injection, from which the emittance dilution factor is obtained [4]. These factors are plotted in figure 4 for 100 sets only for clarity. Emittance growth is unacceptable in the high β mode, in which the β function in x-plane near the dipole magnets is about 520 m. Elsewhere in the line, it does not exceed 125 m. This mode is necessary for accurate definition and determination of the momentum spread. Major contribution to the emittance growth comes from the field errors in quadrupoles Q3 and Q4. Figure 4 also shows the dilution factors for a low β mode in which the maximum β is about 130 m. This mode is quite satisfactory for LEB injection and the emittance growth is below 5% in 95% of the cases studied.
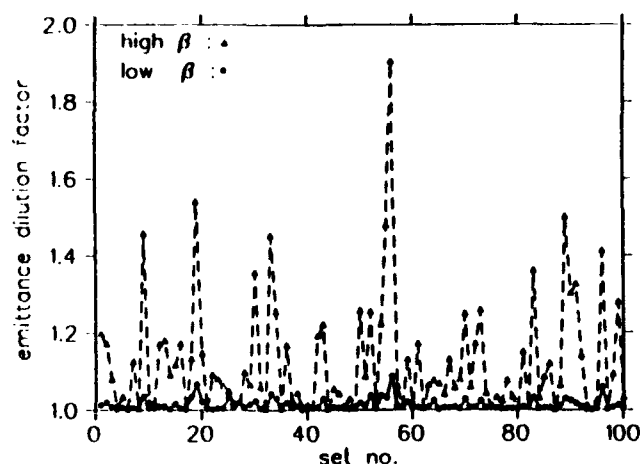
Figure 4. Emittance dilution factors due to quadrupole power supplies' instability of 0.1% of full scale current.

Stripper foil is the single largest source of emittance growth. Initial calculations have been done using the multiple scattering and the plural scattering models. Foil thickness is determined by the desired stripping efficiency. Ideally, all the incoming H⁻ should be stripped to H⁺. The number of beam traversals through the foil during injection process should be minimized. This requirement can be translated into the rate at which the bump field is withdrawn. We have specified [5] that the bump field should fall to 87% of its peak value in 10.8 μs in the Collider filling mode (3 turn injection). In this time interval, physical center of the linac bunch just clears the inner edge of the foil, which is 12 mm wide to intercept, fully, the incident beam. A power supply with such a requirement is difficult but feasible to make. The expected emittance growth is 0.06 π mm-mrad, rms, normalized, as per the multiple scattering model for a lattice β=14.7 m at the foil. The plural scattering model, however, predicts a lower emittance growth, by a factor of almost 2, for the same foil thickness. Foil thickness will be optimized experimentally during the LEB commissioning.

IV. SUMMARY

The Linac to LEB transfer line meets all the requirements for good injection including control of the emittance growth. It will be easy to tune and offers ion optical flexibility.

V. ACKNOWLEDGEMENTS

IV. REFERENCES

[1] R. K. Bhandari, E. Seppi and S. Penner, "Design Characteristics of the Linac-LEB Transfer Line for the SSC," Record of the 1991 Particle Accelerator Conference, Vol. 1, pp. 351-354.

[2] L. Funk, "The SSC Linear Accelerator," these proceedings.

[3] S. Penner, "Injection-By-Stripping Loss Effects," SSCL Internal Note, ADOD-008L February 4, 1991.

[4] M. Syphers, "Injection Mismatch and Phase Space Dilution," Fermilab Note, FN-458, June 1987.

[5] S. Penner, "Conceptual Design of the LEB Injection Girder," SSCL Internal Note, ADOD-019L, April 25, 1991.

200 GeV Beam Transfer Lines at the SSC

Fesseha G. Mariam, John McGill
Superconducting Super Collider Laboratory*
2550 Beckelymeade Avenue, Dallas, TX 75237 USA
Karl Brown
Stanford Linear Accelerator Center, Stanford, CA 94305

Abstract

Two beam lines have been designed to transfer 200 GeV protons from the Medium Energy Booster (MEB) to the High Energy Booster (HEB) of the SSC injector complex. At 850 m and 2200 m in length, these are the longest beam transfer lines at the SSC and are intended to inject beam into the bipolar HEB in the clockwise and counter-clockwise directions, respectively. The beam optics is designed so as to facilitate easy tuning and commissioning of these lines. Sources of emittance dilution are identified and estimates of their contribution calculated which serve as basis for specifications of dipole field homogeneity and power supply stability.

I. INTRODUCTION

The SSC injector complex consists of a 600 MeV linac, the Low Energy Booster (LEB) - 600 MeV to 12 GeV, the Medium Energy Booster (MEB) - 12 GeV to 200 GeV, and the bipolar High Energy Booster (HEB) - 200 GeV to 2 TeV. The last synchrotron, which uses superconducting magnets, feeds the clockwise and counter-clockwise collider rings alternately. Proton beams from the MEB are thus injected into the HEB in clockwise and counter-clockwise directions depending on the state of the its bipolar mode. The planes of the MEB and HEB are parallel to each other but are separated by 27.723 m vertically. The position of the MEB was chosen such that, in the plan view, the extraction straight for the clockwise (CW) transfer line is collinear with the HEB injection straight. For collider operations the normalized rms emittance of the beam is 0.7 π.mm.mrad. The transfer line design calls for transporting this beam with negligible emittance growth. The optical design was done by using the TRANSPORT code[1].

This paper presents the requirements and the rationale for the design of the two beam transfer lines connecting the MEB and the HEB. Extraction out of the MEB and on-axis injection into the HEB are described. Preliminary work on steering analysis and emittance growth are discussed.

II. BEAM EXTRACTION AND INJECTION

The extraction and injection sections of the CW and CCW lines are sufficiently similar that a common description can be given. Extraction out of the MEB is facilitated by means of five 1.43 m long fast kickers at 650 Gauss, located about 90° upstream of vertically bending Lambertson magnets. The kick results in a 31.7 mm horizontal displacement of the beam centroid from the nominal closed orbit of the MEB at the location of the first Lambertson magnet. A second Lambertson magnet

---

and a c-magnet are then employed to bend the 200 GeV beam vertically by a total of 21.9 mrad so that the beam pipe of the transfer line clears the envelop of the closest MEB quadrupole. Injection into the HEB uses Lambertsons and a c-magnet similar to those of the extraction section as well as six 1 m long fast kickers at 500 Gauss. The injection Lambertsons and kickers are separated by a drift space of 70 m so that the beam is injected on-axis. At the exit end of the last Lambertson, the beam is on the plane of the HEB but separated from the nominal closed orbit by 28 mm and with an approach angle of 0.4 mrad. The kickers are then located at the point where the injection trajectory crosses the HEB nominal closed orbit and the kick removes the residual angle of 0.4 mrad. The extraction and

	CW	CCW	Max. Strength [Length]
Length (m)	850	2200	-
Dipoles	4	17	9 T.m [5.8 and 6.5 m]
Quadrupoles	26	53	41 T.m/m [1.5 m]
Lambertsons	4	4	5.6 T.m [5.1 m]
C-magnets	2	2	3.4 T.m [2.7 m]
Extr. Kickers	5	5	0.09 T.m [1.43 m]
Inj. Kickers	6	6	0.05 T.m [1 m]
Trim Dipoles	28	54	0.3 T.m [1 m]
Trim Quads	4	8	6 T.m/m [0.5 m]
BPMs	34	59	[0.25 m]
BLMs	23	50	-

Table 1: Major design parameters of the CW and CCW transfer lines. The no. of trim dipoles is based on preliminary analysis.

injection Lambertsons are located in dispersionless regions.

III. COUNTER CLOCKWISE LINE

The substantial length of the CCW line allows the freedom to achieve optimal conditions for control of beam matching. The vertical bend center V1 (fig. 1) is composed of two unequal bends. The first four quads match the MEB beam into a 90° FODO with a half cell length of 51.5 m which forms the main transport optics. The position and strength of the second bend in V1 was chosen to provide achromaticity. The vertical
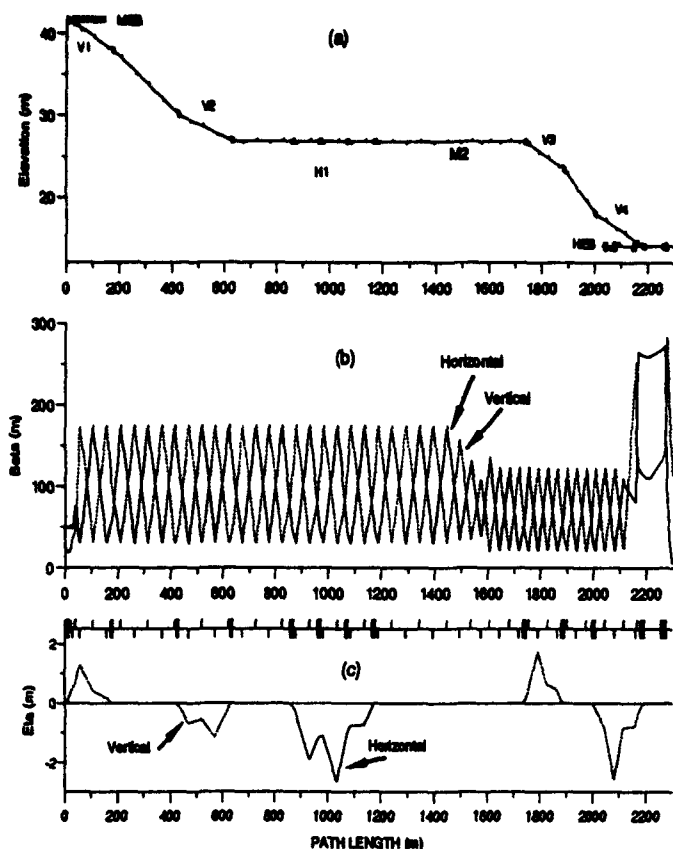
Fig. 1. Layout and lattice functions of the CCW line.

Fig. 2. Layout and lattice functions of the CW line.

bend centers V2 and V3 are symmetric each consisting of two groups of dipoles of equal strength separated by -I[2]. V2 brings the beam into a trajectory that is parallel to the planes of the synchrotrons so that an 83.5 mrad horizontal bend H1 can be implemented without coupling to the vertical plane. H1 consists of four equally spaced groups of identical dipoles embedded within the 51.5 m FODO and spanning a phase advance of $3\pi/2$. This optical arrangement can be viewed as two interlaced -I transformers. The FODO structure and the four equal bends ensure that H1 is achromatic. A set of four quadrupoles (M2) is used to match the 51.5 m FODO to a 36.2 m 90° FODO. The last vertical bend V4 consists of dipoles and Lambertson magnets at the upstream and down-stream ends, respectively. The intervening optics is made up of two cells of the 36.2 m FODO and three families of quads to provide an achromatic match into the HEB.

Since M2 is located in a dispersionless region, α and β matching can be controlled without affecting the dispersion. The modular nature of the 90° FODOs provide dispersion control with pairs of corrector quads on a common power supply. The quads in each pair are located -I apart - one inside any of the symmetric bends and one outside[2]. This scheme is illustrated in the example of fig. 3 where it has been used to correct for hypothetical input dispersions of $\eta_x = \eta_y = 0.7$ m. The perturbations to β and α are confined to the -I region and the corrector quad strengths do not exceed 20% of the main FODO quads.

IV. CLOCKWISE LINE

The main features of the CW line are the 36.2 m FODO transport optics and the bend centers V1 and V2, each of which is individually achromatic (fig. 2). The positions and strengths of the dipoles was dictated by floor layout constraints as well as by a desire to include a portion of the 90° FODO inside V2. The latter allows for one orthogonal control of the vertical dispersion where two trim quadrupoles -I apart may be adjusted in phase as in the case of the CCW line. This line, however, does not have any options for controlling the horizontal dispersion. Since the expected rms $\delta p/p = 5X10^{-5}$ the effect of dispersion mismatch on emittance dilution is negligible[3].

V. BEAM STEERING

Monte calro calculations of beam steering were used to determine beam position monitor locations as well as corrector magnet strengths. Dipole excitation error (rms) of $5X10^{-4}$, quadrupole misalignment error of 0.5 mm and initial beam trajectory errors of 0.5 mm and 0.01 mrad were assumed. With the number of BPMs and steering dipoles indicated in Table 1, the maximum beam excursion was about 2 mm in both planes. Orthogonal x,x' and y,y' corrector dipoles in the transfer lines together with the HEB ring BPMs will be used for final steering into the HEB. The precision of correcting for such systematic errors will be limited by the resolution of the BPMs.
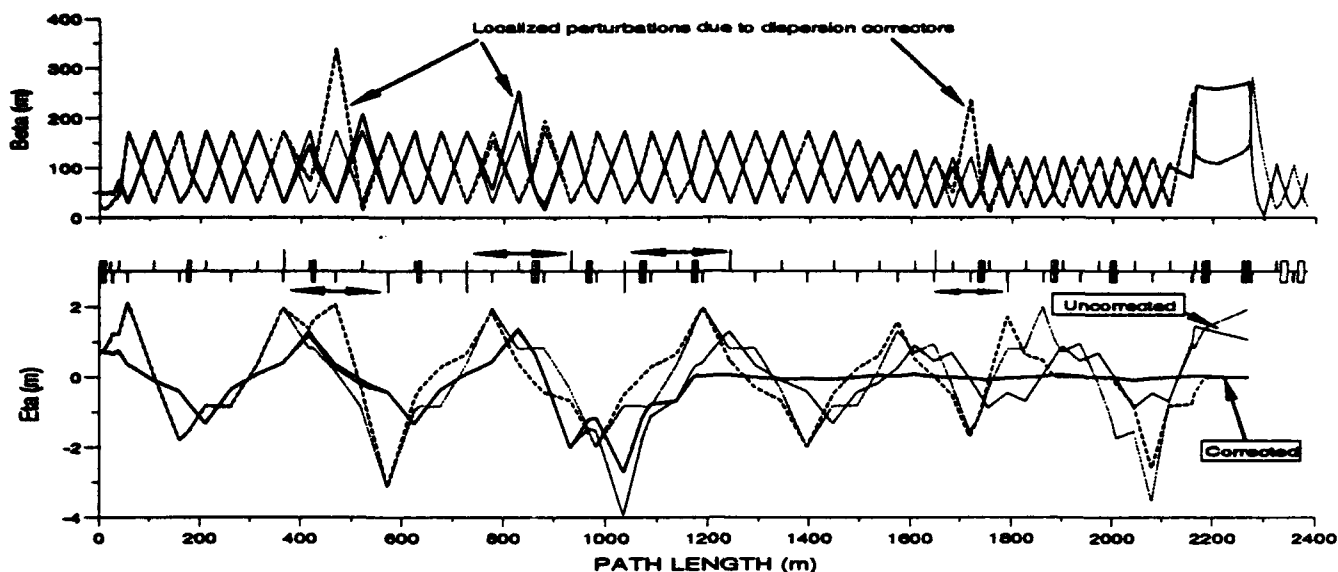
Fig. 3. Dispersion correction using the -I concept. Paired corrector quadrupoles (F and D) are indicated by the arrows.

VI. EMITTANCE DILUTION

Having corrected for systematic quadrupole alignment errors, etc., the most important remaining source of steering errors is random time dependent (pulse to pulse) variations of dipole fields. If the relative field fluctuations ($\Delta B/B$) within each achromat can be made the same by putting the dipoles on a common power supply, it can be shown that, to first order, there is no net injection steering error. In practice this is most

Source	$\Delta B/B$ (rms) (Stability)	$\Delta \varepsilon_{normal}$ (π.mm.mrad)
Extr. Kickers	1×10^{-2}	0.01
Inj. Kickers	1×10^{-2}	0.09
Lambertsons/Dipoles	1×10^{-4}	0.12
Quad Grad.	1×10^{-3}	0.005
Sextupole Errors	1×10^{-3} @12 mm	0.005

Table 2: Expected addition to normalized emittance. The first three entries are correctable with transverse dampers.

easily implementable in the symmetric bend centers V2, H1 and V3 in the CCW line where the dipoles in each achromat are identical in length and strength. Most of the steering errors in both transfer lines are, therefore, expected to come from the kickers and Lambertson magnets as well as from the dipoles in the first and last vertical achromats. The resulting emittance dilution[3] can be shown to be dependent only on the floor layout constraints and the betatron amplitudes at the MEB extraction and HEB injection regions. The expected contributions to emittance dilution, based on attainable power supply stability, are listed in Table 2. For comparison, the allowed growth in emittance due to the MEB and transfer lines combined is about 0.1 π.mm.mrad[4]. It is evident that this require-

ment cannot be met without the use of transverse dampers in the HEB. Systematic or random quadrupole gradient errors lead to mismatches in α and β with attendant emittance growth[3,7]. The effect of sextupole field errors of 1×10^{-3} at 12 mm from the center of the dipole gaps was simulated by using the program TURTLE[5]. These are included in table 2.

VII. CONCLUSION

The regular FODO optics of the transport system is expected to greatly simplify the interpretation of beam diagnostics data as well as the implementation of transfer matrix measurement and correction schemes[6]. In the case of the CCW line the FODO structures enhance tunability by providing independent and mutually exclusive controls over the dispersion and the transverse lattice functions. In view of the relatively large beam size ($\sigma_x = 1$ mm) and the small (40 mm) beam pipe aperture of the HEB, on-axis injection offers simplicity and full use of machine aperture.

While the strength and position of all major dipoles is fixed, the lattice design is periodically updated to meet on-going design changes in the MEB and the HEB without compromising the regular optical structure. Further investigations are planned to determine ways of relaxing the specifications on dipole excitation errors and power supply stability. The implications of kicker failures are yet to be fully understood and safeguards need to be incorporated into the overall design.

VIII. REFERENCES

[1] K.L. Brown, et al., SLAC-91, 1977.
[2] K.L. Brown, R.V. Servranckx, SLAC-PUB-3381, (1984).
[3] D.E. Edwards, M.J. Syphers, "An Introduction to the Physics of Particle Accelerators", Wiley, N. Y. (1993).
[4] "Site Specific Conceptual Design", SSCL-SR-1056 (1990).
[5] D.C. Carey, et al., SLAC-246, UC-28 (1982).
[6] T. Barklow, et al., SLAC-PUB-5695 (1991).
[7] P.J. Bryant, CERN 84-04 (1984).

Effect of Betatron Motion on the Septum Flux in Superslow Extraction at the SSC*

Barry S. Newberger

Institute for Fusion Studies and Department of Physics
University of Texas–Austin, Austin, TX 78712 USA

H.-J. Shih

Superconducting Super Collider Laboratory†
2550 Beckleymeade Ave., Dallas, TX 75237 USA

J. A. Ellison

Department of Mathematics and Statistics
University of New Mexico, Albuquerque, NM 87131 USA

Abstract

A scheme for the superslow extraction of protons from the SSC rings for high energy test beam or precision fixed-target B physics is currently being investigated.[1] The flux onto the extraction septum (a curved Si crystal) is to be generated by diffusion produced by noise injected into the RF system. The extraction rate depends on both the diffusion of the closed orbit (due to dispersion at the crystal) and the horizontal betatron amplitude of the diffusing protons. The diffusion of the closed orbit has previously been described by the one-dimension longitudinal diffusion theory of Dôme and Krinsky and Wang. In this paper, we extend this theory to include the effect of the betatron motion. Comparisons with Monte Carlo tracking simulations are made.

I. INTRODUCTION

It has long been understood that noise in the RF system of a hadron storage ring leads to a slow loss of particles from the circulating beam bunches.[1] It has become of considerable interest to exploit this to create an artificial halo for the purpose of extracting a low intensity beam for precision fixed target experiments or test beams at future hadron colliders.[2,3] A theoretical treatment of the loss process by a diffusion of the longitudinal action have been used for some time[4–6] and do give results which qualitatively describe the observations. These theories have been strictly one-dimensional, taking no account of the betatron motion. Losses are assumed to occur at the separatrix of the longitudinal motion. In actuality, losses occur at a physical aperture stop. This might correspond to an extraction septum in the case of interest to us or, more generally, at any momentum scraper. Indeed, our recent results[6] on diffusion in the presence of filtered noise suggest a scheme for scraping momentum tails. We have conducted Monte Carlo tracking studies in the SSC lattice.[2,6]

The betatron function can be large and the loss rates change significantly when the effect of the betatron motion is

included. Recently, we have obtained a theory of the diffusion process which includes the effect of the betatron motion.[7] Agreement between the particle losses in the simulation and the theory is excellent. In this paper, we briefly describe the theory and present new results on the "marginal" density in longitudinal action. These are also compared with the Monte Carlo tracking results and again the results agree.

II. DIFFUSION THEORY

The theory[4–6] of longitudinal dynamics in a noisy RF system leads to a description of the evolution of an ensemble by a diffusion in the action, J, which is a constant of the unperturbed motion. The time scales of the diffusion in action, the synchrotron period and the betatron oscillation period are disparate with $t_d \gg t_s \gg t_\beta$. Thus the collimation process sweeps a shell in the transverse phase space $(A, A+dA)$, where A characterizes a Courant-Snyder invariant, and a shell $(J, J+dJ)$ in the longitudinal phase space in a time t, $t_s < t < t_d$. The maximum betatron displacement is related to A by $|x_\beta|_{max} = \sqrt{\beta A}$ where β is the usual betatron function.

In the presence of an aperture stop, a particle slowly diffuses toward the periphery of the beam pipe until it strikes the stop. We assume the "image" of the stop in momentum, x_c/D, is inside the bucket. Here D is the dispersion at the position of the stop. The time it takes until the particle is lost, or conversely, the loss rate, depends on both the closed orbit position (equivalently, action) and the betatron displacement.

If we had the joint probability density of J and x_β we would have all the information needed. (Here and throughout the remainder of the paper for ease of notation we have written x_β when we really mean $|x_\beta|_{max}$.) By definition, the joint density can be obtained from the probability conditioned on x_β, $p(J|x_\beta)$:

$$p(J, x_\beta) = p(J|x_\beta)p(x_\beta). \qquad (1)$$

where $p(x_\beta)$ is the marginal density of x_β. These must be probability densities and must be defined throughout the domain of definition of the pair of random variables J, x_β which is the quadrant $J \geq 0$, $x_\beta \geq 0$.

Consider particles which, at a given time, t, have not yet reached the stop. These lie in a domain in the space of the random variables bounded by the coordinate axes and a curve $J_b(x_\beta)$ which is the action for a particle on an energy

surface k defined by $k_b(x_\beta) \equiv (x_c - x_\beta) / D\delta p_s$ where $k \equiv \delta p / \delta p_s$, δp the momentum deviation and δp_s the bucket half-height. For these particles, the conditional density satisfies a diffusion equation of the form considered in earlier work[4-6]:

$$\frac{\partial}{\partial t} p(J,t|x_\beta) = \frac{\partial}{\partial J}\left[D(J)\frac{\partial}{\partial J} p(J,t|x_\beta) \right] \qquad (2a)$$

but with boundary condition:

$$p(J_b,t|x_\beta)=0. \qquad (2b)$$

For these particles, the marginal density in x_β is just the initial distribution.

In the remainder of the domain of the random variables, the conditional density is a δ-function. It is fixed by the requirement that $p(x_\beta)$ be a marginal density; that is, an integral over all $J>0$ of the joint density.

In general, the diffusion equation must be solved numerically. However, analytic solutions have been obtained for diffusion coefficient linear in the action and quadratic in the action. In the former, straightforward separation of variables gives a solution[4] as a Fourier-Bessel series. In the latter, a Fourier integral representation exists.[8] While neither of these exactly correspond to simple noise spectral densities, the diffusion coefficient for small action is linear in the case of white phase noise and quadratic for white amplitude noise.[6] Furthermore, we find the diffusion coefficient for white phase and for white amplitude noise reasonably can be fit over most of the bucket by linear and quadratic approximations respectively; the fit is very good in the latter case. This is illustrated in Fig. 1 where we have shown the diffusion coefficient in the cases of white phase and amplitude noise along with their approximations. The action is normalized to its value at the boundary J_b for a zero betatron amplitude particle. We will now present results obtained from these solutions by use of Eq. (1) and which can be compared to data we obtain from our Monte Carlo simulations.

III. THEORETICAL RESULTS

There are several quantities which typically are of interest when we consider the results of a Monte Carlo extraction simulation.[2,6] Of these, the number of particles reaching the septum at a given time and the distribution in action of the circulating particles are calculable from the diffusion theory. (Other data, such as the initial phase-space coordinates of the particles striking the septum and the distribution of hits on the septum are outside of the scope of a diffusion theory.) In this section, we compare the results of the diffusion theory with the Monte Carlo data.

The number of particles which have hit the septum up to a time, t, is found by integrating the joint density, Eq. (1) over the region of the random variable space, S, occupied by the circulating particles and applying conservation of probability:

$$N(t) = 1 - \iint_S p(J,t|x_\beta) p(x_\beta) dJ dx_\beta. \qquad (3)$$

Explicit expressions have been given in Ref. 7. Here we summarize the results[7] for both white phase and white amplitude noise in Table 1. A typical Monte Carlo simulation follows 1000 tracks for about a million turns or about 5 minutes in real time. Obviously, the simulation extraction rates are substantially higher than would be employed in actual operation but computational constraints necessitate this. This underscores the importance of a theory which allows us to predict the behavior of the extraction process with realistic operating parameters.
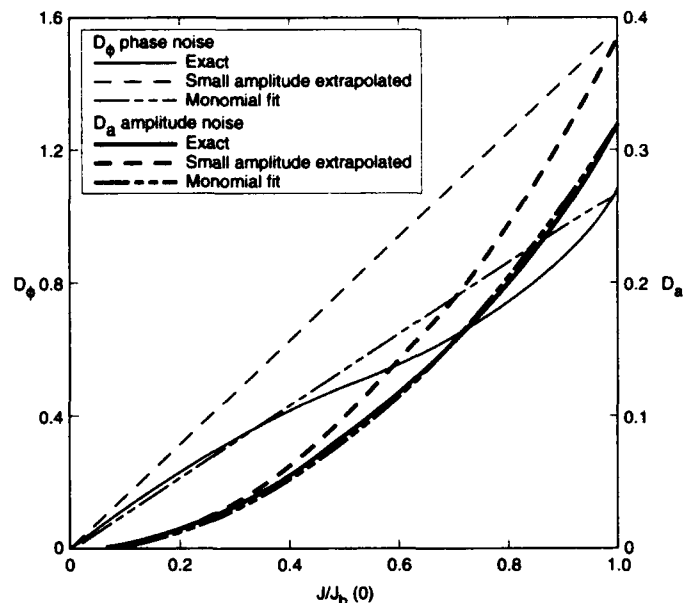
Figure 1. Diffusion coefficients for white noise.

Referring to the table, the first figure in the column of theoretical values is the result using the extrapolated small amplitude diffusion coefficient and the second value was obtained by using the diffusion coefficient fit by forcing the value of the monomial (linear or quadratic as appropriate) approximation to agree with the actual value at J_b (0). The simulation results are from a single realization of the random process. The machine parameters are the nominal values for the SSC collider rings, $\sigma_{\delta p} = 5 \times 10^{-5}$, $\varepsilon_x = 1\,\pi$ mm-mrad. The value of β_x at the aperture stop was 1385 m in all cases but one. The exceptional case is indicated. The dispersion $D = 4$ m. For both simulation and theory, thirty-one transient particles have been taken into account. These are particles which are initialized outside the septum and consequently are lost in a few turns independent of the noise. The agreement between the simulation and theory is generally very good particularly for the monomial fits.

The distribution in action of circulating particles is given by:

$$p(J,t) = \int_0^{x_\beta(J)} p(J,x_\beta',t) dx_\beta' , \qquad (4a)$$

where $x_\beta(J)$ is defined by

$$J_b\left(x_\beta\right) = J. \tag{4b}$$

We simply refer to this as the "marginal" distribution in action but, technically, this is incorrect. It is actually the joint probability of having the "action in an interval dJ about J" and the particle being "inside the aperture".

Table 1
Values of N. Theory values as described in text.

	Phase Noise			Amplitude Noise	
σ_ϕ	N (sim)	N (theory)	σ_a	N (sim)	N (theory)
0.2	584	732/595	0.5	745	772/718
0.2*	343	542/363	0.2	182	211/178
0.1	187	261/179	0.1	67	56/48
0.05	51	69/49	0.05	22	19/17
0.02	13	18/14	0.02	7	7/6

* $\beta_x = 346$ m

We have calculated $p(J,t)$ for both phase and amplitude noise. The integral is done numerically using a standard Romberg routine on a personal computer. The results are shown in Fig. 2a and Fig. 2b for white phase noise and white amplitude noise respectively. The solid curves are for the diffusion coefficient given by the fit while the result using small amplitude extrapolated diffusion coefficient is the dashed curve. These are superimposed on the histogram from the Monte Carlo tracking. The phase noise corresponds to a an rms phase $\sigma_\phi = 0.1$ rad. The rms relative amplitude noise modulation $\sigma_a = 0.2$. In the Monte Carlo results, bar heights of approximately $1. \times 10^{-3}$ correspond to single particles. The agreement is seen to be quite good. Insofar as the marginal densities are concerned, the differences between the result using the small amplitude extrapolation or the fit for the diffusion coefficient is small.

IV. CONCLUSION

We have described a theory of the noise induced diffusion in the longitudinal phase space which accounts for the effect of the betatron motion. The two degrees-of-freedom are coupled at a position with dispersion by any real stop. The problem of interest contemplates noise deliberately introduced into the RF system for superslow extraction of low intensity proton beams. The agreement with Monte Carlo tracking simulations is excellent. The theory could also be applied to momentum scrapers, when the momentum halo production can be described by a diffusive process. The formalism should also apply when the marginal density in x_β has time dependence provided the evolution is independent of J.

V. REFERENCES

[1] D. Boussard, G. Dôme and C. Graziani, "The Influence of RF Noise on the Lifetime of Bunched Proton Beams," in 11th International Conference on High-Energy Accelerators, edited by W. S. Newman, (Birkhäuser, Basel, 1980), p. 620.

[2] B.S. Newberger, H.-J. Shih and J.A. Ellison, Nucl. Instrum. Methods A325, 9 (1993).

[3] S. Weisz, et. al., "Proton Extraction from the CERN-SPS by a Bent Crystal" this conference.

[4] G. Dôme, "Theory of RF Acceleration and RF Noise," in Accelerator School for Antiprotons for Colliding Beam Facilities, CERN Report 84-15, 1984, p 215.

[5] S. Krinsky and J. M. Wang, Particle Accelerators 12, 107 (1982).

[6] H.-J. Shih, J. Ellison, B. Newberger and R. Cogburn, "Longitudinal Beam Dynamics with RF Noise," SSC Laboratory Report SSCL-578, July 1992, submitted to Particle Accelerators.

[7] B. Newberger, J. Ellison and H.-J. Shih, "Effect of Betatron Motion on Particle Loss Due to Longitudinal Diffusion in High-energy Colliders," SSC Laboratory Report SSCL-preprint-205, March 1993, submitted to Physical Review Letters.

[8] H.-J. Shih, J. Ellison and W. Schiesser, "Reliability of Numerical Solutions of a Diffusion Equation Modeling RF Noise-Induced Dilution in Particle Beams" in Advances in Computer Methods for Partial Differential Equations VII, R. Vichnevetsky, D. Knight and G. Richter, eds. (IMACS, New Brunswick, 1992) p. 663.
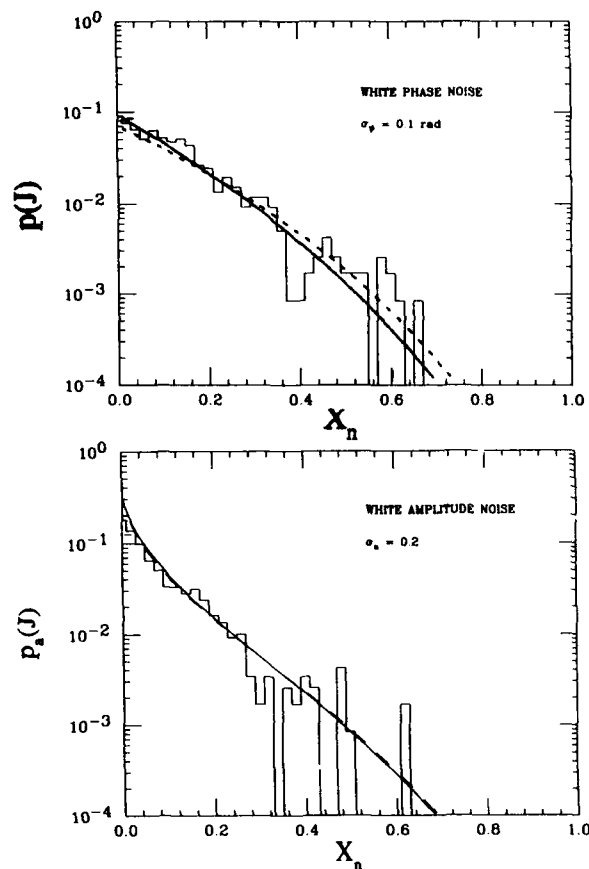
Figure 2. Marginal action density distributions: a) phase noise, $\sigma_\phi = 0.1$ rad b) amplitude noise, $\sigma_a=0.2$.

Study of Energy Ramping Process Applied to the LNLS Synchrotron Light Source (Brazil)

LUCIA JAHNEL*, LNLS, and C.E.T. GONÇALVES DA SILVA, Unicamp and
LNLS Laboratório Nacional de Luz Síncrotron - LNLS/CNPq
Caixa Postal 6192 - 13081-970 Campinas - SP - Brazil.

Abstract

Acceleration cycle studies of the LNLS 1.15 GeV UVX electron storage ring are described. Since this ring will initially be injected at low energies (100 MeV), questions related to the behavior of beam lifetime during the ramping period (about 10 s), especially at the lowest energies, are crucial for the successful operation of the machine. In this work, we present results of Touschek lifetimes, due to single and multiple scattering effects, compared with damping times at various energies. We show that these effects should not lead to appreciable stored current losses.

I. INTRODUCTION

The LNLS 1.15 GeV UVX[1] electron storage ring will be injected using a beam from a linear accelerator. The electrons will be accumulated at low energy - 100 MeV. Ramping to the nominal energy - 1.15 GeV - will follow and the final current will be 100 mA. Two injection schemes will be used: conventional injection (linac pulses at a rate determined by the stored beam oscillation damping time) and injection with anomalous repetition rate (linac pulses at a much faster rate and the stored beam not be damped). Although some other electron synchrotrons are using injection at low energy[2], there is still an appreciable stored current loss during the ramping process.

The ramping period, in our case, is about 10 seconds and during this time, especially at the lowest energies, some coherent and incoherent collective effects could influence the equilibrium beam dimensions, the lifetime and the accumulated current. Initially Touschek scattering, intrabeam scattering (IBS), beam-gas interactions and damping time have been studied. No microwave instability has been considered. All calculations shown here have been done using local computer codes.

II. RAMPING CONDITIONS

Although the energy and the RF voltage are changed during the acceleration cycle, there is an adiabatic change of the parameters of the ring (τ_{i0}, Ω_0, ϕ_0, p_0, R_0 and $\hat{V}$). The condition[3]:

$$\varepsilon = \frac{1}{\Omega_s^2}\frac{d\Omega_s}{dt} \ll 1 \tag{1}$$

from the Boltzman-Ehrenfest adiabatic theorem is still valid for the LNLS UVX ring parameters.

The dipole magnetic field will increase as a sin-function and the RF voltage as two straight lines with different inclinations. The increases are shown in figure 1.
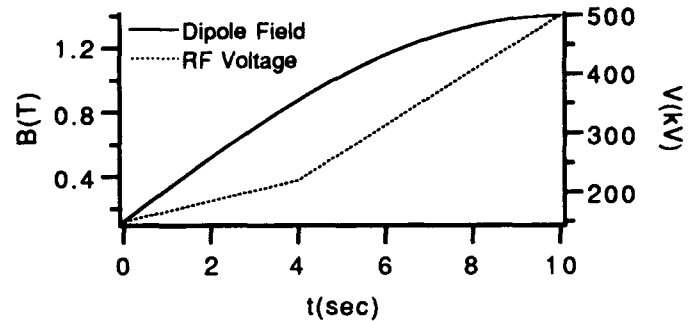
Figure 1- Dipole Magnetic Field and RF Voltage increase during the accelerating cycle.

III. LIFETIME

A. Beam-gas interactions

The interaction of the electron beam with the molecules of residual gas (beam-gas scattering) includes four processes: the elastic scattering of the stored beam on nuclei (in transverse planes x and y, i.e., $1/\tau_{scat}=1/\tau_{scat-x}+1/\tau_{scat-y}$), the bremsstrahlung on nuclei and the elastic and the inelastic scattering on electrons. All these effects lead to particle losses and reduce the beam lifetime.
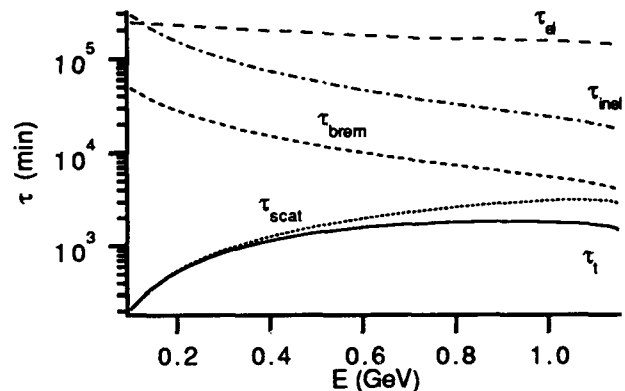
Figure 2 - Lifetime due to beam-gas interactions. τ_{scat} is due to the elastic scattering on nuclei, τ_{brem} is due to the bremsstrahlung on nuclei, τ_{el} is due to the elastic scattering on electrons, τ_{inel} is due to the inelastic scattering on electrons and τ_t is the total lifetime for the four processes.

---

*Graduate student at IFGW - Unicamp

The computation has been carried out using the formulae from references [4] and [5]. For our ring, the residual gases, at the pressure of 0.3 nTorr at 100 MeV and 3.0 nTorr at 1.15 GeV, are: H (90%), CO (4%), CO_2 (4%) and CH_4 (2%) and the current used was I = 100 mA. The results show that the worst-case contribution for the lifetime comes from the elastic scattering on nuclei in the vertical plane, but the full lifetime, resulting from different types of beam-gas interaction, is larger than 3:30 hours at 100 MeV. The results are displayed in figure 2.

B. Intrabeam Scattering

Intrabeam scattering (IBS) is a multiple Coulomb scattering of charged particles in a bunched beam. It induces an increase of bunch dimension and, therefore, a reduction of the beam lifetime due to the collisions of the particles in the vacuum chamber. IBS is in essence a diffusion process in all dimensions.

IBS dominates the emittance during injection energy up to about 500 MeV, for the LNLS UVX ring. Transverse oscillation energy will be transferred into the longitudinal direction through Coulomb scattering among electrons. So, bunch lengthening and emittance growth (transverse and longitudinal) will occur.

The calculations were done using the formulation given by J. Le Duff in reference [6]. Initially, we found the values of σ_E/E and then σ_x and σ_y, where:

$$\sigma_x = [\beta_x U_x + D^2]^{1/2} \frac{\sigma_E}{E}$$

$$\sigma_y = [K\beta_y U_x]^{1/2} \frac{\sigma_E}{E} \quad (2)$$

with

$$U_x = \frac{J_E}{J_x} < \frac{1}{\beta_x}[D^2 + (\beta_x D' - \frac{1}{2}\beta_x' D)^2] > \quad (3)$$

where K is the coupling, J_i is the damping time (see item IV), D is the dispersion. The $\beta_{x,y}$ values used in equations (2) are the average.

In figure 3 the longitudinal beam dimension with and without IBS is shown and in figure 4 the emittance, also with and without IBS. All calculations for IBS were carried out with bunch current of 1 mA and 10% coupling.
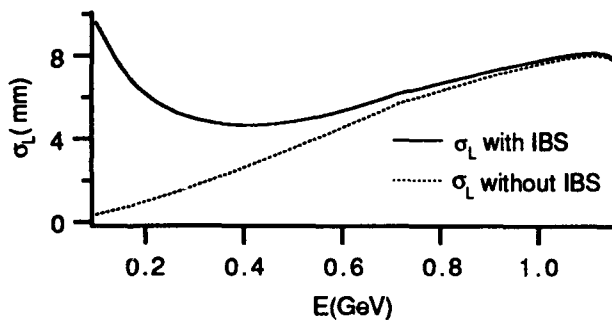
Figure 3 - Longitudinal bunch length during the acceleration cycle with and without IBS. I_{bunch}=1 mA and coupling=10%.

C. Touschek Effect

The Touschek Effect is also caused by Coulomb scattering, but is given by large single scattering events for which only the energy transfer from transverse to longitudinal direction is examined.

As in IBS's computation, we used I_{bunch} = 1 mA and 10% of coupling. The bunch dimensions and the energy acceptance used were obtained from IBS calculations. Because the Touschek lifetime depends on the machine parameters, we computed the average values for the optical functions.
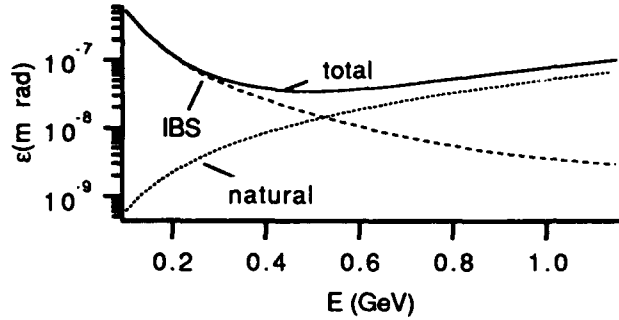
Figure 4 - Emittance during the acceleration cycle with and without IBS. I_{bunch} = 1 mA and coupling = 10%.
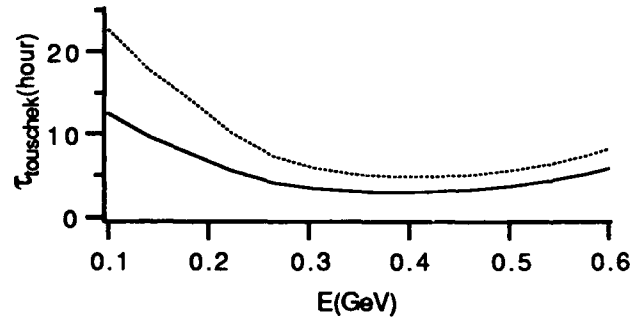
Figure 5 - Touschek lifetime during part of the acceleration cycle (E ≤ 600 MeV), calculated using the emittance total (see figure 4). The dashed line corresponds to the calculation with relativistic approximation and the solid line without relativistic approximation.

There are many formulae to estimate the Touschek lifetime with different approximations[7]. In our study, we used two: one given by J. Le Duff[4] and another, where there is no relativistic approximation, given by U. Völkel[8]. The result is shown in figure 5 only up to 600 MeV. After this energy, the Touschek lifetime increases exponentially up to more than 150 hours. Although there is a small difference between the two calculations, the shortest lifetime is around 3 hours for E ≈ 380 MeV.

D. Total Lifetime

The overall beam decay rate is given by:

$$\frac{1}{\tau} = \frac{1}{\tau_{gas-scat}} + \frac{1}{\tau_{Touschek}} + \frac{1}{\tau_{quantum}} +... \quad (4)$$

In our case we have not included the quantum lifetime, even though the photon emission process alters the electron momentum. The beam-gas interaction, the Touschek scattering and the IBS are dominating.

Although no microwave instability has been considered until now, we can see one significant reduction of beam lifetime at the energy between 350 and 400 MeV. Up to 800 MeV the Touschek lifetime (including the IBS) is dominating. The shortest lifetime is 2:30 hours at 385 MeV. See figure 6.
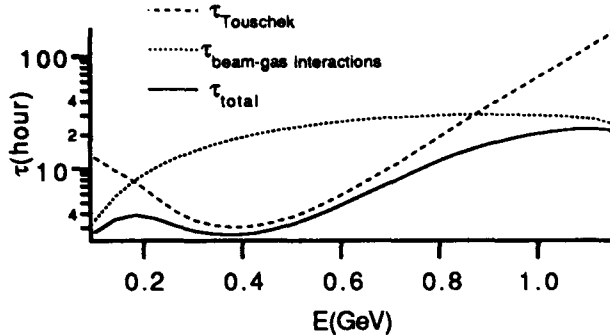
Figure 6 - Total lifetime, during the acceleration cycle, including beam-gas interaction, intrabeam scattering and Touschek effect without relativistic approximation. No microwave instability has been considered. $I_{bunch} = 1$ mA and coupling = 10%.

IV. DAMPING TIME

The damping times of the transversal oscillations or synchrotron oscillations are given by[5]:

$$\tau_i[ms] = \frac{C[m]\rho[m]}{13.2 J_i E^3 [GeV]} \quad (5)$$

where i = x or y (betatron oscillations) or ε (synchrotron oscillation), with $J_x = 1 - D$ and $J_\varepsilon = 2 + D$, where $J_x + J_y + J_\varepsilon = 4$ and $D = I_4/I_2$ (see ref. [5]).
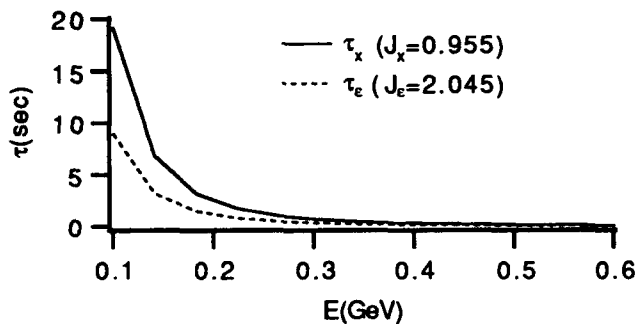
Figure 7 - Damping time during part of the acceleration cycle (E ≤ 600 MeV). τ_x is the solid line and τ_ε is the dash line.

For the LNLS UVX ring, the damping time of the horizontal and synchrotron oscillations are displayed in figure 7. The time for one revolution is 300 nsec and the ramping time is 10 sec, but, on the other hand, τ_ε is ≥ 0.1 sec for $100 \leq E \leq 190$ MeV and τ_x is less than 0.1 sec for $100 \leq E \leq 575$ MeV. If we decrease the damping time of the betatron oscillations (and, consequently, increase the

damping time of the synchrotron oscillations), we will still have no damping in either oscillation during part of the acceleration cycle (E ≤ 600 MeV).

V. CONCLUSIONS

Beam-gas interactions, Touschek single and multiple scattering and damping time have been investigated during the acceleration cycle for the LNLS UVX ring. Although no microwave instability and ion trapping have been included, the result (figure 6) shows that there is a decrease of lifetime at about 400 MeV.

We also have shown that there is no damping of horizontal or synchrotron oscillations up to about 600 MeV. It is not possible to modify these damping times during the acceleration cycle to values on the order of 0.1 sec or less.

Tracking of particles during part of ramping time has also been done, up to 600 MeV using the code TeaPot[9]. The calculation was performed with 230 particles and 1000 turns in the lattice with sextupoles and systematic multipole errors included. The ramping time (3.5 sec for $E_f \approx 610$ MeV) was divided into 14 periods of 0.25 seconds each. Tracking has been done successively for each period using as input the output from previous one. The energy and RF voltage for each period correspond to the values displayed in figure 1. Although we supposed that the energy increased, we used the last beam dimensions because there is no damping. The evolution of the beam shows that there is a reduction of the energy dispersion. No loss has occurred, but each particle was tracked alone, i.e., no collective effect was included.

The future study should contain microwave instability and a tracking computation where all the collective effects (coherent and incoherent) are incorporated.

VI. REFERENCES

[1] Liu Lin, L. Jahnel and P. Tavares, "The LNLS UVX2 Soft X-Ray Source", LNLS Internal Report MeT-09/91 and 3rd European Particle Accelerator Conference 1992 (Berlin).

[2] L. J. Lindgren and M. Eriksson, "Injection and Extraction at Max", NIM 214 (1983) and E . M. Rowe, "Synchrotron Light Sources Experiments: Bringing Aladdin on Line", NIM B24/25 (1987).

[3] B. W. Montague, "Single-Particle Dynamics - RF Acceleration", CERN 77-13 (1977).

[4] J. Le Duff, "Current and Current Density Limitations in Existing Electron Storage Rings", NIM A239 (1985).

[5] J. Murphy, "Synchrotron Light Source Data Book", BNL 42333 (1990).

[6] J. Le Duff, "Single and Multiple Touschek Effects", CERN 89-01 (1989).

[7] R. P. Walker, "Calculation of the Touschek Lifetime in Electron Storage Ring", IEEE Particle Accelerator Conference 1987 (Washington, D.C.).

[8] Uta Völkel, "Particle Loss by Touschek Effect in a Storage Ring", DESY 67/5 (1967).

[9] L.Schachinger and R. Talman, "TEAPOT: a Thin-Element Accelerator Program for Optics and Tracking", Particle Accelerators 22 (1987).

Extraction System Design for the SSC Low Energy Booster

X. Wu, R. York, U. Wienands, T. Hunter and S. Sheynin
Superconducting Super Collider Laboratory*
2550 Beckleymeade Ave., Dallas, TX 75237

Abstract

The Low Energy Booster (LEB) is the first of 3 booster synchrotrons of the SSC accelerator complex. It will accelerate protons from an injection momentum of 1.22 GeV/c to a final momentum of 12 GeV/c, cycling at a frequency of 10 Hz. A single-turn, vertical extraction system has been designed to extract the proton beam from the LEB within the possible machine operation tune range. At extraction, a set of five bump dipoles will be used to vertically displace the central orbit by approximately 1.5 cm at the entrance of the first septum magnet. A fast, ferrite kicker will be used to sweep the proton beam past the septa to initiate the extraction process. The physics parameters and the preliminary designs for the LEB extraction elements are also given.

I. INTRODUCTION

The LEB lattice[1,2,3] has a three-fold symmetry with separate arcs and long straight sections. The overall length is 570 m in order to provide adequate azimuthal space for the required hardware. Each of the three straight sections has a vertical tune of 1.0 effectively increasing the periodicity of the lattice with respect to a polarized beam and therefore reduces the number of depolarizing resonances to be crossed. The horizontal tune across each straight section has been adjusted to achieve the overall non-integer tune in that plane. One of the straight sections (S2) will be used for the extraction process; the other two accommodate the injection and the rf system, respectively. In Figure 1, the lattice functions of the straight section are shown.

The extraction system has been designed to extract a 12 GeV/c proton beam from the LEB in both the collider fill mode and the test beam mode with the normalized transverse beam emittance (rms) being 0.6 π mm-mrad and 4.0 π mm-mrad, respectively. It should provide the same extracted central orbit at the septum magnets for all possible working points; the LEB can be operated with tunes ranging from 10.9 to 11.9 in both horizontal and vertical planes. It is also required that the extraction system fit into the LEB straight section and have no effect on the three fold symmetry of the LEB lattice.
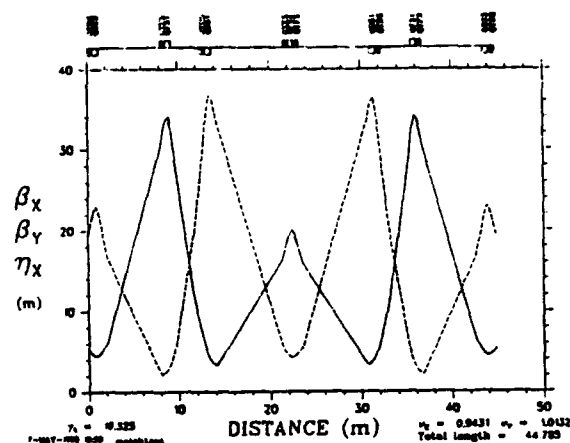
Figure 1. Lattice Functions of the LEB Straight Section

II. THE EXTRACTION SYSTEM DESIGN

A. Beam Optics

Figure 2 shows the layout of the extraction system in the LEB S2 straight section. It also shows the bumped orbits (broken curves) and the extracted orbit (solid curves) in the vertical plane at several different LEB working points. The orbits are calculated by tracking the protons with the code DIMAD.[4] The system consists of a fast kicker, 2 septum magnets and 5 slow bump magnets. The kicker magnet is positioned right after the vertical focusing quadrupole QDS1, and 2 septum magnets one cell downstream. Once the proton beam reaches the final momentum of 12 GeV/c, the slow bump magnets are powered to steer the circulating beam slowly towards the septum several milliseconds before the kick. Then the fast kicker deflects the beam across the septum where it receives additional deflection to leave the machine.

Each of the 5 bump magnets has its own independent power supply so their magnetic field can be independently adjusted in order to generate an adequate vertical displacement at the septum for all possible working points. Once the kicker magnet is turned on, the same extracted orbit will be achieved at the entrance of the first septum regardless of where the LEB is operated, as is evident in Figure 2. Bumps 1 and 2 are positioned before and after the kicker and deflect the orbit by about 15 mm towards the septum depending on the LEB working point. Located right in front of the septum magnet, bump 3 is used to adjust the
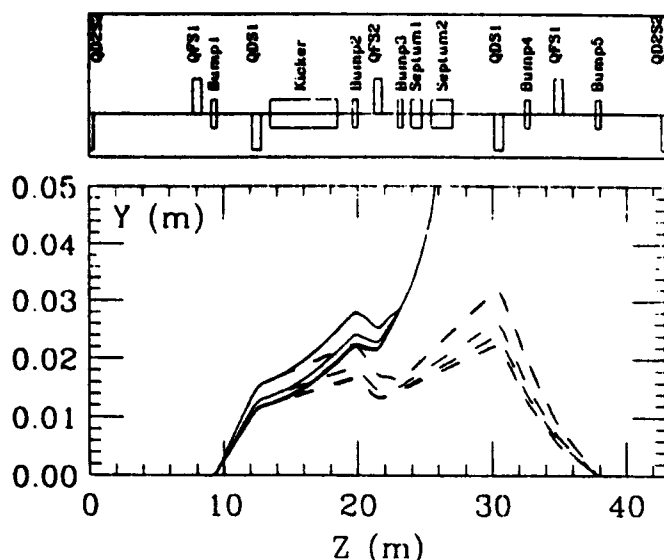
Figure 2. Layout of the Extraction System and the Central Orbit for Bumped and Extracted beam

Figure 3. Cross Section at the Entrance of the First Septum Magnet Showing Sizes and Locations of Beams.

angle of the proton beam entering the first septum magnet. Bumps 4 and 5 bring the bumped orbit back to the median plane within the extraction straight section. The maximum deflection angle required for the bump magnets is about 5.0 mrad.

In order to minimize the kicker strength and achieve the bending required to extract the 12 GeV/c proton beam, two septum magnets are used. The first has a 3 mm thick septum and deflects the proton beam by 5 mrad; the second has a 7 mm septum and provides a 50 mrad deflection angle.

The orbit displacement, Δ, generated by a kick δ at the septum is given by:

$$\Delta = \delta\sqrt{\beta_1\beta_2}sin(\phi_2 - \phi_1) \qquad (1)$$

where β_1, β_2 are the β functions and ϕ_1, ϕ_2 are the betatron phases at kicker and septum, respectively. For a kicker with a length of L, Δ is given by:

$$\Delta = \frac{\delta}{L}\sqrt{\beta_2}\int_0^L \sqrt{\beta_1(s)}sin(\phi_2 - \phi_1(s))ds \qquad (2)$$

The required orbit displacement is determined by the proton beam size at extraction and the thickness of the septum. As indicated above, a 3 mm septum is used in the first septum magnet; the maximum vertical half width of the beam at the first septum is about 4.7 mm (3 σ test beam). More displacement is needed for the closed orbit excursion. About 15 mm orbit displacement at the first septum is required to move the proton beam to the other side of the septum. Figure 3 shows beam sizes and locations at the entrance of the first septum magnet. The kicker strength, δ, is given by:

$$\delta = \frac{\Delta L}{\sqrt{\beta_2}\int_0^L \sqrt{\beta_1(s)}sin(\phi_2 - \phi_1(s))ds} \qquad (3)$$

Both the analytic as well as tracking results show a kicker strength δ of 1.5 mrad will be adequate.

B.   The Kicker Magnet

The extraction kicker has an integrated strength of 600 G-m, and is made up of eight modules to achieve a rise-time of 80 ns. With total magnetic length of about 5.3 m, it has a maximum field of about 115 G. With this rise-time, two to three beam bunches (spaced 16.68 ns apart at 12 GeV/c) are lost due to partial kicker deflection with the head and tail bunches of the extracted beam being sheared somewhat. The aperture of the kicker magnet is 50 mm by 70 mm to accommodate the maximum proton beam size at the injection energy of 600 MeV. The magnetic field variation $\Delta B/B$ is no more than $\pm 1.0\%$ across the good field region of 20 mm by 40 mm. A more detailed paper about the kicker magnet design is included in these proceedings.[5]

C.   The Bump Magnets

Figure 4 shows the cross section of the bump magnet. The required maximum integrated strength is 0.18 T-m. With a magnetic length of 0.45 m, the maximum magnetic field will be 4.0 kG. It is a laminated, H-shaped, 8 turn/pole dipole magnet with a pole gap of 80 mm. A stainless steel vacuum chamber of 75 mm in diameter is placed into the aperture of the bump magnet. The magnetic field variation $\Delta B/B$ is allowed to change no more than $\pm 0.1\%$ within a good field region of 30 mm by 50 mm. The bump magnet is pulsed by a 2 msec half-sine wave with a peak current of 1600 A.

D.   The Septum Magnets

Figures 5 and 6 show the cross sections of the short and
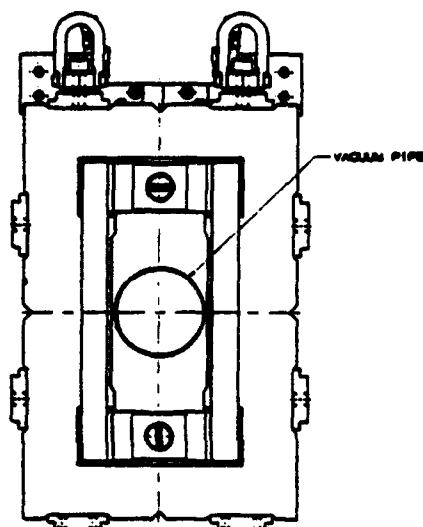
Figure 4. Cross Section of the Bump Magnet
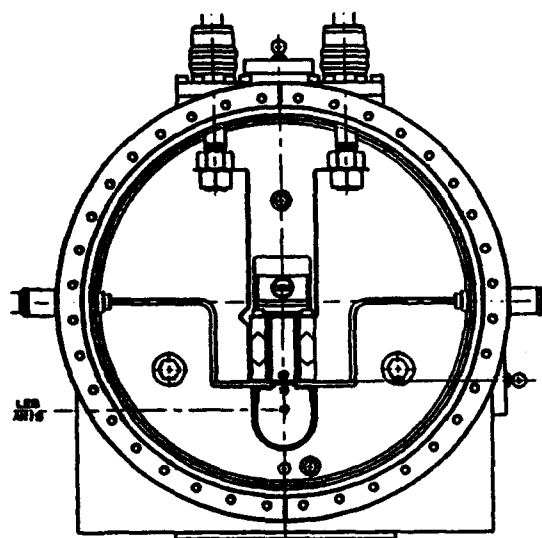
Parameter	Short Septum	Long Septum
$\int Bdl$ (T-m)	0.2	2.0
Magnetic Length (m)	0.8	1.6
Maximum Field (T)	0.25	1.25
Field Uniformity	0.24%	0.1%
Peak Current (A)	4780	20400
Power Pulse	1 msec	1.5 msec

long septum magnets.[6] Single turn current sheet septa are used in both magnets with thicknesses of 3 mm and 7 mm, respectively. The design parameters for the septum magnets are given in Table 1. Both magnets are placed into vacuum tanks and vacuum tight feedthroughs provide power and cooling water to the magnets. Special shielding is required to prevent leakage of the magnetic field outside the septa that otherwise would cause emittance growth on the last few hundreds turns prior to powering the kicker. This shielding is accomplished by a U-shaped low carbon steel shell which is brazed to the conductor assembly and is a part of the conductor support structure.

III. REFERENCES

[1] R. C. York, et. al. "The Superconducting Super Collider Low Energy Booster: A Status Report", *Conference Record of the 1991 IEEE Particle Accelerator Conference*, Vol. 1, pp. 62-64.

[2] U. Wienands, et. al. "Status of the SSC Low Energy Booster", these proceedings.

[3] U. Wienands, et. al. "The H-γ_t Lattice of the SSC Low Energy Booster", *Conference Record of the XVth International Conference on High Energy Accelerators*, (Hamburg, 1992).

[4] R. V. Servranckx, et. al. "User's Guide to the Program DIMAD", SLAC Report 285 UC-28, May 1985.

[5] D. Anderson, et. al. "Low Energy Booster Extraction Kicker Magnet Design Status at SSC", these proceedings.

[6] S. Sheynin, et. al. "Preliminary Design Review of the LEB Extraction System", SSC Internal Document, December 1992.

Figure 5. Cross Section of the Short Septum Magnet

Figure 6. Cross Section of the Long Septum Magnet

Tests and Analysis for SLC Damping Ring Data*

J.E. Spencer

Stanford Linear Accelerator Center, Stanford University

Stanford, California 94309

Abstract: Beyond typical, open-loop or feedback use, fast, turn-by-turn bunch monitors provide recursive data that determines system dimensionality d and K-entropy whose time fluctuations provide useful diagnostic tools. For injection and extraction, one can study variations in the dimensionality of the attractor with matching, jitter, current and tunes. Comparison to dynamical models then helps to optimize control. Experimental and theoretical examples and their signatures are discussed e.g. the evolution of the distribution function after injection is studied as a solution of Liouville's equation.

I. Introduction

Optimal injection and extraction in storage rings can be approached in several ways. We can try to understand the problem with an explicit Hamiltonian or in a purely heuristic way using feedback/forward or, as argued earlier, with a closed system whose structure is based on dynamical models [1]. Since chaotic dynamics are controllable [2] with data of sufficient accuracy and sampling bandwidth, we study the information content in time series, how it varies with time and how we can control and use it.

II. Tests of data

For N equi-spaced samples $(\vec{x}_i(i\tau) : i = 1 \cdots N)_t$, we can write the correlation function as:

$$C(\rho) = \frac{2}{(N-n+1)^2} \sum_{j>i=1}^{N-n+1} \Theta(\rho - |\vec{x}_i - \vec{x}_j|) \qquad (1)$$

with ρ the correlation length, Θ the Heaviside function and n the number of variables assumed to span the problem [3]. d is the limit of $d\mathrm{Log}C(\rho)/d\mathrm{Log}\rho$ with $n_{max}>d>D$ where D counts the number of degrees of freedom.
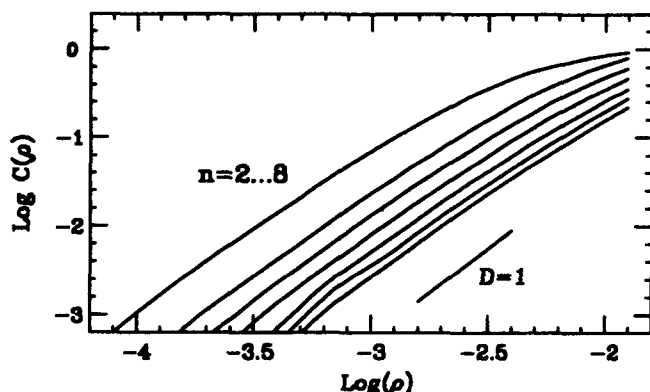
Fig. 1: Dependence of correlation integral on size.

Fig. 1 shows the analysis for Δx from Fig. 3. All curves in Fig. 3 give $D \approx 1$, including 1000 particle tracking. The collective motion is well represented by a single particle with 1D. Two constraints on decimated 'data' are to avoid obvious correlations e.g. $n > 5$ in Fig's. 1&3 and to have enough data to unfold deterministic and stochastic effects (large d). For contrast, Fig. 2 shows the expected result for 1000 random points. For $C(\rho) \ll 1$, all curves in Fig. 1 are parallel whereas none are in Fig. 2.

III. Analytic model for injection

Even when one reduces particle losses along a closed orbit at injection by adjusting the transverse tunes to avoid resonances, injection may still not be optimal due to the cumulative effect of nonlinear fields on the beam over many turns. In terms of the lowest order moments, one observes decoherence in the center-of-mass motion $\langle x \rangle_t$ and filamentation of the phase space e.g. growth in $\langle x^2 \rangle_t$. Examples are given below: first from Moshammer's analytic model [4], then tracking and finally from measured SLC data.
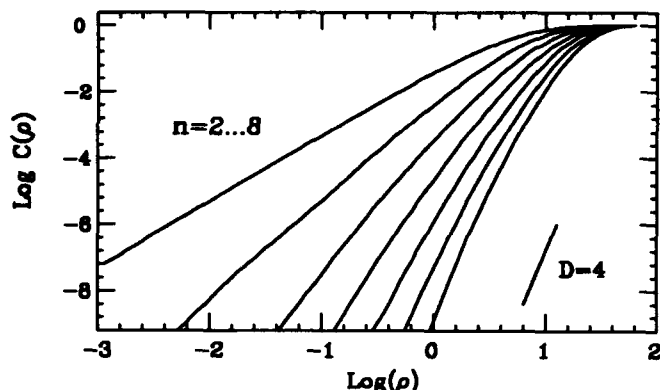
Fig. 2: Correlation data for 1000 random turns.

A. Assumptions

1. One can replace the Hamiltonian of single particle motion $H(x, p, s)$ by an Hamiltonian, averaged over the fast evolving variables

$$\hat{H}(I) = \omega_0 \sum_{n=1}^{N} \mu_{n-1} \frac{I^n}{n!} . \qquad (2)$$

The quantity ω_0 denotes the revolution frequency times the tune. The linear motion is described with $\mu_0 = 1$ and $N = 1$ and μ_1 contains first order octupole plus second order sextupole contributions etc. Once the Hamiltonian is transformed into an integrable Hamiltonian, the equation of motion and thus the time evolution of the phase space distribution is determinable.

2. The beam distribution at injection is assumed Gaussian.

The only requirement is that the initial distribution is well approximated by a positive definite, but not necessarily smooth, function of the phase space variables.

3. Normal coordinates (ξ, η), related to the transverse betatron coordinates (x_β, p_β) are used:

$$\xi = \frac{x_\beta}{\sqrt{\beta}} , \quad \eta = \frac{\alpha x_\beta + \beta p_\beta}{\sqrt{\beta}} , \quad \eta + i\xi = \sqrt{2I}e^{i\phi} .$$

Their relation to action-angle variables is given by the transformation from cartesian to polar coordinates.

The corresponding distribution function in (I, ϕ) at $t = 0$ is:

$$\Psi = \frac{1}{2\pi\epsilon_{x0}} \exp\left(-\frac{b+c}{\epsilon_{x0}}[\sqrt{I}\cos(\Omega) - \sqrt{I_0}\cos(\Omega_0)]^2\right.$$

$$\left. -\frac{b-c}{\epsilon_{x0}}[\sqrt{I}\sin(\Omega) - \sqrt{I_0}\sin(\Omega_0)]^2\right) \quad (3)$$

with

$$\Omega = \phi - \int_0^t dt\; \partial\widehat{H}(I)/\partial I - \bar{\phi} \qquad \Omega_0 = \phi_0 - \bar{\phi} ,$$

$$I_0 = \frac{1}{2}(\eta_0^2 + \xi_0^2) , \qquad \phi_0 = \arctan(\xi_0/\eta_0) ,$$

where the center-of-mass at injection is given by the coordinates η_0, ξ_0 and ϵ_{x0} denotes the injected emittance. The coefficients b and c describe the injected beam ellipse in the lattice of the storage ring. They are composed of the Twiss parameters associated with the injection point in the storage ring (α, β) and the Twiss parameters that describe the injected beam ellipse α_b, β_b. The distribution function in Eq. (3) will be an exact solution of Liouville's equation. From Ref. [4] we have

$$b = \frac{1}{2}\left(\frac{\beta_b}{\beta} + \frac{\beta}{\beta_b} + \frac{\beta}{\beta_b}\left[\alpha_b - \frac{\beta_b}{\beta}\alpha\right]^2\right)$$

and $c, \bar{\phi}$ are given by

$$ce^{2i\bar{\phi}} = \frac{\beta}{2\beta_b}\left(\left[\frac{\beta_b}{\beta} - i(\alpha_b - \frac{\beta_b}{\beta}\alpha)\right]^2 - 1\right) .$$

Notice that: $c^2 = b^2 - 1$. For $b = 1$, the initial distribution is described in phase space by circular contours centered around I_0, ϕ_0. In this case the beam is said to be matched to the lattice. The parameter b is known as the β−mismatch parameter which quantifies the increase of effective beam size after filamentation.

B. First Moments

It is possible to obtain a closed expression for the first and second moments if we limit $N = 2$ for the linear and quadratic terms in Eq. (2). From Ref. [4], the result for the first moment from Ψ in Eq. (3) is:

$$\langle \eta + i\xi \rangle = \iint \Psi\sqrt{2I}\exp(\phi)\,dI\,d\phi$$

$$= \frac{A\sqrt{2I_0(b^2 - c^2)}}{\kappa^2(1-z^2)^{3/2}}e^{-I_0[b+c\cos(2\Omega_0)]/\epsilon_{x0}}e^{i(\omega_0 t + \bar{\phi} + \tilde{\Omega}_0)}$$

$$\times \left(1 - ze^{-2i\tilde{\Omega}_0}\right)\exp\left(\lambda - \lambda z\cos(2\tilde{\Omega}_0)\right) , \quad (4)$$

with

$$\kappa = b - i(\omega_0\mu_1 t\epsilon_{x0}) , \qquad z = c/\kappa , \qquad \lambda = \frac{A^2 I_0}{\kappa(1 - z^2)\epsilon_{x0}}$$

and

$$\tan(\tilde{\Omega}_0) = \frac{b-c}{b+c}\tan(\Omega_0), \quad A = \sqrt{b^2 + c^2 + 2cb\cos(2\Omega_0)}$$

Using the definitions of A and $\tilde{\Omega}_0$ below Eq. (3) it is straightforward to show that Eq. (4) fulfills the initial condition $\langle \eta + i\xi \rangle_{t=0} = \sqrt{2I_0}\exp(i\phi_0)$. Since $|\kappa|$ increases with time, the asymptotic value of the first moment tends to zero: $\langle \eta + i\xi \rangle_{t\to\infty} = 0$. In this context one talks about the decoherence of the center-of-mass motion. This is illustrated in Fig. 3. One thousand particles were tracked over 2000 revolutions in the lattice of the SLC damping ring which contains 72 permanent sextupoles. The stars in Fig. 3 describe the analytic solution based on Eq. (4) whereas the lighter solid line refers to tracking. There is a small but stable phase error.

Equation (4) reduces considerably if we assume a matched beam at injection with $b = 1$. In this case Eq. (4) describes the decoherence of an initial Gaussian beam that has been deflected from the reference orbit.
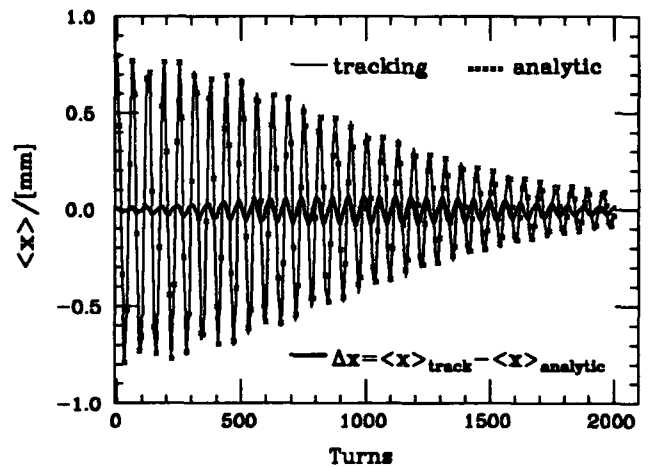
Fig. 3: Center-of-mass motion after injection.
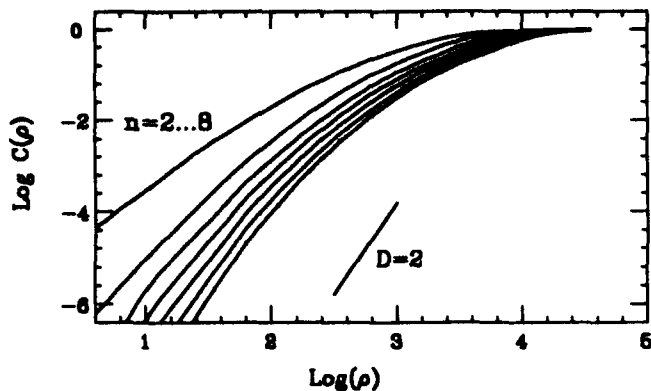
Fig. 4: Correlation data for a turn-by-turn BPM.

Fig. 6: Correlation data for a 'turn-by-turn' SLM.

C. Two or more degrees of freedom

With betatron coupling or chromaticity, the series $(x)_t$ reflects a Hamiltonian with $D \geq 2$. Still it is possible to derive analytic solutions for the center-of-mass motion after injection but the number of parameters that have to be determined from data increases considerably. One way to overcome this is to filter the data in the frequency domain and reduce the 2 or 3 degrees to one. The discussion here is limited to tests of calculations *and* the available data types.

D. Higher dimensionality of different 'data' types

An analysis of $(x)_t$ from 3D tracking with DESPOT for the first 1000 turns implied a value consistent with $D \approx 1.5$ as though the different degrees of freedom were nearly uncoupled. The result for the energy was especially clean with $D = 1$. At 1000 turns, coherent oscillations from injection errors in position and energy had nearly damped whereas at 500 turns $D \approx 2$ for $(x)_t$.

A BPM monitor [5] that gives turn-by-turn data for an FFT has $D \geq 2$ as implied above. Fig. 4 shows an example for the first 1000 turns after injection when there is no betatron coupling. For a synchrotron light monitor (SLM) we expect a similar or higher D.

Fig's. 5&6 show some results [6] for a damped beam that is first perturbed by an extraction kicker and then again by an injection kicker near turn 130. The effects in x are more emphatic and a good example of a matched beam

Fig. 5: $\langle y \rangle$ vs turns for kicked data from a SLM.

with $b = 1$ that decoheres and filaments when deflected. Analysis of the 500 turns for x give a result similar to Fig. 4 with $D \approx 2$, but the y data look totally different and appear noisy so that one expects a higher phase space dimensionality. The result for all 500 turns is shown in Fig. 6. The $D = 1$ trend at the larger correlation lengths disappears when one analyzes only the turns for $N > 130$ which may indicate coupling from the extraction kicker.

IV. Conclusions

Dimensional analysis of real data show insignificant noise [7]. Decimating data, to filter, compress or match sampling capacity should extend the applicability. More SLM data for different orbits could study coupling from the kickers. The analysis is simple for $n < 10$ so it should be interesting for many accelerator studies such as nonlinear resonances or coupling in multi-bunch or flat beams (*e.g. from the kickers*) as well as the parameter dependence of stochastic effects in the beam-beam interaction or in long-term tracking.

V. REFERENCES

[1] J.E. Spencer, IEEE PAC (1991)1440. Dynamical models may be used to define *and* train neural nets.

[2] See Ref. [1] and Edward Ott, Celso Grebogi and James Yorke, Phys. Rev. Lett. 64(1990)1196. They might argue that because most attractors are chaotic, structural stability is mostly irrelevant and even an impediment.

[3] N.H.Packard, J.P.Crutchfield, J.D.Farmer and R.S. Shaw, Phys. Rev. Lett. 45(1980)712 and P. Grassberger and I. Procaccia, Phys. Rev. Lett. 50(1983)346. Alternative algorithms for on-line control will be discussed elsewhere.

[4] H. Moshammer, SLAC-PUB-6063.

[5] See R. Stege, K. Jobe and M. Ross, this conference.

[6] The data are M. Minty's. See SLAC-PUB-5993.

[7] The only other analysis for accelerator data we are aware of was Voelker Ziemann's. It showed large stochastic effects in linac BPM data but that data was necessarily taken differently.

RF Capture Studies for Injection into a Synchrotron*

E. S. Lessner, Y. Cho

Argonne National Laboratory, 9700 So. Cass Ave., Argonne, IL 60439

Abstract

The capture process for a rapid cycling protron synchrotron is studied by numerical simulation. The rf programming is optimized to allow efficient capture such that minimum particle losses and reasonable capture voltage are attained. The total capture time is constrained to be less than 700 μseconds. Two methods of trapping the injected beam by the synchrotron rf system are examined: by stationary adiabatic capture and by synchronous injection in a standing bucket of the ring. In the adiabatic method, the non- linear function of Lilliequist and Symon is employed. The simulation allows the "tracking back" of the original distribution of any set of particles, in particular of those not captured at a given time, which is useful in studying injection alternatives such as shaping the phase-space density prior to injection. The simulation results will be used to design a chopper system to facilitate loss-free injection.

I. INTRODUCTION

A One Megawatt Spallation Neutron Source is being proposed for the upgrade of Argonne's Intense Pulsed Neutron Source. An overview of its conceptual design is given elsewhere in these Proceedings [1]. The new accelerator system (a 400–MeV linear accelerator and a 2.2–GeV rapid cycling synchrotron) will deliver a time-averaged current of 0.5 mA at a 30–Hz repetition rate. At such high intensity beams, it is essential to minimize beam losses to avoid problems with the ensuing induced radioctivity. In this paper, we present the results of preliminary studies of the injection and capture processes and possible ways of maximizing the capture efficiency. We examined two methods of trapping the injected beam by the synchrotron rf system: by stationary adiabatic capture and by synchronous injection in a standing rf bucket of the ring.

The guide magnetic field has a flat-bottom of 0.5–0.7 msec duration, a rising field of 20 Hz, and a falling field of 60 Hz to maintain the overall required 30–Hz repetition rate. The introduction of a constant magnetic field during injection allows for easier manipulation of the capture process. The rf voltage is programmed such that it is minimized during injection and capture and maintains an approximately constant bucket area determined by the bucket area at B_{max}. The minimum voltage at capture insures that one does not have a larger bucket area at the small synchronous phases and high dilution of the phase-space. The capture efficiency is calculated at 2 msec after the start of the acceleration. Our simulation code tracks a number of macro particles in longitudinal phase-space. A pair of Hamiltonian difference equations is solved for each macro particle for each turn. The phase-space coordinates are the total energy and the phase angle measured with respect to the energy E_s and phase angle ϕ_s of the synchronous particle. The equations of motion for particle i, on turn n, are [2]:

$$E_{i,n} = \frac{\beta_{s,n}}{\beta_{s,n-1}} E_{i,n-1} + e\hat{V}(sin\Phi_{i,n-1} - sin\Phi_{s,n-1}) \quad (1)$$

$$\Phi_{i,n} = \Phi_{i,n-1} + \frac{2\pi h \eta_{s,n}}{\beta_{s,n}^2 E_{s,n}} E_{i,n} + (\Phi_{s,n} - \Phi_{s,n-1}) \quad (2)$$

where h = harmonic number, and $\eta = \alpha - \gamma^{-2}$. These equations are sympletic to first order.

For a given final particle distribution, the program can "track back" the initial distribution of any set of particles, which is very useful in determining the initial coordinates of lost particles. A particle is considered to be "lost" if it is outside the separatrix at a specified time.

II. ADIABATIC CAPTURE

In the stationary adiabatic capture method, the non-linear function of Lilliequist and Symon [3] is employed. At any given time t, the rf voltage amplitude is given by:

$$V(t) = \frac{V_2(t_2)}{(\sqrt{\frac{V_2}{V_1}} - \alpha \frac{t-t_1}{\tau_{p2}})^2} \quad (3)$$

where V_1 is the initial voltage at time t_1, V_2 and τ_{p2} are the final voltage and the phase oscillation period at time t_2, respectively, and α is a constant that determines the degree of adiabaticity.

The capture efficiency for several degrees of adiabaticity and phase-space dilution was studied extensively. However, it has been observed experimentally that in adiabatic capture processes that are constrained by time and capture voltage values (a high capture voltage implies high dilution and particle losses when the bucket shrinks during acceleration), there is always a "band" of particles that is not captured. Their initial distribution extends from the unstable fixed points to the energy extreme values, with a roughly linear variation in phase angles (see Figure 2). One possible way of avoiding these losses is to paint the longitudinal phase-space by injecting a beam of small energy spread, with its central energy modulated during the injection period to match the bucket area of the ring and chopped at appropriate phase angles. In our simulation of injection by painting, we have assumed the following conditions:

- the magnetic guide field is kept constant during injection and capture, giving a maximum bucket area for a given voltage;

- the linac pulse duration is 0.5 msec long;

- injection stacks of 100–keV energy spread; and

- the central energy is raised linearly during the injection period.

In the simulation, stacks are sampled at 25 μsec intervals. The rf programming is shown in Figure 1. The initial voltage is kept constant at 1 kV during injection and raised rapidly to 7 kV in 1/4 of the final oscillation period (0.2 msec), right at the start of the acceleration period. The capture voltage of 7 kV is determined by the requirement that the bucket area at $\dot{B} = 0$ be equal to the bucket area at $\dot{B}_{max}$, corresponding to a bucket area of 3 eV-sec. For a momentum deviation $\Delta p/p = 1.5E\text{-}3$ and without beam chopping (bunch length equal to the circumference length), the capture efficiency measured at 2 msec into the accelerating regime ($\Phi_s = 26°$) is 88%. The initial distribution of the uncaptured particles can be seen in Figure 2. To avoid these losses, we injected stacks with the lower energy particles chopped at the end of the bunch (positive phase angles) for increasing periods of time, and the higher energy particles chopped at the beginning of the bunch (negative phase angles) for decreasing periods of time (see Figure 2). With this procedure all of the beam is captured, but 25% of the total beam area must be chopped, requiring a higher duty factor and a dilution of the order of two. The particle distribution at the end of 2 msec can be seen in Figure 3.

For comparison, we examined the case when the voltage is raised immediately from 1 kV to 7 kV, in a "step-

Figure 2

Schematic initial phase-space distribution of particles not captured at t=2 msec of acceleration for an adiabatic capture and unchopped beam. To ensure total capture, the beam is chopped prior to injection along the indicated continous lines.

as before, the capture efficiency at 2 msec of acceleration drops to 80%. To avoid losses, the beam would have to be cut slightly more than 25%, using a more complex scheme than in the previous case, since many of the particles of higher energy and phase angles which are captured in the adiabatic process are lost in the non-adiabatic one. We also examined the capture efficiency for particles injected with lower momentum spread, namely, $\Delta p/p=1.2E\text{-}3$ and 7.0E-4. The capture efficiency for all the cases examined is displayed in Table 1.

Table 1
Capture Efficiency measured at 2 msec

	Δp/p		
	1.5E-3	1.2E-3	0.7E-3
Unchopped Adiabatic	89.17	89.99	90.56
Unchopped Non-Adiabatic	82.68	83.56	84.20
Chopped Adiabatic	100.00	–	–
Waiting Bucket	99.60	99.82	99.98

Figure 1

RF voltage programming from the start of injection to the end of acceleration. The magnetic field is held constant for 700 μsec; the beginning of the accelerator clock is set at t=0.

"like" fashion, thus shortening the flat-bottom field duration requirement. For a momentum variation of 1.5E-3,

III. STACKING IN A STANDING RF BUCKET

In the second study, we injected stacks of 100–keV energy spread cut at +/- 120° into a standing bucket of area 3 eV-sec and momentum spread of $\Delta p/p=1.5E\text{-}3$. As in the adiabatic process, the central energy of the stacks is modulated during the injection period. Figure 4 depicts the phase-space configuration right after injection, showing a dipole distribution, with a hot core of particles around 401 MeV which remains even after several synchrotron oscillations. Since space charge effects are likely to be maximum at the beginning of acceleration [4], this configuration is
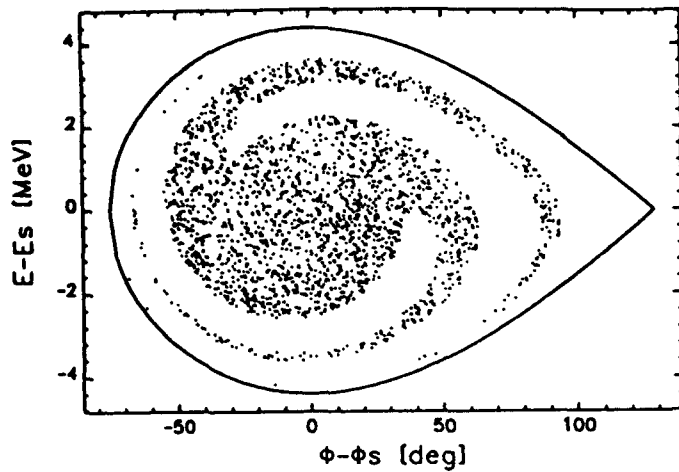
Figure 3
Phase-space distribution at the end of 2 msec of acceleration for the chopped beam.

not desirable. As an alternative, we examined the injection of stacks with no modulation of the central energy and for the three values of momentum deviation. As previously, the stacks are chopped at +/- 120°. For the higher momentum spread case, the phase-space distribution, right after injection, is fairly uniform in energy and phase angle, as shown in Figure 5. Tracking back the initial distribution of the lost particles indicates that chopping the beam at +/- 100° (55% cut) would insure total capture.
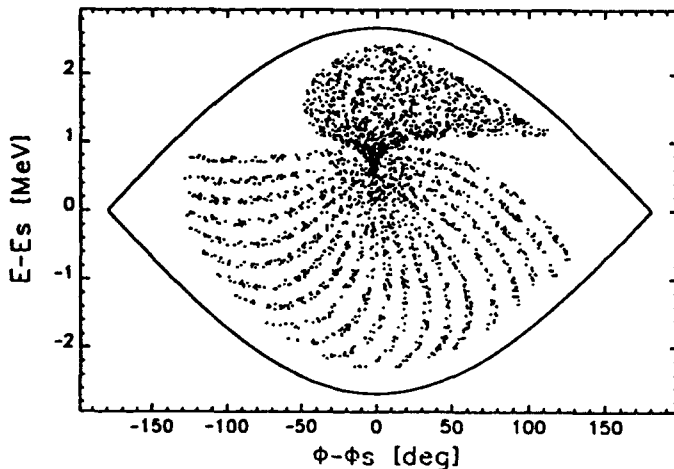
Figure 4
Distribution at the end of injection for energy modulated stacks injected into a waiting bucket of the ring, showing a high density of particles around 401 MeV.

IV. CONCLUSIONS

Several options for the injection and capture into a stationary bucket of a synchrotron are studied by numerical simulation. In the adiabatic case, within the time and voltage requirements, 100% capture efficiency can be achieved
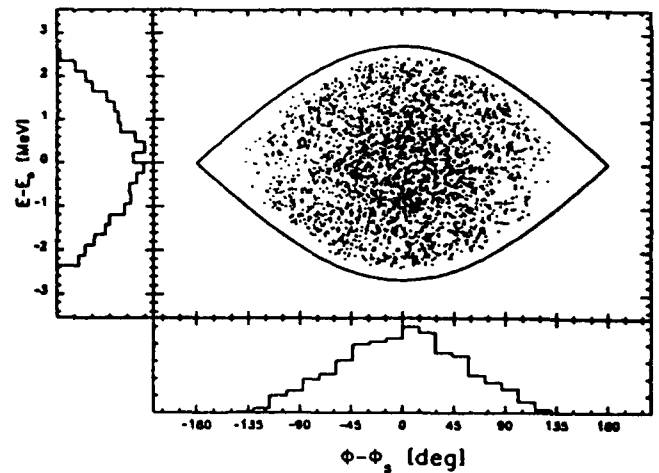
Figure 5
Distribution at the end of injection for stacks injected without energy modulation. The particle distribution in Φ and E space is shown respectively at the bottom and sides of the figure.

by modulating the central energy and chopping the beam prior to injection. In the synchronous capture by a standing bucket case, modulation of the central energy leads to an undesirable phase-space distribution after injection. If the stacking is done without energy modulation, with the injected beam spread to fill the rf bucket acceptance, however, the phase-space distribution is acceptably uniform but requires a higher duty factor than the adiabatic process. In this case, if the energy spread is further reduced by a factor of two, the capture efficiency is nearly 100%.

V. REFERENCES

[1] Y. Cho *et al*, "Conceptual Design for a One Megawatt Spallation Source at Argonne National Laboratory," these proceedings.

[2] S. R. Koscielniak, "The Long1d Simulation Code," *European Particle Accelerator Conference*, 743-745 (1988).

[3] C. G. Lilliequist and K. R. Symon, "Deviations from Adiabatic Behaviour During Capture of Particles into an R.F. Bucket," *MURA-491* (1959).

[4] Y. Cho, "Capture and Acceleration Considerations in the SNQ-SRA," *ANL-83-13, AAD-N-5* (1982).

Results from Beam Diffusion and Collimation Measurements in Preparation for Fermilab Tevatron Crystal Extraction

G. Jackson
(for the Experiment 853 Collaboration[†])
Fermi National Accelerator Laboratory*
P.O. Box 500   MS 341
Batavia, IL 60510

Abstract

In order to extract stored beam from the Tevatron Collider in a controlled and transparent manner, protons must be diffused from the core of the beam into the lattice of the bent crystal without inducing higher background rates in the high energy physics detectors CDF and D0. The experimental study of diffusion, collimation, and detector backgrounds are part of the larger effort of the Fermilab experiment E853. Reported in this paper are results showing the effect of RF noise on beam size evolution, proton diffusion from the beam core, and detector backgrounds.

I. INTRODUCTION

In preparation for the Fermilab Tevatron crystal extraction experiment 853 [1] parasitic colliding beam studies and some dedicated proton only experiments were performed. The purpose of this work was to perform preliminary exploratory experiments on the effect of RF noise and collimation on a proton beam and on the background rates measured in the high energy physics detectors CDF and D0.

Three basic sets of experiments were performed. First, the effect of RF noise on the beam in the absence of collimation (but in the case where protons spill out of the RF buckets confining the bunches) is studied during a proton only store at 900 GeV. Second, the effects of a steel collimator during the above RF noise induced diffusion is observed in the same store. Finally, a test of collimation with a unbent crystal during a normal colliding beam store is reported.

II. EXPERIMENTAL SETUP

The Tevatron stores 6 proton and 6 antiproton counter-rotating bunches at 900 GeV. At the crystal the horizontal dispersion and beta are 2.02 m and 90.8 m respectively. The transition gamma has a value of approximately 18. The synchrotron frequency is 39 Hz. Typical beam dimensions are an rms horizontal betatron width of 0.60 mm, an rms horizontal divergence of 166 μr, an rms bunch length of 60 cm (2 nsec), and an rms relative energy spread of 166×10^{-6}.

The RF system is split into two sets of 4 cavities each. Four cavities accelerate either protons or antiprotons, but generate a net voltage of zero for the other beam. This is accomplished by spacing pairs of cavities 90° apart at the RF frequency 53.104705 MHz (bucket length of 18.8 nsec). Each beam sees a net RF voltage of 1.1 MV/turn (corresponding to an RF bucket half height of 446 MeV). External noise (white in the band between 50 and 100 Hz) was added to the RF amplitude program to induce longitudinal dilution. An external voltage of 10 V changes the RF voltage by 100 kV (10%). Applied at twice the synchrotron frequency, this noise causes quadrupole oscillations and longitudinal diffusion.

There are a series of steel collimators in the ring. They are oriented both vertically and horizontally, where the horizontal collimators are placed on the radial inside of the vacuum chamber. This orientation allows the steel to intercept particles which have fallen out of an RF bucket and are decelerating due to synchrotron radiation emission at the rate of 5 eV/turn toward the radial inside. A single horizontal silicon unbent crystal sits on the radial outside for studies.
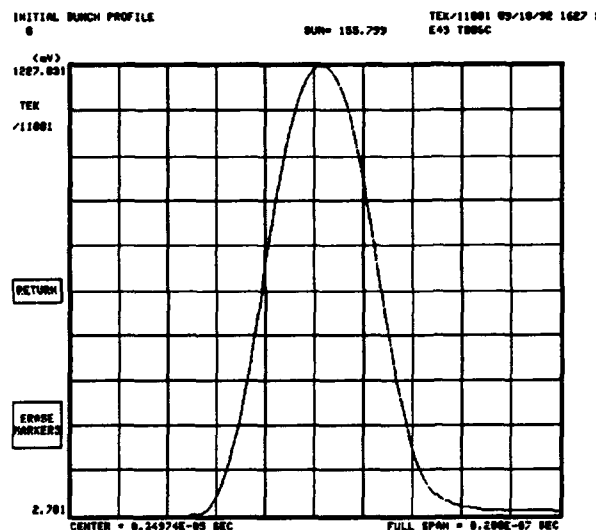
Figure 1: Initial longitudinal beam distribution as measured by a broadband resistive wall monitor and oscilloscope. The scale of the time axis is 2 nsec/div.

III. MEASUREMENTS

A. Diffusion without Collimation

Two levels of external random noise were applied to the RF amplitude program. The first experiment was performed with an rms external voltage of 500 mV, which corresponds to a rms RF gradient fluctuation of 5 kV/turn. Due to the proton diffusion caused by this noise and the fact that the separatrix of the bucket acts as an aperture, the longitudinal density distribution of the beam changes into a new equilibrium shape. Figures 1 and 2 show the longitudinal shape of a typical proton bunch before and after RF amplitude noise was applied. Note that the equilibrium shape has a narrower FWHM than the initial distribution, but has many more particles at large amplitude near the bucket separatrix (the left and right edges of the plot).
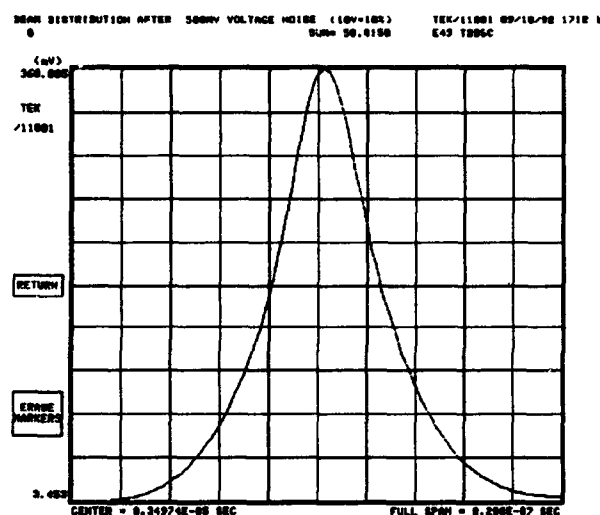
Figure 2: Equilibrium longitudinal distribution generated by RF amplitude noise and the RF bucket separatrix. The scale of the time axis is still 2 nsec/div.

Once the equilibrium shape of the longitudinal bunch distribution was established, an exponential particle loss rate was established. In the 5 kV/turn case, the relative proton loss rate was 1.4×10^{-3}/sec (over 3 orders of magnitude to large a rate). This corresponds to an intensity time constant of 12 minutes.

The next experiment used a reduced external noise level of only 50 mV, corresponding to an RF voltage jitter of 500 V rms. Figure 3 shows the DC and bunched beam intensities vs. time during the study. The equilibrium loss rate in this case was measured to be 1.6×10^{-5}/sec (for a time constant of 17 hours). The nominal intensity time constant for the protons in the Tevatron Collider varies anywhere from 40 to 120 hours, depending on beam-beam effect variations store to store. Note that a factor of 10 reduction in noise amplitude was responsible for a factor of 100 reduction in the proton loss rate. The DC beam (total beam intensity in the accelerator,

both bunched and unbunched) lags the bunched beam loss (the sum total intensity in the 6 primary proton RF buckets) due to the fact that the 5 eV/turn deceleration rate of each proton requires approximately an hour for the particles to hit the inside edge of the horizontal aperture.
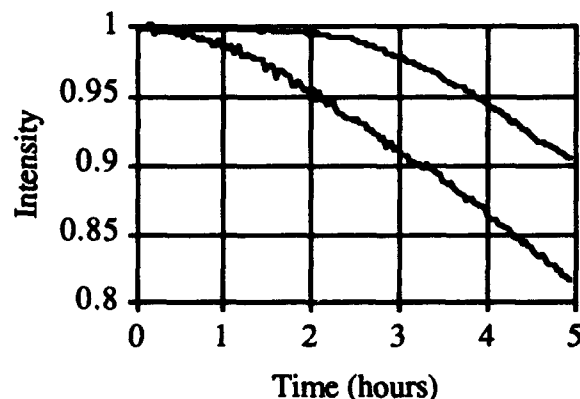
Figure 3: DC beam (top) and bunched beam (bottom) normalized intensity vs. time during RF amplitude noise excitation at the 500 V rms/turn level.

During the latter measurement the bunch length was monitored. One of the potential negative impacts of this extraction technique is that the external noise will increase the bunch length. Since the vertex detectors of the collider experiments and the β^* at the interaction point are comparable to the bunch length, lengthening would cause a reduction in luminosity. While the rms bunch length increased from 55 cm to 75 cm (see figure 4), the FWHM bunch length decreased from 150 cm to 140 cm. This seemingly contradictory result is due to the shape change in the longitudinal bunch distribution. Since the core width (as measured by the FWHM parameter) is basically unchanged, there is no adverse effect of crystal extraction on luminosity.
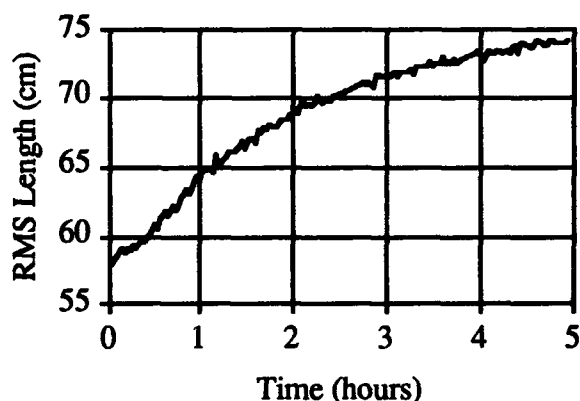
Figure 4: Proton bunch length vs. time during the period when 500 V rms/turn of RF amplitude noise was being applied. At this noise level it takes approximately 6 hours for the bunch length to come to an equilibrium value.

B. Collimation without Diffusion

Before addressing the question of background counting rates in the high energy physics detectors in the presence of externally driven diffusion and collimation, it is useful to measure the diffusion rate during typical colliding beam conditions. This measurement is carried out by monitoring the rate at which single protons are deposited into the CDF high energy physics detector when a momentum aperture defining horizontal collimator (a collimator in a region of high dispersion) is retracted by a small distance. By measuring the time it takes for the loss rate to return to its original value, the average diffusion rate can be calculated.

In this experiment a collimator was retracted by 100 μm. It was observed that the proton loss rate in the CDF detector initially dropped from approximately 4 kHz to 2 kHz, and then required 2000 seconds to approach the original loss level again. Therefore, the diffusion rate was measured to be 0.01 Angstroms/turn. If a crystal replaced the collimator, this would be the average diffusion rate which would be observed at the face of the crystal.

C. Steel Collimator

Again applying an rms RF amplitude noise level of 500 V/turn, a steel horizontal collimator was place next to the beam. Since the edge of the bucket in the horizontal plane (the bucket half height times the horizontal dispersion) is 1 mm from the center of the beam, and the total bunch width at the crystal is 0.7 mm, a collimator would have to scrape away almost half of the beam intensity before it would become the dominant bunched beam aperture. But since the collimator is on the radial inside, it will eventually intercept all of the diffused beam particles. Even though the above noise level induces a loss rate 10 times that which is desired for crystal extraction, the maximum proton background rate measured in the CDF detector was 5 kHz. Depending on the value of luminosity, a background rate below 10 to 5 kHz is considered acceptable.

In addition to slowing down the extraction rate, it should be possible to employ other collimators as "shadows". These collimators are not primary apertures, but they intercept particles which have interacted with the primary aperture and have either large betatron or energy deviations.

D. Silicon Crystal Collimator

In order to assure that the measurements made with the steel collimator were meaningful for crystal extraction calculations, an unbent silicon crystal was installed in the Tevatron. Unfortunately, the crystal was installed on the radial outside of the accelerator, so that it cannot intercept DC beam. On the other hand, large betatron amplitude particles will strike the silicon crystal as their momentum error increases.

Under the same diffusion conditions as the previous section and using the silicon crystal as the primary aperture, it was

found that the CDF loss increased from approximately 2 kHz to 10-15 kHz. Again, remember that this diffusion rate is 10 time that desired for crystal extraction experiments.

At this point, a steel horizontal collimator at the A0 location was brought in as a shadow. The proton background rate in CDF decreased immediately to a value of approximately 5 kHz. Upon removal of the A0 collimator, the losses rose immediately to the 10-15 kHz level again.

IV. CONCLUSIONS

It has been shown in this paper that the diffusion and collimation required to simulate the effects of crystal extraction have little or no deleterious effects on a high energy physics collider experiment. Therefore, it should be possible to perform parasitic studies of crystal extraction during the next Tevatron collider run. In addition, major concerns regarding the compatibility of crystal extraction and collider physics have been answered.

At the accelerator physics level, it has been learned that the momentum spread is so large and the dispersion so small that a horizontal collimator cannot supersede the RF bucket separatrix as the dominant aperture in the Tevatron Collider. Therefore, in order to simulate the crystal extraction process to be employed in the SSC, it will be necessary in the Tevatron to either decrease the longitudinal emittance of the proton bunches or increase the local horizontal dispersion at the crystal. Both solutions are currently under study.

V. REFERENCES

1. G. Jackson, "Extraction from the Fermilab Tevatron using Channeling with a Bent Crystal", Proc. 1993 Part. Acc. Conf., Washington D.C. (1993).

Operational Experience with Third Harmonic RF Cavity for Improved Beam Acceleration Through Transition in the Fermilab Main Ring

C. M. Bhat, J. Dey, J. Griffin, I. Kourbanis, J. MacLachlan, M. Martens,
K. Meisner, K. Y. Ng, J. Shan and D. Wildman

Fermi National Accelerator Laboratory*
P.O. Box 500, Batavia, IL 60540

Abstract

An RF cavity operating at three times the frequency of the present Main Ring rf system at Fermilab has been installed to minimize the beam loss and longitudinal emittance (ϵ_l) growth related to the transition crossing. Tests have been carried out with beam intensities ranging from 3×10^9 to 2.3×10^{10} ppb and $\epsilon_l \simeq .07$ eVs . No beam loss conditions have been attained. Attempts have been made to reduce emittance growth after the transition.

I. An Overview of the Transition Crossing RF System at FNAL

One of the major problems encountered in many medium energy proton synchrotrons is the beam loss due to longitudinal emittance dilution during transition crossing. A number of remedies have been discussed by A.Sorenssen[1]. Very recently a focus-free transition crossing (FFTC) scheme has been proposed[2] as an alternative to the previously suggested methods. The basic principle of this scheme has been explained elsewhere[3]. Implementation of the FFTC requires addition of a second or third harmonic rf system (or combination of these) to the fundamental rf system. The feasibility and limitations of this technique in the Fermilab Main Ring (MR) has been examined using the computer program ESME[4].

The MR at FNAL did not have any specific scheme to reduce beam loss or emittance growth during transition crossing other than normal transition phase jump (NTPJ) scheme. In the NTPJ scheme one accelerates the beam up to the transition energy with a positive phase angle on rising side of rf wave. At the transition the phase is suddenly changed to the falling side of the rf wave form to maintain the rf focusing. Earlier studies made[5] with NTPJ scheme for initial ϵ_l in the range of .09 to .22 eVs showed that the beam loss at transition increases with initial beam intensity and initial ϵ_l. The emittance growth was about

---

*Operated by the Universities Research Association, under contracts with the U.S. Department of Energy

60% at higher intensities. Hence, the MR is one place to test the new scheme for transition crossing.

At Fermilab a third harmonic rf system was developed and installed in the MR during the June 1992 shut down period to test the FFTC scheme. We report our operational experience with this rf system and plans for improvements.

The implementation of the FFTC scheme in MR included development of a 1) 159 MHz rf cavity, 2) perpendicularly biased tuner, 3) power amplifier, (PA) and 4) low level rf system and necessary software programs. Ref. 6-9 explain the details of various hardware and software developments of the third harmonic rf system.

II. Measurements and Discussion

With the third harmonic rf cavity in the MR, measurements have been made with the beam to understand the beam dynamics for the FFTC scheme and compare with the NTPJ. Initial studies were done with a 4 s long MR ramp having a 1.0 s front porch at 8.9 GeV and a 0.5 s front porch at 40 GeV . The beam was aborted after about 2.1 s. The front porches were mainly to facilitate measurements of ϵ_l before and after the transition crossing. For later studies we switched to the regular pbar production ramp, 2.56s long with final energy 120 GeV . All the studies were carried out using a short batch of 13 bunches of protons. There were a number of parameters that needed to be optimized to get the best performance for FFTC scheme viz; the duration of the third harmonic rf, the initial and final rf phase angles, the ratio of 159 MHz to 53 MHz rf voltages, choice of rf curve to keep the growth of ϵ_l minimum, etc. The tests have been carried out for different initial ϵ_l and beam intensities.

Table I gives results of measurements for different intensities at low longitudinal emittances. The RF-curves I, II and III represent three different rf accelerating voltage curves. RF-curve I had bucket area S_A of 0.42 eVs at 8.9 GeV and increasing up to 1.7 eVs at 40 GeV in the acceleration cycle. This had a minimum $S_A = 0.25$ eVs at about 14.7 GeV . The RF-curve II had a an approximately

increasing S_A from 0.18 eVs to 1.0 eVs . The third one, RF-curve III had almost constant S_A of about .3 eVs .

Table I. Comparison of NTPJ and FFTC measurements.

I_{Beam} (ppb) and ϵ_{Init} (eVs)	Mode of Tran. Crossing	Beam Loss	$\%\epsilon_l$ Growth*
2.7x10⁹ .064(±7%) RF-curve I	NTPJ FFTC (sym.)	No loss no loss	67% 77%
2.3x10¹⁰ .08(±12%) RF-curve II	NTPJ FFTC (non-sym. 6.5ms)	5-6% No loss	132% 72%
1.93x10¹⁰ .085(±12%) RF-curve III	NTPJ FFTC (non-sym. 6.5ms)	No loss No loss	60% 40%

* Error on emittance growth measurement $\simeq$ 15% of the value.

To start with, the ratio of 159 MHz to 53 MHz rf voltage amplitudes was 0.129 and the FFTC time was selected in the range of 13 ms to 15 ms symmetric around the transition time in the MR. In this case, one expects to see a distinct bunch shearing in $(\Delta p, \Delta \phi)$-space during transition crossing with the third harmonic cavity on. This arises from the partial de-bunching and then re-bunching of the beam during the focus-free time. For similar operational conditions in the NTPJ scheme, bunches narrow in $\Delta \phi$ direction as the transition energy is approached and reach a minimum value at transition. $\Delta \phi$ grows slowly after the transition. The bunch length monitor and mountain range pictures taken during transition crossing for FFTC clearly showed bunch shearing. Fig 1a and 1b display a typical mountain range pictures for NTPJ and symmetric FFTC schemes respectively. However, the emittance growth observed was essentially the same for both cases as shown in first row of Table I.

Similar measurements done with higher beam intensities and low emittances showed a beam loss up to 6% and a larger emittance growth. In this case the space charge force and wall impedances play important role in beam

loss and emittance growth. For example the space charge forces counteract rf forces before the transition and help rf force after the transition. This causes the bunch to oscillate about the equilibrium bunch length resulting emittance growth as well as beam loss (when beam hits the momentum apperture of the accelerator). Hence in case of symmetric and long FFTC, the bunch matching after the transition becomes difficult. This can be encountered by keeping the third harmonic rf cavity on for a shorter time after the transition. To avoid the unnecessary additional de-bunching of the beam before the transition the third harmonic rf cavity on time was made shorter. This non-symmetric and shorter FFTC improved the performance of the beam during transition crossing. The total FFTC time was varied in the range of 6 ms to 10 ms. As shown in second row of Table I we find an FFTC time of 6.5 ms (with third harmonic rf cavity on at 4 ms before transition and off at 2.5 ms after the transition) gave no beam-loss and smaller emittance growth as compared with NTPJ. Considerable emittance growth after the transition for this case was perhaps due to very large bucket area offered by RF-curve II. An rf curve with parabolically increasing bucket area ($S_A = .35-.72$ eVs) gave no beam-loss for FFTC but about similar emittance growths.
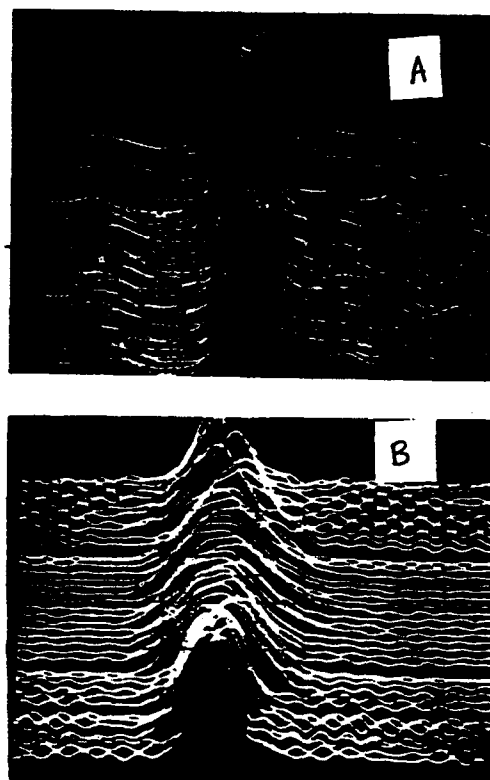
Fig. 1 Comparison of mountain range pictures for NTPJ(A) and FFTC(B) schemes. The third harmonic rf cavity was on for 13ms.

Studies in the MR showed that one of the causes for large beam emittance growth after the transition was the rf-bucket mis-match. For $(\epsilon_l)_{Init} \simeq 0.08$ eVs an rf curve with constant bucket area in the range of 0.35 eVs to 0.45 eVs (which has S_A about a factor of two smaller than previously used) gives a better bucket match. With this type of rf curve (RF-curve III in Table I) we found only about 40% emittance growth which is better than the NTPJ scheme.

III. SUMMARY AND FUTURE PLANS

A third harmonic rf system has been added to the fundamental 53 MHz rf system of the MR at Fermilab to reduce beam loss and emittance growth arising due to transition crossing. No beam-loss conditions have been reached. By properly selecting an rf accelerating voltage curve the emittance growth was reduced.

Detailed ESME simulations are being carried out for higher beam intensities in the MR. Preliminary results show that an rf waveform with a tilt obtained by increasing or decreasing the phase difference between the 53 MHz and 159 MHz rf can be used to ameliorate bunch shape distortion arising from space charge and image current forces. This would require only a small modification in our LLRF system.

REFERENCES

1. A. Sorenssen, Part. Accelerators, Vol. 6 (1975) 141.

2. J. Griffin, Fermilab internal note, TM-1734 (1991) and J. Griffin and C. M. Bhat, Fermilab internal note, MI-0062.

3. J.Griffin, " A new method for control of longitudinal emittance dilution during transition crossing in proton synchrotrons", this conference.

4. J.A. MacLachlan, "Particle tracking in E-ϕ space for synchrotron design and diagnosis", FERMILAB-Conf-92/333(Nov. 92).

5. I. Kourbanis et al, Fermilab internal note, TM-1696, page 141,

6. J.Dey et al, "High level RF system for transition crossing without RF focusing in the Main Ring at Fermilab", this conference.

7. C.M. Bhat, "Measurements of higher order mode in 3rd harmonic RF cavity at Fermilab", this conference.

8. B. Scala and K. Meisner, "Fermilab Main Ring low level RF system modifications for focus free transition beam tests", this conference.

9. M. Martens,"Controlling the third harmonic cavity during focus free transition crossing in the Fermilab Main Ring", this conference.

NEW METHOD FOR CONTROL OF LONGITUDINAL EMITTANCE DURING TRANSITION IN PROTON SYNCHROTRONS

James E. Griffin
Fermilab (ret.)
P.O. Box 261, Wayne, IL 60184

Abstract

A new method for controlling longitudinal emittance growth during transition crossing in proton or heavy ion synchrotrons is described. Longitudinal focusing forces are eliminated near transition through the use of rf harmonics. The rf system provides only the required accelerating voltage to each particle in each bunch during the non-adiabatic period near transition, hence momentum growth is minimized. Bunch length is maximized just at transition, minimizing space charge forces and associated instabilities.

I. INTRODUCTION

A bit of history. All synchrotrons operate on a principle of phase stability [1,2] whereby ensembles (bunches) of particles with momenta slightly removed from a 'synchronous' momentum receive, on average, the same acceleration by engaging in small oscillations about the 'synchronous' phase on an rf accelerating voltage wave. Deviations in the orbit lengths of off-momentum particles can be related to a synchronous orbit length C_o by

$$\frac{\Delta C}{C_o} = \alpha_o \left(\frac{\delta p}{p_o}\right) + \alpha_1 \left(\frac{\Delta p}{p_o}\right)^2 + \cdots. \quad (1)$$

Similarly, with the advent of the strong focusing lattice [3,4], to first order in α The deviation in rotation period of off momentum particles has been expressed

$$\frac{\Delta T}{T} = \left(\alpha_o - \frac{1}{\gamma^2}\right)\frac{\Delta P}{P_o}$$
$$= \left(\frac{1}{\gamma_t^2} - \frac{1}{\gamma^2}\right)\frac{\Delta p}{p_o} = \eta \frac{\Delta p}{p_o}. \quad (2)$$

γ is the particle total energy divided by its rest energy, E/E_o. The 'momentum compaction factor' α has been related to an 'energy' γ_t; $\alpha = \gamma_t^2$, and a 'momentum slip factor' η has been defined in terms of γ and γ_t.

The average accelerating voltage per turn for a synchronous particle with fixed orbit length is,

$$V_{acc} = eV\sin(\phi_s) = \frac{C}{c}\frac{d(pc)}{dt} = \beta^2 E_o T_o \dot{\gamma}. \quad (3)$$

ϕ_s is the phase angle at which synchronous particles cross the rf accelerating gap(s). An off-momentum particle, arriving at the rf accelerating gap(s) at some angle ϕ will see accelerating voltage $V\sin(\phi)$.

These considerations lead to derivation of a harmonic oscillator equation for small amplitude motion of non-synchronous particles. The period of oscillation, expressed in terms of the rotation period of a synchronous particle, is;

$$T_\phi = T_o \left[\frac{2\pi E_o \gamma}{eVh\eta}\right]^{1/2}. \quad (4)$$

h is the harmonic number of the rf, i.e. $F_{rf} = h F_o$. In order for the phase oscillations to average effectively the energy delivered to all off-momentum particles the period of oscillation must be short with respect to the time over which the synchronous energy changes appreciably. Indeed the phase oscillation equation was derived under the assumption that the parameters V, γ, and η remained sufficiently constant during a phase oscillation so that the change in frequencu during one period is a small fraction of the frequency. This is the condition of 'adiabaticity'.

The very small values of α available in a strong focusing lattice reduce drastically the amplitude of radial motion caused by the momentum deviations inherent in synchrotron phase oscillations. The same small value introduces the possibility that η may pass through zero at some point within the momentum range of the accelerator. If this happens the period of phase oscillation appears to become infinite and the condition of adiabaticity is clearly lost. Stable phase oscillations can be established for either sign of η by changing the sign of $\cos(\phi_s)$, (i.e. by changing the operating point from ϕ_s to $\pi-\phi_s$, giving the same accelerating voltage). But the period of interest is the period when adiabaticity cannot exist, i.e. the 'transition' period.

Courant and Snyder pointed out in an early description of the Alternating Gradient (strong focusing) synchrotron that the condition of non-adiabaticy exists when

$$\frac{|\gamma - \gamma_t|}{\gamma_t} < \left[\frac{\gamma_t(eV\sin(\phi_s))^2}{4\pi h E_o eV|\cos(\phi_s)|}\right]^{1/3}. \quad (5)$$

It is useful to express $\gamma(t)$ near transition in terms of time measured from the time at which synchronous particles pass through transition, (assuming that γ is increasing linearly),

$$\gamma(t) = \gamma_t + \dot{\gamma} t. \quad (6)$$

By combining eqns. 3, 5, and 6, an expression for the 'non-adiabatic time period' around transition becomes,

$$T_{m} = \pm T_{o}\left[\frac{\gamma_{t}^{4}\beta^{4}F_{o}E_{o}}{4\pi h\dot{\gamma}eV|\cos(\phi_{s})|}\right]^{1/3} . \quad (7)$$

The non-adiabatic time is affected by the synchronous phase angle which exists just prior to transition. While the accelerating voltage is set by the requirements in eq. 4, ϕ_s is determined by the requirement that adequate bucket area to contain the beam longitudinal emittance be maintained [5].

Adiabaticity exists at times removed from transition by $\pm T_m$. But transition is a local effect, usually occurring at different times for different increments of momenta within the distribution. In the moving reference frame describing the particle phase space distribution γ_t moves from higher to lower momentum, i.e. higher momentum particles pass through transition before lower momentum particles. In order to ensure adiabaticity for all particles within a distribution it is necessary to determine the period required for the entire ensemble to cross transition. This 'non-linear' time has been shown to be [12,13],

$$T_{nl} = \frac{\gamma_{t}(\beta^{2}+\alpha_{1}/\alpha_{2}+1/2)}{\dot{\gamma}} . \quad (8)$$

II. TRANSITION PROBLEMS

Problems associated with transition crossing have been extensively discussed in tha literature [6-12]. In many cases it was assumed that the rf voltage would remain constant with fixed ϕ_s until 'transition' at which time the phase would be jumped to $\pi - \phi_s$ and possibly the voltage changed to account for a change in sign of the effective space charge force. Dynamic analyses for this situation indicate that the bunch momentum spread becomes very large while the phase extent of the bunch becomes minimum at transition. During this period the space charge forces within the bunch have been calculated to be sufficient to cause a shift in betatron tune, "Umstätter effect", with possible transverse emittance dilution.

In other cases the rf voltage is allowed to fall toward the minimum required for acceleration while the phase angle moves smoothly through $\pi/2$ toward a new value between $\pi/2$ and π. This has been termed "duck under"[14].

In all cases problems associated with transition can be traced to the fact that for very small values of η there is very little dispersion in the rotation periods regardless of momentum. Particles arriving at the accelerating gap at phases other than the synchronous phase receive either too much or too little acceleration for long periods of time because they are essentially 'frozen' in time. This causes long tail of particles in the distribution which cannot be matched to the accelerating bucket above transition. The result is loss of some particles followed by frequently observed quadrupole oscillation of the remainder of mismatched particles, or 'tumbling', which results in substantial longitudinal dilution.

III. PROPOSED SOLUTION

Many solutions to the problems described here have been proposed. Lattices can be designed with imaginary or infinite γ_t [15], or quadrupoles can be pulsed near transition to force a quick transition (so called γ_t-jump). Although convincing computations have been done, the first alternative needs an existence proof. The second alternative has the possibility for introducing transverse dilution if chromaticity discontinuities are introduced by the jump.

We propose here a solution involving only the rf accelerating system. It is proposed to remove, to the extent possible, all longitudinal focusing during the transition period by moving the phase of the rf wave to near $\pi/2$ and adding of a second or third harmonic component to the rf wave such that the voltage is constant over a substantial phase range around the (approximate) centroid of the charge distribution. In this way, with proper adjustment of the rf amplitude, all particles can receive the necessary accelerating voltage while moving only slightly in phase. a precedent for this exists in isochronous cyclotrons, which operate essentially at transition throughout their accelerating cycle [16,17]. By the addition of 27.5% second harmonic at the proper phase the rf amplitude can be held constant to $\pm 0.25\%$ over a phase range of ± 35 degrees.

Fig. 1 is a graphical picture of what can be expected of this procedure. Part (a) shows the outline of a charge distribution matched to an accelerating bucket prior to the start of the non-adiabatic period. γ_t is represented by a cross-hatched region above the bucket. In part (b) γ_t has moved to the synchronous energy. Particles above the synchronous energy moved initially to earlier time but reversed direction as γ_t moved downward through them. At this time all particles are moving toward later time, the particles with positive energy being above transition, particles with negative energy being below. In part (c) transition has moved below the entire distribution. The harmonic voltage is removed and the distribution can be matched to an accelerating bucket above transition. This procedure is described in detail in [13].

Extensive computer simulations of this procedure, including the effects of space charge forces and ring impedance have been completed [18,19].

At the present time a third harmonic rf system has been installed in the Fermilab Main Ring and beam studies are in process. The apparently simple scheme is difficult to implement because of the necessity for compensation for beam loading of the harmonic cavity and problems associated with verification of correct phases and amplitudes of the combined rf systems. Efforts to resolve these difficulties are reported in [20,21].

(a)

(b)

(c)
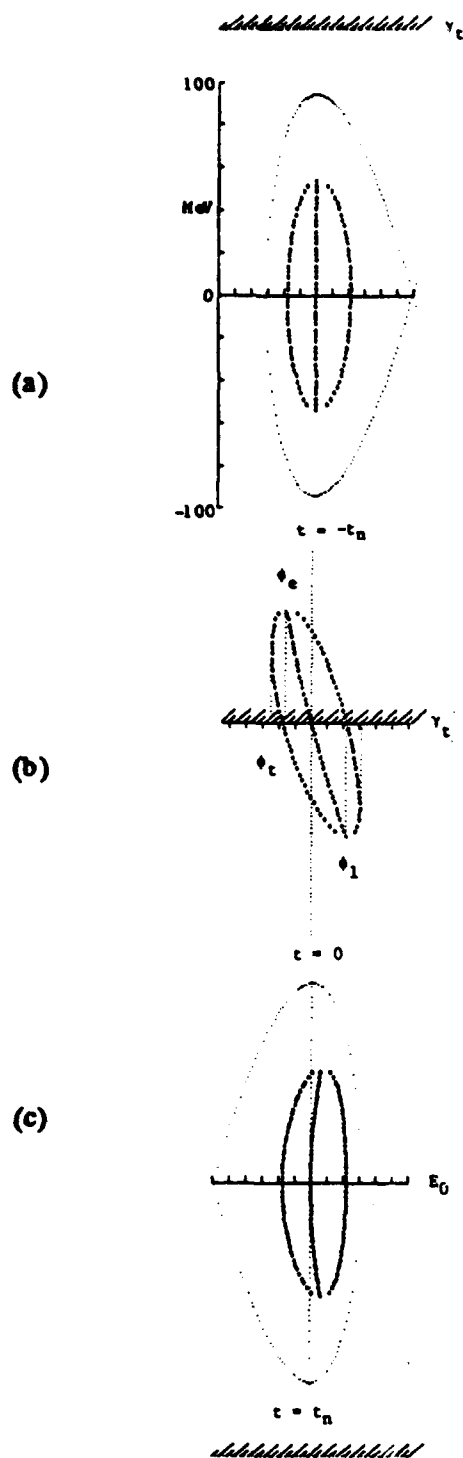
Figure 1. Schematic Representation of Non-Focusing Transition Crossing

IV. REFERENCES

[1] V.Veksler, A New Method of Acceleration of Relativistic Particles, Jour. Phys. U.S.S.R. 9, 153 (1945)

[2] E. M. McMillan, The Synchrotron- A Proposed High Energy Accelerator, The Physical Review, 68: 143-144 (1945)

[3] Nicholas Christofilos, Focussing System for Ions and Electrons, U.S. Patent 2,736,799, [filed March 10, 1950, issued Feb 28, 1956]

[4] E.D. Courant and H.S. Snyder, Theory of the Alternate Gradient Synchrotron, Annals of Physics: 3, 1-48 (1958)

[5] K.R. Symon and A.M. Sessler, Methods of Radio Frequency Acceleration in Fixed Accelerators Proc. of the CERN Symposium on High Energy Accelerators and Pion Physics,1, 46, (1956)

[6] A.A. Kolomenski and A.N. Lebedev, Theory of Cyclic Accelerators, North Holland, Amsterdam, pp190ff

[7] A. Sørenssen, The Effect of Strong Longitudinal Space-Charge Forces at Transition Energy, Proc. 6th Internatl. Conf. on High Energy Accelerators, Cambridge (USA),474, (1957)

[8] L.L. Goldin and D.G. Koshkarev, Nuovo Cimento 2, 1251 (1955)

[9] A. Sørenssen, Crossing the Phase Transition in Strong Focusing Proton Synchrotrons, Particle Accelerators, 6, 141-165,(1975)

[10] J. Wei, Longitudinal Dynamics of the Non-Adiabatic Regime on Alternate Gradient Synchrotrons, PhD Dissertation, State Univ. N.Y. Stony Brook, (1989)

[11] J. Wei and S.Y. Lee, Microwave Instability Near Transition Energy, Workshop on RHIC Performance, BNL-41604,335,(1988)

[12] K. Johnsen, Effects of Non-linearities on the Phase Transition, Proc. of the CERN Symposium on High Energy Accelerators and Pions,1, 106,(1956)

[13] J.E. Griffin, Synchrotron Phase Transition Crossing Using an Rf Harmonic, Fermilab TM-1734 (1991)

[14] N.C. Christofilos, First proposed 'Duck Under' transition crossing. Private Comm. E.D. Courant

[15] D. Möhl, Compensation of Space Charge Effects at Transition by an Asymmetric Q Jump, CERN-ISR/300/GS/69-62

[16] M.K. Craddock, IEEE Trans. Nucl. Sci. NS-24, No.3, 1615 (June,1977)

[17] S   ...m et al, First Operation of a Flattop   ...elerating System in an Isochronous Cyclotron, IE.. Trans. Nucl Sci. NS-28, 2721, (1981)

[18] J.A. MacLachlan and J.E. Griffin, Application of a New Scheme for Passing Through Transition Energy to the Fermilab Main Ring and Main Injector, IEEE Part. Accel. Conf. San Francisco, 2826, (1991)

[19] J. MacLachlan et al,Reducing Bunch Disruption in Transition Crossing by Modification of the RF Waveform, Proc. XVth Internat. Conf. on High Energy Accelerators, 1040,(1992)

[20] J. Dey et al, High Level RF System for Transition Crossing Without RF Focusing in the Main Ring at Fermilab, Sb42, This Conf.

[21] C.M. Bhat et al, Operational Experience with Third Harmonic RF for Improved Beam Acceleration Through Transition in the Fermilab Main Ring.

Remarks on the differential Luminosity in the weak disruption and the transition region

Huschang Heydari

Technische Universität Berlin, EN-2, Einsteinufer 17, D-1000 Berlin 10, Germany

Abstract

The time dependence of the different enhancement factors of the luminosity, in the region of weak disruption, has been discussed here, for the first time, and the corresponding time integral has been explicitly discussed upon. For the case of stronger disruption (transition region), the existing numerical results from various research works, has been checked analytically with the help of a square distribution.

1 Introduction

In order to estimate the parameters [1]..[7] of the future accelerators, especially the e^+/e^- linear colliders accelerator [8]..[11], the increment of luminosity, which results due to disruption, has to be given more consideration. In this paper, the time dependence of the differential enhancement factor (d.e.f.) of a weak disruption D, as well as that of a transition region, is discussed. For the weak disruption region the d.e.f. is expessed in terms of the Gauss' error function. For the transition region, the numerous results available [2] are been checked analytically with the help of a square distribution. The numerical results [2, 9, 11] and our analytical solution are in very good agreement.

2 Differential enhancement factor in the case of weak disruption

As a result of the penetration of the electron in the positron bunch, the respective charged particles do not move along straight but on curved paths. As it is known, this causes the pinch-effect, which then results into the increment of the luminosity. Thus the behaviour of the d.e.f.

$$\frac{dH_D}{dt} = \frac{1}{\mathcal{L}_0}\frac{d\mathcal{L}}{dt} \qquad (1)$$

can be defined with the aid of

$$\mathcal{L} = f \int \frac{dN_1 dN_2}{dA_\perp}$$

$$= f N^2 \int n_1(x,y,z_1,t) n_2(x,y,z_2,t)\, dx\,dy\,dz_1\,dz_2 \qquad (2)$$

where the relationship between z_1, z_2 is $2ct = -z_1 - z_2$ [2]. The d.e.f. can be obtained from equation (2) in terms of cylindrical coordinates for (D = 0)(subscript 0) with the Gauss' radial symmetrical bunchgeometry of the d.e.f.

$$\frac{dH_{D0}}{dt} = \frac{1}{\mathcal{L}_0}\frac{df_0}{dt} = \frac{c}{\sqrt{\pi}\sigma_z}\exp\left\{-\frac{c^2 t^2}{\sigma^2}\right\} \qquad (3)$$

For different logitudinal and radial bunch distribution, The enhancement factor for weak disruption (D≥0) is given by:

$$H_D = 1 + \frac{1}{2}D \cdot \left\{ \begin{array}{l} \frac{1}{2}rad.hom \\ \frac{2}{3}rad.gauss \end{array} \right\} \left\{ \begin{array}{l} \frac{1}{\sqrt{3}}long.hom \\ \frac{1}{\sqrt{\pi}}long.gauss \end{array} \right\} \qquad (4)$$

and the disruption parameter is

$$D = \frac{r_e \sigma_z N}{\gamma \sigma_0}; \quad r_e = \frac{\hbar c \alpha_s}{m_0 c^2} \qquad (5)$$

In addition to the above known results, a new d.e.f. is being introduced.

$$\frac{dH_D}{dt} = \frac{1}{\mathcal{L}_0}\frac{d\mathcal{L}_0}{dt} + \frac{2c^2(2\pi)^3 r_e N}{\gamma} V \tilde{U}(t) \qquad (6)$$

where

$$V = \frac{\int_0^{+\infty} dr\, n_r^3(r)}{\int_0^{+\infty} dr\, n_r^2(r)} = \left\{ \begin{array}{ll} \frac{1}{2}\frac{1}{\sigma_0^2} & hom. \\ \frac{2}{3}\frac{1}{\sigma_r^2} & gauss. \end{array} \right\} \qquad (7)$$

is the radial bunchgeometry and

$$\tilde{U} = \qquad (8)$$

$$\int_0^{+\infty} dz_1\, n_z(z_1) n_z(-z - 2ct)\left[g(t,z_1) + g(t, -2ct - z_1)\right]$$

the longitudinal bunch geometry with respect to dH_0/dt. The functions g in (8) are defined as

$$g(t, z_j) = \frac{1}{4c^2}\int_0^\infty d\tau\, \tau n_z(\tau + z_k) \qquad \begin{array}{l} j = 1 \Rightarrow k = 2 \\ j = 2 \Rightarrow k = 1 \end{array} \qquad (9)$$

The equation (6) can be further formulated for the longitudinal Gauss' distribution:

$$n_z(z) = \frac{1}{(2\pi)^{\frac{1}{2}}\sigma_z}\exp\left\{-\frac{z^2}{2\sigma_z^2}\right\} \qquad (10)$$

as follows

$$\check{U}(t) =$$

$$= \int_{-\infty}^{+\infty} dz_1 n_z(z_1) n_z(z_2) \frac{1}{4c^2} \times$$

$$\times \left[\int_0^{+\infty} d\tau \, \tau \{ n_z(\tau + z_2) + n_z(\tau + z_1) \} \right]$$

$$= \frac{1}{4c^2} \int_{-\infty}^{+\infty} dz_1 n_z(z_1) n_z(-2ct - z_1) \times$$

$$\times \left[\int_0^{+\infty} d\tau \, \tau \{ n_z(\tau + (-2ct) - z_1) + n_z(\tau + z_1) \} \right]$$

$$= \frac{1}{4c^2} \frac{1}{[2\pi\sqrt{2\pi}\sigma_z]} \int_{-\infty}^{+\infty} dz_1 e^{-\frac{z_1^2}{2\sigma_z^2}} e^{-\frac{(2ct + z_1)^2}{2\sigma_z^2}} \times$$

$$\times \int_0^{+\infty} d\tau \, \tau \left\{ e^{-\frac{(r - 2ct - z_1)^2}{2\sigma_z^2}} + e^{+\frac{(r + z_1)^2}{2\sigma_z^2}} \right\} \quad (11)$$

After various substitutions and numerous mathematical steps (not discussed here) the following equation results

$$\check{U}(t) = 2 \sqrt{\frac{2\pi\sigma_z^2}{3}} \frac{1}{4c^2} \frac{1}{(2\pi\sqrt{2\pi}\sigma_z)^3} e^{-\frac{c^2 t^2}{\sigma_z^2}} \times \quad (12)$$

$$\times \left\{ \frac{3\sigma_z^2}{2} e^{-\frac{c^2 t^2}{\sigma_z^2}} + ct\sigma_z \sqrt{3} \frac{\sqrt{\pi}}{2} \left[1 - erf \left\{ \frac{ct}{\sqrt{3}\sigma_z} \right\} \right] \right\}$$

From this equation a new expression for dH_0/dt can be dreived:

$$\frac{dH_D}{dt} = \quad (13)$$

$$= \frac{c}{\sqrt{\pi}\sigma_z} e^{-\frac{c^2 t^2}{\sigma_z^2}} + \frac{c r_e N \left[\frac{1}{2} \int_0^\infty s dr n_r^3(r) \right]}{\gamma \left[\int_0^\infty s dr n_r^2(r) \right]} \frac{\sqrt{3}}{2\pi} \times$$

$$\times e^{-\frac{c^2 t^2}{\sigma_z^2}} \left[e^{-\frac{c^2 t^2}{3\sigma_z^2}} + \frac{ct\sqrt{\pi}}{\sqrt{3}\sigma_z} \left\{ 1 - erf \left(\frac{ct}{\sqrt{3}\sigma_z} \right) \right\} \right]$$

$$= \frac{c}{\sqrt{\pi}\sigma_z} e^{-\frac{c^2 t^2}{\sigma_z^2}} + \frac{\sqrt{3}}{2\pi} \frac{c r_e N}{\gamma} V \frac{1}{2} \times$$

$$\times e^{-\frac{c^2 t^2}{\sigma_z^2}} \left[e^{-\frac{c^2 t^2}{3\sigma_z^2}} + \frac{ct\sqrt{\pi}}{\sqrt{3}\sigma_z} \left\{ 1 - erf \left(\frac{ct}{\sqrt{3}\sigma_z} \right) \right\} \right]$$

3 Analytical results for the transition region

The characteristics of trajectories and those of the density distribution (under the aspect of longitudinal Gauss' distribution), in case of larger disruption parameter

$(1 \le D \le 10)$ can be obtained only numerically. The numerical results mentioned above shall now be proven with the aid of equivalent longitudinal square distribution. The general differential equation [9, 11, 12] for a radial motion is

$$\ddot{r}(t) = \frac{c^2}{c^2 m_0 \gamma} (-4\pi\hbar c\alpha_s N) \frac{1}{r(t)} \int_0^{r(t)} dr^* \, r^* n(t, r^*, z) \quad (14)$$

Considering only the paraxial beams, the Taylor's series can be written as:

$$\ddot{r}(t) = -\frac{4\pi c^2 N r_e}{\gamma} \frac{1}{2} n(t, 0, z) r(t) \quad (15)$$

for which the information regarding the density distribution along the beam axis $(r = 0)$ [2, 9, 11, 12] is necessary. This can be expressed as

$$n(t, 0, z) = \quad (16)$$

$$\frac{1}{(2\pi)^{3/2}\sigma_z} \frac{e^{-\frac{(2ct + z_1)^2}{2\sigma_z^2}}}{\sigma_z^2} \left[1 + \frac{4\pi c^2 N r_e^2}{\gamma\sigma_r^2} g(t, z_1) \right]$$

(15) and (16) lead to the numerical and analytical solutions mentioned in the references [2].

(i) The slope on the focal point (in equation (16) in a first approxiation only the first term "1" is considered):

$$\dot{r}(\tilde{t}_0) = -\frac{3}{4} \frac{c}{\sigma_z} \sqrt{\frac{D}{2}} \quad (17)$$

(ii) The focal point t0 within the limits $D \in [1, 10]$ is

$$\tilde{t}_0 \approx 2 \frac{\sigma_z}{cD} \quad (18)$$

In the differential equation (15) the longitudinal Gauss' distribution

$$n_z(z) = \frac{1}{2\pi} \frac{1}{\sqrt{2\pi}} \frac{1}{\sigma_z} \exp\left(-\frac{z^2}{2\sigma_z^2}\right) \quad (19)$$

is substituted by the areal equivalent quadratic distribution

$$n_z(z) = \begin{cases} \frac{1}{2\pi l} & ; |z_z| \le \frac{l}{2} \\ 0 & ; |z_z| > \frac{l}{2} \end{cases} \quad (20)$$

Neglecting the second term in (16) the differential equation (15)

$$\frac{d^2 r(\tilde{t})}{d\tilde{t}} = -\frac{2\pi}{2\pi} \frac{c^2}{\sqrt{2\pi}} \frac{D}{\sigma_z^2} e^{-\frac{2c^2 t^2}{\sigma_z^2}} \cdot r(\tilde{t}) \quad (21)$$

turns into $\quad \Downarrow$

$$\frac{d^2 r(\tilde{t})}{d\tilde{t}} = -\frac{2\pi}{2\pi} \frac{c^2}{\sqrt{2\pi}} \frac{D}{\sigma_z^2} e^{-\frac{2c^2 t^2}{\sigma_z^2}} \cdot r(\tilde{t}) \quad (22)$$

412

where $z_2 = -2ct - z_1 = 2c\tilde{t}$. From equation (22) we obtain for $|\tilde{t}| \leq L/4c$ a simple differential equation with harmonic solutions

$$r(\tilde{t}) = A_m \sin(W\tilde{t}) + B_m \cos(W\tilde{t})$$
$$\dot{r}(\tilde{t}) = A_m W \cos(W\tilde{t}) - B_m W \sin(W\tilde{t}) \qquad (23)$$
$$W^2 := -2\pi c^2 \frac{D}{\sigma_z} \cdot \begin{cases} \frac{1}{2\pi l} & ; |\tilde{t}| \leq \frac{l}{4c} \\ 0 & ; else \end{cases}$$

The solutions have to be differentiable and must be matched to the the general solution for $|\tilde{t}| \geq L/4c$

$$r(\tilde{t}) = A_l + B_l \cdot \tilde{t} = 1 + 0 \cdot \tilde{t} \quad , \dot{r}(\tilde{t}) = 0$$
$$r(\tilde{t}) = A_R + B_R \cdot \tilde{t} \qquad\qquad , \dot{r}(\tilde{t}) = B_R \qquad (24)$$

Due to the above condition, and $r(t_0) = 0$ the focal point can be written as

$$\tan(W\tilde{t}_0) = \frac{1}{\tan\left(W\frac{l}{4c}\right)} \qquad (25)$$

and the slope $r(\tilde{t}_0)$ as

$$\dot{r}(\tilde{t}_0) = -W \left[\sin\left(W\frac{l}{4c}\right) \frac{\tan\left(W\frac{l}{4c}\right)}{\sqrt{\tan^2\left(W\frac{l}{4c}\right)+1}} + \right.$$
$$\left. + \cos\left(W\frac{l}{4c}\right) \frac{1}{\tan^2\left(W\frac{l}{4c}\right)+1} \right] \qquad (26)$$

Hence the final relation can be given as:

$$\dot{r}(\tilde{t}) = -W = -\frac{c}{\sqrt{2\sqrt{3}}} \frac{\sqrt{D}}{\sigma_z} \qquad (27)$$

This matches amazingly with the numerical results already mentioned above.

$$\frac{1}{\sqrt{\sqrt{3}}} = \frac{1}{\sqrt[4]{3}} = 0,75983 \approx \frac{3}{4} \qquad (28)$$

The equation (26) can lead to a corresponding result for the region $\{3; 6,6\}$, after various series expansions as

$$\tilde{t}_0 \approx 2,4 \frac{\sigma_z}{CD} \qquad (29)$$

4 Conclusion

For the different bunch geometries of the d.e.f in the weak focussing region a time dependency has been established and relation has been derived. Besides, the various results from different references have been evaluated. For the transition region an extremely good match has been obtained between the numerical methods achieved from a series complex mathematical operations and the results quoted. This was possible due to the substitution of longitudinal Gauss' distribution through an equivalent square distribution. This simplified the differential equation upon which the analytical methods could be easily applied.

References

[1] Kauru Yokoya, KEK-Report 85-9, October 1989

[2] Pisin Chen, Kooru Yokoya, SLAC-Pub 439, August 1988

[3] Kauru Yokoya, KEK-Report 85-53, October 1985

[4] Karl Berkelmann, CLIC-Note 154, February 1992

[5] A. Hofmann, CERN LEP-Dt/89-55, April 1989

[6] O. Napoly, P. Sievers, T. Taylor, B. Zotter, CERN Saclay

[7] O. Napoly, B. Zotter, CLIC Note 129, October 1990

[8] W. Schnell, CLIC Note 151 December 1991

[9] Pisin Chen, SLAC Pub., 4823, August 1987

[10] T. Berklow, P. Chen, W. Kozonecki, SLAC Pub. 5718, September

[11] P. Chen, SLAC Pub. 5615, July 1989

[12] H. Heydari, unpublished Habilitation, TU-Berlin

Flat Beam Studies in the SLC Linac*

C. Adolphsen, F.-J. Decker, J. T. Seeman
Stanford Linear Accelerator Center
Stanford University, Stanford, California 94309 USA

Abstract

The Stanford Linear Collider (SLC) was recently converted to flat beam operation ($\gamma\epsilon_x = 10\ \gamma\epsilon_y$), producing a factor of two increase in luminosity[1]. In this paper we review the results of flat beam studies in the SLC Linac. In summary, the injected beams from the damping rings had invariant horizontal emittances as low as 30 mm-mrad and invariant vertical emittances as low as 2 mm-mrad. The emittances measured at the end of the linac after tuning for 3×10^{10} particles are about 5 to 8 mm-mrad vertically and 40 to 50 mm-mrad horizontally. Flat beam operation began 3/17/93.

Introduction

Two bunches (e^- and e^+) are accelerated in the linac from 1.19 to 47 GeV in 3 km of S-band RF structure. Special measurements, component tolerances, and controls are needed to maintain the initial 10 to 1 emittance ratios. Transverse wakefield damping (BNS) is used in the first two-thirds of the linac to control wakefield growth from beam injection jitter[2]. A small energy spread (0.26 %) at 47 GeV is made by careful overall klystron phasing (+/- 0.5 degrees). Along the linac, eight feedback loops (x,x',y,y' for two beams) updating at 30 Hz maintain the trajectory to about 25 μm. Emittance measurements are made at three locations along the linac (at 1.2, 15, and 47 GeV) using three sets of four wires scanners, each with an emittance resolution of 0.5-0.75 mm-mrad. Typical vertical beam sizes (σ_y) at 47 GeV are 35 to 60 μm. The emittance and TWISS parameters are measured automatically by the control computer in all parts of the SLC about every 30 minutes and recorded in long term history buffers for analysis. The linac emittance histories showing the start of flat beam running on 3/17/93 can be seen in Figure 1.

Emittance Optimization

The study of flat and round beam cases allows the comparison of various types of linac emittance enlargements. Betatron mismatches with filamentation cause multiplicative enlargements: $B_{mag}=\epsilon/\epsilon_0$. Dispersion, wakefields, and coupling, followed by filamentation, generates additive growth: $\epsilon=\epsilon_0+f/2$. Sqrt(f) is the normalized 'kick' amplitude.

Prior to the conversion to flat beams, the emittance enlargement effects along the linac were feared to be mostly additive. Thus, changing to flat emittances would lead to minimal overall luminosity gain. However, as it turned out, the multiplicative effects dominated the residual emittance increases with round beams and significant emittance reductions were made with the new smaller initial emittances.

The dispersion and beta-functions are carefully tuned in the ring-to-linac transport line to provide the best injected beam emittances[3]. The linac klystron phases and accelerating gradient must be accurately maintained (a few degrees and 5%, respectively) in the first few hundred meters to avoid chromatic emittance enlargement. Furthermore, the strengths of three quadrupoles in the early linac were empirically adjusted by up to 10% to minimize the emittances at the 15 GeV location. The linac support girders were mechanically clamped to reduce component vibration[4] below 100 nm. These clamps were set at full tunnel temperature to avoid systematic transverse component offsets leading to dispersion and wakefield errors.

The emittance growth from residual dispersion and wakefield effects is reduced by cancellation using "trajectory bumps" located along the linac[5]. In the tuning process, the SLC operators try to minimize the beam emittance at two downstream wire scanner locations (15 GeV and 47 GeV). The setpoints of the linac feedback loops are adjusted for this purpose. For each loop, there is a position and angle setpoint, which when varied, generates a betatron oscillation that extends downstream until the next feedback loop removes it. First, the setpoints of the loop at 8 GeV are tuned looking at emittance and beam tail changes at the 15 GeV point. Second, the setpoints at 16 GeV are used to reduce the emittance at 47 GeV. Occasionally, other loops are tried. Typically, 8 to 12 distinct "trajectory bumps" are in use at any given time with amplitudes of order 100-200 μm with lengths of 200 to 800 m. Most of these bumps are stable to 90% in amplitude over several weeks; however, fine tuning (10%) is often done to track hour-by-hour and diurnal changes. For vertical emittances of order 6 mm-mrad, bump control at the 25 μm level is needed. The tuning procedure typically requires 15-30 minutes per beam. Measured data from tuning two representative feedback setpoints at the 16 GeV location to reduce γε at 47 GeV are shown in Figure 2. Note that the increase in the vertical emittance with bump amplitude is about the same as that of the horizontal because the wakefield and dispersion induced growth is nearly additive for small induced errors.

Emittance versus Beam Charge

In the fall of 1992 the SLC was operated at 10 Hz to study the emittance increase along the linac versus beam charge. At 10 Hz a ring store time longer than the nominal (1/120 sec) is possible, decoupling the exit emittances from the entrance emittances, so smaller values are achieved. The electron results with a mixture of short and long store data are shown in Figure 3. (Positron data is similar.) The increase in the emittances at the entrance to the linac with current is due to bunch lengthening in the damping ring (which doubles σ_z and makes σ_E/E 50% higher) and chromatic effects in the bunch compressors. An increase in emittance along the linac was observed, although there was not sufficient beam time to perform all the tuning techniques described above. Thus, these curves may over estimate the possible emittances. One example is from Figure 1 where an incoming vertical invariant emittance of order 3.5 mm-mrad can be maintained over long
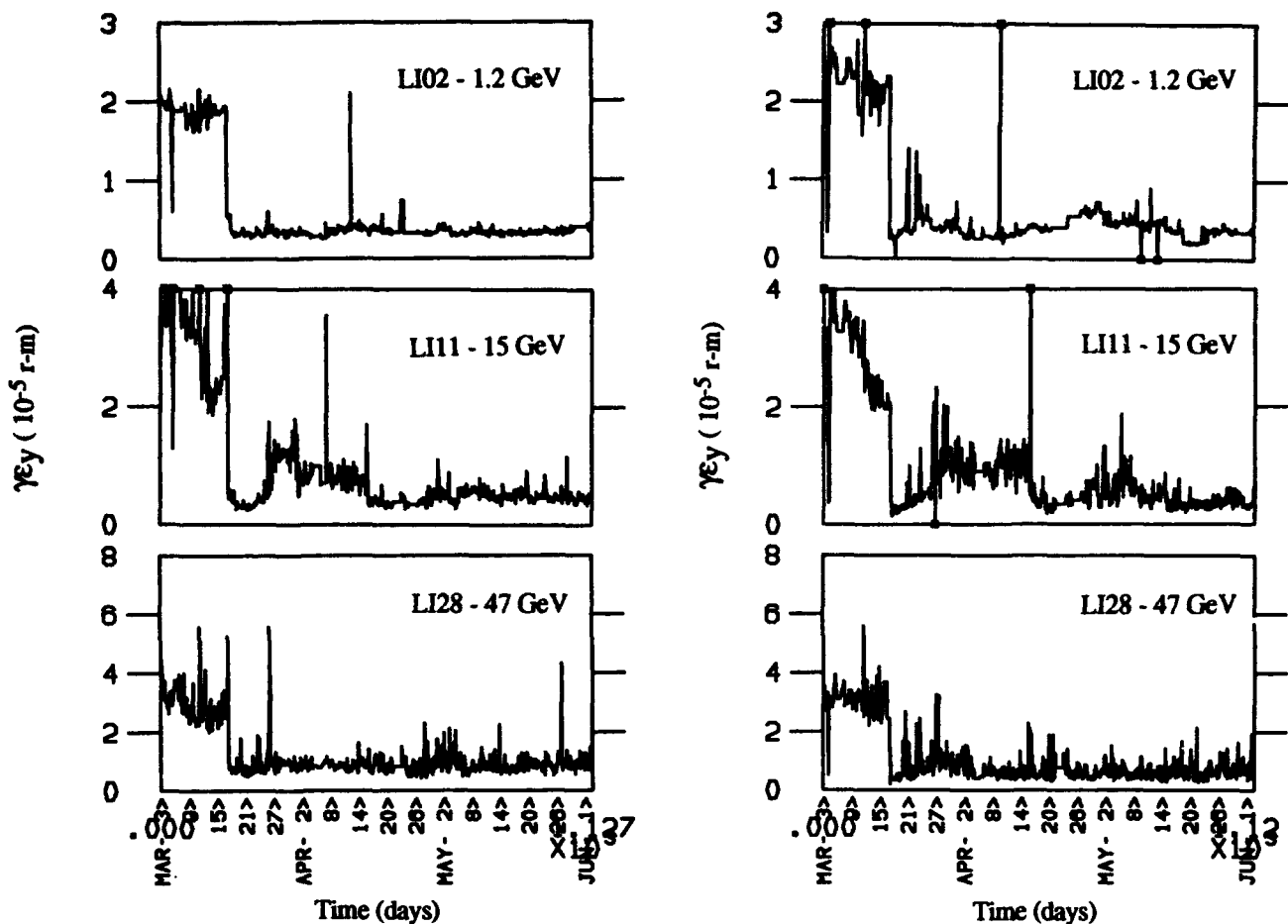
Figure 1   Histories of SLC invariant vertical emittances for e⁻ (left) and e⁺ (right) at 3 x 10¹⁰ at linac locations: entrance
(1.2 GeV, top), 1 km (15 GeV, center), and exit at 3 km (47 GeV, bottom). The period is March 3 - June 2, 1993.
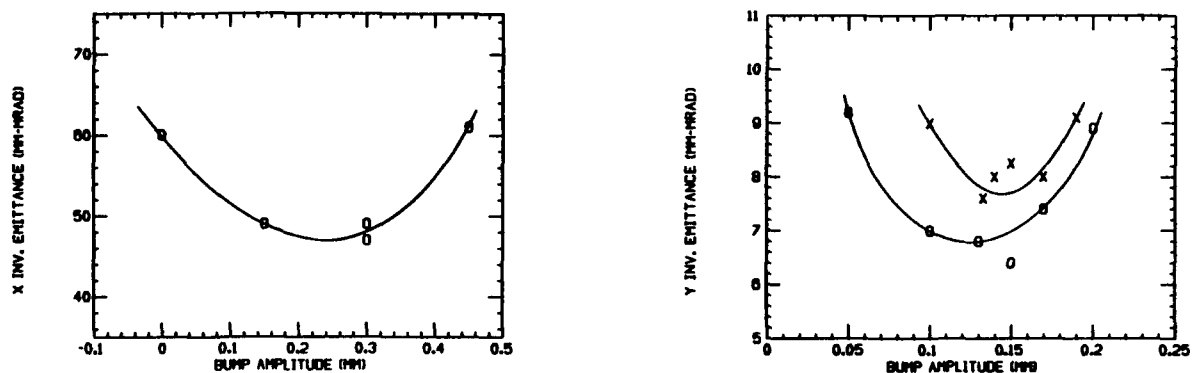
Figure 2   Measured horizontal and vertical emittances for electrons at 47 GeV as a function of amplitude of respective
oscillations induced from 1000 m to 1800 m. Two independent vertical data sets are shown.

times during collisions at 3×10^{10} particles per bunch with
only 50 to 100% enlargement along the linac. The incoming
horizontal emittance can be maintained at about 35. mm-mrad
with just 5-15 mm-mrad increase along the linac. Finally it
should be noted that vertical emittances of about 2.0 mm-mrad
have been produced at 47 GeV at 1×10^{10} / bunch.

Simulations

From previous measurements and simulations, we believe
that the wakefields generated from misaligned accelerator

structures to be the dominate growth mechanism at high
currents. In the simulation model, we assume that the
accelerator sections are misaligned independently at each end
with 300 μm rms offsets. The position monitors and
quadrupoles are assumed to have 100 μm rms errors.

With these misalignments, simulations of the beam
transport were done to compute their effect on the beam
emittance[6]. In addition, beam steering and tuning effects were
included. As in the SLC, a one-to-one steering procedure was
used, where a dipole near each focusing quadrupole is adjusted
to zero the BPM reading at the next focusing quadrupole.

415
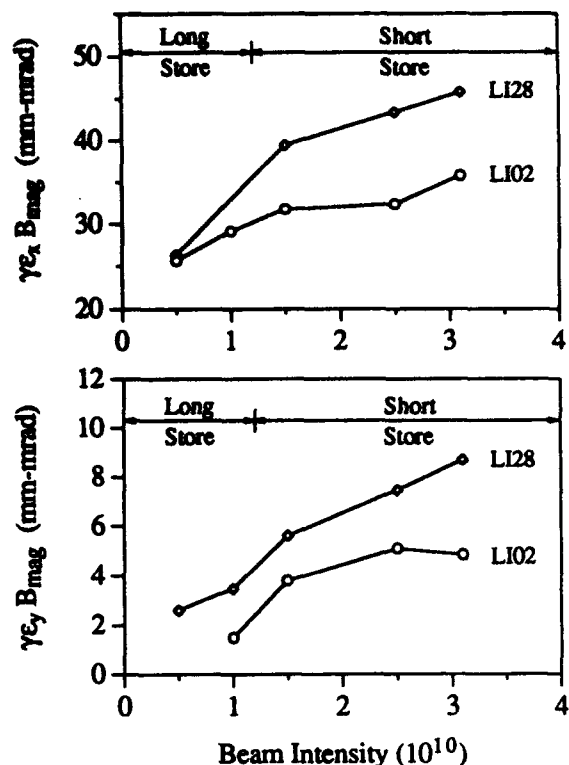
Figure 3 Measured horizontal (upper) and vertical (lower) emittances as a function of beam charge at 47 GeV.

Trajectory bump tuning, as described above, was also done first at 15 GeV and then at 47 GeV, but a least-squares procedure is used to fit for the effective feedback setpoint changes corresponding to the minimum emittances. A beam with a vertical invariant emittance of 3.5 mm-mrad and an intensity of 3.0×10^{10} was assumed to be injected on-axis into the linac.

The simulation program was used to compute the fractional vertical emittance enlargements at 47 GeV for many misalignment configurations. Figure 4 shows the resulting distributions for three linac conditions: 1) no BNS damping and no bumps, 2) BNS damping with no bumps, and 3) BNS with bumps. Thus, BNS damping helps emittance enlargement by a factor of about two and the further addition of trajectory bumps helps by an additional factor of six, a large gain! The mean of the final distribution corresponds to a 52% growth, comparable to the vertical results of the SLC as in Figure 1. [There is slightly poorer agreement when comparing the horizontal data and simulation where a measured growth of 20% or more at 15 GeV was measured when less than 10% was expected. The source of this growth is under investigation but may simply be insufficient tuning.] A final note: if the linac were operated without the large energy spread from the BNS phase configuration, the tuning would further reduce the emittance growth (on average, about 25% at 15 GeV and 60% at 47 GeV). This is the opposite to what happens with one-to-one steering only, where zeroing the BNS phases leads to a 30% (200%) larger growth at 15 GeV (47 GeV). This difference may be related to the nearly 'auto-phased' beam in the upstream end of the linac where the tail growth generated from betatron oscillations is nearly suppressed, making the tuning less efficient.
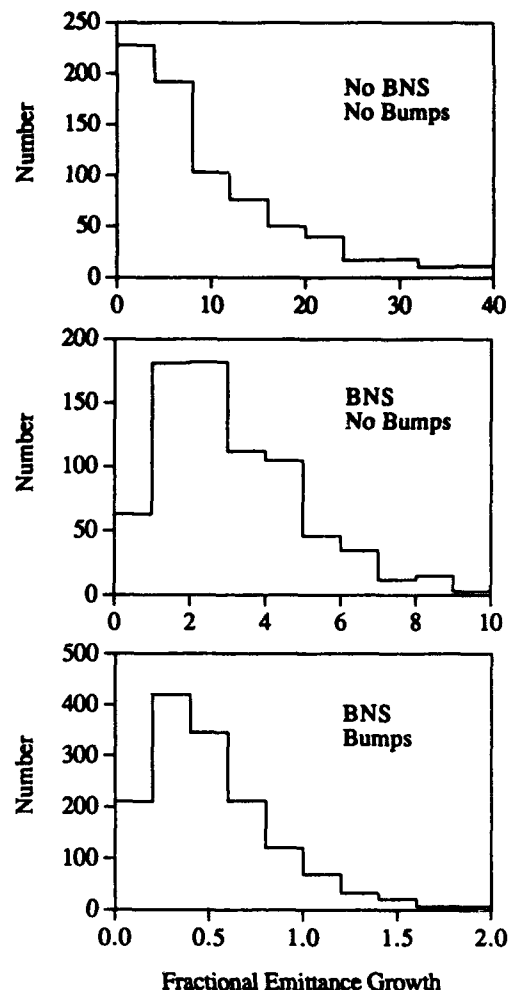
Figure 4 Distributions of final enlargement factors for vertical emittance for simulated linacs with errors without BNS damping (top), with BNS damping (center), and with BNS damping and linac bumps at two locations (bottom).

References

1) C. Adolphsen, et al., *Flat Beams in the SLC*, IEEE PAC 93, Washington, DC 1993.

2) J. Seeman, et al, *Measured Optimum BNS Damping Configuration of the SLC Linac*, Proceedings of 1993 Part. Accel. Conf., Washington, D.C., 1993.

3) F.-J. Decker, et al., *Dispersion and Betatron Matching into the Linac*, IEEE PAC 91, San Francisco, May 1991, p. 905.

4) J. Seeman, R. Holtzapple, and M. Ross, *Induced Beams Oscillations from Quadrupole Vibrations in the SLC*, Proceedings of 1993 Part. Accel. Conf., Washington, D.C., 1993.

5) J. Seeman, F.-J. Decker, and I. Hsu, *The Introduction of Trajectory Oscillations to Reduce Emittance Growth in the SLC Linac*, XV Int. Conf. on HE Accel., Hamburg, Germany, 1992, p. 879.

6) C. Adolphsen, K. Bane, and J. Seeman, *Effect of Wakefields on First Order Transport in the SLC Linac*, IEEE PAC 91 San Francisco, May 1991, p. 3207.

Method to Evaluate Steering and Alignment Algorithms for Controlling Emittance Growth*

Chris Adolphsen and Tor Raubenheimer

Stanford Linear Accelerator Center, Stanford University, Stanford California 94309

Abstract

Future linear colliders will likely use sophisticated beam-based alignment and/or steering algorithms to control the growth of the beam emittance in the linac. In this paper, a mathematical framework is presented which simplifies the evaluation of the effectiveness of these algorithms. As an application, a quad alignment algorithm that uses beam data taken with the nominal linac optics, and with a scaled optics, is evaluated in terms of the dispersive emittance growth remaining after alignment.

I. INTRODUCTION

A major concern in the design of future linear colliders is the emittance growth in the linac. For example, dispersive and wakefield generated growth occurs when the beam travels off-axis as a result of misalignments of the quads, beam position monitors (BPMs) and accelerator structures. Steering and alignment algorithms have been devised to reduce these offsets and their effects [1-3]. The basic method of evaluating these algorithms is to simulate the linac beam transport including misalignments, and then to apply the correction scheme. This is repeated for many misalignment configurations to accurately gauge the effectiveness of the algorithm.

Here we present an analytical approach that makes it much easier to explore the 'parameter space' of an algorithm by eliminating the need to do simulations. This approach is generally applicable in cases where the emittance growth depends quadraticly on the misalignments. Some examples in which it can be easily applied are dispersive growth where there is little filamentation, and wakefield growth where the orbit perturbations are smaller than the orbit offsets in the accelerator structures.

A good way to describe the approach is to apply it to the problem of the dispersive emittance growth that results from misaligned quads and BPMs. We will first define the problem, then formulate a quad alignment algorithm, and finally evaluate the growth from first order dispersion. Briefly, we exploit the fact that the computed misalignments are linearly related to the BPM measurements used in the fit. Since the emittance growth also depends linearly on the misalignments, the growth can be expressed in terms of the measurement errors.

II. ALIGNMENT PROBLEM

As a specific example, we treat the case of misalignments in a linac consisting of a FODO lattice with a BPM located in

the bore of each quad. We assume that a single bunch of constant mean energy and constant energy spread traverses the linac. We also assume a constant spacing, L, between quads, and a constant phase advance per FODO cell, μ. These parameters define the periodic beta function: its maximum value is

$$\beta_{max} = \frac{2L}{\sin(\mu)} \left[1 + \sin(\mu/2) \right]. \qquad (1)$$

We note that the emittance results derived with these assumptions can be simply related to the case of constant gradient acceleration with a $\sqrt{E}$ scaling of beta.

In computing the beam motion, we consider only the steering effect of the quad misalignments. The relation between the resulting beam trajectory and the BPM measurements is illustrated in Figure 1. Here, a quad is offset relative to an alignment axis by x_q, and the BPM located in the quad is offset relative to the quad center by x_b. Not represented in this figure is the BPM measurement error, which we denote by x_r. Including this error, the BPM measurement, x_m, is related to the orbit offset, x, by

$$x_m = x - x_q - x_b + x_r. \qquad (2)$$
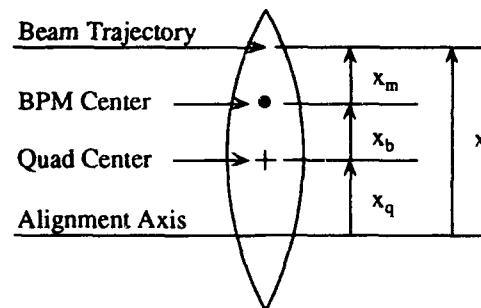
Figure 1. Illustration of a quad offset, x_q, BPM offset, x_b, and BPM measurement x_m for $x_r = 0$.

From this relation, one can see that correcting the orbit by zeroing the BPMs (using steering magnets for example) will result in an rms orbit offset at each quad that is the sum in quadrature of the rms BPM and quad offsets (assumed to be uncorrelated) and the BPM resolution. With this 'One-to-One' steering approach, the resulting dispersion is proportional to the rms orbit offset. In an actual linac, the largest of the three contributions is likely to be from the quad offsets, followed by the BPM offsets. Hence, in a beam-based approach to reducing dispersion, it is reasonable to consider determining the quad offsets from the BPM data. The measurements from N contiguous BPMs can in fact be used to fit for the offsets of

the N quads starting at the quad upstream of the first BPM. These offsets would then be used to correct the orbit by either moving the quads (assumed here for simplicity), or by equivalent adjustments to steering magnets.

One can also use BPM data taken with other lattice configurations to further reduce the quad offsets, or to allow for a fit for the BPM offsets as well. However, just minimizing the residual orbit offsets is not necessarily optimal for dispersion reduction since the correlations that arise between the offsets as a result of the fit affect how the dispersion source terms add. In fact, the results are often counterintuitive, making it all the more useful to have an analytic means of examining the problem.

III. ALIGNMENT ALGORITHM

To further our example, we next formulate a quad alignment algorithm based on two sets of BPM measurements, one taken with the nominal lattice and one taken with a uniform scaling of the quad strengths. This scaling, whose size we denote by Q/Q_0, changes the phase advance per cell while maintaining periodic focusing. (We note that other types of lattice scaling are also possible, and may be more efficient although less simple to implement.)

As a first step, we need to define an alignment axis to which the trajectory offsets are referenced. In practice, one is likely to align a group of N quads at a time, one group immediately after the next, so a good choice for the alignment axis is the line formed between the beam position at the first quad in the group, and the center of the first quad in the next group (*i.e.*, quad N+1). This leaves the initial angle of the beam unconstrained, so it must also be included as a variable in the fit. We assume, however, that it does not change between the two sets of measurements.

As with any fitting procedure, we need to define a χ^2 in terms of the variables and measurements involved, accounting for the errors and their correlations. The errors in this problem are the BPM offsets relative to the quads and the BPM measurement error, each of which we assume to have a mean of zero and an rms width of

$$\sigma_r^2 \equiv \langle x_r^2 \rangle \quad \text{and} \quad \sigma_b^2 \equiv \langle x_b^2 \rangle \qquad (3)$$

for each BPM. The resolution variable, x_r, differs from measurement-to-measurement while the offset variable, x_b, is common to all measurements. If we let $^1\bar{x}_m$ and $^2\bar{x}_m$ be vectors representing the two sets of N+1 BPMs measurements (*i.e.*, the N BPMs at the quads being aligned plus the next downstream BPM, with superscript 1 (2) denoting the measurements with the nominal (scaled) lattice), then we can write the full measurement vector and the corresponding error matrix as

$$\bar{x}_m \equiv \begin{bmatrix} ^1\bar{x}_m \\ ^2\bar{x}_m \end{bmatrix} \qquad \Lambda \equiv \langle \bar{x}_m \bar{x}_m^t \rangle \qquad (4)$$

where the elements of Λ are obtained from equations 2 and 3:

$$\Lambda_{i,j} = \left[\sigma_r^2 + \sigma_b^2 \right] \delta_{i,j} + \sigma_b^2 \left(\delta_{i,j-N-1} + \delta_{i,j+N+1} \right). \qquad (5)$$

The final ingredient for the fit is the functional dependence of the measurements on the fit variables. From equation 2, we need only an expression for x since x_b and x_r are treated as random variables. At quad i,

$$x_i = R_{12_{i,1}} \theta_1 - \sum_{j=1}^{i-1} R_{12_{i,j}} K_j x_{q,j} \qquad (6)$$

and (for future reference),

$$x_i' = R_{22_{i,1}} \theta_1 - \sum_{j=1}^{i-1} R_{22_{i,j}} K_j x_{q,j} - \frac{K_i}{2} x_{q,i} \qquad (7)$$

where $R_{12_{i,j}}$ ($R_{22_{i,j}}$) is the [1,2] ([2,2]) transport element between the center of quad j and i, K_j is the integrated quad strength, θ_1 is the beam angle just upstream of the first quad, and $x_{q,i}$ is the offset of quad i (note $x_{q,N+1} \equiv 0$).

To simplify the algebra, we form a vector, $\bar{x}_d$, that is the difference of the BPM measurements and the fit function:

$$\bar{x}_d \equiv \begin{bmatrix} ^1\bar{x}_d \\ ^2\bar{x}_d \end{bmatrix} \equiv \begin{bmatrix} ^1\bar{x}_m - \left(^1\bar{x} - \bar{x}_q \right) \\ ^2\bar{x}_m - \left(^2\bar{x} - \bar{x}_q \right) \end{bmatrix}. \qquad (8)$$

The expression for χ^2 is then

$$\chi^2 = \bar{x}_d^t \Lambda^{-1} \bar{x}_d \qquad (9)$$

which when expanded yields

$$\chi^2 \propto \sum_{i=1}^{N+1} \left\{ \left(^1x_{d,i} \right)^2 + \left(^2x_{d,i} \right)^2 - \frac{2R^2}{1+R^2} \left(^1x_{d,i} \right)\left(^2x_{d,i} \right) \right\} \qquad (10)$$

where

$$R \equiv \sigma_b / \sigma_r. \qquad (11)$$

In the $R \to 0$ limit, where the BPMs are perfectly aligned, χ^2 reduces to the sum of squares of the two measurements, while in the $R \to \infty$ limit, it reduces to the sum of the measurement differences squared.

With this χ^2, we next solve the set of equations generated when setting its derivative with respect to the fit variables to zero. Skipping this algebra we note only that the resulting fit values are linearly related to the measurements. We express this by

$$\bar{x}_v \equiv \begin{bmatrix} \theta_1 \\ \bar{x}_q \end{bmatrix} \equiv F \bar{x}_m \qquad (12)$$

where F is a matrix which depends on R and on the lattice parameters for the two measurements.

IV. DISPERSION

With the alignment equations, we now compute the beam emittance growth due to the first order dispersion remaining after the alignment process. To begin, we evaluate the dispersion at the center of quad N (quad N+1 is not used since the beam angle at this location is not constrained in the fit: this angle is corrected, however, during the alignment of the next

418
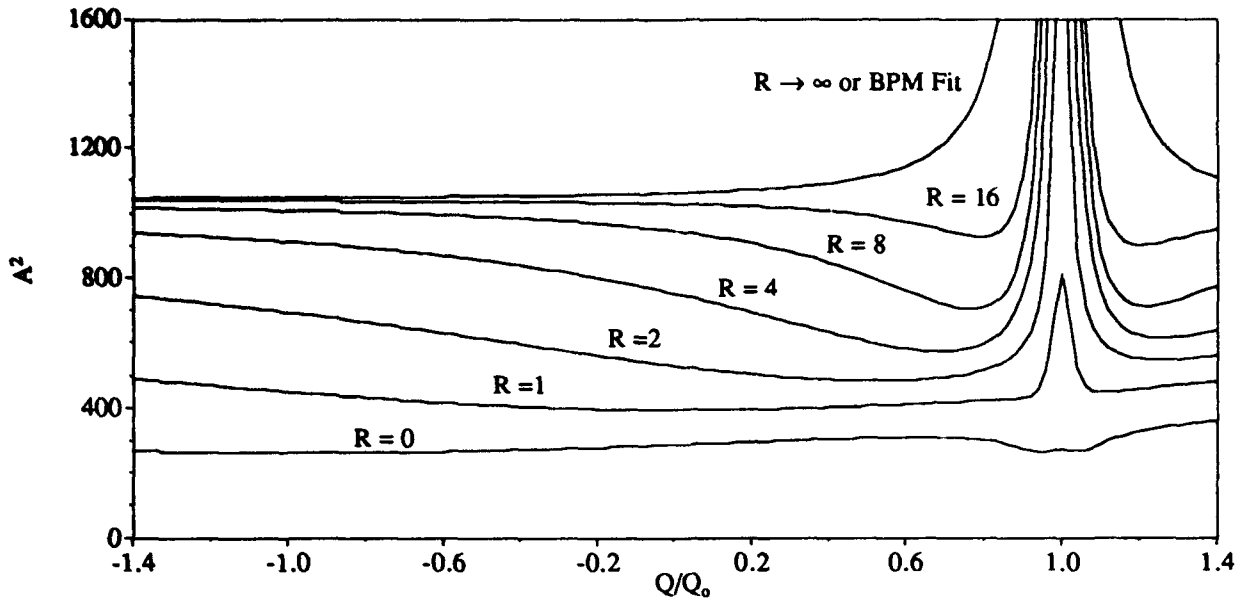
Figure 2. Scaled dispersion amplitude, A^2, as a function of R and Q/Q_0 for $N = 40$ and $\mu = 90°$. The R $\rightarrow \infty$ limit is equivalent to fitting for the BPM offsets.

group of N quads). Using equations 6 and 7, the normalized dispersion amplitude can be written

$$\vec{\eta}_N = \begin{bmatrix} \dfrac{1}{\sqrt{\beta_N}} \dfrac{\partial^l x_N}{\partial \delta} \\ \sqrt{\beta_N} \dfrac{\partial^l x_N'}{\partial \delta} \end{bmatrix} \equiv D \, \vec{x}_V \qquad (13)$$

where **D** is a matrix that depends on the parameters of the nominal lattice, and δ is the fractional energy difference. To evaluate the emittance growth due to this dispersion, we average over the beam energy spread and over the quad alignment results. If ε_0 is the emittance of the beam entering the alignment region and σ_δ^2 is the rms beam energy spread, the rms of the emittance at quad N, ε_N, is

$$\frac{\langle \varepsilon_N^2 \rangle^{1/2}}{\varepsilon_0} = \left(1 + \frac{\sigma_\delta^2}{\varepsilon_0} \mathrm{Tr}\left[\langle \eta \eta^t \rangle \right] \right)^{1/2} \qquad (14)$$

where we ignore the effect of betatron chromaticity. Now we substitute the alignment results to compute the average:

$$\mathrm{Tr}\left[\langle \eta \eta^t \rangle \right] = \mathrm{Tr}\left[\langle D \vec{x}_v \vec{x}_v^t D^t \rangle \right] \qquad (15)$$

$$= \mathrm{Tr}\left[\langle D F \vec{x}_m \vec{x}_m^t F^t D^t \rangle \right] = \mathrm{Tr}\left[D F \Lambda F^t D^t \right].$$

For convenience, we define a scaled dispersion amplitude as

$$A^2 \equiv \frac{\beta_{max}}{\sigma_r^2} \mathrm{Tr}\left[D F \Lambda F^t D^t \right] \qquad (16)$$

which depends only on μ, R and N. The emittance is then

$$\frac{\langle \varepsilon_N^2 \rangle^{1/2}}{\varepsilon_0} = \left(1 + \frac{\sigma_\delta^2 \sigma_r^2}{\beta_{max} \varepsilon_0} A^2 \right)^{1/2}. \qquad (17)$$

From a practical point of view, one wants N to be large in order to reduce the dispersion from the uncorrected quad offsets at the ends of the steering sections, but not too large that systematic effects, such as from common errors in the quad strengths, are large. Based on experience with beam-based alignment in the SLC, a reasonable value is $N = 40$ for $\mu = 90°$. Figure 2 shows A^2 for this choice, and various values of R, as function of Q/Q_0 over the range in which the phase advance per cell is $< 180°$.

For $Q/Q_0 = 1$, where two sets of the nominal lattice data are used, A^2 scales as $1 + 2R^2$ since the effect of the BPM offsets and measurement errors are indistinguishable in the fit. Outside of the $Q/Q_0 = 1$ region, A^2 saturates as R $\rightarrow \infty$ since the difference of the orbits from the two lattices is independent of the BPM offsets, and hence independent of R. This is true even though the orbit offsets after alignment still scale as R for R >> 1. Another interesting result is that if the BPM offsets are included as variables in the fit, the dispersion is the same as the R $\rightarrow \infty$ case. Allowing the BPM offsets to vary apparently leaves the quad offsets sensitive to only the difference orbit. In this case, however, the orbit offsets after alignment are independent of R (the error in determining the BPM offsets is about 1.3 σ_r, independent of N). Finally, we note that A^2 is essentially linear with N at $Q/Q_0 = 1$ and at values outside of the peak region. In the transition region, the widths of the peaks decrease as N increases.

V. REFERENCES

[1] C. Adolphsen et. al., SLAC-PUB-4902, (March 1989).

[2] T.O. Raubenheimer and R. Ruth, Nucl. Instr. and Meth. A302, 191 (1991).

[3] T.O. Raubenheimer, Nucl. Instr. and Meth. A306, 61 (1991).

Experimental Simulation of Ground Motion Effects

M.J. Syphers[a], M. Ball[b], B. Brabson[b], J. Budnick[b], D.D. Caussyn[b], A.W. Chao[a], J. Collins[b], V. Derenchuk[b],
S. Dutt[a], G. East[b], M. Ellison[b], T. Ellison[b], D. Friesel[b], W. Gabella[d], B. Hamilton[b] H. Huang[b],
W.P. Jones[b], S.Y. Lee[b], D. Li[b], M.G. Minty[c], S. Nagaitsev[b], K.Y. Ng[d], X. Pei[b], G. Rondeau[b],
T. Sloan[b], L. Teng[e], S. Tepikian[f], Y. Wang[b], Y.T. Yan[a], P.L. Zhang[a]

Abstract

Synchro-betatron coupling in a proton storage ring with electron cooling was studied by modulating a transverse dipole field close to the synchrotron frequency. The combination of the electron cooling and transverse field modulation on the synchrotron oscillation is equivalent to a dissipative parametric resonant system. The proton bunch was observed to split longitudinally into two pieces, or beamlets, converging toward strange attractors of the dissipative system. These phenomena might be important to understanding the effect of ground vibration on the SSC beam, where the synchrotron frequency is about 4 ~ 7 Hz, and the effect of power supply ripple on the RHIC beam, where the synchrotron frequency ramps through 60 Hz at 17 GeV/c.

Figure 1. Phase amplitude response as a function of the modulation frequency near the synchrotron tune. Solid lines correspond to attractor solutions calculated with the parameter a of Eq.(3).

I. INTRODUCTION

The equation of motion for phase oscillations[1] of a particle in a synchrotron, in the absence of forced oscillations, is given by

$$\ddot{\phi} + \omega_s^2(\sin\phi - \sin\phi_0) = 0.$$

Here $\omega_s = \omega_0\sqrt{\frac{heV|\eta|}{2\pi\beta^2 E}}$ is the small amplitude synchrotron angular frequency at $\phi_0 = 0$, ω_0 is the angular revolution frequency, and h, V, and ϕ_0 are respectively the harmonic number, the peak rf voltage and the synchronous phase angle. The speed of the particle is βc, E is the energy, and η is the phase slip factor. For this experiment, we have $h = 1, \eta \approx -0.86$, $\phi_0 = 0$ and $f_0 = \frac{\omega_0}{2\pi} = 1.03168$ MHz at 45 MeV proton kinetic energy. We chose an rf voltage of 41 V to obtain a synchrotron frequency of 262 Hz in order to avoid odd harmonics of the 60 Hz ripple. The synchrotron tune is given by $\nu_{syn} = \frac{\omega_s}{\omega_0} = 2.54 \times 10^{-4}$.

Transversely, particles are executing *betatron oscillations* about the closed orbit of the accelerator. Horizontal and vertical tunes $\nu_x = 3.828$, and $\nu_z = 4.858$ were chosen for this experiment to avoid nonlinear betatron resonances. The corresponding fractional part of the horizontal betatron frequency was $(4 - \nu_x)f_0 = 177$ kHz.

Coupled motion between the transverse and longitudinal degrees of freedom (synchro-betatron coupling) is important to electron storage rings, where the fractional parts of the synchrotron and betatron tunes are of the same order of magnitude. To the knowledge of the authors, synchro-betatron (SB) coupling has not been observed previously in proton storage rings, where the fractional part of the betatron and synchrotron tunes differ substantially.

The dominant effect of ground vibration or power supply ripple is that of a modulating dipole field. A slow adiabatic dipole modulation gives rise to a closed orbit modulation. Performance degradation can arise from *nonadiabatic modulations*, which occur naturally at resonance conditions, e.g. transverse modulation at the synchrotron frequency. In this paper, we present experimental data for transverse modulations producing SB coupling, similar to what may arise from ground vibrations or power supply ripple.

II. THE EXPERIMENT

The experimental procedure started with a single bunch of about 5×10^8 protons at at 45 MeV kinetic energy. The cycle time was 11 s. The injected beam was electron-cooled and was simultaneously modulated by a small dipole of effective length $\ell = 0.27$ m. The horizontal dispersion function was $D_x \approx 4.0$ m at this dipole's location. At the end
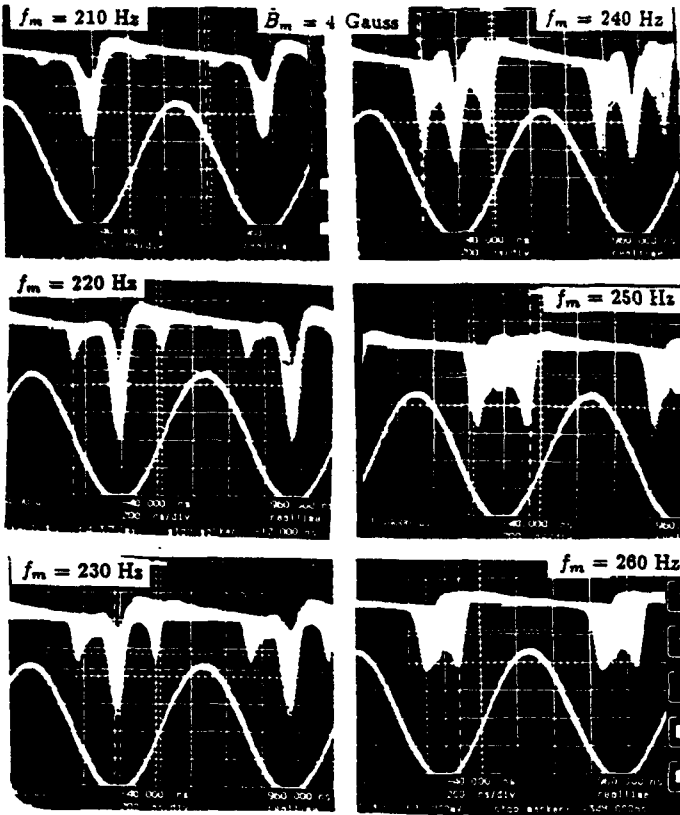
Figure 2. Longitudinal beam profile, observed from a fast sampling oscilloscope, showed the splitting of beam bunch into beamlets below the bifurcation frequency. The modulation amplitude was $\hat{B}_m = 4$ Gauss. The sine waves in this figure are the rf waveform.

of 7 seconds, the beam-centroid displacements were measured, digitized, and recorded from signals of beam position monitors (BPM). The longitudinal phase was measured by comparing the time difference between the peak signal from a wall gap monitor and the signal from an rf clock. A beam position at a high dispersion location was used to measure the momentum deviation, which is related to the off momentum closed orbit by $\Delta x_{co} = D_x \frac{\Delta p}{p}$ with $D_x \approx 3.9$ m. A total of 8 channels were used to obtain 6D phase space maps with 16,384 points recorded at 10 turn intervals. Details of our detection system are reported elsewhere[2].

With a horizontal dipole (vertical field) modulation at location s_0, the horizontal closed orbit becomes[3], $x_{co}(t) = \frac{\sqrt{\beta_x(s)\beta_x(s_0)}}{2\sin\pi\nu_x}\theta(t)\cos(\pi\nu_x - |\phi_x(s) - \phi_x(s_0)|)$, where $\theta(t) = \frac{B_m(t)\ell}{B\rho} = \hat{\theta}\sin\omega_m t$ with $\hat{\theta} = \frac{\hat{B}_m\ell}{B\rho}$. Furthermore, if the dispersion function at the modulating dipole location is not zero, the path length is also modulated. The change of the circumference is given by $\Delta C = D_x\theta(t)$, where D_x is the dispersion function at the modulation dipole location. The corresponding rf phase difference becomes, $\Delta\phi = 2\pi h\frac{\Delta C}{C}$, where $C = 86.8224$ m is the circumference of the IUCF

Cooler Ring. In our experiment, the maximum rf phase shift per turn was $\Delta\phi = 0.78 \times 10^{-5}\hat{B}_m$ [Gauss] radians. The longitudinal phase space coordinates, $(\phi, \frac{\Delta p}{p})$, at the nth and the $(n+1)$th revolutions are transformed according to the following mapping equations,

$$\phi_{n+1} = \phi_n + 2\pi h\eta(\frac{\Delta p}{p})_n + \Delta\phi,$$

$$(\frac{\Delta p}{p})_{n+1} = (\frac{\Delta p}{p})_n + \frac{eV}{\beta^2 E}\sin\phi_{n+1} - \lambda(\frac{\Delta p}{p})_n, \quad (1)$$

where the fractional momentum deviation of particles, $(\frac{\Delta p}{p})$, is the conjugate variable to the synchrotron phase angle ϕ, and λ is the phase space damping parameter related to electron cooling. Thus the synchrotron equation of motion, in the presence of transverse modulation, becomes,

$$\ddot{\phi} + 2\alpha\dot{\phi} + \omega_s^2\sin\phi = \omega_m\omega_s a\cos\omega_m t + 2\alpha\omega_s a\sin\omega_m t, \quad (2)$$

with the damping coefficient $2\alpha = \frac{\omega_0}{2\pi}\lambda$, and a is given by,

$$a = \frac{h\omega_0 D_x\hat{\theta}}{\omega_s C} = \frac{\omega_0}{2\pi\omega_s}\hat{\Delta\phi}. \quad (3)$$

. With electron current 0.75 A, the damping time for the 45 MeV protons was measured to be about 0.4 sec or $\alpha = 2.5$ s^{-1}, which was indeed small compared with $\omega_s = 1646$ s^{-1}.

Even though the cooling was weak, sufficient time was allowed before making measurements that the transient solution of Eq.(2) was damped out. Let the stationary solution of this system be given by, $\phi \approx g\sin(\omega_m t - \chi)$, where we have used a single harmonic approximation. Expanding the term $\sin\phi$ in Eq.(2) up to the first harmonic, we obtain the equation for the modulation amplitude g as,

$$[-\omega_m^2 g + 2\omega_s^2 J_1(g)]^2 + [2\alpha\omega_m g]^2 = [\omega_m\omega_s a]^2 + [2\alpha\omega_s a]^2, \quad (4)$$

where J_1 is the Bessel function[4] of order 1. Fig. 1 shows the longitudinal phase amplitude, measured with the wall gap monitor (diamonds), as a function of sinusoidal transverse modulation frequencies for the modulation amplitude with $\hat{B}_m = 12$ Gauss. The amplitudes of the steady state solutions of Eq.(4) are also shown in Fig.1 with $\alpha = 2.5$ s^{-1} and the parameter a obtained from Eq.(3). Note here that there are multiple solutions of Eq.(4) when the modulation frequency is below the critical bifurcation frequency[5], ω_c.

The existence of a unique phase factor χ for the solutions implies that trajectories are attracted to a single phase space point rotating with modulation frequency ω_m. Fig. 2 gives the measured longitudinal beam profile in time domain integrated over many synchrotron periods as shown on a fast sampling digital oscilloscope, which is triggered at the rf frequency. The modulation amplitude was $\hat{B}_m = 4$ Gauss. The modulation frequencies were 210, 220,..., 260 Hz. Using a fast sampling oscilloscope for a single trace, the bunch was indeed observed to split into two beamlets located at amplitudes corresponding to the steady state solutions of the dissipative parametric system. Both of

Figure 4. Initial phase space coordinates, obtained from numerical simulation of Eq.(1), which converge to the outer attractor are shown for $\hat{B}_m = 4$ Gauss and $f_m = 240$ Hz.

Figure 3. The phase amplitude of outer beamlet measured from a fast sampling oscilloscope and the phase amplitude measured from a wall gap monitor as functions of modulation frequency for the sinusoidal wave at $\hat{B}_m = 2$ Gauss, and for a square wave at $\hat{B}_m = 1.42$ Gauss. Here, $\hat{\phi} = g$.

these two beamlets rotate in the synchrotron phase space at the modulating frequency, measured from the FFT of the phase signal. As the modulating frequency is increased towards the synchrotron frequency, the outer peak moves in and its population intensity increases. When the modulating frequency was set higher than ω_c, the center peak disappeared (see the 260 Hz data of Fig.2).

Fig.3 shows the phase amplitude of the outer beamlet (squares) measured with the oscilloscope and the phase amplitude obtained from the phase detector (diamonds). Note here that our phase detector was not intended for use with more than one beam bunch present. It seems that our phase detector measured the centriod of these two beamlets shown in Figs. 1 and 3. Only when the outer beamlet becomes the dominant charge distribution, the phase detector was able to measure its phase. In the lower part of Fig. 3, the phase response data from a square wave modulation are shown. Since the square wave can be expanded in a Fourier series, $\frac{4}{\pi}\hat{B}_{sq}\sin\omega_{sq}t + \frac{4}{3\pi}\hat{B}_{sq}\sin 3\omega_{sq}t + \cdots$, the

peak response was expected and observed at a modulation frequency of 87.3 Hz.

A computer simulation based on Eq.(1) has been performed to demonstrate the strange attractor nature of the system. One of the results is shown in Fig. 4, where the black region corresponds to initial phase space coordinates converging toward the outer attractor. The complementary phase space coordinates converge mostly to the inner attractor except a small patch of phase space coordinates located on the boundary of the separatrix, which will converge toward two attractors located on the separatrix. The relative population of the inner and outer attractors observed from Fig. 2 can also be understood qualitatively from numerical simulations.

III. REFERENCES

[1] E.M. McMillan, Phys. Rev., **68**, 143 (1945); V.I. Veksler, Compt. Rend. Acad. Sci. U.R.S.S., **43**, 329 (1944); **44**, 365 (1944).

[2] S.Y. Lee, et al., Phys. Rev. Lett. **67**, 3768 (1991); D.D. Caussyn, et al., Physical Review A, **46**, 7942 (1992).

[3] E.D. Courant and H.S. Snyder, Ann. Phys. **3**, 1 (1958).

[4] M. Abramowitz and I.A. Stegun, eds, Handbook of Mathmatical Functions, National Bureau of Standard, (1975).

[5] M. Ellison, et al., Phys. Rev. Lett. **70**, 591 (1993).

BUNCH COALESCING STUDIES FOR THE SSC

N. Mahale , Y. T. Yan and J. Ellison
Superconducting Super Collider Laboratory*
2550 Beckleymeade Avenue
Dallas, TX 75237 USA

Abstract

It may become necessary to enhance the luminosity and increase the bunch spacing in the Superconducting Super Collider (SSC). Here we study the feasibility of bunch coalescing to achieve this. We choose the Medium Energy Booster (MEB) at extraction, momentum 200GeV, to perform the operation. In order to properly align the bunches we propose to linearize the RF using the second and third harmonics. Theoretical studies with simulation are presented. The program ESME is used for the simulation.

I. INTRODUCTION

The fundamental parameters of the collider are, luminosity of 10^{33}, energy of 20 TeV and bunch spacing of 5 meters. This corresponds to about 2 events per bunch crossing. Thus the detector requirement is to handle at least 2 events every 16 nanoseconds. There are several scenarios which may require a change in the bunch spacing. If the detector dead time cannot handle 16 nanosecond time interval between the bunch crossing it may be necessary to increase the bunch spacing. One way to achieve this is bunch coalescing. The design emittance may not be achieved. Then we could increase the luminosity through bunch coalecsing. If the design energy is not achieved this could be compensated by increasing the luminosity. During the comissioning of the detectors it may be desirable to have a larger bunch spacing. Lastly, luminosity upgrade by itself may be required for the new experiments in future. One way to achieve the higher luminosity is through bunch coalescing if one can accept a higher rate of events per bunch crossing. Here we study the feasibility of this option.

II. CHOICE OF MACHINE

The Low Energy Booster is a resonant machine and there fore is out of consideration. To keep the longitudinal emittance, ϵ_l, small and power requirements of subharmonic low, it is necessary to reduce the bunch height before coalescing. Due to high energy and low slip factor it would be difficult to reduce the bunch heights in the High Energy Booster or the Collider. If coalescing is done in the MEB, resulting higher longitudinal emittance and larger

bunch spacing will improve the bunch stability, microwave and multibunch, in the HEB and the Collider Thus, the Medium Energy Booster is the most desirable for the operation.

Next we have to choose between the injection and extraction point. The advantage of the injection point is that slip factor here is higher and therefore the procedure will take a shorter time. On the other hand the required rf voltages of subharmonics will be larger. In the MEB the bunches cross the transition energy. The coalescing process inevitably leads to a large longitudinal emittance. Also the new bunches have a greater number of particles and the ratio of peak to average current will be larger. This gives rise to a higher space charge tune shift. If the bunches are coalsced at injection, resulting larger longitudinal emittance and higher space charge tune shift will have a detrimental effect on transition crossing. At extraction the only disadvantage is a somewhat longer time for the procedure. However, the time for the procedure is not unacceptable. Thus, the extraction point in the MEB is the optimum stage for coalescing.

III. THE BASIC PROCEDURE

The basic procedure is to turn off the primary RF and turn on the subharmonic. Keep the subharmonic for one quarter of synchrotron period so that all the bunches in the longer bucket align along the energy axes in the phase space. Now turn off the subharmonic and recapture the bunch within the bucket of the primary RF. However, the synchrotron periods for different bunches vary. The bunches near the separatrix move too slowly and a good allignement is not possible. To get a better allignment three things are done. The main RF is adiabatically reduced to reduce the bunch height. The bunches further than $90°$ from the synchronous phase($180°$) in the subharmonic bucket are assumed to be chopped off. The RF profile between $90°$ and $270°$ is linearized by superimposing the the second and third harmonics of the subharmonic. These operatons make the bunches align adequately so that the longitudinal emittance and the beam loss during recapture of bunches is kept low. Though we assume that the adiabatic reduction of the bunch height is done after the complete acceleration, it could be done at the tail end of the MEB cycle during the acceleration phase.

IV. REDUCTION OF RF AMPLITUDE

Limiting factors with regard to the reduction of the RF amplitude are, the bunch size, time for the process and the multipactoring limit. Since we do not know the multipactoring limit we assume that an effective lower ring voltage can be obtained by paraphasing the cavities. The bucket area must be adequate for the bunch size; we shall provide the bucket at least twice the 95% emittance.

The remaining important criterion is the time for the process. We define the adiabiticity factor P,

$$P = -\frac{\tau_s}{H_b}\frac{dH_b}{dt},\qquad(1)$$

where, H_b is the bucket height and τ_s is the synchrotron period. The adiabiticity factor, P, will be kept constant during the reduction of the RF amplitude. Then, the equation for the RF amplitude V is,

$$\frac{dt}{dV} = -\frac{\alpha V^{-\frac{3}{2}}}{2P},\qquad(2)$$

where,

$$\alpha = \tau\sqrt{\frac{2\pi\beta^2 E}{e\eta h}}$$

where, τ is the revolution time and η is the slip factor. This gives the profile for the RF amplitude and the time required to change the amplitude. Integrating the above equation we get,

$$t = \frac{\alpha}{P}(\frac{1}{\sqrt{V_f}} - \frac{1}{\sqrt{V_0}})\qquad(3)$$

where V_f and V_0 are the final and the initial RF voltage. We now have to select the adiabaticity parameter P, the final RF amplitude and the time. These parameters will be chosen on the basis of simulation results.

V. LINEARIZATION OF THE RF PROFILE

The RF system used for accelerating and regular bunching we will refer as primary RF. The subharmonic RF system used for coalescing will be referred as the secondary RF system. Let A_1, A_2 and A_3 be the amplitudes of the secondary RF and its second and third harmonics. To align all the bunches in the subharmonic bucket we linearize the RF profile. To linearize we use the second and third harmonics. The scheme we propose is to minimize the integral rms error, the least square fit, in the range of interest between actual RF profile and the linear profile with a slope K. Then we minimize $f(A_i)$, keeping K constant, given by,

$$f(A_i) = \int_{\pi}^{\phi_0} d\phi[V - K(\pi - \phi)]^2,\qquad(4)$$

where,

$$V = A_1 sin(\phi) + A_2 sin(2\phi) + A_3 sin(3\phi).$$

The coefficients A_i are to be found by minimizing the error with respect to the linear profile; that is,

$$\frac{\partial f}{\partial A_i} = 0.\qquad(5)$$

Corresponding to this voltage profile the potential $U(\phi)$ is,

$$U(\phi) = A_1 cos(\phi) + \frac{A_2}{2}cos(2\phi) + \frac{A_3}{3}cos(3\phi),\qquad(6)$$

With this potential we then can calculate the period of oscillation. Let T_0 be the small amplitude period and $T(\phi)$ be the period for the amplitude ϕ; we define the normalized period $T = \frac{T(\phi)}{T_0}$. T is then given by,

$$T = \int_0^{\phi} d\theta\sqrt{\frac{A_1 - 2A_2 + 3A_3}{U(\phi) - U(\theta)}}.\qquad(7)$$

VI. THE SIMULATION

The MEB has 3960m circumference, harmonic number 792 and transition gamma of 25.0. The time available for the operation is about one second. The bunch has $\epsilon_l = 0.076$ eVs and the momentum is 200 GeV/c. At extraction, at frequency of 60 MHz, the RF amplitude is 160 kV which produces a bucket with a height 122.5 MeV and an area 2.6 eVs. The rms dimensions of the bunch are 9.9MeV height and 12.95cm long. Eleven full buckets and eleven empty buckets alternate in the bunch train. We coalesce 11 bunches which requires 22nd subharmonic. Therefore we need additional RF sources at 2.72 MHz., and 5.44 MHz.(the second harmonic) and 8.16 MHz.(the third harmonic).

The RF amplitude corresponding to a bucket area of .30 eVs (this is the least bucket we wish to provide), which is 2.2 kV, is not the limiting factor. Thus, the limiting factor will be multipactoring and paraphasing abiliity in the presence of errors and beamloading. We use the value of 5 kV; this order achieved in the FNAL[1,2,3]. We choose $K = 40kV$ corresponding to 8σ bunch length of 5 meters after the rotation.

The time required to reduce the main RF amplitude from 160 kV to 5kV is about 0.158/P seconds; with $P = 0.25$ this time is about 0.63 seconds. The synchrotron tune with the secondary RF systenm is 2.52×10^{-5}; the revolution time for the machine is $13.21\mu s$. Thus, the time required for quarter rotation is 83.30 ms. After the recapture with primary RF we need to decohere the bunches before transfering to the HEB; about 0.1 to 0.2 seconds- about 7 to 15 synchrotron periods- seem to be adequate. Thus the total time for the procedure is 0.8 s to 0.9 s; This could be further reduced if the primary RF amplitude can be reduced during the acceleration period.

Since the extraction γ_E is larger than γ_t we linearize the secondary RF profile in the range $(\frac{\pi}{2}, \frac{3\pi}{2})$. With $K = 40$ kV, the least square fit gives $A_1 = 52.52kV, A_2 = 13.84kV$ and $A_3 = 2.531kV$. Figure 1 shows the linearized profile.
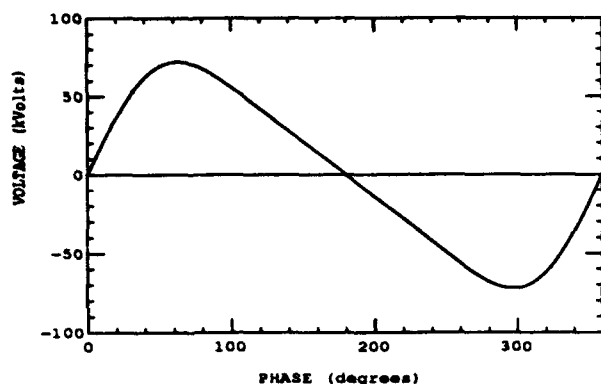
Figure 1. Linearized RF Profile

Figure 3. Bunches Aligned to be Recaptured

Figure 2. Normalized Period vs Amplitude

In Figure 2 we compare the periods as function of amplitude for three cases: (a) single RF system, (b) linearized with second harmonic and (c) linearized with second and third harmonic.

The simulation of the coalescing was done with the program ESME. Figure 3 shows the eleven bunches aligned in the subharmonic bucket ready to be recaptured in the primary RF bucket. At this point the secondary RF is to be turned off and primary RF turned on. After decohering for 0.20 second we get the final longitudinal emittance to be 4.17 eVs with a beam loss of 0.40%; the rms bunch lenght is 65 cm and bunch height is 102 MeV. During the recapture the bucket parametrs are V_c of 800 kV, bucket height of 329 MeV and bucket area of 154 eVs.

VII. DISCUSSION

Figure 2 shows that a great improvement is achieved in the constancy of period as function of amplitude due to the inclusion of the third harmonic. We see that the linearization is rather good up to an amplitude of $120° - 125°$. Here we have studied the coalescing of eleven bunches. There is a factor of four loss in luminosity due to chopped bunches; the net gain in luminosity is by a factor $\frac{11}{4}$. In addtion there is a problem of chopping these bunches. By increasing the range of linearization we may coalesce more

than half of the original bunches; however, this will require higher RF amplitude and will increase the final bunch height and emittance. For this purpose, if necessary, we also may have to add fourth harmonic.

Alternatively, we could coalesce fewer bunches. Consider the coalescing of three bunches. The problem here is not of alligning the bunches- three bunches can always be aligned- but rather how much the bunch will spread when rotated through quarter synchrotron period; this spread can be reduced by linearization. We need to linearize $120°$ about the synchronous phase and can be achieved with three RFs. Here, the gain in the luminosity is 3; which is as good as coalescing of eleven bunches. We remark, without giving deatails, that coalesing six bunches culd be done with three harmonics but beyond that we will need additional harmonics. These cases give more luminosity; however, they need more powerful subharmonic RF cavities.

There could be a problem in reducing the primary RF amplitude, V_f, to 5 kV. To keep the bunch length, which scales as $\left(\frac{V_f}{K}\right)^{\frac{1}{4}}$, after rotation we have to scale K linearly with V_f; we also need to increase the recapture voltage, V_c, linearly with K to keep the beam loss the same.

We thank A. Chao, S. Chen, P. Martin, R. Gerig and M. Syphers for discussions.

VIII. REFERENCES

[1] D. Wildman, P. Martin, K. Meisner and H. W. Miller, " Bunch Coalescing in the fermilab main ring," in *1989 IEEE Particle Accelerator Conference, 1827 (1989)*.

[2] P. Martin, K. Meisner, and D. Wildman, " Improvements in bunch coalescing in the fermilab main ring," in *1987 IEEE Particle Accelerator Conference, 1028 (1987)*.

[3] J. Griffin, J. MacLachlan and J. Bridges, "Preparation and Study of Bunches Containing 10^{11} protons in the fermilab main ring ," in *IEEE Trans. Nucl. Sci. NS-28, No. 3, 2037 (1981)*.

Compensation of RF-Induced Energy Spread in the CEBAF Injector Chopping System[*]

M. G. Tiefenback and G. A. Krafft,
Continuous Electron Beam Accelerator Facility,
12000 Jefferson Avenue, Newport News, VA 23606-1909 USA

Abstract
The CEBAF injector chopping system must generate three interleaved 499 MHz pulse trains of independently variable current from a DC input beam prior to axial compression. The chopper consists of two deflection cavities with an aperture midway between them. Lenses flanking the aperture focus the beam from the first cavity into the center of the second, where the RF deflection from the first cavity is removed. The symmetry of the RF energy spread across any time-slice of the beam is dominantly odd. The inverting optics used to focus the beam into the second cavity causes near cancellation of the energy spread from the two cavities. We present experimental measurements of the energy spread effects from a fundamental frequency (1497 MHz) chopper prototype producing a beam of suitable transverse emittance and energy spread, and discuss the expected performance of the subharmonic chopper system to be used for commissioning starting in January, 1994.

I. INTRODUCTION

The present CEBAF chopper design [1] follows closely the design of the chopper for the NBS microtron [2], and consists of two circularly polarized TM_{210} deflection cavities, an aperture plate, and a pair of solenoid lenses, as shown in Fig. 1. The first cavity (C1) steers the incom-
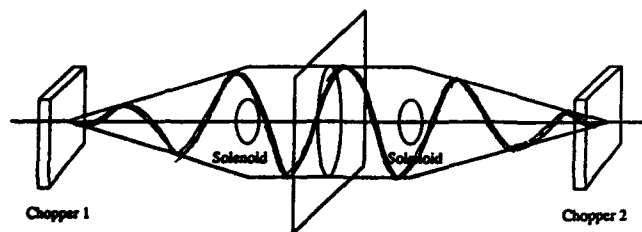
Figure 1. Sketch of the CEBAF injector beam chopping system.

ing DC beam along a divergent cone toward the chopping aperture plate. The first lens directs the beam parallel to the beamline. The second lens directs the beam along a

convergent cone with a focus at the center of the second cavity (C2). Cavities C1 and C2 must provide identical deflections to each slice of the beam in order for the overall deflection to be zero. In the absence of an aperture plate, the entire beam is closely restored to its DC state. The beam outline is helical between the cavities, although each electron follows a path at constant azimuth with respect to the beamline.

For like circular polarizations in the two cavities, multiple equivalent apertures may be placed on the aperture plate. Chopping system operation at the third subharmonic of the fundamental linac frequency with three variable apertures 120° apart on the aperture plate will provide three 499 MHz pulse trains with independently controllable current.

II. SINGLE CAVITY EFFECT

The CEBAF deflecting cavities are square, with inner dimensions of 22.39 cm transverse to and 4.0 cm along the beamline. The mode structure of the vertically deflecting linearly polarized TM_{120} mode is (adapted from [3])

$$E_{vz} = -\sqrt{5}\eta H_0 \cos\frac{\pi x}{a}\sin\frac{2\pi y}{a}\sin\omega t \qquad (1)$$

$$H_{vz} = -H_0\sin\frac{\pi x}{a}\sin\frac{2\pi y}{a}\cos\omega t \qquad (2)$$

$$H_{vx} = -2H_0\cos\frac{\pi x}{a}\cos\frac{2\pi y}{a}\cos\omega t, \qquad (3)$$

in mks units, plus the corresponding expressions for the orthogonal mode. Here a is the transverse dimension of the cavity, ω is the angular frequency of the RF, $\eta = \sqrt{\epsilon_0\mu_0}$, the origin is the center of the cavity, x is positive to the left and y is positive upward with respect to the beam, and z is in the direction of motion of the beam. Fig. 2 illustrates a beam being deflected upward in a left circularly polarized system. The upward deflection is followed by deflection to the left, implying a positive value of H_y for electrons. For maximal vertical deflection, the particles cross the center of the cavity at time $t = 0$, corresponding to zero crossing for E_{vz}.

We will neglect the field distortion at the entrance and exit apertures. For the beam energy of 100 keV, the beam samples RF phases approximately over ±1.2 rad over the 4 cm length of the cavity. The momentum δp_y imparted to the particles from the vertically deflecting mode in the

cavity is

$$\delta p_y = \frac{q_e v_z}{\omega} \int_{-1.2}^{1.2} \mu_0 H_{vx}(\psi) \mathrm{d}\psi \qquad (4)$$

where q_e is the charge and v_z is the velocity of the electron. The longitudinal momentum at this kinetic energy is 335 keV/c and the deflection angle is approximately 10 mrad. The maximum magnetic deflecting field $2\mu_0 H_0$ is then approximately 3.5 G and the maximum gradient in the electric field is $E'_z = 3.3$ MV/m^2.

For the horizontally deflecting mode in a left circularly polarized system,

$$E_{hz} = \sqrt{5}\eta H_0 \cos\frac{\pi y}{a} \sin\frac{2\pi x}{a} \cos\omega t. \qquad (5)$$

Approximations for small deviations off-axis for Eqs. 1 and 5 are

$$E_{vz} = -\frac{2\pi\sqrt{5}}{a}\eta H_0 y \sin\omega t \qquad (6)$$

and

$$E_{hz} = \frac{2\pi\sqrt{5}}{a}\eta H_0 x \cos\omega t. \qquad (7)$$

The energy integral for E_{vz} (an odd function over a symmetric interval) is zero along a line parallel to the z axis, so a constant offset does not affect the energy gain of a particle. To first order in x and y, all particles leave the cavity with the same energy increment from E_{vz}. Approximating the deflection as a uniform force resulting in a deflection $\delta\theta$ over a path of length L, the energy change is approximately

$$q_e E'_z \frac{\delta\theta}{2L} \left(\frac{v_z}{\omega}\right)^3 \int_{-1.2}^{1.2} (\psi + 1.2)^2 \sin\psi \, \mathrm{d}\psi.$$

Only the term linear in ψ survives, and for our parameters ΔE is +4.8 eV. The electric field for the other RF mode, however, is at its maximum during the particle crossing, and the energy change neglecting the slight x deflection is

$$\frac{q_e v_z x}{\omega} E'_z \int_{-1.2}^{1.2} \cos\psi \, \mathrm{d}\psi,$$

for a total energy change of 105 eV per millimeter of horizontal offset from the center of the cavity for particles being
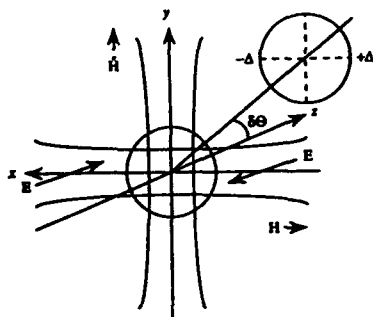
Figure 2. Left circularly polarized deflection cavity, beam deflected upward.

deflected vertically. This pattern rotates in time, so that at any point along the subsequent path of the beam, the particle energies are the same along any radius from the original beamline, but there is a gradient in the azimuthal direction. These analytic results are in good agreement with particle simulations by Liu, et al. [4]. This correlation of energy with position is used to search for the RF energy spread, as described below.

The beam passes through an emittance filter just before entering the first cavity, limiting the radius of the beam to less than 1.85 mm in the cavity. The resulting ±190 eV spread in energy would degrade the final bunching process, especially if increased by passage through the second cavity. The rms energy spread introduced by a single cavity (90 eV), corresponds to an rms momentum spread of 5×10^{-4}. The energy spread from the DC high voltage supply for the gun is less than 10^{-4}, so the relative momentum spread should be less than 6×10^{-5} with no RF on.

III. MEASUREMENT RESULTS

We steered the beam through the chopper system with the RF off and measured the beam diameter at a spectrometer with a horizontal dispersion of 43 cm, using a scanning wire monitor (profile A in Table 1). We repeated this with RF on in C1, using steering magnets to deflect the outgoing beam cone so that first the top portion (profile B) and later the bottom portion (profile C) of the cone passed across the central aperture on the plate. The profiles for these two beam setups are shown in Fig. 3.

With both choppers on, profile D was taken with beam passing through a 60° slot at the top of the circle and profile E was taken with beam passing through a 60° slit at the bottom of the circle. These profiles are narrower than profile A with the choppers off, which may indicate the presence of an instrumental artifact, a current-dependent increase in the measured profile. With the RF on, the central hole passes 11.5° (FWHM) of the RF cycle, so thirty times as much current reaches the profile monitor with the RF off (profile A) as for profiles B and C. Profiles D and E were taken using a 60° slit, and have an intermediate current. Profiles B and C (Fig. 3) are for equal beam currents, as are profiles D and E. The rms beam radii were 0.61 mm and 1.28 mm with one cavity on, and 0.48 mm and 0.56 mm with both cavities on.

Table 1. Variances of beam profiles

label	RF status	x_{rms} (mm)	$\delta\theta_y$ (radian)
A	off	0.63	0
B	C1 on	0.61	+0.01
C	C1 on	1.28	-0.01
D	C1,C2 on	0.48	+0.01
E	C1,C2 on	0.56	-0.01
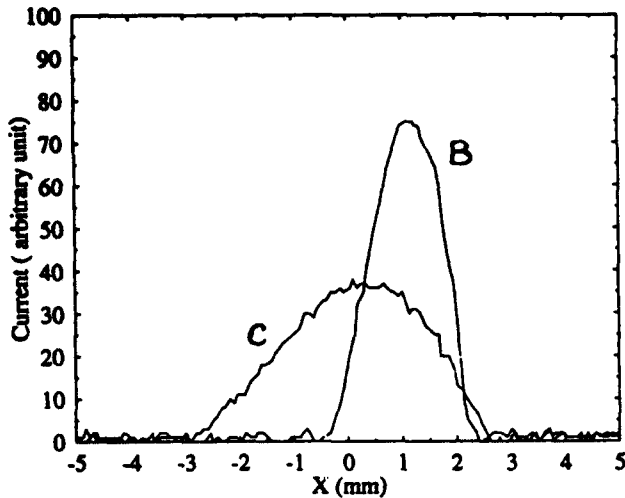
Figure 3. Profiles of the 100 keV beam in a region of horizontal dispersion 43 cm. See text for discussion.

IV. ANALYSIS

The profile asymmetry is due to the $\langle x \delta p_z \rangle$ and $\langle x' \delta p_z \rangle$ correlations introduced by the RF cavities. If the energy spread were uncorrelated with the horizontal coordinate of the beam, there would be no difference between beam from the top of the circle and beam from the bottom. The correlation $\sigma_{11} = \langle x^2 \rangle$ at the profile monitor is related to the correlation matrix at the second chopper cavity by

$$\sigma_{11} = M_{1k} \Sigma_{kl} M_{1l},$$

where M_{ij} is the transfer matrix between the two points and Σ_{kl} is the correlation matrix at the cavity. Samples of the beam taken at the top and bottom of the chopper circle will differ only in the sign of $\langle x \delta p_z \rangle$ (and the consequent $\langle x' \delta p_z \rangle$). Therefore the mean square difference between the downstream profiles for these portions of the beam will be proportional to the momentum correlation terms.

From Table 1, the difference in mean square (not rms) radius between profiles B and C is 12.7×10^{-7} m^2 while the difference between D and E is only 0.8×10^{-7} m^2. Profiles D and E are both smaller than profiles B and C, in spite of the factor of six higher current and even higher relative current density. This indicates a cancellation of the correlated energy spread introduced by a single cavity by approximately a factor of fifteen.

There are some points of disagreement concerning the actual energy spread of the beam with and without the RF cancellation. The overall rms width of profile B plus profile C is 1 mm, which is the profile width that would be measured from summing the two beam distributions at the chopper cavity to remove the correlated energy spread without changing the rms momentum spread. To account for the increase in rms radius with respect to A, D, and E purely through increased energy spread would require an energy spread for a single cavity of 2×10^{-3}, which is more than three times the calculated value. The RF-induced emittance increase from using a single deflection

cavity (limited by the central 11.5° aperture as a stop in the system) should be well under a factor of two, and at this level cannot reconcile the observation and calculation.

V. CONCLUSIONS

A large difference in the measured beam size results from changing the sign of the RF $\langle x \delta p_z \rangle$ correlation for a single cavity. The difference between the mean squares of profiles D and E with both deflection cavities powered (0.29 mm) is smaller by a factor of fifteen than that of B and C (1.13 mm) with one cavity powered. This indicates more than an order of magnitude cancellation for the correlated energy spread induced by one cavity. For either sign of this correlation with both cavities on, the measured beam size is smaller than either of the one-cavity profiles and for the DC beam profile with no RF. In spite of possible instrumental problems, this supports the conclusion that the overall energy spread induced by the chopper system is significantly smaller than the effect of one cavity. The rms momentum spread induced by a single cavity seems to be significantly larger than expected from RF calculations and from the modeling results reported in [4].

Aberrations in the lenses and in the deflecting cavities remain as sources of increased emittance, and energy perturbations of even symmetry are not compensated. The time-of-flight error between the cavities caused by the energy modulation is negligible. Any deviation from unity for the optics magnification from C1 to C2 will result in reduced cancellation of the energy spread.

The subharmonic chopper to be used at CEBAF is scaled from the fundamental frequency system, with one-third of the frequency and three times the deflection angle. The energy spread induced by the RF scales as $\omega \delta \theta$, and should be unchanged from the 1497 MHz system. There is a greater spacing planned between the cavities, but the phase lag from the differential velocity of the particles between the cavities is still unimportant.

VI. REFERENCES

[1] W. Diamond and R. Pico, 1988 Linac Conf., CEBAF-Report-89-001, June, 1989, pp. 403–405.
[2] M A. D. Wilson, et al., "Performance of the 100 keV Chopper/Buncher System of the NBS-Los Alamos RTM Injector," Proc. 1985 Part. Acc. Conf., IEEE Trans. on Nuc. Sci., NS-32 (5), pp. 3089–3091.
[3] Jacob Haimson, "Optimization Criteria for Standing Wave Transverse Magnetic Deflection Cavities," Proc. of the 1966 Linear Acc. Conf., Los Alamos Scientific Laboratory, LA-3609, pp. 303–331.
[4] H. Liu and J. Bisognano, "Simultaneous Cancellation of Beam Emittance and Energy Spread in the CEBAF Nuclear Physics Chopping System," these proceedings.

The North Arc of the SLC as a Spin Rotator*

T. Limberg, P. Emma

Stanford Linear Accelerator Center, Stanford, California 94309

and

R. Rossmanith

CEBAF, Newport News, Virginia 23606

ABSTRACT

The 1992 running cycle of the Stanford Linear Collider (SLC) showed that the orientation of the electron polarization vector at the interaction point was very sensitive to the vertical orbit in the north collider arc. We point out the reason for this sensitivity—the spin tune is equal to the vertical betatron tune. We devise a scheme of closed vertical orbit bumps which provide arbitrary manipulations of the polarization vector at the IP. We have developed an analytical model for the tuning of this 'arc spin rotator' and have performed a detailed numerical analysis to show its effectiveness. We present experimental results.

I. INTRODUCTION

The SLC arcs bend the beams from the end of the linac into the Final Focus area where the beams collide. They are about a mile long and densely stacked with combined function magnets. The quadrupole field of these magnets is very strong —their focal length is 1 meter.

The spin motion, more precisely, the motion of the spin expectation value of the beam, is given by the BMT equation [1],

$$\frac{d\vec{S}}{dt} = \vec{\Omega} \times \vec{S}. \tag{1}$$

The spin $\vec{S}$ rotates around the magnetic field $\vec{\Omega}$ in the rest system of the electron. If an electron is deflected in a transverse magnetic field by an angle φ, the spin is rotated around the field axis by

$$\phi = a\gamma \cdot \varphi, \tag{2}$$

where a is the anomalous momentum of the electron and γ the Lorentz factor.

At the beam energy corresponding to the peak rate of Z particle production (45.6 GeV) the spin phase advance, $\Delta\phi$, and the vertical betatron phase advance are equal (108° per cell). The additional spin rotations experienced by a particle performing vertical oscillations therefore add in resonance. This resonant build-up is shown in Fig. 1. The vertical component of the spin is steadily increasing as the betatron motion of the particle and the spin tune (indicated by the longitudinal spin component) are in phase.
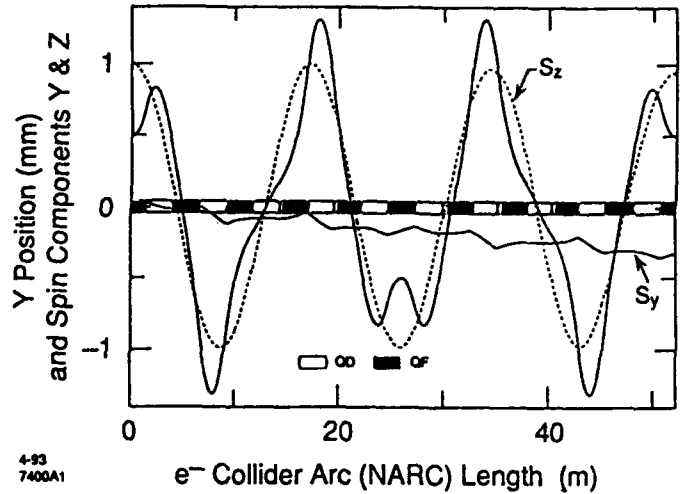
Fig 1. Vertical orbit and the vertical and longitudinal spin components over the first of twenty-three achromatic sections of the arc. The particle is launched with a vertical offset of 0.5 mm, *the spin with longitudinal orientation.*

To illustrate how drastically vertical orbit changes in the arc can alter the arc spin transport, Fig. 2 shows the vertical spin component of two particles with 0.5 and 0.05 m vertical launch offset over the entire arc. The spin at an entrance points again in the longitudinal direction. At the reverse bend section (400 m), a phase slip occurs between spin and betatron phase advance.

Fig 2. Vertical spin component over the entire arc for particles of 0.5 and 0.05 mm vertical launch offset.

The impact on the SLC operation was originally observed as a very sensitive dependence of the longitudinal polarization at the IP on the vertical orbit launch into the arc. The main effect, however, is not caused by depolarization but by a mere rotation of the polarization axis, since the vertical beam size is only 40 μm (20 μm for flat beams). However, the precision of instrumentation and orbit correction in the arcs proved sufficient to provide stable polarization orientation at the IP. The solenoid spin rotator magnets in the damping ring area could be used to compensate for the arc spin rotation and orient the spin at the IP into the longitudinal direction [2].

Colliding flat beams to increase the luminosity of the SLC [3] would have increased the difficulty of optical matching through the solenoid rotators. Beam rotations would have to be compensated and emittance preserved, requiring additional hardware (at least eight skew quadrupole magnets) and new tuning techniques. Therefore, we investigated the possibility of using controlled manipulations of the vertical orbit in the arc to orient the spin at the IP.

II. CONCEPT FOR AN ARC SPIN ROTATOR

A spin rotator is a sequence of magnets which provide control of spin orientation of the beam while leaving the outgoing orbit unaffected. The spin rotators in the damping ring area of the SLC provide an example (Fig. 3).
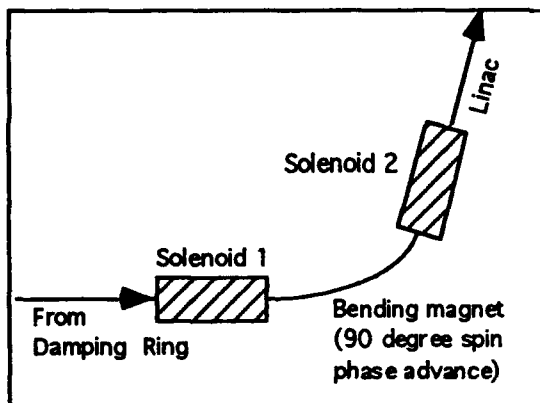
Fig 3. Spin rotator with solenoid magnets in the SLC damping ring area (NRTL - Linac Sector 2)

Two solenoid magnets capable of rotating the spin around the longitudinal axis by up to 90 degrees are separated by horizontal bending magnets which rotate the spin 90 degrees around the vertical axis. Different settings of the solenoid magnets can rotate the spin to any point of a half sphere at the launch into the linac without changing the launch itself.

In the arcs we know that vertical oscillations cause additional rotations around an axis in the horizontal/ longitudinal plane. So in principle two adjustable closed vertical orbit bumps separated by a fixed spin rotation around the vertical axis (two arc magnets provide 108 degrees) work as a spin rotator. The length of the bumps should be a multiple of 6π (one achromat) to minimize the optics perturbations. In practice, we use two interleaved bumps. They each span 42 π in betatron and spin phase and overlap for all but two arc magnets (see Fig. 4).
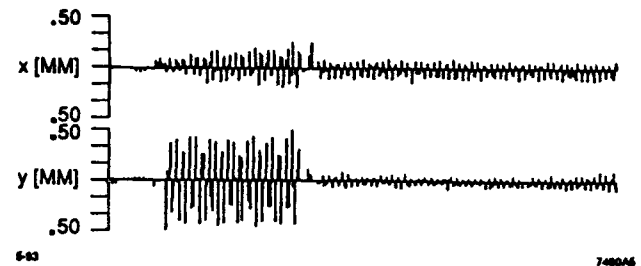
Fig 4. Difference orbit in the North Arc showing typical spin bump. This bump rotates the spin by 60 degrees. Note the x-y coupling due to arc rolls.

III. TUNING CONSIDERATIONS

There is a principle difference between rotating the spin in the arcs and rotating it at linac injection with the solenoid magnets. The absolute orbit in the arcs is only known to about one millimeter. Therefore the absolute spin rotation in the arcs is entirely unknown. The polarization measurement at the Interaction Point (IP) is restricted to longitudinal polarization[4]. Even so, measuring the IP polarization for three different settings of the solenoid magnets, which produce three transverse states of the spin at the launch into the arc, gains enough knowledge about the arc spin rotation to calculate the correct setting of the solenoids for longitudinal spin direction at the IP[5].

A similarly elegant way to set the arc bumps cannot be found because their additional spin rotations (which we assume as known) are interleaved with unknown rotations due to the unknown absolute arc orbit. To tune the arc polarization bumps, we step through a nine-point grid of bump settings for which the measured longitudinal polarization is fitted to the under constrained function

$$\frac{P_z}{|P|} = (a_1 + a_2\cos\theta_1 + a_3\sin\theta_1) \cdot (b_1 + b_2\cos\theta_2 + b_3\sin\theta_2) \quad (3)$$

which reflects that two bump amplitudes (or rotation angles) θ_1 and θ_2 together with unknown rotation parameters shape the outcome of this scan.
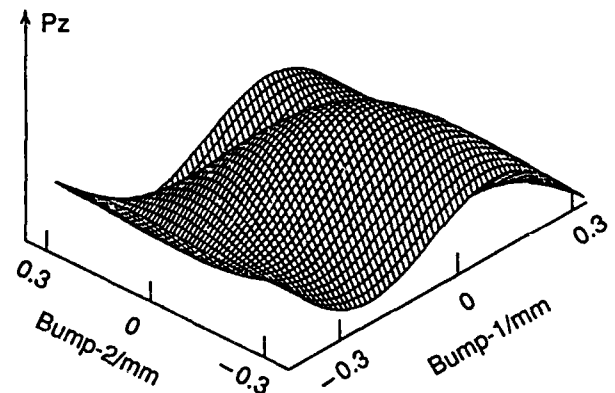
Fig 5. Fit for a 9-point grid scan with the arc polarization bumps. The fit form is given in eqn. 3.

IV. SIMULATION CALCULATIONS

Extensive tests with simulation calculations had been done before the first machine studies. A simulation code was written which tracks single particles and their spin through the arc. The optics are linear, the spin rotations are calculated to all orders, and rolls are included (the SLC arcs have rolls of up to 10 degrees). The code was cross-checked against existing spin tracking codes [6].

First calculations showed that the axis of the additional spin rotation caused by a vertical orbit bump is sufficiently independent of the rotation angle (bump amplitude) as long as the orbit amplitude is confined to 1.0 mm (which is beyond the limits for optical considerations).

Then the complete polarization optimization with vertical arc bumps was simulated. Different initial arc orbits were generated and 9-point grid scans were simulated for each of these. The calculated results of the grid scans was fitted with eqn. 3 and the predicted result verified with a final calculation. In all cases the spin vector could be rotated into the longitudinal direction at the IP within a few degrees.

V. MACHINE STUDIES

To initiate a vertically closed orbit bump in the north arc, one magnet is displaced vertically (the arc is steered by physically moving the main combined function magnets). For design optics, a magnet with a phase difference of 6π downstream closes the bump with the same move in the opposite direction. In practice, a few additional small corrections are applied to achieve bump closure of less than 20µm rms downstream oscillation amplitude (see Fig.4). The same combinations of magnet displacements are then reproducibly scaled to scan the grid.

Optimization with the grid scan was immediately successful. Table 1 shows data for one of the first grid scans taken. It compares the data to the fit values using eqn.3. The peak value predicted by the fit was found within 2% at the specified bump configuration.

Table 1: IP Polarization 9 Point 'Grid-Scan'

Point #	Measured P_Z [%]	Error on P_Z [%]	Fitted P_Z [%]
1	+6.8	1.3	+3.1
2	+16.0	0.8	+17.9
3	–32.0	1.0	–27.9
4	–12.2	0.7	–12.2
5	+8.0	0.9	+8.0
6	+24.0	0.6	+24.0
7	–18.8	0.7	–18.7
8	–33.5	0.6	–33.5
9	+9.0	0.9	+9.0

Fit Results ==>   Set Bump-1 = –298 µm
                   Set Bump-2 = +21 µm
                   P_Z = –41.2% (measured = –39.0%)

VI. CONCLUSION AND OUTLOOK

Rotating the spin at the IP with arc spin bumps proved to be from the first machine experiments an effective and reliable tool. The solenoid spin rotators have remain switched off for the entire 1993 run cycle. Bump optimization requires only a few hours and has been stable for months under normal SLC operating conditions.

The SLC is presently operating with >60% electron polarization. The polarization degree at the beginning of the arc is thought to be around 80%[7]. Spin diffusion due to energy spread (0.3% rms) accounts for 10% relative polarization loss. Studies are under way to recover the additional polarization loss due to diffusion by means of further arc orbit tuning.

VII. ACKNOWLEDGMENTS

We would like to thank T. Barklow, R. Chestnut, R. King, N. Phinney, N. Walker and the operations staff for their support.

VIII. REFERENCES

[1] V. Bargmann, L. Michel, V.L. Telegdi, Phys. Rev. Lett, 2, 435, (1959).

[2] T. H. Fieguth, "The Optical Design of the Spin Manipulation System for the SLAC Linear Collider" , SLAC-PUB-4924, March 1989.

[3] C. Adolphsen, et al., "Flat Beams in the SLC", Proc.Particle Accelerator Conference, Washington,D.C. (May 1993).

[4] G. Shapiro, et al., "The Compton Polarimeter at the SLC", Proc.Particle Accelerator Conference, Washington,D.C. (May 1993).

[5] W. Spence, private communication.

[6] R. King, private communications.

[7] J. Clendenin, et al., "Performance of the SLC Polarized Electron Source with High Polarization", Proc.Particle Accelerator Conference, Washington,D.C. (May 1993).

The Evolution of Tensor Polarization *

H. Huang, S.Y. Lee
IUCF, Indiana University, Bloomington, IN 47405
L. Ratner
Brookhaven National Laboratory, Upton, NY 11973

Abstract

Using the equation of motion for the vector polarization, the spin transfer matrix for spin tensor polarization is derived. We study the evolution equation for the tensor polarization in the presence of an isolated spin resonance and in the presence of a spin rotator, or snake.

I. INTRODUCTION

Polarized beam is used very often as a research tool to study the fundamental interactions between elementary particles. Much has been written about both the theoretical and experimental aspects of spin polarization in particle accelerator for spin-$\frac{1}{2}$ particles. But it is believed that there has been no systematic study on the possibility of accelerating polarized spin-1 particle (e.g., deuteron) beams. The complexity of spin-1 particle comes from the tensor polarization. [1] Recently, two of the authors (Lee and Ratner) studied the possibility of polarized deuteron beams in the AGS and RHIC. [2] To get a basic understanding of the polarized deuteron beam, it is worthwhile to derive the evolution equation of tensor polarization.

Spin motion in circular accelerators follows the Thomas-BMT equation. [3] In a synchrotron, the Thomas-BMT equation can be rewritten in terms of particle coordinates in the synchrotron, i.e., the Frenet-Serret curvilinear coordinates . [4] Expressing the spin vector in terms of its components,

$$\vec{S} = S_1 \hat{x} + S_2 \hat{s} + S_3 \hat{z}, \tag{1}$$

and defining $S_\pm = S_1 \pm iS_2$, the equation of spin motion becomes,

$$\frac{dS_\pm}{d\theta} = \pm iG\gamma S_\pm \pm iF_\pm S_3; \quad \frac{dS_3}{d\theta} = \frac{i}{2}(F_- S_+ - F_+ S_-) \tag{2}$$

where G is the anomalous gyromagnetic g-factor, γ is the relativistic Lorentz factor, and $F_\pm$ characterize the spin depolarization kick. The spin tune, $G\gamma$, is the number of

spin precessions per orbit turn. Eq.(2) is the general spin equation of motion for a particle moving in a synchrotron. Given the periodic nature of circular accelerator, $F_\pm$ can be Fourier analyzed as

$$F_- = \sum \epsilon_j e^{-iK_j\theta} \tag{3}$$

where the Fourier amplitude ϵ_j is called the resonance strength, the corresponding frequency K_j is called resonance tune, and θ is azimuthal orbit rotation angle. When particle is moving at constant $G\gamma$, for a single resonance, i.e., $F_- = \epsilon e^{-iK\theta}$, the equations can be solved analytically. In this paper, we only consider the single resonance case. Transforming the equation of motion into the resonance precessing frame, the eigenvalues σ can be determined as,

$$\sigma = 0, \pm\lambda, \quad \lambda = \sqrt{\delta^2 + |\epsilon|^2} \tag{4}$$

where $\delta \equiv (K - G\gamma)$. The spin closed orbit is given by

$$\hat{n}_{co} = \frac{1}{\sqrt{|\epsilon|^2 + \delta^2}}[\delta\vec{e}_3 + \epsilon_R\vec{e}_1 - \epsilon_I\vec{e}_2] \tag{5}$$

where the unit vectors $\vec{e}_1, \vec{e}_2, \vec{e}_3$ coincide with $\hat{x}, \hat{s}, \hat{z}$ at any azimuth in the ring.

II. TENSOR POLARIZATION

For particles of spin S the polarization state can be completely described by $(2S+1)^2 - 1$ parameters. For spin-$\frac{1}{2}$ particles, three parameters are required for the specification of the most general mixed state. This is referred to as vector polarization. It is just the average value of the particle spin $\vec{S}$, where the average is taken over all the particles in the beam and can be written as $\langle\vec{S}\rangle$. $\langle\vec{S}\rangle$ follows the similar equation as eq.(2) with every spin quantity being averaged. For spin-1 particles, apart from 3 components of the vector polarization, there are in general 5 components of tensor polarization. The explicit forms of the tensor operators in terms of the spin operator $\vec{S}$ are; [1]

$$\langle T_0 \rangle = \frac{1}{\sqrt{2}}(3\langle S_3^2 \rangle - 2),$$

$$\langle T_{\pm 1} \rangle = \mp\frac{\sqrt{3}}{2}\langle(S_\pm S_3 + S_3 S_\pm)\rangle, \tag{6}$$

$$\langle T_{\pm 2} \rangle = \frac{\sqrt{3}}{2}\langle S_\pm^2 \rangle$$

Using the spin vector equation of motion, eq.(2), the spin tensor equation of motion for particles moving in a synchrotron can be derived. The bracket notation is dropped for simplicity.

$$\frac{dT_0}{d\theta} = \frac{1}{\sqrt{2}}(3\frac{dS_3}{d\theta}S_3 + 3S_3\frac{dS_3}{d\theta})$$

$$= -\frac{\sqrt{6}}{2}i(F_-T_1 + F_+T_{-1}) \qquad (7)$$

$$\frac{dT_{\pm 1}}{d\theta} = -\frac{\sqrt{3}}{2}(\frac{dS_\pm}{d\theta}S_3 + S_\pm\frac{dS_3}{d\theta} + \frac{dS_3}{d\theta}S_\pm + S_3\frac{dS_\pm}{d\theta})$$

$$= \pm iG\gamma T_{\pm 1} - \frac{\sqrt{6}}{2}iF_\pm T_0 - iF_\mp T_{\pm 2} \qquad (8)$$

$$\frac{dT_{\pm 2}}{d\theta} = \frac{\sqrt{3}}{2}(\frac{dS_\pm}{d\theta}S_\pm + S_\pm\frac{dS_\pm}{d\theta})$$

$$= \pm 2iG\gamma T_{\pm 2} - iF_\pm T_{\pm 1} \qquad (9)$$

These equations can be rewritten in matrix form as,

$$\frac{d}{d\theta}\begin{pmatrix} T_2 \\ T_1 \\ T_0 \\ T_{-1} \\ T_{-2} \end{pmatrix} = A\begin{pmatrix} T_2 \\ T_1 \\ T_0 \\ T_{-1} \\ T_{-2} \end{pmatrix} \equiv AT \qquad (10)$$

where A is given by

$$A = \begin{pmatrix} 2iG\gamma & -iF_+ & 0 & 0 & 0 \\ -iF_- & iG\gamma & -\frac{\sqrt{6}}{2}iF_+ & 0 & 0 \\ 0 & -\frac{\sqrt{6}}{2}iF_- & 0 & -\frac{\sqrt{6}}{2}iF_+ & 0 \\ 0 & 0 & -\frac{\sqrt{6}}{2}iF_- & -iG\gamma & -iF_+ \\ 0 & 0 & 0 & -iF_- & -2iG\gamma \end{pmatrix} \qquad (11)$$

III. SPIN TENSOR CLOSED ORBIT

For an imperfection resonance, the spin closed orbit for the vector polarisation is well-defined. Since the evolution of tensor polarisation can be derived from the equation of motion of vector polarisation, the tensor polarisation should not change when vector polarisation is on closed orbit. Then corresponding tensor polarisation is spin tensor closed orbit. From section 1, spin closed orbit for vector polarisation is

$$\begin{pmatrix} S_3 \\ S_+ \\ S_- \end{pmatrix}_{co} = \frac{1}{\sqrt{2|\epsilon|^2 + \delta^2}}\begin{pmatrix} \delta \\ \epsilon^* \\ \epsilon \end{pmatrix} \qquad (12)$$

where ϵ^* is the complex conjugate of ϵ. From the definition of tensor polarisation, the corresponding tensor polarisation closed orbit is

$$\begin{pmatrix} T_2 \\ T_1 \\ T_0 \\ T_{-1} \\ T_{-2} \end{pmatrix}_{co} = \begin{pmatrix} \frac{\sqrt{3}}{2}\frac{\epsilon^{*2}}{2|\epsilon|^2+\delta^2} \\ -\frac{\sqrt{3}\epsilon^*\delta}{2|\epsilon|^2+\delta^2} \\ \frac{1}{\sqrt{2}}(\frac{3\delta^2}{2|\epsilon|^2+\delta^2} - 2) \\ -\frac{\sqrt{3}\epsilon\delta}{2|\epsilon|^2+\delta^2} \\ \frac{\sqrt{3}}{2}\frac{\epsilon^2}{2|\epsilon|^2+\delta^2} \end{pmatrix} \qquad (13)$$

IV. TRANSFER MATRIX FOR TENSOR POLARIZATION

When particles are moving at constant $G\gamma$, and a single resonance is considered, the equation of motion for tensor polarisation can be solved analytically. At a constant spin tune $G\gamma$, the equation of motion can be transformed into the resonance precessing frame by following transformation:

$$T = \begin{pmatrix} e^{i2K\theta} & 0 & 0 & 0 & 0 \\ 0 & e^{iK\theta} & 0 & 0 & 0 \\ 0 & 0 & 1 & 0 & 0 \\ 0 & 0 & 0 & e^{-iK\theta} & 0 \\ 0 & 0 & 0 & 0 & e^{-2iK\theta} \end{pmatrix}\begin{pmatrix} \tilde{T}_2 \\ \tilde{T}_1 \\ \tilde{T}_0 \\ \tilde{T}_{-1} \\ \tilde{T}_{-2} \end{pmatrix}$$

$$\equiv \Theta\tilde{T} \qquad (14)$$

Then the equation of motion becomes

$$\frac{dT}{d\theta} = \Theta\frac{d}{d\theta}\tilde{T} + \frac{d\Theta}{d\theta}\tilde{T} \qquad (15)$$

which can be rewritten in matrix form as,

$$\frac{d}{d\theta}\begin{pmatrix} \tilde{T}_2 \\ \tilde{T}_1 \\ \tilde{T}_0 \\ \tilde{T}_{-1} \\ \tilde{T}_{-2} \end{pmatrix} = R\begin{pmatrix} \tilde{T}_2 \\ \tilde{T}_1 \\ \tilde{T}_0 \\ \tilde{T}_{-1} \\ \tilde{T}_{-2} \end{pmatrix} \qquad (16)$$

where

$$R = \begin{pmatrix} -2i\delta & -i\epsilon^* & 0 & 0 & 0 \\ -i\epsilon & -i\delta & -i\frac{\sqrt{6}}{2}\epsilon^* & 0 & 0 \\ 0 & -i\frac{\sqrt{6}}{2}\epsilon & 0 & -i\frac{\sqrt{6}}{2}\epsilon^* & 0 \\ 0 & 0 & -i\frac{\sqrt{6}}{2}\epsilon & i\delta & -i\epsilon^* \\ 0 & 0 & 0 & -i\epsilon & 2i\delta \end{pmatrix} \qquad (17)$$

Now we can find the eigenvalues of R. The five eigenvalues are

$$\sigma_{\pm 2} = \pm 2\lambda, \quad \sigma_{\pm 1} = \pm\lambda, \quad \sigma_0 = 0. \qquad (18)$$

where λ is given by eq.(4). The system has five eigenvalues, $0, \pm i\lambda$ and $\pm i2\lambda$ which correspond to five eigensolutions describing the spin tensor along the spin closed orbit and the spin tensors precessing right/left with respect to $\hat{n}_{co}$ with precessing tunes λ and 2λ.

Given the eigenvalues, the equation of motion could have following solutions

$$T_i = A_i^{(\pm)}e^{\pm i2\lambda\theta}; \quad T_i = B_i^{(\pm)}e^{\pm i\lambda\theta};$$

$$T_i = C_i, \quad i = 0, \pm 1, \pm 2. \qquad (19)$$

where $A_i^{(\pm)}$, $B_i^{(\pm)}$, and C_i are arbitrary coefficients. For each eigenvalue, the 5 coefficients are not independent, they are constrained by the differential equation (10). Because 4 of the 5 equations are independent, the 5 coefficients are reduced to 1 independent coefficient. For 5

433

eigenvalues, there are 5 independent coefficients which are determined by the initial condition $T_i(\theta = \theta_0)$, where θ_0 is the initial orbit rotation angle. By solving the equation of motion, we can get the spin transfer matrix $\tilde{M}(\theta, \theta_0)$

$$\tilde{T}(\theta) = \tilde{M}(\theta, \theta_0)\tilde{T}(\theta_0). \tag{20}$$

To simplify the formalism, let $\theta_0 = 0$. Define two sets of functions m_i and a_{ij}

$$
\begin{aligned}
m_{-2}(\sigma_i) &= 1 \\
m_{-1}(\sigma_i) &= -(\sigma_i - 2\delta) \\
m_0(\sigma_i) &= (\sigma_i - \delta)(\sigma_i - 2\delta) - |\epsilon|^2 \\
m_1(\sigma_i) &= -\sigma_i m_0(\sigma_i) - \frac{3}{2}|\epsilon|^2(\sigma_i - 2\delta) \\
m_2(\sigma_i) &= -\frac{1}{\sigma_i + 2\delta} m_1(\sigma_i)
\end{aligned} \tag{21}
$$

$$
\begin{aligned}
a_{j2} &= \frac{\epsilon^4}{16\lambda^4}(m_j(2\lambda)e^{i2\lambda\theta} + m_j(-2\lambda)e^{-i2\lambda\theta}) - \\
&\quad \frac{\epsilon^4}{4\lambda^4}(m_j(\lambda)e^{i\lambda\theta} + m_j(-\lambda)e^{-i\lambda\theta}) + \frac{3\epsilon^4}{8\lambda^4}m_j(0) \\
a_{j1} &= -\frac{\epsilon^3}{8\lambda^4}[(\delta+\lambda)m_j(2\lambda)e^{i2\lambda\theta} + (\delta-\lambda) \\
&\quad m_j(-2\lambda)e^{-i2\lambda\theta}] + \frac{\epsilon^3}{4\lambda^4}[(2\delta+\lambda)m_j(\lambda)e^{i\lambda\theta} + \\
&\quad (2\delta-\lambda)m_j(-\lambda)e^{-i\lambda\theta}] - \frac{3\delta\epsilon^3}{4\lambda^4}m_j(0) \\
a_{j0} &= \frac{\sqrt{6}\epsilon^2}{16\lambda^4}[(\delta+\lambda)^2 m_j(2\lambda)e^{i2\lambda\theta} + (\delta-\lambda)^2 m_j(-2\lambda) \\
&\quad e^{-i2\lambda\theta}] - \frac{\sqrt{6}\delta\epsilon^2}{16\lambda^4}[(\delta+\lambda)m_j(\lambda)e^{i\lambda\theta} + \\
&\quad (\delta-\lambda)m_j(-\lambda)e^{-i\lambda\theta}] - \frac{\sqrt{6}\delta\epsilon^2}{8\lambda^4}(|\epsilon|^2 - 2\delta^2)m_j(0) \\
a_{j,-1} &= -\frac{\epsilon}{8\lambda^4}[(\delta+\lambda)^3 m_j(2\lambda)e^{i2\lambda\theta} + (\delta-\lambda)^3 m_j(-2\lambda) \\
&\quad e^{-i2\lambda\theta}] - \frac{\epsilon}{4\lambda^4}[(\lambda-2\delta)(\lambda+\delta)^2 m_j(\lambda)e^{i\lambda\theta} + \\
&\quad (-\lambda-2\delta)(-\lambda+\delta)^2 m_j(-\lambda)e^{-i\lambda\theta}] + \frac{3\delta|\epsilon|^2\epsilon}{4\lambda^4}m_j(0) \\
a_{j,-2} &= \frac{1}{16\lambda^4}[(\delta+\lambda)^4 m_j(2\lambda)e^{i2\lambda\theta} + (\delta-\lambda)^4 \\
&\quad m_j(-2\lambda)e^{-i2\lambda\theta}] + \frac{|\epsilon|^2}{4\lambda^4}[(\delta+\lambda)^2 m_j(\lambda)e^{i\lambda\theta} \\
&\quad +(\delta-\lambda)^2 m_j(-\lambda)e^{-i\lambda\theta}] + \frac{3|\epsilon|^4}{8\lambda^4}m_j(0)
\end{aligned} \tag{22}
$$

Then the transfer matrix for the tensor polarization $\tilde{M}(\theta, 0)$ is,

$$
\begin{pmatrix}
\frac{2\epsilon^2}{3\epsilon^3}a_{22} & \frac{2\epsilon^2}{3\epsilon^3}a_{21} & \frac{2\epsilon^2}{3\epsilon^3}a_{20} & \frac{2\epsilon^2}{3\epsilon^3}a_{2-1} & \frac{2\epsilon^2}{3\epsilon^3}a_{2-2} \\
\frac{2}{3\epsilon^3}a_{12} & \frac{2}{3\epsilon^3}a_{11} & \frac{2}{3\epsilon^3}a_{10} & \frac{2}{3\epsilon^3}a_{1-1} & \frac{2}{3\epsilon^3}a_{1-2} \\
\frac{2}{\sqrt{6}\epsilon^2}a_{02} & \frac{2}{\sqrt{6}\epsilon^2}a_{01} & \frac{2}{\sqrt{6}\epsilon^2}a_{00} & \frac{2}{\sqrt{6}\epsilon^2}a_{0-1} & \frac{2}{\sqrt{6}\epsilon^2}a_{0-2} \\
\frac{1}{\epsilon}a_{-12} & \frac{1}{\epsilon}a_{-11} & \frac{1}{\epsilon}a_{-10} & \frac{1}{\epsilon}a_{-1-1} & \frac{1}{\epsilon}a_{-1-2} \\
a_{-22} & a_{-21} & a_{-20} & a_{-2-1} & a_{-2-2}
\end{pmatrix} \tag{23}
$$

V. TRANSFER MATRIX FOR SNAKE

A snake is characterized by the spin rotating angle, ϕ, and the snake axis angle, ϕ_s, with respect to $\hat{s}$ (radially outward direction). A full snake rotates particle spin by π. The transfer matrix for snake with arbitrary ϕ and ϕ_s can be derived easily. To save length, we only consider an accelerator with two snakes with $\phi_s = \frac{\pi}{2}$ and $\phi_s = \pi$, respectively, located at an orbital angle of π from each other. For

$\phi_s = \frac{\pi}{2}$, the spin components at a snake are transformed according to

$$
\begin{pmatrix} S_3(\theta^+) \\ S_+(\theta^+) \\ S_-(\theta^+) \end{pmatrix} =
\begin{pmatrix} -1 & 0 & 0 \\ 0 & 0 & -1 \\ 0 & -1 & 0 \end{pmatrix}
\begin{pmatrix} S_3(\theta^-) \\ S_+(\theta^-) \\ S_-(\theta^-) \end{pmatrix} \tag{24}
$$

where the $\theta^\pm$ depict azimuthal orbit rotation angles just before and after the snake.

The transfer matrix of the tensor polarization for a snake with $\phi_s = \frac{\pi}{2}$ can be derived to be:

$$
\tilde{T}(\theta^+) =
\begin{pmatrix}
0 & 0 & 0 & 0 & 1 \\
0 & 0 & 0 & -1 & 0 \\
0 & 0 & 1 & 0 & 0 \\
0 & -1 & 0 & 0 & 0 \\
1 & 0 & 0 & 0 & 0
\end{pmatrix}
\tilde{T}(\theta^-) \equiv S(\frac{\pi}{2})\tilde{T}(\theta^-) \tag{25}
$$

Similarly, the tensor polarizations are transformed by the following mapping equation for a snake with $\phi_s = \pi$:

$$
\tilde{T}(\theta^+) =
\begin{pmatrix}
0 & 0 & 0 & 0 & 1 \\
0 & 0 & 0 & 1 & 0 \\
0 & 0 & 1 & 0 & 0 \\
0 & 1 & 0 & 0 & 0 \\
1 & 0 & 0 & 0 & 0
\end{pmatrix}
\tilde{T}(\theta^-) \equiv S(\pi)\tilde{T}(\theta^-) \tag{26}
$$

Then the one turn map matrix is given by

$$\tilde{T}(2\pi) = S(\frac{\pi}{2})M(2\pi, \pi)S(\pi)M(\pi, 0)\tilde{T}(0) \tag{27}$$

Since

$$T = \Theta\tilde{T}, \quad \tilde{T}(\theta) = \tilde{M}(\theta, 0)\tilde{T}(0), \tag{28}$$

Finally, $T(\theta)$ is transformed as

$$
\begin{aligned}
T(2\pi) = \Theta(2\pi)S(\frac{\pi}{2})\tilde{M}(2\pi, \pi) \cdot \\
S(\pi)\tilde{M}(\pi, 0)\Theta^{-1}(0)T(0)
\end{aligned} \tag{29}
$$

VI. CONCLUSION

We have discussed tools needed for tracking the spin tensor polarization of spin-1 particles in synchrotrons. The tensor transfer matrix was derived for a single resonance and in the presence of snakes. The evolution of tensor polarization in synchrotron can therefore be studied along with the vector polarization.

REFERENCES

[1] Nuclear Spectroscopy and Reaction, Part A, ed. J.Cerny, Academic Press, New York, 151(1974).

[2] S.Y.Lee and L.G.Ratner, Polarized Collider Workshop, AIP Conf. Proc. No.223,350(1991).

[3] L.H.Thomas, Phil. Mag. 3, 1(1927).

[4] S.Y.Lee, Proc. 8th Intern. Symp. High Energy Spin Physics, AIP Conf. Proc. No.187,1105(1989).

Even Order Snake Resonances

S.Y. Lee

Department of Physics, Indiana University, Bloomington, IN 47405

ABSTRACT

We found that the perturbed spin tune due to the imperfection resonance plays an important role in beam depolarization at snake resonances. We also found that *even* order snake resonances exist in the overlapping intrinsic and imperfection resonances. Due to the perturbed spin tune shift of imperfection resonances, each snake resonance splits into two.

1   Introduction

The spin equation of motion for a spin particle, governed by the magnetic interaction between the magnetic dipole moment of the particle and the static magnetic field in a synchrotron, is given by the Thomas-BMT equation [1] , $\frac{d\vec{S}}{dt} = \frac{e}{\gamma m}\vec{S} \times [(1 + G\gamma)\vec{B}_\perp + (1 + G)\vec{B}_\parallel]$, where $\vec{B}_\perp$ and $\vec{B}_\parallel$ are the transverse and longitudinal components of the magnetic fields with respect to the velocity vector, $\vec{\beta}$. In a planar synchrotron, vertical magnetic fields are needed to guide the orbiting particle around a closed path. Thus the spin vector is precessing with respect to the vertical axis at a frequency $G\gamma f_0$, where f_0 is the revolution frequency, $G = \frac{g}{2} - 1$ is the anomalous magnetic g-factor and γ is the relativistic Lorentz factor. The quantity, $G\gamma$, representing the number of spin precessions per revolution, is called the spin tune.

In a synchrotron, strong quadrupole fields are also needed to focus the beam to a small size. Those particles moving off-center vertically in quadrupoles experience horizontal fields, which will kick the spin vector away from the vertical axis. Since quadrupole magnets and the particle closed orbits are periodic in a circular accelerator and the betatron and the synchrotron motions are quasiperiodic, perturbing kicks to the spin vector can be decomposed into harmonics, K, given by $K = n + m\nu_z + \ell\nu_x + k\nu_{syn}$, where ν_z, ν_x and ν_{syn} are respectively the vertical betatron, the horizontal betatron and the synchrotron tunes, and k, ℓ, m, n are integers. The imperfection resonances, due to the vertical closed orbit errors, are located at integer harmonics, $K = n$. The intrinsic resonances, due to the vertical betatron motion, are located at $K = nP + \nu_z$, where P is the superperiodicity of the accelerator. Other depolarizing resonances arise from linear or nonlinear betatron coupling, vertical dispersion, synchro-betatron coupling and random field errors. When the spin precession frequency is in phase with the harmonics of perturbing kicks, i.e. $G\gamma = K$, these spin perturbing kicks add up coherently every turn around the ring. Therefore the beam can be depolarized.

To avoid a spin resonance condition, Derbenev and Kondratenko [3] proposed to use a local spin rotator, which rotates the spin vector 180° about an axis in the horizontal plane. These spin rotators are called snakes. Using snakes in an accelerator, the spin tune of the particle can become $\frac{1}{2}$ and independent of energy. The resonance condition can be avoided.

2   Snakes and Spin Motion

Snakes are local spin rotators, which rotate particle spin by π radians about a horizontal axis locally without perturbing particle orbits outside a snake region. A partial snake differs only in the amount of spin rotation angle, e.g. a 10% snake rotates spin by 0.1π radians. Thus a snake is characterized by the amount of *spin rotation angle*, ϕ, and the *snake axis angle*, ϕ_s, with respect to $\hat{e}_1$ (radially outward direction). The spinor wave function at a snake will be transformed locally according to $\Psi(\theta^+) = e^{-i\frac{\phi}{2}\hat{n}_s \cdot \vec{\sigma}}\Psi(\theta^-)$, where ϕ is spin rotation angle and $\hat{n}_s = (\cos\phi_s, \sin\phi_s, 0)$ denotes the snake axis with respect to radially outward direction, $\hat{e}_1$. $\theta^\pm$ depict azimuthal orbit rotation angles just before and after the snake. More specifically, at $\phi = \pi$, or the 100% snake, the spinor wave function can be transformed as,

$$\Psi(\theta^+) = e^{-i\frac{\pi}{2}\hat{n}_s \cdot \vec{\sigma}}\Psi(\theta^-) = T_s(\phi_s)\Psi(\theta^-), \qquad (1)$$

where $T_s(\phi_s) = -i\hat{n}_s \cdot \vec{\sigma}$ is the spin transfer matrix for a 100% snake.

Let us consider a perfect circular accelerator with two snakes, $-i\sigma_1, -i\sigma_2$, separated by π orbital angle apart. The one turn spin transfer matrix (OTM) is given by

$$[-i\sigma_2]e^{-i\frac{G\gamma\pi}{2}\sigma_3}[-i\sigma_1]e^{-i\frac{G\gamma\pi}{2}\sigma_3} = i\sigma_3. \qquad (2)$$

Thus the spin tune, obtained from the trace of the one turn spin transfer matrix, is $\frac{1}{2}$ and the stable spin closed orbit is vertical. Now we introduce a small constant local spin angular precessing kick, χ, about an axis $\hat{n}_k$ in the horizontal plane, the spin transfer matrix becomes,

$$T_1 = e^{-i\frac{\chi}{2}\hat{n}_k \cdot \vec{\sigma}}i\sigma_3. \qquad (3)$$

Because $\hat{n}_k$ is in the horizontal plane, the evolution of the spin transfer matrix at the nth revolution becomes,

$$T^{(n)} = [T_1]^n = \begin{cases} [i\sigma_3]^n & \text{if } n = \text{even} \\ T_1[i\sigma_3]^{(n-1)} & \text{if } n = \text{odd} \end{cases}, \qquad (4)$$

which means that the perturbed spin precessing kicks cancel each other every two turns around the accelerator. Thus the snake is effective in correcting imperfection resonances due to a localized constant spin perturbing kick.

435
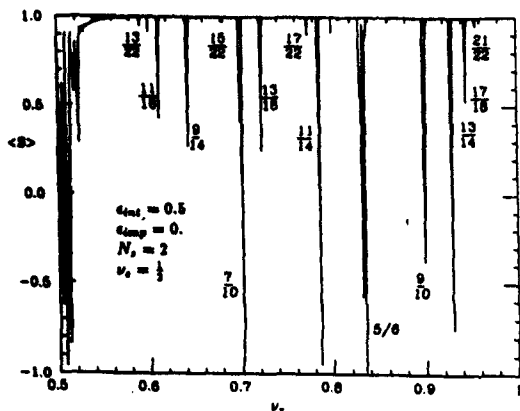
Figure 1: The vertical polarization after passing through an intrinsic depolarization resonance with two snakes is plotted as a function of the vertical betatron tune ν_z.

Extending the model a step further, we assume that the precessing kick is different in each turn, the spin transfer matrix becomes,

$$T^{(n)} = \prod_{m=1}^{n} T_m = e^{-i\frac{1}{2}[\sum_{m=1}^{n}(-1)^{n-m}\chi_m]\hat{n}_k \cdot \vec{\sigma}}[i\sigma_3]^n. \quad (5)$$

The vertical spin vector is given by,
$$S_3^{(n)} = 1 - 2\sin^2[\frac{1}{2}\sum_{m=1}^{n}(-1)^{n-m}\chi_m].$$
Now if the spin perturbation kicks are due to a betatron motion, these kicks are correlated by $\chi_m = \chi_0 \cos 2m\pi\nu_z$, where ν_z is the fractional part of the vertical betatron tune. When the vertical betatron tune is $\nu_z = \frac{1}{2}$, each kick adds up coherently. The spin vector will precess around the $\hat{n}_k$ axis at a precessing tune of $\frac{\chi_0}{2\pi}$, i.e. it takes $\frac{2\pi}{\chi_0}$ turns to complete one revolution around the $\hat{n}_k$ axis.

3 Odd order snake resonances

Subsequent studies show that when the resonance strength is large, new spin depolarizing resonances occur at some fractional betatron tunes. These resonances are called *snake resonances* [4] . Snake resonances, due to coherent higher order spin perturbing kicks, are located at

$$\nu_s + \ell K = \text{ integer}, \quad \ell = 1,3,5,7,\cdots, \quad (6)$$

where ν_s is the spin tune and K is the spin depolarizing resonant harmonic. For $\nu_s = \frac{1}{2}$, we expect that snake resonances occur at the following fractional betatron tunes, $\nu_z = \frac{1}{2}, \frac{1}{6}, \frac{5}{6}, \frac{1}{10}, \frac{3}{10}, \frac{7}{10}, \frac{9}{10}, \frac{1}{14}, \frac{3}{14}, \cdots$, where the lowest order snake resonance has been observed [5] . Other higher order snake resonances have been identified in numerical simulation (Fig. 1). It is interesting to note that the numerical simulations show no apparent even order snake resonances at

$$\nu_s + \ell K = \text{ integer}, \quad \ell = 2,4,6,8,\cdots. \quad (7)$$

Several reasons for the nonexistence of even order snake resonances were given in the past [4,6], which has never been tested in the case of overlapping resonances.

Overlapping resonances are important in high energy accelerators. [6,7] An important imperfection resonance occur usually at the integer nearest to the dominant intrinsic resonance. Therfore overlapping intrinsic and imperfection resonances constitute the most important problem in the spin dynamics during polarized proton acceleration.

4 Even Order Snake Resonances

To understand the effect of imperfection resonances on the spin motion, we reduce intrinsic resonance strength in our calculation to $\epsilon_{int} = 0.137$, where only low order snake resonances at $\nu_z = 1/2$, $1/6$, $5/6$ are important. When an imperfection resonance at $\epsilon_{imp} = 0.13$ is included, we found that even order snake resonances at $\nu_z = 3/4$, $5/8$, $7/8$, $\cdots$ appear. Furthermore, all snake resonances split into double peaks shown in Fig. 2. The distance of these two peaks increases with the strength of the imperfection resonance. Note that the even order snake resonance becomes more important than the odd order snake resonance and the odd order snake resonance is not affected by the imperfection resonance. Note also that double peaks occur for each snake resonance. The feature of double peaks can be understood easily knowing that the imperfection resonance generates a perturbed spin tune shift. The snake resonance condition becomes

$$\frac{1}{2} + \Delta Q_s \pm \ell\nu_z = \text{ integer}, \quad \ell = \text{ integer}, \quad (8)$$

where ΔQ_s is the perturbed spin tune shift from the imperfection resonance given by

$$|\Delta Q_s| \approx \frac{1}{\pi} \arcsin[\sin^2 \frac{\pi\epsilon_{imp}}{N_s}], \quad (9)$$

where the actual magnitude and sign of the spin tune shift depend on the closed orbit of the circular accelerator. The distance of splitting becomes smaller at higher order snake resonances (Fig. (2)) with $\Delta\nu_z = \pm\frac{1}{\ell}\Delta Q_s$. The depolarization line shape of these double peak reflects the important effect of perturbed spin tune shift on the snake resonances at the maximum spin tune shift.

To understand the essential mechanism of the even order snake resonances in the presence of overlapping spin resonances, we consider the model of the spin transfer matrix. The OTM of the overlapping intrinsic and imperfection resonances can be expressed as

$$\tilde{\tau} = e^{-i\frac{\chi}{2}\sigma_1}\tau(\theta_0 + 2\pi, \theta_0), \quad (10)$$

where $\tau(\theta_0 + 2\pi, \theta_0)$ is the OTM without imperfection resonance and we have assumed a small local spin precessing kick, χ, about the $\hat{e}_1$ axis. The resonance strength of the imperfection resonance is given by $\epsilon_{imp} = \chi/2\pi$ at all integer harmonics. Due to the imperfection resonance, the off-diagonal matrix elements now contain a term oscillating at
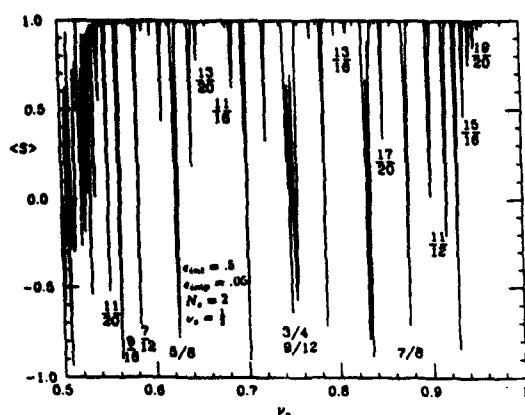
Figure 2: Vertical polarization after passing through an overlapping intrinsic and imperfection resonances with two snakes

Figure 3: The critical snake resonance strength vs the order of snake resonance is plotted for $\dot{p}_0 = 5$ MeV/c per turn on the left. The critical resonance strength vs the acceleration rate is plotted in the middle part and the snake resonance strength for the even order resonance as a function of the imperfection resonance is shown on the right

two times the betatron frequency with an amplitude proportional to $b^2 \sin\frac{\chi}{2}$. Thus the snake resonance condition is given by $\nu_s \pm 2K =$ integer. Performing similar higher order analysis, one obtain all even order snake resonances.

5 Critical Resonance Strength

Let us define the critical resonance strength as the resonance strength that the polarization is preserved to within 1.5% of full polarization. Fig. 3 shows the critical resonance strength for the odd and even order snake resonances at the acceleration rate of 5 MeV/c per revolution. Depending on the acceleration rate, the critical resonacne strength can be described by the following formula fitted to numerical simulation results,

$$\epsilon_{c,5/6} = \ln[1.12(\frac{\dot{p}}{\dot{p}_0})^{0.024}],$$

$$\epsilon_{c,21/26} = \ln[1.64(\frac{\dot{p}}{\dot{p}_0})^{0.024}],$$

$$\epsilon_{c,13/16} = \ln[1.50(\frac{\dot{p}}{\dot{p}_0})^{0.020}],$$

where the reference acceleration rate is $\dot{p}_0 = 5$ MeV/c per revolution. Here we study only $K = \frac{5}{6}, \frac{13}{16}, \frac{21}{26}$ snake resonances with the assumption that the betatron tune are chosen to lie in between $\frac{4}{5}$ and $\frac{5}{6}$ for example for RHIC at BNL.

6 Conclusions

We found that snake resonances, located at $\nu_s + \ell K =$ integer, are the major source of depolarization in synchrotrons with snakes, where the integer ℓ is called the order of snake resonance, K is the spin resonance harmonics. When imperfection resonances are overlapping with intrinsic resonances, even order snake resonances appear. The perturbed spin tune, arising from imperfection resonances, plays an essential role in the depolarization mechanism, it causes each snake resonance to split into two resonances.

References

1. L.H. Thomas, Phil. Mag. 3, 1 (1927); V.Bargmann, L. Michel, and V.L. Telegdi, Phys. Rev. Lett. 2, 435 (1959).

2. E.D. Courant and H.S. Snyder, Ann. Phys. 3,1(1958).

3. Ya.S. Derbenev, and A.M. Kondratenko, Sov. Phys. Doklady, 20, 562 (1976); Ya.S. Derbenev et al., Particle Accelerators, 8, 115 (1978).

4. S.Y. Lee and S. Tepikian, Phys. Rev. Lett. 56, 1635 (1986); S.Tepikian, Ph. D. Thesis, S.U.N.Y. Stony Brook, (1986), unpublished.

5. A.D. Krisch et al., Phys. Rev. Lett. 63, 1137 (1989). J.E. Goodwin et al., Phys. Rev. Lett. 64, 2779 (1990). J.E. Goodwin, Ph.D. Thesis, Indiana University, (1990), unpublished. M. G. Minty, Ph.D. Thesis, Indiana University, (1991), unpublished. M.G. Minty et al., Phys. Rev. D44, R1361 (1991). M.G. Minty and S.Y. Lee, Proc. EPAC p.723 (1992), and Particle Accelerators, to be published.

6. S.Y. Lee, in Proc. of Workshop on Polarized Beams at SSC, A.D. Krisch ed., AIP Conf. Proc. No.145, p. 189 (1985); E.D. Courant, S.Y. Lee and S. Tepikian, ibid. p. 174 (1985); S.Y. Lee, in High Energy Spin Physics, K.J. Heller ed., AIP Conf. Proc. No.187, p. 1105 (1988).

7. S.Y. Lee and E.D. Courant, Phys. Rev. D41, 292 (1990); S.Y.Lee, Phys. Rev. E, in press.

8. K. Steffen, Particle Accelerator 24, 45 (1989).

Wiggler as Spin Rotators for RHIC*

Alfredo Luccio and Mario Conte**
AGS Dept., Brookhaven National Laboratory
Upton, NY 11973

Abstract

The spin of a polarized particle in a circular accelerator can be rotated with an arrangement of dipoles with field mutually perpendicular and perpendicular to the orbit. To achieve spin rotation, a given field integral value is required. The device must be designed in a way that the particle orbit is distorted as little as possible. It is shown that wigglers with many periods are suitable to achieve spin rotation with minimum orbit distortions. Wigglers are also more compact than more established structures [1] and will use less electric power. Additional advantages include their use for non distructive beam diagnostics. Results are igiven for the Relativistic Heavy Ion Collider (RHIC) in the polarized proton mode.

I. INTRODUCTION

Devices to rotate the spin of the proton from vertical to radial and conversely can be built with two series of magnets, each series with magnetic fields directed along the vertical and radial axes respectively. The two series are longitudinally shifted with respect to each other, as schematically shown in Fig. 1. In each configuration the magnetic field integral must be zero, so that a proton entering the structure on axis would also emerge on axis.

Advantages of configurations with more than six dipoles (wiggler rotators) are: (i) smaller overall magnet volumes, (ii) smaller beam displacement from the equilibrium orbit, especially important at lower proton energies (injection), (iii) lower electric power, (iv) possibility of using permanent magnets, (v) use of proton undulator radiation (synchrotron) for non-destructive beam diagnostics. The main disadvantage is the greater rotator length.

We have studied the behavior of a series of wiggler spin rotators, both with conventional and superconducting magnets.

II. EQUATIONS FOR SPIN AND ORBIT

The proton beam propagates along the z-axis (Fig.1). y is the vertical and x the transverse axis. Spin rotation is given by
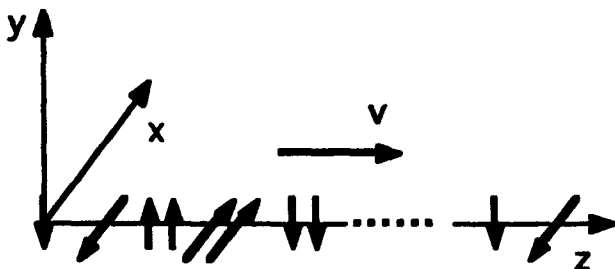
Fig.1 Spin rotator with transverse magnets.

the vector equation for the unitary spin vector in a transverse magnetic field

$$\frac{d\hat{s}}{dt} = \Omega \times \hat{s} = -\frac{e}{m\gamma}(1+G\gamma)B_\perp \times \hat{s} \qquad (1)$$

with γ the relativistic energy of the protons and

$$G = 1.7928 \; ; \frac{e}{m} = 9.58 \, 10^7 \sec^{-1} T^{-1} . \qquad (2)$$

The equation for the trajectory and the first field integral are

$$x,y(z) = \int \frac{I_{x,y}(z)}{\sqrt{1-I_{x,y}^2(z)}} dz \qquad (3)$$

$$I_{x,y}(z) = \frac{e}{\beta\gamma mc}\int B_{x,y}(z)\,dz . \qquad (4)$$

A proton on axis at the entrance will emerge on axis if integral (4) is zero for the whole rotator.

The synchrotron radiation generated by the high energy protons in the wiggler exhibits a line spectrum with fundamental wavelength given by

$$\lambda_1 = \lambda_0 \frac{1+k^2/2}{2\gamma^2} \; ; k = \frac{e}{2\pi mc}\lambda_0 B \qquad (5)$$

where k is a quantity defining the maximum bending angle of the trajectory in units of $1/\gamma$. $\lambda 0$ is the period of the wiggler, i.e. the length of a full field spatial oscillation along the z axis.

III. RESULTS FOR RHIC

The integration of the six equations (3,4) using z as the independent variable was numerically performed by a Runge-Kutta plus Predictor Corrector routine. Results of the calculations for wiggler rotators capable of rotating the polarization between x and y are shown in Table 1. The values are calculated for $\gamma=200$; however, they are in very good approximation valid for a very wide range of proton energies.

Entries in Table 1 are for normal conducting and superconducting magnets. The total length L of a rotator including the two end poles of half strength, and the total relative snake volume V and the relative magnetic field energy W can be estimated as follows

$$L = (n+1)\frac{\lambda_0}{2} \; ; V = L\lambda_0^2 \; ; W = (n+1)\lambda_0^2 B^2 .$$

The expression for the volume relies on the observation that the transverse dimensions of each component dipole (in the normal conducting case) are of the order of the period, and for the energy stored in the field, on the observation that the energy is roughly proportional to the volume of the magnetic gap.

Column 4 is the (odd) number of full field dipoles of half period length. Column 7 is the fundamental wavelength of the radiation. It lies in the infrared; however its harmonics, say

the 5th, 7th and 9th, are in the near infrared or in the visible, then easily detectable.

The product $\lambda_0 B$ needed to appropriately rotate the spin and, accordingly, also the length of a wiggler rotator slowly grows with n. Thus a 15-pole is about twice as long than a 1-pole. However the volume of the magnet decreases, and with it the magnet cost, in spite of the greater complication of fabrication. The energy stored in the magnetic field also decreases for normal conducting snakes. In the SC case, the values given for the volume and energy are indicative.

Figures 2 through 5 show some results (γ=200) of the integration of the spin and orbit equations for a SC 15-pole compared with a NC 1-pole rotator.

IV. REFERENCES

[1] J.Collins, S.F.Heppelman, R.W.Robinett (Eds.)
    "Polarized Collider Workshop", *AIP Proc* **223** (1990)

Table 1
Comparison of wiggler spin rotators

B [T]	λ_0 [m]	L [m]	n	V	W	λ_1 [μm]
Normal Conducting						
1.728	6.0	6.0	1	216	215	85.40
	3.6	7.2	3	93	155	47.25
	2.1	10.2	9	45	132	26.70
	1.63	13.0	15	35	127	20.58
1.85	1.52	12.2	15	28	127	19.19
SuperConducting						
3.2	0.88	7.04	15	6	126	11.11
4.0	0.70	5.60	15	3	125	8.84
6.0	0.47	3.76	15	1	127	5.94
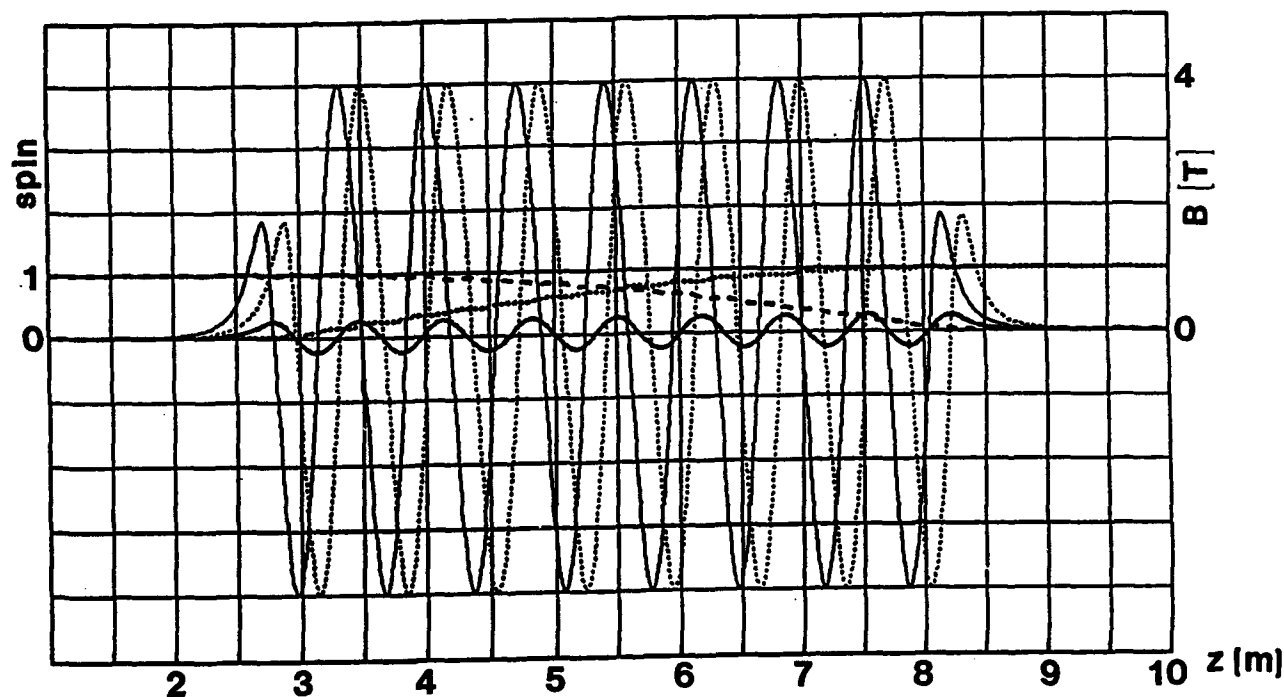
Fig.2. Transition for a 15-pole 4 T SC rotator. Spin from vertical to radial. Thin lines are the field components:B_x (solid), B_y (dotted), thick lines are the spin components: S_x (solid), S_y (dotted), S_z (dashed).
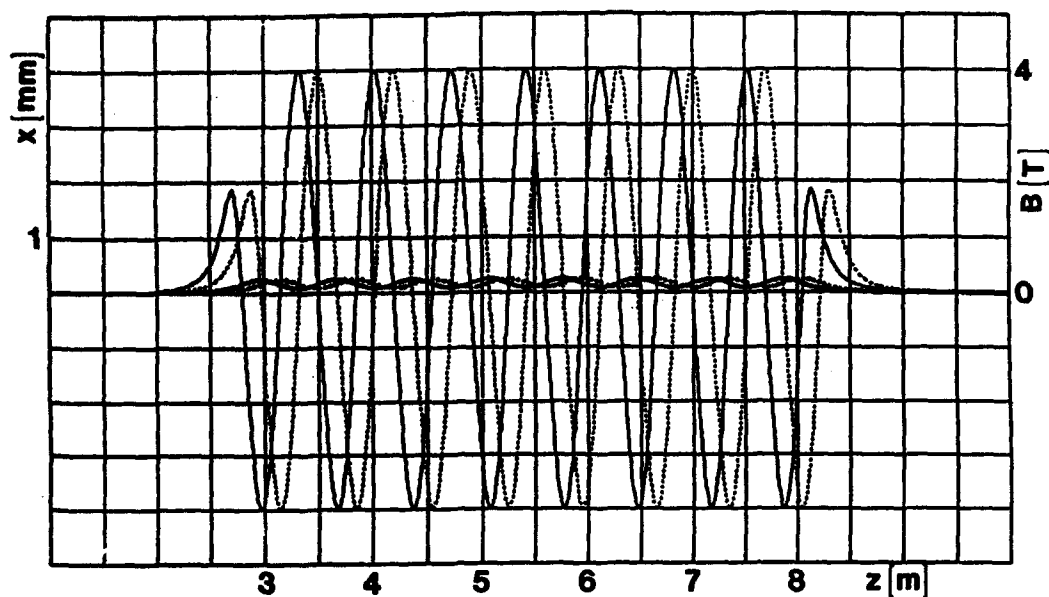
Fig.3. Trajectory in the 15-pole SC rotator of Fig.2. Thin lines are the field components:B_x (solid), B_y (dotted), thick lines are the trajectory: y (vertical, solid), x (radial, dotted).
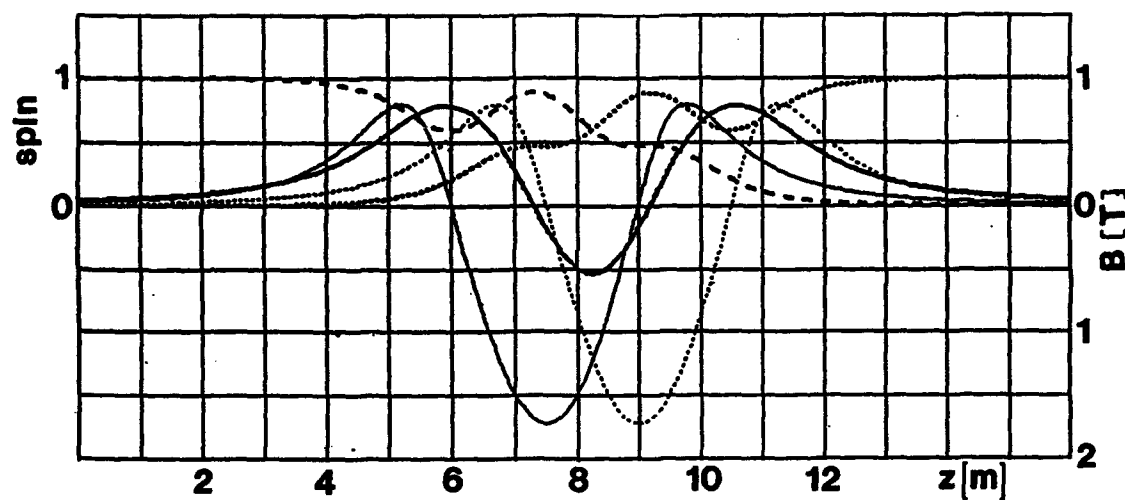
Fig.4. Transition for a 1-pole rotator. Spin from vertical to radial..
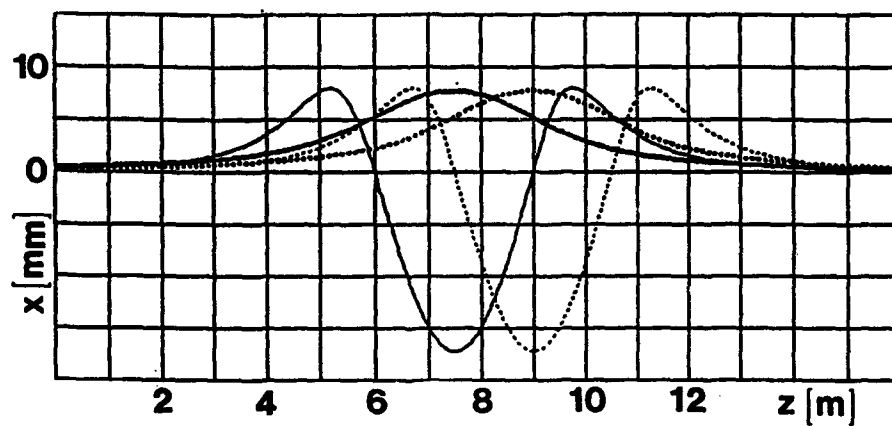
Fig 5. Trajectory in a 1-pole rotator.

Taylor Map and Calculation of Equilibrium Polarization Direction for Proton Storage Rings

V. Balandin and N. Golubeva
Institute for Nuclear Research of the Russian Academy
of Sciences, Moscow

Abstract

The spin-orbital motion in proton storage rings is investigated with help of the methods of Lie operator and computer algebra. The one-turn transfer map is used to obtain the orbital and spin tunes, the invariant functions of the orbital motion and the equilibrium polarization direction.

I. HAMILTONIAN FORM OF CLASSICAL SPIN-ORBIT MOTION EQUATIONS

The system of the ordinary differential equations is called a Hamiltonian system if it can be represented in the form

$$\frac{d\vec{z}}{d\tau} = \{\vec{z}, H\} \qquad (1)$$

where $H = H(\vec{z}, \tau)$ is the Hamiltonian, the binary operation $\{\cdot, \cdot\}$ is the Poisson bracket with the usual properties.

The classical spin-orbit equations of the motion in storage rings or in circular accelerators have the form of a Hamiltonian system if we use the Poisson bracket:

$$\{F(\vec{z}), Q(\vec{z})\} = F_{\vec{q}} \cdot Q_{\vec{p}} - F_{\vec{p}} \cdot Q_{\vec{q}} + [F_{\vec{s}} \times Q_{\vec{s}}] \cdot \vec{S} \qquad (2)$$

and the Hamiltonian:

$$H = H_{orbit}(\vec{z}, \tau) + \vec{W}(\vec{z}, \tau) \cdot \vec{S} \qquad (3)$$

where $\vec{z} = (\vec{x}, \vec{S})$ and $\vec{x} = (\vec{q}, \vec{p})$ are canonical orbit variables, $\vec{S} = (S_1, S_2, S_3)$ is a classical spin vector.

For example, if τ means the time t, $\vec{q}$ and $\vec{p}$ are canonical orbit position and momentum variables in a fixed Cartesian coordinate system, then

$$H = e\Phi + c\sqrt{m_0^2 c^2 + (\vec{p} - \frac{e}{c}\vec{A})^2} + \vec{W} \cdot \vec{S}$$

where

$$\vec{W} = -\frac{e}{m_0 \gamma c}((1 + \gamma G)\vec{B} - \frac{G\gamma^2}{(1+\gamma)c^2}(\vec{v}\vec{B})\vec{v}$$
$$-(G\gamma + \frac{\gamma}{1+\gamma})[\vec{v} \times \frac{\vec{E}}{c}])$$

e, m_0 are the charge and the rest mass of a particle, c is the velocity of light, $\vec{E}$, $\vec{B}$ are electric and magnetic fields, $G = (g - 2)/2$, g is the anomalous spin factor, γ is the Lorentz factor, $\vec{v}$ is the velocity of a particle, $\vec{A}$ and Φ are vector and scalar potentials [1].

The Poisson bracket (2) is degenerated. It has the nontrivial Casimir function $|\vec{S}|^2$. It means that we can decrease the dimension of the system (1) studding the equations on the sphere: $|\vec{S}| = \hbar/2$, where $\hbar$ is Planck's constant. For example, we can do this by introducing a pair of canonical spin variables (J, ψ), J is a projection on the selected axis, ψ is a polar angle in the transverse plane. In this case we obtain the Hamiltonian system with the classical Poisson bracket in eight-dimensional phase space (6 orbital variables and two canonical spin variables J, ψ). But unfortunately, in this case we lose so important property which we would like to keep: the linearity of the initial system in respect of spin variables.

II. ONE TURN MAP AND ITS SIMPLE PROPERTIES

If the Hamiltonian (3) is a periodic function τ, we can consider the one turn map which is defined by the action of the system (1) for one period:

$$\vec{z}_f = \vec{f}(\vec{z}_i) \qquad (4)$$

Let $\vec{z} = \vec{0}$ be the fixed point of the map (4). Using the Taylor series expansion of the function $\vec{f}(\vec{z})$ in respect of spin variables we obtain:

$$\begin{cases} \vec{x}_f = \vec{F}(\vec{x}_i) + O(|\vec{S}_i|) \\ \vec{S}_f = A(\vec{x}_i) \cdot \vec{S}_i + O(|\vec{S}_i|^2) \end{cases} \qquad (5)$$

where $\vec{F}(\vec{0}) = \vec{0}$ and $A(\vec{x})$ is a 3 × 3 matrix. The map (5) preserves the Poisson bracket (2). Using this property we find:

a) The map $\vec{x}_f = \vec{F}(\vec{x}_i)$ is symplectic:

$$\left(\frac{\partial \vec{F}}{\partial \vec{x}}\right)^{\perp} \cdot J \cdot \left(\frac{\partial \vec{F}}{\partial \vec{x}}\right) = J$$

b) Every element of the matrix $A(\vec{x})$ is equal to its own cofactor. It means that $A(\vec{x})$ is an orthogonal matrix and $det A(\vec{x}) = 1$, i.e. $A(\vec{x}) \in SO(3)$.

III. LIE EXPONENTS, ORDER TRUNCATION, AND EXPONENTIAL FACTORIZATION

Using the Poisson bracket (2) we can define the Lie operator $: Q(\vec{z}) :$ and the exponential Lie operator $exp(: Q(\vec{z}) :)$ associated with the function $Q(\vec{z})$ according to the usual rules [2].

The length of the vector $\vec{S}$ is proportional to Planck's constant. Consequently, we will neglect terms of order $\hbar$ in the map (5). It is possible to show that for any given truncation order of the orbital variables m there is the Dragt-Finn's type exponential factorization of the map:

$$: B_{full} : \; = \; : B_{spin} : \; : B_{orbt} : \tag{6}$$
$$: B_{orbt} : \; = \; : A_1 : exp(: F_3 :) \cdots exp(: F_{m+1} :)$$
$$: B_{spin} : \; = \; : A_2 : exp(: \vec{U}_1 \cdot \vec{S} :) \cdots exp(: \vec{U}_m \cdot \vec{S} :)$$

This factorization represents the map (5) with the precision $O(|\vec{S}| + |\vec{x}|^{m+1})$ in the sense that:

$$: B_{full} : \vec{x} \; = \; \vec{F}(\vec{x}) + O(|\vec{S}| + |\vec{x}|^{m+1})$$
$$: B_{full} : \vec{S} \; = \; A(\vec{x}) \cdot \vec{S} + O(|\vec{S}| + |\vec{x}|^{m+1}) \cdot \vec{S}$$

Here $F_k(\vec{x})$ and $\vec{U}_k(\vec{x})$ are homogeneous polynomials of order k.

The exponential representation is comfortable in the sense that it allows to deal not with maps but with their symbols (with algebra of Hamiltonians). It is also possible to find further types of factorizations which we will not mention here.

IV. INVARIANT FUNCTIONS AND EQUILIBRIUM POLARIZATION DIRECTION

The function $V(\vec{z})$ is called an invariant function of the map (4) if

$$V(\vec{z}) = V(\vec{f}(\vec{z})) \tag{7}$$

In this section the conception of the dependent on the spin invariant functions is introduced. Taking into account that we neglect the terms proportional to $\hbar$, it is enough to consider these functions in the form:

$$V(\vec{z}) = b(\vec{x}) + \vec{g}(\vec{x}) \cdot \vec{S} \tag{8}$$

If we substitute (8) in (7), we will see that $b(\vec{x})$ is the usual invariant function of the orbital part of the map. It means that one can find $V(\vec{z})$ only as:

$$V(\vec{z}) = \vec{g}(\vec{x}) \cdot \vec{S} \tag{9}$$

Equation (7) for the function (9) becomes:

$$A(\vec{x}) \cdot \vec{g}(\vec{x}) = \vec{g}(\vec{F}(\vec{x})) \tag{10}$$

From (10) it follows that

a) $|\vec{g}(\vec{x})|^2$ is an invariant function of the map $\vec{F}(\vec{x})$.

b) If $b(\vec{x}) = b(\vec{F}(\vec{x}))$ and $V(\vec{z})$ are invariant functions then $b(\vec{x}) \cdot V(\vec{z})$ is an invariant function also. This allows to identify two invariant functions V_1 and V_2 if $V_1(\vec{z}) = b(\vec{x}) \cdot V_2(\vec{z})$ or $V_2(\vec{z}) = b(\vec{x}) \cdot V_1(\vec{z})$.

We will call the function $V(\vec{z})$ the nondegenerate one if $|\vec{g}(\vec{0})| \neq 0$. In this case it is possible to believe that $|\vec{g}(\vec{x})| = 1$.

The Poisson bracket of two invariant functions $V_1(\vec{z})$ and $V_2(\vec{z})$ is an invariant function $V_3(\vec{z})$ again.

$$V_3(\vec{z}) = [\vec{g}_1(\vec{x}) \times \vec{g}_2(\vec{x})] \cdot \vec{S}$$

It means that if the matrix $A(\vec{0}) \neq I$ then there is not more than one nondegenerate invariant function (with the precision up to the multiplication on the invariant function of the orbital map).

It is possible to show that if the nondegenerate invariant $V(\vec{z})$ in the form (9) exists and the fixed point of the orbital motion $\vec{x} = \vec{0}$ is stable then the vector $\vec{g}(\vec{x})$ defines the direction along which the polarization of a particle is conserved. This definition of the equilibrium polarization direction does not depend on the selection of the coordinate system and on the Hamiltonian form of the orbit motion.

In the case when the action-angle variables I, φ for the orbital motion and the Derbenev and Kondratenko vector $\vec{n}(I, \varphi)$ [3] exist, the introduced vector $\vec{g}(\vec{x})$ gives the one turn boundary conditions for $\vec{n}$.

V. NORMAL FORM METHOD FOR MAPS WITH SPIN VARIABLES

In this part we present an arbitrary order (in respect of the orbital variables) normal form algorithm that allows to obtain the vector $\vec{g}(\vec{x})$ in the formal power series form in the nonresonance case. This algorithm is in the Lie algebraic framework [4], [5] and uses the map factorization (6).

As usually, the algorithm consists of a sequence of coordinate transformations of the map:

$$: C_{full} : \; = \; : C_{spin} : \; : C_{orbt} :$$
$$: C_{orbt} : \; = \; exp(: K_{m+1} :) \cdots exp(: K_3 :) : C_1 :$$
$$: C_{spin} : \; = \; exp(: \vec{P}_m \cdot \vec{S} :) \cdots exp(: \vec{P}_1 \cdot \vec{S} :) : C_2 :$$

Here $: C_{orbt} :$ is the coordinate transformation reducing the orbital part of the map to the normal form:

$$: C_{orbt} : \; : B_{orbt} : \; : C_{orbt} :^{-1} =_m exp(: H_{orbt}(I) :)$$

where $=_m$ indicates that the right and left side agree up to order m and I, $H_{orbt}(I)$ are action variables and pseudohamiltonian of the orbital motion.

The full transformation $: C_{full} :$ reduces the full map to the normal form:

$$: C_{full} : \ : B_{full} : \ : C_{full} :^{-1} =_m$$
$$exp(: H_{orbt}(I) + \Omega_{spin}(I) \cdot S_3 :) \qquad (11)$$

where $\Omega_{spin}(I)$ is the spin tune.

Omitting the details we note that the map (11) has the nondegenerate invariant function $V = S_3$. In the initial variables this function has the form $V = : C_{full} :^{-1} \cdot S_3$.

VI. CONNECTION BETWEEN SO(3) AND SU(2) GROUPS AND ONE TURN MAP COMPUTATION

The orthogonal 3×3 matrix $A(\vec{x}) \in SO(3)$ consists of 9 elements, but for its definition it is enough to have a smaller number of parameters. Usually this fact is used in the spinor formalism. A more classical approach is described in this paper.

In correspondence to the vector $\vec{S}$ we set the matrix

$$L = \begin{pmatrix} S_3 & S_1 + iS_2 \\ S_1 - iS_2 & -S_3 \end{pmatrix}$$

and introduce the matrix B ($B^* = -B$):

$$B = \frac{i}{2} \cdot \begin{pmatrix} W_3 & W_1 + iW_2 \\ W_1 - iW_2 & -W_3 \end{pmatrix}$$

By means of the matrices L and B one can write the spin part of motion equations (1) in form of a Lax equation:

$$\frac{dL}{d\tau} = B \cdot L - L \cdot B \qquad (12)$$

If the matrix $U(\tau)$ satisfies the equation

$$\frac{dU}{d\tau} = B \cdot U, \quad U(0) = I \qquad (13)$$

then $U(\tau) \in SU(2)$ and the solution of (12) for $L(0) = L_0$ is given by the formula:

$$L(\tau) = U(\tau) \cdot L_0 \cdot U^*(\tau) \qquad (14)$$

Thus we only need to calculate the solution of equation (13) for one turn. This approach is advantageous because the calculation with help of $SU(2)$ matrices requires a smaller number of arithmetic operations than with $SO(3)$ matrices.

VII. IMPLEMENTATION IN COMPUTER CODE VASILIE

All algorithms presented in this paper have been implemented up to arbitrary high order in the code VasiLIE [6].

This code allows to obtain one turn Taylor maps for orbital and spin motion, the invariant functions for the orbital motion, the equilibrium polarization direction and the orbital and spin tunes for the proton storage rings. This program is being created specially for computers like IBM PC with small memory $(1 - 2 \ MB)$.

REFERENCES

[1] V. Bargman, L. Michel, and V. L. Telegdi. *Phys. Rev. Lett.*, 2:435, 1959.

[2] A. J. Dragt and J. M. Finn. *Journal of Math. Physics*, 17:2215, 1976.

[3] Ya. S. Derbenev, A. M. Kondratenko. *Sov. Phys. JETP*, 37: No.6 968, 1973.

[4] E. Forest, M. Berz, and J. Irwin. Part. Acc., 24:91, 1989.

[5] K. Yokoya. *KEK Preprint.* 86-90.

[6] V. Balandin and N. Golubeva. *Proceedings of the XV Conf. on High Energy Particle Accelerators, Int. J. Mod. Phys. A*, 2B:998, 1992.

Investigation of Spin Resonance Crossing in Proton Circular Accelerators

V. Balandin and N. Golubeva
Institute for Nuclear Research of the Russian Academy
of Sciences, Moscow

Abstract

The general approach to the problem of the symplectic integration of Hamilton's equations, which is presented in paper [1] and which uses only the common properties of Lie groups, is developed to obtain the numerical tracking methods for both orbital and spin motions. The integration step of these methods is an explicit canonical map. (Here we use the term "canonical" instead "symplectic" for the systems with the spin Poisson brackets.) Some methods of such tape are realized in computer code VasiLIE [2]. With help of this code it is possible to study the dynamics of the polarization during acceleration. The numerical simulation of crossing the depolarizing resonances depending on the different parameters was performed for a lattice under study for the TRIUMF KAON Factory Booster [3]. The effect of nonlinear elements is also discussed.

I. INTRODUCTION

The spin resonance crossing is the main process which does not allow efficiently to accelerate polarized proton beam to high energy. The influence of spin resonances can be so great that in the end we can obtain a completely depolarized beam. This depends on concrete conditions of a passage through resonances. The behaviour of a semiclassic spin of a particle far from resonances is described well by a vector $\vec{n}$ and a spin tune ν_s introduced by Ya.S.Derbenev and A.M.Kondratenko [4]. For every given orbital trajectory a projection of a spin vector on the direction $\vec{n}$ is preserved and the projection on the transverse plane is rotated with a tune ν_s (the correct mathematical definition of $\vec{n}$ and an algorithm of its calculation with help of one turn Taylor map see in [5]). In general case in nonresonance situation it is possible to conserve the beam polarization only along the direction $\vec{n}$ because $\vec{n}$ and a spin tune ν_s depend on the betatron and synchrotron oscillations.

Let consider the situation of one isolated resonance crossing. In this case we have two directions $\vec{n} = \vec{n}_1$ and $\vec{n} = \vec{n}_2$ which describe the spin motion before and after resonance. If we know the angle between an image of $\vec{n}_1$ after resonance and $\vec{n}_2$, we can predict the value of the depolarization of the particle beam. For the first time the depolarization due to passage through a resonance was estimated by M. Froissart and S. Stora [6]:

$$P_2 = P_1 \cdot (2\, exp(-\pi \mid w_k \mid^2 /2\alpha) - 1) \qquad (1)$$

This formula gives a small value of depolarization in cases of very slow or very fast passage of spin resonances. What will happen when we have the intermediate situation or cross one after another several near resonances? The numerical integration methods are a useful addition to analytical investigations of this problem. In this paper we present the numerical integration method, the integration step of which is an explicit canonical map.

II. NUMERICAL INTEGRATION METHOD

The classical spin-orbit equations of the motion in circular accelerators have the form of a Hamiltonian system if we use the Poisson bracket:

$$\{F(\vec{z}), Q(\vec{z})\} = F_{\vec{q}} \cdot Q_{\vec{p}} - F_{\vec{p}} \cdot Q_{\vec{q}} + [F_{\vec{s}} \times Q_{\vec{s}}] \cdot \vec{S} \qquad (2)$$

and the Hamiltonian:

$$H = H_{orb}(\vec{x}, \tau) + \vec{W}(\vec{x}, \tau) \cdot \vec{S}$$

where $\vec{z} = (\vec{x}, \vec{S})$ and $\vec{x} = (\vec{q}, \vec{p})$ are canonical orbit variables, $\vec{S} = (S_1, S_2, S_3)$ is a classical spin vector, τ is generalized machine azimuth or the time (see details in [5]).

So we will use a general approach to the numerical integration of Hamiltonian systems which is presented in paper [1] and which uses only the common properties of Lie groups and Poisson brackets. For simplicity one consider the case when the Hamiltonian does not depend on τ. Usually the effect of the spin on an orbital motion is not taken into account. In this case we can obtain the solution of the system with the Hamiltonian $\vec{W} \cdot \vec{S}$ in the evident form. It means that it is possible to reduce the initial problem to the problem of symplectic integration of an
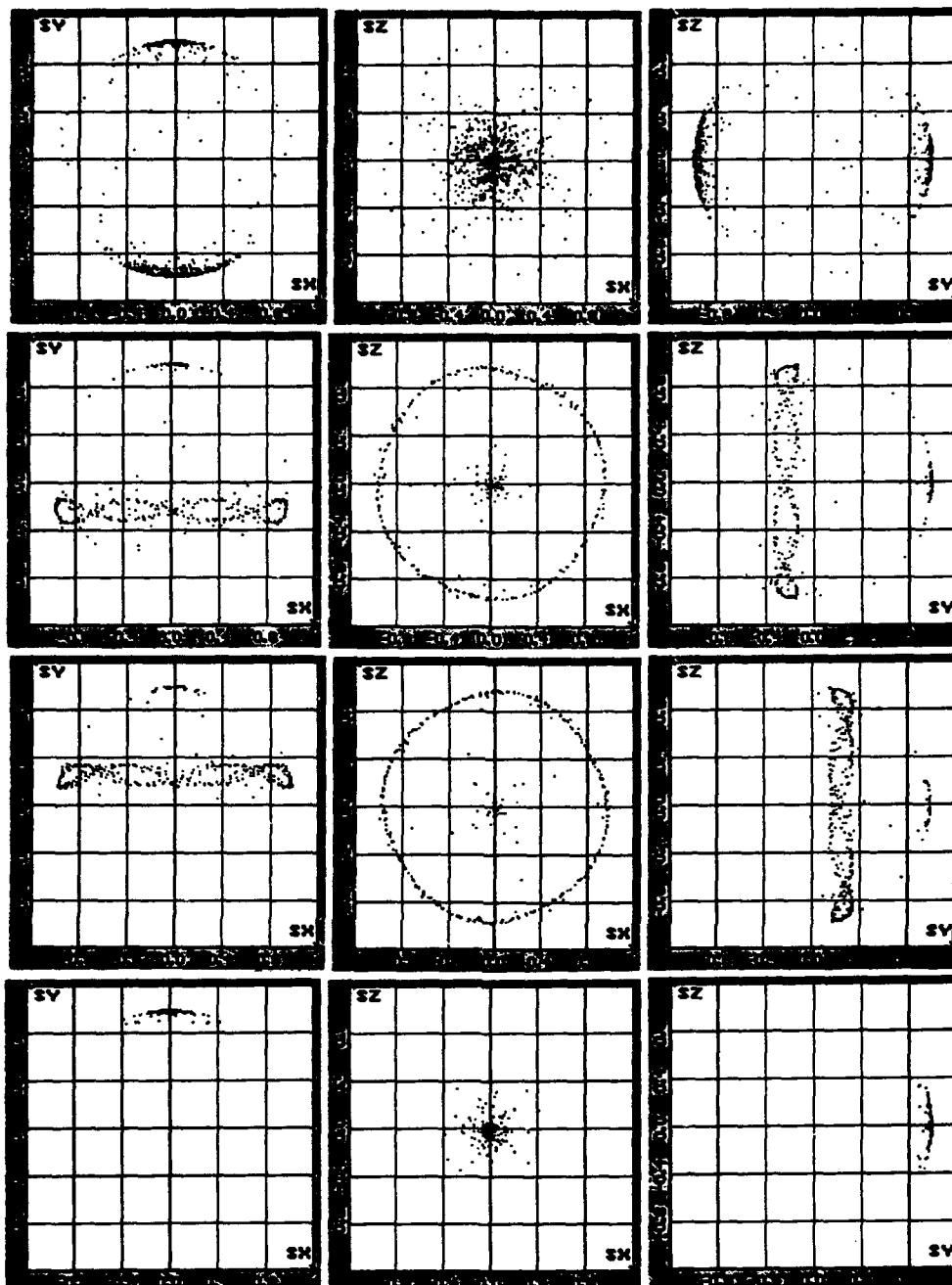
Figure 1:
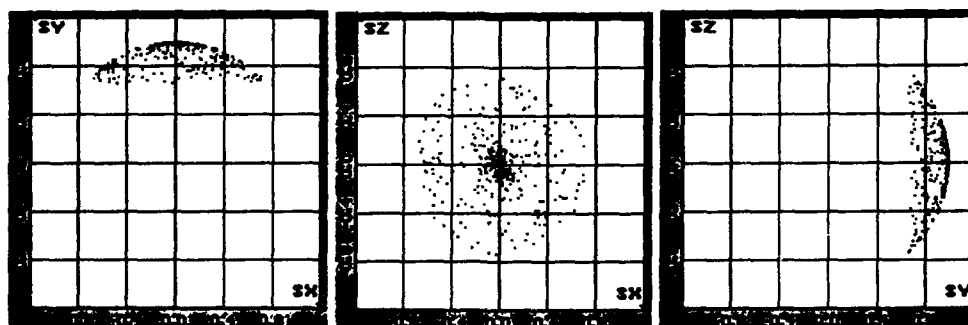
Figure 2:
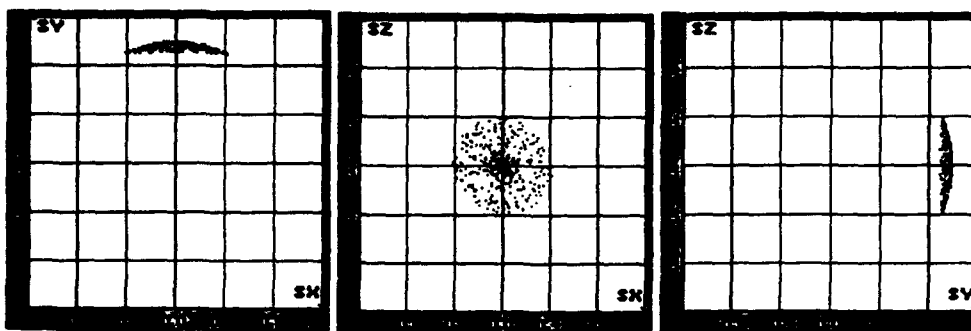
Figure 3:

orbital motion only. Using the Campbell-Baker-Hausdorff formula one can to introduce a new vector

$$\vec{W}_1(\vec{x}, h) = \vec{W} + h \cdot \vec{U}_1 + h^2 \cdot \vec{U}_2 + \cdots$$

so that for any given order k

$$exp(: -\frac{h}{2} H_{orb} :) \cdot exp(: -h\vec{W}_1 \cdot \vec{S} :) \cdot exp(: -\frac{h}{2} H_{orb} :) =$$

$$= exp(: -h(H_{orb} + \vec{W} \cdot \vec{S}) :) + O(|h|^k) \qquad (3)$$

where h is the size of the integration step.

If we use the combination of some symplectic integration method of order k for orbital motion [1] and an evident formula for central Lie exponent in the left side of (3), we will obtain the numerical method of order k which preserves the Poisson bracket (2). Some methods of such tape are realized in computer code VasiLIE [2].

III. NUMERICAL INVESTIGATIONS OF SPIN RESONANCE CROSSING

There are 6 intrinsic spin resonances in the acceleration region of a racetrack lattice under study for the TRIUMF KAON Factory Booster [3]. A part of them is in the intermediate region when a crossing speed is not very slow or very fast. In this part we present the results of numerical investigations of the resonance $\gamma G = 2 - \nu_y$ which is passed at the energy $E_k = 757\,MeV$.

Fig.1 shows turn-by-turn evolution of three spin projections during resonance crossing for a particle with $\delta p/p = 0$. These pictures were obtained with help of computer code VasiLIE [2] and correspond to different speeds α in formula (1).

The spin flip takes place with small depolarization for the crossing speed $\alpha \simeq 2 \times 10^{-4}$ (an upper part of Fig.1). It corresponds to a parameter $I = (\pi \mid w_k \mid^2)/(2\alpha) \simeq 0.6$ in formula (1). The bottom of Fig.1 shows the result of a fast resonance crossing with $I \simeq 0.01$. The rest of pictures show the intermediate cases for $I = 0.17$ and 0.09.

At a sine change of a momentum during acceleration which is proposed for the Booster lattice, $I \simeq 0.3$.

The effect of nonlinearity influence is considered for a resonance $\gamma G = 2\nu_y$. Without sextupoles this resonance is due to the edge magnetic fields and is weak. So this resonance is nonlinear we have taken a large emittance to see its effect more clearly. Fig.2 shows the resonance crossing in the Booster lattice with sextupoles and Fig.3 without sextupoles.

REFERENCES

[1] E. Forest, R. D. Ruth, Fourth-order symplectic integration. *Physica D*, 43:105, 1990.

[2] V. Balandin and N. Golubeva, Nonlinear Spin Dynamics. *Proceedings of the XV Inter. Conf. on High Energy Part. Accelerators, Int. J. Mod. Phys. A*, 2B:998, 1992.

[3] U. Wienands, R. Servranckx, N. Golubeva, A. Iliev, Yu. Senichev. *Proceedings of the XV Inter. Conf. on High Energy Part. Accelerators, Int. J. Mod. Phys. A*, 2B:1073, 1992.

[4] Ya. S. Derbenev, A. M. Kondratenko, and A. N. Skrinsky. *Sov. Phys. Dokl.*, 192:1255-1258, 1970.

[5] V. Balandin and N. Golubeva. Taylor map and calculation of equilibrium polarization direction for proton storage rings. *these proceedings.*

[6] M. Froissart and S. Stora. *Nucl. Inst. and Meth.*, 1:297-305, 1960.

Electron Beam Depolarization in a Damping Ring[*]

M. Minty

Stanford Linear Accelerator Center, Stanford University, Stanford, CA 94309 USA

Abstract

Depolarization of a polarized electron beam injected into a damping ring is analyzed by extending calculations conventionally applied to proton synchrotrons. Synchrotron radiation in an electron ring gives rise to both polarizing and depolarizing effects. In a damping ring, the beam is stored for a time much less than the time for self polarization. Spin flip radiation may therefore be neglected. Synchrotron radiation without spin flips, however, must be considered as the resonance strength depends on the vertical betatron oscillation amplitude which changes as the electron beam is radiation damped. An expression for the beam polarization at extraction is derived which takes into account radiation damping. The results are applied to the electron ring at the Stanford Linear Collider and are compared with numerical matrix formalisms.

1. Introduction

In an ideal synchrotron, the vertical polarization component of a polarized injected beam is conserved. Due to coupling of the spin to the orbital motion, however, the spin motion is perturbed. Depolarizing resonances occur whenever the electron spin tune, ν_s, equals a resonance tune, K, by satisfying $\nu_s = K \equiv n + mP + q\nu_x + r\nu_z + s\nu_{syn}$, where P is the superperiodicity, ν_x and ν_z are the horizontal and vertical betatron tunes, ν_{syn} is the synchrotron tune, while $m, n, q, r,$ and s are integers. In the absence of any longitudinal and radial error fields, the spin tune, ν_s, is equal to $a\gamma$, where $a = 0.011596$ is the anomalous part of the electron magnetic moment and $\gamma = \frac{E}{m_e c^2}$, where E is the electron energy, m_e is the electron mass, and c is the speed of light. In this paper we study the effects of depolarizing resonances on the spin motion of polarized electrons injected into a damping ring.

2. Spin Precession and Depolarizing Resonances

The spin of an orbiting particle in a synchrotron obeys the Thomas-BMT equation[1], which describes the spin motion in the presence of electromagnetic fields in the laboratory frame. With no significant electric fields in the accelerator, the Thomas-BMT equation reduces to

$$\frac{d\vec{S}}{dt} = \frac{e}{\gamma m} \vec{S} \times [(1 + a\gamma)\vec{B}_\perp + (1 + a)\vec{B}_\parallel], \qquad (1)$$

where $\vec{S} = (S_x, S_y, S_z)$ is the spin vector, e is the electric charge, and γ is the relativistic factor, while $\vec{B}_\perp$ and $\vec{B}_\parallel$ are the magnetic field components transverse to and parallel to the instantaneous velocity of the particle.

The magnetic fields in the Thomas-BMT equation may be expressed[2] in terms of the particle coordinates. The corresponding spinor representation is

$$\frac{d\Psi}{d\theta} = \frac{i}{2}\begin{pmatrix} -\kappa & -t - ir \\ -t + ir & \kappa \end{pmatrix}\Psi, \qquad (2)$$

where $\kappa, t,$ and r depend on the particle coordinates. The polarization components are obtained by taking the expectation value of the Pauli matrix vector, $\vec{\sigma}$; i.e. $S_i = \Psi^\dagger \sigma_i \Psi$. The off diagonal matrix elements characterize the effect of spin depolarization due to the coupling between the up and down components of the spinor wave function. Given the periodic nature of a synchrotron, the coupling term may be expanded in terms of the Fourier components; i.e.

$$t + ir = \sum \epsilon_j e^{-iK_j\theta} \qquad (3)$$

in which θ is the particle orbital angle, K_j is the value of the resonant tune for the jth resonance, and ϵ_j is the resonance strength and is given by the Fourier amplitude

$$\epsilon_j = \frac{1}{2\pi}\int (t + ir)e^{iK_j\nu}d\dot{r} \; \dot{=} \; \frac{1 + a\gamma}{2\pi}\sum \frac{\partial B_z/\partial x}{B\rho}z e^{iK_j\theta}. \qquad (4)$$

This corresponds to summing over the precession angles due to each radial error field.

In the single resonance approximation[3], the spin equation in the particle rest frame is given by

$$\frac{d\Psi}{d\theta} = -\frac{i}{2}\begin{pmatrix} a\gamma & -\zeta \\ -\zeta^* & -a\gamma \end{pmatrix}\Psi \quad \text{with} \quad \zeta = \epsilon \cdot e^{-iK\theta}. \qquad (5)$$

Transforming[3] the spin equation to the resonance precession frame using $\Psi_K = e^{i\frac{K\theta}{2}\sigma_z}\Psi$, we obtain

$$\frac{d\Psi_K}{d\theta} = \frac{i}{2}(\delta\sigma_z + \epsilon_R\sigma_x - \epsilon_I\sigma_y)\Psi_K, \qquad (6)$$

where σ_i are the Pauli matrices, $\epsilon = \epsilon_R + i\epsilon_I$, and $\delta = K - a\gamma$ measures the nearness to the resonance.

The general solution of Eq.(6) can be expressed as a linear combination of two eigenmodes: $\Psi_K = C_1\Psi_{K\uparrow} + C_2\Psi_{K\downarrow}$ with $C_1^2 + C_2^2 = 1$. Let S_i be the magnitude of the injected polarization, S_f the magnitude of the extracted polarization, and S_z the vertical component of the stored polarization in the resonance precession frame. For a vertically polarized injected beam, the polarization can be obtained by taking the expectation value of σ_z giving

$$S_z = \frac{\delta}{\lambda}(|C_1|^2 - |C_2|^2) + \frac{|\epsilon|}{\sqrt{+}\sqrt{-}}|C_1 C_2|\cos(\lambda\theta + \phi). \qquad (7)$$

where the phase angle ϕ is given by $\phi = \arg(C_1^* C_2)$, $\sqrt{\pm} = \sqrt{(\lambda \pm \delta)^2 + |\epsilon|^2}$, and $\lambda = \sqrt{\delta^2 + |\epsilon|^2}$.

When $\epsilon = 0$ in Eq. (7) we have $\delta = \lambda$ and therefore $S_z = S_i = |C_1|^2 - |C_2|^2$, where S_i is the polarization far from resonance; i.e. the magnitude of the injected polarization. Averaging over many revolutions around the ring

Figure 1. The ratio of the final to injected beam polarization as a function of the nearness to the resonance for three different resonance strengths.

we find, with $|C_1| = 1$ and $|C_2| = 0$ corresponding to a pure initial state, that

$$\frac{\langle S_z \rangle}{S_i} = \frac{K - a\gamma}{\sqrt{(K - a\gamma)^2 + |\epsilon|^2}}. \qquad (8)$$

On resonance, where $K = a\gamma$, the polarization is zero. Just off resonance we may write $\frac{\langle S_z \rangle}{S_i} = \cos\alpha_i$ so the ratio $\frac{\langle S_z \rangle}{S_i}$ may be interpreted as the projection of the injected polarization onto S. For a constant beam emittance, $\alpha_i = \alpha_f$ and the final polarization, S_f, is given by projecting $\langle S_z \rangle$ onto the vertical direction:

$$S_f = \frac{\langle S_z \rangle}{S_i} S_i \cos\alpha_f = S_i \cos^2\alpha = \frac{(K - a\gamma)^2}{(K - a\gamma)^2 + |\epsilon|^2} S_i. \qquad (9)$$

The dependence of the polarization on the resonance strength is shown in Fig. 1. The ratio of the final to injected polarization, $\frac{S_f}{S_i}$, is plotted as a function of $\delta = K - a\gamma$ for three different resonance strengths.

3. Spin Dynamics in an Electron Ring

Synchrotron radiation gives rise to both polarizing and depolarizing effects. Spin flip radiation tends to polarize the beam on a time scale which is long relative to the damping time and hence the store time. Spin flip radiation need therefore not be considered. However, radiation damping of the betatron oscillations is important because the resonance strength is proportional to the vertical betatron oscillation amplitude. The time dependence of the orientation of the spin vector is accounted for by noting that the turn by turn spin precession is adiabatic. The final polarization, S_f, is then a projection of the precessed spin vector onto the vertical. Thus $S_f = S_i \cos\alpha_i \cos\alpha_f$ or

$$S_f = \frac{K - a\gamma}{\sqrt{(K - a\gamma)^2 + |\epsilon_i|^2}} \frac{K - a\gamma}{\sqrt{(K - a\gamma)^2 + |\epsilon_e|^2}} S_i, \qquad (10)$$

where $|\epsilon_i|$ is the resonance strength at injection and $|\epsilon_e|$ is the strength at extraction.

Figure 2. Graphical representation of Eq. (10).

A graphical representation of Eq. 10 is sh᷃ in Fig. 2. The injected polarization, S_i, is first projected onto the stable spin axis, the orientation of which is determined by the resonance. This projection, $\langle S_z \rangle$, precesses adiabatically to $\langle S_z' \rangle$ as the resonanance strength changes. Then $\langle S_z' \rangle$ is projected back to the vertical to obtain the polarization at extraction, S_f.

We now average over a Gaussian particle density distribution. In emittance space, the distribution function is given by $\rho(\eta) = \frac{1}{\eta_{rms}} e^{-\frac{\eta}{\eta_{rms}}}$, where η is the phase space occupied by a single particle and η_{rms} is the beam emittance. The final polarization is then

$$\frac{S_f}{S_i} = \int \int \frac{(K - a\gamma)\rho(\eta_i) d\eta_i}{\sqrt{(K - a\gamma)^2 + |\epsilon_i|^2}} \frac{(K - a\gamma)\rho(\eta_e) d\eta_e}{\sqrt{(K - a\gamma)^2 + |\epsilon_e|^2}} \qquad (11)$$

where $\rho(\eta_i)$ and $\rho(\eta_e)$ are the distribution functions for the injected and the extracted beam, respectively.

4. Application to the SLC Damping Ring

During the 1992 physics run, polarized electron beams were created and transported to the interaction point for the first time[4]. Vertically polarized electron beams were injected into the damping ring at a nominal energy of 1.153 GeV. The store time was 8.33 ms while the damping time was about 3.7 ms. The resonance strengths at injection and extraction were estimated using DEPOL[2] which calculates the resonance strength based on Eq. 4. An injected to extracted emittance ratio of about 20 was assumed with the normalized beam emittance at extraction equal to 15 mm-mrad. The betatron tunes were 8.23 in x and 3.25 in y. Plotted in Fig. 3 is the extracted polarization as a function of $a\gamma$, where the solid line at $a\gamma = 2.6176$ corresponds to the operating energy of 1.153 GeV. The curve is calculated based on Eq. 11 which takes into account the damping of the betatron oscillations. If the vertical betatron tune is lowered, then both intrinsic resonances could cause slight depolarization. With these tunes however the amount of depolarization is minimal. We also considered the energy spread of the injected beam and the effect of a nonzero chromaticity. The energy spread, which was taken to equal the energy acceptance of the ring, was determined not to

Figure 3. The ratio of the final to injected beam polarization as a function of $a\gamma$ calculated from Eq. 11.

cause significant depolarization. The nonzero chromaticity shifts the $6 - \nu_z$ resonance downwards only slightly.

To compare the analysis with numerical simulation, we make the conservative approximation that the contributions from individual resources add coherently. Then summing over the contributions due to each resonance at a given $a\gamma$ gives, from Eq. (9)

$$S_f = [1 - \Sigma \frac{|\epsilon_j|^2}{(K - a\gamma)^2 + |\epsilon_j|^2}]S_i. \qquad (12)$$

Eq. (12) was used in Fig. 4a to calculated the ratio of the final to the initial polarization as a function of $a\gamma$.

These results include first order linear resonances only. To check the importance of higher order resonances and depolarization due to spin diffusion, we compare the results to those obtained using SLIM[5], which calculates the resulting equilibrium polarization; that is, the polarization one would observe after injecting unpolarized beam and allowing the beam to polarize due to spin flip radiation. The simulation using SLIM is shown in Fig. 4b. Shown in Fig. 4c is a simulation made with SMILE[6], which includes nonlinear resonances.

5. Conclusion

Using the spinor formulation of the Thomas-BMT equation, we emphasized that the measurable polarization depends on the projection of the polarization vector onto the stable spin direction at injection. This direction depends both on the resonance strength and the nearness of the operating energy to the resonance. We then considered the effects arising from synchrotron radiation. We obtained an expression for the final polarization taking into account the damping of the betatron oscillations. The solution was based on the realization that the polarization vector precessed adiabatically as the transverse distribution was damped. We then integrated over an assumed Gaussian transverse particle density distribution and predicted the final polarization at extraction. To test the
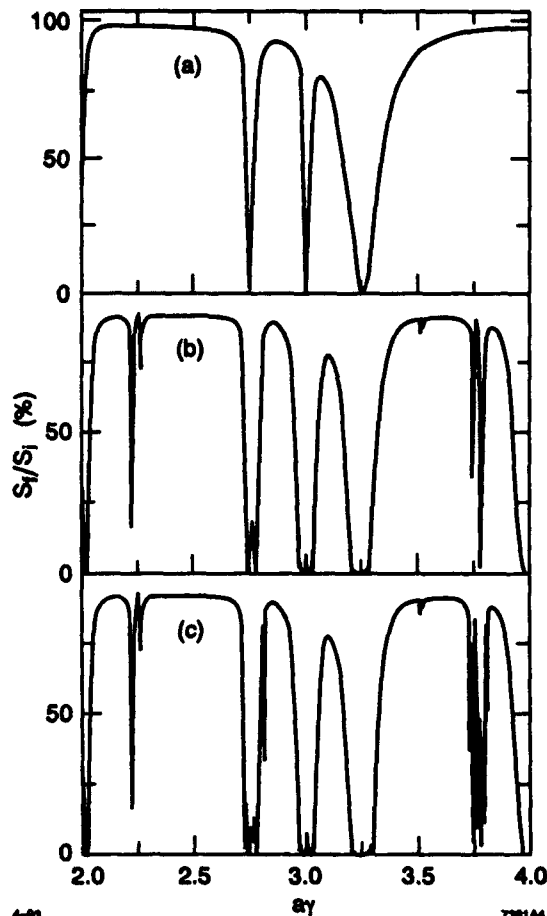
Figure 4. Comparison of ratio of final to injected polarization as a function of $a\gamma$ obtained from analytic calculations (4a), SLIM (4b), and SMILE (4c).

effect of higher order resonances on the spin motion, we compared the predictions to numerical simulations under equilibrium conditions.

I would like to thank R. Siemann, R. Ruth, A. W. Chao, and S.Y. Lee for many interesting discussions and suggestions.

References

[1] L. H. Thomas, Philos. Mag., **3** (1927) 1; V. Bargman, L. Michel, V. L. Telegdi, Phys. Rev. Lett., 2 (1959) 435.

[2] E. D. Courant, R. D. Ruth, "The Acceleration of Polarized Protons in Circular Accelerators," BNL 51270 (1980); E. D. Courant, BNL Report EDC-45 (1962).

[3] S. Y. Lee, S. Tepikian, Phys. Rev. Lett., **56** (1986) 1635-1638; S. Y. Lee, Prospects for Polarization at RHIC and SSC, AIP Conf. Proc., No. 224, (1991) 35.

[4] Spin transport at the SLC is discussed by W. Spence *et al*, these proceedings.

[5] A. W. Chao, Nucl. Instr. and Meth., **180** (1981) 29-36; A. W. Chao, "Polarization of a Stored Electron Beam", AIP Conf. Proc., **87** (1981) 395-447.

[6] S. R. Mane, "Higher Order Spin Resonances", AIP Conf. Proc., **187** (1989) 957-962.

SPINLIE - new computer code for polarization calculation

Eidelman Yu., Yakimenko V.
Budker Institute of Nuclear Physics,
630090 Novosibirsk, Russia

Abstract

The application of the analytical method of spin calculation is described. The calculation of both orbital and spin motion is based on Lie operators technique. The computer code SPINLIE realizing this method is discussed. The input language of SPINLIE is compatible with that of MAD. In SPINLIE elements are described as "thick lenses" for spin motion as well as for orbital calculations. The explicit expressions of Lie operators were found for orbital and spin motion for elements of different type (bending magnets, quadrupoles, sextupoles, RF-cavities, solenoids, kickers). The rules of addition of spin transformations were obtained for the beam passing the collider structure. Good agreement was found for SPINLIE results for the linear spin resonances in comparison with the other codes (SITF [1], SMILE [2]). The first results are presented for the calculation of nonlinear spin resonances.

I. INTRODUCTION

Calculations of the spin motion in colliders are interesting in connection with different schemes of experiments with the polarized beams. There are several computer codes for polarization degree calculations. Since there is a necessity to estimate the influence of nonlinear orbital and spin motion on the polarization degree, the attempts have been made to find more reliable and adequate methods for these calculations. This report presents a new computer code SPINLIE for polarization calculations for accelerators and colliders. The terms of sextupole type for orbital and quadratic for spin motion are precisely taken into account due to the usage of the Lie operator technique.

Most of the problems where the nonlinear character of orbital motion should be taken into account (dynamical aperture, lifetime, ...) require taking into consideration large amplitudes as well. Application of analytical methods for these purposes is not always justified. But these methods have some advantages when we are dealing with problems where small amplitudes are under examination (chromatism, polarization, ...). The analytical methods

have the best accuracy and, as a rule, higher calculation speed, since all elements (linear and nonlinear) are considered to be thick.

II. THE BRIEF COMPARISON OF DIFFERENT CODES FOR SPIN CALCULATION

It is clear, that the main point for comparison in different approaches is the "level" of nonlinearity which is allowed in the codes. As is known, the resonance order is $|k| + |k_x| + |k_z| + |k_s|$ for a resonance $\nu_{sp} = k + k_x\nu_x + k_z\nu_z + k_s\nu_s$, where ν_{sp}, ν_i are spin, betatron and synchrotron tunes respectively and the values k, $k_i (i = x, z, s)$ are integer.

The connection between the order of the resonance and the solution of the spin motion equation is determined, as is known, by the so-called the "resonance denominator" in the form [3] $(1 - e^{2\pi i(\nu + \sum_i k_i \nu_i)})$ and describes the N-order resonance ($N = \sum_i |k_i|$) correspondingly. In this context the "spin" codes SLIM [4], SITF and ASPIRRIN [5] are purely linear [1]. The example of the linear calculations is presented in Fig.1 for code SITF and new code SPINLIE. Good agreement is received.

Codes SpinLie (solid) and SITF (dashed)
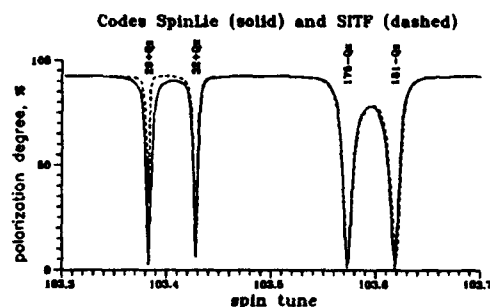
Figure 1: Linear resonanses for LEP structure N21C20.

The nonlinear N-order resonance is caused by three reasons. They are:

---

[1]The code ASPIRRIN estimates the strength of the synchrotron sideband spin resonances due to the usage of enhancement factors [6].

a) the correspondent order term $\vec{\omega}^{(N)}$ of the precession frequency $\vec{\Omega}$ expansion in terms of the orbital vector $\vec{Z}$;

b) all kinds of products of the terms $\vec{\omega}^{(k)}$ such that $\sum k = N$. These products appear from the terms of so-called θ-ordered solution [3] of the spin motion equation and describe noncommutation of the rotation sequences;

c) the terms which take into account the influence of nonlinearity of the orbital motion.

All "linear" codes include the term $\vec{\omega} = \vec{\omega}^{(1)}$ from the item a) because $\vec{\omega}$ has the same (first) order of infinitesimal as orbital vector $\vec{Z}$. The codes SMILE and SODOM [7] take into account item b) only for the high order resonances (for these codes $\vec{\omega}$ is the same as for "linear" codes). The code SITROS [8] involves all items (second order), but the last of them only partially. The terms are omitted, which describe the nonliearity contribution caused by the finite thickness of elements.

All terms a)-c) are taken into account for the second order resonances in the computer code SPINLIE.

III. LIE OPERATORS

There are two completely equivalent methods for nonlinear analytical matrixes calculations: perturbation method [9] and Lie operators technique [10]. As in any correct method, the starting and the final formulae are absolutely the same, but the intermediate steps are different. It seems, that the Lie operator method is shorter but, probably, a more formal way to the result.

A. Operators of the Orbital and Spin Transformations
In accordance with the Lie technique [10], [11] the equation for spin motion has the solution in the following form for the Hamiltonian $\mathcal{H}_{orb} + \vec{\Omega}\vec{n}$, which does not explicitly depend on the azimuth [12]:

$$\vec{n}(\theta) = e^{-\theta:\mathcal{H}_{orb}+\vec{\Omega}\vec{n}:}\vec{n}(0) = \mathcal{M}\vec{n}(0),$$

where the precession frequency vector $\vec{\Omega}$ is defined by BMT's equation [13] and $\vec{n}(0)$ is the initial spin vector for $\theta = 0$. The semicolons emphasize the operator nature of this formula.

In accordance with the Hamilton equations this operator satisfies the equation

$$\frac{d\mathcal{M}}{d\theta} = \mathcal{M} : -(\mathcal{H}_{orb} + \vec{\Omega}\vec{n}) : .$$

Let us separate the total Hamiltonian in two parts: all terms, which describe the linear orbital and spin motion ($\mathcal{H}_0(\vec{Z},\vec{n})$), and all terms of high orders $\mathcal{H}_1(\vec{Z},\vec{n}) + \mathcal{H}_2(\vec{Z},\vec{n})$). The part $\mathcal{H}_0$ includes the polynomial of the 2-nd degree over orbital vector $\vec{Z}$ from $\mathcal{H}_{orb}$ and part $\vec{\Omega}_0 \equiv \omega^{(0)}$ of the spin precession frequency $\vec{\Omega}$, which does not depend on $\vec{Z}$. Similarly, $\mathcal{H}_1$ includes the polynomial of the 3-rd degree from $\mathcal{H}_{orb}$ and the linear (over $\vec{Z}$) part $\omega^{(1)}$ of $\vec{\Omega}$. At last, as we consider here the sextupole order of the nonlinearity only, therefore $\mathcal{H}_2$ includes only the

quadratic part $\omega^{(2)}$ of $\vec{\Omega}$:

$$\mathcal{H}_0 = h_{ij}^{(0)}Z_iZ_j + \omega_\alpha^{(0)}n_\alpha,$$

$$\mathcal{H}_1 = h_{ijk}^{(1)}Z_iZ_jZ_k + \omega_{\alpha i}^{(1)}n_\alpha Z_i,$$

$$\mathcal{H}_2 = \omega_{\alpha ij}^{(2)}n_\alpha Z_iZ_j,$$

where all Roman indexes $i, j, ...$ correspond to $1,2,...,6$ and all Greek indexes $\alpha, \beta, ...$ correspond to x, τ, z.

Let us represent the operator $\mathcal{M}$ as a product of two exponential operators [11], [12]: $\mathcal{M} = \mathcal{M}_r \cdot \mathcal{M}_0$. As is known, operator $\mathcal{M}_0$ is simply matrixes for the linear transformation from the initial to the current azimuth θ: $\mathcal{A}(\theta)$ for orbital or $\mathcal{S}(\theta)$ for spin motion. Using the equation for the operator $\mathcal{M}$, the Lie technique and restricting the sextupole terms only, one can find:

$$\mathcal{M}_r = e^{-:f_2:}e^{-:f_1:} \simeq E - :f_1: - :f_2: + \frac{:f_1:^2}{2},$$

where E is a unit operator and

$$:f_1: = -\int_0^\theta d\theta' : (-\mathcal{H}_1(\mathcal{A}\vec{Z},\mathcal{S}\vec{n})|_{\theta'}):,$$

$$:f_2: = -\int_0^\theta d\theta' : (-\mathcal{H}_2(\mathcal{A}\vec{Z},\mathcal{S}\vec{n})|_{\theta'}): +$$

$$+ \frac{1}{2}\int_0^\theta d\theta' : \left(:f_1|_{\theta'}:\left(-\mathcal{H}_1(\mathcal{A}\vec{Z},\mathcal{S}\vec{n})|_{\theta'}\right)\right): .$$

Thus, we obtain the following rules for the calculation of the Lie operators $\mathcal{F}$, $\mathcal{W}^{(1)}$ and $\mathcal{W}^{(2)}$:

$$:f_1: = \mathcal{F}_{ijk}:Z_iZ_jZ_k: + \mathcal{W}_{\alpha i}^{(1)}:n_\alpha Z_i:,$$

$$:f_2: = \mathcal{W}_{\alpha ij}^{(2)}:n_\alpha Z_iZ_j:;$$

$$\mathcal{F}_{ijk}(\theta) = \int_0^\theta d\theta' h_{lmn}^{(1)}\mathcal{A}_{li}(\theta')\mathcal{A}_{mj}(\theta')\mathcal{A}_{nk}(\theta'),$$

$$\mathcal{W}_{\alpha i}^{(1)}(\theta) = \int_0^\theta d\theta' \mathcal{S}_{\alpha\beta}^{-1}(\theta')\omega_{\beta j}^{(1)}\mathcal{A}_{ji}(\theta'),$$

$$\mathcal{W}_{\alpha ij}^{(2)}(\theta) = \int_0^\theta d\theta'\left(\mathcal{S}_{\alpha\beta}^{-1}(\theta')\omega_{\beta kl}^{(2)}\mathcal{A}_{ki}(\theta')\mathcal{A}_{lj}(\theta') + \right.$$

$$+ \frac{1}{2}e_{\alpha\beta\gamma}\mathcal{W}_{\beta i}^{(1)}(\theta')\mathcal{S}_{\gamma\lambda}^{-1}(\theta')\omega_{\lambda k}^{(1)}\mathcal{A}_{kj}(\theta') +$$

$$\left. + \mathcal{S}_{\alpha\beta}^{-1}(\theta')\omega_{\beta k}^{(1)}\mathcal{A}_{kl}(\theta')J_{lm}\mathcal{F}_{mij}(\theta')\right).$$

B. The rules for transformation of the operators
Let us denote all constructions for the transformation from the azimuth θ_0 to θ' as: $\mathcal{A}|_{\theta_0\to\theta'} \equiv \mathcal{A}^{(u)}$, $\mathcal{S}|_{\theta_0\to\theta'} \equiv \mathcal{S}^{(u)}$, $\mathcal{F}|_{\theta_0\to\theta'} \equiv \mathcal{F}^{(u)}$, $\mathcal{W}^{(1)}|_{\theta_0\to\theta'} \equiv \mathcal{U}^{(1)}$, $\mathcal{W}^{(2)}|_{\theta_0\to\theta'} \equiv \mathcal{U}^{(2)}$. Then

$$Z_i(\theta') = A_{ij}^{(u)}Z_j(\theta_0) + A_{ij}^{(u)}J_{jk}\mathcal{F}_{klm}^{(u)}Z_l(\theta_0)Z_m(\theta_0)$$

$$\vec{n}(\theta') = \mathcal{S}^{(u)}e^{-:\mathcal{U}_{\alpha i}^{(1)}Z_i(\theta_0)n_\alpha(\theta_0):}\cdot e^{-:\mathcal{U}_{\beta jk}^{(2)}Z_j(\theta_0)Z_k(\theta_0)n_\beta(\theta_0):}\cdot\vec{n}(\theta_0)$$

Similarly, let us use for the transformation from θ' to θ the values $A_{ij}^{(v)}$, $\mathcal{S}^{(v)}$, $\mathcal{F}^{(v)}$, $\mathcal{V}^{(1)}$, $\mathcal{V}^{(2)}$ and for "merging"

451

transformation from θ_0 to θ the values $A^{(w)}_{ij}$, $S^{(w)}$, $\mathcal{F}^{(w)}$, $\mathcal{W}^{(1)}$, $\mathcal{W}^{(2)}$. Then, the rules of merging of elements to a unified element from θ_0 to θ are:

$$A^{(w)}_{ij} = A^{(v)}_{ik} A^{(u)}_{kj},$$

$$\mathcal{F}^{(w)}_{ijk} = \mathcal{F}^{(u)}_{ijk} + \mathcal{F}^{(v)}_{lmn} A^{(u)}_{li} A^{(u)}_{mj} A^{(u)}_{nk},$$

$$S^{(w)}_{\alpha\beta} = S^{(v)}_{\alpha\gamma} S^{(u)}_{\gamma\beta},$$

$$\mathcal{W}^{(1)}_{\alpha i} = \mathcal{U}^{(1)}_{\alpha i} + S^{(u)-1}_{\alpha\beta} \mathcal{V}^{(1)}_{\beta j} A^{(u)}_{ji},$$

$$\mathcal{W}^{(2)}_{\alpha ij} = \mathcal{U}^{(2)}_{\alpha ij} + S^{(u)-1}_{\alpha\beta} \mathcal{V}^{(2)}_{\beta kl} A^{(u)}_{ki} A^{(u)}_{lj} +$$

$$+ \frac{1}{2} e_{\alpha\beta\gamma} \mathcal{U}^{(1)}_{\beta i} S^{(u)-1}_{\gamma\lambda} \mathcal{V}^{(1)}_{\lambda k} A^{(u)}_{kj} +$$

$$+ S^{(u)-1}_{\alpha\beta} \mathcal{V}^{(1)}_{\beta k} A^{(u)}_{kl} J_{lm} \mathcal{F}^{(u)}_{mij}.$$

IV. SPIN POLARIZATION CALCULATION

In SPINLIE code the calculation of the equilibrium level polarization is based on the DK - formula [14]. Analytical determination of the spin transformation (the sextupole order is taken into account for both orbital and spin motions) is used. The components of these transformations are the polynoms of orbital variables $\vec{Z}$. These polynoms have been determined for each element type of the collider magnetic structure. The special rules of explicit summing of these polynoms are used for the calculation of one-turn spin transformation (linear and sextupol orders). The periodical solution is found for the equilibrium spin vector from the one-turn transformation. This solution explicitly depends on the first and second powers of $\vec{\mathcal{J}}$ and so one can find the spin chromaticity vector $\vec{d}$ and the degree of the equilibrium polarization.

A. Periodical solution

Let us denote the one turn transformation from θ to $\theta+2\pi$ as $A|_{\theta\to\theta+2\pi} \equiv A^{(w)}$, $S|_{\theta\to\theta+2\pi} \equiv S^{(w)}$, $\mathcal{F}|_{\theta\to\theta+2\pi} \equiv \mathcal{F}^{(w)}$, $\mathcal{W}^{(1)}|_{\theta\to\theta+2\pi} \equiv \mathcal{W}^{(1)}$, $\mathcal{W}^{(2)}|_{\theta\to\theta+2\pi} \equiv \mathcal{W}^{(2)}$. To find the periodical solution $\tilde{n}(\theta; \vec{Z}(\theta)) = \tilde{n}(\theta + 2\pi; \vec{Z}(\theta))$ we use the "gradient" method. It is based on the introduction of small dissipation into transformation and calculation of relaxative solution. Practically, it means introducing synchrotron damping decrements $\alpha^{(\nu)}$ [15] into the one turn orbital matrix A and summing total transformation so many times N that the A^N becomes negligible with computer accurancy. Physically, it corresponds to synchrotron damping of orbital imperfections on azimuth θ (due to photon emission) and summing of spin distortions. The resulting transformation from θ to $\theta + 2\pi N$ will be periodical and is described by the following expressions:

$$A|_{\theta\to\theta+2\pi N} = A^{(w)N} \overset{N\to\infty}{\Longrightarrow} 0,$$

$$S|_{\theta\to\theta+2\pi N} = S^{(w)N},$$

$$\mathcal{F}|_{\theta\to\theta+2\pi N} = \sum_{n=0}^{N} \mathcal{F}^{(w)} A^{(w)n} A^{(w)n} A^{(w)n} \overset{N\to\infty}{\Longrightarrow} \tilde{\mathcal{F}};$$

$$\vec{\mathcal{W}}^{(1)}|_{\theta\to\theta+2\pi N} = \sum_{n=0}^{N} \left(S^{(w)-1}\right)^n \vec{\mathcal{W}}^{(1)} A^{(w)n} \overset{N\to\infty}{\Longrightarrow} \widetilde{\vec{\mathcal{W}}^{(1)}},$$

$$\vec{\mathcal{W}}^{(2)}|_{\theta\to\theta+2\pi N} = \sum_{n=0}^{N} \left\{ \left(S^{(w)-1}\right)^n \vec{\mathcal{W}}^{(2)} A^{(w)n} A^{(w)n} + \right.$$

$$+ \frac{1}{2} \sum_{k=0}^{n-1} \left(S^{(w)-1}\right)^k \left[\vec{\mathcal{W}}^{(1)}, \left(S^{(w)-1}\right)^{n-k} \cdot \right.$$

$$\left. \cdot \vec{\mathcal{W}}^{(1)} A^{(w)n-k}\right] A^{(w)k} A^{(w)k} +$$

$$+ \left(S^{(w)-1}\right)^n \vec{\mathcal{W}}^{(1)} \left[\sum_{k=0}^{n-1} A^{(w)n-k} \cdot \right.$$

$$\left. \left. \cdot J\mathcal{F}^{(w)} A^{(w)k} A^{(w)k}\right]\right\} \overset{N\to\infty}{\Longrightarrow} \widetilde{\vec{\mathcal{W}}^{(2)}}.$$

The summing can be made by two one-turn transformation, two two-turns, two four-turn, ...and so on in powers of 2 this procedure is not too long and 20-25 summings are usually enough. This multiturn transformation corresponds to the condition of periodicity:

$$\tilde{n}(\theta) = \vec{n}_0(\theta) + \widetilde{\vec{\mathcal{W}}^{(1)}}(\theta, \vec{Z}(\theta)) + \widetilde{\vec{\mathcal{W}}^{(2)}}(\theta, \vec{Z}(\theta), \vec{Z}(\theta)).$$

B. Spin Chromaticity and its transformaton

Now we can find the periodical spin vector $\tilde{n}(\theta)$. The spin chromaticity can be determined from it as a derivative over the sixth component of the orbital vector $\vec{Z}$. It is necessary to integrate the spin chromaticity over the ring in order to calculate the polarization degree. There are two possibilities: calculate $\tilde{n}(\theta)$ for each current azimuth θ or calculate $\tilde{n}(\theta_0)$ for initial azimuth and after that "pull" this vector from θ_0 to θ. We found the following rule for the "pulling":

$$\mathcal{W}^{(1)}_{\alpha i}|_{\theta\to\theta+2\pi N} = S_{\alpha\beta}|_{\theta_0\to\theta} \left\{ \mathcal{W}^{(1)}_{\beta j}|_{\theta_0\to\theta_0+2\pi N} - \right.$$

$$\left. - \mathcal{W}^{(1)}_{\beta j}|_{\theta_0\to\theta} \right\} A^{-1}_{ji}|_{\theta_0\to\theta},$$

$$\mathcal{W}^{(2)}_{\alpha ij}|_{\theta\to\theta+2\pi N} = S_{\alpha\beta}|_{\theta_0\to\theta} \cdot$$

$$\cdot \left\{ \left(\mathcal{W}^{(2)}_{\beta kl}|_{\theta_0\to\theta_0+2\pi N} - \mathcal{W}^{(2)}_{\beta kl}|_{\theta_0\to\theta} \right) - \right.$$

$$- \frac{1}{2} e_{\beta\gamma\lambda} \mathcal{W}^{(1)}_{\gamma k}|_{\theta_0\to\theta} \mathcal{W}^{(1)}_{\lambda l}|_{\theta_0\to\theta_0+2\pi N} -$$

$$- \left(\mathcal{W}^{(1)}_{\beta m}|_{\theta_0\to\theta_0+2\pi N} - \mathcal{W}^{(1)}_{\beta m}|_{\theta_0\to\theta} \right) \cdot$$

$$\left. \cdot J_{np} \mathcal{F}_{pkl}|_{\theta_0\to\theta} \right\} A^{-1}_{ki}|_{\theta_0\to\theta} A^{-1}_{lj}|_{\theta_0\to\theta}.$$

V. SOME SPINLIE CALCULATION RESULTS

All presented calculations was performed for the VEPP2-M collider structure. Imperfection was introduced by special skew. Its strength corresponded to the measured width of the coupling resonance. Fig.2 shows the suppression of the some resonances for the different kind of the structure symmetry. As was shown earlier the strength of the nonlinear
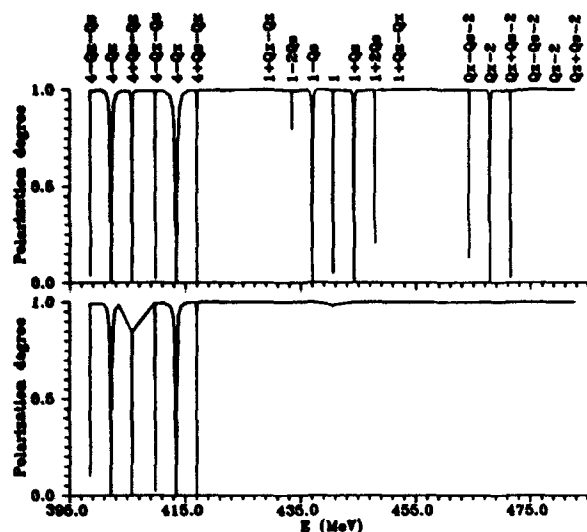
Figure 2: The spin resonances for different kinds of the symmetry of the magnetic structure.

Figure 3: The comparison of each term contributions to the nonlinear resonance. a - $\left[\vec{\omega}^{(1)}, \vec{\omega}^{(1)}\right]$ term; b - term caused by the orbital motion nonlinearity; c - the sextupole order term $\vec{\omega}^{(2)}$ in the expansion of the spin precession frequency; d - all terms together.

resonance is determined by the contribitions of the different terms. We compare them and the result is presented in Fig.3. One can see that all terms have approximately the same values for VEPP2-M. We assume that the relation between the different terms can been changed for different energies and symmetry of collider structures and this is the matter for special investigation.

REFERENCES

[1] A.Ackerman, J.Kewisch, T. Limberg, "The linear polarization calculation program SITF", LEP Note 9999, 1988.

[2] S.Mane, Proc. 8th Int. Symp. on High Energy Spin Physics, Minneapolis, 1988 (Am. Inst. Phys. Conf. no. 187, vol. 2 (1989) p.959).

[3] S.Mane, Phys. Rev. A36 (1987) 120.

[4] A.Chao, Nucl. Instr. Meth. 29 (1981) 180.

[5] V.Ptitshyn, Yu.Shatunov, will be published.

[6] S.Mane, NIM A292 (1990) 52.

[7] K.Yokoya, "Non perturbative Calculation of Equilibrium Polarization of Stored Electron Beams", preprint KEK 92-6, 1992.

[8] J.Kewisch, "Simulation of Electron Spin Depolarization with the Computer Code SITROS, reprint DESY 83-032, 1983.

[9] Braun Karl L., Advances in Particle Physics, vol.1, pp.71-134, 1968.

[10] J.Dragt, "Lecture on Nonlinear Orbit Dynamics", Am. Inst. Phys. Conf. no. 87, (1982) p.147.

[11] J.Dragt, E.Forest, J.Math.Phys. 24(12), pp. 2734-2744, 1983.

[12] Yu.Eidelman, V.Yakimenko, "The Spin Motion Calculation with Using Lie Method in Collider Nonlinear Magnetic Field", preprint INP 90-127 Novosibirk, 1990 (Submited to Particle Accelerators).

[13] V.Bargmann, L.Michel, V.Telegdi, Phys.Rev.Lett. 2(10), pp.435-437, 1959.

[14] Ya.S.Derbenev, A.M.Kondratenko, Zh. Eksp. Teor. Fiz. 64 (1973) 1918 (Sov. Phys. JETF 37 (1973) 966).

[15] H.Mais, G.Ripken, "Theory of Spin-orbit Motion in Electron-positron Storage Ring", preprint DESY 83-062, 1983.

IHEP Polarized Proton Beam

V.N.Zapolsky, Yu.A.Chesnokov, A.S.Dyshkant, N.A.Galyaev, V.I.Kotov, V.I.Kryshkin,
R.A.Rzaev , R.M.Sulyaev , S.V.Tsarik, V.G.Zarucheisky
Institute for High Energy Physics, 142284, Protvino, Moscow Region, Russia

Abstract

The IHEP polarized proton beam with momentum up to 40 GeV/c from the decay of lambda hyperons is described. The measured characteristics of the beam are compared with the calculated ones.

I. INTRODUCTION

The availability of a polarized proton beam may push further the development of the IHEP experiments devoted to the study of hadron interactions with polarized targets and production of high p_t charged hadron (single and pair) in pp and pA collisions. In connection with this the existing multipurpose beam line №22 [1] which used to produce high intensity beams of protons, pions and electrons for two experimental facilities has been modernized. The existance of two working experimental facilities, each with its own requirements for the beam parameters, makes our task more difficult. During the modernization we should be led by following requirements:

- All the possibilities to form particle beams, that the beam line has before the modernization, should be conserved;
- Beam parameters at experimental facility targets should be also conserved;
- The necessary alterations should be minimized;
- The transversely polarized proton beam should have as high intensity I_p and "polarization quality" $I_p \eta^2$ (η - the average particle polarization) as it possible;
- The background contamination in the polarized proton beam should be minimized.

To produce a polarized proton beam, we, similar to [2], used parity-nonconserving decays of Λ hyperons: $\Lambda \Rightarrow p + \pi^-$ [3]. The intensity of Λ hyperons has been maximized by centering the beam line acceptance at 0^0 production angle. Lambda hyperons are produced when 70-GeV/c protons from the IHEP accelerator strike an Al production target. The Λ hyperons then decay into protons that are polarized along the proton direction of motion, as viewed in the Λ rest frame. In these frame, the decay $\Lambda \Rightarrow p + \pi^-$ occurs isotropically and the decay-proton polarization is 64% [4]. A transversally polarized proton beam is produced by selecting a portion of these Λ decays.

II. POLARIZED PROTON BEAM DESCRIPTION

The incoming 70-GeV/c primary proton beam with intensity up to 10^{13} ppp is extracted from the accelerator with the pulse spill $t \sim 0.5 \div 1.5$ sec and focused on the production target into a spot with dimensions 4×2.5 mm^2 (H $\times$ V). The target (see fig. 1) with dimension of its working part $10 \times 3 \times 300$ mm^3 (H $\times$ V $\times$ L) is placed at the clearing magnet yoke entrance.
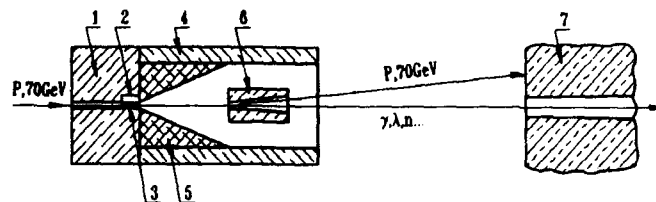
Figure 1. The layout of the head part of beam line №22 (plain view). 1 – local shield; 2 – target chamber; 3 – target; 4 – clearing magnet; 5 – shield in the magnet; 6 – safeguard collimator; 7 – beam absorber P1.

A clearing magnet with radiation resistant coil was designed and manufactured at IHEP [5]. It is 3 m long, its gap is 50 mm and magnetic field strength is 1.8 T. This magnet eliminates unwanted charged particles from the beam. Noninteracting primary beam protons are deflected downward into a beam dump P1. Charged particles produced at the target are bent from the beam line acceptance. Also, the charged particles from Λ decay occurring too close to the production target are swept from the beam. In the second part of the magnet in its aperture there is a brass insert with an expanding hole, which acts as a collimator for the neutral particles. This collimator reduces the number of neutron interactions downstream that could simulate Λ decays. It terminates ~ 50 cm from the end of the magnet so that charged particles produced within the collimator can be deflected away from the beam line acceptance. The primary beam dump P1 starts 11.6 m downstream of the target. This absorber 5 m long has an expanding hole for the beam passage as well as for neutral particle beam. The neutral particles which passed through the holes in the safeguard collimator and in absorber P1 are transported without losses to the absorber P2, located just after the magnet MH2 ~ 35 m downstream of the production target (see fig.2). At the beam line entrance the proton beam is limited in vertical and horizontal directions by two remotely controlled collimators K1 and K2. The vacuum system of the beam line starts at the exit of the clearing magnet to minimize the number of interactions that the beam has with air.
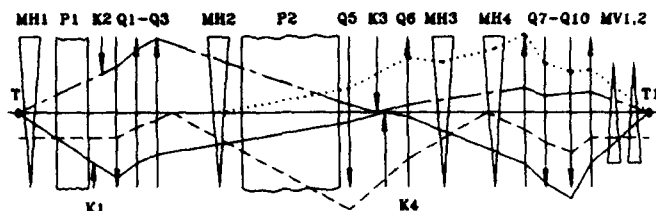
Figure 2. Structure and optical scheme of the beam line. T, T1 – production target and target of experimental facility; P1, P2 – absorbers of charged and neutral particles; K – collimators; Q – quadrupole lenses; MH, MV – bending and correcting magnets; X/X'_o, Y/Y'_o, Y/Y_o, $X/\delta p$ – matrix coefficients: solid line – Y/Y'_o, dotted line – Y/Y_o, dot-dash line – X/X'_o, dots – $X/\delta p$.

III. POLARIZED PROTON BEAM OPTICS

Unfortunately the optical scheme of beam line №22 cannot fulfil all requirements, that usually are imposed on such systems [2,3,6,7,8]. The corresponding modernization of the beam line is impossible due to limited space and other restrictions. Nevertheless, we managed to satisfy basic, undoubtedly essential requirements. The quadrupole lenses Q1, Q2, Q3, Q5 (their polarity is clear from Fig.2) provide the beam focusing in the horizontal plane in the center of the momentum collimator K3, and in the vertical plane they form an intermediate image in the center of the collimator K4. The spatial vertical magnification

Table
Calculated Parameters of the Polarized Beam
at 40 GeV/c.

№	Parameter	Value
1.	Beam dispersion at momentum slit	15.6 mm/1%Δp/p
2.	Space magnification at intermediate focus (collimator K4)	−2.68
3.	Beam profile at final focus: Horizontal Vertical	$\sigma_x = 10.6$ mm $\sigma_y = 8.1$ mm
4.	Angular divergence at final focus: Horizontal Vertical	±6.5 mrad (max) ±6.0 mrad (max)
5.	Momentum band	±4.5% Δp/p
6.	Total intensity of polarized protons at final focus, with incident flux of 10^{13}ppp	$8.1 \cdot 10^7$
7.	Intensity of polarized protons with average polarization ~40%	$2.6 \cdot 10^7$
8.	π^+-meson background from decay $K_s^o \Rightarrow \pi^+\pi^-$	0.8%

at the intermediate focus −2.68 is sufficient for reliable selection of the beam part with required degree of polarization. The linear beam dispersion at the momentum slit is 15.6 mm/1% Δp/p, that provides fairly good momentum analysis of the beam. The quadrupole lenses Q6-Q10 form the beam on the experimental facility target, providing strictly unity first-order transfer matrix in the vertical plane. The linear beam dispersion on the experimental facility target turns out to be practically fully compensated. The main calculated beam parameters of the transversely polarized protons at 40 GeV/c momentum are presented in the table. The calculations of the beam line parameters were carried out with a program TRANSPORT [9], more detailed calculations were based on a modified program TURTLE [10].

IV. EXPERIMENTAL RESULTS AND COMPARISON WITH CALCULATION

The first run on beam line № 22 with polarized protons was in December 1990. Transversely polarized protons were formed at momentum 40 GeV/c and expected degree of average polarization ~ ±40%. The beam tuning was made with the well known method of focal coefficients and consisted in accurate beam steering along the beam line axis, correcting the beam focuses in both transverse planes and choosing the corresponding opening of the collimators. The operation regims of the beam elements practically coincide with the calculated ones. The intensity of the primary proton beam was about ~ $4.4 \cdot 10^{12}$ppp, the total intensity of the beam (unpolarized in a whole) was ~ $3.75 \cdot 10^7$, and polarized proton intensity was ~ $1.5 \cdot 10^7$. The background level measured by threshold Cherenkov counters was ~ 1.4%. The selection of the beam with the required direction and degree of polarization was realized by collimator K4. Fig.3 shows the calculated dependence of the average beam polarization η (line 1), the intensity of polarized beam I_p corresponding to this polarization(line 2), and the "polarization quality" $I_p\eta^2$ (line 3) versus collimator K4 opening. The lower jaw of the collimator is set on the coordinate Y = −60 mm, the upper jaw is moving from −60 mm to +60 mm. The value I_p is normalized to the intensity of the primary beam 10^{13} ppp.
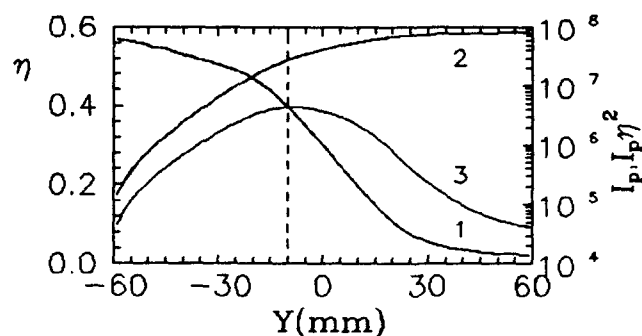
Figure 3. 1 – η, 2 – I_p, 3 – $I_p\eta^2$
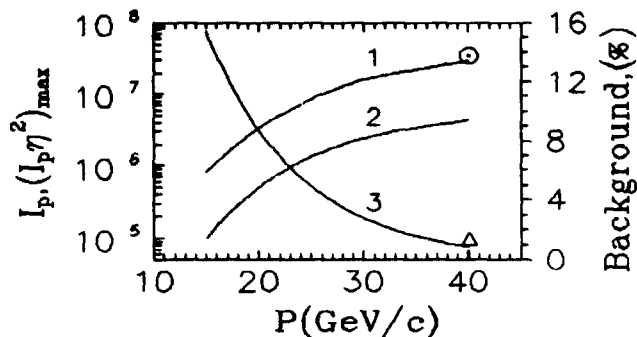
Figure 4. The potentiality of the beam line to form a polarized proton beams at different energies. 2 – the maximum value of the "polarization quality" $(I_p\eta^2)_{max}$; 1 – the corresponding to $(I_p\eta^2)_{max}$ intensity of the polarized beam; 3 – the π^+-meson background from decay $K_s^0 \Rightarrow \pi^+\pi^-$; $\odot$ – the measured (and normalized to primary beam of 10^{13}ppp) intensity of the polarized beam at P=40 GeV/c; $\triangle$ – the measured background of positive particles.

The vertical dotted line on the figure is drawn through the selected operating position of the upper collimator jaw at Y $= -10$ mm where the value of "polarization quality" $I_p\eta^2$ is maximum and average polarization is $\sim 40\%$. The revers of the beam polarization is achieved by changing the position of the K4 collimator jaws from -60 mm and -10 mm to $+10$ mm and $+60$ mm respectively. The use of the collimator for the selection of the beam fraction with the required direction and degree of polarization leads to the effect of vertical displacement of the beam symmetrically relative to the beam line axis. In our case it was ± 10 mm for linear and ± 0.46 mrad for angular displacement. These displacements make extremely difficult the experiments with polarized beams because lead to the apparatus asymmetry. To eliminate the displacements two vertical bending magnets are placed close to the experimental facility target. The selection of the beam fraction with the required direction of polarization vector (up or down) and shifting it on the beam line axis is made automatically now during 3 - 4 accelerator spills with the algorithm determined by an experimentators.
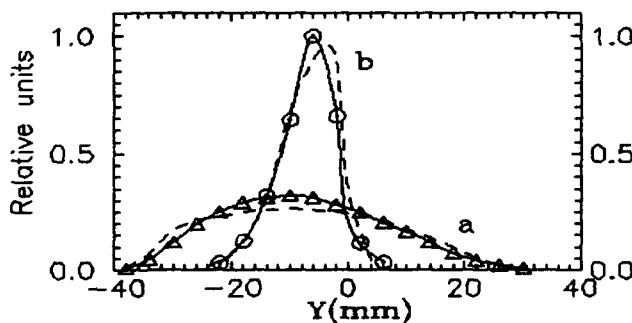
Figure 5.

The potentiality of the beam line to form transversely polarized protons at different energies are illustrated in Fig.4. Fig.5 presents the vertical beam distribution of the polarized protons at 40 GeV/c with expected average polarization about $\sim 40\%$ measured at ~ 5.5 m (a) and ~ 0.9 m (b) upstream of the experimental facility target. The dotted lines correspond to the calculated values. As one can see there is a good agreement between the calculated and measured values. This fact allows one to hope that the polarization degree of the formed beam will be close to the calculated one.

V. CONCLUSION

At the IHEP accelerator there was constructed a polarized proton (antiproton) beam at 40 GeV/c based on the nonconserving parity Λ ($\bar{\Lambda}$) decay. Multifunctional beam line №22 has been modernized to obtain the polarized beam. All potentialities of this beam line — high intensity proton, pion, and electron beams are preserved. The stable position of the beam on the target for reverse of the polarization is provided by two dipole magnets. The degree of average beam polarization is supposed to be measured by the coulomb - nuclear interference method, the rest parameters are close to the calculated ones. The salient features of the polarized proton beam production are:
- High intensity (up to $3.5 \cdot 10^7$ppp) for $\sim 40\%$ average proton polarization;
- Low level of background ($\sim 1 \div 1.5\%$);
- Automatic positioning of the beam on the beam line axis (and onto the experimental target center) at the beam polarization reverse.

In conclusion the authors express their deep gratitude to the Institute colleagues who took part in the beam line modernization and the measurements of the beam characteristics.

VI. REFERENCES

[1] A.G. Afonin et al., Preprint IHEP 90-38. – Protvino, 1990.
[2] D.P. Grosnick et al., NIM. 1990. V. A290. P.269.
[3] O.E. Overseth, J. Sandweiss, NAL 1969 Summer Study Report SS – 120. 1969. V.1.
[4] J.W. Cronin, O.E. Overseth, Phys. Rev. 1963. V.129. P.1795.
[5] V.V. Afanasiev et al., Preprint IHEP 87-70. – Serpukhov, 1987.
[6] J. Jensen et al., Selsk. Fork. 1958. V.6. P.31.
[7] P. Dalpiaz et al., CERN/ECFA/72/4. 1972. V.1. P.284.
[8] S.B. Nurushev et al., Proc. of Intern. Symp. on High Energy Spin Physics with Polarized Beams and Polarized Targets, Lausanne, 1980. P.501.
[9] K.L. Brown et al., CERN Report 80-04. 1980.
[10] D.C. Carey, "The Optics of Charged Particle Beams." (New York. Harwood Academic, 1987).

Measurement of Longitudinal Beam Polarization by Synchrotron Radiation*

I. P. Karabekov[1,2], R. Rossmanith[2]

[1] Yerevan Physics Institute, 2 Alikhanian Brothers Street
Yerevan 375036, Republic of Armenia

[2] Continuous Electron Beam Accelerator Facility
12000 Jefferson Avenue, Newport News, Virginia 23606, USA

Abstract

A method to measure the longitudinal polarisation of an electron beam using synchrotron radiation is proposed. Quantum theory predicts that a longitudinally polarised electron emits a slightly different number of synchrotron photons into the space above and below the orbit plane. The degree of this asymmetry is proportional to the magnetic field strength and the ratio between photon and electron energy. For CEBAF (electron energy $E_e = 4$ GeV and 100 μA beam current), a dedicated bending magnet with the field strength of $B = 6.25$ T permits us to measure a 100% polarised beam with an accuracy of about 1% in one second when the measurement is performed with photons in the range between $E_{\gamma min} = 6.0$ keV and $E_{\gamma max} = 600$ keV. The technique for measuring this asymmetry is also discussed.

I. INTRODUCTION

The standard polarimeters in high-energy electron storage rings and colliders are laser polarimeters [1, 2]. A circularly polarised laser beam is directed against the particle beam and the distribution of the backscattered photon beam is measured.

Several years ago the Novosibirsk polarisation group used the predictions of the quantum mechanical theory of synchrotron radiation to measure the transverse polarisation in a storage ring [3]. They found good agreement between the theory developed by Sokolov and Ternov [4, 5] and the experimental results. The aim of this paper is to show that the longitudinal polarisation can be measured as well by using another prediction of the same theory.

II. PRINCIPAL CONSIDERATIONS

The starting point is the famous quantum mechanical description of synchrotron radiation developed by Sokolov and Ternov [4, 5]. According to this theory the angular and spectral distributions of the intensity of the σ and π polarised synchrotron radiation emitted from an electron with arbitrary spin direction can be calculated by the following formula:

$$W_{\sigma,\pi} = \frac{27}{16\pi} \frac{ce_0{}^2}{R^2 \varepsilon_0{}^{9/2}} \int_0^\infty \frac{y^2 dy}{(1+\xi y)^5} \oint d\Omega \, \Phi_{\sigma,\pi} \quad (1)$$

The indices σ and π refer to the two different planes of synchrotron light polarisation: σ refers to light with a polarisation vector in the orbit plane, π to light polarised perpendicularly to this plane. $\Phi_{\sigma,\pi}$ describes the angular and spectral distribution of the radiation. For longitudinally polarised electrons these functions (neglecting spin-flips caused by synchrotron radiation) are:

$$\Phi_\sigma = \frac{4}{\gamma^4} \frac{(1+\xi y)}{12\pi^2} (1+\alpha^2)^2 K_{2/3}^2(z)$$

$$\left(1 + \zeta\xi y \frac{\alpha}{\sqrt{1+\alpha^2}} \frac{K_{1/3}(z)}{K_{2/3}(z)}\right) \quad (2)$$

$$\Phi_\pi = \frac{4}{\gamma^4} \frac{(1+\xi y)}{12\pi^2} \alpha^2 (1+\alpha^2) K_{1/3}^2$$

$$\left(1 + \zeta\xi y \frac{\sqrt{1+\alpha^2}}{\alpha} \frac{K_{2/3}(z)}{K_{1/3}(z)}\right) \quad (3)$$

where ζ is the electron polarisation, $\varepsilon_0 = 1 - \beta^2$, $z = \frac{\omega}{2\omega_c}(1+\alpha^2)^{3/2}$, $\omega_c = \frac{3}{2}\omega_0\gamma^3$, $\omega_0 = \frac{c}{R}$, c is the speed of light, R is the bending radius, $\gamma = \frac{E}{m_0 c^2}$, e_0 is electron charge, $y = \frac{\omega}{\omega_c}$, $\alpha = \gamma\psi$, ψ is the vertical angle between the orbit plane and the direction of the radiated photons, θ is the bend angle, $K_{1/3}(z)$ and $K_{2/3}(z)$ are modified Bessel functions, $\xi = \frac{3}{2}\frac{H}{H_0}\frac{E}{m_0 c^2}$, and $H_0 = \frac{m_0^2 c^3}{e_0 \hbar} = 4.41 \times 10^{13}$ Oe.

In the case of transverse spin polarisation, (2) and (3) must be replaced by:

$$\Phi_\sigma = \frac{1+\xi y}{3\pi^2\gamma^4}(1+\alpha^2)^2$$

$$\left(1 + \xi y - \zeta\frac{\xi y}{\sqrt{1+\alpha^2}} \frac{K_{1/3}(z)}{K_{2/3}(z)}\right) K_{2/3}^2(z) \quad (4)$$

$$\Phi_\pi = \frac{2+3\xi y}{6\pi^2\gamma^4}\alpha^2(1+\alpha^2)K_{1/3}^2(z) \quad (5)$$

The dependence of the synchrotron radiation intensity on the transverse polarisation described in formulas (4) and (5) was experimentally verified by the Novosibirsk polarisation group [3].

Equations (2) and (3) show that the synchrotron light intensity depends slightly on the longitudinal spin polarisation $\zeta = \pm 1$. This paper discusses the possibility of measuring this asymmetry, which is buried in a highly spin-independent background.

If we combine equations (1), (2), and (3), and assume $\xi y \ll 1$, the angular distribution of the intensity radiated

by n_e electrons into the solid angle $d\psi d\theta$ for a given photon frequency y is

$$d^3W = \frac{9n_e}{16\pi^3}\frac{ce_0^2}{R^2}\gamma^5 y^2 dy F(\alpha)d\psi d\theta \qquad (6)$$

where

$$F(\alpha) = (1+\alpha^2)^2\left[K_{2/3}^2(z)\left(1+\zeta\xi y\frac{\alpha}{\sqrt{1+\alpha^2}}\right)\right.$$

$$\left. +\frac{\alpha^2}{1+\alpha^2}K_{1/3}^2(z)\left(1+\zeta\xi y\frac{\sqrt{1+\alpha^2}}{\alpha}\right)\right] \qquad (7)$$

Integrating (6) over $\psi = \pm\pi/2$ (see Fig. 1) and using $F(\alpha)$ from (7) yields the intensity of radiation emitted into the interval $dyd\theta$. This intensity is

$$d^2W = \frac{9n_e}{16\pi^3}\frac{ce_0^2}{R^2}\gamma^5 y^2 dyd\theta$$

$$\int_{-\pi/2}^{\pi/2}(1+\alpha^2)^2\left[K_{2/3}^2(z)+\frac{\alpha^2}{1+\alpha^2}K_{1/3}^2(z)\right]d\psi \qquad (8)$$

and independent of the spin. The intensity of the photons emitted into the space above the orbit plane is obtained by integrating (8) from 0 to $+\pi/2$ and the intensity of the photons emitted into the space below the orbit plane is obtained by integrating (8) from 0 to $-\pi/2$. The difference of these two integrals is spin-dependent,

$$d^2W = \frac{9n_e}{8\pi^3}\frac{ce_0^2}{R^2}\gamma^5 y^2 dyd\theta\zeta\xi y$$

$$\int_0^{\pi/2}\alpha(1+\alpha^2)^{3/2}\left[K_{1/3}^2(z)+K_{2/3}^2(z)\right]d\psi \qquad (9)$$

For further investigations it is convenient to convert the formulas for intensities into formulas for photon numbers by dividing equations (8) and (9) by the photon energy

$$\epsilon_\gamma = \frac{3}{2}\frac{\hbar c}{R}y\gamma^3 \qquad (10)$$

Taking into account that $e_0^2/\hbar c = 1/137$ and

$$n_e\frac{e_0}{e_0}\frac{c}{R} = 2\pi\frac{I_0}{e_0}, \qquad (11)$$

replacing $d\theta$ by the finite horizontal angle $\Delta\theta$, and $d\alpha = \gamma d\psi$, the total number of emitted photons, N_γ, and the number of photons in the flux difference, $\Delta N_\gamma(\zeta)$, can be presented as follows:

$$N_\gamma = \frac{3}{4\pi^2}\frac{1}{137}\frac{I_e}{e_0}\gamma\Delta\theta$$

$$\int_{y_1}^{y_2}ydy\int_{-\pi/2}^{+\pi/2}F(\alpha,y)d\alpha \qquad (12)$$

and

$$\Delta N_\gamma(\zeta) = \frac{3}{2\pi^2}\frac{1}{137}\frac{I_e}{e_0}\xi\gamma\zeta\Delta\theta$$

$$\int_{y_1}^{y_2}y^2dy\int_0^{\pi/2}F(\alpha,\zeta,\xi y)d\alpha \qquad (13)$$

where $F(\alpha)$ and $F(\alpha,\zeta,\xi y)$ are the unchanged integrands from (8) and (9).

III. RESULTS OF THE CALCULATIONS AND THE MEASURING TECHNIQUE

Equations (12) and (13) were solved in order to find the resolution in the measurement of the asymmetry $\Delta N_\gamma(\zeta)$ which is mainly limited by the quantum fluctuation of N_γ.

Another limitation comes from the fact that the beam has a finite emittance. This is taken into account by performing the integration in (13) with $\alpha_1 \geq \gamma\sigma_{y'}$ as a lower limit.

The detector can be a transparent differential ionisation chamber (DIC) [6] (Fig. 2). It consists of two ionisation chambers with electrodes of identical length and identical interelectrode distance. The collecting electrodes are united and connected with an electrometric amplifier. The high voltage for the electrodes is the same but the voltage has opposite sign. The chambers work in the regime of full ion collection so that the dark current is determined by the cable leakage and the variation of the background radiation within the chamber. Systematic errors can be eliminated by measuring with an unpolarised beam and by reversing the electron polarisation.

In order to calculate the number of photons absorbed in the ionisation chamber the integrands in (12) and (13) have to be multiplied by the absorption function $A(\mu,t)$:

$$A(\mu,t) = 1 - \exp[-\mu(\lambda)\cdot t] \qquad (14)$$

where t is the length of the ionisation chamber, $\lambda = \lambda_c/y$, and $\mu(\lambda)$ is the linear absorption coefficient described by the empirical expression [7]

$$\mu(\lambda) = 0.023\frac{Z}{A}\rho(Z\lambda)^{2.78} \qquad (15)$$

where ρ is the density in g/cm^3, Z is the number of protons and A is the number of nucleons of the ionisation gas, and λ is the wavelength in Å.

The results of the calculations are presented in Table 1, and the parameters used for the calculations—magnetic field strength, type of detector, the gas of the ionisation chamber and the chamber length, and the spectral and the angular limits—are presented in Table 2. In all these calculations $\Delta\theta$ is 10^{-2} rad and $\sigma_{y'}$ is 2×10^{-5}.

The tables cover the energy range of the existing polarised electron machines: CEBAF (0.8–4.0 GeV, $I=$ 0.1 mA), Bates (MIT) (0.4–0.9 GeV, $I=$ 10 mA) and HERA, LEP, and SLC (27–45 GeV).

In the following the polarization detector proposed for CEBAF is described in more detail (Fig. 2). The synchrotron radiation is created by a superconductive three-pole wiggler with a pole length of 10 cm.

A transparent differential ionisation chamber working in the full ion collection regime has a dark current of $I_{dark} \ll 10^{-14}$ A. This corresponds for an air-filled DIC to about 300 photons with an energy of 10 keV. Since the expected current in each part of the differential chamber is higher than 10^{-8} A, the dark current can be neglected.

The ionisation chamber can be centered with the help of the visible part of the synchrotron radiation. For visible light $\xi y \sim 0$ and therefore the asymmetry caused by polarization is negligible. The visible light detectors can be silicon photodiodes [8] with a dark current of about 0.1 fA. In order to protect the photodiodes from the radiation damage caused by hard x rays, mirrors can be used as shown in Fig. 2.

IV. ACKNOWLEDGMENT

V. REFERENCES

[1] K. Nakajima, "A Vector Polarimeter For Measurement of Spin Polarization in Electron Storage Rings," *Proc. Workshop on Advanced Beam Instrumentation*, Vol. 1, April 1991, KEK, Tsukuba, Japan.

[2] M. Placidi and R. Rossmanith, *Nucl. Instrum. Methods* A274, 79 (1989).

[3] A. E. Bondar, E. L. Saldin, "On the Possibility of Using of the Synchrotron Radiation for Measuring the Electron Beam Polarization in Storage Ring," Preprint INP 81-41, Novosibirsk.

[4] A. A. Sokolov, I. M. Ternov, *Radiation From Relativistic Electrons* (American Institute of Physics, Translation Series, New York, 1986).

[5] A. A. Sokolov, I. M. Ternov, *Synchrotron Radiation* "Nauka" Edition, Moscow, 1966).

[6] I. P. Karabekov, E. D. Egikian *et al.*, "An Express Method for Determination of Crystal Perfection Using Synchrotron Radiation," Preprint YERPHI-1117(80)-88, Yerevan, 1988.

[7] M. A. Blochin, *Physics of X-Rays* (Gos. Tech. Izdat. Teor. Phys., Moscow, 1957).

[8] G. Eppeldauer and J. E. Hardis, *App. Opt.* 30 (22) (1991).

Table 1. Results of the Calculations

Energy, current (GeV, mA)	Photon intensity N_γ (photons/s)	Flux asymmetry $\Delta N_\gamma(\zeta)$ (photons/s)	Flux fluctuation $\Delta N_\gamma(fl)$ (photons/s)	Accuracy, time $\Delta\zeta/\zeta$; Δt (%, s)
0.5, 0.1	5.94×10^{10}	4.30×10^5	2.44×10^5	5.1, 120.
0.5, 10.0	5.94×10^{12}	4.30×10^7	2.43×10^6	1.0, 32.
1.0, 0.1	2.03×10^{12}	1.98×10^7	1.42×10^6	1.0, 50.
1.0, 10.0	2.03×10^{14}	1.98×10^9	1.42×10^7	0.7, 1.0
2.0, 0.1	2.65×10^{13}	2.70×10^8	5.14×10^6	1.0, 4.0
3.0, 0.1	6.18×10^{13}	6.85×10^8	7.86×10^6	1.15, 1.0
4.0, 0.1	9.78×10^{13}	1.10×10^9	9.88×10^6	0.9, 1.0
50.0, 0.001	13.93×10^{12}	5.25×10^8	3.37×10^6	0.7, 1.0

Table 2. The Parameters Used in Table 1

Energy (GeV)	Type of detector (filling gas, length in m)	Strength of magn. field (T)	Spectral bandwidth $(\lambda_c/\lambda_1)/(\lambda_c/\lambda_2)$	Lower angle of integration $\psi\gamma$
0.5	Air, 0.5	6.25	4.0/14.0	0.02
1.0	Kr, 0.1	6.25	1.7/14	0.04
2.0	Xe, 0.1	6.25	0.4/10.0	0.08
3.0	Xe, 1.0	6.25	0.18/10.0	012
4.0	Xe, 1.0	6.25	0.1/10.0	0.16
50.0	Shower counter	1.5	0.1/10.0	0.16

1. 3-pole magnet
2. Differential Ionization Chamber (DIC)
3. Electrometer
4. Absorber
5. Mirror
6. Collimator
7. Photodiode
8. Differential Electrometer

Figure 1: Geometrical definitions.
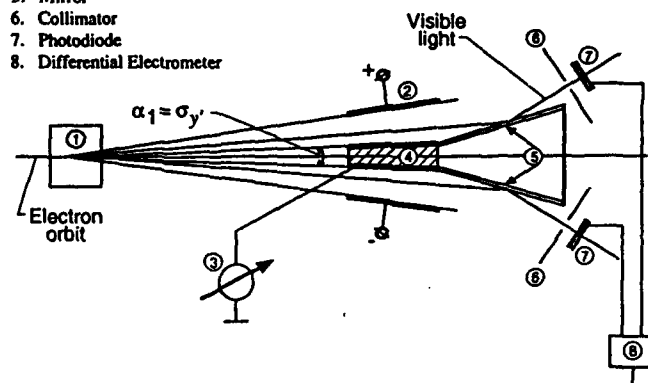
Figure 2: A possible detector design. The synchrotron radiation created by a wiggler is detected by a transparent differential ionization chamber. The chamber measures the asymmetry in the synchrotron radiation distribution. The visible light is used to center the chamber. The detectors for the visible light can be silicon photodiodes with a low dark current.

The Status of Polarization Studies at HERA

M. Böge
for the HERA Polarization Group
DESY, Notkestr. 85, W-2000 Hamburg 52, Germany

Abstract

In August 1992 a vertical electron beam polarization of nearly 60% at 26.7 GeV (spin tune=60.5) was obtained at HERA. This was achieved by optimizing the energy and orbit tunes and by applying harmonic corrections to the closed orbit. The polarization level was reproducible from fill to fill and the calibration of the Compton polarimeter was confirmed by measuring the polarization build up curve. The polarization measurements were made with currents of one to two milliamps. Much higher currents are expected for the 1993 luminosity run ($\sim$ 30 mA were obtained in May 1993). The high polarization level was reproduced at high current. Further polarization studies in parallel with e-p operation are planned. In 1993/94 a pair of spin rotators will be installed in the East straight section so that longitudinal polarization is available at the East interaction point. Simulations with the spin tracking program SITROS are in qualitative agreement with the measurements. Calculations with SITROS show that longitudinal polarizations of up to 50% could then still be achieved.

I. INTRODUCTION

The HERA electron-proton colliding beam facility was designed with the aim of storing polarized electrons. The beam can become polarized parallel to the main bending field through the emission of synchrotron radiation in the arcs.

Vertical polarization of the electron beam at the 8% level was observed in November 1991 at the current operating energy of 26.7 GeV. The HERA polarimeter and these first measurements are described in detail in [1]. The following steps were taken to increase the polarization:

1. the alignment of the quadrupole magnets was checked and selected magnets were realigned,

2. the tilt of the beam ellipse was corrected with orbit bumps distributed around the ring,

3. the orbital tunes were changed to increase the energy separation of the first order resonances,

4. the harmonic spin-orbit correction scheme was prepared and tested with simulations.

Parasitic measurements in April and June 1992 showed that owing to the first two steps the maximum polarization had increased to about 18%. After all optimizations of the orbit nearly 60% vertical polarization was obtained [2].

A. Theoretical Aspects

Centre of mass spin motion in electric and magnetic field is governed by the Thomas-BMT [3][4] equation:

$$\frac{d\vec{s}}{d\theta} = \vec{\Omega} \times \vec{s},$$

where $\vec{\Omega}(\vec{B}, \vec{E}, \gamma)$ is a function of the fields and energy. θ is the azimuthal coordinate.
In a flat ring with the conditions $\vec{B} \parallel \vec{e_z}$, $\vec{E} = \vec{0}$ and after transformation to a frame which is circulating with the beam, $\vec{\Omega}$ becomes:

$$\vec{\Omega} = \frac{e\vec{B}}{cm_e\gamma} \frac{R}{2\pi} \quad \gamma a,$$

where the first part is the relativistic cyclotron frequency $\vec{\omega}$, R the circumference of the ring and γa the spin tune ν. a denotes the electron anomalous g factor.
The emission of synchrotron radiation in an electron storage ring can cause spin flip from up to down and vice versa [5]. An asymmetry in the emission rates leads to an exponential polarization buildup with time against the direction of the bending field [6]:

$$P(t) = P_\infty(1 - \exp{-t/\tau_p}), \quad \tau_p^{-1} \propto \gamma^5 \oint \frac{1}{\rho^3} d\theta$$

with ρ = modulus of bending radius, the equilibrium polarization $P_\infty = 92.4\%$ for a flat ring and the characteristic buildup time $\tau_p = 46$ min for a ring like HERA at 26.67 GeV. So far we have neglected depolarizing effects. Due to the stochastic change of momentum by photon emission betatron oscillations are excited. Especially in the quadrupoles this leads to additional fields which can act on the spin. As a result spin diffusion and hence depolarization with a characteristic depolarization time τ_d is introduced:

$$P(t) = P_\infty \frac{\tau_d}{\tau_p + \tau_d} \left(1 - \exp\left(-\frac{\tau_p + \tau_d}{\tau_p \tau_d} t\right) \right)$$

(HERA: $P_{eff} = 17\%$ corresponds to $\tau_{eff} = 7.5$ min at 26.67 GeV). Spin diffusion is particularly strong when the precession of the spins is synchronous with orbital and energy oscillations which drive the diffusion, i.e. when the spin resonance condition:

$$\nu = m + m_x Q_x + m_z Q_z + m_s Q_s$$

is fulfilled, where Q_x, Q_z, Q_s are the horizontal, vertical and synchrotron tunes and m and $m_{x,z,s}$ are integers. At

460
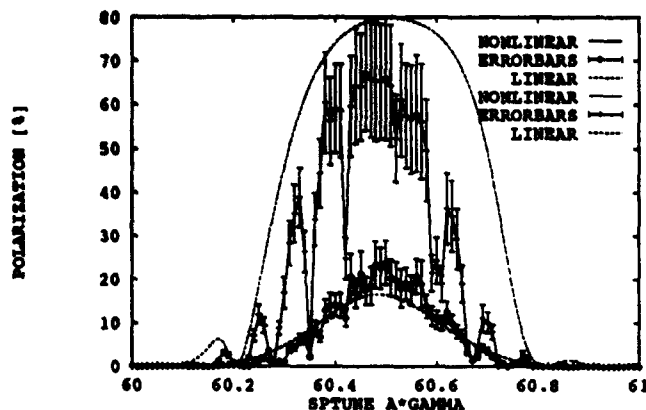
Figure 1: Monte-Carlo simulations (solid curves) of polarization vs. spin tune between two integer resonances (440 MeV). The maximum polarization attained with standard orbit corrections is ∼ 23%. After the corrections with the special bump scheme a value of ∼ 70% is reached. The linear calculations (dashed curves) are shown for comparison

Figure 2: The polarization measurement for a typical run: $\Delta\eta$ is plotted vs. E_γ. The fit gives $\Delta S_3 P_y = 53.1\%$

high energy and large energy spread not only the first order resonances ($|m_x| + |m_z| + |m_s| = 1$) are important. The synchrotron sidebands ($\nu = Q_{x,z,s} + m_s Q_s$) can also be strong. The spin diffusion can be controlled by a proper alignment of the ring elements (especially the quadrupoles) and with a special orbit correction scheme which minimizes the coupling between the orbital and spin motion for a given (but unknown) error distribution of the magnets by empirical optimization of the measured polarization [7]. The scheme used for HERA consists of 8 vertical orbit bumps at "strategic positions" in the arcs of the ring. Using these bumps we are able to control the most important contributions to the spin orbit coupling. The Monte-Carlo calculations with SITROS [8][9] show how effective these bumps should be (Figure 1).

II. THE HERA POLARIMETER

The vertical component of the electron polarization is measured using the asymmetry of the Compton cross section for the scattering of vertically polarized electrons off circularly polarized photons [10]. Laser light of 514 nm is directed against the electron beam and the energy E_γ and vertical position y of the backscattered photons are measured. The polarization P_y is obtained from the difference Δy in the mean vertical positions $\langle y \rangle$ of the distributions measured with left and right circularly polarized light:

$$\Delta y = \frac{\langle y \rangle_L - \langle y \rangle_R}{2} = P_y \Delta S_3 \Pi_y(E_\gamma),$$

with $\Delta S_3 = (S_{3,L} - S_{3,R})/2$ where $S_{3,L}$ and $S_{3,R}$ are the degrees of circular polarization of the laser light and Π_y the analyzing power, is derived from the polarization dependent cross section. The maximum value of Π_y is 180μm at $E_\gamma = 8$ GeV. In practice ΔS_3 is nearly 1, and the vertical

component of the electron beam polarization is proportional to Δy. The HERA polarimeter has been described in detail in [1].

A. The Calorimeter

The energy and vertical position of the backscattered photons are measured using a tungsten-scintillator sampling calorimeter. The calorimeter is split in the middle, and can thus be considered to consist of two calorimeters, one on the top of the other. The energy of an incoming photon is the sum of the energies in the two halves $E_\gamma = E_{up} + E_{down}$ and the vertical position is measured using the asymmetry of the energies:

$$\eta(y) = \frac{E_{up} - E_{down}}{E_{up} + E_{down}}.$$

Figure 2 shows an example of the measured variation of

$$\Delta\eta(E_\gamma) = \frac{\langle\eta\rangle_L - \langle\eta\rangle_R}{2} = P_y \Delta S_3 \Pi_\eta(E_\gamma) \qquad (1)$$

with E_γ together with the result of a fit to (1) using the Monte-Carlo program EGS4 [11] for the calculation of the normalized shower distribution dE/dy which is needed for the derivation of Π_η. The agreement is excellent. For $\Delta S_3 = 1$ the fit corresponds to ∼ 53% polarization.

III. THE MEASUREMENTS

The measurements were made at beam energies near 26.7 GeV (spin tune $a\gamma$=60.5). The chosen working point was at $Q_x = 47.12$ and $Q_z = 47.20$ which has the advantage of an increased energy separation between the first order resonances and higher polarization around the half-integer spin tune (expected by simulations) compared with the old working point at $Q_x = 47.22$ and $Q_z = 47.35$. During the measurements the total circumferential voltage ranged between 140 and 165 MV leading to a synchrotron tune Q_s from 0.061 to 0.082 at 26.67 GeV. This choice of the tunes satisfies $Q_z \approx Q_x + Q_s$ which puts the sidebands to the orbital resonances on top of each other. The rms distortion

461
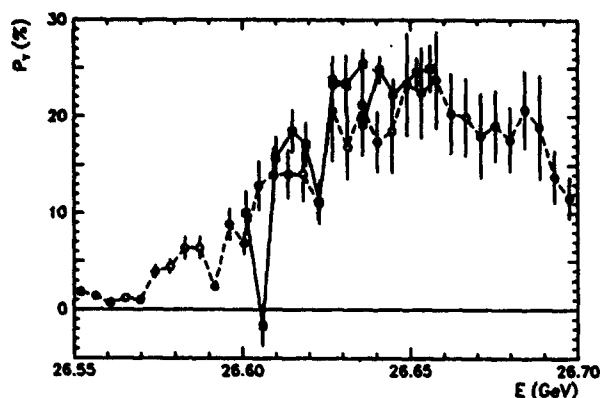
Figure 3: Overlay of simulation results (circles) and measured values (squares) of polarization vs. energy. The data have been shifted in energy by −64 MeV

Figure 4: The buildup of polarization after depolarization (Results of the fit: $P_{max} = 50.6 \pm 1.9\%$)

of the vertical closed orbit achieved by standard orbit corrections was ~ 0.8 mm. The proton ring and the solenoids of the experiments were turned off. The total current had been limited to about 2 mA in 10 bunches with lifetime of about 5 hours. These conditions gave a statistical error of $\Delta P_y \sim \pm 0.03$ for a 1 minute measurement consisting of 40 sec Compton-scattering measurements switching the laser polarization between left and right circular polarizations at 90 Hz, followed by 20 sec background measurements. An energy scan followed by an RF voltage scan was performed to find the maximum polarisation leading to a value of 25.5% at 26.70 GeV. A comparison between measurement and simulation for the scan is made in Figure 3 taking into account the uncertainty in the energy scale of HERA. By application of the special bump scheme the polarization increased to nearly 60%. Figure 4 shows a buildup time measurement at ~ 50%. The measured polarization values (45.6±5.3%) and the polarization calculated by fitting the buildup time are consistent showing that the systematic error of the calorimeter measurement is small.

IV. CONCLUSIONS

An electron polarization of 8% was observed in November 1991. After the realignment of misaligned quadrupoles a maximum polarization of about 18% was observed in spring of 1992. During dedicated beam time in August and September 1992, special orbit correction schemes were successfully tested. After all corrections a maximum polarization of 56.0±1.6±5% (systematic) was achieved. The short and long-term stability of the HERA ring concerning polarization was excellent. Comparisons between measurements and simulations using the Monte-Carlo program SITROS show the predictive power of the program. In forthcoming measurements the aim will be to achieve polarization during luminosity operation (solenoids and compensators of the experiments, multi-bunch feedback and proton ring turned on). An accurate beam energy measurement will be made using resonant depolarization. Spin rotators are
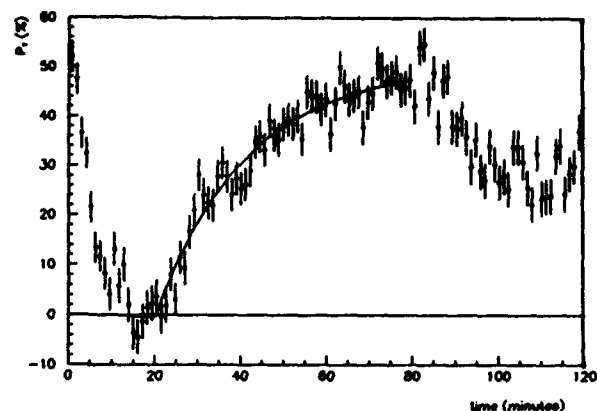
ready for installation in the East area of HERA during the 1993/94 shutdown. Simulations with SITROS indicate that a high degree of polarisation can also be achieved with spin rotators [12].

V. REFERENCES

[1] D.P. Barber,et. al.,*DESY Report* 92-136, October 1992.

[2] D.P. Barber,et. al.,*DESY Report* 93-038, April 1993.

[3] L. Thomas, *Philos.Mag.*, vol.3,p.1, (1927).

[4] V. Bargmann,L. Michel,V.L. Telegdi, *Phys.Rev.Letts.*, vol.2,p.435, (1959).

[5] A.A. Sokolov, I.M. Ternov, *Sov. Phys. Doklady*, vol.8,p.1203, (1964).

[6] A. W. Chao, *Nucl.Inst.Meth.*, vol.180,p.29, (1981).

[7] E. Gianfelice-Wendt, in: F. Willeke (editor), *DESY HERA* 92-07, p.202, (1992).

[8] J. Kewisch, T. Limberg, R. Rossmanith, *Phys.Rev.Letts.*, vol.62,N^04,p.419, (1989).

[9] M. Böge, in: F. Willeke (editor), *DESY HERA* 92-07, p.211, (1992).

[10] U. Fano, *J. Op. Soc. Am.*, vol.39, p.859, (1949).

[11] W.R. Nelson, H. Hirayama, D.W.O. Rogers, *SLAC-265*, (1985).

[12] E. Gianfelice-Wendt, M. Böge, 10th Int. Symp. on High Energy Spin Physics, Nagoya, Nov. 1992

Computer Assisted Accelerator Tuning*

John K. Boyd

Lawrence Livermore National Laboratory

P.O. Box 808, Livermore, CA 94550

Abstract

The challenge of tuning an induction accelerator in real time has been addressed with the new TUNE GUIDE code. The code initializes a beam at a particular position using a tracer particle representation of the phase space. The particles are transported, using a matrix formulation, element by element along the beamline assuming that the field of a solenoid, or steering element is constant over its length. The other allowed elements are gaps and drift sections. A great deal of effort has been spent programming TUNE GUIDE to operate under the IBMPC Windows 3.1 system. This system features an intuitive, menu driven interface, which provides an ability to rapidly change beamline component parameter values. Consequently various accelerator setups can be explored and new values determined in real time while the accelerator is operating. In addition the code has the capability of varying a component value over a range and then plotting the resulting beam properties, such as radius or centroid position, at a down stream position. Element parameter editing is also included along with an on-line hyper text oriented help package.

I. INTRODUCTION

An induction accelerator can be tuned in real time with a responsive code having an intuitive graphical interface. The TUNE GUIDE code uses a matrix formulation to reduce the model complexity, and thus the required run time. TUNE GUIDE has been implemented in the Windows 3.1 system to obtain ease of use. The accelerator is modeled as a number of regions of solenoid focus, drift, dipole steering, or accelerating gap. Results are generated by repetitively applying beam line matrix elements to the initial condition. A real accelerator beamline element has a field with a peak value at its center and then diminishes to zero at large distances. The TUNE GUIDE code models beamline elements as constant fields over a specified length and then zero outside this region. The main part of this paper elaborates on the description of the beam line elements in the TUNE GUIDE code.

The matrix models used by TUNE GUIDE are similar to those of other codes [1]. The main difference is the addition of an element consisting of a steering coil and solenoid in the same location. Also to keep run time down and improve realism a method has been used to select input parameters that involves off line element characterization. The best agreement between the code and a real element is obtained by using an effective length and field strength parameter that differs from the actual physical value and is chosen to account for the step function behavior. Complete agreement is not possible with only one or two free parameters. However, a method is described that gives agreement for the basic effects of a solenoid and steering coil. For a solenoid, a procedure is given for selecting the length and the gauss/amp parameter that produces the correct phase advance and focusing strength. For a steering coil an equation is determined that provides a transverse gauss/amp parameter which results in the same steering kick as the real coil.

II. SOLENOID BEAMLINE ELEMENT MODEL

A solenoid causes an electron beam to focus and also rotate. These effects begin occurring before the beam enters the starting position of the solenoid coil. In the TUNE GUIDE code model there is no focus or rotation until the beam enters a region of constant field. Also upon exiting the region of constant field the model ceases any focus or rotation. In order to preserve the focus and rotation that really results from the solenoid that is being modeled, it is necessary to calculate what values of solenoid length and gauss/amp should be used in TUNE GUIDE. The values that are derived guarantee equivalence along the axis.

A solenoid field $B(0,z) = GI_{ps}h(z)$ near the axis is modeled as a scaled profile function where G is the gauss/amp parameter, I_{ps} is the power supply current and $h(z)$ is a normalized axial variation function. The condition for equivalent focus is obtained by appealing to an axis expansion of the first order matrix for transport of a beam through a solenoid. The equivalence condition from this method requires that the integral of B^2 for the model must equal that of the real solenoid,

$$\alpha^2 G^2 I_{ps}^2 L_{eff} = G^2 I_{ps}^2 L \int_{-\infty}^{\infty} h^2(Z)\,dZ \qquad (1)$$

where α is a G modification factor resulting in focus strength equivalence (to be determined), L_{eff} is the effective model length of the solenoid and L is the actual solenoid length. Note that a normalized axial variable $Z = z/L$ is used in the Eq.(1) integral.

The condition for equivalent rotation is that the integral of B be the same,

$$\alpha G I_{ps} L_{eff} = G I_{ps} L \int_{-\infty}^{\infty} h(Z)\,dZ \qquad (2)$$

Equations (1) and (2) can be solved simultaneously to obtain,

$$L_{eff} = L\frac{\left[\int h\,dZ\right]^2}{\int h^2\,dZ} \qquad (3)$$

$$\alpha = \frac{\int h^2\,dZ}{\int h\,dZ} \qquad (4)$$

where the effective length and modification factor are specified in terms of the $h(Z)$ profile. The $h(Z)$ profile can be determined from analytical expressions for the field.

A. Azimuthal current sheet model

For the case of a solenoid consisting of a single thin layer of azimuthal current, there is an analytical solution for the magnetic field on axis,

$$B = GI_{ps}\sqrt{\frac{1}{4}+A^2}\left[\frac{Z_m}{\sqrt{Z_m^2+A^2}}+\frac{Z_p}{\sqrt{Z_p^2+A^2}}\right] \qquad (5)$$

where $Z_p = 1/2+Z$, $Z_m = 1/2-Z$ and the normalized solenoid radius is $A = a/L$. From the form of Eq.(5) it is readily apparent that,

$$h(Z) = \sqrt{\frac{1}{4}+A^2}\left[\frac{Z_m}{\sqrt{Z_m^2+A^2}}+\frac{Z_p}{\sqrt{Z_p^2+A^2}}\right] \qquad (6)$$

Using Eq.(6) in Eq.(3) and (4),

$$\frac{L_{eff}}{L} = \frac{2}{\int_0^\infty \left(\frac{Z_p}{\sqrt{Z_p^2+A^2}}+\frac{Z_m}{\sqrt{Z_m^2+A^2}}\right)^2 dZ} \qquad (7)$$

$$\alpha = \sqrt{A^2+\frac{1}{4}}\int_0^\infty \left(\frac{Z_p}{\sqrt{Z_p^2+A^2}}+\frac{Z_m}{\sqrt{Z_m^2+A^2}}\right)^2 dZ \qquad (8)$$

Equations (7) and (8) are used to produce values of L_{eff}/L and α as a function of A. These values can be used to determine input for the TUNE GUIDE code.

B. Rectangular cross section current model

At the next level of refinement the analytic model for the solenoid can be based on an azimuthal current that has constant current density in a rectangular cross section. The constant value is,

$$J_\theta = \frac{c}{2\pi L}GI_{ps} \qquad (9)$$

where $G = 2\pi N/(10L(R_2-R_1))$, N is the number of turns, R_1 and R_2 are the normalized inner and outer radius respectively. The corresponding component of the vector potential is,

$$A_\theta(R,Z) = \frac{GI_{ps}L}{2\pi}\iiint\frac{\cos\theta'R'\,dR'\,d\theta'\,dZ'}{\sqrt{D(R,R',0)}} \qquad (10)$$

where $D(x,y,\theta) = x^2 - 2xy(\cos\theta\cos\theta'-\sin\theta\sin\theta') + y^2 + (Z-Z')^2$ and the coordinates are normalized to the solenoid length. Since the magnetic field on axis is desired, the above expression is expanded about $R = 0$ keeping only the first two terms. Then using the scaled

coordinate field definition $B_z = (LR)^{-1}\frac{\partial RA_\theta}{\partial R}$, it is found,

$$B_z = \frac{GI_{ps}}{\pi}\iiint dR'\,d\theta'\,dZ'\left[\frac{(R'\cos\theta')^2}{\left(R'^2+(Z-Z')^2\right)^{3/2}}\right] \qquad (11)$$

Equation (11) can be integrated to obtain the profile function for this model.

$$h(Z) = \frac{Z_m\log\dfrac{R_2+\sqrt{R_2^2+Z_m^2}}{R_1+\sqrt{R_1^2+Z_m^2}}+Z_p\log\dfrac{R_2+\sqrt{R_2^2+Z_p^2}}{R_1+\sqrt{R_1^2+Z_p^2}}}{\log\dfrac{R_2+\sqrt{R_2^2+\frac{1}{4}}}{R_1+\sqrt{R_1^2+\frac{1}{4}}}} \qquad (12)$$

Equation (12) is used in Eq.(3) and (4) to determine L_{eff}/L and α as a function of R_1 where some relationship between the inner and outer radius $R_2 \propto R_1$, must be assumed. For any particular solenoid both the inner and outer radius are known, so the effective length and α can be determined numerically.

III. STEERING BEAMLINE ELEMENT MODEL

A steering element causes an electron beam to deflect to the left, right or up, down, depending on its orientation. The deflection begins occurring before the beam actually arrives at the start of the physical coil. To determine the parameter that allows equivalent steering in TUNE GUIDE, it is sufficient to concentrate on a steering coil set that creates vertical field. The goal is then to select the ζ, gauss/amp parameter so the left or right deflection is equivalent to the on axis value which is

caused by a real steering element. The condition to be satisfied is given by Eq(13),

$$\zeta I_{ps} L = L \int_{-\infty}^{\infty} B_y dZ \qquad (13)$$

On the left side of Eq.(13) is the expression for the steering kick due to a TUNE GUIDE element which only steers over a finite distance. The right side of Eq.(13) is the expression for the total steering caused by a real element. In order to perform this integral the magnetic field of the steering coil is expressed in terms of components of the vector potential.

$$B_y = \frac{\partial A_x}{\partial z} - \frac{\partial A_z}{\partial x} \qquad (14)$$

The steering coil currents that flow in the theta direction contribute to A_x and the currents in the axial or z direction contribute to A_z. Using Eq.(14) in Eq.(13),

$$\zeta I_{ps} = A_x(\infty) - A_x(-\infty) - \int_{-\infty}^{\infty} \frac{\partial A_z}{\partial x} dZ \qquad (15)$$

The first two terms on the right side of Eq.(15) are steering field contributions at great distance from the steering coil. The formula to within a constant, for A_x is given below.

$$A_x = \int_{0}^{2\pi} d\theta' \int_{-\frac{L}{2}}^{L(\theta')} \frac{dZ' \sin\theta'}{\sqrt{D(r, A, \theta)}} \qquad (16)$$

The integral on the right of Eq.(16) has Z in the denominator and thus as Z gets large the integral becomes small, so the A_x terms of Eq.(15) vanish. This means that ζ is completely specified by A_z. To determine this component of the vector potential the longitudinal current of the steering coil is modeled as a sheet,

$$J_z = -\frac{2NI_{ps}}{\pi a} \delta(a - r') \qquad (17)$$

where a is the sheet radius and N is the number of turns. The sheet current has a variable length in angle about the axis and this feature appears below in the z limits of integration. The axial component of the vector potential is then,

$$A_z = -\left(\frac{2NI_{ps}}{\pi c}\right) \int d\theta' \int \frac{dZ'}{\sqrt{D(r, A, \theta)}} \qquad (18)$$

and using this expression in Eq(14),

$$B_y = -\left(\frac{2NI_{ps}}{\pi cL}\right) \int_{0}^{2\pi} d\theta' \int_{Z_1}^{Z_1} \frac{(x - A\cos\theta') dZ'}{(D(r, A, \theta))^{3/2}} \qquad (19)$$

The field at the axis is obtained by applying symmetry and performing the Z' integration,

$$B_y(0, 0, Z) = -\frac{8NI_{ps}}{\pi ca} \int_{0}^{\frac{\pi}{2}} \cos\theta' d\theta' (\Xi(2) - \Xi(1)) \qquad (20)$$

where $\Xi(k) = (Z - Z_k(\theta')) / \sqrt{A^2 + (Z - Z_k(\theta'))^2}$ and the angle dependent axial integration limits are,

$$Z_1(\theta') = -\frac{1}{2} + (1 - \frac{\hat{L}}{L}) \frac{\theta'}{\pi}$$

$$Z_2(\theta') = \frac{1}{2} - (1 - \frac{\hat{L}}{L}) \frac{\theta'}{\pi} \qquad (21)$$

An unrolled steering coil has current turns which run in the axial direction. The shape of these turns is that of a trapezoid. In Eq.(21) L corresponds to the length of the base of the trapezoid and $\hat{L}$ corresponds to the shorter length of the top of the trapezoid. Using Eq.(20) with (21) in Eq.(13), it is found (for current now expressed in amps),

$$\zeta = \frac{1.6N}{\pi a} \left[1 - (1 - \frac{2}{\pi})(1 - \frac{\hat{L}}{L}) \right] \qquad (22)$$

This expression is the gauss/amp factor for the steering coil. In the presence of ferrite it should be increased by approximately a factor of two. Using typical steering coil values of 13.5 and 36.2 cm for the lengths, 44 turns and a radius of 7.3 cm, gives $\zeta = 2.37$ gauss/amp. This compares favorably with the value from reported measurements [2] where 420 gauss-cm at 5 amps is recorded. This is 420[gauss-cm]/(5[amp]x36.2[cm]) or 2.32 gauss/amp.

IV. REFERENCES

[1] A.C. Paul, TRANSPORT: an Ion Optic Program, Lawrence Berkeley Lab., LBL-2697, UC-32, TID-4500-R62 (Feb. 1975).

[2] J. Zentler, private communication

Pulse-to-Pulse Simulation of Orbit Feedback for JLC Final Focus System

Noboru Yamamoto, Kohji Hirata, and Katsunobu Oide
KEK, National Lab. for High Energy Phisics
1-1 Oho, Tsukuba, Ibaraki 305 JAPAN

Abstract

A realistic, pulse-to-pulse, simulation is done to evaluate performance of an orbit feedback system in final focus system for future linear colliders. Accumulation of errors and long time stability of the system including time evolution of ground movement are estimated by this simulation. The result of simulation confirms that the orbit feedback system can maintain nano meter beam size at a colliding point and can keep beams in head-on collision

I. INTRODUCTION

In future linear colliders, 1 μm r.m.s. vertical random displacement of focusing elements in final focus system can cause 10 times larger beam spot at interaction point (IP) than designed nano meter beam size. After the beam based alignment technique [1] recovers the proper alignment of the elements, we still need a feedback against the ground motion.

The authors of reference [2] suggested the use of a simple orbit correction method. With this method, 3 μm r.m.s. random ground motion does not harm 3 nm beam size at IP, if the error is a static one. To manage the time evolution of the errors, a pulse-to-pulse feedback is necessary.

In this paper, we propose a feedback method and check its effectiveness by a more realistic simulation. This feedback method not only corrects the global orbits in both beam lines but also keeps the head-on collision. We also include incoming beam position jitter, BPM jitter, and orbit correctors setting errors in the simulation.

II. SIMULATION OF ORBIT FEEDBACK

a. Beam Optics

The optics used in the simulation is the optics for the final focus system of JLC[3] designed by K.Oide[4]. Figure 1 shows the optical functions of this optics. The beta functions at the interaction point are 10 mm in horizontal and 100 μm in vertical direction.

Assuming the invariant emittances of $\epsilon_x = 3.6 \times 10^{-6}$m·rad and $\epsilon_y = 5 \times 10^{-8}$m·rad at the entrance, the designed beam cross section at the interaction point is 280 nm × 3.5 nm including 15 % increase of emittance due to aberration. Non linearity of sextupole magnets for chromaticity correction is canceled out each other by $-\pi$ transformer between a pair of sextupoles.
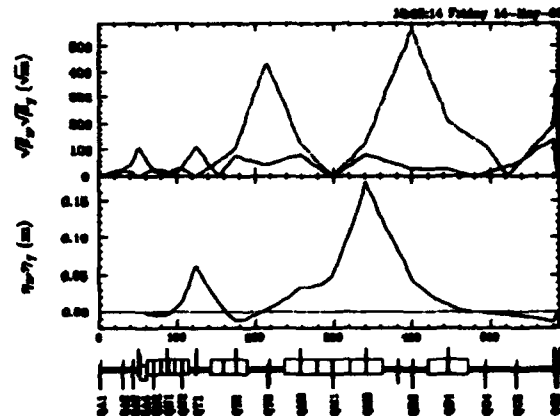
Figure 1: Optical functions of the JLC final focus system. The upper: horizontal and vertical beta functions. The lower: dispersion functions.

b. Feedback System

We consider the feedback system which consists of two kinds of orbit correction methods. Result from each method is summed and applied for the next pulse of the beam.

The first feedback cures the global orbit distortions caused by the transverse displacement of quadrupole and sextupole magnets, such as the ground motion. The orbit correction method discussed in [2] is used as a correction algorithm. The algorithm 1) centers the orbit at each BPM (so-called one to one correction) and 2) keep the beam position at IP unchanged. It follows that any linear dispersion is not produced at IP in the ideal case.

The second feedback keeps beams in collision. The relative distance between colliding beams, Δ_x and Δ_y, will be measured by the beam-beam deflection monitor in future linear colliders. The feedback controls the beam positions at IP by making dispersion-free bump orbits near the IP. Figure 2 shows an example of such a bump orbit.

c. Feedback Loop Parameter

Because of randomness in the error sources, it is necessary to average input data for the feedback loops. The global orbit correction feedback does not directly correct the orbit distortion, $z(s)$, but a filtered quantity $f_i(s) = \alpha z(s) + (1 - \alpha)f_{i-1}(s)$, as a target of i-th pulse. The head-on collision feedback has a similar damping constant β. Search for luminosity-optimum for these parameters by simulations results in $\alpha = 0.25$ and $\beta = 0.5$ as shown in Figure 3. These values are used in the rest of simulation.
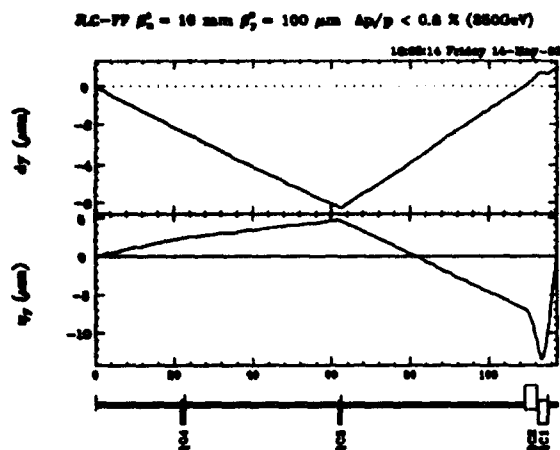
Figure 2: Dispersion-free bump orbit for the head-on collision feedback.

(a) Optimum search of β for α=0.05   (b) Optimum search of α for β=0.5
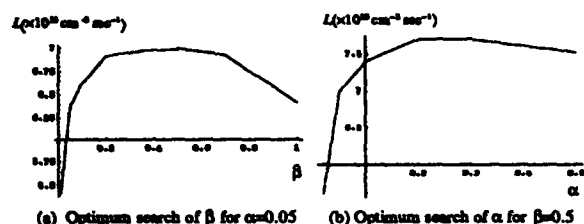
Figure 3: Optimum values of feedback parameters.

d. Luminosity Enhancement by Beam-Beam Interaction

Disruption parameter, $D_{x/y}$, of the colliding beam for the future linear colliders is in the range from 3 to 10. For such an intense beam, luminosity enhancement by beam-beam interaction is important. Luminosity enhancement factor was calculated by simulation in [5]. We used the approximate formula,

$$H_D = (1 + D_y)^{\frac{1}{3}} \frac{15 e^{-\frac{1}{4}\frac{\Delta_y^2}{(1+D_y)^{\frac{3}{2}}}} + D_y e^{\frac{-|\Delta_y|}{1+D_y}}}{15 + D_y}$$

for vertical offsets. This formula agrees well with the result in [5] for flat Gaussian beam with $D_y \leq 10$. For horizontal offset, we used a simple Gaussian overlap formula for the luminosity.

e. Ground Motion

Random transverse displacement of the magnet is generated by using the ATL rule [6]. Although meaning of the ATL rule and its validity are not understood completely yet, we use the ATL rule as a guideline for the estimation of long-term ground motion.

The ATL rule implies squared average of the relative displacement, σ, between two points at distance L after time interval T follows the relation $\sigma^2 = A \times T \times L$. A is a

constant parameter depends on the site. In the reference [6], $10^{-16} \text{msec}^{-1}$ is reported as a value of A. We use this value in the most of simulations. Using the repetition rate 150Hz, we get $AT = 6.67 \times 10^{-19}$ m.

f. Other Error Sources

We used the following numbers for the other error sources.

Error sources	Horizontal	vertical
Beam jitter	0	$1 \times \sigma_y$
correctors error.	0.1%	0.1%
correctors rotation error	1 mrad	1 mrad

g. Simulation Method

Particle tracking simulation in this study was performed by using computer code SAD developed at KEK. SAD tracks particles in full 6 dimension phase space in a symplectic way.

Two computer processes corresponding electron and positron lines are activated simultaneously. Both processes exchange data of beam position at IP for each pulse, and use them for the head-on collision feedback. In this simulation, we do not include the deflection curve with beam-beam effect. We assumed that the offset of two beams can be directly measured. The global orbit correction uses the BPM data supplied by multiparticle simulation with 100 particles/pulse/beam. Synchrotron radiation was turned off due to the limit of computer power.

III. RESULTS OF SIMULATION

Figure 4 summarizes the results of simulation for 10^5 pulses. From the top to the bottom, 1 and 2) are horizontal and vertical relative beam offset at IP as a function of pulse number; 3 and 4) Horizontal and vertical beam sizes at IP for electron beam; 5 and 6) Luminosities without and with the pinch effect. Factor 2 enhancement due to the pinch effect is clearly seen. We have assumed that the beam energy is 250 GeV and the number of particles/bunch 1.11×10^{10}, the number of bunches/rf pulse 72, and the repetition rate 150 H_z. The achieved average luminosity is $7.2 \times 10^{33} \text{cm}^{-2}$ for above parameters.

Figure 5 shows the performance of this orbit feedback. Beam positions and beam sizes at IP are tracked for first 5000 pulses without the orbit feedback. Both beam sizes and beam positions drift away from their nominal values in this period. Feedback loops start at the 5001st pulse. Beam positions and beam sizes recover their nominal values after a few hundred pulses. To visualize an effect of long term ground motion, we used large value of $AT = 10^{-16}$ m in this case, which corresponds to 1 Hz repetition rate. One thousand pulses corresponds to 17 minutes assuming $A = 10^{-16}$ m/sec.

In Figures 4 and 5, there is no clear evidence of long term instability. Such an instability is observed for a quite large value of $AT = 9 \times 10^{-16}$: σ_y^*: decays slowly even with the
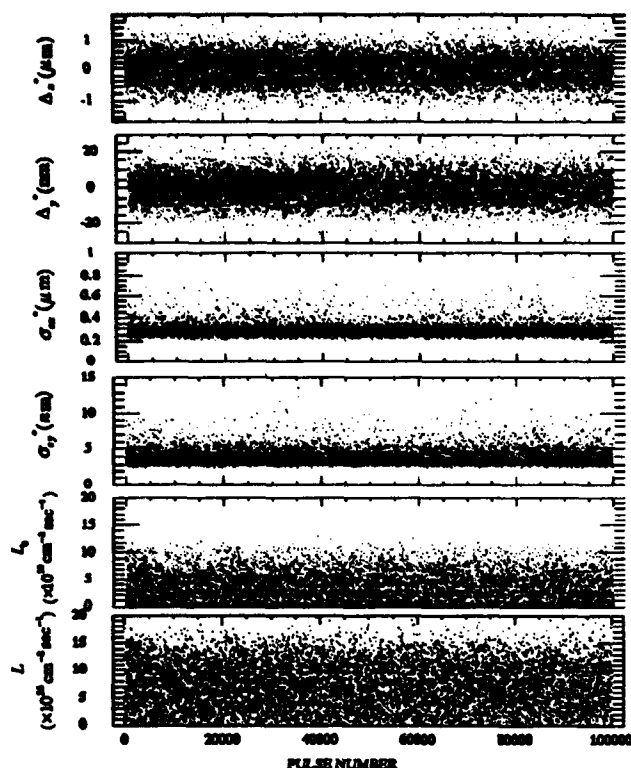
Figure 4: Long term behavior of relative beam displacement, beam size at IP and Luminosity(without/with pinch effect enhancement). Horizontal full scale, 10^5 pulses, corresponds $\sim$ 11 minutes.
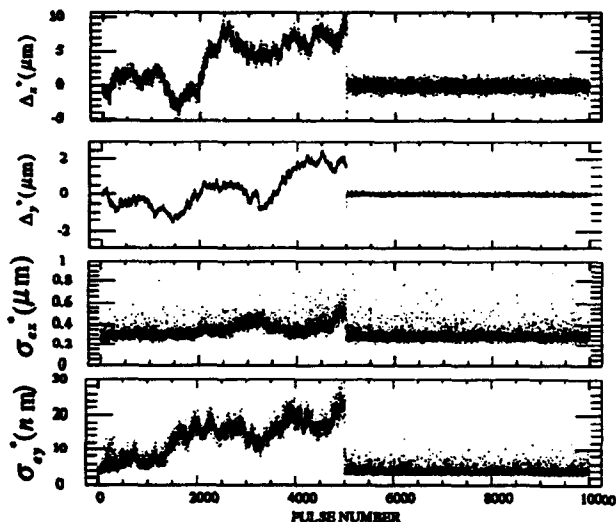
Figure 5: Simulation runs 5000 pulses without feedback. Feedback loops are turned on after 5000 pulses.

feedback. One thousand pulses in this case corresponds 25 hours assuming $A = 10^{-16}$ m/sec.
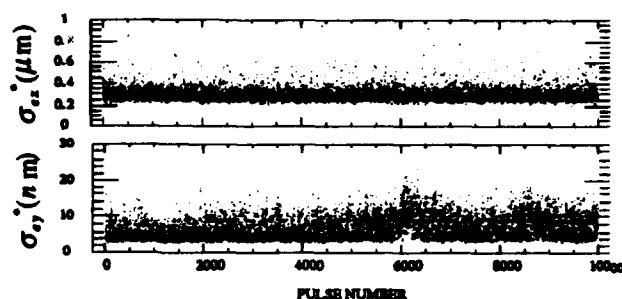
Figure 6: Long term stability of the system. With $AT = 9 \times 10^{-16}$, σ_y^* decays slowly even with the feedback. Horizontal Full scale:25 hours.

IV. SUMMARY AND DISCUSSION

Realistic pulse to pulse simulation of orbit feedback for final focus system of future linear colliders has been performed. The simulation includes several important error sources which may degrade performance of the system. The result of simulation indicates that the final focus system keeps good luminosity with this feedback method for more than 3 hours without any other tuning procedure.

There still remain error sources not included, such as the dynamic range and the nonlinearity of the beam-beam deflection monitoring, drift of strength of components, non-ATL vibrational ground motion, synchrotron radiation in magnets, BPM nonlinearlity, and so on. Simulation including these effects is in progress.

REFERENCES

[1] F. Bulos et al., SLAC-PUB-5488, May 1991. Contributed to IEEE Particle Accelerator Conf., San Francisco, CA, May 1991.

[2] N.Yamamoto and K. Oide, Int. J. Mod. Phys. A(Proc. Suppl) 2A(1993), pp 858

[3] JLC Group,"JLC-I", KEK Report 92-16(1992)

[4] K.Oide, "Final Focus System with Odd-dispersion scheme" in these proceedings, KEK-Preprint-92-58(1992)

[5] Kaoru Yokoya and Pisin Chen,"Beam-Beam phenomena in linear colliders", KEK-Preprint 91-2 (1991)

[6] B. Baklakov, P. Lebedev, B. Parkomchuk, A. Sery, A. Sleptsov, B. Shiltsev, INP-PREPRINT-91-15.

Multi-dimensional Beam Emittance and β-functions

Jean Buon

Laboratoire de l'Accélérateur Linéaire, IN2P3-CNRS
et Université de Paris-Sud, F - 91405 Orsay Cedex

Abstract

The concept of r.m.s. emittance is extended to the case of several degrees of freedom that are coupled. That multi-dimensional emittance is lower than the product of the emittances attached to each degree of freedom, but is conserved in a linear motion. An envelope-hyperellipsoid is introduced to define the β-functions of the beam envelope. On the contrary of an one-degree of freedom motion, it is emphasized that these envelope functions differ from the amplitude functions of the normal modes of motion as a result of the difference between the Liouville and Lagrange invariants.

1. INTRODUCTION

A statistical definition of beam emittance has been originally introduced by P. Lapostolle [1] in a 2-dimensional phase space of an one-degree of freedom motion. The statistical point of view is the most natural way to study the particle spread in phase space. It has been reviewed in [2] and it is here extended to the case of several degrees of freedom that are coupled. The key role is here played by the covariance matrix of the particle coordinates. The emittance is proportional to the square root of its determinant. It is also involved in the expressions of the Liouville and Lagrange invariants that characterize a linear motion.

2. THE STATISTICAL DEFINITION OF MULTIDIMENSIONAL EMITTANCE

The second-order moments give the main statistical characteristics of a set of points in a 2p-dimensional phase space (p is the number of degrees of freedom). With respect to a frame, the origin of which is taken at the barycentre of the points, the moment $<x_\alpha x_\beta>$ is obtained by averaging the coordinate product $x_\alpha x_\beta$ over the set of points (x_α, x_β are two coordinates of one point : α, β = 1,...,2p). The second-order moments are embodied in the covariance matrix V :

$$V = \begin{pmatrix} < x_1\, x_1 > & ... & < x_1\, x_{2p} > \\ ... & ... & ... \\ < x_{2p}\, x_1 > & ... & < x_{2p}\, x_{2p} > \end{pmatrix}$$

Hereafter, it is convenient to write the covariance matrix as the statistical average of a formal product :

$$V = \langle x.\tilde{x} \rangle$$

where x is a coordinate column-vector and $\tilde{x}$ is the transposed coordinate row-vector.

The covariance matrix V is real and symmetric. It can always be diagonalized by a similarity transform, defined by an orthogonal matrix Ω ($\Omega\tilde{\Omega}$ = 1). Assuming that the coordinate frame is orthogonal, that transform corresponds to a change of orthogonal frame with respect to which the new coordinate vector is $X = \Omega x$. One recognizes that the new matrix $W = \Omega V \Omega^{-1}$ is the covariance matrix w.r.t. the new frame :

$$W = \Omega \langle x.\tilde{x} \rangle \Omega^{-1} = \Omega \langle x.\tilde{x} \rangle \tilde{\Omega} = \langle \Omega x.\widetilde{\Omega x} \rangle = \langle X.\tilde{X} \rangle$$

The covariance matrix W w.r.t. the new coordinate frame is :

$$W = \begin{pmatrix} \langle X_1^2 \rangle & 0 & \cdots & 0 \\ 0 & \langle X_2^2 \rangle & \cdots & 0 \\ 0 & 0 & \cdots & \langle X_{2p}^2 \rangle \end{pmatrix}$$

The diagonal element $<X_\alpha^2>$ is the mean square distance to the hyperplane perpendicular to the frame axis OX_α. The square root $\sqrt{< X_\alpha^2 >}$ is the corresponding r.m.s. distance $\sigma(X_\alpha)$.

To measure the spread of points in phase space, it is natural to define the multidimensional emittance ε_p as :

$$\varepsilon_p = 2\sigma(X_1).2\sigma(X_2)\cdots 2\sigma(X_{2p})$$

i.e. :

$$\varepsilon_p = 2^{2p} \sqrt{\det(V)}$$

where one has used the property that V and W have the same determinant, in order to express the emittance ε_p as function of the second-order moments w.r.t. the original frame.

In a two-dimensional phase space that definition reproduces the so-called r.m.s. emittance, first introduced by P. Lapostolle [1] :

$$\varepsilon_1 = 4 \sqrt{\langle x^2 \rangle \langle x'^2 \rangle - \langle xx' \rangle^2}$$

The numerical factor 2^{2p} is optional. It is just introduced to give a realistic and quantitative measure of the volume occupied by the points in the phase space.

It is worth noting that the mean distances $\langle X_\alpha^2 \rangle$ are the eigenvalues of the covariance matrix V and that these eigenvalues are never negative (V is a semi-definite positive matrix). Conversely, any matrix real, symmetric, and semi-definite positive, can be considered as a covariance matrix. Effectively, its positive eigenvalues can be taken as the mean square distances to the hyperplanes perpendicular to the axes of a particular coordinate frame.

Normally, a 2p-dimensional phase space is the product of p two-dimensional subspaces, each one being the phase space for one degree of freedom of the particle motion. For instance, the product of the two-dimensional phase space for the x-transverse motion, of the two-dimensional phase space for the y-transverse motion and of the two-dimensional phase space for the z-longitudinal motion is a six-dimensional phase space. Using a generalization [3] of the Hadamard determinant inequality, it can be shown that the 2p-dimensional emittance ε_p cannot be larger than the product of the emittances $\varepsilon^{(1)}$, $\varepsilon^{(2)},...,\varepsilon^{(p)}$ in the p two-dimensional subspaces :

$$\varepsilon_p \leq \varepsilon^{(1)} \varepsilon^{(2)} ... \varepsilon^{(p)}$$

The equality only occurs when the degrees of freedom are uncorrelated, i.e. when all the correlation moments $\langle x_\alpha x_\beta \rangle$ of two coordinates x_α, x_β corresponding to two different degrees of freedom are vanishing. Usually, a beam is said coupled when the degrees of freedom are correlated. Accordingly, the correlation moments between them will be hereafter named coupling moments. For instance, in the case of the 4-dimensional transverse phase space with coordinates x, x', y, y', there are four such coupling moments : $\langle xy \rangle$,

$\langle xy' \rangle$, $\langle x'y \rangle$, $\langle x'y' \rangle$. The 4-dimensional emittance ε_2 is the product of the emittances ε_x, ε_y, of the x and y transverse motions, only if these four coupling moments vanish.

The preceding inequality geometrically means that the volume occupied by the points in the 2p-dimensional phase space is less than the product of the areas occupied on each two-dimensional subspace, apart when they are uncoupled.

It may even happen that the emittance ε_p vanishes although none of the emittances $\varepsilon^{(1)}$, $\varepsilon^{(2)}$, ... , $\varepsilon^{(p)}$ vanishes. That occurs when two coordinates x_α, x_β corresponding to two different degrees of freedom are linearly dependent, i. e. fully correlated. For instance, in the case of the 4-dimensional transverse phase space with coordinates x, x', y, y', it occurs if the coordinates x and y would be proportional.

3. EMITTANCE CONSERVATION AND INVARIANTS IN LINEAR MOTION

In a linear motion, governed by a quadratic hamiltonian, the conservation of the multidimensional emittance results from the Liouville theorem. If R is the linear and symplectic mapping that connects the particle coordinates at time t to the coordinates at initial time t_0, the covariance matrix V is mapped according to :

$$V(t) = \langle x(t).\tilde{x}(t) \rangle = \langle Rx(t_0).\tilde{Rx}(t_0) \rangle = RV(t_0)\tilde{R}$$

The Liouville theorem implies det(R) = 1 and det(V) is constant.

Moreover, the geometrical shape of the particle spread in phase space can be made more precise by defining an envelope-hyperellipsoid H. With respect to the coordinate frame corresponding to the diagonal covariance matrix W, the equation of H is :

$$\sum_{\alpha=1}^{2p} \frac{X_\alpha^2}{4\langle X_\alpha^2 \rangle} = 1$$

either, with a matrix notation :

$$\tilde{X} W^{-1} X = 4$$

Returning to the normal coordinate frame by an orthogonal transformation, the equation of H keeps the same form :

$$\tilde{x} V^{-1} x = 4$$

470

The volume $\Omega(H)$ of the envelope-hyperellipsoid H is proportional to the emittance ϵ_p :

$$\Omega(H) = \frac{\pi^P}{\Gamma(p+1)} \epsilon_p$$

and the conservation of the emittance expresses the conservation of the volume.

The projection of the envelope-hyperellipsoid H on any 2-dimensional subspace, as x, x', is the envelope-ellipse describing the geometrical shape of the particle spread in that subspace. Its equation is [2] :

$$x^2 \langle x'^2 \rangle - 2xx' \langle xx' \rangle + x'^2 \langle x^2 \rangle = \frac{\epsilon_x^2}{4}$$

In a coupled motion the 2-dimensional emittance ϵ_x is not constant. To define, as usual, the envelope-functions β_x, α_x and γ_x of the beam in the x,x' subspace, one must use the invariant emittance ϵ_p instead of the emittance ϵ_x in that subspace :

$$\beta_x \, \epsilon_p = 4 \langle x^2 \rangle$$

$$\gamma_x \, \epsilon_p = 4 \langle x'^2 \rangle$$

$$\alpha_x \, \epsilon_p = -4 \langle xx' \rangle$$

with the relations :

$$\alpha_x = -\frac{1}{2} \frac{d\beta_x}{ds}$$

$$\beta_x \gamma_x - \alpha_x^2 = \left(\frac{\epsilon_x}{\epsilon_p} \right)^2$$

These envelope-functions, defined in each subspace, together with the coupling moments completely characterize the beam evolution in phase space.

Now, the LHS of the envelope-hyperellipsoid equation : $\tilde{x} \, V^{-1} \, x$ is a quadratic form left invariant by any linear mapping. It is the Liouville invariant expressing the hypervolume conservation in phase space. Another invariant quadratic form can be obtained from the Lagrange invariant [4] :

$$\tilde{x}_i \, \eta \, x_j$$

where x_i and x_j are the coordinate vectors of two particles i and j, and η is the symplectic unit matrix. Squaring that invariant and averaging over the particle j, one obtains the invariant quadratic form :

$$\tilde{x} \, \eta \, V \, \eta \, x$$

For instance, in the 4-dimensional phase space of the coupled transverse betatron motion, these two invariant quadratic forms determine two hyperellipsoids. The particle moves on their intersection that is a bidimensional torus. As well-known, that motion of an individual particle is characterized by two frequencies ω_1, ω_2 and two amplitude functions β_1, β_2. These two amplitude functions are different from the beam envelope-functions β_x, β_y defined above. They become identical only in the case of an uncoupled motion. It is due to the fact that the Liouville invariant and the Lagrange invariant are identical in the case of an one-degree of freedom motion.

4. REFERENCES

[1] P. M. Lapostolle, IEEE Trans. Nucl. Sci. NS-18, n° 3, 1101 (1971).

[2] J. Buon, CERN Accelerator School Proceedings (Ed : S. Turner) CERN 91-04, (1991) p. 30.

[3] M. Faguet, Doklady Akad. Nauk SSSR, 54 (1946) 761.

[4] J. S. Bell, CERN Accelerator School Proceedings (Ed : S. Turner) CERN 87-03 (1991), p. 10-15.

Observation of the Coalescing of Beam Into an Asymmetric RF Bucket by Stochastic Cooling

Alfred Mike Halling, Xian Ping Lu
Fermi National Accelerator Laboratory[†]
P.O. Box 500, Batavia, IL 60510-0500

ABSTRACT

Antiprotons in the debuncher ring at Fermilab have been observed to be bunched outside of the "barrier bucket" when cooled to small $\Delta p/p$ with the stochastic cooling. This bunching occurs in the same location as a very small stable bucket in the RF wave form. The stochastic cooling appears to be causing beam that is originally uniformly distributed to be captured by this stable bucket.

I. INTRODUCTION

During normal stacking operations in the PBAR source antiprotons are injected into the debuncher storage ring and cooled in all three dimensions by stochastic cooling for several seconds before being transferred to the accumulator storage ring. While in the debuncher a barrier bucket RF system is used to preserve a gap in the beam distribution. This ensures that the beam can be injected into the smaller circumference accumulator with high efficiency.
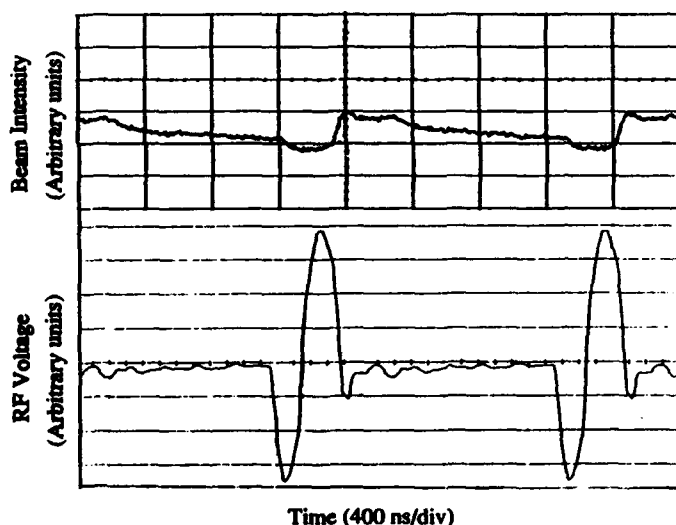
Figure 1. Beam distribution on the gap monitor after 2.4 seconds in debuncher and RF voltage wave form.

II. BEAM DISTRIBUTION AFTER 2.4 SECONDS IN DEBUNCHER

The beam is initially injected uniformly into the space outside of the barrier bucket. After 2.4 seconds of cooling the longitudinal energy distribution is roughly gaussian with a standard deviation of about $\Delta p/p = 0.08\%$. At this time the

beam distribution observed on a gap monitor is shown in Figure 1. The RF voltage is also shown. The relative time of the RF with respect to the gap monitor has been adjusted in the figure to the expected location. The gaps in the beam distribution caused by the barrier bucket are clearly visible, and the distribution is noticeably asymmetric.
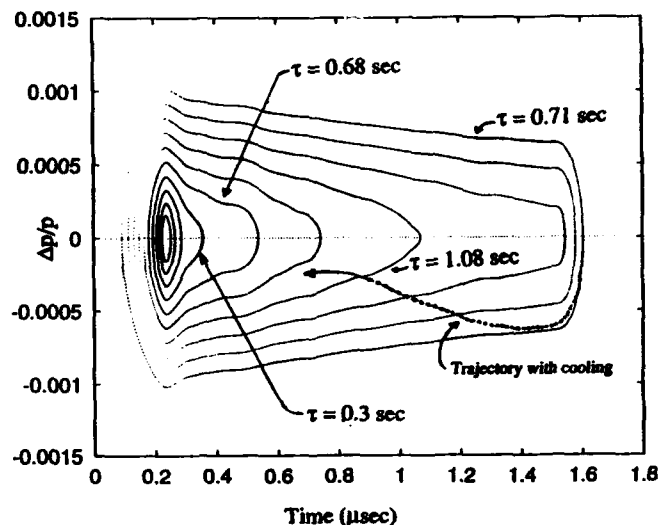
Figure 2. Particle Trajectories in the RF bucket. Contours are 0.01% apart in $\Delta p/p$. The synchrotron period is shown for a few trajectories. The dotted arrow is a possible path that a particle may take as it is cooled by the stochastic cooling.
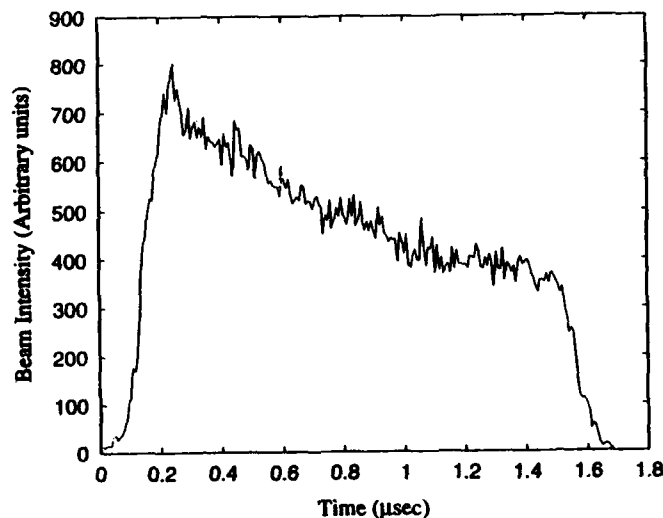
Figure 3. Predicted time distribution of beam injected uniformly into the bucket shown in Figure 2 with no cooling after 2.4 seconds.

[†] Operated by the Universities Research Association, Inc under contract with the U.S. Department of Energy.

III. BEAM DISTRIBUTION AFTER COOLING

The asymmetry in the above distribution has been modeled using a particle tracking code similar to ESME. The initial uniform beam is injected off center into the asymmetric bucket shown in Figure 2. After a few seconds the time distribution of the beam is predicted to look as in Figure 3. It is asymmetric do to the fact that the bucket has more phase space area on the right hand side. There is good qualitative agreement between the two distributions.

If the beam is cooled for about 15 seconds in the debuncher the longitudinal energy distribution will stabilize with an energy spread of about $\Delta p/p = 0.03\%$. The beam on the right hand side of Figure 2 cannot be cooled if it remains on the same contour line. Therefore, as it is cooled it spirals in along a path similar to that shown by the arrow in Figure 2. The beam distribution on the gap monitor after about 15 seconds of cooling is shown in Figure 4. Almost all the antiprotons have been pushed against the edge of the barrier bucket. The large spike and two shoulders in the beam distribution closely match the details in the RF wave form.

Time (400 ns/div)
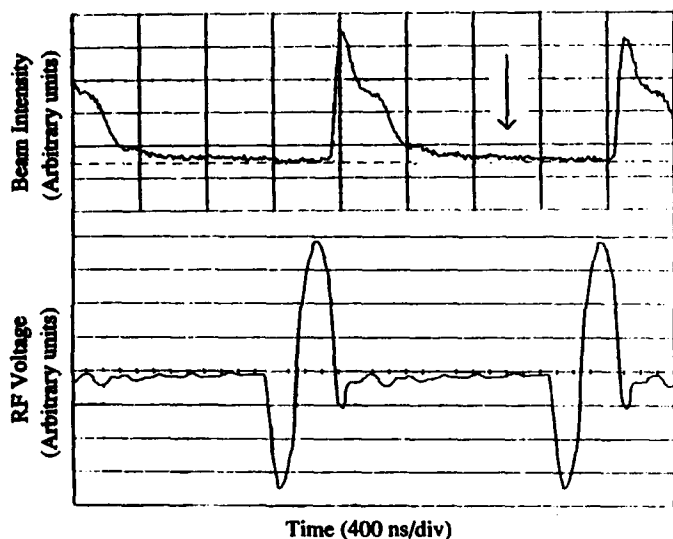
Figure 4. Time distribution of beam in Debuncher after 10-20 seconds of cooling, and the RF wave form.

A series of investigations showed that bunching depended only on how much cooling had been done to the beam, i.e. after cooling for 15 seconds the stochastic cooling could be turned off without effecting the distribution. The amount of bunching did not vary if the cooling system was tuned to give the beam a net increase or decrease in energy.

IV. POSSIBLE USES OF ASYMMETRIC RF BUCKETS FOR STACKING

The coalescing of beam by stochastic cooling opens up the possibility of stacking in the time domain rather than the energy domain, as is now done in the PBAR source at Fermilab. This could allow stacking in an accelerator with a more conventional lattice than the accumulator, where a very high dispersion section is used to physically separate the fresh injected pulse from the accumulated stack.

For instance, a 400 ns wide kicker centered in time at the point indicated by the arrow in Figure 4 could inject a fresh pulse of beam, which the stochastic cooling would then cool into the bunch at the left. In principle this is a much simpler method of stacking than is currently used, it may have some inherent advantage over the existing technique.

V. CONCLUSION

This paper documents another case of bunched beam cooling[1-2], a slowly emerging field. It appears that stochastic cooling indeed cools bunched beams, and in the presence of an asymmetric RF field can cause apparent bunching of the beam.

VI. REFERENCES

[1] J. Claus et. al., "Experimental Cooling Of Bunched Beams In FNAL'S Accumulator Ring". AD/AP-19 (Feb 1990) 75p. Fermilab Library Only.

[2] J. Marriner et. al., "Bunched Beam Cooling in the FNAL Anti-Proton Accumulator", Proc. of the 2nd European Particle Accelerator Conf. Nice, June 12-16, 1990 p 1577..

Effects of Transverse Coupling on Transverse Beam size, Simulation and Measurements

Alfred Mike Halling
Fermi National Accelerator Laboratory[†]
P.O. Box 500, Batavia, IL 60510-0500

ABSTRACT

The equations of motion for particles in an accelerator lattice show that a larger physical aperture is required to hold a beam of constant invariant emittance if there is transverse coupling of the tunes. The results of a tracking simulation of particle motion in the Fermilab accumulator ring are discussed, and results are shown from beam tests carried out in the accumulator to demonstrate this effect.

I. INTRODUCTION

It is well known that transverse coupling in an accelerator lattice can cause the transfer of betatron motion from one transverse plane to another. This effect is easy to demonstrate with modern day beam position monitor (BPM) measurements by injecting beam with a large transverse betatron motion in one dimension. Our present instrumentation does not, however, shed full light on the motion of particles injected with initial transverse motion in both planes.

The operating points of most accelerators are close to the coupling resonance, so it is important to understand the behavior of coupled beams. This report contains a discussion of three methods of exploring this problem, and will show that choosing an operating point without coupling can lead to a smaller physical beam size than a coupled operating point. First, I will summarize an analytical solution to this problem found in the literature. Second, I will show the results of a tracking simulation of this effect. Third, I will show measurements of the beam size with and without coupling in the accumulator storage ring.

II. ANALYTICAL DISCUSSION OF COUPLED MOTION

There have been many discussions in the literature of coupled particle motion in accelerator lattices. One of the simplest is that of P.J. Bryant[1], from which I will quote several results below. In Reference 1 the author derives an approximate solution to the equations of motion:

$$x'' + (Q_x/R)^2 x = bz' - kz$$
$$z'' + (Q_z/R)^2 z = bx' - kx$$

Where:
  Q_x is the tune in x
  Q_z is the tune in z.
  $\kappa_x = Q_x / R$
  $\kappa_z = Q_z / R$
  $k = (1/B\rho)(dB_x/dx)_0 = -(1/B\rho)(dB_z/dz)_0$

$$\delta = (Q_x - Q_z) / R$$
$$\kappa = (Q_x + Q_z) / 2R$$
$$\eta = ((k/\kappa)^2 + \delta^2)^{1/2}$$

In the limit that the coupling strength k=0 the motion of particles is described by the following two equations:

$$x = A e^{i\kappa_x s}$$
$$z = B e^{i\kappa_z s}$$

For this study we are interested in coupling from skew multipole fields, so for the equations below I have set b=0, i.e. no velocity coupling. In the limit that the coupling fields are small w.r.t the normal focusing fields, i.e. when k/κ is much less than 1, and when the difference in tunes δ is very small, an approximate solution for the motion of the particle is given by Equations 10 and 11 from Reference 1. These equations are reproduced below for the special case when the motion of the particle becomes 100% coupled, i.e. as the fractional coupling strength k/κ becomes much larger than the fractional difference in tunes δ.

Let's consider a particle in an accelerator with zero coupling described by the above two equations. At time s=0 we turn on the coupling fields to a strength where the motion is 100% coupled. This is similar to injecting a beam of particles into a coupled lattice. Initially the motion must still be described by the above equations. In this case equations 10 and 11 from Reference 1 can be written as shown below, where I have chosen the new constants A' and B' to match the boundary condition at s=0.

$$x = e^{i\kappa_x s} [(A+B)e^{+(i/2)(\eta-\delta)s} - (B-A)e^{-(i/2)(\eta+\delta)s}]/2$$
$$z = e^{i\kappa_z s} [(B-A)e^{-(i/2)(\eta-\delta)s} + (A+B)e^{+(i/2)(\eta+\delta)s}]/2$$

The above equations describe a particle moving with a fast sinusoidal betatron motion, and with amplitude modulated by the slower functions X and Z described by equations 13 and 14 from reference 1 after correcting for a sign error.

$$|X|^2 = [|A|^2 + |B|^2 - (|A|^2+|B|^2-2AB^*)\cos(\eta s)]/2$$
$$|Z|^2 = [|A|^2 + |B|^2 + (|A|^2+|B|^2-2AB^*)\cos(\eta s)]/2$$

It is clear from the above equations that the amplitude of the coupled motion in general has larger excursions in each dimension than the original uncoupled motion. This means the physical size of the beam is larger in the presence of coupling.

III. SIMULATIONS WITH A TRACKING PROGRAM

To study this effect I performed a tracking calculation using the lattice design program DIMAD. This model includes all dipoles, quadrupoles, and sextupoles, as well as an accurate

---

description of the fringe fields from the dipoles. The values of the sextupoles were adjusted to give chromaticities close to our measured values, and the tunes were adjusted to be 6.612 and 8.612 on the central orbit. To add coupling to this model I added two skew quadrupoles with a strength equal their operating point when used to remove coupling during normal operations.

With the skew quads turned on I launched test particles from a nominally dispersionless location in the lattice with a small amount of dp/p = 0.02%, an energy where the coupling in the lattice is essentially 100%. Figure 1 shows the x and y position of the test particle every other revolution around the machine for particles launched with an initial displacement in x. The motion in the model is very similar to the motion actually measured by the BPM system shown in Figure 2.
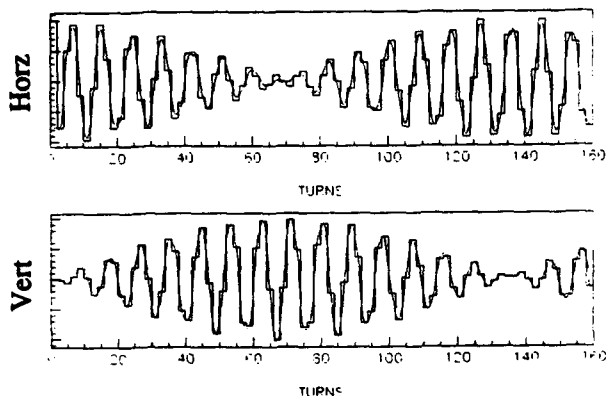
Figure 1. Simulation of horizontal and vertical motion of a particle launched with initial horizontal displacement.
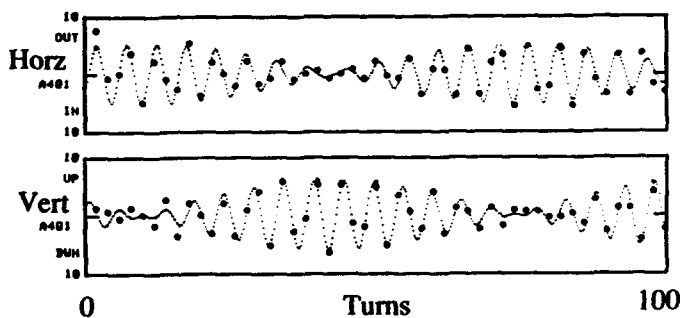
Figure 2. Measured horizontal and vertical motion of a particle injected with initial horizontal displacement.

IV. TRACKING STATISTICAL ENSEMBLES OF PARTICLES

Several ensembles of particles with gaussian distributions in betatron phase space were generated and tracked for 400 turns in the above model. The generated beams had a 95% emittance of 4π in each dimension, roughly equal to the expected size of pbars from the debuncher during normal stacking operations. The ensembles were tracked both with and without coupling to ensure that coupling was indeed the cause of the increased beam sizes.

On each turn the betatron amplitude of each particle was calculated using the known lattice parameters and the position and angle given by the tracking program. The maximum betatron amplitude for each particle was saved and entered into

a histogram after 400 turns, see Figures 3 and 4. Each figure shows two distributions, one for an uncoupled lattice and one for a coupled lattice. The curves are 5th order polynomials meant to guide the eye. The arrows on each distribution show the 90% point of the tail. The effective beam size of coupled beams is roughly twice that of the uncoupled beam, and the distributions appear to be hollow in phase space.
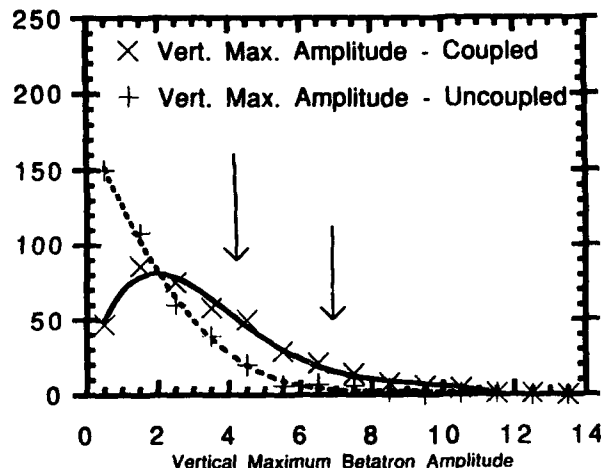
Figure 3. Density of particles as a function of maximum vertical betatron motion with 4π gaussian input beam. The two curves shown are for coupled and uncoupled lattices. The arrows point to the approximate point that contains 90% of the beam.
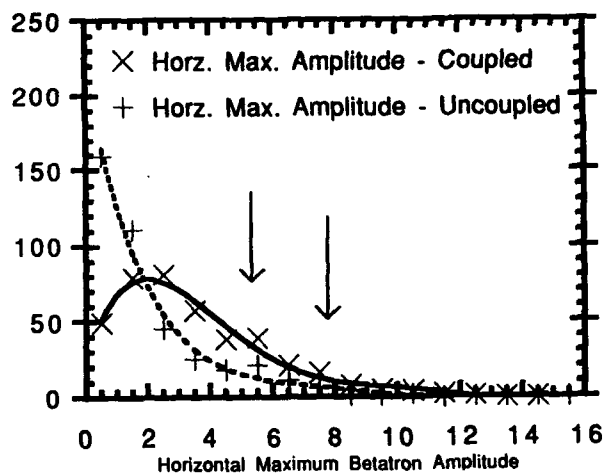
Figure 4. Density of particles as a function of maximum horizontal betatron motion with 4π gaussian input beam. The two curves shown are for coupled and uncoupled lattices. The arrows point to the approximate point that contains 90% of the beam.

V. MEASUREMENTS WITH BEAM

To confirm this effect measurements were made with 8 GeV/c protons injected into the accumulator storage ring. Protons were first injected directly onto the closed orbit and the scraper was used to determine the location of closed orbit, as is shown in Figure 5. The closed orbit location with the skew

quad on is a little difficult to determine from this small reproduction due to the low density of particles with zero betatron amplitude, but is shown by the arrow in the figure. There is very good agreement on the closed orbit location with and without coupling, showing that the skew quad does not steer the beam.
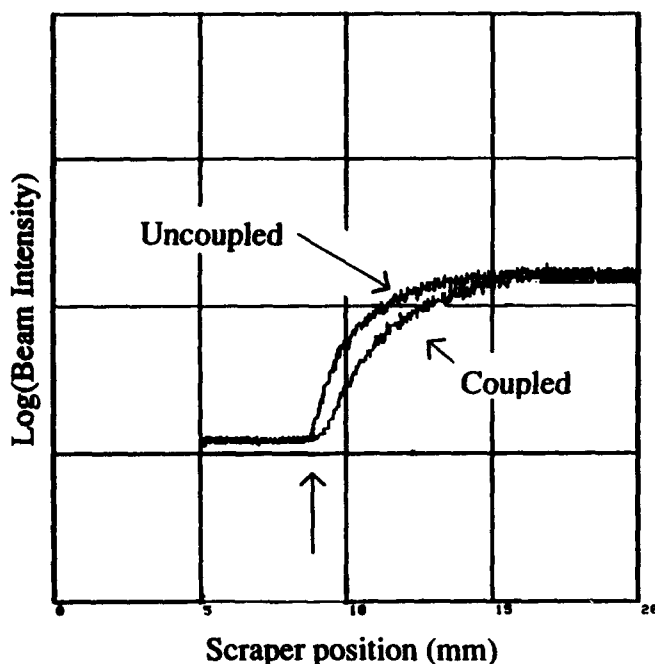
Figure 5. Log(intensity) as a function of scraper location.. The two curves shown are for coupled and uncoupled lattices. The arrow points to the end of the coupled distribution. The closed orbit location is the same with and without coupling, showing that the skew quad does not steer the beam.

Protons were then injected into the accumulator with deliberate injection oscillations in both x and y dimensions. This ensured that the emittance of the beam in the accumulator was uniform from pulse to pulse rather than being determined by factors outside of our control, and made the input emittances large enough for an accurate measurement with the scraper. Figure 6 shows the beam intensity on a linear scale as a function of scraper location for coupled and uncoupled lattice configurations. The arrows in the figure point to the point where 50% of the beam remains for each case.The beam size is clearly larger in a coupled lattice.

To make a quantitative measurement we determined the point where 50% of the beam was scraped away, which is much better determined than the 90% point. We then made a number of measurements summarized in Table I of the maximum betatron amplitude in both dimensions with and without coupling. In all cases the maximum betatron amplitude measured without coupling is smaller than that measured with coupling, giving clear confirmation of the effect described above.

VI. CONCLUSION

This paper has presented both analytical and experimental evidence that beams in a coupled lattice have a larger physical size than expected from their invariant emittance. In a machine where aperture restrictions are important decoupling the tunes can make a significant improvement. The increased effective beam size may also limit the luminosity of colliding beams. On the other hand, increased beam size may be a benefit in some conditions, for example when ion trapping instabilities are limiting the performance as in the PBAR source. The addition of coupling to the accumulator lattice has been used for most of the last year as one of the more reproducible tools for controlling instabilities caused by ion instabilities.

TABLE I

Measured maximum betatron amplitudes for coupled and uncoupled lattice. The numbers given are the maximum amplitude in π-mm-mr that contains 50% of the beam.

Uncoupled		Coupled	
ε_x	ε_y	ε_x	ε_y
1.77	1.44	2.80	2.44
2.06	1.38	2.77	
1.59	1.22	2.60	
1.86			
Average = 1.82	1.35	2.72	2.44
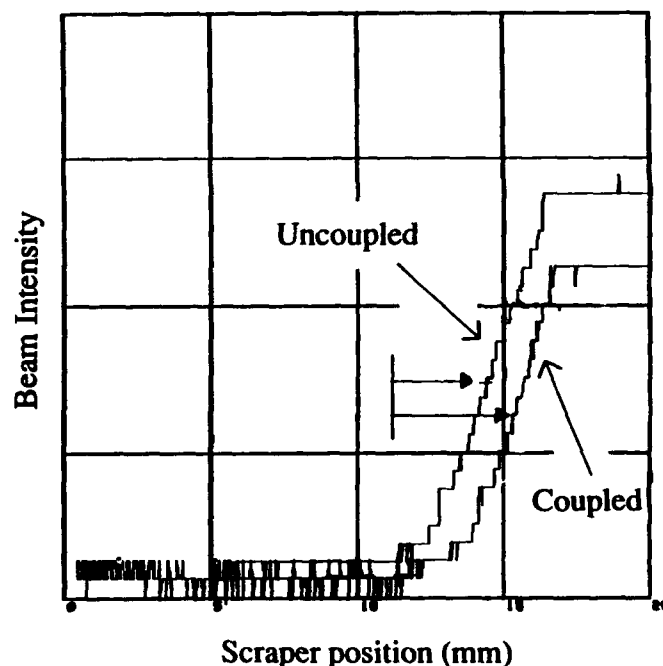
Figure 6. Beam intensity as a function of scraper location.. The two curves shown are for coupled and uncoupled lattices.

VII. REFERENCES

[1] P.J. Bryant, "A Simple Theory For Weak Betatron Coupling", Proc. of the Cern Accelerator School, Salamanca Spain, September 19-30 1988, p50-62, edited by S. Turner.

476

One of Methods to Extract Truncated Taylor Map for Orbital and Spin Motion in Proton Storage Rings

V. Balandin
Institute for Nuclear Research of the Russian Academy
of Sciences, Moscow

Abstract

The Taylor map coefficients obtained by any tracking code with differential algebra techniques accumulate two types of errors: computer rounding errors and errors defined by size of integration step. There is the approach free from defects of second type. That is the method of undetermined coefficients. Unfortunately it is not easy to produce computer code for the usually used form of this method. In this paper we present algorithm combining the advantages of method of undetermined coefficients and the calculating elegance of Lie algebraic techniques. The general approach using only the common properties of Lie groups and Hamilton's equations allows to obtain the truncated Taylor map for orbital and spin motion by the same way.

I. INTRODUCTION

The computer programs for analytical manipulations with polynomials have become an essential tool for the nonlinear design and analysis of circular accelerators [1], [2], [3], [4], [5]. The powerful methods as the numerical integration with using the differential algebra techniques and the direct summing the Lie exponent series with the machine precision allow to obtain the Taylor map coefficients up to the arbitrary hight order of the nonlinearity. The steps number in these methods depends on a desirable precision of the result and the length of computer word. In this paper the algorithm, the number of the steps in which does not depend on a precision, is described (like in the Gauss method of the matrix inversion the number of operations depends on the matrix dimension only). The main idea of this approach can be applied to the wide class of the hamiltonian and nonhamiltonian systems of ordinary differential equations. Lower this method is illustrated for the orbital motion through one magnet element (quadrupoles, sextupoles and etc.) in circular accelerators.

II. REALIZATION FOR ORBITAL MOTION

We will say that the function $g(z,t) \in HP(k)$ if $g(z,t)$ is the homogeneous polynomial of order k in respect to z with t-dependent polynomial coefficients.

Define the order of Taylor map truncation m and consider the initial Hamiltonian in the form

$$H^1(z,t) = H_2^1(z) + H_3^1(z,t) + \cdots + H_{m+1}^1(z,t) \quad (1)$$

where $z = (x,y)$ are the canonical orbital variables $(dim(z) = 2n)$ and $H_l^1 \in HP(l)$.

Introduce two additional canonical variables τ, L and new Hamiltonian

$$H^2(z,\tau,L) = H^1(z,\tau) + L$$

One obtain the autonomous differential equations system in the space of larger dimension

$$\frac{dx}{dt} = \frac{\partial H^2}{\partial y}, \quad \frac{dy}{dt} = -\frac{\partial H^2}{\partial x}$$
$$\frac{d\tau}{dt} = \frac{\partial H^2}{\partial L}, \quad \frac{dL}{dt} = -\frac{\partial H^2}{\partial \tau}$$

All next steps consist of the sequence of canonical variables transformations:

a) So there is the symplectic $2n \times 2n$ matrix A that the second order part of the new Hamiltonian

$$H^3(z,\tau,L) = H^2(A \cdot z,\tau,L)$$

has the form:

$$H_2^3(z) = \bar{H}_2(z) + \tilde{H}_2(z)$$

$$\bar{H}_2(z) = \sum_{j=1}^{n} \lambda_j \cdot x_j \cdot y_j$$

$$\tilde{H}_2(z) = \frac{1}{2} \cdot \sum_{j=1}^{n} \sigma_j \cdot y_j^2 + \sum_{j=1}^{n-1} \epsilon_j \cdot x_j \cdot y_{j+1}$$

where $\{\bar{H}_2(z), \bar{H}_2(z)\} = 0$ ($\{\cdot, \cdot\}$ is the Poisson bracket) and

$$\epsilon = \begin{cases} 0 & \text{if } \lambda_j \neq \lambda_{j+1} \\ 1 & \text{otherwise} \end{cases}$$

$$\sigma = \begin{cases} 0 & \text{if } \lambda_j^2 + \epsilon_j^2 \neq 0 \\ 1 & \text{otherwise} \end{cases}$$

(see ref. [6]).

b) Perform the Lie transformation of the Hamiltonian H^3:

$$H^4(z, \tau, L) = exp(: -\tau \tilde{H}_2(z) :) H^3(z, \tau, L) =$$

$$= \tilde{H}_2(z) + L + \sum_{l=3}^{m+1} H_l^3(exp(: -\tau \tilde{H}_2(z) :)z, \tau)$$

It is possible to proof directly that the series

$$exp(: -\tau \tilde{H}_2(z) :)z$$

contains the finite number of members only. We note also the way which can be applied to non-hamiltonian equations.

Consider the system

$$\frac{dw}{dt} = (D + N) \cdot w + f(w, t)$$

where N is a nilpotent matrix ($N^{k+1} = 0$), $D \cdot N = N \cdot D$, $f(w, t) = f_2(w, t) + \cdots + f_m(w, t)$, $f_l(w, t) \in HP(l)$.

Using the coordinate transformation

$$w = exp(t \cdot N) \cdot u = (I + t \cdot N + \cdots + \frac{t^k}{k!} \cdot N^k) \cdot u$$

one obtain

$$\frac{du}{dt} = D \cdot u + g(u, t) =$$

$$= D \cdot u + exp(-t \cdot N) \cdot f(exp(t \cdot N) \cdot u, t)$$

Here a function $g(u, t)$ has the same structure as a function $f(w, t)$. i. e. $g(u, t) = g_2(u, t) + \cdots + g_m(u, t)$ and $g_l(u, t) \in HP(l)$.

So we obtain after steps a) and b) the Hamiltonian with the diagonal second order part.

c) This part consists of $m - 1$ steps of nonlinear coordinate transformations $l = 3, 4, \cdots, m+1$

$$H^{l+2}(z, \tau, L) = exp(: W_l(z, \tau) :) H^{l+1}(z, \tau, L)$$

where $W_l(z, \tau) \in HP(l)$.

If $W_l(z, \tau)$ satisfies the equation

$$\frac{\partial W_l}{\partial \tau} + \{W_l, \bar{H}_2\} + H_l^{l+1} = N_l \qquad (2)$$

then the final Hamiltonian has the form

$$N(z, \tau, L) = H^{m+3}(z, \tau, L) =_{m+1}$$

$$=_{m+1} \bar{H}_2 + L + N_3(z, \tau) + \cdots + N_{m+1}(z, \tau) \qquad (3)$$

where $=_{m+1}$ indicates that the right and left side agrees up to order $m + 1$.

The equation (2) is divided in independent equations for coefficients of monomials $x^I \cdot y^J$. Each of them has the form:

$$\frac{dw}{d\tau} + \mu \cdot w = n - h \qquad (4)$$

where $\mu = (I - J) \cdot \lambda$. For any given polynomials

$$h(\tau) = h_0 + h_1 \cdot \tau + \cdots + h_k \cdot \tau^k$$
$$n(\tau) = n_0 + n_1 \cdot \tau + \cdots + n_k \cdot \tau^k$$

the equation (4) has the polynomial solution. If $\mu = 0$ then

$$w(\tau) = const+$$

$$+(n_0 - h_0) \cdot \tau + \cdots + \frac{1}{k+1} \cdot (n_k - h_k) \cdot \tau^{k+1}$$

else

$$w(\tau) = w_0 + w_1 \cdot \tau + \cdots + w_k \cdot \tau^k$$

$$\begin{cases} w_k = \frac{1}{\mu} \cdot (n_k - h_k) \\ w_{k-1} = \frac{1}{\mu} \cdot (n_{k-1} - h_{k-1} - k \cdot w_k) \\ \cdots \\ w_0 = \frac{1}{\mu} \cdot (n_0 - h_0 - w_1) \end{cases}$$

d) Using the notation

$$: C(z, \tau) :=$$

$$= exp(: W_{m+1} :) \cdots exp(: W_3 :) exp(: -\tau \tilde{H}_2 :) : A :$$

we obtain finally

$$: C(z, \tau) : H^2(z, \tau, L) =_{m+1} N(z, \tau, L)$$

$$exp(: -H^2 :) =_m : C :^{-1} exp(: -N :) : C : \qquad (5)$$

e) In mathematical sense the equation (2) has the solution for any $N_l \in HP(l)$. Consider the important particular case $N_l = N_l(z)$ and $N = \bar{N}(z) + L$. In this case for any real α we obtain:

$$exp(: -H^2 :) =_m exp(: \alpha L :) : C(z, \tau + \alpha) :^{-1} \cdot$$

$$\cdot exp(: -\bar{N}(z) :) : C(z, \tau + 1 + \alpha) : exp(: -(1 + \alpha)L :) \qquad (6)$$

478

If the initial Hamiltonian $H^1 = H^1(z)$ then from (6) the important representation follows

$$exp(:-H^1:) =_m$$

$$=_m : C(z, \tau + \alpha) :^{-1} exp(:-\bar{N}(z):) : C(z, \tau + 1 + \alpha) : \quad (7)$$

and in z-space we have

$$exp(:-H^1(z):) =_m$$

$$=_m : C(z, \alpha) :^{-1} exp(:-\bar{N}(z):) : C(z, 1 + \alpha) : \quad (8)$$

If $\{\bar{N}(z), \bar{H}_2(z)\} = 0$ then for any given order of Taylor map truncation m the right side in (8) can be calculated for the finite number of operations with polynomials.

The representation (8) includes the normal form decomposition in the nonresonance case [7]. It also includes the more unusual factorization with $\bar{N}(z) = \bar{H}_2(z)$ which exists for any initial autonomous Hamiltonian $H^1(z)$ independently of properties λ_j. If we use the possibility of the arbitrary choice of $N_l(z)(l = 3, \cdots, m + 1)$ we can obtain the another interesting results from formula (8).

III.   COMPUTER IMPLEMENTATION

What are more difficult steps in the computer realization of the described above algorithm? For the arbitrary initial autonomous Hamiltonian it is the finding the matrix A in the point a) and the process of the obtaining the solution of the equation (4) in the case when μ does not equal zero but very small. Fortunately, we never meet this situation when we consider magnet elements like ideal quadrupoles, sextupoles and other multipoles. The method of the map calculation with help of the representation (8) has been implemented in the computer code VasiLIE [3]. To the author surprise the calculation speed of this algorithm is not so slow as it seems before the realization. It is near the same as the speed of the direct summing Lie exponent series with the machine precision (the tests were performed using IBM PC 386 computer for maps of 4 variables and orders $6 - 10$ and $\alpha = 0, -0.5$).

ACKNOWLEDGMENTS

REFERENCES

[1] A. Dragt, et al.. *IEEE Trans. Nucl. Sci.*, NS-32:2311, 1985.

[2] M.Berz. COSY INFINITY Version 6 reference manual. Technical Report MSUCL, 1993.

[3] V. Balandin and N. Golubeva. *Proceedings of the XV Hight Energy Particle Accelerators, Int. J. Mod. Phys. A*, 2B:998, 1992.

[4] Y. Yan. *Proceedings of the Workshop on High Order Effects in Accelerators and Beam Optics, East Lansing*, MSUCL-767, 1991.

[5] L. Michelotti. *Proceedings of the 1989 IEEE Particle Accelerator Conference, Chicago*, 839-841, 1989.

[6] A. D. Bruno. - The restricted three-body problem: Plane periodic orbits. Moscow: Nauka, 1990.

[7] E. Forest, M. Berz, and J. Irwin. *Part. Acc.*, 24:91, 1989.

SKEW QUADRUPOLE EFFECTS IN THE IBM COMPACT SYNCHROTRON

Chas. N. Archie
IBM Semiconductor Research and Development Center
East Fishkill Facility, Route 52
Hopewell Junction, NY 12533-0999 USA

Abstract

The normal operating condition for the IBM x-ray source is to have a skew quadrupole magnet energized to a focal length of -20 m. This paper details the effects seen by synchrotron light monitors as a consequence of varying the strength of this magnet. In particular, the cross section of the electron beam appears vertically expanded and *tilted*. Furthermore, these effects are slightly different in the two dipole magnets. These effects can be understood by deriving the normal modes for the linearly coupled betatron motions for the case of operation far from a coupling resonance line.

INTRODUCTION

The IBM compact synchrotron storage ring Helios, manufactured by Oxford Instruments, has two 180° bending angle superconducting dipole magnets separated by straight sections containing quadrupole magnets, injection magnets, rf cavity, diagnostics, and specialty magnets. One of these specialty magnets is a skew quadrupole designed to couple horizontal and vertical betatron motions if need be. During commissioning it was determined that the beam lifetime at full energy for typical stored currents could be increased significantly by energizing this magnet to 20 A corresponding to a thin lens focal length of -20 m. This effect agrees with Touschek scattering estimates. Since this lifetime enhancement is very desirable, this has become the normal operation condition.

Located at synchrotron light ports looking at the dipoles' centers are two synchrotron light monitors (SLM's). These devices focus the visible synchrotron light to form images of the electron beam cross section on CCD cameras which can then be frame grabbed for electronic processing and storage. Figure 1 shows a collection of images from the two SLM's illustrating the effect of the skew quadrupole. The vertical size at zero skew quadrupole current suggests there are some residual coupling fields in the storage ring. It is speculated that slight misalignment of the dipole coils could account for this residual since there is significant normal quadrupole field through the body of the dipole magnets.

Though the images are qualitatively similar in the two dipoles there are differences. Supported by detailed measurement is the observation that at any given
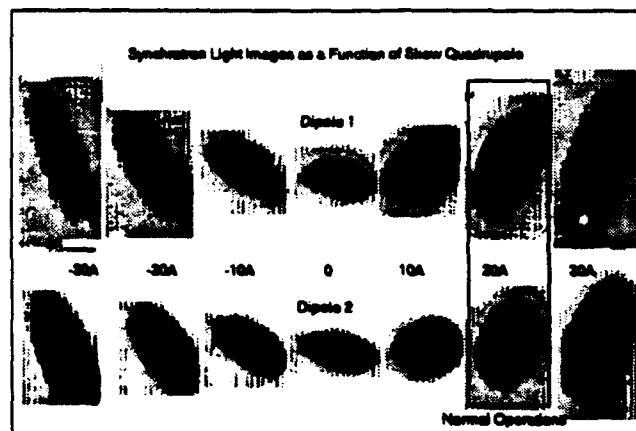
Figure 1. Composite SLM Images from Dipoles. The effect of the skew quadrupole magnet is to produce both vertical extension to the beam and an apparent tilt to the electron beam cross section. Relative image intensities have been adjusted to improve this presentation.

skew quadrupole strength the electron beam is more vertically extended in Dipole 1 than in Dipole 2. Furthermore, the apparent *tilt* of the image is more for Dipole 1.

NONRESONANT OPERATION OF A SINGLE THIN LENS SKEW QUADRUPOLE

The effect of a single thin lens skew quadrupole in a ring can be solved in the absence of higher order magnetic fields. One way to proceed would be to introduce the 4 by 4 transfer matrices of combined horizontal and vertical betatron motion and solve for the normal modes[1]. In the simple case of a single thin lens skew quadrupole, however, there is a 2 by 2 solution that more clearly illustrates several interesting features directly applicable to the Helios observations. The latter treatment is given here.

If we are explicitly seeking the normal modes of this problem then the horizontal (x) and vertical (y) motions should be synchronized and the thin lens skew quadrupole transfer matrix for the tranverse horizontal direction can be expressed as

$$S = \begin{pmatrix} 1 & 0 \\ kR & 1 \end{pmatrix} \quad \text{where} \quad R = \left(\frac{y}{x}\right)_{s=0} . \quad (1)$$

The ratio R is a constant (to be determined) and k is the skew quadrupole strength. The azimuth coordinate s is measured from the skew quadrupole position.

Let M_{x0} denote the transfer matrix in the horizontal direction for one time around the ring in the absence of a skew quadrupole and let M_x be the transfer matrix including the skew quadrupole. The full ring transfer matrix has an explicit form in terms of betatron tune, v for coupled and v_x for uncoupled, and the α, β, and γ lattice parameters. This applies to both M_{x0} and M_x but for uncoupled and coupled values accordingly. Therefore, we can write $M_x = M_{x0}S$ or explicitly

$$\begin{pmatrix} \cos 2\pi v + \alpha_x \sin 2\pi v & \beta_x \sin 2\pi v \\ -\gamma_x \sin 2\pi v & \cos 2\pi v - \alpha_x \sin 2\pi v \end{pmatrix} = \begin{pmatrix} \cos 2\pi v_x + \alpha_{x0} \sin 2\pi v_x & \beta_{x0} \sin 2\pi v_x \\ -\gamma_{x0} \sin 2\pi v_x & \cos 2\pi v_x - \alpha_{x0} \sin 2\pi v_x \end{pmatrix} \begin{pmatrix} 1 & 0 \\ kR & 1 \end{pmatrix}. \quad (2)$$

The equation for the vertical direction is the same except that the x's and y's are interchanged and $R \to R^{-1}$. Equating the traces gives

$$\cos 2\pi v = \cos 2\pi v_x + \tfrac{1}{2}kR\beta_{x0} \sin 2\pi v_x \quad (3)$$

and from the vertical direction,

$$\cos 2\pi v = \cos 2\pi v_y + \tfrac{1}{2}k\frac{1}{R} \beta_{y0} \sin 2\pi v_y . \quad (4)$$

Eliminating R from these two equations gives

$$\cos 2\pi v = \tfrac{1}{2}(\cos 2\pi v_x + \cos 2\pi v_y) \pm \quad (5)$$
$$\tfrac{1}{2}\sqrt{(\cos 2\pi v_x - \cos 2\pi v_y)^2 + k^2 \beta_{x0}\beta_{y0} \sin 2\pi v_x \sin 2\pi v_y} .$$

There are three distinct regions of betatron tune space depending on whether the uncoupled tunes are far from or near to a sum or difference resonance line, $v_x \pm v_y = integer$. The radical of Eqn. (5) becomes imaginary in the stop band of the sum line. On the other hand, a common practice for studying coupling effects in storage rings is to bring the betatron tune operating point close to a difference resonance line [2], thereby amplifying coupling effects near degeneracy. However, the normal betatron tune operating point for Helios, with v_x, v being 1.43,0.64, is far from such a condition. Expanding the square root to second order in k in this case gives

$$\cos 2\pi v_\pm = \cos 2\pi v_{x,y} \pm \frac{\tfrac{1}{4}k^2 \beta_{x0}\beta_{y0} \sin 2\pi v_x \sin 2\pi v_y}{\cos 2\pi v_x - \cos 2\pi v_y} . (6)$$

Corresponding to these two solutions are the amplitude ratios

$$R_+ = \frac{\tfrac{1}{2}k\beta_{y0} \sin 2\pi v_y}{\cos 2\pi v_x - \cos 2\pi v_y}$$
$$\frac{1}{R_-} = \frac{-\tfrac{1}{2}k\beta_{x0} \sin 2\pi v_x}{\cos 2\pi v_x - \cos 2\pi v_y} . \quad (7)$$

These expressions were used to determine starting coordinates for tracking results shown in Figure 2.

Mode +

Dipole 2 Dipole 1

Mode -

Beam Cross Sections for Normal Modes
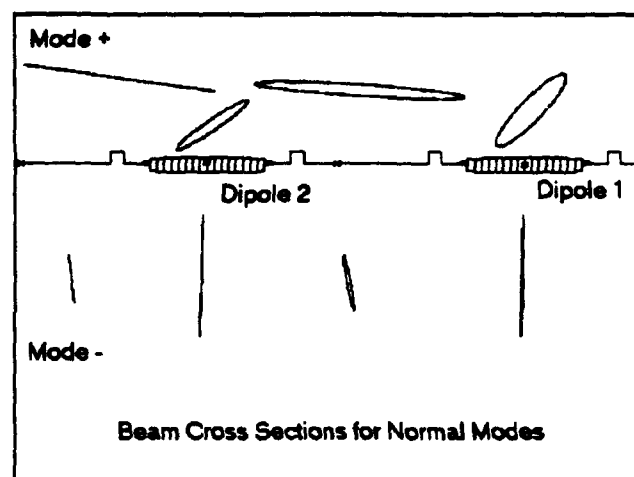
Figure 2. X-Y Tracking Maps for the Normal Modes. Maps for the two normal modes at standard Helios operating conditions are shown for azimuth locations depicted by x's in the beamline schematic.

The other matrix elements of Eqn. (2) provide expressions for modifying the lattice parameters at the skew quadrupole position. In particular,

$$\beta_y = \beta_{y0} \frac{\sin 2\pi v_y}{\sin 2\pi v} \quad \text{and}$$
$$\alpha_y = \alpha_{y0} \frac{\sin 2\pi v_y}{\sin 2\pi v} + \frac{\cos 2\pi v - \cos 2\pi v_y}{\sin 2\pi v} \quad (8)$$

with similar expressions for the x direction.

For each normal mode there is a major member and a minor member in terms of contributions from the uncoupled vertical and horizontal motions. In the weak coupling case one such mode v_+ is close to the uncoupled horizontal tune v_x and the y amplitude is much smaller than the x amplitude. The expressions for β and α (Eqns. (8)) then show that the new Twiss parameters in the x direction are little changed by the

481
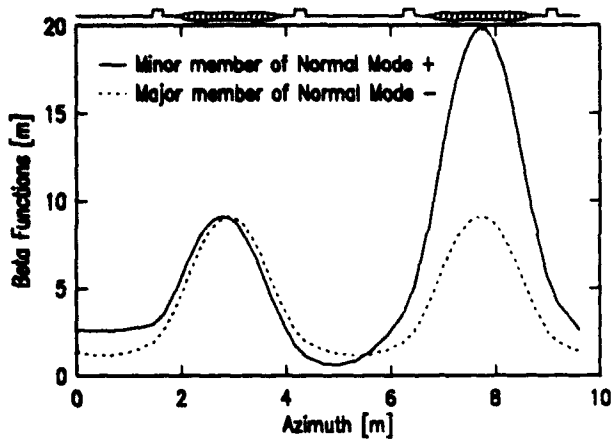
Figure 3. Vertical Beta Functions for Normal Modes

coupling, however, the parameters in the y direction are very much altered.

Figure 3 shows the vertical betatron functions for each of the normal modes. The strongly perturbed function for the minor member of the $+$ normal mode has been calculated in a standard beamline lattice code using a representation with initial values for the Twiss parameters from Eqns. (8). As illustrated by the beamline schematic, the Helios skew quadrupole is not at a high symmetry point. This helps explain the asymmetry in the beta function maxima for the minor member of the $+$ normal mode.

It is a good approximation that the energy change due to emission of synchrotron radiation initially results in a pure horizontal excitation. Expressed in terms of the normal modes, the vertical components of such an excitation must initially cancel. As a consequence, the coupling results in two contributions to
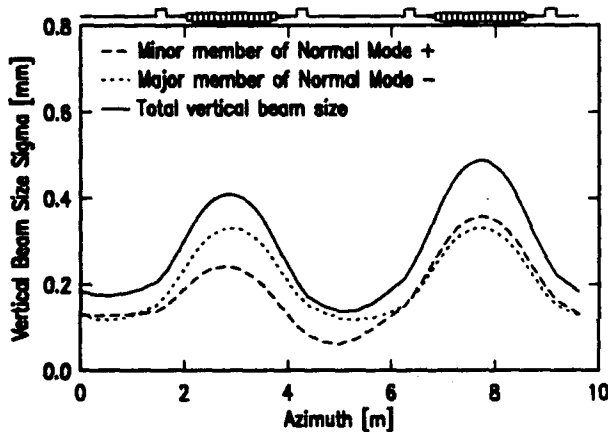
Figure 4. Contributions to the Vertical Beam Size
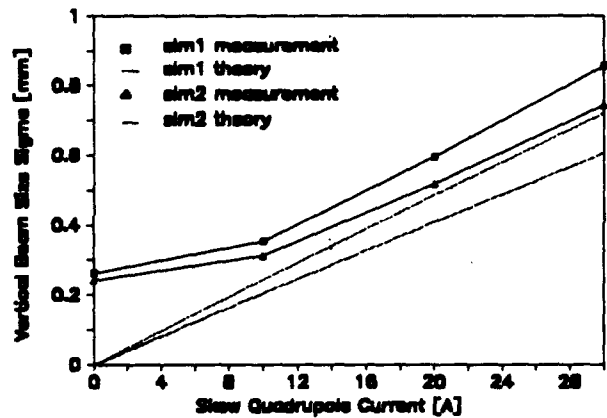
Figure 5. Vertical Beam Size

the vertical beam size. One comes from the y component of the $+$ normal mode:

$$\sigma_{y+}^2(s) = \frac{\beta_{y+}(s)}{\beta_{y+}(0)} \frac{\varepsilon_{x0}\beta_{x0}(0)}{\left(R_+^{-1} - R_-^{-1}\right)^2} \qquad (9)$$

and the other comes from the y component of the $-$ normal mode:

$$\sigma_{y-}^2(s) = \frac{\beta_{y-}(s)}{\beta_{y-}(0)} \frac{\varepsilon_{x0}\beta_{x0}(0)}{\left(R_+^{-1} - R_-^{-1}\right)^2} \qquad (10)$$

where ε_{x0} is the total emittance. Over time with incommensurate phase advances in general, the vertical components of the two normal modes will have random relative phase. They will, therefore, add as uncorrelated contributions: $\sigma_y^2(s) = \sigma_{y+}^2(s) + \sigma_{y-}^2(s)$. Figure 4 shows these contributions to the vertical beam size for the case of normal Helios operating conditions.

In Figure 5 the measured vertical beam sizes at the two SLM's as a function of skew quadrupole strength are compared with calculation. The discrepancy at zero skew quadrupole strength due to residual coupling effects is not addressed by this calculation.

REFERENCES

1. D. Edwards amd L. Teng, *Parameterization of Linear Coupled Motion in Periodic Systems*, IEEE Trans.Nucl. Sci., NS-20, No. 3, (1973).

2. P. Bagley and D. Rubin, *Correction of Transverse Coupling in a Storage Ring*, Conference Record of the 1989 IEEE Particle Accelerator Conference, Vol. 2, pp. 874-876.

A SIMULATION STUDY OF LINEAR COUPLING EFFECTS AND THEIR CORRECTION IN RHIC*

G. Parzen

Brookhaven National Laboratory
Upton, NY 11973, USA

Abstract

This paper describes a possible skew quadrupole correction system for linear coupling effects for the RHIC92 lattice. A simulation study has been done for this correction system. Results are given for the performance of the correction system and the required strength of the skew quadrupole corrections. The location of the correctors is discussed. For RHIC92, it appears possible to use the same 2 family correction system for all the likely choices of β^*. The simulation study gives results for the residual tune splitting that remains after correction with a 2 family correction system. It also gives results for the beta functions before and after correction.

I. INTRODUCTION

An important effect of linear coupling in RHIC is to shift the tune ν_x, ν_y, sometimes called tune splitting. Most of this tune splitting can be corrected with a two family skew quadrupole correction system. For RHIC92, the same 2 family correction system will work for all likely choices of β^*. This was not the case for the RHIC91 lattice where different families of correctors were needed for different β^*.

The tune splitting described above which is corrected with a 2 family correction system is driven primarily by the $\nu_x - \nu_y$ harmonic of the skew quadrupole field given by the field multipole a_1. There are several other effects of linear coupling present which are driven primarily by the $\nu_x + \nu_y$ harmonics of the skew quadrupole field, a_1. These include the following

1. A higher order residual tune shift that remains after correction with the 2 family correction system. This tune shift is roughly quadratic in a_1.
2. Possible large changes in the beta functions.
3. Possible increase in the beam size at injection due to the beta function distortion and the emittance distortion at injection.

The simulation study computes the magnitude of two of these effects, the higher order residual tune shift and the change in the beta functions.

II. THE 2 FAMILY CORRECTION SYSTEM

The 2 family correction system is based on canceling the driving term for the nearby difference resonance, $\nu_x - \nu_y = p$, p being an integer. For the $\nu_x - \nu_y = 0$ resonance the driving term may be written as

$$\Delta\nu = \frac{1}{4\pi\rho} \int ds \, (\beta_x\beta_y)^{\frac{1}{2}} \, a_1 \exp\left[i\bar{\nu}\left(\theta_x - \theta_y\right)\right]$$
$$\bar{\nu} = \left(\nu_x + \nu_y\right)/2 \tag{1}$$
$$\theta_x = \psi_x/\nu_x \ , \ \theta_y = \psi_y/\nu_y$$

One needs two families of a_1 correctors to correct both the real and imaginary parts of $\Delta\nu$. The phase of the exponent in (1) is nearly $\psi_x - \psi_y$, so the two families should be located at places where $\psi_x - \psi_y$ differ by $\pi/2$. One obvious place to put the a_1 correctors is near the high beta quadrupoles Q2 and Q3, where they are most effective. It will be seen from Fig. 1 that all the high beta quadrupoles have $\psi_x - \psi_y \simeq 0$, and thus another family of a_1 correctors is needed at a location where $\psi_x - \psi_y \simeq \pi/2$.

Fig. 1 plots $(\psi_x - \psi_y)/2\pi$ against the path distance s for a RHIC92 lattice with six $\beta^* = 10$ insertions and also for six $\beta^* = 2$ insertions. Looking at the $\beta^* = 10$ case, one sees that $\psi_x - \psi_y \simeq 0$ at the high beta quadrupoles Q2,Q3, while a_1 correctors near Q4 and Q5 have $\psi_x - \psi_y \simeq \pi/2$. It is proposed that one family of a_1 correctors be located near each Q2 or Q3, which will be called the Q23 family and one family be located near each Q4 or Q5, which will be called the Q45 family. For the $\beta^* = 2$ case, the phases are not as perfectly chosen but these two families will be adequate in this case too, although about 20% less effective.

Fig. 2 plots $(\psi_x - \psi_y)/2\pi$ against s for $\beta^* = 1, 2, 10$ and 16. From this plot, it seems likely that the proposed 2 families will work for the entire range of $\beta^* = 1$ to $\beta^* = 16$. The $\psi_x - \psi_y$ for $\beta^* = 1$ nearly overlaps the curve for $\beta^* = 2$ except for the indicated points for $\beta^* = 1$.

III. SIMULATION STUDY RESULTS

For this simulation study the random a_1 and b_1 present in the magnets have a magnitude given at the end of this section. If the random a_1 and b_1 can be reduced then the effects, the tune shift and beta function shifts, can be scaled in an appropriate way. In this study the random a_1 and the random b_1 are both assumed to be present. However, the tune shift due to random b_1 is

corrected using the QF and QD quadrupoles. Thus the tune shifts shown below are due to the random a_1 errors and the a_1 correctors.

Table 1 gives the results for the tune, ν_1, ν_2, and the maximum beta functions at QF and QD, β_1, β_2 for ten different distributions of the random a_1 and b_1. Results are shown before the 2 family correction system is applied, the uncorrected case, and after the correction is applied, the corrected case. The correctors are set to cancel the driving term $\Delta\nu$ given by Eq. (1). The RHIC92 lattice has 6 $\beta^* = 2$ insertions.

Table 1

Results for the correction of the tune splitting for a RHIC92 lattice with six $\beta^* = 2$ insertions using a 2 family correction system set to make $\Delta\nu = 0$. The unperturbed tune is 28.826, 28.821. β_1 is the maximum β_1 at a QF and β_2 is the maximum β_2 at a QD. The maximum unperturbed beta function is 50 m.

Field Error	ν_1	ν_2	— uncorrected — $\lvert\nu_1 - \nu_2\rvert$ /10^{-3}	β_1 (m)	β_2 (m)
1	.854	.792	62	67	65
2	.860	.791	69	78	69
3	.835	.814	21	61	62
4	.868	.801	67	103	94
5	.840	.791	49	88	80
6	.892	.807	85	127	101
7	.906	.779	127	120	94
8	.941	.709	232	92	105
9	—	—	unstable	—	—
10	.782	.870	88	69	75

	ν_1	ν_2	— corrected — $\lvert\nu_1 - \nu_2\rvert$ /10^{-3}	β_1 (m)	β_2 (m)
1	.828	.819	9	62	66
2	.829	.822	7	63	58
3	.829	.819	10	64	63
4	.839	.830	9	79	94
5	.829	.820	9	62	65
6	.857	.836	21	66	68
7	.872	.831	41	102	72
8	.832	.817	15	65	59
9	.876	.856	20	94	86
10	.834	.821	13	63	72

Table 1 shows that one can get tune splittings as large as $\lvert\nu_1 - \nu_2\rvert = 232 \times 10^{-3}$ before correction. One error distribution leads to unstable motion before correction, although this error distribution would not be unstable for the $\beta^* = 10$ lattice. After correction, with the correctors set to cancel the driving term $\Delta\nu$, there remains a residual tune shift with the largest $\lvert\nu_1 - \nu_2\rvert = 41 \times 10^{-3}$. Previous studies [1] indicate that this residual tune shift is roughly quadratic in a_1 if ν_x, ν_y are close to the difference resonance.

Table 1 also shows large shifts for the beta functions, as much as $\Delta\beta/\beta = 100\%$ after correction. It has been
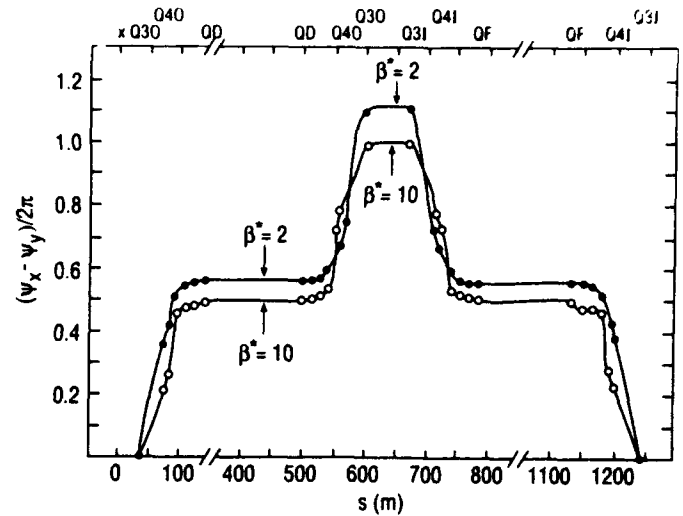
Figure 1: Plot of $(\psi_x - \psi_y)/2\pi$ against s for the RHIC92 lattice with 6 $\beta^* = 10$ and 6 $\beta^* = 2$ insertions. Each dot on the curves indicates the location of a quadrupole.
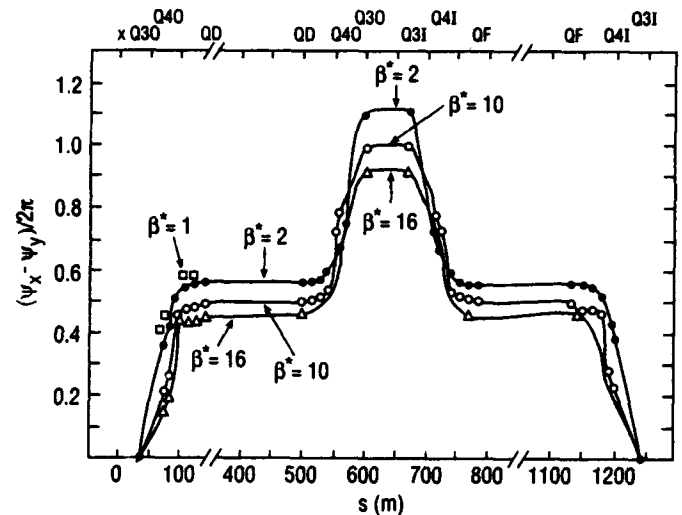
Figure 2: Plot of $(\psi_x - \psi_y)/2\pi$ against s for RHIC92 lattices with $\beta^* = 1, 2, 10, 16$. The $\beta^* = 1$ curve nearly overlaps the $\beta^* = 2$ curve except for the indicated points for $\beta^* = 1$.

shown that the beta function shift [2] and the higher order residual tune shift [3] are driven primarily by the harmonics of a_1 close to $\nu_x + \nu_y$. Part of the beta function shift is due to random b_1 which can cause a maximum $\Delta\beta/\beta$ of about 20%. [4]

Similar results have also been computed for a RHIC lattice with 6 $\beta^* = 10$ insertions. In this case the effects are smaller, and the largest residual tune splitting found is $\lvert\nu_1 - \nu_2\rvert = 14 \times 10^{-3}$, and the largest beta function found at QF or QD is $\beta_1 = 61$ at a QF after correction.

In Table 1, the 2 family correction system was set to cancel the driving term $\Delta\nu$, Eq. (1). In operating accelerators, the correction system is usually set to minimize the tune splitting, as $\Delta\nu$ is not known. Table 2 gives the results for ν_1, ν_2 and β_1, β_2 when the 2 family correction is set to minimize $|\nu_1 - \nu_2|$. The lattice is a RHIC92 lattice with 6 $\beta^* = 2$ insertions. Table 2 gives the results only after correction.

Table 2
Results for the correction of the tune splitting for a RHIC92 lattice with six $\beta^* = 2$ insertions using a 2 family correction system set to minimize $|\nu_1 - \nu_2|$. Results are shown after correction.

Field Error	ν_1	ν_2	$|\nu_1 - \nu_2|/10^{-3}$	β_1	β_2
1	.824	.823	1	59	59
2	.828	.824	4	56	55
3	.827	.821	6	54	55
4	.836	.833	3	72	71
5	.825	.821	3	65	63
6	.856	.837	19	58	64
7	.856	.838	18	64	63
8	.831	.818	13	63	58
9	.876	.856	20	93	86
10	.829	.826	3	74	67

In Table 2, the results for the tune splitting is somewhat smaller than found in Table 1. The largest tune splitting found after correction is $|\nu_1 - \nu_2| = 20 \times 10^{-3}$. The largest beta function shift after correction is $\Delta\beta/\beta \simeq$ 86%. The results are smaller but still appreciable.

For a RHIC92 lattice with 6 $\beta^* = 10$ insertions, and the correctors set to minimize the tune splitting, the largest residual tune splitting found is $|\nu_1 - \nu_2| = 8 \times 10^{-3}$ and the largest beta function at QF or QD after correction is $\beta_1 = 59$ at a QF.

Reducing the tune splitting and the beta function distortion further would require more families [1] of skew quadrupole correctors to correct the effects of the harmonics of a_1 near $\nu_x + \nu_y$.

Required Correction Strengths
In the above simulation, the largest corrector strengths needed are the following

$$\int ds\, B_0\, a_1 = 15 \text{ kG}, \quad \text{family Q45}$$

$$\int ds\, B_0\, a_1 = 6 \text{ kG}, \quad \text{family Q23}$$

Random a_1 and b_1 Errors Assumed in Study

The random quadrupole errors are due to a number of sources that include construction errors in the magnet coils, effective length errors in the quadrupoles, and rotational errors in the positioning of the quadrupoles.

a_1 and b_1 are defined so that the field due to a_1 and b_1 on the median plane is given by

$$B_y = B_0 b_1 x$$

$$B_x = B_0 a_1 x$$

where B_0 is the main dipole field.

The rms random a_1, b_1 used in this study are given in the following table.

Source	$a_1/10^{-5}$ (cm^{-1})	$b_1/10^{-5}$ (cm^{-1})
Dipole coil error	16.8	8.4
Quadrupole coil error	15	15
Quadrupole effective length	—	40
Quadrupole rotation error	40	—

The assumed effective length error in the quadrupoles is $\Delta L/L = 2 \times 10^{-3}$ rms. The assumed rotational error in the quadrupoles is $\Delta\theta = 1 \times 10^{-3}$ rad rms.

IV. REFERENCES

1. G. Parzen, Tune Shifts and Beta Function Shifts Due to Linear Coupling, Advanced Beam Dynamics Workshop, AIP Conf. Proc. No. 255 p. 131 (1991).

2. G. Parzen, Theory of the Beta Function Shift Due to Linear Coupling, BNL Report AD/RHIC-102 (1991).

3. G. Parzen, Theory of the Tune Shift Due to Linear Coupling, BNL Report AD/RHIC-100 (1991).

4. G. Parzen, Linear Random Quadrupole Effects, BNL Report AD/RHIC-AP-71 (1988).

EIGENFUNCTIONS OF THE TRANSFER MATRIX
IN THE PRESENCE OF LINEAR COUPLING*

G. Parzen

Brookhaven National Laboratory
Upton, NY 11973, USA

Abstract

This paper presents an approach to computing the change in the linear orbit parameters, due to a perturbing field that couples the x and y motions, by computing the change in the eigenfunctions of the transfer matrix and then using the relationship between the eigenfunctions and the orbit parameters. This can be compared with the approach [1] that computes the change in the transfer matrix and uses the relationship between the elements of the transfer matrix and the orbit parameters. For the case of coupled motion, the eigenfunction approach appears to be easier to apply than the transfer matrix approach, partly because the relationship between the transfer matrix and the linear orbit parameters is considerably more complicated in this case. Results are found for the change in the four eigenfunctions of the transfer matrix in the presence of linear coupling, and for the relationship between the eigenfunctions and the orbit parameters.

I. THE EIGENFUNCTIONS AND THE LINEAR ORBIT PARAMETERS

The eigenfunctions may be defined in terms of the transfer matrix, $T(s, s_0)$,

$$x(s) = T(s, s_0) x(s_0) \tag{1a}$$

In Eq. (1) $T(s, s_0)$ is a 4×4 matrix, $x(s)$ is a 4×1 column vector

$$x = x, p_x, y, p_y \tag{1b}$$

In the absence of solenoids, $p_x = x'$ and $p_y = y'$. The eigenfunctions are those $x(s)$ that satisfy

$$T(s + L, s) x = \lambda x, \tag{1c}$$

where L is the period of the magnetic guide field.

It can be shown [1] that there are 4 eigenfunctions $x_i(s), i = 1, 2, 3, 4$ with eigenvalues λ_i, and which occur in pairs such that for stable motion,

$$x_2 = x_1^*, \quad x_4 = x_4^*, \quad \lambda_2 = \lambda_1^*, \quad \lambda_4 = \lambda_3^*.$$

It can be shown [2] that the eigenfunctions are solutions of the equations of motions, and that

$$\begin{aligned} x_1(s) &= \exp(i 2\pi \nu_1 s / L) \; f_1(s), \\ x_3(s) &= \exp(i 2\pi \nu_2 s / L) \; f_3(s). \end{aligned} \tag{2}$$

$f_1(s), f_3(s)$ are periodic in s with period L, and ν_1, ν_2 are the normal mode tunes. Note x_i and f_i are both 4×1 column vectors.

A. The Transfer Matrix in Terms of the Eigenfunctions

Given the four eigenfunctions $x_i, i = 1, 4$ which are normalized such that $\tilde{x}_i^* S x_i = 2i,$ (3) where S is

$$S = \begin{bmatrix} 0 & 1 & 0 & 0 \\ -1 & 0 & 0 & 0 \\ 0 & 0 & 0 & 1 \\ 0 & 0 & -1 & 0 \end{bmatrix}$$

then it will be shown that one can find the transfer matrix $T(s, s_0)$ from

$$T(s, s_0) = (-1/2i) U(s) \overline{U}(s_0)$$

$$\overline{U} = \tilde{S} \tilde{U} S \tag{4}$$

$$U = [x_1 x_2 x_3 x_4].$$

U is a 4×4 matrix and x_i is a 4×1 column vector.

Eq. (4) will be derived for the 2-dimensional case. The generalization to 4 or more dimensions is clear. In two dimensions a solution of the equation of motion can be written as

$$x = a_1 x_1 + a_2 x_2, \quad x_2 = x^*,$$

$$a_1 = \tilde{x}_1^* S x / 2i, a_2 = a_1^* = \tilde{x}_2^* S x / (-2i) \tag{5}$$

Evaluate a_1 and a_2 using $x(s_0)$. Then

$$x = (1/2i) \left(x_1(s) \, \tilde{x}_1^*(s_0) - x_2(s) \, \tilde{x}_2^*(s_0) \right) S \, x(s_0)$$

$$x = (1/2i) \left(x_1(s) \, \tilde{x}_1^*(s_0) - x_1^*(s) \, \tilde{x}_1(s_0) \right) S \, x(s_0)$$

$$x = (1/2i) [x_1(s) \quad x_1^*(s)] S \begin{bmatrix} \tilde{x}_1(s_0) \\ \tilde{x}_1^*(s_0) \end{bmatrix} S \, x(s_0) \tag{6}$$

$$x = (-1/2i) U(s) \overline{U}(s_0) x(s_0).$$

Thus
$$T(s, s_0) = (-1/2i) U(s) \overline{U}(s_0) \tag{7}$$

One may note that $V = (-2i)^{-\frac{1}{2}} U(s)$ is symplectic as $T(s, s) = I$ and $V \overline{V} = I$.

Eq. (7) shows that knowing the eigenfunctions x_i is equivalent to knowing the transfer matrix $T(s, s_0)$. Eq. (7) also shows that $T(s, s_0)$ is symplectic as it is the product of two symplectic matrices, $V(s)$ and $\overline{V}(s_0)$.

B. Relationship Between Eigenfunctions and the Linear Orbit Parameters

The eigenfunctions will now be related to the 10 linear orbit parameters for the coupled motion.

In two dimensions, the eigenfunction is related to the 3 orbit parameters β, α, ψ by

$$x_1 = \begin{pmatrix} \beta^{\frac{1}{2}} \\ \beta^{-\frac{1}{2}}(-\alpha + i) \end{pmatrix} \exp(i\psi) \tag{8}$$

and $x_2 = x_1^*$. x_1 obeys the normalization condition

$$\tilde{x}_1^* S x_1 = 2i \tag{9}$$

In four dimensions, one can go from the coordinates, x, p_x, y, p_y to an uncoupled set of coordinates v, p_v, u, p_u the normal coordinates, by the transformation [3]

$$x = R\, v \qquad (10)$$

$$R = \begin{pmatrix} I \cos\varphi & \overline{D}\sin\varphi \\ -D\sin\varphi & I\cos\varphi \end{pmatrix} \qquad (11)$$

I and R are 2×2 matrices. I is the 2×2 identity matrix. $\overline{D} = D^{-1}$ and $|D| = 1$. R is a symplectic matrix,

$$\overline{R}R = I$$
$$\overline{R} = \tilde{S}\tilde{R}\,S \qquad (12)$$

φ and the 3 independent elements of D may be considered as 4 of the orbit parameters. They are periodic in s. The other 6 orbit parameters are the $\beta_1, \alpha_1, \psi_1$ and $\beta_2, \alpha_2, \psi_2$ of the 2 normal modes.

It can be shown that $\tilde{x}^{*}\,Sx$ is a constant [1] of the motion. Also if x and v are related by a symplectic matrix then

$$\tilde{x}^{*}\,Sx = \tilde{v}^{*}\,Sv \qquad (13)$$

The transfer matrix for the v coordinates is given by

$$v(s) = U(s, s_0)\, v(s_0)$$
$$U = \overline{R}(s)\, T R(s_0) \qquad (14)$$

It can then be shown that the eigenfunction of U, v_i, and the eigenfunctions of T are related by

$$x_i = R\, v_i \qquad (15)$$

The v coordinates are uncoupled, so the v_i eigenfunctions can be written down using Eq. (8) as

$$v_1 = \begin{pmatrix} \mu_1 \\ 0 \end{pmatrix} \qquad v_3 = \begin{pmatrix} 0 \\ \mu_2 \end{pmatrix}$$

$$\mu_1 = \begin{pmatrix} \beta_1^{\frac{1}{2}} \\ \beta_1^{-\frac{1}{2}}(-\alpha_1 + i) \end{pmatrix} \exp(i\psi_1), \qquad (16)$$

$$\mu_2 = \begin{pmatrix} \beta_2^{\frac{1}{2}} \\ \beta_2^{-\frac{1}{2}}(\alpha_2 + i) \end{pmatrix} \exp(i\psi_2)$$

$$v_2 = v_1^{*}, \qquad v_4 = v_3^{*}$$

one may note that $\tilde{v}_1^{*} Sv_1 = \tilde{v}_3^{*} Sv_3 = 2i$. The x_i can then be written down using $x = RV$ as

$$x_1 = \begin{pmatrix} \mu_1 \cos\varphi \\ -D\mu_1 \sin\varphi \end{pmatrix}$$

$$x_3 = \begin{pmatrix} \overline{D}\mu_2 \sin\varphi \\ \mu_2 \cos\varphi \end{pmatrix} \qquad (17)$$

Eq. (17) relates the eigenfunctions x_i to the 10 orbit parameters. Also $\tilde{x}_1^{*} Sx_1 = \tilde{x}_3^{*} Sx_3 = 2i$.

If the eigenfunctions are known, then Eqs. (17) can be inverted to find the 10 orbit parameters. One can use the additional relationships

$$\frac{d\psi_1}{ds} = \frac{1}{\beta_1}, \qquad \frac{d\psi_2}{ds} = \frac{1}{\beta_2} \qquad (18)$$

$$\alpha_1 = -\frac{1}{2}\beta_1' + \beta_1 \tan\varphi\, d\varphi/ds, \qquad \alpha_2 = -\frac{1}{2}\beta_2' + \beta_2 \tan\varphi\, d\varphi/ds$$

which are valid in absence of solenoidal fields.

To further illustrate how expressions for the eigenfunctions can be used to compute the linear orbit parameters, consider the problem of finding β_1, the beta function of the normal mode with ν_1, assuming that the eigenfunctions are known (see section II).

The eigenfunction x_1 may be written as

$$x_1 = \begin{bmatrix} x_{11} \\ x_{12} \\ x_{13} \\ x_{14} \end{bmatrix} \qquad (19)$$

From Eq. (17)

$$x_{11} = \beta_1^{\frac{1}{2}} \cos\varphi \exp(i\psi_1) \qquad (20)$$

which gives the two relations

$$\psi_1 = ph\,(x_{11}), \beta_1^{\frac{1}{2}} \cos\varphi = |x_{11}| \qquad (21)$$

where $ph\,(x_{11})$ means the phase of x_{11}.

Assuming x_{11} is known, ψ_1 can be found from Eq. (21) and one can find β_1 from $\beta_1 = d\psi_1/ds$. Once β_1 is known, one can find $\cos\varphi$ from Eq. (21). One may note that the results for the tune ν_1 and ν_2 comes directly out of solving the equations of motion for the eigenfunctions (see section II).

To find the emittance ϵ_1 from the eigenfunctions, one can use the relationship [4]

$$\epsilon_1 = |\,\tilde{x}_1^{*}\, S\, x_1|^2 \qquad (22)$$

II. PERTURBATION SOLUTIONS FOR THE EIGENFUNCTIONS

The skew quadrupole field is described by $a_1(s)$. On the median plane, the field B_x is given by

$$B_x = -B_0\, a_1\, x, \qquad (23)$$

where B_0 is the main dipole field. ρ is the radius of curvature of the main dipole.

The solutions of Eq. (23) were found in two previous papers [5,6] when ν_x, ν_y are near the resonance line $\nu_x = \nu_y + p$. These solutions may be written as

$$\eta_x = A \exp(i\nu_{x,s}\theta_x)\left\{1 + \sum_{n \neq -p} f_n\right\} \qquad (24)$$

$$f_n = \frac{(\nu_{x,s} - \nu_x)}{\Delta\nu} \frac{2\nu_x b_n \exp[-i(n+p)\theta_x]}{(n - \nu_x - \nu_y)(n + p)}$$

$$\eta_y = B \exp(i\nu_{y,s}\theta_y)\left\{1 + \sum_{n=p} g_n\right\}$$

$$g_n = \frac{(\nu_{y,s} - \nu_y)}{\Delta\nu^{*}} \frac{2\nu_y c_n \exp[-i(n-p)\theta_y]}{(n - \nu_x - \nu_y)(n - p)}$$

$$\Delta\nu = (1/4\pi\rho)\int ds\,(\beta_x\beta_y)^{\frac{1}{2}} a_1 \exp[i(-\nu_{x,s}\theta_x + \nu_{y,s}\theta_y)]$$

$$b_n = \frac{1}{4\pi\rho}\int ds\,(\beta_x\beta_y)^{\frac{1}{2}} a_1 \exp[i((n - \nu_y)\theta_x + \nu_y\theta_y)]$$

$$c_n = \frac{1}{4\pi\rho}\int ds\,(\beta_x\beta_y)^{\frac{1}{2}} a_1 \exp[i(\nu_x\theta_x + (n - \nu_x)\theta_y)]$$

$$\theta_x = \psi_x/\nu_x, \qquad \theta_y = \psi_y/\nu_y$$

$\nu_{x,s}$ and $\nu_{y,s}$ are the solutions of

$$\nu_{x,s} = \nu_{y,s} + p, \qquad (\nu_{x,s} - \nu_x) = |\Delta\nu|^2 \qquad (25)$$

There are two solutions of Eq. (25) corresponding to the two normal modes. For the mode for which $\nu_{x,s} \to \nu_x$ when $a_1 \to 0$, we will put $\nu_{x,s} = \nu_1$, $\nu_{y,s} = \nu_1 - p$. For the mode for which $\nu_{y,s} \to \nu_y$ when $a_1 \to 0$, we will put $\nu_{y,s} = \nu_2$, $\nu_{x,s} = \nu_2 + p$. The A and B coefficients are related by

$$B_1 = \frac{-(\nu_1 - \nu_x)}{\Delta \nu} A_1 \text{ for the } \nu_1 \text{ mode}$$
$$A_2 = \frac{-(\nu_2 - \nu_y)}{\Delta \nu^*} B_2 \text{ for the } \nu_2 \text{ mode}$$
(26)

The results for the eigenfunctions, Eq. (24) were found by solving the equations of motion to first order terms in a_1. It has been assumed that ν_x, ν_y the unperturbed tune, is close to the coupling resonance $\nu_x = \nu_y + p$ and the $\nu_x - \nu_y - p$ can be considered to be small, of the same order as a_1. This last assumption allows the equations to be simplified and it is the case of most interest to us.

The A and B coefficients in Eq. (24) have now to be chosen so that the eigenfunctions are properly normalized, which means the eigenfunctions can be then expressed in terms of the orbit parameters like $\beta_1, \alpha_1, \psi_1$ and $\beta_2, \alpha_2, \psi_2$. To understand this better consider the 2 dimensional case. If we wish the eigenfunction to be related to β, ψ by

$$x = \beta^{1/2} \exp(i\psi),$$

then

$$p_x = x' = \beta^{-1/2} (-\alpha + i) \exp(i\psi)$$

and the two eigenfunctions are given by x_1, x_1^* where

$$x_1 = \begin{bmatrix} \beta^{\frac{1}{2}} \\ \beta^{-\frac{1}{2}} (-\alpha + i) \end{bmatrix} \exp(i\psi)$$
(27)

These eigenfunctions are normalized so that

$$\tilde{x}_1^* \, S \, x_1 = 2i$$
(28)

$$S = \begin{bmatrix} 0 & 1 \\ -1 & 0 \end{bmatrix}$$

$\tilde{x}_1$ is the transpose of x_1.

The normalization given by Eq. (28) gives the relationship between x_1 and β, α, ψ given by Eq. (27). It is shown in section I, that in the 4 dimensional case the normalization Eq. (28) will allow the eigenfunctions x_1, x_3 to be related to $\beta_1, \alpha_1, \psi_1$ and $\beta_2, \alpha_2, \psi_2$ in a corresponding way. In this case, S is now the corresponding 4×4 matrix. Eq. (28) will be used to determine the coefficients A, B. This gives the relationship, see Ref. 7 where the following relationship is derived,

$$|A|^2 (\nu_{x,s}/\nu_x) + |B|^2 (\nu_{y,s}/\nu_y) = 1.$$
(29)

Eq. (29) together with Eq. (26) determine A and B.

For the ν_1 mode

$$B_1 = -\frac{\nu_1 - \nu_x}{\Delta \nu} A_1,$$
$$|A_1|^2 \left(\frac{\nu_1}{\nu_x} + \frac{\nu_1 - p}{\nu_y} \left| \frac{\nu_1 - \nu_x}{\Delta \nu} \right|^2 \right) = 1.$$
(30)

For the ν_2 mode

$$A_2 = -\frac{\nu_2 - \nu_y}{\Delta \nu^*} B_2,$$
$$|B_2|^2 \left(\frac{\nu_2}{\nu_y} + \frac{\nu_2 + p}{\nu_x} \left| \frac{\nu_2 - \nu_y}{\Delta \nu} \right|^2 \right) = 1.$$
(31)

A case of particular interest is when the linear coupling has been corrected to make $\Delta \nu \simeq 0$. There are then two solutions of interest,

1. $|\Delta \nu| \ll |\nu_x - \nu_y - p|$
2. $|\nu_x - \nu_y - p| \ll |\Delta \nu|$

In case 1., $\Delta \nu$ has been made small enough so that the tune ν_x, ν_y is well outside the width of the difference resonance. This may not always be achieved. ν_x, ν_y may be very close to the difference resonance, and the best setting of the correction system to minimize the tune splitting does not have to correspond to $\Delta \nu = 0$.

If $|\Delta \nu| \ll |\nu_x - \nu_y - p|$, one finds
$$|A_1| = 1, \qquad B_1 = 0,$$
$$|B_2| = 1, \qquad A_2 = 0.$$
(32)
The two modes appear to be decoupled.

If $|\nu_x - \nu_y - p| \ll |\Delta \nu|$, one finds
$$|A_1| = |B_1| = 1/\sqrt{2}$$
$$|A_2| = |B_2| = 1/\sqrt{2}$$
(33)
The two modes appear completely coupled.

Examples of using the eigenfunction approach to compute the linear orbit parameters are given in Ref. 4,7.

V. REFERENCES

1. E.D. Courant and H. Snyder, Theory of the AG Synchrotron, Annals of Physics, 3, No. 1, p. 1 (1958).
2. F. Willeke and G. Ripken, Methods of Beam Optics, DESY 88-114 (1988).
3. D. Edwards and L. Teng, Parameterization of Linear Coupled Systems, IEEE PAC, p. 885 (1973).
4. G. Parzen, Emittances and Beam Size Distortion Due to Linear Coupling, BNL Report AD/AP-51 (1992).
5. G. Parzen, Theory of the Tune Shift Due to Linear Coupling, BNL Report AD/RHIC-100 (1991).
6. G. Parzen, Theory of the Beta Function Shift Due to Linear Coupling, BNL Report AD/RHIC-102 (1991).
7. G. Parzen, Beta Functions, Rotation Angle, and Eigenfunctions due to Linear Coupling, BNL Report AD/AP-49 (1992).

EMITTANCE AND BEAM SIZE DISTORTION
DUE TO LINEAR COUPLING*

G. Parzen

Brookhaven National Laboratory
Upton, NY 11973, USA

Abstract

At injection, the presence of linear coupling may result in an increased beam emittance and in increased beam dimensions. Results for the emittance in the presence of linear coupling will be found. These results for the emittance distortion show that the harmonics of the skew quadrupole field close to $\nu_x + \nu_y$ are the important harmonics. Results will be found for the important driving terms for the emittance distortion. It will be shown that if these driving terms are corrected, then the total emittance is unchanged, $\epsilon_x + \epsilon_y = \epsilon_1 + \epsilon_2$. Also, the increase in the beam dimensions will be limited to a factor which is less than 1.414. If the correction is good enough, see below for details, one can achieve $\epsilon_1 = \epsilon_x$, $\epsilon_2 = \epsilon_y$, where ϵ_1, ϵ_2 are the emittances in the presence of coupling, and the beam dimensions are unchanged. Global correction of the emittance and beam size distortion appears possible.

I. THE EMITTANCE FOR COUPLED MOTION

One definition for the emittances when the particle motion is coupled was given by Edwards and Teng.[1] In four dimensions, one can go from the coordinates x, p_x, y, p_y to an uncoupled set of coordinates v, p_v, u, p_u by the transformation [1]

$$x = R\, v$$

$$x = \begin{pmatrix} x \\ p_x \\ y \\ p_y \end{pmatrix} \qquad v = \begin{pmatrix} v \\ p_v \\ u \\ p_u \end{pmatrix} \tag{1}$$

$$R = \begin{pmatrix} I\cos\varphi & \overline{D}\sin\varphi \\ -D\sin\varphi & I\cos\varphi \end{pmatrix}.$$

I and D are 2×2 matrices. I is the 2×2 identity matrix. $\overline{D} = D^{-1}$ and $|D| = 1$. R is a symplectic matrix

$$\overline{R}\, R = I$$

$$\overline{R} = \widetilde{S}\widetilde{R}\, S \tag{2}$$

$$S = \begin{bmatrix} 0 & 1 & 0 & 0 \\ -1 & 0 & 0 & 0 \\ 0 & 0 & 0 & 1 \\ 0 & 0 & -1 & 0 \end{bmatrix}.$$

$\widetilde{R}$ is the transpose of R.

v, p_v and u, p_u are uncoupled. Thus v, p_v satisfy differential equations with periodic coefficients whose solutions have the form

$$v = \beta_1^{\frac{1}{2}} \exp(i\psi_1)$$
$$p_v = \beta_1^{-\frac{1}{2}}(-\alpha_1 + i)\exp(i\psi_1). \tag{3}$$

A second solution exists with $\psi_1, \beta_1, \alpha_1$ replaced by $\psi_2, \beta_2, \alpha_2$. As in the case of 2 dimensional motion

$$\epsilon_1 = \gamma_1 v^2 + 2\alpha_1 v p_v + \beta_1 p_v^2 \tag{4a}$$

is an invariant. $\gamma_1 = (1 + \alpha_1^2)/\beta_1$. Similarly, ϵ_2 is an invariant,

$$\epsilon_2 = \gamma_2 u^2 + 2\alpha_2 u p_u + \beta_2 p_u^2. \tag{4b}$$

For two dimensional motion, one can find α, β from the one turn transfer matrix $M(s + L, s)$.

In 4 dimensions, α_1, β_1 and α_2, β_2 can be found from the one turn transfer matrix. The process is quite involved [1], and using Eq. (4) to find ϵ_1, ϵ_2 when the transfer matrix is known is also involved.

A second definition of the emittance was suggested by A. Piwinski [2] which seems easier to apply. The emittance ϵ_1 is defined by

$$\epsilon_1 = \left| \widetilde{x}_1^* S\, x \right|^2 \tag{5a}$$

x_1 is the 4 vector for the eigenfunction of the transfer matrix, which are assumed to be $x_1, x_2 = x_1^*, x_3, x_4 = x_3^*$.

Since $\widetilde{x}_1^* Sx$ has the form of the Lagrange invariant [3] ϵ_1 is an invariant. It will be shown below that ϵ_1 defined by Eq. (5a) and ϵ_1 defined by Eq. (4) are the same. In a similar way, ϵ_2 is defined by

$$\epsilon_2 = \left| \widetilde{x}_3^* S\, x \right|^2 \tag{5b}$$

Note that x_1 and x_3 have to be normalized so that

$$\widetilde{x}_1^* S\, x_1 = \widetilde{x}_3^* S\, x_3 = 2i \tag{6}$$

Analytic expressions for x_1, x_3 were given in a previous paper. [4] These results for x_1, x_3 when put in Eq. (5) give an analytic expression for ϵ_1 and ϵ_2.

To show that ϵ_1, ϵ_2 defined by Eqs. (4) and Eqs. (5) are equal, one may note that since v, p_v, u, p_u are uncoupled coordinates, the eigenfunctions in this coordinate system may be written as

$$v_1 = \begin{bmatrix} \beta_1^{\frac{1}{2}} \\ \beta_1^{-\frac{1}{2}}(-\alpha_1 + i) \\ 0 \\ 0 \end{bmatrix} \exp(i\psi_1),$$

$$(7)$$

$$v_3 = \begin{bmatrix} 0 \\ 0 \\ \beta_2^{\frac{1}{2}} \\ \beta_1^{-\frac{1}{2}}(-\alpha_2 + i) \end{bmatrix} \exp(i\psi_2)$$

One can then show that

$$\tilde{v}_1^* s\, v_1 = \tilde{v}_3^* s\, v_3 = 2i,$$

and

$$\left| \tilde{v}_1^* s\, v \right|^2 = \gamma_1 v^2 + 2\alpha_1 v p_v + p_v^2,$$

which is ϵ_1 according to Eq. (4).

One can show that since $x = Rv$ and R is symplectic, that

$$\left| \tilde{x}_1^* s\, x \right|^2 = \left| \tilde{v}_1^* s\, v \right|^2, \qquad (8)$$

and thus the ϵ_1 defined by Eq. (5) is the same as ϵ_1 defined by Eq. (4). One may note that $x_1 = R\, v_1$.

It also can be shown that

$$\int dx\, dp_x\, dy\, dp_y = \epsilon_1 \epsilon_2, \qquad (9)$$

where the integral is over the region of 4-space which lies inside the two surfaces

$$\begin{aligned} \epsilon_1(x, p_x, y, p_y) &= \epsilon_1 \\ \epsilon_2(x, p_x, y, p_y) &= \epsilon_2 \end{aligned} \qquad (10)$$

This can be shown by transforming the integral in Eq. (10) from the x coordinates to the v coordinates and using the result $|R| = 1$.

II. ANALYTICAL RESULTS FOR THE EMITTANCE DISTORTION AND ITS CORRECTION

Analytical results for the eigenfunctions of the 4×4 transfer matrix were found in Ref. 4. Assuming the eigenfunctions are known the ϵ_1, ϵ_2 can be computed as follows

$$\begin{bmatrix} x \\ \nu_x \\ y \\ p_y \end{bmatrix} = G \begin{bmatrix} \eta_x \\ p_{\eta x} \\ \eta_y \\ p_{\eta y} \end{bmatrix} \qquad (11)$$

$$G = \begin{bmatrix} G_x & 0 \\ 0 & G_y \end{bmatrix}$$

$$G_x = \begin{bmatrix} \beta_x^{\frac{1}{2}} & 0 \\ -\alpha_x \beta_x^{-\frac{1}{2}} & \beta_x^{-\frac{1}{2}} \end{bmatrix}, \quad G_y = \begin{bmatrix} \beta_y^{\frac{1}{2}} & 0 \\ -\alpha_y \beta_y^{-\frac{1}{2}} & \beta_y^{-\frac{1}{2}} \end{bmatrix}$$

The eigenfunctions being known, see Ref. 4,5, one can now compute ϵ_1 and ϵ_2

$$\epsilon_1 = \left| \tilde{x}_1^* S\, x \right|^2 = \left| \eta_1^* S\, \eta \right|^2 \qquad (12)$$

since G is symplectic.

$$\eta_1 = \begin{bmatrix} \eta_{x1} \\ p_{\eta x1} \\ \eta_{y1} \\ p_{\eta y1} \end{bmatrix} \qquad (13)$$

one finds

$$\begin{aligned} \epsilon_1 &= |\eta_{x1}|^2 p_{\eta x}^2 + |p_{\eta x1}|^2 \eta_x^2 - \eta_x p_{\eta x} (p_{\eta x1}^* \eta_{x1} + \text{c.c.}) \\ &+ |\eta_{y1}|^2 p_{\eta y}^2 + |p_{\eta y1}|^2 \eta_y^2 - \eta_y p_{\eta y} (p_{\eta y1}^* \eta_{y1} + \text{c.c.}) \\ &+ p_{\eta x} p_{\eta y} (p_{\eta x1}^* p_{\eta y1}^* + \text{c.c.}) + \eta_x \eta_y (p_{\eta x1}^* p_{\eta y1}^* + \text{c.c.}) \\ &- p_{\eta x} \eta_y (\eta_{x1}^* p_{\eta y1} + \text{c.c.}) - \eta_x p_{\eta y} (p_{\eta x1}^* \eta_{y1}^* + \text{c.c.}) \end{aligned}$$

$$p_{\eta x} = (1/\nu_x)\, d\eta_x/d\theta_x, \quad p_{\eta y} = (1/\nu_y)\, d\eta_y/d\theta_y$$

$$(14)$$

One can now find analytic expressions for ϵ_1 by substituting for η_1 the results found in Ref. 4, 5. This result is usually quite complicated. One interesting case is when a correction system has been used to cancel the b_n and c_n for $n \simeq \nu_x + \nu_y$, which generate the larger terms in the expressions for the eigenfunctions. Let us assume that enough b_n, c_n have been corrected so that, see Ref. 4,5, the eigenfunctions can be written as

$$\begin{aligned} \eta_x &= A\, \exp(i\nu_{xs}\theta_x) \\ \eta_y &= B\, \exp(i\nu_{ys}\theta_y) \\ p_{\eta x} &= iA\, \exp(i\nu_{xs}\theta_x) \\ p_{\eta y} &= iB\, \exp(i\nu_{ys}\theta_y) \end{aligned} \qquad (15)$$

It has been assumed that the difference resonance has also been corrected, and that ν_x, ν_y is very close to the nearby difference resonance $\nu_x - \nu_y = p$, so that $\nu_{xs}/\nu_x \simeq 1$ and $\nu_{ys}/\nu_y \simeq 1$. It will be seen that correcting the b_n, c_n for $n \simeq \nu_x + \nu_y$ and the nearby different resonance will essentially correct the emittance distortion and the beam size distortion.

Putting the corrected results for the eigenfunctions Eq. (15) into the emittance result Eq. (14) one finds

$$\begin{aligned} \epsilon &= |A|^2 (p_{\eta x}^2 + \eta_x^2) + |B|^2 (p_{\eta y}^2 + \eta_y^2) \\ &+ p_{\eta x} p_{\eta y} (A^* B + \text{c.c.}) \\ &+ \eta_x \eta_y (A^* B + \text{c.c.}) \\ &- p_x \eta_y (-iA^* B + \text{c.c.}) \\ &- \eta_x p_{\eta y} (-iA^* B + \text{c.c.}) \end{aligned} \qquad (16)$$

There are two solutions of interest corresponding to how well one can correct $\Delta \nu$,

$$
\begin{aligned}
&\text{Case 1.} \quad |\Delta \nu| \ll |\nu_x - \nu_y - p| \\
&\text{Case 2.} \quad |\nu_x - \nu_y - p| \ll |\Delta \nu|
\end{aligned}
\tag{17}
$$

For the first case, $|\Delta \nu| \ll |\nu_x - \nu_y - p|$, then the coefficients A, B in the eigenfunctions satisfy [4]

$$
\begin{aligned}
|A_1| = 1 \qquad B_1 = 0 \\
|B_2| = 1 \qquad A_2 = 0
\end{aligned}
\tag{18}
$$

Then for case (1) Eq. (16) gives

$$
\epsilon_1 = \epsilon_x, \epsilon_2 = \epsilon_y
\tag{19}
$$

where use has been made of the results

$$
\begin{aligned}
\eta_x + p_{\eta x}^2 &= \gamma_x x^2 + 2\alpha_x x p_x + \beta_x p_x^2 = \epsilon_x \\
\eta_y^2 + p_{\eta y}^2 &= \gamma_y y^2 + 2\alpha_y y_\gamma p_y + \beta_y p_y^2 = \epsilon_y
\end{aligned}
\tag{20}
$$

Thus in case 1, ϵ_1, ϵ_2 are the same as ϵ_x, ϵ_y.

For case (2), $|\nu_x - \nu_y - p| \ll |\Delta \nu|$ then [4]

$$
\begin{aligned}
|A_1| = |B_1| &= 1/\sqrt{2} \\
|A_2| = |B_2| &= 1/\sqrt{2} \\
A_1^* B_1 + A_2^* B_2 &= 0
\end{aligned}
\tag{21}
$$

Then for case (2), Eq. (16) gives

$$
\epsilon_t = \epsilon_1 + \epsilon_2 = \epsilon_x + \epsilon_y
\tag{22}
$$

We no longer have $\epsilon_1 = \epsilon_x$, $\epsilon_2 = \epsilon_y$ as in case (1) however ϵ_t is not increased by the linear coupling.

Thus, if one corrects enough of the b_n, c_n for $n \simeq \nu_y + \nu_x$ and also corrects $\Delta \nu$, the driving term of the nearby difference resonance, $\nu_x - \nu_y = p$, then the emittance distortion has also been corrected. We will either obtain $\epsilon_1 = \epsilon_x$, $\epsilon_2 = \epsilon_y$ or $\epsilon_1 + \epsilon_2 = \epsilon_x + \epsilon_y$ depending on how well $\Delta \nu$ has been corrected.

III. ANALYTICAL RESULTS FOR THE BEAM SIZE DISTORTION AND ITS CORRECTION

In the previous section, results were found for the emittance distortion, and it was f⁒ nd that if the b_n, c_n for $n \simeq \nu_x + \nu_y$ and $\Delta \nu$ are corrected, then the emittance distortion is also largely corrected. For 4 dimensional motion, the connection between the beam size and the emittance is not as simple as it is in the 2 dimensional uncoupled case. In this section the maximum beam size will be computed when the b_n, c_n and $\Delta \nu$ are corrected. It will be shown that the beam size distortion is also largely corrected, although in one case it may be increased by a factor which is ≤ 1.414.

The results for $x_{\max}, y_{\max}$ are given below. See Ref. 4 for details.

For case 1, $|\Delta \nu| \ll |\nu_x - \nu_y - p|$ then

$$
\begin{aligned}
x_{\max} &= \sqrt{\beta_x \epsilon_x} \\
y_{\max} &= \sqrt{\beta_y \epsilon_y}
\end{aligned}
\tag{23}
$$

and there is no growth in beam size.

For case 2, $|\nu_x - \nu_y - p| \ll |\Delta \nu|$ then

$$
\begin{aligned}
x_{\max} &\leq (\beta_x (\epsilon_x + \epsilon_y))^{\frac{1}{2}} \\
y_{\max} &\leq (\beta_y (\epsilon_x + \epsilon_y))^{\frac{1}{2}}
\end{aligned}
\tag{24}
$$

For the case where $\epsilon_x = \epsilon_y$, then $x_{\max} \leq 1.4 (\beta_x \epsilon_x)^{\frac{1}{2}}$ and the coupling may increase $x_{\max}$ by the factor 1.414. So in case (2) $|\nu_x - \nu_y - p| \ll |\Delta \nu|$, then when the b_n, c_n and $\Delta \nu$ are corrected one may still have a beam size increase of the factor 1.414.

IV. OTHER BEAM DISTORTIONS

This section applies the eigenfunction method to computing the change in the beta functions and the normal mode rotation angle. Expressions are found for the important driving terms of these orbit parameters. The results are given below. For the details see Ref. 4.

$$
\begin{aligned}
\frac{\beta_1 - \beta_x}{\beta_x} = - \sum_{\text{all } n} &\left\{ \frac{\nu_1 - \nu_x}{\Delta \nu} \frac{b_n}{n - \nu_x - \nu_y} \right. \\
&\left. \exp\left[-i(n + p)\theta_x \right] + \text{c.c.} \right\}.
\end{aligned}
\tag{25}
$$

$$
\cos \varphi = |A_1| \left(1 + \frac{1}{2} \frac{\nu_1 - \nu_x}{\nu_x} + \sum_{n \neq -p} (f_n + f_n^*) \left(\frac{1}{2} - \frac{n + p}{4\nu_x} \right) \right)
\tag{26}
$$

$$
f_n = \frac{\nu_1 - \nu_x}{\Delta \nu} \frac{2\nu_x b_n}{(n - \nu_x - \nu_y)(n + p)} \exp\left[-i(n + p)\theta_x \right]
$$

$$
|A_1|^2 \left(\frac{\nu_1}{\nu_x} + \frac{\nu_1 - p}{\nu_y} \left| \frac{\nu_1 - \nu_x}{\Delta \nu} \right|^2 \right) = 1
$$

The results for the beta functions, Eq. (25) and the results for $\cos \varphi$, Eq. (26), show that they have the same important driving terms b_n, c_n for $n \simeq \nu_x + \nu_y$. The higher order ν-shift also has the same driving terms. Thus a correction system that corrects these driving terms might be able to correct all these three effects simultaneously.

V. REFERENCES

1. D. Edwards and L. Teng, IEEE 1973 PAC, p. 885 (1973).
2. A. Piwinski, DESY 90-113 (1990).
3. E.D. Courant and H. Snyder, Ann. Phys. 3, 1 (1958).
4. G. Parzen, BNL Report AD/AP-49 (1992).
5. G. Parzen, These proceedings.

Use of Regularization Method in the Determination of Ring Parameters and Orbit Correction *

Y.N. Tang and S. Krinsky

National Synchrotron Light Source, Brookhaven National Laboratory, Upton, NY 11973

Abstract

We discuss applying the regularization method of Tikhonov to the solution of inverse problems arising in accelerator operations. This approach has been successfully used for orbit correction on the NSLS storage rings, and is presently being applied to the determination of betatron functions and phases from the measured response matrix. The inverse problem of differential equations often leads to a set of integral equations of the first kind which are ill-conditioned. The regularization method is used to combat the ill-posedness.

1 Introduction

Inverse problems of differential equations, which determine the physical properties (*e.g.* betafunctions, phases) and causes (corrector strengths) from measured data (orbit displacements) have wide applications in many fields. Unfortunately, these problems are inherently ill-posed computationally [3]. Their solutions do not smoothly depend on the input data. Small errors in the input data will cause big changes in their solutions. If we solve them directly on finite precision computers without applying special techniques and if the dimension of the problem exceeds some limit, oscillations will occur and the results may diverge if under iteration.

This paper gives a simple illustration of why the inverse problem is ill-posed, and introduces the regularization method, which is used in the orbit correction of NSLS storage rings and a simulation model for determination of ring parameters from the measured local bump ratios.

2 Inverse Problems and Ill-Posedness

To study a dynamic system, people solve differential equations. The motion of a particle in the storage ring is governed by a second-order differential equation [1]. If the coefficients (*i.e.* the system parameters) of the equation and the driving force satisfy certain conditions, finding its solution is well- defined and conditioned. To solve a differential equation is to integrate the effects of all the sources. However, the reverse process of finding the distributed sources from the cumulative effects is a totally different matter. The immediate question is the uniqueness of its solution

because the effects caused by some sources could cancel each other. Generally speaking, the inverse problem of differential equations leads to integral equations [3]. This is expected because the differentiation and integration are inverse operations. However, to solve the produced integral equations is far more difficult than solving the original differential equations.

Let's take a simple example of solving the inverse problem of the following equation:

$$\frac{d^2x}{ds^2} + K(s)x = F(s) \qquad (1)$$

with some boundary or initial conditions, where $a \leq s \leq b$. The inverse problem is to determine $K(s)$ from the known solution $x(s), a \leq s \leq b$.

It is not possible to find analytical solutions of inverse problems in most of the cases. In practice, the following iterative procedure is employed.

Let

$$K_{n+1} = K_n + \delta K_n \quad and \quad x = x_n + \delta x_n \qquad (2)$$

be the $(n+1)$th iterates of K and x. K_0 is the initial guess. Substituting Eq. (2) into Eq. (1) and neglecting terms of $O\{\delta x_n \delta K_n\}$, one obtains

$$\frac{d^2x_n}{ds^2} + K_n(s)x_n = F(s) \qquad (3)$$

and

$$\frac{d^2(\delta x_n)}{ds^2} + K_n(s)\delta x_n = -x_n \delta K_n(s) \qquad (4)$$

By applying the Green function to Eq. (4),

$$\int_a^b G_n(s,s')(-x_n(s')\delta K_n(s'))ds' = \delta x_n(s) \qquad (5)$$

Eq. (5) tells that what relates δK_n to δx_n is a Fredholm integral equation of the first kind, which is notorious for its ill-posedness. It presents a great challenge to obtain $\delta K_n(s)$ from the known $\delta x_n(s)$, especially in the case when $\delta x_n(s)$ is derived from the measured data and inevitably has errors.

To make description simple, let's rewrite Eq. (5) in a more general form

$$\int_a^b G(s,s')\theta(s')ds' = p(s), \quad c \leq s \leq d \qquad (6)$$

where $p(s), c \leq s \leq d$ is the known function and $\theta(s), a \leq s \leq b$ is unknown. Suppose $\theta_1(s)$ is a solution of Eq. (6). Let

$$\theta_2(s) = \theta_1(s) + N \sin ns \qquad (7)$$

where N and n are arbitrary numbers. Using Eq. (6) one finds

$$\int_a^b G(s,s')(\theta_1(s') + N \sin ns')ds'$$
$$= p(s) + N \int_a^b G(s,s') \sin ns' ds'$$

Theoretically, in order to make $\theta_2(s)$ the solution of Eq. (6), the following equation must hold,

$$N \int_a^b G(s,s') \sin ns' ds' = 0, \quad c \le s \le d \quad (8)$$

On a computer with finite precision, Eq. (8) always holds for sufficiently large n.

Suppose we solve Eq. (6) numerically on a grid $s_i, i = 1, 2, \cdots, M$, where $s_1 = c$ and $s_M = d$. By using a well-known theorem,

$$\lim_{n \to \infty} \int_a^b f(s) \sin ns ds = 0, \quad (9)$$

it is easy to show that we can make $N \int_a^b G(s_i, s') \sin ns' ds'$ arbitrarily small for $i = 1, 2, \cdots, M$ if n is large enough. If they are smaller than the precision of the digital computer on this grid, $\theta_2(s)$ becomes a solution of Eq. (6).

Note that it is very easy to apply the previous analysis to the orbit correction problem and obtain the same conclusion. As a matter of fact, the analysis is much simpler. The response matrix in the orbit correction is the discretized form of the Green's function.

3 The Regularization Method

The regularization method was devised and developed by Tikhonov et al. [2] for the purpose of reformulating ill-posed problems into problems of a more well-posed nature. The revised problems do not have the same exact solution as the original problems, but in most practical cases, the data is inexact and thus no method can possibly extract the exact solution. However, as the errors in the original posed problem tend to vanish, the regularized solutions are designed to converge to the exact solution. The convergence can be weak, uniform, or of higher orders depending upon the order of regularization chosen.

The regularization method uses stabilizers to form a new regularizing operator to replace the original ill-posed operator. Different stabilizers produce different regularizing operators. Which type of stabilizers to use depends on the nature of the ill-posed problem. This method is widely used to solve many kinds of ill-posed problems such as the integral equations of the first kind and of the convolution type, optimum control, linear algebraic equations *etc.* Tikhonov used functional analysis and gave this method a rigorous mathematical deduction and proof. To introduce it in detail goes far beyond the scope of this paper. What

interests us here is how to use it to solve the ill-posed linear algebraic system:

$$A\theta = x. \quad (10)$$

If we use $\| \theta \|_2^2$ as the stabilizer, the regularization method minimizes the following functional

$$\| A\theta - x \|_2^2 + \alpha \| \theta \|_2^2 \quad (11)$$

where $\| x \|_2 = (\sum x_i^2)^{1/2}$ stands for the geometric norm (or 2-norm) of the vector x, and α is a positive constant and called the regularization parameter.

After some manipulations, the new equation used in the regularization is

$$(A^T A + \alpha I)\theta = A^T x, \quad (12)$$

where A^T is the transpose of matrix A and I is the unit matrix.

Note: If we use different stabilizers, we will get different equations. However, we want to minimize the corrector strengths in our case and hence choose $\| \theta \|_2^2$ as the stabilizer.

The matrix $A^T A$ in Eq. (12) is non-negative symmetric and its eigenvalues are non-negative. If we add a positive constant α to its diagonal, its eigenvalues will be greater or equal to α. If we select suitable α, the system of Eq. (12) becomes well-conditioned.

How to select α is very important in the real computations. The bigger the α is, the more stable Eq. (12) becomes and the farther the regularized solution is from the true solution. However, if the α is chosen too small, Eq. (12) would not be well-conditioned. If α equals zero, Eq. (12) becomes the normal equation of the least square method, which provides a way to solve an overdetermined or underdetermined linear system but does not address or control the ill-posedness of the problem.

4 Orbit Correction

In a circular machine, the orbit change due to a change in the corrector strengths is expressed as

$$A\theta = x. \quad (13)$$

where $\theta = [\theta_i], 1 \le i \le N_c, x = [x_j], 1 \le j \le N_m$, and matrix A is the $N_m \times N_c$ response matrix, N_m and N_c are number of monitors and correctors, respectively. Eq. (13) is widely used in the orbit correction.

Eq. (13) could be overdetermined ($N_c > N_m$), determined ($N_c = N_m$) or underdetermined ($N_c < N_m$). The least square method yields

$$A^T A\theta = A^T x. \quad (14)$$

Theoretically, Eq. (14) may have one solution or infinitely many solutions.

According to the analysis in the previous section, Eq. (14) is not well-conditioned. Since the dimension of matrix

$A^T A$ is N_c by N_c, how ill-posed is Eq. (14) mainly depends on how large N_c is. When doing study on our VUV and X-ray rings, it was found that in many cases if no more than some numbers of correctors were used, we could solve Eq. (14) directly. Once we used more than this number of correctors, bad oscillation started to occur and Eq. (14) started to give unreasonably large kick values. The more correctors were used, the worse the results became.

In order to combat the ill-posedness, several algorithms have been developed in the accelerator community.

- The Micado method [4] selects N (normally 2 to 4 in our operations) "most effective" correctors. That is, it does not solve the whole Eq. (14). Instead, it selects only a small number N equations in Eq. (13) and the dimension of the resulted normal equation Eq. (14) is N (2 to 4 in our case). Because the number of correctors used are very small, the ill-posedness is effectively controlled.

- Recently, the singular value decomposition (SVD) method has entered the orbit correction field [6, 7]. The SVD method is very powerful tool to solve least square problems. It not only diagnoses the problem, it also solves it. If the dimension of matrix A is large, its singular value set has very small numbers and possibly zeros. The SVD method simply ignores these small and zero singular values to control the ill-conditionedness.

The regularization method has been used successfully in the orbit correction in the NSLS storage rings both for study and operation.

According to the analysis in the previous section, This method solves the equation

$$(A^T A + \alpha I)\theta = A^T x, \tag{15}$$

instead of solving Eq. (14).

The key to a successful execution of the regularization method is choosing a good α, which depends on the degree of the ill-posedness of the problem and also depends on the magnitude of the elements in the matrix A. For example, suppose we selected a very good α to solve Eq. (15) and suppose now we use different units to measure the response matrix A and all elements in A become 10 times in magnitude of the original elements. The elements in the matrix $A^T A$ will be 100 times of the original values. In order to solve the new Eq. (15), the α has to be chosen 100 times larger.

In practice, we simply use the trial-and-error method to find the best α. At first, we pick a typical number in the matrix A and divide it by 3 or 4 and use the quotient as the initial guess of α. Normally, after a few trials, the α could be determined. Fortunately, once a good α is chosen, it could be used in successive sessions unless the lattice of the accelerator changed. Generally speaking, the resulting θ values are not very sensitive to α if it is not chosen too small. For example, when doing orbit correction on the

VUV ring, we use 0.2 as α for the vertical plane and 0.25 for the horizontal. While working on the X ray ring, 0.1 is used for both the vertical and horizontal planes. However, if we use 0.05 or 0.2 as α for the X ray ring, the results do not differ much. Let's take a case in the horizontal correction (55 correctors were used) of the X ray ring as an example. If $\alpha = 0.05$, the corrector kicks ranged from 3 to 460 digits, and the RMS difference after correction was 0.0605mm; if $\alpha = 0.10$, kicks 1 to 291 and RMS 0.0675; if $\alpha = 0.20$, kicks 3 to 185 and RMS 0.0750. Zero α gave unreasonably large kick values. The SVD method with optimization gave similar results. However, the Micado and harmonic methods were able to reduce the RMS to only 0.10 and 0.16, respectively. We have many similar data sets.

The regularization method not only makes the orbit correction process more stable, but also minimizes the corrector strengths. All the available correctors are used. The results show that it uses much smaller corrector strengths than the traditional methods and gives very good corrections. Generally speaking, The results generated by the regularization method are comparable with the SVD method with optimization, and better than the harmonic [5] and Micado method.

5 Concluding Remarks

We have discussed applying the regularization method of Tikhonov to the solution of inverse problems arising in accelerator operations. This approach has been successfully used for orbit correction on the NSLS storage rings. We have obtained high precision correction with weak corrector strength, eliminating the "fighting" of corrector against one another. In this case, the regularization method corresponds to a least square minimization of the orbit deviations, with an additional constraint to minimize a weighted measure of the corrector strengths.

At present, we are applying this method to the determination of betatron functions and phase from the measured response matrix

$$A_{ij} = \sqrt{\beta_i \beta_j} \cos \nu \left(|\phi_i' - \phi_j| - \pi \right) \tag{16}$$

Preliminary results seem promising and we hope to report on this work in the future.

I. References

[1] E.D. Courant and H.S. Snyder, Annals of Phys., 3, No. 1, p. 1–48, (1958).

[2] A. N. Tikhonov etc, Solutions of Ill-Posed Problems, John Wiley and Sons, New York (1977).

[3] Y. M. Chen, Inverse Problems, Lecture notes, SUNY at Stony Brook, New York (1984).

[4] B. Autin and Y. Marti, CERN ISR-MA/73-17 (1973).

[5] A. Jackson, SRS/NS/76/103 (1976).

[6] E. Bozoki and A. Friedman, In this proceeding.

[7] Y. Chung, G. Decker, In this proceeding.

Automatic Differentiation of Limit Functions

Leo Michelotti

Fermilab*, P.O.Box 500, Batavia, IL 60510

Abstract

Automatic differentiation can be used to evaluate the derivatives of and set up Taylor series for implicitly defined functions and maps. We provide several examples of how this works, within the context of the MXYZPTLK class library, and discuss its extension to inverse functions.

I. INTRODUCTION.

The techniques of automatic differentiation [2] and differential algebra [1, 3, 9] are rapidly becoming a standard part of accelerator physicists' arsenals. That automatic differentiation can be used to calculate the derivatives of recursively or iteratively[1] defined functions is not as well appreciated as it should be. Applying recursive algorithms directly to DA variables[2] provides an easy method for obtaining derivatives of such functions. In the following sections we shall (a) sketch the essential argument needed to prove this assertion, (b) discuss two examples written using the C++ classes in MXYZPTLK [5, 6], and (c) provide C++ code fragments for a general program. This paper builds on work done previously [7] but remains necessarily short. Applications of the techniques described are too numerous to mention and so obvious that there is no need to do so.

II. HEURISTICS FOR A PROOF

Following [7], a mathematically correct proof that recursions can be extended to DA variables was published by Gilbert [4] for single derivatives; its extension to higher derivatives is implied. The proof's correctness makes it

---

*Operated by the Universities Research Association, Inc. under contract with the U.S. Department of Energy.

[1] I confess to being confused about the distinction between "recursive" and "iterative."

[2] A DA variable carries information about derivatives of functions as well the value of the functions. It is a computer implementation of a "jet" structure [8].

---

formal, and how it works is not obvious to naive intuitionists. It is hoped that the following heuristic argument will be easier to understand while retaining essential points of the proof.

Let $f : R \to R$ possess a fixed point, x^*. The sequence $x_{n+1} = f(x_n)$, started "close enough" to x^*, converges to x^* provided that $|f'(x^*)| < 1$. Now consider the recursion,

$$x_{n+1}(m) = F(x_n(m), m) , \qquad (1)$$

and assume that it converges to a fixed point, $x^*(m)$, for a given m. This requires that

$$x^*(m) = F(x^*(m), m) \text{ and } |\partial_1 F(x^*(m), m)| < 1. \quad (2)$$

Differentiating both Eqs.(1) and (2), we get the following result.

$$x^{*'}(m)(1 - \partial_1 F(x^*(m), m)) = \partial_2 F(x^*(m), m)$$

$$x'_{n+1} = x'_n \partial_1 F(x_n, m) + \partial_2 F(x_n, m) ,$$

where primes denote differentiation with respect to m, and ∂_k means differentiation with respect to the kth argument. The defect between x'_{n+1} and $x^{*'}(m)$ can therefore be estimated as follows.

$$
\begin{aligned}
x'_{n+1} - x^{*'}(m) &= (x'_n - x^{*'}(m)) \partial_1 F(x_n, m) \\
&\quad - [x^{*'}(m)(1 - \partial_1 F(x_n, m)) - \partial_2 F(x_n, m)] \\
&\approx (x'_n - x^{*'}(m)) \partial_1 F(x^*(m), m) \\
&\quad - [x^{*'}(m)(1 - \partial_1 F(x^*(m), m)) - \partial_2 F(x^*(m), m)] \\
&= (x'_n - x^{*'}(m)) \partial_1 F(x^*(m), m)
\end{aligned}
$$

As long as Eq.(2) is satisfied, i.e., as long as the *original sequence converges to a fixed point*, the defect decreases and $\lim_{n \to \infty} x'_n = x^{*'}(m)$. Higher derivatives work as well. The important thing is to recognize that simultaneously,

$$
\begin{aligned}
x^{*[k]}&(m)(1 - \partial_1 F(x^*(m), m)) \\
&= \Lambda(x^{*[k-1]}(m), x^{*[k-2]}(m), \ldots, x^*(m), m) , \text{ and} \\
x^{[k]}_{n+1} &= x^{[k]}_n \partial_1 F(x_n, m) + \Lambda(x^{[k-1]}_n, x^{[k-2]}_n, \ldots, x_n, m) .
\end{aligned}
$$

The demonstration of a convergent sequence then goes through exactly as with the first derivative. The *only*

condition that enters into play is Eq.(2), which is nothing more than the original requirement of convergence. These arguments still go through for a dimension greater than one, but the condition Eq.(2) becomes a statement about the spectral radius of the Jacobian, $\underline{\partial F}(\underline{x}^*(\underline{m}), \underline{m})$.

III. IMPLICIT FUNCTIONS

Consider the function $x(m)$ defined implicitly by the equation

$$x(m) = \cos(m \cdot x(m)) \quad . \qquad (3)$$

Simple recursion can be used to construct $x(m)$ for m in the approximate range, $m \in (-1.2, 1.2)$, determined by the condition $|m\sin(m \cdot x(m))| < 1$. A fragment of source code that uses the MXYZPTLK DA object (class) to implement this is shown below.

```
coord m ( 0.5 );
DA x;
x = cos( m );
for( i = 0; i < 15; i++ ) x = cos( m * x );
```

This example used a coord variable for m, set to evaluate derivatives of $x(m)$ at $m = 0.5$. coords are the atomic DA variables used to start calculations, basically the implementation of a projector. The behavior of the weighted derivatives — which would be the coefficients in a power series representation of $x(m)$ — is shown in Figure 1; the first five are plotted versus loop index. Convergence is seen to be rapid, although, as suggested by the proof, a derivative does not begin to converge until the ones at lower order have already done so.

IV. INVERSE FUNCTIONS

One of the most frequent application of recursion is to compute the inverse of a given function. For example, applying Newton's method to the equation $\tan(x(m)) = m$ provides the recursion

$$x_{n+1} = x_n - \cos x_n (\sin x_n - m \cos x_n) \quad ,$$

which converges to the function $x(m) = \arctan m$.[3] The recursion can be applied *directly* to DA variables. Using MXYZPTLK, the following short, simple C++ program follows the recursion explicitly through six steps and prints out the value and derivatives of x for a given value of m.

```
#include "mxyzptlk.rsc"
main( int argc, char** argv ) {
  const int dim      = 1;
  const int maxWeight = 5;
  DASetup( dim, maxWeight, dim );
  double a = atof( argv[1] );
```

---

[3] As an acceptable seed, we could set $x_0(m) = m$ when $|m| \le 1.4$ and $x_0(m) = 1.4$ when $|m| > 1.4$.

```
  coord m ( a );
  DA x, s, c;
  int i, j, d[1];
  x = m;
  for( i = 0; i < 6; i++ ){
    s = sin( x );
    c = cos( x );
    x = x - c*( s - m*c );
    printf( "%-7.4lf  ", x.standardPart() );
    for( j = 1; j < 6; j++ ) {
      d[0] = j;
      printf( "%-7.4lf  ", x.derivative(d) );
    }
    printf( "\n" );
  }
}
```

When compiled and run with a command line argument of 1.2 it produced the output lines:

1.0198	1.0581	1.7697	4.7170	-1.6753	-30.666
0.9027	0.6776	1.9990	19.1460	119.009	531.937
0.8769	0.4280	-0.0384	7.3912	124.051	2092.93
0.8761	0.4099	-0.4015	0.5231	2.2807	101.790
0.8761	0.4098	-0.4031	0.4571	-0.3575	-0.8372
0.8761	0.4098	-0.4031	0.4571	-0.3575	-0.8414

Notice the repetition of the earlier pattern: derivatives settle down to their limiting value in sequence. In particular, the highest order derivatives can undergo unsettlingly large excursions before convergence kicks in. However, this is not a danger, as evaluation of higher order derivatives could be suppressed, if needed, until the lower order ones have converged.

The wonderful thing is that we could start the recursion using any DA variable for m, not just atomic projectors. We could, for example, use a code fragment like the following

```
coord y ( ay ), z ( az );
DA m, x, s, c;
m = sqrt( y*y + z*z );
x = m;
while( x.isChanging() ){
  s = sin( x );
  c = cos( x );
  x = x - c*( s - m*c );
}
```

to find derivatives of $\arctan \sqrt{y^2 + z^2}$ evaluated at $(y, z) = (\text{ay}, \text{az})$. This little loop thus becomes the computational core of a DA -valued function that returns the arctangent of any DA argument.

V. A GENERAL PROGRAM

Because DA variables possess a differentiation operation, Newton's method can be used to write a general method that works with "arbitrary" DA functions F. The key line that sets up the solution[4]

---

[4] This is written inefficiently; it would be better to avoid evaluating F twice.
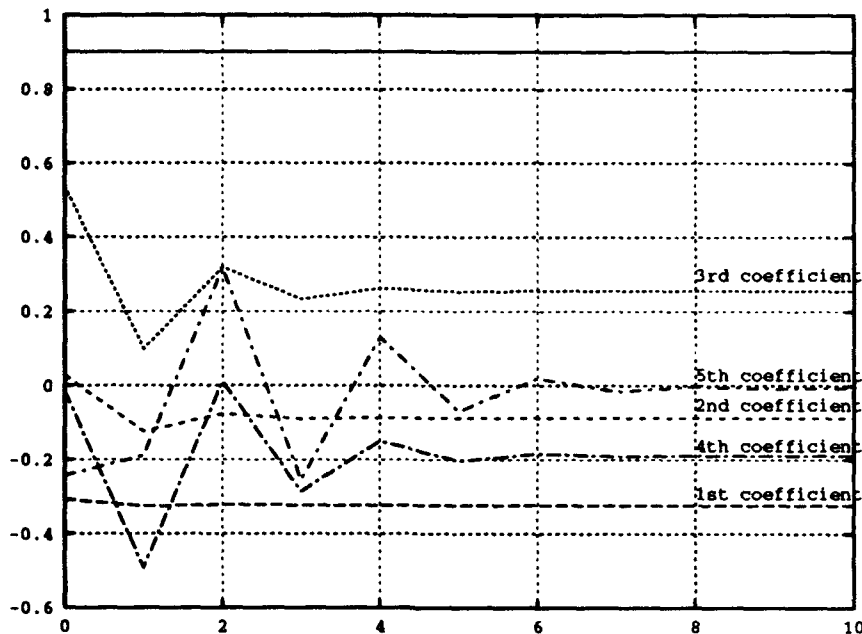
Figure 1: Behavior of the coefficients with iteration number.

```
G = x - ( F(x) / F(x).D(n) );
```

where G and x are DA variables, F is a DA -valued function of a DA argument, and .D is the differentiation operator.[5] G will be a DA variable corresponding to a single Newton step. Once it is constructed, iterating the line

```
x = G.multiEval( x );
```

will make x, with all its derivatives, converge to a zero of F. To repeat the example of Eq.(3), we then define

```
DA F( DA& x ) { return ( x - cos( m*x ) ); }
```

before entering the main function. The complete program, although short (about 60 lines) is too long to be included here. For those would like to experiment with the program and who have a C++ compiler, it and the MXYZPTLK package can be obtained *as is* via anonymous ftp from calvin.fnal.gov in the directory /pub/outgoing/michelotti/mxyzptlk or /pub/outgoing/michelotti/beamline.[6]

REFERENCES

[1] Martin Berz. Differential algebraic description of beam dynamics to very high orders. *Particle Accelerators*, 24(2):109, March 1989.

[2] G. Corliss and A. Griewank, editors, *Automatic Differentiation of Algorithms: Theory, Implementation, and Application.* SIAM, 1991. Philadelphia, PA.

[3] Etienne Forest, Martin Berz, and John Irwin. Normal form methods for complicated periodic systems: A complete solution using differential algebra and lie operators. *Particle Accelerators*, 24:91, 1989.

[4] Jean Charles Gilbert. Automatic differentiation and iterative processes. *Optimization: Methods and Software*, 1(1):13–21, 1992.

[5] Leo Michelotti. MXYZPTLK and BEAMLINE: C++ objects for beam physics. In *Advanced Beam Dynamics Workshop on Effects of Errors in Accelerators, their Diagnosis and Correction. (Corpus Christi, Texas. October 3-8, 1991).* American Institute of Physics, 1992. Conference Proceedings No.255.

[6] ———— MXYZPTLK: A practical, user-friendly C++ implementation of differential algebra: User's guide. Fermi Note FN-535, Fermilab, January 31, 1990.

[7] ———— A note on the automated differentiation of implicit functions. Technical Memo 1742, Fermilab, June, 1991.

[8] Gordon Pusch. Private communication.

[9] Joseph Fels Ritt. *Differential Algebra.* American Mathematical Society, New York, 1950.

---

[5] n is an integer array needed by .D; essentially, n tells .D which derivative is desired.

[6] These files may be moved eventually.

Corrector Ironing in the SLC Final Focus*

V. Ziemann
Stanford Linear Accelerator Center
Stanford University
Stanford, Ca. 94309

Abstract

A method to minimize corrector excitations while maintaining a set of constraints on the orbit is described. This method, which is based on a singular value decomposition algorithm, was successfully applied in the final focus of the Stanford Linear Collider in order to remove "fighting correctors" and improve their tuning range.

I. INTRODUCTION

In beam lines with a large number of corrector magnets individual corrector excitations can acquire large values while the orbit remains bounded. In this case the effect of different correctors cancel. Having correctors at large values is operationally inconvenient, because it limits the range of correction. Here we describe an algorithm which minimizes the sum of squares of corrector excitations and, at the same time, maintains orbit constraints, such as position or angle at certain points in the beam line.

II. ALGORITHM

First we have to find out how each corrector affects each constraint. In linear beam lines the response of the orbit at one point to a corrector upstream is given by the transfer matrix elements R_{pq} between the corrector and the constraint point. In general the total effect of all correctors on the constraint is then

$$c_i = \sum_j R_{p(i),q(j)}\Theta_j = \sum_j A_{ij}\Theta_j \qquad (1)$$

where $p(i) = 1,3$ if we have a x/y-position constraint and $p(i) = 2,4$ if we have a x/y-angle constraint. $q(j) = 2$ if corrector j is a x-corrector and $q(j) = 4$ if it is a y-corrector. Θ_j is the kick angle of corrector j. We will call the matrix A the *response matrix* and the vector c the *constraint vector*. Note that in the case where we have more correctors than constraints the matrix A has more columns than rows and we are dealing with an *under determined linear system*.

Assume now that we have a corrector configuration with corrector strengths $\bar{\Theta}_j$. The objective is to find new corrector strengths Θ_j such that the constraints are maintained and that $\sum_j \Theta_j^2$ is minimum. The first objective can be fulfilled by making Θ_j the solution of

$$\sum_j A_{ij}\bar{\Theta}_j = \sum_j A_{ij}\Theta_j . \qquad (2)$$

We require that the new corrector values Θ_j must produce the same constraint vector as the old corrector values $\bar{\Theta}_j$.

The second objective, namely to make $\sum_j \Theta_j^2$ minimum is automatically fulfilled by using a *Singular Value Decomposition* (SVD) Algorithm [1] to solve eq. 2. SVD finds a solution to eq. 2 and also explicitly constructs the null space of the under determined linear system. It then subtracts the projection of the solution onto the null space from the solution and thereby minimizes the norm of the solution [1], i.e. $\sum_j \Theta_j^2$.

Note that we can simply add an extra vector to the left hand side of eq. 2 to modify the orbit at one constraint point, e.g. to steer through the center of magnets with known misalignments.

III. APPLICATION

The algorithm described in the previous section is implemented in a computer code that reads the

quadrupole and corrector values in the Final Focus of the Stanford Linear Collider (SLC). It then updates an offline model of the beam line and generates a table with the current corrector values and a few sample constraints. The user can then remove correctors he does not want to include in the ironing process and can also modify the constraints. This table is then used to set up the response matrix A and constraint vector c and subsequently performs the singular value decomposition using routines from ref. 1. Finally the new corrector values are printed, the old and new orbits are displayed and a file is generated that can be read by the SLC control system to linearly interpolate the corrector values from the old to the new configuration.

We have applied this algorithm successfully to the correctors near the interaction point (IP) which had acquired large values. Here we choose the constraint that the horizontal and vertical position and angle of the orbit at the IP and the position in two sextupoles are to remain fixed for a total of eight constraints. All ten included correctors were allowed to vary. The procedure brought the rms of the 10 included correctors down to 30 % of their initial value. Despite ing. Despite the rather large predicted orbit changes in the intermediate region beam position monitor readings downstream of the affected region showed very little changes. The newly found corrector configuration proved to be operationally more convenient, because the correctors' tuning range were increased considerably.

IV.   Conclusion and Outlook

We have described an algorithm to minimize corrector strengths in beam lines which contain more correctors than orbit constraints. The method was implemented in a computer code and applied to correctors near the IP of the SLC. The rms of the involved correctors was successfully reduced to 30 % of their initial rms.

We need to note that the method relies on an accurate knowledge of the optics of the beam line as determined by the quadrupole lattice, because the trading off of corrector effects depends strongly on the transfer matrices between the correctors and the constraint points.

This method is directly applicable to circular accelerators. Either by constraining position and angles at one point the modification of the corrector configuration can be made transparent to the rest of the accelerator. In this way the corrector changes act similar to a local closed orbit bump. Alternatively, instead of using the transfer matrices R in eq. 1 one can use the closed orbit response coefficient matrix $C = R(1 - S)^{-1}$ where S is the one turn transfer map starting at the corrector. In this case the bump is not closed but the constraints are still satisfied.

The described algorithm can easily be extended to incorporate other constraints such as fixed vertical position at the end of a synchrotron radiation (photon) beam line of length L. In this case the response matrix element A_{ij} between corrector j and the special constraint reads $R_{34} + L R_{44}$. The presented method was adapted for SPEAR and successfully used in the initial setup of SPEAR after a long shut down [2]. In general the response matrix element is the derivative of the constraint condition (the quantity to remain unaffected) with respect to the corrector strength. Following this prescription very general constraints can easily be included.

Acknowledgements

References

1. W. Press, ‹   ι., *Numerical Recipes*, Section 2.9, Cambridge University Press, Cambridge, 1986.

2. W. Corbett, et. al., *Optimum Beam Steering of Photon Beam Lines in SPEAR*, these proceedings.

General Normal Form Procedure to Correct Tune–Shift and Non–Linear Chromaticity for Large Accelerators like the LHC

M. Giovannozzi and F. Schmidt
SL Division, CERN
CH 1211 - Geneva 23

Abstract

In future hadron colliders such as the LHC very high fields are needed to reach the design energy. Only super-conducting magnets can produce such high fields and only at the cost of strong multipolar errors up to high order. This leads to a large non–linear shift of the tunes (detuning) both in amplitude and momentum, which may forbid a safe operation of the accelerator. The best solution to decrease these effects is to introduce a quasi–local correction via placing a set of non–linear elements in each cell near the source of the errors. A sequence of programs were used to perform this kind of correction. SIXTRACK was used to produce the high order transfer map in five variables using the DA–package of Berz. The tune–shift functions are derived with the Lielib package of E. Forest. Then, based on the approach proposed by A. Bazzani and G. Turchetti and first applied by E. Todesco, we developed a correction procedure to minimise these detuning functions up to fifth order (decapole contribution) considering four–dimensional tune–shift with the momentum deviation as a parameter. For different machine versions we computed correction schemes and compared the results with tracking simulations. In all cases a considerable improvement of the detuning was established.

I. INTRODUCTION

In the design of magnets for the new accelerators one can not completely avoid high order multipole errors which limit the dynamic aperture of these new machines. The strategy to tackle this problem is twofold: one has to set reasonable specifications for the magnet errors and propose a proper correction scheme for the residual non–linear content of the magnets. In both cases a profound knowledge of the sources for the aperture limiting effects is needed. A good indicator of the nonlinearity of the machine is the tune–shift as a function of amplitude and momentum. The correction schemes will deal with minimizing the detuning. The straightforward approach is to carry out the optimization by tracking methods [1]. In that process it is not obvious how the different multipole components enter into the detuning functions especially when there are interfer-

ing terms.

There are different analytical methods to derive the tune–shift as a function of multipole errors and phase space co-ordinates. One of the possible approaches is using normal forms [2, 3]. This choice has the convenient advantage that there are ready–to–use software packages [4, 5] to attack the problem.

II. CORRECTION METHOD

The correction procedure is carried out using an order–by–order approach. We first determine the values of the sex-tupolar correctors needed to optimize the first order tune–shift. Then the computation of the decapoles is carried out working on the second order tune–shift. The approach used can deal with both amplitude–dependent contribution in the tune–shift and momentum–dependent effects (at the present the correction of the mixed terms is not considered but it is possible as well). In the former case there are $i + 2$ coefficients at order i, while in the later one there are always only two coefficients which we denote by $\alpha_{x,i}(K_l), \alpha_{y,i}(K_l)$ where K_l is the integrated gradient of order l. Given a sufficient number of free correctors it is in principle possible to set to zero the tune–shift at order i. If this can not be fulfilled we can always define a norm in the tune–shift space which we can try to minimize. The choice commonly used [3, 6, 7] is:

$$\chi_{i,0}^2 = \frac{1}{R^{2i+1}} \int_{\rho_1+\rho_2=R} [\delta\nu_{x,i}(\rho_1,\rho_2;K_l)]^2 \, d\rho_1 d\rho_2$$
$$+ \frac{1}{R^{2i+1}} \int_{\rho_1+\rho_2=R} [\delta\nu_{y,i}(\rho_1,\rho_2;K_l)]^2 \, d\rho_1 d\rho_2 \quad (1)$$

for the amplitude–dependent case, where $\delta\nu_{x,i}, \delta\nu_{y,i}$ are the horizontal and vertical tune–shift functions at order i respectively. For the momentum–dependent effect we use:

$$\chi_{0,i}^2 = [\alpha_{x,i}(K_l)]^2 + [\alpha_{y,i}(K_l)]^2. \quad (2)$$

Both $\chi_{i,0}, \chi_{0,i}$ are low order polynomial functions of the integrated gradients K_l only. Therefore the correction strategy does not depend on a particular value of ρ_1, ρ_2, δ, but represents a global minimization over the whole phase space.

The computation of the functions $\chi_{i,0}, \chi_{0,i}$ is carried out using SIXTRACK [8] and the Lielib package of E. Forest [5]. As a first step the one turn transfer map is produced including δ and the corrector strength as additional parameters. The result is a polynomial map in $N_{cor} + 5$ variables, where N_{cor} is the number of free correctors. Then the tune–shift is computed using Lie–algebraic techniques. Finally we have added a special routine to minimize $\chi_{i,0}, \chi_{0,i}$.

III. LATTICE MODEL

We consider two realistic models of the LHC including the differences between odd and even octants as well as insertions each having a different purpose. The differences between the models consist mainly in the cell layout. In the first case (LHC version 1) there are eight dipoles per cell and two central correctors consisting of sextupole, octupole and decapole magnets. Near the cell quadrupoles there are additional correctors. In this case the sextupoles are used to set to zero the linear chromaticity.

In the second case (LHC version2) there are only six longer dipoles per cell and each of them has a corrector at both ends: a sextupole and a decapole. Again additional sextupoles are placed near the focusing and defocusing quadrupoles to correct the linear chromaticity.

As far as the errors are concerned only the contributions due to the dipoles have been taken into account. The values of the systematic multipole errors forseen for the LHC dipoles and used in our studies are listed in Table 1.

Table 1

Normal dipole field errors in units of 10^{-4} at $R_r = 10mm$

Order n	Systematic at injection LHC Version 1	Systematic at injection LHC Version 2
0	–	5.00
1	−1.40	±1.15
2	−3.35	−2.19
3	±0.05	±0.11
4	0.45	0.34

The double sign is a feature introduced by the two–in–one geometry of the magnets and it produces a change in the sign of the error from odd to even octants. Therefore in the case of the octupole components there is a sort of self–compensation of the error along the whole ring. Because of this symmetry we decided to introduce in our models only the sextupole and decapole components of the field errors.

IV. CORRECTION SCHEMES FOR DIPOLE ERRORS

Each correction scheme has to take care of linear chromaticity. This imposes a linear relation between the sextupoles and it fixes the values of the chromatic correctors

as a function of the M cell correctors

$$\begin{cases} K_{2,F} = \alpha_F + \beta_{1,F}K_{2,1} + \cdots \beta_{M,F}K_{2,M} \\ K_{2,D} = \alpha_D + \beta_{1,D}K_{2,1} + \cdots \beta_{M,D}K_{2,M} \end{cases} \quad (3)$$

Therefore the number of free correctors available to minimise $\chi_{i,0}, \chi_{0,i}$ is reduced. For the LHC version 1 there are three free correctors:

$$K_{2,C}, K_{4,C}, K_{4,D} \quad (4)$$

The decapoles near the cell quadrupoles have been set equal $K_{4,D} = K_{4,F}$ so that the mid–cell symmetry is not broken. In this case we can fix the value of $K_{2,C}$ by minimizing the first order tune–shift (amplitude or momentum). The decapoles can then be used either to correct exactly the second order momentum–dependent tune–shift or to optimise $\chi_{2,0}$. The results are showed in Fig. 1: solid lines represent the detuning computed with normal forms, while dashed lines are obtained by direct tracking. The
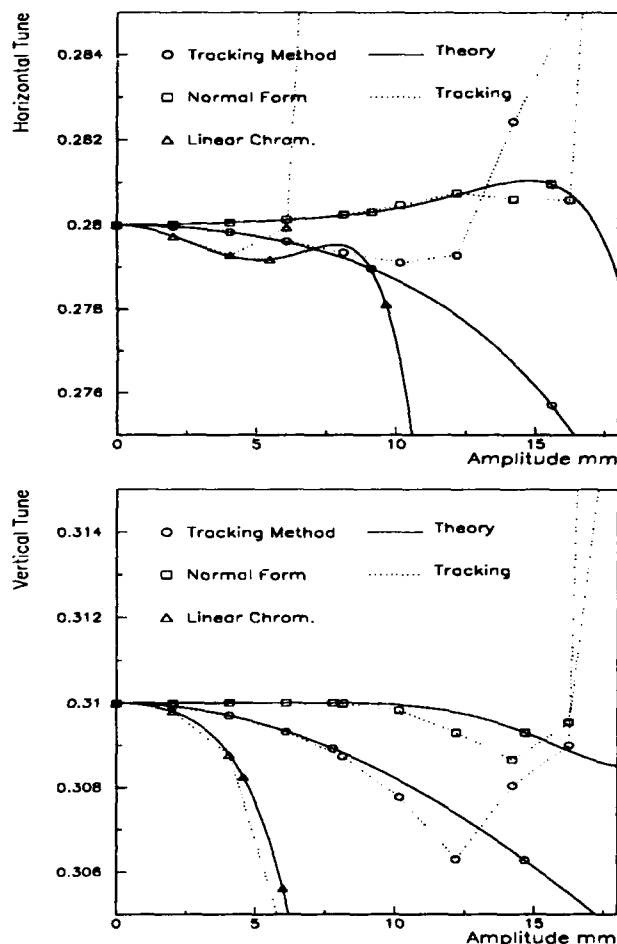
Figure 1: Detuning curves for LHC Version 1

tune–shift of the machine in which only the linear chromaticity is corrected and the results of a tracking–based

correction [1] is shown. Due to the better control on the higher order terms the normal form procedure allows to correct the machine so that a good agreement with the tracking can be found up to the dynamic aperture.

The scheme used for the second lattice, LHC version 2, is completely different. Only two free correctors are used:

$$K_{2,C}, K_{4,C} \qquad (5)$$

in order to reduce the number of independent power supplies needed. In this situation the only choice is to minimise one of the functions $\chi_{i,0}, \chi_{0,i}$ using the two correctors. Due to the quasi–locality of the optimisation scheme, correcting one of the two tune–shift functions (amplitude or momentum) implies a good correction of the other one (this holds also for LHC version 1). However for the latest version there are cases in which one correction type disturb the other. We found that dropping the concept of having a mid–cell corrector has the price that the effectiveness of the sextupole correction is reduced (compare the corresponding curves in Figs. 1,2).

The situation concerning the correction of the second order tune–shift with the decapoles is different. The correction can be performed almost perfectly. The reason for this difference is the fact that the sextupole strengths enter quadratically in the first order tune–shift, while the second order detuning functions depend linearly on the decapoles. It is interesting to stress that the results of the second order optimisation depend on a good correction of the first order detuning because this reduces the interfering terms between sextupoles and decapoles: without this precondition it would be very difficult to achieve an optimal solution using decapoles. The results are shown in Fig. 2 where we compare two different sets of correctors obtained by minimising $\chi_{1,0}$ and $\chi_{2,0}$ or by using $\chi_{0,1}$ and $\chi_{0,2}$. Besides the problems with the sextupole stated above also in this case a satisfactory correction has been achieved.

V. CONCLUSIONS

We have shown the effectiveness of the normal form approach to correct the tune–shift due to field errors. Both the amplitude-dependent and the momentum–dependent tune–shift can be corrected applying this technique. However, we would like to stress that these correction results have always to be tested against tracking results. This is necessary to avoid solutions which are dynamically not acceptable.

Finally a user–friendly option to perform these corrections in SIXTRACK is in preparation.

ACKNOWLEDGEMENTS
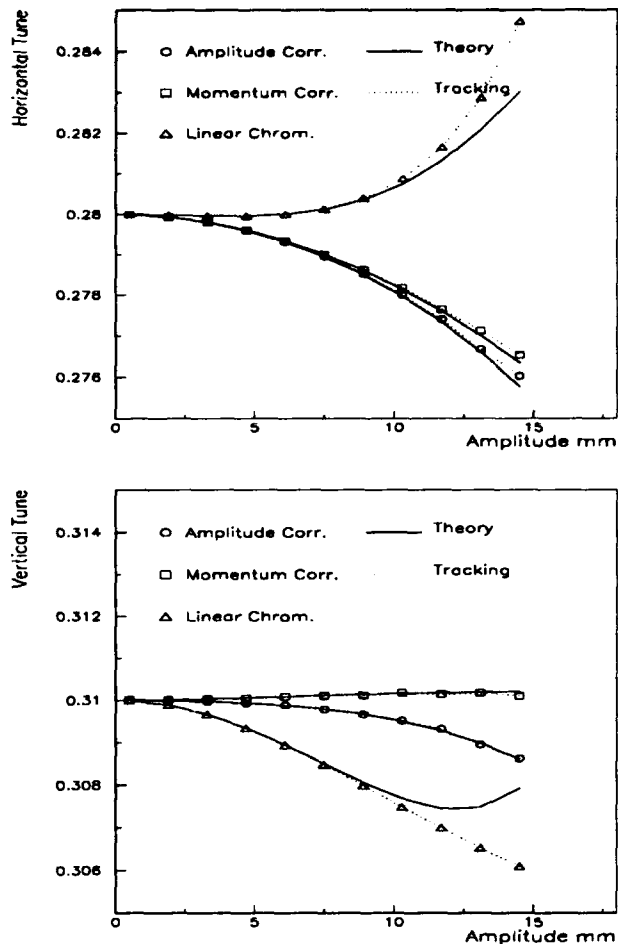
Figure 2: Detuning curves for LHC Version 2

REFERENCES

[1] F. Galluccio, W. Scandale, CERN/SPS/89-51 (AMS) (1990).

[2] A. Bazzani, P. Mazzanti, G. Servizi, G. Turchetti, Il Nuovo Cim., No. 102 B, 51 (1988).

[3] E. Todesco, University of Bologna Master Thesis (1990).

[4] M. Berz, Part. Accel., No 24, 109 (1989).

[5] M. Berz, E. Forest, J. Irwin, Part. Accel., No 24, 91 (1989).

[6] W. Scandale, E. Todesco, F. Schmidt, Part. Accel., No. 35, 53 (1991).

[7] M. Giovannozzi, University of Bologna PhD Thesis (1992).

[8] F. Schmidt, CERN/SL/91-52 (AP) (1991).

Review of recent optical issues in LEP

F. Ruggiero,
CERN
CH-1211 Geneva 23

Abstract

We review some optical measurements and correction strategies adopted for the new lattice with 90° phase advance used in LEP during 1992. In particular, we compare three different techniques used to measure beta-beating: a multi-turn orbit measurement in presence of betatron excitation, a method based on the variation of chromaticity due to opposite trims in the strength of two sextupole families and an orbit measurement with two orthogonal kicks. The average vertical beating measured by these three methods (up to 37%, depending on the optical configuration) shows a substantial agreement among them. We also discuss a resonant method of correction for residual dispersion by special orbit bumps. The amplification factors for such bumps range from 200 to more than 700, i.e., a 1 mm orbit bump can give rise to more than 70 cm peak dispersion and these bumps have been routinely used to control beam size and optimize machine performance without any appreciable effect on the closed orbit.

I. MEASUREMENTS OF BETA-BEATING

During 1992, the behaviour of the beta-functions in LEP did not correspond to the theoretical predictions. In particular, for an optical configuration supposed to yield a vertical beta value of 5 cm at the IP's, the actual measured beta value was around 7 cm. This effect was corrected by applying an empirical trim $\Delta K/K = 7.24 \times 10^{-4}$ to the strength of the low-beta quadrupoles (QS0's). A more general study of the associated beta-beating was then started to understand the origin of such discrepancies and their consequences on the available aperture of the machine. The three different techniques used to measure the beating of the beta-functions [1] are described below.

A. Multi-turn orbit measurement

This method consists in the analysis of the turn by turn readings of the monitors (up to 1024 turns) in presence of betatron excitation. The data is then Fourier analyzed at the excitation frequency (usually close to the betatron frequency) yielding the amplitude and phase of the driven betatron oscillations around the machine [2].

B. Sextupole method

The strength of one of the two defocussing sextupole families (SD1) is increased by some amount, whereas the strength of the second family (SD2) is decreased by the same amount. This should leave the vertical chromaticity

Q' of the machine unchanged if the β-values are the same in all the SD sextupoles, since the phase advance between two successive SD2 is π (this still holds in case of beating of the dispersion). The variation of chromaticity is related to the difference between the vertical β's at the SD1 and SD2 sextupoles by [3]:

$$\Delta Q' = \frac{1}{4\pi} D_{x,SD} L_{SD} \Delta K'_{SD1}(\beta_{SD2} - \beta_{SD1}).$$

C. Orthogonal kicks

Closed orbit distortions are created by subsequently exciting two corrector magnets with a phase advance of $\pi/2$ between them. In an ideal machine without beating, squaring the readings of the two orbits and adding them eliminates the phase-dependent term in the orbit response, and directly yields the values of the β-function. In presence of beating, however, the values β_1 and β_2 at the two correctors may be different and the phase advance between them may deviate from the nominal value $\pi/2$ by some amount ϵ. In general, the β-function is given by

$$\beta(s) = ay_1^2(s) + by_2^2(s) + cy_1(s)y_2(s),$$

where $y_1(s)$ and $y_2(s)$ denote the measured (difference) orbits corresponding to the excitation of each corrector and the three coefficients a, b and c have the following theoretical values:

$$a = F/\beta_1, \qquad b = F/\beta_2, \qquad c = -2F\sin(\epsilon)/\sqrt{\beta_1\beta_2}.$$

Here $F = [2\sin(\pi Q)/\cos(\epsilon)\Delta y']^2$ and $\Delta y'$ is the common (angular) strength of the two correctors.

The coefficients a, b and c have been estimated using two independent methods, both giving the correct result when applied to orbits simulated with MAD. The first method makes use of the (vertical) orbit values $y_1(s_1)$, $y_2(s_2)$ at the PU's closest to the correctors in order to obtain β_1 and β_2. It can be shown that the 'cross terms' $y_1(s_2)$ and $y_2(s_1)$ should have the same value y_{12} given by

$$y_{12} = \frac{1}{2}\Delta y' \sqrt{\beta_1\beta_2} \left[\frac{\sin(\epsilon)}{\tan(\pi Q)} + \cos(\epsilon) \right].$$

Therefore the equality of the cross terms can be used as a self-consistency test and ϵ can be estimated from their common value y_{12}. This method is independent of the nominal β-function, but requires the measured tune Q.

A second method to estimate the coefficients a, b and c consists in a five-parameter fit of the nominal β-function

$$\beta_N = ay_1^2 + by_2^2 + cy_1y_2 - \beta_N \left[A\cos(2\phi_N) + B\sin(2\phi_N) \right],$$

Octant	$\beta_y^* = 21$ cm multi-turn	kicks	$\beta_y^* = 7$ cm multi-turn	kicks	$\beta_y^* = 5$ cm multi-turn	kicks
1	19	17	41	41	16	19
2	14	15	42	40	18	24
3	9	6	33	29	6	12
4	11	5	34	29	7	11
5	10	4	34	28	12	9
6	7	9	32	33	9	14
7	16	4	42	30	24	10
8	13	6	40	36	18	14
$\langle \Delta\beta/\beta \rangle$	12	8	37	33	14	14
sextupoles	9		37		13	

Table 1: Vertical beta-beating (in per cent) for the detuned optics, for the nominal squeezed optics and for the squeezed optics with trimmed QS0's: results for multi-turn analysis and orthogonal kicks are octant by octant, while only the average beating is given for the sextupole method.

where the harmonic terms in square bracket take into account the beating at twice the nominal betatron phase ϕ_N. Applying this method to simulated orbits, we have found that the correlation of the fit becomes poor when the beta-beating is produced by a few localized sources (e.g. QS0's), but that a good correlation can be recovered by introducing a different harmonic amplitude for each arc: therefore we effectively perform a fit with 3 plus 8 parameters. This method is more stable against PU noise, since it makes use of the information at all the PU's, but the resulting amplitude of beta-beating in each arc depends somewhat on the criterion adopted for the rejection of bad PU's.

We have used the first method to have a rough estimate of a, b and c: then we have discarded monitors where $\Delta\beta/\beta$ was larger then 3 times its r.m.s. value and finally we have used the second method, based on the fit, to arrive at our final result. Typical values for a, b and c were 1.5, 1 and 0.25, respectively, thus showing a significant deviation from the simple rule of summing the squares of the two orbits.

D. Comparison of the results

In Table 1, we report the vertical beta-beating measured by the multi-turn and by the orthogonal kick method in each LEP octant for three different optics, together with the corresponding average beating measured by the sextupole method. In Table 2, which refers to a perturbed squeezed optics, the results of the sextupole method are reported quadrant by quadrant. The average vertical beta-beating measured by our three independent methods shows a substantial agreement among them, with the results of the sextupole method typically lying below those of the multi-turn and above those of the orthogonal kicks. The comparison of the beating amplitudes octant by octant suggests a larger spread in the results of the three methods, possibly associated with the criterion adopted for bad PU rejection. Finally, all methods confirm a large vertical beating for the nominal machine with $\beta_y^* = 7$ cm and a significant reduction of this beating as a consequence of

the trim applied to the QS0 magnets in order to bring β_y^* down to 5 cm.

During the last LEP shutdown, the longitudinal position of the QS0 and QS1 magnets was found to be wrong by significant amounts (up to 9 mm). According to recent simulations [4], these quadrupole shifts are largely sufficient to explain the observed beta-beating.

Octant	multi-turn	kicks	sextupoles
1	22	16	22
2	22	18	
3	20	10	15
4	20	12	
5	21	14	23
6	25	20	
7	33	18	22
8	29	23	
$\langle \Delta\beta/\beta \rangle$	24	16	20

Table 2: Vertical beta-beating (in per cent) for the perturbed optics with $\beta_y^* = 5$ cm and KQS0.L2= -0.0004: multi-turn analysis, orthogonal kicks and results of the sextupole method (in each quadrant).

II. RESONANT DISPERSION BUMPS

During LEP start-up in 1992, large r.m.s. values of residual vertical dispersion (up to 60 cm) have been observed, both with the 94/100 optics and with the 91/97 optics. It was later shown by simulation [5] that large fluctuations of D_y can be generated when a reduced number of orbit correctors (typically 16) is used in each iteration. As a consequence, the initial strategy for closed orbit correction was modified (using 64 correctors per iteration) and the residual dispersion was much reduced. Meanwhile we developed a resonant method of correction [6] that turned out to be very useful during physics runs.

Since D_y is mainly driven by the vertical orbit harmon-

504

ics closest to the vertical tune, we looked for special orbit bumps having a Fourier spectrum dominated by the line at the integer betatron tune, i.e., orbit bumps as close as possible to a pure betatron oscillation. The dispersion created by such a 'resonant' excitation could then be used to cancel the corresponding betatron component of the measured residual dispersion, by more than an order of magnitude, without any appreciable deterioration of the closed orbit (and of the coupling compensation). In order to apply this resonant excitation with the right phase, one has to determine the correct amplitude for two independent bumps in quadrature.

Let us consider a series of orbit bumps with the same amplitude, each of them extending over a large fraction of a machine arc. With the 90° optics, each bump can be excited by two correctors, close to the beginning and to the end of the corresponding octant. For any given optics, and thus for given betatron phase advances across the straight sections, it is always possible to choose the relative phases of the arc bumps such that their contributions to dispersion add up almost coherently. In fact there are two independent choices giving rise to 'resonant families' of arc bumps in quadrature: the corresponding D_y is either symmetric or antisymmetric around the IP's.

To estimate the amplification factor A, defined as the ratio between normalized dispersion (outside the bump) and normalized bump amplitude, we write the vertical closed orbit $y_{co}(s)$ and the associated dispersion $D_y(s)$ for a single orbit bump with normalized amplitude Y, starting at the beginning s_i of arc i:

$$y_{co}(s) = Y\sqrt{\beta(s)}\sin[\mu(s) - \mu_i],$$

$$D_y(s) = -y_{co}(s) - \frac{Y\sqrt{\beta(s)}}{2\sin(\pi Q)}\int_{bump}ds'\,[\beta(K - K'D_x)]_{s'}\,f(s,s').$$

Here $f(s,s') = \cos[\pi Q - |\mu(s) - \mu(s')|]\sin[\mu(s') - \mu_i] = \{\sin[\pi Q + 2\mu(s') - \mu(s) - \mu_i] - \sin[\pi Q - \mu(s) + \mu_i]\}/2$ (for $\mu(s) > \mu(s')$). The first term in curly brackets oscillates at twice the betatron frequency and thus changes sign at each cell (if the phase advance is 90°), while the second term is independent of the integration variable s'. Therefore for a two-family sextupole arrangement, the contribution of the first term to the integral vanishes and neglecting the first term in the expression of D_y, we get

$$\frac{D_y(s)}{\sqrt{\beta(s)}} = \frac{Y\sin[\pi Q - \mu(s) + \mu_i]}{4\sin(\pi Q)}\int_{bump}ds'\,[\beta(K - K'D_x)]_{s'}.$$

The last integral equals $4\pi N_{cell}Q'_{cell}$, where N_{cell} is the (even) number of regular cells covered by the bump and Q'_{cell} the chromaticity of a single cell. Thus the amplification factor A for a vertical bump extending over a single arc is $A = \pi N_{cell}Q'_{cell}/\sin(\pi Q)$.

If the number of cells covered by orbit bumps in each octant is the same, the global amplification factor is $A_{tot} = 8C\,A$, where the coherence factor $C \leq 1$ is given by

$$C = \frac{1}{8}\sqrt{8 + \sum_{i \neq j} p_i p_j \cos(\mu_i - \mu_j)}.$$

Here $p_i = \pm 1$ denotes the *sign* of the orbit bump starting at betatron phase μ_i in octant i. We choose the signs p_i and the starting cells (i.e., the phases μ_i) such that the coherence factor is as large as possible. For the 90° injection optics and for an arc bump extending over 26 cells in each octant, our formula gives a global amplification factor $A_{tot} \sim 282$, while using MAD, we find global amplification factors of 280 and 276, respectively, for symmetric and antisymmetric resonant bumps.

In the case of a *four-family* sextupole arrangement, as in the squeezed optics, the term oscillating at twice the betatron frequency also contributes to vertical dispersion

$$\int_{bump}ds'\,[\beta(K - K'D_x)]_{s'}\sin[\pi Q + 2\mu(s') - \mu(s) - \mu_i] =$$

$$-\frac{N_{cell}}{2}\int_{cell}ds'\,\beta(s')\Delta K'(s')D_x(s')\sin[\pi Q + 2\mu(s') - \mu(s) - \mu_i],$$

where $\Delta K'$ is the difference in sextupole strength between two SF or two SD families. This difference increases for decreasing values of β^* and, if the bump phase μ_i is shifted by an odd number of cells (i.e., by a multiple of $\pi/2$) the sign of $\Delta K'$ is reversed. Since the main difference in sextupole strength occurs for the two SD families (corresponding to an effective *three-family* sextupole arrangement) and since the vertical phase advance from a vertical corrector to the defocussing sextupole in the same cell is almost $\pi/2$, the contribution to vertical dispersion is proportional to the same trigonometric factor as the previous contribution due to Q'_{cell} and the amplification factor becomes

$$A \simeq \frac{N_{cell}}{\sin(\pi Q)}\left|\pi Q'_{cell} \pm \frac{1}{8}(\beta\Delta K'LD_x)_{SD}\right|.$$

For the 5 cm squeezed optics, the cell chromaticity is $Q'_{cell} = 0.45$ and the contribution of the SD sextupoles is $(\beta\Delta K'LD_x)_{SD} \simeq 6.5$. Therefore the symmetric and antisymmetric bumps now have rather different global amplification factors, approximately given by $A_{tot} \simeq 470 \pm 270$. These estimated factors are again very close to those computed by MAD, namely 203 and 735.

III. References

[1] D. Brandt, R. Giachino, E. Keil, G. Morpurgo, F. Ruggiero and A. Verdier, 'Beta-beating in LEP for various optics configurations'. SL-MD Note 61 (1992).

[2] A. Burns, 'BOM Software', in Proceedings of the Second Workshop on LEP Performance, Chamonix, 1992, Ed. J. Poole, SL/92-29 (DI), p. 95 (1992).

[3] H. Burkhardt and A. Verdier, SL-MD Note 31 (1992).

[4] E. Keil, 'Quadrupole position and beta-beating', SL-MD Note 83

[5] E. Keil. Note 11 (1992).

[6] F. Ruggiero and A. Zholents, 'Resonant correction of residual dispersion in LEP', SL-MD Note 26 (1992).

Emittance and Damping of Electrons in the Neighborhood of Resonance Fixed Points*

Edwin A. Crosbie

Argonne National Laboratory, 9700 S. Cass Avenue, Argonne, IL 60439

Abstract

The stable fixed points generated by nonlinear field harmonics in a cyclic lattice define a multiturn stable orbit. The position of the orbit for each turn in each magnet of the lattice determines the betatron tunes and lattice dispersion functions describing the linear motion of charged particles with respect to the stable orbit. Since the position of the fixed points is dependent in part on the central orbit tune, it turns out that the multiturn orbit dispersion function depends to a large extent on the central orbit chromaticity. In particular, the horizontal partition number can be made to vary from values less than zero (horizontal antidamping for electrons) to values greater than three (longitudinal antidamping). The central orbit chromaticity therefore plays a major role in determining the characteristic emittance of an electron beam with respect to the multiturn orbit.

I. INTRODUCTION

Nonlinear resonance studies at the University of Wisconsin electron storage ring, ALADDIN, have been reported previously [1,2]. During those studies it was observed that electrons kicked to the neighborhood of the third integer resonance fixed points had betatron oscillations that damped to the fixed points. Subsequent experiments at ALADDIN have been devoted to measuring the island lifetimes and rates of diffusion of the beam from the islands to the central region [3]. Damping and quantum growth rates of the beam in the islands are determined by the linear characteristics of the betatron oscillations about the stable fixed points which define a three-turn closed orbit.

Figure 1 shows a computer simulation of the damping of two phase points with initial starting points almost (but not quite) equal. One particle damps to the separatrix and ends up damping to the central orbit. The other particle also damps to the separatrix but then proceeds to damp to the third integer resonance stable fixed points. In this simulation the damping rates have been artificially increased. The tracking is stopped before the damping is complete.

II. SIMULATIONS OF THE THREE-TURN CLOSED ORBIT

The ALADDIN storage ring has four long straight sections and normally operates with betatron tunes of $v_x = 7.14$, $v_y = 7.23$. Each of the four sectors contains sextupoles used to control the horizontal and vertical chromaticity. The third integral resonance is produced by changing the horizontal tune to about
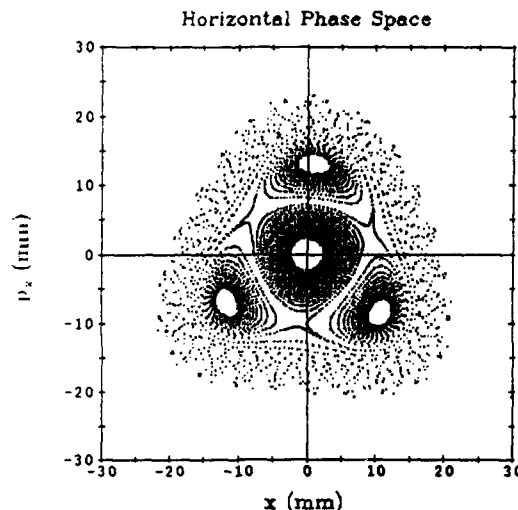
Figure 1.   Damping of two almost equal phase points.

resonance is produced by changing the horizontal tune to about 7.33 and turning on an extra sextupole to produce the 22nd harmonic.

To determine the linear characteristics of oscillations about the fixed points one first uses a tracking program to find the position of the three-turn closed orbit at all of the magnets. These positions are used to define new elements which can be used to build a lattice for the three-turn machine. Each quadrupole or sextupole becomes a gradient bending magnet for the three-turn machine. For example, the bend in a quadrupole is determined by the change in angle of the fixed point orbit in passing through the quadrupole, i.e.

$$\theta = -\Delta x' = \frac{B'\ell}{B\rho} < x > = \frac{\ell}{< \rho >}$$

where $B'/B\rho$ is the quadrupole strength. The edge angles are also determined by slopes of the orbit on entering and leaving the magnet.

III. LINEAR CHARACTERISTICS OF THE THREE-TURN ORBIT

The lattice elements described in the preceding section describe a machine with well-defined betatron and dispersion functions. The horizontal tune is about 22.033. (One can verify the tune by tracking the oscillations about the stable fixed points using the central nonlinear machine.)

The interesting feature of the new three-turn machine is the dependence of the dispersion function on the chromaticity of

506

the oscillations with respect to the original central orbit. This dependence on chromaticity is explained as follows. The position of the fixed point is determined by the central orbit tune and an average amplitude-dependent tune shift. Near resonance the amplitude-dependent tune shift is not very sensitive to change in the chromaticity correcting sextupoles. Therefore, the fixed points for a positive momentum particle are at either a greater or smaller amplitude depending on whether the chromaticity is respectively negative or positive. Figures 2 and 3 show the dispersion functions for normalized chromaticities of ± 0.3. In general, the two dispersion functions have a phase difference of about π. (Note that the dispersion function generated by the three-turn lattice can be verified by off-momentum tracking using the original nonlinear lattice.)
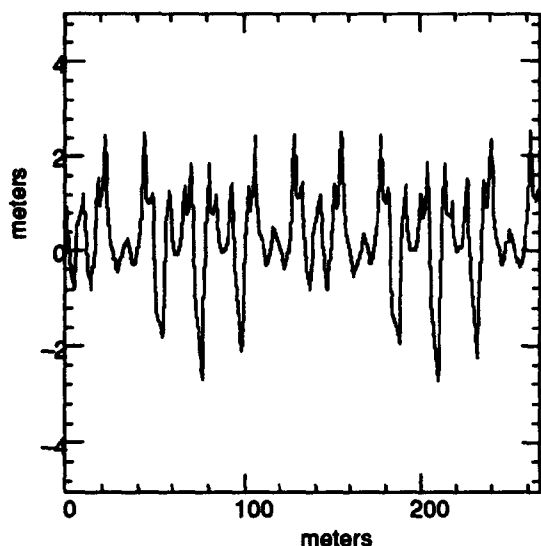
Figure 2.   Dispersion function with normalized chromaticity = .3.
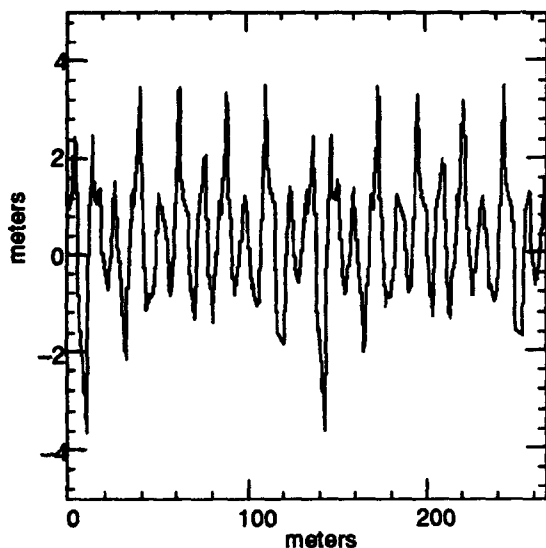
Figure 3.   Dispersion function with normalized chromaticity = −.3.

This dependence of the dispersion function on the central orbit chromaticity has a large effect on the damping partition numbers J_x and J_E. The damping time constants are given by [4]

$$\tau_i = \frac{2E_o}{J_i P_\gamma} \qquad i = x, y, E$$

$$J_x = 1 - D \qquad J_y = 1 \qquad J_E = 2 + D$$

$$D = \frac{-\int \eta G \,(G^2 + 2K)\, ds}{\int G^2 ds}$$

where η is the dispersion function, G is the reciprocal bend radius, and K is the gradient focusing force in the magnet.

For the central orbit (and almost all machines), D is a small quantity. However the gradient terms in the new dipoles defining the three-turn machine are not small. In addition, the sign of the contributions to D in these magnets depends on the sign of the dispersion which in turn depends on the central orbit chromaticity.

Figures 4 and 5 show the contributions to the integrand for D for opposite signs of the central chromaticity. It turns out that the dependence of D (and hence J_x) on the chromaticity is almost linear as shown in Figure 6.
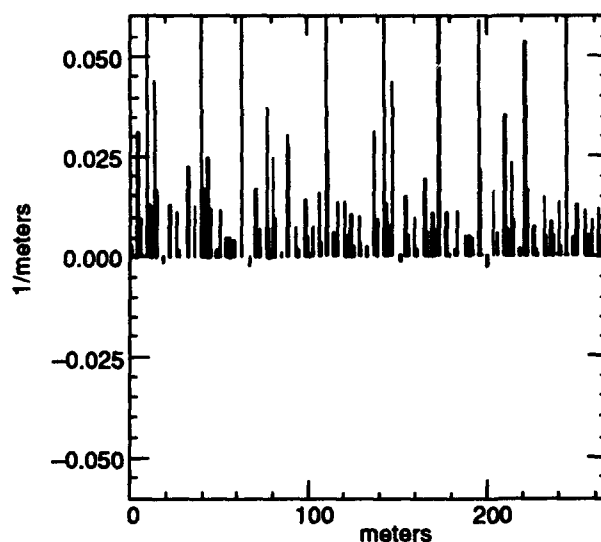
Figure 4.   Contribution to the integrand of D with chromaticity = .2.

This dependence of the dispersion function on the central orbit chromaticity has a large effect on the damping partition numbers J_x and J_E.

On the other hand, the quantum fluctuation emittance growth rate depends on the square of the dispersion function. Hence, the plot of this function versus the chromaticity shows a minimum near small positive values (Figure 7). The resultant natural emittance (Figure 8) determined by the growth rate and the damping time constant shows a very shallow minimum at a moderate positive value of the chromaticity. The minimum

value is about 10% smaller than the corresponding emittance for the central orbit.
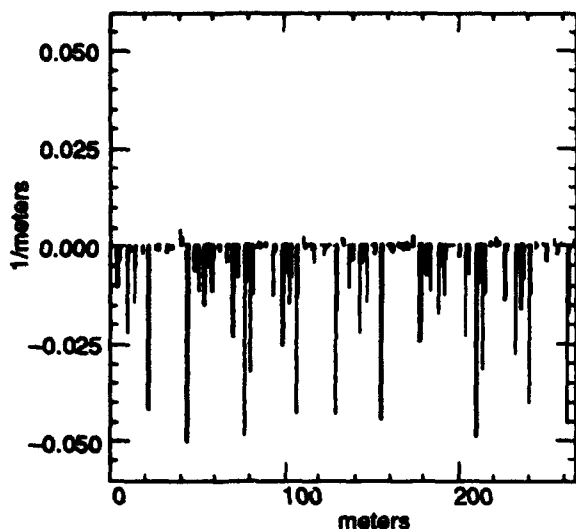
Figure 5. Contribution to the integrand of D with chromaticity = –.3.
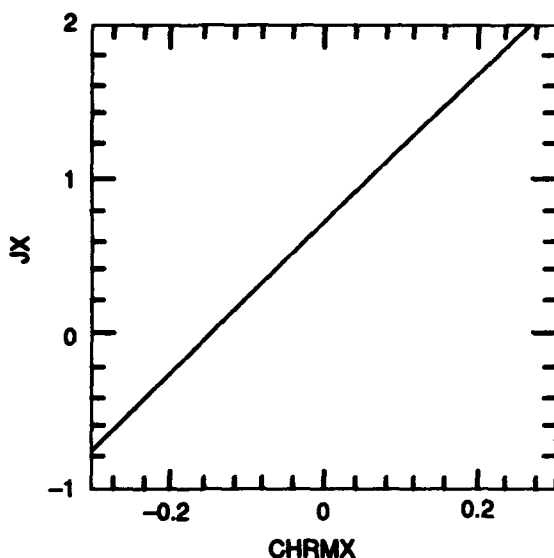
Figure 6. Dependence of J_x on chromaticity.

Figure 7. Quantum growth rate as a function of chromaticity.
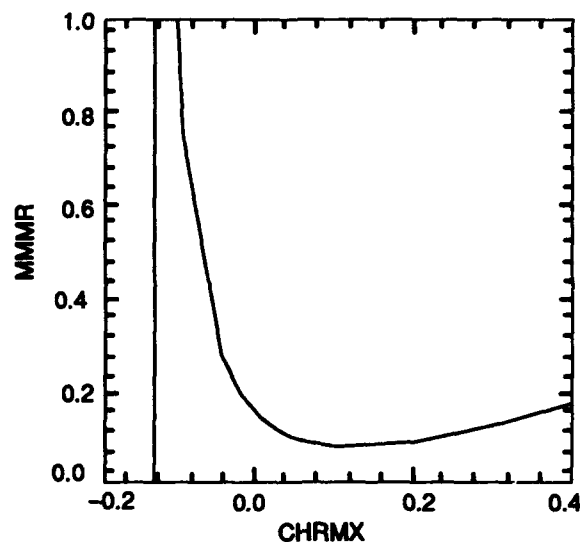
Figure 8. Island natural emittance as a function of chromaticity.

V. REFERENCES

[1] E. Crosbie, et. al.,"Non-linear Resonance Studies at the Synchrotron Radiation Center, Stoughton, Wisconsin," Conference Record of the 1991 IEEE Particle Accelerator Conference, Vol. 3, pp. 1624–1626, 1991.

[2] J. Bridges, et. al., "Dynamic Aperture Measurement on ALADDIN," Particle Accelerators, 1990, Vol. 28, pp. 279-487.

[3] J. Liu, et. al., "Particle Diffusion from Resonance Islands in Aladdin at SRC," these proceedings.

[4] M. Sands, "The Physics of Electron Storage Rings--An Introduction," SLAC-121, May, 1979.

Effects of the Third Order Transfer Maps and Solenoid on a High Brightness Beam

Zohreh Parsa
Physics Department
Brookhaven National Laboratory, -
Upton, NY 11973

Abstract

We present a sketch of the formulation for obtaining Lie algebraic transfer maps for the solenoid through third order and its effect on the beam of charged particles. We discuss simulation results showing effects of solenoids on the laser driven high brightness photoelectrons for the proposed alternate injection system for Brookhaven Accelerator Test Facility.

I. INTRODUCTION

A brief overview of a Lie algebraic formulation is given in section II. Using Hamiltonian dynamics we describe the motion of a charged particle through electromagnetic fields. With Lie transformations we obtain the maps and trajectories for a particle along the beamline in a magnetic field (e.g. of solenoid). We discuss the transfer maps for magnetic elements and solenoid through third order and their effects on the beam of charged particles. In section III we discuss the effects of the solenoids used in the design of the proposed alternate injection system for the Brookhaven Accelerator Test Facility (ATF) [1].

II. FORMALISM

In this section we present an overview of the formalism used to obtain the trajectories of a particle along the beamline via Lie transformation. Using Maxwell's equations, axisymmetrical fields, and the relativistic equations for the charged particles motion along the beamline we can obtain the magnetic field components everywhere (e.g. of a solenoid given the on axis longitudinal component of the field $B_z = (B, 0, 0)$) and its effect on the particles motion.

We express the canonical equations in 2n-Dimensional phase space (e.g 6 Dim., in our calculation), as

$$\frac{d\psi_i}{dt} = [\psi_i, H], \qquad i = 1, 2, \dots 2n \qquad (1)$$

and in terms of the Lie transformations as

$$\frac{d\psi_i}{dt} = - : H : \psi_i, \qquad i = 1, 2, \dots 2n \qquad (2)$$

Where the Lie operator ($: H :$) is generated by the Hamiltonian, (H), and Lie transformation,

$$M = e^{-t : H :}, \qquad (3)$$

could generate the solution to Eq. (2) as

$$\psi_i = M \psi_i (0) \qquad (4)$$

where ψ_i is the value of $\psi_i (t)$ at $t > 0$ and $\psi_i (0)$ is the initial trajectory. The interest is to find solutions to equations of motion which differ slightly from the reference orbit (e.g. the design orbit of an accelerator beamline. Design orbit for solenoid is along z-axis). Thus, we choose the canonical variables, from the values for the reference trajectory (for small deviations) and Taylor expand the Hamiltonian (H) about the design trajectory:

$$H = H_2 + H_3 + \dots . \qquad (5)$$

Where H_n is a homogeneous polynomial of degree n in the canonical variables. After transformations to the normalized dimensionless variables, we obtain the effective Hamiltonian H^{New}, expressed as

$$H^{New} = F_2 + F_3 + F_4 \dots . \qquad (6)$$

Thus the particle trajectory $\vec{\psi} = (X, P_X, Y, P_Y, \tau, P_\tau)$ through a beamline element of length L can be described by

$$\psi_i^f = - : H^{New} : \psi_i, \qquad i = 1, 2, \dots 2n \qquad (7)$$

The exact symplectic map that generates the particle trajectory through that element is,

$$M = e^{-L : H^{New} :}, \qquad (8)$$

where, M describes the particle behavior through the element of length L. Using the factorization and expanding H^{New} as in Eq. (6), we obtain

$$M = e^{-L : H^{New} :} = e^{: f_2 :} e^{: f_3 :} e^{: f_4 :} \dots , \qquad (9)$$

(for a map through 3rd order we need to include terms of f2, f3, and f4). Where $f_2 = LF_2$, $f_3 = LF_3$, $f_4 = LF_4$, etc.

To illustrate the above formalism, consider the evolution of the motion of particles in an external electromagnetic field described by the Hamiltonian

$$H = \sqrt{m^2 c^4 + c^2 \left[(p_x - qA_x)^2 + (p_y - qA_y)^2 + (p_z - qA_z)^2 \right]}$$
$$+ e\phi (x, y, z; t) \qquad (10)$$

where m and q are the rest mass and charge of the particle, A and ϕ are the vector and scalar potentials such that $\vec{B} = \nabla \times \vec{A}$, $\vec{E} = -\nabla\phi - \nabla\vec{A}/\partial t$.

Making a canonical transformation from H to H_1 and changing the independent variable from time t to z (for convenience) for a particle in magnetic field (e.g. of solenoid) results in:

$$p_z = \left[(p_x - qA_x)^2 + (p_y - qA_y)^2 + p_t^2/c^2 - m^2c^2\right]^{1/2}.$$

(11)

Where $H = -p_t$, $H_1 = -p_z$ and $t = (z/v_{0z})$ the time as a function of z. We next make a canonical transformation from H_1 to H^{New}, with a dimensionless deviation variables (for convenience), $X = x/l$, $Y = y/l$, $\tau = c/l(t - z/v_{0z})$, $P_x = p_x/p_0$, $P_y = p_y/p_0$, $P_\tau = (p_t - p_{0t})/p_0 c.$, where l is a length scale (taken as 1 m in our analysis), with $\mathbf{P} = \vec{P}x + \vec{P}y$ and $\mathbf{Q} = \vec{X} + \vec{Y}$ defined as two dimensional vectors [3]. p_0 and p_0c are momentum and energy scales. Where p_0 is the design momentum, v_{0z} is the velocity on the design orbit and p_{0t} is value of p_t on the design orbit $(p_{0t} = \sqrt{m^2c^4 + p_0^2c^2})$ (reminding that design orbit for the solenoid is along the z-axis).

Thus, expanding the new Hamiltonian (eq.(6)) leads to:

$$F_2 = \frac{P_\tau^2}{(2\beta^2\gamma^2)} - \frac{1}{2}B_0\left(\vec{Q} \times \vec{P}\right) \cdot \hat{z}$$
$$+ \frac{1}{8}B_0^2 Q^2 + \frac{P^2}{2}$$

(12)

$$F_3 = \frac{P_\tau^3}{(2\beta^3\gamma^2)} - \frac{P_\tau}{2\beta}B_0\left(\vec{Q} \times \vec{P}\right) \cdot \hat{z}$$
$$+ \frac{P_\tau}{8\beta}\left(B_0^2 Q^2 + 4P^2\right)$$

(13)

$$F_4 = \frac{P_\tau^4\left(5 - \beta^2\right)}{8\beta^4\gamma^2} + \frac{P_\tau^2 Q^2 B_0^2\left(3 - \beta^2\right)}{16\beta^2}$$
$$- \frac{P_\tau^2}{2}\left(\vec{Q} \times \vec{P}\right) \cdot \hat{z}\frac{B_0\left(3 - \beta^2\right)}{2\beta^2}$$
$$+ \frac{P_\tau^2}{2}\frac{P^2\left(3 - \beta^2\right)}{2\beta^2} + \frac{Q^4}{16}\left(B_0^4 - 4B_0B_2\right)/8$$
$$+ \frac{Q^2}{4}\frac{P^2\,3B_0^2}{4} + \frac{Q^2}{4}\left(\vec{Q} \times \vec{P}\right) \cdot \hat{z}\left(B_2 - B_0^3\right)/4$$
$$- \frac{1}{8}\left(\vec{P} \cdot \vec{Q}\right)^2 B_0 - \frac{P^2}{4}\left(\vec{Q} \times \vec{P}\right) \cdot \hat{z}B_0 + \frac{P^4}{8}$$

(14)

Following the hamiltonian flow generated by $H^{New} = F_2 + F_3 \ldots$ from some initial ψ_0 to a final ψ_f coordinates we can calculate the transfer map M (eq. 9) for the solenoid. Where F_2, F_3, and F_4 would lead to the 1st, 2nd, and 3rd order maps. The effects of which can be seen from eqs. (12-14). For example, the 2nd order effects due to solenoid transfer maps are purely chromatic aberrations (eq. 13). In addition to chromatic effects, we note the third order geometric aberrations (eq. 14). The coupling between X, Y planes produced by a solenoid is rotation about the z-axis which is a consequence of rotational invariance of the Hamiltonian H^{New} shown by eqs.(12-14), due to axial symmetry of the solenoid field.
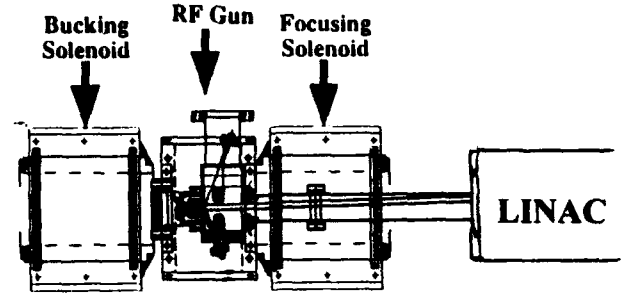
Figure 1: Sketch of the alternate injection system for ATF. A solenoid + gun + solenoid combination is placed straight ahead into the linac. (Not scaled).

For beam simulations, M can be calculated to any order using numerical integration techniques such as Runge-Kutta method depending on the computer memory and space available [3].

III. BNL ATF INJECTION SYSTEM

In this section we present some of our calculations and simulation results obtained for the proposed alternate (straight-ahead) injection system which consists of a pair of solenoids and an rf gun placed directly into the linac [1,7].
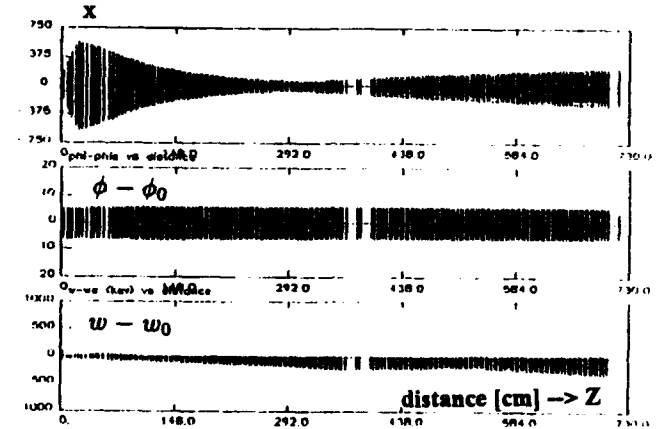
Figure 2: Shows the change in position x [cm], phase $\phi - \phi_0$ [degree] and energy $w - w_0$ [KeV] of particles at each element location, from the cathode through the linac exit. With solenoid current of 2140 A and $d = 62cm$ and $\sigma_r = .9mm$, $\sigma_z = 5ps$.

Present injection system consists of 2 sets of quadrupole triplets and a 180° achromatic double bend [1], where beam diverges quickly as it exits the gun and gets large as it traverses through the dipoles and the linac. We have used a pair of solenoids (placed before and after the gun such that B=0 on the cathode) shown in Fig. 1, which controls the beam divergence at the gun exit, reduces the emittance dilution due to space charge forces, and improves the conditions for production of high brightness low emittance beam needed e.g., for Free Electron Laser, and Inverse Free Electron Laser experiments. Figure 2 shows how the beam size increases as it drifts from the
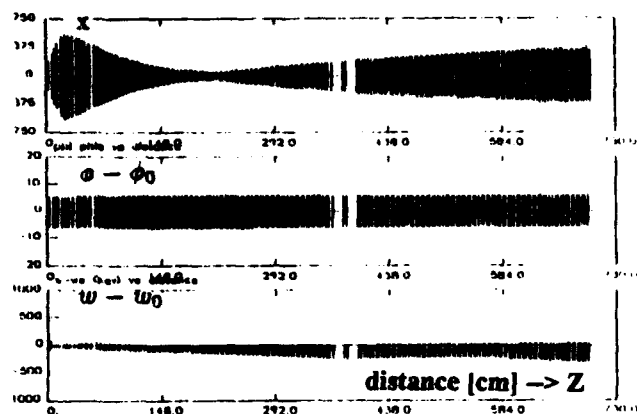
Figure 3: Shows the change in position x [cm], phase $\varphi - \phi_0$ [degree] and energy $w - w_0$ [KeV] of particles at each element location, from the cathode through the linac exit. With solenoid current of 2180 A and $d = 62cm$ and $\sigma_r = .9mm$, $\sigma_z = 5ps$.

gun into the linac. The Beam converges to a waist in the linac resulting in a beam of smaller emittance at the linac exit which is of interest at ATF.

Comparison of Figs. 2 and 3 show locations of the beam waist and beam envelopes along the beamline from cathode through the linac. In Fig. 3, a 2% increase in the solenoid current resulted in the shift in the position of the beam waist in the linac and an emittance increase from ($\epsilon_x^{N,rms} = .278$, $\epsilon_y^{N,rms} = .243$) to ($\epsilon_x^{N,rms} = .390$, $\epsilon_y^{N,rms} = .333$) at the linac exit (as compared to Fig. 2). This illustrates the effects due to variation of the solenoid strength on the beam dynamics. In this analysis we used an initial $E = 100$ MV/m on the cathode, laser pulse length ($2\sigma_z$) of 10 ps, spot size $\sigma_r = 0.9mm$, initial phase of $43°$, and d = 62 cm, (the distance from cathode to linac entrance). The solenoid for this design can vary up to 4.0 KG in strength. For example with a 2.2 KG solenoid strength we can preserve the beam quality and achieve high brightness, low emittance beam at the linac exit, which is needed for the FEL and laser acceleration experiments at ATF. With program PARMELA [6], with $\sigma_r = 1mm$ and 0.9 mm (uniform beam distribution) we obtained beam emittance of few tenths of cm-mrad with energies of about $46MeV$ and brightness ($B = I^{peak}/\pi\epsilon_x^N \epsilon_y^N$) of orders of 10^{13} for the beam emerging from the exit of the linac.

IV. SUMMARY

We presented a sketch of the formalism used to obtain Lie algebraic maps through third order for magnetic elements e.g. a solenoid. Note that, the 2nd order aberration due to solenoid is purely chromatic. We discussed effects of solenoids used in the design of the alternate injection system for the ATF at Brookhaven National Lab. Where a pair of solenoids and an rf gun is placed directly into the linac, to improve the beam loss and the emittance growth at the linac exit (as may be with the present double bend system). With solenoid+gun+solenoid straight

injection into the linac scheme we reduce the emittance dilution due to space charge forces, and produce the beam needed for FEL, IFEL and other laser acceleration experiments. We obtained small emittance (few tenths of cm-mrad) and high brightness of orders of 10^{13}. The solenoids used in the alternate injection system, controls the beam divergence at the gun exit, reduces the emittance dilution due to the space charge forces on the beam and produces a smaller beam emittance needed for the experiments at ATF.

V. REFERENCES

*Work performed under the auspices of the U.S. Department of Energy, Contract Number DE-ACO2-76-CH00016.

1. Z. Parsa, *"Development of the Alternate Entry Port for the ATF"*, Proc. IEEE May 17-20 PAC, Washington D.C. (1993).

2. Z. Parsa, *"Lie Algebraic Transfer Maps of Magnet System and Nonlinear Aberrations in the Beam"*, BNL Tech. Note ADD/CAP/TN 5 (1/21/89) and References therein. Additional Lie transfers maps for drifts, quadrupole, dipole etc. were included in this reference.

3. A. Dragt, Program MARYLIE, Private comm.; ibid *"Numerical third-order transfer map for solenoid "*, NIM, A298 (1990), and References therein. MARYLIE includes 3rd order maps for solenoid with soft-edge "bump" function model for the field. We thank A.Dragt for discussions and providing his code. We did not include any results with MARYLIE for our analysis of the ATF alternate injection system with solenoids, since this code does not provide acceleration through the rf gun and the linac. Results with MARYLIE for the beamline without rf and linac accelerations will be given in a separate note.

4. Z. Parsa, *"Preliminary Emittance Measurements and Calculations of the Laser Excited Beam from the BNL Accelerator Test Facility Radio Frequency Electron Gun"*, Vol.II, Sec.II, p1-54, BNL-52292 (1991) and References therein; K. McDonald et al., Proc., EPAC88, June (1988); K. Batchelor et al., *"Operational Status of Brookhaven Accelerator Test Facility"*, Proc. 1989 IEEE Particle Accelerator Conf. Chicago, Ill, March 20-23, 1989, #89CH2669-0 (1990).

5. Z. Parsa, *"On Beam Emittance and Invariants - Applications to ATF Beamline"*, Proc. 2nd EPAC, Nice - France, Nile Ed., Frontiers, (1990); BNL Report BNL-44364 (1990) and Ref. therein.

6. Z. Parsa, and L. Young, *"The BNL Photocathode Gun with the Code PARMELA"*, Nucl. Inst. & Meths. A318; BNL-46804 (1991); L. Young, (Private comms.), PARMELA (1993 version).

7. Z. Parsa, *"An Alternate Injection System for the BNL Accelerator Test Facility"*, BNL-48403, APS April 12-15, Washington D.C. (1993).

Simultaneous Cancellation of Beam Emittance and Energy Spread in the CEBAF Nuclear Physics Injector Chopping System *

H. Liu and J. Bisognano

CEBAF, 12000 Jefferson Ave., Newport News, VA 23606

Abstract

The CEBAF nuclear physics injector will utilize a unique chopping system consisting of two identical square box RF cavities with an inverting lens and a chopper aperture inbetween. This system produces three interleaved 499 MHz cw electron beams from a 100 kV input beam. In this paper, we present our theoretical and numerical studies on how both emittance and energy spread are cancelled simultaneously in the dechopping process in the second cavity.

I. INTRODUCTION

The CEBAF nuclear physics injector chopping system consists of two identical square box RF cavities with a Newtonian lens and a chopper aperture inbetween. The system produces three interleaved 499 MHz cw electron beams from a 100 kV input beam. In the first cavity, a beam is deflected radially and swept into a circle at the chopper aperture by two orthogonal electromagnetic modes (TM_{120} and TM_{210}) in the cavity. Each complete circle of the beam is chopped into three bunches continuously with three equally spaced notches at the chopper aperture. Then the bunches are brought back onto axis using the second cavity.

One interesting issue is whether the energy spread of electrons introduced in the first cavity due to finite beam spot size is cancelled or not as the beam is dechopped in the second cavity. In this paper, we present our theoretical and numerical studies.

II. LAYOUT OF THE SYSTEM

The layout of the initial part of the CEBAF nuclear physics injector is shown in Fig. 1. Following a 100-kV
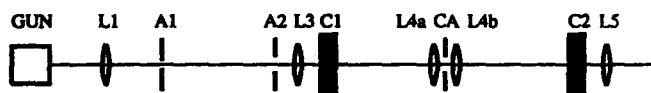
Fig. 1 Layout of the system

thermionic gun, a pair of apertures (A_1 and A_2) are used for limiting the emittance of the beam, which is 66 nm divided by the beam energy in MeV as the rms geometric emittance for the machine at high energies [1]. Then a pair of chopper cavities (C_1 and C_2) are used to chop a cw beam through an aperture (CA). The first lens (L_1) focuses the beam to a waist at the first aperture; the third lens (L_3) makes an image-to-image transform from A_1 to

CA; and the lens pair L_{4a}-L_{4b} makes an image-to-image transform between the centers of C_1 and C_2. The chopper system is symmetric with respect to the chopper aperture. The chopping process is shown in Fig. 2.
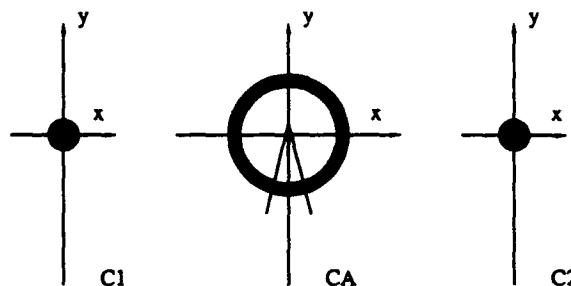
Fig. 2 Chopping process

III. CHOPPER CAVITY

Each chopper cavity is simply a square box operating at two orthogonal electromagnetic modes. Although the field distributions will be affected more or less by the beam pipe and coupling waveguide, the ideal field expressions for these two modes remain very useful and provide the most powerful means for us to get the most clear insight into the issue. We write these expressions as follows:

TM_{210} :

$$E_z = E_0 \sin\left(2\pi x/a\right) \cos\left(\pi y/a\right) \sin\left(\omega t\right), \quad (1.1)$$

$$B_x = -(\pi E_0/a\omega) \sin\left(2\pi x/a\right) \sin\left(\pi y/a\right) \cos\left(\omega t\right), \quad (1.2)$$

$$B_y = -(2\pi E_0/a\omega) \cos\left(2\pi x/a\right) \cos\left(\pi y/a\right) \cos\left(\omega t\right), \quad (1.3)$$

TM_{120} :

$$E_z = E_0 \sin\left(2\pi y/a\right) \cos\left(\pi x/a\right) \sin\left(\omega t\right), \quad (2.1)$$

$$B_y = (\pi E_0/a\omega) \sin\left(2\pi y/a\right) \sin\left(\pi x/a\right) \cos\left(\omega t\right), \quad (2.2)$$

$$B_x = (2\pi E_0/a\omega) \cos\left(2\pi y/a\right) \cos\left(\pi x/a\right) \cos\left(\omega t\right), \quad (2.3)$$

where a is the transverse dimension of the square box, and ω the angular RF frequency. The wavelength $\lambda = 2a/\sqrt{5}$.

As can be seen from the above expressions, when its spot size is small, the beam centered on axis will experience a strong B_y field component from the TM_{210} mode and a strong B_x field component from the TM_{120} mode. When these two modes are excited in quadrature phase and equal amplitude, the electrons in an RF cycle will be swept into a circle in the transverse plane, and hence the longitudinal motion of the beam will be converted into transverse motion, providing an approach to chopping the

beam into bunches in the transverse plane by using a number of notches. If the second cavity is added, the trasverse momentum spread introduced in the first cavity can be compensated for from a reverse process. However, according to Eqs. (1.1) and (2.1), the finite beam spot size will introduce an additional energy spread as a side-effect. Will this energy spread be undone as the beam is dechopped in the second cavity? This is the issue we will study in this paper.

IV. INVERTING LENS

Before analysing the performance of the chopping system, we introduce one crucial element in the system which is in fact an inverting lens consisting of two solenoidal lenses L_{4a} and L_{4b}.

Given that the system from C_1 to C_2 is symmetric with respect to the chopper aperture, the transfer matrix of the system is

$$R = \begin{pmatrix} R_{11} & R_{12} \\ R_{21} & R_{22} \end{pmatrix}$$

with

$$R_{11} = (1 - \frac{d_1}{f})(1 - \frac{2d_2}{f}) - \frac{d_1}{f}, \qquad (3.1)$$

$$R_{12} = 2(1 - \frac{d_1}{f})(d_1 + d_2(1 - \frac{d_1}{f})), \qquad (3.2)$$

$$R_{21} = -2(1 - \frac{d_2}{f})\frac{1}{f}, \qquad (3.3)$$

$$R_{22} = R_{11}, \qquad (3.4)$$

where d_1 is the distance from $C_{1(2)}$ to $L_{4a(b)}$, d_2 the distance from $L_{4a(b)}$ to the chopper aperture, f the focal length of the lenses. It is seen that for $d_1/f = 1$ and $d_2/f \ll 1$ the transfer matrix of the system becomes

$$R = \begin{pmatrix} -1 & 0 \\ -2/f & -1 \end{pmatrix}, \qquad (4)$$

which describes a 180° flip to an electron. Since $f \gg d_2$, the crossover will take place between L_{4b} and C_2.

The magnetic field of the solenoidal lens has been carefully measured[2]. We also calculated it using POISSON. Fig. 3 shows its field configuration from POISSON, and Fig. 4 shows the comparison of the on-axis field profile between the measurement and the calculation. The agreement in field profile is excellent. However, the calculated peak field actually was a few percent higher than the measurement. For example, for the same current of 0.9 A, the measured peak field is 153 Gauss, whereas the calculated one is 162 Gauss.
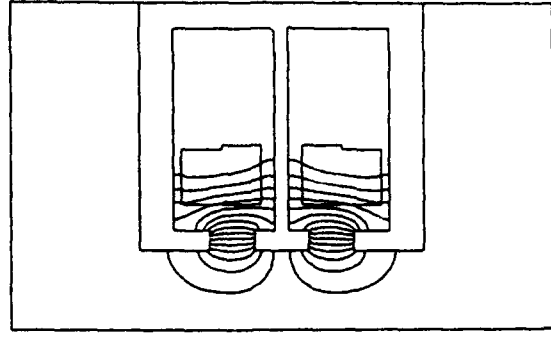
Fig. 3 Field configuration of the lens $L_{4a(b)}$ (POISSON)
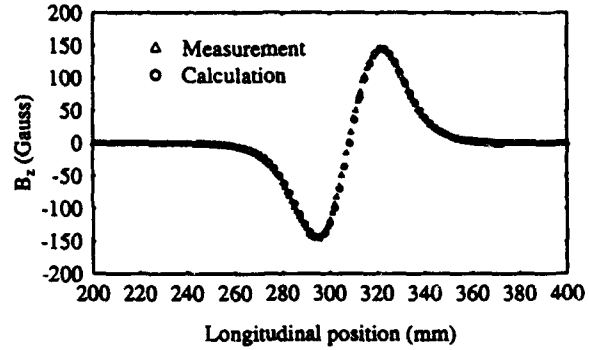
Fig. 4 Comparison of the field profiles for $L_{4a(b)}$

V. THEORETICAL ANALYSIS

The electromagnetic fields in a chopper cavity cause RF deflection and acceleration to electrons. From the TM_{210} mode, we have, to the first order of x and y,

$$\Delta x' = -\theta_0[\sin(\phi) - \sin(\phi_{01})], \qquad (5.1)$$

$$\Delta W_1 = W_0(x/a)[\cos(\phi) - \cos(\phi_{01})], \qquad (5.2)$$

$$\Delta x = x_0'\Delta z + a_0[\cos(\phi) - \cos(\phi_{01}) - \phi_z \sin(\phi_{01})], \qquad (5.3)$$

where $\Delta x' = x'(t) - x'(t_0)$; $x' = v_x/v_z$ is the divergence angle; $x_0' = x'(t_0)$; $\theta_0 = (|e|/m_0c^2\gamma)(E_0\lambda/ka)$ is the deflection amplitude; $\phi = \omega t$ is the RF phase; $\phi_{01} = \omega t_0$ is the initial RF phase; $\gamma = 1/\sqrt{1 - \beta^2}$ is the relativistic factor; $\Delta W_1 = W_1(t) - W_1(t_0)$; $W_0 = |e|E_0\lambda\beta_z$ is the energy spread amplitude; $\Delta z = z(t) - z(t_0)$; $a_0 = \theta_0\beta_z/k$; $\beta_z = v_z/c$; $\phi_z = k\Delta z/\beta_z$; $\Delta z = z(t) - z(t_0)$; and all the other symbols have their conventional meanings.

Similarly, from the TM_{120} mode, we have

$$\Delta y' = -\theta_0[\sin(\phi) - \sin(\phi_{02})], \qquad (6.1)$$

$$\Delta W_2 = W_0(y/a)[\cos(\phi) - \cos(\phi_{02})], \qquad (6.2)$$

$$\Delta y = y_0'\Delta z + a_0[\cos(\phi) - \cos(\phi_{02}) - \phi_z \sin(\phi_{02})], \qquad (6.3)$$

where ϕ_{02} is the initial RF phase of the mode.

It is seen from Eqs. (5.2) and (6.2) that the maximum energy spread in a slice of a beam takes place from top to bottom or from right to left in the beam spot. So the

maximum energy spread for a slice of a beam, induced in a chopper cavity, is

$$\Delta W = m_0 c^2 \gamma k d \theta_o \beta_z, \qquad (7)$$

where d is the spot size diameter of the beam going through the cavity. Note that the maximum energy spread is proportional to the beam diameter. For the 1497 MHz chopping system, the slope is 100 eV/mm.

The maximum energy spread is related to the emittance in view of the fact that $\epsilon = d\theta_o/2$ is the beam emittance. Since the energy spread is induced due to the finite beam size, it must be a linear relationship between the emittance and the energy spread introduced, to the first order. This tells us that energy spread comes together with the emittance and therefore it is possible for it to vanish with the emittance as the latter is recovered in the second cavity.

In fact, there are two methods to recover the emittance and/or energy spread. One is to go through the same process that happened in chopper 1 reversely in chopper 2; the other is to go through the same process in the same direction in chopper 2 to make a closed course. It is pointed out that by the first method we can not recover the energy spread, since the energy spread is caused by the finite beam spot size and depends on electron trajectories, and the electrons can not suddenly move in the reverse direction because of the inertial effect. But we can recover both energy spread and emittance by the second method. Correspondingly, the first method requires that if the phase difference of the TM_{210} mode and the TM_{120} mode in the first chopper cavity is $+90°$, it must be $-90°$ in the second chopper cavity. For the second method it requires that the phase difference must be $+90°$ in both chopper cavities.

VI. NUMERICAL MODELING

We used the code PARMELA for calculations. However, the conventional version of PARMELA assumes a hard-edge field profile for a solenoidal lens. It additionally requires that the length of the hard-edge field profile be the same as that of the rf element when the two elements overlap each other. The chopping process is treated using a zero-length transform. All these assumptions fail to apply to our case. We modified the code to meet the requirements for our modeling [3].

Numerically we easily found out that the phase difference between the two orthogonal modes must be $+90°$ in both cavities, instead of $+90°$ in one cavity and $-90°$ in the other. This is consistent with the experiment. Then we found that the relative phase difference between the two identical modes in the two cavities governs the cancellation of emittance, and the energy spread follows exactly the same process as for the emittance, as shown in Fig. 5, given that the lenses L_{4a} and L_{4b} have been properly powered satisfying Eq. (4). The underlying mechanism is that an electron is flipped $180°$ in the transverse plane by

the inverting lens; and therefore it will experience an accelerating or decelerating process which is opposite to that which occurred in the first cavity.
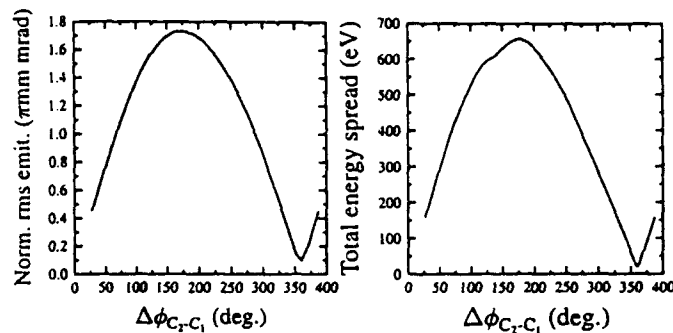
Fig. 5 Emittance and energy spread of the beam exiting the second chopper cavity versus the RF phase difference between the two identical modes in the two 1497 MHz cavities. The input bunch length in simulation is 360°, and 69° of it is chopped at the chopper aperture.

However, because of the finite transit angle, the cancellation both in emittance and energy spread could be incomplete. For example, for an RF cycle of electrons with an initial total energy spread of 10 eV and an initial normalized rms emittance of 0.08 mm mrad, the minimum energy spread and minimum normalized rms emittance at the exit of the second cavity in the 1497 MHz chopping system are 43 eV and 0.25 mm mrad, respectively, for the unchopped beam. However, for 69° of it chopped by the chopper aperture, the energy spread and normalized rms emittance are 23 eV and 0.11 mm mrad, respectively, as shown in Fig. 5. This issue will be further studied.

Some experiments carefully conducted by M. Tiefenback et al. will be presented in a separate paper [4].

VII. DISCUSSION

We believe this mechanism is not only important to our chopper performance but also of general interest. We point out that the extent of cancellation of the energy spread may depend on the coherence of the beam. The finite transit angle and any system aberrations will result in incmplete cancellation. In the future, we may do some more experiments on this issue as our commissioning schedule permits.

ACKNOWLEDGEMENTS

REFERENCES

1. H. Liu, CEBAF TN# 93-022.
2. C. K. Sinclair, private communication.
3. H. Liu, CEBAF PR-93-006.
4. M. Tiefenback and G. Krafft, this conference.

The Linkage of Zlib to TEAPOT for
Auto-Differentiation Map Extraction And Nonlinear Analysis*

Ning Sun, Yiton T. Yan, Fulvia Pilat, and George Bourianoff

Superconducting Super Collider Laboratory, 2550 Beckleymeade Avenue
Dallas, TX 75237, USA

ABSTRACT

The differential Lie algebraic numerical library, **Zlib** [1], has been linked to the **Teapot** [2], the accelerator simulator code. This makes possible the use of the operational correction features of Teapot to produce a corrected lattice, and then choose either map or thin element-by-element tracking for tracking studies. Because thin-element tracking is more accurate but slower than map tracking, the option of choosing one or the other is very desirable.

I. INTRODUCTION

Element-by-element tracking with Teapot for the Superconducting Super Collider (SSC) (more than 20,000 thin elements) for a thousand turns takes many hours of Sun workstation cpu time. The results are used to analyze the properties of the lattice, such as linear aperture, resonances, and short-term stability. One way to reduce the computing time is to use vectorized or parallel computing such as Ztrack [3] and Hypertrack [4]; another way is to use a nonlinear mapping method to map the lattice, such as Automatic Differentiation maps, which have been applied to the study of the long-term stability of the SSC lattices with the use of Zlib and its related programs [5], [6].

However, no attempt has been made so far to use maps for short-term tracking because the extraction of very-high-order maps takes long time and therefore gives no advantage over direct tracking. However, experience shows that maps of relatively low orders give quite reliable results for the analysis of some features of the accelerator lattice. To take the advantage of the fast speed of one-turn map tracking, we have started the implementation of Zlib directly in Teapot. We present the preliminary results on the reliability and tracking speed of the low-order maps and show how to combine the tools of Zlib and Teapot for convenient comprehensive studies.

II. MAP EXTRACTION AND TRACKING

First, we take the collider lattice of 20,000 elements, extract maps of various orders , record the time it takes to extract each of them, track the particles and compare the results with those obtained from the Teapot. The lattice we are using is the one with collision optics, including IR regions, all errors, corrections and crossing angle of 135 μrad (3B specifications for alignment and multipole errors; triplets have 0.1 mm misalignment and 0.2 mrad rotation errors). The time taken by the map extraction is proportional to the number of elements in the lattice and the number of monomials in the map, of which the latter is given by

$$nm = (nv+no)!/(nv! \; no!) \qquad (1)$$

for a *no*-order and *nv*-variable map.
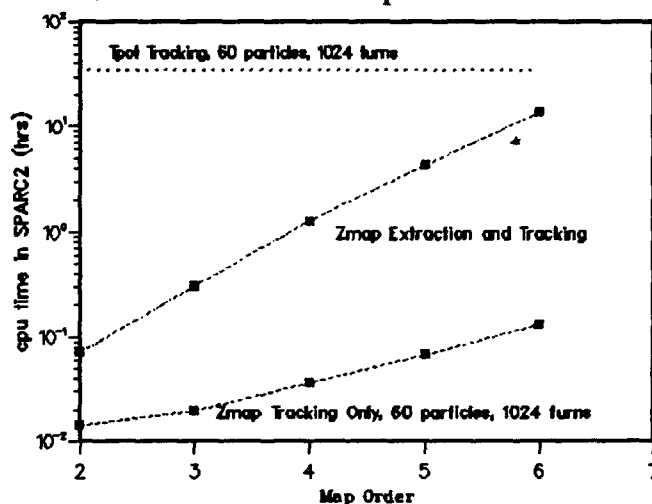
Fig.1 Speed of Zmap and Teapot Tracking for the Collider Lattice

In Fig.1, the extraction and tracking times are plotted vs. map orders from 2 to 6, with the Teapot tracking as a reference. We use a SUN Sparc2 workstation and take a typical case (for smear and linear aperture studies) in which 60 particles are tracked 1024 turns along the lattice. All maps are 6x6, i.e, 6-dimensional 6-variable. We notice the following:

(a) The extraction and tracking time for Zmap of order 4 or 5 are significantly shorter than direct element-by-element tracking.
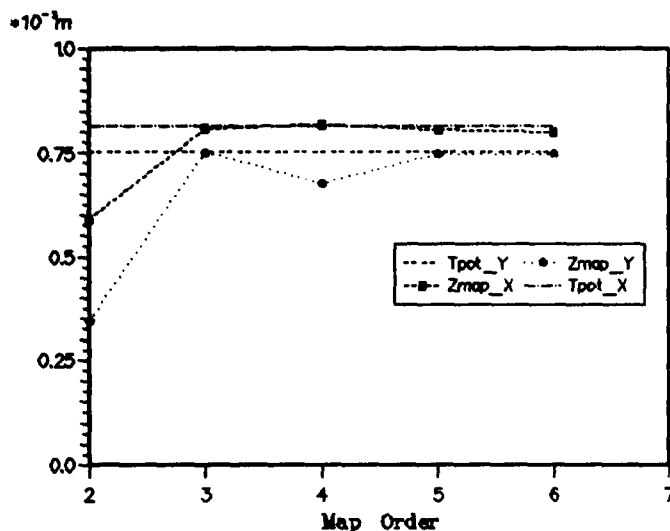
Fig.2 Horizontal(x) and vertical(y) linear apertures of the collider lattice

(b) Once a map has been obtained, tracking of 1,024 turns takes just a few minutes because the whole lattice is represented by one element (the map). This opens the possibility of tracking bunches of particles to get the detailed features of the phase space.

III. LINEAR AND DYNAMIC APERTURES

All trackings are performed with respect to the closed orbits. The turn-by-turn data from every tracking case is analyzed to find the smear and tune shifts with amplitude so that the linear apertures (defined as occurrence of 5% smear or 0.5% tune shift, whichever comes first) can be determined. The results are shown in Fig.2 for the Collider Lattice; and results from Teapot direct tracking are plotted as references.
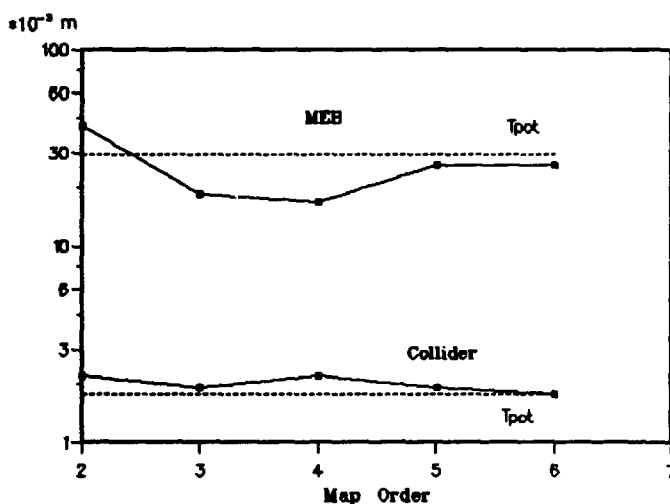
Fig.3 Horizontal(x) and vertical(y) linear apertures of the MEB lattice

What we can see from these figures is that the 5th order map is very accurate compared with the direct tracking; and the horizontal result is better than the vertical one for lower orders.

In Fig. 3 we show linear apertures calculated from maps extracted for the SSC Medium Energy Booster lattice (MEB20-version). In this case, the convergence toward the results from direct tracking (shown as parallel horizontal lines in the figure) looks even more consistent with the increment of map orders.

In Fig. 4, the dynamic apertures calculated for the Collider and MEB lattices by Zmap and Teapot are plotted. Although one cannot expect by either method to obtain an accurate dynamic aperture from the tracking of only 1,024 turns, the map results are still in very good agreement with those from Teapot with the use of 5th order maps in both cases; and we expect to get even better agreement from map tracking if more than 1,024 turns are tracked: because as the dynamic aperture shrinks with longer turns, the map will definitely become more accurate.
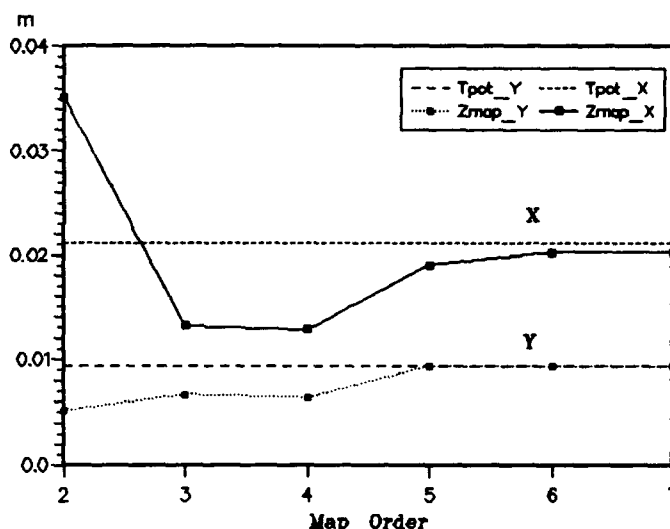
Fig.4 Dynamic apertures of the collider and MEB lattices calculated from map tracking

IV.IMPLEMENTATION OF ZLIB IN TEAPOT

Teapot and Zlib (and other Z-family programs) were originally independently written and compiled, with a nonlinear machine "Zfile" as the only readable input data structure of the Z-family program. Most variables were defined differently in the two systems and thus were incompatible with one another for direct communication. We made some changes and created some subprograms which link both programs and could be read and executed by Teapot. We load Zlib in Teapot, so that Zlib's functions and subroutines could be

516

directly called in Teapot. The following are some commands that we propose to be used by the Teapot user:

1) **maptrk**: a command similar to **trackclo** of Teapot. Its appearance switches the program to the "map mode" and it must be preceded by **analysis** command.

2) **order = :** an integer number from 2 to 10 could be assigned to specify the map's order to be extracted or tracked.

3) **mapname = :** a string of characters of max size 16 could be assigned to specify the desired name for the map.

4) **getzmap :** a command for extracting the map of order in "**order =**" by using Zlib , and the absence of it means the map of the name in "**mapname =**" already exists so that the map extracting process could be skipped.

Here is an example of a section of Teapot input data:

readfile

analysis, energy = 2.0e4, xtyp=1.e-6, pxtyp=1.e-06, ytyp=1.e-06, pytyp=1.e-06, dptyp=1.e-6, delta=0.0000

maptrk, energy = 2.0e4, eigenamp, getzmap, order = 5, mapname = nov1map5th

start, x=1.4690e-04, px=0.0, y=1.4849e-04, py=0.0, dp=0.000

start, x=2.9380e-04, px=0.0,   y=2.9380e-04, py=0.0, dp=0.000

and so on; and the rest is the same as in the original Teapot .

V. CONCLUSION

The implementation of Zlib in Teapot gives the user more choices to choose from when tracking particles. Thin-element tracking gives more accurate results, and is convenient when dealing with most accelerator lattices for routine analysis. Fast map tracking with Zlib is now also available in an easy-to-use form, and our preliminary results indicate that for a well-corrected lattice, low order maps provide useful and effective perspectives about the accelerator lattices for efficient analysis of some of their properties.

VI. REFERENCES

[1] Y. Yan and C. Yan, "Zlib - A Numerical Library for Differential Algebra", *SSCL-300* (1990).

[2] L. Schachinger and R. Talman, "Teapot: A Thin-Element Accelerator Program for Optics and Tracking", *Particle Accel.* 22, 35 (1987).

[3] Y. Yan, G. Bourianoff and L. Schachinger,"A Typical 'Ztrack' Long-term Tracking Results for the SSC Aperture Study", *Proc. of Workshop on Nonlinear Problems in Future Part. Accelerators*, Capri, Italy, p.297 (1990).

[4] B. Cole, G. Bourianoff, F. Pilat, "Particle Orbit Tracking on a Parallel Computer: Hypertrack",*IEEE Particle Accelerator Conference*, San Francisco, p.204 (1991).

[5] Y. Yan, "Applications of Differential Algebra to Single Particle Dynamics in Storage Rings", *SSCL-500* (1991).

[6] Y. Yan, T. Sen, A. Chao, G. Bourianoff, A. Dragt, and E. Forest, " Comment on Round-off errors and on One-Turn Taylor Maps", *SSCL-301* (1990).

Influence of the ionization loss in the diagnostic foil on the phase motion in the phasotron

O.N. Borisov   L.M. Onischenko

Joint Institute for Nuclear Research, Dubna, Russia

Abstract

In the present paper it is shown that the influence of the ionization loss in the foil on the longitudinal motion consists of the synchronous phase shift followed by the phase oscillation amplitude compression.

The secondary emission monitors (SEM) [1] are used for the beam diagnostics of the JINR phasotron [2]. An SEM consists of the aluminium foil the several μm thick and $3 \div 5$ mm in radial size. The foil plane forms an angle of 45° to the horizontal plane (the plane of the beam circulation); the foil is places on the fixed azimuth and is moved along the radius.

Secondary electrons emitted by the proton beam passing through the foil are collected and this signal is used to measure the intensity and some other parameters of the proton beam.

The SEM influence on the transversal motion of the beam particles is analyzed in the [3]. The SEM influence on the longitudinal beam particle motion is discussed in the present paper. The beam particles passing through the SEM have a lower energy gain because of the ionization loss in the SEM. The value of the energy loss ΔW depends (for the chosen foil) on the beam energy. It is $3 \div 10$ keV per revolution and makes up a considerable part of the synchronous particle energy gain eV $cos\,\varphi_S$ which is about 20 keV per revolution [4].

When the accelerated particles do not pass through the foil their full energy E changes as [5]

$$\frac{1}{f}\frac{dE}{dt} = eV cos\,\varphi\,, \qquad (1)$$

where f — particle revolution frequency,

φ — particle phase relative to the accelerating voltage.

If the parameters of the synchronous particle (whose revolution frequency is exactly equal to the accelerating voltage frequency f_0 at the moment) are given an index 's', then the synhronous phase will be

$$cos\,\varphi_S = \frac{1}{eVf_S}\frac{dE_S}{dt}\,. \qquad (2)$$

Let us introduce $K = -\frac{E_s}{f_s}\left(\frac{\partial f}{\partial E}\right)_s$, which only depends on the magnetic field structure and describes the phase stability properties of this type of accelerator. Then we obtain the following expression for $cos\varphi_S$

$$cos\,\varphi_S = -\frac{E_S}{eV f_S^2 K}\frac{df_0}{dt}\,. \qquad (3)$$

In the presence of ionization loss equation (1) comes to

$$\frac{1}{f}\frac{dE}{dt} = eV cos\,\varphi - \Delta W\,. \qquad (4)$$

Emergence of the term $\Delta W < eV$ on the right-hand side of the equation can be interpreted as a change of the synchronous phase, the expression for which now will be

$$cos\,\varphi_S = -\frac{E_S}{eV K f_S^2}\frac{df_0}{dt} + \frac{\Delta W}{eV}\,. \qquad (5)$$

The both terms on the right-hand side of (5) are positive. Thus, ionization loss causes the increasing of $cos\varphi_S$, i.e. the decreasing of the phase stability region. Therefore, the phase oscillation amplitudes have to change.

To verify this conclusion the numerical solution of the equation (4) was done. The computer program LONMOT [6] was used with the real magnetic field and the real accelerating voltage frequency dependence on time.

Two modes of the acceleration process were investigated — slow ($cos\varphi_S = 0.003$) and fast ($cos\varphi_S = 0.17$). In fig. 1 the particle with the initial energy 650 MeV and the initial phase 65° is accelerated in the slow mode with dee voltage 15 kV. In fig. 1-a the particle is accelerated without ionization loss, while in fig. 1-b the energy loss is 10 keV per revolution. Obviously, the synchronous phase is changed and the phase oscillation amplitude decreases.

In fig. 2 the same process is shown, but for the initial phase 90°. In this case the synchronous phase is also changed, but the phase oscillation amplitude increases.

In both above cases the value of energy losses in the acceleration process was fixed. The real situation, when the SEM is used for measuring, is different. At first the particles are accelerated without passing through the foil, but after gaining some radius (energy) they begin to pass through the foil and lose the energy. At the transition from acceleration without losses to acceleration with losses the phase oscillation parameters should be changed. It is obviously from the qualitative considerations that the oscillation amplitudes smaller than the synchronous phase shift should be increased and large ones should be decreased.

In fig. 3 the results of modelling this process are shown. In fig. 3-b the particle with the initial phase 90° is accelerated in the slow mode, at first it does not pass through the foil. Its oscillation amplitude is small. When its energy reaches 651 MeV the energy losses of 20 keV are introduced. The synchronous phase then moves to 40°, and the oscillation amplitude is increased. The results of such a manipulation with the particle of the 65° initial phase are shown in fig. 3-a.

In fig. 4-a the results of the same calculation are shown for the fast mode ($cos\varphi_S = 0.17$) of acceleration of a number of the particles with initial phases from 20° to 100° and initial energy 650 MeV. At first the particles are accelerated

without energy losses, and after gaining the energy of 654 MeV they begin to interact with the foil and to lose 10 keV per revolution. The significant damping of the phase and energy oscillations is seen.

In fig. 4-b the results of the similar calculation are shown for other initial energy 649 MeV.

Thus, we can conclude, that the influence of the interaction between accelerated particles and the foil on the phase motion consists in

— the shift of the synchronous phase, $\Delta\varphi_S$ which increases with the energy losses;

— the change of the phase oscillation amplitude. For the slow acceleration process small amplitudes (less then $\Delta\varphi_S$) are increased but the large ones are decreased, i.e. the amplitude spectrum is compressed. For the fast acceleration all amplitudes are decreased, independently of the initial amplitude. It can be explained by the phase with which the particle comes to the foil. For the slow acceleration this phase is always almost equal to the synchronous one. For the fast acceleration this phase depends on the oscillation amplitude, but it is always found at that part of the phase trajectory, where the phase and the energy are increased.

The influence of the ionization loss in the foil may be significant in the multiturn injection of heavy ions with a stripping foil.

References

[1] A.V.Demjanov et al. JINR Phasotron and its Beams. XIII Meeting on Particle Acc., JINR, D9-92-380, Dubna, 1992.

[2] V.V.Kolga, et al. Proc. of the XI Meeting on Particle Acc. JINR D9-89-52, v.2, p.178, Dubna, 1989.

[3] A.L.Beljajev et al. JINR 13-88-575, Dubna, 1988.

[4] L.M.Onischenko et al. JINR P9-91-226, Dubna, 1991.

[5] A.A.Kolomensky, A.N.Lebedjev. Theory of cyclic acc. Physmatgis, Moscow, 1962.

[6] O.N.Borisov, L.M.Onischenko. Beam stretching by phase displacement. XIII Meeting on Particle Acc., JINR, D9-92-380, Dubna, 1992.
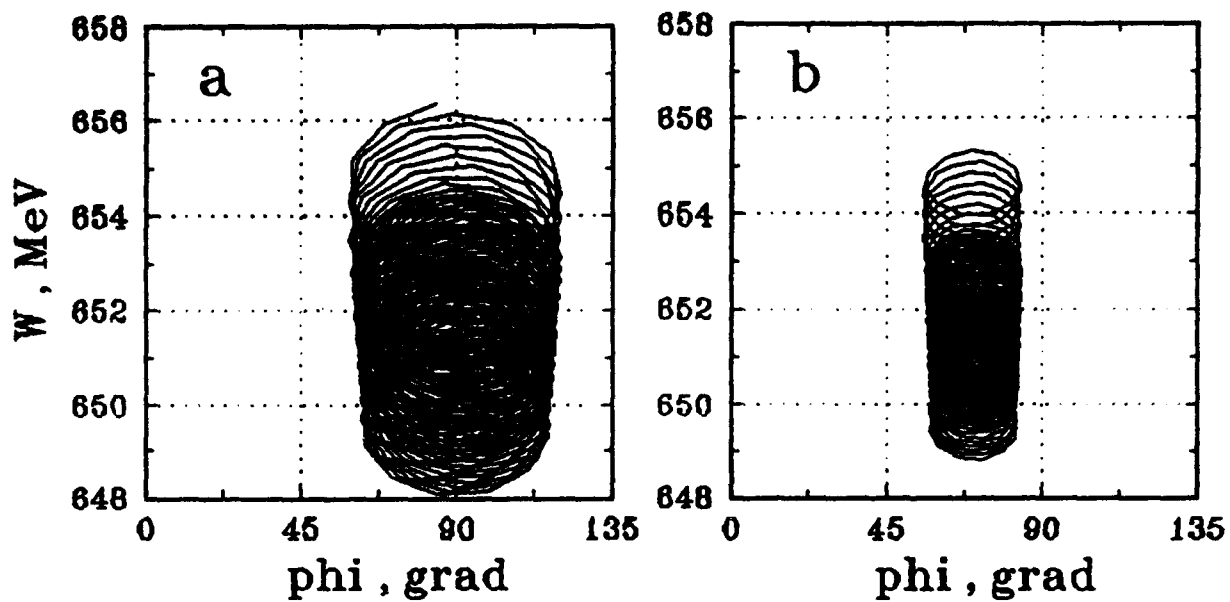
Figure 1: $df_o/dt = -8.3 \cdot 10^6 \ s^{-2}$, $\varphi_o = 65°$,   a) $\Delta W = 0$,   b) $\Delta W = 10$ keV
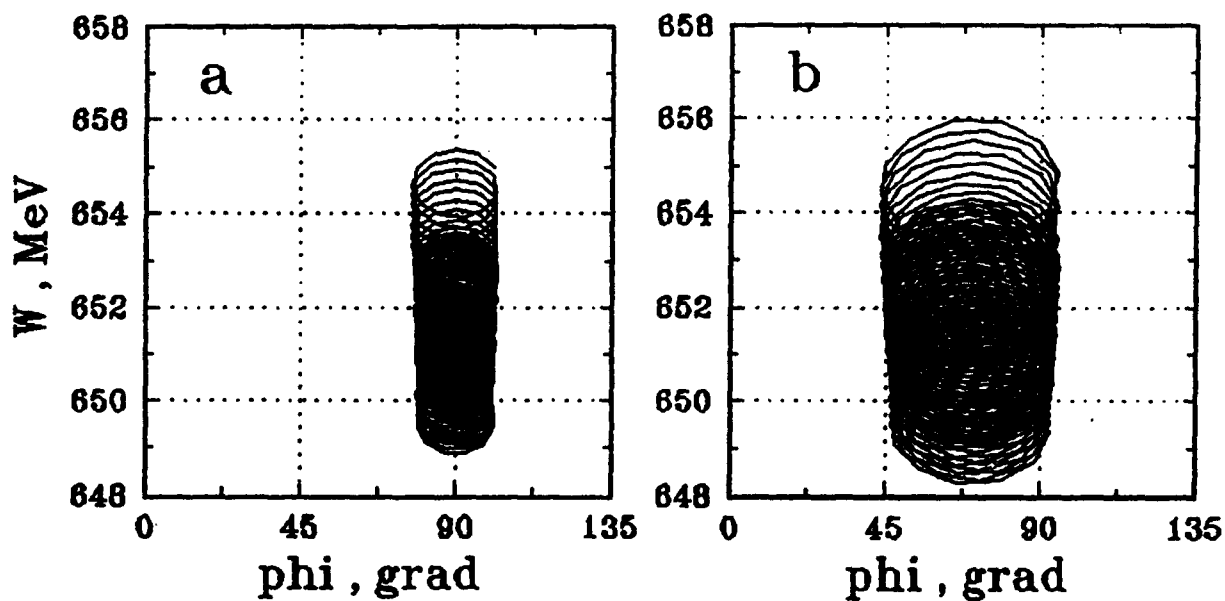
Figure 2: $df_o/dt = -8.3 \cdot 10^6 \ s^{-2}$, $\varphi_o = 90°$,   a) $\Delta W = 0$,   b) $\Delta W = 10$ keV

Figure 3: $df_o/dt = -8.3 \cdot 10^6 \ s^{-2}$, $\Delta W = 20$ keV for $W > W_1$,
a) $\varphi_o = 65°$, $W_1 = 652$ MeV;   b) $\varphi_o = 90°$, $W_1 = 651$ MeV.
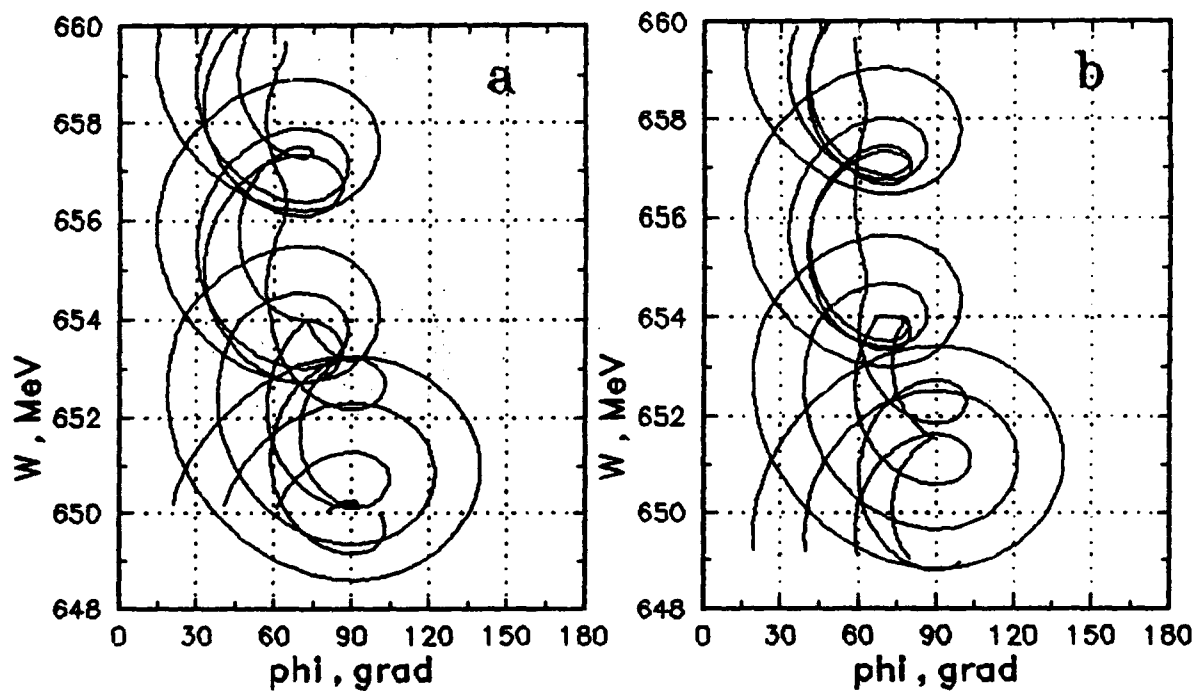
Figure 4: $df_o/dt = -5 \cdot 10^8 \ s^{-2}$, $\Delta W = 10$ keV for $W > W_1$, $W_1 = 654$ MeV,
$\varphi_o = 20°, 40°, 60°, 80°, 100°$,   a) $W_o = 650$ MeV,   b) $W_o = 649$ MeV

RECENT SLC DEVELOPMENTS

Marc Ross

Stanford Linear Accelerator Center

Stanford, California 94309

Abstract

The SLAC Linear Collider (SLC) is the forerunner of a new generation of high energy accelerators. As such, it incorporates many novel features that must be fully exploited to achieve optimum performance. In this paper we present an overview of the frontiers of collider performance at SLC. Recent developments have centered on polarization, intensity and emittance preservation issues. A polarized source and spin transport system were successfully commissioned in 1992 and operated with high reliability. Practical intensity limits associated with rapid growth ($< \tau_s$) bunch length instabilities have been observed in the damping rings. Ring RF voltage manipulations are used to suppress the instabilities. Emittance preservation technique development has focused on controlling system-wide instabilities and improving feedback and tuning procedures. Control of instabilities of all time scales, pulse to pulse, fast and slow, is one of the most challenging aspects of the collider. The challenge is met with 1) very high level of control and automation required for general tuning and optimization, 2) real-time transport line optical correction and monitoring, 3) coupled, high level, trajectory and energy feedback, 4) high order multipole optical correction and monitoring, 5) feedback-based linac beam emittance preservation, and 6) interaction region luminosity optimization. The common thread beneath all of these is the SLC control system which must provide a level of control, diagnosis and feedback not required for simpler machines.

I. Introduction

The novel features incorporated in linear colliders are the small beam size at the interaction point and the low repetition rate which for SLC are about 1μm and 120Hz. Table 1 shows some typical SLC operating parameters.

The challenges for the linear collider are: 1) produce the high intensity bunches, 2) preserve their emittance throughout the system, 3) produce the aberration-free spots at the interaction point and 4) control instabilities. At SLC there are the additional challenges of polarized beam production and transport. Other luminosity related topics such as

repetition rate, detector backgrounds and system reliability will not be discussed in this paper[1].

Parameter	1992	1993	Design (1985)
Energy (GeV)	45.6	45.6	50
Intensity (10^{10})	3.0	3.2	7.2
Polarization (%)	24	60	-
Linac Emittance ($\gamma\epsilon, 10^{-5}$ m-rad)	3.5 x 3.5	4 (x) 0.7 (y)	3
Interaction Point beam size (μm)	2.1(x) x 1.7 (y)	2.3 x 0.7	1.7 x 1.7
σ_z(mm)	1	1	1.5
σ_E/E (% rms)	.3	.3	.25
Luminosity (10^{29} cm^{-1} s^{-2})	2.4	3.6	60
Luminosity (Z events/hr)	26	40	650
Enhancement from disruption		~1.1	2.2
Rep. rate (Hz)	120	120	180

Table 1. SLC Beam parameters at the interaction point, (except where specified).

II. Review of Performance

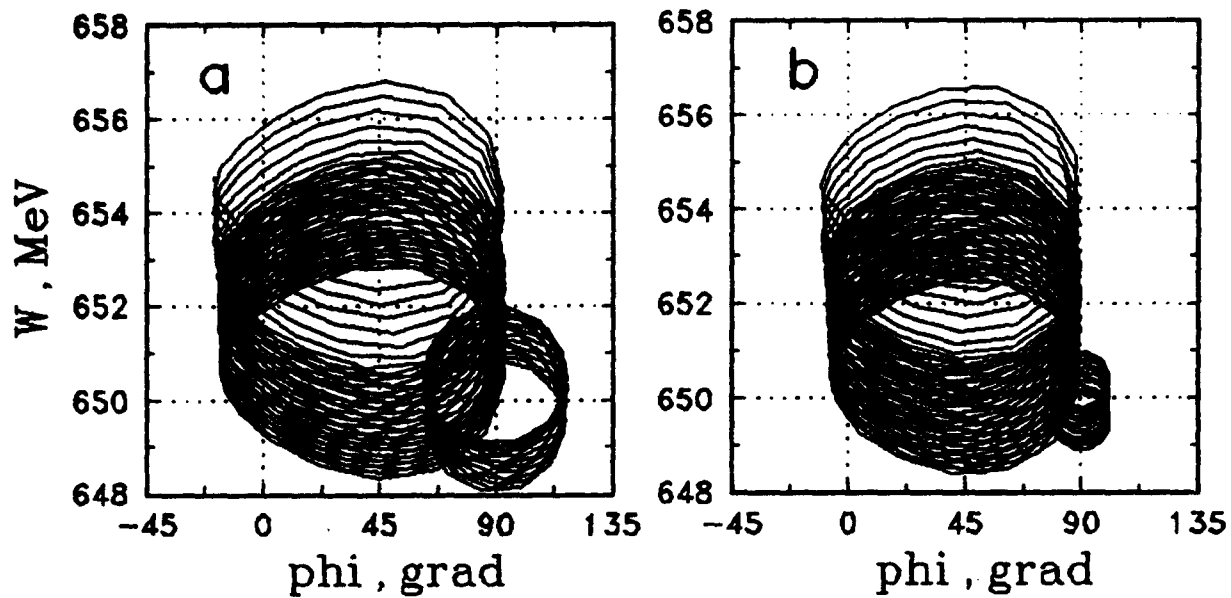The design luminosity of the SLC with 7.2 x 10^{10} per bunch and 180 Hz operation is 6 x 10^{30} cm^{-1} s^{-2}. The design estimates also included a factor of 2.2 for disruption which is expected to be 1.1 at the lower currents. The design luminosity calculated for 1993 intensities and repetition rate is 4 x 10^{29}. Present peak performance is 40 Z_0 events per hour or approximately 3.6 x 10^{29} cm^{-1} s^{-2}. Typical average luminosity, (neglecting downtime) is about 80% of that, or 32 Z_0 per hour.

The first collisions involving polarized electrons occurred in April 1992. At that time, a large, unanticipated, spin precession was observed in the arcs. The cause is the fact that the arc vertical betatron tune and spin tune are close enough to one another to be in resonance. While the spin resonance introduces some depolarization (about 15% relative), it can be used with benefit for spin direction manipulation using vertical trajectory bumps[2]. A

fortunate side effect of this is that it allows the spin rotators at the ring exit and linac entrance to be powered off. Since the superconducting rotator solenoids introduced significant x-y coupling (which was harmless if the beams were round ($\varepsilon_x \approx \varepsilon_y$)), disconnecting them made it easier to transport damping ring flat ($\varepsilon_y < \varepsilon_x$) beams to the linac.

Emittance dilution occurs more strongly in the horizontal plane so the flat beam spot area at the IP is significantly reduced. Flat beams also facilitate the operation of the vertical final triplet focusing at the optimum between the linear and higher order aberrations. With round beams this is difficult due to the detector background generated in the final triplet. Flat beam operation has provided a gain of 1.5 in luminosity. The beam size reduction in the final triplet has also significantly reduced the detector's sensitivity to backgrounds.

Goals set for the 1993 operating cycle (1/1 - 9/1) include 50K Z_0 events recorded on tape with a polarization of greater than 40%. Early in the cycle, the polarized electron source[3], using a strained lattice GaAs photocathode, achieved much higher polarization. Typical polarization at the IP is greater than 60%. The luminosity performance is also good, with an average of about 500 Z_0 delivered per day. With some improvements expected during the cycle from improved feedback and tuning procedures, our goals should be surpassed by a good margin.

III. Intensity

Intensity limitations come from a charge limit effect of the polarized source and single bunch longitudinal instabilities[4] in the damping ring. Because of these two effects, prolonged operation at intensities higher than 3.5×10^{10} has not been done in the linac and positron system.

Soon after the polarized electron photocathode gun was tested online in late 1991, a 'charge limit' effect was discovered that limits the single bunch charge that can be extracted from the gallium arsenide photocathode in a 2 ns full width pulse[5]. The limit is proportional to the low laser light quantum efficiency and the resulting saturation has the benefit of reducing the impact that laser light intensity instability has on the electron beam operation. Testing is proceeding on a gun with twice the cathode area which should provide more than 5×10^{10} in the damping ring.

A practical limit to the present damping ring intensity is the observed bunch lengthening instability which occurs at a threshold of 3.0×10^{10} in each bunch. The onset of this instability is marked by a phase error of the bunch at extraction from the ring. The errant bunch is not properly longitudinally compressed and therefore does not propagate through the linac to 47 GeV with the proper phase space volume. The associated losses usually provoke a response from the beam loss power limiting protection system which forces a momentary 4 second shut down. Production running is effectively stopped if this occurs too often.

The cause of the instability is the high impedance of the damping ring vacuum chamber[6] which has a computed inductance of 37.5nH. By reducing the RF voltage with a slow ramp after injection and restoring it before extraction, the peak bunch current is decreased during the damping cycle. The generator gap voltage is reduced a factor of 4 requiring the use of a wide bandwidth feedback to maintain centroid stability[7]. In order to compensate for the small bunch lengthening that results after the ramp completes, the extracted bunch can be shortened using timed RF voltage pulses just before extraction[8]. With this technique, the onset of the instability can be prevented up to intensities of about 4×10^{10}.

The positron source operates at the design yield of one damped positron per incident 30GeV electron on the positron target. The yield of 150 MeV positrons from the target is 4. The large losses throughout the positron transport and damping ring are accompanied by intensity instabilities of typically 3 to 6% at the output of the damping ring. Efforts are underway to identify the instabilities that cause the increase in relative intensity jitter from the target to the damping ring exit.

IV. Emittance Preservation

Emittance or spot size issues have been addressed successfully. With the flat beam operation, first tested in 1992 and implemented in 1993, the normalized luminosity, (L/N+N-), has surpassed the design with vertical IP beam sizes as low as 800nm. Emittance issues involve all systems downstream and including the damping rings. The phase space orientation and coupling in the arcs and final focus must also be controlled and corrected.

In the last two years the performance of each SLC subsystem has been improved through the widespread use of phase space monitors and careful application of transfer function mapping techniques[9]. For each SLC subsystem automated or semi-automated emittance control and tuning procedures have been implemented.

Damping ring studies done in 1991 showed a significant dependence of the damping time on the tune[10] leading to a 20% increase in the extracted emittance for a 0.1 change in the tune. Studies showed the probable cause to be related to alignment effects. As a result of these studies, the ring radius was changed, reducing the transverse partition numbers at the expense of an increase in the longitudinal partition number. The electron ring damping time was reduced 10% from 3.8 to 3.4 ms.

Optical tuning techniques are required due to the tight alignment tolerances placed on items such as the chromatic correction sextupole magnets and the linac disk loaded waveguide. These techniques have been developed and automated where typical time constants make it necessary. Examples of these are: 1) Linac emittance tuning using orbit bumps, 2) Higher order optical tuning in the ring to linac bunch compressor using phase space monitors, 3) Arc coupling and emittance growth tuning using transfer function grid maps, 4) Final Focus dispersion correction using phase space monitors[11], and 5) Final Focus sextupole alignment correction using bumps and beam size monitors[12].

Items 1) and 3) from the list above are important since they allowed flat beam operation[13]. In the linac, wire scanner emittance measurements made at 1.2, 15 and 47GeV provide information used to correct beam tail and emittance growth coming from residual dispersion and transverse wakefields[14]. Typical trajectory oscillation amplitudes used for the correction are 100 to 200μm. The fast steering feedback loops used throughout the linac are used to maintain the bumps to the $\pm15\mu$m level. At nominal operating intensities, emittance growth can be kept below 50%. Normalized emittances as low as 1.5×10^{-6} m-rad have been observed at low intensities (10^{10}).

Grid mapping techniques have been used for controlling the phase space transformation in the arcs for several years[15]. During the 1993 start-up, this technique was used to reduce cross plane coupling to levels acceptable for flat beam operation.

V. Interaction Region Optimization

The most extreme application of automated tuning is found in the IP spot size optimization. Waist, skew, dispersion and chromatic correction scans are used for testing and making corrections for slow drifts of the incoming beam parameters and for changes in the performance of the final focus correction systems. Among new items for 1993 are the special handling of the flat beam-beam deflection fit[16] and the implementation of a radiative Bhabha pulse to pulse luminosity monitor. The latter device has proven to be a useful check on the luminosity estimated from the beam beam deflection fits and a valuable indicator of short time scale instabilities.

VI. Stability Control

It is perhaps improvements in the control of instabilities of all sorts that have made the most contribution to the good performance of the last two years[17]. Table 2 shows a rough categorization of collider instabilities, categorized both by their time scales and the response they evoke.

Clearly the goals, as broadly indicated in table 2, are to 1) directly fix or control pulse to pulse instabilities using techniques tailored to the problem, 2) move as many as possible into the 'fast' category and 3) build control system tools and mechanical protection for beam power related instabilities. The underlying key to dealing with these issues is a very strong control system which provides the high level programming environment necessary for generating robust feedback and tuning tools.

The introduction, in 1992, of high level fast steering and energy feedback[18], has provided 5 important benefits to SLC operation: 1) operability (through rapid recovery from simple faults), 2) orthogonalization of beam parameters through calibrated fit of BPM data, 3) improvements over the single instrument resolution through constrained fits of many BPM's, 4) immunity from first order thermo-mechanical effects and 5) decoupling of upstream and downstream systems. The final item in the list may be the most significant since it allows fine optical optimization to proceed continuously without complications due to downstream centroid displacements. Several such tuning procedures are non- or minimally invasive and take place during routine operation.

The use of the feedback loops to orthogonalize and record beam parameters such as position, angle and energy has provided clues leading to the cause of slow instabilities. In many cases tunnel air temperature stabilization has made a significant improvement. In addition to recording the centroid value and correction required for stabilization, the feedback loops also record the pulse to pulse stability or the rms variance of each parameter. The stability record provides a similar tool for tracking down sources of pulse to pulse instabilities. By using this and related techniques, linac disk loaded waveguide girder vibrations were identified in early 1992. The 2μm vibrations were reduced by a factor of 20 using simple support struts[19].

VII. Planned Improvements

Two major upgrades are planned for the coming SLC downtime; 1) a new, low impedance damping ring arc vacuum chamber and 2) a major final focus optics upgrade that will reduce remaining aberrations and provide tuning diagnostics.

The new vacuum chamber will have an inductance that is 7 times lower than the present one. It will be built using novel wire electro-discharge machining (EDM) construction techniques and will have a greatly reduced number of flexible bellows. In order to accommodate the rigid chamber, a clearance between the chamber and the quad and bend magnet poles of ±1 mm has been introduced. This requires the installation of separate vacuum chamber and BPM supports and also requires an upgrade of the existing magnet supports. This improvement should put the microwave single bunch instability safely out of reach of other practical limits.

The final focus optics upgrade addresses residual third order aberrations of the system. For this project a single, high field quad will be placed at the closest waist to the IP. This quad will eliminate the largest remaining aberration. Octupoles are also planned which will allow the generation of 320nm vertical spot sizes at the IP with present emittances. The introduction of these elements tightens the tolerances and the tunability of the final telescope. In order to stabilize the optics of the final telescope as well as provide more powerful tuning tools, six new wire scanners are planned per final focus.

These two upgrades have the potential to provide a fivefold luminosity increase.

VIII. Conclusion

The success of the SLC as a prototype of the next generation of electron positron colliders is striking. The number of papers and workshops dealing with linear collider accelerator physics has grown rapidly in the last 5 years and shows strong signs of continued growth. Most major accelerator laboratories worldwide now have large ongoing linear collider research and development programs. The SLC provides a unique laboratory for testing practical collider issues. Of the many challenges that face the next linear collider, perhaps none is more clearly illustrated at SLC than the need for an extremely powerful instrumentation and control system which can be used to perform tuning and feedback processes.

IX. Acknowledgments

I would like to acknowledge the assistance of the SLC Accelerator Department physicists in the preparation of this paper. Of course, the SLC itself is the product of the ongoing efforts of the operators and the engineering groups and I acknowledge their contribution here.

Class	Definition	Sources	Examples	Diagnostic
Pulse to pulse	Not amenable to beam based feedback - truly random process	Pulsed Devices (e.g. thyratron driven) Beam dynamics Vibration	Kicker Girder vibration Source	Synchronous coded data acquisition
Fast	Quickly detected and corrected with no interference	Power Converters Thermal Operator tuning	Power line phase synchronous	Fast feedback Optimized tuning procedure
Slow	Complex analysis requiring expert - fix is interfering	Ground settling Thermal Power Converters	Optics tuning RF phases	Dither control Synchronous acquisition
Rate	Beam power limiting machine protection system	Beam Dynamics Pulsed device breakdown	Klystron Fault	Trip driven snapshot Data acquisition traps

Table 2. Table of linear collider instabilities and examples. Instability classifications are determined in part by the rate with which the problem can be cured. Synchronous data acquisition techniques, whereby data from diverse monitors throughout the complex are taken on the same or related pulses, is an powerful tool for the diagnosis of instabilities.
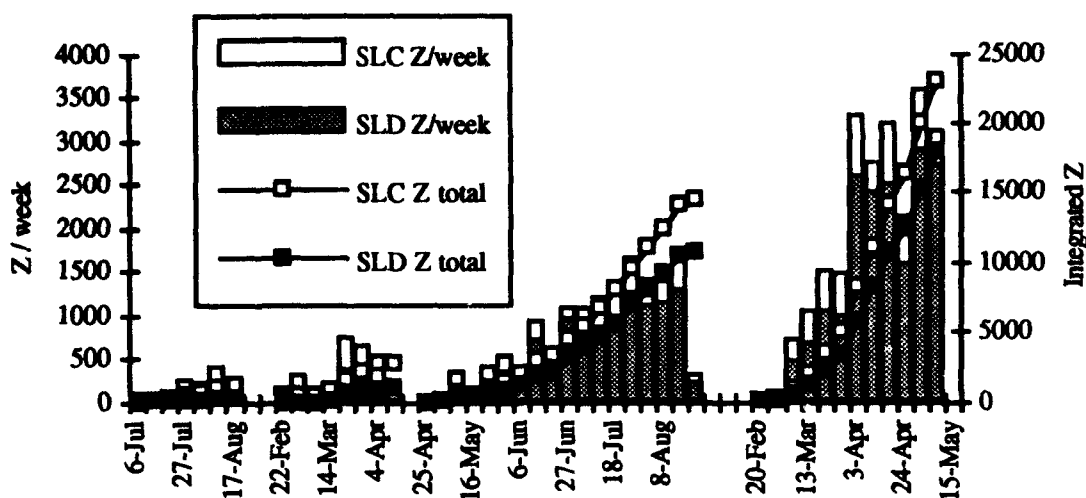
Figure 1. SLC Performance from 1991 to mid-May 1993. The left hand scale is in Z/week and the right hand scale is total integrated Z's delivered. SLC Z's are projected from luminosity monitors and SLD Z's are actually identified events.

X. References

[1] See for example: N. Phinney, 'Review of SLC Performance', Proceedings of the XVth International Conference on High Energy Accelerators, Hamburg, 1992, p45.

[2] T. Limberg, et. al., 'The North Arc of the SLC as a Spin Rotator', These proceedings

[3] J. E. Clendenin et. al., 'Performance of the SLC Polarized Electron Source with High Polarization', These proceedings.

[4] P. Krejcik et. al., 'High Intensity Bunch Length Instabilities in the SLC Damping Rings', These proceedings.

[5] M. Woods et.al., 'Observation of a Charge Limit for Semiconductor Photocathodes', SLAC-PUB-5894, submitted to Journal of Applied Physics

[6] K. Bane, 'Bunch Lengthening in the SLC Damping Rings', SLAC-PUB-5177, Contributed to the Impedance and Bunch Instability Workshop, Argonne, 1989.

[7] P. Krejcik, et. al., 'RF Feedback for Beam Loading Compensation in the SLC Damping Rings', These proceedings.

[8] F.-J. Decker, et.al., 'Pre-Compression of Bunch Length in the SLC Damping Rings', Proceedings of the XVth International Conference on High Energy Accelerators', Hamburg, 1992.

[9] P. Emma and W. Spence, 'Grid Scans - A Transfer Map Diagnostic', Proceedings of the 1991 Particle Accelerator Conference, San Francisco, 1991.

[10] T. Limberg, et.al., ' Calculations of Emittance and Damping Time Effects in the SLC Damping Rings', 3rd EPAC, SLAC-PUB-5789.

[11] P. J. Emma, et.al., 'Beam Dispersion Measurements with Wire Scanners in the SLC', These proceedings.

[12] P. J. Emma, et.al., 'Beam Based Alignment of the SLC Final Focus Sextupoles', These proceedings.

[13] C. Adolphsen, F.-J. Decker and J. Seeman, 'Flat Beam Studies in the SLC;, These proceedings.

[14] J. T. Seeman, et.al., ' Introduction of Trajectory Oscillations to Reduce Emittance Growth in the SLC Linac', Proceedings of the XVth International Conference on High Energy Accelerators', Hamburg, 1992., SLAC-PUB-5705.

[15] T. Barklow, et.al., 'Review of Lattice Measurement Techniques at the SLC', Proceedings of the 5th ICFA Advanced Beam Dynamics Workshop, Corpus Christi, 1991. SLAC-PUB-5695.

[16] P. Raimondi, Private Communication

[17] M. Ross, 'Requirements for Linear Collider Instrumentation', Proceedings of the First European Workshop on Beam Instrumentation and Diagnostics for Particle Accelerators', Montreux, Switzerland, May 1993, SLAC-PUB-6143

[18] T. Himel, et. al., 'Adaptive Cascaded Beam-Based Feedback at the SLC', These proceedings.

[19] J. Seeman, et.al., 'Induced Beam Oscillations from Quadrupole Vibrations of about 2 Microns at SLC', These proceedings.

CEBAF Commissioning Status*

Andrew Hutton
for the CEBAF Commissioning Group
Continuous Electron Beam Accelerator Facility
12000 Jefferson Avenue, Newport News, VA 23606-1909 USA

Abstract

CEBAF is a 4 GeV, 200 μA CW electron accelerator, recirculating the beam five times through two superconducting linacs. The accelerator itself is not due to be completed until January 1994 but CEBAF has been accelerating beams for more than a year and has already validated many of the design concepts. In the injector, 340 μA have been accelerated to 45 MeV. In a recirculation experiment, 215 μA have been accelerated to 80 MeV, demonstrating by extrapolation that the full 5 pass machine will operate well below the recirculating beam break-up threshold. In the north linac, beam has been accelerated to over 245 MeV using 99 superconducting cavities at an average gradient of 5 MeV/m. The beam characteristics mostly meet or exceed specifications. Beam has been taken around 135° of the first arc and the optical properties have been studied. High current tests in the north linac resulted in several runs of more than 100 μA being accelerated through more than 120 superconducting cavities.

I. INTRODUCTION

CEBAF is a 4 GeV, 200 μA CW accelerator with 5 passes through two 400 MeV superconducting linacs. The superconducting linacs use 1497 MHz five-cell niobium cavities operated at 2° K with a nominal gradient of 5 MeV/m and a Q_0 of 2.4×10^9. There will be three interleaved beams at 499 MHz with independent current control. Beam from any recirculation pass can be delivered to any of three experimental halls using RF separators Exceptional beam quality is required for the physics program: 4 σ emittance less than 2×10^{-9} m-rad above 1 GeV and 4 σ energy spread less than 10^{-4}.

II. CONSTRUCTION STATUS

A. General

The civil construction is complete, including the three experimental halls. The accelerator is now 88% complete and 92% committed, with completion due in January 1994. The first experiment will be ready for test beam in June 1994 with the other experiments coming later as dictated by the funding profile. The entire installation should be complete by summer 1996. The east spreader, recombiner, and the five east arc lines are complete, under vacuum, and aligned. The four west arc lines are 75% complete and 75% under vacuum.

B. Rf Superconductivity

The 5-cell superconducting cavities are based on a Cornell/CEBAF design and are made of high RRR niobium, supplied by CEBAF for fabrication by industry (Siemens AG). The vendor does the initial field flattening and tuning of the cavity frequency. CEBAF completes the cavity tests, and assembles them in the cryostat. To date, $28^1/_4$ cryomodules (each containing eight 5-cell cavities) have been completed and installed in the machine (113 active meters) out of a total of $42^1/_4$ (169 active meters); of these 15 have been used to accelerate beam. A production rate of two cryomodules per month has been maintained for over twelve months, and this rate will continue through the completion of the second linac.

The cavities are significantly better than design specification, with a mean usable accelerating gradient of 7.2 MV/m defined as the minimum gradient defined by one of three limits:

$$Q_0 = 2.4 \times 10^{-9}, \text{ or}$$

Field emission heat load = 1 W, or

1 MV/m lower than the quench gradient.

There is little or no systematic degradation seen between vertical dewar cavity tests and tests of cavities installed in the tunnel. The detailed performance figures are given in another paper in this conference[1].

C. RF Power System Status

The RF power sources consist of one 5 kW klystron per 5-cell cavity with eight klystrons having a common high voltage power supply, low level controls, and CAMAC interface. There are 43 of these systems, 20 in each linac, and 3 in the injector (or to be exact $2^1/_4$). At present 31 systems have completed low level checkout, and 28 have passed high level checkout (full power into waveguide shorts). The control system performance has been validated in the Front End Test (Table 1) and the master oscillator has passed the acceptance test.

Table 1. RF Control System Performance	
Uncorrelated gradient noise	$< 1.5 \times 10^{-4}$
(Specification	$< 2 \times 10^{-4}$)
Correlated gradient noise	$< 1.1 \times 10^{-5}$
at 60 Hz	$< 2 - 3 \times 10^{-5}$
(Specification	$< 1.1 \times 10^{-5}$)
Phase noise	$< 0.1°$
Slow phase variations not yet measured	
(Specification	$< 0.25°$)

D. Cryogenic System

There are three major refrigeration systems. The cryogenic test facility provides 2° K and 4.5° K helium for the SRF Test Laboratory to support cavity production and measurements of the experimental magnets. It now has 32,000 hours of operation with no major problems.

The end station refrigerator with its 0.6 km of transfer line supports the experimental hall magnets and is rated at 1.5 kW at 4.5° K. Purification of the liquid helium is now in progress and cool-down of the Hall C dipole is scheduled for June 1993.

The central helium liquifier with its 1.4 km of transfer lines supports accelerator operation and is rated at 4.8 kW at 2° K. During the running period, the cold compressors were not available due to a series of electrical failures. A vacuum pump was installed to support accelerator pre-commissioning and 16,000 hours operation have now been accumulated with vacuum pumps at 2.0° K-4.2° K. A second pump was commissioned in February to provide additional capacity but it shattered its rotor after 1 hour of operation. At present, the cold compressors have been redesigned, reinstalled, and have achieved 3.35° K operation. Commissioning will continue this summer.

Beam energy during the pre-commissioning was always limited by the available cryogenic capacity and operation was at 2.3° K rather than 2.0° K to minimize the load on the vacuum pump.

III. COMMISSIONING

A. Strategy

The commissioning is organized around Teams. Each Team consists of a small group of people with different skills and backgrounds who, together, search for the "best solution" to a particular problem. The principal thrust of the entire commissioning and operations efforts is to make the machine operate well for experimental physics. The interaction between different disciplines is maximized to make this process as efficient as possible, where efficiency is defined as the shortest commissioning time to provide quality beams to the experiments.

The commissioning Teams that have been established to date are:

- Harp Team
- Diagnostics Checkout Team
- Control System Speed Team
- RF Commissioning Team
- High Current Team
- High Gradient Team
- Arc Commissioning Team

The commissioning studies described in this paper are largely the work of these Teams.

B. Commissioning Schedule

There is a global commissioning plan which is shown in Table 2. Pre-commissioning started in January 1992 in the injector region and continued through April 1993. During this time, temporary shielding walls were put up to enable installation to occur downstream of the zone with beam. The whole machine is currently down to complete installation. Tests of the upgraded injector will begin in October 1993 and commissioning of the whole machine is scheduled to start in January 1994.

Table 2. Commissioning Overview
Phase 1 Pre-Operational Tests-low power (<17 kW)
Stage 1 Front end test (completed)
Stage 2 North linac low power beam test (completed)
Stage 3 East arc low power beam test (completed)
Phase 2 Pre-Operational Tests-high power (<120 kW)
Stage 1 North linac high power beam test (completed)
Stage 2 South linac high power beam test
Phase 3 Commissioning
Stage 1 Commission single-pass operation, start delivery of nominal 800 MeV, 200 μA beam to Hall C
Stage 2 Tests of 2, 3, 4 and 5 pass operation to 4 GeV (nominal)
Stage 3 Three-beam distribution tests

IV. INJECTOR

A. Performance

The injector consists of a thermionic gun, copper cavities accelerating to 500 keV, 1497 MHz choppers and $2^1/_4$ cryomodules (9 active meters of superconducting cavities). The nominal beam energy of 45 MeV was easily achieved The nominal average beam current of 200 μA CW was also easily achievable, indeed 340 μA CW was obtained without great heroics. The transverse emittance is below 20 nm-rad in both planes (spec. = 44 nm-rad), the longitudinal emittance is below 5π keV-degree (spec. = 15π keV-degree). In routine operation, the bunch length obtainable is 0.4 degrees at 1.497 GHz (spec. = 1.5 degrees or 2.8 ps).

B. Turnkey Operation

A considerable amount of effort was devoted to trying to make the operation of the injector complex "turnkey". These tests were a prelude to establishing similar performance for the entire north linac.

"Turnkey operation" was defined as:
Start-up with all systems un-powered and obtaining spec. 45 MeV beam entering north linac, verifying:

- Beam momentum at nominal 500 keV
- Beam momentum at nominal 5 MeV
- Beam momentum at nominal 45 MeV
- Bunch length at entrance to first cryomodule
- Proper steering through entire beam line

The goal established for this was 25 minutes. On the best day, the entire sequence was repeated three times in succession in an average time of 24 minutes. However, start-up after a weekend shutdown was considerably slower, mainly due to problems with the phase reproducibility of the warm copper cavities. The whole injector complex is currently being rebuilt to include 499 MHz choppers and the new installation should correct the problems found. In addition, the early production cavities that were installed in the injector are being replaced by two of the very best late-production cryomodules. This should provide an operational safety margin when running the injector day in and day out.

C. Front End Test

In the Front End Test, two 180° doubly achromatic bends were installed in the injector region to permit beam to be recirculated through the two cryomodules. Fourteen quadrupoles were installed to provide dispersion-free beam transport and independent adjustment of the x and y planes.

Using this experimental set-up it was possible to examine the beam break-up instabilities which could be caused by the superconducting cavities. It was demonstrated that a total of 215 μA could be accelerated in two passes to an energy of 80 MeV. Since the injection energy into the two cryomodules was only 5.5 MeV compared to the nominal energy of 45 MeV for injection into CEBAF, this result indicates that the full 5-pass machine will operate well below the recirculating beam break-up threshold. This experiment and the simulations are described in another paper at this conference[2].

V. LOW CURRENT TESTS

The low current tests were the first attempts to operate a large number of superconducting cavities simultaneously, but only part of the north linac was involved. At that time, a total of 104 five-cell cavities, each with its own klystron and independent controls, was available for acceleration. Due to the cryogenic limitations discussed in Section IIB, it was not possible to sequentially set up each cavity at the nominal accelerating gradient. Instead, each cavity was set up and phased at a gradient of 2 MeV/m and the cryostats were overfilled with helium. All the cavities were then simultaneously ramped in gradient up to the nominal value. The tests were scheduled over a four week period with operation for two days every week, the remaining time being spent correcting problems and increasing the number of cavities that could be operated simultaneously.

On the best run, 99 superconducting cavities (93% of those available) operated at the design gradient of 5 MV/m. Beam was accelerated to 245 MeV and the energy confirmed with a spectrometer.

Energies over 200 MeV could be obtained only briefly due to the cryogenic limitations but several multi-hour beam runs were completed at up to 148 MeV.

During all these runs, the average current was limited to approximately 1 μA, both for machine protection reasons and because a suitable high-power dump was not yet available.

These tests demonstrated successful operation of multiple RF systems from high level screens, and a large amount of operational experience (both personnel and equipment) was gained.

VI. HIGH CURRENT TESTS

A. RF Considerations

For these tests, the high power dump had been installed, the beam loss monitors calibrated, and the machine protection system set up[3]. As before, the energy was limited to 130 MeV by the cryogenic system rather than the nominal 400 MeV.

The maximum current achieved was 110 μA CW, maintained for over 10 minutes (compared to the specification of 200 μA). The limitation was the time available for adjusting the beam loss monitors to provide adequate, redundant coverage without causing spurious trips. There was no obvious technical limitation, indeed the stability of the beam was impressive since none of the feedback systems were operational during these runs.

However, the first tests of the energy vernier system were successfully carried out[4], demonstrating that the errors in beam energy could be detected and corrected on a slow (≈3 Hz) time scale.

The neutron source terms from the beam dump were measured by lowering detectors down a penetration. These measurements are needed to cross-check the shielding calculations to ensure that CEBAF will be operated within the safety envelope.

B. Cavity Considerations

Many theoretical calculations and operational measurements were carried out to support high current running. Cavity phasing algorithms[5] and an algorithm for an automated search for the resonant frequency of the cavity[6] were developed and tested successfully. Cavity steering and focusing effects were measured but the measurements are hard to interpret and are not in agreement with the theory[7]. Beam loading algorithms[8] and techniques for bypassing un-powered cavities and cryomodules were developed, coded and successfully tested with beam.

RF performance was confirmed under heavy beam loading conditions by comparing the signals picked up by a probe in the cavity during operation at different beam currents. The probe signals are essentially identical, indicating that the RF control module was performing correctly.

C. Optics and Beam Quality Measurements

An auto-steering algorithm was developed and tested[9] and initial tests of semi-automated beam quality measurement techniques were performed.

The beam characteristics of a 36 μA pulsed beam were measured at 121 MeV at the end of the north linac. The energy spread was 9×10^{-4} (spec. = 5×10^{-4}) and the horizontal and vertical emittances were 0.7 and 1.8 nm-rad (spec. = 4 nm-rad). The extremely small emittance is confirmed by the experimental observation that it is possible to drift the electron beam down the entire linac without focusing. The measurement of energy spread is believed to be larger than specification due to drift in the injector region as was discussed in Section IVB.

VII. HIGH GRADIENT TEST

A. Cryomodule Limitations

When superconducting cavities are installed in cryomodules, their performance is limited by interlocks designed to protect the cavities from irreparable damage. In the CEBAF cryomodule, there are arc and infrared detectors for cold and warm windows on the input waveguide and an interlock on the waveguide vacuum.

The maximum usable gradient is limited to values defined during the cavity commissioning. The limits are given by the requirement that the field emission power should be less than 1 W and that the maximum gradient should be 1 MV/m less than the level at which the cavity quenches.

With these constraints, the average usable gradient for the CEBAF cryomodules is 7.2 MV/m compared to the average gradient of 8.4 MV/m for the bare cavities. This is a fairly typical result for complex superconducting cavities

Operation in the commissioning phase was limited by the cryogenics as discussed above. However, by running most of the cryomodules at low gradient, it was possible to push a complete cryomodule to the limit given by the cavities.

Table 3. Measured Accelerating Gradients

Cavity	Gradient	Limitation
1	6.8 MV/m	Field Emission
2	8.2 MV/m	Field Emission
3	9.2 MV/m	Quench
4	8.7 MV/m	Quench
5	9.6 MV/m	Quench
6	10.9 MV/m	Quench
7	7.7 MV/m	Field Emission
8	6.3 MV/m	Quench

B. Results

Initially, the gradient was limited to 5 MV/m by the infrared detectors. It was determined that the trip levels could be raised without endangering the windows. In subsequent runs, a complete cryomodule (8 cavities) was operated at an average accelerating gradient of more than 8 MeV/m (specification = 5 MeV/m) and this gradient was cross-calibrated with a spectrometer. This gradient was maintained for up to a shift.

The detailed list of achieved gradients in the 8 cavities is given in Table 3.

VIII. EAST ARC TEST

A. Description of Layout and Optics

The optics of the Linac is a straightforward 120° FODO lattice for the lowest energy passage and a proportionally smaller phase advance for the higher energy beams. At the end of the linac, the different beam energies are separated into their respective arcs in the spreader region and then matched into the arcs in the extraction region. At the other end of the arcs the beams are brought together in the recombiner region, which is almost a mirror image of the spreader region.

Beam tests of the optics were done at 130 MeV, rather than the nominal 400 MeV for which the first arc was designed. This caused some difficulty in matching magnets in the spreader region, which are on a common bus. These magnets were matched at the nominal energy and they have different saturation characteristics at lower energies. This provided more stringent requirements on measuring and correcting optical errors than will be required for the nominal conditions.

The CEBAF arcs are designed to be both achromatic and isochronous. There are four similar achromats per arc and the required conditions should be reproduced at the 45°, 90°, and 135° points as well as the complete 180° arc. As installation of the south linac was proceeding in parallel with the beam commissioning in the north linac and east arc, a low power beam dump was inserted at the 135° with a shielding wall behind it.

The section of the machine that was available for pre-commissioning therefore enabled all the relevant properties of the linac optics, spreader, matching region and arcs to be tested.

B. Initial Beam Transport

It was first determined that it was possible to bring beam, loss-free, to the beam dump at the 135° point using a simple 120° optics. This demonstrated that all of the hardware was correctly hooked up. A calibration problem was also diagnosed and corrected at this time.

The nominal, isochronous and achromatic optics was then used and the beam run to the dump for extended periods to support commissioning of the diagnostics, particularly the arc beam position monitors[10,11] and the beam loss monitors[3].

C. Optical Checks

Optics tuning procedures were developed and tested for the entire beam line from the gun to the dump. Specifically: the north linac FODO cells were tuned to exactly $120°$; the spreader dispersion was tuned to the theoretical value of zero; and the phase advance across the extraction region was set to $180°$[12].

Operational procedures are being developed for measuring and correcting: the arc momentum compaction factor; high dispersion tuning of the arc to support studies of linac energy variation; and fine tuning of the transverse optics.

The first optical checks using difference orbits were initiated. Data was taken off-line and analysis is currently in progress.

D. Isochronicity Measurement and Correction

The linac energy was modulated by $\pm 0.1\%$ with a square wave applied to the drive of one of the superconducting RF cavities. A precision 1500 MHz phase detector was used to measure the phase difference between a reference signal derived from one of the RF control modules in the linac and a beam signal from a BPM at the $90°$ point of the arc.

Two optics sets were calculated using DIMAD to give different values of the M_{56} beam transfer matrix element (change of path length with energy). These were used in the arc and measured using this technique. The results are as follows[13].

nominal M_{56}　1.0 m　　measured M_{56}　1.4 m
nominal M_{56}　0.0 m　　measured M_{56}　18 cm

Applying small tweaks to the optics corrected the M_{56} of the latter case to:

measured M_{56} 1.8 cm　specification　10 cm

The accuracy of the measurement technique is better than 3 mm.

IX. CONCLUSION

A.. Present Strengths

Pre-commissioning of CEBAF has now been underway for more than a year. An experienced commissioning team is in place, with members of the team having prior experience from CERN, DESY, FermiLab, KEK, and SLAC. A trained and qualified team of operators is now in place and used to working together.

The safety procedures are well documented and enforced. Examples of each element of the safety system have been tested with beam and proven procedures exist for testing the expanded system.

The Team approach is now part of the commissioning culture and is accepted by all (this was not initially the case). There are clearly defined and understood goals which incorporate the best ideas of the entire staff. It has been clearly demonstrated that working together produces better results.

B. Long Term Improvements Planned

There are a number of areas where improvements are necessary.

The main limitation to accelerator operation up till now has been the cryogenic system. We expect to commission the cold compressor this summer and demonstrate reliable operation.

The control system, TACL, was also a weakness. Initially, the main problem was system response time and this was successfully rectified by modifying the configuration. The enhancements now foreseen are:

　　more "canned" procedures on the computer
　　more, and better, high level screens
　　higher reliability of the system
　　better operator interface

We are benefiting from interaction with the FermiLab controls group and may well incorporate some of the functionality of their ACNET control system.

The beam position monitors need improvement to correct problems seen during operation. The arc monitors (which see a single beam) will be modified to improve the signal-to-noise ratio. The cost will be offset by multiplexing monitors from the different arcs. The linac beam position monitors (which see multiple super-imposed beams) also need improved front-end electronics which is not completely defined at this time.

X. REFERENCES

[1] F. Dylla. This conference, "Operating Experience with SRF Cavities."

[2] N. S. Sereno and L. S. Cardman. This conference, "Studies of Multipass Beam Breakup and Energy Recovery Using the CEBAF Injector Linac."

[3] J. Perry, et al. This conference, "The CEBAF Beam Loss Sensors."

[4] G. Krafft et al. This conference, "Energy Vernier System for CEBAF."

[5] S. Simrock et al. This conference, "Phasing Schemes for the CEBAF Cavities."

[6] R. Li et al. This conference, "Automated Measurement of Cavity Frequency and Cavity Tuning at CEBAF."

[7] Z. Li et al. This conference, "Transport Properties of the CEBAF Cavity."

[8] L. Merminga et al. This conference, "Operation of the CEBAF Linac with High Beam Loading."

[9] B. Bowling et al. This conference, "Orbit Correction Implementation at CEBAF."

[10] A. Hofler et al. This conference, "Performance of the CEBAF Arc Beam Position Monitors."

[11] B. Bowling et al. This conference, "CEBAF Beam Viewer Imaging Software."

[12] Y. Chao et al. This conference, "Commissioning and Operating Experience with the CEBAF Recirculation Arc Beam Transport System."

Overview of Linear Collider Designs

R. H. Siemann*

Stanford Linear Accelerator Center, Stanford University, Stanford, CA 94309

I. INTRODUCTION

Linear collider design and development have become focused on a center-of-mass energy $E_{CM} = 0.5$ TeV and a luminosity $L \sim 5 \times 10^{33} cm^{-2} sec^{-1}$. There are diverse approaches to meeting these general objectives. The diversity arises from different judgements about the ease of developing new and improving existing technology, costs, extension to higher energies, experimental backgrounds and center-of-mass energy spectrum, and tolerances and beam power.

The parameters of possible colliders are given in Table 1 which is based on a compilation made by G. Loew at the LC-92 Conference and is reproduced with his permission.[1] The colliders described in that table are:

TESLA (being developed by an international collaboration) which is based on superconducting RF. All the others would use room temperature RF.

DLC (DESY/Darmstadt) which uses S-band (3 GHz) RF where there is extensive operating experience.

NLC (SLAC) which uses higher frequency X-band (11.4 GHz) RF in a modulator-klystron-accelerator configuration similar to S-band linacs.

JLC-I (KEK) which has three frequency options, S-band, C-band (5.7 GHz), and X-band. Multiple bunches are accelerated in each RF pulse as they are in TESLA, DLC, and NLC.

VLEPP (INP) which employs a single high intensity bunch rather than multiple bunches.

CLIC (CERN) which is a "two-beam" accelerator with klystrons replaced by an RF power source based on a high-current, low-energy beam travelling parallel to the high energy beam.

The discussion below focuses on some of the common themes of these designs and the differences between them.

II. EFFICIENCY AND MULTIPLE BUNCHES

The AC mains power is large for any of the colliders, and energy efficiency is critically important.[2] One way to achieve good efficiency is by accelerating multiple beam bunches per RF pulse.

For example, in the DLC a 150 MW, 2.8 μsec long RF pulse powers two 6 m long sections to a gradient of 17 MV/m. The beam has 172 bunches with 2.1×10^{10} particles per bunch spaced 10.7 nsec apart. The RF pulse has 420 J of energy; a single bunch extracts 0.685 J from the accelerator RF fields, and the bunch train extracts a total of 118 J leading to an efficiency, η_B, for converting RF to beam energy of η_B

= 0.28. If only a single bunch was accelerated, the RF pulse could be shortened to 1 μsec, the accelerator filling time, but the efficiency would be low, $\eta_B = 0.0046$. A major advantage of multiple bunches is that the cost of filling the accelerator with RF energy has been amortized over a large number of bunches.

Multiple bunches have implications for both the fundamental and higher modes. The energy spread of the beam must be small to minimize emittance blow-up from dispersive effects in the linac and to minimize chromatic aberrations in the final focus. The bunch train lengths are comparable to filling times, and the accelerator structure must be prefilled and the RF amplitude ramped so that each bunch gains the same energy.[3]

The bunches are closely spaced, and they interact through higher modes. The transverse modes can cause emittance blow-up that is in addition to that from the short range transverse wakefield. The interaction between bunches must be reduced by damping higher order modes or by "detuning", varying cell dimensions to spread mode frequencies, leading to destructive interference between the deflections from different cells.[4] Detuning and damping may have to be combined to get adequate reduction of the long range wakefields.

VLEPP has a single, large bunch, 2×10^{11} particles, and that results in $\eta_B = 0.12$. The large bunch and relatively high RF frequency impose stringent tolerances on the linac for emittance preservation and requires a novel final focus, the "traveling focus" where a head-tail energy shift is introduced to shift the focal point during the collision and prevent enormous disruption. CLIC has parameters for between one and four bunches, and studies of energy compensation and transverse modes for four bunches are in progress.[5]

III. POWER SOURCES

Present day, conventional linacs are modular with each module consisting of a modulator, klystron, possibly an RF pulse compression system, and, finally, one or more accelerator sections powered in parallel. The modulator converts AC power to high voltage, pulsed power. Most use a low voltage, lumped element transmission line for energy storage, thyratrons as switches, and a pulse transformer to step-up the output voltage. SLAC modulators are typical and are roughly 75% efficient.[6] A substantial fraction of the inefficiency comes from the rise- and fall-times of the pulse transformer. Improving modulator efficiency would be significant. Ideas under consideration are a capacitor bank and high voltage switch tube rather than a pulse transformer (DLC) and a DC high voltage supply and avoiding the modulator by using a gridded klystron (VLEPP).

Table 1: Parameters for E_{CM} = 0.5 TeV Linear Colliders from LC-92[1,2]

	TESLA	DLC	JLC-I(S)	JLC-I(C)	JLC-I(X)	NLC	VLEPP	CLIC
Linac RF Frequency (GHz)	1.3	3.	2.8	5.7	11.4	11.4	14.	30.
Beam Loaded Gradient (MV/m) [3]	25.	17.	18.4	32.5	28.	37.6	96.	78. - 73.
Repetition Rate (Hz)	10.	50.	50.	100.	150.	180.	300.	1700.
Bunches/RF Pulse	800	172	55	72	90	90	1	1 - 4
σ_x/σ_y (nm) (with Disruption)*	310/50	250/190	300/1.9	260/1.9	260/2.0	300/2.2	1590/4	40/5.5
Beam Power/Beam (MW)	16.5	7.5	1.6	3.6	3.8	4.2	2.4	0.4 - 1.6
Υ [4]*	0.063	0.070	0.24	0.21	0.16	0.096	0.076	0.34
n_γ [4]*	5.7	3.1	1.6	1.4	0.9	0.8	5.1	4.6
Beam Posit. Monitor Precision(μm) [5]*	10.	10.	NA	NA	1.	1.	0.1	0.1
Luminosity (10^{33}cm^{-2}s^{-1}) [4]	11.1	6.5	4.4	6.5	6.3	8.2	15.	2.2 - 8.9
Particles/Bunch (10^{10})	5.15	2.1	1.3	1.0	0.63	0.65	20.	0.6
Bunch Separation (nsec)	1000.	10.7	5.6	2.8	1.4	1.4	-	0.33
Unloaded Gradient (MV/m)	25.	21.	22.	40.	40.	50.	108.	80.
Active Two-Linac RF Length (km)	20.	30.	28.	16.7	17.	14.	6.4	6.6
Section Length (m)	1.04	6.	3.6	2.	1.3	1.8	1.01	0.273
Two-Linac Number of Sections	19232	4900	7776	8360	13600	7778	5200	24000
Two-Linac Number of Klystrons	1202	2450	1944	4180	3400	1945	1300	2
Sections/Klystron	16	2	4	2	4	4	4	"12000"
Klystron Peak Power (MW)	3.25	150.	85.	45.	70.	94.	150.	700.
Klystron Pulse Length (μsec)	1300.	2.8	4.5	3.6	0.84	1.5	0.7	0.011
Pulse Length to Section (μsec)	1300.	2.8	1.2	0.6	0.21	0.25	0.11	0.011
Pulse Compression Ratio	-	-	3.7	6.	4.	6.	6.3	-
Pulse Compression Gain	-	-	2.4	4.2	3.2	4.	4.22	-
a/λ Ratio (Input/Output Cavity)	0.15	.154/.108	0.13	.160/.120	.236/.138	.210/.147	0.140	0.2
Total Two-Linac AC Power (MW) [6]	137.	114.	106.	193.	86.	152.	91.	175.
Damping Ring Energy (GeV)	3. or 14.	3.13	1.98	1.98	1.98	1.8	3.0	3.0
σ_L (μm)	1000.	500.	80.	80.	67.	100.	750.	170.
$\gamma\varepsilon_x/\gamma\varepsilon_y$ (10^{-8} m)	2000/100	500/50	330/4.5	330/4.5	330/4.5	500/5	2000/7.5	180/20
β_x^*/β_y^* (mm)	10/5	16/1	10/0.1	10/0.1	10/0.1	10/0.1	100/0.1	2.2/0.16
σ_{x0}/σ_{y0} (nm) (no Disruption)	640/100	400/32	300/3	260/3	260/3	300/3	2000/4	90/8
Disruptions, D_x/D_y	1.2/7.9	0.69/8.6	0.13/13.	0.13/11.5	0.07/6.	0.08/8.3	0.4/ -[7]	1.3/15.
H_D^*	4.1	2.7	1.6	1.6	1.5	1.4	1.3	3.2
δ_B [4]*	0.13	0.078	0.098	0.081	0.043	0.027	0.14	0.35
Crossing Angle (mrad)	1. - 2.	2.	7.3	8.	7.2	3.	NA	1.

Notes

1) Based on a compilation made by Gregory A. Loew for LC92, ref. [1]. Modifications of and additions to his original table are indicated with a *.

2) Symbols are defined in the text.

3) Before applying further gradient reductions for off-crest running, BNS damping, etc (VLEPP excepted).

4) Including the effects of disruption, ref. [7].

5) From ref. [8].

6) DLC bases its number on a combined klystron-modulator efficiency of 45%. JLC and NLC have assumed this number to be closer to 35%. In addition, SLED-I (used for JLC-I(S)) and SLED-II (used for JLC-I(C), JLC-I(X), NLC and VLEPP) are assumed to be about 65% efficient. Power for klystron focusing is not included.

7) VLEPP employs a "traveling focus".

A short, high power RF pulse is the ideal for high frequencies because short sections and high group velocities are favored by efficiency and wakefields. The input power must be multiplied by $\tau^2/(1 - e^{-\tau})^2$ for the same average accelerating gradient ; $\tau \propto \zeta/(\lambda^{1.5}\beta_g)$ where ζ is the section length, β_g is the (normalized) group velocity, and λ is the RF wavelength.[9] The wavelength dependence comes from the skin effect. The maximum transverse wakefield behaves as $1/(a^3(\lambda/a)^{-.8}))$ where a is the radius of the waveguide iris.[10] Increasing λ/a reduces the wakefield with the side effect of raising the group velocity.[9]

It is impractical to generate short RF pulses directly. Modulator efficiency would be poor because pulse rise-and fall-times would be a large fraction of the pulse and klystron peak power would be enormous. Pulse compression[11] which raises the peak power while shortening the RF pulse is used for matching klystron capabilities to an optimum accelerator configuration and is a feature of the high RF frequency colliders.

TESLA has unique power source requirements. The high Q and long pulse length reduce the peak power to 3.25 MW, but the modulator must be capable of delivering that power for over a millisecond.

All except CLIC have a large number of klystrons each of which is a major piece of apparatus requiring maintenance, etc. CLIC is a two-beam accelerator which replaces all of this with a single, low-energy beam travelling parallel to the high energy beam. This low-energy beam has a time structure appropriate for generating 30 GHz RF. It is accelerated by a superconducting RF system, and energy is extracted with transfer structures spaced roughly 1.5 m apart. If the two-beam approach is developed successfully, it will be a major simplification of linear collider design that could be key to reaching multi-TeV energies.

IV. EMITTANCE PRESERVATION

The vertical invariant emittances, $\gamma\varepsilon_y$, are small, and emittance preservation during acceleration is an important consideration. Emittance growth caused by the combination of injection jitter and wakefields must be controlled by tight tolerances on injection elements and BNS damping.[12] Those tolerances range from about 1 μm for NLC and JLC-I(X) to about 10 μm for the S-band accelerators and TESLA.[8]

Misalignments in the main linac cause emittance growth through wakefields and dispersion, that is different central trajectories for different energies. With straight one-to-one orbit correction, i. e. steering to the middle of beam position monitors, there would be extremely tight tolerances on accelerator, quadrupole, and beam position monitor alignment. As examples, those tolerances would be about 10 μm for DLC and half that for NLC.

Beam-based orbit correction procedures, where optical elements are varied and orbit changes measured, relieve these tolerances substantially.[8] The strengths of all the quadrupoles are increased, or decreased, in dispersion free (DF) steering to measure momentum dependence of the central trajectory;

then, the orbit is corrected to minimize the dispersion. The strengths of focusing quadrupoles are reduced while those of defocusing quadrupoles are raised to approximate the defocusing effect of wakefields in wakefield free (WF) steering. WF steering requires good local alignment between quadrupoles and accelerator sections. Since these procedures depend on measuring orbit changes, the beam position monitor must be precise. Estimates of the required precisions are included in Table 1 and range from 0.1 μm for CLIC and VLEPP to 10 μm for DLC and TESLA.[8]

V. FINAL FOCUS

The beams are flat at the interaction point to minimize backgrounds (see below) with $\gamma\varepsilon_x \gg \gamma\varepsilon_y$ and $\beta_x^* \gg \beta_y^* > \sigma_L$ (for all but VLEPP with its traveling focus) where σ_L is the bunch length. The vertical dimension is the most demanding with the vertical sizes before disruption ranging from 100 nm (TESLA) to 3 nm (JLC, NLC).

The vertical spot sizes quoted are the first order sizes, $(\beta_y^*\varepsilon_y)^{1/2}$, and up to third order geometric and chromatic aberrations must be corrected to reach those sizes. This is done by using dipoles to introduce dispersion in a region with sextupoles separated by a -I transformation. Synchrotron radiation losses in the chromatic correction section and in the final quadrupoles introduce important aberrations.

There are extremely tight pulse-to-pulse jitter tolerances. For all but the final doublet those tolerances are about $10\sigma_y$ while for the final doublet they are roughly σ_y.[13] The Final Focus Test Beam (FFTB) at SLAC will test many of the techniques for reducing aberrations to the required level and will provide a test bed for studying and specifying jitter tolerances.

The beams cross at an angle. This avoids unwanted collisions for colliders with closely spaced bunches, and it allows the channel for focusing the incoming beam to be independent of the channel for the exiting disrupted beam. Crab crossing,[14] tilting the bunches with an RF deflector, prevents luminosity loss due to incomplete overlap.

VI. ELECTROMAGNETIC FIELDS AT THE COLLISION POINT

The luminosity is given by

$$L = \frac{N^2 f_c}{4\pi\sigma_{x0}\sigma_{y0}} H_D = \frac{N^2 f_c}{4\pi\sigma_x\sigma_y} ; \qquad (1)$$

N is the number of particles/bunch and f_c is the collision frequency. Focusing during the collision, disruption, is accounted for by an enhancement factor, H_D, in the left-hand expression where the beams sizes without disruption are used, and by using the disrupted beam sizes in the right-hand expression.

The electromagnetic fields at the collision point are parametrized by[7]

$$T = \frac{5r_e^2}{6\alpha} \frac{\gamma N}{\sigma_L(\sigma_x + \sigma_y)} . \tag{2}$$

Field enhancement due to disruption is accounted for approximately by using the disrupted sizes. This increases T for TESLA, DLC and CLIC because the horizontal size is reduced about 50% by disruption in those cases. The mean energy beamstrahlung energy loss, $\delta_B \propto T^2$, and backgrounds from beamstrahlung, e^+e^- pairs, and hadronic events depend on T. When $T << 1$ and $\sigma_x >> \sigma_y$, the mean number of beamstrahlung photons per incident particle is[7]

$$n_\gamma = \frac{5\alpha^2 \sigma_L}{2r_e\gamma} T = \frac{2\alpha r_e N}{\sigma_x} . \tag{3}$$

This parameter, n_γ, serves as an approximate measure of backgrounds.

The luminosity can be rewritten in terms of only three free parameters: n_γ, σ_y, and the beam power, $P_B = Nf_c\gamma mc^2$,

$$L = \frac{1}{8\pi\alpha r_e mc^2} \frac{P_B n_\gamma}{\gamma \sigma_y} . \tag{4}$$

VII. JUDGEMENTS

Table 1 shows the diverse approaches to meeting the general objectives of a 0.5 TeV collider. The diversity arises from different judgements about the following.

The ease of developing new and improving existing technology - DLC and JLC-I(S) are the most conservative in this regard. They take advantage of over forty years of experience with S-band RF. NLC, JLC-I(C), and JLC-I(X) extend the basis of present day linacs, high peak power klystrons and modulators, to higher frequencies. Klystrons and accelerator structures must be developed for those frequencies. TESLA relies on substantial improvements in the cost and accelerating gradient of superconducting RF. VLEPP requires innovations to meet demanding tolerances and relies on novel beam dynamics in the linac and final focus. CLIC has stringent tolerances because of its high frequency, and the RF power source development by itself is a major undertaking comparable to the complete development of other colliders.

Costs - Cost reduction and cost control must be dominant considerations as designs are developed. New technologies promise significant, but uncertain, cost reductions. Older technologies have better established costs, but these tend to be high and must be lowered through engineering and mass production.

The experience of the SSC, an accelerator based on mature technology and a detailed design, teaches us that present linear collider cost estimates should not be taken seriously.

Extension to higher energies - A recent ICFA Seminar[15] strongly endorsed an 0.5 TeV linear collider as the next natural step for high energy physics after the LHC and the SSC and as an important opportunity for international collaboration. It was stressed that this collider should be a step towards multi-TeV energies. High gradients and high RF frequencies tend to be better for reaching high energies with room temperature RF. NLC, JLC-I(X), and VLEPP are optimized for 0.5 - 1 TeV while it would be difficult to directly extend S-band colliders beyond 0.5 - 1 TeV. CLIC is a multi-TeV collider scaled down to 0.5 TeV for purposes of comparison. The energy reach of TESLA depends on how close the fundamental gradient limit of ~50 MV/m in Nb can be approached.

There are considerations that transcend specifics like the choice of RF frequency. Colliders based on room temperature RF have beam dynamics and technologies in common and, at the same time, substantially different from those for superconducting RF. The energy reaches of the generic approaches of room temperature and superconducting RF need to be understood and compared.

Experimental backgrounds and center-of-mass energy spread - The effects of beamstrahlung have been captured in eq. (4) above with a single parameter, n_γ. This parameter doesn't account for the energy spectra of photons, e^+e^- pairs, and hadronic events, and it doesn't account for the overlap of events in the detector. The complicated interface between collider and experiment cannot be reduced to a single number, and it is only through the ongoing studies of that interface that tolerable background levels can be estimated.

Tolerances and beam power - The trade-off is given in eq. (4). Increasing the beam power relaxes injection tolerances, beam position monitor precision, and pulse-to-pulse jitter in the final focus by allowing a larger σ_y. However, there are limits to beam power from efficiency and beam handling, collimation and accelerator protection.

Narrowing the range of choices depends on continuing operation of the SLC and on prototype research and development. The SLC is the foundation for future linear colliders. There there is a clearly measured bottom line, integrated luminosity in a low background environment. The system integration needed to meet it has shown what is and what is not possible and has lead to the development of numerous diagnostic and control procedures that are sure to be at the heart of any future collider.

There are system prototypes addressing beam dynamics and system engineering of the different colliders in Table 1. These include:

A 500 MeV TESLA prototype to be constructed at DESY to demonstrate a gradient of 15 MV/m, to meet cost goals, and to test a high gradient superconducting linac with beam.

A 450 MeV DLC prototype that will test long pulse, high power, multiple bunch operation of an S-band linac.

The Accelerator Test Facility at KEK that combines a 1.5 GeV, S-band linac with a prototype damping ring. The damping ring will produce beams with brightness, single bunch charge, and bunch train structure covering many of the colliders in Table 1. New levels of tolerances, control of beam generated fields, extraction kicker stability, etc will be reached in accomplishing this.

Interaction region optics and stability will be studied at the Final Focus Test Beam at SLAC. In addition, strong field QED, the regime of beamstrahlung in high energy linear colliders, will be explored experimentally.

A 540 MeV prototype NLC linac has the goals of constructing, reliably operating, and studying beam dynamics in an X-band linac.

A ~500 MeV VLEPP prototype will test the klystrons, accelerator, and beam dynamics of that collider.

A beam with the time structure of the CLIC drive beam will be generated by an RF gun, accelerated and used for demonstrating energy extraction at the CLIC Test Facility.

We can look forward to several years of interesting developments as this work proceeds and plans for a high energy linear collider emerge.

VIII. ACKNOWLEDGEMENTS

IX. REFERENCES

1. Gregory A. Loew, *Beam Line*, Vol.2, No. 4, 21 (1992), and the proceedings of LC-92.
2. For comparison, the average AC mains power for the SSC is anticipated to be ~100 MW. *Site-Specific Conceptual Design of the SSC.*
3. K. A. Thompson and R. D. Ruth, *Proc of the 1993 Part Accel Conf*, SLAC-PUB-6154 (1993).
4. K. A. Thompson, C. Adolphsen and K. L. F. Bane, *Proc of the 1993 Part Accel Conf*, SLAC-PUB-6153 (1993).
5. I. Wilson and W. Wuensch, *Proc of the 1993 Part Accel Conf*, CERN-SL/93-20.
6. P. Wilson, private communication.
7. Pisin Chen, *Photon-Photon Collisions*, p. 418 (1992).
8. T. Raubenheimer, *Proc of the 1993 Part Accel Conf.*
9. Z. D. Farkas and P. B. Wilson, SLAC-PUB-3688 (1985).
10. P. B. Wilson, SLAC-PUB-3688 (1985).
11. P. B. Wilson, Z. D. Farkas and R. D. Ruth, SLAC AP-78 (1990).
12. V. Balakin, A. Novokhatski and V. Smirnov, *Proc of 12th Int Conf on High Energy Accel*, p. 119 (1983).
13. J. Irwin, private communication.
14. R. B. Palmer, *Proc DPF Summer Study Snowmass '88*, p. 613 (1988).
15. ICFA Seminar held at DESY, May, 1993.

Progress Report on the TESLA TEST FACILITY

The TESLA Collaboration
reported by
H. T. Edwards
DESY/FNAL*

Abstract

An R&D RF cavity production and test program is underway to evaluate the practicality of superconducting RF cavity systems for future linear collider applications in the 500 GeV energy region. An international collaboration[1] organized by DESY is assembling a TESLA test facility to assess gradient, systems, and manufacturing cost issues of the superconducting RF collider option. Construction of a state of the art cavity processing facility is underway. It is proposed to build four 12 m long cryounits each with eight 9-cell superconducting cavities operating at 1.3 GHz. Two 4.5 Mwatt, 2 msec pulse length klystrons will distribute power to the total 32 cavities. An electron gun and injector section will be included in this test facility, and beam tests with energies of about 500 MeV will be carried out.

Introduction

There is wide spread consensus amoung the HEP community that an e^+e^- collider with a center-of-mass energy of 500 GeV and luminosity of a few time $10^{33} cm^{-2} sec^{-1}$ should be considered as the next accelerator after the SSC/LHC. Such a collider would provide for top analysis via $t - \bar{t}$ production and also have the potential for discovery such as Higgs with mass below ≈ 350 GeV.

Within the accelerator community a number of alternate linear collider design efforts are being pursued that meet the above stated energy and luminosity requirements. These designs have many features in common such as the overall linear collider/injector layout, but differ mainly in the choice of spot size, bunch charge and frequency. The differences mainly come down to a trade off between the amount of beam power that is accelerated vs the spot size which has to be provided at the interaction point. The greater beam intensity can be used to balance more relaxed beam emittance and final focusing requirements. Typically, bunch intensities vary by an order of magnitude and vertical spot sizes by more than that. Also the different designs span a variety of rf frequencies from 1.3 to 30 GHz.

The TESLA approach lies at the low frequency, high intensity end of the present parameter range.[2] The use of superconducting rf cavity structures aids in achieving the higher beam intensity design. The resulting beam power could as well be applied toward higher luminosity design values if more stringent emittance and focusing were employed. However the major appeal of the scrf approach is that it allows for the more relaxed tolarances and less ambitious extraploations from todays state of the art operation at SLC.

The technical advantages of the superconducting rf cavaties stem from their high Q values and low wall losses. This allows for the use of large aperture structures operating at relatively low frequency, with relatively long pulse lengths, and low peak rf power requirements. The large aperture of the cavities are perceived to be a major advantage as it results in substantially reduced wake effects for both longitudinal and transverse wake fields. (the longitudinal wake scales with the aperture (a) as $1/a^2$, and the transverse wake as $1/a^3$.) As the aperature of an L band sc cavity is $\approx$ 70mm diameter, or about ten times larger than in some of the higher frequency designs, relaxed linac alignment and vibration tolarances should result even with the large bunch charge contemplated. With the larger emittance, more dilution can be tolerated in the linac, in the optics after the linac and the final focus. In addition the focusing strength, optical quality and alignment needed is not so stringent because of the higher beam power and larger spot. The result for the detector is more longitudinal space after the last focusing element, a long beam pulse with considerable time between bunch interactions. Just how much easier the alignment/vibration and field quality tolarances will be and how favorable the result will be for the detectors, will require a serious design study employing all the knowledge that has been learned at SLC and with other collider design efforts.

Though the use of superconducting rf cavities appears to greatly reduce the overall technicial difficulty of a linear collider, the difficulty has been concentrated in the one area of the sc cavities themselves. Reliable accelerating gradients at the 20 - 30 MeV/m must be achieved in a cost effective cryogenic assembly. Conventional wisdom in the past has used 5MV/m for a reliable operating

value of the gradient. Costs for production of a few cavities have been typically 200k$/m, or 40k$/MV. In order for the superconducting approach to become a viable alternative, this figure of merit must be reduced to the range of about 2k$/MV (or say 50k$ per meter with a gradient of 25MV/m). Though this would appear a somewhat daunting goal, it is to be noted that CEBAF is typically achieving averages of 12MV/m on their recent production. New cavity processing techniques such as heat treatment and high pulsed power rf processing show that gradients of 15 - 20 Mv/m can be reached in multi-cell structures. This work is reported in depth in other papers at this conference. Many tests on single cell cavities by the same techniques show accelerating gradients between 25 - 35 MV/m demonstrating that there are no fundamental limitations to the desired gradients for TESLA. Engineering design for economies of scale must be adressed as well, for whereas CEBAF for instance needs 360 cavities a linear collider would require typically 20,000. The goal of the TESLA R&D program is to build a test string of cavities of a modular design suitable for the linear collider application and to address the operating systems issues of the string as well as the all important gradient performance and cost effective design of the cavities and their cryostat. The goal is to have a 50m string of 32 cavities operational with beam in the 97 time scale and to be able to at that point make a rational judgement as to potential achieveable gradient and cost extrapolation to mass production scales.

The TESLA Test Facility (TTF)

The gradient goal of the R&D program is 15MV/m at Q's of 3×10^9. The long term collider design goal is 25MV/m at 5×10^9. Individual cavities are standing wave pi mode 9 cell structures; they are about one meter long and have individual coaxial input couplers and HOM couplers. Needed power for each cavity is 206kW at 25MV/m and 8ma of beam.

As cost savings is a major point of the R&D, it is important to come up with an efficient, simple, and reliable arrangement for the cavity cryostat. To this end, long cryomodules (12m) will be built which contain a linear array of 8 cavities with their associated input and HOM couplers. The end of each module near the interface will contain quad focusing, beam detectors, steering, and an annular space for high frequency HOM absorber cooled to 70K. The magnetic elements are superconducting and operate at 4K.

Each cavity has its own helium container, connected in series to the adjacent components. All vacuum flanges are arranged so there are no helium to vacuum flange interfaces but rather beam vacuum to cryostat vacuum, or cryostat vacuum to air. All helium to vacuum joints are welded. The input couplers are coaxial with two ceramic windows; one at 70K, the other at room temperature. These couplers have bellows which allow for an order of magnitude adjustment in the external Q, and for longitudinal thermal contraction of the cavity array over the length of the cryomodule.

The cavities are suspended and aligned off the large 300mm helium gas return pipe. The whole cryostat and shield arrangement is similar to the HERA or SSC magnet cryostats. Three support posts derived from the SSC posts provide the warm to cold support transition from the outside of the cryostat to the helium gas header[3].

The RF system will consist of two 4.5 MW modulators and Thomson Th2104 klystrons capable of 2ms RF pulse at 10 Hz. Each modulator is capable of providing 1.5 times the power needed for 16 cavities under full beam current and gradient (25MV/m).

One of these high power systems will also be used for RF processing at high peak power(HPP) of the individual cavities. It is expected that 1 MW RF levels will be required for HPP. An additional RF system will be used for the TTF injector.

A cryogenic system which supplies 200W at 1.8K and 200W at 5K is envisioned using an existing DESY refrigerator and an additional 1.8K cold box. The budgeted heat load at 1.8 and 4.5K respectively per meter is: static 0.4/1.25 W, total with rf power and beam 1.35/1.45 W. The fundamental RF power is 3/4 W, and HOM power 1/4 W at 2K. (Assuming 15MV/m, Q= 3×10^9, 10% HOM power at 2K.)

Infrastructure is being set up at DESY. An industrial building is being devoted to the Tesla activity. The final processing and preparation of the industrially produced cavities will be carried out with state of the art facilities. These include or make use of: cleanrooms (classes 100 and 10,000), chemical treatment and high purity water rinse; 1200C vacuum oven for improvement of the RRR and thermal conductivity of the Nb cavities; and vertical dewar high peak power (HPP) RF processing, gradient, and Q measurements of the bare cavitiy units. Finally the helium containment shell is attached and the couplers and tuners are mounted, and followed by a test of individual "dressed" cavities. This operation is performed in a horizontal test cryostat prior to the final assembly in the 8 cavity cryomodule. As experience is learned at obtaining reliable high gradient cavity performance, simplification and cost savings in the processing steps will be attempted. The initial infrastructure will be as complete as possible in order to assure the highest probability of success.

It should be pointed out that the push to high gradients in multi-cell 1.3 GHz cavities is already underway at Cornell[4] and CEBAF continues to gain experience at 1.5 GHz.

The four cryomodules, consisting of 32 cavities and 4 sets of focusing–steering elements at the cryo interfaces will be configured as a test string for beam as well as engineering systems tests. Two types of injectors, both operating at $\approx 8mA$ are under consideration. The first would be a low bunch charge injector with a conventional thermonic gun, chopper and buncher section operating at 300kV into one

of the standard 1m sc cavities. The injector beam energy would be 14 MeV. The second injector under consideration would provide the 5×10^{10} bunch charge at 1 microsec spacing. An effort is underway to evaluate this gun; a high gradient rf photocathode gun looks most promising. A thermionic gun will also be evaluated. Simulations with asymetric emittances will be carried out to see what emittance looks possible. For the TTF tests bunch charge is important but design emittance is not as important. A warm section between the injector and the standard cryomodules will provide an optics match and beam analysis area. Similarly there will be an analysis area after the four modules. Provision will be made to allow for beam offset of 1 cm or more in order to produce large transverse wakes.

Test Program for the TTF

Cavity Performance–Transfer full RF pulse power to beam at full pulse length. Attempt in-situ HPP processing of cavities in the string at the 1 MW level and experiment with different failure modes which might effect the cavity operation (e.g., vacuum failure).

Measure Q vs gradient with and without beam. As this will need to be done calorimetrically in the string, only low Q's below 10^9 will be detectable. Most Q measurements will come from the test cryostat data.

Measure the higher order mode power produced by the 5×10^{10} bunches and determine the fraction removed by: the HOM couplers, the microwave absorbers at the interfaces of the cryomodules (every 8 cavties), and that dissipated at 2 K in the helium. Look for transverse mode excitation by the beam as a function of beam position and see if one can measure cavity alignment by looking for a minimun in the transverse exicitation. Measure dark current, radiation patterns and energy spectrum without beam and determine the extent of captured dark current transported through the string.

RF System and Control–Develop a cavity, coupler tune up proceedure to control voltage, phase and coupling of the 16 cavities connected to one RF modulator. Measure the gradient and phase in each cavity as a function of time. Develope a quench, spark detection, protection system that allows for sufficient RF uptime. Develop cavity tune adjustment, radiation pressure compensation, and beam loading compensation. Look for and learn to control microphonics, coupler vibration, and radiation pressure effects that result in cavity tune , voltage or phase variations.

Beam Measurements–Measure the beam energy,energy spread, and energy and positional stability bunch by bunch as a function of bunch intensity, RF phase, bunch length, etc. Look for wake field and transverse mode excitation, and perform measurements of emittance blow up of off axis beams. (Many of the wake field measurements will require high intensity bunches.)

Cryogenics–Measure heat leak with and without RF and beam to determine static, RF fundamental, and HOM

losses. Be able to detect cavities with low Q (10^9) and detect quenches. Measure operating performance as a function of temperature and measure the temperature profile for each cell and coupler on at least one cavity (this might be best done in the horizontal single cavity test cryostat.

Alignment and Vibration–Measure the cryomodule alignment stability and reproducibility during cooldown/warm-up. Measure the vibrational properties and transfer function of the cavities and quadrupoles.

Operation–Develop tune up procedure, practice beam alignment and focusing, simulate fault conditions for the subsystems. Check the beam position system operation and stability, and try to make precission measurements of beam transmittion (or losses).

Schedule for the TTF

- two model cavities to test infrastructure - summer 93

- infrastructure: cleanroom, chemistry, furnace - fall 93

- cryosystem & HPP rf - winter 93

- treatment/test of first 8 cavities - spring/summer 94

- assembly 1st cryomodule - fall 94

- install and operate 1st cryomodule winter - 94/95

- beam test 1st cryomodule - summer/fall 95

- cavities for 2nd -4th modules - mid 95/mid 96

- install modules 2-4 in test string - 96/97

- beam tests complete TTF - 97

References

[1] The TESLA R&D effort (TESLA=TeV electron superconducting linear accelerator) is being carried out by an international collaboration led by DESY. A number of institutions have joined this collaboration and include IHEP Beijing, Tech Univ Berlin, CEN Saclay, CERN, Cornell, TH Darmstadt, DESY,Fermilab, Univ. Frankfurt, INFN Frascati-Milan, Univ. Karlsruhe, KEK, LAL Orsay, IPN Orsay, SETF Finland, Univ. Wuppertal.

[2] M. Tigner, SLAC Beamline, Fall 1992, Vol. 22, #3.

[3] D. Trines *et al*, Proceedings, International Accelerator Conference, Hamburg, July 1992.

[4] J. Kirchgessner *et al*, this conference.

The CERN Linear Collider

The CLIC Study Group
CERN, 1211 Geneva 23, Switzerland

Abstract

The CERN study of an electron-positron linear collider is concerned with a two-beam system powered via a superconducting drive linac. The study pursues the development of suitable technologies for a 2 TeV (centre-of-mass) collider in the longer term but concentrates, now, on a 500 GeV first stage for which the two-beam system developed by us appears very suitable. Results are reported on the 30 GHz main linac, the drive beam and the final focus system.

INTRODUCTION

Without abandoning the long-term goal of a 2 x 1 TeV machine, the study of a CERN Linear Collider - CLIC - now follows specific physics interests in concentrating on a 2 x 250 GeV version for which the system under development appears to be a very serious contender. It is considered of paramount importance, however, that such a relatively low-energy project should be readily extendible into the TeV range. Much emphasis is put, therefore, on developing a technology which permits a reasonably high accelerating gradient.

The tentative design aims at 80 MeV/m. Since the main linacs for such a gradient have to be normal-conducting, an unusually high frequency - 30 GHz in fact - has to be chosen if the high gradient and a high macroscopic repetition rate are to be reconciled with tolerable power dissipation. Both choices of basic parameters - 80 MeV/m and 30 GHz - have been confirmed by a systematic parameter optimisation study [1]. With this gradient, the length of a 2 TeV (centre of mass) collider is about equal to the LEP circumference of roughly 30 km; an 0.5 TeV version is closer to a LEP diameter - where it would actually find a good site from all points of view.

The proposed solution is a two-beam scheme in which an intense *drive beam* of a few GeV average energy, accelerated by continuous-wave superconducting cavities, travels parallel to the main beam along the entire length of the accelerator. Pulsed microwave power is extracted from the bunched drive beam and fed into the main linac by means of *transfer structures* and short waveguide feeders. Two kinds of problems have to be faced, therefore, namely those presented by tolerance requirements and wake fields of a high main-linac frequency and those connected with the drive beam.

In an 0.5 TeV collider the drive beam, once preaccelerated to 3 GeV in the injector complex, requires no reacceleration. In a 2 TeV machine, reacceleration by superconducting cavities *is* required but can be concentrated in three local stations at about 4 km spacing. In either case, therefore, the main accelerator tunnel requires access pits at 4 km distance only and is kept free of any equipment connected with high power transfer, high voltage, cryogenics or limited operational life, a feature which turned out very important in LEP experience. A crossection of the CLIC tunnel is shown in Fig. 1.
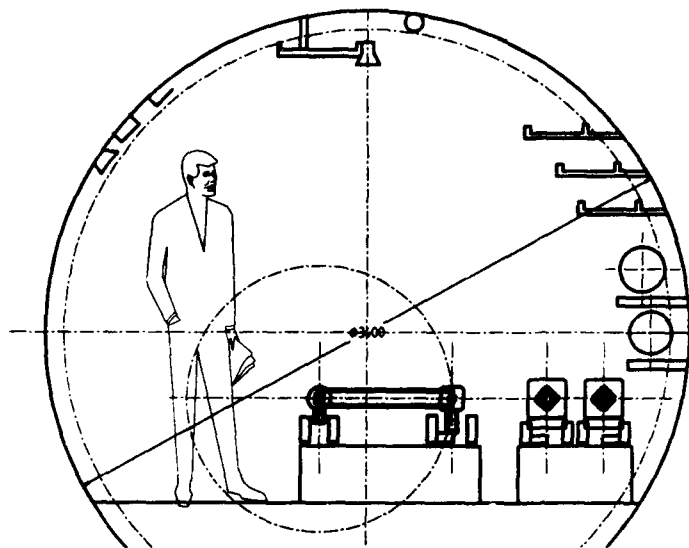
Fig. 1 Crossection of the CLIC tunnel. Shown from left to right is the drive beam (transfer structures and focusing) the main beam (high-gradient structures, microalignment and focusing) and beam transport for both beams at injection energy (3 and 9 GeV respectively) from a central injector complex to the linac input. The large circle is the outline of the superconducting drive linac which is *not* situated in the main tunnel but determines the distance between main and drive beams if the machine is to be readily extendible beyond 2 x 250 GeV.

THE MAIN LINEAR ACCELERATORS

Special technologies have been developed for cost effective fabrication of the main accelerating structure meeting the requirements (tolerances and surface finish) of a microwave frequency ten times above present-day practice. As a result, two full-length 30 GHz structures have been built and tested [2].

An iris-loaded section contains 84 cells and has a coupler (to WR 28 waveguide) at each end. The aperture diameter is 4 mm, the cell diameter 8.7 mm and the group velocity 8.2% c. The outer diameter of the structure (35 mm), machined to ±1 μm precision and concentricity with the beam aperture, serves as the reference for alignment. The cells are pumped through four radial holes via brazed-on manifolds. Parallel channels for water cooling are drilled into the copper. Each cell can be deformation-tuned by forming a pair of diametrically opposite dimples, but the precision attainable in diamond machining and vacuum brazing is such as to make us consider elimination of any tuning. So far, our accelerating structures are constant-impedance structures. Our attempts to accommodate a modest amount of multibunching by stagger tuning are described elsewhere at this conference [3, 4]. BNS-

damping within a bunch will be provided with the help of microwave quadrupoles [5] formed by giving some accelerating structures flat-shaped cells but normal, circular apertures. About 5% of the accelerator will be of this kind.

About 2×10^4 accelerating sections containing 2×10^6 discs will be required for an 0.5 TeV collider. In considering mass fabrication it becomes apparent that the fabrication cost will be dominated by the seemingly trivial operations of disc-forming, roughing, drilling, cleaning, inspection and handling. Therefore, an industrial study of suitable fabrication processes has been launched with a view to obtaining a first-order cost estimate.

It might be suspected that a potential problem at the high acceleration gradient of CLIC could be the accumulation of *dark current* formed by field-emitted electrons which are trapped in the accelerating field. However, the threshold gradient scales linearly with frequency and computer simulations [6, 7] show it to be well above 100 MeV/m at 30 GHz. It is, nevertheless, reassuring that a structure made by the CERN technology but scaled down to 11.4 GHz and tested at KEK Japan in the frame of a collaboration, readily exceeded 100 MeV/m gradient, the limit being set by available power.

The strong transverse wakefields associated with the high accelerating frequency and the strong BNS damping required for stability lead to tolerances of only a few micrometer of rms jitter for structures, quadrupoles and beam position monitors [1, 8]. This, therefore, has led to two hardware developments.

One the one hand, the beam position with respect to the accelerating structures (not the quadrupoles) will be measured to sub-micron resolution by means of E_{110} cylindrical cavities, fabricated integrally with the accelerating structures [9].

Fig. 3 Output of beam position monitor for $\pm 2 \, \mu m$ travel of a beam-simulating electrode.
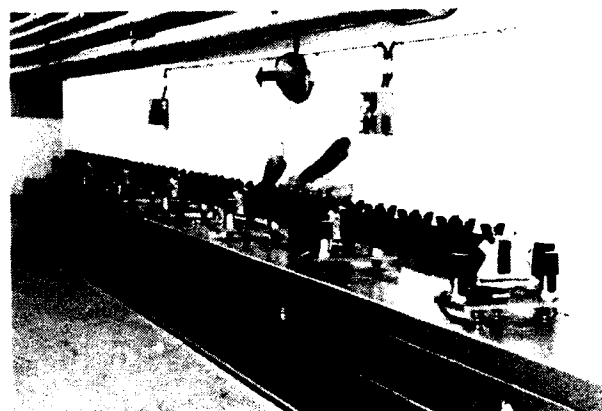
Fig. 4 Six-unit prototype of submicron self-aligning support structure.

On the other hand, sub-micron automatic alignment in an underground test facility has already been demonstrated and reported two years ago [10]. Together with the results with the beam position monitor reported above these tests form a demonstration in principle that the micrometer tolerances required for a 30 GHz system can indeed be met. A ten meter complete prototype of self-aligning structure is nearing completion. It is shown in Fig. 4.

THE DRIVE BEAM

The multibunch high-intensity drive beam runs parallel to the main beam at about 1 m distance. The drive beam delivers energy to 30 GHz travelling-wave transfer structures which thus form the pulsed RF power sources of the main linac sections to which they are connected by rectangular wave-guides. The drive beam is accelerated by superconducting cavities.

A multi-frequency scheme has been worked out for this superconducting drive linac [11]. Firstly, the beat between closely spaced fundamental frequencies will compensate the transient beam loading. Secondly, the addition of beam-driven

Fig. 2 Microwave set up for testing sub-micron beam position monitor. Above: probe holder and micro-mover. Below: the diamond-machined E_{110} cell, two diametrically opposite output waveguides, a magic-tee and a flexible waveguide for the differential output.

Fig. 2 shows a setup in which a small antenna like probe is moved across the aperture of a prototype monitor with the help of mechanical micro-movers. The result, shown in Fig. 3, clearly demonstrates a resolution better than 0.1 μm.

541

cavities at two harmonics will linearize the waveform over half a wavelength, so as to permit an extension of the drive-beam train - with concomitant reduction of charge - by up to a factor of four compared with single-frequency operation. Further charge reduction by the addition of RF pulse compression at the transfer structure output is under development.

Since the drive bunches suffer different and strong decelerations in the absence of longitudinal focusing, it is clear that the drive beam will accumulate a large energy spread along its path, as well as a large increase of transverse emittance.Tracking the beam energy spread and the associated chromatic growth of transverse emittance through a suitable FODO focusing system confirmed [12] that the beam survives the full (active) length of 12.5 km of a 1 TeV main linac, albeit with over 20% energy spread and filling the available aperture at the end. Preacceleration to about 6 GeV and three reacceleration stations, located at discrete access points to the machine, are foreseen for this case of a 2 TeV collider. No reacceleration is required in a 0.5 TeV machine where each of the two drive beams - after being preaccelerated to 3 GeV in the injector complex - travels the entire linac length of about 4 km (3.2 km active) without further acceleration.
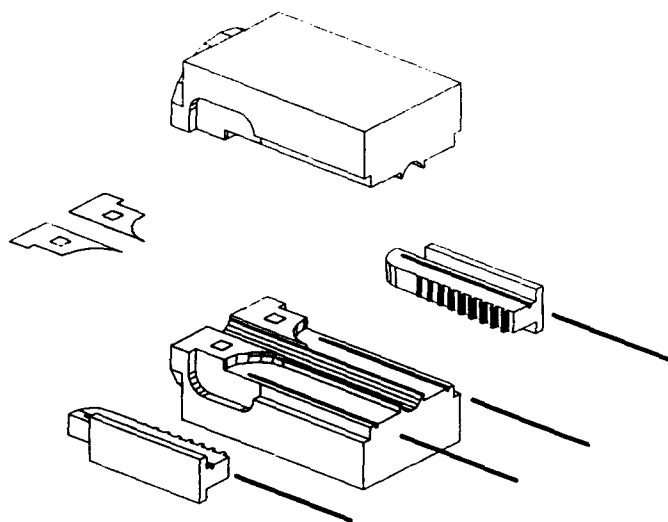
Fig. 5 One end of a 30 GHz transfer structure made of two halves. Total length: 60 cm. Central bore: 12 mm. The black lines (lower right) and the thin foils (middle left) indicate the placing of the brazing alloy (Curtesy KM kabelmetal)

The transfer structures for pulsed power generation take the form of smooth beam tubes of 12 mm diameter with two periodically loaded power-collecting waveguides running in parallel and coupled to the tube by continuous slots. The particle beam is in synchronous interaction with a forward $2\pi/3$ mode. Transverse wake fields, excited by an off-centre drive beam, are nearly synchronous with the bunches but have a 90° phase offset, affecting mostly the head and the tail (and in opposite signs). Tracking results indicate that this effect

remains tolerable. So far, the transfer structure has been developed with the help of 9 GHz scale models as well as by computation. A 30 GHz prototype is being constructed by industry (Fig. 5). Details of the transfer structure development are given in three compagnon contributions [12, 13, 14] to this conference.

The generation of the required drive beam is a difficult problem for which several solutions have been proposed. One of these employs a battery of laser-driven photocathodes in high-gradient r.f. guns. This has been the subject of a test facility which has begun operation. Short bunches are obtained from a CsI cathode excited at 209 nm wavelength and exposed to 100 MV/m peak extraction field in a 3GHz gun. So far, 2.7 MW of peak 30 GHz power have been produced in one of the prototype main linac structures using this beam.

A promising scheme under active study employs a single-pass free electron laser for bunching. Only one preinjector is required which directly generates the complete configuration of drive bunches. An experimental test carried out in collaboration with a specialised laboratory is in preparation. This is described in another contribution to this conference [15]. Other proposals make use of bunch compression at different stages of preaccelaration [16, 17].

THE FINAL FOCUS

Chromaticity-corrected final focus systems for 2 TeV and 0.5 TeV have been developed [18]. In the latter case the critical-photon-to-particle energy ratio is 0.15 and the beamstrahlung energy spread is 5.9%. Work is in progress concerning the effect of the crossing angle (including crab crossing), collimation and masking and compensation of the solenoid field of the detector by an antisolenoid

REFERENCES

[1] G. Guignard, These proceedings.
[2] I. Wilson, W. Wuensch, C. Achard, *Proc. 2nd European Particle Accel. Conf. EPAC*, Nice 1990, p. 943.
[3] G. Guignard, These proceedings.
[4] I. Wilson, W. Wuensch, these proceedings.
[5] W. Schnell, I. Wilson, *Proc. 1991 IEEE Particle Accel. Conf.*, San Francisco p. 3237.
[6] R. Parodi, Genoa, private communication, 1991.
[7] S. Yamaguchi, LAL Orsay report LAL/RT 92-18, 1992.
[8] C. Fischer, these proceedings.
[9] J.P.H. Sladen, W. Wuensch, these proceedings.
[10] W. Coosemans, I. Wilson, P. Poirier, *Proc. 1991 IEEE Particle Accel. Conf.*, San Francisco p. 2070.
[11] L. Thorndahl, *Proc. XVth International conf. on high energy Accel.*, HEACC '92, 1992 Hamburg, P. 885.
[12] G. Guignard et al., These proceedings.
[13] A. Millich, These proceedings.
[14] L. Thorndahl, G. Carron, These proceedings.
[15] C.D. Johnson CERN, J. Gardelle, J. Grenier CESTA le Barp, These proceedings.
[16] A.A. Mikhailichenko, CLIC note 186, 1992.
[17] J.P. Delahaye, private communication, 1993.
[18] O. Napoly CERN reports SL/92-28 (AP) and SL/92-34 (AP).

THE NEXT LINEAR COLLIDER TEST ACCELERATOR†

R.D Ruth, C. Adolphsen, K. Bane, R.F. Boyce, D.L. Burke, R. Callin, G. Caryotakis, R. Cassel, S.L. Clark, H. Deruyter, K. Fant, R. Fuller, S. Heifets, H. Hoag, R. Humphrey, S. Kheifets, R. Koontz, N.M. Kroll,‡ T. Lavine, G.A. Loew, A. Menegat, R.H. Miller, C. Nantista,* J.M. Paterson, C. Pearson, R. Phillips, J. Rifkin, J. Spencer, S. Tantawi, K.A. Thompson, A. Vlieks, V. Vylet, J.W. Wang, P.B. Wilson, A. Yeremian, B. Youngman

Stanford Linear Accelerator Center, P.O. Box 4349, Stanford, California, 94309, USA

ABSTRACT

During the past several years, there has been tremendous progress on the development of the RF system and accelerating structures for a Next Linear Collider (NLC). Developments include high-power klystrons, RF pulse compression systems and damped/detuned accelerator structures to reduce wakefields. In order to integrate these separate development efforts into an actual X-band accelerator capable of accelerating the electron beams necessary for an NLC, we are building an NLC Test Accelerator (NLCTA). The goal of the NLCTA is to bring together all elements of the entire accelerating system by constructing and reliably operating an engineered model of a high-gradient linac suitable for the NLC. The NLCTA will serve as a testbed as the design of the NLC evolves. In addition to testing the RF acceleration system, the NLCTA is designed to address many questions related to the dynamics of the beam during acceleration. In this paper, we will report on the status of the design, component development, and construction of the NLC Test Accelerator.

INTRODUCTION

In order to control the linac length of the NLC, current designs at SLAC and KEK use acceleration gradients which begin at 50 MV/m for the 0.5-TeV linear collider (phase one) and finish with 100 MV/m in the upgraded 1-TeV collider (phase two)[1]. These gradients are provided by an 11.4-GHz RF system (X-band). Although there has been experience with short X-band accelerators in industrial and medical applications, there are presently no high-gradient X-band accelerators in operation.

During the past several years much experience has been gained with this RF frequency at SLAC and KEK. We have powered 11.4-GHz structures to reach peak surface fields in excess of 500 MV/m[2]. Short travelling wave accelerating structures have been powered to accel-

erating fields in excess of 100 MV/m[3,4]. High-power klystrons have been constructed which reach 50 MW in pulses one microsecond long and 85 MW in pulses 200 nsec long[5]. We have constructed high-power RF pulse-compression systems which achieve a factor of five in peak-power multiplication[6,7]. Designs for more efficient modulators have been completed[8]. Finally, we are developing low-loss components for manipulation of high-power pulses of 11.4-GHz RF[7].

The first goal of the NLC Test Accelerator, the subject of this paper, is to construct and reliably operate a high-gradient X-band linac in order to integrate the accelerator structures, RF sources, and RF systems being developed for the NLC.

The second goal of the NLCTA is to study the dynamics of the beam during the high-gradient acceleration of many bunches on each RF fill of the structure. The dynamics of transient beam loading is of particular interest in order to test strategies for multibunch energy compensation and higher-order mode suppression. It will also be possible to measure the residual transverse wakefield effects in the NLCTA.

The NLCTA is primarily a high-gradient X-band linac consisting of six 1.8-meter-long accelerator sections. These sections are fed by three 50-MW klystrons which make use of SLED-II pulse compression to increase the peak power by a factor of four. This yields an acceleration gradient of 50 MV/m so that the total unloaded energy gain of the beam in the X-band linac is 540 MeV.

The NLCTA parameters are listed in Table 1. The right-hand column of Table 1 lists the parameters for an upgrade of the X-band linac to 100 MV/m by the use of six 100-MW klystrons.

INJECTOR

The NLCTA injector will consist of a 150-kV gridded thermionic cathode gun, an X-band prebuncher, a capture section with solenoid focusing, and a rectangular chicane magnetic bunch compressor.

The prebuncher will be a velocity-modulating cavity. The capture section will be a standard linac section modified to comprise two half-sections, each with its own input and output couplers. The first half-section, with a minor modification of the first few cells, will capture the beam. The second half-section will provide additional acceleration, up to 90 MeV, to improve the spectrum and

---

Table 1. NLCTA Parameters

Parameter	Design Value	Energy Upgrade
Energy	540 MeV	1280 MeV
Active linac length	10.8 m	
Accelerating gradient	50 MV/m	100 MV/m
Injection energy	90 MeV	
RF frequency	11424 MHz	
Number of klystrons	3	6
Klystron peak power	50 MW	100 MW
Klystron pulse length	1.0–1.5 μs	
Compression power gain	4.0	
Accelerating mode	$2\pi/3$	
HOM suppression	Detuning	

to reduce the transverse emittance at the entrance to the NLCTA linac.

The injector will produce trains of 1600 bunches with 0.09-nanosecond (11424 MHz) bunch spacing. The total charge in the bunch train will be 10^{12} e. The average current matches (or exceeds) that required for the NLC bunch train. This beam will be adequate for the energy gain measurements of the X-band accelerator. It will allow the study of multibunch loading and compensation techniques to achieve a small bunch-to-bunch energy spread, and will also allow studies of residual transverse beam breakup.

In the future, we plan to upgrade the injector to produce a train of bunches identical to that required for the NLC, in order to carry out additional beam dynamics studies. The present specification for the NLC bunch structure calls for total charge of $6 \times 10^{11}e$ in trains of 90 bunches with 1.4-nanosecond (714 MHz) bunch spacing. Injecting the proper NLC multi-bunch structure in the NLCTA will allow us to measure true single-bunch beam loading, and to further verify the beam-loading compensation techniques necessary for maintaining small bunch-to-bunch energy spread. Proper suppression of the higher-order modes in the accelerating structure can be verified by measuring the bunch-to-bunch energy offsets and bunch-to-bunch position offsets. We are presently investigating alternatives for this gun upgrade.

RF SYSTEM

The high-gradient accelerator will be fed with RF power through overmoded circular waveguides which penetrate the shielding blocks above the accelerator. Three 50-MW klystrons will be positioned along the accelerator, outside the shielded enclosure[5]. Each klystron is powered by an independent modulator, allowing the flexibility needed for multibunch energy control and adequate power for an upgrade to a 100-MV/m accelerating gradient with six 100-MW klystrons, as indicated in Table 1. Each klystron feeds a SLED-II pulse compressor[6,7]. The pairs of delay lines of the SLED-II pulse compressors are overlapped, parallel to the accelerator, outside the shielding. The output of each SLED-II is split to feed two accelerator sections. In the case of the injector, the SLED-II output is split to feed the two short injector sections to provide overhead for beam loading.

ACCELERATOR STRUCTURE[9]

In order to increase the luminosity of an NLC well beyond the minimum levels necessary for high-energy physics experiments, a train of bunches must be accelerated on each RF pulse. The primary impact of this choice is in the design of the RF structure. As each bunch traverses the structure, it excites wakefields which can remain until the next bunch passes. If this happens, each bunch resonantly drives all the bunches behind it. This leads to transverse multibunch beam-breakup. However, beam-breakup can be eliminated by choosing an RF structure in which the wakefields damp significantly between bunches.

There are two methods which can be used to achieve this damping. In the first, the higher-order modes in the structure can be damped by coupling them to radial waveguides which are terminated with matched loads. This causes the energy to radiate out of the structure between bunches. The second technique involves changing the frequency of the higher-order modes (HOMs) of each cell. Qualitatively, the total wakefield is then composed of a sum of wakefields, one from each cell. Behind the driving bunch, the wakefield decoheres because of the differing frequencies, and the net effect is a reduction of the wakefield. With this technique, the frequency distribution is important in determining the subsequent decay of the wakefield behind the driving bunch. Both of these techniques have been tested experimentally[10,11].

For the NLCTA, we plan to use a detuned structure. It is a $2\pi/3$ "constant-gradient-like" structure which is modified every half meter to include four symmetric pumping holes. These holes lead to parallel vacuum manifolds which provide sufficient pumping speed despite the small beam aperture. The cavities are machined to provide a precise mechanical reference from the inside dimensions to the exterior of the structure[12].

In order to achieve the reduced wakefield, the structure is configured to be very nearly constant gradient. The decoherence of the wakefield between bunches will be achieved by a Gaussian distribution of HOM frequencies with a standard deviation of 2.5%, which results in a Gaussian decay in time for the initial wakefield. This distribution can be obtained by tailoring a constant-gradient section so that more cells are near the central frequency

while fewer are near the ends of the frequency band. This choice results in a structure in which the iris size along the structure first decreases rather quickly, then decreases slowly in the middle, and finally decreases quickly along the structure towards the output end[13].

With this distribution of HOMs, the wakefield decoheres to less than 1% of its peak value[14]. This decoherence is sufficient to eliminate beam breakup in the NLC or NLCTA[15]. Because of the low injection energy, the NLCTA has a sensitivity to transverse wakefields comparable to the much-longer NLC linac. The NLCTA will permit the verification that detuned structures can indeed supress wakefields to the levels necessary for stable acceleration.

BEAM ANALYSIS

A magnetic spectrometer has been designed which will analyze the bunch train after acceleration in the linac in order to determine beam energy and energy spread, and bunch-to-bunch offsets. The optics in the beam analysis region allow for the measurement of emittance in both transverse planes. A vertical kicker magnet upstream of the spectrometer provides a method for separating the bunches vertically so that the energy, energy-spread and horizontal offsets can be independently measured along the bunch train. After initial commissioning, an extensive set of experiments is planned to verify that the NLCTA can indeed stably accelerate trains of low-emittance bunches suitable for a full-scale NLC.

SUMMARY AND PLANS

The conceptual design for the NLCTA is complete and detailed engineering is presently underway. The facility to house the NLCTA is under construction in End Station B at SLAC. Prototypes of the klystron, pulse compression system and the accelerating structure are under construction and will be complete in 1993. These prototypes will be tested in the Accelerator Structure Test Area at SLAC[16]. The wakefield of the detuned structure will be measured in the Accelerator Structure Setup in the SLC[17]. We plan to complete the NLCTA and begin beam dynamics experiments in 1996.

REFERENCES

[1] R.D. Ruth, "The Development of the Next Linear Collider at SLAC," *Proc. of Workshop on Physics and Experiments with Linear Colliders*, Saariselka, Finland, September 9–14, 1991; also in SLAC–PUB–5729.

[2] J.W. Wang *et al.*, "High-Gradient Studies on 11.4-GHz Copper Accelerator Structures," *Proc. of the 1992 Linac Conference*, Ottawa, Canada, August 23–28; also in SLAC–PUB–5900.

[3] J.W. Wang, "High-Power Experiments in X-Band Accelerator Structures," these proceedings.

[4] T. Higo *et al.*, "High Gradient Testing of an 11.4 GHz Accelerating Structure for KEK/CERN Linear Collider Studies," CERN CLIC-Note 187 (1993).

[5] G. Caryotakis, "Development of Multimegawatt Klystrons for Linear Colliders: A Progress Report," these proceedings; also in SLAC–PUB–6168.

[6] P.B. Wilson *et al.*, "Progress at SLAC on High-Power RF Pulse Compression," *Proc. of the 15th Int. Conf. on High-Energy Part. Acc.*, Hamburg, Germany, July 20–24, 1992; also in SLAC–PUB–5866.

[7] C. Nantista *et al.*, "High-Power RF Pulse Compression with SLED-II at SLAC," these proceedings; also in SLAC–PUB–6145.

[8] K. Harris *et al.*, "600 kV Modulator Design for the SLAC Next Linear Collider Test Accelerator," *Proc. of the 20th Int. Power Modulator Symp.*, Myrtle Beach, South Carolina, June 23–25, 1992; also in SLAC–PUB–5851.

[9] R.H. Miller *et al.*, "Accelerator Structure Work for NLC," *Proc. of the 15th Int. Conf. on High-Energy Part. Acc.*, Hamburg, Germany, July 20–24, 1992; also in SLAC–PUB–5865.

[10] H. Deruyter *et al.*, "Damped and Detuned Accelerator Structures," *Proc. of the 1990 Lin. Acc. Conf.*, Albuquerque, NM, Sept. 10–14, 1990; also in SLAC–PUB–5322.

[11] J. Wang *et al.*, "Wakefield Measurements of SLAC Linac Structures at the Argonne AATF," *Proc. of the 1991 IEEE Part. Acc. Conf.*, San Francisco, California, May 6–9, 1991; also in SLAC–PUB–5498.

[12] H. Hoag *et al.*, "Accelerator Structure Development for NLC," these proceedings; also in SLAC–PUB–6183.

[13] J.W. Wang and E. Nelson, "Design of the Detuned Accelerator Structure," these proceedings; also in SLAC–PUB–6142.

[14] K.L.F. Bane and R.L. Gluckstern, "The Transverse Wakefield of a Detuned X-Band Accelerator Structure," to be published in Particle Accelerators; also in SLAC–PUB–5783.

[15] K. Thompson *et al.*, "Multibunch Beam Breakup in Detuned Structures," these proceedings; also in SLAC–PUB–6153.

[16] A. Vlieks *et al.*, "Accelerator and RF System Development for NLC," these proceedings; also in SLAC–PUB–6148.

[17] C. Adolphsen *et al.*, "Measurement of Wakefields Generated in Accelerator Test Structures Using the SLC," *Proc. of the 15th Int. Conf. on High-Energy Part. Acc.*, Hamburg, Germany, July 20–24, 1992; also in SLAC–PUB–5941.

High Power CW Linac in PNC

S. Tōyama, Y. L. Wang, T. Emoto, M. Nomura, N.Takahashi, H. Oshita,
K. Hirano, Y. Himeno
Power Reactor and Nuclear Fuel Development Corporation
4002 Narita, Oarai-machi, Ibaraki, 311-13 Japan
I. Sato, A. Enomoto, M. Ono
National Laboratory for High Energy Physics
1-1 Oho, Tsukuba-shi, Ibaraki, 305 Japan

Abstract

Power Reactor and Nuclear Fuel Development Corporation(PNC) is developing a high power electron linac for various applications. The electron beam is accelerated in CW operation to get maximum beam current of 100mA and energy of 10MeV. Crucial components such as a high power L-band klystron and a high power traveling wave resonant ring(TWRR) accelerator guides were designed and manufactured and their performance were examined. These design and results from the recent high power RF tests were described in this paper.

1. INTRODUCTION

The development of a high intensity CW electron linac to study feasibility of nuclear waste transmutation was started in 1989[1]. Its purpose is to establish the high current beam acceleration technique with more than 50% efficiency. The specifications of the PNC linac are described in Table 1. An accelerating guide and klystron was newly developed in L-band 1249 MHz RF so as to achieve high efficiency. The accelerator facility building was constructed in August, 1991. The exterior of the building is shown in Figure 1. The facility has three floors, where there are the accelerator in the basement, klystrons and its power supply in the first floor. The base floor has 2.3 m concrete shielding on its roof. The high power RF test for the components started in 1992. The study of high current beam operation will be started in 1996 after the injector test in 1995 using partially built accelerator.

Figure 1. View of accelerator facility.

2. STRUCTURE OF HIGH POWER CW ELECTRON LINAC

A conceptual RF diagram of PNC accelerator is shown in Figure 2. The accelerator consists of eight normal conducting accelerator guides which each have TWRR including one buncher guide.
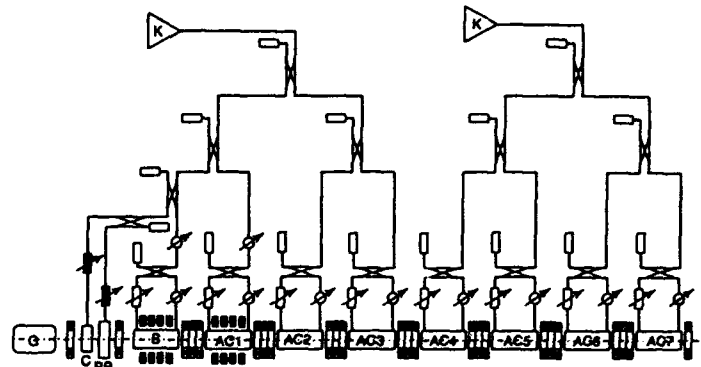
Figure 2. Conceptual diagram of PNC accelerator:
G is the electron gun; C, a chopper; PB,
a prebuncher; B, a buncher; AC, a acc.guide;
K, a klystron.

The injector section consists of an electron gun, a prebuncher, a chopper and a buncher guide. A water cooled chopper slit is designed because of high heat removal of 11 kW. Prebuncher system with two standing wave cavities is designed to compress phase angle of beam bunch without large energy dispersion which happens to escape from beam transportation. Two high power CW klystrons feed RF into four accelerator guides respectevely. The linac accelerates 10MeV-100mA electrons with the duty factor of 20~100%. A 5 mmφ impregnated cathode generates electron beam of 200kV and average current 100mA. It is very important to keep low beam emitance in order to avoid beam break up(BBU) in the case of high current beam acceleration. The high quality LaB$_6$ cathode which can emit stable and brilliant electron beam will be future candidate for the smaller emitance electron gun besides of thermionic cathode. The buncher guide was designed in constant gradient structure for uniform power dissipation along the buncher cavity wall. Klystron is driven by 90kV DC power supply to produce 1.2

MW RF with the efficiency of more than 65%. The 1.2MW RF power is fed into four TWRR through two 3 dB directional couplers.

The constant gradient regular accelerator guide and phase shifter and stub tuner form a recirculating wave guide called TWRR, which get high accelerating efficiency using traveling wave. This guide has a efficiency 65% and field multiplication factor two with full beam loading, which is almost same efficiency by standing wave type. The advantage to employ TWRR rather than standing wave accelerator guide is as follow; simplicity of cavity structure, larger aperture size of disk hole, less effort of fabrication, and easy mechanical separation from the recirculating wave guide. These make it easy to handle under heavy radiation field.

3. RESULTS FROM RECENT DEVELOPMENT

Low power RF characteristic of an accelerator guide was measured in preceding experiment[2]. The maximum RF power from the klystron was limited to 330 kW by unexpected heat generation from the klystron ceramic window. High power RF characteristic of a accelerator guide and a klystron output window was examined by using the klystron powered by a 90kV DC power supply in the national laboratory for high energy physics(KEK).

A. Accelerator guide

The experiment of an accelerator guide is performed with a one TWRR unit and one klystron. The RF power was loaded into the TWRR unit with CW and long pulse (~4 ms) aging to squeeze the RF spark and gas emission inside of the TWRR. It took about two weeks to reach the final RF power level, which power dissipation was equivalent to full beam loading.

Unexpected heating of a phase shifter in the TWRR occurred when RF power level reached 35 kW. One of the phase shifter choke cylinder temperature increased more than 100 degree. This phenomenon came from incomplete electromagnetic contact of a finger strip between a stub and a outer cylinder of choke component. It was turned out the RF attenuation of the phase shifter must be reduced less than 0.05 nep. After the phase shifter was replaced by straight wave guide, the accumulated power in the TWRR achieved 800 kW in CW operation. The Q value was 1150 which is in accordance with calculation. The temperature changes and changes of resonant frequency along TWRR RF power are summarized in Figure 3 a and b. The following values can be

1. frequency deviation per RF   -50.1 kHz/100kW
2. temperature deviation per RF   2.1 °C/100kW
3. frequency deviation per temperature   -23.4 kHz/ °C.
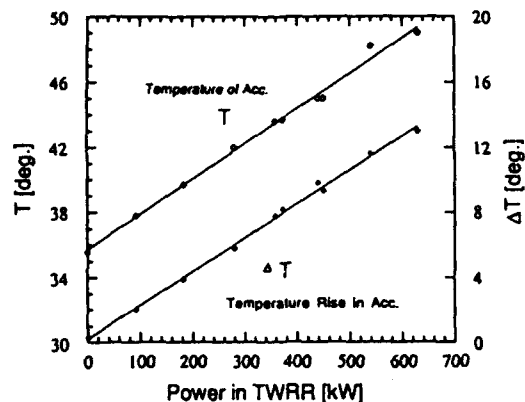
Figure 3 a. RF power dependence of acc. temperature.
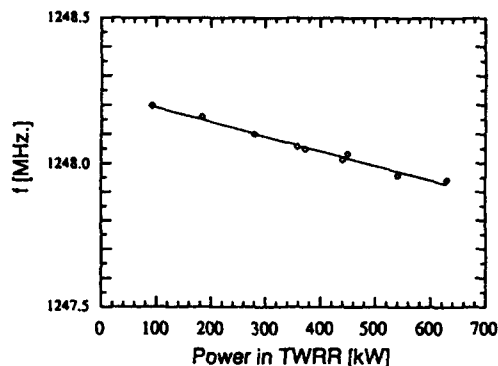
Figure 3 b. RF power dependence of resonant frequency.

The result is in good agreement with the result from low power experiment carried out in preceding experiment, which means there is no local heating inside the accelerator guide in final use. The field multiplication factor M for TWRR was three, which was reasonable from the expectation by calculation with no beam loading. The choke structure of phase shifter should be modified in next development.

B. Klystron window

The maximum power of the klystron is limited to 330 kW, because the temperature of ceramic window increased up to 90 degree, which is one third of the critical points of destruction by thermal stress. So the modified output window was designed and three different pieces of pill-box type windows were tested with TWRR unit replaced the accelerator guide. The materials, dimension and VSWR of each piece are summarized in Table 2. The high power test was done by increasing RF in TWRR with the careful watch by video camera for light emission from ceramic surface and by infrared-thermometer for the surface temperature. The aging of these windows is done by CW and long pulse (duty factor 5~20% at 50 Hz). The results from three test windows are shown in Figure 4. The beryllia window which has long dimension was able to endure the 1.7 MW CW RF power. The temperature increase is 48 degree and there was no glow discharge by multipactoring effect on the ceramic surface. Only some light spots was observed from the small dust

547

attached to the ceramic surface. The alumina window which has shorter dimension was broken down at power of 0.5 MW in CW. The crack was caused by thermal stress. The test of higher power with long pulse was carried out to look for the possibility to produce more than 1.2MW from klystron with long pulse operation. The experiment was done by using 2 ms and 4 ms pulse and duty factor of 10 % and 20 %. There was no multipactoring bellow 4 MW and weak light emission was observed above 4.25 MW.
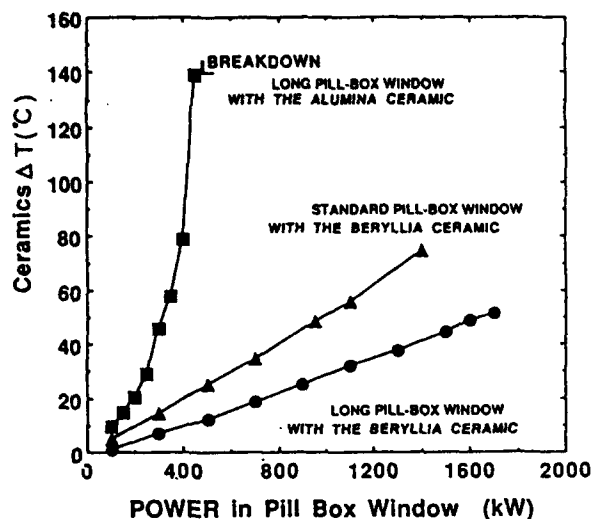
Figure 4. Temperature increase of test windows.

The result agrees with the characteristic of field decrease and reduction of VSWR by the design and suggests that the klystron will be able to produce more than 1.2MW RF after changing the design of the window.

4. SUMMARY

The high power CW electron linac is designed using normal conducting TWRR and high power CW klystron to accelerate electron beam with 10MeV-100mA at peak current. The efficiency of acceleration is designed to get more than 65% at full beam loading and 65% efficiency for klystron. The high power component test was carried out to check the design parameters. It was turned out that an accelerator guide and klystron output window are able to show sufficiently enough performance for high power CW operation, however the phase shifter in TWRR should be modified to get less attenuation.

5. ACKNOWLEDGEMENT

This study is collaborated between PNC and KEK. The authors sincerely would like to acknowledge the member of KEK, especially, Dr. S. Fukuda for his advice and discussion of klystron window, Dr. S. Yoshimoto for his help and discussion of DC power supply and RF system, and Dr. H. Nakanishi for his help of construction of cooling system for high power experiment.

6. REFERENCES

[1] S. Toyama et al , "Transmutation of Long-lived Fission Product (137Cs,90Sr) by a Reactor-Accelerator system," Proceedings of The 2nd International Symposium on Advanced Nuclear Energy Research, (1990)
[2] A. Enomoto et al ,"Development of the CW Electron Linac Using Traveling Wave Resonant Ring," Proceeding of European Particle Accelerator Conference, (1992)

Table 1. Parameter of The PNC Linac

operation mode	CW	pulse			CW	pulse
General				Resonant ring		
pulse width	-	0.8 ms		transmission(no load)	0.946	
repetition rate	-	250 pps		transmission(load)	0.850	
energy	10MeV	18MeV		multiplication(no load)	3.0	
current	100mA	55mA		multiplication(load)	2.0	
total length	20 m			Klystron(target)		
Accelerator section				power	1.2MW	4.1MW
type	traveling wave			beam voltage	90kV	147kV
	constant-gradient			micro-perveance	0.8	
mode	2π/3			gain	50 dB	55 dB
frequency	1249MHz			efficiency	65%	50%
gain(max)	1.4 MV/m	2.0MV/m		modulation	modulating anode	

Table 2. Parameters of window test

No.	material	length of pill-box	dia. of pill-box	VSWR	phase length
A	BeO	402mm	190.5mm	1.04(measured)	751.6deg.
B	Al₂O₃	412mm	193.7mm	1.30(measured)	777.8deg.

A mm-wave Planar Microcavity Structure for Electron Linear Accelerator System *

Y. W. Kang, H. Henke,[†] R. Kustom, F. Mills, and G. Mavrogenes
Accelerator Systems Division
Argonne National Laboratory
9700 S. Cass Ave., Argonne, IL 60439

Abstract

The muffin-tin cavity structure is planar and well suited for mm-wave accelerator with silicon etching techniques. A constant impedance traveling-wave structure is considered for design simplicity. The RF parameters are calculated and the shunt impedance is compared with the shunt impedance of a disk loaded cylindrical structure.

I. INTRODUCTION

A double-sided muffin-tin structure was proposed for acceleration of relativistic electrons at 120 GHz [1]. At very high frequencies, around 100 GHz, the standard technology for the fabrication of RF structures is no longer applicable. In recent years, micrometer silicon technology [2, 3] has become so well developed that large-scale wafers in the range of 10cm are available and, when metalized, could support planar RF structures for acceleration.

The structures can be made with high precision, on the order of one micrometer, and can be of nearly arbitrary shape. Glass fibers in V-grooves allow for alignment precisions of about 1 to 5 micrometers between wafers. Copper coating of these structures is well established and has been proven to withstand very high fields around 100 MV/m under DC conditions. Additionally, silicon has a very good thermal conductivity, only a factor 2.5 lower than copper at room temperature and even better than copper at liquid nitrogen temperature. Micro channels at the bottom of the wafer could therefore provide very effective cooling.

II. GEOMETRY AND MODE OF OPERATION

The operating frequency we are considering is 120 GHz (the wavelength λ =2.5 mm). For RF cavities of this size, planar structures are well suited. One such structure is the double-sided muffin-tin structure. The structure has a series of advantages:

- it is of simple geometry and best suited for microfabrication techniques,

- it is simple to cool from top and bottom,

- it has low higher-order modes which can be damped easily using the side openings,

- the side openings provide vacuum pumping slots in a natural way,
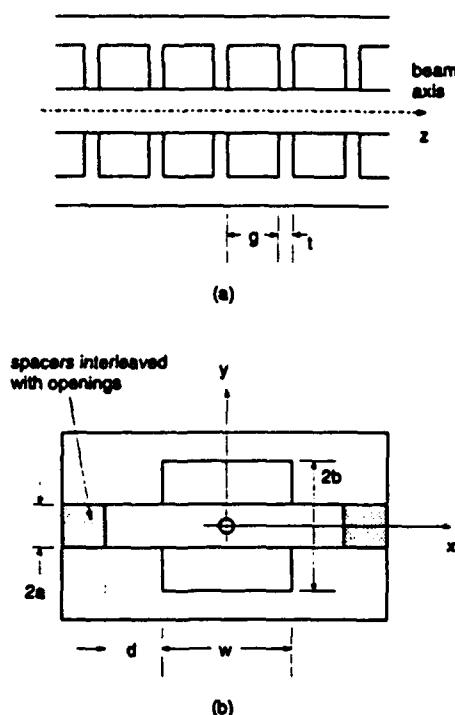
Figure 1
The double-sided muffin-tin structure. a) longitudinal b) transverse cut

- on axis the RF fields cause transverse forces of quadrupole character which can be used for focusing.

For SW acceleration, one has to use a $\pi - mode$ in order to get a high shunt impedance. Operation at the $\pi - mode$, without excitation of neighboring modes, requires the mode bandwidth to be smaller than the distance to the next mode. Taking k=0.05 and Q=2000 (Q scales with $\omega^{-1/2}$) only N=15 cells can be coupled which means that every 2 cm we would need a feed. This is probably too small a number. $\pi - mode$ operation also means increased sensitivity to frequency deviations and dimensional tolerances and a cell-to-cell phase deviation to compensate for the losses [4]. The resulting phase shift over the entire structure is

$$\Delta\phi = (1 - k)^{\frac{1}{2}}\frac{N^2}{kQ} \qquad (1)$$

or 2.2 radians for the above example, clearly excessively large.

SW operation also causes a somewhat higher average heat dissipation than traveling wave (TW) operation where

---

Table 1
Comparison of TW shunt impedance and Q-factor of disk-loaded and muffin-tin designs.

t	Disk-loaded		Muffin-tin	
(mm)	r_o $(M\Omega/m)$	Q	r_o $(M\Omega/m)$	Q
0.04	441	2456	366	2460
0.08	431	2401	358	2380
0.12	417	2342	347	2310
0.16	401	2280	335	2240
0.20	385	2214	312	2160

Figure 2
Dispersion relation of the muffin-tin structure with dimensions (2).

the filling time is shorter and the left-over RF power is taken out after the beam passage. This difference may be important, since due to the tininess of the structure the cooling will be at the limit of what is possible.

TW operation can be done in either a constant impedance (CI) structure or a constant gradient (CG) structure. For simplicity, we have chosen a CI structure. But, higher peak electrical fields and the non-uniform heat dissipation may either dictate the use of CG structures or split the structure in several sections of different but constant impedances. This is possible with different aspect ratios w/b (see Fig. 1) as will be shown in the next section. Other advantages a CG structure normally has as compared to a CI structure are lower sensitivity to errors in frequency, dimensions, and beam break-up. They are, we believe, less important since the muffin-tin is very open with correspondingly large coupling and small higher modes. In both cases, CI and CG, a $2\pi/3 - mode$ will be used. This gives the highest shunt impedance, especially for thicker iris walls as are needed here.

Clearly the conclusions have to be reconsidered if the cooling problem turns out to be insurmountable or if the RF power available from the source is not high enough to reach the desired gradients of at least 10 MV/m. If one has to go to cryogenic temperatures, SW operation may be preferable.

III. RF PARAMETERS

The cavity shunt impedances are calculated using the finite difference computer code MAFIA for the muffin-tin design in Figure 1 and for the 120GHz $2\pi/3 - mode$ disk-loaded design [5], as shown in Table 1. The shunt impedance of a disk-washer design at 120GHz is expected to be ~390 MΩ/m for t=0.12mm. (The 2.83GHz SLAC cavity has a shunt impedance of ~60 MΩ/m [6].)

For 120 GHz (λ =2.5 mm) the dimensions in mm were found to be
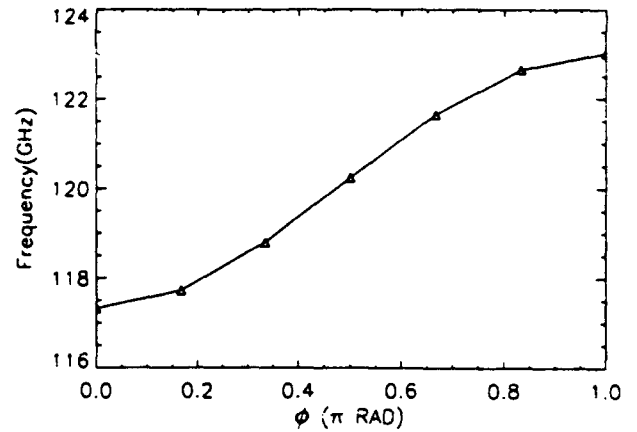
$$a = 0.3, \quad b = 0.9$$
$$w = 1.8, \quad d = 0.8 \qquad (2)$$
$$g = 0.633, \quad t = 0.2.$$

The period length g + t was chosen for the $2\pi/3 - mode$

$$2\pi\frac{g+t}{\lambda} = \frac{2\pi}{3} \qquad (3)$$

and the iris thickness t fixed through practical reasons. The length of the side openings was taken large enough such that the fields have decayed sufficiently. The aperture 2a is in principle a free parameter and influences the passband bandwidth as well as Q-value, shunt impedance, and wakefields. The value given above is a trade-off between the different requirements.

The dispersion relation is given in Fig. 2. It is well approximated by the theoretical cosine-shape

$$\omega_n \simeq \omega_\tau(1 - \frac{1}{2}k\cos\phi_n), \quad \phi_n = \pi\frac{n}{N}, \quad n = 0, 1, 2, ..., N \qquad (4)$$

with $k = \frac{\omega_N - \omega_a}{\omega_r} = 0.0475$ for $f_r = 120GHz$. From (4) we derive the group velocity as

$$\frac{v_g}{c_o} = \frac{\partial\omega}{\partial\beta} = \frac{(g+t)}{c_o}\frac{\partial\omega}{\partial\phi} = \frac{\pi}{3}k\sin\frac{2\pi}{3} = 0.043. \qquad (5)$$

Knowing the group velocity, the structure attenuation follows from

$$\alpha = \frac{\omega_r}{2v_g Q_o} = 13.5m^{-1}. \qquad (6)$$

A particle sitting on the crest of the RF wave gains an energy V in a structure of length ℓ

$$V = \sqrt{2\tau}\frac{1 - e^{-\tau}}{\tau}\sqrt{r_o\ell P_o}, \quad \tau = \alpha\ell \qquad (7)$$

where P_o is the input power. Since r_o changes only slowly with the cavity dimensions, one can assume it to be constant and optimize V, yielding

$$V_{opt} \simeq 0.9\sqrt{r_o\ell P_o} \ for \ \tau_{opt} = 1.26. \qquad (8)$$
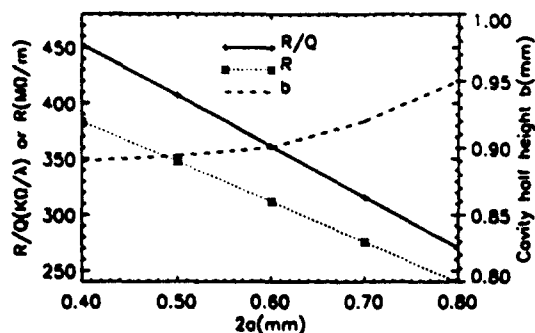
Figure 3

Shunt impedance, r_o/Q, and cavity depth b versus aperture 2a at constant cavity width w = 1.8 mm.

Figure 4

Shunt impedance r_o, r_o/Q, coupling constant k, and cavity depth b versus cavity width w at constant aperture 2a = 0.6 mm.

The optimum is very flat and not critically dependent on τ. Substituting α from (6) into (8) gives $\ell = \tau_{opt}/\alpha$=9.3 cm. This is about the maximum length one can reasonably achieve with silicon wafers. We choose it a little shorter

$$\ell = 7cm \quad \text{yielding} \quad \tau = 0.945 \tag{9}$$

to have reserve in the wafer length and also to have a somewhat higher energy conversion. With this structure length we get

$$V = 4.1\sqrt{P_o}\ KV. \tag{10}$$

The ratios of input to output gradient and power loss are

$$\frac{E_{(s=0)}}{E_{(s=\ell)}} = 2.6, \quad \frac{P'_{(s=0)}}{P'_{(s=\ell)}} = 6.6 \tag{11}$$

and the number of cells per section is $N = \ell/(g+t) = 84$. To get an accelerating gradient $E = V/\ell$ of 10 MV/m we need, following Eq. (10), a peak input power of

$$P_o = \left(\frac{E\ell}{4.1 \times 10^3}\right)^2 = 29.1\ KW.$$

For small beam currents one may tolerate even smaller apertures than the chosen 2a = 0.6 mm. In that case the shunt impedance goes up as shown in Fig. 3.

If it turns out that the strong dependence of power dissipation along the structure, Eq. (11), is not tolerable for cooling reasons, we can choose a quasi CG structure with a few CI subsections. The energy gain, Eq. (10), will only change marginally but the power dissipation can be made nearly uniform along the structure. Fig. 4 shows the necessary aspect ratio w/b in order to adjust the coupling constant k and, therefore, v_g (see Eq. 5).

The current threshold for the regenerative multi-bunch beam break-up was estimated as [3]

$$I_{th} \simeq \pi \frac{|v_g|}{c_o} \frac{1}{\lambda r_\perp/Q} \frac{pc_o}{e} \left(\frac{\lambda}{2\ell}\right)^3.$$

If the deflecting HEM_{11} mode is around 150GHz (λ =2mm), beam energy pc_o =10 MeV, $v_g = 0.05c_o$, and $\lambda r_\perp/Q = 200\Omega$, the current threshold is 23 mA.

IV. CONCLUSION

A double-sided muffin-tin structure is ideally suited for mm-wave frequencies and microfabrication techniques. A traveling wave mode with a $2\pi/3$ phase advance per cell has adequate RF parameters and could even form an approximated constant gradient structure. In addition, it has transverse fields of quadrupole character which can be used, at least partially, for focusing.

V. REFERENCES

[1] H. Henke, Y. W. Kang, and R. L. Kustom, "A mm-wave RF structure for relativistic electron acceleration," APS Note MMW-1, September 1992.

[2] H. Guckel, K. J. Skrobis, T. R. Christenson, J. Klein, S. Han, B. Choi, and E. G. Lovell, "Fabrication of Assembled Micromechanical Components via Deep X-Ray Lithography," MEMS 1991, Nara, Japan. Jan. 1991.

[3] R. T. Howe, R. S. Muller, K. Y. Gabriel, and W. S. N. Trimmer, IEEE Spectrum, p. 29, July 1990.

[4] G. A. Loew and R. B. Neal, Linear Accelerators, chapters B.1.1 and B.1.4, North-Holland Publishing Co., 1970.

[5] R. Klatt, F. Krawczyk, W. R. Novender, C. Palm. B. Steffen, T. Weiland, T. Barts, M. F. Browman. R. Cooper, C. T. Mottershead, G. Rodenz, and S. G. Wipf, Proc. of the 1986 Linear Acc. Conf., SLAC-Report-303, Sept. 1986.

[6] G. A. Loew, R. H. Miller, R. A. Early, and K. L. Bane, "Computer Calculations of Traveling-Wave Periodic Structure Properties," IEEE Trans. on Nuclear Science, Vol. NS-26, No. 3, June, 1979.

SCANUR:
A Subcritical Reactor with Electron Linacs
for Transmutation of Nuclear Wastes

† - A. Krasnykh, Yu. Popov, V. Rudenko, and L. Somov,
‡- L. Men'shikov, V. Prusakov, and S. Subbotin
†- Joint Institute for Nuclear Research, Dubna, Russia and
‡- Russia Research Center "Kurchatov Institute", Moscow
email: krasnykh@main1.jinr.dubna.su

II. REACTOR TRANSMUTATOR

Our point of view is the following. All actinide fission fragments besides ^{129}I should be buried. Only high actinides ^{241}Am, ^{243}Am, ^{237}Np, ... and ^{129}I should be incinerated in SCANUR. Plutonium should be return back to the nuclear plant. So, SCANUR must incinerate $J_a = 3 \cdot 10^{18}$ nuclei per second for the 3 GW power plant. The total cross section for n,γ and n,f reactions with actinides is rather high (about 500 $barn$). The wastes could be incinerate in a conventional slow reactor but this way is connected with the high nuclear hazard. The subcritical melted actinide fluoride salt reactor for transmutation of nuclear wastes has a whole row of the advantages. The main one is the guaranteed safety when there is a high level of the effective neutron multiplication coefficient. The reactor fuel is a liquid melted salt of the fluoride actinides. There are of this kind experimental running reactors but with other salt as a fuel. The designed reactor has a closed external contour. The melted salts circulate by thermal convection. The heat and product of nuclear reaction are removed from the active zone by the natural convection process. The soft driving and tuning of SCANUR is achieved by the changing of the salt concentration. There is a dilution process in the ^6LiF salt. As a result, there is radiation safety of the SCANUR operating with a high level of the reliability and with the effective neutron multiplication coefficient up to

$$k_{eff} = 1 - \beta = 0.997$$

where β is a fraction of slow neutrons for actinides.

It should be mentioned that

$$k_{eff} = 1 - 10 \cdot \beta$$

for the solid fuel reactors. The SCANUR has a high level of neutron multiplication (about 300). In this case a simple, cheap and existing electron linac system could be adopted to solve the nuclear transmutation problem. As it will be shown bellow k_{eff} will determine the general parameters for the SCANUR linac.

Abstract

Subcritical Actinide Nuclear Reactor (SCANUR) guided by the electron - gamma -neutron chains is considered. It incinerates the nuclear wastes of one nuclear power plant with power about 3 GW. The main requirements for the reactor system and electron linac are formulated. In this paper the outline of the main linac system and parameters is discussed.

I. INTRODUCTION

The conception of the melted salt subcritical reactor for the transmutation of high actinides such as ^{241}Am, ^{243}Am, ... and including longlived ^{129}I is considered. The fuel of SCANUR is melted salt of fluoride actinides that circulate in the external loop by thermal convection. The actinide fission fragments are extracted from the loop by the radiochemical method. Simultaneously the heat removal by the external loop is allowed. The total average e-beam power needs about 1.5-4 MW for transmutation of nuclear wastes from one block of a plant with power 3 GW. The reactor version with the effective neutron multiplication coefficient $k_{eff}=0.997$ is discussed. The experimental results and the experience gained at the existing melted salt reactors are taken into account here. The SCANUR is driven and fed by the external neutron source which it is based on the system of S-band linacs. The linacs are situated in the horizontal plane around the active section (core). This design solves the problem of injecting the e-beam into reactor. The well known pulse rf-technology is used in the SCANUR conception. Most of the rf-equipment which is required to build the linac system is a part of well developed technology or could be scaled from systems that have been running for many years.

III. CONCEPTION OF ELECTRON LINAC FOR TRANSMUTATION OF WASTES

The needed average e-beam power P_{av} is:

$$P_{av} = J_a(1 - k_{eff})\nu C_n \qquad (1)$$

where:

$\nu \simeq 3$ is the neutron multiplicity for actinides;

$C_n = E_e/\chi_n$ is the "neutron price";

E_e is the incident energy of the e-beam and

χ_n is efficiency of the photonuclear reaction for neutrons that were born inside the active zone.

The neutron price for the $\sim$100MeV incident e-beam is $\simeq$ 1.1 GeV for natural uranium. The price for high actinides will be $\simeq$0.8 GeV. So, the total average beam power should be up to $\simeq$ 4 MW for the 3 GW nuclear plant and SCANUR would incinerate about J_a =3 10^{18} nuclei per second. It is clear from (1) that the total beam power is determined by the effective neutron multiplication coefficient k_{eff}. Different kind of accelerators (linear and cyclic, conventional linacs and new ones, induction or rf-linacs, superconducting or warm rf-linacs etc.) were discussed and the analysis was carried out. Their comparison with a proton linac was carried out of course. The analysis showed us that the S-band e-beam linac could have a number of advantages (for this time) as compared with others. The main advantage of this combination of an e-beam linac and a liquid melted salt of the fluoride actinides reactor is a total low cost (the final price that include R&D and operation cost, safety, time of running, ecology etc.) and its "chamber" and proper relation to the nuclear block of plant.

The needed total beam power is too high to be obtained by only one electron linac but it could be spread in space and time. The preliminary estimates was showed, for example, that the perimeter of the SCANUR active zone in the horizontal plane could be about 6 m. For the SCANUR project could be used a several separate S-band linacs. The total number of linacs is 16, for example. Each one could have conventional (not record!) parameters. The linac system is based on the use of well developed technology that have been in successful operation for a many years. It seems to us that a SLAC-like $2\pi/3$ traveling wave constant gradient structure can be used. It is more cheaper relative L-band stuctures. Instead of the single bunch operation mode, the SCANUR linac should get the multibunch one.

SCANUR, for example, has got of 16 linacs, which are situated around the active zone. The output target is made of tantalum, which is more suitable for a high level of average $e-$, γ, $e+$ and n power fluxes. The general parameters of the SCANUR linac system are presented in Table 1.

The operation cyclogram was chosen as follows in order to decline the target heating problems. Linac operates consistently and in turn. The pulse length of each electron beam is about 4.15 μsec. The total illumination time of

Parameter	Value
Energy	112 MeV
Average beam power	1972 kW
Linac length (each one)	$\sim$ 25m
Number of linacs	16
Repetition rate	600 Hz
Linac efficiency	0.74

Table 1: SCANUR Linac Parameters

Parameter	Value
RF-frequency	2856 MHz
Pulse duration of rf-power	$\simeq$ 5μsec
Beam pulse length	$\sim$ 4.15μsec
Average output power	123 kW
Average beam current	0.0011 A
Average pulse current	0.46 A
Pulse beam current	5.4 A
Energy of beam	112 MeV
Bunch charge	161 pC
Bunch length	3 mm
Distance between bunches	10.5 cm

Table 2: The Main SCANUR Linac Parameters

the target is about of 70.5 μsec followed by a relatively long (about 1.6 msec) pause for the technological process in the SCANUR active zone. The EGS3-code was used to estimate the energy deposition on the target. It should be mentioned that there is a possibility of using the coherent bremsstralung from the crystal target for to get of the additional gain for the neutron flux. The using of crystal target allow to reduce some the neutron price for SCANUR. The estimates of coherent bremsstralung is shown that for $E_e \simeq$ 40 MeV the neutron price could reach up to $C_n \simeq$ 300 MeV. Than the total average power could decline to 1.5 MW.

It seems to us that accumulation of the defects in the crystal converter target is not so much significant because there is a continuous annealing process by electron beam. The value of the gain should be specified by experiment in the nearest future. The using of the coherent bremsstralung from the crystal target could be useful and for design of positron source for electron/positron colliders with a high average luminosity. This is the important moment both for the SCANUR project and the design of positron sources with a high yield.

In Table 2 was given the main parameters for one linac. There was the analysis of several variants of the SLAC-like structures in the range $a/b = 0.25 \div 0.35$ where a is the beam hole radius and b is the inner radius of the accelerating structure. The aim of the study was to determinate the beam loss parameter for the operation and HOM frequencies. The broad band of the structure is an important parameter for the multibunch operation mode. It was studied by the URMELT and TBCI codes. It was interested to compare the URMELT dates with dates that had get from Handbook on Disk Loaded Structure by O.Val'dner

a/b	0.24	0.3	0.35
Transmittance for f_0	12 MHz		56 MHz
Transmittance on f_{HOM}	49 MHz	105 MHz	198 MHz
k_{loss} for f_0	1.1 V/pC	0.88 V/pC	
k_{loss} for f_{HOM}	0.088 V/pC	0.1 V/pC	0.3 V/pC

Table 3: Comparison of Linac Structures

and et al. In Table 3 some data are presented.

The structure with a/b= 0.3 could get the next stage of the SCANUR linac design. There is not so bad agreement between computer and the Handbook data for the operating frequency. The different is not more than 8%. The different increase when the dipole mode parameters are calculated The thermoproblem of the disk will be considered on the next stage of the study.

The Russian klystron "Bereg" could be used as the pulse rf-power supply. It is a multibeam high pulse power klystron. The output pulse power is of 10 MW and the average power is about 25 kW. The pulse length of rf-power is 5 μsec. The anode voltage is rather low (about 80 kV) and the pulse power supply is not so large as for the single beam tube power supply. This fact could be very useful for the SCANUR linac.

The beam loading problem for the multibunch operation mode was also studied for optimization of the energy spectrum. The energy spectrum of the beam would be to have the minimum if the injection start had shifted before the time of the rf-filling $0.335 \cdot t_f$ were t_f is the filling time of the section (it is about 0.83 μsec for the standard SLAC-section). In this case the energy spectrum will be no more than 14%. The preliminary study of the transverse wake fields (TBCI-code) for the SCANUR linac regime gives the hope that there will not be any problems for the beam stability with the gradient about 5.3 MeV/m and accelerating train of bunches with $\sigma_z = 3$ mm and 160 pC per bunch.

IV. CONCLUSION

The use of the combination subcritical melted actinide fluoride salts reactor and S-band linac system for the transmutation of nuclear wastes would allow to large reduce the cost of R&D for the solving problems of the incineration of the longlieved nuclear wastes of the plants. The SCANUR systems is rather compactly relative the system of the nuclear plant and could place on the direct on the plant. The most of the details and the ground system that are required to start the experimental study of the transmutation nuclear wastes are a part of well development technology. In this case there is a possibility to start the draft proposal for the solving this problem.

New Irradiation Field Shaping Systems of High Voltage Electron Accelerators for Industry

A.S.Ivanov, V.P.Ovchinnikov, M.P.Svinin, N.G.Tolstun

The D.V.Efremov Scientific Research Institute of Electrophysical Apparatus,
189631, P.O.42, St.Petersburg, Russia

The competitiveness of high voltage accelerators for industry is determined by their cost, operational conveniences and sizes, provided their main parameters are equal. These characteristics have been essentially improved in the machines with the extended cathodes that provides their wide usage in such spheres of technologies as for example the treatment of thin coating layers [1]. The accelerators for higher energy range have far more large sizes and high costs that restrains their industrial application, though the electron beam modifications of thicker materials are in high demands. The dimensions of high voltage accelerators in the energy range of 0,3 to 3,0 MeV are determined mainly by their sizes and mutual arrangement of their main systems: an accelerator itself which includes a high voltage generator and an acceleration structure and an irradiation field shaping system (IFSS). The height of a 1 MeV accelerator with an outlet window width of 150-200 cm is about 4,5-6 m, if designed to a traditional schematic and thus requires higher premises to provide service (see Fig.1.). The height of accelerators often is a restricting factor because customers would like to install them in common industrial premises.
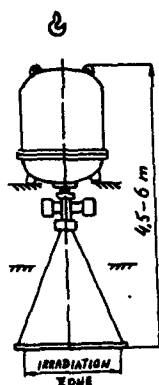
Figure 1.The lay-out of traditional scheme of industrial electron accelerator

The IFSS with an extended bending magnet designed in our institute uses the principles of cylindrical electron optics and allows to decrease the vertical size of accelerator by several times. Such type of IFSS and the projection of electron trajectories in it obtained by numerical simulation are represented in Fig.2. Another merit of such field shaping system is practically normal angles of electron trajectories on the outlet window foil, as shown in Fig.2. It must be emphasized that such IFSS demands higher quality and smaller beam size at the inlet than conventional ones because the bending magnet field enlarges the beam size on the foil plane by several tens. When using a double shaping system of such a type an accelerator beam can be extracted through the two outlet windows facing opposite sides,
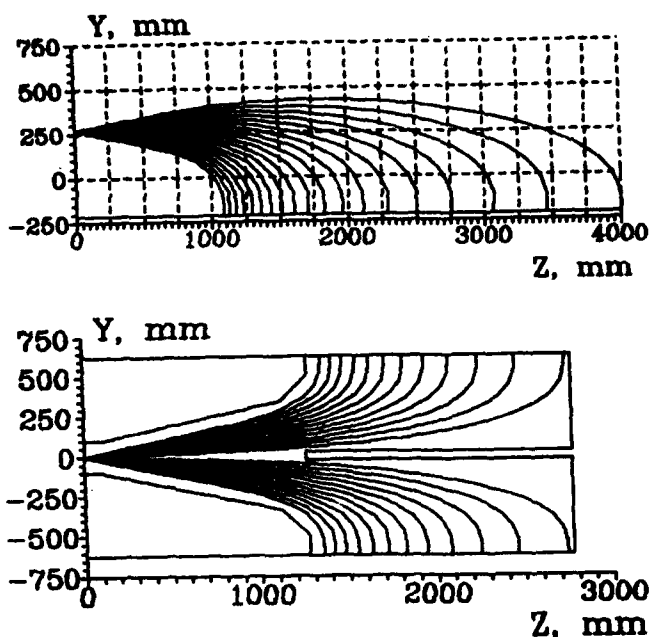
Figure 2. Projection of electron trajectories in the IFSS with bending magnets

providing double-sided or staged irradiation of materials (see Fig.2.).

On the other hand one of the most compact and convenient in operation type of high voltage electron accelerators is that on the basis of a single-phase transformer-rectifier with the particle accelerating channel situated on its axis [3,4]. The alternating magnetic field of an axially-symmetric primary winding induces the e.m.f. in the sections of a secondary winding. The alternating current in each section is rectified by a voltage-doubler scheme and the separate DC outputs are connected in series. The power supply system of such accelerators is the reliable mass production frequency converters.

These accelerators are designed and successfully operate in industrial and pilot plants at the energies from 0,5 to 2,5 MeV and beam power up to 100 kW.

So we have put the task to design the compact and convenient industrial accelerators by means of combining these two technical decisions in the one machine.

The main problems to be solved in such accelerators are associated with the beam passage through the accelerating tract in the presence of the transformer

magnetic field. The value of this field on the system axis is 100-150 G. The tube screening by means of copper rings provides an axial magnetic field decrease from 50 to 60 times on the tube axis, but the main influence on the accelerated electrons, naturally, is from radial and crossed components of the field. The radial component of axial symmetric winding equals zero on the winding axis, but the location of the electron optical axis may not coincide with the magnetic one, moreover the nonsymmetrical elements of primary winding produce a crossed field component on the optical axis.

It was necessary to conduct a special study to get at the accelerating tube outlet an electron beam suitable for utilization in the IFSS with the extended turning magnet. All the beam experiments and the magnetic field measurements were accomplished on the 1 MeV accelerator. The magnetic field amplitude was 110 G on the axis of the transformer-rectifier with the frequency from 500 to 800 Hz.

The measurements of the crossed magnetic field distribution along the accelerating tube axis were carried out to study the possibility of combining the magnetic and electron optical axes. The crossed magnetic field minimization was done by the primary winding movement and inclination with respect to the accelerating tube. The results of measurements of the primary winding crossed magnetic fields · after their optimization on the tube axis are shown in Fig.3. The corresponding beam axis trajectories and their deflection angles, that have been calculated according to the crossed magnetic field distribution, are represented in the same figure. It was necessary to reduce this deflection by several times
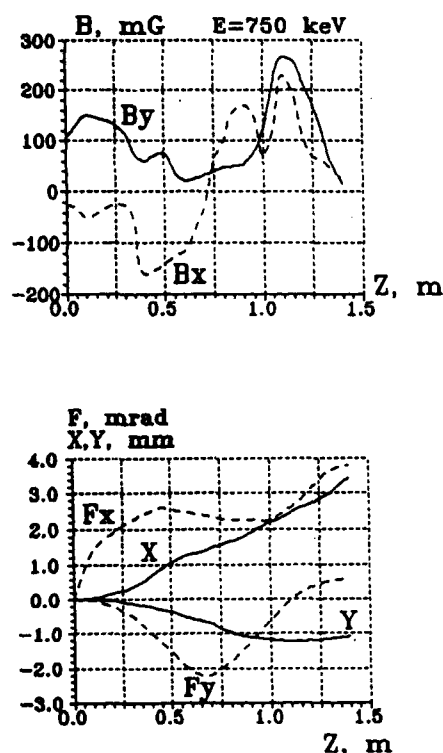
within the acceptable limits for the beam usage in IFSS with extended bending magnets.

The possibilities to screen a tube aperture with the electrodes having high magnetic permeability were considered to decrease the crossed field as well as the copper rings to decrease the axial component.

To determine the screen coefficient (Cs) dependence on different factors, the magnetic field measurements within the aperture of the ferro-magnetic electrodes have been made. The electrodes were put in a special device which permitted to fasten them at different distances. As a source of magnetic field the primary winding of the accelerator was used that gave sufficient magnetic field distribution homogeneity.

The dependence of Cs on the distance between the flat electrodes is represented in Fig. 4. As these measurements show, the use of ferro-magnetic electrodes decreases the alternating crossed magnetic field by several tens at the typical for high voltage accelerator correlations of the electrode sizes and the space between them. The experiments on electron beam passing through the accelerating tube thus screened confirmed the high effect of such solution. The beam track photographs, which have been done on the outlet window foil at the various energies, showed the absence of beam swing. Another experiment with a 2° inclination of primary winding, as referred to the accelerating tube, showed the full coincidence of beam track on the window foil and the beam track from primary winding fixed at the right angle.

Thus, this way of the accelerating channel screening permits to exclude the influence of winding magnetic field on the beam dynamics in the accelerator with a single-phase transformer-rectifier.

When this task has been solved there was designed a series of accelerators embodying these technical principles. The height of all the machines is less then 2.2 m thus permitting their location in the standard industrial premises and there is no need of any special lifting devices for theirs technical service.

The accelerator for the energy of 1 MeV, beam current 80 mA and 150 cm width outlet window is represented in Fig.5. Thanks to the horizontal lay-out of its main parts it might be easy integrated in the production lines.

Figure 4. Dependence of screen coefficient (Cs) on the distance between flat electrodes

Figure 3. Crossed magnetic field distribution on the tube axis, deflection and angles of electron trajectories in the accelerating tube

The installation on the basis of the electron
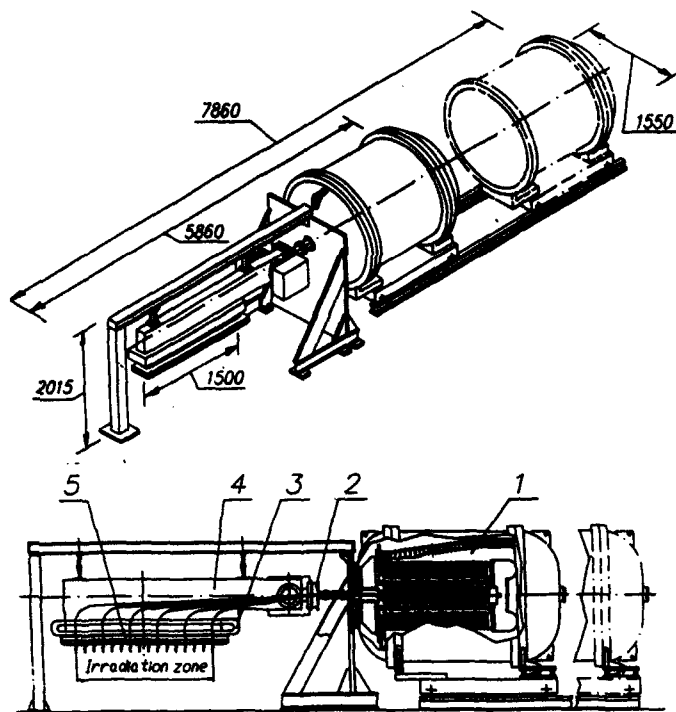
I-Irradiator   4- Vacuum Chamber
2-Scanning magnet   5-Outlet window
3-Turning magnet

Figure 5. The electron accelerator for the energy 1 MeV

accelerator for the energy of 300 keV and a 200 cm width outlet window is placed inside an iron-lead radiation shielding and is presented in Fig.6.
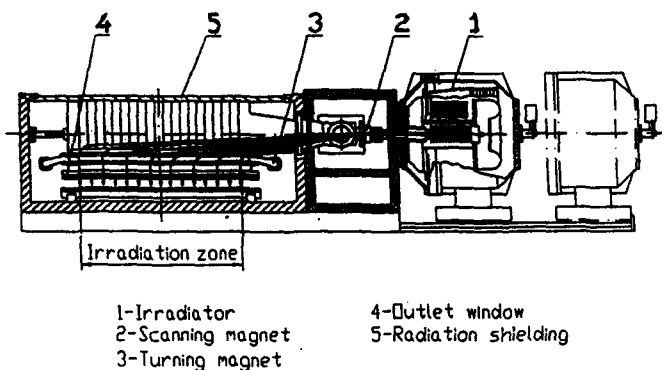
1-Irradiator   4-Outlet window
2-Scanning magnet   5-Radiation shielding
3-Turning magnet

Figure 6. The installation on the basis of the electron accelerator for the energy of 300 keV

The accelerator for the energy of 750 keV and 100 mA beam current with two windows facing opposite sides 150 cm in width each is shown in Fig.7. The accelerator is placed inside a metal radiation shielding and meant for the double-sided irradiation of flexible materials. The electron beam is scanned in each window with frequency about 500 Hz and transferred from window to window with frequency of 40 Hz. The homogeneity of distribution of beam current in each window is better then +/- 5%. Double-sided irradiation allows to increase the thickness of treated material from two to four times in comparison with the one-side irradiation at the same energy and besides provides a complete absorption of accelerated electrons in the material.
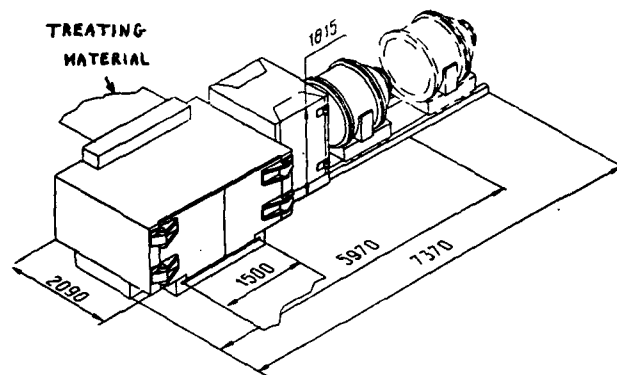
Figure 7. The installation on the basis of the electron accelerator for the energy of 750 keV for double-sided irradiation of flexible materials

Thus, the solution of the problem of combining the two most compact main systems of high voltage accelerator in one unit permits to decrease considerably the sizes of industrial electron accelerators and fully adapt these machines to the demands of industrial production.

REFERENCES

[1] Aaronson J.N., Nablo S.V. Performance Characteristics and Typical Industrial Application of Selfshielded lectron Accelerator (< 300kV), *Nucl.Inst.& Meth.Ph.R. B10/11* (1985), pp. 998-1003

[2] Ovchinnikov V.P., Lamzin E.A., Sukharev Y.V., Tolstun N.G. The Investigation of the Irradiation Field Shaping System of the Accelerators for the Radiation Technology. *Preprint NIIEFA P-D-B-0689*, Moscow., TSNIIATOMINFORM, 1985.

[3] Auslender V.L., Salimov R.A. The Electron Accelerators of Nuclear Physics Institute SO AS USSR for National Economy. *Atomnaya energiya*, 1978, v.64, 5, pp.403-408.

[4] Akulov V.V. and others. High Voltage Accelerator ELECTRON-6 *Abstr. of Sixth All Union Conf. for Part. Accelerators Using in National Economy* (Leningrad, 11-13 oct.1988.) p.5.

A Versatile 2 MeV, 200 mA Compact X-Band Linac

C. E. Clayton and K. A. Marsh
Department of Electrical Engineering
University of California at Los Angeles
56-125B Engineering IV
Los Angeles, CA 90024

Abstract

A small, high performance electron linear accelerator is described. It is a modified version of a commercially available portable x-ray source. The fixed power supplies were replaced with remote controllable supplies allowing a systematic exploration the linac's parameter space. A condition in which the linac performs nearly in accordance with its theoretical limits was found. The 9.3 GHz RF linac and beamline deliver a 2 nsec train of approximately 10 psec pulses with a peak current, limited by beam loading of the RF structure, of more than 200 mA and a beam energy of around 2 MeV with a 5% FWHM energy spread. The small energy spread is due largely to the focusing of the beam through a 500 μm lead pinhole early in the beamline. A 6 μm Mylar vacuum window covers the pinhole allowing the use of the beam in a rough vacuum environment with minimal degradation of the beam emittance. The unnormalized beam emittance is 6π mm-mrad and the final spot size is 260 μm diameter for f/20 focusing.

INTRODUCTION

A compact, reliable, inexpensive, and easy to operate electron linac was required for experiments on the plasma beat wave accelerator concept at UCLA.[1,2] Such a linac was realized through the modification of a commercially-available x-radiography machine. This paper will briefly describe the hardware as well as some of the operational experience of the linac.

ACCELERATOR HARDWARE

The Linac

The electron linac started out as a commercial portable x-ray generator, the MINAC 1.5 (Refs. 3 and 4) manufactured by Schonberg Radiation Corporation[5]. The modifications we made to this unit are described in greater detail in Ref. 6. Essentially, the modifications were the following. First, the tungsten target (the x-ray source) at the end of the linac was removed and the linac attached to a vacuum system. The remainder of the modifications was essentially to replace the gun-voltage, grid-bias voltage, cathode-heater, and grid-pulser power supplies, which were not all independently adjustable in the commercial unit, with adjustable and remote-operable units. The 9.3 GHz magnetron was also upgraded from a 200 to a 250 kW unit.

These changes allowed us to freely explore parameter space and fine-tune the operating parameters. The net result of these modifications was to increase the beam energy from 1.5 MeV to 2 MeV and the beam current from 2 mA to 25 mA average current.

Vacuum system

The pressure in the vacuum chamber at the interaction point in the beat wave experiment is typically 150 mT of hydrogen gas. However, the pressure at the gun of the linac must be kept below 10^{-7} T. One solution is to use differential pumping techniques to drop the pressure between the gun and the interaction point but this would have added a level of complexity that we could not afford. A simpler solution is to use a thin vacuum window to separate the rough vacuum of the experiment from the high vacuum of the linac. But at these low beam energies, even the thinnest foils adds a finite angular spread to the beam. However, if the foil is located at a tight waist, the degradation to the emittance is minimized.
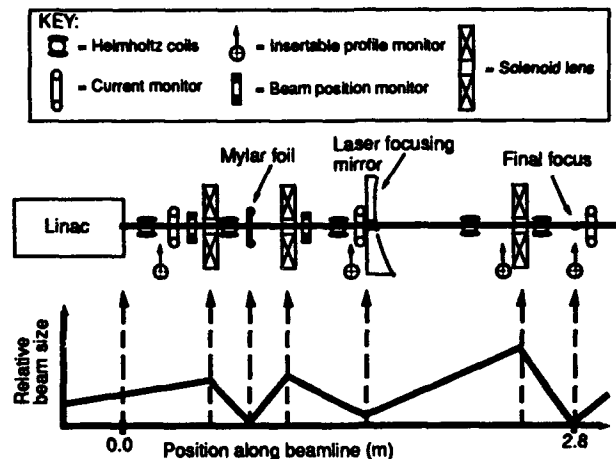
Figure 1: Cartoon of electron beamline and the variation of the beam spot size along the beamline.

Figure 1 shows the electron beam line with its three solenoidal lenses and three waists. A 6 μm thick Mylar foil is located at the first waist. We find that the emittance increases from 4π to 6π mm-mrad in traversing the foil. For added mechanical strength, the foil is supported against the higher pressure downstream by a thin lead disk with a 500 μm, centrally located pinhole. The presence of the pinhole has the added benefit of selecting the momentum of the beam due to the chromatic aberration of the solenoid lens. Thus the fairly wide energy spread coming out of the linac is scraped down to a 5% spread after the pinhole.

Beamline

After the pinhole, the beam has two more waists, again from solenoid lenses. The beam line has five Helmholtz coils to keep the beam centered on the lenses and at the interaction

point as well as various profile monitors and current monitors as shown in Fig. 1. Between the first two profile monitors, the beam is confined to a 3/4" tube so that beam-position monitors are required to verify proper alignment of the beam.

The second waist in the beamline is at a small (≈5 mm) hole drilled in the final, off-axis-parabolic focusing mirror of the experiments large diameter (15 cm) CO_2 laser beam. Beyond this point, the electrons are collinear with the laser beam, as is required for the experiment. At the last lens, the beam has a diameter of about 1 cm and is focused down to a spot of 260 μm FWHM at a distance of about 20 cm from the lens.

OPERATIONAL EXPERIENCE

For all these measurements, the rf power is about 230 kW, the gun voltage is 10 kV, the cathode temperature is well above the emission vs. temperature "knee", the grid bias is -90 V and the pulse amplitude applied to the grid is about 250 V, well into saturation.

Pulse width control

As the width of the square pulse applied to the grid is varied from 10 to 20 nsec, the output current measured on the first current monitor rises from zero to about 100 mA with a 10 nsec FWHM. For longer applied pulses, the current essentially droops with time. Energy measurements indicate that the longer pulses have severe energy droop as well. What is happening is that the first 10 nsec of the output pulse substantially loads down the rf fields, perhaps most strongly in the early cavities. For our experiment, we operate with a 15 or 20 nsec drive pulse to stay just on the edge of severely loading down the rf fields and thus maximize extracted current
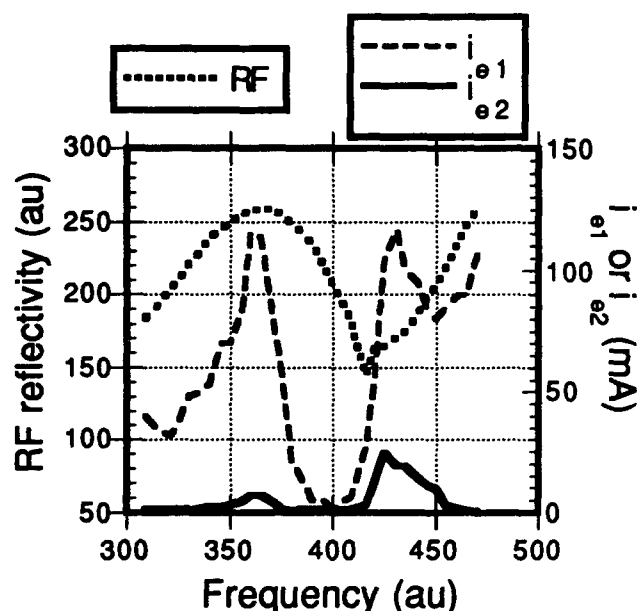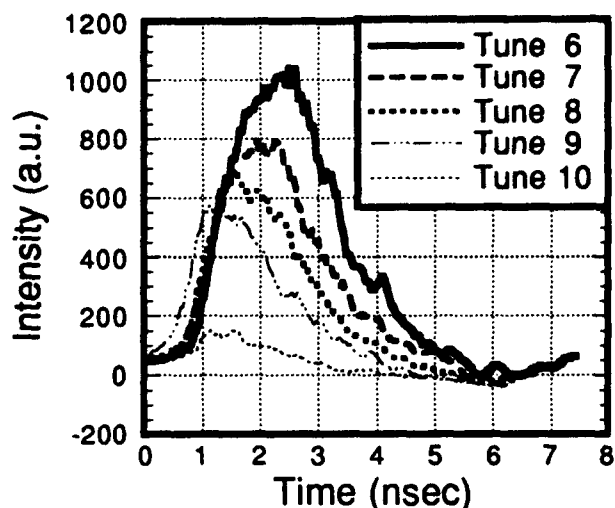
Figure 3: The output pulse shape measured at the interaction point for various frequency tunings of the magnetron.

while avoiding substantial energy droop on the beam.

Tuning curve and macropulse structure

The accelerating mode of the linac was designed to capture 10 keV electrons and accelerate them to near light speed over the first third of the linac structure. As we increase the rf frequency in the vacinity of the design frequency, we see a glitch in the curve of rf reflectivity vs. frequency (top curve in Fig. 2) as the accelerating mode becomes excited. At the same time, the signals on the first and second current monitors rise rapidly. The second monitor measures *after* the lead pinhole so essentially it measures the 2 MeV portion of the beam whereas the first monitor sees all energies. As the frequency increases further, the second monitor falls off slowly as the rf reflectivity rises indicating that we are depositing less and less energy into the stored rf fields.

The output pulse shape at the interaction point was measured as a function of this tuning. Some of the results are shown in Fig. 3. The top curve labeled "Tune 6" is at the optimum frequency from Fig. 2. As the frequency was increased up to this optimum (Tunes 1 through 5, not shown) the pulse shape was constant, only the amplitude changed. This may be due to the poor capture efficiency in the early cavities at frequencies below the optimum. But for higher frequencies (Tunes 7 through 10 in Fig. 3), the pulse shape changes as the rear of the pulse is lost due to a saturation in the current at progressively lower levels. This is the slow drop seen in Fig. 2 and is probably due to beam loading since we store less and less energy in the accelerating mode as we move up in rf reflectivity.

Micropulse structure

The micropulse structure was measured with a Cherenkov emitter located at the interaction point. The emitter was a short piece of 1 mm diam quartz fiber optic rotated such that the beam entered at 47° to the fiber axis. In this case, a

Figure 2: Tuning curves for the linac showing the variation of the reflected rf power and the beam currents measured before (i_{e1}) and after (i_{e2}) the momentum-selecting lead pinhole.

portion of the Cherenkov cone is directed along the fiber axis. This light was relayed with lenses to an optical streak camera and the signal was recorded at several different sweep speeds. Figure 4 shows the entire micropulse with a time resolution of about 20 psec. The variation from one micropulse to the next is dominated by the streak camera photoelectron statistics. (The signal was intentionally kept weak for optimal time resolution). A single micropulse from a faster streak is shown in Fig. 5. The time resolution for this streak was about 6 psec which implies the true pulse width is around 10 psec FWHM. The current monitors measure an average current of > 20 mA which means that the peak current in one micropulse is in excess of 200 mA at 2 MeV.

Figure 5: Lineout of a streak camera record of the Cherenkov emitter intensity (proportional to instantaneous beam current) vs. time for a fast sweep (6 psec resolution). The deconvolved pulse width is closer to 10 psec.

SUMMARY

In summary, a linac with the interaction-point parameters of: 2 MeV energy, 10 psec/200 mA micropulses, 2 ns/20 mA macropulses, 6π mm-mrad emittance, 260 μm FWHM spot

REFERENCES

[1] C. E. Clayton, K. A. Marsh, A. Dyson, M. Everett, A. Lal, W. P. Leemans, R. Williams, and C. Joshi, "Ultrahigh-gradient acceleration of injected electrons by laser-excited relativistic electron plasma waves", Phys. Rev. Lett. 70, 37 (1993).

[2] C. E. Clayton, K. A. Marsh, M. Everett, A. Lal, and C. Joshi, "Demonstration of Plasma Beat Wave Acceleration of Electrons from 2 MeV to 20 MeV", this proceedings.

[3] R. H. Miller, H. Deruyter, W. R. Fowkes, J. M. Potter, R. G. Schonberg, and J. N. Weaver, "RF phase focusing in portable x-band, linear accelerators", IEEE Trans. Nuc. Sci. NS-32, 3231 (1985).

[4] R. G. Schonberg, H. Deruyter, W. R. Fowkes, W. A. Johnson, R. H. Miller, J. M. Potter, and J. N. Weaver, "Portable, x-band, linear accelerator systems", IEEE Trans. Nuc. Sci. NS-32, 3234 (1985).

[5] Schonberg Radiation Corp., Mountain View, CA.

[6] C. E. Clayton and K. A. Marsh, "A 2 MeV, 100 mA electron accelerator for a small laboratory environment", Rev. Sci. Instr., 64, 728 (1993).

Figure 4: Lineout of a streak camera record of the Cherenkov emitter intensity (proportional to instantaneous beam current) vs. time for a slow sweep (20 psec resolution).

size, and single shot (but capable of high repetition rates) was built by modifying a commercial x-ray source. The beam can be delivered to a course vacuum environment. The linac is reliable and easy to operate and can be switched on, tuned up, and characterized in under 30 minutes.

Emittance Measurements of the 4.5 MeV UCLA RF Photo-Injector*

S. C. Hartman, N. Barov, S. Park,
C. Pellegrini, J. Rosenzweig, G. Travish, R. Zhang
Department of Physics, University of California, Los Angeles 90024

P. Davis, C. Joshi, G. Hairapetian
Electrical Engineering Department, University of California, Los Angeles 90024
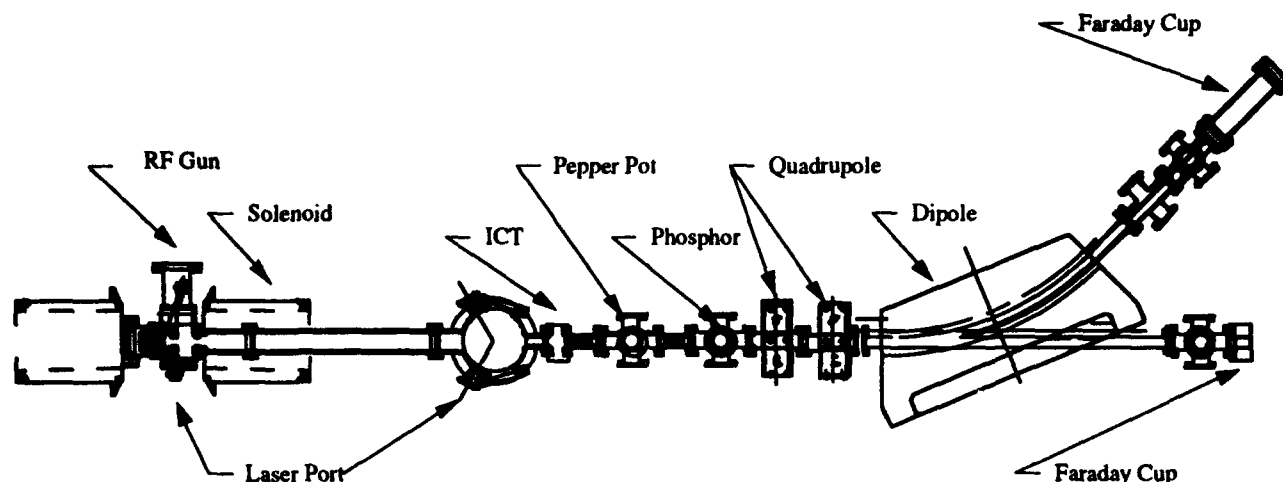
Figure 1.

Abstract

The 1.5 cell RF photo-injector(1, 2) has been operated for the past several months using a copper cathode illuminated by 4 ps long pulses of UV (266nm) light, with a variable energy of between 0 to 300μJ. This typically produces up to 3 nC of charge per bunch. Because space charge forces dominate the electron beam transport a pepper pot measurement system is used to measure the emittance. The emittance is measured as a function of charge, peak accelerating field, laser spot size and initial phase with respect to the RF field. This is accomplished with an automated control and data acquisition system which can measure single shot emittances at a rate of 5 Hz developed at UCLA. The experimental results obtained are then compared with theory and simulations.

I. INTRODUCTION

The UCLA photo-injector produces a very high peak current beam, up to 250 amps, at relatively low energy, 4.5 MeV. The consequence of this is that electron beam transport is in the highly non-linear space charge dominated regime. Since the beam is space charge dominated, linear beam transport formalisms such as matrix transformations do not apply. This means that the usual quadrupole scan technique is not valid for the UCLA photo-electron beam. To overcome this problem a pepper pot emittance measurement apparatus has been designed and implemented. The pepper pot is designed such that upon the electron beams passage through the pepper pot it is transformed from a space charge dominated beam to an

emittance dominated beam. Once the electron beam is in the emittance dominated regime one can use linear transform theory to calculate the emittance. Because of pulse to pulse fluctuations in the beam charge the measurement must be made single shot. All the beam parameters are measured every shot via fast sample and hold electronics.

II. EXPERIMENTAL DESIGN

A. RF Photo-Injector and Drive Laser

The UCLA photo-injector is a one and half cell standing wave accelerator operating in the π-mode with peak accelerating fields of the order of 100 MV/m. The photocathode is illuminated by frequency chirped, pulse compressed, frequency quadrupled Nd-YAG laser. This laser system delivers 0-300 μJ of energy on the cathode in less than 4 ps and can be injected on axis or at a 70° angle of incidence.

B. Diagnostics

Figure 1 shows the beam line configuration and the location of the diagnostics used in this experimet. Phosphor screens are employed at three locations to measure spot size and emittance patterns. The phosphors used were experimentally confirmed to be linear so no distortions in spot size are due to non linear phosphor response. Faraday cups are used to measure the charge and some of the phosphor screens are floating and can double as faraday cups. This way one can gather image and charge data simultaneously. To measure the charge when taking emittance measurements we use an Integrating Current Transformer, ICT, which measures the total charge which passes through it. Because it is designed to

respond to time scales of the order of ps it automatically ignores the dc like dark current background.

III. PEPPER POT AND DATA ACQUISITION

A. Pepper Pot Considerations

The pepper pot used in these experiments is actually an array of eight slits. After the electron beam traverses the slits it drifts approximately 20 cm onto a phosphor screen. The image then gives the full phase space, emittance, and other beam parameters. The width of the slit was chosen by considering the envelope equation, eq. 3.1. For a round beam A is the normalized beam transverse dimension, β is the normalized velocity, γ is the normalized energy, and ε is the normalized emittance.

$$A'' - \frac{\beta \gamma k}{A} - \frac{\varepsilon_n^2}{A^3} = 0 \quad \text{where} \quad A = a[\beta \gamma]^{\frac{1}{2}} \quad (3.1)$$

Taking the ratio of the space charge to emittance term yields,

$$\Re = \frac{2a^2 I_p}{(\beta \gamma)^{\frac{1}{2}} \varepsilon_n^2 I_A} \quad (3.2)$$

where I_p is the peak electron beam current and I_a is the Alfven current of 17 kA. When this ratio is greater than unity space charge forces dominated the electron beam and when the ratio is less than unity emittance effects dominates the electron beam transport. By choosing the slit widths wisely we can go from the space charge dominated regime to the emittance dominated regime. Now if we scale the transverse dimension by η,

$$I_p' = \eta^2 I_p; \quad a' = \eta a; \quad \varepsilon_n' = \eta \varepsilon_n \quad (3.3)$$

the ratio of the space charge term to the emittance term becomes.

$$\Re' = \Re \eta^2 \quad (3.4)$$

Using this expression and plugging in the numbers for the UCLA experiment we get η=0.01 which corresponds to a slit size of 50μm.
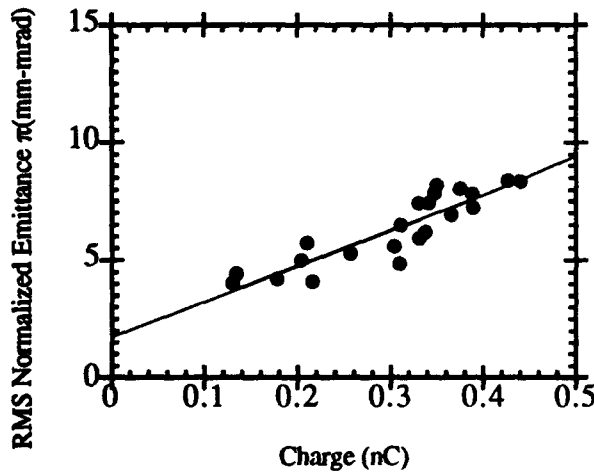
Figure 2.

IV. EMITTANCE MEASUREMENTS

A. Definition of Emittance

Electron beams do not typically have sharp boundaries so the definition of emittance is ambiguous at times. Some laboratories define emittance for a certain percentage of the beam particles enclosed within an ellipse, commonly 63% or 90%(3). For the following measurements we define our emittance as the root-mean-square emittance given by

$$\varepsilon_{rms} = \left(\langle x^2 \rangle \langle x'^2 \rangle - \langle x \cdot x' \rangle^2 \right)^{\frac{1}{2}} \quad (4.1)$$

and the normalized emittance is given by

$$\varepsilon_n = \beta \gamma \varepsilon_{rms} \quad (4.2)$$

C. Emittance Vs Charge

The electron beam emittance in all of the following was done with a beam momentum of 3.5 MeV/c. The first step in measuring the emittance is to measure the linear increase as a function of charge. The laser energy delivered to the cathode was varied and the emittance was measured as a function of charge transported through the ICT and to the slits. For all other parameters fixed one expects the emittance to be linear in charge as in the following equation(4)

$$\varepsilon_x^{sc} = \frac{\pi}{4} \frac{1}{\alpha \kappa} \frac{1}{\sin(\vartheta_0)} \frac{I}{I_A} \mu \quad (4.3)$$

Each emittance verses charge plot takes approximately thirty to sixty seconds to complete. So one can adjust on-line the

RF INJECTION PHASE (Degrees)
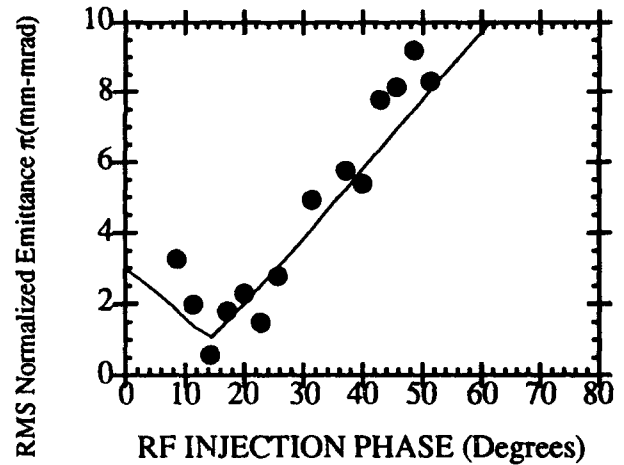
Figure 3.

beam parameters to minimize the electron beam emittance. This is a very powerful diagnostic.

D. RF induced Emittance Vs Laser Injection Phase

To measure the rf induced emittance verses laser injection phase many emittance verse charge data runs were taken with different laser injection phases. The procedure for extracting the rf induced emittance is as follows. For each laser injection phase the data is plotted and fit to a line. The slope and intercept of this line are then extracted. The zero charge intercept gives the rf induced emittance. The following graph

is a plot of the zero intercepts of many rf injection phases. The data is then fit to the equation(4)

$$\varepsilon_x^{rf} = \alpha\kappa\langle x^2\rangle\sqrt{\langle(\Delta\phi)^2\rangle}|\cos(\phi)| \qquad (4.4)$$

Notice that the data has the correct scaling as one would expect.

E. Emittance Vs Peak Accelerating Field

To explore the effect of the variation of the peak electric field the rf power into the photoinjector was varied. Since the final beam energy is proportional to the peak accelerating field we recover the expected linear decreasing of the emittance .

BEAM Momentum (MeV/c)
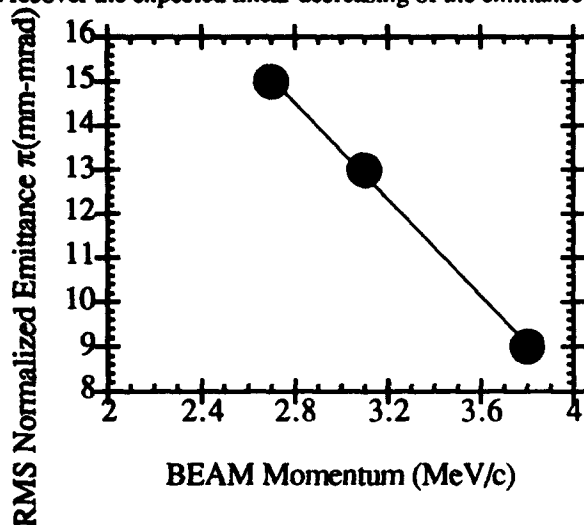
Figure 6

F. Rf Injection Phase Calibration

The beam energy verse rf injection phase was measured in order to calibrate the absolute phase. The equations of motion were then integrated and compared to the experiment. This data highlights the fact that the rf gun was unbalanced. The field in the full cell was 1.8 times that in the half cell. This was confirmed with a bead pull experiment after the gun was removed for a postmortem cold test.

RF Phase (Deg)
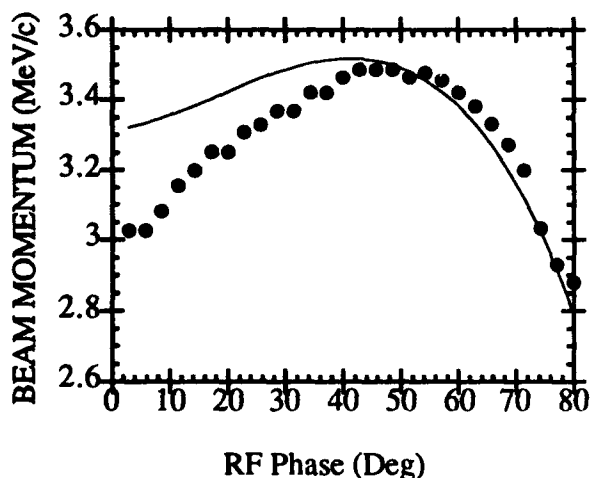
Figure 5

V. DISCUSSION

The emittance measurements presented above are the first round results and suffer from a few problems. The first is that upon installation of the photo-injector the micrometer which holds the cathode in place was bumped. This caus ' the gun to become detained. The gun was then retuned on-line by adjusting the cathode position until the shunt impedance was maximized. Since the shunt impedance of the full cell is larger than the half cell the peak fields in the full cell were favored. The second artificial emittance growth mechanism was that the phosphor screens which were use to measure the spots were at 45° angles with respect to the beam. This enlarged the spot size artificially and due to short depth of focus induced some parallax broadening and blurring of the image. These problems were eliminated in a subsequent attempt to re measure the emittance but due to time limitations the measurements were not completed in time for this conference. The emittance values given are thus a set of worse case values.

VI. CONCLUSION

The UCLA photo-injector has been operated successfully. The measurements show that the emittance scales as expected. The important thing to note is that for these set of emittance runs the rf photo-injector had a field imbalance. The filled in the full cell was 1.8 times that in the half cell. This contributed to emittance blowup as did the phosphor screens used to measure the emittance. The phosphor screens were placed onto the beamline at a 45° angle. This created broadening of the line widths

References

1.   S. C. Hartman et al., Photocathode Driven Linac at UCLA for FEL and Plasma Wakefield Acceleration Experiments, Particle Accelerator Conference Sanfransisco, CA., 1991), pp. 2967.

2.   K. Batchelor et al, European Particle Conference Accelerator Conference Rome, Italy, June 7-12, 1988),

3.   C. Lejeune, J. Aubert, Eds., *Emittance and Brightness Definitions and Measurements* (Academic, New York, 1980).

4.   K.-J. Kim, *Nuclear Instruments and Methods in Physics Research* **A275**, 201-218 (1989).

Commissioning of the SIBERIA-2 Preinjector and First Beam Results

V.Korchuganov, G.Kulipanov, E.Levichev, O.Nezhevenko, G.Ostreiko,
A.Philipchenko, G.Serdobintsev, E.Shaimerdenov, V.Ushakov,
Institute of Nuclear Physics, Novosibirsk 630090, Russia,

A.Kadnikov, Yu.Krylov, S.Kuznetsov, V.Ushkov, Yu.Yupinov,
Kurchatov Institute, Moscow, Russia

Abstract

The DAW structure linac - the preinjector for the SIBERIA SR complex was commissioned on November 1, 1992 when the 62.5 MeV electron beam is obtained. A 6-m-long high impedance (92 MOhm/m) linac operates at 2.8 GHz. The paper describes the experimental RF characteristics of the linac structure and beam measurements obtained during the commissioning. The results of electron current, energy spectrum, beam profiles and emittance measurements are presented.

I. INTRODUCTION

A SR facility SIBERIA is being constructed at the Kurchatov Institute in Moscow. The injection part comprises a 80 MeV preinjector-linac operating in the stored energy mode. The paper reports the successful commissioning of the linac in November of 1992.

II. GENERAL DESCRIPTION OF THE LINAC

The 6.1 m linear accelerator (Fig. 1) consists of an electron gun, 6 regular accelerating sections (Fig. 2) and a power input unit which is housed in the center of the accelerator. Each section comprises 18 identical cavity cells

spaced with the period equal to $\lambda/2$ [1],[2].

The linac design is based on the 2.8 GHz modified DAW structure. Each disk is supported by three radial stems, whose length is close to one quarter of the wave length. The DAW structure operates in the stored energy mode and enables us:

- to reach maximum accelerating voltage due to high shunt impedance;
- to accelerate the beam with a maximum number of particles due to large stored energy;
- to make an accelerating structure in the form of single resonance section with a single power input due to a high group velocity and, thus,
- to avoid phasing of separate sections and to simplify the requirements for the accuracy of manufacturing and tuning.

The DAW structure measured parameters are given in Table 1.

Table 1. The parameters of the accelerating structure

Operation mode	$TM02\pi$
Shunt impedance	92 MOhm/m
Frequency	2797.2 MHz
Quality factor	28000
Characteristic impedance	3.5 kOhm/m
Calculated overvoltage coefficient	5.6

The linac has a simple injection system without a special buncher. The longitudinal bunching and transverse size shaping of the electron beam are the effect of RF field in the accelerator only. The nonbunched 40 keV electron beam formed by a diode gun is injected directly into the first cavity cell of the structure.

Note that the first cell was made twice shorter than the
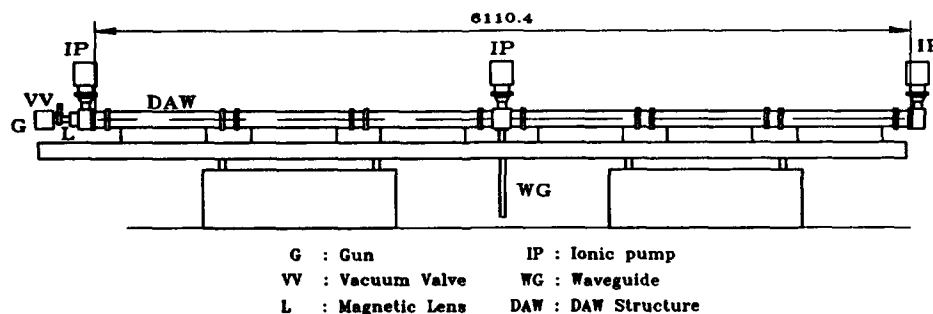
Figure 1:

Fig.1: The preinjector layout

G : Gun	IP : Ionic pump
VV : Vacuum Valve	WG : Waveguide
L : Magnetic Lens	DAW : DAW Structure

Figure 2: The regular accelerating section

atm. This ceramic window is inserted because the klystron ceramic window of the cone type has not provided the reliable klystron operation with the vacuum waveguide in January of 1992, when training the waveguide and lattice a breakdown in ceramics was happened at a power of the incident wave 11 MW [3].

III. COMMISSIONING

The stable, 9 MW level of RF power in the linac was achieved by October 28, after a week training of the lattice and waveguide with the nitrogen-filled insertion. We want to note that the multipacting in the vacuum section of the waveguide was overcame during 8 hours by training and increasing the power level from 0.3 MW to 5.5 MW. Fig. 3 shows the oscillograms of: 1) the incident wave voltage in the waveguide; 2) the reflected wave voltage in the waveguide; 3) the voltage in the linac structure.

Figure 3: The oscillogram of RF signals

regular one with the aim to obtain a uniform distribution of the accelerating field amplitudes in the cavity cells, to reach the required emittance and the conditions for the longitudinal bunching. There is a grid to exclude the defocussing effect of RF fields on the low energy electrons at the entrance of the first cell. The linac aperture is 8.7 mm in diam.

The linac has a minimum necessary and sufficient set of devices for the initial transverse focussing of the beam and its following tracking along the structure, namely:
- the x,z-correctors are placed at the accelerating structure entrance in the region of a 40 keV electron beam crossover,
- a single short axial-symmetry focussing lens is installed after x,z-correctors for matching the beam emittance and accelerator acceptance,
- the four pairs of windings of the long distributed correctors with separate power sources are spaced at the first and second halfs of the linac structure to compensate the influence of the small parasitic magnetic fields in the vicinity of the linac axis.

The structure exitation is reached by means of a special co-axial cavity. It is installed in the middle of the structure and splits it into two equal parts. The proper choice of the dimention of a coupling hole in this cavity matches the structure and the RF generator.

The linac is fed by an industrial RF S-band generator which is based on the 18 MW klystron.

The klystron and the accelerating structure is connected by a 90 × 45 mm^2 rectangular waveguide whose length is a multiple of $\lambda/2$. This permits us to have minimum overvoltage during the unstable operation. The waveguide consists of gas and vacuum sections and a ceramic window between them. The gas part of the waveguide which is adjacent to the klystron is filled with nitrogen at about 6

On November 1, 1992 we first emitted the electron beam from the linac to a transfer line. The current measurement, the beam position monitoring and beam collimation are performed by a movable pickup at the first accelerating cell entrance. The emitted beam parameters are measured in the transfer line.

Fig. 4 shows the elements of the magnetic and diagnostic

Figure 4: The magnetic and diagnostic system of the transfer line

systems of the transfer line. The electrons come out the linac in horizontal plane and move along an about 4-m-long straight section to the 12° vertical bending magnet (2M1). This bending magnet deflects the beam downwards to the

septum magnet of the SIBERIA-1 or upwards in the diagnostic section and the Faraday cup (FC).

The three secondary-emission wire monitors are intended to observe and measure the intensity, the center-of-mass position, the transverse dimensions of the beam. The first one (DS01) is placed behind the linac, two others are installed after (2M1), at the end of the diagnostic section (DS02), and in the injection straight section before the septum magnet (DS03). A step between the wires of the monitor is as much as 1 mm in both directions and the charge sensibility is equal to 2×10^{-15} C.

At first the beam current and beam sizes were measured by means of the Faraday cup specially mounted at the initial part of the transfer line. The DS01 monitor current measurements were calibrated with the FC. After that, the movable remote-controlled vertical probe (lead cylinder-LD) was installed instead FC, and FC was positioned behind the vertical bending magnet (2M1). The beam was then led to the SIBERIA-1 input straight section.

The transversal distributions of the electron density which are reached by the secondary-emission wire monitors DS01, DS02, DS03 have shown very small angle spreads of the electrons. The measured transverse profile of the electron beam at the linac exit has standard sizes of $1.1 \div 1.3$ mm, the standard angle spread is 2.4×10^{-4} rad. When supposing the Gauss distribution we estimate the beam emittance as large as 3×10^{-5} cm-rad. The beam profile images are presented in Fig. 5.

We note that the transverse sizes of the beam measured

Figure 6: The energy spectrum of the linac electron beam

current selected by the slit is measured by the Faraday cup. The achieved dependence of FC current versus deflection angle is converted to the energy spectrum, Fig.6. Taking into account the geometry of the dispersion part of the transfer line, the width of the slit (3 mm), the transverse beam size at the slit (about 3 mm at one half level), and subtracting the background of the scattered electrons the relative width of the energy spectrum distribution is no more than 7 %.

The measured parameters of the electron beam at the exit of the linac are in Table 3:

Table 3.

Maximum energy	E = 69 MeV
Energy spectrum width	$\Delta E/E_{max} \leq 7\%$
Electron current	I = 370 mA
Pulse duration	$\tau = 18$ ns
Pulse repetition frequency	$f_{rep} = 2 Hz$
Electron beam emittances	$\epsilon_x = \epsilon_z \simeq 3 \times 10^{-5}$ cm $\times$ rad
Beam transverse size at 1600 mm apart from linac	$2\Delta r_{1/2} = 3$ mm

The measured parameters of the beam enable us to take up the works with SIBERIA-1. The circulating electron beam at SIBERIA-1 was first generated using the new injector in December, 1992. The energy of the injected beam was 67.7 MeV. In March, 1992 the work was continued with the electron energy equal to 70 MeV at the injection in SIBERIA-1. Now SIBERIA-1 operates at a designed 450 MeV. The one-time capture current is up to 20 mA at the equilibrium orbit that sufficiently agrees with the expected current at this energy. By the end of 1993 the works on linac are assumed to be focused on increasing the energy up to 80 MeV and the current of the emitted beam

Figure 5: The beam profile images.

with FC and the movable remote-controlled probe after the linac were in good agreement with those of the wire monitor DS01 (Table 2).

Table 2.

	DS01	FC	Probe	DS02	FC
σ_x, mm	1.22	1.3	1.23	2.5	2.3-2.8
σ_z, mm	1.41			3.6	

The Faraday cup with a slit collimator before it and a vertical bending magnet 2M1 serve as a spectrometer intended for electron energy spectrum measurements. When changing the deflection angle of the magnet 2M1 the electron beam scans the slit of the collimator and the beam

REFERENCES

[1] M.M.Karliner et al. Proc. of the EPAC, Rome, June 7-11, 1988. Vol.1. pp 602-604.

[2] O.A.Nezhevenko et al. IEEE Part. Acc. Conf.San Francisco, Cal., May 6-9, 1991. Vol.5, pp.935-937.

[3] V.N.Korchuganov, M.M.Samorukov. Proc. of the EPAC 92, Berlin, March 24-28, 1992. Vol.1, pp.474-476.

Emittance Measurement and Modeling of the ALS 50 MeV Linac to Booster Line *

J. Bengtsson, W. Leemans and T. Byrne
Lawrence Berkeley Laboratory, University of California
1 Cyclotron Road, Berkeley, CA 94720, USA

Abstract

The Twiss parameters and emittance have been measured for the ALS LINAC through non-linear χ^2 fitting of the measured beam size (fixed location) vs. focal strength of a quadrupole triplet. The obtained values have been used to calculate the expected beam size and dispersion along the linac-to-booster transport line giving good agreement with measurements. The efforts resulted in superior injection into the booster.

I. INTRODUCTION

The Advanced Light Source at LBL has a 50 MeV linac, a booster which increases the electron energy to 1.5 GeV and a storage ring which is expected to need refilling every 6 - 8 hours. In between refills the 50 MeV electron will be transported into an experimental vault and will be used to conduct a number of experiments such as plasma lens focusing, generation of femtosecond X-ray pulses and interaction of the electron beam with a variety of electromagnetic cavities [1].

To be able to design a beam transport line optimized for the different experiments, we have measured the beam's initial conditions after the linac. In addition, these values have also been used to calculate the beam size and dispersion along the Linac-To-Booster (LTB) transport line and compared with measurements.

II. THEORETICAL MODEL

A. Equations of motion

The linearized transverse motion of the beam is described by [2]

$$x(s) = \sqrt{\varepsilon_x \beta_x(s)} \cos[\mu_x(s) + \varphi_x] + \eta_x(s) \delta$$

using the phase space coordinates $\bar{x} = (x, p_x, y, p_y, \delta)$, where β is the beta-function, μ the phase advance, η the dispersion and ε a constant of motion known as the emittance. The beam is parameterized by the six parameters α_x, β_x, ε_x, α_y, β_y and ε_y at each point along the transport line. Since we have three parameters in each plane but can only observe configuration space, i.e. beam sizes, we need at least three different observations of beam size in each plane to be able to determine the corresponding beam parameters at a given point along the transport line.

B. Statistical Analysis by Non-linear χ^2

The horizontal beam size x is a function of α_x, β_x and ε_x

$$x(\bar{q}, \bar{a}) = \sqrt{\varepsilon_x \left[m_{11}^2 \beta_x(\bar{q}) - 2 m_{11} m_{12} \alpha_x(\bar{q}) + m_{12}^2 \frac{1 + \alpha_x^2(\bar{q})}{\beta_x(\bar{q})} \right]}$$

with $\bar{a} = (\beta_x, \alpha_x, \varepsilon_x)$ as parameters, $\bar{q} = (q_f, q_d)$ as independent variables and m_{ij} being the elements of the transport matrix $\bar{x}_f = M \bar{x}_i$. The χ^2 merit function is

$$\chi^2(\bar{a}) = \sum_{i=1}^{N} \left[\frac{x_i - x(\bar{q}_i; \bar{a})}{\sigma_i} \right]^2$$

where N is the number of data points, i.e. measured and computed beam size. χ^2 is minimized by solving the system

$$\sum_{l=1}^{N} v_{kl} \, \delta a_l = u_k, \quad u_k \equiv -\frac{1}{2} \frac{\partial \chi^2}{\partial a_k} = \sum_{i=1}^{N} \frac{[x_i - x(\bar{q}_i; \bar{a})]}{\sigma_i^2} \frac{\partial x(\bar{q}_i; \bar{a})}{\partial a_k}$$

$$v_{kl} \equiv \frac{1}{2} \frac{\partial^2 \chi^2}{\partial a_k \partial a_l} = \sum_{i=1}^{N} \frac{1}{\sigma_i^2} \frac{\partial x(\bar{q}_i; \bar{a})}{\partial a_k} \frac{\partial x(\bar{q}_i; \bar{a})}{\partial a_l} + O(\partial^2)$$

and iterating [3]. The second order derivatives have been neglected to stabilize the iterations. We find

$$u_1 = -\frac{1}{2} \frac{\partial \chi^2}{\partial \beta_x} = \sum_{i=1}^{N} \frac{[x_i - x(\bar{q}_i; \bar{a})]}{\sigma_i^2} \frac{\varepsilon_x \left(m_{11}^2 - m_{12}^2 \frac{1 + \alpha_x^2(\bar{q}_i)}{\beta_x^2(\bar{q}_i)} \right)}{2\sqrt{}},$$

$$u_2 = -\frac{1}{2} \frac{\partial \chi^2}{\partial \alpha_x} = \sum_{i=1}^{N} \frac{[x_i - x(\bar{q}_i; \bar{a})]}{\sigma_i^2} \frac{\varepsilon_x \left(-m_{11} m_{12} + m_{12}^2 \frac{\alpha_x(\bar{q}_i)}{\beta_x(\bar{q}_i)} \right)}{\sqrt{}},$$

$$u_3 = -\frac{1}{2} \frac{\partial \chi^2}{\partial \varepsilon_x} = \sum_{i=1}^{N} \frac{[x_i - x(\bar{q}_i; \bar{a})]}{\sigma_i^2}$$

$$\times \frac{m_{11}^2 \beta_x(\bar{q}_i) - 2 m_{11} m_{12} \alpha_x(\bar{q}_i) + m_{12}^2 \frac{1 + \alpha_x^2(\bar{q}_i)}{\beta_x(\bar{q}_i)}}{2\sqrt{}}$$

where

$$\sqrt{} \equiv \sqrt{\varepsilon_x \left[m_{11}^2 \beta_x(\bar{q}_i) - 2 m_{11} m_{12} \alpha_x(\bar{q}_i) + m_{12}^2 \frac{1 + \alpha_x^2(\bar{q}_i)}{\beta_x(\bar{q}_i)} \right]}$$

The confidence interval is given by

$$\delta a_i = \pm \sqrt{\Delta \chi^2 (v)_{ii}^{-1}}$$

where we choose $\Delta\chi^2 = 4$ for a 95.4 % confidence interval.

III. EMITTANCE MEASUREMENT

A. Linac parameters

The parameters of the linac are given in Table 1. The LTB line transports the beam towards the 1.5 GeV booster and must be tuned to provide the correct matching conditions into the ring.

Maximum Energy	50 MeV
Charge	1-2 nC/bunch
Bunch Length (σ_z)	10-15 ps
Emittance rms (unnorm)	0.3 mm-mrad
# bunches/macro pulse @ 125 MHz	1 - 10 (max 100)
Macro pulse rep. rate	1 - 10 Hz

Table 1: ALS Linac parameters

Typically, emittance measurements are done with a pepper pot and beam profiles are measured with wire scans or harps. We have carried out the measurements by measuring the beam size on a fluorescent screen as a function of the focal strength of the focusing element, Q_{12}, of a quadrupole triplet, while keeping the defocusing element, Q_{11}, at a fixed strength.

The beam size is obtained as follows: light emitted by the fluorescent screen, is imaged onto a CCD-camera. The video signal output is frame-grabbed with 8 bit resolution on a Macintosh computer and analyzed using commercial image processing software. For the particular choice of magnification, the intrinsic spatial resolution of the system is about 110 μm but the statistical analysis, discussed previously, improves this about five-fold to 20 μm. For fixed imaging conditions, we have evaluated the linearity of the system by measuring the peak number of counts on the image as a function of number of bunches per macro pulse. The complete imaging system was found to be linear, for beam intensities below those resulting in 200 counts on the image. The noise floor is typically 15 counts.

After acquisition of an image, horizontal and vertical line-outs were fit to a Gaussian distribution using a non-linear Levenberg Marquardt fitting routine [3] with 3 parameters: noise floor (counts), amplitude (counts) and rms beam size.

C. Emittance measurement.

The measurements were carried out as follows. First, all quadrupole magnets were cycled. At the end of the cycling procedure the current was brought up to 90 % of the final set-value and then slowly increased to the 100% value. Without these procedures, preliminary measurements indicated that hysteresis effects led to irreproducible results. For a given current setting of the focusing (defocusing) element, the current delivered to the defocusing (focusing) element was varied from 0 to 8 A (maximum current) in steps of 0.5 A. An example of the horizontal and vertical beam sizes as a function of current is shown in Fig. 1.

The experimental results were modeled with TRACY [4] using the measured location of the different beam line

components (dipole and quadrupole magnets, fluorescent screens); magnetic lengths and strengths. The magnetic length for each quadrupole was calculated from the measured B'L$_{eff}$ line integral value and the calculated field gradient, for a given current setting. All the current supplies were carefully calibrated. The measured transfer functions of the quadrupoles were used to calculate the focusing strength .
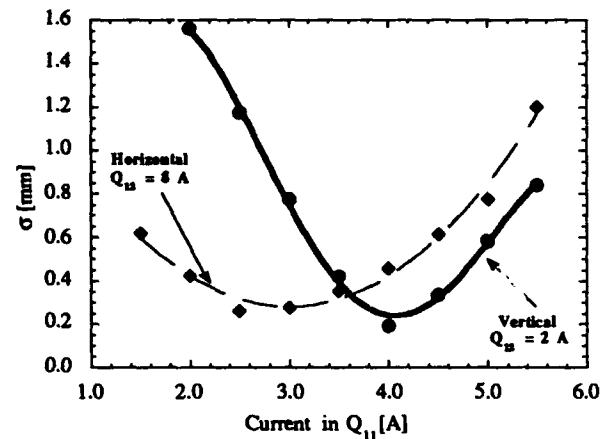
Figure 1: Horizontal and vertical beam sizes as a function of current in Q_{11} for fixed current in Q_{12}. The lines through the data are polynomial fits used in the modeling.

The results of the non-linear χ^2 from are summarized in Table 2.

α_x	1.31 ± 0.12
β_x [m]	3.09 ± 0.29
ε_x rms, unnorm. [mm-mrad]	0.32 ± 0.02
α_y	-0.19 ± 0.11
β_y [m]	1.00 ± 0.10
ε_y rms, unnorm. [mm-mra]	0.33 ± 0.03

Table 2: Measured initial conditions for the 50 MeV beam.

IV. MODELING OF THE LTB-LINE

The measured initial conditions allow us to calculate the beam sizes and dispersion along the linac-to-booster (LTB) line and to compare with measured values. Previous operation of the LTB-line utilized quadrupoles set points giving predicted beam sizes shown in Fig. 2. Visual inspection of beam profiles, aided by image enhancing software, indicated beam scraping. Furthermore, one could also notice considerable beam motion at the injection point. This is explained by rather large dispersion at that point and the pulse to pulse energy jitter of the linac.

However, the measured initial conditions allow us to calculate the proper settings of the quadrupole power supplies for matching the beam into the booster. The beam profiles were measured at 5 different locations along the LTB-line for these settings. Th comparison between experimental and theoretical results is given in Table 3. Notice, that a small modeling error of the dispersion at one point will be substantially magnified in downstream quadrupoles. No

fluorescent screen is present after B1 preventing us from measuring dispersion after the achromat (BS, Q2 and B1).
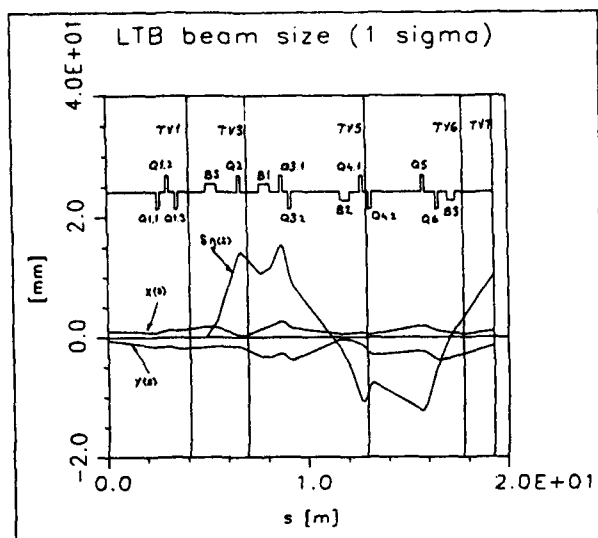
Figure 2: Original predicted beam profile along the LTB line and the effect of dispersion.

The predicted beam profiles for the optimized settings are shown in Fig. 3.
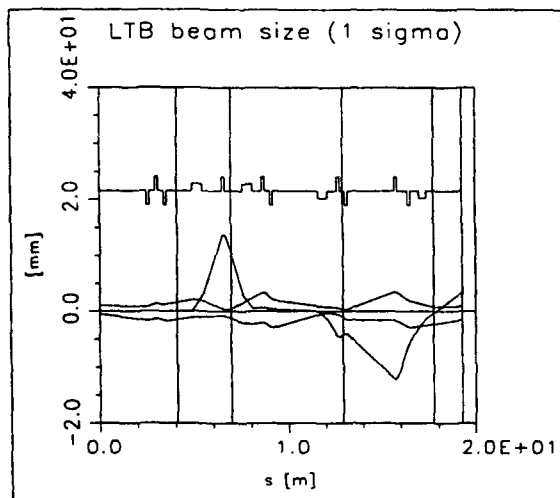
Figure 3: Optimized LTB-line, tuned for minimum dispersion at injection into the booster.

The experimentally measured vertical beam sizes is given by $\sigma = \sqrt{\epsilon \beta}$. However, analysis of the horizontal beam profiles is complicated by the fact that beam loading of the accelerator structure leads to systematic energy difference between consecutive bunches of 0.8 %. This causes only partial spatial overlapping of the beam profiles on screens located in dispersive sections. The need for running more than 1 bunch arose from the limited light sensitivity of the imaging system. With the present LINAC performance, adding consecutive images to increase the dynamic range cannot be done: the energy jitter between consecutive macro-pulses was found to be as high as 1%. We are currently working on improving the sensitivity of the imaging system by an order of magnitude.

Loc.	Measured σ_{hor} [mm]	Model σ_{hor} [mm]	Measured σ_{ver} [mm]	Model σ_{ver} [mm]
tv1	1.67	1.53, 1.53	1.76	1.52
tv3	9.15	10.69, 0.33	1.16	1.28
tv4	2.88	4.69, 0.37	0.99	1.06
tv5	2.49	1.08, 0.70	1.76	2.36
tv6	0.81	4.30, 0.88	1.30	1.52

Table 3: Experimental and theoretical beam sizes along the LTB-line. The first and second entry in the third column are with and without dispersion taking into account, respectively.

To obtain the linear dispersion, the change of beam location Δx on TV3 (Q2 off) was measured as a function of the strength of the upstream BS dipole magnet. By using

$$\Delta x = \delta\, \eta_x = \delta\left[\rho_0(1 - \cos\phi) + L_{drift} \sin\phi\right],$$

$$\delta = -\Delta B_\perp \frac{\rho_0}{(B_\perp \rho)_0} + O(2)$$

we find a measured dispersion $\eta_x = 1.18$ m which agrees well with the predicted value of 1.13 m.

CONCLUSIONS

A detailed quantitative analysis has been presented on a) the measurement of the beam emittance and Twiss parameters of the ALS Linac, and b) on the modeling and optimization of the LTB line. The solution for the beam's initial conditions was propagated down the LTB-line. Good agreement between the calculated and measured beam sizes and dispersion was obtained. Furthermore, the quantitative and qualitative analysis of beam profiles helped us to diagnose incorrect operation of the Linac sub-harmonic bunching system, calibration problems with power supplies and.the importance of magnet cycling to avoid systematic errors caused by hysteresis effects. Finally, it has led to a substantial improvement of injection stability of the beam into the booster.

ACKNOWLEDGMENT

REFERENCES

[1] W. Leemans et al., these proceedings.

[2] E. D. Courant and H. S. Snyder, Ann. Phys. Vol 3, p. 1 (1958).

[3] W. H. Press, B. P. Flannery, S. A. Teukolsky and W. T. Vetterling, "Numerical Recipes" (Cambridge University Press) 1989.

[4] J. Bengtsson, E. Forest and H. Nishimura, unpublished.

Extended Version of an S–Band RF Gun*

Sanghyun Park and Claudio Pellegrini

Department of Physics, University of California, Los Angeles, CA 90024

Abstract

A 4.5 MeV rf gun has been in operation at UCLA as a part of a 20 MeV linac. To improve the photoelectron beam parameters without changing the major characteristics of the driving laser and rf systems, a revised and extended version of the present rf gun has been investigated. The new gun consists of 6 full cells terminated at either end by one half cell each. The gun operates in π–mode at 2.856 GHz. Accelerating fields and mode structures have been studied, and based on this, particle dynamics has been simulated. An aluminum prototype has been built for cold tests. Description of the gun is presented along with initial computational and experimental results.

Introduction

Photoinjectors have been successfully used at a number of laboratories to produce high brightness, low emittance electron beams[1,2,3]. The electron beam out of a photoinjector is subjected to further acceleration by a linac that follows the injector. At UCLA, a 4.5 MeV beam will be boosted by the plane wave transformer(PWT) to a 20 MeV beam energy[4].

When high brightness means more charge per bunch and lower emittance, these two compete against each other because of space charge effect. A solenoid focusing the beam to reduce the divergence produced at the gun exit, tends to distort the phase space distribution. The angular divergence at the gun exit and space charge effects decrease with increasing beam energy, which pushes us to design a higher energy gun[5]. Also, the radial electric fields provide periodic focusing and defocusing forces to the beam, whereas the axial fields accelerate the beam so that the beam energy is roughly linear to the axial length of the structure. This gives rise to a net focusing of the beam[6].

From the engineering point of view, combination of photoinjector and a linac introduces some complexity in distribution of the driving rf power, in terms of amplitude and phase. If one klystron can drive one structure to generate a beam of comparable energy and probably better

quality, this minimizes requirements for hardware in handling high power rf. And this is partly the motive behind investigation of a multicell structure.

Computational Modelling

The starting point of the new structure is the $1\frac{1}{2}$–cell photocathode rf gun, to be referred to as Gun A, which is in operation at UCLA and at Brookhaven. The Gun A has two resonance modes, 0–mode and π–mode. They are about 2 MHz apart. There are more resonance modes as more cells are added, but the frequency span between the 0–mode and π–mode remains about the same. The separation of the π–mode and the nearest neighboring mode becomes smaller accordingly. As the inner radius of the aperture is increased, a larger separation between the modes is realized.

To be sure that we drive only the π-mode we require a mode separation much larger than the klystron bandwidth. For a klystron pulse duration of 2.5 μs we have $1/\tau_{rf} = 0.4$MHz. When the aperture radius is increased from 1.0 cm to 1.5 cm for a $(6 + 2 \times \frac{1}{2})$–cell structure, to be referred to as Gun B, the $\frac{6}{7}\pi$ and π modes are roughly 1 MHz apart. Enlargement of the aperture is accompanied by overall upshift in resonance frequencies of all the modes, which is compensated for by an increase in cell diameter.

We chose the present configuration to achieve a beam energy of 20 MeV. The second half cell gives larger angular divergence, but it was needed to maintain the field balance between the cells. This will be changed in the future. The frequencies of resonance modes are found by SUPERFISH[7] in a frequency scan. The field distribution and other relevant parameters are found from the output of the code and by using post processor. Some of the results are shown in Figure 1.

The design parameters of the Gun B are summarized in Table 1.

Based on SUPERFISH output data, we computed a set of Fourier coefficients for the PARMELA[8] code to use for spatial distribution of the wave electric and magnetic fields. Using the same initial conditions, the two guns were simulated with a space charge effect of 1 nC photo-

Figure 2: Emittance along the z-axis for the guns A and B.

Figure 3: Transverse beam size along the z-axis for the guns A and B.
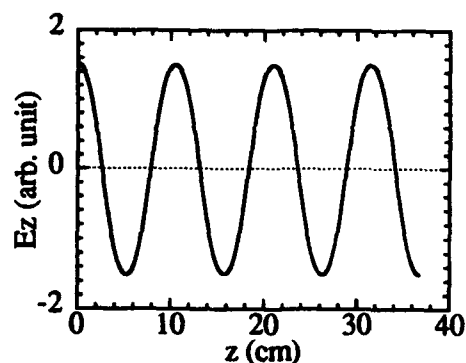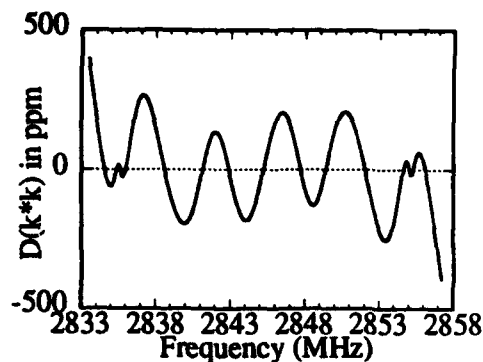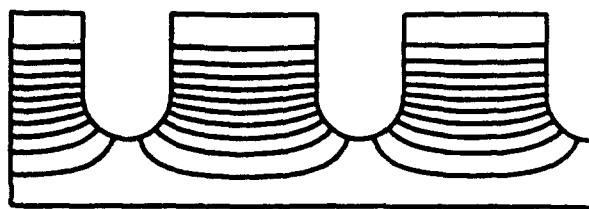
Figure 1: SUPERFISH output for the Gun B. The first half cell followed two full cells of the structure, with the electric field lines(top). The resonance frequencies are when the curve crosses zero from the positive side (middle). The axial electric field along the axis(bottom)

Table 1: Design parameters of Gun B

overall length	36.75cm
cell inner radius	4.30cm
cell length	5.25cm
aperture inner radius	1.50cm
shunt impedance	84MΩ
beam energy	20MeV
photocharge	1nC

electron bunch included. The normalized rms transverse emittance of the two cases are shown in Fig. 2 for comparison. Solenoidal focusing with a compensating bucking coil is the only active focusing applied externally.

While the electron bunch is being accelerated in the gun, the emittance growth rate is small. After passing the exit, the space charge forces the emittance to grow until the bunch loses some of its particles. Even with the energy about four times higher, the growth rate and overall emittance is lower for the case of Gun B. Other parameters of interest from this particle simulation are final transverse beam size, bunch length, beam energy, and energy spread for the two cases at distances farther than two gun lengths. These are given in the Table 2 below.

Table 2: Comparison of beams from the guns A and B

Gun		A	B
beam radius	cm	0.58	0.51
bunch length	mm	0.44	0.31
Energy	MeV	4.5	19.0
$< \delta\gamma > / \gamma$	%	0.13	0.01

571

The above data are preliminary, and thus are subject to modification as the particle code is improved as well as the input data is better prepared. However, the contrast between the two cases will remain unchanged.

Experimental

Based on results from the computational studies, an aluminum prototype has been built. The assembly is made to be versatile, so that the configuration can be changed as needed. There are some extra cells made for the purpose. When all the primary tests are done, the gun will be eventually powered through a waveguide coupling at the center. Presently, however, there is no rf coupling structure and field quantities are measured by launching the rf waves at the end of the structure through an electric dipole probe on axis. This preserves a two dimensional nature computed by SUPERFISH.

With one end of the gun terminated by a flat metal plate, the reflected wave from the probe was monitored over a band of frequencies. The local minimum in reflection is where resonance occurs, and from a network analyzer measurement, there were seven resonances observed. According to SUPERFISH, there are eight resonances with $(n-1)\pi/7$ modes where the integer n ranges from 1 to 8. The measured frequencies were about 1.8% higher than computed values. The discrepancy may be due to poor electrical contact between the cells and/or inaccuracy in machining.

The present setup is assembled by axially clamping the cells by 16 each of 5/16-28 threaded rods with a bolt circle radius of 6.5 cm, where the cell inner radius is 4.3 cm. Geometric dimension of every cell will be checked for consistency and end faces will be contoured to improve the electrical contact between the cells. For the axial electric field distribution measurements, a frequency perturbation method[9,10] will be employed. After each modification of the cell is made, the Q value, resonance frequencies, and axial electric field will be measured. This process will continue until the parameters are within permissible ranges.

The next step is to install waveguide coupling to the cell. Numerical study in three dimension may well be made, but the limitations in resolution and computer resources can be avoided by adopting an experimental trial and error in shaping of the coupling structure. Again, the present $1\frac{1}{2}$ gun will be our baseline. One magnetic rf probe and one tuner for each cell will be used to balance the rf power between the cells. The driving rf waves may be launched through this probe for the purpose of tuning individual cells.

Conclusion

A framework for the study of multicell photocathode rf gun has been setup. Computer codes need to be refined to reveal the details of the wave fields and particle dynamics.

For example, SUPERFISH does not distinguish metal and vacuum on axis, and its shunt impedance calculation on multicell structure is not realistic. In particle dynamics, preparing good input parameters is very important. The need for long computer time is now partially satisfied by running the code on NERSC Cray.

For the hardware part of the problem, optimal coupling of the rf wave to the cavity must be achieved as well as mechanical precision. The opposite end of the photocathode is presently terminated by a flat metal. This will be replaced by a small aperture iris. Breaking of axial symmetry will be compensated for by individual tuning of the cells. Realistic cold test may be done if the entire cavity is copper plated. We will continue this study in the near future.

Acknowledgement

We wish to thank Dr. J. Rosenzweig of UCLA, Drs. R. Cooper, R. Ryne, J. Stovall of Los Alamos and Drs. J. Gallardo and I. Lehrman of Brookhaven/Grumman collaboration for useful discussions and providing computer codes.

References

[1] C. Pellegrini *et al.* Initial operation and beam characteristics of the UCLA S-band RF photoinjector, these proceedings.

[2] K. Batchelor *et al.* Proceedings of the 1992 Linear Accelerator Conference (Ottawa, Canada), p 178 (1992)

[3] D.W. Feldman *et al.* p 603, *op. cit.*

[4] R. Zhang *et al.* The plane wave transformer development at UCLA, these proceedings.

[5] K.-J. Kim, Nucl. Instr. and Meth. **A275**, 201 (1989)

[6] J. Rosenzweig and S. Hartman, these proceedings.

[7] M.T.Menzel and H.K.Stokes, User's guide for the POISSON/SUPERFISH group of codes, Los Alamos Natl Lab. Rep. LA-UR-87-15 (Jan. 1987)

[8] K.R.Crandall and L. Young, PARMELA, *in* The Compendium of Computer Codes, H. Deaven and K.C. Chan, Los Alamos Natl Lab. Rep. LA-UR-90-1766 (May 1990) 137.

[9] K.T. McDonald, IEEE Trans. Nucl. Sci. **NS-32**, 1794 (1988)

[10] E.L. Ginzton, *Microwave Measurement*, McGraw-Hill, New York (1957).

Progress Report on the Commissioning of the Lisa 25 MeV SC Linac

F.Tazzioli, M.Castellano, M.Ferrario, S.Kulinski, M.Minestrini, P.Patteri,

INFN, LNF, P.O. Box 13, 00044 Frascati (Italy)

L.Catani, S.Tazzari

INFN , Sez. Roma II, Via E. Carnevale, 00178 Roma (Italy)

Abstract

The 25 MeV linac, called Lisa, equipped with 4-cell, 500 MHz superconducting cavities, is in the commissioning stage. Data on the performance of the various components are presented together with the results of the first beam tests.

I. INTRODUCTION

The 25 MeV, 2 mA, SC linac LISA, the characteristics of which have been described in various conferences [1], has now been completely assembled and its commissioning is well advanced.

The beam has been transported through the 1 MeV injector to the entrance of the SC accelerating section.

The four 500 MHz, 4-cells SC cavities have all been partially reconditioned with RF power, reaching on the average an accelerating field of 3.5 MV/m, with quality factor $Q_0=1.5 \times 10^8$ limited by electron loading; the low field Q value is of the order of 2×10^9. Peak field is not limited by quench; in pulsed operation a peak value above 4 MV/m has been obtained. Further conditioning is required to reach the design goals.
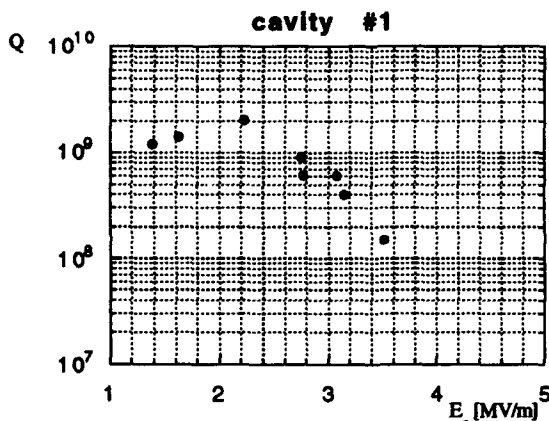
Figure 1. Q vs. E_{acc} for cavity n.1

Progress has also been made in the construction of the transport channel to the FEL experimental station. Magnetic elements, including the undulator, are in place and ready for alignment and the vacuum chamber has been delivered.

II. THE INJECTOR

The RF control circuits of the 1 MeV injector elements, inflector, chopper, prebuncher and capture section, are operational, though still needing improvement, and under computer control. A preliminary optimization of their parameters has been performed by maximizing the current transported through the 1 MeV, 180° bending arc that has a momentum acceptance of approximately 5%.

Table 1
Beam transport measured data

Gun voltage	90 KV
Gun current	120 mA
Chopping angle	90 deg
Pulse length	1 msec
Avg. current after capt. sect.	1 mA
Avg. Current after 180° arc	0.5 mA

The chopper performance is at present not at its best, because the original design structure has been provisionally replaced by a fluorescent oxidized Aluminum collimator with a hole of larger diameter (8 mm instead of 4 mm) and at a less favorable optical position. The replacement was motivated by the difficulty of transporting the beam through the aperture without additional beam position diagnostics.

The beam transport measured performance is summarized in Table 1.

The transverse diagnostics, consisting in fluorescent targets and strip-line electrodes, is working satisfactorily.

Oxidized Aluminum targets have given good results, avoiding the adverse effects of charge build-up observed with ceramic targets at low energy and high charge levels.

III. THE SC CAVITIES

The four 500 MHz, 4-cell, bulk Nb cavities have all been partially reconditioned after several months of idleness.

They had been kept evacuated by ion pumps, but one of them had been, by accident, sealed off in static vacuum. Notwithstanding this, no particular difficulty has been found in restarting them up to fields of about 3 MV/m. Above this threshold heavy electron loading impaired the Q factor but a rapid improvement was brought about by pulsing the RF at high power .

In some of the cavities the apparent field limit for electron emission onset (evidenced by X ray emission) was somewhat lower than 3 MV/m and this was attributed to unflatness of the field distribution, producing higher peak fields in some cells. To check this we have measured the

dispersion curves of the four cavities and compared them with the theoretical one. Two of them are shown in Fig.2.

The cavities with mode frequencies farther away from the theoretical ones are in fact those with lower field thresholds.
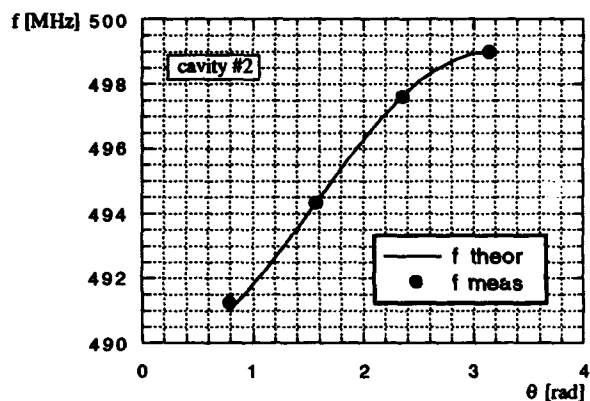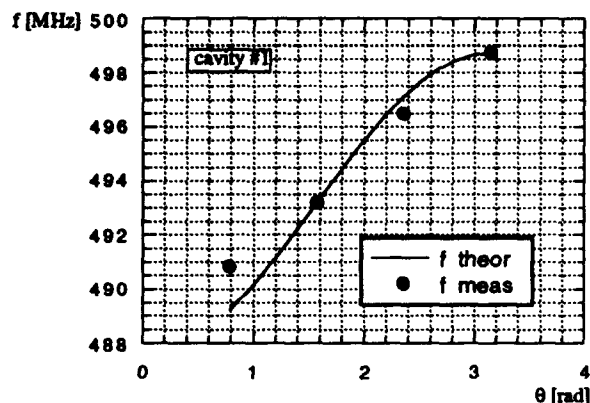
Figure 2. Dispersion curves of cavities 1 and 2.

The Q factor has been measured by measuring the level of liquid helium in the bath.
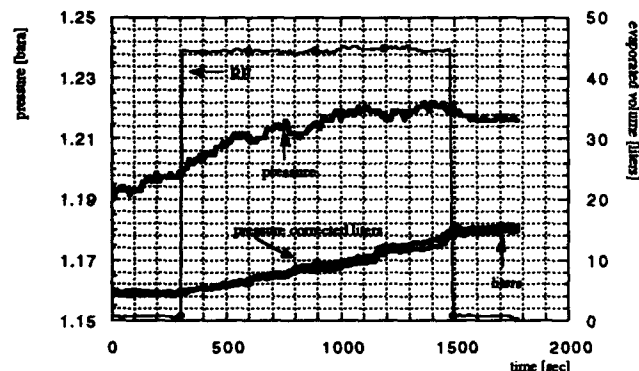
Figure 3. LHe level variation vs. time

Using the built-in heating resistors on the LHe container, we first introduce a known amount of power, much larger than

static losses, in the cryostat and with the refrigerator in automatic operation wait until an average equilibrium state is reached. Under such conditions the LHe inlet valve performs small oscillations around its average position. Once the latter position has been determined, the valve is blocked there manually. The fixed LHe input then almost exactly compensates the overall heat input and the level remains sufficiently constant for tens of minutes. We can then switch on the RF and measure the liquid level fall rate $\Delta V/\Delta T$ and from this evaluate the dissipated RF power P_c. The Q factor is then determined from the value of the RF electric field, measured through a calibrated probe.

The method has been improved by taking into account pressure variations. In Fig. 3 we show the behaviour of pressure and a corrected level variation curve.

A description of these measurements will be published separately [2].

Q measurement data for cavity n.1 are reported in Tab.2.

Table 2
Cavity n.1 Q measurement data

duty cycle	c.w.	25 %	25 %	20 %	20 %	20 %
$\Delta V/\Delta T$ [l/s]	0.29	1.01	1.41	1.92	2.75	9.55
P_c [W]	7.9	27.2	38.2	51.9	74.3	258.1
E_a [MV/m]	2.22	2.75	2.77	3.08	3.15	3.51
$Q/10^9$	2	0.9	0.6	0.6	0.4	0.15

The mechanical tuning system has been tested on the cold cavities. The electronics consists of a phase detector that compares the incident voltage with that transmitted to the field probe. The output from the phase detector, above a given threshold, drives the step-motor that moves the mechanical actuator.

On the phase detector signal, in addition to some drift, we observe slow fluctuations with frequencies in the range of several tens of Hz, that however are well within the cavity bandwidth ($\approx$ 100 Hz); they are eliminated by a low-pass filter with a cut-off frequency of a few Hz. Fast phase and amplitude fluctuations are counteracted by electronic loops. No special problem has been encountered although the cavity external Q is in the range of 10^8.

IV. REFERENCES

[1] M. Castellano et al.- Proc.EPAC 92- p. 611.

[2] M. Castellano et al. "On line calorimetric measurement of the quality factor of superconducting accelerating cavities"- LNF 93/006 (P) Submitted to Nucl. Instr. & Meth

The Plane Wave Transformer Linac Development at UCLA*

R. Zhang, S. Hartman and C. Pellegrini,
Dept. of Phys., UCLA, 405 Hilgard Ave., Los Angeles, CA 90024, USA

Abstract

A plane wave transformer linac (PWT), offering advantages of high efficiency, compactness, fabrication simplicity and cost, is being developed at UCLA. The PWT prototype at UCLA is an 8-cell, π-mode, S-band standing-wave linac. To fully understand its physical properties, numerical modeling of the PWT prototype has been carried out by using the 3-D code MAFIA. A microwave test-stand with a network analyzer has also been set up to test these properties. In this paper, we present the important physical features, such as mode structures, dispersion curves, wake field, from the computation and/or the experiment. The measurements show good agreement with the numerical computation.

I. Introduction

A compact RF linac with a laser-driven RF electron gun is being under development at UCLA. This linac system, as shown schematically in Fig.1, is dedicated to study of high brightness electron beam physics, high gain free electron laser (FEL) experiments, plasma focusing and plasma wake field acceleration[1] . For these experiments, especially the FELs, to be carried out successfully, a high quality beam will be very important.
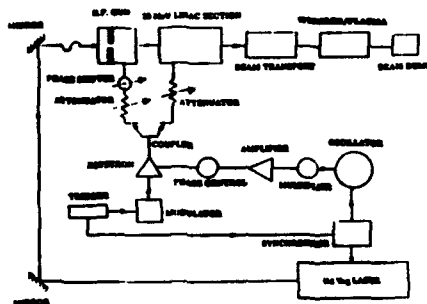
Fig.1 UCLA RF linac system schematic.

The rf electron gun consists of one and a half cells operating at π-mode at frequency 2856 MHz, with copper as a photocathode. The injector can generate electron charge up to 1 nC and a bunch length as short as 4 pico-seconds (FWHM). The exit energy of the electron beam can reach 4.5 Mev with a normalized emittance of about 10 π mm-mrad. The recent experimental results of the rf gun are reported in another paper[2] .

The rf linac under development at UCLA is a prototype of the plane-wave transformer (PWT) structure[3] . Its cross section is schematically shown in Fig.2. The history of the PWT linac can be dated back to 1960s. This similar structure first was analyzed by V.G. Andreev[4] . The PWT is basically a disk-washer type linac. However,

the disk-washer array in the PWT is separated from the cylindric tube. Therefore, the array acts as a center conductor to support a TEM-like plane wave traveling back and forth along the structure and transforms the transverse field of the plane wave into a longitudinal field for acceleration. It is the TEM mode which provides the coupling between the individual cells. In other words, this structure transform a plane wave (TEM mode) into a longitudinal electric field for acceleration of particles.
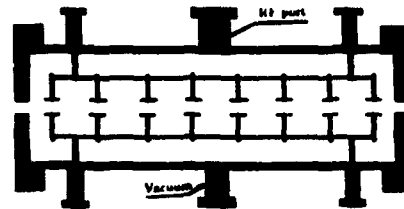
Fig.2 The cross section of the PWT prototype.

Different from the other known rf linac, the PWT operates on the high order TM_{02}-like mode instead of the fundamental TM_{01}-like mode. This feature concerns us about the frequency separation of the different modes, the mode structure and the wake field. To understand these properties are important to operate this linac. In this paper, these characteristics of the PWT structure are described. The rf modes found from the numerical simulation by the 3D code MAFIA[5] and from the microwave cold test are presented. Then the short range wake-field calculation is discussed. We conclude the paper by a summary and the discussion of further work.

II. Electrical Characteristics of the PWT

The PWT linac prototype consists of eight cells. It is a π-mode standing-wave rf linac. The field pattern of the operation mode, shown in Fig.3(a), is a TEM-like one excited between the outer tube wall and the inner disk-washer structure. The field distribution at certain cross section along the tube, shown in Fig.3(b), shows that the PWT is operated at TM_{02}-like mode instead of the conventional TM_{01n}-like mode. These electrical parameters are listed in Table I.

Table I. Electrical Parameters of the PWT

resonant frequency	2856.0 MHz
unloaded Q factor	35000
effective shunt impedance	78 MΩ/m
transit time factor	0.77
$E_{surface}/E_{axis}$	2.5

The high unloaded Q-value, thus a high impedance, is due to the fact that very little rf power is dissipated on the outer tube of the structure. The larger of the diameter of the outer tube is, the larger the unloaded value. Considering the finite rf pulse length in our system, a medium Q-value is better for our purpose. Besides, the mechanical tolerance of dimensions for the PWT structure is very high because of the large coupling between cells. The operation frequency has little dependence upon the diameter of the outer tube. We do the minor tuning by slightly changing the dimensions of the end cells. However, the misalignment of the central array with the tube and the unequal distance between cells may probably induce other modes around the operation mode.

a)

b)

Fig.3 The feild pattern of the operation mode: a)longitudinal field; b) transverse field.

III. Numerical simulation and Cold Test Results

In order to hold the disk-washer array in the PWT, some support rods are used. In practice, there are a lot of ways to place the rods. Besides the way shown in Fig.2, we can u~: straight rods connected to the end walls, which has the advantage for preserving the uniformity from cell to cell.

Because of these supporting rods, the cylindrical symmetry of the PWT is broken. Thus, the 3-D code MAFIA is used to numerically simulated this structure. From the field pattern we can identify different modes. Fig. 4 shows these mode frequencies as a function of phase advance. The dashed line is the dispersion curve of the π-mode without the support rods. Thus the introduction of the rods reduces the coupling between the cells. As long as the π mode dispersion curve is concerned, there is little difference for the ways to place the support rods.

There are two kinds of modes we are concerned. One is the modes whose resonance frequencies are very close to the operation frequency. As a result, it is possible
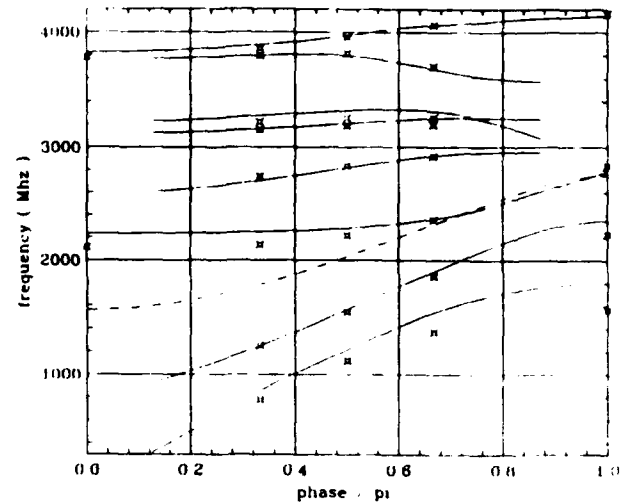
Fig.4 The mode frequencies vs. phase advance: solid lines — simulation for the prototype; dashed lines — simulation for the PWT without the support rods; marks — from measurements.

for those modes to be excited by the rf power supply due to the finite frequency band width of the klystron. The numerical simulation by MAFIA indicates the closest mode is separated about 10 MHz from the π-mode. In the measurement, we found the most close mode separation is about 16 MHz, which is beyond the bandwidth of the klystron. Besides, the alignment of the central array with the outer tube must be done carefully, otherwise, new undesired modes could be excited. Another kind of modes are those whose phase velocities are close to the velocity of electron beam, which could be excited by the electron beam. One of these modes is shown in Fig.5. The excitation of the undesired modes will increase the energy spread, cause the emittance growth and even induces the beam break up (BBU). In order to get a high quality beam, some measures have to be taken to damp these modes out.
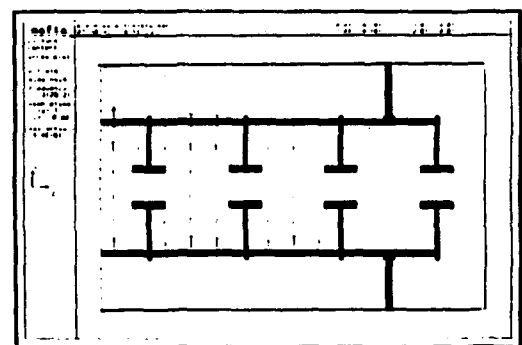
Fig.5 The field distribution of a high order mode.

To check the results obtained from the simulation by using MAFIA, we set-up a cold test stand with a network analyzer to measure the PWT. The measured

unloaded Q-value is a little lower than the computation value due to the roughness of the disk surfaces. The electrical field distribution along the axis is, measured by perturbation method, shown in Fig. 6. The measured characteristic impedance (R/Q) agrees well with that found from numerical simulation. To measure the dispersion curves, one way is to measure the phase advance by pulling a metal bead along the axis. It is effective for modes with a high Q-value, but fails for low-Q and high order modes. To measure these high order modes, we measure a module with different cells. In this way, we can find most of the modes. These measurement results are shown in Fig. 4 by marks.
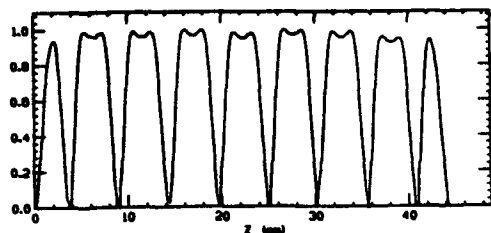
Fig. 6 The field distribution along the axis, from which we find the $R/Q = 3.3\ k\Omega/m$.
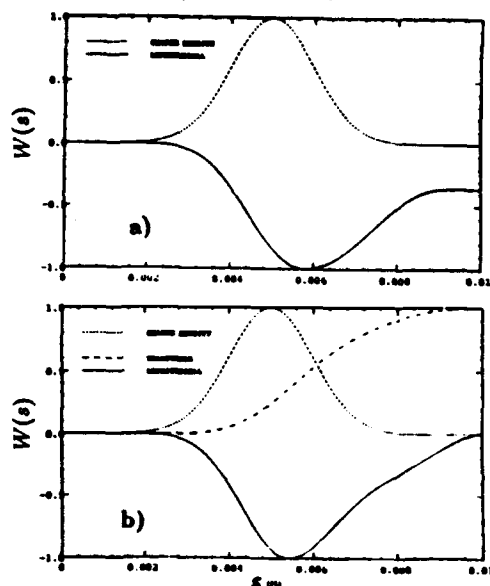
Fig.7 The wake field potential for an electron bunch of $\sigma = 1mm$. a) monopole wake;   b) dipole wake.

IV. The Wake Field Calculation

When a bunched electron beam with high peak current traverses an accelerating structure, strong wakefield will be excited. The longitudinal wake will induce an energy spread of the electrons in the bunch; while the transverse wake leads to emittace growth. However, these effects may be compensated, at least partially, by the rf field when the appropriate injection phase is chosen. Therefore, it is helpful to calculate the wakefield in order to preserve a high brightness beam during the acceleration process.

As for the wakefield calculation, there are several codes available. ABCI[6] is used for 2-dimension geometry, while MAFIA is for 3-D structures. There are, however, some restrictions: the computing time and the memory size, in using MAFIA for short electron bunch wakefield calculation, which is as short as about 1 mm (1σ) for the beam at UCLA. On the other hand, there is no much error to be induced if we ignore these rods, even reduce the diameter of the outer tube, as far as the short range wake field is concerned[7] . Thus, we use the 2D code ABCI, to do the wakefield calculation. The results are shown in Fig.7. Fig. 7(a) shows the wake potential for monopoles, and Fig.7 (b) for dipoles. The maximum energy loss (longitudinal wake) is about 40 keV, which will induce an energy spread of about 0.3%. The maximum transverse kick is about 0.2 kV/cm, which is negligible comparing the transverse rf field. In the future, we will use an analytic formula to approximate the wake function and find out the optimal injection phase to preserve the beam quality.

V. Summary

The PWT linac has many advantages like compactness, high efficiency, low cost, etc. over other known structures. Because the separation of the cylindrical tube and the central disk-washer array, this structure is very easy to manufacture. These advantages make it attractive for this structure to be used in medical and industrial application. However, the operation of high order mode (TM_{02}-like) makes it difficult to build a long structure because of its small frequency separation from undesired modes. For the acceleration of multi-bunch electron beam, the high order mode damping becomes important to preserve a high quality beam and increase the BBU threshold. The approaches to this end are under study.

V. Acknowledgement

References

1. S. Hartman, et al., Proc. 1991 IEEE Particle Accelerator Conf., San Francisco, CA., (1991) 2967.

2. C. Pellegrini, et al., this Proc. (1993).

3. D.A. Swenson, European Particle Accel. Conf., 2, 1988, Rome, Italy, ed. S.Tazzari, pp 1418..

4. V.G. Andreev, Accelerating Structure for a High-Energy Linear Proton Accelerator, Sov. Phys. - Tech. Phys., 13, (1969) pp.1070.

5. F. Ebeling, et al., MAFIA User Guide, LA-UR-90-1307, (1989).

6. Yong Ho Chin, LBL-33091, CERN SL/92-49 (AP), (1993).

7. K. Bane and M. Sands, SLAC-PUB-4441 (1987).

NANOSECOND MOSFET GUN PULSER FOR THE
CESR HIGH INTENSITY LINAC INJECTOR

C. R. Dunnam and R. E. Meller

Laboratory of Nuclear Studies ◆

Cornell University, Ithaca. NY 14853

Abstract

A fast solid-state pulser (PFH) for the Cornell CESR linac injector system is described. Stripline-packaged high-voltage power MOSFET devices are arranged in a novel cascode output topology to achieve extremely low transition times. In the present CESR injector, the PFH driver outputs pulses of 3 nanoseconds FWHM and 20 amperes peak current through an Eimac Y-796 cathode-grid assembly. Recovery time is approximately 10 nsec. Advantages of the MOSFET pulser over its hard-tube predecessor include a substantial increase in peak beam current, an order-of-magnitude reduction of gun interpulse recovery time and precise control of the unequal output pulse amplitudes required for e^+ vs e^- injection modes. Reduction of physical size permits collocating the pulser with the linac electron gun assembly to minimize transmission line artifacts arising from unavoidable impedance mismatch over the gun's bias range. Successful implementation of the MOSFET linac gun pulser is an initial step to a future CESR B-factory injector.

Introduction

Injection rate into the CESR storage ring strongly affects collider integrated luminosity, principally due to time lost during replenishment of the beams. Upgrades of the CESR injector's gun, linac and synchrotron over the past decade have thus far yielded more than an order of magnitude improvement in average charge transport during fill periods. A significant step forward has been achieved by replacing the previous linac hard-tube gun pulser with a solid-state module of markedly superior performance. Cornell has recently begun investigating multibunch train operation as an avenue to higher luminosity, and the MOSFET linac gun pulser described here (Figure 1) is an essential component of that program.

Key parameters for a CESR multibunch-train compatible injector gun driver are: peak pulse current of 20 amperes, pulse FWHM 3-5 nanoseconds, maximum repetition rate 72 MHz and recovery time less than 12 nanoseconds. Although

Figure 1. Nanosecond gun pulser assembly.

solid-state pulsers exist in many forms, including the familiar avalanche bipolar and step recovery types, output capabilities of these and other fast pulser solutions are either inadequate or the technologies are too costly for CESR injector use. Several years ago, preliminary work at Cornell using SPICE simulations and breadboard measurements indicated a power MOSFET cascode output topology could meet specifications at reasonable cost, if and when r.f.-packaged H.V. pulse power MOSFET devices became available.

Eventually, commercial r.f.-packaged high-voltage, high pulse power MOSFET's were located, and a stripline pulser breadboard utilizing the devices was then assembled. With specific MOSFET parameters in hand, SPICE modeling proved useful for successfully "fine tuning" the cascode design. Performance of the prototype met expectations for peak output and pulse width, the only shortfall being a longer than expected recovery interval. The longer recovery time did not affect contemporary 7 bunch CESR operations, so a MK I version of the MOSFET gun pulser was installed in the Cornell High Intensity Linac Injector[1] (CHILI) in mid-1991.

After approximately one year of service, the pulser (and spares) were upgraded in preparation for CESR multibunch-train studies. A troublesome energy storage mechanism was found to exist in the intermediate driver stages. By substituting custom stripline packages for the earlier

paralleled DIP arrays in these stages, recovery time constant and pulse to pulse crosstalk were reduced to a negligible level.
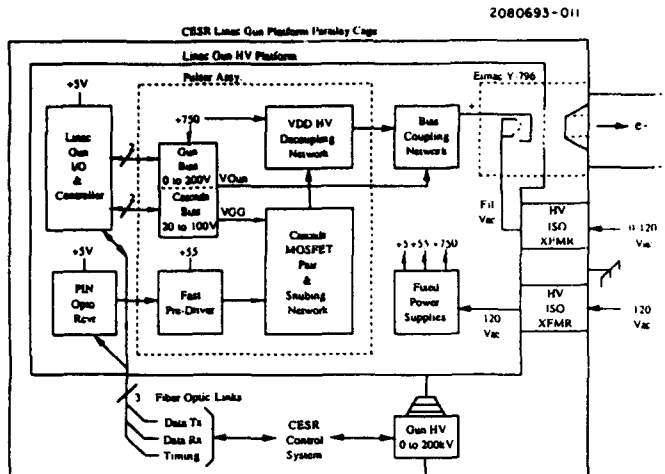
Figure 2. CESR CHILI injector HV platform.

CHILI systems

A block diagram of linac gun support systems is presented in Figure 2 with MOSFET pulser circuit board subsystems shown in the dashed area. Peripherals in the gun tank include fixed power supplies and I/O controller. The nanosecond pulser is mounted in the high-voltage tank approximately two centimeters from the EIMAC cathode assembly to minimize transmission line artifacts which can degrade pulse to pulse isolation. Timing signals are sent to the pulser over a fast (tr, tf ≈ 2.5 nanoseconds) fiber optic link. Control data sent over a lower bandwidth CESR control system optical link determine the level of the V_{GUN} and V_{GG} bias supplies associated with the gun pulser. Upstream serial information includes readback of all supply voltages and the detected pulser output level.

Pulser design

A simplified schematic of the nanosecond gun pulser is shown in Figure 3. Fast response in all stages is obtained by avoiding operation in or near the MOSFET devices' depletion-transition region. This is accomplished by maintaining $|V_{DS}| - |V_{GS}| > 5$ volts under worst-case conditions (e.g., when the cascode pair is biased for minimum pulse amplitude). All critical MOSFET signal paths are controlled-impedance striplines within the multilayer circuit board.

Predriver and drivers consist of a paralleled array of 74ACT-series high-current gates followed by two discrete stages, shown in Figure 4, which provide level conversion and additional power gain. Both stages consist of a single MOSFET die bonded to a small circuit board which serves as a stripline substrate, as seen in Figure 4. The technique is known as chip-on-board, or COB, fabrication[2] and is a cost-effective r.f. construction method.

Output devices DE101N05 and DE102N05 are stripline-packaged, commercially available[3] power MOSFETs. The input (lower) device is selected for small input C_{iss} and relatively low R_{Don}, while the output (upper) device is specified for high (1 KV) V_{DS} capability. Both devices exhibit good r.f. characteristics to the 400 MHz region. By arranging the output devices in a cascode topology to minimize Miller-effect loading, charge gain remains high and the inherent device bandwidth is retained. The cascode arrangement also permits wide-range adjustment of output amplitude via programmable bias voltage source, V_{GG}, applied to the DE102N05 gate. Details of the output section, including the output H.V. decoupling network, are displayed in Figure 5.
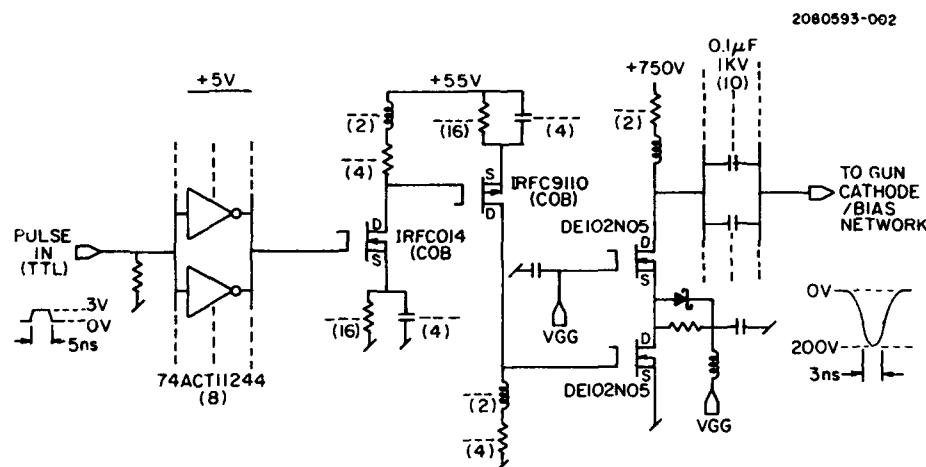
Figure 3. Driver and output schematic.
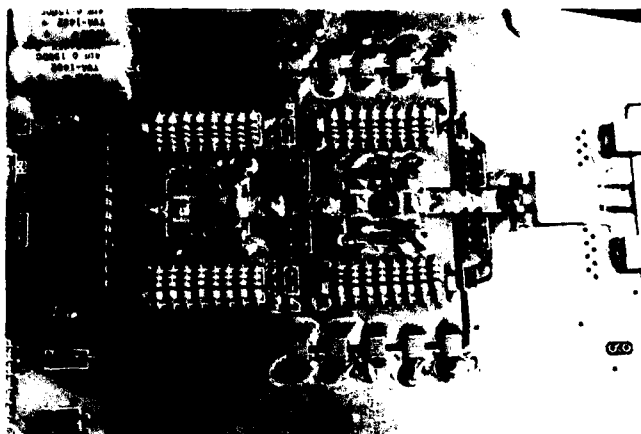
Figure 4. Intermediate driver stage detail.
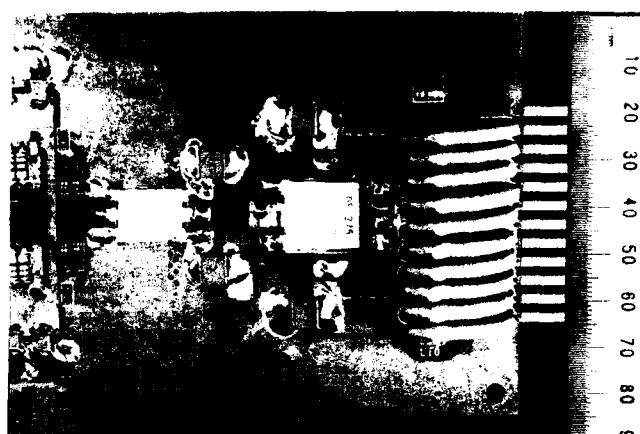
Figure 5. Pulser output and coupling network detail
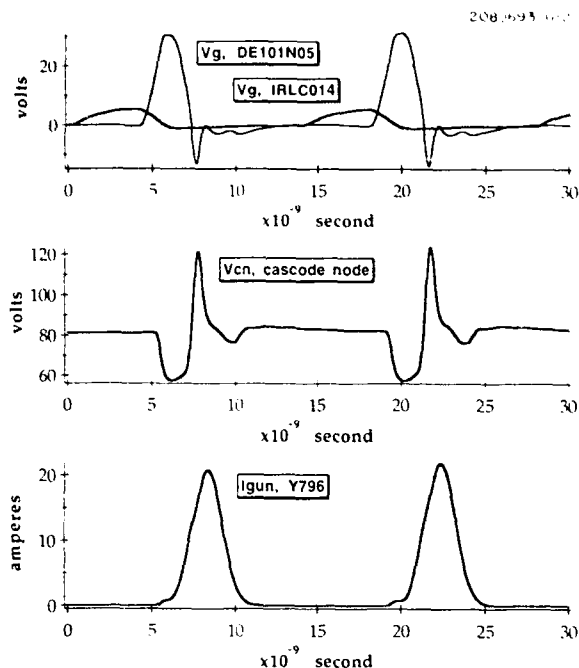
Figure 6. Pulser waveforms under e^+ injection conditions.

Figure 7. Pulser waveforms under e^- injection conditions

Performance

Measurements of electron bunch charge exiting the gun assembly under varying bias conditions are in good agreement with SPICE predictions, as revealed by bench observations of the cascode node and output waveforms. We find that level 3 MOSFET modeling provides correspondence within a few percent of observed fast pulser characteristics. Simulation waveforms of Figure 6 (e^+) and Figure 7 (e^-) accurately depict pulser behavior over an order of magnitude programmed output range (injection intensity is attenuated during CESR electron filling to avoid space charge induced loss through the linac pre-bunchers and excess radiation). For both waveform sets, a noteworthy feature is the relatively small variation in output pulse amplitude evident in comparison of the first gun current pulse to subsequent 14 nanosecond-spaced pulses.

Conclusions

We have found, for present and projected CESR injection parameters, the stripline-MOSFET solid state pulser provides superior performance when compared with hard-tube or other solid-state alternatives. A MK II version of the CESR MOSFET "Pulser from Hell" is presently operational in the CESR injector and meets critical parameters for B-factory-compatible 14 nanosecond CESR multibunch-train injection.

---

[1] E.B. Blum et al, "Performance of the Cornell High Intensity Linac Injector", LNS CBN 83-8, 1983

[2] Argo Transdata Corp., Clinton, CT, 203-669-2233

[3] DEI, Inc., Fort Collins, CO, 303-493-1901

PROGRESS OF PLS 2-GeV LINAC*

W. Namkung, I. Ko, M. Cho, C. Ryu, J. Bak, S. Nam, and H. Lee
Pohang Accelerator Laboratory, POSTECH
P. O. Box 125, Pohang 790-600, Korea

Abstract

Pohang Accelerator Laboratory (PAL) is constructing the 2-GeV Pohang Light Source (PLS). The 2-GeV electron linear accelerator will be used as a full energy injector to the storage ring. There are 42 accelerating columns in the 150-m long linac. The linac is powered by 11 klystrons of 80-MW maximum output power, which are driven by 200-MW modulators. Two 200-MW modulators connected to the klystrons are already under normal operation, and assembly work for the nine remaining modulators is in progress. In the tunnel, about half of the linac has been installed. The cooling system is completed along with the precision temperature controllers. The installation work will be completed by the end of 1993. We present the updated construction progress of the PLS 2-GeV linac.

I. INTRODUCTION

The PLS 2-GeV linear accelerator is a full energy injector to the storage ring (SR) which will serve as a low-emittance light source for various research: basic science, applied science, and industrial and medical applications [1]. There will be 11 klystrons and modulators, and 10 SLAC-type pulse compressors in the linac gallery. In the linac tunnel, which is 6-m below the gallery floor, there will be 42 accelerating columns, 6 quadrupole triplets, and various components to form the 150-m long linac.

The approximately 215-m long linac building is completed. The installation work started on July 1, 1992 is progressing smoothly. As of May 1, 1993, up to K6 module in the tunnel has been completed. This location is about 80-m from the e-gun. There are 22 accelerating columns and four quadrupole triplets up to this place. The completion of the installation is expected by the end of 1993. The commissioning of the 2-GeV linac will be carried out during the first half of 1994.

II. TECHNICAL DESCRIPTION

A. General Description

The nominal beam energy of the PLS linac is 2-GeV and the operating frequency is 2,856 MHz. The maximum repetition rate of the linac is 60 Hz. However, this repetition rate will be reduced to 10 Hz when the linac serves as an injector to the storage ring due to limitation on the SR injection system. The higher repetition rate will be useful for the testing of the machine or other purposes in the future.

The normalized emittance for the electron beam of the linac is 0.015π MeV/c cm rad. It corresponds to $7.5 \times 10^{-8} \pi$ m rad at 2 GeV. The energy spread of the electron beam is $\pm 0.6\%$ at FWHM. Major parameters are summarized in Table 1.

B. Preinjector

The PLS 2-GeV linac is considered to consist of two parts: the preinjector and the main linac. The preinjector is the first 60 MeV section of the whole linac. It consists of a triode type e-gun, an S-band prebuncher and buncher, two accelerating columns, and various components. It is powered by a 25-MW klystron.

The preinjector was completed on February 28, 1992. At that time, 61.2 MeV electron beam was achieved [2]. Since then, it is being used to train PLS personnel.

Table 1: Major parameters of PLS 2-GeV linac.

Beam Energy	2 GeV
Accelerating Gradient	15.5 MV/m (min.)
Energy Spread	< 0.6 %
Machine Length	150 m
RF Frequency	2,856 MHz
Repetition Rate	60 Hz max.
E-gun	> 2 A, 2 nsec
Emittance	0.015π MeV/c cm rad
Klystron Output Power	80 MW max.
Number of Klystrons	11 (=1+10)
Number of Pulse Compressor	10
Number of Accelerating Column	42
Number of Quadrupole Triplet	6
Number of Support & Girder	22
Beam Exit	at 80 MeV, 1 GeV, 2 GeV

C. Main Linac

The electron beams from the preinjector are accelerated to 2-GeV by 10 high-power klystrons and 10 SLAC-type pulse compressors [3]. Each klystron provides 80 MW maximum output power, and feeds RF power to four accelerating columns. Ten pulse compressors are employed to obtain a higher accelerating gradient. The accelerating gradient exceeds 15.5 MeV/m. To obtain the 2-GeV beam, the klystron output power is about 64 MW and the energy gain factor of the pulse compressor is 1.5. In this way, we can avoid operating the klystron at its maximum power level, and can, therefore, extend the lifetime of the klystron.

There are 40 accelerating columns in the main linac. The 3.072-m long accelerating column has a SLAC-type constant gradient structure with $2\pi/3$ operating mode. Its distinctive feature is the conflat flanges for easy installation. There are six quadrupole triplets altogether in the 2-GeV linac. These will be sufficient to focus and guide the electron beam even in event of a power failure in any one of the klystron, with the exception of the preinjector klystron, which provides the driving power to the rest of the klystrons.

III. INSTALLATION STATUS

A. Klystron and Modulator

The high power klystron used in the PLS linac is Toshiba's E3712 model [4]. The first two units were already delivered in June 1992 and installed in the klystron gallery as K2 and K3, respectively. The K4 klystron was delivered in March this year, and is now undergoing power testing in the klystron test lab which is annexed to the klystron gallery. The K5 unit is arrived at PLS in April 1993 and is waiting to be tested. Six more klystrons are being manufactured in Toshiba's Nasu factory, Japan, and all of them will be shipped to Pohang by this summer. A SLAC 5045 klystron was also delivered to PLS in September, 1992. This unit will be used as a reference klystron.

The matching modulator of 200-MW rated power is being manufactured in-house [5]. A prototype of the 150-MW modulator was completed in February, 1992. This unit now serves as a klystron test unit in the test lab. In the klystron gallery, ten modulator cabinets are placed in their final positions. The size of this modulator cabinet is 3.2 m (L) x 1.5 m (W) x 2.7 m (H). Two units are completed, and are under normal operation with matching klystrons. Most of heavy components such as transformers, choke coils, capacitors are already assembled in the remaining modulators. Subsystems such as thyratron assembly, SCR circuit, diode and transistor banks are being installed. Assembly work for remaining 8 modulators in the gallery will be finished by this summer.

The klystron and modulator for the preinjector will be replaced later this year with a higher power unit in order to drive 10 klystrons in the downstream.

B. Tunnel Components

Out of 44 accelerating columns ordered from the Institute of High Energy Physics (IHEP) in Beijing, China, 36 columns have been shipped to Korea. Eight sets of girders and supports have also arrived. Besides the preinjector, twenty accelerating columns have been already installed as of May 1, 1993, along with two beam current monitors, one beam profile monitor, and three quadrupole triplets. Therefore, approximately 80-m of the linac is completed. All waveguide components were delivered from IHEP. By using a standard girder with two accelerating columns on it, the whole waveguide network will be installed well before the accelerating column installation, which will save time and effort during the installation. All the centerline components will be installed by November this year.

C. Cooling System

The main cooling system was completed in April this year. This includes piping work, pump station, cooling towers, low conductivity water generation, and precision temperature control system. The PC-based temperature control system is under normal operation. The temperature of $45 \pm 0.2^\circ$C is routinely achieved. The quartz crystal oscillator is used as a temperature sensor. The preinjector cooling is also connected to a new cooling system.

D. Microwave System

In order to drive 10 klystrons, the drive line is being installed from the first klystron. Two IPA (Isolator, Phase shifter, Attenuator) units are under test. The IPA unit will provide suitable input RF power and correct RF phase to the klystrons. The first pulse compressor was delivered and the cold test was completed. The result shows that the energy gain factor is 1.68. This unit can be detunable.

E. Control System

We made significant changes in the linac control system even though the basic structure is still VME based system. There are three layers in the control hierarchy as shown in Fig. 1. Three

Fig. 1: Linac control system
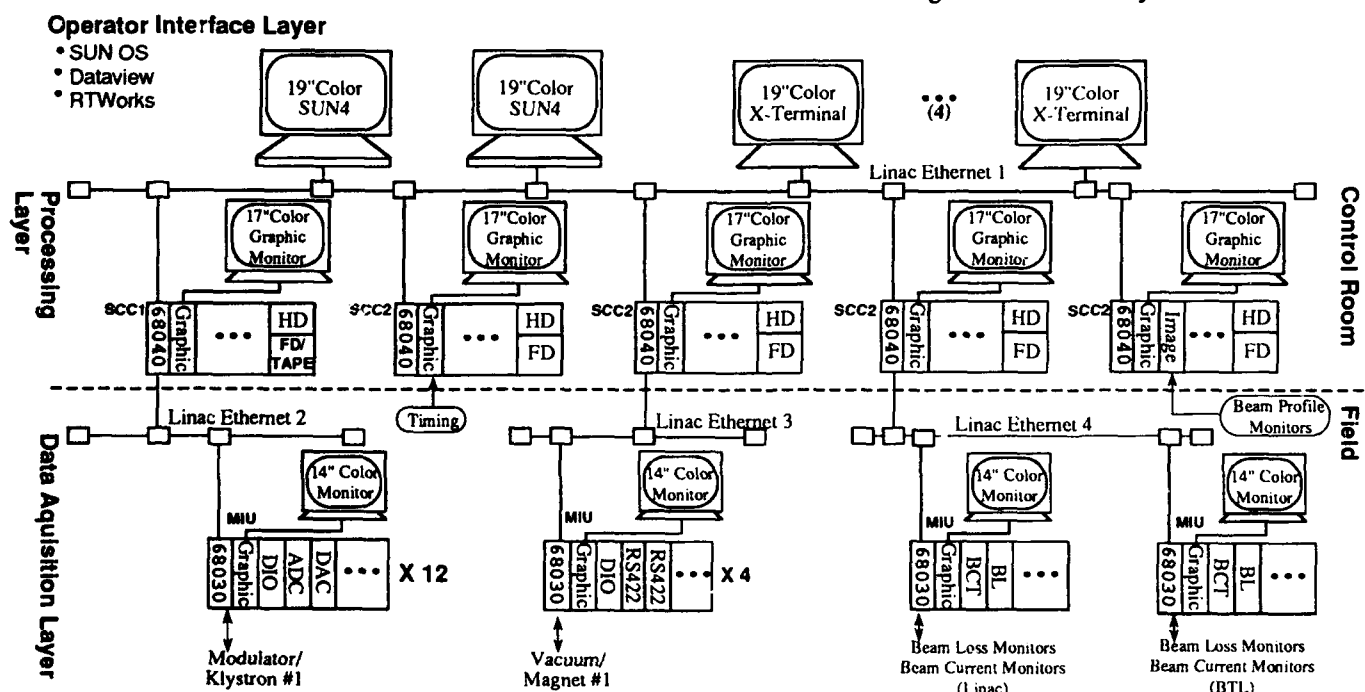
layers are connected with several Ethernets. Replacing a MIL-STD-1553B network by Ethernet is one of major changes.

The operator interface layer is composed of two SUN sparcstations and four X-terminals. Several graphic windows will be provided for the operators. In order to optimize the graphics and data acquisition in this layer, commercial S/W packages such as RTworks[TM] and Dataview[TM] are being used.

The data processing layer and the data acquisition layer are both VME based systems. The operating system is OS-9. The difference between the data processing layer and the data acquisition one is based on their functions. All CPU boards and many of I/O boards are commercial products.

The data acquisition layer is directly connected to the individual devices to be controlled or monitored. There are 11 units for the modulator control, and 3 units for the magnet power supply (MPS) control. One unit is assigned to control the pneumatic gate valves and several vacuum monitors. One unit is also dedicated to the beam current monitors and the beam loss monitors. Every CPU board in this layer is equipped with a 14" color graphic monitors, a keyboard, and a mouse. On-demand local computer control is available to all CPUs in this layer. This feature is extremely useful for local commissioning of an individual device, especially 200-MW modulators. All CPUs are located in the klystron gallery.

The data processing layer is divided into four different functions: modulator/klystron, MPS/vacuum, beam monitoring, and timing system. The run-time data collected by the data acquisition layer are stored in a RAM memory area temporarily and, later, in a hard disk permanently. This Motorola 68040 based CPU board has two independent Ethernet ports: one for data acquisition and one for operator interface layer. A 19" color monitor is attached to individual CPU board in this layer. All CPUs are located in the linac control room.

One special CPU is assigned to beam profile monitors which produce large image data. The beam profile image captured by a CCD camera is directly sent to this CPU board. After the image processing is completed, numeric data such as beam sizes are sent to the operator console through the Ethernet instead of image data itself. The isolation of image data can reduce the data traffic in the Ethernet significantly.

For fast signals such as modulator beam voltage, RF signals from pulse compressors, we will use digital sampling oscilloscopes connected to the CPU board via a GPIB port. Using oscilloscopes, we can reduce a lot of cumbersome hardware and software development works in handling fast signals.

The signal conditioning units will be used to isolate noises from the modulator. Isolation transformers and noise filters will also be used at the AC input terminal for all control cabinets.

F. Commissioning

The preinjector commissioning was completed by February, 1992. Last December, a combined system test for the preinjector and K2 module was performed. The main purpose of this test was the commissioning of first 200-MW modulator with matching 80-MW klystron. In this test, a 200-MeV beam was obtained. Even though many subsystems were operated by manual control, it showed that there were no significant flaws in the system integration for the 2-GeV linac.

IV. CONVENTIONAL FACILITIES

A. Linac Building

The linac building was completed in April this year. The machine tunnel includes three beam switch yards and beam dumps. The beam transport line (BTL) tunnel is also completed except the injection area in the storage ring. In the second floor, thirteen air handling units (AHUs) are installed. These units can be controlled remotely in the linac control room.

B. Cooling Station

The linac cooling station is located near 1-GeV beam switch yard. It includes the AHU pump system and the machine cooling system. All systems are completed and are under normal operation. The parameters for the precision temperature control system and normal cooling system are summarized in Table 2.

Table 2: Design parameters for linac cooling system

Description	Precision System	Normal System
Heat Load (max.)	250 kW	710 kW
Flow Rate	960 gpm	320 gpm
Pressure Drop	72 psi	93 psi
Temperature	$45 \pm 0.2\ ^\circ C$	$35\ ^\circ C$
Conductivity	0.2~0.5 μS/cm	0.2~0.5 μS/cm
Cooling Tower	50 RT	220 RT

C. Linac Substation

The linac substation is located between the linac and the storage ring. Several transformers and switch gears are located in this building. Power lines for modulators and computers are separated in this station in order to avoid unnecessary interference. On November 30, 1992, the 154-kV main power station was completed. This power line is directly connected to the national power grid.

V. ACKNOWLEDGMENTS

VI. REFERENCES

[1]. *Design Report of Pohang Light Source*, Revised ed. (Pohang Accelerator Laboratory, POSTECH, 1992).

[2]. W. Namkung, et al., "Installation and Commissioning of PLS Preinjector Linac," *Proc. of the Third European Particle Accelerator Conference*, Vol. 1, pp. 507-509 (1992).

[3]. W. Namkung, et al., "The Status of PLS Linac," *1992 Linear Accelerator Conference Proceedings*, Vol. 1, pp. 302-304 (1992).

[4]. M. Cho, et al., "Performance Characteristics of the Pulsed High Power Klystron Tube for PLS 2-GeV Linac," these proceedings.

[5]. S. Nam, et al., "High Power Pulse Modulator for PLS Linac," these proceedings.

Lattice Design Principles for a Recirculated, High Energy, SRF Electron Accelerator*

David R. Douglas
Continuous Electron Beam Accelerator Facility
12000 Jefferson Avenue,
Newport News, Va. 23606

Abstract

Issues critical to the design of a high energy (over 10 GeV), recirculated, superconducting RF (SRF) based electron accelerator are discussed. These include injection energy, number of passes, type of linac focussing structure (constant gradient or constant focal length), quantum excitation in recirculation arcs, method of beam separation for recirculation, and use of isochronous or nonisochronous transport. An example lattice for a 16 GeV SRF linac with a CEBAF-like footprint is presented.

I. INTRODUCTION

This paper will discuss lattice issues relevant to the design of the CEBAF 4 GeV SRF electron accelerator [1], and extrapolate to determine their interactions and impact on a high energy (> 10 GeV or higher) multipass electron linac based on SRF technology. An example lattice, for a 16 GeV linac with a CEBAF-like footprint, is given.

II. FUNDAMENTAL DESIGN ISSUES

Several technical issues have arisen during the design of the CEBAF 4 GeV linac. Their impact in that context has been discussed elsewhere [2]. We now examine how they influence the design of a linac of final energy of over 10 GeV.

Certain features are assumed common to all designs. The machine will comprise an injector, multiply recirculated superconducting linac(s), and a recirculator. The recirculator will either commonly transport beams at multiple energies, or will have individual beam lines transporting monoenergetic beams, using a "spreader" to separate the beams for transport following the linac(s), and a "recombiner" to combine them for reinjection.

The intent of any design is to produce a lattice supporting specific performance goals. In the following, we attempt to achieve electron beam currents of 10–100 μA with $E_{\text{final}} > 10$ GeV, beam emittances $\epsilon_{\text{rms}} < 10$ nm-rad, and energy spread $\sigma_{\Delta E/E} < 2.5 \times 10^{-4}$. A desire for minimum cost, easy operability, and upgradibility is assumed. SRF technology is adopted as the preferred method to achieve high duty factor and superior beam quality.

A. Injection Energy

Injection energy is primarily cost limited. Higher values provide better performance, by reducing peak betatron envelope values in multiple passes; higher front end linac energy has associated with it higher focussing strength. For example, the peak betatron function values in the four pass 4 GeV CEBAF design (45 MeV at injection) were over 200 m in x and y [3]. In an optically identical 16 GeV linac design discussed below (1 GeV at injection), the peak betatron function values are only about 130 m in x and y. This stronger focussing also provides greater stability against multipass beam breakup. It enhances ease of operation, by lowering error sensitivity due to pass-to-pass betatron mismatch. Finally, use of high injection energy and a short linac (low single pass linac energy gain) may allow use of low linac focussing (e.g. quadrupole excitations at constant gradient, instead of constant focal length). This simplifies pass-to-pass betatron matching of the recirculation transport system.

B. Number of Passes, N_{pass}

To first order, this is a cost optimization issue: trade linac cost ($\propto 1/N_{\text{pass}}$) off against recirculator costs ($\propto N_{\text{pass}}$), and seek the cost minimum.

Higher order effects may be significant. As N_{pass} increases, mechanical and operational complexity of the recirculator (in particular, the spreaders and recombiners) increases, driving costs up at a rate $\propto N_{\text{pass}}^2$ or higher. The choice of single vs. split linac can affect cost in an N_{pass}-dependent manner. A split linac is relatively more complex than a single linac; in the limit of a short linac and many passes the split linac will have higher costs (due to the need for two spreader/recombiner pairs per pass).

Betatron mismatch and error sensitivity increase with N_{pass}, the former due to lowered first pass linac focussing, the latter due to increased total beam path length. Both cause an increase in operational complexity and a decrease in machine performance.

C. Single vs. Split Linac

A split linac is an effective use of tunnel length and minimizes the cost of unit acceleration per unit tunnel length. However, the cost and performance optimum for a given machine also depends on the type of beam transport used for recirculation and the number of passes. A highly modular, many pass transport system requires relatively complex spreaders and recombiners; tunnel cost savings achieved by using a split linac could be offset by the incremental cost of the additional required spreader/recombiner pair. The use of a split linac also entails some operational complexity as the number of betatron phase space matches of recirculator transport to linac and the number of linac reinjections is doubled, as is the number of adjustments of beam path length to match the beam to linac accelerating phase.

Certain designs are not amenable to split or multiple linacs. Microtron-like recirculators are most easily designed for a single linac; use of multiple linacs can force utilization of complex magnetic components with severe error tolerances. Finally, a machine may be site-limited to the choice of either single or split linac; in particular, a short, wider, site will favor the use of a split linac.

D. Type of Linac Focussing Structure

Linac focussing structure can be either constant gradient focussing (which has zero gradient—no focussing—as a sub-case), or focussing varying in gradient along the linac (typically, constant focal length focussing).

584

Constant gradient allows simple optical matching for multi-pass operation. However, the maximum focussing strength is set by transverse (betatron) stability of the injected beam, and is thus limited by injection energy. On higher energy passes, the linac will appear more and more "drift-like"; the maximum betatron excursion is thus dictated by the linac length. This type of focussing is therefore best suited to a machine with short linac(s) and high injection energy, such as a cascaded microtron.

In constant focal length optics, focussing along the linac is limited by betatron stability of the first pass; thus, on higher passes, the beam experiences more focussing in the back end of the linac than it would with constant gradient focussing. This "back-end focussing" can, with proper choice of reinjection condition, compensate for lack of focussing of recirculated beams, and provide greater betatron stability than constant gradient focussing. Constant focal length optics are thus well suited for use in a long linac with low injection energy. If the injection energy is raised, the performance improves (as in constant gradient focussing).

A comparison of these focussing methods for a 16 GeV machine described below is given in Table 1, in which peak beta functions and total phase advance through a four pass linac are tabulated. The linac comprises 50 cryomodules embedded in 19.2 m long FODO cells; the first linac quad is set to give 120° phase advance per cell on the first pass. Constant focal length focussing provides about 50% lower peak envelope functions, and much higher total phase advance, than does constant gradient, for the specified front-end FODO cell betatron tune.

Table 1
Comparison of Focussing Structures for 16 GeV Linac

	Constant Gradient				Constant Focal Length			
Pass	β_x (m)	ψ_x	β_y (m)	ψ_y	β_x (m)	ψ_x	β_y (m)	ψ_y
1	82	3.00	63	3.02	41	8.34	41	8.34
2	99	1.08	99	1.08	62	2.97	85	2.98
3	143	0.68	149	0.69	98	1.85	93	1.88
4	193	0.49	199	0.49	132	1.34	121	1.37

E. Degree of Functional Modularity

It is important to specify the degree of functional modularity to be employed. In the limit of nonmodularity, a microtron-like machine could be designed, in which recirculated beams of all energies are transported by a common (set of) dipole(s). Toward the limit of higher modularity, accelerated beams of various energies could be separated for recirculation by individual transport channels. Given this, a second level of modularity must be set, in which various transport functions of the mono-energetic beam lines are accomplished either globally, or locally, in a modular fashion. The CEBAF 4 GeV accelerator [4] is an example of a modular transport system, in which only a few parameters are coupled to any particular control variable.

Modularity trades construction costs off against operational costs, flexibility, and upgradability. Modular systems generally require more parts than nonmodular systems. They therefore may have higher construction costs, though the complexity of components for nonmodular systems can reduce the cost differential. However, modular transport allows use of simple tuning algorithms and provides operational flexibility absent in nonmodular recirculators. (See the following discussion of isochronous vs. nonisochronous transport.)

F. Quantum Excitation in Recirculator Arcs

Emittance and momentum spread growth from quantum excitation can be estimated [5]. The absolute energy spread, σ_E^2, and the emittance, $\Delta\epsilon$, generated by bending a monoenergetic, zero emittance beam through 180° are

$$\sigma_E^2 = 1.18 \times 10^{-33} \text{ GeV}^2\text{m}^2 \frac{\gamma^7}{\rho^2}$$

$$\Delta\epsilon = 7.19\pi \times 10^{-28} \text{ m}^2\text{rad} \frac{\gamma^5}{\rho^2}\langle\mathcal{H}\rangle,$$

$$\langle\mathcal{H}\rangle = \left(\frac{1}{L}\right) \int_{\text{bends}} ds\{(\frac{1}{\beta})[\eta^2 + (\beta\eta' - \frac{1}{2}\beta'\eta)^2]\},$$

where $L=$ orbit length, and $\rho=$ orbit radius, in bends.

At a given energy, σ_E^2 is a function of ρ only; $\Delta\epsilon$ is a function of both ρ and $\langle\mathcal{H}\rangle$. Thus, bend radii are limited by the final momentum spread specification; betatron parameters are then optimized to control emittance. It is particularly useful to keep dispersion, η, small in the dipoles. This is readily achieved if achromatic, isochronous transport is invoked.

G. Method of Beam Separation for Recirculation

Assuming use of modular transport, a mechanism for separation or recombination of the multiple energy beams on the linac axis (axes) is needed. Small, recirculated single linacs may easily separate beams in the plane of recirculation. High energy machines are, however, constrained by tunnel size. It is then best to separate out of the recirculation plane, so that the various energy-specific beam lines can be stacked vertically. They are then presented for easy installation and maintenance.

The separation of beams will generate transverse dispersion. Control of this dispersion is desirable to limit quantum excitation. If the separation is in the recirculation plane, dispersion may be suppressed locally (in the spreader itself), or matched to the dispersion inherently present in the recirculator. If spreading is out of the recirculation plane, dispersion can be locally suppressed, or mapped to the recirculation plane through the use of a skew-quad rotator, and matched to the recirculator dispersion. The latter entails significant operational complexity.

There are several modular methods of dispersion suppression. In the CEBAF 4 GeV design, two methods were examined: a simple achromatic transverse (vertical) translation [6], which was rejected because of high error sensitivity generated by strong focussing, and a "staircase" (vertical) spreader [7], which has been built. Although optically superior, the staircase suffers from some mechanical complexity due to congestion of transport elements immediately following the linac. In a following section, we describe an asymmetric chicane based spreader, which lacks some optical symmetries of other solutions, but avoids component congestion and seems to have low error sensitivity.

H. Use of Isochronous vs. Nonisochronous Transport

In non-modular systems there is typically little tuning range for momentum compaction. It is set by the geometry of the transport. Careful consideration of the use of nonisochronous transport vs. isochronous transport is therefore needed at the design stage.

Functionally modular transport systems have demonstrably tunable momentum compaction [8]. Therefore, no

design decision is required; momentum compaction can be adjusted to meet operational needs.

I. Error Sensitivity

Error sensitivities must be considered in all design choices. They tend to grow as the square root of number of machine elements and/or machine length, for uncorrelated errors, and linearly in number of elements and/or machine length, for correlated errors. In addition, sensitivity is greater in designs with greater betatron mismatch. It therefore interacts with the number of passes, the type of linac focussing, injection energy, use of a single or split linac, and degree of functional modularity.

An analysis of error sensitivities should be conducted for any particular design. Appropriate design modifications must then be made, and error analyses iterated.

III. A 16 GEV SRF LINAC

The following design is an exercise promulgated on two assumptions. First, the following example of a 16 GeV machine will fit on a CEBAF-sized site. Secondly, it is assumed that currently available gradients in CEBAF SRF cavities [9] continue to rise to ~ 20 MV/m. The target beam performance for the design is as discussed above.

Injection energy is selected to be 1 GeV, to reduce the injection-to-final-energy ratio of the machine from the current CEBAF value of 90 to 1 to the level of 16 to 1. The advantages of this are discussed above.

It is assumed that SRF production costs rise only modestly in going to 20 MV/m, while beam transport costs increase significantly in going from 4 to 16 GeV final energy. The optimum number of passes will therefore fall; we choose four passes as a design value. We are site constrained to a split linac. The data of Table 1 suggest that constant focal length linac focussing is to be desired; we duplicate the present CEBAF linac focussing structure of 12 1/2 120° FODO cells in each linac. The resulting linacs use 25 eight cavity cryomodules, with each cavity supplying 9.375 MeV energy gain, for a single pass energy gain of 3.75 GeV.

A high degree of functional modularity is preferred operationally. Beams are separated vertically for recirculation using a spreader based on a dispersion-suppressed asymmetric chicane. This is depicted in Figure 1. Beam recombination and reinjection matching occur as in a time-reversed propagation through the spreader.
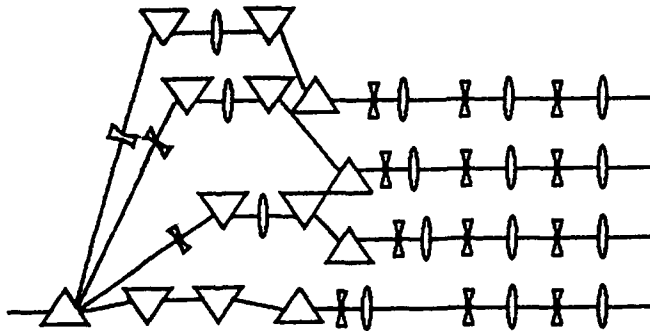
Figure 1. Schematic of spreader/recombiner.

Preliminary computations suggest dispersion suppression and matching of linac beam envelope functions to arc acceptance require modest quadrupole strengths and generate little betatron mismatch. Error sensitivity will therefore be low.

The seven recirculation arcs proper are configured to provide large bend radius (to control energy spread generation) and strong focussing (to limit emittance excitation). Initial studies indicate that combined function dipoles are required to limit quantum excitation of emittance. Each arc consists of six superperiods of the following "six-cell" alternating gradient focussing structure.

$\frac{1}{2}$QD1-BF-BD-QF-BD-BF-QD2-BF-BD-QF-BD-BF-$\frac{1}{2}$QD1

Each superperiod is tuned to 7/6 wavelength horisontally and 5/6 wavelength vertically. The resulting arc is thus a second order achromat. Three quadrupole families allow operational control of tunes and momentum compaction. (Dipole field indices are selected to give small superperiod matched dispersion for isochronous arc transport and to allow for a broad tuning range on momentum compaction.) On the final pass, for isochronous transport, net relative energy spread excitation is $\sigma_{\Delta E/E} = 1.6 \times 10^{-4}$, quantum excitation is specified by $\langle \mathcal{H} \rangle = 0.167$ m, and net emittance excitation is $\Delta \epsilon_x = 2.1 \times 10^{-9}$ m-rad. Relevant magnetic parameters are summarized in Table 2.

Table 2: Arc Transport System Parameters for 16 GeV Recirculator

Global focussing structure	2nd order achromat
Superperiodicity	6
Superperiod focussing structure	6 "cell" a - g
#dipoles	48
Bend radius (m)	53.476
Bend index, $n = -(\rho/B)\partial B/\partial x$	-310.56
Bend magnetic length (m)	3.5
Peak bend field (kG)	8.811
Minimum quadrupole focal length (m)	1.39
Superperiod phase advance, $\psi_{x,y}$	$2\pi \times 7/6, 5/6$
M_{56} range (m)	$|M_{56}| < 1$
Superperiod matched $\beta_{x,y}$ (m), ($M_{56} = 0$)	29.58, 31.47
Superperiod matched η_x (m), ($M_{56} = 0$)	0.17
Superperiod $\partial\nu_{x,y}/\partial\delta$, ($M_{56} = 0$)	$-3.02, -1.43$

IV. ACKNOWLEDGMENTS

V. REFERENCES

[1] B. Bowling *et al.*, "The CEBAF Beam Transport System Lattice Design," *Proc. 1991 IEEE Part. Acc. Conf.*, San Francisco, CA, May, 1991, pp. 446–448.

[2] *ibid.*

[3] R. C. York and D. R. Douglas, "Optics of the CEBAF CW Superconducting Accelerator," *Proc. 1987 IEEE Part. Acc. Conf.*, Washington, D.C., March, 1987, pp. 1292–1294.

[4] B. Bowling, *op. cit.*

[5] R. C. York and D. R. Douglas, *op. cit.*; M. Sands, "Emittance Growth From Radiation Fluctuations", SLAC Report SLAC/AP-47, Dec., 1985.

[6] R. C. York and D. R. Douglas, *op. cit.*

[7] D. R. Douglas *et al.*, "Optical Design of the CEBAF Beam Transport System," *Proc. 1989 IEEE Part. Acc. Conf.*, Chicago, IL, March, 1989, pp. 557–559.

[8] Y. Chao *et al.*, "Commissioning and Operation Experience With the CEBAF Recirculation Arc Beam Transport System", these proceedings.

[9] F. Dylla, "Operating Experience with SRF Cavities", these proceedings.

Commissioning and Operation Experience with the CEBAF Recirculation Arc Beam Transport System*

Y. Chao, M. Crofford, N. Dobeck, D. Douglas, A. Hofler, C. Hovater, G. A. Krafft,
R. Legg, J. Perry, E. Price, S. Suhring, M. Tiefenback, and J. van Zeijts
CEBAF, 12000 Jefferson Avenue, Newport News, Va. 23606

Abstract

Results of the initial beam tests and early operation of the CEBAF recirculation beam transport system are presented.

I. INTRODUCTION AND SCOPE OF TESTS

From October 1992 to April 1993, pre-commissioning checkout and beam tests of the CEBAF accelerator were conducted. This paper documents the scope and results of these tests and relates experience gained.

The CEBAF superconducting accelerator is a recirculating cw electron linac consisting of a 45 MeV injector linac, two 0.4 GeV main linacs, and a recirculator. The design is unchanged from previous reports [1], and comprises lattices of five subsystems: injector, linacs, spreader/recombiners, extraction regions, and semicircular arcs. Here, we describe initial tests of the system through the 135° point of the lowest energy arc. The subsystem tested consisted of the injector and north linac lattices, the lowest energy spreader and extraction transport lines, and three of the four superperiods of the lowest energy east arc recirculation transport line.

Accelerator beam operations resumed on 23 November 1992 after an extended construction-related shutdown. By 4 December, 135 MeV beam had been brought to the end of the spreader, and on 11 December, beam was taken to a dump at the 135° point of the low energy east arc beam line. Testing continued until 9 April 1993.

Tests conducted during this period fell into three categories. Firstly, algorithms for setup and tuning of the transport system were developed. Secondly, comparisons were made between observed machine behavior and that predicted by design and modeling of the system. Finally, descrepancies between modeling and observations were detailed, and possible reconciliations tested.

II. SETUP AND TUNING

Numerous procedures for accelerator setup and tuning were developed during this running period. These are designed to utilise values from machine modeling and previous accelerator runs, and, with a minimum of operator intervention, propagate well-tuned beam losslessly through the accelerator. We now describe the major algorithms.

A. Betatron Phase Space Matching

At the end of the injector and following the spreader, betatron phase matching regions allow for a match of the beam ellipse from the upstream transport to the acceptance of the downstream beamline. This is accomplished by making an emittance measurement, which specifies the betatron parameters at the front end of the phase matching region (see section IIE). These values are used as initial conditions for a DIMAD computation of quadrupole excitations required to provide the desired betatron match. Simple downloading of the resulting quadrupole values, with no additional trimming of quadrupole strengths, produced no observable betatron mismatch through either a well tuned linac or arc. A measurement of beam properties at the end of the linac implies agreement of observed and computed betatron functions to the 20–30% level, which is consistent with the error of measurement in the initial values provided by the emittance measurement.

B. Linac FODO Tuning

The linac 120° FODO lattice is tuned using an algorithm in which betatron oscillations are excited by steering magnets and driven to nodes every third half-cell by quadrupoles. The resulting optics has phase advances with absolute errors of 2–5° along the length over which the nodal pattern is constructed; no betatron mismatch is evident in the beam spots down the linac. Use of this procedure gives agreement in phase advance, quadrupole excitation curves, and beam energy, to a level of 1–2%. The distance over which the procedure is applicable is limited by horizontal/vertical coupling induced by RF cavities; this is discussed in more detail in section IIID.

C. Spreader Dispersion Suppression

Following the linac, the spreader is dispersion suppressed by using two vertically focussing quadrupoles 1/4 betatron wavelength apart to create dispersion nodes at beam position monitors that are, respectively, 1/4 and 1 1/2 betatron wavelengths from the second quad. The transport is achromatic and has a momentum acceptance of $\sim 3\%$; the measurement is described in section IIF. The quadrupole excitations required for good dispersion suppression were noted to be 5–10% different from those predicted by the machine model and quadrupole excitation curves. This discrepancy is now understood to be due to end fields in transport system dipoles.

D. Adjustment of Arc Momentum Compaction

In section IV, we describe tests of isochronicity in this system. Here, we note that the momentum compaction is adjustable over a broad range by varying a pair of quadrupoles, a half-wavelength apart, in each arc superperiod. This was successfully performed as a part of the isochronicity measurement described below, and serves as a first step in the development of algorithms to tune simultaneously arc phase advances, dispersion, and momentum compaction.

In summary, the testing of setup and tuning algorithms resulted in successful procedures for machine operation. No undue system sensitivities were encountered, and any discrepancies were attributable to errors in quadrupole excitation curves (which are now resolved to the 1–2% level) and/or dipole end fields (which are now being understood quantitatively). The resulting algorithms behave in accordance with observation and modeling, and can be readily automated. Two major procedures remain to be developed. The first will provide fine-tuning of phase matches between machine modules; the second will provide detailed control of arc transport parameters. Both will depend on applications of difference orbit techniques presently under development (see section IIIE).

587

We note that these tests were carried out at 120–135 MeV, which is 1/4 to 1/3 the design energy. The energy off-set was readily accommodated by application of measured dipole and quadrupole excitation curves at lower currents, and by careful attention to standardizing hysteresis loops, to avoid errors due to magnet remnant fields.

We will now discuss a pair of measurements that were frequently performed as a part of setup and for verification of proper beamline tuning.

E. Emittance/Momentum Spread Measurements

Emittance measurements were performed to obtain β function values for use in matching computations. Table 1 summarizes typical results obtained at the injector (20 MeV), the arc (121 MeV, 10 μA), and the spreader entrance (121 MeV, 36 μA).

In general, measurements were performed in a regime (pulsed mode, low current) that does not represent beam characteristics at design operating conditions; however, the observed β functions agree with design values. The measurement is estimated to resolve betatron function values in excess of 10 m to 20–30% and values under 5 m to a factor of two.

Table 1: Emittance Data

Energy (MeV)	ϵ_x (nm-rad)	ϵ_y (nm-rad)	Average Current (μA)	Macropulse Width (μsec)
20	10.8	8.2	10	150
121	0.7	1.8*	10	150
121	0.7	—	36	100

*We note that the value $\epsilon_y = 1.8$ nm-rad measured in the recirculator was corrupted by residual dispersion and should be regarded as an upper bound.

The value $\epsilon_x = 0.7$ nm-rad measured in the arc is adiabatically damped from the 10.8 nm-rad value observed in the injector. An emittance measurement performed at a higher current indicated that ϵ_x values remained consistent with values obtained at lower currents. A measurement of energy spread conducted in conjunction with the high current ϵ_x measurement yielded $\sigma_{\delta p/p} = 9 \times 10^{-5}$ [2].

Horizontal-vertical coupling [3] was a detriment to this measurement. Discrepancies in the 20 and 121 MeV emittances (which should adiabatically vary by only a factor of 6) may be due to this. Coupling was alleviated when the injector was well tuned.

F. Dispersion Measurements

Detailed dispersion measurements were made during difference orbit measurements; a separate vertical dispersion measurement indicated good agreement with design. Residual and error dispersions were nominally at the 10 cm level. As noted, spreader momentum acceptance is ~ 3%.

III. COMPARISON OF DESIGN, MODELING, AND OBSERVATION

Tests of the above procedures provided opportunities to compare design and simulation predictions against observation. Points of comparison were thereby established.

A. Quadrupole Excitation Curves

Quadrupole excitation curves from magnetic measurment were verified by tuning of the linac FODO lattice to ~ 1%. Hysteresis effects were important, as remnant fields could change quad excitation at low energies by 50% or more. Standardized quadrupole cycling avoided errors of this type.

B. Dipole Excitation Curves

Excitation curves were verified by spreader and arc orbit setup to ~ 1/2% if hysteresis effects were ignored; agreement between magnetic-measurement-based predictions and observeration was estimated to be better than 0.1% if magnets were operated on a standard hysteresis loop.

C. Dipole End Fields

Effects of end fields in arc dipoles were observed. Behavior was consistent with measurement and modeling [4]. The focussing effect of the end fields of a dipole was equivalent, in the arc, to trim of 1–3% of arc quads; in spreader magnets (with larger sagitta), the effect was equivalent to trims of 2–10% of dispersion suppressor quads. This is consistent with observation (see sections IIC and IV); these effects will be included in improvements to the machine model.

D. Horizontal/Vertical Coupling

RF-cavity-generated coupling was observed in the injector and linac, and, when evident, limited the distance over which linac FODO tuning was possible to approximately 1 to 1 1/2 betatron wavelengths. Behavior was consistent with simulation of cavity coupling effects [5].

Horizontal/vertical coupling was not observable in the arcs provided the orbit was well corrected (residual of a few millimeters) though arc dipoles. If beam steering was poor (residual of several millimeters), dipole end-field-generated coupling could be observed.

As noted above, this experience suggested two possibly useful tuning algorithms that are yet to be developed: fine tuning of phase matching regions and fine tuning simultaneously of arc phase advances, dispersion and momentum compaction. Development of these procedures will depend on use of difference orbit measurements for detailed understanding of the optics.

E. Difference Orbit Measurements

Detailed verification of lattice properties can be obtained through use of difference orbit measurement techniques. A program is therefore under development to measure transfer matrices through the system using BPM readings of trajectories with different launch conditions covering the 5-dimensional phase space $(x, x', y, y', \delta p/p)$. Localized sections of beamline are used as a basis for inferring global optical behavior. This difference orbit method has been employed successfully in measurements elsewhere [6].

The program includes procedures for determining the full linear transfer matrix. This is done by utilizing BPM readings of specific orbit offsets. Injection conditions can be established by fitting to these readings, with BPM reading errors being established from separate measurements. A number of features in the program allow for flexible operation. For example, algorithms allow for the use data from an arbitrary number of BPMs in the fitting process, along with the exact propagation of errors. In addition, defective data are eliminated by an iterative screening process. All contributions to the final error analysis, including BPM errors, signal/noise ratio in every set of trajectories, as well as errors incurred during the nonlinear fitting procedure, are propagated to the final transfer matrix elements. This yields information on both the nonlinear optical behavior in the system and on the accuracy of the optics setup in the local sections.

Test versions of this program were used to measure the optics in the spreader and east arc. Preliminary results imply that the divergence in the rms BPM data is consistent with the expected deviations due to nonlinear optical effects and the measured transfer matrix elements. This method of insuring proper optical behavior is expected to be increasingly useful as the program evolves; it will become the principal tool for checking lattice behavior and verifying proper beamline tuning during next running period.

IV. MEASUREMENT OF ISOCHRONICITY

A major test of design and modeling against observation was provided by a measurement of the M_{56} linear transfer matrix element from the front end of the east arc spreader to the 90° point. This was done using a modified version of the phase transfer measurement detector [7] (Figure 1), and provides a test of the isochronicity and tuneablity of the transport system. A 1500 MHz precision phase detector is used to measure the phase difference between a reference signal derived from one of the final RF control modules in the linac and an amplified beam signal originating in the BPM at the 90° point. The variable phase shifter is used to calibrate the measurement; drifts are negligible on the measurement time scale. Simultaneously a modulator changes the linac energy.

Precision Phase Detector
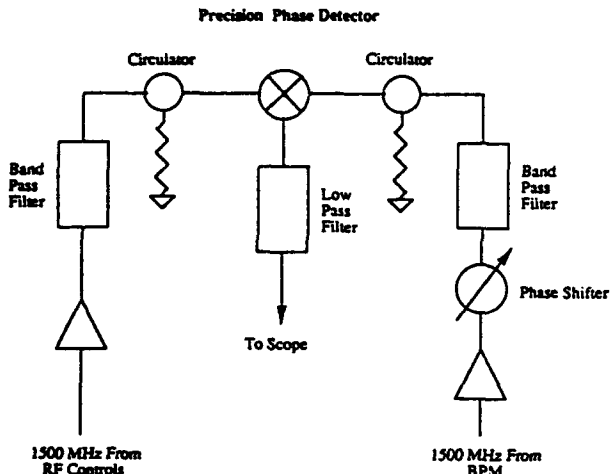
Figure 1. Schematic for M_{56} measurement.

Two optics sets were calculated using DIMAD. The first was the nominal isochronous arc tuning, with a nominal M_{56} of 0 m. The second was a special tuning with a nominal M_{56} of −1 m, and was generated from the first by varying the excitation of a specific family of arc quadrupoles (which, by design, control M_{56}) by 15% while trimming the 3 remaining families to restore the design tunes and dispersion suppression. The special tuning was measured to have an M_{56} of absolute magnitude 1.4 m; the deviation from design is equivalent to a quadrupole excitation error of 6% in the family used to control momentum compaction, which, together with the effects of dipole end fields, is consistent with the type of error observed in other tests. The nominal tuning was measured to have an M_{56} of 18.5 cm. Small corrections of 1–2% were iteratively applied to the compaction control quadrupoles while M_{56} was repeatedly measured. After these quads were shifted by an average of 3%, the M_{56} was measured to be 1.8 cm. This deliberately generated shift in M_{56} is consistent with the 0.4 m per 6% quad excitation offset observed above, and is also consistent with the effect of dipole end fields (section IIIC).

This technique can probably be used to measure M_{56} to an accuracy of better than 3 mm, as compared to the presently estimated resolution of ~ 1 cm.

V. FUTURE DIRECTIONS

The experience gained during this testing period suggests a number of additions to machine hardware, control, and operating procedures that will be useful during the next running period. Regular use of difference orbit measurements will be made to verify machine tuning and resolve discrepancies between design and observed behavior. Incorporation of measured dipole end-field effects into machine modeling will improve the robustness of tuning computations; algorithms for fine-tuning of module-to-module betatron phase matches and for arc tuning are under development. Installation of shims on low energy arc dipoles will reduce the magnitude of end field effects.

Hysteresis effects influence system reproducibility. Automated procedures for standardizing magnets at start-up and after machine tuning will therefore be implemented, and will insure that magnet excitations remain on a standard cycle. The RF vernier system will provide control of linac energy drifts by stabilizing both gradient and phase [8]. Additional control system utilities, including automated beam threading and steering as well as tuning of transport line focusing properties, will assist in machine setup [9].

Improvements will be made in emittance measurement techniques, which at present are limited by profile monitor cycle time. These could be implemented through simultaneous use of multiple harps, and/or use of beam steering across a fixed wire profile monitor. Finally, an analog monitoring system is being implemented, which will allow access to various useful signals, such as output from beam loss monitors distributed around the machine.

In summary, this test period has provided confirmation of many design choices. The transport system behaves predictably and in general accordance with design and modeling. Many automated procedures are under development, and guidance has been obtained for the resolution of outstanding questions.

VI. REFERENCES

[1] B. Bowling et al., "The CEBAF Beam Transport System Lattice Design", Proc. 1991 IEEE Part. Acc. Conf., San Francisco, CA, May, 1991, pp. 446–448.

[2] Work performed in collaboration with L. Merminga and members of the CEBAF High Power Test Team.

[3] M. Tiefenback et al., "Emittance Measurements and Transverse Cavity Transfer Matrix in the CEBAF Nuclear Physics Accelerator", these proceedings.

[4] D. Douglas, "The Effect of Observed Dipole End Fields On Beam Transport System Optics", CEBAF-TN-91-095, 10 December 1991.

[5] Z. Li et al., "Transport Properties of the CEBAF Cavity", these proceedings; M. Tiefenback et al., op. cit.

[6] T. Barklow, SLAC-PUB-4969; T. Barkow, P. Emma, and N. Walker, unpublished SLAC seminars.

[7] C. G. Yao, "A Method to Measure Phase Distribution of Charge in Bunch", CEBAF-TN-0131, 20 June 1989.

[8] G. A. Krafft et al., "Energy Vernier System for CEBAF", these proceedings.

[9] B. Bowling et al., "Orbit Correction Implementation at CEBAF", these proceedings.

Linac Upgrade Plan for the KEK B-Factory

Atsushi Enomoto, Shozo Anami, Takuya Kamitani, Hirofumi Hanaki, Tetsuo Shidara, and Isamu Sato
National Laboratory for High Energy Physics (KEK)
1-1 Oho, Tsukuba-shi, Ibaraki-ken, 305, Japan

Abstract

In the KEK B-Factory plan, e^+/e^- collider rings with 3.5-GeV positrons and 8-GeV electrons are being considered, and full-energy injection from the existing linac is required. The acceleration energy of the linac must be upgraded from 2.5 to 8 GeV. The most effective way has been searched from several points of view, such as the beam quality, ease of beam handling, and construction. This article describes the basic plan of the energy upgrade and recent progress regarding this project.

I. INTRODUCTION

The KEK 2.5-GeV linac [1] was completed in early 1982 in order to inject electron beams for the Photon Factory (PF) storage ring. Three years later (1985), a 250-MeV positron generator [2] was constructed for TRISTAN, and then combined at the 250-MeV point of the linac (Fig.1). In 1986, routine-injection into TRISTAN was started with 2.5-GeV, 2-ns, 25-pps electron /positron (e^-/e^+) beams. In 1988, the storage beam in the PF ring was changed from electrons to positrons in order to realize more stable operation. Table 1 summarizes the major specifications.

A linac upgrade plan has been considered for the last two years concerning the KEK B-factory project. The ideas have been classified into two parts. One involves combining a moderate linac upgrade (roughly 4 GeV), which is essential for a positron increase, as well as a change in the TRISTAN accumulation ring (AR) to a rapid-cycle synchrotron. The other involves an 8-GeV upgrade of the linac for full-energy injection into the collider ring. Though the latter plan is harder regarding the linac, it came to be considered desirable from the viewpoint of efficient utilization of the existing facility; e.g., high-energy synchrotron-radiation experiments will still be conducted in the AR.

II. BEAM REQUIREMENTS FOR THE LINAC

The KEK B-factory will be normally operated at 8 GeV (e^-) x 3.5 GeV (e^+); however, a maximum energy slightly higher than 8 GeV will be required for experiments involving higher states. Although the linac will deliver single-bunch beams at a repetition rate of 50 pps, the possibility of multi-bunch injection still remains. When the linac beam has 2×10^9 particles per bunch, injection can be completed within 30

Table 1
General parameters of the KEK 2.5-GeV injector linac

Main linac beam		
Energy (50 mA loaded)		
(Total rf power : 840 MW)	2.5 GeV	
Beam pulse length	1.5 ns ~ 2.0 μs	
Repetition rate (max)	25(50) pps	
Accelerator (main linac)		
Type of structure	TW. 5 type Semi-C.G.	
Frequency	2856 MHz	
Length of section	2 m (with couplers)	
Total number of sections	160	
Length of acceleration unit	9.6 m	
Number of acceleration units	40	
Number of sectors	5	
RF source		
Peak power of klystron	30 MW	
Number of klystrons	40+1 (main linac)*	
	6+1 (e^+ generator)*	
RF pulse length	3.5 μs	
Pre-injector		
Type of gun	Triode	
Gun voltage	200 kV (max.)	
Output energy	50 MeV (max.)	
Positron generator		
Primary electron, energy	250 MeV	
Charge (per pulse)	20 nC,	80 nC
Pulse width	2 ns,	40 ns
Positron linac, energy	250 MeV	
Charge at e^+ gen. end	160 pC,	960 pC
(at 2.5-GeV end	70 pC,	250 pC)

* 1 for pre-injectors

minutes for a storage beam of 2.6 A from vacancy (the ring circumstance is 3 km). The beam requirements for the linac are summarized in Table 2.

Of these requirements, both an energy upgrade and a positron intensity increase are the most important. After the energy upgrade is achieved, the positron production target will be moved from the present (250-MeV) position to the ~4-GeV point. Primary electrons, which have a higher beam-power by more than an order of magnitude will hit the target and produce sufficient positrons, taking account of the fact that the present linac produces more than 4×10^8 positrons per pulse (5-bunch, 2-ns pulse). However, we need to make
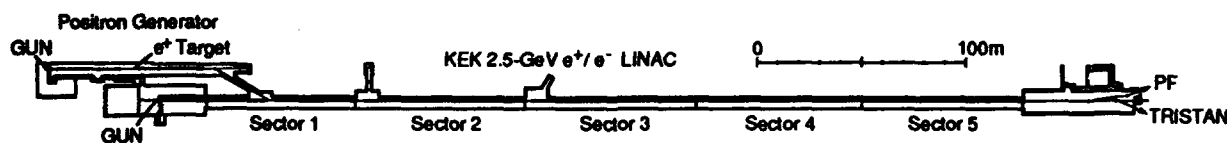
Figure 1.   The KEK 2.5-GeV injector linac.

	Present			8-GeV Upgrade	
	e^+(PF)	e^+(TR)	e^-(TR)	e^+(BF)	e^-(BF)
Energy (GeV)	2.5	2.5	2.5	3.5	8
Pulse width (ns)	40	2	2	Single bunch	
Particles/pulse	1.6×10^9	4.4×10^8	$>2.5 \times 10^9$	$\sim 4 \times 10^9$	
(Charge (pC))	(250)	(70)	(>400)	(~ 640)	
Repetition (pps)	25	25	25	50	
$\delta E/E$ (σ) (%)	0.35	0.22	0.20	0.25	
ε (m.rad)	1.0×10^{-6}		0.3×10^{-6}		

intense single-bunch beams, each of which will contain nearly 10^{11} electrons; we must be very careful regarding beam breakup (BBU) in accelerating such intense beams used to produce positrons. The phase-space specifications seem to be reasonable compared with the measured values for the present 2.5-GeV beams [3], [4].

III. ENERGY UPGRADE OF THE LINAC

Several ideas concerning the linac energy upgrade have been discussed, such as a beam-recirculating system, an accelerator structure with a resonant ring, and an rf pulse compression system. The important criteria for choosing one of these are as follows: stability under high-gradient operation of the existing accelerator; accelerated beam quality and beam handling; construction cost and schedule. In high-gradient tests, though they have been limited to the six existing accelerator sections, after rf processing they could be operated at average fields of 17 to 25 MeV/m without any serious trouble. The time-schedule is also an important subject, since the linac must continue injection for the PF storage ring.

From the viewpoints mentioned above, the best way to carry out the linac energy upgrade is to make the rf peak power fed into the accelerator sections as high as possible. However, if we want to realize an energy upgrade by only increasing the rf power, it must be nearly one order of magnitude. We conclude that a cost-effective way is to combine increasing the rf power with a short extension of the entire linac length.

Because of the building capacity and construction costs, the pulse energy of the pulse modulators will be increased by at most a factor of two; this will be achieved by increasing the PFN total capacitance while maintaining the same charging voltage. This is a reasonable way to use commercially available 50- to 60-MW klystrons with an rf pulse-multiplication system, such as a SLED (SLAC energy doubler) [5], [6]. Table 3 shows the modulator upgrade required for two examples of the pulse modes.

Table 4 gives examples of the energy gain by upgraded klystrons and the SLED system, when they are applied to the existing acceleration units, each of which comprises four 2m-sections. The average field gradient of the accelerator will reach 24 MeV/m due to the SLED system. The last column of Table 4 shows the net number of acceleration units to obtain a total energy of 8 GeV. This number does not include any margins necessary for practical operation, such as standby units for klystron faults and off-crest operation units for energy adjustments. The margins should be at least several

units; we are proposing a plan using 60 acceleration units. Fourteen units are the increments from the existing 46 acceleration units (see Table 1); these units can be installed by a small extension of the linac upstream building. We have started with the 4-μs mode , since we can use lower peak-power klystrons and the advantage of the 3-μs mode in the energy gain is not so large.

Table 3
An example of the pulse modulator upgrade. The pulse energy is increased by a factor of two.

	Present	SLED	
		4-μs mode	3-μs mode
Modulator			
Pulse: energy (J)	299	588	588
Width, FWHM. (μs)	3.5	5.5	4.5
Peak power (MW)	84	107	131
Peak voltage (kV)	22.5	22.5	22.5
PFN: number of caps.	20	40	40
Total capacitance (μF)	0.294	.588	.588
Charging voltage (kV)	45	45	45
Impedance (W)	6	4.7	3.9
Pulse transformer			
Step-up ratio	12	13.5	14.6
Voltage x width	0.95	1.7	1.5
Klystron			
Beam voltage (kV)	270	304	329
Beam current (kA)	295	352	397
Output power (MW)	36	46	56
Output average (MW)	26	41	51
Pulse flat-top (μs)	2.0	4.0	3.0

Table 4
Energy gain by upgraded klystrons with the SLED system, applied to the existing acceleration units.

	Present	SLED	
		4-μs mode	3-μs mode
Input RF pulse			
Flat-top (μs)	2.0	4.0	3.0
Ave. peak power (MW)	21	41	51
Power multiplication	1	4	3.5
Energy gain (MeV/m)	8.3	23	24
Total energy (GeV)	2.5	8	8
Net number of acc. units*	40	51	49

IV. PROGRESS

A. High-Gradient Acceleration

In order to realize the linac energy upgrade, the accelerator gain should be extensively increased. It should thus be first checked whether the accelerator works stably at this level of the accelerator field.

A high-gradient acceleration test was carried out at an acceleration unit of the linac by feeding the rf power from one 30-MW klystron into one 2-m accelerator guide; the power became four-times as much as that under normal operation. After rf-processing for several weeks, full power could be fed without any severe electric breakdown. The measured energy gain was roughly 20 MeV/m.

After the test described above, the 2-m section was moved to a new section with a traveling-wave resonant ring. Using the resonant ring the rf peak-power built up in the accelerator section was further increased by nearly a factor of two. This section was also stably operated after some rf processing; the measured gain was ~25 MeV/m.

B. RF System

A test upgrading of the klystrons from 30-MW to 60-MW class was carried out using a SLAC 5045 klystron during 1990-1991 at a test bench. An output power of 58 MW with a pulse width of 1μs was achieved at an applied beam voltage of 345 kV; the rf conversion efficiency was 44%.

The other task is to try to upgrade the presently used 30-MW klystron (MELCO-PV3030) by carrying out small modifications, which may provide the possibility of an efficient upgrade regarding cost. The first test was carried out by just increasing the beam voltage from 270 kV to 300 kV while limiting the pulse width and repetition rate from 3 μs, 50 pps to 1 μs, 10 pps, respectively. After adjusting the beam-focusing magnets, a maximum output of 47 MW was obtained. Recently, 51 MW was obtained at 3 μs, 50 pps by a new tube, the gun-insulator of which was improved [7].

In November, 1992, a SLED system was installed in the linac. This SLED is based on a system which was newly designed and tested by the Japan Linear Collider (JLC) group [8]; the design was slightly modified for our linac by changing the cavity coupling coefficient and adding RF monitors. Installing this system in an existing acceleration unit, an average energy gain of 19.4 MeV/m was measured at a klystron output of ~32 MW, 3.7 μs. By comparing energy gain between the tuned and detuned conditions of the SLED cavity, the energy-gain multiplication was measured to be 1.9. This result agreed with a prediction in our design work.

C. Others

Various works have been carried out regarding the B-Factory project, such as beam breakup of high-current beams [9], improvement of the 250-MeV positron generator [10] and the high-current pre-injector [11]. The development of beam monitors has been started recently; those are a wire-line type beam position monitor, a wire-scanner and a optical transition-radiation bunch monitor [12]. Investigations for the beam control and the triggering system for the B-Factory injector linac have also been started.

V. FUTURE

The feasibility study of high-gradient acceleration by the existing accelerator will further proceed with more units. In eight of forty units, the modulators and the klystron will be upgraded; in four of these, the SLED system will be installed by the end of March 1994. More studies regarding the B-Factory project, such as a single-bunch beam acceleration, will also be started this year.

VI. REFERENCES

[1] J. Tanaka et al., "OPERATION OF THE KEK 2.5 GeV ELECTRON LINAC", *The 1984 Linear Accelerator Conference*, Darmstadt, Germany, May 7-11, 1984.

[2] A. Enomoto et al., "FOCUSING SYSTEM OF THE KEK POSITRON GENERATOR", *Nucl. Instr. Meth. (NIM)*, A281, 1989, pp.1-9.

[3] T. Shidara et al., "Improvements to the Monitoring System of the KEK 2.5-GeV Linac and Its Performance Tests", *The XIV International Conference on High-Energy Accelerators*, Tsukuba, Japan, August 22-26, 1989, pp.-.

[4] S. Ohsawa and T. Mitsuhashi, "Present Status of Positron Beam Production and Injection into the PF Ring", *Journal of the Japanese Society for Synchrotron Radiation Research*, Vol.2, No.4, 1989, pp.23-31 (in Japanese).

[5] Z. D. Farkas et al., "SLED: A METHOD OF DOUBLING SLAC's ENERGY", *the IX International Conference on High-Energy Accelerators*, SLAC, CA, U.S.A., May 2-7, 1974, pp.1-9.

[6] A. Fiebig et al., "Design Considerations, Construction and performance of a SLED-type Radiofrequency Pulse Compressor Using Very High Q Cylindrical Cavities", *CERN/PS* 87-45 (RF) March 1987.

[7] S. Fukuda et al., "Upgrade of an RF Source of the KEK Linac for B-Factory Project", these proceedings.

[8] H. Matsumoto et al., "High Power Test of a SLED System with Dual Side-Wall Coupling Irises for Linear Colliders", Submitted to *Nucl. Instr. Meth.*

[9] Y. Ogawa et al., "Experimental Investigation of a Transverse Wake-Field Instability at the KEK Electron Linac", *The XIV International Conference on High-Energy Accelerators*, Hamburg, Germany, July 20-24, 1992.

[10] A. Enomoto et al., "Performance of the Upgraded Positron Generator at KEK", *The third European Particle Accelerator Conference*, Berlin, Germany, March 24-28, 1992, pp.524-526.

[11] S. Ohsawa et al., "New Pre-injector of the KEK 2.5-GeV Linac and its Performance", these proceedings.

[12] Y. Ogawa et al., "Beam Monitor Utilizing Transition Radiation", these proceedings.

Performance Characteristics of the Pulsed High Power Klystron Tube for PLS 2-GeV Linac*

M.H. Cho, S.H. Nam, J.S. Oh, S.S. Park, H.S. Lee, J.S. Bak, I.S. Ko, and W. Namkung
Pohang Accelerator Laboratory, POSTECH
P. O. Box 125, Pohang 790-600, Korea

Abstract

PLS 2-GeV Linac employs the E-3712 klystron tubes manufactured by the TOSHIBA as one of the pulsed high power microwave sources. The rated power of the tube is 80-MW at 4 μs pulse width with 60Hz pulse repetition rate. As a part of the main linac we have completed the installation of two units of the E-3712 klystron tubes and the matching 200-MW modulators together with the accompanying waveguide networks and the accelerating columns. Since all the components are exposed as a virgin to high power microwave, careful power conditioning procedures are underway. The rest of linac components installation is also underway. We present the performance characteristics of the E-3712 klystron tube measured with the water load. The result of the initial power conditioning operation for the waveguide network and the accelerating structures installed as a part of the PLS 2-GeV linac is also presented.

I. INTRODUCTION

The PLS 2-GeV electron linac design [1] employs SLAC type S-band accelerating structures tuned at the frequency of 2856MHz, and the microwave output power requirement is more than 60 MW with the pulse width of minimum 4 μs. Following this design requirement the allowed high power klystron tubes available in the world are the SLAC-5045 and E-3712 klystron tubes manufactured by the Stanford Linear Accelerator Center in U.S. and the Toshiba company in Japan, respectively.

The type of the S-band pulsed klystron tubes under operation for the several large linear accelerators currently in operation or under construction world wide are shown in Table 1.

Table 1. Type of the pulsed high power S-band klystron tubes used in the large electron linacs.

e⁻-Linac	Energy	Klystron type	Power	No.
SLAC/USA	56	SLAC-5045	65 MW	247*
PF-KEK/Japan	3.0	Mitsubishi PV3030	30	40
ATF-KEK/Japan	1.54	Toshiba E-3712	85	9*
BEPC/China	1.4	HK-1	22	16*
ORSEY/France	1.85	----	24	15
ELETTRA/Italy	1.5	Thomson TH-2132	45	8*
PLS/Korea	2.0	Toshiba E-3712	80	10*
	(GeV)	& SLAC-5045	65	1

* System design includes energy compressors.
(Note: Data based on the private communication and the "Catalogue of High Energy Accelerators" by HEACC '89, Tsukuba, Japan. This table is not the complete list of the large linacs.)

This paper presents the performance characteristics of the E-3712 klystron tube and the result of the initial power conditioning operation for the waveguide network and the accelerating structures installed as a part of the PLS 2-GeV Linac.

II. CHARACTERISTICS OF THE E-3712

The dimensional outline drawing of E-3712 klystron tube is shown in Fig. 1, and the operational parameters are listed in Table 2. The electron gun is made out of the dispenser cathode (9cm dia.) and the gun ceramic is tapered to have larger diameter at the anode side. The tube has five integral cavities, and the output cavity has two output waveguide coupling irises facing 180 degree apart each other, which allow more symmetrical distribution of the power flow to the output waveguides. The output waveguides are bent by E-band (go upward) and followed by H-corner (directing forward). Two output ceramic windows are placed such that the dominant electric field is in horizontal direction. The two output waveguides are combined to have a single waveguide by a power combiner. The single ceramic window is designed to withstand approximately 50MW at 4 μs pulse width, and has approximately 40A thick TiN coating to suppress multifactoring. The weight of the tube including solenoid is approximately 1,000kg (tube only: 300kg).

Table-2. E-3712 Klystron tube parameters

Description	Parameter	Description	Parameter
Frequency	2,856 MHz	Peak RF power	84 MW*
Pulse width	4 μsec	Avg. power	18 kW
Rep. Rate	60 Hz max.	Drive Power	500 W max.
Beam Voltage	400 kV	Gain	53 dB max.
Beam Current	500 A	Efficiency	42 %
μ-perveance	2.0	Focusing	electromag.

*100MW at short pulse (1 μs) operation.

III. 200MW MODULATOR FOR E-3712

Main design specification of the power modulator is listed in Table 3. The detailed design features are described in elsewhere [2,3]. Among those design parameters there are several key features that should be noted. To keep the maximum high voltage of the primary side below 50 kV, 1 to 17 turn ratio is chosen for the pulse transformer. The three phase primary voltage control (from 0 to 440 V, 120 kVA max.) is designed to use SCR phase control circuit with the active feedback control using the signal from the DC high voltage output. This SCR circuit replaces the bulky IVR or VVT that commonly used in most of the high power modulators in existing electron linacs.

The active feedback mechanism is providing less than ±0.5% fluctuation in the PFN charging voltage without too much diffi-

culty in the presence of the somewhat high noise level coming from the firing of the thyratron tube. Typically PFN charging voltage stability is achieved using the De-Q'ing method, inspite of energy loss, in many accelerator applications.

Fig.1 E-3712 Klystron tube dimensional outline

Table 3. Design specifications and the operational parameters of the 200MW modulator

Peak power	80 MW	Peak beam voltage	400 kV
Avg. power	85 kW	Peak beam cur.	500 A
Pulse width(flat)	4.3 μs	Pulse rise time	<1.0 μs
ESW	~7 μs	Pulse fall time	<2.0 μs
PFN impedance	2.6 Ω	Pulse flatness	±0.5 %
Pulse trans turn R	1 : 17	Primary AC-	SCR phase
Thyratron tube	ITT F-303	voltage control	(feedback)

IV. PROTECTION INTERLOCKS

The power modulator has number of interlocks to protect the klystron tube, modulator circuit, waveguides, and accelerating structures. The summarized list is shown in Table 4. Among those list many of the interlocks are intended for the protection of the maintenance crew of the modulator. During the system operation the most frequently activated interlocks are vacuum and VSWR. Table 5 is the summary of the vacuum and VSWR interlock action set levels and protection methods. The vacuum pressure set values are intended to protect severe multifactoring on the microwave ceramic windows.

It is observed that the general vacuum outgasing during the power conditioning operation tends to be very short bursting type, so it is very important to have very fast interlock action

time (action before next trigger pulse) to prevent multiple exposure of microwave pulses.

Table 4. Interlock list for the protection of the klystron tube and the modulator (interlock indicator template).

We used internal interlock relays of TPG-300 (Balzers) cold cathode gauge, and the measured action time was approximately 60msec. We are testing an electronic type relay for making action time approximately 10msec not to make double firing during the 60Hz operation.

Table-5. Vacuum and VSWR interlock conditions

Vacuum	Actions
$P \geq 1.0 \times 10^{-7}$ torr	Trigger hold off
$P < 5.0 \times 10^{-8}$	Automatic recovery
$P \leq 5.0 \times 10^{-7}$	Trigger off & high voltage off locked (manual reset required)*
VSWR	Actions
VSWR > 1.5	Trigger hold off
1st/2nd/3rd/4th Fault	1/2/4/8 sec trigger hold (auto reset)
Accumulated 8 faults	Trigger hold off locked (manual reset required)

* When high voltage shut down occurs soft restart computer controls the ramping rate of H.V. rise depending on the vacuum pressure (P is the vacuum pressure near the klystron windows).

V. KLYSTRON PERFORMANCE

The initial tube performance was measured using the microwave absorbing water-load. The water-load provides accurate rf output power by means of the calorimetric measurement. The magnitude and wave forms of the drive power, the forward, and reflected power are measured by the crystal detectors. Fig. 2 shows the rf output power characteristics measured by varying the beam voltage with the pulse width of 4 μsec. Fig. 3 shows the power transfer characteristics for the drive input power level. The output power saturation starts at about 300 W. Tube to tube variation of the beam voltage for the 80MW output power operation ranges from about 390 kV to about 405 kV.

For the beam voltage ripple less than ±0.5%, which is the performance requirement of the modulator, it is expected from the Fig. 3 that the output power fluctuation is approximately ±1.5% (equivalent to about ±1.2MW) of the 80MW. The phase

variation due to the beam voltage variation is also measured using the double balance mixer, and the result shows approximately 1 degree/kV, which makes approximately ±2° fluctuation when the PFN is tuned at the best performance level. Typical wave forms of the beam voltage, drive power, and output rf power are shown in Fig. 4.
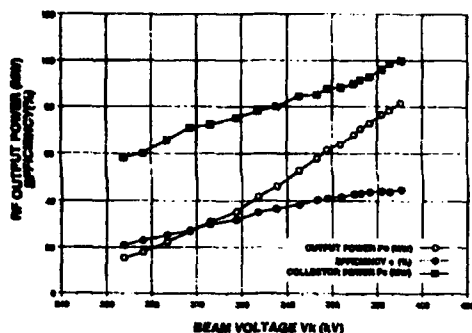
Fig. 2. Microwave output power characteristics of the E-3712 klystron (serial number of PLS-002).
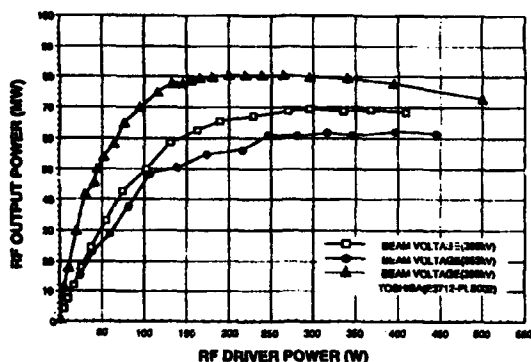
Fig 3. Microwave power transfer characteristics of the E-3712

Beam Voltage and Output Power
(X-axis:1µs/div. Vk=3f2 V,Po= 82 MW)

Drive Power and Output Power
(X-axis:1µs/div. Pd=26í W,Po= 82 MW)
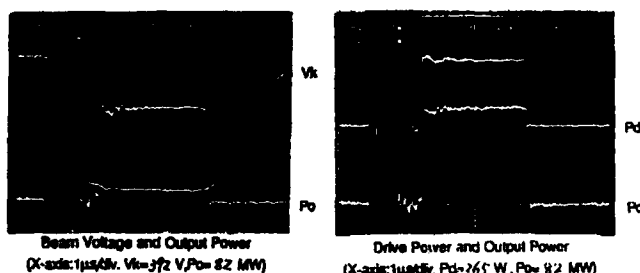
Fig 4. Wave form of the pulses; the klystron beam voltage (Vk), drive power(Pd), and the output power(Po).

The vacuum behavior during the initial power conditioning operation (no electron beam and no SLED operation, i.e. detuned mode) for the one module of accelerating structures is shown in Fig. 5 (data taken near the input coupler of the 3rd accelerating structures). Total waveguide length for the one module is approximately 16m, and there are 4 sections of 3.07 m long accelerating structures. The schematic structure and vacuum system for one module are illustrated in Fig. 6. Typical residual gases measured near the accelerating structure were hydrogen, nitrogen, and molecules of water vapors.
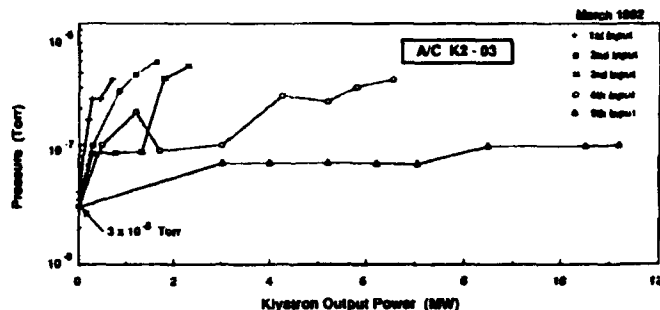
Fig. 5. Vacuum history of the accelerating structures during the power conditioning operation.

It was observed that the large amount of gas released by a burst tends to move upward near the microwave window before they are pumped away by the nearby ion pumps. The migration of burst gas seems responsible for making consecutive vacuum outgasing caused by the multifactoring near the high gas pressure region. Other interesting phenomena observed during the conditioning operation was that one can make audible sound detection (using such as sound noise detector or stethoscope) for the region of frequent multifactoring, especially inside the waveguide.

Due to the installation schedule conflict with the other utility the conditioning operation was performed up to near 50 MW. Overall observation gave series of lessons, especially the importance of vacuum measurement together with the VSWR and the reflected microwave power. It contains many informations about what is happening during the pulsed high power microwave is passing through the long waveguide networks including many vacuum flanges, and acce ting structures.
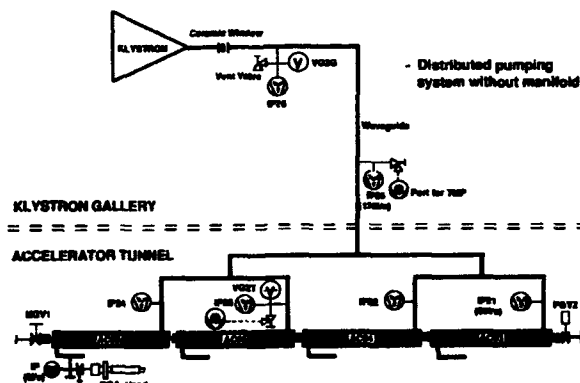
Fig. 6. Schematic diagram of the vacuum system and overall structure for the one linac module powered by a klystron.

VI. REFERENCES

[1]. W. Namkung et al., "Status of PLS 2-GeV Linear Accelerator," *Proc. of the Third European Particle Accelerator Conference*, Vol.1, pp. 501-503 (1992).

[2]. M.H. Cho, S.H. Nam, J.S. Oh, and W. Namkung, "Design of 200MW Pulse Modulator for PLS 2-GeV Electron Linac," *ibid.*, Vol.2, pp. 1591-1593 (1992).

[3]. S.H. Nam et al., "High Power Pulse Modulator for PLS Linac," these proceedings.

Electron Transport of a Linac Coherent Light Source (LCLS) Using the SLAC Linac*

K. L. BANE, T. O. RAUBENHEIMER, J. T. SEEMAN

Stanford Linear Accelerator Center, Stanford University, Stanford, CA 94309

Introduction

A linac configuration providing a low emittance high peak current electron beam is under study for a potential Linac Coherent Light Source (LCLS) based on the SLAC accelerator [1]. The parameters of the final electron bunch are nearing the technological limits of present accelerators in both transverse and longitudinal phase space. In this note we describe a layout of the RF gun, linac, and bunch compressors to deliver the required bunch properties.

We consider a bunch that is generated by an rf gun and accelerated to 7 GeV in 900 m of SLAC linac structure before it enters the wiggler. We assume that the rf gun generates a gaussian beam with an energy of 10 MeV, a population $N = 6 \times 10^9 e^-$, an rms length $\sigma_z = 0.5$ mm, an rms energy spread $\sigma_\delta = 0.2\%$, and normalized rms emittances $\gamma\epsilon_{x,y} = 3$ mm-mrad. At the end of the linac, we require that the peak current $\hat{I} \gtrsim 2.5$ kA and the peak-to-peak energy spread $\Delta\delta \lesssim 0.2\%$.

To obtain the required high peak current, we need to compress the bunch length by a factor greater than 10. In deciding at what position in the linac to compress we need to consider three issues: (i) the longitudinal wakefield in the linac, this increases the beam's energy spread and is harder to compensate with short bunches, (ii) the transverse wakefield and rf deflections in the linac, these increase the transverse emittance of the beam and are more severe for long bunches, and (iii) the effects of phase and current jitter which will change the bunch length and therefore the peak current of the beam.

In the next sections, we will describe how we compress the bunch to meet these three criteria. Then, we will briefly describe the bunch compressor optics and finally we will mention some details specific to the SLAC site.

Longitudinal and Transverse Wakefields

Previously, we have studied the longitudinal and transverse wakefield effects in the linac [2]; the results are summarized in Fig. 1. Here, we have plotted the peak-to-peak energy spread in the beam and the transverse emittance dilution versus the bunch length after acceleration from 100 MeV to 7 GeV in the linac. The transverse points are calculated from the average of 10 random distributions of alignment errors with rms's typical of the SLAC linac. Finally, no emittance correction trajectory bumps have been utilized [3]; although the use of trajectory bumps could reduce the emittance dilution, we have chosen not to include them to select more conservative parameters.
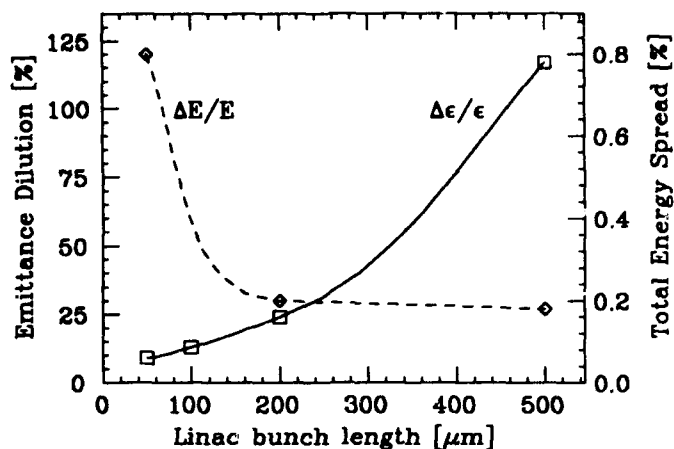
Fig. 1 Transverse emittance dilution (solid) and peak-to-peak energy spread (dashed) as a function of the linac bunch length. The emittance dilution is in units of the initial emittance $\gamma\epsilon_{x,y} = 3$ mm-mrad and the energy spread is in percent with a scale on the right. The plotting symbols are the values calculated.

As Fig. 1 shows, the transverse emittance dilution forces us to consider partially compressing the bunch before the main acceleration but the energy spread induced by the longitudinal wakefield prevents us from fully compressing right at the beginning. Thus, in Ref. 2 we concluded that we should compress to $\sigma_z \approx 200\,\mu$m at roughly 100 MeV and then fully compress at the end of the acceleration to achieve the necessary peak current.

Jitter

Previous work, described in Ref. 2 ignored the sensitivity of the peak current to phase and intensity jitter. The phase jitter arises from timing errors between the laser for the RF gun and the RF generated by the klystrons; the intensity jitter arises from the intensity jitter of the laser. Both of these effects will change the correlation between the energy deviation (δ) and longitudinal position (z) along the bunch $\langle\delta z\rangle$. In the case of phase jitter, the $\langle\delta z\rangle$ correlation varies because of the non-linearity of the RF while with intensity jitter the variation occurs because a more intense bunch generates larger wakefields.

A simple single stage bunch compressor consists of an acceleration section, where an energy-longitudinal position correlation is introduced, followed by a dispersive region where the path length depends linearly upon the energy deviation, i.e. the R_{56} transfer matrix element is non-zero; this rotates the bunch in longitudinal phase space. But, when the $\langle\delta z\rangle$ correlation is changed, the degree of rotation changes and thus phase and intensity jitter causes the compressed bunch length and peak current to change.
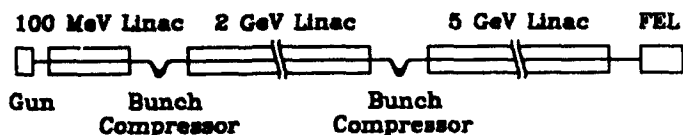
Fig. 2 Schematic illustration of beam transport.

Fig. 3. Phase space after the 2nd compression. The bunch head points to negative values of z.

In the LCLS, the longitudinal emittance from the RF gun is extremely small and thus we cannot operate with a fully compressed bunch; we must either under-compress or over-compress. Therefore, the longitudinal phase space is either rotated less than 90° or it is rotated more than 90°. In this case, changes of the $\langle \delta z \rangle$ correlation cause a linear variation of the bunch length. For example, if we are under-compressing and the $\langle \delta z \rangle$ correlation decreases, the bunch length will increase. In contrast, if the correlation increases, the bunch length decreases. The opposite is true if we over-compress the bunch.

With phase jitter the bunch length change can be simply estimated. When the longitudinal emittance is extremely small, we can neglect the uncorrelated energy spread and calculate the bunch length after a single compression:

$$\sigma_z(\Delta\phi) = \sigma_{z0}\left|1 - R_{56}k_{RF}\frac{\sin(\phi+\Delta\phi)}{\cos\phi}\right| \quad , \qquad (1)$$

where $\Delta E = V_{RF}\cos\phi \gg E_0$, σ_{z0} is the initial bunch length, ϕ is the nominal RF phase and $\Delta\phi$ is the phase jitter. Now, the change in the bunch length is:

$$\frac{1}{\sigma_z^\star}\frac{d\sigma_z}{d\Delta\phi} = \frac{\sigma_{z0}^\star}{\sigma_z^\star}\left[\left(\frac{\sigma_z^\star}{\sigma_{z0}^\star}\pm 1\right)\cot\phi\right] \quad , \qquad (2)$$

where the $\star$ denotes the design values and the negative sign corresponds to under-compressing while the positive sign is for over-compressing. Notice that the sensitivity depends upon the compression factor σ_z/σ_{z0} and upon the RF phase, although the RF phase is also determined by the required energy gain and the correlated energy spread.

At this point, we can perform a similar calculation to include the effect of a second compression. In this case, we find two terms in the expression that can be chosen to cancel. Assuming that the bunch is forward of the RF crest so that the bunch head has a higher energy than the tail, the two terms can cancel provided that the second compression is an over-compression; this can be understood from the simple arguments given above and noting that the phase jitter is under- or over-compressed along with the bunch length. If the bunch is behind the RF crest, then the second compression must be an under-compression for the two terms to cancel. Finally, similar calculations can be made for the intensity changes, but the results are poorer because the effects are more non-linear. -

Thus, to satisfy all three conditions: preservation of the transverse emittance, reduction of the longitudinal energy spread, and reduction of the jitter sensitivity, we propose compressing in two stages. We would under- or over-compress once near the beginning of the linac and then over-compress in the middle of the acceleration; this achieves the desired high peak current while causing the jitter effects of the two compressors to cancel. The scheme is illustrated schematically in Fig. 2.
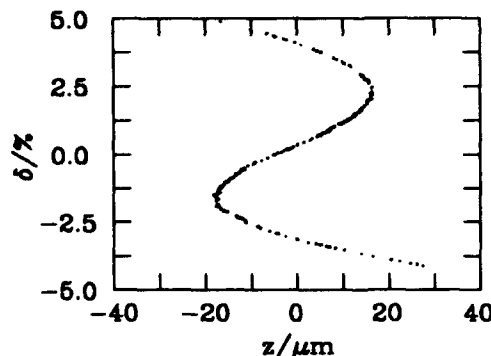
Longitudinal Phase Space Simulations

As described, without wakefields a solution that has very relaxed jitter tolerances can be found analytically. The wakefields, however, make the problem more complicated. So we have developed a computer program to study the development of longitudinal phase space, one that considers the effects of both the longitudinal wakefields in the SLAC linac [4] and the curvature of the rf wave, and that does compression to first order. A parameter search was done to find good a solution. One example solution is sketched in Fig. 2. We first run the beam at 18° with respect to the rf crest to 112 MeV, where with an $R_{56} = 2.3$ cm we compress to an rms length of 0.25 mm. (Our convention is that a negative phase is toward the front of the bunch. Therefore a positive R_{56} will move a high energy particle more toward the back of the bunch.) Next we run the beam at 54° up to 2.0 GeV, where with an $R_{56} = 0.97$ cm, we over-compress to a double horned distribution with a full width of 35 μm (phase space is shown in Fig. 3). Then finally we accelerate at the top of the rf crest to 7.0 GeV. In the simulations, we have used an acceleration gradient of 14 MeV/m which is 25% less than that achieved in the SLAC linac. This will allow for flexibility in the operation of the LCLS.

The final beam phase space, the bunch shape, and the energy distribution are shown in Fig. 4. Note that between the horns of the bunch distribution the peak current is everywhere ≥ 5.0 kA and that the full-width of the energy distribution is 0.04%, both of which satisfy our requirements. Let us define the jitter tolerance as the amount of change in a parameter that changes the full-width of the bunch distribution by 10%. We find that in this example the tolerance to incoming current jitter is ±2.2% and to incoming phase jitter is ±0.45°. For comparison, when we consider a scheme that uses only one compression, at 100 MeV, to obtain the desired peak current we find an unacceptable energy distribution width of 1.4%, a current jitter tolerance of ±2%, and a phase jitter tolerance of ±0.15°. Alternately, if we consider a single compression at the end of the acceleration, we can achieve the desired energy bandwidth, but the phase jitter tolerance is reduced to 0.04° and the transverse emittance growth is too large.

The branches in phase space that point upward and downward in Fig. 4c will not contribute to lasing, and it might be desirable to remove them. This can be conve-
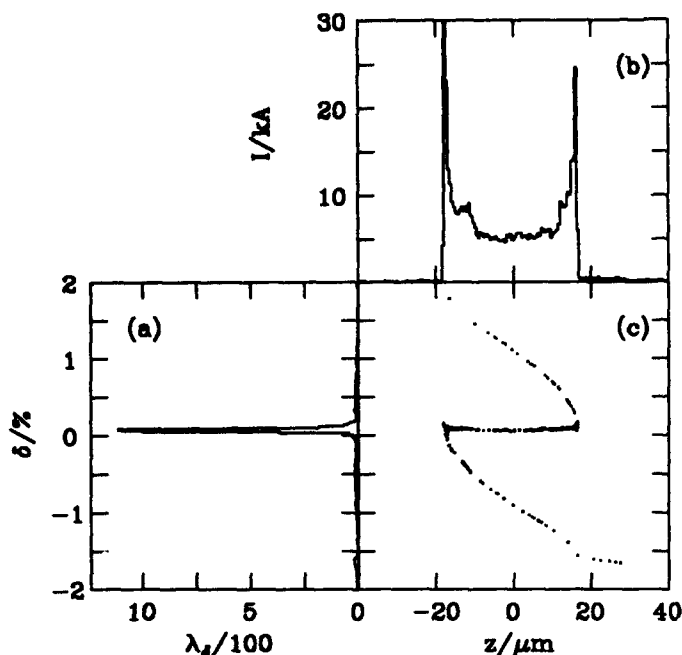
Fig. 4. The energy spectrum (a), the charge distribution (b), and the shape of phase space (c) at the end of the linac.
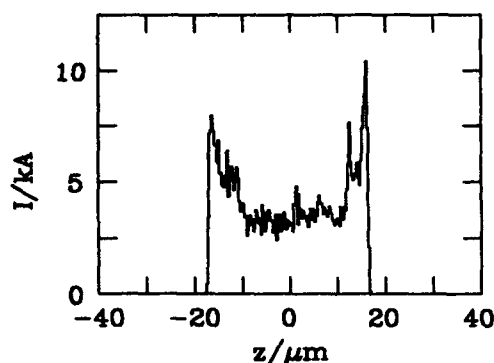
Fig. 5. The bunch shape for the example of Fig. 4 except that after the 2nd compression particles with energy deviations $\delta > 2.0\%$ and $\delta < -1.5\%$ are removed.

niently done immediately after the second compression by clipping in energy. By removing particles with relative energy variation $\delta > 2.0\%$ and $\delta < -1.5\%$, which will remove about half of the beam, we obtain the bunch distribution shown in Fig. 5. Now $I \geq 3.0$ kA between the horns.

One important comment about these results: The wakefields obtained from Ref. 4 were not intended to be used for bunches as short as 35 μm. We estimate that the wakefield effect after the second compressor may be underestimated by as much as 25%. If we artificially increase the wakefield by 25% in the last acceleration section we find that the final bandwidth becomes 0.2%, which can be reduced by changing the compressor parameters. Note that with the very short bunches that we have after the second compressor we can't compensate the correla   a energy spread by going off crest in the last acceleration region; instead, we compensate by adjusting the correlated energy

spread at the exit of the second compressor which is shown in Fig. 3. Finally, we intend to obtain a better wakefield for future work.

Solutions have also been found which do not have a double horned bunch distribution, but rather are more gaussian-like, though more highly peaked and with longer tails. Some of these solutions have much looser jitter tolerances than presented here, however they tend to have larger energy bandwidths than desired. Note that for the example presented here, after the second compression the bunch tail is at higher energy than the head, which will therefore tend to compensate the effect of the longitudinal wakefield in the final acceleration section.

Compressor Optics

The optics of the bunch compressors are quite straightforward. We have studied various optical solutions for the LCLS; a similar study is described in Ref. 5. The emittance dilution due to the bunch compressors should be small because the required R_{56}'s are small and the beam energy is high so that space charge is not significant.

SLAC Site Specifics

The upgrade of the SLAC linac to include an RF gun, preaccelerator, and two bunch compressors is straightforward. The bulk of the acceleration would be done in the main SLAC linac with existing equipment. The first and second compressors would be either magnetic s-bends or chicanes. The injection-extraction locations would be provided for by removing 12 m accelerating sections. The gun would likely be placed about 700 m from the end of the linac to provide sufficient acceleration downstream with (1) 8 GeV maximum beam energy, (2) 10% of the klystrons as spare or in maintenance, (3) sufficient energy feedback overhead, (4) bunch phase offsets up to 55 degrees, and (5) space for length compressors. Specific plans are under investigation. Finally, it should be noted that, operationally, single bunches of 3×10^{10} particles with vertical emittances of 3 mm-mrad have been stably transported in the SLAC linac [6].

References

[1] H. Winick, et. al., "A 2-4nm Linac Coherent Light Source (LCLS) Using the SLAC Linac," Presented to this conference, Washington, DC. (1993).

[2] C. Pellegrini, et. al., "A 2 to 4nm High Power FEL on the SLAC Linac," Presented at the 13th Int. FEL Conf., Kobe, Japan (1992).

[3] J. T. Seeman, F.-J. Decker, I. Hsu, "The Introduction of Trajectory Oscillations to Reduce Emittance Growth in the SLC Linac," Proc. of the 15th Int. Conf. on High Energy Acc., Hamburg, Germany (1992).

[4] K. Bane and P.B. Wilson, Proc. of the 11th Int. Conf. on High-Energy Acc., CERN (1980), p.592.

[5] J. T. Seeman and R. Holtzapple, "Short Bunch Length Test Area Using the SLAC Linac," Presented to this co ference, Washington, DC. (1993).

[6] C. Adolphsen, et. al., "Flat Beam Studies in the SLC Linac," Presented to the conference, Washington, DC. (1993).

PHASING SCHEMES FOR THE CEBAF CAVITIES*

S. N. Simrock, R. Kazimi, G. A. Krafft, L. Merminga, L. Ninan, S. Witherspoon
Continuous Electron Beam Accelerator Facility
12000 Jefferson Avenue, Newport News, VA 23606-1909 USA

Abstract

The CEBAF accelerator requires accurate phasing of the 338 superconducting cavities to achieve the design rms energy spread of $2.5 \cdot 10^{-5}$. The rms phase error along each linac, with 160 cavities over a length of 200 m, may not exceed 2.6°, assuming that the whole linac is operated on crest. The common procedure is to maximize the energy gain with a spectrometer. At CEBAF, however, phase-dependent cavity steering effects cause deflections of the beam of several mrad, requiring steering corrections in the linac, which makes this method very time consuming. Beam-induced transients can also be used in pulsed operation to determine the zero-energy-gain phase with high accuracy. Better than 2° accuracy is achieved when the signal-to-noise ratio is improved by signal averaging. These and other approaches for the phasing of cavities are compared and accuracy and feasibility are discussed.

I. PHASE STABILITY REQUIREMENTS

The overall specification for the CEBAF accelerator is given in Table 1.

Table 1: Accelerator Parameters

Energy	E = 0.5-4.0	GeV
Energy spread	$\sigma_E/E \leq 2.5 \cdot 10^{-5}$	at 1 GeV
Beam current	0 – 200	μA

The low energy spread of the beam requires strict amplitude and phase control of the RF field in the superconducting cavities according to table 2.

Table 2: RF amplitude and phase stability requirements with vernier system maintaining linac on crest

	uncorrelated	correlated
σ_A/A: gradient error	$2 \cdot 10^{-4}$	$1.1 \cdot 10^{-5}$
σ_f: fast phase error	0.25°	0.13°
σ_s: slow phase error	2.6°	-

The rms phase error along a linac with 160 cavities may not exceed 2.6°. A phase vernier system will maintain the overall phase of the linacs on crest while a gradient vernier [1] system will maintain constant energy at the end of the linac. With the overall phase of the linac being on crest, the individual cavities need to be phased better than ±5.2° to meet the specification in table 2. The goal is to initially phase cavities better than ±2°.

II. PHASING SCHEMES

During accelerator operation the phase of the accelerating field of individual cavities must be maintained better than ±5.2°. When the RF system is turned on for the first time, the actual accelerating phase is not known, since the electrical length of the probe cables may differ by more than ±180°. The electrical length can be measured with a TDR or network analyzer and be used to calculate the actual phase as described in Section VII. This method is not very accurate, since RF control module internal phase shifts and the geometry of the cavities to calculate the drifttime of the beam have to be taken into account. More accurate are measurements which use the beam as reference. The following phasing methods have been evaluated during north linac operation at typical energies between 100 MeV and 150 MeV with more than 100 superconducting cavities operational:

- Phasing of cavities by maximizing energy with a spectrometer as energy detector.
- Phasing of cavities by minimizing beam-induced transients during pulsed beam operation to determine the phase with zero energy gain.
- Phasing of cavities by measurement of the phase of the beam-induced field with a phase detector in the RF control module.
- Phasing by minimizing residual gradient fluctuations due to beam current modulation to determine the phase with zero energy gain.

In some cases the phase for maximum energy gain (crest phase) is determined directly; in other cases the phase for zero energy gain (zero crossing of the accelerating field) is determined and a 90° offset added or subtracted to set the crest phase.

III. PHASING WITH SPECTROMETER

Cavity phasing with the spectrometer makes use of the dependency between energy gain of the cavity and phase of the accelerating field. The energy gain is maximized using a spectrometer. This method can be automated and computer controlled.

Manual Phasing

For the initial cavity phasing a spectrometer at the end of the north linac was used. Changes in energy were observed on a view screen with a radius of 17.5 mm corresponding to an energy change of ≈1% at an energy of 100 MeV. In the spreader region at a location with a dispersion of 1.1 m, a position resolution of 0.1 mm corresponding to an energy

change of $1 \cdot 10^{-4}$ can be detected. At a field gradient of 5 MV/m the achieved phase resolution is

$$\phi = \cos^{-1}\left(1 - \frac{\Delta E}{E_0} \cdot \frac{E_0}{E_{acc}/2}\right) = 2.56°$$

for a spectrometer resolution of $(\Delta E / E) = 1 \cdot 10^{-4}$

with $E_0 = 100$ MeV and $E_{acc} = 5$ MeV/m.

Cavity steering effects are significant and require correction of the beam optics especially if cavities at the beginning of the linac are phased. Manual phasing with the spectrometer has been proven to be very time consuming but is required only once for initial phasing of the accelerator. Periodic phase corrections are performed using automated algorithms. It is expected that the resolution will increase significantly when a Beam Position Monitor (BPM) in the arc at a location with a higher dispersion of 10 m is used.

Automated Phasing

The above described method has been automated. The view screen for the beam position measurement is replaced by reading from a beam position monitor with a position resolution of 0.2 mm. It is also possible to use a harp reading. The BPM is located in the spreader section at a location with a dispersion of 1.1 m resulting in an energy resolution of $1 \cdot 10^{-4}$. The algorithm changes the phase in an individual cavity by $\Delta\phi = \pm 30°$, measures the initial beam position and the beam positions following the changes in phase, and calculates the crest phase from the three measured positions according to

$$\phi_{crest} = \tan^{-1}\left[\frac{x_1 - x_2}{x_1 + x_2 - 2x_3} \cdot \sin\left(\frac{\Delta\phi}{2}\right)\right] + \phi_0$$

ϕ_0 : initial phase setting

x_3 : beam position for $\phi = \phi_0$

x_2 : beam position for $\phi = \phi_0 - \Delta\phi$

x_3 : beam position for $\phi = \phi_0 + \Delta\phi$

$\Delta\phi$: change in phase setting

For a final energy of 100 MeV and a cavity gradient of 5 MV/m, a phase change of 30° results in a position change of 7.4 mm assuming a dispersion of 1.1 m.

The accuracy of this method is $\approx \pm 2.5°$ and takes 20 seconds per cavity. Most of the time is required for the averaging of the BPM signal to achieve a resolution of 0.1 mm. This takes about 4 seconds. The automated phasing is only successful if the phase is set within $\pm 90°$. Therefore initial manual phasing is required. The experimental verification of this algorithm showed that the linac energy was increased by 1.8 MeV at an initial energy of 119.6 MeV. Reproducibility has been verified by changing the initial phase by 5° and 10°, and the automated algorithm determined the same crest phase within $\pm 2.5°$.

IV. PHASING WITH BEAM-INDUCED TRANSIENTS

This method requires pulsed beam. Typical beam conditions are $I_0 = 200$ μA, $\tau_b = 20$ μs (pulse length), and $f_r = 60$ Hz. The average beam current is less than 1 μA and therefore does not require machine protection by the beam loss system. The expected transients for the gradient signal have been discussed in [2]. Unity gain of the control loop is typically ≈ 10 kHz and therefore the effect of the gradient control loop is small during such a short pulse. The control system regulates the average of the gradient.

The observed transient amplitudes for the above described beam conditions are 170 mV for $\approx 0°$ (on crest) and ± 1.5 mV for phase settings $\pm 5°$ from the zero crossing at $\pm 90°$. The result of a measurement is shown in Figure 1. The observed amplitudes are consistent with the calculations except close to zero crossing. The transients at zero crossing are a result of the beam loading in the buncher, which causes the phase of the electron beam to change by $\approx 2°$ during the macropulse of 20 μs. This is due to the fact that the buncher cavity is not operated at zero crossing and that the RF control system is not designed to correct for fast transients. The signals in Figure 1 are averaged over 64 samples to improve the signal-to-noise ratio. This method allows cavity phasing better than $\pm 2°$ if only the first 2 μs of the transients are observed to determine a change in sign for the transients.
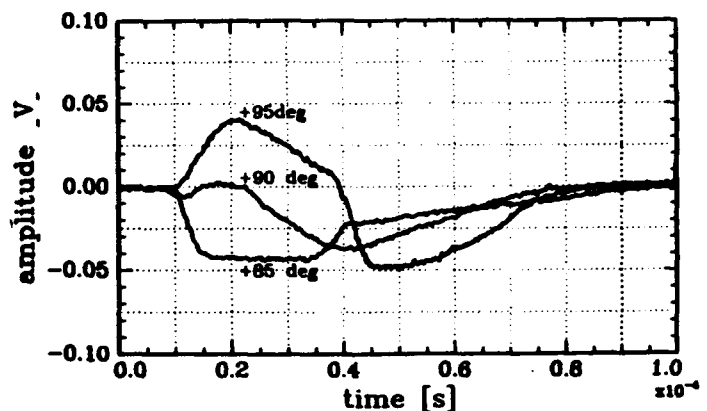
Figure 1. Measured beam-induced transients. Phase at zero crossing and $\pm 5°$. $I_0 = 250$ μA, $\tau_b = 20$ s, $f_r = 60$ Hz. Signal amplified by 30 dB.

It is possible to implement the transient phasing method in the embedded microprocessor code for the RF control module using the module internal digitizer. The gradient error signal is amplified by 50 dB and will be sufficiently large compared to 2.5 mV ADC resolution to determine the phase better than $\pm 5°$.

V. PHASING WITH BEAM MODULATION

This method is similar to the phasing with transients since it uses beam-induced gradient fluctuations to determine the phase at zero crossing. The beam current is modulated as

$$I = I_0 + \Delta I \cdot \sin(\omega_m t)$$

ΔI : amplitude of current modulation (typ. 1 μA)

ω_m : frequency of current modulation (typ. 100 Hz)

The beam-induced gradient will be 6.4 kV/m resulting in a detector error of 6.4 mV (5 V=5 MV/m) if the gradient loop is open. This translates into ~ 6 mV gradient modulator drive (at 100 Hz) if the gradient loop is closed. The spectrum of the gradient modulator drive is shown in Figure 2. The dominant microphonic noise component at 56 Hz has twice the amplitude, and the broadband noise within a bandwidth of 50 kHz as acquired by RF control module internal ADC is 20 mV$_p$. The signal is too small to be analyzed within the RF control module, but if processed in the machine control room using the analog monitor system [3], it is possible to phase cavities better than ±5°.
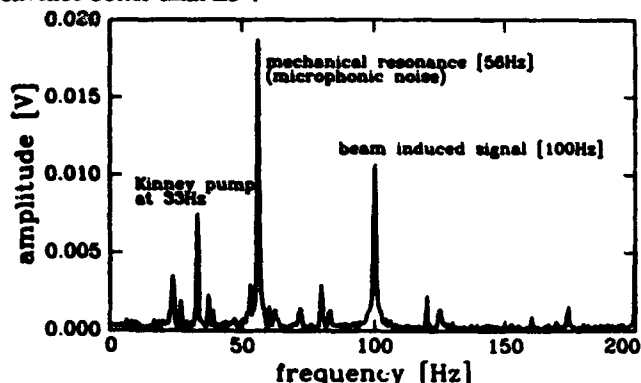
Figure 2. Spectrum of gradient modulator drive with modulated beam. $\Delta I = 1$ μA and $f_m = 100$ Hz.

VI. PHASING WITH BEAM-INDUCED GRADIENT

This method requires CW beam. At least 10 μA of beam current is required to excite a sufficiently large field gradient to measure a phase error relative to the phase reference derived from the master oscillator. The cavity is not powered by the klystron. The phase setpoint is adjusted to null the phase error signal. Typical sensitivity is 100 mV/degree at 5 MV/m or 1.27 mV/degree for 10 μA of beam current which excites a field of 63 kV/m. The slope of the zero crossing must be negative to guarantee that the phase of the beam is 0° and not 180° out of phase. The phase setpoint determined by this method is then used with gradient and phase loop closed to accelerate beam on crest.

The phase of the beam-induced voltage is offset by the detuning angle which is measured with an accuracy of ±5°. The precision of the detuning angle measurement limits therefore the accuracy of this otherwise very precise measurement.

VII. CALCULATED PHASE SETTINGS

The phase of the accelerating field relative to the beam can be calculated from known electrical length of cables, other control module components such as the down converter, and the time of flight of the electron beam converted to phase. All signals are referenced to a common master oscillator. Cable length of more than a kilometer over the whole accelerator site and effects from temperature changes do not allow for high accuracy. Nevertheless it is possible to calculate the phase difference between the cavities in one cryomodule within ±5°. The probe cable length and phase offsets in the control module can be measured better than ±2° as achieved in recent tests. Also errors in time of flight due to mechanical position of the cavity, which can change by up to ±0.5 cm as function of tuner position, contribute to the overall error.

VIII. CONCLUSION

Several methods for the adjustment of the phase of the accelerating field have been tested in the CEBAF accelerator during the commissioning phase of the north linac. Phasing with the spectrometer is time consuming especially for the initial phasing for the accelerator. Once the cavity phase is adjusted within ±40° an automated algorithm will correct for drifts. Only one cavity can be done at a time. Other methods allow for simultaneous phasing of several cavities and are therefore, since faster, more desirable during accelerator operation. The cavity phasing using beam modulation can possibly be used while beam is delivered to the experiments. A comparison of the different methods is given in Table 3. The most sensitive method is the phasing using beam-induced gradient in CW mode, but it relies on precise knowledge of the detuning angle.

Table 3: Comparison of the Phasing Methods

Method	Accuracy aver. (best)	Dedicated beam time	Multiple cavities simultaneously
Spectrometer	±3° (±2°)	No	No
Beam ind. trans.	±2° (±1°)	Yes	Yes
Beam modulation	±5° (±2°)	No	Yes
Beam ind. grad.	±5° (±3°)	Yes	Yes
Calculation	±5° (±2°)	No	Yes

IX. REFERENCES

1. G. Krafft, J. Bisognano, L. Merminga, S. Simrock, these proceedings.
2. G. A. Krafft, S. N. Simrock, and K. L. Mahoney, *Proceedings of the 1990 Linear Accelerator Conference*, p. 300.
3. K. Crawford, M. O'Sullivan, S. Simrock, these proceedings.

Initial data of Linac Preinjector for SPring-8

S.Suzuki, H.Yoshikawa, T.Hori, K.Yanagida, A.Mizuno, K.Tamezane, K.Mashiko and H.Yokomizo
JAERI-RIKEN SPring-8 Project Team
JAERI,Tokai-mura,Naka-gun,Ibaraki-ken,319-11,Japan

Abstract

The construction of the SPring-8 (Super Photon ring 8 GeV) linac was started in 1991 March. The preinjector of linac (2856 MHz, 60 pps) was already installed in Tokai Establishment of JAERI, and its commissioning is under way. We obtained the initial data of the electron gun, bunching section and several monitors. The electron beam is emitted by thermal cathode assembly, and extracted by 200 kV high voltage. Three types of grid pulsers were prepared to generate different pulse length, 1 nsec, 10~40 nsec and 1 μsec. On the 1 nsec mode, this gun generated 22 A peak currents. The electrons were transported to the prebuncher along the magnetic field, about 600 Gauss, by eight helmholtz coils. The bunching efficiency was obtained to be 64~65 %, and the energy spread was obtained ±2 % at the enertgy of 9 MeV after the buncher with 2 MW RF power.

I. INTRODUCTION

SPring-8 has constructed in Harima Science Garden City, 100 km west of Osaka, near Himeji. And it is composed by three accelerators, linac, synchrotron and storage ring. Electron or positron is accelerated up to 1.15 or 0.9 GeV by this linac, and injected into the synchrotron then, accelerated to 8 GeV.

SPring-8 linac will have 26 acceleration tubes, 3 m length, accelerated 16 MeV/m. The linac will operate five beam modes. It's shown in the Table 1. In the table 1, single pulse mode means the single bunch in synchrotron and storage ring. Positron will generate at an area, where electron energy is 250 MeV, having a movable target for electron / positron conversion. When they request the positron beam, we will insert the target into the beam line. We assume the conversion efficiency to be 0.1 %. So, before the target, it requests high currents (over 10 A) electron beam. The preinjector of the SPring-8 linac was installed in Tokai Establishment of JAERI, and its commissioning is under way.

Table 1. Linac control modes

	pulse width	electron	positron
Long pulse mode	1 μs	100 mA	X
Short pulse mode	10 - 40 ns	300 mA	10 mA
Single pulse mode	1 ns	300 mA	10 mA

II. GENERAL DESCRIPTION

A. Layout of Preinjector

The preinjector system is consists of electron gun, two prebunchers, one buncher that driven by one booster klystron (Mitsubishi Electric Co. model PV2012, 7 MW peak) and several beam monitors. The arrangement of linac preinjection system is shown in Figure 1.

A distance between electron gun and first prebuncher is far, about 900 mm. In this space, there are a gate valve and the monitors of the electron beam, like two types current transfers (CT) and a profile monitor.

The gaps between first prebuncher (PB1), second prebuncher (PB2) and buncher are 222 and 152 mm respectively. After buncher, one Q-triplet and several monitors like CTs, bending magnet and Faraday cup for energy measurement, slits and wire grid monitor for emittance measurements and beam windows and streak camera for bunch length measurements, are placed.

B. Electron Gun

The electron gun is the traditional thermonic gun with three grid pulsers. The electron beam is generated by a cathode assembly: model Y796 (EIMAC) with a cathode area of 2 is able to produce 10 A/mm^2 [1] pulsed beam currents at an extraction voltage of 200 kV. Three grid pulsers stay in high voltage station. And the generated pulses are transported through long coaxial tube, 1068 mm, with 12 ohm impedance. The grid pulser for long pulse is traditional transistor pulse
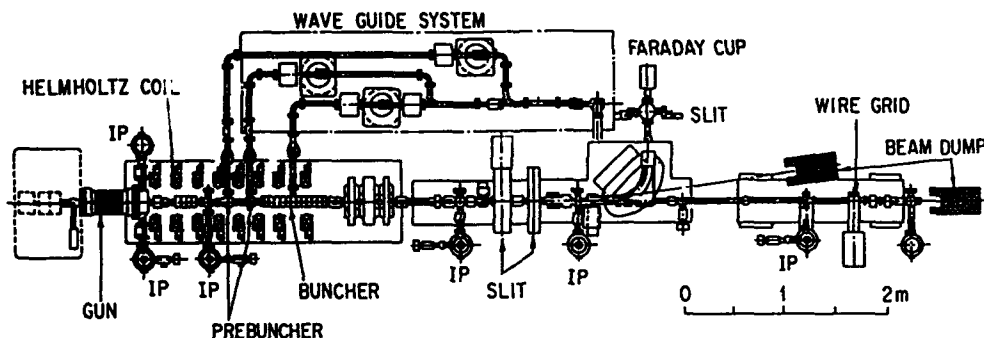
Figure 1   Arrangement of the Linac Preinjector

generator. The beam current is obtained to be 3 A of 1 μsec pulse beam, and its fluctuation is less than ±1.5 % within a flat-top of 3 μsec. The grid pulser for short pulse is Kentech nanosecond pulser. Generated short pulse is led to 12 ohm coaxial tube by four 50 ohm coaxial cables for impedance matching. The beam current is obtained to be 12 A of 40 nsec pulse beam The grid pulser for single pulse is Kentech model HMPS. Rise time of the generated pulse is 60 ps with output impedance of 50 ohm. Output impedance is converted to 12 ohm by impedance converter, and output pulse is formed to 1 ns pulse by clip line method with short stab, then output voltage becomes 200~320 V. The layout of 1 nsec pulse transport line is shown in Figure 2. The beam current is obtained to be 22 A peak of 1 nsec pulse beam. The emission characteristics versus gun high voltage, grid voltage at grid bias 60 V of single pulse beam are shown in Figure 3,4. The jitters of single pulses are less than 100 psec. Typical gun emissions of short and single pulse modes are shown in Figure 5. The current form of long pulse is measured by Peason current transformer. Short and single pulse beam are measured by wall currents monitor.

Figure 4. Emission current characteristics versus grid voltage

Short Pulse Mode 40 nsec

Single Pulse Mode 1 nsec

Figure 3. Emission current characteristics versus gun high voltage
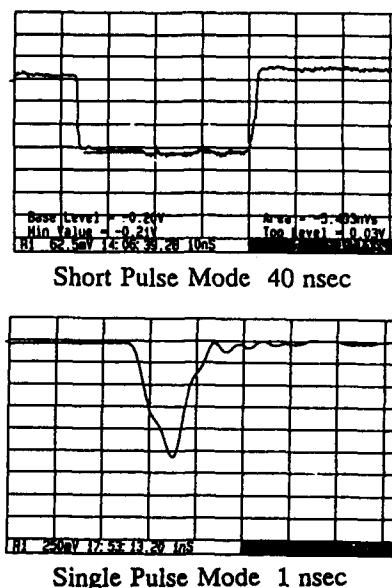
Figure 5. Typical gun emission of short and single pulse modes

C. RF system

The diagram of the RF system is shown in Figure 6. The master trigger synchronizes with AC power line, 50 Hz. When it injects the synchrotron, this trigger will get from the synchrotron control system.

RF master oscillator is the synthesizer, Hewlet-Packard model 8664A. Low power RF, about 1 dBm, from the master oscillator inputs to the 300 W TWT amplifier,

Figure 2 Layout of pulse transport line

LogiMetrics model A500/S. TWT amplifier output is led the klystron input.

A modulator of the booster klystron has a good stability of an output voltage, that is, the fluctuation is less than ±0.2 %. This is required to have a good stability because this is used for a microwave source for all high-power klystrons. The modulator has a 16-steps line type pulser. The FWHM of this modulator's output is 5 μsec, and the flat top is 2.4 μsec.

Wave guide line filled with SF6 gas is divided three lines by directional coupler for PB1, PB2 and buncher. The driven power of PB1, PB2 and buncher is 20 kW, 40 kW and 2 MW. For power and phase control, IφA is in a way.

When the injector system is moved to the SPring-8 site, 26 high power klystron's drive power is supplied with this wave guide line divided by directional coupler.
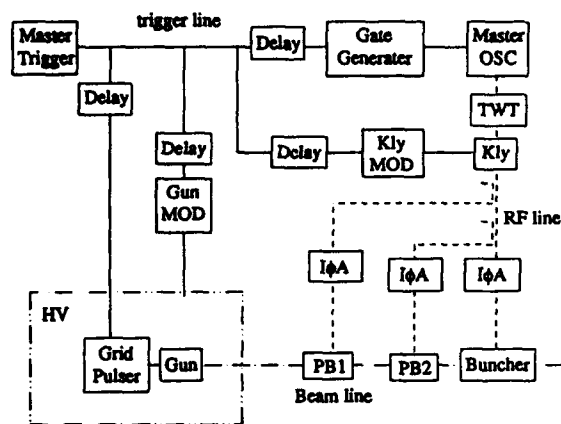
Figure 6. Diagram of RF system

D. Bunching Section

The gap voltage of the prebunchers is 20 kV and 30 kV, respectively, and the drift distance between two prebunchers is 222 mm. The velocity modulation by the prebunchers causes 68 % of the electrons to be bunched into 50 degrees in phase spread at the entrance of the buncher, which is located at the place of 152 mm away from the second prebuncher. The beam is finally bunched to 5 degrees in phase, and a beam energy is expected to be 9 MeV at the exit of the buncher. The energy spectrum of singlepulse beam mode is shown in Figure 7.
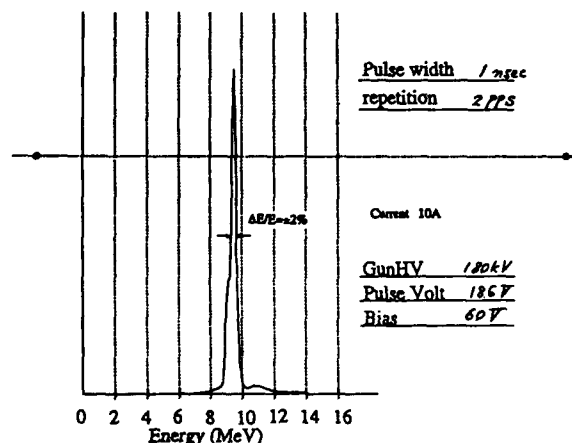
Figure 7. Energty spectrum of single pulse beam

E. Monitor

Several types of the beam monitors are prepared for a long pulse and a short pulse. The monitors are grouped into five types, which are for beam profile, currents, energy, emittance and bunch length. The profile monitors are the traditional fluorescent monitors, Demarquest AR995F, with CCD camera. It uses the operation of beam transport. The current of a long pulse is measured by Peason current transformers, and that of a short pulse is measured by wall current monitors and an amorphous-core type current transformer. The gun emission current tests about the wall current monitor show a good characteristic of the time response of less than 250 psec, that is good enough to observe a beam current of a single pulse. The cross section of the wall current monitor is shown in Figure 8. The set of a bending magnet of 90 degrees and a Faraday cup after a Q triplet measures the energy spectrum at a point after the buncher, with electron energy to be 9 MeV. Before the bending magnet of energy analyzer, there is another bending magnet of 8 degrees defraction. This beam line is used for the bunch length monitor using the streak camera by Cherenkov light radiation.
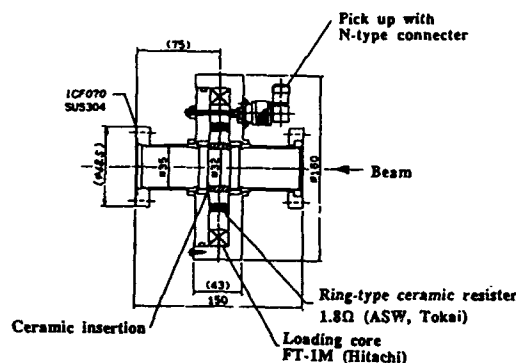
Figure 8. The cross section of wall current monitor.

III. CONCLUSION

The preinjector system of SPring-8 linac has been temporarily installed in Tokai Establishment, 700 km the East of Harima Garden City. We are testing the performance of the preinjector system, electric gun, bunching section, modulator and klystron system, monitors, control system and total beam characteristics. In result, the performance of preinjector system is enough to fill the request of the SPring-8.

Further experiments will be continue to examine the endurance for the long term of operation on SPring-8 injector, especially the life time of the gun cathode.

IV. Reference

[1] R. F. Koontz, "CID Thermonic Gun System", SLAC-PUB-2824, Oct. (1981)

Status of the Advanced Photon Source (APS) Linear Accelerator *

M. White, W. Berg, R. Fuja, A. Grelick, G. Mavrogenes, A. Nassiri, T. Russell, and W. Wesolowski
Advanced Photon Source
Argonne National Laboratory
Argonne, IL 60439

Abstract

A 2856-MHz S-band, 450-MeV electron/positron linear accelerator is the first part of the injector for the Advanced Photon Source (APS) 7-GeV storage ring. Construction of the APS linac is currently nearing completion, and commissioning will begin in July 1993. The linac and its current status are discussed in this paper.

I. INTRODUCTION

Electrons are accelerated to 200-MeV by the electron linac, and then impinge on a tungsten positron converter target. The resulting positrons are accelerated to 450 MeV in the positron linac and are accumulated in the positron accumulator ring prior to injection into the synchrotron. Positron energy is increased from 450 MeV to 7 GeV in the synchrotron before injection into the storage ring at final energy.

The injector portion of the electron linac consists of a thermionic gun, a single gap prebuncher, a constant impedance buncher with $v_p = 0.75c$, and a 3-meter-long constant gradient travelling wave accelerating structure. The prebuncher, buncher, and accelerating structure are powered by a single klystron. Rf power from a second klystron is transmitted to a SLED [1] cavity assembly. The SLED compresses the rf power in time, proportionally increasing the peak power. The shorter but higher peak power pulse is split four ways, powering the final four accelerating structures in the electron linac. A dipole magnet is installed at the end of the electron linac for energy optimization and analysis.

The 200-MeV beam from the electron linac is focussed down to a 3-mm spot by a set of triplet quadrupoles and it impinges on a 2 X_0 (7 mm) thick water-cooled tungsten target. A pulsed solenoidal coil just downstream of the target produces a 1.5 T field focussing the beam into the positron linac, where nine accelerating structures accelerate the positrons to 450 MeV. The first two accelerating structures are surrounded by solenoidal magnets for focussing and containment of the low energy beam, and the final seven have 24 FODO quadrupoles mounted around them. Steering magnets are positioned throughout the linac. The positron linac is powered by three klystrons and two SLEDs, as shown in Figure 2.

Lead and Heavimet shielding have been incorporated into the water-cooled target housing for protection of upstream and downstream equipment. Beam positioning on

the target is aided by beam diagnostic readouts and by minimizing collected charge on a foil iris located in front of the tungsten target.

The linac beamline is shown in Figure 1, and some parameters are listed in Table 1.

Table 1
Electron and Positron Linac Beam Parameters.

	e$^-$ Linac	e$^+$ Linac
Particle Type	e$^-$	e$^+$
Beam Energy	200 MeV	450 MeV
Pulse Rate	48 pps	48 pps
Pulse Length	30 nsec	30 nsec
Particles/Pulse	3.125 x 10^{11}	1.563 x 10^9
Beam Current	1.7 A	8 mA
Beam Power	480 W	5.4 W
Beam Emittance (mm-mrad)	≤ 1.2	6.6
($\Delta E/E$)	± 0.08	± 0.01
# of Acc. Str.	5	9

II. RF SYSTEM

A. High Power RF

Klystron amplifiers (Thomson TH 2128) are powered by line type pulsed modulators which provide 100 MW peak power to the klystrons. Regulation is done with a command charge tetrode system and operates at a repetition rate of up to 60 Hz. Thirty MW of rf power at 2856 MHz is fed into the accelerating structures which produces an electric field gradient of about 20 MV/m. The modulators are discussed in more detail in another paper presented at this conference [2].

B. Low Level RF

The 2856-MHz low level output of a highly stable master oscillator is amplified by a 10-W GaAs FET amplifier, and is then divided into two separately distributed signals. One of these signals is distributed to the five klystron drivers, and the other provides the reference to the VXI-based phase measurement system.

The klystron driver uses a preamplifier and a 400-W pulsed driver amplifier [3] which follows it. Both the

preamplifier and the pulsed driver amplifier are based on bipolar transistor technology.

III. BEAM DIAGNOSTICS

Twelve beam position monitors (BPMs) [4], three wall current monitors, and eight fluorescent screens [5], measure the beam position and current in the APS linac. The gun current and pulse width are measured by a toroidal current monitor located just downstream of the electron gun. Stripline BPMs, shown schematically in Figure 3, measure the beam's position and intensity both horizontally and vertically with sensitivities of 1.805 ± 0.15dB/mm. The beam's relative position, spot size, and shape are measured by fluorescent screens. The video image is frame grabbed, processed, and displayed. The resulting image is accurate to approximately 600μm. Prototypes of these devices were successfully used to analyze beam characteristics in a pretest of the linac injector [6]. BPMs, fluorescent screens, as well as average current monitors are installed throughout the linac.

IV. READOUT AND CONTROLS

The linac control system uses the Experimental Physics and Industrial Control System (EPICS) tools which are being developed by the Controls and Computing group at APS/ANL and by the AT8-GTA groups at LANL [7]. Eight microprocessor-based Input/Output Controllers (IOCs) provide real-time control, monitoring, and data acquisition services to the linac equipment. Two IOCs accommodate the beamline equipment, including vacuum, magnets, cooling water, etc. Each of the five rf stations has a dedicated IOC which acquires its rf and diagnostic measurements at a 60-Hz rate. An eighth IOC handles the image processing requirements for the fluorescent screen cameras. The IOCs are connected to a common ethernet by which they can communicate with each other and with the Unix-based Operator Interface workstations (OPIs). Several tools are available on the OPIs to support data archiving, alarm management, interactive equipment control, and backup/restore of machine settings, and are described in Reference [7].

Beam diagnostics readout and rf phase and amplitude measurements have been integrated, together with the dedicated microprocessor-based IOCs mentioned above, into a common VXI based system. LANL [8] VXI modules were upgraded for faster pulse response and are used with ANL's trigger timing module, constituting the central part of the system. Rf phase is measured using two VXI modules, a downconverter, and a vector detector, plus conversion software which computes phase from the detected I and Q vectors. Measurements repeatable to ±0.1 degree have been demonstrated after appropriate averaging.

V. CONCLUSION

Installation of the APS linac began in earnest in Octo-

ber of 1992. The electron linac installation has been completed, the beamline is under vacuum, most of the rf power system is in place, and control systems are operational. The positron linac installation will be complete by July of 1993 so that commissioning can begin. Relevant safety documentation and startup procedures are being prepared and reviewed now to ensure a timely startup.

VI. ACKNOWLEDGEMENTS

VII. REFERENCES

[1] Z.D. Farkas, H.A. Hogg, G.A. Loew, and P.B. Wilson "SLED: A Method of Doubling SLAC's Energy," SLAC-PUB-1453, June 1974.

[2] Thomas J. Russell, "Noise Reduction Techniques Used on the High Power Klystron Modulators at Argonne National Laboratory," these proceedings.

[3] 400 Watt solid state amplifier originally manufactured by SGS Thomson (now MPD).

[4] Raymond Fuja and Youngjoo Chung, "The APS Linac Beam Position Monitors and Electronics," *Acc. Instr. Wkshp. Proc.*, Berkeley, CA, Oct. 1992.

[5] W. Berg and K. Ko, "Fluorescent Screens and Image Processing for the APS Linac Test Stand," ibid.

[6] W. Berg, R. Fuja, A. Grelick, G. Mavrogenes, A. Nassiri, T. Russell, W. Wesolowski, and M. White, "Beam Measurements of the ANL-APS Linac Injector Test Stand," *Linac Conf.*, Ottawa, Can. Aug. 1992

[7] McDowell, William P. , "Status and Design of the Advanced Photon Source Control System," these proceedings.

[8] C. Ziomek, "Accelerator RF Instrumentation Implemented with the VXIbus," *Proc. ATE & Instr. Conf.* January, 1991.
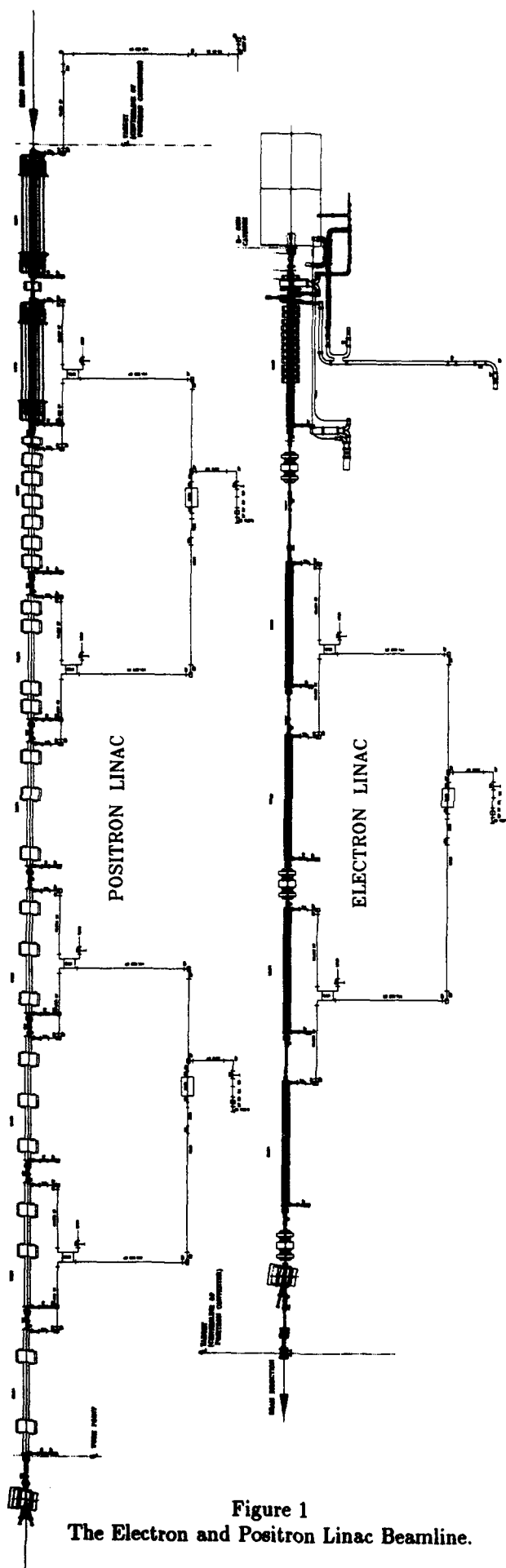
Figure 1
The Electron and Positron Linac Beamline.
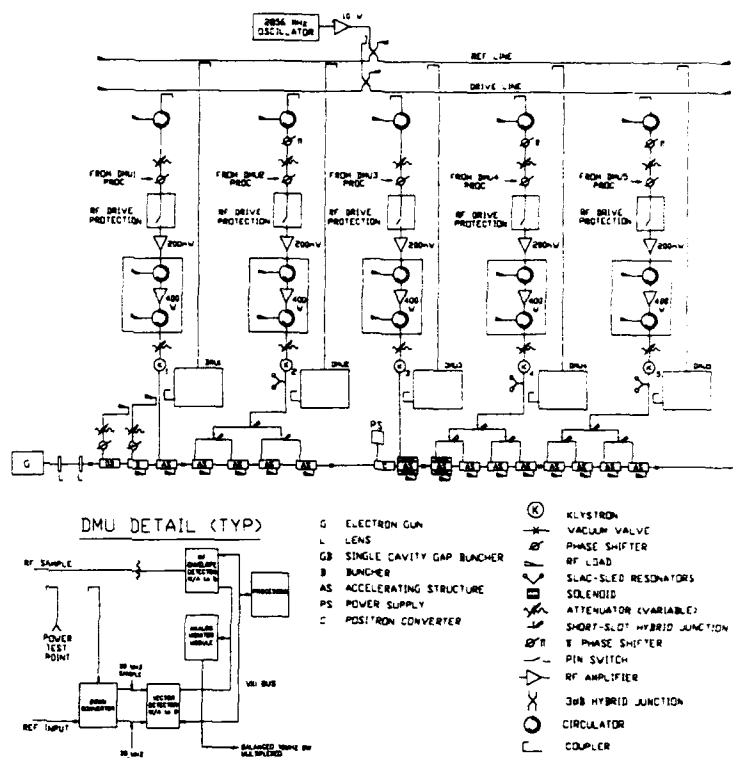
Figure 2
The Linac RF Circuit Diagram.
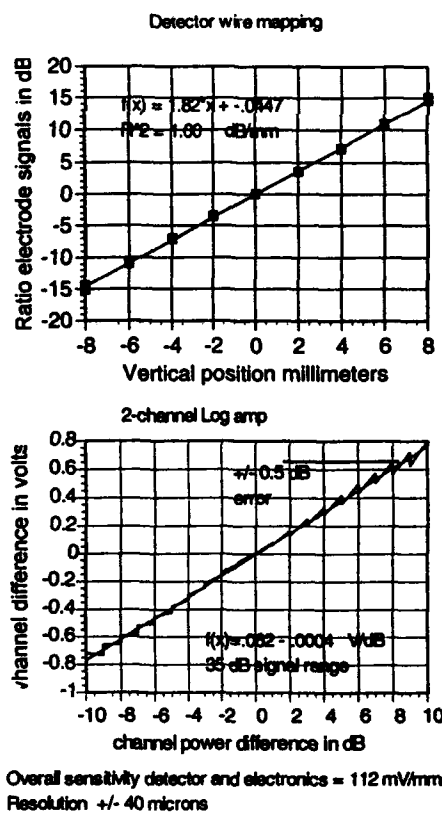
Figure 3
The Beam Position Monitors (BPMs) allow a simple,
accurate determination of the beam position.

200 MEV RF Linac for Brookhaven National Laboratory

K. Whitham, H. Anamkath, S. Lyons, J. Manca,
R. Miller, P. Treas, T. Zante
Titan Beta, 6780 Sierra Ct., Dublin, CA 94568

R. Miller
Stanford Linear Accelerator Center (SLAC)
2575 Sand Hill Rd., Stanford, CA 94025

R. Heese, J. Keane
Brookhaven National Laboratory, Building 355
50 Brookhaven Avenue, Upton, NY 11973

I. INTRODUCTION

A 200 MeV RF linac was designed and built for Brookhaven National Laboratory. Factory tests have now been completed and it is in final assembly for use at Brookhaven. Table 1 gives the overall requirements of the linac. The system consists of four 3 m sections of S-Band accelerator waveguide powered by three 45 MW Thomson klystrons. The injector is comprised of a triode gun, prebuncher, and a four cavity buncher. The system provides over 1 amp of beam at 1 ns to 10 ns at 10 pps.

Table 1: Brookhaven Linac Requirements

RF Frequency	2856 MHz
Beam Energy	Variable from 40 MeV - 200 MeV
Beam PW	1-10ns
PRF	1-10Hz
Energy Spread at 200 MeV	±1%
Peak Beam Current	1A @ 1-10ns
Beam Emmittance	<1E^{-6}mR, geometric
Synchronization, (RF Phase Locked)	35.25 MHz
Vacuum	10^{-8} Torr
RF PW	1.2μs Flat top
Modulator Pulse Flatness	±0.25%
Klystron Peak Power	45MW x 3 Tubes

II. GENERAL SYSTEM DESCRIPTION

A. Beamline

The conceptual design of the Brookhaven National Laboratory 200 MeV linac is patterned after the original SLAC injector, which ran for 20 years delivering beams from a few nanoamps to 2 amps. The BNL linac injector consists of the following components:

1. A 120 kV thermionic triode (with a mesh grid) gun with a 2 sq cm dispenser cathode capable of currents up to 10 amps.

2. A single resonant cavity prebuncher, which bunches about $^3/_4$ of the electrons into a 90° bunch in the 20 cm prebuncher drift.

3. A 10 cm long travelling wave buncher with phase velocity equal to 0.75c, which bunches the beam by about a factor of 3 to about 30° and accelerates the electrons up to about 320 kV.

4. A 3 meter long constant gradient, velocity of light accelerator section, which completes bunching the beam to about 5° FWHM and accelerates the beam to about 45 MeV. According to the program PARMELA, which was used to design the injector, 84% of the beam from the gun should be captured and accelerated, and 84% of the captured beam should be within a 1% full width spectrum. The RMS normalized emittance is calculated to be 30 pi mm-mr at the end of this section.

5. A magnetic focussing system consisting of one iron core magnetic thin lens which matches into a solenoid consisting of 10 large aperture coils placed within the Helmholtz spacing. The beam from the injector is focussed by quadrupole triplets placed between accelerator sections.

Figure 1 shows a portion of the beamline.

Figure 2

Figure 1

The E-gun pulser is required to generate a low jitter, fast risetime pulse to the gun cathode (grounded grid configuration). A fast avalanche transistor based pulser was developed at Titan Beta to meet these requirements. Amplitude control of the pulser is via a PIN diode attenuator stack that was developed for this purpose. The E-gun output has been shown to be at least 2 amps with rise and fall times of less than 800 picoseconds.

Control and trigger of the E-gun pulser is via fiber optic links providing pulse width, amplitude, and fault detection through serial communication. The E-Gun pulse width is remotely settable between 1 and 10 ns in 1 ns increments using an on-board digital pulse width generator.

The E-gun floating deck is connected to a 150 kV DC power supply which provides the acceleration potential for the injector.

B. Magnetics

The low energy transport magnetics consist of a bucking coil at the E-gun, focus coil between the E-gun and prebuncher, and ten air core focus coils over the first accelerating section. The field in this open solenoid structure is 1.2 K gauss. Beam focusing is accomplished by using quadrupole triplets between accelerating sections. Steering is provided by X-Y corrector sets at the beam input to each accelerating section. Figure 2 shows one of the quadrupoles on the beamline assembly.

C. Modulators and Klystrons

Each of the three 45 MW klystrons are driven by three identical modulators with 10 stage PFN's capable of delivering 100 MW peak power video pulses with 1.2 microsecond flattop at 10 pps. A high voltage, high frequency switching power supply is used to charge the PFN and to achieve pulse to pulse amplitude stability of ± 0.1%.

The Thomson TH 2128 klystrons operate at 45 MW to provide the 1.2 microsecond flattop. This allows for the accelerator guides to fill and provides adequate RF flattop for the guides to be used in the stored energy mode.

Evacuated rf waveguide is used throughout the system.

D. Control System

The control system is distributed into various subsystem chassis located in the main control rack. Each chassis has built-in fault detection circuitry to detect any fault condition and display all of the faults and indicate the first fault occurrence. In addition, all faults are summed in the master system controller for subsystem fault identification.

A bussed architecture is used to reduce the number of control cable wires. The fault detection system uses a multiplexed buss to the master system controller instead of individual wires for each fault (16 lines instead of >140 lines).

The entire system can be operated locally, or through CAMAC based computer control. Although Titan Beta was not contracted to provide the operational software, we operated the system at our facility with a 386SX based IBM clone computer running National

Instruments LABWINDOWS control software.

The linac system timing was established by various digital generators built into the system. A sophisticated phase-lock loop timing system was developed to allow linac injection to be synchronized with the synchrotron ring timing. This system allows injection into the ring at 60° increments of the synchrotron frequency with very low jitter.

E. Factory Tests

For factory test, the system was divided in two segments to fit the test cells and space in the Titan Beta facility. The first half was tested with beam from the E-gun through the injector and the first two accelerator sections. These two sections are driven by a single klystron. The RF system for the buncher includes a high power waveguide phase shifter and attenuator. The other two accelerator sections were operated with one klystron powering each to the full 45 MW output of the klystron. The accelerator sections held 45 MW with no problem after conditioning.

Gun tests were performed and the injector output was measured at 1.6 A max for 1 ns, 2 A for 1.25 ns, and 3.1 A max for 10 ns. Rise and fall times were 800 ps. Jitter was measured at less than 100 ps.

With accelerator structures 1 and 2, the energy was measured using beam deflection at 75 MEV and the emittance was measured at less than 150 pi mm mrad. Max current for 10 ns was measured at 1.61 A. A heat run was satisfactorily completed.

F. Conclusions

The performance of a 200 MeV accelerator designed and built at Titan Beta was satisfactory during factory tests. We achieved design parameters and stability required for successfully operation of the linac at BNL. The accelerator was delivered and is being assembled at Brookhaven.

References

1. K. Whitham et al., "200 MeV RF Linac for Synchrotron Injection", *AECL Research 1992 Linear Accelerator Conference Proceedings*, Vol. 2, pp. 615-617.

Design Of The e⁺/e⁻ Frascati Linear Accelerator For DAΦNE

K. Whitham, H. Anamkath, S. Lyons, J. Manca,
R. Miller, T. Zante, P. Treas, D. Nett
Titan Beta, 6780 Sierra Ct., Dublin, CA 94568

R. Miller
Stanford Linear Accelerator Center (SLAC)
2575 Sand Hill Road Stanford, CA 94025

R. Boni, H. Hsieh, S. Kulinski, F. Sannibale,
B. Spataro, M. Vescovi, G. Vignola
Istituto Nazionale Di Frascati Nucleare
Frascati, Rome

I. INTRODUCTION

The electron-positron accelerator for the DAΦNE[1] project is under construction at Titan Beta in Dublin, CA. This S-Band RF linac system utilizes four 45 MW sledded[2] klystrons and 16-3 m accelerating structures to achieve the required performance. It delivers a 4 ampere electron beam to the positron converter and accelerates the resulting positrons to 550 MeV. The converter design uses a 4.3T pulsed tapered flux compressor along with a pseudo-adiabatic tapered field to a 5 KG solenoid over the first two positron accelerating sections. Quadrupole focusing is used after 100 MeV. The system performance is given in Table 1. This paper briefly describes the design and development of the various subassemblies in this system.

Table 1. DAΦNE Linac Parameters

General

RF Frequency	2856 MHz
Klystron Power	45 MW
No. of Klystrons	4
No. of SLED Cavities	4
No. of Sections	16
Repetition Rate	50 Hz
Beam Pulse Width	10 nsec

High Current Electron Linac

No. of Accelerating Sections	6
Input Current	up to 10.0 A
Input Energy (nominal)	120 kV
Output Current	>4.0 A
Output Energy	250 MeV
Output Emittance (geometric)	≤1π mm mrad
Energy Spread	± 5%
Focused Beam Spot	~1 mm radius

Positron Linac Mode

No. of Accelerating Sections	10
Output Energy	≥550 MeV
Input Energy (mean)	8 MeV
Resolved Output Current	36 mA
Emittance (geometric)	≤5π mm mrad
Energy Spread	± 1%

High Energy Electron Linac Mode

Full Beam Energy	550 MeV
Peak Current	150 mA
Energy Spread	±0.5%
Emittance (geometric)	≤1π mm mrad

II. GENERAL SYSTEM DESCRIPTION

A. The Linac System

The linac system consists of:

1. A high current linac designed to produce 250 MeV with 4 amperes of beam current with a 1 mm focus spot on the positron target. This section includes the electron gun and injector which is useable in both the electron and positron modes. This linac utilizes a series of discreet solenoid coils over the first section and quadrupole focussing over the remaining 4 sections. A final focus triplet brings the beam to the 1 mm spot on the positron target.

2. An electron to positron converter based on the SLAC design.

3. A low current accelerator designed to produce 550 MeV for accelerating either the positron beam or a low current (150ma) electron beam. This section includes a 5 kG solenoid over the first two sections followed by an electron-positron separator prior to the remaining ten sections.

4. The system is computer controlled using a bussed architecture and a MacIntosh Quadra 700 computer running Labview.

B. *Injector*

The conceptual design of the first few meters of the DAΦNE linac is patterned after the original SLAC injector, which ran for 20 years delivering beams from a few nanoamps to 2 amps. The DAΦNE Linac injector consists of the following components:

1. A 120 kV thermionic triode (with a mesh grid) gun with a 3 sq cm dispenser cathode capable of currents up to 15 amps.

2. A single resonant cavity prebuncher, which bunches about $^{3}/_{4}$ of the electrons into a 90° bunch in the 21 cm prebuncher drift.

3. A 5 cell, 13 cm long, travelling wave buncher with phase velocity equal to 0.75c, which bunches the beam by about a factor of 3 to about 30° and accelerates the electrons up to about 0.5 MeV.

4. A 3-meter long constant gradient, velocity of light accelerator section, which completes bunching the beam to about 5° FWHM and accelerates the beam to about 45 MeV. According to the program PARMELA, used to design the injector, 80% of the beam from the gun should captured and accelerated, and 87% of the captured beam is within a 15° bunch.

5. The magnetic focussing system consisting of one iron core magnetic thin lens which matches into a solenoid consisting of 14 large aperture coils placed at the Helmholtz spacing around the prebuncher, buncher, first 3 meter long accelerator section. The solenoid has a nominal maximum axial magnetic field in the accelerator section of 1.25 kG. The beam from this section is focussed by a quadrupole doublet placed after this first accelerator section. This doublet matches the beam into a FODO array consisting of two large quadrupoles between sections.

This system is designed to be capable of running well for a wide range of currents from 7 amps (for producing positrons) down to the nominal 150 mA required for injecting electrons into the DAΦNE storage ring and indeed down to 1 mA or less.

C. *E-Gun Pulser*

The E-gun pulser was required to generate a low jitter, fast risetime pulse to the E-gun cathode (groun-ded grid configuration). A fast avalanche transistor based pulser has been developed to meet these requirements. Amplitude control of the pulser is via a PIN diode attenuator stack that was developed for this purpose. Previously the E-gun output has been shown to have rise and fall times of less than 800 picoseconds.

Control and trigger of the E-gun pulser is via fiber-optical links providing pulse width, amplitude, and fault detection through serial communication. Up to four 8-bit analog and six digital signals are transmitted over a single pair of fiber optical cables. The E-gun pulse width is fixed at 10 nanoseconds, but is locally settable between 1 and 10 nanoseconds in 1 ns increments using an on-board digital pulse width generator.

The E-gun floating deck is connected to a 150 kV DC power supply which provides the acceleration potential for the injector.

D. *Positron Source*

The positrons are produced by focussing a high current (4 to 7 amps) 250 MeV electron beam which has been accelerated through the first 5 three-meter sections of the linac onto a tungsten converter, creating an electromagnetic cascade of electrons, positrons and photons. The electrons are focussed onto the converter by close-spaced quadrupole triplet mounted about 1 meter upstream of the converter. The positron source was designed (as was the electron injector) using the simulation program PARMELA obtained from L.M. Young at LANL. We are using a SLAC SLC style source with a pulsed "Flux Concentrator" which produces a field tapering from 43 kG at the input to 0 kG in about 15 cm. Superimposed on this pulsed field is a DC magnetic field which tapers from 12 kG down to a uniform field of 5 kG which continues through the first 6 meters of acceleration.

The RF is phased to initially decelerate the positrons. The positrons which debunch because of the spread in pathlengths and velocities are rebunched in order to achieve a much better spectrum. With this design, over 2% yield was achieved into a ±1% spectrum with 250 MeV incident electrons.

After acceleration through 2 three-meter sections immersed in a solenoid, the positrons pass through a chicane consisting of 4 rectangular dipoles which deflect the positrons 2 cm off axis and then back on axis. The secondary electrons from the positron converter (the converter produces roughly twice as many electrons as positrons) are deflected in the opposite direction, and thus can be stopped on a collimator. Such a chicane is achromatic to all orders. The chicane makes the positron and current monitors between this point and the end of the linac effective for tuning the positron beam, since beyond the chicane the beam has only positrons. Beyond the chicane the beam

is focused by a FODO array of large aperture quadrupoles mounted around the accelerator sections: six around the first 3 meter accelerator section; four around each of the next 3 sections; and 2 around the remaining 4 sections.

E. Modulators

Titan Beta is building four identical line modulators capable of delivering 100 MW peak power video pulse with 4.5 μsec flat top at 50 pps. There is a 8 stage PFN in each modulator, resonantly charged with requirement of ±0.1% pulse to pulse amplitude stability.

The system will also have a modulator to drive the positron flux concentrator. The design of this unit is based on existing SLAC unit and is expected to run at 50 Hz driving 12 k amp peak current through a 1 μh load.

F. Control System

The control system is distributed into various subsystem chassis located throughout the linac system. Each chassis has built-in fault detection circuitry to detect any fault condition and display all of the faults and indicate the first fault occurrence. In addition, all faults are summed in the master system controller for subsystem fault identification.

A bussed architecture is used to reduce the number of control cable wires. The fault detection system uses a multiplexed buss connected to the master system interface instead of individual wires for each fault. The first subsystem to detect a fault acquires the buss via logic located in the master control interface. This allows the use of 16 lines instead of >140 lines to monitor all possible fault conditions.

The entire system is operated through a CAMAC based computer control system. An Apple MacIntosh Quadra 700 Computer is used to run the National Instruments Labview 2 software. The computer is integrated with the control system and provides all system operating and monitor functions via software control with the exception of the safety interlocks which are hardwired. The computer can be located at the CAMAC rack location or can be remotely located up to 100m away using a fiber-optic IEEE-488 buss extender. A small control chassis is co-located with the computer to provide hardwire basic operating control functions.

G. Mechanical Systems

1. Vacuum System

Ultra high vacuum is maintained by the use of ion pumps distributed throughout the system. There are two pumps at the injector, a pump between each accelerating section and one at the beam output of the system. Additionally there is an ion pump at each SLED cavity as well as at each klystron window. Beamline valves are used to divide the system into four separate volumes.

2. Temperature Control

Temperature stability for the system is accomplished using two separate water systems. One system (accessory) removes waste heat from the klystron/pulse transformer tank assembly, beam line magnetics, and accelerating section RF output loads.

The second system regulates the temperature of the prebuncher, buncher 15 accelerating sections, 4 SLED cavities and the RF transmission waveguide system. Regulation is accomplished by mixing hot and cold water, followed by SCR controlled high power heaters. Heaters are located at the inlet to each accelerating section. Temperature stability is ±1°C.

H. Acknowledgements

Schonberg Radiation Corp is supplying the accelerating structures and SLED cavities which are based on the SLAC design. Hermosa Electronics provided the electron gun. SLAC has provided support through the participation of several scientists, H. Hoag, H. DeRuyter, A. Kulikov, and through access to drawings and design information. In addition, a Technical Review Committee was established consisting of scientists from laboratories around the country including to review our designs and critique our approaches. Their input has been invaluable.

I. Conclusion

The DAΦNE accelerator is under construction at Titan Beta. It is proceeding on schedule and is expected to be delivered early in 1994.

References

(1) G. Vignola, INFN-LNF; "DAΦNE, The Frascati Φ-Factory", PAC '93 Conference Ib4, May 17-20, 1993.

(2) Z.D. Farkas, H.A. Hogg, G.A. Loew and P.B. Wilson, "SLED: A Method of Doubling SLAC's Energy", IXth Int'l Conf on High Energy Accelerators, SLAC, May 2-7, 1974.

The Possibility of Introducing Additional Focusing Caused by the Circular Irises in Iris Loaded Accelerator Sections *

M. Kurz, P. Hülsmann, H.-W. Glock, H. Klein

Institut für Angewandte Physik
Robert-Mayer-Straße 2-4, D-6000 Frankfurt am Main, Fed. Rep. of Germany

Abstract

To reach high luminosities in future linear colliders short range wakes have to be controlled in the range of X-band frequencies or higher. Rectangular irises can be used to introduce strong focusing quadrupole-like rf-fields. Even circular irises in iris-loaded accelerator structures have the capability of focusing if the particle velocity differs from phase velocity. Theoretical investigations concerning the focusing strength to be expected are presented. Their applicability for linear colliders is discussed.

I. INTRODUCTION

Almost all schemes proposed for future linear colliders rely on travelling-wave iris structures. In order to reach the high luminosities required by experiments wake field effects must be taken into account. Since transversal wakes scale with ω^3 [1] colliders operating at X-band or higher have to care for single bunch beam breakup (SBBU). Additional focusing is required. This can be achieved in several ways. One is to use an external quadrupole system, another is to use microwave quadrupoles (MWQ) [2], [3], and in the special case of an X-band collider it is possible to use short sections of conventional iris structures forming a FOFO-lattice to provide focusing power.

II. THEORY

A. Forces on a Particle

We consider a conventional Iris Structure with circular aperture. If we restrict our considerations on points not far from the beam axis we can write the accelerating E_z-component of a TM_{01}-wave travelling through the structure (see Fig. 1.) as

$$E_z = E_0 \cos(\omega t - kz) \tag{1}$$

where $k = \omega/\beta c$ and $\beta = v_{ph}/c$. From $\mathrm{div}\,\vec{E}$ we get:

$$E_r = -\frac{kr}{2}E_0 \sin(\omega t - kz) \tag{2}$$

Looking for the H_ϕ-component we find from $\mathrm{curl}\,\vec{H} = \varepsilon \partial_t \vec{E}$:

$$H_\phi = -\varepsilon\frac{r}{2}E_0 \sin(\omega t - kz) \tag{3}$$

Assuming the velocity of the particle $v_p = c$ and $\beta = 1$ we see an exact cancellation of electric and magnetic forces, $F = F_{el} + F_{mag} = 0$.

We now consider the situation when v_p is different from c and $\beta \neq 1$. The total force on a particle can then be expressed as (see also Fig. 2):

$$F = q\frac{\omega r}{2c}E_0\left(\frac{\beta_p\beta - 1}{\beta}\right)\sin(k_0 z\delta) \tag{4}$$

where $k_0 = \omega/c$, $\delta = (\beta-\beta_p)/\beta\beta_p$, and q is the charge of the particle. Equation (4) holds for the case that the structure covered by the particle is very short or β and β_p do not differ very much.
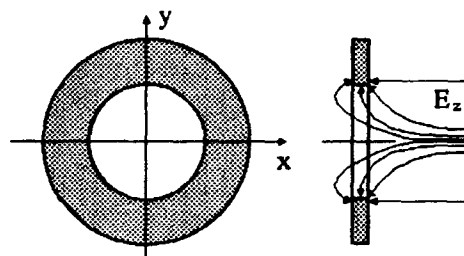
Figure 1. Electric field at an iris. The cavity is operated in $\pi/2$-mode.
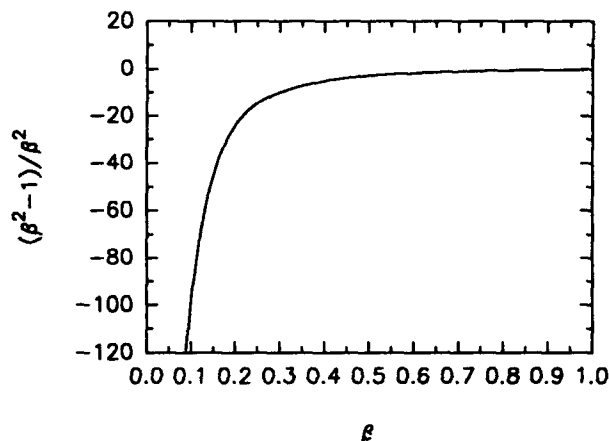
Figure 2. Total force on a particle plotted versus $\beta = \beta_p$. It can be seen that cancellation of electric and magnetic forces only takes place for velocities near c.

B. Focusing Properties

Since we have to deal with structures of finite length we have to take into account the time a particle needs to traverse the structure. Seeking the transversal momentum gain a charge q experiences while inside the accelerator section this leads to the following expression:

$$\Delta P_\perp = qE_0 \frac{\omega r}{2c^2}\left(\frac{\beta_p\beta - 1}{\beta_p\beta}\right)\frac{\sin(\frac{\omega\delta}{2c}\iota)}{\frac{\omega\delta}{2c}\iota}\iota\sin\Phi \quad (5)$$

where ι denotes the length of the cavity, and Φ the phase of the particle with respect to the rf. The velocity of the particle must not change while flying through the structure. This condition can · be fulfilled by chosing $\Phi = 90°$ or the particle's velocity equal to c. In electron linacs the latter condition is fulfilled for almost every location along the accelerator. In order to achieve a non-zero transversal momentum gain towards the beam axis we look for the optimum velocity difference $\Delta\beta$, where $\beta = \beta_p + \Delta\beta$. Equation (5) can be rewritten:

$$\Delta P_\perp = q\frac{E_0 r}{c}\sin(\frac{\omega\iota}{2c}\tau)\sin(\Phi) \quad (6)$$

where $\tau = \Delta\beta/(1 + \Delta\beta)$. As can be seen the charge experiences a portion of a magnetic field of strength E_0/c. Assuming $E_0 = 100MV/m$ one gets 0.33T magnetic field strength. The maximum of $\Delta P_\perp$ is found for

$$\tau = -\frac{\pi c}{\omega\iota} \quad (7)$$

where $\Phi = 90°$. It is also possible to choose $\Phi = -90°$ and therefore get a positive τ as long as a phase-slip occurs between particle and wave.

The longitudinal momentum gain ΔP_z is then given by:

$$\Delta P_z = 2q\frac{E_0}{\pi c}\iota \quad (8)$$

The focusing uses up approximately one third of the maximum accelerating gradient for 0° rf-phase.

Provided that the path of the particle is not changed while traversing the cavity the structure can be considered a thin lens of focal length f.

$$f = -\frac{r P_z}{\Delta P_\perp} \quad (9)$$

where r denotes the axis offset and P_z the longitudinal momentum of the particle. If it's energy is big compared to it's rest-mass this leads to:

$$f = \frac{U}{E_0 \sin(\frac{\omega\iota}{2c}\tau)\sin(\Phi)} \quad (10)$$

Here U denotes the voltage seen by the particle. Taking an X-Band cavity of length $\iota = 0.5m$, $E_0 = 100MV/m$, and $U = 3GV$ one gets $\Delta\beta = -0.026$ and a focal length $f = 30m$.

The transversal momentum gain per unit charge is $\Delta P_\perp = 333.56Vs/m^2$.

C. FOFO-Lattice

In principle it is possible to construct a constantly focusing channel by adding up many of these sections. The accelerating gradient is then reduced by one third because this fraction of the rf is used to build up the focusing field. Another way is to arrange the cavities such that a FOFO-lattice is formed (see Fig. 3). The section consists of the focusing cavities F and the drift spaces O of length d.

We now look at the x-component (say) of the motion of a particle through a FOFO. We have to consider the following equation:

$$\begin{pmatrix} x \\ x' \end{pmatrix} = \begin{pmatrix} 1 & d \\ -\frac{1}{f} & 1-\frac{d}{f} \end{pmatrix}\begin{pmatrix} x_0 \\ x_0' \end{pmatrix} \quad (11)$$

From this one can derive the cosine of the phase advance:

$$\cos(\mu) = 1 - \frac{d}{2f} \quad (12)$$
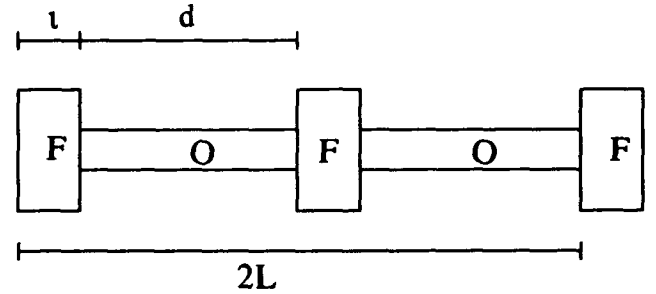
Figure 3. Picture of a FOFO-lattice of structure length L. The focusing sections F are separated by drift sections O of length d.
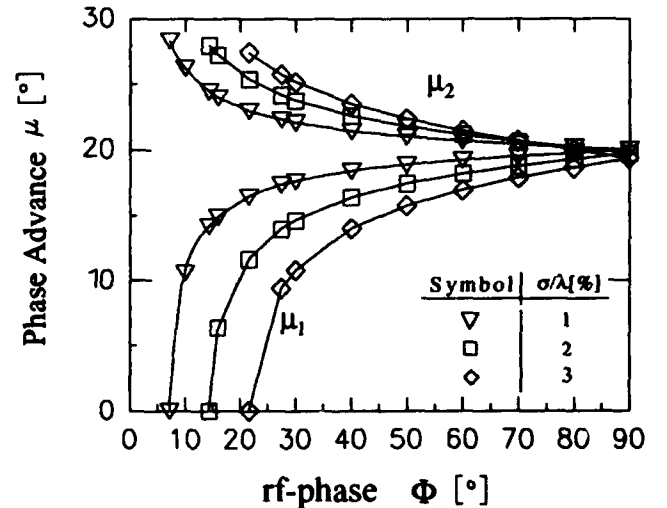
Figure 4. Phase advance for different Φ_0. Plotted for several values σ/λ.

615

The transversal momentum gain depends on the phase Φ at the entrance. We define the beginning and the end of a bunch of rms-length σ at $\pm 2\sigma$. The corresponding rf-phases are then $\Phi_0 \pm (4\pi\sigma/\lambda)$, where λ denotes the wavelength. Inserting (10) into (12) gives:

$$\frac{\sin^2(\frac{\mu_{1,2}}{2})}{\sin(\Phi_{1,2})} = \frac{\sin^2(\frac{\mu_0}{2})}{\sin(\Phi_0)} \qquad (13)$$

The phase advance of the head (μ_1)and tail particle (μ_2) in a bunch is drawn in Figure 4, where a $\mu_0 = 20°$ is chosen arbitrarily.

D. Additional External Focusing

By adding additional external focusing strength, e.g. by using external quadrupoles the resulting phase advance of the lattice is determined by the superposition of both focusing fields. One gets:

$$\sin^2(\frac{\mu}{2}) = \frac{L E_0}{4U}\left(\sin(\Phi) + \frac{L c \eta_e G_e}{2 E_0}\right) \qquad (15)$$

where η_e is the filling factor of external focusing system. By denoting external focusing strength by $m = L c \eta_e/2 E_0$ one comes to an expresion similar to (14).
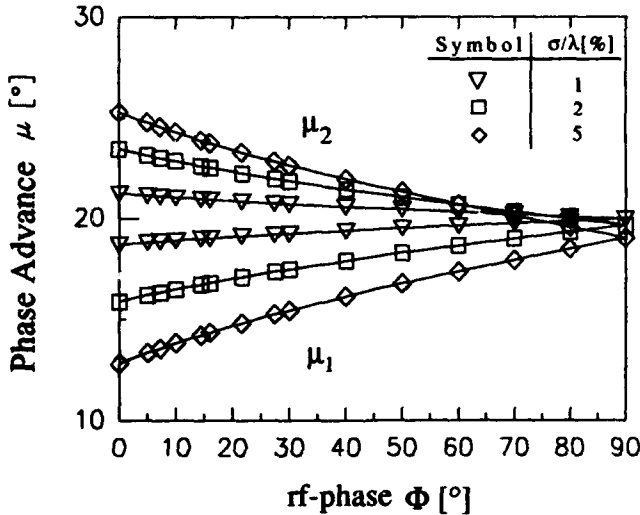
Figure 5. Phase Advance for different Φ_0. Plotted for several values σ/λ. External focusing strength is m = 1.

$$\frac{\sin^2(\frac{\mu_{1,2}}{2})}{m + \sin(\Phi_{1,2})} = \frac{\sin^2(\frac{\mu_0}{2})}{m + \sin(\Phi_0)} \qquad (16)$$

Taking m = 1 a rf-phase of 0° is possible. The Variation in phase advance over the bunch is 12.5° (see Figure 5). Taking $\mu_0 = 60°$ instead of 20° one gets 41° phase width which is only half the value in a quadrupole-FODO.

E. BNS-damping

Since focusing in these structures is phase dependent they can be used for BNS-Damping [4]. Combining (10) (maximum deflection) with (12) and differentiating with respect to the rf-phase (note that $d/d\Phi = (\lambda/2\pi)d/ds$) leads to the BNS-criterion:

$$2Uk_\beta\frac{dk_\beta}{ds} = \frac{\pi\mu^2 E_0}{\lambda L \sin^2(\frac{\mu}{2})}\cos(\Phi) \geq q\frac{dW_\perp}{ds} \qquad (14)$$

It should be mentioned that the rf-wavelength is changed by a factor $1 + \Delta\beta$.

Taking a X-band structure at 11.4GHz of length $\iota = .25m$, $\Phi = 10°$, L = 2m, $E_0 = 100MV/m$, and $\mu = 20°$ this leads to $\Delta\beta = -5\%$ and a BNS-damping strength of $1.13\cdot10^{10}Vm^{-3}$.

III. DISCUSSION

Taking a X-band structure (e.g. NLC [5]) the rms bunch length is foreseen to be $\sigma = 0.1mm$ which corresponds to a $\sigma/\lambda = 0.4\%$. The transversal wake potential can be approximately calculated to $eNdW_\perp/ds = 13.73GV/m^3$ [6] assuming an aperture of 8.6mm and a bunch charge of 1.44nC. The above example shows a BNS-damping strength which is nearly sufficient to compensate for transversal wakes. It is of course possible to change the example-lattice such that BNS-damping is increased (i.e. chose shorter L and ι). Still this type of focusing remains limited to frequencies not higher than X-band for the reason that there is a limitation in the possible accelerating gradient..

IV. REFERENCES

[1] H. Henke, CLIC Note 100, CERN 1989

[2] W. Schnell, CERN-LEP-RF/87-24, CLIC Note 34, 1987

[3] R.B. Palmer, Private Communication

[4] V.E. Balakin, A.V. Novokhatsky, V.P. Smirnov, Proc. 12th HEACC, p. 119, Fermilab, 1983

[5] R. Ruth, "The Status of NLC", Proc. 3rd Int. Workshop on Linear Colliders, vol. 1, pp. 107-140, Protvino 1991

[6] R.B. Palmer, "Prospects for High Energy e+-e- Linear Colliders", SLAC-PUB-5195, 1990

Disruption Effects from the Collision of Quasi-Flat Beams*

Pisin Chen

Stanford Linear Accelerator Center

Stanford University, Stanford, CA 94305

Abstract

The disruption effects from the collision of round beams and flat beams in linear colliders have been studied in the past, and has by now been well understood. In practice, however, in the current SLC running condition and in several designs of the next generation linear colliders, the *quasi-flat* beam geometries are expected. Namely, the beam aspect ratio $R \equiv \sigma_x/\sigma_y > 1$, but not infinitely large. In this regime the disruption effects in both x and y dimensions should be carefully included in order to properly describe the beam-beam interaction phenomena. In this paper we investigate two major disruption effects for the the quasi-flat beam regime: The luminosity enhancement factor and the effective beamstrahlung. Computer simulations are employed and simple scaling laws are deduced.

I. INTRODUCTION

One of the most important issues in the design and operation of e^+e^- linear colliders is the effect of the beam-beam interaction. The single-pass nature of linear colliders demands that a high luminosity can only be achieved by colliding tiny, intense bunches of electrons and positrons. In this circumstance, these bunches interact strongly with one another, inducing large *disruption*, or pinch, effect between the colliding beams, and producing intense radiation called *beamstrahlung*.

In the case of the disruption effects, there have been detailed studies for the *round* beam, i.e., $R = \sigma_x/\sigma_y = 1$, and for the *flat* beam collisions[1][2]. Typically, in the flat beam limit where $R \gg 1$, the horizontal motion of beam particles is nigligible, and the problem has been studied in the one-dimensional approximation. However the current SLC running condition lies in the regime where R is larger, but not so much larger than one. As a result the horizontal motion of particles cannot be ignored. It happens that several of the next generation linear colliders, i.e., CLIC, DLC and TESLA, call for beam dimensions which also fall into this catagory. There is thus a need for a scaling law which can help estimate the disruption effect in the quasi-flat beam regime. In addition, in this regime it is also important that the calculation on beamstrahlung has the disruption effect properly included.

II. LUMINOSITY ENHANCEMNET FACTOR

The collective fields in one beam deform the other beam during collision, by an amount controlled by global

disruption parameters, which may be different in the two transverse directions[1][2]:

$$D_{x,y} = \frac{2Nr_e\sigma_z}{\gamma\sigma_{x,y}(\sigma_x + \sigma_y)} \quad . \tag{1}$$

The deformation of the colliding bams results in effective beam sizes, $\bar{\sigma}_x$ and $\bar{\sigma}_y$, which are different from their nominal values. This in turn gives an effective luminosity different from the nominal one. The luminosity enhancement factor is defined as the ratio of the effective luminosity to the nominal luminosity due to the change of beam size:

$$H_D \equiv \frac{\bar{\mathcal{L}}}{\mathcal{L}} = \frac{\sigma_x\sigma_y}{\bar{\sigma}_x\bar{\sigma}_y} \quad . \tag{2}$$

The luminosity enhancement factor is calculable analytically only in the $D_{x,y} \ll 1$ limit. Beyond this limit the dynamics of beam-beam interaction becomes nonlinear, and one must use simulations. For the case of round beams, simulations produce the behavior[2]:

$$H_D = 1+D^{1/4}\left(\frac{D^3}{1+D^3}\right)\left\{\ln(\sqrt{D}+1)+2\ln(0.8/A)\right\}, \tag{3}$$

where for round beam $D \equiv D_x = D_y$ and $A \equiv A_x = A_y = \sigma_z/\beta^*$, and β^* is the β-function at the interaction point. This scaling law is valid to about 10% accuracy. The largeness of H_D in the $D_{x,y} \gg 1$ limit was recognized to be associated with the near equilibrium pinch-confined transverse beam profiles[2]. In this regime the beam particles undergo multiple betatron oscillations during the collision, and tend to be traped in a much narrower focusing potential of the opposing beam.

In the flat beam limit where one-dimensional approximation is employed, simulation gives the following scaling law[2]:

$$H_D(R \gg 1) \simeq H_D(R = 1)^{1/3}, \tag{4}$$

when D_y and A_y are fixed and $D_x, A_x \to 0$.

It was later shown that there is actually a theoretical basis for such a cubic relationship[3]. The near equilibrium pinch-confined states are approached through collisionless damping due to mixing and filamentation in phase space. It was already pointed out[1] that the disruption parameter D is related to the square of the wave-number (of the betatron oscillation), κ_β. The emittance growth due to the disruption effect occurs in a length scale of κ_β^{-1}, but the beam rethermalizes in a length β^* due to the nonlaminar effects of the finite emittance. Thus the

fundamental quantity which governs the luminosity enhancement is evdently $\sqrt{D_y}/A_y \simeq \kappa_\beta \beta_y^*$ in the 1-D calculation. Indeed, this is precisely the leading logarithmic behavior in (3) for H_D. When the same prescription is applied to round beams, it was shown that the cubic relationship between the two limits can be deduced.

The less than quadratic dependence, which one might naively assume, can also be appreciated intuitively. In the round beam case the change of beam size in either x or y direction will enhance the pinching of the other dimension, i.e., the focusing in the two dimensions are fully coupled. On the other hand, it is well-known that the field strength in a non-round, i.e., $R > 1$, charge distribution is mainly determined by its major dimension, σ_x. This means that the lack of horizontal disruption renders a milder pinch effect for the flat beams.

From (2) we see that for round beams the effective beam size is given by

$$\bar{\sigma} = \sigma H_D^{-1/2} \quad , \qquad R = 1 \quad . \tag{5}$$

On the other hand, since in the flat beam limit the horizontal beam size is assumed to be fixed, the cubic relationship (4) suggests that

$$\bar{\sigma}_y = \sigma_y H_{D_y}^{-1/3} \quad , \qquad R \gg 1 \quad . \tag{6}$$

It was therefore proposed recently that the luminosity enhancement factor for quasi-flat beams scales as[4]:

$$H_D = H_{D_x}^{1/2} H_{D_y}^{1/3} \quad , \tag{7}$$

Noteice, however, that although this scaling law approaches the right flat beam limit of (4), it does not converge to the correct round beam scaling of (3). It is evident that the power law of the H_{D_y} dependence should be more complex than the simple cubic scaling when $R \to 1$.
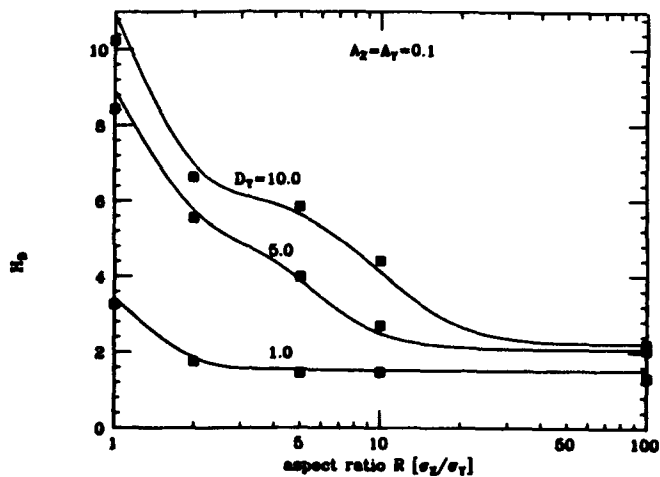
Fig.1 Evolution of H_D as a function of R

Computer simulation using ABEL[5] was performed to study the evolution of H_D as a function of R. This is done by fixing D_y, A_x, and A_y in the calculations, while varying D_x. Figure 1 shows the simulation results of H_D as a function of R, with $A_x = A_y = 0.1$ and three choices of D_y. We find that these results (shown in squares) agrees very well with the following scaling behavior (shown in solid curves):

$$H_D = H_{D_x}^{1/2} H_{D_y}^{f(R)} \quad ,$$
$$f(R) = \frac{1 + 2R^3}{6R^3} = \begin{cases} 1/2 & , \quad R \to 1 \\ 1/3 & , \quad R \to \infty \end{cases} . \tag{8}$$

This new scaling law now applies to all values of R.

III. EFFECTIVE BEAMSTRAHLUNG

High energy e^+e^- beams generally follow Gaussian distributions in the three spatial dimensions, and their local field strength varies inside the beam volume. In the weak disruption limit, where particle motions have small deviations from the z direction, it is possible to integrate the radiation process over this volume and derive relations which depend only on averaged, global beam parameters. It is found in such para-axial, or fixed impact parameter, approximation, that the beamstrahlung intensity is controlled by a global *beamstrahlung parameter*[6][7],

$$\Upsilon_0 = \gamma \frac{\langle B \rangle}{B_c} = \frac{5}{6} \frac{r_e^2 \gamma N}{\alpha \sigma_z (\sigma_x + \sigma_y)} \quad , \tag{9}$$

where $\langle B \rangle$ is the mean electromagnetic field strength of the beam, $B_c = m_e^2/e \simeq 4.4 \times 10^{13}$ Gauss is the Schwinger critical field, N is the total number of particles in a bunch, γ is the Lorentz factor of the beam, r_e is the classical electron radius, and α is the fine structure constant.

In the most general designs for linear colliders, the photon spectrum due to beamstrahlung is not a factorized function of the electron and positron sources and depends on the detailed evolution of the bunches in the collision process. In general, then, the spectrum of radiation depends on the disruption process and must be computed by detailed simulation.[5] However, typical beams in linear colliders are very long and narrow. Since all particles oscillate within the focusing potential that is defined by the geometry of the oncoming beam, the oscillation amplitudes are small compared with their periodicity in z. Then the assumption of small deviations from the z direction remains approximately valid. The main effect of disruption on beamstrahlung is therefore the change of effective EM fields in the bunch due to the deformation of the transverse beam sizes. Thus, beamstrahlung is in practice still factorizable even under a non-negligible disruption effect, if one computes its magnitude using an effective beam size which takes the global disruption into account. This means one shall only replace the nominal beam size σ_x, σ_y in (9) by the corresponding effective size $\bar{\sigma}_x$ and $\bar{\sigma}_y$ following the prescription in (8):

$$\bar{\sigma}_x = \sigma_x H_{D_x}^{-1/2} \quad , \qquad \bar{\sigma}_y = \sigma_y H_{D_y}^{-f(R)} \quad . \tag{10}$$

Then the effective beamstrahlung parameter is given by

$$\Upsilon = \frac{5}{6}\frac{r_e^2 \gamma N}{\alpha \sigma_z (\bar{\sigma}_x + \bar{\sigma}_y)} \quad . \tag{11}$$

As long as the effect of disruption on beamstrahlung can be grouped under the globle beamstrahlung parameter, the recently derived beamstrahlung photon spectrum[8], which invokes the mean-field approximation, is readily applcable. The number of soft photons radiated per unit time, calculated by the classical theory of radiation, is

$$\nu_{cl} = \frac{5}{2\sqrt{3}}\frac{\alpha^2}{r_e \gamma}\Upsilon \quad . \tag{12}$$

Note that for a given field strength ν_{cl} is independent of the particle energy. This expression applies to the infrared limit of the spectrum where photon energies approach zero. For a hard photon, up to the initial energy of the electron, the quantum mechanical calculation gives a more general formula:

$$\nu_\gamma = \nu_{cl}[1 + \Upsilon^{2/3}]^{-1/2} \quad . \tag{13}$$

In a multi-photon radiation process, it was found useful to introduce a linear interpolation between these two values. Let x be the energy fraction of the initial electron carried by the photon. Then define

$$\begin{aligned}\bar{\nu}(x) &= \frac{1}{1-x}\int_x^1 dx'[x'\nu_{cl} + (1-x')\nu_\gamma] \\ &= \frac{1}{2}\Big[(1+x)\nu_{cl} + (1-x)\nu_\gamma\Big] \quad .\end{aligned} \tag{14}$$

With these basic parameters introduced, $f_r(x)$ is given by[8]

$$\begin{aligned}f_r(x) &= \frac{1}{\Gamma(1/3)}\Big(\frac{2}{3\Upsilon}\Big)^{1/3} x^{-2/3}(1-x)^{-1/3} \\ &\times \exp\Big[-\frac{2x}{3\Upsilon(1-x)}\Big]\cdot G(x) \quad ,\end{aligned} \tag{15}$$

where Υ is given by (11),

$$\begin{aligned}G(x) &= \frac{1-w}{g(x)}\Big\{1 - \frac{1}{g(x)n_\gamma}\Big[1 - e^{-g(x)n_\gamma}\Big]\Big\} \\ &\quad + w\Big\{1 - \frac{1}{n_\gamma}\Big[1 - e^{-n_\gamma}\Big]\Big\} \quad ,\end{aligned} \tag{16}$$

$$g(x) = 1 - \frac{\bar{\nu}}{\nu_\gamma}(1-x)^{2/3} \quad ,$$

and

$$w = \frac{1}{6}\sqrt{\frac{3\Upsilon}{2}} \quad , \qquad n_\gamma = \sqrt{3}\sigma_z \nu_\gamma. \tag{17}$$

n_γ is the mean number of photons radiated per electron throughout the collision. The approximations are valid for $\Upsilon \leq 5$.

IV. EXAMPLE

To varify the validity of our handling of the disruption effect in beamstrahlung, we calculate the beamstrahlung spectrum in TESLA with center-of-mass energy at 1 TeV[9]. In this design, $N = 5.8 \times 10^{10}, \sigma_x = 404$nm, $\sigma_y = 50.5$nm, $\sigma_z = 1100\mu$m, $\beta_x^* = 8$mm, and $\beta_y^* = 2.5$mm. Therefore $D_x = 1.95, D_y = 15.6$ ($R = 8$), and $A_x = 0.14, A_y = 0.44$. This gives $\bar{\sigma}_x = 172$nm and $\bar{\sigma}_y = 27.0$nm form (10). In turn, we find $H_D = 4.4$ from (8). According to our prescription the disruption effect changes the beamstrahlung parameter from $\Upsilon_0 = 0.10$ to $\Upsilon = 0.24$. With this effective beamstrahlung parameter, we calculate the beamstrahlung spectrum using (15). This is then compared with the simulation result, shown in Fig. 2. We see that our prescription indeed agrees very well with the simulation.
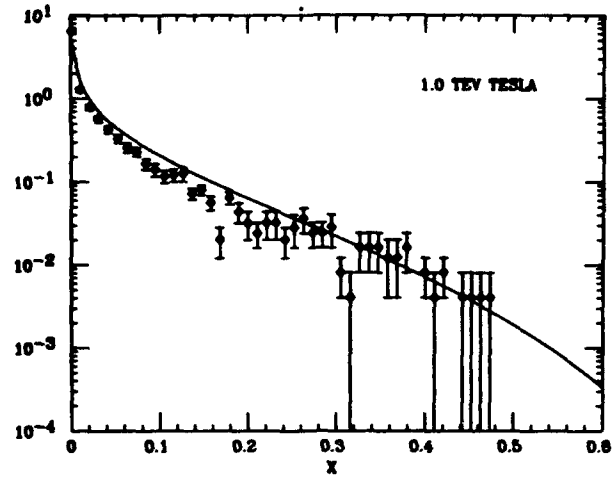
Fig.2 Beamstrahlung spectrum in a 1 TeV TESLA.

V. REFERENCES

[1] R. Hollebeek, *Nucl. Instr. Meth.* bf 184, 333 (1981).

[2] P. Chen and K. Yokoya, *Phys. Rev.* D38, 987 (1988); K. Yokoya and P. Chen, "Beam-Beam Phenomena in Linear Colliders", in *Frontiers of Particle Beams: Intensity Limitations*, Lecture Notes in Physics 400, Springer-Verlag, 1992.

[3] J. B. Rosenzweig and P. Chen, in *Proc. of IEEE PAC 91CH3038-7*, M. Allen, ed. (1991).

[4] P. Chen, in *Photon-Photon Collisions*, ed. D. Caldwell and H. Parr, World Scientific (1992).

[5] K. Yokoya, KEK Report 85-9 (1985).

[6] R. J. Noble, *Nucl. Instr. Meth.* A256, 427 (1987).

[7] P. Chen, "An Introduction to Beamstrahlung and Disruption", in *Frontiers of Particle Beams*, Lecture Notes in Physics 296, Springer-Verlag, 1988.

[8] P. Chen, *Phys. Rev.* D46, 1186 (1992).

[9] H. Padamsee, *TESLA Calculations Program, Cornell report (unpublished) 1991*.

Accelerator and RF System Development for NLC*

A. E.Vlieks, R. Callin, H. Deruyter, R. Early, K. S. Fant, Z. D.Farkas, W. R. Fowkes, C. Galloway,
H. A. Hoag, R. Koontz, G. A. Loew, T. L.Lavine, A. Menegat, R. H. Miller, D. Palmer, C. C. Pearson,
R. D. Ruth, S. G. Tantawi, P. B. Wilson, J. W. Wang, C. Yoneda
Stanford Linear Accelerator Center, Stanford, CA 94309 USA
N. Kroll, UC San Diego and SLAC, C. Nantista, UCLA

Abstract

An experimental station for an X-band Next Linear Collider has been constructed at SLAC. This station consists of a klystron and modulator, a low-loss waveguide system for rf power distribution, a SLED II pulse-compression and peak-power multiplication system, acceleration sections and beam-line components (gun, pre-buncher, pre-accelerator, focussing elements and spectrometer). An extensive program of experiments to evaluate the performance of all components is underway. The station is described in detail in this paper, and results to date are presented.

I. INTRODUCTION

In order to test new high-gradient accelerator structures for a Next Linear Collider (NLC), an experimental test area is required to study the detailed properties of these devices. Such a facility must be capable of measuring the energy and energy distribution of a tightly bunched accelerator beam as well as that of dark current produced by electron emission from accelerator cavity walls. We have completed the construction of an accelerator structure test area (ASTA) that consists of a gun/beam focussing section, and a spectrometer section capable of analyzing up to 200 MeV electrons. The gun assembly and accelerator structures are mounted on precision rails to permit the testing of structures up to 4 m in length. Part of ASTA but external to the housing is a high-power X-band klystron and a SLED II rf pulse-compression system. The facility itself is constructed from concrete with wall thicknesses 1.22 m and ceiling thickness 0.61 m. Extensive lead shielding (up to 20 cm thick) is incorporated in the spectrometer area to keep the expected radiation to a safe level.

II. GUN AND BEAM FOCUSSING

A schematic of the accelerator beamline is shown in Figure 1. The electron gun consists of a planar Pierce triode operating at a nominal beam voltage of 80 kV. The design-beam current is 25 mA with a pulse width of 10 ns. The rise and fall times of this pulse will be <1 ns. The pulse width and rise times will be determined by a grid pulser. The beam will be first focussed to an "alpha" magnet by means of a thin-lens solenoid. The alpha magnet effectively bends the beam 105° so that its trajectory will coincide with the main accelerator axis after passing through the magnet. The purpose of this magnet is to prevent the gun from viewing the accelerator structure directly. If the thermionic cathode faces the accelerating structure directly, Barium, boiling off the cathode surface, could contaminate the structure. The accelerator could also bombard the cathode with reverse-accelerated electrons. A second thin lens, positioned after the alpha magnet, will focus the beam through a pre-buncher. This-single cavity pre-buncher is used to improve the capture efficiency of the beam. The pre-buncher will be driven by a TWT driver. Following the pre-buncher, a third thin lens is positioned to focus the beam through a pre-accelerator, into the accelerator. The pre-accelerator, identical in design to the
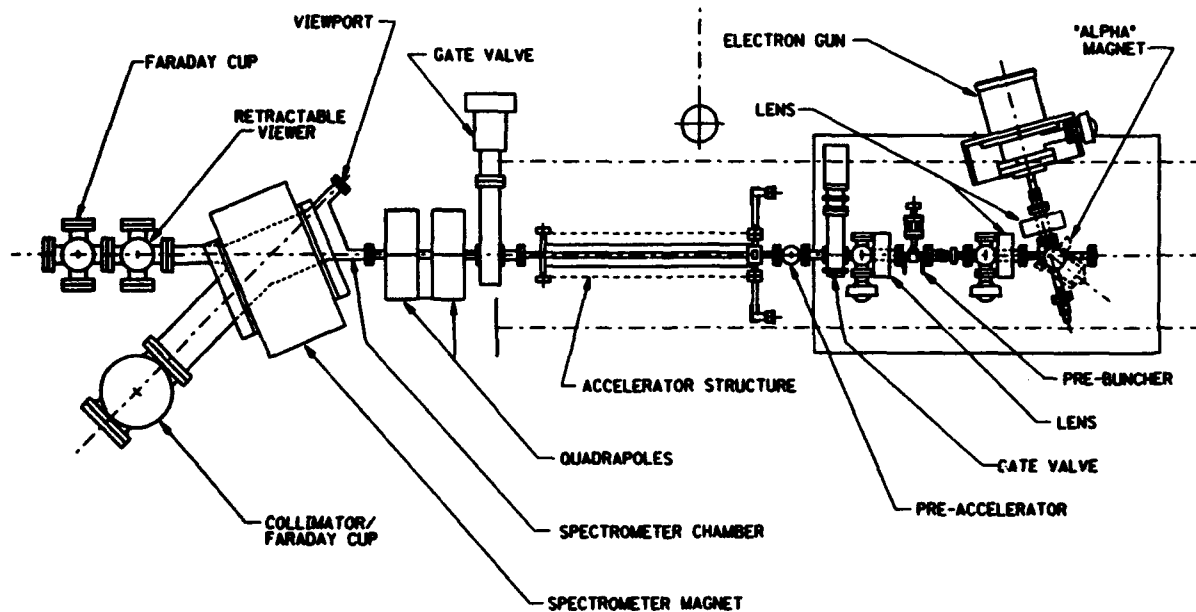
Figure 1. ASTA beam line.

pre-buncher and located directly in front of the accelerator, will be used to accelerate the beam to energies high enough that beam capture is possible even at low injector voltages and acclerator drive powers. The rf power for this pre-accelerator will be derived from the main accelerator drive power through a 20 dB coupler. Control of power and phase will be accomplished by a magic Tee and moveable shorts arrangement (see Figure 2). The complete gun and focussing system is mounted on a metal plate which slides on a pair of precision rails. This will permit the testing of accelerator sections of various lengths with a minimum of redesign or alignment to the support structure. The beam current can be measured at three positions along the beamline by means of beam-gap monitors.

III. SPECTROMETER

The spectrometer is designed to measure the total beam current through an exit port aligned along the acclerator axis or to measure a momentum analyzed beam through an exit port positioned at 45° to the accelerator axis. A 1.6 T analyzing magnet is capable of bending a 200-MeV electron beam 45° through the analyzing beam line and into a Faraday cup. Detailed measurements of the magnetic-field profile in the vicinity of the beam trajectory have been performed and calibration curves of current versus field strength have been made. In addition, a precision hall probe has been positioned within the spectrometer for accurate field determination. A

pair of collimating slits in front of this Faraday cup permits ± 0.5 % energy resolution. A second Faraday cup, positioned at the end of the 0° exit path measures the total beam current. A moveable scintillating viewport in this beam line also permits the viewing of the beam. Using this viewport and a pair of quadrapoles at the entrance of the spectrometer, the beam profile can be optimized.

IV. RF POWER

The source of rf for ASTA is a high-power X-band klystron which feeds power to a SLED II pulse-compression setup. The general layout of this setup is shown in Figure 3. The initial design goal is to obtain a 50 MW, 1µs rf pulse from a klystron. This will be pulse compressed with SLED II, resulting in a 225-MW pulse having a pulse width of 150 ns. Currently, a reduced pulse-width SLED II scheme has been completed (pulse width of 70 ns) and initial high-power testing has been performed [1]. The klystron (XC-2) currently used is capable of generating 35–40 MW rf power at 1 µs which is sufficient for initial accelerator testing. A great deal of rf component development work has gone into the construction of SLED II. Since X-band power is rather lossy in rectangular waveguide and since the SLED II pulse-compression scheme requires rf power to travel long distances in its storage waveguides, the use of the low-loss TE_{01} mode in circular waveguides is required. This, in turn has required the development of new high-power components
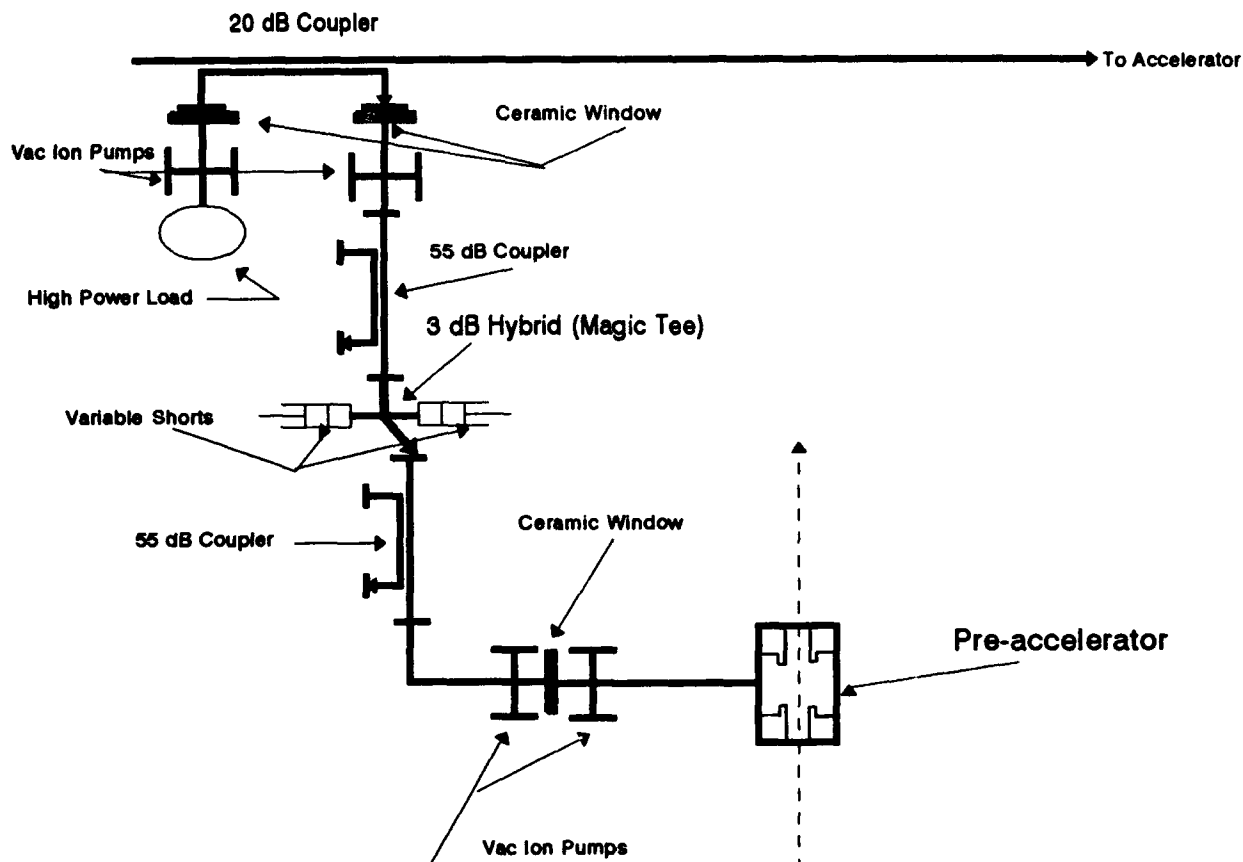
Figure 2. Pre-accelerator rf line.
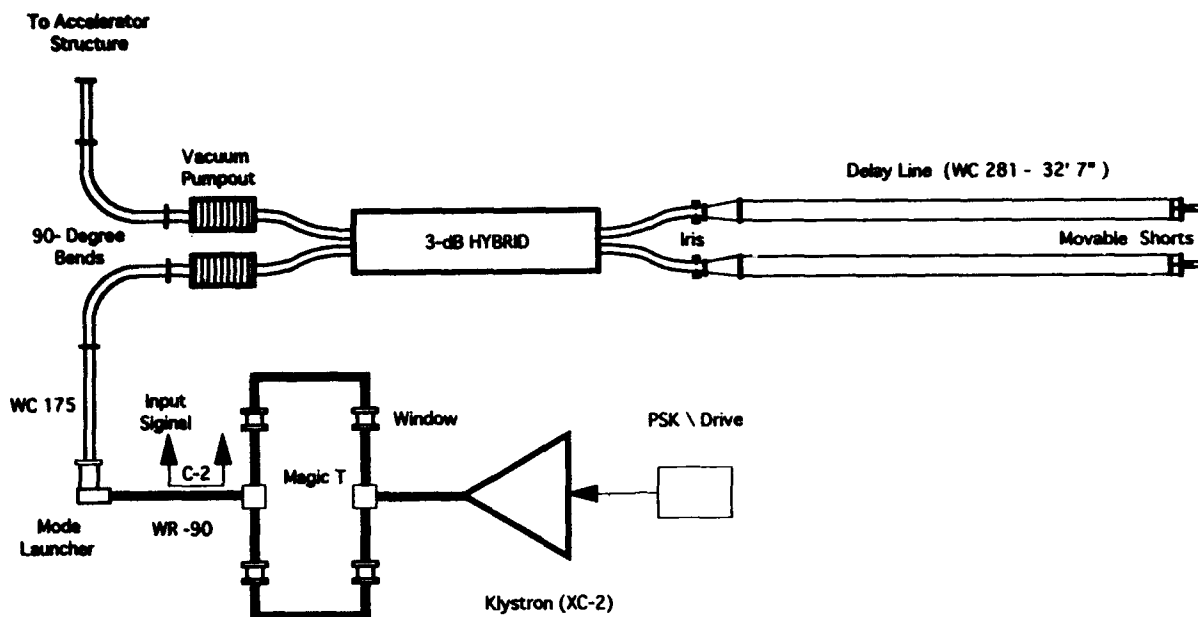
Figure 3. SLED II pulse compression for ASTA.

to transport the rf power. We have recently designed and tested a flower petal mode converter [2] that converts rf power from the rectangular TE_{10} mode to the circular TE_{01} mode with less than 0.7% loss (reflection plus spurious mode conversion). This device has recently been successfully tested in a traveling-wave resonant ring to 150 MW. In addition, low-loss circular 90° bends and nonlinear tapers (purchased from General Atomics Corp.), pumpout/mode filters, and directional couplers [3] were developed and are being tested.

V. TESTING PROGRAM

In the next year several additional high-gradient structures will be tested. Currently the facility is being readied to test a .75 m constant-gradient structure. Initially, only dark-current measurements will be performed. The peak accelerating gradients to be measured will be 100 MV/m. The next series of tests will be with a 1.8-m, detuned structure. In these tests both dark-current measurements and bunched-beam tests will be performed at accelerating gradients up to 100 MV/m. A third series of tests will then be performed with two 1.8-m structures operated at peak accelerating gradients of 50 MV/m. In addition to testing accelerator structures, different types of high-power waveguide component will be tested by being incorporated into the rf transport line. New, reduced sized 90° bends, 3 dB hybrids, and pumpouts/mode filters will be the first components to be tested in the next few months.

ACKNOWLEDGEMENTS

REFERENCES

[1] High Power RF Pulse Compression with SLED I System, Sb33 1993 Particle Accel. Conf., Washington DC.

[2] Flower-Petal Mode Converter for NLC, H. A. Hoag et al., Sb3 1993 Particle Accel. Conf., Wash DC.

[3] Mode Selective Directional Coupler for NLC, S. G. Tantawi, Sb6 1993 Particle Accel. Conf., Washington DC.

Rise Time of the Amplitudes of Time Harmonic Fields in Multicell Cavities *

H.-W. Glock, M. Kurz, P. Hülsmann, H. Klein

Institut für Angewandte Physik
Robert-Mayer-Straße 2-4, D-6000 Frankfurt am Main, Fed. Rep. of Germany

Abstract

Wall losses can cause a coupling between eigenmodes in a cavity. The magnitude of the effect can be determined by means of eigenmode expansion. The influence on rise time of forced oscillations is calculated. Results for a brick resonator and a six-cell iris structure are presented.

I. INTRODUCTION

The operation of superconducting and conventional linear colliders under multibunch conditions requires the recovery of the accelerating field and damping of wake fields being completed before the arrival of the next bunch in the train. In either case the study of time behaviour of the accelerating resp. wakefields is essential. For example, for TESLA [1] a train of 800 bunches, following each other in 1μs distance, is foreseen. For TESLA accelerator sections there have been experiments and calculations based on lumped circuit theory showing good agreement between measurement and calculations [2].

In order to investigate the time behaviour of generator or beam driven cavities we decided to use a more general approach.

II. GENERAL THEORY

A. Basic Equations

We consider a driven cavity and want to express the solutions of the time dependent Maxwell equations (1) in terms of cavity eigenmodes.

$$\nabla \times H = \varepsilon_0 \partial_t E + J \quad , \quad \nabla \times E = -\mu_0 \partial_t H \qquad (1)$$

The eigenmodes satisfy the following set of equations [3]:

$$\nabla \times H_j = i\omega_j \varepsilon_0 E_j \quad , \quad \nabla \times E_j = -i\omega_j \mu_0 H_j \qquad (2)$$

The solutions of the time dependent equations (1) may be expanded as

$$E(r,t) = \sum_j a_j(t) E_j(r) \quad , \quad H(r,t) = \sum_j b_j(t) H_j(r) \qquad (3)$$

if the driving term can be expressed in the same way.

$$J(r,t) = \sum_j c_j(t) E_j(r) \qquad (4)$$

As shown in (5) the eigenmodes are normalized to unity.

$$\left\{ \begin{array}{c} \mu_0 \\ \varepsilon_0 \end{array} \right\} \iiint_V \left\{ \begin{array}{c} H_j^* \cdot H_k \\ E_j^* \cdot E_k \end{array} \right\} dV = \delta_{jk} \qquad (5)$$

Wall losses are taken into account by assuming the following boundary condition for the parallel electric field on the surface, R_a being the surface impedance [3].

$$E_{tan} = (1+i) R_a H_{tan} \times n \qquad (6)$$

We multiply equations (1) with E_j^*, H_j^* resp., use (3), (4), and (5), integrate both equations over the cavity volume and apply Gauss' integral identity. The appearing integral of the function $E \times H_j^*$ can be evaluated (using (6)) to a sum of $b_k(t)$ with coefficients depending only on the magnetic eigenfields. These interaction terms are denoted by A_{jk}.

$$\oint_{\partial V} \left(E \times H_j^* \right) \cdot n \, ds = (1+i) R_a \sum_k b_k(t) \oint_{\partial V} H_j^* \cdot H_k \, ds$$

$$=: (1+i) R_a \sum_k A_{jk} b_k(t) \qquad (7)$$

Now we are able to set up a first order system of linear differential equations describing the behaviour of the coefficients for the evaluation of the fields. The dimension is twice the number of modes under consideration.

$$\begin{array}{llll} \dot{a}_j(t) & -i\omega_j b_j(t) & = -\dfrac{1}{\varepsilon_0} c_j(t) \\[2mm] \dot{b}_j(t) & -i\omega_j a_j(t) + (1+i) R_a \sum_k (A_{jk} b_k(t)) & = 0 \end{array} \qquad (8)$$

This is equivalent to a second order system:

$$\ddot{b}_j(t) + (1+i) R_a \sum_k \left(A_{jk} \dot{b}_k(t) \right) + \omega_j^2 b_j(t) = -\frac{\omega_j}{\varepsilon_0} c_j(t) \qquad (9)$$

One can observe the driven harmonic oscillator characteristic which is modified by the mode interaction in the first order time derivative terms.

B. Treatment of the Exchange Terms A_{jk}

The $A_{jj} \cdot R_a$ are proportional to the wall losses in the mode j. The single-mode Q is given by:

$$Q_j = \frac{\omega_j}{A_{jj}R_s} \qquad (10)$$

The A_{jk} describe power exchange between modes. From (7) it is apparent that:

$$A_{jk} = A_{kj}^* \qquad (11)$$

Further it can be shown with aid of the sentence of Bunjakowski-Schwarz [4] that there is an upper limit for the value of the A_{jk}.

$$|A_{jk}| \leq \sqrt{A_{jj}A_{kk}} \qquad (12)$$

For some simple geometries like brick or pillbox cavities there are analytical solutions for the A_{jk}. In general a numerical determination of fields has to be done, e.g. use of MAFIA [5] or similar codes.

III. NUMERICAL AND ANALYTICAL EXAMPLE

Starting with (8) one first seeks the solution of the homogenous system. For simplicity, in the following we restrict ourselves to two modes. This is no limitation of the procedure.

$$\begin{pmatrix} \dot{a}_1 \\ \dot{b}_1 \\ \dot{a}_2 \\ \dot{b}_2 \end{pmatrix} = \begin{pmatrix} 0 & i\omega_1 & 0 & 0 \\ i\omega_1 & -(1+i)R_sA_{11} & 0 & -(1+i)R_sA_{12} \\ 0 & 0 & 0 & i\omega_2 \\ 0 & -(1+i)R_sA_{12}^* & i\omega_2 & -(1+i)R_sA_{22} \end{pmatrix} \begin{pmatrix} a_1 \\ b_1 \\ a_2 \\ b_2 \end{pmatrix} \qquad (13)$$

The general solution of the homogenous system can be written as:

$$f(t) = u_1 V_1 e^{\lambda_1 t} + \ldots + u_4 V_4 e^{\lambda_4 t} \qquad (14)$$

where $f^T = (a_1, b_1, a_2, b_2)$, λ_j and V_j are the eigenvalues and eigenvectors of the system matrix, and u_j are arbitrary constants. To solve the inhomogenous system variation of constants u_j is used. With the assumption of the same harmonic time dependence of both c_1, c_2 (they may differ in phase and amplitude) we get for the inhomogenous part of (8):

$$-\frac{1}{\varepsilon_0} \begin{pmatrix} c_1(t) \\ 0 \\ c_2(t) \\ 0 \end{pmatrix} = \kappa e^{i\omega_0 t} s(t) = \begin{pmatrix} \kappa_1 \\ 0 \\ \kappa_2 \\ 0 \end{pmatrix} e^{i\omega_0 t} s(t) \qquad (15)$$

where $s(t)$ is an arbitrary function controlling the complex amplitude of the excitation. The solution is, e.g. $u_1(t)$:

$$u_1(t) = \frac{\det(\kappa, V_2, V_3, V_4)}{\det(V_1, V_2, V_3, V_4)} \int_0^t \frac{e^{i\omega_0 \tau} s(\tau)}{e^{\lambda_1 \tau}} d\tau \qquad (16)$$

Inserting into (14) gives the result.

The figures 1.-4. show the envelope of the values $|a_1|$, $|a_2|$ of the forced $\exp(i\omega_0 t)$-oscillations. The eigenvectors and

OME0 5.49020e9
OME1 5.49055e9
OME2 5.49055e9
KAP1 1
KAP2 0
AR11 2.1672e7
AR22 2.1190e7
AR12 0
AI12 1.253e6
Ro 2e-3
NEND 300000
STEP 263
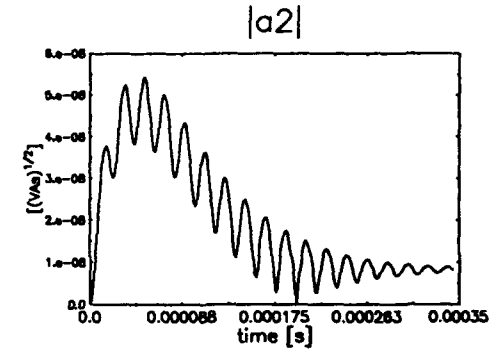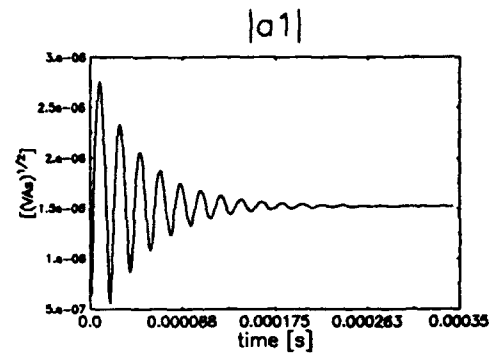
Figure 1. Brick resonator driven slightly below resonance of both degenerated modes (TM$_{111}$, TE$_{111}$). In the parameter block the generator (OME0), the two angular eigenfrequencies (OME1, OME2), direct coupling constants according to (15) (KAP1, KAP2), the A_{jk} and the wall impedance are printed.

OME0 5.49053e9
OME1 5.49055e9
OME2 5.49055e9
KAP1 1
KAP2 0
AR11 2.1672e7
AR22 2.1190e7
AR12 0
AI12 1.253e6
Ro 2e-3
NEND 300000
STEP 1283
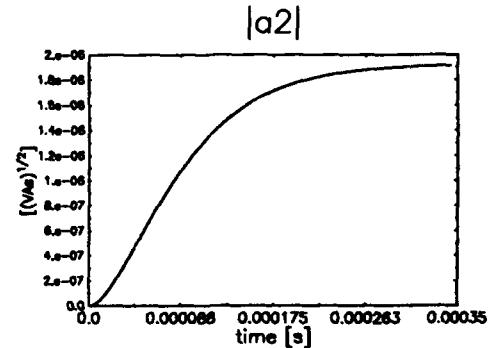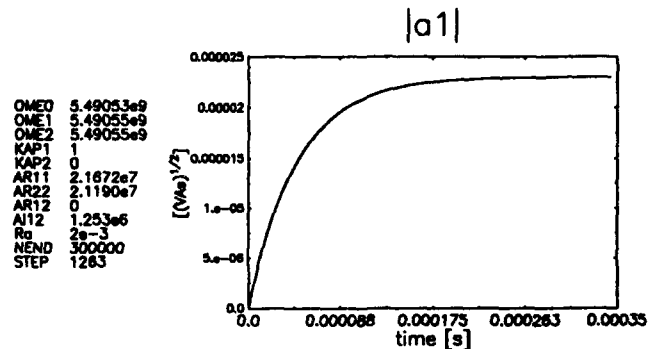
Figure 2. Brick resonator driven very close to resonance. $|a_2|$ reaches about 10% of $|a_1|$.

|a1|

OMEG	5.4806e+6
OME1	5.4806e+6
OME2	5.4806e+6
KAP1	1
KAP2	0
AR11	2.1673e7
AR22	2.1190e7
AR12	0
AI12	1.253e6
Ro	2e-3
NEND	300000
STEP	1263

|a2|
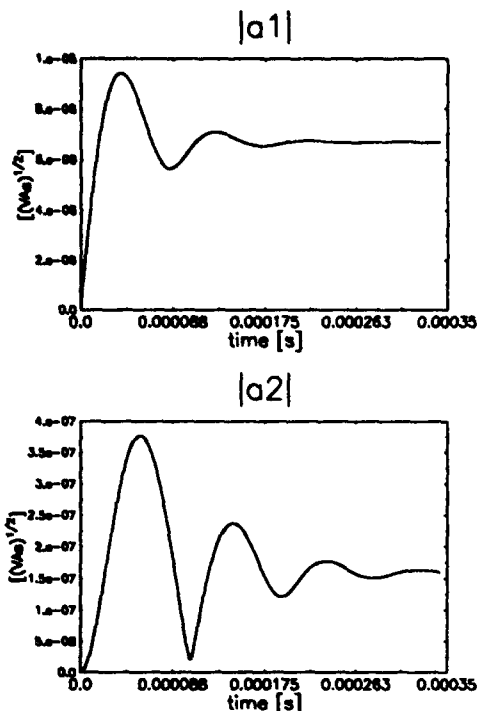
Figure 3. Brick resonator driven above resonance. Stabilization of second mode takes twice the time of the first.

|a1|

OMEG	3.89103e10
OME1	3.77792e10
OME2	3.89103e10
KAP1	1
KAP2	0
AR11	1.97342e9
AR22	2.02636e9
AR12	-8.77515e8
AI12	0
Ro	2e-3
NEND	13000
STEP	4638

|a2|
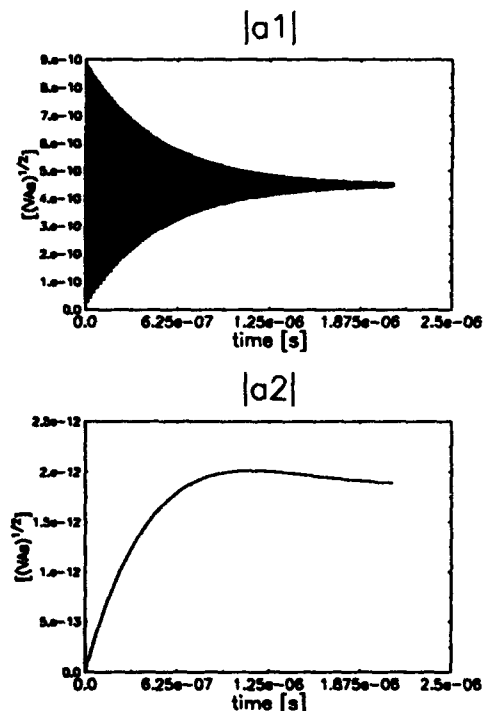
Figure 4. Six-cell iris structure. First mode is $\pi/6$, second mode is $\pi/3$. Excitation at eigenfrequency of second mode. The relatively far distance to ω_1 causes a fast oscillation of $|a_1|$. $|a_2|$ reaches about 0.5% of $|a_1|$.

eigenvalues as well as the $u_j(t)$ were calculated numerically. The function s(t) has been chosen

$$s(\tau) = \begin{cases} 0.5\left[1 - \cos(\frac{\tau}{T_{st}}\pi)\right] & \tau \leq T_{st} \\ 1 & \tau > T_{st} \end{cases} \quad (17)$$

that analytical time integration is possible.

For the brick resonator ideal degeneration of modes is possible. Therefore we investigated the interaction between the TM_{111} and the TE_{111} mode. The A_{jk} werde determined analytically.

As an example of a multicell structure we chose a six-cell iris cavity. The TM_{010}-$\pi/6$ and the neighbouring $\pi/3$ mode were calculated by means of MAFIA, then the magnetic surface fields had to be extracted from the result file in order to compute the A_{jk}.

IV. CONCLUSIONS

There is a coupling between modes due to wall losses. The effect depends on the distance of frequencies of the involved modes, the value of wall impedance, and the geometrically determined interaction terms A_{jk}. The coupling strength is limited according to (12). In most cases there is no need to take care of the effect. But it can be of some importance for degenerated modes or multicell accelerator structures with low coupling between cells, equivalent to narrow passbands. A similar coupling mechanism is to be expected for HOM-damped structures.

V. ACKNOWLEDGEMENTS

VI. REFERENCES

[1] A Proposal to Construct and Test Prototype Superconducting R.F. Structures for Linear Colliders, The TESLA Collaboration, Hamburg, February 1992

[2] D. Proch, Private Communication, November 1992

[3] H.-G. Unger, Elektromagnetische Theorie für die Hochfrequenztechnik, Teil 2, pp. 275, Heidelberg 1981

[4] Bronstein-Semendjajew, Taschenbuch der Mathematik, p. 124, Thun und Frankfurt/Main 1985

[5] T. Weiland, Solving Maxwell's Equations in 2D and 3D by Means of MAFIA, Proc. Conf. on Computer Codes and the Linear Accelerator Community, pp.3, Los Alamos 1990

CLIC Drive Beam Generation by Induction Linac and FEL Experimental Studies for the CERN Linear Collider

R. Corsini, C.D. Johnson
CERN, 1211 Geneva 23, Switzerland
J. Gardelle, J. Grenier
CESTA, 33114 Le Barp, France

Abstract

Generation of the intense 30 GHz drive beam for the CERN Linear Collider project (CLIC) presents several interesting technological challenges. Following recent suggestions to generate this beam using a Linear Induction Accelerator (LIA) and Free Electron Laser (FEL), this option is now actively studied. Newly introduced schemes for harmonic acceleration of the CLIC drive beam, possibly including rf pulse compression, require four or more trains of many bunchlets at 30 GHz and these requirements are well matched to the known performance of the induction linac and FEL. A test facility is being set up at CESTA with the initial aim to generate and measure the properties of a low-energy bunched beam close to the needs of CLIC. An electron beam (1 MeV, 1 kA, 50 ns) created by the LELIA induction injector [1] will be transported through a dipole wiggler in order to generate the low-energy beam bunched by FEL effects. This spatial modulation will be measured by using the Cerenkov radiation analysed by a high-speed streak camera in the picosecond regime. The experimental programme is supplemented by theoretical studies relating to the problems of post-acceleration without significant loss of the essential bunch structure and to the control of phase jitter.

1 INTRODUCTION

CLIC design study explores the technologies that would be required to construct a two- beam linear collider in the center-of-mass energy range from 500 GeV to 2 TeV [2]. The drive beam, that supplies microwave power to a 30 GHz main linac in this two-beam scheme, must be capable of providing trains of intense electron bunches at 30 GHz. Each train, or group of trains within the main linac filling time of 12 ns must contain a total charge of 7 μC and this will be repeated at 1.7 kHz.

Various schemes for generating these bunch trains are under study, mainly involving individually formed bunchlets from thermionic or laser photocathode guns that are compressed to 1 mm bunch length and then combined into groups with 1 cm spacing, i.e. at 30 GHz. The aims are to create bunch structures ranging from four trains of 11 bunchlets each containing 160 nC of charge, the trains being seperated by 2.85 ns to permit acceleration over 45 degrees of phase in 350 MHz cavities, to 32 trains of 43 bunchlets of much lower charge, the post-acceleration over 180 degrees of phase being achieved by the use of cavities of second and higher harmonics [3]. In the extreme case

the charge would be spread over three or four filling times with a stage of microwave pulse compression between the drive beam transfer cavity and the main linac accelerating cavity [4]. The trend towards more trains of many bunchlets of relatively low charge favours a solution to the drive beam generation that was initially proposed by Yu in 1989 [5] and then elegantly presented by Shay et al. in 1991 [6].

In the latter proposal a beam of electrons from a LIA is bunched in a single-pass FEL at 30 GHz and the continuous (over 12 or more ns) bunched beam is then chopped into four trains of 11 (or more) bunchlets before post-acceleration in 350 MHz superconducting cavities. This scheme has the extremely attractive feature of requiring just one source of electrons and gives automatic relative phasing of the bunchlets – a non-negligible problem in schemes where the trains are built up from several sources. The chief drawback arises from the need to create the bunchlets at an energy high enough to avoid subsequent debunching from longitudinal space charge forces, since the following acceleration at 350 MHz provides no longitudinal focussing. Also, despite the continuous formation of bunchlets, there will be some bunchlet to bunchlet phase jitter that is mainly related to energy jitter in the electron beam entering the FEL.

The debunching problem can be solved, at the cost of providing sufficient LIA voltage, by increasing the energy at which the beam is first bunched in the FEL. According to the bunchlet charge that we choose, this FEL energy may be from 20 to 200 MeV.

2 POST-ACCELERATION

The mainstay of the CLIC design is the acceleration of the drive beam to GeV energies in 350 MHz superconducting cavities similar to those developed for the CERN electron-positron collider LEP. The cost of acceleration by this means is an order of magnitude less than by the use of LIA. However, because of beam loading and high order mode excitation in the superconducting cavities, to obtain the beam quality needed for correct FEL operation it seems that the LIA is the only candidate for acceleration up to the FEL energy. Hence, there is ample motivation to keep this energy as low as possible. A preliminary study has shown that for a drive beam comprising 4 trains of 22 bunchlets each with 80 nC charge the energy of the FEL should be in the region of 100 MeV. Bunching at a lower energy would result in some loss of 30 GHz structure due to the effect of longitudinal space charge. Reducing the bunchlet charge by increasing the number of bunchlets or

trains of bunchlets (always maintaining the total charge at 7 μC, or more if the inefficiencies of microwave bunch compression have to be compensated) would allow the FEL energy to be reduced, but then we run into the problem of debunching due to the relatively large transverse emittance of the drive beam.

3 PHASE STABILITY

To obtain the desired conversion efficiency in the CLIC transfer structure, the position of individual bunchlets composing a train should be stable in phase within some degrees. It is therefore essential to know under what experimental conditions this restriction is satisfied.

An analysis has been made to understand the dependence of the position of the bunches on the various experimental FEL parameters. This analysis has been carried out both analytically and numerically. It has shown that the main contribution to the phase difference between the bunchlets comes from initial variations in the electron beam energy along the macropulse, and has substantially confirmed the phase sensitivity evaluations given in [6]. An approximate analytical expression has been derived which gives an upper limit for the variation of the bunchlet phase as a function of energy sweep along the electron pulse:

$$\Delta\Theta \leq 4\pi N_w \left(1 - \frac{X}{2}\right)\frac{\Delta\gamma}{\gamma} \qquad (1)$$

where N_w is the number of wiggler periods and $X = k_\perp^2/k_w k_\parallel = \lambda\lambda_w/b^2$ is the TE01 waveguide parameter; λ_w is the wiggler period, λ the FEL radiation wavelength and b the waveguide height.

The above expression is valid in the FEL linear regime, prior to saturation, and for an energy variation $\Delta\gamma/\gamma \leq \rho$ where ρ is the fundamental FEL parameter (typically of the order of 5 10^{-2}). In steady state condition [7] the waveguide parameter $X = 1$, so the sensitivity is ≤ 0.06 N_w (rad / %) $\Delta\gamma/\gamma$. A wiggler tailored to the CLIC drive beam generation will have a number of periods between 10 and 30, depending on electron beam current and energy. The effective phase variation (numerically evaluated) ranges from 0.4 to 1.3 (rad / %) $\Delta\gamma/\gamma$. This will limit the acceptable energy sweep during the electron pulse to values of the order of 5 10^{-3}. A more accurate investigation on acceptable phase jitter in the CLIC transfer structure will set the exact limit.

4 TEST FACILITY

To study the FEL concept for CLIC drive beam generation we shall use the LELIA induction linac at CESTA. This accelerator can deliver a 1 kA, 50 ns electron beam at 1 MeV and will be upgraded to 2.5 MeV before summer '93. A preliminary bunching experiment will use a short hybrid wiggler built to study electron trajectories. As indicated in figure 1 the electron beam is transported from LELIA to the wiggler where it interacts with a copropagating 35
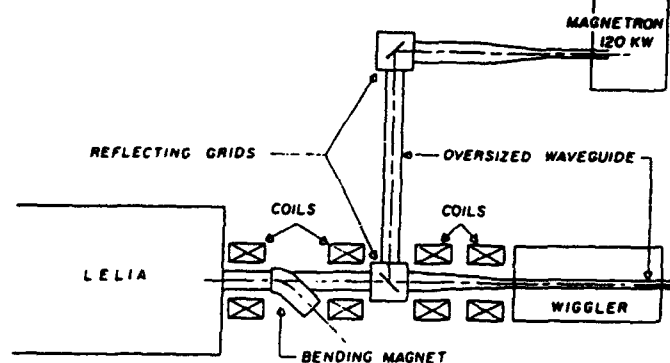
Figure 1: Lay-out of the LELIA facility for the CLIC drive beam experiments

GHz wave delivered by a 120 kW magnetron. The beating of the electromagnetic wave and the wiggler magnetostatic field gives rise to an axial ponderomotive force and a consequent bunching of the electron beam. This process causes the amplification of the injected radiation pulse. The existing wiggler parameters (8 periods of $\lambda_w = 8$ cm; $B_w \simeq 1500$ Gauss) impose a low energy ($\simeq 1$ MeV) operation for 35 GHz amplification. The challenge of this experiment comes from space charge forces, which can cause a loss of beam current during transport between LELIA and the wiggler and, worse, can induce FEL gain degradation and bunching delay. By increasing the electron beam energy such effects can be minimized, permitting higher spatial modulation of the electron beam in the wiggler.

This year is dedicated to electron beam transport along the experimental line at 1.2 MeV and 2.5 MeV, paying particular attention to beam injection and matching into the wiggler. Next year we shall couple the 1.2 MeV resonant electron beam to the 35 GHz microwave radiation delivered by the magnetron; we estimate that at least 50 kW out of the initial 120 kW power generated by the magnetron can be transported and launched in the TE01 mode in the interaction region. Then, once a significant rf power amplification is measured, we shall use the bunching diagnostic to measure the longitudinal electron beam current modulation at the rf frequency.

4.1 The Wiggler

The existing hybrid wiggler is made of permanent magnets alternating with soft iron poles. These are curved in such a way as to assure equal beam focussing in both transverse planes [8]. The wiggler magnetic field inside the structure and near the propagation axis z will approximate the desired field given by:

$$B_x = B_w \sinh k_x x \sinh k_y y \cos k_w z$$
$$B_y = B_w \cosh k_x x \cosh k_y y \cos k_w z$$
$$B_z = \sqrt{2}B_w \cosh k_x x \sinh k_y y \sin k_w z$$

where $k_x = k_y = k_w/2$ and $k_w = 2\pi/\lambda_w$.

The magnetic field is measured using a fully automatic Hall probe bench enabling us to obtain the three magnetic
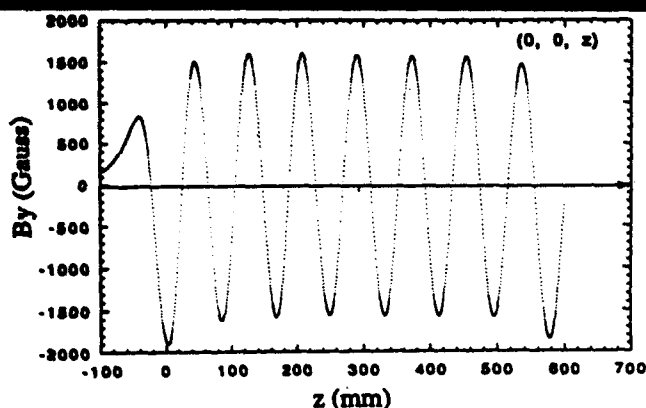
Figure 2: Example of the B_y field measurement on the z axis for a 53 mm wiggler gap showing fringing field to be corrected at the wiggler entrance
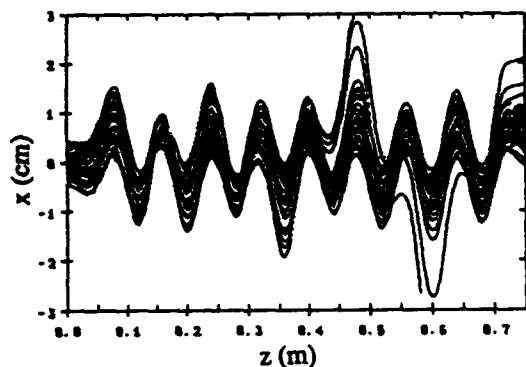
Figure 3: 1 MeV, 1 kA, 10 mm diameter, 400 π mm mrad beam propagation through the wiggler using the ELECTRA propagation code. $B_w = 1600$ Gauss at $z = 0.1$ m Some current is lost in this example but a better matching is possible by changing adjustments in the wiggler entrance section $z < 0.1$ m

field components in the desired locations. An example of the main field component B_y measurement on the z axis is given in figure 2.

4.2 Electron Beam Trajectories

Solenoidal focusing is used inside the accelerator and in the transport line. Initially the required coil current values are evaluated with an envelope code and then adjusted with the help of the PIC code ELECTRA, developed at CESTA, to obtain a 1 kA, 10 mm diameter exit waist.

Figure 3 gives an example of a 1 MeV electron beam beginning its propagation at a 10 mm diameter waist. These results are obtained with the ELECTRA code including transverse space charge. We have built a shuttle with a Cherenkov screen to measure the beam radius at different locations in the wiggler to confirm these calculations.

4.3 FEL computations and bunching previsions

Simulations of the FEL process have been made using the SOLITUDE code [9], developed at the "Commissariat à l' Energie Atomique" (CEA) a few years ago, and benchmarked against previous experiments.

This code is a multimode steady-state amplifier FEL code, with a version for rectangular waveguides and planar wigglers, taking into account longitudinal space charge.

Gain reduction and shift in resonant frequency due to longitudinal space charge for various sets of parameters have been studied numerically. The bunching achievable with low-energy operation is quite low and may be difficult to observe.

A great improvement is obtained for 2.5 MeV operation with adequate wiggler parameters (λ_w =10 cm, $B_w \simeq 3000$ Gauss, total length $\simeq 1.5$ m); in this case a value of the bunching parameter of $\simeq 0.5$, is shown by the computer simulations.

5 CONCLUSIONS

The FEL bunching scheme for the CLIC Drive Beam requires the development of a high energy 30 GHz FEL with good phase stability. This novel use of an FEL to generate bunched electron beams rather than as a source of radiation requires some studies into the electron beam characteristics within a high-gain microwave FEL amplifier. An experimental approach to this work has now begun at CESTA. The initial two-year programme calls for the generation and transport of a 1 kA electron beam from an induction linac into a hybrid wiggler. After a study of the amplification of input rf power in the fundamental waveguide mode, the electron bunch structure will be measured using a Cherenkov radiator and a high-speed camera.

The experiment will be extended to energies beyond the scope of the existing wiggler, and a suitable 2.5 MeV 35 GHz wiggler is sought. At this energy the quality and phase stability of the bunchlets can be well established.

6 REFERENCES

[1] J. Bardy et al., *Nucl. Inst. and Meth.*, Vol. A204, p. 311, 1991.

[2] W. Schnell, *Proceedings of the ECFA Workshop on e^+ e^- Colliders*, Garmish, 25 July - 2 August 1992

[3] L. Thorndahl, "A multi-frequency preacceleration system for the CLIC drive linac with beam loading compensation", *Proceedings of the XVth International Conference on High Energy Accelerators*, Hamburg, 20-24 July 1992.

[4] L. Thorndahl, private communication and The CLIC Study Group, These Proceedings.

[5] S.S. Yu, BRM89-29 (1989).

[6] H.D. Shay et al. *Nucl. Inst. and Meth.*, Vol. A304, pp. 262-267, 1991.

[7] R. Bonifacio and L. De Salvo Souza, *Nucl. Inst. and Meth.*, Vol. A296, p. 394, 1989.

[8] E.T.Scharlemann, *J. Appl. Phys.*, Vol.58, No. 6, pp. 2154-2161, September 1985.

[9] Ph. Gouard, CEA internal report.

Beam Instabilities Related to Different Focusing Schemes in TESLA

Alban Mosnier

DAPNIA-SEA, CE Saclay, 91191 Gif/Yvette, France

Abstract

The preservation of beam emittances during the transport through the main linac is essential to achieve maximum luminosity. An increase of the beam area in transverse phase space occurs when beam trajectories are displaced from the accelerator axis : Chromatic effects due to the finite energy spread are generated by the focusing magnets while beam instabilities due to the excitation of wakefields are induced by the accelerating structures. The major sources of emittance growth of a beam accelerated in the TESLA main linac are studied for different focusing schemes, including the constant β and the energy dependent β lattices. Since the accelerating structures have a low rf frequency and a large iris aperture, very weak or even no BNS damping is necessary to cure the single bunch instability from coherent betatron oscillations. In addition, different orbit correction techniques have been tested and the resulting emittance dilutions are compared. However, the choice of the steering method will be determined mainly by the effects of the wakefields, both short-range and long-range, induced by the randomly displaced cavities, which are allowed to have a large scatter in their misalignments.

INTRODUCTION

An increase of the beam area in tranverse phase space arises from a variety of errors and is mainly driven by 3 phenomena : the short-range and long-range dipole wakefields and the dispersion resulting from the finite beam energy spread. The errors of main concern are quadrupole and cavity static misalignments, injection jitter, and quadrupole jitter due to ground motion. The effects of the major errors can be reduced in some cases thanks to various techniques (BNS damping, steering algorithms, de-Q'ing ...) and their maximum allowed magnitudes are then fixed once a limit on the emittance growth has been prescribed. A typical set of machine parameters for TESLA 500 with the high charge option [1] is listed below and have been used throughout this study.

Energy / Linac (GeV)	250
Injection energy (GeV)	3
Bunch population	$5\ 10^{10}$
Bunch length σ (mm)	1
Number of bunches	800
Bunch separation (μS)	1.
Eacc (MV/m)	25
Tot number of cavities	10000

Two focusing schemes have been considered : the FODO lattice with a constant focusing strength all along the linac (focal length and beta function); and the $E^{1/2}$ beta scaling suggested in [2] because it provides a BNS damping criterion

[3] independent of energy. Since eight cavities per cryomodule are assumed, the modules are grouped in sections with matching cells in between such that the beta function best fits the $E^{1/2}$ law. The resulting beta function at the focusing quadrupoles and the exact scaling are shown in figure 1 for starting cells filled with one module. We should emphasize that the matching cells were assumed ideal and their quadrupoles perfectly aligned for the simulations.
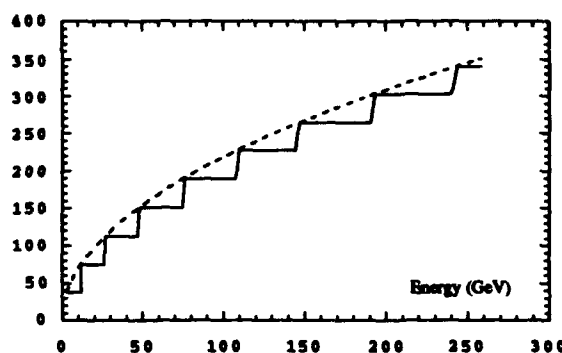
Figure 1 : Beta function for the actual scaling (full line) and for the exact scaling law (dashed line) at the focusing quads.

SINGLE BUNCH INSTABILITY

Injection jitter

When a beam is injected off-axis, the tail particles are driven on resonance by the wakefield of the head particles and oscillations will grow along the linac. Figure 2 shows the development of the emittance growth along the linac assuming a beam offset of 28.5 μm (half the beam size) for the constant (β = 66m) and energy dependent (starting β = 22m) beta lattices
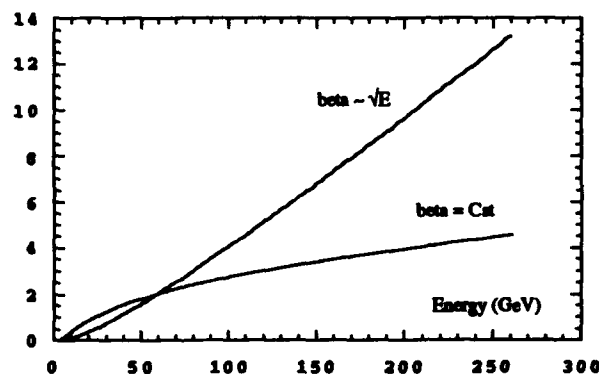
Figure 2 : Vertical emittance growth for both focusing lattices (beam offset = 28.5 μm).

The instability driven by the short-range wakefields could be controlled by means of BNS damping by simply shifting the rf phase in such a way that the tail is more focussed. Although the damping is more efficient for the √E beta scaling, the damping conditions are barely achieved for the whole bunch. After optimization of the rf phase, the same dilution of about 1 % is found for both focusing lattices but the energy spread has been multiplied by a factor of 4, increasing the chromatic effects induced by the alignment errors. We conclude that BNS damping is not necessary for the constant β case since the final dilution is small (4 %) while keeping the energy spread to the minimal value of $5.5\ 10^{-4}$.

Alignment errors

In order to prevent a continually growing trajectory in the presence of quadrupole errors, the beam must be steered all along the linac. Different correction techniques have been tested on the TESLA linac and are recalled below.

1) The "one to one" correction : the BPM readings are zeroed such a way the beam is steered to the center of the quadrupoles. Chromatic dilution arises because the actual orbit follows the BPM errors, however.

2) The Dispersion Free correction [4] : the dispersive errors are cancelled by measuring the difference of 2 trajectories with effective different energies. The difference orbit and the original trajectory are then simultaneously corrected. The measurement of the difference orbit is then independent of the BPM errors but some errors remain due to the finite BPM resolution.

3) The Wake Free correction [5] : two difference orbits must be minimized to correct both the dispersive errors and the wakefields effects (one by varying only the QF's and one by varying only the QD's).

These 3 correction algorithms were first tested on the TESLA linac (constant β = 66m) with a final energy spread of $1.5\ 10^{-3}$ assuming only quadrupole and BPM errors, and without any cavity errors. Figure 3 shows the beam slice centroids emerging from the linac as well as the beam ellipses of the first and last slices. This points out the benefit of the DF and WF algorithms (beam slices nearly superimposed) compared to the one to one algorithm (beam slices strongly diluted) where the dispersive errors are not corrected.
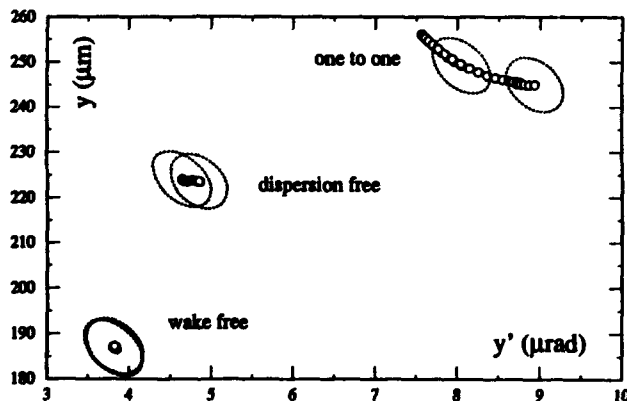
Figure 3 : Beam slice centroids and beam ellipses of the first and last slices at the linac exit in transverse phase espace.

The WF correction cancels the wakefields effects for a corrected trajectory but not the wakefields effects induced by the random errors of cavity misalignments. A less spectacular improvement is hence expected when using these non dispersive corrections in case of large cavity random offsets. Figure 4 gives the emittance growth for 10 sets of random errors for the constant beta lattice with different beta values for the 3 corrections. The √E beta scaling lattice with a starting beta of 22m gives about the same results than the constant β=66m lattice. The linac is corrected section by section, with each section containing 20 cells. The rms values of the errors chosen for these computations are :

cavity scatter	500 µm
quadrupole scatter	100 µm
BPM scatter	100 µm
BPM resolution	10 µm
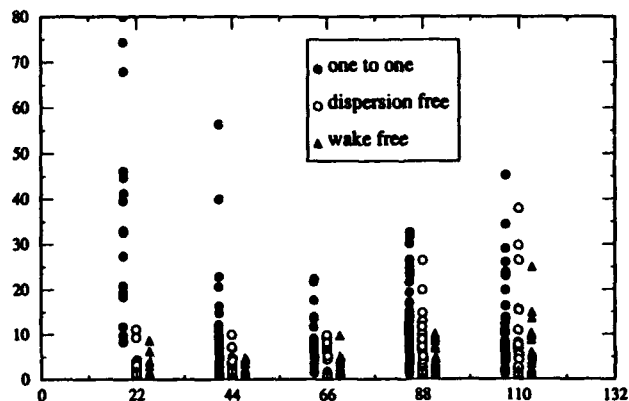
Figure 4 : Vertical emittance growths (%) for the 3 correction algorithms vs. beta (m) for the constant beta lattice

We note that the dilution has clearly decreased when using the DF or WF corrections, especially in the region of stronger focussing (higher number of cavities / half cell), as expected. The maximal emittance dilution is lowered by a factor of 2 to 4 with respect to the "one to one" correction used with the optimal lattice (β=66m). This improvement has however to be balanced by the fact that the simple "one to one" algorithm allows for a fast correction and then a feedback within the bunch train (bunch repetition frequency = 1 MHz).

MULTIBUNCH INSTABILITY

The growth of the transverse motion of the bunches due to the long-range wakefields are controlled in TESLA both by damping of the modes and by the frequency spread of each mode which spoils the coherence. We assume a mode frequency spread due to fabrication tolerances of 1 MHz and Q values of around or below 10^5 for the highest R/Q modes, in agreement with the measurements [6].

Injection jitter

When the beam is launched off-axis, both lattices (always with a starting beta value of 22 m for the √E scaling and 66m for the constant beta) give about the same results : a multibunch emittance of only 0.6 % of the single bunch emittance design value for a beam offset of 1 mm at the entrance of the linac when the dispersive errors are neglected. But if some bunch to bunch energy spread is introduced, the emittance dilution arises mainly from the partial filamentation due to the chromatic phase advance. The emittance growth is then 2 % of the design value for an injection jitter of 28.5 μm and an energy spread of 10^{-3}.

Alignment errors

Finally, we study the effects of cavities randomly misaligned with an rms value of 1 mm and neglecting any energy spread. The emittance at the exit would be only a few percent higher than the design bunch emittance for the constant β lattice with a mean beta of 66 m [7], while the emittance was found to be about 3 times higher for the energy dependent lattice with a starting beta of 22 m.

However, if a bunch to bunch energy spread is introduced, due, for example, to a systematic fluctuation of the cavity fields, the emittance becomes 10 times more, e.g. $0.4 \ 10^{-6}$, for an energy spread of 10^{-3}. Figure 5 shows the 800 bunches emerging from the linac in transverse phase space both with and without energy spread.
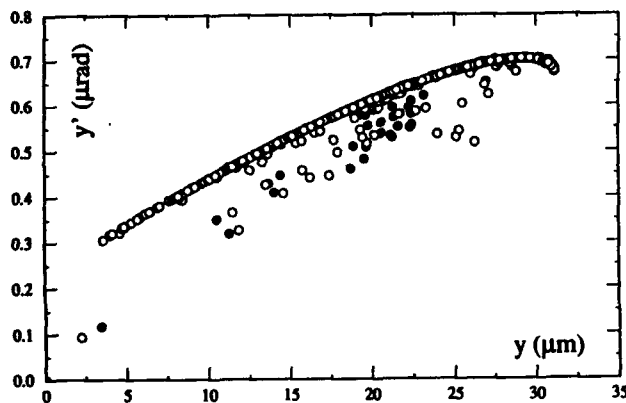
Figure 5 : Coordinates in phase space of the 800 bunches without (full circles) and with energy spread (empty circles).

For vanishing energy spread (full circles) the first bunches are slightly scattered but the others bunches form a dense core. For the energy spread of only 10^{-3} (empty circles), the plot reveals a large chromatic effect. In fact, the steady state regime is rapidly achieved in TESLA because of the strong mode damping, and after approximately 150 bunches, the next bunches follow the same trajectory, resulting in a small rms emittance if no energy spread is present. However, the beam is strongly displaced from the accelerator centerline as we can see in figure 6, where the trajectory of the last bunch is plotted

along the linac exhibiting a betatron oscillation of final amplitude 20 μm. If the filamentation was complete, occuring at $\sigma_E/E = 5.10^{-3}$, the emittance would be 6.10^{-6} instead of $0.03 \ 10^{-6}$ without dispersive errors.
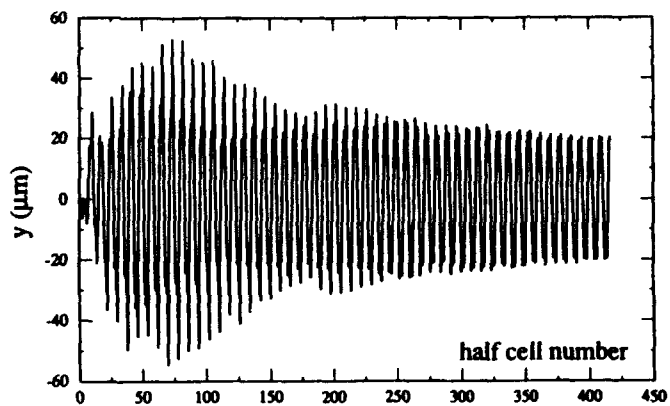
Figure 6 : Trajectory of the last bunch (steady state regime) for an energy spread of 10^{-3}.

In order to get rid of this wakefield-chromatic combined effect, which demands a stringent tolerance on the bunch to bunch energy spread (a few 10^{-4}), we could imagine a correction scheme which measures the trajectory once the steady state is achieved. This method was successfully applied by using the one to one correction where the wakefields effects can be easily taken into account with BPM readings on the last bunch. The initial emittance growth of a few percent obtained without energy spread was fully recovered with 10^{-3} energy spread assuming the BPMs perfectly aligned. Some computations were carried out with BPM and quadrupole alignment errors: the emittance becomes $0.13 \ 10^{-6}$ with a rms BPM error of 100 μm; and $0.22 \ 10^{-6}$ if an additional rms quadrupole error of 100 μm is added.

REFERENCES

[1] H. Padamsee, "Review of the superconducting approach to linear colliders", *Proc. 3rd Eur. Part. Acc. Conf.*, Berlin, Editions Frontieres, 1992

[2] V. Balakin, A. Novokhatsky and V. Smirnov, *Proc. 12th Int. Conf. on High Energy Accelerators*, Fermilab, 1983

[3] R. Ruth, "Emittance Preservation in Linear Colliders", *Frontier of Particle Beams* 296, Springer-Verlag

[4] T. Raubenheimer and R. Ruth, "A dispersion-free trajectory correction technique for linear collider", *Nucl. inst. and Methods*, A302, 1991

[5] T. Raubenheimer, "A new technique of correcting emittance dilutions in linear colliders", *Nucl. Inst. and Methods*, A306, 1991

[6] A. Mosnier and J. Sekutowicz, TESLA collaboration meeting, Fermilab, March 1993, unpublished

[7] A. Mosnier and O. Napoly, "Wakefield effects in a Superconducting Linear Collider", *Proc. 15th Int. Conf. on High Energy Accelerators*, Hamburg, World Scientific, 1992

A Large Aperture Final Focus System for TESLA

Olivier Napoly

DAPNIA-SEA, CE Saclay, F-91191 Gif/Yvette, France

Abstract

An alternative set of beam parameters at the IP is presented for TESLA. Thanks to a larger aspect ratio, it allows a substantial reduction of the beamstrahlung effect. The optics of a final focus system based on the standard sextupole correction of the chromatic aberrations is described. The particularity of this system is, along with the 3 m long last drift space, the large aperture of the last quadrupoles, possibly superconducting, which permits the clearance of the disrupted beams and beamstrahlung photons. Due to the large bunch separation in TESLA, head-on collisions are therefore possible with this system. Its energy acceptance and misalignment tolerances are analyzed.

I. BEAM PARAMETERS

The beam sizes at the interaction point (IP) usually proposed [1] for the 500 GeV center of mass energy, high current option of TESLA, with $N = 5.10^{10}$ particles per bunch and 800 bunches per 10Hz pulse, are

$$\sigma_x^* = 640\,\text{nm}\ ,\ \sigma_y^* = 100\,\text{nm}\ \text{and}\ \sigma_s = 1\,\text{mm}, \qquad (1)$$

yielding the Gaussian luminosity $\mathcal{L} = 2.5\ 10^{33}\text{cm}^{-2}\text{s}^{-1}$. Given the normalized emittances considered in the TESLA linac, namely

$$\epsilon_{n,x} = 20.10^{-6}\,\text{m.rad}\ ,\ \epsilon_{n,y} = 10^{-6}\,\text{m.rad}\ , \qquad (2)$$

these beam sizes are achieved with $\beta_x^* = 10$ mm and $\beta_y^* = 5$ mm . These parameters are rather conservative as far as the aspect ratio $R = \sigma_x^*/\sigma_y^* = 6.4$ is concerned. A much flatter beam at the IP can be easily produced by the final focus optics. The limit on the large aspect ratio arises from 3 constraints:

1. the "hour-glass" luminosity reduction imposes $\beta_y^* > \sigma_s$.
2. the spot sizes at the IP are limited by the emittance growth due to synchrotron radiation in the last quadrupoles ("Oide effect"). For the optics described in the next section and the normalized emittances given above, this limit is around 35 nm for the vertical spot size, and 400 nm for the horizontal one.
3. the disruption parameter must be small enough to prevent a kink instability from occurring when the two beams collide with a vertical offset.

The beam spot sizes

$$\sigma_x^* = 1000\,\text{nm}\ \text{and}\ \sigma_y^* = 64\,\text{nm}\ , \qquad (3)$$

corresponding to $\beta_x^* = 24.5$ mm and $\beta_y^* = 2$ mm, lead to the same Gaussian luminosity with an aspect ratio $R = 15.6$. This parameter set obviously fulfills the first two constraints and the vertical disruption parameter only increases from 8.0 to 8.7. In order to check the third constraint, a plot of the luminosity as a function of the vertical offset as calculated with the program RBEAM [2] is shown in Figure 1. The observed reduction
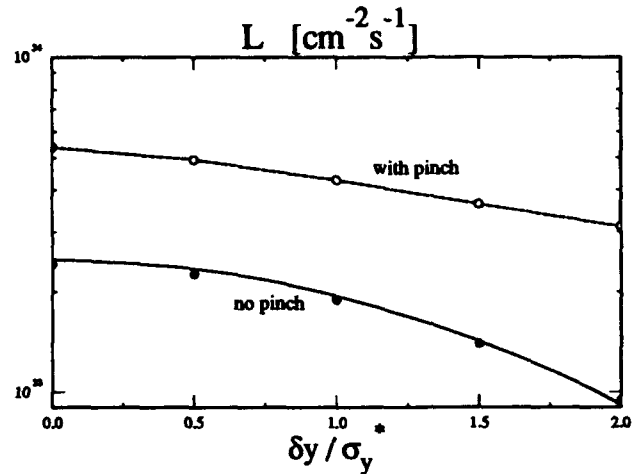
Figure 1 Luminosity vs. vertical offset (full and empty circles are results from RBEAM, the full curve is the analytic prediction)

is not faster than predicted analytically when the beam-beam forces are neglected (full curve). This expected behaviour strongly suggests that the kink instability does not show up, even for the flat beam parameters.

The beneficial effect expected on the beamstrahlung reduction from the large aspect ratio is illustrated in Figure 2 and in Table 1. The integral of the differential luminosity $\int_s^{s_{max}} (d\mathcal{L}/ds')ds'$, calculated with RBEAM, is plotted in Figure 2. It is higher for $R = 15.6$ than for $R = 6.4$ as
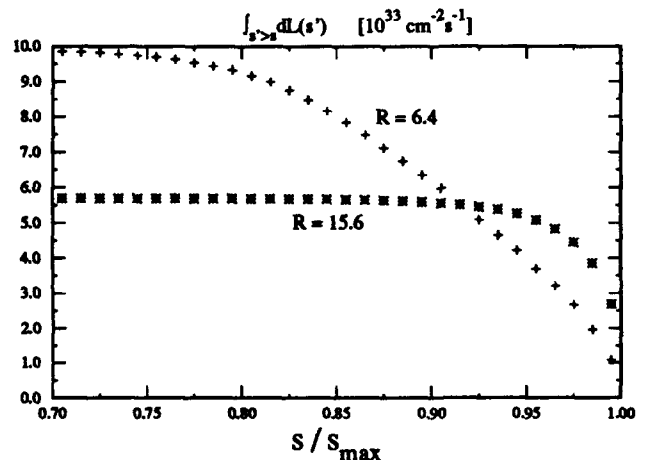
Figure 2 Integrated differential luminosity spectrum for TESLA

long as the c.m. energy is larger than 95% of the maximum energy. This is true even though the total luminosity is about a

factor 2 larger for $R = 6.4$ due to a larger pinch enhancement factor. The average relative c.m. energy loss, calculated from these luminosity spectra, is equal to 1.0% in the flat beam case and 4.6% in the other case, showing a substantial improvement in the energy resolution of the collisions. This is in agreement with the results, given in Table 1, of the comparison of 3 different beam-beam simulation programs [3] for the e^+e^-, $e\gamma$ and $\gamma\gamma$ luminosities and for the average relative energy loss ("beamstrahlung parameter"). Although slightly different, the

R	Program	$\mathcal{L}_{ee}$	$\mathcal{L}_{e\gamma}$	$\mathcal{L}_{\gamma\gamma}$	δ
	MACPAR	11.7	19	43	9.3%
6.4	ABEL	13.7	23	57	9.5%
	RBEAM	13.2			7.8%
	MACPAR	8.0	7.2	8.8	3.0%
15.6	ABEL	8.8	7.9	9.3	2.9%
	RBEAM	7.3			1.9%

Table 1 Luminosity per crossing (in units of 10^{29}cm^{-2}) and beamstrahlung parameter for two sets of TESLA parameters

results derived from the 3 programs are consistent in showing that the flat beam parameters lead to a significant reduction of the beamstrahlung photon emission and background. Accordingly, and as a last comparison between the two parameter sets, the quadratic average of the beam disruption angle drops from 520 μrad to 270 μrad for the flat beam case.

II. THE LARGE APERTURE OPTICS

A final focus system (FFS) is essentially a low-beta telescopic system transfering the beam from the end of the collimation section after the linac, to the IP. The strong chromaticity of the last focusing doublet is corrected, in the standard way [4], by placing sextupole pairs into a region where non-zero dispersion is created by bending magnets. The system described here derives from the CLIC FFS design [5], adapted and optimized for the flat beam parameters introduced in the preceding section. A system optimized for the other parameter set would have very similar characteristics.

A. General description

We assume upright beam ellipses with $\beta_x = 113.4$ m and $\beta_y = 19.5$ m at the entrance of the FFS, corresponding to a 250 GeV beam exiting from a 90° constant beta FODO lattice with 24 TESLA superconducting cavities per half-cell [6]. The total demagnifications to achieve with the FFS are therefore 68.0 horizontally and 98.7 vertically. The lattice of the FFS, displayed in Figure 3, contains 3 modules:

1. a matching telescope of 8.5×5.8 demagnifications.
2. a chromatic correction section (CCS) containing two pairs of identical sextupoles, all separated by π phase-shift. The first pair, correcting the horizontal chromaticity, is located at the maxima of β_x (full line), and the second pair, for the vertical correction, is located at the maxima of β_y (dashed line).
3. a final telescope of 8×17 demagnifications.
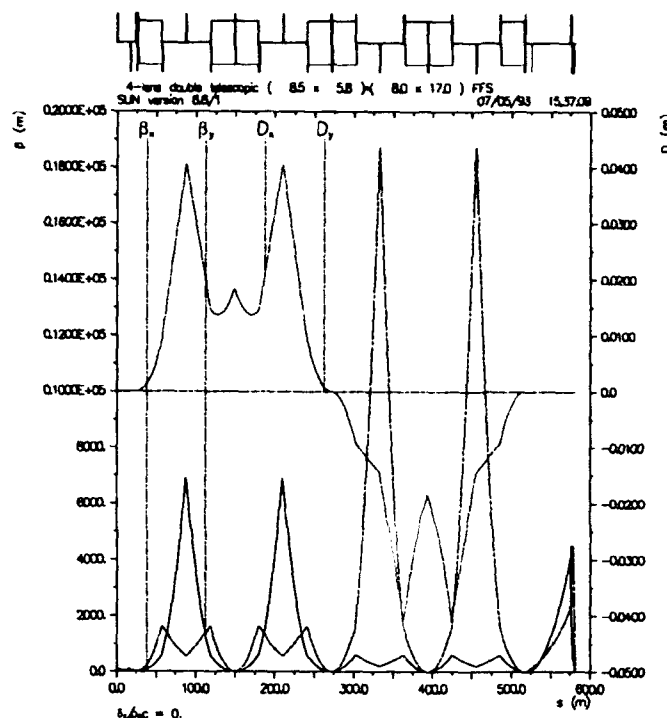
Figure 3 Lattice layout and orbit functions of the final focus sytem

The total length of the system is less than 600 m. The matching of the imperfect vertical and horizontal beam ellipses from the linac can be done at the first sextupole by using the 4 quadrupoles of the matching telescope and the first 2 quadrupoles of the CCS. The dispersion in the CCS is created by 8 identical 29 m long dipoles. The dipole field is 170 Gauss and the synchrotron power deposited by the beam is negligible. The final telescope is composed of a weak and a strong doublet separated by 50 m. The length of the final drift space before the IP is 3 m.

B. The energy acceptance

Dividing the total demagnifications between the matching and the final telescopes is done in such a way as to maximize the energy acceptance of the FFS. This acceptance can be estimated by calculating with MAD [7], the dependence of β_x^* and β_y^* on the energy offset δ. The bandwith of the system, defined as the doubling of the beta-functions, is $\pm 1.1\%$. The energy acceptance can also be characterized, as in Figure 4, by the dependence of the spot sizes and luminosity on the Gaussian energy spread σ_δ of the beams.

C. The aperture of the last doublet

The integrated gradient of the quadrupoles of the last doublet are inversely proportional to their focal length. For a 3 m long last drift, the gradient can be as low as 300 T/m. In our design, the two quads then have a length of 1.2 m and 1.7 m, and are separated by 30 cm. This gradient can be obtained with 1.4 T pole-tip field permanent magnets of about 1 cm aperture. It also opens the possibility of using superconducting quadrupoles with an aperture of the order of 3.5 cm. For the flat beam parameters, these apertures are very

633

large compared to the 407 μm horizontal and 110 μm vertical 1-σ maximum extension of the incoming beams. A 10-σ beam collimation could therefore be contemplated. Moreover, beamstrahlung simulations [3,8] indicate that the maximum angle of the outgoing disrupted electrons and emitted photons, are about 0.5 mrad and 1.1 mrad. Hence, even with an aperture of 1 cm, the central region of the opposing last doublet could clear the disrupted beams and no photon would hit the quadrupole face on the detector side. As a consequence head-on collisions, i.e. with zero crossing-angle, seem feasible with this large aperture optics. All these aspects must, however, be carefully studied by tracking simulations.
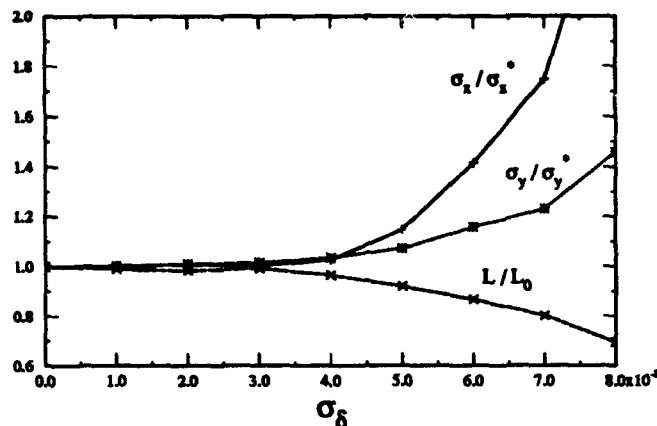
Figure 4 Energy acceptance of the final focus sytem

D. Separation of the beams

At zero crossing-angle it is necessary to separate the bunches in order to avoid unwanted collisions. The bunch spacing is foreseen to be 300 m (1 μs) in TESLA, and separation may thus easily take place in the 50 m free space after the last doublet. A 250 KV electrostatic voltage over a 4 cm gap, compensated by a magnetic field to keep the trajectory of the incoming bunch straight, induces a transverse separation of 6 cm with a deflection angle of 2.5 mrad after 50 m. This should allow to further deflect the outgoing beam by using a septum magnet.

III. ALIGNMENT TOLERANCES

In order to investigate the sensitivity of this beam line to misalignments, we first consider the loss of luminosity resulting from ground vibrations affecting all magnets *on both sides of the* IP, except the last doublets which are then treated separately. Luminosities are calculated from the beam distributions at the IP and the pinch enhancement is not taken into account.

Assuming uncorrected (jitter) and uncorrelated vibrations of identical amplitudes $\sigma_{\delta x}$ and $\sigma_{\delta y}$, the luminosity loss induced by each element adds up quadratically, to yield

$$\mathcal{L} = \mathcal{L}_0\left(1 - 0.64(\sigma_{\delta x}/\sigma_x^*)^2 - 0.13(\sigma_{\delta y}/\sigma_y^*)^2\right). \quad (4)$$

Hence, a 10% luminosity loss corresponds to vertical vibrations of around 56 nm rms.

The issue of the alignment of the last doublet quadrupoles is of course critical, especially in the case of SC quadrupoles envisaged above. Most probably the two opposing doublets will have a common support to ensure the best possible alignment of the 4 quadrupoles relative to each other. Neglecting the weak sensitivity to the absolute displacement of the two doublets (i.e. that of the common support), the luminosity is found to depend only on the relative misalignments of the opposing focusing quadrupoles $\Delta x_F = (\delta x_F^+ - \delta x_F^-)$ and $\Delta y_F = (\delta y_F^+ - \delta y_F^-)$ on the one hand, and of the opposing defocusing quadrupoles $\Delta x_D = (\delta x_D^+ - \delta x_D^-)$ and $\Delta y_D = (\delta y_D^+ - \delta y_D^-)$ on the other. For small displacements the luminosity loss is given by

$$\delta\mathcal{L}/\mathcal{L}_0 = 3.8(\Delta x_F/\sigma_x^*)^2 + 1.9(\Delta x_D/\sigma_x^*)^2 - 5.3\Delta x_F\Delta x_D/\sigma_x^{*2}$$
$$+0.22(\Delta y_F/\sigma_y^*)^2 + 0.94(\Delta y_D/\sigma_y^*)^2 - 0.91\Delta y_F\Delta y_D/\sigma_y^{*2}. \quad (5)$$

Finally, let us point out that one might obtain better tolerances by trying different optimizations of the FFS and compromising on the momentum bandwidth.

V. REFERENCES

[1] M. Tigner, "Superconducting Linear Colliders", *Proc. 15th Int. Conf. on High Energy Accelerators*, Hamburg (HEACC92), World Scientific (1992)

[2] L.Wood, "The CLIC beam-beam interaction program", unpublished

[3] D. Schülte, "Simulation of the Background due to Incoherent Pair Creation in Linear Colliders", *Diplomarbeit*, II. Institut für Experimentalphysik der Universität Hamburg, (March 1993)

[4] J.J. Murray, K. Brown and T. Fieguth, "The Complete Design of the SLC Final Focus System", *Proc. IEEE Particle Accelerator Conf.*, Washington D.C. (1987)

[5] O. Napoly, T. Taylor and B. Zotter, "A Final Focus Design for the CERN Linear Collider CLIC", *Proc. 14th Int. Conf. on High Energy Accelerators*, Hamburg (HEACC89), Part. Accelerators Vol.30, pp.137-142 (1990)

[6] A. Mosnier and O. Napoly, "Wakefield effects in a Superconducting Linear Collider", *Proc. 15th Int. Conf. on High Energy Accelerators*, Hamburg (HEACC92), World Scientific (1992)

[7] F.C. Iselin and H. Grote, "The MAD Program", CERN/SL/90-13 (AP) (1991)

[8] R. Brinkmann, private communication.

Chicane and Wiggler Based Bunch Compressors
for Future Linear Colliders[*]

T. O. RAUBENHEIMER, P. EMMA, S. KHEIFETS

Stanford Linear Accelerator Center, Stanford University, Stanford, CA 94309

Abstract

In this paper, we discuss bunch compressors for future linear colliders. In the past, the bunch compression optics has been based upon achromatic cells using strong sextupoles to correct the dispersive and betatron chromaticity. To preserve the very small emittances required in most future collider designs, these schemes tend to have very tight alignment tolerances. Here, we describe bunch compressors based upon magnetic chicanes or wigglers which do not need sextupoles to correct the chromatic emittance dilution. The dispersive chromaticity cancels naturally and the betatron chromaticity is not a significant source of emittance dilution. Thus, these schemes allow for substantially reduced alignment tolerances. Finally, we present a detailed design for the NLC linear collider.

Introduction

Bunch compressors are needed in the NLC [1], a future linear collider design, to compress the bunch length from roughly 5 mm at the exit of the damping rings to 100 μm. The principal problem that arises is the preservation of the transverse emittances. This becomes difficult because the beam energy spread is increased as the bunch length is decreased (the longitudinal emittance is conserved). Thus, it is extremely important to design a compressor that is insensitive to the inevitable errors and that is tunable so that the emittance dilutions can be corrected easily.

In the past, many bunch compressor designs relied on achromatic arcs to generate the necessary correlation between energy and path length; this correlation is referred to as the R_{56} matrix element or the I_1 synchrotron integral. The dispersive and betatron chromaticities were corrected with sextupoles distributed through the arc. An example of such a system is the Ring-to-Linac (RTL) transport line [2] at the Stanford Linear Collider (SLC). The RTL is designed to compress the bunch by a factor of 10. Unfortunately, the system has proven difficult to operate, partially due to a larger than expected bunch length from the damping rings. Many additional tuning elements, quadrupoles, sextupoles, and even octupoles have been added to the line and yet the emittance is still increased by roughly 25% [3]. The primary source of dilution is thought to be higher order dispersion that is not fully cancelled.

In the NLC, the situation would probably be even worse because the design emittances are much smaller and because the collider is designed to operate with flat beams: $\epsilon_x = 100\epsilon_y$. To preserve the vertical emittance with flat beams, the vertical alignment tolerances on the sextupoles

---
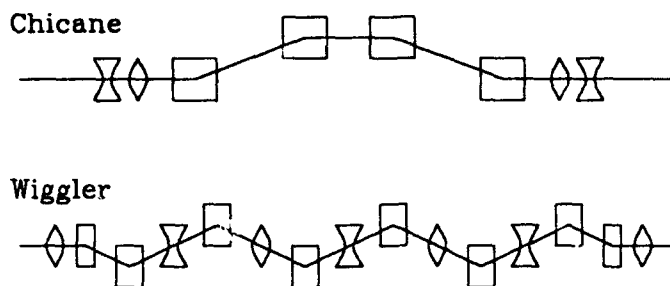
Chicane

Wiggler

Fig. 1 Schematic of wiggler and chicane to be used for bunch compressors.

must be very tight; vertical misalignments of sextupoles cause skew fields that will couple the beam and increase the vertical emittance. An initial design of the NLC bunch compressor [4,5] required a 2 μm vertical alignment of the sextupoles [6].

For these reasons, we are considering using wigglers or magnetic chicanes to generate the necessary R_{56} for the compressor. It is straightforward to show that in a system consisting only of rectangular bending magnets, all non-linear contributions to the dispersive chromaticity are cancelled when the first order dispersion is cancelled [7]; the betatron chromaticity is not a significant source of emittance dilution.

Finally, in the NLC, we are considering performing two bunch compressions, one immediately after the damping ring at 1.8 Gev and one at 10 to 20 GeV so that the relative energy spread never exceed 1%; this reduces the tolerances on the compressors and the linacs downstream of the compressors. To perform the first compression, we want to rotate the longitudinal phase space by 90° so that the beam energy spread is translated into the bunch length and the bunch length is translated into energy spread. This will prevent phase deviations in the damping rings from becoming phase deviations in the linac. But, in the next compressor, we want to prevent energy deviations that arise in the linac from becoming phase deviations in the next linac. Thus, we want to perform a "180°" compression in the second compressor where the bunch is rotated by $n\pi$ in longitudinal phase space. This requires at least two R_{56} elements with RF between them.

Wigglers and Chicanes

Figure 1 schematically illustrates a wiggler and a chicane bunch compressor. Both systems have an energy dependant path length and thus can be used for a bunch compressor. In the wiggler system, quadrupoles can be placed at locations where the dispersion goes through zero; this does not generate non-linear dispersion and allows control

of the beta functions. We only would need to introduce a few weak correction elements for tuning in the dispersive regions that would have nominal strengths of zero. Finally, one can choose the phase advance across the wiggler to be equal to 2π so that systematic errors in the bends cancel.

The R_{56} and Synchrotron Radiation

We can use very simple formula to calculate the R_{56} matrix element for a chicane of wiggler system. The P_{56} is equal to the I_1 synchrotron integral:

$$R_{56} = \int ds \frac{\eta}{\rho} \quad , \qquad (1)$$

where η is the dispersion and ρ is the instantaneous bending radius.

In the case of a chicane, constructed from four equal bending magnets of length L_B, bending angle Θ_B, and separated by a distance ΔL, the R_{56} is:

$$R_{56} = 2\Theta_B^2 \left(\Delta L + \frac{2}{3} L_B \right) \quad . \qquad (2)$$

Similarly, in a wiggler with N_p periods, each period constructed from two bending magnets with length $2L_B$ and angle $2\Theta_B$, and separated by a distance $2\Delta L$, the R_{56} is:

$$R_{56} = 4N_p \Theta_B^2 \left(\Delta L + \frac{L_B}{2} \right) - (2N_p + 1)\Theta_B^2 \frac{L_B}{3} \quad . \qquad (3)$$

Next, we can estimate the emittance dilution due to the synchrotron radiation. As mentioned, in the NLC, we are considering performing two bunch compressions, one immediately after the damping ring at 1.8 Gev and one at 10 to 20 GeV. In the high energy compressor, synchrotron radiation becomes a significant source of emittance dilution. In a transport line, the emittance growth can be estimated using the formalism of Refs. 8 or 9:

$$\Delta\gamma\epsilon_x \text{ [m-rad]} \approx 4 \times 10^{-8} E^6 \text{ [GeV] } I_5 \text{ [m]} \quad , \qquad (4)$$

where E is the beam energy in GeV and I_5 is the fifth synchrotron integral.

In a chicane, the emittance growth is approximately

$$\Delta\gamma\epsilon_x \approx 8 \times 10^{-8} E^6 \frac{\Theta_B^5}{L_B^2} \left[(\Delta L + L_B) + \frac{\check{\beta} + \hat{\beta}}{3} \right] \quad , \qquad (5)$$

while in a wiggler the emittance growth is:

$$\Delta\gamma\epsilon_x \approx 2 \times 10^{-7} E^6 N_p \frac{\Theta_B^5}{L_B^2} \frac{(\Delta L + L_B)}{\sin\psi_c} \quad , \qquad (6)$$

where $\check{\beta}$ and $\hat{\beta}$ are in minimum and maximum beta values across the chicane and ψ_c is the phase advance per cell in the wiggler. Notice that for the same length and the same R_{56}, the synchrotron radiation contribution to the emittance is much larger in a wiggler than in a chicane. Finally, more exact calculations of the emittance growth need to consider the match of the synchrotron radiation contribution to the beam [10], but this is unnecessary for our purposes; Eqs. (5) and (6) will tend to over-estimate the growth.
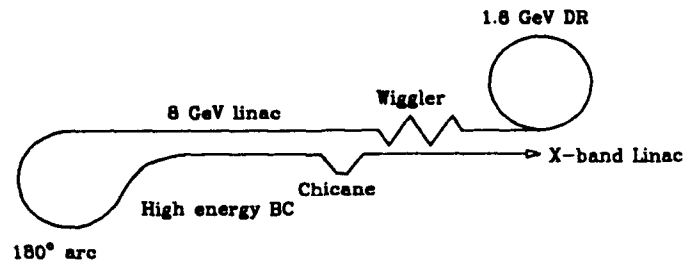
Fig. 2 Schematic of the NLC bunch compression.

Low Energy Compressor

The NLC low energy bunch compressor is located immediately after the damping ring as illustrated in Fig. 2. It must provide a 10:1 bunch length reduction while preserving the small transverse emittances from the damping rings. The compressor consists of a 2.5 meter S-band structure with a voltage of 67 MV followed by a four period wiggler. This rotates the longitudinal phase space by roughly 90°, compressing the bunch length from 5 mm to 500 μm while increasing the energy spread from 0.1% to 1%. The optics are shown in Fig. 3.

The main wiggler section is made up of four 90 degree cells such that each bend magnet (with the exception of the first and last) has an opposing pair at a $-I$ transform separation. This symmetry provides cancellation of systematic dipole magnet errors (e.g. sextupole component). Each main quadrupole is placed where the horizontal dispersion crosses through zero. This placement eliminates the generation of dispersive chromaticity and also locates the quadrupoles where the beam size is small which eases quadrupole field quality tolerances.

Operational experience in the SLC bunch compressors has made clear the need for tuning elements which are designed into the beamline. In addition to a high degree of symmetry and the absence of strong focusing elements at dispersive locations, the low energy bunch compressor incorporates eight small dispersion tuning quadrupoles — four skew and four normal — for orthogonal control of residual angular and spatial dispersion in both planes. Each tuning quad has a $-I$ opposing pair so that dispersion can be controlled independent of beta functions and betatron coupling by varying the quad pair's difference setting and holding the sum setting to zero. There are two skew pairs separated by 90° and two normal pairs separated by 90°.

A set of ≥ 4 wire scanners (not addressed here) must be well placed immediately following the wiggler section in order to measure horizontal and vertical emittance and beta functions. This section will require magnified beta functions (especially vertically) in order to measure beam sizes of 5 to 100 μm rms. Linear combinations of the tuning quads can then be formed to orthogonally correct all dispersion by simply minimizing the emittance with each of the four linear combinations.

In order to test the tuning capability of the wiggler

636
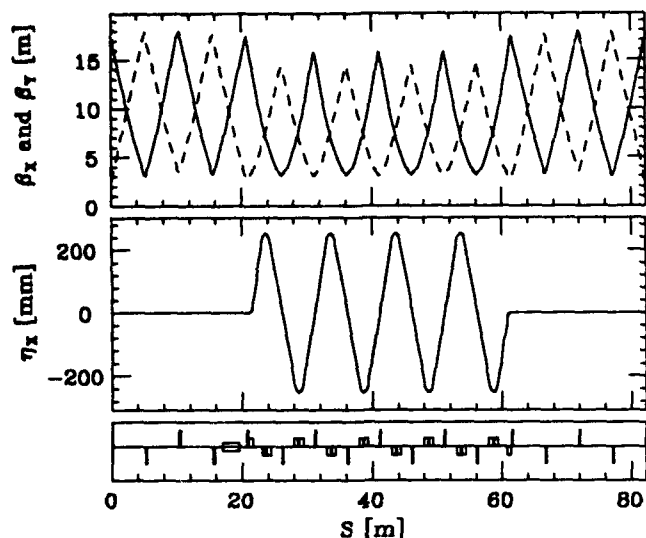
Fig. 3 Optical functions β_x (solid), β_y (dashes), and η_x in the low energy compressor. The RF cavity is a 2.5 meter S-band structure with a voltage of 67 MV. The tuning quadrupoles are located at the bending magnets.
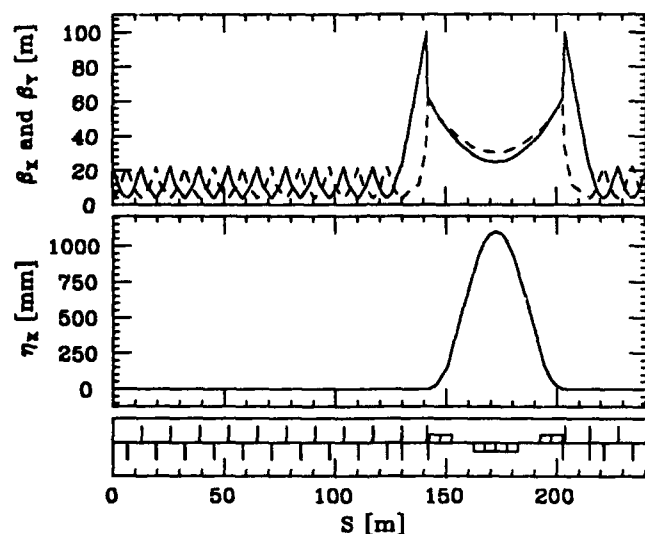
Fig. 4 Optical functions β_x (solid), β_y (dashes), and η_x for the 1.3 GeV S-band correlation linac and chicane of the high energy compressor.

section, several simulations were run using TRANSPORT and TURTLE tracking. Bend magnet rolls of 1°, bend magnet field errors of 1%, and large orbit distortions of 1 mm were each introduced independently and, *in all cases*, the huge emittance dilution, sometimes 50 times the initial emittance, was fully recovered by correcting dispersion with the tuning quads.

High Energy Compressor

A schematic layout of the high energy compressor is illustrated in Fig. 2. The rms bunch length exiting the low energy compressor is ≈ 0.5 mm. After acceleration from 1.8 GeV to 10.1 Gev, the uncorrelated energy spread

is 0.2%. At this point, the bunch passes through an arc which reverses its direction of motion and acts as the first stage of the "180°" compressor. The arc is composed of 156 FODO bending cells; sextupoles are not necessary since the beam energy spread is small. Next, a 1.3 GeV S-band linac creates an energy-position correlation which is used in the subsequent chicane to decrease the rms length of the bunch to 0.1 mm; the rms energy spread is increased to 1.0%, correspondingly. The R_{56} of the reversing arc is 0.5 m while that of the chicane is 0.1 m; the optics of the 1.3 GeV linac and the chicane are illustrated in Fig. 4. The synchrotron radiation contribution to the emittance is less that 0.2% at 10 GeV. We are currently studying the effects the effects of errors and the tunability of the system.

Discussion

We have described a bunch compression system that is based upon a wiggler and a chicane. In such devices, the higher-order dispersion cancels naturally without the sextupole magnets that can lead to severe alignment tolerances. Furthermore, in future linear colliders, it is essential that emittance correction elements and procedures be integrated into the design. This appears straightforward in the chicane and wiggler designs. Although we have not completed study of the high energy compressor, the tunability of the low energy compressor is extremely promising.

References

[1] The NLC is a 500 GeV to 1 TeV c.m. linear collider that is being designed at SLAC. Current parameters can be found in: *Proc. of ECFA Workshop on e^+e^- Linear Colliders: LC92*, Garmisch-Partenkirchen, Germany (1992).

[2] T. H. Fieguth and J. J. Murray, "Design of the Stanford Linear Collider Damping Ring to Linac Transport Lines," *XIIth Int. Conf. on High Energy Acc.*, Fermilab, IL (1983).

[3] C. Adolphsen, P. Emma, T. Fieguth, W. Spence, "Chromatic Correction in the SLC Bunch Length Compressors," *Proc. of the 1991 IEEE Part. Acc. Conf.*, San Francisco, CA (1991).

[4] S. Kheifets, R. Ruth, J. Murray, T. Fieguth, "Bunch Compressor for the TLC: Preliminary Design," *Proc. of the 1988 DPF Summer Study: Snowmass '88*, Snowmass, CO (1988).

[5] S. Kheifets, R. Ruth, T. Fieguth, "Bunch Compressor for the TLC," *Proc. of XVth Int. Conf. on High Energy Acc.* Tsukuba, Japan (1989).

[6] R. Rogers and S. Kheifets, "Misalignment Study of the NLC Bunch Compressor," *Proc. of the 1991 IEEE Part. Acc. Conf.*, San Francisco, CA (1991).

[7] K. Steffen, *High Energy Beam Optics*, Interscience Pub., New York (1965).

[8] M. Sands, "Emittance Growth from Radiation Fluctuations," SLAC–AP–47 (1985).

[9] G. Leluex, P. Nghiem, A. Tkatchenko, "Synchrotron Radiation Perturbations in Long Transport Lines," *Proc. of the 1991 IEEE Part. Acc. Conf.*, San Francisco, CA (1991).

[10] W. L. Spence, private communication.

An "NLC-Style" Short Bunch Length Compressor in the SLAC Linac*

John T. Seeman and Robert Holtzapple
Stanford Linear Accelerator Center
Stanford University, Stanford, California 94309 USA

I. Abstract

Experimental tests of a "second bunch length compressor" in a linac is important for the next generation of linear colliders and for other future accelerators. These future accelerators need bunches with lengths of order 0.06 - 0.2 mm. At these lengths, new accelerator dynamics will be encountered. We have studied the possibility of constructing a second compressor with the present SLAC linac and have found a reasonable design[1]. The core of this project is to reconfigure an old beamline (BL-90) at the 1000m location in the linac to: (1) extract a 10 GeV bunch, (2) pass it through a new 96 m long transport line in which length compression is done, and (3) reinject the beam into the main linac in an available drift section. Using the resulting compressed bunch, accelerator physics tests would be performed in the remaining downstream linac with the resulting very high charge density.

The bunch compression in this transport line results from

the TRANSPORT element R_{56} as determined from the optics of the transport line. $\Delta z = R_{56} \Delta E/E$. For example, if $\Delta z = -0.5$ mm, $\Delta E/E = 0.5\%$, $R_{56} = -0.1$ m, a bunch of 5×10^{10} particles would have a final length (σ_z) of about 0.08 mm with a peak current of 9600 A.

II. Decription of the Project

This project would use as much existing SLAC equipment as possible: including the SLC accelerator complex, old SPEAR injection line magnets, spare power supplies and diagnostics. No civil construction is required. The design is aimed at a rapid construction and installation schedule, maintaining flexibility and with no operational impact on other SLAC programs: SLC, FFTB, or B-Factory.

A schematic layout of the bunch compressor is shown in Fig. 1. The basic beam parameters are listed in Table 1. The compressor is to be installed in Sector 10 of the SLAC Linac tunnel. The beam is deflected into the south isle where it travels through a 96 m long lattice of large bore (8 cm) dipole and quadrupole magnets and is then reinjected into the SLAC linac at the drift section at linac Girder 10-9.

Eight large bore dipoles (10D37) and 14 quadrupoles (3 1/4 Q 20) will be used to bend and focus the beam along the transport line. Three pair of correction dipoles are available for steering. Two additional linac style quadrupoles (QE4) will be installed along the main linac to provide for betatron matching. Two sextupoles will be installed at the center of the line to provide for chromatic corrections to reduce horizontal emittance growth.

Table 1 General Parameters of the Bunch Compressor

Parameter	Case #1	Case #2	Case #3
Beam:			
Number of particles (10^{10})	1.0	3.0	5.0
Damping ring:			
Energy (GeV)	1.19	1.19	1.19
Bunch length σ_z (mm)	0.50	0.50	0.50
Energy spread after 1st compression (%)	1.0	1.0	1.0
Linac (Sectors 2-9):			
Peak accel. energy (GeV)	9.0	9.3	11.0
Bunch RF Phase (degrees)	-7.0	13.7	31.0
Second compressor:			
R_{56} (m)	-0.06	-0.06	-0.05
Final energy (GeV)	10.0	10.0	10.2
Final bunch length* σ_z (mm)	0.06	0.083	0.08
Energy spread after 2nd compression (%)	0.60	0.60	0.60

* Determined from FWHM / 2.354.
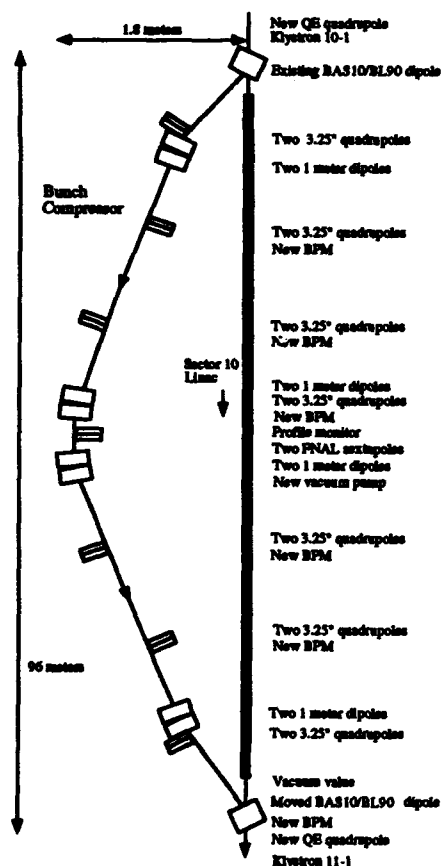
Figure 1   Schematic layout of the short bunch compressor.

Five 3-inch diameter position monitors will be built to provide for steering and energy analysis in the compressor. A profile monitor (screen type) will be located in the center of the transport line to provide for energy spread monitoring and control. Existing RF controls in Sectors 2-9 will be used to create the beam energy and energy spread needed for the compressor. Existing wire scanners in Sector 11 (50 m downstream) will be used for emittance and betatron phase space monitoring of the reinjected beam. The existing wire and screen profile monitors at the end of the linac will be used to measure the energy spread of the beam. When coupled with the RF phase controls from Sectors 11-30, these monitors will determine the bunch length[2] to about 30-50μm. The existing collimators in Sectors 18, 29, and 30 will be used to measure collimator steering. The geometry of this beam line was chosen so that no RF changes are needed.

III. Beam Line Optics

The optics of the transport line provides for proper compression, matched betatron functions, corrected dispersion, and second order corrections with sextupoles. The transport line is symmetrical about the mid-point. The transverse extent of the line was adjusted to provide clearance in the south isle of the tunnel for the widths of the magnets and for access. The quadrupoles in the compressor are relatively strong producing the desired "reversed dispersion function" at the center where all the compression is done. The resulting dispersion is shown in Fig. 2. The quadrupole pair at the center of the line is adjusted to remove any residual dispersion at the end of the compressor. The betatron matching is done by the two new linac quadrupoles and others in the linac. The β- functions are shown in Fig. 2.

Bunch length reduction can be adjusted by changing the

energy spread of the bunch or by a change of the lattice phase advance per cell of the quadrupoles between the end and center bends. R_{56} values from -0.15 m to 0. m can be handled.

IV. Bunch Compression

The bunches are extracted from the damping ring and compressed to 0.5 mm in the Ring-To-Linac transport line. They are then accelerated to 10 GeV with the appropriate RF phase to introduce the required head-tail energy spread for the second compression. The sign of R_{56} was chosen to allow the present BNS phases and resulting energy spreads to remain nearly intact, thus preserving our existing emittance control procedures. An explicit example of bunch compression is shown in Fig. 3 for a bunch charges of 5×10^{10} electrons per bunch. Other beam parameters for this and other cases are listed in Table 1. The bunch lengths quoted here are for the core of the beam which contains about 80-90% of the particles and have the long tails excluded. For the case of 5×10^{10} the resulting peak current is about 9600 A.
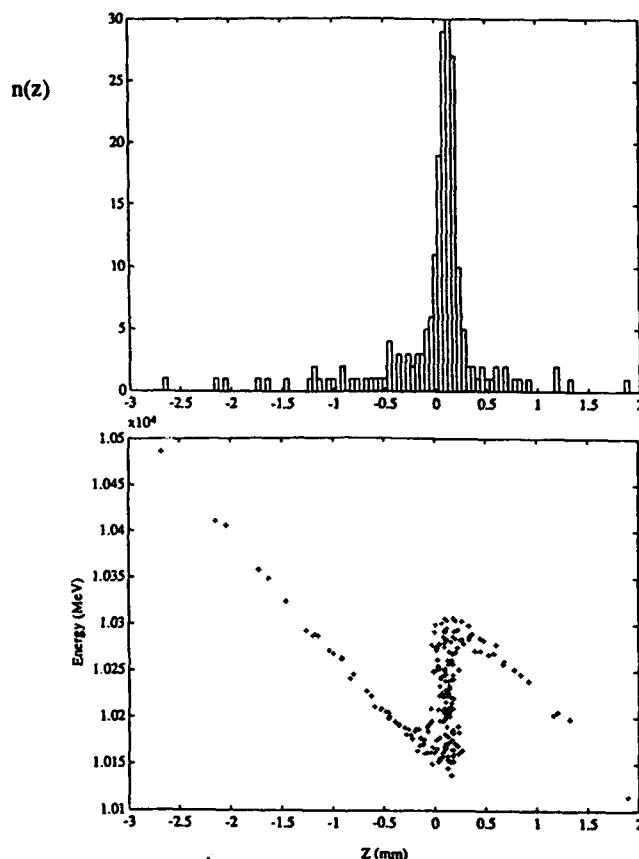
Figure 3   Bunch compression example for $N = 5 \times 10^{10}$ e⁻ and $\sigma_z = 0.08$ mm. The energy versus longitudinal position (z) correlation after compression is shown in the lower plot. The longitudinal density distribution is shown in the upper plot.

This compressor can also be configured to study the effectiveness of a "transformer" style compressor. In this case the R_{56} is raised to over-compress the bunch followed by a RF phase change of downstream klystrons to remove the remaining energy spread. A combination of increasing the

Figure 2   β-functions and dispersion along the compressor

magnet strengths and reducing the beam energy will accommodate this study.

Several studies of tolerances required of the input beam parameters and the accelerator and compressor conditions have been done. For 5×10^{10}/bunch, the changes in the resulting bunch length from variation of the input bunch charge indicate that the bunch charge should be kept constant to 10%. Also, for 5×10^{10}/bunch, the changes in the resulting bunch length with the transport line R_{56} values suggest that the "compressor strength" should be held to about 5-10%. Finally, studies of the effects on compression from changes of the phase of the linac RF shows that the linac RF phase should be set to about 1 degree.

With the quadrupole lattice and the sextupole corrections properly set for this compressor, the transverse emittance growth should be kept below 10% or $\Delta\gamma\epsilon_x < 0.3 \times 10^{-5}$ r-m, invariant. The vertical emittance, in principle, should be unaffected. However, due to small quadrupole roll errors, coupling of horizontal dispersion into the vertical must be controlled with a few weak skew quadrupoles.

IV. Potential Accelerator Investigations

Wakefields in the short bunch length regime: Theoretical calculations[3] for the longitudinal wakefields of a short bunch in a series of accelerating cavities are strongly dependent on the ratio of the bunch length to the iris radius of the cavities and on the number of cells over which the wakefields are integrated. Using the bunch lengths produced with this compressor and accelerating the bunches to 40 GeV, longitudinal wakefields can be measured in a regime where the uncertainties are on the order of 25 to 50%. The expected energy spread at the end of the accelerator versus the linac RF phase is shown in Fig. 4 for the nominal SLAC longitudinal wake and for a value twice as large. Given our ability to measure the energy spread to about 0.1%, we can measure the longitudinal wakes to about 5 - 10%.
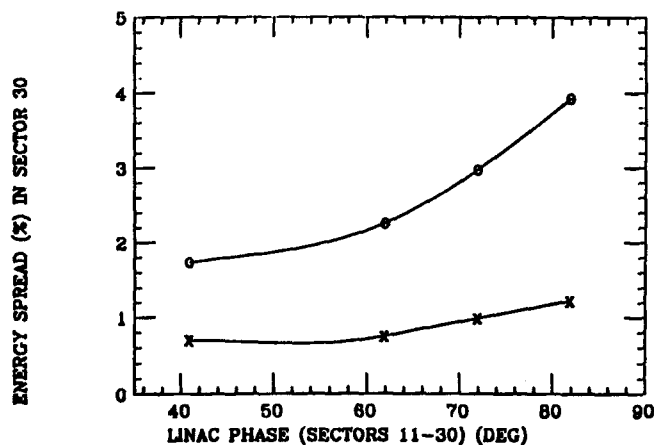
Figure 4   Energy spread at the end of the linac versus linac phase downstream of the compressor. The bunch charge is 3 $\times 10^{10}$ compressed to $\sigma_z = 0.083$ mm in Sector 10. The (x) points used the nominal longitudinal wakefields in the Sectors 11-30. The (o) points used twice the nominal wakefields. The final beam energies are 25-35 GeV.

Tolerances for the Next Linear Collider: The second bunch compressor for the NLC must preserve both the horizontal and vertical emittances of the incoming bunches[4]. The compressor described here has been designed to test many of the required tolerances including alignment, RF phasing, magnet strengths, coupling, second order optics, as well as energy and energy spread control of multiple bunches.

Instrumentation for Short Bunch Lengths: The required bunch lengths in the new generation of accelerators are on the order of 0.05 to 0.2 mm. There are no proven methods of measuring bunch lengths below about 1.0 mm, except for RF-energy spread manipulation techniques which require a long linac[2] (50 μm resolution) such as the SLAC linac. There are several proposed non-invasive methods using coherent synchrotron radiation, normal synchrotron radiation, or high frequency cavities. With this new compressor and the SLAC linac, these new monitors can be tested and calibrated aga: known RF-energy spread measurement technique.

Collimator deflections: Collimators are used to remove unwanted halo from the bunches in a linear collider. However, if the bunch passes through the collimator off-axis, then transverse forces from image currents deflect the core of the bunch increasing the beam emittance[5]. The next linear collider with its small emittances is particularly sensitive to these deflections. As a result, very complicated collimation sections have been designed[6]. It is important that these transverse effects be experimentally verified. The expected deflection for the charge density of a compressed beam (3 $\times 10^{10}$ at 0.08 mm) is about 10 μrad which is 5 times the natural angular size. This deflection can be measured to ~10%.

Short bunch lengths for the FFTB: With this compressor bunch lengths below 0.08 mm can be provided to the FFTB[7]. Bunch intensities of about 1 $\times 10^{10}$ at full energy and 2 $\times 10^{10}$ at a reduced energy (~40 GeV) are possible. This reduced length would allow the entire bunch to be simultaneously focused in the FFTB with a design β_y^* of 100 μm.

V. References

1. J. Seeman, et al, "Beam Parameters of a Possible Emittance-Dynamics Test Area for NLC Studies at the SLC," XV Int. Conf. on High Energy Accelerators, Hamburg, Germany, p. 821 (1992).
2. L. Merminga, et al., " Bunch Length Measurements in the Linac," SLC Experimental Report #116, Stanford (1990).
3. S. A. Heifets and S. A. Kheifets, "High Frequency Limit of the Longitudinal Impedance of an Array of Cavities," SLAC-PUB-4625, Stanford (1988).
4. S. Kheifets, et al., "Bunch Compression for the TLC," *Particle Accelerators*, Vol. 30, p. 1037 (1990).
5. K. Bane and P. Morton, "Deflections by the Image Current and Charges of a Beam Scrapper," 1986 Linear Accelerator Conf., SLAC-Report-303, p. 490, (1986).
6. N. Merminga, et al., "Optimizing a Nonlinear Collimation System for Future Linear Colliders," SLAC-PUB-5507, Stanford (1991).
7. "Final Focus Test Beam Project Design Report," SLAC-Report-376, Stanford, (1991).

Multibunching Studies for CLIC

I. Wilson, W. Wuensch

CERN, CH-1211 Geneva 23, Switzerland

Abstract

Studies aimed at increasing the luminosity of the CERN Linear Collider (CLIC) for a given power by introducing multiple bunches during a single RF fill are described. Long range transverse wakefields are reduced by detuning the dipole mode frequencies and beam loading is compensated by partial section filling and tapered power pulses.

INTRODUCTION

Operation of CLIC in a multibunch mode is being studied in an attempt to increase luminosity without significantly increasing power consumption, and to reduce the charge per bunch. Lower bunch charges result in less disruption at the interaction point consequently there is less energy spread in interactions and easier physics analysis. Multiple bunches during a single RF fill can be accelerated to the same energy by adding extra energy to compensate the beam loading. The compensation must however be compatible with the rather small ± 0.23% energy acceptance of the final focus system and the physics requirement of a small energy spread.

As a starting point, a train of *four* bunches with 4.24×10^9 particles per bunch has been chosen - this doubles the present single bunch luminosity (6×10^9 particles) and reduces the bunch charge by a factor $\sqrt{2}$. Beam simulations with such charges in the 500 GeV version of CLIC indicate that long range transverse wakefields must be reduced by factors between 200-1000 (depending on the way the linac is optimised) for the passage of a second bunch without excessive loss in luminosity [1]. This value is a factor 10 more severe than that needed for X-band multibunching [2]. The major difference comes from the cubic dependence of wakefield on frequency, but some ground is regained on the shorter linac length due to higher accelerating gradients, and tighter alignment tolerances.

BEAM LOADING COMPENSATION

The simplest beam loading compensation scheme minimises energy spread by having the section only partially filled when the first bunch passes but completely filled when the final bunch passes. The energy flowing in during the time between bunches ($\Delta s/c$) balances the energy being taken out by the bunches thus keeping the net voltage constant. The energy gain of the bth of n bunches is given by,

$$\Delta E_b = E_0[L-(n-b)\Delta s\frac{v_g}{c}]-(b-\frac{1}{2})2k'qL+k'q\Delta s\frac{v_g}{c}b(b-1)$$

Using $E_0 = 80 \text{MV/m}$, $q = 4.24 \times 10^9 \times 1.6 \times 10^{-19}$ C and assuming

$k' = 1.25 \times 10^{15}$ V/Cm, $v_g/c = 6.3\%$ for a stagger-tuned CLIC section, the optimum bunch spacing is $\Delta s = 0.3 \text{ns} \approx 9$ RF cycles resulting in energy variations well within the energy acceptance of the final focus.

DETUNED DIPOLE FREQUENCY DISTRIBUTIONS

The level of the transverse wakefield can be significantly reduced by creating a spread in the frequencies of the first dipole modes. The transverse wakefield in a section is given approximately by the Fourier transform of this distribution. Decay characteristics are nearly optimum for truncated Gaussians [3]. To evaluate major effects Fourier transforms of continuous distributions were first used. A reduction in the wakefield by a factor 1000 as required by beam simulations in 0.3 ns (see Fig.1) would require a distribution with a frequency span $\Delta f = 13.3$ GHz (36%) and a $\sigma = 2$ GHz (5.4%). The value of the ratio of $\sigma/\Delta f$ results from a compromise between a fast rolloff time (large ratio) and low sinx/x behaviour (small ratio) and has been set to 1/6.7 to have an attenuation of 1000 at the first lobe.
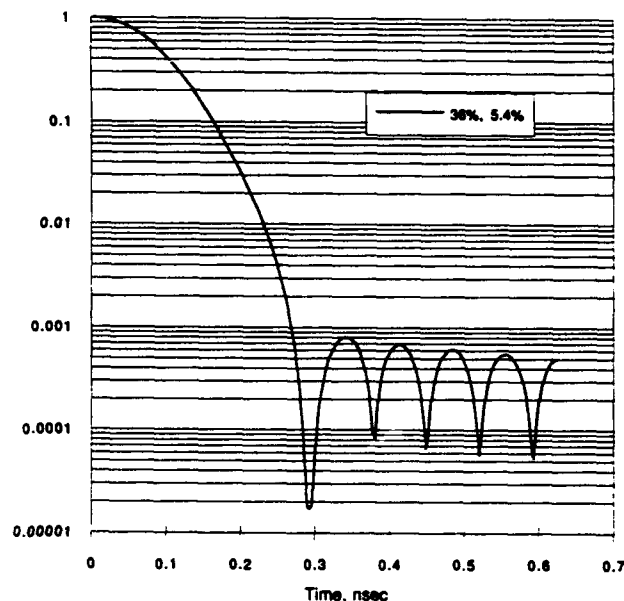
Fig.1: Wakefield resulting from a *continuous* truncated Gaussian distribution ($\Delta f = 36\%$, $\sigma = 5.4\%$)

Such bandwidths are unfortunately well outside practical limits. The smallest iris (giving the highest dipole mode frequency) which can be machined is about 3.5 mm. The largest iris (giving the lowest frequency) is limited to 5.0 mm

- this is the largest iris with a dispersion curve which does not cross the fundamental frequency. The risk here is that fundamental power would be fed into the dipole mode by imperfections if the two modes were degenerate. These two limiting iris dimensions fix the practical dipole mode frequency span to be 3.89 GHz (10.4% of the center frequency 37.4 GHz). The fundamental and dipole mode characteristics over this range are shown in Figs. 2 and 3 as a function of iris diameter.
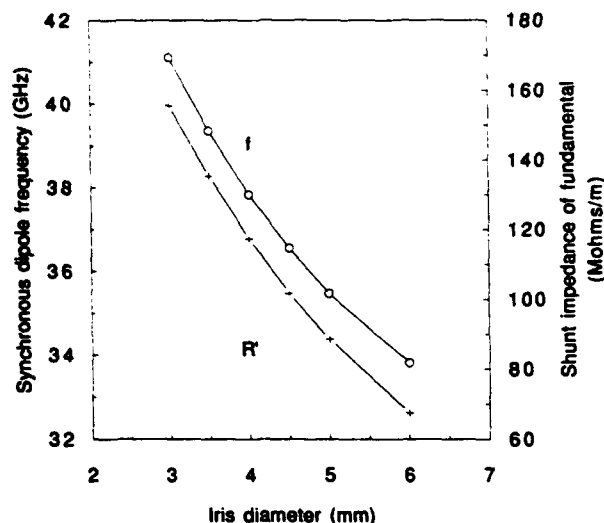
Fig. 2: Synchronous dipole mode frequency and fundamental mode shunt impedance versus iris diameter
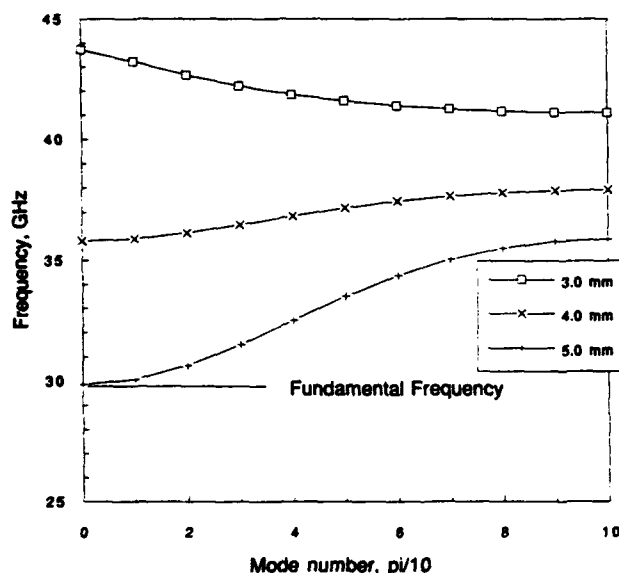
Fig. 3: Lowest dipole mode dispersion curves for iris diameters of 3, 4, and 5 mm

The wakefield resulting from the use of this reduced bandwidth is shown in figure 4. An attenuation of 1000 can now only be achieved after 1 nsec. With bunches spaced at 1 nsec intervals the simple beam loading scheme gives an unacceptable energy spread and has to be modified - too much

power is flowing into the sections compared to the amount being taken out by the bunches [4]. One way to bring the differences in energy gained by the four bunches back within the energy acceptance of the final focus is to taper the voltage of the power pulse linearly downwards by 15% during the passage of the bunch train. With such a large bunch spacing compared to the total fill time, the effective accelerating gradient due to partial filling is now reduced by a factor $1-3/11.4 = 0.73$. If the length of the linac and the total beam energy are kept constant a higher nominal gradient requiring a $1/.73^2 = 1.9$ increase in input power is needed. In addition there is a loss of shunt impedance in the detuned structure compared with the constant impedance geometry of about 5% because the iris diameters are on average larger. Multibunching has therefore only improved our luminosity to power consumption ratio by 5%. It would be much simpler to get the two-fold increase in luminosity for the same increase in power by doubling the repetition rate.

The problems of tolerance on charge, the effect of the non linear distribution of the accelerating gradient (due to the non linear distribution of shunt impedance), the effect of a non linearly varying group velocity, and the effect of dispersion on the finite bandwidth power pulse have not been considered.
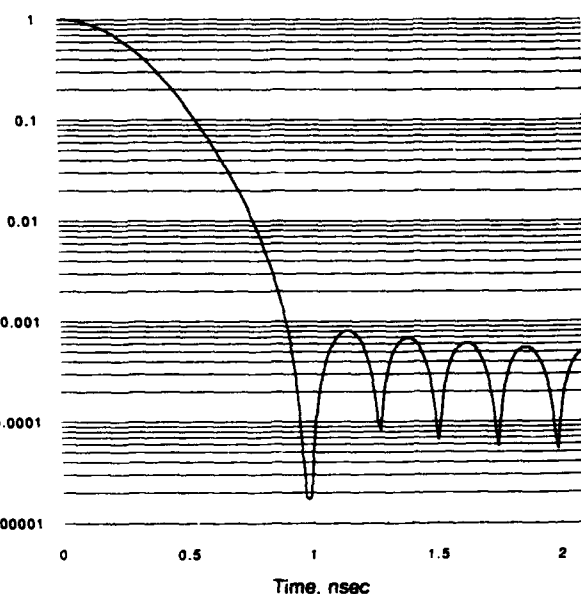
Fig. 4: Truncated Gaussian ($\Delta f=10.4\%$, $\sigma=1.6\%$)

WAKEFIELDS FROM DISCRETE CELL DISTRIBUTIONS

In order to have a better approximation to the wakefield in a section, discrete frequencies as opposed to continuous distributions will now be used. To maintain a power attenuation $\alpha=0.5$, an accelerating section with a range of iris diameters from 3.5 to 5.0 mm will have 101 cells. The fit of the discrete dipole frequencies of the 101 cells to the truncated Gaussian of $\Delta f=3.89$ GHz and $\sigma=0.58$ GHz is shown in Fig.5
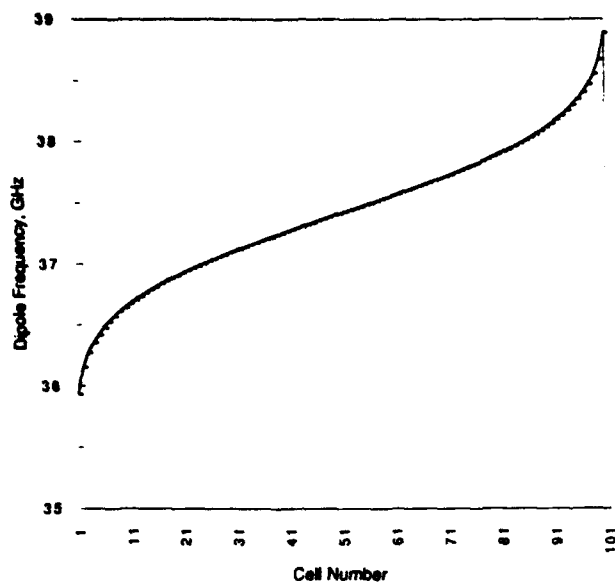
Fig. 5: Dipole frequency versus cell number

Fig. 7: Wakefield from 1001 cells

The wakefield in this case (see Fig.6) is approximately the sum of the wakefields of all the cells considered individually (uncoupled cell model). The wakefield attenuation is degraded from 1000 to 100 when the distribution becomes discrete. The limiting value of attenuation factor seems to be of the order of the number of cells. Thus one could recover by distributing the frequencies over 1000 cells which would mean over many sections. The wakefield from 1001 cells is shown in fig. 7. This assumes however that the two coupler cells of each section are accurately included in the distributions, otherwise they represent an attenuation limit of about 101/2. All of these calculations ignore coupling between cells and have assumed that the voltage produced in each cell is the same, which is of course not true if iris diameters vary.

FREQUENCY BEATING

A scheme in which only two frequencies Δf apart are used was also investigated. The wake in this case

$$w(t) = A\sin\{\pi(f_1 + f_2)t\}\cos\{\pi(f_1 - f_2)t\}$$

would have a null at a time $t=1/2\Delta f$ after the passage of the first bunch. For $t=0.3$ns, Δf would be 1.6 GHz. The rate of change of the envelope of the wakefield with frequency however at this null $dw/d\Delta f=\pi t$ requires that for a tolerable residual wakefield of say 0.004 (an attenuation of 250) the frequencies would have to be correct to within 2 MHz - this is considered unrealistic.

CONCLUSIONS

Doubling the luminosity of CLIC by passing four bunches of reduced charge through stagger-tuned structures during one RF fill seems to be difficult and would in any case have to be paid for by almost doubling the power.

The two-frequency beating technique requires too tight a tolerance on the dipole frequencies and is considered unrealistic.

REFERENCES

[1] G.Guignard, Transverse Stability in Multibunch Mode for CLIC, this conference.

[2] M.Yamamoto et al., KEK Preprint 91-153, Nov. 1991.

[3] K.A.Thompson and J.W.Wang, SLAC-PUB-5465, 1991.

[4] Z.D. Farkas, LINAC Proc. p.410, Ottawa August 1992.

Fig. 6: Wakefield from 101 cells

Linear Collider Systems and Costs*

G.A. Loew
Stanford Linear Accelerator Center
Stanford, CA 94309 USA

I. ABSTRACT AND INTRODUCTION

The purpose of this paper is to examine some of the systems and sub-systems involved in so-called "conventional" e^+e^- linear colliders and to study how their design affects the overall cost of these machines.

There are presently a total of at least six 500 GeV c. of m. linear collider projects [1] under study in the world. Aside from TESLA (superconducting linac at 1.3 GHz) and CLIC (two-beam accelerator with main linac at 30GHz), the other four proposed e^+e^- linear colliders [2] can be considered "conventional" in that their main linacs use the proven technique of driving room temperature accelerator sections with pulsed klystrons and modulators. The centrally distinguishing feature between these projects is their main linac rf frequency: 3 GHz for the DESY machine, 11.424 GHz for the SLAC and JLC machines, and 14 GHz for the VLEPP machine. The other systems, namely the electron and positron sources, pre-accelerators, compressors, damping rings and final foci, are fairly similar from project to project. Probably more than 80% of the cost of these linear colliders will be incurred in the two main linacs facing each other and it is therefore in their design and construction that major savings or extra costs may be found.

II. WHAT MAKES UP THE COST OF A LINEAR COLLIDER ?

The total cost (C_T) of a linear collider can be expressed as the sum of five parts:

$$C_T = C_{RD} + C_L + C_P + C_F + C_{OP} \quad (1)$$

where C_{RD} is the R&D cost of the project, C_L is the cost of all components scaling with length ($C_L = c_L L$), C_P is the cost of all components scaling with peak rf power ($C_P = c_P P_{PK}$) where c_L and c_P are per-unit costs, C_F is the fixed cost of the injectors, positron source, damping rings, compressors and final foci, and C_{OP} is the cost of operating, maintaining and powering the facility, once it is running.

Since in a linac the total energy E is proportional to $(P_{PK}L)^{1/2}$, the product $C_L C_P$ is constant for a fixed E and it can be shown that C_T has a broad minimum when $C_L = C_P$, provided that the other three costs do not dominate.

For reference, the cost of the original SLAC linac with upgrades for the 100 GeV c. of m. SLC, including salaries, and escalation from 1962-1967 to 1993 (factor of 5.7) is shown in Table I [3].

Note that the costs of some of the sub-systems such as the rectangular waveguides, valves, vacuum, supports, etc., in this table have been apportioned somewhat arbitrarily to both C_L and C_P because they are a function of machine length as well as number of power sources. The balance between C_L and C_P in the original SLAC linac was close. However, the subsequent SLC upgrade of the linac energy from about 23 to 55 GeV which used mostly power-related components (while decreasing the repetition rate from 360 to 120 Hz) slanted the cost heavily towards C_P. Including the C_F costs in Table I but excluding the cost of the original R&D, the cost of the SLC, integrated over time, is about $600M.

TABLE I: COST OF ORIGINAL SLAC LINAC UPGRADED TO SLC STANDARDS (INCLUDING SALARIES) 1993$ (1967$X5.7)

C_L (PROPORTIONAL TO LENGTH)	K$/M	TOTAL M$
Accelerator Housing	9	26.8
Klystron Gallery	6.8	20.5
Accelerator Sections	5.1	15.4
Rectangular Waveguides, Valves, etc.	2.9	8.6
Quads, Correctors, BPMs		6.8
Vacuum, Supports, Cooling	5.7	17.1
Phase & Drive	1.9	5.7
I & C		_13.7_
		114.6

C_P (PROPORTIONAL TO POWER)	K$/Unit	TOTAL M$
245 Klystrons (24 MW, 22 kV at 360 pps)	79	19.4
245 Modulators (250 joules x 360 pps)	107	26.2
Rectangular Waveguides, Valves, etc.	35	8.6
Vacuum, Supports, Cooling	69	17.1
Phase & Drive	23	5.7
Electrical System & Utilities		31.9
I & C		_13.7_
		122.6

	M$
(C_L+C_P) unloaded	237.2
Engineering, Design and Inspection (16%)	38.0
Indirect Administrative Costs (18.5%)	43.9
Subsequent SLC Upgrades (64 MW Klystrons, Modulators, SLED, New Focusing, Beam Position Monitors, etc.)	_113.4_
(C_L + C_P) loaded	432.5
C_{RD}(Original pre-construction R&D)	_103.2_
(C_L + C_P + C_{RD})*	535.7

*C_F and C_{OP} are not included above. For reference, in FY 1993$ the original SLC injector cost about $3.2M, the two damping rings with vaults $22.3M, the positron source $12.8M, the arcs and final focus $40M, the collider hall $16M, extra controls $24M. EDI and Indirect costs added another $17.5M and $16M respectively for a total C_F of $151.8M. The annual direct operating cost of the SLC is about $60M.

III. 500 GeV (C. of M.) EXAMPLES

To look at future machines, let us now take two "generic" examples, one at S-Band (DESY type) and one at X-Band (SLAC/NLC type), and let us first examine the specifications and block diagrams of their main linacs. The general parameters of the two machines are summarized in Table II. Note that the S-Band example is roughly ten times as long as SLAC and twice as long as the NLC. Its luminosity, compared to the NLC, is obtained by using twice the number of bunches, three times the charge per bunch and fourteen times the IP spot size, at a repetition rate of 50 Hz instead of 180 Hz. Its damping rings will clearly need greater circumferences than the X-Band example to accommodate the longer bunch trains. On the other hand, the S-Band example needs only one compressor per beam because the bunches do not have to be compressed from the pre-accelerator linac to the main linac since it will operate at the same frequency.

Fig. 1 shows a generic block diagram of an X-Band main linac module. The only difference between this case and the S-Band case is that in the latter, the klystron may drive only two accelerator structures and does not include any pulse compression. The X-Band gradient is twice the S-Band gradient.

TABLE II: GENERAL PARAMETERS OF TWO GENERIC CONVENTIONAL LINEAR COLLIDERS 500 GeV (CENTER-OF-MASS)

	S-BAND	X-BAND
RF frequency of main linacs(GHz)	3	11.4
Nominal luminosity (10^{33} cm^{-2}s^{-1})	2.4	6
Luminosity w/pinch (10^{33}cm^{-2}s^{-1})	6.5	8.2
Linac repetition rate (Hz)	50	180
No. of particles/bunch at IP (10^{10})	2.1	0.65
No. of bunches/pulse	172	90
Bunch separation (nsec)	10.66	1.4
Active two-linac RF length (km)	30	14
Actual gradient (MV/m)	16.6	35.7
Beam power/beam (MW)	7.5	4.2
Total two-linac AC power (MW)†	147	152
Damping ring energy (GeV)	3.13	1.8
Final Focus:		
σ_x^*/σ_y^* (nm)	400/32	300/3
σ_z^* (μm)	500	100

† This is the AC power consumed by the klystrons and modulators alone. The efficiency of both S- and X-Band klystrons is assumed to be 45%, that of the modulators 80% for S-Band and 72% for X-Band. Pulse compression for the X-Band case is assumed to be about 65% efficient. Power requirements for klystron focussing supplies, pumps, vacuum, quadrupoles, etc. are not included here. They probably add another 50 MW.

Cost estimates for the two cases are shown in Tables III and IV respectively. These estimates are based on a number of assumptions, many of which may be debatable, and some of which are discussed below:

a) The accelerator housing and klystron gallery are assumed to consist of two parallel tunnels. The cost per unit length for the two examples is assumed to be the same.

b) The cost per meter of the S-Band accelerator sections is assumed to be half that of the X-Band ones because the S-Band tolerances are looser and there are less couplers per unit length. In both cases, a large degree of automation in fabrication will be necessary.

c) The klystrons for the two examples are assumed to have equal costs: the S-Band klystrons are heavier and larger but the X-Band ones are more complex. Uncertainties exist in the focussing method and cost (R.T. or superconducting solenoids, or preferably periodic permanent magnets) as well as in possible economies of scale. Indeed, according to G. Caryotakis at SLAC, there is experience in the microwave tube industry that if a manufacturer must produce, say 1000 tubes, and starts with an increment of 10 units at a per-unit cost of X, the per-unit cost of the next 20 units will go down to 0.9X, and so on for every doubling. Hence, on such a learning curve, for 1000 tubes, the average per-unit cost would come down to about 0.6X. This would be a very favorable trend.

d) The modulators for the two examples are also assumed to have equal costs even though the X-Band ones require 40% higher average power. As suggested by R. Cassel at SLAC, it may be possible to reduce costs by sharing the power supply (Box 1 in Fig. 1) among several modules, by replacing conventional discrete PFN elements by water-filled triax lines in Box 2, and by immersing the thyratron and pulse transformer in Box 3 in a single oil tank.

e) High power prototypes for pulse compressors (SLED-II type) are not yet operational and their costs are still very uncertain.

f) Many of the other costs are patterned after escalated original SLAC costs.

We see that the S-Band machine, under the above assumptions, is about 1 Billion dollars more costly than the X-Band one, also assuming that the fixed costs (C_F) are the same for both. The dominant reason for this difference is that the S-Band linacs are twice as long as the X-Band ones. Note that this difference could be wiped out if tighter X-Band tolerances for sections, transverse alignment, klystrons, power compressors, modulators and focussing were to be much more costly than assumed, or simply, if the up-front
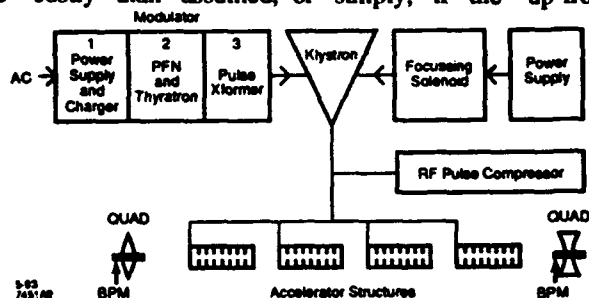
Figure 1. Generic module for main linacs.

TABLE III: COST OF S-BAND EXAMPLE
1993$

LINACS

Total length (km)	33
Total RF length (km)	30
No. of sections	4900
Section length (m)	6
No. of quadrupoles, correctors, BPMs	2450
Klystron peak power (MW)	150
No. of klystrons and modulators	2450

C_L	K$	TOTAL M$
Housing (double tunnel)	16/m	528
Accelerator Sections	15/m	450
Rectangular Waveguides, etc.	2.9/m	86
Quads, correctors, BPMs	30/unit	74
Vacuum, Supports, Cooling	8/m	240
Phase & Drive	2/m	66
Backward Transport Lines	2/m	66
I & C (18.5%)		280
		1790

C_P	K$	TOTAL M$
Klystrons	100/unit	245
Modulators	120/unit	294
Rectangular Waveguides, etc.	35/unit	86
Vacuum, Supports, Cooling	60/unit	147
Phase & Drive	30/unit	74
Utilities (200 MW)		180
I & C (18.5%)		190
		1216

$(C_P + C_L)$ unloaded	3006
EDI (16%)	481
INDIRECTS (18.5%)	556
LINACS SUB-TOTAL	4043
C_F (rough estimate, loaded)	400
$(C_L+C_P+C_F)$ loaded	4443

TABLE IV: COST OF X-BAND EXAMPLE
1993$

LINACS

Total length (km)	16
Total RF length (km)	14
No. of sections	7778
Section length (m)	1.8
No. of quadrupoles, correctors, BPMs	1600
Klystron peak power (MW)	94
No. of klystrons, pulse compressors and modulators	1945

C_L	K$	TOTAL M$
Housing (double tunnel)	16/m	256
Accelerator Sections	30/m	420
Circular Waveguides, etc.	5/m	70
Quads, correctors, BPMs	30/unit	48
Vacuum, Supports, Cooling	8/m	112
Phase & Drive	2/m	32
Backward Transport Lines	2/m	32
I & C (18.5%)		179
		1149

C_P	K$	TOTAL M$
Klystrons	100/unit	195
Modulators	120/unit	233
Circular Waveguides, etc.	35/unit	68
Pulse Compressors	50/unit	97
Vacuum, Supports, Cooling	60/unit	116
Phase & Drive	30/unit	58
Utilities (200 MW)		180
I & C (18.5%)		175
		1122

$(C_P + C_L)$ unloaded	2271
EDI (16%)	363
INDIRECTS (18.5%)	420
LINACS SUB-TOTAL	3054
C_F (rough estimate, loaded)	400
$(C_L+C_P+C_F)$ loaded	3454

R&D effort at X-Band took too long. Conversely, if tunnel and other C_L costs were to be greater, the balance would tilt in the opposite direction.

One of the main reasons for carrying out this admittedly sketchy study is not simply to predict costs but rather to indicate, at an early time, where serious attention must be paid to designs so that costs may be controlled and hopefully cut drastically.

Acknowledgements

References

[1] G.A. Loew, "Toward The Next Linear Collider," SLAC *Beam Line*, Winter 1992, Vol. 22, No. 4, from a talk presented at the European Committee on Future Accelerators (ECFA) Workshop on e+e- Linear Colliders in Garmisch-Partenkirchen, Germany, July 26-August 1, 1992.

[2] G.A. Loew, "Review of Studies on Conventional Linear Colliders in the S- and X-Band Regime," presented at the XVth International Conference on High-Energy Accelerators in Hamburg, Germany, July 20–24, 1992. HEACC '92 Hamburg, Vol. II.

[3] The Stanford Two-Mile Accelerator, R.B. Neal (W.A. Benjamin, Inc., 1968), chapter 4.

Application of the Monte Carlo Method to Estimate the Tenth-value Thickness for X-rays in Medical Electron Accelerators

José Ródenas, Gumersindo Verdú
Departamento de Ingeniería Química y Nuclear
Universidad Politécnica de Valencia
Apartado 22012, 46071 Valencia (SPAIN)

Abstract

DIN-6847 is the most suitable standard to estimate shielding requirements in medical radiotherapy installations using linear electron accelerators. Its calculation method is based on the tenth-value thickness concept for which values given by curves and tables are recommended in DIN-6847. These parameters have been estimated for both primary and secondary X-ray beams using the MCNP code based on the Monte Carlo method. Results show that DIN-6847 values are conservative for secondary X-ray beam, but not always for direct radiation. The methodology used has been tested using the mentioned code and results are well consistent.

I. INTRODUCTION

There is a great number of medical installations using particle accelerators for radiotherapy. The importance of an accurate estimation of the doses due to these installations that can be received by health workers, patients or public is obvious. The lower limits of doses established in the new ICRP recommendations [1] imply a recalculation of items concerning such installations [2].

There are only two known standards [3], [4] to estimate shielding requirements in medical installations using linear accelerators, i. e. NCRP-51 and DIN-6847. The last one is more suitable for this type of calculations. NCRP-51 is incomplete and difficult to apply, while DIN-6847 is fairly comprehensive and easy to apply [2], [5]. However, it is based on various semiempirical approaches which should be adequately verified. In the paper, the tenth-value thickness included in DIN-6847 for various materials for primary and secondary X-rays produced in electron accelerators has been verified using the MCNP code based on the Monte Carlo method [6].

II. CALCULATION METHODOLOGY

A. Shielding Calculation

In DIN-6847 standard [4], the shielding thickness is given by the following expression:

$$s_i = z_i \, \log_{10} \left(\frac{W_A \, U \, T \, K_i \, q_i}{H_w} \right) \tag{1}$$

where, s_i is the shielding thickness for the ith radiation, referring to electrons, X-rays (primary, secondary, leakage, tertiary) or neutrons (primary and scattered beam); z_i is the tenth-value thickness; W_A is the weekly workload at the reference distance of a_0 meters (Gy/week); U is the use factor; T is the occupancy factor; K_i is the reduction factor; q_i is the quality factor; and H_w is the equivalent weekly dose.

The calculation scheme is as follows: (a) establish the geometrical features of the reference point; (b) identify all types of radiation involved in the calculation; and (c) obtain the shielding thickness s_i, from the general equation (1) and the actual variations according to the type of radiation.

For *primary X-ray beam*, $q_i = 1$ and the reduction factor is given by:

$$K_i = \frac{a_0^2}{a_n^2} \tag{2}$$

where, a_0 is the reference distance (1 m) and a_n is the distance in meters from the source to the shielding. The tenth-value thickness, $z_i = z_r$, depending on the shielding material can be obtained from curves recommended by DIN-6847 that are reproduced in Figure 1, it is seen that the same curve is used for aluminum and concrete, and also for iron and copper.
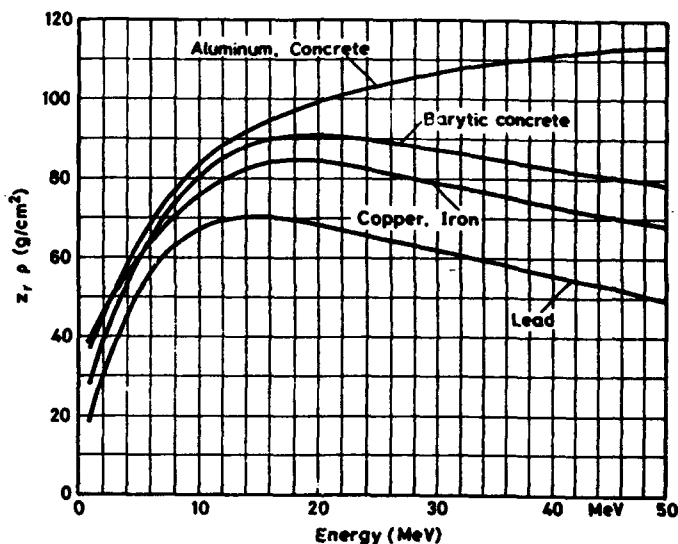
Figure 1. Mass tenth-value thickness for primary X-rays.

For the *scattered X-ray beam*, the use factor is U = 1; the tenth-value thickness, $z_i = z_s$, obtained from DIN-6847 (see Table 1) does not depend on energy; and the reduction factor K_s is given by:

$$K_s = \frac{10^{-2} \, F_s \, k}{a_s^2} \qquad (3)$$

where, F_s is the illuminating surface (normally ~ 0,04 m²); k equals 1 for X-rays; and a_s is the distance from the scatterer to the reference point.

Table 1
Mass Tenth-value Thickness for Secondary X-rays.

Material	Concrete	Barytic concrete	Iron	Lead
$x_s \rho$	37	29	38	17

B. *Tenth-value Thickness Estimation*

The following expression for the equivalent dose rate H_w can be obtained from eq. (1):

$$H_w = \frac{C}{a_n^2} \left(\frac{1}{10} \right)^{\frac{s}{z}} \qquad (4)$$

where C includes all the terms depending on the installation and radiation involved.

In order to verify the adequacy of eq. (4) a photon source produced by Bremsstrahlung in aluminum from monoenergetic 23 MeV electrons has been considered. With a lineal spectrum taken from Chilton [7], MCNP calculates doses for shielding thickness from 0 up to 130 cm. The correlation coefficient between $\log(H_w \, a_n^2)$ and s has been found and it is equal to 0.999613. Therefore, they are linearly related and consequently the tenth-value thickness can be estimated in terms of dose rates calculated for two different values of shielding thickness and related distances, as follows:

$$z = - \frac{s_2 - s_1}{\log_{10} \dfrac{H_{2w} \, a_2^2}{H_{1w} \, a_1^2}} \qquad (5)$$

MCNP code has been used to determine doses at distances considered, for various energy values up to 50 MeV and materials of interest. The photon source was point isotropic and monoenergetic, with all the particles being emitted inside a small solid angle (cos α = 0.9997) to avoid the leakage radiation. Surface counters have been used, placed in maximal dose zones. Cell importance has been the only variance reduction technique used, due to geometric features of the problem and the type of counters used.

The photon interaction cross sections come from the Storm and Israel [8] plus ENDF/B evaluations and cover the energy range from 0.001 to 100 MeV. MCNP takes account of incoherent (using an inverse fit rather than a rejection scheme on the Klein-Nishina distribution) and coherent scattering, the possibility of fluorescent emission following photoelectric absorption, and absorption in pair production with local emission of the annihilation quanta.

III. RESULTS

Calculation has been carried out for a radiotherapy room with two perpendicular walls made of the same material. The first one that receives primary beam is located at 500 cm away from the radiation source and the second one where falls in the scattered beam is 350 cm away from the source. MCNP has been run for energies from 0,5 up to 50 MeV for direct radiation and from 5 up to 50 MeV for the scattered one.

Shielding thickness values have been taken in such a way that for each energy the doses obtained differ by a magnitude order at least. 100,000 photons for direct radiation and 200,000 for the scattered one for each energy have been generated. Concrete, barytic concrete, aluminum, iron, copper and lead have been considered for primary beam and all except aluminum and copper for the scattered one.

Results are shown in Figure 2 for *direct radiation*. Comparing this figure with Figure 1, one can see that values obtained by MCNP match reasonably with those from DIN-6847 except for lead. At the lowest energy (0.5 MeV) the Monte Carlo values are slightly lower than the DIN ones, but for higher values of energy they are higher too: always for concrete, up to 40 MeV for aluminum, up to 10 MeV for barytic concrete, and up to 15 MeV for iron and copper. For the rest of energy values, the Monte Carlo obtained values are lower, but differences are small.

For lead the behavior is completely opposite and we think that the Monte Carlo calculated values should be discarded for this material. MCNP does not include the transport of photoelectrons, Compton electrons and electron-positron pairs. At higher energies these electrons collide with hard atomic nuclei producing the electromagnetic radiation (Bremsstrahlung) obviously not considered by the code. These phenomena are very important in lead and the calculated tenth-value thicknesses are clearly lower than those of the guide, they might be less safe.
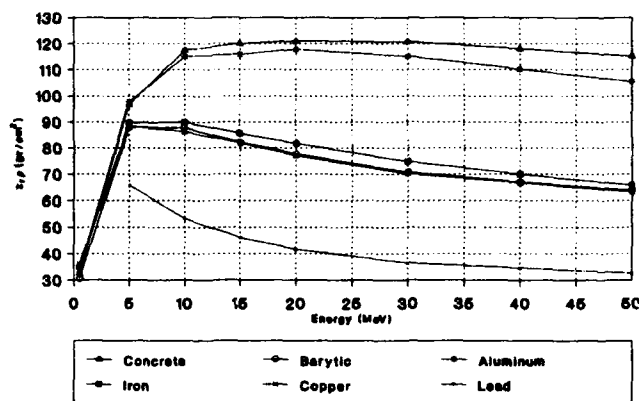
Figure 2. MCNP results for direct radiation.

Concordance would has been better if we had considered a continuous actual spectrum rather than a monoener-

getic source, but unfortunately we could not get these data from manufacturers.

Thus, DIN-6847 is less conservative for direct radiation than expected, as it was discussed by authors in an early paper [9] comparing tenth-value thickness from DIN-6847 with those from NCRP-49 [10] for concrete, up to 10 MeV.

On the other hand, the obtained curves for concrete and aluminum are very similar, furthermore the curves not only for iron and copper but also for barytic concrete match very well.

For the *scattered radiation* the Monte Carlo results are shown in Figure 3. Note that the obtained tenth-value thicknesses are practically constant, always lower than the DIN-6847 recommended values although differences are less significant.
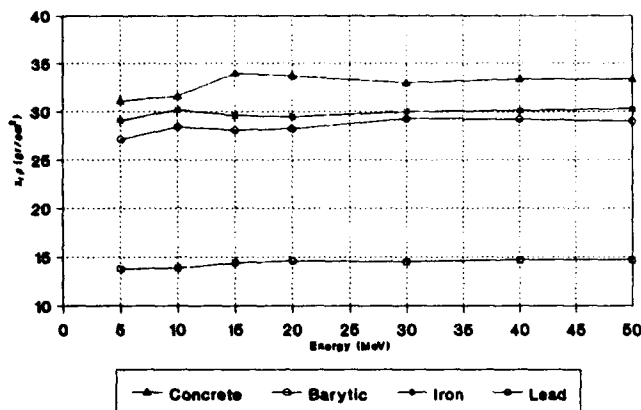
Figure 3. MCNP results for scattered radiation.

MCNP determines error for each calculated dose. With these data a statistical analysis has been performed to prove that results are significant, practically at 100% for relative error of 5%.

IV. CONCLUSIONS

Monte Carlo method has been used to estimate tenth-value thickness for X-ray direct and scattered beams in medical electron accelerators. Results have been compared with values recommended by the DIN-6847 standard.

It has been verified for primary radiation that without significant errors the same curve may be used for different materials, in particular for concrete and aluminum and for barytic concrete, iron and copper, respectively, though "a priori" it did not look very logical.

For secondary radiation, results proved that the single table given by the guide is sufficient to obtain tenth-value thickness independently of incident beam energy. Furthermore, the Monte Carlo obtained data are very similar to those proposed by the guide.

Since the primary beam spectrum in an accelerator is generally unknown, a monoenergetic source has been considered. For a continuous actual spectrum there should be used the maximal value of z within the spectrum energy range. If the spectrum is well known, the tenth-value thickness can be obtained by decomposition.

In order to get more conservative shielding barriers the Monte Carlo calculated values for the primary beam may be used, except for lead for which the DIN-6847 curve has to be used. For the scattered beam, values recommended by DIN-6847 may be safely used.

V. REFERENCES

[1] ICRP Publication 60, *New Recommendations of the Commission*, approved on 9 November 1990.

[2] G. Verdú, J. Ródenas and J. M. Campayo, "Radiation Protection for Particle Accelerators", *I International Conference on Implications of the new ICRP Recommendations*, Salamanca (Spain), 26-29 November 1991.

[3] NCRP Report 51, *Radiation Protection Design Guidelines for 0.1-100 MeV Particle Accelerator Facilities*, National Council on Radiation Protection and Measurements, 1977.

[4] DIN-6847, *Medizinische Elektronenbeschleuniger-Anlagen; Teil 2: Strahlenschutzregeln für die Errichtung*, (Medical electron accelerators; Part 2: Radiation protection rules for installation), DIN Deutsches Institut für Normung e. V., 1977.

[5] J. Ródenas and G. Verdú, "Análisis de la normativa aplicable al cálculo de blindajes en aceleradores lineales", *PROTECCIÓN RADIOLÓGICA*, Revista de la Sociedad Española, núm. 2, Mayo 1992.

[6] W. L. Thompson, (Monte Carlo Group Leader), *MCNP - A General Monte Carlo Code for Neutron and Photon Transport*, Version 3, Los Alamos Monte Carlo Group, Los Alamos National Laboratory, Los Alamos, New Mexico, 1983.

[7] A. B. Chilton, J. K. Shultis and R. E. Faw, *Principles of Radiation Shielding*, Prentice Hall, 1984.

[8] E. Storm and H. I. Israel, *Photon Cross Sections from 0.001 to 100 MeV for Elements 1 through 100*, LA-3753, 1967.

[9] J. Ródenas, G. Verdú and R. Máiquez, "Aplicación del método de Monte Carlo al cálculo de blindajes en un acelerador lineal", *XVIII Reunión Anual de la Sociedad Nuclear Española*, Jerez de la Frontera — Puerto de Santa María (Spain), 28-30 October 1992.

[10] NCRP Report 49, *Structural Shielding Design and Evaluation for Medical Use of X-Rays and Gamma Rays of Energies up to 10 MeV*, National Council on Radiation Protection and Measurements, 1976.

Burst-Mode Electron Gun Pulser
for FEL with the ISIR Linac

K. Tsumori*, S. Okuda, T. Yamamoto, S. Suemine and S. Takamuku
Radiation Laboratory. The Institute of Scientific and Industrial Research,
Osaka University
8-1 Mihogaoka, Ibaraki, Osaka, 567 Japan

Abstract

Infrared free-electron lasers (FEL's) are being developed at The Institute of Scientific and Industrial Research (ISIR). For a FEL oscillator, a burst-mode electron gun pulser with short pulse widths and high repetition rates is effective to obtain multi bunch beams of high peak currents. In order to produce narrow pulses at a 36.9ns interval, rf of two different frequencies, 27 MHz (fundamental) and 81 MHz (the third harmonic), has been combind with a 3 dB hybrid coupler. The pulses have been directly supplied to the cathode of a high-current electron gun (Model-12, ARCO). The electron beam from the gun at an energy of 100 keV has a peak current of 440 mA in a micropulse with a width of 4.5 ns (FWHM), whose frequency is 27MHz for a macropulse duration of 4micro second. After acceleration at an energy of 23MeV, the charge of an electron bunch and energy spread have been measured to be 1nC and 0.9%, respectively, which shows good performance of the present pulser for FEL oscillator experiments.

The grid pulser will be improved to make the repetition rate of the micropulse changeable.

1. INTRODUCTION

The ISIR L-band linac was constructed in 1978. After the improvement of the subharmonic prebuncher (SHPB) system the charge of the single bunch beam was remarkably increased from 7 to 67 nC. [1], [2]   The beams have been applied to various studies for analyzing the transient phenomena in the fields of radiation physics and chemistry. Recently, the FEL project has started to realise an oscillator and an amplifier at 10-60 micrometer wavelengths.

For a FEL oscillator, an electron gun pulser with a very high repetition rate (more than 10 MHz) and a short pulse width (less than 5 ns) is effective. Such a high frequency is not realized with the ordinary grid pulsers using the avalanche transistors nor the discharge tubes. For time-of-flight experimens at SLAC [3], the burst-mode grid pulser which consists of a V-MOS transistor and a snap diode has been

---

* Present address: Sumitomo Electric Industries, Elect. Power Syst. Tech. Res. Lab., 1-1-3 Shimaya, Konohana-ku, Osaka 544, Japan

developed: a pulse width is less than 1 ns and a repetition rate is above 20 MHz during a 1.6 micro-second rf macropulse. For the FEL experiments with an S-band linac at CLIO,[4] a grid pulser using a very fast frequency divider and a wideband solid state amplifier of 10-500 MHz has been developed: The pulser with a 0.9 ns width at 4-32 ns intervals drive a Y646B(EIMAC) cathode.

In this work, a new bursut-mode pulser having a simple circuit and the same performance as above system have been developed.

2. ISIR LINAC

The ISIR linac consists of a 120 kV electron gun (Model-12,ARCO), three SHPB's (two twelfth SHPB's and one sixth), a prebuncher, a buncher and an accelerating waveguide 3m long. The accelerating waveguide is driven by a 20 MW L-band klystron (TV-2022B,THOMSON) and both the buncher and the prebuncher are driven by a 5 MW klystron (E3775A,TOSHIBA). The SHPB has a coaxial single-gap cavity at one end of the inner conductor. To SHPB's pulsed rf of 20 micro-second duration and 20 kW peak power is supplied. Beam characteristics at the single bunch mode

Figure 1. A wave form given by calculation. Solod line: Fundamental wave form of 27 MHz. Dotted line: combind wave form of 27MHz and 81MHz(third harmonic).

Figure 2. Schematic diagram of the burst-mode gun pulser.

operation, the energy, the energy spread and the charge per single bunch, are 38 MeV, 0.9% and 67 nC, respectively.

3. BURST-MODE GUN PULSER

For the FEL oscillator experiments, the interval between the micropulses of the accelerated beam can be determined by the round-trip time of light in an optical resonator. In the present case, the interval is 36.9 ns(27 MHz), corresponding to four rf periods at the first SHPB. The maximum pulse width of the beam from the gun acceptable for the first SHPB (108 MHz) is 4.5 ns. In order to produce such narrow pulses by the gun pulser, rf of two different frequencies, 27 MHz (fundamental) and 81 MHz (the third harmonic) have been combined.

The schematic diagram of the present grid pulser system is shown in Fig. 2. The pulser consists of rf processing circuits on the ground potential and the gun-cathode driver which is installed in a high voltage deck in an injecter tank. In the processing circuit, 54 MHz rf from the master oscillator of the linac is converted to rf at two frequencies, 27 and 81 MHz. The pulsed rf which modulated by a PIN diode switch is amplified to about 10 W and then fed to coupling coils working over a voltage diffrence of 100 kV in the injector tank filled with Freon gas at a pressure of 5 PSI. The width of the gap between these coils is 85 mm. An attenuation of rf power between the coils is about 20 dB.

For driving the gun cathode, the two pulsed rf of 27 and 81 MHz are independently amplified up to 300 W and combined by using a 3 dB hybrid coupler. In this case a phase shifter and attenuaters placed in the rf processing circuit are adjusted. A wave form given by calculation is shown with a dotted line in Fig 1. The combined rf is supplied to

the cathode through a dc-cut capacitor. The bias supplied to the cathode to avoid emission due to the small peaks shown in Fig.1 decreases the injection current to some extent. The driving voltage at the cathode is measure rate of 400 V peak to peak as shown in Fig.3.
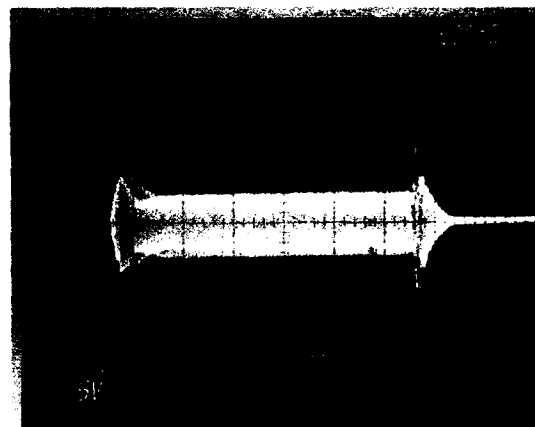
Figure 3. Pulse shape of the combined rf at the cathode voltage is measured of 400 V peak to peak.

The electron beam generated by the gun at an energy of 100 kV has a peak current of 440 mA for a 4.5 ns pulse width. For an electron beam acclerated at an energy of 23 MeV, micropulses having a repetition rate of 27 MHz (36.9 ns interval) over a 4 micro-second macropulse duration is shown in Fig. 4. This measurment has been made with a bi-planar phototube (60 ps rise time) by observing Cherenkov radiation from the electron beam in the air atmosphere. Measurements have also been made with an ultrafast streak camera. The charge per micropulse is 1 nC.

651
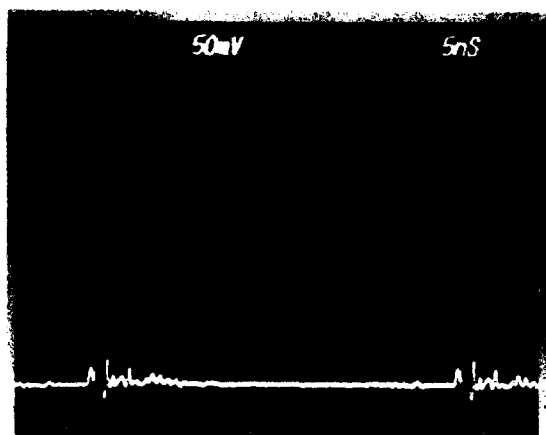
Figure 4. A part of the accelerated micropulses having a repetition rate of 27 MHz (36.9 ns interval).

4. GUN PULSER UPGRADE

On the burst-mode operation for common use of electron beams, the repetition rate of the micropulse is desired to be changeable. In order to realize this feature a micropulse-elimination circuit will be added to the present gun pulser. Fig.5 shows the schematic diagram of the main part of the new circuit.
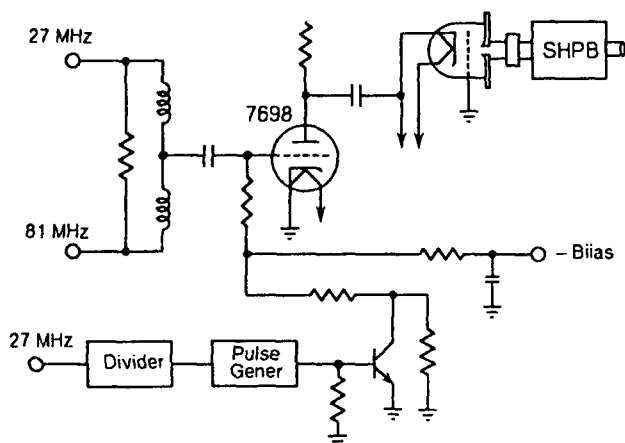
Figure 5. A pert of the micropulse-elimination circuit a gun control triode is added to the present gun pulser.

The plana triiord 7698 (EIMAC) is inserted between the hybrid coupler and the gun cathode. Only when positive short pulse which has the same width as the micropulse is imposed on the dc bias, the triode works. The rate of elimination can be determined by the rf frequency divider. This system will be tested by November in 1993.

6. REFERENCES

[1] K. Tsumori, N. Kimura, T. Yamamoto, T. Hori, S. Takeda, J. Ohkuma, T. Sawai, M. Kawanishi, H. Sakurai and K. hayashi, Proc. 3rd Symp. on Accelerator Sci. and Technol. (1980) 49.

[2] S. Takeda, K. Tsumori, N. Kimura, T. Yamamoto, T. Hori, T. Sawai, J. Ohkuma, S. Takamuku, T. Okada, K. Hayashi and M. Kawanishi, IEEE Trans Nucl. Sci. NS-32 (1985) 3219.

[3] R.F, Koontz, "One nanosecond pulse electron gun systems" IEEE Trans. Nucl. Sci. NS-26, No.3, 4129 (1978).

[4] R. Chaput, "Electron gun for the FEL CLIO" Proc. 2nd Europ. Particle Accelerator Conf. Nice, 1990.

Positron Accumulation Ring for the SPring-8 Project

Yoshikazu Miyahara
JAERI-RIKEN SPring-8 Project Team
Honkomagome, 2-28-8, Bunkyo-ku, Tokyo 113, Japan

Abstract

Design of a positron accumulation ring (PAR) for the SPring-8 project has been considered as an option to increase the injection rate into the storage ring via a synchrotron. The beam energy and the circumference of the PAR are 500 MeV and 28.294 m, respectively. The injection rate can be increased by about 10 times. Reduced bunch length in the PAR and RF synchronism between the PAR and the synchrotron are favorable to produce a pure single bunched beam in the storage ring.

I. INTRODUCTION

In the SPring-8 project, a 900 MeV positron beam is injected from a linac into a synchrotron, accelerated up to 8 GeV in the synchrotron, and stored in an 8 GeV storage ring with a repetition of 1 Hz. In this scheme, 8 pulses of positron beam with a beam current of 10 mA and a pulse length of 10 ns are accumulated in the synchrotron in the injection period. There is no synchronism of the RF frequensies between the linac and the synchrotron, but a synchronism between the synchrotron and the storage ring. Thus assuming an injection efficiency of 50 % and 100 % into the synchrotron and the storage ring, respectively, it is expected to take about 20 min to store a beam current of 100 mA in the storage ring. The assumption is rather simple, and the injection efficiency might be reduced much. Accordingly a positron accumulation ring (PAR) similar to those of DESY[1] and APS[2] has been considered as an option.

The PAR is to be placed between the linac and the synchrotron. Since the repetition of the linac is 60 Hz, about 55 pulses of the positron beam can be accumulated in the PAR during the ramping cycle (1 Hz) of the synchrotron, which increases the injection rate drastically. In addition, the reduction of emittance, energy spread and bunch length in the PAR and also RF synchronism between the PAR and the synchrotron are expected to increase the injection efficiency into the synchrotron, and especially favorable to produce a pure single bunched beam in the storage ring.

In this design, conversion of the components of a 300 MeV electron storage ring JSR, to be shut down soon, was taken into account.

II. LATTICE OF PAR

Fig.1 shows the structure of PAR placed between the linac and the synchrotron. The circumference of PAR is $2\pi R=28.294$ m, which is 1/14 of the circumference of the synchrotron. The revolution period is To=94 ns, long enough for the rize time of a kicker magnet in the PAR for beam extraction. The lattice is mainly composed of 8 bending magnets and 3 families of quadrupole magnets.

Figure 1. Structure of PAR placed between linac and synchrotron.
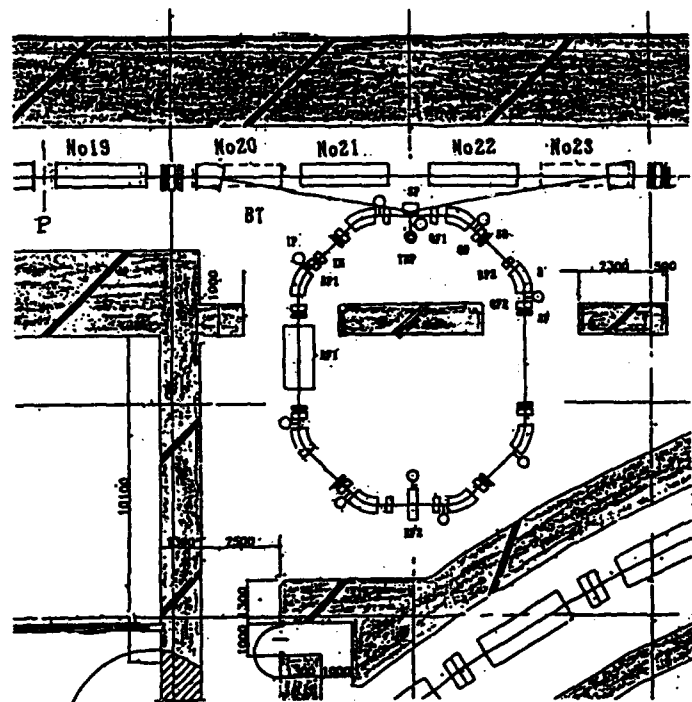
The radiation damping time in the PAR should be comparable with the repetition period 16.7 ms of the linac beam. Assuming to use the bending magnets of JSR with a length of 0.874 m, the orbit curvature was taken as ρ =1.113 m. For a small beta function and a stable operation and also for a smooth variation of beta function, a weak focusing of bending fields is quite favorable. In addition the radiation damping time can be reduced considerably by the use of the weak fucusing. The damping time is given by

$$\tau_x = 2ET_o/J_xU_o = 2.5\times10^{-4}\times2\pi R/BE^2 \ (J_x=1)$$

where E is the beam energy, Jx the horizontal partition number, Uo the radiation energy and B the bending field. The partition number is given by $J_x=1-D$ with

$$D = \frac{1}{2\pi}\oint_B \eta(s)\frac{1-2n}{\rho^2}\ ds$$

where $\eta(s)$ is the dispersion function along the circumference, and n the n-value of the bending field. Thus an increase of n increases Jx, and consequently decreases the damping time. Fig.2 shows the relation of the damping time and the bending field with respect to the beam energy for Jx=1 or n=0.5. To avoid a strong field saturation, B=1.5 T and E=500 MeV are
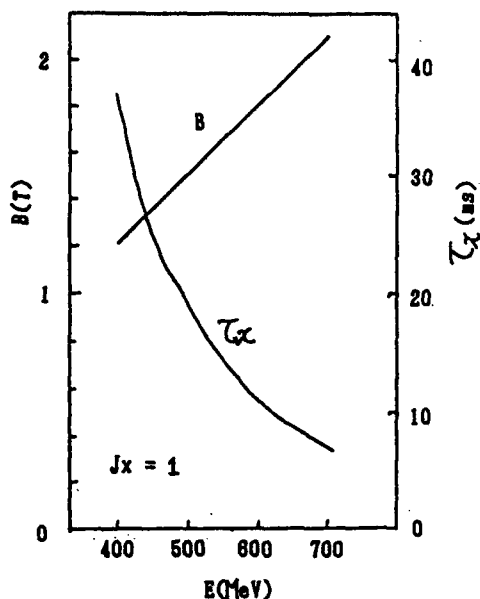
Figure 2 Relation of radiation damping time and the bending field with respect to the beam energy.

Table 1 Parameters of PAR.

Beam energy	E	500	MeV
Circumference	$2\pi R$	28.294	m
Revolution period	T_0	94.38	ns
Momentum compaction fac.	α	0.276	
Tune	ν_x/ν_y	1.76/1.38	
Chromaticity	ξ_x/ξ_y	-2.47/-0.004	
Partition number	$J_x/J_y/J_\epsilon$	1.224/1.0/1.776	
Emittance	ϵ_x	0.44	mmrad
Energy spread	σ_E/E	2.6×10^{-4}	
Radiation energy	U_0	4.97	keV/turn
Damping time	$\tau_x/\tau_y/\tau_\epsilon$	15.5/19.0/10.7	ms
RF frequency	$f1/f2$	10.596/116.55	MHz
Harmonic number	$h1/h2$	1/11	
RF voltage	$V1/V2$	50/35	kV
RF bucket height	$\Delta E/E$	1.40/0.34	%
Bunch length	σ_τ	0.81/0.29	ns
Bending field	B	1.5	T
Curvature of bend	ρ	1.1128	m

favorable, which gives τ_x=19 ms. Further increase of n reduces the damping time. The weak fucusing also reduces the emittance. Thus the pole pieces of the magnets of JSR are changed from a constant field type to a weak focusing type for the PAR with an n-value of 0.6, which gives a damping time of 15.5 ms.

Fig.3 shows the lattice functions of PAR. The dispersion is zero in the beam injection/extraction region, and becomes the maximum 3.2 m in the long straight section. The dispersion function is mainly determined by quadrupole magnets QF2, and the tune mainly by QF1 and QD. Sextupole magnets SF and SD are installed close to QF2 and QD to avoid the head-tail instability. The lattice parameters are shown in Table 1. The beam is injected and extracted through the same septum magnet at an angle of 9 degrees, and the beam passes QF1s between the poles and yoke. Two bump magnets and a kicker magnet are placed in short straight sections at a phase advance of $\pm\pi/2$ from the septum magnet. The horizontal excursion of the injected beam becomes the maximum of 50 mm at QF2.

III. RF SYSTEM

The RF system of PAR is composed of two cavities. One(RF1) is excited at the revolution frequency and a voltage of 50 kV, and the other(RF2) at the 11th harmonic or 116.55 MHz and 35 kV. For the latter the RF system of JSR can be converted. The 11th harmonic frequency can be generated by down counting and a phase lock loop as shown in Fig.4. RF1 is excited continuously, and RF2 just before beam extraction for 50 ms, so that about 55 macro-pulses of linac beam can be accumulated in one cycle of the synchrotron. During the accumulation, RF2 cavity is detuned by swithing to a matched load to avoid a beam bunching with an induced voltage.

Fig.5 shows the relation of RF bucket height and length compared with bunch length and energy spread. The damped bunch length in RF2 is $4\sigma_\tau$=1.2 ns, short enough for the beam injection into the RF bucket of

7.073 m

Figure 3. Lattice functions of PAR.

Figure 4. Generation of the 11th harmonic frequency with a phase lock loop.

654

Figure 5. Relation of RF bucket height and length with respect to energy spread and bunch length in RF1, RF2 and synchrotron.

IV. MAGNETS

Bending magnets and the power supply of JSR can be converted to PAR with some modifications. The orbit curvature and the pole pieces are changed as shown in Fig.8. The pole gap is also reduced from 55 mm to 42 mm to produce an increased field of 1.5 T instead of 1.2 T of JSR with the same power supply. But we need two additional bending magnets and their power supply.

JSR has three families of Q magnets with 3, 8 and 6 each. The PAR needs three families with 4, 4 and 4 each, and the field strengths in the PAR is much weaker than those in JSR because of the use of weak focusing in bending magnets. Thus Q magnets and the power supplies of JSR can be converted to the PAR. The pole pieces of Q magnets should be changed to increase the good field region.

Sextupole magnets and the power supplies can be used, but the pulse magnets (septum, bumps and kicker) need to be newly constructed.

V. BEAM TRANSPORT

In the beam tranport line from the linac to the synchrotron via the PAR shown in Fig.1, 10 Q magnets are installed, and two acceleration sections of the linac are replaced with bending magnets, which deflect the beam by 9 degrees. Fig.7 shows the magnet arrangement and matched lattice functions of the beam transport line.

VI. REFERENCES

[1] A. Febel and C. Hemmie, IEEE Tr. NS-26, 3244 (1979).

[2] E. A. Crosbie, ANL Rept. Light Source Note, LS-109 (March, 1988).

the synchrotron with a bucket length about 2 ns. Expected threshold current of the microwave instability is 13 A at peak for a longitudinal coupling impedance $Z_{\parallel}/n=10\,\Omega$, while the accumulated peak current is 7.5 A with an injection efficiency of 100 %, so that the bunch lengthening would not be induced.

Figure 6. Bending magnet modified for PAR.

Figure 7. Matched lattice functions of beam transport line.

Induction Accelerator Development for Heavy Ion Fusion*

Louis L. Reginato for the HIFAR EngineeringGroup**
University of California Lawrence Berkeley Laboratory
1 Cyclotron Road, MS 47-112, Berkeley, CA 94720 USA

Abstract

For approximately a decade, the Heavy Ion Fusion Accelerator Research (HIFAR) group at LBL has been exploring the use of induction accelerators with multiple beams as the driver for inertial fusion targets. Scaled experiments have investigated the transport of space charge dominated beams (SBTE), and the current amplification and transverse emit'ance control in induction linacs (MBE-4) with very encouraging results. In order to study many of the beam manipulations required by a driver and to further develop economically competitive technology, a proposal has been made in partnership with LLNL to build a 10 MeV accelerator and to conduct a series of experiments collectively called the Induction Linac System Experiments (ILSE).

The major components critical to the ILSE accelerator are currently under development. We have constructed a full scale induction module and we have tested a number of amorphous magnetic materials developed by Allied Signal to establish an overall optimal design. The electric and magnetic quadrupoles critical to the transport and focusing of heavy ion beams are also under development. The hardware is intended to be economically competitive for a driver without sacrificing any of the physics or performance requirements.

This paper will concentrate on the recent developments and tests of the major components required by the ILSE accelerator.

I. INTRODUCTION

The LBL approach to a HIF driver using multiple beams in one induction accelerator and combining them into fewer beams has many unique advantages, such as high repetition rate, reliability, high efficiency, and electromagnetic focusing which allow long stand-off from the target. To further investigate the feasibility of this approach beyond MBE-4, the HIFAR group has proposed a series of scaled experiments called the Induction Linac Systems Experiments (ILSE) [1]. In ILSE we will not only investigate beam transport physics but will also develop accelerator technology and a capital cost database which will confirm the technological soundness and economics of this approach to HIF.

In ILSE, four potassium beams will be accelerated from a 2 MeV injector to 5 MeV by the electrostatic focusing section, combined into a single beam, and accelerated to 10 MeV by the magnetic focusing section. The line charge density will be the same as for a full scale driver, 0.25μC/m, and charge compression or current amplification occurs continuously throughout the accelerator. To maintain longitudinal stability, the acceleration waveforms are also continuously changing throughout the accelerator; initially the acceleration waveforms are ramped or trapezoidal with 1.5 μs duration while the final stages will have square waveforms with 400 ns duration. To transport the four space charge dominated beams, electrostatic quadrupoles with a half lattice period of 33 cm and 41 cm will be used. After the beams reach the 5 MeV acceleration, a four-to-one beam combiner will be used to inject a single beam into the magnetic quadrupole transport section. This section with a half lattice period of 50 cm will accelerate the ions from 5 MeV to 10 MeV. This paper will describe the accelerator design and the technology development.

II. MAGNETIC MATERIALS

The induction accelerator is inherently a very low gradient (< 1 MeV/m) but very high current device (10s of kA). The drive system for an induction linac is typically a distributed or a lumped pulse forming network with the proper impedance to supply both the beam current (I_B) and the core magnetizing current (I_M) at the desired voltage. The efficiency is simply the ratio $I_B/(I_B + I_M)$. For an accelerator such as the ATA where the magnetizing current was 800 A and the beam current 8 kA, the efficiency is very high. In a driver for inertial confinement fusion, a very large fraction of the induction linac will be required to accelerate many kiloamperes of beam. The induction cores will no doubt be large in diameter and likewise require several kiloamperes of magnetizing current, making this approach to acceleration reasonably efficient (> 50%). The front end of a driver, prior to large charge compression or current multiplication, will be accelerating tens to hundreds of amperes which will make the efficiency quite small (< 10%). ILSE is basically the front end of driver and in order to optimize the design, a magnetic material should be chosen with a maximum flux swing (ΔB) and a minimum magnetization current (ΔH). The ferromagnetic material is, therefore, one of the most important components of an induction linac because it sets the requirements for the acceleration waveform drive system. Historically, short pulse (< 100 ns) induction accelerators have utilized ferrite as the magnetic material of choice, whereas those for longer pulses have used nickel-iron and amorphous materials.

The voltage gradient and the pulse duration will establish the volt-seconds required by the cells. For ILSE, a voltage gradient of 300 to 400kV/m and a pulse duration of one to two microseconds will require cores of one to two meters in diameter. It is imperative to find a material with the maximum flux swing and the minimum magnetizing current. A significant effort has already been invested in the investigation of the magnetic materials which are appropriate for this application [2] There are several materials which satisfy the technical requirements for ILSE. The conventional Ni-Fe alloys that have been used for many decades and the

relatively new amorphous materials (Metglas[*]) satisfy these requirements. The choice of materials is therefore based on economic advantages. Recent investigation shows that the Metglas alloys hold an advantage over the conventional Ni-Fe alloys. The Allied Metglas amorphous material 2605 series can be mass produced as a thin ribbon (15-20 μm) with high resistivity and practically any width. This material is used extensively by the 60Hz power industry. For this application, annealing is essential in order to achieve maximum flux swing and minimum loss. Annealing is typically done after the ribbon is wound into a core without interlaminar insulation. Interlaminar insulation is not required for the 60 Hz application because the volts per layer of ribbon are very small (mV). For the ILSE application where the rates of magnetization are between 2-6 Tesla/μs and 10-20 V per layer can be generated, some insulation will be required to maintain low eddy current losses. Previous efforts have concentrated on finding interlaminar insulation which allows annealing after the material is wound into a core. Annealing embrittles the material, and winding a core afterwards is not practical. After several years of effort, insulators were found which held off sufficient volts per layer and that could withstand annealing temperatures without degradation of the magnetic properties. Application of those coating, however, resulted in a considerable cost increase for the finished core. Clearly, the most cost effective option for ILSE is to use Metglas as-cast (unannealed) and wound with thin mylar insulation (2.5μm) to achieve turn-to-turn insulation and a high packing factor. Experimental data [3] has shown that at high magnetization rates, magnetic losses can be described fairly closely by saturation wave theory. In this model, unlike the 60Hz case where hysterisis losses are dominant, the losses depend on the square of the ribbon thickness, the rate of magnetization, and the inverse of the resistivity. Extensive testing and comparison between annealed and unannealed Metglas showed that for the latter there is slight rounding of the B-H loop, but the flux swing and the magnetization losses are nearly the same (Fig.1). A number of alloys were tested (Fig.2) and it appears that the unannealed 2605 SC material is optimal for ILSE. The flux swing is 2.5-3 Tesla, the losses with 1 μs saturation times are about 1000 Joules/m^3, and the packing factor with 2.5 μm mylar is greater than 80%.

The recent conceptual design report (CDR) used this material for our baseline cost estimates. Studies of other magnetic materials such as the Metglas TCA and the conventional Ni-Fe is continuing, and a final decision on the most cost effective material will not be made until after the project is approved.

A. *Induction Cell*

The principle of linear acceleration by magnetic induction has been thoroughly covered in many publications. Heavy ion induction accelerators, however, are unique in their requirements. The acceleration waveforms are continuously variable throughout the ILSE acceleration cycle and the focusing half lattice periods (HLP) varies accordingly from an initial 33 cm for the first 16 modules to 41 cm for the next 16 and finally 50 cm for the remainder of the accelerator. A

---

[*] Metglas is a trademark of Allied Signal Corporation.
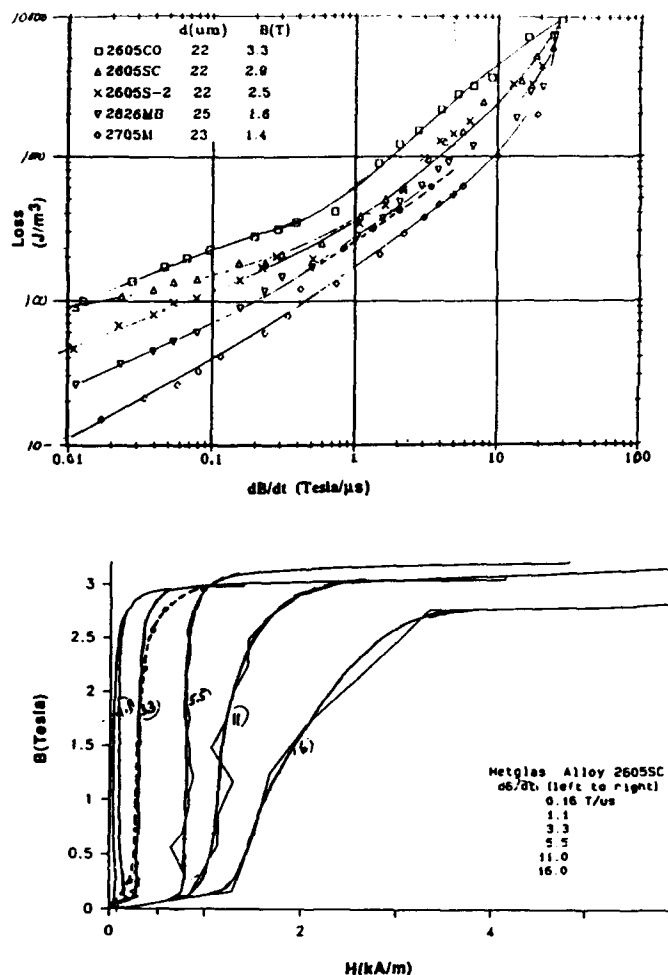
Figure 1. Top: Losses (J/m^3) at different rates of magnetization dB/dt (T/μs) measured by Allied for annealed 2605SC Metglas. Bottom: B-H loops, dB/dt (T/μs), at different rates of magnetization, measured by Allied, for annealed 2605SC Metglas. The dotted lines represent LBL data for the same material unannealed with 2.5 μm of Mylar wound between turns.
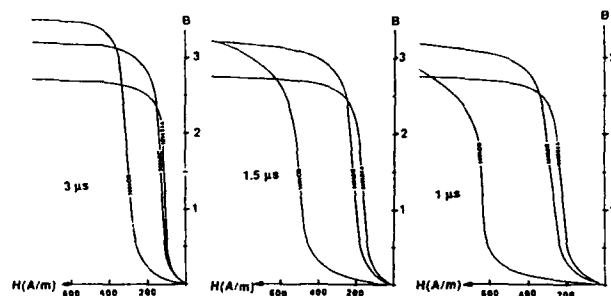
Figure 2. Dynamic magnetization curves taken at constant voltage and different saturation times for unannealed 2605 alloys.

number of factors influenced our decision to choose the 2" wide Metglas for our induction cells. First of all, it gave us the flexibility to use identical cells for the different half lattice periods. For example, the 33 cm HLP uses three cells, the 41 cm four cells and the 50 cm five cells bolted together to form a module. Between each module there is axial space for high voltage feedthrough, magnet power, and most importantly, alignment and structural supports for the quadrupoles. A second reason for the 2" width was the fact that we wanted to avoid cumbersome liquid insulation (oil) in the acceleration gap. With the 2" width, the voltage per gap is 33 kV which can be held off reliably with gas insulation (SF$_6$ or CO$_2$ + N$_2$). Another argument for maintaining acceleration voltages of 33 kV is that the line modulators which drive the core can utilize reliable and inexpensive glass thyratrons rather than expensive high voltage ceramic units or unreliable spark gaps. Another advantage of using a narrower ribbon is that the voltage per layer is lower, thus allowing a thinner interlaminar insulation (2.5 μm) to hold off the voltage, and this results in a higher packing factor (0.8 to 0.9). The inside diameter of the induction cell is determined by the size of four beam electrostatic quadrupole and the voltage hold off requirements. The gradient and pulse duration now dictate the volt-seconds, hence the outside diameter. Allowing 50% more volt-seconds than the minimum dictated by the 1 μs pulse, the outside diameter is 1.5 m. The magnetic field H is related to magnetizing current I by $H = I/2\pi r$. Because the outside radius is about three times the inside radius, the inside portion of the core will saturate before the outer portion is fully magnetized. Saturation of the inner portion will cause nonlinear current flow which makes pulse shaping more difficult. In order to maximize utilization of the magnetic material, the core is segmented radially into three sections. The three cores are now driven in parallel and will approach saturation very nearly at the same time. The voltage will, of course, be one-third as high, while the drive current will be three times higher. An additional benefit of segmenting the core is that the thyratron switch will operate at a more conservative voltage level (22 kV charge), resulting in a more reliable system. A detailed cross-section of the segmented cell is shown in Figure 3.

Each induction core is supported by a mandrel and flanked by a thick plate on one side and a thin one on the other. The thick plate constitutes the ground return and the thin one terminates the high-voltage cable feed. On each side of the core are several layers of Mylar to insulate the high voltage from the ground. The high voltage will be fed through standard high-voltage connectors to the outer core and will be connected to the two inside cores by means of high-voltage wire embedded in the thick plate.

Three cells are bolted together to form a 33 cm HLP module, and eight modules are assembled together to form a section or cell-block with complete diagnostics capability. Figure 4 shows a complete cell block for the 33 cm HLP electrostatic focus section with quadrupoles inside. The space between three-cell modules is required for quadrupole support, high voltage feed-through, and articulation devices.

B. Waveform Generator

The acceleration schedule for ILSE will require careful tailoring of the voltage waveforms at each gap in order to provide energy gain, current multiplication, and longitudinal
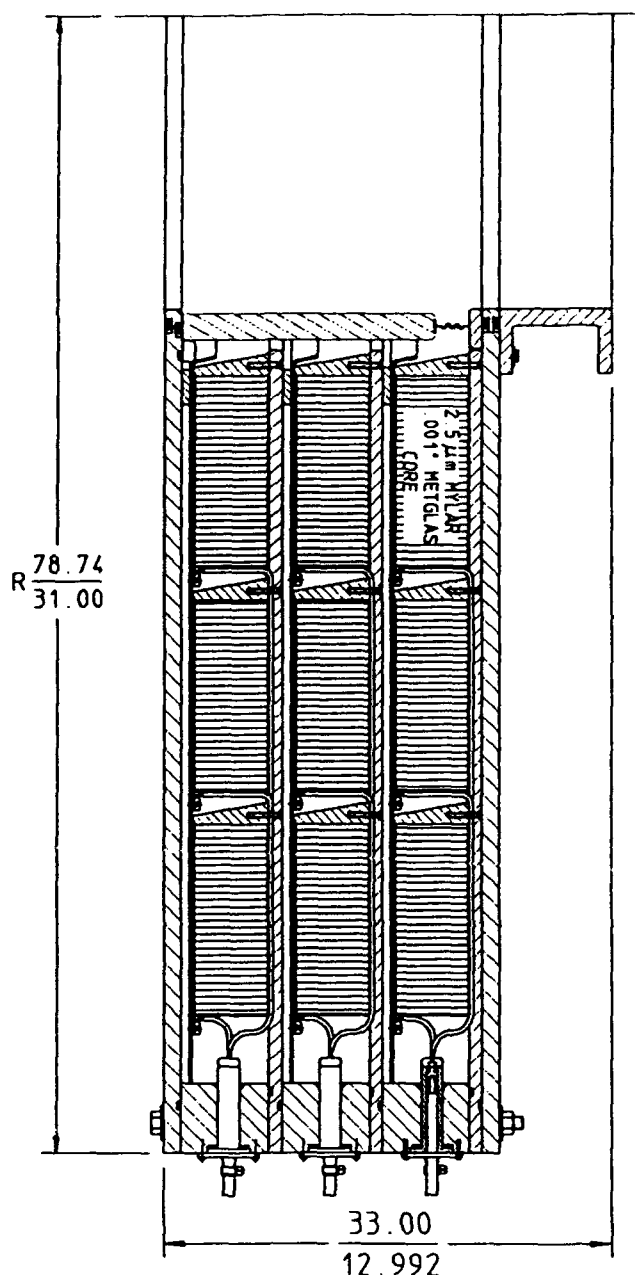
Figure 3. Detailed cross section of radially segmented induction cells for the electrostatic focus section.
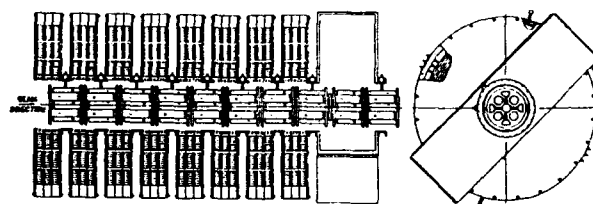
Figure 4. Eight modules of three cells each (33-cm HLP) form a "cell block" in the electrostatic focus section.

658

focusing. Figure 5 shows the acceleration waveforms dictated by heavy ion beam transport physics. Initially, the voltage is sawtooth with over 1 µs duration and then becomes rectangular with shorter and shorter duration. These waveforms should be replicated to within a percent of the ideal. To satisfy these requirements, we have chosen to build pulse-forming networks (PFN) switched by a thyratron. This technology can produce the desired waveforms to within a few percent and will have to be augmented by some active or fast correction devices to meet the specifications. This combination is the most cost-effective way to satisfy all the requirements. Active solid state devices or hard tube modulators to produce all the desired waveforms would be prohibitively expensive. To achieve the desired accuracy, each PFN will be designed with time varying impedance in order to complement the nonlinearity of the induction cell. As can be seen from the magnetizing current, the impedance of the induction cell decreases as the magnetic material approaches saturation; the PFN will likewise have an impedance which "decreases in time." Using this approach, we hope to be within a few percent of the ideal wave shape. The fast correction will then be required to handle a very small fraction of the total current. The voltage to the cell will be slightly higher than required, and the fast correction will basically act as a shunt regulator in a feedback system to lower the voltage to the desired level. The shunt regulator has not been designed yet, but it will consist of a stepdown transformer with FET to act as variable resistors.
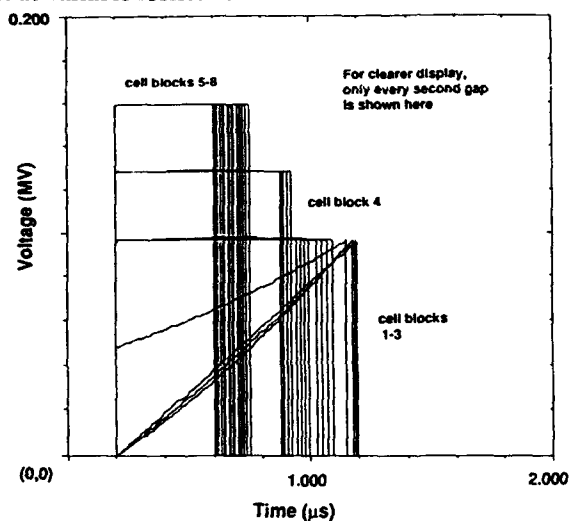
Figure 5. Ideal accelerating waveforms. This figure shows the ideal voltage waveforms for every second accelerating gap needed to achieve self-simi ar current amplification through the accelerator portion of ILSE.

The block diagram of the complete drive system is shown in Figure 6. The DC power supply charges the command resonant charger (CRC) which pulse charges the tapered impedance pulse-forming network (PFN) which powers the induction accelerator cores once the thyratron is triggered. During the charge cycle from the CRC to the PFN, the current flows through the cores and partially resets them. Because of their large diameter, however, this charging current is insufficient to fully reset them, and a separate reset pulse is required.
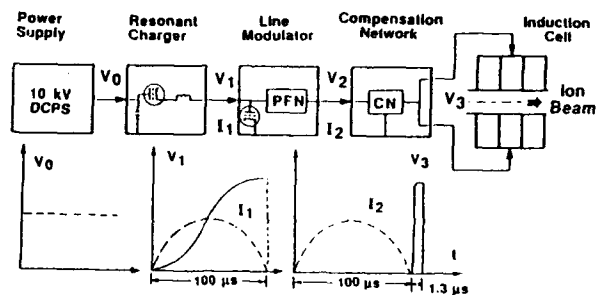
Figure 6. Block diagram of a drive system that generates the acceleration voltage for the induction cells.

The desired sawtooth and rectangular pulses are generated by ladder-type PFNs. These networks use discrete components to build a series of harmonics that together approximate the desired wave shape. Each component or stage of the network is associated with a different portion of the pulse. Taking the load impedance as the instantaneous value of the voltage divided by the current for a particular cell, the impedance of each stage can be matched to that load at the time associated with that stage. The two types of networks for generating the sawtooth and rectangular pulses are simulated on the computer prior to building full-scale prototypes. Figure 7 shows a simplified circuit for a rectangular pulse generator with computer simulation and the actual waveform. Figure 8 is the computer simulation for a sawtooth generator.
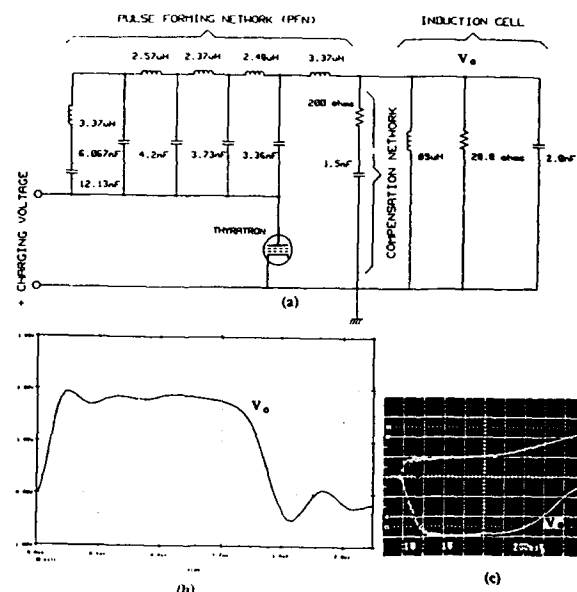
Figure 7. The schematic, computer-simulation results, and actual test results of the square-wave pulse generator.
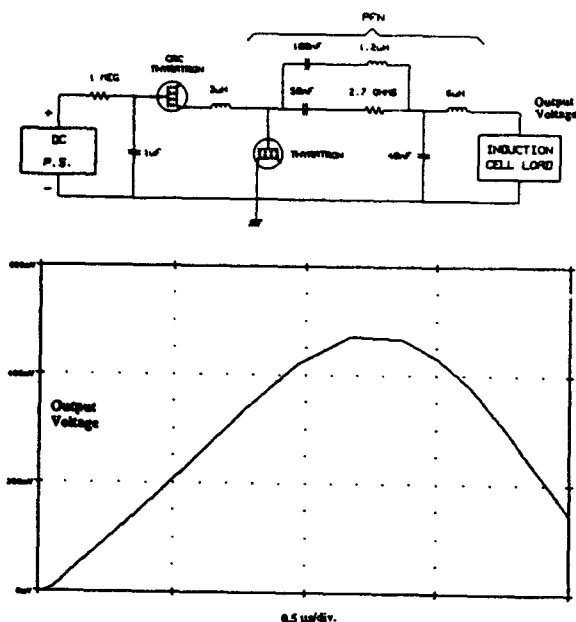
Figure 8. Unipolar network design to generate a ramp, along with the resulting waveform in computer simulation.

C. Test Stand

During the past year we have constructed a full scale test stand to study the issues associated with a heavy ion induction accelerator. The test stand consists of three full-scale cells which simulate the 33 cm HLP module. This module is driven by PFNs which deliver rectangular pulses to the cells. Reset to the cells is provided by a SCR pulser which can drive the magnetic material below $-B_r$ to obtain a greater flux swing. The initial cores were all wound using the 2605 S3A material since approximately one tonne was left over from a previous project at a small cost to us. This materials is not the optimum for ILSE, but it did allow us to assemble the system and develop all the hardware associated with the drive system. We have since tested a variety of other alloys, chosen the optimal material for ILSE, and are currently in the process of replacing the S3A material with SC or other material which will be more suitable. This test stand will eventually house the electrostatic quadrupole and the magnetic quadrupole for in situ testing. The alignment and articulation systems for the quadrupoles will also be prototyped once the project is approved.

III. SUMMARY

The HIFAR group at LBL has undertaken the development of an induction accelerator for heavy ion fusion. This accelerator is somewhat unique when compared to the standard ones for electrons in that the waveforms are continually changing throughout the acceleration cycle. This accelerator will address many of the transport issues for driver scale beams and will help resolve many technology issues associated with magnetic materials, waveform generators, alignment, and electrostatic and magnetic quadrupoles. Most importantly, this accelerator will answer many questions associated with the economic viability and reliability of an eventual driver for inertial confinement fusion.

IV. ACKNOWLEDGMENTS

V. REFERENCES

[1]   T. Fessenden et al., Proc. 14th Intl. Conf. Plasma Physics and Controlled Nuclear Fusion Research, Germany, September 30 - October 7, 1992.

[2]   A. Faltens et al., *J. Appl. Phys.* 57(1) April 15, 1985.

[3]   C.H. Smith, *IEEE Trans. Magn.* MAG20, 1320 (1984).

Generation and Focusing of High Energy, 35-kA Electron Beams for Pulsed-Diode Radiographic Machines: Theory and Experiment*

R.L. Carlson and M.J. George
Los Alamos National Laboratory
P.O. Box 1663
Los Alamos, NM 87545
and
T.P. Hughes and D.R. Welch
Mission Research Corp.
1720 Randolph Road SE
Albuquerque, NM 87108

Abstract

Cathode ball and anode planar-foil geometries used to generate self-focused beams onto x-ray conversion targets via beam-induced ionization in gas cells have been investigated since the early 1970's by J. C. Martin et al at Aldermaston, U.K. The building of a succession of increasingly higher voltage, pulsed-diode machines tailored for flash x radiography has resulted. Given sufficient dose to penetrate an object, the spot size of the x-ray source generally determines the resolution of a radiograph. Reported are particle-in-cell code simulations applied to beam generation in the A-K gap and the self-focusing onto the target. A Monte Carlo code for neutron, photon, and electron transport converts the beam particles at the target to photons with transport to a film plane used to calculate the spot size. Comparisons are made to experiments using the Ector (3.5-4 MeV) and PIXY (4-8 MeV) pulsed-diode radiographic machines at Los Alamos.

I. INTRODUCTION

The study of explosively driven systems at Los Alamos has been enhanced since the mid-1960's by flash radiography [1], a technique in which a pulsed beam of electrons interacts with a converter target to produce x-rays that penetrate an object and are detected and recorded by a film pack. Pulsed power diodes, such as Mogul-D attributed to J.C. Martin and his colleagues, can produce high doses (240 R/pulse at 1 m with collimation), energies of 8 MeV, and reasonably small spot sizes (7-mm diam) [2,3]. Although a variety of machines with differing energy, dose, and spot size have been and are continuing to be built, all figures of merit emphasize the importance of a small spot size for high resolution flash radiography [4,5].

Figure 1 shows the anode-cathode (A-K) region of the Ector pulsed diode machine at Los Alamos. This machine (formerly Mogul C) was originally built in the 1960's at Aldermaston and shipped to Los Alamos in 1981. The output of a Blumlein feeds a magnetically insulated transmission line stalk that terminates in a field-shaping electrode or "beam stopper". The cathode consists of a 12.7-mm-diam polished stainless steel ball on an 18-mm stem; the frontal area (90%)

of the ball is painted with silver to aid in the start of explosive cold cathode emission. The resultant 3.5-4 MeV electrons are accelerated across the 13-mm A-K gap and impinge upon a 25-μm aluminum-foil anode. Figure 2 shows an average of five shots using a 200-MHz digitizer to record the voltage across the axial insulator stack and the diode current.
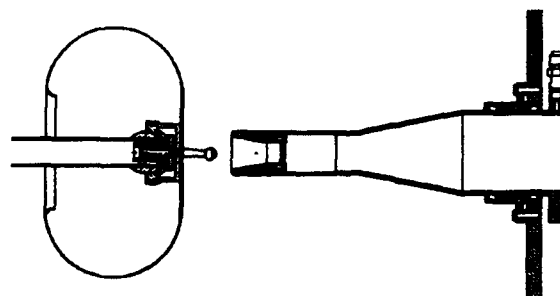
Figure 1. Ector Diode Region.

Figure 2. Ector Stack Voltage and Diode Current.

The beam then encounters a low pressure (typically 0.8 to 1.2 torr) drift section of air where direct impact ionization of the gas results in electrons and ions. The electrons, being light and mobile, are repelled by the beam leaving behind a region of positive charge that cancels out the beam's self-radial electric field. The beam's high current (~35 kA) together with the plasma return current create a net self-magnetic field that focuses the beam over a drift distance of 45 mm onto the x-ray conversion target with a spot size of 9- to 10-mm diam. The x-ray spot size is a time-integrated value and includes any beam motion in the focal plane.

II. THEORY AND EXPERIMENT

Figure 3 shows the results of a SPEED [6] calculation that gives the equipotential contours and electron trajectories for the 13-mm A-K gap of Ector at 3.5 MeV and 33.8 kA. The total current is reduced to 27.2 kA by limiting the emission to the 90% frontal area of the cathode ball; conversely, at fields above 800 kV/cm the rear of the ball and part of the stem would also emit, raising the total current to 36.0 kA. In all cases, it is presumed that the silver paint enhances the initial area of emission which is elsewhere suppressed by the lower fields and highly polished rear area of the ball and stem.
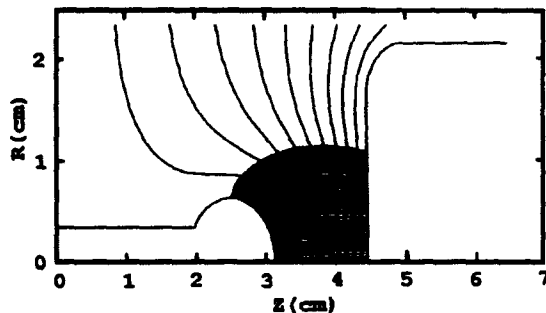
Figure 3. Ector at 3.5 MV with 13-mm A-K gap.

The output of SPEED is then post-processed to include the effects of scatter by the 25-μm aluminum-foil anode and then input to the IPROP [7] PIC code. IPROP models gas conductivity generated by direct impact and secondary ionization and uses a semi-implicit electromagnetic field solver. The simulation for Ector is shown in Fig. 4.
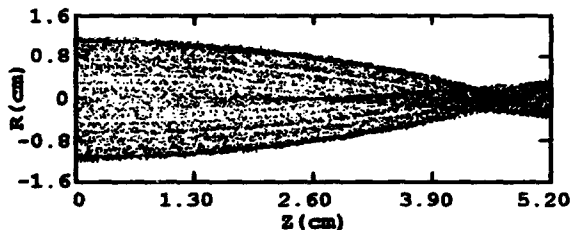
Figure 4. Transport in Ector Gas Cell at 1.2 Torr Air.

At lower energies the beam is divergent and larger in diameter at the foil which results in a longer focal length. At constant beam energy, a wider A-K gap (lower field on the ball) or a smaller cathode (reduced area of beam emission) produces much the same result. The beam at the target ($z=45$ mm) is 2.2-mm diam (rms). How does this compare to the radiographic spot size of Ector, which is about 9-mm diam? A similar question arose from the predictions [8] of IPROP and the measured 7-mm-diam spot size of Mogul D at 8 MeV during the design of the Los Alamos 8-MeV PIXY machine [9]. After optimizing the diode geometry, the radiographic spot size of PIXY was measured to be 9.5 ± 0.6-mm diam for 18 shots at Ector voltages (3.5-4 MV) and A-K gaps of 12-, 13-, and 14-mm. It was anticipated that the measured spot size

would be smaller than Ector's in light of the IPROP predictions and the more trapezoidal voltage and current pulse of PIXY vs the half-sine-like pulse of Ector (Fig. 2).

SPEED and IPROP were next used to make detailed time-dependent calculations of the beam transport to the target. For this case, the driving voltage pulse of Ector was approximated as a half-sine having a base width of 85 ns and a peak of 3.5 MV. The beam's rms radius vs axial position in the drift cell is shown in Fig. 5 for the first 75 ns of the 85-ns pulse in successive time slices of 8.33 ns. The focus of the beam moves from past the target ($z=45$ mm) to a minimum value on the target of 2.2-mm diam (rms) at 33.3 ns; this is the same instantaneous condition as calculated in Fig. 4. At later times, the focus continues to move away from the target and toward the anode foil.
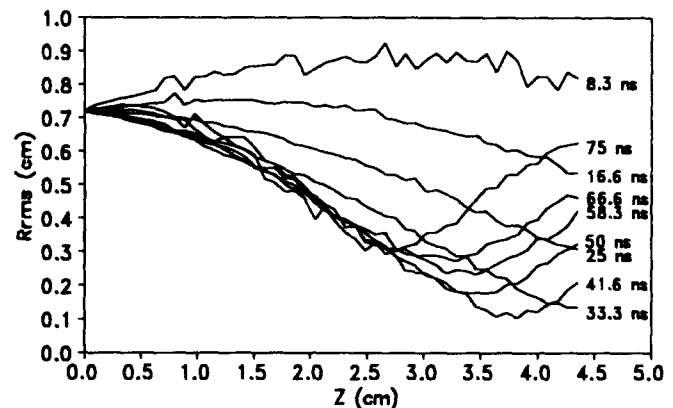
Figure 5. Beam Radius vs Axial Distance in Gas Cell.

Figure 6 shows the corresponding calculation of the beam and net current versus time in the 1.2-torr drift cell. At early time, the beam rapidly ionizes the gas and drives radial and axial return currents in the drift space. When high conductivity is reached, the net current (beam current minus plasma return current) increases slowly with time until the beam current drops below the net current. This continued increase in net current causes the self-magnetic field for focusing to increase with time. Figure 5 shows that the focal plane of the beam moves from past, through, and finally in front of the target. This is contrary to the expectation that the focal plane of the beam would move toward and past the target as the beam current and voltage drop late in time. The inductive nature of the plasma and the experimentally verified behavior of the net current [8] suggest that the temporal evolution of the net current is somewhat independent of the driving voltage and resulting beam current pulse shape. This effect could explain why the spot-size results obtained with the trapezoidal pulse of PIXY were essentially the same as those obtained with the sinusoidal-like pulse of Ector. The time-integrated electron beam size on the target of Fig. 5 is 5.4-mm-diam (rms).

To quantify the relationship between the electron beam distribution and the radiographic spot-size at the target, each particle from the output of IPROP was dose-weighted. The dose-weighting factor used was the 2.8 power of the voltage

multiplied by the charge of the particle. This calculation gives a dose distribution versus radius which is then converted to the radiographic spot size [3,5]. The results are spot sizes of 7.1- and 2.7-mm diam for the time-integrated and instantaneous cases of Fig. 5, respectively.
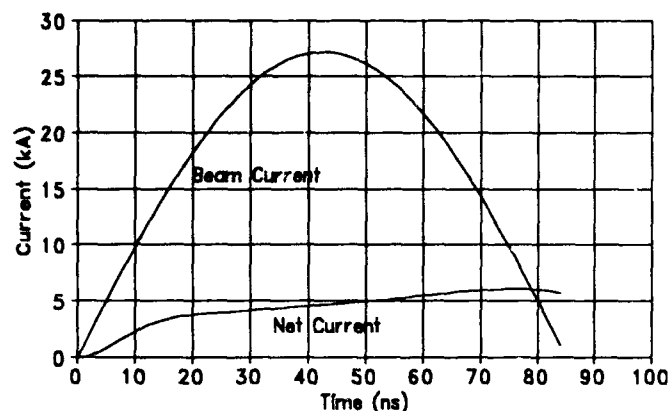
Figure 6. Beam and Net Current for Fig. 5 Simulation.

Although the above computed spot size is in close agreement with the measured results, it does not include the electron and photon transport processes that occur in the x-ray converter. The momentum and position of each particle from IPROP was used as an input to the MCNP [10] code to convert each particle at the 0.5-mm-thick tungsten target to photons. These photons were then transported to a film plane to calculate the radiographic spot size via an edge-projection technique [3]. To improve the photon statistics, two sets of source particles from IPROP ($\sim 10^3$ in the first set averaged over 1 ns centered at 33.3 ns, and $\sim 8 \times 10^4$ in the second set time-averaged over the 85-ns pulse) were replicated with azimuthal symmetry in the plane of the target. This technique increased the number of particles input to MCNP by 500-fold for the 1-ns and 10-fold for the 85-ns cases. Figure 7 shows the computed step-responses across an opaque edge as projected onto a film plane with a source magnification of 5 for the two data sets. The radiographic spot sizes are 3.15- and 7.44-mm diam for the near-instantaneous and time-integrated cases, respectively.
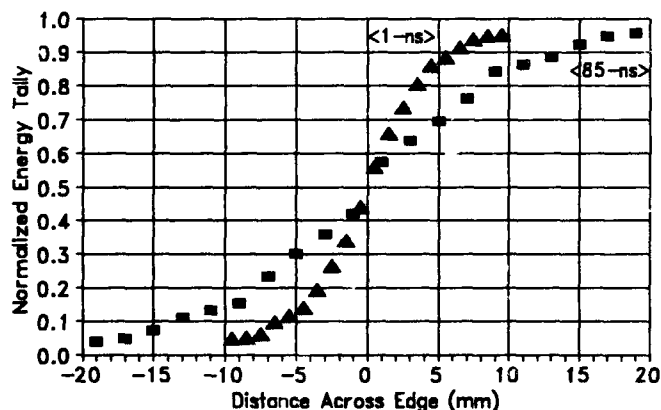
Figure 7. Edge Step-Responses via MCNP in Film-Plane.

III. CONCLUSION

Several codes, used in tandem, have modeled the beam generation, transport, gas-cell focusing, and x-ray conversion for a class of pulsed diode machines dedicated to flash x-radiography. The major parameters that control the focused size of the electron beam and its relationship to the radiographic spot size have been studied. The spot size is dominated by time-dependent motion of the beam's focal plane and not the emittance, foil scatter, nor the non linear forces that focus the beam. This movement is due to the temporal behavior of the net current, which appears to be independent of the voltage or current pulse shape. This motion might be minimized by using a shorter pulse length or tailoring the voltage to rise during the pulse. There is good agreement between either the dose-weighted (7.1-mm diam) or the MCNP (7.44-mm diam) methods and the measured 9.5-mm-diam spot sizes. The SPEED and IPROP codes along with the simpler dose-weighted method can be used to predict and guide improvement efforts for various machines.

IV. REFERENCES

[1] T.J. Boyd, Jr., B.T. Rogers, F.R. Tesche, and Douglas Venable, "PHERMEX - A High-Current Electron Accelerator for Use in Dynamic Radiography," Rev. Sci. Instr. 36 (10), October 1965, pp. 1401-1407.

[2] Private Communication with Mike Goodman of AWE, Aldermaston, U.K. and K.H. Mueller of Los Alamos.

[3] K.H. Mueller, "Measurement and Characterization of X-Ray Spot Size," Proceedings of the 1989 Flash Radiography Topical, American Defense Preparedness Association, pp. 383-394.

[4] J.C. Martin, "Aids to Estimating the Quality of Flash Radiographs," British Note SSWA/JCM/788/266, AWRE, Aldermaston, United Kingdom, August 1978.

[5] J.C. Dainty and R. Shaw, Image Science, Academic Press Inc., New York, 1974.

[6] SPEED was written by Jack Boers, Thunderbird Simulation, Inc.

[7] M.M. Campbell, B.B. Godfrey, and D.R. Welch, "IPROP User's Manual: Post-processor Version," MRC/ABQ-R-1397, Mission Research Corporation, March 1991.

[8] M.A. Mostrom, M.M. Campbell, R.M. Clark, and L.A. Wright, "Electron Focusing in the Neutral Gas Drift Tube," MRC/ABQ-R-1197, Mission Research Corporation, August 1989.

[9] R.A. Lucht and S. Eckhouse, "Intense X-Ray Machine for Penetrating Radiography," Proceedings of the 1989 Flash Radiography Topical, American Defense Preparedness Association, pp. 333-346.

[10] J.F. Briesmeister, ed., "MCNP: A General Monte-Carlo Code for Neutron and Photon Transport, Version 3A," LA-7396-M, Revision 2, (Version 4 includes electrons), Los Alamos National Laboratory, September 1986.

Numerical Investigation of High-Current Ion Beam Acceleration and Charge Compensation in Two Accelerating Gaps of Induction Linac

Nadya G. Belova

Institute of Physics and Technology Russian Academy of Sciences

117218 Krasikov Str. 25a, Moscow, Russia

Vyacheslav I. Karas'

Kharkov Institute of Physics and Technology Ukrainian Academy of Sciences

310108 Akademicheskaya Str. 1, Kharkov-108, Ukraine

Abstract

The numerical investigation of the hollow high-current ion beam (HHCIB) dynamics in two magnet-isolated accelerating gaps of induction linac are presented. It has been shown that the applied electric field destroys partially the charge and current compensations, and impairs the brightness of the ion beam when the electron beam energy is not sufficient to overcome the potential difference. The acceleration, the charge and current compensations, and the stability of the high-brightness ion beam can be achieved under the optimum parameters choice.

I INTRODUCTION

Several approach to producing high-current ion beams by means of induction accelerators are now considered for controlled thermonuclear fusion research [1].

One of these methods involves the transport of several beams with sourse currents of $\sim 1A$ in a vacuum with subsequent current enhancement by raising the energy through combining the beams and bunching in an accelerating pulse [2]. Another way of obtaining a large beam current at low kinetic energy makes use of the collective focusing techniques in which the space-charge forces are balanced by neutralizing the beam ions with electrons, while the electron current is suppressed by the magnet-isolated accelerating gaps. At present kiloampere ion beams are obtained from this type of linear high-current induction accelerator (linac) (see e.g. [3] and Refs. in that). A number of important physical problems discussed in [3] must be studied since the power and brightness requirements for ion beams in the controlled thermonuclear research are very stringent.

The previous study [5] has shown that without the accelerating field i) charge and current compensations of the ion beam by the specially injected electron beam occur; ii) the ion beam is stable for the time greater than the reciprocal Larmor and Langmuir ion frequencies. Here we present the results of our numerical investigation of the electron and ion beams dynamics in a two magnet-isolated accelerating gaps.

II EQUATIONS

ınce The dynamics of a collisionless plasma in both the self-consistent and the external electromagnetic fields in axisymmetric ($\partial/\partial\theta = 0$) geometry, is described by the set of relativistic Vlasov's equations for the distribution functions of a given type (s) of particles $f_s(\vec{p}, \vec{R}, t)$. Here $\vec{p} = m_s \vec{v} \gamma$, $\vec{v} = \{\dot{r}, r\dot{\theta}, \dot{z}\}$, $\gamma = [1 - (|\vec{v}|/c)^2]^{-1/2}$, $\vec{R} = \{r, z\}$.

The self-consistent electromagnetic fields in Vlasov's equation are determined by Maxwell's equations, which in the Lorenz gauge ($div\vec{A} + \frac{1}{c}\frac{\partial\phi}{\partial t} = 0$) take the form of wave equations for the dimensionless scalar $\phi(r, z)$ and vector $\vec{A}(r, z)$ potentials the right hand of which is defined as

$$\rho = \sum_s \int q_s f_s(\vec{p})d\vec{p}, \quad \vec{J} = \sum_s \int q_s \vec{v} f_s(\vec{p})d\vec{p}$$

We use the dimensionless quantities defined by $[v] = c$; $[r, z] = c/\omega_{pe}$; $[t] = \omega_{pe}^{-1}$; $[n] = n_{0e}$; $[q] = e$; $[m] = m_0$; $[\phi, A] = \mathcal{E}_{ch}/e$; $[E, B] = (4\pi n_{0e}\mathcal{E}_{ch})^{1/2}$; $[J] = en_{0e}c$; $[P_\theta] = [\psi] = c^2/\omega_{pe}$, where $\omega_{pe} = (4\pi n_{0e}e^2/m_0)^{1/2}$ is the electron plasma frequency, $\mathcal{E}_{ch} = m_0 c^2$ is the rest energy of the electron, n_{0e}, m_0, e are the initial density, rest mass and charge of the electrons respectively, γ is the relativistic factor.

The equations of motion, obtained as characteristic equations of Vlasov's equation have the form:

$$\frac{du_r}{dt} = \frac{1}{\gamma}\frac{q}{m}\left(\frac{\psi}{r^2}\frac{\partial(rA_\theta)}{\partial r} - \gamma\frac{\partial A_r}{\partial t} - u_z\left(\frac{\partial A_r}{\partial z} - \frac{\partial A_z}{\partial r}\right)\right) - \frac{q}{m}\frac{\partial\phi}{\partial r} + \frac{1}{\gamma}\frac{\psi^2}{r^3} \quad (1)$$

$$\frac{du_z}{dt} = \frac{1}{\gamma}\frac{q}{m}\left(\frac{\psi}{r^2}\frac{\partial(rA_\theta)}{\partial z} - \gamma\frac{\partial A_z}{\partial t} + u_r\left(\frac{\partial A_r}{\partial z} - \frac{\partial A_z}{\partial r}\right)\right) - \frac{q}{m}\frac{\partial\phi}{\partial z} \quad (2)$$

where $\vec{u} = \gamma\vec{v}$, $\psi = \gamma r^2\dot{\theta} = P_\theta - \frac{q}{m}rA_\theta$. ($P_\theta$ is the dimensionless generalized particle momentum), $\gamma = [1 + u_r^2 + (\psi/r)^2 + u_z^2]^{1/2}$.

The boundary conditions for the potentials are

$r = 0:$ $\partial\phi/\partial r = 0$ $\partial A_z/\partial r = A_r = \partial A_\theta/\partial r = 0$;

$r = r_L:$ $\phi = \phi(z)$ $A_z = A_r = A_\theta = 0$;

$$\phi(z) = \begin{cases} 0, & 0 \le z \le \Delta_z \\ (n-1)\Delta_\phi + \\ \quad + \frac{\Delta_\phi}{\Delta_z}(z - (2n-1)\Delta_z), & (2n-1)\Delta_z \le z \le 2n\Delta_z \\ n\Delta_\phi, & 2n \le z \le (2n+1)\Delta_z \end{cases}$$

$z = 0:$ $\left.\begin{array}{c}\\ \\\end{array}\right\}$, $\frac{\partial A_z}{\partial z} = -\frac{1}{r}\frac{\partial(rA_r)}{\partial r}, \frac{\partial A_r}{\partial z} = \frac{\partial A_\theta}{\partial z} = 0$
$z = z_L:$

$$\phi|_{z=0} = 0, \phi|_{z=z_L} = \phi_L$$

whe $\Delta_\phi = (\phi_L - \phi_0)/K$, $\Delta_z = z_L/(2K + 1)$ are the potential difference accross the accelerating gap and the length
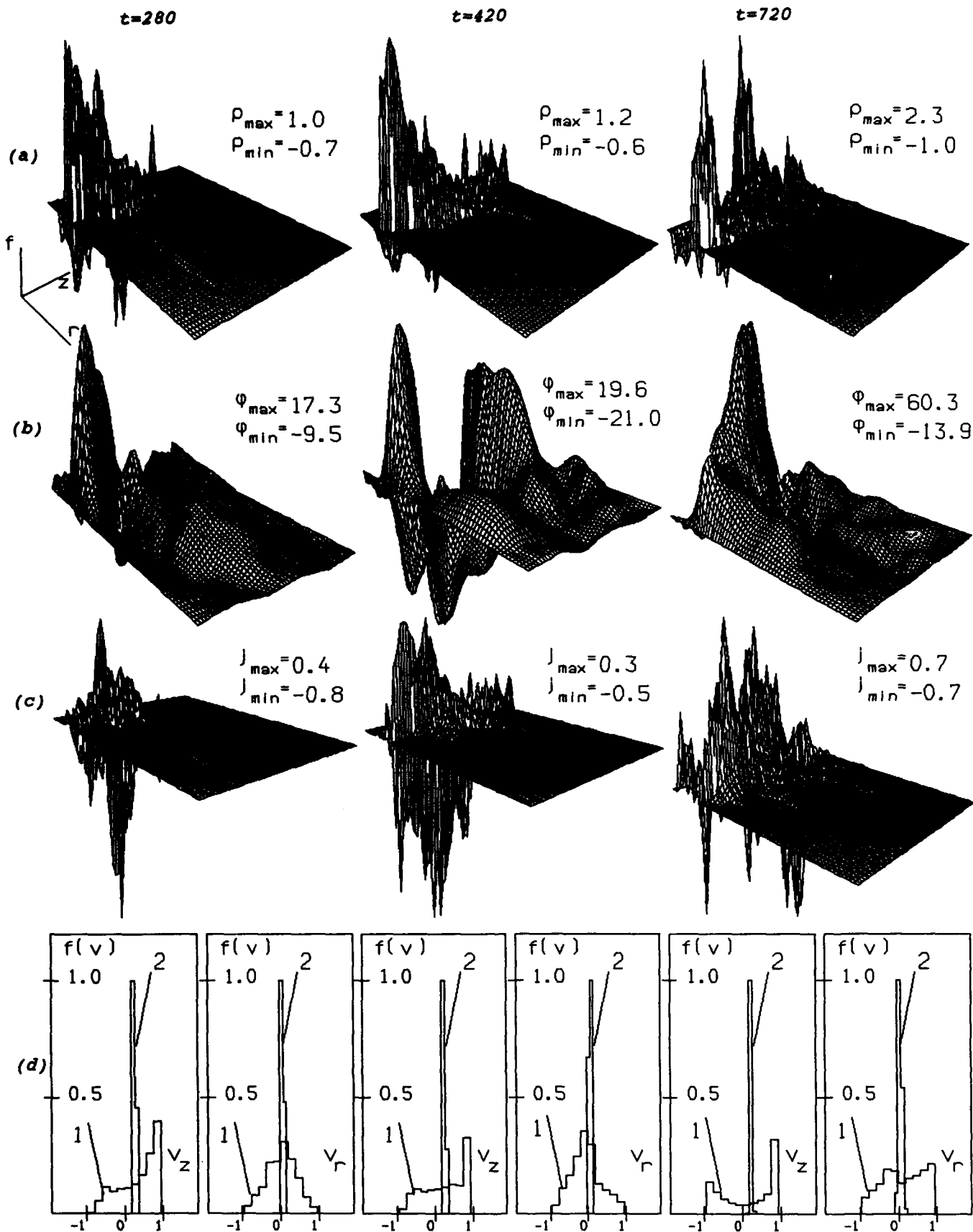
Figure 1: Distributions of the total charge density $\rho(r,z)$ (a), scalar potential $\phi(r,z)$ (b), axial current density $j_z(r,z)$ (c), and the distribution functions $f(V)$ (d) of electron (1) and ion (2) beams versus the longitudinal (V_z) and transverse (V_r) velocities at $t = 280, t = 420$ and $t = 720$.

of that, $n = 1, \ldots, \mathcal{K}$, $\mathcal{K}$ is the total number of cusps. The initial conditions for the self-consistent fields are $\Delta\phi = A_z = A_r = A_\theta = 0$ (here Δ is Laplassian).

The boundary conditions for the distribution functions set the hollow beams injection at $z = 0$: $f_s(\vec{p}, \vec{R}, t) = f_s(m_s\vec{u}, \vec{R}, t) = \delta(u_r)\delta(u_z - u_{0s})\delta(u_\theta)$ at $r_{min}{\le}r{\le}r_{max}$ and $p_z > 0$, they are equal to zero at $z = z_L$. Here r_{min} and r_{max} are the minimum and maximum beams radii respectively, $u_{0s} = V_s/(1 - V_s^2)^{1/2}$, V_s is a beams velocity. At $(r = 0, r = r_L)$ set the reflection regime: $f_s(\vec{p}, \vec{R}, t) = f_s(-p_r, p_z, p_\theta, \vec{R}, t)$, $z{\in}[0, z_L]$. At the initial time, the distribution functions are equal to zero.

The external magnetic field is defined by the expression $A_\theta = -\frac{B_0}{k}I_1(kr)\cos(kz)$ where $I_1(kr)$ is the first order modified Bessel function, B_0 is the amplitude of magnetic field, and $k = \mathcal{K}\pi/z_L$.

The method and algorithm of the solution of presented equations are described in [5]. The above model was carried out as a 2.5-dimensional cylindrical computer code [4, 5].

III   RESULTS AND DISCUSSION

Let a hollow magnetized electron beam with velocity V_e and a hollow high-current unmagnetized ion beam with velocity V_i be injected along the z-axis into the external magnetic field. The beam current densities are equal to $q_e n_{0e} V_e = q_i n_{0i} V_i$.

In the calculations we assumed the mass ratio to be $m_i/m_e = 100$, $m_e = 20 m_0$, the number of particles in the cell was $N_e = 64$, $N_i = 180$. The ion beam velocity was supposed $V_i = 0.285$. The minimum and maximum beams radii were $r_{min} = 30$ and $r_{max} = 32.5$. The length and radius of the chamber were $z_L = 157.5$ and $r_L = 157.5$. The amplitude of the external field was $B_0 = 1.76$. In all cases two cusps $\mathcal{K}$ were considered. The number of points and the time step for solving Maxwell's equations were (64×64) and $\Delta\tau = 0.025$. The time step for solving of the equation of the motion was equal to $\Delta t = 0.05$.

The potential difference and the electron beam velocity were changed as follows:

No. of case	1	2	3
$\Delta\phi$	0.8	2.0	5.0
V_e	0.85	0.85	0.8

The results of the calculations are shown for case 1 in figure 1. Cases 2 and 3 are not displayed because of the limited scope of paper.

The distributions of $\rho(r, z)$ (a), $\phi(r, z)$ (b), $j_z(r, z)$ (c), presented in figure 1 show that the applied external electric field, which accelerates ions and retards electrons, does not disrupt the electron beam drift through the accelerating gaps. From the functions $j_z(r, z)$ (fig.1c) it is clearly seen that not only the charge (fig.1a,b) but also the current compensation of the ion beam occur. Figure 1d shows the distribution functions $f(V)$ of the electron (1) and ion (2) beams versus the longitudinal (V_z) and transverse (V_r) velocities at $t = 280$, $t = 420$, and $t = 720$ respectively. It is seen that the ion beam generally retains monoenergetic shape, because its spread in

V_z and V_r does not exceed 10%. The electron beam spread in the velocities is nearly 100% , but this does not prevent the charge compensation of the ion beam by electrons.

In variants 2 and 3 the electron beams energy $\mathcal{E}_{eb}$ was not sufficient to overcome the potential difference in the accelerating gaps. They have demonstrated that the electrons localize mainly in the drift region of the channel in the case 2. In third case the electrons have retarded predominently by the electric field of the first accelerating gap. Only a slight part of electrons pass to the second gap following the ion beams therefore the ion beam is retarded and the substantial radial spread occures as the space charge compensation of beam is not quite. The distribution functions has also shown the significant spread both the longitudinal and transverse velocities with the displacement of the distribution function maximum into the positive direction of the transverse velocity about ≈ 0.1.

The above presented results of the computer simulation are correspond to the real model of a high-current linac [3]. The length of the accelerating gap is $L{\approx}5$ cm, the radius of the chamber is $R{\approx}10$ cm, the characteristic magnetic field value is $B_0{\approx}7.5$ kG, the Larmor radius of electrons is $r_{Le}{\approx}0.045$ cm ($r_{Le}{\ll}L$), the Larmor radius of ions is $r_{Li}{\approx}20$. cm ($r_{Le}{\gg}L$), the electron beam density $n_{0e} = 8 \cdot 10^{13}$ cm^{-3}. The maximum of the electric potential ϕ (fig.1b) in the drift gap obtained in the computer simulation can be easily rectified by the cold electrons injection to that for the space charge compensation. In the real linac this is also no difficult as the external electric field is not in the drift gap which is sufficiently extended in comparison with the accelerating gap.

Thus the high-current beams can be accelerated in the linac with the substantial space-charge and current compensations without disturbing the stability in deciding on the optimal parameters.

IV   REFERENCES

[1] A. I. Faltens and D. Keeffe, "Review of induction Linac," *Proc of the 1981 Lin.Accel.Conf.*, Santa Fe, **LA-9234c**, pp. 205-208.

[2] R. O. Bangerter, "Heavy Ion Fusion – progress and prospects," *Part. Accel.* **37-38**, 3 (1992).

[3] V. I. Karas', V. A. Kiyashko, E. A. Kornilov, Ya. B. Fainberg, "Theoretical and experimental investigations of a neutralized ion induction linac for inertial confinement fusion," *Nuclear Instruments and Methods in Physics Research* **A278**, 245 (1989).

[4] N. G. Belova, V. I. Karas' "Numerical simulation of high-current ion beam acceleration and charge compensation in magnet-isolated systems," *Part. Accel.* **37-38**, 225 (1992).

[5] N. G. Belova, V. I. Karas', Yu. S. Sigov, "Numerical simulation of the dynamics of charged particle beams in an axisymmetric nonuniform magnetic field," *Fiz.Plazmy* **16**, 209 (1990) [*Sov. J. Plasma Phys.* **16**, 115 (1990)]

THE LIGHT-ION PULSED POWER INDUCTION ACCELERATOR FOR THE LABORATORY MICROFUSION FACILITY (LMF)*

M. G. Mazarakis, D. L. Smith, L. F. Bennett, T. R. Lockner, R. E. Olson, J. W. Poukey, J. Boyes
Sandia National Laboratories
P. O. Box 5800, Albuquerque, NM 87185-5800 USA

Abstract

In order to initiate ignition and substantial energy yield from an inertial confinement fusion target (ICF), a light-ion pulse of ~700 TW peak power and 15-20 ns duration is required. The pre-conceptual design presented here provides this power. The HERMES-III technology of linear inductive voltage addition in a self-magnetically insulated transmission line (MITL) is utilized to generate the 25-36 MV peak voltage needed for lithium ion beams. The 15-20 MA ion current is achieved by utilizing many accelerating modules in parallel.

The lithium ion beams are produced in two-stage extraction diodes. To provide the two separate voltage pulses required by the diode, a triaxial adder system is incorporated in each module. The accelerating modules are arranged symmetrically around the fusion chamber in order to provide uniform irradiation onto the ICF target. In addition, the modules are fired in a preprogrammed sequence in order to generate the optimum power pulse shape onto the target.

In this paper we present an outline of the LMF accelerator conceptual design with emphasis on the architecture of the accelerating modules.

I. INTRODUCTION

The Laboratory Microfusion Facility has both near and long-term goals. The near-term goals are to study high gain Inertial Confinement Fusion (ICF) targets with yields of the order of 500 MJ, to study nuclear weapon physics, and to provide an improved nuclear weapon simulation source. Among the long-term goals, the most important is to provide the technical development necessary to demonstrate scientific feasibility for fusion energy production. To achieve these goals, the LMF driver must deliver to the ICF target energies equal to or higher than 10 MJ with the ability to vary the magnitude and pulse shape of the deposited energy as a function of time.

The light-ion LMF pre-conceptual design is based upon the ion beam input requirements of the 500-MJ yield ICF target. These requirements are established by a combination of numerical calculations and the existing ICF database. The driver design is modular and consists of 24 modules of two different types: A and B. These modules are fired in a two-step sequence to provide the desired power pulse shape on the target (Figure 1). The first pulse to arrive at the target, generated by the 12 A modules, has a 65-TW flat top and a 60-ns duration. The main pulse, delivered by the 12 modules B, arrives at the target 40 ns later. It has higher peak power (650 TW) but shorter duration (20 ns). The pulses overlap during the last 20 ns to provide the target with the required 715 TW peak power.
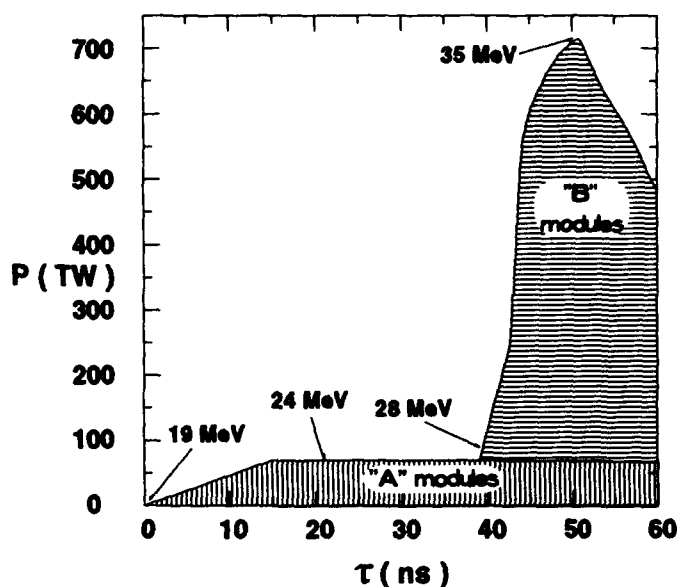
Figure 1. ICF Target Power Requirement for a 500-MJ Yield

II. THE LMF ACCELERATOR

The LMF pulsed power accelerator (Figure 2) is based on the successful HERMES-III[1] (Figure 3) technology developed in Sandia during the last ten years in collaboration with Pulsed Science Inc. Each of the 24 modules of Figure 2 are similar or identical to HERMES III. This technology is fairly simple and couples the self-magnetically insulated transmission line (MITL)[2] principle with the N. Christophilos invention of the induction linac[3] to generate a new family of linear induction accelerators, such as HELIA,[4] HERMES III, RADLAC/SMILE,[5] and SABRE,[6] which we call linear inductive voltage adders. In these accelerators there is no beam drifting through the multiple cavities as is the case with conventional induction linacs. The place of the beam is taken by a central conductor which extends along the entire length of the device and effectuates the voltage addition of the accelerating cavities. The beam is produced at the end of the voltage adder in a single or multistage diode. These devices can operate in either polarity to produce negatively or positively charged particle beams. In a positive polarity voltage adder (Figure 4), the center conductor is positively charged relative to the outer conductor which is interrupted at regular intervals by the cavity gaps. The HERMES-III voltage adder is of negative polarity. A linear inductive voltage adder can be converted from negative to positive polarity and vice versa by a rotation of 180° around a vertical axis of the center conductor or equivalently of each of the accelerating cavities. This was

demonstrated on HERMES-III which operated with equal success in positive and negative polarity.[7] SABRE has a positive polarity inductive voltage adder. The LMF voltage adders also are of positive polarity, and the beam particles produced by the diodes are singly charged positive lithium ions.
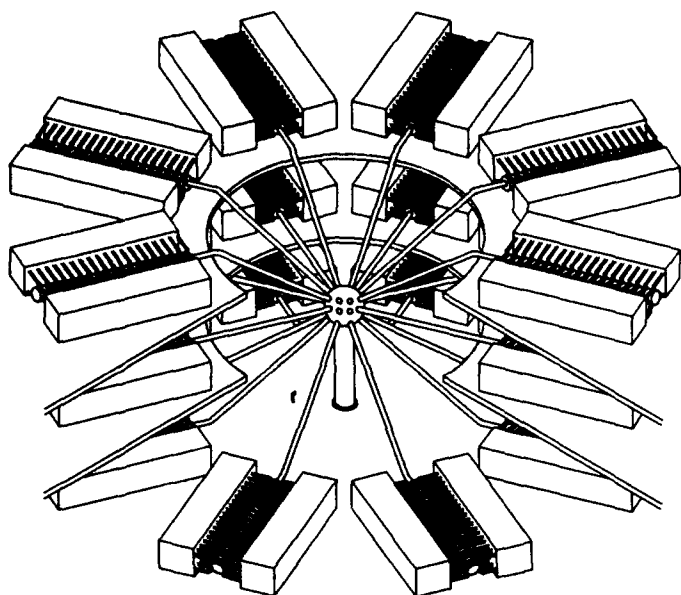
Figure 2. Cutaway View of the Light-Ion Microfusion Accelerator
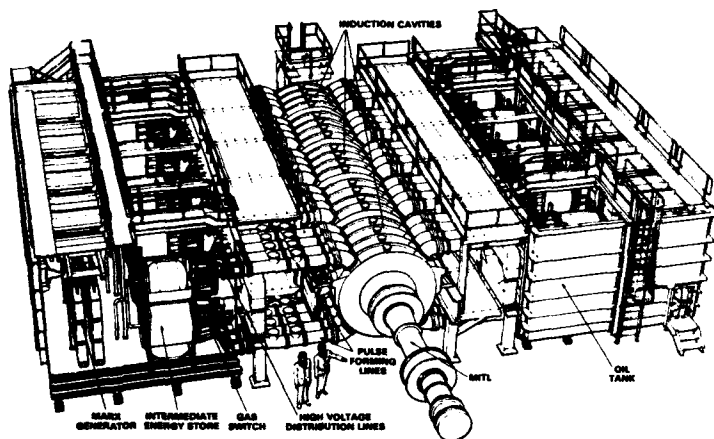
Figure 3. The HERMES III Accelerator

The selected number of modules, 24, is a trade-off between cost, pulse uniformity on the target, and number of diodes that can be fit at the 4 m radius outside wall of the interaction chamber. Each module has its own diode, producing the 24 separate ion beams focused on the ICF target. The beams propagate fully space charged and current neutralized in a 1 Torr helium atmosphere. In the first 3 meters of transport the beam annular cross section remains constant with the particle trajectories being slightly divergent. The principal focusing occurs in a main solenoidal lens 1 meter from the 1 cm radius ICF target. The beam transport system is achromatic.[8] The achromaticity is achieved by combining the final focusing solenoid with the self-
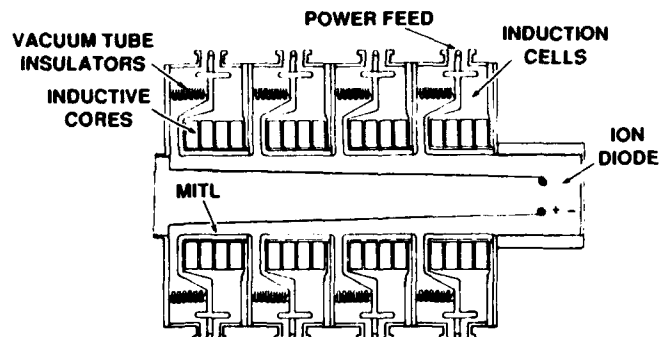
Figure 4. A Simple Positive Voltage Adder of the SABRE Type Providing Power to a Single Stage Ion Diode

filled focusing effect at the ion diode. The ion trajectories are ballistic between the diode and the lens and between the lens and the target.

The power and kinetic energy of the ions delivered to the target are shown in Figure 1. The electrical power delivered by the voltage adders to the diodes is somewhat higher due to certain inefficiencies in the diode and in the transport system. We assume a 70% peak power efficiency from the diode to the target. Hence, the modules A deliver to the diodes at total peak electrical power of 91 TW and the modules B of 457 TW. Table 1 summarizes the electrical output parameters for both types of modules.

The beams from the modules B are bunched by a factor of 2 during transport to the target, driven by a ramped voltage pulse provided to the second stage gap by the inductive voltage adders. Bunching doubles the peak ion power delivered to the target and shortens the pulse duration from 40 ns (Table 1) to 20 ns (Figure 1).

Table 1
Electrical Output Parameters per Module

	Module A	Module B
P(TW)	7.6	38
V(MV)	24.7	36
I(MA)	0.31	1.06
τ(ns)	60	40
W(MJ)	0.46	0.83

III. ACCELERATING MODULE DESIGN

The accelerating voltage of the first stage for both A and B diodes is a constant 10 MV (not ramped). The second stage voltage for the modules A is a constant 15 MV while the modules B voltage is ramped from 18 to 26 MV. A triaxial adder system is designed for each module (Figure 5) to provide the two separate voltage pulses to the diode. The cavities of each module are grouped into two stages, and the voltage addition occurs in two separate MITLs nested one inside the other. The center hollow cylinder (anode) of the second MITL also serves as the outer cathode electrode for the extension of the first voltage adder MITL.
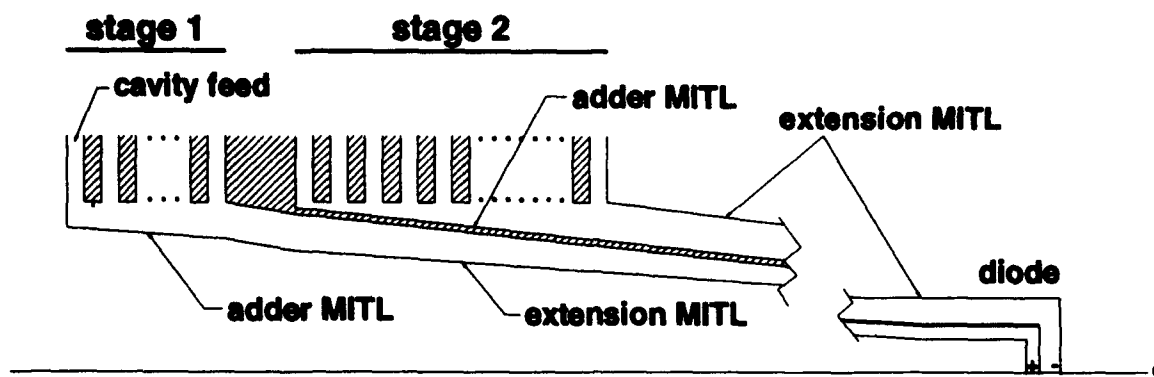
Figure 5. The Triaxial Voltage Adder Configuration for the Two-Stage Extraction Diodes of the LMF Accelerator.

Each voltage adder is connected to the corresponding stage of the diode via a long extension MITL which time-isolates the diode from the voltage adder. Thus the diode can operate at lower impedance than the voltage adder without affecting the voltage adder operation. Undermatching the diode load reduces the sheath electron current in the extension MITL and provides for more efficient pulse power coupling. The power coupling efficiency for this design depends on the final voltage of each adder, typically 80% to 85%.

The LMF driver can be built with components similar or identical to those of HERMES III. The modules A are HERMES-III accelerators with 4 more cavities (24 total) operating at half power, using half of the 5 Ω pulse-forming and transmission lines that power each of the HERMES-III cavities.

There are two design options for the modules B: one that is again composed solely of HERMES-III components and the other made up of 2.6 MV cavities of entirely new design. The modules B can be built by two HERMES-III accelerators connected in series (40 cavities in total) or by seventeen 2.6-MV cavities. Table 2 summaries the two design options for the B modules.

Table 2
Design Options for the B Modules

	HERMES-III Option	2.6 MV Cavity Option
Cavity Voltage (MV)	1.1	2.6
Number of Cavities	40	17
PFLs/Cavity	4	4
PFL Impedance (Ω)	5	8
I matched (MA)	0.88	1.15

IV. CONCLUSION

This LMF accelerator design is based on the HERMES-III robust technology. It has a flexible modular configuration which offers risk control by an anticipated staged construction. Half of the 24 modules are identical to HERMES III, and the other half can be built with HERMES-III or similar 2.6-MV components. This provides a confident base for realistic cost estimates and offers additional assurance for the success of the project.

REFERENCES

[1] J. J. Ramirez, et al., "HERMES-III—A 16-TW, Short Pulse Gamma Ray Simulator," *Proc. 7th International Conf. on High Power Particle Beams*, Karlsruhe, Germany, July 4-8, 1988, pp. 148-157.

[2] J. H. Creedon, "Magnetic Cutoff in High-Current Diodes," *J. Appl. Phys.*, 48, No. 3, 1070 (1977).

[3] N. Christophilos, et al., "High Current Linear Induction Accelerator for Electrons," *Rev. Scient. Instrum.*, 35, No. 7, 886 (1964).

[4] J. J. Ramirez, et al., "The Four Stage HELIA Experiment," *Proc. 5th IEEE Pulsed Power Conf.*, Arlington, Virginia, June 10-12, 1985, p. 143-146, IEEE #85C2121-2.

[5] M. G. Mazarakis, et al., "SMILE—A New Version for the RADLAC II Linear Accelerator," *Proc. of the 1990 Linear Accelerator Conference*, Albuquerque, New Mexico, September 10-14, 1990, pp. 438-440, LA-12004-C.

[6] J. Corley, et al., "SABRE, A 10-MV Linear Induction Accelerator," *Proc. 8th IEEE Pulsed Power Conference*, San Diego, California, June 16-19, 1991, pp. 920-923, IEEE #91CH3052-8.

[7] D. L. Johnson, et al., "Hermes-III Positive Polarity Experiment," *Proc. 7th IEEE Pulsed Power Conference*, Monterey, California, June 11-14, 1989, pp. 32-35, IEEE #89CH2678-2.

[8] C. L. Olson, "Achromatic Magnetic Lens Systems for High Current Ion Beams," *Proc. of the 1988 Linear Accelerator Conference*, Williamsburg, Virginia, Oct. 3-7, 1989, pp. 34-37, CEBAF Report 89-001.

FIRST OPERATION OF THE LELIA
INDUCTION ACCELERATOR AT CESTA

Ph. Eyharts, Ph. Anthouard, J. Bardy, C. Bonnafond, Ph. Delsart, A. Devin, P. Eyl, P. Grua, J. Labrouche,
J. Launspach, P. Le Taillandier, J. de Mascureau, E. Merle, A. Roques, M. Thevenot, D. Villate

Commissariat à l'Energie Atomique (C.E.A.)
Centre d'Etudes Scientifiques et Techniques d'Aquitaine (CESTA)
B.P. n° 2 - 33114 LE BARP (FRANCE)

Abstract

An induction linac has been studied and built in order to acquire induction technology for free electron laser (FEL) and other applications. It comprises a 1.5 MeV injector with a thermionic cathode which can deliver a high current electron beam (1 to 2kA) and a 12 cells accelerating block which raises the electron energy up to 3 MeV. The injector has been tested and fully characterized and the accelerator is now being completed. We describe the induction cells and the high voltage generator designed to feed the cells with 150 kV pulses at 1 kHz repetition rate.

I - INTRODUCTION

The LELIA accelerator has been designed and built at CESTA to produce a high current (1-3 kA) and high brightness (10^8 A m^{-2} rad^{-2}) electron beam with an energy of 3 MeV. Initially devoted to microwave FEL experiments [1] it is also used as a test bed for the AIRIX induction accelerator [2] especially in beam transport studies and diagnostic development.

The LELIA accelerator consists of a ten cells induction injector, a twelve cells induction accelerator and a high voltage generator that can deliver 150 kV/80 ns feeding pulses . An osmium coated dispenser cathode is used to produce the electron beam.

Since june 1991 the injector is under operation and has been fully characterized. By the beginning of this year the accelerating module has been assembled and partially tested.

In the following sections we describe the different components of the machine and we present the results obtained.

II - ACCELERATOR ENGINEERING

A - Induction cells

LELIA induction cells are constructed around a core of seven TDK PE 11 B ferrite torroids (250 mm I.D., 500 mm O.D., 25 mm thick) housed in a non magnetic stainless steel body [3]. The beam pipe diameter is about 185 mm and the accelerating gap is 8 mm wide. Oil is used as dielectric and cooling fluid surrounding the ferrites. A pure alumina insulator brazed on the cell provides the oil-vacuum interface and eliminates any possibility of cathode poisoning by hydrocarbons.

Accelerator and injector cells are similar; but for beam transport, only the cells located in front of the cathode are provided with a solenoid capable of producing a 2 kG axial magnetic field (fig. 1)
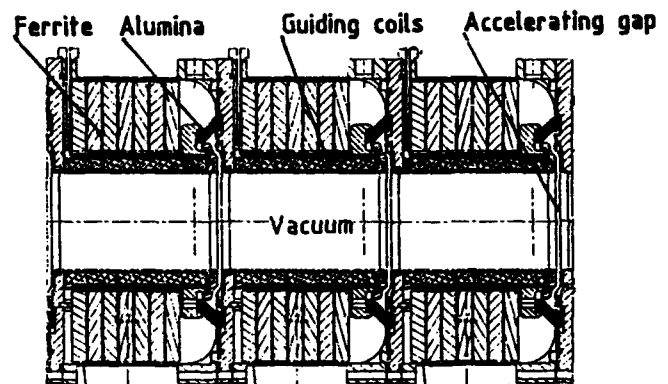
Figure 1 : LELIA induction cells

B - Pulse power

Cells are driven through 100 Ω coaxial cables by a H.V. pulse generator consisting of two parts [3] :
- a command resonant charging system (CRCS)
- a pulse forming and compression device (MAG)

One generator is sufficient to drive the twenty two accelerator cells with 100 to 150 kV/80 ns flat top pulses at 1 kHz repetition rate.

Timing between the cells is controlled by adjusting the length of the cables. A typical feeding signal on resistive load is shown on figure 2.

C - Electron gun

The electron beam is generated by a triode consisting of an 85 mm diam. osmiun coated dispenser cathode, an intermediate electode and an anode.
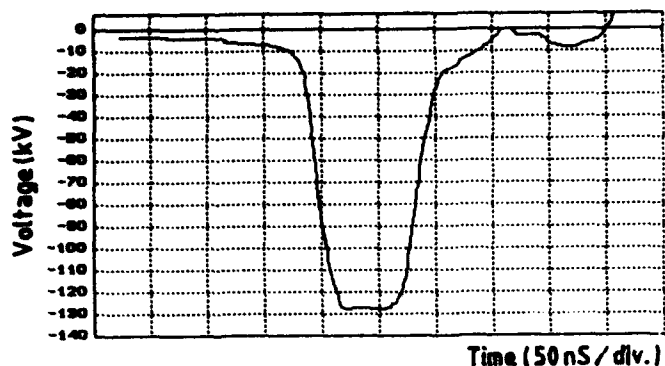
Figure 2 : H.V. Generator output

The geometry has been calculated with FLUX-2D and E-GUN numerical codes in order to minimize the beam emittance.

The cathode has a 300 mm spherical radius and is surrounded by a focusing electrode. The distance between the cathode and intermediate electrode can be adjusted from 25 to 75 mm to control the beam intensity.

The anode internal diameter has been recently increased from 84 mm to 112 mm; it is located 50 mm from the intermediate electrode.

D- Vacuum system

The vacuum in the beam pipe is ensured by three 4500 l/s cryogenic pumps (two are located on injector near the cathode) associated with turbomolecular pumps for rough vacuum.

In operation, with cathode at 1200°C, the pressure was easily maintained at 10^{-8} Torr in the injector section which is consistent with the use of a dispenser cathode.

E - Reset and matching circuit

After each shot the magnetic cores are saturated and must be reset before the next pulse, otherwise the cells will be short circuited.On LELIA this is performed by supplying an inverse D.C. current (30 A) to the cell from a reset circuit equipped with a choke coil for high voltage isolation. In addition this circuit comprises a resistor placed in parallel with the beam to electrically match the cell with the generator and limit overvoltages.

F - Control system

At first level LELIA control system comprises programmable controllers (TELEMECANIQUE TSX 6740) connected to the machine through several I/O standard cards. They are used to control all the accelerator components (vacuum apparatus, power supplies, ancillary system, interlocks) as well as personnel safety system.

The second level centers around a HP 9000 computer that supports an ethernet network connected to the operator consoles. It allows supervision of the accelerator through the programmable controllers and ensures data acquisition by monitoring LE CROY oscilloscopes via GPIB interface.

III - EXPERIMENTAL RESULTS

A - Alignments

Mechanical alignment of LELIA cells has been measured with optical instruments . An error of ± 500 μm between the mechanical axis and a reference line defined by an helium-neon laser has been observed.

Magnetic aligment of guiding solenoid has been checked using the stretched wire technique.

Measurements lead to offset errors of ± 700 μm and tilt errors of ± 5 mrad. These latest errors have been easily minimized by energizing the trim coils installed around each solenoid.

B - Cathode current

After a step by step cathode heating up to 1200 °C the electrical tests have begun first with a cable pulser and then with the H.V. pulse generator. During these experiments cathode current I_k was measured versus cathode temperature θ_k. The I_k (θ_k) curves plotted on figure 3 at 0.35 and 1.3 MV accelerating voltage show a knee that determines the transition between emission limited and space charge limited operation.

To maintain a space charge limited operation, where temperature inhomogeneities present less influence, we decided to run the cathode at 1200° C during next experiments.
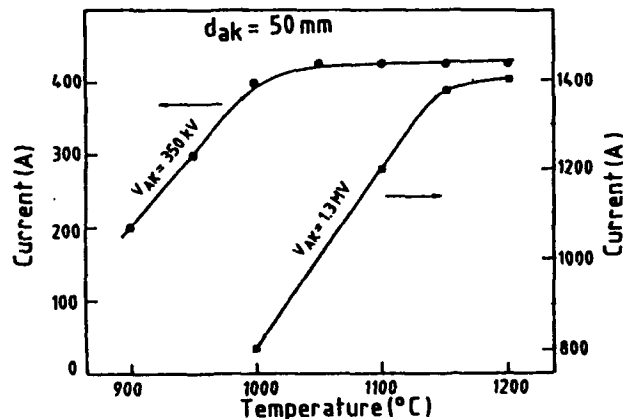
Figure 3 : Cathode current vs temperature

By varying the distance between cathode and intermediate electrode a maximum emission current of 2.5 kA has been obtained. This result corresponds to a high emission density (45 A/cm²) which indicates a good cathode formation.

C - Beam transport

Using the guiding solenoids, current emitted from the cathode has been transported through the anode stalk and the accelerator beam pipe. With a 84 mm anode diameter we observed that a part of cathode current was lost on anode pipe and only 70 % of total amount was effectively extracted from the injector. This constatation has led us to increase anode internal diameter up to 112 mm in order to transport 95 % of emitted current as predicted by TETHYS numerical code. Results obtained experimentally have been in good agreement with the calculations as shown on figure 4 where current profiles measured with Rogowski coils are presented at different locations along the accelerator.
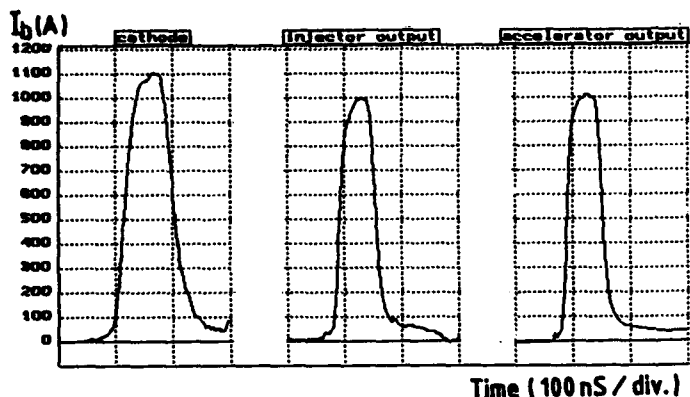
Figure 4 : Beam current

D - Energy spectrum

A magnetic spectrometer placed at the injector output was used to characterize the electron beam. A maximum peak energy has been measured at 1.36 MeV; but, due to problem of H.V. breakdown in gap cells, accelerating voltage has been limited around 1 MV for routine operations.

During the last weeks accelerator cells have been energized at low voltage; the peak energy raised up to 2.1 MeV preserving a good spectrum quality (see figure 5). Experiments at higher energy are in development and will give results soon.

E - Emittance - Brightness

Measurements have been performed at the injector output with 1.2 MV accelerating voltage and 1 kA
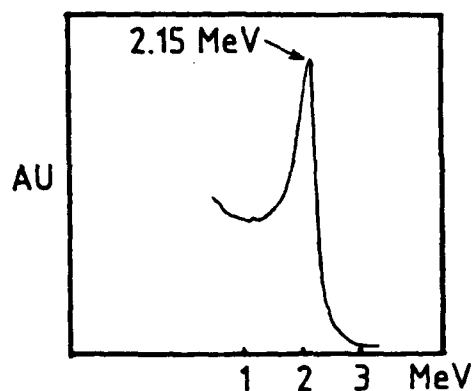
Figure 5 : Energy spectrum

beam current using pepper pot technique. The measured emittance was close to 200 π.mm.mrad on the two axis, leading to a normalized brightness of 5×10^8 A m^{-2}. rad^{-2} which is higher than the design value. We have not yet performed measurements at the accelerator output.

F - Beam stability

Beam centroid position measured with four " B$_\theta$ loops " between injector and accelerator module indicates a good stability all the more as trim coils have not still been used. The beam centroid motion was around 2 mm on each transverse axis over 25 ns indicating a relatively low corkscrew instability.

REFERENCES

[1] Microwave FEL experiments at CESTA
J. Launspach, Ph. Anthouard, J. Bardy, C. Bonnafond, H.Bottollier-Curtet, Ph. Delsart, A. Devin, Ph. Eyharts P. Eyl, J. Gardelle, D. Gardent, G. Germain, P. Grua, J. Labrouche, P. Le Taillandier, J. de Mascureau, E. Merle, A. Roques, M. Thevenot, D. Villate
CEA/CESTA - B.P. 2 - 33114 Le Barp -(FRANCE)
Proceedings of the 14 [th] Int. FEL Conference, KOBE, Japan - Aug 23-28, 1992 (to be published)

[2] Design and progress of the AIRIX Induction Accelerator
J. de Mascureau et al.
CEA/CESTA - BP 2 - 33114 LE BARP (FRANCE)
Proceedings of this conference

[3] LELIA : An Induction Linac Developed for FEL Application
Ph. Eyharts, J. Bardy, Ph. Anthouard, P Eyl, M. Thevenot
CEA /CESTA - BP 2, 33114 Le Barp (FRANCE)
Proceedings of the 1991 PAC, May 6-9, 1991, San Fransisco, Ca - Volume 5, p. 3204 - 3206

An Induction Linac and Pulse Power System at KEK

J.Kishiro, K.Ebihara, S.Hiramatsu, Y.Kimura, T.Ozaki, K.Takayama
and D.H.Whittum
National Laboratory for High Energy Physics, Japan, KEK
Oho 1-1, Tsukuba, Ibaraki 305, Japan
K.Saito
The Graduate University for Advanced Studies at KEK

Abstract

A R&D program on a free electron laser(FEL) in the microwave regime is currently in progress at KEK, intending to investigate the feasibility of an FEL as a promising GW order high power microwave source for the two beam accelerator(TBA) scheme[1][2] in a future high energy linear collider. The first prototype of the KEK FEL was an induction linac driven X-band(9.4GHz) FEL energized by a 800keV, 1kA electron beam[3]. The rf power amplification exceeded 30MW[4], however, theoretical work indicated that the 800keV operation was in the Raman regime and the FEL gain was limited by a strong space charge effect. To cure problems arising from the space charge effect, a new generation of the KEK FEL has been completed, in which the driving electron beam energy was upgraded to 1.6MeV and about 700A beam current was successfully transported through a wiggler magnet.

In parallel to the FEL investigation, several types of high current induction linacs and a pulse power system were also developed. The pulse power system consists of two gate-turn-off thyristor(GTO) switch modules, two magnetic pulse compressors and a dc high voltage source. A 1.6kV dc high voltage is resonantly discharged by the GTO switches and its pulse duration is compressed to 200kV, 100ns pulse power by a combination of two step-up transformers and three saturable inductors. The induction linacs are of two types. One is loaded by a ferrite magnetic cores (TDK PE14) and the other is loaded by amorphous cores (Metglass 2605S). The details of the induction linacs and pulse power system design and a performance will be reported in this article.

I. INDUCTION LINAC

To get the 1.6MeV high current electron beam, eight induction units were installed, four of which have been used in the previous 800keV operation. These were formed by 12 ferrite cores of 50.8cm outer dia., 29cm inner dia. and 2.54cm thickness. The other four units are newly designed for improving the vacuum seal and consist of 5 amorphous cores, Metglass 2605s, of 49.3cm outer dia., 31.5cm inner dia. and 4.4cm thickness. The previous version of the unit has only an acrylic resin to insulate the oil filled and vacuum region. This resulted in rather poor vacuum because of the evaporation of the acrylic compound. An additional ceramic insulator has been installed

in the vacuum region in the new design and less than $10^{-7} Torr$ is possible throughout the whole beam region. Figure 1 shows the inner structure of the new induction unit.
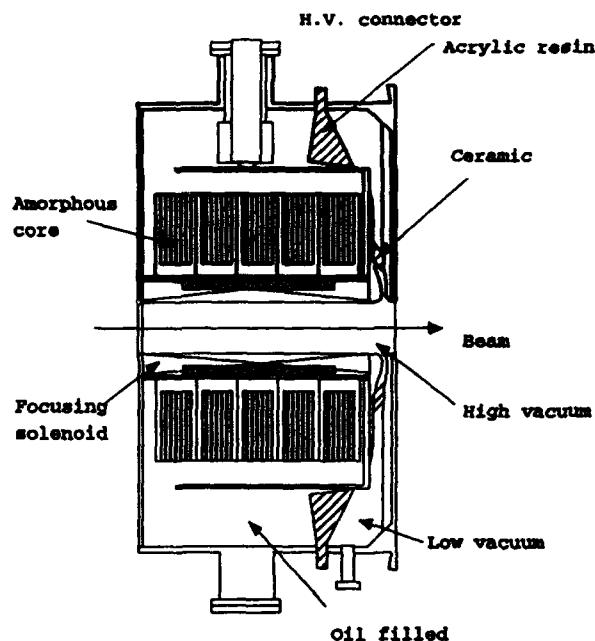
Figure 1. New induction unit.

The use of amorphous core is motivated by the lower magnetic coercive force than the ferrite core: this provides lower magnetic reset current and results in lower heat dissipation in the unit. Moreover the higher saturation magnetic field, B_S, of the amorphous material is suitable to reduce the unit size. The heat dissipation of the pulse operation in the unit volume depends on the material; however, the concern is not in the unit volume but in the whole volume. The high saturation material, like amorphous, in general, has high loss but requires small volume to realize the same volt-time product. Thus the total dissipation is almost independent of the ferromagnetic material.

The other consideration for choice of the material is the magnetization current, I_M, which is required to be as small as possible, because it detracts from the beam current, i.e. beam current I_b is $I_b = I_{ps} - I_M$, where I_{ps} is the current from a power supply. The size of I_M can be measured by examining the unit impedance without the beam

loading, i.e. $R_M = V_{IDU}/I_M$. Too good electrical conductivity of the amorphous core will lower the impedance. The table I shows the measured induction unit impedance of both the ferrite and amorphous core loaded.

Table I   Impedance of the induction unit.

cell number	1	2	3	4	5	6	7	8
$R_M(\Omega)$	118	94	105	79	91	86	81	100
magnetic core	Ferrite(TDK PE14)				Metglass(2605S)			

The fabricated units almost meet the design goal of $R_M \geq 100\Omega$, required to insure the impedance matching

between the induction unit and the power feeder (50Ω coaxial cable) from the power supply, for a 2kA beam. The new design has not been optimized the core size, and took the other structures, like cooling channel etc. Then the whole unit size became almost the same as the previous version in spite of the advantage of high B_S of the amorphous core. In the third design it is foreseen an optimization work.

II. PULSE POWER SYSTEM

The pulse power system was designed to energize the two units of induction linac. The system consists of a high voltage source, two modules of solid state switches and two magnetic pulse compressors(MPC).
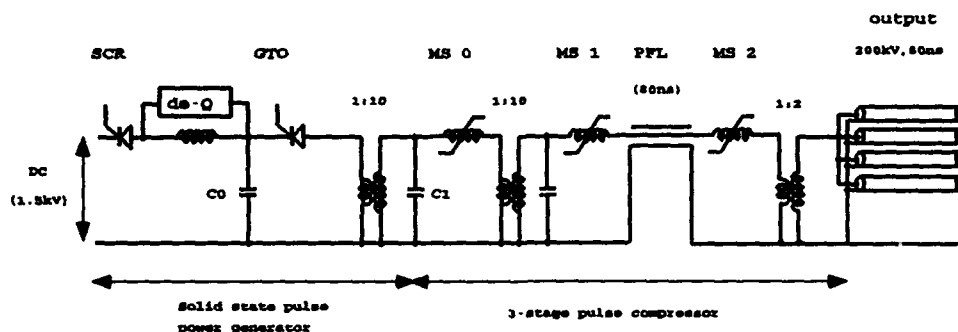
Figure 2.   MPC circuit diagram.

A. Magnetic pulse compressor

Among the several types of pulse power system, MPC is the most preferable system because it consists of only passive components, thus making possible huge power switching. The KEK MPC is three stage saturable inductor switch, compressing a power pulse from $7\mu s$ to 80ns. A schematic drawing is shown in Figure 2. The characteristics of the MPCs are:

Output voltage	200kV
Output current	16kA
Output impedance	12.5Ω
Output pulse duration	80ns(FWHM)
Input voltage	2.6kV
Input pulse duration	7μs(half-sinusoidal)

Figure 3.   MPC output wave form.

The output power from the dc high voltage source(1.6kV) is resonantly charged into the capacitor C_0(2.7kV). Two

1:10 step-up transformers increase the voltage up to 250kV and three stages of amorphous inductor switches compress the power pulse down to 80ns. The output pulse is formed by a pulse forming line(PFL), which has a length corresponding to 80ns and an impedance of 3.1Ω, and at the final end of the MPC a 1:2 step-up transformer is installed for recovering the charging voltage to the PFL. Figure 3 shows a typical output wave form on a resistive matched dummy load.

B. Power station

The dc power source is the conventional type of rectifier from 420V primary AC power to 1.6kV DC power. The high voltage pre-pulser is formed by ten GTO switches, each of which has a capability of switching the high voltage power of 3kV, with current ramp rate of up to 6kA/μs. The charged DC 1.6kV power in a capacitor is resonantly charged into the capacitor C_0 and discharged into C_1 by the GTOs through a 1:10 transformer and successively compressed in duration by the MPC.

The charging voltage of the capacitor C_0 is continuously examined and automatically cuts off the power line between the power supply and C_0 by exciting a de-Q circuit. The stabilization of the MPC output voltage by the de-Q circuit was established within 1% and the advantage of the solid state switches was confirmed in the timing jitter of the output pulse, observed to be less than ±2ns.

III. 1.6MeV X-band FEL test stand

The re-assembling of the 800keV stand to the new 1.6MeV FEL test stand has been completed. Figure 4 shows the whole view of the 1.6MeV X-band FEL test stand. Two sets of the four induction units generate 1.6MV on a 40mm dia. field emission metal cathode. A carbon cloth is attached on the cathode surface, which has a good electric conductivity and makes the beam quality stable. A mesh-less type anode is placed at 89mm downstream of the cathode. This diode is operated in the sense of "laser-based foilless diode"[5], because laser-induced ion channel guiding is used as a means of high current beam transport. Thus the diode is surrounded by dense ions; however, the electrode is designed neglecting this effect by using the EGUN code. A stable 1.2kA beam current is generated from the cathode and about 800A beam is constantly transported into the wiggler magnet. The beam is transported by employing ion channel guiding alone, without any external focusing magnets.
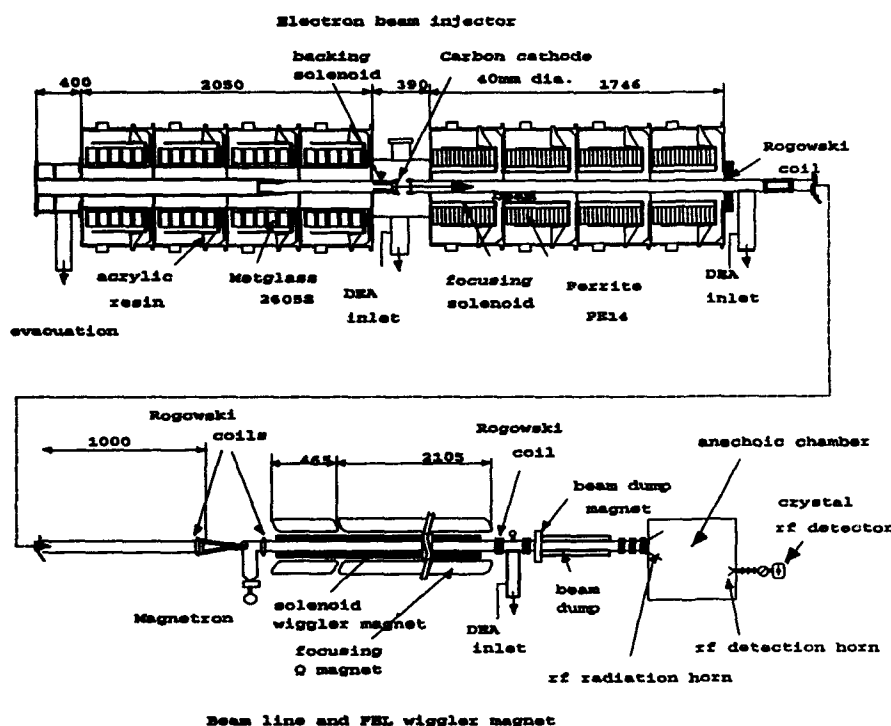
Figure 4. 1.6MeV KEK X-band FEL test stand.

The wiggler magnet is the planar type magnet, which consists of 12 small solenoid coils and an additional 4 similar coils. The 9.4GHz rf is injected from a magnetron into the over-sized waveguide and amplified rf is ejected into an anechoic room where power and mode contamination etc are measured.

IV. Preliminary FEL experiment at 1.6MeV

Figure 5 shows preliminary results for beam transmission in the wiggler section.
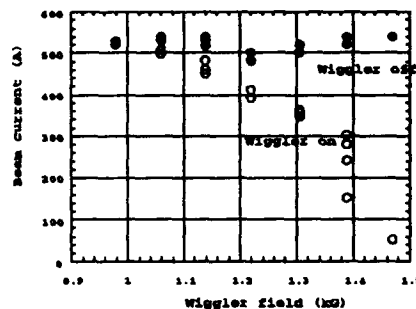
Figure 5. Preliminary result for beam transmission in the wiggler section.

With no wiggler excitation, the beam is completely guided by ion channel focusing. However, we have considerable beam loss for wiggler field higher than 1.2kG. Since maximum FEL gain at 1.6MeV is expected at a wiggler field of 1.4~1.5kG, improvement of the beam transmission at higher field is essential and is under way.

In preliminary operation, rf amplification by the FEL was observed as shown in Figure 6 and maximum power of 16MW was obtained. Due to the beam loss in Fig.5, amplified rf power degrades toward the high wiggler field side. Meanwhile, a 1-D FEL theory "benchmarked" at 1.6MeV predicts a saturated power in excess of 50MW, for 0.5kA beam.
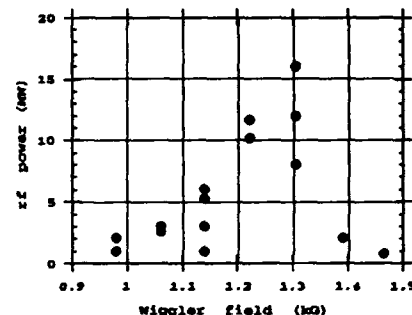
Figure 6. Amplified rf power in preliminary studies.

V. REFERENCES

[1] A.M.Sessler, AIP Conf.Proc.No.91, New York 1982
[2] S.Hiramatsu et.al.,Nucl.Instr.and Meth. A285(1989)83
[3] J.Kishiro et.al.,Particle Accelerators 31(1990)83
[4] T.Ozaki et.al.,Nucl.Instr.and Meth. A318(1992)101
[5] S.L.Shope et.al.,Phys.Rev.Lett. 58(1987)551

Design and Operation of Inductive Acceleration Modules
for FEL with Controlled Voltage Ramp

S.Kawasaki[a], H.Ishizuka[b], A.Tokuchi[c], Y.Yamashita[d], S.Nakajima[e], K.Sakamoto, H.Maeda and M.Shiho

Japan Atomic Energy Research Institute, Naka Laboratory

Nakamachi, Ibaraki 311-01 JAPAN

Abstract

A new pulse compression system is fabricated for grading up the induction accelerator LAX-1, which is currently used for Raman FEL research at JAERI[1]. It is designed so that the capacitance of PFL can be varied partly, and the output voltage ramp be controlled within ± 20 %. The system consists of a series of PFLs and magnetic switches for pulse compression from $2\mu s$ and 30 kV to 130 ns and 250 kV. The final output is supplied with to 2 × 4 units of accelerating cavity. The design, circuit parameters, mechanism of varying the PFL parameters and the results compared with those of the numerical simulation are presented. Relation to the beam dynamics and FEL performance is also considered.

I. INTRODUCTION

The instantaneous energy spread and emittance of the electron beam are well recognized to give great influence to FEL performance. The evolution (and/or fluctuation) of the beam energy and intensity in time, can as well t: the cause of the degradation of the resulted radiation on an average, through the beam dynamics and the slippage[2][3]. We have studied a Raman FEL in the microwve frequency range at JAERI, using an intense electron beam of 1 MeV and 2 kA generated with an induction linac. The plasma cathode used there has an intrinsic time-dependent impedance and the electron beam rather differs from being constant in both energy and intensity although the driving voltage was shaped nearly rectangular of 150 ns in duration. Stable transport of the beam in the wiggler field over the whole duration was not obtained and an effective FEL amplification of the input microwave was realized only in a narrower span (~40 ns)[4] (Fig.1). In the design of upgrading of LAX-1 in view of

a) Saitama Univ., Fac. of Sci., Urawa 338 JAPAN.

b) Fukuoka Inst. of Tech., Fukuoka 811-02 JAPAN.

c) Nichicon Co. Ltd., Kusaru, Shiga 525 JAPAN.

d) Hitachi Metal Ltd., Magnetic and Electric Materials Res. Lab., Kumagaya, Saitama 360 JAPAN.

e) Hitach Ltd., Kokubu Works, Hitachi, Ibaraki 316 JAPAN.

its application of the resulted FEL radiation to control the plasma parameter in a medium-sized Tokamak JFT-2M, the driving acceleration pulse is required to be tailored for the beam to produce an intense microwave of 30-120 GHz over the full beam duration (130 ns), by means of a variable PFL compression scheme.

II. PFL AND MAGNETIC SWITCH

Fig. 2 shows a schematic of the circuit of the magnetic compression device, including PFLs and magnetic switches. The operation of the circuit depends mainly on the magnetic characteristics of the core material, and on the arrangement of the successive stages. We had investigated various plans with many kinds of core materials and PFLs, and finally chose the components as shown in the figure. The circuit consists of a pulse step-up transformer PS, an intermediate capacitor ISC, and a series of 11 PFLs between magnetic swithes MS. Thin foils of amorphous metal "Finemet" and "AC10" available from Hitachi Metals and TDK, are used for the cores. The capacitance and characteristic impedance in the PFLs can be varied in a large range in three sections of the PFLs, to control the final waveform; the rising and falling times and the voltage ramp of the flat part. In these sections the circuit forms a folded planar PFL, where the central and outer electrodes are immersed in pure water with dielectric material inserted between them. The position of the dielectric layer can be moved mechanically in vertical direction to change the capacitance of the PFL within ± 50 %. Two of the PFLs (PFL2 and PFL11) are for getting the leading and falling edges of the pulse shorter than 20 ns and the group of PFL3-9 is for the ramp control. The pulse form is thus subject to fine control when it should be ajusted to the time-dependent impedance change of the electron beam diode. The pulsed waveform of the voltage and current in each stage were numerically simulated with the same computer code as used for the design of LAX-1. The results of the simulation are shown in Fig.3, for the cases of the pulse with a flat top and a positive/negative voltage ramp, assuming the load of pure resistance.

III. EXPERIMENTAL RESULTS

The device is composed of 2 systems identical with one described in the previous section. The either of their outputs is divided into 4 channels to feed independently to 4 accelerating cavities a pulse of 250 kV respectively. We will have thus an inductive acceleration of 1 MV/system, or 2 MV in all. The device was tested with a dummy load of pure resistance of 50 ohms/each channel. The circuit voltage(V) at several nodal points were measured as well as the flowing currents(I) between them, and from them the values of power transported(P) through the successive stages of the circuit are calculated. Energy losses(E) in the stages are to compare with the values expected from the core characteristics. Some of the results are shown in the Fig. 4a)-d). Fig. 4a) is the input voltage to and the current through MS1. Fig. 4b) is for those measured at the entrance of the PFLs, and Fig 4c) for the voltage at the load when the impedances of PFLs are fine-ajusted to get a flat top within ± 1.7% over 120 ns. Changing the impedances of the PFLs we obtain the pulses as shown in the Fig. 4d):typical examples of the output for the cases of a flat top, positive and negative ramp, which should be compared with the Fig. 3. The coincidence of the measurements and the simulation is fairly good. The input energy from the primary capacitor is 1390 J and the power consumed at the load 860 J approximately. The transmission efficiency is then 62 %. The accelerating cavities are under construction at present and the first operation of the electron beam is expected before the end of the fiscal year 1993.

IV. DISCUSSION AND CONCLUSION

It was successfully demonstrated that the output pulse of the pulse modulator for generating an intense relativistic electron beam for Raman FEL research could be controlled in the shape with a variable voltage ramp by adjusting the impedances of the PFLs inserted btween the magnetic switches. The modulator will be matched to the impedance evolutiom of the electron beam diode and get the beam of constant particle energy. The planar PFLs the capacitance of which is changeable with a relatively simple mechanism work well and show a moderate power loss. At the Raman FEL experiment the transmission of the beam through and the satbilty in the wiggler are affected quite seriously by the particl energy with collective effects related to the intense self-field. It is necessary to keep the energy constant within a

few % over the pulse length at least in our geometry of the experiment[5]. The beam with time-dependent energy may also produce the radiation with a large spectral width on an average. If we use a cavity to confine the FEL radiation to enhance the gain, the fluctuation of the beam energy will affect the spectral characteristics through the slippage and the competition between the possible modes[3]. We will be able to investigte these issues experimentally in detail with the new driver, while so far the effect was discussed mostly for a low gain continuous beam FEL.

IV. REFERENCES

[1] M. Shiho, K. Sakamoto, S. Maebara, A. Watanabe, Y. Kishimoto, S. Kawasaki, T. Nagashima, and H. Maeda, "JAERI millimeter FEL experiment by using focusing wiggler", *Nucl. Instr. Meth.* **A 304** 141 (1991).

[2] C.M.Tang, B.Hafizi, E. Esarey, A. Ting, W. Marable, and P. Sprangle, "Key issues affecting the performance of free electron lasers", *AIP Conf. Proc.* No. **249** 1020 (1992).

[3] T. M. Antosen, Jr. and B. Levush,"Spectral characteristics of a free electron laser with time-dependent beam energy", *Phys. Fluids* **B 2** 2791 (1990).

[4] K. Sakamoto, T. Kobayashi, S. Kawasaki, Y. Kishimoto, S.Musyoki, A. Watanabe, M. Takahashi, H. Ishizuka, M. Sato, and M. Shiho, "Millimeter wave amplification in a Free Electron Laser with a focusing wiggler", submitted to *Journal of Appl. Phys.*

[5] K.Sakamoto, T. Kobayashi, Y. Kishimoto, S. Kawasaki, S.Musyoki, A. Watanabe, M. Takahashi, H. Ishizuka, and M. Shiho,"Beam divergence with harmonic gyroresonance in focusing wiggler and axial field", *Phys. Rev. Lett.* **70** 441 (1993).
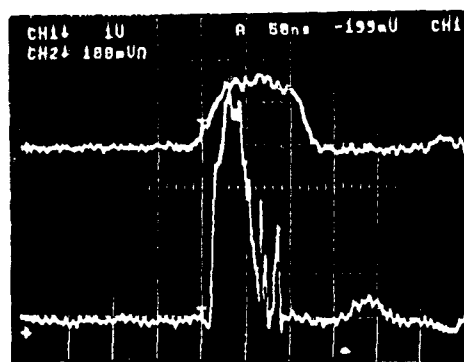
Figure 1. Accelerating Pulse of LAX-1 and Amplified RF
upper:output 500 kV/div.   time scale:50ns/div.
lower:amplified FEL of 35 GHz.

Figure 2. Schematic of the Device and Equivalent Circuit of PFLs.

mm

| 700 | 400 | 850 | 1000 | 700 | 1650 |

PS   ISC   MS1   PFN   MS2   MS3

PFLs.

PFL1 L1 PFL2 PFL3 L2 PFL4 L3 PFL5 PFL6 PFL7 L4 PFL8 L5 PFL9 .PFL10 L6 PFL11

C12 C37 C22 C37 C32 C47 C42 C57 C52 C67 C62
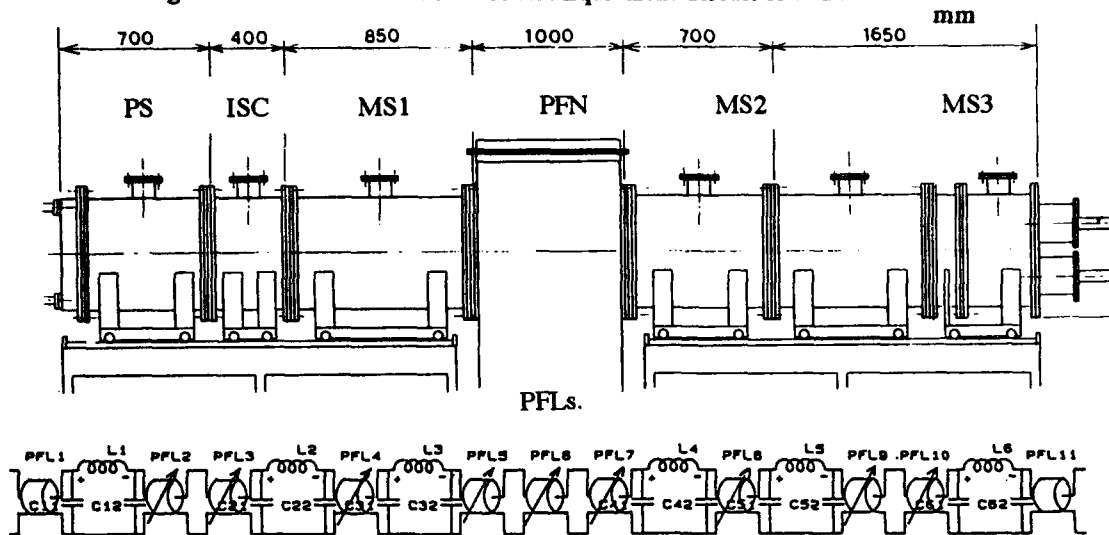
Figure 3. Simulation of the Output Waveforms.
case 2: flat impedances for PFL2-10.
case 3: PFL impedances decreasing from 2 to 10.
case 4: PFL impedances increasing from 2 to 10.

CASE 2 CONSTANT IMPEDANCE.
CASE 3 DECREASE IMPEDANCE.
CASE 4 INCREASE IMPEDANCE.
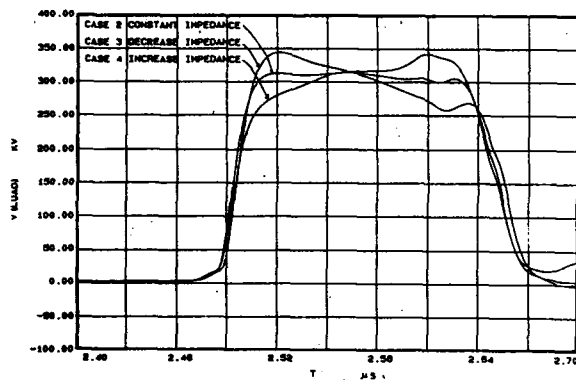
Figure 4. Voltages and Currents in the Compression Circuit.
4a) Input to MS1.
4b) Input to PFLs.
4c) Load voltage with a flat top.
4d) Outputs with various ramp.
    100 kV/div.

4a)
(4) Ems1 (in)
(3) Pms1 (in)
(2) Vms1 (in)
(1) Ims1 (in)

4b)
(3) Ppfn (in)
(4) Epfn (in)
(1) Ipfn (in)
(2) Vpfn (in)

4c)
Vdc=29.5kV
RISE TIME 22ns
(10%-90%)
FWHM 168ns
FLATNESS ±1.7%
Vload

4d)

678
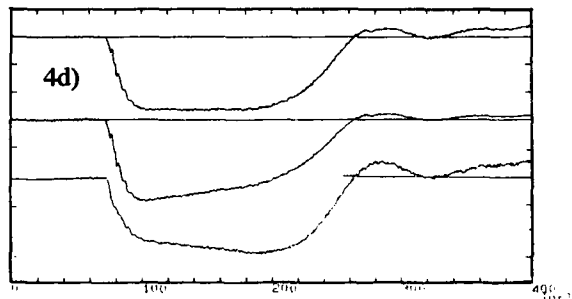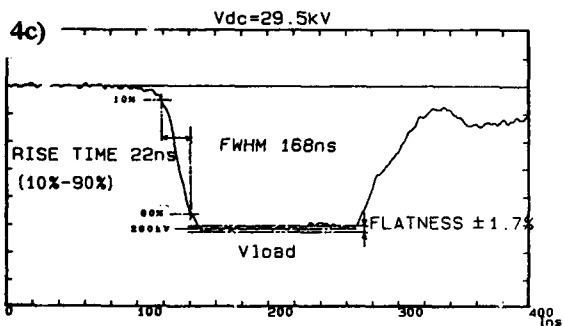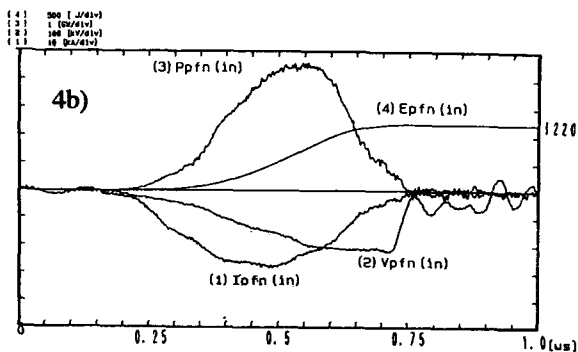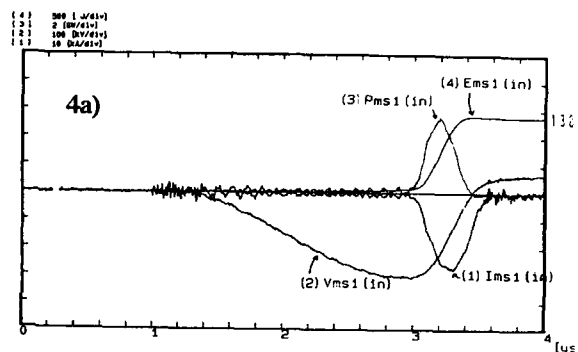
Study on Induction Accelerator for Industrial Applications

Y. S. Cho, K. H. Baik, K. H. Chung

Department of Nuclear Engineering, Seoul National University

Seoul 151-742, Korea

and

B. H. Choi

Korea Atomic Energy Research Institute

Daejun 305-606, Korea

Abstract

The design of electron induction accelerator for industrial applications, for example sterilization, is presented. The injector, the accelerating column, the Blumlein circuit pulse power supply and the beam extraction system of movable (Compact and Light) electron induction accelerator with 5 MeV electron energy and 100 kW electron beam power are described.

I. INTRODUCTION

The electron induction accelerator can be industrially used for sterilization, deinsectization and sewage treatments. As to movability, it has strong-point since it requires less auxiliary equipments and can be operated by the commercial electric power.

Considering the electron beam applicability, the movability through compact and light equipment design, and at least one-year maintenance-free operation as well as low manufacturing costs, the specifications of designed industrial induction accelerator are presented as Table 1.

Table 1. Design parameters

Peak Energy	5 MeV
Peak Current	200 A
Pulse duration	1 μs
Pulse repetition rate	100 ppm
Average beam power	100 kW
Maintenance-free life shots	$> 10^9$
Weight	~15 t
Length	~12 m

II. INJECTOR

The injector consists of 4 induction cavities and electron gun and it has been designed to produce electron beams with 400 keV, 200 A, and 1 μs duration time. Considering life time and heating availability, the cathode material of electron gun has been adopted as LaB_6 with flat surface whose diameter is 50 mm. Induction cavities have aluminum electrodes and 0.1 V·sec core, whose material is 0.05 mm thick silicon steel. Polyamide film is used for intermediate layer insulation and cross-linked polystyrene for vacuum interface. The electron beam is focused by coils that is set both inside induction cavity and at anode. It can produce electron beams with 30 mm diameter along 500 Gauss guiding magnetic fields, which was calculated and verified by ETP (Electron Trajectory Program) Computer Code. The simulated electron trajectory in the injector is shown as Figure 1.

III. ACCELERATING COLUMN

Accelerating column is made up of induction cavities for 100 kV accelerating voltage and 1 μs pulse duration and the electron beam energy can be adjusted on the number of induction cavities. The materials of accelerating column are the same as those of induction cavities. Its bore radius is relatively small to 50 mm diameter. One of induction cavities is shown as Figure 2.

IV. POWER SUPPLY SYSTEM

The power supply system of induction cavities consists of high-voltage charging power supply, Blumlein circuit, pulse transformer and core reset
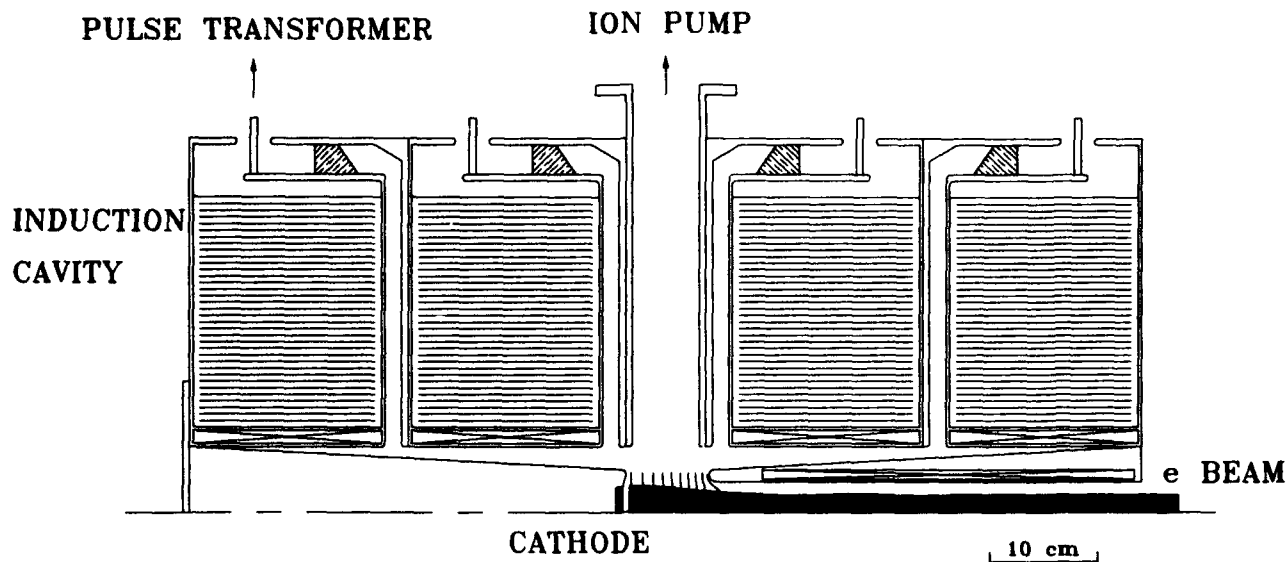
Figure 1. Injector

circuits. 20 kV charging voltage has been determined in that high efficiency solid-state switching power supplies are available as well as capacitors and thyratron switches which have 100 pps repetition rate and can be maintained over 10^9 shots.

For compact and light design, Blumlein circuits [1] are made up of capacitors and inductors, which can apply the full charging voltage to pulse transformer. The turn ratio of pulse transformer is 1:5 and the output voltage 100 kV. Since the pulse transformer like induction cavities is put in the same case and the 20 kV output pulse of Blumlein circuits enters induction cavity case, the power feeding can be facilitated. The core reset circuit supplies currents on the primary windings of pulse transformer. All the induction cavity cores can be reset on rotating switch connected to the same shaft. Figure 3 is the equivalent circuit diagram of all power supply components.

PULSE TRANSFORMER

LAMINATED SILICON STEEL CORE

GUIDING FIELD COIL
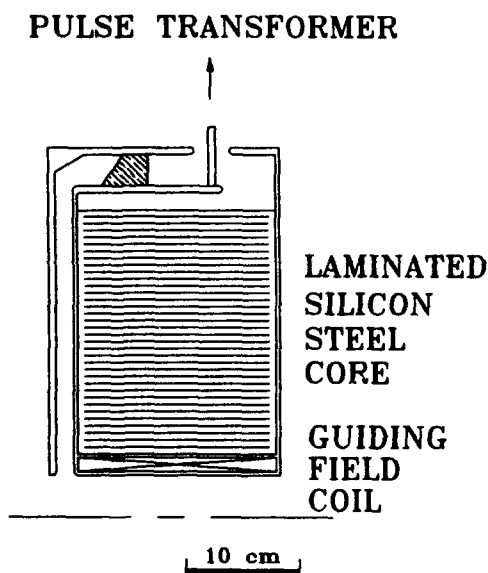
Figure 2. Induction Cavity
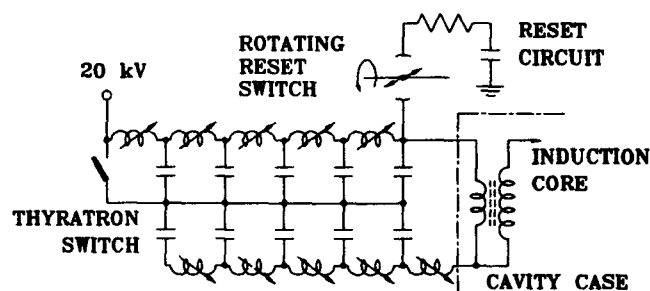
Figure 3. Power Supply System

V. BEAM EXTRACTION SYSTEM

The accelerated electron beams are extracted into the air through 20 μm thick Ti foil. For the extraction of pulse currents with 5 MeV, 200 A and 1 μs duration, the extraction window area requires over 10 cm^2 [2]. Multi-extraction methods with 10 windows are used, for its pulse repetition rate is 100 ppm. For high beam extraction efficiency, the

extraction window is spherically shaped. The extraction window can be air-cooled down by nozzles. The electron beam is guided to extraction window by solenoid focusing electromagnet and deflecting electromagnet. Figure 4 is the diagram of designed beam extraction window.
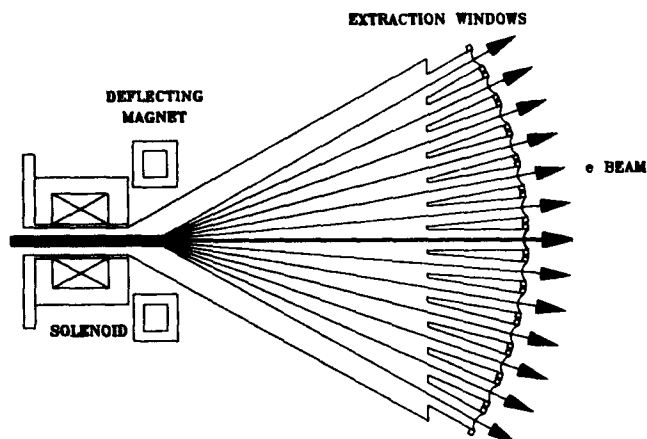
Figure 4. Beam Extraction System

VI. CONCLUSION

The electron induction accelerator for industrial applications has been designed with 5 MeV electron energy and 100 kW average beam power. The overall schematic of the designed electron induction accelerator is Figure 5. The movable accelerator will be useful for electron beam processings.

VII. REFERENCES

[1] G. N. Glasoe and J. V. Lebacqz, "Pulse Generators", McGraw-Hill Book Co., New York, 1948.

[2] E. A. Abramyan, "Industrial Electron Accelerators and Applications", Hemisphere Publishing Co., Washington, 1988.
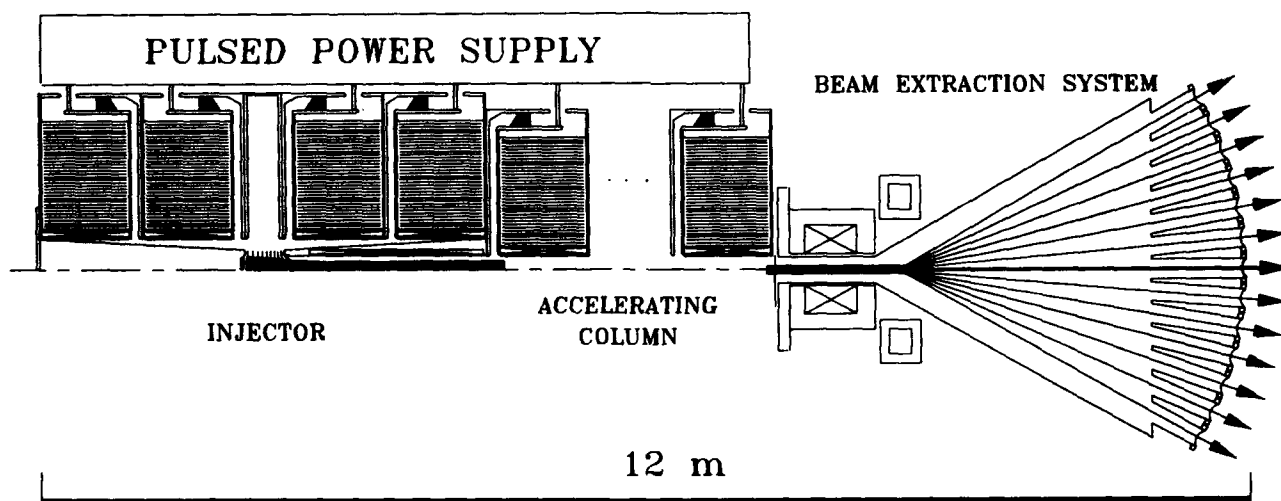
Figure 5. Total System

LINEAR INDUCTION ACCELERATORS FOR INDUSTRIAL APPLICATIONS

M. I. Demsky, Yu. P. Vakhrushin, A. E. Baranovsky, A. A. Volzhev, A. P. Kuprianov, D. E. Trifonov

D.V.Efremov Scientific Research Institute of Electrophysical Apparatus (NIIEFA)
St.Petersburg, Russia

A technology of Linear Induction Accelerators (LIA) is developed in Research Institute of Electrophysical Apparatus (NIIEFA) during more than 25 years. The first LIA - LIA-3000 started to work in 1967 in Joint Institute for Nuclear Research (JINR), Dubna.

This accelerator was constructed for researches of collective acceleration of heavy ions by electron rings. It produced an electron beam with energy up to 3 MeV, current up to 200 A and pulse duration about 500 ns. The second accelerator LIA-5000 was performed for the same purposes in Theoretical and Experimental Physics Institute (Moscow). At this accelerator the following parameters of the electron beam were achieved: 5 MeV, 2 KA, 50 ns. Than the first section of LIA-30/250 was adjusted in JINR (250 A, 3 MeV, 500 ns).

The experience received during the designing and adjusting of these accelerators was used further in the works for creation of industrial LIA. Two types of accelerators were designed: powerfull long pulse LIA for power-consuming processes and compact short pulse LIA - the source of brake radiation (X-ray source). In the first case it is supposed to realise unique potential posibilities of LIA to produce powerfull electron beams for high energy technological processes. In the second case it is supposed to create X-ray apparatus on the base of two sections of LIA induction system with total voltage on the tube up to 1 MeV.

The industrial LIA of NIIEFA as earlier constructed LIA for scientific researches have a small section induction system and pulse generators with hydrogen thyratrones workings without heighten transformers. The cores of the long pulse accelerators LIA-1.25-200 are performed from 50 NiFe permalloy tape 10 mkm width, and short pulse accelerator LIA-1-5 is performed from nickel-zinc ferrites. The injector of the accelerator LIA-1.25-200 looks like a diod with 120 mm diameter oxide thermocathode and 100 mm curvature radius, works with perveance about $2 \times 10^{-6} AV^{-3/2}$. Electron-optical system of injector and its general view are shown in fig. 1 and 2. Maximum cathode voltage reaches 400 KV and output beam current about 600 A.
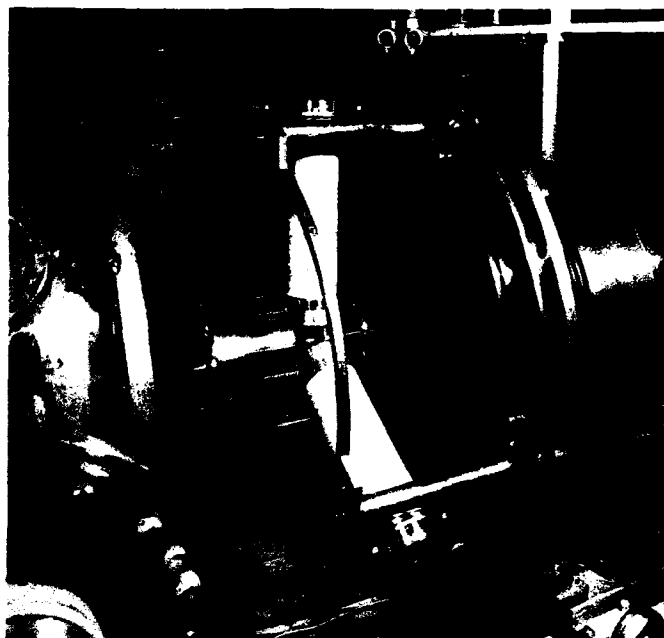
Fig. 1. General view of the injector
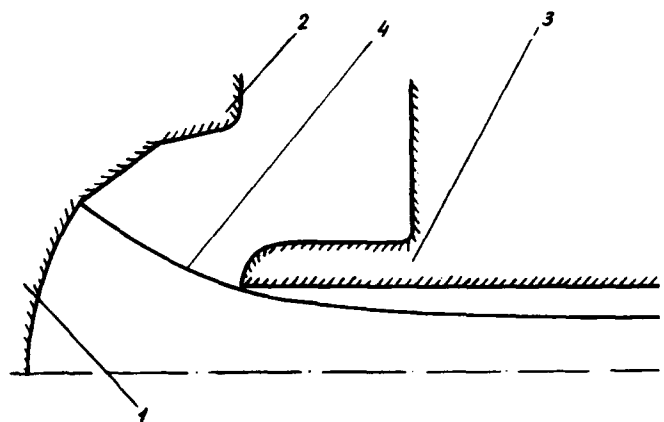
Fig. 2. Electronic-optical system of the electron gun: 1 - cathode; 2 - focusing electrode; 3 - anode; 4 - beam envelope

The injector induction system is supplied from a set of pulse generators with pulse hydrogen thyratrones. The stable work in the regimes close to the industrial exploatation was demonstrated on the injector and first acceleration section for two combinations of the parameters:

voltage on the injector, KV – 400; 200
beam current, A – 600; 250
pulse length, ns – 250; 500
pulse repetition rate, 1/s – 400; 1000

Taking into account that LIA is built usually from the succession of the same type modules, on the base of received parameters two variants of the accelerator performing can be suggested:

acceleration rate, KV/m – 100; 200
rate of beam power
collection, KW/MeV – 100; 50

As the accelerator turnes out rather bulky, actual task becomes to reduce energy expenses on beam transportation, that is reached first of all by improving its quality. The scientific researches of beam parameters at the output of the first acceleration section were carried out. The emittance measurement apparature was performed on the base of widely spreaded scheme: chink aperture, fluorescent screens, mirrors system and registration system. In our case the registration system has at the output the electron-optical transformer with electron "shutter", that makes possible to measure beam emittance in the separate time layer of the current pulse. Transverse phase beam volume versus the part of the current included in it for the beam current about 600 A in various parts of the pulse and integraly for all pulse (without strobing) are shown in fig. 3. The received experimental and calculated data allow the conclusion that for transportation the beam in the 100 mm diameter channel the transverse magnetic field with induction about 0.7 T is enough.

The further works at this accelerator are concentrated on the creation of the accelerator for a smoke clean-up from sulphur and nitrogen oxydes with average power about 500 KW and the total efficiency net-beam not less than 40%.

Compact LIA is performed on the base of hydrogen thyratron with the magnetic compressor (the scheme in fig. 4). In the magnetic compressor the pulse duration is
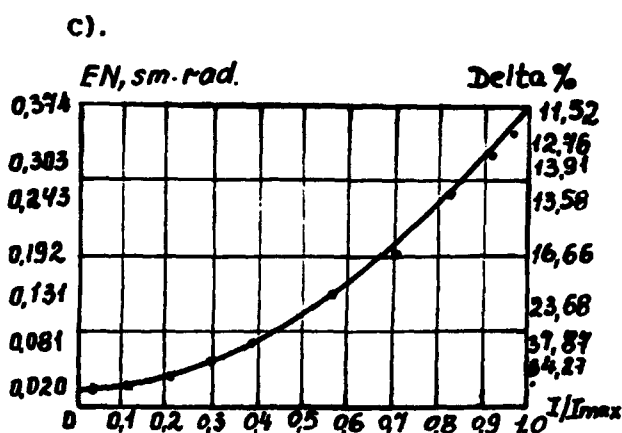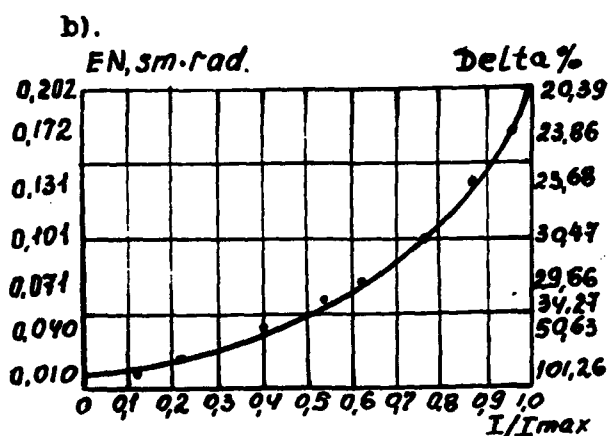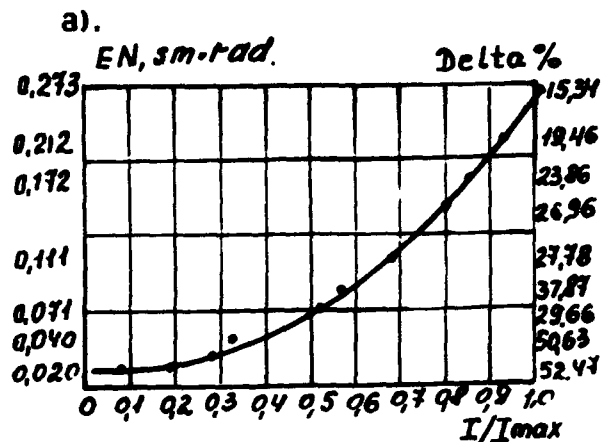
Fig. 3. Dependence of transverse phase beam volume upon the part of the current included in it:
a) t=0.25 T_p
b) t=0.5 T_p
c) t=0.75 T_p
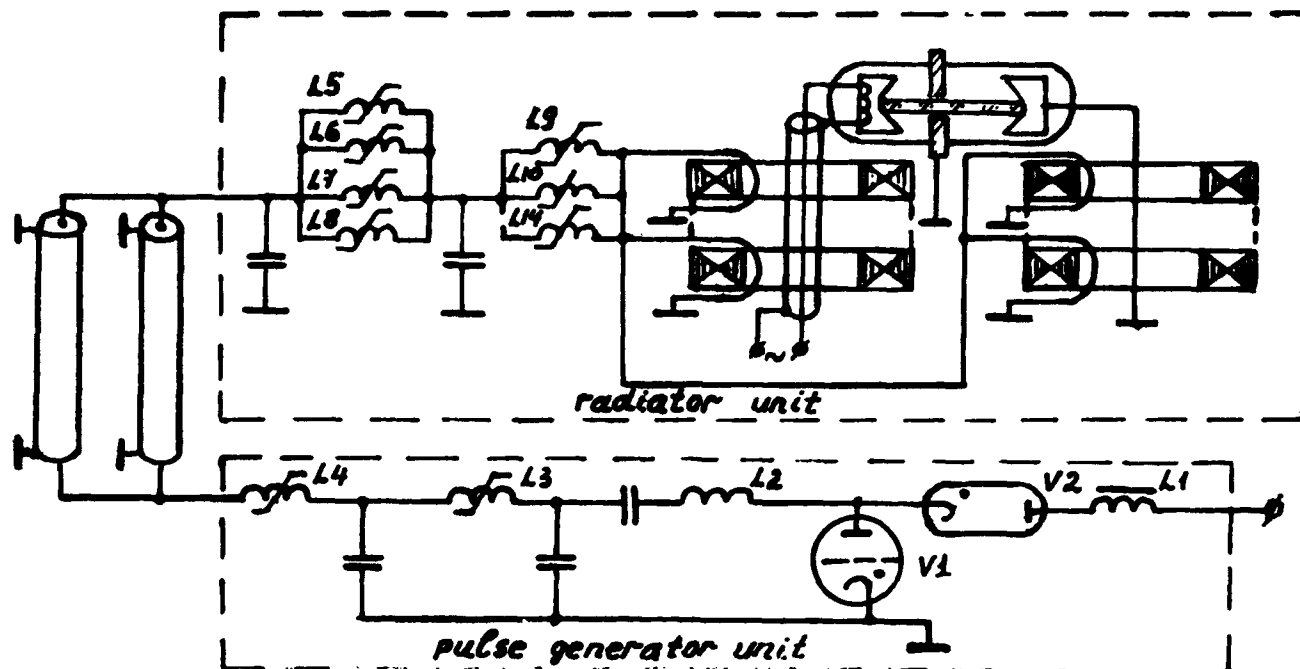
Fig. 4. Scheme of compact LIA with a magnetic compressor

reduced more than 100 times up to about 20 ns. During designing the main problem was to transmit such a short pulse into load. The load of two ferrit cell sections was pulse metal-glass X-ray tube with the thermocathode. The section, X-ray tube and two last compression units are mounted in the radiator block with dimensions 800x460x260 mm. The rest of equipment is mounted in the block with dimensions 1000x600x1200 mm connected with the radiator by 10 m length cables. The accelerator control is performed from carried out control panel. In recent time the voltage about 600 KV with average power about 3 KW and pulse frequency 5 kHz is obtained on the X-ray tube and the works on construction modernization are carried out for the purpose of receiving the voltages up to 1 MV and increasing the stability of the output pulse parameters with the repetition rate more than 3 kHz.

High Power, High Brightness Electron Beam Generation in a Pulse-Line Driven Pseudospark Discharge

W. W. Destler, Z. Segalov, J. Rodgers, K. Ramaswamy, and M. Reiser

Electrical Engineering Department and Laboratory for Plasma Research
University of Maryland, College Park MD 20742

Abstract

High brightness ($\sim 3 \times 10^{10}$ A/m^{2}rad^2), high power density ($\sim 10^{10}$ W/cm^2) electron beams have been generated by the mating of a hollow-cathode discharge device operating in the pseudospark regime to the output of a high power pulse line accelerator. Very small diameter (~ 1 mm) electron beams with currents in the range 500-1000 A and energies in the range 150-300 keV have been generated with measured effective emittances of about 85 mm-mrad. Such emittances are comparable to those achieved in conventional electron beam sources at current densities several orders of magnitude lower than those observed in these experiments.

Figure 1: Basic experimental configuration.

I. INTRODUCTION

During the last decade, considerable research has been conducted on pseudospark discharges of the type first explored by Christiansen and Schultheiss[1] in 1978. Interest in this novel discharge configuration has been driven by potential applications of such discharges to such areas as high power switch development.[2] In addition, the observation of high current density electron beams generated by such discharges has spurred interest in their possible application as high brightness electron beam sources for such diverse uses as electron beam lithography, plasma processing, Free Electron Lasers, and next-generation accelerators.

Over the last decade, several experiments have been reported in which high-brightness electron beams have been produced in pseudospark devices operating in the voltage range 20-50 kV.[3-5] Ion-focused electron beams with normalized brightness values as high as 10^{12} A/m^{2}rad^2 have been observed to propagate out from the discharge region in these experiments. Although these studies have been encouraging, the extraction of such ion-focused beams into vacuum for possible applications is complicated by the low energy and very high current density of the beam. In this report, we detail initial experiments in which a high-power pulse line accelerator has been mated to a hollow cathode discharge experiment operating in the pseudospark regime in an attempt to reproduce the attractive beam qualities observed in low voltage experiments at electron energies in the range 150-300 keV.

II. EXPERIMENTS

The experimental configuration is shown schematically in Figure 1. A pulse line accelerator which normally operates at 200-800 kV, 40-120 kA, 100 ·s was modified to produce a longer pulse duration by eliminating the output pulse forming switch and connecting the load directly to the output of the pulse transformer via a water coax section. The resulting pulser is capable of routine operation at 150-600 kV, 5-40 kA, 1 μsec. A multigap hollow cathode discharge device was connected to the output of the pulser in series with a 10 Ω resistor to ensure that the pulser would be well matched should the hollow cathode discharge impedance short out late in the discharge cycle. The multigap hollow cathode device consists of ten sets of electrodes and insulators as shown with an effective gap between electrodes
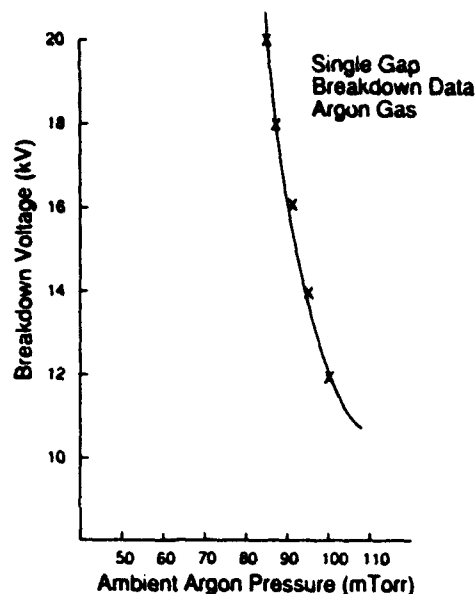
Figure 2: Single gap hollow cathode breakdown data.

of about 1 cm. An on-axis aperture 0.63 cm in diameter was drilled in the electrodes and electrons generated in the hollow cathode region were accelerated through these apertures to the extraction point on the anode side of the device. The discharge was initiated in Argon gas with ambient gas pressures in the range 30-100 mTorr.

In order to ensure that the multigap hollow cathode device would operate in the pseudospark regime, single gap breakdown characteristics were measured using a 20 kV pulser with a pulse duration similar to the 1 μsec pulse of the modified pulse line accelerator. Data from these studies, shown in Figure 2, indicates that operation of the multigap device in the pseudospark regime is possible at voltages of 100-300 kV with ambient Argon gas pressures in the range 50-100 mTorr, providing that the breakdown voltage of the multigap device is approximately that of a single gap times the number of gaps employed.

Typical pulse line voltage and current waveforms observed upstream of the multigap hollow cathode discharge device are shown in Figure 3. The voltage is seen to rise smoothly to a maximum of about 200 kV prior to voltage collapse, and a peak line current of greater than 20 kA is observed after the collapse occurs with the expected pulse duration (100 ns) equal to the electrical length of the coaxial line feeding the device. A typical ejected electron beam current waveform measured with the exit current
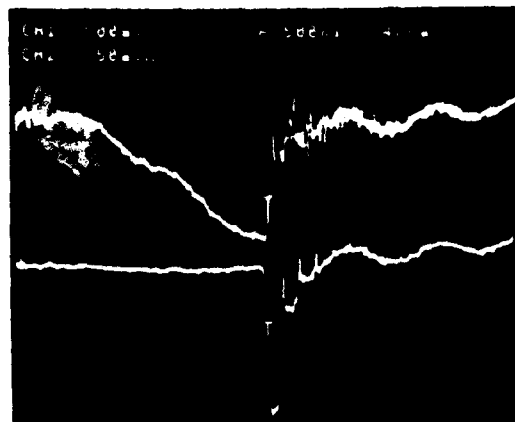
Figure 3: Typical pulse line voltage (top, 92.5 kV/div) and current (bottom, 3.7 kA/div) waveforms.

monitor is shown in Figure 4a. It is readily seen that the ejected beam current begins to rise about 20 ns prior to the onset of voltage collapse (which occurs at $t = 0$ on the scale accompanying the waveform) to a current of about 2 kA, and then increases to about 3 kA after voltage collapse. The peak ejected electron beam current, therefore, is seen to be a small fraction of the observed line current, an indication that most of the post-collapse current flows from electrode to electrode and is returned to ground at the anode. The post-collapse electron beam current, moreover, is comprised almost entirely of low energy electrons. Thus the high voltage electrons are produced in a short burst of approximately 20 ns duration prior to voltage collapse. To confirm this interpretation of the ejected beam current waveform, the ejected beam was then passed through a thin copper foil calculated to cut off all electrons below 140 keV. The current waveform obtained downstream of the foil is shown in Figure 4b, and it is readily seen that only that part of the ejected beam pulse that was initiated before voltage collapse had sufficient energy to penetrate the foil. It is therefore expected that the electrons that produced the current pulse shown in Figure 4b were accelerated to energies comparable to those associated with the full anode-cathode voltage (200 keV) prior to voltage collapse. The measured post-foil beam current of 120 A is consistent with range-energy theoretical expectations for a 1 kA, 200 keV electron beam passing through a foil of sufficient thickness to stop 140 keV electrons.

Both the damage pattern on the copper stopping foil and the image left by the beam on a heat sensi-
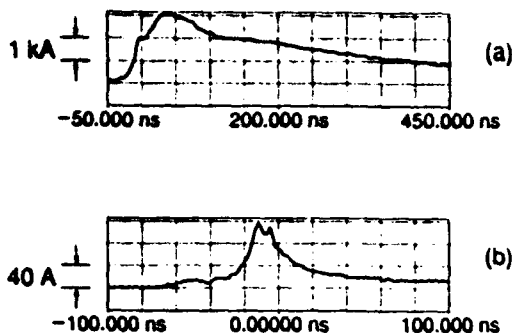
Figure 4: (a) Typical ejected beam current waveform. (b) Current waveform downstream of copper stopping foil. In both cases, t = 0 is the time when voltage collapse begins.
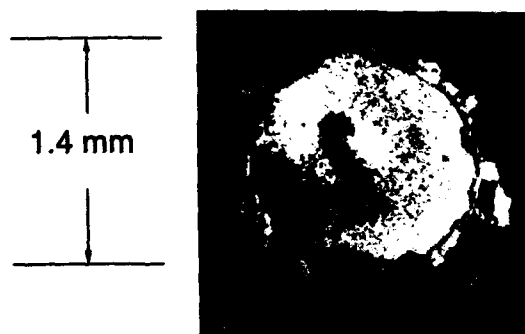
Figure 5: Photograph of typical beam damage pattern on copper foil. The dark spot in the damage pattern is a hole 0.17 mm in diameter produced by the beam.

tive polycarbonate sheet placed on the downstream side of the copper stopping foil were used to provide a simple means of estimating the diameter of the high energy component of the electron beam. These measurements were typically obtained 3.5 cm downstream of the anode plate, although similar measurements have been obtained at distances as great as 12 cm downstream of the anode. The measured beam diameter obtained from these experiments was in the range 0.2–1.4 mm. A microscope photograph of a typical damage pattern is shown in Fig. 5.

In a previous report[6], the measurements of beam energy, current and diameter were used to estimate the effective (4× rms) emittance and corresponding normalized brightness of the high energy component of the beam. Assuming a beam energy of 200 keV, I = 1 kA, and full charge neutralization, the effective emittance was calculated to be ≤ 174 mm-mrad for

a beam radius of 0.5 mm. Recent measurements of beam emittance made by passing the beam through a multi-slit aperture and recording the beam image on an electron-sensitive film 2 cm downstream of the aperture yield an actual measured effective emittance of about 85 mm-mrad. Normalized brightness is calculated to be 3×10^{10} A/m^{2}rad^2.

Future studies are planned to explore the scaling laws that determine beam parameters and to explore their injection into vacuum in the presence of confining magnetic fields. In addition, methods of delaying voltage collapse in the hope of increasing the high energy beam pulse duration are also under study.

III. REFERENCES

[1] J. Christiansen, Ch. Schultheiss, *Z. Phys.* **A2990**, 35 (1979).

[2] W. Hartmann and M. A. Gundersen, *Phys. Rev. Lett.* **60**, 2371 (1988).

[3] K. K. Jain, E. Boggasch, M. Reiser, and M. J. Rhee, *Phys Fluids* **B2**, 2487 (1990).

[4] W. Benker, J. Christiansen, K. Frank, H. Gundel, W. Hartmann, T. Redel, and M. Stelter, *IEEE Trans. Plasma Sci.* **PS-17**, 754 (1989).

[5] P. Choi, H. H. Chuaqui, M. Favre, and E. S. Wyndham, *IEEE Trans. Plasma Sci.* **PS-15**, 428 (1987).

[6] W. W. Destler, Z. Segalov, J. Rodgers, K. Ramaswamy, and M. Reiser, *Appl. Phys. Lett.* **62**, 1739 (1993).

Experimental Study of Post-Acceleration and Transport of a Pseudospark-Produced Electron Beam*

C. J. Liu[a] and M. J. Rhee
Laboratory for Plasma Research and Department of Electrical Engineering
University of Maryland, College Park, Maryland 20742 U. .A.

Abstract

Preliminary results of post-acceleration and transport experiment of a pseudospark-produced electron beam are presented. The electron beam propagating in a low-pressure gas is accelerated by a simple induction linac system. The beam transport characteristic in the gas filled drift tube is determined and the beam appears to be in the ion-focusing regime. The brightness of the post-accelerated beam is found to be -2×10^{10} A/(m rad)^2.

I. INTRODUCTION

Recently, high-brightness electron beam produced by a simple pseudospark device has been reported.[1] Such high-brightness beam sources would find immediate application in high-current accelerators[2] and in rf sources such as free-electron lasers.[3],[4] In this work, preliminary experimental results of post- acceleration and transport of a triggered pseudospark produced electron beam are reported. The electron beam, produced and propagated in the same low-pressure background gas, is accelerated by a simple induction linac system. The current, emittance and time-resolved energy spectrum of the electron beam are measured in conjunction with the study of the post- acceleration and transport of the beam.

II. EXPERIMENTS

A. Experimental Setup

The experimental setup is shown in Fig. 1. The discharge chamber consists of a planar cathode with a hollow cavity, two sets of intermediate electrodes and insulators, and a planar anode. The hollow cavity is a 2.54-cm diam 4-cm long cylindrical cavity in which a trigger electrode made of 6.35-mm diam semirigid coaxial cable is inserted. All the electrodes are made of brass and the insulators are of plexiglas. A 3.2-mm diam center hole is present through the entire electrode system. The storage capacitor used in this experiment is a 2.7 nF low- inductance type door knob capacitor. A homemade compensated resistive divider is used to monitor the cathode voltage. A Rogowski coil is built into the downstream side of the anode flange to monitor the electron beam current extracted through the anode hole. A diagnostic chamber, which is placed below the linac module, can accommodate various diagnostics such as a movable Faraday cup, a movable emittance meter and a time-resolved energy spectrometer.
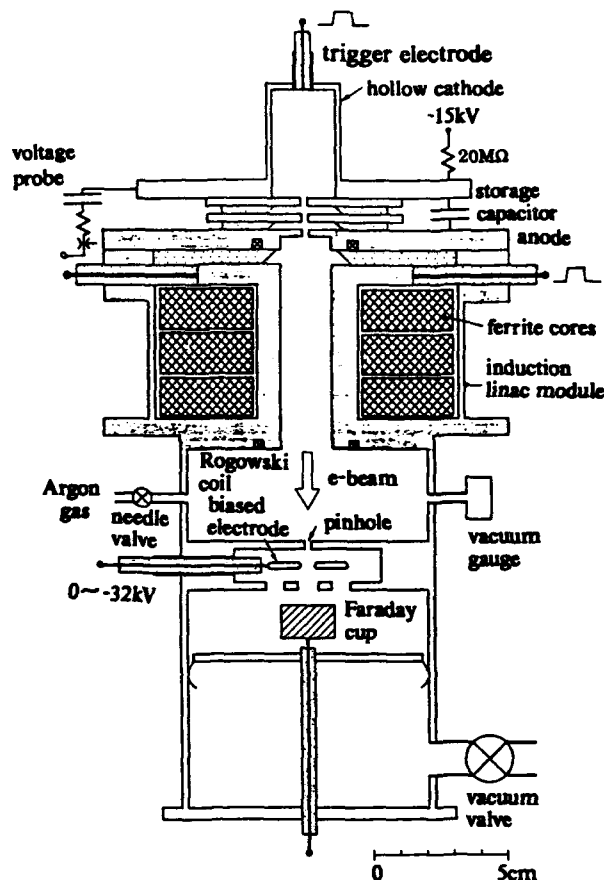
FIG. 1 Experimental setup.

B. Time-Resolved Energy Spectrum

Experimental setup as shown in Fig. 1 is used in this experiment. The cathode is charged to -15 kV with respect to the grounded anode through a 20 MΩ charging resistor. The entire chamber is initially evacuated by an oil diffusion pump typically down to 10^{-5} Torr. A time-resolved energy spectrometer system,[5] which consists of a 0.5-mm diam pinhole, a biased electrode, and a Faraday cup, is placed downstream of the anode. Argon gas is then slowly filled at a slow flow rate through a needle valve in the upper chamber while the pinhole allows the gas leak into the downstream chamber maintaing a constant differential pressure in the upper chamber and vacuum in the downstream chamber. The pressures used in this experiment are 55 and 75 mTorr, which are measured by a capacitance-manometer type vacuum gauge. By applying +20 kV pulse to the trigger electrode, the main discharge is triggered with low

jitter time of <1 ns. The cathode voltage during the discharge
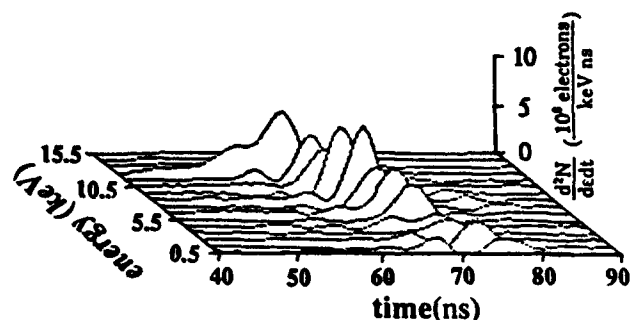
FIG. 2 The time-resolved energy spectrum of
the pseudospark- produced electron beam.

is measured by the resistive probe. The electron beam gener-
ated by this discharge is sampled by the 0.5 mm diam pinhole,
allowing the sampled beamlet to propagate in the vacuum cav-
ity of the spectrometer. Only electrons of energy higher than
that corresponding to a given bias voltage can pass through the
center hole of the biased electrode and arrive at the Faraday
cup. The bias voltages are varied from 0 to -16 kV in 1 kV
increments, and the corresponding Faraday cup current signals
are recorded in a digital oscilloscope. The differences between
two digital waveforms of adjacent bias voltages are computed
by using a personal computer. The time-resolved energy spec-
trum is then constructed by plotting the resultant differential
waveforms as functions of energy as shown in Fig. 2.

C. Post-Acceleration

An induction linac module is attached to the downstream
side of the anode as shown in Fig. 1. The linac module is
terminated by a matched load 25 Ω. This is done by two 50-Ω
cables (not shown in Fig. 1), one of which is conveniently
used for monitoring the voltage across the accelerating gap.
The electron beam generated by this discharge propagates
through the induction linac. The induction linac is powered
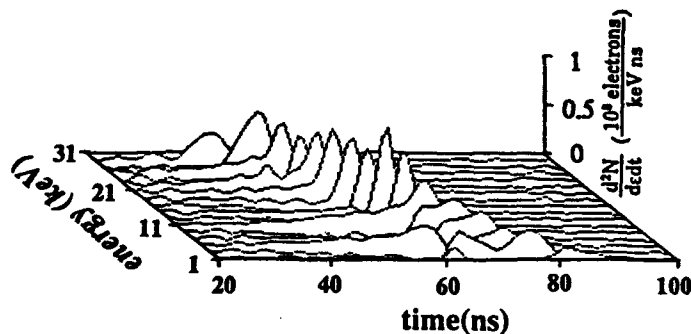
FIG. 3 The time-resolved energy spectrum of the post-
accelerated pseudospark-produced electron beam.

by the Blumlein modulator that also triggers the pseudospark.
Thus, the beam generation and accelerating voltage are in good
synchronization. For this experiment the bias voltage is varied
from zero to -32 kV in 2 kV increments and the time-resolved
energy spectrum is constructed by analyzing the Faraday cup

signals as described in the previous section. The resulting
spectrum is plotted in Fig. 3.

It is found that the both time-resolved energy spectra
shown in Figs 2 and 3 have relatively narrow spreads: instanta-
neous energy spreads of <1.5 keV and temporal spreads of < 2
ns. The projection of peak intensity points of each differential
waveform for both cases onto the energy-time space is shown
in Fig. 4. It is observed that the plots of peak intensity points
for the beam before the post-acceleration follow closely the
cathode voltage waveform. The plots for the post-accelerated
beam are also in good agreement with a curve that is the sum
of the cathode voltage waveform and the accelerating voltage
waveform of the induction linac.
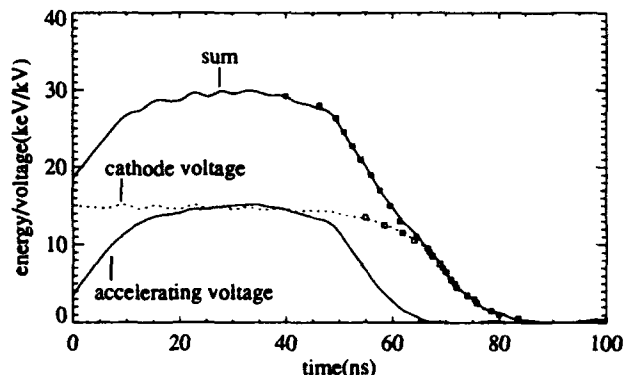
FIG. 4 Comparison of the projection of peak points of the
spectra onto energy-time space with the voltage waveforms.

D. Beam Transport

The pseudospark chamber is operated at -15 kV with two
different gas pressures 55 mTorr and 75 mTorr. The same gas
pressure is filled in the drift tube and the accelerating gap of
the induction linac. The current at downstream is measured
with a movable Faraday cup at various axial positions ranging
from 0.5 to 10 cm. The measurements are done for the
both pressures and also with and without the post-acceleration.
The typical peak current measured at anode is -1 kA. The
peak values of the downstream beam current normalized to
that at the anode hole are plotted as functions of the axial
distance as shown in Fig. 5. The results are qualitatively in
agreement with the beam propagation characteristic in the ion-
focusing regime in which beam induced ionization results in
self- focusing of the electron beam. The radial profile of the
beam is also measured at different axial positions by using
a slit plate and a radiachromic film (emittance meter). The
radiachromic film is exposed to a number of consecutive beam
pulses so as to produce an appropriate density profile, with the
peak value of optical density not exceeding 0.5. This ensure
that the measured optical density distribution is linear to the
beam density. The exposed film is then scanned by an optical
microdensitometer. The resultant profiles are curve fitted to
Gaussian as shown in Fig. 6.
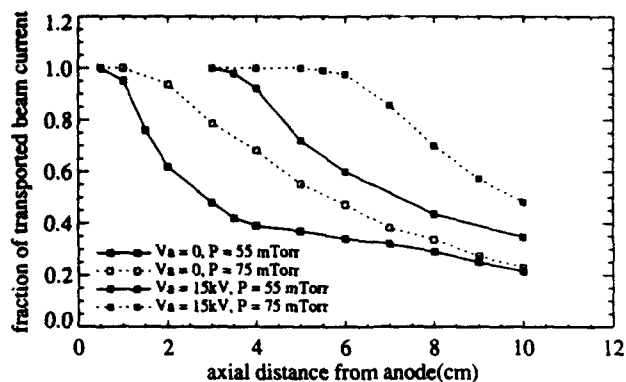
FIG. 5 Fraction of transported beam current in argon gas as a function of the axial distance.
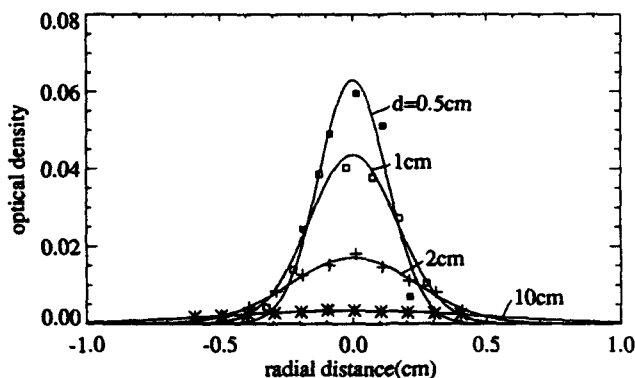
FIG. 6 The beam profiles measured at various axial positions.

E. Emittance and Brightness

The emittance of the post-accelerated beam is measured at 10 cm downstream of the anode by using the emittance meter. The procedure of the measurement and analysis are detailed

in Ref.[6] The effective emittance[7] of the beam is found to be ϵ = 243 mm-mrad with the measured beam current I = 450 A. The normalized brightness[8] may be defined as B_n = $I/(\beta\gamma\pi\epsilon)^2$. Assuming an average beam energy of 25 keV, the normalized brightness is found to be B_n = 2×10^{10} A/(m rad)2.

IV. CONCLUSION

Post-acceleration and transport of the electron beam produced by a triggered pseudospark device have been experimentally studied. The electron beam that is propagating in a low-pressure gas is accelerated by a simple induction linac system. Time- resolved energy spectrum reveals that the instantaneous beam energy is equal to the sum of the cathode voltage and the accelerating voltage of the induction linac. The beam transport in a low-pressure gas is qualitatively in agreement with characteristic of beam propagation in the ion-focusing regime. The normalized brightness of the post-accelerated beam is found to be -2×10^{10} A/(m rad)^2.

V. REFERENCES

a) Permanent address: China Academy of Engineering Physics, P. O. Box 523–56, Chengdu, Sichuan, China

[1] K. K. Jain, E. Boggasch, M. Reiser, and M. J. Rhee, "Experimental investigation of a pseudospark-produced high-brightness electron beam," Phys. Fluids B 2, 2487 (1990).

[2] R. Stiening, "The status of the Stanford linear collider," in Proceedings of the 1987 Particle Accelerator Conference, edited by E. R. Lindstrom and L. S. Tailor (IEEE,New York,1987),p.1.

[3] C. W. Robertson and P. A. Sprangle, "A review of free-electron lasers," Phys. Fluids B 1, 3 (1989).

[4] T. J. Kwan and C. M. Snell, "Efficiency of free-electron lasers with a scattered electron beam," Phys. Fluids 26, 835 (1983).

[5] B. N. Ding, T. J. Myers, and M. J. Rhee, "Time-resolved energy spectrum of a pseudospark-produced electron beam," Rev. Sci. Instrum. 64 (6), (1993).

[6] M. J. Rhee and R. F. Schneider, "The root-mean-square emittance of an axisymmetric beam with a Maxwellian velocity distribution," Particle Accelerators 20, 133 (1986).

[7] J. D. Lawson, The Physics of Charged-Particle Beams, 2nd ed. (Clarendon, Oxford, 1988), p. 192

[8] M. J. Rhee, "Refined definition of the beam brightness," Phys. Fluids 4, 1674 (1992).

COMPOUND-LENS INJECTOR FOR A 19-MeV, 700-kA ELECTRON BEAM*

T. W. L. Sanford, J. W. Poukey, J. A. Halbleib, and R. C. Mock†

Sandia National Laboratories

P. O. Box 5800, Albuquerque, NM 87185-5800 USA

Abstract

A robust injector capable of controlling the radius and angle of incidence of the intense, pulsed, annular electron beam extracted from the HERMES-III accelerator is described. The injector, called the compound lens, uses a tapered anode to control the beam electrostatically, followed by a gas cell with externally applied current to control the beam magnetically. Adjustment of the anode-cathode gap and external current of the injector permits the mean radius and injection angle of the beam to be defined independently of one another. Measurements of these quantities confirm model expectations.

I. INTRODUCTION

The extended planar-anode diode[1] with a thin anode window has been used to inject[2] a 25-ns, 19-MeV, 700-kA, annular electron beam into gas-filled drift cells for beam transport to bremsstrahlung targets located downstream of the HERMES-III accelerator.[3] By adjusting the anode-cathode (AK) gap of the diode, the radius and angle of incidence of the annular beam at injection can be varied. Increasing the AK gap increases the radius and simultaneously decreases the angle. This adjustment enables injection angles as low as ~20° (zero degrees being parallel to the beam propagation direction) to be achieved before significant beam is lost to the side wall upstream of injection. This restriction in injection angle limits the subsequent transport efficiency achievable in a downstream drift cell.[2]

By using the compound-lens diode as an injector,[4] this limitation is removed. This diode was developed to improve the uniformity of the radiation[5] generated by HERMES III, which was designed to produce an intense burst of bremsstrahlung for the study of radiation effects induced by γ rays.[3] In this diode, the beam is accelerated to a thin, conical anode window separating the vacuum AK gap from a gas-filled lens (Fig. 1). As in the extended planar-anode diode, increasing the AK gap increases the radius and simultaneously decreases the angle of the annular beam at the anode. After passage through the window, the beam is rapidly charge and effectively current neutralized by the 3 Torr of N_2 gas contained within the lens. With no applied external current, the beam propagates nearly ballistically in the lens, owing to the radial distribution of the net-current density.[6] However, application of an external current I_B produces an azimuthal magnetic field that enables a given angle of incidence at the exit of the lens to be achieved independently of the incident radius.

In this paper, we theoretically model and experimentally characterize the electron flow in the compound-lens diode when it is used as a bremsstrahlung source (Fig. 1).[5] Results when it is
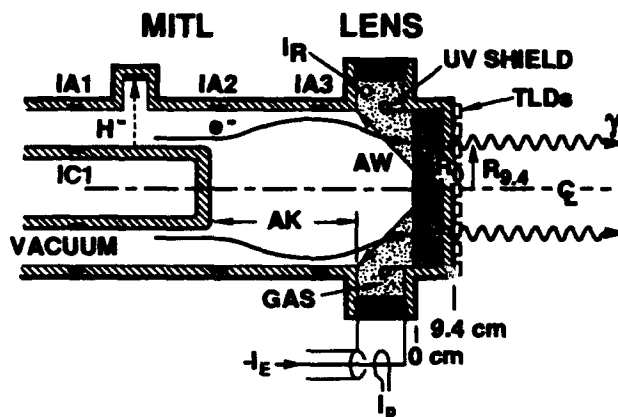
Figure 1. Schematic of compound-lens diode.

used as an injector for a short drift cell with a 20-cm AK gap are given in Ref. 7. Here we emphasize results obtained as the AK gap is increased to 40 cm. The model combines the MAGIC code[8] to simulate the time-dependent electron flow in the AK gap and lens with the CYLTRAN code of the ITS system[9,10] to model window effects and the subsequent transport in the target. MAGIC is a two-dimensional, time-dependent, electromagnetic, particle-in-cell code. CYLTRAN is a two-dimensional, time-independent, Monte-Carlo electron-photon, transport code. The model is similar to that described in Ref. 1. It uses the voltage pulse measured at the diode as input to MAGIC. MAGIC then generates the time-dependent space-angle distribution of the electron beam at the lens. This distribution is time integrated and, along with an experimental electron kinetic-energy distribution, is used as input to CYLTRAN.

Section II describes the experimental arrangement, including some details of the diode. Section III describes the operation of the diode and presents some model results and comparisons. Section IV summarizes our conclusions.

II. EXPERIMENTAL ARRANGEMENT

The general arrangement, operating conditions, and diagnostics are those discussed in Refs. 1, 2, and 5. Briefly, current shunts in the anode (IA1) and cathode (IC1), as shown in Fig. 1, measure the incident current and permit the voltage pulse to be estimated from parapotential flow theory.[11] For a 20-cm AK gap, the time dependence of voltage, current, beam radius, and output beam angle are given in Fig. 3 of Ref. 7. The peak voltage is corroborated within 4% by simultaneously measuring the range of H⁻ ions[12] for selected shots. For the data presented here the peak voltage was measured to be 19.0±0.5 MV, where the uncertainty corresponds to shot-to-shot variation. This value is identical to that measured previously under nominal operating conditions.[13]

The N_2 gas within the lens is contained by two 0.3-mm thick Ti windows welded at a 5-cm radius, and held apart at a 52-cm radius by a Lucite insulator 28-cm long (Fig. 1). The gas is held at pressures between 3 and 10 Torr to facilitate rapid charge and current neutralization of the incident beam. Below an I_B of 160 kA, the lens is operated at 3 Torr—the pressure that optimizes the neutralization ($\geq 96\%$) of the beam current.[6] Above 160 kA, to prevent breakdown across the insulator from the higher inductive voltage drop, we operate the lens at 10 Torr. This higher pressure is within the capability of the windows to contain the gas without significant distortion—20 Torr is the estimated maximum. The calculated multiple-Coulomb-scattering produced by the two windows results in a beam divergence of about $\pm6°$. This divergence is similar in magnitude to the intrinsic dispersion ($\pm4°$) about the mean angle of incidence at the anode (to be discussed in the next section). The energy loss through the windows is calculated to be 0.45 MeV.

An optimized bremsstrahlung target was placed immediately downstream of the lens (Fig. 1). Measurements of the annular radiation pattern from images taken with the X-ray pinhole camera enabled the time-integrated radial impact position R_o of the annular beam at the exit ($z=0$ cm) of the lens to be estimated. Combining R_o with measurement of the radius of the peak off-axis radiation dose $R_{9.4}$ obtained from TLDs (thermoluminescent dosimeters) at the downstream face ($z=9.4$ cm) of the target permits the angle of incidence θ_o of the time-integrated beam to be determined ($\theta_o = \tan^{-1}[(R_o-R_{9.4})/9.4]$).

III. DIODE OPERATION AND MODEL RESULTS

The compound-lens diode provides a matched load to the upstream magnetically-insulated transmission line[3] of HERMES III for the 20- to 40-cm AK gaps considered here. The MAGIC simulations indicate that once an electron sheath forms above the cathode for these AK gaps, the sheath, together with the flow near the tip of the cathode, leads to a well-defined annulus of beam electrons that moves towards the lens. As the voltage and associated current ramp up at the tapered anode window (aw), the radius R_{aw} of this annular ring sweeps radially inward, attains a minimum radius near the time of peak voltage, and then sweeps radially outward as the voltage ramps down.[7] The sweeping is due to the shorting of the repulsive radial electric field at the anode window and the continued presence of the pinching self-magnetic field, which increases or decreases with beam current.

Early and late in the voltage pulse, the low-energy electrons are lost to the side anode wall, or are swept into the insulator (when a finite I_B is flowing in the lens). These combined losses are small for our parameters.[7] Once the energy of the electrons exceeds 3 MeV, the electrons are injected forward. Comparison of the forward current pulse with the voltage pulse also shows that, after the voltage exceeds about 9 MV, the voltage and current pulses have nearly the same shape. Thus, over this range the diode impedance is almost constant.

Figures 2A and 2B show the corresponding simulated radial and angular distribution of the beam at the anode window at peak voltage. Figure 2 is the result for an AK gap of 40 cm and $I_B = 90$ kA. Figure 2A indicates the presence of the dominant annular

beam, showing that R_{aw} equals 19 cm and has a full-width at half-maximum of about 8 cm. The electrons at smaller radii originate from the cathode front face. As the radial impact position of the electrons increases at the anode window, more beam current is enclosed within that radius, and the self-magnetic pinching force increases. Because the repulsive radial electric field (which prevents the beam from pinching far upstream of the anode window) is shorted at the anode, the angle of incidence θ_{aw} thus increases with increasing radius (Fig. 2B). At $R_{aw}=19$ cm, the associated angle of incidence θ_{aw} is 15.4°.
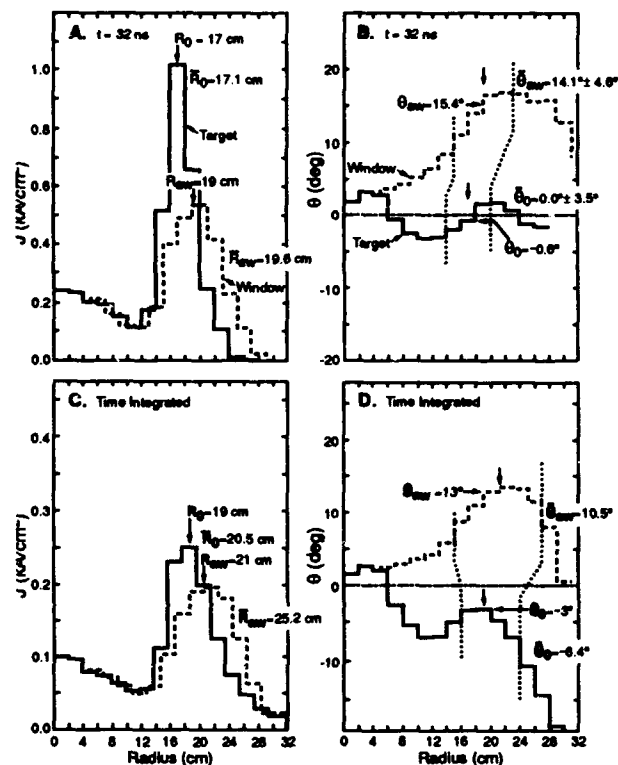
Figure 2. (A) Simulated electron beam radial current-density profiles and (B) associated angular distributions at the anode window [aw] (dashed lines) and lens exit [z=0 cm] (solid lines) at peak voltage. Corresponding (C) electron beam radial current density profiles and (D) associated angular distributions at the anode window and lens exit, time-integrated over the voltage pulse. Configuration is that of Fig. 1 with AK=40 cm and I_B=90 kA. The dotted lines in (B) and (C) indicate the radii corresponding to the full-width at half-maximum of the radial beam distributions of (A) and (C), respectively. Notation: radial averages indicated by bars over the symbol; time averages by bold face.

For times earlier or later than that corresponding to the time of peak voltage (32 ns), the radial impact position R_{aw} is increased, and the associated pinch angle θ_{aw} is reduced, owing to the reduced magnetic pinching from the lower beam current. Thus, the time-integrated radial (Fig. 2C) and angular (Fig. 2D) distributions at the anode window are modified relative to those shown at peak power. Specifically, because of the larger radii and smaller pinch angles at lower voltage, the radial distribution is skewed toward larger radii and the angular distribution is skewed toward smaller angles, especially at large radii. Both distributions retain, however, the main characteristics calculated

at peak voltage, because the bulk of the beam occurs near those conditions. For the 40-cm AK-gap case, the radius R_{av} of the time-integrated annular beam is 21 cm (Fig. 2C), which is an increase of only 2 cm over that calculated at peak voltage. The associated angle θ_{av} at R_{av} is also close to the θ_{av} of 15.4° calculated at peak voltage (Fig. 2D).

Because the repulsive radial electric force exceeds the pinching magnetic force far upstream from the anode window, as the AK gap is increased, the beam experiences a longer region over which it expands radially before being pinched due to the shorting of the radial electric field and the continued presence of the magnetic pinching field at the anode window. Accordingly, adjusting the AK gap permits the radius and the correlated angle at the anode window to be varied. Over the range of AK gaps from 20 to 40 cm, R_{av} increases from 16 cm[7] to 21 cm (Fig. 2C) and the correlated θ_{av} decreases from 17° to 13° (Fig. 2D).

When using a bremsstrahlung target to generate uniform radiation fields (Fig. 1), normal angles at the target are desired. By adjusting I_B, the associated external magnetic field (which turns the annular beam in the lens) is controlled, enabling the desired angle of incidence at the exit of the lens (z=0 cm) to be achieved independently of AK gap. Simulations show, for example, that for I_B=90 kA and AK = 40 cm, the time-integrated angle of incidence averaged over radius is reduced from $\overline{\theta}_{av}$ = 10.5° at the entrance of the lens to $\overline{\theta}_e$= -6.4° at the exit (Fig. 2D). At peak voltage, the corresponding angles are changed from θ_{av} = 14.1°±4.6° at the entrance to θ_0=0.0°±3.5° at the exit (Fig. 2B). Thus the simulation predicts normal incidence for this case.

Figure 3 compares the simulated and measured time-averaged lens exit angle θ_e of the beam at R_e, for AK= 40 cm, as a function of I_B. The measured values systematically exceed the simulation values. The measured values are based on R_e and R_{9A} (Fig. 1). R_e is derived from the radial profile on the film, where distortion leads to an overestimate by several cm.[7] A 1-cm shift in R_e leads to a 6° shift in θ_e. If this systematic error is combined in quadrature with the statistical measuring error (shown in Fig. 3), then the simulation point falls within the experimental uncertainty.

IV. SUMMARY

The predicted radial sweeping of the electron beam, leading to a well-defined annular beam at the entrance and exit of the lens, is confirmed by the measurements.[7] Adjustment of the AK gap over the range 20 to 40 cm causes the time-integrated radial impact position R_e at the exit to increase from 11 to 16 cm when no external current I_B is present. Over this range, the corresponding angle of incidence θ_e decreases from about 17° to about 13°.

According to simulation and measurement, increasing I_B does not change R_e much. The major effect of adjusting I_B is to change the exit angle, independent of the incident radius, as in Fig. 3. For a 40-cm AK gap, for example, increasing I_B from 0 to 75 kA reduces θ_e from 13° to 0°, and simultaneously increases R_e by only 3 cm. When the beam is incident on bremsstrahlung targets (Fig. 1) or injected into long drift cells, such angles are useful for producing uniform radiation fields and for efficient transport, respectively.

In conclusion, we have shown theoretically and experimentally on HERMES III that the compound lens provides an efficient method for controlling the radial and angular distributions of intense, pulsed, annular electron beams.
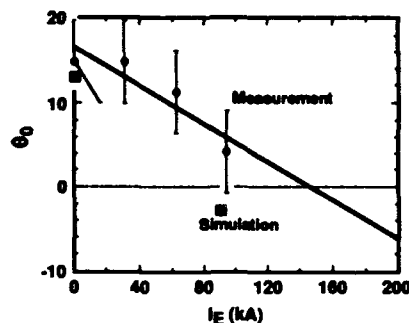
Figure 3. Comparison of measured estimate (●) and simulated (■) time-averaged lens-exit angle θ_0 at R_0 as a function of I_E for geometry of Fig. 1, with AK=40 cm.

REFERENCES

[1] T. W. L. Sanford, Phys. Fluids B3, 2387 (1991) and references therein.

[2] T. W. L. Sanford, J. A. Halbleib, W. H. McAtee, K. A. Mikkelson, R. C. Mock, J. W. Poukey, D. R. Welch, J. Appl. Phys. 70, 1778 (1991).

[3] J. J. Ramirez, K. R. Prestwich, and I. D. Smith, Proceedings of the IEEE, 80, 946, (1992) and references therein.

[4] T. W. L. Sanford, J. A. Halbleib, J. W. Poukey, T. Sheridan, D. Muirhead, C. E. Yagow, K. A. Mikkelson, R. Mock, P. W. Spence, and H. Kishi, in Digest of Technical Papers of 7th IEEE Pulsed Power Conference, Monterey, CA. (IEEE, New York, 1989), pp. 441-444.

[5] T. W. L. Sanford, J. A. Halbleib, W. H. McAtee, K. A. Mikkelson, R. C. Mock, and J. W. Poukey, J. Appl. Phys. 69, 7283 (1991).

[6] T. W. L. Sanford, J. W. Poukey, R. C. Mock, and D. R. Welch, J. Appl. Phys. 71,472 (1992).

[7] T. W. L. Sanford, J. W. Poukey, J. A. Halbleib, and R. C. Mock, in press, J. Appl. Phys. 73, (1993).

[8] T. D. Pointon, J. Comput. Phys. 96, 143 (1991).

[9] J. A. Halbleib and T. A. Mehlhorn, Nucl. Sci. Eng., 92, 338 (1986).

[10] J. A. Halbleib, Monte Carlo Transport of Electrons and Photons, edited by T. M. Jenkins, W. R. Nelson, and A. Rindi (Plenum, New York, 1088), pp. 249-284.

[11] J. M. Creedon, J. Appl. Phys. 46, 2946 (1975); 48, 1070 (1977).

[12] S. Lapin, G. W. Cooper, L. Davis, J. Bailey, W. A. Stygar, A. Carlson, and P. Reyes, Rev. Sci. Instrum. 63, 4895 (1992).

[13] T. W. L. Sanford, J. A. Halbleib, L. J. Lorence, J. G. Kelly, P. J. Griffen, J. W. Poukey, W. H. McAtee, and R. C. Mock, Rev. Sci. Instrum. 63, 4795 (1992).

Electron Flow in the SABRE Linear Induction Adder in Positive Polarity

J. R. Smith[+], J. W. Poukey, M. E. Cuneo, D. L. Hanson, S. E. Rosenthal, and M. Bernard
Sandia National Laboratories
Albuquerque, NM 87185

Abstract

In a positive polarity induction adder each of the induction cavities is a cathode, which emits electrons at a unique potential. These broad spectrum electrons strongly affect Magnetically Insulated Transmission Line (MITL) behavior. Electron flow decreases the cavity-to-MITL coupling efficiency, and reduces the power transport efficiency along the system. Also the operating impedance of the MITL is lowered, reducing the diode impedance required for good coupling and good total system power efficiency [1-4]. It is therefore imperative to understand the details of MITL electron flow. In previous work, measurement of MITL electron flow for a twenty-stage linear induction adder (Hermes III), operated in positive polarity, was compared with simulations [1]. There was qualitative agreement, but some differences were noted. For example, measured electron flow in the first cavities was greater than in the simulations. We have extended the work on this subject with detailed current measurements on a ten-stage linear induction adder (SABRE). Time resolved electron flow is determined from the difference between anode and cathode currents at several axial locations. A time-resolved mapping of electron flow versus adder length is constructed. Measurements of electron flow in the initial cavities agreed well with simulations. Electron flow for times near the current peak exhibits a monotonic increase with length, except at the adder end.

I. INTRODUCTION

The technologies of the inductive cavity and MITL have been combined as the basis of several high-voltage, high-current particle accelerators at SNL (Hermes III, Helia, SABRE). Voltage addition is achieved by stacking cavities. A coaxial, center conductor is stepped to smaller
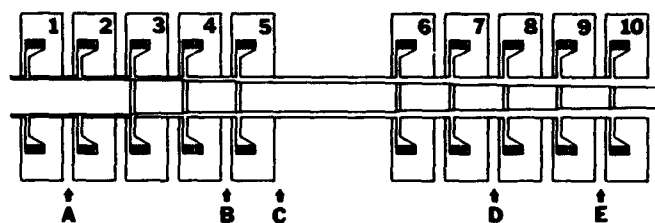
Figure 1. SABRE ten-stage adder. Arrows denote B-dot locations. Cavities are numbered 1-10.

radius at each cavity gap to match the total drive impedance as voltages are added along the MITL. Insulation between the center conductor and cavity bore is obtained via high magnetic fields associated with the large cavity currents. Linear induction accelerators have been operated in both negative and positive polarity for x-ray simulation and ion fusion applications, respectively. In both cases electrons which are emitted from the cathode surfaces are insulated by the self-magnetic fields. In negative polarity operation, the cathode is one continuous conductor, the center conductor. However, in positive polarity, a separate cathode exists at each induction cavity. Electrons are emitted from the inner surface of each cavity, at a unique potential, and travel along parapotential lines toward the diode end of the adder. At any location inside the adder, the total electron flow is the sum of the flow from the upstream cavities. Therefore, in going from beginning to end of the adder, an increase in electron flow is expected.

In this paper we present measurements on electron flow in the SABRE adder section, as a function of time and space. SABRE was constructed to investigate light-ion inertial confinement fusion issues (e.g. accelerator physics, ion sources, beam transport).
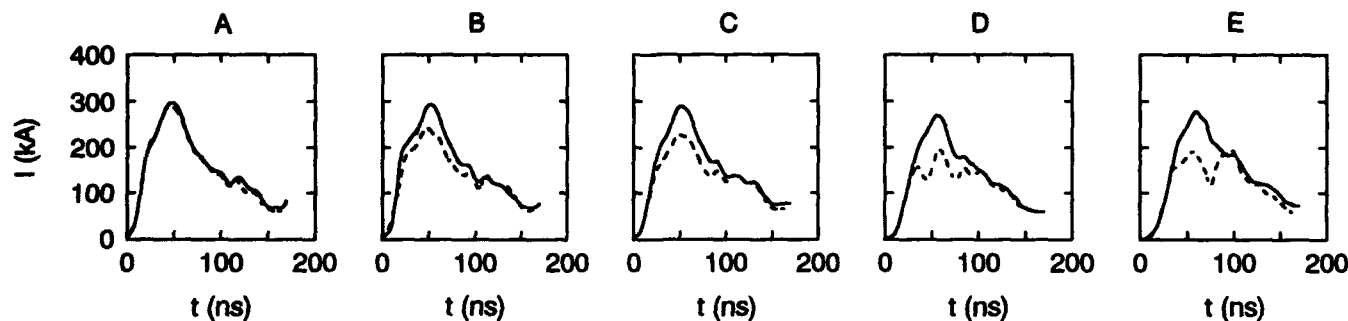
Figure 2. Adder B-dot signals at 5 axial locations.

[———] Anode current. [- - -] Cathode current.

The SABRE MITL is terminated with an applied-B extraction ion diode 4-m downstream from the final cavity [4].

II. ELECTRON FLOW

A. SABRE Adder

A line drawing of the SABRE voltage adder is given in Figure 1. There are two sets of five cavities. Each set is charged through an electrically triggered gas switch. Firing of the switch on the downstream set is delayed (6 - 17 ns) to compensate for the transit time between the two cavity sets. B-dot monitors were used to obtain the inner conductor (anode) current and outer conductor (cathode) current at five axial locations, between the following cavities: 1-2, 4-5, 5-6, 7-8, and 9-10. Each B-dot assembly consists of a B-dot pair configured for common mode noise rejection. At each location, a set of two anode B-dots and two cathode B-dots are positioned 180 degrees apart. The average anode and cathode currents measured at each axial location for a sample shot (with 13 ns switch delay) are given in Figure 2.

B. Measurements

In order to more easily visualize MITL electron flow along the length of the adder, the data of Fig. 2 are displayed as plots of current vs axial position (frames), at equally spaced time intervals (Fig. 3a). The difference between anode and cathode currents is the electron flow displayed in the corresponding frames of Fig. 3b.

We make the following observations from this data.

(1) The anode and cathode currents near the beginning of the adder are equal (within measurement error) for the entire pulse.

(2) *Frames during the pulse risetime (10-30 ns).* Electron flow initially appears in the first set of five cavities, which is energized before the second set of cavities.

(3) *Frames near the peak of the pulse (40-60 ns).* The anode current is roughly constant along the entire adder, which indicates no current losses to the anode. There is a general decrease in cathode current in the downstream direction, corresponding to an increase in electron flow with increasing cavity number. In two of these frames, there is a marked decrease in electron flow at the end of the adder.

C. Simulations

Simulations were performed using a 2½ - d particle code (TWO-QUICK) with parameters relevant to SABRE experiments. The results of a simulation with a 14 ns gas switch delay, similar to the delay of the shot in Fig. 3, are given in Fig. 4. Observations from this data are:
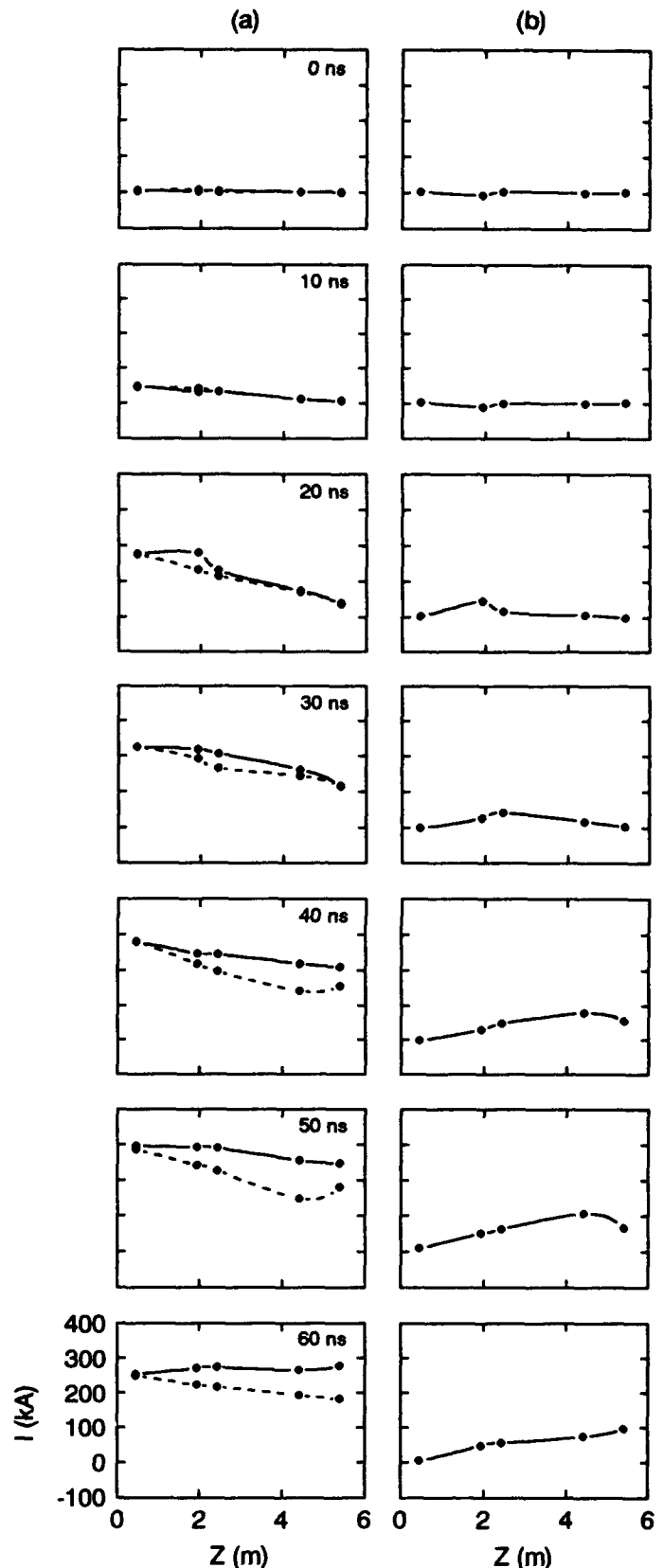
Figure 3. (a) Measured anode current [——] and cathode current [– – –] vs axial position.
(b) Difference in anode and cathode current = electron flow.

695

(1) The anode and cathode currents near the beginning of the adder are equal for the entire pulse, just as they were for the measurements.

(2) *Frames during the pulse risetime (10-30 ns)*. Electron flow initially appears in the first set of five cavities, similar to the measurements.

(3) *Frames near the peak of the pulse (40-60 ns)*. Electron flow follows a general increasing trend with cavity number, as it did in the measurements. There is one exception, no decrease was observed at the adder end.

III. SUMMARY

Current efficiency may be defined as the ratio of cathode current/anode current at the adder end. Near the peak of the pulse, the current efficiency was approximately 65%. Accurate determination of energy loss associated with electron flow must take into account the broad electron energy spectrum. Future work will address this topic.

Measurements and simulations of electron flow in the SABRE adder are generally in good agreement. Agreement in the initial cavities was particularly good, unlike the Hermes-III case [1]. At the adder end, there was a decrease in electron flow in some frames (40-50 ns) which was not present in the simulations. This could be caused by electron particle loss or electron energy loss.

Analysis of electron flow in the format given here will be valuable in future work to gauge the success of attempts to decrease electron emission and therefore increase adder efficiency. Construction of the plots showing current vs position has been automated, so that analysis is readily available for each shot.

IV. REFERENCES

[1] S. E. Rosenthal, "Characterization of Electron Flow in Negative- and Positive-Polarity Linear Induction Accelerators," *IEEE Trans. Plasma Sci.*, Vol. 19, No. 5, 822 (1991).

[2] D. L. Johnson et al., "Hermes-III Positive Polarity Experiment," in *Proceedings of the 7th IEEE Pulsed Power Conference*, p. 32 (1989).

[3] J. P. Corley et al., "Positive Polarity Voltage Adder MITL Experiments on Helia," in *Proceedings of the 7th IEEE Pulsed Power Conference*, p. 571 (1989).

[4] D. L Hanson et al., "Operation of a High Impedance Applied-B Extraction Ion Diode on the SABRE Positive Polarity Linear Induction Accelerator," in *Proceedings of the 9th International Conference on High-Power Particle Beams*, (1992).
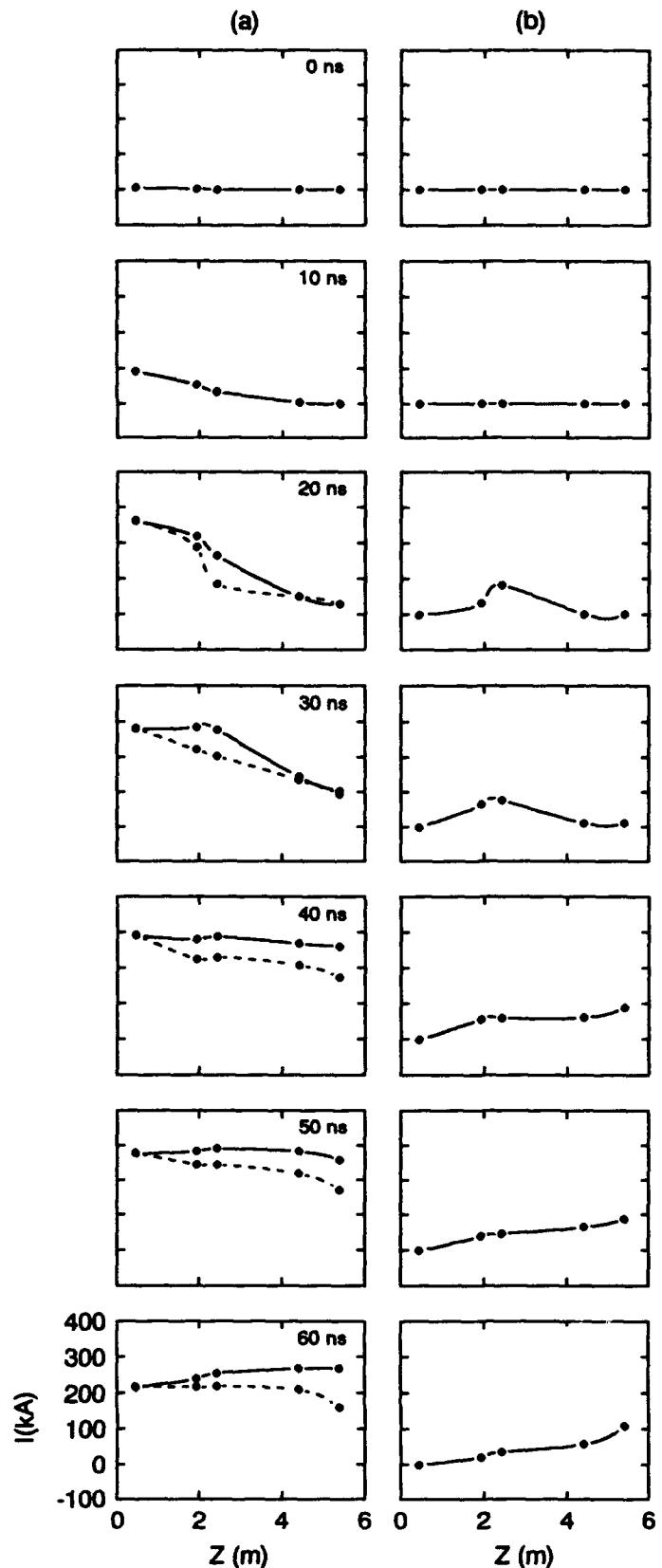
Figure 4. (a) Simulation of anode current [——] and cathode current [– – –] vs axial position.
(b) Difference in anode and cathode currents = electron flow.

DESIGN AND PROGRESS OF THE AIRIX INDUCTION ACCELERATOR

J. de Mascureau, Ph. Anthouard, J.Bardy, C. Bonnafond, Ph. Delsart, A. Devin, Ph. Eyharts, P. Eyl, P. Grua, J. Labrouche, J. Launspach, P. Le Taillandier, E. Merle, A. Roques, B. Sacepe, M. Thevenot, D. Villate

Commissariat à l'Energie Atomique, Centre d'Etudes Scientifiques et Techniques d'Aquitaine
B.P. n° 2
33114 LE BARP - FRANCE

Abstract

A new electron accelerator is now being studied and designed for Flash Radiography Application. It consists of a pulsed injector (4 MeV-3,5 kA - 60 ns) and an Induction Accelerator increasing the energy of the electrons up to 20 MeV. We briefly describe the Injector built by PSI [1] and similar to the DARHT injector at LANL [2]. We present studies and experimental tests carried out in order to design and build new induction cells and high voltage generators suitable for this application.

Information is given on the PIVAIR milestone planned for a beforehand validation of the whole AIRIX machine.

I - INTRODUCTION

The main goal of the AIRIX [3] facility is the production of high quality powerful Radiographic Flashes. On that purpose the exclusive advantage of Induction Accelerator is its ability to accelerate high intensity (multi-kilo-ampère) electron beams and to focus them on a small point. The main physical parameter of the beam is its emittance at the output of the accelerator. In order to minimize it, a high brightness electron beam emission is needed with an energy high enough to prevent the beam emittance increase due to space charge effects. A 4 MeV electron beam accelerated up to 20 MeV by the means of induction cells is anticipated. The accelerator design, comprises 8 modules of 8 cells, each module being driven by 4 high voltage (250 kV) generators.

II - INJECTOR

The injector, now under fabrication, is the same type as the one used at Los Alamos on the ITS facility for the DARHT program. It comprises a prime power Transformer charging a glycol Blumlein through four laser triggered spark gaps and three output lines transforming the 1.8 MV pulse from the Blumlein to 4.0 MV on a 150 ohm vacuum tube load. The diode cavity is separated from the last output line by a segmented radial insulator interface with a water resistor allowing the resistance matching of the diode. The electron beam is generated by a 7.5 cm diameter velvet cathode. The injector designed performances have been summarized on Table 1.

Diode voltage	≥ 4 MV
Voltage flatness	$\leq \pm 1$ %
Beam current	$\geq 3,5$ kA
Pulse width	≥ 60 nsec (flat top)
Voltage reproducibility	± 1 %
Jitter	$\leq 1,5$ nsec
Normalized emittance	$\leq 1200\ \pi$ mm. mrad
Shot Rate	One per minute

Table 1

Complementary studies are currently carried through at CESTA in order to improve the reliability and the performances of the machine. In a second step, a new Induction Injector could be a way of improving the overall performances of the AIRIX facility.

III- AIRIX INDUCTION CELLS

A Prototype Induction cell suited for the AIRIX Accelerator has been studied, designed and built, and is now being tested (figure 1). The FLUX-2D electrostatic code was extensively used in order to analyze the E field and voltage repartitions and determine the best gap geometry. It uses an alumina insulator brazed on the body of the cell to hold the 250 kV pulse applied to the gap and ensure vacuum insulation between the beam pipe and the oil-insulated ferrite cores. Elsewere Rexolite insulators are being considered as an alternative solution to the use of Alumina and cells without insulators (ferrite cores under vacuum) are being tested. The accelerating gap has been carefully shaped in order to minimize the beam coupling with the gap cavity and hence reduce the BBU instability. The prototype cell uses, as ferrite cores, 11 torroids

from TDK (PE 11 B - 250 mm ID, 500 mm OD, 25 mm thick).

The device has been equipped with specific probes (Rogowski coils, current loops, resistive and capacitive probes) in order to understand the electrical behaviour of the cell and to adjust and compare the electrical diagnostics.

Other studies connected with beam - cell interaction are currently being carried out :

- Transverse Impedance measurements of a gap cavity mock-up (figure 2) have been undertaken and compared with results given by the PALAS electromagnetic code [4].

- Prototype solenoid magnets have been designed and built, and longitudinal B_z field uniformity is being characterized with and without homogenizer rings.

IV- HIGH VOLTAGE GENERATORS

A high voltage generator has been designed and built and is now being tested. It is able to feed 2 cells by the means of 4 (50 Ω) cables.

This high voltage generator, as it appears on the rough drawing of figure 3 can be divided into 4 main parts :

- a water blumlein, 2 m long, horizontaly placed for a more convenient handling in the future AIRIX building . It has a 12,5 Ω total impedance,

- a coaxial structure spark gap designed at CESTA with specific features including a V/3 ... ization of the triggering electrodes and a 18 mm g ... ween the main electrodes which can be dismantled.

- a Blumlein charging device using a step-up transformer (1:11) and two EEV Cx 1722 thyratrons

- a two stage spark gap triggering circuit able to generate a triangular pulse with an amplitude over 160 kV and a rise time shorter than 15 ns.

This generator is now in operation, giving a pulse in the 300 kV range with a 70 nsec flat top, and is planned for coupling to the prototype cell in the near future.

V - PIVAIR MILESTONE

Next year, we shall have the injector in operation at CESTA. A first accelerating module (8 cells = 2 MeV) will be built and installed by that time, and then a second one in 1995. These two blocks of cells with the 8 associated generators, coupled to the injector, will make up the so called PIVAIR set up, giving rise to an 8 MeV electron beam. This facility is intended to allow a complete validation of AIRIX (cells and HV generators, technology, alignment, beam transport and focusing, X-ray generation).

VI - REFERENCES

[1] Pulse Science Inc. 600 Mc Cormick street - San Leandro CA 94577

[2] J. Downing et al. " Pulse Power Systems for the DARHT Accelerators " 8 th IEEE International Pulsed Power Conference, San Diego, CA, June 1991.

[3] AIRIX stands for " Accelerateur à Induction de Radiographie par Imagerie X "

[4] F. Delaurens, F. Charlet
Calcul par le code Palas des impédances de couplage d'une cavité résonnante
Internal Report 1991
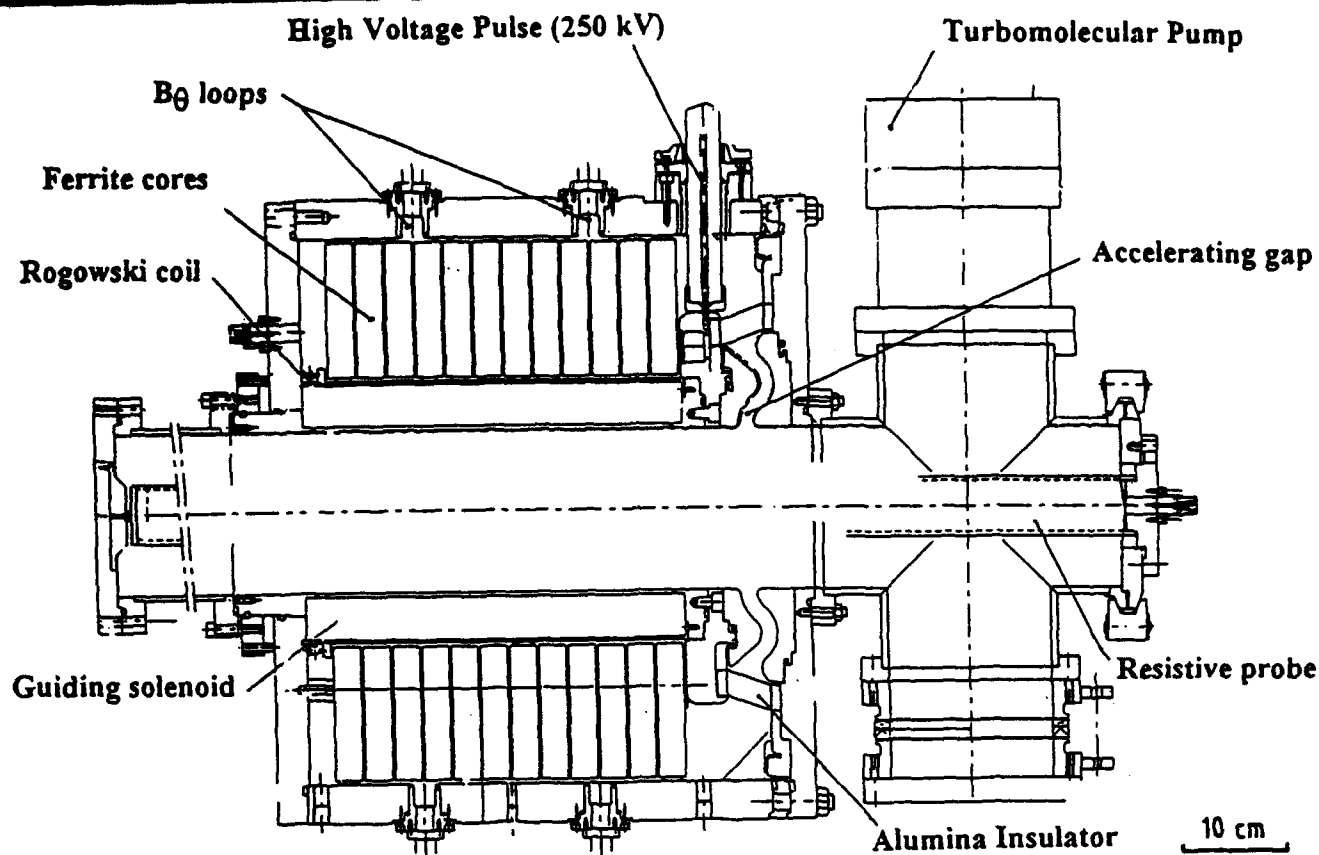
Figure 1 : AIRIX Prototype Induction Cell
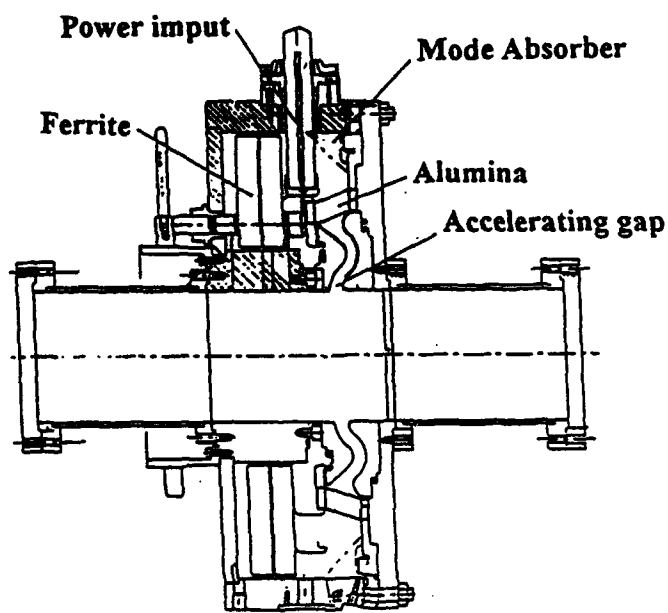
Figure 2 : Accelerating gap mock-up
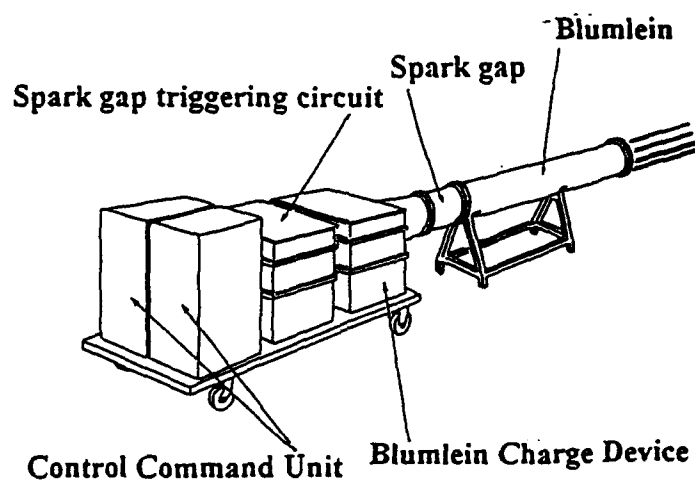
Figure 3 : High Voltage Generator
General view

699

Nuclear Fusion of Protons with Ions of Boron*

Alessandro G. Ruggiero
Brookhaven National Laboratory
Upton, Long Island, New York 11973, USA

Abstract

This paper describes a method of extracting energy from the fusion events occurring between the collision of a beam of protons with a beam of ions of Boron 11. The two beams are circulating in separated and intersecting storage rings where they collide head-on in a common long-straight section. Requirements on the luminosity of the low-energy collider are shown. Limitations due to space-charge and intrabeam scattering are described. Very fast electron cooling is needed to compensate these effects.

I. INTRODUCTION

One of the most interesting fusion reaction [1] is a proton colliding with an ion of Boron 11. For a very brief period of time, an ion of Carbon 12 is formed which then immediately decays in three α particles. In order for this reaction to occur, assuming the ion of Boron at rest, the proton needs a sufficiently large energy. There is a broad resonance [2] centered around 675 keV which exhibits a large cross-section of 0.9 barn. The low energy combined with the large fusion cross-section makes the reaction a good choice as a method for obtaining fusion nuclear power. Once the lowest bound state is reached, a total energy of 8.7 MeV is released under the form of kinetic energy given to the α particles.

Since it is relatively easy to control the energy of the particle beams with today's accelerator technology, the fusion reaction here proposed can be easily ignited with no other possible channels of interaction involved. In particular no neutrons or gamma rays are produced. Another interesting feature is the large state of electric charge (Z=6) of the final products which suggests methods employing electricity for the immediate conversion of the nuclear energy to electric power.

A method [3] which makes use of two beams, one of protons and one of ions of Boron, colliding periodically with each other is presented in Section II. We report on the beam requirements for a small size device producing a 1 MW power in Section III. Section IV is a discussion of the limitations due to space-charge and of the possible cure by beam-charge neutralization with electrons. The effects of intrabeam scattering are discussed in Section V. Finally, electron cooling requirements are reported in Section VI.

II. THE COLLIDER

This is shown in Figure 1. The proton beam is generated with hydrogen-ion sources followed by RFQ devices [4] operating at few tens to few hundred of MHz. Average currents of a hundred milliampere are possible. The proton beam is injected in a cooling and storage ring. Cooling is needed to reduce or to maintain the beam transverse dimensions to sufficiently small values to enhance the collision events in the collider.

The beam of ions B^{11} is also prepared already completely stripped from similar RFQ devices fed by ECR sources. The ECR sources [5] should be capable to deliver an amount of beam intensity matching the one of the proton beam. Also the ion beam will be injected in its own cooling and storage ring which is placed sidewise next to the proton ring. There is thus a continuous streaming of beams at both sides, from the sources to the RFQ's, to the storage rings and to the collision region. The two beams are circulating in the same direction in the respective storage rings and collide head-on in the common straight section of the collider. In this location protons and ions will fuse. During collision the two beams have essentially the same bunching structure, transverse dimensions and intensity. The long straight section where the two beams collide is surrounded by the reactor vessel itself.
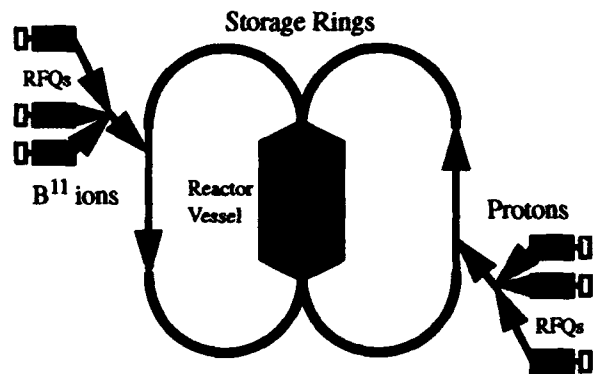
Figure 1. Nuclear Reactor with Colliding Beams

Each storage ring has a circumference $2\pi R = 3.3$ m and is made of a sequence of 16 FODO cells, each having a phase advance of 90° and a length of 21 cm. Quadrupoles and dipoles are made of permanent magnets. Quadrupoles are 2 cm long. There are 16 dipoles, each 8 cm long, placed in the arcs. The long straights are made of 4 cells each without dipoles. Matching is assumed to provide zero dispersion in the long straights.

III. BEAM REQUIREMENTS

Let T_p and T_B be the energies respectively of protons and Boron ions. We require $T_p + T_B = 675$ keV. The solution yielding equal velocities is $T_p = 56$ keV and $T_B = 619$ keV, corresponding to the velocity $\beta = 0.011$. Let N be the number of particles in each beam that at any one time travel in the interaction region. Let also S be the common cross-section of the two beams where they collide. The frequency of particle encounter f_{enc} is the revolution frequency. The number of fusion events per unit of time in this configuration is then given by

$$dn/dt = \sigma \, (N^2 / S) \, f_{enc} = \sigma \, L \qquad (1)$$

where $\sigma = 0.9 \times 10^{-24}$ cm^2 is the fusion cross-section and L is

the *luminosity* of the collision.

If each fusion event releases an amount of energy W, the instantaneous power produced is

$$P_g = W (dn/dt) \qquad (2)$$

At the same time there is a depletion of both beams which will occur at the rate

$$dN/dt = -dn/dt \qquad (3)$$

The ion sources have then to replenish the beams also at these rates. One can estimate the amount of power, respectively P_p and P_B, which will be required just for the beam production

$$P_p = T_p (dn/dt) \quad \text{and} \quad P_B = T_B (dn/dt) \qquad (4)$$

To this we add the power P_{acc} that is dissipated for the operation of the entire complex. The equation for the power P_{exc} produced in excess is

$$P_{exc} = P_g - P_p - P_B - P_{acc}$$
$$= (W - T_p - T_B) (dn/dt) - P_{acc} \qquad (5)$$

It is seen that, in order for the process to produce useful power, P_{exc} has to be positive, which requires that

$$T_p + T_B < W \qquad (6)$$

In our case W = 8.7 MeV and $T_p + T_B$ = 675 keV. Also

$$\sigma L > P_{acc} / (W - T_p - T_B) \qquad (7)$$

Neglecting the amounts of beam power, a break-even situation is obtained when the power delivered equals the power just needed for the operation of the system, which gives

$$L = P_{acc} / (\sigma W) \qquad (8)$$

Since it is not clear what value one should take for the operation power P_{acc} we shall assume that the nuclear power from the collisions of the two beams is entirely available as excess power. We shall set as a goal P_{exc} = 1 MW, so that the required luminosity of the collision is

$$L = P_{exc} / (\sigma W) \sim 10^{42} \text{ cm}^{-2} \text{ s}^{-1} \qquad (9)$$

At the same time, the rate of fusion events is

$$dn/dt \sim 10^{18} \text{ events per second} \qquad (10)$$

This is also equal to the rate of depletion of the beams and to the rate particles are produced at their sources and are entering the system. Beam currents at injection are not excessive since they are about 100 mA-particle for both types of beam. Protons can be produced with a single source; the production of ions of boron requires improvement of the sources available. Eventually several ECR sources can be used in parallel.

If the circumference $2\pi R$ of the collider is 3.3 meter, the frequency of encounter f_{enc} is 1 MHz. Assuming a beam cross-section at collision S = 10^{-4} cm^2, then each beam is made of about N = 10^{16} particles. Each particle will spend in average ten milliseconds in the collider, that is it will survive in average ten thousand revolutions.

IV. SPACE CHARGE LIMITATIONS

There is a very serious limitation due to the beam space-charge. It is customary to measure this limit [6] in terms of the maximum value $\Delta \upsilon$ that can be allowed for the betatron-tune depression

$$\Delta \upsilon = N r_p Q^2 / (2 \beta^2 \gamma^3 B A \varepsilon) \qquad (11)$$

where r_p = 1.535 x 10^{-18} m is the classical radius of a proton, N the total number of particles, Q the charge state and A the mass number of the particle specie, B the bunching factor defined as the ratio of average beam current to the peak current and which we take here to be unit, and ε is the full betatron emittance. A reasonable limit of $\Delta \upsilon$ is about a unit. To keep the beam within the space-charge limit, one derives $\varepsilon > 50 \pi$ m rad.

It is very difficult to achieve the required beam spot size of 0.1 mm at the interaction region with such large beam emittance. An ordinarily conceived method is the focussing of the particle motion with quadrupole magnets placed on both sides. Typically a small value of β^* is few centimeters. In turn this requires a beam emittance $\varepsilon = 10^{-6} \pi$ m rad, that is eight orders of magnitude smaller than the space-charge limit. This figure is also about what one can expect for the beam emittance from the source and therefore at injection into the storage rings.

It is possible to compensate space-charge effects with neutralization of the beam electric charge by trapping electrons produced by ionization of the atoms of the residual gas in the vacuum chamber of the storage rings. It has been experimentally demonstrated [7] at INP (Novosibirsk, Russia) that it is possible to store with this method a current ten times larger than the value otherwise set by the space-charge limit. A factor of a thousand is also believed possible.

Let P_{mmHg} be the vacuum in the storage rings expressed in mmHg. At room temperature, the number of molecules per unit of volume is given by

$$n_{mol} = (3 \times 10^{16}/\text{cm}^3) P_{mmHg} \qquad (12)$$

which corresponds to the following density

$$\rho = (1.4 \times 10^{-6} \text{ g/cm}^3) P_{mmHg}. \qquad (13)$$

A vacuum pressure of 1 x 10^{-8} mmHg corresponds to an energy loss of less than 1 keV, by atom excitation and ionization, for a particle spending the average 10 milliseconds in the storage ring. This vacuum pressure is thus adequate and it is assumed in the following.

The ionization rate can be estimated with the equation

$$dn_i/dt = \beta c \sigma_\iota n_{mol} N \qquad (14)$$

where σ_ι = 2.5 x 10^{-18} cm^2 is the ionization cross-section. With the vacuum pressure of 10^{-8} mmHg, the number of electrons produced is 10^{15} per second. It takes about ten seconds to produce a number of electrons equal to number of particles to achieve complete space-charge neutralization. As the electrons are being produced and accumulate within the beam dimensions, the potential barrier decreases continuously until vanishes. Beyond that point the electrons produced in excess will leave the beam and the neutralization should persist for a long

period of time. There should be an initial period where the beam is slowly established toward full intensity and density in combination of electron cooling and ionization. It is important that the ionization method for space-charge neutralization is also used in a controllable fashion during cooling to avoid that the space-charge limit is exceeded during the storage.

V. INTRABEAM SCATTERING

Because of the large density, particles in the same beam will scatter with each other by Coulomb repulsion. This effect will cause a considerable increase of the beam dimensions and particle losses as well.

We have estimated the rates of diffusion using available computer programs for the purpose [8]. The storage rings operate below the transition energy and the following features have been observed. For sufficiently small energy spread ($< 10^{-4}$) there is actually a reduction of the transverse dimensions at cost of increasing the energy spread. The situation is inverted for larger initial energy spreads ($> 10^{-3}$) when the beam emittance will grow and the momentum spread actually reduces. There is an intermediate range where growth occurs in all dimensions. The exact behavior depends of course on the choice of the storage ring lattice. For large energy spreads, the relative growth rate of the betatron emittance is about 10^9 s^{-1}.

There are several methods to cope with this large diffusion caused by intrabeam scattering. We mention below few of the possibilities.

A. Electron Cooling. This will be discussed in the next Section VI.

B. Chose the storage ring lattice and the beam parameters in such a way that the intermediate energy-spread range discussed above vanishes, and an equilibrium is found where the diffusion rates are identically zero in all dimensions.

C. Diffusion rates are directly proportional to the Coulomb Log, which is the logarithm of the ratio of the largest to the lowest impact parameters

$$\text{Log} = \log (b_{max}/b_{min}). \qquad (15)$$

It may be possible to chose beam dimensions so that the two impact parameters are equal, in which case Log = 0.

The smallest impact parameter is given by the largest scattering angle

$$b_{min} = 2\pi Q^2 r_0 \, \beta_L / A\varepsilon \, \beta^2 \qquad (16)$$

where β_L is the average value of the amplitude lattice function. For a very dense beam, the large impact parameter is given by the Debye radius, that is the range above which particles are effectively screened from each other

$$b_{max} = \varepsilon \, \beta \sqrt{AR / 2\pi Q^2 r_0 N} \qquad (17)$$

It is seen that if $\varepsilon = 0.1 \, \pi$ mm mrad and all the other parameters are unchanged, then $b_{max} = b_{min}$.

D. It may be possible [9] to employ very fast cooling to "freeze" the particles in the beam in a cold, high-ordered state, where they are essentially equally spaced ("crystalline beam").

Once this configuration is reached, all particles would be effectively screened from each other, and scattering among each other is thus removed. Of course it remains to check what happens to the ordered state when the two beams collide with each other.

VI. ELECTRON COOLING

The most important requirement, in order for cooling to be effective, is to provide velocity matching between the ion beam and the electrons. Since $\beta = 0.011$ this corresponds to an electron kinetic energy of only 30 eV. Whether a beam with such low energy is feasible over an extended length depends on other parameters like intensity and transverse dimensions which in turn depend on the required cooling rate. Cooling should proceed to maintain the beam at the space charge limit. Moreover cooling has to balance the diffusion rates due to intrabeam scattering which happens to be by far the most important effect. Thus a cooling rate $\lambda = 10^9$ s^{-1} may be required.

The formula for the cooling rate [10] is

$$\lambda = (4\pi \, Q^2 \, r_e \, r_p \, L \, \mu \, J/e) / (A \, \beta^4 \, \gamma^5 \, \theta^3) \qquad (18)$$

where $r_e = 2.818 \times 10^{-15}$ m is the electron classical radius, μ the ratio of the length of the electron beam to the circumference, J the electron beam density, $L \sim 10$ the Coulomb Log, and θ the angular divergence of the ion beam which we can assume to be larger than the angular divergence of the electron beam. With our parameters $\theta = 1$ mrad. If we take $\mu = 10\%$, the electron beam density for the cooling of the protons is $J = 4$ A/cm^2. With a radius of 1 millimeter, the electron current is then 0. 13 A.

VII. ACKNOWLEDGMENTS

VIII. REFERENCES

[1] L.M. Lidsky, "The Trouble with Fusion", Technology Review, Oct 1983. Edited by M.I.T.

[2] F. Ajzenberg-Selove and C. Langell Busch, Nuclear Physics A336, p. 73 (1980).

[3] A.G. Ruggiero, "Nuclear Fusion of Protons with Boron", BNL - 47989 and AD/AP-48 (Sept. 1992).

[4] J.W. Staples, "RFQs - An Introduction", AIP Conf. Proc. 249, Vol.2, p. 1483. The Physics of Particle Accelerators. (1992).

[5] R. Geller, "ECR Source Scaling Concepts", IEEE Particle Accel. Conf. March 1989, Chicago, IL. Vol. 2, p. 1088.

[6] L.J. Laslett, "On Intensity Limitations imposed by Transverse Space Charge Effects in Circular Particle Accelerators", BNL 7534 (1963).

[7] G.I. Dimov and V.E. Chupriyanov, Particle Accelerators, 14, p. 155 (1984).

[8] M. Martini, PS/AA/Note 84-7. CERN, May 1984.

[9] A.G. Ruggiero, these proceedings.

[10] T. Ogino and A.G. Ruggiero, Particle Accelerators, 10, p. 197 (1980).

Heavy Ion Fusion Injector Program*

S. Yu, S. Eylon, W.W. Chupp, A. Faltens, T. Fessenden, E. Henestroza, R. Hipple, D. Judd, C. Peters, L. Reginato,
H. Rutkowski, J. Stoker, D. Vanecek; LBL
J. Barnard, G. Caporaso, Y.J. Chen, F. Deadrick, A. Friedman, D. Grote, D. Hewett, LLNL
University of California Lawrence Berkeley Laboratory
1 Cyclotron Road, MS 47-112, Berkeley, CA 94720 USA

Abstract

A program is underway to construct a 2 MV, 800 mA, K$^+$ injector for heavy ion fusion. The Electrostatic Quadrupole (ESQ) injector configuration consists of a zeolite source, a diode of up to 1 MV, together with several electrostatic quadrupole units to simultaneously focus and accelerate the beam to 2 MV. The key issues of source technology, high voltage breakdown, beam aberrations, and transient effects will be discussed. Results from ongoing experiments and simulations will be presented.

I. INTRODUCTION

A new high current ion injector for heavy ion fusion is under construction at Lawrence Berkeley Laboratory . The objective is to build a one-beam version of the 4-beam injector needed for the Induction Linac System Experiments (ILSE). As such, the machine must have high reliability, and the technology must be scalable to the ultimate full-scale fusion driver. The design goals for the K$^+$ ion beam are driver-scale line charge density (0.25 μC/m A), driver scale particle energy (2 MV), very low emittance (normalized emittance of less than 1π mm-mr) repetition rate of 1 Hz, and pulse length of 1 μs. While all previous injectors in the Heavy Ion Fusion Accelerator Research (HIFAR) group at LBL have been based on electrostatic aperture column (ESAC) designs, a six-month study at LBL and LLNL from March to September 1992 has led to the choice of the electrostatic quadrupole (ESQ) injector as the most suitable for the long term need of induction linac-based heavy ion fusion research work. The ESQ is a concept which uses a set of electrostatic quadrupoles to simultaneously focus and accelerate an ion beam. The front end of the ESQ is an axisymmetric diode containing a large source (of up to 7" in diameter according to present designs). The concept originated with Abramyan [1] and has been studied extensively by the Magnetic Fusion Energy group at LBL for a number of years [2]. As a high energy , high current injector, the ESQ concept has the distinct advantage of reduced voltage breakdown risks (as compared to ESAC), resulting from the intrinsically lower accelerating gradient and the presence of large transverse fields to sweep out deleterious secondary electrons.

II. INJECTOR DESIGN

A schematic of the one-beam injector is shown in Figure 1. The key components of the injector are a 2 MV MARX generator, a large hot alumino-silicate source (of ≤ 7"

diameter), a diode column in which the ion beam is accelerated to ~ 1 MV after extraction, and a number of electrostatic quadrupoles to bring the ion beam to 2 MV. Furthermore, external to the accelerating columns, protection devices (metal oxide varisters and guard rings) are built in to prevent irreversible damage in the case of major breakdowns.
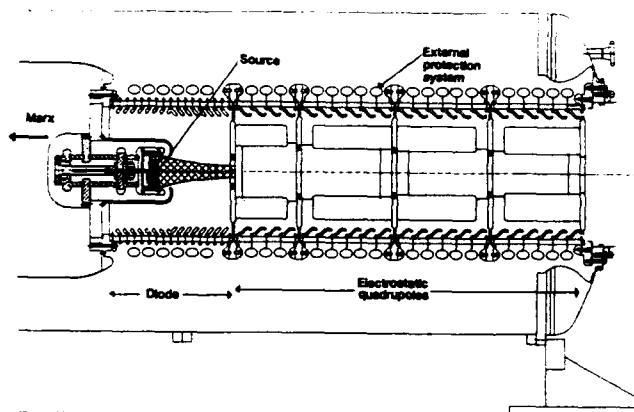
Fig. 1. Schematic of the one-beam injector.

The new MARX is a 36-stage pulse-forming network designed to produce a 2 MV pulse with 1 μs rise and 5 μs voltage flat top. This flat top can maintain constant voltage for the 1 - 2 μs long ion pulse during its transit through the length of the injector (~ 2 μs transit time). To minimize beam-induced transients, the electrical system as designed is quite stiff. The total resistance is 5 kΩ.

Source development is reported in a separate paper in this conference [3]. Tests with a small 1" hot alumino-silicate source over the past year has produced very encouraging results. The measured current density of 20 mA/cm^2, the temperature and emission uniformity, as well as life time have been shown to exceed ILSE requirements under normal operating conditions. A 4" source and a 6" source have been fabricated and initial tests have yielded similar emission characteristics.

The key design constraint for an ESQ injector arises from a distortion of the particle phase space which may lead to an unacceptable increase in beam emittance. This effect arises from a large spread in particle energy with varying radial position when a low energy beam traverses a strong electrostatic quadrupole structure. The phase space distortion resulting from this "energy effect" is further enhanced by the higher order multipole fields intrinsic in an interdigital electrostatic quadrupole structure. Earlier designs with a low energy diode (500 keV) show unacceptable growth in

emittance. 3D simulations of these effects have been confirmed quantitatively in a scaled experiment [4].

Three design paths have been identified for the reduction of these deleterious beam dynamics effects. First of all, if the diode energy is increased to 1 MV, the emittance growth through an ESQ is shown to be significantly reduced. Secondly, increased quad voltages lead to a reduced beam envelope with corresponding reduction of nonlinear effects. Thirdly, simulations have shown that the distortions are entirely attributable to fourth order single particle effects. Hence, external correction schemes are straightforward in principle, although the actual implementation may be somewhat involved.

The most cost-effective way to design a ESQ with acceptable emittance is to increase diode energy as well as quad voltage. Both of these measures would enhance breakdown risks. Hence, the choice of the optimal ESQ parameters involves a proper balance between breakdown risks and emittance growth.

To determine the quad breakdown voltage for our ESQ designs, we constructed a full-size quad unit with electrodes as well as X-ray shields, and tested the voltage holding capabilities in the absence of beam (Figure 2). The pulsed voltage from an existing MARX generator has a 30 μs rise, and ~10 μs flat-top (Figure 3). For two electrode to end-plate gap spacings of 5.5 cm and 7.6 cm, the breakdown voltages were determined to be 550 kV and 700 kV, respectively. On the basis of these data, we have designed our ESQ quads for voltages of up to 350 kV (7 cm gap spacing).

Figure 3. Voltage waveform for quad breakdown test. Peak voltage = 700 kV, pulse length = 80 μs

The diode is designed to hold up to 1 MV. A hot alumino-silicate source with a large (< 7") curved surface is surrounded by a thick copper "extraction electrode." An extraction pulser switches the source from -80 kV to +80 kV relative to the extraction electrode during beam turn-on. The waveform for a low voltage bench test of the extraction pulser is shown in Figure 4. The insulator column is a brazed 16-ring ceramic unit (1.5" per ring) with 1 cm thick stainless steel shields to protect against secondary electrons and X-rays produced by the beam.

t (400 ns/div)

Figure 4. Beam extractor waveform.
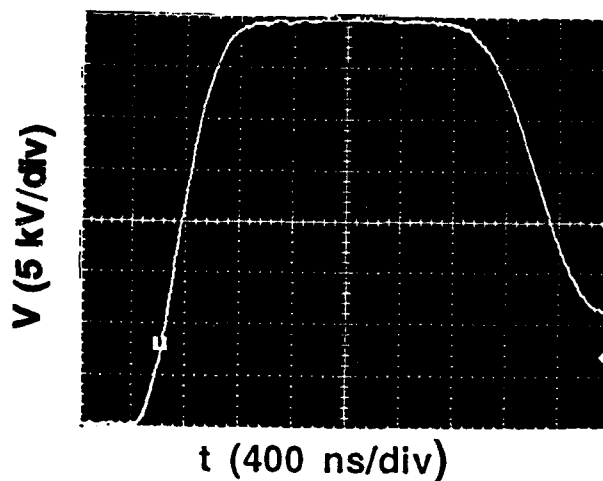
The geometry of the diode, as calculated by the EGUN code, is shown in Figure 5. At 1 MV operation, the highest surface field (at the extraction electrode) is about 85 kV/cm, whereas the peak field at the shields is about 65 kV/cm. The average field along the insulator is about 15 kV/cm. The normalized emittance at the exit of the diode is calculated to be less than 0.4π mm-mr.

Figure 2. Schematic of the full-size quad breakdown test.
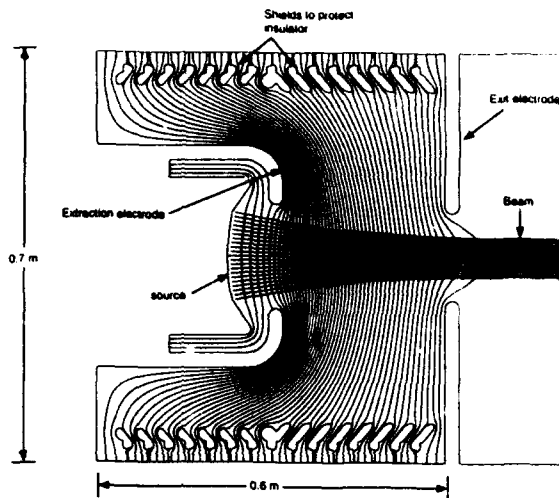
Figure 5. EGUN output showing the geometry of the axisymmetric injector diode, the beam envelope, and field equipotential surfaces.
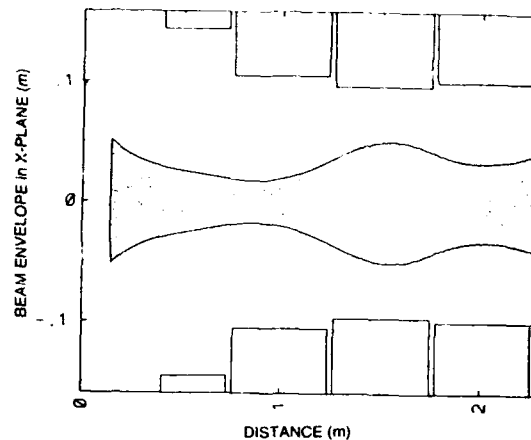
Figure 6. WARP3D calculations of the beam envelopes in the injector.

The ESQ section consists of 4 quadrupoles with representative parameters given in Table 1. The beam envelopes as calculated by the 3-D particle-in-cell code WARP3D are shown in Figure 6. The normalized emittance at the exit is predicted to be less than 0.7π mm-mrad.

	Unit 1	Unit 2	Unit 3	Unit 4
Length, cm	30	46	46	46
Quad aperture radius, cm	12	10.5	10.5	10.5
Quad voltage, kV	206	259	308	281

Table 1. Parameters of the 4 quadrupole units in the ESQ section.

III. REFERENCES

[1] E.A. Abramyan and V.A. Gaponov, Atomnaya Energiya **20**, 385 (1966).

[2] O.A. Anderson et al., Proceedings of the 1989 Particle Accelerator Conference, Chicago, March 20-23, 1989.

[3] S. Eylon et al., Proceedings of the 1993 Particle Accelerator Conference, Washington, DC, May 17-20, 1993.

[4] E. Henestroza et al., Proceedings of the 1993 Particle Accelerator Conference, Washington, DC, May 17-20, 1993.

ION PULSE PROPAGATION THROUGH A PREVIOUSLY UNFILLED ELECTROSTATIC APERTURE LENS ACCELERATING COLUMN

H. L. Rutkowski, S. Eylon, D. S. Keeney
Lawrence Berkeley Laboratory

Y. J. Chen, D. W. Hewett, J. Barnard
Lawrence Livermore National Laboratory

ABSTRACT:

Heavy Ion Fusion experiments require very high current beams with excellent beam quality during a short pulse. Scaled experiments planned at LBL require very short pulses (μsec) compared to what one expects in an HIF driver (20-30 μs). A 1MV acceleration column composed of aperture lenses has been constructed at LBL in order to study the propagation effects on such ion pulses. The column is initially empty of space charge but with the full acceleration potential applied. A short current pulse is then injected into the column with a planar diode "current valve." Effects on the pulse propagation due to rise time, pulse duration, and beam size have been studied. Experiments on transported beam current and emittance have been conducted using a carbon arc plasma source (2" and .5" diameter) and a 1" diameter alumino-silicate potassium ion source. Computer simulations using a 2.5D time dependent code are compared with the experimental data.

INTRODUCTION

In the case of using induction linacs for heavy ion fusion one wishes to build an injector that can accommodate a short pulse 20-30 μs long and at very high current of typically amperes per beam while preserving a high quality electrical pulse. This means that one must have some sort of gating mechanism to inject the pulse into the accelerating column which has already been brought up to voltage, but which contains no charged particles. The column-beam system must come to equilibrium after beam starts to enter the column. Significant distortions in the pulse will cause problems in the succeeding linac transport system.

We have studied pulsed injection into a 1MV electrostatic aperture lens column using carbon arc ion sources and K^+ alumino-silicate sources. The puls lengths in this case are 1-2 μs because the injector is intended for a scaled experiment which cannot accommodate the longer pulse of a driver because of the cost limit on Metglas available for the machine. The column was originally designed to accelerate a 2 inch diameter 500 mA C^+ ion beam.

EXPERIMENTAL SYSTEM

The injector accelerating column is shown in Fig. 1. It is an electrostatic aperture lens column that operates at a full design voltage of 944 kV. the carbon arc ion source is shown on the left. After the column is brought to full voltage with an approximately critically damped pulse (30 μs risetime) the beam is gated into the column with a "current valve" diode. The valve diode is a planar 9mm gap that can be operated up to 15 kV. There is a 90% transmitting nickel mesh at the exit into the accelerating column. The arc plasma is kept from entering the valve before hand by use of an electrostatic plasma switch.[1] Two versions of this source were used, 2 inch and 0.5 inch diameter, the smaller beam being produced by aperturing the plasma switch. The pulse length and current are varied by changing the pulse forming network that drives the planar current valve diode. The beam was diagnosed in several ways. The most reliable method was the use of a calibrated ferrite core current transformer placed on the back-side of the second ground plate behind the electron trap. Downstream from this transformer a 5 inch diameter aperture, deep (12"), Faraday cup was placed as a beam dump and electron trap. The 5 inch deep collector cup was modified by placing a graphite disk on the rear surface to reduce production of secondary electrons by the beam. The cup suppresser ring (also 5 inches deep) in front of the collector cup and the collector cup could be biased up to 10kV positive to trap secondary electrons. Failure to use this beam dump results in backstreaming secondary electrons passing through the current transformer giving anomolously high current readings. This effect occurs even if the beam is allowed to hit the vacuum chamber wall which is approximately two feet from the column exit. Use of the current transformer allows one to measure total beam current at high levels without intercepting the beam. Using capacitive coupling, collected current can also be measured from the beam dump and from the electron trap electrode. Calculations with the EGUN (2) code were used to verify that the beam would be completely deposited in the beam dump collector only and that secondary electrons would be completely trapped in the dump. Therefore all anomolous beam behavior would have to be due to departures from ideal beam optics. Later on, emittance measurements were carried out using a double slit emittance scanner capable of .2 mrad angular resolution.

COMPUTER MODELING

The column was originally designed using the EGUN code for a steady state, 2 inch, 0.5A C^+ beam at full 944kV design voltage. The 0.5 inch carbon source
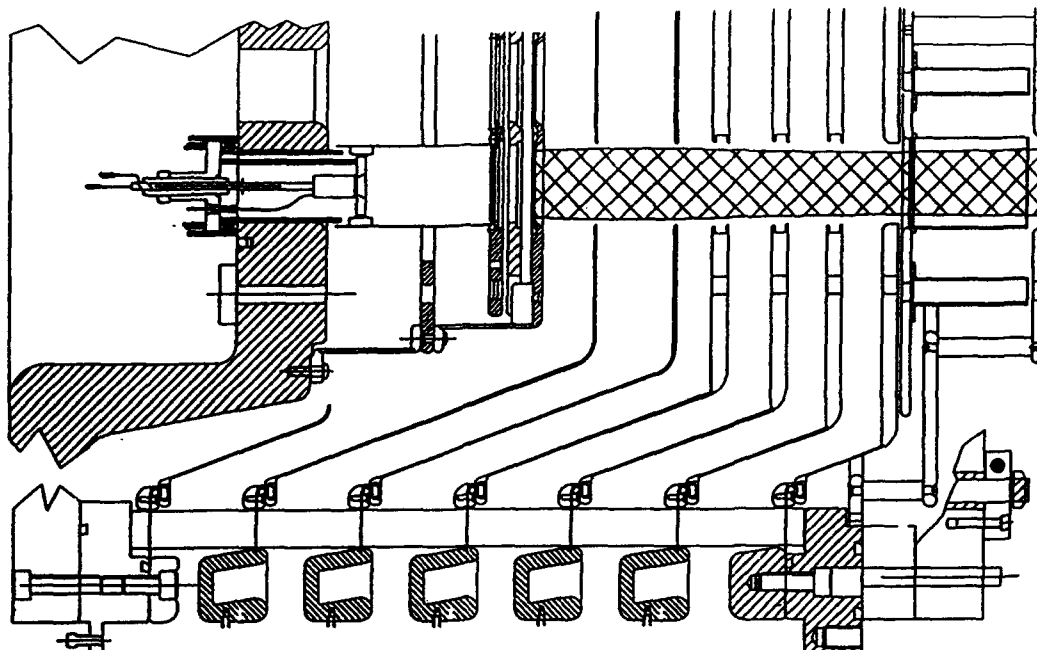
Fig. 1 Accelerating column with carbon arc source installed on left followed by plasma drift region, plasma switch, and current valve diode. Crosshatched area is the calculated beam envelope for a 2" source and starts at current valve exit. Electron trap is the cylindrical electrode before exit ground plate

measurements were modeled in the same way. Beam clearance in the large aperture case was a few millimeters at closest approach, but the ideal beam propagated all the way to the exit without touching electrodes in calculations. The small aperture beam had minimum beam clearances of 18mm. A time dependent simulation using the GYMNOS code was performed for both the small carbon source and a 1 inch diameter K+ alumino-silicate source. Both simulations ran until the 1 μs (nominal) injected current pulse left the column at 2 μs after start. The beam was not seen to hit the electrodes and predicted current levels agreed substantially with EGUN predictions.

EXPERIMENTAL RESULTS

At the beginning of injector tests the carbon arc source was used without the current valve by putting the plasma switch grid at the location of the current valve exit grid. Long pulses were extracted at reduced current because of the geometry change. the extracted currents agreed reasonably with computer predictions. However, when the current valve was installed the propagated pulses were not well behaved even though preliminary tests on a test stand showed that good pulse shapes were coming out of a duplicate valve diode. The thought was that the rise time was playing a role in the behavior of the beam and the rise time was slowed. Some

negative spikes were visible on the pulse rise even after it was gradually increased to 1.5 μs.

Tests were then performed using 2.5 μs wide pulses with a 250 ns rise time. The current was measured with the current transformer combined with the beam dump to trap secondary electrons. 500 mA currents at full column voltage were measured which is the expected Child-Longmuir current from the valve diode. However, a negative notch appeared at approximately 0.5 μs into the pulse. The current after the notch was flat. Reducing the pulse width to 1.5 μs resulted in negative current signals from the current transformer. In other words, electrons were exiting the column in sufficient quantities to more than cancel the ion signal. The current signal from the electron trap had the same shape as the negative signal from the beam, but was a positive signal. This indicated that the beam was hitting the electron trap, generating secondaries which then flowed with the beam out of the column. The beam dump showed very similar negative signals compared to the current transformer. Under these conditions the central portion of the pulse was negative and there was a weak positive signal at the beginning and the end of the pulse.

In an attempt to find better beam propagation the carbon source was masked to 0.5 inches aperture. this should have resulted in a 28 mA C^+ beam propagating for the 11.6 kV current valve voltage applied. With the much larger beam clearance provided in this case
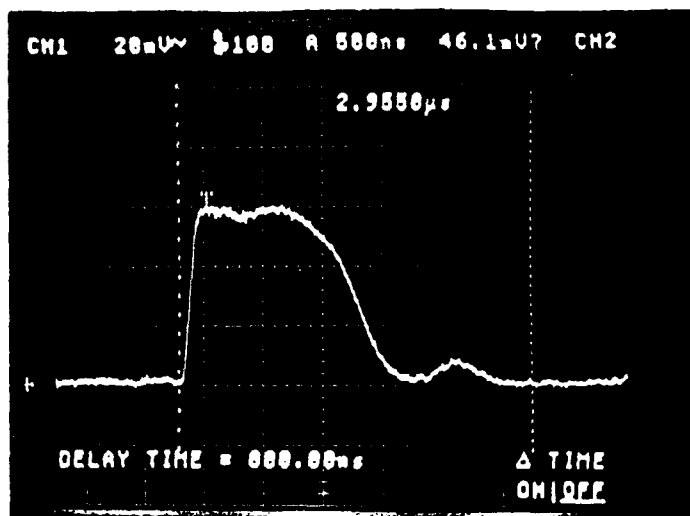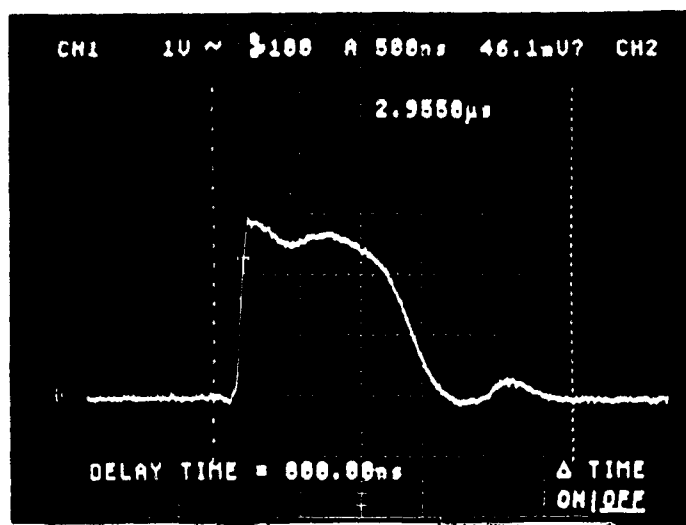
Fig. 2   Current measurements at column exit, (left) beam dump, (right) current transformer, for 1 inch
potassium alumino-silicate source, 800kV column voltage, peak current 59 mA in each case.

positive signals were seen, but they were quite erratic in magnitude. The beam dump measurements gave a current of 24 mA ± 4mA at full operating voltage on the column. The current transformer signals were much higher, about twice the expected current and with very large error bars. Both the EGUN simulations and the GYMNOS simulations showed the beam propagating down the column without hitting electrodes.

The one inch alumino-silicate source was installed. After calibrating the temperature of the source as a function of input power, beam was propagated down the column. The current signals from the column became much more reproducible and there was almost exact agreement between the current transformer and the computer simulations. The beam dump current was low, but this was later shown to be a result of a defective capacitor in a coupling box which attenuated the beam signal while maintaining voltage on the beam dump collector cup. The beam propagated was 82 mA, K$^+$ at 904 kV column voltage with a 1.5 μs (0 to 0) pulse width.

After the initial current measurement with the hot potassium source, the column had to be used at reduced voltage because of breakdown problems not related to the source. Operating at 800 kV column voltage, beams were propagated using different grids in the current valve. Substituting a 200 x 200, 50% transmitting stainless steel mesh gave 79 mA beams with normalized emittance of 2.6 x 10^{-7} π m-rad. Removing the grid altogether gave a current of 20 mA and a normalized

emittance of 5 x 10^{-8} π m-rad. This second case had a very narrow beam of 2.4 mm diameter. These results were in agreement with GYMNOS simulations.

CONCLUSIONS

These experimental results indicate that in propagating the large diameter carbon beam from the plasma source, the beam hit at least the electron trap at the column exit. This was probably caused by an unstable ion emission surface at the plasma switch. Substituting the solid surface hot source improved propagation and agreement with simulations to such an extent that the emission surface stability must be the prime suspect in causing poor beam propagation. The hot source is now being used as the main approach to building an injector for these scaled experiments.

REFERENCES

1) H. L. Rutkowski, D. W. Hewett, I. Humphries Jr., IEEE Trans. Plasma Sci. 19, pg. 782, Oct. 1991.

2) W. B. Herrmannsfeldt, SLAC-226, Nov. 1979

ACKNOWLEDGEMENT

ILSE-ESQ Injector Scaled Experiment*

E. Henestroza, S. Eylon, and S. Yu
Lawrence Berkeley Laboratory,
University of California
Berkeley, California 94720

D. Grote
Lawrence Livermore National Laboratory,
University of California
Livermore, California 94550

Abstract

A 2 MeV, 800 mA, K^+ injector for the Heavy Ion Fusion Induction Linac Systems Experiments (ISLE) is under development at LBL. It consists of a 500keV-1MeV diode pre-injector followed by an electrostatic quadrupole accelerator (ESQ). One of the key issues for the ESQ centers around the control of beam aberrations due to the "energy effect": in a strong electrostatic quadrupole field, ions at beam edge will have energies very different from those on the axis. The resulting kinematic distortions lead to S-shaped phase spaces, which, if uncorrected, will lead eventually to emittance growth. These beam aberrations can be minimized by increasing the injection energy and/or strengthening the beam focusing. It may also be possible to compensate for the "energy effect" by proper shaping of the quadrupoles electrodes. In order to check the physics of the "energy effect" of the ESQ design a scaled experiment has been designed that will accommodate the parameters of the source, as well as the voltage limitations, of the Single Beam Transport Experiment (SBTE). Since the 500 KeV pre-injector delivers a 4 cm converging beam, a quarter-scale experiment will fit the 1 cm converging beam of the SBTE source. Also, a 10 mA beam in SBTE, and the requirement of equal perveance in both systems, forces all the voltages to scale down by a factor 0.054. Results from this experiment and corresponding 3D PIC simulations will be presented.

I. INTRODUCTION

The US Heavy-Ion Fusion Accelerator Research (HIFAR) Program at Lawrence Berkeley Laboratory has proposed a sequence of experiments that collectively are called the Induction Linac Systems Experiments, or ILSE. A principal design criterion was that the beams in ILSE should be at the same line charge density expected in a full-scale heavy-ion driver. A key element in the ILSE project is the ion injector that will provide 0.8A of 2-MeV K^+ ions, equivalent to a line charge density of 0.25 μC/m; it is further specified that the beams must have a low normalized-emittance ($\approx 1 \pi$ mm-mr). Two main options that could meet the requirements were considered, namely the Electrostatic Aperture Column (ESAC) and the Electrostatic Quadrupole Injector (ESQ). The ESAC option consists of a number of axisymmetric electrodes arranged in a conventional Pierce electrode geometry. The key

issue for this option is high-voltage breakdown and beam emittance. The ESQ option consists of an axisymmetric front end (which could be a diode or a multiple aperture column) followed by a sequence of quadrupoles arranged to focus and accelerate the beam at the same time. The key issue for this option is the beam aberration produced by the "energy effect". Based on reliability, driver scaleability, and beam specifications the ESQ option was selected for the ILSE injector.

III. THE ILSE-ESQ INJECTOR

The ESQ concept was first proposed by Abramyan *et al.* in the late 1960's . More recently, the Magnetic Fusion Energy program at LBL has worked towards the construction of a MeV-class ESQ injector. As compared to the ESAC, the ESQ is generally a longer machine with correspondingly lower gradients. The secondary electrons are swept out by the large transverse fields, which reduces significantly the breakdown risks. In addition, the sources in an ESQ are generally smaller, so their intrinsic emittance is reduced. The ESQ is also attractive from the standpoint of driver scaling; it has the potential advantage of operating at energies much higher than 2MeV, since the critical issues in an ESQ tend to center in the transition from preinjector into the first accelerating quadrupoles. The ILSE-ESQ injector was designed to provide four beams of K^+ at driver line charge densities. It is followed by a matching section that shapes the beams to the proper radius and "squeezes" them together for insertion into the electrostatically focused induction linac.

III. THE "ENERGY EFFECT"

One of the key issues for the ESQ centers around the control of beam aberrations due to the "energy effect": in a strong electrostatic quadrupole field, ions at beam edge will have energies very different from those on the axis. This effect can be analyzed by a perturbation treatment of the particle orbits to leading order. Expanding the single-particle equations of motion to fourth order in the external electrostatic potential ϕ we obtain:

$$v_x = v_{x0} + v_{x1}$$

$$\phi = V_{00} + [V_{20} + V_{22}\cos 2\theta]\left(\frac{r}{R}\right)^2 +$$

$$[V_{40} + V_{42}\cos 2\theta + V_{44}\cos 4\theta]\left(\frac{r}{R}\right)^4$$

$$\frac{dv_{x1}}{dz} = \frac{v_{z0}}{2}\left\{\begin{array}{l}\left[\frac{1}{8}\left(\frac{eV_{22}}{T_0}\right)^2 + \frac{eV_{44}}{T_0}\right]\left[-\frac{\partial}{\partial x}\left(\frac{r}{R}\right)^4\cos 4\theta\right] + \\[2mm] \left[\frac{1}{2}\left(\frac{eV_{22}}{T_0}\right)\left(\frac{eV_{20}}{T_0}\right) + \frac{eV_{42}}{T_0}\right]\left[-\frac{\partial}{\partial x}\left(\frac{r}{R}\right)^4\cos 2\theta\right] + \\[2mm] \left[\frac{1}{8}\left(\frac{eV_{22}}{T_0}\right)^2 + \frac{1}{4}\left(\frac{eV_{20}}{T_0}\right)^2 + \frac{eV_{40}}{T_0}\right]\left[-\frac{\partial}{\partial x}\left(\frac{r}{R}\right)^4\right]\end{array}\right\}$$

The second order terms in the potential give rise to the "energy effect". The fourth order terms (octupoles) are due to the "inter-digital" structure of the quadrupoles. The resulting kinematic distortions lead to S-shaped phase spaces, which, if uncorrected, will lead eventually to emittance growth. These beam aberrations can be minimized by increasing the injection energy and/or strengthening the beam focusing. It may also be possible to compensate for the "energy effect" by proper shaping of the quadrupoles electrodes to include octupole corrections.

Fig. 1   Schematics of the ESQ-Scaled Experiment. Cross-sectional view.

IV. NUMERICAL SIMULATIONS

The dynamics of the beam in the ESQ was simulated by the 3-D particle-in-cell codes WARP3D[1] and ARGUS[2]. A full 3D simulation code was required to incorporate the beam space charge field as well as the self-consistent fields from the accelerating quadrupoles, including their "inter-digital" structure. Large normalized-emittance growth ($\approx 2\,\pi$ mm-mr) was obtained for the case of a 500keV beam injected into the ESQ. A smaller normalized-emittance growth ($\approx 0.6\,\pi$ mm-mr) was obtained for the case of a 1MV injected beam. The initial normalized-emittance in both cases was $0.4\,\pi$ mm-mr.

V. SCALED EXPERIMENT

We are presently building a one-beam prototype of the ILSE-ESQ Injector. The prototype consists of a 500keV-1MeV diode followed by an ESQ that will focus and accelerate the beam to 2MeV. In order to check the physics of the "energy effect" of this design a scaled experiment has been designed that will accommodate the parameters of the source, as well as the voltage limitations, of the Single Beam Transport Experiment (SBTE). Since the 500 KeV pre-injector delivers a 4 cm converging beam, a quarter-scale experiment will fit the 1 cm converging beam of the SBTE source. Also, a 10 mA beam in SBTE, and the requirement of equal perveance in both systems, forces all the voltages to scale down by a factor 0.054. The SBTE source normalized-emittance was measured to be $0.06\,\pi$ mm-mr. A schematic of the scaled experiment is shown in Fig. 1. Two set of measuremts were taken corresponding to scaled versions of a 570keV,787mA (36keV,12.6mA) and a 1MeV,787mA (30keV,4.1mA) beams. Fig. 2 and Fig 3. shows the experimental results as well as the WARP3D numerical simulations. Further measurements taken by scanning the injection energy for a given quadrupole voltage setting shows a consistent agreement between experimental results and 3D numerical calculations (Figs. 4a and 4b).
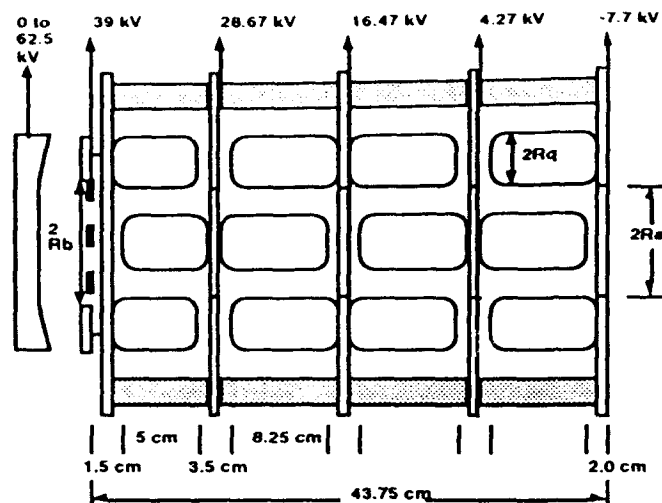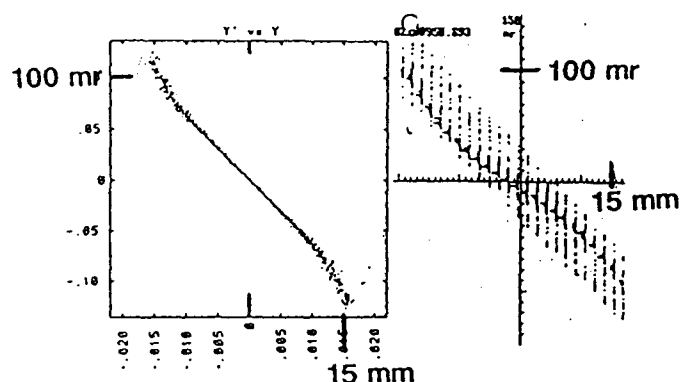
Fig. 2   WARP3D simulation and measured phase-space distributions. Scaled version of a 570keV,787mA (36keV,12.6mA) beam.
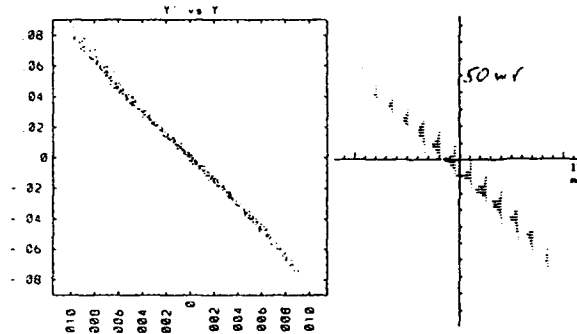
Fig. 3   WARP3D simulation and measured phase-space distributions. Scaled version of a 1MeV,787mA (30keV,4.1mA) beam.

V. CONCLUSIONS

Phase space distortions predicted by simulations have been observed in the 570keV scaled experiment leading to a factor of 8 growth in the beam normalized emittance. A growth of less than a factor of 2 in the beam emittance observed in the 1MeV scaled experiment is in agreement with the numerical simulation and the expected decrease in emittance growth by an increase in injection energy. We found consistent agreement between 3D numerical simulations and experimental results.

ACKNOWLEDGEMENTS

REFERENCES

[1] A. Friedman, D. Grote, and I. Haber, "Three-dimensional particle simulation of heavy-ion fusion beams", *Phys. Fluids* B4,2203(1992).

[3] C.L. Chang, D. Chernin, A. Drobot, K. Ko, M. Kress, A. Mankofsky, A. Mondelli, and J. Petillo, "Three-Dimensional Modeling of Accelerators", *Proc. Conf. on Computer Codes and the Linear Accelerator Community* (Los Alamos National Laboratory, January 22-25, 1990, LA-11857-C), pp. 27-56.
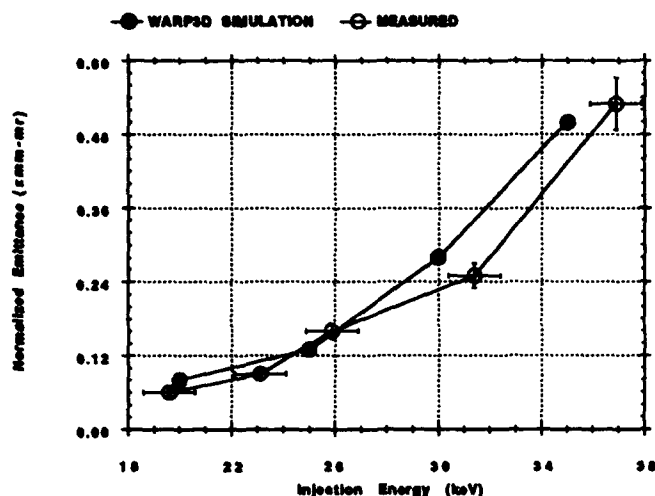
Fig. 4a Scan of the normalized emittance versus the injection energy for the quadrupole voltage setting corresponding to the scaled version of a 570keV,787mA (36keV,12.6mA) beam.
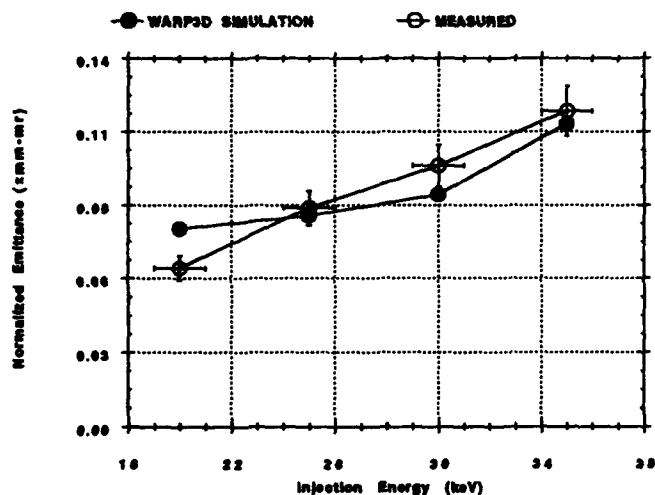
Fig. 4b Scan of the normalized emittance versus the injection energy for the quadrupole voltage setting corresponding to the scaled version of a 1MeV,787mA (30keV,4.1mA) beam.

One Dimensional Simulations of Transients in Heavy Ion Injectors*

J.J. Barnard, G.J. Caporaso

Lawrence Livermore National Laboratory, L-440, Livermore, CA 94550

S.S. Yu, and S. Eylon

Lawrence Berkeley Laboratory, MS 47-112, Berkeley CA 94720

Abstract

A fast-running time-dependent one-dimensional particle code has been developed to simulate transients in both electrostatic quadrupole and electrostatic column heavy-ion injectors. Two-dimensional effects are incorporated through the use of an approximation to the transverse part of the Laplacian operator. Longitudinal electric fields are solved on a mesh. An external circuit is coupled to the column, and the effect of the beam on the circuit is modeled. Transients such as initial current spikes, space-charge debunching, and beam loading of the circuit, are simulated. Future directions for the code include introduction of envelope and centroid equations to provide beam radius and displacement information and the modeling of secondary electron currents arising from beam-spill.

I. INTRODUCTION

We have used the 1-dimensional, time-dependent code HINJ (for Heavy-ion INJector) in order to study transient effects in both the electrostatic quadrupole (ESQ) and electrostatic column (ESAC) heavy ion injector configurations. The ESAC uses an increasing longitudinal accelerating electric field which causes a radial convergence of the electric field lines, and hence a focusing component to the electric field. The ESQ uses alternating gradient electrostatic quadrupoles to provide the focusing. The most accurate simulations have been done using 2-D codes (e.g GYMNOS, [1]) in the case of the axisymmetric ESAC or the axisymmetric diode in an ESQ, or 3-D codes (e.g WARP3d, [2]) for the non-axisymmetric ESQ. However, it has been valuable for physical understanding, to develop a fast running 1D code which examines longitudinal dynamics, and thus shed light on the transient behavior of the injector.

In this paper, we first briefly discuss the types of transients that may be investigated by using the code HINJ. The physics which is included in HINJ is discussed in section III. In section IV we provide an example of a benchmark of the code against a diode experiment, and an example of code results for one possible ESQ design that is being planned for the Induction Linac Systems Experiment (ILSE) [3] now being planned for the Lawrence Berkeley Laboratory (LBL).

II. TYPES OF TRANSIENTS

We divide injector transients that may be modeled using HINJ into at least four classes: 1. initial current spikes, 2. space-charge debunching, 3. beam loading of the circuit, and 4. secondary electron currents arising from beam spilling. Initial current spikes arise because during the initial transit of the beam across the injector, the space charge electric fields are not the same as those that occur during the "D.C." part of the pulse. In particular, during the initial part of the pulse there is no space charge in front of the head of the beam so that the electric fields are larger than the steady state fields, and so more current is drawn from the emitting surface than occurs in steady state. This oversupply of space-charge inhibits emission from the emitter and produces a paucity of current following the current spike, which then induces an over-supply and so forth. These oscillations are damped on approximately the transit time scale after which steady state conditions are reached. Space-charge debunching is a result of the line-charge density gradients at the head and tail of the beam. These gradients result in an electric field which causes the head and tail of the pulse to expand relative to the center, and causes the length of the flat top in the current pulse to decrease in duration as rarefaction waves propagate inward from the head and tail. Beam loading arises as the magnetic field of the beam induces return currents, and the electric field of the beam induces image charges, in the accelerating structure. These act as current and voltage sources in the circuit, altering the voltages on the accelerating electrodes, which in turn alters the beam current. Finally, if errant beam particles strike an electrode, electrons may be emitted and accelerated producing large current perturbations, which will again alter the accelerating electrode voltages.

III. THE PHYSICS OF HINJ

As stated earlier, HINJ is a 1-D (z), electrostatic, time-dependent particle code. The particles are moved using the non-relativistic equations of motion:

$$\frac{dz_i}{dt} = v_i \quad \text{and} \quad \frac{dv_i}{dt} = -\frac{qe}{m}\frac{\partial \phi}{\partial z} \quad (1)$$

where q is the charge state of the ions, e it the proton charge, z_i and v_i are the longitudinal position and velocity of the ith ion, and m is the ion mass. The on-axis potential ϕ is solved on a grid. In diode geometries, however, there is an option which allows calculation of the potential by summation of the known greens function for each particle. In the multi-electrode geometries used in the ESAC and

ESQ the calculational grid is used. One novel feature of the code, is the incorporation of 2-dimensional effects by the use of an approximation to the transverse part of the Laplacian operator [4].:

$$\nabla^2\phi \cong \frac{\partial^2\phi}{\partial z^2} + \frac{V_{ext} - \phi}{a_*^2} = -\frac{\rho}{\epsilon_0} \qquad (2)$$

Here, $a_*^2 \equiv (1+g)a^2/4$, $g \equiv 2\ln r_p/a$, ϕ is the electrostatic potential on axis, V_{ext} is the external potential at the pipe radius r_p and a is the beam radius. The equation reduces to the correct expression in the two extreme limits:

$\frac{\partial^2\phi}{\partial z^2} \cong -\frac{\rho}{\epsilon_0}$ if $L_\nabla << a_*$, and

$\phi \cong V_{ext} + \frac{(1+g)\lambda}{4\pi\epsilon_0}$ if $L_\nabla >> a_*$ (3)

Here $L_\nabla \equiv \phi/|\partial\phi/\partial z|$. Since in both the ESAC and ESQ, the beam has much smaller radius than length, the beam rapidly transfers from the $L_\nabla << a_*$ regime to the $L_\nabla >> a_*$ regime and the 2-D equation is essential in order to get meaningful computational results. One may get a qualitative understanding of the two dimensional effects, by examining the greens function for eq. (1) in the diode geometry. A charge slab of unit total charge with radius a, at position z_p in a diode of length d with external voltage $V_{ext} = V_o(1 - z/d)$, has a solution to eq. (2) which satisfies:

$$\phi_{sc} = \begin{cases} \frac{a_*\sinh(z/a_*)\sinh([d-z_p]/a_*)}{\epsilon_0\sinh(d/a_*)} & z < z_p \\ \frac{a_*\sinh(z_p/a_*)\sinh([d-z]/a_*)}{\epsilon_0\sinh(d/a_*)} & z > z_p \end{cases} \qquad (4)$$

Here $\phi_{sc} \equiv \phi - V_{ext}$. For the case $a_* \longrightarrow \infty$, The 1-D greens function is obtained:

$$\phi_{sc} = \begin{cases} z(d - z_p)/(\epsilon_0 d) & z < z_p \\ z_p(d - z)/(\epsilon_0 d) & z > z_p \end{cases} \qquad (5)$$

In the 1-D case, the contribution to the space charge field from a particle falls off linearly with distance from the charge sheet, vanishing at $z = 0$ and $z = d$, while the greens function falls off exponentially after a distance from the charge sheet $\sim a_*$ in the 2-D case. This indicates that the effect of the radial boundaries, i.e. image charges on the walls, limits the extent over which the space charge has a significant influence. This affects the initial transients, since the relative transit time in the 2-D case is approximately a_*/v rather than d/v, and v is an average velocity.

The external voltage at various discrete locations in z is determined by a circuit equation. The external circuit is divided into a Marx bank power supply and accelerating column, which accelerates the beam by creating a decreasing voltage at discrete electrodes along the column. The equivalent circuit is shown in figure 1 [5]. The potential and current of the beam act as voltage and current sources in the circuit [6]. For example, the equation for relating the voltages on $i^{th} - 1$ through $i^{th} + 1$ electrode is given by:

$$C_{pi}\frac{dV_{i-1}}{dt} - (C_{pi} + C_{pi+1} + C_{si} + C_{gi})\frac{dV_i}{dt} + C_{pi+1}\frac{dV_{i+1}}{dt}$$

$$= -\frac{V_{i-1}}{R_i} + (\frac{1}{R_i} + \frac{1}{R_{i+1}})V_i - \frac{V_{i+1}}{R_{i+1}} - N_b(I_{bi} - I_{bi+1}) - C_{gi}\frac{d\phi_i}{dt} \qquad (6)$$

Here C_{pi} is the capacitance between the $i^{th} - 1$ and i^{th} electrode, (where the emitting surface is the 0th electrode), R_i is the resistance between the $i^{th} - 1$ and i^{th} electrode, C_{si} is the stray capacitance between the ith electrode and ground, C_{gi} is the capacitance between the electrode and the on-axis potential, V_i is the voltage on the ith electrode, I_{bi} is the current in a single beam (out of N_b beams) at the ith electrode, C_d is the capacitance of the high voltage dome (which is at the voltage of the emitting surface). The external voltage is assumed to linearly vary between electrodes. Wire grids may replace a given electrode (for which $\phi = V_{ext}$).

Marx bank circuit (N_m stages):
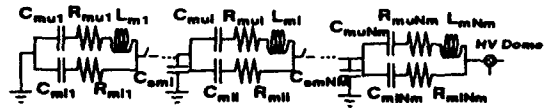
Injector column circuit (N electrodes):
Beam acts as both current source I,
and voltage source V.
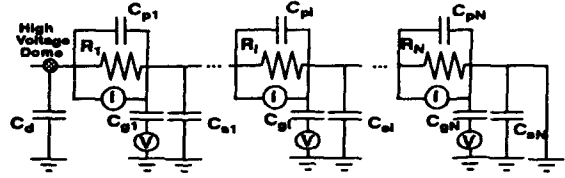
Figure 1. Circuit diagram for marx bank and injector modeled in HINJ.

Other features that are in the process of being incorporated into HINJ, include the following: 1. Envelope equations to self-consistently determine a_*. 2. The effects of spurious electron currents on the circuit equations, by injection of negative return currents at various electrodes, proportional to the current intercepted at an electrode, as determined by the radius of the electrode and the envelope radius.

IV. EXAMPLES OF RESULTS FROM HINJ

One test of HINJ was made by comparing the results from a simulation to an experiment performed on the Multi-Beam Experiment at LBL (MBE-4) by one of the authors (S. Eylon). It consisted of a 13.3 cm diode followed by a 1.8 m drift section. An aperture at the diode exit reduced the current by a factor of approximately 0.4. In simulating the experiment, we used a constant beam radius a such that the total current matched the total current in the experiment. Since the diode region did not have a definite outer "pipe" radius, and since r_p is defined as that radius at which the external voltage linearly decreases from V_0 to 0, we estimate that the equivalent $r_p \sim 2d$ where d is the diode length. Because r_p enters in the longitudinal dynamics only logarithmically, the results are not sensitive to the exact value of r_p. Fig. 2 shows simulation results of

the current and energy at the diagnostic station (LP0) at the end of the drift region, for two different voltage waveforms applied to the diode, and used as input to HINJ. Figure 3 shows the same quantities as measured in the experiment. The qualitative features of the experiment are seen in the simulation results. (Note that the time axes are displaced by ~2 μs, reflecting different zero points.)
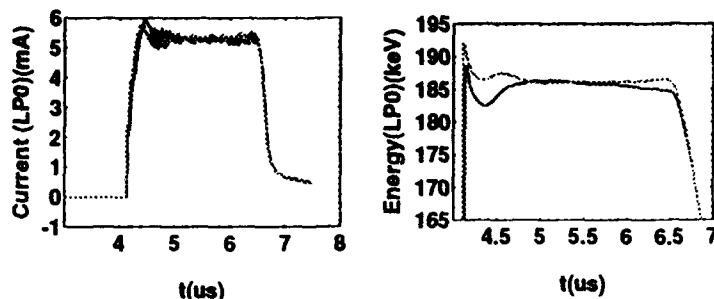
Figure 2. HINJ simulation of an MBE-4 experiment.
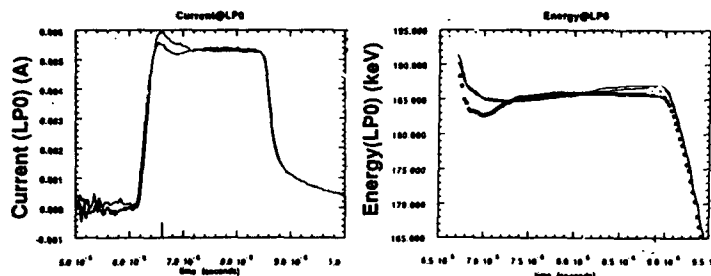
Figure 3. Experimental results of an MBE-4 experiment.

Another example of HINJ results is shown in figs. 4 and 5. A simulation of an ESQ that has circuit parameters which are typical of a possible ILSE [3] injector is shown. Fig. 4 shows the current at the emitter, diode exit, and injector exit. Both the initial current spike, and the erosion of the beam flattop due to space-charge debunching are evident. In fig. 5 the difference in final energy for a beam with and without beam loading of the circuit is shown. Beam loading effects of order ten keV are apparent. The ESQ column modeled consisted of 11 electrodes and the circuit values used were (cf. fig. 1): $R_1 = 1080$ Ω, $R_2 = 216$ Ω, $R_{i>2} = 432$ Ω, $C_d = 200$ pF, $C_{pi} = 400$ pF, $C_{gi} = 10$ pF, $C_{si} = 20$ pF. The Marx bank was modeled as a single stage ($N_m = 1$) with the values: $R_{mu1} = 864$Ω, $R_{ml1} = 2070$Ω, $C_{mu1} = 1306$ pF, $L_{m1} = 0.0378$ mH.

V. CONCLUSIONS

We have developed a 1-D, time-dependent particle code HINJ in which 2-D effects are incorporated into the code approximately, and in which beam loading is included self-consistently. The code has been compared to analytic, computational, and experimental results, and has been found to capture many of the physical details in the transient behavior.
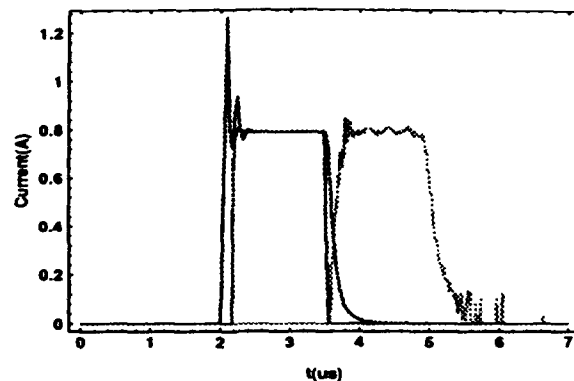
Figure 4. HINJ simulation of ESQ current pulse.
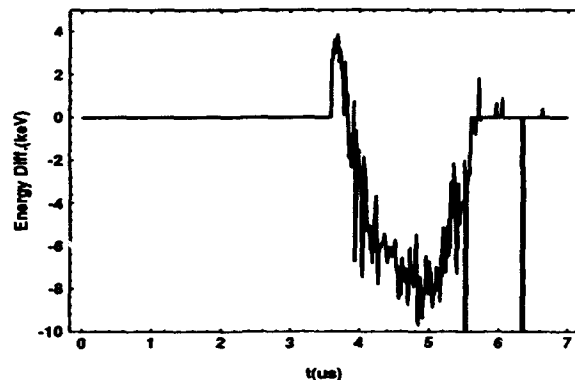
Figure 5. HINJ simulation of the difference in ion final energy between a beam-loaded and unloaded circuit in an ESQ.

VII. REFERENCES

[1] Y.J. Chen, D. Hewett, "Simulation of Transient Effects in the Heavy Ion Fusion Injectors," Particle Accelerator Conference Proceedings, this volume (1993).

[2] D. Grote, A. Friedman, I. Haber, "Three Dimensional Simulation of Heavy Ion Fusion Beams: Recent Improvements to and Applications of WARP," Particle Accelerator Conference Proceedings, this volume (1993).

[3] S. Yu, et al, "Heavy Ion Fusion Injector Program," Particle Accelerator Conference Proceedings, this volume (1993).

[4] Bruce Langdon, LLNL, private communication (1992).

[5] Lou Reginato, LBL, private communication (1992).

[6] G. J. Caporaso and J.J. Barnard, "Beam Loading Effects in Heavy Ion Injectors," Particle Accelerator Conference Proceedings, this volume (1993).

Analysis of Beam Loading in Electrostatic Columns*

George J. Caporaso and John J. Barnard
Lawrence Livermore National Laboratory
Box 5508, Livermore, CA 94550 USA

Abstract

A lumped element circuit model is derived which accounts for both electric and magnetic coupling of the beam to the electrodes and drive circuitry of an electrostatic column. A modified one dimensional Poisson equation which incorporates two dimensional effects is discussed. An effective capacitance between the beam and the column electrodes which affects the electric coupling is estimated. Simple analytic cases which treat electric and magnetic coupling separately are solved and compared against a numerical simulation. Scaling laws are given for the magnitude of the beam loading.

I. INTRODUCTION

This paper briefly discusses a beam loading model for an injector column system and how 2-D effects can be incorporated in a one dimensional code. We will show that the loading arises from two different effects which can be tied to electrostatic and magnetic fields.

II. BEAM LOADING MODEL

We wish to consider beam loading in a cylindrical column such as shown figure 1. A large insulator supports several electrodes or plates. There are external resistors which help to grade the applied voltage to the electrodes. There is a substantial capacitance between each electrode. The column assembly is enclosed in a large tank so that there is an additional capacitance from each electrode to the tank (which is assumed to be at ground potential).
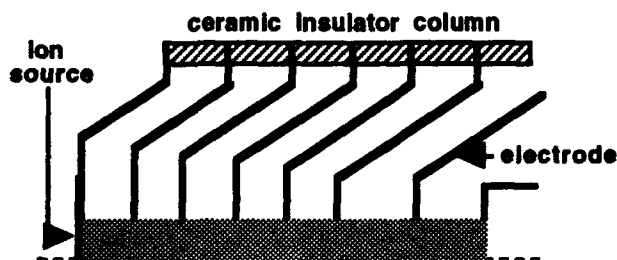
Figure 1. Typical ion injector column.

Figure 2 shows the effects of the beam's azimuthal magnetic field. Since the electrodes are good conductors the transient magnetic field generated by the beam cannot penetrate them on the time scale of the pulse. Ampere's law then requires that surface currents are generated in order to set up a magnetic field that cancels the beam's field inside the electrodes. The total surface current is equal and opposite to the beam current and can be approximately modeled as a current source in parallel with the inter-plate capacitance and resistance as shown in the bottom half of figure 2 (also shown

in the circuit is a stray capacitance C_S between each plate and the outer tank (ground)).
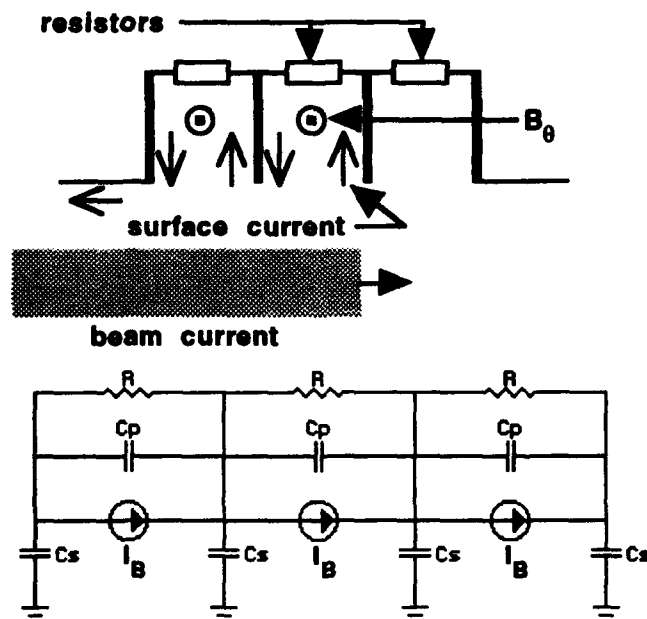
Figure 2. The beam's azimuthal magnetic field drives a return current on the electrode surfaces. The circuit equivalent is also shown.

Next consider the effect of the beam's radial electric field on the electrodes. If we imagine an isolated conducting aperture in a conducting cylinder as a uniform coasting beam passes through we would see electrons rushing in radially on the aperture as the head of the beam passes by.
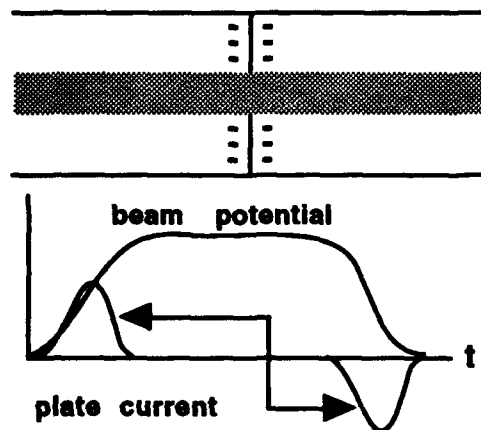
Figure 3. The beam's radial electric field draws in charges onto the plate. The current that flows in response to the passage of the beam appears to be a capacitive charging current.

715

This current would look like the derivative of the potential difference between the axis of the system and the plate. If the beam is long and of constant density, no additional radial current will flow. As the tail of the beam passes underneath the aperture the electrons which initially rushed in will be expelled and the radial current will reverse sign as the potential difference between the axis and the plate returns to zero. The radial current looks like a capacitive charging current that is proportional to the time derivative of a the potential difference between the axis and the plate. This is represented as a capacitance C_g in series with a voltage source between the plate and ground. The value of the voltage source is the value of the potential on the axis.
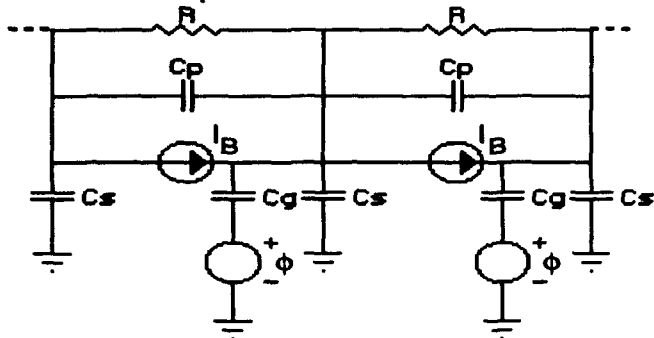
Figure 4. The circuit representation of the column showing both the return current and capacitive loadings.

In order to evaluate the loading we need to estimate both the value of the "beam capacitance" and the value of the potential along the axis.
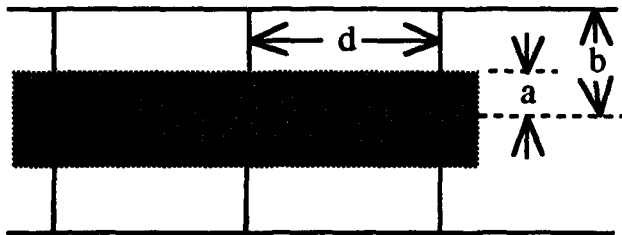
Figure 5. Geometry for the "beam capacitance" calculation.

We first look at estimating the value of the capacitance. We consider a uniform coasting beam just touching a periodic array of conducting apertures in an infinitely long cylinder. We will solve for the axial component of electric field and find the total charge induced on each aperture from the boundary condition $E_z = \sigma/\varepsilon_0$. We will then calculate the potential difference across the beam and define the "beam capacitance" as the total charge on the aperture divided by the potential difference across the beam. The capacitance is a function of the cylinder radius, aperture radius and aperture separation as is shown in figure 6. The presence of other apertures acts to reduce the local radial electric field of the beam thus reducing the amount of charge induced on a given aperture. Hence, the capacitance of a given plate will decrease as the inter-plate spacing decreases. For d/2b greater than approximately 2.0 the other plates have no effect and this solution is almost indistinguishable from that of a single plate in an infinite cylinder. The capacitance can

be found analytically as $C_g = 16\pi\varepsilon_0 b\ f(a/b,d/b)$ where $f(a/b,d/b)$ is given as

$$f(\frac{a}{b},\frac{d}{b}) = \sum_{n=1}^{\infty} \frac{J_o\left(\frac{x_{on}a}{b}\right)}{x_{on}^2 J_1(x_{on})}\left[1-\frac{a}{b}\frac{J_1\left(\frac{x_{on}a}{b}\right)}{J_1(x_{on})}\right]\tanh\left(\frac{x_{on}d}{2b}\right). \quad (1)$$
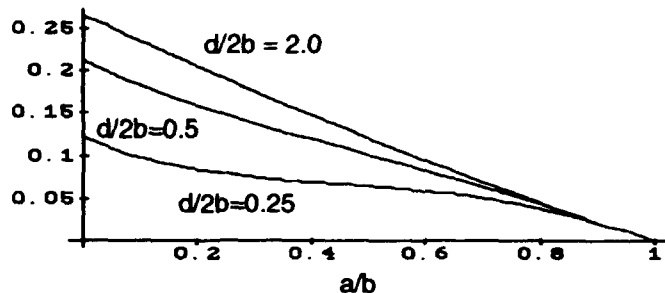
Figure 6. $f(a/b,d/b)$ as a function of inter-plate spacing.

We next turn to the problem of calculating the potential along the axis. The correct way to do this of course is to solve the 2-D Poisson equation. However, we would like to use this model in a 1-D code so we need some way of accounting for 2-D effects. A "field equation" that fits this requirement was suggested by Langdon [1]. It basically approximates $\nabla_{\perp}^2 \phi$ by the quantity $(V-\phi)/a^{*2}$ where V is the potential along the outer wall of the problem and ϕ is the potential on axis. The quantity a^* is defined as

$$a^* \equiv \frac{a}{2}\sqrt{1+2\ln\left(\frac{b}{a}\right)} \quad (2)$$

and is a characteristic length over which potential changes axially. Thus, the 2-D Poisson equation is to be replaced by the approximate equation

$$\frac{\partial^2\phi}{\partial z^2}+\frac{(V-\phi)}{a^{*2}} = -\frac{\rho}{\varepsilon_o} \quad (3)$$

where ϕ now represents the on-axis potential.

We can see how well this equation works on a test problem. Imagine a conducting cylinder with conducting end caps. Inside this cylinder we put a charged column of uniform radial density of radius a and arrange for the axial variation of density to correspond to that of steady state Child-Langmuir flow (the density varies as $z^{-2/3}$).
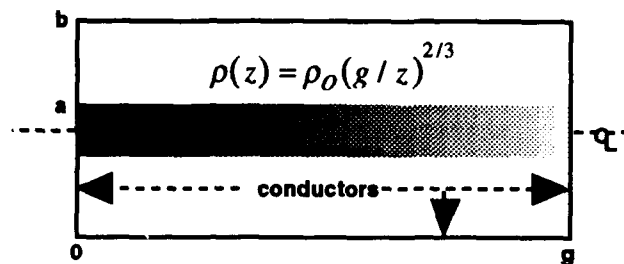
Figure 7. Geometry for Child-Langmuir flow density problem in a conducting cylinder with end plates.

We can solve this problem using the exact 2-D Poisson's equation and by using the "field equation". The solutions are overlaid on figure 8. We see that the field equation is remarkably accurate and correctly incorporates the 2-D effects of the end caps shorting out the radial electric fields.

than one then essentially the entire beam potential appears on the plate and raises the column voltage. When this ratio is less than one, however, the column is raised to something on the order of the maximum beam potential multiplied by this ratio.
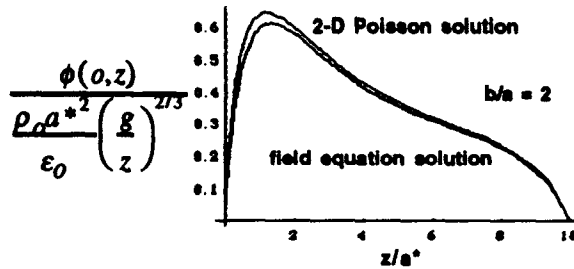
Figure 8. Comparison of field equation result with 2-D Poisson solution for a Child-Langmuir problem.

III. ANALYTIC SOLUTION AND SCALING LAWS

We now wish to put all these elements together to see the effects of beam loading. We will try a simplified problem so that we can solve it analytically to use as a check against the HINJ implementation [2]. We take the continuum limit of a discrete network in order to use differential equations in both z and t. We first look at the effects of the "beam capacitance" alone without the current source. In addition, to simplify the problem we assume that the column source impedance is zero and we eliminate the stray capacitance (that is in figure 4 we remove the current source and set C_s to zero. We take a coasting beam of constant density that is traveling at speed v. We take the length of the column to be 10 a* and assume that both ends of the column are grounded.

We plot the solution as a dimensionless voltage as a function of length along the column for successive times. We see that without a source impedance the column voltage rises reaching a maximum at about the time that the head of the beam reaches the end of the column (x=10) and then decays asymptotically to zero (for an infinitely long beam) as the resistance discharges the capacitors to ground. The quantity v_0 is given by

$$v_o = \left(\frac{C_g a^{*2}}{C_p} \right)\left(\frac{\rho_o a^{*2}}{\varepsilon_o} \right)$$ (3)

while x is defined as $x \equiv \beta ct / a^*$.

From this and other simple test problems (not discussed) we can draw some conclusions about beam loading. The beam capacitance and plate capacitance form a divider along which the beam potential appears. From our test problem for the field equation we see that the electric field from a sharply rising beam front actually spreads out over a distance roughly equal to a^*. The column forms a divider with series capacitance equal to C_p/a^* and with shunt capacitance equal to $C_g a^*$. When $C_g a^{*2}/C_p$ is greater
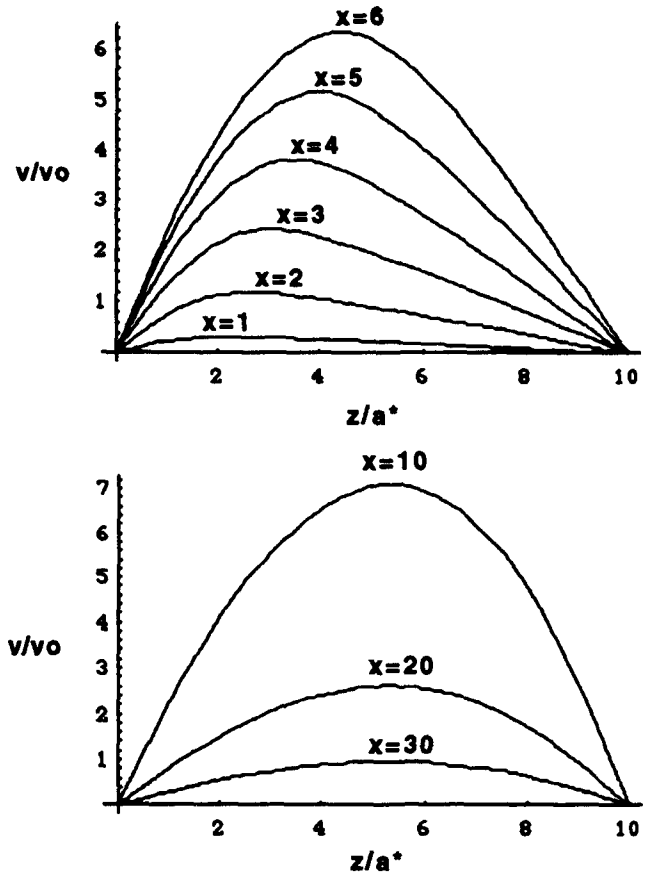
Figure 9. Solution to the simplified network discussed in the text.

The current sources will ̦ aise the column voltage if there is no source impedance. The effect is qualitatively similar to the case of just voltage sources alone. In this case the effective length for the circuit is roughly given by the velocity of the beam and the RC time constant per unit length. Multiplying this length by the resistance per unit length gives an effective resistance through which the return current is flowing raising the voltage.

When the source impedance is included in the picture the column voltages now go negative (we are speaking of the *perturbation to the column voltages caused by the loading*). This occurs because the return current is flowing through this impedance and represents the mechanism by which the source of the column voltage is coupling energy into the beam.

IV. REFERENCES

[1] B. Langdon, Private communication.
[2] J. Barnard, G. Caporaso, S. Yu and S. Eylon, these proceedings.

Simulation of Transient Effects in the Heavy Ion Fusion Injectors *

Yu-Jiuan Chen and Dennis W. Hewett
Lawrence Livermore National Laboratory
University of California
Livermore, California 94550

Abstract

We have used the 2-D PIC code, GYMNOS[1], to study the transient behaviors in the Heavy Ion Fusion (HIF) injectors. GYMNOS simulations accurately provide the steady state Child-Langmuir current and the beam transient behavior within a planar diode. The simulations of the LBL HIF ESAC injector experiments[2,3] agree well with the experimental data and EGUN[4] steady state results. Simulations of the nominal HIF injectors have revealed the need to design the accelerating electrodes carefully to control the ion beam current, particularly the ion loss at the end of the bunch as the extraction voltage is reduced.

I. INTRODUCTION

The transient effects in an injector can be caused by the time-varying emission of the ion source due to the time varying gap voltage pulses, the time-varying space charge redistribution within the beam pulse (or space charge debunching), secondary electron current arising from beam spilling and the beam loading effects[5,6]. These transient behaviors of a ion beam may lead to undesirable head-to-tail variations in beam energy and current, and even current loss. The transient problem is one of main concerns in an injector for the proposed Induction Linac Systems Experiments (ILSE)[7] where the ion pulse length is comparable to the injector length. Two options are considered for the ILSE injector[8]: one uses a set of axisymmetric electrodes arranged in an electrostatic accelerating Pierce column (ESAC), and the other uses an axisymmetric front end, such as a small ESAC pre-injector, followed by a sequence of electrostatic accelerating quads (ESQ). We have used the 2-D code, GYMNOS, to study beam emittance and the ion transient effects in several of the ILSE injector variants that have been proposed and tested during the design phase and have found excellent agreement in most cases in which comparison was possible.

We have found that the beam transients can be controlled easily by adding a low time-varying voltage "current valve" wire mesh[9,10] located closely to the the anode while fixing all other downstream electrodes at their steady-state values. However, to use the current valve transient control with a spherical anode would require fragile, curved current valve meshes in a very hostile environment. We have also found that careful design of the accelerating electrodes is needed to control the ion beam current, particularly the ion loss at the end of the bunches as the extraction voltage is reduced.

II. TESTS OF EMISSION ALGORITHM

In this section, we show the simulation results of an 1-D potassium (A=39) diode with a gap distance of 1.6 cm and a voltage of -6.56 kV that verify that GYMNOS simulations can provide the accurate beam transients and current. The GYMNOS calculated steady state current is 0.057 mA, within PIC noise, as predicted by the Child-Langmuir law for the cases of varied number of mesh points (8-240) in the A-K gap and a relatively small time step (0.5 ns) in the simulations[11].

Since one of the purposes of doing the time-dependent simulations is to study the effect of transients, we show in Figs. 1a and 1b the simulation results of the same 1-D potassium diode using the A-K voltage waveform given by

$$\phi(t) = \left[\frac{4}{3} \frac{t}{t_{rise}} - \frac{1}{3} \left(\frac{t}{t_{rise}} \right)^4 \right] \phi_0, \qquad t \le t_{rise} \ ,$$

$$\phi(t) = \phi_0, \qquad\qquad\qquad t > t_{rise} \ , \quad (1)$$

where t_{rise} is the rise time of the voltage pulse. Only 8 mesh points in the A-K gap were used in the simulations. For the case in Fig. 1a, we used the Lampel-Tiefenback voltage waveform[12] with the rise time equal to the ion transit time for crossing the A-K gap, t_{trans}, We obtained the predicted constant current profile for the front end and the flat-top of the beam pulse. When $t_{rise} < t_{trans}$, we expect the same asymptotic Child-Langmuir current at the flat-top portion of the beam pulse led by a higher current during the rise time (shown in Fig. 1b). In the case $t_{rise} = 150$ ns, the current during the rise time is estimated to be roughly 0.08 mA.
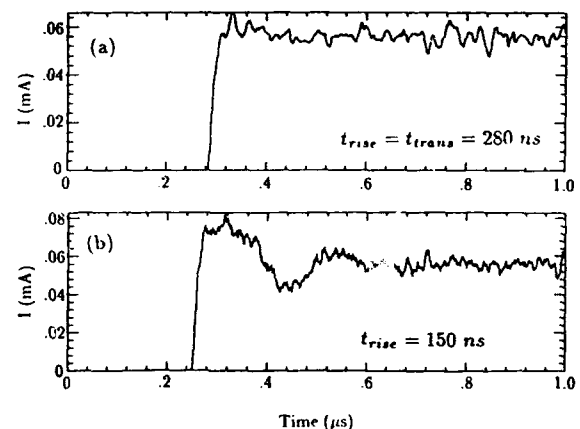
Fig. 1 The current profile calculated by GYMNOS when the A-K gap voltage waveform's rise time is (a) equal to and (b) less than the ion transit time, respectively.

III. LBL HIFAR ESAC INJECTORS

The GYMNOS results for the first prototype ILSE E-SAC injector are presented in Ref. [2]. The simulation results of the ILSE ESAC injector scaled experiment[3] with and without a current valve located closely to the anode are shown in Figs. 2a and 2b in this section. Tables I and II show that GYMNOS calculations of current, normalized emittance, beam envelope radius, and beam divergence agree very well with the experimental measurements, and EGUN's results[3] for both cases. The range of EGUN calculated emittance given in the Tables were obtained by using different initial transverse beam velocity distribution functions at the current valve location to characterize the initial transverse temperature and the emittance in the EGUN calculations. When a current valve mesh was used to control the beam pulse, the beam radius is comparable to the electrodes' aperture size as shown in Fig. 2a. Hence, the beam experiences a large nonlinear external field and its normalized beam emittance grows from its intrinsic value of 0.05 mm-mr at the source to 0.25 mm-mr at the emittance diagnostics location.

aperture size, the external field seen by the beam is linear. There is no normalized emittance growth in this case. We did not use enough resolution to simulate the small beam size (1mm) and beam divergence properly. Nevertheless, we have obtained very good agreement in the values of current and normalized emittance with experiments and EGUN calculations as given in Table II.

Table I The ESAC injector with a current valve

	GYMNOS	EXP	EGUN
Current (mA)	82	80	80
Normalized emittance (mm-mr)	.26	.25	0.07-0.2
Beam radius (mm)	32.5	31.2	31.0
Beam divergence (mr)	34.5	38.4	36.0

Table II The ESAC injector without a current valve

	GYMNOS	EXP	EGUN
Current (mA)	20	> 24	19
Normalized emittance (mm-mr)	.06	.04	0.05
Beam radius (mm)	5.0	1.2	0.9
Beam divergence (mr)	19	6	8

IV. ILSE INJECTORS

GYMNOS simulation results of the ILSE ESAC injector with a wire mesh located closely to the anode show that the transient effects in this injector configuration is small (as given in Fig. 3 and Fig. 4). The injector voltage pulse used in all the ILSE injector simulations has a 300 ns rise time and a 300 ns fall time with a 1 μs long flat-top. An early version of the ILSE ESQ pre-injector has a simple diode configuration without any current extraction control

Fig. 2 The ESAC injector (a) with and (b) without a current valve

When the current valve was removed, the voltage on the emitting anode and the first electrode (at $z=1.2$ cm in Fig. 2b) were the same. This voltage arrangement results in curved equipotential surfaces near the anode so that the beam is pinched by a very strong radial focusing force near the ion emitting surface and the first electrode, and focused roughly to a 1mm radius spot size at the injector exit. The space-charge limited current is then reduced. Since the beam radius is much smaller than the electrodes'

Fig. 3 GYMNOS simulation of the ILSE ESAC injector
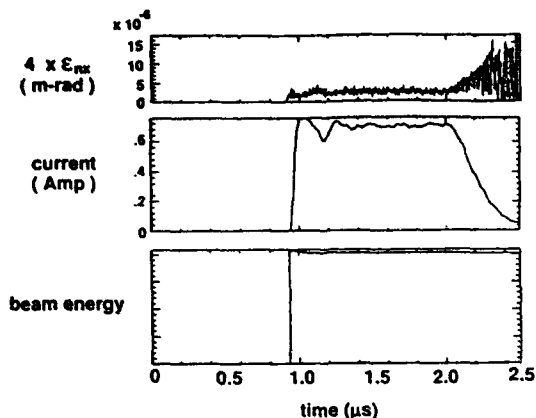
Fig.4 GYMNOS calculated normalized emittance, current and beam energy at the ILSE ESAC injector exit
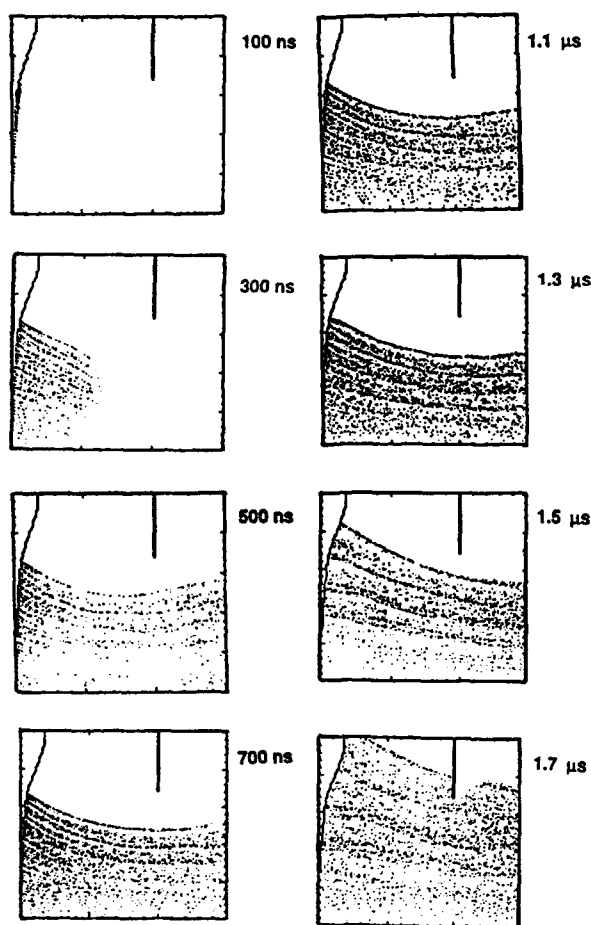
Fig. 5 GYMNOS simulation of an ILSE ESQ pre-injector

electrode. The simulation of this ILSE pre-injector indicates a large ion loss at the end of the current pulse as the time-varying injector voltage is turned off (see Fig. 5). Comparing the simulation results of these two injector configurations, we found that transients in an ILSE injector can be controlled easily by using a time-varying low voltage wire mesh, "current valve", located closely to

the anode while fixing all other downstream electrodes at their steady-state values. The current valve divides the injector into two parts. In the region between the anode and the current valve, the transient behaviors are controlled by the current valve's voltage waveform. From the current valve to the injector exit, the transient behaviors caused by the time varying current valve voltage are negligible if the current valve voltage is much smaller than the full injector voltage. While this vavle is a good current controller in a planar configuration, a spherical anode would require fragile, curved current valve meshes in a very hostile environment. We are now investigating the new injector configuration needed to control transients without using the current valve.

V. ACKNOWLEDGMENT

VI. REFERENCES

[1] D.W. Hewett and D.J. Larson, "The Best of GYMNOS: A User's Guide", LLNL Report No. UCRL-UR-110499, May 4, 1992.

[2] H. Rutkowski, et. al., "Ion Pulse Propagation Through a Previously Unfiled Electrostatic Aperture Lens Accelerating Column", thes proceedings, (1993).

[3] E. Henestroza, S. Eylon, and S. Yu, "ILSE-ESO Injector Scaled Experiment", this conference, (1993).

[4] W.B. Herrmannsfeldt, "Electron Trajectory Program", SLAC Report No. SLAC-226, UC-28 (A), Nov. 1979.

[5] J. Barnard, G. Caporaso, and S.S. Yu, "One Dimensional Simulations of Transients in Heavy Ion Injectors", thes proceedings, (1993).

[6] G. Caporaso and J. Barnard, "Analysis of Beam Loading in Electrostatic Columns", thes proceedings, (1993).

[7] "Induction Linac Systems Experiments Conceptual Engineering Design Study", LBL Report No. PUB-5219, March 1989.

[8] S. Yu, et. al., "Heavy Ion Fusion Injector Program", thes proceedings, (1993).

[9] H.L. Rutkowski, D.W. Hewett, and S. Humphries Jr., 'Development of Arc Ion Sources for Heavy Ion Fusion", *IEEE Trans. Plasma Sci.* 19, No. 5, 782 (1991).

[9] D. W. Hewett, M. R. Gibbons, and H. L. Rutkowski, "Extracting Low Emittance Ion Beams through a Current Valve/Switch Mesh", (in preparation, 1993).

[11] D. W. Hewett and Y.-J. Chen, "PIC Space-Charge Emission with Finite Δt and Δz", *Proc. of 1993 Comp. Acce. Phys.*, Pleasanton, Ca. Feb. 23-26, 1993.

[12] M. Lampel and M. Tiefenback, "An Applied Voltage to Eliminate Current Transients in a One-dimensional Diode", *Appl. Phys. Lett.* 43, No. 1, 1 (1983).

Electrostatic Quadrupoles for Heavy-Ion Fusion[*]

Peter Seidl and Andy Faltens
Lawrence Berkeley Laboratory
Berkeley, CA 94720 USA

Abstract

Voltage-holding data for three quadrupole electrode sizes and inter-electrode spacings are reported. The dependence of the breakdown voltage on system size and its influence on the optimum quadrupole size for beam transport in a multiple beam array are discussed.

I. INTRODUCTION

A number of designs for a heavy ion induction linac to be used as a driver for inertial confinement fusion (ICF) incorporate electrostatic quadrupoles as elements in an alternating-gradient-focusing lattice in the low-energy portion. This arises from the efficiency of the electrostatic quadrupole, in particular at low ion velocity, when compared to the magnetic quadrupole. Important objectives in designing a driver in this application intended for commercial electricity generation are efficiency and cost minimization, and thus, optimization of the beam current transported along the accelerator. To accelerate the large charge necessary to drive ICF, about 400 μC/pulse, it is advantageous to use multiple parallel beams which are focused in individual transport channels but are accelerated by common induction modules. Other things being equal, the cost of the accelerator decreases as the volume occupied by this charge decreases. The advantages of *electrostatic* quadrupoles are low manufacturing cost, economical operation, and the ability to transport a large amount of charge. The primary disadvantage is the risk of electrical breakdown either between the quadrupole electrodes, across the insulating supports or at the high-voltage feedthrough.

Figure 1 shows a schematic of the quadrupole geometry transverse to the beam axis. Field quality is an important issue, due to the necessity of maintaining low emittance so that beam combining and final focusing requirements may be achieved. In this work we have used the "ideal quadrupole geometry" which has circular cylindrical electrodes with 8/7 of the aperture diameter for their diameter. With this ratio the fields in the overlap region are almost purely quadrupolar and the dodecapole component vanishes[1]. Longitudinally, the structure is interdigitated, shown in Fig. 3, where the quadrupole electrodes are cantilevered from opposite polarity end plates, and peripheral insulators hold the assembly together. The basic electrode structure in Figs. 1 and 3 is repeated in order to accommodate multiple beams in a single induction core. If perfect manufacturing and alignment were possible, then the optimum solution would be a very large number of microscopic beams -- the examination of this possibility was

advocated by Maschke[3] with the Meqalac concept. Closely related to the question of the number of beams to be used is the beam-combining process. The geometric and space charge dilution of emittance from combining and the low emittance required by the final focusing system limit the number of beam combinings to one or two. In the low energy section a very large number of beams is desired, whereas, in most of the accelerator, the lowest cost is found for a small number of beams. For final focusing, however, a larger number is desirable again. With the present understanding of these matters, the driver would have about 80 electrostatically-focused beams in the front end, and 20 magnetically-focused beams in the remainder.

A common formulation of the beam transport is given by solutions to the Kapchinskij-Vladimirskij envelope equations, in terms of hard-edge equivalent fields with an occupancy of focusing fields, η, and a half period, L. Using the tables and equations of Ref. 2 in the limit of extreme space-charge dominance, we will establish a figure of merit (FOM) for transport in an electrostatically-focused, multiple-beam array that depends on the voltage holding characteristics of the quadrupoles, and the clearance limits of the beam edge to the physical aperture.
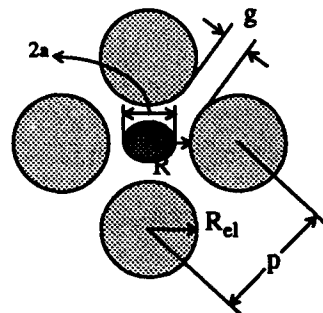
Figure 1. Schematic of electrode layout transverse to the beam direction. p is the repeat size of the quadrupole array geometry, a is the beam size, g is the inter-electrode gap size, R is the aperture radius and R_{el} is the electrode radius.

First, the longitudinal dimensions of the quadrupole determine the maximum η available. At a low beam energy, the end plates and high-voltage clearance around them take up most of the "dead space", $(1-\eta)L$; this is a consequence of needing large radii of curvature around the beam holes. It appears that 10-13 cm of dead space are necessary; for example, this implies $\eta \approx 0.5$ and $L \approx 30$ cm at T=2.5 MeV.

The transportable line charge density, λ, is

$$\lambda = 2\pi\varepsilon_o\gamma^2 kV_q\left(\frac{a}{R}\right)^2 \qquad \text{(EQ 1)}$$

where a is the maximum beam radius, R is the aperture radius and $\gamma=(1-\beta^2)^{-1/2}$ is the Lorentz transformation parameter. The

factor k is a scaled intensity/(beam envelope area) parameter which is a monotonically increasing function of η and the undepressed tune (single-particle, betatron phase advance per cell) σ_0. Beam stability considerations dictate a maximum allowable σ_0 of $85°-90°$[4]. The standard clearance prescription has been

$$R = 1.25a + 1 \ (cm)$$

(EQ 2)

This is based on experiments [5] and simulations which showed undesirable image effects for high-intensity beams which filled more than about 80% of the aperture (the factor 1.25) and the expected growth with distance of coherent oscillations from misalignment, field errors and mismatches (the $+1$ cm term[†]). With these constraints, it can be shown that λ is an increasing function of T, with the greatest increase in the first several MeV of the accelerator. The optimum transportable charge per unit volume (ρ) may be considered as the figure of merit, which is proportional to λ/p^2. Obviously, there is no limit on λ as the channel size is increased.
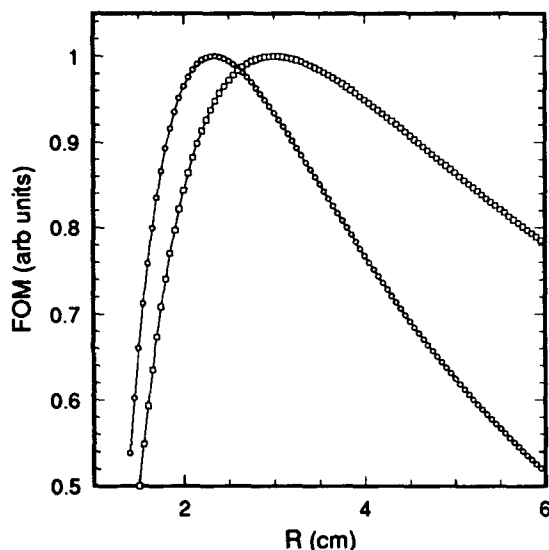
Figure 2. Figure of merit for electric focusing beam transport is proportional to λ/p^2, shown here in arbitrary units for two functional dependences of V_{max} on the quadrupole aperture radius. The squares and the circles are for a linear and a square-root dependence, respectively.

The dependence of V_q on R has been unknown due to the complicated three-dimensional nature of the fields, the presence of insulators, and the ambiguities of the breakdown process. The vacuum breakdown dependence for simpler situations has been measured to be linear for gaps smaller than 1 cm, and $\propto g^{0.5}$ for $g > 5$ cm, with a transition region in between. Based partly on these simpler systems, and the clearance prescription of Eq. 2, it has long been thought that the optimum aperture radius is near 3 cm, with an electrode to electrode gap near 2 cm. Figure 2 illustrates the FOM for the

[†]The +1 cm clearance is excessive right at the entrance to the accelerator, because the coherent oscillations require some distance to develop. Therefore, the clearance could initially be decreased from that given by eq. 2, and λ increased.

linear and square root dependences. The impact on the cost of an induction linac driver is significant, since an aperture difference of $\Delta R = 0.6$ cm translates into a 20% reduction in p, and in the overall focusing array diameter. For typical parameters this is a 15% change in the amount of induction core material needed to supply the required acceleration gradient.

The quadrupoles should be operated at approximately one-half of their breakdown voltage, V_{max}, which is consistent with the operation of other high-voltage apparatus. V_{max} is not a well defined quantity because it varies with electrode materials, surface finish, contaminants and high-voltage conditioning. For a multiple beam array nested inside the induction cores, it would not be practical to bake such a large system in situ, nor would it be desirable to heat the quadrupoles because of their precision alignment. In this application, the statistics and physics in the operation of a large array would lower the operating voltage, as would small, unavoidable beam spills.

II. EXPERIMENTAL SETUP

The issues of alignment tolerances and the difficulties associated with supporting the quadrupoles horizontally in an accelerator lead to consideration of hollow electrode designs and insulator supports that are not necessarily normal to the endplates or parallel to the electrodes. In order to expedite and simplify the interpretation of the results, these considerations were not included in the design of the quadrupoles tested in the experiment described here (see Fig. 3).
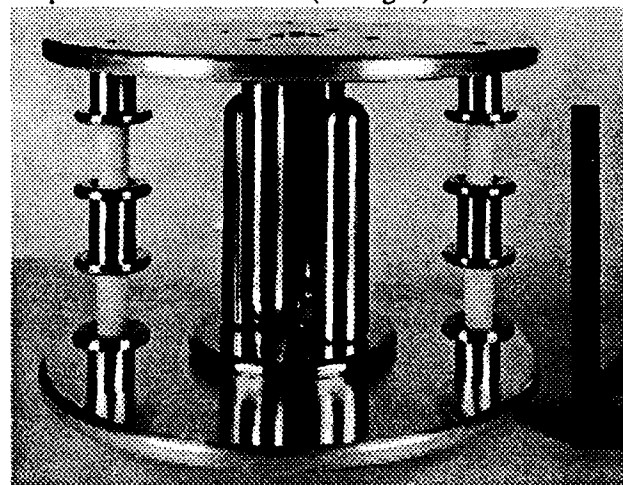
Figure 3. Quadrupole A is shown with the R_{el}=2.54 cm, L=21.5 cm electrodes. The scale on the right is 1 ft high.

The goal of the experiment was to study the voltage holding characteristics of the quadrupolar electrode geometry in order to determine the optimum electrode size and spacing. Once this is established, future studies will address the issues of alignment and compact design, based on V_{max} determined in this simpler experiment.

Since it was desired to have the controlling mechanism for breakdown be vacuum discharges between electrodes, the insulating supports were placed rather far away from the quadrupole electrodes. The electrodes and end-plates were solid stainless steel, and the insulating supports were made of 98% alumina (Al_2O_3). Three sets of electrodes with hemispherical ends were constructed and arranged as described in Table I.

Events at the interface between vacuum, dielectric, and conductor (triple-point) have been known to be controlling mechanisms for surface breakdown due to the high field concentration and field emission at the junction. To mitigate these effects, conducting shielding structures ("flower pots") were designed to reduce the field stress at the triple point. These flower pots also shielded the potentially high field region at the end of the supporting set screw that secured the insulator. For each of the three measurements, high voltage from two (−300kV/1.0mA maximum and +80kV/15mA maximum) Glassman DC power supplies was supplied to the opposing endplates. The quadrupole rested vertically on a high-voltage feedthrough connected to the −300-kV power supply. The pressure in the 1 m diameter x 3 m long vacuum tank was measured to be $0.5\text{-}5\times10^{-6}$ Torr with an ionization gauge a few meters away from the quadrupole.

TABLE 1. Electrode sizes (R_{el}), spacings and voltages.

Quad #	R (cm)	R_{el} (cm)	p (cm)	g (cm)	V_{max} (kV)
A	2.20	2.53	6.67	1.63	230
B	3.00	3.44	9.09	2.22	270
C	3.49	4.00	10.58	2.58	289

III. RESULTS AND DISCUSSION

The breakdown voltage for each quadrupole geometry was reached after about one day of pumping followed by about one-half day of conditioning, during which the vacuum system -- including the quadrupole under test -- was outgassing. Breakdown was evident by current and voltage fluctuations on the power supplies, by pressure fluctuations, concurrent visible light emission from the electrodes and fluorescence from the insulators. Slightly above V_{max}, the frequency of breakdown increased sharply, while slightly below V_{max} the voltage stability improved substantially. This stability was, however, not complete: occasional surface discharges were still visible from the supporting insulators below V_{max}. In addition, X-ray production was detected below V_{max}. The source of these X-rays is not completely clear, though it was determined to be associated with imperfections in the geometry of the 300-kV vacuum feed-through. In fact, the voltage-holding capability of the 300-kV feed-through alone was inferior to that of the tested quadrupoles, and this enigmatic behavior is still under study. The possible impact of the flux of X-rays on the voltage holding of the quadrupoles was a serious concern, and was studied and minimized by varying the bias between the positive and negative power supplies.

It is clear from Fig. 4 that the experimentally-determined V_{max} varies nearly as $\sqrt{g}$ in the R=2-3 cm region of interest. Thus the relevant figure of merit curve has a maximum at R≈2.3 cm in Fig. 2. Regarding the breakdown between the stainless steel electrodes, possible mechanisms of high-voltage vacuum breakdown have been discussed in the literature extensively in the past few decades, and no single mechanism has been uniquely identified as responsible. For example: electrons produced from microprotrusions on the cathode surface heat both the anode and the cathode and the melted

microprotrusions may give rise to metallic ejection which could initiate a spark. Another mechanism is that the electrons bombard the anode surface producing desorbing gas which may have adverse effects on the local vacuum pressure.
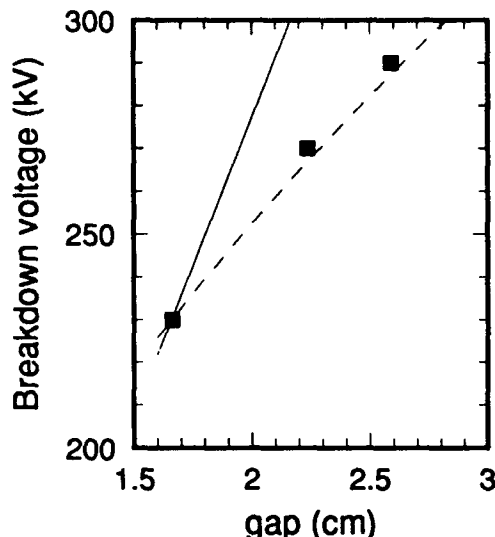
Figure 4. The experimentally determined breakdown voltage (squares) follows a $g^{0.5}$ dependence (dashed line). The solid line is a linear dependence.

In summary, we have measured the breakdown voltage vs. size relation for electrostatic quadrupoles designed for use in induction linacs for heavy ion fusion drivers. The breakdown dependence (measured in a beam-free vacuum) is proportional to $R^{0.5}$ in the region of interest, and the optimum aperture radius is 2.3 cm. Assuming the aperture-filling prescription of Eq. 2, the resulting transportable charge may be estimated: Assuming that a conservative operating point is $V_q \cong \pm 0.6\,(V_{max}/2) = \pm 71\,kV$ the corresponding line charge density approaches $\lambda = 0.19$ μC/m at T≈65 MeV. Likewise, the beam volume charge density averaged over the quadrupole structure would be $\lambda/p^2 = 38$μC/m^3 in a multiple beam array. This does not include edge effects of electrode packing and space required for high voltage holdoff at the periphery, which are minor corrections for a large array.

IV. ACKNOWLEDGEMENTS

V. REFERENCES

[1] For another possible design see C. M. Celata, *Proceedings 1987 Particle Accelerator Conf.*, p. 996 (1987).

[2] *Selected works of L. Jackson Laslett*, Lawrence Berkeley Laboratory Pub-616, Vol. III, chapter 6 (1987).

[3] A. W. Maschke, Brookhaven National Laboratory BNL-51029 and BNL-51419 (1979).

[4] M. G. Tiefenback and D. Keefe, *IEEE Trans. Nucl. Sci.*, NS-32, No. 5, 2483 (1985).

[5] A. W. Maschke et al., *IEEE Trans. Nucl. Sci.*, NS-30, No. 4, 2558 (1983).

Simulation Studies of Space-Charge-Dominated Beam Transport in Large Aperture Ratio Quadrupoles*

W.M. Fawley, L.J. Laslett, C.M. Celata, A. Faltens
Lawrence Berkeley Laboratory, University of California
Berkeley, CA 94720 USA
I. Haber
Naval Research Laboratory
Washington, D.C. USA

Abstract

For many cases of interest in the design of heavy-ion fusion accelerators, the maximum transportable current in a magnetic quadrupole lattice scales as $(a/L)^2$ where a is the useful dynamic aperture and L is the half-lattice period. There are many cost benefits to maximizing the usable aperture which must be balanced against unwanted effects such as possible emittance growth and particle loss from anharmonic fringe fields. We have used two independent simulation codes to model space-charge dominated beam transport both in an azimuthally-pure quadrupole FODO lattice design and in a more conventional design. Our results indicate that careful matching will be necessary to minimize emittance growth and that (a/L) ratios of 0.2 or larger are possible for particular parameters.

I. Introduction

An important issue in the design of heavy ion fusion (HIF) drivers is the dynamic aperture of short quadrupoles which immediately follow the transition from electrostatic to magnetostatic focusing. This importance stems from the maximum transportable current for a highly space-charge depressed beam scaling as the usable beam aperture, a_b, squared:

$$ I_{max} \approx \left(\frac{a_b}{2L}\right)^2 I_o \frac{A\gamma^3\beta^3}{2Q}\sigma_o^2 \qquad (1) $$

Here I_o is the proton "Alfven current", 31.07 MA, σ_o is the phase advance per lattice period $2L$, A and Q are the atomic mass and charge state respectively of the ion species, and γ and β have the normal Lorentz definitions. Since a large I_{max} permits decreasing the required number of beamlets and thus more efficient use of the accelerating core cross-section, there is a great premium in making the inverse aperture ratio (a_b/L) as large as possible.

The usable beam aperture a_b may be defined as that above which the beam suffers unacceptable emittance growth and/or particle loss over transport distances of interest. Both these phenomena generally occur due to non-linearities in the net focusing forces (i.e. external minus space charge). Such nonlinearities are inevitably present whenever the external focusing contains higher order multipole (e.g. dodecapole) moments or fringe fields (e.g. pseudo-octupoles [1] which arise from the second longitudinal derivative of the quadrupole moment). Although these effects are present to some degree in all strong focusing systems, FODO lattices in HIF induction accelerators are somewhat unusual in two respects: 1) Beam space-charge forces lead to very high tune depressions ($\sigma_o/\sigma \geq 10$ or more where σ is the space-charge depressed phase advance); this makes it unclear whether the usable beam aperture can be estimated from "single particle" results. 2) The high σ_o's ($\sim 72°$) true for many HIF driver designs imply relatively large AG flutter motion which may lead to poor net cancellation of fringe field and multipole forces compared to the more usual low σ_o case.

II. Magnet Designs

A. "Conventional" Multipole Suppression

As a/L becomes large and the relative contribution of fringe fields increases, serious attention must be paid to the coil end topology. Our present work builds upon earlier designs [2] in which higher order multipoles disappear in the z-integrated sense, i.e.

$$ \int_{-\infty}^{+\infty} dz \int_{-\pi}^{+\pi} d\theta \, A_z(r,\theta,z) \cos(4l+2)\theta = 0 \qquad (2) $$

for $l \neq 0$. Presuming time-independent coil currents, the zth component of the vector potential may be replaced by that of the current density J. In the absence of transverse motion, particles traveling through isolated magnets with this topology will suffer no net kick due to the higher order multipoles. In the real world, however, transverse motion associated with emittance and AG flutter prevents the cancellation from being absolute.

The simplest (and probably most compact) coil end topology is that of right angles with the coil turns of each individual half-period quadrant being rectangles in the developed view (ignoring the necessary turn-to-turn connections). The angular position of each wire is then determined by replacing Eq. (2) by

$$ \sum_{k=1}^{n_{wire}} L_k \cos(4l+2)\theta_k = 0 \quad \text{for } l = 1, 2, \ldots \qquad (3) $$
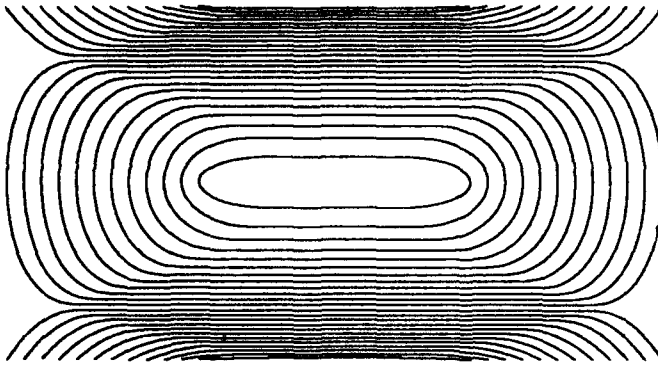
Figure 1: Top view of current windings for an ILSE prototype magnet with elliptical coil ends.

where L_k is the specified length of the kth wire.

Most HIF driver designs require magnetic field magnitudes and electrical efficiencies that are possible only with superconducting cables. Present day SC cable technology requires radii of curvature ≥ 1 cm, which rules out rectangular coil ends. In addition, tight corners tend to be regions of enhanced magnetic field strength which can lead to quenching difficulties. Ref. [2] gives an analytic framework for determining a family of curves that satisfy Eq. (2). For magnetic quadrupole development associated with the Induction Linac Systems Experiment (ILSE) project, we are examining elliptical coil end curves. Fig. 1 shows a top view of the windings in one-half period; a prototype magnet with this topology is currently undergoing electrical and mechanical tests at LBL.

B. "Pure" Quadrupole Magnet Design

The multipole suppression described above is strictly relevant only to an isolated magnet. In a periodic lattice, fringe field leakage from adjacent magnets can reduce this suppression in each half-period. Moreover, AG flutter motion prevents effective suppression in the integral sense even over a full period. To overcome these limitations, one of us [LJL] suggested examining winding patterns that result in a *pure* quadrupole dependence of the fields azimuthally. The necessary surface current at radius a is

$$\vec{J}(\theta, z) = \sum_{n=1,3,5\ldots}^{\infty} \alpha_n \left[\cos\left(\frac{n\pi z}{L}\right) \cos 2\theta\, \vec{e}_z \right. +$$
$$\left. \frac{n\pi a}{2L} \sin\left(\frac{n\pi z}{L}\right) \sin 2\theta\, \vec{e}_\theta \right] \quad (4)$$

and the resultant interior magnetic scalar potential is

$$\Phi_m(r,\theta,z) = \frac{\mu_0 a}{2} \sin 2\theta \sum_{n=1,3,5,\ldots}^{\infty} \alpha_n \left[\frac{n\pi a}{L}\right] K_2'\left(\frac{n\pi a}{L}\right) \times$$
$$I_2\left(\frac{n\pi r}{L}\right) \cos\left(\frac{n\pi z}{L}\right) \quad (5)$$

where I_2 and K_2 are modified Bessel functions. While the above formulas are exact only for infinite lattices, they are quite good approximations to long, periodic lattices whose wire topologies and currents change only slowly with z.

For a given choice of the longitudinal Fourier components α_n, the behavior of $K_2'(\zeta)$ for $\zeta \geq 2$ implies that the contribution of components with $n \geq 3$ near the axis become exponentially small for $a/L \geq 0.3$. In other words, as the aperture ratio a/L of a periodic lattice becomes large, the $z-$dependence of the quadrupole field components asymptotically approaches a simple sinusoid with period $2L$. Consequently, our transport studies have concentrated on the limiting case of $\alpha_n \equiv 0$ for $n \neq 1$, which we call a "one-term" magnet.

Although the magnetic fields corresponding to Eq. (5) are azimuthally pure quadrupoles, the resultant focusing has anharmonic terms due to the radial dependence of the I_2 function. To estimate the strength of these nonlinearities in a one-term magnet, we compute an average over the AG-flutter motion in one lattice period, resulting in

$$\sigma_o^2(r,\theta) = \sigma_o^2(0)\left(1 + \frac{3}{8}\left(\frac{\pi r}{L}\right)^2 - \frac{1}{8}\left(\frac{\pi r}{L}\right)^2 \cos 4\theta\right) \quad (6)$$

through terms second order in r/L. Here $\sigma_o(0)$ is the on-axis value of σ_o. One should remember that although the second and third terms on the RHS are small compared to the undepressed tune for $r \leq 0.2L$, they are relatively much larger components of the net focusing of space-charge dominated beams with $\sigma \ll \sigma_o$.

III. Simulation Code Studies

A. Code Descriptions

We employed two independently developed, electrostatic, 2D particle simulation codes for our transport studies. The first, SHIFTXY[3], solves fields on a uniform Cartesian $x - y$ grid and thus permits study of all azimuthal modes. The second, HIFI, uses an $r - \theta$ grid and presumes even symmetry about the x and y planes, thereby restricting azimuthal modes to $\cos 2m\theta$ dependences. Both codes include non-paraxial terms and $v_\perp \times B_z$ forces in the equation of motion and determine $\vec{B} \equiv -\nabla\Phi_m$ from Eq. (5). The initial particle loads follow either a KV or semi-Gaussian distribution in phase space (*i.e.* uniform in configuration space). The simulation "walls" are fully absorbing with radii generally $\geq$ twice the initial beam radius.

B. Emittance Growth

There are at least two related agents for emittance growth for beams transported by large aperture quadrupoles. The first arises from phase-mixed damping of macroscopic mismatch oscillations. Due to the growing relative strength of non-linearities such as the pseudo-octupole, it becomes harder and harder [*cf.* Eq.(6)] to match accurately the beam envelope parameters (x, x', y, y') as a_b/L increases. When $a_b/L \leq 0.25$, a surprisingly good match can be obtained by running an envelope code that evaluates the *total* focusing forces at the
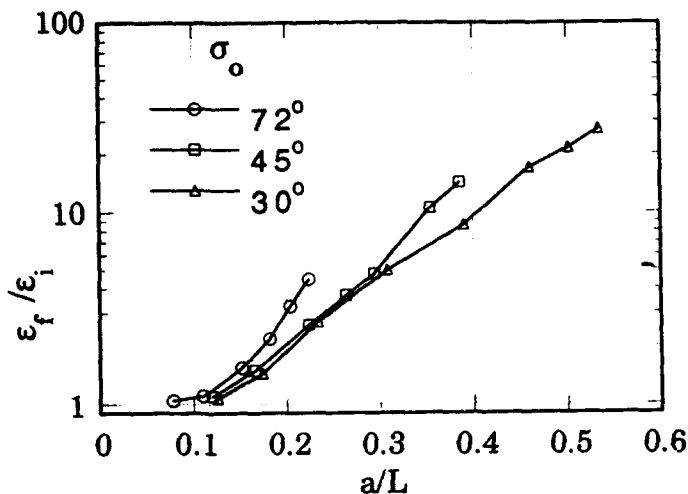
Figure 2: Relative emittance growth over 100 periods of transport in a "one-term" sinusoidal lattice versus a_b/L for three values of σ_0. Each curve was terminated when particle losses exceeded a few per cent.

Figure 3: The dynamic aperture of a "one-term" sinusoidal periodic lattice for both space-charge dominated ($\sigma \ll \sigma_0$) and emittance-dominated ($\sigma = \sigma_0$) beams. The dotted curve labeled λ_{max} refers to the maximum line charge density that can be transported ($\sigma \ll \sigma_0$) with negligible particle loss.

envelope *edge* (as opposed, for example, to an algorithm that uses area-weighting). For larger values of a_b/L, this scheme becomes inaccurate and a full particle simulation must be done iteratively to obtain the predicted macroscopic match quantities.

Even when the macroscopic match is "correct", the microscopic deviation of the beam's internal profile from the nonlinear equilibrium value can lead to strong emittance growth. In agreement with expectations from Eq. (6), it appears that the equilibrium profile must have a space-charge density $\rho(r)$ increasing with r and a small, but non-zero octupole moment. Our simulations show both characteristics developing within a few plasma periods when $a_b/L \geq 0.2$. It then takes ≈ 30 lattice periods for the beam to settle down near its new equilibrium. This adjustment normally leads to the formation of a halo in velocity space.

When $a_b/L \leq 0.1$, the focusing nonlinearities are small and there is very little emittance growth for a well-matched beam. Fig. 2 plots the ratio of final to initial emittance versus beam radius for three values of σ_0. The initial beam brightness was kept constant (*i.e.* $\varepsilon \propto \lambda^{1/2}$) and the tune depression was $\sim 12:1$ for $\sigma_0 = 72°$ and $a_b/L \approx 0.08$. We define the maximum dynamic aperture a_{max} as the radius beyond which significant numbers of beam particles will be lost. Plots of a_{max} versus σ_0 for both space-charge and emittance-dominated beams are shown in Fig. 3. For $\sigma_0 \approx 72°$, the instability boundary appears to be associated with unstable fixed points whose (undepressed) pahse advance is $90°$. When σ_0 is relatively small, there is not such a clear association with fixed points. We find it intriguing that throughout this large range in σ_0, the instability boundary is barely perturbed by the presence of strong space-charge effects, at least for well-matched beams.

Fig. 3 also plots the (normalized) maximum line charge density that can be transported over 100 lattice periods with little or no loss. We stress that although one can transport greater λ at $\sigma_0 = 30°$ than at $72°$, the emittance growth is so severe for $\lambda \geq 0.25\lambda_{max}$ at $30°$ that few applications could use the resultant beam. Scans of emittance growth for well-matched beams with $\lambda = 0.8\lambda_{max}(\sigma_0 = 72°)$ versus σ_0 show a minimum value in the $65°$ to $75°$ range. The growth is larger for either much lower σ_0 values or higher values (where particle loss, too, is a problem). Consequently, our present results support the present bias in HIF driver design to set $\sigma_0 \approx 72°$.
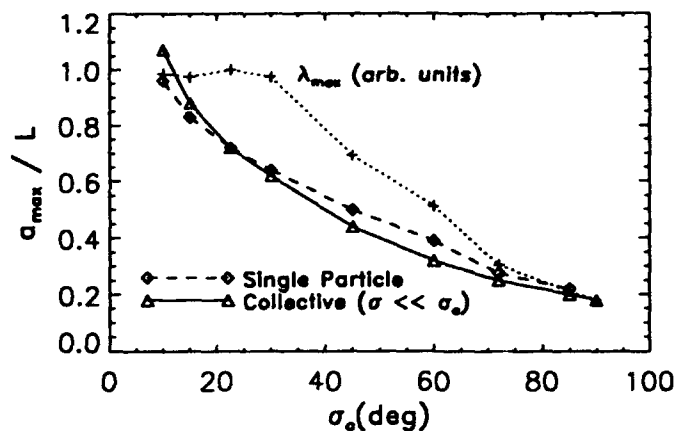
This paper is dedicated with deep affection to the memory of our co-author, L. J. Laslett.

References

[1] P. Krejcik, "Nonlinear Quadrupole End-Field Effects in the CERN Antiproton Accumulators," *Conference Record of the 1987 IEEE Particle Accelerator Conference*, Vol. 2, pp. 1278-1280.

[2] Laslett, L.J., Caspi, S., Helm, M., *Particle Accel.*, **22**, 1 (1987).

[3] Haber, I., "High Current Simulation Codes," *High Current, High Brightness, High Duty Factor Ion Injectors*, Ed. George H. Gillespie *et al.*, **AIP Conf. Proc. 139**, (AIP, New York, 1986), p. 107.

Three Dimensional PIC Simulation of Heavy Ion Fusion Beams: Recent Improvements to and Applications of WARP *

David P. Grote and Alex Friedman
Lawrence Livermore National Laboratory
P.O. Box 808, Livermore CA, 94550-0808 USA
and Irving Haber
Naval Research Laboratory
Washington D.C. 20375 USA

Abstract

The multi-dimensional particle simulation code WARP is used to study the transport and acceleration of space-charge dominated ion beams in present-day and near-term experiments, and in fusion drivers. The algorithms employed in the 3d package and a number of applications have recently been described.[1] In this paper we review the general features and major applications of the code. We then present recent developments in both code capabilities and applications. Most notable is modeling of the planned ESQ injector for ILSE, which uses the code's newest features, including subgrid-scale placement of internal conductor boundaries.

I.   INTRODUCTION

Heavy-ion particle accelerators are attractive candidates for inertial fusion drivers.[2] The required beams have high current and must have a low transverse emittance, so the beam can be focused down onto a small (few mm) spot at the fusion target. Nonlinearities of the self-fields of the beam, as well as manipulations of the beam, can lead to emittance growth. A self-consistent description of the space-charge fields is thus needed: the particle-in-cell method is well suited to such simulations. The WARP3d code is being developed to study the transport and acceleration of space-charge dominated heavy ion beams; it combines features of particle-in-cell simulation with those of an accelerator code.

II.   CODE OVERVIEW

The code's accelerator "lattice" consists of a fully general set of focusing and bending elements. These elements are described in the laboratory frame and can be periodic. The description includes the strengths of the fields, location of the elements, and other properties specific to the types of elements. For flexibility, each multipole component is specified separately- this allows the possibility of overlapping elements. The lattice fields are calculated in the local

lab frame for each particle at each time step. These fields, along with the self-consistently calculated self-fields, are used in the Lorentz force law to advance the particles at each time step. For efficiency, the lattice information is loaded onto a one-dimensional local grid which moves with the beam at the beginning of each time step. This avoids having to search the master list to find the information for each particle.

The code's particle-in-cell sections calculate particle trajectories and self-consistent electrostatic fields from the particles' positions. The particle trajectories are calculated with the leapfrog advance, using either full steps for efficiency or split steps to have the particle's velocity and position synchronized in time for diagnostics. Residence corrections are used to account for differing number of steps through sharp-edged elements; without residence corrections, particles landing inside an element more times or fewer times would receive dramatically different impulses. The self-potential ϕ is calculated via a Poisson solver on a co-moving mesh that is only large enough to hold the beam. The electric fields are applied by directly differencing ϕ for each particle.

In a bend, each particle is described in its own Cartesian frame; as the particle advances around the bend, the frame changes. Assuming a small inverse-aspect-ratio, an approximate algorithm is used. The dipole or bend field is augmented with a "pseudo-gyrofrequency" that accounts for the rate of change of the velocity angle due to the frame transformation. The algorithm is inexact since it does not account for the changes in beam position and velocity during the time step. The self-potential is calculated assuming a gentle bend. It is first calculated in Cartesian coordinates and then modified through iterations to include the non-Cartesian terms.[1]

Additional features include a full set of RMS particle moment calculations, including emittance, in both the beam frame and the lab frame. A multitude of phase space plots can also be generated.

III.   APPLICATIONS

A.   *Drift Compression in a Misaligned Lattice*

Current amplification from drift compression can lead to emittance growth, especially in the presence of misaligned

quadrupoles. With the side-to-side oscillations from the misalignments and fattening of the beam from the compression, particles will sample more non-linear fields from the focusing structure and from the images on the surrounding pipe. In one case, with 1 mm (RMS) random misalignments and a square surrounding pipe, the beam experienced an increase in emittance of 25%. When the walls were moved out farther (from 7 cm to 9 cm), the emittance growth went away almost completely.

B. *Beam Equilibria*

The code allows us to follow beams over long distances. Beams have been followed for as long as 175 strong-focusing lattice periods, or 210 meters in 10500 time steps. The bulk of the beam remained quiescent over this time. The ends of the beam did show some emittance growth because the initial state was not a true equilibrium. Other runs show equilibration between transverse and longitudinal temperature ($T_{x,y}$ and T_z). When T_z is much less than $T_{x,y}$, there is (over a certain range of physical parameters) a rapid, collective process that equilibrates the two temperatures. Equilibrium in the other direction ($T_{x,y} < T_z$) is observed to proceed more slowly, on a collisional timescale.

C. *MBE-4 Experiment*

Drift compression experiments on the MBE-4 facility at LBL showed anomalous emittance growth.[6] Simulations show that the growth, in large part, results from the dodecapole components of the focusing fields. As the beam compresses and grows fatter, the particles experience more of the non-linear dodecapole field.

D. *Bent Beams in an ILSE Lattice*

The transport of beams through bent lattices is being studied. Simulations have shown that beams that are axially cold do not exhibit any emittance growth during a bend, whereas beams that are axially hot ($T_{x,y} \sim T_z$) do show emittance growth. We believe this growth arises as a result of dispersion in the bend; this has been described in more detail in reference [1].

IV. RECENT ADDITIONS

A. *Injection*

A simple model of injection has been added to WARP3d. At each time step, a preset number of particles are injected from the plane of injection. The injection is not space-charge-limited. The region into which the particles are injected extends from the plane of injection to the axial distance traveled in one time step. That distance includes acceleration from any potential gradients along the beam axis. The particles are distributed as if they were injected uniformly in time and accelerated along a uniform electric field given by the ratio of the potential across the region of injection to the length of the region.

B. *SOR Field Solver With Internal Conductors*

In order to simulate the transport of beams through complex conducting structures, the field solver must be able to include those conductors in the field solution self-consistently. For that purpose, a successive overrelaxation (SOR) iterative Poisson solver was added to the code. SOR was chosen because of its simplicity, ease of use, and flexibility in dealing with internal conductors. The seven point finite-difference form of Poisson's equation is used with the three-dimensional extension of red-black ordering. The potential of the conductors internal to the field mesh is enforced by setting the grid points inside the conductors to the appropriate potential before each iteration. For more accuracy, a scheme for allowing subgrid-scale placement of boundaries was implemented.

Subgrid-Scale Placement of Boundaries: The conductors that produce the quadrupole focusing fields consist of round, cylindrical rods, but the field mesh is a rectangular Cartesian grid. The round rods would be represented by stacks of rectangular blocks or "legos." This leads to inaccuracy of the fields. With space-charge dominated beams, the focusing fields need to be accurate in order to produce the correct beam envelope. A scheme was developed to solve for the potential near conducting surfaces that are not aligned with the computational grid.

The finite-difference form of Poisson's equation near conducting surfaces is changed to explicitly include the location of the boundary. In the finite-difference equation, one (or several) of the points will be inside a conductor, so ϕ at these points can be used as a free parameter. In one dimension, the potential at the surface of the conductor is given by linear interpolation from the two surrounding points, one outside the conductor, the other inside.

$$\phi_{\text{surface}} = (1 - \delta)\phi_{\text{outside}} + \delta\phi_{\text{inside}} \qquad (1)$$

where δ is the distance between the surface and the point outside. This is rearranged to give an expression for ϕ_{inside} which is put into the finite-difference equation. The resulting expression is rearranged to make it fully explicit. The altered equation is used to calculate ϕ_{outside} in the iteration in place of the finite-difference equation used for the bulk. This process is done for all points near conducting surfaces. With multiple dimensions, several nearby points may be inside a conductor. Each point is handled separately as above. The linear interpolations for ϕ_{surface} in each direction are used to give separate equations for the ϕ_{inside}. These are all place into the seven point finite-difference equation which is then rearranged to be fully explicit.

V. ESQ INJECTOR

The electrostatic quadrupole injector that is being designed for ILSE uses ESQ's for both focusing and acceleration. The quadrupoles are arranged to give a net acceleration along the axis while maintaining alternating gradient focusing. A major issue of concern is emittance growth from both the nonlinear multipole components of the focusing fields and the "energy effect". The cause of this effect are the focusing potentials, which are a large fraction of the particle's energy. Particles which are off axis

have a significantly different axial velocity than those on axis and are focused differently, causing beam distortion. Note that this effect is present in all electrostatic focusing systems but is generally insignificant, since the focusing potentials are a small fraction of the beam energy.

A. *Description of the Computer Runs*

Only steady state phenomena are of interest, so the runs are made in a quasi time dependent fashion. The time step over which the fields are calculated is larger than the time step of the particle advance. This process converges in just over one transit time across the injector, between five and ten field solutions. Transient behavior is lost and only steady-state is obtained. The dimensions of the field grid, including the conductors, are typically 50×50 in the transverse directions and between 200 and 600 in the axial direction, depending on the number of quadrupoles in the system. The lengths of the runs are between 300 and 1000 time steps, again depending on the number of quadrupoles. From 70,000 to 300,000 particles are used. Runs take typically from 3 to 30 minutes on the NERSC Cray C-90. We are effectively able to use WARP3d as a design tool.

B. *Simulation of the ILSE Injector*

The injector is required to supply 1 Amp of 2 MeV singly charged potassium ions at low transverse emittance, less than .5 π-mm-mrad. The initial design was done using an envelope code that does not include the energy effect. The three-dimensional simulations of that design did show significant emittance growth, up to 2 π-mm-mrad. By selectively canceling various multipole components, it was found that about half of the emittance growth was the result of the V_{42} potential component ($\phi_{42} = V_{42}r^4 \cos 2\theta$). The effect of that component is greatest where the beam gets closest to the conductors.

Analysis of single particle motion shows that the energy effect is fourth order ($\phi \sim r^4$) and is the result of the interaction of the difference in kinetic energy between particles on axis and off axis and the quadrupole field. By analytically applying additional fourth order fields, the energy effect can be canceled. Doing this showed that the energy effect accounted for the other half of the emittance growth. When the correction to the energy effect is applied and the V_{42} field is canceled, the beam experiences no emittance growth. This is a favorable result since it shows that the emittance growth is the result of external fields only and not the result of nonlinear space-charge fields. There is confidence, then, that the emittance growth can be greatly reduced or eliminated.

C. *Optimization of Design*

We looked at three ways of optimizing the design to reduce the emittance growth: changing the focusing fields to make the envelope as small as possible, changing the quadrupole structure to reduce the effect of the nonlinear fields, and increasing the beam energy from the source. Decreasing the size of the envelope was simple but of limited help. The envelope reduction is limited by the nature of alternating gradient focusing. Changing the structure was the next most useful. The biggest gain was from moving the focusing rods out and the defocusing rods in. While maintaining the same focusing strength, that moved the rods away from the fattest parts of the beam.

The most effective way of reducing the emittance growth is to increase the beam energy from the source. By increasing the energy before it enters the ESQ, the beam is stiffer and maintains a smaller envelope, reducing the effect of both the nonlinear fields and the energy effect. Also, with a higher beam energy, the energy effect is directly reduced. Simulations show that it is possible to have no emittance growth. Unfortunately, due to experimental constraints, increasing the beam energy at the source is difficult to do in practice.

D. *Comparison With Experiment*

A scaled-down version of the ILSE injector that was tested at LBL was simulated. There was good agreement between experiment and simulation. Scans, varying the diode energy, were made with both WARP3d and the experiment. Comparisons of the final beam phase space show good agreement. The beam's transverse size and velocities agree to within a few percent. Qualitatively, phase space looked the same and both displayed the same distortions that result in emittance growth.

VI.   ACKNOWLEDGEMENTS

REFERENCES

[1] A. Friedman, D. P. Grote, and I. Haber, "Three-dimensional particle simulation of heavy-ion fusion beams," *Phys. Fluids B* **4**, 2203 (1992).

[2] T. J. Fessenden and A. Friedman, Nucl Fusion, **31**, 1567 (199)

[3] D. P. Grote, A. Friedman, and I. Haber, Bull. Am. Phys. Soc., **36**,2415 (1991)

[4] T. J. Fessenden, Nucl. Instrum. Methods Plasma Res. A **278**,13 (1989)

[5] E. P. Lee, Nucl. Instrum. Methods Plasma Res. A **278**,178 (1989)

[6] Shmuel Eylon et. al.,Proceedings of the Fourteenth Biennial IEEE/APS Particle Accelerator Conference, (1991)

Longitudinal Beam Dynamics For Heavy Ion Fusion*

Debra A. Callahan, A. Bruce Langdon, Alex Friedman
Lawrence Livermore National Laboratory, Livermore, CA 94550
Irving Haber
Naval Research Laboratory, Washington, DC 20375

Abstract

The longitudinal wall impedance instability is of potential importance for a heavy ion fusion (HIF) driver because complete stabilization of this mode via momentum spread is impractical due to the requirement of focusing the beam onto the inertial confinement fusion target. This instability is being studied with the WARPrz particle-in-cell code. The impedance of the induction linac modules is modeled as a wall impedance corresponding to a continuum of resistors and capacitors in parallel. We discuss simulations of the this instability, including reflection of perturbations off the beam end, the effect of finite temperature on the growth rate, and errors in intermittently-applied axial confining fields as a seed for this instability. We also present very long simulations in which we study the approach to equilibrium.

I. INTRODUCTION

Because of the large cost involved in building a full scale heavy ion fusion (HIF) accelerator, much effort has gone into simulating the physics of space-charge-dominated beams needed for HIF. These simulations have been successfully compared with existing experiments. The WARP family of codes [1] has been developed to study driver issues. The code is made up of five major physics packages: a 3d particle-in-cell code in Cartesian geometry, a 3d electrostatic field solver, a cylindrically symmetric (r, z) particle-in-cell code, an r, z electrostatic field solver, and an envelope code. This family of codes is being used to study a variety of heavy ion fusion issues.[2, 3, 4, 5]

To model the longitudinal dynamics of these beams, the r, z portion of the WARP code was developed. This code is a 2.5 dimensional, cylindrically symmetric particle-in-cell code. Calculation of the field solution is done in a window that moves with the beam. In this window, the

fields are very close to purely electrostatic, since the force due to magnetic fields is down by $(u/c)^2$ compared with the force due to the electric fields where u is the velocity in the beam frame. The beam frame velocity for a heavy ion fusion driver is much less than 1% of the speed of light.

II. LONGITUDINAL INSTABILITY

This instability is of concern for a HIF driver because it amplifies small perturbations launched from the beam head. These perturbations may be caused by errors in the accelerating fields, or errors in applying axial confining fields ("ear" fields). The instability has the same mechanism used in "resistive wall" amplifiers with the impedance coming from the accelerating modules. This mode can be stabilized by a sufficiently large longitudinal momentum spread; however, chromatic aberration in the focusing lens system restricts the amount of momentum spread allowed. Since HIF driver beams travel at a fraction of the speed of light ($\leq c/3$), growth from this instability can be reduced by using "feed-forward" techniques in which perturbations are detected at one point along the accelerator, a signal is sent ahead, and a correcting field is applied downstream. One dimensional feed-forward simulations by K. Hahn [6] were successful in reducing growth due to this instability. Although these techniques enable suppression of the instability, the low growth rate makes the instability difficult to study experimentally. Experiments are underway at the University of Maryland [7, 8] to study longitudinal beam dynamics including the longitudinal instability in a small scale experiment by using space-charge-dominated electron beams. We are using simulations to understand such issues as the reflection of waves off the beam ends, the effects of finite temperature on this instability and errors which can result in finite amplitude seeds for the instability.

The longitudinal instability can be seen via a simple fluid model. If we consider an incompressible beam with radius a traveling down a pipe of radius r_{wall}, 1-d linear cold fluid theory shows that two waves will develop in the beam frame–a forward traveling wave and a backward traveling wave. These waves propagate with a phase velocity in the

beam frame given by

$$v_{\text{phase}} = \sqrt{\frac{Ze\lambda g}{4\pi\epsilon_0 m}} \quad (1)$$

where Z is the charge, λ is the line charge density (with units of charge/length), m is the mass, $g = \ln(r^2_{\text{wall}}/a^2)$. Adding a wall composed of a continuum of resistors and capacitors in parallel to this model results in decay of the forward traveling wave while the backward traveling wave grows. This growth is largest when the perturbation wavelength is large compared with the pipe radius. In a heavy ion fusion driver, the impedance that drives this instability comes from the induction acceleration modules.

To study this instability, we added a model for a wall with a continuum of resistors and capacitors in parallel to WARPrz.[9] This approximation for the induction modules contains the relevant physics, and also corresponds well with much of the analytic work being done. We calculate the resistive wall contribution to the electric field using the Poisson solve at the boundary. This is smoother and more physical than using the explicit beam current.

Simulations including a purely resistive wall in which a perturbation is launched from the beam head have shown growth of the backward traveling wave. The measured growth rate is down from the cold beam theory by about 15%. We believe this is due to the effects of finite transverse temperature. This is an area of current research.

The perturbation reflects off the beam tail. During reflection we see a steepening of the perturbation. This appears to be a non-linear effect as it is greater in larger perturbations than in small ones. The narrowing of the perturbation puts it in a dispersive regime, so that as the perturbation travels from beam tail to head, it decays and slower wavelengths begin to lag behind the main perturbation.

Cold beam fluid theory predicts that a capacitive component of the impedance will reduce the growth rate as well as lengthen the wavelength of the most unstable mode. This has been seen in WARPrz simulations. Very long wavelength ($\sim$ beam length) perturbations are excited, but little growth is seen. These perturbations slosh back and forth from beam head to tail with little change in size.

III.   INTERMITTENTLY-APPLIED "EAR" FIELDS

To get a realistic look at the effects of the longitudinal instability, sources of finite amplitude perturbations on the beam need to be considered. One source of such perturbations is the intermittency of applied axial confining electric fields ("ear" fields). In most of our simulations, ear fields are applied at each time step and are designed to keep the beam from expanding or contracting. In an experiment, these fields will be applied at fixed locations along the accelerator and the beam will expand and contract between applications. The application of these fields can cause a

train of perturbations to be launched from the beam head and these perturbations will be amplified by the longitudinal instability.

In our simulations, each application of the ears was made up of the following steps:

1. Let the beam expand for .48 μs (48 m at $c/3$)

2. Apply ears fields to both ends of the beam for .0875 μs and reverse expansion velocities.

3. Let the beam expand for .48 μs. At the end of this expansion, the beam should be back to its original length.

The perturbations on the beam were minimized when we applyed an electric ear field which was proportional to the average particle velocity in the beam frame as a function of z after the first expansion. The proportionality constant was varied until the beam was close to its original state after one application. The same ear field was used for each application. We found that we were able to apply these ear fields more than 20 times without significant perturbations developing on the beam, even in the presence of a 100 ohms/meter resistive wall.[9]

We then added an error to the ear fields. In the first case, the error added was a "bump" which had the algebraic form of one half the period of a sine wave with magnitude 5% of the local ear field. The same error was added at each application and this error made the ear fields too large. We believed that by applying an error in the same direction each time, we would see a worst case since there was no way for the errors to cancel one another out. We found this was not the case. We ran the simulation for 25 applications of the intermittent ears and saw that the first few applications excited a perturbation on the beam. Later in time, however, we saw that the beam adjusted itself to the error in the ear fields.

This phenomenon has also been seen in experiments done by A. Faltens. [10] These experiments were designed to test longitudinal bunch control in the beam tail on the SBTE at LBL. In this experiments, no attempt was made to match the waveform of the applied ear fields to the beam profile. Instead, fields of the form $[1 - \exp(-at)]$ were applied. In the experiment, mismatches in the ear fields caused waves to be launched from the beam tail in the early pulsers, but at later times the beam reached a new steady state configuration.

After seeing the beam adjust to a systematic error in the ears, we applied errors to the ears of random size and sign. The shape of the error was the same as in the last case, but the size of the errors varied randomly from 5% too large to 5% too small (+5% $\geq$ error $\geq$ -5%). In this case, we see the expected train of perturbations launched from the beam head, growing as they approach the beam tail. The width of these perturbations is measured to be approximately the wavelength of the most unstable mode of the longitudinal instability. Figure 1 shows the electrostatic potential on axis vs z after 15 applications of the ear fields with 100 ohms/meter wall resistance.
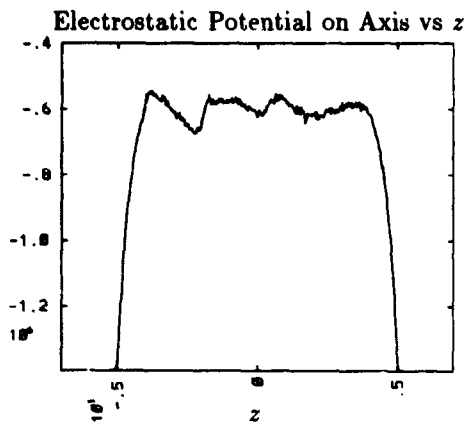
Figure 1: Random size errors in ears fields produce perturbations at the most unstable wavelength

IV. Beam Equilibria

The initial loading of the particles assumes a beam current profile as a function of z which is constant in the center and a parabolic falloff in the beam ends. The transverse emittance is scaled such that it is proportional to the beam current. This leads to constant phase advance along the beam. Simulations done with WARP3d[11] showed little emittance growth in the flat, center section of the beam, but emittance growth in the parabolic beam ends. This suggested that our assumed profile is not an equilibrium and lead us to undertake longer simulations with WARPrz in search of an equilibrium state.

Simulations were done on HIF driver scale beams (3000 Amps current, $c/3$ beam velocity). A 5 meter beam length was chosen for computational convenience with 50% of the beam length in the flat center section and 50% in the parabolic ends (25% in each end). Ear fields composed of an electric field to offset the space charge force plus an electric field component to offset the pressure were calculated based on the initial loading and applied at every time step.

The simulation was run for 96 μs in which time the beam traveled 9.6 km. Over the long run, the transverse thermal velocity in the beam center grows by about 10% and a corresponding increase in emittance is seen in the beam center. The transverse thermal velocity in the beam ends increases considerably and by the end of the run is constant over most of the beam.

V. Conclusions and Future Work

The WARPrz code has been used to model three aspects of the longitudinal dynamics of space-charge-dominated beams needed for heavy ion fusion. By modeling the impedance of the accelerating modules, we have simulated the longitudinal instability and seen growth of the back-ward traveling wave, reflection of perturbations off the beam end, and the partially stabilizing effects of the capacitive component of the module impedance. We have modeled intermittently-applied axial confining fields including errors and have seen the beam adjust to systematic errors in these fields, while randomly sized errors excite the most unstable mode of the longitudinal instability. We have run very long simulations in search of an equilibrium state and found that the beam tends toward a constant transverse temperature over most of the beam, even in the beam ends.

In the future, we will study the effects of finite transverse temperature on the growth rate of the longitudinal instability. We believe the transverse temperature is responsible for the decrease in growth rate that we see in warm beam simulations. We will also simulate feed-forward stabilization as a mechanism for correcting errors on the beam and reducing the growth rate of the instability. We also hope to couple our observations about beam equilibria with a more complete theory.

References

[1] A. Friedman, D. A. Callahan, D. P. Grote, A. B. Langdon, and I. Haber, Proc. of the Conference on Computer Codes and the Linear Accelerator Community, Los Alamos, NM, Jan 1990.

[2] A. Friedman, D. P. Grote, D. A. Callahan, I. Haber, and A. B. Langdon, Proc. Computational Accel. Phys. Conf. 1993, R. Ryne, Ed., Los Alamos National Laboratory, Pleasanton, CA, Feb. 23-26, 1993.

[3] D. P. Grote, A. Friedman, and S. S. Yu, ibid.

[4] D. P. Grote, A. Friedman, and I. Haber, this meeting.

[5] I. Haber, D. A. Callahan, A. B. Langdon, M. Reiser, D. X. Wang, J. G. Wang, this meeting.

[6] K. Hahn, Bul. Am. Phys. Soc., Seattle, WA, 1992.

[7] J. G. Wang, D. X. Wang, D. Kehne, M. Reiser, this meeting.

[8] D. X. Wang, J. G. Wang, D. Kehne, M. Reiser, this meeting.

[9] D. A. Callahan, A. B. Langdon, A. Friedman, and I. Haber, Proc. Computational Accel. Phys. Conf. 1993, R. Ryne, Ed., Los Alamos National Laboratory, Pleasanton, CA, Feb. 23-26, 1993.

[10] A. Faltens, LBL Half Year Report LBL-19501, June 1985.

[11] D. P. Grote, A. Friedman, and I. Haber, Particle Accelerators, 37-8, 141, (1992).

Correction of Longitudinal Errors in Accelerators for Heavy-Ion Fusion*

W. M. Sharp, D. A. Callahan, J. J. Barnard, and A. B. Langdon
Lawrence Livermore National Laboratory, University of California
Livermore, California 94550

T.J. Fessenden
Lawrence Berkeley Laboratory, University of California
Berkeley, California 94720

Abstract

Longitudinal space-charge waves develop on a heavy-ion inertial-fusion pulse from initial mismatches or from inappropriately timed or shaped accelerating voltages. Without correction, waves moving backward along the beam can grow due to the interaction with their resistively retarded image fields, eventually degrading the longitudinal emittance. A simple correction algorithm is presented here that uses a time-dependent axial electric field to reverse the direction of backward-moving waves. The image fields then damp these forward-moving waves. The method is demonstrated by fluid simulations of an idealized inertial-fusion driver, and practical problems in implementing the algorithm are discussed.

I. Introduction

Axial confinement of the high-current beams needed for heavy-ion fusion (HIF) must be provided by the accelerating waveforms. The longitudinal electric field required for this confinement ideally is proportional to the axial derivative of the beam line-charge density in the beam frame, and if it could be applied continually, it would have no effect except to balance the axial space-charge force of the beam. However, these so-called "ear" fields can only be applied periodically in induction accelerators, at an amplitude that gives the correct average force. Moreover, the high cost of time-dependent pulsers favors the widest allowable spacing of these "ear cells."

Numerical modeling [1,2] indicates that the periodic application of ear fields initiates low-amplitude space-charge waves near the beam ends, even if the fields are applied every lattice period. The waves moving toward the beam head are shown theoretically to decay, but waves moving back from the head grow exponentially due to the "longitudinal instability," which is driven by the interaction of a line-charge perturbation with its resistively retarded image field. These growing waves can increase the longitudinal emittance of the beam and thereby frustrate the final focus of the beam onto a target. Additional sources of space-charge waves on ion pulses are the inevitable errors in measuring the line-charge density, the imperfect generation of ear fields, and the timing errors in applying them.

In this paper, a simple algorithm is proposed for correcting errors in either the line-charge profile or average longitudinal velocity of a HIF pulse. The method is briefly described in the next section, and it is demonstrated using

a one-dimensional fluid code in Section III. Some warnings about the limited applicability of the method are mentioned in a final section.

II. Model

A. Basic Equations

Beam longitudinal dynamics is modeled here by treating slices of the beam as Lagrangian fluid elements. This approach is acceptable for studying longitudinal perturbations because of the long time scales involved and because there are no significant single-particle effects. In adopting a cold-fluid model, we implicitly assume that the beam has a negligible longitudinal temperature and that the slices remain approximately collinear. An approximate equation for the longitudinal velocity v is obtained by retaining only the electrostatic force in the single-particle motion equations and averaging the axial component over the beam cross-section. For a beam with a line-charge density λ, an ion mass M, and charge state q transported in a straight lattice, we obtain

$$\frac{dv}{dt} = \frac{qe}{M} \left(E_{ext} - g\frac{\partial \lambda}{\partial z} - \eta \lambda v \right). \qquad (1)$$

Here, E_{ext} is the radially averaged axial component of the external electric field, and the following term accounts for the radially averaged longitudinal space-charge field of the beam, with the coupling factor g being given by

$$g \approx \frac{1}{4\pi\epsilon_0} \ln\left(\frac{R^2}{r_0}\right) \qquad (2)$$

for a beam-pipe radius R and a matched beam radius of r_0. In deriving this space-charge field, the radial electrostatic field is assumed to vary over a much shorter scale length than λ, and we have used the fact that the charge density of an equilibrium beam is approximately constant except near the ends. The final term on the right side of Eq. (1) models the electric field that results when the image current in the accelerator wall is retarded due to an average resistance per unit length η [3]. In this simple description, the beam transverse dynamics only enter through the logarithmic coupling factor g. We treat this factor as a constant here to obtain a one-dimensional description. This choice is equivalent to assuming a matched beam with uniform axisymmetric focusing. An independent equation for λ is obtained by averaging the continuity equation over the beam cross section:

$$\frac{\partial \lambda}{\partial t} + \frac{\partial (\lambda v)}{\partial z} = 0. \qquad (3)$$

To obtain tractable equations, we assume that the unperturbed beam has a constant and uniform line-charge density λ_0 and fluid velocity v_0. If we then change variables to the beam-frame distance $\zeta \equiv z - v_0 t$ and assume perturbations of the form $v = v_0 + \tilde{v}$ and $\lambda = \lambda_0 + \tilde{\lambda}$, then we obtain a pair of linearized equation for $\tilde{v}$ and $\tilde{\lambda}$:

$$\frac{\partial \tilde{\lambda}}{\partial t} + \lambda_0 \frac{\partial \tilde{v}}{\partial \zeta} = 0 \qquad (4a)$$

$$\frac{\partial \tilde{v}}{\partial t} = \frac{qe}{M} \left[\tilde{E}_{ext} - g \frac{\partial \tilde{\lambda}}{\partial \zeta} - \eta(\lambda_0 \tilde{v} + v_0 \tilde{\lambda}) \right]. \quad (4b)$$

Here, we have included an unspecified correction field $\tilde{E}_{ext}$ that depends on the correction algorithm.

B. Dynamics of Uncorrected Perturbations

For a perfectly conducting accelerator with no correction field, the perturbed equations of Eq. (4) reduce to a homogeneous wave equation for $\tilde{v}$ or $\tilde{\lambda}$. The general solution can be written in the form

$$\tilde{\lambda}(\zeta,t) = F_+(\zeta + v_p t) + F_-(\zeta - v_p t) \qquad (5a)$$

$$\tilde{v}(\zeta,t) = -\frac{v_p}{\lambda_0} F_+(\zeta + v_p t) + \frac{v_p}{\lambda_0} F_-(\zeta - v_p t), \quad (5b)$$

where the wave phase velocity $v_p = (qeg\lambda_0/M)^{1/2}$ is typically small compared with v_0. This solution describes a slow wave moving backward at v_p in the beam frame and a fast wave moving forward at v_p. The two simplest examples are a pure velocity perturbation, which initially has $F_+(\zeta) = -F_-(\zeta)$, and a pure density perturbation with $F_+(\zeta) = F_-(\zeta)$. In the examples shown in this paper, a pure parabolic velocity perturbation is always used, but equivalent results are obtained with a density perturbation.

A non-zero resistance has been shown to cause bunching of backward waves and damping the forward waves [3]. If we assume that perturbations depend on ζ and t according to $\exp(ik\zeta - i\omega t)$, then the resulting dispersion relation shows for small v_p/v_0 that backward waves grow with a growth rate $\Gamma = \eta v_0 v_p/2g$, while forward waves damp with a decay rate $-\Gamma$. This "longitudinal instability" can be seen in the numerical solution of the perturbed equations of Eq. (4) shown in Fig. 1. For this illustration, parameters resembling those of a HIF driver have been used, with an ion mass M of 200 amu, a charge state q of unity, an ion kinetic energy of 10 GeV, and a beam current $\lambda_0 v_0$ of 3 kA. The coupling factor g has been taken to be 1.4×10^{10} m/F, and a resistance $\eta = 150$ Ω/m has been used. For these parameters, the initial perturbation is expected to grow by a factor of about 5.8 during the 8 μs duration of the simulation, and the calculated value is in almost exact agreement. The forward wave is seen in the figure to damp by a similar factor.

C. Correction Algorithm

The strategy adopted here for correcting longitudinal perturbations is to apply a suitable axial electric field $\tilde{E}_{ext}$ to reverse any backward waves, relying on the accelerator
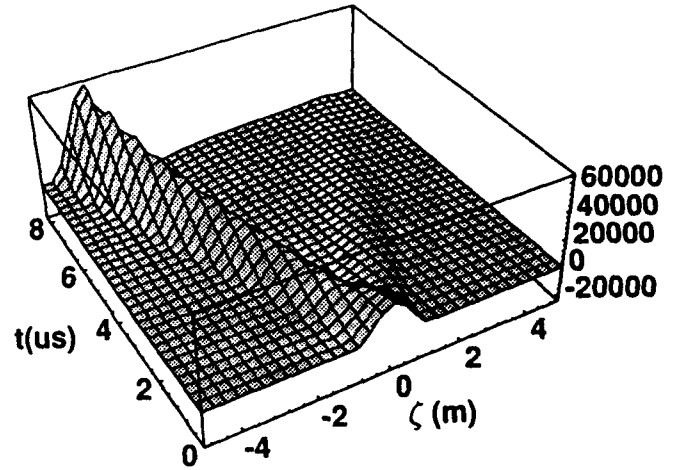
Fig. 1   Uncorrected evolution of a parabolic velocity perturbation in an accelerator with $\eta = 150$ Ω/m resistance.

resistance to subsequently damp them. The required velocity change is calculated by noting the relation between line-charge density and velocity for a forward going wave:

$$\tilde{\lambda}(\zeta,t) = F(\zeta - v_p t) \qquad (6a)$$

$$\tilde{v}(\zeta,t) = \frac{v_p}{\lambda_0} F(\zeta - v_p t). \qquad (6b)$$

To correct perturbations at some time t_c, we then take $\tilde{\lambda}_{new}(\zeta,0) = F(\zeta) = \tilde{\lambda}_{old}(\zeta,t_c)$ and change the velocity so that $\tilde{v}_{new}(\zeta,0) = (v_p/\lambda_0)F(\zeta)$. The required velocity change is then

$$\Delta \tilde{v}(\zeta) = \frac{v_p}{\lambda_0} \tilde{\lambda}_{old}(\zeta,t_c) - \tilde{v}_{old}(\zeta,t_c). \qquad (7)$$

From Eq. (6), this velocity change is seen to vanish for purely forward-going waves, and it equals $2(v_p/\lambda_0)\tilde{\lambda}_{old}$ for purely backward perturbations.

As written, this velocity change requires an electric field to be applied simultaneously to the full length of the beam. Such application is difficult because the accelerating field in induction accelerators is confined to relatively short gaps. Instead, we use the fact that v_p/v_0 is normally small to replace the ζ-dependent field at t_c with a time-dependent field in a gap of length L_g located at the beam-head position at t_c. The required electric field is then

$$\tilde{E}_{ext}(t) = \frac{Mv_0}{qeL_g} \Delta \tilde{v}[\zeta = v_0(t - t_c)]. \qquad (8)$$

III. Results

When the correction field from Eq. (8) is applied to an idealized perturbation in the absence of resistance, the method works as expected. Since the correction field is zero when the forward wave is traversing the gap, that portion of the wave is unaffected, but the backward wave is seen to change direction as the velocity perturbation changes sign The final state is a pair of undamped perturbations moving forward in the beam frame at v_p. If an accelerator resistance of 150 Ω/m is included, the correction
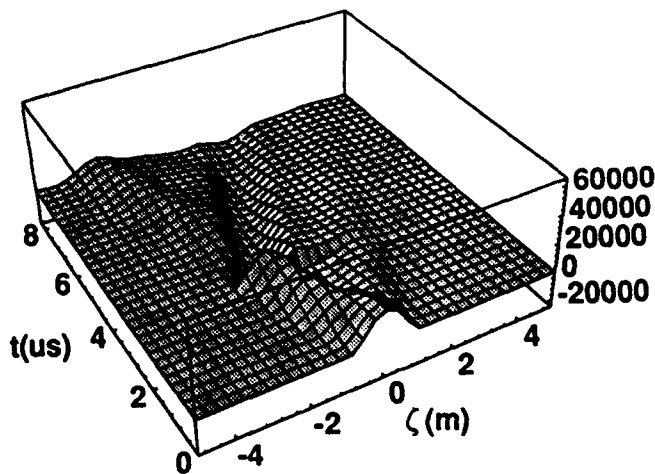
Fig. 2   Evolution of a parabolic velocity perturbation in an accelerator with $\eta = 150$ Ω/m making a single correction.
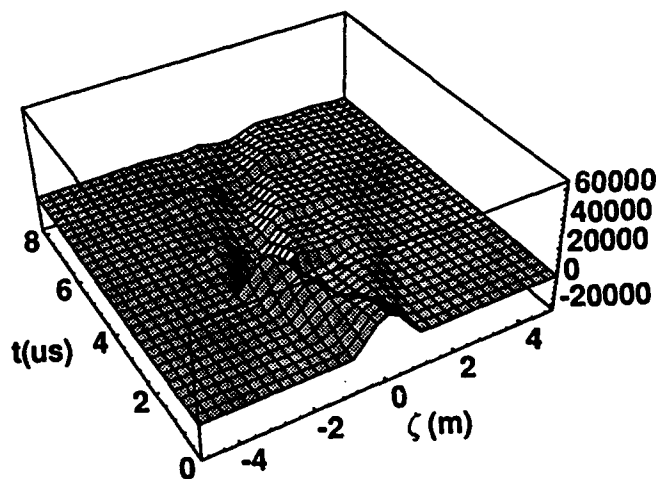
Fig. 3   Evolution of a parabolic velocity perturbation in an accelerator with $\eta = 150$ Ω/m making three corrections.

method works imperfectly, as seen in Fig. 2. Although the backward wave is substantially reversed, a small backward component remains and is the dominant perturbation by the end of the run. Reversal of the backward wave is incomplete in this case because the wave-equation solution Eq. (5), from which the correction field of Eq. (8) is obtained, is only exact in the absence of resistance.

Regrowth of backward waves can be controlled by periodically applying corrections with the form of Eq. (8). Fig. 3 shows the same initial velocity perturbation corrected at three locations about 170 m apart. At the end of the simulation there is no visible backward wave, although there has not been sufficient time after the last correction for significant regrowth. The main conclusion from this case is that periodic correction can control but probably not eliminate backward waves.

IV. Discussion

It should be stressed that the numerical results here are the best that might be obtained using the proposed correction algorithm. Perfect measurement of the perturbations

was assumed, and the exact correction field was applied. In fact, measuring $\tilde{v}$ independently from $\tilde{\lambda}$ is difficult with currently available diagnostic techniques. Current loops can measure $I_b = \lambda v$ with an accuracy of about $\pm 1\%$ for the currents levels expected near the end of a HIF driver, and methods for obtaining the line-charge density λ, such as capacitive probes, are less accurate. Consequently, any scheme for combining these measurements to obtain the relative velocity error $\tilde{v}/v_0$ will have an error greater than 0.01, whereas final focus requirements limit $\tilde{v}/v_0$ to less that 0.005. Probably some as yet unproven method like laser "tagging" of ions is needed to measure $\tilde{v}$ directly. Generating the required correction field $\tilde{E}_{ext}$ is also challenging because of the magnitude and complicated time dependence of the correction signal. If we assume that the 1% uncertainty in I_b represents the smallest measurable perturbation, then the minimum correction signal from Eq. (8) for a gap length L_g of 3 cm is about 5×10^7 V/m. To avoid electrical breakdown, this voltage may have to be applied piecemeal in several successive cells.

The proposed correction algorithm effectively reduces the level of space-charge waves on a beam provided that the growth rate Γ is sufficiently high. When backward waves are repeatedly reversed with an interval δt between corrections, the peak amplitude of space-charge waves is reduced by about $\exp[\Gamma(\delta t - L_b/v_p)]$ compared with an uncorrected beam, where L_b is the beam length. For a growth length v_p/Γ equal to L_b, this reduction factor is at most about 0.37, making the utility of the correction scheme questionable. Furthermore, since incompletely damped perturbations reflect coherently at the beam head and begin to regrow, repeated corrections in effect trap the waves in a region approximately $v_p \delta t$ long near the beam head, most likely causing excessive emittance growth there as the waves phase mix. Because of these problems, the method is not useful at low energy, because $v_p/\Gamma \sim v_0^{-1}$. Also, work by Lee and Smith [4] shows that inclusion of a realistic amount of cell capacitance in the electric-field model substantially increases the growth length by reducing Γ, again reducing the effectiveness of the method.

References

[1]   W. M. Sharp, J. J. Barnard, and S. S. Yu, "Pulse Control in an Accelerator for Heavy-Ion Fusion," in *Proceedings of the 1992 Linear Accelerator Conference AECL-10728* (Chalk River Laboratories, Ontario, Canada, 1992), p. 486.

[2]   D. A. Callahan, A. B Langdon, A Friedman, and I. Haber, "Longitudinal Beam Dynamics for Heavy Ion Fusion" in these proceedings.

[3]   E. P. Lee, "Resistance Driven Bunching Mode of an Accelerated Ion Pulse," in *Proceedings of the 1981 Linear Accelerator Conference*, Los Alamos National Laboratory report LA-9234-C, p. 263.

[4]   E. P. Lee and L. Smith, "Asymptotic Analysis of the Longitudinal Instability of a Heavy Ion Induction Linac" in *Proceedings of the 1992 Linear Accelerator Conference AECL-10728* (Chalk River Laboratories, Ontario, Canada, 1992), p. 716.

System Modeling for the Longitudinal Beam Dynamics Control Problem in Heavy Ion Induction Accelerators*

Anthony N. Payne
Lawrence Livermore National Laboratory
Livermore, California 94550

Abstract

We address the problem of developing system models that are suitable for studying the control of the longitudinal beam dynamics in induction accelerators for heavy ions. In particular, we present the *preliminary* results of our efforts to devise a general framework for building detailed, integrated models of accelerator systems consisting of pulsed power modulator circuits, induction cells, beam dynamics, and control system elements. Such a framework will permit us to analyze and design the pulsed power modulators and the control systems required to effect precise control over the longitudinal beam dynamics.

I. INTRODUCTION

An important problem in the design of heavy ion accelerators for the inertial confinement fusion application is the control of the longitudinal beam dynamics. Space-charge-dominated beams are accelerated, compressed, and transported over large distances, and the interaction of the beam with the impedance of the induction modules gives rise to the longitudinal instability [1]-[3].

Conceptually, the acceleration waveforms consist of three components (cf. Fig. 1). First, there are the main acceleration pulses. Then bipolar "ear pulses" serve to compensate for the deleterious effects of space-charge forces. Finally, "fast" pulses correct for errors in the main acceleration waveforms and compensate for the interaction between acceleration modules and the beam or for other disturbances.

The induction cells and pulsed power modulators must be designed to provide these three components. In each case, the required pulses must meet stringent requirements on shape and timing, and these requirements vary as a function of location along the accelerator. Furthermore, accurate pulse-waveform tailoring and timing requires some form of closed-loop feedback control. The performance requirements become even more stringent for recirculators and multi-pulse accelerators. Then issues such as modulator pulse repetition rate, efficiency, cell reset, and pulse-to-pulse stability become critical. Clearly this is a complex analysis and design problem. To achieve a satisfactory design, many design parameters must be adjusted

and system performance evaluated in terms of multiple, and possibly, conflicting design objectives.
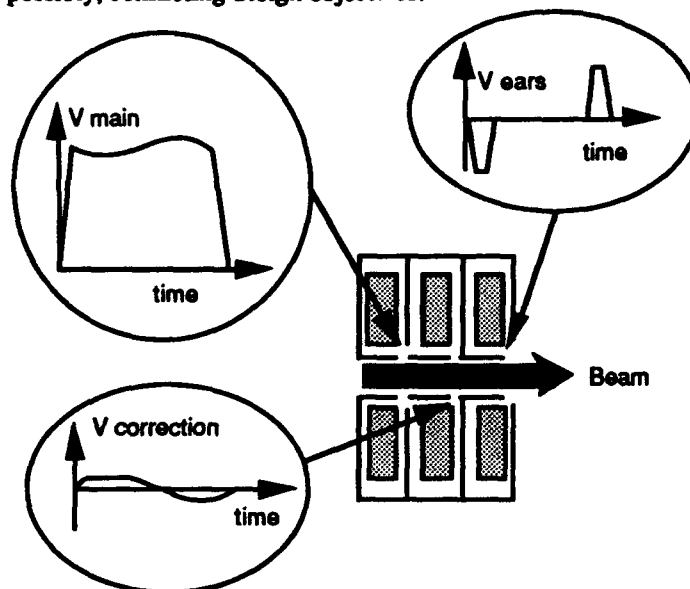
Fig. 1. Waveforms required for control of longitudinal beam dynamics.

To evaluate possible designs for main acceleration modules, ear pulsers and fast waveform correction modulators, the need arises for a computational modeling and design methodology possessing two features. First, it must permit the formulation of high fidelity, integrated system models comprised of multiple subsystems—pulsed power modulator circuits, induction cells, control system circuits, and beam dynamics (cf. Fig. 2). Second, it must provide an efficient means of exercising these models to explore the design parameter space, evaluate design-performance objectives, and arrive at optimal designs.
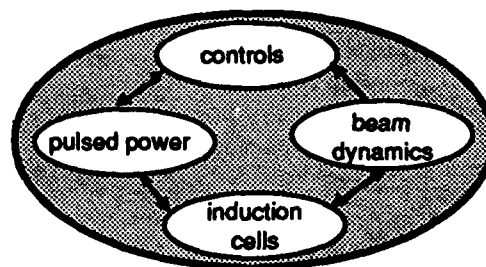
Fig. 2. Integrated system model comprised of four classes of subsystems.

We are developing a general system modeling and design methodology that is well-suited for studying the engineering issues that arise in the control of longitudinal beam dynamics. This methodology will provide a general framework for building detailed, integrated models of accelerator systems. It will also permit us to design and evaluate possible modulator designs and control strategies and allow us to explore important design issues, such as requirements on sensor accuracy, control system bandwidth, and the number and location of sensors and correction modulators required to achieve satisfactory longitudinal beam control. It will ultimately enable us to apply modern control techniques to the longitudinal beam instability problem. In this paper, we give a brief overview of the methodology and its planned application in the study of the longitudinal beam dynamics control problem.

II. THE METHODOLOGY

The anatomy of the methodology that we are developing is depicted in Fig. 3. It consists of three stages. In the input stage, the system is defined in terms of its topology and its components or elements. Parameter "knobs" by which design parameters can be varied and performance objectives and constraints are also defined at this stage. Then the particular tool is selected for a desired analysis or design task. Next comes the computational stage, in which the system model and the selected analysis or design task is formulated mathematically. These mathematical models are then operated upon by specific algorithms for performing the particular task selected. Finally, the output stage provides the results of the computational phase.

INPUT STAGE ⟶ COMPUTATIONAL STAGE ⟶ OUTPUT STAGE
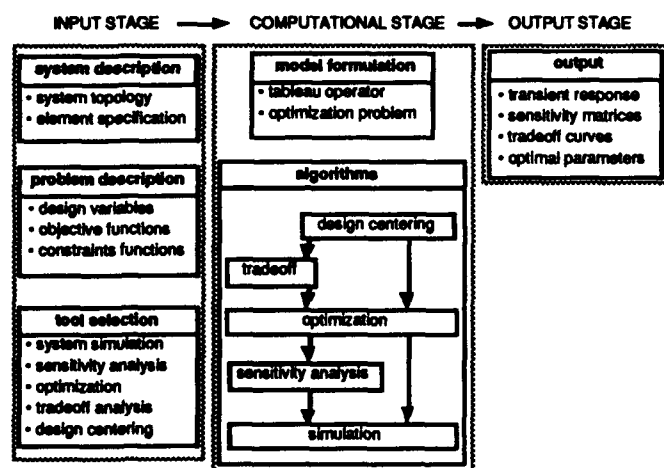
Fig. 3. Simplified anatomy of the methodology.

The analysis or design tasks are performed by one or more of five tools or algorithms, as shown in Fig. 3. The *simulation tool* computes the time-domain responses of all system variables or "states." It is the foundational tool in the sense that it serves as the "calculator" for the remaining four

tools. The *sensitivity analysis tool* ascertains the sensitivity of a given point-design to variations in design parameters. The *optimization tool* permits us to tune design parameters in order to optimize a given performance measure. The *tradeoff tool* allows us to identify tradeoffs and arrive at designs that achieve an acceptable compromise among multiple, conflicting design objectives. Finally, the *design-centering tool* seeks design parameter values that insure that design objectives are met even in the presence of component tolerances and parameter variations.

To date, we have built a prototype code called PRISMA, which realizes the simulation tool and provides the capability of building models of systems comprised of diverse subsystem types. We have used this code successfully to analyze pulsed power problems at LLNL, particularly in the area of magnetically-switched modulators [4]-[5]. The code presently possesses a collection of basic circuit component models (e.g., capacitors, inductors, sources, transmission lines, nonlinear magnetic cores) and control system element models (e.g., transfer functions, integrators, saturation, dead zone, etc.). To this repertoire of components, we are now adding those elements that are required to model accelerator systems (e.g. beam dynamics, beam current monitors, acceleration gaps, drift sections, etc.).

The code utilizes a free-format input language for describing the topology and components of the system to be simulated. The user simply describes the system in a "net list," each line of which specifies a component type and its name, its connection points to the system (nodes) and its defining parameters. From this description of the system, the mathematical model of the complete system is constructed.

The simulator employs a sparse tableau formulation [6] of the system equations. In this formulation, the system model takes the form of a system of simultaneous differential-algebraic equations

$$f(x(t), \dot{x}(t), t) = 0 \quad t \geq t_0 \tag{1}$$
$$x(t_0) = x_0$$

The vector function f includes the topological constraints of the system (e.g., Kirchhoff's current and voltage laws for circuits) and the component constitutive equations. The vector x consists of node variables and component variables that are defined or constrained through each component's mathematical model. The advantage a general network and systems formulation has over a problem or application specific formulation is that changes in system topology, components, and parameters can be made and evaluated easily.

We obtain the solution of (1) by discretizing the differentiation operator by a backward differentiation formula. We then solve the resulting system of nonlinear difference equations by a modified Newton-Raphson method, which exploits the sparsity of the Jacobian of f. A stiffly stable, adaptive step-size, adaptive order solver permits the simulation of highly nonlinear and stiff dynamical systems.

III. Beam Model

At present, we model the longitudinal beam dynamics by a simple one-dimensional cold-fluid model [1]-[3], consisting of the continuity equation and the momentum transfer equation, which in the laboratory frame (z,t) take the form

$$\frac{\partial \lambda}{\partial t} + \frac{\partial I}{\partial z} = 0 \qquad (2)$$

$$\frac{\partial v}{\partial t} + v\frac{\partial v}{\partial z} = \frac{F}{m} \qquad (3)$$

with

$$I = v\lambda \qquad (4)$$

where $\lambda(z,t)$ is the line charge density and $v(z,t)$ is the fluid velocity, and $I(z,t)$ is the total beam current. The force F is given by

$$F = qE - gq\frac{\partial \lambda}{\partial z} + F^a \qquad (5)$$

where E is the longitudinal field induced by the interaction of the beam current with the induction gaps. In general, interaction of E and I can be modeled by a circuit model of the the induction module. The second term in (5) is the space-charge force, and F^a is the force applied by induction cells.

To incorporate the beam model into the tableau equation (1), we transform equations (2)-(5) into a Lagrangian coordinate system and discretized them in both time and space. Eventually, we plan to solve the equations by the method of lines to take advantage of the adaptive time-step algorithm of the stiffly stable solver in PRISMA.

IV. Conclusion

Once the beam model and models for other accelerator system components are fully integrated into PRISMA, we plan to study the longitudinal beam control problem. In particular, we plan to use the code to explore control strategies and to analyze modulator designs for ear-pulse and fast correction waveform generation. In the near future we also hope to add the sensitivity analysis and optimization tools, which should greatly enhance the effectiveness of the code as a engineering tool.

References

[1] J. Bisognano, I. Haber, L. Smith, and A. Sternlieb, "Nonlinear and Dispersive Effects in the Propagation and Growth of Longitudinal Waves on a Coasting Beam," *IEEE Transactions on Nuclear Science*, Vol. NS-28, No. 3, June 1981, pp. 2513-2515.

[2] E. P. Lee and L. Smith, "Asymptotic Analysis of the Longitudinal Instability of a Heavy Ion Induction Linac," *Proc. 1990 Linear Accelerator Conference*, Albuquerque, NM, September 10-14, 1990, pp. 716-718.

[3] E. P. Lee and L. Smith, "Analysis of Resonant Longitudinal Instability in a Heavy Ion Induction Linac," *Conference Record of the 1991 IEEE Particle Accelerator Conference*, San Francisco, CA, pp. 1737-1739.

[4] A. N. Payne, "Modeling Magnetic Pulse Compressors," *Conference Record of the 1991 IEEE Particle Accelerator Conference*, San Francisco, CA, pp. 3091-3093.

[5] A. N. Payne, "Modeling Magnetically Switched Pulse Modulators," to be presented at the *9th IEEE Pulsed Power Conference*, Albuquerque, NM, June 21-23, 1993.

[6] G. D. Hachtel, R. K. Brayton and F. G. Gustavson, "The sparse tableau approach to network analysis and design," *IEEE Trans. Circuit Theory*, Vol. CT-18, No. 1, pp. 101-113, Jan. 1971.

Development of FET-Switched Induction Accelerator Cells for Heavy-Ion Fusion Recirculators

M. A. Newton, W. R. Cravey, S.A. Hawkins, H.C. Kirbie, C. W. Ollis
Lawrence Livermore National Laboratory
Livermore, California 94550

Abstract

The "recirculator", a recirculating heavy-ion induction accelerator, has been identified as a promising approach for an inertial fusion driver. One of the technical challenges to building a recirculator is the requirement for a modulator that can drive the induction accelerator cells at repetition rates $\geq$ 100 kHz with variable pulse width and pulse repetition rate capability. A high repetition rate modulator and cell is presently being developed for use on a proposed heavy-ion recirculator. The goal is to develop an array of field-effect transistors to switch 5 kV, 1 µs pulses onto a Metglas induction core at pulse rates exceeding 100 kHz. Each transistor in the array is driven by a fiber-optic isolated gate signal that is powered by a dc/dc converter. The circuit architecture provides for core reset between pulses and produces bursts of pulses that are variable in pulse width and prf. The transistor switching array, energy storage capacitors, reset circuit and cell core are all combined into a single compact, low-impedance package. Progress of this development work will be presented with supporting data.

I. INTRODUCTION

Background on HIF

Heavy Ion Fusion (HIF) is one of the promising alternatives for using inertial fusion to generate commercial electrical power in the 21st century. There have been numerous studies that evaluate the different types of accelerators that might be used as "drivers" for heavy-ion-driven inertial fusion. Systems studies conducted at Lawrence Livermore National Laboratory (LLNL) have shown that a recirculating induction accelerator, "recirculator", can provide substantial reductions in driver costs over the more conventional linear induction accelerator.[1]

What is a recirculator and how is it different?

A recirculator is an induction accelerator which accelerates the particles and bends them in a closed path. The methods for acceleration and focusing are nearly identical to a linear induction accelerator where induction accelerator cells couple the accelerating potential to the beam and quadrupole magnets provide the focusing. Unlike the linear machine, the acceleration and focusing components are re-used many times to accelerate the ions to their final energy resulting in a significant reduction in the number of acceleration and focusing components. In a recirculator however, dipole magnets and power supplies are required to bend the ion beam, which are unnecessary in a linear machine.

While the recirculator may afford significant cost reductions through the reuse of many of the induction accelerator components, it does require more advanced technology which partially offsets the cost savings. One of these areas of technology that is critical to the feasibility of a recirculator is the modulator system which generates the pulses that accelerate the ion beams. This paper will describe the modulator characteristics required by a recirculator and the work that is being done to achieve these characteristics for near term experiments.

II. MODULATOR REQUIREMENTS

Performance requirements

Re-use of the induction accelerator cells results in a significant reduction in the amount of magnetic material required to accelerate the ion beam. However, the induction cell drive requirements are very different and much more complex than those in a linear accelerator.

The first major difference is the repetition rate requirement for the modulators. The repetition rates for a recirculator are determined by the time it takes the ion beam to traverse one lap of a ring. This time depends on the mass and kinetic energy of the ion as well as the circumference of the ring. Figure 1 is a plot of the required repetition rates for various ion masses in a driver with a ring circumference of 2 kilometers. This time period can be as short as 10 - 20 µs for a driver-scale recirculator. In addition, the velocity of the ions increase as they are accelerated, thus reducing the amount of time required to traverse a ring from one lap to the next. The time required for an ion to complete the first lap could be 100 µs with the last lap requiring only 15 µs.
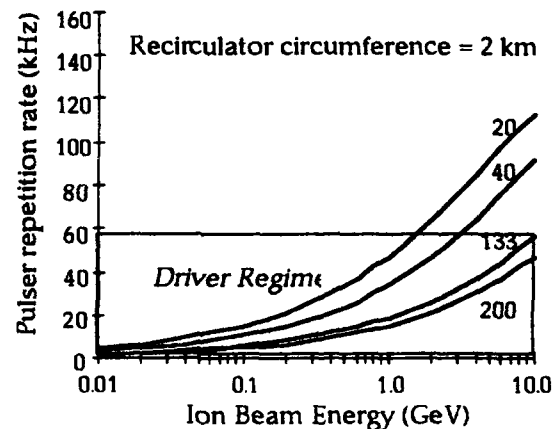
Figure 1. Modulator repetition rates required for various mass ions in a recirculator with a 2 km circumference.

The primary objective of the heavy-ion driver is to deliver the full energy of the ion beam to the fusion target in a few 10's of nanoseconds. Stability criteria on the maximum amount of transportable current in an alternating-gradient quadrupole transport system limit the current that can be

transported at the lower energies for a given quadrupole field.[2] For this reason, the ion beam is compressed to increase the current as the particle energy increases. In the recirculator, this compression occurs continuously throughout acceleration. In order to maximize the efficiency of the recirculator, the pulse duration of the acceleration potential generated by the modulators should closely track the duration of the beam pulse as it is compressed. In a driver scale recirculator the pulse duration in a single ring can change by an order of magnitude, e.g. 2.5 µs to 250 ns, during the acceleration sequence.

An example of the desired pulse format is shown in figure 2. Although there are several possible formats that might be used, a variable pulse duration was shown to be the most desirable on the basis of beam physics and accelerator efficiency.[1]
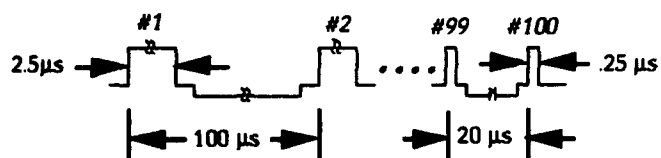
Figure 2. Example of pulse format that might be required for a recirculator.

An acceleration format with pulse width agility is desirable for two reasons. The first reason is that pulse agility allows a constant and more gentle compression of the beam during the acceleration sequence. Elimination of abrupt changes in beam size and velocity eases some of the physics concerns associated with maintaining the ion beam quality.

The second reason is that the magnetic core losses are significantly reduced by continuously decreasing the pulse duration. As the acceleration pulse gets shorter the peak flux density used in the core becomes less resulting in a significant reduction in overall losses. Figure 3 is a graph of the induction core losses as a function of pulse number for three different acceleration schedules.

In addition to having an extremely flexible pulse format capability, the induction cell modulator must be capable of driving a time-varying load. This load consists of the ion beam in parallel with the nonlinear magnetic material in the induction cell which must be reset after each acceleration pulse. An inverse voltage and current must be supplied to reset the magnetic material. Insufficient reset would allow saturation of the induction cell core material resulting in little or no voltage appearing at the acceleration gap. The amplitude of the reset pulse is dependent on the time available for reset because $\int V dt$, where V is the amplitude of the modulator output, must be equal for the both main accelerating pulse and the reset pulse.

III. MODULATOR DEVELOPMENT

Objectives

The use of heavy-ion accelerators as drivers for inertial fusion is at least 20 - 30 years in the future based on the present development plans for inertial fusion energy (IFE). The purpose of present development work is not to develop a modulator with the capabilities that we believe a modulator

will need in the year 2020, but instead to determine the feasibility of the modulator concept based on present day technology and to develop the capability necessary to build a recirculator in the near term as part of an overall driver
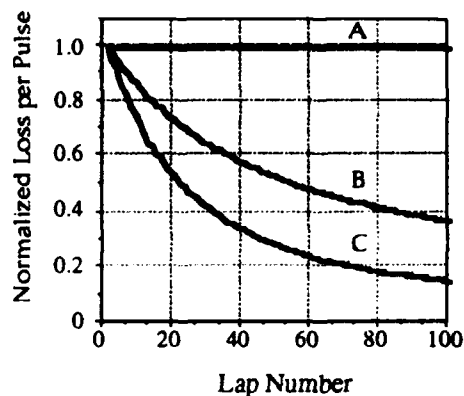
Figure 3. Losses on each pulse for three different acceleration schedules where A) τ_p = constant, B) $\tau_p = \beta^{-1}$ C) $\tau_p = \beta^{-2}$ where τ_p is the pulse duration and $\beta = v/c$

development program. Presently the most immediate test of a recirculator is likely to be on the proposed ILSE accelerator to be built at LBL. This modulator development work is specifically focused on developing a modulator that can answer the needs of the proposed ILSE recirculator experiment in several years. For this experiment, we estimate that the modulator must be able to supply 50 - 100 pulses to drive an induction accelerator cell at repetition rate from 100 - 200 kHz at voltages on the order of 5 kV.

Development Plan

The development of this technology is being undertaken in a series of incremental steps. The first step was to develop a conceptual circuit topology for generating the acceleration pulse and resetting the magnetic material in the induction cell. This concept was then validated using computer modeling and bench top testing. The first significant testing of the concept consisted of a modulator with two devices in series and two devices in parallel. This testing was quickly followed by the design and fabrication of a modulator with four parallel strings of MOSFETs each with six devices in series. This 6 x 4 modulator is presently being tested and evaluated. The next step in the development is to build a modulator capable of meeting the ISLE recirculator requirements.

Circuit Description

The performance requirements dictated by the recirculator are so challenging that the choices available for the modulator technology are limited. There are few switch choices available with the capability of operating at several 100 kHz and opening as well as closing. Several solid-state switch types were evaluated and power MOSFETs were selected as the basis for our initial development work. Based on power MOSFET technology we have developed a circuit topology that is capable of driving a nonlinear magnetic load at 100's of

kilohertz and providing the energy required for reset between pulses.

The modulator circuit components can be grouped into four functional units, i.e. energy storage, switching, reset and load. The diagram in figure 4 shows a simplified schematic of the modulator and its functional units. The energy storage unit supplies enough energy to provide a flat voltage pulse to the nonlinear load for ≈ 1μs. The switch unit, which is a series-parallel combination of MOSFET switches, controls the flow of energy to the load. It has the capability to both initiate and interrupt current flow at repetition rates >100 kHz. The load is a nonlinear magnetic material , Metglas, in parallel with the ion beam. In early recirculator experiments, the ion beam load will be insignificant compared to the magnetic load. This reset portion of this circuit recovers the energy stored in the magnetic field of the induction core and uses it to reset the core material before the next pulse arrives.
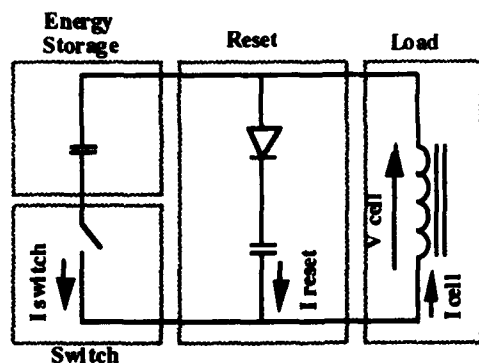
Figure 4. Simplified schematic of high repetition rate modulator.

The gate drive circuitry is a significant part of the modulator both in terms of cost and performance. The rise and fall times of the gate drive circuits are critical to the successful operation of these series-parallel stacks of MOSFETs. A fiber optic gate drive system was developed to provide unlimited flexibility in pulse widths and to provide precise control over the rise and fall times of each gate signal.

Modulator Packaging

A unique packaging configuration was chosen to facilitate efficient transfer of energy to the induction cell and thus avoid reflections due to impedance mismatches. This efficient energy transfer is accomplished through closely coupling the modulator to the load and making the modulator an integral part of the induction cell. This also provides a very low impedance drive to the cell which helps suppress any longitudinal beam instabilities that result from finite cell impedances. A picture of the cell packaging is shown in figure 5. Four parallel stings of series power MOSFETs are shown assembled on the outer radius of a magnetic core.

Performance status

The first demonstration modulator has been built and is presently being evaluated. This modulator (6x4) has operated at 3 kV, 160 A, 100 kHz and pulse durations of .4 - 1 μs as shown in Figure 6. The modulator has performed as expected and the next version is being designed using the latest in

MOSFET technology to achieve the voltages (5 kV) and currents (1 kA) required for a recirculator on ILSE.
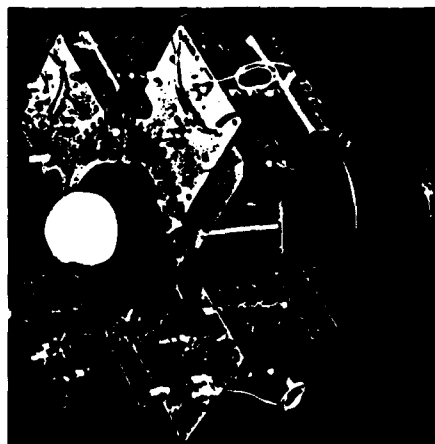
Figure 5. Photo of 6 x 4 modulator
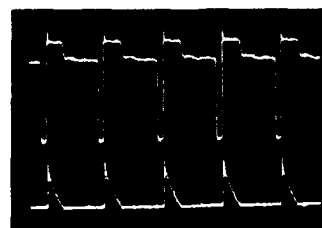
Figure 6. Cell voltage and reset current during 100 kHz

IV. CONCLUSIONS

Early test results on our 6 x 4 modulator indicate that the high repetition rates and pulse to pulse agility desired for a recirculator are feasible. There is a high degree of confidence that the performance required for near term recirculator experiments can be achieved with existing MOSFET technology. Modulators for a driver scale recirculator will require much greater voltages (≈100 kV) than the 5 kV we are attempting to achieve for an ILSE scale recirculator. Significant innovation and development will be necessary to achieve these higher voltages at affordable costs.

V. REFERENCES

[1]J. Barnard, "Study Recirculating Induction Accelerators as Drivers for Heavy Ion Fusion," Lawrence Livermore National Laboratory report no. UCRL-LR-108095 (1991)

[2]E. Lee, T. Fessenden, and L. Laslett, "Transportable Charge in a periodic Alternating Gradient System," IEEE Trans. of Nucl. Sci. NS-26, 2489 (1985)

Parametric Studies for Recirculating Induction Accelerators as Drivers for Heavy-Ion Fusion

Robert L. Bieri

W. J. Schafer Associates, Inc.

303 Lindbergh Avenue, Livermore, CA 94550

Abstract

A computer model for the cost and performance of a recirculating induction heavy-ion accelerator for driving inertial fusion reactions has been developed. This code has been used to examine the driver design space in an effort to reduce driver costs while maintaining high driver efficiency and target gain. The driver model is described, and the results of parametric studies are reported. The design parameters examined include driver energy, maximum magnetic field allowed at the superconducting windings, maximum bending field in each ring, axial quadrupole field packing fraction for the focusing magnets in each ring, and ion mass.

I. INTRODUCTION

Inertial fusion energy (IFE) power plant concepts produce energy by compressing and heating a target made of heavy hydrogen isotopes (D-T or D-D) until the nuclei become close enough that fusion occurs. The driver used to compress and heat the target must deliver a large amount of energy (MJs) in a very short period of time (10s of nanoseconds). Both particle accelerators (using light ions or heavy ions) and lasers have been proposed as drivers for IFE, with particle accelerators having the advantage of higher inherent efficiency.

Heavy-ion fusion (HIF) driver research in the U.S. has focused on induction accelerators. Recirculating induction accelerators (RIAs) have been proposed as a less-expensive alternative to linear induction accelerators (linacs) for IFE drivers [1].

II. DESCRIPTION OF AN RIA

An induction accelerator accelerates an array of ion beams through transformer action and continually focuses the beam using a lattice of alternating focusing and defocusing quadrupoles. In a multiple-beam accelerator, the cost of the acceleration systems can be reduced if a single ferromagnetic induction cell surrounds all of the beams to provide an acceleration voltage for all of them. Each beam still requires its own focusing lattice, so compact arrays of quadrupoles are required along the length of the accelerator.

An RIA adds arrays of dipole magnets between the quadrupoles in each half-lattice period in order to bend the beams in a circle and allow the beams to pass through each induction cell up to a few hundred times. An RIA generally consists of one to four rings. Because each quadrupole array and inductor is used many times per shot, the required focusing and acceleration costs are greatly reduced. The added costs for the dipole magnets are more than offset by the cost savings for the acceleration and focusing systems. Driver efficiency is kept high (>30%) by using combined function (CF) superconducting focusing magnets (quadrupoles with a constant dipole offset) in high energy rings and by using energy recovery circuits for all pulsed resistive dipoles.

There are additional design constraints on an RIA that are not relevant to a linac. Because the lattice period must remain constant in each ring, the undepressed tune of the beam will decrease as the ion energy increases. This defocusing effect limits the useful energy gain per ring and leads to designs which use several rings (three rings were used in LLNL's most cost-effective "C" design [1]). Rapidly pulsed injection and extraction systems are needed for each ring. The need for dipoles between the quadrupoles limits the space available for acceleration gaps. Constraints on available circumferential space lead to designs which use induction cores surrounding the quadrupoles. Each induction core uses voltage leads to connect it to the narrow acceleration gaps located between quadrupole arrays.

III. DESCRIPTION OF RECIRC CODE

The RECIRC code was created to model three ring RIA drivers and examine the dependence of driver cost and target gain on the large number of available driver design parameters. The driver includes an injector, a low-energy ring (LER), a medium-energy ring (MER), a high-energy ring (HER), and a final compression and focusing section. For a given driver energy and set of input driver parameters (see Table 1), the code calculates the final ion energy and beam current. The injection and extraction beam parameters for each ring are then calculated, and the cost of the driver is calculated. The final beam parameters are used to give ion ranges (gm/cm^2) and spot sizes (mm) needed to calculate target gain. Spot sizes are calculated assuming auto-neutralization of the ion pulse by co-injected electrons following the final focusing magnets [2].

A. Beam Modeling

The models used for transportable current in an alternating-gradient lattice are improvements to those first studied by Maschke [3], the improved approximations were derived by Lee, Fessenden, and Laslett [4] at Lawrence Berkeley Laboratory. The four equations used are:

$$2\left(1 - \cos(\sigma_0)\right) = \left(1 - 2\eta/3\right)\eta^2 \left(B'/[B\rho]\right)^2 L^4$$

$$\varepsilon_n = \beta\gamma \, \sigma/(2L) \, \bar{a}^2$$

$$2\left(1 - \cos(\sigma)\right) = 2\left(1 - \cos(\sigma_0)\right) - \kappa\left(2L/\bar{a}\right)^2$$

$$\kappa = 2I/\left[(\beta\gamma)^2 [B\rho]\left(4\pi\varepsilon_0 c^2\right)\right]$$

where

σ_0 = the undepressed phase advance per lattice period,

σ = the depressed phase advance per lattice period

η = the occupancy factor for the quadrupole fields,

B' = the field gradient in the quadrupoles,
Bρ = the ion beam rigidity,
L = the half-lattice-period length,
ā = the average beam radius,
κ = the dimensionless line charge,
e_n = the normalized emittance,
βγ = the relativistic velocity, and
I = the transportable current.

B. Determining Ring Parameters

The relations in the previous section can be used to give the transportable beam current as a function of the cumulative acceleration voltage, V. For a constant current beam, the transported power is given by P = I(V) V, so the final voltage needed for a given final driver energy, E, and pulse duration, τ, can be obtained by solving the final power balance,

$$P_{beam} = V\,I(V) = \frac{E}{N\,\tau}$$

for V. The final beam current can then be obtained from I(V). The injection voltage and current for the HER and the injection and extraction voltage and current for the MER are then calculated from the transport parameters and energy gain (V_{ext}/V_{inj}) for each of these rings. The energy gain for the LER is obtained by dividing the injection voltage for the MER by the 3 MV injection voltage for the driver. The required beam size and injection current for the LER are then determined by the required injection current for the MER. The diameters for the MER and HER are given by the bending strength of the dipoles and the beam rigidity; the diameter of the LER is set by the assumption that the LER circumference must be twice the injected beam length to allow time to reset the acceleration cells.

C. Component Costing and Scaling

The number and size of the quadrupole arrays, dipole arrays, and induction cores in each ring are calculated from the packing fractions, ring diameters, injection and extraction pulse durations, and the input magnetic fields allowed in each component. The size and cost scaling for the acceleration and bending systems are taken from the "C" design in Reference [1], but the scaling of the quadrupole array is given by a more detailed model [5] taken from an earlier study of linac drivers [6,7]. The more detailed quadrupole model gives slightly larger quadrupole arrays and thus slightly increases the cost of the quadrupoles and inductor cells relative to those estimated in [1].

Key cost assumptions are a unit cost of $5/kg for the Metglas used in the inductor cells and a wound cost of $300/kg of NbTi and $50/kg of Cu in the quadrupole or CF magnet windings.

D. Key Driver Parameters

Key driver parameters which may be varied in parametric studies are given in Table 1.

Table 1
Key Input and Output Parameters

Input Parameters	driver energy
	final pulse duration
	ion mass and charge state
	quad field gradients
	quad packing fractions
	dipole fields in CF magnets
	max dipole field in LER
	pulse compression exponents for each ring, $(\tau \sim \beta^{-a} \sim V^{-a/2})$
	ion energy gain ratio (E_{ext}/E_{inj}) for MER and HER
Output Parameters	dipole packing fractions
	Max. dipole fields in MER and HER
	Inj. and Ext. beam parameters: $(E_{ion}, I_{beam}, \tau_{pulse})$ for each ring
	ring diameters
	total direct cost for driver
	estimated target gain

IV. RESULTS OF PARAMETRIC STUDIES

Two parametric studies were done. First the "C" design assumptions were scaled through a range of energies; then a parameter search was done to find lower cost options for 1.5, 4, and 6 MJ three-ring drivers. In the second study, all parameters were varied except final pulse duration and ion charge state. Figure 1 shows the direct costs (including installation and controls), target gain, and pulsed-power efficiency for the drivers in both studies. Table 2 compares the parameters used for the low-cost 4 MJ driver with those used in the "C" design.

Only drivers with three rings and four beams were considered. Although these are reasonable assumptions for 4 MJ drivers, the range of energies examined was large enough that other design choices may be more cost effective at different energies. At 1.5 MJ, two-ring drivers may have lower costs and less emittance growth. Drivers with more beams (e.g., 12) will give lower ion energies and smaller rings; they may give higher gains (because of the lower ion ranges) at comparable costs for higher-energy drivers.

The pulsed-power efficiency is the ratio of the driver beam energy to the total pulsed energy for the inductors and dipoles. The actual driver efficiency will also include constant power terms for refrigeration, vacuum pumps, etc.

Minimizing driver cost is only one way of choosing a driver design. The eventual goal will be to optimize figures of merit, such as cost of electricity, for IFE plants. Better figures of merit will include the effects of target gain and driver efficiency on reactor and plant scaling and costs.

Innovative and aggressive magnet design may also lower the estimated cost of RIA drivers. The quadrupole (or CF)

743

arrays assumed in this study are very conservative in that each magnet NbTi winding is surrounded by a structural collar and enough iron to isolate it from the fields of adjacent magnets.

Total Direct Costs for 3 Ring Drivers
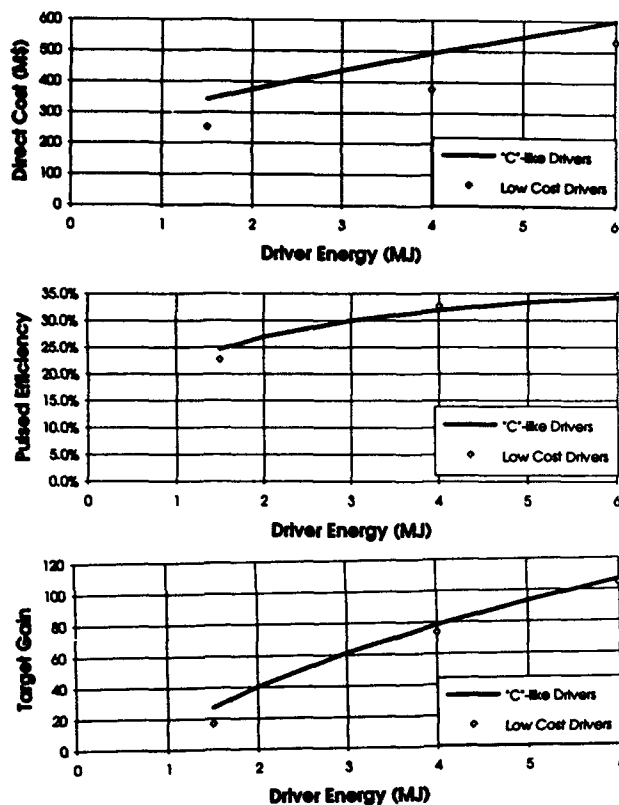
Figure 1. Cost and Performance Parameters

Table 2
4 MJ Driver Parameter Comparison

Parameter	"C"-Like 4 MJ Driver	Low-Cost 4 MJ Driver
Ion Mass (amu)	200	140
Ion GeV-HER	1.1-11	0.73-8.76
Ion MeV -MER	55 - 1,100	61 - 730
Ion MeV-LER	3 - 55	3 - 61
HER Diameter	615 m	252 m
MER Diameter	259 m	176 m
LER Diameter	245 m	391 m
CF Dipole Field-HER	1.0 T	1.5 T
CF Dipole Field-MER	0.75 T	0.62 T

More aggressive designs using high-performance superconductors (such as Nb_3Sn), using less iron, and/or using less structural material may be possible. More compact magnet arrays would reduce the dimensions and costs of the inductor cells as well as the focusing magnets.

V. RESULTS AND CONCLUSIONS

A. Cost Reductions for Three Ring Drivers

Parametric studies on 3 ring RIA drivers ranging from 1.5 to 6 MJ gave a cost reductions of 11 to 27%. Cost reductions resulted from

* using lower ion masses,
* using higher bending field in the CF magnets, and
* using smaller energy gains in the MER and HER.

B. Potential Future Studies

This study was limited in scope to the analysis of three ring recirculating drivers. Other work that would be of great interest includes

Examination of low-energy RIAs with one or two rings and examination of high-energy RIAs with more beams.

Examination of hybrid drivers: Cost savings may be possible if a linac is used before the first recirculating ring. The cost and performance of such "hybrid" drivers should be examined.

Sensitivity Studies: The effect of significant changes in anticipated beam performance (e.g., emittance growth) or unit cost (e.g. superconductor cost) on optimum designs and costs should be explored.

Cost comparisons between optimized linacs and RIAs: A comparison of optimized drivers using consistent assumptions has yet to be done.

VI. REFERENCES

[1] J. J. Barnard et al., Study of Recirculating Induction Accelerators as Drivers for Heavy Ion Fusion, Lawrence Livermore National Laboratory report UCRL-LR-108095 (Sept. 21, 1991).

[2] L. D. Stewart and E. L. Hubbard, "Heavy Ion Beam Driver Final Drift, Compression, and Focusing Design," Fusion Technology, 21, Num. 3, 1594 (May 1992).

[3] A. W. Maschke, Brookhaven National Laboratory, BNL-20297 (1975).

[4] E. P. Lee, T. J. Fessenden, and L. J. Laslett, "Transportable Charge in a Periodic Alternating Gradient System," IEEE Trans. Nucl. Sci. NS-26, 2489 (1985).

[5] R. L. Bieri, "Inertial Confinement Fusion Driver Enhancements: Final Focusing Systems and Compact Heavy-Ion Driver Designs," MIT Nuclear Engineering Ph.D. thesis, Ch.5&6 (1991).

[6] R. L. Bieri, et al, "Heavy-Ion Driver Design and Scaling," Fusion Technology, 21, Num. 3, 1583 (May 1992).

[7] R. L. Bieri and W. R. Meier, "Heavy-Ion Parametric Studies and Choice of a Base 5 Mega-Joule Driver Design," Fusion Technology, 21, Num. 3, 1589 (May 1992).

A FUSION DEVICE OF THE CONTINUOUS ELECTRON BEAM CONFINEMENT USED BY THE ACCUMULATING RING WITH THE CONTINUOUS INJECTION

Gao Shuyang,   Qian Guangyu

China Institute of Atomic Energy

P.O.Box 275(3),P.R.C.102413,Beijing,P.R.China

Abstract

In this paper the design of a accumulating storage ring for the electron beam with ultra−fast automatic cooling is given.The electron beam can be continuously injected and accumulated in more than 1 MA at the enough high eneregy.It can contain deuterium and tritium about one per cent and confine them to realize the fusion.The choice of the cooling magnet and the lattice design are introduced.

1.INTRODUCTION

J.P.Schiffer proposed the possibility of achieving a condensed crystalline state in cooled particle beams.Thier calculations have shown that a plasma of one kind of particle under the influence of such a field as $f = k.r$ can undergo a phase transition and form a crystalline aray in a certain conditions[1].In the case of the nonneutral plasma,when Budker limits are fullfilled[2]

$$\frac{1}{\gamma^2} < \frac{Z.N_i}{N_e} < 1$$

In that case,the critical intensity of the electron beam could be unlimited. The self−electric field is expressed

$$E_r = [\frac{2.I}{c.\beta_z.r_b}].\frac{r}{r_b}$$

When

$$r_b = 1 \ cm, I = 1 \ MA, E_r = \frac{59 \ MV}{cm}$$

Such a super intense field is quite fitted to the above demand for the condensed crystalline.Of course,it can be used to the fusion.Besides,the Ultra−Fast Automatical Cooling for Beams was found out[3],which makes the accumulating ring with the continuous injection realize easily.In other words,the technically simple and remarkably feasible way has turned up.

This new idea of the fusion has such characteristics as follows:Its confinement is the super−intense static electric field produced by the intense electron beam.In the nonneutral plasma,the electron beam intensity is unlimited.Because the electron beam of any high energy can also be accumulated,the electron energy is unlimited.In general,the energy of the electron beam must be equal to or larger than 2 Mev.Because the nonneutral plasma system is self−constricted and stable,the plasma dencity can be much higher than the magnetic confinement fusion and approximating to the initial confinement fusion.It is useful to improve the action rate.Besides,the device is not only minimal and cheap,but also technically simple and remarkably feasible,it is easy to combine with the magnetic or the initial confinement.

In this paper,a minimal accumulating storage ring with the continuous injection is illustrated.Condensed plasma confined by the intense electron beam can be obtained and used to the fusion.

2. DESIGN OF THE LATTICE

As usual,the accumulating storage ring with ultra−fast automatic cooling consists of the two straight line sections and N identical periodic sections or "unit cells",which is called a lattice.There is no specific distinction from the ordinary storage ring,except that the bending magnet should play a part in the automatic cooling.In the case of the linear approximation,the current standard treatment of the betatron oscillation can be used[4],except that the edge−focusing angle of the bending magnet must be satisfied with the requirement for the automatic cooling.By other words, there is a strict constraint in the edge−focusing angle of the bending magnet. In order to simplify the structure,we had better choose a group of the double quadrupole lenses as focusing element.Then the motion of particles can be expressed in terms of the linear transformation

$$X(s) = M(s,s_i) \cdot X(s_i) \tag{2.1}$$

$$M(s,s_i) = \begin{bmatrix} x_1(s) & x_2(s) \\ x'_1(s) & x'_2(s) \end{bmatrix}$$

$$x_1(s_i) = 1, x'_1(s_i) = 0$$
$$x_2(s_i) = 0, x'_2(s_i) = 1$$

As usual,where X stands for both horizontal and vertical direction matrices.Using the piecewise method of solution,we have

$$M = M_{a3} \cdot M_{f2} \cdot M_{a2} \cdot M_{f1} \cdot M_{a1} \cdot M_b \cdot M_e \quad (2.2)$$

Where M_e is of the matrix in the edge—focusing,so that

$$M_{ex} = \begin{bmatrix} 1 & 0 \\ k_b \cdot tan(\varphi) & 1 \end{bmatrix} \quad (2.3)$$

$$M_{ey} = \begin{bmatrix} 1 & 0 \\ -k_b \cdot tan(\varphi) & 1 \end{bmatrix}$$

$$k_b = \frac{e}{p_0} \cdot B$$

In the bending magnet region,we have

$$M_{bx} = \begin{bmatrix} Cos(k_b s) & \frac{1}{k_b} Sin(k_b s) \\ -k_b Sin(k_b s) & Cos(k_b s) \end{bmatrix}$$

$$M_{by} = \begin{bmatrix} 1 & s \\ 0 & 1 \end{bmatrix} \quad (2.4)$$

$$k_b = \frac{e}{p_0} \cdot B$$

In the conditions of the automatical coolng,we know

$$M_{bmx} = M_{bx} . M_{ex} \quad (2.5)$$

$$= \begin{bmatrix} (Cos(\varphi))^{-1} & (k_b)^{-1} \cdot Sin(\varphi) \\ 0 & Cos(\varphi) \end{bmatrix}$$

The matrix in the section of a free drift space or in the section of a quadrupole lens is the same as usual expression[4].

The optimum parameters are obtained in considering of that μ does not approach to $\frac{\pi}{2}$.The results are as follows:

$$N = 6; \varphi = \frac{\pi}{3}; k_b = 0.05; l_1 = l_2 = 10 \ Cm; l_3 = 35 \ Cm;$$

$$l_i = 6 \ Cm; k_{f1} = 0.13077; k_{f2} = 0.10196; \mu_x = 1.2939;$$

$$\mu_y = 1.6624$$

The envenlope can also be obtained.

3.THE NONLINEAR TRANSFORMATION
OF THE TRANSVERSE EMITTANCE

In the linear approximation,as well known,the emittance is an invariant of the motion

$$\frac{\varepsilon}{\pi} = \gamma \cdot x^2 + 2 \cdot \alpha \cdot x \cdot x' + \beta \cdot (x')^2 = Const. \quad (3.1)$$

But according to the principle of ultra—fast automatic cool-

ing,the transverse emittance of a beam with constant energy should be shrinked in the nonlinear motion.In order to prove that deduction,we must consider the nonlinear transformation of the transverse emittance.

In the region of the quadrupole lenses,we still use the exactly linear tranfer matrix.But only in the region of the bending magnet with ultra—fast automatic cooling,the formulas (2.5) in the paper [3] are used for calculation of the nonlinear transformation.

We should point out that the magnetic field in the median plane is only dependent on the transverse coordinate.Therefore it is the simplest way for the field to equal a constant.Then

$$B_n = B = Const.; K = \frac{e}{p_0} \cdot B;$$

$$\frac{e}{p_0} \cdot A(\xi) = -K \cdot \xi$$

Then the formulas (2.5) in the paper [3] become

$$x_k = \{ \frac{x_i}{Cos(\theta_{ei}) + x'_i \cdot Sin(\theta_{ei})} \quad (3.2)$$

$$+ \int_{\xi_i}^{\xi_k} [\frac{f}{\sqrt{1-f^2}} - \frac{f_e}{\sqrt{1-f_e^2}}] \cdot d\xi \}$$

$$\cdot [Cos(\theta_{ek}) + x'_k \cdot Sin(\theta_{ek})]$$

$$x'_k = -\frac{Sin(\delta\theta_k)}{\sqrt{1 - Sin^2(\delta\theta_k)}}$$

$$f = Sin(\theta_{ei} + \delta\theta_i) + K \cdot \xi$$

$$f_e = Sin(\theta_{ei}) + K \cdot \xi$$

$$Sin(\delta\theta_k) = [C_i + Sin(\theta_{ek})] \cdot Cos(\theta_{ek})$$

$$- Sin(\theta_{ek}) \cdot \sqrt{1 - (C_i + Sin(\theta_{ek}))^2}$$

$$C_i = \frac{Sin(\theta_{ei})}{\sqrt{1 + (x'_i)^2}} - Cos(\theta_{ei}) \cdot \frac{x'_i}{\sqrt{1 + (x'_i)^2}}$$

$$- Sin(\theta_{ei})$$

That can be considered as the analytical solution of the nonlinear equation of motion in the natural coordinate system. can be used for calculation of the nonlinear transformation.

We have taken two groups of the initial conditions

$$x_i = 0; \ x'_i = 0.1 \ Radian$$

$$x_i = 0; \ x'_i = 0.05 \ Radian$$

Then the calculations follow the tracks of the emittance phase points in the 360 periodicities or 60 turns.The corresponding emittance phase diagrams are illustrated in firgure 1 and 2,from which we can get some inspirations

3.When the amplitude of the betatron oscillation is smaller,the emittance phase trajectory is quite similar to a ellipse,while there is obvious damping.Therefore it is not true that the emittance is an invariant in the
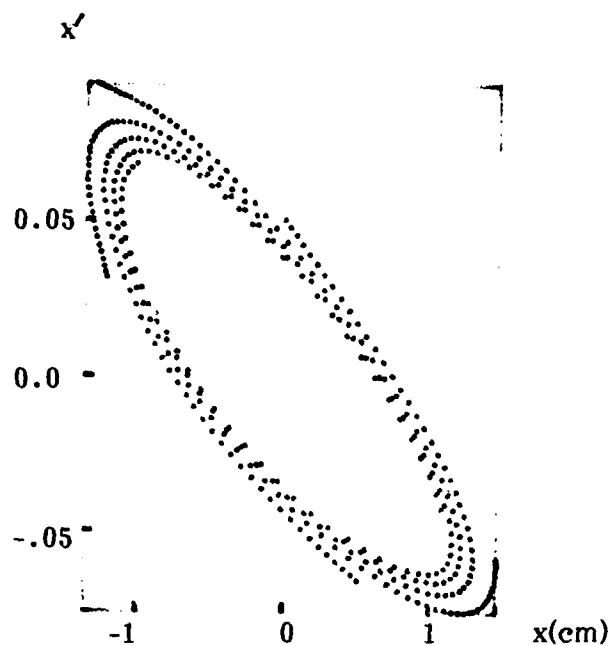
Fig.1,the phase diagram in small amplitude
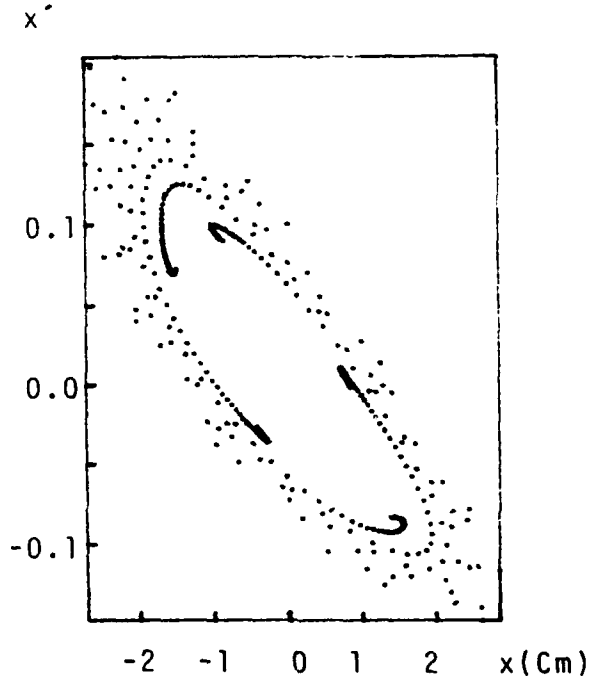
Fig.2,the phase diagram in large amplitude

1.The emittance phase trajectory is devided into five curves,which is not a closed ellipse any longer.The emittance phase points always approach to the center $x = 0, x' = 0$.That is a typical damping diagram.In the case of both larger and smaller amplitudes,there is the steady damping in the phase diagram in the stable regioin.The results show that the deduction from the principle of ultra-fast automatic cooling for beams is true indeed.

2.When the amplitude of the betatron oscillation is larger,there is obvious distortion in the emittance phase diagram.From the figure 2 we knom,it takes 15 turns or about 0.3 μs that the first phase point on each curve reach thefinal one.The phase area has contracted by a factor of $1 / e$ in 15 turns or 0.3 μs.Therefore the corresponding cooling rate is much more rapid than the stochastic or the fast electron cooling by six or seven orders of magnitude. It is useful to realize continuous injection.

tranditional theory.If only the emittance entirely is equal to zero,it really becomes an invariant.

4.The bending magnet as a cooling element may be got widespread use in various storage rings,because only the proper edge-focusing angle is need.Therefore the reliability and feseability are very clear.

5.In the case of the larger amplitude,the phase area is shrinked so fast that the continuous injection can be realized.

References

[1] J.P.Schiffer,AIP Conf.Proc. 150,345,(1986)

[2] R.B.Miller,AIP Conf. Proc. 184,1729,(1989)

[3] Gao Shuyang and Qian Guangyu,the Principle of Ultra-fast Automatic Cooling for Beams, (the same proceedings)

[4] E.Courant and H.Snyder,Ann.Phys.,3,1,(1958)

Conference Author Index

C

Cai, S. Y. 3075
Cai, Y. 203, 2781
Calabrese, R. 3243
Calame, J. P. 2667, 2670
Calderon, M. 3836
Callahan, D. A. 730, 733, 3660
Callin, R. 543, 620, 1106
Calloway, D. 2172
Calo, A. 3127
Calvert, J. 1160, 3748
Camas, J. 2498
Cameron, P. 1166
Cameron, P. R. 2328
Campbell, B. 1402
Campisi, I. E. 1115, 1220
Capista, D. 2252
Caporaso, G. 703
Caporaso, G. J. 712, 715
Cappi, R. 3570
Cardito, M. 2154
Cardman, L. S. 3246
Carey, D. C. 47
Carlé, P. 1735
Carlini, R. 2136, 3103
Carlisle, L. 1718
Carlson, R. L. 661
Carlsten, B. 2675
Carlsten, B. E. 2537, 2664
Carmel, Y. 2714
Carpenter, J. 3757
Carr, R. 1596
Carroll, F. E. 1448
Carron, G. 1066, 3426
Carson, J. 2769
Carter, A. 2054
Carwardine, J. 1709
Carwardine, J. A. 3210
Caryotakis, G. 543, 1106, 1259
Casella, R. 1277
Caspers, F. 2157, 3381
Cassel, R. 543, 1318
Castellano, M. 573
Castro, P. 2103
Catani, L. 573
Caussyn, D. 3745
Caussyn, D. D. 29, 224, 227, 420, 3536
Cavallari, G. 806
Celata, C. M. 724, 3748
Cerniglia, P. 2310
Chabert, A. 1789
Chae, Y. 282
Chae, Y. C. 182
Chamberlain, O. 2172
Champion, M. 809, 918, 1127
Champion, M. S. 989
Chan, C. F. 3157, 3160
Chan, K. D. C. 2970
Chanel, M. 2157
Chang, C. H. 1943, 2886
Chang, C. R. 122, 812, 3585
Chang, H. P. 1943
Chang, J. S. 1345
Channell, P. J. 38
Chao, A. 3781

Chao, A. W. 29, 224, 227, 420, 3345, 3348
Chao, Y. 587
Chapman, L. 1914, 2249
Chappelier, J. 158, 161
Charruau, G. 858
Chase, B. E. 2355
Chattopadhyay, S. 83, 2638, 3042
Chautard, F. 267, 2720
Chechetenko, V. 1480
Chehab, R. 3093
Chel, S. 855
Chen, B. 3345, 3348
Chen, C. 2656
Chen, H. 2151
Chen, J. 1095
Chen, J. R. 1635
Chen, J. S. 1878
Chen, P. 617, 2638
Chen, S. 200, 3255
Chen, S. C. 2575, 2696, 2699
Chen, S. J. 1878
Chen, T. 3479
Chen, Y. 303, 718, 2841
Chen, Y. J. 703, 706
Cheng, J. 2659, 2667
Cheng, W. 221
Cheng, Y. 1262, 1393, 2269
Chepurnov, A. S. 2059
Chesnokov, Y. A. 454
Chester, N. 2826
Chester, N. S. 2823
Chevallier, M. 3093
Chiaveri, E. 806, 849
Chida, K. 41
Chimenti, V. 3906
Chin, J. 1572, 1584
Chin, Y. H. 3347, 3414
Ching, C. H. 3351
Chiou, T. C. 2635
Chirkov, P. 2769
Chmielewski, A. G. 1890
Cho, C. 2151
Cho, M. 581, 1521
Cho, M. H. 593, 1315
Cho, Y. 399, 3757
Cho, Y. S. 679
Choi, B. H. 679, 3196
Choi, J. 2516, 3273
Choi, J.-Y. 3087, 3705
Chojnacki, E. 815, 1844, 2596, 3071
Chou, P. J. 3363
Chou, W. 818, 2281, 3444, 3609, 3781, 3888
Christensen, K. 1712, 2947
Christiansen, C. F. 1098, 2139
Christianson, M. 2757
Chu, C. 306, 2841
Chubar, O. V. 1626, 2474, 2510
Chubarov, O. V. 2059
Chugun, T. 2205
Chung, K. H. 679, 3196
Chung, Y. 188, 1814, 2112, 2263, 2266, 2275, 2304
Chupp, W. W. 703, 3199
Church, M. 330
Chuvilo, I. V. 1675
Ciapala, E. 1903, 2358

Ciardullo, D. J. 1241
Ciarlette, D. 285
Ciarlette, D. J. 1814
Cifarelli, F. 3099
Ciullo, G. 3243
Claborn, G. 2222
Clark, D. 369, 3888
Clark, D. J. 1724, 1727
Clark, S. L. 543
Clarke, J. A. 1494, 1638, 3594, 3672
Claudet, S. 2956
Claus, J. 2895
Clay, W. 3888, 3891
Clayton, C. 2976, 3003
Clayton, C. E. 558, 2551, 3543
Clayton, T. 1369, 2781
Clément, M. 1363
Clendenin, J. 3033
Clendenin, J. E. 2978, 3027, 3036
Clerc, G. 1184
CLIC Study Group 540
Clifft, B. E. 1694
Cline, D. 2051, 2638
Clout, P. 1801
Clozza, A. 3906
Coacolo, J. C. 3567
Coadou, B. 798
Cobb, J. K. 2838
Codutti, A. 1587
Cohen, S. 369
Colby, E. 3021
Colchester, R. J. 2495
Cole, B. 128, 203
Cole, M. 821, 3012
Cole, R. 1669
Coleman, P. 824
Coleman, P. D. 1033, 1256, 3252
Colestock, P. 3294
Colestock, P. L. 3303, 3306, 3384, 3540
Collet, G. J. 3030
Collet, P. 1187
Collier, P. 1937, 2001
Collins, J. 29, 224, 227, 420
Collins, J. P. 2823
Colton, E. 3297
Combs, C. 1703
Combs, C. M. 846
Conciauro, G. 1524, 1569
Conde, M. E. 3042
Condé, H. 1771
Connolly, R. 1669
Conte, M. 32, 438
Conway, P. 2388
Coombes, R. 2769
Cooper, R. 3297
Cooper, R. G. 2400
Cooper, R. K. 3267
Cooper, W. S. 3169
Coosemans, W. 44
Corbett, J. 173
Corbett, W. J. 108, 114, 1483, 2275
Cork, C. 1575
Corlett, J. N. 2109, 3318, 3408, 3411
Cornacchia, M. 173
Cornelis, K. 2001, 3429